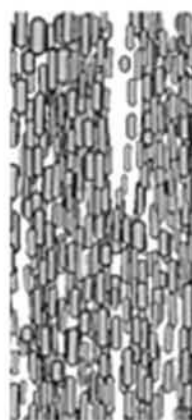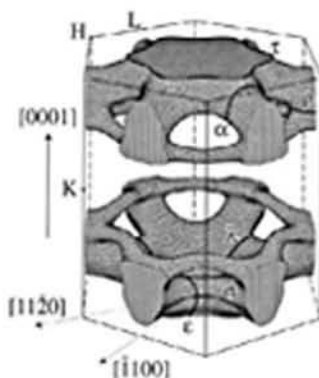# CONCISE ENCYCLOPEDIA OF

MAGNETIC AND SUPERCONDUCTING MATERIALS

SECOND EDITION

Editor

K.H.J. BUSCHOW

CONCISE ENCYCLOPEDIA OF

MAGNETIC & SUPERCONDUCTING MATERIALS

SECOND EDITION

Elsevier Internet Homepage - http://www.elsevier.com
Consult the Elsevier homepage for full catalogue information on all books, major reference works, journals, electronic products and services.

Elsevier Titles of Related Interest

K.H.J. BUSCHOW
The Encyclopedia of Materials: Science and Technology
Major reference work
2001, ISBN: 0-08-043152-6

R. CAHN
Concise Encyclopedia of Materials Characterisation
2004, ISBN: 0-08-044547-0

F. FIORILLO
Characterisation and Measurement of Magnetic Materials
2004, ISBN: 0-12-257251-3

K.H.J. BUSCHOW
Handbook of Magnetic Materials
Book Series, 15-Vol set.
2003, ISBN: 0-44-485311-1

Related Journals:
Elsevier publishes a wide-ranging portfolio of high quality research journals, encompassing the materials science field. A sample journal issue is available online by visiting the Elsevier web site (details at the top of this page). Leading titles include:

Journal of Magnetism and Magnetic Materials
Materials Science in Semiconductor Processing
Physica C: Superconductivity and its Applications
Material Science and Engineering: A
Materials Science and Engineering: B
Progress in Material Science
Materials Letters
Mechanics of Materials
Materials Today

All journals are available online via ScienceDirect: www.sciencedirect.com

To contact the Publisher
Elsevier welcomes enquiries concerning publishing proposals: books, journal special issues, conference proceedings, etc. All formats and media can be considered. Should you have a publishing proposal you wish to discuss, please contact, without obligation, the publisher responsible for Elsevier's Composites and Ceramics programme:

Amanda Weaver		
Publisher		
Elsevier Ltd		
The Boulevard, Langford Lane	Phone:	+ 44 1865 84 3634
Kidlington, Oxford	Fax:	+ 44 1865 84 3920
OX5 1GB, UK	E.mail:	a.weaver@elsevier.com

General enquiries, including placing orders, should be directed to Elsevier's Regional Sales Offices – please access the Elsevier homepage for full contact details (homepage details at the top of this page).

CONCISE ENCYCLOPEDIA OF
MAGNETIC & SUPERCONDUCTING MATERIALS

SECOND EDITION

Editor
K.H.J. BUSCHOW
University of Amsterdam, The Netherlands

CONTENTS

This page intentionally left blank

EDITOR'S PREFACE TO SECOND EDITION

The *Concise Encyclopedia of Magnetic and Superconducting Materials* combines in a single volume articles written by leading authorities in these fields, aiming at giving a complete cross-section of the science and technology of magnetic and superconducting materials. It is a successor of the *Concise Encyclopedia of Magnetic and Superconducting Materials* edited by Jan Evetts and published in 1992. In the present volume, the majority of articles deal with the advances of recent years, combining new developments in the field of magnetism and superconductivity with earlier articles describing the achievements reached in those topological areas that have kept their fires burning. Already many decades ago, physicists have abandoned the idea that the occurrence in the same material of localized magnetic moments and superconductivity is mutually exclusive. The advent of high-T_c superconductors in particular has shown that magnetism and superconductivity are intimately connected and theoretical and experimental studies of the interplay between magnetism and superconductivity have become an area of its own right. But it is not only the strong mutual interest of scientists working in the field of magnetic and superconducting materials that has made it desirable to combine both issues in a single volume. Also from the applications side there is an increasing overlap between superconductivity and magnetism, magnetic bearings based on high-T_c superconductors and superconducting permanent magnets being prominent examples. One can even go one step further and say that electrical conduction and magnetic polarization have increasingly become intertwined in many materials in recent years. The recognition that the magnetoresistive effect can advantageously be utilized in magnetic sensor and read head applications has led to a proliferation of research in this area, eventually culminating in the observation of the giant- and colossal magnetoresistance effects. New exciting phenomena have surfaced including spin-, charge- and orbital ordering in a variety of magnetic and superconducting materials.

The majority of articles contained in the present version of the *Concise Encyclopedia of Magnetic and Superconducting Materials* have been drawn from the *Encyclopedia of Materials: Science and Technology* (*EMSAT* for short). This encyclopedia consists of 10 volumes containing about 2000 articles. It was published only recently, in 2001. Included in the present volume are about 40 newly commissioned articles that will also appear in the electronic updated version of *EMSAT*. Bearing in mind that progress in materials technologies cannot occur without the benefit of the underlying science, both encyclopedias have aimed at a proper balance between articles dealing with technology of materials and fundamental science. The present volume has been tailored to meet the demands of smaller institutions, industrial companies and individual scientists for which research and development in the field of magnetic and superconducting materials is at a premium. In the last decade, research in the field of magnetism has received substantial impetus from information technology. Therefore, it is not surprising that a considerable number of magnetism articles in the present volume deal with magnetic and magneto-optic recording and the physics behind it. The articles in the present volume have been selected to provide the readership with a comprehensive coverage of materials properties, the design and principles of operation of devices in which particular materials have been applied and the fundamental phenomenology of magnetism and superconductivity. Each of the articles contains a reference list opening the way to more detailed and more deepened studies. Considerable attention has been paid to cross-reference various articles appearing in this volume with each other, providing as far as possible a coupling between materials, devices and phenomenology.

I wish to thank all authors who have responded affirmatively to my invitation to contribute an article on magnetism or superconductivity. In retrospect, I realize that I may have twisted the arms of some of my colleagues somewhat too strongly when convincing them to finish their article in time, presenting a comprehensive coverage of their specialistic topic and complying with the requirements of style and length set by the Publisher.

The task to provide the readership with an extensive coverage including novel trends and achievements in the areas of magnetism and superconductivity would have been extremely difficult without the professionalism of Pergamon Press. I am particularly indebted to Ms. Amanda Weaver and Mr. David Sleeman for their great help and expertise.

K.H.J. Buschow
Editor

FOREWORD TO FIRST EDITION

In the time since its publication, the *Encyclopedia of Materials Science and Engineering* has been accepted throughout the world as the standard reference about all aspects of materials. This is a well-deserved tribute to the scholarship and dedication of the late Editor-in-Chief, Professor Michael Bever, to the Subject Editors and to the numerous contributors.

During its preparation, it soon became clear that change in some areas is so rapid that publication would have to be a continuing activity if the Encyclopedia were to retain its position as an authoritative and up-to-date systematic compilation of our knowledge and understanding of materials in all their diversity and complexity. Thus, the need for some form of supplementary publication was recognized at the outset. The Publisher has met this challenge most handsomely: both a continuing series of Supplementary Volumes to the main work and a number of smaller encyclopedias, each covering a selected area of materials science and engineering, are in the process of publication.

Professor Robert Cahn, the Executive Editor, was previously the editor of an important subject area of the main work and many other people associated with the Encyclopedia have contributed or will contribute to its Supplementary Volumes and derived Concise Encyclopedias. Thus, continuity of style and respect for the high standards set by the *Encyclopedia of Materials Science and Engineering* are assured. They have been joined by some new editors and contributors with knowledge and experience of important subject areas of particular interest at the present time. Thus, the Advisory Board is confident that the new publications will significantly add to the understanding of emerging topics wherever they may appear in the vast tapestry of knowledge about materials.

The appearance of the Supplementary Volumes and the series *Advances in Materials Science and Engineering* is an event which will be welcomed by scientists and engineers throughout the world. We are sure that it will add still more luster to a most important enterprise.

Walter S Owen
Chairman
Honorary Editorial Advisory Board

This page intentionally left blank

EXECUTIVE EDITOR'S PREFACE TO FIRST EDITION

As the publication of the *Encyclopedia of Materials Science and Engineering* approached, Pergamon Press resolved to build upon the immense volume of work which had gone into its creation by embarking on a follow-up project. This project had two components. The first was the creation of a series of Supplementary Volumes to the Encyclopedia itself. The second component of the new project was the creation of a series of Concise Encyclopedias on individual subject areas included in the Main Encyclopedia to be called *Advances in Materials Science and Engineering*.

These Concise Encyclopedias are intended, as their name implies, to be compact and relatively inexpensive volumes (typically 400–600 pages in length) based on the relevant articles in the Encyclopedia (revised where need be) together with some newly commissioned articles, including appropriate ones from the Supplementary Volumes. Some Concise Encyclopedias offer combined treatments of two subject fields which were the responsibility of separate Subject Editors during the preparation of the parent Encyclopedia (e.g., dental and medical materials).

Eleven Concise Encyclopedias have been published. These and their editors are listed below.

Concise Encyclopedia of Advanced Ceramic Materials	Prof. Richard J Brook
Concise Encyclopedia of Building & Construction Materials	Prof. Fred Moavenzadeh
Concise Encyclopedia of Composite Materials	Prof. Anthony Kelly CBE, FRS
Concise Encyclopedia of Magnetic & Superconducting Materials	Dr Jan Evetts
Concise Encyclopedia of Materials Characterization	Prof. Robert W Cahn FRS & Dr Eric Lifshin
Concise Encyclopedia of Materials Economics, Policy & Management	Prof. Michael B Bever[†]
Concise Encyclopedia of Medical & Dental Materials	Prof. David Williams
Concise Encyclopedia of Mineral Resources	Dr Donald D Carr & Prof. Norman Herz
Concise Encyclopedia of Polymer Processing & Applications	Mr Patrick J Corish
Concise Encyclopedia of Semiconducting Materials & Related Technologies	Prof. Subhash Mahajan & Prof. Lionel C Kimerling
Concise Encyclopedia of Wood & Wood-Based Materials	Prof. Arno P Schniewind

Many of the new or substantially revised articles in the Concise Encyclopedias have been or will be published in one of the three Supplementary Volumes, which are designed to be used in conjunction with the Main Encyclopedia. The Concise Encyclopedias themselves, however, are "free-standing" and are designed to be used without reference to the parent Encyclopedia.

The Executive Editor was personally responsible for the selection of topics and authors of articles for the Supplementary Volumes. In this task, he has had the benefit of the advice of the Senior Advisory Editor and of other members of the Honorary Editorial Advisory Board. The Executive Editor was responsible for appointing the Editors of the various Concise Encyclopedias and for supervising the progress of these volumes.

Robert W Cahn FRS
Executive Editor

This page intentionally left blank

EDITOR'S PREFACE TO FIRST EDITION

The *Concise Encyclopedia of Magnetic & Superconducting Materials* draws together in a single volume articles that cover all major aspects of the science and technology of magnetic and superconducting materials. When I was asked by Professor Robert W. Cahn, the Executive Editor of the series, to edit this volume, I was immediately attracted by the challenge of producing a unified and balanced work that would enable readers to draw parallels and experience contrasts in the conceptual treatment and practical technology of these materials. Having myself worked with magnetic and superconducting materials since the 1960s, I have become acutely aware that these two important classes of material have much in common, both in the phenomenology that underlies their behavior and in many of the issues that relate to their fabrication and optimization as bulk materials or thin films for application in technology. I believe that the treatment of these distinct materials, each at their own characteristic stage of development, in a single volume brings a conceptual freshness to our appreciation of both classes of material that helps to highlight deficiencies in our overall knowledge base and corresponding opportunities for new advances. Although the emphasis is on materials science and technology, the subject matter extends from physics to engineering design and applications and it is expected that the *Concise Encyclopedia of Magnetic & Superconducting Materials* will be useful to engineers, teachers, managers and scientists from a wide range of disciplines and many areas of manufacturing industry.

Because of the remarkable advances of recent years, this Concise Encyclopedia is based mainly on newly commissioned articles; about a third of the entries are drawn from the *Encyclopedia of Materials Science and Engineering* which was published in 1986, although many authors of articles in rapidly developing fields have rewritten or extensively updated their articles for this volume. In the area of magnetic materials there are 30 updated articles and 32 articles that are essentially new, while in the area of superconductivity three articles have been updated and 52 articles have been newly commissioned. The articles have been selected to give comprehensive and balanced coverage to each of three broad subject areas: first, there are articles devoted to particular classes of material; second, there are those that describe and elucidate material properties and phenomena that are common to different materials; and, third, there are articles that treat the general area of applications dealing with issues of materials selection and fabrication as well as the design and principles of operation of devices for particular applications. Extensive coverage has been given to articles concerned with the phenomenology of technical magnetism and superconductivity since the effective characterization and optimization of magnetic and superconducting materials depends critically on an understanding of the mechanisms underlying their various properties.

I am grateful to all the authors who responded to my invitation to write for this Concise Encyclopedia; they are all recognized authorities in their fields and I respect the special efforts they made with their contributions to accommodate the guidelines on length, style and content that were necessary to achieve a balanced and comprehensive coverage of the subject. Although the work is not intended as a source book for data on materials, an effort has been made to include, at every point, sufficient data to equip the reader with a reasonably quantitative understanding of the subject. An important part of each article is the list of references; these are selective rather than comprehensive and provide the reader with avenues for further study. At a time when much public attention has been focused on developments in the field of high-temperature superconductivity, considerable effort has been made to retain objectivity in the selection of topics and coverage. The aim has been to produce a work that will have lasting value and relevance over many years. In practice, this has not been too difficult as there is no area of high-temperature super-conductivity that cannot be seen, on pragmatic inspection, to have roots that go back over many years and, sometimes, over decades. In such an extensive work with so many contributing authors there is, inevitably, the occasional overlap; where this occurs articles are cross-referenced to each other. Considerable attention has been given to harmonizing notation, equations and preferred units, although I have

chosen not to force total uniformity where the common practice differs from one area of the subject to another. I have, however, insisted on the use of SI units as the primary unit throughout, although other units are sometimes given in parentheses.

I would like to acknowledge the encouragement and guidance of Professor Robert Cahn, the Executive Editor, and to thank Mr Michael Mabe and Mr Peter Frank of Pergamon Press for their support and advice. I am also particularly indebted to Mr Paul Aslin for his assistance in maintaining day-to-day contact with authors and in coordinating and assembling the manuscript copy. Finally, it is with sadness and regret that I acknowledge the valued contributions of two authors who are now deceased.

Professor John Bardeen, who inspired so many through his contributions to the theory of superconductivity over 35 years, completed a balanced and carefully worked article *Superconducting Materials: BCS and Phenomenological Theories* in January 1991, a few days before he died. Dr Gilbert Y. Chin, who recently retired as director of the Passive Components Research Laboratory at AT&T Bell Laboratories, passed away in May 1991. Dr Chin contributed the key introductory article *Magnetic Materials: An Overview* and coauthored with his friend and colleague Dr Jack Wernick a further ten articles on specialist magnetic materials.

Jan Evetts
Editor

GUIDE TO USE OF THE ENCYCLOPEDIA

This Concise Encyclopedia is a comprehensive reference work covering all aspects of materials characterization. Information is presented in a series of alphabetically arranged articles which deal concisely with individual topics in a self-contained manner. This guide outlines the main features and organization of the Encyclopedia, and is intended to help the reader to locate the maximum amount of information on a given topic.

Accessibility of material is of vital importance in a reference work of this kind and article titles have therefore been selected not only on the basis of article content but also with the most probable needs of the reader in mind. An alphabetical list of all the articles contained in this Encyclopedia is to be found on pp. xvii–xix.

Articles are linked by an extensive cross-referencing system. Cross-references to other articles in the Encyclopedia are of two types: in text and end of text. Those in the body of the text are designed to refer the reader to articles that present in greater detail material on the specific topic under discussion at that point. They generally take one of the following forms:

…which is fully described in the article *Magnetic Recording Devices: Future Technologies*.

…other applications of this technique (see *SQUIDs: Magnetic Microscopy*).

The cross-references listed at the end of an article serve to identify broad background reading and to direct the reader to articles that cover different aspects of the same topic.

The nature of an encyclopedia demands a higher degree of uniformity in terminology and notation than many other scientific works. The widespread use of the SI system of units has determined that such units be used in this Encyclopedia. It has been recognized, however, that in some fields Imperial units are more generally used. Where this is the case, Imperial units are given with their SI equivalent quantity and unit following in parentheses. Where possible, the symbols defined in *Quantities, Units, and Symbols*, published by the Royal Society of London, have been used.

All articles in the Encyclopedia include a bibliography giving sources of further information. Each bibliography consists of general items for further reading and/or references which cover specific aspects of the text. Where appropriate, authors are cited in the text using a name/date system as follows:

…as was recently reported (Smith 2002).

Jones (1984) describes...

The contributors' names and the organizations to which they are affiliated appear at the end of all articles. All contributors can be found in the alphabetical List of Contributors.

The most important information source for locating a particular topic in the Encyclopedia is the multilevel Subject Index, which has been made as complete and fully self-consistent as possible.

This page intentionally left blank

ALPHABETICAL LIST OF ARTICLES

This page intentionally left blank

A

Actuator Materials for Small-scale Devices

The fabrication of a microsystem requires the processing of a large variety of different materials in order to realize their different electronic, sensor, and actuator components. The fabrication processes of these materials should be compatible with microsystem technologies, i.e., with silicon micromachining. One possibility for the realization of sensors and actuators in microsystems is the use of "smart" materials that directly transduce electrical, magnetic, or thermal energy into mechanical energy or vice versa. The related physical effects are the piezoeffect, magnetostriction, or the shape memory effect.

In general, thin film technologies are an attractive approach to integrate these materials into microsystems as this approach has almost no materials limitations, offers easy down-scaling into the micrometer range by a cost-effective manufacturing technology, avoids assembly and interconnection processes, allows the protection of the microsystem by protective layers (Quandt and Holleck 1998), and provides the possibility to design new materials as, for example, metastable phases, multilayers or gradient layers. Physical vapor deposition (PVD) techniques, in particular magnetron sputtering, offer the opportunity of tailoring the constitution of the thin films. Additionally, the interaction with the substrate enables fabrication of highly textured films which, in the case of piezoelectric materials, show improved properties compared to conventional polycrystalline bulk materials. Furthermore, it can be expected that the integrated sensing features of smart film actuators—e.g., the resistive effects present in all three classes of materials—will provide means to realize "intelligent" actuators by using thin film "smart" materials.

Thin film actuators in the case of piezoelectric or magnetostrictive materials are always used as compounds with micromachined substrates working as bending transducers, whereas in the case of shape memory thin films both free-standing thin film actuators and compounds with metallic or silicon substrates are realized. Since free-standing shape memory films have to be trained for the two-way effect to introduce internal stresses into the material, which is quite complicated in small dimensions, the film substrate compounds represent the generally more important approach for all smart film materials. In this case the materials development target has to be modified compared to bulk actuator materials. Whereas in bulk materials the strain has to be maximized, the resulting bending stress of a thin film substrate compound is proportional to the strain and Young's modulus of the film. As a consequence, this stress of the thin film actuator material should be as large as possible. In the following sub-sections the main results for magnetostrictive, piezoelectric, and shape memory thin films for actuators will be discussed in view of their main application areas.

1. Magnetostrictive Films

The development of room temperature giant magnetostrictive bulk and thin film materials is based on the rare earth Fe_2 Laves phase, while at low temperatures the highest strains are found in hexagonal Tb_xDy_{1-x} and body-centered $Tb_xDy_{1-x}Zn$ alloys. The giant magnetostrictive materials were optimized in terms of their magnetostriction to magnetic anisotropy ratio in order to attain large strains at reasonable magnetic fields (see *Magnetostrictive Materials*). Different approaches have been taken based on the Laves phases $(Tb,Dy)(Fe,Co)_2$ with positive or $Sm(Fe,Co)_2$ with negative magnetostriction. The fabrication of these rare earth based materials is restricted to PVD methods, the most prominent being magnetron sputtering.

Because the magnetic saturation field is proportional to the magnetic anisotropy constant and inversely proportional to the saturation magnetization, its reduction is achieved either by decreasing the magnetic anisotropy constant and/or by increasing the saturation magnetization. To reduce the macroscopic anisotropy, amorphous rare earth–iron thin film materials have been fabricated in a wide composition range. It was found that increasing the rare earth content compared to the Laves phase composition results in the highest low-field magnetostriction in amorphous thin films. For amorphous TbFe films with an inplane magnetic easy axis an important improvement of the low-field magnetostriction and the hysteresis can be observed in comparison to nanocrystalline $(Tb,Dy)Fe_2$ films.

Assuming the same local environment in the amorphous compared to the crystalline state, a further approach to lower the remaining anisotropy is by Tb/Dy substitution, which was investigated over a wide composition range for rare earth–iron or –cobalt thin film materials. This approach leads to a further reduction in the magnetic saturation field, but the lower Curie temperature due to the dysprosium alloying significantly reduces the saturation magnetostriction, resulting in negligible gain in low-field magnetostrictive strain of these ternary films.

The second route to lower the macroscopic anisotropy is by increasing the saturation magnetization. The magnetostrictive thin films discussed so far have rather low magnetizations, owing to their ferrimagnetic nature. Unfortunately, an increase of the saturation magnetization using amorphous homogeneous rare earth–transition metal materials is impossible, because the compositions of interest contain

30–45 at.% rare earth elements. The rare earth moments dominate and thus any decrease will further reduce the magnetization, while an increase of their content results in a lowering of the Curie temperature and consequently a lowering of the room temperature magnetization.

However, using multilayers, it is possible to develop new composite materials which show properties that overcome these limitations. One layer is composed of the giant magnetostrictive amorphous $Tb_{0.4}Fe_{0.6}$ alloy, while the other is magnetically very soft and has a very high magnetization as well as considerable magnetostriction itself ($Fe_{0.5}Co_{0.5}$). By fabricating these layers with thicknesses smaller than the ferromagnetic exchange length, domain wall formation at the interfaces is prevented and the magnetic properties of such an exchange-coupled multilayer system are determined by the average of those of each individual layer. The comparison of the magnetostriction of this multilayer with the state-of-the-art amorphous and nanocrystalline single-layer materials demonstrates that these novel multilayers give the highest magnetostrictions at very low fields with a saturation field of only 20 mT (Fig. 1).

The most important advantages of magnetostrictive actuators are the possibility of wireless operation and the anisotropic behavior of the magnetostriction. The former is especially attractive for ultrasonic motors and for valves or pumps operating in harsh environments or on rotating or moving parts. The anisotropy of the magnetostriction can be employed for the realization of a two-dimensional scanner using a simple cantilever geometry in combination with the excitation of bending and torsion modes.
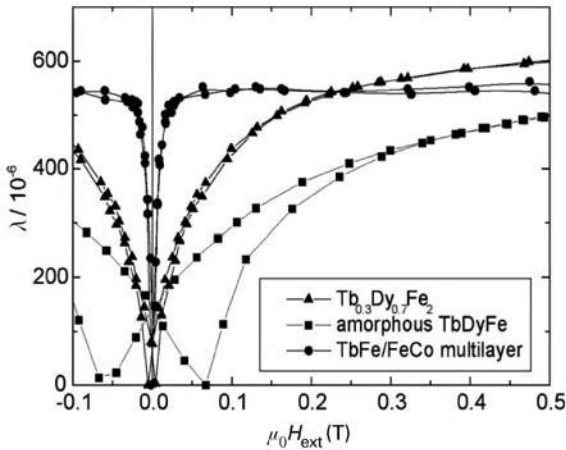
Figure 1
Magnetostriction (λ) versus external magnetic field (H_{ext}) of different thin film materials: nanocrystalline $Tb_{0.3}Dy_{0.7}Fe_2$ single layer, amorphous TbFe single layer, and TbFe/FeCo multilayer.

2. Piezoelectric Films

The development of piezoelectric thin films for actuators is related either to wurtzite-type structure materials (e.g., ZnO, AlN) or to ferroelectric perovskite materials (e.g., $Pb(Zr,Ti)O_3$). The general merits of piezoelectric thin film actuators are their low power consumption and their driving voltages compatible with transistor–transistor logic (TTL) signal levels. The drawbacks are their high fabrication temperatures, especially in the case of ferroelectric thin films, their comparably low sputtering rates, and the high precision of stoichiometry control required.

In the development of piezoelectric thin film materials, high piezoelectric strains, breakdown field strengths, electrical resistivity, Young's modulus, long-time stability and fatigue strength, and in the case of the ferroelectric materials high Curie temperature, are further important targets. The wurtzite-type piezoelectric films can be fabricated by chemical or physical vapor deposition (CVD or PVD) methods, the latter being mainly sputtering or laser-ablation routes. Even more fabrication methods exist in the case of ferroelectric thin film materials; the most prominently used are CVD, PVD and sol–gel methods.

Although their piezoelectric constants are one or two orders of magnitude lower than in $Pb(Zr,Ti)O_3$ (PZT), wurtzite-type thin films are of interest for many applications, predominantly because of their simpler fabrication, mainly owing to lower fabrication temperatures, their hysteresis-free response, and their higher temperature range of use. Furthermore, their much higher Young's moduli compensate in part for their lower piezoelectric constants in the case of bending-type thin film actuators. In order to obtain high piezoelectric constants, highly c-axis-textured wurtzite-type films are required having low resistivity perpendicular to the substrate. It has been found that the microstructure and the texturing depend critically on the deposition conditions. By adjusting the sputtering conditions, highly c-axis-oriented films can be obtained. Although ZnO shows the higher piezoelectric strain, AlN films are very promising owing to their higher resistivity and their better compatibility with microelectronics batch fabrication processes.

Ferroelectric thin films having a perovskite structure are of wide interest mostly because of their high dielectric constant and high remanence, e.g., as capacitors for dynamic random access memories (DRAMs). The high piezoelectricity in PZT materials leads to further interest in these materials for applications as microsystem actuators, especially as bulk PZT is widely used for high precision or ultrasonic actuators. In general, PZT films can be fabricated either by a single-step process with substrate temperatures of approx. 550 °C or by a two-step process using postdeposition crystallization for the

Table 1
Measured piezoelectric and dielectric coefficients. $d_{33,f}$ describes the strain x_3 in the normal direction ($x_3 = d_{33,f} E_3$), $e_{31,f}$ the in-plane strain ($\sigma_{1,2} = e_{31,f} E_3$) of thin film materials, where E_3 is the applied electric field in the normal direction (Muralt 1997).

	AlN	PZT
$d_{33,f}$	3.9	90 … 200
$e_{31,f}$	−0.9	−4 … −6
ε_{33}	11	1100 … 1300

amorphous as-deposited films. Employing this two-step process, crystallization in the perovskite structure was found at temperatures between 550 and 600 °C, whereas the texture of the films depends strongly on the bottom electrode and the substrate being used. Owing to the inherent film stress and its texture the unpoled polycrystalline PZT films being fabricated by sputtering already exhibit a polarization and a piezoelectric response which reach approximately half the values of poled or single crystal thin film materials.

The piezoelectric data of both classes of materials are compared in Table 1, which demonstrates the special potential of PZT films provided that all fabrication issues are solved. The most important features of piezoelectric thin film actuators are the low voltage, low power, high-frequency operation being compatible to TTL signal levels. Consequently, high frequency applications such as surface acoustic wave (SAW) devices, ultrasonic motors, and resonant sensors for mechanical quantities are the domain of piezoelectric thin film actuators.

3. Shape Memory Thin Films

The development of shape memory thin films is based on TiNi, which is superior to other potential shape memory materials with respect to attainable strains and stresses. Owing to the low transformation temperatures of binary TiNi films, the materials research is concentrated on Ni/Pd substitution for an increase in transformation temperature and Ni/Cu substitution for a reduction in transformation hysteresis. Furthermore, it is known that TiNiCu films are much less sensitive in their transformation temperatures to variations in the titanium content. Further interest is related to the training procedures as well as to the actuator design to achieve the two-way behavior in either free-standing films or in combination with a substrate.

It has been found that Ni/Pd substitution is very effective in adjusting the transformation temperatures between room temperature and temperatures above 500 °C, whereas the measured austenite finish

temperatures of sputtered films are in good agreement with the reported data of bulk materials (Fig. 2) (Quandt *et al.* 1996).

By Ni/Cu substitution it is possible to reduce the transformation hysteresis. In the case of the ternary system Ti–Ni–Cu this substitution affects almost only the martensite finish temperatures, which are raised by increasing the copper content. The martensite and austenite finish temperature (M_f, A_f, respectively), as well as the hysteresis A_f–M_f are shown in Fig. 3 as a function of the copper content while the titanium content was kept constant. The results show that
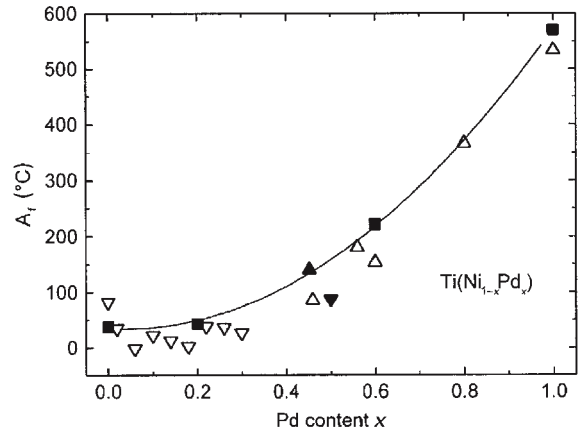
Figure 2
Austenite finish temperature A_f of Ti(Ni$_{1-x}$Pd$_x$) bulk (open symbols) and thin film (closed symbols) materials, as a function of palladium content (after Quandt and Holleck 1998).
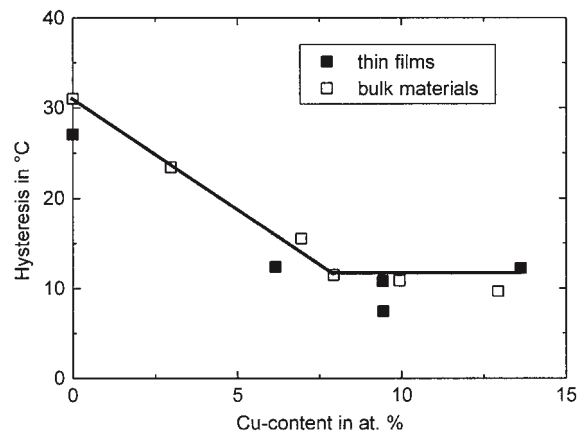
Figure 3
Hysteresis of Ti(Ni,Cu) bulk (open symbols) and thin film (closed symbols) materials (after Miyazaki *et al.* 1996).

3

Ni/Cu substitution of about 20% leads to a reduction of the hysteresis from 70 K to approx. 20 K for free-standing, stress-free thin-film materials, which is not further reduced by higher copper contents.

Compounds of substrates and shape memory films are an attractive approach to realize actuators that do not require a special training treatment, which is necessary in the case of free-standing films. The internal stress resulting in a two-way behavior is introduced after the crystallization upon cooling, owing to different thermal expansion coefficients of substrate and shape memory film. In the case of lower thermal expansion coefficients of the substrate (e.g., silicon, molybdenum) the shape memory films are under tensile stress while higher thermal expansion coefficients of the substrate (e.g. $Fe_{72}Cr_{18}Ni_{10}$) result in compressive film stress. Below the martensite start temperature these stresses vanish, owing to the formation of selected martensite variants corresponding to the lowest free energy of the system.

Upon heating, the shape memory effect leads to a restoration of the original stress state. Thus high stresses exceeding 400 MPa are restored in a narrow temperature range defined by the transformation hysteresis of the shape memory material (Fig. 4). Using these shape memory compounds it is possible to fabricate shape memory bending transducers in a fully batch technology by sputtering the metallic substrate layer in combination with sacrificial layers. This two-way actuator does not require any training procedures.

The unique feature of shape memory actuators is the very high energy density, which is considered to be of special importance, owing to the small volumes of actuators in microelectromechanical systems (MEMS). Applications realized so far make use of this feature, e.g., in the case of microvalves to be employed in pneumatics or hydraulics.

See also: Giant Magnetostrictive Materials

Bibliography

Miyazaki S, Hashinaga T, Ishida A 1996 Martensitic transformations in sputter-deposited Ti–Ni–Cu shape memory alloy films. *Thin Solid Films* **281–2**, 364–7

Muralt P 1997 Piezoelectric thin films for MEMS. *Integr. Ferroelect.* **17**, 297–307

Quandt E, Halene C, Holleck H, Feit K, Kohl M, Schloßmacher P, Skokan A, Skrobanek K D 1996 Sputter deposition of TiNi, TiNiPd, and TiPd films displaying the two way shape memory effect. *Sensors Actuat. A* **53**, 433–8

Quandt E, Holleck H 1998 Transducer and protective PVD-films for applications in microsystem components. *Microsyst. Technol.* **26**, 49–58

Winzek B, Quandt E 1999 Shape memory Ti–Ni–X films (X = Cu, Pd) under constraint. *Z. Metallkd.* **90**, 796–802

E. Quandt
*Center of Advanced European Studies and Research
Bonn, Germany*

Figure 4
Stress–temperature curve of a TiNiCu shape memory film on molybdenum. A_s and A_f denote the austenite start and finish temperature; M_s and M_f are the martensite start and finish temperature.

Alloys of 4*f* (R) and 3*d* (T) Elements: Magnetism

Ordered metallic alloys with a well-defined crystal structure are classified as intermetallic compounds, or intermetallics. Owing to the metallic character of bonding, the crystal structures of intermetallics tend to reach the highest symmetry, highest space filling, and highest coordination number.

The R–3*d* intermetallics are ordered alloys of rare earth (RE) and 3*d* transition (T) elements and can involve one or both elements with magnetic moments. These compounds exist in a relatively narrow compositional range, and the R and T atoms are distributed at proper and definite positions in the crystallographic cell. Accordingly, two magnetic sublattices (*f*- and *d*-electron subsystems) can be distinguished in R–3*d* intermetallics. While the number of pure magnetic 3*d* and 4*f* elements is about 20, there are several hundred binary R–3*d* intermetallics and thousands among the ternary R–3*d*–M systems. It has been established that in most cases the same crystal structure is stabilized for variable R elements and to some extent for variable T elements so that helpful comparison of magnetic properties can be made, giving enlightenment as to the basic interactions involved in various cases.

1. 4f *and* 3d *Magnetism in* R–3d *Intermetallic Compounds*

The nature of magnetism is different in the two electron subsystems involved in the magnetic interactions in R–3d intermetallics. Most of the lanthanide ions retain the localized atomic character of the 4f orbitals and their magnetism can usually be well described by atomic characteristics, L, S, and J, of a free R^{3+} ion (see *Localized 4f and 5f Moments: Magnetism*). In contrast, the 3d electrons of transition metals are itinerant and the 3d states form an energy band crossed by the Fermi level, ε_f, with natural consequences for magnetism (see *Itinerant Electron Systems: Magnetism (Ferromagnetism)*). The interaction between the RE and transition metal sublattices is mostly realized by the hybridization of the 5d (4d for Y) states of the RE and the 3d states of the transition metal, which mediates the strength of the 4f–3d exchange interaction.

The effect of the RE sublattice on the magnetic properties of the d subsystem is in most cases considered as resulting in an additional shift of the majority ("up," or "+") and minority ("down," or "–") d subbands, whereas the effect of the d electrons on the RE sublattice consists of a modification of the energy level scheme of the R^{3+} ions.

Because of a spatial localization of the 4f electronic shells, no direct overlap between the 4f wave functions takes place in R–3d intermetallics. The f–f exchange occurs via the conduction electrons and is therefore weaker than the f–d and d–d exchange interactions. The interactions related to the d sublattice increase successively along with the content of the transition metal and the d–d interaction becomes dominant in T-rich compounds.

1.1 *Itinerant Magnetism of the* d *Electrons*

A distinct feature of the d magnetism in R–3d intermetallics is the hybridization between the narrow 3d band ($\sim$3eV) of the transition metal with a high density of states (DOS), $N_{3d}(\varepsilon)$, and the broader 5d band ($\sim$10eV) of the lanthanide (the 4d band of yttrium) with a lower DOS. The contribution to the total DOS from the 6s (5s) band is negligible because of very low values of $N_s(\varepsilon)$. The magnetic properties of the d-electron subsystem are hence determined by the energy dependence of $N_d(\varepsilon)$ near the Fermi level, ε_f, and the position of ε_f itself (Barbara *et al.* 1990, Franse and Radwanski 1993).

The electronic structure of the hybridized d band can be represented schematically by one of the three characteristic curves shown in Fig. 1. Figure 1(a) shows the weak (unsaturated) ferromagnetic case: the majority and minority subbands are both partly filled. This class involves all the iron intermetallics, the cobalt series R_2Co_7, RCo_3, R_4Co_3, and the nickel
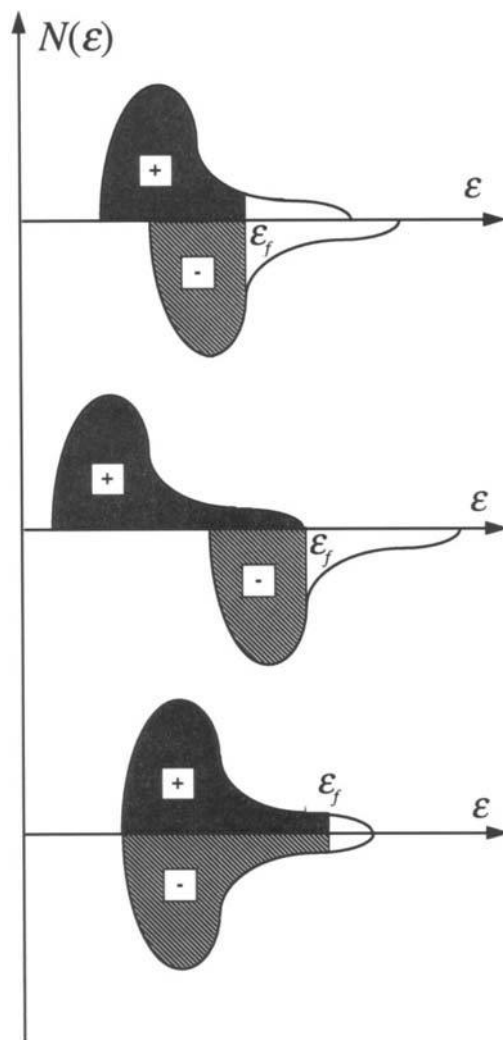
Figure 1

Schematic representations of the density of d states of the hybridized d band of R–3d intermetallic compounds for a weak, unsaturated, ferromagnetic (top), strong, saturated, ferromagnetic (center), and paramagnetic (bottom) states.

series R_2Ni_7, RNi_3. For these compounds ε_f lies in the region with high DOS where the contribution from the 5d states is essentially important. Figure 1(b) illustrates the strong (saturated) ferromagnetic case. The majority subband is filled and the Fermi level is in the high DOS region where the contribution of the 3d states dominates. The cobalt-rich compounds R_2Co_{17} and RCo_5 belong to this class. Figure 1(c) shows the paramagnetic case, for which ε_f lies in the region with low DOS formed primarily by the 5d (4d) electron states of R.
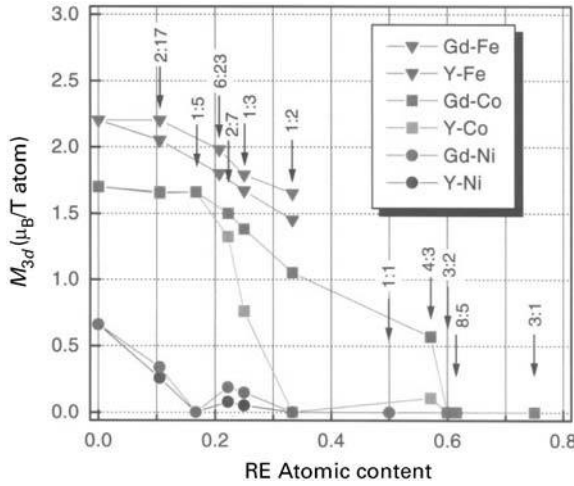
Figure 2
Magnetic moment of the *d*-electron subsystem per one T atom vs. RE content (data taken from Burzo *et al.* 1991).

The magnetic behavior of the *d* subsystem is found to be almost independent of the RE within each given $R_m T_n$ series. However, a strong variation of the *d* magnetism vs. stoichiometry is one of the most important factors, along with the crystal structure, in determining the magnetic properties of R–3*d* intermetallics with different chemical formulas.

The *d* magnetic moment vs. the chemical formula is depicted in Fig. 2 for compounds with nonmagnetic yttrium and magnetic gadolinium partner elements. While in the T-rich compounds μ_d is close to the value for the given partner T metal, with increasing RE content its value falls substantially. In the Y–Fe system, μ_d takes the value $1.45\mu_B$ (YFe$_2$), while in metallic iron it is $2.2\mu_B$. In the Y–Co and Y–Ni systems μ_d varies in a nonmonotonic way: YCo$_2$ and YNi$_5$ have paramagnetic ground states, whereas ferromagnetism appears in Y$_4$Co$_3$ ($T_C \approx 7$K), Y$_2$Ni$_7$ (58K), and YNi$_3$ (32K). With further increasing RE content the *d* subsystem becomes paramagnetic in both series.

In some series, substitutions of nonmagnetic yttrium by a magnetic RE can induce a substantial increase of μ_d (cf. yttrium and gadolinium systems in Fig. 2). Within the scope of the itinerant model, this is ascribed to the *f–d* exchange interaction. The total molecular field acting on the *d* subsystem is given by:

$$H_{\text{mol}}^{(d)} = n_{dd}M_d + n_{Rd}M_R \qquad (1)$$

where

$$n_{dd} = \frac{z_d I_{dd}}{2\mu_B^2}$$

and

$$n_{Rd} = \frac{(g_R - 1)z_R I_{Rd}}{2g_R\mu_B^2}$$

are the corresponding molecular field coefficients, I_{dd} and I_{Rd} denote the *d–d* and R–*d* exchange integrals, and z_d and z_R are the numbers of T and R atoms in the nearest neighbor surrounding a T atom.

The description of the *d*-electron subsystem in the itinerant model presumes the existence of spin fluctuation (SF) excitations at elevated temperatures. In T-rich intermetallics with stable *d* moments and high values of T_C, the mean square SF amplitude, $\langle m_{SF}^2 \rangle$ (in the paramagnetic state), and the local spin density amplitude, $\langle m_{loc}^2 \rangle$ (in the ordered state), at the T-atom positions are both almost temperature independent and also depend weakly on external fields. Hence, the *d* subsystem can be considered to a good approximation as a stable magnetic sublattice. In the molecular field approach, the following expression for T_C is derived:

$$T_C = \frac{1}{2}\left(T_d + T_R + \sqrt{(T_d - T_R)^2 + 4T_{Rd}^2}\right) \qquad (2)$$

where T_d, T_R, and T_{Rd} represent the contributions to T_C arising from the *d–d*, R–R, and R–*d* interactions, respectively. The characteristic temperatures are given by $T_{dd} = n_{dd}C_d$, $T_{RR} = n_{RR}C_R$, and $T_{Rd} = n_{Rd}\sqrt{C_R C_d}$, where C_R and C_d are the corresponding Curie constants.

For weakly magnetic and exchange-enhanced paramagnetic *d* subsystems, the temperature and field dependence of the *d* magnetization is substantial. In these systems, temperature-induced SF as well as critical fluctuations near T_C become important. In weakly ferromagnetic itinerant electron systems both $\langle m_{SF}^2 \rangle$ and $\langle m_{loc}^2 \rangle$ are substantially temperature dependent in a wide region around T_C (Brooks and Johansson 1993). Therefore, the spontaneous magnetovolume effect, $\omega_s = (V_m - V_0)/V$, reaches 10^{-3}–10^{-2} in intermetallics with unsaturated *d* magnetism (see *Itinerant Electron Systems: Magnetism (Ferromagnetism)* and *Magnetoelastic Phenomena*), whereas a much lower magnetovolume effect originates from the RE sublattice ($\sim 10^{-4}$). The thermal expansion is therefore widely used in investigating aspects of the *d* magnetism in R–3*d* intermetallics (see *Magnetoelastic Phenomena*).

1.2 Localized RE Magnetism

Electronic properties of the 4*f* ions can be described within a single-ion Hamiltonian including the spin–orbit (SO), crystal field (CF), and exchange (EX) interactions:

$$H_R = H_{SO} + H_{CF} + H_{EX} \qquad (3)$$

For most of the RE ions, the spin–orbit term dominates in the Hamiltonian of Eqn. (3). Thus, the *L–S* coupling scheme remains valid in R–3*d* intermetallics (*J* is said to be a "good quantum number"). The expectation value of J_z varies then between $L + S$ and $|L-S|$. In agreement with Hund's rules, for the heavy (light) RE the ground-state multiplet has the highest (lowest) value of $J = L + S$ ($J = |L-S|$). The level scheme is determined by a combined action of the CF and the exchange interaction (see *Magnetism in Solids: General Introduction*; *Electron Systems: Strong Correlations*).

In the molecular field approximation, the molar magnetization of the RE sublattice as a function of the external field, H_{ext}, and *T*, expressed through the partition function, $Z_R(\mathbf{n})$ ($n_i = x, y, z$), takes the form:

$$M(\mathbf{n}, T, H_{ext}) = NkT \frac{\partial Z_R(\mathbf{n})/\partial H_{ext}}{Z_R(\mathbf{n})} \qquad (4)$$

The free energy, $F_R(T, \mathbf{n}) = -NkT Z_R(\mathbf{n})$, and hence the energy level scheme, depend on the crystallographic direction. The anisotropic part of the free energy determines the magnetocrystalline anisotropy that is responsible for the spontaneous orientation of the magnetization vector in the crystal. This direction is called the easy axis (EA). For a weak exchange interaction energy, E_{EX}, the CF anisotropy—single-ion anisotropy—can lead to a reduction of the 4*f* moment. In these intermetallics, anisotropy of the magnetization is observed under strong magnetic fields.

1.3 Exchange Coupling Between the 4*f* and *d* Sublattices

The models suggested for the *f–d* exchange involve a direct on-site 4*f*–5*d* exchange interaction and take into account the space localization of the *d*-electron states (Yamada 1988). Since the intra-atomic exchange integral on a T atom is larger than that on an R atom, the exchange splitting of the local density of *d* states of T atoms with up and down spins is substantially larger than the splitting of the local DOS of R atoms. Then, the difference, $\Delta\varepsilon$, between the effective atomic potentials on R and T atoms for up-spin electrons becomes larger than that for down-spin electrons. As the strength of hybridization weakens with increasing value of $\Delta\varepsilon$, the *d* states in the up-spin subband mix with each other less than those in the down-spin subband. This difference in mixing is of prime importance for the sign of the 4*f*–3*d* magnetic coupling (Brooks and Johansson 1993).

Under the external magnetic field the numbers of *d* electrons of R-atom character with spins up and down are not equal, $n_{d\uparrow}(R) < n_{d\downarrow}(R)$, and the *d* polarization, $m_d(R) = (n_{d\uparrow}(R) - n_{d\downarrow}(R))\mu_B$, is negative (if considering $m_d(T) = (n_{d\uparrow}(T) - n_{d\downarrow}(T))\mu_B$ positive). Thus, the molecular fields on R atoms created by
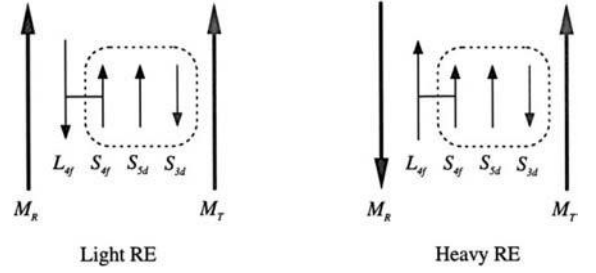
Figure 3
Schematic illustration of the 4*f*–3*d* exchange coupling between the R and T magnetic moments. The dashed areas show that part of the interactions for which the sign remains unchanged. Note that the magnetic moments are antiparallel to the corresponding mechanic moments.

$m_d(R)$ and $m_d(T)$ are opposite to each other, and the local DOS of the R atoms with up and down spins will split in the opposite direction with respect to the local DOS of T atoms. This scheme remains also valid for the R–3*d* compounds with a magnetic RE. Numerical calculations as well as Mössbauer data give the value of $m_d(R)$ as about $-0.3\mu_B$ per T atom in R–Fe compounds.

In R–3*d* intermetallics with a magnetic RE the spin moments, $\mathbf{S}_{4f}$, of the R atoms are always oriented parallel to the 5*d* spin moments, $\mathbf{S}_{5d}$, owing to the positive intra-atomic exchange interaction. This means that the 4*f* spin moment is oriented antiparallel to the 3*d* moment. Therefore, the total magnetic moment, $M_R = g_R\mu_B J_R$, is oriented opposite (parallel) to M_T for heavy (light) RE elements, as shown in Fig. 3.

2. Basic Properties of Binary R–3d Intermetallics

The Curie temperatures of binary Gd–3*d* and Y–3*d* intermetallics are given in Table 1. Since the molecular fields due to the *f–f* and *f–d* interactions reach their maximum in the gadolinium compounds (S_{Gd} is a maximum among all RE), T_C of $R_m T_n$ with other magnetic RE range between the respective values for the compounds with R = Y and Gd. These data show the weakening of the RE contribution (primarily through the *f–d* interaction) in the total exchange energy with increasing content of the T partner element.

2.1 Compounds with a Nonmagnetic 3d Sublattice

In these compounds the magnetic properties are almost exclusively determined by the 4*f* electrons. The itinerant *d* states contribute only because of a polarization induced by the *f–d* exchange interaction. Among various magnetic states and magnetization processes, one may quote metamagnetic transitions

Table 1

Symmetry of the crystal cell and the Curie (Neel) temperatures (in K) of Gd_mT_n and Y_mT_n (T_C (R $=$ Gd)/T_C (R $=$ Y)) intermetallics.[a]

m:n	Crystal cell, space group[b]	Mn	Fe	Co	Ni
3:1	o, *Pnma*			127/PM	100/PM
8:5	m, $P2_1/c$			–/PM	
3:2	o, *Pnmm* (Co) t, $P4_12_12$ (Ni)			–/PM	–/PM
4:3	h, $P6_3/m$			230/13	
1:1	o, *Cmcm* (Gd) m, $P2_1/c$ (Y)				73/PM
1:2	c, *Fd3m* (Fe, Co, Ni) h, $P6_3/mmc$ (Mn)	110/$\sim$100	790/542	409[c]/PM	75/PM
1:3	r, $R\bar{3}m$ or h, $P6_3/mmc$		725/569	611/301	115/32
2:7	r, $R\bar{3}m$ (Ni, Co) or h, $P6_3/mmc$ (Ni)			771/639	116/57
5:19	r, $R\bar{3}m$ or h, $P6_3/mmc$			–/721	
6:23	c, *Fd3m*	461/486	569/495		
1:5	h, $P6_3/mmc$			953/987	28/PM
2:17	r, $R\bar{3}m$ or h, $P6_3/mmc$		478/324	1209/1186	187/150
1:12	T, $I4/mmm$	125/110			
T metal		95	1043	1394	631

a Only R_3Co, R_3Ni, RFe_2, RCo_2, RNi_2, RCo_5, RNi_5, and R_2Ni_{17} exist with any R and with the same crystal structure. The following stoichiometries have nonmagnetic *d* sublattices and exist with very limited R and T: 5:2 (m, $C2/c$, R $=$ Pr, Nd, Sm, T $=$ Co); 7:3 (h, $P6_3/mc$, R $=$ La, Ce, Pr, Nd, T $=$ Ni); 24:11 (h, $P6_3/mc$, R $=$ Ce, T $=$ Co); 12:7 (m, $P2_1/c$, R $=$ Gd, Tb, Dy, Ho, Er, T $=$ Co); 1:1 $-\delta$ ($\delta \approx 0.85$, h, $P6_3/mmc$, R $=$ La, Pr, Nd, T $=$ Co); 2:3 (o, *Cmca*, R $=$ La, T $=$ Co, Ni). $LaCo_{13}$ (c, *Fd3m*, $T_C = 1290$K). PM $=$ Pauli paramagnet. b c, cubic; h, hexagonal; m, monoclinic; o, orthorhombic; r, rhombohedral; t, tetragonal. c In $GdCo_2$ the cobalt subsystem is magnetic due to itinerant electron metamagnetism.
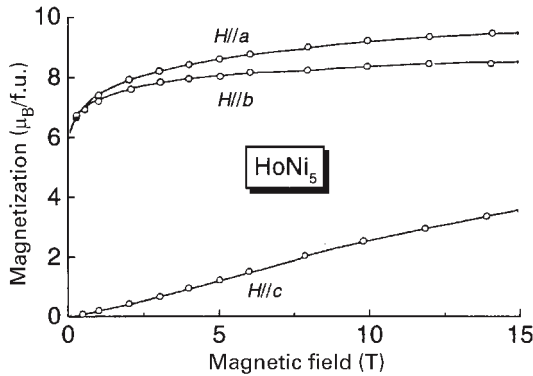
Figure 4
Magnetization curves of the hexagonal compound $HoNi_5$ at 1.5K measured along different crystallographic axes, orthorhombic set (data taken from Franse and Radwanski 1993).

associated with a field-induced crossing and anti-crossing of CF energy levels in paramagnetic systems (as in $PrNi_5$), metamagnetic transitions in ferromagnetic compounds associated with a crossing of the CF levels, spin-flop transitions in low-anisotropy systems, and stability of long-period and incommensurate structures owing to the oscillation character of the indirect exchange interactions.

The magnetization curves of hexagonal $HoNi_5$ ($T_C = 5$K) represent an example of large anisotropy of magnetization originating from CF effects (Fig. 4).

The theoretical curves are calculated with the use of the perturbing Hamiltonian (Eqn. (3)) and give the following CF parameters (in Ka_0^{-n}) : $A_2^0 = -686$, $A_4^0 = -56$, $A_6^0 = 0.3$, and $A_6^6 = +55.0$.

2.2 Compounds with a Magnetic 3d Sublattice (Unstable 3d Moments)

The strong field dependence of the magnetic characteristics of the *d*-electron system implies a strong field-induced change of DOS in the vicinity of ε_f. Hence, the *d*-electron subsystem may exhibit a magnetic instability. A first-order-type change of the magnetic state induced by an external magnetic field is known as itinerant electron metamagnetism (IEM), which can occur both from paramagnetic and weakly ferromagnetic ground states (see *Magnetic Units*).

In combination with a magnetic RE, the metamagnetic *d* subsystem can be the cause of a number of intriguing effects, e.g., a first-order-type transition at T_C and its controlled transformation in a second-order type by RE substitutions. By varying the second term in Eqn. (1), conditions for magnetic instability at a low external critical field, H_{crit}, can be reached in pseudobinary compounds of the $(R_{1-x}Y_x)_mT_n$ type:

$$H_{crit} = |n_{Rd}x\mu_R - H_M| \qquad (5)$$

where H_M is the critical field in the absence of the intersublattice interaction, μ_R is the magnetic moment of the R ion, and *x* is the RE concentration.

2.3 Compounds with a Magnetic 3d Sublattice (Stable 3d Moments)

Owing to a strong *f–d* exchange interaction, most of the R–3*d* intermetallics are collinear ferrimagnets. They have, therefore, all the attributes that collinear ferrimagnets can show. Figure 5 illustrates the regular change of the magnetic compensation point in the
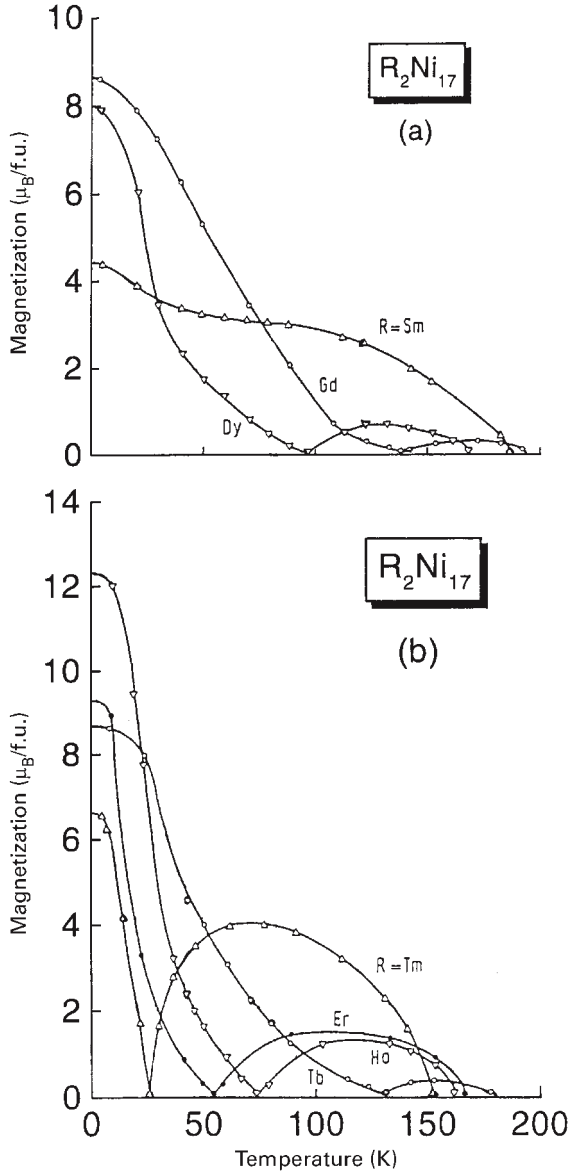
Figure 5
Temperature dependence of the spontaneous magnetization of the R_2Ni_{17} compounds (data taken from Burzo *et al.* 1991).

Table 2
f–d and *d–d* molecular fields of some gadolinium- and yttrium-rich compounds evaluated from values of T_C.

Compound	$H_{RT}^{(R)}$ (T)	Compound	H_{TT} (T)
Gd_2Co_{17}	225	Y_2Co_{17}	1450
$GdCo_5$	188	YCo_5	1210
$GdCo_2$	126	YCo_2	PM[a]
Gd_2Fe_{17}	275	Y_2Fe_{17}	390
Gd_6Fe_{23}	272	Y_6Fe_{23}	554
$GdFe_3$	278	YFe_3	690
$GdFe_2$	230	YFe_2	680
Gd_2Ni_{17}	51	Y_2Ni_{17}	296

a PM = Pauli paramagnet.

R_2Ni_{17} series. Within a two-sublattice approximation the basic intra- and intersublattice exchange interactions can be determined by analyzing the temperature dependence of the spontaneous magnetization, paramagnetic susceptibility, and values of T_C.

Values of the molecular field, $H_{RT}^{(R)} = n_{RT}M_T$ and $H_{TT} = n_{TT}M_T$, are listed for some Gd–T and Y–T intermetallics in Table 2. They show the role of a magnetic RE in compounds with stable 3*d* sublattices. The *f–f* interaction is weak in these compounds. The strength of the *f–d* interaction for other R–3*d* intermetallics can be estimated from these data using the respective relations between n_{RT} and I_{RT} and considering I_{RT} to be weakly dependent on R within the same R_mT_n stoichiometry (Franse and Radwanski 1993).

A direct determination of the strength of the intersublattice exchange interaction in the ferrimagnetic R–3*d* compounds can be made by the observation of field-induced noncollinear magnetic structures. When the anisotropy effects are neglected, the magnetization process is characterized by a critical field, H_{C1}, of a spin-flop transition into a noncollinear magnetic phase, given by:

$$H_{C1} = -n_{RT}|M_R - M_T| \qquad (6)$$

The magnetic saturation is then reached at the second critical field:

$$H_{C2} = -n_{RT}(M_R + M_T) \qquad (7)$$

In the intermediate state, $H_{C1} < H_{ext} < H_{C2}$, the magnetic configuration is canted, and the net magnetization, $M = |M_R - M_T|\cos\theta$, varies linearly as $M = H_{ext}/n_{RT}$.

In the R–3*d* intermetallics the *d*-electron subsystem is responsible for high T_C, whereas the large magnetic anisotropy and the anisotropic magnetostriction are considered mainly due to the RE sublattice. Nevertheless, the contribution of the *d* sublattice to anisotropic interactions is not negligible. In YCo_5 the
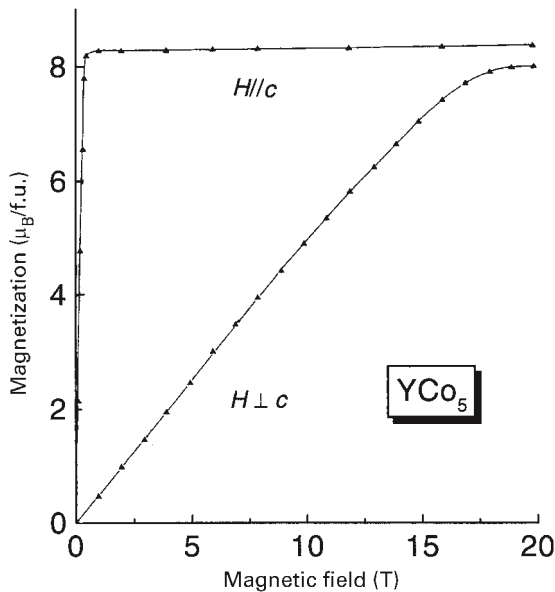
Figure 6
Magnetization curves of the hexagonal compound YCo$_5$ at 4.2K for fields applied parallel and perpendicular to the *c*-axis (data taken from Franse and Radwanski 1993).

Frustration) often present in the manganese crystallographic sublattice, various complex magnetic structures are stabilized in these intermetallics. The noncollinear magnetic structure of YMn$_{12}$ ($T_N = 110$K) is characterized by a moment arrangement which cancels the effects of possible *f–d* exchange interactions (Ballou 1994). When yttrium is replaced by a magnetic RE, the R sublattice orders only due to the *f–f* exchange interaction, leading to two distinct ordering temperatures. In the R$_6$Mn$_{23}$ intermetallics, Y$_6$Mn$_{23}$ has the highest T_C in contrast to the general characteristics found for iron, cobalt, and nickel compounds. The magnetic ordering temperatures in this series are around 450K, which indicates that the magnetism is primarily controlled by the Mn–Mn exchange interactions. The interplay of exchange interactions results in complex magnetic structures.

A magnetic structure with a long-wavelength helical component, strongly distorted by a large local anisotropy, is stabilized in YMn$_2$ through a first-order transition. The existence of long-range order in RMn$_2$ with a magnetic RE depends on several

anisotropy field, H_A, reaches about 16.5T (Fig. 6) and the anisotropy constant $K_1 = 47.0$K f.u.$^{-1}$. These values are comparable with the total anisotropy of highly anisotropic SmCo$_5$: $H_A = 60$T and $K_1 = 162.0$K f.u.$^{-1}$. In the RCo$_5$ series the cobalt anisotropy explains the existence of temperature-induced spin-reorientation phase transitions. The transitions take place around the temperatures where the absolute value of the R and cobalt sublattice anisotropies are equal (for R = Nd, Tb, Dy, and Ho).

Combination of high T_C with a high anisotropy energy in R–Co intermetallics was the basis for development of a new generation of permanent magnets in the 1960s using SmCo$_5$ as the basic component (see *Rare Earth Magnets: Materials*). In the 1980s ternary compounds based on Nd$_2$Fe$_{14}$B were discovered as prospective permanent magnet materials (Buschow 1997). Another instructive example of exploiting for practical purposes the magnetic properties of both the sublattices is provided by the cubic RFe$_2$ intermetallics (Clark 1986). These compounds show large anisotropic magnetostriction originating from the R sublattice, the high T_C being provided by the iron sublattice (see *Magnetoelastic Phenomena*).

Manganese-based intermetallics are characterized by antiferromagnetic Mn–Mn exchange coupling. As a result of the competition with the negative *f–d* exchange along with geometrical frustration (see *Magnetic Systems: Lattice Geometry-originated*

Table 3
Curie temperatures of ternary intermetallics with NaZn$_{13}$-, ThMn$_{12}$-, and CaCu$_5$-type structures and some interstitial phases formed by nonmagnetic RE.[a]

Compound	T_C (K)
NaZn$_{13}$-type	
YFe$_{11.5}$Si$_{1.5}$	198
YNi$_{11}$Si$_2$	PM
ThMn$_{12}$-type	
YFe$_{11}$Ti	524
YCo$_{11}$Ti	943
YFe$_{10}$Si$_2$	540
YFe$_{10}$Ti$_2$	498
YFe$_{10}$V$_2$	532
YFe$_{10}$Cr$_2$	450
Y$_{1.1}$Fe$_{10}$Mo$_2$	360
YFe$_{10}$W$_2$	500
YCo$_{10}$V$_2$	611
YFe$_4$Co$_6$Si$_2$	820
YFe$_8$V$_4$	350
LuCr$_6$Al$_6$	PM
YFe$_6$Al$_6$	308
CaCu$_5$-type	
YCo$_4$B	382
LuCo$_4$B	396
LuFe$_4$B	573
Interstitial phases	
Y$_2$Fe$_{17}$C	502
Lu$_2$Fe$_{17}$C	490
Y$_2$Fe$_{17}$N$_{2.6}$	694
Lu$_2$Fe$_{17}$N$_{2.7}$	678

a PM = Pauli paramagnet.

factors, such as the Mn–Mn distance and the strength of the *f–d* exchange interaction.

3. Ternary Compounds Containing R and 3d Elements

In the search for novel magnetic compounds the ternary intermetallics containing both RE and T elements provide wide possibilities (Li and Coey 1991, Szytula 1991). Some crystal structures which do not exist in R–T binary phase diagrams can be stabilized by substitutions. An example of this approach is the stoichiometry 1:13 in which only $LaCo_{13}$ ($T_C = 1290K$) crystallizes. The pseudobinary systems $La(Fe_{1-x}Me_x)_{13}$ with Me = Al ($0.08 \leqslant x \leqslant 0.54$) and Si ($0.12 \leqslant x \leqslant 0.19$) have higher iron concentration than the binary R_2Fe_{17}. A number of new intermetallics with iron and cobalt have been synthesized with the 1:12 stoichiometry existing only in binary R–Mn systems. Iron-rich $R(Fe_{1-x}Me_x)_{12}$ compounds are known with Me = Al, Si, Ti, V, Cr, Mn, Mo, Ta. Their magnetic properties determined by the R and T sublattices follow in general the regularities established for binary intermetallics with stable 3*d* moments.

The intermetallics with true ternary structure types, $R_mT_nM_p$, form the biggest group. They can also be synthesized with chromium. Another way of generating a ternary structure is by introducing small, interstitial atoms X, such as carbon or nitrogen, into binary compounds, e.g., $R_2Fe_{17}X_{3-\delta}$, which are interstitial ternary phases. Tables 3 and 4 give the crystal structures and Curie temperatures of some of the most studied ternaries with nonmagnetic yttrium. The effect of the magnetic RE sublattice is similar to the case of binary R–3*d* intermetallics.

See also: Crystal Field Effects in Intermetallic Compounds: Inelastic Neutron Scattering Results; Magnetism in Solids: General Introduction; Metal Hydrides: Magnetic Properties; Spin Fluctuations

Bibliography

Ballou R 1994 The role of R–M compounds in the understanding of magnetism. *J. Magn. Mater.* **129**, 1–9

Barbara B, Gignoux D, Vettier C 1990 *Lectures on Modern Magnetism*. Springer, Berlin

Brooks M S S, Johansson B 1993 Density functional theory of the ground state magnetic properties of rare earths and actinides. In: Buschow K H J (ed.) *Handbook on Magnetic Materials*. Elsevier, Amsterdam, Vol. 7, Chap. 3, pp. 139–230

Burzo E, Chelkowski A, Kirchmayr H R 1991 Compounds between rare earth elements and 3d, 4d or 5d elements. In: Wijn H P J (ed.) *Landolt-Börnstein Numerical Data and Functional Relationships in Science and Technology, New Series III/19d2*

Buschow K H J 1997 Magnetism and processing of permanent magnet materials. In: Buschow K H J (ed.) *Handbook on Magnetic Materials*. Elsevier, Amsterdam, Vol. 10, Chap. 4, pp. 463–594

Clark A E 1986 Magnetostrictive rare earth–Fe_2 compounds. In: Wohlfarth E P (ed.) *Ferromagnetic Materials*. Elsevier, Amsterdam, Vol. 1, Chap. 7, pp. 531–89

Franse J J M, Radwanski R 1993 Magnetic properties of binary rare-earth 3d-transition-metal intermetallic compounds. In: Buschow K H J (ed.) *Handbook on Magnetic Materials*. Elsevier, Amsterdam, Vol. 7, Chap. 5, pp. 307–501

Li H-S, Coey J M D 1991 Magnetic properties of ternary rare-earth transition-metal compounds. In: Buschow K H J (ed.) *Handbook on Magnetic Materials*. Elsevier, Amsterdam, Vol. 6, Chap. 1, pp. 1–83

Szytula A 1991 Magnetic properties of ternary rare-earth transition-metal compounds. In: Buschow K H J (ed.) *Handbook on Magnetic Materials*. Elsevier, Amsterdam, Vol. 6, Chap. 2, pp. 85–180

Yamada H 1988 Electronic structure and magnetic properties of the cubic Laves phase transition metal compounds. *Physica B* **149**, 390–402

A. S. Markosyan
Czech Academy of Sciences, Prague, Czech Republic and Moscow State University, Russia

Table 4
Symmetry of the crystal cell and the Curie (Neel) temperatures of R–T–Me intermetallics with ternary structure types formed by nonmagnetic RE (notations as Table 1).

Compound	Crystal cell, space group	T_C, T_N (K)
$Y_6Fe_{62}B_{14}$	c, *Im3m*	510
$Y_6Co_{12}B_6$	r, *R$\bar{3}$m*	151
$Lu_2Fe_{14}C$	t, *P4$_2$/mnm*	495
$Lu_2Fe_{14}B$	t, *P4$_2$/mnm*	532–539
$YNiAl_2$	o, *Cmcm*	PM
$LaMnSi_2$	o, *Cmcm*	386
$LuFeSi_3$	t, *I4mmm*	PM
YCo_2Si_2	t, *I4mmm*	PM
$LuCo_2Si_2$	t, *I4mmm*	PM
YCo_2Ge_2	t, *I4mmm*	PM
YMn_2Si_2	t, *I4mmm*	460
$LaMn_2Si_2$	t, *I4mmm*	303–310
YMn_2Ge_2	t, *I4mmm*	395
$LaMn_2Ge_2$	t, *I4mmm*	306–310
$LuMn_2Ge_2$	t, *I4mmm*	453

Alnicos and Hexaferrites

The traditional permanent magnets based on ferrites and Al–Ni–Co alloys are still of substantial commercial importance because of their low cost, although some of their magnetic properties are much inferior

to those of rare earth permanent magnets (see *Rare Earth Magnets: Materials*).

Hard ferrites are ceramic materials that have hexagonal crystal structures. Their formula composition can be represented as $n(\text{MeO}) \cdot m(\text{Fe}_2\text{O}_3)$, where n and m are natural numbers and Me is a divalent metal. For $n = 1$ and $m = 6$ one obtains the formula for the so-called M-type ferrites, $\text{MeO} \cdot 6(\text{Fe}_2\text{O}_3)$, which can also be written as $\text{MeFe}_{12}\text{O}_{19}$. The most common M-type ferrites are those where Me = Ba, Sr, or Pb. For $n = 3$ and $m = 8$ one obtains the formula composition $3(\text{MeO})\, 8(\text{Fe}_2\text{O}_3)$. There are usually two (or more) types of divalent metals, Me, involved. The formula composition of the so-called W-type ferrites is therefore most conveniently represented by $\text{Me}_1\underline{\text{Me}}_2\text{Fe}_{16}\text{O}_{27}$. Well-known examples of such compounds are formed with Me = Ba or Sr and $\underline{\text{Me}}$ consisting of Fe(II) and large amounts of magnesium, zinc, copper, nickel, cobalt, or manganese. Most applications deal with the M-type ferrites. For this reason only this type will be discussed below. A more detailed description of both types of hard ferrites can be found in the review by Buschow (1997). (See also *Ferrites*.)

Alnico magnets are composed of iron, cobalt, nickel, aluminum, and various types of additives. These are magnets of metallic character obtained by casting. One of the advantages of alnico alloys is that the melting can be performed in air, although sometimes an apron of inert gas is blown over the melt. Alnico alloys can also be prepared by sintering powders of the raw materials, aluminum being always added in the form of a prealloy with one or more of the other constituent metals.

Compared to hard ferrites, alnico alloys have a rather insignificant magnetocrystalline anisotropy. They derive their magnetic hardness from shape anisotropy. This implies that the microstructure of the alloys is of paramount importance. Alnico magnets can be characterized as fine-particle alloys in which elongated ferromagnetic particles are dispersed in a basically nonmagnetic matrix. This particular microstructure can be attained by a heat treatment leading to the so-called spinodal decomposition of the alloy, which is described briefly below. For more details the reader is referred to the review by McCaig and Clegg (1987).

1. Alnico Alloys

It has been mentioned already that alnico alloys are multicomponent systems. All these systems have in common the fact that they form homogeneous solid solutions at high temperatures. At lower temperatures there is a miscibility gap. This miscibility gap leads to phase separation of the homogeneous alloy into two phases, α_1 and α_2, where α_1 represents a strongly ferromagnetic b.c.c. phase rich in cobalt and iron. By contrast, α_2 is a nonmagnetic or only weakly ferromagnetic b.c.c. phase rich in aluminum and nickel.

The standard heat treatment of alnico alloys usually consists of a homogenization treatment at about $1250\,^\circ\text{C}$ at which temperature the alloys still consist of a single phase (α). The alloy is subsequently annealed under conditions corresponding to the region within which decomposition into two phases can occur. This spinodal decomposition of the α phase into the α_1 and α_2 phases can occur spontaneously, but its rate is diffusion controlled. It can proceed therefore only at relatively high temperatures (above $800\,^\circ\text{C}$). The concentrations of the Fe(Co) atoms show a periodic variation (assumed to be sinusoidal after decomposition has set in) and the amplitude of the composition fluctuations increases with time until the phase separation into α_1 and α_2 is complete. The whole process takes only a very short time. Depending on the temperature, it can be completed in a matter of seconds or minutes. Formation and subsequent growth of the ferromagnetic α_1 particles to their final shape and size occurs almost completely during the spinodal decomposition reaction at 800–$850\,^\circ\text{C}$. The driving force for the growth is the decrease of the interfacial energy between the particles (α_1) and the matrix (α_2).

Optimization of the magnetic properties requires a further tempering treatment generally performed at $600\,^\circ\text{C}$. Its main purpose is to increase the difference in magnetic saturation polarization, J_s, between the somewhat elongated Fe(Co)-rich particles and the surrounding matrix (Ni–Al-rich). During this low-temperature anneal a continuous change in the composition takes place owing to diffusion of iron and cobalt atoms into the ferromagnetic particles. The spinodal decomposition alone does not produce a sufficiently large shape anisotropy in the ferromagnetic α_1 phase particles. This is because the difference in the saturation magnetizations between the α_1 particles and the matrix is relatively modest so that the effective shape anisotropy field of the particles (proportional to $J_s(\alpha_1) - J_s(\alpha_2)$, see below) is also modest in spite of the elongation. The heat treatment at $600\,^\circ\text{C}$ is therefore desirable for producing a sufficiently high magnetization anisotropy, which makes it possible to obtain the highest coercivities and the optimum permanent magnet properties. The latter treatment commonly consists of an anneal for several hours.

The interfacial energy of the alloy depends on the crystallographic orientation of the boundaries between the α_1 and α_2-type particles. Particle growth is therefore anisotropic, and results in an elongation parallel to the $\langle 100 \rangle$ directions. This opens the possibility of obtaining substantial improvements in magnetic properties by controlled cooling of the alloys after the homogenization treatment at about $1200\,^\circ\text{C}$ to about $800\,^\circ\text{C}$ in the presence of a

saturating magnetic field. This so-called thermomagnetic treatment promotes the formation of anisotropic magnets in which the easy magnetization direction of the grains formed during the spinodal decomposition is parallel to the direction of the magnetic field applied during cooling. The elongation of the particles in the field direction originates from the decrease of the magnetic free energy of the particles when the axis with the lowest demagnetizing factor is along the direction of the applied field. For an oriented single crystal, optimum properties would be obtained when the thermomagnetic field is applied parallel to one of the $\langle 100 \rangle$ directions. In practice, use is made of so-called columnar crystallized alnico alloys instead of expensive single crystals.

It is possible to obtain such highly textured alloys by a grain orienting process preceding the thermomagnetic and tempering treatment. The alloys are then cast in heated or exothermic molds onto water-cooled steel or copper slabs. During solidification of the alloy on the cold surface, the grains tend to grow with their long axis parallel to the $\langle 100 \rangle$ directions, perpendicular to the cold surface. This leads to a semicolumnar alloy in which the columnar axes are parallel to one of the $\langle 100 \rangle$ directions, for instance, parallel to the [001] direction. It has become common practice to refer to alloys manufactured in this way as alnico DG (directed grain). The thermomagnetic treatment for this type of textured alloy is applied with the magnetic field parallel to the elongated direction of the columnar particles, i.e., parallel to the [001] direction. As mentioned above, the magnetic properties in the easy magnetization direction can be further improved by subsequent tempering of the ingots for several hours at about 600 °C.

The relatively high coercivities and remanences in alnico alloys are due to the shape anisotropy associated with the elongated Fe(Co)-rich particles imbedded in the nonferromagnetic matrix. The Stoner–Wohlfarth theory predicts that the coercivity is proportional to the saturation polarization, J_s, of the Fe(Co)-rich particles and also proportional to a factor related to the difference in the effective demagnetization factors perpendicular (N_ζ) and parallel (N_ψ) to the preferred direction of magnetization in the particles. For magnetization reversal proceeding by uniform rotation, this leads to the formula

$$\mu_0 H_A = \mu_0 H_c = f(\theta)[N_\psi - N_\zeta]J_s \qquad (1)$$

where $f(\theta)$ is an averaging factor that accounts for the various orientations of the preferred axes of the particles with respect to the direction in which H_c is measured.

For an assembly of noninteracting uniaxial single-domain particles arranged at random, $f(\theta)$ has the value 0.5. In highly elongated particles $f(\theta)$ may approach unity. In the case of spheroid particles there is a considerable difference in the demagnetizing factor

Table 1

Nominal chemical compositions and magnetic properties of cast alnico magnets. The balance of composition is iron for all alloys. Taken from Magnetic Producers Association listing.

	Composition (wt.%)							
Type	Al	Ni	Co	Cu	Ti	BH_{max} (kJm^{-3})	B_r (T)	$_JH_c$ (kAm^{-1})
1	12	21	5	3		5.6	0.72	38.4
2	10	19	13	3		13.6	0.75	46.4
3	12	25		3		10.8	0.70	40.0
5	8	14	24	3		44.0	1.28	51.2
5DG	8	14	24	3		52.0	1.33	53.6
6	8	16	24	3	1	31.2	1.05	64.0
8	7	15	35	4	5	42.4	0.82	148.8
9	7	15	35	4	5	81.0	1.06	120.0

for particles magnetized perpendicular or parallel to the flat surface of the spheroid. In the limit of an extremely flat and elongated spheroid one has $N_\psi - N_\zeta = 1 - 0 = 1$. Equation (1) shows that the coercivity in such materials may reach an upper limit equal to $H_c = J_s/\mu_0 = M_s$. With $M_s = 1.7\,\text{MAm}^{-1}$, this upper limit becomes $H_c = 1.7\,\text{MAm}^{-1}$. Even for the less favorable case $N_\psi - N_\zeta = 0.5$, the coercivity could become $850\,\text{kAm}^{-1}$. The latter value is much higher than the actual values found in alnico materials, as listed in Table 1.

The comparatively low values of the coercivity in alnico alloys can partly be attributed to the less ideal shape of the thin ferromagnetic particles and also to the fact that the matrix is magnetic to some extent. Considerable experimental evidence exists, showing that the magnetization reversal does not proceed by uniform rotation, as is assumed in the discussion above. Instead magnetization reversal can occur by a complex incoherent mechanism known as "curling" (McCurrie 1982). It can proceed in lower fields, which accounts for the lower observed coercivities.

The various grades of alnico-type alloys are usually referred to by plain numbers, as indicated in the first column of Table 1. More details of the preparation and second quadrant characteristics of these and other alnico-type permanent magnet materials can be found in the review of McCaig and Clegg (1987). One of the favorable magnetic properties of alnico alloys is their very high Curie temperature (700–850 °C). The small negative reversible temperature coefficient, $\delta(B_r) \sim -0.02\%\text{K}^{-1}$, leads to excellent flux stability at elevated temperatures. Alnico alloys are chemically and metallurgically very stable. In fact, alnico 5 is the only magnet material that has some long-term utility at temperatures up to 500 °C (see also *Magnets: High-temperature*).

As may be inferred from Table 1, a drawback of alnico alloys is that their coercivity is low in comparison to rare earth-based magnets (see *Rare Earth Magnets: Materials*). Generally, the $B(H)$ curves of alnico magnets in the second quadrant display a nonlinear behavior. This implies a serious disadvantage in device design and dynamic operation. Also it limits the attainable energy products, in spite of the high remanences that are comparable to NdFeB-type magnets (see *Magnets: Sintered*).

Alnico magnets are best suited in applications involving magnetic circuits of high permeance because the maximum energy product corresponds to permeance ratios larger than five. In practice, this implies that alnico magnets have to be comparatively long in the easy direction and that their cross-sectional area has to be relatively small. Alnico magnets are used as sensors and in devices such as electron tubes or watt hour meters (see also *Permanent Magnets: Sensor Applications*). They are also applied in several types of motors and in generators operating at high temperatures.

2. Hard Ferrites

The hard magnetic properties of hexaferrites originate from their comparatively large magnetocrystalline anisotropy. Hard ferrites still play a dominant role in the permanent magnet market owing to the low price per unit of available energy, the wide availability of the raw materials, and the high chemical stability.

The so-called M-type ferrites crystallize in the magnetoplumbite structure characterized by close packing of oxygen and Me ions with iron atoms at the interstitial positions. The structure can be described as consisting of cubic blocks with the spinel structure and hexagonal blocks containing the Me ions. There are two formula units $MeFe_{12}O_{19}$ per unit cell and the Fe^{3+} ions are distributed over five nonequivalent crystallographic positions.

An important feature governing the occurrence of hexagonal ferrites is that substitutions are only possible when the rule of charge conservation is obeyed. Two well-known examples demonstrating this charge conservation are $BaFe_{12-2x}Ti_x^{4+}Co_x^{2+}O_{19}$ and $Ba_{1-x}La_x^{3+}Fe_{12-x}Fe_x^{2+}O_{19}$, where iron is trivalent when not indicated differently. A detailed survey of various types of substitution in M-type ferrites is given in the reviews of Kojima (1982) and Kools (1986).

The complicated nature of the magnetic couplings in hard ferrites may be illustrated by means of $BaFe_{12}O_{19}$. Each of the Fe^{3+} ions in this compound carries a large magnetic moment equal to $5\,\mu_B$ at 4.2 K. The moments of the iron ions occupying the same crystallographic position are ferromagnetically aligned. By contrast, the coupling between iron moments belonging to different crystallographic positions is ferromagnetic for some sites and antiferromagnetic for other sites. All these couplings are determined by a superexchange interaction, mediated by the oxygen atoms. As described in detail in the review of Kojima (1982), there is a strong preference for ferromagnetic coupling when the Fe–O–Fe angle approaches $180°$ and the Fe–O–Fe distance is comparatively small. The resultant spin structure is ferrimagnetic. The partly antiparallel coupling of the iron moments leads to a net moment per unit cell of only $40\,\mu_B$ (at 4.2 K), which is considerably below the value $12 \times 5\,\mu_B = 60\,\mu_B$ expected for ferromagnetic alignment.

The Curie temperatures of hexagonal ferrites are fairly high and fall into the temperature range 700–750 K. Of particular interest is their temperature dependence of the saturation polarization J_s. Results for $BaFe_{12}O_{19}$ are shown in Fig. 1. The value of J_s is seen to decrease with increasing temperature much faster than would be expected on the basis of a Brillouin function. This is the main reason that these materials have a relatively low value of J_s at room temperature, much lower than the value corresponding to the saturation moment of $40\,\mu_B$ per formula unit mentioned above. The temperature coefficient of J_s is fairly high ($-0.2 \times K^{-1}$), being
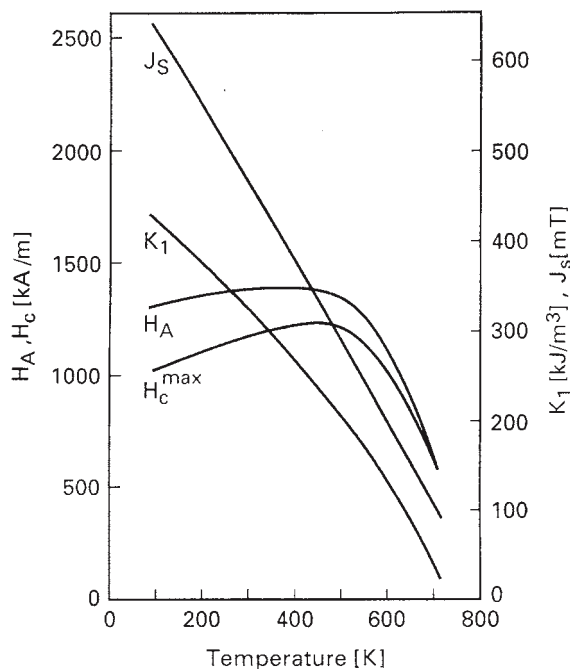
Figure 1
Temperature dependence of saturation polarization, J_s, anisotropy constant, K_1, anisotropy field, H_A, and maximum attainable coercivity, H_c^{max}, for M-type barium ferrite (after Kools 1986).

roughly an order of magnitude higher than that found in alnico magnets.

The magnetocrystalline anisotropy in hard ferrites is generally considered as arising from spin–orbit coupling. The anisotropy energy is characterized by a comparatively high positive value of the anisotropy constant K_1 (for a definition, see *Hard Magnetic Materials, Basic Principles of*), higher order constants (K_2, K_3, etc.) being negligibly small. This corresponds to an easy magnetization direction along the *c*-axis.

The temperature dependence of K_1 for $BaFe_{12}O_{19}$ is included in Fig. 1, together with the temperature dependence of the anisotropy field $H_A = 2K_1/J_s$. The magnetic polarization, J_s, decreases more strongly with temperature than K_1 in the lower temperature range. This leads to the rather peculiar case that H_A first (slightly) increases with temperature before it eventually decreases. A similar temperature dependence is expected for the maximum attainable coercivity, H_c^{max}.

Compounds of M-type ferrites are usually formed by calcination of appropriate mixtures of Fe_2O_3, $BaCO_3$, or $SrCO_3$ and minor additives at high temperatures (about 1250 °C). After this so-called prefiring process the resulting product is milled to very fine particles (below 1 μm), which is usually performed in water. The slurry is dried by heating in ovens or by spray drying. After mixing the dried ferrite powders with lubricants and small amounts of additives the material is compacted by pressing. The pressed magnet bodies are sintered in air at high temperatures. This operation is commonly indicated as firing. The magnets obtained in this way are isotropic, meaning that the orientation of the powder particles has a random distribution.

Anisotropic sintered magnets can be manufactured by wet pressing and sintering. Compound formation proceeds in the same way during prefiring as described above. Contrary to dry pressing, a different choice of additives (SiO_2 and/or B_2O_3) is used in order to better control grain growth and densification. The hard, prefired material is wet milled in water using steel balls. The result of this process is a thick suspension, the so-called slurry. The fine powder particles (preferably single crystals) have sufficient mobility in this slurry to align themselves along the preferred magnetization direction in an external field during wet pressing. The pressed compacts are first dried and then sintered in air at about 1250 °C. Considerable anisotropic shrinkage occurs during the sintering process. Therefore, the pole faces of the sintered magnet bodies have to be ground afterwards when accurate dimensional control of the magnets is desired. More details regarding general processing can be found in the review of Stäblein (1982). Several optimization procedures for reaching higher performances have been described by Horiishi and Yamamoto (1992), Taguchi *et al.* (1992), and Harada (1992).

Mechanical alloying has also been proposed as a method to produce ferrite magnets of high coercivities (Ding *et al.* 1995). The starting material is $BaO_2 + 6Fe_2O_3$. After high-energy ball milling the material is annealed at temperatures between 750 °C and 1000 °C, resulting in coercivities close to 450 kAm^{-1}.

Castro *et al.* (1996) have prepared nanostructured particles of barium hexaferrite by means of the combustion method, starting from a solution of the metal nitrates and using a reducing agent (tetraformal trisazide or oxalic acid dihydrazide) as a fuel. For the submicrometer-sized particles of $BaFe_{12}O_{19}$ thus prepared, coercivities of 425 kAm^{-1} and magnetizations of 57.8 Am^{2}kg^{-1} are obtained.

The coercivity in ferrite magnets is usually described in terms of nonuniform magnetization reversal. It has been mentioned briefly above that the main purpose of some additives is to control the microstructure of the ultimate magnets by reducing the grain growth during prefiring as well as during sintering. For describing the relationship between coercivity and microstructural parameters, Kools (1986) uses the expression

$$_JH_c = \alpha H_A - N_{eff}(J_s + B_r)/\mu_0 \qquad (2)$$

where α depends on the grain size and N_{eff} depends on the grain shape (see also *Coercivity Mechanisms*). Also the fraction of the ferrite phase present in the magnet and the degree of alignment are important since they largely determine the value of the remanence B_r. For more details the reader is referred to the reviews of Kools (1986) and McCaig and Clegg (1987). A most helpful tool in studying the coercivity mechanism in permanent magnet materials is the magnetic aftereffect (Givord *et al.* 1990). From a study of the field and temperature dependence of the magnetic aftereffect constant in M-type strontium and barium ferrite magnets, it was concluded that the coercivity mechanism (see also *Coercivity Mechanisms*) in these sintered magnets is of the nucleation type.

Hard ferrite magnets can be classified as low-cost, low-performance magnets. Their application is widespread, including anisotropic segments for electric motors, anisotropic rings for loudspeakers, and large anisotropic blocks for ore separators. Applications in which the temperature can become substantially higher than room temperature may profit from the fact that the ferrite magnets have a high chemical stability. Another advantage is that they are electrical insulators. Furthermore, the coercivity increases rather than decreases with temperature. This is again beneficial for high-temperature applications, although the temperature coefficients of coercivity and remanence are undesirably high. The most prominent disadvantage of magnets made of hard ferrites is their low $(BH)_{max}$ value, remaining below 30 kJm^{-3} even for anisotropic sintered magnets. This generally

requires magnets of comparatively large size, excluding application of magnetic devices in which weight and space are at a premium. The unequalled low cost of ferrite magnets is because of the very inexpensive raw materials.

See also: Ferrite Magnets: Improved Performance

Bibliography

Buschow K H J 1997 Magnetism and processing of permanent magnet materials In: Buschow K H J (ed.) *Magnetic Materials*. Elsevier, Amsterdam, Vol. 10, Chap. 4

Castro S, Gayoso M, Rivas J, Greneche J M, Mira J, Rodrigues C 1996 Structural and magnetic properties of Ba hexaferrite nanostructured particles prepared by the combustion method. *J. Magn. Magn. Mater*. **152**, 61–9

Ding J H, Yang H, Miao W F, McCormick P G, Street R 1995 High coercivity Ba hexaferrite prepared by mechanical alloying. *J. Alloys Compounds* **221**, 70–3

Givord D, Lu Q, Rossignol M F, Tenaud P, Viadieu T 1990 Experimental approach to coercivity analysis in hard magnetic materials. *J. Magn. Magn. Mater*. **83**, 183–8

Harada H 1992 The recent progress of hexagonal hard ferrite magnets. In: Yamaguchy T, Abe M (eds.) *Proc. 6th Int. Conf. on Ferrites*. Japan Society of Powder and Powder Metallurgy, Tokyo-Kyoto, Japan, pp. 1112–7

Horiishi N, Yamamoto S 1992 Ferrite powder for bonded magnets. In: Yamaguchy T, Abe M (eds.) *Proc. 6th Int. Conf. on Ferrites*. Japan Society of Powder and Powder Metallurgy, Tokyo-Kyoto, Japan, pp. 1041–5

Kojima H 1982 Fundamental properties of hexagonal ferrites with magnetoplumbic structure. In: Wohlfarth E P (ed.) *Ferromagnetic Materials*. North Holland, Amsterdam, Vol. 3, Chap. 5

Kools F 1986 Hard magnetic ferrites. In: Bever M B (ed.) *Encyclopedia of Materials Science and Engineering*. Pergamon, Oxford, Vol. 4, p. 2082

McCaig M, Clegg A G 1987 *Permanent Magnets in Theory and Practice*. Pentech Press, London

McCurrie R A 1982 The structure and properties of alnico permanent magnets. In: Wohlfarth E P (ed.) *Ferromagnetic Materials*. North Holland, Amsterdam, Vol. 3, Chap. 3

Stäblein H 1982 Hard ferrites and plastoferrites. In: Wohlfarth E P (ed.) *Ferromagnetic Materials*. North Holland, Amsterdam, Vol. 3, Chap. 7

Taguchi H, Hirata F, Takeischi T, Mori T 1992 High performance ferrite magnet. In: Yamaguchy T, Abe M (eds.) *Proc. 6th Int. Conf. on Ferrites*. Japan Society of Powder and Powder Metallurgy, Tokyo-Kyoto, Japan, pp. 1118–21

K. H. J. Buschow
University of Amsterdam, The Netherlands

Amorphous and Nanocrystalline Materials

Amorphous metals (often also referred to as metallic glasses) are characterized by the absence of atomic long-range order and reveal only a short-range order (SRO) with a structural correlation length in the order of atomic distances (O'Handley 1987). Nanocrystalline materials have a limited long-range order (which is the same as the short-range order) with a structural correlation length (the grain size) on the nanometer scale, typically 5–20 nm.

Regarding their magnetic properties, the key point for amorphous and nanocrystalline $3d$ metals is that their structural correlation length D in many cases is smaller than the ferromagnetic correlation length $L_0 = \sqrt{A/K_1}$, which is determined by the exchange interaction constant A and the local magnetocrystalline anisotropy K_1. L_0 is closely related to the domain wall width and defines the minimum length scale over which the direction of the magnetization can vary appreciably. For iron-based alloys, as an example, typical values are $L_0 = 20$–40 nm.

As a consequence, if $D < L_0$, the magnetization cannot follow the randomly oriented magnetic easy axis defined by the SRO, but is increasingly forced to align parallel by exchange interaction. Thus, the anisotropy effective for the magnetization process is an average over the randomly fluctuating local anisotropies scaling down like $(D/L_0)^6$ and, hence, is considerably reduced in magnitude (see *Nanocrystalline Materials: Magnetism*).

As a result, amorphous and many nanocrystalline alloys reveal virtually no or only a very small macroscopic magnetocrystalline anisotropy which is the precondition for superior soft magnetic behavior as observed in these material classes.

As an example, Fig. 1 summarizes the typical variation of the coercivity, H_c, over the whole range of structural correlation lengths starting from atomic distances in amorphous alloys over grain sizes, D, in the nanometer regime up to macroscopic grain sizes—the permeability shows an analogous behavior being essentially inversely proportional to H_c (Herzer 1990, 1997). The $1/D$-dependence of coercivity for large grain sizes (Pfeifer and Radeloff 1980) reflects the conventional rule that good soft magnetic properties require very large grains ($D > 100\,\mu m$). Thus, the reduction of particle size to the regime of the domain wall width increases the coercivity towards a maximum controlled by the anisotropies present. Lowest coercivities, however, are again found for structural correlation lengths smaller than the domain wall width like in amorphous alloys ("grain size" of the order of atomic distances) and in nanocrystalline alloys for grain sizes $D < 20$ nm.

An interesting consequence of the exchange softening mechanism at small structural correlation lengths is that these materials simultaneously combine magnetic soft and mechanical hard behavior (like high yield strength and high hardness) unlike conventional soft magnetic crystalline alloys.

Apart from a low magnetocrystalline anisotropy superior soft magnetic behavior additionally requires a low or vanishing magnetostriction, λ_s, which
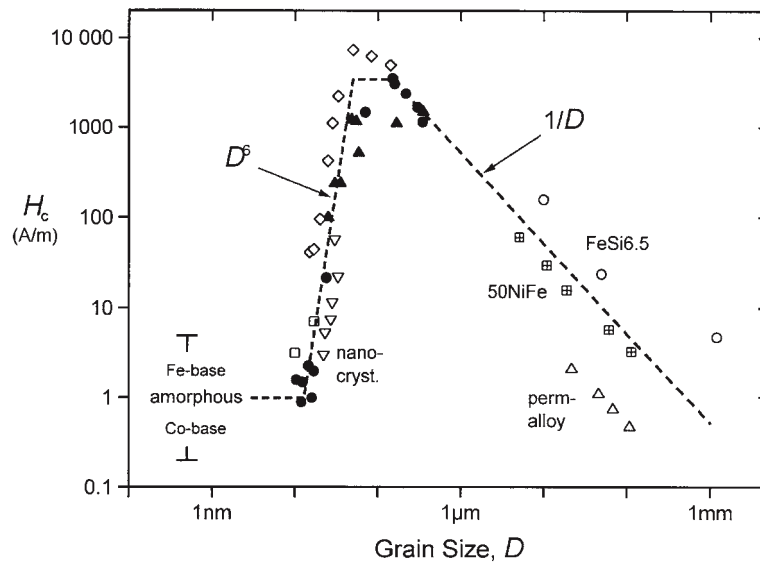
Figure 1
Coercivity, H_c, vs. grain size, D, for various soft magnetic metallic alloys: Fe–Nb–Si–B (▲), Fe–Cu–Nb–Si–B (●), Fe–Cu–V–Si–B (▽), Fe–Zr–B (□), Fe–Co–Zr (◇), NiFe-alloys (⊞ and △) and FeSi6.5 wt% (○).

reduces magnetoelastic anisotropies arising from internal or external mechanical stresses. While magnetocrystalline anisotropy (characterized by a second rank tensor) is randomly averaged out at small structural correlation lengths, magnetostriction (characterized by a fourth rank tensor) is not. Thus, amorphous and nanocrystalline magnetic materials, except from certain compositional ranges, generally exhibit magnetostriction and, accordingly are grouped into magnetostrictive and near-zero magnetostrictive alloys. The latter are of particular interest for application since they reveal highly reproducible and superior soft magnetic properties comparable or even better than those of permalloys. Still, the exchange softening at small structural correlation lengths results in an isotropic magnetostrictive behavior, i.e., it can be described by a single coefficient—the saturation magnetostriction λ_s. As a consequence, zero saturation magnetostriction really results in stress-insensitivity of the magnetic properties, unlike large-grained crystalline systems where an average zero saturation magnetostriction does not generally imply stress-insensitivity of the hysteresis loop.

Fig. 2 gives an example for the typical magnetic properties of near-zero magnetostrictive amorphous, nanocrystalline, and crystalline soft magnetic alloys. The clear advantage of nanocrystalline alloys is that they combine the highest achievable permeabilities (up to $\mu_i \approx 200 \times 10^3$) and the simultaneously highest saturation magnetization of typically $J_s \approx 1.2$–1.3 T. The benefit of amorphous materials is that they allow a much wider range of property variation by alloying.
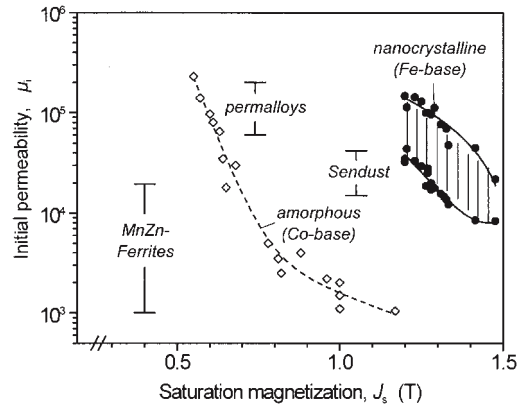
Figure 2
Typical initial permeabilities and saturation magnetization for near-zero magnetostrictive, soft magnetic materials with flat-type hysteresis loop.

Thus, the initial permeability of near-zero magnetostrictive amorphous alloys can be varied continuously by more than two orders of magnitude from about $\mu_i \approx 1 \times 10^3$ up to $\mu_i \approx 300 \times 10^3$.

Due to the absence of an appreciable magnetocrystalline anisotropy both amorphous and nanocrystalline materials are very susceptible to magnetic field annealing which induces a uniaxial anisotropy with an easy axis parallel to the direction of the magnetic field applied during the heat treatment.

17

Indeed, field induced anisotropies have a tremendous practical impact for tailoring the soft magnetic properties according to the demands of various applications. As an example, Fig. 3 shows the hysteresis loop and the impedance permeability for various heat treatments with and without magnetic field. Thus, almost perfect rectangular or flat shaped hysteresis loops can be obtained after annealing in a magnetic field along or transverse to the magnetic path in the application. Conventional annealing without magnetic field typically results in a more round shaped hysteresis loop. Even in this case uniaxial anisotropies are induced although with an angular distribution of directions which is defined by the domain structure during annealing. The induction of a magnetic anisotropy along the axis of the spontaneous magnetization is related to directional atomic pair ordering along this axis, which minimizes spin-orbit coupling energy. The induced anisotropy energy K_u directly controls the soft magnetic properties. Thus, for example, transverse field annealing results in a permeability μ which is constant up to ferromagnetic saturation and inversely proportional to K_u, i.e., $\mu = J_s^2/(2\,\mu_0 K_u)$. For a rectangular loop, for example, low induced anisotropies facilitate domain refinement which results in good dynamic properties like, e.g., reduced anomalous eddy current losses. Moreover, the mechanisms responsible for anisotropy formation also control the thermal aging of the material. Hence, good thermal stability of the magnetic properties requires a possibly high activation energy and slow kinetics of anisotropy formation.

Finally, both amorphous and nanocrystalline alloys generally reveal low losses and a high permeability even at elevated frequencies up to several hundred kilohertz. The favorable high-frequency behavior, comparable to or even better than in Mn–Zn ferrites (see *Ferrites*), is essentially related (i) to the thin ribbon gauge of $d \approx 20\,\mu m$ inherent to the production technique, and (ii) to a relatively high electrical resistivity of typically $\rho \approx 100$–$130\,\mu\Omega$ cm, which both reduce eddy current losses. In particular, low remanence ratio materials show the best dynamic properties due to the homogeneous change of magnetization by rotation, which avoids *anomalous* eddy current losses. Lowest losses are hereby found in near zero-magnetostrictive alloys due to (i) their low coercivity which minimizes the hysteresis losses and (ii) to the absence of magnetoelastic resonances, which in magnetostrictive alloys can produce very significant excess losses.

Figure 3
Typical d.c.-hysteresis loops and 50 Hz permeability after various forms of field annealing. The material shown is nanocrystalline $Fe_{73.5}Cu_1Nb_3Si_{13.5}B_9$ annealed for 1 h at 540 °C without (R) and with a magnetic field applied parallel (Z) and transverse (F2; $K_u \approx 20\,Jm^{-3}$, $\mu \approx 30 \times 10^3$) to the magnetic path. Sample F1 ($K_u \approx 6\,Jm^{-3}$, $\mu \approx 100 \times 10^3$) was first crystallized at 540 °C and subsequently transverse field annealed at 350 °C.

1. Preparation and Alloy Systems

Amorphous materials can be principally synthesized by a variety of techniques such as rapid solidification from the liquid state, mechanical alloying, plasma processing, and vapor deposition. For soft magnetic applications the material is mostly produced by rapid solidification from the melt (Cahn 1993) as thin ribbons usually about 20–30 μm thick and about 1–100 mm wide.

Nanocrystalline soft magnetic alloys, actually, are also cast as an amorphous ribbon which is subsequently annealed above its crystallization temperature to produce the nanocrystalline state. Actually, controlled crystallization from the amorphous state seems to be the only method presently available to synthesize nanocrystalline alloys with attractive soft magnetic properties.

The range of compositions which can be prepared in the glassy state by rapid solidification from the melt is wide. Typical compositions are given by the formula $T_{70-90}X_{10-30}$ (at.%). Here, T stands for a practically arbitrary combination of transition metals

which, for magnetic applications, are of course given by Fe, Co, and Ni. The letter X refers to metalloid atoms like Si and B and/or refractory metals like Nb, Mo, Zr, Hf, etc. These "nonmagnetic" additions are necessary for glass formation and in order to stabilize the amorphous structure.

The most common compositions for soft magnetic applications either in the amorphous or in the nanocrystalline state are metal-metalloid based (Fe,Co, Ni)-(Si,B) alloys with small additions of manganese, niobium, carbon, and, for the nanocrystalline case, copper. This alloy system has a good glass forming ability and is easily accessible by rapid solidification as a thin ribbon in large-scale production.

The final alloy design is largely determined by (i) the desired magnetic properties, (ii) good glass forming ability, (iii) thermal stability, and, for the nanocrystalline alloys (iv), a well-defined crystallization behavior.

2. Amorphous Alloys

The saturation magnetization J_s is the highest in the iron-rich alloys and decreases with increasing nickel and cobalt content. It is generally lower than in crystalline alloys due to the nonmagnetic additions of silicon and boron necessary for glass formation. The J_s maximum observed for crystalline Fe–Co alloys is only weakly developed and shifted to the iron-rich side.

For the iron-rich alloys the saturation magnetostriction λ_s is positive, typically $\lambda_s \approx 20$–40 ppm, while for the cobalt-rich alloys, λ_s is negative, typically $\lambda_s \approx -5$ to -3 ppm (Fig. 4). The decrease of λ_s with

increasing nickel content is correlated to the simultaneous decrease of the saturation magnetization ($|\lambda_s| \propto J_s^2$). Thus, the apparent disappearance of λ_s at high nickel contents (Fig. 4) occurs because the system becomes paramagnetic. A true zero of magnetostriction only occurs on the cobalt-rich side of Co–Fe (Fujimori *et al.* 1976) or Co–Mn (Hilzinger and Kunz 1980) based systems at iron or manganese concentrations of about 3–8 at.% (Fig. 4).

According to their magnetostriction, amorphous materials are commonly divided into two major groups: iron-based and cobalt-based alloys. The iron-based amorphous alloys are based on inexpensive raw materials, have a high saturation magnetization, but their magnetostriction is large which limits their soft magnetic behavior. On the other hand, cobalt-based amorphous alloys with small additions of iron or manganese reveal nearly zero magnetostriction. Accordingly, they can offer a superior soft magnetic behavior, but their saturation magnetization is considerably lower than that of the iron-based materials.

Apart from the metallic components, the magnetic properties are also significantly influenced by the metalloid-contents. Fig. 5 gives an example for near-zero magnetostrictive cobalt-based alloys. For example, a saturation magnetization up to 1.2 T can be achieved in cobalt-based alloys by reducing the metalloid contents below 20 at.%. However, these high J_s alloys are close to the boundary of glass formation and reveal a low crystallization temperature, T_x, which at the same time diminishes the thermal stability of the magnetic properties.

Fig. 6 shows the characteristic features of field-induced anisotropies in amorphous metals which can
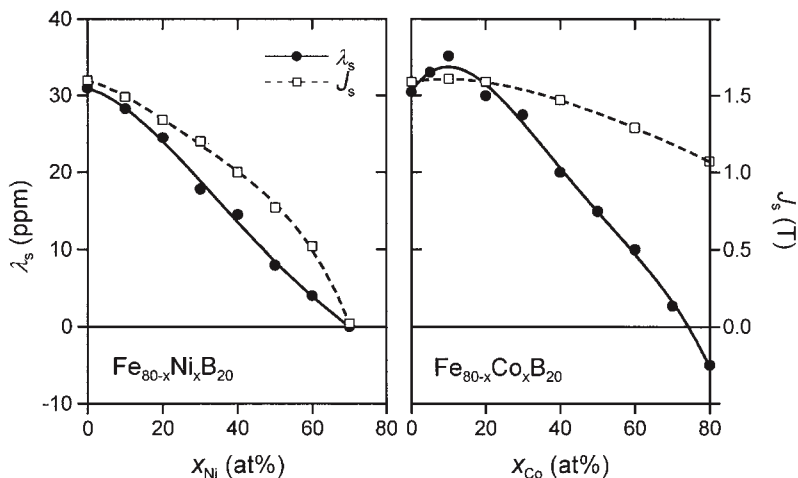
Figure 4
Saturation magnetostriction, λ_s, (——) and saturation magnetization, J_s, (- - -) in amorphous Fe–Ni and Fe–Co-base alloys (after Boll *et al.* 1983 and references cited therein).

be summarized as follows (Fujimori 1983). (i) An anisotropy is only formed by annealing below the Curie temperature T_c, i.e., the driving forces are magnetic interactions. The equilibrium value of K_u achieved after infinite time of annealing approximately scales with the square of the saturation magnetization at the given annealing temperature. (ii) The anisotropy formation is governed by thermal activation. At lower annealing temperatures the kinetics are too slow to reach the equilibrium value, which results in the typical maximum of K_u at a certain annealing temperature. (iii) Alloys with two or more different kinds of magnetic metallic elements show considerably stronger field-induced anisotropies than amorphous alloys with only one transition element.

Principally any level of K_u can be adjusted by appropriate choice of the annealing temperature and time. The annealing conditions which can be realized in practice, however, only allow a K_u variation of about a factor 3–5 around the maximum in the K_u vs. T_a curve in Fig. 6. The latter is determined by the alloy composition. Accordingly, low values of K_u, i.e., high permeabilities, are only achievable in alloys with preferably only one magnetic transition metal and a possibly low Curie temperature, which at the same time means a low saturation magnetization (Fig. 5). Thus, highest permeabilities of $\mu_i > 100 \times 10^3$ can only be obtained in cobalt-base alloys with $J_s < 0.6\,T$ and $T_c < 250\,°C$ and an accordingly high metalloid content.

The spectrum of amorphous alloys used in application is wide and ranges from inexpensive iron-base or Fe–Ni-base alloys over Fe–Co–Ni-alloys to the extremely soft magnetic near-zero magnetostrictive cobalt-base alloys. Accordingly wide is the spectrum of magnetic properties. Permeability, for example, can be adjusted from less than one thousand to several hundred thousand with the help of induced anisotropies and proper alloy design.

3. Nanocrystalline Alloys

The first example of soft magnetic behavior in the nanocrystalline state was given by O'Handley *et al.* (1985) for a devitrified glassy *cobalt* base alloy. However, the soft magnetic properties were inferior to the

Figure 5
Saturation magnetization, J_s, Curie temperature, T_c, and crystallization temperature, T_x, of near-zero magnetostrictive Co-base alloys vs. the total metalloid contents.
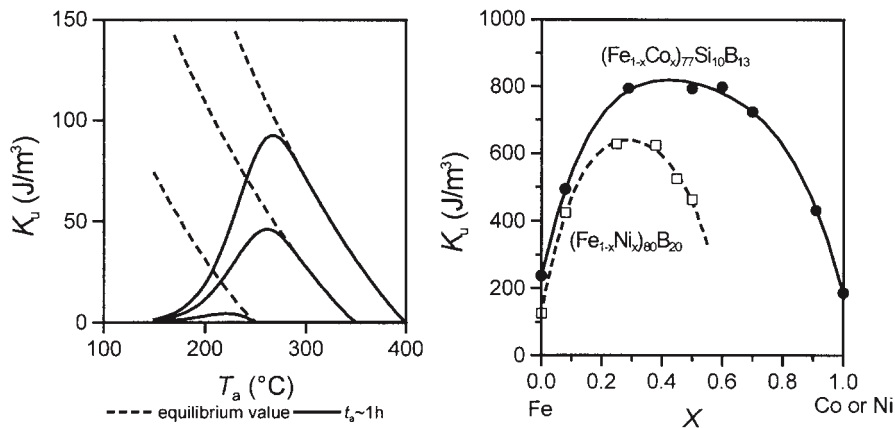
Figure 6
Dependence of the field induced anisotropy, K_u, in amorphous alloys on the annealing temperature, T_a, and the composition. The K_u vs. T_a curves on the left are a sketch of the typical behavior in near-zero magnetostrictive Co-base alloys with different Curie temperatures. The figure on the right shows the equilibrium K_u of Fe–Ni-base and Fe–Co-base alloys annealed at 225 °C and 300 °C, respectively (after Fujimori 1983).

amorphous state and, thus, not very attractive, which actually seems to be typical for cobalt-based nanocrystalline materials. Indeed, the most promising properties so far have been found in iron-based alloys. This is related to the fact that the magnetostriction in iron-based alloys can be virtually reduced to zero by nanocrystallization. Another aspect of iron-based nanocrystalline materials is the low raw material costs of iron, which ultimately makes this system highly attractive for application.

The crystallization of conventional metallic glasses optimized for soft magnetic applications usually yields a relatively coarse grained microstructure of several crystalline phases with grain sizes of about 0.1–1 μm and, correspondingly, deteriorates the soft magnetic properties. A typical nanocrystalline structure with good soft magnetic properties occurs only if the amorphous state is crystallized by the primary crystallization of b.c.c. iron, before intermetallic phases like Fe–B compounds may be formed. Both an extremely high nucleation rate and slow growth of the crystalline precipitates are needed to obtain a nanoscaled microstructure. Such crystallization characteristics seem to be rather the exception than the rule and can be obtained only with a particular alloy design.

The optimum alloy composition originally proposed (Yoshizawa *et al.* 1988) and subsequently not much changed is $Fe_{73.5}Cu_1Nb_3Si_{13.5}B_9$ (at.%) and can be considered as a typical Fe–Si–B metallic glass composition with small additions of copper and niobium (or other group IV to VI elements). The combined addition of copper and niobium is essentially responsible for the formation of the particular nanocrystalline structure: copper enhances the nucleation of the b.c.c. grains while niobium impedes grain coarsening and, at the same time, inhibits the formation of boride compounds.

The nanocrystalline state is achieved by annealing above the first crystallization temperature, typically for 1 h at temperatures between about 500 and 600 °C which leads to primary crystallization of b.c.c. iron. The resulting microstructure is characterized by randomly oriented, ultrafine grains of b.c.c. Fe–Si 20 at.% with typical grain sizes of 10–12 nm embedded in a residual amorphous matrix which occupies about 20–30% of the volume and separates the crystallites at a distance of about 1–2 nm. These features are the basis for the excellent soft magnetic properties indicated by the high values of the initial permeability of about 10^5 and correspondingly low coercivities of less than $1\,Am^{-1}$. The magnetic properties and the underlying microstructure are rather insensitive to the precise annealing conditions within a wide range of annealing temperatures, T_a, of about $\Delta T_a \approx 50$–$100\,°C$. They develop in a relatively short period of time (about 10–15 min) and do not much alter even after prolonged heat treatment of several hours. Only annealing at more elevated temperatures above

600 °C leads to the precipitation of small fractions of boride compounds like Fe_2B or Fe_3B with typical dimensions of 50–100 nm, while the ultrafine grain structure of b.c.c. Fe–Si still persists. Further increase of the annealing temperature above 700 °C, finally yields grain coarsening. Both the formation of Fe-borides and grain coarsening deteriorates the soft magnetic properties significantly (Herzer 1997).

The small grain size in $Fe_{73.5}Cu_1Nb_3Si_{13.5}B_9$ or similar alloy compositions is decisive for its soft magnetic behavior, but is only a prerequisite. The actual highlight of the nanocrystalline iron-base alloys is that the phases formed on crystallization simultaneously can lead to low or vanishing saturation magnetostriction, λ_s. Fig. 7 summarizes the
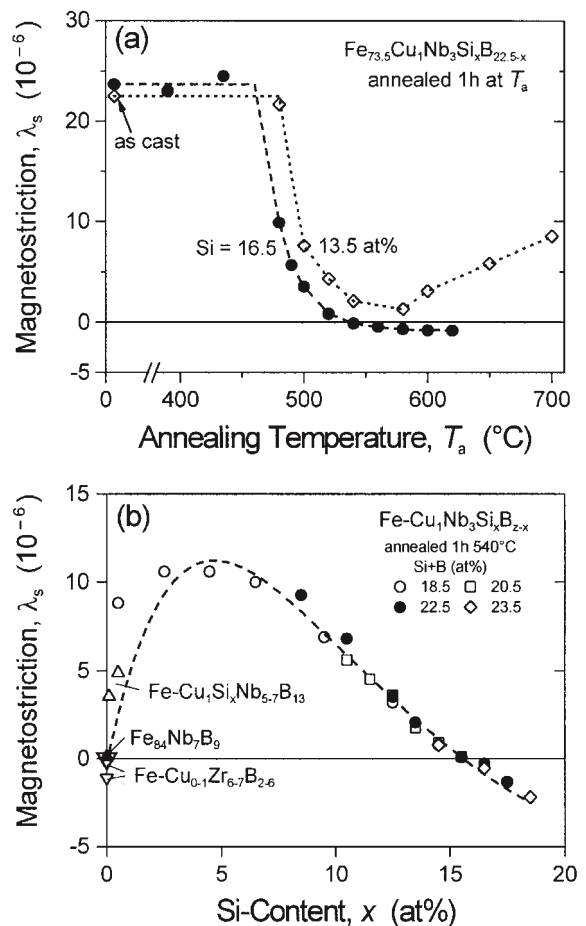
Figure 7
Saturation magnetostriction, λ_s, of Fe–Cu–Nb–Si–B alloys: (a) influence of the annealing temperature, T_a, and (b) influence of the Si-content in the nanocrystalline state. The figure includes the data for Fe–Nb–B (▲) and Fe–(Cu)–Zr–B alloys (▽) from Suzuki *et al.* (1991).

situation in the Fe–Cu–Nb–Si–B system. It is the decrease of λ_s that is ultimately responsible for the simultaneous increase of the initial permeability upon nanocrystallization. Otherwise, the soft magnetic properties would be only comparable to that of stress-relieved amorphous iron-based alloys.

While λ_s is high and fairly independent of the composition in the amorphous state it depends sensitively on the silicon content in the nanocrystalline state. Zeros of magnetostriction are realized at low silicon concentrations in Fe–Zr–B alloys (Suzuki *et al.* 1991) and at high silicon concentrations around 16 at.% in the Fe–Cu–Nb–Si–B system. The detailed behavior of λ_s can be understood from the balance of magnetostriction among the structural phases present in the nanocrystalline state (see *Nanocrystalline Materials: Magnetism*, Herzer 1997).

A major driving force in the search for further alloy compositions was to increase the saturation magnetization towards the value of pure α-iron while maintaining near-zero magnetostriction. The major hindrance towards such high iron content alloys results from the requirement of a good glass forming ability. Thus, for the sake of a good glass forming ability, the silicon content in the Fe–Cu–Nb–Si–B alloys cannot be simply reduced without substituting other glass formers for it. A relatively low boron content is a further requirement in order to inhibit the formation of Fe–B compounds, which would degrade the soft magnetic properties (Herzer 1997).

Ultimately, the only way to reduce the silicon content is to add refractory metals with large atoms and low *d*-electron concentrations, i.e., particularly zirconium, hafnium, niobium, and tantalum.

In this way the second family of near-zero magnetostrictive, nanocrystalline alloys has been established which is based on $Fe_{\sim 84-91}(Cu_1)–(Zr,Nb)_{\sim 7}B_{2-9}$ and exhibits a very high saturation magnetization up to 1.7 T (Suzuki *et al.* 1991). Although the outstanding soft magnetic properties of the original Fe–Cu–Nb–Si–B alloys could not be reached up to now, the soft magnetic properties are better than those of amorphous iron-base alloys or comparable to those of crystalline 50–60% Ni–Fe but combined with low magnetostriction and lower losses. These alloys and derivatives are currently still under intensive research. Their major drawback is a lower glass forming ability and/or castability due to the oxygen reactivity of the zirconium addition. Thus, these alloys presently are still restricted to the laboratory scale, since they require a far more sophisticated production technology than the more conventional Fe–Si–B compositions.

It should be finally mentioned that the spectrum of accessible nanocrystalline systems can still be considerably expanded by thin film sputtering techniques. One example is hafnium carbide dispersed nanocrystalline Fe–Hf–C films crystallized from the amorphous state (Hasegawa *et al.* 1993). They combine good

thermal stability, good high frequency properties in the megahertz range with low magnetostriction and high saturation induction of $J_s = 1.7$ T which can be even increased up to 2.0 T by multilayering these films with iron. Another example is (Fe,Co,Ni)–(Si,B)–(F,O,N) granular alloy films (Fujimori 1995) which at a saturation induction of about 1 T possess a uniquely high electrical resistivity of 10^3–10^4 μΩcm.

Similar to amorphous alloys, the final adjustment of the soft magnetic properties is achieved with uniaxial anisotropies induced by magnetic field annealing. The principal features of anisotropy formation in nanocrystalline alloys are summarized in Fig. 8.

If the material is nanocrystallized first without applied field and subsequently field annealed at lower temperatures, the resulting anisotropy K_u depends on the annealing temperature, T_a, and time, t_a, and behaves similar to the amorphous case. However, the kinetics are considerably slower (Yoshizawa and
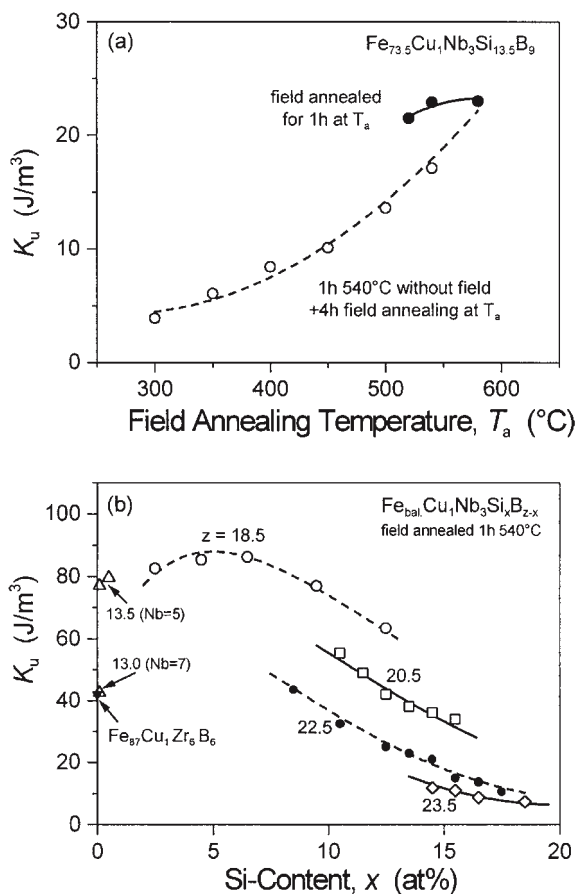
Figure 8
Field induced anisotropy, K_u, in nanocrystalline Fe–Cu–Nb–Si–B alloys as a function of (a) the annealing conditions and (b) the composition.

Yamauchi 1990) which shifts the maximum of the K_u vs. T_a curve to considerably higher annealing temperatures. This circumstance allows to tailor lowest induced anisotropies, i.e., highest permeabilities but with a significantly better thermal stability than in amorphous alloys, or even in permalloys.

If the field annealing is performed during nanocrystallization, the induced anisotropy reaches a maximum value which is relatively insensitive to the precise annealing conditions and, thus, corresponds to the equilibrium value characteristic for the alloy composition.

The Curie temperature of the b.c.c. grains ranges from about $T_c = 600$–$750\,°C$ (depending on composition) and is considerably higher than the T_c of the amorphous matrix (200–$400\,°C$). Thus, the anisotropy induced by a magnetic field applied during nanocrystallization at $540\,°C$ primarily originates from the b.c.c. grains (Herzer 1994). Accordingly, the induced anisotropy in nanocrystalline Fe–Cu–Nb–Si–B alloys is mainly determined by the silicon content and the fraction, v_{cr}, of the b.c.c. grains.

A more detailed analysis (Herzer 1994) shows that the dependence of K_u/v_{cr} on the silicon content in the b.c.c. grains is comparable with that observed for conventional α-FeSi single crystals where the formation of the field induced anisotropy has been proposed to arise from the directional ordering of silicon atom pairs. The decrease of K_u with increasing silicon content, in terms of (Néel's 1954) theory, can be related to the formation of a DO_3 superlattice structure for silicon concentrations above about $10\,at.\%$: for completely ordered Fe_3Si, the lattice sites for the iron and silicon atoms are entirely determined by chemical interactions, allowing no degree of freedom for an orientational order. However, for a composition $Fe_{1-y}Si_y$ with less than $25\,at.\%$ Si a complete DO_3 order cannot be reached and iron atoms will occupy the vacant sites in the silicon sublattice. The way the latter is done provides the necessary degrees of freedom for an orientational order.

The low K_u-level due to the superlattice structure at higher silicon contents is an additional key factor for the high initial permeabilities which can be achieved in these alloys despite their high Curie temperature and their high saturation induction.

In contrast to amorphous alloys the spectrum of nanocrystalline alloys presently used in soft magnetic application is relatively narrow and essentially limited to the low magnetostrictive compositions around $Fe_{bal}Cu_1Nb_3Si_{13-16}B_{6-9}$ with a saturation magnetization of 1.2–$1.3\,T$. The initial permeability in these alloys can be adjusted in a range between $\mu_i \approx 20 \times 10^3$ and $\mu_i \approx 200 \times 10^3$ by magnetic field annealing.

4. Conclusions

In summary, the best static and dynamic soft magnetic properties are presently achieved as well in amorphous cobalt-base as in nanocrystalline iron-base alloys. Both alloy systems reveal isotropic near-zero magnetostriction. Apart from its higher saturation induction, however, the nanocrystalline material shows a much better thermal stability of its magnetic properties than its amorphous counterpart and, additionally, is based on the inexpensive raw materials iron and silicon. Accordingly, nanocrystalline alloys provide an invaluable supplement to the existing soft magnetic materials manifested in a steadily increasing number of applications. Yet, the variability of their soft magnetic properties, as well as their form of delivery so far, is still restricted compared to amorphous or other soft magnetic materials. Thus, amorphous alloys may reveal good soft magnetic properties already in the as quenched state or after moderate annealing. They can be delivered as a semi-finished, ductile product useful for, e.g., flexible magnetic screening or for sensor applications, most noticeably in electronic article surveillance. Accordingly, the major drawback of the nanocrystalline materials is the severe embrittlement upon crystallization, which requires final shape annealing and restricts their application mainly to toroidally wound cores. Yet, the situation is similar for highly permeable amorphous alloys due to the necessary stress relief treatment, which also causes embrittlement.

See also: Magnetoelasticity in Nanoscale Heterogeous Materials; Magnets, Soft and Hard: Domains; Magnetic Materials: Domestic Applications

Bibliography

Boll R, Hilzinger H R, Warlimont H 1983 Magnetic material properties and applications of metallic glasses. In: Hasegawa R (ed.) *The Magnetic, Chemical and Structural Properties of Glassy Metallic Alloys*. CRC Press, Boca Raton, FL, pp. 183–201

Cahn R W 1993 Background to rapid solidification processing. In: Liebermann H H (ed.) *Rapidly Solidified Alloys*. Dekker, New York, pp. 1–15

Fujimori H 1983 Magnetic anisotropy. In: Luborsky F E (ed.) *Amorphous Metallic Alloys*. Butterworths, London, pp. 300–16 and references therein

Fujimori H 1995 Structure and 100 MHz soft magnetic properties in multilayers and granular thin films. *Scr. Metall. Mater.* **33**, 1625–36

Fujimori H, Kikuchi M, Obi Y, Masumoto T 1976 New Co–Fe amorphous alloys as soft magnetic materials. *Sci. Rep. Res. Inst. Tohoku Univ. Ser. A.* **26**, 36

Hasegawa N, Saito M, Kataoka N, Fujimori H 1993 Soft magnetic properties of carbide-dispersed nanocrystalline films with high thermal stability. *J. Mater. Eng. Perform.* **2**, 181–92

Herzer G 1990 Grain size dependence of coercivity and permeability in nanocrystalline ferromagnets. *IEEE Trans. Magn.* **26**, 1397–402

Herzer G 1994 Magnetic field induced anisotropies in nanocrystalline Fe–Cu–Nb–Si–B alloys. *Mater. Sci. Eng.* **A181–2**, 876–9

Herzer G 1997 Nanocrystalline soft magnetic alloys. In: Buschow K H J (ed.) *Handbook of Magnetic Materials*. Elsevier, Amsterdam, Vol. 10, Chap. 3, pp. 462–75

Hilzinger H R, Kunz W 1980 Magnetic properties of amorphous alloys with low magnetostriction. *J. Magn. Magn. Mater*. **15**, 1357–8

Néel L 1954 Anisotropie magnétique superficielle et substructures d'orientation. *J. Phys. Radium*. **15**, 225–39

O'Handley R C 1987 Physics of ferromagnetic amorphous alloys. *J. Appl. Phys*. **62**, R15–59

O'Handley R C, Megusar J, Sun S-W Hara, Grant Y 1985 Magnetization process in devitrified glassy alloy. *J. Appl. Phys*. **57**, 3563–5

Pfeifer F, Radeloff C 1980 Soft magnetic Ni–Fe and Co–Fe alloys—some physical and metallurgical aspects. *J. Magn. Magn. Mater*. **19**, 190–207

Suzuki K, Makino A, Kataoka N, Inoue A, Masumoto T 1991 Soft magnetic properties of nanocrystalline bcc Fe–Zr–B and Fe–M–B–Cu alloys with high saturation. *J. Appl. Phys*. **70**, 6232–7

Yoshizawa Y, Oguma S, Yamauchi K 1988 New Fe-based soft magnetic alloys composed of ultrafine grain structure. *J. Appl. Phys*. **64**, 6047–9

Yoshizawa Y, Yamauchi K 1990 Induced magnetic anisotropy and thickness dependence of magnetic properties in nanocrystalline alloy "Finemet." *IEEE Trans. Magn*. **5**, 1070–6

G. Herzer
Vacuumschmelze GmbH, Hanau, Germany

Amorphous Intermetallic Alloys: Resistivity

Many intermetallic alloys can be prepared in a glassy or amorphous state simply by quenching rapidly from the melt at rates of the order of $10^6 \, \mathrm{K s}^{-1}$ using, amongst other techniques, melt spinning and splat quenching to produce bulk samples, or sputtering, evaporation, and electrodeposition to produce thin films. The resulting material is rich in unusual and often unique phenomena and for the last 30 years of the twentieth century amorphous alloys were the focus of extensive experimental and theoretical interest, particularly in the investigation of the effects of extreme atomic disorder on conductivity, electron localization, magnetic order, spin fluctuations, and even superconductivity. In this context the anomalous resistivity of amorphous alloys has, perhaps, received the most attention and, although the resistivity is not fully understood, it reveals a fascinating and complex interplay of structural scattering processes and quantum corrections arising principally from weak localization and electron–electron interactions. In this section the general features of the temperature dependence of the resistivity of amorphous intermetallic alloys will be briefly reviewed, and the major contributions to the resistivity introduced.

1. Resistivity, Order, and Disorder

According to Bloch theory, an electron in a perfect periodic potential experiences no collisions, and therefore no resistance. The familiar features of the temperature-dependent resistivity of structurally ordered metals and alloys are therefore a consequence of modest deviations from the underlying translational and orientational periodicity of a perfect crystalline lattice. On the one hand static defects, such as impurities, vacancies, or dislocations, act as localized scattering centers, contributing to an essentially temperature-independent residual resistivity, ρ_o. On the other hand, thermal vibrations result in dynamic displacements of the atoms from their equilibrium positions thereby perturbing the lattice periodicity and contributing a temperature-dependent term, $\rho_L(T)$, to the resistivity. The latter term, generally known as the ideal or lattice resistivity, is well described by the Gruneisen formula (see, e.g., Ziman 1972)

$$\rho(T) = 4A \left(\frac{T}{\theta_D} \right)^5 \int_0^{\theta_D/T} \frac{e^x x^5}{(e^x - 1)^2} \, \mathrm{d}x \qquad (1)$$

where θ_D is the Debye temperature.

Because ρ_o and $\rho_L(T)$ result from entirely independent scattering processes they can be linearly combined, through Mattheissen's rule, to give a total resistivity of

$$\rho(T) = \rho_o + \rho_L(T) \qquad (2)$$

For most crystalline metals and alloys $\rho_L(T)$ is generally the dominant contribution and consequently Eqn. (2) predicts a resistivity, which tends to ρ_o at the lowest temperatures, but varies as T^5 below θ_D and increases linearly with T at and above θ_D.

For rapidly quenched amorphous intermetallic alloys, however, the deviations from perfect periodicity arising from static topological disorder are extreme. Although the near neighbor distances between constituent atoms in an amorphous alloy may vary randomly by only a few percent about those of their crystalline counterparts, and local atomic coordinations and configurations may remain closely similar to the corresponding crystalline phases (Fig. 1), any translational symmetry of the lattice is entirely lost (Elliot 1983).

It might be expected that such pronounced topological disorder would lead to a considerably enhanced residual resistivity. Indeed, the measured resistivities of amorphous metals and alloys are much greater than those of ordered crystalline phases of similar composition, but additionally the experimentally determined temperature dependence of the resistivity is observed to be highly anomalous. Marked deviations from the simple form of Mattheissen's rule, given by Eqn. (2), are found in which the temperature coefficient of resistivity, $\alpha \, (= \rho^{-1}(\partial\rho/\partial T))$, is
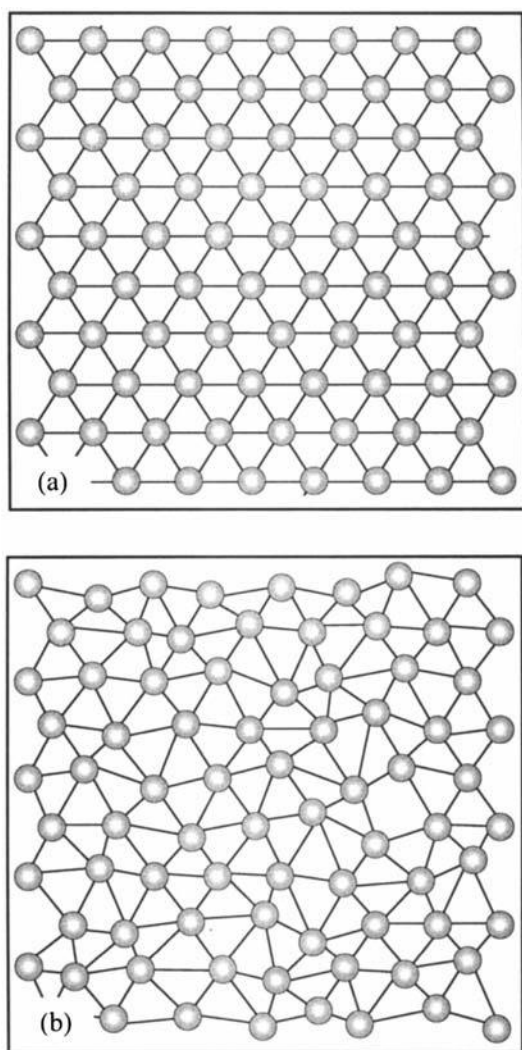
Figure 1
A schematic representation of (a) a crystalline lattice and (b) the corresponding amorphous lattice formed by applying small random deviations to the atomic bond lengths. Note that in (b) translational symmetry is lost, although a vestige of orientational symmetry remains.

Figure 2
The Mooij correlation showing the variation of the temperature coefficient of resistivity with the magnitude of the resistivity for several amorphous alloys (▼), thin films (●), and bulk alloys (▲). The inset provides a schematic illustration of the temperature dependence of the resistivity of amorphous compounds corresponding to the Mooij correlation (after Cote and Meisel 1981).

generally very small ($\sim 10^{-4}\,\text{K}^{-1}$) and can be either positive or negative (Mooij 1973).

2. The Mooij Correlation

Mooij (1973) was the first to note an approximate but striking "universal" correlation between the anomalous temperature coefficient, α, and the magnitude, ρ, of the resistivity for amorphous metallic alloys. Experimental resistivity data collected over a wide range of transition metal-based amorphous alloys revealed that the sign of α changes from positive to negative as the room-temperature resistivity exceeds a threshold magnitude of approximately $150\,\mu\Omega\text{cm}$. Moreover, for both positive and negative α, the resistivity is always found to approach to a similar limiting value of $150\,\mu\Omega\text{cm}$ at high temperatures. A schematic representation of the Mooij correlation is given in Fig. 2.

The limiting or threshold value for the resistivity is close to that expected when the effective mean free path of the conduction electrons approaches a length scale comparable to the mean interatomic near neighbor distance ($0.3\text{–}0.5\,\text{nm}$). This implies that the Mooij correlation should be quite generally applicable to materials with short mean free paths. Extensive surveys of amorphous intermetallic alloys do indeed show the Mooij correlation to be effectively independent of either atomic or electronic structure, and this correlation is even followed by many highly resistive disordered *crystalline* alloys.

3. The Faber–Ziman Theory

Despite the apparent insensitivity of the Mooij correlation to the underlying atomic structure, many

theoretical treatments of the resistivity of amorphous alloys have focused entirely upon this underlying structure (Cote and Meisel 1981).

The absence of translational symmetry in amorphous alloys necessitates a probabilistic description of the atomic positions in terms of a radially averaged distribution function dominated by short-range atomic correlations. Such radial distributions are very similar to those used to describe the structure of liquids. Consequently a particularly useful starting point for theory has been the generalized Faber–Ziman model based upon modifications to the Ziman diffraction theory of conductivity in *liquid* metals and alloys (Cusak 1987).

The Faber–Ziman theory is a nearly free electron approach. It treats the conduction electrons as plane waves with a wave vector k_F, corresponding to the Fermi momentum, which are coherently diffracted by the amorphous structure. Within this formalism the resistivity, ρ is given by

$$\rho = \frac{12\pi\Omega}{e^2\hbar v_F^2} \int_0^1 S^\rho(k)|t(k)|^2 \left[\frac{k}{2k_F}\right]^{3d} \left[\frac{k}{2k_F}\right] \mathrm{d}k \qquad (3)$$

where Ω is the atomic volume, v_F the Fermi velocity and $|t(k)|$ the scattering matrix element or t-matrix. In Eqn. (3), the resistivity static structure factor $S^\rho(k)$ is approximately related to the equilibrium structure factor $S(k)$, as measured directly in conventional neutron or x-ray structural studies, through

$$S^\rho(k) \approx 1 + [S(k) - 1]e^{-2W(k,T)} \qquad (4)$$

where the Debye–Waller factor, $e^{-2W(k,T)}$, introduces the important effects of thermal vibrations (Rao 1983).

The structure factor, $S(k)$, takes the typical form shown schematically in Fig. 3. Of particular significance is the extremely large first peak in $S(k)$ at $k = k_p$. There is considerable evidence that for most amorphous alloys $2k_F$ lies close to k_p, generally within the range $0.9 < 2k_F/k_p < 1.1$. This situation leads directly to back scattering of conduction electrons, a process that correspondingly dominates the integral in Eqn. (3) and leads to the characteristic high resistivity.

Within the diffraction theory the Mooij correlation is thus a consequence of the relative position of $2k_F$ with respect to k_p. Compositional effects are related to $2k_F$ moving through k_p as the concentration of the alloy is changed, whilst Eqn. (4) shows that the negative α observed at high values of resistivity is associated with the back scattering condition $2k_F \approx k_p$, and is a direct reflection of the reduction in scattering due to the temperature dependence of the Debye–Waller factor for situations where $S(k = 2k_F) > 1$.

More precisely, the Faber–Ziman diffraction theory predicts a T^2 increase in resistivity at low
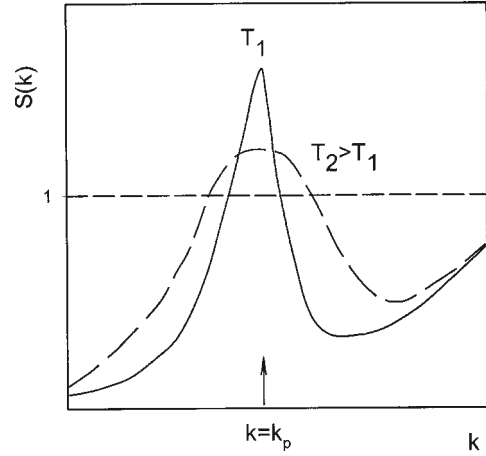
Figure 3
A schematic representation of the equilibrium structure factor, $S(k)$ at low (T_1) and high (T_2) temperatures.

temperatures ($T < \theta_D/2$) and a positive or negative linear dependence with T at higher temperatures ($T > \theta_D/2$), according to the proximity of $2k_F$ to k_p. Correspondingly, a shallow maximum is predicted in the resistivity of those alloys at the crossover from positive to negative α (Rao 1983).

These predictions are certainly in broad agreement with experimental measurements and provide a simple qualitative explanation for the general features of the temperature dependence of the resistivity and also for the Mooij correlation (Fig. 4). A more quantitative agreement can be achieved when additional modifications, such as a limitation of the effectiveness of the electron–phonon interaction with decreasing electron mean free path, are introduced (Cote and Meisel 1981). However, even with such modifications the diffraction theory does seem better suited to those alloys with lower resistivity for which α is positive rather than negative.

As the particular characteristics of the atomic structure of amorphous materials lies at the heart of the Faber–Ziman approach, the diffraction theory unfortunately provides little insight into the generalization of the Mooij correlation beyond amorphous alloys to disordered crystalline materials. This issue was elucidated to some extent by a simple but elegant approach suggested by Markowitz (1977) in which the temperature-dependent Debye–Waller factor is introduced multiplicatively in Mattheissen's rule, i.e.,

$$\rho(T) = [\rho_o + \rho_L(T)]e^{-2W(k,T)} \qquad (5)$$

to account for higher order phonon processes. This correction is entirely negligible for the general case of $\rho_o \ll \rho_L(T)$ but becomes increasingly important for
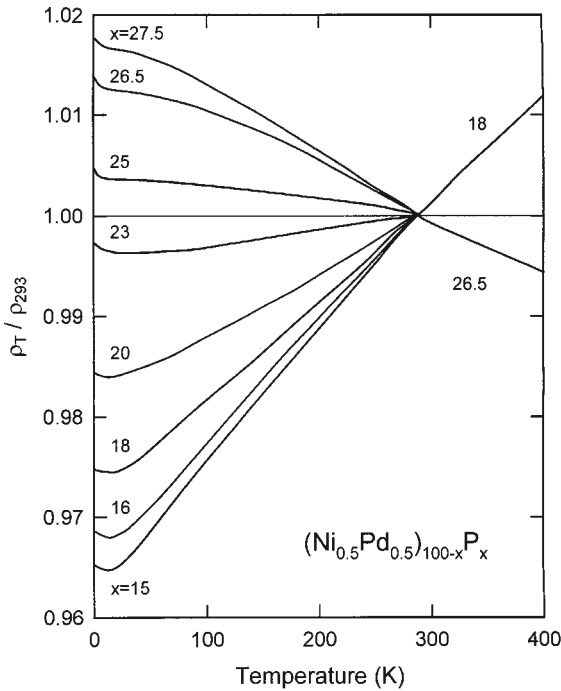
Figure 4
Temperature dependence of the resistivity (normalized to the value at $T = 293\,\text{K}$) of the amorphous alloy series $(Ni_{0.5}Pd_{0.5})_{100-x}P_x$. Note the crossover from $\alpha > 0$ to $\alpha < 0$ with increasing x, and also the occurrence of a low-temperature logarithmic term at all concentrations (after Harris and Strom-Olsen 1983).

Figure 5
Relative low-temperature resistivity as a function of $T^{1/2}$ for ($\blacktriangledown$) $Y_{77.5}Al_{22.5}$, ($\blacktriangle$) $Fe_{40}Ni_{40}(P, B)_{20}$, ($\diamond$) $Cu_{60}Zr_{40}$, ($\bigcirc$) $Fe_{79}Cr_1B_{20}$, ($\bullet$) $Pd_{82}Cr_{18}$ (after Cusak 1987).

$\rho_o \gg \rho_L(T)$ causing the sign of α to change from positive to negative, in line with the Mooij correlation.

A more severe limitation of the Faber–Ziman approach is the inability of the diffraction theory to account for an "additional" prominent feature observed in the low-temperature ($T < 50\,\text{K}$) resistivity of many amorphous metals (Fig. 4). This feature, which can be loosely characterized as a logarithmic increase in the resistivity towards low temperatures, is seemingly uncorrelated with the sign of α (although there are very few examples of materials with positive α for which no logarithmic term is observed) (Harris and Strom-Olsen 1983).

The apparent $-\ln(T)$ dependence of the low-temperature resistivity, which leads to a distinctive minimum for those alloys with positive α, has provoked comparisons with Kondo processes observed in crystalline alloys. However, unlike the conventional Kondo effect, the $-\ln(T)$ term observed for the amorphous alloys is entirely insensitive to the presence of either spin glass or ferromagnetic order.

The $-\ln(T)$ description of the low-temperature resistivity is only approximate and the heuristic form,

$-\ln(T^2 + \Delta^2)$, with $\Delta \sim 1\,\text{K}$, often provides a better description. It has been widely suggested that this term is not magnetic in origin, but is instead a structural analogue of the Kondo effect. This model assumes that the liquid-like structure of the amorphous state provides internal degrees of freedom allowing atoms to tunnel between two local equilibrium positions (Harris and Strom-Olsen 1983). However it is not clear that such two-level scattering processes are sufficiently effective to produce contributions of the magnitude observed experimentally.

Some authors have argued convincingly that the low-temperature logarithmic term is better described as a $T^{1/2}$ term, as illustrated in Fig. 5. This will be discussed in the next subsection.

4. Quantum Corrections: Localization and Interaction Effects

The theoretical models discussed so far have all been based upon conventional "Boltzmann" transport theory, a weak-scattering approximation in which the nearly free electrons are considered to follow classical trajectories between scattering events (see *Boltzmann Equation and Scattering Mechanisms*). Unfortunately, such assumptions are of questionable validity for topologically disordered amorphous alloys in general and for the highly resistive alloys with negative α in particular.

In the strong scattering regime, where the electron mean free path is comparable to the interatomic spacing, it becomes necessary to consider quantum corrections to the conductivity, and in some cases

27

these corrections can dominate the temperature dependence of the resistivity.

Mechanisms of electron localization resulting from a high degree of structural disorder have been extensively discussed in the literature (Howson and Gallagher 1988, Dugdale 1987). In addition to the possibility of weak incipient localization of electron states, the weak localization that arises from a quantum interference effect known as "$2k_F$-scattering" is of particular relevance to amorphous alloys. This phenomenon is associated with a diffusing conduction electron returning to its primary scattering point, after a series of intermediate elastic scattering collisions with nearby ions, with a probability that is significantly enhanced due to the phase coherence between scattered partial waves. The higher than classical probability of the electron being found at its starting point is interpreted as a tendency towards localization. These quantum considerations increase the probability of back- (hence "$2k_F$"-) scattering, a process that has already been shown to be significant in amorphous alloys.

This quantum interference mechanism is particularly sensitive to any factor that is effective in suppressing the coherent summation of the amplitudes of the scattered partial waves. So, for example, inelastic electron–phonon scattering, spin-orbit effects, or external magnetic fields can inhibit localization by changing the phase of the electron wave function on its closed path.

An appropriately corrected form of the Boltzmann conductivity, $\sigma_B = e^2 k_F^2 l_e / 3\pi^2 \hbar$, is therefore

$$\sigma = \sigma_B \left[1 - \frac{3}{(k_F l_e)^2} \left(1 - \frac{l_e}{L} \right) \right] \qquad (6)$$

where l_e is the elastic mean free path, and L is the inelastic diffusion length (related to the inelastic mean free path, l_i, through $L^2 = l_i l_e / 2$) or the cyclotron radius, $(c\hbar/2eH)^{1/2}$, in a magnetic field H, whichever is the shorter (Howson and Gallagher 1988).

Using a scaling approach to localization, and with some simplifications, it is found that the correction to the Boltzmann conductivity arising from the temperature dependence of the mean free path for inelastic scattering, i.e., $\Delta\sigma_{wl} = e^2/3\pi^2 \hbar L(T)$, takes the form

$$\Delta\sigma_{wl} \propto T \qquad \text{for } T < \theta_D/3$$

$$\Delta\sigma_{wl} \propto T^{1/2} \qquad \text{for } T > \theta_D/3.$$

The quantum interference effects leading to weak localization do not include electron–electron interactions. However localization processes can significantly enhance the effective Coulombic electron–electron interaction causing a gap, or at least a minimum, to form in the density of states at the Fermi energy and leading to a further correction to

the Boltzmann conductivity of

$$\Delta\sigma_{ee} \propto T^{1/2}$$

This electron–electron interaction correction term is significant only at low temperatures below a limit (typically 15–20 K) determined by the electron diffusion coefficient, the dynamic screening of the Coulomb interaction and the temperature-dependent mean free path for inelastic scattering, $l_i(T)$. It is this contribution that has been identified with the Kondo-like $-\ln(T)$ term in the resistivity discussed in the previous section (Howson and Gallagher 1988), and shown in Fig. 5.

The unmodified Boltzmann conductivity is here associated with the Faber–Ziman weak scattering model that predicts either a positive or negative thermal coefficient of resistivity, α. However, each of the quantum corrections to the conductivity increases with temperature and therefore contributes a negative α. Moreover, in the strong scattering regime, for which $l_e \ll l_i$, the temperature dependence of the resistivity will be entirely dominated by the quantum "corrections," thereby reinforcing the Mooij correlation for the highly resistive amorphous alloys. It should also be emphasized that the quantum corrections discussed above are not based upon considerations of the structure of amorphous alloys and are thus equally valid for disordered *crystalline* alloys, providing that the appropriate conditions for weak localization are met.

The low-temperature $T^{1/2}$ behavior has already been encountered in Fig. 5, whereas a typical progression from the $T^{1/2}$-, through a T-, then back to a $T^{1/2}$-dependence of the correction to the Boltzmann conductivity with increasing temperature can be clearly seen in Fig. 6 where the data for several amorphous $(Ni_{0.5}Zr_{0.5})_{1-x}Al_x$ alloys is shown (Nath and Majumdar 1997).

It therefore appears that the quantum corrections can account for all the principal features in the conductivity of the highly resistive amorphous alloys, at least up to θ_D. Beyond this it is likely that other processes, such as phonon assisted tunneling, thermal expansion effects, and thermal smearing of the Fermi function will become increasingly significant.

Finally, a particular shortcoming of the Faber–Ziman diffraction model has been is its inability to explain satisfactorily the magnitude of the magnetoresistivity observed for many amorphous alloys. A fractional magnetoresistance of the order of 10^{-4} at 1 T is often measured at low temperatures, even for those alloys which contain no magnetic constituents. This is some four orders of magnitude greater than the effect calculated using nearly free electron models. However, both the weak localization and electron–electron interaction models predict magnetoresistivities of this order (Howson and Gallagher 1988).
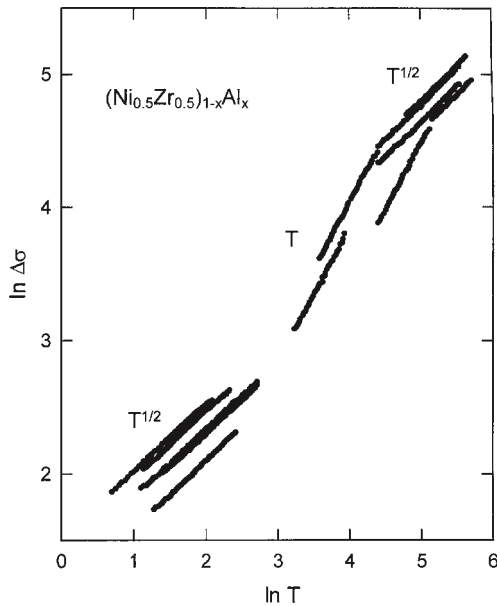
Figure 6
The logarithm of the correction to the Boltzmann conductivity as a function of ln(T) for several amorphous (Ni$_{0.5}$Zr$_{0.5}$)$_{1-x}$Al$_x$ alloys. The progressive transitions from $T^{1/2}$- to T- then back to $T^{1/2}$-dependence are clearly seen (after Nath and Majumdar 1997).

5. Magnetism, Spin Fluctuations, and Superconductivity

The magnetic properties of amorphous intermetallic compounds are extremely varied. Manifestations of almost all of the classes of magnetic behavior found in crystalline alloys and compounds are represented and, as in crystalline alloys, are determined by the magnitude and stability of the magnetic moment, and the balance between the exchange interaction and magnetic anisotropy. The superposition of topological disorder and consequent randomization of local magnetic anisotropy axes can additionally lead to magnetic phenomena which are peculiar to the amorphous state, particularly in those alloys containing non-S-state rare earth ions (for a review see, e.g., Chudnovsky 1995). In most cases, however, the transition from a low-temperature magnetically ordered state to a high-temperature paramagnetic state is accompanied by an increase in resistivity associated with spin disorder scattering, similar to that observed for crystalline alloys. In comparison with the underlying resistivity of the amorphous alloy this contribution is relatively modest.

However, in several amorphous transition metal alloys, 3d elements that are normally considered as "magnetic" (e.g., Fe, Co, Ni) do not support localized magnetic moments over relatively wide compositional ranges. For example in amorphous Fe$_{1-x}$Zr$_x$ the loss of weak itinerant ferromagnetism with increasing zirconium composition is accompanied by a collapse of the iron moment itself. Close to and at either side of the critical concentration for ferromagnetism (approximately 65 at.% Zr) the resistivity shows clear evidence of spin fluctuations (see *Spin Fluctuations*), with a large contribution of the characteristic form

$$\rho_{sf} \propto AT^2$$

At higher Zr concentrations in the Fe$_{1-x}$Zr$_x$ system, in common with other TM$_{1-x}$Zr$_x$ amorphous alloys (with TM = Co, Ni, Cu, Rh), a low-temperature ($T_c < 3$ K) superconducting phase is recovered. The observed spin fluctuations are generally held responsible for the suppression of superconductivity, a view reinforced by resistivity measurements under pressure, which show a reduction in the spin fluctuation contribution, and a concomitant rapid increase in the superconducting transition temperature with increasing applied pressure (Hamed *et al.* 1995 and references therein, Poon 1983).

6. Summary and Conclusions

Even the simplest nonmagnetic amorphous intermetallic alloys exhibit an anomalous temperature-dependent resistivity that reflects a complex combination of electron scattering, localization, and interaction processes. Nevertheless, the general features of the temperature dependence of the resistivity and the widely applicable Mooij correlation that relates the magnitude and temperature coefficient of resistivity are generally well explained by a combination of the Faber–Ziman amorphous structural diffraction model and the appropriate quantum corrections.

However, in the literature, there remains a tendency, on the one hand, to emphasize the importance of the topologically disordered structure of amorphous alloys, and on the other hand to categorize the alloys as either weak scattering ($\rho < 150\,\mu\Omega$cm, $\alpha > 0$) or strong scattering ($\rho > 150\,\mu\Omega$cm, $\alpha < 0$) and to develop theoretical models accordingly. This belies the Mooij observations that the characteristic features of the resistivity of amorphous intermetallic alloys can also be found in highly disordered but nevertheless fully crystalline alloys, and that the progression from the weak to the strong scattering limit is entirely continuous.

It is apparent that there is considerable scope for further theoretical and experimental studies of electron transport in these fascinating materials.

See also: Amorphous and Nanocrystalline Materials; Amorphous Materials: Electron Spin Resonance; Amorphous Materials: Nuclear Magnetic Resonance, New Techniques; Amorphous Materials: Nuclear Spin Relaxation; Amorphous Superconductors; Magnetic Systems: Disordered

Bibliography

Chudnovsky E M 1995 Random anisotropy in amorphous alloys. In: Fernandez-Baca J A, Ching W-Y (eds.) *The Magnetism of Amorphous Metals and Alloys*. World Scientific, Singapore, Chap. 3, pp. 143–74

Cote P J, Meisel L V 1981 Electrical transport in glassy metals. In: Güntherodt H-J, Beck H (eds.) *Glassy Metals I*. Springer, Berlin, Chap. 7, pp. 141–66

Cusak N E 1987 The physics of structurally disordered matter. In: Brew D F (ed.) *Graduate Student Series in Physics*. Hilger, Bristol, UK

Dugdale J S 1987 Electron transport in metallic glasses. *Contemp. Phys.* **28**, 547–72

Elliot S R 1983 *Physics of Amorphous Materials*. Longman, London

Hamed F, Razavi F S, Bose S K, Startseva T 1995 Spin fluctuations in metallic glasses $Zr_{75}(Ni_xFe_{1-x})_{25}$ at ambient and high pressures. *Phys. Rev. B* **52**, 9674–8

Harris R, Strom-Olsen J O 1983 Low-temperature electron transport in metallic glasses. In: Beck H, Güntherodt H-J (eds.) *Glassy Metals II*. Springer, Berlin, Chap. 10, pp. 325–42

Howson M A, Gallagher B L 1988 Electron transport properties of metallic glasses. *Phys. Rep.* **170**, 267–324

Markowitz D 1977 Calculation of electrical resistivity of highly resistive metallic alloys. *Phys. Rev. B* **15**, 3617–9

Mooij J H 1973 Electrical conduction in concentrated disordered transition metal alloys. *Phys. Stat. Solidi (a)* **17**, 521–30

Mott N F, Davis E A 1979 *Electronic Processes in Noncrystalline Materials*. Clarendon, Oxford

Nath T K, Majumdar A K 1997 Quantum interference effects in $(Ni_{0.5}Zr_{0.5})_{1-x}Al_x$ metallic glasses. *Phys. Rev. B* **55**, 5554–7

Poon S J 1983 Superconducting properties of amorphous metallic alloys. In: Luborsky F E (ed.) *Amorphous Metallic Alloys*. Butterworths, London, Chap. 22, pp. 432–50

Rao K V 1983 Electrical transport properties. In: Luborsky F E (ed.) *Amorphous Metallic Alloys*. Butterworths, London, Chap. 21, pp. 401–31

Ziman J M 1972 *Principles of the Theory of Solids*. Cambridge University Press, Cambridge

R. Cywinski and S. H. Kilcoyne
University of Leeds, Leeds, UK

Amorphous Materials: Electron Spin Resonance

Electron spin resonance (ESR) is a spectroscopic technique that uses the spin magnetic moment of the electron as a probe of its local environment. Only unpaired electrons can participate in ESR. In most insulating materials virtually all electrons are paired and their magnetic moments cancel. However, a few unpaired electrons may be present in the form of electrons or holes trapped at point defects or located in partially filled *d* or *f* shells of transition group ions. ESR is sufficiently sensitive to detect unpaired electrons in concentrations sometimes as low as a few parts per billion.

1. ESR Theory and Practice

The spin **S** and spin magnetic moment μ of the electron are related quantum mechanical vectors:

$$\boldsymbol{\mu} = -g\beta\mathbf{S} \qquad (1)$$

where $\beta = |e|h/4\pi mc$ is the Bohr magneton, *e* is the charge of the electron, *m* is its mass, *h* is Planck's constant, *c* is the speed of light, and *g* is a dimensionless number. For the free electron $g = g_e = 2.00232$, and $\boldsymbol{\mu} = \boldsymbol{\mu}_e \equiv -g_e\beta\mathbf{S}$. When any magnetic dipole $\boldsymbol{\mu}$ is placed in an external magnetic field **H**, its Zeeman interaction energy is given by the scalar product

$$E_{\text{Zeeman}} = -\boldsymbol{\mu} \cdot \mathbf{H} \qquad (2)$$

A quantum-mechanical property of spin angular momentum is that its projections on the direction of **H** are limited to the values $M_S = S, S-1, \ldots, -S$, where the scalar quantity *S* is termed the "spin." For the free electron, $S = \frac{1}{2}$. In general, atoms or assemblies of atoms binding *N* electrons may assume net spins as large as $N/2$, but in practice $S = \frac{1}{2}$ for most point defects, and *S* for transition group ions can be no larger than $\frac{1}{2}$ multiplied by the number of electrons in *d* and/ or *f* orbitals.

The most common ESR spectrometer exposes samples to microwaves of a fixed frequency υ and an applied magnetic field **H**. The allowed transitions between the Zeeman levels of Eqn. (2) are those for which $\Delta M_S = \pm 1$. Near thermodynamic equilibrium there are more electrons in the lower energy Zeeman states than the higher ones, resulting in a net absorption of microwave power when $|\mathbf{H}| = H_{\text{res}}$, given by the "resonance condition"

$$H_{\text{res}} = \frac{h\upsilon}{g\beta} \qquad (3)$$

There is also a magnetic moment associated with the orbital angular momenta of electrons circling about atoms. However, when atoms are embedded in solids, local electric fields ("crystal fields") tend to "quench" the orbital angular momentum of their ground states leaving a magnetic moment due mostly to the spin, i.e., $\boldsymbol{\mu} \approx \boldsymbol{\mu}_e$. Nevertheless, the spin-orbit and orbit-Zeeman interactions admix small amounts of orbital angular momentum back into the ground state. These residual orbital effects require the

replacement of $g\mathbf{S}$ in Eqn. (1) with $\mathbf{g} \cdot \mathbf{S}$. The so-called "$g$ matrix" is expressed by (e.g., Weil *et al.* 1996)

$$\mathbf{g} = g_e\mathbf{1} + 2\lambda\mathbf{\Lambda} \qquad (4)$$

where $\mathbf{1}$ is the unit matrix and λ is the spin-orbit coupling constant. The elements of the matrix $\mathbf{\Lambda}$ take the form (correct to second order in perturbation theory):

$$\mathbf{\Lambda}_{ij} = \sum_n \frac{\langle 0|L_i|n\rangle \langle n|L_j|0\rangle}{(E_n - E_0)} \qquad (5)$$

where L_i and L_j are orbital-angular-momentum operators and $|0\rangle$ and $|n\rangle$ are the ground- and nth-excited-state wavefunctions, respectively, of the paramagnetic species and E_0 and E_n are their energies.

The energetics of unpaired electrons subjected to electric and/or magnetic fields are contained in the "spin Hamiltonian" $\mathscr{H}$ operator, (e.g., Weil *et al.* 1996). For the case of the Zeeman interaction in the presence of crystalline electric fields

$$\mathscr{H} = \beta\mathbf{H} \cdot \mathbf{g} \cdot \mathbf{S} + \mathbf{S} \cdot \mathbf{D} \cdot \mathbf{S} \qquad (6)$$

where $\mathbf{g}$ is given by Eqns. (4) and (5) and the second term on the right (sometimes called the fine-structure interaction) is nonzero only for $S > \frac{1}{2}$. When $|\mathbf{H}| = 0$, $\mathbf{S}$ is quantized along the set of axes which diagonalize $\mathbf{D} = \lambda^2\mathbf{\Lambda}$, where $\mathbf{\Lambda}$ is given by Eqn. (5). In its diagonalized form, the diagonal elements of $\mathbf{D}$ are commonly expressed as $\frac{1}{3}D - E$, $\frac{1}{3}D + E$, and $-\frac{2}{3}D$, where D and E ($|E| \leqslant |\frac{1}{3}D|$) are the axial and orthorhombic fine-structure splittings, respectively.

In general, solutions of Schrödinger's equation using Eqn. (6) as the energy operator yield resonance conditions which depend on the angles between the direction of the applied field $\mathbf{H}$ and the principal axes of $\mathbf{g}$ and $\mathbf{D}$ (which in turn relate to axes of crystalline symmetry). For example, in the case of a paramagnetic center with $S = \frac{1}{2}$ located on a high-symmetry site in a crystal with a three-fold axis of symmetry or higher (i.e., a c axis), the value of g to be used in the resonance condition of Eqn. (3) is found to be

$$g = \sqrt{g_\parallel^2\cos^2\theta + g_\perp^2\sin^2\theta} \qquad (7)$$

where θ is the angle between $\mathbf{H}$ and the c axis.

Many atomic nuclei have nonzero quantum mechanical spin vectors $\mathbf{I}$ and, by analogy with Eqn. (1), nuclear magnetic moments $\boldsymbol{\mu}_N \equiv g_N\beta_N\mathbf{I}$, where g_N is the nuclear g factor and $\beta_N = |e|h/4\pi Mc$ is the nuclear magneton (M is the proton mass). The projections of $\mathbf{I}$ on the direction of an imposed magnetic field can take only integral or half-integral values given by $M_I = I, I-1, ..., -I$, where the scalar quantity I is called the "nuclear spin." A single unpaired electron whose ground-state orbital bears a fixed geometric relationship to a companion "magnetic"

nucleus ($I \neq 0$) is therefore subjected to the vector sum of the applied magnetic field $\mathbf{H}$ and one of $2I+1$ possible magnetic field values corresponding to the $2I+1$ possible orientations of the nuclear magnetic moment vector $\boldsymbol{\mu}_N$. In these cases, a hyperfine term $\mathscr{H}_{hf} = \mathbf{S} \cdot \mathbf{A} \cdot \mathbf{I}$, must be added to the spin Hamiltonian of Eqn. (6). In an actual experiment (usually involving $> 10^{13}$ unpaired electrons) a paramagnetic species with $S = \frac{1}{2}$ which is associated with a single nuclide of spin I gives rise to a manifold of $2I+1$ equally intense hyperfine lines with spacings which depend on the angles between the field $\mathbf{H}$ and the principal axes of the hyperfine matrix

$$\mathbf{A} = A_{iso}\mathbf{1} + \mathbf{T} \qquad (8)$$

where A_{iso} is the isotropic hyperfine coupling constant and $\mathbf{T}$ is a traceless matrix accounting for the angular dependence. A second-order-perturbation-theory resonance condition for $\mathscr{H} = \beta\mathbf{H} \cdot \mathbf{g} \cdot \mathbf{S} + \mathbf{S} \cdot \mathbf{A} \cdot \mathbf{I}$ assuming axial symmetry and collinear g and A matrices can be found, e.g., in Griscom (1990) or Weil *et al.* (1996). For the special case of a p orbital centered on the magnetic nucleus, $\mathbf{T}$ is diagonal with elements $-B$, $-B$, and $2B$.

Many point defects in insulators are characterized by sp hybrid-molecular-orbital ground-state wavefunctions of the form

$$\psi_0 = c_s|ns\rangle + c_p|np\rangle + \sum c_i|k_i\rangle \qquad (9)$$

where $|ns\rangle$ and $|np\rangle$ are, respectively, s- and p-state valence orbitals of an atom at the apex of a triangular or trigonal-pyramidal cluster of atoms and $|k_i\rangle$ are the remaining valence orbitals of the cluster. Where the apex atom incorporates a magnetic isotope, the coefficients c_s and c_p can be determined from the experimental hyperfine coupling constants according to $c_s^2 = A_{iso}/A_0$ and $c_p^2 = B/B_0$, where A_0 and B_0 are s-state and p-state coupling constants of the free atom, respectively, available from tables (e.g., Weil *et al.* 1996). In general, there is a direct relationship between the hybridization ratio c_p/c_s and the apex bond angles (see, for example, references in Griscom 1990).

2. ESR in Crystals and Powders

Figure 1(a) exhibits a plot of the expected positions of $H_{res}(\theta)$ specified by Eqns. (3) and (7) for a particular set of parameters ($g_\parallel = 2.185$, $g_\perp = 1.999$, and $\nu = 9.23 \text{GHz}$). If this crystal were to be crushed into a fine powder, the resulting ESR signal would become "smeared" between the field values $H_{min} = h\nu/g_\parallel\beta$ and $H_{max} = h\nu/g_\perp\beta$. However, this smearing is not random. In practice, all solid-angle orientations Ω of the particle's c axes with respect to the direction of $\mathbf{H}$ are represented with equal probability. This uniform orientational distribution, $P_\Omega(\Omega) = constant$, transforms into a function $P_H(H_{res}) = P_\Omega(\Omega) \cdot |J_H(\Omega)|$,
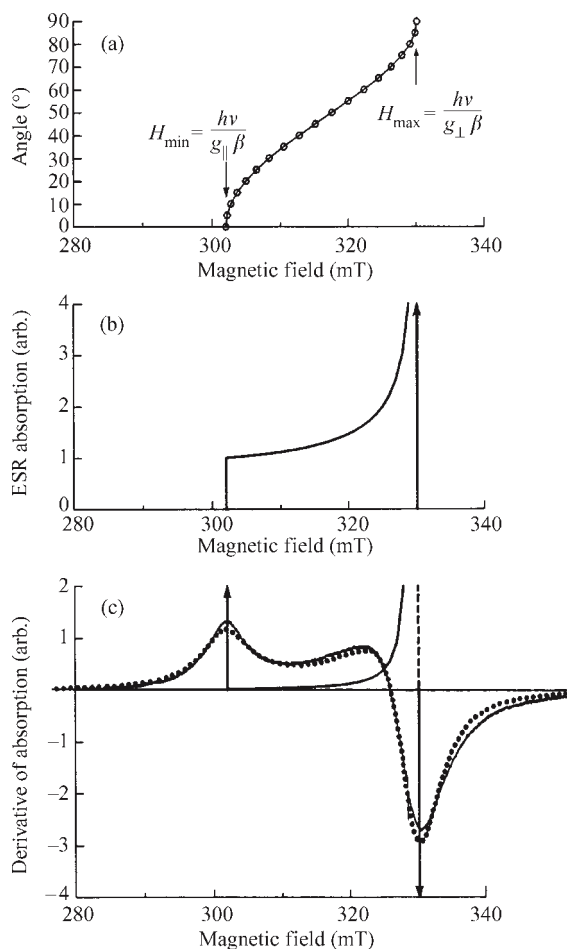
Figure 1
ESR of crystals and powders using the example of a resonance condition specified by Eqns. (3) and (7): (a) simulated angular dependence data for a hypothetical single crystal; (b) "powder pattern" absorption in the case of an infinitesimally narrow single-crystal linewidth; (c) first derivative of the powder pattern (bold curves) with superposed experimental (thin curve) and simulated (dots) spectra due to O_2^- ions in polycrystalline Na_2O_2. The simulation assumed an axially symmetric g matrix (which is only approximately true of the experimental spectrum) and a Lorentzian single-crystal line-broadening function whose (finite) width was used as a fitting parameter.

where $J_H(\Omega)$ is the Jacobian of the transformation $\Omega \rightarrow H$. $P_H(H_{res})$ is called a powder pattern and expresses the probability of resonance absorption per unit interval of H.

Figure 1(b) is the powder pattern for the case in point, where $J_H(\Omega) = [\partial H_{res}(\cos \theta)/\partial \cos \theta]^{-1}$ and H_{res} is given by Eqns. (3) and (7) (the vertical arrow marks

a mathematical singularity which would occur if the single-crystal linewidth were infinitesimally narrow). The first derivative of this envelope is shown as the bold lines in Fig. 1(c). The thin curve in Fig. 1(c) is an experimental first-derivative spectrum (solid curve) arising from superoxide ions (O_2^-) in polycrystalline Na_2O_2. The dotted curve is a computer simulation based on the (approximately valid) assumption of an axially symmetric g tensor. This simulation is the result of convoluting the powder pattern with a Lorentzian single-crystal line shape of an appropriate finite width (Griscom 1990).

3. ESR in Amorphous Materials

Glasses and other amorphous materials differ from powdered crystals in a fundamental way. Whereas each particle of a crystalline powder has a structure and density identical to all others, the structure of each nanoregion of a glass differs randomly from other nanoregions of equivalent size. In particular, glasses display spatial density fluctuations. Thus, a simplistic but instructive way to visualize a glass would be as a nanocrystalline solid wherein the ensemble of randomly oriented nanocrystallites is characterized by a statistical distribution of densities.

3.1 How ESR Spectra of Amorphous Materials Differ from Those of Powders

It can be shown theoretically that an O_2^- ion in free space (or in a material of zero density) is characterized by $g_\parallel = 4$, $g_\perp = 0$, whereas in a hypothetical material of infinite density $g_\parallel = g_\perp = g_e$. Figure 2(a) illustrates the predicted angular dependencies of the ESR spectra of O_2^- ions in a material of finite density subjected to ten incrementally different isostatic pressures. The decreases of $g_\parallel$ and correlated increases of $g_\perp$ with increasing pressure were calculated from the theory of Känzig and Cohen (1959) by approximating their formulae to axial symmetry. Figure 2(b) shows the result of adding together the powder patterns corresponding to each of these 10 cases according to a bell-shaped weighting function. The subtly rounded shape of the "glass pattern" which would be obtained by replacing the 10-element summation of Fig. 2(b) with a continuous integral over the same weighting function contrasts with the sharply angular powder pattern of Fig. 1(b).

Figure 2(c) (unbroken curve) illustrates the experimental first-derivative spectrum of O_2^- ions in an amorphous peroxyborate material (Griscom 1990). The dotted curve in Fig. 2(c) is a computer simulation based on the correlated skew-symmetric g-value distributions of Fig. 2(d), which in turn were derived by assuming a Gaussian distribution $P_\Delta(\Delta)$ in the crystal-field-imposed splittings Δ of the $2p\pi_g$ energy levels of the O_2^- ion in a solid (Känzig and Cohen 1959).
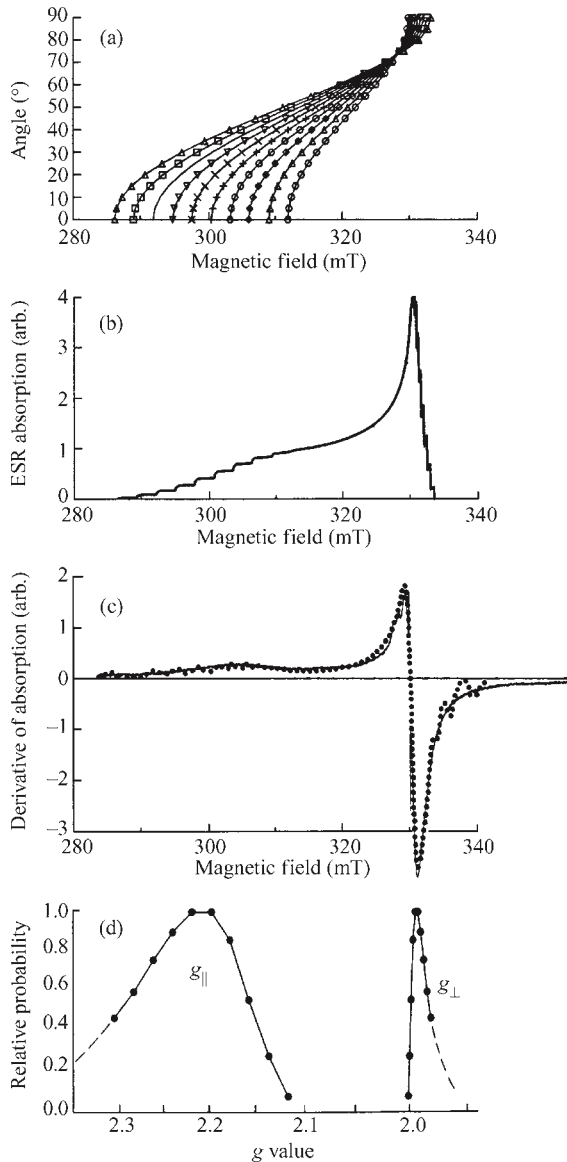
Figure 2

Conceptualization of the ESR spectrum of a glass: (a) simulated angular dependencies of the spectra of O_2^- ions in a hypothetical single crystal subjected to a range of isostatic compressions; (b) powder patterns of the foregoing ten cases summed according to a bell-shaped weighting function; (c) experimental spectrum of O_2^- ions in an amorphous peroxyborate preparation (solid curve) and its computer simulation (dots) based on a statistically weighted set of powder patterns deriving from (d) correlated distributions of $g_\parallel$ and $g_\perp$ values semiempirically determined under the constraints of the g-value theory of Känzig and Cohen (1959).

The O_2^- ion is a special case used above for illustrative purposes because $g_\parallel$ and $g_\perp$ depend in different ways on a single energy difference Δ. In more common cases where the ground-state wavefunction is given by Eqn. (9), $g_\parallel \approx g_e$ while $g_\perp$ is calculated from Eqns. (4) and (5). Redefining Δ as $E_1 - E_0$ in Eqn. (5), skew-symmetric distributions in $g_\perp$ can result according to $P_g(g) = P_\Delta(\Delta) \cdot |J_g(\Delta)|$, where $J_g(\Delta) \equiv (\partial g/\partial \Delta)^{-1}$ is the Jacobian of the transformation $\Delta \to g$ (Peterson *et al.* 1974) and again $P_\Delta(\Delta)$ is taken to be a Gaussian. Skew-symmetric g-value distributions arising in this way are endemic to glasses.

3.2 Use of Hyperfine Interactions to Determine the Ground State of a Point Defect in an Amorphous Material

One of the common radiation-induced point defects in amorphous SiO_2 is the so-called "peroxy radical" (POR). As discovered from ESR (Friebele *et al.* 1979, Stapelbroek *et al.* 1979, Griscom 1990), the POR comprises an O_2^- molecular ion covalently bonded to a silicon in the glass network. The most important knowledge concerning the POR derives from measurements of its hyperfine interactions with the magnetic nuclides ^{29}Si ($I = \frac{1}{2}$, natural abundance 4.7%) and ^{17}O ($I = \frac{5}{2}$, natural abundance 0.038%). Figure 3(a) shows the experimental spectrum of a neutron-irradiated SiO_2 sample enriched to 36 at.% ^{17}O. The inset to Fig. 3 shows the structural model of the POR; this model implies that oxygens O(1) and O(2) are chemically inequivalent. For finite amounts of both isotopes, there are four distinguishable cases which must simultaneously contribute to the observed spectrum: $^{16}O(1)$–$^{16}O(2)$, $^{17}O(1)$–$^{16}O(2)$, $^{16}O(1)$–$^{17}O(2)$, and $^{17}O(1)$–$^{17}O(2)$. For 36% ^{17}O, the relative probabilities of these four cases are calculated to be 0.41:0.23:0.23:0.13, respectively. The first-mentioned case effectively corresponds to zero isotopic enrichment; the spectrum for this case (not shown) was first computer-simulated to determine the g-value distributions (Stapelbroek *et al.* 1979). Using these g-value distributions as given, the synthetic spectra of Figs. 3(c) and 3(d) were devised (Friebele *et al.* 1979) for the cases $^{17}O(1)$–$^{16}O(2)$ and $^{16}O(1)$–$^{17}O(2)$, respectively. Finally, these two synthetic spectra were added together in the required 1:1 ratio to achieve the simulation of Fig. 3(b), which successfully replicates all of the main ^{17}O hyperfine lines. (The central part of the spectrum due to the case $^{16}O(1)$–$^{16}O(2)$ is not simulated here.) The diagonal elements of the hyperfine matrices, $A_\parallel = A_{iso} + 2B$ and $A_\perp = A_{iso} - B$, were determined from this simulation for both cases. As a check, the same coupling constants were used successfully to predict the positions of the more numerous but weaker lines of the $^{17}O(1)$–$^{17}O(2)$ case (vertical bars in Fig. 3(a)). The resulting values of A_{iso} and B were

(a)

Experimental

Gain $\times \frac{1}{4}$

(b)

Simulations:
^{17}o(1)^{16}o(2) + ^{16}o(1)^{17}o(2)

(c)

Site I
^{17}o(1)^{16}o(2)

(d)

Site II
^{16}o(1)^{17}o(2)

300   320   340
Magnetic field (mT)
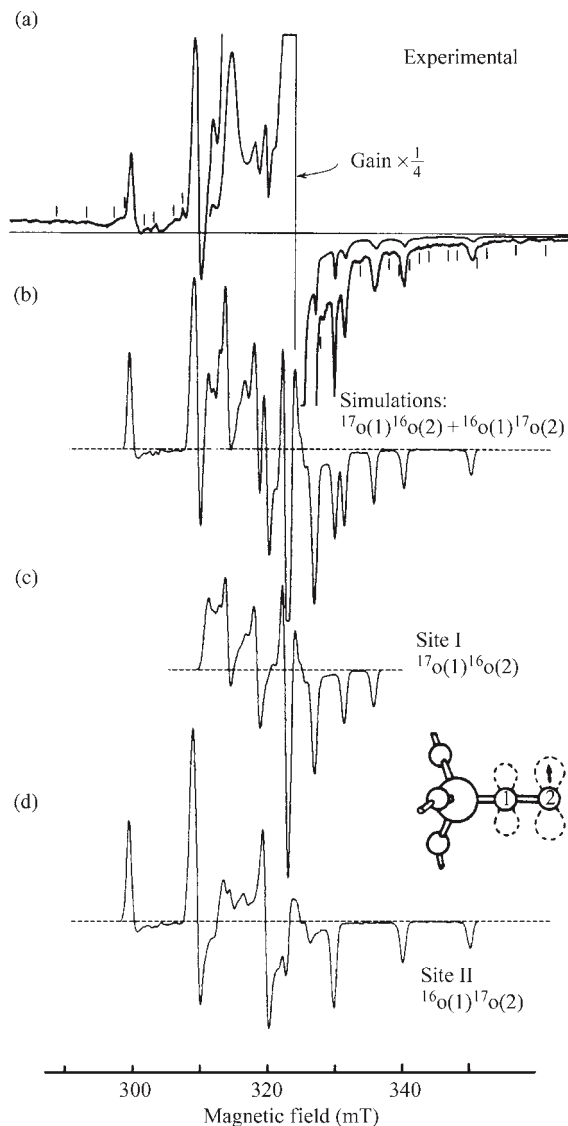
Figure 3
ESR spectra of peroxy radicals (PORs) in 36% ^{17}O-enriched silica glass: (a) experimental spectrum and (b) simulation of the highly structured parts of (a) assuming a POR model with one ^{17}O ($I = \frac{5}{2}$) and one ^{16}O ($I = 0$) per defect. Under the assumption that the two oxygen sites are chemically inequivalent (see inset), the simulation of (b) perforce comprises an equally weighted sum of the simulated component spectra (c) and (d).

then used to determine the coefficients in Eqn. (9), namely, $c_s(1) \approx c_s(2) \approx 0$, $c_p(1) = 0.26$ and $c_p(2) = 0.74$. Thus, the ground-state wavefunction of the POR in amorphous SiO_2 was deduced to comprise a $2p\pi$ antibonding orbital asymmetrically partitioned over

two chemically inequivalent oxygen atoms. As inferred from ESR measurements of samples enriched in ^{29}Si, the reason for this chemical inequivalence is that one of the oxygens is bonded to a single silicon atom in the glass network (c.f., Griscom 1990).

3.3 Transition Group Ions in Glasses

For a single electron ($S = \frac{1}{2}$) in a d or f orbital of a transition group ion involving a nonmagnetic isotope, the resonance condition is given by Eqns. (3), (4), (5), and (7). In this event, the skew-symmetric g-value distributions which occur in glasses are simply calculated by assuming Gaussian distributions in the energy denominators of Eqn. (5) and effecting the transformation $\Delta \to g$ as described above (Peterson *et al.* 1974). However, in many cases where more than one electron is found in a d or f shell, details of the coordination sphere and crystal-field strengths determine not only the matrix elements of **D** but also the value of S (e.g., Griscom 1990, Weil *et al.* 1996). For $S > \frac{1}{2}$ the spin Hamiltonian of Eqn. (6) applies. Perturbation-theory-based resonance conditions have been derived for the cases $h\nu \gg |D|$ and $|D| \gg h\nu$. Notable is the case of Fe^{3+} ions ($S = \frac{5}{2}$) in glasses, where the conditions $|D| \gg h\nu$ and $|E| \approx \frac{1}{3}|D|$ commonly prevail, leading to an isotropic absorption at an effective g value of ~ 4.3 (reviewed, e.g., in Griscom 1990). However, situations where $h\nu$ and D have comparable magnitudes necessitate exact matrix diagonalization of Eqn. (6).

Figure 4(b) shows the allowed transitions of an $S = \frac{5}{2}$ state determined by matrix diagonalization of Eqn. (6) for **H** parallel to each of the principal axes of **D**; these transitions are plotted here as normalized resonance fields, $g_e\beta H_{res}/h\nu$, versus the normalized fine-structure coupling constant, $|D|/h\nu$, for the special case $|E| = |D|/3$ (Griscom and Griscom 1967). This diagram pertains to Fe^{3+} and (neglecting ^{55}Mn hyperfine interactions) also to Mn^{2+}. ESR spectra of Mn^{2+} in an alkali borate glass recorded at two separate microwave frequencies are displayed in Fig. 4(a). Note that the normalized magnetic field scale for the Ka-band spectrum ($\nu = 35$ GHz) is compressed by a factor of ~ 4 relative to the X-band spectrum ($\nu = 9$ GHz). Figure 4(c) represents a single Gaussian distribution in $|D|$ values plotted as $P_{|D|}(|D|/h\nu)$ for two separate values of ν (9 and 35 GHz). On the basis of the correspondences indicated by the dotted lines, it has been proposed that a single bell-shaped distribution $P_{|D|}(|D|)$ might account for all details of the experimental spectra at both microwave frequencies (Griscom 1990).

In any event, the diagram of Fig. 4(b) appeared to account for the Mn^{2+} spectrum in the $Li_2O \cdot 4B_2O_3$ polycrystalline compound by assuming a single discrete value of $|D|$ corresponding to $|D|/h\nu = 0.4$ at X band (Griscom and Griscom 1967). Actual computer
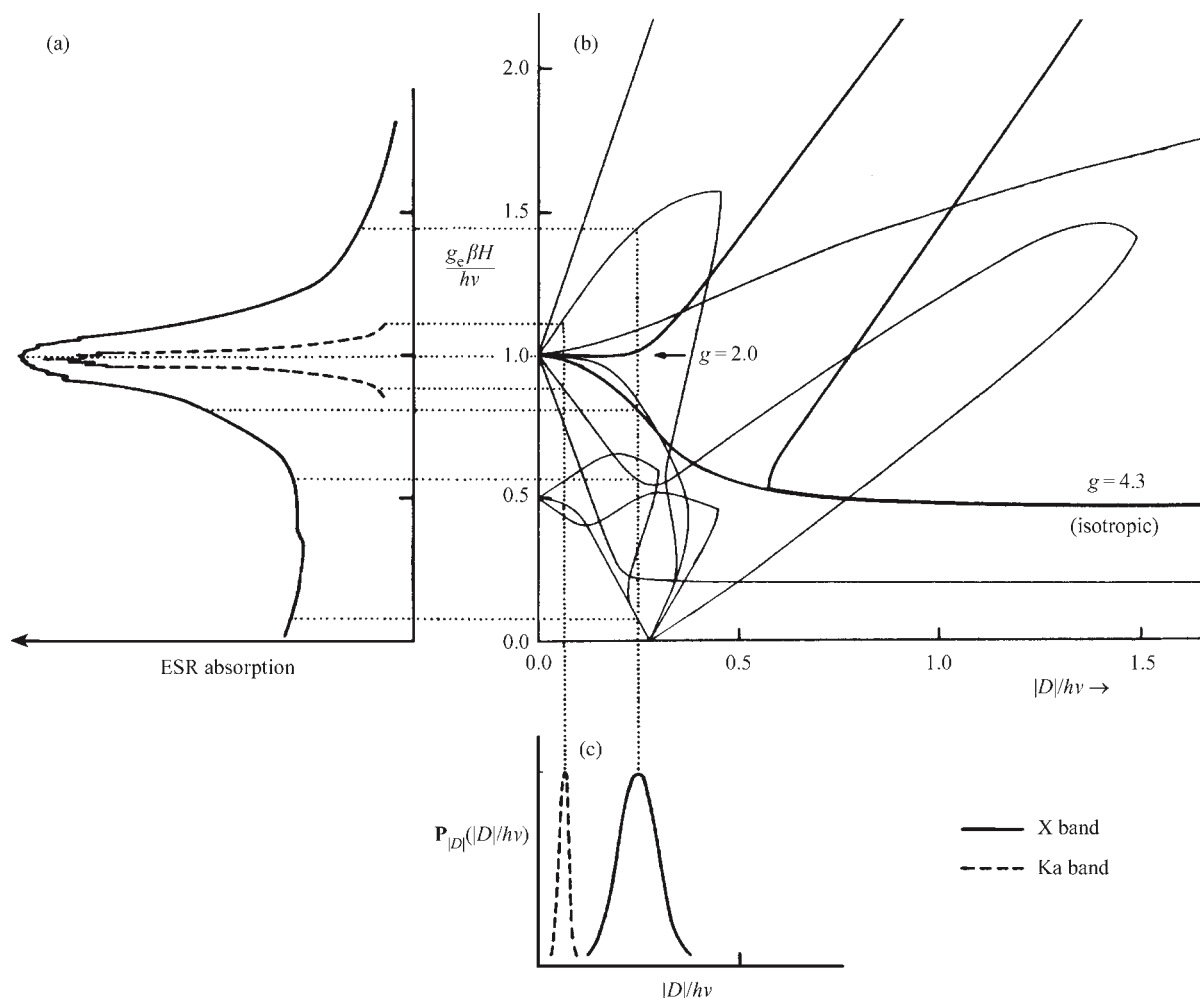
Figure 4
ESR of Mn^{2+} in an alkali borate glass: (a) absorption spectra recorded at $\nu = 9\,GHz$ (solid curve) and $\nu = 35\,GHz$ (dashed curve); (b) calculated resonance conditions (neglecting ^{55}Mn hyperfine splittings) $g_e\beta H_{res}/h\nu$ for H parallel to each of the principal axes of the tensor D (for the special condition $|E| = \frac{1}{3}|D|$) shown as functions of $|D|/h\nu$; (c) a Gaussian distribution of $|D|$ values plotted as $P_D(|D|/h\nu)$ for the two values of ν pertaining to the spectra of (a).

line-shape simulations of glassy-state ESR spectra based on matrix diagonalization in this parameter regime have been carried out by only a few workers to date (e.g., Kliava and Purāns 1980, Cugunov *et al.* 1994, Legein *et al.* 1993).

3.4 The Bigger Picture

For convenience, the examples given above have pertained to a single paramagnetic species, O_2^-, and its occurrences as point defects in the amorphous peroxyborates (Sect. 3.1) and irradiated silica glasses (Sect. 3.2) and to a single transition group ion, Mn^{2+},

in an oxide glass system (Sect. 3.3). Critical reviews of the application of continuous-wave (c.w.) ESR to much broader ranges of point defects and transition group ions in oxide glasses have been given by Griscom (1980, 1990). The importance of carrying out comparative studies of both glassy and polycrystalline forms of the same material system when attempting to model paramagnetic centers in the former has been stressed in a review paper featuring point defects in the alkali borate system (Griscom 1993a).

Continuous-wave ESR of point defects in chalcogenide and multicomponent fluoride glasses have been reviewed by Griscom (1980) and (1993b), respectively. Examples of ESR investigations of

35

transition metal ions doped into fluoride and chalcogenide glasses can be found in Legein *et al.* (1993) and El Mkami *et al.* (1996), respectively. Street (1991) has reviewed applications of ESR to hydrogenated amorphous silicon (a-Si:H).

Continuous-wave ESR has also been employed to good advantage in the characterization of ferro- and ferrimagnetic particles precipitated in both synthetic and natural glasses (Griscom 1980, 1984). ESR studies of ferrimagnetic particles in 65-million-year-old glasses have a bearing upon the theory that an asteroidal impact triggered the extinction of the dinosaurs (Griscom *et al.* 1999).

Modern pulsed-ESR spectrometers afford several new capabilities over and above those inherent in c.w. methods. These include the possibility of separating overlapping spectra of paramagnetic centers characterized by differing spin-lattice relaxation times and the ability to resolve weak hyperfine interactions with ligand magnetic nuclei by the study of electron spin echo envelope modulation (ESEEM). ESEEM studies of defect centers in alkali borate glasses (Kordas 1997, Shkrob *et al.* 1999) appear to compel revision of some of the defect models proposed earlier on the basis of c.w. ESR results. Isoya *et al.* (1993) have used ESEEM to probe the spatial distribution of deuterium near dangling-bond defects in deuterated amorphous silicon.

Morigaki (1993) reviews the results of electron-nuclear double resonance (ENDOR) and optically detected magnetic resonance (ODMR) studies of dangling bonds in a-Si:H. Electron-hole recombination processes in a-Si:H have been investigated by a time-resolved ODMR technique (Mao and Taylor 1995). Shkrob and Trifunac (1997) comprehensively review time-resolved pulsed ESR and ODMR in radiation chemistry, including applications to amorphous silicon dioxide and a-Si:H.

Bibliography

Cugunov L, Mednis A, Kliava J 1994 Computer simulations of the EPR spectra for ions with S-greater-than-$\frac{1}{2}$ by eigenfield and related methods. *J. Magn. Reson. Ser. A* **106**, 153–8

El Mkami H, Deroide B, Zanchetta J V, Rumori P, Abidi N 1996 Electron paramagnetic resonance study of Mn^{2+} and Cu^{2+} spin probes in $(Ag_2S)_x(GeS_2)_{1-x}$ glasses. *J. Non-Cryst. Solids* **208**, 21–8

Friebele E J, Griscom D L, Stapelbroek M, Weeks R A 1979 Fundamental defects in glass: the peroxy radical in irradiated, high-purity, fused silica. *Phys. Rev. Lett.* **42**, 1346–9

Griscom D L 1980 Electron spin resonance in glasses. *J. Non-Cryst. Solids* **40**, 211–72

Griscom D L 1984 Ferromagnetic resonance of precipitated phases in natural glasses. *J. Non-Cryst. Solids* **67**, 81–118

Griscom D L 1990 Electron spin resonance. In: Uhlmann D R, Kreidl N J (eds.) *Glass Science and Technology: Advances in Structural Analysis*. Academic Press, New York, Vol. 4B, Chap. 3, pp. 151–251

Griscom D L 1993a Electron spin resonance spectroscopy of radiation-induced defect centers in insulating glasses. In: Simmons C J, El-Bayoumi O H (eds.) *Experimental Techniques of Glass Science*. The American Ceramic Society, Westerville, OH, pp. 161–84

Griscom D L 1993b Defect centers in heavy metal fluoride glasses: a review. *J. Non-Cryst. Solids* **161**, 45–51

Griscom D L, Beltrán-López V, Merzbacher C I, Bolden E 1999 Electron spin resonance of 65-million-year-old glasses and rocks from the Cretaceous–Tertiary boundary. *J. Non-Cryst. Solids* **253**, 1–22

Griscom D L, Griscom R E 1967 Paramagnetic resonance of Mn^{2+} in glasses and compounds of the lithium borate system. *J. Chem. Phys.* **47**, 2711–2

Isoya J, Yamasaki S, Okushi H, Matsuda A, Tanaka K 1993 Electron-spin-echo envelope-modulation study of the distance between dangling bonds and hydrogen atoms in hydrogenated amorphous silicon. *Phys. Rev.* **47**, 7013–24

Känzig W, Cohen M H 1959 Paramagnetic resonance of oxygen in alkali halides. *Phys. Rev. Lett.* **3**, 509–10

Kliava J, Purans J 1980 Simulation of EPR spectra of Mn^{2+} in glasses. *J. Magn. Reson.* **40**, 33–45

Kordas G 1997 N(= 1,2,3)-dimensional Fourier-transform–electron paramagnetic resonance (FT-EPR) spectroscopy measurements in the B_2O_3–Li_2O System. *Phys. Chem. Glasses* **38**, 21–4

Legein C, Buzaré J Y, Jacoboni C 1993 EPR structural investigations of transition metal fluoride glasses (TMFG). *J. Non-Cryst. Solids* **161**, 112–7

Mao D, Taylor P C 1995 Optically detected ESR studies of recombination processes in a-Si:H. *J. Non-Cryst. Solids* **190**, 48–57

Morigaki K 1993 ENDOR and ODMR characterization. In: Sakurai Y, Hamakawa Y, Matsumoto T, Shirae K, Suzuki K (eds.) *Current Topics in Amorphous Materials: Physics and Technology*. Elsevier, Amsterdam, pp. 323–8

Peterson G E, Kurkjian C R, Carnavale A 1974 Random structure models and spin resonance in glass. *Phys. Chem. Glasses* **15**, 52–8

Shkrob I A, Trifunac A D 1997 Spin and time-resolved magnetic resonance in radiation chemistry. Recent developments and perspectives. *Radiat. Phys. Chem.* **50**, 227–43

Shkrob I A, Tadjikov B M, Trifunac A D 1999 Magnetic resonance studies on radiation-induced point defects in mixed oxide glasses. I. Spin centers in B_2O_3 and alkali borate glasses. *J. Non-Cryst. Solids* **262**, 6–34

Stapelbroek M, Griscom D L, Friebele E J, Weeks R A 1979 Oxygen-associated trapped hole centers in high-purity fused silicas. *J. Non-Cryst. Solids* **32**, 313–26

Street R A 1991 *Hydrogenated Amorphous Silicon*. Cambridge University Press, Cambridge 104–14

Weil J A, Bolton J R, Wertz J E 1996 *Electron Paramagnetic Resonance: Elemental Theory And Practical Applications*. Wiley, New York

D. L. Griscom
Naval Research Laboratory, Washington, DC, USA

Amorphous Materials: Nuclear Magnetic Resonance, New Techniques

The elucidation of the structure and dynamics of solid or highly viscous amorphous materials represents a major challenge for techniques of characterization.

This holds, in particular, if atomistic resolution is desired. Here solid-state NMR offers unique possibilities, owing to its selectivity and versatility, in particular if multidimensional techniques are employed. This article describes advances in the field, emphasizing multidimensional exchange and double-quantum NMR. These techniques allow one, for example, to probe the *conformation* of macromolecules and their *packing* in both the solid state and the melt, as well as the *connectivity of building blocks* in inorganic glasses, and both the geometry and memory effects of complex dynamics.

1. Multidimensional Exchange NMR

In two-dimensional (2D) exchange NMR, information on the structure of the material is obtained by monitoring the transfer of nuclear magnetization between different building blocks, which can be distinguished in the NMR spectrum if differences in the chemical structure, conformation, or orientation of the distinct residue are reflected in different resonance frequencies. For optimum spectral resolution, magic-angle spinning (MAS) is employed, while nonrotating samples often yield better geometric information. Magnetization exchange can result from the dipole–dipole interaction between the nuclear spins; this leads to through-space spin diffusion, from which the spatial proximity and mutual orientation of molecular moieties, i.e., valuable *structural* information, can be determined.

Alternatively, magnetization exchange can result from a spatial movement of the moiety under study, thereby changing its NMR frequency, and thus providing information about *dynamics*. From the time needed for the exchange to occur, the *time scale* of the dynamic process can be directly obtained in real time. Moreover, the mutual orientation of molecular moieties before and after the move can be read from the off-diagonal exchange patterns (*geometry of dynamics*). This experiment provides information on *slow* dynamic processes on time scales between 1 ms and 100 s, which is equivalent to that available via incoherent neutron scattering on *fast* dynamics. By extending the NMR technique to three and four dimensions, *memory* effects concerning the *orientation* as well as the *rate* of molecular dynamics become experimentally accessible. For organic materials, ^{13}C and ^{2}H are widely used, while in inorganic systems, spin 1/2 nuclei such as ^{31}P are most popular (Schmidt-Rohr and Spiess 1994).

1.1 Structure

Multidimensional exchange and other solid-state NMR techniques are used to determine the *packing* of amorphous polymers in the glassy state (Klug *et al.* 1997, Tomaselli *et al.* 1997) and the *connectivity* of

building blocks in inorganic glasses (Eckert 1994). Advanced approaches then combine the information provided by spectroscopy with computer simulations of the packing. Similarly, information about the conformation of macromolecules is readily available from an analysis of the observed ^{13}C chemical shift, making use of *ab initio* calculations of this spectroscopic parameter (Born and Spiess 1997).

1.2 Dynamics

The molecular dynamics is probably most complex in amorphous melts close to the glass transition. Nevertheless, applying various 2D exchange NMR techniques it has been possible to show that molecular dynamics, in both low molar mass glass-formers and synthetic polymers, consists of small-angle fluctuations causing total displacements of 2–4° and occasional jumps through 10–25° (Spiess 1997). By extension to 3D or even 4D NMR, the orientation of individual moieties can be probed at three, or even four, subsequent times, and memory effects concerning the geometry as well as the rate of the molecular dynamics in vitrifying polymer melts can be elucidated. Studies along these lines lead to the notion of *dynamic heterogeneities*, as shown schematically in Fig. 1. By combining 4D exchange NMR with spin diffusion, the length scale of these heterogeneities has been determined (Tracht *et al.* 1998).

2. Double-quantum Solid-state NMR

In 2D exchange NMR, direct magnetization transfer cannot readily be distinguished from transfer via a third spin or orientation. Likewise, it is difficult to distinguish transfer back to the original moiety or orientation from no transfer at all. Such problems do not occur in double-quantum (DQ) NMR, where a DQ coherence is generated within selected spin pairs. These can either be introduced by isotope labeling, in particular ^{13}C–^{13}C, or separated from others by fast MAS. The latter approach even allows one to use solid-state ^{1}H NMR, which makes the technique widely applicable. Although mainly aimed at determining *structure*, the connectivity of functional groups provided by this technique also yields information about *dynamic* processes on mesoscopic length scales (Spiess 1997).

2.1 Structure

The advantages of DQ solid-state NMR have already been exploited for both inorganic and organic amorphous materials. In inorganic phosphate glasses, the connectivity between coordination polyhedrons has been elucidated with previously inaccessible detail by fast MAS DQ NMR, with motifs involving sequences of at least three polyhedrons of the same kind being
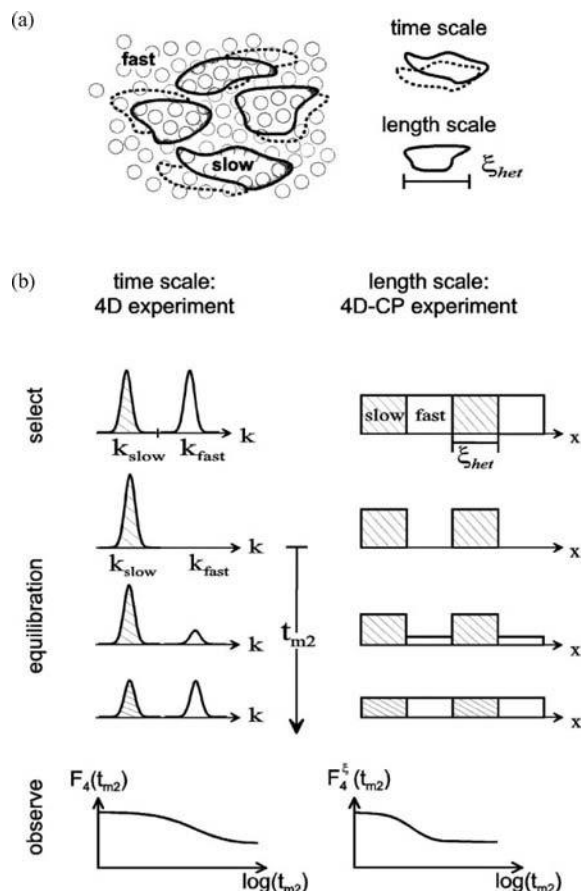
Figure 1
Schematic of (a) dynamic heterogeneities and (b) how their time and length scales can be measured by multidimensional NMR (after Tracht *et al.* 1998).

Figure 2
Schematic of (a) experimental scheme for measuring residual dipole–dipole couplings for selected proton–proton pairs in (b) *trans*-1,4-polybutadiene from (c) a ¹H DQ MAS NMR spectrum (after Graf *et al.* 1998).

identified in such glasses for the first time (Feike *et al.* 1998). The conformation of organic polymers can be probed by the determination of torsional angles between nearby groups via DQ NMR on systems containing ^{13}C–^{13}C labels, and clear-cut differences between crystalline and amorphous regions have been elucidated (Schmidt-Rohr 1996). Moreover, using fast MAS DQ ^{1}H NMR, the structure of *hydrogen bonds* in disordered organic materials is now readily accessible. Owing to the high sensitivity of ^{1}H NMR, such experiments can be performed with samples of about 10 mg and measuring times as short as 30 minutes, thus seriously challenging the use of neutron scattering for this purpose (Schnell *et al.* 1998).

2.2 Dynamics

The application of DQ NMR with MAS to viscous melts even allows one to probe both the conforma-

tion of chains on mesoscopic scales as well as translational dynamics. This is due to the fact that the chain motion in entangled polymer melts is not completely isotropic, resulting in residual dipole–dipole couplings. From these residual couplings, *dynamic order parameters* can be determined, which are defined in the same way as the conventional order parameters in liquid crystals. As shown in Fig. 2, the spectral resolution of DQ MAS ^{1}H NMR of polymer melts is high enough to probe the order parameters for the *chain direction*. The values found are about an order of magnitude higher than anticipated from standard theory of polymer melts (Doi and Edwards 1986). From the time, molecular weight, and temperature dependence of the *dynamic order parameter*, information about *translational* chain motion as well as the length scale of the regions with partially ordered chains could be deduced (Graf *et al.* 1998).

3. Conclusions

The specific examples of advanced solid-state NMR discussed here indicate the potential of this technique. Moreover, it is possible to cover all length scales from molecular via mesoscopic to macroscopic levels (Spiess 1997). For example, the combination of spin-diffusion experiments with filters, which can discriminate between different dynamic behavior, allows one to probe the phase behavior and the interphase structure of heterogeneous polymers such as block copolymers, core-shell particles and organic–inorganic

hybrid materials, while NMR imaging can detect subtle differences in molecular dynamics resulting from nonlinear plastic deformation of solid polymers. Close analogies exist between solid-state exchange NMR and *incoherent* neutron scattering. Moreover, DQ solid-state NMR provides information even equivalent to *coherent* neutron scattering, albeit for much slower processes in the region of milliseconds. In short, advanced solid-state NMR is already an indispensable tool for the characterization of amorphous materials, and its importance is expected to increase further in the future.

See also: Amorphous Materials: Nuclear Spin Relaxation; Nuclear Magnetic Resonance Spectrometry

Bibliography

Born R, Spiess H W 1997 *Ab initio* calculations of conformational effects on ^{13}C NMR spectra of amorphous polymers. In: *NMR—Basic Principles and Progress*. Springer, Heidelberg, Germany, Vol. 35

Doi M, Edwards S F 1986 *The Theory of Polymer Dynamics*. Clarendon Press, Oxford, UK

Eckert H 1994 Structural studies of non-crystalline solids using NMR. New experimental approaches and results. In: *NMR—Basic Principles and Progress*. Springer, Heidelberg, Germany, Vol. 33 pp. 125–98

Feike M, Jäger C, Spiess H W 1998 Connectivities of coordination polyhedra in phosphate glasses from ^{31}P double-quantum NMR spectroscopy. *J. Non-Crystalline Solids* **223**, 200–6

Graf R, Heuer A, Spiess H W 1998 Chain-order effects in polymer melts probed by ^{1}H double-quantum NMR spectroscopy. *Phys. Rev. Lett.* **80**, 5738–41

Klug C A, Zhu W L, Tasaki K, Schaefer J 1997 Orientational order of locally parallel chain segments in glassy polycarbonate from [13]C–[13]C dipolar couplings. *Macromolecules* **30**, 1734–40

Schmidt-Rohr K 1996 A double-quantum solid-state NMR technique for determining torsion angles in polymers. *Macromolecules*. **29**, 3975–81

Schmidt-Rohr K, Spiess H W 1994 *Multidimensional Solid-State NMR and Polymers*. Academic Press, London

Schnell I, Brown S P, Low H Y, Ishida H, Spiess H W 1998 An investigation of hydrogen bonding in benzoxazine dimers by fast magic-angle spinning and double-quantum ^{1}H NMR spectroscopy. *J. Am. Chem. Soc.* **120**, 11784–95

Spiess H W 1997 Multidimensional solid state NMR: a unique tool for the characterization of complex materials. *Ber. Bunsenges. Phys. Chem.* **101**, 153–68

Tomaselli M, Zehnder M M, Robyr P, Grob Pisano C, Ernst R R, Suter U W 1997 Local conformations in the glassy polycarbonate of 2,2-bis(4-hydroxyphenyl)propane (bisphenol-A). *Macromolecules* **30**, 3579–83

Tracht U, Wilhelm M, Heuer A, Feng H, Schmidt-Rohr K, Spiess H W 1998 Length scale of dynamic heterogeneities at the glass transition determined by multidimensional nuclear magnetic resonance. *Phys. Rev. Lett.* **81**, 2727–30

H. W. Spiess
Max-Planck-Institut für Polymerforschung, Mainz Germany

Amorphous Materials: Nuclear Spin Relaxation

Nuclear spin relaxation (NSR) techniques are widely used to investigate the dynamic properties of amorphous materials over a very wide time scale ranging from seconds to nanoseconds. Application of strong magnetic field gradients allows the measurement of tracer diffusion coefficients down to about $10^{-15} m^2 s^{-1}$ on mesoscopic-length scales (Geil 1998). The techniques are extensively employed to amorphous polymers to study rotational and translational motions of molecular groups as well as glass-transition dynamics. In particular, incorporated site-specific deuterium probes yield very detailed information about molecular dynamics in polymers (Schmidt-Rohr and Spiess 1994). Until now, however, only a few NSR studies have been performed on amorphous metals. For instance, (Tang *et al.* 1998) have observed the diffusion of beryllium in a beryllium-containing metallic glass by means of [9]Be NSR.

In inorganic glasses containing alkali ions, three processes are important which occur in different temperature regions. At low temperatures low-frequency transitions take place between energetically nearly equivalent positions of atomic configurations which are intrinsic to the glassy state (Dieckhöfer *et al.* 1997). At elevated temperatures, ionic diffusion becomes dominant, whereas close to the glass-transition temperature the shear viscosity decreases rapidly corresponding to fast-growing density fluctuations. The present contribution focuses on the study of ionic diffusion by NSR.

1. Diffusion-induced Nuclear Spin Relaxation

Atomic diffusion gives rise to a time evolution of the nuclear magnetization in a sample towards the thermal equilibrium. The time constant (NSR time) T_1 of the process is given by the relation

$$1/T_1 = J(\omega_0) + 4J(2\omega_0) \tag{1}$$

where

$$J(\omega_0) = \mathrm{Re} \int_0^\infty G(t) \mathrm{e}^{-\mathrm{j}\omega_0 t} \mathrm{d}t \tag{1a}$$

denotes the spectral density of the diffusional pair correlation function

$$G(t) = \sum_{i<j} \langle \omega_{ij}(0) \cdot \omega_{ij}(t) \rangle_{\mathrm{therm.av}} \tag{1b}$$

at the applied Larmor frequency ω_0 of the nuclear probes. $\omega_{ij}(t)$ represents the time fluctuation of the coupling frequency between a resonant probe nucleus i and a neighboring species j (resonant or

nonresonant nuclear spin, electron spin, local charge, etc.) caused by the atomic movements.

For probe nuclei with spin $I = 1/2$ (such as ^{1}H, ^{19}F, ^{29}Si, and ^{31}P) ω_{ij} is due to mutual magnetic dipolar interactions, while for nuclei with $I > 1/2$ (alkali atoms like ^{7}Li, ^{23}Na, ^{85,87}Rb, ^{11}B, and ^{27}Al) the coupling is dominated by the interaction between the nuclear quadrupole moment of the probe and electric field gradients at the probe site created by neighboring charges, e.g., ionic point charges. In either case ω_{ij} is related to the distance r_{ij} of the particles by $\omega_{ij} \propto 1/r_{ij}^3$.

For a thermally activated diffusion of dilute particles in an ordered lattice, $G(t)$ can be expressed to a very good approximation by $G(t) \cong \langle \omega_c^2 \rangle \exp(-t/\tau)$ which corresponds to a Debye-like behavior of the diffusion-induced NSR rate $1/T_1|_{\mathrm{Diff}}$ in accordance with $J(\omega) = \langle \omega_c^2 \rangle \tau/(1 + \omega^2 \tau^2)$. Here, $1/\tau = 1/\tau_\infty \exp(-E/kT)$ is the jump rate of the moving particles with E being the corresponding activation energy and

$$\langle \omega_c^2 \rangle = \frac{1}{N} \cdot \sum_{i<j}^{N} \langle \omega_{ij}^2 \rangle$$

denotes the mean-square coupling frequency.

In practice, $\langle \omega_c^2 \rangle^{1/2}$ is roughly equal to the width of the respective NMR line at sufficiently low temperatures ("rigid line width"). Moreover, one should note that the diffusive motion is observable not only by the NSR rate of the mobile particles but also by measuring the NSR rate of immobile probe nuclei. This is caused by the pair character of the coupling frequency ω_{ij} which becomes time dependent for both mobile and immobile probes whenever a hopping event occurs. Finally, as mentioned in the introduction, the measured NSR rate $1/T_1$ can be induced by different relaxation processes. If the processes are independent of each other, the related rates add up to the observed rate:

$$1/T_1 = 1/T_1|_{\mathrm{Diff}} + \sum_{\mathrm{other}} 1/T_1$$

2. Ionic Diffusion in Glasses by Nuclear Spin Relaxation

Ionic diffusion in glasses gives rise to a NSR rate that does not exhibit the classical Debye-like features described above. As shown as an example in Fig. 1 (diffusion-induced ^{19}F NSR in the glassy fluorine ion conductor $27\mathrm{ZrF}_4 \cdot 27\mathrm{HfF}_4 \cdot 20\mathrm{BaF}_2 \cdot 3\mathrm{LaF}_3 \cdot 3\mathrm{AlF}_3 \cdot 20\mathrm{NaF}$ (ZBLAN20) (Kanert *et al.* 1996) the Arrhenius representation of $1/T_1|_{\mathrm{Diff}}$ exhibits an asymmetric peak with remarkably different slopes on either side of the maximum. Further, the frequency dependence of $1/T_1|_{\mathrm{Diff}}$ on the low-temperature side does not obey the ω^{-2} law proposed by the Debye relation.
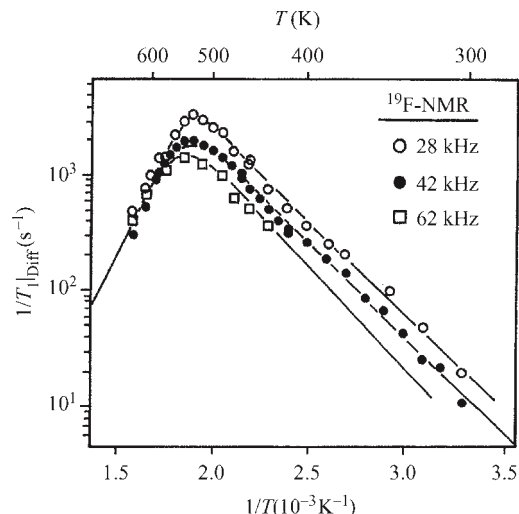
Figure 1
Arrhenius plot of the diffusion-induced ^{19}F NSR rates in the glassy fluorine ion conductor ZBLAN20 observed in the rotating frame at three different frequencies (after Kanert *et al.* 1996).

Two theoretical approaches exist to interpret this unusual behavior. On the basis of the random structure of the glassy network, the correlation time τ (and correspondingly the activation energy E) is assumed to be distributed according to an appropriate distribution function $g(\tau)$ (Svare *et al.* 1993). Then, $G(t)$ is formed by a superposition of exponential decays according to

$$G(t) = \int_0^\infty g(\tau) \mathrm{e}^{-t/\tau} \mathrm{d}\ln\tau \qquad (2)$$

This approach represents the motion of a single particle in a random landscape. As discussed in detail by Beckmann (1988), a large variety of functions $g(\tau)$ can be used to fit properly the experimental data to the model.

There is strong evidence, however, that $G(t)$ decays inherently nonexponentially due both to the Coulomb interaction between the mobile ions and to their interactions with the glass skeleton. There exist different theoretical approaches dealing with the complex coupled motion of charged particles in a random matrix—e.g., Monte Carlo simulations (Maass *et al.* 1995), an analytical jump relaxation model (Funke 1993), a diffusion-controlled relaxation model (Elliott and Owens 1991), and a phenomenological coupling model (Ngai 1993)—which all result in a nonexponential time evolution of $G(t)$. So far, the models do not take into account the real structure of the glasses, i.e., a quantitative agreement cannot be expected between the experimental data and such calculations. In

future, molecular dynamics simulations will offer more realistic results of ionic diffusion-induced NSR in vitreous solids.

However, from the different models the following general features can be extracted: above a lower cross-over time $t_c (\sim 10^{-11}$s) the complexity of the ionic motion enhances the initial ionic jump time $\tau = \tau_{0,\infty} \exp(V/kT)$ to the apparent jump time

$$\tau(t) = f(t_c, n) \cdot \tau_0^{1/(1-n)} = \tau_\infty \exp\left(\frac{V}{(1-n)kT}\right) \quad (3)$$

where V is the microscopic barrier height for the hopping ion and n denotes the so-called coupling coefficient where $0 \leq n \leq 1$. Instead of n, often the coefficient $\beta = 1 - n$ is used in the literature. In consequence, the mean-square displacement $\langle r^2(t) \rangle$ of a moving ion becomes sublinear in time between t_c and $\tau(T)$ ($\langle r^2(t) \rangle \propto t^{1-n}$) which corresponds to a frequency dispersion of the apparent diffusion coefficient (Funke 1993) and gives rise to the non-Debye behavior of the NSR rate. For $t > \tau(T)$ the ion enters the Gaussian region where $\langle r^2(t) \rangle \propto t$. Here one observes the d.c. activation energy E which is related to the barrier height V by $E = V/(1-n)$.

The corresponding correlation function $G(t)$ can be expressed to a good approximation by a stretched exponential function in the relevant time regime $10^{-3} \leq t/\tau \leq 10^2$:

$$G(t) = \langle \omega_c^2 \rangle \exp[-(t/\tau)^{1-n}] \quad (4)$$

The diffusion-induced NSR rate is given by Eqns. (1), (1a), and (4), where for arbitrary exponents $1-n$ the Fourier transformation has to be performed numerically. The following analytical relation, however, represents a good approximation to the numerical results (Maass *et al.* 1995):

$$1/T_1|_{\text{Diff}} = \langle \omega_c^2 \rangle \left(\frac{\tau}{1 + (\omega_0 \tau)^{2-n}} + \frac{4\tau}{1 + (2\omega_0 \tau)^{2-n}} \right) \quad (5)$$

Applying this relation to Fig. 1 one obtains from the slopes $E = 1.15$ eV and $V = 0.34$ eV, i.e., $n = 0.70$. The data confirm also the ω^{n-2}-dependence of $1/T_1$ as proposed by Eqn. (5) for $\omega_0 \tau \gg 1$. Moreover, the temperature dependence of the NSR rate maxima, which is given by the condition $\omega \tau \cong 0.6$, leads to a temperature-dependent correlation time $\tau = 10^{-16}$s. $\exp$ (E/kT) with $E = 1.15$ eV equal to $V/(1-n)$ in accord with Eqn. (3).

Approaching the glass-transition temperature T_g, the shear viscosity η and, therefore, the related correlation time τ_η of the glass both decrease rapidly. The question whether the diffusion-induced NSR rate is affected by the process in the vicinity of T_g is answered by the actual magnitude of the decoupling coefficient $R = \tau_\eta/\tau$. For $R \gg 1$ the glass structure is

rigid on the time scale of the ionic hops, i.e., the observed NSR rate is dominated by the diffusion.

By use of site-selective spin excitation, NSR is able to detect the ionic diffusion separately in different environments. Kim *et al.* (1997) observed the motion of lithium ions in $Li_2S \cdot B_2S_3$ glasses near $3(BS_3)$- and $4(BS_4^-)$-coordinated boron atoms by measuring the temperature dependence of the ^{11}B NSR rate of different parts of the ^{11}B NMR spectrum belonging to BS_3 and BS_4^- units, respectively. They obtained two well-separated NSR rate peaks. From the position of the maxima they drew the conclusion that the lithium ions move much faster close to the 3-coordinated boron than to the 4-coordinated boron. Such site-selective NSR experiments should also be applied to highly-resolved magic angle spinning (MAS)-NMR spectra (Eckert 1992) of glasses, opening new insights into the ionic motion at different sites of the glassy network.

With increasing temperature, the correlation time τ reaches the magnitude of the inverse NMR line width, and the width starts to decrease. Such motional line-width narrowing offers a simple possibility to distinguish diffusing from immobile probe nuclei: while for mobile probes the line width approaches zero for sufficiently high temperatures, the corresponding width of the immobile probes remains finite (Kanert *et al.* 1996).

3. Comparison Between Nuclear Spin Relaxation and Ionic Conductivity

It is very instructive to compare the results of diffusion-induced NSR with those obtained from complex ionic conductivity ($\tilde{\sigma}$) measurements. Though both $1/T_1(\omega, T)$ and $\tilde{\sigma}(\omega, T)$ measurements are probing the same physical process, in practice the results can differ due to the different structure of the underlying correlation functions $G(t)$ and $G_\sigma(t)$. While $G(t)$ is a pair correlation function of the coupling frequencies ω_{ij}, G_σ is a particle autocorrelation function of the ionic velocities v_i (Ngai 1993). In practice, however, the results of NSR and ionic conductivity agree fairly well, i.e., both the correlation functions can be approximated by a stretched exponential (Eqn. (4)) with the same coupling coefficient n but different time constants τ and τ_σ.

This is due to the fact that τ is the mean waiting time (correlation time) of an ion between consecutive hops, while τ_σ denotes the relaxation time of the decaying electric field under constant dielectric displacement. According to Funke (1993), τ and τ_σ are related by

$$\tau = \frac{nq^2 x_0^2}{6\varepsilon_0 \varepsilon_\infty kT} \tau_\sigma = C \cdot \tau_\sigma \quad (6)$$

where n is the density and q the charge of the ions, and x_0 denotes the mean jump distance of a hopping

ion. Using appropriate values for the different quantities (see below) one finds $C \cong 5 \div 100$, i.e., $\tau \gg \tau_\sigma$ in qualitative accord with experimental findings (Kanert *et al.* 1996).

For a uniform correlation function $G(t/\tau)$ for both NSR and conductivity differing only with regard to the time constant τ (i.e., $\tau_\infty \neq \tau_{\sigma,\infty}$), the NSR rate $1/T_1$ can be linked to the imaginary part of the electric modulus, M'', by the following general expression (Funke 1993)

$$1/T_1(\omega_0\tau(T)) \propto [M''(\omega_0\tau_\sigma) + 2M''(2\omega_0\tau_\sigma)]/\varpi_0 \quad (7)$$

This relation turns out to be very useful for comparative NSR and conductivity experiments on ionic transport in glasses.

Unfortunately, until now only a limited number of investigations exists on ionic diffusion in inorganic glasses comparing in detail NSR and conductivity data. Blache *et al.* (1998) performed an extended study on a series of lithium silicophosphate glasses measuring the temperature dependence of Li^+ diffusion by NMR and electrical conductivity for different glass compositions. Part of the results are shown in Fig. 2 exhibiting the dependence of the activation energy E and barrier height V on the concentration $c(Li)$ of the lithium ions for a fixed ratio of the network formers SiO_2 and P_2O_5. The data were obtained from electrical conductivity, ^7Li and ^{31}P NSR, and ^7Li tracer diffusion $D_T(T)$ using the NMR field-gradient technique (Geil 1998). As expected for the diffusion of a single species of charged carriers, $D_T(T)$ was found to be in accord with the diffusion constant $D_\sigma(T)$ calculated from the dc conductivity σ_{dc} by

$D_\sigma = k/(q^2 n) \cdot \sigma_{dc} \cdot T$, i.e., the Haven ratio D_T/D_σ is about 1.

The figure demonstrates that the corresponding quantities V and E obtained from the different experiments agree well, resulting in a uniform coupling coefficient $n = 0.67$ for $c \geqslant 2$ at.%. For $c \leqslant 2$ at.% the data indicate a slight decrease of n as proposed by the coupling model (Ngai 1993). The observed monotonic decrease of the activation energy E with increasing amount of lithium ions could be interpreted fairly well by the simplified Anderson–Stuart relation (Patel and Martin 1992) $E = E_1 + E_2 \cdot c(Li)^{1/3}$ using $E_1 = 1.5$ eV and $E_2 = 1.52$ eV $(at.\%)^{-1/3}$ as best-fit parameters.

Moreover, the authors measured the dependence of τ and τ_σ on temperature and on the concentration of lithium ions. Evaluation of the data revealed that the following relation is approximately valid:

$$\tau \cong 10\tau_\sigma = 5 \times 10^{-14}\text{s} \exp\left(\frac{E(c(Li))}{kT}\right)$$

for $c(Li) \geqslant 5$ at.%. This result seems to confirm Eqn. (6): using the suitable values $\langle n \rangle \cong 0.8 \times 10^{28}\text{m}^{-3}$ ($\hat{=} 10$ at.% Li), $\langle T \rangle = 500$K, $\varepsilon_\infty = 3$, $x_0 = 2.4$Å, one obtains $C \cong 10$ in accord with the experimental findings. It has to be noted, however, that in some glassy ionic conductors the activation energy E observed by NSR was found to be somewhat larger than the corresponding energy E_σ measured by dc conductivity, i.e., $n > n_\sigma$ using the relation $E = V/(1 - n)$ (Kanert *et al.* 1996). Such deviations were proposed also by Monte Carlo simulations (Maass *et al.* 1995). At present, however, a final decision whether Eqn. (6) is correct and E equals E_σ cannot be made because of a lack of sufficient experimental data.

See also: Amorphous Materials: Nuclear Magnetic Resonance, New Techniques; Nuclear Magnetic Resonance Spectrometry

Figure 2
Dependence of the activation energy E and barrier height V of lithium diffusion on the amount of lithium in the glassy lithium ion conductor $Li_2O \cdot SiO_2 \cdot P_2O_5$ observed by different methods (see text). Solid curve is a fit by the Anderson–Stuart model (after Blache *et al.* 1998).

Bibliography

Beckmann P A 1988 Spectral densities and nuclear spin relaxation in solids. *Phys. Rep.* **171**, 85–128
Blache V, Förster J, Jain H, Kanert O, Küchler R, Ngai K L 1998 Ionic motion in lithium silicophosphate glasses by nuclear spin relaxation and electrical conductivity. *Solid State Ionics* **113–5**, 723–31
Dieckhöfer J, Kanert O, Küchler R, Volmari A, Jain H 1997 Composition dependence of low-frequency excitations in lithium silicophosphate glasses by NMR and electrical conductivity. *Phys. Rev. B* **55**, 14836–46
Eckert H 1992 Structural characterization of nanocrystalline solids and glasses using solid state NMR. *Progr. NMR Spectrosc.* **24**, 159–293
Elliott S R, Owens A P 1991 Nuclear spin relaxation in ionically conducting glasses: application of the diffusion-controlled relaxation model. *Phys. Rev. B* **44**, 47–59

Funke K 1993 Jump relaxation in solid electrolytes. *Prog. Solid State Chem.* **22**, 111–95

Geil B 1998 Measurement of translational molecular diffusion using ultrahigh magnetic field gradient NMR. *Concepts Magn. Res.* **10**, 299–321

Kanert O, Dieckhöfer J, Küchler R 1996 Recent progress in the area of NMR characterization of ionic transport and relaxation in glasses. *J. Non-Cryst. Solids* **203**, 252–61

Kim K H, Torgeson D R, Borsa F, Cho J P, Martin S W, Svare I, Majer G 1997 Evidence of complex ionic motion in $xLi_2S \cdot (1-x)B_2S_3$ glassy fast ionic conductors from ^{7}Li and ^{11}B NMR and ionic conductivity measurements. *J. Non-Cryst. Solids.* **211**, 112–25

Maass P, Meyer M, Bunde A 1995 Non-standard relaxation behavior in ionically conducting materials. *Phys. Rev. B* **51**, 8164–77

Ngai K L 1993 Difference between nuclear spin relaxation and ionic conductivity relaxation in superionic glasses. *J. Chem. Phys.* **98**, 6424–30

Patel H K, Martin S W 1992 Fast ionic conduction in $Na_2S \cdot B_2S_3$ glasses: compositional contribution to non-exponentiality in conductivity relaxation in the extreme low-alkali-metal limit. *Phys. Rev. B* **45**, 10292–300

Schmidt-Rohr K, Spiess H W 1994 *Multidimensional Solid State NMR and Polymers*. Academic Press, London

Svare I, Borsa F, Torgeson D R, Martin S W 1993 Correlation functions for ionic motion from NMR relaxation and electrical conductivity in the glassy fast-ion conductor $(Li_2S)_{0.56} \cdot (SiS_2)_{0.44}$. *Phys. Rev. B* **48**, 9336–44

Tang X P, Busch R, Johnson W L, Wu Y 1998 Slow atomic motion in Zr–Ti–Cu–Ni–Be metallic glass studied by NMR. *Phys. Rev. Lett.* **81**, 5358–61

O. Kanert
Universität Dortmund, Germany

Amorphous Superconductors

Amorphous superconductors are a class of superconducting materials that lack long-range, translational ordering in their atomic arrangement. Since the discovery of superconductivity in amorphous bismuth and gallium (a-Bi, a-Ga) by Bückel and Hilsch in the 1950s, noncrystalline superconductors have been the subject of numerous experimental and theoretical studies. Recently, interest in this field has been focused on amorphous transition-metal (TM) superconductors as opposed to the amorphous non-transition-metal (non-TM) superconductors investigated earlier.

The techniques used to synthesize amorphous superconducting materials include quenching from the vapor (obtained by evaporation or sputtering), particle irradiation, ion mixing or ion implantation, and liquid quenching. The technique of quenching from the melt is capable of producing large quantities of metallic glasses in the form of ribbons, flakes or powder suitable for large-scale engineering applications. Vapor deposition and particle bombardment methods are used to prepare thin films amenable to small-scale electronic device applications.

In general, the Cooper pairs in superconductors are formed from time-reversed electron states, no matter how complicated these states are in real space as a result of scattering from various disorders. Hence, the basic mechanism of superconductivity is not expected to be different in disordered or crystalline materials. There are, however, several interesting differences between amorphous superconducting materials and their crystalline counterparts; these differences will be discussed.

1. Systematics of the Transition Temperature

1.1 Nontransition Metals

Amorphous non-TM superconductors usually show an enhancement in transition temperature T_c over that of corresponding crystalline phases. For example, a-Bi thin films become superconducting at about 6 K, whereas the crystalline phase, a semimetal, remains normal down to 0.05 K. The value of T_c for a-Ga is found to be 8.4 K, significantly higher than the T_c of the crystalline phases ($T_c = 1.08$ K for α-Ga and 6 K for β-Ga). A more complete listing of the T_c values of amorphous superconductors and their crystalline counterparts is given in Table 1. It is

Table 1
The T_c of some amorphous (or highly disordered) superconductors and their crystalline counterparts.

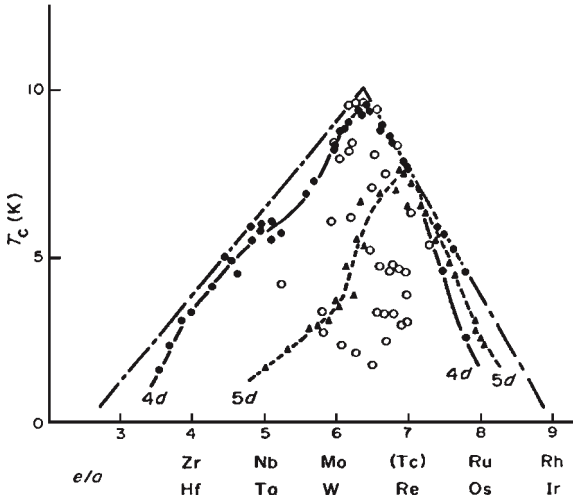| Metals	Amorphous or highly disordered (K)	Crystalline (K)
Nontransition metals		
Pb	7.16	7.2
$Pb_{50}Bi_{50}$	6.99	8.1
Ga	8.4	6 (β-Ga)
		1.08 (α-Ga)
Bi	6.1	< 0.05
Be[a]	10	0.026
Al[a]	6	1.18
Transition metals		
Nb	5.7	9.2
Mo	8–9	0.9
Nb_3Ge	3.6	23
Nb_3Si	3.9	18
Nb_3Sn	3	18
V_3Si	1.5	17
Mo_3Si	7.5	1.4

a Extrapolated values.

noted that T_c for amorphous non-TM superconductors tends to increase with valence and with atomic number for a given valence (Johnson 1981; Bergmann 1976).

1.2 Transition Metals

A systematic study by Collver and Hammond (1973) on amorphous 4*d* and 5*d* TM elements and alloys thereof indicates that the well-known Matthias rule for crystalline superconductors (see *Superconducting Materials, Types of*) is significantly altered for the amorphous state. The variation of T_c as a function of e/a (the average valence electrons–atom ratio) shows a sharp peak at $e/a = 6.4$, corresponding to a half-filled *d* shell (see Fig. 1). More recent work has revealed that T_c as a function of e/a is more symmetric than the original Collver–Hammond curve and similar systematics are also observed in some liquid-quenched TM-metalloid metallic glasses. The T_c of amorphous TM alloys made from elements widely separated in the periodic table is always significantly lower than that of the original Collver–Hammond alloys composed of nearest 4*d* or 5*d* elements. The T_c of alloys mixing the 4*d* and 5*d* elements shows an even more intriguing behavior. For example, whereas the values of T_c for a-MoRe alloys are slightly higher than those for the a-MoRu alloys, lower T_c values

have been found for all the a-MoRh alloys in the same range of e/a. The T_c values for a-NbIr, a-NbRh, a-TaRh and a-TaIr alloys are considerably lower than those for corresponding amorphous near-neighbor TM alloys and show essentially no variation of e/a. These data along with others are plotted in Fig. 1. (Recent T_c data on amorphous alloy systems containing 3*d* elements and noble metals, for example a-ZrCu, a-ZrFe and a-ZrNi, are not included in this plot and should be treated separately.) It is clear from Fig. 1 that there is no universal curve of T_c as a function of e/a for all amorphous TM alloys. It has been suggested that the effects of spin fluctuations and charge transfer may be responsible for this.

At present, there is no satisfactory interpretation for all the systematics of T_c previously described. The data shown in Fig. 1 do suggest, however, that there is an upper limit of T_c for a given e/a in amorphous 4*d* and 5*d* TM alloys as roughly outlined by the modified Collver–Hammond curve. The fact that the peak of this upper-bound curve coincides with half-filled *d* shells suggests that there is an atomic parameter characterizing the e/a dependence of T_c. This point can be qualitatively discussed with the aid of the well-known McMillan formula:

$$T_c(\theta_D/1.45)\exp\left[\frac{-1.04(1+\lambda)}{\lambda - \mu^*(1 + 0.62\lambda)}\right] \qquad (1)$$

where λ is the dimensionless electron–phonon coupling parameter, μ^* is the effective electron–electron Coulomb pseudopotential and θ_D is the Debye temperature. The parameter λ can be expressed as

$$\lambda = N(E_F)\langle I^2 \rangle/M\langle \omega^2 \rangle \qquad (2)$$

where $N(E_F)$ is the bare electronic density of states at the Fermi level, $\langle \omega^2 \rangle$ is an average square phonon frequency and $\langle I^2 \rangle$ is the Fermi-surface average of the electron–phonon interaction strength.

In terms of tight-binding models, it has been suggested that the Collver–Hammond curve essentially reflects the e/a dependence of $N(E_F)$ and that the ratio $\langle I^2 \rangle/\langle \omega^2 \rangle$ is a constant throughout the 4*d* series. A systematic study of the low-temperature specific heat of some of the more stable Collver–Hammond alloy films is crucial in determining $N(E_F)$ quantitatively as a function of e/a. It should be pointed out that the empirical and calculated values of $\langle I^2 \rangle$ for the 4*d* transition metals (Butler 1977) are insensitive to structural change and their e/a variation closely mimics the T_c upper limit shown in Fig. 1.

Figure 1
The T_c of amorphous TM elements and alloys as a function of e/a. The original Collver–Hammond curves for amorphous TM superconductors are shown for ($\bullet$) 4*d* and ($\blacktriangle$) 5*d* metals; also shown are ($\bigcirc$) the T_c values of various amorphous TM alloys made from elements widely separated in the periodic table and from mixing the 4*d* and 5*d* metals. For a given e/a, there is an upper limit of T_c as outlined by the triangular peak ($-\cdot-\cdot$)

2. Strength of the Electron–Phonon Interaction

The coupling between electrons and phonons is fundamentally important to the occurrence of superconductivity and is of particular interest in the case of amorphous superconductors in view of possible

enhancement of the coupling strength through structural disorder as suggested by several theories. The strength of the electron–phonon interaction can be estimated from (a) the ratio of Bardeen–Cooper–Schrieffer (BCS) energy gap to transition temperature, $2\,\Delta(0)/k_B T_c$, and (b) the parameter λ (see *Superconducting Materials*: *BCS and Phenomenological Theories*). The BCS gap can be measured directly by superconductive tunnelling experiments or estimated indirectly from calorimetric measurements. The parameter λ can be determined using either the McMillan formula for T_c or the technique of superconductive tunnelling spectroscopy through

$$\lambda = 2 \int_0^\infty d\omega\, \omega^{-1} \alpha^2(\omega) F(\omega) \qquad (3)$$

where $\alpha^2(\omega) F(\omega)$ is the Eliashberg electron–phonon spectral function.

The results accumulated so far clearly lead to three conclusions.

First, amorphous non-TM superconductors are all characterized by a very strong electron–phonon coupling (i.e., $2\,\Delta(0)/k_B T_c \sim 4$–5 and $\lambda > 2$), as are their crystalline counterparts.

Second, amorphous TM or TM-based superconductors are found to be in the BCS weak-coupling limit. In particular, the electron–phonon coupling strength of several strong-coupled A15 superconductors is found to be reduced to the BCS limit in the amorphous state. These experimental findings suggest that structural disorder alone does not necessarily give rise to a significantly enhanced electron–phonon interaction.

Third, a detailed analysis of the tunnelling data for various amorphous non-TM superconductors has revealed that the Eliashberg function is enhanced and varies linearly with ω in the low-frequency region as predicted by various theories. There is no significant low-frequency enhancement found in $\alpha^2 F(\omega)$ for amorphous nitrogen-stabilized niobium and molybdenum films. The function $\alpha^2 F(\omega)$, in fact, follows the phonon density of states $F(\omega)$ based on a structural model of dense random packing of hard spheres. From this finding, it is concluded that the observed low-frequency enhancement in $\alpha^2 F(\omega)$ for amorphous non-TM superconductors is essentially a manifestation of an increase in the electron–phonon interaction caused by structural disorder. The lack of such enhancement in amorphous TM superconductors is attributed to the "nearly localized" nature of d electrons, which are relatively insensitive to structural disorder.

In a more general perspective, this result can also be understood by noting the difference between the TM and non-TM amorphous superconductors in the effectiveness of the phonon modes in contributing to the electron–phonon coupling. Unlike amorphous TM superconductors, the phonon density of states in non-TM superconductors (crystalline and amorphous) is distributed over a range from 0 to approximately 10 meV and is most efficient in achieving a strong electron–phonon interaction (Tsuei 1981).

3. Critical Fields

Amorphous superconductors are all characterized by relatively large upper critical fields H_{c2} in view of their generally low T_c values. This is mainly a manifestation of a short electron mean free path ($l \lesssim 1\,\text{nm}$) leading to a short zero-temperature coherence length $\xi(0)$ (see *Coherence Length*, *Proximity Effect and Fluctuations*). The upper critical field at 0 K is related to $\xi(0)$ by

$$H_{c2}(0) = \Phi_0 / 2\pi \xi^2(0) \qquad (4)$$

where $\Phi_0 = h/2e$ is the flux quantum. Typical values of $\mu_0 H_{c2}(0)$ are about 2–5 T (20–50 kG) for amorphous non-TM superconductors and are in the range 10–40 T (100–400 kG) for the noncrystalline TM or TM-based superconductors. The lower critical field $H_{c1}(T)$ for several metallic glasses has been measured; $\mu_0 H_{c1}(0)$ values are typically of the order of 1–10 mT (10–100 G). Both $H_{c2}(T)$ and $H_{c1}(T)$ are found to vary linearly with temperature over a wide range of temperatures below T_c ($\sim 0.5 T_c$ to T_c). Examples of dH_{c2}/dT near T_c are about $-2\,\text{T K}^{-1}$ to $-3\,\text{T K}^{-1}$ for amorphous TM superconductors and about $-0.5\,\text{T K}^{-1}$ for amorphous simple metals. The values of dH_{c1}/dT are about $1\,\text{mT K}^{-1}$.

From critical-field measurements, values for $\xi(0)$ and the Ginzburg–Landau parameter κ can be estimated; the values are of the order of 5 nm and 60, respectively. Such large values of κ represent a true indication of the extreme type II, or "dirty limit," behavior expected for amorphous superconductors. Detailed studies of the temperature dependence of $H_{c2}(T)$ for several amorphous TM alloys indicate that H_{c2} is enhanced at low temperatures by the effect of weak localization as predicated by the FEM theory (Fukuyama *et al.* 1984). The amount of the H_{c2} enhancement depends on the alloy system and can be as large as 20% (Poon 1985a,b). It should be mentioned that the quantum correction effects of weak localization and interaction also manifest themselves in suppressing T_c (Fukuyama *et al.* 1984) and reducing the temperature coefficient of the normal-state resistivity.

4. Flux Pinning Phenomena

The pinning of the flux line lattice (FLL) in superconductors can be studied by measuring the critical current density $J_c(T, H)$ as a function of temperature and applied field. Results of critical-current measurements on amorphous superconductors show that J_c at $H = 0$ is in general relatively low ($\sim 10^7$–$10^8\,\text{A m}^{-2}$)

and that it decreases rapidly with increasing field. Such a weak FLL pinning can probably be attributed to the homogeneity and isotropy, on a scale of $\xi(0)$, intrinsic in all amorphous materials. It is exactly this characteristic property which makes direct use of amorphous superconductors in high-field applications less attractive. A possible solution to this problem is to incorporate, by appropriate heat treatments, some second-phase precipitates in an amorphous superconducting matrix (Johnson 1981). Homogeneous amorphous superconductors, however, are ideal for studying flux pinning phenomena in terms of existing theory (see *Electrodynamics of Superconductors: Flux Properties*). The fact that amorphous TM or TM-based superconductors are weak coupled and in the extreme type II limit simplifies the analysis of the experimental data considerably, because theoretical expressions in the dirty limit are highly developed. Furthermore, pinning behavior in these materials (in the form of carefully prepared thin films) is expected to be insensitive to complications arising from pinning by surface irregularities, edge dislocations and buckling of the flux lines.

A recent fundamental study of flux pinning in amorphous films of Nb_3Ge and Nb_3Si (Kes and Tsuei 1981) led to the following results.

(a) Owing to the large κ and low J_c, the FLL in amorphous thin-film superconductors is essentially two dimensional.

(b) The pinning force density $F_p (= J_c B$, where B is flux density) as a function of perpendicular field and temperature is found to be in good agreement with the theory of collective pinning.

(c) A sharp peak in F_p is observed near H_{c2}. A pinning-mediated renormalization of the shear modulus of the FLL is probably responsible for this peak effect.

(d) The F_p for samples with relatively large J_c shows a domelike behavior characteristic of strong pinning. By annealing, J_c decreases by up to two orders of magnitude and both two-dimensional collective pinning and the peak effect are recovered, supporting the view that weak pinning is an essential requirement to observe the collective behavior. It has also been demonstrated that the flux pinning can serve as a sensitive probe to study structural relaxation in amorphous metals.

The concept of collective flux pinning along with the consideration of the thermal fluctuation effects has been used to understand the flux-creep-related phenomena in high-T_c cuprate superconductors (Feigel'man and Vinokur 1990). It is interesting to note that both amorphous superconductors and high-T_c copper oxides are characterized by short coherence length and relatively high normal-state resistivity except that there is a large difference in T_c and temperature scale.

5. Potential Applications

Most amorphous non-TM superconductors are structurally stable only at very low temperatures. For example, a-Bi films are found to crystallize at 20 K and the amorphous phase of gallium films transforms into a crystalline state (β-Ga, $T_c = 6.4$ K) at about 15 K. Further annealing at 60 K results in the room-temperature stable phase α-Ga with a T_c of 1.08 K. In sharp contrast, many TM or TM-based superconducting alloys can resist crystallization at temperatures up to more than 1000 K. In addition to this phase stability, these materials are ductile, flexible and possess extremely high mechanical strength, comparable with that of single crystals. Potential areas for using amorphous superconductive materials include high-field magnets, especially for use in an environment of high-level radiation, and possibly some specialized vortex memory devices for computer applications.

See also: Thin Films, Multilayers and Devices, Superconducting

Bibliography

Bergmann G 1976 Amorphous metals and their superconductivity. *Phys. Rep.* **27**, 159–85
Butler W H 1977 Electron–phonon coupling in the transition metals. *Phys. Rev. B* **15**, 5267–82
Collver M M, Hammond R H 1973 Superconductivity in "amorphous" transition-metal alloy films. *Phys. Rev. Lett.* **30**, 92–5
Feigel'man M V, Vinokur V M 1990 Thermal fluctuations of vortex lines, pinning, and creep in high-T_c superconductors. *Phys. Rev. B* **41**, 8986–90
Fukuyama H, Ebisawa H, Maekawa S 1984 Bulk superconductivity in weakly localized regime. *J. Phys. Soc. Jpn.* **53**, 3560–7
Johnson W L 1981 Superconductivity in metallic glasses. In: Guntherodt H, Beck H (eds.) 1981 *Glassy Metals 1*. Springer, Berlin, Chap. 9, pp. 191–223.
Kes P H, Tsuei C C 1981 Collective flux pinning phenomena in amorphous superconductors. *Phys. Rev. Lett.* **47**, 1930–4
Poon S J 1985a Amorphous and highly disordered metallic superconductors. *Physica B* **135**, 259–66
Poon S J 1985b Localization effects on superconductivity in homogeneous metallic glasses. *Phys. Rev. B* **31**, 7442–5
Tsuei C C 1981 Amorphous superconductors. In: Foner S, Schwartz B B (eds.) 1981 *Superconductor Materials Science*. Plenum, New York, Chap. 12, pp. 735–56.

C. C. Tsuei
IBM, Yorktown Heights, New York, USA

B

Boltzmann Equation and Scattering Mechanisms

When an external force is applied to the conduction electron system of a solid, a drift velocity results. Random scattering effects tend to restore a dynamical balance between the acceleration caused by the external forces and restoring forces due to scattering processes.

In general we expect currents J_i to develop as a response of the system to generalized external forces X_k. If these responses can be considered to be linear the relation between the forces X_k and the currents J_i can be written as

$$J_i = \sum_{k=1}^{n} L_{ik} X_k \qquad (1)$$

The coefficients L_{ik} are called the linear transport coefficients. Their physical nature depends on which current is connected to which force. If the forces and the currents are properly selected so that the internal entropy production per unit time is

$$\frac{\mathrm{d}S_i}{\mathrm{d}t} = \sum_{i=1}^{n} J_i X_i \qquad (2)$$

then they are canonically conjugated in the sense of irreversible thermodynamics. In this case Onsager's theorem provides the symmetry relation

$$L_{ik}(\vec{B}) = L_{ki}(-\vec{B}) \qquad (3)$$

for these transport coefficients, where $\vec{B}$ is an external magnetic field.

In principle two different kinds of force can induce a current J_i. The first and the more familiar type is an electric field acting on the electron system. The second type of force has its origin in statistics; it is not a "force" in the usual sense but arises from concentration and temperature gradients. It should be noted that an external magnetic field is influencing the transport phenomena but does not contribute to a current in the sense discussed above.

In order to give a theoretical description of the transport phenomena (electrical and thermal resistivity, thermopower, Peltier effect, etc.) the Boltzmann formalism may be used as one among a number of different other theoretical concepts.

1. Distribution Function

The Boltzmann formalism is based on the assumption that a distribution function in phase space $(\vec{r}, \vec{k})$ can be defined. Since we are dealing with a strongly interacting quantum mechanical system it is by no means clear that such a function can be defined because of the Heisenberg uncertainity principle. In many cases, however, one considers the distribution function to be a function of k only; the Heisenberg uncertainty principle does not preclude the use of this distribution. When an $\vec{r}$-dependence is considered at all, the position in real space usually occurs through the dependence of the distribution function on external position dependent parameters, such as the $\vec{r}$-dependence of the temperature in the case of an applied temperature gradient. This expression makes sense if the electrons can be localized over macroscopic distances. This can be done by using wave-packets which contain a small number of wave-numbers. In this limited sense one can use a distribution function which is a function of both $\vec{k}$ and $\vec{r}$ (Butcher 1973).

1.1 Bloch Electrons

For an electron interacting with a periodic potential

$$V(\vec{r} + \vec{R}_l) = V(\vec{r}), \; \vec{R}_l \text{ lattice vector} \qquad (4)$$

the stationary eigenstates are given by the solutions of the Schrödinger equation

$$\left(-\frac{\hbar^2}{2m}\Delta + V(\vec{r})\right)\psi_{n\sigma\vec{k}}(\vec{r}) = E_{n\sigma}(\vec{k})\psi_{n\sigma\vec{k}}(\vec{r}) \quad (5)$$

where n, σ, and $\vec{k}$ denote the band index, the spin, and the wave-vector of the conduction electrons, respectively.

The eigenstates are usually written as Bloch functions

$$\psi_{n\sigma\vec{k}}(\vec{r}) = \frac{1}{\sqrt{N}} e^{i\vec{k}\cdot\vec{r}} u_{n\sigma\vec{k}}(\vec{r}) \qquad (5a)$$

with the periodic amplitude

$$u_{n\sigma\vec{k}}(\vec{r} + \vec{R}_l) = u_{n\sigma\vec{k}}(\vec{r}) \qquad (5b)$$

where N is the number of the unit cells of the crystal. The eigenvalues $E_{n\sigma}(\vec{k})$ of Eqn. (5) are functions of the wave-vector $\vec{k}$. From Kramer's degeneracy

$$E_{n,-\sigma}(-\vec{k}) = E_{n,\sigma}(\vec{k}) \qquad (5c)$$

it follows that the electrical (and the thermal) currents for a thermodynamical equilibrium state are zero.

1.2 Semiclassical Motion of Wave-packets

In order to describe the movement of an electron through the periodic array of the ions in the lattice, the electrons are represented by wave-packets. Constructing a wave-packet from Bloch states in the vicinity of a wave vector $\vec{k}$ in the energy band $n\sigma$, we can consider the time dependence of the shape of this wave-packet in real space as well as in reciprocal space corresponding to a classical particle with position $\vec{r}$ and momentum $\vec{p}$.

The corresponding semiclassical equations describing the movement of a wave-packet are:

$$\vec{v} = \frac{\mathrm{d}\,\vec{r}}{\mathrm{d}t} = \frac{1}{\hbar}\vec{\nabla}_k E_{n\sigma}(\vec{k}) \qquad (6a)$$

$$\frac{\mathrm{d}\,\vec{k}}{\mathrm{d}t} = \frac{1}{\hbar}\,\vec{F} \qquad (6b)$$

$\vec{F}$ is an external force acting on the electron (for an electromagnetic field this force is the Lorentz force). The mechanical momentum $\vec{p}$ is connected in the usual way with the wave vector: $\vec{p} = \hbar\,\vec{k}$.

1.3 Electrical and Heat Current

Using Eqns. (6a) and (6b) each electron in an energy band $n\sigma$ gives a trajectory in the 6-dimensional phase space $(\vec{k},\,\vec{r})$. We therefore define (in analogy to classical statistical mechanics) a distribution function $f(n,\sigma,\,\vec{k},\,\vec{r},\,t)$ with the following properties

$$\frac{1}{(2\pi)^3}\,\Delta^3 k \Delta^3 r$$

$$\times f(n,\,\sigma,\,\vec{k},\,\vec{r},\,t) = \begin{cases} \text{number of electrons} \\ \text{in the energy band } n\sigma \\ \text{within the phase space} \\ \text{volume } \Delta^3 k \Delta^3 r \end{cases} \qquad (7)$$

The factor $1/(2\pi)^3$ ensures, that the distribution function $f(n,\sigma,\vec{k},\vec{r},t)$ for a local thermodynamical equilibrium state (characterized by the local temperature $T(\vec{r})$ and the local chemical potential $\mu(\vec{r})$) is identical with the local Fermi distribution function

$$f(n,\,\sigma,\,\vec{k};\,T(\vec{r}),\,\mu(\vec{r})) = f_0\!\left(\frac{E_{n\sigma\,\vec{k}} - \mu(\vec{r})}{k_B T(\vec{r})}\right) \quad (8)$$

whereby

$$f_0(x) = \frac{1}{e^x + 1}$$

Using the distribution function we are able to calculate the mean values of all single electron properties.

In the following the abbreviation γ is used for all three quantum numbers n, σ, and $\vec{k}$ ($\gamma \equiv n, \sigma, \vec{k}$) in order to characterize the Bloch states. Furthermore we use the notation

$$\sum_\gamma \cdots = \sum_{n,\sigma} \frac{Vol}{(2\pi)^3} \int_{1.\mathrm{BZ}} \mathrm{d}^3 k \ldots \qquad (9)$$

where the integral is over the 1st Brillouin zone. The local electron density can now be written as

$$n(\vec{r},\,t) = \frac{1}{Vol}\sum_\gamma f(\gamma,\,\vec{r},\,t) \qquad (10)$$

with the total number of electrons N_e

$$N_e = \int \mathrm{d}^3 r\, n(\vec{r},\,t) \qquad (11)$$

It then follows that the electrical current density, $\vec{I}$, may be expressed as

$$\vec{I}(\vec{r},\,t) = \frac{1}{Vol}\sum_\gamma f(\gamma,\,\vec{r},\,t)(-e\,\vec{v}_\gamma) \qquad (12)$$

whereby $e = |q_e|$ is the absolute value of the electric charge of an electron.

A similar expression may be derived for the thermal heat current density $\vec{J}$,

$$\vec{J}(\vec{r},\,t) = \frac{1}{Vol}\sum_\gamma f(\gamma,\,\vec{r},\,t)(E_\gamma - \mu)\,\vec{v}_\gamma \qquad (13)$$

The energy is measured relative to the chemical potential μ; this is the correct heat-current for a statistical force caused by a temperature gradient. Then we obtain the usual relation between the thermopower S and the Peltier coefficient Π: $\Pi = TS$.

2. Boltzmann Equation

For the calculation of the current densities $\vec{I}$ and $\vec{J}$ the distribution function f is needed (see Eqns. (12) and (13)). This distribution function is a solution of the Boltzmann equation in presence of external forces $\vec{F}$. The Boltzmann equation describes the time development of the distribution function and can be written in the form

$$\frac{\partial f(\gamma,\,\vec{r},\,t)}{\partial t} + \frac{1}{\hbar}\vec{F}\cdot\vec{\nabla}_k f(\gamma,\,\vec{r},\,t)$$
$$+ \vec{v}\cdot\vec{\nabla}_r f(\gamma,\,\vec{r},\,t) = \left(\frac{\partial f}{\partial t}\right)_C \qquad (14)$$

The left hand side describes the time development of the distribution function caused by the semiclassical equations of motion (see Eqns. (6a) and (6b)). These terms are called drift terms. The right hand side is the

collision term. It takes into account the changes of the distribution function due to scattering processes.

2.1 Collision Term

The change of $f(\gamma, \vec{r}, t)$ caused by scattering processes may be subdivided as follows:

Scattering processes from electron state γ' to electron state γ result in an increase of $f(\gamma, \vec{r}, t)$:

$$f(\gamma')[1 - f(\gamma)]P_{\gamma' \to \gamma} \tag{15a}$$

Scattering processes from electron state γ to electron state γ' result in a decrease of $f(\gamma, \vec{r}, t)$:

$$f(\gamma)[1 - f(\gamma')]P_{\gamma \to \gamma'} \tag{15b}$$

The factor f gives the probability that the initial state is occupied whereas the factor $(1-f)$ ensures that the final state is empty. $P_{\gamma \to \gamma'}$ is the quantum mechanical probability per unit time for the transition from the state γ to the state γ'. It is expressed using first order perturbation theory by Fermi's golden rule

$$P_{\gamma \to \gamma'} = \frac{2\pi}{\hbar} \sum_{\psi \psi'} g_\psi |\langle \gamma\psi | H_{\text{int}} | \gamma'\psi' \rangle|^2 \delta(E_{\gamma\psi} - E_{\gamma'\psi'}) \tag{16}$$

In this equation H_{int} is the interaction Hamiltonian between the Bloch electrons and the system (rest of the solid) characterized by quantum states ψ and ψ'. g_ψ is the probability that one finds the system in the state ψ. If a thermodynamical description of the system is possible, this factor corresponds to the Boltzmann factor

$$g_\psi = \frac{e^{-\beta E_\psi}}{\sum_\psi e^{-\beta E_\psi}} \tag{17}$$

whereby β is proportional to the inverse temperature: $\beta = 1/(k_B T)$ (k_B is the Boltzmann constant, T is the temperature). The collision term is now the sum over all possible scattering processes which contribute to a change of the distribution function at γ:

$$\left(\frac{\partial f(\gamma)}{\partial t}\right)_{\text{C}} = \sum_{\gamma'} \{ f(\gamma')[1 - f(\gamma)]P_{\gamma' \to \gamma}$$
$$- f(\gamma)[1 - f(\gamma')]P_{\gamma \to \gamma'} \} \tag{18}$$

2.2 Thermal Equilibrium

The thermal equilibrium distribution function f_0 is characterized by a vanishing collision term:

$$\left(\frac{\partial f}{\partial t}\right)_{\text{C0}} = \sum_{\gamma'} \{ f_0(\gamma')[1 - f_0(\gamma)]P_{\gamma' \to \gamma}$$
$$- f_0(\gamma)[1 - f_0(\gamma')]P_{\gamma \to \gamma'} \} = 0 \tag{19}$$

Because this equilibrium condition must be fulfilled for any interaction, it follows that each term of this sum is zero and hence:

$$f_0(\gamma')[1 - f_0(\gamma)]P_{\gamma' \to \gamma} = f_0(\gamma)[1 - f_0(\gamma')]P_{\gamma \to \gamma'} \tag{20}$$

This equation allows the definition of a symmetric equilibrium transition rate

$$W_{\gamma'\gamma} = f_0(\gamma')[1 - f_0(\gamma)]P_{\gamma' \to \gamma}$$
$$= f_0(\gamma)[1 - f_0(\gamma')]P_{\gamma \to \gamma'} = W_{\gamma\gamma'} \tag{21}$$

which will be used in the treatment of the linearized Boltzmann equation.

The thermal equilibrium distribution function f_0 is the Fermi–Dirac function

$$f_0(\beta(E_\gamma - \mu)) = \frac{1}{e^{\beta(E_\gamma - \mu)} + 1} \tag{22}$$

characterized by a temperature T and a chemical potential μ. With this function we obtain from Eqn. (20) the relation

$$e^{\beta E_\gamma} P_{\gamma' \to \gamma} = e^{\beta E_{\gamma'}} P_{\gamma \to \gamma'} \tag{23}$$

which has to be fulfilled by the transition probabilities $P_{\gamma \to \gamma'}$ for any scattering process.

3. Linearized Boltzmann Equation

Assuming that there is simultaneously a time-independent electric and magnetic field applied to the system of conduction electrons we can make use of the Lorentz force

$$\vec{F} = -e \left(\frac{1}{c} \vec{v} \times \vec{B} + \vec{E} \right) \tag{24}$$

For this time-independent force we can look for a time-independent distribution function $f(\gamma, \vec{r})$ which fulfils the Boltzmann equation (Eqn. (14))

$$-\frac{e}{\hbar c} (\vec{v}_\gamma \times \vec{B}) \cdot \vec{\nabla}_k f(\gamma, \vec{r}) - \frac{e}{\hbar} \vec{E} \cdot \vec{\nabla}_k f(\gamma, \vec{r})$$
$$+ \vec{v}_\gamma \cdot \vec{\nabla}_r f(\gamma, \vec{r}) = \left(\frac{\partial f}{\partial t}\right)_{\text{C}} \tag{25}$$

As it is shown in Eqn. (18) the collision term depends also on the distribution function.

3.1 Linearization of the Boltzmann Equation

Due to the external forces the local thermodynamical equilibrium distribution function $f_0(\gamma, T(\vec{r}), \mu(\vec{r}))$ is disturbed. Assuming this distortion to be small we can use

$$f(\gamma, \vec{r}) = f_0(\gamma, T(\vec{r}), \mu(\vec{r})) + f_1(\gamma, \vec{r}) \tag{26}$$

The Boltzmann equation thus splits into equations of zero, first, and higher order. Terms of higher than first order will not be included in the further discussion.

The zero order equation reads:

$$-\frac{e}{\hbar c}(\vec{v}_\gamma \times \vec{B}) \cdot \vec{\nabla}_k f_0(\gamma, \ \vec{r}) = \left(\frac{\partial f}{\partial t}\right)_{C0} \qquad (27)$$

with the zero order collision term given in Eqn. (19). A thermodynamic state characterized by a local temperature distribution $T(\vec{r})$ and a local chemical potential $\mu(\vec{r})$ has the undisturbed distribution function

$$f_0(\gamma, \ \vec{r}) = \frac{1}{e^{\beta(\vec{r})[E_\gamma - \mu(\vec{r})]} + 1} \qquad (28)$$

and therefore Eqn. (27) is fulfilled since both sides are zero.

The first order equation reads:

$$-\frac{e}{\hbar} \ \vec{E} \cdot \vec{\nabla}_k f_0(\gamma, \ \vec{r}) + \vec{v}_\gamma \cdot \vec{\nabla}_r f_0(\gamma, \ \vec{r})$$
$$= \left(\frac{\partial f}{\partial t}\right)_{C1} + \frac{e}{\hbar c} \ [\vec{v}_\gamma \times \vec{B}] \cdot \vec{\nabla}_k f_1(\gamma, \ \vec{r}) \qquad (29)$$

with the first-order collision term

$$\left(\frac{\partial f}{\partial t}\right)_{C1} = \sum_{\gamma'} \{f_1(\gamma')[1 - f_0(\gamma)]P_{\gamma' \to \gamma} - f_0(\gamma')f_1(\gamma)P_{\gamma' \to \gamma}$$
$$- f_1(\gamma)[1 - f_0(\gamma')]P_{\gamma \to \gamma'} + f_0(\gamma)f_1(\gamma')P_{\gamma \to \gamma'}\} \qquad (30)$$

Equation (29) is frequently called linearized Boltzmann equation and it is used to calculate the linear transport coefficients.

Using the symmetric equilibrium transition rate from Eqn. (21) the linear collision term can be written as:

$$\left(\frac{\partial f}{\partial t}\right)_{C1} = \sum_{\gamma'} \left\{ \frac{f_1(\gamma')}{f_0(\gamma')[1 - f_0(\gamma')]} - \frac{f_1(\gamma)}{f_0(\gamma)[1 - f_0(\gamma)]} \right\} W_{\gamma\gamma'} \qquad (31)$$

Using for f_0 the local thermodynamic distribution function given by Eqn. (28) we can calculate the gradient of this function. The linearized Boltzmann equation is then given by:

$$-\frac{\partial f_0(\gamma, \vec{r})}{\partial E_\gamma} \ \vec{v}_\gamma \cdot \left(\underbrace{e\vec{E} + \vec{\nabla}_r \mu}_{e\vec{E}'} + \frac{E_\gamma - \mu}{T} \ \vec{\nabla}_r T \right)$$
$$= \left(\frac{\partial f}{\partial t}\right)_{C1} + \frac{e}{\hbar c}(\vec{v}_\gamma \times \vec{B}) \cdot \vec{\nabla}_k f_1(\gamma, \vec{r}) \qquad (32)$$

We have assumed that a spatial variation of the temperature $T(\vec{r})$ and the chemical potential $\mu(\vec{r})$ are represented by first-order terms.

3.2 Operator Formalism

Instead of describing the distortion of the distribution function by f_1 we use a function ϕ, which is connected to f_1 through the relation

$$f_1(\gamma, \ \vec{r}) := -\frac{\partial f_0(\gamma, \ \vec{r})}{\partial E_\gamma} \phi(\gamma, \ \vec{r})$$
$$= \beta f_0(\gamma, \ \vec{r})[1 - f_0(\gamma, \ \vec{r})]\phi(\gamma, \ \vec{r}) \qquad (33)$$

Equation (31) is now used to define the linear collision operator C

$$C\phi(\gamma, \ \vec{r}) := \left(\frac{\partial f}{\partial t}\right)_{C1}$$
$$= \beta \sum_{\gamma'} W_{\gamma\gamma'}[\phi(\gamma', \ \vec{r}) - \phi(\gamma, \ \vec{r})] \qquad (34)$$

The second term on the right hand side of Eqn. (32) is used in an analogous fashion to define a magnetic operator Ω:

$$\Omega\phi(\gamma, \ \vec{r}) := \beta f_0(\gamma, \ \vec{r})[1 - f_0(\gamma, \ \vec{r})]$$
$$+ \frac{e}{\hbar c}(\vec{v}_\gamma \times \vec{B}) \cdot \vec{\nabla}_k \phi(\gamma, \ \vec{r}) \qquad (35)$$

With these two operators the linearized Boltzmann Eqn. (32) can be written in the short notation

$$(C + \Omega)\phi(\gamma, \vec{r}) = -\frac{\partial f_0(\gamma, \ \vec{r})}{\partial \varepsilon_\gamma} \ \vec{v}_\gamma \cdot \vec{X} \qquad (36)$$

with the general force $\vec{X}$ defined as

$$\vec{X} = e\vec{E}' + \frac{\varepsilon_\gamma}{T} \ \vec{\nabla}_r T \qquad (37)$$

and a modified electron energy

$$\varepsilon_\gamma = E_\gamma - \mu \qquad (38)$$

4. Linear Transport Coefficients

Using Eqn. (26) we can calculate the stationary electrical current density I and the stationary heat current density J according to Eqns. (12) and (13)

$$\vec{I}(\vec{r}) = -\frac{e}{Vol} \sum_\gamma [f_0(\gamma, \ \vec{r}) + f_1(\gamma, \ \vec{r})] \ \vec{v}_\gamma \qquad (39a)$$

$$\vec{J}(\vec{r}) = \frac{1}{Vol} \sum_\gamma [f_0(\gamma, \ \vec{r}) + f_1(\gamma, \ \vec{r})][E_\gamma - \mu] \ \vec{v}_\gamma \qquad (39b)$$

There is no contribution to both current densities due to f_0. Using the function ϕ (see Eqn. (33)) the

expressions for the current densities are

$$\vec{I}(\vec{r}) = +\frac{e}{Vol} \sum_{\gamma} \frac{\partial f_0(\gamma, \vec{r})}{\partial \varepsilon_\gamma} \vec{v}_\gamma \phi(\gamma, \vec{r}) \quad (40a)$$

$$\vec{J}(\vec{r}) = -\frac{1}{Vol} \sum_{\gamma} \frac{\partial f_0(\gamma, \vec{r})}{\partial \varepsilon_\gamma} \varepsilon_\gamma \vec{v}_\gamma \phi(\gamma, \vec{r}) \quad (40b)$$

For the calculation of the heat current the modified electron energy ε_γ is used according to Eqn. (38). The function ϕ obtained as a solution of the linearized Boltzmannn equation (Eqn. (36)) can be written formally as:

$$\phi(\gamma, \vec{r}) = -(C + \Omega)^{-1} \frac{\partial f_0(\gamma, \vec{r})}{\partial \varepsilon_\gamma} \vec{v}_\gamma \cdot \vec{X} \quad (41)$$

The current densities thus obtained are given by:

$$\vec{I}(\vec{r}) = -\frac{e}{Vol} \sum_{\gamma} \frac{\partial f_0(\gamma, \vec{r})}{\partial \varepsilon_\gamma} \vec{v}_\gamma (C + \Omega)^{-1} \frac{\partial f_0(\gamma, \vec{r})}{\partial \varepsilon_\gamma} \vec{v}_\gamma \cdot \vec{X} \quad (42a)$$

$$\vec{J}(\vec{r}) = +\frac{1}{Vol} \sum_{\gamma} \frac{\partial f_0(\gamma, \vec{r})}{\partial \varepsilon_\gamma} \varepsilon_\gamma \vec{v}_\gamma (C + \Omega)^{-1}$$
$$\times \frac{\partial f_0(\gamma, \vec{r})}{\partial \varepsilon_\gamma} \vec{v}_\gamma \cdot \vec{X} \quad (42b)$$

4.1 Phenomenological Transport Coefficients

Using the expression for the general force $\vec{X}$ (see Eqn. (37)) these current densities are linear functions of the general electric field strength $\vec{E}'$ and the temperature gradient $\vec{\nabla}_r T$:

$$\vec{I}(\vec{r}) = e^2 \overleftrightarrow{\mathbf{K}}_{00} \cdot \vec{E} + e k_B \overleftrightarrow{\mathbf{K}}_{01} \cdot \vec{\nabla}_r T \quad (43a)$$

$$\vec{J}(\vec{r}) = -e k_B T \overleftrightarrow{\mathbf{K}}_{10} \cdot \vec{E} - k_B^2 2 T \overleftrightarrow{\mathbf{K}}_{11} \cdot \vec{\nabla}_r T \quad (43b)$$

It is important to note that the coefficients $\overleftrightarrow{K}_{ij}$ represent tensors which are functions of the external magnetic field:

$$\overleftrightarrow{\mathbf{K}}_{ij}(\vec{B}) := -\frac{1}{Vol} \sum_{\gamma} \left(\frac{\varepsilon_\gamma}{k_B T}\right)^i \frac{\partial f_0(\gamma, \vec{r})}{\partial \varepsilon_\gamma} \vec{v}_\gamma \circ (C + \Omega)^{-1}$$
$$\times \frac{\partial f_0(\gamma, \vec{r})}{\partial \varepsilon_\gamma} \vec{v}_\gamma \left(\frac{\varepsilon_\gamma}{k_B T}\right)^j \quad (44)$$

Equations (43a) and (43b) are now compared with the phenomenological transport equations as

obtained in the scope of irreversible thermodynamics

$$\vec{E} = \overleftrightarrow{\rho} \cdot \vec{I} + \overleftrightarrow{S} \cdot \vec{\nabla}_r T \quad (45b)$$

$$\vec{J} = \overleftrightarrow{\Pi} \cdot \vec{I} - \overleftrightarrow{\lambda} \cdot \vec{\nabla}_r T \quad (45b)$$

The different transport tensors: electrical resistivity $\overleftrightarrow{\rho}$, thermopower $\overleftrightarrow{S}$, Peltier coefficient $\overleftrightarrow{\Pi}$, and thermal conductivity $\overleftrightarrow{\lambda}$ can now be written as:

$$\overleftrightarrow{\rho}(\vec{B}) = \frac{1}{e^2}(\overleftrightarrow{\mathbf{K}}_{00}(\vec{B}))^{-1} \quad (46a)$$

$$\overleftrightarrow{S}(\vec{B}) = -\frac{k_B}{e}(\overleftrightarrow{\mathbf{K}}_{00}(\vec{B}))^{-1} \cdot \overleftrightarrow{\mathbf{K}}_{01}(\vec{B}) \quad (46b)$$

$$\overleftrightarrow{\Pi}(\vec{B}) = -\frac{k_B T}{e} \overleftrightarrow{\mathbf{K}}_{10}(\vec{B}) \cdot (\overleftrightarrow{\mathbf{K}}_{00}(\vec{B}))^{-1} \quad (46c)$$

$$\overleftrightarrow{\lambda}(\vec{B}) = k_B^2 T [\overleftrightarrow{\mathbf{K}}_{11}(\vec{B}) - \overleftrightarrow{\mathbf{K}}_{10}(\vec{B}) \cdot (\overleftrightarrow{\mathbf{K}}_{00}(\vec{B}))^{-1} \cdot \overleftrightarrow{\mathbf{K}}_{01}(\vec{B})] \quad (46d)$$

In the following we consider homogeneous materials and therefore there is no r-dependence.

4.2 Relaxation Time Approximation

If we use for the collision term the relaxation time approximation

$$\left(\frac{\partial f}{\partial t}\right)_C = -\frac{f_1}{\tau_\gamma} \quad (47)$$

we see, that in this approximation the collision operator C reduces to a factor:

$$C = \frac{\partial f_0}{\partial \varepsilon_\gamma} \frac{1}{\tau_\gamma} \quad (48)$$

Without a magnetic field the coefficients $\overleftrightarrow{\mathbf{K}}_{ij}$ are then:

$$\overleftrightarrow{\mathbf{K}}_{ij} = -\frac{1}{Vol} \sum_{\gamma} \left(\frac{\varepsilon_\gamma}{k_B T}\right)^{i+j} \frac{\partial f_0(\gamma)}{\partial \varepsilon_\gamma} \vec{v}_\gamma \circ \vec{v}_\gamma \tau_\gamma \quad (49)$$

For an isotropic material (or a material with cubic symmetry) these tensor coefficients are proportional to the unit tensor

$$\overleftrightarrow{\mathbf{K}}_{ij} = K_{ij} \overleftrightarrow{I} \text{ with } K_{ij} = \tfrac{1}{3}\text{Tr} \overleftrightarrow{\mathbf{K}}_{ij} \quad (50)$$

where

$$K_{00} = -\frac{1}{3Vol} \sum_\gamma \frac{\partial f_0(\gamma)}{\partial \varepsilon_\gamma} \, \vec{v}_\gamma^2 \tau_\gamma = -\frac{1}{e^2} \int d\varepsilon \, \frac{\partial f_0}{\partial \varepsilon} \, \sigma(\varepsilon)$$

(51a)

$$K_{01} = K_{10} = -\frac{1}{3Vol} \sum_\gamma \frac{\varepsilon_\gamma}{k_B T} \frac{\partial f_0(\gamma)}{\partial \varepsilon_\gamma} \, \vec{v}_\gamma^2 \tau_\gamma$$

$$= -\frac{1}{e^2} \int d\varepsilon \, \frac{\varepsilon}{k_B T} \frac{\partial f_0}{\partial \varepsilon} \, \sigma(\varepsilon)$$

(51b)

$$K_{11} = -\frac{1}{3Vol} \sum_\gamma \left(\frac{\varepsilon_\gamma}{k_B T} \right)^2 \frac{\partial f_0(\gamma)}{\partial \varepsilon_\gamma} \, \vec{v}_\gamma^2 \tau_\gamma$$

$$= -\frac{1}{e^2} \int d\varepsilon \left(\frac{\varepsilon_\gamma}{k_B T} \right)^2 \frac{\partial f_0}{\partial \varepsilon} \, \sigma(\varepsilon)$$

(51c)

$\sigma(\varepsilon)$ is a short notation for the energy-dependent electrical conductivity defined by:

$$\sigma(\varepsilon) := \frac{e^2}{3Vol} \sum_\gamma \delta(\varepsilon - \varepsilon_\gamma) \vec{v}_\gamma^2 \tau_\gamma$$

$$= \frac{e^2}{3} \underbrace{\frac{1}{Vol} \sum_\gamma \delta(\varepsilon - \varepsilon_\gamma)}_{N(\varepsilon)} \underbrace{\frac{\sum_\gamma \delta(\varepsilon - \varepsilon_\gamma) \vec{v}_\gamma^2 \tau_\gamma}{\sum_\gamma \delta(\varepsilon - \varepsilon_\gamma)}}_{\langle v^2 \tau \rangle_\varepsilon}$$

(52)

The energy dependence of $\sigma(\varepsilon)$ derives principally from the energy dependence of the density of states $N(\varepsilon)$, whereas the mean value of $v^2 \tau$ shows little variation with energy.

Applying a series expansion

$$\sigma(\varepsilon) = \sigma(0) + \sigma'(0)\varepsilon + \cdots$$

(53)

and taking into account only the leading terms it follows that

electrical conductivity:

$$\sigma = -\int d\varepsilon \, \frac{\partial f_0}{\partial \varepsilon} \, \sigma(\varepsilon) = \sigma(0)$$

(54a)

thermopower:

$$S = -\frac{\pi^2}{3e} k_B^2 T \frac{\sigma'(0)}{\sigma}$$

(54b)

thermal conductivity:

$$\lambda = \frac{\pi^2 k_B^2 T}{3e^2} \sigma(0)$$

(54c)

In the expression for λ the second term in the square bracket of Eqn. (46d) has been neglected.

From Eqns. (54a) and (54c) the Wiedemann–Franz law follows:

$$\lambda = \frac{\pi^2 k_B^2}{3e^2} T\sigma = L_0 T\sigma$$

(55)

with L_0, the Lorenz–number

$$L_0 = \frac{\pi^2 k_B^2}{3e^2} = 2.45 \times 10^{-8} \frac{V^2}{K^2} = 24.5 \frac{mW}{cm \, K} \cdot \mu\Omega cm \cdot \frac{1}{K}$$

(56)

4.3 Variational Principle

For the diagonal elements of the electrical conductivity and the thermal conductivity tensor it is possible to formulate a variational principle. If a finite set of basis functions $\phi_s(\gamma)$ $(s = 0, 1, \ldots, r-1)$ has been selected one can determine the distribution function using this variational principle. The result can formally be written as (Gratz *et al.* 1987)

$$[C + \Omega]^{-1}h(\gamma) := \sum_{s=0}^{r-1} \sum_{t=0}^{r-1} \phi_s(\gamma)([\hat{C} + \hat{\Omega}]^{-1})_{st}$$

$$= \frac{1}{Vol} \sum_{\gamma'} \phi_t(\gamma')h(\gamma')$$

(57)

where $h(\gamma)$ denotes an arbitrary function. Note: $[\hat{C} + \Omega]^{-1}$ is the inverse of the matrix $\hat{C} + \Omega$ with the matrix elements

$$(\hat{C} + \hat{\Omega})_{st} := \frac{1}{Vol} \sum_\gamma \phi_s(\gamma)[C + \Omega]\phi_t(\gamma)$$

(58)

This matrix describes the effect of the sum of the collision operator C and the magnetic operator Ω on the selected set of basis functions. Using Eqn. (57) for the calculation of the coefficients $\overleftrightarrow{K}_{ij}$ (see Eqn. (44)) allows to calculate the transport coefficients (see Eqns. (46a)–(46d)).

(a) Scalar transport coefficients
For a material with cubic symmetry or a polycrystalline sample the transport coefficients in zero magnetic field are scalars (see Eqn. (50)). Therefore the tensor component $(\overleftrightarrow{K}_{ij})_{xx}$ corresponds to the scalar coefficient K_{ij}, which can be written as:

$$K_{ij} = -\sum_{s,t} h_s^i (\hat{C}^{-1})_{st} h_t^j$$

(59a)

with

$$h_s^i := -\frac{1}{Vol} \sum_\gamma \left(\frac{\varepsilon_\gamma}{k_B T} \right)^i \frac{\partial f_0(\gamma)}{\partial \varepsilon_\gamma} v_x(\gamma)\phi_s(\gamma)$$

(59b)

The transport coefficients which then follow from Eqns. (46a)–(46d) are:

electrical conductivity:

$$\sigma = e^2 K_{00} \tag{60a}$$

thermopower:

$$S = -\frac{k_B}{e} \frac{K_{01}}{K_{00}} \tag{60b}$$

Peltier coefficient:

$$\Pi = -\frac{k_B T}{e} \frac{K_{10}}{K_{00}} \tag{60c}$$

thermal conductivity:

$$\lambda = k_B^2 T \left(K_{11} - \frac{K_{10} K_{01}}{K_{00}} \right) \tag{60d}$$

(b) The simplest variational approach

From the relaxation time approximation (Eqn. (48)) it can be seen, that the function ϕ (Eqn. (41)) is proportional to $v_x(\gamma)$ or $v_x(\gamma)\varepsilon_\gamma$ depending on which external force is acting in the x-direction. If we operate in a two-dimensional variation space with the two basis functions

$$\phi_0(\gamma) = v_x(\gamma), \quad \phi_1(\gamma) = v_x(\gamma)\varepsilon_\gamma \tag{61}$$

the simplest result within the scope of the variational approximation is obtained:

electrical conductivity: $\sigma = e^2 K_{00} = -e^2 h_0^0 \frac{1}{\hat{C}_{00}} h_0^0$ (62a)

thermal conductivity: $\lambda = k_B^2 T K_{11} = -k_B^2 T h_1^1 \frac{1}{\hat{C}_{11}} h_1^1$
$$\tag{62b}$$

thermopower: $S = -\frac{k_B}{e} \frac{K_{01}}{K_{00}} = \frac{k_B}{e} \frac{h_1^1}{h_0^0} \frac{\hat{C}_{01}}{\hat{C}_{11}}$ (62c)

where the inequalities

$$\hat{C}_{00}\hat{C}_{11} \gg \hat{C}_{10}\hat{C}_{01}, \quad h_0^0, \ h_1^1 \gg h_0^1, \ h_1^0 \tag{63}$$

have been used.

The electrical and the thermal resistivity are then expressed by:

electrical resistivity: $\rho = -\frac{1}{e^2} \frac{1}{h_0^0 h_0^0} \hat{C}_{00}$ (64a)

thermal resistivity: $W = -\frac{1}{k_B^2 T} \frac{1}{h_1^1 h_1^1} \hat{C}_{11}$ (64b)

ρ and W are proportional to only one matrix element of the collision operator C whereas in the expression for the thermopower two matrix elements $\hat{C}_{01}$, $\hat{C}_{11}$ enter (see Eqn. (62c)). However, when multiplying W and S, the product contains only one matrix element

$$WS = -\frac{1}{ek_B T} \frac{1}{h_0^0 h_1^1} \hat{C}_{01} \tag{65}$$

4.4 Sum Rules

If there are two or more independent scattering mechanisms (e.g., A and B) for the Bloch electrons then the transition probabilities can be added. In terms of the collision operator this can be written as:

$$C^{AB} = C^A + C^B \tag{66}$$

For the relaxation time approximation it follows from Eqn. (48) that:

$$\frac{1}{\tau^{AB}} = \frac{1}{\tau^A} + \frac{1}{\tau^B} \tag{67}$$

where τ^{AB} denotes the total relaxation time.

Since the electrical and the thermal resistivity (Eqns. (64a) and (64b)) are proportional to the collision operator, the sum rules for ρ and W are:

$$\rho^{AB}(T) = \rho^A(T) + \rho^B(T) \tag{68a}$$

$$W^{AB}(T) = W^A(T) + W^B(T) \tag{68b}$$

or

$$\frac{1}{\lambda^{AB}(T)} = \frac{1}{\lambda^A(T)} + \frac{1}{\lambda^B(T)}$$

Equations (68a) and (68b) are known as Matthiessen's rules. Even if more than two scattering mechanisms exist Matthiessen's rule is applicable, provided the different scattering processes are independent.

For the thermopower no such simple relation exists, however from Eqn. (65) it can be seen, that for the thermopower S multiplied by thermal resistivity W a similar rule follows:

$$W^{AB}(T)S^{AB}(T) = W^A(T)S^A(T) + W^B(T)S^B(T) \tag{69}$$

Inserting Eqn. (68b) than gives the Kohler rule for the thermopower:

$$S^{AB}(T) = \frac{W^A(T)}{W^A(T) + W^B(T)} S^A(T)$$
$$+ \frac{W^B(T)}{W^A(T) + W^B(T)} S^B(T) \tag{70}$$

It follows from this equation that the thermopower S^{AB} in the presence of two independent scattering

processes lies between the thermopowers S^A and S^B. The weighting factors depend on the respective thermal resistivities. The thermal conductivity is frequently not known, and there is the additional problem in determining the contribution of the lattice thermal conductivity. However, it is possible to replace the thermal resistivities in Eqn. (70) by the electrical resistivities using the Wiedemann–Franz law (Eqn. (55)):

$$S^{AB}(T) = \frac{\rho^A(T)}{\rho^A(T) + \rho^B(T)} S^A(T) + \frac{\rho^B(T)}{\rho^A(T) + \rho^B(T)} S^B(T)$$
(71)

This is the well-known Nordheim–Gorter rule.

5. Scattering Mechanism

Three of the most important scattering mechanism will be considered in the following: elastic potential scattering, inelastic phonon scattering, and magnetic scattering.

5.1 Potential Scattering

Since these scattering processes are elastic, no energy transfer from the conduction-electron system to the scatterer takes place. Such scattering may occur from dislocations, foreign atoms and grain boundaries. However, if the material includes magnetic moment carrying atoms also, a disorder in the static moment arrangement will contribute to these scattering mechanism.

The transport coefficients due to this kind of interaction are given by

$$\rho_0(T) = C_0^\rho$$
(72a)

$$W_0(T) = C_0^w / T$$
(72b)

$$S_0(T) = -C_0^s T$$
(72c)

where the different constants C_0 are temperature independent (the subscript 0 characterize potential scattering and the suffices ρ, w, and s the type of the corresponding transport coefficient). The constants C_0^ρ and C_0^w are proportional to the interaction strength (this means the electrical and thermal resistivity becomes lower for a smaller interaction strength). This is not the case for the constant C_0^s of the thermopower (the thermopower must not become lower if the interaction strength decreases). The simplest approximation for this constant is given by

$$C_0^s = \frac{\pi^2 k_B}{3|e|} \frac{d}{d\varepsilon} \ln v^2(\varepsilon)$$
(73)

whereby the energy dependence of the square of the electron velocity is given analogous to Eqn. (52) by the equation

$$v^2(\varepsilon) = \frac{\sum_\gamma \delta(\varepsilon - \varepsilon_\gamma) \, v_\gamma^{\rightarrow 2}}{\sum_\gamma \delta(\varepsilon - \varepsilon_\gamma)}$$
(74)

In the schematic pictures shown below the temperature variation of ρ_0, W_0 and S_0 is depicted together with ρ_p, W_p, S_p and ρ_m, W_m, S_m, the subscripts p and m referring to phonon and magnetic scattering.

5.2 Phonon Scattering

Using the Debye model to describe the lattice dynamics, the simplest results (Gratz and Nowotny 1985) for the transport coefficients are (in what follows the subscript p denotes phonon scattering)

$$\rho_p(T) = C_p^\rho T F_p^\rho(\Theta_D/T)$$
(75a)

$$W_p(T) = C_p^w F_p^w(\Theta_D/T)$$
(75b)

$$S_p(T) = -T(C_p^{sf} F_p^s(\Theta_D/T) + C_p^{sg} G_p^s(\Theta_D/T))$$
(75c)

where the different constants C_p are again temperature independent (because the formula for the thermopower consists now of two terms, the suffix s is extended to sf or sg, corresponding to the function F or G). The functions F_p and G_p are given by

$$F_p^\rho(x) = J_5(x)$$
(76a)

$$F_p^w(x) = J_5(x) + \frac{3}{4\pi^2} x^2 \left(J_5(x) - \frac{4}{9} J_7(x) \right)$$
(76b)

$$F_p^s(x) = \frac{1}{F_p^w(x)} \left(F_p^\rho(x) + F_p^w(x) - \frac{3}{8\pi^2} x^2 J_5(x) - F(x) \right)$$
(76c)

$$G_p^s(x) = \frac{1}{F_p^w(x)} (F_p^\rho(x) + F_p^w(x) - 2F(x))$$
(76d)

where the generalized Debye integrals $J_n(x)$ are

$$J_n(x) = \frac{n-1}{x^{n-1}} \int_0^x d\omega \, \frac{\omega^n}{(e^\omega - 1)(1 - e^{-\omega})}$$
(77a)

and the function $F(x)$ is

$$F(x) = \left(1 + \frac{1}{4\pi^2} x^2 \right) \frac{x^2}{(e^x - 1)(1 - e^{-x})}$$
(77b)

The functions F_p^ρ, F_p^w and F_p^s are normalized, having the limit one for very high temperatures, whereas G_p^s vanishes in the high temperature region (see insert in Fig. 3).

The temperature dependence of the electrical resistivity ρ_p given in Eqn. (75a) corresponds to the well known Bloch–Grüneisen law. The constant C_p^ρ includes the electron–phonon coupling constant, the atomic masses of the different types of atoms and the characteristic temperature Θ_D for the phonons. From Eqn. (75a) (together with Eqns. (76a) and (77a)) it follows for the low and the high temperature region

$$\rho_{ph}(T) \propto C_p^\rho T^5 \text{ for } T \ll \Theta_D \tag{78a}$$

$$\rho_{ph}(T) = C_p^\rho T \text{ for } T \gtrsim \Theta_D \tag{78b}$$

The derivation of these equations is based on the assumptions that the Boltzmann formalism is applicable. Basically this means that the scattering events are separated spatially by a sufficient numbers of wavelengths of the conduction electrons so that an electron recovers from a previous collision before experiencing the next one. Another important simplification is the assumption that the Debye model for the description of the phonon dynamics is valid. Therefore one of the parameters in the theoretical model calculation is the Debye temperature Θ_D, which can most easily be obtained from a fit of the Bloch–Grüneisen law to the resistivity data (for examples see *Intermetallic Compounds: Electrical Resistivity*).

The thermal resistivity due to the electron–phonon scattering given in Eqn. (75b) corresponds mainly to a formula obtained by Wilson (see e.g., Ziman 1962). For the low and high temperature ranges the thermal resistivity follows simple relations:

$$W_p(T) \propto C_p^w T^2 \text{ for } T \ll \Theta_D \tag{79a}$$

$$W_p(T) = C_p^w \text{ for } T \gtrsim \Theta_D \tag{79b}$$

For the high temperature region the Wiedemann – Franz law follows from these equations.

The temperature variation of the thermopower its not as simple as for the electrical and thermal resistivity even for simple nonmagnetic compounds, since the thermopower can take positive or negative signs depending on temperature. This is because its sign is determined by the conduction electron properties at the Fermi level. The parameters C_p^{sf} and C_p^{sg} are proportional to the energy derivative of the velocity and the density of states of the conduction electrons at the Fermi level:

$$C_p^{sf} \propto \frac{\mathrm{d}}{\mathrm{d}\varepsilon} \ln v^2(\varepsilon), \; C_p^{sg} \propto \frac{\mathrm{d}}{\mathrm{d}\varepsilon} \ln N(\varepsilon) \tag{80}$$

The calculation of $S_p(T)$ requires the knowledge of these two model parameters (Durczewski and Ausloos 1996).

5.3 Spin-dependent Scattering Mechanism

For a magnetic RE-compound the existence of scattering processes of the conduction electrons on the localized 4f spins of the RE-ions has to be taken into consideration. We will describe a ferromagnetic system of localized 4f-moments by a Heisenberg-Hamiltonian in the molecular field approximation and the magnetic scattering processes between the conduction electrons and the localized 4f moments by a s-f interaction Hamiltonian. When neglecting a possible influence of the crystal field or short range correlations, one obtains after some simplifications the following magnetic contributions to the electrical resistivity, the thermal resistivity, and the thermopower (the subscript m denotes magnetic scattering):

$$\rho_m(T) = C_m^\rho F_m^\rho(T/T_c) \tag{81a}$$

$$W_m(T) = C_m^w F_m^w(T/T_c)/T \tag{81b}$$

$$S_m(T) = -T(C_m^{sf} F_m^s(T/T_c) + C_m^{sg} G_m^s(T/T_c)) \tag{81c}$$

T_c represents the ferromagnetic ordering temperature (Curie temperature). Above T_c the function G_m^s vanishes and the functions F_m^r, F_m^w and F_m^s are equal to one (see inset of Fig. 3). Within this paramagnetic region ($T > T_c$) the magnetic scattering processes are called spin–disorder scattering. The results for this spin–disorder scattering are similar to those for potential scattering because of the elastic nature of these interactions:

$$\rho_{spd}(T) = C_m^\rho \tag{82a}$$

$$W_{spd}(T) = C_m^w/T \tag{82b}$$

$$S_{spd}(T) = -C_m^{sf} T \tag{82c}$$

In the ferromagnetic region ($T < T_c$) the magnetization $M(T/T_c)$ mostly determines the temperature dependence of the transport coefficients. This magnetization is proportional to the average value of J_z given in the molecular field theory by

$$\langle J_z \rangle = J B_J(2J\eta) \tag{83a}$$

where B_J is the Brillouin function for localized spins with the fixed total momentum J

$$B_J(x) = \frac{2J+1}{2J} \coth \frac{2J+1}{2J} x - \frac{1}{2J} \coth \frac{1}{2J} x \tag{83b}$$

and η is a function of the reduced temperature T/T_c determined by

$$B_J(2J\eta) = \frac{2(J+1)}{3} \frac{T}{T_c}\eta \qquad (83c)$$

The functions F_m^{ρ}, F_m^w, F_m^{sf} and F_m^{sg} are given by:

$$F_m^{\rho}(T/T_c) = R_J^0(T/T_c) \qquad (84a)$$

$$F_m^w(T/T_c) = R_J^0(T/T_c) + R_J^2(T/T_c) \qquad (84b)$$

$$F_m^s(T/T_c) = \frac{R_J^0(T/T_c)}{R_J^0(T/T_c) + R_J^2(T/T_c)} \qquad (84c)$$

$$G_m^s(T/T_c) = \frac{R_J^2(T/T_c)}{R_J^0(T/T_c) + R_J^2(T/T_c)} \qquad (84d)$$

with the abbreviations

$$R_J^0(T/T_c) = \frac{1}{J(J+1)}\left(\langle J_z^2 \rangle - \langle J_z \rangle^2 + \frac{\eta\langle J_z \rangle}{\sinh^2\eta}\right) \quad (85a)$$

$$R_J^2(T/T_c) = \frac{4}{\pi^2} \frac{1}{J(J+1)} \frac{\eta^3\langle J_z \rangle}{\sinh^2\eta} \qquad (85b)$$

whereby $\langle J_z \rangle$ is given by Eqn. (83a), η has to be determined from Eqn. (83c) and $\langle J_z^2 \rangle$ is given by

$$\langle J_z^2 \rangle = J(J+1) - \langle J_z \rangle\coth\eta \qquad (85c)$$

The parameters C_m^{sf} and C_m^{sg} are again proportional to the energy derivative of the velocity and the density of states at the Fermi level (see Eqn. (80)). Below T_c, $S_m(T)$ can show a maximum, whereby the magnitude of the maximum strongly depends on the ratio of the parameters C_m^{sf} and C_m^{sg} (see Fig. 3). It should be noted, that such a maximum (or minimum) observed below T_c in magnetically ordered materials is caused by the inelastic spin flip scattering of the conduction electrons. Such a behavior has sometimes been interpreted to be a drag effect (magnon drag, phonon drag; hereby magnons and/or phonons are taken along with the conduction electrons). Such drag effects may have some influence at very low temperatures, but each maximum (or minimum) in the temperature dependence of the thermopower is not an indication of a drag effect.

The contribution to the total electrical or thermal resistivity depends strongly on whether the material is magnetically ordered or is in the paramagnetic state. If the magnetically ordered state is not ferromagnetic no general rules can be given for the electrical resistivity or for those of W and S since the magnetic order in general can show a complex non collinear arrangement of the spins (see also *Localized 4f and 5f Moments: Magnetism*). Mainly at low temperatures

the temperature variation is sensitively dependent on the spin dynamic which itself might be very complex in an antiferromagnetic ordered state (this spin wave scattering also occurs in ferromagnetic material and is not included in the formulas given above).

In the following figures the temperature dependencies for the different contributions to electrical resistivity, thermal resistivity and thermopower are sketched.
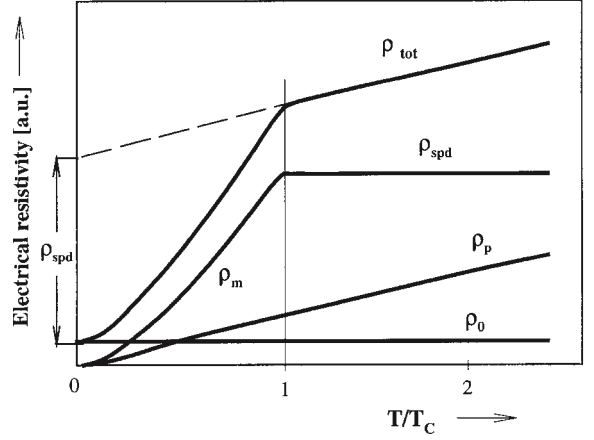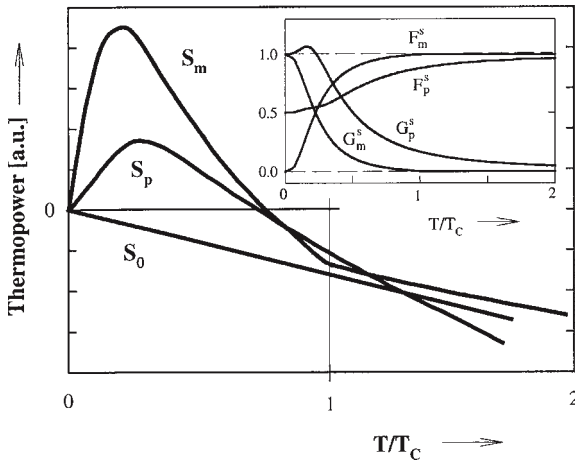

Figure 1
The calculated temperature dependence of the electrical resistivity for a magnetic compound is shown assuming that the total resistivity is the sum of the residual, the phonon, and the magnetic resistivity.
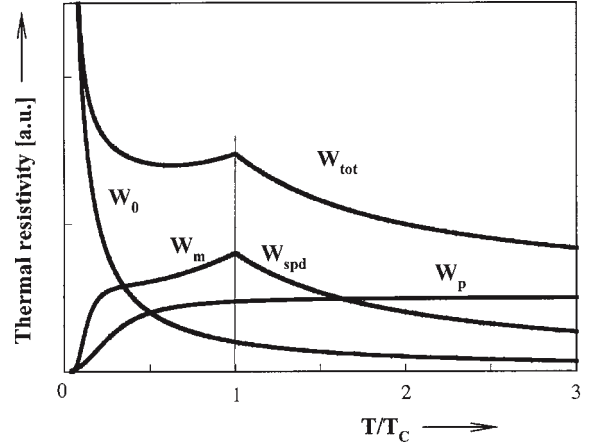
Figure 2
The calculated temperature dependence of the electronic thermal resistivity W due to impurity, phonon and magnetic scattering (schematic). The total electronic part of the thermal resistivity is the sum of the residual, the phonon, and the magnetic thermal resistivity.

Figure 3
The calculated temperature variation of the thermopower S for a ferromagnetic compound due to impurity, phonon, and magnetic scattering (the inset shows the functions F_m^s, F_p^s, G_p^s, and G_m^s.

Fig. 1 shows schematically the temperature variation of the electrical resistivity due to potential scattering (ρ_0), phonon scattering (ρ_p) and magnetic scattering (ρ_m and ρ_{spd}). The total resistivity ρ_{total} is the sum of the residual, the phonon and the magnetic resistivity. That means we assume that Matthiessen's rule holds.

Fig. 2 shows in an analogous way to Fig. 1 the temperature variation of the thermal resistivities W due to impurity, phonon and magnetic scattering. The total thermal resistivity W_{total} is again the sum of these three thermal resistivities (Matthiessen's rule).

In Fig. 3 the temperature variation of the thermopower due to potential scattering (S_0), phonon scattering (S_p) and magnetic scattering (S_m) are sketched. The inset shows the functions F_m^s, F_p^s, G_p^s and G_m^s.

6. Conclusion

In this section the electronic transport coefficients (ρ, W, S and Π) have been considered in the scope of the linearized Boltzmann equation. To use this classical formalism it is necessary that

(i) the conduction electrons can be described by Bloch wave-packets (characterized by $\gamma = k, n, \sigma$)

(ii) scattering processes can be described as transitions from a state γ into a state γ'

(iii) the time in between two successive scattering processes has to be long enough in order to establish the formation of a wave packet.

From the latter point it follows that the mean free path of a conduction electron has to be much longer

than the interatomic distances. This means that only a limited number of collisions per unit time can be experienced by an electron (for a normal metal this gives an upper limit for the electrical resistivity of about 200–300 $\mu\Omega$ cm). If these conditions are not fulfilled the classical treatment of transport phenomena fails and a quantum mechanical consideration is necessary (Kubo 1959). For an example, see YMn$_2$ in *Intermetallic Compounds: Electrical Resistivity*. In the scope of the Boltzmann formalism the external fields change the distribution function which is used in order to calculate the corresponding current densities (see Eqns. (39a) and (39b)).

The linear relations between these current densities and the external fields determine the linear transport coefficients (see Eqns. (46a)–(46d)). The necessary distribution functions were calculated as a solution of the linearized Boltzmann equation. In this section, two of the most simplest solution methods for the Boltzmann equation have been discussed

(i) Relaxation time approximation

(ii) Variational method (however with only two trial functions)

An important result of these simple approximations are the sum rules, since these rules are very helpful for the analysis of experimental data (see also *Intermetallic Compounds: Electrical Resistivity*, *Kondo Systems and Heavy Fermions: Transport Phenomena*). As independent scattering mechanisms, the potential scattering, the phonon scattering and spin dependent scattering are considered and the corresponding temperature dependence of ρ, W and S are outlined. In the figures this temperature dependencies are schematically shown according to Eqns. (72a)–(72c) (potential scattering), Eqns. (75a)–(75c) (phonon scattering) and Eqns. (81a)–(81c) (magnetic scattering).

Bibliography

Butcher P N 1973 Basic electron transport theory. In: Salam A (ed.) *Electrons in Crystalline Solids*. IAEA, Vienna, pp. 103–65

Durczewski K, Ausloos M 1996 Theory of the thermoelectric power or Seebeck coefficient: the case of phonon scattering for a degenerate free-electron gas. *Phys. Rev. B.* **53**, 1762–72

Gratz E, Bauer E, Nowotny H 1987 Transport properties in rare earth intermetallics. *J. Magn. Magn. Mater.* **70**, 118–25

Gratz E, Nowotny H 1985 Thermopower in rare earth intermetallics. *Physica* **130B**, 75–80

Kubo R 1959 *Lecture in Theoretical Physics*. Interscience, New York, Vol. 1 Chap. 4

Ziman J M 1962 *Electrons and Phonons*. Clarendon, Oxford

H. Nowotny
Vienna University of Technology, Austria

E. Gratz
Vienna University of Technology, Austria

Bulk Magnetic Materials: Low-dimensional Systems

The magnetism in space dimension D reduced to one or two shows very interesting and nontrivial features which result essentially from the enhancement of both the thermal and quantum fluctuations. The ground and excited states of low-dimensional magnetic systems appear more exotic as the spin dimension, n, increases ($n = 1$, 2, or 3) and the spin value, S, decreases ($S = \frac{1}{2}$, 1 …). Thus, the largest effect is expected for the one-dimensional (1D) $S = \frac{1}{2}$ Heisenberg ($n = 3$) system. The nature of the ground state also depends strongly on the type of spin–spin couplings which are involved (see *Magnetism in Solids: General Introduction*): ferromagnetic, antiferromagnetic, or frustrating, at short or long range. The most interesting cases are predicted (and observed) for exchange interactions favoring antiferromagnetic or frustrated spin configurations, this resulting from the enhancement of quantum effects at low dimension. As a direct consequence of the strengths of both the thermal and quantum fluctuations in one or two dimensions, in most cases the spin system can no longer develop a long-range ordering at finite temperature and thus remains disordered down to $T = 0\,\mathrm{K}$.

This article outlines the main features of magnetism at low dimension, emphasizing in particular the role played by quantum fluctuations, frustration, and doping.

1. Generalities and Definitions

A one-dimensional magnetic system is one in which the spin interactions are strong only along a well-defined direction in space, thus defining a quasi-isolated chain of spins. When the spin interactions are large along two directions in space and weak along the third one, the spin system can be viewed as a stacking of quasi-isolated magnetic layers. Figure 1 gives examples of 1D, 2D, and "intermediate" antiferromagnetic lattices. Figure 2 shows an example of a spin-ladder spin-chain system ($Sr_{14}Cu_{24}O_{41}$). Following the general theory of phase transitions (Domb and Green 1972, 1976; Domb and Lebowitz 1983, 1988), a spin system at a given temperature T is characterized by an order parameter which is generally defined as the thermal expectation value of the spin S_i at site i, $|\langle S_i \rangle_T|$. The magnetic system exhibits a phase transition towards long-range ordering if the order parameter becomes nonzero below some characteristic temperature T_C called the critical temperature.

Generally, the spin fluctuations are characterized by the space- and time-dependent spin–spin correlation functions:

$$G_{ij}^{\alpha\beta}(t) = \langle \mathbf{S}_i^\alpha(R_i, 0) \cdot \mathbf{S}_j^\beta(R_j, t) \rangle_T \qquad (1)$$
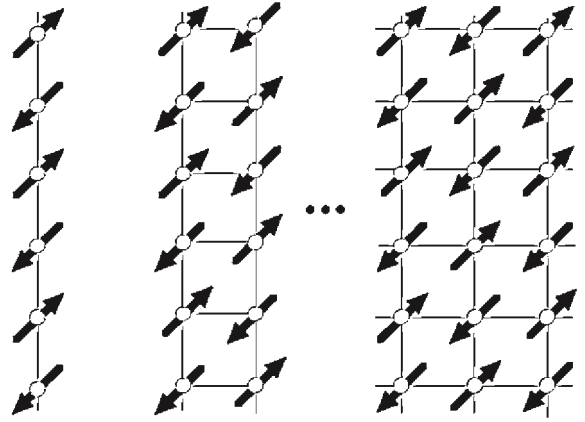

Figure 1
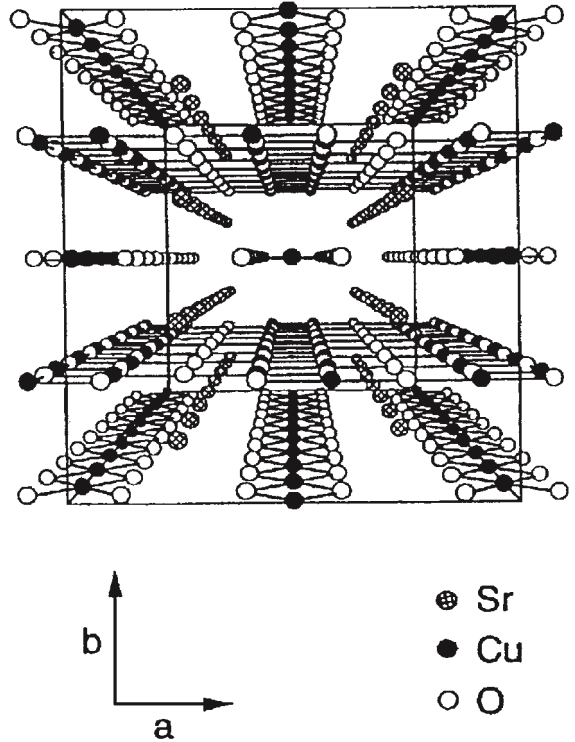The n-leg antiferromagnetic spin-ladder system: the 1D–2D crossover.

Figure 2
An example of a low-dimensional system: crystallographic structure of the spin-ladder dimer-chain compound $Sr_{14}Cu_{24}O_{41}$.

where α and β label the various spin components. Some experimental techniques such as NMR (Slichter 1990) or inelastic neutron scattering (INS) (Lovesey 1987) probe more or less completely the various

dynamical structure factors $S^{\alpha\beta}(\mathbf{q}, \omega)$ which are nothing else than the Fourier transforms of the spin–spin correlation functions $G_{ij}^{\alpha\beta}(t)$. The quantities $S^{\alpha\beta}(\mathbf{q}, \omega)$ contain all the physics of spin fluctuations and spin excitations. They are related to the wave vector and energy-dependent generalized susceptibilities $\chi^{\alpha\beta}(\mathbf{q}, \omega)$ through the well-known fluctuation–dissipation theorem:

$$\chi^{\alpha\beta}(\mathbf{q}, \omega) = \frac{1}{\pi}(1 - \exp(-\hbar\omega/kT))S^{\alpha\beta}(\mathbf{q}, \omega) \quad (2)$$

Information on $\chi^{\alpha\beta}(\mathbf{q}, \omega)$ can be obtained from various techniques such as susceptibility ($\chi^{\alpha\alpha}(\mathbf{q} = 0, T)$), magnetization ($M^{\alpha}(H, T)$), specific heat ($C(T)$), and ESR measurements (Abragam and Bleaney 1970). In the absence of long-range ordering, the spin system is characterized in the direction v by a length scale $\xi_v(T)$ (the correlation length), defined as the average distance over which two spins are correlated. $\xi_v(T)$ can be determined from INS studies of the q-dependencies of the energy-integrated structure factors:

$$S_v(\mathbf{q}) = \int S_v(\mathbf{q}, \omega)d\omega \quad (3)$$

In the vicinity of a "classical" critical point (when it exists), the quantities $|\langle \mathbf{S}_i \rangle_T|$, $\xi(T)$, and $\chi(T)$ are expected to exhibit power-law dependencies of $T_C - T$:

$$|\langle \mathbf{S}_i \rangle_T| \propto (T_C - T)^{\beta} \quad (4)$$

$$\xi(T) \propto (T_C - T)^{-\nu} \quad (5)$$

$$\chi(T) \propto (T_C - T)^{-\gamma} \quad (6)$$

allowing one to define critical exponents β, ν, and γ, whereas at T_C the "instantaneous" correlation function $\langle \mathbf{S}_0 \cdot \mathbf{S}_r \rangle$ should behave at large distance as $1/r^n$.

2. Critical Phenomena in Low-dimensional Classical Systems

It is now accepted that the existence of a magnetic phase transition at finite temperature depends in a crucial way on both the space dimension (D) and spin dimension (n). Following the usual terminology, $n = 1$, 2, and 3 correspond, respectively, to the so-called "Ising," "XY," and "Heisenberg" models (see *Magnetism in Solids: General Introduction*).

In the space dimension $D = 2$, there exists a true phase transition only for the Ising model (de Jongh and Miedema 1974, de Jongh 1990). The general characteristics of this phase transition depend only weakly on the type of lattice under consideration, even in the presence of "frustration" (as in the case of the antiferromagnetic triangular lattice (see *Magnetic*

Systems: Lattice Geometry-originated Frustration)). Owing to the Ising character, the spin excitation spectrum displays a gap $\Delta_I \approx 2zJS^2$ (z being the number of adjacent spins), whereas both the longitudinal susceptibility and the specific heat follow thermal activation laws ($\sim \exp(-\Delta_I/kT)$). Theoretical predictions for the critical exponents of the 2D Ising model for a square lattice ($\beta = 1/8$, $\nu = 1$, $\gamma = 7/4$, and $\eta = 1/4$) have been quantitatively verified by quasi-elastic neutron scattering experiments on the prototype compound K_2CoF_4 (Ikeda and Hirakawa 1974). Figure 3 shows, for example, that the sublattice magnetization closely obeys the well-known Onsager formula established for that model:

$$\frac{M_S(T)}{M_S(0)} \approx \left(1 - \sinh^{-4}\left(\frac{2JS^2}{kT}\right)\right)^{1/8} \quad (7)$$
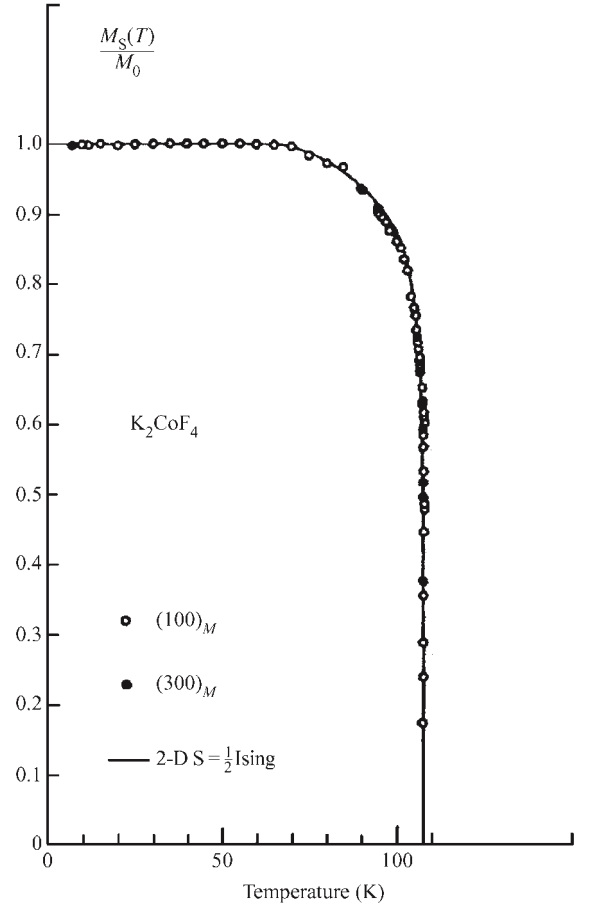
Figure 3
Temperature dependence of the normalized magnetic intensities in the two-dimensional Ising material K_2CoF_4.

For such a system, the magnetization $M_S(T)$ vanishes at $kT_C \approx 1.8JS^2$. For the frustrated antiferromagnetic triangular lattice, $kT_C \approx 1.5JS^2$ is smaller, reflecting closely the change of nearest-neighbor number z.

For $D = 2$, $n = 2$ and $D = 2$, $n = 3$, no phase transition towards long-range ordering can exist, owing to the increase of thermally activated spin fluctuations: $|\langle \mathbf{S}_i \rangle_T| = 0$. For $n = 3$, the correlation length diverges exponentially as $T \rightarrow 0$, according to the relationship:

$$\xi(T) \propto \exp(cJS^2/kT) \tag{8}$$

where c is a constant of the order of 2π. The spin excitation spectrum of the 2D Heisenberg model is gapless, and linear or quadratic in q, respectively, for antiferromagnetic or ferromagnetic couplings. At wave vectors q smaller than some cut-off value q_c (roughly corresponding to the relationship $\hbar\omega(q_c) \approx kT$), the spin dynamics become of the diffusive type. The case $D = 2$, $n = 2$ is quite pathologic.

For the 2D XY model, there exists a very peculiar phase transition (the so-called Kosterlitz–Thouless (KT) transition) below some finite temperature T_{KT} towards a new "topological" order (Kosterlitz and Thouless 1973). The low-temperature phase is characterized by the absence of long-range ordering together with a divergence of the spin susceptibility ($\chi(T)$ remains infinite down to $T = 0K$). The instantaneous correlation function decays following a power-law relationship:

$$\langle \mathbf{S}_0 \cdot \mathbf{S}_r \rangle \propto 1/r^{\eta(T)} \tag{9}$$

where $\eta(T_{KT}) = kT/2\pi JS^2$ (indeed defining a line of critical points with $\eta(T_{KT}) = 1/4$ and $T_{KT} = \pi JS^2/2$). The physical origin of this nonconventional behavior has been attributed to the existence in the low-temperature phase of "topological" vortex–antivortex pairs melting at the KT transition.

This gives rise to a very special temperature dependence of the correlation length which behaves exponentially according to the well-known relationship:

$$\xi(T) \propto \exp\left(\frac{b}{\sqrt{\dfrac{T}{T_C} - 1}}\right) \tag{10}$$

where $b = \pi/\sqrt{2}$. At $T \approx 0K$, the low-energy magnetic excitation spectrum of the 2D XY model is gapless, as expected for any quasi-isotropic system. It is, moreover, linear in q at small q (even for the ferromagnetic case), giving rise to a T^2 term in the specific heat. There are no good experimental realizations of the classical $D = 2$, $n = 2$ and $D = 2$, $n = 3$ systems (de Jongh and Miedema 1974, de Jongh 1990). For the former case, this situation is mainly ascribed to the

fact that the KT ground state is marginal and easily destroyed by any small corrective term (interlayer coupling or axial anisotropy), which should be inherent to all real materials. Both tend to induce a long-range ordering when the temperature becomes sufficiently low.

Experimental investigations exist for the quasi-2D planar compounds K_2CuF_4, Rb_2CrCl_4, $BaNi_2(PO_4)_2$, or $BaCo_2(AsO_4)_2$ (de Jongh 1990), which give some evidences for the exponential behavior of the correlation length above T_{KT}. Concerning the 2D Heisenberg model, prototype systems like Rb_2MnCl_4 or K_2MnF_4 exist (de Jongh 1990). Unfortunately, they all order at finite temperature owing to non-negligible interlayer couplings and to the presence of a small axial single-ion anisotropy term, preventing the observation of the true 2D behavior.

In the space dimension $D = 1$, the strength of spin fluctuations increases so much that no spontaneous magnetization can appear down to $T = 0K$, even for the Ising system (Steiner *et al.* 1976). For $D = 1$, $n = 1$, the correlation length obeys the quasi-exponential relationship:

$$\xi(T) = \frac{a}{|\ln(\tanh(JS^2/kT))|} \tag{11}$$

where a is the intrachain spin–spin spacing. The excitation spectrum has a spin gap, implying an exponential decay of both the longitudinal susceptibility $\chi(T)$ and the specific heat $C(T)$ at low temperature. For $D = 1$, $n = 2$ and $D = 1$, $n = 3$, the correlation length behaves linearly in T according to the simple relationship:

$$\xi(T) = \xi_0 JS(S+1)/kT \tag{12}$$

where prefactors $\xi_0 = 2$ and 1, respectively. The excitation spectrum is gapless ($\hbar\omega(q) \propto q$ at small q) for both systems, a result again in agreement with the isotropic character of this spin system. As for the 2D case, there exists a cut-off wave vector $q_c \approx \xi^{-1}(T)$ separating the diffusive regime from the quasi-propagating spin wave regime. The specific heat $C(T)$ is linear in T and $\chi(T)$ remains finite at low temperature.

One of the best prototypes of the classical Heisenberg chain is probably the manganese-based $(S = 5/2)$ chain compound $((C_2H_3)_4NH_4)NMnCl_3$ (TMMC), which exhibits magnetic properties in very quantitative agreement with the theoretical predictions of that model. In particular the relevance of nonlinear excitations (also known as solitons) in the thermal properties (Mikeska 1980) has been clearly demonstrated in TMMC by very comprehensive NMR and INS studies as functions of temperature and field (Regnault *et al.* 1982).

Indeed, in real materials there always exists either a small interchain coupling (quasi-1D system) or a small interlayer coupling J' (quasi-2D system) which

finally leads to the occurrence of a phase transition towards a true long-range ordering at finite temperature. Qualitatively, the critical temperature T_C can be determined from the implicit relationship:

$$2J'S^2\xi^D(T_C) \approx kT_C \qquad (13)$$

which means that the phase transition takes place as soon as the thermal energy is comparable to the exchange energy of adjacent correlated segments. For the quasi-1D isotropic chain, this relationship gives:

$$kT_C \approx 2S^2\sqrt{JJ'} \qquad (14)$$

For the quasi-2D Heisenberg system this implies a logarithmic dependence on the ratio J'/J:

$$kT_C \approx \frac{4\pi JS^2}{|\ln(J'/J)|} \qquad (15)$$

The latter relationship explains why very good prototypes of the ideal 2D Heisenberg and XY systems are lacking (de Jongh 1990).

3. Effects of Quantum Fluctuations

Quantum fluctuations are expected to become stronger as the spin value, S, decreases from infinity (classical limit) to $\frac{1}{2}$ (strongly quantum limit). However, the space dimension, D, the number of adjacent spins, and the sign of the intrachain or intralayer couplings, J, also play an important role. Qualitatively, one finds that the smaller D, the larger the quantum effects. Antiferromagnetic interactions are particularly suitable for the existence of strong quantum fluctuations, the more so if they are frustrating the spin system. This is especially the case in the antiferromagnetic triangular lattice, for the J_1–J_2 antiferromagnetic model of the square lattice, or in the J_1–J_2 $S=\frac{1}{2}$ antiferromagnetic chain.

3.1 The Two-dimensional Case

In space dimension $D=2$, for evident topology arguments the predictions are not much different from the classical case. The thermal behavior is qualitatively the same as to some renormalization of coefficients or prefactors. Thus, the 2D Ising model exhibits a phase transition at finite temperature, whereas the 2D XY model exhibits again the topological phase transition. For the 2D Heisenberg model, the ground and excited states correspond to the so-called "spin-liquid" state, as far as the frustration is absent from the problem. The predictions are qualitatively the same for both the ferromagnetic and the antiferromagnetic system. Basically, the quantum antiferromagnetic system exhibits no phase transition at finite temperature and remains short-range ordered down to $T=0\,$K. The temperature dependence of the

in-plane correlation length is again exponential, given by an expression similar to that predicted for the classical model (as to some renormalization of the prefactors).

The excitation spectrum at $T=0\,$K is gapless and behaves linearly at small wave vector, $\hbar\omega_q \approx cq$, with a spin wave velocity, c, only slightly renormalized with respect to its classical value. The best realizations of the 2D $S=\frac{1}{2}$ Heisenberg antiferromagnetic system are the two layered compounds La_2CuO_4 ($T_N \approx 320\,$K, $J \approx 1500\,$K) and $YBa_2Cu_3O_6$ ($T_N \approx 410\,$K, $J \approx 1300\,$K), well known for their very good high T_C superconducting properties appearing upon hole doping. In both materials, comprehensive INS studies (Furrer 1998) have allowed an accurate determination of magnetic excitation spectra and a quantitative comparison with the main predictions of the $S=\frac{1}{2}$ antiferromagnetic square lattice (in particular $\xi(T)$).

3.2 The One-dimensional Case

In space dimension $D=1$, the strength of quantum fluctuations is considerably enhanced. The magnetic behavior depends not only on the sign of the spin–spin couplings, but also on the parity of the quantity $2S+1$. The case of the antiferromagnetic Heisenberg chain is the most interesting because in that case the magnetic properties are found to be very different for $2S+1$ even ($S=\frac{1}{2}, \frac{3}{2}...$) or $2S+1$ odd ($S=1, 2...$).

(a) The $S=\frac{1}{2}$ antiferromagnetic chain

The main difference in comparison with the classical system is seen in the excitation spectrum. As shown from analytical as well as numerical calculations (Steiner *et al.* 1976, Schulz 1986), the spin excitation spectrum of the $S=\frac{1}{2}$ Heisenberg antiferromagnetic chain consists of a continuum of triplet ($S=1$) excitations limited on the low-energy side by the threshold energy:

$$\hbar\omega_1(q_c) = \frac{\pi}{2}J\sin(2\pi q_c a) \qquad (16)$$
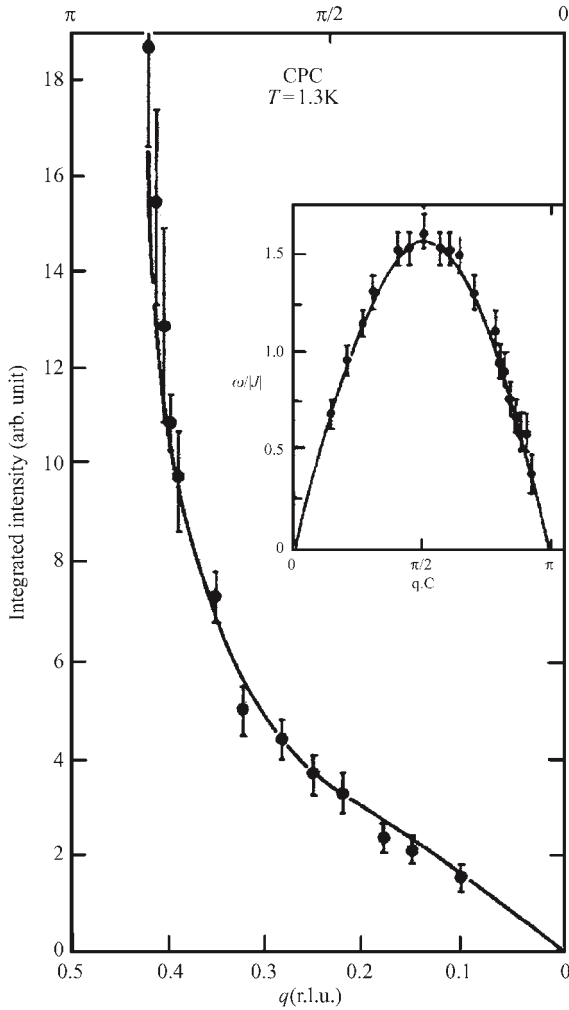
and on the high-energy side by the threshold energy:

$$\hbar\omega_2(q_c) = \pi J\sin(\pi q_c a) \qquad (17)$$

The excitation spectrum (unbound spinon continuum (Schulz 1986)) is gapless and the ground state is not ordered, even at $T=0\,$K. The equal-time spin–spin correlation function behaves according to the algebraic relationship $\langle S_0 S_n \rangle \propto (-)^n \ln(n)/n$, whereas the magnetic susceptibility at very low temperature remains finite and the magnetic specific heat is linear in T. The most important predictions of the $S=\frac{1}{2}$ Heisenberg antiferromagnetic chain have been quantitatively verified in the two prototype materials $CuCl_2 \cdot 2N(C_5H_5)$ (CPC) (Endo *et al.* 1974) and

KCuF$_3$ (Tennant *et al.* 1993). Figure 4 shows, for example, the dispersion relationship along the chain axis and the wave vector dependence of the energy-integrated intensity in CPC, both found to be in good quantitative agreement with the corresponding theoretical predictions.

The $S = \frac{1}{2}$ Heisenberg antiferromagnetic chain in the presence of non-negligible spin–lattice interactions shows a quite different behavior. As shown by Pytte (1974), the strong 1D spin fluctuations induce a lattice instability (indeed a dimerization) below a well-defined temperature, T_{SP}, called the spin-Peierls transition temperature. As a consequence of the presence of alternating couplings induced by the dimerization, the ground state of the spin-Peierls system is a nonmagnetic singlet ($S = 0$) state. It is well separated from the first excited triplet ($S = 1$) states by a gap energy of $\Delta_{SP} \approx 1.75 \, kT_{SP}$, directly related to T_{SP} through a Bardeen–Cooper–Schrieffer (BCS)-type relationship, as in phonon-mediated superconductivity. Under an applied magnetic field, the triplet excited states are linearly split by the Zeeman effect into three components of energy $\Delta_v \approx \Delta_{SP} + v g \mu_B H$, with $v = -1, 0, 1$.

Above a critical field $H_c \approx 0.84 \Delta_{SP}/g\mu_B$, the spin-Peierls system undergoes a first-order phase transition towards a new incommensurate magnetic phase which can be viewed as a regular stacking of undistorted regions magnetized along the field direction and distorted nonmagnetic regions (defining the so-called soliton lattice structure). The period, L, of the soliton lattice is directly controlled by the homogeneous magnetization, M, according to $M \approx \mu_B a/L$. This relationship means that each soliton bears a total spin $\frac{1}{2}$. The major predictions of the standard spin-Peierls model (lattice distortion, singlet ground state, gap in the excitation, high-field incommensurate phase, etc.) have been quantitatively verified in several good prototype compounds such as TTF–Cu–BDT ($T_{SP} \approx 12 \, K$) (Bray *et al.* 1975) or CuGeO$_3$ ($T_{SP} \approx 14 \, K$) (Hase *et al.* 1993, Boucher and Regnault 1996). As an example, Fig. 5 shows the temperature dependence of the static susceptibility in CuGeO$_3$, which confirms the spin-Peierls scenario.

Figure 4
Wave vector dependence of the energy-integrated intensity in CPC. Comparison with the theoretical prediction for the $S = \frac{1}{2}$ Heisenberg antiferromagnetic chain.
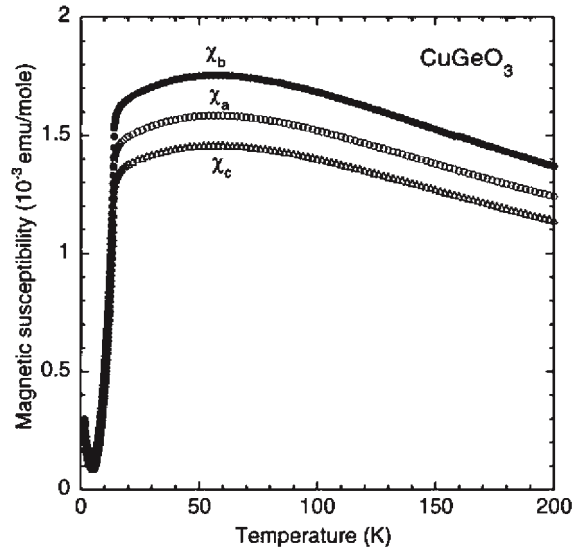
Figure 5
Temperature dependence of the magnetic susceptibility along the crystalline directions *a*, *b*, and *c* (chain axis) in the $S = \frac{1}{2}$ spin-Peierls compound CuGeO$_3$.

(b) The $S = 1$ antiferromagnetic chain

The spin $S = 1$ Heisenberg antiferromagnetic chain displays quite different magnetic properties. As shown by Haldane (1983) and Affleck (1990), for a spin $S = 1$ the ground state is a nonmagnetic singlet ground state well separated from the first excited triplet states by a large energy gap $\Delta \approx 0.41J$, where J is the intrachain coupling constant. Contrary to the $S = \frac{1}{2}$ Heisenberg antiferromagnetic case, the spin–spin correlation function behaves exponentially:

$$\langle \mathbf{S}_{0i}\mathbf{S}_n \rangle \propto (-)^n \frac{\exp(-na/\xi)}{\sqrt{n}} \qquad (18)$$

with a correlation length ξ which is directly related to the gap energy Δ by the relationship $\xi \approx c/\Delta$, with $c \approx 2.7Ja$ (c being the spin wave velocity for the model). As a consequence of the spin-gap opening, both the susceptibility and the magnetic specific heat vanish exponentially at low temperature, according to:

$$\chi(T) \propto \frac{\exp(-\Delta/kT)}{\sqrt{T}} \qquad (19)$$

and

$$C(T) \propto T\exp(-\Delta/kT) \qquad (20)$$

In agreement with numerical calculations, the correlation length of the $S = 1$ chain remains finite at $T = 0\,\mathrm{K}$ ($\xi \approx 6.5a$). Under an applied field the Haldane ground state disappears at a critical field $H_c \approx \Delta/g\mu_B$, above which a more conventional magnetic phase is recovered. Experimentally, the nickel-based organic compound $Ni(C_2H_8N_2)_2NO_2ClO_4$ (NENP) is probably the best and most studied prototype of the Haldane gap system. In this material, the large Haldane triplet is split into three components by the presence of an intrinsic orthorhombic single-ion anisotropy. Macroscopic as well as microscopic measurements have clearly demonstrated the existence at low temperature of a Haldane phase and the opening of three quantum gaps (Renard *et al.* 1987). Figure 6 shows, for example, the disappearance of the static magnetic susceptibility along the three main crystallographic directions in NENP, a clear signature of the existence of both a singlet ground state and a spin gap at low temperature.

For a larger spin value S, the Haldane gap vanishes exponentially according to the semiclassical relation $\Delta \approx 2JS\exp(-\pi S)$ (Haldane 1983, Affleck 1990) and the quantum fluctuations are not strong enough to prevent the interchain couplings from inducing a 3D long-range order.

3.3 The Spin-ladder System

At the crossing between chain and plane (see Fig. 1), the n-leg $S = \frac{1}{2}$ ladder system displays quite interesting magnetic properties, depending drastically on the
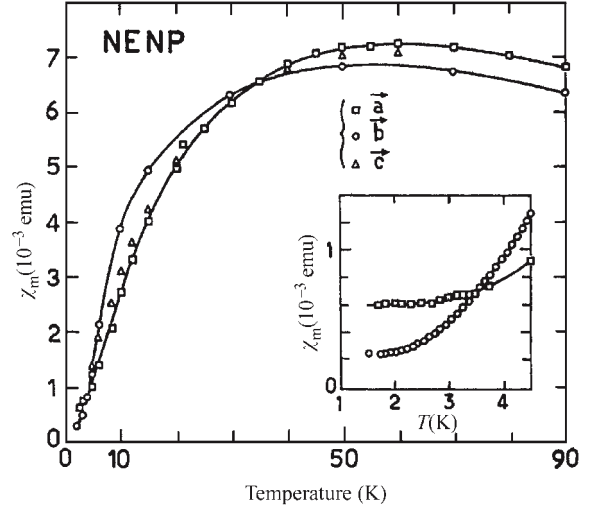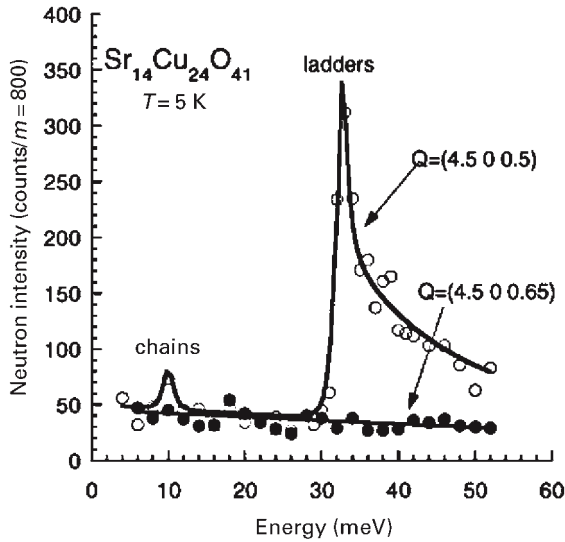

Figure 6
Temperature dependence of the magnetic susceptibility along a, b (chain), and c axes in the quasi-1D $S = 1$ antiferromagnetic chain compound NENP.

parity of n, the number of legs. As in the purely 1D case, the most pronounced effects are expected when the spin couplings are antiferromagnetic, both along the legs and the rungs. For n odd, the spin system behaves like the $S = \frac{1}{2}$ chain: gapless magnetic ground state and power-law decay of spin–spin correlation functions. For n even, the spin system exhibits a nonmagnetic singlet ground state separated from the first triplet states by a gap energy $\Delta \propto J\exp(-n)$ and behaves like a Haldane system (Dagotto and Rice 1996). The largest quantum effect is predicted for the two-leg ($n = 2$) antiferromagnetic ladder with a gap energy amounting to about $0.53J$. Basically, the singlet ground state results from the formation of strongly coupled $S = 0$ dimers along the rungs. The main interest of the two-leg spin-ladder system is in the very interesting conducting properties supposed to appear upon charge doping (e.g., hole doping). As shown theoretically (Dagotto and Rice 1996), if the antiferromagnetic couplings along the legs and the rungs are strong enough to cancel the Coulomb repulsion, the charge carriers tend to be confined to the rungs, leading to an anisotropic pairing mechanism of charge carriers of d-wave symmetry, very reminiscent of that existing in high T_C superconductors.

Experimentally, the n-parity effect has been unambiguously observed from susceptibility measurements in the series $Sr_{n-1}Cu_{n+1}O_{2n}$ (Azuma *et al.* 1994). In agreement with theoretical studies, $SrCu_2O_3$ (a two-leg ladder compound) exhibits a susceptibility vanishing exponentially at low temperature, characteristic of a spin-gap opening. In contrast, $Sr_2Cu_3O_5$ (a three-leg ladder compound) displays a finite

Figure 7
A typical INS result showing the presence of a gap in the magnetic excitation spectrum of the $S = \frac{1}{2}$ two-leg spin-ladder dimer-chain material $Sr_{14}Cu_{24}O_{41}$.

susceptibility at $T = 0\,K$, characteristic of a gapless system. The existence of the singlet ground state and the spin gap has been seen in the insulating ladder cuprate $Sr_{14}Cu_{24}O_{41}$ from comprehensive NMR (Kumagai *et al.* 1997) and INS studies (Eccleston *et al.* 1998). This compound is very interesting because its crystallographic structure (see Fig. 2) can be described as a stacking of magnetically inert Cu_2O_3 two-leg ladder layers and CuO_2 chain layers, separated by strontium layers (forming a so-called "composite" structure).

Figure 7 shows a typical INS experimental result obtained for a single-crystalline sample, demonstrating clearly the presence in this material of a forbidden energy window below 33 meV. Interestingly, the chain subsystem contains a large amount of intrinsic quasi-ordered holes ($\sim 0.6/Cu$) and plays the role of charge reservoir. When substituting calcium for strontium, a part of these holes is released to the Cu_2O_3 ladders, and the new material (of chemical formula $Sr_{14-x}Ca_xCu_{24}O_{41}$) undergoes an insulator–metal transition at ambient pressure and finally a nonconventional superconductivity is induced under pressure. For calcium content of $x \approx 13.6$, the superconducting transition temperature T_C reaches a maximum value of 10 K at 30 kbar (Uehara *et al.* 1996, Mayaffre *et al.* 1998).

4. Effects of Impurities

Chemical substitution takes on different aspects depending on the substituted element. In the most

frequent case, a part of the magnetic ions in the parent material is replaced by magnetic or nonmagnetic elements of the same chemical nature (e.g., substitution of zinc for copper or nickel for copper). The magnetic properties of the doped system will depend on several factors, among which is the nature of the ground state (long-range ordered or quantum disordered), the space dimension of the lattice ($D = 1$ or $D = 2$), and the nature of the impurity itself (valence state, spin). In some cases, the substitution leads to a real charge doping and the formerly insulating material acquires a metallic character and superconductivity can even occur.

4.1 Dilution by Magnetic or Nonmagnetic Impurities

The introduction of randomly distributed impurities breaks the regular network of exchange links coupling the magnetic ions. The effect is particularly dramatic for a 1D system because the impurity cuts a chain more or less completely, depending on its spin value. Obviously, the topology of the parent lattice plays a large role. The size of the region disturbed around the impurity will also depend on the strength of quantum fluctuations. The strongest effects are again expected for the $S = \frac{1}{2}$ spin-Peierls system or the $S = \frac{1}{2}$ alternating antiferromagnetic chain, two systems exhibiting a singlet ground state and a spin gap. In the gapless quasi-1D or quasi-2D systems, the main effect of impurities is to reduce the correlation length (and thus the 3D ordering temperature) and to bring an additional $1/T$ contribution to the susceptibility (assuming noninteracting impurities, which is the case if the impurity density, n_i, is small). This is easily understandable by assuming that the impurity is "dressed" by a magnetic defect of finite size.

Within this picture, the correlation length at low temperature is mainly controlled by the impurity–impurity distance d_i. This distance is directly related to n_i by the geometrical relationship $d_i \approx a/n_i^{1/D}$. At finite temperature, both the impurity and temperature effects are at first order additive: $\xi^{-1}(n_i, T) \approx d_i^{-1} + \xi_{int}^{-1}(T)$. Both the magnetic defects created around each impurity and the intradefect correlated segments contribute to the spin dynamics. At low temperature, quasi-propagating damped spin wave modes exist for wave vectors larger than a cut-off value $q_c \approx 2\pi/d_i$, whereas at low q a diffusive quasi-elastic mode appears. This classical behavior has been quantitatively observed in the $S = 5/2$ Heisenberg antiferromagnetic chain compound TMMC slightly substituted with copper for manganese (Dupas and Renard 1978).

The case of strongly quantum antiferromagnetic chain systems displaying a spin gap Δ is less intuitive. Basically, in such systems the correlation length of spin fluctuations is strongly reduced by the quantum fluctuations and remains finite at $T = 0\,K$ ($\xi \approx c/\Delta$,

where c is the spin wave velocity, i.e., typically $\xi \approx (3-7)a$ depending on the particular system). The main role of impurities is to suppress the quantum fluctuations and thus the doped system recovers a more conventional magnetic behavior, with spin excitations appearing in the gap. In some cases, simultaneously with the destruction of the singlet ground state, a true long-range ordered antiferromagnetic phase occurs, coexisting with the singlet phase. This puzzling result (order by disorder!) is attributed to the fact that around each impurity a magnetic defect is formed (a soliton in this case) developing a staggered magnetization $S(\mathbf{R}_i)$ and extending over a characteristic length scale of the order of the quantum correlation length ξ.

Each soliton bears a total spin $\frac{1}{2}$ which can be detected, for example, by susceptibility or ESR measurements. Such a scenario has been observed in the $S = 1$ Heisenberg antiferromagnetic chain compound NENP doped with a small amount of copper or cadmium. The case of the spin-Peierls compound $CuGeO_3$ is even more interesting. For this system, the substitution of a small amount x of silicon for germanium or y of zinc for copper is enough to considerably reduce T_{SP} ($\Delta T_{SP}/T_{SP} \approx -35x$ for silicon doping), meaning that the coherence length of the dimerization associated with the spin-Peierls transition decreases strongly, even at small doping. Neutron diffraction measurements reveal the presence of a true long-range ordered antiferromagnetic phase coexisting with the short-range dimerized phase (Fukuyama *et al.* 1996, and references therein). An explanation has been proposed for such a coexistence based on the solitonic model (Fukuyama *et al.* 1996). Doping by zinc or silicon has qualitatively the same effect: that of modifying locally the magnetic couplings, either by breaking completely the exchange links (zinc doping) or by changing the value and/or the sign of J (silicon doping).

Topological solitons bearing a total spin $\frac{1}{2}$ are created around each impurity. These objects are associated with weakly distorted regions extending over a length scale ξ and cut the nonmagnetic distorted chain segments of characteristic length $\sim a/x$ (this value corresponding roughly to the average soliton–soliton distance). For x large enough, the solitons overlap and the phase can propagate, giving rise to the nonzero staggered magnetization detected by neutron diffraction. Such coexistence is indeed a general feature of low-dimensional systems. It has also been observed in doped spin-ladder materials.

4.2 Charge Doping

In the doping mechanism previously considered, the substitution between chemical elements having the same valence states (e.g., Zn^{2+} for Cu^{2+}) does not change the global charge balance. In most cases the

material remains electrically inert. However, there are systems for which the substitution of elements of different valence states generates charge carriers in the material. This is, for example, the case when substituting Sr^{2+} for La^{3+} in the "high T_C" material La_2CuO_4, for which holes are created in the CuO_2 planes. In some other cases, the host material contains intrinsically an amount of charge carriers (holes or electrons) confined to crystallographic entities playing the role of a charge reservoir. This is the case in the quasi-2D material $YBa_2Cu_3O_{6+x}$ (YBCO) or, as previously seen, in the spin-ladder compound $Sr_{14}Cu_{24}O_{41}$, for which the charge carriers (indeed holes) are confined to the CuO chain layers. The change in oxygen content for the former or the substitution of calcium for strontium for the latter induces a charge transfer and some holes are released, respectively, in the CuO_2 planes and in the Cu_2O_3 ladders, which become metallic. The superconductivity can occur either at ambient pressure (as in YBCO) or under strong pressure (as in the ladder compound). The presence of holes in the CuO_2 or Cu_2O_3 layers not only affects the exchange links but also distorts the surrounding lattice, thus creating magnetoelastic defects (usually called polarons). As in the previous case, the magnetic coherence length should reflect directly the hole–hole distance, $\sim a/\sqrt{n_h}$, where n_h is the hole density, whereas the spin dynamics should be analogous to that of the diluted system (assuming n_h is sufficiently small).

The presence of such large-size magnetic defects is the origin of the strong decrease of T_N which is observed in the high T_C cuprates upon doping, just before entering the metallic regime. As shown from comprehensive neutron scattering investigations in LSCO and YBCO, the antiferromagnetic long-range ordering disappears for a hole density as small as 2–2.5% hole Cu^{-1}. Above this critical value, the previously gapless excitation spectrum starts to develop a spin gap directly related to the superconducting order parameter. In this nontrivial regime, a clear non-Fermi liquid behavior is observed which originates from the existence of strong antiferromagnetic (more or less incommensurate) correlations persisting in the superconducting state (Furrer 1998).

5. Conclusion and Perspectives

The magnetism in low-dimensional systems often shows quite nonconventional features resulting in a large part from an increase in both the thermal and quantum fluctuations. The general properties of a given material depend on the subtle balance between several factors: the spin fluctuations and magnetic correlations, the (more or less dynamical) charge ordering, and the spin–lattice or electron–lattice couplings. Depending on their relative strengths, quite different ground states can be realized (e.g., insulating

long-range ordered, nonmagnetic singlet, spin-liquid, Lüttinger-liquid, and superconducting ground states). In most cases, the magnetic behavior can be well described by considering spin Hamiltonians involving only the spin degrees of freedom. However, there is a tendency to reconsider the role played by the orbital degrees of freedom in the strongly correlated electron systems. Techniques probing directly both the spin and orbit correlations (such as spherical neutron polarimetry or polarized x-ray resonant magnetic diffraction) should bring particularly relevant information for the understanding of the roles played by the spin and orbital ordering.

Bibliography

Abragam A, Bleaney B 1970 *Electron Paramagnetic Resonance*. Clarendon, Oxford

Affleck I 1990 In: Brezin E, Zinn-Justin J (eds.) *Fields, Strings and Critical Phenomena*. North-Holland, Amsterdam

Azuma M, Hiroi Z, Takano M, Ishida K, Kitaoka Y 1994 Observation of a spin gap in $SrCu_2O_3$ comprising spin-$\frac{1}{2}$ quasi-1D two-leg ladders. *Phys. Rev. Lett.* **73**, 3463–6

Boucher J P, Regnault L P 1996 The inorganic spin-Peierls compound $CuGeO_3$. *J. Phys. I* **6**, 1939–66

Bray J W, Hart H R, Interrante L V, Jacobs I S, Kasper J S, Watkins G D, Wee S H, Bonner J C 1975 Observation of a spin-Peierls transition in a Heisenberg antiferromagnetic linear-chain system. *Phys. Rev. Lett.* **35**, 744–7

Dagotto E, Rice T M 1996 Surprises on the way from one- to two-dimensional quantum magnets: the ladder materials. *Science* **271**, 618–22

De Jongh (ed.) 1990 *Magnetic Properties of Layered Transition Metal Compounds*. Kluwer, Amsterdam

De Jongh L J, Miedema A R 1974 Experiments on simple magnetic model systems. *Adv. Phys.* **23**, 1–260

Domb C, Green M S 1972 *Phase Transition and Critical Phenomena*. Academic Press, London, Vol. 1

Domb C, Green M S 1976 *Phase Transition and Critical Phenomena*. Academic Press, London, Vol. 2

Domb C, Lebowitz J L 1983 *Phase Transition and Critical Phenomena*. Academic Press, London, Vol. 8

Domb C, Lebowitz J L 1988 *Phase Transition and Critical Phenomena*. Academic Press, London, Vol. 12

Dupas C, Renard J P 1978 Effect of impurities on the Néel temperature and the low-temperature susceptibility of the quasi one-dimensional antiferromagnet TMMC. *Phys. Rev. B* **18**, 401–7

Eccleston R S, Uehara M, Akimitsu J, Eisaki H, Motoyama N, Uchida S 1998 Spin dynamics of the spin-ladder dimer-chain material $Sr_{14}Cu_{24}O_{41}$. *Phys. Rev. Lett.* **81**, 1702–5

Endo Y, Shirane G, Birgeneau R J, Richards P M, Holt S L 1974 Dynamics of an $S = \frac{1}{2}$ one-dimensional Heisenberg antiferromagnet. *Phys. Rev. Lett.* **32**, 170–3

Fukuyama H, Tanimoto T, Saito M 1996 Antiferromagnetic long-range order in disordered spin-Peierls systems. *J. Phys. Soc. Jpn.* **65**, 1182–5

Furrer A (ed.) 1998 *Neutron Scattering in Layered Copper Oxide Superconductors*. Kluwer, Dordrecht, The Netherlands

Haldane F D M 1983 Nonlinear field theory of large-spin Heisenberg antiferromagnets: semi-classically quantized easy-axis Néel state. *Phys. Rev. Lett.* **50**, 1153–6

Hase M, Terasaki I, Uchinokura K 1993 Observation of the spin-Peierls transition in linear Cu^{2+} (spin-1/2) chains in the inorganic compound $CuGeO_3$. *Phys. Rev. Lett.* **70**, 3651–4

Ikeda H, Hirakawa K 1974 Neutron scattering study of two-dimensional Ising nature of K_2CoF_4. *Solid State Commun.* **14**, 529–32

Kosterlitz J M, Thouless D J 1973 Ordering, metastability and phase transition in two-dimensional systems. *J. Phys. C: Solid State Phys.* **6**, 1181–203

Kumagai K, Tsuji S, Kato M, Koike Y 1997 NMR study of carrier doping effects on spin gaps in the spin ladders $Sr_{14-x}A_xCu_{24}O_{41}$ (A = Ca, La and Y). *Phys. Rev. Lett.* **78**, 1992–5

Lovesey S W 1987 *Theory of Neutron Scattering from Condensed Matter*. Clarendon, Oxford

Mayaffre H, Auban-Senzier P, Nardone M, Jerome D, Poilblanc D, Bourbonnais C, Ammerahl U, Dhalenne G, Revcolevschi A 1998 Absence of spin gap in the superconducting ladder compound $Sr_2Ca_{12}Cu_{24}O_{41}$. *Science* **279**, 345–8

Mikeska H J 1980 Nonlinear dynamics of classical one-dimensional antiferromagnets. *J. Phys. C: Solid State Phys.* **13**, 2913–23

Pytte E 1974 Lattice distortions in one-dimensional Heisenberg chains. *Phys. Rev. B* **10**, 2039–43, 4637–42

Regnault L P, Boucher J P, Rossat-Mignod J, Renard J P, Bouillot J, Stirling W G 1982 A neutron investigation of the soliton regime in the one-dimensional planar antiferromagnet $(CD_3)_4NMnCl_3$. *J. Phys. C: Solid State Phys.* **15**, 1261–82

Renard J P, Verdaguer M, Regnault L P, Erkelens W A C, Rossat-Mignod J, Stirling W G 1987 Presumption for the existence of a quantum gap in the one-dimensional $S = 1$ antiferromagnet NENP. *Europhys. Lett.* **3**, 949–54

Schulz H J 1986 Phase diagrams and correlation exponents for quantum spin chains of arbitrary spin quantum number. *Phys. Rev. B* **34**, 6372–85

Slichter C P 1990 *Principles of Magnetic Resonance*. Springer, Heidelberg, Germany

Steiner M, Villain J, Windsor C G 1976 Theoretical and experimental studies on one-dimensional magnetic systems. *Adv. Phys.* **25**, 87–209

Tennant D A, Perring T G, Cowley R A, Nagler S E 1993 Unbound spinons in the $S = \frac{1}{2}$ antiferromagnetic chain $KCuF_3$. *Phys. Rev. Lett.* **70**, 4003–6

Uehara M, Nagata T, Akimitsu J, Takahashi H, Mori N, Kinishita K 1996 Superconductivity in the ladder material $Sr_{0.4}Ca_{13.6}Cu_{24}O_{41.84}$. *J. Phys. Soc. Jpn.* **65**, 2764–7

L.P. Regnault
CEA, Grenoble, France

C

Coercivity Mechanisms

Since the early days of the commercial use of permanent magnets (PMs) the coercive field has been a topic of theoretical discussion concerning its quantitative interpretation (Becker and Döring 1939, Kersten 1942). With the development of the theory of micromagnetism in the 1930s and 1940s the basic concepts became available for a quantitative treatment of magnetization processes and of the hysteresis loop. At the beginning of the twentieth century the application of magnetic materials was mainly based on iron, cobalt, nickel, carbon steels, and natural iron oxides such as magnetite (Fe_3O_4). As a consequence of the quantum theoretical interpretation of spin order by Heisenberg, Bloch, and Néel, combined with the development of the theory of micromagnetism by Landau and Lifshitz (1935), Becker and Döring (1939), and Brown (1945), a more systematic tailoring of magnetic materials became possible. The characterization of the constitution and of the microstructure allowed an analysis of the microstructure–property relationships. The development of high-permeability, high-coercivity, high-remanence, giant-magnetoresistive, and giant-magnetostrictive materials combined with suitable electrical and mechanical properties has influenced the whole field of magnetic devices ranging from the energy technique to high-density recording systems.

The hysteresis loops of these high-quality magnetic materials are characterized by three main parameters: coercive field, H_c, remanence, J_r, and initial susceptibility, χ_0 (see *Magnetic Hysteresis*). In particular, nanocrystalline alloys have become the leading material for high-technology applications. These applications, the applied experimental techniques, and the underlying physical effects are summarized in Table 1. In all these materials the coercive field is the basic

property that should be either very large for permanent magnets or extremely small for high-permeability or sensor materials. For high-density recording systems H_c values of $100–200\,kA\,m^{-1}$ are used. The characteristic parameters of the hysteresis loop depend on the main intrinsic material parameters, such as the spontaneous polarization, $J_s = \mu_0 M_s$ ($M_s =$ magnetization, $\mu_0 = 4\pi \times 10^{-7}\,V\,s\,A^{-1}\,m^{-1}$), the magnetocrystalline constants, K_1 and K_2 (see *Magnetic Anisotropy*), and the magnetostriction, λ. Furthermore, the microstructure has a strong influence on H_c and χ_0. The important role of the anisotropy constant K_1 is demonstrated by Fig. 1 where the dependence of H_c of different prominent material groups is presented schematically as a function of K_1. Here the coercive field varies over eight orders of magnitude from $10^{-1}\,A\,m^{-1}$ up to $10^7\,A\,m^{-1}$. This very large range of variation is due to the large variations of K_1 and the microstructures with length scales varying from nano- to centimeters. The main mechanisms governing the coercive field are nucleation and domain wall pinning processes. Sometimes also combinations of rotation and nucleation processes exist. In the following the micromagnetic backgrounds of nucleation and pinning in inhomogeneous regions are reviewed.

1. Brown's Paradox on and the Role of Microstructures

The ideal coercive field of an ellipsoidal, single-domain uniaxial particle for a uniform rotation process (Brown 1963) is given by the so-called nucleation field:

$$\mu_0 H_N = \mu_0 H_c = \frac{2K_1}{M_s} - (N_\parallel - N_\perp)J_s \qquad (1)$$

According to Eqn. (1), H_c is independent of the size of particles but depends only on the shape via the

Table 1
Nanocrystalline, high-quality magnetic materials.

Application	Experimental technique	Physical phenomena
High-coercivity–high-remanence magnets: $H_c > 1.5\,T$; $J_r > 1\,T$	Nanocrystalline melt-spinning Mechanical alloying	High anisotropy Intergrain exchange coupling
High-permeability–high-remanence magnets: $J_r > 1\,T$; $\mu > 10^5$	Nanocrystalline melt-spinning Amorphous crystallization	Low anisotropy Random anisotropy effect
Giant-magnetostrictive alloys $\lambda > 10^{-4}$	Ion d.c. sputtering	Single ion anisotropies of 4f electrons
Giant-magnetoresistive alloys $\Delta R/R > 50\%$	Laser ablation	Double exchange Magnetic phase transition
High-density recording: $> 1\,Gb\,cm^{-2}$	Multilayers Ion d.c. sputtering Self-organization of substrates and particles on substrates	Single-domain granular systems Perpendicular anisotropy
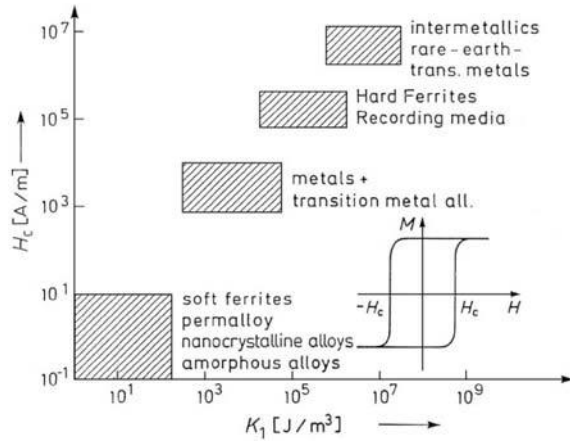
Figure 1
Schematic plot of coercive field H_c vs. crystal anisotropy K_1 for prominent soft, hard, and extremely hard magnetic materials.
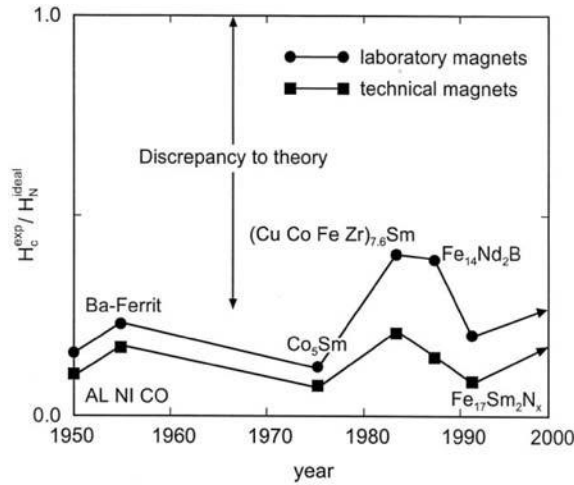
Figure 2
Ratio H_c^{exp}/H_N of permanent magnets developed since the 1950s.

demagnetization factors $N_{\parallel}$ and $N_{\perp}$ parallel and perpendicular to the easy axis. The coercive fields predicted by Eqn. (1) so far have not been realized for technical materials. Only in the case of elongated iron whiskers could the theoretical values of the curling mode be approached (Luborsky and Morelock 1964). According to Fig. 2, for the most prominent PMs only 20–30% of the theoretically predicted coercive field could be realized for many years. It is now generally accepted that this discrepancy has to be attributed to magnetic imperfections that lead locally to a drastic reduction of the ideal nucleation field. The main sources of this phenomenon, originally known as Brown's paradoxon (Brown 1945), are the following: (i) reduced anisotropy constant at grain surfaces, (ii) misaligned grains that are exchange coupled with neighboring grains, and (iii) enhanced local demagnetization fields at sharp edges and corners of polyhedral grains.

A relationship that has been shown to be very useful in describing the role of the microstructure and the temperature dependence of H_c is a modification of Eqn. (1) (Kronmüller 1987, Kronmüller *et al.* 1988, Sagawa and Hirosawa 1988):

$$\mu_0 H_c = \frac{2K_1}{M_s}\alpha - N_{eff}J_s \qquad (2)$$

where two microstructural parameters, α and N_{eff}, have been introduced. Here $\alpha < 1$ describes the reduction of the ideal crystal field $2K_1/M_s$ owing to lattice imperfections and atomic disorder at grain surfaces. The effective demagnetization factor takes care of the enhanced stray fields at edges and corners of polyhedral grains. Equation (2) not only applies to nucleation-hardened PMs but also describes H_c of thin films and multilayers and the coercive field of the pinning hardened Sm_2Co_{17}-based PMs. The parameter α subsumes the above described microstructural effects and is composed of three subparameters (Kronmüller *et al.* 1987, Bauer *et al.* 1996):

$$\alpha = \alpha_K \alpha_\psi \alpha_{ex} \qquad (3)$$

where α_K, α_ψ, and α_{ex} describe the effect of a reduced anisotropy constant, of misaligned grains, and of exchange coupling between grains. An explicit determination of α is based on solutions of the micromagnetic equations for special models of microstructures.

2. Nucleation Field in Regions of Reduced Anisotropy Constants

Nucleation fields are usually derived as the eigenvalues of the linearized micromagnetic equations. For example, the nucleation field for uniform rotation has been obtained for constant material constants J_s, K_1, and A ($A =$ exchange constant). Similarly the curling and the buckling mode have been determined for constant material parameters (Aharoni 1962). In magnetically inhomogeneous regions in general all three material parameters vary spatially. However, K_1 is much more sensitive with respect to atomic disorder than J_s and A, as known from amorphous alloys. To a first approximation J_s and A therefore may be considered to be constant and only variations of K_1 are taken into account. In the case of a planar grain boundary or a deteriorated surface, the main parameters characterizing the magnetic defect are the half width, r_0, and the change, ΔK, of the anisotropy
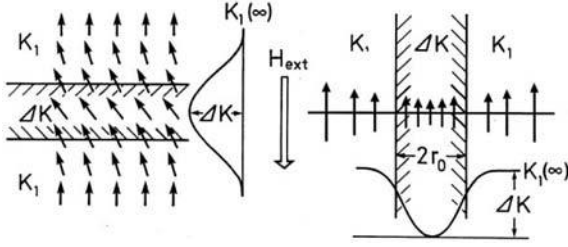
Figure 3
Nucleation of a reversed domain within a planar intergranular phase of reduced anisotropy. Left: perpendicular stripe; right: parallel stripe.

constant. A suitable one-dimensional equation for the position dependence of $K_1(z)$ allowing a quantitative solution of the nucleation problem is given by (Kronmüller 1987).

$$K_1(z) = K_1(\infty) - \Delta K / ch^2(z/r_0) \quad (4)$$

In the case of a one-dimensional problem, e.g., a planar grain boundary as shown in Fig. 3, the linearized micromagnetic equation is then

$$2A\frac{\mathrm{d}^2\varphi}{\mathrm{d}z^2} - \left\{ 2\left[K_1(\infty) - \frac{\Delta K}{ch^2(z/r_0)} \right] \right.$$
$$\left. - J_s(H_{ext} + N_{eff}M_s) \right\} \varphi = 0 \quad (5)$$

where φ is the angle between $\underline{J}_s$ and the easy axis. The solution of Eqn. (5) leads to hypergeometric functions and the parameter α_K follows from the lowest eigenvalue of possible solutions:

$$\alpha_K = 1 - \frac{1}{4\pi^2} \frac{\delta_B^2}{r_0^2} \left(1 - \sqrt{1 + \frac{4\pi^2 r_0^2}{\delta_B'^2}} \right)^2 \quad (6)$$

where $\delta_B = \pi\sqrt{A/K_1(\infty)}>$ denotes the wall width of the perfect crystal and $\delta_B' = \pi\sqrt{A/\Delta K}$ corresponds to a fictitious wall width of a material with anisotropy ΔK. The parameter α_K is presented in Fig. 4 as a function of δ_B/r_0 and for ΔK as a parameter. From Eqn. (6), three interesting limiting cases can be derived:

1. $2\pi r_0 < \delta_B; \alpha_K = 1 - \pi^2 \frac{\delta_B^2}{\delta_B'^4} r_0^2$

2. $2\pi r_0 \geqslant \delta_B; \alpha_K = \frac{1}{\pi} \frac{\delta_B^2}{\delta_B'} \frac{1}{r_0} + \frac{K_1 - \Delta K}{K_1} \quad (7)$

3. $2\pi r_0 \gg \delta_B; \alpha_K = \frac{K_1 - \Delta K}{K_1}$

In the case where $\Delta K = K_1$, α_K in the three limits is $\alpha_K = 1 - \pi^2 r_0^2/\delta_B^2$, $\alpha_K = (1/\pi)(\delta_B/r_0)$, and $\alpha_K = 0$. Inserting
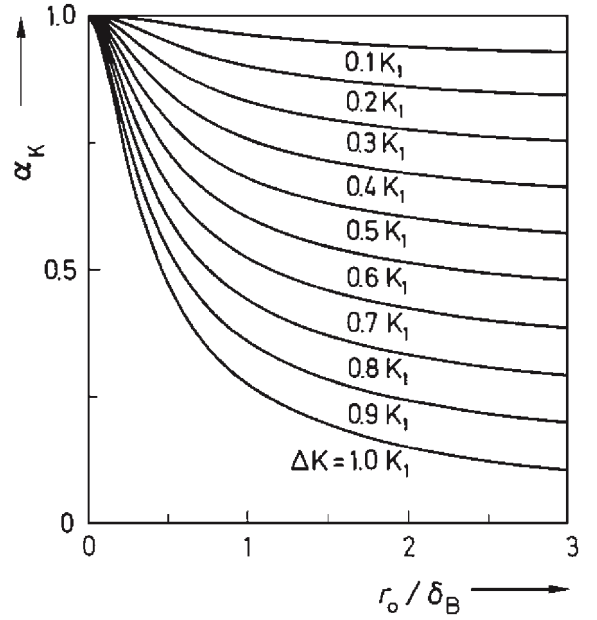
Figure 4
Variation of α_K as a function of r_0/δ_B for various ΔK.

α_K of the second limit into Eqn. (2) gives

$$H_N = H_c = \frac{2K_1}{J_s} \frac{\delta_B}{\pi r_0} - N_{eff}M_s = \frac{\gamma_B}{2J_s} \frac{1}{r_0} - N_{eff}M_s \quad (8)$$

where $\gamma_B = 4\sqrt{AK_1}$ denotes the wall energy per unit area.

3. Nucleation Field of Misaligned Grains

The nucleation field is reduced by a factor α_ψ if the field is applied under an angle ψ_0 with respect to the negative c-axis. Stoner and Wohlfarth (1948) have determined α_ψ for a uniaxial particle and the anisotropy constant K_1. An expansion of the Stoner–Wohlfarth result including the second anisotropy constant K_2 is given by (Kronmüller *et al.* 1987)

$$\alpha_\psi = \frac{1}{[(\cos\psi_0)^{2/3} + (\sin\psi_0)^{2/3}]^{3/2}}$$
$$\times \left[1 + \frac{2K_2}{K_1 + K_d} \frac{(\tan\psi_0)^{2/3}}{1 + (\tan\psi_0)^{2/3}} \right] \quad (9)$$

The angle φ_N by which $\underline{J}_s$ is rotated before spontaneous nucleation takes place is given by

$$\varphi_N = \tan^{-1} \sqrt[3]{\tan\psi_0} + \frac{2}{3} \frac{K_2}{K_1 + K_d} \quad (10)$$
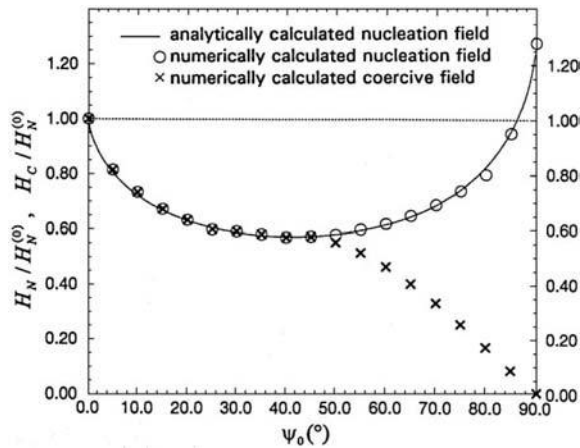
Figure 5
Angular dependence of the nucleation and the coercive field of a $Nd_2Fe_{14}B$ sphere in reduced units ($\alpha_\psi = H_N/H_N^{(0)}$).

1. High-Coercivity, Two-Phase Magnets

$Nd_2Fe_{14}B$ + dipolar coupling

2. High-Remanence, Single-Phase Magnets

exchange + dipolar coupling

3. High-Remanence, Composite, Two-Phase Magnets

$\alpha - Fe$ + $Nd_2Fe_{14}B$

Figure 6
Schematic microstructures of nanocrystalline melt-spun permanent magnets.

where $K_d = (1/2)\mu_0(N_\perp - N_\parallel)M_s^2$. The parameter α_ψ, defined as $\alpha_\psi = H_N(\psi)/H_N(0)$, is shown in Fig. 5 for the extended theory with $K_2 \neq 0$ for the case of $Nd_2Fe_{14}B$ and $K_d = 0$ (sphere). Also shown in Fig. 5 are the coercive fields which for $\psi_0 < \pi/4$ coincide with the nucleation fields, but decrease for $\psi_0 > \pi/4$, because nucleation takes place in the third quadrant.

4. Coercive Fields of Assemblies of Grains

In the case of assemblies of grains three types of permanent magnets have to be distinguished that are characterized by special microstructures, as shown schematically in Fig. 6 and leading to hysteresis loops presented in Fig. 7:

(i) High-coercivity PMs where the grains are magnetically decoupled by a paramagnetic intergranular film. In the case of $R_2Fe_{14}B$-based magnets, this microstructure is realized by an overstoichiometry of R and suitable additives such as gallium and niobium (Kronmüller *et al*. 1996) (see *Magnets: Sintered*). There still exists a long-range dipolar interaction between the grains, which, however, becomes rather small in the case of nanograins (Rieger *et al*. 1999).

(ii) High-remanence–high-coercivity PMs are obtained if nanograins are magnetically coupled by exchange interactions (Kneller and Hawig 1991, Kronmüller *et al*. 1996). These types of PMs are realized by highly stoichiometric alloys.

(iii) Composite high-remanence PMs (Coehoorn *et al*. 1988, Bauer *et al*. 1996, Goll *et al*. 1998, Neu *et al*. 1996) are obtained by melt-spinning of alloys with overstoichiometric content of α-Fe. In this case, in addition to the effect of exchange coupling

between the grains, the large magnetization of α-Fe also enhances the remanence (see *Magnets: Remanence-enhanced*).

4.1 Isotropic Distribution of Decoupled Grains

In the case of decoupled grains, α_ψ has to be replaced by an effective value, α^{eff}, which takes care of the fact that the demagnetization process takes place by irreversible nucleation processes and also by reversible rotational processes. Owing to the angular dependence of α_ψ all those grains oriented symmetrically around $\psi_0 = \pi/4$ reorient their magnetization first. Neglecting the reversible rotations in the remaining grains the demagnetization to zero polarization is performed by those grains with misalignment angles in the range $30° < \psi < 60°$. In this range the average, $\langle \alpha_\psi \rangle$, is of the order of 0.53, i.e., this value is very near to the minimum value $\alpha_\psi^{min} = 0.5$ at $\psi_0 = \pi/4$. The value of 0.53 is even lowered if the contributions of the reversible rotations are taken into account. Consequently, in the case of an isotropic distribution of
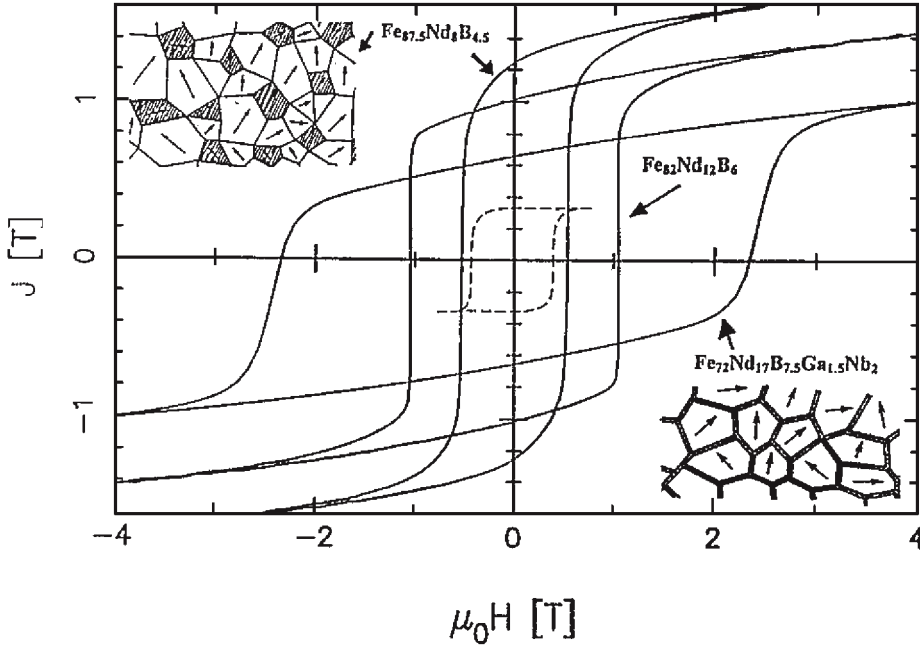
Figure 7
Hysteresis loops of nanocrystalline PMs with the microstructures of Fig. 6. The broken curve represents the conventional (Ba, Sr)-based ferrite. The intermediate loop results from the stoichiometric $Nd_2Fe_{14}B$.

easy axes, it is a reasonable approximation to use for α_ψ the minimum value α_ψ^{min}, given by (Kronmüller 1990)

$$\alpha_\psi^{min} = \frac{K_1 + K_2}{2K_1} \cong \frac{1}{2} \qquad (11)$$

4.2 Isotropic Distribution of Exchange-coupled Grains

In nanocrystalline PMs with exchange coupling between the grains the coercive field is in general smaller as compared to exchange-decoupled grains. Several sources may contribute to this decrease of H_c. The random anisotropy effect (Herzer 1990) leads to a reduction of the effective anisotropy constant if the grain sizes are smaller than the wall width. In the case of hard magnetic materials, $\delta_B < 5$ nm holds whereas in most nanocrystalline PMs D is larger than δ_B (10–20 nm) and therefore the random anisotropy effect becomes ineffective. Another source of reduced coercive fields are grains with misalignment angles $\psi_0 > \pi/4$. According to Fig. 5 the coercive field of these grains decreases to zero for $\psi_0 = \pi/2$ where $H_N > H_c$, i.e., they contribute to the demagnetization process only by reversible rotations.

Owing to the exchange coupling these strongly misaligned grains increase the rotation of J_s within

the neighboring grains which leads to an enhancement of the reversal of magnetization in these neighboring grains because the critical angle, φ_N, is achieved at lower fields. The demagnetization process of exchange-coupled grains therefore is a collective process where a cluster of grains becomes reversed by the grain of largest misalignment. It can therefore be assumed that the demagnetization process in assemblies of exchange-coupled grains is governed by the grains with misalignment angles $\pi/4 < \psi < \pi/2$. The average coercive field of these grains is of the order of $(1/4)(2K_1/J_s)$, i.e., $\alpha_{ex} \sim 1/2$.

5. Analysis of Temperature Dependence

5.1 The Nucleation Model

The analysis of hardening mechanisms and of the temperature dependence of H_c starts from Eqn. (2). In general it is assumed that the grains with the smallest H_c values determine the global H_c, i.e., the grains that are characterized by α_ψ^{min} of Eqn. (11). A precise value of α_ψ^{min} including K_2 has been determined by Martinek and Kronmüller (1990). With $H_N^{min} = \alpha_\psi^{min} \cdot H_N$, Eqn. (2) may be written as

$$\mu_0 H_c = \alpha_K \alpha_{ex} \mu_0 H_N^{min} - N_{eff} J_s \qquad (12)$$

71
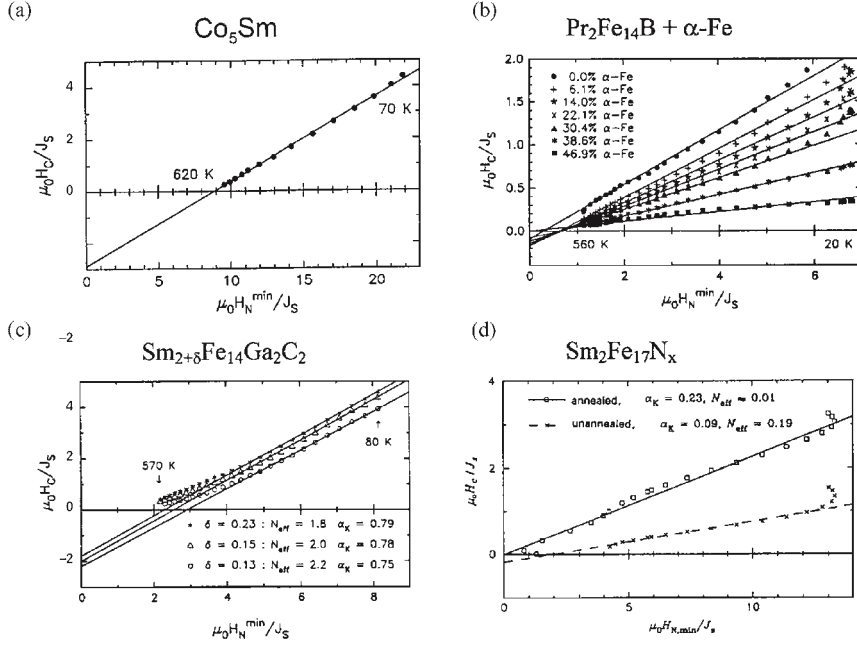
Figure 8
Plots of $\mu_0 H_c/J_s$ vs. $\mu_0 H_N^{\min}/J_s$ to determine the microstructural parameters α_K and N_{eff}: (a) Co_5Sm sintered PM; (b) composite $Pr_2Fe_{14}B + \alpha$-Fe melt-spun PMs; (c) $Sm_{2+\delta}Fe_{14}Ga_2C_2$ carbides with $\delta = 0.0$, 0.05, 0.14; (d) $Sm_{10.7}Fe_{89.3}N_x$ nitride annealed at $T_a = 850\,^\circ C$ for $t_a = 17\,\text{min}$ and nitrided at $460\,^\circ C$.

from which it is possible to derive the plot

$$\mu_0 H_c(T)/J_s(T)|_{\exp} \text{ vs. } \mu_0 H_c^{\min}(T)/J_s(T)|_{\text{theor}} \quad (13)$$

The left-hand side represents the experimental and the right-hand side the theoretical values. In the case of a linear plot the parameters $\alpha_K \cdot \alpha_{\text{ex}}$ and N_{eff} are obtained as the slope and the ordinate intersection of the straight line, respectively. These parameters have been determined for a large number of rare-earth-based PMs. Figure 8 shows the $\mu_0 H_c(T)/J_s(T)$ plots for sintered Co_5Sm, nanocrystalline $Pr_2Fe_{14}B + \alpha$-Fe, $Sm_{2+\delta}Fe_{14}Ga_2C_2$ (with $\delta = 0.0$, 0.05, and 0.14), and the nitride $Sm_{10.7}Fe_{89.3}N_x$. In all cases a linear relationship is found with minor deviations in the case of the carbide, because the determination of $H_N^{\min}$ suffers from a large error in K_1 and K_2 at high temperatures. The results presented so far clearly show that linear plots of Eqn. (13) are obtained for nanocrystalline and sintered PMs. The validity of the nucleation model therefore seems clear. From the measured α parameters with the assumption $\alpha_{\text{ex}} = 1/2$ for nanocrystalline and $\alpha_{\text{ex}} = 1$ for sintered and decoupled PMs, values of α_K are obtained between 0.3 and 0.8, which corresponds to a width of the inhomogeneity region of $0.3\delta_B < 2r_0 < \delta_B$. For example, in the case of Co_5Sm with $\alpha_K = 0.33$ and $\alpha_{\text{ex}} = 1/2$, r_0 is of the order

of 1 nm. Similar results have been obtained previously for $Nd_2Fe_{14}B$ PMs (Kronmüller *et al.* 1988). Another interesting result is the range of α parameters of nanocrystalline $Pr_2Fe_{14}B$ PMs (Goll *et al.* 1998). For decoupled PrFeB PMs with excess praseodymium α_K values of ~ 0.8 are obtained, whereas the stoichiometric exchange-coupled and composite PMs show α values in the range 0.06–0.32. These small α values of nanocrystalline PMs are due to the parameter α_{ex}, which reduces the α values by at least 50%. Furthermore, it should be noted that the N_{eff} values of sintered magnets are large with $N_{\text{eff}} \geqslant 1$, whereas the values of nanocrystalline PMs range from 0 to 0.2 because the grains have a spherical shape.

5.2 The Nucleus Expansion Model

Besides the spontaneous nucleation model discussed in Sect. 5.1 a so-called phenomenological "global model" has been discussed (Givord and Rossignol 1996). In this model it is assumed that the expansion of a preformed nucleus takes place by means of a thermally excited process within the lifetime of the reversed nucleus that is given by an Arrhenius equation: $\tau = \tau_0 \exp(-\Delta E/kt)$. The pre-exponential factor is of the order of magnitude $\tau_0 \cong 10^{-11}\,\text{s}$ and ΔE
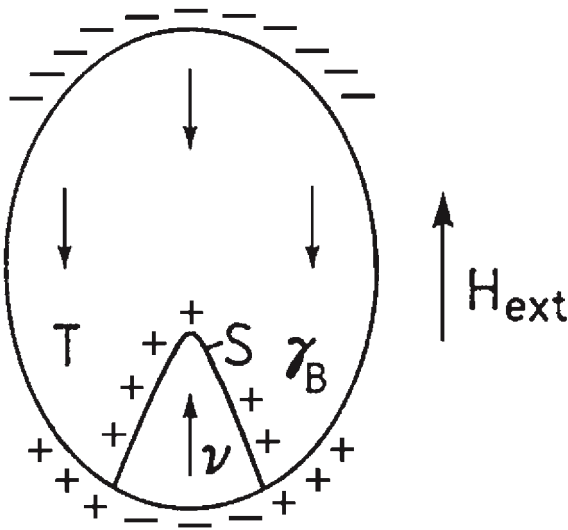
Figure 9
Spike-type nucleus of volume v, surface area s, and wall energy γ'_B.

denotes the activation enthalpy required to expand the nucleus of volume v spontaneously. For usual measuring times of $t = 1 - 10^3$ s the activation enthalpy $\Delta E(t) = kT\ln(t/\tau_0)$ is of the order of $\Delta E \cong 25kT$ (Givord and Rossignol 1996).

The activation energy ΔE is required in order to overcome the magnetic enthalpy required for the expansion of the nucleus. As shown in Fig. 9, at the coercive field H_c the three terms of the magnetic enthalpy are balanced by ΔE, which leads to

$$s\gamma'_B - \mu_0 M_s H_c v - \mu_0 N_{\text{eff}} M_s^2 v = \Delta E = 25kT \quad (14)$$

with the domain wall energy, the magnetostatic energy of the external field at H_c, and the demagnetization energy. Since it is suggested that the nucleus is formed in a perturbed region, the specific wall energy γ_B is reduced as compared to the value of the perfect crystal, giving $\gamma'_B = \alpha_B \gamma'_B = \alpha_B \times 4\sqrt{AK_1}$, where α_B corresponds to a microstructural parameter less than unity. The surface, s, of the nucleus may be related to the volume, v, by $s = \alpha_s v^{2/3}$, where α_s corresponds to a geometrical parameter relating the nucleus surface to the nucleus volume. From Eqn. (14), one now obtains

$$\mu_0 H_c = \frac{\alpha_s \alpha_B \gamma_B}{M_s v^{1/3}} - \mu_0 M_s \cdot N_{\text{eff}} - \frac{25kT}{vM_s} \quad (15)$$

Measurements of the activation volume, v, by means of relaxation curves have shown that v obeys a similar temperature dependence as δ_B^3. Therefore, with

$v = \alpha_v^3 \delta_B^3$, Eqn. (15) can be rewritten as

$$
\begin{aligned}
\mu_0 H_c &= \frac{\alpha_s \alpha_B}{\alpha_v} \frac{1}{M_s} \frac{\gamma_B}{\delta_B} - \mu_0 M_s \cdot N_{\text{eff}} - \frac{25kT}{vM_s} \\
&= \frac{2K_1}{M_s} \frac{2\alpha_s \alpha_B}{\pi \alpha_v} - \mu_0 M_s \cdot N_{\text{eff}} - \frac{25kT}{vM_s} \quad (16)
\end{aligned}
$$

Here it becomes obvious that the coercive field of the global model is described by the same Eqn. (2) or Eqn. (8) as in the case of the nucleation model. The only difference seems to be that the nucleation model is based on the micromagnetic equations whereas the global model starts from an energetic approach, i.e., the integrated micromagnetic equations. Since the thermal fluctuation field $\mu_0 H_f = 25kT/vM_s$ corresponds only to 5–10% of the coercive field, the micromagnetic energy terms are the dominant ones. Naturally the fluctuation field can also be introduced into the nucleation model as a term reducing the nucleation field. The microstructural parameters α_s and α_B can be derived from the plot

$$\left. \frac{H_c + H_f}{M_s} \right|_{\text{exp}} \text{ vs. } \gamma_B/\mu_0 M_s^2 v^{1/3} \text{ or vs. } \mu_0 \gamma_B/J_s^2 v^{1/3} \quad (17)$$

where H_c, v, and H_f are determined experimentally and M_s and γ_B are obtained from the intrinsic material parameters. Figure 10 shows the temperature dependence of the activation volume of three types of magnets (melt-spun, sintered and annealed, and as-sintered). The corresponding plots, according to Eqn. (17), are shown in Fig. 11 (Becher *et al.* 1998). For all three magnets linear plots are obtained and the microstructural parameters vary between 0.66 and 1.07. For a nucleus of spherical or conical shape (apex angle $\theta = 15°$) α_s varies between 4.8 and 2.3. In the case of the nanocrystalline melt-spun magnet this means that α_B varies between 0.2 and 0.4.
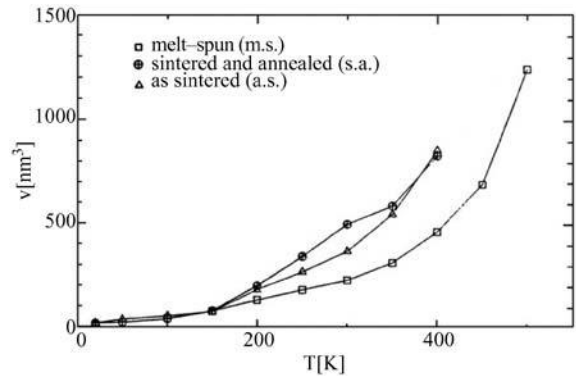
Figure 10
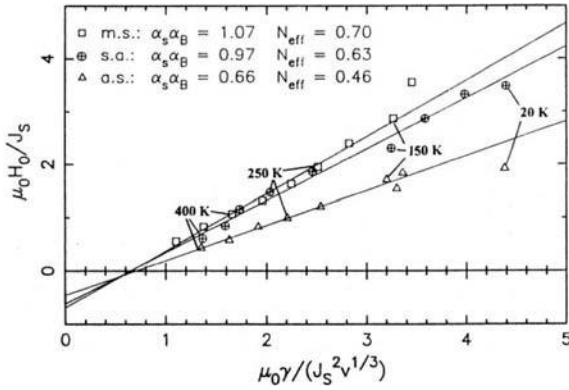Temperature dependence of the activation volume of three types of magnets.

Figure 11
Plots for the determination of $\alpha_s\alpha_B$ and N_{eff} for the global model of the PMs of Fig. 10.

Since the measured activation volumes are of the order of $300\,\text{nm}^3$ the reduction of the wall energy should extend over dimensions of $\sim 5\delta_B$ ($\sim 20\,\text{nm}$). The problem arising here is the fact that from high-resolution transmission electron microscopy images (Kronmüller *et al.* 1996) it is known that the nanocrystalline grains are perfect with the exception of the grain boundaries of width 1–3 nm. Accordingly, neither the values measured for v nor for α_B are compatible with the real microstructure. The situation is different for the nucleation model where the reversion of magnetization starts in regions of width 0.5–2 nm in agreement with the microstructure. Since the global theory is just the integrated expression of the micromagnetic equation, the microstructural parameters, α_s, α_B, and α_v may be identified with the parameters α_K and α_{ex}, i.e., $4\alpha_s\alpha_B/\pi\alpha_v\equiv\alpha_K\alpha_{ex}$, which enlightens one as to the seeming existence of two different theories.

6. Pinning of Domain Walls by Planar Barriers in Sm₂Co₁₇-based Magnets

Planar defects of atomic width are stacking faults, phase and antiphase boundaries, and planar precipitates as the cell walls of copper-doped Sm_2Co_{17} PMs. The pinning of domain walls by planar defects has been treated by the continuum theory of micromagnetism (Kronmüller 1973, Friedberg and Paul 1975, Hilzinger 1977, Gaunt and Mylvaganam 1981) and on the basis of the Heisenberg model (Hilzinger and Kronmüller 1975). The pinning effect is due to the modification of the wall energy by the planar defect. If the planar defect has extensions larger than the wall width the coercive field is given by

$$H_c = \frac{1}{2J_s}\frac{1}{\cos\psi_0}\left.\frac{d\gamma(z)}{dz}\right|_{max} - N_{eff}M_s \qquad (18)$$

where $d\gamma(z)/dz|_{max}$ denotes the maximum slope of wall energy. In the case of a linear barrier, $d\gamma(z)/dz|_{max}$ is given by $|\gamma^{II}-\gamma^{I}|/D$, where $\gamma^{I,II}$ denote the wall energies in the two neighboring phases and D corresponds to the width of the defect.

In the case of a narrow defect with $D < \delta_B$ the coercive field is determined by the discrete Heisenberg model (Hilzinger and Kronmüller 1975) where the planar defect is described by its n individual lattice planes of distance d. Each plane, i, is characterized by a local anisotropy constant, K^i, and an exchange constant, $A^{i,i+1}$, between neighboring planes. The result of a lengthy calculation is

$$H_c = \frac{\pi}{3\sqrt{3}}\frac{2K_1}{J_s}\frac{1}{\cos\psi_0}\frac{d}{\delta_B}\sum_{i=1}^{n-1}\left|\frac{A}{A^{i,i+1}}-\frac{K_1^i}{K_1}\right| \qquad (19)$$

where A, K_1, and J_s are the material constants of the matrix phase and δ_B is the wall width. Equation (19) has a wide range of applications and may be applied for the interpretation of the Sm_2Co_{17}-based magnets with additives of iron, copper, and zirconium. For these PMs the largest coercivities of the order of 3–4 T have been found. These hard magnetic properties are obtained after a homogenizing treatment at 1100–1200 °C (30 min), isothermal aging at 850 °C (10–25 h), and a subsequent slow cooling (0.5–1.0 °C min⁻¹) to 400 °C followed by quenching to room temperature. During the annealing procedure a cellular pyramidal structure develops composed of three phases (Livingston and Martin 1977, Hadjipanayis 1982): cells of about 100 nm in size corresponding to an iron-rich 2:17 matrix, cell walls of $SmCo_5$ structure separating the cells enriched in copper and poor in iron and zirconium, and a zirconium-rich lamellar platelet phase, called a Z-phase, which is oriented perpendicular to the c-axis of the cells. The cell walls of width 5–10 nm may act as a barrier or pinning center depending on the copper content and the degree of order in the 1:5 cell wall. In the particular case of $Sm(Co_{bal}Cu_{0.08}Fe_{0.22}Zr_{0.02})_{8.5}$ Goll *et al.* (2000) have performed an analysis of the element distributions within the cells and cell walls by HRTEM-EDX. The corresponding profile of the copper and iron distribution and of the anisotropy constant is shown in Fig. 12 (Goll 2001). The anisotropy constant varies from a value of $K_1^{2:17} = 2.9\,\text{MJ m}^{-3}$ to $K_1^{1:5} = 8.1\,\text{MJ m}^{-3}$ within a narrow width of ~ 2 nm. Assuming that this increase of nearly a factor 3 takes place over 10 atomic layers, where $d = 0.2$ nm and $\delta_B = 5$ nm, $\mu_0H_c = (2K_1/M_s) \times 0.22$ is obtained from Eqn. (19) for a constant exchange energy. With the α parameter for the pinning $\alpha^{pin} = 0.22$ for room temperature a coercive field of 2.8 T is obtained, in excellent agreement with the experimental results. Figure 13 shows plots of μ_0H_c/J_s vs. $2\mu_0K_1/J_s^2$ for different annealing treatments of sintered magnets. Over a wide temperature range between 170 K
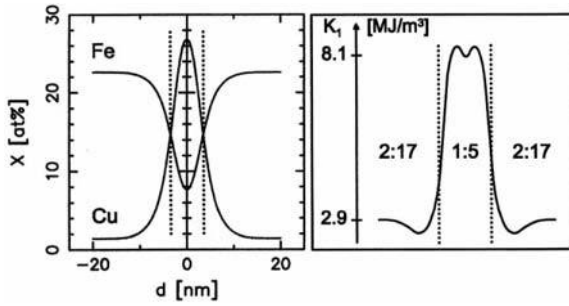
Figure 12
Copper and iron profiles of the cell wall in
$Sm(Co_{bal}Cu_{0.08}Fe_{0.22}Zr_{0.02})_{8.5}$ as measured by high-
resolution EDX transmission electron microscopy and
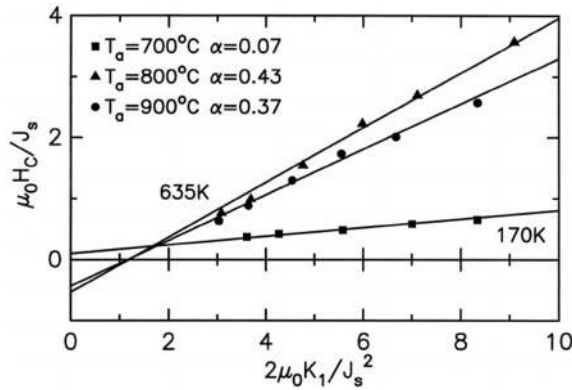the corresponding profile of the anisotropy constant.

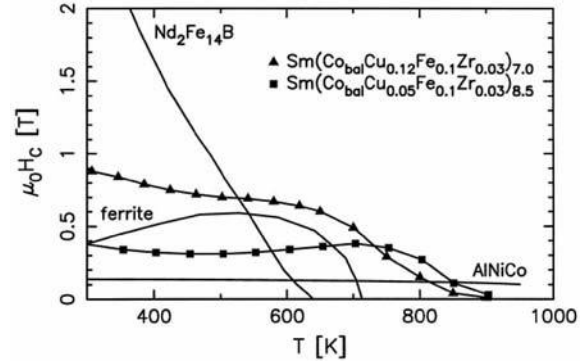*Figure 14*
Comparison of the temperature dependence of different
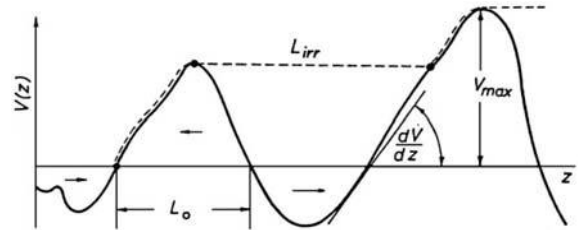types of PMs showing the dominance of the Sm_2Co_{17}-
type PMs at high temperatures.

Figure 13
Plots of $\mu_0 H_c/J_s$ vs. $2\mu_0 K_1/J_s^2$ for different annealing
treatments of a sintered $Sm_2(CoCuFeZr)_{17}$ PMs
showing the validity of Eqn. (2).

Figure 15
Characteristic parameters of the statistical field of force.

and 635 K a linear relationship is found with α pa-
rameters between 0.07 and 0.43. As is well known
annealing at 800 °C gives the optimal values of the
coercive field. The dominance of the 2:17-based PMs
above 650 K is clearly shown by Fig. 14 where the
coercive fields of several prominent PMs are com-
pared with each other.

7. Statistical Pinning Theory of Domain Walls

In soft magnetic materials based on amorphous,
crystalline, or nanocrystalline alloys the coercive field
is determined by the interaction of domain walls with
a large number of imperfections such as grain bound-
aries, dislocations and point defects, or impurity
atoms. In the case of a dislocation density of
$10^{10}\,cm^{-2}$, there are 10^4 dislocations within a domain
wall (DW) of cross-section $10^{-6}\,cm^2$. The resulting

force acting on a DW in this case has to be deter-
mined by statistical methods. The force of a defect at
position z_j acting on a DW at position z is described
by $v(z-z_j)$, where z is the coordinate parallel to the
DW normal. The total force acting on a DW is then
given by (Kronmüller 1997)

$$V(z) = \sum_j v(z - z_j) \qquad (20)$$

where the sum extends over all defects. The statistical
field of force, shown schematically in Fig. 15, is char-
acterized by three parameters:
  (i) the average wavelength $2L_0$ defined as twice the
distance between neighboring zeros $\overline{V}(z) = 0$;
  (ii) the average value V_{max} of the maximum of
$V(z)$; and
  (iii) the average of the reciprocal slopes of $V(z)$ at
$V(z) = 0$ given by $\overline{1/R} = \overline{1/(dV/dz)}$.
  These parameters may be determined by means of
correlation functions under the assumption that the
total forces V obey a Gaussian distribution function
$f(V)$. The probability, f, of finding an interaction
force between V and $V + dV$ or a slope $R = dV/dz$

between R and $R + dR$ is given by

$$f(V) = \frac{1}{(2\pi B_0)^{1/2}} \exp\left(\frac{-V^2}{2B_0}\right);$$

$$f(R) = \frac{1}{(2\pi B_1)^{1/2}} \exp\left(\frac{-R^2}{2B_1}\right) \quad (21)$$

The correlation functions B_0 and B_1 are related to the individual interaction forces, v, by the following integrals:

$$B_0 = \frac{F_B N}{L_3} \int_{-L_3/2}^{L_3/2} [v^2(z) - \langle v(z) \rangle^2] dz$$

$$B_1 = \frac{F_B N}{L_3} \int_{-L_3/2}^{L_3/2} \left\{ \left[\frac{dv(z)}{dz}\right]^2 - \left\langle \frac{dv(z)}{dz} \right\rangle^2 \right\} dz \quad (22)$$

where F_B is the DW area, L_3 the DW distance, and N the defect density. The characteristic parameters of the statistical potential are related to the correlation functions as follows:

$$2L_0 = 2\pi (B_0/B_1)^{1/2}; \quad \bar{V}_{\max} = (B_0/2\pi)^{1/2};$$

$$\overline{1/R} = (\pi/2B_1)^{1/2} \quad (23)$$

In the following the relationship of the coercive field is considered. It is given by

$$\mu_0 H_c = \frac{\pi^{1/2}}{M_s F_B |\cos\psi_0|} \bar{V}_{\max} \left(\frac{\ln L_3}{2L_0}\right)^{1/2}$$

$$\frac{\chi_0 H_c}{M_s} = |\cos\psi_0| \frac{\pi^{1/2}}{2} \frac{L_0}{L_3} \left(\frac{\ln L_3}{2L_0}\right)^{1/2} \quad (24)$$

From Eqns. (23) and (24) the dependence of H_c and χ_0 on the defect density is obtained as

$$H_c \propto \sqrt{N}; \qquad \chi_0 \propto 1/\sqrt{N} \quad (25)$$

Equation (25) has been tested for plastically deformed nickel single crystals where the dislocation density, N, is related to the applied flow stress, τ, by (Kronmüller 1972)

$$\tau - \tau_0 = 0.36 Gb(Nl)^{1/2} \quad (26)$$

where τ_0 is the initial flow stress, G the shear modulus, and l the length of dislocation lines interacting with the DW. In this case the interaction force is due to the magnetoelastic coupling energy (Kronmüller 1997) and is proportional to the magnetoelastic stresses of the DW. As a function of the applied flow stress according to Eqns. (25) and (26) a linear relationship is expected for H_c and $1/\chi_0$ as demonstrated by Fig. 16, which also shows the dependence of the Rayleigh constant α (Kronmüller 1997) following a $1/N \propto 1/(\tau - \tau_0)^2$ law. Another interesting feature is the temperature dependence of H_c, which,
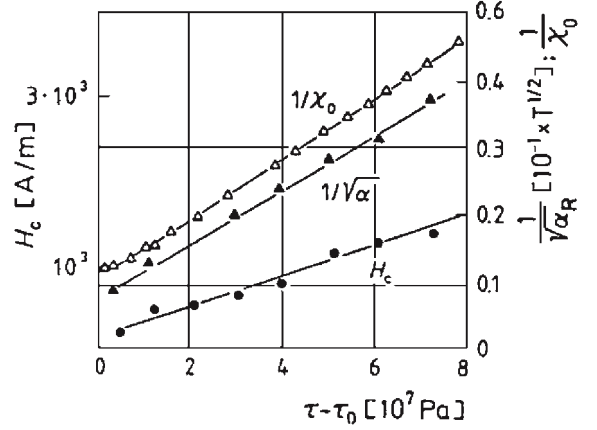
Figure 16
Test of the dependence of H_c, χ_0, and the Rayleigh constant, α_R, on the dislocation density of plastically deformed single crystals (Kronmüller 1972).

in the case of straight dislocations, is determined by the intrinsic material parameters M_s, K_1, and the magnetostriction λ_s, and is given by

$$\mu_0 H_c(T) \propto \frac{\lambda_s}{M_s} \delta_B^{1/2} \propto K_1^{-1/4} \quad (27)$$

With increasing anisotropy constant K_1, i.e., decreasing wall width δ_B, the pinning strength of dislocations decreases. If one deals with dislocation dipoles the interaction forces are proportional to the gradients, $\nabla\sigma$, of the magnetoelastic stresses of the DW leading to a temperature dependence of H_c given by

$$\mu_0 H_c(T) \propto \frac{\lambda_s}{M_s} \delta_B^{-1/2} \propto K_1^{1/4} \quad (28)$$

In contrast to the case of individual dislocations, H_c increases in the case of dislocation dipoles with decreasing wall width because this leads to an increase of, $\nabla\sigma$, i.e., of the pinning force v. According to Eqn. (28) the temperature dependence of H_c follows a $K_1^{1/4}$ law that has been demonstrated to be valid for amorphous FeNi-based alloys (Kronmüller 1997) where the stress sources correspond to dipole type precipitates of free volume. The existence of the $K_1^{-1/4}$ and the $K_1^{1/4}$ dependence of H_c has been found for the case of nickel single crystals as shown in Fig. 17. In as-grown nickel single crystals the main pinning centers are dislocations leading to the $K_1^{-1/4}$ law, whereas in neutron-irradiated single crystals dislocation dipoles exist owing to the agglomeration of vacancies giving rise to the $K_1^{1/4}$ law for H_c. H_c and χ_0 are governed by the self-consistency relationship of Eqn. (24), which may be written as

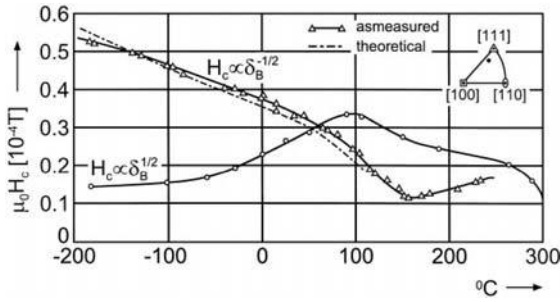$$\chi_0 \cong \frac{M_s}{H_c} \cdot \frac{\delta_B}{L_3} \quad (29)$$

Figure 17
Temperature dependence of the coercive field of a nickel single crystal owing to dislocations ($\propto \delta_B^{1/2}$) and to dislocation dipoles ($\delta_B^{-1/2}$) after heavy neutron irradiation ($xxx = 3 \times 10^{18}\,\text{n cm}^{-2}$) (Kronmüller 1966).
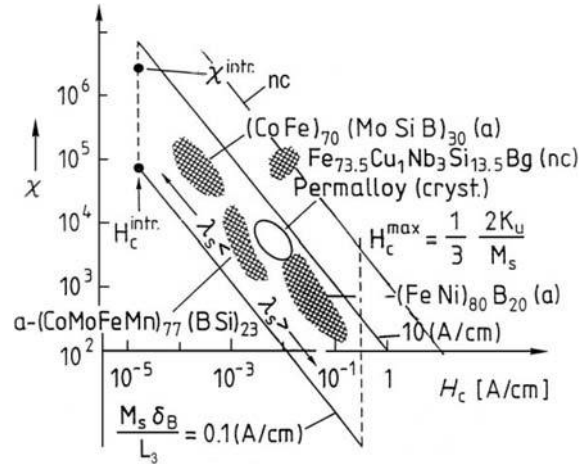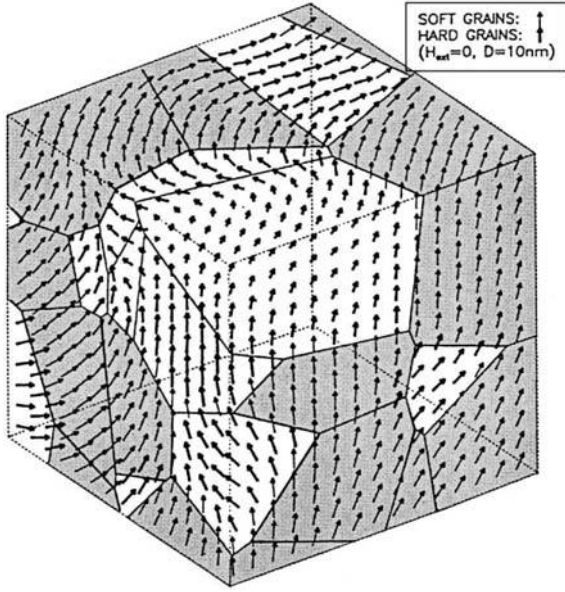

Figure 18
Upper and lower bounds for the χ_0 vs. H_c self-consistency relationship (Eqn. (24)) for crystalline, nanocrystalline, and amorphous alloys. The upper bound for χ^{intr} and the lower bound for H_c^{intr} are obtained for $K_1 = 0$ and $\lambda_s = 0$ (Kronmüller 1981).

if one takes into account that the average wavelength, $2L_0$, of the pinning force is of the order of $2\delta_B$. Owing to Eqn. (29), χ_0 and H_c may vary only between upper and lower bounds as determined by the ratio δ_B/L_3. This ratio with $L_3 \sim 100\delta_B$–$10\,000\delta_B$ may vary between 10^{-4} and 10^{-2} giving values of $10\,\text{A m}^{-1} < M_s\delta_B/L_3 < 10^3\,\text{Am}^{-1}$ for $M_s = 100\,\text{kA m}^{-1}$. The double logarithmic plot of Fig. 18 shows that the CoFe- and NiFe-based amorphous and crystalline alloys in fact lie between these two limits, which means that L_3 has been chosen correctly. Nanocrystalline materials (see *Amorphous and Nanocrystalline Materials*) such as FeSiNbCuB alloys (Herzer 1990) have a position with $M_s\delta_B/L_3 = 5\,\text{kA m}^{-1}$, which reflects the fact that in nanocrystalline materials owing to the random anisotropy effect the DW widths are a factor of 5–10 larger than in amorphous alloys. Figure 18 also includes the absolute lower and upper limits of H_c and χ_0, respectively, as expected in ideal amorphous materials with $K_1 \to 0$ and $\lambda_s \to 0$ (Kronmüller 1981).

8. Computational Micromagnetism of Coercivity

The experimental results for H_c of hard magnetic materials show a discrepancy by a factor of 4–5 with respect to the theoretical predictions. In Sects. 2–4 this is attributed to the role of the microstructure, the effect of which is described by the microstructural parameters α and N_{eff}. In the case of assemblies of grains, an explicit calculation of the parameters α and N_{eff} is not possible. Therefore, numerical calculations have been performed by means of the finite element method (FEM) (Schrefl *et al.* 1994). Simulations of magnetization processes of assemblies of grains start from a minimization of the magnetic free enthalpy G with respect to the direction of the spontaneous polarization $\underline{J}_s$:

$$\delta G = \delta \int (\phi_A + \phi_K + \phi_s + \phi_H)\mathrm{d}V = 0 \qquad (30)$$

The free enthalpy is composed of four contributions: exchange energy $\phi_A = A(\nabla\varphi)^2$, crystal anisotropy $\phi_K = K_1\sin^2\varphi + K_2\sin^4\varphi$, stray field energy $\phi_s = -(1/2)\underline{H}_s \cdot \underline{J}_s$, and magnetostatic energy $\phi_H = -\underline{H}_{ext} \cdot \underline{J}_s$. The stray field, $\underline{H}_s$, follows from a scalar potential U by $\underline{H}_s = -\nabla U$ and U obeys Poisson's equation $\Delta U = \mu_0^{-1}\text{div}\,\underline{J}_s$.

For three-dimensional numerical calculations usually a cubic particle composed of polyhedral regular or irregular grains is considered. This model allows the variation of the average grain size, the modification of the magnetic material parameters within grain boundaries, and the formation of composite PMs. As an example of the FEM calculations, Fig. 19 shows the distribution of $\underline{J}_s$ in the remanent state within a model composite PM of 35 grains with an average grain diameter of 10 nm with easy axes distributed isotropically and 51% of soft magnetic grains of α-Fe, embedded in hard magnetic grains of $Nd_2Fe_{14}B$ (Fischer *et al.* 1995). At the grain boundaries the direction of $\underline{J}_s$ changes smoothly from one easy direction to the other within a region of width $2\delta_B$. Under the assumption of a perfect exchange coupling between the grains, Fig. 20 illustrates the dependence of J_r, μ_0H_c, and $(BH)_{\text{max}}$ on the grain size D for the irregular grains shown in Fig. 19, and also for a hypothetical regular grain structure of dodecahedral grains. All three quantities decrease with increasing grain size and J_r and H_c can be fitted empirically by the following logarithmic laws
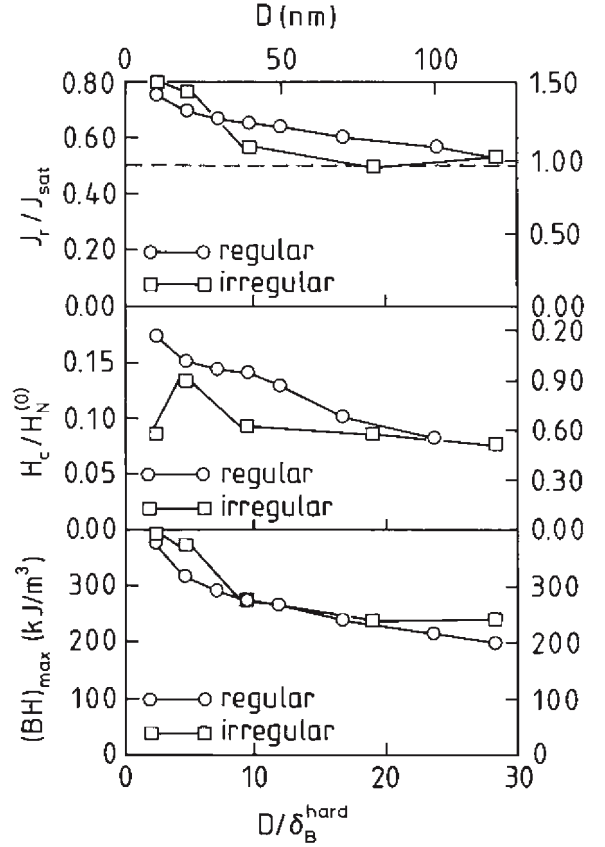
Figure 19
Distribution of polarization within 35 irregular grains of average diameter 10 nm within a cube with volume fraction of 51% α-Fe (shaded) and 49% $Nd_2Fe_{14}B$.

(Fischer *et al.* 1996):

$$J_r = J_{sat}\left[0.84 - 0.085\ln\left(\frac{D}{\delta_B^{hard}}\right)\right]$$

$$H_c = H_c^{(0)}\left[0.22 - 0.041\ln\left(\frac{D}{\delta_B^{hard}}\right)\right] \quad (31)$$

with $H_N^{(0)} = 2K_1^{hard}/J_s$ and $J_{sat} = J_s^{hard}v^{hard} + J_s^{soft}v^{soft}$, where the superscripts refer to the saturation polarizations and volume fractions of the hard and soft magnetic phases. It turns out that for grain sizes of 20 nm, i.e., $5\delta_B^{hard}$, the coercive field is only 15% of the ideal field $H_N^{(0)}$, and the remanence is considerably larger than the isotropic value of $0.5J_s$. Figure 21 shows the numerical results for the three characteristic properties of the hysteresis loops as a function of the percentage of α-Fe content (Fischer *et al.* 1995). Whereas the numerical results for J_r agree fairly well with the experimental data, the theoretical predictions for μ_0H_c and $(BH)_{max}$ are appreciably larger than the experimental values. In the case of $(BH)_{max}$, this is due to the fact that for the experimental results the condition $\mu_0H_c > 0.5 J_r$ is only valid for α-Fe concentrations $<30\%$ whereas the numerical results fulfill this condition up to 50% α-Fe. The observed discrepancy between numerical and experimental results can be explained by allowing a modification of the intrinsic material

Figure 20
Remanence J_r, coercivity μ_0H_c, and maximum energy product $(BH)_{max}$ for the irregular configuration of Fig. 19 and a regular dodecahedral grain structure as a function of mean grain size D.

parameters within the grain boundaries. Owing to the atomic disorder within a grain boundary it can be assumed that in particular A and K_1 have reduced values (Fischer and Kronmüller 1996). Figure 22 shows the influence of the reduction of these two parameters on the demagnetization curve for a cube of 64 grains of average diameter 20 nm (Fischer and Kronmüller 1998). For the model calculations a width of 3 nm of the grain boundaries is assumed where A and K_1 suffer a step-like reduction. With decreasing A and K_1 within the grain boundaries μ_0H_c and J_r also decrease. If the parameter $f = A^{gb}/A = K_1^{gb}/K_1$ is introduced where the superscript gb refers to the grain boundary, H_c and J_r obey the following relationships:

$$H_c/H_N^{(0)} = 0.304 + 0.098f$$
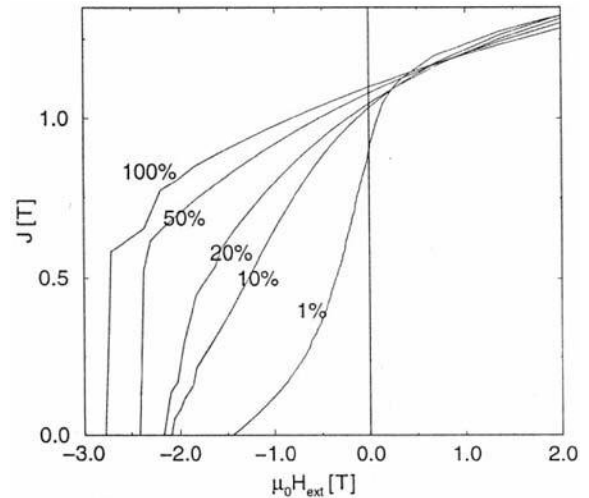
$$J_r/J_{sat} = 0.646 + 0.036f \quad (32)$$
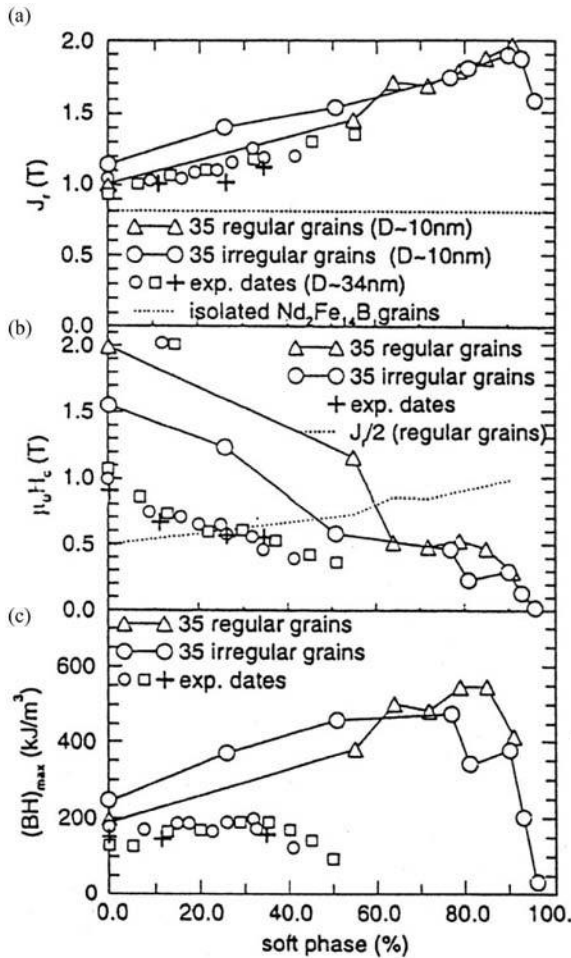
Figure 21
Numerical results for J_r, $\mu_0 H_c$, and $(BH)_{max}$ of nanocrystalline composite magnets for regular and irregular distributions of grains (average grain size 10 nm) as a function of the α-Fe percentage. Experimental results: +, Wilcox *et al.* (1994); ○, Bauer *et al.* (1996); □, Goll *et al.* (1998).

Figure 22
Demagnetization curves for an assembly of 64 NdFeB grains of average grain diameter 20 nm and an intergranular phase of reduced anisotropy and exchange constant.
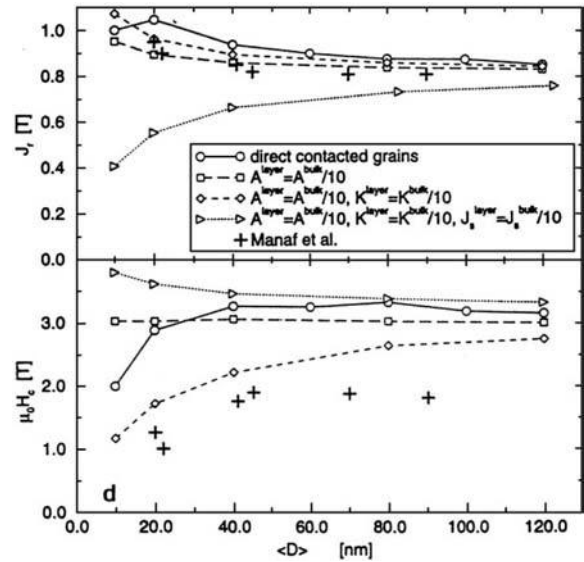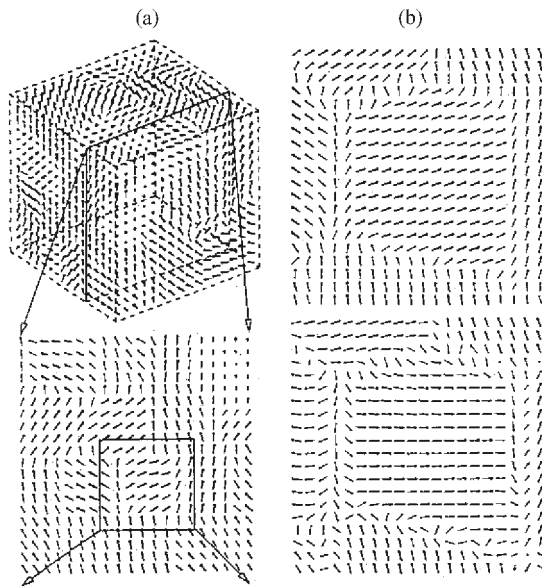

Figure 23
Coercive field as a function of the mean grain diameter $\langle D \rangle$ and grain boundaries of reduced material parameters. The computed points ($\diamond$) with $f = 0.1$ describe the experimental results of Manaf *et al.* (1991) fairly well.

As a further interesting property, the dependence of the coercive field as a function of the average grain diameter, $\langle D \rangle$, is shown in Fig. 23. Here it turns out that the experimental results obtained by Manaf *et al.* (1991) for nanocrystalline $Nd_{13.2}Fe_{79.6}B_6Si_{1.2}$ can only be simulated by the modification of A and K_1 within the grain boundary. Modifications of J_s lead to completely controversial results (Fischer and Kronmüller 1996). Figure 24 shows the magnetization reversal process for an individual grain surrounded by grains of different easy direction. Here it is evident that the reversal of magnetization primarily nucleates within the grain boundaries and the neighboring regions whereas in the bulk of the grain the magnetization starts to rotate reversibly into the direction of the applied field.

(a)   (b)

Figure 24
Vector plots of the magnetization of a nanocrystalline assembly of grains with $\langle D \rangle = 20\,\text{nm}$. (a) Remanent state. Top: magnetization at the surfaces of the cube; bottom: magnetization along a cut through the PM. Strong arrows refer to the bulk of the grains, weak arrows refer to the magnetization within grain boundaries. (b) Vector plots of magnetization within the square of (a) for nonideal grain boundaries with $f = 0.1$. Top: remanent state ($H_{ext} = 0$); bottom: applied opposite field $\mu_0 H_{ext} = 0.6\,\text{T}$ showing the nucleation of reversed magnetization within the grain boundaries (Fischer and Kronmüller 1998).

See also: Magnets Soft and Hard: Magnetic Domains; Micromagnetics: Finite Element Approach

Bibliography

Aharoni A 1962 Theoretical search for domain nucleation. *Rev. Mod. Phys.* **34**, 227–38

Bauer J, Seeger M, Zern A, Kronmüller H 1996 Nanocrystalline NdFeB permanent magnets with enhanced remanence. *J. Appl. Phys.* **80**, 1667–73

Becher M, Seeger M, Bauer J, Goll D, Kronmüller H 1998 Magnetic viscosity measurements on nanocrystalline NdFeB and PrFeB magnets. In: Schultz L, Müller K H (eds.) *Proc. 10th Int. Symp. on Magnetic Anisotropy and Coercivity in Rare-Earth Transition Metal Alloys*. Werkstoff-Informationsgesellschaft, Frankfurt, Germany, pp. 307–16

Becker R, Döring W 1939 *Ferromagnetismus*. Springer, Berlin

Brown W F Jr. 1945 Virtues and weaknesses of the domain concept. *Rev. Mod. Phys.* **17**, 15–9

Brown W F Jr. 1963 *Micromagnetics*. Interscience, New York

Coehoorn R, de Mooij D B, Duchateau J P, Buschow K H J 1988 Novel permanent magnetic materials made by rapid quenching. *J. Phys. (Paris) Colloq.* **49**, 669–70

Fischer R, Kronmüller H 1996 Static computational micromagnetism of demagnetization processes in nanoscaled permanent magnets. *Phys. Rev. B* **54**, 7284–94

Fischer R, Kronmüller H 1998 The role of grain boundaries in nanoscaled high-performance permanent magnets. *J. Magn. Magn. Mater.* **184**, 166–72

Fischer R, Schrefl T, Kronmüller H, Fidler J 1995 Phase distribution and computed magnetic properties of high-remanent composite materials. *J. Magn. Magn. Mater.* **150**, 329–44

Fischer R, Schrefl T, Kronmüller H, Fidler J 1996 Grain size dependence of remanence and coercive field of isotropic nanocrystalline composite permanent magnets. *J. Magn. Magn. Mater.* **153**, 35–49

Friedberg R, Paul D 1975 New theory of coercive force of ferromagnetic materials. *Phys. Rev. Lett.* **34**, 1234–7

Gaunt P, Mylvaganam C K 1981 Domain wall pinning and nucleation in $SmCo_5$: I. Thermal activation and coercive field. *Phil. Mag. B* **44**, 569–80

Givord D, Rossignol M F 1996 Coercivity. In: Coey J M D (ed.) *Rare-Earth Iron Permanent Magnets*. Clarendon Press, Oxford, UK Chap. 5

Goll D 2001 Ph.D. thesis, University of Stuttgart

Goll D, Kleinschroth I, Sigle W, Kronmüller H 2000 Melt-spun precipitation-hardened $Sm_2(Co,Cu,Fe,Zr)_{17}$ magnets with abnormal temperature dependence of coercivity. *Appl. Phys. Lett.* **76**, 1054–6

Goll D, Seeger M, Kronmüller H 1998 Magnetic and microstructural properties of nanocrystalline exchange coupled PrFeB permanent magnets. *J. Magn. Magn. Mater.* **185**, 49–60

Hadjipanayis G C 1982 Microstructure and magnetic domain structure of 2:17 precipitation-hardened rare-earth cobalt permanent magnets. In: Fidler J (ed.) *Proc. 6th Int. Workshop on Rare Earth–Cobalt Permanent Magnets*. Technical University of Vienna, Austria, pp. 609–30

Herzer G 1990 Grain size dependence of coercivity and permeability in nanocrystalline ferromagnets. *IEEE Trans. Mag.* **26**, 1397–402

Hilzinger H R, Kronmüller H 1975 Investigation of Bloch wall pinning of antiphase boundaries in RCo_5 compounds. *Phys. Lett.* **51A**, 59–60

Hilzinger H R 1977 The influence of planar defects on the coercive field of hard magnetic materials. *Appl. Phys.* **12**, 253–60

Kersten M 1942 Grundlagen einer Theorie der ferromagnetischen Hysterese und Koerzitivkraft. Doctoral thesis, Technische Hochschule Stuttgart, Germany

Kneller E F, Hawig R 1991 The exchange-spring magnet: a new material principle for permanent magnets. *IEEE Trans. Mag.* **27**, 3588–600

Kronmüller H 1966 Magnetisierungskurve der Ferromagnetika. In: Seeger A (ed.) *Moderne Probleme der Metallphysik*. Springer, Berlin, Vol. 2, pp. 24–156

Kronmüller H 1972 Magnetic techniques for the study of dislocations in ferromagnetic materials. *Int. J. Nondestr. Testing* **3**, 315–50

Kronmüller H 1973 Microstructure and micromagnetism. In: Graham C D, Rhyne J J (eds.) *Proc. 18th AIP Conf. on Magnetism and Magnetic Materials*. American Institute of Physics, New York, pp. 1006–25

Kronmüller H 1981 Theory of coercive fields in amorphous ferromagnetic alloys. *J. Magn. Magn. Mater.* **24**, 159–67

Kronmüller H 1987 Theory of nucleation fields. *Phys. Stat. Sol. (b)* **144**, 385–96

Kronmüller H 1990 Micromagnetism and magnetization processes in modern magnetic materials. In: Hadjipanayis G C, Prinz G A (eds.) *Proc. NATO Advanced Study Institute on Science and Technology of Nanostructured Magnetic Materials*. Kluwer, Dordrecht, The Netherlands, pp. 657–75

Kronmüller H 1997 Micromagnetism and the microstructure of modern magnetic materials. In: Hadjipanayis G C (ed.) *Proc. NATO Advanced Study on Magnetic Hysteresis in Novel Magnetic Materials*. Kluwer, Dordrecht, The Netherlands, pp. 85–108

Kronmüller H, Durst K D, Martinek G 1987 Angular dependence of the coercive field in sintered $Fe_{77}Nd_{15}B_8$ magnets. *J. Magn. Magn. Mater.* **69**, 149–57

Kronmüller H, Durst K D, Sagawa M 1988 Analysis of the magnetic hardening mechanism in REFeB permanent magnets. *J. Magn. Magn. Mater.* **74**, 291–302

Kronmüller H, Fischer R, Seeger M, Zern A 1996 Micromagnetism and microstructure of hard magnetic materials. *J. Phys. D* **29**, 2274–83

Landau L, Lifshitz E 1935 On the theory of the dispersion of magnetic permeability in ferromagnetic bodies. *Physikalische Zeitschrift Sowjetunion* **8**, 153–69

Livingston J D, Martin D L 1977 Structure of aged $(Co,CuFe)_7Sm$ magnets. *J. Appl. Phys.* **48**, 1350–4

Luborsky F E, Morelock C R J 1964 Magnetization reversal in almost perfect whiskers. *J. Appl. Phys.* **35**, 2055–66

Manaf A, Buckley R A, Davies H A, Leonowicz M 1991 Enhanced magnetic properties in rapidly solidified NdFeB based alloys. *J. Magn. Magn. Mater.* **101**, 360–2

Martinek G, Kronmüller H 1990 Influence of grain orientation of the coercive field of FeNdB permanent magnets. *J. Magn. Magn. Mater.* **86**, 177–83

Neu V, Eckert D, Schultz L 1996 Nanocrystalline two phase Nd–Fe–B powders with Co and small additions of Zr and Si. In: Missell F B, Villas-Boas V, Rechenberg H R, Landgraf F J G (eds.) *Proc 9th Int. Symp. on Magnetic Anisotropy and Coercivity in Rare-Earth Transition Metal Alloys*. World Scientific, Singapore, pp. 42–8

Rieger G, Seeger M, Kronmüller H 1999 Microstructural parameters in high-remanent sintered NdFeB magnets. *Phys. Stat. Sol. (a)* **171**, 583–95

Sagawa M, Hirosawa S 1988 Coercivity and microstructure of REFeB sintered permanent magnets. *J. Phys. (Paris) Colloq.* **49**, 617–22

Schrefl T, Fidler J, Kronmüller H 1994 Remanence and coercivity in isotropic nanocrystalline permanent magnets. *Phys. Rev. B* **49**, 6100–10

Stoner E C, Wohlfarth E P 1948 A mechanism of magnetic hysteresis in heterogeneous alloys. *Phil. Trans. R. Soc. A* **240**, 599–644

Wilcox M, Williams J, Leonowicz M, Manaf A, Daves H 1994 Relations between phase constitution, determined by Mössbauer spectroscopy, and the enhanced magnetic properties for nanocrystalline FeNdB alloys. In: Manwaring C A F, Jones D, Williams A, Harris I (eds.) *Proc. 8th Int. Symp. on Magnetic Anisotropy and Coercivity in Rare Earth–Transition Metal Alloys*. University of Birmingham, Birmingham, UK, pp. 87–94

H. Kronmüller
Max-Planck-Institut für Metallforschung, Stuttgart Germany

Coherence Length, Proximity Effect and Fluctuations

The phenomenological London theory for superconductivity was able to explain the Meissner effect in terms of a rigid wave function under the application of an external magnetic field. Under this assumption, F. and H. London calculated the value of the London penetration depth λ_L:

$$\lambda_L^2 = \frac{m}{\mu_0 e^2 n_s} \tag{1}$$

where m is the effective mass of the electron and n_s is the superfluid density, which at $T = 0$ is equal to the electron density in the normal state. Since the ratio m/n does not vary by more than one order of magnitude among common metals, λ_L does not vary much from one superconductor to another: roughly by a factor of 4 from say lead (39 nm) to the high-T_c oxides (about 140 nm in $YBa_2Cu_3O_7$). No explicit dependence of λ_L on T_c is predicted.

The main modification to the London theory proposed by Ginzburg and Landau (GL theory) was the introduction of a finite correlation length ξ, somewhat unfortunately called the coherence length. This is the minimum length scale over which the superfluid density may vary with only a moderate increase of the free-energy density. Ginzburg and Landau showed that under small applied fields, the spatial variation of the superfluid density remains negligible and the London result (Eqn. (1)) is recovered, whatever the respective values of λ and ξ. The effect of a finite coherence length is only apparent in strong applied fields and when the GL parameter $\kappa = \lambda/\xi$ is larger than $1/\sqrt{2}$. As shown by Pippard, when $\xi > \lambda$ nonlocal corrections lead to an effective value of λ somewhat larger than that given by the London theory.

1. Coherence Length

1.1 Coherence Length in the GL Theory

Ginzburg and Landau introduced the coherence length in the framework of their treatment of the superconducting phase transition as a second-order transition, occurring at the critical temperature T_c. The existence of a coherence length that diverges at the transition is a general property of all second-order phase transitions:

$$\xi(t) = a\xi_0 (1-t)^{-\nu} \tag{2}$$

where a is a numerical coefficient of order unity, ξ_0 is the zero temperature coherence length, t is the reduced temperature (T/T_c) and ν is the critical exponent for the coherence length. In the mean-field approximation $\xi(t)$ can be obtained from the GL

free-energy functional:

$$\mathbb{F}_s = \mathbb{F}_n + A|\Delta|^2 + \frac{B}{2}|\Delta|^4 + C|\nabla\Delta|^2 \qquad (3)$$

where the coefficients $A = N(0)\,(t-1)$, $B = 0.098 N(0)/(k_B T_c)^2$, $C = 0.55\,\xi_0^2\,N(0)\chi(\alpha)$, $N(0)$ is the normal state density of states and $\chi(\alpha)$ is the Gorkov impurity function. Here Δ is the pair potential, equal to the superconducting energy gap when it is uniform across the sample.

The pair potential Δ is related to the order parameter Ψ by $|\Delta|^2 = \hbar^2|\Psi|^2/(4mC)$. In some cases the free-energy functional is written in terms of the *reduced*-order parameter $\psi = \Psi/\Psi_\infty$, where Ψ_∞ is the equilibrium order parameter at the temperature under consideration. Sometimes it is convenient to use the pair *amplitude* $F = \Delta/V$, where V is the BCS interaction parameter (e.g., in a normal metal with $V = 0$ in contact with a superconductor, the pair potential is zero but the pair amplitude is finite, as will be discussed in Sect. 3). In simplified terms $(FV)^2$ and $(F/\pi N(0))^2$ are proportional to n_s in the two regions.

In the notation used here

$$\xi^2 = \frac{C}{|A|} \qquad (4)$$

Since $A \propto 1 - t$, $v = \frac{1}{2}$ and λ is found in this approximation to diverge with the same exponent. In the clean limit, therefore, $\xi(t) = 0.74\,\xi_0(1-t)^{-1/2}$ while in the dirty limit $\xi(t) = 0.85\,(\xi_0 l)^{1/2}(1-t)^{-1/2}$ where l is the normal state electron mean free path. The applicability of the mean field approximation to the superconducting phase transition will be returned to later.

The GL theory is phenomenological and does not predict what the value of ξ_0 should be. However, it does offer a simple method for measuring $\xi(t)$ through the expression for the nucleation field:

$$\mu_0 H_{c2}(t) = \frac{\Phi_0'}{2\pi\xi^2(t)} \qquad (5)$$

where $\Phi_0 = 2.07 \times 10^{-15}\,\mathrm{T\,m^2}$ is the flux quantum. If the superconductor is type II, H_{c2} as given by Eqn. (5) is the upper critical field. If it is type I, H_{c2} is the supercooling field. Coherence lengths in the clean and dirty limits, obtained from H_{c2} measurements, are given in Tables 1 and 2, respectively. Measurements of the supercooling field are usually affected by the Saint James–de Gennes surface nucleation phenomenon which occurs at a field $H_{c3} = 1.69\,H_{c2}$ in regions of the sample where the surface is parallel to the applied field (Saint James and de Gennes 1963, Deutscher 1967). Once the superconducting state has nucleated in some region, it spreads all over the sample. Hence H_{c3} rather than H_{c2} is usually the measured nucleation field and ξ must be calculated accordingly.

Table 1
Coherence lengths in the clean limit.

	T_c (K)	ξ_0 (µm)	$\xi_0 T_c$ (µm K)
Aluminum	1.19	1.20	1.4
Indium	3.40	0.33	1.1
Tin	3.72	0.26	0.97
Gallium	5.90	0.16	0.94
Lead	7.20	0.08	0.58
Niobium	9.25	0.035	0.32
$YBa_2Cu_3O_7$	93	0.0015	0.14

Table 2
Coherence lengths in the dirty limit (practical superconductors).

	T_c (K)	$\xi(T = 0)$ (µm)
Nb–56 at.% Ti	10	0.0050
Nb_3Sn	17	0.0040
$(Nb, Ta)_3Sn$	18	0.0035

When $H_{c3} > H_c$, a stable superconducting surface sheath of thickness ξ exists below the nucleation field. Its thickness has been measured directly in lead and was found to be about twice the coherence length (Deutscher 1967).

1.2 Coherence Length in the BCS Theory

The microscopic origin of ξ became clear only with the advent of the BCS theory: it is the average radius of a Cooper pair. The value of ξ_0 can be simply estimated from the uncertainty principle:

$$\xi_0 \simeq \frac{hv_F}{\pi\Delta} \qquad (6)$$

where v_F is the Fermi velocity and 2Δ is the energy necessary to break a Cooper pair. In the weak coupling limit of the BCS theory, $2\Delta = 3.5\,k_B T_c$. Since v_F does not vary much from one metal to another, the coherence length is essentially inversely proportional to the critical temperature (Table 1). As a rule of thumb, $\xi_0(\mu m) \simeq T_c^{-1}(K^{-1})$. Since λ_L is basically independent from T_c, low-T_c superconductors should be type I and high-T_c superconductors should be type II. This is well borne out experimentally. Superconductors with a T_c lower than that of lead (7.2 K) are type I, superconductors with a higher T_c are type II (niobium, the A15 compounds, the Chevrel phases and the high-T_c oxides).

The effect of impurities on λ and ξ has been calculated by Gorkov. In the limit where the electron

mean free path l is much shorter than ξ_0 (the so-called dirty limit):

$$\lambda = 0.64\,\lambda_L(\xi_0/l)^{1/2} \tag{7a}$$

$$\xi = 0.85(\xi_0 l)^{1/2} \tag{7b}$$

As first observed by Shubnikov, the introduction of impurities can turn a type I superconductor into a type II material. Nonmagnetic impurities do not affect the critical temperature (Anderson theorem). However, magnetic impurities strongly depress T_c; for a low concentration x of paramagnetic impurities with total angular momentum J this is given by the BCS Gorkov theory

$$\frac{dT_c}{dx} \simeq \frac{-\pi^2 N(0) f^2 (g-1)^2 J(J+1)}{2k_B}$$

where f is the exchange coupling constant and g is the gyromagnetic ratio. Eqns. (5) and (7b) show that H_{c2} is inversely proportional to the mean free path and, hence, proportional to the normal state resistivity, that is, to the concentration of impurities. This result is in excellent agreement with experiment (Serin 1969) and is put into practice in the commercial Nb–Ti wires, which have an upper critical field of about 10 T, roughly 30 times larger than that of pure niobium.

A short coherence length, achieved either in a clean high-T_c superconductor or in a dirty low-T_c superconductor, is therefore the key to practical applications of superconductivity in strong applied fields. However, in general, ξ remains much larger than interatomic distances. The high-T_c oxides are an exception to that rule: along the CuO planes, ξ is about 2 nm in $YBa_2Cu_3O_7$; in the perpendicular direction it is only 0.3 nm. Practical superconductors such as NbTi and Nb_3Sn have coherence lengths of the order of 5 nm.

2. Thermal Fluctuations of the Superconducting Order Parameter

2.1 Quasi-mean-field Regime

Thermodynamic fluctuations of the superconducting order parameter can be estimated from the GL free-energy functional. The lowest free energy is achieved for $\Delta = \Delta_0$, $\Delta_0 = (-A/B)^{1/2}$ below T_c and $\Delta_0 = 0$ above T_c. Any other configuration $\Delta = \Delta_0 + \delta\Delta(r)$ can be decomposed into its Fourier components, each of them being characterized by an amplitude and a wavelength. The Fourier components with the largest amplitude have a wavelength of order ξ. This is because, for larger wavelengths, the energy cost is high because of the large volume involved and, for shorter wavelengths, the gradient term in Eqn. (3) is prohibitive. Hence, the volume of a typical fluctuation is ξ^3.

Its amplitude can be estimated by taking its energy to be of the order of $k_B T$. Developing $\mathbb{F}_s$ to second order in $\delta\Delta$, one obtains below T_c

$$-2A\langle|\delta\Delta|^2\rangle\xi^3 \simeq k_B T \tag{8}$$

Apart from numerical coefficients, the relative amplitude of the fluctuations is given by:

$$\frac{\langle|\delta\Delta|^2\rangle}{\Delta_o^2} = \frac{k_B T}{\Delta\mathbb{F}\xi^3} \tag{9}$$

where $\Delta\mathbb{F}$ is the condensation energy per unit volume at equilibrium, $\Delta\mathbb{F} = A^2/2B = \mu_0 H_c^2/2$, where H_c is the thermodynamic critical field.

The relative amplitude of the fluctuations is thus essentially given by the ratio of the thermal energy $k_B T$ to the value of the condensation energy per coherence volume. Eqn. (9) can be immediately generalized to the case of a general dimensionality d by replacing ξ^3 by ξ^d. The relative amplitude of the fluctuations diverges as

$$\frac{\langle|\delta\Delta|^2\rangle}{\Delta_o^2} \propto (1-t)^{-(4-d)/2} \tag{10}$$

where $d < 3$ is achieved when one or more of the dimensions of the sample is smaller than the coherence length $\xi(t)$.

In the preceding analysis the fluctuations have been treated as independent of each other (quasi-mean-field approximation). Equations (9) and (10) are thus only valid in the limit where the relative amplitude of the fluctuations is much smaller than unity. This approximation is in general excellent for conventional low-T_c superconductors (LTS), but not for the high-T_c oxides (HTS).

The effects of fluctuations are very small in bulk LTS (e.g., their effect on the heat capacity is negligible; this is not the case for the high-T_c oxides). They are larger for low dimensionalities (thin films, wires, small grains) because the relative amplitude of the fluctuations then diverges with a stronger exponent (see Eqn. (10)). The most easily detected fluctuation effect is an excess conductivity $\Delta\sigma$ above T_c. In two dimensions within the quasi-mean-field approximation (Azlamazoff and Larkin 1968)

$$\Delta\sigma = \frac{e^2}{16\hbar}(t-1)^{-1} \tag{11}$$

where the conductivity is expressed in $(\Omega/\text{square})^{-1}$. In a d-dimensional sample, the conductivity diverges as $(t-1)^{-(4-d)/2}$, that is, with the same exponent as that of the relative amplitude of the fluctuations given by Eqn. (10). Additional terms to the excess conductivity considered by Maki and Thompson lead to a stronger divergence.

The effect of fluctuations on the conductivity is most easily detected when the background normal state conductivity is small, that is, in dirty films (Glover 1971) or wires. Another case where the excess conductivity is easily observed is that of granular superconductors (Deutscher and Dodds 1977).

On the contrary, the effect of fluctuations on the diamagnetism (which diverges with the same exponent as that of the conductivity) is most easily observed in clean samples, with a large coherence length. Fluctuation diamagnetism has been studied in low-T_c intercalated compounds.

2.2 Critical Fluctuation Region

The mean-field approximation is valid as long as the relative amplitude of the fluctuations as given by Eqn. (10) is much smaller than unity. However, since this amplitude diverges at T_c, there exists a temperature range near T_c where this approximation fails. This range is called the critical region (for a recent review see Ginzburg 1988). It is customary to measure it on the reduced temperature scale $\varepsilon = (T - T_c)/T_c$. If ε_c is the reduced temperature at which the relative amplitude of the fluctuations is of order unity, it follows from Eqn. (9) that

$$\varepsilon_c = \alpha \left[\frac{k_B T_c}{\Delta \mathbb{F}(0) \xi_0^3} \right]^2 \tag{12}$$

where α is a numerical factor (actually important, $\alpha = 2^{-11} \pi^{-2}$) and $\Delta \mathbb{F}(0)$ is the condensation energy at $T = 0$. According to the BCS theory:

$$\Delta \mathbb{F}(0) = \frac{1}{2} N(0) \Delta(0)^2 \tag{13}$$

where $N(0)$ is the normal state density of states. In the weak coupling limit, $\Delta(0)$ is proportional to T_c and since as seen before $\xi_0 \propto T_c^{-1}$, it follows that $\varepsilon_c \propto T_c^4$. ε_c is extremely small for LTS, typically $\varepsilon_c < 10^{-12}$. This fully justifies the use of the GL mean-field approximation. However, for the HTS ε_c is much larger ($\varepsilon_c \simeq 10^{-3}$) and the critical region can be studied experimentally (Salamon *et al.* 1990).

As seen from Eqn. (12), the width of the critical region is determined by the value of the condensation energy in a coherence volume at $T = 0$, compared with $k_B T_c$. However, $U_0 = \Delta \mathbb{F} \xi^3$ is also the typical energy scale for core pinning of vortices. Through the coherence length, there exists therefore an intimate relationship between the critical temperature, the width of the critical region and the ability of the superconductor to pin vortices. Notice that as T_c goes up, the upper limit for U_o (clean limit) goes down ($U_o \propto T_c^{-1}$). In LTS, ε_c is small and vortices are easily pinned even close to T_c but, in HTS, ε_c becomes significant and vortex pinning cannot be achieved when T is of the order of T_c (Deutscher 1990). Full use of their extremely high upper critical field (several hundred tesla) can only be made at temperatures significantly lower than T_c. Furthermore, the quasi-mean-field approximation appears to be inadequate for the description of the vortex state near $H_{c2}(T)$ in the bismuth- and thallium-based oxide superconductors (Kes *et al.* 1992).

3. Proximity Effect

When a normal metal (N) is in good electrical contact with a superconductor (S), Cooper pairs can leak from S to N. If the electron–electron interaction in N is zero ($V_N = 0$), and in the absence of magnetic impurities and applied magnetic fields, Cooper pairs in N are only destroyed by the thermal energy $k_B T$. Their decay length is then given by (Deutscher and de Gennes 1969)

$$\xi_N = K^{-1} = \frac{\hbar v_{FN}}{2\pi k_B T} \tag{14}$$

where v_{FN} is the Fermi velocity in N. When pair breaking is also induced by magnetic impurities and applied magnetic fields, a multipair breaking model in which the various depairing factors simply add can be used. The value of K is then expressed in terms of a depairing variable α (see Yang and Finnemore 1984).

The probability amplitude for finding a Cooper pair in N at a distance $|x|$ from the SN interface is given by

$$F(x) = \varphi(x) \exp(-K|x|) \tag{15}$$

where $\varphi(x)$ is a slowly varying function of x. The probability amplitude F is defined as the ratio of the pair potential Δ to the BCS interaction parameter V. If $V_N = 0$, $\Delta_N = 0$, but F is finite (see later for the boundary conditions for F at the SN interface).

Eqn. (14) is valid when the mean free path in N, l_N, is large compared to the decay length as given by Eqn. (14) (clean limit). In the dirty limit

$$K^{-2} = \left(\frac{\hbar D_N}{2\pi k_B T} \right) \tag{16}$$

where D_N is the normal state coefficient of diffusion in N, $D_N = v_{FN} l_N / 3$.

If N is a superconductor at some lower temperature $T_{cN} < T$, K^{-1} diverges as $T \to T_{cN}$. Properties of the SN contact near T_{cN} can be treated with the GL formalism. Very close to T_{cN}, $K^{-1} \propto (T - T_{cN})^{-1/2}$, symmetrical with the temperature dependence of the coherence length in the superconducting state below T_{cN}. At $T = T_{cN}$, the exponential decay law (Eqn. (15)) must be replaced by a power law dependence $F(x) = F(0) [x_0/(x + x_0)]$ (Deutscher and de Gennes 1969). At temperatures slightly above T_{cN}, this power

law persists near the interface. It crosses over to the exponential decay far from the interface where the pair amplitude is sufficiently small so that the non-linear term in the GL functional becomes negligible.

At low temperatures, K^{-1} is a macroscopic length scale. For instance, in copper at 1 K, K^{-1} is of the order of 1 μm. This allows the easy observation of the proximity effect in superconductivity. This is in contrast to other ordering phenomena, such as magnetism, where the basic length scale is much shorter.

In the absence of any significant boundary resistance (which may arise either from imperfections of the boundary, such as a thin insulating layer, or from a mismatch of the normal state properties, that is, different Fermi velocities and electron effective masses), the boundary conditions at the SN interface are (de Gennes 1964)

$$F/N(0) \text{ continuous} \tag{17a}$$

$$D(dF/dx) \text{ continuous} \tag{17b}$$

The pair amplitude is depressed on the S side over a length $\xi(T)$ and has a tail on the N side over a length $K^{-1}(T)$ (see Fig. 1). For this reason K^{-1} is alternatively expressed as the normal state coherence length.

The consequences of the proximity effect are (Deutscher and de Gennes 1969) (a) in zero field, a depressed critical temperature of SN bilayers, an excitation spectrum showing states within the gap if measured from the S side and gapless superconductivity if measured from the N side; (b) in strong applied fields, a reduction of the upper critical field of thin films and suppression of the surface sheath above H_{c2} in bulk superconductors; and (c) in weak applied fields, existence of a Meissner effect on the N side of the contact.

A simplified discussion of the proximity effect on the transition temperature and on the upper critical field can be made in terms of a length b defined by

$$\left| \frac{dF}{dx} \right| = \frac{E}{b} \tag{18}$$

where the value of F and its derivative are taken at the interface on the S side. According to Eqn. (18), b is equal to the distance from the interface to the intercept of the linear extrapolation of $F(x)$ (into N) with the x axis, which is why it is called the extrapolation length (Fig. 1).

In the dirty limit, and in the absence of any boundary resistance, b is given by:

$$b = (\rho_N/\rho_S)K^{-1} \coth(Kd_N) \tag{19}$$

where ρ_N and ρ_S are the normal state resistivities and d_N and d_S are the thicknesses of N and S, respectively. The critical temperature T_{cNS} of a bilayer is given by

$$T_{cNS} = T_{cS} - \frac{\pi^2}{8}\xi_S^2(T=0)\frac{1}{(d_S+b)^2} \tag{20}$$

This expression is only valid in the GL approximation, that is, when T_{cNS} is not too different from T_{cS}.

In the same approximation, the parallel upper critical field of a bilayer is given by (Orsay Group 1966)

$$B_{c2}^2 = \frac{1}{\beta}\left(\frac{2\Phi_0}{\pi d_S^2}\right)^2 \frac{d_S^2}{\xi^2(0)}(1 - t_{cNS}) \tag{21}$$

where β is a function of (b/d_s).

One of the most fundamental manifestations of the proximity effect is the existence of a Meissner effect on the N side of SN contacts. This induced Meissner effect was revealed by the study of the susceptibility of SN contacts in weak fields, which showed that a field applied parallel to the interface is screened out at a distance ρ_{scr} from the interface (Deutscher *et al.* 1969). This induced diamagnetism is easily identified because it is destroyed in fields that are much smaller than the characteristic fields of the S side. The screening length ρ_{scr} was found to be typically of the order of 100 nm in the conventional liquid (helium) range. If N is itself a superconductor at a temperature T_{cN}, ρ_{scr} diverges when T_{cN} is approached. This effect is felt well above T_{cN}, $\rho_{scr} = 1$ μm in zinc ($T_{cN} = 0.92$ K) at 1.6 K. If N is a "truly" normal metal, ρ_{scr} diverges as $T \to 0$. In the limit of very small applied fields and large N thickness ($d_N \gg \rho_{scr}$)

$$\rho_{scr} = K^{-1}\{\ln[K^{-1}/\lambda(0)] - 0.116\} \tag{22}$$
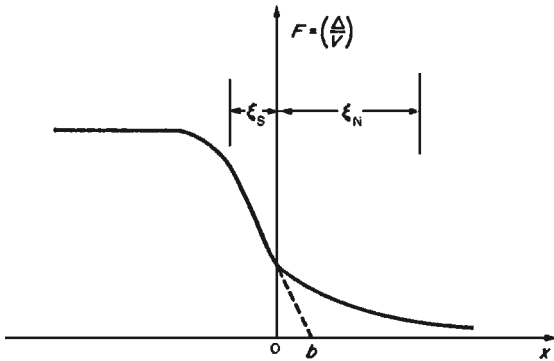
Figure 1
Behavior of the pair amplitude F near an SN interface. For simplicity, it is assumed that the normal state density of states is the same in N and in S (otherwise, F is discontinuous at the interface) and that the boundary resistance is negligible (which also leads to a discontinuity of F). A case is illustrated where the coefficient of diffusion in S is shorter than in N. In this case, the extrapolation length b is shorter than $K^{-1}(= \xi_N)$.

where $\lambda(0)$ is the value of the local penetration depth at the SN interface. As soon as the temperature is sufficiently low that $[K^{-1}/\lambda(0)] > 1$, ρ_{scr} is typically of the order of K^{-1}.

At low temperatures, as ρ_{scr} becomes larger, it is also more sensitive to the applied field:

$$\sigma_{scr}(H) = K^{-1} \ln(2H_0/H) \qquad (23)$$

where H_0 is a field characteristic of the N side, $H_0 = [\Phi_0 K/2\pi\lambda(0)]$. Notice that $H_0 \to 0$ as $T \to 0$.

These relations apply for a semi-infinite N layer. The main effect of a finite N thickness is that for $d_N \simeq K^{-1}$ and $[K^{-1}/\lambda(0)] > 1$, a first-order transition is observed at a breakdown field H_b at which the pair amplitude in N collapses and ρ_{scr} varies essentially from d_N to zero (Orsay Group 1967). A good approximation for H_b is

$$H_b = 3.8H_0 \exp(-Kd_N) \qquad (24)$$

There are at least two important applications where the proximity effect is important. One is in the fabrication of practical Josephson devices. For LTS electronics, niobium, being a refractory metal, is a preferred choice of material for stable, cyclable devices. Unfortunately, it does not have a good insulating oxide. The solution is then to use a niobium film with a thin aluminum coating and to oxidize the surface of the aluminum. The operation of the device is based on the proximity-induced superconductivity in the aluminum coating (see *SQUIDs: Biomedical Applictions; SQUIDs: The Instrument; Josephson Junctions: Low-T_c*). Another example is in the design of ultrathin filamentary wires, composed of very fine Nb–Ti filaments in a copper matrix, for ac applications. In these wires, the distance between the filaments is so small that the copper matrix is effectively superconducting; to minimize ac losses the proximity coupling has to be reduced either by separating the filaments or by suppressing the proximity coupling by alloying the copper with magnetic impurities such as manganese (see *Superconducting Wires and Cables: Materials and Processing*).

Special mention should be made of proximity effects where the S side is a high-T_c oxide. In this case ξ_s is very small, typically of the order of 1 nm. This makes the fabrication of high-T_c devices quite difficult, since electron tunnelling occurs into a surface region of thickness ξ_s, whose quality is hard to control. One solution consists of using a high-T_c–low-T_c (or normal metal) contact, taking care, however, to use a *high-resistivity* normal side. This is essential because of the high normal state resistivity of the oxides: as can be seen from Eqn. (19), the extrapolation length b is very small when $\rho_N \ll \rho_S$, and if b is very small the pair amplitude will be destroyed right at the interface (Fig. 1).

Proximity-coupled weak link structures and tunnel junctions have been made using thin proximity-coupled layers of silver or gold deposited onto $YBa_2Cu_3O_7$ and other high-T_c oxides. Various device heterostructures have been investigated including SNS, SNS′ and SNIS′ junctions, where S′ is usually lead or niobium (Akoh *et al.* 1990, Gijs *et al.* 1990). Properties of these junctions have been calculated within a BCS framework by Kupriyanov and Likharev (1991). Recently, proximity effects have been measured using a semiconducting layer of perovskite-type oxide (e.g., $La_{1.5}Ba_{1.5}Cu_3O_{7-y}$). It appears that the proximity decay length K^{-1} can be as large as 65 nm in this system (Tarutani *et al.* 1991).

The small leakage of Cooper pairs into an insulator is sufficient to weaken the pair amplitude at the interface of an HTS with an insulator (Deutscher and Muller 1987). The extrapolation length b at an SI interface is of the order of ξ_0^2/a where a is an interatomic distance: since in the oxides ξ_0 is only a few interatomic distances, b is not much larger than ξ_0 and as a rule the pair amplitude will be reduced at all surfaces and interfaces. This explains small critical currents and granular behavior in polycrystalline oxides; a disordered region at grain boundaries is sufficient to depress the pair amplitude at the surfaces of the adjacent grains. This depression results in an anomalous temperature variation of the critical current of grain boundary junctions, $I_c \propto (T - T_c)^2$ instead of the linear dependence of usual Josephson junctions (Gross *et al.* 1990). It also explains why I_c scales with the normal state resistance R_N of the junction as R_N^{-2} instead of the usual dependence R_N^{-1} (Deutscher and Chaudhari 1991). Both effects contribute towards reducing the critical current density in randomly oriented polycrystalline samples.

See also: Electrodynamics of Superconductors: Flux Properties; Electrodynamics of Superconductors: Weakly Coupled

Bibliography

Akoh H, Camerlingo C, Takada S 1990 Anisotropic Josephson junctions of YBaCuO/Au/Nb film sandwiches. *Appl. Phys. Lett.* **56** (15), 1487–9

Azlamazoff L G, Larkin A L 1968 Effect of fluctuations on the properties of a superconductor above the critical temperature. *Sov. Phys. Solid State* **10**, 875–80

de Gennes P G 1964 Boundary effects in superconductors. *Rev. Mod. Phys.* **36**, 225–37

Deutscher G 1967 Contribution a l'étude expérimentale de la supraconductivité de surface. *J. Phys. Chem. Solids* **28**, 741–82

Deutscher G 1990 The potential for large critical currents in the high T_c oxides. Transport properties of superconductors. *Prog. High Temp. Supercond.* **25**, 2–10

Deutscher G, Chaudhari P 1991 Scaling behavior of the critical current of grain boundary junctions. *Phys. Rev. B* **44**, 4664–5

Deutscher G, de Gennes P G 1969 Proximity effects. In: Parks R D (ed.) 1969 *Superconductivity*. Dekker, New York, pp. 1005–34

Deutscher G, Dodds S 1977 Critical field anisotropy and fluctuation superconductivity in granular aluminium films. *Phys. Rev. B* **16**, 3936

Deutscher G, Hurault J P, van Dalen P A 1969 Electrodynamic properties of superconducting contacts. *J. Phys. Chem. Solids* **30**, 509–20

Deutscher G, Muller K A 1987 Origin of extrinsic critical currents and glass behavior in the high-T_c oxides. *Phys. Rev. Lett.* **59**, 1745–7

Gijs M A M, Sholten D, van Rooy Th, Gerrits A M 1990 YBa$_2$Cu$_3$O$_{7-x}$/Ag–Al/Al$_2$O$_3$/Pb tunnel junctions based on the superconducting proximity effect. *Appl. Phys. Lett.* **67**, 2600–2

Ginzburg V L 1988 Macroscopic theory for superconductors with small coherence length. *Phys. C* **153**, 1617–21

Glover R E III 1971 Superconducting fluctuation effects above the transition temperature. In: Chilton F (ed.) 1971 *Superconductivity*. North-Holland, Amsterdam, pp. 3–31

Gross R, Chaudhari P, Dimos D, Gupta A, Koren G 1990 Thermally activated phase slippage in high-T_c grain boundary Josephson junctions. *Phys. Rev. Lett.* **64** (2), 228–31

Kes P H, van der Beek C J, Maley M P, McHenry M E, Huse D A, Menken M J V, Menovsky A A 1992 Field suppression of the phase transition in Bi$_2$Sr$_2$CaCu$_2$O$_8$. *Phys. Rev. Lett.* (in press)

Kupriyanov M Yu, Likharev K K 1991 Towards the quantitative theory of the high-T_c Josephson junctions. *IEEE Trans. Magn.* **27**, 2460–3

Orsay Group 1966 Strong field effects at the surface of a superconductor. In: Brewer D (ed.) 1966 *Quantum Fluids*. North-Holland, Amsterdam, pp. 26–67

Orsay Group 1967 Field dependence of the superconducting properties induced by the proximity effect: breakdown fields. *Phys. Kondens. Mater.* **6**, 307–24

Saint James D, de Gennes P G 1963 Onset of superconductivity in decreasing fields. *Phys. Lett.* **7**, 306–9

Salamon M B, Inderhees S E, Rice J P, Ginsberg D M 1990 Heat capacity of untwinned YBa$_2$Cu$_3$O$_7$ in magnetic fields: dimensional cross-over near T_c. *Phys. A* **168**, 283–90

Serin B 1969 Type II superconductors: experiments. In: Parks R D (ed.) 1969 *Superconductivity*. Dekker, New York, pp. 925–76

Tarutani Y, Fukazawa T, Kabasawa U, Tsukamoto A, Hiratani M, Takagi K 1991 Superconducting characteristics of a planar-type HoBaCuO–LaBaCuO–HoBaCuO junction. *Appl. Phys. Lett.* **58**, 2707–9

Yang H C, Finnemore D K 1984 Pair-breaking mechanisms in superconductor–normal metal–superconductor junctions. *Phys. Rev. B* **30** (3), 1260–5

G. Deutscher
Tel Aviv University, Tel Aviv, Israel

Colossal Magnetoresistance Effects: The Case of Charge-ordered Pr$_{0.5}$Ca$_{0.5}$MnO$_3$ Manganite Thin Films

Recently, perovskite type manganites such as RE$_{1-x}$A$_x$MnO$_3$ (RE = rare-earth and A = alkaline-earth ion) have received renewed interest due to the fact that they display colossal magnetoresistance (CMR), a huge decrease in resistance when applying a magnetic field (Chahara *et al.* 1993, Von Helmolt *et al.* 1993, McCormack *et al.* 1994, Prellier *et al.* 2001). Since most of the technological applications require thin films, it is essential to understand the effects of the substrate-induced strains on the properties of these manganites. These materials are very sensitive to the strains and even very small perturbations may result in observable effects on the properties. These effects have indeed been studied experimentally on various compounds (Prellier *et al.* 1999, Biswas *et al.* 2000). Moreover, among all the properties of these manganite materials, the phenomenon of charge ordering (CO) is probably one of the most remarkable effects which occurs for certain values of x and for a particular average A-site cation radius. It corresponds to an ordering of the charges in two different Mn sublattices. In fact, the metallic state becomes unstable, below a certain temperature (T_{CO}) and the material goes to an insulating state. T_{CO} decreases with increasing field and the insulating CO state can be totally suppressed by the application of an external magnetic field (Rao *et al.* 2000). As an example, a 25 T magnetic field is required to melt the CO state in bulk Pr$_{0.5}$Ca$_{0.5}$MnO$_3$ (Tokunaga *et al.* 1998) leading to huge CMR effect.

The substrate-induced strain effects and the thickness of the films influence the structural and physical properties of manganite thin films. As an example, Pr$_{0.5}$Ca$_{0.5}$MnO$_3$ (PCMO), thin films grown on LaAlO$_3$ (LAO) and SrTiO$_3$ (STO) using the pulsed laser deposition (PLD) technique are considered here. The focus is on the changes in the lattice parameters, the orientation and the transport measurements of the film. On the basis of these results, a temperature–field phase diagram for CO thin films is determined and compared with the bulk material.

Thin films of PCMO were grown *in situ* using the PLD technique on [100]-SrTiO$_3$ (cubic with $a = 3.905$ Å) and [100]-LaAlO$_3$ (pseudocubic with $a = 3.789$ Å) substrates. Detailed optimization of the growth procedure was completed and described previously (Prellier *et al.* 2000, Haghiri-Gosnet *et al.* 2000). The structural study was carried out by X-ray diffraction (XRD) using a Seifert XRD 3000P for the Θ–2Θ scans and a Philips MRD X'pert for the in-plane measurements (Cu Kα, $\lambda = 1.5406$ Å). The in-plane parameters were obtained from the $(1\,0\,3)_C$ reflection (where C refers to the ideal cubic perovskite cell). An electron microscope JEOL 2010 was used for the electron diffraction (ED) study. The resistivity (ρ) was measured by a four-probe method with a Quantum Design PPMS and magnetization (M) was recorded using a Quantum Design MPMS SQUID magnetometer as a function of the temperature (T) and the magnetic field (H). The composition of the films was checked by energy-dispersive scattering analyses. It is homogenous and corresponds exactly
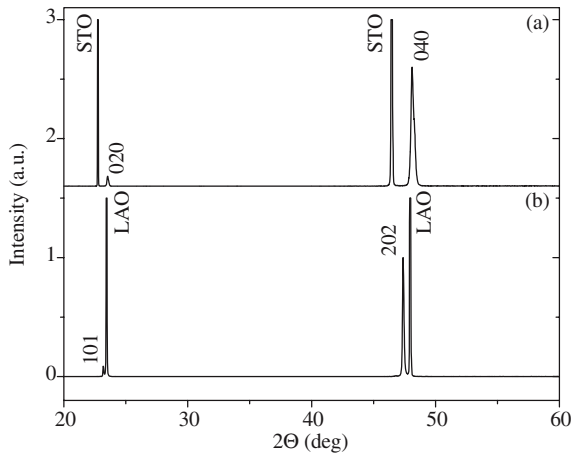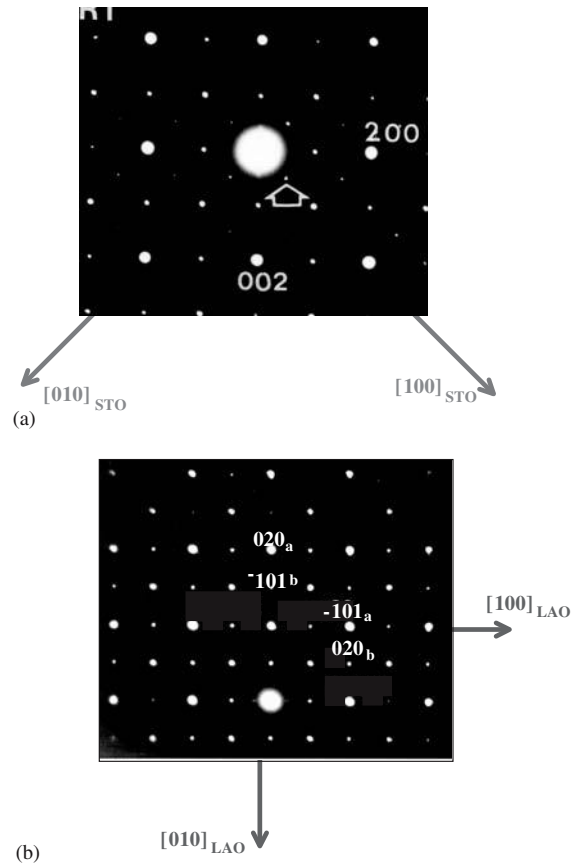
Figure 1
Room temperature Θ–2Θ XRD pattern of a 75 nm thick film on (a) STO and (b) LAO. Note the high intensity and the sharpness of the peaks.

to the composition of the target (i.e., Pr$_{0.5}$Ca$_{0.5}$MnO) in the limit of the accuracy.

The structure of bulk PCMO is orthorhombic (*Pnma*) with $a = 5.395$ Å, $b = 7.612$ Å and $c = 5.403$ Å (Jirak *et al*. 1985). Figure 1 shows a typical Θ–2Θ scan recorded for a 750 Å thick film deposited on STO (a) and LAO (b). Note that the same type of pattern is obtained for all of the films. This shows that the films are single phases and highly crystallized. From the XRD pattern, the out-of-plane lattice parameter is, respectively, calculated to be 3.78 Å on LAO and 3.85 Å on STO indicating that the film is under compression on LAO and under tension on STO as already reported.

Figure 2 shows the ED pattern recorded along a direction perpendicular to the substrate plane. It is clear that the orientations of the films with respect to the substrate are different. In fact, the film is [010]-oriented, i.e., with the [010] axis perpendicular to the substrate plane when grown on STO and [101]-oriented on LAO. This surprising orientation results from the lattice mismatch. Indeed, the mismatch (σ) between the film and the substrate can be evaluated using the formula $\sigma = 100(a_S - a_F)/a_S$ (where a_S and a_F, respectively, refer to the lattice parameter of the substrate and the film). The smaller mismatch on LAO is obtained for a [010]-axis in the plane ($\sigma_{LAO} = -0.4\%$), i.e., the [101]-axis is perpendicular to the substrate plane ($\sigma_{LAO} = -0.7\%$ for a [101] axis in the plane). In contrast, the smaller mismatch on STO ($\sigma_{STO} = 2.2\%$) is found for a [101]-axis in the plane ($\sigma_{STO} = 2.5\%$ for a [010]-axis in the plane). Thus, the [010]-axis is normal to the surface of the substrate as found experimentally (Prellier *et al*. 2000, Haghiri-Gosnet *et al*. 2000).

Figure 2
Room temperature electron diffraction of PCMO on STO (a) and LAO (b); reproduced from W. Prellier *et al*. (2000) Spectacular decrease of the melting magnetic field in the charge-ordered state of Pr$_{0.5}$Ca$_{0.5}$MnO$_3$ films under tensile strain. *Appl. Phys. Lett*. **77**, 1023–5.

The samples were cooled down to 92 K. The diffraction patterns recorded at low temperature in the strained film systematically exhibit a system of extra reflections characteristic of an incommensurate CO parallel to the a^* direction on both substrates (not shown). The q values of the modulation vector are close to 0.45 and STO and 0.38 on LAO and do not vary with the temperature below T_{CO}, contrary to what is observed in the bulk samples. This modulation disappears at T_{CO}. Small film fragments separated from the substrate were also observed. In this case, a modulation vector close to 0.5 was observed. This value is similar to that of the bulk samples (Barnabé *et al*. 1998). Since the composition is the same, this reinforces the assumption that the deviation from the ideal q value originates from the strain induced by the substrate. This demonstrates that the
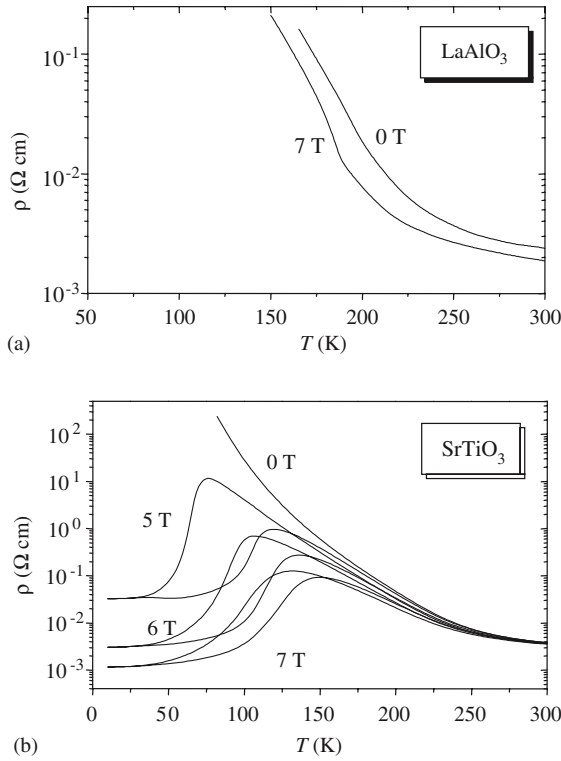
Figure 3

$\rho(T)$ in different magnetic fields (0 T, 5 T, 7 T, and 9 T) applied in the plane of the substrate for different films on (a) LAO and (b) STO.

orthorhombic distortion induced by the CO ordering is strongly reduced by the presence of the substrate, preventing the locking of the q value of the CO on the 1/2 value contrary to the bulk sample of the same composition, leading to $q = 0.45$ for the film grown on STO and $q = 0.38$ for the one deposited on LAO.

The $\rho(T)$ curves are presented in Fig. 3. Different magnetic fields (0 T, 5 T, 6 T, and 7 T) were applied perpendicular to the substrate. The behavior of both films is very different. Clearly, the film grown on STO (Fig. 3(b)) shows an insulating behavior in the whole temperature range when the magnetic field is below 4 T. A small anomaly in the resistivity (around 240 K) is associated with the CO. But the most interesting feature is observed when applying a magnetic field of 7 T. The film then becomes metallic at low temperatures and shows an insulator-to-metal transition (T_{IM}) at 120 K. When a magnetic field is applied, the T_{IM} upon heating occurs at a higher temperature ($= 140$ K) indicating a clear hysteresis. This melting field of 7 T is much lower than the 20 T one which is necessary to induce the metallic phase in the bulk

sample. On the contrary, this effect is not observed for [101]-PCMO films grown on LAO (Fig. 3(a)) with fields up to 7 T.

Figure 4 shows the temperature dependence with different applied magnetic fields (0 T, 5 T, and 9 T) for three film thicknesses deposited on STO. In the absence of an applied field, one always observes a semiconducting behavior with an anomaly around 225 K corresponding to the T_{CO} (this value is close to the one found in the bulk material). On the contrary, the results are drastically different under application of external magnetic fields. A field up to 9 T has almost no effect on the thinner film (15 nm): the film is still semiconducting and the magnetoresistance is very small (Fig. 4(a)). For the intermediate thickness (75 nm), while a 5 T magnetic field keeps the film semiconducting, a field of 9 T renders it metallic with a T_{IM} close to 125 K (see Fig. 4(b)). This feature is a typical characteristic of the melting of the CO state. On the thicker film (110 nm), the melting magnetic field is reduced to 5 T (Fig. 4(c)). The thickness dependence of the properties suggests that the strains play an important role in determining the melting magnetic field. When the thickness of the film is increasing, there is a reduction of the strain on the film at room temperature. However, the properties of the film do not approach those of the bulk as the substrate-induced strain is reduced. In PCMO single crystal, with a 6 T magnetic field, the material remains insulating (Tomioka *et al.* 1996), whereas the 110 nm film becomes metallic.

The magnetic field dependence of the resistivity shows a strong decrease on a logarithmic scale at a critical field (H_C) indicating the field-induced melting of the CO state (see insets of Fig. 4). This field-induced insulator-to-metal transition, which accompanies the collapsing of the CO state takes place below T_{CO}. The critical fields in the field-increasing scan and in the field-decreasing scan will be represented by H_C^+ and H_C^-, respectively. This decrease of the resistivity versus magnetic field can be viewed as CMR of about five orders of magnitude at 75 K. A clear hysteresis is seen at these temperatures as previously reported on several CO compounds (Kuwahara *et al.* 1995, Tomioka *et al.* 1996). This hysteretic region is more pronounced when the temperature is decreasing. The temperature dependence of the large hysteresis region is a feature of a first-order transition and has been extensively studied for the composition Nd$_{0.5}$Sr$_{0.5}$MnO$_3$ (Kuwahara *et al.* 1995). From the resistivity measurements, a phase diagram for the 110 nm thick film (Fig. 5) and for the 75 nm film (inset of Fig. 5) can be derived. Two remarks should be made: First as already mentioned, the transition to the metastable state (i.e., the field-induced metallic state) is easier or requires a lower field in case of a thin film than in the bulk (Tomioka *et al.* 1996) (5 T for a 110 nm thick film and 9 T for a 75 nm thick film); second, the shape of the H–T phase diagram is totally different as
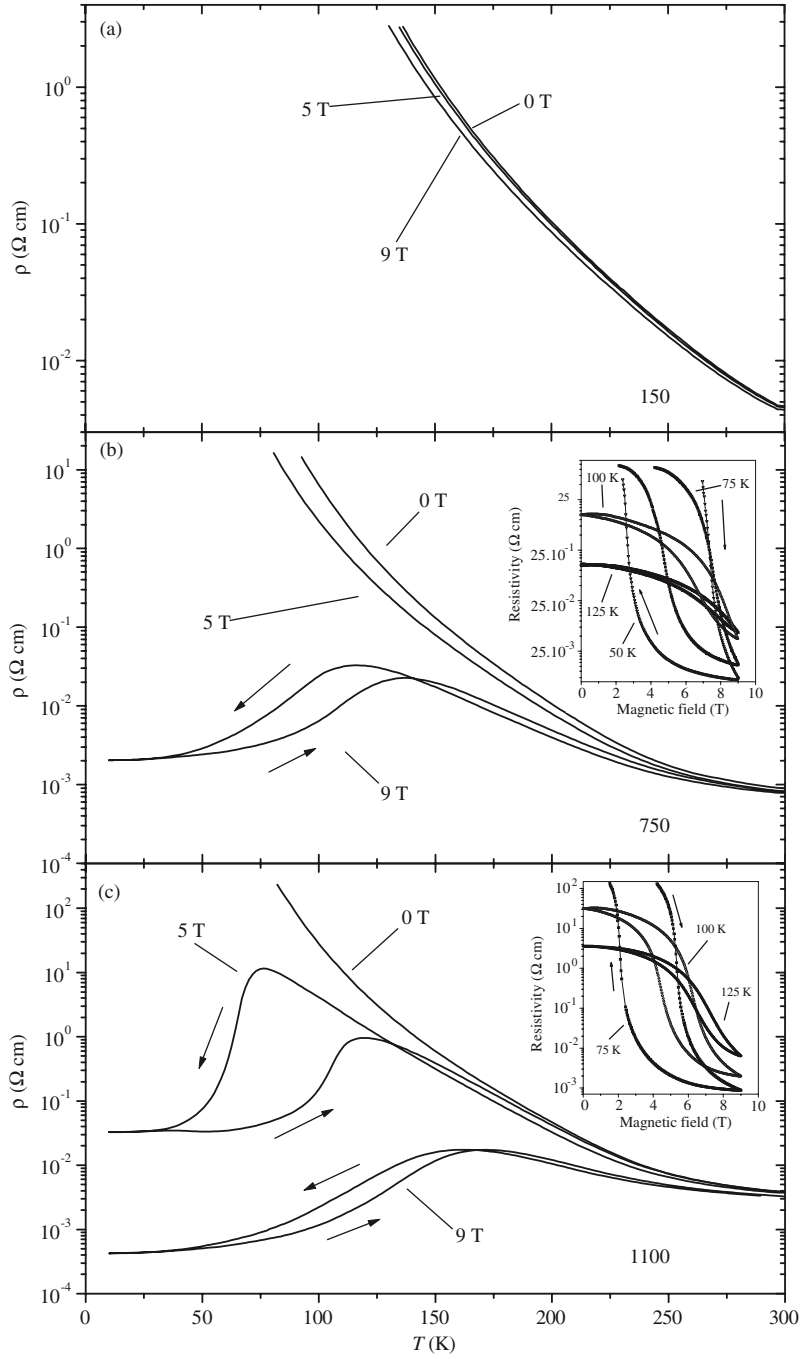
Figure 4

$\rho(T)$ in different magnetic fields (0 T, 5 T, and 9 T) applied in the plane of the substrate for different PCMO films on STO: (a) 15 nm, (b) 75 nm, and (c) 110 nm. Arrows indicate the direction of the temperature variation. Experimental points were taken with a stabilized temperature and a control of the sample film itself. The crossing of the curves ramping up and down in temperature is real. The insets of (b) and (c) depict the $\rho(H)$ for a 75 nm and 110 nm film, respectively. Runs with increasing field and decreasing field are denoted by arrows. Reproduced from W. Prellier *et al.* (2000) Thickness dependence of the stability of the charge-ordered state in Pr$_{0.5}$Ca$_{0.5}$MnO$_3$ thin films. *Phys. Rev. B* **62**, R16337.
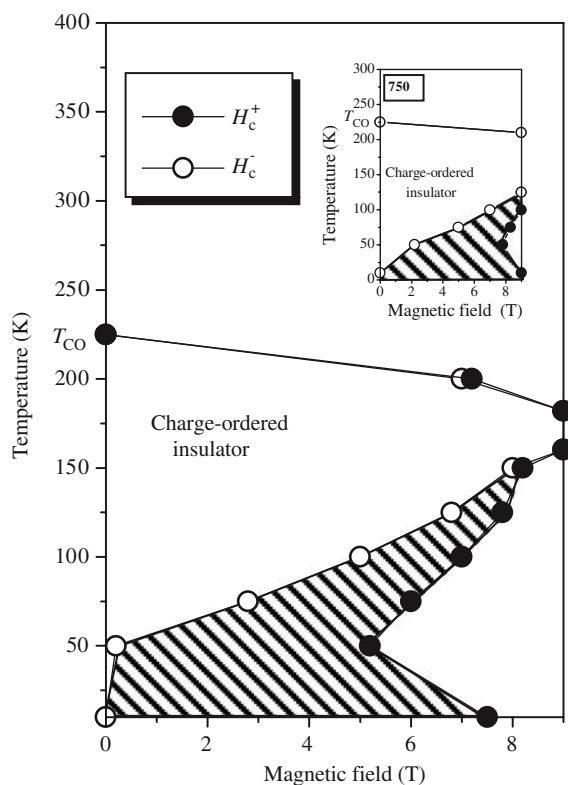
compared to the bulk single crystal Pr$_{0.5}$Ca$_{0.5}$MnO$_3$. The hysteretic region grows when the temperature is decreasing and rapidly vanishes at 8 T. In other words, H_C is smaller than 9 T at low temperature, then H_C is decreasing when the T is increasing. Above 50 K, H_C begins to increase again to 8 T. In the mean time, the hysteretic region is shrinking. Note that this region is larger in the case of the 75 nm film, indicating that the CO state is more stable as previously seen from the $\rho(T)$ curves (Fig. 3). In fact, the phase diagram of the 110 nm film has almost the same profile as a Pr$_{1-x}$Ca$_x$MnO$_3$ single crystal with $0.35 < x < 0.45$. This suggests that the whole electronic structure of Pr$_{0.5}$Ca$_{0.5}$MnO$_3$ thin films grown on STO is similar, though the charge transfer is different ($x = 0.5$ instead of 0.4 in Pr$_{1-x}$Ca$_x$MnO$_3$). The interesting point is that the modulation vector q is equal to 0.45 in PCMO on STO (Prellier *et al.* 2000), whereas

q is always equal to 0.5 in bulk Pr$_{1-x}$Ca$_x$MnO$_3$ compounds ($0.35 < x < 0.45$) (Barnabé *et al.* 1998).

In summary, the melting magnetic field of the insulating charge-ordered state, in Pr$_{0.5}$Ca$_{0.5}$MnO$_3$ films, is strongly sensitive to the substrate-induced strain and thickness of the film. When deposited on SrTiO$_3$ (tensile stress), the application of magnetic fields up to 9 T has almost no effect on the resistivity of a very thin film, but a 5 T magnetic field can completely melt the CO state of a 110 nm thick film. When the film is under compression (on LaAlO$_3$), the films are insulating in a magnetic field of 7 T. By growing thin films, the properties of the materials can be modified compared to the bulk compounds. We have studied the case of Pr$_{0.5}$Ca$_{0.5}$MnO$_3$ on two different substrates that are able to induce two different types of strains (tensile on SrTiO$_3$ and compressive on LaAlO$_3$) and their effects on various parameters. We observed that the lattice parameters of the film, the orientation of the film with respect to the substrate, the transport properties of the film and the stability of the charge/orbital ordered state are influenced by the strains suggesting some similarities between strain and pressure effects in oxides (Wang *et al.* 1995).

Acknowledgements

See also: Boltzmann Equation and Scattering Mechanisms; Giant Magnetoresistance: Metamagnetic Transitions in Metallic Antiferromagnets; Intermetallic Compounds: Electrical Resistivity; Magnetoresistance, Anisotropic; Magnetoresistance: Magnetic and Nonmagnetic Intermetallics; Magnetoresistance in Transition Metal Oxides

Bibliography

Barnabé A, Hervieu M, Martin C, Maignan A, Raveau B 1998 Role of the A-site size and oxygen stoichiometry in charge ordering commensurability of Ln$_{0.5}$Ca$_{0.5}$MnO$_3$ manganites. *J. App. Phys.* **84**, 5506–14

Biswas A, Rajeswari M, Srivastava R C, Li Y H, Venkatesan T, Greene R L, Millis A J 2000 Two-phase behavior in strained thin films of hole-doped manganites. *Phys. Rev. B* **61**, 9665–8

Chahara K, Ohno T, Kasai M, Kozono Y 1993 Magnetoresistance in magnetic manganese oxide with intrinsic antiferromagnetic spin structure. *Appl. Phys. Lett.* **63**, 1990–2

Haghiri-Gosnet A M, Hervieu M, Simon Ch, Mercey B, Raveau B 2000 Charge ordering in Pr$_{0.5}$Ca$_{0.5}$MnO$_3$ thin films: a new form initiated by strain effects of LaAlO$_3$ substrate. *J. Appl. Phys.* **88**, 3545–51

Jirak Z, KrupiImageka S, Simca Z, Dlouhá M, Vratislav S 1985 Neutron diffraction study of $Pr_{1-x}Ca_xMnO_3$ perovskites. *J. Magn. Mat.* **53**, 153–66

Kuwahara H, Tomioka Y, Asamitsu A, Moritomo Y, Tokura Y 1995 A first-order phase transition induced by a magnetic field. *Science* **270**, 936–61

McCormack M, Jin S, Tiefel T H, Fleming R M, Phillips J M, Ramesh R 1994 Very large magnetoresistance in perovskite-like La-Ca-Mn-O thin films. *App. Phys. Lett.* **64**, 3045–7

Prellier W, Biswas A, Rajeswari M, Venkatesan T, Greene R L 1999 Effect of substrate-induced strain on the charge-ordering transition in $Nd_{0.5}Sr_{0.5}MnO_3$ thin films. *Appl. Phys. Lett.* **75**, 397–9

Prellier W, Haghiri-Gosnet A M, Mercey B, Lecoeur Ph, Hervieu M, Simon Ch, Raveau B 2000 Spectacular decrease of the melting magnetic field in the charge-ordered state of $Pr_{0.5}Ca_{0.5}MnO_3$ films under tensile strain. *Appl. Phys. Lett.* **77**, 1023–5

Prellier W, Lecoeur Ph, Mercey B 2001 Colossal magnetoresistive manganite thin films. *J. Phys. Condens. Matter* **13**, R915–44

Rao C N R, Arulraj A, Cheetham A K, Raveau B 2000 Charge ordering in the rare earth manganates: the experimental situation. *J. Phys.: Condens. Matter* **12**, R83–106

Tokunaga M, Miura N, Tomioka Y, Tokura Y 1998 High-magnetic-field study of the phase transitions of $R_{1-x}Ca_xMnO_3$ (R = Pr, Nd). *Phys. Rev. B* **57**, 5259–64

Tomioka Y, Asamitsu A, Kuwahara H, Moritomo Y, Tokura Y 1996 Magnetic-field-induced metal-insulator phenomena in $Pr_{1-x}Ca_xMnO_3$ with controlled charge-ordering instability. *Phys. Rev. B* **53**, R1689–92

Von Helmolt R, Wecker J, Holzapfel B, Schultz L, Samwer K 1993 Giant negative magnetoresistance in perovskitelike $La_{2/3}Ba_{1/3}MnO_x$ ferromagnetic films. *Phys. Rev. Lett.* **71**, 2331–3

Wang H Y, Palstra T T M, Cheong S W, Batlogg B 1995 Pressure effects on the magnetoresistance in doped manganese perovskites. *Phys. Rev. B* **52**, 15046–9

W. Prellier
Laboratoire CRISMAT
CNRS UMR 6508 6 Boulevard du Marechal Juin
F-14050 Caen Cedex, France

Crystal Field and Magnetic Properties, Relationship between

The crystal-field (CF) model has been very successful in the analysis of $4f^N$ configurations of the triply ionized rare-earth R ions in solids whose energy levels are reproduced through a Hamiltonian which involves both free-atom and CF operators (Morrison and Leavitt 1982, Görller-Walrand and Binnemans 1996). A satisfactory simulation of the experimental scheme of energy levels can be achieved if the number and quality of the operators is adequate. The procedure also provides good quality wave functions associated to the Stark levels, which can be used to simulate other physical properties, depending on them and the energies only. Thus, if there are no magnetic interactions between the lanthanide ions, the effective magnetic moment, the thermal evolution of the paramagnetic susceptibility χ for any crystallographic direction, as well as the g-values of the magnetic splitting factor for each Kramers doublet, can be calculated when the same $L + g_eS$ tensorial operator is applied to the wave function of a level, according to the Van Vleck formalism (Van Vleck 1932).

This article outlines the importance of the CF effects on the explanation of the magnetic properties in a wide group of R-containing materials, prepared as polycrystalline powders. In them, the one single crystallographic position occupied by R has a point symmetry ranging from a relatively high symmetry, S_4 for both $R_3Sb_5O_{12}$ and $Na_5R(MoO_4)_4$ series, to a very low symmetry, C_s for $R_3WO_6Cl_3$ and C_1 for $R_2Te_4O_{11}$ and $MgR(BO_2)_5$ families (Cascales *et al.* 1995, 1999). The very good agreement found between the calculated paramagnetic susceptibility curves, derived through phenomenological and/or estimated crystal field parameters (CFPs), and the observed χ vs. T plots constitutes an excellent test of the ability of the CF model to provide correct wave functions for the $4f^N$ configurations.

1. Crystal-field Analysis and Simulation of the Energy Level Schemes

In the development of a complete Hamiltonian for $4f^N$ configurations, the central-field approximation allows considering separately the Hamiltonians corresponding to the gaseous free-ion and to the CF interactions, which arise when R is in a crystalline environment. Thus the total Hamiltonian (Carnall *et al.* 1989) consists of two parts, $H = H_{FI} + H_{CF}$. The H_{FI} free-ion part includes the spherically symmetrical one-electron term of the Hamiltonian, the electrostatic interaction between equivalent f electrons, the spin-orbit interaction, and terms accounting for higher-order corrections, as it is described in Carnall *et al.* 1989.

In the presence of a crystalline electric field the degeneracy of each state of the free-ion will be lifted according to the site symmetry of R in the crystal lattice. Calculations are usually carried out within the single-particle CF theory, and following Wybourne's formalism (Wybourne 1965), the CF H_{CF} Hamiltonian is expressed as a sum of products of spherical harmonics and CFPs.

$$H_{CF} =$$

$$\sum_{k=2}^{4,6} \sum_{q=0}^{k} \left[B_q^k (C_q^k + (-1)^q C_{-q}^k) + iS_q^k (C_q^k - (-1)^q C_{-q}^k) \right]$$

Whereas for the S_4 symmetry of the R^{3+} site in $R_3Sb_5O_{12}$ the serial development of the CF potential

involves five real B_q^k and two complex S_q^k parameters, for the lowest C_1 symmetry found in $MgR(BO_2)_5$ all 27 CFPs are kept nonzero. For R ions with low point-group symmetries the constraints imposed by group theory are weak and it becomes difficult, with polycrystalline samples but even with polarized optical absorption and emission measurements on single crystals, to unravel the optical spectra unambiguously. Even if this has been done, it is not straightforward to fit the data with a total Hamiltonian. The number of adjustable parameters are very large, and the nonlinear least square fits are unreliable, unless a good initial set of CFPs is known. Besides *the descent of symmetry* method (Wybourne 1965), various theoretical models for calculating the CF interactions have been proposed (Garcia and Faucher 1995). The *simple overlap model* SOM (Porcher *et al.* 1999), a simplified semi-*a priori* calculation model used to obtain the initial set of CFPs from the crystallographic structure (Malta *et al.* 1991), was used for the limit situations represented by the $Na_5R(MoO_4)_4$ or $R_3Sb_5O_{12}$ series, and by the $MgNd(BO_2)_5$ compound. Finally, to verify the consistency and reliability of the final fitted parameters, simultaneous simulations performed for different $4f^N$ configurations either in the same or in an isostructural crystalline matrix, should provide sets of CFPs with only smooth variations (Morrison and Leavitt 1982).

2. Magnetic Susceptibility and Crystal-field Levels

The calculation of the magnetic susceptibility for above R-compounds (Cascales *et al.* 1993, 1995, 1996, 1997, 1999) has been carried out from the consistent sets of wave functions and energy levels previously determined (Cascales *et al.* 1990, 1992a, b, c, 1998), by diagonalizing the total Hamiltonian. This is done using the Van Vleck formalism (Van Vleck 1932) the result of an application of the perturbation theory,

$$\chi^{(i)} = N\beta^2$$

$$\sum_a \left[\frac{\langle \phi_a|H|\phi_a \rangle^2}{kT} - 2\sum_b \frac{\langle \phi_a|H|\phi_b \rangle \langle \phi_b|H|\phi_a \rangle}{E_a - E_b} \right] B_a$$

in which N is the Avogadro's number, β the Bohr magneton, k the Boltzmann constant, and E and ϕ the nonperturbed energy levels and wave functions, respectively, described in the $|SLJM_J\rangle$ basis, and H is the magnetic tensor operator $L + g_eS$. The different values of the tensor components (or combinations of them) destroy the isotropy observed for the free-ion or even for an ion in a cubic symmetry. For polycrystalline samples, the mean observed paramagnetic susceptibility is $\chi_{av} = (\chi_x + \chi_y + \chi_z)/3$. The sums run over thermally populated levels, according to the

Boltzmann population,

$$B_a = \exp(-E_a^{(0)}/kT)/\sum_a \exp(-E_a^{(0)}/kT).$$

In the expression, the matrix elements are calculated using the Racah algebra rules.

The formula is the sum of a temperature-dependent diagonal term and a temperature-independent off-diagonal term, which is reminiscent of the classical Curie–Weiss law. The off-diagonal term, a result of the second order perturbation, usually has little importance, with the exception of the ground states with $J = 0$. The sum runs over all other states $(b \neq a)$. Energy levels up to $5000\,cm^{-1}$ and $10000\,cm^{-1}$, for the diagonal and off-diagonal terms, respectively (which are largely sufficient to cover the thermal population effect above 300K), were accounted in the calculation along with the J mixing of the levels.

The simulation of Stark levels for $4f^N$ configurations as well as the calculations of the χ vs. T curves were performed by the programs REEL and IMAGE (Porcher personal communication, 1989).

3. Results

The calculation of the thermal variation of the paramagnetic susceptibility (Cascales *et al.* 1993, 1995, 1996, 1997, 1999) has been carried out with two different collections of energy levels and associated wave functions: (i) Those derived from CFPs obtained through spectroscopic data. (ii) Calculated from CFPs obtained by using SOM, through crystallographic data. Values of χ have been found to be independent of the field because of the relatively weak applied field. With the well-known exceptions of Eu and Sm-compounds, χ^{-1} vs. T curves at high temperatures follow a Curie–Weiss-type behavior. Deviations from linearity observed at low temperature can be attributed to the splitting of the corresponding free-ion ground state under the influence of the CF, and the Weiss constants for these materials are entirely due to CF effects since they do not undergo any magnetic exchange interactions.

Figure 1 presents the comparison between experimental and calculated average χ^{-1} (or χ for R $=$ Eu^{3+}) vs. T curves for some selected compounds of $R_3Sb_5O_{12}$ and $MgR(BO_2)_5$. The choice of these series is related to the very different number of real and complex parameters that the CF potential involves in each case. As it can be seen, a very satisfactory concordance is found between the experimental and calculated curves, especially when these last ones are from optical data. The observed slight discrepancy between them when the temperature increases is related with a variation of the CF, usually assumed to be temperature-independent, since, in fact, the network parameters smoothly vary with the temperature.
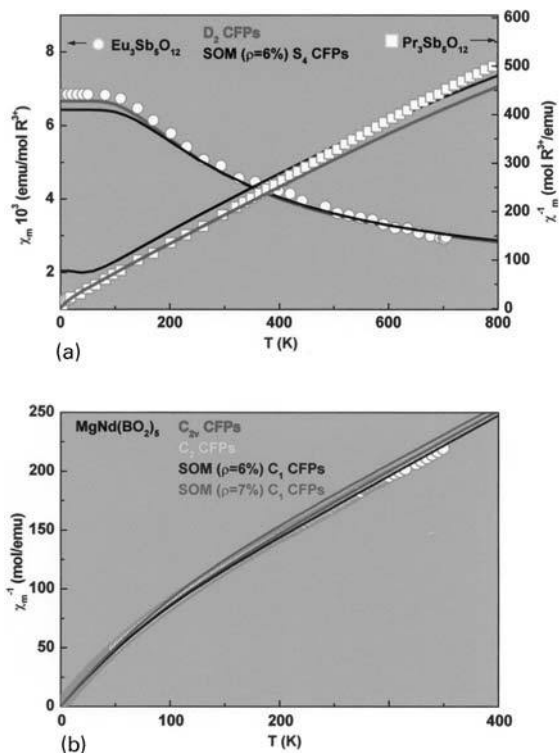
Figure 1
Comparison between experimental (symbols) and
calculated (solid lines) χ^{-1} (or χ for the Eu^{3+}
compound) curves: (a) for selected $R_3Sb_5O_{12}$
compounds; (b) for $MgNd(BO_2)_5$ (reproduced by
permission of Elsevier Science from *J. Solid State
Chem.*, 1995, **114**, 52–6; *Chem. Phys.*, 1999, **240**, 291–
301).

4. Concluding Remarks

The good reproduction of experimental data, espe-
cially the observed deviation from the Curie–Weiss
behavior at low temperature in the χ^{-1} vs. T plots,
underscores that the standard CF treatment of $4f^N$
configurations can explain the magnetic properties of
these ions, whatever the number of parameters in-
volved in the simulation, with no need to consider
any sort of exchange interactions between them.
These calculations are extremely dependent on the
composition of the CF wave functions; hence the
comparison with experimental measurements consti-
tutes an excellent opportunity to test the ability of the
model to give adequate wave functions for the con-
sidered ion. Anyway, the correct simulation of phys-
ical properties can be considered as a proof of
obtaining "good wave functions" if it is done through
"good CFPs," i.e., those deduced from a high-quality
spectroscopically-observed energy level scheme for

the given $4f^N$ configuration. The oversimplified SOM
model seems to be useful at providing estimations of
CFPs, especially when the point symmetry of R in-
volves a reasonable number of nonzero CFPs. This
kind of calculation is of particular interest for opaque
materials, for which only a reduced number of Stark
levels can be observed from experimental techniques.

See also: Crystal Field Effects in Intermetallic
Compounds: Inelastic Neutron Scattering Results;
Localized $4f$ and $5f$ Moments: Magnetism.

Bibliography

Carnall W T, Goodman G L, Rajnak K, Rana R S 1989 A
systematic analysis of the spectra of the lanthanides doped
into single crystal LaF$_3$. *J. Chem. Phys.* **90**, 3443–57

Cascales C, Antic Fidancev E, Lemaitre Blaise M, Porcher P
1990 Spectroscopic properties of Eu^{3+} in lanthanum chloro-
tungstates. *J. Sol. State Chem.* **89**, 118–22

Cascales C, Antic Fidancev E, Lemaitre Blaise M, Porcher P
1992a Spectroscopic properties of Pr^{3+} doped LaWO$_4$Cl and
La$_3$WO$_6$Cl$_3$. *Eur. J. Solid State Inorg. Chem.* **29**, 273–82

Cascales C, Antic Fidancev E, Lemaitre Blaise M, Porcher P
1992b Optical properties and crystal field calculations of
europium tellurium oxide. *J. Alloys Comp.* **180**, 111–6

Cascales C, Antic Fidancev E, Lemaitre Blaise M, Porcher P
1992c Spectroscopic properties and simulation of the energy
level scheme of Nd^{3+} and Pr^{3+} ions in rare earth tellurium
oxides. *J. Phys.: Condens. Matter* **4**, 2721–34

Cascales C, Porcher P, Sáez Puche R 1993 Crystal field effects
on the magnetic susceptibility of rare earth tellurium oxides.
J. Phys. Chem. Solids **54**, 1471–4

Cascales C, Porcher P, Sáez Puche R 1996 Paramagnetic sus-
ceptibility simulations from crystal-field effects on rare-earth
double molybdate and tungstate Na$_5$RE(XO$_4$)$_4$. *J. Phys.:
Condens. Matter* **8**, 6413–24

Cascales C, Porcher P, Sáez Puche R 1997 Paramagnetic sus-
ceptibility simulations from crystal-field effects on rare-earth
antimonates R$_3$Sb$_5$O$_{12}$. *J. Alloys Comp.* **250**, 391–5

Cascales C, Sáez Puche R, Porcher P 1995 Crystal-field effect
on the magnetic susceptibility of rare-earth (Pr, Nd, Eu)
mixed oxides. *J. Sol. State Chem.* **114**, 52–6

Cascales C, Sáez Puche R, Porcher P 1998 Crystal-field effects
and simulation of the energy level scheme of Nd^{3+} in mag-
nesium borate MgNd(BO$_2$)$_5$. *J. Alloys Comp.* **277**, 384–7

Cascales C, Sáez Puche R, Porcher P 1999 Paramagnetic sus-
ceptibility simulations from crystal-field effects on Nd^{3+} in
magnesium borate MgNd(BO$_2$)$_5$. *Chem. Phys.* **240**, 291–301

Garcia D, Faucher M 1995 In: Gschneider K A, Eyring L (eds.)
*Handbook on the Physics and Chemistry of Rare Earths, Vol.
21, Crystal Field in Non-metallic (Rare Earth) Compounds.*
Elsevier, Amsterdam

Görller-Walrand C, Binnemans K 1996 In: Gschneider K A,
Eyring L (eds.) *Handbook on the Physics and Chemistry of
Rare Earths, Vol. 23, Rationalization of Crystal-field Par-
ametrization.* Elsevier, Amsterdam

Malta O L, Ribeiro S J L, Faucher M, Porcher P 1991 The-
oretical intensities of 4f–4f transitions between Stark levels of
the Eu^{3+} ion in crystals. *J. Phys. Chem. Solids* **52**, 587–93

Morrison C A, Leavitt R P 1982 In: Gschneider K A, Eyring L
(eds.) *Handbook on the Physics and Chemistry of Rare Earths,*

Vol. 5, Spectroscopic Properties of the Triply Ionized Lanthanides in Transparent Host Crystals North-Holland, Amsterdam

Porcher P, Dos Santos C M, Malta O 1999 Relationship between phenomenological crystal field parameters and the crystal structure: The simple overlap model. *Phys. Chem. Chem. Phys.* **1**, 397–405

Van Vleck J H 1932 *The Theory of Electric and Magnetic Susceptibilities.* Oxford University Press, London

Wybourne B G 1965 *Spectroscopic Properties of Rare Earths.* Wiley, New York

C. Cascales
Instituto de Ciencia de Materiales de Madrid, Spain

R. Sáez-Puche
Universidad Complutense de Madrid, Spain

Crystal Field Effects in Intermetallic Compounds: Inelastic Neutron Scattering Results

The crystal field (CF) interaction in rare-earth compounds is responsible for an enormous variety of magnetic phenomena. The electrostatic interaction experienced by the rare-earth ion, arising from the presence of near neighbor ions and outer valence electrons, is much smaller than the spin–orbit coupling, because of the minute spatial extent of the 4*f*-wave functions. This CF interaction gives rise to splittings of the ground-state multiplet of the order of tens of meV for the lanthanides. A precise determination of CF parameters is a necessary precondition for detailed analysis of bulk magnetic properties such as the static susceptibility, magnetic contribution to the specific heat, and complex magnetization processes and transitions in a large host of magnetic materials. The CF interaction intimately reflects the crystallographic point symmetry of the lanthanide ion and splits the $(2J + 1)$-fold degeneracy of the ground state according to rules dictated by group theory. In combination with an exchange interaction, the result is a truly phenomenal array and variety of magnetic properties. The situation pertaining to compounds, such as those based on Ce, with an unstable or delocalized 4*f*-shell leads to complications due to the manner in which conduction electrons can couple to 4*f*-electrons, giving rise to valence fluctuating or Kondo systems (see *Intermediate Valence Systems*; *Kondo Systems and Heavy Fermions: Transport Phenomena*). Similar circumstances are also pertinent for 5*f*-electron heavy-fermion systems.

The most direct experimental method for the determination of CF eigenvalues and eigenfunctions in crystalline rare-earth intermetallics is provided by inelastic neutron scattering (INS), a truly fundamental and unique investigative probe of the microscopic magnetization which yields the spatial and time dependence of the dynamical magnetic susceptibility. In the specific case of CF effects, the neutron induces transitions between CF levels and these are most easily observed by the INS technique. The investigation of the CF interaction in more than 1000 rare-earth intermetallic compounds by INS and complementary techniques has been reviewed in detail by Moze (1998) whilst a briefer review of the INS technique, with specific reference to tetragonal REAg and RNi_2Si_2 compounds, has been compiled by Blanco (1998). The INS technique is also widely used for the determination of CF parameters and associated linewidth of CF transitions in rare-earth-based high-temperature superconductors (Furrer *et al.* 2001). The CF interaction and INS for rare-earth ions in icosahedral and amorphous environments have been briefly summarized by Moze (1998).

1. Crystal Electric Field

The CF Hamiltonian is most commonly expressed as

$$H_{CF} = \sum_{m,n} B_n^m O_n^m \tag{1}$$

where B_n^m and O_n^m are, respectively, CF energy parameters (typically in meV) and Stevens operator equivalents (Hutchings 1964). Alternatively, it can be expressed in terms of CF coefficients A_n^m:

$$H_{CF} = \sum_{m,n} A_n^m \langle r^n \rangle \theta_n O_n^m \tag{2}$$

where $\langle r^n \rangle$ are radial averages over the 4*f*-electron wave functions and θ_n are the Stevens coefficients α_J, β_J, γ_J for $n = 2$, 4, 6, respectively. These expressions are only valid for the CF split ground-state multiplet. A well-known exception to the rule is the case of the Sm^{3+} ion. The number of CF parameters required to characterize the interaction appropriate to the point symmetry in which the rare-earth ion resides are tabulated in Table 1. For triclinic and monoclinic crystal point groups, where imaginary terms appear, the relevant matrix elements have been derived by Takegahara (2000).

The interaction represented in Eqn. (1) or (2) splits the $(2J + 1)$-fold degenerate ground-state multiplet into a series of CF energy level eigenvalues with energy E_i and corresponding eigenstate, labeled by its irreducible representation Γ_i. The uniqueness of the INS technique in this regard is that CF eigenstates can be obtained from the intensities of observed INS transitions whilst eigenvalues are determined from the energy positions of these transitions. It still remains by far the most indispensable and direct

Table 1
CF parameters relevant for the 32 point groups. Complex values are indicated by $\underline{B_n^m}$.

Symmetry	Point group (Schoenflies)	Point group (International)	CF parameters
Triclinic	$C_1 C_i$	1 $\bar{1}$	$B_2^0 \underline{B_2^1} \underline{B_2^2} B_4^0 \underline{B_4^1} \underline{B_4^2} \underline{B_4^3} \underline{B_4^4} B_6^0 \underline{B_6^1} \underline{B_6^2} \underline{B_6^3} \underline{B_6^4} \underline{B_6^5} \underline{B_6^6}$
Monoclinic	$C_2 C_{2h}$	2 $2/m$	$B_2^0 \underline{B_2^2} B_4^0 \underline{B_4^2} \underline{B_4^4} B_6^0 \underline{B_6^2} \underline{B_6^4} \underline{B_6^6}$
Orthorhombic	$D_2 C_{2v} D_{2h}$	222 $2mm$ mmm	$B_2^0 B_2^2 B_4^0 B_4^2 B_4^4 B_6^0 B_6^2 B_6^4 B_6^6$
Trigonal	$C_3 S_6$	3 $\bar{3}$	$B_2^0 B_4^0 \underline{B_4^3} B_6^0 \underline{B_6^3} \underline{B_6^6}$
Trigonal	$C_{3v} D_{3d} D_3$	$3m$ $\bar{3}m$ 32	$B_2^0 B_4^0 B_4^3 B_6^0 B_6^3 B_6^6$
Hexagonal	$C_{3h} D_{3h} C_{6v} D_6 C_6 D_{6h} C_{6h}$	$\bar{6}$ $\bar{6}m2$ $6mm$ 622 6 $6/mmm$ $6/m$	$B_2^0 B_4^0 B_6^0 \underline{B_6^6}$
Tetragonal	$D_{4h} D_{2d} C_{4v} D_4$	$4/mmm$ $\bar{4}2m$ $4mm$ 422	$B_2^0 B_4^0 B_4^4 B_6^0 B_6^4 B_6^6$
Tetragonal	$C_4 S_4 C_{4h}$	4 $\bar{4}$ $4/m$	$B_2^0 B_4^0 \underline{B_4^4} B_6^0 \underline{B_6^4} B_6^0$
Cubic	$T T_d T_h O O_h$	23 $\bar{4}3m$ $m3$ 432 $m3m$	$B_4^0 B_6^0$

experimental technique for investigating the ground-state properties of a large class of modern magnetic materials. These cover a wide range of interests, from fundamental to technological, and in many cases their magnetic properties are partially governed by the CF interaction. It is hence of utmost importance to be able to determine the characteristics of the CF, for example, and for this purpose INS plays a very prominent role in experimental magnetism.

2. Inelastic Neutron Scattering

The parameters of the CF Hamiltonian invariably need to be determined by a number of different experimental techniques, of which INS is undoubtedly the most powerful, since it is extremely sensitive to the details of the CF. With no exchange interactions between rare-earth ions, which is the case for a pure CF system, the dynamic magnetic susceptibility is simply related to the CF eigenstates $|\Gamma_m^n\rangle$. The widely used equation for the INS cross-section for transitions within a purely CF split multiplet was first derived and presented by de Gennes (1963). The INS master formula for CF transition intensities and energies is given by the double differential magnetic scattering cross-section from N rare-earth ions, in the dipole approximation, for neutrons scattered into an element of solid angle $d\Omega$ and with a corresponding energy change given by $\hbar\omega = E_i - E_f$ (where E_i is the incident neutron energy and E_f is the final neutron energy after scattering) as

$$\frac{d^2\sigma}{d\Omega\,dE} = N \frac{k_f}{k_i}(\gamma r_0)^2 e^{-2W} \left[\frac{1}{2} g_J f(Q)\right]^2$$
$$\times \sum_{i,j} p_i \langle \Gamma_i | \boldsymbol{J}_\perp | \Gamma_j \rangle \langle \Gamma_i | \boldsymbol{J}_\perp^* | \Gamma_j \rangle$$
$$\times \delta(\hbar\omega - E_i + E_j) \qquad (3)$$

The terms in this equation are defined by the usual nomenclature: k_i is the initial neutron wavevector, k_f the final neutron wavevector, γ, the neutron

gyro-magnetic ratio, $= -1.913$, $r_0 = (e^2/m_e c^2)$, the classical electron radius, $(0.2818 \times 10^{-15}\,\text{m})$, exp$(-2W)$ is the Debye–Waller factor, representing the thermal vibrational motion of atoms, g_J the Landé g-factor, $f(Q)$ the Fourier transform of the magnetization density of unpaired electrons and comprises both spin and orbital magnetization terms, p_i the CF thermal occupation factor, $J_\perp$ the component of the angular momentum operator perpendicular to the scattering vector $\boldsymbol{Q}$. The term $(\gamma r_0)^2$ corresponds to a magnetic cross-section of 0.2906 barn (1barn $= 10^{-28}\,\text{m}^2$). The subscripts i and j refer to different CF eigenfunctions.

The delta function $\delta(\hbar\omega - E_i + E_j)$ is appropriate only for vanishing CF linewidths, but in practice the linewidth always has an intrinsic temperature-dependent CF component, with a distribution characterized by a Lorentzian component $P(\hbar\omega, T)$. In such cases, the delta function is replaced by

$$P(\hbar\omega,\ T) = \frac{1}{\pi}\left(\frac{\Gamma}{\Gamma^2 + (\hbar\omega)^2}\right) \qquad (4)$$

The Lorentzian full width at half height maximum 2Γ is inversely proportional to the relaxation rate of the magnetization fluctuation energy. Intrinsic CF linewidths are usually associated with magnetic interactions at low temperatures by a Korringa law. CF excitations are nondispersive and are most conveniently studied with polycrystalline material. The relative intensities between CF levels, suitably averaged for a powder, are given by the squared matrix elements:

$$\langle \Gamma_i | J_\perp | \Gamma_j \rangle^2 = \tfrac{1}{3}\Big(\langle \Gamma_i | J_+ | \Gamma_j \rangle^2$$
$$+ \langle \Gamma_i | J_- | \Gamma_j \rangle^2 + 2\langle \Gamma_i | J_z | \Gamma_j \rangle^2\Big) \quad (5)$$

As can be appreciated by inspection of Table 1, a lowering of the point symmetry corresponds with an increase in the number of parameters needed to completely specify the CF interaction. For systems with cubic point symmetry there exists an ingenious and

widely employed method (commonly referred to as LLW) of parametrizing the eigenfunctions and eigenvalues of the CF Hamiltonian by setting the two parameters required for description of the CF in terms of parameters x and W defined by

$$B_4^0 = \frac{Wx}{F(4)}, \quad B_6^0 = \frac{W(1-|x|)}{F(6)} \quad (6)$$

where $-1 \leq x \leq 1$, and listing all the eigenvalues and eigenfunctions as functions of only one parameter x (the factors $F(4)$ and $F(6)$ are functions only of J; Lea *et al.* 1962). In the context of the INS cross-section for CF excitations, the matrix elements for magnetic dipole transitions for cubic symmetry in terms of the LLW parameter x have been conveniently tabulated by Birgeneau (1972). Once the intensities of CF transitions have been determined, it is a relatively simple matter to determine the two CF parameters using this tabulation. With further reference to cubic symmetry, an important point which has been recently brought to light is a subtle difference in the CF eigenfunction composition and INS transition probabilities between point groups (T_h, T) and (O_h, O, T_d), respectively (Takegahara *et al.* 2001). For systems with a lower point symmetry, no similar method of the same ingenuity and simplicity as the LLW method is available for parametrizing the CF parameters.

CF transitions in the INS spectrum are usually identified by their unique dependence on temperature and the scattering vector Q. Analysis of the neutron polarization can be used in specific circumstances when it is necessary to isolate a particularly weak magnetic scattering signal from scattering due to nonmagnetic lattice vibrational modes (Janoušavá *et al.* 2003).

3. Complimentary Techniques

When the crystal point group is progressively lowered, the INS technique used on its own is generally not sufficient to give a unique set of parameters. In this context, bulk techniques are most vital for verification of parameters determined by the INS technique for rare-earth intermetallic compounds (Moze 1998). The most widely used and significant of these are summarized in brief in the following sections.

3.1 Magnetic Susceptibility

A limited amount of information about the CF interaction can be obtained from the temperature dependent magnetic susceptibility in the noninteracting regime via the Van Vleck susceptibility

$$X_z^{VV}(T) = N_A (g_J \mu_B)^2 \left\{ \sum_n p_n \frac{\langle \Gamma_n | J_z | \Gamma_n \rangle^2}{k_B T} + 2 \sum_{n,m} p_n \frac{|\langle \Gamma_m | J_z | \Gamma_n \rangle|^2}{E_m - E_n} \right\} \quad (7)$$

with E_n and $|\Gamma_n\rangle$ eigenvalues and eigenfunctions, respectively, of the CF Hamiltonian and Z the partition function. There is an explicit dependence on the energy of the CF levels and the matrix elements connecting the eigenstates, but the limiting proviso is that the sum is over all levels at any particular temperature and hence any information about one particular level or set of levels is lost. However, a determination of the three paramagnetic Curie temperatures θ_z, θ_x, and θ_y, as measured along the three principal axes of a single crystal, the CF parameters, B_2^0 and B_2^2 are uniquely determined, viz.

$$k_B \theta_z = -\frac{1}{5} B_2^0 (2J-1)(2J+3)$$

$$k_B \theta_x = -\frac{1}{10}(B_2^0 - B_2^2)(2J-1)(2J+3)$$

$$k_B \theta_y = -\frac{1}{10}(B_2^0 + B_2^2)(2J-1)(2J+3) \quad (8)$$

If such data are available, B_2^0 can be specified immediately for tetragonal and hexagonal CFs, whilst for an orthorhombic CF, B_2^0 and B_2^2 are similarly determined (Wang 1971, Boutron 1973).

3.2 Magnetization

In the presence of combined CF, exchange and applied magnetic fields, the expectation value of the magnetization can be calculated in the mean field approximation. The magneto-crystalline anisotropy energy at any particular temperature is determined by calculation of the variation of the magnetic moment with the direction of the applied magnetic field. The thermal variation of the component $\alpha (\alpha = x, y, z)$ of the magnetic moment (in Bohr magnetons) is given by

$$\langle \mu_z \rangle = \frac{\sum_n \langle \Gamma_n'(h) | g_J J_z | \Gamma_n'(h) \rangle \exp(-\beta E_n(h))}{\sum_n \exp(-\beta E_n(h))} \quad (9)$$

with $\beta = 1/k_B T$ and $|\Gamma_n'\rangle$ the eigenstates of the Hamiltonian if exchange and applied fields are included. In the paramagnetic regime, rather high magnetic fields are required to mix the different CF eigenstates. In the ordered regime, when an exchange field is present, the ordered moment as a function of temperature is calculated, in standard fashion, by obtaining self-consistent solutions which simultaneously satisfy the above equation and the molecular field condition

$$h = \lambda N g_J \mu_B^2 \langle \mu_z \rangle \quad (10)$$

The molecular field constant λ is determined by a measurement of the ordering temperature. When the CF is a small perturbation of a dominant rare-earth–transition metal exchange interaction, simple relationships exist between the anisotropy constants and

CF parameters (Rudowicz 1987). The transferibility of CF parameters obtained from investigation of systems where the CF is the dominant interaction to those where the exchange dominates must, however, be treated with some caution (Moze and Buschow 1996).

3.3 Specific Heat Measurements

The magnetic specific heat is sensitive only to the eigenvalues of the magnetic system (see *Magnetic Systems: Specific Heat*). In the paramagnetic phase, where CF effects are important, the CF levels are evidenced via a Schottky-type contribution. The level degeneracy can also be deduced and the technique is now routinely used in analyses of systems with a significant CF interaction. For a sequence of CF-only eigenstates E_i, at a temperature T, the magnetic part of the specific heat is given by

$$C(T) = \frac{R_0}{Z^2} \left\{ Z \sum_i (\beta E_i)^2 \exp(-\beta E_i) \right. $$
$$\left. - \left(\sum_i \beta E_i \exp(-\beta E_i) \right)^2 \right\} \qquad (11)$$

Limitations in the accuracy of this technique arise from spin-phonon contributions and experience has shown that several sets of CF parameters can equally well fit the specific heat data.

Raman scattering can be used to induce CF transitions in rare-earth intermetallics (Martinho *et al.* 2001), but the selection rules for transitions are more restrictive than the INS technique. A recent novelty is the joint use of experimental determinations of CF parameters in rare-earth intermetallics and predictions of the ground-state charge density using density functional theory (DFT) (Liu *et al.* 1999, Strässle *et al.* 2003). This allows at least the low-order CF parameters to be calculated approximately. The relevant full set of CF parameters can then be refined from INS data. This innovative and important methodology is expected to be widely employed in the future.

4. Recent INS Results

Since the appearance of a review and compilation of INS investigations concerning the CF interaction in stable rare-earth intermetallic compounds (Moze 1998), further studies have been reported on a wide variety of novel compounds which encompass an equally wide variety of magnetic properties. Amongst these are the following types of compounds: $TmCu_{2-}Si_2$ (Kosaka *et al.* 1997), $Nd_3Pd_{20}Ge_6$ (Dönni *et al.* 1998), PrPdSb (Adroja *et al.* 1999), RNiSb (Karla *et al.* 1999), $PrInAg_2$ (Kelley *et al.* 2000), $HoCr_2Si_2$

(Moze *et al.* 2000), $Tm_{0.05}Y_{0.95}Ni_2^{11}B_2C$ (Sierks *et al.* 2000), ErNiAl (Javorský *et al.* 2001), TmT_2Si_2, with $T = Co, Ni, Cu$ (Harker *et al.* 2002), and $ErAl_xGa_{2-x}$ (Strässle *et al.* 2003). For Ce-based compounds displaying valence fluctuation, heavy-fermion, or Kondo-type behavior, a broad INS spectrum is usually the norm, as the CF coexists with other magnetic interactions (Christianson *et al.* 2002, Knafo *et al.* 2003) but well localized CF excitations have been recently observed, for example, in $CeTe_2$ (Liu *et al.* 2003).

In order to illustrate briefly the unique advantages of the INS technique, displayed in Fig. 1, are the intensities and energies of dipole CF transitions directly observed by INS in the hexagonal compound $NdAl_3$ (Strässle *et al.* 2003). At low temperatures two transitions from the ground state are clearly identified, $\Gamma_9^{(1)} \to \Gamma_7$ and $\Gamma_9^{(1)} \to \Gamma_9^{(2)}$ respectively, as well as an excited state transition $\Gamma_8^{(1)} \to \Gamma_8^{(2)}$. The pressure dependence of these transitions has also been reported and their energy-level scheme at ambient and elevated pressure is displayed in Fig. 2, together with the energy-level scheme determined for $PrAl_3$ at ambient pressure. There are four CF parameters which need to be determined, as the appropriate point group is of hexagonal symmetry. DFT predictions of the CF parameters at ambient and elevated pressures for $NdAl_3$ were also compared with those obtained from a careful fitting of the INS spectra. The parameters calculated within DFT predict the same signs and orders of magnitude (within at least 50%) for all four CF terms: B_2^0, B_4^0, B_6^0, B_6^6. The only parameter which is seriously underestimated is B_4^0. Overall, this is highly encouraging given that within a DFT approach applied to CF interactions it is still difficult to accurately treat highly correlated 4*f*-electron states.
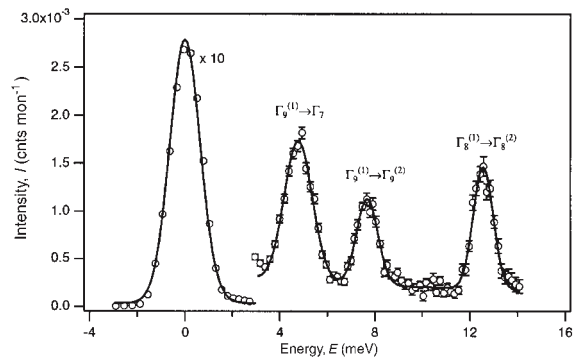
Figure 1
Dipole CF transitions and energies for $NdAl_3$ as observed by INS at ambient pressure and $T = 10$ K (reproduced by permission of Strässle *et al.* (2003) from *J. Phys.: Condens. Matter* **15**, 3257–66; © IOP Publishing).
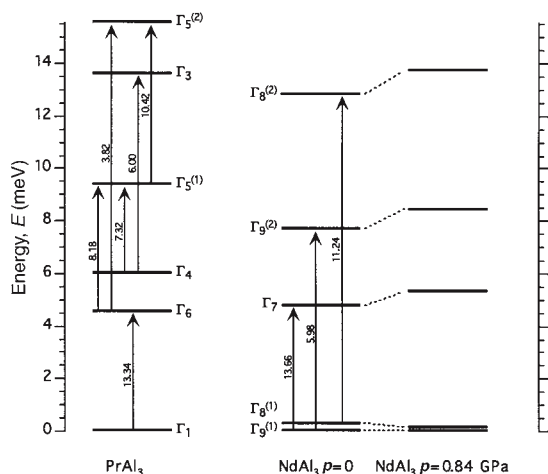
Figure 2
Energy-level schemes, as determined by INS, for PrAl$_3$ at ambient pressure and for NdAl$_3$ at ambient and elevated pressure. Arrows refer to the observed dipole transitions whilst numbers refer to the INS transition matrix elements as presented in Eqn. (3) (reproduced by permission of Strässle *et al*. (2003) from *J. Phys.: Condens. Matter* **15**, 3257–66; © IOP Publishing).

5. Summary

The technique of neutron inelastic scattering is a unique and hugely successful spectroscopic technique which has been used with large effect for the determination of CF levels and level composition in a vast number of rare-earth intermetallic compounds. An intimate knowledge of the CF interaction allows for detailed microscopic modeling and subsequent understanding of the principal mechanisms responsible for complex magnetic structures and phase transitions in systems composed of lanthanide intermetallics. In systems where the R-ion resides in a site of low symmetry, a determination of the large number of CF parameters is an enormously difficult task, and the energy-level scheme and level composition can only be determined by combined analysis of INS and bulk measurements. On a more recent note, experimental INS data combined with DFT calculations of the ground-state charge density are a novel and extremely promising methodology for an unambiguous determination of CF parameters. The field is very vibrant and rich and there are many systems, relevant for either fundamental or technological reasons, which will surely be investigated by INS in the future.

See also: Crystal Field and Magnetic Properties, Relationship between; Electronic Configurations of 3*d*, 4*f*, and 5*f* Elements: Properties and Simulation;

Localized 4*f* and 5*f* Moments: Magnetism; Magnetic Excitations in Solids

Bibliography

Adroja D T, Rainford B D, Malik S K, Takeya H, Gschneidner K A Jr., Pecharsky V K 1999 Neutron scattering studies on CeRhSb and PrTSb (T = Rh and Pd) compounds. *J. Alloys Compnds.* **288**, 7–12

Birgeneau R J 1972 Transition probabilities for *f*-electron *J*-multiplets in cubic crystal fields. *J. Phys. Chem. Solids* **33**, 59

Blanco J A 1998 The determination of crystal field parameters in rare-earth intermetallic compounds. *J. Alloys Compnds.* **275–277**, 518–25

Boutron P 1973 Exact calculation of the paramagnetic susceptibility of a single crystal with arbitrary crystal field and exchange interactions. *Phys. Rev. B* **7**, 3226

Christianson A D, Lawrence J M, Pagliuso P G, Moreno N O, Sarrao J L, Thompson J D, Riseborough P S, Kern S, Goremychkin E A, Lacerda A H 2002 Neutron scattering study of crystal fields in CrRhIn$_5$. *Phys. Rev. B* **66**, 193102-1/193102-4

de Gennes P G 1963 Theory of neutron scattering by magnetic crystals. In: Rado G T, Suhl H (eds.) *Magnetism*. Academic Press, New York, Vol. 3, p. 115

Dönni A, Keller L, Fischer L, Aoki Y, Sato H, Fauth F, Zolliker M, Komatsubara T, Endoh Y 1998 Magnetic order and crystal-field excitations in Nd$_3$Pd$_{20}$Ge$_6$. *J. Phys.: Condens. Matter* **10**, 7219–29

Furrer A, Strässle T, Temprano D R 2001 New excitement with crystal field excitations. *J. Alloys Compnds.* **323–324**, 649–53

Harker S J, van Dijk B D, Mulders A M, Gubbens P C M, Stewart G A, de Vroege C F, Buschow K H J 2002 Crystal fields and magnetic interactions in TmT$_2$Si$_2$ (T = Co, Ni, Cu). *J. Phys.: Condens. Matter* **14**, 2705–14

Hutchings M T 1964 Point-charge calculations of energy levels of magnetic ions in crystalline electric fields. In: Seitz F, Turnball B (eds.) *Solid State Physics*. Academic Press, New York, Vol. 16, p. 227

Janoušavá B, Kulda J, Diviš M, Sechovsky V, Komatsubara T 2003 Neutron polarization analysis study of crystal field excitations in CePtSn. *Physica B* **335**, 26–9

Javorský P, Diviš M, Mutka H 2001 Crystal field and magnetocrystalline anisotropy in ErNiAl. *Phys. Rev. B* **65**, 014404-1/014404-08

Karla I, Pierre J, Murani A P, Neumann M 1999 Crystalline electric field in RNiSb compounds investigated by inelastic neutron scattering. *Physica B* **271**, 294–303

Kelley T M, Beyermann W P, Robinson R A, Trouw F, Canfield P C, Nakotte H 2000 Crystal-field spectrum and linewidths in the heavy-fermion system PrInAg$_2$. *Phys. Rev. B* **61**, 1831–5

Knafo W, Raymond S, Fåk B, Canfield P C, Flouquet J 2003 Study of low-energy magnetic excitations in single-crystalline CeIn$_3$ by inelastic neutron scattering. *J. Phys.: Condens. Matter* **15**, 3741–9

Kosaka M, Onodera H, Ohoyama K, Ohashi M, Yamaguchi Y, Nakamura S, Goto T 1997 Crystalline electric field and magnetic properties of the TmCu$_2$Si$_2$ intermetallic. *J. Phys. Soc. Japan* **66** (9), 2844–50

Lea K R, Leask J M, Wolf W P 1962 The raising of angular momentum degeneracy of *f*-electron terms by cubic crystal fields. *J. Phys. Chem. Solids* **23**, 1381

Liu Z, Richter M, Diviš M, Eschrig H 1999 Calculation of paramagnetic susceptibilities and specific heats by density-functional-crystal-field theory: $PrPd_2X_3$ and $NdPd_2X_3$ (X = Al, Ga). *Phys. Rev. B* **60**, 7981–92

Liu Z S, Park J G, Kwon Y S, McEwen K A, Bull M J 2003 Crystal-field excitations and model calculations of $CeTe_2$. *J. Magn. Magn. Mater.* **256**, 151–7

Martinho H, Sanjurjo J A, Rettori C, Canfield P C, Pagliuso P G 2001 Raman scattering study of crystal field excitations in $ErNi_2B_2C$. *J. Magn. Magn. Mater.* **226–230**, 978–9

Moze O 1998 Crystal field effects in intermetallic compounds studied by inelastic neutron scattering. In: Buschow K H J (ed.). Elsevier, Amsterdam, Vol. 11, pp. 493–624

Moze O, Buschow K H J 1996 Magnetic structure of $ErCo_{12}Mo_2$ and $TbCo_{12}Mo_2$ determined by time-of-flight neutron diffraction. *Z. Phys. B* **101**, 521–6

Moze O, Rosenkranz S, Osborn R, Buschow K H J 2000 Magnetic excitations in tetragonal $HoCr_2Si_2$. *J. Appl. Phys.* **87**, 6283–5

Rudowicz C 1987 On the derivation of the superposition-model formulae using the transformation relations for the Stevens operators. *J. Phys. C: Solid State Phys.* **20**, 6033–6037

Sierks C, Loewenhaupt M, Freudenberger J, Müller K-H, Schober H 2000 Magnetic excitations in $TM_{0.05}Y_{0.95}$ $Ni_2^{11}B_2C$. *Physica B* **276–278**, 630–1–6033

Strässle Th, Altorfer F, Furrer A 2001 Crystal-field interactions in the pseudo-ternary compound in $ErAl_xGa_{2-x}$ studied by inelastic neutron scattering. *J. Phys.: Condens. Matter* **13**, 6773–85

Strässle Th, Diviš M, Rusz J, Janssen S, Juranji F, Sadykov R, Furrer A 2003 Crystal-field excitations in $PrAl_3$ and $NdAl_3$ at ambient and elevated pressure. *J. Phys.: Condens. Matter* **15**, 3257–66

Takegahara K 2000 Matrix elements of crystal electric fields in rare-earth compounds. *J. Phys. Soc. Japan* **69** (5), 1572–3

Takegahara K, Hisatomo H, Yanase A 2001 Crystal electric fields for cubic point groups. *J. Phys. Soc. Japan* **70** (5), 1190–3

Wang Y-L 1971 Crystal-field effects of paramagnetic Curie temperature. *Phys. Lett. A* **35**, 383–4

O. Moze
Modena University, Italy

D

Demagnetization: Nuclear and Adiabatic

1. Principles of the Method

Adiabatic demagnetization (AD) is one of the cooling methods that have a common principle: the entropy of the working medium (helium, spins, etc.) is controlled by some parameter like pressure or magnetic field. The working medium in AD is a system of magnetic moments (nuclear spins, electronic spins, or orbital moments) and the magnetic field is the control parameter when the magnetocaloric effect is employed. The magnetization, M, of a paramagnet or a ferromagnet increases with an applied magnetic field, H, and simultaneously both the energy of magnetic moments in the field and the internal energy of their exchange interaction decrease. Supposing negligible pressure and volume effects, the entropy can be expressed by the following thermodynamic relation:

$$\mathrm{d}S = \frac{1}{T}\left(\frac{\partial U}{\partial T}\right)_H \mathrm{d}T + \frac{1}{T}\left[\left(\frac{\partial U}{\partial H}\right)_T + M\right]\mathrm{d}H \quad (1)$$

The internal energy, U, is a function of the temperature, T, of the sample, and in general it increases with temperature. Consequently, if the magnetization of a paramagnetic sample is reduced adiabatically, the sample temperature should decrease. The cooling cycle of the AD method consist of two steps:

(i) *Isothermal magnetization*. The sample is in thermal contact with a constant temperature bath kept at T_i. The magnetic field is increased from zero to H_i and the heat released to the bath compensates for the work done on the sample. It leads to an increase in the order of the magnetic moments and, consequently, reducing their entropy, S, by

$$\Delta S = \int_0^H \left(\frac{\partial M}{\partial T}\right)_H \mathrm{d}H \quad (2)$$

This entropy change is determined by the rate of change of magnetic energy with respect to the thermal energy. The efficiency of the process increases with decreasing temperature.

(ii) *Adiabatic demagnetization*. The sample is thermally isolated from the bath, and the field is then reduced from H_i to H_f. It is an adiabatic process, i.e., $\mathrm{d}Q = T\mathrm{d}S = 0$ and the entropy remains constant. Since the sample performs magnetic work by demagnetizing at the expense of internal energy, it decreases

in temperature towards T_f at a rate given by:

$$\mathrm{d}T_{(\mathrm{d}S=0)} = -\frac{T\left(\dfrac{\partial M}{\partial T}\right)_H}{C_H}\mathrm{d}H \quad (3)$$

where C_H is the specific heat.

AD is a one-shut process. After demagnetization the system will warm up owing to a parasitic heat load. The energy which can be absorbed, $Q = \int T\mathrm{d}s$, is proportional to the shaded area in Fig. 1.

In modeling a system of noninteracting moments, μ, the entropy is simply a function of H/T. For an isoentropic process $T_f = T_i H_f / H_i$ and absolute zero temperature could be reached for $H_f = 0$, in contradiction to the third law of thermodynamics. This does not happen in a real system, however, because the assumption of noninteracting spins breaks down and the energy levels in zero applied field are not degenerate. The lowest temperature achievable by the AD method is limited by the existence of an internal interaction in a spin system. This interaction causes spin ordering at sufficiently low temperatures and a spontaneous decrease of the entropy of a system. The detailed nature of the interactions may be complicated. It may be, for example, the direct dipolar interaction between magnetic moments in the case of dielectrics or the RKKY interaction in metals. It simplifies matters to define an effective internal field,
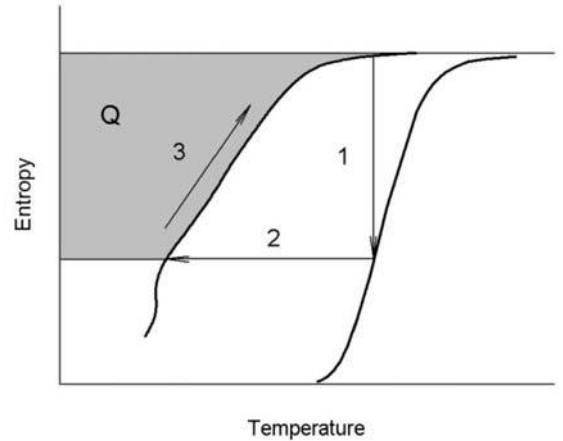
Figure 1
Graphical representation of the processes of isothermal magnetization (1) and adiabatic demagnetization (2). The shaded area shows the cooling power during a warm up (3).
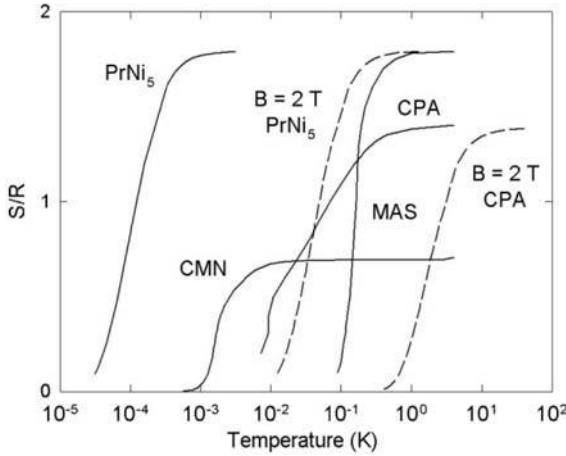
Figure 2
Entropies per mole of substance, S/R, of four salts and $PrNi_5$ in zero field (solid curves) and in a 2 T field (dashed curves).

h, such that it would produce a Zeeman splitting equal to the splitting, ε, due to the interaction, i.e., $\varepsilon = \mu\mu_0 h$. Then:

$$T_f = T_i \sqrt{\frac{H_f^2 + h^2}{H_i^2 + h^2}} \qquad (4)$$

The temperature dependence of the entropy of some substances used for this cooling method is shown in Fig. 2.

2. Practical Aspects

The most common substances used for the AD method are paramagnetic salts such as $MAS = Mn^{2+}SO_4(NH_4)_2SO_4.6H_2O$ ($T_c \approx 0.17$ K; $b \approx 80$ mT), $FAA = Fe_2^{3+}(SO_4)_3(NH_4)_2SO_4.24H_2O$ (0.03 K; 50 mT), $CPA = Cr_2^{3+}(SO_4)_3K_2SO_4.24H_2O$ (0.01K; 10 mT), $CMN = 2Ce^{3+}(NO_3)_33Mg(NO_3)_2.24H_2O$ (0.002K; 4mT), $Gd_2(SO_4)_3.8H_2O$ (0.18 K), van Vleck paramagnets such as $PrNi_5$ (0.0004 K; 16 mT) and $PrCu_6$ (0.0026 K), and pure metals such as copper (58 nK; 0.3 mT) and silver (0.56 nK). The ordering temperature and the effective internal field are given in parentheses.

Besides cooling magnetic moments by AD, for any practical use it is also necessary to cool the lattice of which the magnetic atoms form a part. The exchange of energy between the spins and the lattice is characterized by the spin–lattice relaxation time, τ_1. For metals the exchange is mediated by the conduction electrons and τ_1 is given by the Korringa relation. In nonmetals, owing to their poor thermal conductivity, τ_1 can reach hours or days at very low temperatures.

The use of the magnetocaloric effect to produce temperatures well below 1 K was proposed by Giauque and Debye in 1926. A practical realization of AD cooling was announced in 1933 by Giauque and MacDougall, reaching 0.53 K using $Gd_2(SO_4)_3$. $8H_2O$ at starting conditions of 3.4 K and 0.8 T. On the other hand, de Haas, Wiersma, Kramers used CeF_2, and after demagnetization from 3 T to 0.1 T decreased the temperature from 1.26 K to 0.27 K. According to present knowledge, 0.001 K is the estimated lower limit achievable by the AD technique employing electronic paramagnetism.

In 1934 Gorter proposed nuclear magnetic refrigeration but owing to severe experimental problems it was only in 1956 that Kurti succeeded in reducing the nuclear spin temperature in copper wires to about 20 μK. Osgood and Goodking in 1966 were the first to achieve considerable electron and lattice refrigeration. The progress made in the AD technique enabled the Helsinki group, in 1982, to observe spontaneous nuclear order of copper below the Néel temperature $T_N = 58$ nK (Oja and Lounasmaa 1997). The nuclear order in silver with $T_N = 560$ pK has been investigated and the long spin–spin relaxation time of silver made it possible to produce a negative nuclear spin temperature and to find ferromagnetic order in silver above $T_C = -1.9$ nK (Oja and Lounasmaa 1997). The lowest temperature achieved is 280 pK and -750 pK is the highest temperature obtained (Oja and Lounasmaa 1997).

Using the known potential of van Vleck paramagnets for nuclear refrigeration, Andres and Lounasmaa (1982) tested many of them. The electronic ground states of van Vleck paramagnets are nonmagnetic singlets. Owing to the nuclear hyperfine interaction of nuclear and electronic spins a magnetic moment is induced into the ground state. This can be formally described by assuming that the nuclear magnetic moment is enhanced by a factor

$$1 + K \equiv 1 + \frac{A\chi_{VV}}{g_J\mu_B g_N\mu_N} \qquad (5)$$

where A is the hyperfine interaction constant and χ_{VV} the van Vleck temperature-independent susceptibility. For Pr or Tm compounds, K is typically 10–100. $PrNi_5$ (hyperfine interaction-enhanced nuclear ferromagnet, $T_C = 0.4$ mK) or $PrCu_6$ ($T_N = 2.6$ mK) serve in a lower stage in many nuclear refrigerators. The starting conditions for demagnetization, $B/T \approx 500$–1000 TK^{-1}, are fulfilled by available dilution refrigerators and superconducting magnets. Advantages of these materials are a huge cooling power and a short τ_1.

3. Outlook

AD is mostly used in the temperature range below 1 mK but its ability to work in zero gravity has led to the development of prototypes for satellite

applications. It is a prospective method as AD can reach higher efficiency than traditional vapor compression technology. To apply this method to a wide temperature range up to room temperature, considerable progress in materials research is needed. Materials with a large magnetocaloric effect are fundamental for AD but they are also suitable for regenerators in other types of refrigerators. For devices suitable for cooling at room temperature (see *Magnetocaloric Effect: From Theory to Practice*).

Bibliography

Andres K, Lounasmaa O V 1982 Recent progress in nuclear cooling. In: Brewer D F (ed.) *Progress in Low-Temperature Physics*. North-Holland, Amsterdam, Vol. 8, pp. 222–87
Betts D S 1976 *Refrigeration and Thermometry Below One Kelvin*. Sussex University Press, Brighton, UK
Hagmann C, Richards P L 1995 Adiabatic demagnetization refrigerators for small laboratory experiments and space astronomy. *Cryogenics* **35**, 303–9
Hudson R P 1972 *Principles and Application of Magnetic Cooling* North-Holland, Amsterdam
Oja A S, Lounasmaa O V 1997 Nuclear magnetic ordering in simple metals at positive and negative nanokelvin temperatures. *Rev. Mod. Phys.* **69**, 1–136
Pecharsky V K, Gschneidner K A Jr. 1999 Magnetocaloric effect and magnetic refrigeration. *J. Magn. Magn. Mater.* **200**, 44–56
Pobell F 1992 *Matter and Methods at Low Temperatures*. Springer, Berlin

J. Sebek
Institute of Physics ASCR, Prague, Czech Republic

Density Functional Theory: Magnetism

Spin density functional theory (SDFT) is the basis of most of the modern electronic structure calculations. It has been reviewed in detail by Jones and Gunnarsson (1989), Trickey (1990), Eschrig (1996), and many others, and is only briefly outlined here.

1. Spin Density Functional Theory

1.1 General Theory

At the quantum mechanical level, magnetic properties of materials are usually well described within the Born–Oppenheimer (*adiabatic*) approximation: the electrons, moving much faster than the heavier atomic nuclei, are considered in the Coulomb potential $v(\mathbf{r}) = \sum_s -Z_s/|\mathbf{r}-\mathbf{R}_s|$ created by the nuclei of charge Z_s in their instantaneous positions $\mathbf{R}_s$. In most cases, the values of $\mathbf{R}_s$ are approximated by the rest positions of the atoms in a regular structure.

For each set of $\{\mathbf{R}_s\}$ there is a state of the electrons with the lowest energy, the ground state $|\psi_0\rangle$. Its energy can be written as a functional of the potential, $E_0[v]$, i.e., the ground state energy depends on the Coulomb potential of the nuclei at each point $\mathbf{r}$ of space. The exact functional dependence $E_0[v]$ is in general unknown, but reasonable approximations will be discussed below. They allow for a determination of the atomic rest positions in molecules and solids with an accuracy of a few percent, by minimization of the energy $[E_0 + \sum_{ss'} Z_s Z_{s'}/|\mathbf{R}_s-\mathbf{R}_{s'}|]$ with respect to $\{\mathbf{R}_s\}$ (Moruzzi *et al.* 1978).

The calculation of observable quantities from the true wave function ψ_0 is not feasible in the case of many, strongly interacting electrons, since ψ_0 depends on the coordinates $\mathbf{r}_i$ and on the spin quantum numbers σ_i of all N electrons, although the total energy may be expressed in terms of the spin and pair densities. Hohenberg and Kohn (1964) went further and proved that the ground state density function $n_0(\mathbf{r})$ alone determines $v(\mathbf{r})$ and hence ψ_0, together with all ground state properties uniquely. Since the ground state spin density matrix $\mathbf{n}_0(\mathbf{r})$

$$
\begin{aligned}
\mathbf{n}_0(\mathbf{r}) &= n_{0,\sigma\sigma'}(\mathbf{r}) \\
&= N \sum_{\sigma_2} \int d^3 r_2 \ldots \sum_{\sigma_N} \int d^3 r_N \psi_0 \\
&\quad \times (\mathbf{r},\, \sigma,\, \mathbf{r}_2,\, \sigma_2,\, \ldots,\, \sigma_N) \\
&\quad \times \psi^*{}_0(\mathbf{r},\, \sigma',\, \mathbf{r}_2,\, \sigma_2,\, \ldots,\, \sigma_N)
\end{aligned}
\tag{1}
$$

comprises the information on the electron density, $n = \mathrm{tr}\,\mathbf{n}$, the unique determination of the ground state by the spin density follows as a corollary. It allows, as an important generalization, the inclusion of the action of an external magnetic field $\mathbf{B}$ on the spin, by the definition of the spin-dependent external potential $\mathbf{v} = v + \mu_B \boldsymbol{\sigma}\mathbf{B}$. Here, $\boldsymbol{\sigma} = (\sigma_x, \sigma_y, \sigma_z)$ denote the Pauli spin matrices. The vector spin density is given as $\boldsymbol{\Sigma} = \mathrm{tr}(\boldsymbol{\sigma}\mathbf{n})$. Further, the total spin in a given volume V is $\boldsymbol{S} = \int_V d^3 r\, \boldsymbol{\Sigma}/2$, and the related spin magnetic moment is defined by $\boldsymbol{\mu}_s = -\mu_B \cdot 2\boldsymbol{S}$.

The calculation of E_0 and $\mathbf{n}_0$ becomes possible with the help of the Hohenberg–Kohn variational principle:

$$
\begin{aligned}
E_0[\mathbf{v}] &= \min_{\psi} \langle \psi | \hat{H} | \psi \rangle \\
&= \min_{\mathbf{n}} \left\{ \int d^3 r\, \mathrm{tr}(\mathbf{v}\mathbf{n}) + \min_{\psi_{\mathbf{n}}} \langle \psi_{\mathbf{n}} | \hat{T} + \hat{U} | \psi_{\mathbf{n}} \rangle_{\int d^3 r n = N} \right\}
\end{aligned}
\tag{2}
$$

where $\psi_{\mathbf{n}}$ means the class of all normalized fermionic wave functions with the spin density $\mathbf{n}$. The electronic

Hamiltonian $\hat{H}$ consists of the potential $\mathbf{v}$ plus the operators of the kinetic energy, $\hat{T}$, and of the electron–electron interaction energy, $\hat{U}$. The latter terms are further subdivided (Kohn and Sham 1965):

$$\min_{\psi_{\mathbf{n}}} \langle \psi_{\mathbf{n}} | \hat{T} + \hat{U} | \psi_{\mathbf{n}} \rangle = T_{\mathrm{s}}[\mathbf{n}] + E_{\mathrm{H}}[n] + E_{\mathrm{xc}}[\mathbf{n}] \quad (3)$$

Here, T_{s} is the ground state kinetic energy of a model system of electrons that are assumed to have no mutual Coulomb interaction and to possess the spin density matrix $\mathbf{n}$:

$$T_{\mathrm{s}}[\mathbf{n}] = \sum_i^N \sum_\sigma \langle \phi_i(\sigma) | - \Delta/2 | \phi_i(\sigma) \rangle,$$

$$\delta_{ij} = \sum_\sigma \langle \phi_i(\sigma) | \phi_j(\sigma) \rangle \quad (4)$$

$$n_{\sigma\sigma'} = \sum_i^N \phi_i(\sigma) \phi_i^*(\sigma') \quad (5)$$

The ϕ_i denote the N lowest single-particle eigenstates in a corresponding, yet unknown, effective potential. Further, E_{H} is the spin-independent Hartree energy:

$$E_{\mathrm{H}} = \frac{1}{2} \int \int \mathrm{d}^3 r \mathrm{d}^3 r' \frac{n(\mathbf{r}) n(\mathbf{r}')}{|\mathbf{r} - \mathbf{r}'|} \quad (6)$$

and $E_{\mathrm{xc}}[\mathbf{n}]$, the so-called exchange-correlation (xc) energy, is an unknown functional of the spin density matrix, containing all contributions beyond the mean field approximation from electron–electron interactions in the ground state.

The essence of the Kohn–Sham procedure is to subdivide the total energy into large contributions that are either well-known functionals ($\int \mathrm{d}^3 r \; \mathrm{tr}(\mathbf{vn})$ and E_{H}), or at least computable quantities (T_{s}), and a much smaller remaining part (E_{xc}). Then, approximations applied to the latter part are expected to introduce only reasonably small errors. However, all known approximations to E_{xc} are unfortunately on a heuristic level and cannot be systematically improved. Thus, the spin density functional theory (SDFT) described here and in the following has to be considered as a model theory, in the sense that the applicability of any chosen approximation is justified *a posteriori* by experience from comparison with experiment. On the other hand, within a given approximation, the calculations are usually carried out without adjustable parameters. In this way, after validating the approximation for a certain class of materials, reliable forecasts of experimental results on this class can be expected from theory.

For this aim, a numerically tractable formulation is needed to allow for the calculation of $\mathbf{n}_0$ and E_0. Such a formulation is given by the Kohn–Sham equations that are obtained by: (i) inserting Eqn. (3) in Eqn. (2), (ii) using the Ansatz Eqn. (5) also in the case with

electron–electron interaction, and (iii) varying with respect to the ϕ_i^*:

$$\sum_{\sigma'} \left[-\frac{\Delta}{2} \delta_{\sigma\sigma'} + v_{\mathrm{eff},\sigma\sigma'} \right] \phi_i(\sigma') = \varepsilon_i \phi_i(\sigma) \quad (7)$$

The Kohn–Sham equations (Eqn. (7)) contain the above-mentioned effective potential:

$$v_{\mathrm{eff},\sigma\sigma'} = v_{\sigma\sigma'}(\mathbf{r}) + \int \mathrm{d}^3 r' \frac{n(\mathbf{r}')}{|\mathbf{r} - \mathbf{r}'|} \delta_{\sigma\sigma'} + v_{\mathrm{xc},\sigma\sigma'} \quad (8)$$

consisting of external, Hartree, and xc potentials. The latter is defined by: $v_{xc,\sigma\sigma'} = \delta E_{xc}[\mathbf{n}] / \delta n_{\sigma\sigma'}$.

Together with Eqn. (5), these equations form a nonlinear system of integro-differential equations which have to be solved by iteration (*self-consistent solution*). Due to the complexity of the Kohn–Sham equations (reflecting part of the complexity of nature), more than one stationary solution may exist. The further solutions can be related to physically relevant metastable magnetic states (for instance, low-spin/high-spin states, see Sect. 3.3, or different magnetic moment arrangements). This problem is investigated in some detail by Moruzzi and Marcus (1993).

1.2 Approximations

The most widely used approximation for $E_{\mathrm{xc}}[\mathbf{n}]$ is the local spin density approximation (LSDA):

$$E_{\mathrm{xc}}[\mathbf{n}] \approx E_{\mathrm{xc}}^{\mathrm{LSDA}}[\mathbf{n}] = \int \mathrm{d}^3 \mathbf{rn}(\mathbf{r}) \varepsilon_{\mathrm{xc}}^{\mathrm{hom}}(\mathbf{n}^\uparrow(\mathbf{r}), \; \mathbf{n}^\downarrow(\mathbf{r})) \quad (9)$$

Here, $\varepsilon_{\mathrm{xc}}^{\mathrm{hom}}$ means the exchange-correlation energy per electron of the spin-polarized homogeneous electron gas, a model system frequently used in electronic structure theory. The quantities $n^\uparrow$ and $n^\downarrow$ denote spin-up and spin-down densities. They are obtained by rotating the spin quantization axis at each point in space in the direction that yields a diagonal spin density matrix.

Another, more recent, approximation is called the generalized gradient approximation (GGA). At variance with the LSDA, it takes into account not only the local value of $\mathbf{n}$, but also its spatial derivatives.

If electrons in one of the open shells do not contribute to the chemical bonding, like 4f states in most rare-earth systems, they should be distinguished from the valence electrons in the theoretical treatment as well. Then, the so-called open-core approximation, or the self-interaction-corrected (SIC) LSDA, are modern approximations to be used (Richter 1998). The latter approximation is also relevant to finite systems like atoms and small molecules.

The energy $\varepsilon_{\mathrm{xc}}^{\mathrm{hom}}$ can be subdivided into $\varepsilon_{\mathrm{xc}}^{\mathrm{hom}} = \varepsilon_{\mathrm{x}}^{\mathrm{hom}} + \varepsilon_{\mathrm{c}}^{\mathrm{hom}}$. Here, $\varepsilon_{\mathrm{x}}^{\mathrm{hom}}$ describes the effect of exchange interaction: according to the Pauli exclusion

principle, electrons with the same spin quantum number should have a zero probability density of being at the same point in space. For this reason, the Coulomb energy between pairs of electrons with the same spin is lower than between pairs with different spin, and $\varepsilon_x^{hom} < 0$. The energy ε_c^{hom} describes the effect of Coulomb correlation: electrons with arbitrary spin do not move in a stochastic way either, but tend to avoid each other due to their mutual Coulomb repulsion. This correlated motion yields a smaller total energy than estimated by a mean field treatment, and $\varepsilon_c^{hom} < 0$ holds as well.

1.3 Hund's Rules

In atoms, exchange interaction is the reason for incompletely filled shells to maximize their spin polarization (SP) in the ground state. This behavior is known as Hund's First Rule (see *Magnetism in Solids: General Introduction*). It is driven by an energy gain $E_{SP} \sim S(S-1/2)$ in comparison to an unpolarized shell (Melsen *et al.* 1994), where the total spin S is zero. If LSDA is applied to an atom, then $E_{SP} \approx \Delta E_{xc} = E_{xc}^{LSDA}(S) - E_{xc}^{LSDA}(0) \approx -IS^2$, yielding a good approximation for the relation above in the case of large total spins. This fact indicates that LSDA is particularly suited for extended systems which are closer to the idealized homogeneous electron gas than atoms are. The prefactor I is called the Stoner parameter.

While free atoms in their ground state always carry a maximum spin moment, this is not the case in condensed matter. The reason for this difference is that band splitting lifts the degeneracy of the atomic states. As a consequence, energy is gained when the spin polarization is reduced, since then states at the majority spin Fermi surface with a higher Fermi momentum are emptied in favor of states at the minority spin Fermi surface with a lower Fermi momentum. The energy gain ΔT_s is the bigger the broader the band is, and vanishes in the atomic limit.

This consideration is the essence of Stoner theory (see *Itinerant Electron Systems: Magnetism (Ferromagnetism)*), which evaluates the counterbalance of ΔE_{xc} and ΔT_s to give a criterion for the onset of long-range spin order when starting from a spin-compensated state. The condition for the instability of the Pauli paramagnetic state is that:

$$IN(E_F) > 1 \qquad (10)$$

where $N(E_F)$ denotes the density of states at the Fermi energy for one spin direction. Detailed discussion of the first-principles investigation of the magnetic ordering is given in Sect. 2.

Orbital magnetism also plays a big role in solids, e.g., for the phenomenon of magnetocrystalline anisotropy. It arises if the other two of Hund's rules are considered. Hund's Second Rule states that of all

atomic terms with maximum spin, the term with the largest total angular momentum L is the lowest in energy. The related energy gain is called orbital polarization (OP) energy, E_{OP}, which vanishes for s- and p-shells. Coulomb correlation is the reason behind OP. Though the LSDA accounts for a part of Coulomb correlation contributions, OP cannot be obtained in a local approximation, since any definition of an angular momentum density is ambiguous, due to the gauge freedom of this quantity. Reasonable heuristic approximations, called OP corrections, (Eriksson *et al.* 1989) use the local gauge where the angular momentum density vanishes in the interstitial regions. The angular momenta of the individual atomic shells are assumed to give contributions to the xc energy of the form $E_{OP} \approx E_{xc}(L) - E_{xc}(0) =$ const. $\cdot L^2 < 0$, resembling the form of the SP term.

Finally, Hund's Third Rule determines the coupling between spin and orbital degrees of freedom to be antiparallel or parallel in the ground state of less or more than half-filled atomic shells, respectively. This behavior is a relativistic effect: the fast-moving electrons experience a magnetic field generated by the relative motion of the nuclear charges with respect to the rest system of the electrons. This field interacts with the individual electron spins and yields an additional contribution to the kinetic energy of the form: $E_{SO} = \sum_i \xi_i \langle \sigma_i l_i \rangle_i$, where ξ_i are radial integrals called spin-orbit coupling (SOC) constants, and $\mathbf{l}_i$ are single-particle angular momentum operators. The important role of SOC in solid state magnetism is discussed in more detail in Sects. 2 and 3.

Figure 1 shows the range of energies related to Hund's rules couplings in those atomic shells that are most important in solid-state magnetism: transition metal 3d, rare-earth 4f, and actinide 5f shells. The spin polarization energy, E_{SP}, is maximum for half-filled shells, while the orbital polarization energy, E_{OP}, and the spin–orbit coupling energy, E_{SO}, are large for shell fillings close to 1/4 and 3/4. In metals and compounds, spin and orbital polarization energy can be much smaller, or even zero, since losses of T_s and E_H due to polarization compensate at least part of the polarization gains: for instance, $E_{SP} \approx 0.4$ eV in iron metal. In general, the atomic values given in Fig. 1 put an upper boundary on the energy scales observed in solids.

1.4 Single Particle Excitations

The Kohn–Sham orbitals ϕ_i, with related single-particle energies ε_i, have been introduced above as auxiliary quantities needed to compute the spin density matrix. In a hypothetical system without electron–electron interaction, these Kohn–Sham states would coincide with the quasi-particle excitations of the system, which can be probed by optical, x-ray or electron spectroscopies (Sections 3.4 and 3.5). To
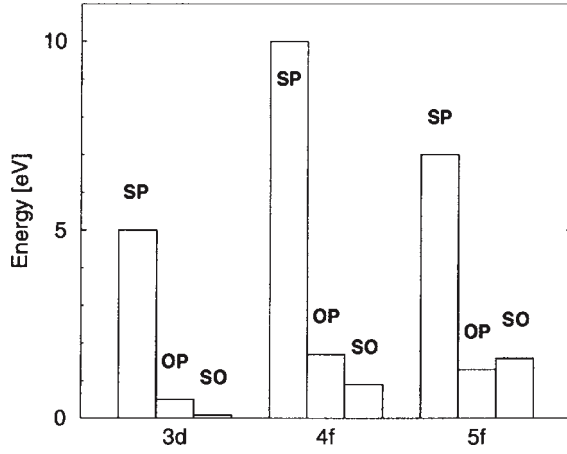
Figure 1
Range of energies related to Hund's rules in atoms: transition metal 3*d* shells, rare-earth 4*f* shells, and actinide 5*f* shells. The labels **SP**, OP, and SO denote the maximum values, within the related shell, of the energies E_{SP}, E_{OP}, and E_{SO} (Hund's First, Second, and Third Rule coupling energies, respectively).

evaluate single-electron or single-hole excitations ψ_i close to the Fermi level of a realistic system, the Dyson equation:

$$\left[-\frac{\Delta}{2} + \int d^3 r' \frac{n(\mathbf{r}')}{|\mathbf{r} - \mathbf{r}'|} \right] \psi_i(\sigma, \mathbf{r})$$
$$+ \sum_{\sigma'} \left[v_{\sigma\sigma'} + \int d^3 r' M_{\sigma\sigma'}(\mathbf{r}, \mathbf{r}'; E_i) \right] \psi_i(\sigma', \mathbf{r}')$$
$$= E_i \psi_i(\sigma, \mathbf{r}) \qquad (11)$$

has to be solved. However, full knowledge of the self-energy operator kernel M is even further away than full knowledge of v_{xc}; both quantities must rather be approximated on the basis of physical intuition. As a matter of fact, the replacement of $M_{\sigma\sigma'}$ by $\delta(\mathbf{r}-\mathbf{r}')v_{xc,\sigma\sigma'}(\mathbf{n})$, i.e., the LSDA, turns out to work fairly well for many systems (*weakly correlated systems*). In particular, the spectra related to s and p valence states of simple and transition metals, as well as rare-earth 5d and actinide 6d states, are well described.

These states form broad bands; the quasi-particle is extended over many atoms due to the large hopping rate, and thus correlation effects are small. If the bands become narrower, the hopping rate is lower, and hence a stronger intra-atomic Coulomb repulsion/attraction is felt by additional electrons/holes. Strong on-site correlations result in a jump of M, as a function of energy, at the Fermi level E_F by an amount U_{eff}. This quantity is related to the on-site Coulomb matrix element U, but is strongly screened

in metals. A simple approximation for this situation is called LSDA + U, where the energy dependence of M is reduced to the jump at E_F and otherwise the LSDA is used. A certain problem in this approach is that the screening depends much on chemical composition and on local structure, such that the value of U_{eff} is not just an atomic property as U is; it has to be estimated for each individual situation.

Finally, the relationship between U_{eff} and the band width W determines if the related states contribute to the chemical bonding or not. Accordingly, these states may exhibit itinerant or localized magnetic behavior. The rare-earth 4f shells where $U_{eff} \gg W$ show local moment behavior in most cases. On the other hand, elemental 3d metals ($U_{eff} < W$) are itinerant magnets. Actinide systems as well as transition metal compounds may show both types of behavior.

1.5 Model Parameters

Model parameters like U_{eff} may be obtained by means of *constrained* SDFT calculations (Dederichs *et al.* 1984). The general idea behind this method is to impose a symmetry restriction on the considered system that models, in a static way, a certain quasi-particle excitation. If the time-scales of the excitation and of the remaining degrees of freedom are different enough, the response of the latter, treated in a self-consistent calculation, provides a fairly realistic description of the screening process (Gunnarsson 1990).

Prominent examples are so-called frozen magnon calculations, where the atomic spin directions are fixed to form a periodic wave. Then, the ground-state energy is calculated for both the relaxed and the constrained system, and the energy difference is equated with the related excitation energy. Heisenberg model parameters describing the interatomic exchange coupling may be fitted to frozen magnon spectra or to other constrained magnetic configurations. They are used to describe thermodynamic properties of magnetic substances.

Finally, crystal field model parameters should be mentioned. They enter model theories for the description of magnetism related to localized 4f states (see *Localized 4f and 5f Moments: Magnetism*). The parameters may be obtained by applying shape restrictions on the atomic 4f charge density (Brooks *et al.* 1997, Richter 1998).

2. Magnetic Ordering

One of the major tasks of the SDFT is the first-principles description of the ground-state magnetic order. There is a great variety of possible magnetic ground states, for example: Pauli paramagnetism in vanadium, ferromagnetism in nickel, antiferromagnetism in chromium, spiral magnetic structures in γ-iron and rare-earth metals, complex noncollinear magnetic

structures in compounds of the transition metals and actinides, and disordered magnetic state in amorphous iron. In principle, the machinery of the SDFT allows one to start with an arbitrary magnetization and, by calculating to self-consistency, to determine the ground state magnetization. However, in this general approach the study of even the simplest magnetic system becomes a complex computational problem. This kind of calculation is unavoidable for the systems with no regular magnetic structure, but otherwise available experimental and theoretical information about the magnetic ground state is usually used to simplify calculations.

According to its basic theorems (Sect. 1.1), the SDFT supplies physical information about the state of the system which realizes the minimum of the energy-functional. The applications of the theory can, however, be extended by the possibility of the constrained calculations, where the process of minimization takes place under certain restricting conditions (Dederichs *et al.* 1984) imposed upon, for example, the symmetry of the magnetic density and effective potential.

An important example of the constraint is the constraint of zero magnetisation: $\mathbf{m}(\mathbf{r}) = 0$ for any $\mathbf{r}$. Even for magnetic systems, it is possible to calculate the lowest energy nonmagnetic state and to study the physical reasons for the instability of this state with respect to the formation of the magnetic structure (see *Magnetism in Solids: General Introduction*).

2.1 Ferromagnetic Structure

The best-studied magnetic crystals are the elementary 3d metals with ferromagnetic magnetic ordering: α-iron (iron with the body-centered cubic lattice), cobalt, and nickel. The instability of the nonmagnetic state of a 3d metal with respect to the formation of a ferromagnetic structure can be studied with the help of the Stoner criterion, Eqn. (10). The density of states (DOS) of the nonmagnetic α-iron is shown in *Itinerant Electron Systems: Magnetism (Ferromagnetism)* (Fig. 3). The DOS has a peak at the position of the Fermi level that indicates the instability of the nonmagnetic state. Indeed, if the constraint of zero magnetization is removed by placing a small magnetic moment at each iron site, the calculation results in the ferromagnetic state with the atomic magnetic moment which is close to the observed value (e.g., $2.15\,\mu_B$ in the calculation of Moruzzi *et al.* (1978)). One obtains a similar situation in cobalt and nickel (Moruzzi *et al.* 1978).

2.2 Antiferromagnetic Structure

For chromium, the Stoner product is less than 1. Still the nonmagnetic state of chromium is unstable, but in this case with respect to the formation of an antiferromagnetic structure. The antiferromagnetic structure can be treated as a magnetic structure with the spatial variation of the atomic magnetic moments defined by the wave vector $\mathbf{q} = \frac{1}{2}\mathbf{K}$, where $\mathbf{K}$ is a vector of the reciprocal lattice. The Stoner criterion generalized to the case of the magnetic structures characterized by an arbitrary value of $\mathbf{q}$ takes the form:

$$I\chi(\mathbf{q}) > 1 \tag{12}$$

where $\chi(\mathbf{q})$ is the unenhanced magnetic susceptibility of the nonmagnetic state of the system in a nonuniform static magnetic field, with spatial variation defined by vector $\mathbf{q}$. For a ferromagnet, $\mathbf{q} = 0$ and the susceptibility is equal to the density of states at the Fermi level.

For a finite $\mathbf{q}$, the susceptibility is given by the formula:

$$\chi(\mathbf{q}) = \sum_{\mathbf{k}\nu\mu} \frac{f(\varepsilon_{\nu\mathbf{k}}) - f(\varepsilon_{\mu\mathbf{k}-\mathbf{q}})}{\varepsilon_{\mu\mathbf{k}-\mathbf{q}} - \varepsilon_{\nu\mathbf{k}} + \mathrm{i}\delta} \left| \langle \mathbf{k}\nu | \mathrm{e}^{\mathrm{i}qr} | \mathbf{k} - \mathbf{q}\mu \rangle \right| \tag{13}$$

and cannot be expressed through the DOS. Here, ν and μ are band indices, δ is an infinitesimal, and $f(\varepsilon)$ is the Fermi–Dirac distribution function.

In Fig. 2, we compare the calculated $\mathbf{q}$-dependences of the susceptibility of α-iron and chromium. The two curves are essentially different. In the case of α-iron, the susceptibility is maximum for $\mathbf{q} = 0$ and decreases monotonically with increasing $\mathbf{q}$, clearly revealing the origin of the ferromagnetic instability. In the case of
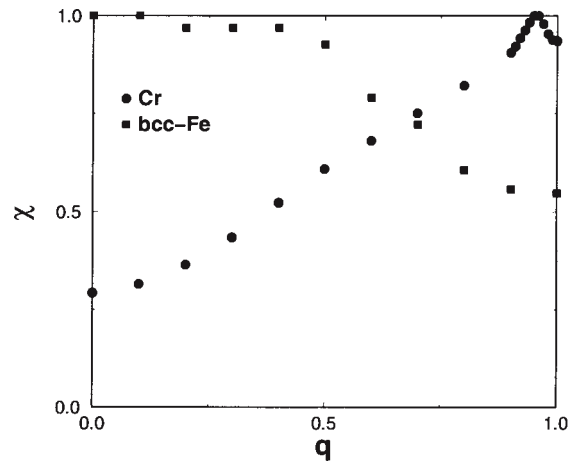
Figure 2
$\mathbf{q}$-dependence of the unenhanced magnetic susceptibility of α-Fe (lattice parameter $a = 5.27$ atomic units) and Cr ($a = 5.45$ atomic units); $\mathbf{q}$ is given in units of $2\pi/a$. The susceptibilities are scaled to assume a unity value at the point of maximum. Calculation was carried out with the scheme of Sandratskii and Kübler (1992).

chromium, the behavior is the opposite: the susceptibility for $\mathbf{q} = 1$ (in units of $\frac{1}{2} > \mathbf{K}$) is more than three times that for $\mathbf{q} = 0$. The difference between these two cases reflects the tendency for systems with half-filled d-bands to be antiferromagnetic, in contrast to the systems at the end of the 3d series, which order ferromagnetically (Heine and Samson 1983).

From Eqn. (13), it is seen that the largest contribution to the susceptibility is given by the pairs of states which are separated in reciprocal space by the vector $\mathbf{q}$ and are close in energy. Since the energy difference contains one occupied and one unoccupied state, these states lie close to the Fermi level. Indeed, the Fermi surface of chromium possesses two similar sheets shifted in the reciprocal space by the vector $\mathbf{q}$, which is close to $\frac{1}{2}\mathbf{K}$ (see Fawcett (1988) for details). This nesting of the sheets of the Fermi surface is important for the formation of the antiferromagnetic instability.

2.3 Spiral Magnetic Structure

The spatial variation of the directions of the atomic magnetic moments in the simplest magnetic structures—ferromagnetic and two-sublattice antiferromagnetic—can be described by the wave vectors equal, respectively, to 0 or $\frac{1}{2}\mathbf{K}$. Also, the magnetic structures described by an intermediate value of vector $\mathbf{q}$ were found experimentally.

The spiral magnetic structure can be defined by the formula:

$$\mathbf{m}_n = m(\cos(\mathbf{q} \cdot \mathbf{R}_n)\sin\theta, \ \sin(\mathbf{q} \cdot \mathbf{R}_n)\sin\theta, \ \cos\theta) \quad (14)$$

where $\mathbf{m}_n$ is the magnetic moment of the nth atom and $(\mathbf{q} \cdot \mathbf{R}_n)$, θ are polar coordinates. For vector $\mathbf{q}$ incommensurate with the vectors of the reciprocal lattice, the magnetic unit cell representing a translationally invariant part of the magnetic crystal is infinite. The spiral structure possesses, however, a special symmetry which, for an arbitrary $\mathbf{q}$, allows reduction of the consideration to the unit cell of the *chemical* lattice.

The spiral structure, Eqn. (14), is invariant with respect to the translation of the crystal by an arbitrary lattice vector $\mathbf{R}_n$, accompanied by the rotation of all atomic moments by an angle $\mathbf{q}\mathbf{R}_n$ about the z axis. Such operations, $\{(\mathbf{q}\mathbf{R}_n)|\mathbf{R}_n\}$, are called generalized translations. The Kohn–Sham Hamiltonian of the magnetic moments of the spiral structure (Sandratskii 1998) commutes with the generalized translations $\{(\mathbf{q}\mathbf{R}_n)|\mathbf{R}_n\}$. As a consequence of the generalized translational symmetry, a generalized Bloch theorem can be formulated:

$$\{(\mathbf{q}\mathbf{R}_n)|\mathbf{R}_n\}\psi_{\mathbf{k}}(\mathbf{r}) = \exp(-i\mathbf{k}\mathbf{R}_n)\psi_{\mathbf{k}}(\mathbf{r}) \quad (15)$$

where the vectors $\mathbf{k}$ lie in the first Brillouin zone of the chemical lattice. The theorem, Eqn. (15), is

sufficient for the reduction of the problem, for an arbitrary value of $\mathbf{q}$, to the consideration of the chemical unit cell of the crystal.

The formation of spiral structure leads to the hybridization of the states of the nonmagnetic crystal which are separated in the reciprocal space by vector $\mathbf{q}$. The importance of this hybridization is reflected in the formula for the susceptibility, Eqn. (13), and is closely related to the phenomenon of the Fermi surface nesting discussed in the case of chromium.

Figure 3 shows the calculated $\mathbf{q}$-dependence of the total energy for a number of transition metals (Sandratskii and Kübler (1992); see also the paper by Mryasov *et al.* (1991) for the first, first-principles calculation of γ-iron). In agreement with experiment, the ground state was found to be ferromagnetic for all metals, except for the case of γ-iron. In γ-iron, the minimum of the total energy occurs at a finite value of $\mathbf{q}$, i.e., the ground state is spiral.

Another example of the spiral structure is that in the heavy rare-earth metals (REM) (see *Localized 4f and 5f Moments: Magnetism*; *Magnetism in Solids: General Introduction*). The intra-atomic exchange interaction between the 4f states and the valence 5d and 6s states leads to the spin polarization of the valence states. In the crystal, the valence states of different atoms hybridize and form energy bands. The energy of the hybridized valence states depends on the directions of the 4f moments of different atoms.
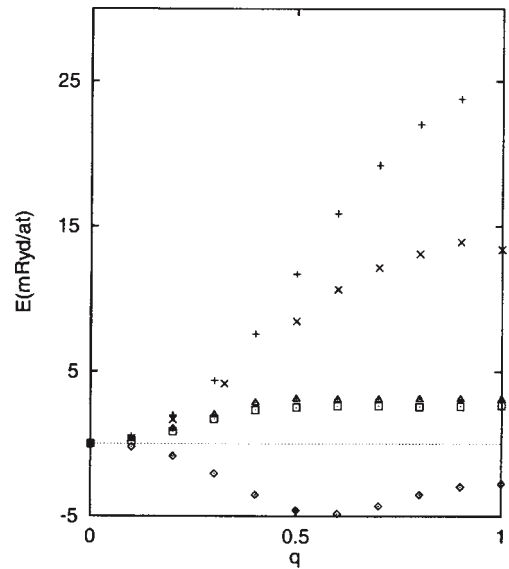
Figure 3
The total energy as a function of $\mathbf{q}$ for the (001) direction. $\diamond = \gamma$-Fe; $+ = \alpha$-Fe; $\square =$ fcc-Co; $\times =$ hcp-Co; $=$ Ni. In all calculations $\theta = 90°$. (Sandratskii and Kübler (1992)).
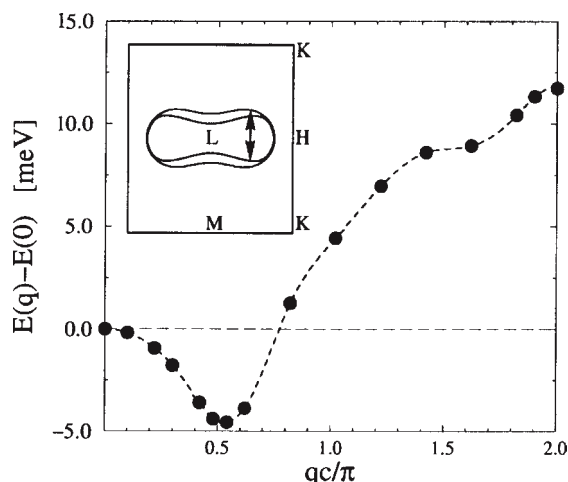
Figure 4
The *q*-dependence of the total energy of T_m. The inset shows the nesting property of the Fermi surface. (Nordström and Mavromaras (1999))

Early calculations of the **q**-dependence of the unenhanced susceptibilities (Jensen and Mackintosh 1991) gave the maximum at the **q** values close to the experimentally determined wave vectors of the spiral structures. In Fig. 4, a first-principles calculation by Nordström and Mavromaras (1999) of the total energy of thulium as a function of **q** is shown.

2.4 Role of the Spin–Orbit Coupling

In the calculations of the magnetic structure discussed up to now, the SOC (see Sect. 1.3) was not taken into account. With the SOC being neglected, an arbitrary rotation of all atomic magnetic moments by the same angle does not change the energy. However, the dependence of the energy of the system on the direction of the magnetic moments with respect to the lattice, that is, the magnetic crystalline anisotropy, is a property of primary importance in numerous technical applications (see also Sect. 3).

In bcc iron, the energy of magnetic anisotropy is of the order of 10^{-4} mRy per atom, and is five orders of magnitude smaller than the interatomic exchange interaction. In the case when the SOC energy becomes comparable with the interatomic exchange interaction, it influences substantially not only the direction of the atomic moments with respect to the lattice, but also the relative directions of the moments. Indeed, experimental determination of the magnetic structure in heavy REM revealed a distortion of the spiral structure due to the influence of the magnetic anisotropy (Jensen and Mackintosh 1991).

The influence of the SOC on the formation of the magnetic structure increases further when one moves

from the 4f systems (see *Localized 4f and 5f Moments: Magnetism*) to the 5f systems (see *5f Electron Systems: Magnetic Properties*). The most effort has been devoted to the magnetic structure of uranium compounds. The hybridization of the 5f states with the states of other atoms is essential for the physics of the uranium compounds. On the other hand, the 5f states experience strong spin–orbit coupling.

The importance of the SOC can be illustrated by the phenomenon of the symmetry-predetermined noncollinearity of the magnetic structure. To introduce this effect, let us consider a collinear magnetic structure, and let θ be a parameter which describes the noncollinear magnetic structures obtained with the deviation of the magnetic moments from the collinear directions. $\theta_0 = 0$ corresponds to the collinear structure. The following criterion of the instability of the magnetic structure can be formulated: the structure corresponding to $\theta = \theta_0$ can be stable only in the case that this state is distinguished by symmetry, compared to the states obtained with infinitesimal variation of parameter θ (Sandratskii (1998) and references therein). Indeed, only in this case can the minimum of the total energy be at $\theta = 0$.

The effect of the symmetry-predetermined noncollinearity is illustrated in Fig. 5 by the example of U_3P_4. The inset shows the experimentally determined magnetic structure of U_3P_4. An SDFT calculation starting with the collinear ferromagnetic
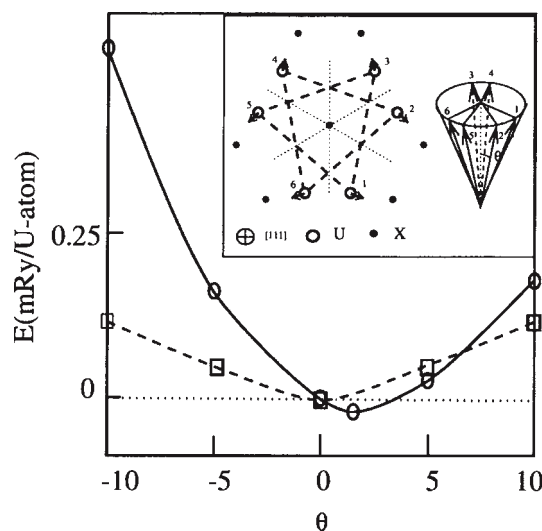
Figure 5
The total energy of U_3P_4 as a function of the deviation of the magnetic moments from the (111) axis. Solid/ dashed line shows the result of the calculation with/ without the spin–orbit coupling, respectively. The inset shows the projection of the crystal and magnetic structure to the (111) plane. The magnetic moments form a cone structure.

configuration results immediately in the noncollinear magnetic structure similar to the structure found in the experiment. The deviation of the magnetic moments does not influence the symmetry of the magnetic structure. The minimum of the total energy is at an accidental point.

With the SOC being neglected, the curve of the total energy as a function of the deviation angle θ is symmetrical with respect to the change of the sign of θ (Fig. 5). Therefore, the collinear configuration corresponding to $\theta = 0$ is distinguished by symmetry and is stable. The reason for different symmetry properties of the total energy in relativistic and nonrelativistic problems is the different types of symmetry groups which describe the relativistic and nonrelativistic problems.

The phenomenon of the symmetry-predetermined noncollinearity observed in U_3P_4 has the same physical nature as the effect of weak ferromagnetism in Fe_2O_3, where the iron moments deviate from their antiparallel directions and result in a finite ferromagnetic component.

3. Calculated Magnetic Properties

Magnetic ordering in itinerant magnets is driven by the spin density, but the orbital contribution to the magnetic moment,

$$\mathbf{m}_{or} = \mu_B \sum_{i,\mathbf{k}}^{occ} \langle \phi_{i,\mathbf{k}} | \mathbf{L} | \phi_{i,\mathbf{k}} \rangle \qquad (16)$$

where $\phi_{i,\mathbf{k}}$ is an energy band eigenfunction for the ith branch, with wave vector $\mathbf{k}$ and angular momentum $\mathbf{L}$, is responsible for such technologically important effects as intrinsic magnetocrystalline anisotropy energy (MAE), magnetostriction, the magneto-optical Kerr effect, and magnetic circular dichroism in itinerant magnets. In iron, cobalt, and nickel, the calculated spin (orbital) contributions to the magnetic moment are, respectively, $2.13 \mu_B$ ($0.08 \mu_B$), $1.52 \mu_B$ ($0.14 \mu_B$) and $0.57 \mu_B$ ($0.05 \mu_B$) and are parallel (Ebert *et al*. 1988, Eriksson *et al*. 1990). The orbital moment is carried almost entirely by the $3d$ electrons, whereas the spin contribution is the sum of local ($3d$) and diffuse (sp) parts aligned antiparallel. However, the calculated orbital moments are smaller than measured (Ebert *et al*. 1988, Eriksson *et al*. 1990).

Experimental information on ground-state spin and orbital magnetization densities may be obtained from elastic neutron scattering measurements (see *Magnetism in Solids: General Introduction*; *Magnetic Excitations in Solids*). The neutron magnetic form factor, *f(Q)*, where *Q* is the momentum transfer ($= 4\pi \sin\theta / \lambda$) is a direct measure of the Fourier transform of the magnetization. In the dipole approximation the form factor is given by:

$$f(Q) = \langle j_0 \rangle + \mu_L \langle j_2 \rangle / \mu \qquad (17)$$

where $\langle j_n \rangle = 4\pi \int r^2 n_s(r) j_n(r)$ is a Bessel transform of the calculated spin density, μ is the total and μ_L the orbital magnetic moment. The orbital contribution to the magnetic moment is small for transition metal systems, but can be large in rare earths and actinides (Brooks and Kelly 1983). Analysis of the form factors of actinides has been used to show that they have large orbital moments. In systems that do not order, or above the ordering temperature in systems that do order, the application of a magnetic field allows the induced form factor to be measured. Calculations have been used to show that the relationship between spin and orbital moments can be quite different when the form factor is induced, compared with the ordered state due to the breaking of Hund's rules by the applied field (Hjelm *et al*. 1993).

3.1 Hyperfine Interactions

The interactions between the nuclear and electronic charge and current densities produce hyperfine structure, for which a comparison of calculated and measured contributions is therefore an excellent test of density functional theory. Since the length scale of the nucleus ($r_N \approx 10^{-4} a_0$) is small compared with the atomic length scale of one Bohr radius, ($a_0 = \hbar^2/me^2$), the Coulomb potential, $-Ze^2/r$, is large in the region of the nucleus, and the concomitant large electronic kinetic energy makes relativistic effects important. Therefore either the Dirac equation, or some approximation to the Dirac equation that takes proper account of the boundary condition for the relativistic case at small values of radius, should be used in any theory of hyperfine interactions. The interaction between nuclear and electronic charges and currents is usually expressed in terms of a multipole expansion:

$$H_{\text{int}} = \sum_{k=0}^{k=2} \mathbf{T}_n^k \cdot \mathbf{T}_e^k \qquad (18)$$

since the contribution of multipoles with rank greater than 2 is negligible.

The monopole ($k = 0$) interaction gives rise to the isomer (or chemical) shift, which is proportional to the contact charge density at the nuclear radius and is used to study trends in charge transfer, particularly in Mössbauer experiments (see *Mössbauer Spectroscopy*). For example, the isomer shift at the iron site in dilute FeX alloys is essentially periodic across the periodic table, being a minimum (more contact charge) if X is at the start of a row and maximum (less contact charge) if X is at the end (Akai *et al*. 1986). The self-consistently calculated isomer shifts are in good agreement with measurements, and broadly follow the argument that charge flows from atoms at the beginning of a period to those at the right which are more electronegative. However, detailed calculations show that there is a strong angular

momentum dependence in the charge transfer and that, particularly in the case of transition metals, *sd*-hybridization is important.

The dipole ($k = 1$) interaction may be separated into Fermi contact, dipolar, and orbital contributions. The Fermi contact interaction is between the electronic spin density at the nucleus and the nuclear dipole moment which experiences a magnetic field:

$$H_{hf}^1 = \frac{8\pi}{3}\mu_B m_{av} \qquad (19)$$

where $m_{av} = \int \delta_T(\mathbf{r})\mu_s(\mathbf{r})d^3r$ is the average spin magnetic moment density over a sphere with the diameter of the Compton radius, $r_T = Ze^2/mc^2$.

$$\delta_T(\mathbf{r}) = (1/4\pi r^2)(\partial S(\mathbf{r})/\partial r),$$

where $S^{-1}(\mathbf{r}) = 1 + ((\varepsilon - v_{eff}(\mathbf{r}))/2mc^2)$ is the relativistic mass enhancement.

The dipolar interaction is between the electronic vector spin density and the nuclear moment which experiences a field:

$$H_{hf}^2 = \mu_B \int \left[\Sigma(\mathbf{r}) - 3\frac{\mathbf{r}\cdot\Sigma(\mathbf{r})}{r^2}\mathbf{r} \right]\frac{d^3r}{r^3} \qquad (20)$$

Finally, the orbital interaction is between the electronic current distribution and the nuclear moment which experiences a field:

$$H_{hf}^3 = -2\mu_B L_{av} \qquad (21)$$

where $L_{av} = \int L(\mathbf{r})S(\mathbf{r})/r^3$ is the weighted orbital moment density measured in units of $\hbar$.

The Fermi contact interaction, which is proportional to the spin density at the nucleus, is normally far larger than the dipolar and orbital contributions, especially in crystals with cubic symmetry and small spin–orbit interaction, where the dipolar term is negligible. The spin density at the nucleus, which arises entirely from *s*-states, is composed of the contribution from the unpaired spins of the valence electrons and a contribution from core polarization. Detailed calculations have shown that the contact interaction is dominated by core polarization. For example, in iron the calculated hyperfine field due to core polarization is 235 kG, compared with a valence contribution of 42 kG (Ebert 1988, Ebert *et al.* 1988).

The most thoroughly studied itinerant electron metals are the transition metals iron, cobalt, and nickel (Ebert *et al.* 1988). The *s*-electrons—both core and valence—are polarized by exchange interactions with the *d*-electrons. Since the core spin density is dominant, comparison with measured hyperfine fields is a severe test of the calculated exchange interactions between transition metal *d*-states and core *s*-states. In practice, the calculated and measured hyperfine fields for cobalt are 194 kG and 215 kG, respectively, where in addition to the Fermi contact contribution, the

contribution from the orbital currents (moment) of the *d*-electrons of -50 kG is included. Although this result is quite reasonable, the calculated hyperfine fields for iron and nickel are poor.

In iron, the measured and calculated hyperfine fields are 339 kG and 253 kG, respectively; and in nickel the corresponding quantities are 75 kG and 39 kG. Since the calculated dipolar contribution from the orbital currents is relatively small in iron (-24 kG), the errors are due to the calculated core polarization. In nickel, the orbital current contribution is relatively larger (-37 kG), but is of the wrong sign to rectify the errors. Since the calculated magnetic moments of the transition metals compare well with experiment, it is difficult to escape the conclusion that errors in LSDA are connected with its description of core polarization (Akai *et al.* 1990).

The hyperfine fields at impurity sites in transition metal alloys have also been studied in some detail. When the impurity atom is non-magnetic, the measured hyperfine field is due to the induced *s*-spin density at the impurity nucleus, which arises from hybridization with the magnetic transition metal *d*-electrons and, since the core of the impurity atom is unpolarized (there is no impurity *d*-moment to do this), core polarization plays no role. The induced spin density at the impurity nucleus depends both upon the local occupation of the spin-up and spin-down states and the magnitude of the spin-up and spin-down wave functions. When transition metal *d*-states hybridize with conduction electrons from other atoms, the sign of the wave function at the impurity site can change as the energy in the hybridized bands changes, passing from bonding to antibonding orbitals. The effect upon the spin density at the impurity nucleus is a quite remarkable systematic trend throughout the periods in the periodic table, illustrated by the measured and calculated hyperfine fields for impurities in nickel (Akai *et al.* 1990) (see Fig. 6).

The hyperfine fields are negative at the beginning of each period and change sign, reaching a maximum near the end of each period before changing sign again at the beginning of the next period. When the impurities are themselves transition metals the mechanism controlling the hyperfine fields is different, since *d*–*d* hybridization is important and an impurity *d*-moment is induced which, particularly in the case of 3*d* impurities, can be quite large. At the beginning of a period, the less tightly bound impurity *d*-bands lie higher in energy than the nickel 3*d*-bands, and an impurity *d*-moment is induced anti-parallel to the nickel 3*d*-moment. However, for impurities towards the end of the transition metal series, the induced moment can flip to ferromagnetic alignment. On the whole, although there are some discrepancies, both trends and magnitude of the hyperfine fields at the impurity sites are obtained from LSDA calculations.
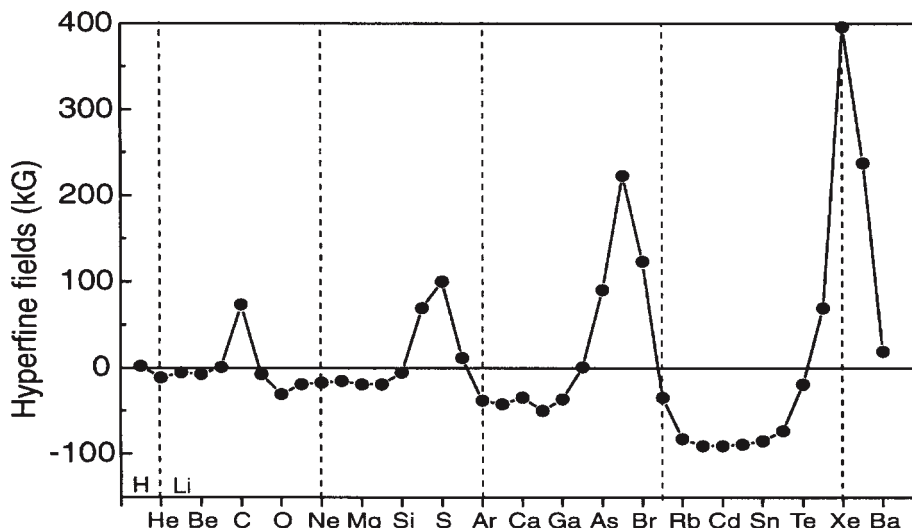
Figure 6
The calculated hyperfine fields for impurities from the short periods in Ni (Akai *et al.* 1990).

The next term in the multipole interaction ($k = 2$) is the interaction between the nuclear electric quadrupole moment and the electric field gradient produced by the electron density:

$$E_{zz} = \sqrt{\frac{5}{\pi}} \lim_{r \to 0} \frac{v_{20}(r)}{r^2} \qquad (22)$$

where v_{20} is the quadrupolar electronic charge density. The accurate calculation of electric field gradients requires accurate treatment of non-spherical components of the charge density. In particular the quadrupolar charge density, when weighted by $1/r^3$, is directly related to the field gradient. The field gradient vanishes for cubic crystals, but it has been found for hcp transition metals that, due to the radial weighting, the *p*-electron contribution to the field gradient becomes dominant, since the first radial node of the *p*-states lies inside that of the *d*-states (Blaha *et al.* 1988).

3.2 Magnetocrystalline Anisotropy

The magnetic anisotropy energy (MAE) is normally calculated as the difference in total energy for moment alignment along an easy and a hard axis. For iron, cobalt, and nickel, the magnetic anisotropy energy is of the order of μeV, which demands extremely accurate numerical treatment. The magnitude of the MAE from self-consistent calculations is too small for iron and cobalt, and has the wrong sign for nickel (Daalderop *et al.* 1990, Jansen 1990). Inclusion of the

orbital polarization correction term improves the results, except for nickel.

The magnetic anisotropy constants are the coefficients in the expansion of the energy in terms of spherical harmonics which depend upon the moment direction. In cubic crystals, the lower order anisotropy constants vanish by symmetry; consequently the anisotropy energy is small. Of the non-cubic symmetries where the magnetic anisotropy is larger, the most important is tetragonal, since this is the symmetry of many thin films and multilayers. It is possible to take the crystal symmetry from fcc to bcc via tetragonal along a Bains path, simply by changing the *c/a* ratio. Self-consistent total energy calculations have shown that the anisotropy energy should increase by orders of magnitude as the structure is taken to tetragonal and, since the final structure is also cubic, it has at least one maximum along the path, which for cobalt is about $600\,\mu$eV. If the exchange splitting were larger than the bandwidth (which is seldom true) and the spin–orbit interaction, a small perturbation in the magnetic anisotropy would be proportional to the anisotropy of the orbital moment (Bruno 1989). No such approximations are made in total energy calculations, but experience has shown that the easy (hard) direction is that in which the orbital moment is largest (smallest).

3.3 Magnetovolume, Invar Effect, and Magnetostriction

Magnetostriction is the lattice deformation which accompanies magnetization (see *Magnetoelastic*

Phenomena). Since magnetostriction is due to the coupling of magnetic and elastic forces, it is of immense technological importance for the conversion of energy between magnetic and elastic degrees of freedom. The magnetovolume effect is the isotropic (or volume) component of magnetostriction. Itinerant magnetic materials may have quite large magneto-volume effects, since the electrons responsible for the magnetism are also responsible for chemical bonding. For example, the Friedel (1969) model of transition metal bonding attributes to the cohesive energy a term proportional to $f(1-f)$, where f is the fractional occupation of the *d*-band, which is responsible for the parabolic trend in cohesive energy across a transition metal series.

More detailed modelling has shown that the change of this term with volume, contributes an electronic pressure:

$$P = (2l+1)^2 W_d[g^2 - f(1-f)]/3V \qquad (23)$$

where W_d is the width of the *d*-band, $l = 2$ for *d*-states, $f_\pm$ are the fractional occupations of the spin-up and spin-down bands and g is the fractional magnetic moment, $(f_+ - f_-)/2$. The magneto-volume effect is due to the repulsive contribution proportional to g^2, which is a maximum when $f = m = 1/2$ and the spin-up band is filled.

The Invar effect (see *Invar Materials: Phenomena*) arises when high and low volume magnetic states have about the same energy, such that the latter may be populated by thermal excitations, thus compensating thermal expansion due to lattice vibrations. The low volume magnetic state was proposed by Weiss (1963) to be anti-ferromagnetic, but both the paramagnetic state and the ferromagnetic state can be simultaneously stable if the Fermi level of the paramagnetic state density lies in a dip between two peaks. Williams *et al.* (1982) used SDFT to show that in iron–nickel alloys, the total energy of the low volume paramagnetic state is a function of composition, and lies about 10 meV above the total energy of the high volume ferromagnetic state for Fe_3Ni. Subsequently, the low volume state has been shown to be disordered when non-collinear spin ordering is included in the simulation (van Schilfgaarde *et al.* 1999).

The anisotropic part of the magnetostrictive energy may be obtained from self-consistent calculations if the anisotropy energy is calculated as a function of strain. Calculations for transition metals (James 1999) reveal proportionality between the magnitude of the magnetostriction energy and the MAE, and between the MAE and the anisotropy of the orbital magnetic moment. Although the absolute values of the calculated magnetostrictive energy for Fe/Co and Co/Ni alloys tend to be too large by up to an order of magnitude, the correct trend as a function of cobalt concentration is reproduced.

3.4 X-ray Magnetic Circular Dichroism

First-principles calculations of optical properties are usually made in two stages. Firstly, the self-consistent ground state charge and spin densities are calculated; then the optical conductivity tensor is calculated for the Kohn–Sham energies and wave functions corresponding to the ground-state density (Sect. 1.4). The conductivity tensor, $\sigma(\omega)$, derived from linear response theory, is:

$$\sigma(\omega) = \frac{-ie^2}{3m^2\hbar v} \sum_{\mathbf{k}} \sum_{nn'} \frac{f(\varepsilon_{n\mathbf{k}}) - f(\varepsilon_{n'\mathbf{k}})}{\omega_{nn'}(\mathbf{k})} \frac{|\Pi_{n'n}(\mathbf{k})|^2}{\omega - \omega_{nn'}(\mathbf{k}) + i/\tau} \qquad (24)$$

where v is the volume of the unit cell, $f(\varepsilon_{n\mathbf{k}})$ is the Fermi function, $\hbar\omega_{nn'}(\mathbf{k}) = \varepsilon_{n\mathbf{k}} - \varepsilon_{n'\mathbf{k}}$, the energy difference of the Kohn–Sham energies $\varepsilon_{n\mathbf{k}}$, τ is the average lifetime of excited electron states, and $\Pi_{n'n}(\mathbf{k})$ are the matrix elements of the momentum operator.

When circularly polarized x-rays are absorbed by a magnetic material, the absorption depends upon whether the light is left-or right-polarized. The absorption is determined by the imaginary part of conductivity tensor, where the initial states are the core states of the x-ray edge. The source of X-ray magnetic circular dichroism (XMCD) is that the off-diagonal elements of the conductivity tensor are non-zero, which is due to spin–orbit interaction in either initial or final states. Calculations for transition metals (Ebert 1996) have shown that pronounced XMCD can occur when there is a large spin–orbit splitting of the core states and a small moment in the conduction bands, as for the $L_{2,3}$ edges of 5*d* impurities in magnetic 3*d* transition metal hosts. Alternatively, in pure transition metals the 2*p*-core state spin–orbit splitting is relatively small, but the conduction band moment is large. In both cases agreement with measurements is good (for experimental aspect of XMCD, see *Demagnetization: Nuclear and Adiabatic*).

3.5 Magneto-optical Kerr Effect

When linearly polarized light is reflected from a magnetized sample, the reflected light becomes elliptically polarized, with the plane of polarization rotated (see *Faraday and Kerr Rotation: Phenomenological Theory*). The complex Kerr rotation angle, $\phi = \theta + i\varepsilon$ where θ is the rotation and ε the ellipticity, is given by:

$$\phi \approx \frac{\sigma_{xy}}{\sigma_{xx}\sqrt{1 + (4\pi i/\omega)\sigma_{xx}}} \qquad (25)$$

The sign of the Kerr angle changes when the magnetization is reversed; therefore, information stored in the form of a reversed magnetization may be read by measuring the Kerr rotation. Since high data density is desirable, and blue light is easier to focus than

red, a large Kerr rotation in the 2–3 eV region is considered optimal. Since the Kerr rotation is proportional to the off-diagonal elements of the conductivity tensor, which increase with spin–orbit interaction, materials with large magnetic anisotropy are also likely to have a large Kerr rotation for some energy of incident light (Oppeneer 1998). However, the fact that the Kerr rotation should be large in the 3 eV region has made Fe/Pt and Co/Pt intermetallics of particular interest.

The magnitude of the Kerr rotation for transition metal compounds rarely exceeds $0.5°$, but for Heusler alloys, particularly the half-metallic ferromagnets XMnSb (X = Ni, Pd, Pt), it can have higher values (see *Half-metallic Magnetism*). Calculations, which are in good agreement with experiment, for PtMnSb yield a Kerr rotation of over $1°$ at 1.6 eV (Ebert 1996). The Kerr rotation for actinide compounds, where the $5f$ state spin–orbit interaction is large, can reach several degrees (Oppeneer *et al.* 1998). Magnetic multilayers possessing perpendicular anisotropy are excellent candidates for recording materials since, apart from the fact that they yield a polar Kerr effect, the magnetic layers may be tailored. Here theoretical predictions are most useful, and extensive investigations of, for example, multilayers of the type nA/mB (A = Fe, Co and B = Cu, Ag, Au, Pd, and Pt) have been made (see *Magneto-optics: Inter- and Intraband Transitions, Microscopic Models of*).

Bibliography

Akai H, Akai M, Blügel S, Drittler B, Ebert H, Terakura K, Zeller R, Dederichs P H 1990 Theory of hyperfine interactions in metals. *Progr. Theor. Phys. Suppl.* **101**, 11

Akai H, Blügel S, Zeller R, Dederichs P H 1986 Isomer shifts and their relation to charge transfer in dilute Fe alloys. *Phys. Rev. Lett.* **56**, 2407–10

Blaha P, Schwarz K, Dederichs P H 1988 First-principles calculation of the electric-field gradient in h.c.p. metals. *Phys. Rev. B* **37**, 2792–6

Brooks M S S, Eriksson O, Wills J M, Johansson B 1997 Density functional theory of crystal field quasi-particle excitations and the *ab initio* calculation of spin Hamiltonian parameters. *Phys. Rev. Lett.* **79**, 2546–9

Brooks M S S, Kelly P J 1983 Large orbital-moment contribution to 5f band magnetism. *Phys. Rev. Lett.* **51**, 1708–11

Bruno P 1989 Tight-binding approach to the orbital magnetic moment and magnetocrystalline anisotropy of transition-metal monolayers. *Phys. Rev. B* **39**, 865–8

Daalderop G H O, Kelly P J, Schuurmans M F H 1990 First-principles calculation of the magnetocrystalline anisotropy energy of iron, cobalt, and nickel. *Phys. Rev. B* **42**, 11919–37

Dederichs P H, Blügel S, Zeller R, Akai H 1984 Ground states of constrained systems: application to cerium impurities. *Phys. Rev. Lett.* **53**, 2512–5

Ebert H 1988 Two ways to perform spin-polarized relativistic linear muffin-tinorbital calculations. *Phys. Rev. B* **38**, 9390–7

Ebert H 1996 Magneto-optical effects in transitional metal systems. *Rep. Prog. Phys.* **59**, 1665–736

Ebert H, Strange P, Gyorffy B L 1988 The influence of relativistic effects on the magnetic moments and hyperfine fields of Fe, Co and Ni. *J. Phys. F* **18**, L135–40

Eriksson O, Brooks M S S, Johansson B 1990 Theoretical aspects of the magnetism in the ferromagnetic AFe₂ systems (A = U, Np, Pu, and Am). *Phys. Rev. B* **41**, 9087–94

Eriksson O, Johansson B, Brooks M S S 1989 Meta-magnetism in UcoAl. *J. Phys.: Condens. Matter* **1**, 4005–12

Eschrig H 1996 *The Fundamentals of Density Functional Theory*. Teubner, Stuttgart

Fawcett E 1988 Spin-density-wave antiferromagnetism in chromium. *Rev. Mod. Phys.* **60**, 209–83

Friedel J 1969 Transition metals. Electronic structure of the d-band. Its role in the crystalline and magnetic structures. In: Ziman (ed.) *The Physics of Metals*. Cambridge University Press, Cambridge, p. 341

Gunnarsson O 1990 Calculations of parameters in model Hamiltonians. *Phys. Rev. B* **41**, 514–8

Heine V, Samson J H 1983 Magnetic, chemical and structural ordering in transition metals. *J. Phys. F* **13**, 2155–68

Hjelm A, Eriksson O, Johansson B 1993 Breakdown of Hund's third rule for induced magnetism in uranium metal. *Phys. Rev. Lett.* **71**, 1459–61

Hohenberg P, Kohn W 1964 Inhomogeneous electron gas. *Phys. Rev.* **136**, B864–71

James P 1999 Calculation of magnetism and its crystal structure dependence. *Ph.D. thesis*, Uppsala University, Sweden

Jansen H J F 1990 Origin of orbital momentum and magnetic anisotropy in transition metals. *J. Appl. Phys.* **67**, 4555–7

Jensen J, Mackintosh A R 1991 *Rare Earth Magnetism*. Oxford University Press, Oxford

Jones R O, Gunnarsson O 1989 The density functional formalism, its applications and prospects. *Rev. Mod. Phys.* **61**, 689–746

Kohn W, Sham L J 1965 Self-consistent equations including exchange and correlation effects. *Phys. Rev.* **140**, A1133–8

Melsen J, Wills J M, Johansson B, Eriksson O 1994 Calculations of valence stabilities for the lanthanide metals. *J. Alloys Compounds* **209**, 15–24

Moruzzi V L, Janak J F, Williams A R 1978 *Calculated Electronic Properties of Metals*. Pergamon, New York

Moruzzi V L, Marcus P M 1993 Energy band theory of metallic magnetism in the elements. In: Buschow K H J (ed.) *Handbook of Magnetic Materials, Vol. 7*. North-Holland, Amsterdam, p. 97

Mryasov O N, Liechtenstein A I, Sandratskii L M, Gubanov V A 1991 Magnetic structure of f.c.c. iron. *J. Phys.: Condens. Matter* **3**, 7683–90

Nordström L, Mavromaras A 1999 Magnetic ordering of the heavy rare earths. *Europhys. Lett.* **49**, 775–81

Oppeneer P M 1998 Magneto-optical spectroscopy in the valence band energy regime: relationship to magnetic anisotropy. *J. Magn. Magn. Mater.* **188**, 275

Oppeneer P M, Perlov A Y, Antonov V N, Yaresko A N, Kraft T, Brooks M S S 1998 Optical and magneto-optical spectroscopy of uranium and plutonium compounds: recent theoretical progress. *J. Alloys Compounds* **271–273**, 831

Richter M 1998 Band structure theory of magnetism in 3d–4f compounds. *J. Phys. D: Applied Physics* **31**, 1017–48

Sandratskii L 1998 Noncollinear magnetism in itinerant electron systems: theory and applications. *Adv. Phys.* **47**, 91–160

Sandratskii L M, Kübler J 1992 Static nonuniform magnetic susceptibility of selected transition metals. *J. Phys.: Condens. Matter* **4**, 6927–42

Trickey S B 1990 Density functional theory of many-Fermion systems. *Advances in Quantum Chemistry*. Academic Press, San Diego, CA, Vol. 21

van Schilfgaarde M, Abrikosov I A, Johansson B 1999 Origin of the Invar effect in iron-nickel alloys. *Nature* **400**, 46–9

Weiss R J 1963 The origin of the Invar effect. *Proc. Phys. Soc. London* **82**, 281–8

Williams A R, Moruzzi V L, Gelatt C D 1982 Aspects of transition-metal magnetism. *J. Appl. Phys.* **53**, 2019–23

M. S. S. Brooks
European Commission Joint Research Centre Karlsruhe, Germany

M. Richter
Institut für Festkörper- und Werkstofforschung Dresden, Germany

L. M. Sandratskii
Institut für Festkörperphysik, Technische Universität Darmstadt, Germany

Dilute Magnetic Semiconductors

This family of materials encompasses standard semiconductors, in which a sizable portion of atoms is substituted by elements which produce localized magnetic moments in the semiconductor matrix. Usually, magnetic moments originate from $3d$ or $4f$ open shells of transition metals (TMs) or rare-earth metals (lanthanides), respectively, so that typical examples of diluted magnetic semiconductors (DMS) are $Cd_{1-x}Co_xSe$, $Ga_{1-x}Mn_xAs$, $Pb_{1-x}Eu_xTe$ and, in a sense, Si:Er. A strong spin-dependent coupling between the band and localized states accounts for outstanding properties of DMS. This coupling gives rise to spin-disorder scattering, giant spin-splitting of the electronic states, and strong indirect exchange interactions between the magnetic moments, the latter leading to collective spin-glass, antiferromagnetic or ferromagnetic spin ordering.

Owing to the possibility of controlling and probing magnetic properties by the electronic subsystem or vice versa, DMS have successfully been employed to address a number of important questions concerning the nature of various spin effects in various environments and at various length and time scales. At the same time, DMS exhibit a strong sensitivity to the magnetic field and temperature as well as constituting important media for generation of spin currents and for manipulation of localized or itinerant spins by, e.g., strain, light, and electrostatic or ferromagnetic gates. These properties, complementary to both nonmagnetic semiconductors and magnetic metals, allow applications of DMS as functional materials in spintronics devices.

1. Historical Background and Survey of Growth Methods

Extensive studies of DMS started in the end of the 1970s, when appropriately purified manganese was employed to grow bulk II–VI Mn-based alloys by various modifications of the Bridgman method. Compared to magnetic semiconductors, such as europium chalcogenides (e.g., EuS) and chromium spinels (e.g., $CdCr_2Se_4$) which were investigated earlier, DMS exhibited smaller defect concentrations and were easier to dope by shallow impurities. Accordingly, it was possible to examine their properties by powerful magneto-optical and magnetotransport techniques. Since, in contrast to magnetic semiconductors, neither narrow magnetic bands nor long-range magnetic ordering affected low-energy excitations, DMS were named *semimagnetic semiconductors*. More recently, studies of DMS have been extended towards materials containing magnetic elements other than manganese as well as to IV–VI, III–VI, and III–V compounds. As a consequence, a variety of novel phenomena have been discovered, including effects associated with narrow-bands and magnetic phase transformations, making the borderline between properties of DMS and magnetic semiconductors more and more elusive.

Rapid progress of DMS research in the 1990s stemmed, to a large extent, from the development of methods of crystal growth far from thermal equilibrium, primarily by molecular beam epitaxy (MBE), but also by laser ablation. These methods have made it possible to obtain DMS with the content of the magnetic constituent beyond thermal equilibrium solubility limits. Similarly, the doping during the MBE process allows the electrical activity of shallow impurities to be increased substantially. In the case of III–V compounds, in which divalent magnetic atoms supply both spins and holes, the use of the low-temperature MBE (LT MBE) provides thin films of, for example, $Ga_{1-x}Mn_xAs$ with x up to 0.07 and the hole concentration in excess of $1 \times 10^{20}\,cm^{-3}$, in which ferromagnetic ordering is observed above 100 K. Remarkably, MBE and processes of nanostructure fabrication make it possible to add magnetism to the physics of semiconductor quantum structures.

2. Magnetic Impurities in Semiconductors

A good starting point for the description of DMS is the Vonsovskii model, according to which the electron states can be divided into two categories: (i) localized magnetic d or f shells and (ii) extended band states built up of s, p, and sometimes d atomic orbitals. The former give rise to the presence of local magnetic moments and intracenter optical transitions. The latter form bands, which are alike as in the case of nonmagnetic semiconductor alloys. Indeed,

the lattice constant of DMS obeys the Vegard law, and the energy gap E_g between the valence and the conduction band depends on x in a manner qualitatively similar to nonmagnetic counterparts. According to the Anderson model, the character of magnetic impurities in solids results from a competition between (i) hybridization of local and extended states, which tends to delocalize magnetic electrons, and (ii) the on-site Coulomb interactions among electrons, which stabilize magnetic moments.

Figure 1 shows positions of local states derived from $3d$ shells of TM impurities in respect to the band energies of the host II–VI compounds. The levels labeled *donors* denote the ionization energy of the magnetic electrons ($TM^{2+} \to TM^{3+}$ or $d^n \to d^{n-1}$), whereas the *acceptors* correspond to their affinity energy ($TM^{2+} \to TM^{1+}$ or $d^n \to d^{n+1}$). The difference between the two is the on-d-shell Coulomb (Hubbard) repulsion energy U in the semiconductor matrix. In addition, the potential introduced by either neutral or charged TM can bind a band carrier in a Zhang-Rice-type singlet or hydrogenic-like state, respectively. Such bound states are often experimentally important, particularly in III–V compounds, as they correspond to lower energies than the competing d-like states, such as presented in Fig. 1.

In the case of manganese, in which the d shell is half filled, the d-like donor state lies deep in the valence band, whereas the acceptor level resides high in the conduction band, so that $U \approx 7\,eV$ according to photoemission and inverse photoemission studies. Thus, manganese-based DMS can be classified as charge transfer insulators, $E_g < U$. The manganese ion remains in the $2+$ charge state, which means that it does not supply any carriers in II–VI materials. However, it acts as a hydrogenic-like acceptor in the case of III–V arsenides. According to Hund's rule the

total spin $S = 5/2$ and the total orbital momentum $L = 0$ for the d^5 shell in the ground state. The lowest excited state d^{*5} corresponds to $S = 3/2$ and its optical excitation energy is about $2\,eV$.

Thus, if there is no interaction between the spins, their magnetization is described by the Brillouin function. In the case of other transition metals, the impurity-induced levels may appear in the gap, and then compensate shallow impurities, or even act as resonant dopant, e.g., scandium in CdSe, iron in HgSe, and copper in HgTe. Transport studies of such systems have demonstrated that intersite Coulomb interactions between charged ions lead to the Efros–Shklovskii gap in the density of the impurity states, which makes resonant scattering inefficient in semiconductors. Furthermore, spin-orbit interaction and the Jahn–Teller effect control positions and splittings of the levels in the case of ions with $L \neq 0$. If the resulting ground state is a magnetically inactive singlet there is no permanent magnetic moment associated with the ion, as in the case of Fe^{2+}, whose magnetization is of the Van Vleck-type at low temperatures.

3. Exchange Interaction Between Band and Localized Spins

The important aspect of DMS is a strong spin-dependent coupling of the effective mass carrier into the magnetic electrons. Neglecting nonscalar corrections that can appear for ions with $L \neq 0$, this interaction assumes the Kondo form,

$$H_K = -\sum_i \hat{I}(\vec{r} - \vec{R_i})\, \vec{s}\, \vec{S_i} \qquad (1)$$

where $\hat{I}$ is the short-range exchange energy operator. When incorporated to the kp scheme, its effect is described by matrix elements $\langle u_i|\hat{I}|u_i \rangle$, where u_i are the Kohn–Luttinger amplitudes of the corresponding band extreme. In the case of carriers at Γ point of the Brillouin zone in zinc-blende DMS, the two relevant matrix elements $\alpha = \langle S|\hat{I}|S \rangle$ and $\beta = \langle X|\hat{I}|X \rangle$ involve s-type and p-types wave functions, respectively.

There are two mechanisms contributing to the Kondo coupling: (i) the exchange part of the Coulomb interaction between the effective mass and localized electrons and (ii) the spin-dependent hybridization between the band and local states. Since there is no hybridization between Γ_6 and d-derived (e_g and t_{2g}) states in zinc-blende structure, the s-d coupling is determined by the direct exchange. The experimentally determined values are of the order of $\alpha N_o \approx 0.25\,eV$, where N_o is the cation concentration, somewhat reduced from the value deduced from the energy difference between $S \pm \frac{1}{2}$ states of the free singly ionized manganese atom $3d^5 4s^1$, $\alpha N_o = 0.39\,eV$. In
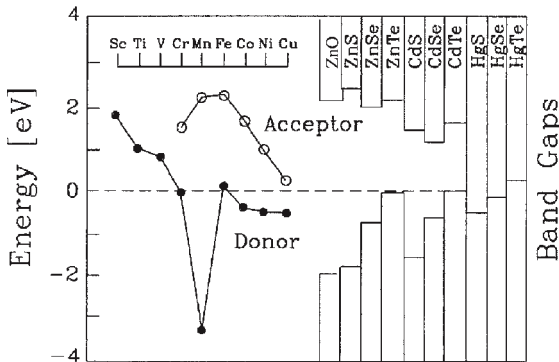
Figure 1
Approximate positions of donor (full points) and acceptor (open circles) levels derived from d-states of transition metal impurities in II–VI DMS (courtesy of Heiman and Dobrowolski, data after Zunger 1986 and Langer *et al.* 1988).

contrast, there is a strong hybridization between Γ_8 and t_{2g} states, which affects their relative position, and leads to a large magnitude of $|\beta N_o| \approx 1$ eV. If the relevant effective mass state ε_k is above the t_{2g} level (e.g., Mn-based DMS), $\beta < 0$ but otherwise β can be positive (e.g., $Zn_{1-x}Cr_xSe$).

4. Electronic Properties

4.1 Effects of Giant Spin Splitting

In the virtual-crystal and molecular-field approximations, the effect of the Kondo coupling is described by $\langle u_i | \hat{I} | u_i \rangle \vec{M}(\vec{r}) \vec{s} / g\mu_B$, where $\vec{M}(\vec{r})$ is magnetization (averaged over microscopic regions) of the localized spins, and g is their Landé factor. Neglecting thermodynamic fluctuations of magnetization (the mean-field approximation) $\vec{M}(\vec{r})$ can be replaced by $M_o(T, H)$, the temperature and magnetic field dependent macroscopic magnetization of the localized spins available experimentally. The resulting contribution to the spin-splitting of s-type electron states is given by

$$\hbar\omega_s = \frac{\alpha M_o(T, H)}{g\mu_B} \qquad (2)$$

The effect is known as the giant Zeeman splitting, as in moderately high magnetic fields and low temperatures $\hbar\omega_s$ attains values comparable to the Fermi energy or to the binding energy of excitons and shallow impurities. For effective mass states, whose periodic part of the Bloch function contains spin components mixed up by a spin-orbit interaction, the exchange splitting $\hbar\omega_s$ does not depend only on the product of M_o and the relevant exchange integral, say β, but usually also on the magnitude and direction of $\vec{k}$, confinement, and strain. The giant Zeeman splitting is clearly visible in magneto-optic phenomena as well as in the Shubnikov–de Haas effect, making an accurate determination of the exchange integrals possible, particularly in wide-gap materials, in which competing Landau and ordinary spin splittings are small.

The possibility of tailoring the magnitude of spin splitting in DMS structures offers a powerful tool to examine various phenomena. For instance, spin engineering has been explored to control by the magnetic field the confinement of carriers and photons, to map atom distributions at interfaces, as well as to identify the nature of optical transitions and excitonic states. Furthermore, a subtle influence of spin splitting on the quantum scattering amplitude of interacting electrons with opposite spins has been put into evidence in DMS in the weakly localized regime.

The redistribution of carriers between spin levels induced by spin splitting has been shown to drive an insulator-to-metal transition as well as to generate universal conductance fluctuations in DMS quantum wires. Since the spin splitting is greater than the cyclotron energy, there are no overlapping Landau levels in modulation-doped heterostructures of DMS in the quantum Hall regime. This has made it possible to test a scaling behavior of wave functions at the center of Landau levels. At the same time, it has been confirmed that in the presence of a strong spin-orbit coupling (e.g., in the case of p-type wave functions) the spin polarization can generate a large extraordinary (anomalous) Hall voltage. Finally, optically and electrically controlled spin-injection has been observed in all-semiconductor structures containing DMS.

4.2 Spin-disorder Scattering

Spatial fluctuations of magnetization, disregarded in the mean-field approximation, lead-to-spin disorder scattering. According to the fluctuation-dissipation theorem, the corresponding scattering rate in the paramagnetic phase is proportional to $T\chi(T)$, where χ is the magnetic susceptibility of the localized spins. Except in the vicinity of ferromagnetic phase transitions, a direct contribution of spin-disorder scattering to momentum relaxation turns out to be small. In contrast, this scattering mechanism controls the spin lifetime of effective mass carriers in DMS, as evidenced by studies of universal conductance fluctuations, line-width of spin-flip Raman scattering, and time-resolved magneto-optics. Furthermore, thermodynamic fluctuations contribute to the temperature dependence of the bandgap and band off-set. In the case when the total potential introduced by a magnetic ion is greater than the width of the carrier band, the virtual crystal and molecular field approximations break down, a case of the holes in $Cd_{1-x}Mn_xS$. Various nonperturbative schemes have been developed to describe nonlinear dependencies of the band gap on x and of the spin splitting on M observed in such situations.

4.3 Magnetic Polarons

Bound magnetic polaron (BMP), that is a bubble of spins ordered ferromagnetically by the exchange interaction with an effective mass carrier in a localized state, modifies optical, transport, and thermodynamic properties of DMS. BMP is formed inside the Bohr radius of the occupied impurity state but also around a trapped exciton, as the polaron formation time is typically shorter than the exciton lifetime. The BMP binding energy is proportional to the magnitude of local magnetization, which is built up by two effects: the molecular field of the localized carrier and thermodynamic fluctuations of magnetization. The latter enlarges width of optical lines, particularly in the case of quantum dots and wires, in which self-trapped magnetic polaron is stable even without pre-localizing potential. In contrast, a free magnetic polaron—a

delocalized carrier accompanied by a traveling cloud of polarized spins—is expected to exist only in magnetically ordered phases. This is because coherent tunneling of quasi-particles dressed by spin polarization is hampered, in disordered magnetic systems, by a small quantum overlap between magnetizations in neighboring space regions.

5. *Exchange Interactions Between Localized Spins*

As in most magnetic materials, classical dipole–dipole interactions between magnetic moments are weaker than exchange couplings in DMS. Direct *d–d* or *f–f* exchange interactions, known from properties of magnetic dimmers, are thought to be less important than indirect exchange channels. The latter involve a transfer of magnetic information via spin polarization of bands, which is produced by the exchange interaction or spin-dependent hybridization of magnetic impurity and band states. If magnetic orbitals are involved in the polarization process, the mechanism is known as *superexchange*, which is merely antiferromagnetic and dominates, except for *p*-type DMS. If fully occupied band states are polarized by the *sp–d* exchange interaction, the resulting indirect *d–d* coupling is known as the *Bloembergen–Rowland mechanism*. In the case of *Rudermann–Kittel–Kasuya–Yosida* (RKKY) interaction, the *d–d* coupling proceeds via spin polarization of partly filled bands, that is by free carriers.

Since in DMS carrier concentrations are usually much smaller than those of localized spins, the energetics of the latter can be treated in the continuous medium approximation, an approach referred to as the *Zener model*. Within this model the RKKY interaction is ferromagnetic, and particularly strong in *p*-type materials, because of large magnitudes of hole mass and exchange integral β. Finally, in the case of systems in which magnetic ions in different charge states coexist, hopping of an electron between magnetic orbitals of neighboring ions in differing charge states tends to order them ferromagnetically. This mechanism, dubbed the double exchange, can operate in, for example, *n*-type (Zn,Co)O.

In general, the bilinear part of the interaction Hamiltonian for a pair of spins *i* and *j* is described by a tensor *J*,

$$H_{ij} = -2S_i J_{ij} S_j \qquad (4)$$

which in the case of the coupling between nearest neighbor cation sites in the unperturbed zinc-blende lattice contains four independent components. Thus, in addition to the scalar Heisenberg-type coupling, $H_{ij} = -2J_{ij}S_iS_j$, there are nonscalar terms (e.g., Dzialoshinskii–Moriya or pseudo-dipole). These terms are induced by the spin-orbit interaction within the magnetic ions or within nonmagnetic atoms mediating the spin–spin exchange. The nonscalar terms, while smaller than the scalar ones, control spin-coherence time and magnetic anisotropy. Typically, $J_{ij} \approx -1\,\text{meV}$ for nearest-neighbor pairs coupled by the superexchange, and the interaction strength decays fast with the pair distance.

Thus, with lowering temperature more and more distant pairs become magnetically neutral, $S_{\text{tot}} = 0$. Accordingly, the temperature dependence of magnetic susceptibility assumes a modified Curie form, $\chi(T) = C/T^{\gamma}$, where $\gamma < 1$ and both C and γ depend on the content of the magnetic constituent *x*. Similarly, the field dependence of magnetization is conveniently parameterized by the Brillouin function B_S,

$$M_o(T,\ H) = Sg\mu_B N_o x_{\text{eff}} B_S[Sg\mu_B H/k_B(T + T_{\text{AF}})] \quad (5)$$

in which two *x*- and *T*-dependent empirical parameters, $x_{\text{eff}} < x$ and $T_{\text{AF}} > 0$, describe the presence of antiferromagnetic interactions.

6. *Magnetic Collective Phenomena*

In addition to magnetic and neutron techniques, a variety of optical and transport methods, including subpicosecond spectroscopy and $1/f$ noise study of nanostructures, have successfully been employed to characterize collective spin phenomena in DMS. Undoped DMS belong to a rare class of systems, in which spin-glass freezing is driven by purely antiferromagnetic interactions, an effect of spin frustration inherent to the randomly occupied f.c.c. sublattice. Typically, in II–VI DMS, the spin-glass freezing temperature T_f increases from $0.1\,\text{K}$ for $x = 0.05$ to $20\,\text{K}$ at $x = 0.5$ according to $T_f \sim x^{\delta}$, where $\delta \approx 6$, which reflects a short-range character of the superexchange. For *x* approaching one, antiferromagnetic type III ordering develops, according to neutron studies. Here, strain imposed by the substrate material—the strain engineering—can serve to select domain orientations as well as to produce spiral structures with a tailored period.

Particularly important is the carrier-density controlled ferromagnetism of bulk and modulation-doped *p*-type DMS. The observed values of the Curie temperature T_C are below $5\,\text{K}$ in $\text{Zn}_{1-x}\text{Mn}_x$Te:N but in the case of $\text{Ga}_{1-x}\text{Mn}_x$As, in which manganese supplies both spins and holes, T_C reaches $110\,\text{K}$ for $x = 0.05$. At the same time, strain engineering makes it possible to design the direction of the easy axis. In the case of *p*-type quantum structures, the hole concentration, and thus the magnetic phase, can be changed isothermally, by light or gate voltage. Furthermore, observations of an exchange coupling via nonmagnetic layers have been followed by demonstrations of giant magnetoresistance (GMR) and tunneling magnetoresistance (TMR) effects in ferromagnetic III–V DMS.

7. Concluding Remarks

In addition to being a valuable playground in which to examine various novel phenomena, DMS have already been commercialized as Faraday effect-based optical insulators as well as intracenter light emitters. Future studies will certainly attempt to explore a great potential of ferromagnetic semiconductors and their quantum structures. This requires preparation of ferromagnetic semiconductors with T_C above room temperature, a feasible task according to some theoretical predictions. Indeed, promising results on T_C above 300 K in chalcopirite (Cd,Mn,Ge)P$_2$ and wurzite (Zn,Co)O:Ga have been reported.

Properties of short period ferrimagnetic superlattices containing two different magnetic elements, such as Mn and Co, but perhaps also different rare earths or actinides, are to be explored. Other possible functional materials are hybrid structures of semiconductors and ferromagnetic metals, the latter in the form of overgrowth or inserted layers or inclusions. Magnetoresistance over 10 000% that has been found at room temperature in such a granular system constitutes a good example of the many opportunities ahead.

See also: Giant Magnetoresistance; Spintronics in Semiconductor Nanostructures

Bibliography

Averous M, Balkanski M 1991 *Semimagnetic Semiconductors and Diluted Magnetic Semiconductors*. Plenum, New York, pp. 1–274

Awschalom D D, Samarth N 1999 Spin dynamics and quantum transport in magnetic semiconductor quantum structures. *J. Magn. Mater*. **200**, 130–47

Dietl T 1994 (Diluted) magnetic semiconductors. In: Moss T C (ed.) *Handbook on Semiconductors*. North-Holland, Amsterdam, Vol. 3B, pp. 1251–342

Furdyna J K 1998 Diluted magnetic semiconductor thin films and multilayers. In: Bain J A, Rubin K, Nolan T, Bogy D, Stadler B J H, Levy M, Lorenzo J P, Mansuripur M, Okamura Y, Wolfe R (eds.) *High-Density Magnetic Recording and Integrated Magneto-Optics: Materials and Devices*. Warrendale, Pennsylvania, PA, pp. 613–24

Furdyna J K, Kossut J 1988 Diluted magnetic semiconductors. In: Willardson R K, Beer A C (eds.) *Semiconductors and Semimetals*. Academic Press, Boston, Vol. 25, pp. 1–462

Gałazka R R, Kossut J, Story T 1999 Semimagnetic semiconductors. In: Rössler U (ed.) *Landolt-Börstein, New Series*. Springer, Berlin, Vol. 41B, pp. 650–721

Jain M (ed.) 1991 *Diluted Magnetic Semiconductors*. World Scientific, Singapore, pp. 1–652

Kossut J, Dobrowolski W 1997 Properties of diluted magnetic semiconductors. In: Capper P (ed.) *Narrow Gap II–VI Compounds for Optoelectronic and Electromagnetic Applications*. Chapman and Hall, London, pp. 401–29

Langer J M, Delerue C, Lannoo M, Heinrich H 1988 Transition-metal impurities in semiconductors and heterojunction band lineups. *Phys. Rev. B* **38**, 7723–39

Nagaev E L 1979 *Physics of Magnetic Semiconductors*. Mir, Moscow, pp. 1–388

Ohno H 1999 Properties of ferromagnetic III–V semiconductors. *J. Magn. Magn. Mater*. **200**, 110–29

Ohno H 2000 Ferromagnetic III–V heterostructures. *J. Vac. Sci. Technol. B* **18**, 2039–43

Zunger A 1986 Electronic Structure of 3d Transition-atom Impurities in Semiconductors. In: Seitz F, Turnbull D (eds.) *Solid State Physics*. Academic Press, New York, Vol. 39, pp. 275–464

T. Dietl
Institute of Physics, Warsaw, Poland

DNA Microarrays using Magnetic Labeling and Detection

There are myriad applications for biosensors—from antiterrorism, to food safety, to point-of-care clinical diagnostics. The goal is to create systems that mimic the sensitive and specific sensing abilities that come effortlessly to naturally occurring organisms. A common approach to detecting biological molecules is to attach to the target molecule a chemical label that produces an externally observable signal. Traditionally, this is accomplished using biomolecular recognition between the target molecule and a specific receptor (e.g., an antibody) that incorporates a label such as a radioisotope, enzyme, or fluorescent molecule. Sensing methods have been developed based on a range of transduction mechanisms, including optical, electrical, electrochemical, thermal, and piezoelectrical means, which are covered eloquently by numerous reviews (see, e.g., Pearson *et al.* 2000, Vo-Dinh and Cullum 2000).

Recently, magnetic particles have been developed as labels for biosensing. Magnetic labels have several potential advantages over other labels. They are not subject to degradation over time or photobleaching, making their properties very stable. In addition, magnetic fields are not attenuated by biological material, offering the possibility of *in vivo* sensing. Magnetism may also be used to remotely manipulate the particles. Finally, there are a number of sensitive magnetic field detection methods arising from advances in microelectronics and magnetic storage technologies that will enable the design of compact, low-power sensor systems. Recently described detection methods include the Maxwell bridge (Kriz *et al.* 1996), micro-cantilever-based force amplified biological sensor (Baselt *et al.* 1997), superconducting quantum interference device (SQUID) (Kötitz *et al.* 1997), giant magnetoresistive bead array counter (Baselt *et al.* 1998), frequency-dependent magnetometer (Richardson *et al.* 2001), and silicon Hall sensor (Besse *et al.* 2002).

1. Basic Biomolecule Labeling and Detection with Magnetic Particles

As for many other biomolecular labels, magnetic labeling can be easily accomplished using specific ligand–receptor interactions, as illustrated generically in Fig. 1. The illustrated "sandwich" configuration proceeds as follows:

(i) Receptor molecules specific for the target biomolecules are attached to the surface of a solid substrate. Often arrays of different probe spots are used to simultaneously detect multiple targets.

(ii) When target molecules are present in a sample solution, they are captured by the surface.

(iii) Magnetic particles coated with a second set of receptor molecules for the target are introduced, labeling the previously captured targets.

(iv) The label particles are detected by a magnetic sensor.

Sandwich assays are commonly performed using antibody–antigen pairs and complementary DNA strands, and often use the strongly binding biomolecular combination of streptavidin and biotin to attach the particle labels to the receptor molecules.

For biosensing applications, the magnetic particles used as labels should be paramagnetic, i.e., only have a magnetic moment when a magnetic field is applied. The absence of a permanent magnetic moment prevents agglomeration of the particles in solution which would render them ineffective as labels. When selecting label particles, properties of importance include the size and size uniformity, the type of magnetic material and its volume fraction within the particle, and the particle surface chemistry. For example, though nanometer-scale particles are matched in size

Figure 1
Generic illustration of magnetic labeling of targets captured onto a solid substrate in a "sandwich" configuration using specific biomolecular ligand–receptor recognition.

to biological macromolecules such as DNA, the small magnetic fields they generate are difficult to detect. Second, the surface of the particles must be suitable for chemical attachment of biomolecules. A variety of paramagnetic beads with biocompatible polymer or silica shells are commercially available with diameters that range from 1 μm to 5 μm.

Because magnetic particles experience a force in the presence of a magnetic field gradient, they may be manipulated by magnets. This phenomenon can be used to apply a controlled force that selectively pulls off only those labels not bound to the surface by specific binding (Lee *et al.* 2000). Such a force discrimination assay increases the sensitivity of detection by greatly reducing the background signal and thereby permitting very low signal levels to be detected with confidence.

2. Magnetic Particle Detection

The detection of magnetic particles can be accomplished by a number of methods, as mentioned above. Here we will focus on the use of solid-state magnetic field sensors embedded in the substrate, a method that illustrates many of the advantages of magnetic labeling for biomolecule detection. For example, such an approach has the potential to eliminate the requirement for an external detection system, thereby reducing the size, cost, and power of the sensor system.

One of the simplest solid-state magnetic field sensors to incorporate into a microelectronic substrate is a giant magnetoresistive (GMR) wire (Baselt *et al.* 1998). GMR materials are multi-component thin films with alternating magnetic and nonmagnetic layers (see *Giant Magnetoresistance*). The relative orientation of the magnetic moments of these layers is altered in the presence of a magnetic field, changing the electrical resistance of the wire. When a magnetic particle is present above a GMR sensor, the resistance of the sensor changes; the larger the number of particles present, the larger the change. The availability of suitably sensitive GMR sensors was made possible by recent advances in magnetic materials for high-density data storage, including magnetic disk drive read-out sensors and nonvolatile magnetic memory elements (Prinz 1998).

When paramagnetic microbeads are used, such as those commercially available, GMR sensors have been designed that are only sensitive to a planar component of the dipolar magnetic field induced in the particles, as illustrated in Fig. 2. As discussed by Miller *et al.* (2001), when an external magnetic field is applied normal to the plane of the GMR sensor, the field strength at the sensor is given by

$$B \sim m/z^3 \qquad (1)$$

where m is the magnetic moment of the bead and z is the distance from the center of the bead to the sensor. Therefore, the resistance change in the sensing wire is roughly proportional to the number of magnetic particles present above it, a signal that can be easily measured. For maximum signal, the particle should have as large a magnetization as possible and be as close to the sensor as possible.

Figure 2
Schematic of the magnetic field induced around a paramagnetic microbead on top of a magnetic field sensor when an external field is applied normal to the substrate.

3. Detection with a GMR Sensor Microarray

A well-developed system that uses a GMR microarray to detect different DNA sequences in a sample is the bead array counter (BARC) sensor (Baselt *et al.* 1998, Edelstein *et al.* 2000, Miller *et al.* 2001). In this system, the test is performed inside a small, quartz flow cell mounted over the sensor chip. The chip itself is wire bonded to a printed circuit board housed in a disposable plastic cartridge that contains the required liquid reagents. The cartridge plugs into an automated electronic controller and connects to a miniature pumping system (Tamanaha *et al.* 2002).

Before assembly, the surface of the sensor chip is coated with a biocompatible polymer film (polyethylene glycol (PEG)) and an array of single-stranded DNA capture probes (Fig. 3(a)). Note that the GMR sensors and associated interconnects must be protected from the reactive and conductive salt solution used in the biochemical test, in this case by a film of
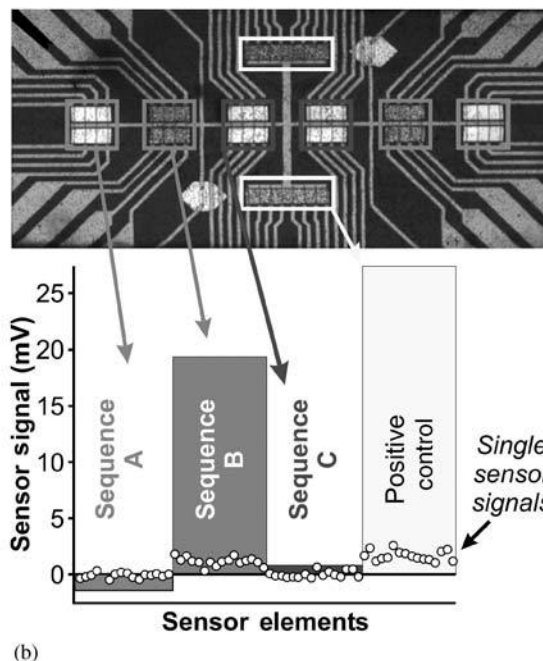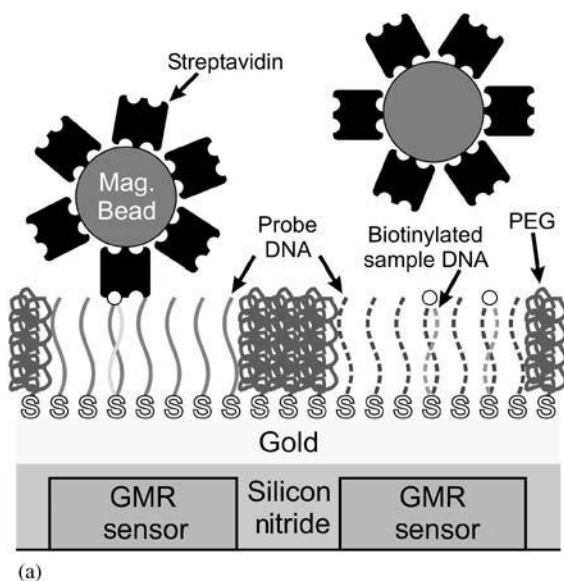
Figure 3
(a) An illustration of the BARC biosensor approach. Note that the elements are not to scale; in particular, the beads and sensors are much larger in proportion to the biomolecules. (b) A micrograph of a BARC chip after a DNA test, with the eight sensing zones outlined. For each of the probe zones, the graph shows the measured signals from the individual sensing elements (open circles) and the integrated signal for all 16 elements (colored bar). The assay for sequence "B" was performed with 10 nM DNA hybridized for 30 min. The total test required about ~60 min.

silicon nitride. The chip is also coated with a thin gold layer so that the DNA probes and PEG can be attached to the surface by strong gold–sulfur bonds. Each sensor zone is covered with strands of DNA complementary for a different target strand. The PEG film inhibits undesirable, nonspecific, sticking of target DNA and magnetic particles in the areas outside of the DNA probe spots.

To test for the presence of specific target DNA sequences, the sample is introduced into the flow cell and allowed to hybridize with the capture probes. In the illustrated example, the target strands have been pre-modified to have biotin molecules attached at one end. Therefore, the presence of target in the sample will result in double-stranded, biotin-tagged DNA bound above a sensor. The captured targets are then labeled with streptavidin-coated magnetic microbeads. Beads just resting on the surface can be removed by a magnetic force, and the remaining beads detected by the underlying GMR sensors.

The results of an actual experiment performed in this way are shown in Fig. 3(b) on a chip with eight sensor zones (Miller *et al.* 2001). A micrograph shows the surface of the chip after the test. In this test, each of the three different DNA sequences and the positive control (a probe with biotin already on it) were each applied to two zones. Introducing a sample containing only sequence ''B'' results in the complementary zones and the positive control being covered with beads (appearing dark). The presence of the beads is accurately detected by the eight GMR sensors in each zone.

4. Summary

Magnetic labeling and detection holds great promise for sensing biomolecules. As demonstrated by the BARC system, advances in microelectronics and materials can be adapted to analytical applications in the biosciences with great success. Magnetic particles, magnetic force manipulation, and magnetoelectronic detection can be combined to create relatively simple, compact, sensor systems. Such technology promises to fulfill the need for ever faster, more sensitive, and more portable systems in fields as diverse as homeland defense, clinical diagnostics, genomics, proteomics, and forensics.

See also: SQUIDs: Biomedical Applications

Bibliography

Baselt D R, Lee G U, Hansen K M, Chrisey L A, Colton R J 1997 A high-sensitivity micromachined biosensor. *Proc. IEEE* **85**, 672–80

Baselt D R, Lee G U, Natesan M, Metzger S W, Sheehan P E, Colton R J 1998 A biosensor based on magnetoresistance technology. *Biosens. Bioelectron.* **13**, 731–9

Besse P-A, Boero G, Demierre M, Pott V, Popovic R 2002 Detection of a single magnetic microbead using a miniaturized silicon hall sensor. *Appl. Phys. Lett.* **80**, 4199–201

Edelstein R L, Tamanaha C R, Sheehan P E, Miller M M, Baselt D R, Whitman L J, Colton R J 2000 The BARC biosensor applied to the detection of biological warfare agents. *Biosens. Bioelectron.* **14**, 805–13

Kötitz R, Matz H, Trahms L, Koch H, Weitschies W, Rheinländer T, Semmler W, Bunte T 1997 SQUID based remanence measurements for immunoassays. *IEEE Trans. Appl. Supercond.* **7**, 3678–81

Kriz C B, Rådevik K, Kriz D 1996 Magnetic permeability measurements in bioanalysis and biosensors. *Anal. Chem.* **68**, 1966–70

Lee G U, Metzger S, Natesan M, Yanavich C, Dufrêne Y F 2000 Implementation of force differentiation in the immunoassay. *Anal. Biochem.* **287**, 261–71

Miller M M, Sheehan P E, Edelstein R L, Tamanaha C R, Zhong L, Bounnak S, Whitman L J, Colton R J 2001 A DNA array sensor utilizing magnetic microbeads and magnetoelectronic detection. *J. Magn. Magn. Mater.* **225**, 138–44

Pearson J E, Gill A, Vadgama P 2000 Analytical aspects of biosensors. *Ann. Clin. Biochem.* **37**, 119–45

Prinz G 1998 Magnetoelectronics. *Science* **282**, 1660–3

Richardson J, Hawkins P, Luxton R 2001 The use of coated paramagnetic particles as a physical label in a magneto-immunoassay. *Biosens. Bioelectron.* **16**, 989–93

Tamanaha C R, Whitman L J, Colton R J 2002 Hybrid macro–micro fluidics system for a chip-based biosensor. *J. Micromech. Microeng.* **12**, N7–N17

Vo-Dinh T, Cullum B 2000 Biosensors and biochips: advances in biological and medical diagnostics. *Fresenius J. Anal. Chem.* **366**, 540–51

Cy. R. Tamanaha
Geo-Centers, Washington, DC, USA

Lloyd J. Whitman
Naval Research Laboratory, Washington, DC, USA

E

Electrodynamics of Superconductors: Flux Properties

The "mixed state" of type II superconductors occurs when magnetic flux penetrates the material in the form of flux lines (vortices) without destroying the superconducting ground state (Tinkham 1996). Above the field of first flux penetration, H_p, the repelling flux lines spontaneously order into a triangular (Abrikosov) lattice with sixfold symmetry. The state of zero resistivity is destroyed by vortex motion, which, however, is retained up to a critical current density, J_c, when the flux lines are pinned by crystalline defects. Vortex motion can also be driven by thermal fluctuations. When they are sufficiently large, the vortex lattice melts to a vortex liquid and the superconducting ground state is destroyed.

1. Flux Line Lattice

Thermodynamically, a flux line is stable above the lower critical field, H_{c1} (Abrikosov 1957). The flux line (or vortex) consists of a "normal" core in which the density of Cooper pairs decreases to zero over a length scale $\xi(T)$, the Ginzburg–Landau (GL) coherence length. Around the core superconducting screening currents circulate, which generate a local magnetic field of about $2\mu_0 H_{c1}$, where μ_0 is the magnetic permeability of vacuum. Away from the core both the field and the screening currents decay over a length scale $\lambda(T)$, the GL penetration depth. The line energy of a flux line per unit length is given by

$$\varepsilon = \varepsilon_0 \ln \kappa \equiv (\Phi_0^2 / 4\pi\mu_0\lambda^2) \ln \kappa \qquad (1)$$

where Φ_0 is the flux quantum, which is also the magnetic flux carried by a flux line. The GL parameter κ is the ratio λ/ξ.

Usually, the first penetration of flux occurs at a field H_p, which is considerably different from H_{c1}, because the flux line has to enter through the surface or across the edges of the superconductor. This means that H_p is determined by surface and geometrical barriers which depend on sample shape and field orientation.

Well above H_p the flux lines form a triangular Abrikosov lattice with lattice parameter $a_\Delta = (2/\sqrt{3})^{1/2} a_0$, where $a_0 = (\Phi_0/B)$ and B is the flux density. Because of the electromagnetic origin, the range of the vortex interactions is λ, which is generally much larger than a_0. Elastic deformations of the Abrikosov lattice are described by elasticity moduli for uniaxial compression (c_{11}), for tilt deformations (c_{44}), and for shear deformations (c_{66}). Both c_{11} and c_{44} strongly depend on the wavelength of the deformation fields.

Especially for small wavelengths the effect of the deformations is considerably reduced by averaging over the vortex interaction range λ, i.e., the flux line lattice is very soft on scales smaller than λ.

For very anisotropic materials, such as high-temperature superconductors, the flux lines caused by a magnetic field perpendicular to the CuO_2 planes break up into pancake vortices located in the superconducting layers (Blatter et al. 1994). The tilt modulus is now reduced by a factor equal to the anisotropy parameter, Γ, which can be as large as 10^5. Above a crossover field $B_{cr} = \Phi_0/\Gamma s^2$ (s is the interlayer distance) the tilt deformations become irrelevant and a quasi two-dimensional interaction results in which only compression and shear modes between pancake vortices in the same layer survive. When the magnetic field is parallel to the CuO_2 plane it penetrates in the form of Josephson vortices (Bulaevskii 1973), which possess no normal core. For arbitrary field directions crossing lattices of Abrikosov pancake vortex stacks and Josephson vortices may coexist (Koshelev 1999).

2. Thermodynamics

Usually the mixed state is represented by the magnetization curve $M(H)$ which in principle consists of five regimes: up to H_{c1} in the Meissner state $M = -H$, just above H_{c1} it drops exponentially, for $H_{c1} < H < H_{c2}$ it is characterized by $M \propto \ln(H_{c2}/H)$, near H_{c2} it is linearly proportional to $H_{c2} - H$, and above H_{c2} $M = 0$. Because of surface and geometrical effects there may occur deviations from this ideal behavior. In this picture it was believed that the phase transition to the superconducting state takes place at the upper critical field, $H_{c2}(T)$. It is now generally accepted that the real thermodynamic phase transition occurs at the melting line, $H_m(T)$. In pure single crystals of high-temperature superconductors the melting transition is of first order. It manifests itself by a jump in B, the flux liquid is slightly denser than the solid (Zeldov et al. 1995). In the presence of quenched disorder the transition becomes of second order.

Melting occurs when thermal fluctuations generate elastic modes in the lattice that are strong enough to destroy its shear strength (Nelson 1988). In a three-dimensional lattice both shear and tilt deformations determine the mean square displacement $\langle u^2 \rangle^{1/2}$. According to the Lindemann criterion the lattice melts when this quantity is a significant fraction of the lattice parameter, i.e., $\langle u^2 \rangle^{1/2} = c_L a_0$, where c_L is the Lindemann number ($c_L = 0.1$–0.3). This criterion gives a good description of the melting line. For thin films in a perpendicular field the tilt modes of the flux lines do

not contribute to the thermal disorder and the system should be considered as a two-dimensional solid consisting of rigid flux bars. Thermal fluctuations in two dimensions give rise to the formation of edge dislocation pairs, which unbind at a second-order melting line in accord with the Kosterlitz–Thouless theory for two-dimensional melting.

In very anisotropic materials the low-temperature phase consists of a solid of flux lines (stacked pancake vortices) which at the first-order transition line decays to a plasma of decoupled pancake vortices. In all situations the state of true superconductivity is destroyed at the melting line and ohmic behavior is recovered.

3. Flux Pinning and the Critical Current

A moving flux line lattice (FLL) dissipates energy. When this motion is driven by a transport current with density J, a steady state with velocity v is reached when the driving force, $J\Phi_0$, on each vortex is compensated by a frictional force ηv. An illustrative model for the friction coefficient, η, is that of Bardeen and Stephen in which the vortex core is treated as a moving cylinder of normal metal. The ratio between flux flow resistivity, ρ_f, and normal state resistivity, ρ_n, is then simply represented by the normal fraction, i.e., B/B_{c2}, which leads to $\eta = \Phi_0^2 \rho_n^{-1}/2\pi\xi^2$.

A moving FLL should thus be considered as a normal metal with a (much) smaller resistivity ρ_f. Obviously, for applications, the flux flow state should be suppressed. In practice, most materials can be made with a high density of inhomogeneities acting as pinning centers which trap the flux lines up to a critical force $J_c\Phi_0$, where J_c is the critical current density. Defects deviate from the background material by a different local density, elasticity, electron–phonon coupling, electron mean free path P, etc. The first three properties give rise to a local change in T_c, whereas the latter leads to a variation in P. Consequently, one may distinguish between δT_c pinning and δP pinning, each with its characteristic temperature and field dependence (Kes 1991).

The collective action of the pinning centers breaks up the FLL in domains of average size L_c parallel to the field and transverse size R_c perpendicular to the field. Its volume is $V_c \approx R_c^2 L_c$. The critical current density follows from the statistical average over distributions of pinning centers with pinning strength $W = n_p\langle f^2\rangle$, where n_p is the concentration of pins and $\langle f^2\rangle$ the squared average of the pinning force of a single defect. This leads to the well-known collective pinning relationship (Larkin and Ovchinnikov 1979)

$$J_c B \approx (W/V_c)^{1/2} \tag{2}$$

In the original theory the domain sizes were determined by the balance of pinning energy and the energy of the *elastic* deformations in the FLL. However, when the pinning is strong, the local strains in the FLL may grow beyond the elastic limit so that topological defects such as edge dislocations are created. These now determine the positional disorder in the FLL and the domain size V_c. Optimal pinning occurs when the transverse order is totally destroyed, i.e., $R_c \approx a_0$, and individual flux line segments of length L_c make up the average domain size. In anisotropic high-temperature superconductors this length can be as small as the height, s, of a single pancake vortex. The transition from elastic to plastic disorder may be seen as a peak effect in J_c. It usually happens near H_{c2} or near the melting line. Interesting finite size effects may occur in thin films in a perpendicular field leading to two-dimensional collective pinning.

When the pinning is weak, as is the case in amorphous thin films, L_c can be larger than the film thickness. Now only shear deformations are relevant, which makes the analysis conveniently transparent (Kes and Tsuei 1983).

4. Thermal Effects, Depinning, and Creep

The FLL in the presence of pinning centers may be seen as an elastic medium in a disorder potential with each domain sitting in a local potential minimum. With increasing temperature thermal fluctuations will give rise to positional fluctuations of the domains and thermal smearing of the potential roughness. When the mean square displacement is of the order of the range, r_f, of the disorder potential, this effect (called thermal depinning) is large enough to cause a considerable decrease of the pinning force and of J_c. The corresponding depinning or irreversibility line in the temperature–field diagram separates a strong pinning regime at low temperatures from a weak pinning regime at high temperatures.

Thermal fluctuations also make the FLL domains jump over energy barriers between different potential minimums of almost equal energy. In the presence of a driving force this process leads to a unidirectional creep of the FLL with an average velocity $\sim \exp(-U_p/k_B T)$, where U_p is the typical height of the energy barrier and k_B is the Boltzmann constant. For relatively small values, $U_p/k_B T \lesssim 10$, one thus gets linear resistivity at small J, called thermally assisted flux flow (TAFF):

$$\rho_{\mathrm{TAFF}} = \rho_f \exp(-U_p/k_B T) \tag{3}$$

Although ρ_{TAFF} may be extremely small, TAFF does not describe a true superconducting state with zero resistance at small J, but rather a normal metal with ohmic resistance. The reason is that U_p is supposed to be finite and independent of J. It has been shown, however, that for collective creep of an elastic

medium in random disorder the domain size, the distance between available metastable states, and the corresponding energy barriers should grow when J decreases in order to maintain the balance between deformation energy and work done by the driving force. In fact, $U_p \sim (J_c/J)^\mu$ with μ of order one, which leads to true zero resistance for $J \to 0$, according to $\rho \sim \rho_f \exp[-c(J_c/J)^\mu]$. A similar result is obtained in the vortex glass model where the flux flow is supposed to be triggered by the motion of topological defects in the FLL. It shows once more that the mixed state with strong pinning not only is a very practical phenomenon, but that it is a rich area of research for solid-state and statistical physics.

See also: Electrodynamics of Superconductors: Weakly Coupled

Bibliography

Abrikosov A A 1957 On the magnetic properties of superconductors of the second group. *Sov. Phys. JETP* **5**, 1174
Blatter G, Feigelman V M, Geshkenbein V B, Larkin A I, Vinokur V M 1994 Vortices in high-temperature superconductors. *Rev. Mod. Phys.* **66**, 1125–388
Bulaevskii L N 1973 Magnetic properties of layered superconductors with weak interaction. *Sov. Phys. JETP* **37**, 1133
Kes P H 1991 In: Cahn R W, Haasen P, Kramer E J (eds.) *Materials Science and Technology*. VCH, New York, Vol. 3A, Part I
Kes P H, Tsuei C C 1983 Two-dimensional collective flux pinning, defects and structural relaxation in amorphous superconducting films. *Phys. Rev. B* **28**, 5126–39
Koshelev A E 1999 Crossing lattices, vortex chains, and angular dependence of melting line in layered superconductors. *Phys. Rev. Lett.* **83**, 187–90
Larkin A I, Ovchinnikov Yu N 1979 Pinning in type II superconductors. *J. Low Temp. Phys.* **34**, 409
Nelson D 1988 Vortex entanglement in high-T_c superconductors. *Phys. Rev. Lett.* **60**, 1973–6
Tinkham M 1996 *Introduction to Superconductivity*. McGraw-Hill, New York, 2nd edn
Zeldov E, Majer D, Konczykowski M, Geshkenbein V B, Vinokur V M, Shtrikman H 1995 Thermodynamic observation of first-order vortex lattice melting in $Bi_2Sr_2CaCu_2O_8$. *Nature* **375**, 373–6

P. H. Kes
Leiden University, The Netherlands

Electrodynamics of Superconductors: Weakly Coupled

Systems consisting of two superconducting samples connected by a weak electrical contact possess several unusual properties. First, the net current flowing across the contact—the Josephson junction (see *Josephson Junctions: Low-T_c*; *Josephson Junctions: High-T_c*)—contains a supercurrent I_S. If I_S is smaller than the critical current of a junction, I_C, then its flow does not lead to a voltage drop across the structure. The supercurrent depends on the phase difference $\varphi = \chi_1 - \chi_2$ of the superconductor order parameters $\Delta_1 \exp(i\chi_1)$ and $\Delta_2 \exp(i\chi_2)$ of the samples (stationary Josephson effect). This function is exactly 2π periodic and, in the simplest cases, is sinusoidal:

$$I_S(\varphi) = I_C \sin(\varphi) \tag{1}$$

The critical current, I_C, is a constant determined by the transport parameters of the contact material and the shape of the Josephson junction. At $I_S > I_C$ there is a voltage drop, V, across the junction, which is related to φ by the fundamental law (nonstationary Josephson effect)

$$\frac{d\varphi}{dt} = \frac{2e}{\hbar} V \tag{2}$$

where e is the electron charge and $\hbar$ is Planck's constant.

The physical origin of the stationary Josephson effect lies in the specific form of electron reflection from a superconducting interface. Electrons with energy ε smaller than the superconducting gap, Ω, of the electrodes are trapped in a contact material. They cannot penetrate into an electrode since there is a gap in the density of states near the Fermi level of a superconductor. However, if the energy ε of an electron is in the interval $0 \leqslant \varepsilon \leqslant \Omega$, its interaction with an electrode results in the creation, with a probability equal to one, of an extra pair of correlated electrons (Cooper pair) in the superconductor and a hole with energy $-\varepsilon$ in the contact material. The latter moves in the direction opposite to that of the initial electron (so-called Andreev reflection). This hole, in turn, interacts with another electrode and causes annihilation of a pair of correlated electrons and the creation of an electron with energy ε, which moves in the same direction as that of the initial particle. As a result of this cycle, a pair of correlated electrons transfers from one superconductor to another leading to a supercurrent flow across a junction, i.e., to the stationary Josephson effect.

The nonstationary Josephson effect is a direct consequence of the Schrödinger equation. In the stationary state the wave function of correlated electrons has the form $\psi(r, t) = \psi(r) \exp(iEt/\hbar)$, and the Schrödinger equation for the phase of the wave function reduces to $\hbar \partial \chi_{1,2}/\partial t = -E_{1,2}$, where $E_{1,2}$ is the energy of the superconducting condensate in the samples. Thus $\hbar \partial \varphi/\partial t = E_2 - E_1$ and this latter difference should be equal to the difference $E_{F2} - E_{F1}$ of the electrochemical potentials E_{F2} and E_{F1} across the junction, which is exactly equal to $2eV$.

1. Current Components

In the general case, the net current, I, across a Josephson junction has several components in addition to $I_S(\varphi)$:

$$I = I_S(\varphi) + I_N(V) + I_D(V) + I_F(t) \qquad (3)$$

where I_N is the normal (quasiparticle) current, I_D the displacement current, and I_F the fluctuation current.

1.1 Supercurrent

In accordance with Eqn. (1) a d.c. supercurrent in the range

$$-I_C \leqslant I_S(\varphi) \leqslant I_C \qquad (4)$$

can flow across the junction as a result of a constant phase difference φ. An external system supporting this phase difference represents work on the supercurrent and, thus, stores potential energy in the junction given by

$$U(\varphi) = E_C[1 - \cos(\varphi)] + \text{const}, \; E_C = \frac{\hbar I_C}{2e} \qquad (5)$$

Since the energy is conserved in the form of persistent current, the Josephson junction can be considered as having a nonlinear inductance

$$L_S^{-1} = L_C^{-1}\cos(\varphi), \; L_C = \frac{\hbar}{2eI_C} \qquad (6)$$

This means that for weak signals the supercurrent is equivalent to an inductance L_S dependent on $\varphi(t)$ and on the critical current of the junction.

The most impressive property of a supercurrent is its ability to oscillate (*Josephson oscillations*) with a frequency

$$f_J = \frac{\omega_J}{2\pi} = \frac{2e}{h}\bar{V}, \; \frac{2e}{h} \approx 483 \text{ MHz}\mu\text{V}^{-1} \qquad (7)$$

if a nonzero d.c. voltage, $\bar{V}$, is fixed across the junction. At typical voltages (10^{-6}–10^{-2} V) the oscillation frequency, f_S, is of the order of 10^9–10^{13} Hz.

1.2 Normal Current

The scale of the normal current is given by the normal conductance of a junction G_N. Independent of transport properties of the contact material at voltages larger than $(\Delta_1 + \Delta_2)/e$, the $I_N(V)$ dependence of the junction is close to Ohmic at all temperatures:

$$I_N = G_S V + \delta I \qquad (8)$$

The voltage-independent factor δI in Eqn. (8) is the so-called "excess" ($\delta I \propto (\Delta_1 + \Delta_2)$) or "deficit" ($\delta I \propto -(\Delta_1 + \Delta_2)$) current observed if the contact

material has a metallic type of conductivity (*SNS weak links*). In structures with transparent interfaces between the contact material and superconducting samples there is excess current on $I_N(V)$. Andreev reflection of electrons is responsible for this effect. Owing to a gap in the density of states, an electron with energy ε in the interval

$$E_{F2} + eV - \Omega_2 \leqslant \varepsilon \leqslant E_{F2} + eV + \Omega_2 \qquad (9)$$

cannot penetrate into the superconductor as an electron, as in the normal case. Instead, in accordance with the Andreev process, it creates a pair of correlated electrons and a hole in the contact material. Thus, in this energy interval, (as in the normal case) two electrons instead of one are injected into the electrode leading to an "excess" current.

In structures with small transparent interfaces between the contact material and superconducting samples (*SINIS double barrier structures*) there is a current "deficit" on $I_N(V)$. The probability of Andreev reflection for an electron with energy defined by Eqn. (9) is proportional to D^2, where $D \ll 1$ holds for the transparency of an interface. Thus, in contrast to the normal case, there is no electron injection into the superconductor if the electron energy is in the range given by Eqn. (9) and, therefore, a current deficit should be observed on $I_N(V)$.

In junctions with tunneling-type conductivity of the contact region (*SIS tunnel Josephson junction*), $\delta I = 0$.

1.3 Displacement Current

For most practical Josephson junctions the displacement current is defined by

$$I_D = CV = C\frac{dV}{dt} \qquad (10)$$

where the junction capacitance, C, has the same value as in the normal state and depends on both the junction type and its size. The effect of the capacitance on the processes in the junction is characterized by the dimensionless parameter

$$\beta = \frac{2e}{\hbar}I_C R_N^2 C \qquad (11)$$

introduced by McCamber (1968) and Steward (1968). It compares the normal and displacement currents. Junctions with $\beta \ll 1$ have small capacitance or *high damping* ($I_N \gg I_D$), and junctions with $\beta \gg 1$ have large capacitance or *low damping* ($I_N \ll I_D$).

1.4 Fluctuation Current

The necessity of taking fluctuations ("noise") into account often arises in an analysis of the sensitivity of

superconducting devices. In most cases this is carried out by including some fluctuation current, $I_F(t)$, in the whole current across the junction. There are several sources of current fluctuation. These are *external noise sources*, *1/f noise*, *thermal noise*, and *shot noise*.

Usually, in experimental setups the intensity of an external noise is effectively suppressed to a level that is negligibly small compared to that provided by other sources.

The cutoff frequency of $1/f$ noise is relatively low. In a low-temperature Josephson junction it scales from 1 Hz to 10 Hz, while in high-temperature junctions it is in the range 100–1000 Hz. This means that at typical Josephson frequencies $\omega \approx \omega_J$ the net effect of this noise is very small. Nevertheless, in some practical devices (e.g., see *SQUIDs: Biomedical Applications*) the useful signal is contaminated with $1/f$ noise and special techniques such as signal or bias modulation are used for suppression of this noise component.

Thermal noise and shot noise are two types of classical fluctuations which exist since there is a dissipative current, I_N, across a junction. The relative intensity of the thermal fluctuations can be characterized by the ratio of the thermal energy, $k_B T$, to the Josephson energy, E_C:

$$\gamma = \frac{k_B T}{E_C} = \frac{I_T}{I_C} = \frac{2e}{\hbar}\frac{k_B T}{I_C}, I_T[\mu A] \approx 0.0417[K] \quad (12)$$

Thus, if the critical current of the junction is much larger than I_T the influence of thermal fluctuations should be small.

Shot noise is important if the voltage across the junction is large compared to $\hbar\omega/e$ and $k_B T/e$ and can be characterized by the spectral density

$$S_I(\omega) = \frac{1}{2\pi} e I_N = \text{const} \quad (13)$$

Equations (2) and (3) form the system of the basic equations for the Josephson junction. The concrete expressions for the current components in Eqn. (3) depend on the type of conductivity of the contact material and the geometry of the junction. The problem of finding the relationship between the current and voltage was solved in solid-state theory (Werthamer 1966, Larkin and Ovchinnikov 1966) only for structures with tunnel-type conductivity of the contact material. For this reason, even now the majority of dynamics problems in systems with Josephson junctions are solved in the framework of phenomenological models, which provide approximations of the real properties of various junctions. The resistively shunted junction (RSJ) model introduced by McCamber (1968) and Steward (1968) is the simplest and the most widely used tool for studying the processes in junctions.

2. RSJ Model

The RSJ model is based on Eqns. (1) and (8) with $\delta I = 0$, on Eqn. (10) for the current components in Eqn. (3)

$$I = I_C \sin(\varphi) + G_N V + C\frac{dV}{dt} + I_F(t) \quad (14)$$

and on the Josephson relationship (Eqn. (2)).

Quantitatively this model is valid for SIS and SNS Josephson junctions only in a narrow temperature interval in the vicinity of the critical temperature of the superconductor. At lower temperatures G_N becomes a nonlinear function of voltage and often the $I_S(\varphi)$ relationship is no longer sinusoidal.

Nevertheless, this model is widely used for describing the processes in Josephson junctions of any type, if they are shunted by a conductance $G_e \gg G_N$. A shunted junction can be considered as a new Josephson contact with linear normal conductance, G_e, which should replace G_N in Eqn. (14). A real form of the $I_S(\varphi)$ relationship can be taken into account by representing a junction as a junction with $I_S(\varphi) = I_C \sin(\varphi)$ and effective inductance connected in series (Zubkov *et al.* 1981).

The RSJ model is of great importance, since it provides the possibility of studying the processes in a variety of devices employing Josephson junctions without having the exact solutions of solid-state physics problems for the current components in Eqn. (3).

There are two experimental tests that are generally used to verify how close the behavior of real Josephson contacts are to the predictions of the RSJ model. These are the specific reactions of the structure to external magnetic and microwave fields.

3. Josephson Junctions in a Magnetic Field

In an external magnetic field, B, the phase difference, φ, across a junction depends on a space coordinate, x, along the junction and is a solution of the equation

$$\lambda_J^2 \frac{d^2\varphi}{dx^2} = J(x,t) \quad (15)$$

where J is the local value of a current (Eqn. (3)) through the junction and λ_J is the Josephson penetration depth given by

$$\lambda_J^2 = \frac{\Phi_0}{2\pi\mu_0(d + \lambda_1 + \lambda_2)J_C} \quad (16)$$

where d is the distance between the superconducting samples, Φ_0 the magnetic flux quantum, μ_0 the vacuum magnetic constant, and $\lambda_{1,2}$ the London penetration depths of the superconducting samples.

Solution of Eqns. (14) and (15) essentially depends on the relationship between the length of the junction, L, and λ_J.

In a long Josephson junction with $L \gg \lambda_J$ the magnetic field penetrates inside the structure in the form of a Josephson vortex. This is a region with a length of the order of $\pi\lambda_J$, filled by magnetic flux lines, which are screened by the supercurrent, J, circulating around:

$$B = \frac{\pm\Phi_0}{\pi d\lambda_J}\cosh^{-1}\left(\frac{x-x_0}{\lambda_J}\right),$$

$$J = \frac{\pm 2J_C\sinh[(x-x_0)/\lambda_J]}{\cosh^2[(x-x_0)/\lambda_J]}$$

In a short junction with $L \ll \lambda_J$ the phase difference is a linear function of B:

$$\varphi(x) = \frac{Bd}{\Phi_0}x + \eta, \; \eta = \text{const} \tag{17}$$

The critical current of a junction

$$I_C = \max_\eta\left\{\int_0^W J_C\sin[\varphi(x)]\mathrm{d}x\right\} = I_{C0}\left|\frac{\sin(\pi\Phi/\Phi_0)}{(\pi\Phi/\Phi_0)}\right| \tag{18}$$

depends in this case on the magnetic flux, Φ, inside the junction and exactly equals zero at $\Phi = n\Phi_0$. The form of $I_C(\Phi)$ dependence is similar to the pattern of Fraunhofer diffraction of waves passing through a slit and has been termed the "Fraunhofer pattern."

4. *Josephson Junctions in a Microwave Field*

In his original paper Josephson (1962) also predicted the appearance of a set of vertical current steps on the current–voltage characteristics of short Josephson junctions under the influence of microwave radiation, $V(t) = V_1\cos(\omega t)$.

If the normal current component across the junction is large compared to the supercurrent, then the solution of Eqns. (2) and (3) has the simple form

$$\varphi = \frac{2e}{\hbar}\bar{V}t + \frac{2e}{\hbar\omega}V_1\sin(\omega t) + \alpha \tag{19}$$

Substituting Eqn. (19) into the expression for I_S (Eqn. (1)) of the RSJ model gives

$$I_S = I_C\sum_{m=-\infty}^{\infty} J_m\left(\frac{2eV_1}{\hbar\omega}\right)\sin\left[\left(m+\frac{\omega_J}{\omega}\right)\omega t + \alpha\right] \tag{20}$$

where $J_m(x)$ are Bessel functions of the first kind. It is clear from Eqn. (20) that synchronization of the nth harmonic of the external radiation with the frequency of the Josephson oscillation ($n\omega = \omega_J$) should result in formation of steps, which look like "spikes" in the current–voltage characteristic and have amplitude

$I_C J_m(2eV_1/\hbar\omega)$. According to the well-known properties of Bessel functions, as the signal amplitude increases the nth step first increases, reaches a maximum, and then slowly decreases, oscillating with a period approximately equal to 2π.

These oscillating steps were first observed by Shapiro (1967) and are referred to as Shapiro steps.

Both effects discussed above (Fraunhofer pattern, Eqn. (18), and Shapiro steps, Eqn. (20)) are the direct consequence of the sinusoidal relationship between supercurrent and phase difference φ. It is for this reason that they are used as a standard experimental test for the applicability of the RSJ model for the description of the properties of a Josephson junction of any type and configuration.

See also: Electrodynamics of Superconductors: Flux Properties

Bibliography

Barone A, Paterno G 1982 *Physics and Application of Josephson Effects*. Wiley, New York

Josephson B D 1962 Possible new effects in superconducting tunneling. *Phys. Lett.* **1**, 251–4

Kulik I O, Yanson I K 1970 *Josephson Effect in Superconducting Tunnel Structures*. Nauka, Moscow (in Russian); 1972, Keter Press, Jerusalem (in English)

Larkin A I, Ovchinnikov Yu N 1966 Tunnel effect between superconductors in alternating field. *Zh. Eksp. Teor. Phys. (Sov. Phys. JETP)* **51**, 1535

Likharev K K 1986, 1991 *Dynamics of Josephson Junctions and Circuits*. Gordon and Breach, Reading, UK

McCamber D E 1968 Effect of AC impedance on DC volatage-current characteristics of superconductor weak-link junctions. *J. Appl. Phys.* **39**, 3113

Shapiro S 1967 Josephson currents in superconducting tunneling: the effect of microwaves and other observations. *Phys. Rev. Lett.* **11**, 80

Solymar L 1972 *Superconducting Tunneling and Application*. Chapman and Hall, London

Steward W C 1968 Current-voltage characteristics of Josephson junctions. *Appl. Phys. Lett.* **12**, 277

Werthamer N R 1966 Nonlinear self-coupling of Josephson radiation in tunnel junctions. *Phys. Rev.* **147**, 255

Zubkov A A, Kupriyanov M Yu, Cemenov V K 1981 Stationary Properties of Josephson Structure with Ohmic conductivity. *Fiz. Nizk. Temp. (Sov. J. Low Temp. Phys.)* **7** (11), 1365–71

M. Kupriyanov
Moscow State University, Russia

5f Electron Systems: Magnetic Properties

5f electron systems are characteristic of actinides, i.e., elements between actinium, atomic number $Z = 89$, and lawrencium, $Z = 103$. These elements

are characterized by a gradual filling of the 5*f* electronic shell, in analogy to the 4*f* shell filling in lanthanides. The filling tendencies for free-ion states with increasing *Z* resemble strongly those in lanthanides, but as part of a solid the behavior of the 5*f* electrons resembles 3*d* materials more. The reason is the spatial extent of the 5*f* wave functions, being larger compared with the 4*f* states in lanthanides. Therefore the magnetism of most 5*f* electron systems is more similar to the *d*-band magnetism than to the localized 4*f* magnetism of lanthanides. This is particularly true for light actinides (up to plutonium), whereas for the heavier actinides (from americium onwards) 5*f* localization has been documented for the pure elements. More systematic information on magnetism of heavy-actinide compounds is missing.

The specific characteristics of the 5*f* electron magnetism are manifest in systems based on elements up to plutonium. The higher actinides behave in an analogous way to the corresponding 4*f* systems. The main characteristics of the 5*f* magnetism comprise strong spin-orbit interaction, leading to large orbital moments formed even in the case of band-like states, exchange interactions mediated or assisted by the hybridization of the 5*f* states with the ligand states, and enormous magnetic anisotropy arising from the anisotropy of the hybridization (bonding anisotropy). Another characteristic is a high sensitivity of magnetic properties to external variables, such as pressure and magnetic field, and to fine details of composition.

1. General Features of Electronic Structure and Magnetism of Light-actinide Systems

The fundamental difference between the character of the 4*f* electron states in lanthanides (see *Localized 4f and 5f Moments: Magnetism*) and 5*f* states in light actinides can be attributed to a much larger spatial extent of the 5*f* wave functions, and thus a much stronger interaction with the metallic environment, compared to the 4*f* case. The 5*f* electrons are, as a rule, delocalized due to their participation in bonding, which leads to a considerable hybridization of the 5*f* states with the valence states of neighboring atoms (5*f* ligand hybridization). The delocalization of the 5*f* electrons has serious consequences. The most important one is, that the 5*f* states form a more or less narrow 5*f* band intersected by the Fermi energy E_F (the bandwidth W_{5f} is of the order of several eV) rather than discrete energy levels. Consequently, the magnetic moments due to the itinerant 5*f* electrons are much smaller than expected for a free ion, and magnetic moments can disappear in a broad-band limit leading to weak (Pauli) paramagnetism.

This situation resembles to a certain extent the 3*d* transition metals. The strength of magnetic coupling in cases of existing 5*f* moments is typically much larger than for the 4*f* moments interacting via the RKKY interaction. The impact on magnetic excitations is even more dramatic, no crystal-field excitations could be observed by inelastic neutron scattering in a vast majority of systems studied so far. Instead, one observes typically a rather broad quasielastic response reflecting the 5*f* moment's instability in analogy to, for example, cerium mixed valence materials. However, the high density of states at E_F is projected into high γ-values of the low temperature specific heat (which are further renormalized by strong *e*–*e* correlations), and into highly anomalous transport properties, resulting from the hybridization of such "heavy" electron states with the non-*f* states carrying the electrical current.

2. Pure Actinide Elements

The small separation of the ions in the pure elements leads to large overlap of the 5*f* wave functions of nearest neighbors, formation of a broad 5*f* band and weakly paramagnetic behavior. With increasing 5*f* occupation the value of the Pauli-type susceptibility increases due to the increase of $N(E_F)$, the density of states at the Fermi level, which is corroborated by a similar increase of the low-temperature electronic specific heat coefficient γ (see Table 1). This tendency

Table 1
Overview of essential properties of elemental actinides, summarizing available data on the γ-coefficient of the low-temperature specific heat, temperature independent susceptibility χ_0, Néel temperature T_N and Curie temperature T_C.

	Th	Pa	U	Np	Pu	Am
γ (mJ mol^{-1} K^{-2})	4	6.6	10	14	22	2
χ_0 (10^{-8} m^3 mol^{-1})	0.12	0.34	0.48	0.68	0.64	0.85
	Cm	Bk	Cf	Es		
T_N (K)	64	34	51(T_C)			
μ_{eff} (μ_B)	7.55	9.7	9.7	11.3 (?)		

is interrupted between plutonium and americium, where the 5*f* states localize, and do not contribute to bonding for heavier actinides. The reason for the localization (and loss of the 5*f* bonding energy) can be found qualitatively in the gain of electron correlation energy for atomic-like 5*f* states (which is partly lost in the 5*f* band case). For details see Johansson and Brooks (1993).

Thus the Stoner criterion (see *Itinerant Electron Systems: Magnetism (Ferromagnetism)*) is not fulfilled in light actinides because of too small $N(E_F)$ and the Coulomb interaction parameter U. But these materials can lower their electron energies by forming different open crystal structures, sometimes of a very low symmetry (in analogy to Jahn–Teller effect). The best example of this phenomenon is plutonium, having six allotropes, with the ground-state allotrope, α-plutonium, showing a complicated monoclinic structure. A similar situation occurs in α-uranium, the structure of which is orthorhombic, but an incommensurate charge-density wave is formed below $T = 43$ K (Lander *et al.* 1994).

Due to the weakly magnetic character, superconductivity can appear at the beginning of the actinide series. The critical temperatures T_c are 1.368 K for thorium, 1.4 K for protactinium, 0.68 K for α-uranium. For heavier actinides, superconductivity was found for americium ($T_c = 0.625$ K).

Plutonium, the element on the verge of localization, exhibits the most complex behavior. Its room temperature phase, α-plutonium, is monoclinic with 16 atoms per unit cell. At $T = 395$ K it undergoes a phase transition to an even more complicated monoclinic β-phase with 34 atoms per unit cell. From the remaining phases, most of the data is on the f.c.c. δ-phase with four atoms per unit cell, which has its atomic volume expanded by 26% compared to the α-phase, and which can be stabilized by several percent by doping with aluminum, cerium, or gallium. Comparing to the data for α-plutonium given in Table 1, γ is strongly enhanced to 53 ± 10 mJmol^{-1} K^{-2}. For details see Méot-Reymond and Fournier (1996), where the properties of δ-plutonium are discussed in terms of a Kondo effect with the characteristic Kondo temperature T_K higher than the room temperature.

The elements behind plutonium behave rather similar to the lanthanide series. The analogy starts with crystal structures. Americium, curium, berkelium, and californium all have d.h.c.p. structures, but the structures change and the 5*f* states delocalize under external pressure, yielding low symmetry structures of the light-actinides type (Benedict and Holzapfel 1993).

The nonmagnetic ground state of americium (exhibiting low γ and quite high Van Vleck susceptibility), can be understood in the framework of either L–S or j–j coupling for the 5*f*^{6} configuration. Most information on curium was obtained on a fast

decaying isotope ^{244}Cm (half-life 18 years), which is available in large amounts (milligrams) but displays high self-heating and radiation damage. A maximum magnetic susceptibility indicating antiferromagnetic (AF) ordering was observed at $T = 52$ K for this isotope, and a simple AF order was indeed confirmed by neutron diffraction. For ^{248}Cm, which has longer half-life, but is available in smaller amounts only, the AF order was indicated at $T = 64$ K. Values of effective moment are compatible with $\mu_{eff} = 7.55\,\mu_B$ expected for the intermediate coupling model. Besides the ground-state d.h.c.p crystal structure, a high temperature f.c.c phase can occur in a low-temperature metastable state. Its magnetic ordering temperature is enhanced to $T = 205$ K. Berkelium and californium could be studied only in submilligram quantities. For berkelium, AF ordering was deduced below $T = 34$ K; californium is probably ferromagnetic below approx. 51 K. Both materials display μ_{eff} values compatible with free-ion theoretical values in the paramagnetic state. Einsteinium, which could be studied in submicrogram quantity only, yields a moment of 11.3 μ_B, which is even somewhat higher than the theoretical value (Huray and Nave 1987).

3. Magnetic Properties of Actinide Intermetallic Compounds

Similar to the pure actinide elements, the magnetic properties of the compounds also reflect the gradual filling of the incomplete 5*f* shell. In thorium compounds the very small filling of the 5*f* states cannot give rise to 5*f* magnetic moments, and compounds are typically Pauli paramagnets with a susceptibility χ_0 of the order of 10^{-9}–10^{-8} m^{3}mol^{-1} for intermetallic compounds, where its value reflects the density of states at E_F. The ground state is frequently superconducting. Exceptions are compounds such as Th$_2$Fe$_{17}$ ($T_C = 295$ K) and Th$_2$Co$_{17}$ ($T_C = 1035$ K), in which magnetism is dominated by transition-metal components.

In the compounds of uranium, neptunium, and plutonium, magnetic ordering can appear in those cases in which the actinide–actinide spacing is increased to such an extent, that the 5*f* band narrowing and consequent increase of the density of states at E_F leads to the fulfillment of the Stoner criterion. The proximity of these elements to the boundary between the localized and itinerant character of the 5*f* electronic states makes them very sensitive to variations of the environment. In the first approximation the width of the 5*f* band can be taken as a function of the overlap of the 5*f* atomic wave functions centered on nearest neighbors, and the increase of the overlap can be taken as a principal delocalizing mechanism of the 5*f* electrons. The situation is best documented for uranium compounds, where the inter-uranium spacing $d_{U\text{-}U} = 340$–360 pm, called the Hill limit, is an

approximate boundary value of the spacing, corresponding to the critical $5f$–$5f$ overlap. For smaller spacings most of the compounds are nonmagnetic (often superconducting). For d_{U-U} larger than the Hill limit they incline to a magnetically ordered ground state. The value of the Hill limit should be taken as very approximate; the width of the $5f$ band is naturally affected also by the coordination number.

For compounds with d_{U-U} larger than the Hill limit, the principal control parameter is not the U–U spacing, but the hybridization of the $5f$ states with electronic states of other components. In particular, in compounds with transition metals it is mainly the overlap of the $5f$ states with the d states of the transition metal component in the energy scale which affects the strength of the hybridization. The $5f$ states remain pinned at the Fermi level in most cases, whereas the late transition metals (as well as noble metals), being much more electronegative, have particular d states shifted towards higher binding energies thus leaving the $5f$–d overlap in energy scale small. The reduced $5f$–d hybridization leads to the onset of $5f$ magnetism, whereas the d-states are occupied more than in the pure d-element. Even if the d-element itself is magnetically ordered (cobalt, nickel, iron), in the compound with uranium it behaves essentially as nonmagnetic (a similar effect appears in thorium compounds).

Exceptions are compounds with very high content of the transition metal component, in which the d-magnetism can prevail. In compounds with earlier d-metals such as iron or ruthenium the d-states appear closer to the Fermi energy and the $5f$–d overlap increases, leading typically to a nonmagnetic ground state (as in UFeAl). But in some cases magnetic

moments appear both on uranium and transition-metal ions. Prominent examples are Laves phases with iron, all ordering ferromagnetically. Relatively high T_C values (UFe$_2$ 162 K, NpFe$_2$ 492 K, PuFe$_2$ 564 K, AmFe$_2$ 613 K) point to the dominance of the iron–sublattice exchange interactions, but actinide magnetic moments are non-negligible, reaching 1.1 μ_B per neptunium or 0.45μ_B for plutonium. The tiny total moment in the case of uranium in fact consists of orbital (0.23 μ_B) and spin (0.22 μ_B) component, nearly canceling each other.

In compounds with non-transition metals, it is mainly the size of ligand atoms that affects the hybridization. Compounds with larger ligands are typically magnetic (e.g., UIn$_3$), whereas those where smaller ligands make the hybridization stronger form broad bands with low $N(E_F)$ and are weakly paramagnetic (USi$_3$). Several characteristic groups of uranium compounds can thus be distinguished in Table 2.

The last group, heavy-fermion materials, comprises those having a substantially enhanced γ-coefficient of specific heat, showing a coexistence of magnetic ordering and superconductivity of an unconventional type (see *Heavy-fermion Systems*). In all uranium compounds mentioned, the $5f$ states remain essentially band-like, i.e., contributing to the bonding, and therefore appearing at the Fermi level. The only exception known (at least from binary compounds) is UPd$_3$, for which the $5f$ localization has been confirmed by microscopic methods. Photoelectron spectroscopy exhibits in this case the $5f$ spectral intensity displaced from the Fermi level to higher binding energies. Neutron scattering shows clear crystal electric field (CEF) excitations, normally absent in spectra of

Table 2
Overview of the most characteristic groups of uranium intermetallics.

Characteristics	Examples
Very high U content, small d_{U-U}, weakly paramagnetic, superconducting	U$_6$Fe, U$_6$Co, U$_6$Ni
Higher U content, small d_{U-U}, weakly paramagnetic, normal ground state	UCo$_2$, U$_3$Si$_2$
Low d_{U-U} (<340 pm), magnetic order of $5f$ moments (very weak itinerant magnetism)	rare case (UNi$_2$)
Intermediate d_{U-U} (340–360 pm), typically ferromagnetic ground state, itinerant magnetism, typically $T_C < 100$ K	URh, UPt
Low U content, large d_{U-U}, low $5f$-ligand hybridization, ferromagnetic ground state	rare case (UGa$_2$)
Low U content, large d_{U-U}, weak $5f$-ligand hybridization, AF ground state	UIn$_3$, UGa$_3$
Low U content, large d_{U-U}, strong $5f$-ligand hybridization, normal ground state	USi$_3$, UNi$_5$, UPt$_5$
Low U content, large d_{U-U} spacing, heavy-fermion behavior with different types of ground state	UPt$_3$, UBe$_{13}$, URu$_2$Si$_2$, UPd$_2$Al$_3$, U$_2$Zn$_{17}$, UCu$_5$, UCd$_{11}$

uranium intermetallics, and the coefficient γ reaches only $5\,\mathrm{mJ\,mol^{-1}\,K^2}$.

Besides binary compounds there exist large groups of ternary compounds, often including a transition metal T and a non-transition metal X (UTX, U_2T_2X, UT_2X_2), which follow the tendencies of the 5f ligand hybridization mentioned above. The advantage of studies of the 5f magnetism in such groups is that both the transition and the non-transition metal component can be varied, while the structure type, i.e., the symmetry of environment of actinide atoms, is preserved. This makes it possible to trace out in more detail the cross-over from a nonmagnetic to magnetic ground state.

Materials which are in the boundary region (i.e., nearly or weakly magnetic) show a variety of spin-fluctuation features. Those with nonmagnetic ground state exhibit Curie–Weiss behavior of magnetic susceptibility at high temperatures, but at low temperatures a broad maximum in $\chi(T)$ appears (e.g., URuAl, UCoAl). Other types of spin fluctuators are characterized by a plateau in $\chi(T)$ below a characteristic temperature, and a low-temperature upturn as in URuGa (see Sechovský and Havela 1998).

High ordering temperatures can be achieved, for example, in ternary compounds of the $UT_{10}Si_2$ type (ThMn$_{12}$ structure type), in which both uranium and the transition metal T (iron, cobalt) carry magnetic moments. The highest $T_C = 750\,\mathrm{K}$ was recorded for $UFe_5Co_5Si_2$.

The occurrence of magnetic ordering in neptunium-based compounds is dominated by mechanisms analogous to their uranium counterparts. Important information is obtained using ^{237}Np Mössbauer spectroscopy, which allows determination of microscopic parameters of neptunium magnetism. In particular, the magnetic hyperfine field B_{hf} on the neptunium nuclei was found to be approximately proportional to the local neptunium magnetic moment μ_{Np} (Dunlap and Kalvius 1985): $B_{hf}/\mu_{Np} = 215\,(T/\mu_B)$. The fact that the boundary between the magnetic and nonmagnetic behavior for different materials is not far from the uranium isotopes demonstrates that for neptunium compounds the mechanisms of the 5f delocalization play a comparable role. Thus the nonmagnetic behavior of neptunium in NpGe$_3$ and NpRh$_3$ has to be attributed to the 5f–p and 5f–d hybridization in analogy to UGe$_3$ and URh$_3$. However, differences exist, too. For example, NpSn$_3$ is an itinerant antiferromagnet, whereas USn$_3$ is a spin-fluctuator not undergoing magnetic ordering. Such differences can be generally attributed to a higher 5f count or weaker 5f delocalization.

However, Np$_2$Rh$_2$Sn is a nonmagnetic spin fluctuator, whereas U_2Rh_2Sn undergoes AF order ($T_N = 24\,\mathrm{K}$). ^{237}Np Mössbauer spectroscopy under high pressure has been a convenient tool to distinguish different types of magnetically ordered compounds. For those with more stable 5f moment the

neptunium moment does not decrease with pressure in the gigapascal range while the ordering temperature increases (e.g., NpCo$_2$Si$_2$), whereas a pronounced decrease of both parameters points to a stronger 5f-moment instability e.g., in neptunium Laves phases NpOs$_2$ or NpAl$_2$.

4. Magnetic Properties of Other Actinide Compounds

A large majority of actinide compounds, even with nonmetallic elements, has a metallic character. The magnetic behavior is dominated by the f–p hybridization, which plays a dual role. It leads to a delocalization of the 5f states and mediates the exchange interaction. The metallic character appears in most of the rocksalt type of compounds, monopnictides AnX (An = U, Np, Pu; X = P, As, Sb, Bi) and monochalcogenides AnY (An = U, Np; Y = S, Se, Te), which are magnetically ordered and reach appreciable magnetic phase transition temperatures e.g., $T_N = 213\,\mathrm{K}$ in USb or $285\,\mathrm{K}$ in UBi. However, plutonium monochalcogenides are semimetallic and nonmagnetic. Carbides, which are slightly under-stoichiometric (AnC$_{1-x}$), are weakly magnetic for An = Th, Pa, U. NpC$_{1-x}$ is ferromagnetic below $T = 225\,\mathrm{K}$, whereas AF ordering is found up to about 300 K, depending on the x values. PuC$_{1-x}$ undergoes AF ordering with T_N ranging between 100 K and 30 K, depending on the stoichiometry. A large data set exists for nitrides AnN. Whereas ThN and AmN are weakly magnetic, magnetic ordering appears for UN ($T_N = 53\,\mathrm{K}$), NpN ($T_C \approx 90\,\mathrm{K}$), presumably also in PuN ($T_N = 13\,\mathrm{K}$) and CmN ($T_C = 109\,\mathrm{K}$), and data exist even for BkN ($T_C = 88\,\mathrm{K}$). Of the other compounds, a high magnetic ordering temperature can be found, for example, in U_3As_4 ($T_C = 196\,\mathrm{K}$), U_3Sb_4 ($T_C = 146\,\mathrm{K}$), even 400 K for AF ordering in U_2N_2As. USb$_2$ and UAs$_2$ are antiferromagnets with $T_N = 205\,\mathrm{K}$ and 273 K, respectively.

Of the numerous oxides, the dioxides are the most common. UO$_2$ and NpO$_2$ are antiferromagnets ($T_N = 31\,\mathrm{K}$ and 25 K, respectively). These systems are examples of the 5f localized magnetism, with attributes such as crystal-field excitations and spin waves, but the latter exhibits certain mysterious features as tiny magnetic moments $< 0.1\,\mu_B/\mathrm{Np}$. For further discussion see *Localized 4f and 5f Moments: Magnetism*. PuO$_2$ is a weak paramagnet, presumably due to a singlet crystal-field ground state for the $5f^4$ ionic state. With hydrogen, uranium forms a trihydride known as a ferromagnet ($T_C = 180\,\mathrm{K}$). AF order was found in PuH$_2$ ($T_N = 30\,\mathrm{K}$), whereas PuH$_3$ is ferromagnetic ($T_C = 100\,\mathrm{K}$). Neptunium hydrides are weakly paramagnetic, which can be understood as being due to CEF effects in the case of the $5f^4$ ionic state (for details see Wiesinger and Hilscher 1991). Hydrogen can be absorbed also by a number of

binary and ternary intermetallic compounds. Similar to elemental light actinides, it strongly supports the tendency to form local 5*f* magnetic moments and to give rise to magnetic order. This can at least partly be attributed to 5*f*-band narrowing due to enhanced inter-actinide spacing.

5. Orbital Moments in Light Actinides

Although the majority of the light actinides and their intermetallic compounds is characterized by itinerant 5*f*-states, an important difference with 3*d* magnetics is the energy of the spin-orbit coupling Δ_{S-O} and the width of the 3*d* (5*f*) band W_{3d} (W_{5f}). Whereas $\Delta_{S-O} \ll W_{3d}$, the respective values in the light actinides become of comparable magnitude because Δ_{S-O} is of the order of eV. Due to the strong spin-orbit inter-action, typically a large orbital magnetic moment μ_L is induced. It is antiparallel to the spin moment for uranium, in analogy with the light lanthanides and the third Hund's rule stating that the total angular momentum is given by $J = L - S$. The existence of such orbital moments for the 5*f*-band systems was first revealed from band structure calculations in-volving a spin-orbit interaction term coupling the spin and orbital moment densities (see *Density Func-tional Theory: Magnetism*). Experimentally this was confirmed by studies of the neutron form-factor, which adopts a very specific shape with a maximum, especially if spin and orbital moments are of the same size. Such a case, at which the total moment is close to zero, but the spatial extent of spin and orbital moment densities is different, was observed, for ex-ample, in UNi$_2$ or UFe$_2$. In the latter case the ura-nium moment consists of the orbital part $\mu_L = 0.23 \mu_B$ and a spin part $\mu_S = -0.22 \mu_B$. Recently, orbital mo-ments became accessible also in x-ray scattering stud-ies using synchrotron radiation (see *Magnetism: Applications of Synchrotron Radiation*).

A different sensitivity of spin or orbital moments to external variables led to the assumption that the ratio of orbital and spin moment should reflect the degree of the 5*f*-delocalization. Indeed, as seen from Fig. 1, the compounds showing the least delocalized nature of the 5*f* states (UO$_2$, USb, NpAs$_2$, PuSb) are located on the line representing values of $-\mu_L/\mu_S$ of a free 5f^n ion. On the other hand, magnetically ordered materials with presumably the most itinerant 5*f* states (UFe$_2$, UNi$_2$, NpCo$_2$, PuFe$_2$) have this ratio close to 1.

Relatively large orbital moments induced by mag-netic field exist probably even in weakly paramag-netic materials such as uranium metal. Surprisingly, in an external magnetic field the spin and orbital magnetic moments orient parallel, as shown by a simple balance of the Zeeman and spin-orbit energy in the case of weak susceptibility (for details see Sechovský and Havela 1998).
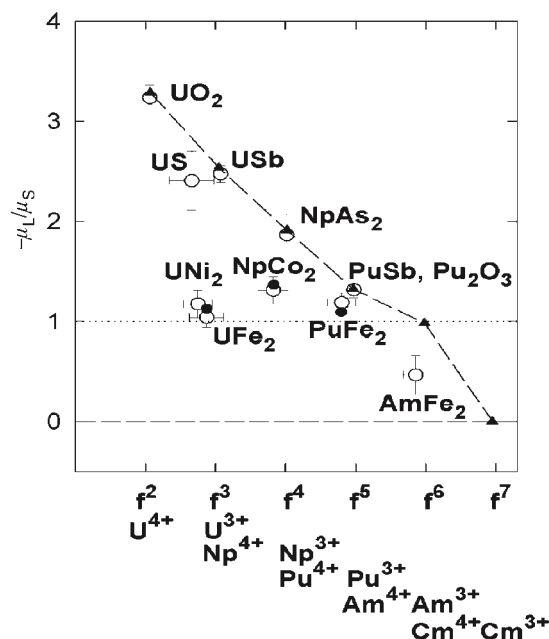
Figure 1
Ratio of the orbital μ_L and spin μ_S moments in a number of magnetically ordered materials plotted as a function of the number of the 5*f* electrons. The triangles, connected by a dashed line, are the values derived from single-ion theory including intermediate coupling. Experimental results are shown by open circles. Results of band structure calculations are shown by solid circles. For details see Sechovský and Havela 1998.

6. Exchange Interactions and Magnetic Anisotropy

Exchange interactions in materials with localized 5*f* states can be seen as being analogous to regular lan-thanides, for which the indirect exchange of the RKKY type is a good approximation. The other limit, systems with strongly itinerant 5*f* states, can be understood in terms of the Stoner–Edwards–Wohlf-arth theory for itinerant magnets (see *Itinerant Elec-tron Systems: Magnetism (Ferromagnetism)*), in which the ordering temperature is proportional to the ordered moment. For intermediate delocalization, when the direct 5*f*–5*f* overlap is negligible, a dual role of the 5*f* ligand hybridization has to be taken into account. It is a primary mechanism of destabilizing the 5*f* magnetic moments, but because the spin in-formation is conserved in the hybridization process, it leads to an indirect exchange coupling. Maximum ordering temperatures can consequently be expected for a moderate strength of hybridization, because a strong hybridization completely suppresses magnetic moments, whereas a weak one leaves the moments intact, but their coupling is weak.

A model leading to realistic results have been worked out by Cooper *et al.* (1985) on the basis of the Coqblin–Schrieffer approach. The mixing term in the hamiltonian of the Anderson type is treated as a perturbation, and the hybridization interaction is replaced by an effective *f*-electron-band-electron resonant exchange scattering. Considering an ion-ion interaction as mediated by different covalent-bonding channels, each for particular magnetic quantum number m_l, the strongest interaction is for those orbitals that point along the ion–ion bonding axis, which represents the quantization axis of the system. The two 5*f* ions maximize their interaction by compression of the 5*f* charge towards the direction to the nearest 5*f* ion. This has serious impacts on magnetic anisotropy, because it means a population of the 5*f* states with orbital moments perpendicular to the bonding axis. This interaction prefers a strong ferromagnetic coupling of the actinide moments along the bonding direction. There is no special general tendency to ferro- or antiferromagnetism in the perpendicular direction, where the interaction is much weaker, and can be of a size comparable to that of the "background" isotropic exchange interaction of the standard RKKY type.

Unlike such two-ion hybridization mediated anisotropy, crystal electric field (single-ion) effects control the type and strength of magnetic anisotropy for materials with the localized 5*f* states, in analogy to lanthanide systems.

The two-ion anisotropy, for which orbital moments are necessary prerequisite, has been observed especially in numerous uranium compounds, for which single-crystal magnetization data exist. The tendency for moments to orient perpendicular to the U–U bonding links leads to a uniaxial anisotropy in crystal structures with uranium atoms organized in planes with a short in-plane U–U spacing and larger inter-plane spacing. The case of uranium linear chains leads to a planar type of anisotropy (see Fig. 2). The strength of the anisotropy, which is well observable both in magnetically ordered and paramagnetic phases, can be estimated in some cases from the difference of the paramagnetic Curie temperatures (see *Magnetism in Solids: General Introduction*) when the susceptibility is studied with the magnetic field along different crystallographic directions. Another estimate can be obtained from the anisotropy field, at which the extrapolated magnetization curves along different directions would intersect each other. Typically values of 10^2–10^3 K or 10^2–10^3 T are obtained in this way (see Figs. 3 and 4).

For large groups of isostructural compounds, the same type of anisotropy is, as a rule, found irrespective of the non-actinide components. Examples are the strong uniaxial anisotropy of UTX compounds (with hexagonal structure of the ZrNiAl type) or tetragonal UT_2X_2 compounds, both with strong uranium bonding within planes perpendicular to the
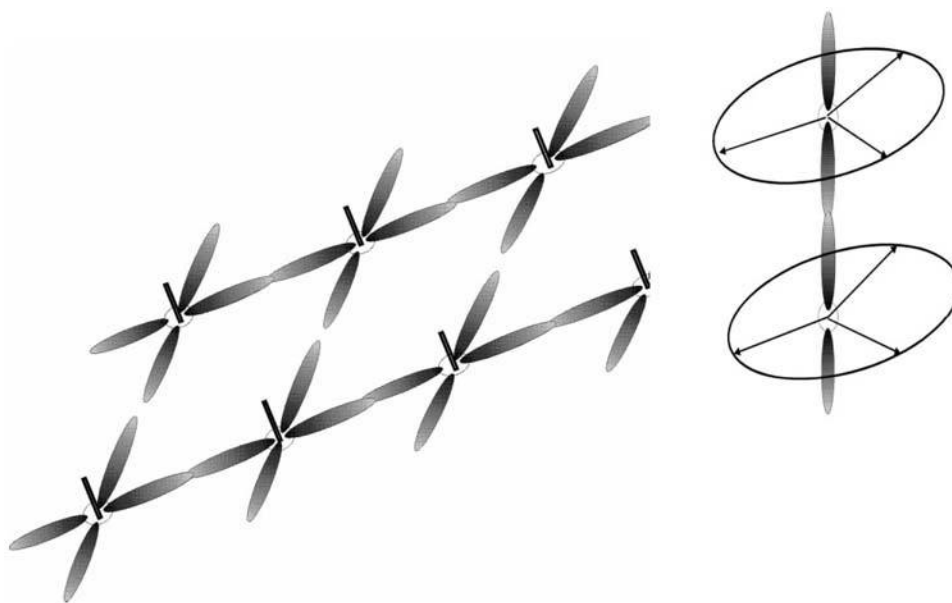
Figure 2
Schematic view illustrating how the bonding and easy-magnetization directions are related in light actinides. On the left, the easy-axis anisotropy for planar bonding; on the right, the easy-plane anisotropy for columnar bonding.
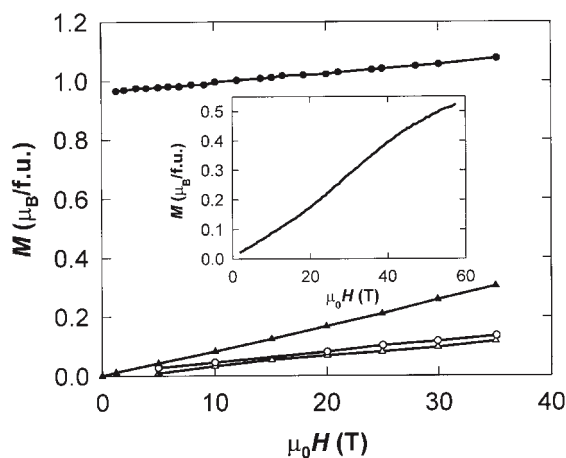
Figure 3
Illustration of the strong uniaxial anisotropy observed in the hexagonal UTX compounds (ZrNiAl structure type), in particular in URhAl–ferromagnet, $T_C = 27\,K$ (circles), and URhAl–paramagnet (triangles). Magnetization at $T = 4.2\,K$ was measured as a function of magnetic field applied along the c-axis (filled symbols) and a-axis (open symbols). The comparison shows that the response along the a-axis is practically the same, unaffected by ordered magnetic moments oriented along the c-axis in URhAl. The inset shows a similar experiment on field-oriented powder of URuAl extending the field range. The noticeable S-shape is attributed to the suppression of spin fluctuations in high magnetic fields (see Sechovský and Havela 1998).
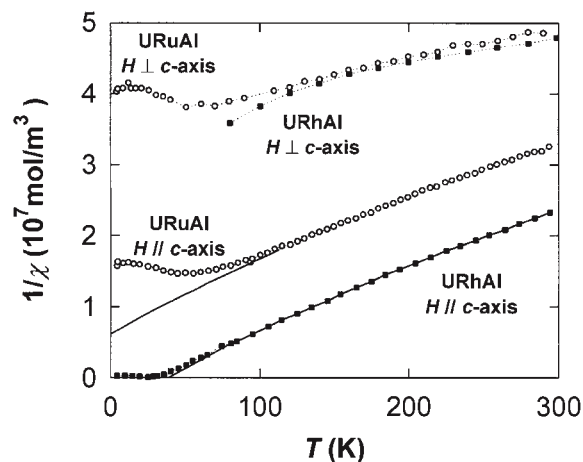
Figure 4
Temperature dependence of inverse magnetic susceptibility for the same materials as shown in Fig. 3, illustrating the same type of anisotropy of the paramagnetic behavior.

hexagonal (tetragonal) axis, and uranium moments (or higher susceptibility) along this axis.

7. Magnetic Structures

Both specific mechanisms in light-actinide materials, the magnetic anisotropy and exchange interactions, affect their magnetic structure types. Strong anisotropy frequently leads to collinear modulated structures (spin-density waves), which are preferred over noncollinear equal moment structures. The reason is that the anisotropy energy is typically stronger than the exchange coupling energies. Noncollinear magnetic structures are stable if the easy-magnetization directions on different sites are noncollinear, as in U_2Pd_2Sn, where they are orthogonal. Also in cases in which the lattice symmetry imposes no special requirements on the moment's directions (see Sandratskii 1998), noncollinear equal-moment structures appear (e.g., UPtGe). Types of magnetic structures are also affected by the strong ferromagnetic coupling along strong bonding directions (see the hybridization-induced exchange model, above). For example, UTX compounds with hexagonal structure of the ZrNiAl type, form magnetic structures consisting of ferromagnetic basal-plane sheets, whereas the inter-sheet exchange interaction is weaker and can be of ferro- or antiferro-type, leading to a variety of stacking sequences along the hexagonal axis. In this case, ferromagnetic-like alignment can be obtained in moderate magnetic fields applied along the AF stacking direction.

See also: Electronic Configuration of 3d, 4f and 5f Elements: Properties and Simulations

Bibliography

Benedict U, Holzapfel W B 1993 High-pressure studies—Structural aspects. In: Gschneidner K A Jr, Eyring L, Lander G H, Choppin G R (eds.) *Handbook on the Physics and Chemistry of Rare Earths*. Elsevier, Amsterdam, Vol. 17, pp. 245–300

Cooper B R, Siemann R, Yang D, Thayamballi P, Banerjea A 1985 Hybridization-induced anisotropy in cerium and actinide systems. In: Freeman A A, Lander G H (eds.) *Handbook on the Physics and Chemistry of the Actinides*. Elsevier, Amsterdam, Vol. 2, pp. 435–500

Dunlap B D, Kalvius G M 1985 Mössbauer spectroscopy on actinides and their compounds. In: Freeman A, Lander G H (eds.) *Handbook on the Physics and Chemistry of the Actinides*. Elsevier, Amsterdam, Vol. 2, pp. 329–434

Huray P G, Nave S E 1987 Magnetic studies of transplutonium actinides. In: Freeman A A, Nave S E (eds.) *Handbook on the Physics and Chemistry of the Actinides*. Elsevier, Amsterdam, Vol. 5, pp. 311–72

Johansson B, Brooks M S S 1993 Theory of cohesion in rare earths and actinide. In: Gschneidner K A Jr, Eyring L, Lander G H, Choppin G R (eds.) *Handbook on the Physics*

and Chemistry of Rare Earths. Elsevier, Amsterdam, Vol. 17, pp. 149–244

Lander G H, Fisher E S, Bader S D 1994 The solid-state properties of uranium—a historical perspective and review. *Adv. Phys.* **43**, 1–110

Méot-Reymond S, Fournier J M 1996 Localization of 5f electrons in δ-plutonium: evidence for the Kondo effect. *J. Alloys Compound.* **232**, 119–25

Sandratskii L M 1998 Noncollinear magnetism in itinerant electron systems—theory and applications. *Adv. Phys.* **47**, 91–160

Sechovský V, Havela L 1988 Intermetallic compounds of actinides. In: Wohlfarth E P, Buschow K H J (eds.) *Ferromagnetic Materials*. Elsevier, Amsterdam, Vol. 4, pp. 309–491

Sechovský V, Havela L 1998 Magnetism of ternary intermetallic compounds of uranium. In: Buschow K H J (ed.) *Handbook of Magnetic Materials*. Elsevier, Amsterdam, Vol. 11, pp. 1–289

Wiesinger G, Hilscher G 1991 Magnetism of hydrides. In: Buschow K H J (ed.) *Handbook of Magnetic Materials*. Elsevier, Amsterdam, Vol. 6, pp. 511–84

L. Havela
Charles University, Prague, Czech Republic

Electron Systems: Strong Correlations

The physics of strongly correlated electron systems originates primarily from the presence of an inner d or f shell in one of the atoms embedded in the system considered. The d electrons in transition elements and the 4f or 5f electrons in rare earths or actinides are generally well localized and correlated. The physics of strongly correlated electron systems is the subject of many experimental and theoretical studies and we will summarize here the main points.

The correlations tend firstly to favor the existence of magnetism which is because of open inner d or f shells, as observed in pure iron, cobalt, or nickel in the 3d series, in the rare-earth metals, and in actinide metals after americium. Magnetism is also observed in many ionic, insulating, or metallic systems containing these magnetic elements.

The generic term of strongly correlated electron systems is mostly reserved to metallic systems where there exists a strong interaction or hybridization between the inner d or f electrons and the conduction electrons. This type of physics started from the experimental observation of the resistivity minimum in dilute alloys such as CuFe, CuMn, LaCe, or YCe, the theoretical concept of "virtual bound state" introduced by Friedel (1956), (1958), the derivation of the hybridization Anderson (1961) model, and the explanation by Kondo (1964) of the resistivity minimum. After the exact solution of the Kondo effect at low temperatures for a single impurity (Wilson 1975), there are many topics involved in the physics of strongly correlated electron systems. The main topic

concerns the so-called "heavy-fermion" behavior observed in many cerium or other anomalous rare-earth compounds, after its first observation in $CeAl_3$ (Andres *et al*. 1975). In the "Kondo lattice," there exists a strong competition between the Kondo single impurity behavior and the magnetism, and the behavior around the quantum critical point of the Doniach (1977) diagram has been extensively studied.

The metal–insulator transition, introduced by the work of Mott (1974), and the study of compounds such as manganites are also a very important part of this type of physics. The discovery of superconductivity in the $CeCu_2Si_2$ compound by Steglich *et al*. (1979), and in some cerium compounds at high pressure and uranium compounds at normal pressure is also a very noteworthy result. Strong correlations appear to be the origin of the high T_c superconductivity, which was discovered by Bednorz and Muller (1986), but this question is still not answered. Finally, the study of strongly correlated electron systems has considerably contributed to the development of new experimental techniques, such as high-accuracy photoemission or related experiments, neutron scattering, and NMR or muon spectroscopy, as well as to all kinds of magnetic and transport measurements at extremely low temperature and high pressures, and under very large magnetic fields.

1. The Series of Rare-earth and Actinide Metals

The first systems studied that could be considered as strongly correlated electron ones were dilute alloys with 3d transition element impurities embedded in a host such as copper; now the most studied systems contain rare earths and actinides.

Most of the rare-earth metals have a magnetic moment given by Hund's rules (see *Magnetism in Solids: General Introduction* and *Localized 4f and 5f Moments: Magnetism*), corresponding to the $4f^n$ (*n* an integer) configuration. For example, gadolinium, in the middle of the series, has a $4f^7$ configuration with a magnetic moment equal to $7\,\mu_B$ in the ferromagnetic phase below the Curie temperature of 293 K, and there is no change in the number of 4f electrons under pressure, even a very high one. It follows that the "valence," taken here as equal to the number of conduction electrons, remains constant and equal to 3. Thus, most of the rare-earth metals have a stable valence of 3 and are called "normal" (Coqblin 1977).

However, some rare-earth metals undergo a change of valence under different experimental conditions (pressure, temperature, or relative composition in the case of alloys and compounds containing these metals) and they are called "anomalous." The best example of the series is cerium, the first element after lanthanum, which varies or fluctuates between the two configurations $4f^0$ and $4f^1$. Cerium metal has a very peculiar phase diagram with several phases,

which is discussed below. However, dilute cerium alloys such as LaCe or YCe, which are magnetic with a magnetic moment corresponding to the $4f^1$ configuration, show at low temperatures a resistivity minimum which was first accounted for by Kondo (1964). This Kondo effect, which has since been observed in many alloys and compounds containing cerium or other anomalous rare earths, has been the subject of many studies.

The actinide series (see *5f Electron Systems: Magnetic Properties*) corresponds to the filling of the 5f inner shell, but clearly the 5f electrons are less localized than the 4f electrons of the rare-earth metals. In fact, the degree of localization of the 5f electrons lies between that of the 4f electrons and that of the d electrons of the transition elements. The actinide metals of the first series up to americium are not magnetic and magnetism arises only in the middle of the series for curium. Thorium and protactinium, at the beginning of the series, are not magnetic. Uranium, neptunium, and plutonium are close to being magnetic, and most of the properties of neptunium and plutonium can be accounted for by the classical model of spin fluctuations. Finally, the ionic model becomes valid for americium and the following actinides; americium is not magnetic because of the presence of the $5f^6$ configuration, while the following two actinides have magnetic moments corresponding to the $5f^7$ and $5f^8$ configurations. A strong hybridization between the 6d and 5f electrons, which yields an effective broadening of the 5f band and gives a nonmagnetic situation, has been proposed to explain this phenomenon (Jullien *et al.* 1972). Many compounds of uranium, neptunium, and plutonium have been studied and various physical situations have been observed, from a clear magnetic situation with a magnetic order at low temperatures to a nonmagnetic, heavy-fermion situation. Moreover, some uranium compounds are both magnetically ordered, with a heavy-fermion behavior, and superconducting at low temperatures.

2. The Friedel Sum Rule and the Anderson Hamiltonian

As previously explained, transition or rare-earth elements in dilute alloys can be magnetic and in an ionic configuration, but many dilute alloys or compounds contain d or f elements that are in an intermediate situation. This is typically the case for CuMn alloys or cerium compounds. There is a strong interaction between the localized electrons (d or f) on the impurity sites and the conduction electrons that are almost free in the lattice and are generally scattered by the localized electrons. Localized magnetism on the impurity comes from the Coulomb integral, U, and the criterion for the occurrence of localized magnetism is $U\rho(E_F) > 1$, corresponding, therefore, to

strong electron correlations and a large density of states, $\rho(E_F)$, at the Fermi energy. Pioneering work discussing this problem provided the "Friedel sum rule" (Friedel 1954), which connects the difference of charge, Z, between the localized electrons on the impurity and the conduction electrons to the phase shifts introduced by the scattering of the conduction electrons. For example, in CuMn dilute alloys, Z represents the difference of charge between copper and manganese and corresponds to essentially the difference in occupation of the 3d shell.

The Friedel sum rule gives a relationship between Z and the phase shifts, δ_l, at the Fermi energy corresponding to the different partial wave functions scattered by the impurity:

$$Z = \frac{1}{\pi} \sum_{l,\sigma} (2l + 1)\delta_l^\sigma \tag{1}$$

The phase shifts correspond to the different l values of the orbital momentum. Friedel (1956, 1958) developed the model of "virtual bound state" to describe the case of dilute aluminum- or copper-based alloys with 3d impurities. The only nonzero (or multiple of π) phase shift is that of $l = 2$ and δ_2 increases from 0 to π when the 3d shell fills up, passing roughly through a maximum value of $\pi/2$ for manganese. Since the residual resistivity varies as $\sin^2\delta_2$, this derivation explains the maximum of the residual resistivity observed in the 3d series for aluminum-based dilute alloys with 3d impurities. The same type of derivation explains the two maxima observed in the case of copper-based alloys that are magnetic, because there are two different phase shifts for the two spin directions.

Anderson (1961) introduced a Hamiltonian given by

$$H = \sum_{k,\sigma} \varepsilon_k n_{k\sigma} + E_0 \sum_\sigma n_{f\sigma} + U n_{f\uparrow} n_{f\downarrow}$$
$$+ \sum_{k,\sigma} (V_{kf} c_{k\sigma}^* c_{f\sigma} + V_{fk} c_{f\sigma}^* c_{k\sigma}) \tag{2}$$

where the 3d (or 4f or 5f) level located at the energy E_0 is hybridized with the conduction electrons by the hybridization parameter V_{kf}. The Coulomb integral, U, for the localized electrons is generally taken as very large, corresponding, therefore, to the case of strong correlations. For a single impurity, the density of states for the localized electrons has a Lorentzian shape with a width of $\Delta = \pi\rho_s V_{kf}^2$ (where ρ_s is the density of states of the conduction band at the Fermi energy), which leads to a nonintegral number of localized electrons. The Hamiltonian is self-consistently solved within the Hartree–Fock approximation and this model has also been applied to describe the occurrence of magnetism in transition element-based alloys. For example, CuMn alloys are magnetic while AlMn alloys are not, because the density of states at

the Fermi energy, E_F, for the localized electrons hybridized with the conduction electrons is larger in copper than in aluminum.

3. The Kondo Effect

The starting point of the history of the Kondo effect is the first calculation performed by Kondo (1964) to account for the observed experimental evidence of a resistivity minimum in magnetic dilute alloys such as CuMn, CuFe, YCe, or LaCe. The first observed resistivity minimum in CuFe dates from 1931. In such dilute alloys, the transition element impurities are magnetic and the system is well described by the classical exchange Hamiltonian given by

$$H = -J s_c S_f \qquad (3)$$

where the localized spin, S_f, on the impurity interacts with the spins, s_c, of the conduction electrons coming from the host. The exchange constant, J, can be either positive (corresponding to a ferromagnetic coupling) or negative (antiferromagnetic coupling). It follows that a localized spin, S_f, on site i interacts with another localized spin on site j by an indirect mechanism involving the conduction electrons through the exchange interaction given by Eqn. (3). This indirect interaction between two localized electron spins is called the "Ruderman–Kittel–Kasuya–Yosida" (RKKY) interaction (Ruderman and Kittel 1954). The RKKY interaction (see *Magnetism in Solids: General Introduction*) decreases as a function of the distance, R, between the two sites i and j as $\cos(k_F R)/(k_F R)^3$.

Kondo computed the magnetic resistivity, ρ_m, up to third order in J (or in second-order perturbation) and found the following:

$$\rho_m = A|J|^2 S(S+1)\left[1 + J\rho\log\left(\frac{k_B T}{D}\right)\right] \qquad (4)$$

where ρ is the density of states for the conduction band at the Fermi energy, A is a constant, and S is the value of the spin for the localized electrons. We see that, for a negative J value, the magnetic resistivity decreases with increasing temperature. Thus, the total resistivity, which is the sum of the magnetic resistivity and the phonon resistivity which increases with temperature, passes through a minimum (Kondo 1964, 1969). A negative J value corresponds to an antiparallel coupling between the localized and conduction electron spins and the preceding treatment is valid only at sufficiently high temperatures above the so-called "Kondo temperature," T_k, given by

$$k_B T_k = D\exp\left(-\frac{1}{|J\rho|}\right) \qquad (5)$$

where D is a cut-off corresponding roughly to the conduction band width. The magnetic susceptibility decreases above T_k as $1/T$, as in a Curie–Weiss law (see *Magnetism in Solids: General Introduction*). The different transport, magnetic, and thermodynamic properties of a Kondo impurity have been extensively studied by perturbation in the so-called "high-temperature" regime (i.e., above T_k). It is clear that, below T_k, the perturbative treatment is not valid and the low-temperature behavior is completely different from the previously described high-temperature behavior.

At "low temperatures" ($T \ll T_k$), a so-called heavy-fermion behavior (see Heavy-fermion Systems) has been observed in many cerium Kondo compounds, such as CeAl$_3$, CeCu$_6$, or CeCu$_2$Si$_2$. This behavior was first observed experimentally in CeAl$_3$, where Andres *et al.* (1975) found an extremely large electronic specific heat constant $\gamma = 1.62\,\text{Jmol}^{-1}\text{K}^{-2}$ and an AT^2 law for the resistivity with a very large coefficient $A = 35\,\mu\Omega\text{cmK}^{-2}$. An extremely high value of $\gamma = 8\,\text{Jmol}^{-1}\text{K}^{-2}$ has been obtained in the YbBiPt compound, which is the maximum observed γ value (Lacerda *et al.* 1993).

The theoretical problem of a single Kondo impurity has been exactly solved at $T = 0$ by Wilson (1975) using the renormalization group technique on the exchange Hamiltonian (Eqn. (3)) with a negative J value. Wilson was the first to show numerically that the exact $T = 0$ solution is a completely compensated singlet formed by the antiparallel coupling between the conduction electron spin, $s_c = 1/2$, and the localized electron spin, $S_f = 1/2$. An analytical exact solution of the single Kondo impurity problem has been obtained by the Bethe–Ansatz method for both the classical exchange and the Coqblin–Schrieffer Hamiltonians (Andrei *et al.* 1983, Schlottmann 1982, Tsvelick and Wiegmann 1982). The exact solutions have given a clear description of the Kondo effect, but since it is difficult to use them for computing the different physical properties, sophisticated mean field-type methods have been introduced, such as the "slave boson" method (Read and Newns 1983, Coleman 1984) or the method using correlators (Lacroix and Cyrot 1979). A dynamical mean-field theory that takes the limit of infinite dimension (or a very large lattice coordination number) has been introduced because this limit can yield an exact mapping of lattice models onto quantum impurity models (Georges *et al.* 1996). We can also mention many works describing dynamical effects or spectroscopic properties and both the impurity Kondo and Anderson problems including dynamical properties have been solved by different theoretical techniques, in particular by the renormalization group technique (Allen *et al.* 1986). There is a tremendous literature on this subject and the reader can find very interesting reviews in Hewson (1992) or Bickers (1987).

The low-temperature (i.e., $T \ll T_k$) properties of a Kondo impurity are those of a "Fermi liquid" and can be summarized as follows:

• The electronic specific heat constant, γ, and the magnetic susceptibility, χ, are much larger than those corresponding to normal magnetic behavior, but the Wilson ratio, $R = \gamma/\chi$, remains constant between 1 and 2 in suitable units. The values of γ are typically of the order of $1000\,\mathrm{mJmol^{-1}K^{-2}}$ in the case of compounds that remain nonmagnetic at low temperatures and of the order of $100\,\mathrm{mJmol^{-1}K^{-2}}$ in the case of compounds which order magnetically. The term "heavy fermions" originates from these high values of γ and χ, and Table 1 gives some examples of heavy-fermion systems (see *Heavy-fermion Systems*).

• Direct evidence of the heavy-fermion behavior has been obtained by de Haas van Alphen effect experiments in many Cerium compounds, such as $CeCu_6$, CeB_6, and $CeRu_2Si_2$, and some uranium compounds. An effective mass up to roughly $100m_e$ (where m_e is the electron mass) has been observed in cerium compounds (Onuki and Hasegawa 1995).

• The transport properties of cerium Kondo compounds are described by the Fermi liquid formalism at low temperatures. In particular, the electrical resistivity follows a T^2 law and the coefficient, A, of this term is particularly large in heavy-fermion systems.

The exchange Hamiltonian (Eqn. (3)) describes well the case of a magnetic impurity embedded in a normal matrix. The Anderson Hamiltonian (Eqn. (2)) is in fact richer, because it can describe different situations, such as the nonmagnetic and the magnetic case or the intermediate valence (see *Intermediate Valence Systems*) and the almost integer valence. However, in the special case of a magnetic impurity with a valence close to an integer (3 in the cerium case), Schrieffer and Wolff (1966) have shown that the Anderson Hamiltonian is equivalent to a Kondo Hamiltonian with a J value given by

$$J = -\frac{|V_{kf}|^2}{|E_0 - E_F|} \qquad (6)$$

and we immediately see that the J value is negative. Thus, this so-called Schrieffer–Wolff transformation allows one to show that the Anderson Hamiltonian in the almost ionic limit yields automatically a negative J value and, therefore, the Kondo effect.

Table 1
Some examples of heavy-fermion compounds.

Compound	Crystal structure (ground state)	CEF splitting (K)	T_N (K)	γ (mJmol$^-$K^{-2})
CeAl$_3$	Hexagonal	60–90		1600
CeCu$_2$Si$_2$	Tetragonal	140–360		1000
CeCu$_6$	Orthorhombic	100–240		1500
CeRu$_2$Si$_2$	Tetragonal	220		350
CeInCu$_2$	Cubic (Γ_7)	90		1200
CeCu$_4$Ga	Hexagonal	100		1800
CeAl$_2$	Cubic (Γ_7)	100	3.85	135
CeB$_6$	Cubic (Γ_8)	500	3.2	300
CeRh$_2$Si$_2$	Tetragonal	150	36	23
Ce$_3$Al$_{11}$	Orthorhombic	100	$T_c = 6.2$ (Ferro)	120
CeIn$_3$	Cubic (Γ_7)	100	10	140
CeAl$_2$Ga$_2$	Tetragonal	66–122	8.5	80
CeCu$_2$	Orthorhombic	200	3.5	82
CeCu$_2$Ge$_2$	Tetragonal	200	4.15	100
Ce$_2$Sn$_5$	Orthorhombic	70–155	2.9	380
YbCu$_4$Ag	Cubic	45		245
YbBiPt	Cubic			8000
YbNi$_2$B$_2$C	Tetragonal	40–200		530
YbCu$_2$Si$_2$	Tetragonal	216		135
YbNiAl	Hexagonal	35	2.9	350
U(Pt$_{0.95}$Pd$_{0.05}$)$_3$	Hexagonal		6	500
UPd$_2$Al$_3$	Hexagonal		14.3	150
UNi$_2$Al$_3$	Hexagonal		4.6	120
NpSn$_3$	Cubic		9.5	240
YMn$_2$	Cubic		100	160
LiV$_2$O$_4$	Cubic			400

4. The Case of Cerium Metal and Compounds: The Introduction of Spin and Orbital Magnetism

The Anderson and the exchange Hamiltonians have been used to describe the situation of magnetic systems with only a spin magnetic moment and a quenched orbital magnetic moment, as in the alloys with 3d transition elements, where we deal with $S = 1/2$ or $S = 5/2$ spins. However, the physical situation of rare earths is more complicated, because the magnetic moment has both spin and orbital components and the states are labeled according to the z-components of the total angular momentum $J = L + S$. For example, in magnetic cerium systems, the spin–orbit is sufficiently large to split the $4f^1$ configuration into a ground state $J = 5/2$ and an excited state $J = 7/2$. Then, the six-fold degenerate level $J = 5/2$ is split by the crystalline field effect which has a typical energy splitting of the order of 100 K and, therefore, of the same order as the usual temperature of the experiment. Thus, both the orbital degeneracy and the crystalline field effect are important in the study of anomalous rare earths like cerium or ytterbium, which have the configurations $4f^1$ and $4f^{13}$, respectively (see *Localized 4f and 5f Moments: Magnetization*).

Thus, it is necessary to include the orbital degeneracy owing to the seven orbitals corresponding to $l = 3$ and $m = l_z = -3, -2, -1, 0, +1, +2, +3$. The Anderson Hamiltonian including the orbital degeneracy is given by

$$H = \sum_{k,\sigma} \varepsilon_k n_{k\sigma} + E_0 \sum_{m,\sigma} n_{m\sigma} + \sum_{k,m,\sigma} (V_{km} c_{k\sigma}^* c_{m\sigma} + V_{mk} c_{m\sigma}^* c_{k\sigma})$$

$$+ \frac{1}{2} \sum_{m,m',\sigma(m \neq m')} (U_{mm'} - J_{mm'}) n_{m\sigma} n_{m'\sigma}$$

$$+ \frac{1}{2} \sum_{m,m',\sigma} U_{mm'} n_{m\sigma} n_{m'-\sigma} \tag{7}$$

This Hamiltonian has been used to explain the phase diagram of cerium metal, which provides a very fascinating example of many features of strong correlations. Cerium, the first element in the series after lanthanum, varies or fluctuates between the two configurations $4f^0$ and $4f^1$. The phase diagram of cerium metal, shown in Fig. 1, is very peculiar and has several phases (Jayaraman 1965). The phase occurring at normal temperature and pressure is the γ phase, which is paramagnetic with a magnetic moment of roughly 2.5 μ_B corresponding to a valence of 3 and a $4f^1$ configuration. The α phase which exists at high pressure is not magnetic and has a valence larger than 3, and is an "intermediate valence" phase. The γ–α transition is of first order at room temperature, but the intensity of this transition decreases with increasing pressure and tends to zero at a critical point, C, of the order of 600 K and 20 kbar. Thus, the existence of a critical point is unique in pure metals and looks like that of the liquid–vapor diagram. At low
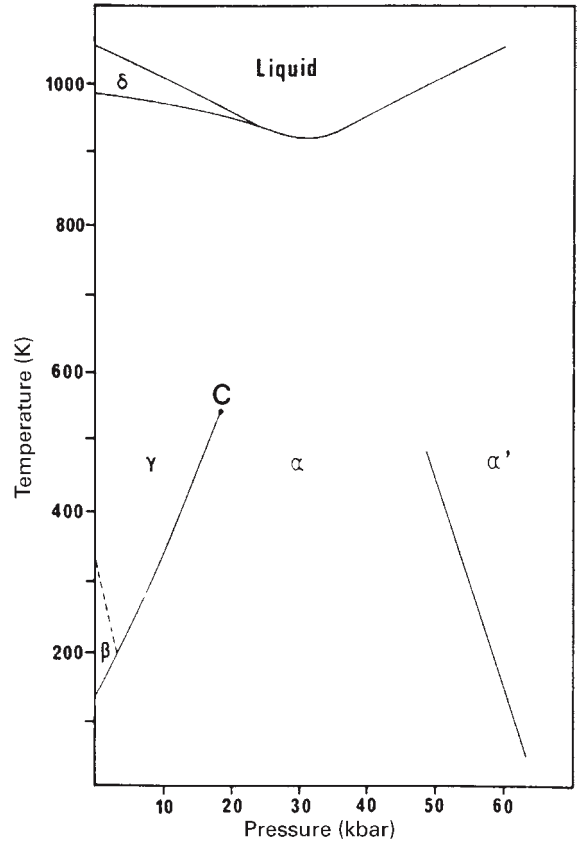
Figure 1
Phase diagram of cerium metal.

temperatures, the β phase orders antiferromagnetically at roughly 12 K, while at very high pressures above 50 kbar, cerium undergoes another phase transition to the α' phase, which becomes superconducting at very low temperatures. At high temperatures, the δ phase has a transition temperature that decreases with increasing pressure.

The theoretical explanation of the γ–α transition of cerium with the existence of a critical point has been the subject of several explanations and many discussions. One explanation of the γ–α transition is based on a Hartree–Fock treatment of the Hamiltonian of Eqn. (7) and yields a first-order transition accompanied by a change of valence from the magnetic trivalent γ-cerium to the nonmagnetic α-cerium that has an intermediate valence of the order of 3.5 (Coqblin and Blandin 1968). Another explanation is based on the Kondo effect with a very large Kondo temperature for the α phase (Allen and Martin 1982, Lavagna *et al.* 1983) and sophisticated band calculations have been performed to account for the phase diagram of cerium (Svane 1996). There have also

been many experiments, in particular those yielding spectroscopic data, that give an estimate of the valence change in cerium.

In the so-called "Kondo limit," i.e., when the number of 4f electrons (or holes) is close to 1, corresponding to the $4f^1$ configuration of cerium (or the $4f^{13}$ configuration of ytterbium), an effective Hamiltonian has been derived using the Schrieffer–Wolff transformation (Coqblin and Schrieffer 1969). We start from the Anderson Hamiltonian with orbital degeneracy and a large spin–orbit coupling. Thus, we define the operators c_M that destroy a localized 4f electron in the $l = 3$, $s = 1/2$, $j = 5/2$ for cerium ($j = 7/2$ for ytterbium), and $j_z = M$ state. Then, the only conduction electrons that are hybridized with the 4f electrons correspond to the partial waves with the same quantum numbers, because the hybridization parameter mixes only localized and conduction electrons with the same values of l, s, j, and j_z. Thus, the resulting so-called "Coqblin–Schrieffer" Hamiltonian can be written as follows:

$$H = - \sum_{k,k',M,M'} J_{MM'} c_{k'M'}^* c_{kM} c_M^* c_{M'} + \sum_{k,k',M} V_{MM} c_{k'M}^* c_{kM}$$

$$(8)$$

with the exchange parameters given by

$$J_{MM'} = \frac{1}{2} |V_{kf}|^2 \left(\frac{1}{E_M} + \frac{1}{E_{M'}} \right) \qquad (9)$$

When the crystalline field effect is not considered there is a unique exchange parameter corresponding to the unique value, E_0, of the 4f level compared to the Fermi level, E_F. However, $J_{MM'}$ are not equal to a unique value when the crystalline field is considered; for example, a cubic crystalline field splits the $j = 5/2$ state into a doublet Γ_7 of energy E_1 and a quartet Γ_8 of energy E_2 and there are three different exchange integrals J_{11}, J_{22}, and J_{12}.

The Coqblin–Schrieffer Hamiltonian including crystalline field effects has been extensively used to derive many transport and magnetic properties of cerium Kondo compounds. The magnetic resistivity (Cornut and Coqblin 1972), calculated by perturbation theory at "high temperatures," i.e., for $T > T_k$, for a cubic crystalline field of energy splitting Δ, shows a maximum at a temperature roughly equal to Δ and two log T behaviors above and below Δ. The slopes of these log T behaviors are characteristic of the respective degeneracies, α_i, of the levels:

$$\frac{d\rho_i}{d\log T} = A_0 \rho J^3 \frac{\alpha_i^2 - 1}{4j(j+1)} \qquad (10)$$

where A_0 is a constant independent of α_i.

Figure 2 shows the log T plot of the magnetic resistivity, ρ_m, of the $CeAl_2$ compound (Nicolas-Francillon et al. 1972). At low temperatures, $CeAl_2$ becomes antiferromagnetic at $T_N = 3.85$ K and the
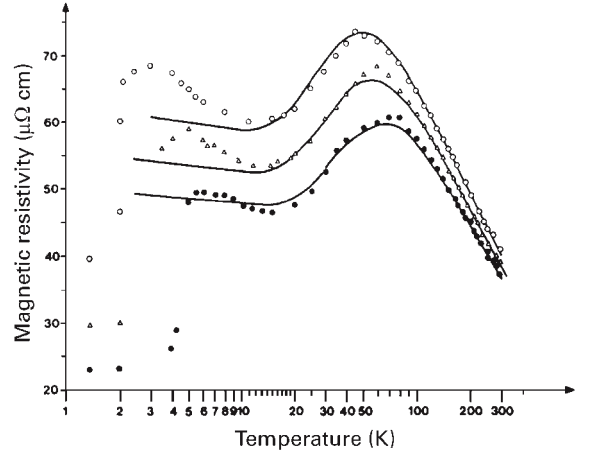
Figure 2
Magnetic resistivity of $CeAl_2$ vs. log T at normal pressure ($\bullet$), 8 kbar ($\triangle$), and 16 kbar ($\bigcirc$). The lines correspond to the theoretical calculations according to Nicolas-Francillon et al. (1972).

magnetic resistivity drops rapidly below T_N. Figure 2 also shows the large effect of pressure: the absolute value of the log T slopes increases rapidly with pressure, which is accounted for by a decrease of $|E_M|$ and an increase of $|J_{MM'}|$ with pressure. Although the results of Fig. 2 were obtained some time ago, they are worth presenting here because they were probably the first to show very well the effects of both the crystalline field and the pressure. These effects have been observed subsequently in other transport and magnetic properties and have been found in many cerium compounds (Coqblin et al. 1993).

The decrease of the magnetic resistivity in log T is considered as a clear signature of the Kondo effect in magnetic cerium compounds and has been observed in more than 100 compounds (Coqblin et al. 1996). The increase of the absolute value of the log T slope is also characteristic of the pressure effect in cerium Kondo compounds. Moreover, the available highest pressures are now much larger and there exist new experiments on such cerium or ytterbium compounds. In fact, the values of $|J_{MM'}|$ first increase with pressure, then at very high pressures they pass through a maximum and then decrease, finally yielding a nonmagnetic state at very high pressures, as for example in YCe alloys (Maple and Wittig 1971).

5. Heavy-fermion Compounds

In the series of rare-earth metals, three are anomalous in the sense that they do not have a stable valence of 3. Cerium has a very peculiar phase diagram with intermediate valence phases, while europium and

ytterbium metals are divalent under normal conditions of temperature and pressure. Thus, as discussed below, many cerium and ytterbium alloys or compounds and only a few europium-based systems have an anomalous behavior.

An anomalous behavior has also been observed in alloys or compounds containing three other rare earths which are trivalent normal metals: praseodymium ($4f^2$), samarium ($4f^5$), and thulium ($4f^{12}$). However, no anomalous behavior has been detected and consequently the normal trivalent character remains very stable even at very high pressures in systems with the other rare earths and in particular with the heavy ones (gadolinium, terbium, dysprosium, holmium, and erbium) (Coqblin 1977).

Examples of anomalous behavior are known for systems containing praseodymium, samarium, or thulium. For example, $PrSn_3$ and TmS show a decrease of the magnetic resistivity characteristic of the Kondo effect. SmS shows, under pressure, a metal–insulator transition that is accompanied by a valence change. $TmSe$, which is insulating at low temperatures in the antiferromagnetic domain, has an intermediate valence, roughly equal to 2.5 at stoichiometry and varying with the departure from stoichiometry. A semiconducting or low carrier behavior has also been observed in other compounds, such as $CeNiSn$, SmB_6, and cerium or ytterbium pnictides.

We now discuss cerium and ytterbium compounds that have a Kondo or heavy-fermion behavior. In fact, there are more than 100 of such compounds, which are reviewed elsewhere (Coqblin *et al.* 1996). Moreover, there are several types of cerium and ytterbium systems, depending on the valence (i.e., intermediate valence and Kondo systems have clearly different behaviors), on the existence of a magnetic moment (yielding a Curie–Weiss law at sufficiently high temperatures), and on the existence of a magnetic order at low temperatures. For example, when x increases, the compound $CeSi_x$ passes through several situations: first a Kondo system which orders antiferromagnetically at low temperatures, then the Néel temperature tends to zero and the compound is no longer magnetically ordered but still magnetic at high temperatures, and finally a nonmagnetic intermediate valence state is reached (Lee *et al.* 1987).

We now discuss the case of Kondo systems that have a heavy-fermion behavior. Table 1 gives some examples of heavy-fermion compounds of cerium, ytterbium, and uranium, with the corresponding values of the crystalline field splittings deduced from the high-temperature behavior, the Néel temperatures when the compounds order, and the very low-temperature values of γ. In fact, it is difficult in some cases to estimate the values of γ, which are not really constant at low temperatures. In spite of these possible difficulties, the values of γ given in Table 1 are very large and characteristic of the heavy-fermion behavior. The cerium compounds that order magnetically at low

temperatures generally show an antiferromagnetic order and only some of them (such as Ce_3Al_{11} in Table 1) order ferromagnetically.

A similar behavior is observed in ytterbium compounds, except that the effect of pressure is reversed. When pressure is applied, the system goes from a nonmagnetic to a magnetically ordered state, and the Néel temperature increases with pressure, as, for example, observed in $YbCu_2Si_2$ (Jaccard *et al.* 1999). There are also examples of heavy-fermion compounds of uranium. Table 1 includes the compound $U(Pt_{0.95}Pd_{0.05})_3$ that orders antiferromagnetically at 6 K because the parent compound UPt_3 seems to have a very peculiar short-range magnetic order, as observed by sophisticated neutron scattering or muon spectroscopy experiments (Koike *et al.* 1999). The three uranium compounds listed in Table 1 have a fascinating behavior, because they combine a heavy-fermion behavior with an antiferromagnetic order and a superconducting state; this last point is discussed in Sect. 7. Finally, very large values of γ have been found in the two compounds YMn_2 and LiV_2O_4 containing 3d transition elements. Table 1 gives the corresponding values of γ for these compounds as well as, for example, for the actinide compound $NpSn_3$, which orders antiferromagnetically at low temperatures. The heavy-fermion character of actinide systems is also a very interesting subject that can be connected to the multichannel Kondo effect (see also *Heavy-fermion Systems*).

6. Competition Between the Kondo Effect and Magnetism: The Doniach Diagram

The competition between the Kondo effect on each atom, which tends to suppress the magnetic moment with decreasing temperature, and the RKKY interaction, which, on the contrary, tends to give a magnetic ordering between different rare-earth atoms is described by the well-known "Doniach diagram" (Doniach 1977), as shown in Fig. 3. Let us call T_{ko} the Kondo temperature for a single impurity and T_{No} the Néel (or Curie in a few cases) temperature as if there were no Kondo effect. For the exchange Hamiltonian (Eqn. (3)), T_{ko} is proportional to $\exp(-1/|J\rho|)$ and T_{No} to $|J\rho|^2$, where ρ is the density of states for the conduction band at the Fermi energy. Thus, for small $|J\rho|$ values, T_{No} is larger than T_{ko} and the system tends to order magnetically, often with a reduction of the magnetic moment owing to the Kondo effect. On the contrary, for large $|J\rho|$, T_{ko} is larger than T_{No} and the system tends to become nonmagnetic and does not order magnetically. The real ordering temperature, T_N, therefore increases initially with increasing $|J\rho|$, then passes through a maximum, and tends to zero at a critical value, $|J\rho|_c$, corresponding to the so-called "quantum critical point" (QCP) I of Fig. 3.
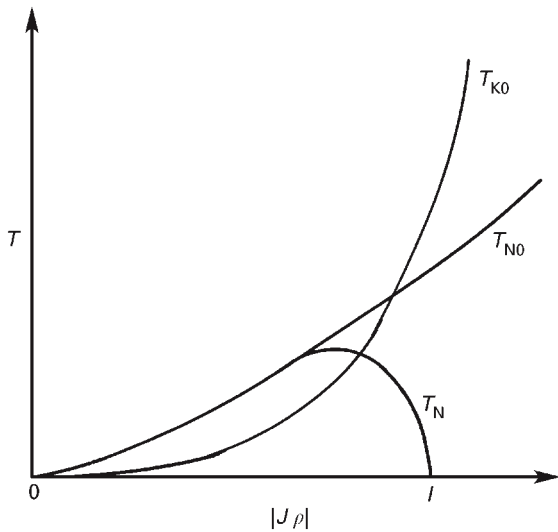
Figure 3
The Doniach diagram.

Such behavior of T_N has been experimentally observed with increasing pressure in several cerium Kondo compounds, such as $CeAl_2$, $CeAg$, $CePd_2Al_3$, $CePtGa$, $CeIn_3$, $CePd_2Si_2$, $CeAu_2Si_2$, $CeCu_2$, and $CeRh_2Si_2$. A maximum in the ordering temperature has been observed in some of them, such as $CeAg$, which is ferromagnetic, or $CePd_2Al_3$, but in all these compounds, the Néel temperature decreases and tends to zero at high pressures. A similar variation of T_N has been observed in $Ce(Ru_xRh_{1-x})_2Si_2$ with a variation of the relative concentration x. In the compounds mentioned above there is no change of valence, but another type of transition to an intermediate valence and eventually to a nonmagnetic state has been observed in the systems $CeSi_x$, $CeNi_xPt_{1-x}$, and $Ce(Cu_xPd_{1-x})_2Si_2$.

Above the QCP corresponding to the magnetic–nonmagnetic instability (or to the disappearance of the Néel temperature, T_N), several behaviors have been observed: a departure from the Fermi liquid (FL) behavior, called "Non-Fermi liquid" (NFL), has been observed experimentally in many cerium compounds under high pressure, such as $CeCu_{6-x}Au_x$ or Ce_7Ni_3 (see *Non-Fermi Liquid Behavior: Quantum Phase Transitions*). For example, $CeCu_{5.8}Au_{0.2}$ alloys (Löhneysen *et al*. 1997) are magnetic with a Néel temperature equal to 0.25 K at normal pressure and become nonmagnetic above 3.2 kbar. Above this critical pressure, the electronic specific heat constant, γ, decreases logarithmically vs. temperature and the slope of γ vs. log T decreases with pressure, i.e., when one goes farther away from the QCP. A similar behavior is observed in the compound Ce_7Ni_3 (Umeo *et al*. 1996), which shows successively a magnetic ordering up to roughly 3 kbar, then a NFL behavior up

to roughly 6–7 kbar, and finally a FL behavior at higher pressures with a coefficient of the resistivity T^2 law decreasing rapidly with pressure and disappearing above 12 kbar. The NFL behavior of the Kondo lattice near the magnetic instability has been theoretically studied within the scaling theory of critical phenomena (Continentino *et al*. 1989) and within the self-consistent renormalized theory of spin fluctuations (Moriya and Takimoto 1995). This latter theory predicts a log T law for γ and a $T^{3/2}$ law for the magnetic resistivity, ρ_m, just at the QCP. As one goes farther away from the QCP, the behavior tends to return to FL behavior, with a decrease of the log T slope of γ and a power law for ρ_m approaching the T^2 law.

In fact, the FL behavior exists above the QCP in some cerium compounds, such as $CeRh_2Si_2$, and the real Kondo temperature has been found to remain roughly constant with $|J|$ or with pressure in the nonmagnetic domain. A theoretical model taking into account both the intrasite Kondo interaction and an additional intersite Heisenberg-type interaction can explain the observed decrease of the real Kondo temperature with respect to the one-impurity Kondo temperature, as a function of the increase of the intersite interaction (Iglesias *et al*. 1997) and of the decrease of the number of conduction electrons (Coqblin *et al*. 2000). The latter result corresponds to the idea of "exhaustion" (Nozieres 1999), which yields a decrease of the Kondo effect when there are not enough conduction electrons to screen the localized electrons. The separation between the FL and the NFL behaviors above the QCP, which depends on the cerium compounds considered, is still a subject of research, but it has been proposed that the FL–NFL separation temperature increases with $|J|$ above the QCP (Continentino *et al*. 1989).

There are in fact several different NFL behaviors, in contrast to the obviously unique FL behavior, and also several theoretical explanations for such experimentally observed NFL behaviors. In addition to the NFL behavior directly connected to the proximity to the QCP described above, a second observed NFL behavior is because of an effect of the disorder. A simple model of a disordered Anderson lattice has been proposed and the disorder introduces a distribution of Kondo temperatures. This simple mechanism leads to logarithmic behaviors in thermodynamic properties and a linear temperature dependence of the resistivity (Miranda *et al*. 1997), as experimentally observed in some cerium and uranium alloys.

The third case of NFL behavior observed in cerium and uranium compounds arises from the so-called "multichannel Kondo model" (Nozieres and Blandin 1980). The regular Kondo effect corresponds to a complete screening of the localized electrons by the conduction electrons, while the multichannel Kondo effect corresponds to either an underscreening or to an overscreening of the localized electrons by the

conduction electrons. The multichannel Kondo model for a single impurity has been completely solved analytically by the Bethe–Ansatz method and numerical solutions have been obtained to describe the different physical properties (Schlottmann and Sacramento 1993).

In the "underscreened" Kondo effect with $2S > n$ (where n is the number of channels for conduction electrons), a part, $n/2$, of the impurity spin is compensated, while the part $S' = S - n/2$ is not compensated. It follows that the magnetic susceptibility is diverging in $1/T$, as for a Curie law, which is obviously different from the constant magnetic susceptibility obtained at low temperatures for the regular screened Kondo effect ($2S = n$). A ferromagnetic coupling between the resulting spin S' and the conduction electron spin is finally obtained in the underscreened Kondo model.

In the "overscreened" Kondo effect with $2S < n$, there remain $(n - 2S)$ uncoupled conduction electrons and the spin, $S' = n/2 - S$, is antiparallel to S. The magnetic susceptibility, χ, and the electronic specific heat constant, γ, have been numerically computed (Schlottmann and Sacramento 1993). For $S = 1/2$, constant values of χ and γ are obtained at low temperatures for the screened Kondo effect corresponding to $n = 1$. Conversely, for $S = 1/2$ and $n = 2$, a logarithmic dependence of χ and γ is obtained, while for $S = 1/2$ and $n > 2$, the temperature dependence of χ and γ is given by a power law in T^n. A particular model within the overcompensated case is the "quadrupolar Kondo effect" introduced by Cox (1987), corresponding to the two-channel case. A logarithmic dependence for γ, a linear dependence for the magnetic resistivity, and an unusual value for the entropy (corresponding to half the value of the entropy for the regular Kondo effect) have been obtained, and these theoretical results have been used to account for the NFL behavior observed in $Y_{1-x}U_xPd_3$.

In conclusion, at and above the QCP several different experimental and theoretical behaviors have been found. First, the FL behavior has been found in many compounds, but even there the real (i.e., for the lattice) Kondo temperature can be either roughly constant with $|J\rho|$ or pressure, as observed in $CeRh_2Si_2$, or can increase rapidly, as observed in some other cerium compounds. Second, a NFL behavior is obtained above the QCP for three possible cases, namely the proximity to the QCP, the disorder, and the overscreened Kondo effect. But, in fact, a given physical case can be relevant to two NFL features, as for example the proximity to the QCP and the disorder for disordered alloys or also the disorder and the multichannel Kondo effect for disordered uranium alloys. The questions of the relative stability of the FL and NFL phases and of the FL–NFL separation have not been solved. In the case of disordered alloys, there can also exist a spin glass state and the relative stability between the spin glass, the FL,

and the NFL states is studied. Finally, a superconducting phase occurs in the proximity of the QCP and this, which will be discussed in the next section, is not really understood.

There has been a tremendous improvement in the experimental techniques used for the study of heavy-fermion compounds and more generally of strongly correlated electron systems. The conditions of transport, calorimetric, and magnetic experiments, using for instance SQUID magnetometry, have reached some millikelvin for temperature, several hundreds of kilobar for pressure, and at least 50 T for pulsed magnetic fields. Also, sophisticated new techniques have been developed: spectroscopic experiments, starting with photoemission, have contributed very much to the determination of the electronic structure of many cerium compounds and other systems; the de Haas van Alphen effect has determined the heavy-fermion character in many cerium and uranium compounds; neutron scattering and muon spin relaxation spectroscopy have been able to determine very small magnetic moments and have been used to study complicated magnetic transitions, as, for example, in $U(Pt_{1-x}Pd_x)_3$ or $CeCoGe_{3-x}Si_x$ alloys (Krishnamurthy *et al.* 1999).

7. Superconductivity and Strong Electron Correlations

Superconductivity was discovered experimentally in 1911 by Kamerlingh Onnes (1911) in mercury metal below $T_c = 4.15\,K$. The theoretical explanation of superconductivity was given by Bardeen *et al.* (1957) who explained the superconductivity by a collective pairing mechanism between electrons of opposite spins. The observed maximum T_c values up to 1986 were $9.25\,K$ for niobium at normal pressure, $12.9\,K$ for lanthanum at 200 kbar, $20.3\,K$ for bulk Nb_3Ga, and $23.2\,K$ for a thin film of Nb_3Ge (Vonsovsky *et al.* 1982, Tominez *et al.* 2000).

Since the mid-1980s there has been considerable interest and progress in the study of superconducting materials, after the discovery by Bednorz and Muller (1986) of "high T_c superconductivity." There are several series of high T_c superconducting materials: the $LaSrCuO_4$ systems are superconducting below roughly 40 K, the $YBaCu_3O_7$ systems have a T_c larger than 90 K, and the mercury-based compounds show the maximum T_c value of 133 K at normal pressure. The origin of superconductivity in cuprates is attributed to the CuO_2 planes and T_c appears to increase with the number of such planes. The alloys $HgBa_2Ca_{n-1}Cu_nO_{2n+2+\delta}$ are superconducting at 94 K, 129 K, 133 K, and 126 K for, respectively, $n = 1$, 2, 3, and 4 layers of CuO_2, showing an increase of T_c with n that unfortunately stops above $n = 3$. The $n = 3$ system Hg-1223 shows, under pressure, a very large increase of T_c, which reaches the
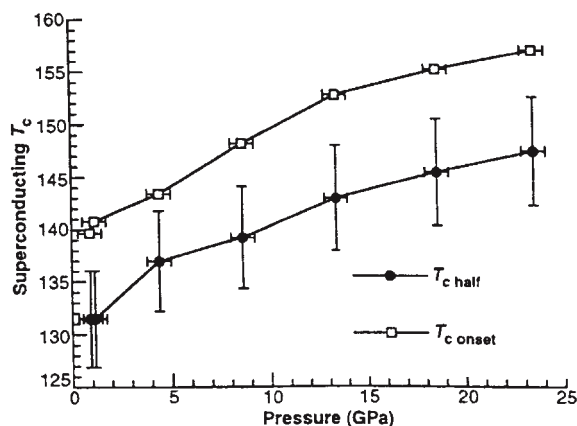
Figure 4
Pressure dependence of the superconducting transition temperature in the Hg-1223 compound. $T_{c\ onset}$ is defined as the temperature at which the resistance turns visibly away from the high-temperature behavior. $T_{c\ half}$ corresponds to the temperature halfway between 80% and 20% of the resistive transition.

value of 157 K at 235 kbar, as shown in Fig. 4 (Nunez-Regueiro *et al*. 1993). Thus, the experimental value of T_c has increased from a value of 23 K in 1986 to more than 150 K in 1993, but is still roughly half the room temperature, the goal of many solid-state physicists. A theoretical explanation of this phenomenon has not yet been found, but there are several possibilities. Superconductivity comes from the CuO_2 planes and the most plausible explanation for the high transition temperature comes from strong magnetic correlations and several models have been built under this assumption. The two-dimensional character of the superconducting CuO_2 planes, which yields a large increase of the density of states, has also been invoked to account for the increase of T_c. There are many experimental works in the field of high-temperature superconductivity, in particular those attempting to increase T_c. Many theoretical studies are based on strong magnetic correlations.

The coexistence of magnetism and superconductivity occurs in several systems, such as the Chevrel phases RMo_6S_8 and RMo_6Se_8 (R being a rare earth Re or tin, lead, or mercury) (Fischer *et al*. 1975) or the borocarbides $ReRh_4B_4$ and $ReNi_2B_2C$ (Mazumdar *et al*. 1993, Tominez *et al*. 2000), but in these cases magnetism comes from the rare earths and superconductivity from the other atoms of the complex chemical structure of these compounds.

Another remarkable and unsolved problem is the "heavy-fermion" superconductivity occurring at low temperatures around the QCP in several cerium compounds. The discovery of superconductivity at $T_c = 0.6$ K in $CeCu_2Si_2$ at normal pressure (Steglich

et al. 1979) is very fascinating. It is known that the compound $CeCu_2Si_2$ is very close to being magnetic and that a small departure from stoichiometry yields a magnetic phase. Superconductivity has been found at very high pressures around the QCP in several cerium compounds, namely $CeCu_2Ge_2$ at $T_c = 0.6$ K above 77 kbar, $CePd_2Si_2$ at $T_c = 0.5$ K above 23 kbar, $CeRh_2Si_2$ at $T_c = 0.4$ K above 9 kbar, $CeCu_2$ around 60 kbar, $CeIn_3$ below 0.2 K at 25 kbar, and $CeNi_2Ge_2$ below 0.1 K at normal pressure (Mathur *et al*. 1998, Gegenwart *et al*. 1999). The two compounds $CeCu_2Si_2$ and $CeNi_2Ge_2$ are nonmagnetic at normal pressure, but in fact they are very close to being magnetic. Thus, we can say that, in all these cerium compounds, this peculiar heavy-fermion superconductivity occurs around the QCP when the Néel temperature disappears but when the heavy-fermion character is very large. (For more details see *Non-Fermi Liquid Behavior: Quantum Phase Transitions*.)

Thus, both the high T_c and the heavy-fermion superconductivities appear to be closely connected with the occurrence of strong electron correlations and further work is necessary to understand better this fascinating subject.

Superconductivity has also been observed in some uranium compounds at low temperatures. The compound UPt_3 is interesting since it undergoes, below 5 K, a transition to a kind of short-range magnetic order and becomes superconducting below $T_c = 0.5$ K, while heavy-fermion behavior characterized by a large electronic specific heat constant, $\gamma = 0.4$ J mol^{-1}K^{-2}, and a T^2 term of the resistivity is observed at low temperatures. A real long-range antiferromagnetic ordering occurs when the concentration, x, increases in alloys $U(Pt_{1-x}Pd_x)_3$ and the Néel temperature is equal to 6 K for $x = 0.05$, as given in Table 1. Some uranium compounds show, when the temperature decreases, first a transition to an antiferromagnetically ordered state at T_N and then a transition to a superconducting state at T_c. The values of T_N and T_c are, respectively, 8.8 K and 0.85 K in UBe_{13}, 17.5 K and 0.8 K in URu_2Si_2, 4.6 K and 1 K in UNi_2Al_3 (Geibel *et al*. 1991b), and 14 K and 2 K in UPd_2Al_3 (Geibel *et al*. 1991a). The physics of such uranium compounds is difficult to understand. We can invoke the underscreened Kondo effect in order to understand better the apparent coexistence observed in such compounds of the heavy-fermion character owing to the Kondo effect and a weak magnetic order resulting from the RKKY interaction, but clearly the occurrence of superconductivity at low temperatures is not yet explained.

8. Manganites

A rapidly developing subject is the experimental and theoretical study of mixed-valence manganites with the perovskite structure. Typical examples are given

by compounds $(La_{1-x}T_x)MnO_3$ or $(Pr_{1-x}T_x)MnO_3$, with T being calcium or strontium. The magnetic phase diagrams show, with varying x, many magnetically ordered phases that are insulating or metallic. In these systems, manganese can be in the two configurations $3d^4$ (corresponding to Mn^{3+}) or $3d^3$ (corresponding to Mn^{4+}). When divalent calcium replaces trivalent lanthanum, the valence of manganese changes from Mn^{3+} to Mn^{4+} resulting in the system being a mixed-valence one. The crystallographic and magnetic structures for the $(La_{1-x}Ca_x)MnO_3$ compounds have been determined in a neutron and x-ray diffraction study as a function of Mn^{4+} (Wollan and Koehler 1955). The system is found to be antiferromagnetic and insulating for x close to 0 and 1, while it is metallic and ferromagnetic with a Curie temperature of 220 K for $x = 0.3$. Zener (1951) presented an explanation of the behavior of such compounds by considering the indirect magnetic exchange between manganese atoms of different charges via an oxygen ion and Goodenough (1955) studied the role of covalence. The "double exchange" corresponding to a simultaneous transfer of an electron from the Mn^{3+} to the oxygen and from the oxygen to the neighboring Mn^{4+} and the classical superexchange that involves a virtual electron transfer were both considered to account for the different magnetic structures, because the double exchange is always ferromagnetic and the superexchange is frequently antiferromagnetic.

Thus, the interest in the study of this quite "old" subject arises from both the discovery of new phenomena such as the so-called "colossal magnetoresistance" which presents interesting new applications in magnetoelectronic devices and the formulation of important physical concepts such as the double exchange and the Jahn–Teller polaron. Excellent reviews are available (Coey *et al.* 1999). Considerable progress has been achieved in several directions: the study by different experiments (transport, magnetic, optical, etc.), the availability of single crystals, the study of systems such as $La_{2-x}T_{1+x}Mn_2O_7$ (with $T = Ca, Sr$), the development of possible applications, and the important progress in the development of theoretical models treating the magnetic polaron and the metal–insulator transition. (See also *Transition Metal Oxides: Magnetism*.)

9. Conclusion

There has been considerable improvement in the development of the field of strongly correlated electron systems since the pioneering works of Mott, Friedel, Anderson, and Kondo. Alloys and compounds of cerium or other anomalous rare earths and obviously heavy-fermion systems are relevant to this field. Manganites also have a strongly correlated electron behavior. The explanation of the high T_c and heavy-

fermion superconductivity has certainly to be looked for in strong electron correlations. Spin-ladder compounds, such as $(Sr,Ca)_{14}Cu_{24}O_{41}$, and low-dimensional systems, such as the ruthenate Sr_2RuO_4 or the compound $CuGeO_3$, can show superconducting and magnetic properties and strong correlations are certainly important in such systems.

Finally, very interesting reviews on strongly correlated electron systems (SCES) have been given at SCES Conferences (SCES Conference Proceedings 1997, 1999, 2000).

See also: Magnetic Excitations in Solids; Rare Earth Intermetallics; Thermopower of Cerium, Samarium and Europium Compounds

Bibliography

Allen J W, Martin R M 1982 Kondo volume collapse and the γ–α transition in cerium. *Phys. Rev. Lett.* **49**, 1106–10

Allen J W, Oh S J, Gunnarsson O, Schönhammer K, Maple M B, Torikachvili M S 1986 Electronic structure of cerium and light rare-earth intermetallics. *Adv. Phys.* **35**, 275–316

Anderson P W 1961 Localized magnetic states in metals. *Phys. Rev. B* **124**, 41–53

Andrei N, Furuya K, Lowenstein J H 1983 Solution of the Kondo problem. *Rev. Mod. Phys.* **55**, 331–402

Andres K, Graebner J E, Ott H R 1975 4f-Virtual-bound-state formation in CeAl$_3$ at low temperatures. *Phys. Rev. Lett.* **35**, 1779–82

Bardeen J, Cooper L N, Schrieffer J R 1957 Theory of superconductivity. *Phys. Rev.* **108**, 1175–204

Bednorz J G, Muller K A 1986 Possible high T_c superconductivity in the Ba–La–Cu–O system *Z. Phys. B* **64**, 189–93

Bickers N E 1987 Review of techniques in the large-N expansion for dilute magnetic alloys. *Rev. Mod. Phys.* **59**, 845–939

Coey J M D, Viret M, von Molnar S 1999 Mixed-valence manganites. *Adv. Phys.* **48**, 167–293

Coleman P 1984 New approach to the mixed-valence problem. *Phys. Rev. B* **29**, 3035–44

Continentino M A, Japiassu G M, Troper A 1989 Critical approach to the coherence transition in Kondo lattices. *Phys. Rev. B* **39**, 9734–7

Coqblin B 1977 *The Electronic Structure of Rare-Earth Metals and Alloys: The Magnetic Heavy Rare-Earths*. Academic Press, London

Coqblin B, Arispe J, Bhattacharjee A K, Evans S M M 1993 Kondo effect and heavy fermions. *Frontiers in Solid State Sciences. Vol. 2: Selected Topics in Magnetism*. World Scientific, Singapore, pp. 75–105

Coqblin B, Arispe J, Iglesias J R, Lacroix C, Le Hur K 1996 Competition between the Kondo effect and magnetism in heavy fermion compounds. *J. Phys. Soc. Jpn Suppl. B* **65**, 64–77

Coqblin B, Blandin A 1968 Stabilité des moments magnétiques dans les métaux. *Adv. Phys.* **17**, 281–366

Coqblin B, Gusmao M A, Iglesias J R, Lacroix C, Ruppenthal A, da R, Simoes A 2000 Effect of conduction band filling on the competition Kondo magnetism in the Kondo lattice. *Physica B* **281–2**, 50–2

Coqblin B, Schrieffer J R 1969 The exchange interaction in alloys with cerium impurities. *Phys. Rev.* **185**, 847–53

Cornut B, Coqblin B 1972 Influence of the crystalline effect on the Kondo effect of alloys and compounds with cerium impurities. *Phys. Rev. B* **5**, 4541–61

Cox D L 1987 Quadrupolar Kondo effect in uranium heavy-electron materials. *Phys. Rev. Lett.* **59**, 1240–3

Doniach S 1977 The Kondo lattice and weak antiferromagnetism. *Physica B* **91**, 231–4

Fischer Ph, Treyvaud A, Chevrel R, Sergent M 1975 Superconductivity in the $RE_xMo_6S_8$. *Solid State Commun.* **17**, 721–4

Friedel J 1954 Electronic structure of primary solid solutions in metals. *Adv. Phys.* **3**, 466–507

Friedel J 1956 Electrical and magnetic properties of metallic solid solutions. *Can. J. Phys.* **34**, 1190

Friedel J 1958 Metallic alloys. *Nuovo Cimento*. **VII**(Suppl.), 287–311

Gegenwart P, Kromer F, Lang M, Sparn G, Geibel C, Steglich F 1999 Non-Fermi-liquid effects at ambient pressure in a stoichiometric heavy-fermion compound with very low disorder: $CeNi_2Ge_2$. *Phys. Rev. Lett.* **82**, 1293–6

Geibel C, Schank C, Thies S, Kitazawa H, Bredl C D, Böhm A, Rau M, Grauel A, Caspary R, Helfrich R, Ahlheim U, Weber G, Steglich F 1991a Heavy-fermion superconductivity at $T_c = 2\,K$ in the antiferromagnet UPd_2Al_3. *Z. Phys. B* **84**, 1–2

Geibel C, Thies S, Kaczorowski D, Mehner A, Grauel A, Seidel B, Ahlheim U, Helfrich R, Petersen K, Bredl C D, Steglich F 1991bb A new heavy fermion superconductor UNi_2Al_3. *Z. Phys. B* **83**, 305–6

Georges A, Kotliar G, Krauth W, Rozenberg M J 1996 Dynamical mean-field theory of strongly correlated fermion systems and the limit of infinite dimensions. *Rev. Mod. Phys.* **68**, 13–125

Goodenough J B 1955 Theory of the role of covalence in the perovskite-type manganites $(La,M)MnO_3$. *Phys. Rev.* **100**, 564–73

Hewson A C 1992 *The Kondo Problem to Heavy Fermions*. Cambridge University Press, Cambridge

Iglesias J R, Lacroix C, Coqblin B 1997 Revisited Doniach diagram: influence of short-range antiferromagnetic correlations in the Kondo lattice. *Phys. Rev. B* **56**, 11820–6

Jaccard D, Wilhelm H, Alami-Yadri K, Vargoz E 1999 Magnetism and superconductivity in heavy fermion compounds at high pressure. *Physica B* **259–61**, 1–7

Jayaraman A 1965 Fusion curve of cerium to 70 kilobar and phenomena associated with supercritical behavior of f.c.c. cerium. *Phys. Rev. A* **137**, 179–82

Jullien R, Galleani d'Agliano E, Coqblin B 1972 Hybridized non-degenerate 6d and 5f virtual bound states model for actinides metals. *Phys. Rev. B* **6**, 2139–55

Kamerlingh Onnes 1911 *Leiden Comm.*, 122b–4c

Koike Y, Metoki N, Kimura N, Yamamoto E, Haga Y, Onuki Y, Maezawa K 1999 Neutron scattering study of the antiferromagnetic ordering in UPt_3 at mK temperatures. *Physica B* **261**, 662–3

Kondo J 1964 Resistance minimum in dilute magnetic alloys. *Prog. Theoret. Phys. (Kyoto)* **32**, 37–69

Kondo J 1969 Theory of dilute magnetic alloys. *Solid State Phys.* **23**, 184–281

Krishnamurthy V V, Watanabe I, Ohira S, Nishiyama K, Nagamine K, Ishikawa M, Eom D H, Takeda N 1999 μ^+ SR observation of magnetic ordering and non-Fermi liquid scaling in $CeCoGe_{1.8}Si_{1.2}$. *Physica B* **261**, 374–5

Lacerda A, Movshovich R, Hundley M F, Canfield P C, Arms D, Sparn G, Thompson J D, Fisk Z, Fischer R A, Phillips N

E, Ott H R 1993 Doping and pressure studies on YbBiPt. *J. Appl. Phys.* **73**, 5415–7

Lacroix C, Cyrot M 1979 Phase diagram of the Kondo lattice. *Phys. Rev. B* **20**, 1969–76

Lavagna M, Lacroix C, Cyrot M 1983 The γ–α transition in cerium compounds. *J. Phys. F* **13**, 1007–15

Lee W H, Shelton R N, Dhar S K, Gschneidner K A Jr. 1987 Competition between the Kondo effect and exchange interactions in the system $CeSi_x$. *Phys. Rev. B* **35**, 8523–7

Löhneysen H V, Huster F, Mock S, Neubert A, Pietrus T, Sieck M, Stockert, Waffenschmidt M 1997 Non-Fermi liquid behavior in strongly correlated electron systems. *Physica B* **230**, 550–6

Maple M B, Wittig J 1971 Low temperature electrical resistivity of $\underline{Y}$Ce under pressure. *Solid State Commun.* **9**, 1611–5

Mathur N D, Grosche F M, Julian S R, Walker I R, Freye D M, Haselwimmer R K W, Lonzarich G G 1998 Magnetically mediated superconductivity in heavy fermion compounds. *Nature* **394**, 39–43

Mazumdar C, Nagarajan R, Godart C, Gupta L C, Latroche M, Dhar S K, Levy-Clement C, Padalia B D, Vijayaraghavan R 1993 Superconductivity at $12\,K$ in Y–Ni–B system. *Solid State Commun.* **87**, 413–6

Miranda E, Dobrosavljevic V, Kotliar G 1997 Disorder-driven non-Fermi-liquid behaviour in Kondo alloys. *Phys. Rev. Lett.* **78**, 290–3

Moriya T, Takimoto T 1995 Anomalous properties around magnetic instability in heavy electron systems. *J. Phys. Soc. Jpn.* **64**, 960–9

Mott N F 1974 *Metal–Insulator Transitions*. Taylor and Francis, London

Nicolas-Francillon M, Percheron-Guegin A, Achard J C, Gorochov O, Cornut B, Jerome D, Coqblin B 1972 Measurements of the $CeAl_2$ and $LaAl_2$ resistivities under pressure: variations of the Kondo effect and the crystalline field of cerium. *Solid State Commun.* **11**, 845–9

Nozieres P 1999 Some comments on Kondo lattices and the Mott transition. *Eur. Phys. J. B* **6**, 447–57

Nozieres P, Blandin A 1980 The Kondo effect in real metals. *J. Phys.* **41**, 193–211

Nunez-Regueiro M, Tholence J-L, Antipov E V, Capponi J-J, Marezio M 1993 Pressure-induced enhancement of T_c above $150\,K$ in Hg-1223. *Science* **262**, 97–9

Onuki Y, Hasegawa A 1995. In: Gschneidner Jr. K A, Eyring L (eds.) *Handbook on the Physics and Chemistry of Rare-Earths*. Elsevier, Amsterdam

Read N, Newns D M 1983 On the solution of the Coqblin–Schrieffer Hamiltonian by large-N expansion technique. *J. Phys. C* **16**, 3273–95

Ruderman M A, Kittel C 1954 Indirect exchange coupling of nuclear magnetic moments by conduction electrons. *Phys. Rev.* **96**, 99–102

SCES 1997 Conference proceedings. *Physica B*, **230–2**

SCES 1999 Conference proceedings. *Physica B*, **259–61**

SCES 2000 Conference proceedings. *Physica B* **281–2**

Schlottmann P 1982 Bethe–Ansatz solution of the ground state of a model for mixed-valent Ce and Yb impurities in metals. *Z. Phys. B* **49**, 109–14

Schlottmann P, Sacramento P D 1993 Multichannel Kondo problem and some applications. *Adv. Phys.* **42**, 641–82

Schrieffer J R, Wolff P A 1966 Relation between the Anderson and the Kondo Hamiltonians. *Phys. Rev.* **149**, 491–2

Steglich F, Aarts J, Bredl C D, Lieke W, Meschede D, Franz W, Shäfer H 1979 Superconductivity in the presence of strong Pauli paramagnetism: $CeCu_2Si_2$. *Phys. Rev. Lett.* **43**, 1892–6

Svane A 1996 Electronic structure of cerium in the self-inter-action corrected local spin-density approximation. *Phys. Rev. B* **53**, 4275–86

Tominez E, Alleno E, Berger P, Bohn M, Mazumdar C, Godart C 2000 Chemical and superconducting properties of the quaternary borocarbides Ln–M–B–C (Ln = rare earths, Y; M = Ni, Pd). *J. Solid State Chem.* **154**, 114–29

Tsvelick A M, Wiegmann P B 1982 Exact solution of the degenerate exchange model (Kondo problem for alloys with rare-earth impurities). *J. Phys. C* **15**, 1707–12

Umeo K, Kadomatsu H, Takabatake T 1996 Non-Fermi-liquid behaviour at the pressure-induced antiferromagnetic to non-magnetic transition in a heavy-fermion compound, Ce$_7$Ni$_3$. *J. Phys.: Cond. Matter* **8**, 9743–57

Vonsovsky S V, Izyumov Tu A, Kurmaev E Z 1982 Superconductivity of transition metals, their alloys and compounds. *Springer Series in Solid State Science*. Springer, Berlin, Vol. 27 Chap. 1

Wilson K G 1975 The renormalization group: critical phenomena and the Kondo problem. *Rev. Mod. Phys.* **47**, 773–840

Wollan E O, Koehler W C 1955 Neutron diffraction study of the magnetic properties of the series of perovskite-type compounds La$_{1-x}$Ca$_x$MnO$_3$. *Phys. Rev.* **100**, 545–63

Zener C 1951 Interaction between the d shells in the transition metals. *Phys. Rev.* **81**, 440–4; **82**, 403–5

B. Coqblin
Université Paris-Sud, Orsay, France

Electronic Configurations of 3*d*, 4*f*, and 5*f* Elements: Properties and Simulation

The development of crystalline spectroscopy of the transition elements and more particularly of the rare earths was strongly connected to the chemical purity of the rare earth elements and of their compounds as well as to their availability on the market. This problem was partially resolved around the 1950s and a litany of works appeared from that time when scientists like Dirac, Bethe, Racah, Stevens, Wybourne, Judd, and others published the works which constitute the basis of this specialty.

From a theoretical point of view, the rare earth elements are one of the most convenient fields for the elaboration and testing of the quantum theories of atomic spectroscopy and their application to an ion included in a crystal. These techniques allow the energy level scheme, deduced from experiment, to be simulated. Moreover, knowledge of the associated wave-functions extends the technique towards the reproduction of other physical properties, mainly involving the magnetic operator (see *Crystal Field and Magnetic Properties, Relationship Between*).

The ability to perform such simulations is entirely due to the great development in computer technology, particularly PCs which make possible sophisticated calculations in a short time at a reduced cost. This rather recent tool, but largely generalized in
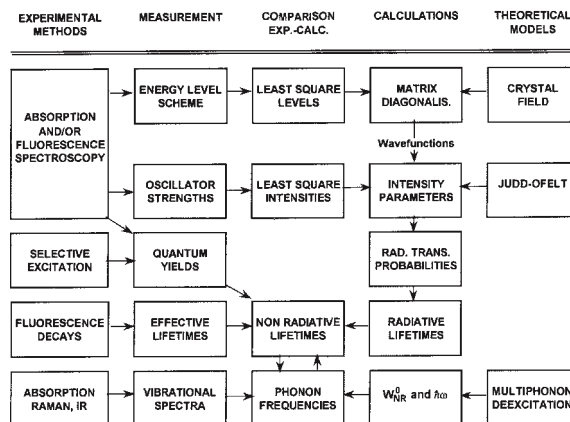
Figure 1
Organigram of the rare earth spectroscopic properties. From Delsart C 1973 Thesis, University of Orsay (ref: CNRS-AO8332), reprinted with the permission of the author.

modern science, has transformed the traditional *Theory–Experiment–Calculation* triptych into a new *Theory–Experiment–Simulation* one in which the physical phenomenon is always accompanied by its image.

In such a concept, the crystalline spectroscopy of transition elements can be summarized in an organigram (Fig. 1) illustrating how the steps of the triptych are connected. The present article is devoted to the simulation of the energy level positions.

The experimental part of the "static" optical spectroscopy that is presented in this article constitutes an energy level scheme deduced from transitions between states of the electronic configuration. It is mainly deduced from absorption and/or emission measurements performed in the wavelength range from the infrared to the ultraviolet. Other techniques, like inelastic neutron scattering, specific heat measurements, etc., can also yield some of the lowest energy levels. The quantum mechanics technique provides the basic theory for the models developed in the case of an ion located in a chemical neighborhood. This is also connected to the nature of the chemical bonding, knowledge of which is so important for the solid-state chemist.

1. Electronic Configurations of the Transition Elements

Simulation of the rare earth (or 3d) elements' electronic configurations is based on the one-center model. In this analytical approach the central ion is submitted to various interactions, quantified, and parameterized according to the perturbation methods. All interactions are considered together in a

unique secular determination. The diagonalization gives the energy levels, which have to be compared with the experimental ones. On the basis of the intermediate coupling, the interactions are formally divided into free ion and crystal field interactions. The framework of the description is the Racah algebra (Judd 1963, Wybourne 1965) which permits a quantitative description of the coupling between angular moments, whereas the qualitative rules are a consequence of the elegant use of group theory.

All trivalent rare earth ions have the $[Xe]4f^N$ configuration as a ground configuration, in which [Xe] represents the filled electronic layers of the rare gas xenon. They are usually considered as isolated from other configurations located at a distance in the energy level energy scale, which is not necessarily a good approximation for other transition elements. The influence of the excited configurations on the ground state is small, but included in the simulation technique through effective operators. This assumption appears to be rather realistic with an energy gap between the ground configuration and the first excited state of ($4f^{N-1}5d$ for RE^{3+}) ca. $120\,000\,cm^{-1}$. The description is based on the $|\eta SLJM\rangle$ kets, in which η, S, L, J, and M are the quantum numbers of the intermediate coupling description. The number of kets is equal to the degeneracy of the configuration, i.e., the number of possible elementary states according to the Pauli exclusion principle. In the group theory aspect, each momentum is associated to a reducible representation of the R_{3i} rotation group (or of the R_{3i}' double group for odd number of electrons), D_S, D_L, and D_J. It is noteworthy that some differences often appear when $4f^N$ and $3d^N$ are compared, the latter being traditionally described on the $|\eta SM_S LM_L\rangle$ basis, in which the total angular momentum (spin–orbit coupling) is not included. This parametric model gives an approximate solution of the Schrödinger equation, each electron being supposed to move independently in an explicit central field replacing the Coulombian potential. In the perturbation theory framework various interactions of decreasing importance are then introduced to correct that approximation. Judd (1963) and Wybourne (1965) have standardized the formalism generally employed.

1.1 Electrostatic Repulsion

This interaction representing the Coulombian repulsion between pairs of electrons is the most important among the free ion interactions:

$$H_{El} = \frac{1}{2}\sum_{i\neq j}^{n} \frac{e^2}{r_{ij}}$$

The corresponding matrix element is written as a linear combination of products between a radial integral (expressed as the Slater integrals, F_k, or as the Racah parameters, E^k) and of an angular part, tabulated by Nielson and Koster (1964):

$$\langle \alpha SLJM|H_{El}|\alpha'S'L'J'M'\rangle = \delta(S,S')\delta(L,L')\delta(J,J')$$

$$\times\, \delta(MM')\sum_{k=0}^{3} f_k F_k \qquad (1)$$

This interaction is diagonal in S,L,J,M except when the principal quantum numbers are different. It creates the ^{2S+1}L terms of the configuration, associated to the $D_L \otimes D_S$ irreducible representation products of the R_{3i} rotations group. Their degeneracy is $(2S+1)(2L+1)$ (Table 1). The energy difference between two terms is ca. $20\,000\,cm^{-1}$. Values of the F_2 Slater integral for various configurations are reported in Table 2.

1.2 Two- and Three-body Interactions

In addition to the electrostatic repulsion operating between the states of the ground configuration (intra-configuration), correcting interactions are usually added in order to reproduce electrostatic coupling with states of excited configurations (interconfigurations) through effective operators. The two-electron operators (for $4f^N$ with $N \geqslant 2$), are the Tree parameter α operating on the angular momentum L and β and γ

Table 1
Number of terms, levels, and degeneracy of the d^N and f^N configurations.

Configurations nd^N		
Nb Electrons	Nb Terms ^{2S+1}L	Nb Levels $^{2S+1}L_J$	Nb States $^{2S+1}L_{JM}$
1 (9)	1	2	10
2 (8)	5	9	45
3 (7)	8	19	124
4 (6)	16	34	210
5	16	37	252

Configurations nf^N		
Nb Electrons	Nb Terms ^{2S+1}L	Nb Levels $^{2S+1}L_J$	Nb States $^{2S+1}L_{JM}$
1 (13)	1	2	14
2 (12)	7	13	91
3 (11)	17	41	364
4 (10)	47	107	1001
5 (9)	73	198	2002
6 (8)	119	295	3003
7	119	327	3432

Table 2
Order of magnitude of the main interactions in the nl^N configurations (cm^{-1}).

Configuration	Coulomb rep. F_2	Spin–Orbit ζ	Crystal field B_q^k
$3d^N$	70 000	500	15 000
$4d^N$	50 000	1000	20 000
$5d^N$	20 000	2000	25 000
$4f^N$	70 000	1500	500
$5f^N$	50 000	2500	2000

parameters associated to the Casimir operators for the Lie groups G_2 and R_7. When interactions between three electrons (for $4f^N$ with $N \geqslant 3$) are taken into account, the Judd parameters T^k are associated to the t_k operators, also transforming as the irreducible representations of the G_2 and R_7 groups.

1.3 Spin–Orbit Coupling

The most important magnetic interaction is the coupling between the spin and the orbit of an electron. The radial part of the interaction defines the phenomenological spin orbit parameter, ζ:

$$H_{SO} = \zeta_N \sum_{i=1}^{N} \vec{l}_i \cdot \vec{s}_i$$

This interaction is not diagonal in L and S and consequently the L–S coupling is broken and replaced by the intermediate coupling. The matrix element is written as:

$$\langle \alpha SLJM | H_{SO} | \alpha' S'L'J'M' \rangle = \delta(J,J')\delta(M,M')$$
$$\times [l(l+1)(2l+1)]^{1/2} \zeta_{Nl}(-1)^{L+S'+J}$$
$$\times \begin{Bmatrix} L & L' & 1 \\ S & S' & J \end{Bmatrix} \times \langle \alpha SL | V^{11} | \alpha' S'L' \rangle \quad (2)$$

in which l is the orbital quantum number ($l=2$ for 3d elements and $l=3$ for 4f elements), V^{11} is a double tensor whose doubly reduced values are tabulated by Nielson and Koster (1964), and {} represents the 6j symbol for the coupling between three angular moments. The triangular rules of the 6j symbols are that L and S cannot differ by more than one unit. In group theory that interaction is associated to the explicitly direct product $D_S \otimes D_L = \sum_{J=|L-S|}^{J=L+S} D_J$. That interaction creates the $^{2S+1}L_J$ levels associated with the D_J irreducible representation, whose remaining degeneracy is $2J+1$. The energy separation between two terms is about $500\,cm^{-1}$ for the rare earths whereas the coupling constant varies from

$\sim 700\,cm^{-1}$ for Ce^{3+} to $\sim 3000\,cm^{-1}$ for Yb^{3+} (from ~ 200 to $\sim 800\,cm^{-1}$ for 3d elements).

1.4 Other Interactions

Other interactions of minor importance can be included. They have essentially a magnetic origin just like the spin–orbit coupling:

(i) the spin–other–orbit and spin–spin interactions, parameterized by the Marvin integrals M^k ($k = 0, 2, 4$);

(ii) the electrostatically correlated spin–orbit interaction, parameterized by two-body pseudomagnetic operators P^k ($k = 2, 4, 6$).

These interactions are considered practically for the nf^N configurations only when the number of experimental levels is large. They have a significant action on the $4f^2$ and $5f^2$ configurations and on those at the end of the series. Usually only M^0 and P^2 vary freely, while the other parameters keep the Hartree–Fock ratios with M^0 and P^2.

2. Crystal Field Interaction

When embedded in a crystalline matrix the rare earth ion is submitted to an internal electric field due to the ligands, assimilated to point charges in the first approximation. Thus, in the original conception, the crystal field has a purely electrostatic origin (Garcia and Faucher 1995, Görller-Wallrand and Binnemans 1996). This is the point charge electrostatic model (PCEM). For one ligand the potential is written as:

$$V = \frac{1}{4\pi\varepsilon_0} \frac{ge}{|r - \rho|}$$

The potential is developed in Legendre polynomials

$$V = \frac{ge}{4\pi\varepsilon_0} \sum_{k=0}^{\infty} \frac{r^k}{\rho^{k+1}} P_k(\cos\Omega) \quad (3)$$

then in spherical harmonics:

$$P_k(\cos\Omega) = \frac{4\pi}{2k+1} \sum_{q=-k}^{q=k} Y_q^{k*}(\alpha, \beta) Y_q^k(\theta, \phi) \quad (4)$$

The hamiltonian of the systems sums over all ligands and electrons involved

$$H_c = -e \sum_i V(r_i, \theta_i, \phi_i) \quad (5)$$

in Eqns. (3) and (4), the ligand and electron parts are separated

$$H_c = -\frac{e^2}{4\pi\varepsilon_0} \sum_{i,k,q} A_q^k r_i^k Y_q^k(\theta_i, \phi_i) \quad (6)$$

with

$$A_q^k = \frac{4\pi}{2k+1} \sum_j \frac{g_j}{\rho_j^{k+1}} Y_q^{k*}(\alpha_j, \beta_j) \qquad (7)$$

where A_q^k is the lattice sum depending on the spherical coordinates of the ligands and g_j is the electric charge of the jth ligand. Using perturbation theory, the energy is written as:

$$E_{cc}^{(1)} = \langle \Phi^{(0)} | H_c | \Phi^{(0)} \rangle \qquad (8)$$

$\Phi^{(0)}$ being the nonperturbed state, and in that expression appear the radial integrals $\langle R_{4f} | r^k | R_{4f} \rangle = \langle r^k \rangle$. These integrals can be obtained directly from the routine package of Cowan. The crystal field parameters are defined as the product of an angular part by a radial part: $B_q^k = A_q^k \langle r^k \rangle$.

2.1 Limitations of the Crystal Field Potential

Equation (3) indicates a summation over k, an integer without any limitation and in Eqn. (4) a summation over q, also integer. In fact, the physical application to electronic configurations and the group theory rules reduce the possible values:

(i) there is a limitation on k due to the nature of the electrons. If the crystal field potential operates as in Eqn. (8) between states of to the same configuration (which is the case for most of the crystal field analysis), then k is even and $k \leqslant 2l$;

(ii) there is also a limitation on q connected to the symmetry of the point group, for instance:

(a) if there is an inversion center in the group symmetry like O_h, S_6, all odd B_q^k vanish;

(b) if there is a C_n or S_n symmetry axis, q/n must be an integer;

(c) other rules are less evident but are a consequence of the application of the projection operators associated with the point group on the spherical harmonics.

An exhaustive list of nonvanishing B_q^k vs. point symmetries is found in the work of Görller-Wallrand and Binnemans (1996).

2.2 Group Theory and Crystal Field

From the group theory point of view the irreducible representations Γ_x of the point group G, associated with the atomic position occupied by the rare earth ligands are considered. G is a subgroup of the rotation group R_{3i} for an even number of electrons and of the rotation double group R_{3i}' for an odd number of electrons. The number and the type of irreducible representations of the subgroup G involved are determined by decomposition of the D_J irreducible representation of R_{3i} (or R_{3i}') on the basis of the G symmetry operations. The list of the J level

decomposition as a function of the J value and of point groups is found in Görller-Wallrand and Binnemans (1996) or Prather (1961).

2.3 Crystal Field Strength

It is often interesting to classify the compounds as a function of the crystal field strength. This parameter can cover the whole crystal field effect or partial effect as a function of the rank k of the parameters. This quantity is a rotational invariant, connected with the displacements of the centers of gravity of the levels from their free ion values. It allows a simple characterization of chemical bondings. It is written as (Chang *et al.* 1982):

$$S = \left[\sum_{k=2,4,6} \frac{1}{2k+1} \sum_{q=-k}^{q=k} |B_q^k|^2 \right]^{1/2}$$

2.4 The Racah Algebra Formalism of the Crystal Field

Equation (3) supposes that the crystal field potential has a pure electrostatic origin. Except for cases involving ionic ligands, this model is unable to represent the reality. For a quantum mechanical treatment it is more realistic to keep only the symmetry aspect of the mathematical expression. The crystal field hamiltonian is then written as:

$$H_c = \sum_{i,k,q} B_q^k [C_q^k + (-1)^q C_{-q}^k]_i + i S_q^k [C_q^k - (-1)^q C_{-q}^k]_i \qquad (9)$$

The summation runs over all electrons of the system, where B_q^k and S_q^k are the real and imaginary parts, respectively, of the phenomenological crystal field parameters and C_q^k are tensor operators of rank k, connected to the spherical harmonics. The Wigner–Eckart theorem gives a simple expression of the coupling between two angular momentums in the $|\eta SLJM\rangle$ basis:

$$\langle \alpha SLJM | B_q^k C_q^k | \alpha' S'L'J'M' \rangle = \delta(S, S')(-1)^\ell (2\ell + 1)$$

$$\begin{pmatrix} \ell & k & \ell \\ 0 & 0 & 0 \end{pmatrix} \times (-1)^{J-M} \begin{pmatrix} J & k & J' \\ -M & q & M' \end{pmatrix}$$

$$B_q^k \langle \alpha SLJ \| U^k \| \alpha SL'J' \rangle \qquad (10)$$

where () are 3j symbols for two angular moment couplings. The second 3j symbol shows the possibilities of coupling between states of different J (J-mixing), which can never be neglected. U^k is a unitary tensor. Equation (10) can be developed

further:

$$\langle \alpha SLJ \| U^k \| \alpha SL'J' \rangle = (-1)^{S+L'+J+k}[(2J+1)(2J'+1)]^{1/2}$$

$$\begin{Bmatrix} J' & J & k \\ L' & L & S \end{Bmatrix} \langle \alpha SL \| U^k \| \alpha SL' \rangle \qquad (11)$$

in which $\langle \alpha SL \| U^k \| \alpha SL' \rangle$ is a doubly reduced matrix element also tabulated by Nielson and Koster. The order of magnitude of the crystal field splitting is shown in Table 2.

2.5 Correlated Crystal Field

The concept of correlated crystal field corresponds to the two-electron part of the crystal field interaction. This interaction was formalized in the 1970s and implies a "scandalously high number of parameters" (Garcia and Faucher 1995). That interaction creates a term-dependent correction to the one-electron crystal field. It has been somewhat "simplified" by considering separately the spin- and orbital-correlated crystal field effects. Thus, the operators become orthogonal to the one-electron crystal field operators and are easier to manipulate. However, it has not been shown clearly if the simulation of the energy level scheme is significantly improved when these interactions are included. A clever overview on that problem is found in the work of Garcia and Faucher (1995).

3. Simulation of the Rare Earth Electronic Configurations

When all interactions are analyzed and described it is easy to write down the secular determinant. It comprises a great number of matrix elements, written as $\langle \alpha SLJM | H_{Tot} | \alpha'S'L'J'M' \rangle$ in which H_{Tot} represents the sum of elementary hamiltonians previously described:

$$H_{Tot} = H_0 + \sum_{k=0,1,2,3} E_k e^k +_{4f} A_{SO} + L(L+1)$$

$$+ G(G_2) + G(R_7) + \sum_{k=2,4,6} P^k p_k$$

$$+ \sum_{k=0,2,4} M^k m_k \sum_{k=2,3,4,6,7,8} T^k t_k + \sum_{k,q,i} B_q^k C_q^k(i)$$

$$(12)$$

Each interaction follows its own rules, in particular as regards its nonzero values as a function of the quantum numbers $\eta SLJM$. H_0 represents the energy separation between the ground and excited configurations. The diagonalization done by standard techniques provides the energy levels and their associated wave-functions. An estimation of the

phenomenological parameters is made by comparing calculated and experimental energy levels by minimization of the root mean square deviation taken as factor of merit (Porcher 1989, unpublished Fortran routines). For the rare earths the number of free ion parameters match 20 and the number of crystal field parameters can vary between two (for O_h or T_d point symmetry) and 27 (for C_1). This last number could be largely increased if the two-electron crystal field effect is included. Thus, it is very common to take into account some 20 parameters, which creates a problem concerning the real significance of the parameters and the reliability of the phenomenological simulation.

Fortunately, various models help in calculating many parameters whose values are considered as starting values in the refining processes. This is true for the free ion parameters as well as for the crystal field parameters (see Sect. 4).

● Free ion parameters calculated by the Hartree–Fock method (Cowan) reproduce the reality with a precision of $\sim 25\%$, which is reasonable.

● There is a smooth variation of free ion parameters vs. the number of f electrons, whatever the crystalline matrix (Fig. 2).

● If all free ion parameters cannot vary freely, some of them are fixed in predetermined ratios. This is often the case for the M^k and P^k integrals and sometimes for the E^k (or F^k) parameters.

● There is also a smooth variation of the crystal field parameters with the ionic radius of the optically active rare earth embedded in a given matrix or when the crystalline matrices are isostructural (Fig. 3).

● In some cases, a descending symmetry procedure is applied for crystal field calculations, assuming the real point symmetry is close to a higher one involving less parameters.

In spite of the relative simplicity of these calculations, few works deal with the optical properties of all rare earth ions in a unique matrix, in single crystal
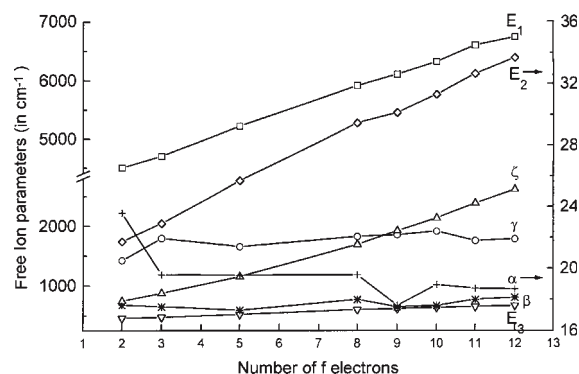
Figure 2
Variation of the free ion parameters in the REOCl series. From Hölsä *et al.* (1998a), reprinted with the permission of the authors.
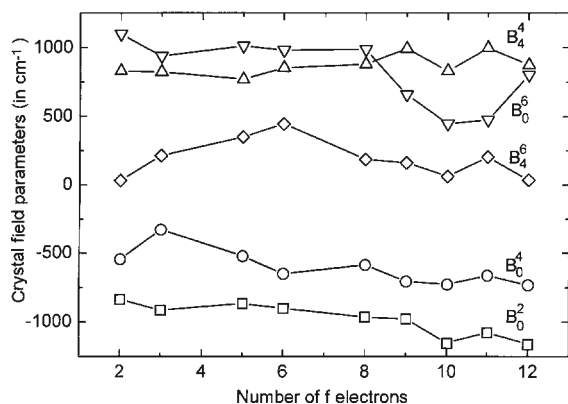
Figure 3
Variation of the crystal field parameters in the REOCl series. From Hölsä *et al.* (1998a), reprinted with the permission of the authors.

form. The most complete work was published by Carnall as early as 1977 for pure rare earth fluoride REF_3 or rare earth doping in lanthanum fluoride LaF_3. This particular matrix is transparent in the far-UV region and therefore gives a great number of experimental energy levels. Initially the simulations were performed with approximated symmetries for the lanthanum (D_{3h} then C_{2v}), the last revision considering the real symmetry (C_2). Later, two other families were systematically studied, but in polycrystalline form, with all trivalent rare earth ions: the rare earth oxychlorides REOCl (Hölsä *et al.* 1998a) and the oxyfluorides REOF (Hölsä *et al.* 1998b), where the rare earth occupies a point site with higher symmetry—C_{4v} for REOCl and C_{3v} for REOF respectively—which means less crystal field parameters (five and six, respectively). The number of observed energy levels is large and SmOF could be added to the *Guiness Book of Records* for rare earth spectroscopy with 191 observed crystal field states! Many other matrices have been studied, not necessary with all rare earth ions, especially with Nd^{3+}, Eu^{3+}, and Er^{3+} which are ions with potential industrial application. Most of the results concerning rare earth energy levels are available in books (Görler-Wallrand and Binnemans 1996, Kaminski 1996) and/or on web sites (NASA, Porcher 2000).

4. Semiempirical Calculation of the Crystal Field Parameters

Newmann (1971) noted that several different interactions should have to be taken into account: ligand point charges of first neighbors and of the rest of the crystalline network, dipolar and quadrulopar polarization of the ligand, exchange and overlap between the rare earth and the ligand, covalency, charge

transfer ligand-to-rare earth and ligand-to-ligand, and triangular interaction. He was able to calculate the different contributions for $PrCl_3$, i.e., in the case of a relatively simple ligand. Others have estimated the influence of the polarizability for some simple covalent ligands (Garcia and Faucher 1995, Morrison and Leavitt 1982). The problem is more complicated when complex ligands, such as borates, molybdates, and sulfates, are involved. Increasing difficulties are presented by organic ligands. For these reasons it seems more realistic to consider semi-empirical calculations. A review of the different models is given by Porcher *et al.* (1999).

4.1 Angular Overlap Model

This model is an extension to the f electrons of the model proposed by Jørgensen (1963) and Schäffer (1969, 1972) for the d electrons. It was initially introduced for explaining the one-electron energy differences between the seven 4f orbitals in lanthanide chromophores, and forms the most "chemical" approach in the sense that the f orbitals are immediately considered. The model expresses the antibonding energy of the molecular orbital created between the central ion and the ligand. One interest of this model is to consider f orbital expressions directly as read on the character table of the point symmetry group, which allows the result to be related to the irreducible representation of a level and consequently to the σ, π, and δ classical bonding of the d elements plus the ϕ bonding specific to the f orbitals. However, difficulties arise when the phenomenological approach of a $4f^N$ configuration simulation is considered as a whole, which also includes the free ion interactions. This model has been applied, coupled with the superposition model in various series of rare earth compounds.

4.2 Superposition Model

Newmann (1971) proposed an empirical approach, where each ligand is characterized by an intrinsic parameter, giving its own contribution to the crystal field. The general expression of B_q^k is:

$$B_q^k = \langle r^k \rangle \frac{4\pi}{2k+1} \sum_j Y_q^{k^*}(j) \bar{A}_k(R_j) \left(\frac{R_0}{R_j}\right)^{t_k} \quad (13)$$

In that expression only the first coordination sphere is considered. There is a distance dependence of B_q^k according to a power law, the rare earth–ligand distance reference R_0 being the shortest in the crystalline network. This semi-*a priori* model is strictly identified with the PCEM if t_k is equal to $2k+1$. t_k could be calculated according to the number and the type of considered interactions. Practically they are considered as adjustable parameters, whose values

are not necessarily integers and can be far from the nominal ones. The interest of that model lies in the fact that each ligand gives its quantitative finger-print which in principle could be transported from one compound to another.

4.3 Effective Charge Model

In this model, the crystal field parameters are written as:

$$B_q^k = (1 - \sigma_k) \frac{\langle r^k \rangle}{\tau^k} A_q^k \qquad (14)$$

This equation differs in four ways from the PCEM of Eqns. (4) and (5) in the expression of the radial as well as in the angular parts.

(i) The radial integrals $\langle r^k \rangle$ are corrected by a spatial expansion parameter τ, which varies linearly with the number of f electrons.

(ii) A shielding factor σ_k is introduced into the multipolar expansion of the crystal field potential.

(iii) A degree of covalence is introduced through effective charges of atoms. These effective charges keep the electric neutrality of the compound.

(iv) A slight shift of the ligand position is introduced in order to take into account their polarizability effect.

The summation runs over all atoms of the crystalline network, which in practice means atoms included within a sphere of ca. 100 Å.

4.4 The Simple Overlap Model

This model developed by Malta retains only the first coordination sphere (Porcher *et al.* 1999). The covalence is represented by the overlap, ρ, between the rare earth and ligand orbitals. The crystal field parameters are written as:

$$B_q^k = \rho \left(\frac{2}{1 \pm \rho} \right)^{k+1} \langle r^k \rangle A_q^k \qquad (15)$$

In that expression the $\langle r^k \rangle$ radial integral is not corrected from the spatial expansion as for the ECM. Lattice sums, A_q^k, are calculated with an effective charge for the ligand. The overlap ρ varies for each ligand as a function of the distance to the central ion and is referred to the closest ligand, as for the super-position model. Finally, this method involves only two adjustable parameters: the overlap and the effective charge of the ligand. The model which offers the possibility of considering the big molecules of coordination chemistry has been successfully applied to a great number of compounds. It was found that the overlap is between 0.05 and 0.08 for the rare earth ions and between 0.10 and 0.25 for 3d elements.

5. The Convenient Case of the Eu^{3+} Ion

Although the $4f^6$ configuration possesses one of the greatest degeneracy (3003) of the trivalent rare earth configurations (Table 2), Eu^{3+} is the most convenient case for characterizing the energy levels of a rare earth ion in a crystalline matrix. This characteristic is due qualitatively to the type of symmetry site analysis of the spectroscopy as well as quantitatively to the relatively simple way of performing crystal field calculations. To a lesser extent, this is also true for intensity calculations. The particular feature of this configuration is a ^7F ground septet and a first excited ^5D quintet relatively well isolated in the energy level sequence.

5.1 Eu^{3+} as a Structural Local Probe

This analytical aspect is a consequence of the even number of electrons in the $4f^6$ configuration. The crystal field lifts more or less completely the degeneracies of ^7F_J levels, according to the endomorphism between crystal field levels and irreducible representations of the local point group, whereas the observability of electronic transitions is related to the electric/magnetic dipole rules, also connected to the point symmetry. Practically, a fluorescence spectrum of europium compounds consists of transitions originating from the ^5D_J levels, more particularly $^5D_0$, the final levels being ^7F_J. Most of the transitions are located in the visible wavelength range. Neither $^5D_0$ nor $^7F_0$ are split by the crystal field, which means that the number of $^5D_0 \rightarrow {}^7F_0$ transitions corresponds to the number of sites occupied by Eu^{3+}. However, this is only true if the group is due to the C_1, C_s, C_n, C_{nv} symmetry point groups, for which that transition is permitted by the electric dipole rules. From the number of observed lines and by application of the same rules on other $^5D_0 \rightarrow {}^7F_J$ ($J = 1,6$) transitions, the symmetry of the point group of the rare earth crystallographic site in the structure is deduced. Another practical consequence is that liquid helium temperature measurements are not necessary, whereas it is required for other rare earth levels to prevent the excited crystal field emitting levels being thermally populated. Thus, only liquid nitrogen measurements are usually performed.

Moreover, the $^5D_0 \rightarrow {}^7F_0$ transition is situated just in the middle of the Rhodamine 6G dye laser wavelength emission range. This low-cost dye can be used for site-selective excitation in the case of multisite compounds. When the excitation wavelength is accorded on a selected $^5D_0 \rightarrow {}^7F_0$ transition each site gives its own "finger-print", any fluorescence response from other sites being almost completely quenched. Figure 4 shows, as an example, the case of $La_2(CrO_4)_3.7H_2O:Eu^{3+}$ in which the rare earth occupies two point sites of low symmetry. The
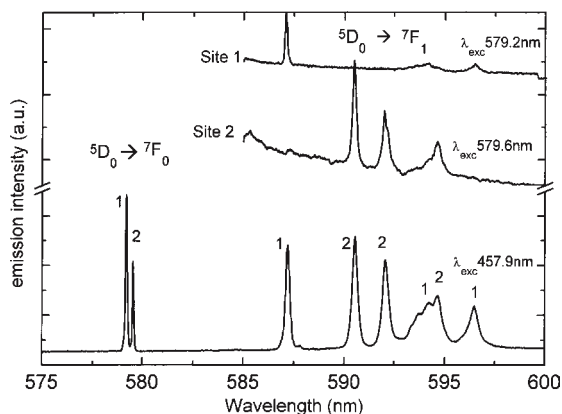
Figure 4
Site selective excitation on $La_2(CrO_4)_3 . 7H_2O:Eu^{3+}$. From Antic-Fidancev *et al.* (1991). Reprinted with the permission of the authors.

fluorescence spectrum excited by the blue lines of the cw-Ar^+ laser shows two lines for $^5D_0 \to {}^7F_0$ (bottom spectrum), whereas $^5D_0 \to {}^7F_{1,2}$ transitions exhibit more lines than expected for one point site. When selectively excited (Fig. 4, middle and top spectra), each site can be analyzed in terms of number and position of lines and the problem is nicely reduced to the case of a single site compound. If one of the sites is due to an impure phase the same result should be obtained. This structural probe aspect has been found to be of great importance in biochemistry.

5.2 Crystal Field Calculations With Eu^{3+}

The particular ^7F ground septet is convenient for fast crystal field calculation because: (i) this term is well isolated from the rest of the configuration with an energy gap of $\sim 12\,000\,cm^{-1}$ between $^7F_6$ and $^5D_0$; (ii) the crystal field operator is a spin operator which allows mixing only between terms of the same parity; (iii) the ^7F term only has this multiplicity; and (iv) the ^7F term wavefunctions are almost pure ($> 95\%$) in $|^7F_{JM}\rangle$ states, the rest being small admixtures of ^5D, ^5G, ^3P, ^3F, and ^1S terms created only by the spin–orbit coupling. Instead, considering the entire configuration even reduced in submatrices according the crystalline quantum number properties, only a 49-square matrix (i.e., the ^7F degeneracy) is diagonalized, which means less than half a second of computation on a standard PC. In this case, the electrostatic repulsion and other interactions operating between terms are completely diagonal in $|^7F_{JM}\rangle$ states except for the spin–orbit coupling. Of course, if a precise knowledge of the wave-functions is necessary, as for paramagnetic susceptibilities and for transition intensity calculations, the full secular determinant has to be diagonalized (see *Crystal Field and Magnetic Properties, Relationship Between*).

5.3 Intensity Calculations With Eu^{3+}

Although it is not the purpose of this article we can mention how the europium ion permits an easier parameterization of the emission intensity, without the usual experimental complexities of absolute measurements. This is due to the simultaneous occurrence of magnetic and electric dipole transitions in the spectrum. Some of the transitions between crystal field states of $^5D_0 \to {}^7F_1$, $^5D_1 \to {}^7F_0$, $^5D_1 \to {}^7F_2$, $^5D_2 \to {}^7F_1$, $^5D_2 \to {}^7F_3$, etc., have a pure magnetic dipole character. The problem is then reduced to the measurements of relative intensities. However, a reference transition for each emitting level is necessary in order to take into account the nonradiative transition processes. When transitions between J levels are studied, Ω_2 and Ω_4, respectively, are deduced directly from the area ratios

$$\frac{^5D_0 \to {}^7F_2}{^5D_0 \to {}^7F_1}$$

and

$$\frac{^5D_0 \to {}^7F_4}{^5D_0 \to {}^7F_1}$$

See also: Crystal Field Effects in Intermetallic Compounds: Inelastic Neutron Scattering Results; Localized 4f and 5f Moments: Magnetism

Bibliography

Antic-Fidancev E, Lemaître-Blaise M, Porcher P, Bueno I, Parada C, Saez-Puche C 1991 Optical and magnetic properties of europium-doped potassium rare earth double chromate. *Inorg. Chim. Acta.* **182**, 5–8

Carnall W T, Goodman G L, Rajnak K, Rana R S 1989 A systematic analysis of the spectra of the lanthanides doped into single crystal LaF_3. *J. Chem. Phys.* **90**, 3443–57

Chang N C, Gruber J B, Leavitt R P, Morrison C A 1982 Optical spectra, energy levels and crystal field analysis of tripositive rare earth ions in yttrium oxide. *J. Chem. Phys.* **76**, 3877–89

Cowan R D, Fortran Routines for Atomic Spectroscopy. *ftp:// aphysics.lanl.gov/pub/cowan/*

Garcia D, Faucher M 1995 Crystal field in non-metallic (rare earth) compounds. In: Gschneidner K A, Eyring L (eds.) *Handbook on the Physics and Chemistry of Rare Earths.* Elsevier, Amsterdam, Vol. 21

Görller-Walrand C, Binnemans K 1996 Rationalization of crystal-field parametrization. In: Gschneidner K A, Eyring L (eds.) *Handbook on the Physics and Chemistry of Rare Earths.* Elsevier, Amsterdam, Vol. 23

Hölsä J, Lamminmäki R-J, Porcher P 1998a Simulation of the energy levels of Dy^{3+} in DyOCl. *J. Alloys Compounds* **275–277**, 398–401

Hölsä J, Sailyonoja E, Ylhä P, Antic-Fidancev E, Lemaître-Blaise M, Porcher P, Deren P, Strek W 1998b Analysis and simulation of the optical spectra of the stoichiometric NdOF. *J. Chem. Soc., Faraday Trans.* **94**, 481–7

Jørgensen C K 1963 Spectroscopy of transition group complexes. *Adv. Chem. Phys.* **5**, 33–146

Judd B R 1963 *Operator Techniques in Atomic Spectroscopy.* McGraw Hill, New York [repr. 1998 Princeton University Press, Princeton, NJ]

Kaminski A A 1996 *Crystalline Lasers: Physical Processes and Operating Systems.* CRC Press, Boca Raton, FL

Morrison C A, Leavitt R P 1982 Spectroscopic properties of the triply ionized lanthanides in transparent host crystals. In: Gschneidner K A, Eyring L (eds.) *Handbook on the Physics and Chemistry of Rare Earths.* North-Holland, Amsterdam, Vol. 5

NASA Website: http://aesd.larc.nasa.gov/gl/laser/elevel/elevel.htm

Newman D J 1971 Theory in lanthanide crystal field. *Adv. Phys.* **20**, 197–256

Nielson C W, Koster G F 1964 *Spectroscopic Coefficients for p^N, d^N and f^N Configurations.* MIT Press, Cambridge, MA

Porcher P 2000 Data base of experimental and calculated crystal field energy levels in rare earths compounds. http://www.enscp.jussieu.fr/labos/LCAES

Porcher P, Couto Dos Santos M, Malta O L 1999 Relationship between phenomenological crystal field parameters and the crystal structure: the simple overlap model. *Phys. Chem. Chem. Phys.* **1**, 397–405

Prather J L 1961 Atomic energy levels of rare earths. *Monograph* **19**, U.S. National Bureau of Standards, Washington

Schäffer C E 1969 A perturbation representation of the weak covalent bonding. *Struct. Bondings* **5**, 68–95

Schäffer C E 1972 Two symmetry parametrization of the angular-overlap model of the ligand-field. *Struct. Bondings* **14**, 69–109

Wybourne B G 1965 *Spectroscopic Properties of Rare Earths.* Interscience, New York

P. Porcher
*Laboratoire de Chimie Appliquée de l'Etat Solide
Paris, France*

Elemental Rare Earths: Magnetic Structure and Resistance, Correlation of

The study of elemental rare earths spans several decades, and in this period there have been many reported studies of resistance and magnetoresistance. The results reveal many magnetic transitions as a function of temperature and applied field. However, as stated in *Boltzmann Equation and Scattering Mechanisms*, there are no general rules that may be applied for the magnetically ordered state, especially in the case of antiferromagnetism. This fact derives from the diversity of magnetic structures.

Electrical resistivity is a sensitive probe in magnetic systems and the construction of magnetic phase diagrams is possible. However, such constructions based on magnetoresistance alone must be made with caution, and this article will look at various aspects

which are important in such determinations. The extent of the field is enormous, and in consequence the review will consider examples of heavy rare earths, with the cases being chosen to exemplify the effects of changing crystal field anisotropy and magnetic exchange interaction. Utilizing the results of elastic and inelastic neutron scattering, it is possible to establish canonical behavior in the resistance in response to changing magnetic structure.

1. Magnetic Order in Rare-earth Elements

As with all physical systems, it is possible to define a Hamiltonian. The spin Hamiltonian is composed of terms intended to represent the possibility of strong anisotropic behavior through crystal field and magnetic exchange. These terms are often linked to the crystal lattice through magnetoelastic coupling. Consideration of the spin Hamiltonian is beyond the scope of the current article, and the reader is referred to Jensen and Mackintosh (1991) and references therein.

The elements chosen for discussion are thulium and erbium. The crystal structure for each of these elements is hexagonal close-packed (h.c.p.), with the three orthogonal symmetry directions being the **a**, **b**, and **c** axes. The crystal field for each element is such that the preferred orientation of the magnetic moments is along different directions. In the case of thulium, the moment is constrained to the **c**-axis. In erbium, the moments are found to develop first along the **c**-axis, and then an additional moment develops along the **a**-axis. In each case, the propagation wave vector for the antiferromagnetic structures is parallel to the **c**-axis. The RKKY-exchange energy (Jensen and Mackintosh 1991) is found to increase going from thulium to erbium. The main consequences of this are an increase in the Néel temperature, and a decrease in the role played by the crystal field within the Hamiltonian.

1.1 Models Proposed to Understand Phenomena

In *Boltzmann Equation and Scattering Mechanisms*, Eqn. (68a) introduces the Matthiessen rule for electrical resistivity. For the systems considered in this article, the rule may be restated (see Eqn. (9) in *Intermetallic Compounds: Electrical Resistivity*) as:

$$\rho_{\text{total}} = \rho_{\text{residual}} + \rho_{\text{phonon}} + \rho_{\text{magnetic}} \tag{1}$$

where ρ_{magnetic} is the component derived from the elastic and inelastic magnetic scattering. This may be represented by the equation:

$$\rho_{\text{magnetic}} = \rho_{\text{magnetic}}^0 \int_{-\infty}^{\infty} d(\hbar\omega) \frac{\hbar\omega/k_B T}{4 \sin h^2(\hbar\omega/2k_B T)}$$
$$\times \sum_{\alpha} \frac{1}{\pi} \langle \chi_{\alpha\alpha}''(\mathbf{q}, \omega) \rangle_{\text{q}} \tag{2}$$

where the weighted **q**-average of the susceptibility tensor components is given by

$$\langle \chi''_{\alpha\alpha}(\mathbf{q},\ \omega) \rangle_q = \frac{3}{(2k_F)^4} \int_0^{2k_F} q\mathrm{d}q \int \frac{\mathrm{d}\Omega_q}{4\pi}$$
$$\times (\mathbf{q} \cdot \hat{\mathbf{u}})^2 \chi''_{\alpha\alpha}(\mathbf{q},\ \omega) \tag{3}$$

The term ρ_{magnetic} may represent a number of different cases of excitations in the magnetic case, ranging from spin-wave scattering (Mackintosh 1963), crystal field (Hessel Andersen *et al.* 1974), and exchange dominated magnetic scattering (Hessel Andersen *et al.* 1980, Ellerby *et al.* 1998). In the high temperature limit, Eqn. (2) predicts the saturation of the spin-disorder scattering and is found to be proportional to the de Gennes factor (see *Intermetallic Compounds: Electrical Resistivity*).

In the heavy rare earths, measurement of the **c**-axis resistivity reveals a pronounced increase at the Néel temperature (Fig. 1). It was proposed (Mackintosh 1962) that this increase derives from a new periodicity along the **c**-axis, associated with the magnetic unit cell. This new periodicity results in additional zone boundaries (superzones), and produces further energy gaps which may appear at the Fermi surface. Watson *et al.* (1968) showed that, for the case of thulium, there was a number of such gaps with an energy of approximately 0.085 eV. Two groups (Elliott and Wedgwood 1963, Miwa 1963) developed a formalism to represent the effects of changing Fermi surface on the resistivity, and this is summarized by:

$$\rho_{\text{total}}^{uu} = \frac{\rho_{\text{residual}}^{uu} + \rho_{\text{phonon}}^{uu} + \rho_{\text{magnetic}}^{uu}}{1 - \Gamma_u M_1/M_1^0} \tag{4}$$

Here Γ_u is determined by the periodicity of the magnetic structure and for the ferromagnetic case, where ordering wave vector $\mathbf{Q} = 0$ and $\Gamma_u = 0$. M_1^0 and M_1 are the zero temperature saturation magnetic
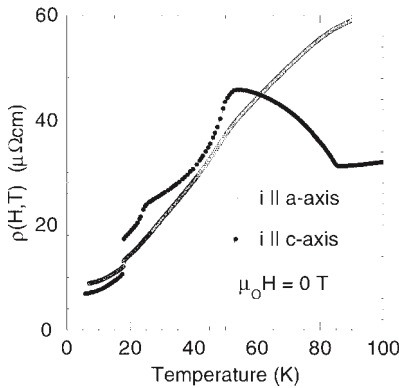
Figure 1
The temperature dependence of the longitudinal **c**($\bullet$) and **a**-axis ($\circ$) resistivity for erbium.

moment and temperature-dependent magnetic moment, respectively, which may be derived from neutron diffraction studies. The subscripts and superscripts, *uu* and *u* represent the axis under consideration. In the case of thulium, $\Gamma_c = 0.73$ and $\Gamma_a = 0$ (Ellerby *et al.* 1998). The influence of the denominator is to increase the resistivity parallel to the **c**-axis as a function of temperature.

The magnetoresistance in magnetically ordered materials has been considered by Yamada and Takada (1973), and has been discussed in *Magnetoresistance: Magnetic and Nonmagnetic Intermetallics*. This model considers the effects, in an antiferromagnetic system, of scattering from enhanced transverse spin fluctuations resulting from an applied magnetic field. The authors also produce a schematic for the effect of spin-flop transitions on the resistivity, where the moments do not fully rotate parallel to the applied field in a single stage, but do so in a series of stages. This model for the magnetoresistance does not accommodate the affects of changing Fermi surface.

2. Discussion

The difference in anisotropy of thulium and erbium has already been alluded to in Sect. 1. The discussion begins in each section by outlining the main features for each of the magnetic phase diagrams shown in Figs. 2(a–c). In each of the phase diagrams, nomenclature is used to describe the magnetic phases and has been left as it appears in the references.

2.1 Thulium

The magnetic phase diagram for thulium (Ellerby *et al.* 1998) is presented in Fig. 2(a). There are five distinct magnetic phase regions. They are labeled as "ferromagnetic," "ferrimagnetic," "**c**-axis modulated" (CAM), "paramagnetic," and "A." The ferrimagnetic structure is such that all the moments are parallel to the **c**-axis with four moments pointing "up" and three moments "down" within the magnetic unit cell, with a wave vector of $\mathbf{Q} = 2/7\mathbf{c}^*$ (**c*** represents the reciprocal lattice vector of the **c**-axis). In the ferromagnetic phase, all the moments point "up" along the **c**-axis. The moments in the paramagnetic phase have no preferred orientation and may point in any direction. The CAM phase is a magnetic structure in which the moments all point along the **c**-axis, but the size of each moment varies from one position to next in a sinusoidal manner (modulation) within the magnetic unit cell. The nature of the phase marked by "A" remains undetermined at this time.

Having outlined the basic magnetic structures, the reader is now referred to Fig. 3. This figure presents two important measurement geometries, with the magnetic field applied parallel to the **c**-axis in both instances. On the left is the magnetoresistance
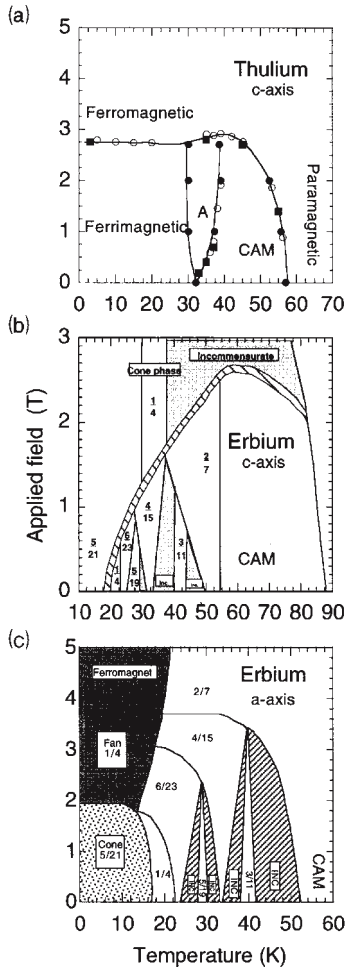
Figure 2
Magnetic phase diagrams for (a) thulium **c**-axis (Ellerby *et al.* 1998); (b) erbium **c**-axis (McMorrow *et al.* 1992); (c) erbium **a**-axis (Jehan *et al.* 1994).

measured along the **c**-axis (longitudinal magnetoresistance), and the magnetoresistance for the **a**-axis (transversal magnetoresistance) is on the right. For the longitudinal geometry at $T = 5$ K, the resistance shows no change with applied field and then a large decrease at 2.8 T, after which there is no change. This may be understood using the model of Fermi-surface modification (Mackintosh 1962, Elliott and Wedgwood 1963, Miwa 1963). The development of the ferrimagnetic structure results in the removal of large sections of the Fermi surface. As the field is increased, the ferrimagnetic structure becomes unstable, and at 2.8 T all the moments flip to form the ferromagnetic phase (see Fig. 2(a)). In doing so the modulation wave-vector changes from $\mathbf{Q} = 2/7\mathbf{c}^*$ to $\mathbf{Q} = 0\mathbf{c}^*$ (ferromagnetic). The additional potential is thus

removed, resulting in an increase of available Fermi surface. In the transverse geometry ($\mu_0 H \| \mathbf{c}$-axis and $i \| \mathbf{a}$-axis) at $T = 5$ K, the features are different, with the resistivity increasing quadratically with field.

Then, as the structure changes, there is a sharp drop, followed by an almost linear increase. The quadratic and linear portion of this behavior is understood to be normal magnetoresistance (Pippard 1989) (discussed in *Magnetoresistance: Magnetic and Nonmagnetic Intermetallics*), and is associated with the Lorentz force acting at the conduction electron motion on the Fermi surface. The sharp decrease suggests that there is a small portion of the Fermi surface removed in the ferrimagnetic structure, which is replaced on entering the ferromagnetic phase. At $T = 45$ K (i.e., in the CAM region in Fig. 2(a)), the longitudinal measurement shows the same overall trend. However, before the large transition there is a smooth decrease. This is associated with the thermal activation of the moments along the **c**-axis. This activation results in fluctuations of the moment parallel and perpendicular to the **c**-axis, and results in spin-fluctuation scattering. The applied field acts to suppress these fluctuations, removing the scattering center and therefore reducing the resistivity until, at 2.7 T, the moments flip parallel to the **c**-axis. Above 2.7 T the applied field suppresses fluctuations of the moment away from the **c**-axis. The transverse magnetoresistance at $T = 45.1$ K shows a smooth increase.

In this orientation, the field is perpendicular to the magnetic moments and thus, as the field increases, fluctuations transverse to the **a**-axis are enhanced, leading to additional scattering centers. This behavior is in accordance with the model (Yamada and Takada 1973). At the transition to the ferromagnetic state, the effects of fluctuations of the moment increase rapidly until full alignment at 2.7 T, after which the effect of the field is to suppress the fluctuations (Yamada and Takada 1973); at 3.2 T this becomes the dominant process. For $T = 53.0$ K, the application of a magnetic field results in a quadratic decrease in the resistivity for the longitudinal geometry. This may be seen as a flipping of the moments in a weak anisotropy field. The crystal field anisotropy has a temperature dependence (Jensen and Mackintosh 1991) which, at higher temperatures, allows the moments to rotate smoothly off the easy axis. The decrease in resistivity is attributed (Ellerby *et al.* 1998) to the replacement of Fermi surface. At $T = 53.0$ K, for the transverse geometry the resistivity is found to increase, and the process may be viewed as a continuous spin-flop process (Yamada and Takada 1973), with the moments eventually aligning parallel to the **c**-axis at 2.3 T. For larger fields, the fluctuations of the moments are systematically suppressed.

To summarize the case of thulium: the dominant influence for the magnetoresistance of the longitudinal geometry comes from the change in the Fermi
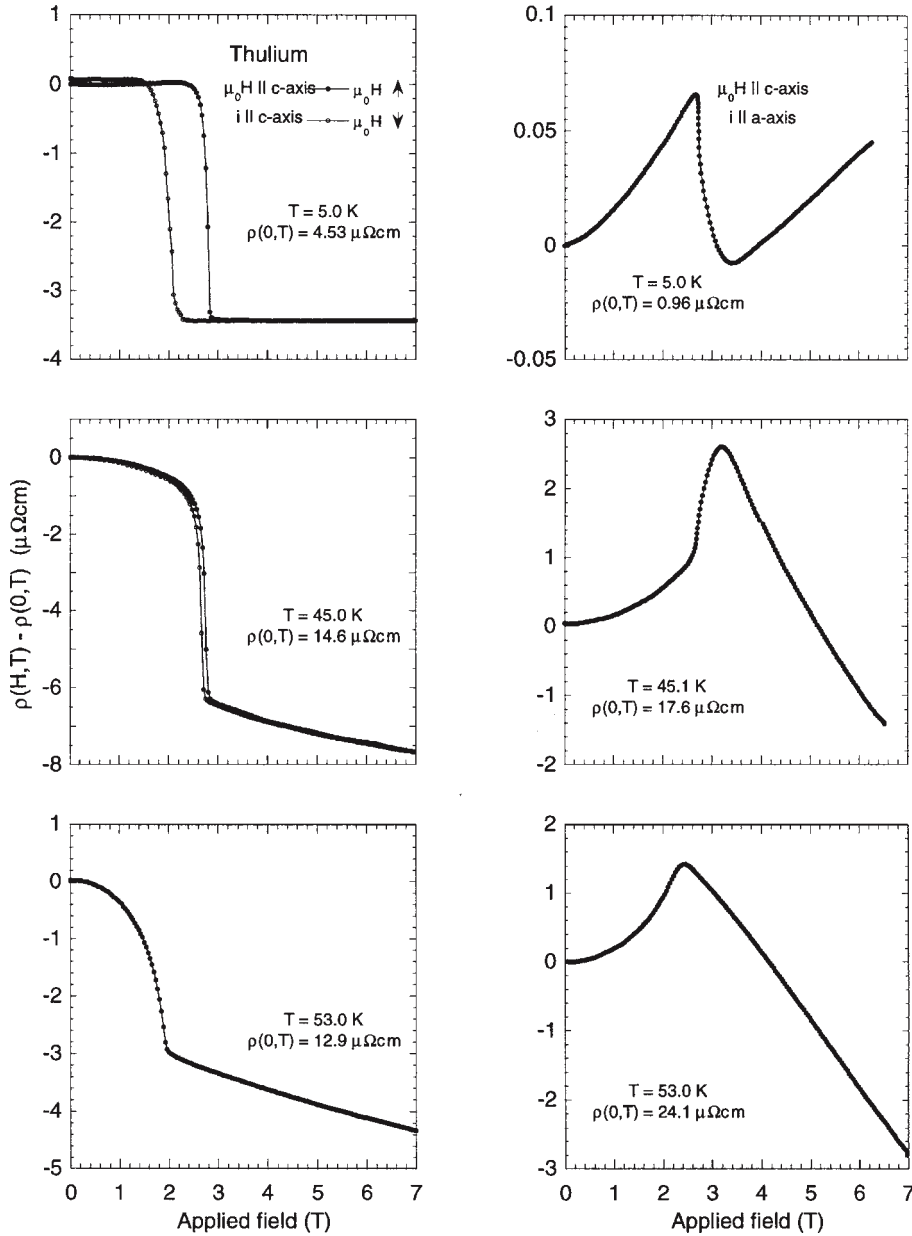
Figure 3
Magnetoresistance for thulium with B‖**c**-axis. Longitudinal **c**-axis on the left and transverse **a**-axis on the right.

surface (Mackintosh 1962, Elliott and Wedgwood 1963). As the temperature is increased, the anisotropy field decreases and spin-fluctuation scattering plays an increasing role. For the transverse geometry, the dominant scattering process derives from spin fluctuations becoming enhanced by the applied magnetic field; there is only a small effect due to the change in Fermi surface, and this can only be

observed at very low temperatures. For the transverse geometry at low temperatures, the Lorentz force acting on the conduction electrons dominates. The temperature dependence of the thulium **c**-axis has been analyzed (Ellerby *et al*. 1998) for zero field and 4 T. From this analysis, Eqn. (4) has been found to provide a good model of the data. The features in Fig. 2(a) are all mapped using the longitudinal **c**-axis

magnetoresistance and temperature-dependent resistivity in fixed fields, and are found to agree with earlier studies.

2.2 Erbium

This introduction to the magnetic phase diagrams of erbium forms an overview, and the reader is encouraged to follow the references below for more detail of this fascinating element.

The magnetic phase diagrams for the **c** (McMorrow *et al.* 1992) and **a**-axes (Jehan *et al.* 1994) are presented in Figs. 2(b) and 2(c). When compared with thulium, it is clear that erbium has a greater number of magnetic structures and, unlike thulium, a moment develops parallel to the **a**-axis. However, as with thulium and other heavy rare earths, the structures are modulated along the **c**-axis. Where fractions appear in each of these figures, the denominator represents the fundamental periodicity. In the region marked CAM, the periodicity is similar to that observed for thulium of $\mathbf{Q} = 2/7\mathbf{c}^*$.

Referring to Fig. 2(b), there appears a region separated and marked by "2/7"; this region of the phase diagram differs in that a moment has developed along the **a**-axis at these temperatures and fields, and this is also reflected in the **a**-axis phase diagram (Fig. 2(c)). In both figures there are regions marked "INC," and these regions are described as incommensurate. This refers to the fact that the modulation wave vector parallel to the **c**-axis bears no simple relation to the crystal lattice. In the **a**-axis phase diagram (Fig. 2(c)) there are three other terms. These are "cone," "fan," and "ferromagnetic." They all refer to the orientation of the moment parallel to the **a**-axis, since the moments parallel to the **c**-axis are aligned ferromagnetically. The "cone" phase refers to the structure in which the moments are parallel to both the **a**-axis and the **b**-axis. These moments are arranged in a helix about the **c**-axis, which, when projected onto a single lattice point, would appear as a "cone." The term "fan" is used to describe a structure in which the moments on the **a**-axis have projected moments aligned parallel to the **a**-axis, but from one site to the next the angle of tilt away from the **a**-axis varies. When this arrangement of moments is projected onto a single lattice position, the moments appear to make a "fan" pattern parallel to the **a**-axis. The "ferromagnetic" phase has all the moments parallel to the **a**-axis.

For both phase diagrams there is a region between $T \sim 20\,\mathrm{K}$ and $55\,\mathrm{K}$, and in this temperature range there is a host of structures. These structures are collectively known as "cycloidal" structures (Cowley and Jensen 1992), and may be "viewed" as moments modulated along the **c**-axis, forming an ellipse with the major axis parallel to the **c**-axis and the minor axis along the **a**-axis. This is an extremely difficult

series of structures to visualize, and the reader is referred to Cowley and Jensen (1992), for a complete description.

Having outlined the magnetic phase diagrams obtained from neutron diffraction experiments, it is now possible to consider the results of magnetoresistance. There are two figures, presenting the effects of magnetic field for two crystal directions.

Figure 4 presents the results for the field parallel to the **c**-axis and measurement of the resistivity parallel to the **c**-axis (longitudinal **c**-axis on left) and parallel to the **a**-axis (transverse **a**-axis on right). For $T = 10\,\mathrm{K}$, erbium is in the "cone" phase, and for the longitudinal geometry there is a small decrease in the resistivity at low fields, associated with the removal of magnetic domains. As the field increases, there is a linear decrease associated with the suppression of spin fluctuations (Yamada and Takada 1973). In the transverse geometry at $T = 5\,\mathrm{K}$, the resistivity at first decreases as spin fluctuations are frozen. However, at approximately $2\,\mathrm{T}$, the magnetoresistance increases linearly resulting from the Lorentz force (Pippard 1989) acting on the motion of the electrons in the applied magnetic field. At $T = 42.2\,\mathrm{K}$, the longitudinal measurement reveals several features. For fields less than $1.2\,\mathrm{T}$, the magnetoresistance increases, revealing two regimes: $0 \rightarrow 0.4\,\mathrm{T}$ and $0.4 \rightarrow 1.2\,\mathrm{T}$. These regimes accord well with the passage through $3/11\mathbf{c}^*$ and $2/7\mathbf{c}^*$ phases.

The behavior in both may be viewed from the perspective outlined by Yamada and Takada (1973), in which the moments antiparallel to the applied field are being turned in the field. At $1.2\,\mathrm{T}$ there is a large decrease in the resistivity passing from the $2/7\mathbf{c}^*$ phase to the incommensurate phase (INC). This is interpreted as the removal of the superzone boundaries and the consequent replacement of Fermi surface (Elliott and Wedgwood 1963). Above $1.2\,\mathrm{T}$, the moments of the incommensurate phase collapse smoothly about the **c**-axis, until at $6.2\,\mathrm{T}$ erbium enters the ferromagnetic phase. The transverse measurement at this temperature is interesting in that the behavior is very similar. This suggests that at this temperature there is strong coupling of the spin fluctuations along each axis. For $T = 64.3\,\mathrm{K}$, the magnetic structure is similar to that observed for thulium, with a CAM arrangement of the moments, and the dominant term in the anisotropy is that which "prefers" the **c**-axis. The behavior at this temperature is described by the same argument used for thulium at $T = 53\,\mathrm{K}$, and this represents the first appearance of "canonical" behavior in the magnetoresistance for these two different elements.

Figure 5 shows the influence of the magnetic field on the **a**-axis resistivity. The graphs on the left represent the longitudinal **a**-axis magnetoresistance, and those on the right represent the transversal **c**-axis resistivity. For the longitudinal magnetoresistance at $T = 4\,\mathrm{K}$, there is a steady increase of resistivity in the
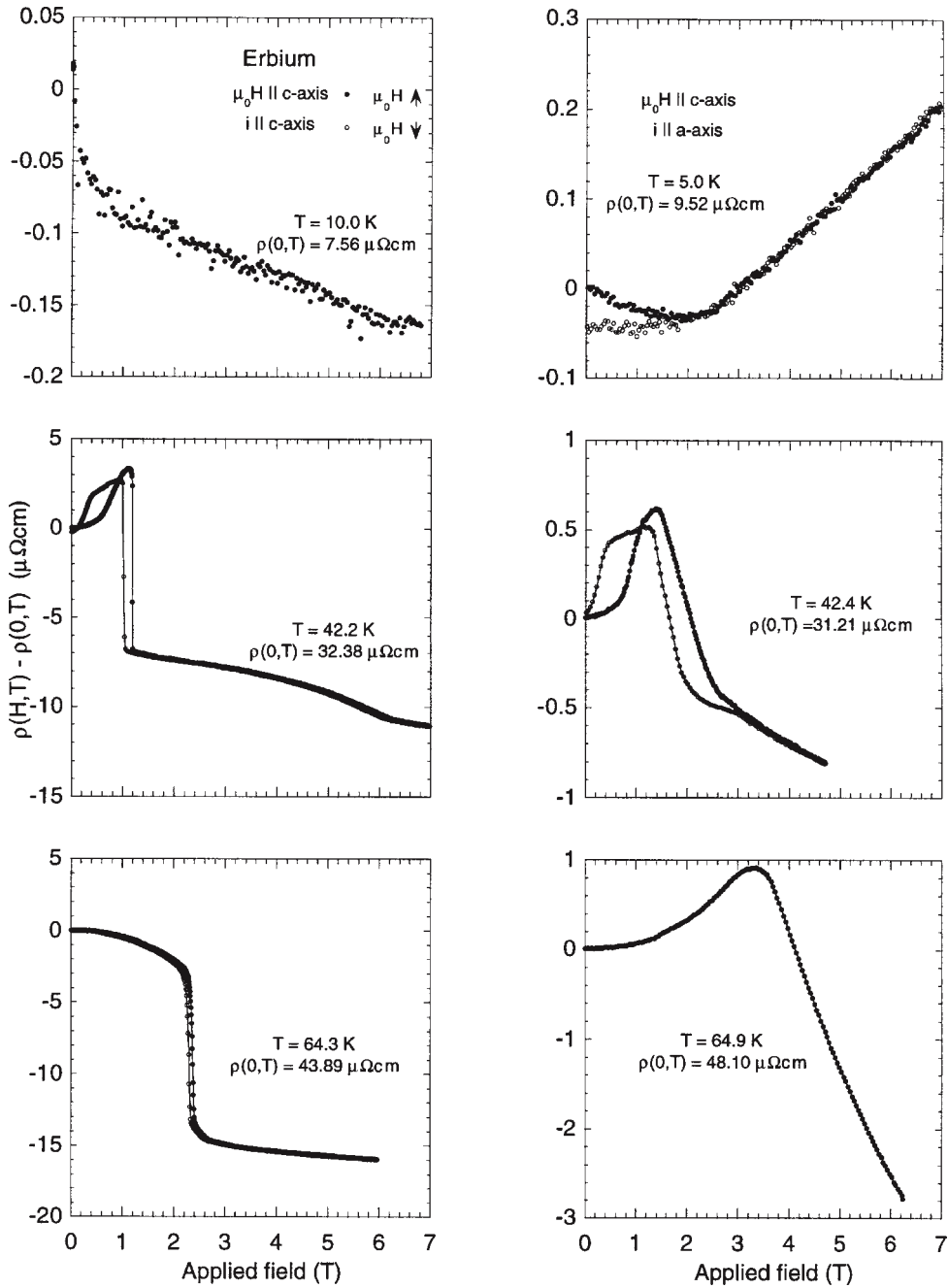
Figure 4
Magnetoresistance for erbium B∥**c**-axis. Longitudinal **c**-axis on the left and transverse **a**-axis on the right. The symbols (●) and (○) represent increasing field and decreasing field, respectively.

"cone" phase, consistent with the Lorentz force distorting the motion of the electrons (Pippard 1989). This is observed for both geometries. When the moments flip into the "fan" phase, there is a removal of Fermi surface. As the magnetic field increases there is smooth collapse of the "fan," formed by moments on the **a**- and the **b**-axes, onto the **a**-axis. There is no model for this process of moment collapse coupled
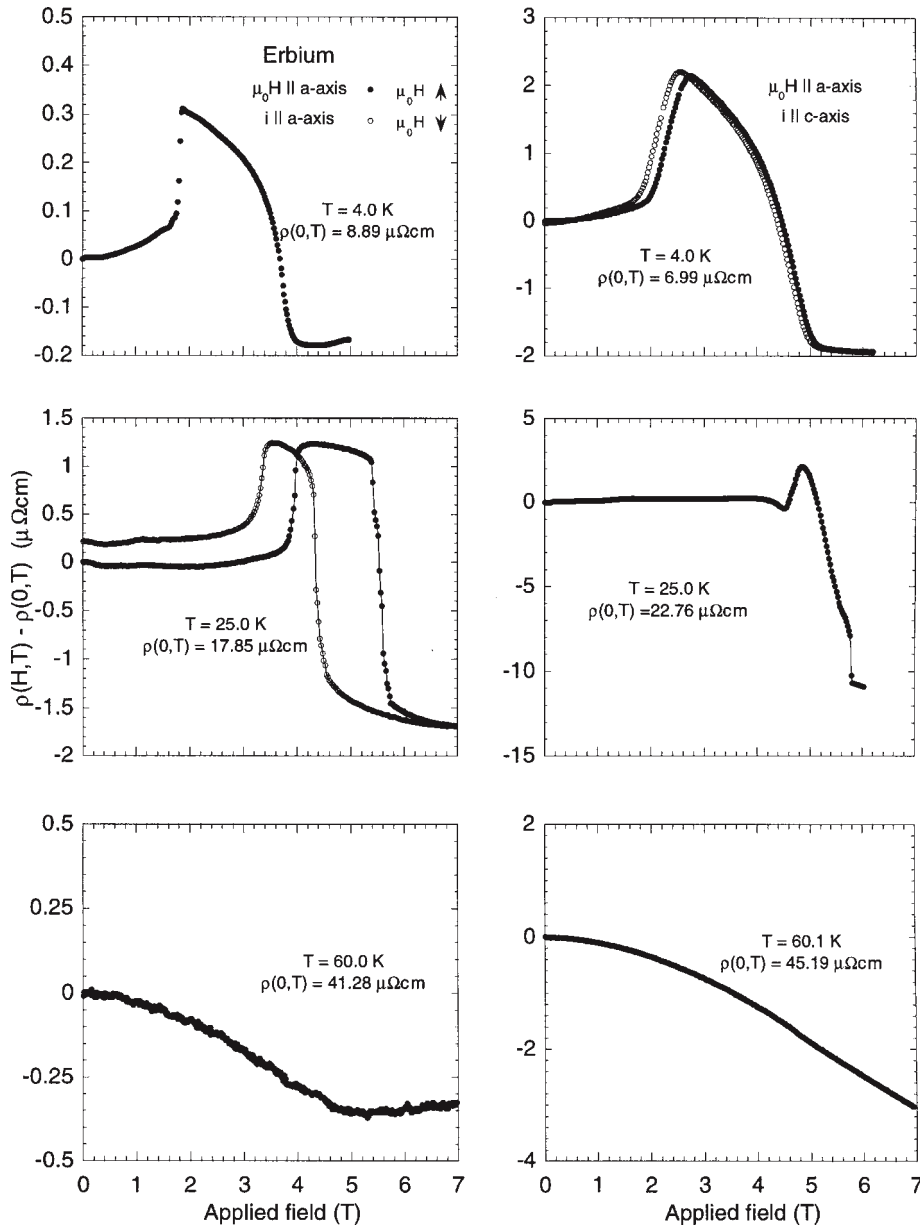
Figure 5
Magnetoresistance for erbium B∥**a**-axis. Longitudinal **a**-axis on the left and transverse **c**-axis on the right.

with a change in Fermi surface. Theoretical consideration of the results for erbium (Ellerby *et al.* 2000) has found that there are gaps in sections of the Fermi surface normal to both the **a** and **c**-axes, and this is certainly responsible for the decrease of the resistivity in the transverse **c**-axis above 5 T. This replacement of Fermi surface arises from the fact that a field parallel to the **a**-axis eventually drives erbium to a fully

ferromagnetic state, as indicated in the phase diagram, and this in turn produces a modulation $\mathbf{Q} = 0\mathbf{c}^*$ and therefore $\Gamma_c = 0$.

The temperature-dependent resistivity for erbium in these two axes (Fig. 1) may be fitted, using Eqn. (4), with values for Γ which have a temperature dependence (Ellerby *et al.* 2000), and values of $\Gamma_c^0 = 0.71$ and $\Gamma_a^0 = 0.14$ for $\mu_0 H = 0$ T. The value of Γ_c is

similar to that found for thulium, where the structure is $\mathbf{Q} = 2/7\mathbf{c}^*$. At a temperature of $T = 25\,\text{K}$, the magnetoresistance remains unaffected along both axes until 4 T, and thus the model of Yamada and Takada (1973), does not apply. The resistivity increases sharply at 4 T as erbium enters the $\mathbf{Q} = 2/7\mathbf{c}^*$ phase, this being in accordance with the removal of a portion of the Fermi surface. As the field is increased further, there is a sharp decrease in both geometries as erbium enters the ferromagnetic phase. As in the case at 4 K, there is no modulation of the magnetic moment, and consequently the superzone boundaries cease to exist abruptly at this boundary, whilst increasing the available Fermi surface. There is significant hysteresis at this transition, suggesting a first-order transition. The results at $T = 60\,\text{K}$ can be understood through the model of Yamada and Takada (1973), in which erbium is paramagnetic along the $\mathbf{a}$-axis, and therefore an applied field systematically suppresses the spin fluctuations along this axis. This is consistent with the dominance of the strong uniaxial anisotropy along the $\mathbf{c}$-axis.

The summary of this section highlights the correspondence of magnetic phase diagrams with the magnetoresistance of erbium. The experimental results presented map well onto the magnetic phase diagrams; however, there are some differences worthy of note. The most prominent derives from the effects of the demagnetizing factor usually present in neutron diffraction studies, which can be of the order 0.5, whilst in longitudinal magnetoresistance the demagnetizing factor can be less than 0.1. The factor results in discrepancies of boundary position, and corrections for this effect can be determined (Stoner 1945). The low-temperature behavior of erbium is dominated by the motion of the conduction electrons in an applied field, with the effects of Fermi-surface modification superposed. A further aspect of phase diagrams concerns the nature of the phase transition. The observation of hysteresis at a transition is a strong indication of a first-order transition, and this can be important in some studies.

3. Concluding Remarks

The preceding sections presented a series of results for the rare earths, chosen to exhibit different anisotropy and exchange. In both cases it has been possible to apply some form of Eqn. (2), incorporating the superzone effects through Eqn. (4) as for the $\mathbf{c}$-axis of thulium and erbium. There is, however, one proviso in the case of erbium. Eqn. (4) requires the inclusion of a temperature dependence in Γ_u which represents the effects of the Fermi surface on the resistivity (Ellerby *et al.* 2000). In addition to this, the $\mathbf{a}$-axis of erbium appears to lose a small portion of the Fermi surface in the cycloidal phase. This is recovered on entry into the cone phase at $T = 20\,\text{K}$ (Fig. 1).

Indeed, Eqn. (2) is particularly versatile in its ability to describe excitations in magnetic systems, and may also be used to analyze systems exhibiting gaps in the spin-wave spectrum.

There were two sets of canonical behavior observed in the magnetoresistance. The first concerned the prominent correlation for the $\mathbf{c}$-axis modulated structures (CAM) of thulium and erbium. The second was found in the magnetoresistance for the "fan" phase in erbium and exhibited in the $\mathbf{a}$-axis measurements a $T = 4\,\text{K}$. This behavior has also been observed in the resistivity for the holmium $\mathbf{b}$-axis in the "fan" phase, where there is quadratic collapse in the resistivity associated with the collapse of the "fan." These responses may be added to the schema derived by Yamada and Takada (1973), to understand the magnetoresistance in spin-flop systems, and the influence of spin/moment fluctuations in ferromagnetic and paramagnetic materials. In both systems discussed, the influence of the magnetic superzones (Mackintosh 1962, Elliott and Wedgwood 1963, Miwa 1963) was found to be of prime importance in the study of the $\mathbf{c}$-axis of these elements. This is true for many of the heavy rare-earth elements.

In comparing results of magnetoresistance with those of neutron diffraction studies, caution is required. In the neutron diffraction studies there is often a large contribution to the position of the phase boundary coming from the demagnetizing field. This can lead to ambiguities. Furthermore magnetoresistance, whilst being one of the most sensitive probes of magnetic systems, can often fail to reveal subtle changes in structural modulation; this is the case with incommensurate structures. Magnetoresistance can only assist in a qualitative fashion when composing magnetic phase diagrams, and will provide allusions as to the type of magnetic structure. However, accurate positions of the phase boundaries may be derived, particularly when using a longitudinal geometry.

Bibliography

Cowley R A, Jensen J 1992 Magnetic structures and interactions in erbium. *J. Phys.: Condens. Matter* **4** (48), 9673–96

Ellerby M, McEwen K A, Bauer E, Hauser R, Jensen J 2000 Pressure-dependent resistivity and magnetoresistivity of erbium. *Phys. Rev. B* **61** (10), 6790–7

Ellerby M, McEwen K A, Jensen J 1998 Magnetoresistance and magnetization of thulium. *Phys. Rev. B* **57** (14), 8416–23

Elliott R J, Wedgwood F A 1963 Theory of the resistance of the rare-earth metals. *Proc. Phys. Soc.* **81**, 846–54

Hessel Andersen N, Gregers-Hansen P E, Holm E, Smith H, Vogt O 1974 Temperature-dependent spin-disorder resistivity in a Van-Vleck paramagnet. *Phys. Rev. Lett.* **32** (23), 1321–4

Hessel Andersen N, Jensen J, Smith H, Spittorf H, Vogt O 1980 Electrical resistivity of the singlet-ground-state system $\text{Tb}_c\text{Y}_{1-c}\text{Sb}$. *Phys. Rev. B* **21** (1), 189–202

Jehan D A, McMorrow D F, Simpson J A, Cowley R A, Swaddling P P, Clausen K A 1994 Collapsing cycloidal

structures in the magnetic phase diagram of erbium. *Phys. Rev. B* **50** (5), 3085–91

Jensen J, Mackintosh A R 1991 *Rare Earth Magnetism*. Clarendon, Oxford

Mackintosh A R 1962 Magnetic ordering and electronic structure of rare-earth metals. *Phys. Rev. Lett.* **9** (3), 90–3

Mackintosh A R 1963 Energy gaps in spin-wave spectra. *Phys. Rev. Lett.* **4** (2), 140–2

McMorrow D F, Jehan D A, Cowley R A, Eccleston R S, McIntyre G J 1992 On the magnetic phase diagram of erbium in a c-axis magnetic field. *J. Phys.: Condens. Matter* **4** (44), 8599–608

Miwa H 1963 Energy gaps and electrical resistance associated with screw-type spin arrangements. *Prog. Theor. Phys.* **29** (4), 477–93

Pippard B 1989 *Magnetoresistance in Metals*. Cambridge University Press, Cambridge

Stoner E C 1945 The demagnetizing factors for ellipsoids. *Phil. Mag.* **36** (263), 803–21

Watson R E, Freeman A J, Dimmock J P 1968 Magnetic ordering and electronic properties of the heavy rare-earth metals. *Phys. Rev.* **167** (2), 497–503

Yamada H, Takada S 1973 Magnetoresistance due to electron-spin scattering in antiferromagnetic metals at low temperatures. *Prog. Theor. Phys.* **49** (5), 1401–19

M. Ellerby
University College, London, UK

ESR Dosimetry: Use of Rare Earth Ions

The trapped electrons (or holes) that are produced in thermoluminescence (TL) phosphors owing to irradiation are thermally released and then recombined with emitting centers, resulting in TL. Therefore, the trapped electrons (or holes) reflecting an accumulated dose are completely released after measuring the TL.

The signal intensity of ESR owing to unpaired electrons produced in irradiated crystals is proportional to the exposure dose. The ESR signal intensity is hardly affected by the measurement because the dose reading with ESR does not require heating, essentially different from the case of TL. Thus, the memory of the irradiation is accurately retained in the crystal after the dose reading. The dose reading can be carried out repeatedly so that the signal/noise ratios are increased. Thus, ESR dosimetry is preferable as a low-dose method to TL dosimetry. Alanine (Regulla and Deffiner 1982), sucrose (Nakajima and Otsuki 1987), and gadolinium ion-doped $K_3Na(SO_4)_2$ (Ohta *et al.* 1997) are known as ESR dosimetry sensors, of which gadolinium ion-doped $K_3Na(SO_4)_2$ is the most sensitive.

ESR and TL properties have been described in $K_3Na(SO_4)_2$ doped with rare earth (Ln = Y, La, Pr, Nd, Sm, Eu, Gd, Tm, Lu) ions after x-ray irradiation. ESR and TL spectra of Ln ion-doped $K_3Na(SO_4)_2$ suggest that these dopants predominately substitute for sodium ions in the $K_3Na(SO_4)_2$ matrix, and the formation of SO_3^- radicals is promoted by the cation vacancy that is produced by the charge compensation, owing to the presence of the trivalent ion. The SO_3^- radical is isotropic and thermally stable. The absorption dependence on the ESR signal intensity of the SO_3^- radical indicates that the ESR signal intensity is proportional to the absorbed dose of x rays from 10^{-4} Gy to 10^2 Gy in yttrium ion-doped $K_3Na(SO_4)_2$ and from 10^{-5} Gy to 10^2 Gy in gadolinium ion-doped $K_3Na(SO_4)_2$.

1. ESR Spectra

The typical ESR spectrum of Ln ion-doped $K_3Na(SO_4)_2$ after x-ray irradiation of about 70 Gy (Fig. 1) consists of a signal at $g = 2.003$, assigned probably to isotropic SO_3^- radicals (Gromov and Morton 1966, Luthra and Gupta 1974). This SO_3^- radical is thermally stable up to about 450 K. Furthermore, the fading of this radical at room temperature is less than 1% yr^{-1} (Ohta *et al.* 1992a).

Figure 2 shows the effect of an amount of blended $Ln_2(SO_4)_3$ on the ESR signal intensity. The ESR signal intensity of SO_3^- radical in stable trivalent yttrium, lanthanum, gadolinium, or lutetium ion-doped $K_3Na(SO_4)_2$ is higher than that in praseodymium, neodymium, or thulium ion-doped $K_3Na(SO_4)_2$, and much lower than that in samarium or europium ion-doped $K_3Na(SO_4)_2$ (Ohta *et al.* 1997).
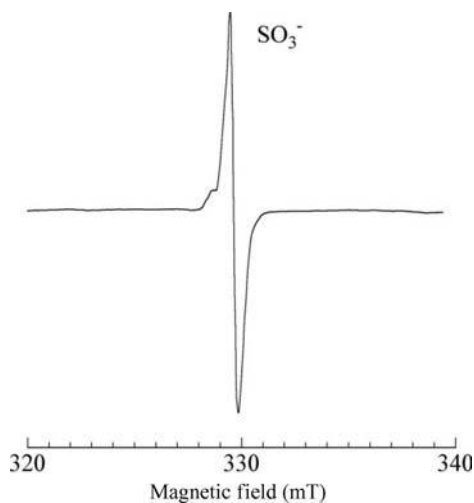
Figure 1
Typical ESR spectrum of Ln ion-doped $K_3Na(SO_4)_2$ without field gradient after x-ray irradiation of about 70 Gy (after Ohta *et al.* 1997).
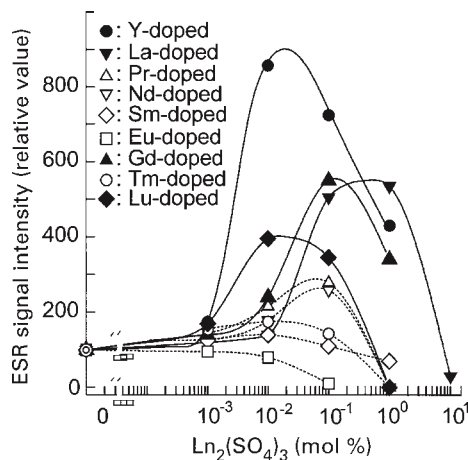
Figure 2
Effect of amount of blended $Ln_2(SO_4)_3$ on ESR signal intensity after x-ray irradiation (after Ohta *et al.* 1997).

Figure 3
ESR signal intensity dependence on x-ray absorbed dose (after Ohta *et al.* 1997).

2. TL Spectra

TL spectra have been measured in order to investigate the valence of the Ln ion-doped $K_3Na(SO_4)_2$ matrix. The TL spectrum of yttrium, lanthanum, or lutetium ion-doped $K_3Na(SO_4)_2$ consists of a broad, weak peak (about 400 nm) owing to the $K_3Na(SO_4)_2$ matrix. In praseodymium, neodymium, gadolinium, or thulium ion-doped $K_3Na(SO_4)_2$, the TL spectrum consists of peaks assigned to the f–f transitions of each Ln^{3+} ion, i.e., the $^1D_2 \to {}^3H_4$ transition of Pr^{3+}, the $^2G_{5/2} \to {}^4I_{13/2}$ and $^2H_{5/2} \to {}^4I_{9/2}$ transitions of Nd^{3+}, the $^6P_{7/2} \to {}^8S$ transition of Gd^{3+}, and the $^1D_2 \to {}^3H_6$, $^1D_3 \to {}^3H_4$, $^1G_4 \to {}^3H_6$, $^1G_4 \to {}^3H_4$, and $^1G_4 \to {}^3H_5$ transitions of Tm^{3+}. The TL intensity of the f–f transition peaks varies according to the following sequence: $Gd^{3+} \ll Pr^{3+}$, $Nd^{3+} < Tm^{3+}$. This is in contrast to the ESR signal intensity (Fig. 2).

The TL spectrum of samarium ion-doped $K_3Na(SO_4)_2$ is affected by the glow peak temperature, i.e., a broad peak owing to the $4f^55d \to 4f^6$ transition of Sm^{2+} and three sharp peaks owing to the $^4G_{5/2} \to {}^6H_{5/2}$, $^4G_{5/2} \to {}^6H_{7/2}$, and $^4G_{5/2} \to {}^6H_{9/2}$ transitions of Sm^{3+} are observed near 380 K and near 430 K, respectively. The TL spectrum of europium ion-doped $K_3Na(SO_4)_2$ consists of a broad, strong peak owing to the $4f^65d \to 4f^7$ transition of Eu^{2+}.

3. Formation Mechanism of SO_3^- Radicals

The formation mechanism of SO_3^- radicals can be interpreted on the basis of the ESR and TL characteristics (Ohta *et al.* 1992b, 1997). Ln ion-doped $K_3Na(SO_4)_2$ after x-ray irradiation reveals that the higher the ESR signal intensity, the lower the TL intensity. Since Ln substitutes mainly for potassium or sodium in Ln ion-doped $K_3Na(SO_4)_2$, cation vacancies are created. Consequently, the SO_4^{2-} ion located in the neighborhood of the cation vacancy can easily capture the free hole released by x-ray irradiation, resulting in an SO_4^- radical. Most of the unstable SO_4^- radicals change immediately into SO_3^- radicals, and some revert to SO_4^{2-} ions with TL emission owing to the electron–hole recombination. The highest ESR signal intensity probably corresponds to a smaller distortion in the $K_3Na(SO_4)_2$ matrix when it is doped with yttrium or gadolinium, because the ionic radii of yttrium and gadolinium are close to that of sodium.

4. Application of SO_3^- Radicals to ESR Dosimetry

Figure 3 shows the ESR signal intensity of SO_3^- radical dependence on the absorption dose in yttrium and gadolinium ion-doped $K_3Na(SO_4)_2$. The net ESR signal intensity, which eliminates the intensity before x-ray irradiation, depends on the absorbed dose of x rays from 10^{-4} Gy to 10^2 Gy in yttrium ion-doped $K_3Na(SO_4)_2$ and from 10^{-5} Gy to 10^2 Gy in gadolinium ion-doped $K_3Na(SO_4)_2$ (Ohta *et al.* 1997).

Bibliography

Gromov V V, Morton J R 1966 Paramagnetic centers in irradiated potassium sulfate. *Can. J. Chem.* **44**, 527–8

Hayakawa T, Ohta M 1999 Role of dopant on the formation of SO_3^- radical induced by x-ray irradiation in radical forms in $K_3Na(SO_4)_2$ crystals. *J. Lumin.* **81**, 313–9

Luthra J M, Gupta 1974 Mechanism of thermoluminescence in Sm- and Eu-doped barium sulfate. *J. Lumin.* **9**, 94–103

Nakajima T, Otsuki T 1987 Development of sucrose radiation dosimeter with free radical. *Ouyo Butsuri (Japan)* **57**, 277–80

Ohta M, Hayakawa T, Furukawa H 1997 Application of lanthanide ion doped alkaline metal sulfates to ESR imaging. *J. Alloys Compds.* **250**, 431–4

Ohta M, Kuroi S, Sakaguchi M 1992a ESR study of x-ray irradiated rare earth (Ln) ion-doped glaserite and Ln ion-doped langbeinite. *Radioisotopes.* **41**, 302–7

Ohta M, Sakaguchi M, Sato M 1992b ESR and luminescence characteristics of glaserite and langbeinite crystals doped with rare earth ion. *Denki Kagaku (Japan)* **60**, 881–6

Regulla D F, Deffiner U 1982 Dosimetry by ESR spectroscopy of alanine. *Int. J. Appl. Radiat. Isot.* **33**, 1101–14

M. Ohta
Niigata University, Niigata City, Japan

F

Faraday and Kerr Rotation: Phenomenological Theory

In 1845 Michael Faraday carried out a series of experiments to determine whether linearly polarized light, when passed though a transparent insulator, was influenced by strong electric fields. Despite Faraday's renowned experimental skills, he failed to observe any effects. Frustrated, he turned instead to the use of magnetic fields. After some initial failures, on the 13th of September he was able to detect a small, though dubious, change when using a poor-quality lead borate glass (Thomas 1991). Fortunately, some 20 years earlier, between 1825 and 1831, Faraday had carried out extensive research into the production of optical-grade glass. Although at the time Faraday considered his research into glasses tedious, his efforts were now to be handsomely repaid. Using one of his own optical-quality glasses he had a sufficiently perfect medium to demonstrate clearly the effect that bears his name to this day. The *Faraday effect* as it is known, demonstrates that the polarization state of electromagnetic radiation may be changed by its passage through an insulating medium when there is a strong magnetic field present (Faraday 1845).

Amazingly, 30 years later in 1875, John Kerr, a close collaborator of William Thompson (later Lord Kelvin), repeated Faraday's quest to demonstrate that electric fields can influence the polarization state of optical radiation as it passes through a transparent material. It is a tribute to the keen experimental skills of Kerr that, where Faraday had failed, he was successful. Using a variety of materials, including glass and later a number of liquids, he demonstrated the electrooptic effect. On the 26th August 1876, at the annual meeting of the British Association for the Advancement of Science held in Glasgow, UK, Kerr announced a further discovery of an effect that has since become known as the *Kerr magnetooptic effect* (Kerr 1877). Using linearly polarized light from a narrow paraffin flame, Kerr showed that a change in polarization state occurred on reflection from a polished, soft iron pole-piece of a strong electromagnet. Given that the changes produced by this effect are usually very small and are difficult to observe, even with modern laser sources, the achievement of Kerr was spectacular. In announcing his discovery Kerr acknowledged the dependence of his success on the earlier work of Faraday and later Verdet, who in 1854 had demonstrated the Faraday effect in semi-transparent paramagnetic media (Verdet 1854).

The Kerr and the Faraday effects are now collectively known as magnetooptical effects and their microscopic origins are well understood (Freiser 1968).

This article is a phenomenological description of the various categories of magnetooptic effects as they may be observed in the laboratory for magnetized media. For obvious historical reasons magneto-optical effects that are observed in transmission are known as Faraday effects. Conversely, effects observed in reflection are referred to as Kerr effects. Often, there is some confusion in referring to the Kerr effect in reflection from materials that are not optically opaque and where radiation may have traveled through the material and back again several times, eventually appearing on the side of reflection as a multiply reflected beam. However, it is convention to refer to effects observed in the reflected field as Kerr effects and in transmission as Faraday effects.

In describing magnetooptical effects it is convenient to categorize them into three principal configurations defined by the orientation of the magnetization vector (**M**) relative to the plane of the reflecting surface and to the plane of incidence of the incident radiation. The three configurations are referred to as the *polar*, *longitudinal*, and *transverse* orientations (Fig. 1).

1. Polar and Longitudinal Effects

In the polar and longitudinal cases, effects occur for incident radiation polarized either in the P-plane (electric vector parallel to the plane of incidence) or the S-plane (electric vector perpendicular to the plane of incidence). Radiation incident in either of these linearly polarized states is, on reflection, converted to elliptically polarized light. The major axis of the ellipse is often rotated slightly with respect to the principal plane and this is commonly referred to as the Kerr rotation. There is also an associated ellipticity and this is called the Kerr ellipticity. At the same time, similar effects occur in transmission, in this case producing Faraday rotation and ellipticity. To first order, the size of these effects is directly proportional to the magnitude of the magnetization vector, **M**. Furthermore the sense of rotation and ellipticity is reversed if the magnetization direction is changed by
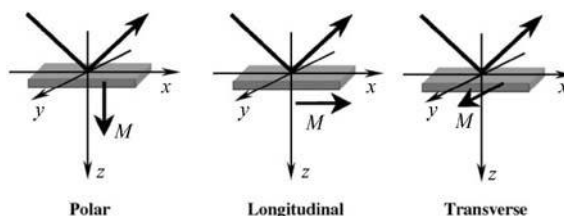
Figure 1
The three principal magnetooptical configurations.
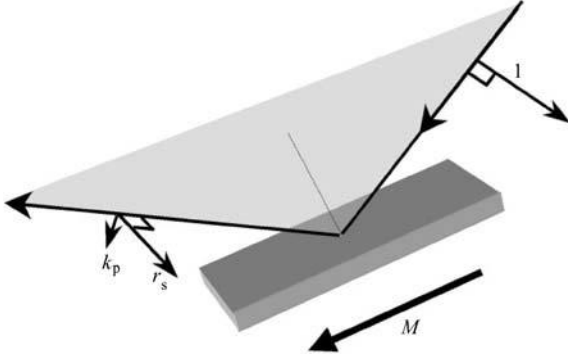
Figure 2
Electric field amplitudes associated with the longitudinal Kerr effect.

Figure 3
Elliptically polarized light showing Kerr rotation, θ_k, and ellipticity, ε_k.

$180°$. In each case the magnitudes of the effects vary with angle of incidence. For the longitudinal case the effect is zero at normal incidence, which is not true for the polar configuration.

It is useful to look at these effects in a little more detail by considering the electric field (**E**) vectors associated with incident and reflected fields. It should be noted that it is the interaction between **E** and **M** (indirectly through spin–orbit coupling) that gives rise to the observed magnetooptical effects. The magnetic component of the wave plays no part at optical frequencies. As an example, Fig. 2 shows the longitudinal configuration although the discussion also applies to the polar case. One can see the specific case of the **E** vector incident in the S-plane. If the incident field amplitude is taken as unity, the reflected beam will consist of two orthogonal complex vectors. One is the usual Fresnel amplitude reflection coefficient, r_s, while the other is a small component, k_p, called the Kerr coefficient. The subscripts p and s refer to the directions parallel and perpendicular to the plane of incidence, respectively. In general, these two vectors represent the amplitudes of oscillating electromagnetic fields and may be out of phase with each other. Together they give rise to elliptically polarized light as illustrated in Fig. 3, where the observer is looking along the reflected beam towards the sample surface. In this case the Kerr rotation, θ_k, is in a clockwise direction and is counted as positive. Likewise, if the locus of the resultant **E** vector rotates in a clockwise direction in time, as indicated in Fig. 3 the ellipticity, ε_k, is positive. In a similar way, the transmitted beam may also become elliptically polarized with amplitude transmission coefficient t_s and Faraday coefficient f_p leading to a rotation θ_f and ellipticity ε_f.

In general, and with reference to Fig. 3, the Kerr rotation and ellipticity are given by the following ellipsometric expressions:

$$\tan 2\theta_k = \tan 2\chi \cos\Delta_k \qquad (1)$$
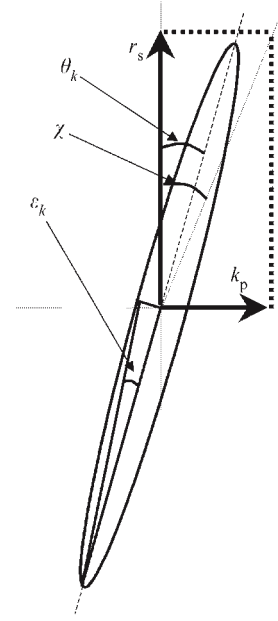
and

$$\sin 2\varepsilon_k = \sin 2\chi \sin\Delta_k \qquad (2)$$

where

$$\tan \chi = \left| \frac{k_p}{r_s} \right| \qquad (3)$$

$$\frac{k_p}{r_s} = \left| \frac{k_p}{r_s} \right| e^{i\Delta_k} \qquad (4)$$

and Δ_k is the angular phase difference between the two orthogonal vectors. In many instances the magnetooptical coefficients are very small; consequently, when $|k_p| \ll |r_s|$ a simple complex Kerr rotation, $\hat{\theta}_k$, may be defined as

$$\hat{\theta}_k = \theta_k + i\varepsilon_k \approx \frac{k_p}{r_s} = \left| \frac{k_p}{r_s} \right| \cos\Delta_k + i\left| \frac{k_p}{r_s} \right| \sin\Delta_k \qquad (5)$$

Similarly, if $|f_p| \ll |t_s|$ a complex Faraday rotation, $\hat{\theta}_f$, may be defined as

$$\hat{\theta}_f = \theta_f + i\varepsilon_f \approx \frac{f_p}{t_s} = \left| \frac{f_p}{t_s} \right| \cos\Delta_f + i\left| \frac{f_p}{t_s} \right| \sin\Delta_f \qquad (6)$$

It should be noted that similar expressions apply for light incident in the P-plane, in which case the associated coefficients are k_s, f_s, r_p, and t_p. In addition, by reversing the magnetization, the signs of the

magnetooptical coefficients are changed and so too is the sense of the complex Kerr rotation.

2. Transverse Effect

The transverse situation is quite different from that described above. First, an effect is only observed for radiation polarized in the P-plane. Second, the radiation remains linearly polarized after reflection, although the reflected intensity changes by a small amount on reversal of the magnetization. This effect varies with angle of incidence and is zero at normal incidence. The situation in reflection is illustrated in Fig. 4 where the incident unit amplitude in the P-plane gives rise to the usual Fresnel amplitude reflection coefficient, r_p, together with a small Kerr component, k_p. The combination of these two vectors, which are not necessarily in phase, results in an intensity reflectivity that changes as the magnetization is switched between the two antiparallel states, $\pm M$. This is illustrated schematically in the amplitude diagram of Fig. 5 where the resultant amplitudes are shown for the two cases. Since the measurable intensity reflectance is equal to the square of the modulus of the resultant amplitude reflectance, the two reflectances, $R_\pm$, are given by

$$R_+ = |r_p + k_p|^2 \text{ and } R_- = |r_p - k_p|^2 \qquad (7)$$

Hence, on magnetization reversal a change, ΔR, occurs with a mean intensity reflectance, R, where

$$\Delta R = R_+ - R_- \text{ and } R = (R_+ + R_-)/2 \qquad (8)$$

3. Permittivity Tensor

As already mentioned, it is the interaction of the electric field vector with the medium that gives rise to magnetooptical effects and for this reason the intrinsic material properties are contained within a skew-symmetric permittivity tensor, [ε]. The form of this tensor may be determined on symmetry grounds since a rotation of the Cartesian coordinate system around the magnetization direction should leave the material properties unchanged. The tensor, for an otherwise isotropic medium, is given below for the magnetization vector pointing along the positive z-direction:

$$[\varepsilon] = \varepsilon_0 n^2 \begin{bmatrix} 1 & -iQ & 0 \\ +iQ & 1 & 0 \\ 0 & 0 & 1 \end{bmatrix} \qquad (9)$$

where ε_0 is the permittivity of free space and n ($= n' + in''$) is the complex refractive index of the material. Q ($= Q' + iQ''$) is the magnetooptic parameter that gives rise to the previously described effects. It should be noted that the positions of the plus and minus signs in this tensor depend upon the particular sign
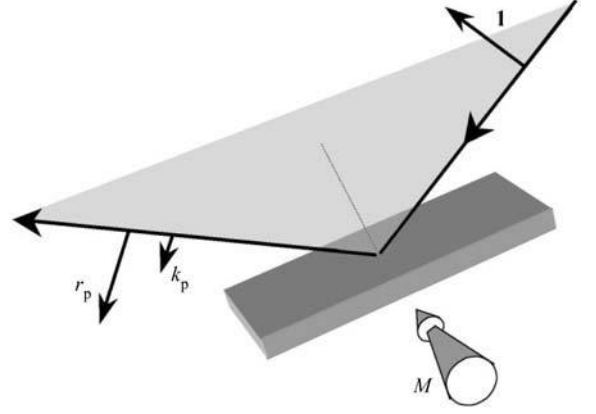
Figure 4
Electric field amplitudes associated with the transverse Kerr effect.
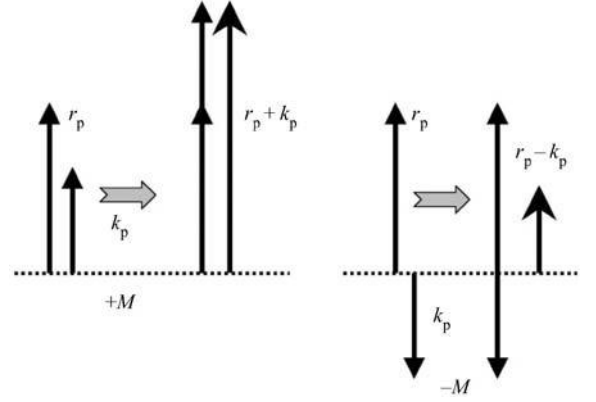
Figure 5
Electric field amplitudes associated with the transverse Kerr effect.

convention chosen to carry out magnetooptical calculations. Moreover the choice of convention has implications for the sense of the complex magneto-optical rotations. For this reason it is important to adopt a clearly defined system. The various options are described in the literature (Atkinson and Lissberger 1992) and it should be noted that the self-consistent preferred scheme described in this reference is used here.

4. Normal Incidence Polar Case

In magnetooptical recording applications the normal incidence polar configuration is most commonly used because the Kerr and Faraday effects are relatively large and normal incidence is convenient from a practical point of view. In such situations the magnetooptical effects can also be understood from the

differential propagation properties of circularly polarized beams or optical modes (Gerber *et al.* 1992). It transpires that a linearly polarized beam may be decomposed into two counter-rotating circularly polarized beams whose **E** vectors are equal and rotate in opposite directions (i.e., clockwise $(+)$ and anticlockwise $(-)$). At normal incidence, these two beams may be considered to propagate separately through the medium with associated refractive indices n_+ and n_- given by

$$n_{\pm} = n(1 \pm Q/2) \qquad (10)$$

At a plane boundary between an incident medium of refractive index n_0 and a semi-infinite medium of refractive index $n_{\pm}$, the amplitude reflection coefficient is simply given by

$$r_{\pm} = \frac{n_0 - n_{\pm}}{n_0 + n_{\pm}} \qquad (11)$$

Consequently, after reflection (or transmission), the amplitudes of these two circular polarized modes are different and when recombined result in the amplitude coefficients r and k (or t and f), as discussed above. Figure 6 is a vector phase diagram that illustrates this. It is clear that after reflection and since $|Q| \ll 1$ these two modes result in amplitude reflection and Kerr coefficients given by

$$r = \frac{r_+ + r_-}{2} \approx \frac{n_0 - n}{n_0 + n} \qquad (12)$$

(Incident beam)

(Reflected beam)
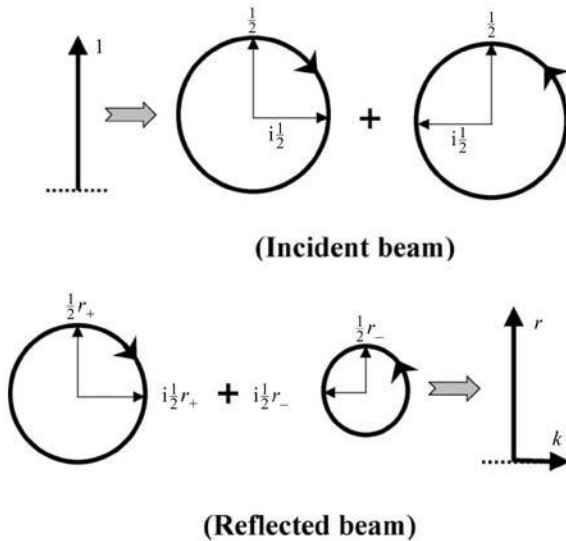
Figure 6
Circular polarized modes leading to the normal incidence polar Kerr effect.

and

$$k = \frac{(r_+ - r)}{2} \approx \frac{-\mathrm{i}n_0 nQ}{(n_0 + n)^2} \qquad (13)$$

In most cases $k \ll r$, in which case it follows that the complex Kerr rotation, as previously defined in Eqn. (5), is given by the following expression:

$$\hat{\theta}_k = \frac{k}{r} \approx -\frac{\mathrm{i}nn_0 Q}{n_0^2 - n^2} \qquad (14)$$

By ignoring boundary effects, a simplified calculation can also be carried out for the Faraday effect in a slab of material of thickness d. In this case the two circular modes suffer differential absorption owing to the differing complex indices n_+ and n_-. A straightforward calculation shows that a simple expression for the complex Faraday rotation is

$$\hat{\theta}_f = \frac{f}{t} \approx -\frac{\pi nQd}{\lambda_0} \qquad (15)$$

where λ_0 is the free-space wavelength of the radiation.

5. Summary

Magnetooptical effects, first discovered by Michael Faraday and John Kerr, can clearly be understood phenomenologically, both in reflection and transmission, in terms of the existence of small electric field amplitudes that appear in the reflected and transmitted fields in addition to the usual Fresnel amplitudes. In longitudinal and polar orientations of the magnetization, with respect to the plane of incidence, these extra magnetooptical components give rise to elliptically polarized light. In the transverse orientation the magnetooptic component results in an intensity change in the reflectivity of P-polarized light. The intrinsic properties of the material, said to be gyroelectric, are fully described by a skew-symmetric permittivity tensor. Formal calculations can be carried out for single surfaces and thin films as well as for multilayered systems. A full discussion of the theoretical techniques used to deal with multilayer systems and their properties is given in *Magneto-optical Effects, Enhancement of* and *Multilayer Optical Film Modelling*.

See also: Magneto-optics: Inter- and Intraband Transitions, Microscopic Models of; Magneto-optic Multilayers

Bibliography

Atkinson R, Lissberger P H 1992 Sign conventions in magnetooptical calculations and measurements. *Appl. Opt.* **31**, 6076–81

Faraday M 1845 Experimental researches in electricity. *Proc. R. Soc.* **5**, 567–9

Freiser M J 1968 A survey of magneto-optic effects. *IEEE Trans. Magn.* **MAG-4**, 152–61

Gerber R, Wright C D, Asti G 1992 *Applied Magnetism.* Kluwer, London

Kerr J 1877 On rotation of the plane of polarisation by reflection from the pole of a magnet. *Philos. Mag.* **3**, 321–43

Thomas J M (1991) *Michael Faraday and the Royal Institution.* Adam Hilger, Bristol, UK

Verdet E 1854 Sur les propriétés optiques développées dans les Corps Transparents par l'Action du Magnétisme. *Ann. Chim. Phys.* **41**, 370–412

R. Atkinson
The Queen's University, Belfast, UK

Ferrite Ceramics at Microwave Frequencies

The term *ferrite* is used to designate ferrimagnetic materials. Ferrites are similar to magnetic alloys in that both possess magnetic domains and exhibit characteristic phenomena of saturation and hysteresis. However, ferrites are generally ceramics that are hard, brittle, and are poor electrical conductors. Typical values for the physical constants of ferrite ceramics are:

Coefficient of linear expansion $= 10^{-5}\,°C^{-1}$
Specific heat $= 0.2\,cal\,g^{-1}\,°C^{-1}$
Thermal conductivity $= 0.015\,cal\,s^{-1}\,cm^{-1}\,°C^{-1}$
Density $= 5\,g\,cm^{-3}$

The chemical formula for ferrites can vary significantly, and they can have cubic or hexagonal crystal structure. Ferrites with spinel structure have the formula MFe_2O_4, where the iron is trivalent and the symbol M denotes a divalent metal from the series Mg^{+2}, Mn^{+2}, Fe^{+2}, Co^{+2}, Ni^{+2}, Cu^{+2}, Zn^{+2}, or Cd^{+2}. Another important family of ferrite compounds are those with the garnet structure with chemical formula $M_3Fe_5O_{12}$, where M is a trivalent metal from the lanthanide period of elements, such as yttrium. Ferrites having hexagonal structure correspond to the formula $MFe_{12}O_{19}$, where M is Ba or Sr, M being divalent and Fe trivalent.

Ferrite ceramics are widely used in microwave devices to control transmission path, frequency, amplitude, and phase of microwave signals. Accurate dielectric and magnetic property measurements at the operational frequency and temperature ranges are needed for optimized development of these devices, as well as to assist in the manufacture of the ferrite itself. Both dielectric and magnetic losses must be determined.

1. Microwave Measurements

A ferrite is characterized electrically and magnetically by its complex permittivity:
$\varepsilon^* = \varepsilon_0(\varepsilon_r' - j\varepsilon_r'') = \varepsilon_0\varepsilon_r'(1 - j\tan\delta_e)$ and its complex permeability:
$\mu^* = \mu_0(\mu_r' - j\mu_r'') = \mu_0\mu_r'(1 - \tan\delta_m)$, where $\tan\delta_e$, $\tan\delta_m$ denote dielectric and magnetic loss tangents, and the free space permittivity ε_0 and permeability μ_0 are given by $8.854 \times 10^{-12}\,F\,m^{-1}$ and $4\pi \times 10^{-7}\,H\,m^{-1}$. The superscript * denotes that the quantity is complex. The complex permittivity and permeability are both temperature- and frequency-dependent.

Dielectric losses for most ceramic ferrites are very small ($\leqslant 5 \times 10^{-4}$) and usually vary linearly with frequency. Magnetic losses depend on saturation magnetization, chemical composition, porosity and grain size, and any applied static magnetic field strength. Magnetic losses vary nonlinearly with frequency, often by seven orders of magnitude over the frequency range from 1 MHz to 25 GHz.

When an applied magnetic field bias is applied in the *z*-direction, the complex permeability becomes anisotropic and is then generally written in diagonalized tensor form:

$$\bar{\bar{\mu}}; = \mu_0 \begin{bmatrix} \mu_x^* & 0 & 0 \\ 0 & \mu_y^* & 0 \\ 0 & 0 & \mu_z^* \end{bmatrix} \qquad (1)$$

For the dielectric case, $\mu_x' = \mu_y' = \mu_z' = 1$ and all magnetic losses are 0. For a demagnetized ferrite, $\mu_x^* = \mu_y^* = \mu_z^* = \mu_d^*$, and magnetic permeability becomes a scalar quantity. For a partially magnetized ferrite, $\mu_x^* = \mu_y^* = \mu_t^*$ and $\mu_z' \neq 1$, $\tan\delta_{z,m} \neq 0$, where $\tan\delta_{z,m}$ denotes the magnetic loss tangent parallel to the applied tuning magnetic bias field and μ_t^* is the magnetic permeability transverse to the bias field. In a saturated ferrite, $\mu_x^* = \mu_y^* = \mu_t^*$, and $\mu_z' = 1$, $\tan\delta_{z,m} = 0$.

The magnetization frequency of a ferrite is defined by $f_M = \gamma_g M_s$, where γ_g is the gyromagnetic ratio (35.19 MHz·m/kA) and M_s is the saturation magnetization (kA/m). At frequencies f less than f_M, ferrites have high magnetic loss and are commonly used as ferrite tiles in anechoic chambers or in other shielding applications. Waveguide transmission line techniques can be used for accurate magnetic characterization for $f < f_M$ (Baker-Jarvis *et al.* 1993).

Wireless communication system applications employing ferrites (circulators and phase shifters) usually operate at frequencies greater than the magnetization frequency. Magnetic losses rapidly decrease above f_M, and transmission line techniques cannot be used for accurate loss characterization. The most accurate methods for measuring ferrite

magnetic properties at microwave frequencies are techniques that use resonant cavities or that incorporate the ferrite specimen as part of a dielectric resonator system (LeGraw and Spencer 1956, Bussey and Steinert 1958, Green and Kohane 1964, Green and Sandy 1974, Ogasawara *et al.* 1976, Muller-Gronau and Wolf 1983, Le Roux *et al.* 1988, Krupka 1991, Krupka and Geyer 1996). Dielectric resonator system techniques have greater sensitivity than cavity methods to magnetic loss for comparably-sized samples. One measurement procedure, illustrated in Fig. 1 for accurate evaluation of ε_r^* and μ_d^* and at frequencies greater than f_M, is to place a cylindrical sample in a parallel plate waveguide (Courtney 1970) and:

Apply a large static magnetic field (beyond ferromagnetic resonance) along the cylindrical z-axis to saturate the ferrite specimen, causing $\mu_z' = 1$ and $\tan\delta_{z,m} = 0$. The ferrite specimen is equivalent to a dielectric resonator, and ε_r and $\tan\delta_e$ may be measured with the TE_{011} mode resonant frequency f and system unloaded Q-factor Q_0.

Demagnetize the specimen and measure the TE_{011} mode resonant frequency f_m and unloaded Q-factor Q_m. The real permittivity and dielectric loss tangent are known from the first step, and the real magnetic permeability μ_d and magnetic loss tangent $\tan\delta_m$ are evaluated from the second.

Another measurement technique is to employ low-loss dielectric sleeves operated with TE_{011} mode structure (Fig. 2). This system (Krupka and Geyer 1996, Geyer 1999) permits broadband permeability characterization of a *single* ferrite sample at frequencies near and far from the magnetization frequency. The measurement bandwidth is realized by the use of commercially available high-Q ceramic or oriented single-crystal quartz resonators. The aspect ratios and permittivities of the sleeve resonators may be chosen so as to enable spectral characterization of a single ferrite sample from 800 MHz to 25 GHz.

In the absence of an applied static field, the ferrite in the demagnetized state is isotropic and is described
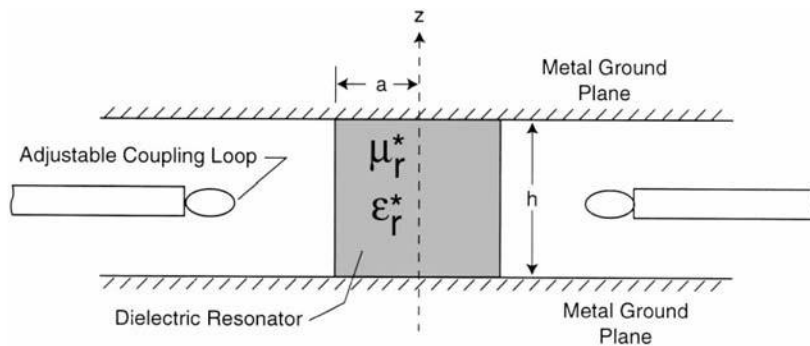
Figure 1
Ferrite employed as dielectric resonator in a parallel plate waveguide.
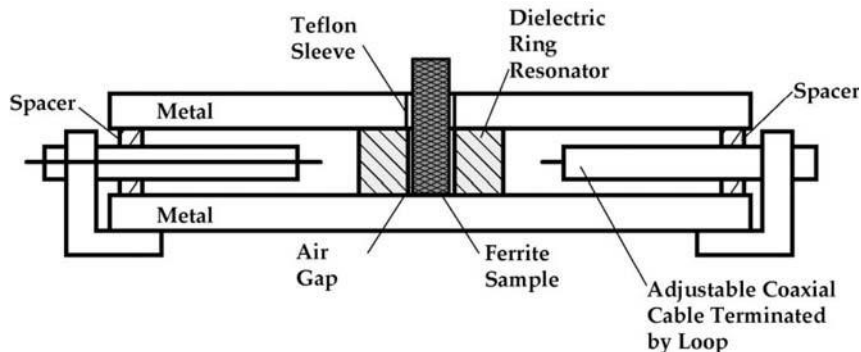
Figure 2
Dielectric resonator system for broadband microwave permeability measurements.

by a scalar frequency- and temperature-dependent relative permeability and complex relative permittivity. The resonators are coupled to the external microwave source through two loop-terminated coaxial cables that are adjustable so that the measured loaded

Q factor is equal to the unloaded Q factor within any prescribed accuracy.

The measurement procedure follows several steps. First, the complex permittivity of the ferrite is determined with a TM_{0n0} cavity. Second, the complex
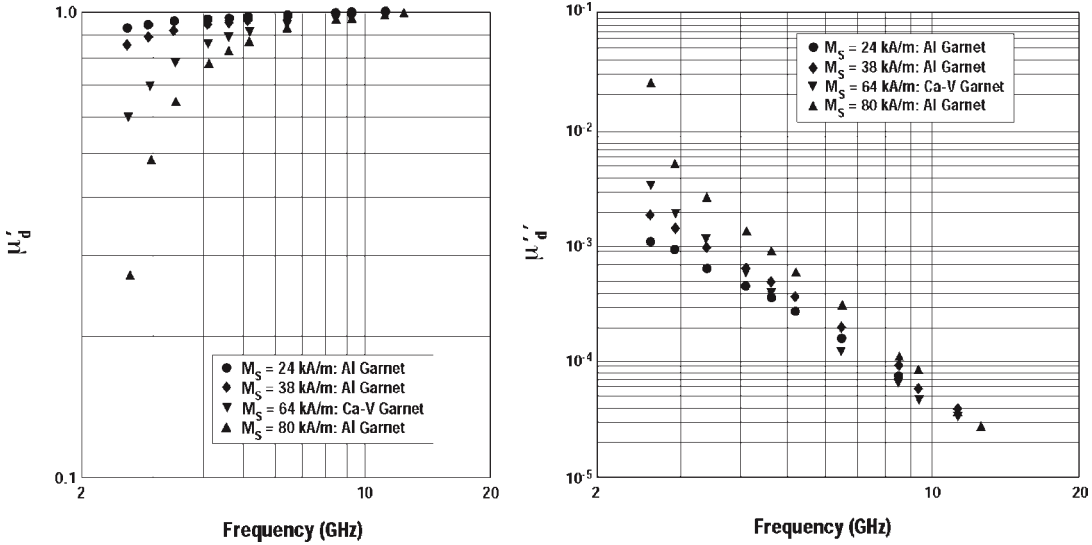
Figure 3
Measured complex permeability, μ_d^*, as a function of frequency for various doped garnets having differing saturation magnetizations. $T = 297\,\mathrm{K}$.
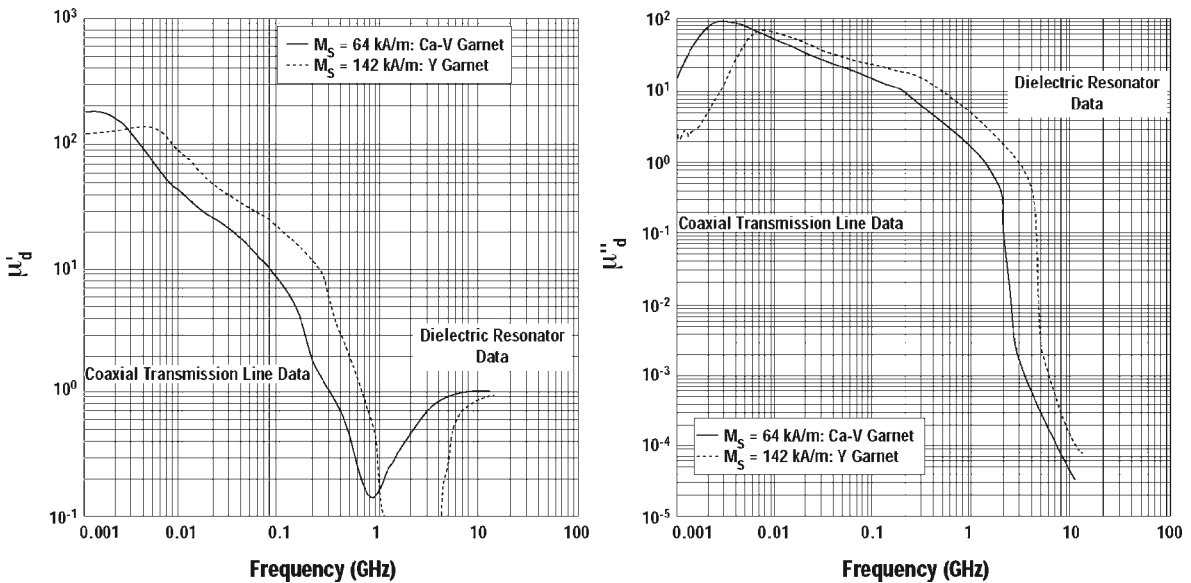
Figure 4
Broadband magnetic permeability spectra of demagnetized ferrite above and below magnetization frequency.

relative permittivity of each dielectric ring resonator is found from measurements of the resonant frequency and unloaded Q-factor of the empty ring resonators operated in the TE_{011} mode, taking into account conductive microwave losses of the upper and lower metal ground planes. The scalar permeability $\mu'_d (f, T)$ at frequency f and temperature T is determined from measurements of the resonant frequency of the ring resonator with ferrite specimen inserted and solving the TE_{011} eigenvalue equation (Geyer in preparation).

After determining μ'_d, the magnetic loss index μ''_d is found as a solution to the equation:

$$\frac{1}{Q} = \frac{1}{Q_c} + p_{\varepsilon'_s}\tan\delta_{e,s} + p_{\varepsilon'_r}\tan\delta_e + p_{\varepsilon'_d}\tan\delta_m \qquad (2)$$

where Q is the unloaded Q-factor for the TE_{011} mode, Q_c is the Q-factor reflecting conductor losses in the metal plates, $p_{\varepsilon'_s}$ is the electric energy filling factor of the dielectric sleeve resonator, $p_{\varepsilon'_r}$, $p_{\varepsilon'_d}$ are the ferrite sample electric and magnetic energy filling factors, $\tan\delta_{e,s}$ and $\tan\delta_e$ are the dielectric loss tangents of the sleeve resonator and ferrite sample, and $\tan\delta_m$ is the magnetic loss tangent of the ferrite. Example complex permeability data for garnets doped with aluminum and calcium-vanadium are given in Fig. 3. Estimated total uncertainty in μ'_d is 1% and in μ''_d is 2×10^{-5}. These data clearly show the shift in magnetization frequency to higher frequencies as saturation magnetization increases, as well as rapidly increasing nonlinear magnetic losses as the magnetization frequency is approached. Dielectric resonator and transmission line data may be combined to yield accurate complex permeability spectra of ferrite ceramics over five decades in frequency (Fig. 4).

When a tuning bias is applied so that the ferrite specimen is partially saturated, two dielectric low-loss sleeve resonators having the same height but differing diameters may be used to evaluate the complex tensor permeability components (Krupka 1991, Geyer *et al.* 1998). In this case, two circularly polarized, oppositely rotating HE^+_{111} and HE^-_{111} resonant modes are used with one sleeve for evaluating μ^*_x and μ^*_y, and the TE_{011} resonant mode with the second sleeve is used for μ^*_z. The aspect ratios of the sleeves are chosen so that, for the nominal measurement frequency of interest, all three resonant modes for both sleeves with ferrite sample insertion occur at the same frequency with zero bias field. For this case, the tensor magnetic properties are evaluated as a function of tuning bias (Geyer *et al.* 1998)

2. Summary

Comparisons between experimentally evaluated demagnetized real permeability spectra of ferrites and quasi-static theoretical formulations given by Schlömann (1970) have been reported (Green and Sandy 1974, Le Roux *et al.* 1988, Geyer 1999). These comparisons show good agreement when $f_M/f < 0.75$. The effect of cooling magnesium spinel ferrite ceramics on both dielectric and magnetic losses at microwave frequencies has also been studied (Geyer 1999) using dielectric resonator techniques. Generally, dielectric losses of a ferrite ceramic decrease as the specimen is cooled, albeit with increasing magnetic loss and decreasing magnetic permeability. Hence, with cooling, the same ferrite ceramic may be used in microwave tuning devices at higher frequencies.

Accurate magnetic characterization from 2 GHz to 25 GHz of a *single* ferrite specimen can be accomplished with low-loss dielectric sleeve resonators, and combined with transmission line measurements to reveal both low-frequency, high-loss and high-frequency, low-loss properties.

See also: Ferrites; Ferrite Magnets: Improved Performance

Bibliography

Baker-Jarvis J, Janezic M D, Grosvenor J H, Geyer R G 1993 Transmission reflection and short-circuit line methods for measuring permittivity and permeability. *Nat. Inst. Stand. Tech. Tech. Note 1355-R*

Bussey H E, Steinert L A 1958 Exact solution for a gyromagnetic sample and measurements on a ferrite. *IRE Trans. Microwave Theory Tech.* **MTT-6**, 72–6

Courtney W E 1970 Analysis and evaluation of a method of measuring the complex permittivity and permeability of microwave insulators. *IEEE Trans. Microwave Theory Tech.* **MTT-18**, 476–85 1970

Geyer R G 1999 Complex permittivity and permeability of ferrite ceramics at microwave frequencies. *Dielectric Ceram. Mater., Ceram. Trans.* **100**, 195–215

Geyer R G Theoretical analysis of sleeve resonators for dielectric and magnetic measurements of rod specimens. *Nat. Inst. Stand. Tech. Note* In preparation

Geyer R G, Jones C, Krupka J 1998 Complex permeability measurements of ferrite ceramics used in wireless communications. *Dielectric Ceram. Mater., Ceram. Trans.* **88**, 93–113

Green J J, Kohane T 1964 Testing of ferrite materials for microwave applications. *Semicond. Prod. Solid State Technol.* **7**, 46–54

Green J J, Sandy F 1974 Microwave characterization of partially magnetized ferrites. *IEEE Trans. Microwave Theory Tech.* **MTT-22**, 641–5

Krupka J 1991 Measurements of all complex permeability tensor components and the effective line widths of microwave ferrites using dielectric ring resonators. *IEEE Trans. Microwave Theory Tech.* **39**, 1148–57

Krupka J, Geyer R G 1996 Complex permeability of demagnetized microwave ferrites near and above gyromagnetic resonance. *IEEE Trans. Magn.* **32**, 1924–33

LeGraw R C, Spencer E G 1956 Tensor permeabilities of ferrites below magnetic saturation. *IRE Con. Rec.* **5**, 66–74

Le Roux P, Jecko F, Forterre G 1988 Nouvelle methode de determination des parties reeles des parametres electriques et magnetiques des resonateurs a ferrites satures et non satures. *Ann. Telecommun.* **43**, 314–22

Muller-Gronau W, Wolff I 1983 A microwave method for the determination of the real parts of the magnetic and dielectric material parameters of premagnetized microwave ferrites. *IEEE Trans. Microwave Theory Technol.* **MTT-32**, 377–82

Ogasawara N, Fuse T, Inui T, Saito I 1976 Highly sensitive procedures for measuring permeabilities ($\mu_\pm$) for circularly polarized fields in microwave ferrites. *IEEE Trans. Magn.* **MAG-12**, 256–9

Schlömann E 1970 Microwave behavior of partially magnetized ferrites. *J. Appl. Phys.* **41**, 204–14

R. G. Geyer
*National Institute of Standards and Technology
Boulder, Colorado, USA*

Ferrite Magnets: Improved Performance

Ferrite magnets, based on the compound $AFe_{12}O_{19}$ (A = Sr, Ba) and the magnetoplumbite or *M* crystal structure, have a dominant position on the magnet market (57% by value and 95% by weight), thanks to the favorable performance/price ratio. The main application for high-grade ferrite magnets is as segments in various d.c. motors for the automotive industry. Their market share would be even larger if their magnetic performance, notably remanence B_r and coercivity H_{cJ}, could be further improved. This can no longer be expected from the conventional technology, which has almost attained its saturation. In recent years, however, it has been recognized that LaCo or related substituents may lead to significantly improved performance. This has initiated a renaissance of its basic research as well as a new generation of high-performance ferrite magnets. After a short survey of the conventional ferrite magnets, the new LaCo–M ferrites are discussed, referring to a recent more extended review article (Kools *et al.* 2002).

1. Conventional Ceramic Ferrite Magnets

The manufacturing process of ceramic ferrite magnets is a classical ceramic process (see *Alnicos and Hexaferrites*), having several specific features (Kojima 1982, Kools 1992). Most characteristic are the wet pressing in a magnetic field to align the powder particles in order to obtain high remanence, the fine milling into alignable particles of $\sim 1\,\mu m$, the natural tendency to lateral grain growth (platelet-shaped crystals), and, finally, the necessity to keep the fired grains small to obtain high coercivity.

In the 1970s and 1980s it became gradually clear that increased magnetic performance can only be attained by further decreasing the particle size of the milled powders. This implies increased milling effort and more difficult wet pressing, two factors which

largely contribute to the production costs. This has led to the following definition of the magnetic performance IP in terms of remanence (B_r) and coercivity (H_{cJ}): $IP(mT) = B_r + 0.4\mu_0 H_{cJ}$. It is governed uniquely by the particle size obtained after milling. For technical and economical reasons, however, there is a lower limit for the latter particle size. The corresponding upper performance level of $IP \approx 550\,mT$ characterizes the saturation state of the conventional technology in the early 1990s.

1.1 Intrinsic Properties

The intrinsic properties stem from the M-crystal structure and, notably, from the five distinct Fe-sublattices, coupled by superexchange. Two intrinsic properties are crucial: the saturation magnetization (J_s^0) determines B_r and the magneto-crystalline anisotropy field strength (H_a) determines H_{cJ}.

The magnitude of J_s^0 derives from the mutual orientations of the five Fe-sublattice moments, as given by the Gorter model: the moments at 2a, 12k, and 2b are mutually parallel and antiparallel to the moments at 4f1 and 4f2. This model is supported by magnetization measurements, Mössbauer spectrometry, and, recently, also by *ab initio* calculation (Fang *et al.* 2003). The $J_s^0 - T$ curve (Fig. 1) is almost linear in the room temperature region with $dJ_s^0/dT = -0.9\,mT\,K^{-1}$.

The anisotropy field H_a represents the hypothetical field that would be able to align the magnetization perpendicular to the easy direction, the *c*-axis. It is defined by $H_a = 2K_1/J_s^0$, where the anisotropy constant K_1 characterizes the associated anisotropy energy. The origin of K_1 is related to spin–orbit
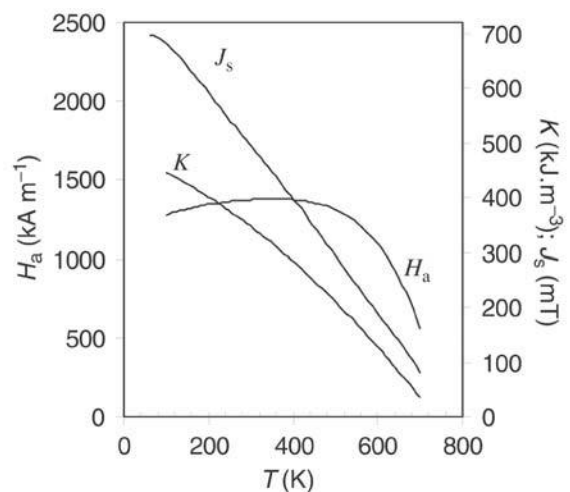
Figure 1
Temperature dependence of J_s, K, and H_a for BaM.

coupling at the 2b and 12k sites, but a detailed model is still lacking. The $K_1 - T$ curve is analogous to the $J_s^0 - T$ curve, but less curved at low temperature, resulting in a flat $H_a - T$ curve with $dH_a/dT \approx 0$ at room temperature (Fig. 1).

1.2 Modeling B_r and H_{cJ}

The formulas given below refer to medium- and high-grade ferrite magnets in which the grains are supposed to be single domain in the remanent state and magnetization reversal inside the grains is supposed to be governed by domain nucleation.

The remanence is described by the formula

$$B_r = k J_s^0 = f(d/d^0) s J_s^0 \qquad (1)$$

The factor k takes account of the influence of the microstructure. It consists of three contributions: the degree of alignment f ($0.5 < f < 1$), the amount of M-phase s, and the relative density d/d^0. Typical values for (unsubstituted) high-performance magnets ($B_r = 420\,\text{mT}$) are: $f = 0.92$, $d/d^0 = 0.98$, $s = 0.98$ ($k = 0.88$). The (relative) temperature coefficient of the remanence, $\text{TC}(B_r)$, derives from the temperature coefficient of the saturation magnetization, $\text{TC}(J_s^0)$, and amounts to -0.19% for nonsubstituted grades.

The coercivity is described by the expression

$$H_{cJ} = aH_a - (N/\mu_0)(B_r + J_s^0)$$
$$= aH_a - (N/\mu_0)(k+1)J_s^0 \qquad (2)$$

Its dependence on the microstructure is described by k and, in particular, by the factors a and N. The factor a increases with decreasing grain size, thus reflecting the well-known H_c-grain size dependency. The factor N is governed by the grain shape and increases when the grains become more platelet shaped. For an unsubstituted high-grade magnet ($H_{cJ} = 270\,kA\,m^{-1}$), typical microstructural factors are: $a = 0.52$ and $N = 0.7$. The value of $\text{TC}(H_{cJ})$ is easily derived from Eqn. (2) by differentiation. Substituting the typical values given above, one obtains $\text{TC}(H_{cJ}) \approx +1\,kA\,m^{-1}\,K^{-1}$ or $\approx 0.4\%\,K^{-1}$.

1.3 Substitutions

Until recently, it seemed impossible to improve the magnet performance by means of substitutions. The J_s^0 can be increased, indeed, but only at the costs of H_a and vice versa. Only the substitution of Al and/or Cr for Fe has been of practical importance, including a decreased J_s^0 at constant K_1, thus leading to increased H_a and H_{cJ}.

1.4 Microstructure

Grain growth and platelet grain shape should be suppressed during high-density sintering, otherwise the H_{cJ} deteriorates. Si-based additions are commonly applied. As the underlying mechanism, the reaction induced grain growth inhibition (RIGGI) has been put forward, being related to the slow incorporation of silica.

2. LaCo-type Substituted M-ferrite Magnets

Scattered over the period 1959–1996, several studies have been published, that included occasionally LaCo-M-type compositions, corresponding to the general formula $A_{1-x}R_xFe_{12-x}B_xO_{19}$ (ARB-M), where A = Ba, Sr, …, R = La^{3+}, Pr^{3+}, Bi^{3+}, …, and B = Co^{2+}, Ni^{2+}, Fe^{2+}, …. The recent recognition that LaCo-type ferrite magnets can represent a new generation of high-performance ferrite magnets has provoked a wave of investigations, being initially practically oriented in order to secure patent rights (Taguchi et al. 1998, Takami et al. 1999). The results obtained share the following general features:

- increased performance (IP ≈ 600 mT), notably from increased H_{cJ}, but B_r/H_{cJ} may vary;
- reduced $\text{TC}(H_{cJ})$, down to ~50% of the unsbstituted value;
- wide composition range ARB-M, including also $(Fe + B)/(A + R) \neq 12$ with optimum properties for SrLaCoM ($x \approx 0.25$), where Co may be partly replaced by Fe^{2+}; and
- classical processing: only the calcination time is longer than usual.

These promising results have provoked an intensive study as to the precise effects and their backgrounds. This is briefly reviewed below, based on our own studies.

2.1 Effects on the Magnet Properties

The main effects illustrated in Figs. 2–5 show the following:

- a significant increase of H_{cJ} up to $x = 0.25$ (25%), followed by a similar decrease for $0.25 < x \leqslant 0.4$;
- reduced $\text{TC}(H_{cJ})$ (50% for $x = 0.3$);
- slight increase of B_r (3.5% for $x = 0.4$); and
- moderate squareness of the demagnetization curve, which strongly deteriorates for high x ($x > 0.2$).

These effects refer to SrLaCo-M, but analogous effects are found for BaLaCo-M.

2.2 Background of the Effects

The coercivity is explained on the basis of the coercivity model (Eqn. (2)), where an increased H_a value is substituted (Fig. 3), as measured by single
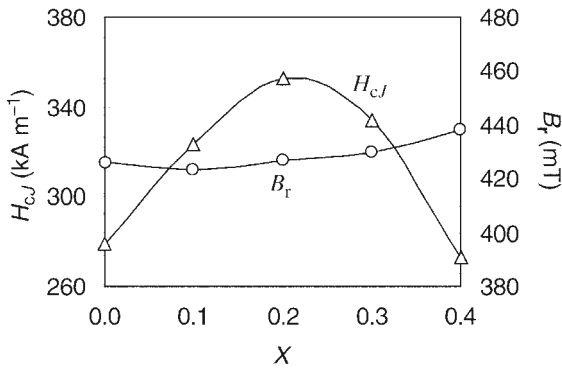
Figure 2
H_{cJ} and B_r vs. x for $Sr_{1-x}La_xFe_{12-x}Co_xO_{19}$ magnets (reproduced by permission of Kools *et al.* (2002) from *J. Magn. Magn. Mater.*, **242–245** (Part 2), 1270–6).

Figure 4
Microstructural factors underlying H_{cJ}, measured magnetically (Morel *et al.* 2000).

Figure 3
SPD data for $Sr_{1-x}La_xFe_{12-x}Co_xO_{19}$ magnets showing H_a vs. x (Grössinger *et al.* 2000).
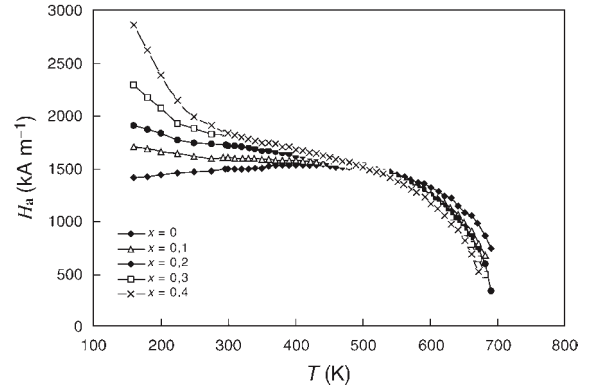
Figure 5
Low-temperature behavior of H_a for $Sr_{1-x}La_xFe_{12-x}Co_xO_{19}$ ($x = 0.2$) (reproduced by permission of Grössinger *et al.* (2000) from *Ferrites, Proc. Int. Conf. on Ferrites*, ICF8, pp. 428–30).

point detection (SPD) H_a measurements (see *Magnetic Measurements: Pulsed Field*). Since the values for B_r, a, and N (Fig. 4) appear to be quite normal, the increased H_{cJ} is dominated by the increased H_a.

The decrease of H_{cJ} for $x > 0.25$ stems from the more pronounced platelet shape. The microstructure parameters a and N were measured both magnetically and by SEM observation. For $x > 0.25$ the N value increases sharply (Fig. 4), while the a value remains essentially constant, thus explaining the drop in H_{cJ}.

The $TC(H_{cJ})$ is explained by the same coercivity model in the differential form, substituting apart from the experimental a and N values, the measured values for dJ_s^0/dT and dH_a/dT (Fig. 5). This formula explains that $TC(H_{cJ})$ deviates significantly from the usual one: dH_a/dT is no longer close to zero

as usual, but has become negative, resulting in a decreased $TC(H_{cJ})$.

The explanation of B_r is based on Eqn. (1) and separate measurements of f, (d/d^0), and s. The factor $J_{s(300\,K)}^0$ is decomposed into two factors: $J_{s(0\,K)}^0$ and a new parameter $R_{jt} = J_{s(300\,K)}^0/J_{s(0\,K)}^0$ characterizing the curvature of the $J_s^0 - T$ curve. Density and $J_{s(0\,K)}^0$ appear to be constant; so the slight increase of B_r is dominated by the alignment factor (f) and the curvature factor (R_{jt}), both showing a slight increase (Fig. 6).

The poor squareness was attributed to chemical and microstructural inhomogeneities. Mössbauer analysis and resistivity measurements showed that the Co substitution is not complete, Co being partly
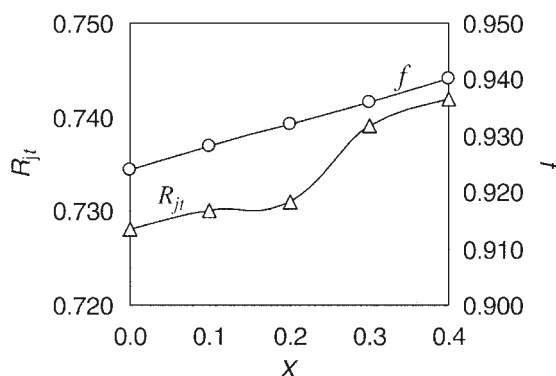
Figure 6
Remanence factors vs. x for $Sr_{1-x}La_xFe_{12-x}Co_xO_{19}$ magnets (reproduced by permission of Kools *et al.* (2002) from *J. Magn. Magn. Mater.*, **242–245** (Part 2), 1270–6).

replaced by Fe^{2+}. The strong deterioration of the squareness for $x > 0.2$ was related to a bimodal grain size distribution.

2.3 Intrinsic Aspects

Substituted M-ferrite magnets are single phase for $0 < x < 0.35$. The cell constant a remains constant, whereas c decreases slightly and linearly up to $x = 0.4$. The latter holds also for T_c.

The analogy between Sr and Ba compounds points to Co as the active ion. The Co sublattice occupation was studied by various techniques, but all being at the limit of detection. The provisional conclusion is that Fe^{2+}/Co is at $2a$ and Co at $4f_2$. For CoTi substituted M-ferrites and related compounds, Co prefers other sites and acts negatively on the anisotropy (Kojima 1982). Apparently, the excess charge of La and its fixed position on the Ba sites forces Co to a special site, where it can contribute to the anisotropy.

The increase of H_a (obtained from SPD data) with increasing x is due to an increase of the magneto-crystalline anisotropy K_1. In addition, H_a increases further when T decreases, similar to $LaFe^{2+}M$ (Lotgering 1974). In view of that, a similar mechanism is assumed: the increased K_1 stems from the single-ion contribution of Fe^{2+}/Co at $2a$ and Co at $4f_2$.

2.4 Microstructural Aspects

There are three major effects: (1) The grain size after calcination decreases with x, (2) the grain size after firing and the platelet grain shape increase with x, and (3) the microstructure becomes more nonuniform when x increases. The first effect is related to incomplete substitution of LaCo during calcining, thus

provoking RIGGI from LaCo. The second effect is also related to the incomplete calcination by means of which Co remains in the secondary phase and counteracts during sintering the RIGGI from silica (Kools *et al.* 2001). The third effect is related to the first one. By optimizing the chemical homogeneity (decreased particle size of the LaCo raw materials) and decreasing the Co/La, ratio, the squareness could be restored to the unsubstituted level (Morel and Tenaud 2002).

3. Concluding Remarks

LaCo-type substituted ferrite magnets can be described by the classical models for M-ferrite magnets, having as a characteristic feature the increased magneto-crystalline anisotropy at 300 K and its increased temperature dependence.

The increased H_{cJ} and reduced $TC(H_{cJ})$ of LaCo-type ferrite magnets allow new applications. Due to the more expensive raw materials (La, Co), the costs are somewhat higher, but optimization will certainly lead to cost reduction. It is expected that the new LaCo-type ferrite magnets will acquire a significant market share in the near future, notably for starter motors and small motors.

See also: Coercivity Mechanisms; Magnetic Hysteresis; Magnetic Materials: Hard; Magnets, Soft and Hard: Domains; Magnets: High-temperature; Magnets: Sintered

Bibliography

Carbone Lorraine commercial data book 2002: www.Ferroxdure.com

Fang C M, Kools F, Metselaar R, de With G, de Groot R A 2003 Magnetic and electronic properties of strontium hexaferrite $SrFe_{12}O_{19}$ from first-principles calculations. *J. Phys. Condens. Matter* (submitted)

Ferrites 2000 *Proc. 8th International Conference on Ferrites, ICF8.* Jap. Soc. Powder and Powder Metallurgy, Kyoto, Japan

Grössinger R, Tellez Blanco J C, Kools F, Morel A, Rossignol M, Tenaud P 2000 Anisotropy and coercivity of M-type Ba and Sr-ferrites containing La and Co. In: *Ferrites, Proc. Int. Conf. on Ferrites, ICF8, Kyoto 2000*, pp. 428–30

Iida K, Minachi Y, Masuzawa K, Kawakami M, Nishio H, Taguchi H 1999 High-performance ferrite magnets: M-type Sr-ferrite containing Lanthanum and Cobalt. *J. Magn. Soc. Japan.* **23**, 1093–8

Kojima H 1982 Fundamental properties of hexagonal ferrites. In: Wohlfarth 1982, Chap. 5, pp. 305–91

Kools F 1992 Hard magnetic ferrites. In: Bever M B (ed.) *Encyclopedia Mater. Sci. and Eng* (2nd edn.) Pergamon Press, Oxford, UK

Kools F, Morel A, Tenaud P 2001 LaCo-substituted ferrite magnets: increased coercivity and improved microstructure. In: *Euro PM2001, Proc. European Powder Metallurgy Congress.* Nice, France, Vol. 2

Kools F, Morel A, Grössinger R, LeBreton J M, Tenaud P 2002 LaCo-substituted ferrite magnets, a new class of high-grade ceramic magnets: intrinsic and microstructural aspects. *J. Magn. Magn. Mater.* **242–245** (Part 2), 1270–6

Lotgering F K 1974 Magnetic anisotropy and saturation of $LaFe_{12}O_{19}$ and some related compounds. *J. Phys. Chem. Solids.* **35**, 1633–9

Morel A, Tenaud P 2002 *International Patent Applications* (1) WO 02/085810 A1 and (2) pending

Morel A, Kools F, Tenaud P, Grössinger R, Rossignol M 2000 Modelling of LaCo substituted M-type ferrite coercivity. In: *Ferrites, Proc. Int. Conf. on Ferrites, ICF8, Kyoto 2000*, pp. 434–6

Morel A, LeBreton J M, Kreisel J, Wiezinger G, Kools F, Tenaud P 2001 Sublattice occupation in $Sr_{1-x}La_x Fe_{12-x}Co_xO_{19}$ hexagonal ferrite analysed by Mössbauer spectrometry and Raman spectroscopy. *J. Magn. Magn. Mater.* **242–248**, 1405–7

Pieper M, Kools F, Morel A 2002 NMR characterization of Co-sites in La + Co Sr hexaferrites with enhanced magnetic anisotropy. *Phys. Rev. B* **65** (184402), 1–5

Taguchi H, Iida K, Masuzawa K, Minachi Y 1998 *Eur. Patent Application* EP 0 905 718 A1

Takami H, Kubota Y, Ogata Y 1999 *Eur. Patent Application* EP 0 964 411 A1

Wiezinger G, Müller M, Grössinger R, Pieper M, Morel A, Kools F, Tenaud P, LeBreton J M, Kreisel J 2002 Substituted ferrites studied by nuclear methods. *Phys. Stat. Sol. (a)* **189** (2), 499–508

Wohlfarth E P (ed.) 1982 *Ferromagnetic Materials* North-Holland, Amsterdam, Vol. 3

F. Kools
Carbone Lorraine-Ferrites, Evreux, France

A. Morel
St Pierre d'Allevard, France

Ferrites

Since their commercial introduction in 1948 by Philips, soft ferrites have found widespread use in electronic applications as inductor or transformer cores, because of their high resistivity in comparison to metallic soft-magnetic materials. This makes soft-magnetic ferrites considerably better suited for applications at frequencies $\geqslant 10\,kHz$. Soft-magnetic ferrites belong to the class of ferrites which have a cubic, spinel lattice structure. These ferrites have the structural formula $MeFe_2O_4$ with Me being a divalent metal ion from the $3d$ transition elements: manganese, iron, cobalt, nickel, copper, zinc, or combinations of these. In addition, also other ions such as Li^+, Mg^{2+}, Cr^{3+}, Ti^{4+}, or Sb^{5+} can be incorporated in the spinel lattice. There is also a class of soft-magnetic ferrites with a hexagonal crystal structure, which has soft-magnetic properties. However, this class of soft ferrites has found limited application thus far, and is not
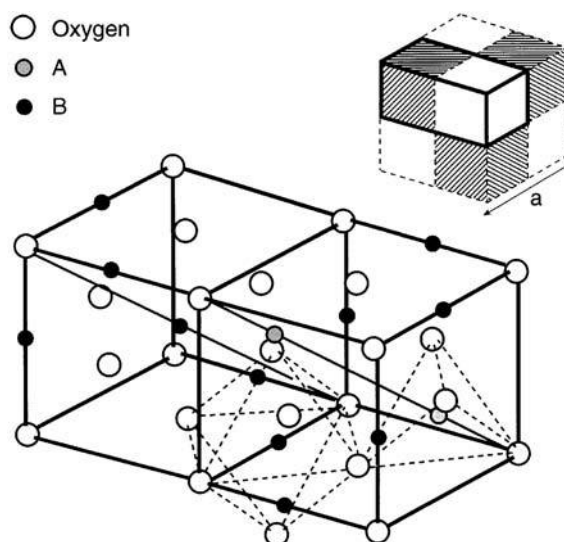
Figure 1
The spinel lattice structure.

treated here. The reader is referred to the treatise by Smit and Wijn (1959).

The spinel-type lattice structure characterizing the conventionally applied ferrites is depicted in Fig. 1. This lattice structure has a lattice parameter a in the range 8.30–8.50 Å depending on the composition of the ferrite (Smit and Wijn 1959). In the unit cell, of which $\frac{1}{4}$ is drawn in detail in Fig. 1, the oxygen ions (O in Fig. 1) form a close-packed face-centered cubic lattice. There are 64 possible tetrahedral (or A) and 32 possible octahedral (or B) interstices or sites in which metal ions can be incorporated. Only eight of the octahedral and 16 of the tetrahedral sites are filled with metal cations. The magnetic interactions are such that the two neighboring magnetic ions on the B-site are ferromagnetically (that is parallel) coupled, whereas the much larger coupling between the magnetic ion on the A-site and the ions on the B-sites is antiferromagnetic (antiparallel). Since, there are two ions antiparallel coupled to each magnetic ion on the A-site, a net magnetic moment still results.

This gives rise to the so-called ferrimagnetism, a net magnetic moment in a magnetic material in which the dominant magnetic interaction is antiferromagnetic. This behaviour can be understood on the basis of super exchange interaction between the magnetic ions as explained by Anderson (1963) and Goodenough (1963).

As shown in Fig. 1 the magnetic ions in ferrites are separated by oxygen ions, which precludes a direct exchange interaction between the magnetic ions. Since, in addition, ferrites are insulators (or very poor semiconductors) exchange interaction by itinerant electrons is also not possible. The explanation for

magnetism in these oxides is that the exchange interaction between the magnetic ions is mediated by the intermediate oxygen ion through super exchange (Anderson 1963, Goodenough 1963). Assuming that the magnetic ions M_1 and M_2 lie on a straight line through the intermediate oxygen ion O, the magnetic super exchange interaction can be explained in the following covalent bonding picture for magnetic ions with at least a half-filled shell: one of the electrons of the oxygen p-orbital directed to the magnetic ions will be excited or transferred to the ion M_1.

On M_1 the electron can only enter an empty orbital with its spin direction antiparallel to the magnetic moment of M_1. The other electron of the p-orbital pointing along the M_1–O–M_2 bond can only be excited to the M_2 ion and lower the total energy of the system, if the magnetic moment of M_2 is oriented antiparallel to M_1. This is so because both electrons involved originate from the same oxygen p-orbital, and thus their spins must be antiparallel according to the Pauli exclusion principle. Hence, the magnetic (spin) moments of both ions should be aligned antiparallel to obtain the lowest energy state and to fulfill the Pauli principle at the same time. More about the super exchange interaction can be found in the reviews by Anderson (1963) and Goodenough (1963). For the super exchange interaction it can be derived that it is strong and antiferromagnetic along a $180°$ bond, i.e. when M_1–O–M_2 form a straight line, while it is weak and ferromagnetic along a $90°$ bond. This explains that the interaction between the magnetic ions on the A- and B-sites in spinel ferrites, which make an angle of around $125°$ (see Fig. 1), is much stronger than between those on the B-sites which make an angle of around $90°$ (Smit and Wijn 1959). Thus in ferrites the dominant magnetic interaction is the AB interaction, which is typically 15–20 times stronger than the BB interaction. This causes the magnetic moments on the A and B sites to be antiparallel oriented whereas those on the B-sites are parallel to each other.

The net magnetic moment of spinel ferrites is thus determined by the sum of the magnetic moments of the two spins on the B-site minus the moment of the A-site. This results in typical saturation magnetizations, M_S, of spinel ferrites between 143–560 kAm^{-1} at $0\,K$ and 120–477 kAm^{-1} at room temperature (Smit and Wijn 1959), which are lower than what can be attained in metallic magnetic materials (where the dominant magnetic interaction is ferromagnetic). Most of the spinel ferrites, with the exception of $ZnFe_2O_4$, have a Curie temperature T_C in excess of room temperature, with typical values ranging from 300 °C for $MnFe_2O_4$ to 670 °C for $Li_{0.5}Fe_{2.5}O_4$ (Smit and Wijn 1959). This T_C of ferrites is acceptable for most applications that require typically an operating temperature of the ferrite of 80 °C. In most commercial applications either MnZn-ferrites or NiZn-ferrites are used. The MnZn-ferrites have the advantage

that high values of the permeability μ can be reached, whereas NiZn-ferrites offer advantageously higher values of the resistivity $\rho \approx 10^5\,\Omega m$ versus $1\,\Omega m$ for MnZn-ferrites. This makes NiZn-ferrites more suited for high frequency application, in particular for frequencies $\geqslant 1\,MHz$. For applications which require a high resistivity and low material costs, MgZn-ferrites ($\rho \approx 10^6\,\Omega m$) are used. For instance, the yoke-rings in the deflection unit of cathode-ray tubes are made of MgZn-ferrites as this makes it possible to directly wind the deflection coil on the ferrite yoke.

For applications the magnetic softness characterized by the permeability $\mu = dB/dH$ is relevant as it gives the response of a ferrite to an applied field H. Depending on intrinsic properties (composition, additions) and extrinsic properties (microstructure, preparation) permeabilities of $\geqslant 15\,000$ can be obtained. The highest permeabilities are typically reached in MnZn-ferrites with large grains, which are free from pores. NiZn-ferrites generally have lower permeabilities, in commercial applications between 100 and 1000. This is because compensation of the magnetocrystalline anisotropy, as can be done in MnZn-ferrites, is not possible in NiZn-ferrites (Smit and Wijn 1959).

The only commercial application in which monocrystalline spinel ferrites are used on a large scale is the magnetic recording head production for VCRs. For most applications ferrites are made by ceramic processing which results in polycrystalline materials. Ceramic processing is done by mixing and calcining of oxide and carbonate powders of the constituent metals. Subsequently, the powder is pressed in the desired shape and the final processing step is a sintering process following a selected temperature profile under a carefully controlled atmosphere. Typically sinter temperatures needed to have the required solid state reactions proceed are 1100 °C or more. Details can be found elsewhere (Smit and Wijn 1959, Snelling 1988).

For further information about soft ferrites the reader is referred to the book by Smit and Wijn (1959) and the review by Brabers (1995) and also to *Transition Metal Oxides: Magnetism.*

1. Applications

Traditionally the main application areas of soft-ferrites are transformer cores, inductors, and yoke-rings in cathode-ray tubes (Snelling 1988). Since the 1990s new applications have arisen, such as cores for induction lighting and magnetic antennas for pagers. The trend in *all* these applications and the driving force for ferrite development is that the operating frequency increases to achieve miniaturization. This trend is illustrated in Fig. 2 which gives the weight and operating frequency of a 100 W power supply since the 1960s. A reduction in weight from approximately 8 Kg to around 100 g has been achieved.
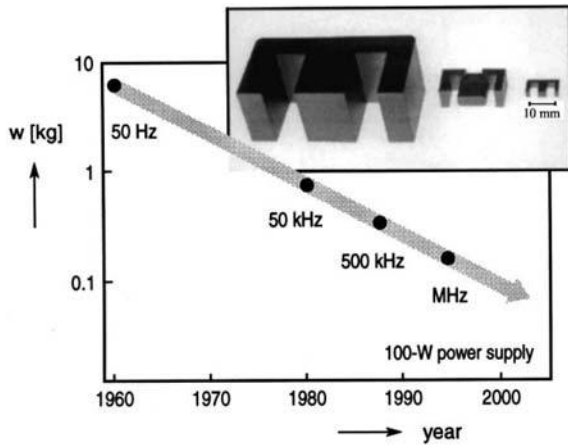
Figure 2
The miniaturization trend in the weight of transformer cores since the 1960s. The resulting operating frequencies are indicated. The inset shows various sizes of E-cores used for transformers.

The reason that miniaturization necessitates higher operating frequencies can be understood by considering the throughput power P_{thr} of a transformer core, which can be given as:

$$P_{thr} = I_{in} \times V_{in} \qquad (1)$$

with I_{in} the input current and V_{in} the input voltage. Expressing V_{in} in terms of the change of flux in time $d\Phi/dt$ gives:

$$P_{thr} = I_{in} \times N\frac{d\Phi}{dt} = I_{in} \times N2\pi fBA \qquad (2)$$

with N the number of turns of the primary winding of the transformer, f the operating frequency, B the induction level in the core, and A the cross-sectional area of the core. Since the maximum induction level within the core is limited by the saturation magnetization of the ferrite, M_S, it is obvious from Eqn. (2) that in order to decrease the size and hence cross-sectional area of the transformer, without sacrificing throughput power, the operating frequency f should be increased. Hence, a key aspect of modern research and development in soft ferrites is to reduce the dissipation, i.e., losses in ferrites at increasing frequencies, in the range of 100 kHz to 3 MHz.

Traditionally, three contributions to the dissipation or loss, P_{tot}, in soft ferrites are distinguished: d.c. hysteresis loss, P_h; eddy current loss, P_e; and residual loss, P_r. The justification for this subdivision resides in part in the differences in frequency response of each contribution, although it is to a large part phenomenological. The d.c. hysteresis loss corresponds to the dissipation incurred by cycling the d.c. *B-H* loop

of a soft-magnetic ferrite. Through the number of times the loop is cycled per unit time, P_h depends on frequency f as $P_h = f\oint BdH$. The standard approach to limit the hysteresis loss in ferrites (Smit and Wijn 1959, Snelling 1988) is to facilitate domain wall movement by using ferrites with a low coercivity, H_C. This is done by selecting ferrite compositions which have a low magneto-crystalline anistropy constant K. Ideally the ferrite should have its anisotropy compensation point, at which K passes through zero, at the required operating temperature. Typically this is 80 °C. In addition, the ferrite composition used should have a low magnetostriction constant and internal and external stress should be avoided to limit adverse magnetostriction effects. Finally, ferrites with a large grain size are used as $H_C \propto D^{-1}$, with D the grain size (see van der Zaag 1999).

The eddy current contribution is the dissipation caused by eddy currents in the ferrite. Although, due to their oxidic character, ferrites have a much higher resistivity than metallic soft magnetic materials, their conductivity is not zero and eddy currents can occur. One can derive that the dissipation P_e is (Snelling 1988):

$$P_e = C_e f^2 B^2 / \rho \qquad (3)$$

with C_e a dimensional constant and ρ the resistivity at the measurement frequency. Hence, the P_e contribution can be separated by plotting P_{tot}/f vs f, as has been done in Fig. 3. Traditionally, the remainder of the dissipation, such as the dissipation due to ferromagnetic resonance (Snoek 1948) has been treated as the residual loss contribution, P_r. The residual loss is thus the extra loss under a.c. measurement conditions not attributable to eddy current loss (i.e., not matching Eqn. (3)). Thus P_r has a higher than quadratic dependence on the frequency f. As Fig. 3 illustrates at higher frequencies both the eddy current and residual loss dominate the ferrite dissipation. Consequently, considerable work was done in the 1990s to determine and minimize the mechanisms responsible for these losses (van der Zaag 1999).

To reduce the eddy current loss, the resistivity of ferrites should be increased. The resistivity of the ferrites used in commercial applications is determined by the resistivity of the grain boundary in these polycrystalline materials. Hence, considerable effort has been devoted to increase the grain boundary resistance by careful control of the processing conditions and by adding dopants such as Nb_2O_5, ZrO_2, and Ta_2O_5 besides the well-known glass-forming additions CaO and SiO_2 (Snelling 1988). The glass formers segregate to the grain boundary to form a secondary phase, which forms an insulating layer around each grain preventing current flow from one grain to the next. At higher frequencies also the capacitive shunting of the grain boundary impedance becomes an issue. It is thought that the addition of
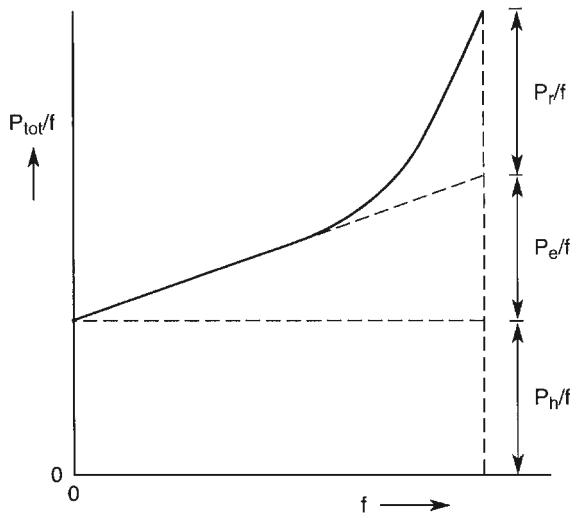
Figure 3
Schematic diagram of the total dissipation, P_{tot}, versus the frequency, f, for soft-magnetic ferrites. The various contributing terms to the ferrite dissipation: hysteresis loss P_h, eddy current loss P_e and residual loss P_r are indicated. All terms have been scaled by the frequency.

dopants like Nb_2O_5, ZrO_2, and Ta_2O_5 play a role in reducing this effect.

The residual loss has been shown to be a dominant contribution to the dissipation of ferrites in the 500 kHz to 3 MHz frequency range. Microscopic mechanisms contributing to the residual loss are: the ferromagnetic resonance loss (Snoek 1948) and the intragranular domain wall loss (van der Zaag 1999). The former is caused by excitation of the uniform spin precession in the ferrite. The latter is due to domain wall movement of intragranular domain walls within the grains of a polycrystalline ferrite. Both contributions can be eliminated by using a fine-grained ferrite material. In the case of the ferromagnetic resonance loss this causes a reduction in the permeability of the ferrite and hence an upward shift of the ferromagnetic resonance (Snoek 1948). In well-developed ferrites the ferromagnetic resonance should be above the frequency at which the ferrite is operated. The intragranular domain wall loss is eliminated by using fine-grained ferrites in which all the grains are monodomain, i.e., intragranular domain walls are absent. Such a situation occurs in fine-grained ferrites, since below a certain grain size the monodomain state has a lower magnetostatic energy than a domain state in which a domain wall is present (van der Zaag 1999). For further reading on the subject of dissipation in ferrites the reader is referred to (Snoek 1948, van der Zaag 1999).

2. New Developments: Ferrite Films

A new development in the field of soft-ferrite research and their application is their deposition and use in thin films (see Brabers 1995). Spurred by the work on high-T_C superconductors, there has been considerable improvement in the deposition of thin film oxides, making it possible to deposit thin film ferrites in the nanometer to micrometer thickness range. The interest in these thin film ferrites is driven in part by the possibility to improve integrated inductors (Suzuki *et al.* 1996).

In the IC industry a problem is that present inductors, amongst others for RF-applications, with typical diameters of 0.2–0.8 mm are huge in comparison to the active elements on ICs. Thus they require a too large surface area to make integration on chip economically attractive. A possible solution would be to apply a magnetic substrate or a thin magnetic film on the coil as this may result in a reduction to a $\frac{1}{4}$ of the area needed for the same inductance while maintaining the quality factor Q (as is illustrated in Fig. 4 by using a ferrite substrate). In view of their resistivity, which makes application at higher frequencies possible, ferrite films deposited on the integrated inductors can provide a possible solution. A problem is the high substrate temperature ($\geqslant 600\,°C$) needed to assure the formation of a ferrite film with a proper cation distribution and an adequate grain size to assure that the ferrite films have a sufficiently high permeability. Wet-chemically prepared films grown by ferrite plating at $80\,°C$ provide a useful method as permeabilities $\geqslant 25$ have been obtained in μm thick films (van der Zaag *et al.* 1999).
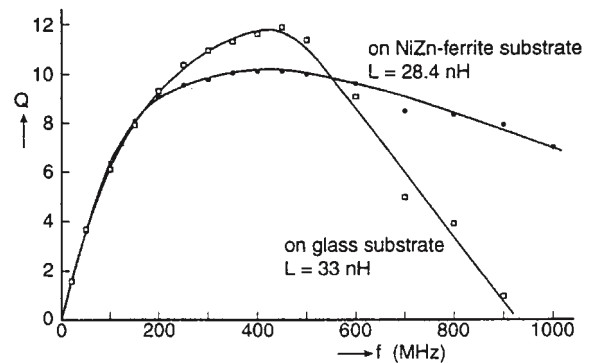
Figure 4
The quality factor, $Q = \omega L/R$ with ω the angular frequency, L the inductance and R the resistance of the inductor, of two planar inductors, one on a glass substrate and the other on a NiZn-ferrite substrate. Although both inductors have comparable inductances ($L = 33$ and 28.4 nH) and Q, the inductor using a ferrite substrate has half the diameter, i.e., needs 1/4 of the area.

Another interesting trend is the work on magnetite, Fe_3O_4, films in view of their intrinsic fully spin-polarized electron transport for magnetoresistive sensors (Coey *et al*. 1998, Seneor *et al*. 1999). Fe_3O_4 is a half-metallic ferromagnet (see *Half-metallic Magnetism*) as it has a gap in the minority spin band, whereas there is no gap in the majority spin band (Brabers 1995). Thus for the majority spins Fe_3O_4 behaves as a metal with spin-polarized electron transport along the B-sites by hopping conduction. This property is of interest as it could be employed in magnetic tunnel junctions leading to a magnetic field sensor element with, theoretically, an infinite magnetoresistance effect, as electrons with minority spin cannot pass the Fe_3O_4 layer. The degree to which a proper Fe_3O_4 layer can be grown in these magnetic tunnel junctions, or needs to be grown to have a positive effect on the magnetoresistance is not known precisely. The same holds for the role played by the interfaces of the Fe_3O_4 layer or anti-phase boundaries, causing so-called ''dead'' magnetic interface layers. A first indication of an increased magneto-resistance effect due to the incorporation of a Fe_3O_4-like layer in a magnetic tunnel junction has been reported by Seneor *et al*. (1999).

See also: Ferrite Ceramics at Microwave Frequencies

Bibliography

Anderson P W 1963 Exchange in insulators: superexchange, direct exchange and double exchange. In: Rado G T, Suhl H (eds.) *Magnetism I*. Academic Press, New York, Chap. 2

Brabers V A M 1995 Progress in spinel ferrite research. In: Buschow K H J (ed.) *Handbook of Magnetic Materials*. Elsevier, Amsterdam, Chap. 3

Coey J M D, Berkowitz A E, Balcells L, Putris F F, Parker F T 1998 Magnetoresistance of magnetite. *Appl. Phys. Lett*. **72**, 734–6

Goodenough J B 1963 *Magnetism and the Chemical Bond*. Wiley, New York, pp. 165–85

Seneor P, Fert A, Maurice J-L, Montaigne F, Petroff F, Vaurés A 1999 Large magnetoresistance in tunnel junctions with an iron oxide electrode. *Appl. Phys. Lett*. **74**, 4017–9

Smit J, Wijn H P J 1959 *Ferrites*. Wiley, New York

Snelling E C 1988 *Soft Ferrites: Properties and Application*, 2nd edn. Butterworths, London

Snoek J L 1948 Dispersion and absorption in magnetic ferrites at frequencies above one Mc/s. *Physica* **14**, 207–17

Suzuki Y, van Dover R B, Gyorgy E M, Philips J M, Korenivski V, Werder D J, Chen C H, Cava R J, Krajewski J J, Peck W F Jr., Do K B 1996 Structure and magnetic properties of epitaxial spinel ferrite thin films. *Appl. Phys. Lett*. **68**, 714–6

van der Zaag P J 1999 New views on the dissipation in soft magnetic ferrites. *J. Magn. Magn. Mater*. **196–7**, 315–9, and references therein

van der Zaag P J, Lubitz P, Kitamoto Y, Abe M 1999 The permeability of plated ferrite films. *IEEE Trans. Magn*. **35**, 3436–8

P. J. van der Zaag
Philips Research Laboratories, Eindhoven
The Netherlands

Ferrofluids: Applications

The first synthesis and application of a magnetic fluid as a magnetocaloric device was reported by Neuringer and Rosensweig (1964), although attempts to create stable ferromagnetic colloids can be traced back to (Elmore 1938). Papell (1965) at NASA was awarded the first patent for the process of making ferrofluid. The fluid was developed for the purpose of retention and orientation of rocket fuel with an external magnetic field under reduced gravity. Although the earlier applications never materialized, the new discovery nonetheless laid the foundation of a whole new industrial sector (Berkovski 1996).

For his lifelong contributions to the field, Ronald Rosensweig is considered the father of the technology. His NASA-funded research, which began in 1965 at AVCO Corporation, demonstrated that ferrofluids can be prepared in a wide variety of carriers and in high magnetization values. His patents in magnetic fluids, staged rotary seals, magneto-gravimetric separators, and display devices created a base for industrial enterprise. Serious marketing efforts began when Ronald Rosensweig and Ronald Moskowitz founded Ferrofluidics Corporation in 1968. The first product based on ferrofluid, introduced in 1969, was the dynamic seal capable of operating under pressure or vacuum. Since then a number of new applications of the technology have been discovered and are listed in chronological order in Table 1. Although the technology may be present in many consumer products, the ferrofluid in the devices is hidden from view. It is estimated that over 200000 rotary vacuum seals, 350 million loudspeakers, 500 million computer disk drives, and 15 million DVD–ROM drives have been built with ferrofluids.

Table 1

Chronology of commercial ferrofluid applications.

1969	Vacuum rotary seal
1970	Ferrofluidic display ''Fluidler''
1973	Loudspeaker
1975	Sensor
1977	Inertia damper
1978	Computer disk drive
1982	Domain visualization
1985	Ferrofluid film bearing
1987	Turbine blade
1989	Stepper motor
1991	Emission seal
1992	Material separation
1998	CD/DVD-ROM
1999	Ferrofluidic adventure science kit

1. Ferrofluids

In ferrofluids, magnetic and liquid states coexist. On the surface, they are deceptively simple systems: a homogeneous phase comprised of three constituents, namely the magnetic particles, surfactant, and the liquid carrier. However, a complex chemistry and a balance of inter-particle forces determine the colloidal stability (Rosensweig 1979). The magnetite particles must be in the range of 10 nm. The surfactant tails should be long enough to prevent particle agglomeration. Ferrofluids synthesized about 30 years previously are still stable.

Both magnetic and liquid properties influence the device performance. The saturation magnetization values of commercial ferrofluids range from 0.0001–0.1 T. Liquid properties such as viscosity, volatility, working temperature range, environmental compatibility, thermal degradation, and dielectric behavior dictate the choice of the carrier in which the particles are suspended. The most commonly used ferrofluids fall in the viscosity range of 1–2000 cp at 27 °C. There exist several different chemical families of ferrofluids such as the petroleum oils, synthetic esters and hydrocarbons, perfluoropolyethers, silicones, water, organic solvents, etc. Within each family a range of physical properties may be achieved by altering the concentration of magnetic solids and the molecular weight of the carrier. Thus, literally hundreds of different commercial magnetic colloid formulations are available.

2. Applications

Ferrofluids offer design solutions to a myriad of complex engineering problems. Patents in the field exceed 2800.

Magnetic and liquid properties in a ferrofluid, although mostly independent of each other, work together to create successful products (Raj and Chorney 1998). The rotary shaft seal relies on the magnetic properties of ferrofluid for pressure capacity, but the liquid carrier determines the service life, operating range, power requirement, and high vacuum performance of the product. In a loudspeaker, the magnetism associated with the colloid simply retains the fluid in the air gap, but the carrier provides the benefits of damping and heat transfer. Similarly the viscosity and lubricity of the base oil are relevant parameters for the performance of a ferrofluid film bearing. When ferrofluid is used in a domain detection application, the particles migrate through the carrier and accumulate at the transition zones of the specimen. The carrier subsequently evaporates making the domain boundaries visible in colorful patterns.

Magnetic fluids exhibit levitation phenomena, a unique feature not found in ordinary liquids. A permanent magnet with density much greater than the fluid floats in the ferrofluid (Rosensweig 1966a). A pool of magnetic colloid exposed to a gradient magnetic field can suspend heavy nonferrous objects (Rosensweig 1966b). These two principles form the basis of several industrial devices such as dampers, sensors, and material separators.

A list of ferrofluid applications, the types of fluids used, and their key properties are presented in Table 2. Devices such as seals and loudspeakers generally require ferrofluid amounts in microliters, material separators in liters and power transformers in gallons. The multistage rotary shaft seal is the oldest and most recognized ferrofluid-based product. This device is used in many industries such as the semiconductor, nuclear, aerospace, laser, and lamp manufacturing industries. The basic construction of the seal is shown in Fig. 1. A magnetic circuit is formed to create alternate regions of high and low magnetic fields in an air gap. The shaft is supported by two high precision ball bearings to allow for rotation. A tooth or ridge structure either on the pole pieces or shaft configures the magnetic field into the desired pattern. A ferrofluid fills the regions of high magnetic field forming a series of liquid O-rings with intervening annular open spaces. Each fluid O-ring sustains a pressure differential dictated by the field strength and the magnetization of the ferrofluid. The total pressure capacity of the seal is the sum of the capacity of individual O-rings and generally exceeds two atmospheres. The use of a low vapor pressure ferrofluid maintains a high vacuum integrity, up to 10^{-9} torr, in the process chamber. The seal is leak tight, essentially nonwearing and consumes low power. It is typically used in gaseous environments but can also withstand occasional liquid splashing.

An example of an application of a ferrofluid vacuum seal is shown in Fig. 2. The seal is mounted on a sterilizer and rotates an impeller at speeds of 1750–3500 rpm inside a chamber charged with a gaseous mixture of ethylene oxide and nitrogen at temperatures close to ambient. The system may be used to sterilize heart pacemakers and sutures. Due to the toxic nature of the gas, the process must be carried out under leak-tight conditions. To ensure personnel safety, dual magnetic fluid seals are employed and the space between the two seals is monitored. If the process end seal fails, escaping gas can be detected while the secondary seal prevents gas emission into the work area.

Manufacturing of integrated circuits requires that the environments be free of any particulate contaminants. In Fig. 3, a coaxial seal is employed in a robotic arm to transport 200 mm silicon wafers in a cluster tool. The arm picks up wafers from a carousel and places them sequentially at different locations. This seal is composed of two coaxial shafts, which provide two independent angular drive mechanisms to the arm.

Thin profile ferrofluid seals with a typical thickness of about 1mm are employed in computer disk drive

Table 2
Types of ferrofluids employed in applications and key properties.

Typical applications	Types of ferrofluids	Main ferrofluid property	Physical parameters (room temperature)
Biomedical/catalysis/ magnetic adhesive/ magnetic shielding	Surfaced magnetite microspheres	Micromagnetics	10 nm supermagnetic particles
Sealing	Perfluropolyethers Polyphenyl ethers Hydrocarbons Silahydrocarbons Esters	Chemically inert Radiation resistant Wide temperature range Hydrolytic stability Good lubricant	0.02–0.06 T 200–2500 cp
Damping/heat transfer/ noise control	Hydrocarbons Esters Perfluoropolyethers Silicones	Low volatility Wide viscosity Fire resistant High viscosity index	0.01–0.04 T 200–10000 cp
Sensing	Mineral oils Hydrocarbons Esters	Large liquid range Thermal stability Boundary lubricant	0.005–0.004 T 2–100 cp
Domain detection/ material separation/ polishing/ magnetic ink/display/inspection	Water	Environmentally safe	0.0001–0.004 T 1–5 cp
Power transmission	Mineral oils Vegetable oils	Improved dielectrics Biodegradable, cooling	0.0001–0.001 T 10–25 cp
Magnetic ink/magnetic polymer/research activities	Organic solvents (heptane, xylene, toluene, MEK)	High volatility	0.005–0.1 T 1–25 cp
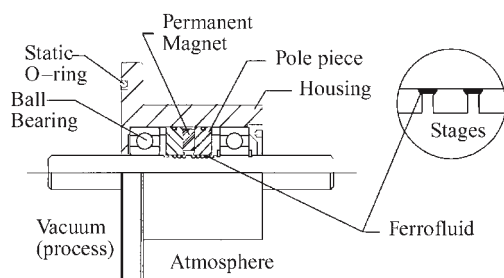
Figure 1
Multistage ferrofluid rotary seal.

spindles, Fig. 4. The seal pressure capacity is in the region of 100 mm H_2O and operating speed 3600–7500 rpm. Several million of these seals are produced each year. The seals prevent the bearing lubricant and other airborne contaminants from reaching the disk cavity. The flying height of the read–write head above the disk surface is only 0.2 µm. The presence of even a

small dust particle (24 µm) can easily cause a head crash or soft error.

As an electromechanical device, a dynamic loudspeaker, Fig. 5, has a natural resonance point in its operating frequency range of 20 Hz to 20 KHz. At resonance the system is underdamped. Also the coil easily burns out when the speaker is over powered. The air surrounding the coil cannot remove heat efficiently. Ferrofluid is incorporated into the speaker gap. Thermal conductivity of ferrofluid is about four times higher than air and consequently the transient power handling of the speaker is increased. The damping requirements of the driver can be achieved with a precise selection of ferrofluid viscosity. The fluid is naturally retained in the gap by the prevailing magnetic field. Ferrofluid also aids with voice-coil centering, reduction in distortion and simplification of cross-over network.

The magnetic permeability of a ferrofluid can produce measurable inductive changes in an electrical circuit. In a tilt sensor, Fig. 6, ferrofluid is used as a movable magnetic core. An angular displacement of the tube moves the fluid partly from one side to the
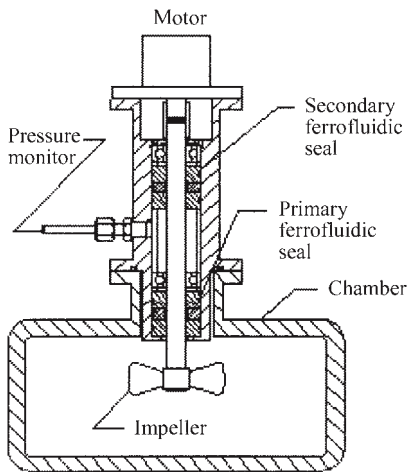
Figure 2
Seal application in a sterilizer.
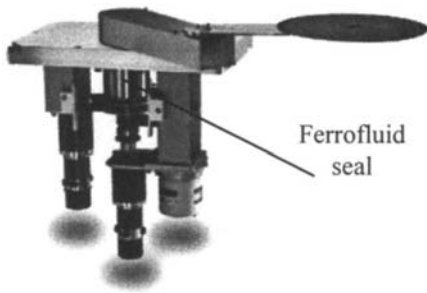
Figure 3
Coaxial seal used in a robot arm.

Figure 4
Computer disk drive with magnetic fluid seals.
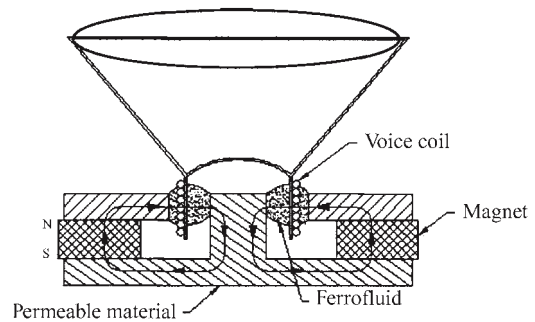
Figure 5
Moving coil loudspeaker using ferrofluid.
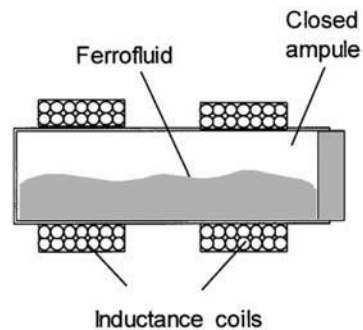
Figure 6
Ferrofluid tilt sensor.

other creating an inductive unbalance and an electronic signal proportional to the tilt angle. These sensors operate in the region of $\pm 45°$ and are utilized in the construction industry to measure the tilt of underground pipes.

The levitation of a permanent magnet in a pool of ferrofluid is the basis of another type of sensing device used in the oil well industry. The position of the freely suspended magnet, influenced by the inclination or acceleration of the encasement, can be detected by means of inductance coils. This rugged sensor accurately measures the orientation of an underground drill bit during oil prospecting.

The apparent density of a ferrofluid increases steadily with increasing magnetic field gradient producing a levitation force upon immersed nonmagnetic objects. Thus, nonferrous materials of various density values float to different levels in the fluid. Two different commercial separators utilize this principle: one is the static (sink/float) apparatus in which ferrofluid is stationary and the other is a dynamic system in which ferrofluid is rotating in a vertical duct. These machines are employed for separation of scrap metals and minerals from ore deposits. Figure 7 is a
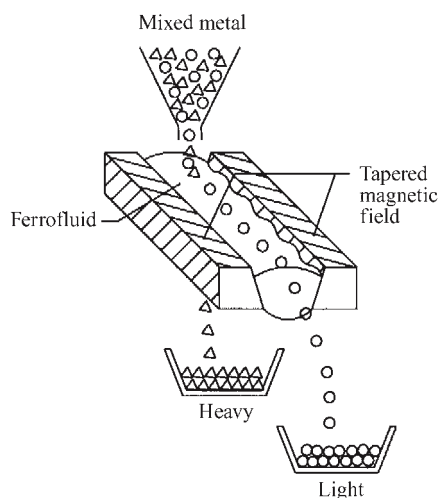
Figure 7
Recycling of scrap metals with sink/float apparatus.

Figure 8
CD/DVD-ROM actuator damping with ferrofluid.

schematic of a sink/float device. A mixture of fine particles is passed through a pool of ferrofluid. The magnetic field gradient is adjusted so that the heaviest metal sinks to the bottom and the remainder floats to the top. The mixed light fraction can be further processed until all grains are sorted out. These scrap metals, which are generally dumped in a landfill as waste, now become a valuable commodity through recycling.

The CD-ROM and DVD-ROM technology, which has revolutionized the entertainment industry with crisp sound and sharp images, relies on ferrofluid for high performance. A laser beam retrieves recorded digital signals from a rotating disk, Fig. 8. A flexible lens assembly, integral to an optical actuator, directs the beam at the disk. The lens is supported by two cross coils: the focusing coil aims the beam precisely on the disk surface and the tracking coil ensures that the beam stays on the optical track. If an error occurs, a feedback signal actuates the coils to reposition the lens and thus the beam. The coils must be damped to minimize settling time and improve the access time. Additionally, the fluid noticeably reduces resonance and hence reading errors.

The mono domain Fe_3O_4 particles in ferrofluids are nontoxic and can pass easily through capillaries of living systems. The particles may be coated with biocompatible dispersants such as dextran or starch and suspended in water. Such a magnetic liquid holds great potential in diagnostic and therapeutic fields (Häfeli *et al.* 1997). Magnetic microspheres based on ferrofluid particles are commercially available for *in vitro* applications such as separation of cells, enzymes, proteins, antibodies, DNA, and RNA, and attachment of bacterial and virus cells
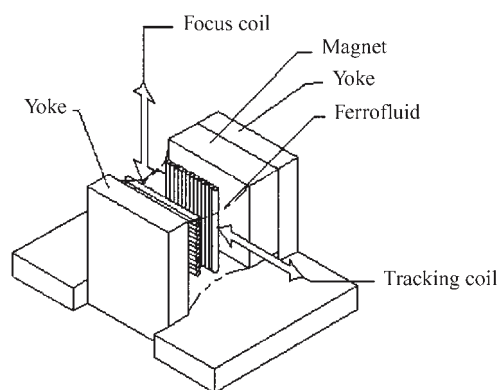
for immunoassays. Immunomagnetic beads can transport drugs to a specific organ or tissue. Thus, radionuclides can be targeted to a lesion for radiation therapy. Also, the magnetic carriers may be heated *in vivo* with an external radio frequency source (hyperthermia) to a temperature of up to 47 °C, thereby destroying AIDS viruses and tumors. The particles have been shown to enhance the magnetic resonance (MR) imaging, thus making it possible to detect metastases. Superparamagnetic iron oxide as a contrast agent has been approved by the FDA for clinical trials.

3. Future Trends

New applications of ferrofluid with significant growth potential include: NMR contrast agents for both biomedical and oil prospecting fields, quiet solenoid valves for the medical industry, environmental seals for pollution control, cooling and dielectric benefits in power transformers, replacement of toxic mercury in switches, displays for education and entertainment markets, a new generation of sensing devices, low noise and efficient steppers, magnetic ink printing, actuator damping, optical shutters, precision fluid film bearings, critical lubrication, magnetically-responsive adhesives, precision grinding, and fabrication of high strength composites. The next generation of ferrofluids may combine magnetism, electrical conductivity, and liquidity into one state, which will undoubtedly uncover new technological frontiers. Magnetic liquids, due to their inherent composition, may also have a role in the development of nanodevices.

See also: Ferrofluids: Introduction; Ferrohydrodynamics; Ferrofluids: Magnetic Properties; Ferrofluids: Preparation and Physical Properties

Bibliography

Berkovski B (ed.) 1996 *Magnetic Fluids and Applications Handbook*. Begell House, New York

Elmore W C 1938 Ferromagnetic colloid for studying magnetic structures. *Phys. Rev.* **54**, 309–10

Häfeli U, Schütt W, Teller J, Zborowski (eds.) 1997 *Scientific and Clinical Applications of Magnetic Carriers*. Academic Press, New York

Neuringer J L, Rosensweig R E 1964 Ferrohydrodynamics. *Phys. Fluids* **7**, 1927–37

Papell SS 1965 Low viscosity magnetic fluid obtained by colloidal suspension of magnetic particles. US Patent 3215575

Raj K, Chorney A F 1998 Ferrofluid technology—an overview. *Indian J. Eng. Mater. Sci.* **5**, 372–89

Rosensweig R E 1966a Buoyancy and stable levitation of a magnetic body immersed in a magnetizable fluid. *Nature* **210**, 613–4

Rosensweig R E 1966b Fluidmagnetic buoyancy. *AIAA4*. **10**, 1751–8

Rosensweig R E 1979 *Fluid Dynamics and Science of Magnetic Fluids*. Advances in Electronics and Electron Physics, Vol. 48. Academic Press, New York, pp. 231–54

K. Raj
Ferrofluidics Corporation, Nashua
New Hampshire, USA

Ferrofluids: Introduction

It is unlikely that any liquid will be found that is intrinsically ferromagnetic. Nickel, cobalt, and iron, for example, are only ferromagnetic in the solid state. It is fluid media composed of solid magnetic particles of very small size, colloidally dispersed in a liquid carrier, that are the basis for the highly stable, strongly magnetizable liquids known as magnetic fluids or ferrofluids, see Fig. 1. Ferrofluids are extremely interesting due to the interplay between hydrodynamic and magnetic phenomena with detailed information the subject of several books (Bashtovoy *et al*. 1988, Berkovsky 1996, Blums *et al*. 1997, Rosensweig 1985, and others). The typical particle size in a ferrofluid is about 10 nm, which is smaller than a magnetic domain, hence each particle is permanently magnetized. The particles experience appreciable thermal translation that maintains them in suspension against the force of gravity, while in the absence of field thermal reorientation of the particles results in zero remanence or coercivity, i.e., ferrofluids are magnetically soft. The ferrofluids behave remarkably as highly homogeneous, magnetizable media that retain their fluid property in the most intense applied magnetic fields and magnetic field gradients.

Following a brief discussion of their origin, this article outlines methods for the synthesis of ferrofluids and discusses physical requirements for their colloidal stability. In addition, basic magnetic and physical properties are described quantitatively.

1. Origin

By remarkable coincidence, ferrofluids were invented in the USA independently at least three times in the 1960s. Of these inventions, the best known is that of Papell (1965) who employed grinding in the presence of a carrier liquid and a surfactant to reduce large grains of magnetite (Fe_3O_4) to colloidal size. The physical chemistry of the process was clarified and the process further developed by Rosensweig *et al*. (1965). O'Connor (1962) synthesized a ferrofluid using chemical precipitation with an ion exchange technique to purify the product. Gable employed chemical synthesis, filing a patent application in 1965 that issued only much later (Gable and Kerr 1977). Dry powders of Gable display remarkable solubility in water. All these ferrofluids use a surface-sorbed layer of a long-chain surfactant, polymer, or protein molecule to provide a short-range repulsion preventing particles from sticking to each other.

Massart (1981) developed ferrofluids in aqueous media that are stabilized by the electric double layer mechanism.

Elmore (1938a, 1938b) produced fine dispersions of magnetite (Bitter colloid) used to detect the boundaries of magnetic domains in bulk ferromagnetic materials. But as the particle size was too large (20 nm) to prevent sedimentation the material does not qualify as a ferrofluid.

2. Preparation

Chemical precipitation is the most often employed process although grinding is useful in some circumstances. Chemical decomposition and vapor-liquid reaction are used to produce certain specialized ferrofluids. In all cases, a repulsive layer is provided that envelopes each particle to prevent them sticking to each other.

The essential chemical reaction in the precipitation of ferrofluid particles is indicated by the reaction:

$$2Fe^{3+} + Fe^{2+} + 8OH^- = FeO \cdot Fe_2O_3 + 8H_2O \quad (1)$$
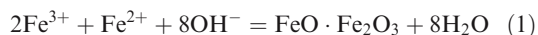
where $FeO \cdot Fe_2O_3$ is magnetite written to emphasize the ratio of divalent to trivalent iron atoms in it, $Fe^{III}/Fe^{II} = 2$. The iron salts used in the preparation may be any combination of soluble salts such as the chlorides or sulfates and the alkali can be ammonium hydroxide, sodium hydroxide, or another base. Following precipitation in the procedure of Khalafalla and Reimers (1974) the small particles are extracted into a mixture of surfactant in an organic solvent. Massart (1996) discusses procedures for bonding species of small ions of a desired electical sign to the

Figure 1
Attraction of ferrofluid against gravity to the poles of a magnet; peaks on the surface result from a competition between gravitational, surface, and magnetic energies (courtesy of Ferrofluidics Corporation).

surface of oxide particles. In this manner, ferrofluids can be conferred stability over ranges of pH values.

In the grinding process, magnetic powder, most commonly magnetite of several microns size, is mixed with 10–20 vol.% of dispersing agent based on solvent volume, and $0.2 \, kg \, l^{-1}$ of magnetite may be used. The proportion of dispersant to solid corresponds closely to a monolayer coating on the particles in the

product liquid. After a prolonged period of grinding in a ball mill (500–1000 h) near-quantitative conversion of the feed solids to colloidal particles of the order of 9–10 nm results. A representative composition consists of magnetite particles, oleic acid dispersant, and an aliphatic hydrocarbon carrier such as hexadecane. Oversize material can be removed by centrifuging or with magnets and the concentration of particles adjusted by the evaporation or addition of the carrier solvent.

The domain magnetization of elemental iron or cobalt exceeds that of magnetite at normal temperatures by three- to four-fold giving incentive to the preparation of more highly magnetizable ferrofluids containing these metals. A problem that arises is the reactivity of the elemental particles with atmospheric oxygen. Nakatani *et al.* (1993) prepared dispersions of iron-nitride particles, e.g., Fe_3N, in oils. Gaseous ammonia is bubbled through a solution of liquid iron carbonyl, $Fe(CO)_5$, dissolved in kerosene containing a polyamine surfactant and produces a well dispersed colloid with particles of highly uniform size. The iron nitrides possess a domain magnetization approaching that of iron and are resistant to oxidation. Ferrofluids having saturation magnetization up to $\mu_0 M = 0.233$ T are reported.

3. Colloidal Stability of the Particles

3.1 Stability Against Sedimentation

Ferrofluids employ the same principle that keeps the atmosphere suspended above the earth, preventing it from collapsing under gravitational pull, to keep the tiny magnetic particles suspended. In addition, the finite size of the particles plays an important role.

Consider a container of ferrofluid exposed to a nonuniform magnetic field of sufficient intensity to magnetically saturate the sample at all points. At an arbitrary point P the magnetic force acting on a unit volume of the fluid in a given direction s is given from the Kelvin force expression for dipolar matter as $\mu_0 mn dH/ds$ where μ_0 is the permeability of free space ($4\pi \times 10^{-7}$ kgms^{-2}A^{-2}), $m = M_d V_d$ is the magnetic moment of a particle, M_d is domain magnetization (4.46×10^5 Am^{-1} for magnetite), V_d particle volume (m^3), n the number concentration of particles (m^{-3}), and H magnetic field magnitude (Am^{-1}) where $B = \mu_0(H + M)$. Balance of the forces acting at equilibrium on a differential slice of the medium centered about P and oriented perpendicular to s yields the relationship:

$$dp = \mu_0 mn dH = \mu_0 M_d \varepsilon \phi dH \qquad (2)$$

where p is osmotic pressure of the particles (regarding the particles as a gas occupying the volume of the fluid space), M_d is domain magnetization (4.46×10^5 for magnetite) ε the volume fraction within a coated

particle that is magnetic, and ϕ the local volume fraction of coated particles in the ferrofluid. An equation of state relates p to the concentration of the particles.

A semi-van der Waals relationship that accounts for the volume occupied by the particles is given by:

$$p\left(\frac{1}{\phi} - \frac{1}{\phi_m}\right) = \frac{kT}{V_d} \qquad (3)$$

where ϕ_m is the maximum value of ϕ to which the colloid can be concentrated as limited by the size of the coated particles, k the Boltzmann constant (1.38×10^{-23} NmK^{-1}), and T absolute temperature (K). A representative value of ϕ_m is 0.74 corresponding to hexagonal close packed spheres, and a typical value of ε is 0.36 corresponding to 10 nm core particles coated with a surfactant of 2 nm thickness. Combining Eqns. (2) and (3) to eliminate p yields a differential equation governing the distribution of the particles. Integration yields the plot of Fig. 2 showing the distribution of the finite size particles as a function of the local field; concentration never exceeds the maximum value which is less than one. A curve showing the distribution for point particles is shown for comparison. In the application of ferrofluids to zero leakage rotary shaft seals and related devices, a concentrated ferrofluid is generally employed. The steric hindrance due to the finite particle size is responsible for the high retention of fluid homogeneity required for the successful operation of these devices.
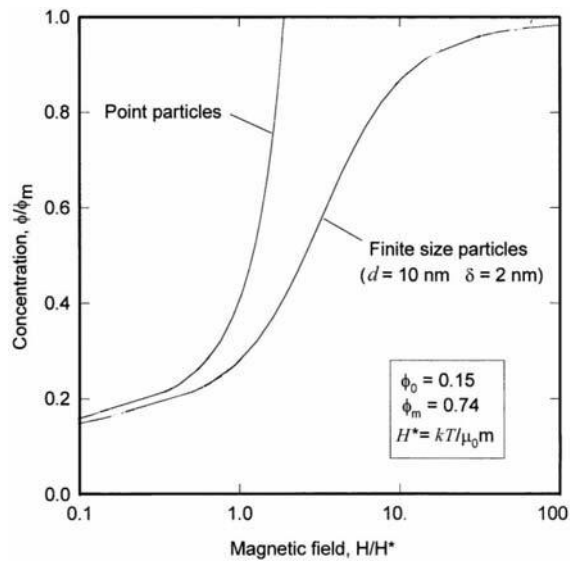
Figure 2
Sedimentation equilibrium of ferrofluid particle concentration in nonuniform magnetic field. The steric hindrance of finite-size particles limits their maximum concentration to a physically realistic value.

3.2 Stability Against Agglomeration

A typical ferrofluid contains on the order of 10^{17} particles per cubic centimeter, and collisions between particles are frequent. Hence, if the particles adhere together, agglomeration will be rapid. The particles are permanently magnetized, so the maximum energy to overcome the magnetic attraction between a pair of particles each of radius, R, occurs when the particles are aligned. The corresponding dipole–dipole magnetic interaction is given by:

$$E_M = -\frac{8\pi\mu_0 M_d^2 R^3}{9(x+2)^3} \qquad (4)$$

where $x = s/R$ with s the surface to surface separation distance.

In addition, van der Waals forces of attraction arise between neutral particles due to the fluctuating electric dipole-induced dipole forces that are always present. It is also necessary to guard against these forces. London's model predicts an inverse sixth power law between point particles which Hamaker extended to apply to equal spheres with the following result.

$$E_V = -\frac{A}{6}\left[\frac{2}{x^2+4x} + \frac{2}{(x+2)^2} + \ln\frac{x^2+4x}{(x+2)^2}\right] \qquad (5)$$

A is the Hamaker constant, roughly calculable from the optical dielectric properties of particles and the medium. For Fe, Fe_2O_3, or Fe_3O_4 in hydrocarbon carrier, $A = 10^{-19}$ Nm is representative within a factor of three.

A technique to prevent particles from approaching too close to one another is the steric repulsion arising from the presence of long chain molecules adsorbed onto the particle surface. A lattice model for the steric repulsion based on the theory of polymer configurations in a good solvent (deGennes 1975) yields an expression for steric repulsion E_S.

$$E_S = kT\frac{\delta^3}{a^3}\left[\ln\left(\frac{1}{1-\phi_s}\right) - \phi_s\right]$$
$$\times \left[\frac{\pi}{12}\left(2 - x\frac{R}{\delta}\right)^2\left(6\frac{R}{\delta}+5\right)\right] \qquad (6)$$

In Eqn. (6) δ is coating thickness, a is the length associated with the lattice spacing, i.e., the correlation length along a chain, and ϕ_s is mean volume fraction of surfactant in the space between the surfaces.

The net sum, E_N, of the magnetic, van der Waals, and steric energy terms is decisive for determining monodispersity of the colloidal ferrofluid.

$$E_N = E_M + E_V + E_S \qquad (7)$$
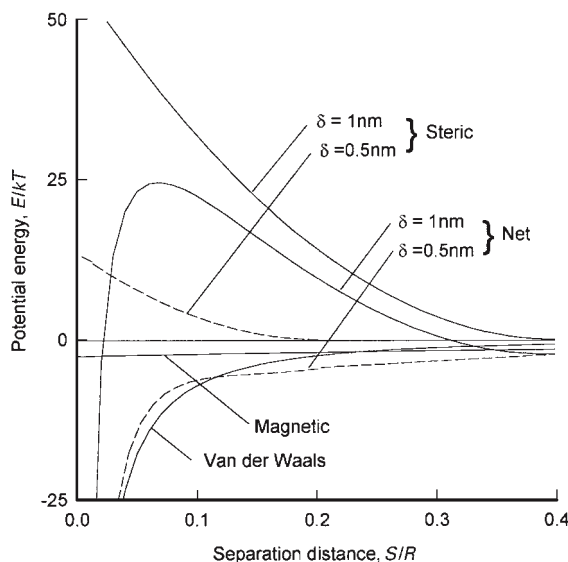
Figure 3
Potential energy versus surface separation distance of sterically protected 10 nm magnetite particles of a ferrofluid. A net energy barrier greater than about 10 kT prevents agglomeration of particles.

Figure 3 illustrates calculated behavior for given size particles with two different thicknesses of coatings. The curve of magnetic energy is the same in both cases as is the distribution of van der Waals energy. Magnetic interaction can nearly be neglected in comparison. Steric repulsion with the thicker coating (1 nm) yields a net energy curve presenting a barrier energy of nearly 25 kT. Statistically, few particles cross the barrier and the colloid is stable against agglomeration. The thin coating (0.5 nm) yields a net energy curve that is attractive at all distances thus yielding an unstable preparation.

Various sorbent configurations that confer steric stability to ferrofluids are illustrated schematically in Fig. 4. A particle coated with a sorbed monolayer of a long tail molecule having a polar head group, e.g., oleic acid, is shown in Fig. 4(a). Figure 4(b) illustrates a polymeric species having multiple polar groups distributed along its length. Loops of polymer rather than tails serve as the protective layer. Because more than one polar group attaches to the particle surface, the colloidal stability at elevated temperatures is enhanced; polybutenylsuccinpolyamines are an example. Figure 4(c) illustrates a double layer configuration with inwardly oriented tails of polar molecules in an outer layer associated with the tails of the surface-sorbed layer. This configuration serves to disperse particles in aqueous media. Example combinations are: sodium oleate/sodium oleate and sodium oleate/sodium dodecyl benzene sulfonate.
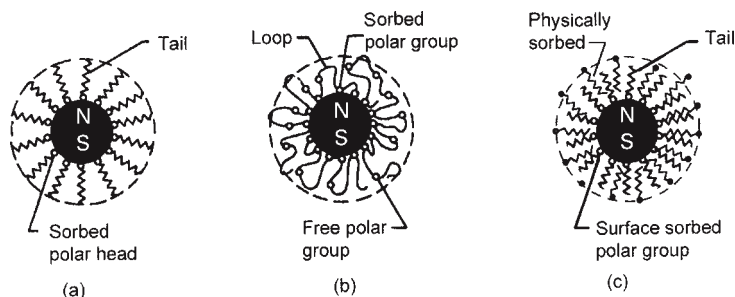
Figure 4
Sorbed protective layers of various types yield stably dispersed particles in a ferrofluid.

Charge stabilized colloids prepared with the Massart technique use the sorption of small moities to adjust electrical charge on the particle. Sorption of tetramethylammonium ion $(N(CH_3)_4^+)$ yields stable dispersions in alkaline solution (pH>9) where hydroxyl ion (OH^-) furnishes the counterion, whereas perchlorate ion (ClO_4^-) and nitrate (NO_3^-) peptize particles in acidic media (pH<5) where hydrogen ions (H^+) are the counterions. Magnetic particles coated with citrate ligands are peptizable at intermediate levels of pH and are candidates for medical application at neutral pH.

4. Phase Transition

Under certain conditions, ferrofluids undergo phase separation in which micronic droplets of a concentrated phase exist in equilibrium with a continuous dilute phase. The appearance of a drop is shown in Fig. 5(a). The phenomenon can be brought on in various ways—by application of magnetic field intensity in excess of a critical value, addition of a foreign solvent, change of pH or counter ion concentration of an electrically stabilized preparation, and by reduction of temperature. It is sometimes possible to take advantage of such a phase separation, e.g., to sort particles by size, or to induce colors in thin layers by diffraction of light. In other cases, where a dilute magnetic fluid is retained by application of a field gradient, the separation can lead to undesired weeping of the dilute phase.

Optical methods are useful for detecting the droplets. Direct microscopic observation via light transmitted through a thin layer is possible for droplets having size of a few micrometers; the layer is transparent red-orange in the homogeneous region. Laser light scattering being very sensitive to the presence of small clusters may be more suitable for direct detection of the very onset of the transition.

Figure 6 shows coexistence curves for a hydrocarbon-based ferrofluid that has particle size $d_{mp} = 7.4$ nm as determined by electron microscopy. Field
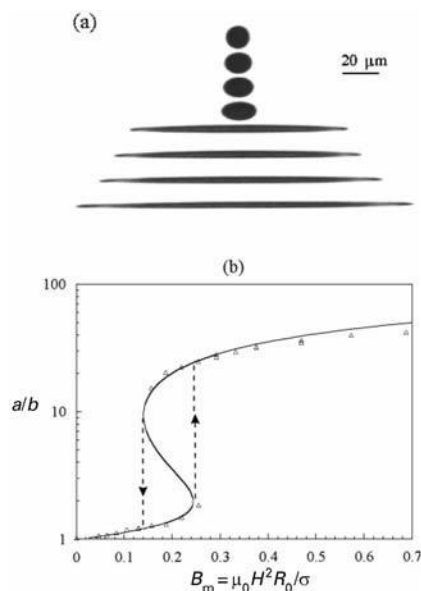
Figure 5
As shown in (a) a stretched droplet of phase-separated ionic ferrofluid exhibits a jump in length as applied field exceeds a critical value; (b): hysteresis results when field is decreased. Viscosity of the drop phase exceeds that of the dilute phase by a factor of more than 300 as determined from birefringence (after Bacri and Salin 1983).

intensity producing transition can be increased using a sample containing smaller size particles. A sample with particle sizes $d = 5.0$ nm tested homogeneous at all concentrations in the highest field applied $(12.7\,\mathrm{Am}^{-1})$.

5. Ferrofluid Modification

If an excess of a polar solvent such as acetone or a lower molecular weight alcohol is added to an
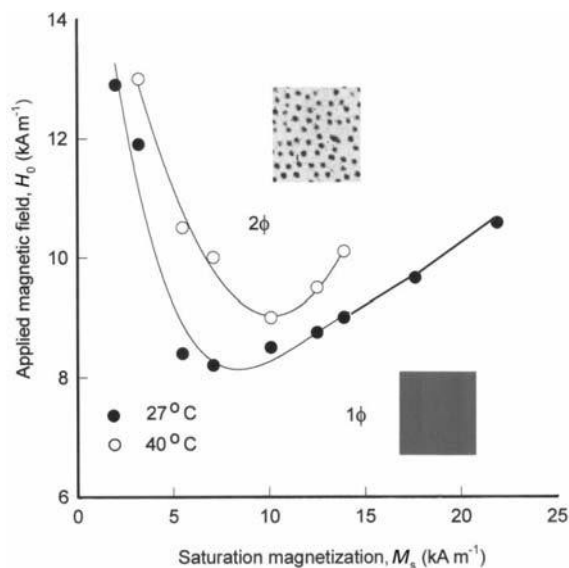
Figure 6
Coexistence curves for a hydrocarbon-based ferrofluid of magnetite particles. Insets show appearance of a thin layer seen through a microscope: one-phase region shows homogeneous coloring; cross-sections of stretched droplets in the two-phase region form a patterned array due to mutual repulsion; applied field is normal to the layer (after Popplewell and Rosensweig 1992).

oleic-acid-stabilized ferrofluid in hydrocarbon carrier the magnetite particles flocculate and settle out in an external force field. Evidently, the surface layer retracts and becomes ineffective in providing steric repulsion. The particles redisperse spontaneously when fresh solvent is added, showing that the surfactant remains bound onto the particle surface. The technique permits the concentration of the colloid to be adjusted and excess surfactant removed. Removing the excess generally reduces the viscosity, especially of high concentration, more magnetic preparations. Also, the initial solvent, e.g., high volatility heptane, can be exchanged for one of low volatility, useful in applications where the ferrofluid is exposed to the atmosphere as in magnetic fluid rotary shaft seals and acoustic drivers.

Certain surfactants are only weakly adsorbed and dissolve off into the polar liquid mixture. Contacting the settled out particles with fresh solvent fails to produce a stable dispersion. An example is aqueous ferrofluid having particles coated with Aerosol C61, an amine complex. After washing the precipitated particles with solvent, a different surfactant may be added which is capable of strongly adsorbing onto the particle surface. The new surfactant can be chosen to confer dispersibility of the particles in a totally

different solvent. The technique confers great flexibility in the production of ferrofluids in diverse carriers such as mineral oils, esters, silicones, etc.

6. Magnetic Properties

6.1 Equilibrium Magnetization

The magnetic torque, τ, experienced by a single particle of volume V and domain magnetization M_d whose moment is oriented at angle θ to applied induction B is given by $\tau = mH\sin\theta$ where $m = M_d V$ is the magnetic moment of the particle. The associated energy to rotate the particle away from alignment with the field is $W = mB(1-\cos\theta)$ with the probability $p(\theta)$ of finding a particle oriented between angle θ and $\theta + d\theta$ proportional to the Boltzmann factor $\exp(-W/kT)$ times the steradians in orientational space, $\sin\theta d\theta$, with the component of the moment along the field direction given by $m\cos\theta$. The mean value of magnetization for monodisperse particles is given by the integration:

$$\frac{\bar{m}}{m} = \frac{\int_0^\pi \cos(\theta)p(\theta)d\theta}{\int_0^\pi p(\theta)d\theta} = \coth\gamma - \frac{1}{\gamma} \equiv L(\gamma) \qquad (8)$$

where $L(\gamma)$ is the Langevin function and $\gamma = mB/kT$. $L(\gamma) = \gamma/3$ for $\gamma \ll 1$ and $L(\gamma) = 1 - 1/\gamma$ for $\gamma \gg 1$. Noting that $\bar{m}/m = M/M_s$ where M is magnetization of the ferrofluid and M_s is the saturation value of M, magnetization curves for monodisperse spherical particles calculated with the domain magnetization of magnetite are shown in Fig. 7.
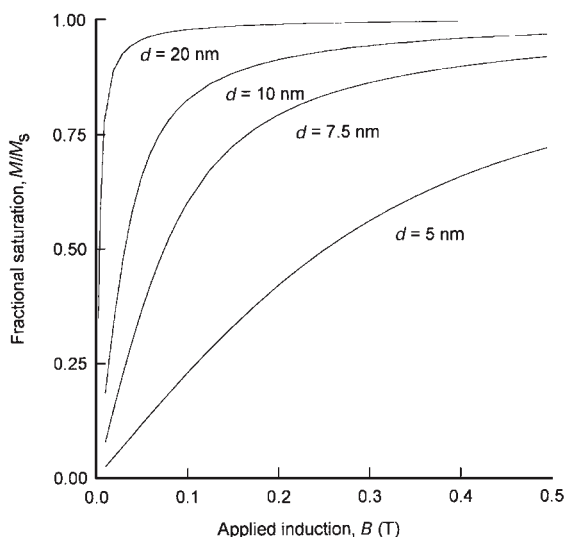
Figure 7
Magnetization curves computed from the Langevin relationship (magnetite, $M_d = 4.46 \times 10^5 \, Am^{-1}$).

For a polydisperse system the shape of the magnetization curve depends on the distribution of particle sizes. Commonly a good fit to the distribution is given by the log normal distribution function $P(d)$ where $P(d)\mathrm{d}(d)$ is the fraction of total magnetic volume having diameter between d and $d + \mathrm{d}(d)$.

$$P(d) = \frac{1}{\sigma d \sqrt{2\pi}} \exp\left[-\frac{\ln^2(d/d_0)}{2\sigma^2}\right] \qquad (9a)$$

and

$$\int_0^\infty P(d)\mathrm{d}(d) = 1 \qquad (9b)$$

where $\ln(d_0)$ is the mean of $\ln(d)$, d_0 is the median diameter, and σ is its standard deviation The most probable diameter is given by $d_{\mathrm{mp}} = d_0 \exp(\sigma^2)$, the mean diameter $\langle d \rangle = d_0 \exp(\sigma^2/2)$, and higher moments $\langle d^n \rangle = d_0^n \exp(n^2\sigma^2/2)$. Taking size distribution into account the magnetization curve is given by:

$$M(H) = \int_0^\infty M(d, H)P(d)\mathrm{d}d \qquad (10)$$

Chantrell *et al.* (1978) used expansions of the Langevin function together with the log normal distribution to obtain the following expressions for median diameter, d_0, and standard deviation, σ, from a magnetization curve of a polydisperse system.

$$\sigma = \frac{1}{3}\sqrt{\ln\frac{3\chi}{M_s/H_0}} \qquad (11a)$$

$$d_0 = \left(\sqrt{\frac{\chi}{3M_sH_0}}\,\frac{18kT}{\pi M_d}\right)^{\frac{1}{3}} \qquad (11b)$$

where χ is the initial susceptility of the fluid and $1/H_0$ is the extrapolation to $M = 0$ of the straight line obtained for high fields when plotting $M = f(1/H)$. Measured values of magnetization for dilute ferrofluids are in good agreement with the superparamagnetic relationship when the distribution of particle size is taken into account. Dipole–dipole interaction between particles elevates the low field portion of the magnetization curve for ferrofluids having parameter $\mu_0 M_d^2 V/kT \approx 30$ or greater.

Temperature dependence of magnetization is of interest in problems of thermal convection. The pyromagnetic coefficient $K = -\partial M/\partial T$ depends on domain magnetization, fluid expansion coefficient, particle volume fraction, and thermal disorientation which can be modeled with the Langevin function.

6.2 Anomalous Susceptibility

The initial susceptibility $\chi = M/H$ of ferrofluid containing noninteracting particles can be computed from the expansion of Eqn. (8) as $L(\gamma) = M/M_s = \gamma/3$ where M_s is the saturation magnetization of the ferrofluid and a is the Langevin argument. Thus $\chi = \pi\mu_0 d^3 M_d M_s/18kT$ where M_d is the domain magnetization of the magnetic particles. For a concentrated phase of 12 nm magnetite particles with $\mu_0 M_s = 0.1T$ the value of χ is 3.27. Polydisperse ferrofluid samples posess susceptibilities that are consistent with this estimate. However, as seen previously, values of χ in the droplets of a phase-separated sample are more than an order of magnitude larger. An *in situ* measurement based on elongation behavior of a droplet as a function of applied magnetic field intensity provides an elegant means for measuring the susceptibility as discussed in the following.

Using ionic ferrofluid the elongated deformation is obtained in fields of very low intensity, of the order of $120\,\mathrm{Am^{-1}}$ (1.5 Oe). Above a threshold value of the magnetic Bond number, $B_m = \mu_0 H^2 R_0/\sigma_t$, where R_0 is radius of an initially spherical drop and σ_t interfacial tension, the drop experiences an elongational shape instability characterized by a steep jump of its aspect ratio. The S-shape curve, see Fig. 5(b) can be fitted to a theoretical expression assuming an ellipsoidal prolate shape allowing susceptibilitiy χ and σ_t to be deduced. The minimum susceptiblity to achieve the hard transition occurs at about $\chi = 18$. For this data $\chi = 75 \pm 10$ and $\sigma = 9 \pm 2 \times 10^{-7}\,\mathrm{Nm^{-1}}$ with $R_0 = 6.5\,\mathrm{mm}$.

Subjected to a rotating magnetic field, the drops first elongate and spin, develop arms reminiscent of starfish, and undergo other transitions depending on field rotational frequency and intensity.

6.3 Nonequilibrium Magnetization

The vectorial magnetization, M_0, in equilibrium with steady magnetic field, H, in motionless fluid is aligned in the direction of H and possesses magnetization magnitude M_0 given, for example, by the Langevin relationship. However, in the presence of time-varying magnetic field magnitude or orientation the magnetization, M, lags behind the field and differs from M_0. Models have been developed (Shliomis 1974, Martsenyuk *et al.* 1973) to treat this behavior which has importance to dynamic flows of ferrofluids.

Measurement of the frequency response of magnetization of a ferrofluid yields information concerning the relaxation mechanism (Fannin *et al.* 1990).

7. Viscosity of Ferrofluid

7.1 Viscosity in Absence of Field

In 1906, Einstein derived the earliest theory for noninteracting spheres suspended in a liquid based on the flow field of pure rate-of-strain perturbed by the presence of the sphere. The resulting formula relates the mixture viscosity, η, to the carrier fluid viscosity,

η_0, and solids fraction, ϕ, in the form $\eta/\eta_0 = 1 + 5\phi/2$. This relationship has been extended by Batchelor to second order in concentration. For higher concentrations, a parameterized expression may be assumed of the form $\eta/\eta_0 = 1/(1 + a\phi + b\phi^2)$ with insistence that the expression (i) reduce to the Einstein relationship for small values of f so that $a = -5/2$; (ii) the suspension becomes effectively rigid at a concentration, ϕ_c, indicative of close packing (0.74 for close packed spheres); and (iii) core particles of volume fraction ϕ coated with dispersing agent of thickness δ occupies volume fraction $\phi(1 + \delta/r)^3$ where r is radius of the core particle. Combining these relationships results in the expression:

$$\frac{\eta - \eta_0}{\phi\eta} = \frac{5}{2}\left(1 + \frac{\delta}{r}\right)^3 - \left(\frac{5\phi_c/2 - 1}{\phi_c^2}\right)\left(1 + \frac{\delta}{r}\right)^6 \phi \quad (12)$$

If particles have a tendency to cluster and form a gel network, the value of ϕ_c is less than 0.74. For ϕ_c less than 0.4 the coefficient of the last term in Eqn. (12), and hence the slope of a plot of $(\eta - \eta_c)/\phi\eta$ vs. ϕ changes sign, a phenomenon that has been observed for certain ferrofluids.

7.2 Viscosity in Magnetic Field

When a magnetic field is applied to a ferrofluid that is sheared, the magnetic particles in the fluid tend to remain aligned in the direction of the orienting field and viscous dissipation in the fluid increases. A theoretical treatment (Shliomis 1974) for dilute suspensions of particles with large Néel time constant and accounting for the Brownian rotational motion gives

$$\frac{\Delta\eta}{\eta} = \frac{3}{2}\phi\left(\frac{\gamma - \tanh\gamma}{\gamma + \tanh\gamma}\right)\sin^2\beta \quad (13)$$

where γ is the Langevin parameter, β the angle between the magnetic field, H, and the fluid vorticity, $\mathbf{\Omega} = \nabla \times \mathbf{v}$, where $\mathbf{v}$ is the fluid velocity vector. The vorticity is twice the local average spin rate of the colloid. Magnetic particles rotate freely when the rotational and magnetic axes are aligned with the local field direction but are hindered otherwise. In laminar flow through a circular tube (Poiseuille flow) the vorticity magnitude is constant on concentric circles in a cross-section normal to the axis of the tube. For field oriented parallel to the axis, $\sin^2\beta = 1$ while for perpendicular orientation of the field relative to the tube axis, averaging over β gives $\langle\sin^2\beta\rangle = 1/2$. Hence, for any applied magnetic field intensity, $\Delta\eta_{||} = 2\Delta\eta_\perp$. As seen in Fig. 8, the theoretical curves (solid lines) agree well with the experimental data of McTague (1969) for a dilute suspension of polymer-stabilized cobalt particles in toluene.

In alternating, linearly polarized magnetic field, the viscosity of a ferrofluid can exhibit a substantial
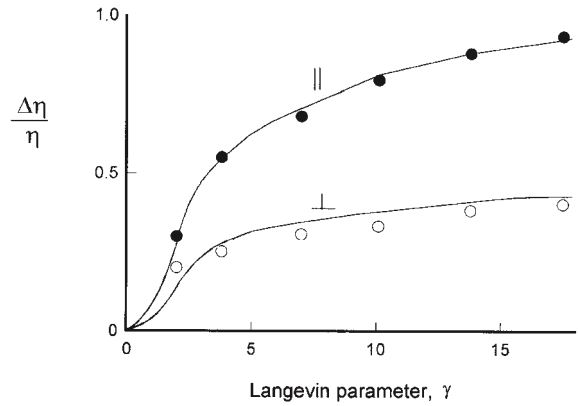
Figure 8
Magnetoviscosity of a dilute ferrofluid containing particles of elemental cobalt. Data of McTague (1963) compared to theory (after Shliomis and Raikher 1980).

reduction, i.e., a negative viscosity component (Shliomis and Morozov 1994). The particles of the ferrofluid act as tiny motors rotating faster than the vorticity spin rate thus helping to propel the fluid.

8. Other Physical Properties

Mass density and specific heat of ferrofluids is estimated as the volumetric average of particle and matrix liquid values assuming surfactant to possess properties of the carrier liquid. Pour point and vapor pressure can be estimated as that of the carrier liquid. Surface tension at ambient temperatures of sterically-stabilized aqueous ferrofluid is reduced from that of water ($72\,\text{mNm}^{-1}$) to a typical value of $26\,\text{mNm}^{-1}$, most likely due to free surfactant concentrated at the air interface. Interfacial tension for ferrofluids in various organic alkanes and esters ranges typically from 20 to $32\,\text{mNm}^{-1}$ depending on the carrier.

The thermal conductivity, λ, of a composite consisting of particles in a matrix fluid is described by the Maxwell formula obtained by comparing the thermal field with the analogous electrical field and it is assumed that ferrofluids can be described in this manner also.

$$\frac{\lambda}{\lambda_c} = \frac{2\lambda_c + \lambda_p + 2\phi_p(\lambda_p - \lambda_c)}{2\lambda_c + \lambda_p - \phi_p(\lambda_p - \lambda_c)} \quad (14)$$

where λ_c is thermal conductivity of the carrier solution, λ_p the thermal conductivity of the particles, and ϕ_p the particle volumetric concentration. Solids conductivity may differ significantly from that of the carrier, e.g., for $\gamma\text{-Fe}_2\text{O}_3$ and perhaps magnetite $\lambda_p \approx 6\,\text{W m}^{-1}\,\text{K}^{-1}$ while for an oil $\lambda_c \approx 0.13\,\text{W m}^{-1}\,\text{K}^{-1}$. Thus, the solids volumetric concentration must considerably affect the

thermal conductivity of the ferrofluid. Data of magnetite-in-kerosene ferrofluid show a range $1.0 < \lambda/\lambda_c < 2.0$ with maximum concentration of $\phi = 0.2$. Magnetic field oriented normal to the temperature gradient does not affect λ.

Ferrofluid solutions when sufficiently dilute or in a thin enough layer transmit a light beam, and the normally isotropic fluid becomes optically anisotropic in an applied magnetic field, H. Properties of interest include birefringence, dichroism, and Faraday rotation.

Birefringence and dichroism in homogeneous samples is attributed to the shape anisotropy of particles and possibly correlations between neighbors. The influence of an individual particle depends on the orientation of its axis relative to the electric field of the incident light ray. Analysis that averages over orientations yields a dependence on applied field intensity that is the same for both phenomena (Shliomis and Raikher 1980).

$$\frac{n_{||} - n_{\perp}}{\Delta n_{\infty}} = \frac{K_{||} - K_{\perp}}{\Delta K_{\infty}} = 1 - \frac{3L(\gamma)}{\gamma} \qquad (15)$$

where n'_i and K_i are components of refractive index and adsorption coefficient, respectively. Figure 9 illustrates the favorable comparison of data and predictions for a sterically-stabilized ferrofluid. Using birefringence detection with a sample having volumetric particle fraction of less than 10^{-3} as a sensor, the viscosity of carrier liquids was measured with an accuracy of 5% over a viscosity range of seven decades (Bacri *et al.* 1985). The viscosity of the solutions was negligibly changed by presence of the particles, less than 2.5 parts per thousand using the Einstein relationship. Bibette (1993) produced a monodisperse emulsion of oil base ferrofluid droplets in an aqueous carrier and optically measured force vs. distance characterizing the electrostatic double layer surrounding the droplets. Modulation of the applied magnetic field was used to control the attraction between droplets, hence their separation distance.
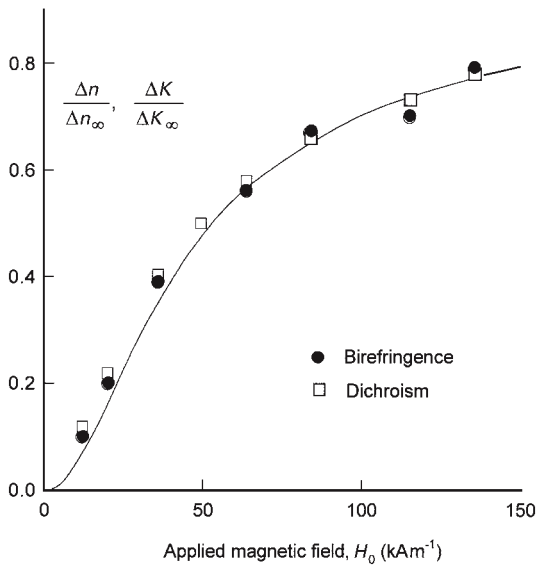
9. Status and Future Directions

Scientific understanding of ferrofluids as a material has progressed greatly. Proceedings of the International Conferences on Magnetic Fluids (Elsevier, North-Holland, Publishers) are a rich source of information including bibliographies of patents and the literature. The influence of magnetic and thermal fields on the hydrodynamics of ferrofluids, i.e., ferrohydrodynamics, is highly developed. Commercial applications of ferrofluids range from tribology to instrumentation to densimetric separation of minerals, and many other uses are in stages of research. Materials research challenges for the future include: development of stable fluids having larger saturation moments, conjugation of ferrofluid particles with protein species for drug delivery and medical imaging, development of ferrofluid inks in various colors, ferrofluids possessing greater monodispersity, stable ferrofluids in liquid metal carrier, and ferrofluid composites with tailored properties.

See also: Ferrofluids: Applications Ferrofluids: Neutron Scattering Studies; Ferrofluids: Preparation and Physical Properties; Ferrohydrodynamics

Figure 9
Dependence on magnetic field of birefringence and dichroism for a hydrocarbon base ferrofluid compared to theory.

Bibliography

Bacri J-C, Dumas J, Gorse D, Perzynski R, Salin D 1985 Ferrofluid viscometer. *J. Phys. Lett.* **46**, L1199–205

Bacri J-C, Perzynski R, Salin D, Cebers A O 1992 Instabilities of a ferrofluid droplet in alternating and rotating magnetic fields. *Mater. Res. Soc. Symp. Proc.* **248**, 241–6

Bacri J-C, Salin D 1983 Dynamics of the shape transition of a magnetic ferrofluid drop. *J. Phys. Lett.* **44**, 415–20

Bashtovoy V G, Berkovsky B M, Vislovich A N 1988 *Introduction to Thermomechanics of Magnetic Fluids*. Hemisphere, Washington, DC

Berkovsky B (ed.) 1996 *Magnetic Fluids and Applications Handbook*. Begell House, New York

Bibette J 1993 Monodisperse ferrofluid emulsions. *J. Magn. Magn. Mater.* **122**, 37–41

Blums E, Cebers A, Maiorov M M 1997 *Magnetic Fluids*. Walter de Gruyter, Berlin

Chantrell R W, Popplewell J, Charles S W 1978 Measurements of particle size distribution parameters in ferrofluids. *IEEE Trans. Magn.* **MAG-16**, 975–7

de Gennes P G 1975 *Scaling Concepts in Polymer Physics*. Cornell University Press, Ithaca, NY, p. 74

Elmore W C 1938a Ferromagnetic colloid for studying magnetic structures. *Phys. Rev.* **54**, 309–10

Elmore W C 1938b The magnetization of ferromagnetic colloids. *Phys. Rev.* **A24**, 1092–5

Fannin P C, Scaife B K P, Charles S W 1990 A study of the complex ac susceptibility of magnetic fluids subjected to a constant polarizing magnetic field. *J. Magn. Magn. Mater.* **85**, 54–6

Gable H S, Kerr G W 1977 Magnetic organo-iron compounds. *US Pat.* 4 001 288 (CIP of copending application Ser. No. 487 564 filed Sept. 15, 1965)

Khalafalla S E, Reimers G W 1973 Magnetofluids and their manufacture. *US Pat.* 3 764 540

Khalafalla S E, Reimers G W 1974 Production of magnetic fluids by peptization techniques. *US Pat.* 3 843 540

Martsenyuk M A, Raikher Yu L, Shliomis M I 1973 On the kinetics of magnetization of suspensions of single domain particles. *Sov. Phys. JETP* **38**, 413–6

Massart R 1981 Preparation of aqueous magnetic liquids in alkaline and acidic media. *IEEE Trans. Magn.* **MAG-17**, 1247–8

Massart R 1996 Dispersion of particles in the base liquid. In: Berkovsky B (ed.) *Magnetic Fluids and Applications Handbook*. Begell House, New York

McTague J P 1969 Magnetoviscosity of magnetic colloids. *J. Chem. Phys.* **51**, 133–6

Nakatani I, Hijikata M, Ozawa K 1993 Iron-nitride magnetic fluids prepared by vapor-liquid reaction and their magnetic properties. *J. Magn. Magn. Mater.* **122**, 10–4

O'Connor T L 1962 Preparation of sols of metal oxides. *Belg. Pat.* 613 716

Papell S S 1965 Low viscosity magnetic fluid obtained by the colloidal suspension of magnetic particles. *US Pat.* 3 215 572

Popplewell J, Rosensweig R E 1992 Influence of concentration on field-induced phase transition in magnetic fluids. *Int. J. Appl. Electromagn. Mater.* **2** (Suppl.), 83–6

Rosensweig R E 1985 *Ferrohydrodynamics, Cambridge Monographs on Mechanics and Applied Mathematics*. Cambridge University Press, New York [Republished 1997. Dover Publications, Mineola, NY]

Rosensweig R E, Nestor J W, Timmins R S 1965 Ferrohydrodynamic fluids for direct conversion of heat energy. Materials Association Direct Energy Conversion Symposium Proceedings. *AIChE—I. Chem. Eng. Ser.* **5**, 104–18 discussion, 133–7

Sandre O, Browaeys J, Perzynski R, Bacri J -C, Cabuil V, Rosensweig R E 1999 Assembly of microscopic highly magnetic droplets: magnetic alignment versus viscous drag. *Phys. Rev. E* **59**, 1736–46

Scholten P C 1980 The origin of birefringence and dichroism in magnetic fluids. *IEEE Trans. Magn.* **MAG-16**, 221–5

Shliomis M I 1974 Magnetic fluids. *Sov. Phys. Usp.* **112**, 153–69

Shliomis M I, Raikher Yu L 1980 Experimental investigations of magnetic fluids. *IEEE Trans. Magn.* **MAG-16**, 237–50

Shliomis M I, Morozov K I 1994 Negative viscosity under alternating magnetic field. *Phys. Fluids* **6**, 2855–61

R. E. Rosensweig
Fondation de l'Ecole Normale Supérieure
Paris, France

Ferrofluids: Magnetic Properties

The magnetic properties of ferrofluids are dominated by the intrinsic magnetic properties of the particles themselves. These are governed by dynamical effects due to Néel relaxation in the solid and Brownian motion in the fluid, and influenced by the interparticle interaction.

1. Single-domain Particles

The particles have diameters in the range of typically 2–20 nm. The size is generally below the critical limit, dependent on the specific ferromagnet, where a magnetic domain structure can form, and so the particles can be considered as single domain. Because of the nanometer-scaled size, finite-size effects are significant. Surface effects influence the intrinsic properties (e.g., magnetization, magnetocrystalline anisotropy). The breaking of symmetry results in site-specific surface anisotropy; the reduced number of magnetic neighbors and specific electronic and structural features lead to magnetic disorder and weakened exchange coupling, with possible effects on atomic moments. All phenomena depend on the surface microstructure and can vary with the surroundings.

Volume effects influence the behavior of the exchange-coupled spin system against excitation. The particle volume, V, is small enough for coherent spin reversal (Stoner–Wohlfarth particle), at least on a macroscopic viewing scale. Because all the spins rotate in unison, except perhaps near the surface, they can be dealt with collectively via the particle moment $\boldsymbol{m}$. Its magnitude is given by

$$\boldsymbol{m} = M_{s}V \tag{1}$$

where M_{s} is the intrinsic magnetization, which is the magnetic moment per unit volume. It can often be considered as constantly neglecting its thermal variation. The orientation of $\boldsymbol{m}$ with respect to the lattice is determined by the total magnetic anisotropy energy, which results generally from bulk magnetocrystalline, magnetostatic (shape), and global macroscopic surface anisotropies. It can often be considered uniaxial and is then given by

$$E = KV\sin^{2}\theta \tag{2}$$

where K (>0) is the effective anisotropy energy density, generally in the range 10^{4}–10^{6} J m^{-3}, and θ is the angle with respect to the symmetry (easy) axis.

Since the anisotropy energy decreases with volume, the energy barriers separating the easy directions can be comparable to the thermal energy, kT, even below room temperature; here, k is Boltzmann's constant and T the temperature. $\boldsymbol{m}$ is then no longer fixed in the lattice, unlike in large crystals, but fluctuates

among the easy directions. Néel performed the first calculation of the relaxation time and this thermo-activated phenomenon is called Néel or superpara-magnetic relaxation. The corresponding magnetic behavior is called superparamagnetism.

A particle responding to a magnetic field rotates its moment. In a solid, the rotation occurs inside the particle (Néel relaxation). In a ferrofluid, it can also occur by bulk rotation (Brownian rotational diffusion). The relaxation rates are generally different and the two processes can often be treated separately.

2. Néel Relaxation

In a uniform magnetic field H of strength H, the free energy of an isolated uniaxial particle with aniso-tropy barrier $E_B = KV$, fixed in space, is given by

$$E = E_B \sin^2\theta - \mu_0 mH(\cos\theta\cos\psi + \sin\theta\sin\psi\cos\varphi) \quad (3)$$

where μ_0 is the permeability of free space, ψ the angle between the easy axis (unit vector e) and field, and φ the longitude of m relative to the plane (e, H). $H_K = 2E_B/\mu_0 m$ is the anisotropy field. The energy has a bistable form if the field is not too large, i.e., $H < H_c(\psi)$ with $1 \geqslant H_c/H_K \geqslant 1/2$. In Brown's model, the equation of motion is given by the Gilbert–Land-au–Lifshitz equation

$$2\tau_{N0}\frac{d\boldsymbol{m}}{dt} = \frac{\mu_0}{kT}\big[m\zeta^{-1}\boldsymbol{m}\times\boldsymbol{H}_e + (\boldsymbol{m}\times\boldsymbol{H}_e)\times\boldsymbol{m}\big]$$
$$\tau_{N0} = \frac{m}{2\gamma kT}(\zeta^{-1} + \zeta) \quad (4)$$

where γ is the gyromagnetic ratio ($1.7 \times 10^{11}\,\text{s}^{-1}\,\text{T}^{-1}$), and ζ ($\approx 10^{-1}$–10^{-2}) the dimensionless damping factor of the precession of m in the effective field $\boldsymbol{H}_e = -\mu_0^{-1}\partial E/\partial\boldsymbol{m} + \boldsymbol{h}(t)$, where $\boldsymbol{h}(t)$ is a random white-noise field. The probability density of m orientations obeys a Fokker–Planck equation, as is the case for Brownian motion.

The effective time to surmount the barrier is given by $\tau_N = 2\tau_{N0}\sum_{n=1}^{\infty} A_n/\lambda_n$, where λ_n is the nth eigen-value, and A_n its amplitude. The lowest ($\neq 0$) eigen-value, λ_1, is associated with the overbarrier mode, and higher ones with intrawell modes. Only the former is frequently considered and then $\tau_N = 2\tau_{N0}/\lambda_1$. If the field is parallel to the easy axis, the energy barrier is $E_B(1\pm h)^2$ with $h = H/H_K$, and τ_N is given by

$$\alpha = \frac{E_B}{kT} \ll 1, \quad \tau_N = \tau_{N0}\big(1 - \tfrac{2}{5}\alpha + \tfrac{48}{875}\alpha^2 + \tfrac{2}{5}\alpha^2 h^2\big)^{-1}$$
$$\alpha \gg 1, \quad \tau_\pm = \tau_{N0}\pi^{1/2}\alpha^{-3/2}\big[(1-h^2)(1\pm h)\big]^{-1}$$
$$\times \exp[\alpha(1\pm h)^2],$$
$$\tau_N^{-1} = \tau_+^{-1} + \tau_-^{-1} \quad (5)$$

τ_+^{-1} and τ_-^{-1} are the probabilities per unit time of m reversal from the lower to upper minimum and vice versa, respectively. For $H = 0$, τ_N is well approxi-mated for all barrier heights by

$$\tau_N = \tau_{N0}\{2\alpha[\pi^{-1/2}\alpha^{3/2}(\alpha+1)^{-1} + 2^{-\alpha-1}]\}^{-1}(e^\alpha - 1) \quad (6)$$

For $\alpha \gg 1$, τ_N is often written as $\tau_N = \tau_0 e^\alpha$, where the factor τ_0 is of the order of 10^{-9}–10^{-11} s.

3. Brownian Rotational Diffusion

If m is blocked in the lattice, along the easy axis ($\theta = 0$), the free energy is

$$E = -\mu_0 mH\cos\psi \quad (7)$$

There is no precessional motion. The equation of motion for Brownian rotation is given by

$$2\tau_{B0}\frac{d\boldsymbol{m}}{dt} = \frac{\mu_0}{kT}[(\boldsymbol{m}\times\boldsymbol{H}_e)\times\boldsymbol{m}], \qquad \tau_{B0} = \frac{3V_h\eta}{kT} \quad (8)$$

where V_h is the hydrodynamic volume of the particle, and η (N s m^{-2}) the kinematic viscosity of the carrier. The longitudinal, $\tau_{B\parallel}(\tau_B)$, and transverse, $\tau_{B\perp}$, relax-ation times are given by

$$\tau_{B\parallel} = \frac{\tau_{B0}\big[\xi - 2L(\xi) - \xi L^2(\xi)\big]}{L(\xi)}$$
$$\tau_{B\perp} = \frac{\tau_{B0}2L(\xi)}{\xi - L(\xi)} \quad (9)$$

with

$$\xi = \frac{\mu_0 mH}{kT}$$

where $L(\xi) = \coth\xi - 1/\xi$ is the Langevin function. For $\xi \ll 1$, $L(\xi) = \xi/3$, so $\tau_{B\parallel} = \tau_{B\perp} = \tau_{B0}$. For $\xi \gg 1$, $L(\xi) = 1 - 1/\xi$ and $\tau_{B\parallel} = \tau_{B\perp}/2 = \tau_{B0}/\xi$. Equations (7)–(9) also apply to the solid-state process (with τ_{N0} replacing τ_{B0}) if the influence of the anisotropy is negligible ($H \gg H_K$).

4. Behavior in Zero Field

A moment rotating by both processes has the effec-tive relaxation time τ_{eff} given by

$$\frac{1}{\tau_{\text{eff}}} = \frac{1}{\tau_N} + \frac{1}{\tau_B} \quad (10)$$

so the process with the shorter time is dominant. In general, $\tau_{N0} < \tau_{B0}$, implying a critical volume V_c satis-fying $\tau_N = \tau_B$ (e.g., for $\tau_{N0}/\tau_{B0} = 10^{-2}$ and $H = 0$, $V_c \approx 8\,kT\,K^{-1}$). Smaller particles will relax mostly by Néel and larger ones by Brownian process. In a zero field, τ_N is in the range of approximately 10^{-10}–10^{20} s, and τ_B of 10^{-8}–10^{-4} s, so τ_{eff} is in the range

10^{-10}–10^{-4} s. A moment will appear blocked or time-averaged to zero depending on whether τ_{eff} is longer or shorter, respectively, than the measuring time, t_{m}. Every moment is time-averaged on the scale for d.c. magnetization measurements, where t_{m} is typically 1–100 s, and so a ferrofluid has no spontaneous magnetization. Moreover, after the removal of the field the system is demagnetized within a time $t \ll t_{\text{m}}$, so ferrofluids are intrinsically perfectly reversible in terms of their d.c. magnetic properties. If particle rotation is frozen out, the relaxation time can reach a geological scale. Under given experimental (t_{m}, T) conditions, a particle can appear unmagnetized ($\tau_{\text{N}} < t_{\text{m}}$) or magnetized ($\tau_{\text{N}} > t_{\text{m}}$) depending on its size and anisotropy (KV).

5. D.c. Magnetization and Initial Susceptibility

When the measuring time is longer than the relaxation time, the system is at thermodynamic equilibrium and Boltzmann statistics can be applied. If $\tau_{\text{B}} < \tau_{\text{N}}$ ($\tau_{\text{B}} < \tau_{\text{N}} < t_{\text{m}}$ or $\tau_{\text{B}} < t_{\text{m}} < \tau_{\text{N}}$), the Néel relaxation is of no consequence and Eqn. (7) leads to the magnetization given by

$$M = \frac{M_s \int_0^\infty \cos\psi \, e^{-E/kT} \sin\psi \, d\psi}{\int_0^\infty e^{-E/kT} \sin\psi \, d\psi} = M_s L(\xi) \quad (11)$$

If $\tau_{\text{N}} < \tau_{\text{B}}$ ($< t_{\text{m}}$), which can occur only in small fields, the system is at equilibrium on the Brownian time scale (Eqn. (3), $M(\psi)$); the easy axis orientation (ψ) is changed after a Brownian event and so the magnetization at global equilibrium will be $M = \frac{1}{2} \int_0^\pi M(\psi) \sin\psi \, d\psi$, which reduces for $\xi \ll 1$ to $M = M_s \xi / 3$. For $\xi \gg 1$, there is no Néel relaxation ($H > H_{\text{K}}$) and $M = M_s(1 - 1/\xi)$ as a first approximation. Langevin's law of paramagnetism describes the result in each case. By analogy with spins, the equilibrium behavior is called superparamagnetic. The initial (low-field) susceptibility follows a Curie law

$$\frac{\mu_0 M_s V H}{kT} \ll 1, \quad \chi_0 = \frac{M}{H} = \frac{\mu_0 M_s^2 V}{3kT} \quad (12)$$

If there are n similar particles per unit volume in the sample, the sample magnetization is $M^* = nM$. In practice, it is necessary to take the size distribution into account. Experimental devices measure the magnetic moment, so $M^* = C_v \langle M \rangle$, where C_v is the volume fraction of particles, and $\langle M \rangle$ the average particle magnetization given by

$$\langle M \rangle = \frac{1}{Z} \int_0^\infty M(V) V f(V) dV$$
$$Z = \int_0^\infty V f(V) dV \quad (13)$$

where $f(V)$ is the volume distribution function. If all particles satisfy the conditions for the low- and high-field approximations of the Langevin function, the magnetization is given by

$$\text{low field} \quad \langle M \rangle = \frac{\mu_0 H M_s^2}{3kTZ} \int_0^\infty V^2 f(V) dV \quad (14)$$

$$\text{high field} \quad \langle M \rangle = M_s \left[1 - \frac{kT}{\mu_0 H M_s Z} \right] \quad (15)$$

where M_s is the average intrinsic magnetization. The data exhibit no remanence and coercivity and show H/T superposition (Fig. 1). In principle, one can make use of the magnetization curve to determine the parameters of the size distribution.

Below the melting temperature of the carrier, the moments will gradually block with decreasing temperature, according to the distribution of energy barriers. A blocking temperature T_B is defined for a particle of volume V as the temperature at which $\tau_{\text{N}} = t_{\text{m}}$. In very small fields, $T_B = KV/k\ln(t_{\text{m}}/\tau_0)$ for $\alpha \gg 1$. If the easy axes are randomly oriented, for
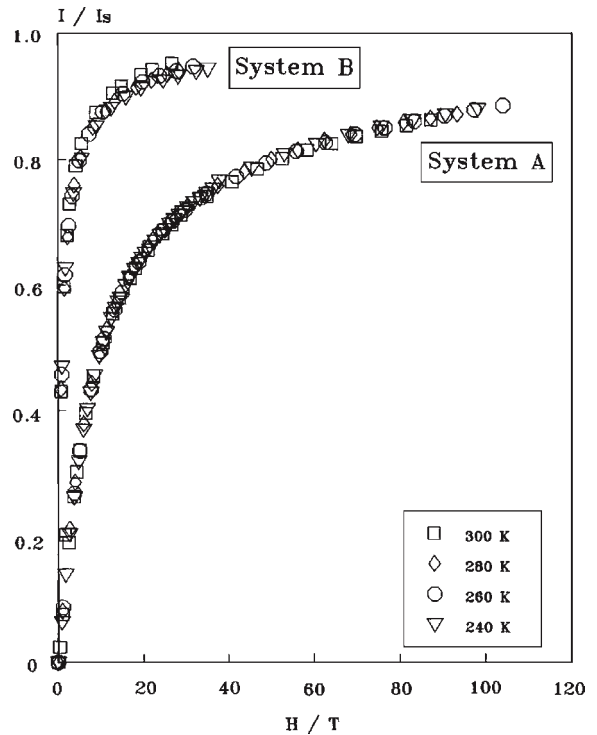
Figure 1
Thermal dependence of reduced magnetization curves of magnetite ferrofluids. Median particle diameter (A) 4.8 nm; (B) 9.6 nm. (Reprinted with permission from Williams *et al.* 1993; © Elsevier Science B.V.)
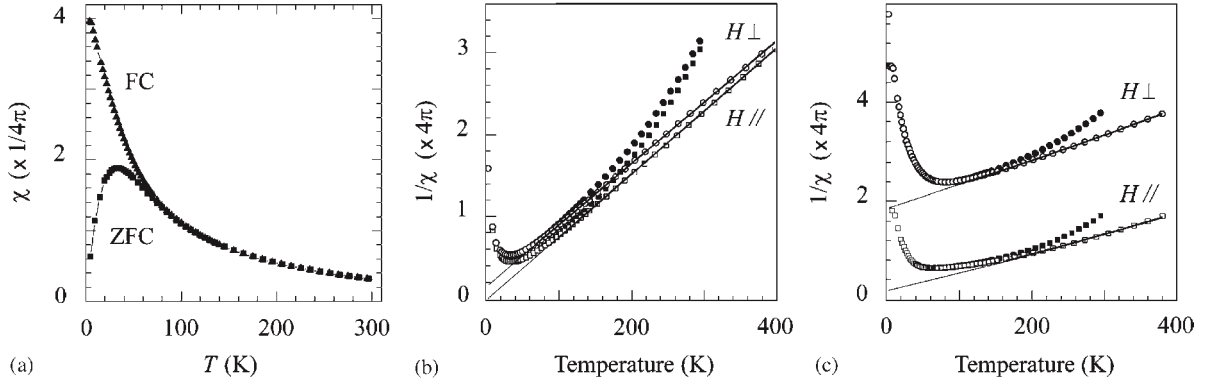
Figure 2
Thermal variation of the initial susceptibility (χ) for polymerized γ-Fe_2O_3 ferrofluids. Applied field $H = 800\,A\,m^{-1}$. (a) Field-cooled (FC) and zero-field-cooled (ZFC) susceptibilities for a dilute sample. (b) Inverse ZFC susceptibility for parallel or perpendicular geometry; and (c) Concentrated sample. Experimental data (filled symbols); corrected (open symbols) for the thermal variation of the intrinsic magnetization. Volume fraction of particles (a, b) 0.0075, (c) 0.195. Average diameter 7.7 nm. (Unpublished data courtesy of M. Nogués).

$T > T_B$ (unblocked state) the particle susceptibility is equal to χ_0. For $T < T_B$ (blocked state), it is given by $\chi_1 = \mu_0 M_s^2 / 3K$. Thus, for a broad volume distribution, the susceptibility will be

$$\chi(T, t_m) = \frac{\mu_0 M_s^2}{3kTZ} \int_0^{V_c} V^2 f(V)\, dV + \frac{\mu_0 M_s^2}{3KZ} \int_{V_c}^{\infty} V f(V)\, dV \tag{16}$$

with V_c such that $T_B(V_c) = T$. The fraction of unblocked particles decreases with temperature so that the χ versus T curve has a maximum. The temperature T_{max} at maximum is proportional to the average blocking temperature according to the type of volume distribution function.

The thermal variation of the initial susceptibility is commonly studied by measurements at very low field of the in-phase a.c. susceptibility $\chi'_{ac}(v) = dM/dH$ with v the frequency, and d.c. susceptibility $\chi = M/H$ (Fig. 2(a)). The d.c. susceptibility measured after cooling the sample in zero field (ZFC susceptibility) shows a maximum, like χ'_{ac}. The d.c. susceptibility measured after cooling the sample under field (FC susceptibility) grows continuously with decreasing temperature, splitting from the ZFC curve at $T_{sp} > T_{max}$, and finally saturating below some temperature T_{sat}. T_{sp} and T_{sat} correspond to the largest and smallest T_B value, respectively. For $T > T_{sp}$, the system is at equilibrium. For $T < T_{sp}$, it is in a non-equilibrium state.

In the blocked state, any change of the magnetic field is followed by a time variation of the magnetization, e.g., both the ZFC and remanent (M_r) magnetizations are time dependent. For a single particle with relaxation time τ_N ($\alpha \gg 1$), an exponential time decay

$$M_r(t) = M_r(0)\exp\frac{-t}{\tau_N} \tag{17}$$

was predicted by Néel. For a volume distribution, $M_r(t) = (1/Z) \int_0^{\infty} M_r(t, V) V f(V) dV$. A decay of the form $M_r(t) = A - S\ln(t)$ is usually found, but deviations can be observed depending on the experimental conditions (e.g., recording time of the relaxation) and sample characteristics. The blocked state gives rise to bulk-like hysteresis cycles, affected by particle size and anisotropy, responsible for the difference in saturation, remanence and coercive force H_c. For uniaxial anisotropy, when all the moments are blocked, $M_r = M_s/2$ and $H_c = H_K/2$ if the easy axes are randomly oriented, and $M_r = M_s$ and $H_c = H_K$ if they are aligned parallel to the field. An orientation texture can easily be induced by freezing a ferrofluid under field.

6. A.c. Susceptibility

The a.c. susceptibility, $\chi(\omega) = \chi'(\omega) - i\chi''(\omega)$, with $\omega = 2\pi v$ the angular frequency, is determined by the moments able to follow the small a.c. field $H = H_0 e^{i\omega t}$. Frequencies of interest for ferrofluids range from hertz to gigahertz, i.e., up to ferromagnetic resonance. For a uniaxial particle where the moment deviates slightly from the easy axis, the resonant condition is $\omega = \gamma \mu_0 H_K$. Far below resonance, for a random assembly of particles with volume V and relaxation time τ, the particle magnetization is given by

$$M(t) = H_0[\chi_0 - (\chi_0 - \chi_\infty)e^{-t/\tau}] \tag{18}$$
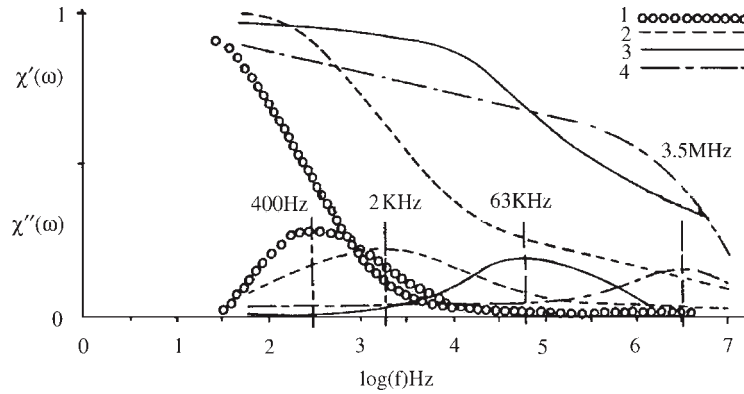
Figure 3
Normalized plots of the real and imaginary parts of the a.c. susceptibility against frequency for cobalt ferrite (1,3) and magnetite (2,4) ferrofluids. Median particle radius of (1–3) 5 nm, (4) 4.5 nm. (Reprinted with permission from Fannin 1994; © Elsevier Science B.V.)

where χ_∞ is the high-frequency susceptibility. The Fourier transform gives the susceptibility according to Debye's theory

$$\chi(\omega) = \frac{\chi_0 + i\omega\tau\chi_\infty}{1 + i\omega\tau}$$

$$\chi'(\omega) = \chi_\infty + \frac{\chi_0 - \chi_\infty}{1 + \omega^2\tau^2}$$

$$\chi''(\omega) = \frac{(\chi_0 - \chi_\infty)\omega\tau}{1 + \omega^2\tau^2} \qquad (19)$$

$\chi'(\omega)$ falls monotonically with increasing ω, whereas $\chi''(\omega)$ has a maximum at $\omega\tau = 1$ (Fig. 3). This enables one to determine the effective relaxation time and particle size in a ferrofluid in a relatively simple way.

A single loss peak will be found if the relaxation time is distributed continuously, in the range 1–100 MHz when the Néel mechanism dominates, and much lower when the Brownian process prevails. For a random assembly of particles, $\chi(\omega)$ can be described in terms of its parallel, $\chi_\parallel(\omega)$, and perpendicular, $\chi_\perp(\omega)$, components according to

$$\chi(\omega) = \frac{\chi_\parallel(\omega) + 2\chi_\perp(\omega)}{3} \qquad (20)$$

$\chi_\parallel(\omega)$ and $\chi_\perp(\omega)$ refer (Eqn. (19)) to longitudinal and transverse relaxation times, respectively. With increasing frequency, $\chi_\parallel(\omega)$ remains purely relaxational in character. $\chi_\perp(\omega)$ is associated with resonance, which corresponds to $\chi'_\perp(\omega)$ going negative. From the frequency dependence of $\chi(\omega)$ in the range 100 MHz−10 GHz, parameters such as H_K, K, and $M_r(t)$ can be determined.

7. Interparticle Interaction Effects

The magnetic dipolar interparticle interaction always exists in a particle assembly. In a ferrofluid, its consequences can range from liquid-like short-range order to highly anisotropic chain configurations as observed in large applied fields. The energy of particle i due to interaction with all other particles is given by

$$E_i = -\mu_0 \boldsymbol{m} \cdot \sum_{i \neq j} \boldsymbol{H}_{ij}, \quad \boldsymbol{H}_{ij} = \frac{3(\boldsymbol{m}_j \cdot \boldsymbol{r}_{ij})\boldsymbol{r}_{ij} - \boldsymbol{m}_j}{4\pi d_{ij}^3} \quad (21)$$

where $\boldsymbol{H}_{ij}$ is the magnetic field seen by particle i due to the interaction with particle j, and $\boldsymbol{r}_{ij}$ and d_{ij} are the unit vector and distance defining the vector connecting the centers of the two particles with moments $\boldsymbol{m}_i$ and $\boldsymbol{m}_j$. The interaction energy adds to the individual anisotropy energy. The particle energies are interdependent and the whole system tends to minimize its magnetostatic energy. A ferrofluid system, unconstrained topologically, will partition itself into an ensemble of subsystems with low magnetostatic energy.

Relaxation in the particles can be assumed blocked and the leading parameter is $\lambda = \mu_0 m^2/4\pi D_h^3 kT$ with D_h the hydrodynamic particle diameter, neglecting size distribution. The stability of the suspension of particles limits the value of λ. No spatial correlation occurs if $\lambda \lesssim 1$. Clustering develops with growing λ and when λ is large enough, all particles are aggregated at equilibrium, as shown by Monte Carlo simulations. Short linear chains (dimers, trimers) predominate at small λ values. Bending and branching appear when λ increases. At medium values, closed magnetic configurations prevail. For large λ values, the cluster structure is more and more isotropic and dense, with the orientation of the moments tending to be randomized. In large applied

fields, the spatial order becomes anisotropic. The orientation effect of the field strengthens the interactions favoring chain-like configurations, which give rise to the anisotropic magneto-optical properties of ferrofluids.

The interactions influence the magnetic properties especially in low applied fields. They cause deviations from the Langevin behavior (Figs. 2(b) and (c)). The equilibrium magnetization is given by the Langevin law, referring to the effective field, H_{eff}, seen by the particle, which is not equal to the applied field, H_{app}, in the presence of interaction. Since the sample is magnetized, boundary phenomena give rise to demagnetizing field effects. The demagnetizing field is constant inside the sample if this is an ellipsoid with an axis parallel to the applied field. The field exterior to the particles is then given by

$$H_{\text{ext}} = H_{\text{app}} - N_{\text{e}} C_v M \qquad (22)$$

with N_{e} ($0 \leqslant N_{\text{e}} \leqslant 1$) the demagnetizing factor of the sample. The measured susceptibility $\chi_{\text{app}} = M/H_{\text{app}}$ depends on the geometrical experimental parameters, unlike $\chi_{\text{ext}} = M/H_{\text{ext}}$.

Different models have been proposed for estimating H_{eff} as a function of H_{ext}. They all lead to first order, with a varying range of applicability, to the same formula for the initial susceptibility

$$\chi_{\text{ext}} = \chi_0 (1 + N_i C_v \chi_0) \qquad (23)$$

where $N_i = 1/3$. This agrees with experimental results, after correcting for size distribution and thermal variations of M_s and C_v, and with numerical simulations for $\chi_0^* = C_v \chi_0 \lesssim 3$. In the limit $\chi_0^* \ll 3$, the susceptibility takes a Curie–Weiss form; it is in no way indicative of a magnetic phase transition. For $\chi_0^* \gtrsim 3$, correlations cannot be neglected and Eqn. (23) does not hold; the influence of the microstructure ($\chi_0^* \approx 8\lambda C_v$) no longer reduces to a concentration effect and Monte Carlo simulations are in practice the only reliable way of modeling. Since the texture varies with field and temperature (λ), the magnetic behavior of ferrofluids can be extremely complex. In real systems, clustering of physicochemical origin may bring extra complexity.

The interactions affect the Brownian dynamics (Fig. 3), especially because a cluster is a rotating Brownian object, with relaxation time proportional to the volume. They modify the dynamics in the particles depending on the topology and relative magnitudes of the anisotropy and interaction energies. In random solid systems, for weak enough interactions, the dynamics can still be described in the framework of the Néel relaxation. The interactions increase the energy barrier. In the Dormann *et al.* (1997) model, valid when all (most) moments are above or near their blocking temperature, the increase for particle i

is approximately given by

$$E_{\text{Bint}}(i) = \sum_j q_{ij} L\frac{q_{ij}}{kT}, \quad q_{ij} = \frac{\mu_0}{4\pi} m_i m_j \frac{3\cos^2 \xi_{ij} - 1}{d_{ij}^3} \quad (24)$$

where ξ_{ij} is an angle parameter of $\boldsymbol{r}_{ij}$. For strong enough interactions, the behavior will become cooperative in type. In any case, typical features (e.g., aging effect on the magnetization relaxation) of correlated disordered systems, such as spin–glass systems, will be observed if the experimental conditions (temperature, time window) are suitably chosen. In ferrofluids, the dynamics in aggregated particles influences the lifetime of their association.

8. Summary

The theoretical models of magnetic dynamics in ferrofluids and main macroscopic experimental features have been outlined. The main difference between Néel and Brownian relaxations lies in their timescales. It is the key to the specific properties of ferrofluids, i.e., a perfectly soft behavior (irrespective of particle size, concentration, and aggregation), an orientational texture under field, and a spatial texture caused by the magnetic interparticle interaction.

See also: Ferrofluids: Applications; Ferrofluids: Introduction; Ferrofluids: Neutron Scattering Studies; Ferrofluids: Preparation and Physical Properties; Ferrohydrodynamics

Bibliography

Brown F J Jr. 1979 Thermal fluctuations of fine ferromagnetic particles. *IEEE Trans. Magn.* **Mag-15**, 11961–208

Chantrell R W, Walmsley N, Gore J, Maylin M 2000 Calculations of the susceptibility of interacting superparamagnetic particles. *Phys. Rev.* **B63**, 024410

Coffey W T, Cregg P J, Kalmykov Yu P 1993 On the theory of Debye and Néel relaxation of single domain ferromagnetic particles. In: Prigogine I, Rice S A (eds.) *Advances in Chemistry and Physics*. Wiley, New York, Vol. 83

Coffey W T, Crothers D S F, Dormann J L, Geoghegan L J, Kennedy E C 1998 Effect of an oblique magnetic field on the superparamagnetic relaxation time. *Phys. Rev.* **B58**, 3249–66

Coverdale G N, Chantrell R W, Martin G A R, Bradbury A, Hart A, Parker D A 1998 Cluster analysis of the microstructure of colloidal dispersions using the maximum entropy technique. *J. Magn. Magn. Mater.* **188**, 41–51

Dormann J L, Fiorani D, Tronc E 1997 Magnetic relaxation in fine-particle systems. In: Prigogine I, Rice S A (eds.) *Advances in Chemistry and Physics*. Wiley, New York, Vol. 98

Dunlop D J, Özdemir Ö 1997 *Rock Magnetism*. Cambridge University Press, Cambridge

Fannin P C 1998 Wideband measurement and analysis techniques for the determination of the frequency-dependent, complex susceptibility of magnetic fluids. In: Prigogine I, Rice S A (eds.) *Advances in Chemistry and Physics*. Wiley, New York, Vol. 104

Kodama R H 1999 Magnetic nanoparticles. *J. Magn. Magn. Mater.* **200**, 359–72

Pshenichnikov A F, Mekhonoshin V V 2000 Equilibrium magnetization and microstructure of the system of superparamagnetic interacting particles: numerical simulation. *J. Magn. Magn. Mater.* **213**, 357–69

Raikher Yu L, Stepanov V I 1997 Linear and cubic dynamic susceptibilities of superparamagnetic fine particles. *Phys. Rev.* **B55**, 15005–17

E. Tronc
C.N.R.S., Université Pierre et Marie Curie Paris, France

D. Fiorani
Institute of Materials Chemistry, C.N.R., Rome, Italy

Ferrofluids: Neutron Scattering Studies

The investigation of the internal structure of magnetic fluids is often carried out by indirect techniques like magnetization measurement or *ex situ* investigations, e.g., the electron micrography of specially prepared fluid samples. This causes strict limitations concerning the interpretation of the fluid microstructure itself as well as of the dependence of macroscopic properties of the fluids on microscopic structural changes.

A possibility to overcome these restrictions is the use of neutron scattering to explore microstructural properties of magnetic fluids. In contrast to normal light, scattering neutrons are able to penetrate ferrofluid samples of reasonable thickness and to give appropriate scattering intensities on experimentally practicable time scales. The intensity of neutrons scattered by a ferrofluid contains an additional anisotropic magnetic part besides the usual nuclear scattering. This magnetic part of the scattering intensity I_m depends on the relative orientation between the scattering vector $\vec{q}$, the neutron polarization $\vec{p}$, and the magnetization of the fluid sample $\vec{m}$ respectively:

$$I_m \propto \{(\vec{q} \times \vec{p}) \cdot (\vec{q} \times \vec{m})\}^2 \tag{1}$$

If unpolarized neutrons are used—and thus the first bracket becomes a constant factor—the scattering intensity of magnetic scattering is anisotropic depending on the relative orientation between scattering vector and sample magnetization:

$$(\vec{q} \times \vec{m})^2 = \begin{Bmatrix} 0 \text{ if } \vec{q} \| \vec{m} \\ \\ 1 \text{ if } \vec{q} \perp \vec{m} \end{Bmatrix} \tag{2}$$

For an unmagnetized sample the $(\vec{q} \times \vec{m})^2$-term equals 2/3 and the scattering becomes isotropic as it
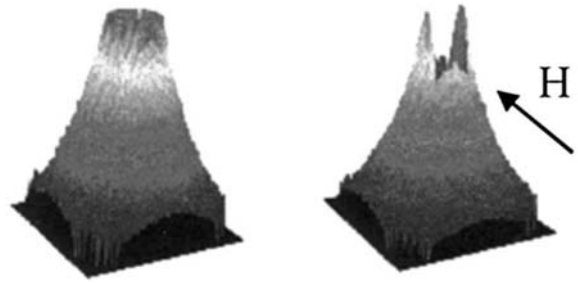
Figure 1
Typical small angle scattering signal from an unmagnetized ferrofluid (left) and from a fluid under influence of a field H in the depicted direction (right) (after Odenbach 2000).

can be seen from Fig. 1. In particular, magnetic neutron scattering allows direct access to the magnetic microstructure and thus to the solutions of questions like magnetic size distribution or cluster and chain formation of magnetic particles. Details concerning the possibility to distinguish between nuclear and magnetic scattering will be discussed in the forthcoming sections.

1. Selection of Experimental Method

The choice of the particular neutron scattering method to be used is determined by the size of the scattering units and the main goal of the investigation itself. The typical particle size range for the particles suspended in a magnetic fluid—which is usually between 5 nm and 30 nm—requires a range of q-vectors to be examined between:

$$q_{min} = \frac{2\pi}{d_{max}} \approx 0.2 \text{Å}^{-1} \text{ and}$$
$$q_{max} = \frac{2\pi}{d_{min}} \approx 1 \text{Å}^{-1} \tag{3}$$

For thermal neutrons with a wavelength λ of about 6 Å to 10 Å, which are usually used for the experiments, this corresponds to scattering angles θ defined by

$$\sin(\theta) = \frac{\lambda q}{4\pi} \tag{4}$$

in the range between $5°$ and $25°$. That means that the method usually chosen for ferrofluid investigations is small angle neutron scattering (SANS). For details on SANS experiments the reader should refer to the basic textbooks by Guinier (1963) and Egelstaff (1965). Figure 2 shows the principal set up for a SANS experiment with magnetic fluids. The sample is subjected to a collimated neutron beam transmitted through the fluid. The scattered neutrons are usually detected
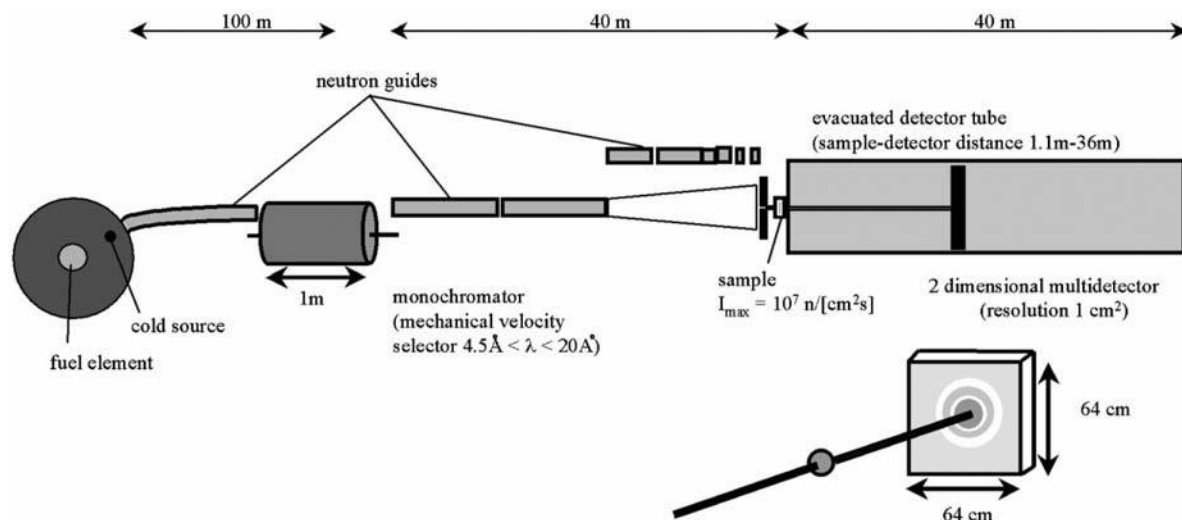
Figure 2
A typical SANS scattering geometry at the example of the small angle scattering instrument D11 at the Institute Laue Langevin in Grenoble.

using a two-dimensional array detector. The detector—sample distance can be altered to vary the maximum momentum transfer detectable. To avoid reduction of scattering intensity, the neutron path to the sample and from the sample to the detector is guided through vacuum tubes.

SANS experiments can be carried out using polarized as well as unpolarized neutrons, providing different kind of information, as can be seen from Eqn. (1). Some basic experimental questions will be discussed, followed by the experiments with unpolarized neutrons that represent the major amount of experimental work performed. Finally, experiments with polarized neutrons and other experimental techniques will be outlined.

2. Nuclear Scattering and Contrast Variation

As was already mentioned, neutron scattering on magnetizable materials provides an anisotropic part of scattering intensity as a result of the interaction between the neutrons magnetic moment and the magnetization of the sample.

Besides this, the most important part of scattering intensity will usually be made by conventional nuclear scattering. The total cross-section for nuclear scattering is composed from the coherent σ_{coh}, incoherent σ_{inc}, and absorption σ_{abs} scattering cross-sections of the particles material, the surfactant, and the solvent. The scattering cross-sections for the most important elements contained in a ferrofluid are given in Table 1.

Table 1
Scattering cross-sections for relevant elements in barns.

Element	σ_{coh}	σ_{inc}	σ_{abs}
Fe	1.86	0.46	1.4
H	1.76	79.7	0.19
D	5.59	2.01	5×10^{-4}
O	4.23	0.01	1×10^{-4}
C	4.52	0.98	3×10^{-3}

Source: Egelstaff (1965).

Essential for scattering experiments is the relation between the coherent scattering providing the signal and incoherent scattering and absorption leading to unwanted noise and signal reduction. For the metallic particles the coherent scattering cross-section is dominant compared to the incoherent part and only weak absorption occurs leading to only small reduction of the scattered intensity. For surfactant and carrier liquid, one has to distinguish between deuterated and nondeuterated material. If nondeuterated substances are used, the scattering behavior will be dominated by the incoherent scattering due to the hydrogen atoms. In this case the scattering from the surfactant and the carrier liquid will dominate the incoherent scattering of the whole sample investigated. The scattering from the particles will be just a small additional part over a strong incoherent noise and thus detection may be difficult. Furthermore, the maximum thickness of the sample in the direction of the beam will be reduced

due to the incoherent scattering by hydrogen. Experiments (Odenbach *et al.* 2000) have shown that the scattering intensity rises by a factor of approximately three if deuterated carrier liquids are used and the necessary counting time for a given sample thickness and for reasonable statistics can be furthermore reduced due to the improvement of the signal/noise ratio in the case of absence of hydrogen.

Beside this, the partial replacement of hydrogen by deuterium allows special experimental approaches providing additional information about the ferrofluid sample. If one defines the excess scattering from the particles over the scattering from the carrier liquid as the scattering contrast (Cebula *et al.* 1983b), one can change the scattering intensity by variation of the scattering from carrier liquid and surfactant. The optimization of the contrast between particles and carrier solvent provides optimum statistics of the signal and ensures that the scattered signal is dominated by the internal particle structure of the ferrofluid. By comparison of scattering intensities from a fluid with deuterated surfactant with that from one having conventional surfactant, information about the thickness of the surfactant layer can be obtained. The best way to do that is the use of a Guinier plot, i.e., a plot of the logarithm of scattered intensity over the square of *q*. This plot provides a linear relation for small q-vectors with a slope proportional to the mean size of the scattering units. Thus in the first case a Guinier plot provides the core size of the particles, in the second case it reflects the size including the surfactant.

3. SANS Experiments for Determination of Size Distribution

Size distribution determination for the particles in a magnetic fluid can be done by electron microscopy or magnetic measurement. In the first case a sample must be prepared by a process that may modify the size distribution, while the second method provides values that strictly depend on the underlying magnetic theory, in particular the question of interaction between the particles can cause serious problems.

From Eqns. (3) and (4) it is seen that the scattering angle depends on the size of the scattering structures, i.e., in the case of a ferrofluid on the size of the particles

$$\sin(\theta) = \frac{\lambda}{2d} \qquad (5)$$

A monodisperse colloid would provide a SANS signal which would directly allow the determination of the particle size from a Guinier plot. For a polydisperse system the situation becomes more difficult, since multiple signal structures are superimposed. Under these conditions a model is needed to fit the data and to obtain the size distribution. Most often
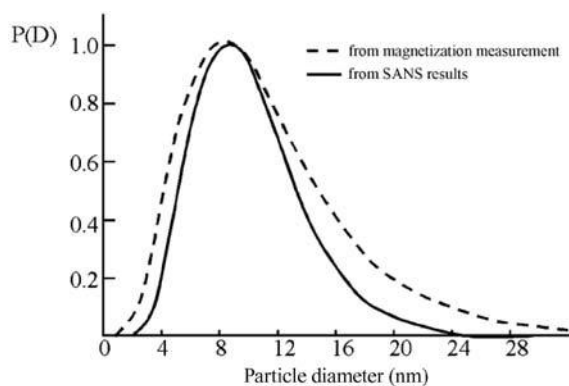
Figure 3
The comparison between particle size distributions measured with conventional magnetization measurement and by SANS. The discrepancy is explained by the neglection of field-induced interaction of the particles in magnetization measurement analysis (after Upadhyay *et al.* 1993).

the usual log normal distribution is used as base model for the fits, but newly developed fitting software at several neutron sources allows more model-independent determination of the distribution. The experimental results obtained in SANS studies show various deviations from the distributions determined with conventional methods like magnetization measurement that shed a light on some basic problems in the understanding of magnetic fluids. In some experiments (e.g., Potton *et al.* 1983) an expansion of the size distribution to larger radii was obtained from the SANS data compared to magnetization measurement, while Upadhyay *et al.* (1993) observed a narrower distribution in neutron experiments (Fig. 3).

The explanations for these discrepancies are usually taken from the lack of knowledge about basic data of the fluids themselves. While the narrower distribution is explained by field-induced magnetic interaction between the particles in magnetization measurement, not accounted for in the data evaluation of these measurements, the expansion to larger radii could be explained by the difference between the bulk saturation magnetization and that of small particles (Söffge *et al.* 1981). Furthermore, the assumption of spherical particles which is usually used when fitting the neutron data together with the considerably large errors of neutron scattering data in general could also lead to discrepancies. Thus it is seen that the underlying model for the data evaluation and the assumptions within as well as the accuracy of the data obtained are of significant influence on the results obtained. While the models used can only be improved on the basis of new experimental results, the quality of the scattering data must be optimized

(e.g., by appropriate choice of deuterated carrier liquids) to avoid additional uncertainties.

4. SANS Experiments for Observation of Cluster Formation

While SANS methods are only an alternative in determining particle size distribution, they provide a unique tool if the formation and development of clusters and cluster like structures of magnetic particles are considered. Aggregation of particles forms structures—determining the scattering process—which have sizes in the order of several hundred nm. Thus the intensity scattered by these structures will be found at even smaller scattering angles of the order of 1° and less. Even the best small angle scattering experiments available nowadays reach with such requirements the edge of their technological possibilities. Nevertheless the influence of the scattering from large structures changes the line shape of the small angle scattering signal even at higher angles easily available in experiments. Such changes can then be taken to obtain information on formation of multiparticle aggregates in magnetic fluids.

In this way, Cebula *et al.* (1983a) investigated the appearance of cluster formation in ferrofluids containing cobalt particles. They found a strong dependence of the scattering signal on the volume fraction of particles at zero field indicating the appearance of cluster formation due to magnetic dipole—dipole interaction. Furthermore, they found interference peaks when a magnetic field was applied, indicating the appearance of ordered structures like chains aligned with the magnetic field direction. Finally reduction of temperature, resulting in a reduction of thermal motion, lead to an anisotropy at $H = 0$, also indicating formation of aggregates and chains. Thus these experiments showed clearly that SANS is a powerful tool for the *in situ* observation of aggregation phenomena in ferrofluids without disturbing effects due to drying in sample preparation for electron micrography.

Extended work on aggregation formation in magnetite-based ferrofluids was carried out by Rosman *et al.* (1990). They combined the SANS measurement in variable magnetic fields with the already discussed contrast variation method providing them with the particle size distribution and the structure of the surfactant layer of the fluids under investigation. Here again the mentioned differences between conventional and neutron scattering methods appeared. Even at low volume fraction and in comparably weak magnetic fields of about 100 mT they found a formation of thin chains of particles in the direction of the applied field. Higher volume concentration enabled formation of three-dimensional rods in field direction. The interparticle distance obtained from the scattering data gave rise to the assumption that the surfactant layers are in contact in the aggregates.

Even larger structures can be observed in ferrofluid mixtures (Hayter *et al.* 1989) when macromolecules are dispersed in a ferrofluid. These nonmagnetic molecules act as magnetic voids in the liquid and arrange to macroscopic structures in presence of magnetic fields. The neutron diffraction patterns obtained show an anisotropy that corresponds to these macrostructures. In this case the neutron diffraction experiments were used to prove the possibility of alignment of nonmagnetic macromolecules by means of magnetic fluids.

5. SANS Experiments with Polarized Neutrons

During the discussion of neutron scattering data obtained from ferrofluids with unpolarized neutrons, it became clear that anisotropies in the scattering pattern can be due to magnetic effects (see Eqn. (1)) as well as due to formation of structures. The use of polarized neutrons can be a powerful help to distinguish between these two kind of anisotropies and thus to eliminate the nuclear scattering background completely. To do so the fluid sample is subjected to a beam of polarized neutrons and a polarization analysis—distinguishing between neutrons scattered with spin flip and those scattered without—is carried out after the scattering process. Coherent nuclear scattering, giving information about the structural phenomena like aggregation by measuring the particle number density, does not flip the neutrons spin. In contrast, the magnetic scattering—which is caused by the component of magnetization perpendicular to $\vec{q}$—causes spin flip for those components of magnetization which are perpendicular to the field, while the parallel one gives nonflip scattering. Therefore measurement of scattered intensity with $\vec{q}$ parallel and perpendicular to the applied field makes it possible to distinguish between nuclear and magnetic scattering signals. This technique has been used by Pynn *et al.* (1983) to analyze the interparticle structure in a cobalt ferrofluid.

The previously discussed problem of the influence of polydispersity on the SANS signal can also be reduced by the use of polarized neutrons (Nunes 1988). Furthermore, a detailed analysis of nuclear and magnetic scattering intensities and of the respective size distributions obtained can shed a light on the existence of magnetically dead layers.

6. Other Experimental Approaches

Up to now we have outlined the use of neutron scattering for determination of structure and agglomeration processes in magnetic fluids using SANS techniques. Beside this, there are a couple of experiments taking neutron scattering for other experimental

goals or using alternative scattering techniques. For example SANS experiments have been used to investigate diffusion phenomena in magnetic fluids (Odenbach *et al.* 1995) by determination of the spatial variation of magnetic scattering anisotropy. Since the anisotropy is proportional to magnetization of the fluid and since this is a measure for the concentration of particles at given magnetic field strength, one can determine the spatial variation and time dependence of concentration in a ferrofluid subjected to a magnetic field gradient. Other SANS experiments have shown that it is possible to use the anisotropy as a measure for local variations of flow velocity in a ferrofluid (Odenbach *et al.* 1999). The shear in the fluid changes the mean alignment of the particles with the magnetic field direction and thus reduces the apparent magnetization in a certain sample volume leading to a change of anisotropy.

In the characterization of a temperature-sensitive magnetic fluid the disappearance of magnetic scattering for temperatures above the Curie point has been used to distinguish between magnetic and nuclear scattering, avoiding the loss of intensity connected with the spin flip method discussed above (Upadhyay *et al.* 1997).

Finally, powder diffraction with polarized neutrons was used as an alternative method to determine the size distribution of the particles and to get information about magnetically-disordered layers (Lin *et al.* 1995).

7. Outlook

It has been discussed that neutron scattering can be a helpful tool to investigate the microstructure of magnetic fluids, the structure of particles and surfactants and the formation of clusters, aggregates, and chains. From this it is astonishing that the amount of work done in this field is not as high as one would expect considering the potential of the method. A possible reason for this could be based on the fact that shortly after the first efforts in this field the two major neutron sources in Europe, providing sufficient intensity for ferrofluid experiments—the high flux research reactors at ILL in Grenoble and at KFA in Jülich, were out of order for approximately five years for maintenance reasons. Now, after restart of both sources, the activities on neutron scattering experiments with ferrofluids have been reactivated and new results are expected in the future. In particular the investigation of structure formation in the presence of magnetic field and shear flow—which is the microscopic reason for the appearance of non-Newtonian effects in ferrofluids—is expected to become a vivid field of interest.

See also: Ferrofluids: Introduction; Ferrofluids: Preparation and Physical Properties; Ferrofluids: Magnetic Properties; Ferrohydrodynamics

Bibliography

Cebula D J, Charles S W, Popplewell J 1983a Aggregation in ferrofluids studied by neutron small angle scattering. *J. Phys.* **44**, 207–13

Cebula D J, Charles S W, Popplewell J 1983b Neutron scattering studies of ferrofluids. *J. Magn. Magn. Mater.* **39**, 67–70

Egelstaff P A 1965 *Thermal Neutron Scattering*. Academic Press, London

Guinier A 1963 *X-ray Diffraction in Crystals*. Freeman, San Francisco, pp. 319–50

Hayter J B, Pynn R, Charles S W, Skjeltorp A T, Trewhella J, Stubbs G, Timmins P 1989 Ordered macromolecular structures in ferrofluid mixtures. *Phys. Rev. Lett.* **62**, 1667–70

Lin D, Nunes A C, Majkrzak C F, Berkowitz A E 1995 Polarized neutron study of the magnetization density distribution within a $CoFe_2O_4$ colloidal particle. *J. Magn. Magn. Mater.* **145**, 343–8

Nunes A C 1988 Effect of magnetic polydispersion in superparamagnetic colloids on neutron scattering line shapes. *J. Appl. Cryst.* **21**, 129–35

Odenbach S, Gilly H, Lindner P 1999 The use of magnetic small angle neutron scattering for the detection of flow profiles in magnetic fluids. *J. Magn. Magn. Mater.* **201**, 353–6

Odenbach S, Schwahn D, Stierstadt K 1995 Evidence for diffusion-induced convection in ferrofluids from small angle neutron scattering. *Z. Phys. B* **96**, 567–9

Potton J A, Daniell G J, Eastop A D, Kitching M, Melville D, Poslad S, Rainford B D, Stanley H 1983 Ferrofluid particle size distributions from magnetization and small angle neutron scattering data. *J. Magn. Magn. Mater.* **39**, 95–8

Pynn R, Hayter J B, Charles S W 1983 Determination of ferrofluid structure by neutron polarization analysis. *Phys. Rev. Lett.* **51**, 710–3

Rosman R, Janssen J J M, Rekveldt M Th 1990 Interparticle correlations in Fe_3O_4 ferrofluids, studied by the small angle neutron scattering technique. *J. Appl. Phys.* **67**, 3072–80

Söffge F, Schmidbauer E 1981 AC susceptibility and static magnetic properties of an Fe_3O_4 ferofluid. *J. Magn. Magn. Mater.* **24**, 54–8

Upadhyay R V, Sutariya G M, Mehta R V 1993 Particle size distribution of a laboratory synthesized magnetic fluid. *J. Magn. Magn. Mater.* **123**, 262–6

Upadhyay T, Upadhyay R V, Mehta R V, Aswal V K, Goyal P S 1997 Characterization of a temperature-sensitive magnetic fluid. *Phys. Rev. B* **55**, 5585–8

S. Odenbach
Universität Bremen, Germany

Ferrofluids: Preparation and Physical Properties

A ferrofluid, or magnetic fluid as it is also commonly referred to, consists of a stable colloidal suspension of single-domain nano-sized particles of ferri- or ferromagnetic materials in a carrier liquid. A wide range of carrier liquids have been employed, and many ferrofluids are commercially available to satisfy particular

applications, e.g., in rotary vacuum lead-throughs, it is essential that the carrier liquid has a very low vapor pressure. In other applications, temperature—either high, low, or both—may be a critical consideration. Theoretically it should be possible to produce dispersions in any liquid thereby being able to tailor the requirements of viscosity, surface tension, temperature and oxidative stability, vapor pressure, stability in hostile environments, etc., to the particular application in mind, whether it be technological or biomedical (see *Ferrofluids: Applications*).

In order to achieve a stable colloidal suspension, and in this context stability refers to situations where the ferrofluid is subjected to a magnetic field, magnetic field gradient, and/or gravitational field, the magnetic particles generally have to be of approximately 10 nm in diameter. Particles of this size, whether they are ferrite or metal, possess a single magnetic domain only, i.e., the individual particles are in a permanent state of saturation magnetization.

As a result, a strong long-range magnetostatic attraction exists between individual particles which would inevitably lead to agglomeration of the particles and subsequent sedimentation unless a means of achieving a repulsive interaction can be incorporated. A repulsive mechanism (see *Ferrofluids: Introduction*) can be achieved by coating the particles with a surface-active material (surfactant) to produce an entropic repulsion or by incorporating a charge on the surface of the particles thereby producing an electrostatic repulsion. In the case of liquid–metal carriers, no such interaction has yet been achieved to produce a stable suspension.

The various methods by which small magnetic particles can be prepared and subsequently colloidally dispersed is described in this article. The preparation of particles and ferrofluids has been the subject of numerous patents and research publications. A comprehensive bibliography of this information can be found updated in each of Proceedings of the International Conference on Magnetic Fluids (ICMF), under the following authors Zahn and Shenton (1980), Charles and Rosensweig (1983), Kamiyama and Rosensweig (1987), Blums *et al.* (1990), Cabuil *et al.* (1993), Bhatnagar and Rosensweig (1995). Reviews of the subject have been given by Rosensweig (1979, 1985, 1988), Charles and Popplewell (1980), Martinet (1983) and Scholten (1978).

1. Preparation of Nano-sized Magnetic Particles

The preparation of nano-sized magnetic particles can be conveniently considered under two headings; one dealing with metal particles and the other with ferrites.

1.1 Metal Particles

There are a number of methods of producing small magnetic metallic particles, the commonest of which

for ferrofluid preparation being the decomposition of organometallic compounds. In addition, reduction of solutions of metal salts and other miscellaneous methods are available. The decomposition of organometallic compounds will be discussed in most detail as it is the easiest and most versatile method of producing metal particles suitable for ferrofluids. In most of these methods, the presence of a surfactant is crucial. By selecting an appropriate surfactant, it has been shown (Charles and Wells 1990) to be an effective method of controlling particle size.

There are two major advantages of using ferrofluids based on metallic particles, such as cobalt and iron particles. First, these metals have high saturation magnetizations compared with ferrites and second, they can be produced easily with very narrow size distributions. However, there is also a major drawback which has restricted their use in most commercial applications and that is their poor resistance to oxidation and subsequent loss of magnetic properties. Only by maintaining these fluids in an inert atmosphere can these fluids possess an extended lifetime.

(a) Decomposition of organometallic compounds

In the 1960s, several groups of workers (Thomas 1966, Hess and Parker 1966) reported the production of colloidal-sized cobalt particles by the thermolysis of dicobalt octa-carbonyl in hydrocarbon solutions containing polymeric materials. The process is very simple in that it only involves refluxing a solution of the carbonyl, usually in toluene, until the reaction is complete, with the formation of cobalt metal particles. Thomas (1966) showed that the particles possess a very narrow size distribution ideal for the production of stable colloids. The particles also possess an f.c.c. structure instead of the b.c.c. structure of bulk cobalt. The absence of a polymer in the thermolysis leads to the formation of large particles (>100 nm). A detailed investigation by Hess and Parker (1966) of the presence of different copolymers of acrylonitrile-styrene in the reaction solution showed that the greater the concentration of polar groups along the polymer chain, the smaller the size of the particles formed.

It was Smith (1981) who proposed that the reaction is polymer-catalyzed, which results in the formation of a polymer–carbonyl complex which then decomposes to form elemental cobalt. Papirer *et al.* (1983) showed that the decomposition could also be catalyzed by the presence of surfactants. They investigated the evolution of carbon monoxide during the decomposition in the presence of diethyl-2-hexyl sodium sulphosuccinate (Manoxol-OT) and in its absence, both experiments carried out as a function of temperature. The results were consistent with the presence of "micro-reactors" and a diffusion mechanism to control the growth. The higher the temperature used, the smaller the particles produced. During the

process of thermolysis in toluene, the presence of $Co_4(CO)_{12}$ was identified as an intermediate.

However, the overall reaction mechanism is complex but it seems likely that a carbonyl complex and/or microreactors are formed which subsequently decompose to produce cobalt particles. Charles and Wells (1990) investigated methods to control the size of the cobalt particles formed by the use of a variety of surfactants and combinations of surfactants. By taking aliquots of the reaction mixture as the reaction proceeded and making observations using electron microscopy, they observed the presence of clusters or microreactors for the first half hour of a four-hour reaction but no particles. Subsequently, observations showed the presence of particles only. They were able to consistently produce particles with median diameters in the range 5 to 15 nm. The median diameter refers to a lognormal volume distribution (see Sect. 1.3).

In many of the papers quoted so far, little information has been presented concerning the saturation magnetization of the particles compared to that of the bulk. Charles and Wells (1990) found the saturation magnetization of the particles to be consistently lower (75%) than that of the bulk value of 17900 Gauss (1.79 T). This result is in agreement with the work of Hess and Parker (1966). There are several possible reasons for this, namely oxidation, spin-pinning/canting, or poor crystallization. Experiments where care had been taken to avoid oxidation still showed the reduced saturation magnetization. However, evidence from x-ray diffraction indicated that the particles were poorly crystallized or amorphous with similar results being obtained for iron particles produced by a similar process (Wonterghem *et al*. 1986). X-ray diffraction and Mössbauer studies indicated the presence of carbon in the particles which is thought responsible for the poorly crystallized state.

The particles, when annealed, showed an x-ray pattern consistent with α-Fe and χ-Fe$_5$C$_2$. Some researchers, using transmission electron diffraction, have reported that the particles produced by thermolysis have a crystalline structure. Whether this is a true indication of the structure of the particles or that annealing has taken place in the electron beam is not known. Measurements of the magnetic anisotropy of cobalt particles have been undertaken by several groups of workers (Chantrell *et al*. 1980, Charles and Wells 1990).

Iron particles of colloidal dimensions can also be produced by thermolysis (Wonterghem *et al*. 1986); in this case of iron pentacarbonyl in decahydronaphthalene. Particle size is again controlled by the presence of surfactants. The actual structure of the particles is open to question. Some groups have reported a crystalline structure (Kilner *et al*. 1984), whilst others (Wonterghem *et al*. 1986) reported an amorphous structure which undergoes crystallization on annealing.

(Hoon *et al*. 1983) have reported the preparation of colloidal nickel particles by the irradiation of nickel carbonyl with ultraviolet light and by the reduction of nickelocene. The particles were reported to have an f.c.c. structure from transmission electron diffraction.

Nakatani and Furubayashi (1990) and Nakatani *et al*. (1993) have prepared iron nitride particles by two methods. First, by a plasma CVD reaction of iron pentacarbonyl and nitrogen gas and second, by heating a solution of iron pentacarbonyl in kerosene containing a surfactant through which a constant stream of ammonia is passed. The crystal structure observed is ε-Fe$_3$N.

It is also possible to prepare alloy particles of the transition metals by the thermolysis of mixed-metal organometallic compounds in the presence of surfactants. Lambrick *et al*. (1985, 1987) prepared organometallic compounds from which particles of Fe–Co and Ni–Fe alloys with median diameters ~ 8 nm were obtained. The saturation magnetizations of the particles are 84% of that of the bulk values.

(b) Reduction of metal salts in aqueous solution

Much of the work on the formation of particles by the reduction of metal salts in aqueous solution using reducing agents such as sodium hypophosphite or sodium borohydride stemmed from an interest in producing particles suitable for magnetic recording media. The particles produced were typically of micron size, which precluded their use in ferrofluids because of their large magnetic moments and consequent strong magnetostatic interactions.

However, there have been a few reports of the formation of particles of nanometer size which could be used in ferrofluids. The solutions used in the preparation contain the salts of ferromagnetic elements, a reducing agent, complexing agents, and buffers to control the pH during reaction. The formation of particles is induced by the addition of PdCl$_2$ to the solution. By the introduction of water-soluble viscosity-increasing materials, it has been shown (Akashi and Fujyama 1969) that particle size can be reduced so that the particle can remain in stable suspension. There have been a few other reports of the formation of such particles. Harada *et al*. (1972) have reported the formation of Co-P particles, using sodium hypophosphite as reducing agent, in aqueous solutions containing protein or synthetic polypeptides. Similar studies on Fe-P particles have also been undertaken.

The at.% of phosphorus or boron in the particles is very dependent on the conditions used. Above a critical concentration of boron, phosphorus, and indeed carbon, the particles possess an amorphous structure very similar to structures produced by rapid-quench techniques. The incorporation of phosphorus, boron, and carbon is a disadvantage in one respect, in that the saturation magnetization of the particles may be

significantly reduced. Small acicular particles of cobalt have been prepared using this method, performed in the presence of a uniform magnetic field (Charles and Issari 1986).

(c)   Inverse microemulsion techniques
Numerous papers have been published on the preparation of small nano-sized metal particles, some of which are ferromagnetic, via the use of reverse micelles. The stimulus for much of this work has been an interest in the production of small-particle catalysts. A reverse micelle can be described as a water-in-oil microemulsion in which two immiscible liquids are stabilized by a surfactant. As it is a three-component system, a triangular phase diagram of the three-component system is used to describe the various structures other than microemulsions that may be formed. For detailed information on micelles and particle formation, the reader is recommended to study a review edited by Pileni (1989). The method of preparation of particles involves the preparation of two microemulsions, one containing an aqueous solution of a metal salt or mixture of metal salts and the other an aqueous solution of a reducing agent, e.g., sodium borohydride.

By simply mixing the two in the appropriate ratio, metal particles, in which some boron is usually incorporated, are produced within the micelles. Because of the incorporation of boron, the particles often have an amorphous structure. Using pure surfactants, the micelle size distribution is very narrow, with the result that the particles themselves also possess a narrow particle size. It has been shown by Lopez-Quintela and Rivas (1992) that it is possible to subsequently coat the metal particles formed with another metal using a further microemulsion. This process is of particular interest in that by the use of an appropriate second metal it may be possible to overcome the recurring problem of oxidation of ferromagnetic particles of iron, cobalt, etc.

(d)   Miscellaneous methods
Fine particles of most of the metallic elements can be produced by evaporation of the metals in an inert gas atmosphere. The size of the particles so produced is very dependent on the gas used and its pressure. As was the case using the reduction of aqueous solutions of metal salts, the same stimulus for this work was the production of micron-sized particles suitable for magnetic recording.

However, ferrofluids have been prepared this way containing particles of iron, cobalt, or nickel by the vacuum evaporation on to a running oil substrate containing a surfactant (Nakatani *et al*. 1987). The particles produced by this method are very small (~ 2 nm in diameter). On heating the product to $270\,^{\circ}\mathrm{C}$ in an argon atmosphere for a few minutes, the particle size can be increased. Fluids produced by this method are gravitationally stable.

This method has also been used to produce dispersions of particles of gadolinium and transition metal alloys in mercury. Unfortunately, these fluids are not colloidally stable despite attempts to stabilize the dispersions with metallic additives.

Spark erosion has been used to produce ferrofluids. A wide range of particle sizes is produced, the smaller particles of which are suitable for dispersion to form a ferrofluid. The method suffers from disadvantages in that the process is slow and the particle distribution is very wide. However, it does have an advantage in that novel particles with similar properties to the bulk can be produced, e.g., TbFeB, which possess a large magnetostriction.

1.2   Ferrite Particles

Ferrites may possess a normal or inverse spin structure. Detailed reviews of the structures and magnetic properties of ferrites have been given by Dormann and Nogues (1990). The name spinel is given to those ferrites which have the formula MFe_2O_4 (where M is a divalent ion) and which have the cubic crystal structure of the mineral spinel ($MgAl_2O_4$). The oxygen atoms are arranged in layers in such a way that there are two types of interstitial sites, tetrahedral (A) sites and octahedral (B) sites. The net magnetic moment of each ferrite is determined by the moment of each cation, the arrangement of the cations in the A and B sites, and the interaction between cations.

The most commonly used ferrites in commercial ferrofluids are magnetite ($FeO.Fe_2O_3$) and maghemite (γ-Fe_2O_3). Because magnetite can be oxidized to maghemite with only a relatively small reduction in moment, the actual structure of the particles in commercial and other ferrofluids usually involves the presence of both ferrites in an undefined ratio. In magnetite, the moment of the two Fe^{3+} ions are split between an A site and a B site and are antiferromagnetically coupled so that the moments cancel, whereas the Fe^{2+} ion situated on the B site gives rise to the overall moment. This opposite and unequal arrangement of the moments gives rise to ferrimagnetism.

The original method of producing ferrofluids based on ferrites is attributed to Papell (1965). The method involved wet-grinding ferrites in a ball mill in the presence of a suitable surfactant until the ferrite is in a colloidal state. Centrifugation was usually employed to remove larger particles, which could lead to agglomeration and sedimentation. Many other workers subsequently studied and used this method. However, this process usually takes a very long time (~ 1000 hours) and it is mainly for this reason that the process has been superceded by a rapid and simple method involving the coprecipitation of metal salts in aqueous solution using a base. This method is the subject of the next section. No further reference will be made to wet grinding.

(a) Coprecipitation method

The coprecipitation method for the preparation of particles of magnetite, maghemite, and substituted ferrites suitable for use in ferrofluids is now well established and has been the subject of many patents and publications (see Introduction to this article *Ferrofluids: Preparation and Physical Properties*). Because the process is usually carried out at room temperature, the cation distribution on the A and B sites may not conform to the distribution in bulk-annealed crystals of the same material. Nevertheless, it is well established by x-ray diffraction that the particles formed are crystalline. Further, their magnetic characteristics with regard to magnetic crystalline anisotropy and Curie temperature are not that far removed from that of the bulk crystals.

For most technological applications, the carriers used are nonaqueous. Thus, the colloidal suspension is usually stabilized by coating the particles with a surfactant. In aqueous colloidal suspensions, surfactants can also be used to stabilize the system but suspensions can also be stabilized by the presence of a charge on the particles. The latter method has been studied extensively by Massart (1981) and his coworkers (Bacri *et al.* 1990, Bee *et al.* 1995). As magnetite and maghemite are the most commonly used materials, the discussion of the coprecipitation method is divided into two sections, one involving these materials and the other, substituted ferrites.

(b) Magnetite and maghemite particles

In the case of magnetite, particles can be prepared from the coprecipitation of hydroxides from an aqueous solution of Fe^{2+} and Fe^{3+} in the mole ratio of approximately 1:2 using a base (Khalafalla and Reimers 1973). The reaction is complex and involves the conversion of the hydroxide particles to magnetite. Oxidation of Fe^{2+} leads to the stoichiometry of the particles not being purely magnetite, which can be circumvented by adjusting the ratio of the Fe^{2+} and Fe^{3+} concentrations.

Some oxidation of the particles themselves may occur during the preparation or may subsequently oxidize over a period of time to maghemite (γ-Fe_2O_3). However, oxidation appears to be of little consequence in most technological application as the oxidation has little effect, if any, on the colloidal stability, and results in only a relatively small decrease in the magnetic moment of the particles, at most 10%. In cases where maghemite is preferred, it is a relatively simple process to oxidize the particles of magnetite by heating the particles to $90\,^{\circ}C$ for thirty minutes in a $0.34\,M$ solution of ferric nitrate (Bee *et al.* 1995).

The co-precipitation process is an extremely versatile method of producing ferrite particles in that particles of different size and magnetic properties may be prepared by simply controlling the experimental conditions. (Massart and Cabuil 1987) have

shown that control of the mole fraction ratio of Fe^{3+}:Fe^{2+}, their concentrations, nature and concentration of the alkali medium can enable particles to be prepared of the desired size. This work has been extended by Davies *et al.* (1993) to include studies of the effect of precipitation temperature on particle size, the effect of heating the precipitate in the alkaline medium, and the effect of addition of surfactant to the reaction mixture.

They have shown that the particle size increases when uncoated particles are heated in the alkaline medium and that the extent of this increase depends on the temperature to which the particles are heated. For an increase in precipitation temperature (between $2\,^{\circ}C$ and $90\,^{\circ}C$) and without subsequent heating in the alkali media, an increase in particle size is observed. The effect of changing the initial Fe^{3+}:Fe^{2+} molar ratio from 2:1 to 1.5:1 and also changing the bases (KOH, NaOH and NH_4OH) have been shown to have an effect on the particle size.

The particle size distribution obtained on changing these various parameters is attributed to changes in the nucleation and growth rate, which in turn depend on the relative supersaturation of the solute, S, the rate of nucleation, R_N, and the critical size for formation of a particle, r^*. The clustering of molecules and subsequent particle precipitation depends on the relative supersaturation of the solute, where the relative supersaturation is the ratio of the activity of the solute in the supersaturated solution to that at equilibrium. A level of supersaturation, S, exists below which nucleation is slow and above which R_N increases rapidly. Nuclei below a critical size, r^*, may either dissolve or grow, but above which nuclei grow and precipitation occurs.

Expressions for r^* and R_N are given by Walbridge (1987) which depend on the interfacial tension and free energy of dilution per unit volume of the precipitating phase. During the precipitation, the supersaturation level falls and the rate of nucleation, R_N, decreases. It follows that with an increase in S, the critical size, r^*, decreases. Consequently, as nucleation is occurring, the supersaturation level falls and the critical size increases. As r^* increases, the smaller particles dissolve preferentially resulting in a narrower size distribution (Ostwald ripening). Particle growth may also occur whereby smaller particles adhere to the larger particles, thereby promoting growth.

In addition to simple straightforward precipitation, it is possible to produce particles using the microemulsion technique as described in 1.1(c) (Gobe *et al.* 1984).

(c) Substituted ferrites

Coprecipitation is not only a very versatile method of producing particles suitable for ferrofluids but it also enables one to produce a wide range of substituted ferrites. The Fe^{2+} ion is simply replaced or partially

replaced by another or combination of divalent metal ions such as Co^{2+}, Mn^{2+}, Ni^{2+}, Zn^{2+}, etc. Ions of other valency, e.g., Li^+ can also be used to prepare substituted ferrites. Numerous papers and patents have been published on this subject. See the references given in the Introduction to this article (*Ferrofluids: Preparation and Physical Properties*). The method of precipitation of the particles is essentially the same as that used to prepare magnetite. Thus it is not important that details of individual preparations be given here, except to say that in some cases the precipitate needs to be hydrotheramally aged to facilitate the conversion of the precipitated hydroxides to the ferrite.

The interest in substituted ferrites stems from differences in the magnetic properties of these materials (Dormann and Nogues 1990). For example, in the case of cobalt ferrites, the magnetocrystalline anisotropy can be very high (Davies *et al.* 1995) so even for nano-sized particles, the magnetic moment is "blocked." Other ferrites, which have relatively low Néel temperatures ($\sim 100\,°C$) and thus high thermomagnetic coefficients at these temperatures, have been used in studies of thermomagnetic convection (Fujita *et al.* 1990) and heat transfer (Nakatsuka *et al.* 1990).

1.3 Particle-size Distribution

An important parameter in characterization of fluids is knowledge of the particle-size distribution in ferrofluids. It is not only a pointer to the likely stability of the fluid in the presence of a magnetic field gradient but also is a means of monitoring the reproducibility of the method of particle preparation. It is an obvious advantage to have a narrow particle-size distribution since large particles, which may adversely affect the performance of the fluid, are absent.

Particle-size distribution is best monitored by using transmission electron microscopy. However, another method based on measurement of the magnetization curve of the fluid is particularly convenient (Chantrell *et al.* 1978). To obtain the particle size, the saturation magnetization of the particles is needed. Use of the bulk value may lead to erroneous values, particularly in the case of ferromagnetic particles where values of the saturation magnetization of the particles and bulk can differ greatly. The method also assumes that the particle-size distribution can be described by a log-normal volume distribution (O'Grady and Bradbury 1983). This distribution has been found to be a good representation for most systems studied whether they are based on metallic or ferrite particles.

X-ray diffraction and use of the Debye-Scherrer expression is a satisfactory pointer to the particle size for well-crystallized particles. This method is obviously of no value for particles such as some of the metal particles, which have an amorphous structure.

2. Preparation of Ferrofluids

For most applications low viscosity, low vapor pressure, and chemical inertness are desirable for the carrier liquid and surfactant. Scholten (1978) gives a review of the chemical and physical problems associated with these parameters and lists the advantages and disadvantages associated with different carrier liquids.

2.1 Using Metal Particles

One drawback exists in producing ferrofluids containing metal particles using the methods described in Sect. 1.1; in those cases where a surfactant is chosen to produce particles of a particular size, that surfactant may not be compatible with the carrier liquid needed for a particular application. Although the surfactants used in the preparation can be removed prior to dispersion in another carrier liquid containing an appropriate surfactant, this is not always an easy option. Thus, sometimes a compromise has to be made. To achieve compatibility between the surfactant and carrier liquid, one may have to be flexible in one's choice of particle size, which is dictated by the surfactant used in the preparation of the particles.

Alternatively, sometimes it is possible to achieve a stable colloid by the addition of a secondary surfactant. Transfer of the coated particles to the carrier of choice is best facilitated by rotary evaporation under reduced pressure of the solvent used in the preparation, in the presence of the carrier liquid. The volume of the latter dictates the value of the saturation magnetization of the ferrofluid. This value will in turn be dictated by the requirements of viscosity for particular applications. For particles of iron, cobalt, and Fe_3N, saturation magnetizations of 2000 Gauss (0.2 T) are feasible (Scholten 1983), representing a volume fraction of the metal particles between 10% and 20%.

2.2 Using Ferrite Particles

(a) Surfactant-stabilized particles

Various methods of coating particles prior to dispersion in a carrier liquid have been described but all are basically the same with small differences in procedure. As an example of one method, magnetite can be coated with oleic acid by adding the acid to the precipitated phase in alkaline solution at pH ~ 9.5. The mixture is usually left stirring for approximately one hour after which time it is heated to $95\,°C$ to facilitate the conversion of hydroxides formed to ferrite. After cooling, the product is acidified to pH 5.0 using nitric acid. The oleate ion produced chemisorbs strongly on to the magnetite particles, and the precipitate coagulates and falls out of solution. The coagulation may also be accompanied by the appearance of a thin film of oleic acid on the surface of the supernatant liquid

which is unadsorbed oleate ions reconverted to oleic acid in acid solution.

Sufficient oleic acid must be added to form a monolayer coverage (Davies *et al.* 1993). The supernatant liquid can be decanted and the agglomerated hydrophobic precipitate of coated particles washed several times to remove salts such as nitrates and sulfates. Water and any physisorbed oleic acid can be removed by washing with acetone. By adding the appropriate carrier liquid to the acetone-wet slurry and gently heating, the acetone and any residual water can be removed leaving a colloidal dispersion of magnetite. If any aggregates are present it may be necessary to centrifuge the fluid or subject the fluid to a high-gradient magnetic field separator (HGMS) (O'Grady *et al.* 1986). If the washing procedure with water has not been carried out carefully, the presence of small quantities of micron-sized particles of salt may be present, which must be filtered.

Using this method with the appropriate surfactant it is possible to produce stable colloids in low vapor pressure carriers such as diesters (Wyman 1984), polyphenyl ethers (Bottenberg and Chagnon 1982), silicone oils (Chagnon 1982), hydrocarbons (Khalafalla and Reimers 1973), perfluorocarbons, perfluoropolyethers, etc.

Stable water-based fluids can be produced by this method by the addition of a variety of secondary surfactants to oleate-coated particles (Shimoiizaka *et al.* 1978).

As with fluids prepared from metal particles, the limiting value of saturation magnetization of ferrite-based fluids depends on the desired viscosity of the fluids. Fluids with magnetization up to approximately 1000 Gauss (0.1 T) can be prepared (Scholten 1983), which represents approximately 25 vol.% of ferrite. Most ferrites have saturation magnetizations at 20 °C up to a maximum value of 5000 Gauss (0.5 T).

(b) Ionically stabilized particles

Massart (1981) developed the method of producing stable colloidal dispersions in alkaline and acidic aqueous media. He and his coworkers have subsequently made extensive and detailed studies of such dispersions, e.g., Bacri *et al.* (1990), Bee *et al.* (1995).

The production of particles of magnetite and maghemite, the latter produced by oxidizing magnetite particles in ferric nitrate solution (see Sect. 1.2(b)), are produced using a similar method to that already described. The particles produced by this method are macroions in which the electric changes are due to specific adsorption of the amphoteric hydroxyl group. In an alkaline medium, the particles are negatively charged and in an acidic medium, positively charged. These particles can be stabilized in water by the presence of low-polarizing counter-ions such as $N(CH_3)_4^+$ in alkaline medium, or ClO_4^- in acidic medium. Strongly polarizing counter-ions lead to flocculation.

For the -OH ligand, the point-of-zero-charge (PZC) occurs at approximately pH = 7.5. The small surface-charge density in this region of pH precludes the formation of a stable colloidal suspension. Using OH^- ligands, stable suspensions are restricted to pH values outside the range 6–10. Massart and co-workers (Bacri *et al.* 1990) overcame this problem by modifying the nature of the surface charges by substituting the -OH surface ligands by citrate ligands. In so doing, they were able to synthesize stable fluids in the pH range 3–11.

2.3 Assessment of Colloidal Stability

In many applications of magnetic fluids, such as exclusion seals, loudspeakers, etc. (see *Ferrofluids: Applications*), the fluids are subjected to large magnetic fields and field gradients. It is thus of paramount importance that the fluids are free from the presence of large agglomerates or large particles so that fluid stability can be maintained and sedimentation averted. A review of the role that aggregation plays in determining the properties of magnetic fluids has been presented by Charles (1988) as well as the various techniques by which aggregation can be studied, both experimentally and theoretically.

The stability of a fluid can be best monitored by simply measuring the saturation magnetization of the fluid and the magnetic particle size (Chantrell *et al.* 1978) before and after subjecting the fluid to a strong magnetic field gradient. An effective and simple way of studying the effect of a magnetic field gradient on colloidal stability is by the use of a high-gradient magnetic field separator (HGMS) (O'Grady *et al.* 1986). Other methods to monitor the presence of agglomerates and large particles include ac-susceptibility measurements (Fannin *et al.* 1987), light scattering (Beresford and Smith 1973), or small-angle neutron scattering (SANS) (Cebula *et al.* 1983).

A simple method to undertake routine and reproducible measurements of stability and thereby make meaningful comparisons between different fluids is by means of a system based on a Colpitts oscillator (Bissell *et al.* 1984). In this method, a long (15 cm) narrow tube is filled with ferrofluid. Measurements of inductance along the length of the tube enable variations in the concentration of the particles to be monitored. Application of a magnetic field gradient allows a comparison of the concentration profile to be made before and after exposure.

3. Physical Properties of Ferrofluids

An overview of the requirements for the stability of ferrofluids and some of the basic magnetic and physical properties is given in *Ferrofluids: Introduction*. The ferrohydrodynamics of ferrofluids, including such processes as convection, mass, and heat transfer, are

discussed in *Ferrohydrodynamics*. Magneto-optic effects have been discussed by Scholten (1980), and thermal conductivity studies made by Popplewell *et al.* (1982).

For many applications of ferrofluids, a knowledge of the saturation magnetization of the fluid, initial magnetic susceptibility, viscosity, operating temperature range, surface tension, and thermal conductivity are required. Much of this information is to be found in Table 2.4 of the monograph by Rosensweig (1985).

In this section, because of their important role in technological applications, discussion of the physical properties will be confined to the viscosity of ferrofluids in the presence of an applied field, and phase separation.

3.1 Viscosity

In the absence of an applied field, a ferrofluid has rheological properties similar to any other colloidal suspension. A colloidal suspension will exhibit a viscosity greater than that of the pure carrier liquid due to the presence of suspended particles, increasing the energy dissipation during viscous flow. In ferrofluids, where unbound dispersants are present, the viscosity will also be enhanced.

The viscosity of the suspension depends on the volume fraction, φ, of the coated particles, which for $\varphi < 0.1$ follows the well-known Einstein relation

$$\eta_\mathrm{f}/\eta_\mathrm{o} = (1 + 2.5\alpha\varphi) \qquad (1)$$

where η_f is the viscosity of the fluid, η_o is that of the carrier, and α is a factor dependent on the shape of the particles, which is unity for spheres.

The above relation is not valid for higher concentrations and so various other relations have been proposed which all, more or less, describe the φ-dependent viscosity satisfactorily. De Bruyn (1960) proposed the following relationship for spherical particles.

$$(\eta_\mathrm{f} - \eta_\mathrm{o})/\eta_\mathrm{f} = 2.5\varphi - (2.5\varphi_\mathrm{c} - 1)\varphi^2/\varphi_\mathrm{c}^2 \qquad (2)$$

where $\varphi_\mathrm{c} = 0.74$ represents a critical concentration at which the liquid becomes solid. In the case of ferrofluids, φ represents the volume fraction of coated particles. In situations where the particles are acicular, then the coefficient in Eqn. (1) can increase significantly and thereby the viscosity, which in most applications is to be avoided.

Experimental and theoretical studies of the viscosity in the presence of a magnetic field have been reported. The magnetic field dependence of the viscosity is dependent on whether the magnetic moments within the suspended particles are "blocked" or are free to rotate within the time scale of the measurements, i.e., superparamagnetic. In a situation where the moments cannot rotate freely, the magnetic

moments in the fluid are subjected to a torque $\boldsymbol{\mu} \times \mathbf{H}$ where $\boldsymbol{\mu}$ is the magnetic moment of a particle and $\mathbf{H}$ is the applied field. As a result, the moments tend to align with the direction of the field with the result that it changes the state of rotation of the particles causing increased viscous dissipation.

When the fluid vorticity and magnetic field are parallel, the particle can rotate freely and thus the viscosity of dilute suspensions should be unaffected. When perpendicular, the viscosity should increase and reach an asymptotic value for high fields at which the particles are prevented from rotating. If the moments were completely free to rotate within the particle (superparamagnetism) then the field effects would be negligible in either orientation. Good agreement was found between the experimental observations of McTague (1969) and the theoretical calculations of Shliomis (1974). Shliomis showed that non-Newtonian behavior, i.e., shear thinning, should occur.

In the case of concentrated suspensions or poorly dispersed systems where agglomeration is prevalent, shear thinning can be pronounced. Studies by Rosensweig *et al.* (1969) of the field- and shear-dependent viscosity of ferrofluids showed a significantly greater enhanced viscosity with field than predicted by Shliomis. These results were attributed to the presence of agglomerates.

3.2 Field-induced Agglomeration and Phase Separation

In most technological applications, the presence of field-induced agglomeration is to be avoided as it will ultimately lead to sedimentation and failure of the device. For good well-dispersed systems, the problem of field-induced agglomeration is not a problem. This is well established by the fact that ferrofluids have operated successfully for long periods in devices in which strong fields are present and where shear is absent which could otherwise break up agglomerates.

In certain applications, field-induced agglomeration is a property that is essential, for example, for the observation of magnetic domain boundaries (Jones and Puchalska 1979), and for the observation of magneto-optic effects, e.g., birefringence, in ferrofluids (Scholten 1980).

Theoretical studies using Monte Carlo methods have been carried out by Chantrell *et al.* (1982) to investigate the effects of particle interaction on chaining in ferrofluids (see *Ferrohydrodynamics*).

In any device employing a ferrofluid, it is essential that the ferrofluid remains stable under all conditions of operation. However, it has been reported by Bacri and Salin (1982), Rosensweig and Popplewell (1991) and others that a phase separation into liquids of different concentrations can occur. In this phenomenon, the concentrated phase consists of droplets

which in the presence of a field are elongated in the field direction. In the case of field-induced phase separation, removal of the field causes break-up of the droplets into small droplets, which subsequently disappear by diffusion. This phenomenon has been studied theoretically by Cebers (1983) and Buyevich and Ivanov (1992) using a thermodynamic model, Sano and Doi (1983) using a lattice-gas model, and Berkovsky *et al.* (1987) using a cell model. Coexistence curves, in which the concentrated phase and dilute phase of the ferrofluid in the presence of a magnetic field as a function of dipole–dipole interactions, have been presented. For small particles, in which the dipole–dipole interactions are small, no phase-separation occurs in very strong fields.

If large particles are present then phase-separation can occur in zero field. Factors, other than a magnetic field, which may induce a phase transition include lowering of the temperature, variation of free surfactant concentration for sterically stabilized particles, and an increase of ionic strength for electrostatically stabilized fluids. Bacri *et al.* (1990) have studied magnetic field-induced phase separation, ionic-strength induced phase separation and the reversibility of phase separation and the effect of polydispersity. Coexistence curves have been presented. Recent studies have been made by Rosensweig and Popplewell (1991) of the influence of concentration and temperature on the magnetic field-induced phase transition of surfactant-stabilized fluids. They observed phase separation for which a coexistence curve was produced.

One of the problems in any analysis of phase separation is how to distinguish between fluids in which the particles are well-dispersed, i.e., no agglomerates present, and those in which agglomerates, too small to be seen optically, are nevertheless present. In the latter case, the presence of a field will transform the agglomerates from having no resultant moment (flux closure) to one in which a large moment is present. In these circumstances, chaining will arise leading to the presence of elongated structures, which, on removal of the field, will break up and disappear.

Whether phase separation exists or agglomerates are present in a fluid, both effects are unwelcome when it comes to consider fluids for use in devices. These problems can be circumvented by the use of fluids in which the particles are small and agglomeration negligible.

See also: Ferrofluids: Magnetic Properties; Ferrofluids: Neutron Scattering Studies; Ferrohydrodynamics

Bibliography

Akashi G, Fujyama M 1969 Process for the production of magnetic substances. US Patent 3 607 218

Bacri J-C, Salin D 1982 Optical scattering on ferrofluid agglomerates. *J. Phys. Lett.* **43**, L771–7

Bacri J-C, Perzynski R, Salin D, Cabuil V, Massart R 1990 Ionic ferrofluids: a crossing of chemistry and physics. *J. Magn. Magn. Mater.* **85**, 27–32

Bee A, Massart R, Neveu S 1995 Synthesis of very fine maghemite particles. *J. Magn. Magn. Mater.* **149**, 6–9

Beresford J, Smith F M 1973 In: Parfitt G D (ed.) *Dispersion of Powders in Liquids.* Publ. Appl. Science

Berkovsky B M, Kalikmanov V I, Filinor V S 1987 On equilibrium properties and phase diagrams of magnetic fluids. *J. Magn. Magn. Mater.* **65**, 191–4

Bhatnagar S P, Rosensweig R E 1995 Magnetic fluids bibliography. *J. Magn. Magn. Mater.* **149**, 198–232

Bissell P R, Chantrell R W, Spratt G W D, Bates P A, O'Grady K 1984 Long-term stability measurements on magnetic fluids. *IEEE Trans. Mag.* **MAG-20**, 1738–40

Blums E, Ozols R, Rosensweig R E 1990 Magnetic fluids bibliography. *J. Magn. Magn. Mater.* **85**, 303–82

Bottenberg W R, Chagnon M S 1982 Low vapor-pressure ferrofluids using surfactant-containing polyphenyl ether. US Patent 4 315 827

Buyevich Y A, Ivanov A O 1992 Equilibrium properties of ferrocolloids. *Physica A* **190**, 276–94

Cabuil V, Neveu S, Rosensweig R E 1993 Magnetic fluids bibliography. *J. Magn. Magn. Mater.* **122**, 437–82

Cebers A O 1983 Thermodynamic stability of magnetofluids. *Magnetohydrodynamics.* **2**, 146–50

Cebula D J, Charles S W, Popplewell J 1983 Aggregation in ferrofluids studied by neutron small angle scattering. *J. Phys.* **44**, 207–13

Chagnon M S 1982 Stable ferrofluid compositions. US Patent 4 356 098

Chantrell R W, Popplewell J, Charles S W 1978 Measurements of particle-size distribution parameters in ferrofluids. *IEEE Trans. Mag.* **MAG-14**, 975–7

Chantrell R W, Popplewell J, Charles S W 1980 The coercivity of a system of single domain particles with randomly oriented easy axes. *J. Magn. Magn. Mater* **15–18**, 1123–4

Chantrell R W, Bradbury A, Popplewell J, Charles S W 1982 Agglomerate formation in a magnetic fluid. *J. Appl. Phys.* **53** (3), 2742–4

Charles S W, Popplewell J 1980 Ferromagnetic liquids. In: Wohlfarth E P (ed.) *Ferromagnetic Materials.* North-Holland, Amsterdam, Vol. 2, pp. 509–59

Charles S W, Rosensweig R E 1983 Magnetic fluids bibliography. *J. Magn. Magn. Mater.* **39**, 190–220

Charles S W, Issari B 1986 The preparation and properties of small acicular particles of cobalt. *J. Magn. Magn. Mater.* **54–57**, 743–4

Charles S W 1988 Aggregation in magnetic fluids and magnetic fluid composites. *Chem. Eng. Comm.* **67**, 145–80

Charles S W, Wells S 1990 Magnetic properties of colloidal suspensions of cobalt. *Magnetohydrodynamics.* **26**, 288–92

Davies K J, Wells S, Charles S W 1993 The effect of temperature and oleate adsorption on the growth of maghemite particles. *J. Magn. Magn. Mater.* **122**, 24–8

Davies K J, Wells S, Upadhyay R V, Charles S W, O'Grady K, El Hilo M, Meaz T, Mørup S 1995 The observation of multiaxial anisotropy in ultrafine cobalt ferrite particles used in magnetic fluids. *J. Magn. Magn. Mater.* **149**, 14–8

De Bruyn H 1960 In: Kruyt H R (ed.) *Colloid Science, Vol. I.* Elsevier, Amsterdam

Dormann J-L, Nogues M 1990 Magnetic structure of substituted ferrites. *J. Phys: Condens. Mater.* **2**, 1223–37

Fannin P C, Scaife B K P, Charles S W 1987 The study of the complex susceptibility of ferrofluids and rotational Brownian motion. *J. Magn. Magn. Mater*. **65**, 279–81

Fujita T, Mamiya M, Jeyadevan B 1990 Basic study of heat convection pipe using temperature sensitive magnetic fluid. *J. Magn. Magn. Mater*. **85**, 203–6

Gobe M, Kon-No K, Kitahara A 1984 Preparation of magnetite superfine sol in w/o microemulsion. *J. Coll. Int. Sci*. **93**, 293–5

Harada S, Yamanashi T, Ugaji M 1972 Preparation and magnetic properties of cobalt alloy particles. *IEEE Trans. Mag*. **MAG-8**, 468–72

Hess P H, Parker P H 1966 Polymers for stabilization of colloidal cobalt particles. *J. Appl. Polymer Sci*. **10**, 1915–7

Hoon S R, Kilner M, Russell G J, Tanner B K 1983 Preparation and properties of nickel ferrofluids. *J. Magn. Magn. Mater*. **39**, 107–10

Jones G A, Puchalska I B 1979 Interference colors of colloid patterns associated with magnetic domain structures. *Philos. Mag*. **B40**, 89–96

Kamiyama S, Rosensweig R E 1987 Magnetic fluids bibliography. *J. Magn. Magn. Mater*. **65**, 401–39

Khalafalla S E, Reimers G W 1973 Magnetofluids and their manufacture. US Patent 3 764 540

Kilner M, Hoon S R, Lambrick D R, Potton J A, Tanner B K 1984 Preparation and properties of metallic iron ferrofluids. *IEEE Trans. Magn*. **MAG-20**, 1735–7

Lambrick D B, Mason N, Harris N J, Russell G J, Hoon S R, Kilner M 1985 An iron–cobalt alloy magnetic fluid. *IEEE Trans. Magn*. **MAG-21**, 1891–3

Lambrick D B, Mason N, Hoon S R, Kilner M 1987 Preparation and properties of Ni-Fe magnetic fluids. *J. Magn. Magn. Mater*. **65**, 257–60

López-Quintela M A, Rivas J 1992 Covering of magnetic particles to produce stable magnetic fluids. Spanish Patent 9 201 984 (see also 1994, Structural and magnetic characterization of cobalt particles coated with silver. *J. Appl. Phys*. **76**, 6564–6)

Martinet A 1983 The case of ferrofluids. In: *Aggregation Processes in Solution*. Elsevier, New York, Chap. 18, pp. 1–41

Massart R 1981 Preparation of aqueous magnetic liquids in alkaline and acidic media. *IEEE Trans. Magn*. **MAG-17**, 1247–8

Massart R, Cabuil V 1987 Effect of some parameters on the formation of colloidal magnetite in alkaline medium. *J. Chim. Phys*. **84**, 967–73

McTague J P 1969 Magnetoviscosity of magnetic colloids. *J. Chem. Phys*. **51** (1), 133–6

Nakatani I, Furubayashi T, Takahashi T, Hanaoka H 1987 Preparation and magnetic properties of colloidal ferromagnetic metals. *J. Magn. Magn. Mater*. **65**, 261–4

Nakatani I, Furubayashi T 1990 Iron–nitride magnetic fluids prepared by plasma CVD technique. *J. Magn. Magn. Mater*. **85**, 11–3

Nakatani I, Hijikata M, Ozawa K 1993 Iron–nitride fluids prepared by vapor-liquid reaction. *J. Magn. Magn. Mater*. **122**, 10–4

Nakatsuka K, Hama Y, Takahashi J 1990 Heat transfer in temperature-sensitive magnetic fluids. *J. Magn. Magn. Mater*. **85**, 207–9

O'Grady K, Bradbury A 1983 Particle-size analysis in ferrofluids. *J. Magn. Magn. Mater*. **39**, 91–4

O'Grady K, Stewardson H R, Chantrell R W, Fletcher D, Unwin D, Parker M R 1986 Magnetic filtration of ferrofluids. *IEEE Trans. Mag*. **MAG-22**, 1134–6

Papell S S 1965 Low-viscosity magnetic fluid obtained by the colloidal suspension of magnetic particles. US Patent 3 215 572

Papirer E, Horny P, Balard H, Anthore R, Petipas R, Martinet A 1983 The preparation of a ferrofluid by the decomposition of dicobalt octacarbonyl. *J. Coll. Int. Sci*. **94**, 207–20

Pileni M P 1989 *Structure and Reactivity of Reverse Micelles*. Elsevier, Amsterdam

Popplewell J, Al-Qenaie A, Charles S W, Moskowitz R, Raj K 1982 Thermal conductivity measurements on ferrofluids. *J. Coll. Poly. Sci*. **260**, 333–8

Rosensweig R E, Miskolczy G, Ezekiel F D 1969 Viscosity of magnetic fluid in a magnetic field. *J. Coll. Int. Sci*. **29** (4), 680–6

Rosensweig R E 1979 Fluid dynamics and science of magnetic liquids. In: Martin M (ed.) *Advances in Electronics and Electron Physics*. Vol. 48, Academic Press, New York, pp. 103–99

Rosensweig R E 1985 *Ferrohydrodynamics*. Cambridge University Press, Cambridge

Rosensweig R E 1988 Special Issue on Ferrofluids. *Chem. Eng. Commun*. **67**, 1–340

Rosensweig R E, Popplewell J 1991 Influence of concentration on field-induced phase transitions in magnetic fluids. *Int. Symp. Electromagnetic Forces*. Institute of Fluid Science, Sendai, Japan

Sano K, Doi M 1983 Theory of agglomeration of ferromagnetic particles in magnetic fluids. *J. Phys. Soc. Jpn*. **52**, 2810–5

Scholten P C 1978 In: Berkovsky B M (ed.) *Thermomechanics of Magnetic Fluids*. Hemisphere, Washington, DC, pp. 1–26

Scholten P C 1980 The origin of magnetic birefringence and dichroism in magnetic fluids. *IEEE Trans. Magn* **MAG-16**, 221–5

Scholten P C 1983 How magnetic can a fluid be? *J. Magn. Magn. Mater*. **39**, 99–106

Shimoiizaka J, Nakatsuka K, Chubachi R 1978 Rheological characteristics of water-based magnetic fluids. In: Berkovsky B M (ed.) *Thermomechanics of Magnetic Fluids*. Hemisphere, Washington, DC, pp. 67–76

Shliomis M I 1974 Magnetic fluids. *Soviet Phys. Uspekhi (Eng. transl.)* **17** (2), 153–69

Smith T W 1981 Surfactant-catalyzed decomposition of dicobalt octacarbonyl. US Patent 4 252 673

Thomas J R 1966 Preparation and magnetic properties of colloidal cobalt particles. *J. Appl. Phys*. **37** (7), 2914–5

Walbridge D J 1987 Preparation of solid/liquid dispersions. In: Tadros F (ed.) *Solid–Liquid Dispersions*. Academic Press, Dublin

van Wonterghem J, Mørup S, Charles S W, Wells S, Villadsen J 1986 Formation of a metallic glass by thermal decomposition of Fe(CO)$_5$. *Phys. Rev. Lett*. **55**, 410–3

Wyman J E 1984 Ferrofluid composition and method of making the same. US Patent 4 430 239

Zahn M, Shenton K E 1980 Magnetic fluids bibliography. *IEEE Trans. Mag* **MAG-16** (2), 387–415

S. W. Charles
University of Wales, Bangor, UK

Ferrohydrodynamics

Ferrohydrodynamics describes the study of the flow behavior of magnetic fluid media. The basic equations of ferrohydrodynamics are introduced. The basic equations of hydrodynamics of a magnetic fluid

consist of three conservation laws of mass, momentum and energy which differ from those of ordinary fluid by the inclusion of a magnetic tensor which is known as the Maxwell stress tensor. The momentum equation is constructed by two different treatments depending on the particle size dispersed in the base liquid. In the case of relatively small particles which behave superparamagnetically, the magnetization of the magnetic fluid is treated as being collinear with the magnetic field. On the other hand, in the case of relatively large particles, it is necessary to treat the fluid as a micropolar fluid.

Pipe flow problems are explained as representative examples of ferrohydrodynamics. The effect of uniform and nonuniform magnetic fields on steady pipe flow resistance of laminar and turbulent flow states is described. The experimental data for laminar flow show a large increase in the flow resistance due to the applied magnetic field which means that the particles in a fluid partially aggregate in the applied magnetic field even in a flowing state. Gas–liquid two-phase flow and oscillatory flow characteristics in a pipe are also taken up in the application of stationary and alternating magnetic fields.

Finally, the ordinary fluid flow around a circular cylinder coated with a magnetic fluid film is described to clarify the drag reduction mechanism of the flow around a blunt body.

1. Basic Equations of Ferrohydrodynamics

1.1 Magnetic Body Force

If the local magnetization vector is collinear with the local magnetic field vector in any volume element, Eqn. (1) for the magnetic stress tensor in magnetic fluids can be obtained in the general form (Rosensweig 1985):

$$T_{ij} = -\left\{ \mu_0 \int_0^H \left(\frac{\partial Mv}{\partial v} \right)_{H,T} \mathrm{d}H + \frac{\mu_0}{2}H^2 \right\} \delta_{ij} + B_i H_j \quad (1)$$

where M is magnetization, H the magnetic field, B the magnetic flux density, v the specific volume ($\mathrm{m^3 kg^{-1}}$), δ_{ij} the Kronecker delta, and μ_0 the permeability of free space which has the value of $4\pi \times 10^{-7}\,\mathrm{Hm^{-1}}$. In Cartesian coordinates, j is a component of the vectorial force per unit area, or traction, on an inflinitesimal surface whose normal is oriented in i direction.

The magnetic body force density is given by $\mathbf{f}_m = \nabla \cdot \mathbf{T}$. Its component are represented by:

$$f_i = (\nabla \cdot \mathbf{T})_j = \sum_i \frac{\partial T_{ij}}{\partial x_i} \quad (2)$$

The vector expression for the magnetic body force may be written as:

$$\mathbf{f}_m = -\nabla \left\{ \mu_0 \int_0^H \left(\frac{\partial Mv}{\partial v} \right)_{H,T} \mathrm{d}H \right\} + \mu_0(\mathbf{M} \cdot \nabla)\mathbf{H} \quad (3)$$

1.2 Quasi-stationary Hydrodynamics

To analyze the magnetic fluid flow, it is necessary to formulate a momentum equation for magnetic fluids which was first proposed by Neuringer and Rosensweig (1964). They considered the limiting case that the relaxation time for magnetization is zero; that is, the magnetization $\mathbf{M}$ is collinear with the magnetic field $\mathbf{H}$. Collinearity is a good approximation for sufficiently small size particles which behave superparamagnetically. The direction of magnetic moment $\mathbf{M}$, then, rotates freely within the solid particle.

The system of ferrohydrodynamics equations is described as follows. The continuity equation is:

$$\frac{\partial \rho}{\partial t} + \nabla \cdot (\rho \mathbf{u}) = 0 \quad (4)$$

the equation of motion is

$$\rho \frac{\mathrm{D}\mathbf{u}}{\mathrm{D}t} = -\nabla p + \mu_0(\mathbf{M} \cdot \nabla)\mathbf{H} - \rho\mathbf{g} + \eta \nabla^2 u \quad (5)$$

the energy equation is

$$\rho c \frac{\mathrm{D}T}{\mathrm{D}t} + \mu_0 \left(\frac{\partial M}{\partial T} \right)_H \frac{\mathrm{D}H}{\mathrm{D}t} = \nabla \cdot (\kappa \nabla T) + \mathbf{\Phi} \quad (6)$$

the Maxwell equation is

$$\nabla \times \mathbf{H} = \mathbf{j} \approx 0, \ \nabla \cdot \mathbf{B} = 0 \quad (7)$$

the equation of state is

$$p = p(\rho, \ T) \quad (8)$$

and the expression of magnetization M is

$$M = M_0(\rho, \ T, \ H) \quad (9)$$

where $\mathbf{u}$ is the flow velocity, η the fluid viscosity, c the specific heat, κ the thermal conductivity, and Φ the viscous dissipation energy.

The boundary condition at a boundary between two different media as illustrated in Fig. 1 is obtained as follows. From Eqn. (1), the traction on a surface element with unit normal $\mathbf{n}$ is:

$$\mathbf{n} \cdot T_{ij} = -\mathbf{n} \left(\mu_0 \int_0^H \frac{\partial Mv}{\partial v} \mathrm{d}H + \frac{\mu_0}{2}H^2 \right) + \mathbf{n} \cdot \mathbf{BH} \quad (10)$$

The difference in this magnetic stress across an interface between media is a force oriented along the normal which may be expressed as:

$$[\mathbf{n} \cdot \mathbf{T}] = \mathbf{n}[T_{nn}] = \mathbf{n} \left(\mu_0 \int_0^H \frac{\partial Mv}{\partial v} \mathrm{d}H + \frac{\mu_0}{2}M_n^2 \right) \quad (11)$$

The square brackets denote the difference between the quantities across the interface.
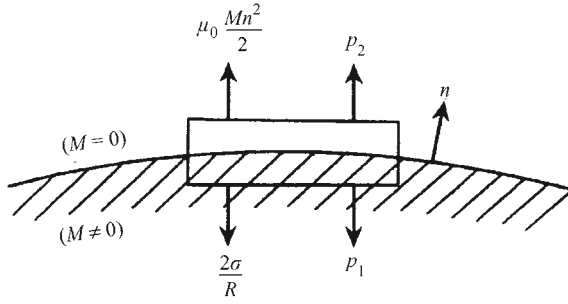
Figure 1
Balance of forces in the boundary condition.

1.3 Treatment as Micropolar Fluids

If a magnetic fluid includes relatively large particles, the relaxation time for magnetization of the fluid is determined by Brownian rotation. In this case, the particles can be considered as rigid magnetic dipoles; that is, one can assume that the magnetic moment of a particle changes its orientation only for rotation of the particle itself. Then, the presence of an external magnetic field results in the prevention of the rotation of the particle and in the appearance of the mechanism of rotational viscosity.

The basic equations in this case were derived using the treatment of micropolar fluids by Shliomis (1967) and Shaposhinikov and Shliomis (1975). The fluid is treated as a fluid with internal angular momentum. The volume density of internal angular momentum is denoted by

$$\mathbf{S} = I\omega \qquad (12)$$

Here $I = 8\pi r^5 \rho_s n/15$ is the sum of moments of inertia of the sphere particle per unit volume and ω is the angular velocity of their ordered rotation, where r is the particle radius, ρ_s the particle density and n is the number density of the particles:

$$\rho\frac{\mathrm{D}\mathbf{u}}{\mathrm{D}t} = -\nabla p + \mu_0(\mathbf{M}\cdot\nabla)\mathbf{H} + \eta\nabla^2\mathbf{u} + \frac{1}{2\tau_s}\nabla\times(\mathbf{S}-I\mathbf{\Omega})$$
$$(13)$$

$$\frac{\mathrm{D}\mathbf{S}}{\mathrm{D}t} = \mu_0(\mathbf{M}\times\mathbf{H}) - \frac{1}{\tau_s}(\mathbf{S}-I\mathbf{\Omega}) + \gamma\nabla^2\mathbf{S} \qquad (14)$$

Here $\mathbf{\Omega} = (1/2)\nabla\times\mathbf{u}$ is angular velocity of fluid, $\gamma = 2r^2/(3\tau_B)$ is diffusion coefficient, $\tau_s = r^2\rho_s/(15\eta_0)$ is the relaxation time of particle rotation, and $I/2\tau_s$ is the rotational viscosity. To obtain a closed system of equations, it is necessary to add the equation for $\mathrm{D}\mathbf{M}/\mathrm{D}t$ to Eqns. (13) and (14); that is

$$\frac{\mathrm{D}\mathbf{M}}{\mathrm{D}t} = \omega\times\mathbf{M} - \frac{1}{\tau_B}\left(\mathbf{M} - M_0\frac{\mathbf{H}}{|H|}\right) \qquad (15)$$

where τ_B is relaxation time of Brownian motion, and M_0 the equilibrium magnetization of magnetic fluid. Eqns. (4), (6)–(9) and (13)–(15) form a complete system of equations.

2. Pipe Flow Problems

The pipe flow problems of magnetic fluids in an applied magnetic field are very important in basic studies of the hydrodynamics of magnetic fluids, which is closely related to the development of engineering applications such as energy conversion systems, viscous dampers and actuators (Kamiyama 1992). Therefore, the various pipe flow problems have been investigated.

2.1 Theoretical Analysis of Steady Laminar Flow

(a) Flow in an axial magnetic field

Let us consider the steady laminar pipe flow in an axial magnetic field $H_z(z)$ and apply the basic equations derived in Sect. 1.3 for the micropolar fluid. If the particle radius is on the order of 10^{-8} m (10 nm), then the values of τ_s becomes the order of 10^{-11} s and hence the left-hand side and the third term on the right-hand side of Eqn. (14) may be neglected. Therefore, eliminating $\mathbf{S}$ from Eqns. (13) and (14), Eqn. (13) reduces to

$$\frac{\mathrm{d}p}{\mathrm{d}z} = \eta\frac{1}{r}\frac{\mathrm{d}}{\mathrm{d}r}\left(r\frac{\mathrm{d}u_z}{\mathrm{d}r}\right) + \mu_0 M_z\frac{\mathrm{d}H_z}{\mathrm{d}z} - \frac{\mu_0}{2r}\frac{\partial}{\partial r}(rM_rH_z) \qquad (16)$$

Also, the following relations are obtained:

$$M_r = \frac{\Omega\tau_B M_z}{1 + \dfrac{\mu_0\tau_s\tau_B M_z H_z}{I}} \qquad (17)$$

and

$$u_z\frac{\partial M_z}{\partial z} = \frac{1}{\tau_B}\left\{M_0 - M_z - \frac{(\Omega\tau_B)^2 M_z}{\left(1 + \dfrac{\mu_0\tau_s\tau_B M_z H_z}{I}\right)^2}\right\} \qquad (18)$$

Here, the equilibrium magnetization M_0 is assumed to be expressed by the Langevin function L; that is,

$$M_0 = nmL(\xi) \qquad (19)$$

where $L(\xi) = \coth\xi - \xi^{-1}$, $\xi = \mu_0 mH/kT$. In the case of a uniform magnetic field, the second terms on the right-hand side of Eqn. (16) and on the left-hand side of Eqn. (18) vanish (Kamiyama *et al.* 1979).

(1) Solution in the case of $\Omega\tau_B \ll 1$

Under the condition that the rotary Péclet number $P_{\mathrm{er}} = 2\Omega\tau_B \ll 1$ holds, the following relation is obtained from Eqn. (18),

$$M_z \approx M_0 \qquad (20)$$

Now, let us introduce the following dimensionless quantities:

$$r^* = \frac{r}{r_0} \qquad z^* = \frac{z}{r_0}$$

$$u_z^* = \frac{u_z}{u_0} \qquad h^* = \frac{H_z}{H_{max}}$$

$$M_z^* = \frac{M_z}{M_{0max}} \qquad p^* = \frac{pr_0}{\eta u_0} \tag{21}$$

$$L^* = \frac{L(\xi)}{L(\xi_{max})} \qquad A = \frac{\mu_0 \tau_s \tau_B H_{max} M_{0max}}{I}$$

Here r_0 is the pipe radius and u_0 is the mean flow velocity. Then, Eqn. (16) is expressed as

$$\frac{d\rho^{*\prime}}{dz^*} = \frac{2}{r^*}\left(1 + \frac{\Delta\eta}{\eta}\right)\frac{du_z^*}{dr^*} \tag{22}$$

where

$$\Delta\eta = \frac{3}{2}\phi\eta_0\frac{Ah^*L^*}{1 + Ah^*L^*}$$

$$p^{*\prime} = p^* - \frac{r_0 nkT}{\eta u_0}\ln(\xi^{-1}\sinh\xi) \tag{23}$$

where $\phi = (4/3)\pi a^3 n$ is volumetric concentration of particles, a is the particle radius and η_0 is the viscosity of the solvent of the magnetic fluid.

Applying the boundary condition $u_z^* = 0$ at $r^* = 1$ to Eqn. (22), we obtain the solution:

$$u_z^* = \frac{\frac{dp^{*\prime}}{dz^*}(r^{*2} - 1)}{4\left(1 + \frac{\Delta\eta}{\eta}\right)} \tag{24}$$

Eqn. (24) shows that the Poiseuille flow of a Newtonian fluid has an apparent viscosity of $\eta_e = \eta + \Delta\eta$. Applying the continuity equation, the velocity profile is also represented by:

$$u_z^* = 2(1 - r^{*2}) \tag{25}$$

Integrating Eqn. (22), the pressure difference between two arbitrary points z_1^* and z_2^* in the applied magnetic field region is given by:

$$p_1^* - p_2^* = -\frac{r_0 nkT}{\eta u_0}|\ln(\xi^{-1}\sinh\xi)|_{z_1^*}^{z_2^*}$$
$$+ 8(z_2^* - z_1^*) + 8\int_{z_1^*}^{z_2^*}\frac{\Delta\eta}{\eta}\,dz^* \tag{26}$$

The first term on the right-hand side of Eqn. (26) is the static pressure difference due to the magnetic body force, the second and third terms correspond to the pressure drop due to friction loss without magnetic field and additional loss with magnetic field, respectively.

(2) Solution in the case of $\Omega\tau_B \sim 1$

It is very difficult to solve Eqn. (16) directly in the case of $P_{er}(= 2\Omega\tau_B) \geqslant 1$. However, an approximate solution is obtained by putting

$$M_z^*(r^*, z^*) = M_0^*(z^*)\delta(r^*, z^*) \tag{27}$$

Then, the solution of Eqn. (16) is obtained as:

$$\frac{du_z^*}{dr^*} = \frac{r^*}{2\left(1 + \frac{\Delta\eta}{\eta}\right)}\left\{\frac{dp^*}{dz^*} - \frac{r_0\mu_0 M_{0max}H_{max}}{\eta u_0}\delta L^*(\xi)\frac{dh^*}{dz^*}\right\} \tag{28}$$

where

$$\Delta\eta = \frac{3}{2}\phi\eta_0\frac{Ah^*L^*\delta}{1 + Ah^*L^*\delta} \tag{29}$$

It is clear from Eqns. (28) and (29) that the apparent viscosity depends on the flow shear rate Ω; that is, the magnetic fluid shows the non-Newtonian fluid property.

(b)   Flow in a transverse magnetic field
In a similar treatment in the case of an axial magnetic field, the solution of Eqn. (16) is obtained for the case where $P_{er}(= 2\Omega\tau_B) \ll 1$ as:

$$\frac{dp^{*\prime}}{dz^*} = \left(1 + \sin^2\theta\frac{2\Delta\eta}{\eta}\right)\frac{d^2u_z^*}{dr^{*2}}$$
$$+ \left(1 + \cos^2\theta\frac{2\Delta\eta}{\eta}\right)\frac{du_z^*}{r^*dr^*} \tag{30}$$

where

$$\Delta\eta = \frac{3}{4}\phi\eta_0\frac{Ah^*L^*}{1 + Ah^*L^*} \tag{31}$$

The increase in the apparent viscosity $\Delta\eta$ in a transverse magnetic field is just half of that in a longitudinal magnetic field.

2.2   Steady Pipe Flow Resistance in Laminar and Turbulent Flows

In the case of ordinary Newtonian fluid, the pressure drop in a laminar pipe flow is expressed by using the pipe friction coefficient $\lambda(= 2d\Delta p/\rho u_0^2 l)$ with $\lambda = 64/Re$, where $Re = \rho u_0 d/\eta$, $d = 2r_0$ is the pipe diameter, and l is the pipe length between measuring points of Δp. Experimental studies of the flow in the axial and transverse magnetic fields were carried out using a similar technique to the ordinary fluid (Kamiyama *et al.* 1979, 1983, 1987).Typical experimental results are sketched in Fig. 2. Figure 2 shows clearly that the pressure increases with the field strength H in the entrance region of magnetic field, due to the magnetic body force, and decreases in the outlet region. Moreover, the pressure drop caused by friction loss is larger in an applied magnetic field than in no
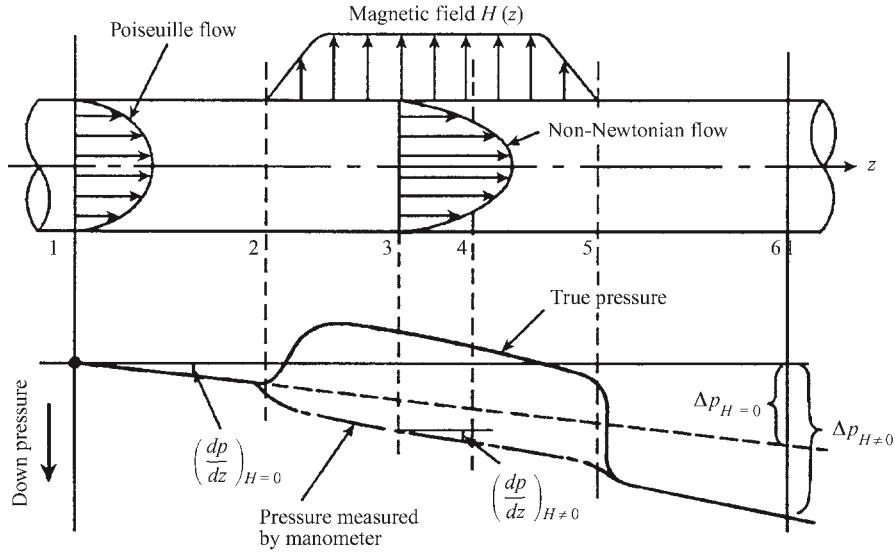
Figure 2
Typical experimental result of pressure distribution measured by transducer and manometer.

magnetic field. The true pressure distribution shows the profile as indicated by solid line in Fig. 2. However, if the pressure in the magnetic field region is measured by a manometer outside the magnetic field, the pressure difference in the manometer indicates only the pressure drop due to pipe friction loss shown by the chain line. In such a case, the magnetic pressure also acts on the fluid in the connecting tube across the magnetic field and cancels the magnetic static pressure in the pipe.

Now, we would like to examine in some detail the pressure distribution measured by the manometer using the test tube in the axal magnetic field distribution as shown in Fig. 3 where the pressure coefficient C_p along the pipe axis is plotted

$$C_p = \frac{p - p_1}{\rho u_0^2 / 2} \tag{32}$$

where p_1 is the pressure at the upstream reference point. It is clearly shown that a peculiar pressure drop occurs at the edge of the imposed magnetic field. The following loss coefficients may be defined from Fig. 3:

$$\zeta = \lambda_0 \frac{l_1 + l_3}{d} + \lambda_H \frac{l_2}{d} + \zeta_{in} + \zeta_{out} \tag{33}$$

where λ_H denotes the resistance coefficient in uniform magnetic field and λ_0 in the absence of magnetic field. ζ_{in} and ζ_{out} are loss coefficients in nonuniform magnetic field regions at the inlet and outlet. Since the pressure gradient is supposed to be nearly constant in
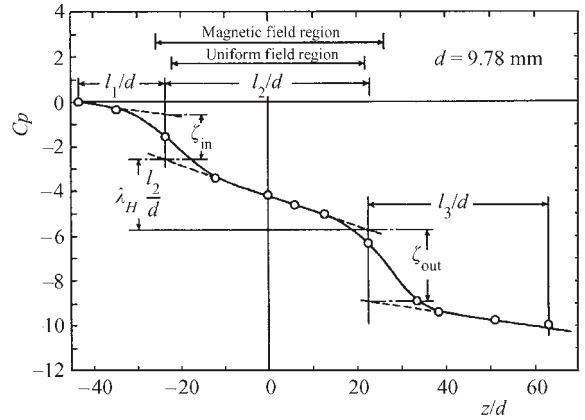
Figure 3
Measured pressure distribution along the pipe axis measured by manometer.

the uniform field region, the resistance coefficient λ_H was estimated. The relation between the resistance coefficient λ, which corresponds to λ_H and the modified Reynolds number Re^* is shown in Fig. 4 where

$$\lambda = \frac{64}{Re^*} \quad \text{and} \quad Re^* = \frac{\rho u_0 d}{\eta + \Delta \eta} \tag{34}$$

It is clear that in the laminar flow regime the resistance coefficient λ increases with the intensity of magnetic flux density B. In particular, the coefficient λ for water-based fluid is much larger than that for
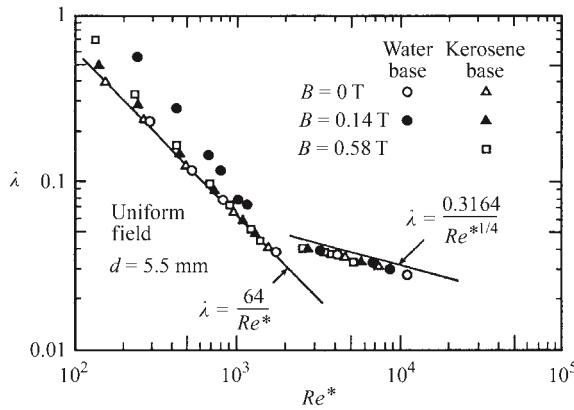
Figure 4
Effect of magnetic field on the relation of resistance coefficient λ versus Reynolds number Re^* in a uniform magnetic field.

Figure 5
Distribution of magnetic flux density in the test section.
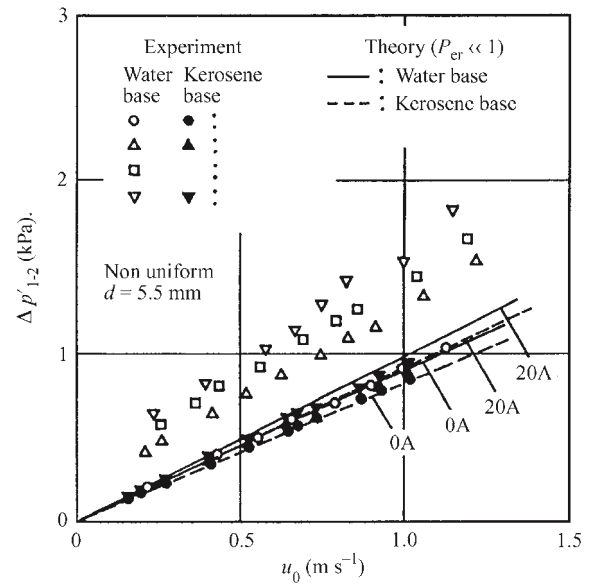
Figure 6
Pressure difference as a function of mean flow velocity.

kerosene-based fluid. On the other hand, λ for turbulent flow is not influenced by the application of magnetic field; it has a slightly lower value compared to the Blasius formula as a Newtonian fluid.

Since it is observed that the large pressure drop occurs at the nonuniform field region, it is important to examine the effect of nonuniform magnetic field on the flow resistance. An experimental study was, therefore, done to clarify the effect of nonuniform magnetic field on the flow resistance. The nonuniform magnetic field distribution was generated by adjusting the pole gap of the electromagnet as shown in Fig. 5. Figure 6 shows the experimental results of the pressure change Δp_{1-2} against mean flow velocity at several values of current I supplied to the electromagnet for both water-based and kerosene-based fluids. $\Delta p'$ denotes the pressure drop over the pipe length L:

$$\Delta p' = \lambda \frac{L}{d} \rho \frac{u_0^2}{2} \qquad (35)$$

In this case, subscript 1–2 denotes the change between the locations z_1 and z_2 in Fig. 5. The theoretical values obtained from Eqn. (26), modified for the transverse magnetic field, are also shown in Fig. 5. The experimental values for the kerosene-based fluid agree well with the predicted ones as indicated in Fig. 5. On the other hand, it is easy to see that the experimental values for the water-based fluid are much larger than the predicted ones.

Measurements of the flow resistance were also made for other pipes with variable cross-sectional area such as venturi and long orifice tubes (Kamiyama *et al.* 1987).

2.3 Unsteady Flow

(a) Oscillatory pipe flow characteristics

The unsteady pipe flow problem is also important in relation to development in the application to magnetic fluid dampers and actuators. As an example of unsteady pipe flow problems, oscillatory flow in a straight pipe in a transverse magnetic field is considered here. Theoretical analysis of the oscillatory flow is made under the assumption that the shape of aggregated particles in the magnetic fluid is a rigid prolate spheroid as shown in Fig. 7 (Tsebers 1974). When the basic equations are simplified by the same

221
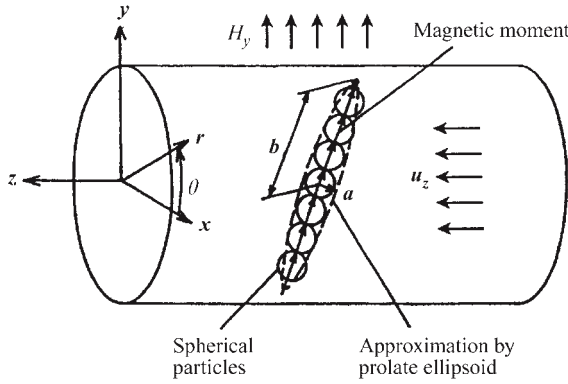
Figure 7
Model of aggregated particles in a magnetic field.

procedure as for steady flow in Sect. 2.1, the following dimensionless equation is obtained:

$$W^2\left(\frac{\mathrm{d}u^*}{\mathrm{d}t^*}\right) = -\frac{\mathrm{d}p^{*\prime}}{\mathrm{d}z^*} + \left(1+\frac{2\Delta\eta_1}{\eta}\right)\frac{\partial^2 u^*}{\partial r^{*2}}$$
$$+ \left(1+\frac{2\Delta\eta_2}{\eta}\right)\frac{\partial u^*}{r^*\partial r^*} + \left(1+\frac{2\Delta\eta_3}{\eta}\right)\frac{\partial^2 u^*}{r^{*2}\partial\theta^2}$$
$$(36)$$

together with the boundary conditions

$$r^* = 1: \quad u^* = 0; \quad r^* = 0: \quad \frac{\mathrm{d}u^*}{\mathrm{d}r^*} = 0 \qquad (37)$$

Here, $W = r_0/\sqrt{\omega\rho/\eta}$ is Womersley number,

$$p^{*\prime} = p^* - \frac{nkT}{\eta\omega}\ln(\xi^{-1} - \sinh\xi),$$

$$\Delta\eta_1 = \frac{\alpha}{8}\left[\left\{\frac{\xi - \tanh\xi}{\xi + \tanh\xi} + \lambda\left(3L_2 - \frac{L_3}{\xi}\right)\right\}\sin^2\theta\right.$$
$$\left. + \frac{\lambda}{\xi}\left(2L_1 - \frac{L_2}{\xi}\right)\right]$$

$$\Delta\eta_2 = \frac{\alpha}{8}\left[\left(\frac{\xi - \tanh\xi}{\xi + \tanh\xi} + \lambda L_2\right)\cos^2\theta\right.$$
$$\left. + \lambda\left(2L_2 - \frac{L_3}{\xi}\right)\sin^2\theta + \frac{\lambda}{\xi}\left(2L_1 - \frac{L_2}{\xi}\right)\right]$$

$$\Delta\eta_3 = \frac{\alpha}{8}\left[\left\{\frac{\xi - \tanh\xi}{\xi + \tanh\xi} + \lambda\left(3L_2 - \frac{L_3}{\xi}\right)\right\}\cos^2\theta\right.$$
$$\left. + \frac{\lambda}{\xi}\left(2L_1 - \frac{L_2}{\xi}\right)\right] \qquad (38)$$

and

$$\alpha = \frac{4\phi\eta_0}{3}\frac{1-\delta^4}{(2-\delta^2)\frac{\delta^2}{\sqrt{1-\delta^2}}\ln\frac{1+\sqrt{1-\delta^2}}{\delta} - \delta^2}$$

is the rotational friction per unit fluid volume and

$$L_1 = \coth\xi - \xi^{-1} \quad L_2 = 1 - \frac{3}{\xi}$$
$$L_3 = L_1 - \frac{5L_2}{\xi} \quad \lambda = \frac{1-\delta^2}{1+\delta^2}$$
$$\delta = \frac{a}{b} = \frac{1}{Nu} \quad r^* = \frac{r}{r_0} \qquad (39)$$
$$z^* = \frac{z}{r_0} \quad u^* = \frac{u}{u_0}$$
$$p^* = \frac{p/\eta u_0}{r_0} \quad t^* = \omega t$$

where u_0 is the amplitude of oscillating mean flow velocity and Nu is the number of aggregated particles.

When the oscillating flow rate is given, the velocity distribution is obtained by solving Eqn. (36) using difference calculus. Also, fluctuating pressure difference between two points in a pipe is expressed by Eqn. (40):

$$\Delta\bar{p}^{*\prime} = -u_0^*\int_0^{l^*}\frac{\mathrm{d}z^*}{\frac{1}{\pi}\iint U^* r^* \,\mathrm{d}r^* \,\mathrm{d}\theta} \qquad (40)$$

where $U^* = u^*/(\mathrm{d}p^{*\prime}/\mathrm{d}z^*)$, $l^* = l/r_0$, and l is the length between two measuring points in a pipe.

Figure 8 shows the calculated results of the effect of magnetic field on the pressure difference in the pipe compared with the experimental data obtained by using the water-based magnetic fluid with 20% mass concentration of particles (Shimada and Kamiyama 1993). The vertical axis shows the increase rate of the pressure difference of the first mode oscillatory flow between two pressure transducers installed apart for 160 mm apart with an applied magnetic field. The abscissa is the Womersley number. The Reynolds number Re is defined as $2r_0u_0/\nu$, where ν is the kinematic viscosity. $I = 20$ A is the current supplied to the electromagnet which produces a nonuniform magnetic field with $H_{max} = 120$ kAm^{-1}. The results show that the fluctuating pressure difference increases with the magnetic field strength especially at low Womersley numbers. The scatter of the experimental data is shown with error bands in Fig. 8. Theoretical analysis can also explain the experimental results well by assuming that the aggregated particle number Nu depends on the Womersley number.

(b) Pulsating flow characteristics
As another example of the unsteady pipe flow, we consider here pulsating pipe flow, that is, the velocity
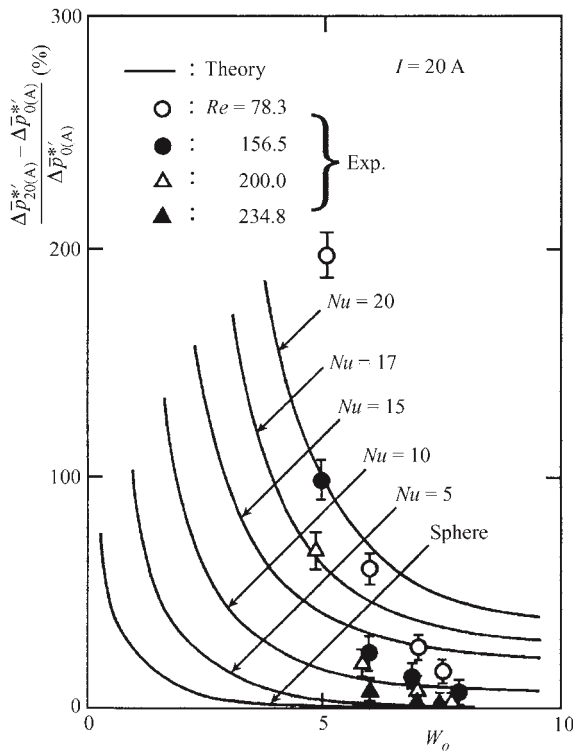
Figure 8
Increase rate of pressure difference versus Womersley number.

Exp. $u_1/u_0 = 1/2$

	Pulsating flow		Oscillatory flow		Steady mag.
	β		β		
$Re,1$	$-45°$	$0°$	$-45°$	$0°$	
40	O	△			
60	◑	▲			
80	◒	▲			●
100	◖	△	■	▼	◆

Theory
Pulsating flow $\left\{ \begin{array}{l} \text{———} : \beta = 0° \\ \text{—·—} : \beta = -45° \end{array} \right.$
Oscillatory flow: ----

Figure 9
Comparison of pressure difference between pulsating and oscillatory flows.

of the fluid is composed of steady and oscillatory flow ($u_0 + u_1$) in a pulsating magnetic field ($H_0 + H_1$). Eqn. (36) is solved numerically by assuming that each time-varying variable is expanded in a series of number $n (= 1, 2 \ldots n)$ and then ordering the resulting terms with respect to the power of n (Shimada and Kamiyama 1994). Time-varying velocity profiles in a circular pipe are obtained as a function of the Womersley number W and the magnetic field parameter. Generally speaking, it is clear from the numerical calculations that the velocity profiles are mainly influenced by W in the same way as the ordinary fluid flow; for smaller W, the velocity profile is parabolic-like and for larger W, it becomes a profile with a maximum near the wall.

Figure 9 shows the results calculated for increasing rate of pressure difference with the application of pulsating magnetic field compared with the experimental results. The results in the case of the oscillatory flow both in the steady and the pulsating magnetic field are also shown for comparison, where β denotes the phase difference between fluctuating velocity and magnetic field. It is easy to see that the experimental data for the pulsating flow are smaller than those for oscillatory flow in the pulsating magnetic field and

this result is similar to the theoretical analysis. However, the experimental data also show that the difference in the oscillatory flow characteristics appears between the cases of the pulsating and steady magnetic field. The cause seems to be the complicated effect of the magnetic field on the particles aggregation in the unsteady flow state.

2.4 Gas–Liquid Two-phase Flow

Gas–liquid two-phase pipe flow problems are closely connected with the development of a new energy conversion system utilizing magnetic fluid. The use of the gas–liquid two-phase flow is very effective in increasing the driving force of circulating fluid in this device.

(a) Theoretical analysis
Let us consider one-dimensional two-phase flow in the vertical pipe. Figure 10 shows schematically the system used in the theoretical analysis as well as in the experiment. A temperature sensitive magnetic
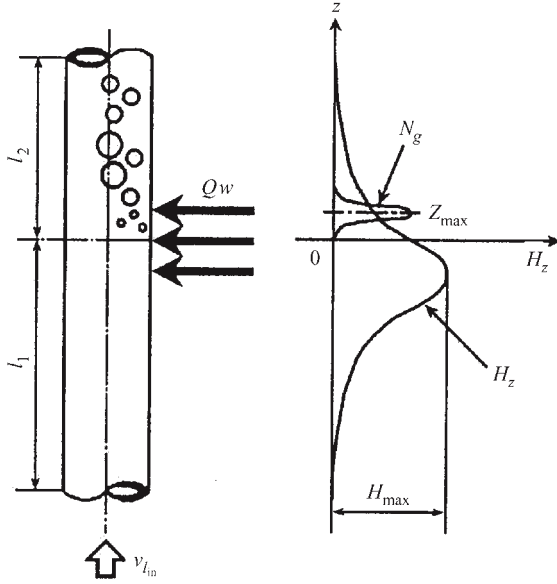
Figure 10
Analytical model of two-phase flow in a nonuniform magnetic field.

fluid is assumed to be heated passing through the point of the maximum magnetic field strength toward the downstream side region and boiled to form the gas–liquid two-phase flow. Under the above conditions, the governing equations of the boiling two-phase flow based on the thermal nonequilibrium two-fluid model are derived as follows (Kamiyama and Ishimoto 1995). The equations of continuity are:

$$\frac{d}{dz}(\rho_g v_g \alpha) = \Gamma_g$$

$$\frac{d}{dz}\{\rho_l v_l(1-\alpha)\} = \Gamma_l \quad (41)$$

where α is the void fraction, v is the velocity, and Γ is the phase generation rate. The subscript g and l denote gas and liquid phase respectively. Γ_g and Γ_l are expressed by

$$\Gamma_g = -\Gamma_l = \Gamma_{(e)} - \Gamma_{(c)} \quad \text{for } T_l \geqslant \bar{T}_l$$
$$= 0 \quad \text{for } T_l \leqslant \bar{T}_l \quad (42)$$

where $\bar{T}_l = (T_{l_{in}} + T_s)/2$, $T_{l_{in}}$ is the liquid-phase temperature at the inlet section $(z = -l_1)$ and T_s is the evaporation temperature. $\Gamma_{(e)}$ and $\Gamma_{(c)}$ are the mean evaporation and condensation rates (Dobran 1988) and are given by

$$\Gamma_{(e)} = \varepsilon_{(e)}^{-\frac{1}{3}} A_1(1-\alpha)\rho_l \alpha (\bar{T}_l R_G)^{\frac{1}{2}}\left(\frac{T_l - \bar{T}_l}{T_s}\right) \quad \text{for } T_l \geqslant \bar{T}_l$$
$$= 0 \quad \text{for } T_l < \bar{T}_l \quad (43)$$

$$\Gamma_{(c)} = \varepsilon_{(c)}^{-\frac{1}{3}} A_2(1-\alpha)\rho_g \alpha (T_s R_G)^{\frac{1}{2}}\left(\frac{T_s - T_g}{T_s}\right) \quad \text{for } T_g \leqslant T_s$$
$$= 0 \quad \text{for } T_g > T_s \quad (44)$$

where $\varepsilon_{(e)}$ and $\varepsilon_{(c)}$ are the relaxation parameters for the evaporation and the condensation and R_G is the gas constant. The variables A_1 and A_2 are proportional to the contact area between the gas and liquid phases. They include the effect of the number density of the vapor bubbles generation $N_g[1/(m^3 s^{-1})]$ which is assumed to have normal distribution in the region of $z = 0 - 2z_{max}$. The combined momentum equation is:

$$\frac{d}{dz}\{\rho_g \alpha v_g^2 + \rho_l(1-\alpha)v_l^2\} = -\frac{dp_l}{dz} - (1-\alpha)\rho_l g$$
$$+ (1-\alpha)\mu_0 M_z \frac{dH_z}{dz}$$
$$+ \Gamma_g(v_g^{(i)} - v_l^{(i)})$$
$$- \frac{32\{\eta_g \alpha v_g + \eta_l(1-\alpha)v_l\}}{d^2} \quad (45)$$

where g is acceleration of gravity and suffix (i) denotes the interface between the gas and liquid phases.

To consider the effect of slip and radial expansion of the bubbles, the equation of motion for the gas phase is replaced here by the translational motion of a single bubble (Ishimoto *et al.* 1994). The equation of motion for the gas phase is:

$$\frac{4}{3}\pi \bar{R}^3 \rho_g v_g \frac{dv_g}{dz} = -\frac{4}{3}\pi \bar{R}^3 \frac{dp_l}{dz} - \frac{4}{3}\pi \bar{R}^3 \rho_g g$$
$$- F_D - F_{VM} - F_B \quad (46)$$

where $\bar{R}$ is the mean radius of the bubble defined by Eqn. (51) below. F_D is the drag force, F_{VM} is the virtual mass force considering the expansion of the bubble, and F_B is the Basset term which takes into account the effect of deviation in a flow pattern from the steady state.

The energy equations for the gas and liquid phases expressed as follows:

$$\frac{d}{dz}\left\{\rho_g \alpha v_g\left(h_g + \frac{v_g^2}{2}\right)\right\} = -\rho_g \alpha v_g g + \Gamma_g h_g^{(i)} + q_g^{(i)} a^{(i)} \quad (47)$$

$$\frac{d}{dz}\left\{\rho_l(1-\alpha)v_l\left(h_l + \frac{v_l^2}{2}\right)\right\}$$
$$= -\rho_l(1-\alpha)v_l g + \Gamma_l h_l^{(i)} + q_l^{(i)} a^{(i)}$$
$$- (1-\alpha)\mu_0 T_l\left(\frac{\partial M_z}{\partial T_l}\right)_H v_l \frac{dH_z}{dz} + Q_w \quad (48)$$

where $q_g^{(i)}$ and $q_l^{(i)}$ are the heat fluxes through the gas–liquid interface ($q_g + q_l = 0$). $h_g^{(i)}$ and $h_l^{(i)}$ are the respective enthalpies as the interface. $a^{(i)}$ is the interface area concentration and Q_w is the heat transfer rate per unit volume. It is assumed that the energy transfer is caused by the heat transfer between an isothermal spherical bubble and the surrounding liquid. With the assumption of a spherical bubble with an equivalent radius $\bar{R}$, the expression for $a^{(i)}$ is obtained as $a^{(i)} = 3\alpha/\bar{R}$ (Kataoka 1986).

To close the basic equations in this system, the following three equations are introduced.

The equation of the ideal gas law:

$$\frac{p_g}{\rho_g} = R_G T_g \qquad (49)$$

where R_G is the gas constant.

The equation of the pressure balance between the gas and liquid phases:

$$p_g - p_l = \frac{2\sigma}{\bar{R}} \qquad (50)$$

where σ denotes the surface tension in the liquid phase.

The mass conservation equation for the single gas bubble:

$$\frac{4}{3}\pi\frac{d}{dz}(\rho_g \bar{R}^3) = \frac{d}{dz}\left(\frac{\sum \Gamma_g}{\sum N_g}\right) \qquad (51)$$

where N_g is the number density of the generation of the vapor bubbles.

(b) Experimental study

An experimental study to measure precisely the liquid phase pressure, the temperature, and the mean velocity was conducted using a test loop tube, the inner diameter and the total length of which are 8.0 mm and 3.3 m, respectively. Taking advantage of the high permeability of an ultrasonic wave in the magnetic fluid, the ultrasonic imaging technique was applied to the investigation of a boiling two-phase flow in the magnetic field.

Figure 11 shows a schematic diagram of the experimental set-up for the boiling two-phase flow of the magnetic fluid. The ultrasonic wave probe is closely attached to the flow pipe through the gel pad. The ultrasonic wave echo visualizes a bubble in the magnetic fluid. The magnetic fluid is heated by a YAG laser, with a constant heat flux passing through the point of the maximum magnetic field strength toward the downstream side.

Figure 12 shows the experimental results of the pressure distribution in the liquid phase, Δp_{IT} compared with the numerical analysis. Δp_{IT} is the pressure difference at the inlet section of the applied magnetic field region and is defined by $\Delta p_{IT} = p_l - \rho_l g(l_2 - z) - p_{l_{in}}$.
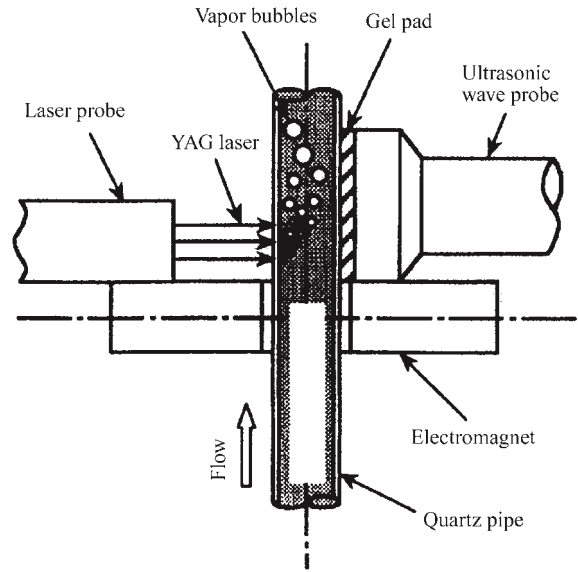
Figure 11
Experimental set-up for two-phase flow in a magnetic field.
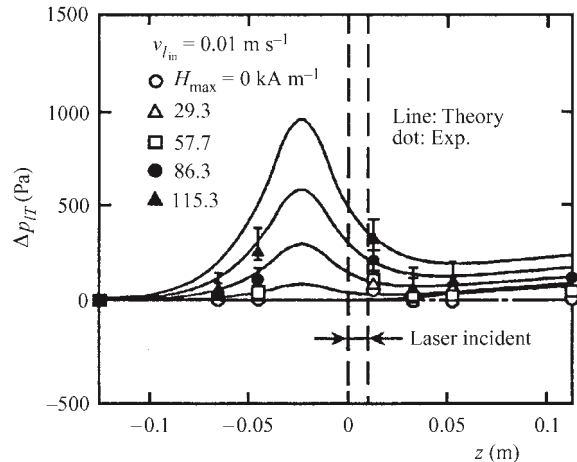
Figure 12
Pressure distribution in liquid phase as a function of z coordinate for different magnetic field strength.

The measured pressure distribution agrees reasonably with the numerical results. Also, because of the appearance of the gas phase and the temperature increase after passing through the heated region, Δp_{IT} at the exit position increases with the maximum magnetic field strength H_{max}. These experimental and theoretical results explain the effectiveness of the two-phase flow in increasing the driving force of the magnetic fluid flow in a nonuniform magnetic field.

3. Flow Around a Blunt Body Coated with a Magnetic Fluid

To reduce the drag and enhance the heat transfer by controlling flow separation in the flow around a blunt body, the magnetic fluid coating on a solid body is investigated. A cylinder coating is made by using a permanent magnet cylinder magnetized transverse to its axis or an electrically conducting cylinder carrying the electric current. The magnetic field keeps the magnetic fluid as the coating which has a constant thickness (its radius $= a$). The shape of this coating changes under the action of the viscous flow as shown in Fig. 13.

The numerical calculation of this flow problem with a transforming the boundary shape was carried out using a new finite element method technique and compared with experimental data (Krakov and Kamiyama 1995). Figure 14 shows the calculated results of a drag reduction ratio G as a function of the initial radius ratio a/R in the case when the viscosity ratio of the outer fluid (η_2) and the magnetic fluid (η_1) equals 100. The Reynolds number is defined as $Re = \rho_2 U_0 2R/\eta_2$. The experimental data were obtained by free fall of a cylindrical permanent magnet coated with the magnetic fluid in silicon oil (Berkovsky *et al.* 1990). It is clear from Fig. 14 that the drag reduction with the film coating is effective in high viscous fluid flow around the blunt body.

See also: Ferrofluids: Applications; Ferrofluids: Magnetic Properties; Ferrofluids: Preparation and Physical Properties

Figure 13
Flow past a circular cylinder coated with a magnetic fluid.
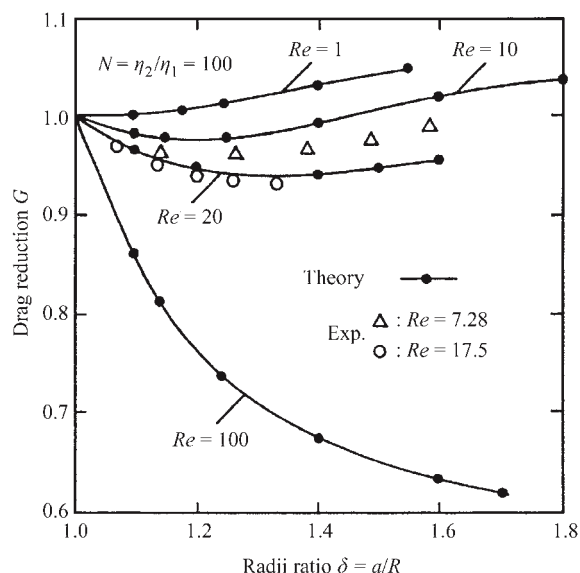
Figure 14
Drag reduction ratio as a function of radii ratio.

Bibliography

Berkovsky B M, Bashitovi V G, Krakov M S 1990 Flow and heat transfer under influence of magnetic fluid coating. *J. Magn. Mater.* **85**, 190–5

Dobran F 1988 Liquid and gas-phase distributions in a jet with phase change. *Trans. Am. Soc. Mech. Eng. J. Heat Transf.* **110**, 955–60

Ishimoto J, Okubo M, Kamiyama S 1994 Study of the MHD power-generation system using two-phase flows of temperature-sensitive electrically conducting magnetic fluids (Analysis of flow characteristics in a pipe and the power-generation characteristics). *Trans. Jpn. Soc. Mech. Eng. Ser. B* **60** (571), 891–8, (in Japanese)

Kamiyama S 1992 Pipe flow problems of magnetic fluids. *Jpn. Soc. Mech. Eng. Int. J., Ser. II* **35**, 131–7

Kamiyama S, Ishimoto J 1995 Boiling two-phase flows of magnetic fluid in a non-uniform magnetic field. *J. Magn. Magn. Mater.* **149**, 125–31

Kamiyama S, Koike K, Iizuka N 1979 On the flow of a ferromagnetic fluid in a circular pipe (Report 1, Flow in a uniform magnetic field). *Bull. Jpn. Soc. Mech. Eng.* **22**, 1205–11

Kamiyama S, Koike K, Oyama T 1983 Pipe flow resistance of magnetic fluids in a nonuniform transverse magnetic field. *J. Magn. Magn. Mater.* **39**, 23–6

Kamiyama S, Htwe J, Koike K, Oyama T 1987 Some peculiarities of pipe flow characteristics of water-based magnetic fluid. *J. Magn. Magn. Mater.* **65**, 317–20

Kataoka I 1986 Local instant formulation of two-phase flow. *Int. J. Multiphase Flow* **12** (5), 745–58

Krakov M S, Kamiyama S 1995 Steady flow past a circular cylinder coated with a magnetic fluid: Flow structure, drag reduction and coating deformation. *J. Fluid Mech.* **295**, 1–22

Neuringer J L, Rosensweig R E 1964 Ferrohydrodynamics. *Phys. Fluids* **7**, 1927–37

Rosensweig R E 1985 *Ferrohydrodynamics*. Cambridge University Press, Cambridge, pp. 100–10

Shaposhinikov I C, Shliomis M I 1975 Hydrodynamics of magnetic fluids. *Magnetohydrodynamics* **10**, 381–93

Shimada K, Kamiyama S 1993 Oscillatory pipe flow of magnetic fluid in a strong magnetic field. *J. Magn. Magn. Mater.* **122**, 214–6

Shimada K, Kamiyama S 1994 Pulsating flow of magnetic fluids in a pipe under fluctuating magnetic field. *Jpn. Soc. Mech. Eng. Int. J. Ser. B* **37**, 71–6

Shliomis M I 1967 Hydrodynamics of a liquid with intrinsic rotation. *Sov. Phys. JETP* **24**, 173–7

Tsebers A O 1974 Flow of dipole fluids in external fields. *Magnetohydrodynamics* **10**, 381–93

S. Kamiyama
Akita Prefectural University
Honjo, Japan

Films and Multilayers: Conventional Superconducting

Thin-film multilayers are artificially fabricated materials that consist of thin slabs of various materials deposited sequentially on a substrate. In general, when the individual layer thicknesses are comparable with certain physical length scales for electronic interactions, the electronic transport takes on new characteristics which could be quite different from the electronic properties of the constituent layers. Superconductivity is one property particularly amenable to layered modifications due to its rather long coherence length in many materials.

The superconducting materials community has historically paid particular attention to films and multilayers, mostly for uncovering new superconducting mechanisms, but also in studying superconducting phenomena in "tunable" model systems. Superconducting thin films are also technologically important as they are a basis for superconducting electronics. Besides artificially structured multilayers, layered structures also exist naturally in transition-metal dichalcogenide superconductors such as $NbSe_2$ and high-T_c cuprate superconductors such as $YBa_2Cu_3O_y$ and $Bi_2Sr_2CaCu_2O_y$ (see *High-temperature Superconductors: Thin Films and Multilayers*).

In this article the focus is on presenting a framework for understanding the physics of superconductivity in layered materials. The discussion centers on one of the interesting aspects of the layered superconductors which is their static anisotropic magnetic properties and dimensional cross-over. For more detailed reviews of materials systems involved see, for example, Ruggiero and Beasley (1984), Matijasevic and Beasley (1987), and Schuller *et al.* (1990). The

phenomenological framework of Ginzburg–Landau (GL) that is presented here provides for a simple understanding of the macroscopic superconducting properties of multilayers. However, if the layering affects the fundamental interactions that bring about the superconductive electronic pairing, this picture will be inadequate, and a microscopic model is needed.

1. Types of Multilayers

Superconducting multilayer structures typically consist of two different layers which alternate in a one-dimensional layering lattice. One material is the primary superconductor (S) and the second material can be an insulator (I), another superconductor (S'), a normal metal (N), or a ferromagnet (F) (see Fig. 1). The wavelength of the modulation is usually denoted by s, with $s = d_S + d_X$, where d_S and d_X are the thicknesses of the superconducting and mediating layers, respectively. In reality materials issues are often more complicated, producing, for example, an interfacial layer which could be another superconducting phase, so that there are S/S'/N multilayers rather than simply S/N.

1.1 Superconductive Coupling

In practice there are two different mechanisms for Josephson coupling of superconductivity between the superconducting layers in a multilayer: pair tunneling and superconducting proximity effect coupling (extension of Cooper pairs into a normal metal). Pair
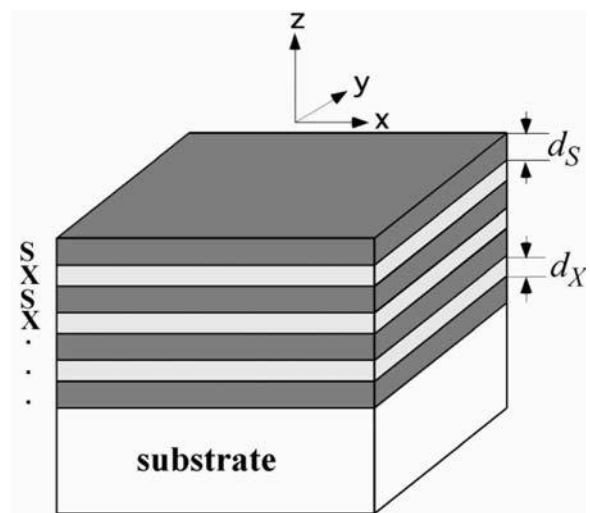
Figure 1
Schematic of a multilayer. X represents an insulator, a second superconductor S', a normal metal N, or a ferromagnet F.

tunneling is relevant for the S/I systems and proximity effect for the others. Both couplings decay exponentially with the separation of the S layers, but the decay scale is different. For tunneling the range is typically 1–2 nm, while proximity effect coupling is typically at 10–1000 nm. Pair tunneling is temperature-independent, for example, so the details of the coupling are different in the two cases, but for many macroscopic properties the actual nature of the coupling is not relevant.

There has been increasing interest in superconductive coupling via ferromagnetic metallic layers. In the case of coupling through ferromagnetic materials the magnetic pair breaking reduces the coupling distance typically to about 1–10 nm. In a ferromagnet adjacent to a superconductor, the exponentially decaying superconducting pair function is presumed to oscillate, as was first suggested by Buzdin *et al.* (1982) and Radovic *et al.* (1988). This behavior is akin to the description of an oscillatory superconducting order parameter that is generated in the presence of an exchange field, described by the Fulde–Ferrell–Larkin–Ovchinikov (FFLO) effect (Fulde and Ferrell 1964, Larkin and Ovchinikov 1964).

The oscillating order parameter reveals itself in an oscillating T_c as a function of d_F and therefore is manifestly different from other types of couplings. Jang *et al.* (1995) and Mühge *et al.* (1996) have shown such behavior in two different S/F systems, but the experimental situation is not yet clarified. When the coupling is negative between the S layers it is presumed that there would be a π phase shift between the superconducting layers to give a so-called π-junction. Subsequent reports by Ryazanov *et al.* (2001) have provided strong evidence for such an oscillatory superconducting wave function.

Figure 2 contrasts the different types of mediating layers and the relevant length scales for the coupling. The present discussion focuses on macroscopic thermodynamic properties of the superconducting
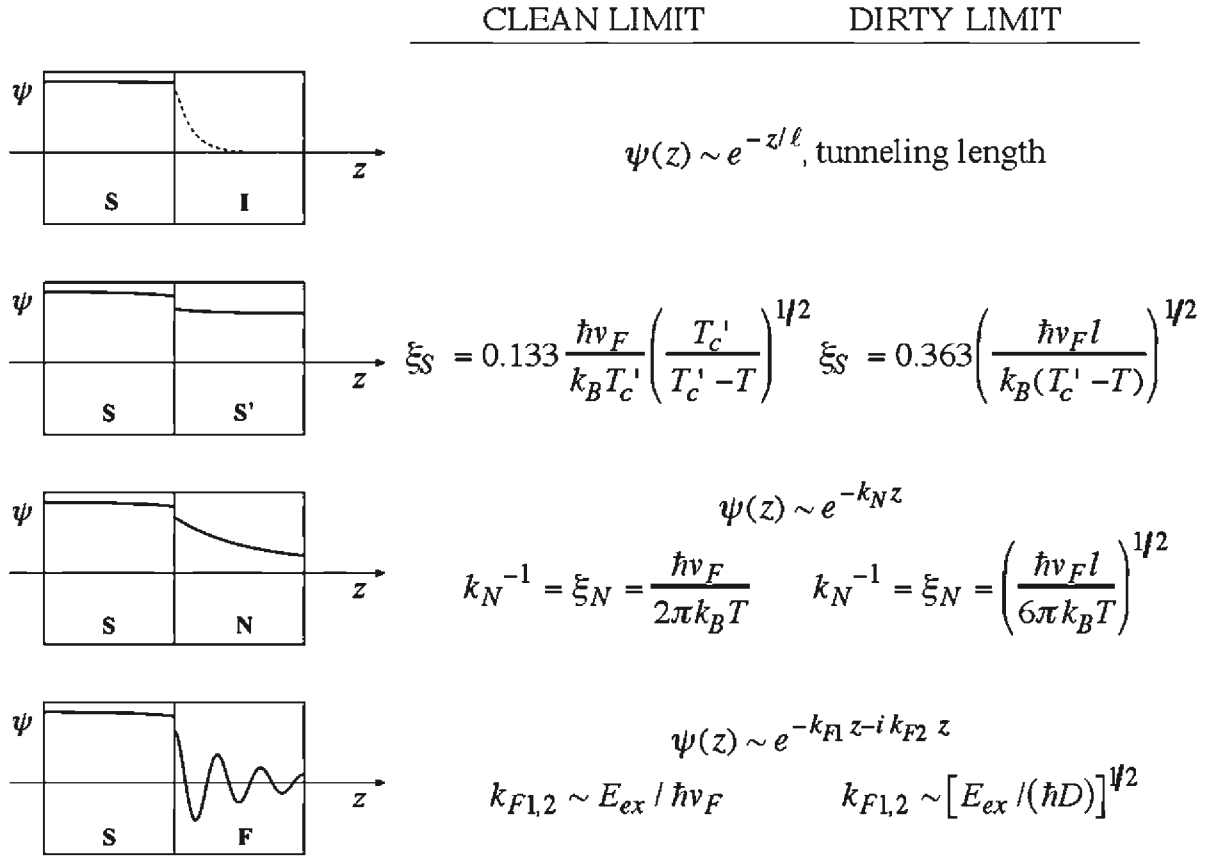
Figure 2
Comparison of the superconducting order parameter across various interfaces and their relevant length scales in the clean and dirty material limits. T_c' is the transition temperature of the S′ superconductor, v_F is the Fermi velocity, l is the mean free path, D is the diffusion constant, and E_{ex} is the exchange splitting in the ferromagnet.

multilayer. For a discussion of, for example, electronic transport perpendicular to the layers see *Josephson Junctions: High-T_c*. A number of properties of superconducting multilayers have been studied experimentally, with transition temperature and upper critical fields being among the most commonly studied. When a conducting material is adjacent to the superconductor the overall T_c can be reduced due to an averaging of the pairing function with the N or F layer. For the case of the magnetic material in contact with the superconductor, there is additional proximity-induced magnetic pair breaking in the S layers.

1.2 Dimensionality of Superconducting Multilayers

Multilayer superconductors can be distinguished according to whether the individual superconducting layers are thick or thin compared with their intrinsic, i.e., intralayer, temperature-dependent GL coherence length $\xi(T)$. If the layer thickness $d_S > \xi(T)$ then the layers themselves are three-dimensional and exhibit bulk material properties. In this case the layering only introduces planar defects to the superconductor which could be of interest for flux pinning and critical currents when a registration of the vortex lattice occurs with the multilayer lattice. If $d_S < \xi(T)$, then the individual layers are two-dimensional. The behavior of the whole system will depend on the strength of the coupling across the mediating layers.

The dimensionality of a superconducting multilayer is not dependent on the detailed nature of the coupling, but can be described macroscopically by a coherence length in the direction perpendicular to the layers, called ξ_z. This perpendicular coherence length reflects the coupling between the S layers. For $\xi_z(T) \gg s$ the system will behave as a bulk anisotropic superconductor. For systems where the $\xi_z(T) \lesssim s$ one can expect a cross-over from three-dimensional to two dimensional behavior as a function of temperature when $\xi_z(T)$ reaches $\sim s$. This classification is summarized in Table 1. The theoretical model

Table 1
Classification of superconducting multilayers according to dimensionality.

Length scale condition	Dimensionality of the system	Behavior of macroscopic superconducting properties
$\xi_S < d_S$	3D; weakly coupled	3D isotropic
$\xi_S > d_S$, $\xi_z < s$	2D; weakly coupled	2D single film-like
$\xi_S > d_S$, $\xi_z > s$	Quasi-2D; strongly coupled	3D anisotropic

described below illustrates this cross-over behavior quantitatively.

2. Magnetic Properties of Superconducting Multilayers

The upper critical field phase boundary is one of the macroscopic properties that directly reflects on the size of the superconducting coherence length in the material and the dimensionality of superconductivity. Another example, which is not discussed here in detail, are the superconducting fluctuations above T_c, where the size of the volume for averaging the fluctuations is also $\xi(T)$.

2.1 Ginzburg–Landau Description of Anisotropic Superconductors

The GL description of superconductivity follows the Landau theory for a two-component order parameter phase transition. The GL free energy of a superconductor in the presence of a magnetic field can be written as

$$F = F_0 + \int \left[\alpha|\psi|^2 + \frac{\beta}{2}|\psi|^4 + \frac{1}{2m^*}\left|\left(\frac{\hbar}{i}\nabla - \frac{e^*}{c}\mathbf{A}\right)\psi\right|^2 + \frac{1}{8\pi}B^2 \right] d^3r$$

where $\alpha = \alpha'(T - T_c)$ and $m^* = 2m$, $e^* = 2e$, and upon variation with respect to ψ, the usual GL equation is obtained:

$$\alpha\psi + \beta|\psi|^2\psi + \frac{1}{2m^*}\left(\frac{\hbar}{i}\nabla - \frac{e^*}{c}\mathbf{A}\right)^2\psi = 0 \qquad (1)$$

The GL formulation is often generalized to an anisotropic form where the mass m^* is replaced by an effective-mass tensor, such as

$$\frac{\mathbf{1}}{\mathbf{m}^*} \equiv \begin{pmatrix} \dfrac{1}{m_x} & 0 & 0 \\ 0 & \dfrac{1}{m_x} & 0 \\ 0 & 0 & \dfrac{1}{m_z} \end{pmatrix} \qquad (2)$$

for a uniaxial system as a multilayer where z axis is the symmetry direction.

Associated with this anisotropic mass tensor are the anisotropic GL coherence lengths and magnetic field penetration depths,

$$\xi_{x,z} \equiv \left(\frac{\hbar^2}{2|\alpha|m_{x,z}}\right)^{1/2} \quad \text{and} \quad \frac{1}{\lambda_{x,z}} = \left(\frac{4\pi e^* 2|\psi|^2}{c^2 m_{x,z}}\right)^{1/2}$$

In a layered superconductor $\xi_z(T)$ reflects the effective coupling across superconducting layers and not

an intrinsic property of a single layer. As $T \to T_c$ the coherence length always diverges and the superconductor inherently averages over many layers in a multilayer. This means that the anisotropic GL model described here is always applicable and $\xi_z(T)$ can be defined.

The upper critical field of a Type II superconductor is the field at which superconductivity is destroyed via a second-order phase transition. Theoretically it can be obtained by determining the temperature at which the linearized Eqn. (1),

$$\alpha\psi + \frac{1}{2m^*}\left(\frac{\hbar}{i}\nabla - \frac{e^*}{c}A\right)2\psi = 0 \qquad (3)$$

in an applied magnetic field **H**, along the **z** direction, has a nontrivial solution. Using the Landau gauge, $\mathbf{A} = H_0\hat{\mathbf{y}}x$, and, separating variables, one obtains the following eigenvalue equation

$$\frac{\hbar^2}{2m^*}\left[-\frac{d^2}{dx^2} + \left(\frac{e^*Hx}{c}\right)^2\right]\psi = -\alpha\psi = \varepsilon(H)\psi \qquad (4)$$

where $H_{c2}(T)$ is given by the implicit relation $\varepsilon(H) = -\alpha(T) = \hbar^2/[2m^*\xi(T)^2]$, where $\xi(T) = \xi(0)\sqrt{(T_c/T_c-T)}$. Equation (4) is equivalent to a Schrödinger equation of a harmonic oscillator with frequency $\omega_c = |e^*|H_0/m^*c$ and Landau levels. Hence, the lowest eigenvalue, corresponding mathematically to the highest field at which superconductivity can nucleate, is $\varepsilon(H) = \hbar e^*H/2m^*c$, from which it follows that

$$H_{c2} = \frac{\Phi_0}{2\pi\xi(0)^2}\frac{T_c - T}{T_c} \qquad (5)$$

where $\Phi_0 = hc/e^*$ is the superconducting flux quantum. At H_{c2} the density of vortices $\sim \xi^{-2}(T)$ is such that the superconductor becomes filled with normal cores of vortices.

From Eqn. (5) the temperature dependence of H_{c2} is linear near T_c for a three-dimensional superconductor. Note that it is the coherence lengths in the two directions perpendicular to the applied field H that enter into Eqn. (5).

2.2 Superconducting Thin Films

In a superconducting thin film of thickness d, T_c will usually decrease as d is reduced due to changes in electronic interactions and reduced dimensionality. Neglecting these effects, however, and by treating $\tilde{T}_c$ and d independently, one can solve Eqn. (3) for the case of a parallel magnetic field. The appropriate boundary condition for a free surface is

$$\left(\nabla - \frac{ie^*}{\hbar c}A\right)\psi \cdot \hat{\mathbf{n}} = 0,$$

where **n** is the unit vector normal to the surface. One can apply a solution (see Ketterson and Song 1999,

for example) of the form $\psi = u(z)e^{ik_xx+ik_yy}$ and obtain

$$H_{c2\parallel} = \frac{\sqrt{12}\Phi_0}{2\pi\xi(T)d} \qquad (6)$$

In comparison with Eqn. (5), one $\xi(T)$ factor is replaced with $d/\sqrt{12}$, and therefore the critical field has a square root temperature dependence instead of a linear one. These two behaviors are referred to as 2D (square root) and 3D (linear). In the perpendicular direction thin films have the critical field, $H_{c2\perp}$, the same as the bulk value of Eqn. (5).

2.3 Superconducting Multilayers and Dimensional Crossover

In a multilayer superconductivity can have either 2D or 3D character. These behaviors and their cross-over can be illustrated with a simple GL model. Lawrence and Doniach (1971) first described the modified GL free-energy functional of a series of superconducting layers which are Josephson coupled—a 1D Josephson lattice.

$$F = \sum_n \int d^2r \left[\alpha|\psi_n|^2 + \frac{\beta}{2}|\psi_n|^4 + \frac{1}{2m^*}\left|\left(\frac{\hbar}{i}\nabla - \frac{e^*}{c}A\right)\psi\right|^2 + \eta|\psi_{n+1} - \psi_n|^2\right]$$

From the free energy functional the GL equation can be derived by variation as

$$\alpha\psi_n + \beta|\psi_n|^2\psi_n + \frac{1}{2m^*}\left(\frac{\hbar}{i}\nabla - \frac{e^*}{c}A\right)^2\psi_n$$
$$- \eta(\psi_{n+1} - 2\psi_n + \psi_{n-1}) = 0 \qquad (7)$$

The first part of this equation is the 2D result, where individual layers are indexed with n. The second part represents the Josephson coupling energy, scaled by the coupling parameter η. In the limit of strongly coupled layers, i.e., when ψ_n varies slowly across the layers, the solution is the same as the anisotropic GL, with the mass

$$m_z = \hbar^2/2s^2\eta$$

Within the LD model one can solve for arbitrary coupling of the layers, i.e., not assuming strong coupling. The linearized GL equation in a parallel magnetic field becomes

$$\left[-\frac{\hbar^2}{2m^*}\frac{d^2}{dx^2} + \frac{\hbar^2}{m_z^*s^2}\left(1 - \cos\frac{2eHxs}{\hbar c}\right)\right]\psi = -\alpha\psi$$

From this equation the critical field follows as

$$H_{c2\parallel} = \frac{\Phi_0}{2\pi s^2(1 - s^2/2\xi_z(T)^2)^{1/2}}\left(\frac{m_x^*}{m_z^*}\right)$$
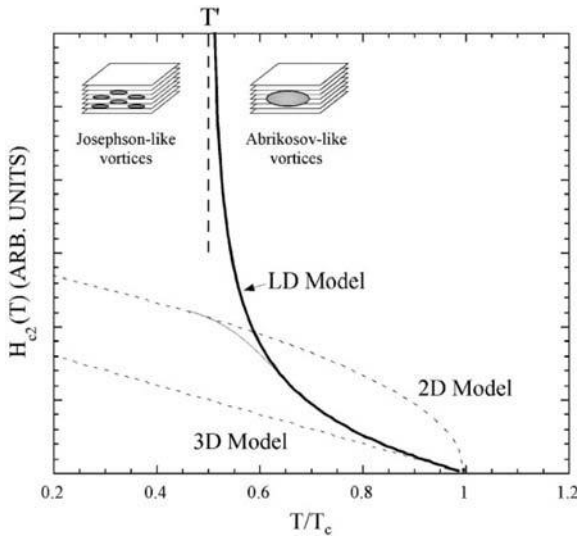
Figure 3
Temperature dependence of the upper critical field for
the Josephson coupled Lawrence–Doniach (LD) model.
Comparison is shown with the 3D GL and 2D GL
models. In reality the critical field will not diverge at T'
as in the LD model, but will cross over to a 2D behavior.
Below T' vortices fit between the superconducting layers
and become Josephson type. Above T' vortices are
averaging over several layers and are Abrikosov-type.

This equation leads to a divergence of the critical field
at T' defined by $\xi_z(T') = s/\sqrt{2}$ (see Fig. 3).
   Above T' the multilayer behaves as a 3D aniso-
tropic superconductor. As the temperature is lowered
the coherence length decreases its zero temperature
value. When the coherence length becomes compa-
rable to the spacing of the superconducting layers,
the normal cores of the vortices can fit between the
superconducting layers where they have a reduced
pair-breaking effect. Hence the critical field will in-
crease at this temperature and in the LD model the
critical field becomes infinite. In reality the critical
field will not diverge because it is limited by the single
film value, such as that described above. However,
the essential physics is captured in this simple model
for dimensional crossover. Below T' the vortices
change from Abrikosov-like to Josephson-like when
the X layers are nonsuperconducting.
   Dimensional crossover was experimentally con-
firmed by a number of experimental reports. The first
most compelling result was by Ruggiero *et al.* (1980).
Other reports can be found in the reviews mentioned
above. Ruggiero *et al.* studied Nb/Ge (S/I) multilay-
ers as a function of different layer thicknesses in or-
der to observe dimensional crossover. Figure 4 shows
the upper critical field of several Nb/Ge multilayer
samples with 3D, 2D, and crossover behavior. Later
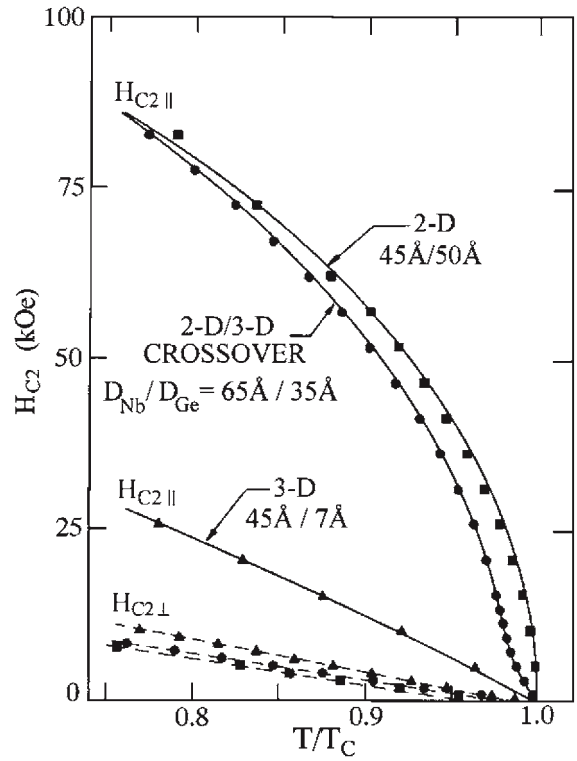
Figure 4
Upper critical fields near T_c for Nb/Ge multilayers. As
the Ge layer thickness increases the system evolves from
3D behavior to "crossover" behavior and finally to
decoupled 2D. Solid lines are fits to the theory (after
Ruggiero *et al.* 1980).

studies have observed the crossover more elaborately
in S/N systems (see, for example, Banerjee *et al.*
1983).

2.4 Takahashi–Tachiki Effect in S/S′ Multilayers

Takahashi and Tachiki (1986a, 1986b) examined the
behavior of the upper critical field in S/S′ multilayers
within a microscopic theory. For the case of widely
differing diffusion constants, i.e., differing ξ, but with
similar bulk T_c of the two superconducting layers,
they observed two possible solutions for nucleation of
superconductivity. One solution is for nucleation of
the superconducting order parameter in the dirty
superconductor, here labeled S, and the other for
nucleation of superconductivity in the clean super-
conductor, or S′, layers. The actual critical field will
be the larger of the two solutions.
   The Takahashi–Tachiki effect is a discontinuity in
the parallel upper critical field exhibiting an upward
curvature at low temperatures. This happens when
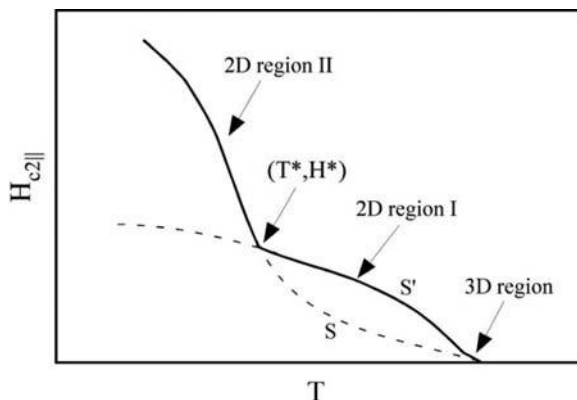
Figure 5
Schematic of the Takahashi–Tachiki effect (after Takahashi and Tachiki (1986b).

nucleation of superconductivity switches from S′ to S layers. Figure 5 illustrates the behavior of the critical field for a particular set of material parameters where this effect may be observed. The effect is only observed for a ratio of diffusion constants above a certain value, or equivalently above a minimum $\xi_{S'}/\xi_S$.

For temperatures very close to T_c the parallel critical field has the usual linear 3D behavior. At some temperature below T_c there is a crossover to 2D behavior with nucleation in the S′ layers. As the temperature decreases further and the coherence length becomes shorter than d_S, the order parameter is constrained inside the S layers and superconductivity behaves as it would in the bulk S material which has a high critical field. At T^* superconductivity crosses over from being nucleated in the S′ to the S layers and there is a discontinuity in the critical field.

The theoretical prediction of the effect was subsequently experimentally confirmed in the Nb/NbTi multilayer system by Karkut *et al.* (1988). For the proper choice of materials, as in $Nb_{0.6}Ti_{0.4}$ and Nb, the two layers have similar T_c but their diffusivities differ by a factor of 20. Karkut *et al.* observed an upturn in the parallel critical field at a particular temperature T^* as predicted by the Takahashi–Tachiki theory.

See also: Superconducting Materials, Types of; Superconducting Thin Films: Materials Preparation and Properties; Superconducting Thin Films: Multilayers

Bibliography

Banerjee I, Yang Q S, Falco C M, Schuller I K 1983 Anisotropic critical fields in superconducting superlattices. *Phys. Rev. B* **28**, 5037–40

Buzdin A I, Bulaevskii L N, Panyukov S V 1982 Critical-current oscillations as a function of the exchange field and thickness of the ferromagnetic metal (F) in an S–F–S Josephson junction. *JETP Lett.* **35**, 178–80

Fulde P, Ferrell R A 1964 Superconductivity in a strong spin-exchange field. *Phys. Rev.* **135A**, 550–63

Huebener R P 1979 *Magnetic Flux Structures in Superconductors*. Springer-Verlag, Berlin

Jiang J S, Davidovic D, Reich D H, Ghien C L 1995 Oscillating superconducting transition temperature in Nb/Gd multilayers. *Phys. Rev. Lett.* **74**, 314–7

Karkut M G, Matijasevic V, Antognazza L, Triscone J -M, Missert N, Beasley M R F, 1988 Anomalous upper critical fields of superconducting multilayers: verification of the Takahashi–Tachiki effect. *Phys. Rev. Lett.* **60**, 1751–4

Ketterson J B, Song S N 1999 *Superconductivity*. Cambridge University Press, Cambridge, UK

Larkin A I, Ovchinnikov Yu N 1964 Inhomogeneous state of superconductors. *Zh. Eksp. Teor. Fiz.* **47**, 1136 [*Sov. Phys. JETP* **20**, 762 (1965)]

Lawrence W E, Doniach S 1971 Theory of layer-structure superconductors. In: Kanda E (ed.) *Proc. 16th Int. Conf. on Low Temperature Physics*, pp. 361–2

Matijasevic V, Beasley M R 1987 Superconductivity in superlattices. In: Shinjo T, Takada T (eds.) *Metallic Superlattices: Artificially Structured Materials*. Elsevier Science, The Netherlands

Mühge Th, Garif'yanov N N, Goryunov Yu V, Khaliullin G G, Tagirov L R, Westerholt K, Garifullin I A, Zabel H 1996 Possible origin for oscillatory superconducting transition temperature in superconductor/ferromagnet multilayers. *Phys. Rev. Lett.* **77**, 1857–60

Radovic Z, Dobrosavljevic-Grujic L, Buzdin A I, Clem J R 1988 Upper critical fields of superconductor–ferromagnet multilayers. *Phys. Rev. B* **38**, 2388–93

Ruggiero S T, Barbee T W, Beasley M R 1980 Superconductivity in quasi-two-dimensional layered composites. *Phys. Rev. Lett.* **45**, 1299–302

Ruggiero S T, Beasley M R 1984 Synthetically layered superconductors. In: Chang L L, Giessen B C (eds.) *Synthetic Modulated Structures*. Academic Press, New York

Ryazanov V V, Oboznov V A, Rusanov A Yu, Veretennikov A V, Golubov A A, Aarts J 2001 Coupling of two superconductors through a ferromagnet: evidence for a π-junction. *Phys. Rev. Lett.* **86**, 2427–30

Schuller I K, Guimpel J, Bruynseraede Y 1990 Artificially layered superconductors. *MRS Bull.* **15**, 29–36

Takahashi S, Tachiki M 1986a Theory of the upper critical field of superconducting superlattices. *Phys. Rev. B* **33**, 4620–31

Takahashi S, Tachiki M 1986b New phase diagram in superconducting superlattices. *Phys. Rev. B* **34**, 3162–4

V. Matijasevic
Oxxel GmbH, Germany

Fullerene Formation

Diamond and graphite constitute two natural crystalline forms of pure carbon. Their properties and characteristics are completely different, a fact that can be explained in terms of the way carbon atoms

bond to each other within the structure. For diamond, sp^3 hybridization prevails, four bonds from each carbon atom being directed towards the corners of a regular tetrahedron. The resulting three-dimensional network is extremely rigid, which is one reason for the hardness of diamond. In graphite, sp^2 hybridization results in three bonds per carbon atom, distributed evenly (120°) in the *xy* plane, with a weak π bond along the *z* axis. The C–C bond length is 1.42 Å, and the sp^2 set creates the honeycomb (hexagonal) lattice typical of a single sheet of graphite. The π (van der Waals) bond is responsible for weak interactions between the layers, which are 3.35 Å apart.

For generations, diamond and graphite were the only known allotropes of carbon. However, in 1985 a new form of carbon, buckminsterfullerene (C_{60}) (Kroto *et al.* 1985), appeared on the scene.

C_{60} is a soccer-ball-like cage composed of 60 carbon atoms with a diameter of 7.1 Å. The shape and symmetry of C_{60} is that of a truncated icosahedron, consisting of 20 hexagons and 12 pentagons (Fig. 1). Curvature is due to the presence of the pentagons.
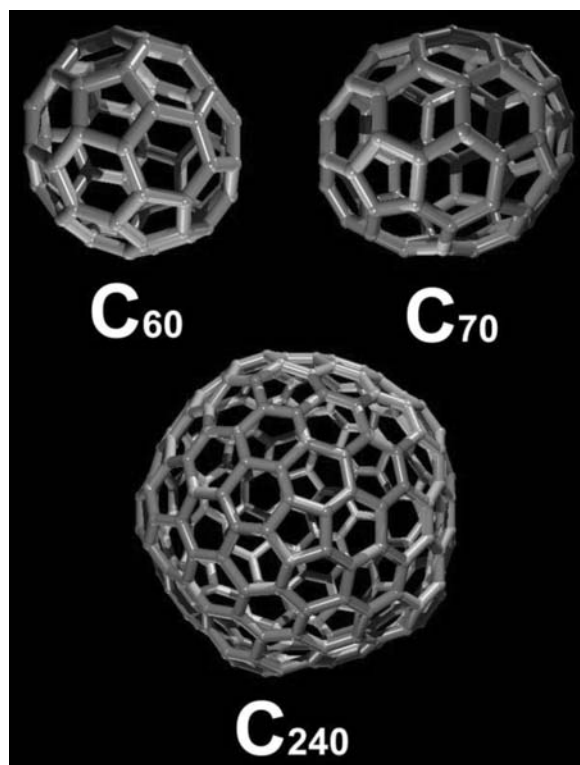
Figure 1
(a) Buckminsterfullerene (C_{60}), the third carbon allotrope, discovered in 1985. (b) C_{70} with D_{5h} symmetry. (c) C_{240}, an icosahedral giant fullerene.

The relationship between the vertices, faces, and edges of C_{60} finds expression in Euler's law (see Sect. 3). C_{60} is but one example of closed structures made up of any number of hexagons (except one) and 12 pentagons now styled fullerenes.

1. Discovery of C_{60}

One part of this story starts in the 1970s, when the chemists Harry Kroto and David Walton at Sussex University were studying cyanopolyynes $H(C\equiv C)_nC\equiv N$ (chain-like molecules, in which carbon atoms are linked by alternating single and triple bonds, being end-capped with hydrogen and nitrogen). These compounds display characteristic microwave spectra commensurate with their linear dipole structure (Kroto 1992).

The two Sussex scientists together with Anthony Alexander (a BSc-by-thesis student) succeeded in preparing HC_5N and, with Colin Kirby (a research student), HC_7N. Subsequently, with Canadian astronomers Takeshi Oka and co-workers, radio waves emitted from HC_nN ($n = 5, 7, 9$) in the center of our galaxy were detected (Kroto 1992).

In 1984 Kroto visited Robert Curl at Rice University (Houston, Texas) and was introduced to Richard Smalley, who was generating clusters of atoms by laser-vaporizing solids. Kroto was interested in subjecting graphite to this treatment in order to simulate the conditions thought to prevail in red giant stars.

In late August 1985 Kroto traveled to Houston in order to participate in the graphite experiment, which involved evaporating carbon from the surface of a rotating graphite disk in the presence of a high density helium flow. The resulting carbon clusters were allowed to expand though a nozzle and were detected by a time-of-flight mass spectrometer (Kroto *et al.* 1985).

The mass-spectral profile for carbon, obtained in these experiments, had in fact already been observed by Rohlfing *et al.* (1984) and consisted of two main groups of clusters: (a) those with low mass (<30 carbon atoms) consisting of odd numbers of carbon atoms and (b) high-mass clusters (>36 atoms) containing only even numbers of carbon atoms (Fig. 2). Rohlfing *et al.* (1984) proposed that clusters with less than nine carbon atoms were linear chains, and that the odd masses between 11 and 23 were due to rings. No comment was made regarding the structure of higher clusters other than that they were exceptional and possibly carbyne-like (consisting of linear carbon chains with alternating single and triple bonds, i.e., polyynes).

In the experiments carried out at Rice University, the dominant role played by the cluster of 60 carbon atoms was noted and its stability was ascribed to the unique nature of the truncated icosahedral cage (see above) without "dangling" bonds (Fig. 1). C_{60} was named buckminsterfullerene by the Sussex/Rice
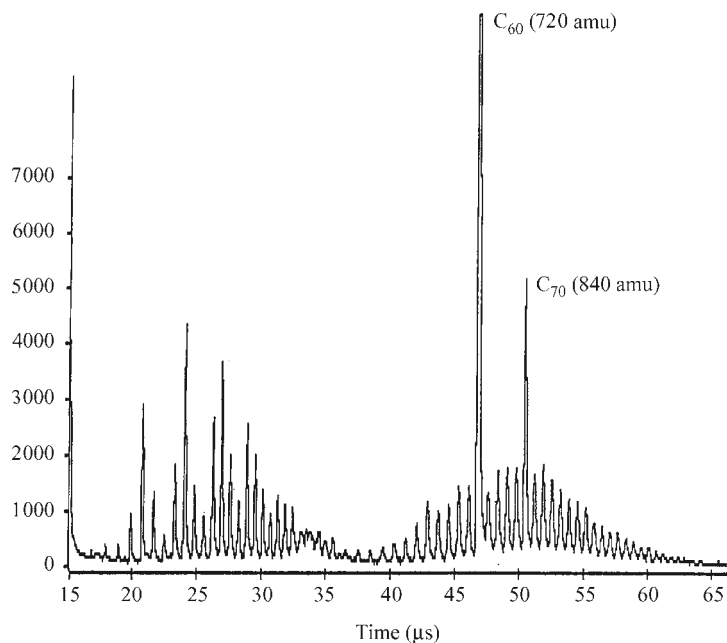
Figure 2
Mass-spectral profile obtained by the Sussex/Rice team, showing C_{60} and C_{70} as the most intense peaks. Additionally, they observed two groups of clusters: those with lower mass (<30 carbon atoms) consisting of odd numbers of carbon atoms and high-mass clusters (>36 atoms) exhibiting only even numbers of carbon atoms (courtesy of H. W. Kroto).
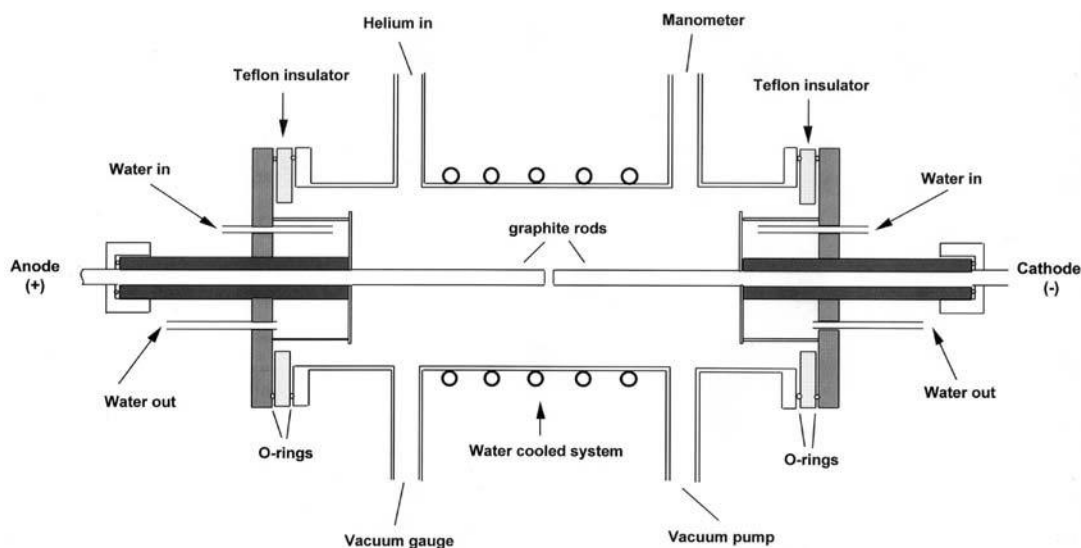
Figure 3
Schematic diagram of a d.c. arc discharge chamber used for fullerene production.

team, in recognition of the US architect R. Buckminster Fuller, who designed geodesic domes with similar topologies.

In order to verify the structure of C_{60}, bulk quantities were needed. However, at the time only picogram amounts were available.

2. Bulk Production and Characterization of C_{60}

In 1990 Krätschmer and Huffman succeeded in preparing milligram quantities of C_{60}, accompanied by smaller amounts of higher fullerenes (e.g., C_{70}, C_{76}, etc.) by extracting soluble material from soot deposits formed in an arc discharge between graphite electrodes in a helium atmosphere (Fig. 3). Subsequently, C_{60} and C_{70} were separated and characterized by the Sussex team using conventional chromatography and NMR techniques. Fullerenes have also been obtained by combustion and by pyrolysis of hydrocarbons such as naphthalene.

In the solid state, C_{60} crystallizes as a cubic structure with a lattice constant of 14.17 Å, a nearest-neighbor C_{60}–C_{60} distance of 10.02 Å, and a density of $1.72\,\mathrm{g\,cm^{-3}}$ (Fig. 4(a)). At room temperature, C_{60} clusters rotate rapidly in an f.c.c. structure about their lattice positions (Tables 1 and 2). However, a transition to a simple cubic phase ($a = 14.17$ Å consisting of four C_{60} clusters per unit cell) occurs below 261 K (Tanigaki and Prassides 1995).

The first fullerene isolated other than C_{60}, was C_{70} (isolated by Taylor *et al.*), which consists of two C_{60} hemispheres connected by a ring of 10 carbons (resembling a rugby ball; Fig. 1). Crystalline C_{70} has different crystallographic arrangements depending on the temperature: the most stable phases are the f.c.c. structure with a lattice constant of 15.01 Å and the hexagonal phase with $a = b = 10.56$ Å and $c = 17.18$ Å. Higher fullerenes such as C_{76}, C_{78}, C_{82}, C_{84}, were subsequently isolated and characterized.

3. Geometry of Fullerenes

Fullerenes are closed polyhedrons made of carbon, and understanding their geometry may eventually shed light on the way they are constructed. As mentioned above, Euler's law expresses the proportions of polygon types (pentagons and hexagons) needed to form C_{60}. For any polyhedron $F - E + V = \chi$, where F is the number of faces, E is the number of edges, V is the number of vertices, and χ is the Euler characteristic, which is a geometric invariant that describes structures with the same shape or topology. For all closed polyhedrons $\chi = 2$. For example, in C_{60}, $F = 32$ (12 pentagons and 20 hexagons), $E = 90$, $V = 60$, and $\chi = 2$; for C_{70}, $F = 37$ (12 isolated pentagons, 25 hexagons, and D_{5h} symmetry), $E = 105$, $V = 70$, and $\chi = 2$. All closed polyhedrons have the same topology as the sphere, which means that any polyhedron can
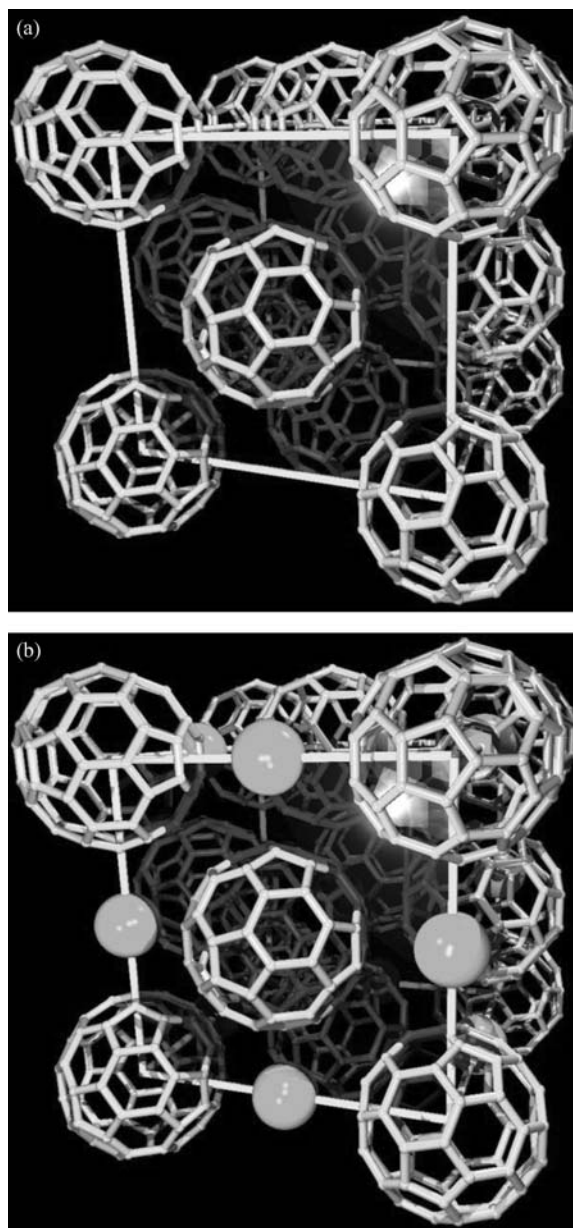
Figure 4
(a) F.c.c. crystal structure of C_{60}. (b) Structure of the M_1C_{60} intercalated compounds showing the metal intercalated between the C_{60} spheres. Note that the size of the intercalated atoms has been chosen arbitrarily.

be transformed into a sphere by bending and stretching without cutting or tearing. In addition, no fullerene can be formed from an odd number of atoms.

For a ''graphitic'' network, considering only pentagonal, hexagonal, heptagonal, and octagonal rings

Table 1
Physical constants for C_{60}.

Quantity	Value
Average C–C distance	1.44 Å
C–C bond length on a pentagon	1.46 Å
C–C bond length on a hexagon	1.40 Å
C_{60} mean ball diameter	7.10 Å
C_{60} ball outer diameter	10.34 Å
Moment of inertia	$1.0 \times 10^{43}\,\mathrm{Kg\,m^2}$
Volume per C_{60}	$1.87 \times 10^{-22}\,\mathrm{cm^{-3}}$
Number of distinct carbon sites	1
Number of distinct C–C bonds	2
Binding energy per atom	7.40 eV
Heat of formation (per g carbon atom)	10.16 Kcal
Electron affinity	2.65 ± 0.05 eV
Cohesive energy per atom	1.4 eV
Spin–orbit splitting of carbon (2p)	0.000 22 eV
First ionization potential	7.58 eV
Second ionization potential	11.5 eV
Optical absorption edge	1.65 eV

Source: Dresselhaus *et al.* (1995).

Table 2
Physical constants for crystalline C_{60} in the solid state.

Quantity	Value
F.c.c. lattice constant	14.17 Å
C_{60}–C_{60} distance	10.02 Å
C_{60}–C_{60} cohesive energy	1.6 eV
Tetrahedral interstitial site radius	1.12 Å
Octahedral interstitial site radius	2.07 Å
Mass density	$1.72\,\mathrm{g\,cm^{-3}}$
Molecular density	$1.44 \times 10^{-21}\,\mathrm{cm^{-3}}$
Compressibility ($-\mathrm{d}\ln V/\mathrm{d}P$)	$6.9 \times 10^{-12}\,\mathrm{cm^2\,dvn^{-1}}$
Bulk modulus	6.8–8.8 GPa
Young's modulus	15.9 GPa
Transition temperature (T_{01})	261 K
$\mathrm{d}T_{01}/\mathrm{d}p$	$11\,\mathrm{K\,bar^{-1}}$
Volume coefficient of thermal expansion	$6.1 \times 10^{-5}\,\mathrm{K^{-1}}$
Optical absorption edge	1.7 eV
Work function	4.7 ± 0.1 eV
Velocity of sound, v_t	$2.1 \times 10^5\,\mathrm{cm\,s^{-1}}$
Velocity of sound, v_l	3.6–$4.3 \times 10^5\,\mathrm{cm\,s^{-1}}$
Debye temperature	185 K
Thermal conductivity (300 K)	$0.4\,\mathrm{W\,m^{-1}\,K^{-1}}$
Electrical conductivity	$1.7 \times 10^{-7}\,\mathrm{S\,cm^{-1}}$
Phonon mean free path	50 Å
Static dielectric constant	4.0–4.5
Melting temperature	1180 °C
Sublimation temperature	434 °C
Heat of sublimation	$40.1\,\mathrm{kcal\,mol^{-1}}$
Latent heat per C_{60} unit	1.65 eV

Source: Dresselhaus *et al.* (1995).

of carbon, Euler's law can be written:

$$N_5 - N_7 - 2N_8 = 6\chi = 12 \qquad (1)$$

where N_n is the number of polygons with n (5, 7, and 8) sides. As Eqn. (1) shows, N_5, N_7, and N_8 are defects in a "graphitic" structure which contribute to the curvature and topology of the arrangement (Terrones and Mackay 1992). N_6 is absent since hexagons do *not* contribute to curvature of the structure. In addition, Eqn. (1) demonstrates that it is possible to introduce heptagons and octagons in a closed graphitic cage if their proportion is maintained. Therefore, if pentagons are present in C_{60}, one cannot rule out the presence of higher-membered rings (e.g., heptagons) in larger fullerenes.

It turns out that there are 1812 possible ways of arranging 12 pentagons and 20 hexagons in C_{60}, so what is special in buckminsterfullerene? It is the smallest cage in which each pentagon is surrounded by five hexagons, thus leading to icosahedral (I_h) symmetry (the highest symmetry than can be obtained by a polyhedron). This suggests that curved graphite follows an isolated pentagon rule to form fullerenes, and explains why smaller fullerenes (less than 60 atoms) are difficult to produce.

4. Fullerene Growth

Although the precise growth mechanism leading to C_{60} and other fullerenes is not well understood, it is worth reviewing ways in which they might be formed.

First, the mass spectrometry data obtained by laser vaporization and arc discharge experiments indicate that there are three main groups of structures, depending upon the size: chains, rings, and fullerenes. In other words, for a small number of atoms (<10) carbon chains are the most stable (one dimension); subsequently rings start to appear (>10 atoms), thus avoiding dangling bonds at the ends (two dimensions); and finally fullerenes emerge in order to avoid dangling bonds in larger, three-dimensional structures.

According to Euler's law, the smallest fullerene that can possibly exist is the dodecahedron with 20 atoms or 12 pentagons (C_{20}; Fig. 5). Although this structure is quite regular (one of the five Platonic solids), with icosahedral symmetry, building it from sp^2 carbons introduces considerable strain. This is because the internal angle in a regular pentagon is 108°, which differs substantially from the internal (hexagon) 120° angles in graphite. Therefore, in order to relieve this strain, hexagons are required to stabilize larger fullerenes. At the same time, with 20 atoms, it is also possible to obtain a ring (cyclic polyyne) or a
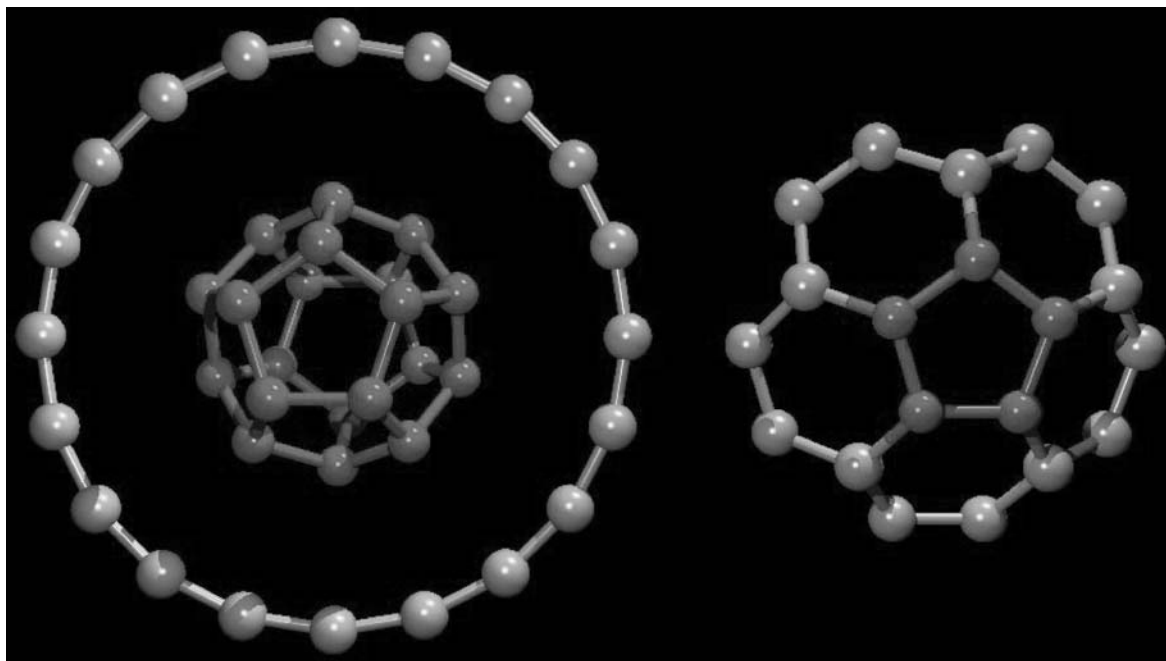
Figure 5
Possible isomers of C_{20}: (a) ring, (b) cage, and (c) bowl (corannulene-like molecule).

corannulene-like molecule (a bowl-shaped structure composed of one pentagon surrounded by five hexagons; Fig. 5). Various theoretical simulations have been carried out in order to ascertain which is the most stable structure composed of 20 atoms. The results show that, depending upon the computational method used, the ring, the corannulene-like molecule, and the dodecahedron are stable and feasible. However, for fullerene formation (under nonequilibrium conditions), corannulene and the dodecahedron might be relevant due to the presence of pentagons in their structures. Nevertheless, neither of them has ever been observed as a stable product.

It is worth noting that fullerenes are formed in a plasma at 3500 °C and under these conditions a wide variety of carbon clusters are present, e.g., dimers, trimers, rings, and small clusters. Thus, structures of the corannulene type or the dodecahedral C_{20} may play a crucial role in the formation of C_{60} since C_2 or bigger units can become attached to the pentagons, thus stimulating growth.

Two main mechanisms have been proposed to account for fullerene formation (Dresselhaus *et al.* 1995). They are based upon: (a) absorption of C_2 units and (b) Stone–Wales (S–W) transformations. The absorption of a C_2 cluster creates an extra hexagon within the structure; therefore, the addition of several C_2 units into a fullerene would generate a larger cage. An S–W transformation involves rotating a C_2 unit by 90°, thus changing the symmetry but

maintaining connectivity. A combination of these two mechanisms is necessary in order to attain a stable "graphitic" cage. Nevertheless, the amount of energy involved in an S–W transformation is large (~ 7 eV). In this context, it has been shown that autocatalytic effects might overcome the potential barrier involved in this type of transformation (Eggen *et al.* 1996). It is also worth noting that fullerenes smaller than C_{60} have been detected only in mass spectrometers, with one exception being the D_{6h} isomer of C_{36}, isolation of which has been claimed (Piskoti *et al.* 1998).

5. Endohedral Complexes, Intercalated Compounds and Superconductivity

Kroto *et al.* (1985) suggested that it should be possible to encapsulate atoms within the C_{60} cage. Shortly afterwards a Rice University student, Jim Heath, succeeded in trapping lanthanum in C_{60} by laser vaporizing a graphite disk impregnated with $LaCl_3$ (Heath *et al.* 1985). Following the bulk production of C_{60}, fullerenes containing encapsulated elements, denoted $M@C_n$, have been described, e.g., $Ar@C_{60}$, $He@C_{60}$, $Hf@C_{28}$, $Ti@C_{28}$, $U@C_{28}$, $U_2@C_{28}$, $Zr@C_{28}$, $U@C_{36}$, $Co@C_{60}$, $Sc@C_{74}$, $Er@C_{82}$, $La@C_{82}$, $La_2@C_{82}$, $Sc@C_{82}$, $Sc_2@C_{82}$, $Sc_3@C_{82}$, $La@C_{84}$, $La_2@C_{84}$, etc. (Dresselhaus *et al.* 1995). The separation and isolation of these endohedrals is difficult because the amounts available are minute,
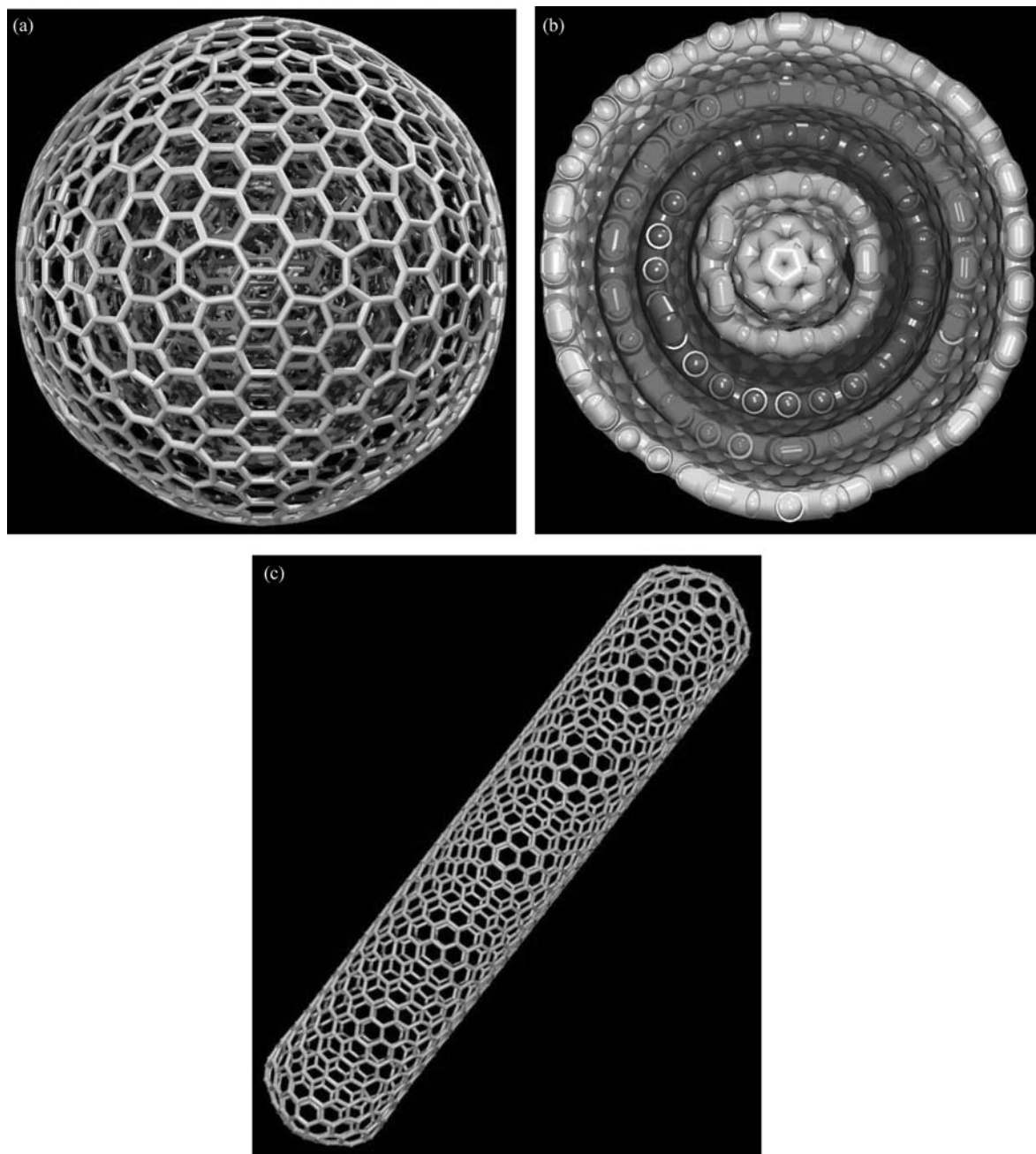
Figure 6
(a) Graphitic onion-like structures: concentric giant fullerenes with heptagons and additional pentagons. (b) Cross-section of the structure shown in (a) exhibiting concentric shells. (c) Elongated fullerene: a carbon nanotube.

there are solubility problems, and the products may be oxygen sensitive.

In 1991 Haddon and co-workers succeeded in inter-calating alkali metals with C_{60} in order to produce materials of stoichiometry M_3C_{60} (M = K, Rb, Cs). These products displayed a relatively high, supercon-ducting, value of T_c (18–33 K) (Tanigaki and Prassides 1995). Other stable phases of intercalated C_{60} were

prepared (e.g., M_1C_{60}, M_3C_{60}, and M_6C_{60}; Fig. 4(b)). All possess lattice constants greater than that of C_{60} ($a = 14.24$ Å) due to the introduction of the metal ion into the crystal phase (Fig. 4(b)). It is important to note that superconductivity only arises when the tetrahedral and octahedral sites of C_{60} are fully occupied by alkali atoms, thus creating a M_3C_{60} structure. Other stable phases and crystal structures with one, two, four, and six alkali ions per unit cell have been also described.

6. Giant Fullerenes

In 1992 Daniel Ugarte discovered that carbon soot (generated in plasma arcs), under high-energy electron irradiation, produced what were effectively nested giant fullerenes, termed "graphitic onions" (Figs. 6(a) and 6(b)). It is interesting to note that in 1980 Iijima observed similar round structures in amorphous carbon films prepared by vacuum deposition (the morphology was proposed by Kroto and McKay in 1988). These closed polyhedrons possess millions of carbon atoms. It has been shown theoretically (Terrones *et al.* 1995) that the high sphericity of the onions is due to the presence of heptagons and octagons (Figs. 6(a) and 6(b); Eqn. (1)).

7. Uses of Fullerenes

Current fullerene research is developing rapidly and due to their exceptional properties (Tables 1 and 2), various applications can be envisaged. In particular, the optical properties have facilitated the fabrication of photodiodes and photovoltaic and photorefractive devices, etc. Fullerenes, in conjunction with conducting polymers, could give rise to C_{60}-based transistors and rectifying diodes. However, it should be pointed out that most of these C_{60} devices are unstable in air due to the diffusion and photodiffusion of dioxygen into the large interball sites present in the solid.

From the catalysis point of view, fullerenes can be useful in the hydrocarbon refining industry, where an active catalyst is needed to enhance the efficiency with which hydrogen is used. Fullerenes can be used as a source of pure carbon in order to generate high-purity carbon allotropes such as diamond or nanotubes (see Sect. 8). In the nanotechnology area, C_{60} and other "graphitic" particles may prove useful as scanning tunneling microscopy (STM) tips, lubricants, sensors, and other nanoscale devices.

Finally, C_{60} has proved to be useful as an efficient inhibitor of HIV enzymes and research related to cancer treatments is underway. Therefore, this exciting area of research is likely to give birth to a new technology in the twenty-first century.

8. Elongated Fullerenes (Nanotubes)

The fullerenes reviewed above consist of closed, *round* cages. However, it is possible to generate elongated fullerenes, known as nanotubes (Fig. 6(c)). Iijima (1991) reported the existence of these structures, consisting of concentric graphite tubes, produced in the Krätschmer–Huffman fullerene reactor (operating at low direct current). A few months after Iijima's paper appeared, the first report on the bulk synthesis of nanotubes, by Ebbesen and Ajayan, was published. These authors collected the material from the inner deposit generated by arcing graphite electrodes in inert atmospheres (a similar procedure to that used for fullerenes).

Nanotubes can be produced by several methods (e.g., arc discharge, pyrolysis of hydrocarbons over catalysts, laser vaporization, electrolysis, etc.), with the products exhibiting various morphologies (e.g., straight, curled, hemitoroidal, branched, spiral, helical, etc.).

It has been predicted that carbon nanotubes may behave as metallic, semiconducting, or insulating nanowires depending upon their helicity and diameter. Conductivity measurements on bulk nanotubes, individual multilayered tubes, and ropes of single-walled tubules have revealed that their conducting properties depend strongly on the degree of graphitization, helicity, and diameter. Young's modulus measurements also show that multilayered nanotubes are mechanically much stronger than conventional carbon fibers (Terrones *et al.* 1999).

The advances typified by fullerenes and related structures herald a new age in nanoscale materials engineering. However, this may be only the "tip of the iceberg" since other layered structures (e.g., MoS_2, WS_2, VS_2, etc.) are also capable of creating closed cages.

See also: Fulleride Superconductors

Bibliography

Dresselhaus M S, Dresselhaus G, Eklund P C 1995 *Science of Fullerenes and Carbon Nanotubes*. Academic Press, San Diego, CA

Eggen B R, Heggie M I, Jungnickel G, Latham C D, Jones R, Briddon P R 1996 Autocatalysis during fullerene growth. *Science* **272**, 87–9

Heath J R, O'Brien S C, Zhang Q, Liu Y, Curl R F, Kroto H W, Tittel F K, Smalley R E 1985 Lanthanum complexes of spheroidal carbon shells. *J. Am. Chem. Soc.* **107**, 7779–80

Iijima S 1991 Helical microtubules of graphitic carbon. *Nature* **354**, 56–8

Kroto H W, Heath J R, O'Brien S C, Curl R F, Smalley R E 1985 C_{60}: buckminsterfullerene. *Nature* **318**, 162–3

Kroto H W 1992 C_{60}: buckminsterfullerene, the celestial sphere that fell to earth. *Angew. Chem., Int. Ed. Engl.* **31**, 111–29

Piskoti C, Yarger J, Zettl A 1998 C_{36}: a new carbon solid. *Nature* **393**, 771–4

Rohlfing E A, Cox D M, Kaldor A J 1984 Production and characterization of supersonic carbon cluster beams. *J. Chem. Phys.* **81**, 3322–30

Tanigaki K, Prassides K 1995 Conducting and superconducting properties of alkali-metal C-60 fullerides. *J. Mater. Chem.* **5**, 1515–27

Terrones H, Mackay A L 1992 The geometry of hypothetical curved graphite structures. *Carbon* **30**, 1251–60

Terrones H, Terrones M, Hsu W K 1995 Beyond C$_{60}$: graphite structures for the future. *Chem. Soc. Rev.* **24**, 341–50

Terrones M, Hsu W K, Kroto H W, Walton D R M 1999 Nanotubes: a revolution in materials science and electronics. *Top. Curr. Chem.* **199**, 189–234

M. Terrones
University of Sussex, Brighton, UK

H. Terrones
Instituto Potosino de investigación Científica y Technológica, San Luis Potosí, Mexico

Fulleride Superconductors

The electronic and crystal structures of C$_{60}$ lead to a diverse chemistry based on the intercalation of electropositive elements into the interstitial sites within the solid and concomitant transfer of electrons to the fullerene. This produces solids with partially filled bands and results in a variety of phenomena including superconductivity (Hebard *et al.* 1991) at the highest temperatures yet seen for molecular solids.

1. Crystal and Electronic Structures of Solid C$_{60}$

For a detailed description of fullerene solids (see *Fullerene Formation*). Face-centered cubic solid C$_{60}$ ($a = 14.17$ Å, $r(\mathrm{C}_{60}\text{–}\mathrm{C}_{60}) = 10$ Å) can to a first approximation be considered as the cubic close packing of 5 Å radius hard spheres. Simple radius ratio considerations then allow the calculation of the sizes of two tetrahedral (T, 1.1 Å) and one octahedral (O, 2.06 Å) interstitial site per C$_{60}$. The extensive intercalation chemistry of f.c.c. C$_{60}$ derives from the weak inter-C$_{60}$ forces and the size match between the octahedral and tetrahedral interstitial sites in the f.c.c. C$_{60}$ array and those of the cations of the electropositive elements.
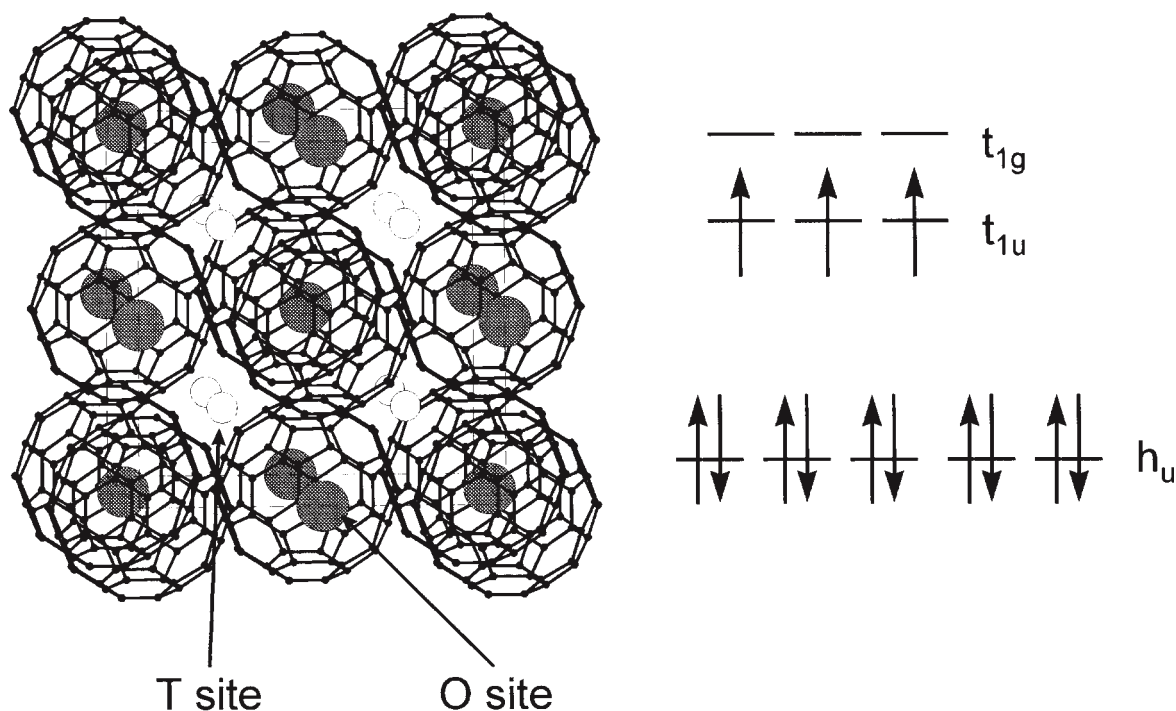
Figure 1
The ordered Fm3 structure of A$_3$C$_{60}$ (most phases, e.g., K$_3$C$_{60}$, have two-fold merohedral disorder of the C$_{60}^{3-}$ in space group Fm3m). Large gray spheres occupy the octahedral (O) site, and small unshaded spheres represent cations on the tetrahedral (T) sites. Rb$_2^{\mathrm{T}}$Cs$^{\mathrm{O}}$C$_{60}$ is a site-ordered A$_3$C$_{60}$ phase. A$_1$C$_{60}$ phases, with only the O sites occupied, are known with both f.c.c. and polymer structures. Na$_2$C$_{60}$ results from occupancy of the T sites. Na$_{4+x}$ groups are found on the O sites in Na$_{6+x}$C$_{60}$. The frontier orbitals of the C$_{60}^{3-}$ anion are shown: the $(t_{1u})^3$ configuration produces a half-filled band and metallic behavior in K$_3$C$_{60}$.

The electronic structure of the molecule is important in determining the properties of the intercalates. The LUMO of C_{60} is almost nonbonding in nature, accounting for the electronegative character of the molecule, and is triply degenerate with t_{1u} symmetry. The t_{1g} "LUMO+1" level is also chemically accessible, with possible anion charges of up to minus 12 (Fig. 1).

2. Intercalate Structures

2.1 Spherical Counterions

Well-defined structural information exists for sodium, potassium, rubidium, caesium, calcium, strontium, barium, europium, samarium, and ytterbium intercalates (Rosseinsky 1998). An A_1C_{60} rock-salt phase with the cation occupying the O site alone is formed for A = K, Rb, and Cs and may polymerize by [2 + 2] cycloaddition on cooling to form a unique air-stable linear-chain polymer if suitable cooling procedures are followed. A Pa3 symmetry Cs_1C_{60} phase is afforded by a particular cooling sequence. Na_2C_{60} with sodium cations solely occupying the T sites forms due to the good size match: there is no analogue of this phase yet known for the other alkali metals.

The A_3C_{60} phases are formed by complete occupancy of the O and T sites in the f.c.c. structure (Fig. 1). Cation ordering is observed when size differences are sufficiently pronounced (e.g., $Rb_2^TCs^OC_{60}$, $Na_2^TRb^OC_{60}$). Anion orientational order is controlled by cation size, with the structures of K_3C_{60} (Fm3m) and Na_2CsC_{60} (Pa3) being related by a 22° rotation of the anions around the [111] direction. Low-temperature polymerization is observed in slow-cooled Pa3 Na_2RbC_{60}, with the interfulleride bonding differing from the A_1C_{60} polymers. $Yb_{2.75}C_{60}$ has a complex defect structure based on the A_3C_{60} f.c.c. model, with vacancy ordering on the O site producing an eight-fold enlargement of the cell (Ozdas *et al.* 1995).

Ba_3C_{60} is an A_3C_{60} phase with b.c.c. packing, adopting the A15 structure of Nb_3Sn, with the caesium cations ordered over half of the interstitial sites in the K_6C_{60} structure (Fig. 2(c)). This structure is also reported for Cs_3C_{60}, where the large Cs^+ cation forces a b.c.c. packing on the C_{60}^{3-} anions due a size mismatch with the tetrahedral site in the f.c.c. structure.

Li_3CsC_{60} adopts f.c.c anion packing with an Li_2Cs unit on the octahedral site, but most A_4C_{60} phases adopt the b.c.c. structure of K_4C_{60}. Cs_4C_{60}, Ba_4C_{60}, and Sr_4C_{60} adopt an orthorhombic distortion of this structure due to anion orientational ordering (Fig. 2(b)). Like Ba_3C_{60}, these are also cation vacancy ordered derivatives of the K_6C_{60} structure. Na_4C_{60} adopts a unique two-dimensional polymerized structure.

A_6C_{60} phases adopt the b.c.c. packing of K_6C_{60} (Fig. 2(a)) with the cations in distorted tetrahedral sites. Alkali metal A_6C_{60} salts are electrical insulators as the $(t_{1u})^6$ configuration produces a filled band. The small sodium cation can retain f.c.c. packing in Na_6C_{60} with Na_4 tetrahedral units on the octahedral site. This f.c.c. structure is retained up to $Na_{11}C_{60}$, with b.c.c. units on the octahedral site. Ca_5C_{60} is f.c.c. but with an as-yet undefined superstructure, thought to be a defect Na_6C_{60} type with similar Ca_{4-x} units on the octahedral site.

2.2 Nonspherical Counterions

The above structures are based on packing of near-spherical objects and all have close analogies in metal

(a)	(b)	(c)
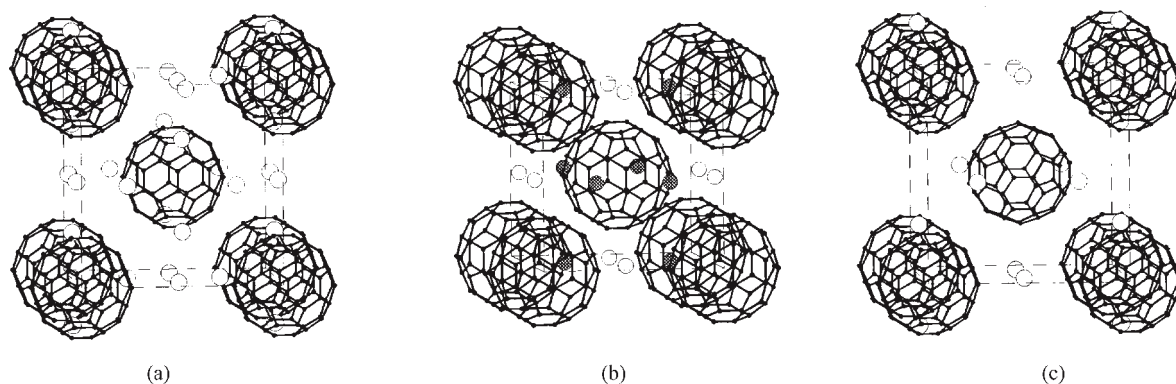
Figure 2
Body-centered fulleride arrays. (a) The Im3 K_6C_{60} structure. The K^+ cations are in distorted tetrahedral sites. (b) The A_4C_{60} structure, generated by ordered removal of one-third of the cations from (a). Cs_4C_{60} and the Sr_4C_{60} and Ba_4C_{60} superconductors adopt an orthorhombic Immm structure with orientationally ordered anions, while K_4C_{60} and Rb_4C_{60} are tetragonal with disordered anions. (c) Ordered occupancy of half of the cation sites in (a) leads to the Pm3n Ba_3C_{60} structure, in which the fulleride anions at the cell origin and body center adopt orientations related by 90° rotation about the cell vectors.

and alloy structures. Coordination of a ligand such as ammonia to the metal ion results in a complex ion whose size and symmetry are controllable and generally nonspherical. This results in new structure types (such as the expanded close-packed $(NH_3)_8$ Na_2C_{60} structure), new metal combinations (the Cs_2NaC_{60} composition is multiphase, but a pure f.c.c. $Cs_2Na(NH_3)C_{60}$ phase is accessible with the linear $Na–NH_3$ unit oriented in a disordered manner along with the [111] directions (Iwasa *et al.* 1997)), and opportunities to control the electronic properties of C_{60}^{3-} phases in new ways (Rosseinsky 1998). The reaction of f.c.c. K_3C_{60} with ammonia affords $(NH_3)K_3C_{60}^{3-}$ with the $NH_3–K$ unit on the octahedral site. This lowers the symmetry to orthorhombic, resulting in the suppression of superconductivity and a metal–insulator transition at 40 K. Ion-exchange techniques allow access to transition metal substituted fullerides such as $Ni(NH_3)_6C_{60} \cdot 6NH_3$.

3. Superconductivity in Fullerides

The interest in fullerene intercalation chemistry stems from the discovery of superconductivity at a critical temperature (T_c) of 19 K in K_3C_{60}—this transition temperature was the highest found for a molecular solid. The interfulleride separation may be tuned by varying the size of the cations intercalated on the octahedral and tetrahedral sites, resulting in a monotonic increase in T_c with lattice parameter (Fig. 3(a)). This is consistent with T_c depending on $N(E_f)$, the density of states at the Fermi level, in a Bardeen–Cooper–Schrieffer (BCS)-like manner, as the increased interfulleride separation narrows the width of the t_{1u} band. The same qualitative dependence of T_c on interfulleride separation is apparent from studies of the pressure dependence of T_c of K_3C_{60} and Rb_3C_{60}, although the quantitative dependence differs slightly.

A range of experiments has clarified the empirical requirements for fulleride superconductivity. The observation of superconductivity in orthorhombic Sr_4C_{60}, Ba_4C_{60}, and $Yb_{2.75}C_{60}$ demonstrate that neither cubic symmetry nor a minus 3 fulleride charge is a prerequisite (Brown *et al.* 1999). However, T_c does appear optimized at an anion charge of minus 3 in the $K_{3-x}Ba_xC_{60}$ and $Li_{2+x}CsC_{60}$ series. The relative orientations of the fulleride anions have a drastic effect on the $T_c(a)$ relationship—a 22° anion rotation about the [111] direction converts the Fm3m K_3C_{60} structure into the Pa3 Na_2CsC_{60} structure, resulting in a much more pronounced $T_c(a)$ slope. The highest reported transition temperature in an f.c.c. phase is 33 K in Cs_2RbC_{60}, while 40 K under 15 kbar pressure is reported for Cs_3C_{60}, which adopts a body-centered structure.

The fullerides present a challenge to theory (Gunnarsson 1997). The sharp peak in T_c at a minus 3 charge (Fischer 1997) (Fig. 3(b)) has been explained using the density of states of an orientationally
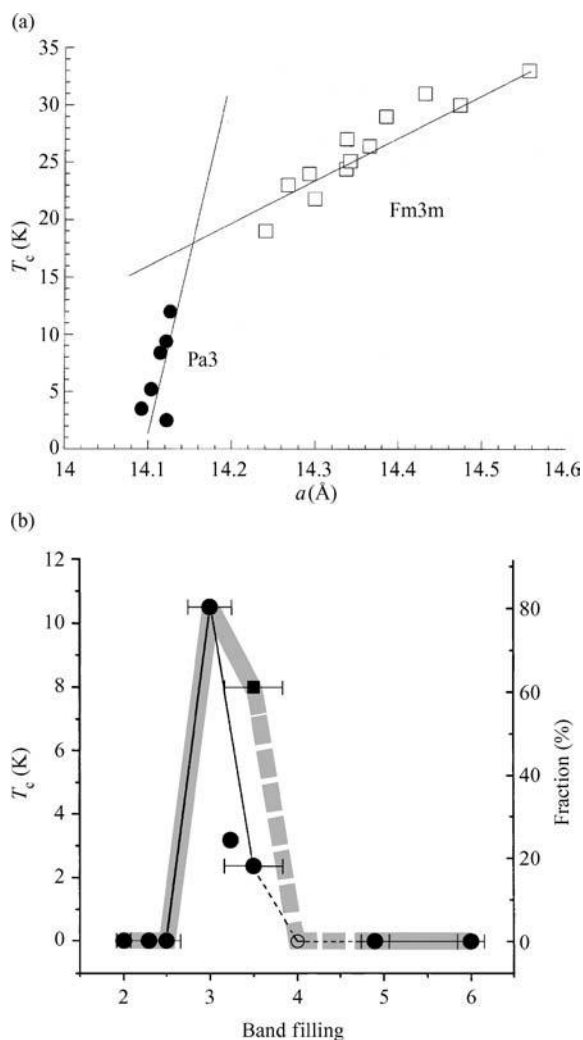
Figure 3
(a) Variation of T_c with lattice parameter in A_3C_{60} phases. Note the much steeper variation of T_c with *a* in the Pa3 family. (b) Variation of T_c with charge per C_{60}^{n-} anion in the Li_xCsC_{60} series. The open circle is $KBaCsC_{60}$ (reproduced by permission of the American Physical Society from *Phys. Rev. B*, 1999, **59**, R6628–30).

disordered f.c.c. A_3C_{60} calculated incorporating both orbital polarization and interelectron repulsion. This is a BCS-type explanation involving pairing of the t_{1u} electrons by phonons. The ^{13}C isotope effect and the strong shifting and broadening of the $H_{(g)}$ symmetry vibrational modes in metallic A_3C_{60} compared with insulating C_{60} and A_6C_{60} support this view. Alternative models point to the inapplicability of a classical BCS model when the electronic bandwidth (approximately 0.5 eV in A_3C_{60}) is comparable to intramolecular

phonon frequencies and on-site electron repulsion energies, and are based on interelectron repulsion between the t_{1u} electrons. These models can reproduce the isotope effect and the sharp peak in T_c at the $(t_{1u})^3$ configuration. Important experimental evidence for the significance of interelectron repulsion in determining the electronic ground states of fullerides has come from the observation of magnetic ordering at the 40 K metal–insulator transition of $(NH_3)K_3C_{60}$. This phase has the same volume per C_{60}^{3-} but adopts a lower symmetry structure (2.1.2). Application of pressure suppresses the magnetic ordering and associated metal–insulator transition, and restores superconductivity ($T_c = 28$ K, pressure = 15 kbar).

The high superconducting transition temperatures of the A_3C_{60} phases are not understood, and considerable further experimental and theoretical detail is required to allow reconciliation between the observed T_c and the parameters describing the normal-state electronic structure deduced from experiment.

Bibliography

Brown C M, Taga S, Gogia B, Kordatos K, Margadonna S, Prassides K, Iwasa Y, Tanigaki K, Fitch A N, Pattison P 1999 Structural and electronic properties of the noncubic superconducting fullerides A_4C_{60} (A = Ba, Sr). *Phys. Rev. Lett.* **83**, 2258–61

Fischer J E 1997 Fulleride solid state chemistry: gospel, heresies and mysteries. *J. Phys. Chem. Solids* **58**, 1939–47

Gunnarsson O 1997 Superconductivity in fullerides. *Rev. Mod. Phys.* **69**, 575

Hebard A F, Rosseinsky M J, Haddon R C, Murphy D W, Glarum S H, Palstra T T M, Ramirez A P, Kortan A R 1991 Superconductivity at 18 K in the potassium doped fullerene K_xC_{60}. *Nature* **350**, 600–1

Iwasa Y, Shimoda H, Miyamoto Y, Mitani T, Maniwa Y, Zhou O, Palstra T T M 1997 Structure and superconductivity in alkali–ammonia complex fullerides. *J. Phys. Chem. Solids* **58**, 1697–705

Kosaka M, Tanigaki K, Prassides K, Margadonna S, Lappas A, Brown C M, Fitch A N 1999 Superconductivity in Li_xCsC_{60} fullerides. *Phys. Rev. B* **59**, R6628–30

Ozdas E, Kortan A R, Kopylov N, Ramirez A P, Siegrist T, Rabe K M, Bair H E, Schuppler S, Citrin P H 1995 Superconductivity and cation-vacancy ordering in the rare-earth fulleride $Yb_{2.75}C_{60}$. *Nature* **375**, 126–9

Rosseinsky M J 1998 Recent developments in the chemistry and physics of metal fullerides. *Chem. Mater.* **10**, 2665

M. J. Rosseinsky
University of Liverpool, UK

This page intentionally left blank

G

Giant Magnetoresistance

The resistance of a ferromagnetic metal changes when one applies a magnetic field. This change is related to the dependence of the resistance on the angle between the magnetization of the ferromagnet and the electrical current direction, and is called anisotropic magnetoresistance (AMR) (see *Magnetoresistance, Anisotropic*). Although AMR in ferromagnets does not exceed a few percent at room temperature, it is used in a number of devices, mainly because the magnetization of a soft ferromagnetic material can be easily manipulated in a low magnetic field. Giant magnetoresistance (GMR) is another type of magnetoresistance (MR) which is observed in magnetic multilayers and is much larger than the AMR of the ferromagnetic metals. It was discovered in 1988 (Baibich *et al.* 1988, Binash *et al.* 1989) on Fe/Cr multilayers (stack of Fe and Cr layers) and Fe/Cr/Fe trilayers. In these structures and at zero magnetic field, the magnetizations of adjacent Fe layers are oriented in opposite directions by antiferromagnetic coupling across Cr (Grünberg *et al.* 1986); when an applied field aligns these magnetizations in parallel, the resistance of the multilayer decreases dramatically and this effect has been called giant magnetoresistance (GMR). The GMR of multilayers is thus associated with a change of the relative orientation of the magnetization in consecutive magnetic layers. Since this pioneering work on exchange coupled multilayers, GMR has been observed in a number of magnetic nanostructures, including uncoupled multilayers, spin valve structures, multilayered nanowires, and granular systems (for an extensive review see Barthélémy *et al.* 1999). In multilayers, GMR has been observed either for current in plane (CIP) or with current perpendicular to the plane of the layers (CPP geometry). CPP GMR has revealed interesting spin accumulation effects which form the basis for further developments.

From the point of view of applications, GMR is already used in various types of devices such as sensors, read-heads, and magnetic memories (MRAM). Reading information from a hard disk, for example, is done in many computers by detecting the resistance change induced by the small field (about 10^{-3} T) generated by the disk. This was achieved with AMR at the beginning of the 1990s and subsequently with GMR. While comparable fields can activate both AMR and GMR devices, the amplitude of GMR is larger, which permits a reduction of the size of the information bits and an increase of the density of stored information to 10–20 gigabits in^{-2} (1.6–3.1 gigabits cm^{-2}).

This article gives an experimental review of GMR. First, we describe the effects observed in multilayers (Sect. 1) or spin valve structures (Sect. 2) when the current flows parallel to the layers. In Sect. 3 the case where the current flows perpendicular to the layers is discussed. In Sect. 4 we give a brief phenomenological overview of the physics of GMR. The theoretical models for the CIP and CPP geometries are summarized in Sect. 5. Finally, inverse GMR and GMR of granular structures are presented in Sects. 6 and 7.

1. CIP GMR in Magnetic Multilayers

GMR was first observed in Fe/Cr superlattices (Baibich *et al.* 1988) and in Fe/Cr/Fe trilayers (Binash *et al.* 1989), in both cases for samples grown by molecular beam epitaxy (MBE). Figure 1 shows the variation of resistance as a function of magnetic field for Fe/Cr superlattices at 4.2 K. As the magnetic field increases, the magnetic configuration of neighboring iron layers goes from antiparallel to parallel. A field H_s is needed to overcome the antiferromagnetic coupling and saturate the magnetization. Between zero field and H_s, the resistance drops significantly as a result of GMR. The MR ratio is defined as the ratio of the resistivity change to the resistivity in the parallel configuration. It reaches 79% at 4.2 K for the sample in Fig. 1 with 9 Å thick chromium layers (and is still 20% at room temperature). For the Fe/Cr system, the GMR ratio can reach 220%
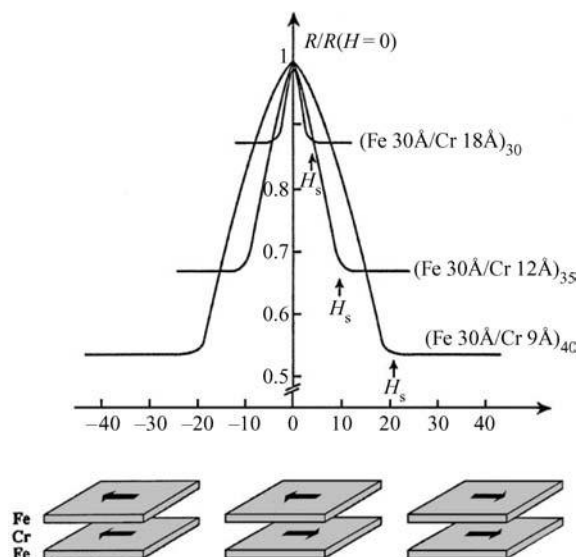
Figure 1

MR of Fe/Cr multilayers at 4.2 K (after Baibich *et al.* 1988).

(Schad *et al*. 1994), which is well above the AMR ratio observed in ferromagnetic films (a few %).

Parkin *et al*. (1990) succeeded in reproducing similar GMR effects in Fe/Cr, Co/Ru, and Co/Cr multilayers deposited by sputtering, i.e., with polycrystalline samples. Regarding applications, this is of definite interest as sputtering is a simpler and faster deposition technique than MBE. In addition, Parkin *et al*. (1990) explored details of the dependence of GMR on spacer layer thickness and found the
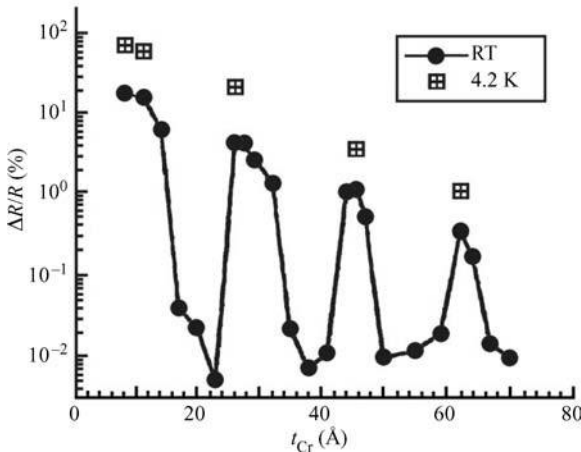
oscillatory behavior which reflects the oscillations of the interlayer exchange coupling. Subsequently, oscillations of GMR with the spacer layer thickness have been found in many systems, as illustrated in Fig. 2 for the case of Fe/Cr multilayers. As shown in Fig. 2, the variation of the MR ratio as a function of chromium thickness presents four well-defined maxima associated with four ranges of antiferromagnetic (AF) coupling. In the ranges corresponding to ferromagnetic (F) coupling GMR vanishes. The height of the maximums is a decreasing function of the chromium thickness. GMR oscillations have been found in a large number of systems, but the typical variation illustrated in Fig. 2 is not always observed. It frequently occurs that, for low spacer layer thicknesses, the AF exchange coupling is reduced by F coupling arising from pinholes in the spacer layer. Indeed, avoiding pinholes is one of the key challenges in the synthesis of such multilayers. However, in some cases, the GMR can be restored by growing discontinuous magnetic layers which, when broken into small islands, reduce the deleterious effect of F coupling by pinholes (Duvail *et al*. 1995).

Not all imperfections are as harmful for GMR as pinholes through the nonmagnetic layers. Other types of imperfection, by introducing spin-dependent scattering potentials, can act in the opposite direction and enhance GMR. For example, introducing cobalt or iron impurities in nickel layers or dusting permalloy/Cu interfaces with cobalt can enhance GMR. It has also been found that, in some cases, GMR can be enhanced by an increase of the roughness of the interfaces. An example of such an influence of the roughness of Fe/Cr multilayers on GMR is shown in Fig. 3.

Figure 2
MR ratio of Fe/Cr multilayers as a function of chromium layer thickness, t_{Cr}, at 4.2 K and 300 K (after Fullerton *et al*. 1993).
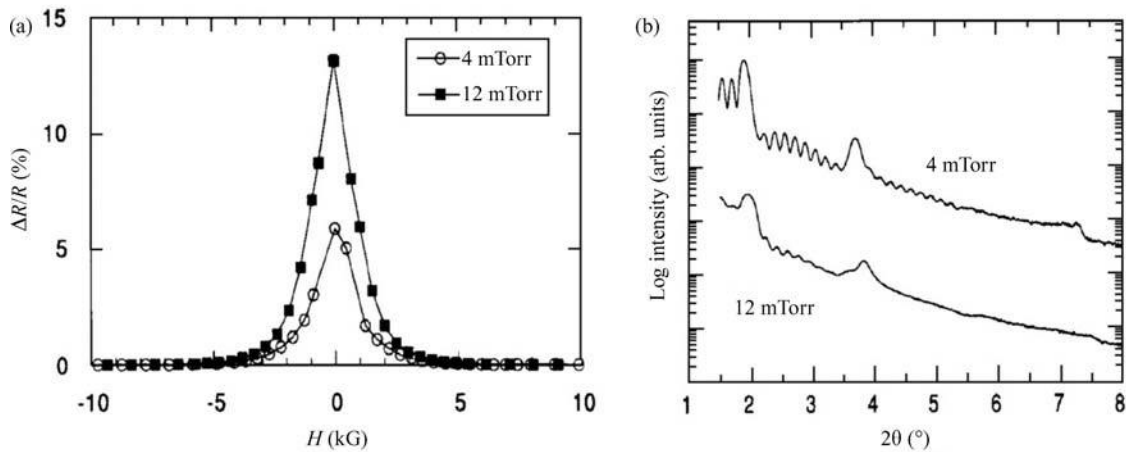
Figure 3
(a) GMR curves at 4 K for two Fe/Cr superlattices sputtered at different argon pressures. (b) Low-angle x-ray diffraction spectra of the same samples. The results show that GMR is enhanced by the presence of roughness (after Fullerton *et al*. 1992).

2. Hard/Soft and Exchange Biased Spin Valve Structures

GMR requires that an antiparallel configuration of the magnetizations can be switched into parallel by applying a magnetic field. AF interlayer exchange is not the only way to obtain an antiparallel configuration. GMR effects can also be obtained with tri- or multilayers combining hard and soft magnetic layers (Shinjo and Yamamoto 1990). As the switching of the magnetizations of the hard and soft magnetic layers occurs at different fields, there is a field range in which they are antiparallel and the resistance is higher. Such structures are often referred as hard/soft spin valves. The best-known structure in which interlayer exchange is not used to obtain GMR is the exchange biased spin valve structure, introduced by Diény *et al.* (1991). As shown in Fig. 4, two soft magnetic layers are separated by a nonmagnetic (NM) layer, one of the magnetic layers having its magnetization pinned by an exchange biasing interaction with an AF pinning layer. The operation of the exchange biased spin valve can be understood from the magnetization and MR curves in Fig. 5. One of the permalloy layers has its magnetization pinned by the AF FeMn layer in the negative direction. When the magnetic field is swept

Figure 5
(a) Hysteresis loop and (b) MR of a spin valve (60 Å NiFe/22 Å Cu/40 Å NiFe/70 Å FeMn) exchange bias structure at room temperature (after Dieny *et al.* 1991).

from negative to positive values, the magnetization of the free layer reverses at very small field, whereas the magnetization of the pinned layer remains fixed in the negative direction. This gives rise to a steep increase of resistance. A large positive field is needed to overcome the exchange biasing interaction and to reverse the magnetization of the pinned layer, which results in a drop of the resistance back to its initial value. The strong and almost reversible resistance variation in a low-field range makes this structure attractive for applications such as sensors or read-heads. Since the mid-1990s, many refinements have been developed to optimize the performances of exchange biased spin valve structures.

Figure 4
Schematic cross-section of an exchange biased spin valve layered structure.

3. CPP GMR

The discussion of the preceding section concerns measurements performed with the electrical current parallel to the plane of the layers (CIP geometry). We now concentrate on GMR effects obtained for CPP geometry (for an extensive review see Bass and Pratt 1999).

The first measurement in CPP geometry was performed by sandwiching the multilayers between two superconducting niobium electrodes in a cross-strip geometry. A comparison between the amplitudes of CIP GMR and CPP GMR for a series of Co/Cu multilayers is shown in Fig. 6. It turns out that the CPP GMR is definitely larger and that the decay as a function of the spacer layer thickness is weaker in the CPP geometry.

Several alternative methods without superconducting contacts have been developed for measurements of CPP GMR at higher temperatures. Some of these methods are based on lithography and microfabrication techniques. Multilayers have been patterned into pillars using lithography by Gijs *et al.* (1993). Although a high-resolution lithography technique was used in these experiments, the aspect ratios were not high enough to ensure a pure CPP geometry without superconducting contacts. Nevertheless, the first temperature dependence of CPP GMR was obtained with these experiments.

CPP GMR has also been obtained by depositing multilayers onto grooved InP substrates. An oblique deposition technique is used, which results in multilayers deposited on one face of the groove. Thus, CPP measurement are achieved when the current flows perpendicular to the grooves, while, in the same sample, CIP GMR can be measured by flowing the current parallel to the grooves (Gijs *et al.* 1995).

Finally, CPP GMR has also been studied in multilayered nanowires electrodeposited into the pores of nuclear track-etched polycarbonate membranes (for an extensive review see Fert and Piraux 1999). As illustrated in Fig. 7(a), the aspect ratio of the nanowires is very high (of the order of 1000), which guarantees that the current is perpendicular to the layers. However, the number of nanowires connected in parallel is generally unknown, which restricts the investigations to the measurements of MR ratios. The Co/Cu and NiFe/Cu multilayer systems have been extensively studied in the nanowire geometry. An example of experimental CPP GMR result is shown in Fig. 7(b).

Figure 6
Comparison of CIP and CPP GMR at 4.2 K for a series of Co (15 Å)/Cu (d_{Cu}) multilayers as a function of t_{Cu} (after Bass and Pratt 1999).
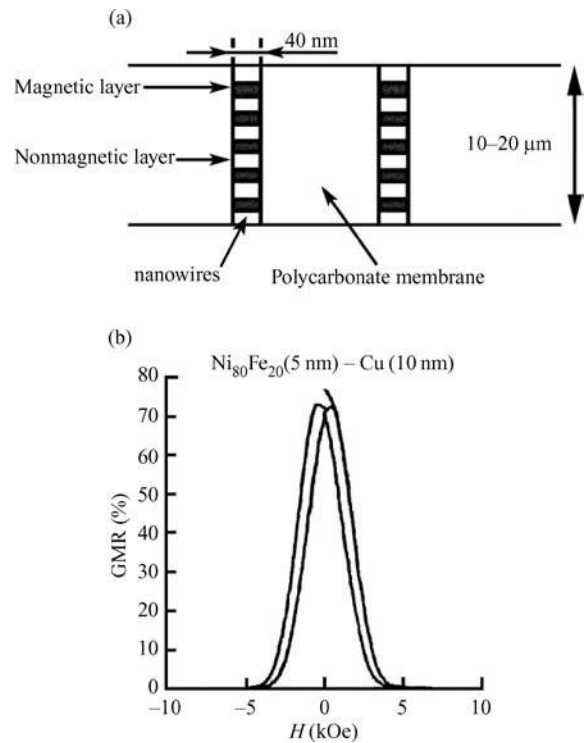
Figure 7
(a) Schematic representation of multilayered nanowires electrodeposited in the pores of a polymer matrix. (b) MR curves at 77 K of NiFe 50 Å/Cu 100 Å multilayered nanowires (after Fert and Piraux 1999).

4. Brief Phenomenological Overview of the Physics of GMR

GMR is related to the spin dependence of the conduction in ferromagnetic metals and alloys (Campbell and Fert 1982). At low temperature, when the spin flip scattering of the electrons by magnons is frozen out, there is conduction in independent parallel channels by the spin ↑ (majority) and spin ↓ (minority) electrons. The resistivity of the ferromagnet is then expressed as:

$$\rho = \frac{\rho_\uparrow \rho_\downarrow}{\rho_\uparrow + \rho_\downarrow} \tag{1}$$

where $\rho_\uparrow$ and $\rho_\downarrow$ are the resistivities of the spin ↑ and ↓ channels, respectively. The asymmetry between the two channels can be characterized by the spin asymmetry coefficient:

$$\beta = \frac{(\rho_\downarrow - \rho_\uparrow)}{(\rho_\downarrow + \rho_\uparrow)} \tag{2}$$

There are several origins of the difference between $\rho_\uparrow$ and $\rho_\downarrow$. First, there is an intrinsic origin, which is related to the spin dependence of the number, the effective mass, and the density of states at the Fermi level of the electrons. There are also extrinsic origins, which are related to the spin dependence of the impurity and defect potentials. In addition, away from the low-temperature limit, it is necessary to take into account the transfer of momentum between the two conduction channels by spin-flip electron–magnon scattering.

Figure 8 shows schematically the mechanism of GMR, in the situation where the mean free path (MFP), λ, of electrons is much larger than the period of the multilayer. Throughout this article, our notation is $+$ and $-$ for the spin directions corresponding to $s_Z = +\frac{1}{2}$ and $s_Z = -\frac{1}{2}$, z being an absolute axis for the whole multilayer, and ↑ and ↓ for the majority and minority spin directions in a given ferromagnetic layer. In the parallel configuration, the electrons of the spin $+$ and spin $-$ channels are, respectively, majority and minority electrons in all the magnetic layers, and this gives different resistances, r_+ and r_- for the two channels. The final resistance is:
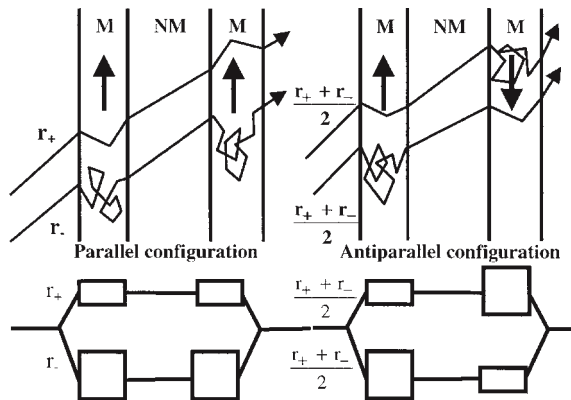
$$r_P = \frac{r_+ r_-}{r_+ + r_-} \tag{3}$$

If, for example, r_+ is much smaller than r_-, the current is shorted by the spin $+$ channel of fast electrons and $r_P \approx r_+$. In the antiparallel configuration, electrons of both channels are alternatively majority and minority spin electrons and the shorting by one of the channels disappears. The resistance is $(r_+ + r_-)/2$ for both channels and the final resistance is:

$$r_{AP} = \frac{r_+ + r_-}{4} > r_P \tag{4}$$

If r_+ is much smaller than r_- then $r_{AP} \approx r_-/4$ is much larger than $r_P \approx r_+$. The general expression for the GMR ratio is:

$$GMR = \frac{r_{AP} - r_P}{r_P} = \frac{(r_- - r_+)^2}{4 r_+ r_-} \tag{5}$$

The above simple picture no longer holds when the thickness of the layers becomes larger than the electron MFP (typically 10 nm in nonmagnetic layers, a few nanometers in ferromagnetic layers), at least for CIP. For example, when the thickness of the nonmagnetic layers, t_N, becomes larger than the MFP in these layers, λ_N, there is no overlap between the respective effects of two consecutive magnetic layers on the electron distribution function, and the GMR decreases as $\exp(-t_N/\lambda_N)$. This is discussed in Sect. 5.1. In CPP geometry, owing to spin accumulation effects, the scaling length becomes the spin diffusion length (SDL), l_{sf}, as discussed in Sect. 5.2. The SDL is related to spin flip scattering and can be much larger than the MFP, which explains that the GMR can be observed for much thicker layers in the CPP geometry. It is only when the thickness, t_N, of the nonmagnetic layers exceeds the SDL, l_{sf}^N, in nonmagnetic materials that CPP GMR decreases as $\exp(-t_N/l_{sf}^N)$.

5. Models of GMR

The theoretical models of GMR are based on the spin-dependent conduction described in the preceding section. However, predicting the GMR of a multilayer is difficult because there are various possible origins of the spin dependence in a given system. This is illustrated in Fig. 9, which shows the spin-dependent potential landscape seen by conduction electrons. One first sees the intrinsic potential of the multilayers

Figure 8
Schematic representation of the GMR mechanism. The scheme holds for both CIP and CPP geometries.

depicted by a periodic arrangement of steps. These steps reflect the band mismatch between the magnetic and nonmagnetic layers or, in simplified language, the different levels of the conduction band in different
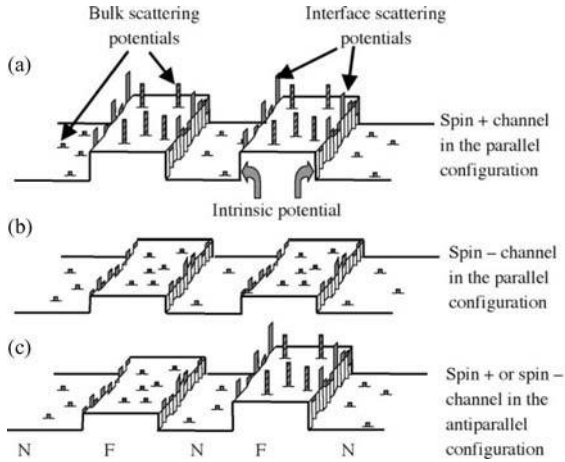
Figure 9
Potential landscape seen by spin + and spin − conduction electrons in the parallel and antiparallel configurations. The intrinsic potential is represented by a periodic array of steps (Kronig–Penney-like potential); the bulk and interface scattering potentials are represented by spikes.

metals. The steps have different heights for the two spin directions, which expresses the exchange splitting of the majority and minority spins in a ferromagnetic metal. In Fig. 9 one also sees spin-dependent spikes which represent random scattering potentials generated by impurities, defects, or interface roughness. The spin dependence of the scattering by impurities or defects is well known in bulk magnetic materials (Campbell and Fert 1982) and it is also obvious that the modulation of the spin-dependent interface steps by roughness produces spin-dependent scattering potentials. The distribution of both the intrinsic and scattering (or extrinsic) potentials is different in the parallel and antiparallel magnetic configurations of the multilayers, as illustrated in Fig. 9 by the alternation of high and low steps or spikes only in the antiparallel configuration. This dependence of the intrinsic and extrinsic potential distribution on the magnetic configuration gives rise to the GMR effect and forms the basis of a number of theoretical models.

5.1 Models of CIP GMR and Analysis of Experimental Data

The first model of GMR was the semiclassical model of Camley and Barnas (1989). This model is based on the picture of free electrons scattered by a distribution of spin-dependent scattering potentials that
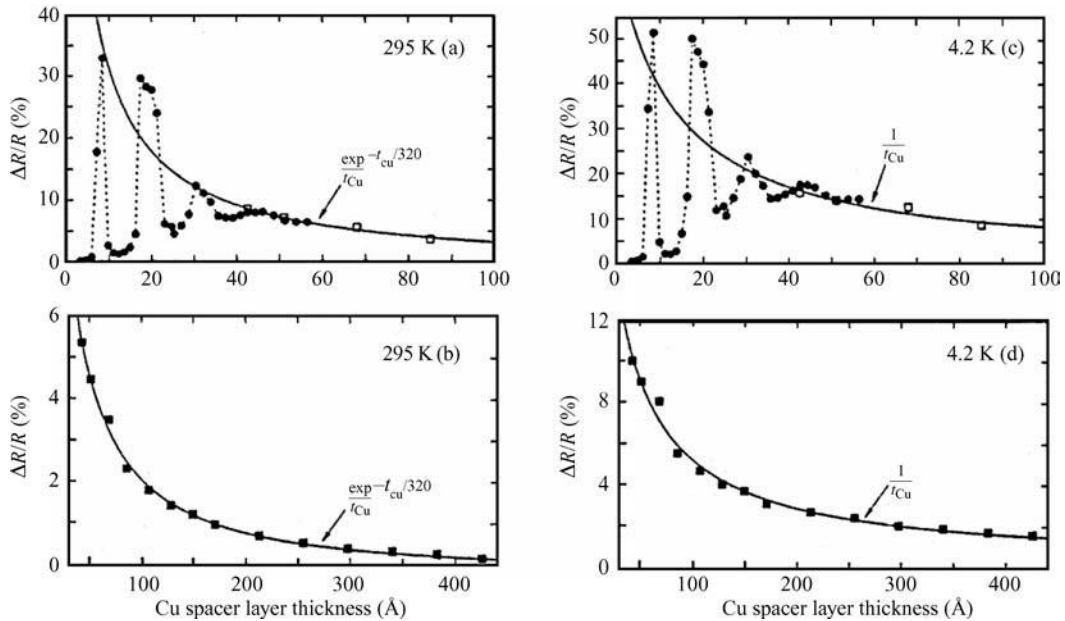
Figure 10
Saturation MR vs. copper spacer layer thickness for several series of (Co (11 Å)/Cu (t_{Cu}))$_N$ multilayers. The number of Co/Cu periods, N, is 20 (filled circles) and 6 (open and filled squares). Data are shown for temperatures of (a) and (b) 295 K, and (c) and (d) 4.2 K. The $N = 6$ data (in (a) and (c)) have been scaled by an empirical factor of 1.6 to make the comparison with $N = 20$ (after Parkin *et al.* 1993).

depends on the magnetic configuration of the multilayer, and uses a Boltzmann equation formalism (see *Boltzmann Equation and Scattering Mechanisms*). Bulk scattering is taken into account by introducing spin-dependent (spin-independent) relaxation times in the magnetic (nonmagnetic) layers. Interface scattering is described by introducing boundary conditions at the interfaces, i.e., by assuming that a proportion, T_σ, of the spin σ electrons are transmitted without scattering, while a proportion $(1-T_\sigma)$ is diffusely scattered (a probability of specular reflection can also be introduced). The major success of this model is that it predicts the thickness dependence of GMR. It shows that the influence of the spin-dependent scattering on the electron distribution function does not extend further than about the MFP inside the nonmagnetic layers, so that the resistance becomes independent of the relative orientation of consecutive magnetic layers when they are apart by more than the MFP.

Analytical expressions of GMR in the Camley–Barnas model have been derived by Barthélémy and Fert (1991) in the simple case where only interface scattering is spin dependent. It is found that, in the limit of thick layers, the MR ratio depends on the nonmagnetic layer thickness, t_N, as $\exp(-t_N/\lambda_N)$, where λ_N is the MFP in this layer. The variation as t_F^{-1} at large values of the thickness, t_F, of the magnetic layers reflects the progressive dilution of the spin-dependent interface scattering.

Figure 10 shows an example of experimental data at 295 K for Co/Cu multilayers where the variation as $\exp(-t_{Cu}/\lambda_{Cu})$ is observed at large thicknesses of copper. At 4.2 K the exponential variation is not observed and it is supposed that, with a larger λ_{Cu} at low temperature, the exponential behavior is repelled above the experimental thickness range.

The first quantum mechanical model of GMR, based on the Kubo formalism of transport, was proposed by Levy *et al.* (1990). As in the model of Camley and Barnas, it neglects the influence of the intrinsic potential of the multilayer and describes the scattering of free electrons by spin-dependent extrinsic potentials. Figure 11 shows an example of the application of the model to experimental data. After 1993 the influence of the intrinsic potential of the multilayer was progressively introduced into the theoretical models and *ab initio* models were also developed. For a general review of the models see Barthélémy *et al.* (1999).

A general result is that the theory of CIP GMR is far from being predictive. This comes from the combination of the intrinsic and extrinsic contributions. *Ab initio* calculations can predict correctly the influence of the intrinsic potential but the nature and distribution of imperfections are generally too poorly known to be introduced realistically into the calculations.
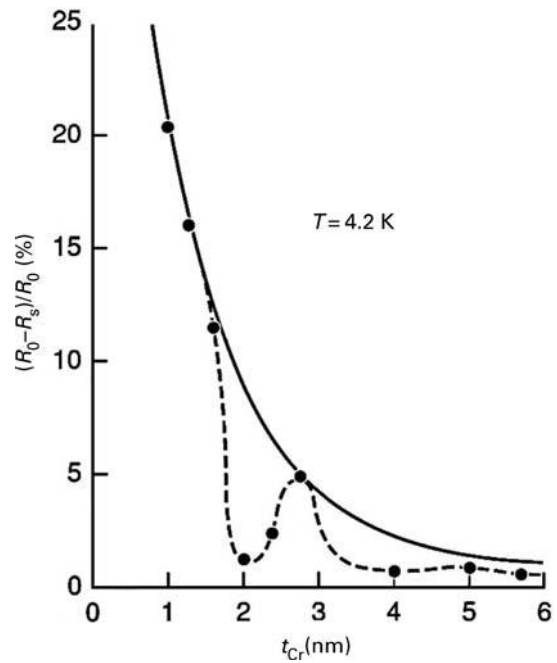
Figure 11
GMR ratio for Fe 30 Å/Cr multilayers vs. chromium thickness. The experimental data (dots) are obtained at 4.2 K. The solid line is calculated within the quantum model of (Levy *et al.* 1990) (after Gijs and Okada 1992).

5.2 Models of CPP GMR and Analysis of Experimental Data

The advantage of CPP geometry for theory is that, in the usual diffuse limit, the contribution from the intrinsic potential (steps in Fig. 9) can be expressed by introducing spin-dependent interface resistances, $r_{\uparrow(\downarrow)} = 2r_b^*[1 - (+)\gamma]$, for the spin $\uparrow$ and spin $\downarrow$ channels. Boltzmann equation models have been developed to express CPP GMR as a function of the interface parameters r_b^* and γ, and the parameters describing the resistivity within the layers $\rho_{\uparrow(\downarrow)}^F = 2\rho_F^*[1 - (+)\beta]$ and ρ_N^* for the magnetic and nonmagnetic layers, respectively. An important point is the treatment of the spin accumulation occurring when the current is perpendicular to the interfaces. Valet and Fert (1993) have shown that, owing to spin accumulation, the SDLs l_{sf}^F and l_{sf}^N in the magnetic and nonmagnetic layers, respectively, become the scaling lengths of the thickness dependence instead of the MFP as in CIP geometry. As the SDL is much larger than the MFP, this explains why CPP GMR decreases more slowly as a function of the layer thickness than CIP GMR.

Valet and Fert (VF) have derived general expressions for CPP GMR as a function of the parameters
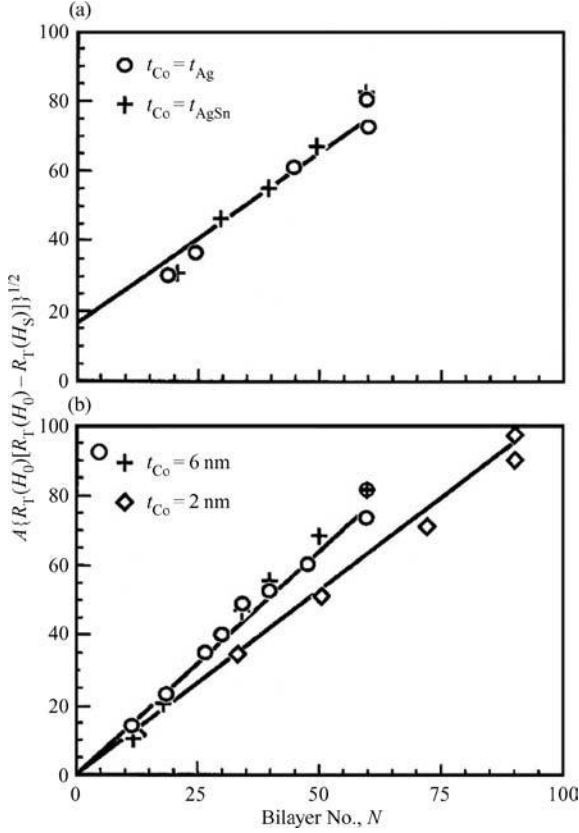
Figure 12
$A\{R_{\mathrm{T}}(H_0)[R_{\mathrm{T}}(H_0) - R_{\mathrm{T}}(H_{\mathrm{S}})]\}^{1/2}$, where A is the sample area, $R_{\mathrm{T}}(H_0)$ the resistance in the virgin state (AP state), and $R_{\mathrm{T}}(H_{\mathrm{S}})$ the resistance at saturation (P state), against N for Ag/Co and AgSn/Co multilayers with a fixed total thickness $L = 0.72\,\mu\mathrm{m}$: (a) $t_{\mathrm{Co}} = t_{\mathrm{Ag}} = t_{\mathrm{AgSn}}$ and (b) $t_{\mathrm{Co}} = 6\,\mathrm{nm}$ and $2\,\mathrm{nm}$ with t_{Ag} varying. The resistivities of the Ag and AgSn layers are $1\,\mu\Omega\,\mathrm{cm}$ and $18\,\mu\Omega\,\mathrm{cm}$, respectively (after Pratt *et al.* 1993).

r_b^*, γ, ρ_F^*, β, ρ_N^*, $l_{\mathrm{sf}}^{\mathrm{F}}$, and $l_{\mathrm{sf}}^{\mathrm{N}}$. In most experiments the layer thicknesses are smaller than the SDL and, in this so-called long SDL limit, the simple expressions of a resistor series model (see Bass and Pratt 1999) can be derived from the general expressions of the VF model. For example, one obtains:

$$[(R^{\mathrm{AP}} - R^{\mathrm{P}})R^{\mathrm{AP}}]^{1/2} = \beta \frac{t_{\mathrm{F}}L}{t_{\mathrm{F}} + t_{\mathrm{N}}}\rho_F^* + 2N\gamma r_b^* \quad (6)$$

where t_{F} and t_{N} are the thicknesses of the magnetic and nonmagnetic layers, N the number of period, and $L = N(t_{\mathrm{F}} + t_{\mathrm{N}})$ is the total thickness. In multilayers with $t_{\mathrm{F}} = t_{\mathrm{N}}$ and a given total thickness L, this gives the linear variation of $[(R^{\mathrm{AP}} - R^{\mathrm{P}})R^{\mathrm{AP}}]^{1/2}$ as a function of N, as illustrated in Fig. 12(a). Once r_b^*, ρ_F^*, and ρ_N^* have been determined from the thickness dependence
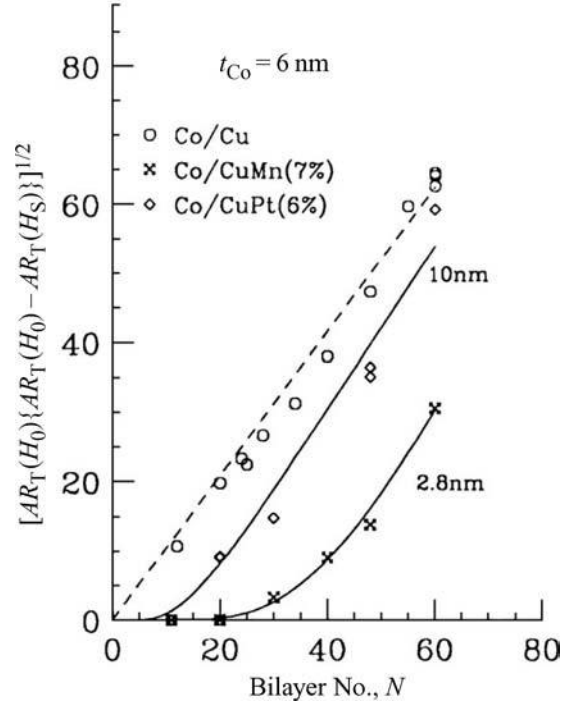
Figure 13
$\{AR_{\mathrm{T}}(H_0)[AR_{\mathrm{T}}(H_0) - AR_{\mathrm{T}}(H_{\mathrm{S}})]\}^{1/2}$ vs. the number of bilayers, N, for Co/Cu, Co/CuMn (7%), and Co/CuPt (6%), where A is the sample area and $R_{\mathrm{T}}(H_0)$ and $R_{\mathrm{T}}(H_{\mathrm{S}})$ the resistances at zero field and saturation field, respectively (after Yang *et al.* 1994). The dashed line corresponds to the linear variation expected when the SDL is much longer than the layer thicknesses. The solid lines are fits with the VF model with $l_{\mathrm{sf}}^{\mathrm{N}} = 10\,\mathrm{nm}$ and $2.8\,\mathrm{nm}$ in CuPt and CuMn, respectively.

of the resistance, the spin asymmetry coefficients, β and γ, can be derived from, respectively, the slope and the intercept with the vertical axis of the straight line in Fig. 12(a). In the same way, for a given value of L and t_{F}, one obtains the linear variations as a function of N with different slopes for different values of t_{N}, as illustrated in Fig. 12(b).

Measurements on extensive series of samples have been analyzed in the above way to determine the parameters r_b^*, γ, ρ_F^*, β, and ρ_N^* for silver, copper, cobalt, and NiFe layers, and Ag/Co, Cu/Co, Ag/NiFe and Cu/NiFe interfaces (Bass and Pratt 1999). Once these parameters have been determined, it turns out that GMR can be predicted for any multilayer composed of the same materials.

Simple expressions for CPP GMR can also be found in the opposite limit, i.e., when the thickness is much larger than the SDL.

For $t_{\mathrm{N}} \gg l_{\mathrm{sf}}^{\mathrm{N}}$ with $t_{\mathrm{F}} \ll l_{\mathrm{sf}}^{\mathrm{F}}$, the VF model predicts a reduction of GMR by a factor $\exp(-t_{\mathrm{N}}/l_{\mathrm{sf}}^{\mathrm{N}})$. This

behavior is observed in Fig. 13 for multilayers in which the SDL of the copper layers has been shortened by doping with manganese or platinum impurities. The fit with the VF expression (solid lines) leads to the values of the SDL indicated in Fig. 13. For pure nonmagnetic metals, the SDL is much larger and can be determined only by measurements on multilayered nanowires with very thick nonmagnetic
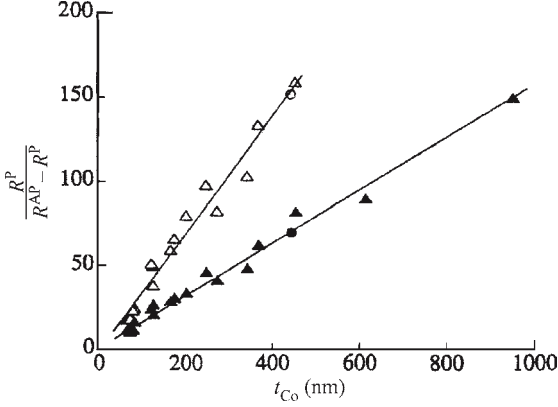
Figure 14
Linear variation of the inverse of the MR vs. cobalt thickness for Co (t_{Co})/Cu (8 nm) multilayered nanowires at $T = 77$ K (filled symbols) and $T = 300$ K (open symbols). The circle refers to data obtained on a Co (435 nm)/Cu (15 nm) sample (after Fert and Piraux 1999).
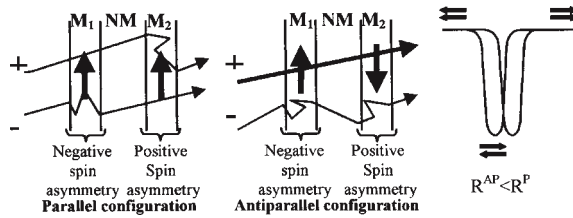
Figure 15
Schematic representation of the inverse GMR effect. The signs + and − are for spins $s_z = +\frac{1}{2}$ and $-\frac{1}{2}$, respectively. The arrows represent the majority spin direction in the magnetic layers. The electron trajectories between two scatterings are represented by straight lines and the scattering by abrupt changes in direction. When M_1 and M_2 are made of two different magnetic materials having opposite spin asymmetries, one of the spin directions (e.g., the spin + direction) is weakly scattered everywhere in the antiparallel configuration. This gives rise to a short circuit effect and a smaller resistance in this antiparallel configuration, and consequently to an inverse GMR effect.

layers (Fert and Piraux 1999). For copper layers, one obtains $l_{sf}^{Cu} = 140$ nm at low temperature.

In the limit $t_F \gg l_{sf}^F$ with $t_N \ll l_{sf}^N$, the VF model predicts:

$$\frac{(R^{AP} - R^P)}{R^P} = \frac{2p\beta^2 l_{sf}^F}{(1 - \beta^2)t_F} \tag{7}$$

where p is the proportion of antiparallel configuration between consecutive magnetic layers. Experimental results on the linear variation of the inverse of GMR as a function of t_F are shown in Fig. 14 and a fit with Eqn. (7) gives $l_{sf}^{Co} = 59 \pm 18$ nm for cobalt at low temperature (45 nm at room temperature). The SDL turns out to be even shorter in permalloy, around 5 nm (Bass and Pratt 1999, Fert and Piraux 1999).
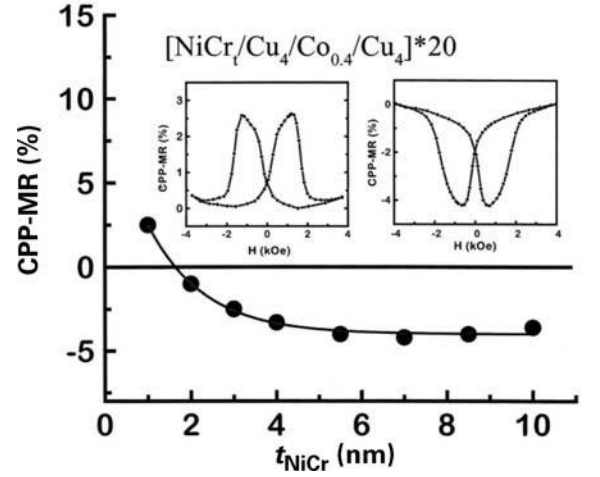
Figure 16
Variation of CPP GMR as a function of the thickness of $Ni_{0.95}Cr_{0.05}$ layers in $\underline{Ni}Cr$/Cu/Co/Cu multilayers. The competition between the bulk scattering (characterized by $\beta_{NiCr} < 0$) and interface scattering (with $\gamma_{NiCr/Cu} > 0$) gives rise to a compensation thickness t_{NiCr}^* at which they cancel each other (t_{NiCr}^* is determined in the long SDL limit by $\beta_{NiCr}\rho_{NiCr}^* t^* + 2\gamma_{NiCr/Cu}r^*_{\underline{Ni}Cr/Cu} = 0$). Below this compensation thickness the interface scattering is predominant, the global spin asymmetry of the $\underline{Ni}Cr$ layer is positive as is that of the cobalt layer (characterized by $\beta_{Co} > 0$ and $\gamma_{Co/Cu} > 0$), and the effect is normal (insert (a)). Above t_{NiCr}^*, the bulk scattering in $\underline{Ni}Cr$ becomes predominant, so that the global asymmetry of the NiCr layers is negative. Consequently, with alternating spin asymmetries for the NiCr and cobalt layers, the effect is the inverse (insert (b)) (after Barthélémy *et al.* 1999).

6. Inverse GMR

Normal GMR, i.e., a smaller resistance in the parallel configuration, is obtained when the spin asymmetry has the same sign in consecutive magnetic layers. This is always the case for multilayers of the type $(F/N)_n$. But it is also possible to fabricate multilayers of the type $(F_1/N/F_2/N)_n$ in which the ferromagnetic layers F_1 and F_2 have opposite asymmetries, e.g., F_1 slowing down more strongly the majority spin electrons and F_2 the minority spin electrons. In these cases, it is in the antiparallel configuration that one of the spin directions propagates easily everywhere and shorts the current (see Fig. 15).

An example of experimental results is shown in Fig. 16 for (NiCr/Cu/Co/Cu) multilayers in CPP geometry. The spin asymmetry coefficients β_{Co}, $\gamma_{Co/Cr}$, and $\gamma_{NiCr/Cu}$ are positive while β_{NiCr} is negative. GMR becomes inverse for $t_{NiCr} > 2$ nm when the contribution from the bulk scattering (related to B_{NiCr}) exceeds the contribution from the interface scattering (related to $\gamma_{Co/Cr}$) in the NiCr layers. Figure 16 shows the variation of GMR as a function of the thickness with a crossover from positive to negative at about 2 nm. An example of an inverse GMR curve can be seen in inset (b). Such experiments on extensive series of $(F_1/N/F_2/N)_n$ multilayers have been performed to determine not only the magnitude but also the sign of the spin asymmetry coefficients of a number of magnetic materials and interfaces (Barthélémy *et al*. 1999).

7. GMR in Granular Systems

GMR effects have also been observed in granular systems, i.e., magnetic clusters embedded in a nonmagnetic matrix (Xiao *et al*. 1992, Berkowitz *et al*. 1992). Figure 17 shows an example of a GMR curve obtained in such systems. The resistivity drops when the magnetic moments of the clusters are aligned by an applied magnetic field. The advantage of granular materials is that they are not very sensitive to the effect of pinholes. The drawbacks are the large magnetic field needed to overcome the anisotropy energy of nonspherical clusters and to saturate the GMR (Fig. 17), and the crossover to superparamagnetic behavior (Fig. 17(b)) above a blocking temperature, which is generally below room temperature.

With the aim of avoiding the propagation of pinhole effects and obtaining a large GMR effect in low field, some attempts have been made to prepare intermediate systems between multilayers and clusters. Interesting results have been obtained starting from multilayers and annealing them to create discontinuous layers of pancake-shaped clusters with low anisotropy energy. Another way to obtain intermediate structures is to grow multilayers with very thin magnetic layers. Hybrid structures combining continuous and discontinuous clustered magnetic layers have also been grown. These kinds of structures lead to large GMR ratios in very low fields (34% in 10 Oe ($796 \, Am^{-1}$)) (Duvail *et al*. 1995).
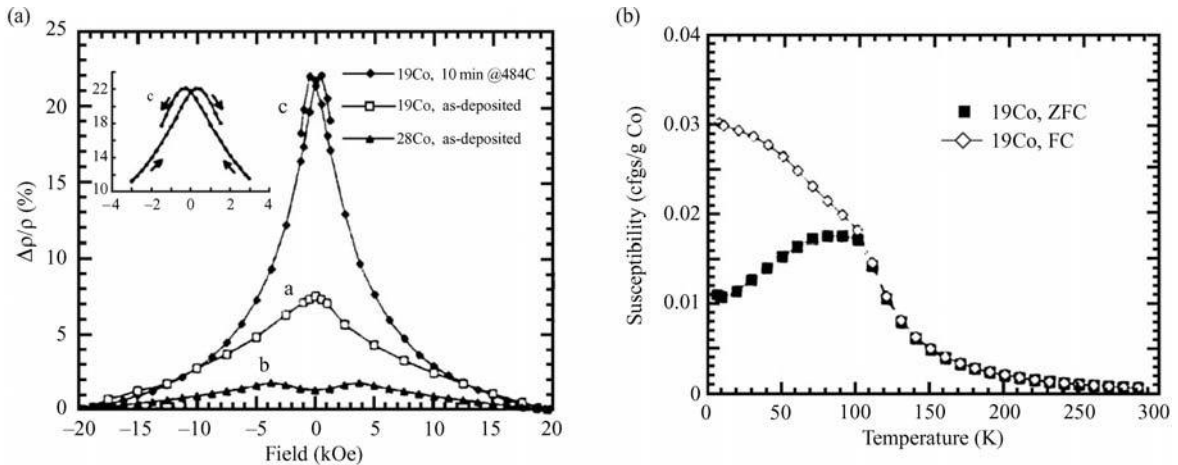
Figure 17
(a) GMR curve obtained in granular alloys by codeposition of immiscible elements such as cobalt and silver. The Co concentration is indicated on the curves. For concentrations above 28% cobalt, the clusters reach their percolation threshold and the whole sample becomes ferromagnetic leading to the disappearance of the GMR effect. (b) Field-cooled and zero field-cooled curves measured in a $Co_{19}Cu_{81}$ granular system. Above a blocking temperature around 100 K, the cobalt clusters are in a superparamagnetic state and a very large magnetic field is needed to obtain the GMR effect (after Berkowitz *et al*. 1992).

See also: Amorphous Intermetallic Alloys: Resistivity; Giant Magnetoresistance: Metamagnetic Transitions in Metallic Antiferromagnets; Magnetoresistance: Magnetic and Nonmagnetic Intermetallics

Bibliography

Baibich M N, Broto J M, Fert A, Nguyen Van Dau F, Etienne P, Creuzet G, Friederich A, Chazelas J 1988 Giant magnetoresistance of (001)Fe/(001)Cr magnetic superlattices. *Phys. Rev. Lett.* **61**, 2472–6

Barthélémy A, Fert A 1991 Theory of the giant magnetoresistance in magnetic multilayers: analytical expressions from a semi-classical approach. *Phys. Rev. B* **43**, 13124–9

Barthélémy A, Fert A, Petroff F 1999 Giant magnetoresistance in magnetic multilayers. In: Buschow K H J (ed.) *Handbook of Magnetic Materials.* Elsevier, Oxford, UK, Vol. 12, Chap. 1

Bass J, Pratt W P Jr. 1999 Current-perpendicular (CPP) magnetoresistance in magnetic metallic multilayers. *J. Magn. Magn. Mater.* **200**, 274–89

Berkowitz A E, Mitchell J R, Carey M J, Young A P, Zhang S, Spada F E, Parker F T, Hutten A, Thomas G 1992 Giant magnetoresistance in heterogeneous Cu–Co alloys. *Phys. Rev. Lett.* **68**, 3745–8

Binash G, Grünberg P, Saurenbach F, Zinn W 1989 Enhanced magnetoresistance in layered magnetic structures with antiferromagnetic interlayer exchange. *Phys. Rev. B* **39**, 4828–30

Camley R E, Barnas J 1989 Theory of giant magnetoresistance effects in magnetic layered structures with antiferromagnetic coupling. *Phys. Rev. Lett.* **63**, 664–7

Campbell I A, Fert A 1982 Transport properties of ferromagnets. In: Wohlfarth E P (ed.) *Ferromagnetic Materials.* North-Holland, Amsterdam, Vol. 3 Chap. 9

Dieny B, Speriosu V S, Parkin S S P, Gurney B A, Wilhoit D R, Mauri D 1991 Giant magnetoresistance in soft ferromagnetic multilayers. *Phys. Rev. B* **43**, 1297–300

Duvail J L, Barthélémy A, Steren L B, Morel R, Petroff F, Sussiau M, Wiedmann M, Fert A, Holody P, Loloee R, Schroeder P A 1995 Giant magnetoresistance in hybrid nanostructures. *J. Magn. Magn. Mater.* **151**, 324–32

Fert A, Piraux L 1999 Magnetic nanowires. *J. Magn. Magn. Mater.* **200**, 338–57

Fullerton E, Conover M J, Mattson J E, Sowers C H, Bader S D 1993 Oscillatory interlayer coupling and giant magnetoresistance in epitaxial Fe/Cr(211) and (100) superlattices. *Phys. Rev. B* **48**, 15755–63

Fullerton E E, Kelly D M, Guimpel J, Schuller I K, Bruynseraede Y 1992 Roughness and giant magnetoresistance in Fe/Cr superlattices. *Phys. Rev. Lett.* **68**, 859–62

Gijs M A M, Johnson M T, Reinders A, Huisman P E, van de Veerdonk R J M, Lenczowski S K J, Gansewinke R M J 1995 Perpendicular giant magnetoresistance of Co/Cu multilayers deposited under an angle on V-grooved substrates. *Appl. Phys. Lett.* **66**, 1839–41

Gijs M A M, Lenczowski S K J, Giesbers J B 1993 Perpendicular giant magnetoresistance of microstructured Fe/Cr magnetic multilayers from 4.2 to 300 K. *Phys. Rev. Lett.* **70**, 3343–6

Gijs M A M, Okada M 1992 Magnetoresistance study of Fe/Cr magnetic multilayers: interpretation with the quantum model of GMR. *Phys. Rev. B* **46**, 2908–11

Grünberg P, Schreiber R, Pang Y, Brodsky M B, Sowers H 1986 Layered magnetic structures: evidence for antiferromagnetic coupling of Fe layers across Cr interlayers. *Phys. Rev. Lett.* **57**, 2442–5

Levy P M, Zhang S, Fert A 1990 Electrical conductivity of magnetic multilayered structures. *Phys. Rev. Lett.* **65**, 1643–6

Parkin S S P, Modak A, Smith D J 1993 Dependence on giant magnetoresistance on Cu layer thickness in Co/Cu multilayers: a simple dilution effect. *Phys. Rev. Lett.* **47**, 9136–9

Parkin S S P, More N, Roche K P 1990 Oscillations on exchange coupling and magnetoresistance in metallic superlattice structures: Co/Cu, Co/Cr and Fe/Cr. *Phys. Rev. Lett.* **64**, 2304–7

Pratt W P, Lee S F, Holody P, Yang Q, Loloee R, Bass J, Schroeder P A 1993 Giant magnetoresistance with current perpendicular to the multilayer planes. *J. Magn. Magn. Mater.* **126**, 406–9

Schad R, Potter C D, Beliën P, Verbanck G, Moshchalkov V V, Bruynseraede Y 1994 Giant magnetoresistance in Fe/Cr superlattices with very thin Fe layers. *Appl. Phys. Lett.* **64**, 3500–2

Shinjo T, Yamamoto H 1990 Large magnetoresistance of field induced giant ferrimagnetic multilayers. *J. Phys. Soc. Jpn.* **59**, 3061–4

Valet T, Fert A 1993 Theory of the perpendicular magnetoresistance in magnetic multilayers. *Phys. Rev. B* **48**, 7099–113

Xiao J Q, Jiang J S, Chien C L 1992 Giant magnetoresistance in nonmultilayer magnetic system. *Phys. Rev. Lett.* **68**, 3749

Yang Q, Holody P, Lee S F, Henry L L, Loloee R, Schroeder P A, Bass J 1994 Spin flip diffusion length and giant magnetoresistance at low temperature. *Phys. Rev. Lett.* **72**, 3274–7

A. Barthélémy, A. Fert
UMR CNRS-Thomson CSF and Université Paris Sud, Orsay, France

F. Nguyen Van Dau
UMR CNRS-Thomson CSF, Orsay, France

Giant Magnetoresistance: Metamagnetic Transitions in Metallic Antiferromagnets

In intermetallic compounds with antiferromagnetic (AF) ordering, a large change in the resistivity (magnetoresistance: MR) occurs within a magnetic field, associated with a metamagnetic transition (MT). The mechanisms responsible are discussed here in relation to several examples.

The MR ratio is defined as:

$$\frac{\Delta\rho(B)}{\rho(0)} = \frac{\rho(B) - \rho(0)}{\rho(0)} \tag{1}$$

where $\rho(B)$ is the resistivity under a magnetic field H ($B = \mu_0 H$).

The term "giant magnetoresistance" (GMR) was first used for the large resistance decrease in magnetic multilayers (MML) associated with the field-induced

change of interlayer coupling from AF to ferromagnetic (F) (Baibich *et al.* 1988). The spin-dependent scattering, namely the difference in the relaxation times between the up- and down-spin electrons, is now recognized to be the origin.

1. GMR in Layered Antiferromagnets

UNiGa (hexagonal ZrNiAl-type structure) was the first intermetallic compound discussed in relation with the GMR in MML (Sechovsky *et al.* 1991). The ground state AF structure in UNiGa is characterized by the *c*-axis stacking of U-moments $\uparrow\uparrow\downarrow\uparrow\downarrow\downarrow$ and oriented along the *c*-axis ferromagnetically ordered within the basal plane sheet. The magnetic field applied along *c* induces a MT at $B_c \sim 0.8$T (at 4.2K) leading to F stacking, and accompanied by a negative GMR. Figure 1 compares the field dependencies of MR and magnetization measured on the same crystal. The GMR is largely anisotropic: $\Delta\rho/\rho_0 = 90\%$ for $B\|i$ and 56% for $B \perp i$. Besides the anisotropy, the geometrical resemblance to the MLL initially led to the conclusion that the GMR in UNiGa has the same origin as MML: the spin-dependent scattering (Sechovsky *et al.* 1993). However, the inherent assumptions for the GMR in MML, the dominance of conduction electron scattering at interlayer boundaries, and the spin-split density of states for each U-monolayer, are not appropriate for UNiGa.
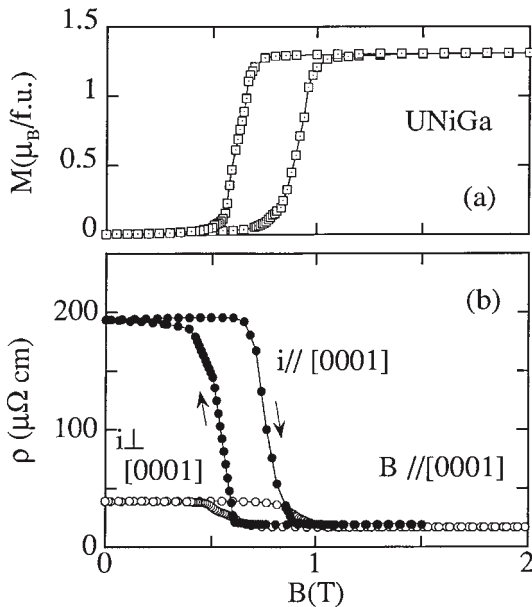
Figure 1
Field dependence of (a) magnetization and (b) magnetoresistance in UNiGa.

2. Mechanisms of GMR–Fermi Surface Reconstruction

The GMR in UNiGa might be more naturally ascribed to a Fermi surface (FS) reconstruction connected with the disappearance of the superzone gap across the MT. Figure 2 shows a simplified model for MT, across which the unit cell size along *c* changes from 2*c* to *c*. As a result, the superzone gap at $\pm\pi/2c$ disappears in the wave vector (**k**-) space. Even from such a simple model, one can infer the reduction of resistance across the MT. The electrical conductivity tensor σ_{ii} along the *i*-axis is given as an integral over FS as (Dugdale 1977)

$$\sigma_{ii} = \frac{e^2}{4\pi^3\hbar} \int \tau(\boldsymbol{k}) v_i(\boldsymbol{k}) \frac{\mathrm{d}S_F}{|v|} \qquad (2)$$

where $\tau(\boldsymbol{k})$ and $v_i(\boldsymbol{k})$ are the relaxation time and the *i*-component of velocity, respectively, for a conduction electron with a wave vector **k**. The change in conduction electron scattering is reflected in $\tau(\boldsymbol{k})$, while those in FS appear both in the FS area through $\int \mathrm{d}S_F$ and in the velocity $v(\boldsymbol{k})$.

Generally, the AF superzone gap reduces the FS area (Elliott and Wedgwood 1963), leading to an isotropic reduction of resistance, as expected from Eqn. (2). In addition, the AF superzone gap reduces the velocity component normal to the Brillouin zone boundary as shown in Fig. 2. Thus, the velocity factor reduces the conductivity along the *c*-axis selectively across the MT, which explains the anisotropic MR in Fig. 1. Antonov *et al.* (1996) have succeeded in ascribing the GMR in UNiGa to the FS reconstruction semiquantitatively by first-principle calculations based on the density-functional band structure. This scenario has been experimentally confirmed both by the specific heat and the Hall effect measurements (Aoki *et al.* 1997, Kobayashi *et al.* 1996).

SmMn$_2$Ge$_2$ (van Dover *et al.* 1993) and FeRh (Schinkel *et al.* 1974), which also posses the AF stacked two-dimensional ferromagnetic planes, exhibit a negative MR accompanying the MT as well.

3. GMR in Nonlayered Antiferromagnets

The AF stacking of two-dimensional ferromagnetic planes is not a necessary condition for the GMR. For more general AF structures, numerous intermetallic compounds have been reported to exhibit a large MR correlated with the MT. NdGa$_2$ ($T_N = 9.5$K) with the AlB$_2$ type hexagonal structure and PrFe$_4$P$_{12}$ ($T_N = 6.2$K) with the cubic filled Skutterudite structure may serve as examples.

Figure 3 shows the transverse MR and magnetization measured on a NdGa$_2$ single crystal at 4.2K below T_t where the magnetic structure is close to the antiphase type. The magnetization exhibits a multistep
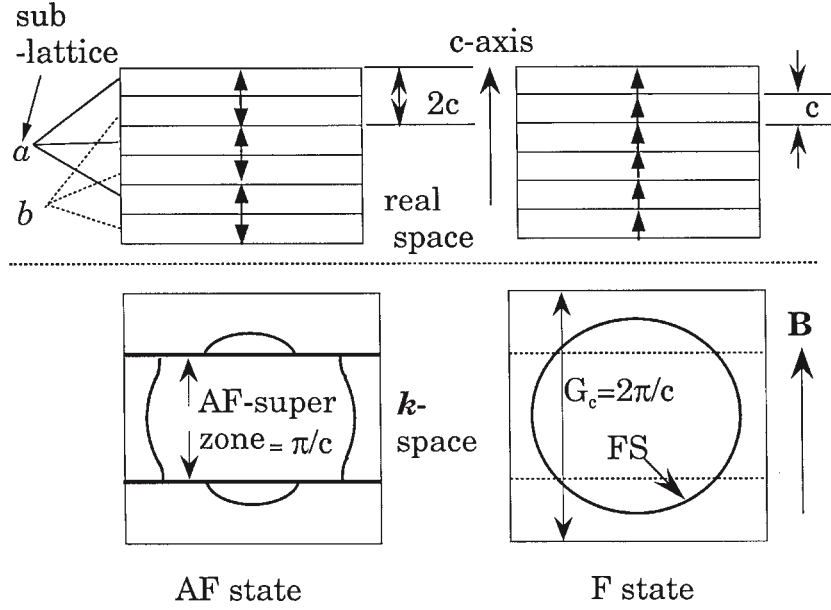
Figure 2
Simplest model for the MT. Top and bottom figures correspond to the real and **k**-space geometry. In zero field (left), two-dimensional ferromagnetic sheets form AF structure made of parallel (a) and antiparallel (b) sublattices. The superzone gap formed in AF state disappears across the MT.
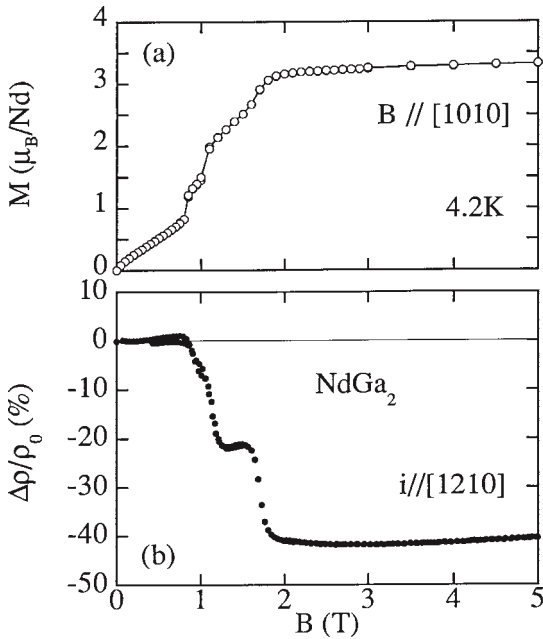
Figure 3
Field dependence of (a) magnetization and (b) MR ratio in NdGa$_2$.

metamagnetic behavior, which is well reflected in the MR curve. Even in the intermediate magnetic configuration, the MR is always negative, which suggests the existence of conduction electron scattering in zero field state resulting from the low energy excitation, as was inferred from the specific heat measurement (Aoki *et al.* 1997).

Figure 4 shows the field dependence of the MR in PrFe$_4$P$_{12}$ along with the magnetization above and below the Néel temperature (T_N) of 6.5K. For this material, the FS reconstruction at T_N can be clearly seen as a jump in the temperature dependence of the resistivity in zero field. This was also manifested in the temperature dependence of the Hall coefficient (Sato *et al.* 2000). A notable feature in Fig. 4 is the initial increase of resistivity in fields below B_M. Yamada and Takada (1973) have explained such an effect by the critically enhanced conduction electron scattering on magnons. They calculated the MR due to electron-spin scattering in a simplest uniaxial AF metal considering the *s–d* interaction. For the field parallel to the easy axis, they found a positive MR below B_M, which results from the increase in the total number of excited magnons. More intuitively, the enhancement of spin fluctuations in the antiparallel sublattice *b* in Fig. 2 overcomes the suppression of spin fluctuations in the parallel sublattice *a*. On the
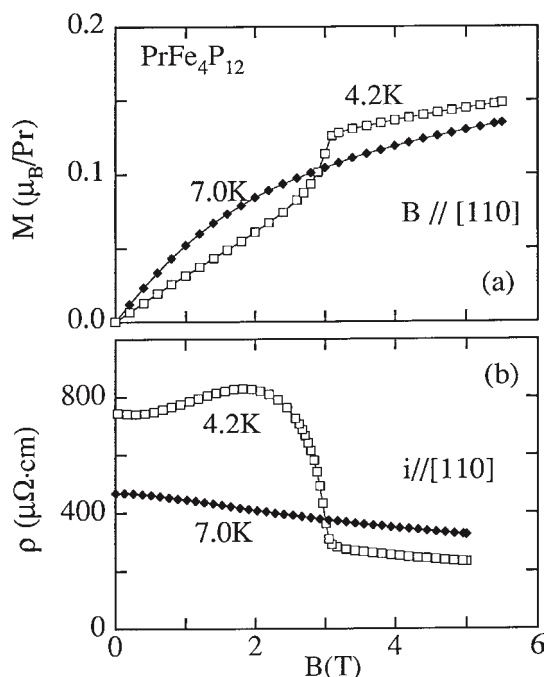
Figure 4
Field dependence of (a) magnetization and (b) MR in $PrFe_4P_{12}$.

other hand, Baranov *et al.* (1993) ascribed the anomalous increase of the resistivity to the conduction electron scattering at interface boundaries separating the phases with different magnetic structures.

To summarize, in the process of the MT from an AF state, the GMR has been observed in variety of intermetallic compounds and ordered alloys. The disappearance of the AF superzone gap across the MT plays the main role in the GMR in many cases. Additional mechanisms, such as the spin fluctuation scattering, the domain wall scattering, etc., should also be taken into account in order to explain the overall behavior including the temperature variation of the MR. Especially for itinerant magnetic electron systems such as UNiGa, the splitting of the up- and down-spin sub-bands might lead to a further change of FS in the high-field ferromagnetic state.

See also: Amorphous Intermetallic Alloys: Resistivity; Giant Magnetoresistance; Magnetoresistance, Anisotropic; Magnetoresistance: Magnetic and Non-magnetic Intermetallic

Bibliography

Aoki Y, Kobayashi Y, Sato H, Sugawara H, Sechovsky V, Havela L, Prokes K, Mihalik M, Menovsky A 1996 Superzone gap formation evidenced by specific heat in UNiGa. *J. Phys. Soc. Jpn.* **65**, 3312–6

Aoki Y, Sato H, Sugawara H 1997 Large T-linear specific heat of $NdGa_2$ below 1K. *Physica B* **230–2**, 770–2

Antonov V N, Perlov A Ya, Oppeneer P M, Yaresko A N, Halilov S V 1996 Mechanism of the giant magnetoresistance in UNiGa from first principle calculations. *Phys. Rev. Lett.* **77**, 5253–6

Ball A R, Gignoux D, Fernandez J R, Schmitt D 1994 Magnetic properties and complex diagram of hexagonal $NdGa_2$. *J. Magn. Magn. Mater.* **137**, 281–92

Baranov N V, Markin P E, Kozov A I, Sintsyn E V 1993 Effect of magnetic interphase boundaries on the electrical resistivity in metallic metamagnets. *J. Alloys Compos.* **200**, 43–50

Baibich M N, Broto J M, Fert A, Van Dau F N, Petroff F, Eitenne P, Creuzet G, Friederich A, Chazelas J 1988 Giant magnetoresistance of (001)Fe/(001)Cr magnetic superlattices. *Phys. Rev. Lett.* **61**, 2472–5

Dugdale J S 1977 *The Electrical Properties of Metals and Alloys.* Arnold, London

van Dover R B, Gyorgy E M, Cava R J, Krajewski J J, Felder R J, Peck W F 1993 Magnetoresistance of $SmMn_2Ge_2$: A layered antiferromagnet. *Phys. Rev. B* **47**, 6134–7

Elliott R J, Wedgwood F A 1963 Theory of the resistance of the rare earth metals. *Proc. Phys. Soc.* **81**, 846–55

Kobayashi Y, Aoki Y, Sugawara H, Sato H, Sechovsky V, Havela L, Prokes K, Mihalik M, Menovsky A 1996 Hall effect and thermoelectric power in UNiGa. *Phys. Rev. B* **54**, 15330–4

Sato H, Henmi H, Kobayashi Y, Aoki Y, Yamamoto H, Shinjo T, Sechovsky V 1994 Giant magnetoresistance related transport properties in multilayers and bulk materials. *J. Appl. Phys.* **76**, 6919–24

Sato H, Abe Y, Okada, Matsuda T D, Sugawara H, Aoki Y, 2000 Unusual behaviors in $REFe_4P_{12}$ (RE: La, Pr and Nd). *Physica B* **281/282**, 306–7

Sechovsky V, Havela L, de Boer F R, Brück E, Suzuki T, Ikeda S, Nishigori S, Fujita T 1993 Specific heat and magnetocaloric effect in UNiGa. *Physica B* **188**, 775–7

Sechovsky V, Havela L, Jirman L, Ye W, Takabatake T, Fujii H, Brück E, de Boer F R, Nakotte H 1991 Giant magnetoresistance in UNiGa. *J. Appl. Phys.* **70**, 5794–9

Schinkel C J, Hartog R, Hochstenbach F H A M 1974 On the magnetic and electrical properties of nearly equiatomic ordered FeRh alloys. *J. Phys. F: Met. Phys.* **4**, 1412–20

Yamada H, Takada S 1973 Magnetoresistance due to electron-spin scattering in antiferromagnetic metals at low temperatures. *Prog. Theoret. Phys.* **49**, 1401–19

H. Sato
Tokyo Metropolitan University, Japan

Giant Magnetostrictive Materials

The magnetostrictive materials exhibit a strain caused by the orientation of the magnetic moment when exposed to a magnetic field (see *Magnetostrictive Materials*). A new class of magnetostrictive materials discovered by Ullakko and co-workers (1995, 1996) is

called magnetic shape memory (MSM) alloys or ferromagnetic shape memory alloy (FSMA) materials. The thermoelastic martensitic phase transformation in MSM materials produces a low-symmetry phase with a large magnetocrystalline anisotropy and highly mobile twin boundaries between the variants. MSM materials exhibit giant magnetic-field-induced strain (MFIS) based on the rearrangement of the crystallographic domains (twin variants). In the magnetic field, those martensite variants having the easy axis of magnetization along the field, start to grow due to twin boundary motion and become dominant. This process lowers the magnetization energy. The MFIS of MSM materials is unique since it produces a large strain with rather high frequencies without a change in the external temperature. Consequently, MSM materials are potentially important for actuator and sensor applications (Tellinen *et al.* 2002).

The currently best working MSM materials are the near stoichiometric Ni_2MnGa Heusler alloys. Their structural, magnetic, and mechanical properties are highly sensitive to the chemical composition and temperature. These have been studied in detail by researchers in several countries (Vasil'ev *et al.* 2003, Söderberg *et al.* 2004). Depending on the martensite crystal structure (5 M or 7 M), one can obtain 6% or 10% strain response in a magnetic field less than $800 \, kA \, m^{-1}$ (Murray *et al.* 2000, Sozinov *et al.* 2003), with the optimum frequencies up to 300–500 Hz (O'Handley and Allen 2001) in the temperature range 150–333 K (Heczko and Straka 2003) and at ambient temperature the MSM fatigue life can be more than 50×10^6 shape change cycles.

The schematic behavior of an MSM material is shown in Fig. 1. In the Ni–Mn–Ga 5 M and 7 M martensitic structures, the *c*-axis is the shortest crystallographic axis and, simultaneously, the easy axis of magnetization. When the material is exposed to a magnetic field, the variants having *c*-axis along the field become dominant and, consequently, the material contracts in the direction of the applied field. Since this MFIS remains after removing the magnetic field (Fig. 1 (1)), the actuation movement is only obtained by turning the magnetic field perpendicular to its original orientation (e.g., applying a rotating magnetic field, Fig. 1 (2)) or with an external spring-back load (Fig. 1 (3)). Consequently, with this way, it is possible to change one single-variant structure to another and to obtain cycling of the giant MFIS.

Figure 2 represents the behavior of the MSM material under compressive stress in a constant transversal magnetic field (*H*). The opposite stress induced by the magnetic field ($\Delta\sigma_{mag}$) is growing with increasing *H* and it saturates at $\Delta\sigma_{mag} = (1 - c/a)^{-1} K_U$, where K_U is the magnetocrystalline anisotropy energy density of martensite (see insert in Fig. 2). Consequently, the giant MFIS is limited to the materials with rather low twinning stress (σ_{tw}) as the requirement for MFIS is $\Delta\sigma_{mag} > \sigma_{tw}$ (Likhachev *et al.* 2001).
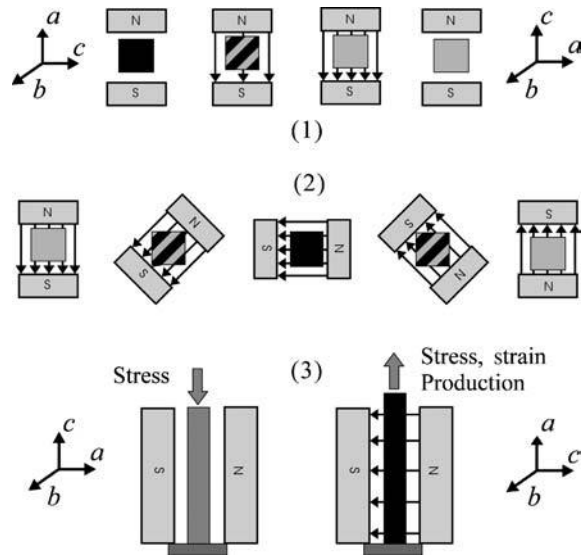
Figure 1
MSM element in (1) unidirectional, (2) rotating magnetic field, and (3) in the actuator. *a*, *b* and *c* are crystallographic axes of martensite ($c < a, b$), *c*-axis is easy axis of magnetization.
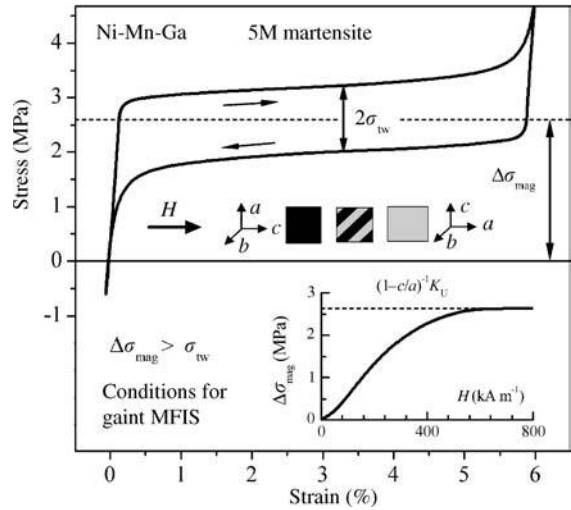
Figure 2
Compression of MSM element in constant transversal magnetic field $H = 800 \, kA \, m^{-1}$. σ_{tw} is twinning stress and $\Delta\sigma_{mag}$ the magnetic stress. Inset shows influence of magnetic field on $\Delta\sigma_{mag}$.

The mechanical behavior of an MSM element in a constant transversal magnetic field (in Fig. 2) resembles the conventional superelastic (SE) behavior of the austenitic alloys: the large strain related to the
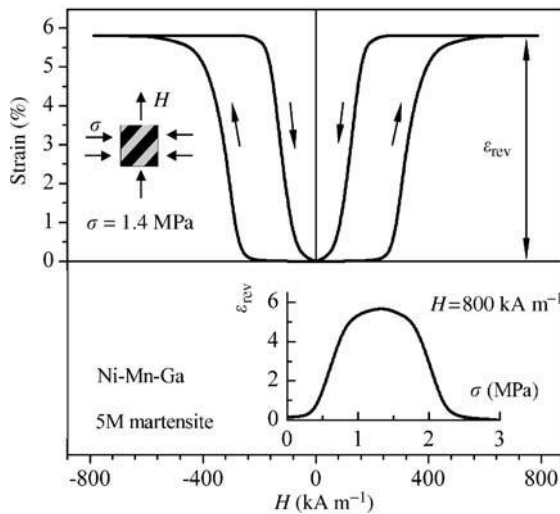
Figure 3
MFIS at constant blocking stress. ε_{rev} is the reversible strain. Inset shows influence of blocking stress on ε_{rev} at constant magnetic field $H = 800\,\mathrm{kA\,m^{-1}}$.

stress-induced phase transformation recovers totally when applied stress is removed. However, as in the conventional case SE behavior is obtained only in a rather narrow temperature region, the magnetically assisted superelasticity of the martensitic MSM alloys can be realized in a broad temperature range.

The behavior of MSM alloys at a variable magnetic field and under constant transversal stress is presented in Fig. 3. This behavior is applied in actuators (Fig. 1 (3)). The reversible strain (ε_{rev}) observed under these conditions (see insert at Fig. 3) has the maximum at a certain optimal value of blocking stress (O'Handley and Allen 2001, Likhachev *et al.* 2001). With this optimum blocking stress, the MSM element is brought back to the initial state when the magnetic field is removed (Fig. 3). In case the stress is below the optimum, it cannot move the twin boundaries back totally and, therefore, the cycling shape change is only partial. Furthermore, if the optimum value is considerably exceeded, this disables the MFIS.

Many other alloy systems (Vasil'ev *et al.* 2003, Söderberg *et al.* 2004) (e.g., Fe–Pd, Fe–Pt, Ni–Mn–Al, Co–Ni, Co–Ni–Al, Co–Ni–Ga and Ni–Fe–Ga) having magnetic and martensitic transformations are at present under intensive investigation as promising candidates for MSM applications.

See also: Magnetostrictive Materials; Magnetoelastic Phenomena; Magnetoelasticity in Nanoscale Heterogeneous Materials; Stress Coupled Phenomena: Magnetostriction

Bibliography

Heczko O, Straka L 2003 Temperature dependence and temperature limits of magnetic shape memory effect. *J. Appl. Phys.* **94**, 7139–43

Likhachev A A, Sozinov A, Ullakko K 2001 Influence of external stress on the reversibility of magnetic-field-controlled shape memory effect in Ni–Mn–Ga. *Proc. SPIE* **4333**, 197–206

Murray S J, Marioni M, Allen S M, O'Handley R C, Lograsso T A 2000 6% magnetic-field-induced strain by twin-boundary motion in ferromagnetic Ni–Mn–Ga. *Appl. Phys. Lett.* **77**, 886–8

O'Handley R C, Allen S M 2001 Shape memory alloys, magnetically activated ferromagnetic shape memory materials. In: Schwartz M (ed.) *Encyclopedia of Smart Materials*. John Wiley and Sons, New York, pp. 936–51

Sozinov A, Likhachev A A, Lanska N, Söderberg O, Ullakko K, Lindroos V K 2003 Effect of crystal structure on magnetic-field-induced strain in Ni–Mn–Ga. *Proc. SPIE* **5053**, 586–94

Söderberg O, Ge Y, Sozinov A, Hannula S-P, Lindroos V K 2004 Giant magnetostrictive materials. In: Buschow K H J (ed.) *Handbook on Magnetic Materials*. Elsevier Science, Amsterdam (to be published)

Tellinen J, Suorsa I, Jääskeläinen A, Aaltio I, Ullakko K 2002 Basic properties of magnetic shape memory actuators. In: Borgmann H (ed.) *Proc. 8th Int. Conf. on New Actuators, Actuator 2002*. Messe Bremen GMBH, Bremen, Germany, pp. 566–9; http://www.adaptamat.com/publications/

Ullakko K 1995 A method for producing motion and force by controlling the twin structure orientation of a material and its uses. *European patent* EP 0 838 095

Ullakko K, Huang J K, Kantner C, O'Handley R C, Kokorin V V 1996 Large magnetic-field-induced strains in Ni_2MnGa single crystals. *Appl. Phys. Lett.* **69**, 1966–8

Vasil'ev A N, Buchel'nikov V D, Takagi T, Khovailo V V, Estrin E I 2003 Shape memory ferromagnets. *Phys. Usp.* **46** (6), 559–88; arXiv:cond-mat/0311433 v1, 19 Nov 2003

O. Söderberg, A. Sozinov and V. K. Lindroos
Helsinki University of Technology, Laboratory of Physical Metallurgy and Materials Science, P.O. Box 6200 (Vuorimiehentie 2A), FIN-02015 HUT Espoo, Finland

Growth and Magnetic Properties of YIG Films

Yttrium iron garnet (YIG), $Y_3Fe_5O_{12}$, is a typical ferrimagnetic material. In this article, "YIG" is used to refer not only to $Y_3Fe_5O_{12}$, but also to any other magnetic garnet crystal, including Fe^{3+} ions, such as $Y_{3-y}R_yFe_{5-x}A_xO_{12}$ and $Bi_{3-y}R_yFe_{5-x}A_xO_{12}$, where R denotes a rare-earth element and A denotes a non-magnetic element. The use of YIG has been studied for a long time. In the 1970s, YIG crystals were used in bubble memory devices for computers.

A bubble memory is created when the magnetic domains in a YIG crystal film are placed under an external static magnetic field. Later, YIG was used in optical isolators, a key device in optical communication systems. The optical isolator is based on the Faraday effect, which is a magneto-optic property of YIG. For these applications, YIG film crystals have been used. On the other hand, spherical YIG crystals have been used in microwave isolators and resonators. These devices are based on spin waves and magnetostatic waves (MSW), which are high-frequency microwaves that propagate through YIG when an external static magnetic field is applied.

Recently, there has been active research on MSW propagating through YIG film. MSW are a mode of electromagnetic wave generated in ferrite crystals (see *Ferrite Ceramics at Microwave Frequencies*) when microwaves are coupled with electron spins in the material. An MSW is characterized by a frequency that changes as the external static magnetic field is varied. In this article, we shall consider the properties of YIG crystals, growth techniques with regard to MSW applications, and an MSW device called an *S/N-enhancer*. The S/N-enhancer is a noise-reduction device that improves the reception of direct-broadcasting satellite receivers.

1. YIG Crystals

The lattice constant of a YIG crystal is 1.2373 nm. The growth techniques for YIG crystals have been developed for applications in bubble memories, microwave devices, and optical devices. A garnet crystal (space group: *Ia3d*) is formed from eight $C_3A_2D_3O_{12}$ sub-units. In a YIG crystal, 24 C-sites with Y^{3+} are each at the center of a dodecahedron whose apexes are occupied by oxygen atoms. Similarly, 16 A-sites with Fe^{3+} and 24 D-sites with Fe^{3+} are each at the center of a tetrahedron and an octahedron, respectively, whose apexes are occupied by oxygen atoms. A YIG crystal can be designed for applications in specific devices, because the composition of a solid solution of YIG can be easily controlled by doping cations.

A fraction of the D-site cations can be replaced with non-magnetic cations, such as Ga^{3+} or Al^{3+}, to decrease the saturated magnetization (*Ms*). On the other hand, a fraction of the A-site cations can be replaced with non-magnetic cations, such as In^{3+}, to increase the *Ms*. In addition, a fraction of the C-site cations can be replaced with Bi^{3+} or rare-earth atoms, such as La^{3+}, to modify the lattice parameter of the YIG and adjust it to that of the garnet substrate for epitaxial growth. For example, the lattice constant of $Gd_3Ga_5O_{12}$ (gadolinium gallium garnet, or GGG), which is usually used as the substrate crystal for YIG epitaxal films, is 1.2383 nm.
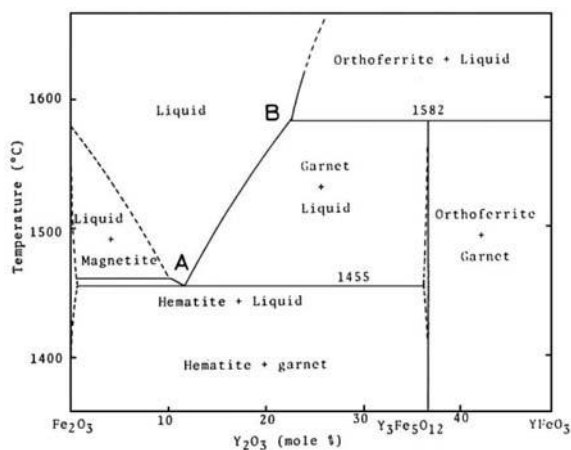
Figure 1
Phase diagram for the Fe_2O_3-$YFeO_3$ system.

Figure 1 shows the phase diagram of the Fe_2O_3–$YFeO_3$ system obtained by Van Hook (1962). As the phase diagram shows, YIG crystals cannot be obtained from a stoichiometric melt, because YIG decomposes into $YFeO_3$ and Fe_2O_3 at around $1580\,^{\circ}C$. Therefore, YIG films are grown by liquid-phase epitaxy (LPE). LPE uses flux, and growth is done under a thermo-equilibrium condition, so the YIG films obtained should have good crystallinity. A solvent mixture of PbO and B_2O_3 is usually used as the flux, and the films are grown on a crystalline substrate with a garnet structure. Although YIG crystals are grown by LPE for both optical and MSW devices, there are great differences between the epitaxial films required for each application. In optical applications, such as optical isolators, the film thickness is at least several hundred micrometers, and the film surface must be polished to prevent optical scattering. In MSW applications, the film thickness is less than a hundred micrometers, and in order to reduce cost, the as-grown films have no surface treatment.

2. Growth of YIG Films

In LPE, the solute for the crystal and the solvent are put into a crucible, and the crucible is kept at a constant temperature under constitutional supercooling condition of the solution. The crystal substrate is then dipped into the solution in the crucible, and the crystal film grows epitaxally on the substrate. There are two important things to note concerning the temperature in the crucible. First, the temperature profile must be kept uniform; and second, temperature fluctuations must be minimized. That is the reason why the crystal grows under quasi-equilibrium conditions.

Figure 2
Schematic cross section of an LPE growth furnace.

Figure 4
Phase diagram for the $PbO-Fe_2O_3-Y_2O_3$ system.

Figure 3
Temperature profile in the growth furnace. The origin of the vertical axis is the gas-melt interface.

platinum reflectors are positioned above the crucible to reflect thermal radiation and control airflow. The temperature distribution in the crucible under optimum furnace conditions is shown in Fig. 3, where the gas-solution interface is set as the origin, and temperature fluctuations are shown by error bars. The temperature gradient in the solution was as small as $0.03\,°C\,mm^{-1}$ at -40 mm, where the LPE growth temperature had a fluctuation of less than $0.5\,°C$. If there had been much temperature difference between the regions above and below the gas–solution interface, or much temperature fluctuation in the solution, YIG crystals could have easily nucleated and clung to the substrate when it was dipped.

Next, the YIG growth example is described. In this case, the YIG films were designed for application in an S/N-enhancer, for which the target composition was $La_{0.07}Y_{2.93}Ga_{0.45}Fe_{4.55}O_{12}$ (LaGa:YIG) with an operating frequency range of 1.03 to 1.35 GHz. The starting materials with a total weight of about 10 kg were Fe_2O_3 (4N), Y_2O_3 (4N), Ga_2O_3 (4N), and La_2O_3 (4N) as the crystal constituents; and PbO (4N) and B_2O_3 (4N) as the flux. Figure 4 shows the phase diagram for the $PbO–Fe_2O_3–Y_2O_3$ system. Fe_2O_3 and Y_2O_3 are the solutes, and PbO is the main constituent of the solvent. The garnet structure can be obtained in a definite region. The B_2O_3 controls the viscosity of the solvent and deters YIG nucleation. The typical compositions of the starting materials are described in Table 1 using Blank's *R*-parameter.

As shown in Fig. 2, the starting materials were mixed and placed in the platinum crucible, 150 mm in diameter and 150 mm in height. Each (111)-oriented GGG substrate of 76 mm in diameter was held horizontally by the platinum holder and dipped into the melt solution during growth. The substrates were

Figure 2 shows a typical growth furnace for LPE. The furnace includes three heater units, which can be controlled independently. The platinum crucible is at the center of the furnace. Five donut-shaped

Table 1
Blank's *R*-parameters. R_i shows the molar ratio.

R-parameter	Molar ratio
$R_1 \equiv \dfrac{[Fe_2O_3]}{[Y_2O_3] + [La_2O_3]}$	20.0–25.0
$R_2 \equiv \dfrac{[Fe_2O_3]}{[Ga_2O_3]}$	20.0–25.0
$R_3 \equiv \dfrac{[PbO]}{[B_2O_3]}$	14.0–16.0
$R_4 \equiv \dfrac{[Fe_2O_3] + [Y_2O_3] + [La_2O_3] + [Ga_2O_3]}{[PbO] + [B_2O_3] + [Fe_2O_3] + [Y_2O_3] + [La_2O_3] + [Ga_2O_3]}$	0.10–0.11
$R_5 \equiv \dfrac{[Y_2O_3]}{[La_2O_3]}$	5.00–7.00
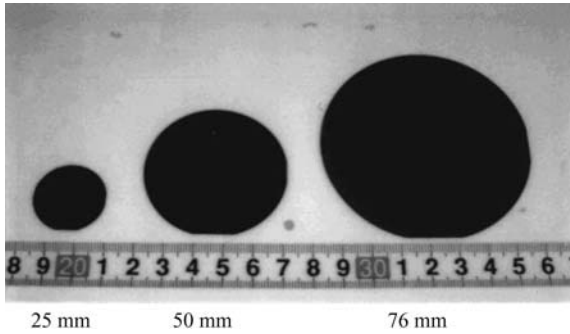
Figure 5
As-grown YIG wafers of 25 mm, 50 mm, and 76 mm in diameter.

rotated horizontally by rotating the holder, and the rotation direction of the substrate was changed at regular intervals. Typical growth temperature was 860 to 920 °C. The rotation rate was 100 rpm, and the intervals between changing the direction were 15 s.

As-grown (111)-oriented YIG wafers of 25 mm, 50 mm, and 76 mm in diameter are shown in Fig. 5. All epitaxial YIG wafers were grown on both sides of the GGG substrate. The thickness distribution, which was measured using an optical-interference thickness-measuring system, was $10.0 \pm 0.5\,\mu m$ for the as-grown YIG films on the 76-mm substrate.

3. Magnetic Properties

For MSW applications, the important magnetic properties of YIG films are the *Ms* and the half-line width of the ferromagnetic resonance (FMR), or ΔH. To examine these properties, FMR spectra were measured using the electric spin resonance (ESR) method with X-band microwaves (9.2 GHz). Square samples $2.0 \times 2.0\,mm^2$ in size were cut from the as-grown YIG wafers, and the YIG film on one side of each sample was removed. After measurement, the ΔH was calculated from peak to peak by Lorenz-type resonance in the FMR spectra. The *Ms-Ha*, where *Ha* is the anisotropic magnetic field, was calculated by using Kittel's resonance equation with the results from applying two resonant external magnetic fields, one parallel to the film and one perpendicular.

For the S/N-enhancer application, the *Ms* must be kept within $120.0 \pm 5.0\,mT$, and the ΔH must be less than $80\,A\,m^{-1}$. For the YIG films above mentioned, both the ΔH and *Ms* (the *Ha* was estimated at 3.0 mT by using other measurements) met the requirements for the S/N-enhancer.

To satisfy the requirement for magnetic properties, there are some important conditions for YIG growth. First, a suitable growth furnace must be used to control the temperature profile. Second, the impurity concentrations of the starting materials must be carefully controlled. For example, nine elements (silicon, titanium, chromium, cobalt, hafnium, tin, germanium, magnesium, and tantalum) degraded the FMR properties, at concentrations ranging from 10 to 50 ppm by weight in the starting materials.

Finally, a periodic layer structure (PLS) in a YIG film is effective in improving the FMR properties. Figure 6 shows an x-ray rocking curve measurement using a monochrometer consisting of four crystals. The main peak corresponds to the YIG (888) reflection, and the second peak corresponds to the GGG (888) reflection. A pair of reflections is found, symmetrical around the main YIG peak. These satellite reflections, indicated by the two arrows, indicate the existence of a PLS, like a superlattice of compound semiconductor

materials. The PLS was estimated to be around 150 nm long, based on the angular difference between the main and satellite peaks. This indicates that the length of the PLS can be controlled by changing the LPE growth

conditions, such as the growth temperature or the interval of changing the rotation direction. Figure 7 shows the FMR spectra with and without a PLS. At a film thickness of 20 μm, both FMR spectra were excellent. However, at 5 μm, only that with a PLS was excellent. This explains why the magnetic direction is ordered above the film-substrate interface for the YIG film with the PLS.

Figure 6
Measured x-ray rocking curve using Cu-Kα$_1$. The main peak shows the YIG (888) reflection.
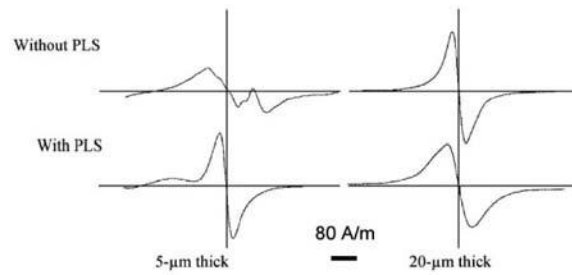
Figure 7
Effect of a PLS on FMR spectra.

4. S/N-enhancer

An S/N-enhancer is an MSW device that cancels noise and emphasizes the signal in direct-broad-casting satellite receivers. It utilizes the nonlinear characteristics of MSW propagation through YIG films, so that the MSW output power finally saturates with increasing input power, as shown in Fig. 8(a). The device operates as shown in Fig. 8(b). The input microwave is divided, and each part passes a separate YIG film. In path (1), the signal amplitude decreases while the noise level does not change, because the signal amplitude is above the saturation level and the noise amplitude is below it. After propagating through the YIG film, the microwave amplitude decreases further at the attenuator (Att-1).

In path (2), both the signal and noise amplitudes decrease at the attenuator (Att-2), but they do not change in the YIG film because they have already decreased below the saturation level. Furthermore, the phase shifter creates a 180° phase difference between paths (1) and (2). The noise amplitude is then reduced after the two microwaves are added, because the noise amplitude through path (1) is almost similar to that through path (2). As a result, the ratio of the signal and noise amplitudes (S/N) is emphasized. Thus, the performance of the two YIG films in the S/N enhancer
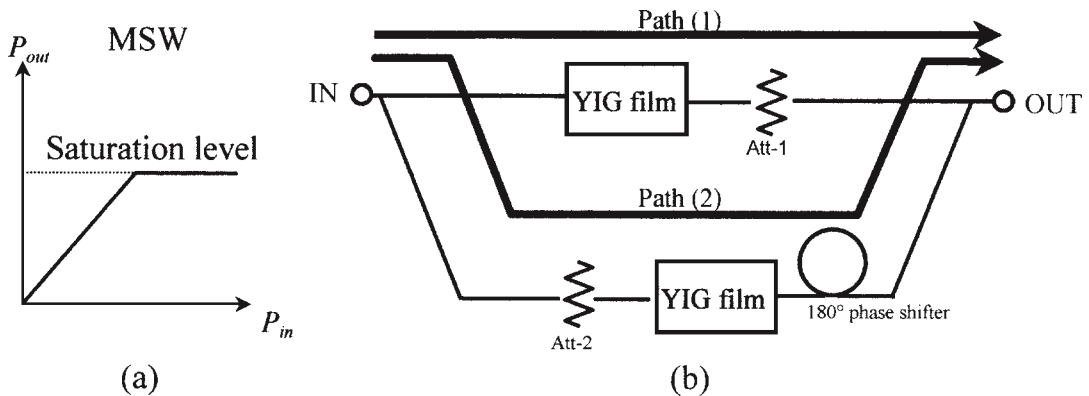
Figure 8
Relationship between input power (P_{in}) and output power (P_{out}) for propagation through a YIG film. P_{out} saturated at a high P_{in} level. (b) Operating principle of a S/N enhancer with two YIG films.

(a)   (b)
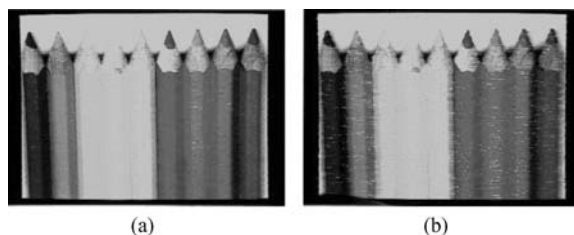
Figure 9
Photographs showing the effect of a S/N enhancer on TV pictures: (a) picture output with S/N enhance; (b) original picture.

must be uniform. As shown in Fig. 9, the S/N enhancer improves the quality of TV pictures.

See also: Ferrite Ceramics at Microwave Frequencies

Bibliography

Blank L S, Nielsen W J 1972 The growth of magnetic garnet by liquid phase epitaxy. *J. Cryst. Growth* **17**, 302–11

Geho M, Fujino M, Fujii T 1999 Growth of magnetic garnet single-crystal films for the S/N-enhancer device. *Key Eng. Mater.* **157–158**, 143–50

Helszajn J 1985 *YIG resonators and filters*. Wiley-Interscience, New York

Small M B, Giess E A, Ghez R 1994 *Handbook of Crystal Growth: 3a—Basic Techniques*. Elsevier, Amsterdam

Shinmura S, Okada T 1997 Murata S/N-enhancers stress signal for dbs receivers. *Nikkei Electronics Asia*. August, pp. 70–3

Spark M 1964 *Ferromagnetic-Relaxatuon Theory*. McGraw-Hill, New York

Stancil D D 1993 *Theory of Magnetostatic Waves*. Springer-Verlag, New York

Tolksdorf W, Welz F 1978 *Crystals—Properties and Applications: 1*. Springer-Verlag, New York

Van Hook J H 1962 Phase relations in the ternary system Fe_2O_3–FeO–$YFeO_3$. *J. Am. Ceram. Soc.* **45** (4), 162–5

Zvezdin A K, Kotov V A 1997 *Studies in Condensed Matter Physics: Modern Magnetooptics and Magnetooptical Materials*. Institute of Physics Publishing, Bristol, UK

T. Fujii and Y. Sakabe
Murata Manufacturing Company Ltd., Shiga Japan

This page intentionally left blank

H

Half-metallic Magnetism

The electronic structure of a magnetic solid can be described by two independent band structures for the two spin directions in the absence of spin–orbit interactions. A half-metal is defined as a solid with metallic properties for one of the spin directions only. As a consequence, the electrical conduction takes place for one spin direction exclusively. Also the magnetic moment of a half-metal is integral. This follows from the integer number of electrons for the nonconducting spin direction as well as the integral total number of electrons. Historically, the possibility of unusual physics in magnetic systems with integral magnetic moments was recognized as early as 1950 (Pickett and Moodera 2001), however, the first discussion on half-metallicity and its origin appeared in 1983 (De Groot *et al*. 1983).

1. Physical Origin of Half-metallicity

A remarkable feature of a half-metal is the occurrence of a bandgap for one spin direction. Bandgaps occur for distinct physical and chemical reasons, leading to distinct behavior as function of pressure, disorder, surface sensitivity, etc. Because of this, the origin of the bandgap is a useful criterion for the classification of half-metals (Fang *et al*. 2002). Three categories exist.

1.1 Systems with Covalent Bandgaps Such As in III–V Semiconductors

Although the origin of the bandgap in this category is the least straightforward, the materials, in which half-metallicity was first described (NiMnSb), fall into this category. NiMnSb crystallizes in the Heusler $C1_b$ structure. This structure consists of a face-centered cubic Bravais lattice with Ni in the origin, Mn at $\frac{1}{4}, \frac{1}{4}, \frac{1}{4}$ and Sb at $\frac{3}{4}, \frac{3}{4}, \frac{3}{4}$. So this structure is quite similar as the zinc-blende structure. Both the Mn and the Sb have the fourfold tetrahedral coordination characteristic for the zinc-blende structure. The band structure and chemical bonding for the minority spin direction is very similar as in the III–V semiconductors. The extra atom, Ni, mediates the interactions, while the role of the *p*-electron of the metal in the III–V semiconductor is played by an Mn t_{2g}-electron in NiMnSb. A bandgap results very similar as for the zinc-blende semiconductors. The metallic spin direction is characterized by four extra *d*-electrons 4 eV lower in energy due to the exchange splitting. Wide bands, without any bandgap, result for the majority spin direction like in an alloy (see Fig. 1). The role of the

t_{2g}-electron in the band formation has two important consequences. First, it implies NiMnSb is a weak ferromagnet: strong magnetism and half-metallicity are mutually exclusive in this category. Second, the $t_{2g}d$-electron can play the role of a *p*-electron in the zinc-blende structure only as long as inversion symmetry is absent. Hence, no half-metallicity in this category exists in the Heuslers $L2_1$ structure, since it possesses inversion symmetry. Several other $C1_b$ Heusler alloys have been investigated.

Isoelectronic PtMnSb shows also half-metallicity (De Groot *et al*. 1984), but the spin–orbit interaction will cause the Fermi energy to cross the top of the valence band. PbMnSb shows a small overlap of the Fermi energy with the top of the valence band for the minority spin directions. In IrMnSb, RhMnSb, PtMnSn, and OsMnSb, the Fermi level overlaps with the top of the valence band (De Groot and Buschow 1986). CoMnSb (Kübler 1984) as well as FeMnSb (De Groot *et al*. 1986) are calculated to be half-metals; however, CoMnSb crystallizes in a super-structure and FeMnSb is always Fe-deficient when synthesized. Extrapolation of the measured moment
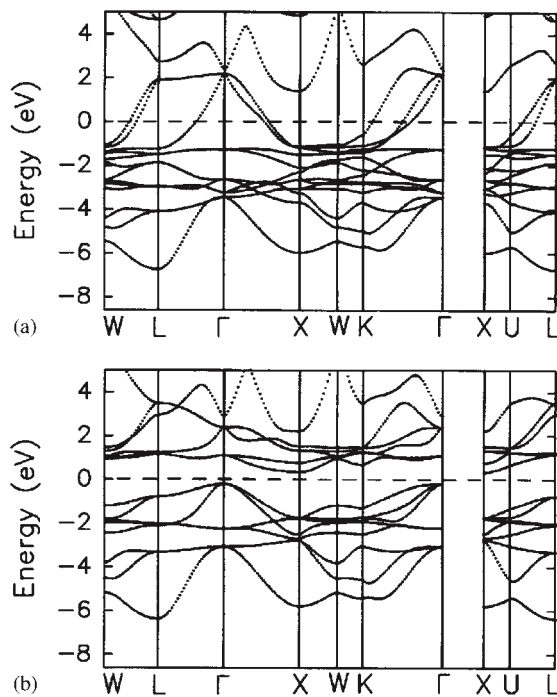
Figure 1

Band structure of NiMnSb for the majority spin direction (a) and minority spin direction (b). The zero of the energy scale coincides with the Fermi level.

267

to the stoichiometric composition leads to the required integral moment $2\mu_\beta$, however. A more recent development is the growth of transition-metal pnictides and chalcogenides in the zinc-blende structure as a meta-stable phase on top of III–V semiconductors. Successful experiments on CrAs (Akinaga *et al.* 2000) as well as CrSb (Zhao *et al.* 2001) have been reported. The magnetic moment in these cases is $3\mu_\beta$.

1.2 Strongly Magnetic, Ionic Compounds

Strong magnetic materials are defined as solids, where a hypothetical increase in exchange splitting does not lead to an increase in magnetic moment. This means, in practice, that for a transition metal the majority spin *d*-states are completely filled or the minority spin *d*-states are completely empty. The former is, for example, the case of Ni. However, there are still itinerant *s–p* electrons present, which show hardly any spin polarization and are responsible for normal metallic behavior. In an ionic compound, these mobile electrons are localized on some anion and half-metallic properties emerge. Up till now, the occurrence of half-metals in this category is confined to systems with an empty minority *d*-shell. The bandgap is of the charge transfer type, whereas the conduction band-minimum has primarily transition-metal *d*-character. Examples in this category are CrO_2 (Schwartz 1986) and the double-exchange perovskite materials (Pickett and Singh 1996).

1.3 Narrow Band Materials

In systems, where bandwidths are smaller than interactions like crystal field and exchange splittings, several bandgaps will show up in a *d*-manifold. Usually, these systems will be Mott insulators. If, however, the bandwidths are not too small and show metallic behavior, the multitude of bandgaps makes the occurrence of half-metallicity likely. The most predominant example in this category is the mineral magnetite, Fe_3O_4 (Yanase and Siratori 1984), above the Verwey transition of 120 K. CoS_2 is nearly half-metallic and can be transferred into a half-metal by substituting part of the Co by Fe (Mazin 2000). Several other half-metals have been reported in this category such as Heusler $L2_1$ phases (Fujii *et al.* 1995, Weht and Pickett 1999) as well as several nitrides (Fang *et al.* 2002). The bandgap of the semiconducting spin direction is of the *d–d* type: both the top of the valence band as well as the bottom of the conduction band are primarily derived from transition-metal *d*-states. Hence, half-metals in this category should be classified as weak magnets.

2. Physical Properties of Half-metals

Most of the early work on half-metallic magnetism was based on electronic structure calculations, presumable because, in spite of the profound influences of half-metallicity, there is no real simple "smoking gun experiment" to prove its existence in a specific compound. The requirement of an integer moment is a necessary but certainly not a sufficient condition. The test of the integral moment should be applied with care on partially substituted systems such as $Fe_{1-x}Co_xS_2$ since an integral moment per formula unit can be obtained with integral number of atoms in the formula unit only. In considering experiments, surface-sensitive ones should clearly be distinguished from bulk measurements. The most stringent one in the last category is without doubt spin-resolved positron annihilation. Positron annihilation measures the Fermi surface of a solid. Since positrons obtained from β-decay are spin polarized and the annihilation process of an electron–positron pair in a singlet state is easily discriminated from that of a triplet pair, the measurement of the Fermi surface can be realized spin dependent. In the case of NiMnSb, it was proven that only for one spin direction a Fermi surface exists (Hanssen *et al.* 1990). Unfortunately, measurements of this type on other half-metals are lacking.

Surface-sensitive measurements are less clear because of the occurrence of surface segregations, surface reconstructions (Ristoiu *et al.* 2000), or simply by the fact that even a perfect surface of a half-metal is not necessarily half-metallic itself. Spin-resolved photoemission showed $La_{1-x}Ca_xMnO_3$ to be half-metallic, although the interpretation of these measurements is not uncontroversial (Park *et al.* 1998). Andreev reflection on NiMnSb showed a spin polarization of the electrons at the Fermi energy of 58% only, whereas spin-polarized tunneling shows 28% polarization only (Tanaka *et al.* 1999). The highest degree of spin polarization of the conduction electrons measured by Andreev reflection is CrO_2: 90% (Soulen *et al.* 1998). Under some conditions, inverse photoemission shows close to 100% spin polarization in NiMnSb (Ristoiu *et al.* 2000).

There exists some confusion in the literature about the influence of disorder, specifically in the first category of half-metals. Since interchange of nickel and manganese in NiMnSb will sacrifice the tetrahedral coordination of the latter atom, it is very effective in destroying the half-metallic properties (Orgassa *et al.* 1999). This has fuelled some belief that the lack of spin polarization at its surface is an indication of such disorder at the surface or even in the bulk. While the latter is in disagreement of the spin-resolved positron-annihilation measurements, the introduction of the former is unnecessary: the presence of the surface itself breaks the tetrahedral symmetry already sufficiently to destroy the half-metallic properties locally (genuine half-metallic *interfaces* are possible, however (De Wijs and De Groot 2001)). Moreover, Ni–Mn interchange is energetically unfavorable. Although it was possible to prepare highly disordered Ni_2MnSb

by molecular beam epitaxy, recent NMR work on thin-film NiMnSb shows a very low amount of disorder and of a type (Mn–Sb interchange) that does not influence the half-metallic properties (Van Roy *et al.* 2003).

3. Half-metallic Antiferromagnetism

The *average* magnetic moment in half-metals in the Heusler structure is well described by a generalized Slater–Pauling curve (Kübler 2000). This calculated curve shows materials with an averaged moment of zero. Besides a nonmagnetic solution this can imply an unusual form of magnetism: half-metallic antiferromagnetism (Van Leuken and De Groot 1994). Half-metallic antiferromagnets differ from traditional antiferromagnets, because local moments on crystallographically different sites cancel. Theoretically, they are predicted to show an unusual form of magnetism (Rudd and Pickett 1998). Experimentally, they have not been realized yet (Pickett 1998).

See also: Spintronics in Semiconductor Nanostructures

Bibliography

Akinaga H, Manago T, Shirai M 2000 Material design of half-metallic zinc-blende CrAs and the synthesis by molecular beam epitaxy. *Jpn. J. Appl. Phys.* **39**, L1118–20

De Groot R A, Buschow K H J 1986 Recent developments in half-metallic magnetism. *J. Magn. Magn. Mater.* **54–57**, 1377–80

De Groot R A, Mueller F M, Van Engen P G, Buschow K H J 1983 A new class of materials: halfmetallic ferromagnetic. *Phys. Rev. Lett.* **42**, 2024–7

De Groot R A, Mueller F M, Van Engen P G, Buschow K H J 1984 Half-metallic ferromagnets and their magneto-optical properties. *J. Appl. Phys.* **55**, 2151–4

De Groot R A, Van der Kraan A M, Buschow K H J 1986 FeMnSb: a half-metallic ferrimagnet. *J. Magn. Magn. Mater.* **61**, 330–6

De Wijs G A, De Groot R A 2001 Towards 100% spin-polarized charge-injection: the half-metallic NiMnSb/CdS interface. *Phys. Rev. B* **64**, 020402

Fang C M, De Wijs G A, De Groot R A 2002 Spin-polarization in halfmetals. *J. Appl. Phys.* **91**, 8340–4

Fujii S, Ishida S, Asano S 1995 A half-metallic band structure and Fe_2MnZ (Z = Al, Si, P). *J. Phys. Soc. Japan* **64**, 185–91

Hanssen K E H M, Mijnarends P E, Rabou L P L M, Buschow K H J 1990 Positron-annihilation study of the half-metallic ferromagnet NiMnSb–experiment. *Phys. Rev. B* **42**, 1533–40

Kübler J 1984 First principles theory of magnetism. *Physica B* **127**, 257–63

Kübler J 2000 Theory of itinerant electron magnetism. Published in International Series of Monographs on Physics, 106

Mazin I I 2000 Robust half-metallicity in $Fe_xCo_{1-x}S_c$. *Appl. Phys. Lett.* **77**, 3000–2

Orgassa D, Fujiwara H, Schulthess T C, Butler W H 1999 First-principles calculation of the effect of atomic disorder on the electronic structure of the half-metallic ferromagnet NiMnSb. *Phys. Rev. B* **60**, 13237–40

Park J H, Vescovo E, Kim H J, Kwon C, Ramesh R, Venkatesan T 1998 Direct evidence for a half-metallic ferromagnet. *Nature* **392**, 794–6

Pickett W E 1998 Spin-density-functional-based search for half-metallic antiferromagnets. *Phys. Rev. B* **57**, 10613–9

Pickett W E, Moodera J S 2001 Halfmetallic magnets. *Phys. Today* **54**, 39–44

Pickett W E, Singh D J 1996 Electronic structure and half-metallic transport in the $La_{1-x}Ca_xMnO_3$ system. *Phys. Rev. B* **53**, 1146–60

Ristoiu D, Noziéres J P, Borca C N, Komesu T, Jeong H K, Dowben P A 2000 The surface composition and spin polarization of NiMnSb epitaxial thin films. *Europhys. Lett.* **49**, 624–30

Rudd R E, Pickett W E 1998 Single-spin superconductivity: formulation and Ginzburg–Landau theory. *Phys. Rev. B* **57**, 557–74

Schwartz K 1986 CrO_2 predicted as a half-metallic ferromagnet. *J. Phys. F* **16**, L211–5

Soulen R J, Byers J M, Osofsky M S, Nadgorny B, Ambrose T, Cheng S F, Broussard P R, Tanaka C T, Nowak J, Moodera J S, Barry A, Coey J M D 1998 Measuring the spin polarization of a metal with a superconducting point contact. *Science* **282**, 85–8

Tanaka C T, Nowak J, Moodera J S 1999 Spin-polarized tunneling in a half-metallic ferromagnet. *J. Appl. Phys.* **86**, 6239–42

Van Leuken H, De Groot R A 1994 Half-metallic antiferromagnets. *Phys. Rev. Lett.* **74**, 1171–3

Van Roy W, Wojcik M, Jedryka E, Nadolski S, Jalabert D, Brijs B, Borghs G, De Boeck J 2003 Very low chemical disorder in epitaxial NiMnSb films on GaAs(III)B. *Appl. Phys. Lett.* **83** (20), 4214–6

Weht R, Pickett W E 1999 Half metallic ferrimagnetism in Mn_2VAl. *Phys. Rev. B* **60**, 13006–10

Yanase A, Siratori K 1984 Band structure of the high temperature phase of Fe_3O_4. *J. Phys. Soc. Japan* **53**, 312–7

Zhao J H, Matsukura F, Takamura K, Abe E, Chiba D, Ohna H 2001 Room-temperature ferromagnetism in zinc-blend CrSb grown by molecular beam epitaxy. *Appl. Phys. Lett.* **79**, 2776–8

R. A. de Groot
University of Nijmegen, The Netherlands

Hard Magnetic Materials, Basic Principles of

The progress in the field of permanent magnets has been dramatic since the 1960s. This would have been impossible without a fundamental understanding of the physical phenomena responsible for hard magnet properties, which led to the discovery of new families of permanent magnet materials based on rare earth(R)–transition metal (T) compounds (see *Rare Earth Magnets: Materials*). The search for new compounds with superior properties focuses on materials

with high values of Curie temperature ($T_C > 500\,K$), high saturation magnetization M_S ($\mu_0 M_S > 1$ T, with μ_0 the permeability of free space ($4\pi \times 10^{-7}$ Tm A^{-1})), and high magnetocrystalline anisotropy, H_A.

In this article, these intrinsic properties which depend on crystal structure and chemical composition will be described. In addition, it will be elucidated that a favorable combination of these values does not automatically lead to a good hard magnet material but can only be regarded as a prerequisite (for more detailed descriptions see Cullity 1972, Coey 1996, Chikazumi 1997 and Buschow 1997). The final suitability can only be assessed when the extrinsic properties such as coercive field H_C, remanent magnetization B_r, and maximum energy product $(BH)_{max}$, derived from the intrinsic properties by the preparation of appropriate microstructures, fulfill certain criteria.

Ferromagnetic materials are characterized by a parallel orientation of the participating magnetic moments below the Curie temperature, i.e., the magnetic ordering temperature. This is caused by an exchange interaction H_{ex} that was described by Heisenberg in 1928 by:

$$H_{ex} = -2J_{ij}S_iS_j \qquad (1)$$

where J_{ij} is the exchange integral, and S_i and S_j are the localized magnetic spin vectors of the ions i and j. For a ferromagnetic interaction, the exchange integral is positive, whereas it is negative for an antiferromagnetic coupling between the two ions. The coupling is sensitive to the interatomic spacing r_{ij} and the ferromagnetic interaction is strongest for cobalt, and significantly weaker for iron and nickel (Bethe–Slater curve).

The above description requires localized electrons and needs to be modified for transition metals (T–T interactions) where the electrons are itinerant: that means the $3d$ ions do not have an integral number of electrons. Nonetheless, the atomic moment m of the transition metal element can be defined as

$$m = gS_T\mu_B \qquad (2)$$

where g is the Landé factor (ratio of the magnetic moment to the angular moment), S_T an effective spin and μ_B the Bohr magneton ($1\,\mu_B = 9.274 \times 10^{-24}$ J T^{-1}). In a weak ferromagnet both spin-up and spin-down bands are partially depleted, and in a strong ferromagnet the majority spin-up band is completely occupied (Fig. 1). Despite its relatively large moment iron is a weak ferromagnet ($2.22\,\mu_B$ at $T = 0$ K) whereas cobalt ($1.72\,\mu_B$) and nickel ($0.61\,\mu_B$) are strong ferromagnets (Slater–Pauling curve, see Fig. 2). If iron were a strong ferromagnet its moment could be extrapolated to $2.7\,\mu_B$

In rare-earth–transition metal compounds three types of exchange interactions may occur: T–T, R–T,
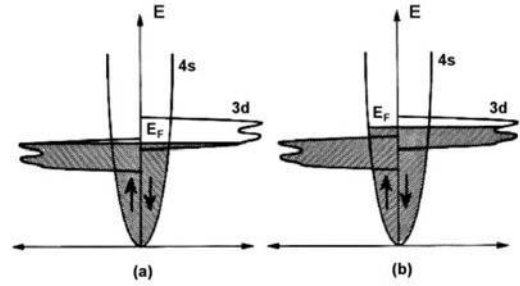
Figure 1
Schematic band structures of (a) weak and (b) strong ferromagnets.
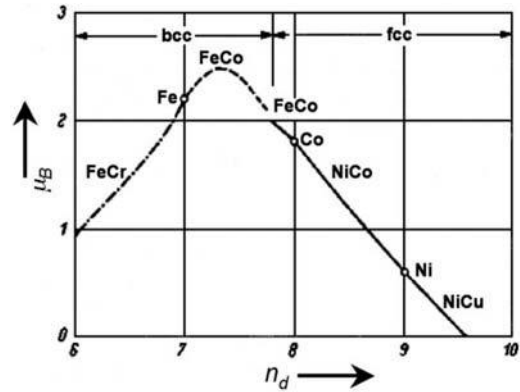
Figure 2
Atomic magnetic moment μ_B of ferromagnetic metals and binary alloys as a function of the number of outer electrons ($3d$) per atom n_d (Slater–Pauling curve).

and R–R. In the case of $SmCo_5$ for example, where the transition metal carries a well-established magnetic moment, the T–T interactions dominate. The strongly ferromagnetic coupling is responsible for the magnetic order up to the very high Curie temperature. The R–R exchange coupling proceeds indirectly via $4f$–$5d$–$5d$–$4f$ and is generally very small compared to the R–T interaction. The latter also proceeds via an indirect mechanism ($4f$–$5d$–$3d$) in which the strong interatomic direct $5d$–$3d$ exchange is transmitted to the $4f$ electrons via the intra-atomic $4f$–$5d$ ferromagnetic interaction (Brooks and Johansson 1993). The $5d$–$3d$ exchange is antiferromagnetic when the $5d$ band is less than half full and the $3d$ band is more than half full, as is the case for compounds of rare-earth metals with ferromagnetic $3d$ metals.

Qualitatively it can be summarized that, as the transition metal spin S_T couples antiparallel to the rare-earth spin S_R, the magnetizations of R and T sublattices couple parallel for the light rare-earth

elements ($J = L - S$) and antiparallel for the heavy rare-earth elements ($J = L + S$). The orbital magnetic moments in rare-earth metals remain unquenched by crystalline fields because the magnetic moments are produced by 4f electrons well inside the atoms and protected from the surrounding atoms. If the total magnetization rotates together with the orbits in the crystal lattice, the electrostatic interaction between the orbits and the lattice favors certain directions of the magnetization. The result of this interaction is an enormous magnetocrystalline anisotropy (see *Magnetic Anisotropy*) as illustrated in Fig. 3 for hexagonal terbium. In that case the shape of the 4f orbit (pancake-like electron cloud) and the crystal symmetry (compressed along the c-axis) finally lead to easy and hard directions of magnetization.

The intrinsic properties are determined by magnetic moments and interactions on an atomic scale and are independent of the microstructure of the specific material. The disappearance of long-range magnetic order at the Curie temperature is a second-order thermodynamic phase transition, as can be seen from specific heat capacity measurements, where a significant magnetic contribution arises. Above this temperature the material becomes paramagnetic. The transition metals cobalt, iron, and nickel exhibit Curie temperatures of 1127 °C, 770 °C, and 358 °C respectively, whereas of the rare-earth metals only gadolinium ($T_C = 16$ °C) is ferromagnetic close to room temperature.
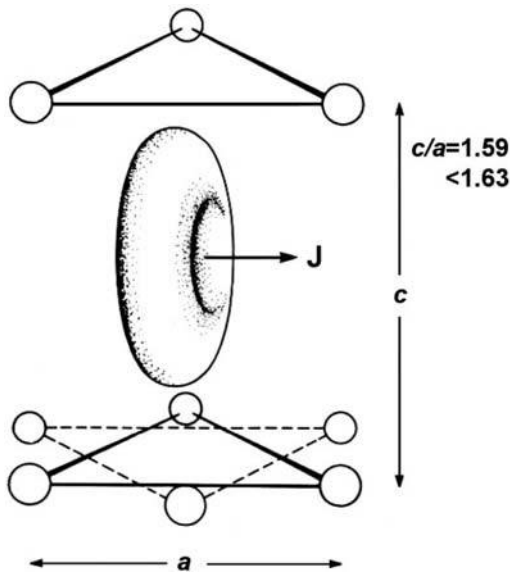
The magnetization of a ferromagnetic material has its origin in the spin and orbital magnetic moments of the electrons. In a continuum description called *micromagnetism*, a local magnetization vector **M** can be defined by summing the elementary contributions per unit volume. In most materials the spatial distribution of the magnetization is dominated by magnetic domains (see *Magnets, Soft and Hard: Domains*). The direction of magnetization varies from domain to domain and normally lies along a crystallographic axis. However, within one domain the magnitude of M is uniform, and it is called the *spontaneous magnetization* M_S. The magnetization over the entire volume of a polycrystalline sample would normally average out to zero, but a net magnetization can be retained when the ferromagnetic material can be prepared in a metastable state.

This remanent state can be achieved after saturation in a magnetic field which corresponds to a complete alignment of all the moments (see also Fig. 4) parallel to the field and which eliminates the domain walls in each crystallite. An easy-axis anisotropy is indispensable for maintaining the metastable domain configuration. The crystalline electric field mentioned above, together with the spin-orbit coupling, gives rise to the single-ion anisotropy on an atomic scale. The atomic moment has local easy directions that reflect the point symmetry of the site. The overall crystal symmetry is described macroscopically by the magnetocrystalline anisotropy that is obtained by summing all single-ion contributions.

In a material with uniaxial symmetry (e.g., hexagonal cobalt) the anisotropy energy of a crystal E_A may be described by

$$E_A = K_1 \sin^2\theta$$
$$+ K_2 \sin^4\theta + K_3 \sin^6\theta + K_4 \sin^6\theta \cos6\phi \quad (3)$$

where K_1, K_2, etc. are the anisotropy constants which vary with temperature and differ for different

Figure 3
Electron cloud of the 4f electron of a terbium atom in a hexagonal lattice (Chikazumi 1997). The c-axis is the hard direction of magnetization. The ideal c/a value for a closed-packed hexagonal lattice is 1.63.
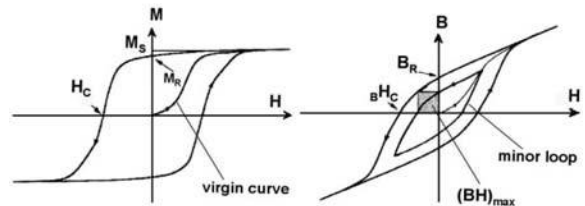
Figure 4
Hysteresis loops for a permanent magnet: (left) M–H loop and (right) B–H loop. The initial magnetization curve after thermal demagnetization starts at the origin; a minor loop arising after the application of fields insufficient for saturation is also shown. The energy product $(BH)_{max}$ is the shaded area in the second quadrant of the B–H loop.

materials; and where the direction of the spontaneous magnetization relative to the single uniaxial direction (*c*-axis) and the *a*-axis is given by the polar angles θ and ϕ, respectively. With K_1 dominating and $K_1 > 0$, the easy direction of magnetization will be along the *c*-axis in hexagonal or tetragonal structures. (SI units of E_A and K_i are J m^{-3}.) The anisotropy field H_A is the intersection of the magnetization curves when measured with the field parallel and perpendicular to the easy magnetization direction and, therefore, can be used as an estimate for K_1 (for materials where K_2 is negligible, this is the case when the magnetization measured with the field applied perpendicular is a straight line, e.g., tetragonal $Nd_2Fe_{14}B$ at room temperature).

$$H_A = (2K_1 + 4K_2)/\mu_0 M_S \qquad (4)$$

The static magnetic properties are described by hysteresis loops as shown in Fig. 4 where either magnetization *M* or magnetic flux density *B* is plotted as a function of field *H* (*M*–*H* or *B*–*H* curves). Provided that the applied field, corrected for the demagnetization effect (the demagnetization factor *N* is a pure number between 0 and 1 and depends only on sample shape, e.g., 1/3 for spherical particles and the sum in the three orthogonal directions is unity), is sufficient to achieve saturation, one symmetric major loop is traced (the intrinsic property M_S is delineated in the *M*–*H* presentation); otherwise minor loops are obtained. In the SI system the relationship between *B*, *M*, and *H* is given by:

$$B = \mu_0(H + M) \qquad (5)$$

M–*H* or *B*–*H* loops have different contours, the former being more relevant for fundamental aspects, the latter of interest from an application point of view and being usually presented in the magnet data sheets.

For an ideal permanent magnet the second quadrant *B*–*H* loop is a straight line, with slope μ_0. The remanence B_r or $\mu_0 M_r$ is the flux density or remanent magnetization that persists after removing the magnetizing field *H*. Another extrinsic property is given when the loop cuts the field axis; with $M = 0$ the coercivity H_c is obtained (often referred to as *intrinsic coercivity*, which is rather unfortunate because the coercivity is not an intrinsic property but is very much microstructure-dependent). The maximum energy density $(BH)_{max}$, or also energy product, of rare-earth permanent magnets is a measure of the magnetostatic energy stored and, thus, describes the performance of the magnet (the shaded area in Fig. 4). It is the most widely spread figure of merit and is found where the product of *B* and *H* is maximized, which is equal to twice the potential energy of the magnetic field outside the magnet divided by its volume.
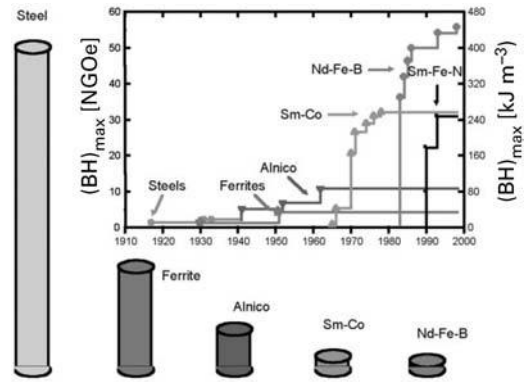
Figure 5
Development in the energy density $(BH)_{max}$ of hard magnetic materials in the twentieth century and presentation of different types of materials with comparable energy density.

$(BH)_{max}$ is limited by the remanence, provided the coercivity has at least half the value of the remanence:

$$(BH)_{max} \leqslant \mu_0 M_r^2/4 \qquad (6)$$

where, for example, the remanent magnetization M_r is half of the saturation magnetization M_S, as postulated by Stoner and Wohlfarth in 1948 for an assembly of isotropic noninteracting single-domain particles (or for an ideal permanent magnet: $M_r = M_S$). $(BH)_{max}$ doubled every 12 years during the twentieth century (see *Rare Earth Magnets: Materials*) and the spectacular development is illustrated in Fig. 5. The progress has been made due to the improvement in coercivity, H_c, and not in magnetization, M_s. The coercivity H_c is usually approximated by (assuming $K_1 \gg K_2$):

$$H_c = 2(K_1/\mu_0 M_S)\alpha - N_{eff}M_S \qquad (7)$$

where α and N_{eff} are microstructural parameters, the former describing the reduction of the crystal field by defects as well as by misaligned grains and the latter taking into account internal stray fields (Adler and Hamann 1985, Durst and Kronmüller 1985).

The mechanism by which a hard magnet is locked in the metastable state described above is controlled by many factors (see *Coercivity Mechanisms*). Here it is only stated that reverse domain nucleation and domain wall propagation result in $H_c \ll H_A$ (the so-called *Brown's paradox*), which means that the anisotropy field represents an upper limit on the coercivity H_c, but typical coercivities in high-performance magnets do not exceed 20% of H_A. This reduction is principally attributed to microstructural effects and it is remarked that the type of coercivity

mechanism can be determined by analyzing the initial magnetization curves after thermal and d.c.-field demagnetization and the demagnetization curves in the respective hysteresis loops.

Larger grains of a ferromagnetic phase are not uniformly magnetized but consist of magnetic domains in order to reduce the magnetostatic energy. The domains are separated by Bloch walls and the wall width δ_w in hard magnets is comparable in size to the exchange length $l_{ex} = \sqrt{(A/K_1)}$ with A being the exchange stiffness in J m^{-1} (proportional to T_C), the latter describing the scale of the perturbed area when a spin is unfavorably aligned. These micromagnetic parameters are especially relevant for exchange-coupled magnets, which are characterized by an unusual coercivity mechanism when consisting of finely dispersed hard and soft magnetic phases ("exchange spring magnets," Kneller and Hawig 1991; see *Magnets: Remanence-enhanced*). The critical single-domain particle size $d_c \sim \mu_0 \sqrt{(A/K_1)}/(\mu_0 M_S)^2$ describes the size of the largest possible crystallite in which the energy cost for the formation of a domain wall is higher than the gain in magnetostatic energy.

Typical values for iron-based rare-earth–transition metal permanent magnets are of the order of $d_c = 200$–300 nm. There are two basic concepts (see *Coercivity Mechanisms*) for the prevention of nucleation and growth of reverse domains from the fully magnetized state (magnetization reversal): (i) for microcrystalline magnets (see *Magnets: Sintered*) and (ii) for single-domain grains found in nanostructured magnets (see *Magnets: Mechanically Alloyed*, *Magnets: HDDR Processed*). The former concept is realized first in the nucleation type, as found in sintered NdFeB-type magnets consisting of multidomain grains in the thermally demagnetized, equilibrium state. The wall motion within a grain is relatively easy but the spontaneous nucleation of reverse domains is hindered by smooth grain boundaries, which also decouple the individual crystallites and thus impede propagation. Second, in the pinning type as found in sintered $Sm_2(Co, Fe, Cu, Zr)_{17}$ magnets where the growth of reverse domains is prevented by pinning the existing domain walls at inclusions or defects. The nucleation- and pinning-types can be easily recognized from their respective initial magnetization curve, the former showing a large low-field susceptibility whereas the latter is characterized by a weak low-field susceptibility.

Stable coercivities and magnetizations at temperatures often exceeding 200 °C are required for applications as in motors, actuators, and electromagnetic machines. Both quantities naturally decline as the operating temperature approaches the Curie temperature. Reversible temperature coefficients of coercivity (dH_C/dT) and remanence (dB_r/dT) are used for magnet specifications in order to design a machine. Ideally, irreversible magnetic losses are avoided, i.e., they are only temporary on heating,

and the original values are recovered when returning to room temperature.

See also: Alnicos and Hexaferrites; Ferrite Magnets: Improved Performance; Magnetic Films: Hard; Magnetic Materials: Hard

Bibliography

Adler E, Hamann P 1985 A contribution to the understanding of coercivity and its temperature dependence in sintered $SmCo_5$ and $Nd_2Fe_{14}B$ magnets. In: Strnat K (ed.) *Proc. 4th Int. Symp. Magnetic Anisotropy and Coercivity in RE–TM Alloys*. Dayton, OH, pp. 747–60

Brooks M S S, Johansson B 1993 Density functional theory of the ground state magnetic properties of rare earths and actinides. In: Buschow K H J (ed.) *Handbook of Magnetic Materials*. Elsevier, Amsterdam, Vol. 7, Chap. 3

Buschow K H J 1997 Magnetism and processing of permanent magnet materials. In: Buschow K H J (ed.) Handbook of Magnetic Materials. Elsevier, Amsterdam, Vol. 10, Chap. 4

Coey J M D 1996 *Rare Earth Iron Permanent Magnets*. Clarendon Press, Oxford

Chikazumi S 1997 *Physics of Ferromagnetism.*, 2nd edn. Oxford Science Publications, Oxford, pp. 276

Cullity B D 1972 *Introduction to Magnetic Materials*. Addison-Wesley, Reading, MA

Durst K D, Kronmüller H 1985 Magnetic hardening mechanisms in sintered Nd–Fe–B and $Sm(Co,Cu,Fe,Zr)_{7.6}$ permanent magnets. In: *Proc. 4th Int. Symp. Magnetic Anisotropy and Coercivity in RE–TM Alloys*. Dayton, OH, pp. 725–35

Kneller E F, Hawig R 1991 The exchange-spring magnet: a new material principle for permanent magnets. *IEEE Trans. Magn.* **27**, 3588–600

Stoner E C, Wohlfarth E P 1948 A mechanism of magnetic hysteresis in heterogeneous alloys. *Philos. Trans. R. Soc. London, Ser. A* **240**, 599

Strnat K, Hoffer G, Olson J, Ostertag W, Becker J J 1967 A family of new cobalt-base permanent magnetic materials. *J. Appl. Phys.* **38**, 1001–2

O. Gutfleisch
IFW, Dresden, Germany

Heavy-fermion Systems

Heavy-fermion metals represent a class of archetypical strongly correlated electron systems (Stewart 1984, Grewe and Steglich 1991). Mostly, these materials are based upon intermetallics containing the *f* electron elements cerium, uranium, ytterbium, or neptunium, and this review will focus entirely on these "classic" heavy fermions. The heavy-fermion-like behavior of a number of compounds not containing these elements is beyond the scope of this work; there is still some controversy over whether the

underlying physical mechanisms here are truly analogous to those of the classic heavy-fermion materials.

Historically, the term heavy fermion (HF) refers to the observation of a largely enhanced electronic contribution to the specific heat C_p at low temperatures T, compared to normal metals. The specific heat of a nonmagnetic metal at $T \ll \Theta_D$ ($\Theta_D = $ Debye temperature) evolves as $C_p = \gamma T + \beta T^3$. The term γT represents the electronic specific heat, βT^3 the phonon part. In free electron approximation the electronic specific heat coefficient is

$$\gamma = \frac{\pi^2 k_B^2 N(E_F)}{3} = \frac{k_B^2 k_F^2 m^*}{3\hbar^2} \tag{1}$$

where $N(E_F)$ is the Fermi level density of states, k_F is the Fermi wave vector, and m^* is the effective electron mass. For simple metals such as sodium the value of γ is of the order of $1\,\mathrm{mJK^{-2}\,mole^{-1}}$, which corresponds to an effective mass m^* almost equal to the free electron mass. In contrast, in HF systems γ values of 100–$1000\,\mathrm{mJK^{-2}\,mole^{-1}}$ are found, reflecting an equally bigger effective electron mass—hence the label *heavy-fermion* or *heavy-electron materials*.

HF behavior is intimately connected to the suppression of magnetic order. In HF systems magnetism is unstable due to the competition between two processes involving the magnetic moment on the f ion site and its hybridization Γ with the surrounding conduction electrons: the indirect magnetic interaction between f moments promotes long-range magnetic order, while a moment screening process, the Kondo effect, tends to suppress magnetic ordering. The strength of the hybridization Γ controls the competition of these two processes, and by variation of Γ a transition from a magnetic to a nonmagnetic ground state can be achieved.

Experimentally, the hybridization of a material can be tuned by applying chemical or hydrostatic pressure. Ideally, both similarly change the material properties, as is the case for $CeRu_2Ge_2$ (Fig. 1). Here, the crystallographic unit cell volume is reduced by 5% by the isoelectronic substitution of silicon by germanium ($x = 1$ in $CeRu_2(Ge_{1-x}Si_x)_2$) or applied pressure $p = 70\,\mathrm{kbar}$, leading to an increase of Γ (Süllow *et al.* 1999). Physically, the ground state of the system is tuned from a local moment ferromagnet (FM) via two reduced moment antiferromagnetic (AFM) phases, through the magnetic instability with $T_N = 0$ into a nonmagnetic Fermi liquid (FL) below a characteristic temperature T_{FL}. The magnetic phase diagram, derived from alloying (shaded symbols, top scale) and pressure (open symbols, bottom scale) studies, is plotted in Fig. 1, with the FM phase I and the two AFM phases II and III. Included in the figure are T_{FL} and the Kondo temperature T_K (filled symbols). The HF regime for $CeRu_2(Ge_{1-x}Si_x)_2$, with large effective electron mass (i.e. $\gamma > 100\,\mathrm{mJK^{-2}}$ $\mathrm{mole^{-1}}$), consists of a narrow pressure range of less
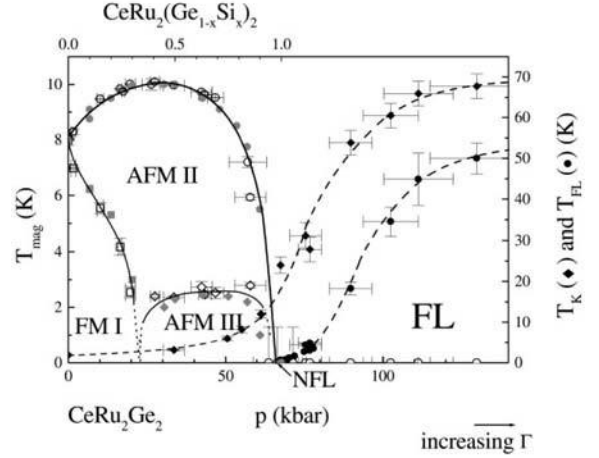
Figure 1
The pressure/chemical pressure phase diagram of $CeRu_2(Ge_{1-x}Si_x)_2$. Open symbols $\square$, $\bigcirc$, and $\diamond$ denote the ferromagnetic FM I, antiferromagnetic AFM II and AFM III transition temperatures determined in a pressure experiment on $CeRu_2Ge_2$, the corresponding shaded symbols those established from an alloying study on $CeRu_2(Ge_{1-x}Si_x)_2$. Further, the single-ion Kondo temperature T_K, derived from a combination of inelastic neutron scattering and pressure dependent resistivity measurements, and the Fermi liquid temperature T_{FL}, representing the temperature range of a resistivity $\rho = \rho_0 + AT^2$, are included in the figure (filled symbols). Note that an increasing pressure corresponds to an increasing hybridization Γ.

than $10\,\mathrm{kbar}$ on both sides of the magnetic instability, with the mass enhancement increasing on approaching the instability. At the instability, with $T_{FL} = T_N = 0$, non-Fermi liquid (NFL) behavior is observed (see *Non-Fermi Liquid Behavior: Quantum Phase Transitions*).

Microscopically, the large mass enhancement in the HF state reflects the appearance of a very large resonance peak, the Kondo resonance, in the enhanced electron density of states at the Fermi energy E_F. Based on inelastic magnetic neutron scattering and dilution studies on prototypical nonmagnetic HF compounds such as $CeCu_6$ or $CeRu_2Si_2$, this resonance at least in part can be traced back to the single-ion Kondo effect, which causes the screening of the local magnetic moments by conduction electrons below a characteristic temperature, the Kondo temperature T_K. On the other hand, the observation of a quasielastic magnetic response at certain distinct wave vectors in reciprocal space attests to the importance of intersite effects, which give rise to short-range and short-lived antiferromagnetic fluctuations. As the intersite interactions compared to the onsite

Kondo interactions gain importance, an antiferromagnetically ordered state will eventually be entered which, sufficiently close to the magnetic instability, is carried by even more strongly mass-enhanced electrons.

While the fundamental properties of HF materials derive from the single-ion Kondo model, they do not fully correspond to it. In particular, as manifestation of single-ion Kondo behavior the resistivity saturates far below T_K with $\rho \propto 1 - (T/T_K)^2$, while in HF compounds below T_{FL} a *metallic* resistivity $\rho = \rho_0 + AT^2$ occurs (ρ_0 being the residual resistivity). This deviation from single-ion Kondo behavior is referred to as the transition into the coherent state. Phenomenologically, it is viewed as the realization of a "Bloch-wave state of Kondo scatterers," i.e., the coherent superposition of scattering amplitudes from Kondo ions with the periodicity of the crystallographic lattice. Because of this transition into a coherent state, HF materials are also called *Kondo lattice systems* (see *Kondo Systems and Heavy Fermions: Transport Phenomena*).

Closely linked to HF behavior, a rich variety of ground state properties and exotic physical phenomena is observed. There is the intricate relationship between the HF state and FL as well as NFL behavior. For a number of HF compounds, superconductivity—possibly unconventional—and unusual types of magnetic order are observed. Further, a gap can open in the enhanced electron density of states at E_F, causing a semiconducting strongly correlated behavior. These, as the most relevant anomalies of the HF state, are briefly discussed below.

1. Fermi Liquid Behavior

The principal feature of nonmagnetic HF compounds below T_{FL}, which is not zero, is that the materials behave as if they were free electron materials, but with largely enhanced electron mass m^*. This highlights the presence of a novel kind of electronic "quasiparticles" (the "heavy fermions"), whose contribution to the electronic specific heat evolves like γT, and whose susceptibility behaves Pauli paramagnetic, saturating at a value χ_0. In addition, the resistivity $\rho - \rho_0$ obeys AT^2, as expected for dominant quasiparticle–quasiparticle scattering. The coefficients γ, χ_0, and A reflect the mass enhanced state with $\gamma \propto \chi_0 \propto \sqrt{A} \propto m^*$. The heavy FL state, coherently formed out of conduction electrons and f electrons, weakly delocalized due to their hybridization with the former, has been studied by de Haas–van Alphen and Shubnikov–de Haas measurements (see *Magnetic Systems: De Haas–van Alphen Studies of Fermi Surface*). The experimentally determined renormalized band structures of HF systems are reproduced by calculations, if the mass renormalization is taken into account as an empirically introduced

parameter. Altogether, the physical properties are linked by a single parameter, the electron mass enhancement. The concept to describe such single-parameter scaling is the Landau theory of the Fermi liquid. Within this concept a one-to-one correspondence between the quasiparticles of the HF state and the electrons in a free electron gas is drawn via a renormalization of the effective mass. In this way, the Fermi liquid theory achieves a mapping of the HF state onto the well-known non-interacting free electron gas.

At the magnetic instability, for $T_N = T_{FL} = 0$, the description of the HF properties within the Landau FL theory appears to fail. Here, temperature dependencies of the physical properties are recorded which do not adhere to the FL predictions, and which are collectively referred to as NFL behavior.

2. Superconductivity and Magnetism

One of the most spectacular and elusive phenomena of HF materials is the appearance of superconductivity in a few compounds (Zwicknagl 1992, Heffner and Norman 1996). Presently, six materials are regarded as heavy-fermion superconductors (HFS): $CeCu_2Si_2$, UBe_{13}, UPt_3, URu_2Si_2, UPd_2Al_3, and UNi_2Al_3. Furthermore, $CeCu_2Ge_2$, $CeRh_2Si_2$, $CePd_2Si_2$, and $CeIn_3$ are probably HFS at high pressure. The unifying aspect of HFS is that superconductivity is carried by the heavy quasiparticles. Thus, superconductivity in HF systems is a property of the strongly correlated state and involves those electrons that also take part in the magnetic exchange, i.e., the f electrons.

The electronic correlations manifest themselves in highly unusual superconducting properties, such as multiple superconducting phases, anomalous pinning behavior, or impurity effects. In analogy to the superfluidity of ^{3}He, it is assumed that in HFS the symmetry of the superconducting order parameter is highly anisotropic and that they behave as unconventional superconductors, i.e., show an order parameter with a lower symmetry than that of the underlying crystal lattice. While for $CeCu_2Si_2$, UBe_{13}, and UPd_2Al_3 the order parameter most probably is of even parity, Knight-shift results suggest an odd-parity superconducting state in UPt_3 (Tou *et al.* 1996). Further candidates for this variant are URu_2Si_2 and UNi_2Al_3. An important question concerns the superconducting pairing mechanism. In contrast to the classical, phonon-mediated superconductors, in HFS the Cooper-pair formation may be, at least partly, mediated by electronic exchange mechanisms. So far, however, neither the unconventional superconducting order parameter nor the specific pairing processes have been established beyond doubt.

The main difficulty in determining the basic physical principles of HFS is the multitude of physical

phenomena observed in this class of compounds, in particular with respect to the interdependence, competition, and coexistence of superconductivity with other ground states. In the cerium-based systems, superconductivity is observed close to the magnetic instability, implying an intimate connection of HFS to the suppression of magnetic ordering. In contrast, in UPt_3, URu_2Si_2, UPd_2Al_3, and UNi_2Al_3, magnetism and superconductivity coexist on a microscopic scale. Yet, in these uranium systems the magnetically ordered ground states are vastly different. In UPt_3 a spin-density-wave (SDW) state of ultralow moments ($\mu_{ord} = 0.02\,\mu_B$) forms. Apparently similar to UPt_3, an ultralow-moment SDW state exists in URu_2Si_2. However, here magnetism probably does not constitute the primary order parameter; instead, quadrupolar ordering mechanisms are considered. UPd_2Al_3 and UNi_2Al_3 both exhibit a more common type of antiferromagnetic order, but the ordered moment in the palladium system ($\mu_{ord} = 0.85\,\mu_B$) is huge compared to the nickel compound ($\mu_{ord} = 0.24\,\mu_B$) and to all other HFS. Again in variance, no long-range magnetic order is observed in pure UBe_{13}, but alloying the system with a few percent thorium triggers ultralow-moment magnetism and leads to a complicated superconducting phase diagram.

Possibly the most remarkable anomaly of HFS is the multiple superconducting B–T phase diagram of UPt_3 shown in Fig. 2. This phase diagram constitutes the strongest evidence for the unconventional superconductivity in HFS. Theoretical proposals to explain the multiple phase diagram started from the assumption of two different anisotropic superconducting states A and C, each with lower symmetry than the crystalline lattice and energetically almost degenerate. The corresponding phase boundaries cross at a tetracritical point. The phase B below
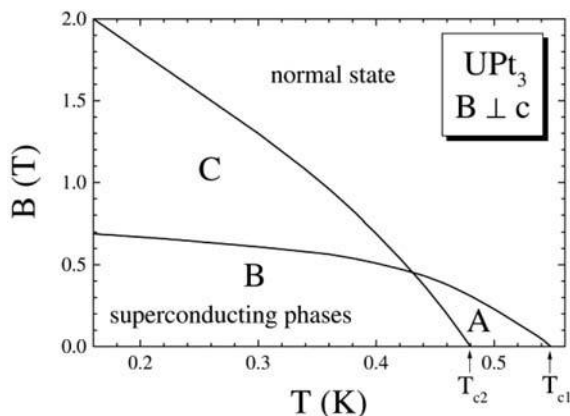
Figure 2
Schematic B–T phase diagram of the three superconducting phases of UPt_3.

T_{c2}, as a combined state of the phases A and C, shows magnetic signatures that have been attributed to the nonunitary property of this state (Tou *et al.* 1998). However, a conclusive experimental verification of unconventional superconducting order parameters in UPt_3 or other HFS is still lacking. An even greater challenge remaining is the determination of the superconducting pairing mechanisms. While there is an abundance of theoretical studies on electronic pairing, only a few experiments have yet been presented in support of such pairing mechanisms in HFS. The nonuniversality of the superconducting phenomena has led to the proposal that more than one coupling mechanism may have to be considered for all HFS.

Aside from the superconducting properties of HF metals, their magnetic behavior is also remarkable (Amato 1997). Most important, low- and ultralow-moment magnetism is observed, i.e., the transition into antiferromagnetically ordered states with staggered magnetic moments as low as $0.001\,\mu_B$. To some extent, this behavior can be understood by proximity of the magnetic instability in HF materials. On approaching the instability within the magnetically ordered phase, the *f* moment is increasingly screened by the Kondo effect, which thus can attain any arbitrary small value.

This mechanism for low-moment magnetism relates the size of the moment to the magnetic transition temperature, which both decrease in a corresponding way. For a number of HF systems, however, such a link does not exist; here additional effects come into play. First, a magnetic order sometimes realized in a SDW indicates that nesting of the renormalized Fermi surface plays a role. Second, in a few HF materials the magnetic ordering appears to be only a secondary, "spurious" effect, which masks the underlying order/disorder transition of the "true" order parameter, frequently being of quadrupolar nature. Finally, for some of the "ultralow-moment" systems, i.e., those with an ordered moment of $\sim 0.01\,\mu_B$, the distinction between "long-range magnetic ordered" and "slowly fluctuating" apparently gradually disappears. For all these materials the magnetic behavior remains very much a mystery to date.

3. Kondo Insulators

These materials are HF or intermediate valence (IV) compounds with a small gap in their quasiparticle density of states (Aeppli and Fisk 1992, Degiorgi 1999). Accordingly, at temperatures $T \gg \Delta$ (Δ = width of the energy gap; typically $\cong 10$–$100\,K$) the magnetic properties of Kondo insulators are those of paramagnetic HF metals, with a Curie–Weiss local *f*-moment susceptibility. But, as T decreases, thermal depopulation controls the T dependence of the susceptibility. Hence, χ goes through a maximum at

$T \approx \Delta$ and saturates at a value χ_0, which is much smaller than in HF metals. Similarly, the transport properties at $T \gg \Delta$ resemble a dirty HF metal, but as T is lowered below Δ, semiconducting behavior develops. The effective carrier mass in the semiconducting state is as large as in HF or IV metals, reflecting a strongly enhanced density of states at the gap edges. And while the electronic specific heat coefficient is small ($\sim 1\,\mathrm{mJK^{-2}\,mole^{-1}}$), upon closing the gap of a Kondo insulator due to doping, semiconductivity is wiped out, and a large γ value ($> 100\,\mathrm{mJK^{-2}\,mole^{-1}}$) is observed in the specific heat. In summary, Kondo insulators are nonmagnetic, mass-enhanced semiconductors at $T \ll \Delta$, while at $T \gg \Delta$ they are reminiscent of HF/IV metals.

The essential properties of Kondo insulators are captured in a simple model of a flat f-band hybridizing with a single broad conduction band, generating the gap Δ. The total number of valence electrons is even, including f electrons in the count. At $T = 0$ the electrons fill the lower hybridized band. Then, for fields H smaller than the energy gap Δ the susceptibility is zero due to the equal number of spin up and spin down electrons. As T increases, χ increases because of a thermally activated Pauli-like susceptibility, until at $T \gg \Delta$ Curie–Weiss paramagnetism develops. Similarly, the transport properties show a transition from semiconducting to metallic behavior as function of temperature. This model represents the realization of an Anderson lattice Hamiltonian, with two electronic states per f site applied to a system containing one f- and one conduction band, and the f onsite Coulomb repulsion U.

This simple picture qualitatively accounts for the fundamental properties of Kondo insulators, but it fails to fully explain the Kondo insulating state. For instance, it has not conclusively been resolved whether the opening of a gap in Kondo insulators is entirely a band structure effect. Surely, electronic correlations do play an important role. Further, four phenomena, which appear to be characteristic features of Kondo insulators, elude simple models: (i) In Kondo insulators the band structure is renormalized in a fashion similar to HF metals. It causes the piling up of states at the gap edges, and thus the mass enhancement. To understand this behavior, electronic interactions have to be taken into account. (ii) The energy gap is renormalized in temperature, i.e., its signatures already disappear well below $T = \Delta/k_B$. (iii) In contrast to magnetic semiconductors or HF metals, in which magnetic interactions play a fundamental role and eventually cause the formation of magnetically ordered ground states, for Kondo insulators the intersite magnetic interaction J vanishes in the limit $\omega \to 0$. Thus, in spite of a dense array of magnetic ions in Kondo insulators the net magnetic exchange is zero. (iv) There are a number of problems related to the gap structure of Kondo insulators. Most important, it is not clear whether a gap or a pseudogap intrinsically opens up in the density of states.

See also: Non-Fermi Liquid Behavior: Quantum Phase Transitions; Electron Systems: Strong Correlations; Intermediate Valence Systems

Bibliography

Aeppli G, Fisk Z 1992 Kondo insulators. *Comments Condens. Matter Phys.* **16**, 155–70

Amato A 1997 Heavy-fermion systems studied by μSR technique. *Rev. Mod. Phys.* **69**, 1119–79

Degiorgi L 1999 The electrodynamic response of heavy-electron compounds. *Rev. Mod. Phys.* **71**, 687–734

Grewe N, Steglich F 1991 Heavy fermions. In: Gschneidner K A, Eyring L (eds.) *Handbook on the Physics and Chemistry of the Rare Earths.* Elsevier, Amsterdam, Vol. 14, pp. 343–474

Heffner R H, Norman M R 1996 Heavy fermion superconductivity. *Comments Condens. Matter Phys.* **17**, 361–408

Stewart G R 1984 Heavy-fermion systems. *Rev. Mod. Phys.* **58**, 755–87

Süllow S, Aronson M C, Rainford B D, Haen P 1999 Doniach phase diagram, revisited: from ferromagnet to fermi liquid in pressurized $CeRu_2Ge_2$. *Phys. Rev. Lett.* **82**, 2963–6

Tou H, Kitaoka Y, Asayama K, Kimura N, Onuki Y, Yamamoto E, Maezawa K 1996 Odd-parity superconductivity with parallel spin pairing in UPt_3: evidence from [195]Pt Knight shift study. *Phys. Rev. Lett.* **77**, 1374–7

Tou H, Kitaoka Y, Ishida K, Asayama K, Kimura N, Onuki Y, Yamamoto E, Haga Y, Maezawa K 1998 Nonunitary spin-triplet superconductivity in UPt_3: evidence from [195]Pt Knight shift study. *Phys. Rev. Lett.* **80**, 3129–32

Zwicknagl G 1992 Quasi-particles in heavy fermion systems. *Adv. Phys.* **41**, 203–302

F. Steglich
Max-Planck-Institut für Chemische Physik fester Stoffe, Dresden, Germany

S. Süllow
Technische Universität Braunschweig, Germany

High-resolution Fourier Transform Spectroscopy: Application to Magnetic Insulators

Optical spectroscopy is used widely for studying magnetic insulators. Various aspects of these studies have been reviewed by Hüfner (1982), Eremenko *et al.* (1986), and Cone and Meltzer (1987). Typically, the spectral resolution of grating spectrometers used for these studies is 0.5–$1\,\mathrm{cm^{-1}}$ in the visible range of the spectrum. For magnetic compounds containing rare earths (REs) the inhomogeneous width of some

spectral lines is less than $0.1\,\mathrm{cm}^{-1}$ (Popova 1998). The most intense optical transitions allowed for a free ion lie in the infrared and occupy broad spectral regions for the majority of RE^{3+} ions. It is advantageous to register such spectra by a Fourier transform spectrometer (FTS) rather than by a classical one.

Substantial gain in sensitivity of a FTS compared with grating spectrometers permits the study of weak spectra of RE ions introduced in a small amount as a probe into a magnetic material, even if the latter is available in a polycrystalline form only. Far-infrared (FIR) study of magnetic compounds that undergo a magnetoelastic phase transition is another field where FTS can be successfully applied. High-resolution Fourier transform spectroscopy offers new possibilities for studying magnetic phase transitions, short-range order, and magnetic structures in magnetic insulators.

1. Fourier Transform Spectroscopy

The principal parts of a FTS are the Michelson interferometer with a moving mirror (see Fig. 1) and a computer that performs the Fourier transform of the interferogram and thus calculates the spectrum of an incident radiation $E(t)$. A detector registers the averaged intensity at the output of the Michelson interferometer

$$\Phi(t) \sim \overline{[E(t) + E(t + \tau)]^2}$$
$$= \overline{E^2(t)} + \overline{E^2(t + \tau)} + 2\overline{E(t)E(t + \tau)} \qquad (1)$$

Here $\tau = l/c$ is the time delay between the two interfering beams, l being the path difference. Under certain conditions, that usually are fulfilled, the first two terms

in Eqn. (1) are equal to the time-independent mean intensity while the third term represents the auto-correlation function

$$\psi(\tau) = \overline{E(t) \cdot E(t + \tau)} \qquad (2)$$

which depends on the time delay τ. The Fourier transformation of $\psi(\tau)$ yields the spectrum, namely,

$$B(\omega) = \frac{2}{\pi} \int_0^\infty \psi(\tau)\cos\omega\tau\,\mathrm{d}\tau \qquad (3)$$

A real instrument delivers $\psi(\tau)$ for the interval [0, L/c], where L is the maximum path difference which depends on the maximum displacement of the moving mirror of the FTS.

The L-dependent instrumental function, that is the response of an instrument to a monochromatic incident light $E(t) = \cos\omega_0 t$, can be written as

$$f_L = \frac{1}{\pi}\frac{\sin(\omega - \omega_0)L/c}{(\omega - \omega_0)} \qquad (4)$$

$f_L \to_{L \to \infty} \delta(\omega - \omega_0)$, where $\delta(\omega - \omega_0)$ is the delta-function; for a finite L, f_L exhibits secondary maxima, and the distance between the first zeros of f_L, $\delta\omega = 2\pi c/L$, or, in wavenumbers ($\sigma = 1/\lambda = \omega/2\pi c$), $\delta\sigma = 1/L$, characterizes the spectral resolution. In high-resolution instruments L may reach several meters which corresponds to the better than $0.01\,\mathrm{cm}^{-1}$ resolution.

The free spectral range $\Delta\sigma$ for the FTS depends on a number N of points registered in the interferogram:

$$\Delta\sigma = N\delta\sigma \qquad (5)$$

Typically, $N \sim 10^6$, and so even for high-resolution ($\delta\sigma \sim 10^{-3}\,\mathrm{cm}^{-1}$) instruments $\Delta\sigma \sim 10^3\,\mathrm{cm}^{-1}$, and thus broadband high-resolution spectroscopy is possible with FTS.

FTS analyzes all the spectral elements simultaneously which results in the so-called Fellgett or multiplex advantage of FTS over conventional instruments in signal-to-noise ratio. For the intensity-independent noise of a detector (infrared spectral region) the Fellgett advantage is maximum, namely, $\sqrt{M}$, where $M = \Delta\sigma/\delta\sigma$ is the number of registered spectral elements. Additional gain comes from the large throughput of a FTS in comparison with a slit spectrometer (Jacquinot advantage). In Fourier transform spectroscopy, the wave number scale is established relative to the frequency of a stabilized laser used for the measurement of the path difference and, as a result, is precise in the whole spectral region (Connes advantage). General advantages of the FTS over conventional instruments make them a useful tool for material research.
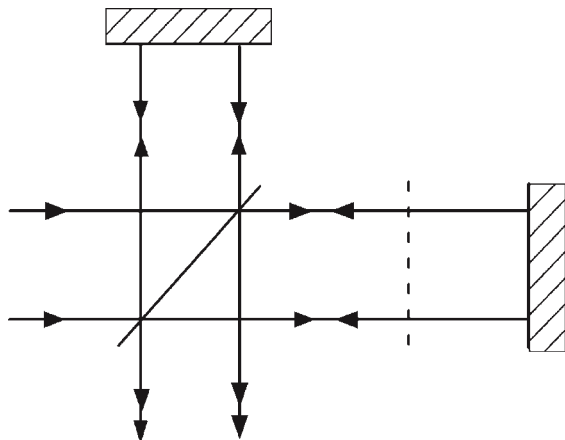
Figure 1
Scheme of the Michelson interferometer.

2. Rare Earth Spectroscopic Probe in a Magnetic Compound

A crystal field of any symmetry lower than cubic raises all but the Kramers degeneracy of the levels of a free RE^{3+} ion with an odd number of electrons. Kramers doublets are further split by the magnetic interactions in a magnetically ordered state. These splittings are usually called exchange splittings. If the crystal unit cell contains n equivalent RE ions, additional so-called Davydov or factor-group splittings of the excited levels into n components occur, due to the interactions between these ions. Usually, Davydov splittings in the RE spectra are small ($\sim 0.1\,cm^{-1}$) and not observable and a single-ion crystal field model shown schematically in Fig. 2 is suitable even for concentrated materials. Each spectral line of a paramagnetic compound splits into a maximum of four components in a magnetically ordered state. Using the fact that the population of the upper component of the split ground Kramers doublet diminishes with decreasing temperature, it is possible to assign all the components of a split spectral line and to find the ground and excited state splittings from optical measurements. Figure 3 gives an example of the spectra of a Kramers ion in a magnetic compound and of the spectral line identification. It shows the absorption of $Er_2Cu_2O_5$ at different temperatures, both higher and lower than the Néel temperature $T_N = 28\,K$. A single-ion crystal field model is true for this concentrated material.

For magnetic compounds containing both RE and transition metal (TM) ions, the main contribution to the splitting comes from the electronic exchange interaction between the RE ion and neighboring TM

Figure 3

Absorption in the region of the $^4I_{15/2} \rightarrow {}^4I_{13/2}$ optical transition in $Er_2Cu_2O_5$ at $88\,K > T_N$ (lower trace) and $6.2\,K < T_N$ (upper trace). Identification is given according to the scheme of Fig. 2. Inset shows the temperature dependence of the line IB. The following values of the level splittings (in cm^{-1}) have been found from the spectra: $\Delta = 20.6$ (19.7); $\Delta_A = 3.3$ (5.7); $\Delta_B = 9.0$ (7.2). Values and notations in parentheses refer to the second crystallographic position for Er^{3+} in $Er_2Cu_2O_5$ (after Popova 1998).

Figure 2
Levels of a Kramers ion in a magnetically ordered crystal.

ions. Usually, the electron clouds of intervening anions are involved, so the superexchange interaction is to be considered. In purely RE compounds, the magnetic dipole–dipole interaction makes comparable or even major contributions to magnetic splittings.

The magnetic dipole–dipole contributions to the splittings of the Kramers levels of a particular RE ion may be described by an action of an effective magnetic field $\mathbf{H}_{dip}$ created by all the magnetic ions of the lattice at the RE site and can be calculated accurately. As for the exchange interaction, a concept of an effective field fails to describe the splittings in this case. The effective exchange potential can be written as an expansion in products of spherical tensor operators for electrons at the two sites, with coefficients that are linear combinations of the two-electron exchange integrals. Only a small number of symmetry-dependent coefficients is required. These may be regarded as empirical parameters and may be found from a set of level splittings measured by optical spectroscopy, which is analogous to the case of crystal field parameters describing the single-ion energy levels of

RE ions in crystals. A review of the two-electron spherical operator method for the description of the interionic exchange interaction and of applications of the method to different RE magnetic compounds has been given by Cone and Meltzer (1987). They have shown in particular that (i) there is a unique set of parameters describing the splittings of both ground and a wide range of excited states; (ii) these parameters vary systematically through the RE series; and (iii) the contributions of anisotropic terms to the splittings are comparable or, in some cases, even appreciably larger than the contribution of the isotopic term.

2.1 Spectral Detection of Magnetic Phase Transitions

High spectral resolution and absolute wavenumber precision in Fourier transform spectroscopy make it possible to measure small line splittings $\Delta \nu$ and also to register the width $\delta \nu$ and shape of spectral lines. The temperature of a magnetic ordering T_c can be determined as the abscissa of the point of inflection in the experimentally measured $\Delta \nu(T)$ dependence (see, e.g., Popova 1996, 1998). As an example, Fig. 4 shows the $\Delta \nu(T)$ dependence for the absorption line IB of Fig. 3. The tail of line splittings at $T > T_c$ is due to the short-range order. Additional evidence of the ordering comes from the spectral line narrowing in the vicinity of T_c (Fig. 4).

In many of the magnetic compounds containing both RE and TM ions (*f–d* compounds) anisotropic interactions lead to spin-reorientation transitions at lower temperatures $T_R < T_c$. Figure 5 illustrates the use of the high-resolution FTS to detect a spin-reorientation transition. It shows the Er^{3+} probe spectrum in Yb_2BaCuO_5 which orders magnetically

Figure 5
Two lines in the $^4I_{15/2} \rightarrow {}^4I_{13/2}$ optical transition of Er^{3+} probe in Yb_2BaCuO_5 at different temperatures. Yb_2BaCuO_5 orders antiferromagnetically at $T_N = 16.5$ K and undergoes a spin-reorientation transition at $T_R = 4.0$ K.

at $T_c = 16.5 \pm 0.5$ K. In the temperature interval 5.5–3.5 K, the spectrum is a superposition of two different spectra with temperature-dependent relative intensities corresponding to two different magnetic phases which is typical for first-order spin-reorientation phase transition.

2.2 Magnetic Structure of the d Subsystem

The level splittings of the RE ion in a magnetically ordered state of a crystal containing both RE (*f*) and TM (*d*) ions are due mainly to RE–TM exchange interactions which are, as a rule, highly anisotropic. Because of this, the spectra of a rare earth probe are extremely sensitive to the alignment of the magnetic moments of the TM ions in the nearest surroundings of the RE ion. On these grounds, it is possible to make a choice between several magnetic structures that fit neutron scattering data equally well (see, e.g., Popova 1996, 1998).

Figure 4
The temperature dependence of the splitting $\Delta \nu$ (squares) of the line IB (see Fig. 3) and of the half-width $\delta \nu$ of the component 1a (circles). The temperature $T_c = 28 \pm 0.5$ K follows from the point of inflection in the $\Delta \nu(T)$ dependence.

2.3 Low-dimensional Magnetic Correlations

For $T > T_c$, the splittings of spectral lines do not vanish—a tail of residual splittings is observed due to short-range magnetic order. This tail is longer the lower the dimensionality of a system. On these

grounds, magnetic Cu–O planes have been investigated in a series of isostructural $R_2Cu_2O_5$ compounds and magnetic chains have been found in Nd_2BaCuO_5 (see, e.g., Popova 1996).

3. Far Infrared Spectroscopy: Detection of Magnetoelastic Transitions

The interaction between magnetic moments and lattice phonons may result in a magnetoelastic phase transition. One of the most fascinating examples is the spin–Peierls transition that occurs in the system of linear spin $-\frac{1}{2}$ Heisenberg antiferromagnetic chains coupled to a three-dimensional phonon field. As a result of such a coupling, magnetic atoms of the chain dimerize and a spin gap opens.

Figure 6 illustrates the use of a high-resolution FTS to study the transition of such a type. It shows FIR spectra of α'-NaV_2O_5 below and above the

Figure 6
FIR transmission of α'-NaV_2O_5 ($T_c = 35\,K$) at $37\,K > T_c$ (dotted line) and $6\,K < T_c$ (solid line). Folded phonon modes are shown by arrows ($E \| b$ polarization). Fano-type resonance ($E \| a$ polarization) is due to the interference of a phonon mode with a continuum. Below T_c, the long-wavelength part of the continuum disappears and the phonon at $90\,cm^{-1}$ demonstrates a Lorentzian lineshape (after Popova *et al.* 1997).

spin–Peierls-like transition ($T_c = 35\,K$). Folded phonon modes of a dimerized lattice as well as a gap opening that leads to a drastic change of a phonon lineshape at the frequency of about $90\,cm^{-1}$ are clearly seen below T_c.

See also: Crystal Field and Magnetic Properties, Relationship between; Localized 4*f* and 5*f* Moments: Magnetism

Bibliography

Bell R J 1972 *Introductory Fourier Transform Spectroscopy*. Academic Press, New York
Cone R L, Meltzer R S 1987 Ion–ion interactions and exciton effects in rare earth insulators. In: Kaplyanskii A A, Macfarlane R M (eds.) *Spectroscopy of Solids Containing Rare Earth Ions*. North-Holland, Amsterdam, Chap. 8
Eremenko V V, Litvinenko Yu G, Matyushkin E V 1986 Optical magnetic excitations. *Phys. Rep.* **132**, 55–128
Hüfner S 1982 Optical spectroscopy of lanthanides in crystal matrix. In: Sinha S P (ed.) *Systematics and the Properties of the Lanthanides*. Reidel, Dordrecht, The Netherlands, Chap. 8
Popova M N 1996 Rare earth spectroscopic probe in physics of magnetics. In: Ryskin A I, Masterov V F (eds.) *10th Feofilov Symp. Spectroscopy of Crystals Activated by Rare-Earth and Transitional-Metal Ions*. Proc. SPIE 2706. SPIE, Bellingham, WA, pp. 182–92
Popova M N 1998 High-resolution spectroscopy of rare earth cuprates and nickelates. *J. Alloys Compounds* **277**, 142–7
Popova M N, Sushkov A B, Vasil'ev A N, Isobe M, Ueda Yu 1997 Appearance of new lines and change in line shape in the IR spectrum of a NaV_2O_5 single crystal at a spin–Peierls transition. *JETP Lett.* **65**, 743–8

M. N. Popova
Russian Academy of Sciences, Moscow, Russia

High-T_c Superconductors: Electronic Structure

An understanding of the electronic structure of the high-T_c cuprate superconductors must start out from an analysis of their chemical composition, valencies, structure, and binding. All cuprate high-T_c superconductors are stacks of alternating anionic CuO_2 layers and block layers which are in gross cationic. The stacking direction is commonly taken as the crystallographic *c*-direction, and the crystal symmetry is generally derived from a simple tetragonal or a body-centered tetragonal (b.c.t.) symmetry, although it is in fact often orthorhombic due to distortions or due to vacancy ordering.

The general composition of the cuprate superconductors is

$$B^{b+}[(CuO_2)^{(2-\delta)-}]_n C_{n-1}^{c+} \qquad (1)$$

where $n = 1, 2, 3, \ldots, c = 2$ or 3, and $b = c + n(2 - \delta - c)$. The block layer B is a cationic metal oxide layer. It is followed by either a single $(CuO_2)^{(2-\delta)-}$ layer or a stack consisting of n such layers with cations C sandwiched in between. So far, the cations C are Ca^{2+}, or RE^{3+} where $RE = Y$, La or any of the lanthanides (see *Superconducting Thin Films: Materials, Preparation, and Properties*).

The main families of cuprate superconductors derive from

(i) $La_{2-x}Sr_xCuO_{4-y}$ which in the systematics of (1) would be $(La_{2-x}Sr_xO_{2-y})^{(2-\delta)+}$ $(CuO_2)^{(2-\delta)-}$ with $n = 1$ and $\delta \approx x$ for $y \approx 0$; related is $M_2CuO_2X_2$ or $(M_2X_2)^{(2-\delta)+}(CuO_2)^{(2-\delta)-}$ with $M = (Ca_{1-x}Na_x)$ or Sr and $X = F$, Cl, or Br;

(ii) $RE_1Ba_2Cu_3O_{6+x}$ which would be $(Ba_2^{2+}(CuO_{2+x})^{(3+2\delta)-})[(CuO_2)^{(2-\delta)-}]_2RE^{3+}$ with $n = 2$ and $\delta = 0$ for $x < 0.3$ and then increasing to $\delta \approx 0.2$ for $x \approx 1$; and

(iii) $B^{(2-n\delta)+}[(CuO_2)^{(2-\delta)-}]_nCa_{n-1}^{2+}$, $n = 1, 2, 3, \ldots$ with $B = (Bi, Pb)_2Sr_2O_{4+x}$ or $TlBa_2O_{2.5+x}$ or $Tl_2Ba_2O_{4+x}$ or $HgBa_2O_{2+x}$, and δ increases with increasing x; Tl may be replaced by B and Hg by Cu or Au; Ca may be replaced by Y, Dy, Er.

The oxygen in the metal oxide block layers B is more or less volatile. Above, it is written in such a way that in all cases the doping level of the cuprate planes is $\delta = 0$ for $x = 0$ or some value of x close to zero. The magnetic properties of these undoped or weakly doped cuprates is a very topical problem of its own because they are more or less ideal model systems of low-dimensional Heisenberg magnets (see Johnston 1997). This is not particularly considered here in this article. Among them are also cuprate structures which are different from the CuO_2 planar structure (chain and ladder structures), some of which become superconductors when doped. They are also not considered here (cf. Müller-Buschbaum (1977) for a structure chemical systematics of all cuprates).

The cation C is always fully ionized; its valence orbitals are unoccupied. The metal oxide block layer B is, depending on composition and on x, either insulating or metallic. The essential conducting component which also carries superconductivity is the $(CuO_2)^{(2-\delta)-}$ layer which is doped by charge transfer to the block layer. The doping level δ may be positive (hole doping) or negative (electron doping). Electron doping is less frequent and is found, in particular, in the family (i) with $B = (Nd_{2-x}Ce_xO_{2-y})$ or $B = (Pr_{2-x}Ce_xO_{2-y})$ instead of $B = (La_{2-x}Sr_xO_{2-y})$. The tetravalent Ce donates one electron.

In traditional metal physics, the electronic structure is characterized by a quasiparticle band structure

where at low temperature, $T \rightarrow 0$, the quasiparticles have a sharp energy–momentum dispersion relation close to the chemical potential (Fermi level ε_F). These also develop a decay rate proportional to the square of their excitation energy, $|\varepsilon - \varepsilon_F|$, due to energy and momentum scattering. This behavior is meant if one speaks of a Fermi liquid (FL) with an arbitrary dispersion relation. The quasiparticle momenta at the Fermi level constitute the Fermi surface (FS) which is measured through quantum oscillations in the magnetic susceptibility (de Haas–van Alphen effect) or in magnetotransport. Experimental evidence on the quasiparticle dispersion relation close to the Fermi level is obtained both from thermal equilibrium properties such as specific heat or magnetic susceptibility and from transport properties. However, the high-energy electronic excitation spectrum (on an eV scale) is obtained mainly from electron removal by photoemission (hole excitations) and from electron injection by inverse photoemission, as well as from electron excitation by electron-energy-loss spectroscopy (EELS) or by x-ray absorption (XAS).

This picture remains even valid for strongly correlated metals like heavy fermion (*f*-electron) systems; only the energy–momentum dispersion relation is scaled down by up to 2 orders of magnitude. There are many experimental indications that this picture breaks down in a certain region of the phase diagram of the superconducting cuprates: while the thermal equilibrium properties are still reminiscent of a (weakly renormalized) metal, the energy dependence of the quasiparticle scattering rate seems to have a singular behavior and the quasiparticle spectral weight seems to fade away.

A generic doping level–temperature phase diagram of the layered cuprates is shown in Fig. 1. More or less understood are the undoped antiferromagnet (AF) phase ($\delta \approx 0$) as a charge transfer insulator and the FL phase ($|\delta| > 0.2$) as a normal metal. A recommended early review of the mean-field quasiparticle band structures, where the mean field is taken to be the Kohn-Sham potential of density functional theory, is that of Pickett (1989).

1. The Undoped Cuprate

For $\delta = 0$, the valence electron number per unit cell of the $(CuO_2)^{2-}$ complex is $11 + 2 \times 4 + 2 = 21$ and hence odd. The mean field band structure for an odd valence electron number per unit cell proposes a metallic state with a half-filled band at least above a possible spin magnetic order temperature. Experimentally, the undoped cuprates are insulators with a gap of ~ 1–2 eV. Below the Néel temperature T_N which, dependent on the block layer, is between 250 K and 540 K, they order antiferromagnetically with an ordered spin moment $\langle \mu \rangle (T \rightarrow 0)$ between $0.25\mu_{Bohr}$ and $0.64\mu_{Bohr}$ at the Cu site. Order is due to
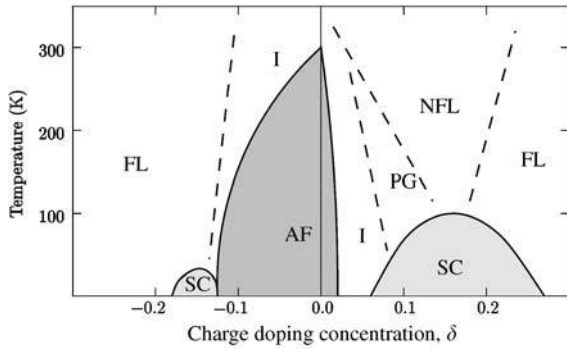
Figure 1
Temperature vs. doping phase diagram of electron- and hole-doped planar cuprates. Full lines are phase boundaries. Dashed lines indicate crossovers. AF: antiferromagnet, SC: superconductor, I: insulator, FL: Fermi liquid, NFL: non-Fermi liquid (maybe marginal Fermi liquid), PG: pseudo-gap phase. The left half is less explored than the right half. The maximum Néel temperature into the AF phase depends on the block layer (not generic). The temperature axis scales down with increasing disorder or dimpling of the cuprate plane. A static stripe phase with alternating high-doped metallic and low-doped AF stripes is sometimes found in the PG region. It is not known whether dynamic (fluctuating) stripes are generic in the PG region (cf. Dagotto 1994, Varma 1997, Tohyama and Maekawa 2000, Damascelli *et al.* 2003).

magnetic interlayer coupling. A two-dimensional square lattice spin $\frac{1}{2}$ Heisenberg AF would have a Néel ground state with an ordered moment of $0.307g\mu_{\rm Bohr}$ where $g \approx 2$ is the Landé factor, but would not order at $T > 0$; it would only develop local AF correlations.

1.1 CaCuO$_2$ As an $n = \infty$ Model Cuprate

The simplest planar cuprate structure is that of CaCuO$_2$ (Fig. 2). It is an infinite stack of CuO$_2$ layers and Ca layers sandwiched in between. Hence, in the systematics of Eqn. (1) one has $n = \infty$ and B is absent. In reality, Ca$_{0.85}$Sr$_{0.15}$CuO$_2$ has been synthesized which is an AF insulator with the highest Néel temperature, $T_{\rm N} \approx 540$ K, of all cuprates and which hardly can be doped. However, the isostructural electron-doped compound Sr$_{1-x}$Nd$_x$CuO$_2$, $x \leqslant 0.16$, was reported to be superconducting with $T_{\rm c}$ up to 40 K.

It is useful to start with the band structure of CaCuO$_2$ in the local spin density approximation (LSDA) and the LSDA + U approximation of density functional theory. The latter accounts in a crude manner for local electron correlations on the copper site by suppressing the $3d^{10}$-configuration in favor of
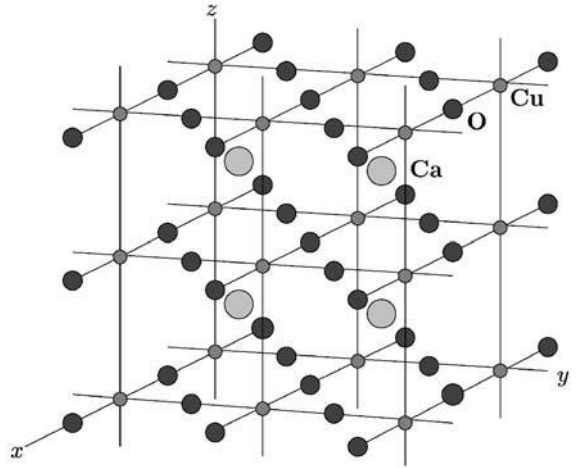
the $3d^9$-configuration. The self-consistent solution of the LSDA converges towards a nonmagnetic ground state. LSDA + U yields a stable AF solution. For the sake of better comparison both the LSDA and LSDA + U results are presented in the AF Brillouin zone (BZ). Within the CuO$_2$ plane the AF order is checkerboard like. In z-direction the simplest structure of a ferromagnetic stacking of equal moments on top of each other is used in order to have the simplest unit cell and BZ geometry (both upright square bricks). Anyhow the magnetic coupling in z-direction is small. (In reality the AF structure has opposite moments stacked on top of each other in z-direction leading to a b.c.t. unit cell instead of a simple tetragonal one; due to the weak coupling in z-direction this does not affect any of the following considerations.) Unit cell and BZ are shown in Fig. 3 together with labels of symmetry points in the BZ.

The LSDA band structure is shown in Fig. 4. In order to visualize the AF downfolding, the self-consistency was stopped shortly before the moment vanishes so that the potential AF splittings of bands are seen on the lines X–M and R–A. The FS of the metallic state intersects the symmetry lines Γ–X and X–M. Its back-folded image in the AF BZ also intersects Γ–M (band above the AF splitting; the FS is sketched in the upper right quadrant of Fig. 3).

The relevant orbitals which form the bands crossing the Fermi level are shown in Fig. 5. Besides the shown oxygen orbital combinations, there are nonbonding combinations of E_u point symmetry for both $2p_\sigma$ and in-plane $2p_\pi$ orbitals, twofold degenerate for $(k_x, k_y) = (0, 0)$, and an A_{1g} nonbonding combination of $2p_\sigma$ orbitals as well as a B_{2g} O–O bonding combination of in-plane $2p_\pi$ orbitals, all of which do not contribute to the bands crossing the Fermi level. Figure 6 shows the same bands as in Fig. 4, weighted

Figure 2
Crystal structure of CaCuO$_2$.
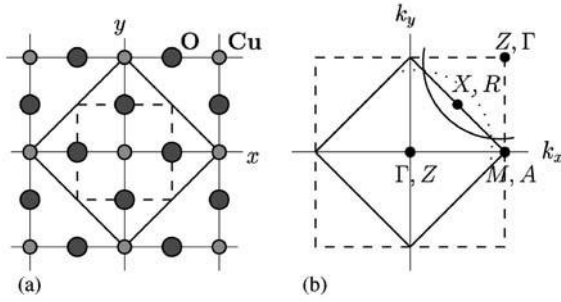
Figure 3
The planar CuO$_2$ structure. Nonmagnetic (dashed line) and antiferromagnetic (full line) unit cell (a) and BZ (b). In the AF unit cell the copper spin in the center of the cell is "up" and in the corners "down." The labeling of symmetry points in (b) is for the antiferromagnetic zone; the first label is for $k_z = 0$ and the second for $k_x = \pi$, X: $(k_x, k_y) = (\pi/2, \pi/2)$, M: $(k_x, k_y) = (\pi, 0)$ (in units of $1/c$ and $1/a$). The solid curve in the right upper quadrant sketches the mean-field FS of the nonmagnetic state which consists of rods around the lines $(\pm\pi, \pm\pi, k_z)$. The dotted curve sketches its back folded image in the magnetic BZ.
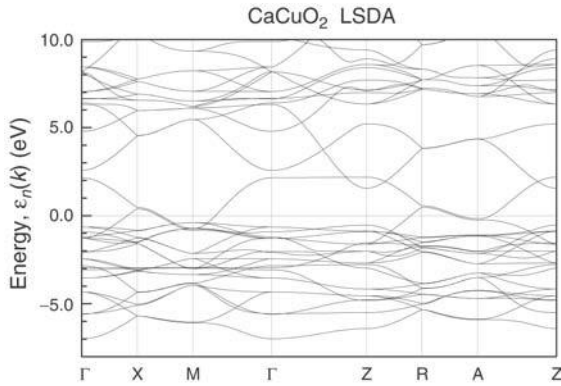
Figure 4
LSDA band structure of CaCuO$_2$. The Fermi level is put to zero. See Fig. 3 for the labels of symmetry **k**-points.

Figure 5
The relevant orbital combinations at $(k_x, k_y) = (\pi, \pi)$ of the nonmagnetic BZ which is equivalent to $(k_x, k_y) = (0, 0)$ of the antiferromagnetic zone (cf. Fig. 3). Oxygen 2p-orbitals having their lobes in the direction of the Cu–O bond are called 2p_σ-orbitals (($m = 0$)-orbitals with respect to the bond direction as quantization axis), and those having their lobes perpendicular to the bond direction are called 2p_π-orbitals (($|m| = 1$)-orbitals). Antibonding means a wave function node (sign change) intersecting the bond, and bonding means no such node. (a) Full line: the antibonding Cu-3$d_{x^2-y^2}$–O-2p_σ orbital combination of B_{1g} symmetry of the point group D_{4h}; dotted: the Cu-4s orbital of A_{1g} symmetry. (b) The O–O antibonding 2p_π-orbital combination of A_{2g} symmetry.

by linewidth with the sums over the AF unit cell of the squares of the expansion coefficients of the Bloch state for in turn Cu-3$d_{x^2-y^2}$, O-2p_σ, in-plane O-2p_π, O-2p_z (that is out-of-plane O-2p_π) and Cu-4s orbitals. In the upper two panels, one recognizes a strong Cu–O covalent splitting of more than 5 eV between the lower bonding and the higher antibonding bands. A weaker peroxidic O–O covalent splitting of the in-plane O-2p_π derived bands of ~ 3 eV is seen in the third panel, and a still weaker splitting of the O-2p_z derived bands is found in the fourth panel. As is

clearly seen, the first two of the above listed orbitals mainly contribute to the bands crossing the Fermi level and only the third and last one contribute in addition. The Ca orbitals and the other Cu orbitals not shown in Fig. 6 do not contribute; the Ca orbitals only contribute well above the Fermi level (hence Ca is fully ionized) as do the Cu-4p orbitals, and the other Cu-3d orbitals only contribute well below the Fermi level. (See also Andersen *et al.* (1995) for similar results for the Y–Ba–Cu–O system; in this case there is an additional metallic CuO$_3$ block layer with additional bands crossing the Fermi level.)

It was already mentioned that due to strong electron correlations on the Cu site the LSDA band structure does not well describe the reality in which CaCuO$_2$ is an insulator. A much better description of the undoped cuprates is given by the so-called rotationally invariant LSDA + U approach for which the resulting band structure is shown in Fig. 7. (The details of the calculations of the bands shown in Figs. 4–8 are given by Eschrig *et al.* 2003.) In this approach, self-consistency yields a stable AF solution with a spin moment $|\langle\mu\rangle|0.71\mu_{\text{Bohr}}$.

Figure 8 shows the same orbital analysis for the LSDA + U bands as in Fig. 6 for the LSDA bands. In the first panel, the lower and upper Hubbard bands of Cu-3$d_{x^2-y^2}$ orbitals and their hybridization with oxygen orbitals in between are clearly seen. The
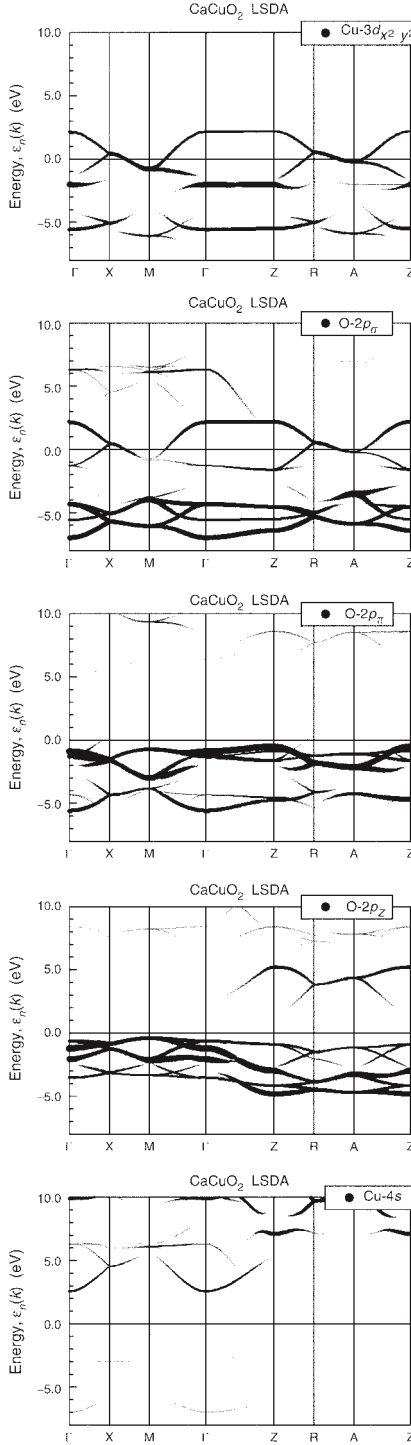
Figure 6
Orbital weighted band structure of Fig. 4 as explained in the text.
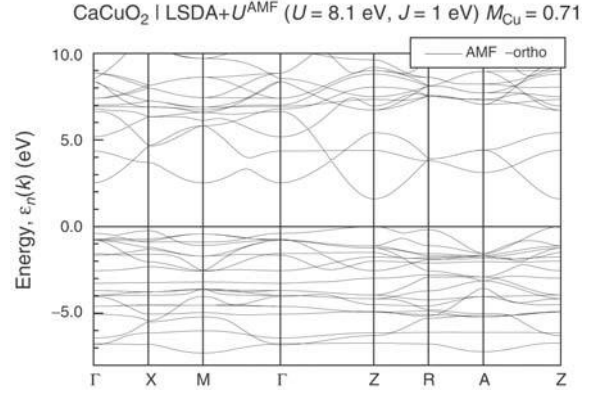
Figure 7
LSDA $+ U$ band structure of CaCuO$_2$ (cf. Fig. 4).

highest occupied state on the line $k = (\pi/2, \pi/2, k_z)$ (with the end points X and R) is a Cu-3$d_{x^2-y^2}$-O-2p_σ-in-plane O-2p_π hybrid as seen in the upper three panels of Fig. 8. (The absolutely highest occupied state is a pure in-plane O-2p_π state in a small k-space region around $k = (0,0,\pi)$ while all Cu-4s contributions are now shifted away from the Fermi level.)

1.2 Angle Resolved Photoemission Spectroscopy on Sr$_2$CuO$_2$Cl$_2$

There is no space here for a detailed description of the angle resolved photoemission spectroscopy (ARPES) experiment. For a clear review in relation to the cuprates, see Damascelli *et al.* (2003). The development of this experimental technique has enormously been triggered by the high-T_c superconductivity physics. For high-resolution measurements on quasi-two-dimensional structures one needs (001)-crystal surfaces as perfect as possible which are available from undoped M_2CuO$_2$Cl$_2$, $M =$ Ca, Sr, and from doped Bi$_2$Sr$_2$CaCu$_2$O$_{8+x}$, because these materials are easily cleaved in ultra-high vacuum in the middle of the M$_2$Cl$_2$ and of the Bi$_2$Sr$_2$O$_{4+x}$ block layers.

Sr$_2$CuO$_2$Cl$_2$ consists of alternating CuO$_2$ layers and insulating Sr$_2$Cl$_2$ block layers. Due to the geometry of the latter, subsequent CuO$_2$ layers are shifted horizontally by (a/2, a/2) relative to each other so that the nonmagnetic structure is b.c.t. Below $T_N \approx 250$ K it orders AF with an orthorhombic magnetic unit cell. However, since there is practically no electronic coupling through the Sr$_2$Cl$_2$ block layer, all considerations may be related to the two-dimensional unit cell and BZ of Fig. 3 and the LSDA $+ U$ band structure in the ($k_z = 0$)-plane of the BZ is practically identical with the left three panels of Figs. 7 and 8.

The quasiparticle low-energy dispersion measured by ARPES (single hole excitation) is shown in Fig. 9.

CaCuO$_2$ | LSDA+U^{AMF} (U = 8.1 eV, J = 1 eV) M$_{Cu}$ = 0.71
● Cu d$_{x^2-y^2}$

CaCuO$_2$ | LSDA+U^{AMF} (U = 8.1 eV, J = 1 eV) M$_{Cu}$ = 0.71
● O 2p$_\sigma$

CaCuO$_2$ | LSDA+U^{AMF} (U = 8.1 eV, J = 1 eV) M$_{Cu}$ = 0.71
● O 2p$_\pi$

CaCuO$_2$ | LSDA+U^{AMF} (U = 8.1 eV, J = 1 eV) M$_{Cu}$ = 0.71
● O 2p$_z$

CaCuO$_2$ | LSDA+U^{AMF} (U = 8.1 eV, J = 1 eV) M$_{Cu}$ = 0.71
● Cu s
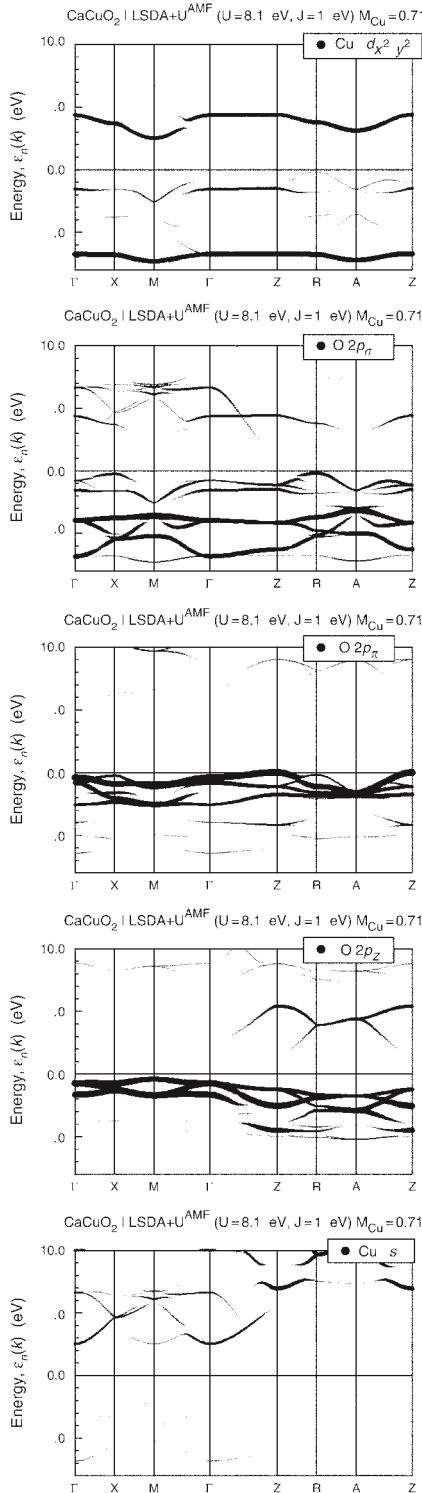
Figure 8
Orbital weighted LSDA + U band structure of CaCuO$_2$.
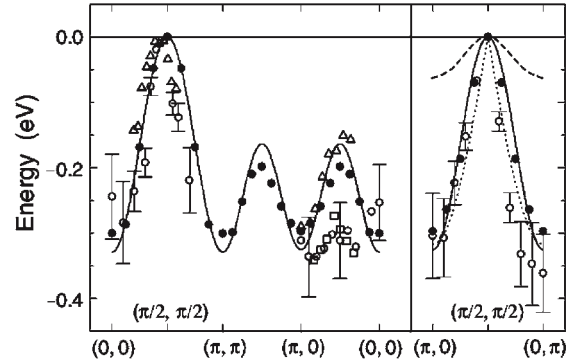
Figure 9
Energy dispersion of quasiparticles for Sr$_2$CuO$_2$Cl$_2$.
The energy zero is put at the top of the band, ~ 0.7 eV
below Fermi level. Open symbols: experimental data;
solid circles: self-consistent Born approximation for a
t–t'–t''–J model; solid line: tight-binding fit; dashed: t–J
model; dotted: spinon model dispersion (reproduced by
permission of Tohyama and Maekawa (2000) from
Supercond. Sci. Technol. **13**, R17; ©IOP Publishing).

A detailed discussion is found in the publications of
Tohyama and Maekawa (2000) and Damascelli *et al.*
(2003). The left part of the experimental spectra
(from (0,0) to ($\pi/2,\pi/2$)) compares nicely with the
O-2p_σ dominated LSDA + U band on the line Γ–X
(second panel of Fig. 8) and the right part (from ($\pi/2$,
$\pi/2$) to (0,π)) with the same LSDA + U band on the
line X–M. Even the reported fading ARPES intensity
when going from X towards M (see also Ronning
et al. 2003) agrees with the fading O-2p_σ projection
of that band. Nevertheless, the experimental bandwidth
is smaller by a factor of ~ 2 and the situation on the
line Γ–M is less clear. After all, LSDA + U accounts
for electron correlations still rather grossly.

2. Theoretical Models

The discrepancy between mean-field band structures,
predicting a metallic state for all cuprates independent
of doping, and experiment calls for models of strong
electron correlation to treat the electronic structure.
Most of these models concentrate on the degrees of
freedom provided by the orbitals Cu-3$d_{x^2-y^2}$ and
O-2p_σ, although it can be inferred from Fig. 8 that the
in-plane O-2p_π orbital is likely playing a role in the
low-energy excitations. Reviews on models of electron
correlations in cuprates have been published, for
instance, by Dagotto (1994), Varma (1997), and
Maekawa and Tohyama (2001). Commonly, the hole
picture is used in which the Hamiltonian acts on the
"vacuum" of the Cu-3d^{10}–O-2p^6 configuration of full
atomic shells and the energy axis of the band structure

is reversed compared to the electron picture of Figs. 4–9. The basic Hamiltonian first proposed by Emery (Emery model) is

$$
\begin{aligned}
\hat{H} = {} & \varepsilon_d \sum_i \hat{n}_i^d + \varepsilon_p \sum_j \hat{n}_j^p \\
& - t_{dp} \sum_{\langle ij \rangle, \sigma} (\hat{p}_{j\sigma}^\dagger \hat{d}_{i\sigma} + \hat{d}_{i\sigma}^\dagger \hat{p}_{j\sigma}) - t_{pp} \sum_{\langle jj' \rangle, \sigma} \hat{p}_{j'\sigma}^\dagger \hat{p}_{j\sigma} \\
& + U_d \sum_i \hat{n}_{i\uparrow}^d \hat{n}_{i\downarrow}^d + U_p \sum_j \hat{n}_{j\uparrow}^p \hat{n}_{j\downarrow}^p + U_{dp} \sum_{\langle ij \rangle} \hat{n}_j^p \hat{n}_i^d
\end{aligned}
$$

$$(2)$$

The on-site Cu-$3d_{x^2-y^2}$ and O-$2p_\sigma$ hole binding energies are ε_d and ε_p, i runs over the Cu sites, j over the O sites, $\langle ij \rangle$ runs over Cu–O bonds, and $\langle jj' \rangle$ over O–O bonds, $\hat{n}$ are the corresponding hole occupation number operators (for spin $\uparrow$ or $\downarrow$ or the sum over both spins if not specified), t are the Cu–O and O–O nearest neighbor hopping amplitudes, $\hat{d}^\dagger, \hat{d}, \hat{p}^\dagger$, and $\hat{p}$ are the Cu-$3d$ and O-$2p$ hole creation and annihilation operators, and U are the on-site and Cu-$3d$–O-$2p$ Coulomb repulsion matrix elements. Standard parameters (in eV) are $\varepsilon_p - \varepsilon_d = 3.6$, $t_{dp} = 1.3$, $t_{pp} = 0.65$, $U_d = 10.5$, $U_p = 4$, and $U_{dp} = 1.2$.

The undoped cuprates have one d-hole per Cu atom which sits in the lower hole Hubbard d-band produced by Eqn. (2) (unoccupied upper electron Hubbard band of Fig. 8). The next band in energy is predominantly of oxygen character without holes present (highest occupied electron band of Fig. 8) which is of central interest, if additional holes are doped into the CuO$_2$ plane or if holes are excited from Cu to O sites. One, therefore, tries to mimic this charge transfer excitation case by an effective one-band Hubbard model

$$
\hat{H} = -t \sum_{\langle ii' \rangle, \sigma} (\hat{c}_{i\sigma}^\dagger \hat{c}_{i'\sigma} + \hat{c}_{i'\sigma}^\dagger \hat{c}_{i\sigma}) + U \sum_i \hat{n}_{i\uparrow} \hat{n}_{i\downarrow} \quad (3)
$$

The $\hat{c}^\dagger$ and $\hat{c}$ now create and annihilate orthogonalized molecular states on CuO$_4$ plaquettes i (Wannier states), and $\hat{n}$ are their occupation number operators; $\langle ii' \rangle$ runs over nearest neighbor Cu pairs. The parameters (again in eV) to reproduce closely the low-energy spectrum of Eqn. (2) are $t = 0.43$ and $U = 5.4$.

In the subspace of the state space of avoided double occupancies of Cu sites by holes, Eqn. (3) may be canonically transformed into the t–J Hamiltonian (with some three-center terms neglected):

$$
\begin{aligned}
\hat{H} = {} & -t \sum_{\langle ii' \rangle, \sigma} (\hat{C}_{i'\sigma}^\dagger \hat{C}_{i\sigma} + \hat{C}_{i\sigma}^\dagger \hat{C}_{i'\sigma}) \\
& + J \sum_{\langle ii' \rangle} (S_{i'} \cdot S_i - \tfrac{1}{4} \hat{n}_{i'} \hat{n}_i)
\end{aligned}
$$

$$(4)$$

where $\hat{C}_{i\sigma} = \hat{c}_{i\sigma}(1 - \hat{n}_{i-\sigma})$, $J = 4t^2/U$, and S_i is a spin-$\frac{1}{2}$ operator at site i. At half-filling, $n_{i-\sigma} = 1$,

the t–J Hamiltonian reduces to the square lattice Heisenberg Hamiltonian

$$
\hat{H} = J \sum_{\langle ii' \rangle} S_{i'} \cdot S_i \quad (5)
$$

The ground state of the latter is now known to be the AF Néel state. It is, however, assumed that the Néel ground state is nearly degenerate with a nearest neighbor resonating valence bond state (RVB) in which neighboring copper spins form singlets ("valence bond singlets") and the RVB state is an eigenstate of total spin, $S = 0$, in which all those singlets resonate (Baskaran *et al.* 1987). This is a state with strong local spin fluctuations which might drive the system into superconductivity. Close to half-filling, $n_{i-\sigma} \approx 1$, Zhang and Rice (1988) derived the Hamiltonian (4) directly from Eqn. (2) by projection to low-energy excitations. The spin part is obtained from the well-known superexchange interaction of the nominal Cu holes. Doped additional holes go into oxygen-dominated states and form spin singlets (Zhang–Rice singlets) with the nominally present Cu hole. If the O-hole from a singlet at site i moves to site i', it leaves behind a spin-$\frac{1}{2}$ Cu-hole at site i and absorbs the Cu-hole present at site i' into a new singlet. Total spin conservation in this process demands that the spin of the created lone Cu-hole at site i has the same direction as had the spin of the previous lone Cu-hole at site i' now absorbed into the new singlet. It looks as if a lone Cu-hole has moved from site i' to i. This lone Cu-hole can only be destroyed at site i' if the site had a lone hole had and no singlet, i.e., the O-hole was not occupied there, $n_{i'-\sigma} = 0$. After the creation of the lone Cu-hole at site i, there is again no O-hole there, $n_{i-\sigma} = 0$. On the other hand, on an AF background with nominal Cu-holes having opposite spin directions on neighboring sites, a Cu-hole moved to the neighboring site has the wrong spin direction which costs an energy $\sim J$ while $t(1 - n_{i'-\sigma})(1 - n_{i-\sigma}) \to 0$ close to half-filling. This is why the bandwidth for the O-hole motion is now $\sim J$ instead of being $\sim t$ in the absence of correlations. (Compare the dramatical reduction of bandwidth from the band crossing the Fermi level in the second panel of Fig. 6 to the corresponding highest occupied band in the second panel of Fig. 8.)

Although the model Hamiltonians (2–4) look rather simple, their excitation spectra and phase diagrams are hard to obtain and not well known.

3. Doped Cuprates

The cuprates of families (i) and (ii) may be doped continuously from the AF insulator at $\delta \approx 0$ into (and eventually beyond) the superconducting state, family (i) with both signs of δ. At the Fermi level and above, spectral weight which is predominantly of in-plane O-$2p$ character is continuously developing

with increasing hole doping as seen in polarization-dependent XAS and orientation-dependent EELS (Fink *et al.* 1994). With electron doping, the situation is not as clear. There is an in-plane O-2*p* pre-edge at the conduction band and a strong in-plane Cu-3*d* peak there, both indicating an upper Hubbard band, but both the EELS and XAS spectra depend in position and intensity only very weakly on doping (Fink *et al.* 1994). Below the Fermi level, ARPES seems to observe developing spectral weight ~ 0.5 eV above the valence band edge of the undoped compound but still below the Fermi level, first around $(\pi, 0)$ and at higher doping level also around $(\pi/2, \pi/2)$, for both hole and electron doping. At low doping the spectra show broad features not crossing the Fermi level and still reminiscent of the AF symmetry of the BZ, before an FS according to the full line of Fig. 3(b) starts to develop, in the hole-doped case beginning near $(\pi/2, \pi/2)$ (Damascelli *et al.* 2003).

3.1 Overdoped Regions

For both signs of doping charge the maximum of the transition temperature T_c into the superconducting state is at $|\delta| \approx \frac{1}{6}$. As was already stated in the introduction, above this doping level, in the so-called overdoped regions, an FL is found consisting of hole-type rods around (π, π) and corresponding to the nonmagnetic BZ (dashed in Fig. 3(b)). The FS and the dispersion of the occupied parts of the electron bands of $(Bi,Pb)_2Sr_2CaCu_2O_{8+\delta}$ as seen in ARPES are shown in Fig. 10. The ARPES exhibits sharp quasiparticle peaks below T_c which become rather broad above T_c. In agreement with mean-field bands, there is a saddle point of $\varepsilon(\boldsymbol{k})$ at $(\pi, 0)$ from which the
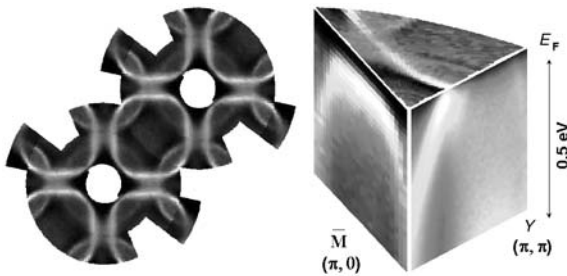
Figure 10
Color plot of ARPES intensity from overdoped (Bi, Pb)$_2$Sr$_2$CaCu$_2$O$_{8+x}$. Left panel: momentum distribution at the Fermi energy taken at 300 K and showing the hole FS rods around (π, π) (center of the dark area, called *Y* in the right panel) and the "shadow FS" rods around (0,0) (center of the white spots) possibly due to AF correlations still present. Right panel: energy and momentum distribution showing also the dispersion of the bands (courtesy of J. Fink).
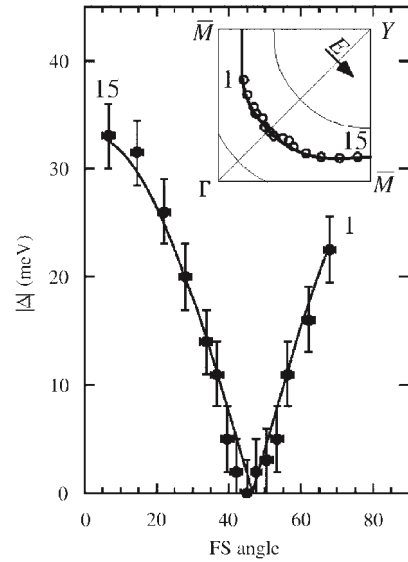
Figure 11
Superconducting gap measured at 13 K on Bi$_2$Sr$_2$CaCu$_2$O$_{8+x}$ ($T_c = 87$ K) and plotted vs. the angle along the normal-state FS, together with a *d*-wave fit (reproduced by permission of Ding *et al.* (1996) from *Phys. Rev. B* **54**, 9678; © American Physical Society).

band disperses downward towards (0,0) (with a flat region close to $(\pi, 0)$ whence the saddle point is called extended) and upward towards (π, π). The saddle point itself is ~ 0.3 eV below the Fermi level for electron overdoping and eventually crosses the Fermi level at hole overdoping. Compared to calculations local density approximation (LDA) the bands are renormalized by roughly a factor of 2.

By very high energy resolution ARPES ($\Delta E \sim 10$-meV), the gap function $|\Delta(\boldsymbol{k})|$ on the FS of the superconducting state well below T_c is measured (Fig. 11). Together with tunneling experiments which measure the phase of Δ, a *d*-wave order parameter

$$\Delta(\boldsymbol{k}) = \Delta_0[\cos(k_x a) - \cos(k_y a)] \qquad (6)$$

is found, where Δ_0 decreases with increasing doping.

3.2 Bilayer Splitting in $(Bi, Pb)_2Sr_2CaCu_2O_{8+\delta}$

In the cuprate families (ii) and (iii) for $n > 1$, there are stacks of n CuO$_2$-layers which in mean-field theory appear electronically coupled across the cation *C* layers even if (as is generally the case) the coupling across the block layers is negligible. Hybridization with Cu-4*s* or with in-plane O-2pπ *C*-*d* orbitals is essential in this coupling. It leads to an *n*-fold splitting of the conduction band of the CuO$_2$-layers which also survives various (but maybe not all) many-body
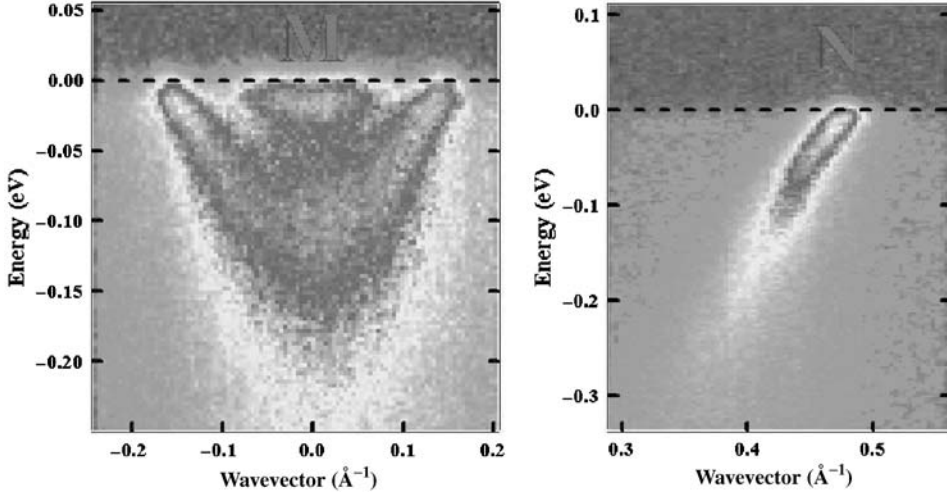
Figure 12
Color plot of ARPES energy–momentum distributions from overdoped (Bi,Pb)$_2$Sr$_2$CaCu$_2$O$_{8+x}$ in the superconducting state at 30 K. Left panel: near $(\pi,0)$ showing the bilayer splitting of the bands; right panel: nonsplit band near the nodal point $k_x = k_y$(N) of the FS (Courtesy of J. Fink).

approaches (Mori *et al*. 2002). For symmetry reasons this splitting is zero for $k_x = k_y$ and maximal at $(\pi, 0)$. It seems to have the symmetry of the superconducting order parameter which led to speculations in the literature. However, one must be cautious with this type of behavior of a number of features; it may simply be related to the mirror plane $k_x = k_y$ of the point symmetry of the crystal and need not be caused by superconducting correlations (which, of course, are also connected with this symmetry).

In particular, for $n = 2$, there is a bilayer splitting (~ 300 meV in LDA) which in the case of (Bi,Pb)$_2$Sr$_2$CaCu$_2$O$_{8+\delta}$ has been intensively studied with ARPES and clearly found in overdoped samples at $(\pi, 0)$ with a value of 90 meV (Fig. 12). Although in underdoped samples the ARPES features are broader and the situation is not as clear, the bilayer splitting in the vicinity of $(\pi, 0)$ was clearly found there by a number of authors recently (Damascelli *et al*. 2003).

3.3 Underdoped Region

The underdoped region of hole doping has been intensively studied because of two striking features (which might be related): the pseudogap and the stripe phase (see Tohyama and Maekawa 2000). It was found in many cuprates but was most intensively studied in Bi$_2$Sr$_2$CaCu$_2$O$_{8+\delta}$ that in the underdoped region away from the nodal point $k_x = k_y$ the ARPES peak (which in this doping region often is merely a broad hump) does not cross the FL but ends at a certain energy distance, the pseudogap value, from the latter. Often it seems to bend away from the

FL again like an AF folded band. It has again the symmetry with respect to $k_x = k_y$ mentioned in the last section.

At optimal doping, $\delta \sim \frac{1}{6}$, the pseudogap equals the superconducting gap, and in the overdoped region it is absent. With δ decreasing into the underdoped region the pseudogap is rapidly increasing extrapolating to ~ 80 meV at very low doping. It is intriguing that the superconducting gap of the overdoped region together with the pseudogap of the underdoped region behave like the gap obtained for RVB superconductivity by Baskaran *et al*. (1987).

Particularly in the cuprate family (i) but not exclusively there, incommensurate AF correlations close to $\boldsymbol{Q} = (\pi, \pi)$ are found which sometimes condense into incommensurate long-range order accompanied by incommensurate charge order. This might be caused by strong electron–lattice interaction leading to a separation into alternating AF and charged stripes. (For instance, the doping level of the charged stripes might be pinned at a higher than the average doping due to Peierls energy gain for rational band filling values, causing low-doped stripes in between.) Whether this is a generic effect and whether it is related to superconductivity is presently unclear.

3.4 Single-electron Self-energy

As was demonstrated by Norman *et al*. (1999), the self-energy of the single-electron Green's function can directly be extracted from ARPES data, if certain assumptions are made, namely that an extrinsic background can be properly subtracted and the

electronic structure has particle–hole symmetry in the close vicinity of the FS point considered.

Earlier ARPES studies of the self-energy focused on the $(\pi, 0)$ point which, however, is masked by bilayer splitting. Recently, a number of investigations (cf. Damascelli *et al.* 2003) at the nodal point $k_x = k_y$ revealed a linear temperature dependence of the imaginary part of the self-energy at optimal doping, which seems to correspond to the linear temperature dependence of the scattering rate in normal state resistivity, but which, in the ARPES results, extends deep into the superconducting state. This would be consistent with the marginal FL model (Varma 1997).

The interest into the self-energy around $(\pi, 0)$ came from the strong effect a magnetic mode at $Q = (\pi, \pi)$ would have in this region (Eschrig and Norman 2000). It would lead to the peak-dip-hump structure of the energy distribution functions measured in ARPES around $(\pi, 0)$. Much but very likely not all of this structure is now attributed to the bilayer splitting. It remains a challenge for further studies to disentangle these features.

4. Summary

The electronic structure of cuprate superconductors is more or less settled in the cases of undoped ($\delta \approx 0$) and overdoped ($|\delta| \gtrsim 0.2$) material. In the former case it is that of an AF charge transfer insulator which can theoretically be described by a t–J model Hamiltonian. It might be necessary to incorporate in-plane O-2p_π orbitals into this model for certain considerations. In the overdoped case, a weakly renormalized LDA band structure of a Cu-3$d_{x^2-y^2}$–O-2p_σ band is experimentally found in the vicinity of the FL in ARPES.

At optimal doping ($\delta \approx \frac{1}{6}$) for superconductivity, experimental evidence seems to accumulate for a marginal FL state at elevated temperature, which is masked by the d-wave superconducting state at low temperature.

Still largely unclear is the situation in the underdoped region where several interactions seem to be interwoven leading to a complex behavior.

See also: High-temperature Superconductors, Cuprate: Magnetic Properties by NMR/NQR; High-temperature Superconductors: Thin Films and Multilayers; High-temperature Superconductors: Transport Phenomena; Superconducting Materials, Types of

Bibliography

Andersen O K, Liechtenstein A I, Jepsen O, Paulsen F 1995 LDA energy bands, low-energy Hamiltonians, t', t'', $t_\perp$ ($\mathbf{k}$), and $J_\perp$. *J. Phys. Chem. Solids* **56**, 1573–91
Baskaran G, Zhou Z, Anderson P W 1987 The resonating valence bond state and high-T_c superconductivity—a mean field theory. *Solid State Commun.* **63**, 973–6

Dagotto E 1994 Correlated electrons in high-temperature superconductors. *Rev. Mod. Phys.* **66**, 763–839
Damascelli A, Hussain Z, Shen Z-X 2003 Angle-resolved photoemission spectroscopy of the cuprate superconductors. *Rev. Mod. Phys.* **75**, 473–542
Ding H, *et al.* 1996 Angle-resolved photoemission spectroscopy study of the superconducting gap anisotropy in Bi$_2$Sr$_2$CaCu$_2$O$_{8+x}$. *Phys. Rev. B* **54**, 9678
Eschrig H, Koepernik K, Chaplygin I 2003 Density functional application to strongly correlated electron systems. *J. Solid State Chem.* **176**, 482–95
Eschrig M, Norman M R 2000 Neutron resonance: modeling photoemission and tunneling data in the superconducting state of Bi$_2$Sr$_2$Ca$_2$Cu$_2$O$_{8+\delta}$. *Phys. Rev. Lett.* **85**, 3261–4
Fink J, Nücker N, Pellegrin E, Romberg H, Alexander M, Knupfer M 1994 Electron energy-loss and x-ray absorption spectroscopy of cuprate superconductors and related compounds. *J. Electron Spectrosc. Relat. Phenom.* **66**, 395–452
Johnston D C 1997 Normal-state magnetic properties of single-layer cuprate high-temperature superconductors and related materials. In: Buschow K H J (ed.) *Handbook of Magnetic Materials*. Elsevier, Amsterdam, Vol. 10, Chap. 1, pp. 1–237
Maekawa S, Tohyama T 2001 Charge and spin in low-dimensional cuprates. *Rep. Prog. Phys.* **64**, 383–428
Mori M, Tohyama T, Maekawa S 2002 Electronic states and superconductivity in multilayer high-T_c cuprates. *Phys. Rev. B* **66**, 064502-1–7
Müller-Buschbaum H 1977 Oxometalates with planar coordination. *Angew. Chem. Int. Ed.* **16**, 674–87
Norman M R, Ding H, Fretwell H, Randeira R, Campuzano J C 1999 Extraction of the electron self-energy from angle-resolved photoemission data: application to Bi$_2$Sr$_2$Ca$_2$Cu$_2$O$_{8+x}$. *Phys. Rev. B* **60**, 7585–90
Pickett W 1989 Electronic structure of the high-temperature oxide superconductors. *Rev. Mod. Phys.* **61**, 433–511
Ronning F, Kim C, Shen K M, Armitage N P, Damascelli A, Lu D H, Feng D L, Shen Z-X, Miller L L, Kim Y-J, Chou F, Terasaki I 2003 Universality of the electronic structure from a half filled CuO$_2$ plane. *Phys. Rev. B* **67**, 035113-1–16
Tohyama T, Maekawa S 2000 Angle-resolved photoemission in high-T_c cuprates from theoretical viewpoints. *Supercond. Sci. Technol.* **13**, R17–32
Varma C 1997 Non-Fermi-liquid states and pairing instability of a general model of copper oxide metals. *Phys. Rev. B* **55**, 14554–80
Zhang F C, Rice T M 1988 Effective Hamiltonians for the superconducting Cu oxides. *Phys. Rev. B* **37**, R3759–561

H. Eschrig
*Institute of Solid State and Materials Research
Dresden, Germany*

High-temperature Superconductors, Cuprate: Magnetic Properties by NMR/NQR

One of the peculiar properties of cuprate high-temperature superconductors (HTSC) is their descent from antiferromagnetic (AF) parent compounds

whose magnetic order arises from Cu^{2+} spins in the CuO_2 planes. For instance, $YBa_2Cu_3O_{7-\delta}$ is obtained by doping $YBa_2Cu_3O_6$ with oxygen while $La_{2-x}Sr_xCuO_4$ results from Sr substitution in La_2CuO_4. Both processes create electron holes in the CuO_2 planes and eventually destroy the AF long-range order. However, AF short-range order is still present in the superconductors and even in the superconducting regime. These properties make cuprate HTSC a unique class of superconductors quite different from conventional superconductors and metals. (see *Superconducting Materials, Types of*).

NMR–NQR spectroscopy has explored many aspects of HTSC and several papers have reviewed these studies: Pennington and Slichter (1990), Alloul (1991), Brinkmann and Mali (1994), Berthier *et al.* (1996), Rigamonti *et al.* (1998). The present article will update results related to magnetic properties of cuprate HTSC: relaxation and Knight shift data in the normal state, the dynamic susceptibility, the single-spin fluid model, the spin–gap effect, and some experiments in the superconducting state.

1. Relaxation Rates and Magnetic Shifts

The information on the microscopic magnetic behavior of cuprate HTSC is contained in the spin susceptibility $\chi(\mathbf{q}, \omega)$ which depends on frequency ω and wavevector $\mathbf{q}$. χ is mainly probed by measuring relaxation times and magnetic frequency shifts. In most NMR studies of HTSC, the external magnetic field B_0 is sufficiently large to render the quadrupole interaction a small perturbation of the Zeeman interaction thus leading to a splitting of the NMR signal. In the case of NQR, internal magnetic fields may give rise to Zeeman perturbed NQR transitions. In nearly all cuprate HTSC, the measured NQR frequencies for both isotopes of in-plane Cu(2) are pure NQR frequencies, thus revealing the absence of long-range magnetic order in these compounds (on the time scale of NQR).

The hyperfine interaction of the nuclear magnetic moment with the local magnetic field contains a static part that induces a magnetic shift of the NMR line, and a dynamic part that causes relaxation (see *Solids, Nuclear Magnetic Resonance of*). The shift tensor consists of an orbital part being predominantly temperature independent in HTSC, and a spin part, usually called the Knight shift $\mathbf{K}^{spin}$, that is temperature dependent and is expected to vanish in the superconducting state due to singlet spin pairing. Each component of $\mathbf{K}^{spin}$ can be expressed by the hyperfine interaction tensor, A_j, and the static spin susceptibility: $K_{\alpha\alpha}^{spin} = (1/g\,\mu_B) \sum_j (A_j)_{\alpha\alpha} (\chi_j)_{\alpha\alpha}$.

The fluctuating part of the hyperfine interactions is the source of relaxation processes. The main contribution to the copper, oxygen, and yttrium spin–lattice relaxation in HTSC compounds arises from electron spin fluctuations. This contribution is related to the imaginary part of the dynamical spin susceptibility $\chi(\mathbf{q}, \omega_0)$ and it is given by the Moriya formula:

$$\left(\frac{1}{T_1 T}\right)_\alpha \equiv \frac{2W_\alpha}{T} = \frac{\gamma_n^2 k_B}{2\,\mu_B^2} \sum_{\mathbf{q}, \alpha' \neq \alpha} F_{\alpha'}(\mathbf{q}) \frac{\chi_{\alpha'\alpha'}''(\mathbf{q}, \omega_0)}{\omega_0}$$

where $F_\alpha(\mathbf{q}) = \left| \sum_j A_{j,\alpha\alpha} \exp(i\mathbf{q} \cdot \mathbf{r}_j) \right|^2$ is the form factor, ω_0 is the nuclear resonance frequency, α denotes the direction of quantization, i.e., the direction of either the maximum component of the electric field gradient tensor V_{zz} in NQR or of B_0 in NMR experiments, and α' is the direction perpendicular to α. A_j is the on-site ($\mathbf{r}_j = \mathbf{0}$) and transferred ($\mathbf{r}_j \neq \mathbf{0}$) hyperfine coupling tensor for the nuclei under consideration.

Therefore, the spin–lattice relaxation time T_1 or better $(T_1 T)^{-1}$ provides information about the $\mathbf{q}$ averaged imaginary part of $\chi(\mathbf{q}, \omega_0)$. Another relaxation time, the spin–spin relaxation time T_2, is related to the real part of $\chi(\mathbf{q}, \omega)$. In many HTSC, the dominating part of $1/T_2$, called $1/T_{2G,ind}$, is due to an enhanced indirect nuclear–nuclear spin coupling mediated by the electronic spin system; this leads to a Gaussian contribution to the spin-echo decay signal. The numerical values of the coupling tensors A_j, which may range up to several thousand oersteds, have been derived from various NMR experiments, in particular from magnetic shift studies (see review papers listed above).

If fluctuating electric field-gradients are present (at the Larmor frequency), additional terms would appear in the Moriya formula. Since these terms are usually small in HTSC, they are neglected; however, as will be discussed in Sect. 3, the presence of quadrupole interactions may have important consequences.

Relaxation times and Knight shift behave quite differently from corresponding data in conventional superconductors or metals. For instance, W has a nonlinear temperature dependence and K is temperature dependent. Furthermore, different nuclei (Cu, O, Y) display different temperature dependences which, in turn, depend on the doping level of the substance. More recent results are discussed by Berthier *et al.* (1996) and Rigamonti *et al.* (1998).

Figure 1 sketches the general behavior of W, $1/T_{2G,ind}$ and K for Cu(2), where the temperature T^* characterizes the spin–gap to be discussed in Sect. 4. When interpreting these data, one usually chooses the Mila–Rice Hamiltonian (Rigamonti *et al.* 1998) as the starting point. Then, the different temperature dependences of W are attributed to differences in the form factors $F_\alpha(\mathbf{q})$ that filter the magnetic fluctuations at different points of the Brillouin zone. This explains, for instance, the striking difference of the W values for copper and oxygen.
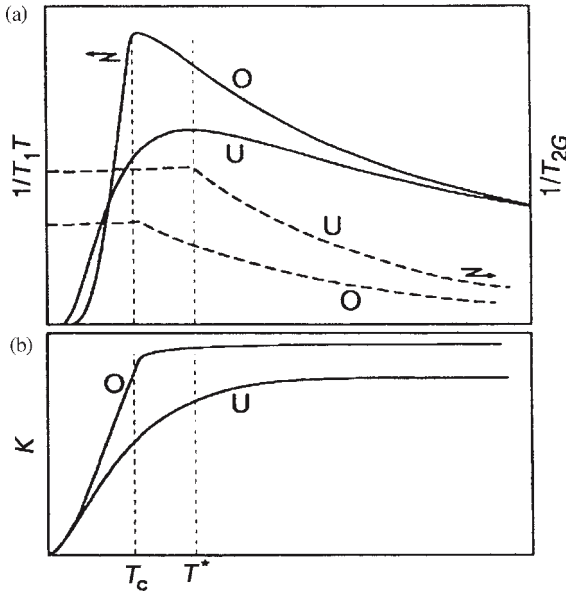
Figure 1
Schematic behavior of relaxation times (a) and Knight shift (b) of planar Cu in optimally (O) and underdoped (U) cuprate HTSC (reproduced by permission of Rigamonti *et al.* 1998).

Figure 2
Calculated temperature dependence of the spin–lattice relaxation rates of ^{63}Cu, ^{17}O, and ^{89}Y in YBa$_2$Cu$_3$O$_7$ (solid lines) compared with experimental data (Brinkmann and Zavidonov 2002).

2. Calculations of the Dynamic Spin Susceptibility

The quality of calculating $1/T_1$ is based on the knowledge of the imaginary part of the dynamic spin susceptibility $\chi''_{+-}(\mathbf{q}, \omega_0)$. Several models have been employed to calculate $1/T_1$ for the normal state of HTSC. Among these are the nearly antiferromagnetic Fermi liquid (NAFL) description of HTSC and the 2DQHAF scaling model which regards a cuprate HTSC as a disordered 2-dimensional quantum Heisenberg AF (Berthier *et al.* 1996, Rigamonti *et al.* 1998). In the NAFL model, the dynamic spin susceptibility is written, in a phenomenological approach, as the superposition of two terms, one for itinerant quasiparticles and the other for localized Cu^{2+} magnetic moments. It seems that the NAFL model is rather well obeyed in overdoped cuprates while the 2DQHAF model describes underdoped cuprates (Berthier *et al.* 1996, Rigamonti *et al.* 1998).

Usually, calculations of the dynamic spin susceptibility start from the *t–J* model (Rigamonti *et al.* 1998) where *t* denotes the hopping energy of the holes and *J* represents the strong repulsion between holes residing on the same square. Then, the susceptibility is usually calculated by using various methods. However, in spite of considerable progress, all theories have some disadvantages which are mainly connected with their phenomenological character. For example, in these theories, the temperature and

doping dependence of the AF correlation length, ξ, which is the essential parameter that governs the temperature and doping dependence of $1/T_1$, are postulated or, at best, are taken from a comparison with experiment. Expressions used for the dynamic spin susceptibility are good approximations only for wave vectors in the vicinity of the AF wave vector, thus the models provide reliable results for $1/T_1$ if ξ is large. In YBa$_2$Cu$_3$O$_{7-\delta}$, for instance, ξ is small and therefore a more detailed theoretical analysis of the NMR data is required.

This has been done, for instance, in an approach where $\chi''_{+-}(\mathbf{q}, \omega_0)$ is calculated within a constraint-free theory based on the presentation of the *t–J* model in terms of Hubbard operators (Brinkmann and Zavidonov 2002). Both electron and AF spin correlations were taken into account. The model is able to reproduce the main features of the temperature and doping dependences of ξ in both the pure Heisenberg AF (e.g. La$_2$CuO$_4$) and doped compounds (La$_{2-x}$Sr$_x$CuO$_4$). Starting form these results, the factors $F(\mathbf{q})\chi''_{+-}(\mathbf{q}, \omega)/\omega$ and hence $1/T_1$ were calculated for ^{63}Cu, ^{17}O, and ^{89}Y in YBa$_2$Cu$_3$O$_{7-\delta}$. Figure 2 demonstrates the good agreement with experimental data.

3. The Single-spin Fluid Model

One of the central issues in understanding the cuprate HTSC has been to determine the minimal number of electronic degrees of freedom which are necessary to describe the physics at the atomic scale of these structures. Adopting the picture of the spin-resonant singlet state with quasi-localized holes at copper (Rigamonti *et al.* 1998), only one spin degree of freedom would be necessary; this is the single-spin fluid (SSF) scenario. However, as was discussed by various

authors (e.g. Berthier *et al.* 1996), this model might be an oversimplification.

NMR provides information about oxygen and copper independently. Studies of the uniform spin susceptibility $\text{Re}\{\chi(q=0,\omega=0)\}$, i.e., of the Knight shift, are in favor of the SSF model. On the other hand, oxygen and copper show a very different temperature dependence of the spin–lattice relaxation, that is of the dynamic spin susceptibility, $\text{Im}\{\chi(q,\omega_L)\}$, thus suggesting independent spin degrees of freedom. However, the hyperfine field, due to antiferromagnetically correlated copper spins, could cancel at the oxygen site and this would explain the different temperature dependences within a SSF model.

There is, however, evidence that this view is incomplete. The ^{17}O NMR in Y-based cuprate HTSC has extensively been studied by various groups. In particular, the pronounced temperature dependence of the anisotropy of the plane oxygen spin–lattice relaxation rate, ^{17}W, is still puzzling (e.g., Suter *et al.* 1997) while the SSF model predicts an almost temperature independent rate anisotropy. Suter *et al.* (1997) pointed out that it is also very difficult to explain, within a simple SSF model, the ratio of the oxygen and the yttrium rate, namely $^{17}W/^{89}W$. Furthermore, a comparison of ^{17}O and ^{63}Cu NMR results from $\text{La}_{2-x}\text{Sr}_x\text{CuO}_4$ with inelastic neutron scattering data suggested that a single-band picture is inadequate (Walstedt and Cheong 1995).

Further support of this conclusion came from a study of the spin–lattice relaxation of plane oxygen in $\text{YBa}_2\text{Cu}_4\text{O}_8$ below 200 K (Suter *et al.* 2000): there is a considerable contribution of quadrupolar fluctuations (i.e., low-frequency charge fluctuations) to the total fluctuating fields. Two degrees of freedom are involved in the low-energy excitations of the electronic system, one of them is the single-spin degree, implying that the single-spin fluid model is partially correct, whereas the other one is the charge degree of freedom with predominantly oxygen character, since it is not observed at the copper sites.

4. The Spin-gap Effect

A dominant characteristic of the normal state of optimally doped and underdoped cuprate HTSC is the occurrence of the so-called pseudogap; its origin still remains unclear. The pseudogap refers to the transfer of low-energy excited states to higher energy. In NMR and neutron scattering experiments, the pseudogap reveals itself as a spin–gap (Brinkmann and Mali 1994, Berthier *et al.* 1996, Rigamonti *et al.* 1998). For instance, in $\text{YBa}_2\text{Cu}_4\text{O}_8$ ($T_c = 81$ K), $(T_1 T)^{-1}$ of Cu(2) increases with falling temperature (see Fig. 1) and reaches a maximum at T^* (≈ 150 K), which serves as a convenient scale for the temperature dependence of the spin–gap onset temperature. Possible relations between the spin–gap and the superconducting gap are still under debate.

A hint to the interdependence of these gaps may be found in the fact that several structure related anomalies have been observed in $\text{YBa}_2\text{Cu}_4\text{O}_8$ around a temperature $T^\dagger = 180$ K. Based on NMR–NQR studies, the anomalies were interpreted as an electronic crossover involving enhanced charge fluctuations in planes and chains (Suter *et al.* 1997). Because of the proximity of $T^\dagger$ and T^*, Eremin *et al.* (1997) suggested that the spin–gap effect in $\text{YBa}_2\text{Cu}_4\text{O}_8$ is caused by a transition due to a charge density wave instability. The authors explained, among others, the strong temperature dependence of the magnetic shift of Cu(2) nuclei and predicted a dependence of T^* on the isotope mass.

Such an isotope effect has been found in a high-accuracy NQR T_1 study of the ^{63}Cu(2) nuclei, supplemented by susceptibility measurements, on ^{16}O and ^{18}O exchanged $\text{YBa}_2\text{Cu}_4\text{O}_8$ samples (Raffa *et al.* 1998). The isotope exponents, defined as $\alpha = -\Delta\ln(T^*)/\Delta\ln(m)$ for T^* and correspondingly for T_c, are $\alpha_{T^*} = 0.061(8)$ and $\alpha_{T_c} = 0.056(12)$. The agreement of the exponents, within the experimental error, suggest a common origin, or at least a relation, for the superconducting and the spin-gap. This result is contrary to a recent ^{89}Y magnetic shift study in $\text{YBa}_2\text{Cu}_4\text{O}_8$ which reported the absence of an isotope effect in the pseudogap (Williams *et al.* 1998). However, Mali *et al.* (2001), by extending the work of Raffa *et al.* (1998) to the ^{63}Cu(2) Knight shift, again found an isotope effect on the spin–gap; both exponents have the same sign. Hence, the controversy on this topic continues.

When T_c is approached from above, one expects enhanced superconducting pairing fluctuations which may, in the presence of strong magnetic fields, influence various normal-state properties, including spin–lattice relaxation (Rigamonti *et al.* 1998). These effects can be used to clarify the origin of the pseudogap (Eschrig *et al.* 1999). Previous experimental results and the corresponding conclusions on the ^{63}Cu(2) relaxation rate in $\text{YBa}_2\text{Cu}_3\text{O}_{7-\delta}$ have been controversial (Rigamonti *et al.* 1998, Gorni *et al.* 2001). Latest high-precision measurements (Gorni *et al.* 2001) found the relaxation rate to be field independent (from 0 T up to 14.8 T) in the normal state; a field dependence develops only below T_c. A field independent ^{63}Cu(2) relaxation has also been observed in the normal state of $\text{YBa}_2\text{Cu}_4\text{O}_8$ (Brinkmann and Mali 1994).

5. The Superconducting State

Again, as in the normal state, magnetic properties of the HTSC are probed mainly via the magnetic shift K and relaxation rates, in particular W and $1/T_{2G}$. The temperature dependence of K below T_c is in accord with a carrier pairing into singlet-spin states and supports the model of d wave pairing. The temperature

dependence of $1/T_{2G}$ is also in accord with this model. The temperature dependence of W is close to a T^3 behavior. The anisotropy of $\chi(\mathbf{q}, \omega)$ is studied by measuring W with the magnetic field parallel and perpendicular to the c axis; the field dependence is explored by comparing NQR and NMR values. The theoretical interpretations are mostly based on models of phenomenological character. Special magnetic effects arise from substituting Cu(2) by diamagnetic Zn and lead to deviations from the T^3 law.

The lattice and dynamics of flux lines (FL) in the superconducting state have attracted special attention. A summary of related NMR experiments is found in Rigamonti *et al.* (1998). NMR spectra and the relaxation times T_1 and T_2 are employed to study statics and dynamics of the FL and their field and temperature dependence. For instance, the temperature dependence of the field distribution inside the bulk $YBa_2Cu_4O_8$, together with a partial melting of the FL lattice, can be inferred from the ^{89}Y linewidth. ^{17}O spectra demonstrate, for a certain temperature range, the coexistence of liquid and solid vortex behavior, e.g., in $YBa_2Cu_3O_7$. The ideal tool to study the FL motion is spin–lattice relaxation: correlation times and pinning barriers can be estimated, for instance in $YBa_2Cu_4O_8$.

Very promising are recent studies to explore the vortex core structure by site-selective and spatially resolved experiments. For instance, $1/T_1$ and $1/T_2$ increase for nuclei close to the vortex core. An NMR imaging experiment has spatially resolved the electronic structure inside and outside vortex cores in near-optimally doped $YBa_2Cu_3O_{7-x}$: strong AF fluctuations are found outside the cores whereas inside unusual electronic states are detected (Mitrović *et al.* 2001). Site-selective $1/T_1$ measurements in $YBa_2Cu_4O_8$ illustrate that the simple interpretation of the data by the density of states of the Doppler-shifted quasiparticles of a d superconductor is problematic (Kakuyanagi *et al.* 2002).

6. Conclusion

NMR and NQR have proven to be suitable tools to investigate the dynamic susceptibility in cuprate HTSC. Experimental results quite often agree with phenomenological models of the susceptibility; but the theoretical approaches still need further refinements to interpret details satisfactorily. The problems of the single-spin fluid model are not yet settled and the spin–gap is still a matter of debate, in particular its relation to other characteristic temperatures of the HTSC. NMR–NQR studies of the superconducting state seem to be an expanding and promising field of research.

See also: High-T_c Superconductors: Electronic Structure; High-temperature Superconductors: Thin Films and Multilayers; Nuclear Magnetic Resonance Spectrometry; Superconducting Thin Films: Materials, Preparation, and Properties

Bibliography

Alloul H 1991 Experimental studies of magnetic properties of cuprates—from the antiferromagnetic to metallic state. In: Tunstall D P, Barford W (eds.) *High Temperature Superconductivity*. Adam Hilger, Bristol, pp. 207–69

Berthier C, Julien M H, Horvatić M, Berthier Y 1996 NMR studies of the normal state of high-temperature superconductors. *J. Phys.* **I 6**, 2205–36

Brinkmann D, Mali M 1994 NMR-NQR studies of high-temperature superconductors. In: Diehl P, Fluck E, Günther H, Kosfeld R, Seelig J (eds.) *NMR—Basic Principles and Progress*. Springer, Berlin, Vol. 31, pp. 171–211

Brinkmann D, Zavidonov A Yu 2002 Nuclear spin-lattice relaxation in cuprate superconductors—some new approaches. *Z Naturforsch.* **57a**, 479–87

Eremin I, Eremin M, Varlamov S, Brinkmann D, Mali M, Roos J 1997 Spin susceptibility and pseudogap in $YBa_2Cu_4O_8$: an approach via a charge-density-wave instability. *Phys. Rev.* **B 56**, 11305–11

Eschrig M, Rainer D, Sauls J A 1999 Effects of strong magnetic fields on pairing fluctuations in high-temperature superconductors. *Phys. Rev.* **B 59**, 12095–113

Gorni K R, Vyaselev O M, Pennington C H, Hammel P C, Hults W L, Smith J L, Baumgartner J, Lemberger T R, Klamut P, Dabrovski B 2001 Magnetic field independence of Cu(2) NMR spin-lattice relaxation rate in the normal state of optimally doped $YBa_2Cu_3O_{7-\delta}$. *Phys. Rev.* **B 63**, 064513/1–6

Kakuyanagi K, Kumagai K, Matsuda Y 2002 Quasiparticle excitation in and around the vortex core of underdoped $YBa_2Cu_4O_8$ studied by site-selective NMR. *Phys. Rev.* **B 65**, 060503/1–5

Mali M, Roos J, Keller H, Conder K, Karpinski J 2001 Oxygen isotope effect in cuprates. Annual Report, Physik-Institut, University of Zürich, pp. 56–7

Mitrović V F, Sigmund E E, Eschrig M, Bachmann H N, Halperin W P, Reyes A P, Kuhns P, Moulton W G 2001 Spatially resolved electronic structure inside and outside the vortex cores of a high-temperature superconductors. *Nature* **413**, 501–4

Pennington C H, Slichter C P 1990 Nuclear magnetic resonance studies of $YBa_2Cu_3O_{7-\delta}$. In: Ginsburg D M (ed.) *Physical Properties of High Temperature Superconductors*. World Scientific, Singapore, Vol. 2, pp. 269–367

Raffa F, Ohno T, Mali M, Roos J, Brinkmann D, Conder K, Eremin M 1998 Isotope dependence of the spin gap in $YBa_2Cu_4O_8$ as determined by Cu NQR relaxation. *Phys. Rev. Lett.* **81**, 5912–5

Rigamonti A, Borsa F, Carretta P 1998 Basic aspects and main results of NMR-NQR spectroscopies in high-temperature superconductors. *Rep. Prog. Phys.* **61**, 1367–439

Suter A, Mali M, Roos J, Brinkmann D 1997 Electronic crossover in the normal state of $YBa_2Cu_4O_8$. *Phys. Rev.* **B 56**, 5542–51

Suter A, Mali M, Roos J, Brinkmann D 2000 Charge degree of freedom and the single spin fluid model in $YBa_2Cu_4O_8$. *Phys. Rev. Lett.* **84**, 4938–41

Walstedt R E, Cheong S-W 1995 $^{63,65}Cu$ and ^{17}O spin-echo decay and the static susceptibility $\chi'(q)$ in $La_{1.85}Sr_{0.15}CuO_4$. *Phys. Rev.* **B 51**, 3163–75

Williams G V M, Tallon J L, Quitly J W, Trodahl H J, Flower N E 1998 Absence of an isotope effect in the pseudogap in $YBa_2Cu_4O_8$ as determined by high-resolution ^{89}Y NMR. *Phys. Rev. Lett.* **80**, 377–80

D. Brinkmann
University of Zurich, Switzerland

High-temperature Superconductors: Thin Films and Multilayers

Since 1986, when high-T_c superconductivity was discovered, stunning achievements have been made in the fabrication of films and multilayers based on these superconducting cuprates despite their complex crystal structures (see also *Superconducting Thin Films: Materials, Preparation, and Properties*, *Superconducting Thin Films: Multilayers*). In this article the key morphologic and electronic properties of high-T_c superconducting thin films, particularly of $YBa_2Cu_3O_{7-\delta}$, and multilayers are described.

Efforts to produce thin films of cuprate superconductors rapidly followed their discovery. The first polycrystalline films of a high-T_c superconductor, $(La,Sr)_2CuO_4$, were deposited by sputtering in February, 1987 (Koinuma *et al.* 1987, Nagata *et al.* 1987). In March, 1987 epitaxial $(La,Sr)_2CuO_4$ films were prepared by sputtering on $(100)SrTiO_3$ substrates (Suzuki and Murakami 1987). Although the latter films were superconducting as grown, their T_c improved greatly after a high-temperature anneal. Later that same month the first superconducting films with a zero resistance critical temperature T_{c0} exceeding the boiling point of nitrogen, 77 K, were grown (Laibowitz *et al.* 1987). These were polycrystalline $YBa_2Cu_3O_{7-\delta}$ films deposited by e-beam evaporation and annealed at high temperatures. In April 1987, the first epitaxial $YBa_2Cu_3O_{7-\delta}$ films were fabricated (Chaudhari *et al.* 1987). This was accomplished by depositing amorphous Y-Ba-Cu-O films via e-beam evaporation on a $(100)SrTiO_3$ substrate and subsequently crystallizing the $YBa_2Cu_3O_{7-\delta}$ film by solid-phase epitaxial regrowth during a high-temperature annealing step.

These were the first superconductors in any form with critical current densities J_c exceeding $10^6\,A\,cm^{-2}$ at 4.2 K, thereby demonstrating the commercial utility of high-T_c superconductivity as well as the importance of epitaxy in producing high-T_c films with useful electrical transport properties. The progress did not stop there. Soon, epitaxial films with good electrical properties, of $YBa_2Cu_3O_{7-\delta}$ (Terashima *et al.* 1988) and other high-T_c superconductors were grown *in situ*, directly in their crystalline state (i.e., without the need of an ex situ annealing step following deposition) on a wide variety of substrates including sapphire, silicon, GaAs, and even on polycrystalline substrates such as stainless steel and alumina, through the use of a highly-textured, intermediate buffer layer. Today, excellent films of a multitude of high T_c compounds are produced by a variety of vapor-phase techniques (see also *Superconducting Thin Films: Materials, Preparation, and Properties*, *Superconducting Thin Films: Multilayers*). Wafer sizes have reached diameters of 8 inches (20.32 cm), and films are deposited in scalable and continuous processes over lengths of up to a meter (Foltyn *et al.* 1999, Park *et al.* 1999).

Due to their outstanding electrical transport characteristics (high T_c, high J_c, low surface resistance R_s), epitaxial films and multilayers, incorporating in some cases Josephson junctions, are very useful for applications involving high-T_c superconductors, including microwave filters, magnetometers, digital circuits, and fault current limiters. Films have also been used with remarkable success to investigate fundamental properties and application-related aspects of high-T_c superconductivity, e.g., analysis of the order parameter symmetry (Tsuei *et al.* 1994, Chaudhari and Lin 1994, Mannhart *et al.* 1996) and measurements of the transport properties of grain boundaries (Hilgenkamp and Mannhart 2001). In addition, the technology developed for the growth of cuprate superconductor films has enabled rapid progress in the deposition of films of other multicomponent oxides including ferroelectrics (Waser *et al.* (eds.) 2001) and manganates that exhibit colossal magnetoresistance (Helmolt *et al.* 1993).

As it is impossible to provide a complete overview of the field within the space available, we have restricted our discussion of the field of high-T_c films and focus on a few illustrative examples based mainly on $YBa_2Cu_3O_{7-\delta}$. We regret that it is impossible to include all of the important work contributed by the large number of groups active in this relatively new and rapidly progressing field (see also *Superconducting Thin Films: Materials, Preparation, and Properties*, *Superconducting Thin Films: Multilayers*). Additional information can be found in other review papers on high-T_c films and multilayers (Humphreys *et al.* 1990, Lemberger 1992, Somekh *et al.* 1992, Matijasevic and Bozovic 1996, Bozovic and Eckstein 1996, Triscone and Fischer 1997, Wördenweber 1999).

1. Substrates for Superconducting Films

A crucial starting point in the growth of high-T_c thin films and multilayers is the selection of the substrate material and its preparation. As large-area single crystal substrates of high-T_c superconductors, a necessity for homoepitaxial growth, are not commercially available, other substrate materials must be used. The ideal substrate is both chemically and structurally compatible with the epilayer. Other

factors, including commercial availability, cost, the potential for integration with other device technologies, thermal expansion coefficient, dielectric constant, and the dielectric loss tangent at microwave frequencies (for high-frequency operation of superconducting circuits) must also be considered (Hollmann *et al.* 1994, Phillips 1996). Unlike the heteroepitaxial growth of semiconductors, where it is imperative to choose a well lattice-matched substrate in order to avoid undesired dislocations in the grown structures, dislocations in superconductors and especially in high-T_c superconductors are effective vortex pinning sites and lead to significantly higher critical current densities (Mannhart *et al.* 1992, Dam *et al.* 1999). Thus, a relatively large lattice mismatch between high-T_c superconductors and substrate materials is, in principle, permissible. Thermal expansion mismatches on the other hand, particularly those that lead to the film being in a state of tension upon cooling (i.e., substrates with smaller thermal expansion coefficients), can lead to film cracking.

The perovskites $SrTiO_3$, $LaAlO_3$, and $NdGaO_3$ have good structural and chemical match to the copper-containing high-T_c superconductors. The excellent structural and chemical match of $SrTiO_3$ to the cuprate superconductors immediately made it the substrate of choice for epitaxial growth (Suzuki and Murakami 1987, Chaudhari *et al.* 1987), and for many purposes it remains the reference substrate. However, the high loss tangent of $SrTiO_3$ bars it from high-frequency applications. $LaAlO_3$ has the lowest loss tangent of these perovskite substrates and is available in diameters as large as 100 mm. MgO has even lower dielectric loss, but the multiple in-plane epitaxial orientations that often exist in oxide superconductor films grown on MgO causes undesirable high-angle grain boundaries in the films. This results in lower critical currents and higher surface resistances (Laderman *et al.* 1991).

The extremely low dielectric loss of sapphire (Al_2O_3) makes it an attractive material for high frequency applications, especially when a device structure with a high quality factor Q is desired. It also has high thermal conductivity at low temperature and is available in large sizes. However, its anisotropic dielectric properties complicate device design and the direct growth of high-T_c superconductors on sapphire is plagued by chemical reactions. Several barrier layers, including $SrTiO_3$, $CaTiO_3$, MgO, Y_2O_3-ZrO_2, and CeO_2, have been implemented to circumvent this reaction. Of these, CeO_2 and $CaTiO_3$ barrier layers on sapphire appear to be the most promising. The surface resistance at microwave frequencies of $YBa_2Cu_3O_{7-\delta}$ films grown on these latter barrier layers on sapphire is comparable to the best values obtained on any other substrate (Merchant *et al.* 1992).

The integration of high-T_c superconductor layers with silicon and GaAs substrates is desirable to form superconductor-semiconductor hybrid electronics

and monolithic microwave integrated circuits (MMIC). The direct growth of cuprate superconductors on silicon or GaAs results in an interface reaction and significant diffusion tails into both substrate and film. However, suitable barrier layers have been found. Critical current densities exceeding 10^6 A cm^{-2} at 77 K have been achieved in $YBa_2Cu_3O_{7-\delta}/Y_2O_3$–$ZrO_2/Si$ and $YBa_2Cu_3O_{7-\delta}/MgO/GaAs$ films (Fork 1994). Due to the higher thermal expansion coefficient of GaAs compared to silicon, crack-free $YBa_2Cu_3O_{7-\delta}$ films may be prepared up to a thickness about five times greater than on silicon substrates, where the onset of cracking is about 50 nm (Fork 1994). Another way to overcome the thermal expansion problem when integrating with silicon is to grow on silicon-on-sapphire, where crack-free $YBa_2Cu_3O_{7-\delta}$ films more than 400 nm thick and critical current densities of 4.6×10^6 A cm^{-2} at 77 K have been demonstrated (Fork *et al.* 1991). In light of the desirable high-frequency properties of sapphire substrates and the progress that has been made in integrating them with high-T_c superconductors, sapphire substrates may be the best substrate choice for monolithic superconductor–semiconductor electronics.

Epitaxial growth of high-T_c films on single crystalline substrates used to be the only way to realize J_c values in excess of 10^6 A cm^{-2} at 77 K. However, the ion-beam-assisted deposition (IBAD) process (Iijima *et al.* 1992) and the rolling-assisted, biaxially-textured, substrates (RABiTS) process (Goyal *et al.* 1996, Norton *et al.* 1996) now allow comparable J_c to be achieved in $YBa_2Cu_3O_{7-\delta}$ films deposited on either roll-textured strips of metals (e.g., nickel alloys) using RABiTS or on polycrystalline or amorphous substrates using IBAD. This freedom from single crystal substrates offers incredible flexibility in the integration of high-T_c superconductors films with other materials.

$SrTiO_3$ was not only the first substrate on which epitaxial high-T_c superconductor films were grown (Suzuki and Murakami 1987), it has also become the best studied and most advanced perovskite substrate in terms of substrate preparation. As the results below describe, it is possible to prepare atomically flat (100)$SrTiO_3$ substrates with relatively straight unit-cell-high steps, where the entire surface is terminated at the TiO_2 layer (Kawasaki *et al.* 1994, Koster *et al.* 1998). Initiating growth on a flat substrate of known termination is key to understanding and eventually controlling the nucleation and growth of high-T_c superconductor films and crucial to the preparation of high-T_c multilayers with structural control at the atomic-layer level.

The surfaces of chem-mechanically polished (100)$SrTiO_3$ substrates (as received from the vendor) and imaged by atomic force microscopy (AFM) and reflection high-energy electron diffraction (RHEED) are shown in Figs. 1(a) and 2(a), respectively. These images are indicative of the untreated $SrTiO_3$ surfaces
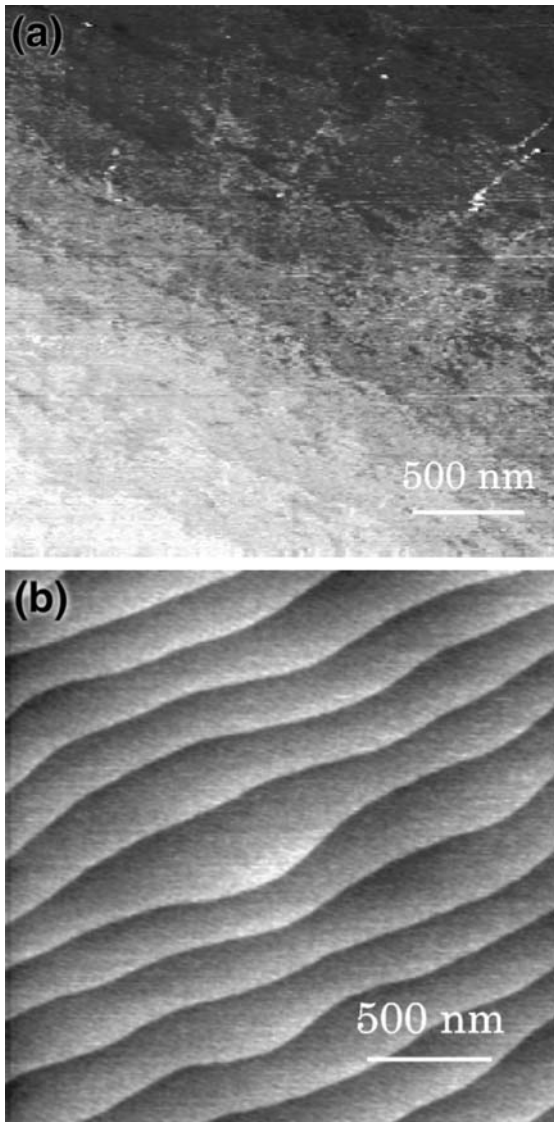
Figure 1
AFM images of (100)SrTiO$_3$ substrate surfaces (a) as-received, following a brief heating to $\sim 650\,°$C in vacuum, and (b) following water soak, buffered-HF etch, and oxygen anneal surface preparation. The vendor of both substrates was ESCETE Single Crystal Technology (reproduced by permission of the American Institute of Physics from *Appl. Phys. Lett.*, 1998, **73**, 2920–2).

Figure 2
RHEED images taken at $\sim 650\,°$C in 15 Pa oxygen of (100)SrTiO$_3$ substrate surfaces (a) as-received and (b) following water soak, buffered-HF etch, and oxygen anneal surface preparation. The vendor of both substrates was ESCETE Single Crystal Technology (reproduced by permission of the American Institute of Physics from *Appl. Phys. Lett.*, 1998, **73**, 2920–2 and of Elsevier Science from *Appl. Surf. Sci.*, 1999, **138–9**, 17–23, respectively).

on which most high-T_c films and multilayers have been grown to date. (100)SrTiO$_3$ can terminate with either the SrO layer or the TiO$_2$ layer and the co-axial impact-collision ion scattering spectroscopy (CAICISS) spectrum in Fig. 3(a) reveals that chem-mechanically polished substrates have mixed SrO and TiO$_2$ termination. The mixed termination remains even after annealing the as-received (100)SrTiO$_3$ surface in oxygen at high temperatures, as shown in Fig. 3(b). However, etching the (100)SrTiO$_3$ in buffered-HF results in a fully TiO$_2$-terminated (100)SrTiO$_3$ surface as revealed by the CAICISS spectra in Fig. 3(c). This buffered-HF process (Kawasaki *et al.* 1994), which has since been enhanced (Koster *et al.* 1998), also makes the surface smoother and more regular as can be seen in the AFM image in Fig. 1(b) and inferred from the RHEED pattern in Fig. 2(b).

2. Properties of YBa$_2$Cu$_3$O$_{7-\delta}$

2.1 Structural Characterization

Improvements in electronic and photonic materials are usually associated with lower defect densities, e.g., lower concentrations of unwanted impurities, dislocations, grain boundaries, twin boundaries, stacking faults, and inclusions, and improved crystalline order. High-T_c superconductors are an exciting case in which defects—of the right kind—are often desired to dramatically improve properties. A clear example of the beneficial potential of such defects is the enhancement of the self-field J_c of single crystals of YBa$_2$Cu$_3$O$_{7-\delta}$ (as well as single crystals of all other high-T_c superconductors studied to date) by over five fold at 4 K and over ten fold at 77 K by subjecting them to heavy-ion irradiation (Civale *et al.* 1991). Although improved, the self-field J_c values of these bombarded single crystals are still an order of magnitude lower than the best films at 77 K, indicating that the films are riddled with even more defects that enhance J_c.

Unraveling which of the defects in the films are beneficial and which are detrimental to a particular

property has been accomplished by correlating transport measurements with structural characterization. In this section we describe some of the defects that exist in high T_c thin films and multilayers, focusing on YBa$_2$Cu$_3$O$_{7-\delta}$ films in which the c-axis is oriented normal to the plane of the substrate (c-axis YBa$_2$Cu$_3$O$_{7-\delta}$ films). We concentrate on YBa$_2$Cu$_3$O$_{7-\delta}$ as it is the best studied of all high-T_c superconductors and on c-axis films as this is generally the most relevant orientation for applications. Note, however, that for most studies and applications there is no obvious reason why yttrium should be the best rare earth (*Re*) to utilize in superconducting *Re*Ba$_2$Cu$_3$O$_{7-\delta}$ films. Indeed, the usage of NdBa$_2$Cu$_3$O$_{7-\delta}$ and SmBa$_2$Cu$_3$O$_{7-\delta}$ films is increasing as they tend to have smoother surfaces and can have slightly higher T_c values than YBa$_2$Cu$_3$O$_{7-\delta}$.

(a) Transmission electron microscopy (TEM)

A cross-sectional transmission electron micrograph of a c-axis YBa$_2$Cu$_3$O$_{7-\delta}$ film grown by PLD on (100)SrTiO$_3$ is shown in Fig. 4 (Eibl and Roas 1990). The dark lines running vertically in this bright-field TEM image are threading dislocations. These dislocations originate in the vicinity of the interface and extend through the film. Although the Burgers vector of the dislocations in Fig. 4 was not determined, subsequent TEM studies of the threading dislocations in YBa$_2$Cu$_3$O$_{7-\delta}$ films grown by PLD on (100) MgO found similar dislocation densities and suggested the Burgers vector to be either [101], [011], or [111] (Aindow and Yeadon 1994, Yeadon *et al.* 1995). Note that when such a threading dislocation intersects the film surface its Burgers vector has a screw component. As described in the next section, atomic force microscopy (AFM) and scanning tunneling microscopy (STM) studies reveal that YBa$_2$Cu$_3$O$_{7-\delta}$ films typically contain comparable densities of dislocations with a screw component at the film surface; thus it is likely that the threading dislocations imaged in Fig. 4 have a Burgers vector with a screw component.

Another important issue that TEM studies have clarified is the chemistry of the interface between high-T_c films and various substrates (Wen *et al.* 1993). Due

Figure 4
Cross-sectional transmission electron micrograph of a YBa$_2$Cu$_3$O$_{7-\delta}$ film epitaxially grown on (100)SrTiO$_3$ by PLD showing $\sim 10^9$ threading dislocations cm^{-2} (reproduced by permission of Materials Research Society from *J. Mater. Res.*, 1990, **5**, 2620–32).
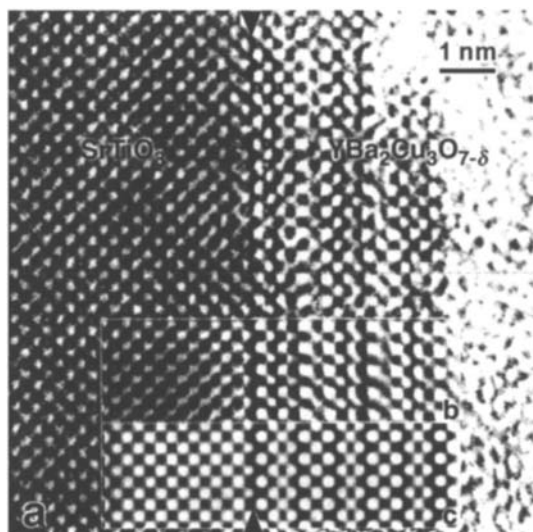
Figure 5
High-resolution cross-sectional TEM of the
$(001)YBa_2Cu_3O_{7-\delta}/(100)SrTiO_3$ interface showing the
TiO_2-termination layer of the $(100)SrTiO_3$ substrate and
the BaO-CuO_2-Y- ... starting layer sequence of the
$YBa_2Cu_3O_{7-\delta}$ film. The arrows indicate the position of
the interface. Regions a, b, and c are the observed image,
the averaged image, and the calculated image
(reproduced by permission of Elsevier Science from
Physica C, 1993, **205**, 354–62).

to the layered structure of all cuprate supercon-
ductors, it is unclear at which specific layer(s)
growth will be initiated, and whether this depends
on the type of substrate or deposition method. A
high-resolution TEM image of the interface between a
c-axis $YBa_2Cu_3O_{7-\delta}$ film and the $(100)SrTiO_3$ subst-
rate upon which it was epitaxially grown is shown in
Fig. 5. Analysis of the interface using TEM image
simulations allowed the starting layer sequence of
the $YBa_2Cu_3O_{7-\delta}$ film to be determined. For c-axis
$YBa_2Cu_3O_{7-\delta}$ grown on TiO_2-terminated $(100)Sr$
TiO_3, the $YBa_2Cu_3O_{7-\delta}$ starts with the BaO mono-
layer followed by the CuO_2, Y, CuO_2, BaO,
CuO, ... monolayers of the $YBa_2Cu_3O_{7-\delta}$ structure,
respectively. This result was found to be independent
of the type of codeposition method used to deposit the
$YBa_2Cu_3O_{7-\delta}$ film (Wen *et al.* 1993). However, the
initial monolayer of a c-axis $YBa_2Cu_3O_{7-\delta}$ film does
depend on the substrate—both the material and its
terminating monolayer.

Due to the narrow composition range within which
the $YBa_2Cu_3O_{7-\delta}$ phase exists, $YBa_2Cu_3O_{7-\delta}$ films
often contain impurity phases. CuO, Y_2O_3, and
$YCuO_2$ are often seen in epitaxial films produced
by *in situ* methods (Catana *et al.* 1993). Other impu-
rity phases including BaO, "$YBa_3Cu_2O_x$" (which is
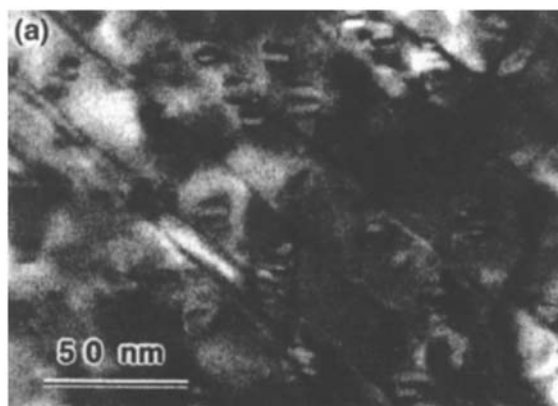
Figure 6
TEM image of a Y_2O_3 precipitate in sputtered
$YBa_2Cu_3O_{7-\delta}$ film. A planar-view image in which the
$\sim 10^{11}$ Y_2O_3 precipitates per cm^2 give rise to the Moiré
fringes (reproduced by permission of the American
Institute of Physics from *Appl. Phys. Lett.*, 1992, **60**,
1016–18).

probably either $YBa_4Cu_3O_{8.5+\delta}$ or $YBa_6Cu_3O_{10+\delta}$),
and Y_2BaCuO_5 have also been reported. Some of
these inclusions can be quite small and epitaxially
oriented to the surrounding $YBa_2Cu_3O_{7-\delta}$ matrix as
is the case for the Y_2O_3 precipitates shown in Fig. 6.

(b) AFM and STM
The morphologies of c-axis oriented $YBa_2Cu_3O_{7-\delta}$
films grown by different vapor phase methods on a
variety of substrates exhibit remarkable similarity,
indicating that the same growth mechanisms are op-
erative (Hawley *et al.* 1991, Gerber *et al.* 1991, Ra-
istrick and Hawley 1994, Schlom *et al.* 1994). The
growth process may generally be described as ledge
growth, emphasizing the energetic preference of the
depositing species to attach to existing ledges (step
edges), which propagate laterally across the substrate
surface as they accommodate species. Depending on
the substrate, its misorientation, the $YBa_2Cu_3O_{7-\delta}$
film thickness, and growth conditions, three different
growth modes are seen in c-axis $YBa_2Cu_3O_{7-\delta}$ films:
spiral growth, layer-by-layer growth, and step-flow
growth. In all three cases STM and AFM reveal a
surface morphology containing closely spaced steps.
These steps, which have a height equal to the c-axis
length of $YBa_2Cu_3O_{7-\delta}$ (1.17 nm), or an integral
multiple of it, separate $(001)YBa_2Cu_3O_{7-\delta}$ terraces.
These terraces are typically only a few tens of nano-
meters wide, indicating the length scale over which
such c-axis $YBa_2Cu_3O_{7-\delta}$ films are atomically flat.
The steps expose (100) and (010) $YBa_2Cu_3O_{7-\delta}$ faces,
which often account for 5–10% of the surface area of
c-axis oriented $YBa_2Cu_3O_{7-\delta}$ films.
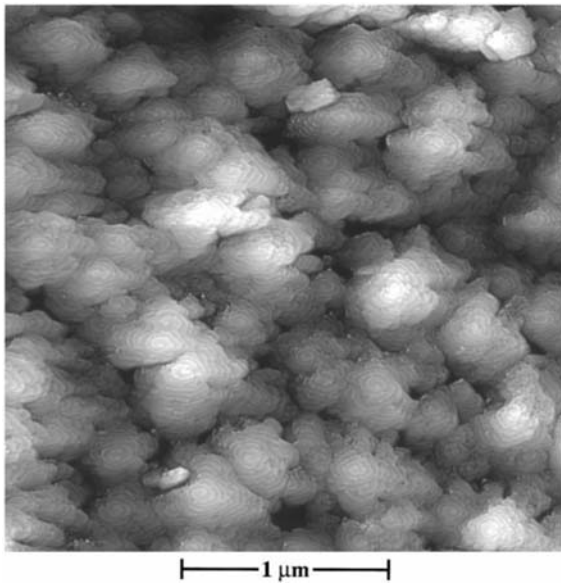
Figure 7
STM image of a *c*-axis oriented, ~ 120 nm thick
$YBa_2Cu_3O_{7-\delta}$ film sputtered on a (100)SrTiO₃ substrate.
Growth spirals emanating from dislocations with a
screw component indicate a density
$(1.4 \pm 0.2) \times 10^9 \, \text{cm}^{-2}$ of dislocations with a screw
component at the film surface (after Schlom *et al*. 1994).

Figure 8
STM image of a *c*-axis oriented ~ 150 nm thick
$YBa_2Cu_3O_{7-\delta}$ film sputtered on a SrTiO₃ substrate. The
image shows a growth spiral with a step height of one
unit cell (~ 1.2 nm). The small dark spots such as the one
pointed to by arrow A are either holes or isolated
insulating regions (e.g., Y_2O_3 precipitates). Clumps of
material with irregular shape, for example at arrow B,
are present at the step edges. The in-plane $\langle 100 \rangle$
directions are indicated (from Schlom *et al*. 1992).

A representative example of the morphology of a
c-axis $YBa_2Cu_3O_{7-\delta}$ film grown under conditions
yielding high T_{c0} (typically 88–90 K) and high
J_c (typically $5 \times 10^6 \, \text{A cm}^{-2}$ at 77 K) on a well-ori-
ented (100) perovskite substrate is shown in Fig. 7
(Schlom *et al*. 1992). The film surface is seen to con-
tain many growth spirals (typically 10^8–$10^{10} \, \text{cm}^{-2}$); a
close-up of a single growth spiral is shown in Fig. 8.
Each spiral emanates from the point at which a dis-
location with a screw component intersects the film
surface. The resulting well-known spiral growth
mechanism (Frank 1949), in which dislocations with
a screw component provide energetically-favorable
attachment sites at the step edges that emerge from
them, occurs frequently in the growth of layered
materials.

A consequence of this growth mechanism is that
the film surfaces are *not* atomically flat over large
distances; instead, the (001) $YBa_2Cu_3O_{7-\delta}$ surface
consists of mounds, each typically 300 nm in dia-
meter. The surface roughness depends on growth
conditions, but height variations of 5–10% of the film
thickness (for films 10–200 nm thick) from the top of
each mound to its intersection with the neighboring
mound are typical in films made by gas phase
codeposition techniques on all of the common
substrates. Figure 9 shows the surface of a *c*-axis

Figure 9
AFM image of a *c*-axis oriented $YBa_2Cu_3O_{7-\delta}$ film
grown by off-axis PLD on a (100)MgO substrate. The
film is characterized by growth spirals emanating from
dislocations with a screw component.

$YBa_2Cu_3O_{7-\delta}$ film grown on (100)MgO; again the growth mode is seen to be spiral growth. How the plethora of dislocations with a screw component are nucleated is not established, although several mechanisms have been proposed (Schlom *et al.* 1992, Burger *et al.* 1994, Schlom *et al.* 1994).

For *c*-axis $YBa_2Cu_3O_{7-\delta}$ films thinner than 10 to 20 nm (Burger *et al.* 1994, Schlom *et al.* 1994), films grown on $YBa_2Cu_3O_{7-\delta}$ substrates (Shimizu *et al.* 1994), or films grown by PLD under conditions where species reach the substrate with significant kinetic energies (Raistrick and Hawley 1994, Dam *et al.* 1998), a layer-by-layer growth mode (also known as "birth and spread") is possible. An example of this growth mode is shown in Fig. 10. The observed morphology, which has been described as "Tower of Hanoi" or "layer-cake-like," is indicative of a growth mode dominated by two-dimensional nucleation coupled with an Ehrlich–Schwoebel step-edge barrier to the diffusion of species from the higher terraces to the incomplete lower terraces. As the surfaces of homoepitaxial $YBa_2Cu_3O_{7-\delta}$ films are free of these high stacks of incomplete terraces (Shimizu *et al.* 1994), the step-edge barrier present in heteroepitaxial growth might be induced by lattice mismatch with the substrate.

If the substrate is misoriented sufficiently (typically a few degrees from the low-index plane on which spiral growth occurs), the growth mode of *c*-axis $YBa_2Cu_3O_{7-\delta}$ changes from spiral growth to step-flow growth (Schlom *et al.* 1992). Step-flow growth occurs by the collective propagation of the terraces

Figure 11
STM image of a *c*-axis oriented ~ 130 nm thick $YBa_2Cu_3O_{7-\delta}$ film sputtered on a vicinal $SrTiO_3$ substrate (misoriented by $\sim 3°$ from (100)) at a substrate temperature of $\sim 750\,°C$. The surface morphology of the film is characterized by growth steps originating from the substrate tilt and from dislocations with a screw component. This image shows the cross-over from spiral growth to step flow (after Mannhart *et al.* 1994).

across the substrate surface. The terraces on vicinal substrate surfaces accommodate the tilt of the substrate and are energetically-favorable incorporation sites. This cross-over in growth mode can be seen in Figs. 11 and 12. In Fig. 11 the misorientation of the substrate is such that both spiral growth and step-flow growth modes are operative. At larger misorientation or higher substrate temperature, as shown in Fig. 12, the growth mode has become purely step-flow.

The impurity phases that occur in $YBa_2Cu_3O_{7-\delta}$ films and have been conclusively identified by TEM, have characteristic morphologies that can be distinguished by AFM (Catana *et al.* 1993). An example is shown in Fig. 13 in which the most common impurity phases found in $YBa_2Cu_3O_{7-\delta}$ films with good transport properties i.e., CuO, Y_2O_3, and $YCuO_2$, are seen.

(c) RHEED
A powerful *in situ* analysis tool used during the growth of high-T_c films is RHEED. The sensitivity of RHEED to surface structure is ideal for monitoring the growth process, and RHEED, in particular, has been key to the atomic-layer engineering of oxide superconductors. RHEED patterns themselves reveal the formation of impurity phases, the in-plane orientation relationship between film and substrate or between the many layers in a multilayer, and allow the relaxation of in-plane lattice constants to be followed in real-time. Growth conditions may be adjusted *during growth* in response to the RHEED pattern.

Figure 10
STM image of a *c*-axis oriented ~ 150 nm thick $YBa_2Cu_3O_{7-\delta}$ film grown on (100)$SrTiO_3$ by PLD. The growth mounds referred to as "wedding cake" towers or "Tower of Hanoi" structures are free of spirals and indicate that the growth mode involves two-dimensional nucleation of unit-cell-high layers and their lateral outgrowth.
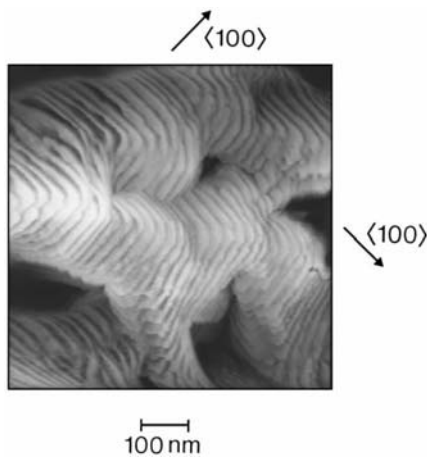
Figure 12
STM image of a *c*-axis oriented, ~ 130 nm thick
$YBa_2Cu_3O_{7-\delta}$ film sputtered on a vicinal (100)$SrTiO_3$
substrate (misoriented by $2.3°$ from (100)) at a substrate
temperature of $\sim 780\,°C$. The surface morphology is
dominated by steps between (001)$YBa_2Cu_3O_{7-\delta}$ terraces
which accommodate the substrate tilt. The
$YBa_2Cu_3O_{7-\delta}$ is growing by step flow. The in-plane
$\langle 100 \rangle$ directions are indicated (after Schlom *et al.*
1992).
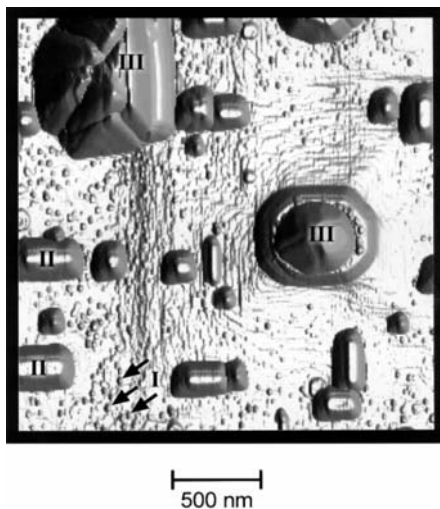
Figure 13
AFM image of the (001) surface of a ~ 100 nm thick
sputtered $YBa_2Cu_3O_{7-\delta}$ film showing densely
distributed outgrowths of three different types: (I)
a-oriented Y_2O_3), (II) $YCuO_2$ and (110)-oriented Y_2O_3,
(III) agglomerates of CuO, Y_2O_3, and a-oriented
$YBa_2Cu_3O_{7-\delta}$) (reproduced by permission of the
American Institute of Physics from *Appl. Phys. Lett.* **63**,
553–5).
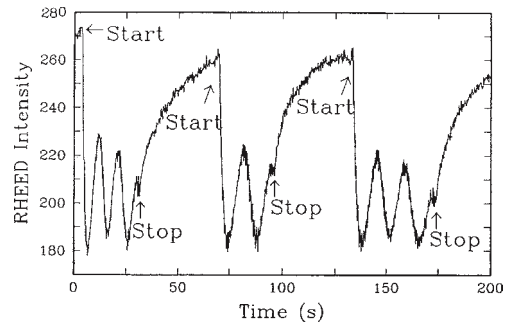
Figure 14
Time dependence of the specular RHEED beam
intensity during deposition of a $YBa_2Cu_3O_{7-\delta}$ film on
(100)$SrTiO_3$ with a $PrBa_2Cu_3O_{7-\delta}$ buffer grown by
growth-interrupted PLD. The growth rate was changed
after the first three layers (reproduced by permission of
the American Institute of Physics from *Phys. Rev. B*,
1994, **49**, 3483–91).

Oscillations in the intensity of the RHEED pattern
allow the thickness of the growing film to be precisely
monitored. In deposition techniques where the spe-
cies are codeposited, the intensity of the RHEED
pattern oscillates as shown in Fig. 14. The period of
these RHEED oscillations corresponds to a deposited
thickness of an electrically neutral formula unit of
each compound (Terashima *et al.* 1990).

For the growth of *c*-axis oriented high-T_c super-
conductor films, this amounts to one *c*-axis unit cell
thickness for $YBa_2Cu_3O_{7-\delta}$ and other high-T_c mate-
rials (e.g., (Ba,K)BiO_3 and $TlBa_2Ca_n-Cu_nO_{2n+3}$)
whose unit cells contain one formula unit, and one
half the *c*-axis unit cell thickness for doped La_2CuO_4
and other high-T_c materials (e.g., $Bi_2Sr_2Ca_{n-1}$
Cu_nO_{2n+4} and $Tl_2Ba_2Ca_{n-1}Cu_nO_{2n+4}$) whose unit
cells contain two formula units. This minimum
growth unit determined by RHEED oscillations is
consistent with the step heights that have been
observed by STM observations on the surfaces of
high-T_c superconductor films and single crystals.

RHEED has traditionally been limited to high-
vacuum deposition techniques like molecular beam
epitaxy (MBE) and ion-beam sputtering, however,
using differential pumping this technique has been
extended to PLD (see *Superconducting Thin Films:
Materials, Preparation, and Properties, Superconduct-
ing Thin Films: Multilayers*, Karl and Stritzker 1992,
Frey *et al.* 1994, Rijnders *et al.* 1997). The rate of
recovery of the RHEED intensity when growth is
interrupted (between the stop and start marks in Fig.
14) provides information on surface diffusion and has
been studied as a function of substrate temperature,
oxidant pressure, and monolayer coverage. These
observations have led to major improvements in PLD
by interrupting and resuming deposition depending

on the RHEED intensity, in order to optimize the smoothness of the films grown (Frey *et al.* 1994, Koster *et al.* 1999).

2.2 Transport Properties

For most studies or applications epitaxial films are required, rather than polycrystalline ones that contain large-angle grain boundaries. This is due to the fact that generally grain boundaries reduce the J_c of high-T_c superconductors and increase their surface resistance (Hilgenkamp and Mannhart 2000). A plot showing the J_c reduction that occurs in $YBa_2Cu_3O_{7-\delta}$ films due to grain boundaries of different angles and different types is shown in Fig. 15. Grain boundaries have also been correlated with an increase in the surface resistance of epitaxial $YBa_2Cu_3O_{7-\delta}$ films (Laderman *et al.* 1991, Lauder *et al.* 1998); this correlation is illustrated in Fig. 16.

The challenges associated with the growth of epitaxial superconducting cuprate films have resulted in such drastic improvements in the deposition technology for multicomponent oxide films, that a large number of groups now routinely grow high-T_c films with superb properties. Of particular significance for basic studies and applications are the J_c and R_s of the films, discussed below. It is important to note that the electrical transport properties, including T_c, J_c, and R_s, depend in different ways on the microstructure and composition of the films. For example, the highest J_c values are obtained in films with a huge density of dislocations, which pin vortices strongly and thus support more current before the resistive losses caused by the movement of vortices set in. These
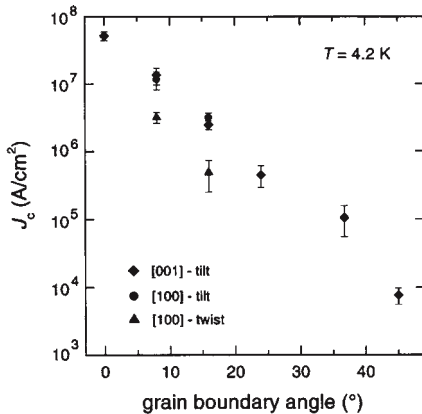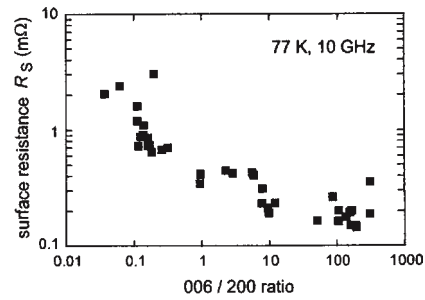
Figure 16
Surface resistance at 77 K and 10 GHz for $YBa_2Cu_3O_{7-\delta}$ films as a function of the intensity of the 006 and 200 X-ray reflections. The 006/200 ratio increases as the amount of *a*-axis grains decreases in the *c*-axis oriented films and is therefore indicative of the number of grain boundaries (reproduced by permission of VCH Verlagsgesellschaft from *Adv. Mater.*, 1998, **10**, 1249–54).

pinning sites, however, reduce T_c. This illustrates that it is not possible to optimize all transport properties with one type of film.

As the density of dislocations and other defects in epitaxial $YBa_2Cu_3O_{7-\delta}$ films is always large compared to that of single crystals, single crystals outperform films in those aspects for which a minimum defect density is key, such as mean free path or T_c. On the other hand, due to their defect structure, films have much higher critical current densities than single crystals. J_c for single crystals are typically in the low 10^5 A cm^{-2} range at 77 K and in the low 10^6 A cm^{-2} range at 4 K (Worthington *et al.* 1987). These J_c values can be increased significantly through the introduction of defects into single crystals, e.g., via irradiation with heavy ions (Civale *et al.* 1991).

The critical current density routinely achieved with *c*-axis oriented epitaxial $YBa_2Cu_3O_{7-\delta}$ films is an impressive 5×10^7 A cm^{-2} at 4.2 K and 5×10^6 A cm^{-2} at 77 K, as shown in Fig. 17. The critical current density is limited by the onset of flux flow, rather than by Josephson decoupling or depairing. As the $YBa_2Cu_3O_{7-\delta}$ films are usually highly twinned, this behavior demonstrates that twin boundaries do not act as Josephson junctions. At first current densities above 10^6 A cm^{-2} (77 K) could only be achieved by films grown on single crystalline $SrTiO_3$ or other perovskite substrates, but now such J_c values are readily obtained in films grown on a large variety of other substrate materials, including sapphire, silicon, silicon-on-sapphire, GaAs, and flexible tapes of stainless steel or nickel, covered by buffer layers such as yttria-stabilized cubic zirconia (Y_2O_3–ZrO_2), MgO, or CeO_2. Such high current densities have been obtained in scalable processes on long, flexible tapes (Foltyn *et al.* 1999, Park *et al.* 1999), or on 8 inch wafers, where a J_c

Figure 15
The intergrain J_c in $YBa_2Cu_3O_{7-\delta}$ films as a function of grain boundary misorientation angle θ for three different types of grain boundaries: [001] symmetric tilt boundaries (◆), [100] symmetric tilt boundaries (●), and [100] twist boundaries (▲) (after Goetz *et al.* 2000).
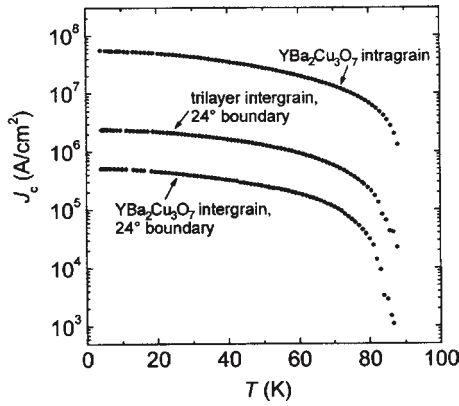
Figure 17
Temperature dependence of the critical current density flowing in the a,b-plane of a $\sim 150\,nm$ thick, c-axis oriented $YBa_2Cu_3O_{7-\delta}$ film. Also shown are the critical current densities across a symmetric $24°$ [001] tilt grain boundary in a $YBa_2Cu_3O_{7-\delta}$ film and in a $Y_{0.7}Ca_{0.3}Ba_2Cu_3O_{7-\delta}/YBa_2Cu_3O_{7-\delta}/Y_{0.7}Ca_{0.3}Ba_2Cu_3O_{7-\delta}$ trilayer.

Figure 18
Superconducting critical current density of a c-axis oriented $YBa_2Cu_3O_{7-\delta}$ film grown by PLD with a dislocation density $n_{disl} = 6 \times 10^8\,cm^{-2}$ at various temperatures as a function of magnetic flux density B applied along the c-direction. The critical current density was measured magnetically using a torque magnetometer. The arrows indicate the field strength of the characteristic field B^* (reproduced by permission of Macmillan Magazines Ltd. from *Nature*, 1999, **399**, 439–42).
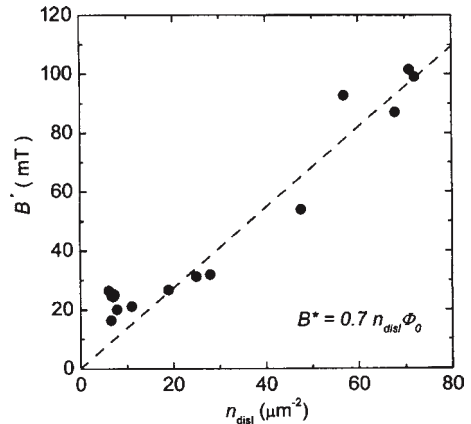
Figure 19
The characteristic magnetic flux density B^* as a function of the dislocation density n_{disl} for $YBa_2Cu_3O_{7-\delta}$ films grown by sputtering and by PLD (reproduced by permission of Macmillan Magazines Ltd. from *Nature*, 1999, **399**, 439–42).

of $3 \times 10^6\,A\,cm^{-2}$ at 77 K varying by only $\pm 5\%$ over the whole wafer area has been achieved (W. Prusseit, personal communication, 2000).

The high critical current densities of $YBa_2Cu_3O_{7-\delta}$ films in the (001) plane are caused by strong pinning of vortices at dislocation cores and weaker pinning at other defects, such as oxygen vacancies and the defects that surround inclusions (Mannhart *et al.* 1992, Douwes *et al.* 1993, Dam *et al.* 1999). This is demonstrated by Figs. 18 and 19. In Fig. 18 the critical current density of a $YBa_2Cu_3O_{7-\delta}$ film is plotted for various temperatures as a function of applied magnetic field. Clearly, as a function of applied field, J_c stays almost constant up to a characteristic field B^*, above which J_c starts to drop rapidly. As shown in Fig. 19, B^* depends almost linearly on the dislocation density in the film, providing evidence that below B^* the flux lines are pinned at the dislocations. At field strengths exceeding B^*, the excessive flux lines are only weakly pinned and J_c is reduced.

For microwave applications, $YBa_2Cu_3O_{7-\delta}$ films have to be grown c-axis oriented on substrates with low dielectric losses such as MgO, $LaAlO_3$, or CeO_2-buffered sapphire. Since grain boundaries cause substantial microwave losses (see for example Habib *et al.* 1998), the films have to be as devoid of grain boundaries as possible. The microwave surface resistance R_s for such films is shown in Fig. 20. In this figure, R_s is plotted as a function of frequency f in comparison to the surface resistance of copper, niobium, Nb_3Sn, and polycrystalline $YBa_2Cu_3O_{7-\delta}$. As can be seen in the figure, at 77 K the surface resistance of $YBa_2Cu_3O_{7-\delta}$ is smaller than R_s of copper for

frequencies below 200 GHz, though still larger than the surface resistance of the conventional superconductors that are measured at much lower temperatures. Good films reach values around 200–300 $\mu\Omega$ at 10 GHz and 77 K. $YBa_2Cu_3O_{7-\delta}$ films have been fabricated in which these values are nearly independent
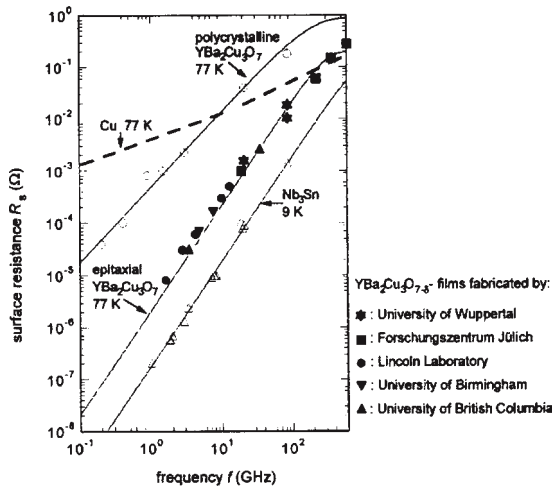
Figure 20
Frequency dependence of the surface resistance R_s at
77 K of high-quality $YBa_2Cu_3O_{7-\delta}$ epitaxial films
fabricated by various laboratories compared to
polycrystalline $YBa_2Cu_3O_{7-\delta}$ samples and copper. Also
shown are the data of Nb_3Sn at 9 K. Note that the data
for the Nb_3Sn samples have been taken at a reduced
temperature $T/T_c \approx 0.5$, whereas the $YBa_2Cu_3O_{7-\delta}$
samples have been measured at $T/T_c \approx 0.85$ (reproduced
by permission of Springer-Verlag from "High-
Temperature-Superconductor Thin Films at Microwave
Frequencies (Springer Tracts in Modern Physics 155),"
1999.)

of the applied microwave power for rf magnetic field
strengths of up to 17 mT at 77 K (Zaitsev *et al.* 1998).

R_s increases with frequency, characteristically var-
ying as f^2. At low temperatures the surface resistance
of $YBa_2Cu_3O_{7-\delta}$ films saturates at values of about
$20\,\mu\Omega$ at $10\,GHz$, which is much larger than the
achievable losses for niobium or Nb_3Sn (Chaloupka
and Müller 1991, Hensen *et al.* 1997, Hein 1999).
It has been shown that the microwave losses are
consistent with the d-wave pairing symmetry of
$YBa_2Cu_3O_{7-\delta}$ (Hensen *et al.* 1997).

An excellent discussion of the microwave properties
of $YBa_2Cu_3O_{7-\delta}$ films as well as $Tl_2Sr_2CaCu_2O_{8+x}$
films (which are also frequently used for microwave
applications) is given in (Hein 1999).

3. Multilayers and Superlattices

High-T_c films, which themselves have a layered
perovskite structure, naturally suggest interspersing
other layers to form a multilayer. Such multilayers
can be divided into three types:

(i) the combination of relatively thick layers of
different compounds, as is done in the integration of

a high-T_c layer with an insulating layer to make a
pick-up coil of a SQUID (see *SQUIDs: The Instru-
ment*);

(ii) the integration of thinner layers of known
compounds as is done in artificial superlattices or in
the fabrication of sandwich-type *SIS* or *SNS* Joseph-
son junctions in which two relatively thick high-T_c
layers are separated by a thin barrier layer of an in-
sulator or conductor; and

(iii) the extreme case in which the high-T_c struc-
tures are altered on the atomic-layer level and the
multilayers produced can be regarded as new high-T_c
phases.

Examples of multilayers consisting of relatively
thick layers of different compounds are $PrBa_2Cu_3$
$O_{7-\delta}/YBa_2Cu_3O_{7-\delta}$ bilayers (Poppe *et al.* 1989) and
field-effect devices in which high-T_c films are layered
with highly insulating $SrTiO_3$ films (Mannhart *et al.*
1991). By cutting diffusion paths by means of arti-
ficial interfaces in $YBa_2Cu_3O_{7-\delta}/Ba_xSr_{1-x}TiO_3/$
$YBa_2Cu_3O_{7-\delta}$ samples, interlayer resistivities as high
as $3 \times 10^{13}\,\Omega\cdot cm$ have been achieved (Frey *et al.*
1996). As multilayer technology is an essential
advantage for many applications, multilayers have
been grown for a variety of studies and applications,
e.g., for superconducting quantum interference
devices (SQUIDs) (Koelle *et al.* 1999) or for tunable
microwave components (Boikov *et al.* 1995). In many
cases it has turned out to be difficult to fabricate
operating multilayers with a high yield; some of the
associated problems are discussed by Wellstood *et al.*
(1994).

Superlattices were first deposited by Triscone and
coworkers, who grew *c*–axis oriented $YBa_2Cu_3O_{7-\delta}/$
$DYBa_2Cu_3O_{7-\delta}$ structures with periods as small as
2.4 nm by sputtering (Triscone *et al.* 1989). Soon
thereafter, *a*-axis oriented superlattices consisting of
$YBa_2Cu_3O_{7-\delta}/PrBa_2Cu_3O_{7-\delta}$ layers were deposited
(Eom *et al.* 1991). Superlattices involving high-T_c su-
perconductors have been applied to many studies of
the physics of high-T_c superconductors, especially
studies of the dimensionality of high-T_c supercon-
ductivity (Triscone *et al.* 1990, Lowndes *et al.* 1990,
Kanai *et al.* 1990), experiments concerning the phys-
ics of Abrikosov vortices (Suzuki *et al.* 1994) or of
phonons in high-T_c superconductors (Storozhuk
et al. 1995). In 1999, doping superlattices consisting
of $YBa_2Cu_3O_{7-\delta}/Y_{1-x}Ca_xBa_2Cu_3O_{7-\delta}$ were deposit-
ed to successfully enhance the grain boundary critical
current density in $YBa_2Cu_3O_{7-\delta}$ films as shown in
Fig. 17 (Hammerl *et al.* 2000). Superlattices contain-
ing other functional materials, such as the CMR-
manganates, have also been grown (Jakob *et al.*
1995).

A very advanced example of multilayers are those
that are engineered on literally the atomic level. MBE
has been particularly successful in creating such mul-
tilayers. This has been used to make device struc-
tures with selectively doped barriers, barriers of new
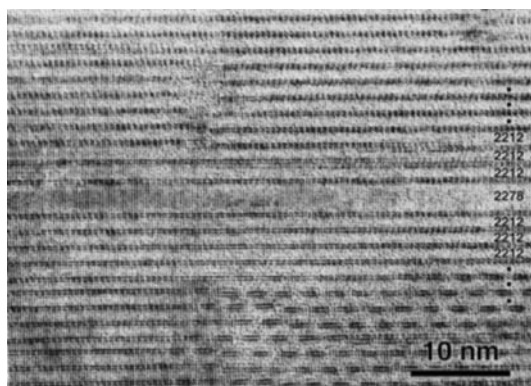
Figure 21
Cross-sectional TEM image of a formula-unit-thick layer of $Bi_2Sr_2Ca_7Cu_8O_{20}$ (2278) sandwiched between thick layers of $Bi_2Sr_2CaCu_2O_8$ (2212) (reproduced by permission of Plenum Publishing Corporation from Bozovic *et al.* 1994).

materials, as well as new high-T_c materials (see *Superconducting Thin Films: Materials, Preparation, and Properties*, *Superconducting Thin Films: Multilayers*, Eckstein and Bozovic 1995, Schlom and Harris 1995). An example is shown in Fig. 21 in which a single formula-unit-thick layer of $Bi_2Sr_2Ca_7Cu_8O_{20}$ (2278) has been grown between thick layers of the superconductor $Bi_2Sr_2CaCu_2O_8$ (2212).

4. Summary and Outlook

As we have described in this article, films and multilayers containing a great number of high-T_c compounds are grown routinely and have exceptional properties—well beyond all expectations when high-T_c superconductivity was discovered in 1986. Multilayers have progressed from combining known materials to literally engineering new materials at the atomic-layer level.

The progress achieved and the knowledge acquired will be applied in the future to the growth of films and heterostructures of other oxide or nitride compounds, into which high-T_c superconducting films will be embedded. As in semiconductors, through doping and material selection, the functionality of individual layers can be tailored in heterostructures. It is expected that the challenges and the potential benefits of such heterostructures will provoke further improvements in the control of film growth.

5. Acknowledgments

See also: Films and Multilayers: Conventional Superconducting; High-temperature Superconductors: Thin Films and Multilayers; Superconducting Materials, Types of; Thin Films Multilayers and Devices, Superconducting

Bibliography

Aindow M, Yeadon M 1994 The origins of growth spirals on laser-ablated $YBa_2Cu_3O_{7-\delta}$ thin films. *Philos. Mag. Lett.* **70**, 47–53

Blank D H A, Rijnders G J H M, Koster G, Rogalla H 1999 *in situ* monitoring by reflective high energy electron diffraction during pulsed laser deposition. *Appl. Surf. Sci.* **138**, 17–23

Boikov Yu A, Ivanov Z G, Kiselev A N, Olsson E, Claeson T 1995 Epitaxial $YBa_2Cu_3O_{7-\delta}/Ba_xSr_{1-x}TiO_3$ heterostructures on silicon-on-sapphire for tunable microwave components. *J. Appl. Phys.* **78**, 4591–5

Bozovic I, Eckstein J N 1996 Superconducting superlattices In: Ginsberg D M (ed.) *Physical Properties of High Temperature Superconductors V*. World Scientific, Singapore, Chap. 3

Burger J, Lippert M, Dorsch W, Bauer P, Saemann-Ischenko G 1994 Observation of the early stages of growth and the formation of growth spirals in epitaxial $YBa_2Cu_3O_{7-\delta}$ thin films by AFM. *Appl. Phys. A* **58**, 49–56

Catana A, Bednorz J G, Gerber Ch, Mannhart J, Schlom D G 1993 Surface outgrowths on sputtered $YBa_2Cu_3O_{7-x}$ films: A combined atomic force microscopy and transmission electron microscopy study. *Appl. Phys. Lett.* **63**, 553–5

Catana A, Broom R F, Bednorz J G, Mannhart J, Schlom D G 1992 Identification of epitaxial Y_2O_3 inclusions in sputtered $YBa_2Cu_3O_7$ films: Impact on film growth. *Appl. Phys. Lett.* **60**, 1016–8

Chaloupka H, Müller G 1991 Applications of HTSC thin films with low microwave losses to linear devices. *Physica C* **180**, 259–66

Chaudhari P, Koch R H, Laibowitz R B, McGuire T R, Gambino R J 1987 Critical-current measurements in epitaxial films of $YBa_2Cu_3O_{7-x}$ compound. *Phys. Rev. Lett.* **58**, 2684–6

Chaudhari P, LeGoues F K, Segmüller A 1987 The microstructure of high-critical current superconducting films. *Science* **238**, 342–4

Chaudhari P, Lin S Y 1994 Symmetry of the superconducting order parameter in $YBa_2Cu_3O_{7-\delta}$ epitaxial films. *Phys. Rev. Lett.* **72**, 1084–7

Civale L, Marwick A D, Worthington T K, Kirk M A, Thompson J R, Krusin-Elbaum L, Sun Y, Clem J R, Holzberg F 1991 Vortex confinement by columnar defects in $YBa_2Cu_3O_7$ crystals: Enhanced pinning at high fields and temperatures. *Phys. Rev. Lett.* **67**, 648–51

Dam B, Huijbregtse J M, Klaassen F C, van der Geest R C F, Doornbos G, Rector J H, Testa A M, Freisem S, Martinez J C, Stäuble-Pümpin B, Griessen R 1999 Origin of high critical currents in $YBa_2Cu_3O_{7-\delta}$ superconducting thin films. *Nature* **399**, 439–42

Dam B, Rector J H, Huijbregtse J M, Griessen R 1998 The transition from 2D-nucleation to spiral growth in pulsed laser deposited $YBa_2Cu_3O_{7-\delta}$ films. *Physica C* **296**, 179–87

Douwes H, Kes P H, Gerber Ch, Mannhart J 1993 Critical currents in $YBa_2Cu_3O_{7-\delta}$ thin films containing screw dislocations. *Cryogenics* **33**, 486–91

Eckstein J, Bozovic I 1995 High-temperature superconducting multilayers and heterostructures grown by atomic layer-by-layer molecular beam epitaxy. *Annu. Rev. Mater. Sci.* **25**, 679–709

Eibl O, Roas B 1990 Microstructure of $YBa_2Cu_3O_{7-x}$ thin films deposited by laser evaporation. *J. Mater. Res.* **5**, 2620–32

Eom C B, Marshall A F, Triscone J -M, Wilkens B, Laderman S S, Geballe T H 1991 A-axis-oriented $YBa_2Cu_3O_7/PrBa_2$-Cu_3O_7 superlattices. *Science* **251**, 780–3

Foltyn S R, Arendt P N, Dowden P C, DePaula R F, Groves J R, Coulter, J Y, Jia Q, Maley M P, Peterson D E 1999 High-T_c coated conductors—performance of meter-long YBCO/IBAD flexible tapes. *IEEE Trans. Appl. Supercond.* **9**, 1519–22

Fork D K 1994 Epitaxial oxides in semiconductors. In: Chrisey D B, Hubler G K (eds.) *Pulsed Laser Deposition of Thin Films*. Wiley, New York, pp. 393–415

Fork D K, Ponce F A, Tramontana J C, Newman N, Phillips J M, Geballe T H 1991 High critical current densities in epitaxial $YBa_2Cu_3O_{7-x}$ thin films on silicon-on-sapphire. *Appl. Phys. Lett.* **58**, 2432–4

Frank F C 1949 The influence of dislocations on crystal growth. *Disc. Farad. Soc.* **5**, 48–79

Frey T, Chi C C, Tsuei C C, Shaw T, Bozso F 1994 Effect of atomic oxygen on the initial growth mode in thin epitaxial cuprate films. *Phys. Rev. B* **49**, 3483–91

Frey T, Mannhart J, Bednorz J G, Williams E J 1996 High-T_c superconductor-insulator-superconductor heterostructures with highly resistive insulator layers. *Jpn. J. Appl. Phys., Part 2* **35**, L384–6

Gerber C, Anselmetti D, Bednorz J G, Mannhart J, Schlom D G 1991 Screw dislocations in high-T_c films. *Nature* **350**, 279–80

Goetz B, Bielefeldt H, Hammerl G, Hilgenkamp H, Mannhart J, Schmehl A, Schneider C W, Schulz R 2000 Critical current densities of tilt and twist grain boundaries in YBCO-bicrystals. To be published.

Goyal A, Norton D P, Budai J D, Paranthaman M, Specht E D, Kroeger D M, Christen D K, He Q, Saffian B, List F A, Lee D F, Martin P M, Klabunde C E, Hartfield E, Sikka V K 1996 High critical current density superconducting tapes by epitaxial deposition of $YBa_2Cu_3O_x$ thick films on biaxially textured metals. *Appl. Phys. Lett.* **69**, 1795–7

Habib Y M, Oates D E, Dresselhaus G, Dresselhaus M S, Vale L R, Ono R H 1998 Microwave power handling in

engineered $YBa_2Cu_3O_{7-\delta}$ grain boundaries. *Appl. Phys. Lett.* **73**, 2200–2

Hammerl G, Schmehl A, Schulz R R, Goetz B, Bielefeldt H, Schneider C W, Hilgenkamp H, Mannhart J 2000 Increasing grain boundary critical currents in high-T_c superconductors at 77 K. *Nature* **407**, 162–4

Hawley M, Raistrick I D, Beery J G, Houlton R J 1991 Growth mechanism of sputtered films of $YBa_2Cu_3O_7$ studied by scanning tunneling microscopy, *Science* **251**, 1587–9

Hein M 1999 *High-Temperature-Superconductor Thin Films at Microwave Frequencies (Springer Tracts in Modern Physics* 155). Springer, Berlin

Helmolt R von, Wecker J, Holzapfel B, Schultz L, Samwer K 1993 Giant negative magnetoresistance in perovskitelike $La_{2/3}Ba_{1/3}MnO_x$ ferromagnetic films. *Phys. Rev. Lett.* **71**, 2331–3

Hensen S, Müller G, Rieck C T, Scharnberg K 1997 In-plane surface impedance of epitaxial $YBa_2Cu_3O_{7-\delta}$ films: Comparison of experimental data taken at 87 GHz with *d*- and *s*-wave models of superconductivity. *Phys. Rev. B* **56**, 6237–64

Hilgenkamp H, Mannhart J 2001 Grain boundaries in high-T_c superconductors. Rev. Mod. Phys. (in press)

Hollmann E K, Vendik O G, Zaitsev A G, Melekh B T 1994 Substrates for high-T_c superconductor microwave integrated circuits. *Supercond. Sci. Technol.* **7**, 609–22

Humphreys R G, Satchell J S, Chew N G, Edwards J A, Goodyear S W, Blenkinsop S E, Dosser O D, Cullis A G 1990 Physical vapour deposition techniques for the growth of $YBa_2Cu_3O_{7-\delta}$ thin films. *Supercond. Sci. Technol.* **3**, 38–52

Iijima Y, Tanabe N, Kohno O, Ikeno Y 1992 In-plane aligned $YBa_2Cu_3O_{7-x}$ thin films deposited on polycrystalline metallic substrates. *Appl. Phys. Lett.* **60**, 769–71

Jakob G, Moshchalkov V V, Bruynseraede Y 1995 Superconductivity and giant magnetoresistance in $YBa_2Cu_3O_7/La_{0.67}Ba_{0.33}O_3$ superlattices. *Appl. Phys. Lett.* **66**, 2564–6

Kanai M, Kawai T, Kawai S 1990 Superconducting superlattices: Verification of two-dimensional nature in high T_c $Bi_2Sr_2(Ca_{1-x}Y_x)Cu_2O_8$ superconductors. *Appl. Phys. Lett.* **57**, 198–200

Karl H, Stritzker B 1992 Reflection high-energy electron diffraction oscillations modulated by laser-pulse deposited $YBa_2Cu_3O_{7-x}$. *Phys. Rev. Lett.* **69**, 2939–42

Kawasaki M, Takahashi K, Maeda T, Tsuchiya R, Shinohara M, Ishiyama O, Yonezawa T, Yoshimoto M, Koinuma H 1994 Atomic control of the $SrTiO_3$ crystal surface. *Science* **266**, 1540–2

Koelle D, Kleiner R, Ludwig F, Dantsker E, Clarke J 1999 High-transition-temperature superconducting quantum interference devices. *Rev. Mod. Phys.* **71**, 631–86

Koinuma H, Kawasaki M, Funabashi M, Hasegawa T, Kishio K, Kitazawa K, Fueki K, Nagata S 1987 Preparation of superconducting thin films of $(La_{1-x}Sr_x)_yCuO_{4-\delta}$ by sputtering. *J. Appl. Phys.* **62**, 1524–6

Koster G, Kropman B L, Rijnders J H M, Blank D H A, Rogalla H 1998 Quasi-ideal strontium titanate crystal surfaces through formation of strontium hydroxide. *Appl. Phys. Lett.* **73**, 2920–2

Koster G, Rijnders G J H M, Blank D H A, Rogalla H 1999 Imposed layer-by-layer growth by pulsed laser interval deposition. *Appl. Phys. Lett.* **74**, 3729–31

Laderman S S, Taber R C, Jacowitz R D, Moll J L, Eom C B, Hylton T L, Marshall A F, Geballe T H, Beasley M R 1991 Resistive loss at 10 GHz in *c*-axis-aligned *in-situ*-grown $YBa_2Cu_3O_7$ films. *Phys. Rev. B* **43**, 2922–33

Laibowitz R B, Koch R H, Chaudhari P, Gambino R J 1987 Thin superconducting oxide films. *Phys. Rev. B* **35**, 8821–3

Lauder A, Myers K E, Face D W 1998 Thin-film high-temperature superconductors for advanced communications and electronics. *Adv. Mater.* **10**, 1249–54

Lemberger T R 1992 Films of high-temperature oxide superconductors In: Ginsberg D M (ed.) *Physical Properties of High Temperature Superconductors III*. World Scientific, Singapore, Chap. 6

Li Q, Xi X X, Wu X D, Inam A, Vadlamannati S, McLean W L, Venkatesan T, Ramesh R, Hwang D M, Martinez J A, Nazar L 1990 Interlayer coupling effect in high-T_c superconductors probed by $YBa_2Cu_3O_{7-x}/PrBa_2Cu_3O_{7-x}$ superlattices. *Phys. Rev. Lett.* **64**, 3086–8

Lowndes D H, Norton D P, Budai J D 1990 Superconductivity in nonsymmetric epitaxial $YBa_2Cu_3O_{7-x}/PrBa_2Cu_3O_{7-x}$ superlattices: The superconducting behavior of CuO bilayers. *Phys. Rev. Lett.* **65**, 1160–3

Mannhart J, Anselmetti D, Bednorz J G, Catana A, Gerber Ch, Müller K A, Schlom D G 1992 Correlation between J_c and screw dislocation density in $YBa_2Cu_3O_{7-\delta}$ films. *Z. Phys. B* **86**, 177–81

Mannhart J, Bednorz J G, Catana A, Gerber Ch, Schlom D G 1994 High-T_c thin films. Growth Modes-Structure-Applications In: Kaldis E (ed.) *Materials and Crystallographic Aspects of HT_c-Superconductivity,* NATO ASI Series Vol. 263. Kluwer, Dordrecht, The Netherlands, pp. 453–70

Mannhart J, Bednorz J G, Müller K A, Schlom D G 1991 Electric field effect on superconducting $YBa_2Cu_3O_{7-\delta}$ films. *Z. Phys. B* **83**, 307–11

Mannhart J, Mayer B, Hilgenkamp H 1996 Anomalous dependence of the critical current of 45° grain boundaries in $YBa_2Cu_3O_{7-x}$ on applied magnetic field. *Z. Phys. B* **101**, 175–9

Matijasevic V, Bozovic I 1996 Thin film processes for high-temperature superconductors. *Curr. Opin. Solid State Mater. Sci.* **1**, 47–53

Merchant P, Jacowitz R D, Tibbs K, Taber R C, Laderman S S 1992 Surface resistance of epitaxial $YBa_2Cu_3O_7$ thin films on CeO_2 diffusion barriers on sapphire. *Appl. Phys. Lett.* **60**, 763–5

Nagata S, Kawasaki M, Funabashi M, Fueki K, Koinuma H 1987 High T_c thin films of $(La_{1-x}M_x)_yCuO_{4-\delta}$ (M = Sr, Ba, Ca) prepared by sputtering. *Jpn. J. Appl. Phys., Part 2* **26**, L410–2

Norton D P, Goyal A, Budai J D, Christen D K, Kroeger D M, Specht E D, He Q, Saffian B, Paranthaman M, Klabunde C E, Lee D F, Sales B C, List F A 1996 Epitaxial $YBa_2Cu_3O_7$ on biaxially textured nickel (001): An approach to superconducting tapes with high critical current density. *Science* **274**, 755–7

Park C, Norton D P, Christen D K, Verebelyi D T, Feenstra R, Budai J D, Goyal A, Lee D F, Specht E D, Kroeger D M, Paranthaman M 1999 Long length fabrication of YBCO on rolling assisted biaxially textured substrates (RABiTS) using pulsed laser deposition. *IEEE Trans. Appl. Supercond.* **9**, 2276–9

Phillips J M 1996 Substrate selection for high-temperature superconducting thin films. *J. Appl. Phys.* **79**, 1829–48

Poppe U, Prieto P, Schubert J, Soltner H, Urban K, Buchal Ch 1989 Epitaxial multilayers of $YBa_2Cu_3O_7$ and $PrBa_2Cu_3O_7$ as a possible basis for superconducting electronic devices. *Sol. State Commun.* **71**, 569–72

Raistrick I D, Hawley M 1994 Scanning tunneling and atomic force microscope studies of thin sputtered films of $YBa_2Cu_3O_7$. In: Shindé S L, Rudman D A (eds.) *Interfaces in High-T_c Superconducting Systems*. Springer, New York, Chap. 2

Rijnders G J H M, Koster G, Blank D H A, Rogalla H 1997 *in situ* monitoring during pulsed laser deposition of complex oxides using reflection high energy electron diffraction under high oxygen pressure. *Appl. Phys. Lett.* **70**, 1888–90

Schlom D G, Anselmetti D, Bednorz J G, Broom R F, Catana A, Frey T, Gerber Ch, Güntherodt H-J, Lang H P, Mannhart J 1992 Screw dislocation mediated growth of sputtered and laser-ablated $YBa_2Cu_3O_{7-\delta}$ films. *Z. Phys. B* **86**, 163–75

Schlom D G, Anselmetti D, Bednorz J G, Gerber Ch, Mannhart J 1994 Epitaxial growth of cuprate superconductors from the gas phase. *J. Cryst. Growth* **137**, 259–67

Schlom D G, Harris J S 1995 MBE growth of high T_c superconductors In: Farrow R F C (ed.) *Molecular Beam Epitaxy: Applications to Key Materials*. Noyes, Park Ridge, NJ, pp. 505–622

Shimizu T, Hirayama F, Oka K, Nonaka H, Matsuda M, Arai K 1994 Growth behavior and surface morphology of homoepitaxial $YBa_2Cu_3O_{7-\delta}$ thin films on flux-grown single crystals. *Appl. Phys. Lett.* **64**, 1289–91

Somekh R E, Barber Z H, Evetts J E 1992 Oxide superconductors: Thin-film deposition In: Evetts J (ed.) *Concise Encyclopedia of Magnetic and Superconducting Materials*. Pergamon Press, Oxford, pp. 431–40

Storozhuk Y, Ham K-M, Teng T, Sooryakumar R, Takeuchi I, Trajanovic Z, Kwon C, Li Q, Venkatesan T 1995 Phonon anomalies in a-axis-oriented $(YBa_2Cu_3O_7)_m$ $(PrBa_2Cu_3O_7)_n$ superconducting superlattices: Evidence for an anisotropic gap function. *Phys. Rev. B* **51**, 6021–7

Suzuki M, Murakami T 1987 Hall effect in superconducting $(La_{1-x}Sr_x)_2CuO_4$ single crystal thin films. *Jpn. J. Appl. Phys., Part 2* **26**, L524–5

Suzuki Y, Triscone J-M, Eom C B, Beasley M R, Geballe T H 1994 Evidence for long localization length along b axis $PrBa_2Cu_3O_7$ in a axis $YBa_2Cu_3O_7/a$, b axis $PrBa_2Cu_3O_7$ superlattices. *Phys. Rev. Lett.* **73**, 328–31

Terashima T, Bando Y, Iijima K, Yamamoto K, Hirata K, Hayashi K, Kamigaki K, Terauchi H 1990 Reflection high-energy electron diffraction oscillations during epitaxial growth of high-temperature superconducting oxides. *Phys. Rev. Lett.* **65**, 2684–7

Terashima T, Iijima K, Yamamoto K, Bando Y, Mazaki H 1988 Single-crystal $YBa_2Cu_3O_{7-x}$ thin films by activated reactive evaporation. *Jpn. J. Appl. Phys., Part 2* **27**, L91–3

Triscone J-M, Fischer Ø 1997 Superlattices of high-temperature superconductors: synthetically modulated structures, critical temperatures and vortex dynamics. *Rep. Prog. Phys.* **60**, 1673–721

Triscone J-M, Fischer Ø, Brunner O, Antognazza L, Kent A D, Karkut M G 1990 $YBa_2Cu_3O_7/PrBa_2Cu_3O_7$ superlattices: Properties of ultrathin superconducting layers separated by insulating layers. *Phys. Rev. Lett.* **64**, 804–7

Triscone J-M, Karkut M G, Antognazza L, Brunner O, Fischer Ø 1989 Y-Ba-Cu-O/Dy-Ba-Cu-O superlattices: A first step towards the artificial construction of high-T_c superconductors. *Phys. Rev. Lett.* **63**, 1016–9

Tsuei C C, Kirtley J R, Chi C C, Yu-Jahnes L S, Gupta A, Shaw T, Sun J Z, Ketchen M B 1994 Pairing symmetry and flux quantization in a tricrystal superconducting ring of $YBa_2Cu_3O_{7-\delta}$. *Phys. Rev. Lett.* **73**, 593–6

Waser R, Speck J, Foster C (eds.) 2001 *Ferroelectric Thin Films*. Springer, Berlin

Wellstood F C, Kingston J J, Clarke J 1994 Thin-film multilayer interconnect technology for $YBa_2Cu_3O_{7-x}$. *J. Appl. Phys.* **75**, 683–702

Wen J G, Traeholt C, Zandbergen H W 1993 Stacking sequence of YBa$_2$Cu$_3$O$_7$ thin film on SrTiO$_3$ substrate. *Physica C* **205**, 354–62

Wördenweber R 1999 Growth of high-T_c thin films. *Supercond. Sci. Technol.* **12**, R86–102

Worthington T K, Gallagher W J, Dinger T R 1987 Anisotropic nature of high-temperature superconductivity in single-crystal YBa$_2$Cu$_3$O$_{7-x}$. *Phys. Rev. Lett.* **59**, 1160–3

Yeadon M, Aindow M, Wellhöfer F, Abell J S, Avenhaus B, Lancaster M J, Woodall P 1995 Microstructures and properties of laser-ablated epitaxial Y-Ba-Cu-O thin films for electronic device applications. *IEEE Trans. Appl. Supercond.* **5**, 1214–7

Yoshimoto M, Maeda T, Shimozono K, Koinuma H, Shinohara M, Ishiyama O, Ohtani F 1994 Topmost surface analysis of SrTiO$_3$(001) by coaxial impact-collision ion scattering spectroscopy. *Appl. Phys. Lett.* **65**, 3197–9

D. G. Schlom
Penn State University, University Park
Pennsylvania, USA

D. G. Schlom and J. Mannhart
Universität Augsburg, Germany

High-temperature Superconductors: Transport Phenomena

The discovery of high-temperature superconductors in 1986 by Bednorz and Müller (1988) started a worldwide explosive growth of research and development in the field of superconductivity. The discovered new class of superconductors shows a critical temperature T_c for the appearance of superconductivity much higher than for the superconductors known before. The value of T_c even exceeds the boiling point (77.3 K) of liquid nitrogen, a result highly important for the technical applications of superconductors. The discovered new class of superconductors are cuprate perovskites with electronic properties which depend sensitively on the admixture of specific doping elements. Up to now the highest critical temperature T_c was observed for the cuprate HgBa$_2$Ca$_2$Cu$_3$O$_{8+\delta}$ with $T_c = 133$ K at room pressure (Tinkham 1996, Waldram 1996).

The common structural element of the copper perovskites are the copper oxide planes in which the superconducting properties are believed to originate. The crystallographic unit cell contains varying numbers of CuO$_2$ planes, depending on the particular oxide compound. Because of the different possible chemical composition there are five main families of high-temperature superconductors, the "parent compounds" of which are listed in Table 1.

In addition to the high values of the critical temperature T_c and the strong anisotropy due to the

Table 1
Parent compounds of the five main families of the cuprate superconductors.

	T_c (K)
La$_{2-x}$Sr$_x$CuO$_4$	38
YBa$_2$Cu$_3$O$_{7-\delta}$	93
Bi$_2$Sr$_2$CaCu$_2$O$_{8+x}$	94
Tl$_2$Ba$_2$Ca$_2$Cu$_3$O$_{10+x}$	125
HgBa$_2$Ca$_2$Cu$_3$O$_{8+\delta}$	133

prominent role of the CuO$_2$ planes, the third novel feature of the cuprate superconductors is the small value of the superconducting coherence length ξ. The length ξ indicates the size of the wave function representing a Cooper pair, i.e., the elementary constituent of superconductivity. The coherence length reaches values as small as only 1–2 nm. Hence, the upper critical magnetic field B_{c2} attains values as high as $B_{c2} = \varphi_0/2\pi\xi^2 = 100$–200 T. Here, $\varphi_0 = h/2e = 2.07 \times 10^{-15}$ Vs is the magnetic flux quantum (h Planck's constant, e elementary charge). The small values of the coherence length in the cuprate superconductors have other important consequences: The number of overlapping Cooper pairs within a "coherence volume" $\frac{4}{3}\pi\xi^3$ is about 20, whereas in the classical superconductors it is about 1×10^6 times larger (since ξ is up to 100 times larger than in the cuprates). Furthermore, the small values of ξ result in a high sensitivity of the superconducting properties of the cuprates to atomic size defects such as, for example, oxygen vacancies (Poole *et al.* 1995).

1. Normal-state Transport Properties

The undoped cuprate perovskites are antiferromagnetic electric insulators, the antiferromagnetism resulting from the arrangement of localized spins on the Cu atoms of the CuO$_2$ planes. Superconductivity only appears after doping, and there exists an optimum doping concentration for each cuprate, where a maximum value of T_c is obtained. Most high-temperature superconductors require hole doping. However, a few electron-doped oxide superconductors have also been found. In many cases doping is accomplished by the variation of the oxygen stoichiometry. Hence, during the preparation of the high-temperature superconductors the oxygen concentration must be carefully controlled (Levin *et al.* 1991, Pickett 1989).

The normal-state *electric resistivity* of the optimally doped high-temperature superconductors is several orders of magnitude larger than in a typical metal. Furthermore, it is highly anisotropic. The electric conduction occurs mainly within the CuO$_2$ planes (oriented parallel to the crystallographic *ab* planes), whereas in the perpendicular direction (along the

crystallographic c axis) it is strongly reduced. The corresponding resistivity values are referred to as ρ_{ab} and ρ_c, respectively. Near room temperature for a typical cuprate such as $YBa_2Cu_3O_{7-\delta}$ we have the values $\rho_{ab} = 200$–$500\,\mu\Omega cm$, compared to $\rho = 2$–$5\,\mu\Omega cm$ for a typical metal. The ratio ρ_c/ρ_{ab} of the anisotropy near room temperature ranges from 30–60 for $YBa_2Cu_3O_{7-\delta}$ up to 1×10^5 for $Bi_2Sr_2CaCu_2O_8$. The fact, that near room temperature ρ_{ab} is about 100 times larger than the resistivity in a typical metal, is partly due to the lower charge carrier concentration and the pronounced anisotropy in the cuprate.

Above the critical temperature T_c near optimum doping the normal-state resistivity of many cuprate superconductors increases linearly with temperature. A prominent exception is the electron-doped cuprate $Nd_{2-x}Ce_xCuO_y$ showing $\rho_{ab} \sim T^2$ near optimum doping. This normal-state resistive behavior can be qualitatively explained in terms of the nature of the scattering processes and the electronic density of states (DOS). It is now well established that in the cuprates the electron scattering processes are dominated by the electron–electron interaction, in contrast to electron–phonon scattering prevailing in metals. An important piece of evidence for this scattering behavior comes from the pronounced increase of the electron mean free path with decreasing temperature below T_c as soon as the quasi-particles (as scattering partners) are frozen out because of the opening of the energy gap. With decreasing temperature this also leads to a sharp upwards turn of the thermal conductivity $\kappa(T)$ at T_c. The thermal conductivity then passes through a maximum near $T_c/2$. If the electron–phonon interaction would dominate, such an abrupt change of the temperature dependence of the electron mean free path at T_c would not be expected.

The $\rho_{ab} \sim T^2$ behavior observed near optimum doping in $Nd_{2-x}Ce_xCuO_y$ is well consistent with the electron–electron interaction as the dominant scattering mechanism. On the other hand, the linear temperature dependence $\rho_{ab} \sim T$ found usually in the optimally hole-doped cuprates can be qualitatively explained by a sharp peak (Van Hove singularity) in the electronic DOS near the Fermi energy E_F. The additional phase space for scattering within this peak region then leads to the proportionality for the scattering rate $\tau^{-1} \sim k_B T$ (marginal Fermi liquid), instead of the usual Fermi liquid behavior $\tau^{-1} \sim (k_B T)^2$. Here, k_B is Boltzmann's constant (Newns *et al.* 1993).

The normal-state *thermopower* (Seebeck coefficient) represents a transport property depending highly sensitively on the electronic structure and the doping level of the cuprates. There exists an interesting correlation between the thermopower and the critical temperature T_c. Depending on the doping level, the thermopower at room temperature of different p doped systems follows a universal curve traversing zero at optimum doping (corresponding to the maximum value of T_c). The typical temperature
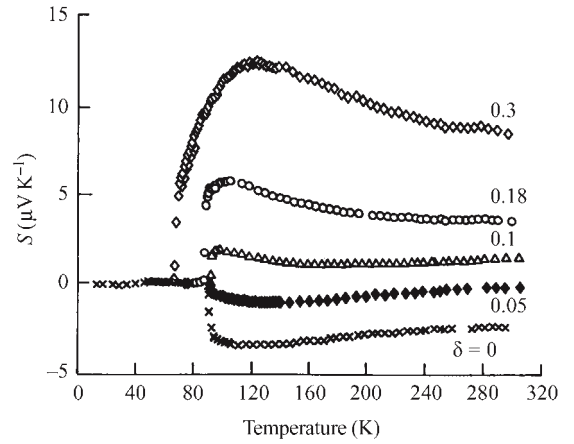
Figure 1
Thermopower S of the cuprate $YBa_2Cu_3O_{7-\delta}$ versus temperature for different values δ of the oxygen depletion (after Cooper *et al.* 1991).

dependence of the thermopower shows an increase of its absolute value above T_c, turning into a flat curve with falling tendency at higher temperatures. This behavior is strongly different from the proportionality to T expected in the limit of a wide ($\gg k_B T$) conduction band. A typical series of curves is shown in Fig. 1 for $YBa_2Cu_3O_{7-\delta}$ at different levels δ of oxygen depletion (Cooper *et al.* 1991).

This dependence of the thermopower on the temperature and the doping level can be understood from standard transport theory in combination with the sharp peak in the electronic DOS near the Fermi level. For the (positive) holes the thermopower is

$$S = \frac{k_B}{|e|} \frac{\int \sigma_E \frac{\partial f}{\partial E} \frac{E - E_F}{k_B T} \, dE}{\int \sigma_E \frac{\partial f}{\partial E} \, dE} \tag{1}$$

with the electric conductivity given by

$$\sigma = -\int \sigma_E \frac{\partial f}{\partial E} \, dE \tag{2}$$

(Kubo–Greenwood formula). Here f is the Fermi function, and σ_E contains the density of states and the scattering processes. We emphasize that, because of the sharp peak in the electronic DOS near E_F, the derivative $\partial f/\partial E$ changes only little in the relevant energy interval. From Eqn. (1) we can predict the following qualitative behavior.

If E_F is smaller (larger) than the energy of the DOS peak, the contribution with $E - E_F > 0$ (< 0) dominates and the thermopower will be positive (negative). Hence, the sign reversal of the thermopower is

expected, when the Fermi energy coincides with the energy of the DOS peak. Alternatively, according to the "Van Hove scenario" of high-temperature superconductivity this location of the Fermi level corresponds exactly to the optimum doping level yielding the maximum value of T_c. The experiments performed with different p doped cuprate systems at varying doping levels mentioned above well confirmed these ideas (Newns *et al.* 1993).

In the orthorhombic form of the cuprate $YBa_2Cu_3O_{7-\delta}$ one of the copper oxide planes per elementary cell contains CuO chains along the b axis, but not along the a axis. This introduces some anisotropy of the transport properties even within the ab planes, in addition to the large anisotropy between the ab plane and the c direction.

The normal state *Hall effect* represents a complicated subject. However, it is this effect that led to the concepts of "hole-doped" and "electron-doped" cuprate superconductors. The Hall coefficient $R_H = 1/nq$ yields information on the nature of the charge carriers involved in the electronic transport. Here n and q are the concentration and elementary charge of the charge carriers, respectively. For hole-doped conductors R_H is positive, whereas for electron-doped materials it is negative. For the magnetic field orientation in c direction in most of the high-temperature superconductors R_H is positive, indicating hole doping. Compounds derived from Nd_2CuO_4 by substitutional alloying ($Nd_{2-x}Ce_xCuO_y$) are the major exception and show electron doping. In the latter case of $Nd_{2-x}Ce_xCuO_y$ an additional complication arises from the fact that a two-band model appears to be necessary, with an electron-like and a hole-like section, for describing the electronic properties.

An unexpected result of the Hall effect measurements is the observed strong temperature dependence of the Hall coefficient, especially near optimum doping. Such a temperature dependence does not arise in a canonical Fermi liquid. In $YBa_2Cu_3O_7$, the most intensively studied cuprate superconductor, for the inverse Hall coefficient the relation $R_H^{-1} = \alpha + \beta T$ has been found, where α and β are constants. An interesting quantity is the Hall angle, θ_H, the angle between the electric current density and the total electric field, which is given by $\tan\theta_H = R_H B/\rho$. From electronic transport theory, one finds that $\tan\theta_H$ is equal to $\langle \omega_c \tau \rangle$, a weighted average for the dominant conducting particles of the product of their cyclotron frequency $\omega_c = qB/m^*$ for the electron orbits in the magnetic field and their scattering time τ (m^* = effective mass).

Hence, $\cot\theta_H$ is expected to be proportional to the scattering rate τ^{-1}. In $YBa_2Cu_3O_{7-\delta}$ across the whole of the metallic doping range the relation $\cot\theta_H = \alpha + \beta T^2$ is valid in good approximation, again, α and β being constants. We conclude that the scattering rate also shows this $\alpha + \beta T^2$ temperature dependence. Noting $R_H^{-1} \sim n$ and $\rho \sim (n\tau)^{-1}$, we see that

the linear temperature dependence of R_H^{-1} and the $(\alpha + \beta T^2)$ behavior of the scattering rate appear consistent with the linear temperature dependence of the resistance observed in many cuprates discussed above. We emphasize that we must restrict our discussion to rough and qualitative remarks only, leaving out many details of the electronic structure of these materials.

2. Granular Structure

Except for the highly specialized procedures for material fabrication developed for the growth of axis-oriented epitaxial films and single crystals, the high-temperature superconductors are usually prepared as ceramics with a granular structure. Within the grain boundary regions superconductivity is strongly weakened or even totally absent. Hence, the grain boundaries in the cuprate superconductors have to date presented a challenging technological problem. It still is an important goal of the present technological developments to minimize the residual electric resistance due to the grain boundaries as much as possible. Recently, special doping processes for the grain boundaries in order to improve the electric conductivity in these regions have been discussed. The important quantity to deal with is the critical current density at which a specific nonzero electric field is generated in the superconductor, resulting in power dissipation. The current flow pattern in a multigranular superconductor has been treated in analogy to the structure of a brick wall (*brick wall model*). In addition to the granular structure, the poor ductility of the cuprate superconductors continues to represent a severe obstacle, in particular for the technological power applications.

For the applications of high-temperature superconductors in microelectronics the critical current density in thin films has received a large amount of attention. Here c axis oriented epitaxial films of $YBa_2Cu_3O_{7-\delta}$ clearly represent the work horse. At 77 K and in zero magnetic field, critical current densities of 1×10^6–1×10^7 Acm^{-2} have been achieved, a highly impressive result of the associated materials science.

Whereas the grain boundaries in the cuprate superconductors are clearly detrimental to many technical applications, in one specific case they turned out to be extremely useful and they represent a well controllable and stable Josephson junction. The grain boundary Josephson junctions are fabricated by growing an epitaxial superconducting cuprate film on a bicrystal acting as the substrate. The grain boundary separating the two single-crystalline pieces of the substrate is then transferred to the epitaxial film deposited subsequently on the bicrystalline substrate. In this way, during recent years Josephson devices and superconducting quantum interferometers (SQUIDs)

operating up to 77 K have been fabricated (see *Josephson Junctions: High-T_c*).

3. Current-induced Vortex Motion

In a magnetic field in the range between the lower and upper critical field, B_{c1} and B_{c2}, respectively, below the critical temperature T_c the superconducting mixed state is established. In the mixed state the superconductor is penetrated by a more or less perfectly ordered 2D lattice of flux lines, each flux line carrying a single magnetic flux quantum φ_0. The regularity of this lattice depends on the spatial homogeneity of the superconductor. The following will be restricted to the case where the magnetic field and, hence, the flux lines, are oriented along the crystallographic c axis. In this case the flux lines degenerate into stacks of pancake vortices (or point vortices) attached to the CuO_2 planes constituting the superconducting structural elements of the cuprates. Under the influence of an external force the flux lines or pancake vortices can be set into motion. This vortex motion represents one of the most important processes in superconductors, since it results in an electric field of quantum mechanical origin and thereby destroys superconductivity (Huebener 2001).

An electric transport current of density j generates the *Lorentz force* $\underline{j} \times \underline{\varphi}_0$ per unit length of flux line. The dynamic state of the vortex lattice is determined by the force equation:

$$\underline{j} \times \underline{\varphi}_0 - \eta \underline{v}_\varphi - \alpha(\underline{v}_\varphi \times n) + \underline{f}_p = 0 \qquad (3)$$

The Lorentz force is balanced by the damping force $\eta \underline{v}_\varphi$, the Hall force $\alpha(\underline{v}_\varphi \times \underline{n})$, and the pinning force $\underline{f}_p$. $\underline{v}_\varphi$ is the vortex velocity, η and α are damping coefficients, $\underline{n}$ is a unit vector in magnetic field direction. Vortex motion always results in an electric field $\underline{E}$ according to the equation:

$$\underline{E} = -\underline{v}_\varphi \times \underline{B} \qquad (4)$$

Equation (4) is derived from the phase change of the macroscopic wave function describing the Cooper pair condensate, effected by the vortex motion. (It is intimately connected with the Josephson voltage frequency relation.) In the absence of the Hall force and the pinning force we see from Eqns. (3) and (4) that $\underline{v}_\varphi$ is perpendicular to $\underline{j}$ and, therefore, $\underline{E}$ is parallel to $\underline{j}$. As a result power dissipation $\underline{E} \times \underline{j}$ per unit volume occurs, and superconductivity is destroyed. It is this mechanism of current induced vortex motion and the appearance of flux-flow resistance which represent the main challenge to maintaining superconductivity. Because of the three characteristic novel features of the high-temperature superconductors (high critical temperature, small coherence length, and large anisotropy) vortex motion and the appearance of flux-flow resistance is highly facilitated in the cuprates and

turns out to be an even more challenging issue than in the classical superconductors.

It is the pinning force in Eqn. (3) which can result in a strong reduction of vortex motion and, hence, contributes to sustaining superconductivity at finite electric transport current. Flux pinning is accomplished by material inhomogeneities (pinning centers) causing a local depression of the Gibbs free energy density of the vortex lattice. Because of the short coherence length in the cuprates, atomic size defects, such as oxygen vacancies in the CuO_2 planes or defects produced by substitutional alloying, already act as important pinning centers. The pinning force eventually acting on the vortex lattice results from the combination of the elementary pinning interaction between a vortex and the pinning center with the elastic properties of the vortex lattice. The elastic properties come in, since the vortex lattice must be deformed in order to accommodate the spatial configuration of the pinning sites. Because of this, flux pinning turns out to be a highly complex phenomenon. However, because of its extreme importance for the technical applications of the cuprate superconductors, the subject of flux pinning has recently attracted a large amount of research and development.

If the damping force $\eta \underline{v}_\varphi$ and the pinning force would be absent in Eqn. (3), the vortices would move parallel to the current density $\underline{j}$, the electric field $\underline{E}$ would be perpendicular to $\underline{j}$ (pure Hall electric field), and the power dissipation $\underline{j} \times \underline{E}$ would vanish. However, for this to happen the quasi-particle scattering time τ must approach the limit $\tau \to \infty$.

According to the Bardeen–Stephen model, valid for the classical superconductors and serving, at best, as a qualitative orientation for the high-temperature superconductors, the flux-flow resistivity ρ_f is given by

$$\rho_f = \rho_n \frac{B}{B_{c2}}$$

where ρ_n is the normal-state resistivity. In this model the vortex core is taken as a normal-state cylinder of radius ξ. The ratio B/B_{c2} then represents the volume fraction of this normal phase. For the damping coefficient η one finds $\eta = \varphi_0 B_{c2}/\rho_n$. In the current-induced flux-flow state the Hall angle θ_H is given by tan $\theta_H = \omega_c \cdot \tau$, similar to the situation in the normal state. In the superconducting mixed state of the cuprates the Hall angle is generally small (typically tan $\theta_H \approx 1 \times 10^{-2}$), and dissipative vortex motion perpendicular to the electric current direction dominates.

In contrast to the classical superconductors, in the cuprate superconductors the description of the vortex core as a normal-state cylinder of radius ξ is only a rough approximation. Here also the symmetry of the pair wave function must be discussed. It is now well established that in the p-doped cuprates the pair wave

function shows d-wave symmetry, with four node lines where the gap energy reaches zero. This has important consequences for the quasi-particle scattering in the mixed state. However, at present the experimental and theoretical clarification of this point is still in progress. Another new aspect of quasi-particle scattering originates from the extremely short coherence length and the corresponding small vortex-core diameter in the cuprates. As a result, quantum effects of the electronic structure of the vortex cores (quantum confinement) can become important. The description of the vortex core as a normal-state cylinder of radius ξ is then highly inadequate. At least in the limit $T \ll T_c$ this can lead to a strong reduction of the phase space available for quasi-particle scattering. Again, at present this issue is still under experimental and theoretical investigation (Huebener 2001).

The peculiar features of the high-temperature superconductors (high critical temperature, short coherence length, and anisotropy leading to the pancake-vortex structure) have important consequences for the dynamic properties of the vortex lattice. There exists an irreversibility line in the phase space of magnetic field and temperature, above which the magnetization is perfectly reversible with no detectable flux pinning. Alternatively, below this line the magnetization becomes hysteretic, and the equilibrium vortex distribution cannot be established any more because of flux pinning. From these observations in the 1990s the new concept of "vortex matter" evolved, with a liquid, glassy, and crystalline state, displaying a complex phase diagram. These novel features strongly influence the transport processes associated with vortex motion.

An immediate result of the different phases of vortex matter appearing in the mixed state is the broadening of the resistive transition in a magnetic field. Whereas in the classical superconductors the drop in the electric resistivity due to the onset of superconductivity is usually shifted to lower temperatures with increasing magnetic field, in high-temperature superconductors the resistively measured onset temperature of superconductivity is only weakly magnetic field dependent, but the transition curve is broadened instead, and the broadening increases strongly with increasing magnetic field. A typical case is shown in Fig. 2a for an epitaxial c axis oriented $YBa_2Cu_3O_{7-\delta}$ film for magnetic fields ranging from 0 to 12 T and oriented in c direction. An exception from this broadening of the resistive transition in a magnetic field has been observed for the electron-doped cuprate superconductor $Nd_{2-x}Ce_xCuO_{4\pm y}$ in the whole doping regime from slightly underdoped to slightly overdoped. Here the whole resistive transition curve is shifted to lower temperatures with increasing magnetic field, more like in classical superconductors.

The motion of the vortex lattice due to the Lorentz force of an electric transport current is accompanied by the transport of entropy carried by the vortex
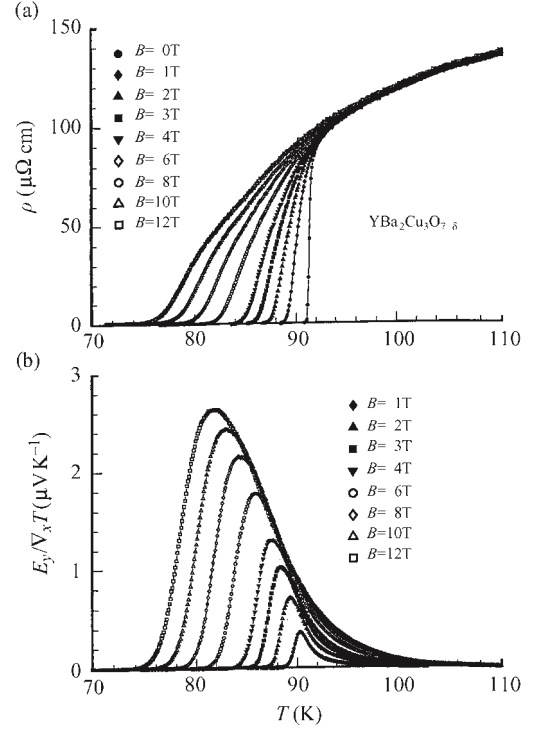
Figure 2
(a) Flux-flow resistivity of the cuprate superconductor $YBa_2Cu_3O_{7-\delta}$ versus temperature for different magnetic fields oriented in c direction. (b) Normalized Nernst electric field $E_y/\nabla_x T$ versus temperature for the same sample and magnetic fields as in (a).

lattice. This entropy transport causes a temperature gradient perpendicular to the directions of the electric current and magnetic field. It is referred to as the Ettinghausen effect and has been observed in a number of high-temperature superconductors. If the electric current density j_x is assumed in x direction and the magnetic flux density B_z in z direction, the heat current density U_y in y direction associated with the entropy transport is

$$U_y = \varepsilon B_z \kappa j_x \tag{5}$$

Here ε is the Ettinghausen coefficient and κ the heat conductivity. The Ettinghausen effect represents one of the major observations supporting the concept of vortex motion as the mechanism generating the electric resistance in the superconducting mixed state.

The experiments on the flux-flow Hall effect in the cuprate superconductors indicated an unexpected reversal of the sign of the Hall voltage at temperatures below the superconducting transition. This effect has been observed in different materials and appears to

represent an intrinsic property. A satisfactory theoretical understanding of this effect has not yet been reached, and the theoretical discussions are still controversial.

4. Vortex Motion in a Temperature Gradient

In a temperature gradient applied to a superconductor in the mixed state the thermal force $-S_\varphi \mathrm{grad}\,T$ acts on the vortex structure, driving the magnetic flux quanta from the hot to the cold side of the specimen. Here S_φ is the transport entropy per unit length of flux line. The thermal force is the driving force in all thermal diffusion phenomena, and the transport entropy represents a characteristic property of the specific type of particle under consideration. (The heat current density U carried by a flux-line lattice moving with velocity $\underline{v}_\varphi$ is $U = nTS_\varphi \underline{v}_\varphi$, where $n = B/\varphi_0$ is the density of flux lines.) For treating the dynamic state of the vortex lattice driven by a temperature gradient, in Eqn. (3) the Lorentz force $\underline{j} \times \underline{\varphi}_0$ must be replaced by the thermal force $-S_\varphi \mathrm{grad}\,T$. If we neglect the Hall effect and flux pinning, take the temperature gradient in x direction and the magnetic field in z direction, we see from Eqn. (4) that the resulting flux-flow electric field is oriented in y direction. This electric field E_y is given by

$$E_y = \nu B_z \frac{\partial T}{\partial x} \qquad (6)$$

and the effect is referred to as the Nernst effect. ν is the Nernst coefficient. The Ettinghausen coefficient ε and the Nernst coefficient ν are coupled through the Bridgman relation of irreversible thermodynamics

$$T\nu = \varepsilon \kappa \qquad (7)$$

The Nernst effect has been investigated in the mixed state of a number of high-temperature superconductors. In Fig. 2(b) we show typical results obtained for the same epitaxial $YBa_2Cu_3O_{7-\delta}$ film and the same magnetic fields as in Fig. 2(a). In the normal state sufficiently far above T_c (of about 91 K in this case) the Nernst electric field E_y is seen to be negligible. With decreasing temperature E_y increases and passes through a maximum. As one expects because of the flux-flow process, E_y increases with increasing flux density B. On the low-temperature end of the curves the Nernst electric field E_y and the resistivity vanish because of flux pinning. From Fig. 2(b) we see also, that the flux-flow Nernst effect clearly extends to temperatures well above the critical temperature T_c measured at zero magnetic field.

This is due to fluctuation effects, which become stronger with increasing magnetic field. These fluctuation effects can be measured with high accuracy, since the Nernst effect is negligible in the normal state, and a special subtraction procedure is not necessary.

Because of the small coherence length, high critical temperature, and large anisotropy in the cuprate, superconductor fluctuations play a much more prominent role than in the classical superconductors. Hence, this subject has received much experimental and theoretical attention.

In thermal diffusion experiments the high sensitivity of the properties of a superconductor to the temperature represents an important point, and the application of a large temperature gradient to the sample often causes complications. However, an interesting exception is a geometry, where the sample dimension in the direction of the temperature gradient is kept small, e.g., about $100\,\mu m$. In this case a large temperature gradient can be achieved even for a small temperature difference between the hot and the cold side of the sample.

In our discussion of the thermal diffusion of magnetic flux quanta we have neglected the Hall force $\alpha(\underline{v}_\varphi \times \underline{n})$. However, if we include the latter force, a finite Hall angle of the resulting vortex velocity $\underline{v}_\varphi$ appears, generating a component $v_{\varphi y}$ perpendicular to the direction of the temperature gradient. This velocity component $v_{\varphi y}$ produces a longitudinal electric field component E_x, i.e., a contribution to the *Seebeck effect*. Furthermore, in the superconducting mixed state the responses of the quasi-particles to the applied temperature gradient also must be discussed, in addition to that of the magnetic flux quanta. However, this subject is beyond the scope of this article, and we refer to the treatments by Huebener (1995, 2001).

5. Concluding Remarks

Since their discovery in 1986 the cuprate superconductors have attracted a large amount of research and engineering developments worldwide. One of the main reasons for this strong interest has been the fact that in many cuprates the critical temperature of superconductivity is well above the boiling point of liquid nitrogen. The layered crystallographic structure of these materials with the CuO_2 planes represents the most prominent characteristic feature dominating the electronic properties. The undoped cuprate perovskites are antiferromagnetic electric insulators and become electric conductors and superconductors only by doping. Most high-temperature superconductors are p doped, but n doping also leads to superconductivity in some cases. While superconductivity is based on Cooper pairs as in the classical superconductors, the pairing mechanism still remains unclear.

It is now well established that in the hole-doped cuprates the pair wave function shows d-wave symmetry, whereas the symmetry is not yet as clearly known in the electron-doped cuprates. In many ways the normal-state electronic transport properties do

not show the canonical Fermi liquid behavior well known for metallic conductors. However, these properties of the normal state continue to provide clues regarding the superconducting pairing mechanism. The critical temperature value of many high-temperature superconductors above the boiling point of liquid nitrogen clearly represents an important asset for practical applications. However, the granular structure and poor ductility still provides a challenge for a technology based on these materials.

See also: Electrodynamics of Superconductors: Flux Properties; Superconducting Thin Films: Multilayers; High-temperature Superconductors: Thin Films and Multilayers

Bibliography

Bednorz J G, Müller K A 1988 Perovskite-type oxides—the new approach to high-T_c superconductivity. *Rev. Mod. Phys.* **60**, 585–600

Cooper J R, Obertelli S D, Carrington A, Loram J W 1991 Effect of oxygen depletion on the transport properties of YBa$_2$Cu$_3$O$_{7-\delta}$. *Phys. Rev. B*. **44**, 12086–9

Huebener R P 1995 Superconductors in a temperature gradient. *Supercond. Sci. Technol.* **8**, 189–98

Huebener R P 2001 *Magnetic Flux Structures in Superconductors*. 2nd edn. Springer, Berlin

Levin K, Kim Ju H, Lu J P, Si Quimiao 1991 Normal state properties in the cuprates and their Fermi liquid based interpretation. *Physica C* **175**, 449–522

Newns D M, Krishnamurthy H R, Pattnaik P C, Tsuei C C, Chi C C, Kane C L 1993 Van Hove scenario for cuprate superconductivity. *Physica B* **186–8**, 801–7

Pickett W E 1989 Electronic structure of the high-temperature oxide superconductors. *Rev. Mod. Phys.* **61**, 433–512

Poole C P, Farach H A, Creswick R J 1995 *Superconductivity*. Academic Press, San Diego, CA

Tinkham M 1996 *Introduction to Superconductivity*, 2nd edn. McGraw-Hill, New York

Waldram J R 1996 *Superconductivity of Metals and Cuprates*. Institute of Physics, Bristol, UK

R. P. Huebener
University of Tübingen, Germany

This page intentionally left blank

I

Intermediate Valence Systems

The group of rare-earth elements comprise the series from lanthanum (atomic number 57) to lutetium (atomic number 71), where the electronic configuration (EC) gradually changes from $[Xe]4f^05d^16s^2$ to $[Xe]4f^{14}5d^16s^2$, respectively (see *Localized 4f and 5f Moments: Magnetism*). Light elements of this series like cerium, elements with a nearly half-filled 4f shell like samarium and europium, or with an almost filled 4f shell like thulium and ytterbium may, however, deviate from such a well-defined EC with integer valency. As a result, the ions exhibit intermediate valence (IV), representing a homogeneous quantum mechanical mixture of two consecutive integer valence configurations. Not only are rare-earth systems known to show such valence instabilities, but about 40 elements (3d, 4d, 5d, 5f) and their compounds can emerge in noninteger valency.

A necessary condition for nonintegral valence to occur is that two bounding states of the rare earth, i.e., $4f^n(5d6s)^m$ and $4f^{n-1}(5d6s)^{m+1}$, are nearly degenerate. The system may then lower its energy by adopting a mixture of both EC and an additional degree of freedom is acquired. On each 4f site charge fluctuations appear between these configurations on a typical time scale τ_{cf}. Experiments probing such samples on scales much shorter than τ_{cf} (like XPS) allow it to observe both configurations, while experiments with a much longer time scale (like Mössbauer effect) reveal just the intermediate configuration. In these systems, the 4f level is pinned to the Fermi energy E_F, provoking f electrons to escape into the conduction band. Hence, the lifetime of the state becomes limited and the former localized level acquires a narrow width Δ with some dispersion and is, therefore, occupied by a nonintegral number of electrons. The inverse of Δ is then given by $\tau_{cf} \sim \Delta/\hbar$.

IV is derived from a quantum mechanical hybridization of two consecutive states $a_n|f^n\rangle$ and $a_{n-1}|f^{n-1}\rangle$ (Lawrence *et al.* 1981), which can no longer be considered as a simple superposition. Rather, fluctuations between both states modify physical properties in a fundamental manner. Features like quenched magnetic moments, an enhanced Pauli susceptibility, and a large electronic contribution to the specific heat may become obvious, which otherwise cannot be found in both integer valent states involved.

Such homogeneously mixed systems are distinguished from the classical "mixed valence" phases like Fe_3O_4 or Sm_3S_4, where at crystallographic inequivalent lattice sites the cations exhibit different oxidation states with distinct electronic configurations.

A lattice-related aspect of IV materials is a soft bulk modulus, indicating the large compressibility of such systems (Wachter 1994). Since the ionic radius of IV materials cannot be considered as a "hard sphere" as for integral valent materials, pressure will change the degree of IV and thus change the f occupation, which in turn is related to the ionic radius. If a pressure induced transition towards an IV state is of first order, the bulk modulus B_0 becomes infinitely small, and as a consequence, the compressibility $\kappa \equiv 1/B_0$ diverges.

IV systems are also known for a negative elastic constant c_{12} which ensures (in the case of cubic crystals) that even under applied uniaxial pressure the crystal structure is preserved as it was firstly observed in TmSe (Batlogg *et al.* 1979). The negative value of c_{12} also causes a negative Poison ratio $c_{12}/(c_{11}+c_{12})$. Measurements of the phonon dispersion relation in IV materials show a common softening of the acoustic and the optical phonon branches when compared to stable isostructural nonmagnetic systems. Moreover, well-defined crystal field (CF) splitting of the 4f state has not been found in IV systems yet studied.

1. Some Theoretical Aspects

The physics of intermediate valent materials is usually accounted for in terms of the periodic (Anderson model 1961, see also *Electron Systems: Strong Correlations*).

A schematic representation of the DOS for the impurity version of the Anderson model is drawn in Fig. 1(a). For large Coulomb repulsion U the f spectral weight is split into two parts located at E_{4f} (binding energy of the localized 4f electrons) and $E_{4f}+U$, having a width $\Delta \sim V^2/W$ (V is the hybridization strength and W is the conduction electron bandwidth). Due to the removal of spin degrees of freedom, a narrow many body resonance occurs in the vicinity of the Fermi energy E_F as a consequence of the crossing of the d- and f bands at the Fermi energy (Martin 1982). IV follows immediately from the Anderson Hamiltonian for $E_{4f} \to E_F$. The Kondo effect, on the contrary, is described by this model, if E_{4f} and $E_{4f}+U$ are well separated from the Fermi level (see *Kondo Systems and Heavy Fermions: Transport Phenomena*).

In the case of a periodic arrangement of the magnetic ions, a two peak structure with a gap develops as a result of the f-d hybridization (Fig. 1(b)). This hybridization gap is complete if V is $\vec{k}$-independent. However, if V vanishes at certain points at the Brillouin zone, the gapping may become incomplete.

If the f and d electron count is even, and if there are no other electrons in the conduction band, the application of Luttinger's theorem causes E_F to be
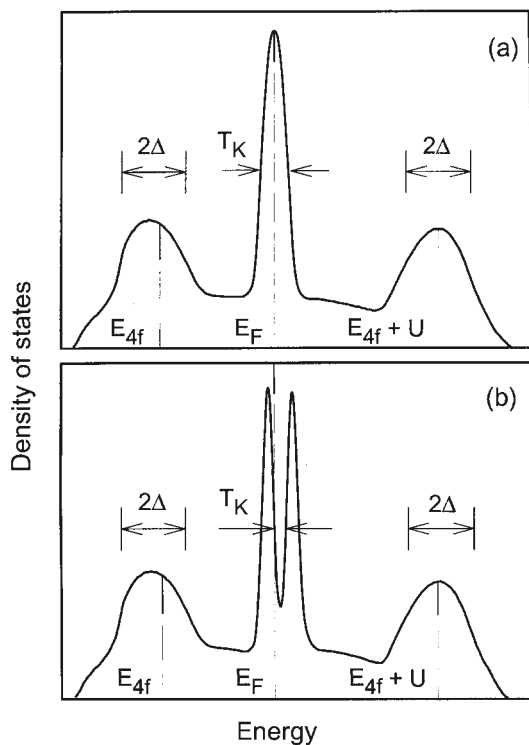
Figure 1
Schematic spectrum of the density of states of (a) the impurity Kondo case and (b) the Kondo lattice. The scale T_K is expanded for clarity.

centered in this gap and the material will be an IV isolator for $T \to 0$. In fact, many examples of IV semiconductors are known, possessing an even electron count such as YbB_{12} with 52 valence electrons per formula unit and an energy gap $E_g \sim 5.2$ meV (Moser *et al.* 1985). Temperatures of the order of 100 k are then sufficient to smear out the gap and thermally activate a huge number of carriers. Such thermal excitations destroy the intersite quantum coherence, responsible for the hybridization gap.

For an odd electron count, the Fermi energy should be situated in one of the density peaks above or below the gap, hence the material will demean as an IV and heavy fermion metal for $T \to 0$.

2. Experimental Evidence of Intermediate Valence

In general, the lattice parameters of an isotypic series of rare-earth intermetallics smoothly decrease from lanthanum to lutetium. This is attributed to the lanthanide contraction and ascribed to the fact that though the electron count of the $4f$ shell increases, it cannot completely screen the increase in the nuclear charge and, therefore, the outer electrons become constricted. However, compounds with cerium, samarium, europium, thulium, or ytterbium may significantly deviate from this simple dependence since their valency can be larger or smaller than three, thus cause a decrease or an increase of the unit cell volume, respectively.

2.1 Samarium and Thulium Monochalcogenides

The monochalcogenides SmS, SmSe, and SmTe crystallize in the f.c.c. structure and are characterized by a semiconducting behavior owing to an energy gap E_g between the $4f^6$ and the $5d$ state of about 0.15, 0.45, and 0.65 eV, respectively (Wachter 1994). CF interaction of cubic symmetry splits the $5d$ orbital into the lower lying t_{2g} band and the e_g band.

The magnetic susceptibility of this series behaves like an inhomogeneous mixing of Sm^{2+} and Sm^{3+}, but the finite values for $T \to 0$ imply that the ground state is homogeneous. The valence fluctuations render the mixture homogeneous; hence the f^5 spin memory is lost when the configuration fluctuates (Lawrence *et al.* 1981).

Pressure applied to such narrow bandgap systems can give rise to a semiconductor-metal instability. In fact, a first order transition was deduced for SmS at $p_c = 6.5$ kbar (Jayaraman *et al.* 1970), accompanied by a volume change of about 20%. Slightly above p_c, SmS turns golden as the plasma edge moves into visible and IV occurs. For SmSe and SmTe the pressure-induced valence transition is continuous and is found at significant higher values of pressure, i.e., 45 and 60 kbar, respectively (Bucher *et al.* 1971).

The approach of the ions due to applied pressure cause the Coulomb potential to increase. Thus CF splitting of the $5d$ band grows and eventually leads to an overlap with the $4f^6$ state. Accordingly, the bandgap closes and $4f$ electrons empty into the d states. Upon the enhanced number of conduction electrons, the lattice starts to shrink, so CF splitting strengthens further, resulting in some avalanche effect and a first order phase transition. Since the reduced lattice parameter stiffens the lattice as a whole, the trivalent state is not attained. Rather, the process stops at $v = 2.75$ (Kaindl *et al.* 1984) where the gain in electronic energy is compensated by the increase of the lattice energy. In the case of SmSe and SmTe, the gap in the density of states at E_F closes before the lattice softens, and consequently only a second-order phase transition is observed.

In the case of Tm, both EC, i.e., Tm^{2+} ($J = 7/2$) and Tm^{3+} ($J = 6$) result in a magnetic ground state. Such systems can exhibit long-range magnetic order even in the IV state, which is in contrast to those based on cerium, samarium, europium, or ytterbium. The thulium monochalcogenides are of particular interest. Binary compounds range from metallic
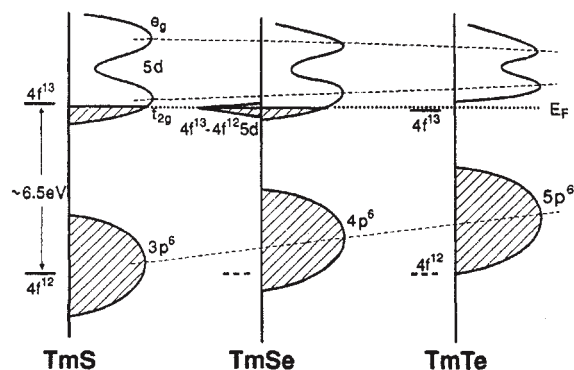
Figure 2
Electronic structure and density of states of the Tm monochalcogenides normalized to the Fermi energy E_F (dotted line). The dashed lines through the density of state peaks serve as a guide to the eyes.

trivalent TmS over IV TmSe to semiconducting divalent TmTe.

A sketch of the electronic structure and the density of states of this series is shown in Fig. 2 (Wachter 1994).There is a cross-over from metallic (TmSe) to isolating behavior (TmTe). The latter exhibits the divalent $4f^{13}$ EC, where the localized $4f$ state is separated by an energy gap $E_g \sim 0.3$ eV from the bottom of the $5d\text{-}t_{2g}$ band.

When proceeding from TmTe to TmSe or TmS, the lattice constant shrinks, thus producing chemical pressure onto the Tm cation. Therefore, crystal field splitting of the $5d$ band increases. The bottom of the conduction band (mostly $5d\text{-}t_{2g}$ states) may then overlap with the $4f^{13}$ level and $4f$ electrons will spill into the conduction band.

Stoichiometric TmSe orders antiferromagnetically below $T_N = 2.9$ K (Bjerrum-Moller *et al.* 1977). The electrical resistivity in both the paramagnetically and the magnetically ordered state shows thermally activated behavior. According to Luttinger's theorem, TmSe should be a metal since the compound is an odd electron system in both EC, $4f^{13}$ and $4f^{12}5d$. Antiferromagnetic order below 2.9 k, however, enlarges the magnetic unit cell which contains an even number (26) of electrons. The hybridization gap can then exist with E_F just in the center, and the system should behave isolating. However, at $\mu_0 H = 0.5$ T, TmSe becomes ferromagnetic, thus the folding of the Brillouin zone vanishes. Consequently, TmSe behaves metallic and the system is an IV ferromagnet (Batlogg *et al.* 1977).

As for many other IV compounds with the Fermi level within the hybridization gap, pressure applied to TmSe ($p_c \sim 30$ kbar) will close the bandgap primarily due to the growing overlap of the crystal field split $5d$ band with the $4f^{13}$ state (Wachter 1994).
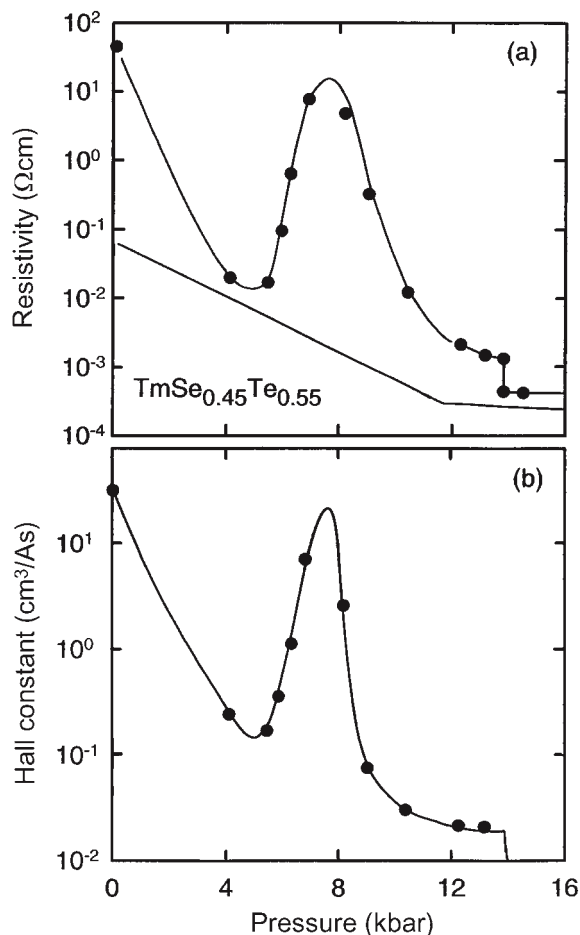
Figure 3
(a) Pressure dependence of the resistivity of $TmSe_{0.45}Te_{0.55}$ at 300 K (lower curve) and at 4.2 K (upper curve). At 300 K the semiconducting to metal transition is at $p_c = 11.5$ kbar and for $T = 4.2$ K at $p_c \sim 14$ kbar. (b) Pressure-dependent Hall constant R_H at 4.2 K.

Besides, the pseudobinary $TmSe_{1-x}Te_x$ allows to realize a novel feature in condensed matter physics, the excitonic insulator, which is characterized by a Bose-Einstein condensation of quasi-particles into a coherent exciton phase (Neuenschwander and Wachter 1990). Figure 3 shows the pressure dependence of the electrical resistivity of $TmSe_{0.45}Te_{0.55}$ at high and low temperatures and the Hall constant. The most striking feature with respect to the resistivity at $T = 4$ K is that after the expected initial decrease of $\rho(p)$, a rapid rise in a narrow pressure range from about 5 kbar to 8 kbar occurs. Beyond this pressure, the resistivity decreases again and furthermore exhibits a first order phase transition near $p = 14$ kbar.

2.2 Cerium and Ytterbium Systems

A large number of cerium compounds and alloys exhibit an EC ranging between the $4f^1$ and the $4f^0$ state, thus behaving as IV materials. The most striking feature of IV, however, occurs in f.c.c. cerium as a response to applied pressure. At a temperature-dependent critical pressure ($p_c = 7$ kbar at room temperature, Franceschi and Olcese 1969) cerium crosses over from the γ state (lattice parameter $a = 5.15$ Å) to the α state ($a = 4.85$ Å). This transition is accompanied by a volume change of about 15% which does not, however, distort the cubic crystal symmetry. While the γ state is primarily trivalent ($4f^1(5d6s)^3$), the α state behaves almost tetravalent ($4f^0(5d6s)^4$), with a valence $v = 3.67$ (Koskenmaki 1978).

Intermediate valence in ytterbium systems is constrained by divalent ytterbium (EC $4f^{14}$) and trivalent Yb (EC $4f^{13}$). While the former is a nonmagnetic state, the latter is magnetic with a total angular momentum $J = 7/2$. Pressure can be used to subtly tune the valence of the ytterbium ion and eventually drive it towards the trivalent magnetic ground state. For proper ytterbium compounds and alloys, intermediate valence is then completely adjustable from the Yb^{2+} towards Yb^{3+} state (Bauer *et al.* 1995).

In addition to pressure, temperature may also cause a dramatic alteration of the ytterbium valence. A temperature driven first order type of transition, as shown in Fig. 4, has been observed for $YbCu_4In$ (Felner and Nowik 1986). The particular transition temperature T_v, however, depends sensitively on details of the stoichiometry (Löffert *et al.* 1999). Qualitatively, the high-temperature state corresponds to the magnetic Yb^{3+} while the low-temperature state is the nonmagnetic Yb^{2+}. Quantitatively,
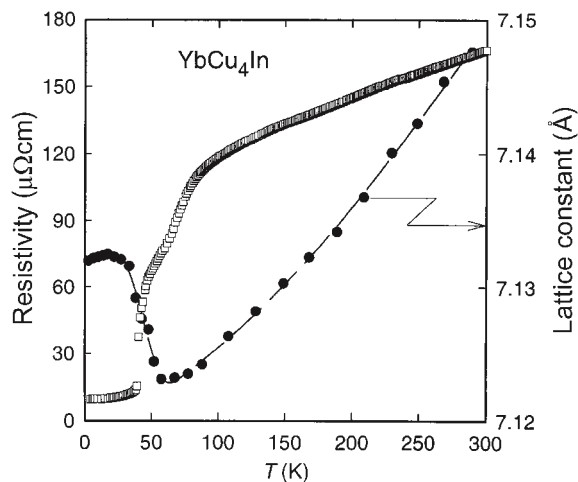
however, the valence at T_v only changes by about 0.2, and the principal effect observed is the nearly complete Kondo compensation of the local moment of ytterbium. This scenario is rendered also from the change of the Kondo temperature, which is small for $T > T_v$ ($T_K^+ \sim 25$ K), but substantially larger for $T < T_v$ ($T_K^- \sim 500$ K) (Cornelius *et al.* 1997).

Concomitantly, there is a large change in the carrier density which occurs at the phase transition, from trivalent semimetallic behavior at high temperature to IV metallic behavior at low temperatures. Although the change of the volume at $T = T_v$ (about 0.5%) is reminiscent of the $\gamma - \alpha$ transition of cerium, a "Kondo volume expansion" in $YbCu_4In$ would require an extraordinary and unrealistic large Grüneisen parameter $\Omega = -\delta \ln T_K / \delta \ln V \sim 4000$ in order to match the conditions of the Kondo volume collapse of cerium.

3. Concluding Remarks

Several rare earth, actinide, and transition metal compounds are characterized by two almost degenerate consecutive f or d levels. Their electronic configuration results from a quantum mechanical mixture of both levels, causing the valence of such systems to adopt noninteger numbers. This hybridization distinguishes IV materials from the classical type of "mixed valent" behavior due to inequivalent lattice sites with different oxidation states.

Intermediate valence can originate in a number of outstanding low temperature features of physical properties. Among them are significantly enhanced Sommerfeld values of the specific heat and Pauli susceptibility, a temperature dependent cross-over from a magnetic to a nonmagnetic state, pressure driven semiconductor to metal transitions, or the formation of an excitonic insulating state.

See also: Heavy-fermion Systems; Kondo Systems and Heavy Fermions: Transport Phenomena

Figure 4
Temperature-dependent resistivity ρ (left axis) and lattice constant a (right axis) of $YbCu_4In$.

Bibliography

Anderson P W 1961 Localized magnetic states in metals. *Phys. Rev.* **124**, 41–52

Batlogg B, Kaldis E, Ott H R 1977 Magnetic mixed valent TmSe. *Phys. Lett. A* **62A**, 270–2

Batlogg B, Ott H R, Kaldis E, Thoni W, Wachter P 1979 Magnetic mixed valent TmSe. *Phys. Rev. B* **19**, 247–59

Bauer E, Tuan L, Hauser R, Gratz E, Holubar T, Hilscher G, Michor H, Perthold W, Godart C, Alleno E, Hiebl K 1995 Evolution of a magnetic state in $YbCu_{5-x}Ga_x$. *Phys. Rev. B* **52**, 4327–35

Bjerrum-Moller H, Shapiro S M, Birgenau R J 1977 Field-dependent magnetic phase transitions in mixed-valent TmSe. *Phys. Rev. Lett.* **39**, 1021–5

Bucher E, Narayanamurti V, Jayaraman A 1971 Magnetism, metal-insulator transition, and optical properties in Sm- and

some other divalent rare-earth monochalcogenides. *J. Appl. Phys.* **42**, 1741–5

Cornelius A L, Lawrence J M, Sarrao J L, Fisk Z, Hundley M F, Kwei G H, Thompson J D, Booth C H, Bridges F 1997 Experimental studies of the phase transition in $YbIn_{1-x}Ag_xCu_4$. *Phys. Rev. B* **56**, 7993–8000

Felner I, Nowik I 1986 First-order valence phase transition in cubic $Yb_xIn_{1-x}Cu_2$. *Phys. Rev. B* **33**, 617–9

Franceschi E, Olcese G L 1969 A new allotropic form of cerium due to its transition under pressure to the tetravalent state. *Phys. Rev. Lett.* **22**, 1299–300

Kaindl G, Kalkowski G, Brewer W D, Perscheid B, Holtzberg F 1984 M-edge X-ray absorption spectroscopy of 4f instabilities in rare-earth systems. *J. Appl. Phys.* **55**, 1910–5

Koskenmaki D C, Gschneidner K A Jr. 1978 Cerium. In: Gschneidner K A Jr., Eyring L (eds.) 1978 *Handbook on the Physics and Chemistry of Rare Earths.* Vol. 1. Elsevier, Amsterdam, pp. 337–7

Jayaraman A, Narayanamurti V, Bucher E, Maines R G 1970 Pressure-induced metal-semiconductor transition and 4f electron delocalization in SmTe. *Phys. Rev. Lett.* **25**, 368–70

Lawrence J M, Riseborough P S, Parks R D 1981 Valence fluctuation phenomena. *Rep. Progr. Phys.* **4**, 1–84

Löffert A, Hautsch S, Ritter F, Assmus W 1999 The phase diagram of $YbInCu_4$. *Physica B* **259–61**, 134–5

Martin R M 1982 Fermi-surface sum rule and its consequences for periodic Kondo and mixed-valence systems. *Phys. Rev. Lett.* **48**, 362–5

Moser M, Wachter P, Hulliger F, Etourneau J R 1985 Point contact spectroscopy of YbB_{12} and $CeAl_3$. *Solid State Commun.* **54**, 241–4

Neuenschwander J, Wachter P 1990 Pressure-driven semiconductor-metal transition in intermediate-valence $TmSe_{1-x}Te_x$ and the concept of an excitonic insulator. *Phys. Rev. B* **41**, 12693–703

Wachter P 1994 Intermediate valence and heavy fermions. In: Gschneidner K A Jr., Eyring L, Lander G H, Choppin G R (eds.) 1994 *Handbook on the Physics and Chemistry of Rare Earths*, Vol. 19. Elsevier, Amsterdam, pp. 383–478

E. Bauer
Technische Universität Wien, Austria

Intermetallic Compounds: Electrical Resistivity

The aim of this article is to show what information can be obtained about the properties of intermetallics from resistivity measurements. The influence of scattering of conduction electrons by impurities, lattice vibrations (phonons), and magnetic moments will be discussed in detail. It will also be shown how changes in the crystallographic structure and in the spin arrangements (magnetic phase transitions) are manifested in the temperature variation of resistivity.

The temperature variation of the electrical resistivity ($\rho(T)$) of different binary yttrium–transition metal compounds is shown in Fig. 1. All these compounds crystallize in the cubic Laves phase structure where the rare-earth (RE) atoms form a diamond lattice.
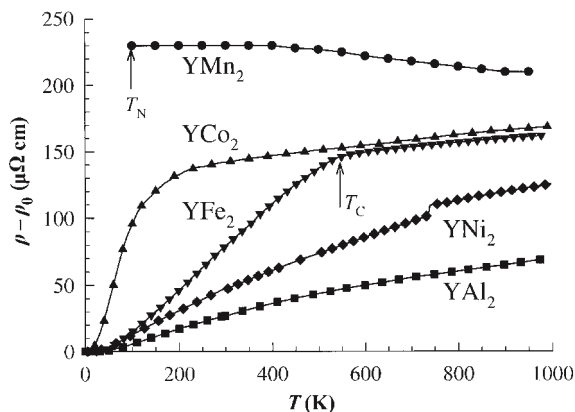
Figure 1
Temperature dependence of the electrical resistivity of yttrium-based cubic Laves phase compounds with 3d transition metals (manganese, iron, cobalt, and nickel) and aluminum.

The remaining space inside the cell is occupied by regular tetrahedrons consisting of the transition metal atoms or aluminum (see below). Figure 1 shows the remarkable variety of behavior within this family of Laves phases when the measurements are performed across an extended temperature range up to 1000 K. With the exception of YMn_2, the residual resistivity (ρ_0) has been subtracted from the ρ vs. T curves.

The reasons for choosing mainly Laves phases to demonstrate the temperature dependence of ρ are as follows:

(i) These compounds have a cubic structure, and therefore the anisotropy of the resistivity in the different crystallographic directions can be neglected.

(ii) The physical properties of these yttrium-based intermetallics are known in great detail, and hence a deeper understanding of the resistivity behavior can be expected. As a consequence, general conclusions can be drawn from a discussion of $\rho(T)$ data.

(iii) More than 730 binary and ternary compounds have been shown to have a cubic Laves phase structure (e.g., Villars 1997), and all have been partially investigated with respect to their physical properties.

Referring to Fig. 1, we note the following.

YAl_2. This is a Pauli paramagnetic compound with a weakly temperature-dependent susceptibility. At room temperature $\chi = 0.106 \times 10^{-3}$ emu mol^{-1}. Band-structure calculations reveal a moderately enhanced electronic density of states (DOS) at the Fermi level owing to $Y(4d)$ states. Investigations of the lattice dynamics have revealed a phonon DOS (PDOS) ranging up to about 30 meV; the center of gravity of the PDOS is approximately 15 meV. YAl_2 is an ideal prototype for demonstrating the electron–phonon scattering mechanism, which in the simplest approximation can be described by the Bloch–Grüneisen relationship.

YNi₂. The resistivity curve of this nonmagnetic compound has been selected in order to demonstrate the influence of a temperature-induced structural transition on the electrical resistivity (Gratz *et al.* 1996). A detailed discussion of the influence of phase transitions on ρ vs. T by means of the pseudobinary $LaAg_xIn_{1-x}$ series is given below.

YCo₂. From a magnetic point of view this is a paramagnetic compound. However, the susceptibility is strongly enhanced and has a maximum in the χ vs. T plot around room temperature. It has been shown that YCo_2 belongs to the group of cobalt-based compounds whose properties are strongly influenced by spin fluctuations (see *Spin Fluctuations*). A comparison of the ρ vs. T plot for YAl_2 and YCo_2 clearly shows the strong influence of spin-fluctuation scattering processes on the resistivity, giving rise to the pronounced negative curvature of $\rho(T)$ around room temperature in YCo_2.

YFe₂. This compound represents a ferromagnetic Laves phase with a Curie temperature of 550 K. Studies of the magnetic properties reveal the localized character of the iron moments which are coupled via a direct $3d$–$3d$ interaction. The breakdown of the long-range magnetic order at T_C can clearly be seen in the kink of the $\rho(T)$ curve at 550 K.

YMn₂. Among all these compounds, YMn_2 exhibits the most complex magnetic properties. There is an antiferromagnetic transition of a first-order type around 110 K (Néel temperature). This magnetic transition is accompanied by a very large volume expansion (about 5%) and a distortion of the cubic unit cell. The enormous volume expansion prevents resistivity experiments in the magnetically ordered state since the sample falls apart. The arrangement of the manganese magnetic moments appears to be sinusoidally modulated along the [111] direction with a very long periodicity. The manganese moments show pronounced temperature dependence. They change from approximately $2.2\,\mu_B$ f.u.$^{-1}$ at 4 K, decreasing to $1.7\,\mu_B$ f.u.$^{-1}$ at the Néel temperature, and then increasing to $2\,\mu_B$ f.u.$^{-1}$ at room temperature. The complex magnetic behavior of YMn_2 is still a matter of discussion. The $\rho(T)$ curve of YMn_2 has been included in order to show that even in a compound with such a relatively simple crystal structure (cubic Laves phase) a temperature variation of the resistivity can be observed for which it is difficult to give a qualitative explanation. This $\rho(T)$ curve is characterized by values of more than $200\,\mu\Omega\,cm$, and a decrease in the whole temperature range above its Néel temperature up to 1000 K. The Boltzmann equation and scattering mechanism conditions are provided in *Boltzmann Equation and Scattering Mechanisms*, detailing the circumstances under which the Boltzmann formalism is no longer applicable, and YMn_2 is a good example of this. A rigorous quantum mechanical treatment would be necessary to give at least a qualitative explanation for this $\rho(T)$ dependence.

1. Analysis of Resistivity Data

A quantitative analysis of resistivity data is in practice only possible if the sum rule can be used (Matthiessen's rule) (see *Boltzmann Equation and Scattering Mechanisms*). This is because a calculation of the temperature dependence of the resistivity in reality is only practicable for a single scattering mechanism (e.g., for the electron–phonon scattering) otherwise the mathematical complexity would be too great. However, the measured temperature dependence of the resistivity (total resistivity) is the result of all the various scattering processes.

Under the assumption that Matthiessen's rule is valid, the total resistivity is simply the sum of all the calculated terms

$$\rho_{tot} = \rho_0 + \rho_{ph} + \rho_{mag} \tag{1}$$

where the subscripts denote the residual resistivity (0), the resistivity owing to phonon scattering (ph) and the resistivity owing to spin-dependent scattering (magnetic scattering processes, mag). If the calculated total and experimental resistivities are in agreement, all the underlying assumptions and being the procedure of the calculation can be taken as being confirmed. If, however, there is no agreement between theory and experiment it is necessary to check whether the experimental conditions (and/or the assumptions) are correct. One of the most serious experimental problems is the correct determination of the sample geometry (sample cross-section), especially if the sample material is brittle and the measured cross-section is uncertain owing to cracks inside the sample. This can be the case for many samples. When the true sample geometry is not known it is often helpful to consider the temperature variation of the normalized resistivity, i.e., $\rho(T)/\rho(300\,K)$ vs. T.

In cases where the conditions for Matthiessen's rule are not fulfilled, i.e., the individual scattering processes are coupled, a quantitative analysis of the resistivity data becomes intractable. Finally, it should be emphasized that for resistivity values of the order of $250\,\mu\Omega\,cm$ and higher, the whole concept of the Boltzmann formalism is not applicable. An estimation of the mean free path, λ, of the conduction electrons reveals that in these cases values of λ are comparable to the size of the interatomic distances. A rigorous quantum mechanical treatment of the transport phenomena may then lead to useful results (Kubo 1959).

1.1 Scattering Mechanism

(a) Impurity scattering
In a nonmagnetic, single-phase sample where scattering contributions from vacancies and dislocations are negligible, the residual resistivity (ρ_0) is solely because of a low concentration of foreign impurity atoms. With the exception of the lowest

temperatures, ρ_0 is much smaller than the temperature-dependent phonon term (ρ_{ph}), and scattering of electrons by impurity defects is invariably elastic. As the temperature rises, ρ_0 remains constant (see *Boltzmann Equation and Scattering Mechanisms*) and ρ_{ph} increases rapidly. The effect of the variable "impurity" scattering can best be seen in pseudobinary systems. The concentration dependence of ρ_0 vs. the concentration of the partner element of three different pseudobinary systems is shown in Fig. 2. The simplest example represents the $Lu_{1-x}Y_xAg$ system, which crystallizes in the cubic CsCl-type structure over the whole concentration range. The ρ_0 vs. x curve is parabolic (see Fig. 2(a)), in good agreement

with the so-called Nordheim rule, which states that the composition-dependent part of ρ_0 is proportional to $x(1-x)$, where x is the composition. However, these contributions to ρ_0 caused by dislocations, stacking faults, etc., are superimposed in any case.

If one of the lattice sites is statistically occupied by a magnetic ion, then a further contribution to ρ_0 appears owing to the disorder in the magnetic moment arrangement. As an example, the pseudobinary $Gd_{1-x}La_xNi$ system is shown in Fig. 2(b). This system crystallizes in the orthorhombic CBr-type structure. Gadolinium bears a magnetic moment, leading to a long-range ferromagnetic order for gadolinium concentrations higher than 30% (Gratz *et al.* 1986). As can be seen from Fig. 2(b), there is a discontinuity in ρ_0 vs. x at about the onset of ferromagnetism. The increase of ρ_0 in the ordered state is obviously because of the domain wall scattering and the disorder in the magnetic moment arrangement within the domains if not all of the RE places are uniformly occupied by gadolinium atoms. Note that ρ_0 is very small in the boundary compound GdNi. The third pseudobinary system, $(Gd_{1-x}Y_x)_4Co_3$ crystallizes in the hexagonal Ho_4Co_3-type structure. In this system a linear increase of the Curie temperature with the gadolinium content has been found, with the highest ordering temperature for Gd_4Co_3 ($T_C = 220\,K$) (Gratz *et al.* 1980). The asymmetric shape of the ρ_0 vs. x curve is referred to the increasing disorder in the magnetic subsystem which exists even at the lowest temperatures. Note that Gd_4Co_3 again shows a comparatively low ρ_0 value.

(b) Electron–phonon scattering

When an electron interacts with a quantized lattice vibration of frequency ω, an energy quantum, $\hbar\omega$, is exchanged and such events are inelastic. Assuming that the conduction electrons are part of one and the same s-conduction band and they are scattered into vacant energy states within the same band, then the $\rho_{ph}(T)$ dependence can be approximated by the Bloch–Grüneisen law, derived using a Debye phonon spectrum and a spherical Fermi surface.

This is expressed by (Blatt 1968)

$$\rho_{ph} = 4R_\Theta \left(\frac{T}{\Theta}\right)^5 \int_0^{\Theta/T} \frac{x^5 dx}{(e^x - 1)(1 - e^{-x})} \quad (2)$$

where the constant R_Θ includes, among other fundamental physical quantities, the electron–phonon coupling constant, an average atomic mass of the different types of atoms, and the Debye temperature Θ (see *Boltzmann Equation and Scattering Mechanisms*).

In order to demonstrate what can be concluded from a fit of Eqn. (2) to experimental data, the temperature variation of the resistivity of three cubic Laves phases (YAl_2, $LaAl_2$, $LuAl_2$) have been

Figure 2
Concentration dependence of the residual resistivity (ρ_0) of three pseudobinary systems with different crystal structures: (a) $Lu_{1-x}Y_xAg$ (cubic CsCl-type structure); (b) $Gd_{1-x}La_xNi$ (orthorhombic CBr-type structure) and $(Gd_{1-x}Y_x)_4Co_3$ (hexagonal Ho_4Co_3-type structure). A ferromagnetic order exists in $Gd_{1-x}La_xNi$ for $0 \leqslant x < 0.7$ (Gratz *et al.* 1986), and in $(Gd_{1-x}Y_x)_4Co_3$ for $0 \leqslant x \leqslant 1.0$ (Gratz *et al.* 1980). Solid lines are guides for the eyes.
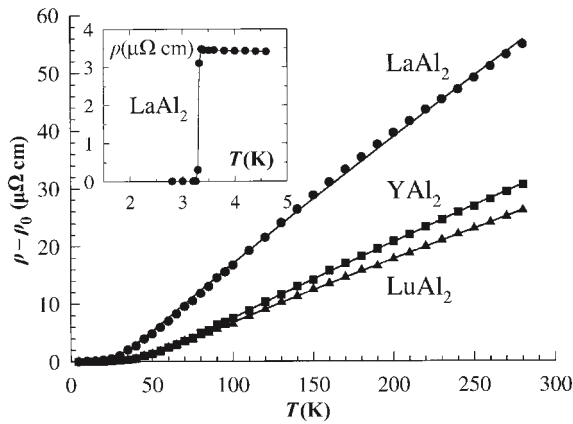
Figure 3
Temperature dependence of the electrical resistivity of three nonmagnetic RAl$_2$ cubic Laves phases (ρ_0 values are subtracted). The solid lines depict the temperature dependence according to the Bloch–Grüneisen relationship, with the fit parameters given in Table 1. The inset shows the superconducting transition of LaAl$_2$ in ρ vs. T at 3.3 K (Bauer *et al.* 1985).

Table 1
Fit parameters obtained by a fit of $\rho(T) = \rho_0 + \rho_{\mathrm{ph}}(T)$ to the experimental resistivity data, with $\rho_{\mathrm{ph}}(T)$ from the Bloch–Grüneisen law (see Eqn. (2)). ρ_0, Θ, and R_Θ are the residual resistivity, the Debye temperature, and the prefactor in the Bloch–Grüneisen law (which depends on the electron–phonon interaction strength).

Compound	ρ_0 ($\mu\Omega$ cm)	Θ (K)	R_Θ ($\mu\Omega$ cm)
LuAl$_2$	7.0	275	24
YAl$_2$	4.4	310	35
LaAl$_2$	3.1	205	45

selected and their $\rho(T)$ curves are depicted in Fig. 3 (Bauer *et al.* 1985). In a fit of the function $\rho(T) = \rho_0 + \rho_{\mathrm{ph}}$ to these experimental data (given by the solid lines in Fig. 3), ρ_0, R_Θ, and Θ are used as fit parameters. These values are listed in Table 1.

One can ask if these fit parameters have any significance. (Note that R_Θ gives the resistivity at the corresponding Debye temperature of a material.) A closer inspection of these parameters reveals an interesting picture, with a much higher Debye temperature obtained for YAl$_2$ ($\Theta = 310$ K), which is related to the higher frequency of the yttrium-dominated optical phonon modes. By contrast, LuAl$_2$ (owing to the larger atomic mass of lutetium) has a lower Debye temperature ($\Theta = 275$ K). The much smaller Debye temperature in LaAl$_2$ ($\Theta = 205$ K), the high R_Θ value (45 $\mu\Omega$ cm), plus the stronger curvature of the experimental $\rho(T)$ data at elevated temperatures

(see Fig. 3) are indicative of a strong electron–phonon coupling. This is a necessary condition for superconductivity and we note that superconductivity is observed in LaAl$_2$ below 3.3 K (Fig. 3 inset).

There are two mechanisms thought to be responsible for the stronger electron–phonon interaction in LaAl$_2$, which might also occur in other lanthanum-based compounds (see below). The first of these comes from band-structure studies. It follows from the calculation that the electronic DOS at E_{F} is enhanced owing to the proximity of the empty 4f band at the Fermi level (Hasegawa and Yanase 1980). The second mechanism comes from studies of the lattice dynamics by inelastic neutron diffraction, which reveal soft phonon modes in LaAl$_2$ (Yeh *et al.* 1981). In this investigation the lattice dynamics of YAl$_2$ and LaAl$_2$ have been compared, and it is shown that the phonon DOS has a pronounced gap at about 17 meV in LaAl$_2$. The trends outlined above have also been observed for LaAg, which is isostructural with YAg and LuAg (Bauer *et al.* 1986).

In conclusion, measurements of the resistivity provide a rough estimate of the electron–phonon interaction strength, especially for cases where isostructural compounds may be compared.

(c) Investigation of structural transitions using resistivity measurements

Changes of the crystal structure influence the resistivity, since if there is a change in symmetry then the lattice dynamics (described by the phonon dispersion relationship) will change resulting from the different interatomic distances in the emerging structure. In addition, changes in structure will be accompanied by a change in the electronic properties (described in the electronic band structure). An example revealing the influence of structural transitions on the resistivity is provided by LaAg$_x$In$_{1-x}$. These pseudobinary compounds crystallize in the cubic CsCl-type structure at room temperature. For $x < 0.95$ the compounds undergo a temperature-induced structural transition (Ihrig *et al.* 1973). Figure 4 shows the resistivity for some x values of this pseudobinary system. The hysteresis in the $\rho(T)$ curves indicates a first-order structural transition. Studies of the lattice dynamics reveal a soft mode in the phonon spectrum (Knorr *et al.* 1980). The underlying mechanism of the anomalies in $\rho(T)$ are a result of a change in the electron–phonon scattering mechanism for the two different structures leading to a destabilization of the cubic structure. These curves present convincing examples that such a martensitic type of transition can be investigated using resistivity measurements.

(d) Spin-dependent scattering

The third term on the right-hand side of Eqn. (1), ρ_{mag}, is introduced to describe spin-dependent
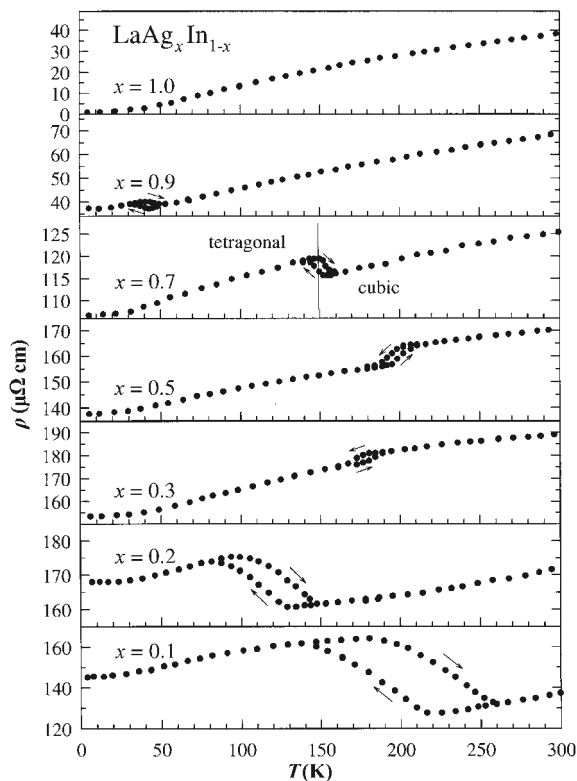
Figure 4
Temperature dependence of the electrical resistivity of the pseudobinary $LaAg_xIn_{1-x}$ series. The hysteresis in the $\rho(T)$ curves indicates structural transitions of martensitic origin.

Figure 5
Temperature dependence of the electrical resistivity of RFe_2 Laves phases in the range up to 1000 K (Gratz *et al.* 1989). The arrows indicate the Curie temperatures (note there is a shift of the zero points).

scattering phenomena. These interactions between the conduction electron system and the matrix naturally depend on the magnetic state of the lattice. Assuming that the lattice contains magnetic ions (e.g., RE ions), any disorder in the arrangement of the associated moments will give rise to magnetic scattering. RFe_2 (R being a heavy RE element) has been selected as an example of the temperature variation of the resistivity in compounds with stable magnetic moments in both sublattices of the Laves phase (Gratz *et al.* 1989). The series is not complete since single-phase samples of light RE elements (praseodymium, neodymium, and samarium) are exceptionally difficult to prepare, with the exception of $CeFe_2$ which is included in the discussion. Among this series there are two examples (YFe_2 and $LuFe_2$) where only the iron moments determine the magnetism. In all the others the RE $4f$ moments *and* the iron moments are involved in magnetism as well as in the scattering of the conduction electrons.

The localization of the iron moments owing to the itinerant character of the $3d$ electrons are less

pronounced than the $4f$ moments. However, the iron moments are much more localized than the cobalt moments in the RCo_2 compounds (see below). The temperature variation of the resistivity of these ferrimagnetic compounds (the RE and iron moments are coupled antiparallel, see *Alloys of 4f (R) and 3d (T) Elements: Magnetism*) is shown in Fig. 5. The kinks in the ρ vs. T curves indicate the Curie temperatures, with the arrows showing the temperature at which there is an inflection point in $d\rho/dT$ vs. T. The high magnetic ordering temperature of RFe_2 is mainly because of the strong interaction between nearest-neighbor iron atoms (these have a separation almost identical to that in elemental iron). There is an increase in T_C when proceeding from $LuFe_2$ to $GdFe_2$ owing to the additional $4f$–$4f$ interaction, which is largest for the gadolinium compound. With the exception of $CeFe_2$, the $\rho(T)$ curves fit to the theoretical $\rho(T)$ curves for a magnetic compound in *Boltzmann Equation and Scattering Mechanisms*.

The ρ_{spd} values (obtained by an extrapolation from high temperatures to $T = 0$) vs. the deGennes factor, $(g-1)^2 J(J+1)$, for the different RFe_2 compounds are given in Fig. 6. It is evident that there is no proportionality $\rho_{spd} \propto (g-1)^2 J(J+1)$, since the ρ_{spd} values in the RFe_2 series are dominated by the $3d$ moment scattering, which is, however, constant within the series. Many RE compounds with nonmagnetic partner elements (e.g., RAl_2) do show the proportionality $\rho_{spd} \propto (g-1)^2 J(J+1)$. Examples of these are RAl_2 and RPt, both of which are included in Fig. 6. At low temperatures in magnetically ordered compounds ($T \ll T_{ord}$) spin waves are often important and spin-wave scattering will dominate the low-temperature increase in ρ vs. T. In the case of ferromagnetism, the

325
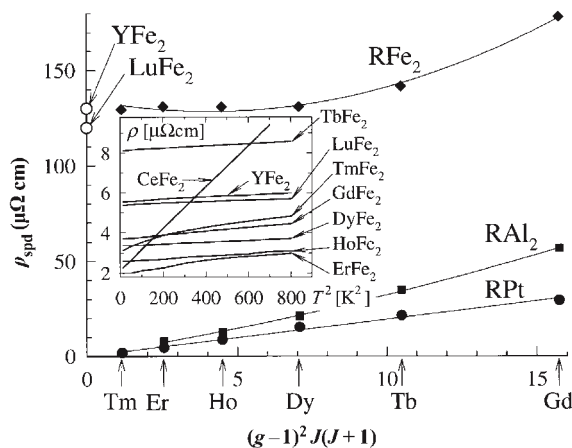
Figure 6
ρ_{spd} as a function of the deGennes factor $(g-1)^2 J(J+1)$ for RFe_2, RAl_2, and RPt. The inset shows ρ vs. T^2 in the low-temperature region for RFe_2.

Figure 7
Temperature dependence of the electrical resistivity of RCo_2 Laves phases (Gratz *et al.* 1995). The arrows indicate the magnetic transition at T_C (first-order type transitions). The inset shows details for $TmCo_2$ at low temperatures (the hysteresis is owing to a further magnetic transition at 3.2 K).

spin-wave dispersion is given by $\hbar\omega = Dq^2$ (where D is the spin-wave stiffness and q the wave vector). For RFe_2 this relationship is obviously fulfilled since there is a T^2 dependence of ρ_{mag} (Fig. 6 inset) (Gratz *et al.* 1989). The curvature in ρ vs. T^2 for $TmFe_2$ and $ErFe_2$ is because of low-lying crystal field excitations.

It can be asked why $CeFe_2$ does not fit into the general behavior of these RFe_2 compounds. In early investigations the unusual situation of $CeFe_2$ had been noted (the much smaller Curie temperature ($T_C = 270$ K), the strongly enhanced electronic specific heat coefficient ($\gamma_{el} = 56$ mJ mol^{-1} K^{-2}), etc.). Eriksson *et al.* (1988) suggested that the cerium $4f$ electron moments may be itinerant in this compound. They suggested that cerium might behave quite differently from the localized $4f$ electrons associated with the other RFe_2 compounds. It is found experimentally that the net moment on the cerium site is $0.15\,\mu_B$, consisting mostly of the spin component and being polarized opposite to the iron moment of $1.2\,\mu_B$. The latter value is much smaller than that in the other RFe_2 compounds. The delocalization of both the cerium $4f$ and the iron $3d$ moments are because of the hybridization of both states (Eriksson *et al.* 1988). $CeFe_2$ is an example of an itinerant ferromagnetic system, where spin fluctuations are important for the physical properties. In the temperature variation of the resistivity of $CeFe_2$ there are basically two features. These are the much stronger T^2 dependence at low temperatures and the negative curvature at elevated temperatures in the magnetically ordered state (see below).

Figure 7 shows the resistivity variations of RCo_2 compounds (Gratz *et al.* 1995). The reason for having selected these compounds is to show the effect of spin-fluctuation scattering on resistivity (see *Spin Fluctuations*). Whereas ρ_{mag} in YCo_2 is determined by the spin fluctuations in the cobalt sublattice only (see Fig. 1 and earlier comments), in RCo_2 compounds containing R atoms with an intrinsic moment, the magnetization is a result of the strong interplay between the two magnetic sublattices, and thus ρ_{mag} depends on both. It leads to magnetic ordering at temperatures indicated by the arrows in Fig. 7. In the paramagnetic state (above T_C) there are spin fluctuations in the cobalt sublattice that cause the pronounced negative curvature in ρ vs. T (as in YCo_2, see Fig. 1). However, there is a temperature-independent spin-disorder scattering, ρ_{spd}, superimposed (owing to the disordered $4f$ moments). The onset of long-range magnetic order in the R sublattice below T_C causes a suppression of the spin fluctuations in the cobalt $3d$ band, and an induced moment of the order of $1\,\mu_B$ per cobalt atom on the cobalt sites. Interestingly, this strong interaction of both sublattices causes the magnetic transition at T_C to be of first order (normally second order) in the compounds with R = Dy, Ho, Er, and Tm. The sudden disappearance of the spin-fluctuation scattering below T_C gives rise to the decrease in resistivity, within a few tenths of a degree, by approximately a factor six in the case of $ErCo_2$.

Below T_C, ρ_{mag} depends on the dynamics of the localized moments only. This turns out to be much smaller than the spin-fluctuation scattering contribution to ρ_{mag}. The magnitude of the discontinuity in ρ vs. T depends on the temperature at which the magnetic transition takes place. The higher is T_C the smaller is the discontinuity in ρ vs. T. These

first-order transitions have a strong dependence on external parameters such as pressure or external magnetic fields. These transitions can also be driven into a second-order-type transition by a substitution of the magnetic R atoms by yttrium, e.g., $Er_{1-x}Y_x$ Co_2 (Hauser *et al.* 1997). The resistivities of these RCo_2 compounds underline convincingly the sensitivity of the resistivity to spin-fluctuation scattering. The influence is more pronounced when compared to other dynamic measuring methods such as NMR or neutron scattering experiments. It has been argued that a reason for the dominant influence of spin-fluctuation scattering on the resistivity derives from the characteristic timescales of spin fluctuations and the transport phenomena (such as the electrical resistivity), which are of the same order of magnitude. A successful attempt to prove this argument, where inelastic neutron experiments and resistivity data for YCo_2 have been compared, seems to confirm this timescale argument (Gratz *et al.* 2000).

2. Conclusion

In this article we have selected compounds of relatively simple crystal structures in order to present the influences of the different scattering mechanisms on the temperature dependence of the resistivity, and to discuss what can be learned from resistivity measurements with respect to properties of a given material. The contribution of the phonon scattering to the resistivity is discussed using the Bloch–Grüneisen law. Furthermore, it is shown that the temperature-induced changes of the crystal structure are readily detected using resistivity as a probe. The influence of the spin-dependent scattering processes on the resistivity is shown on selected cubic Laves phases (RFe_2). A pronounced kink at T_C or T_N in ρ vs. T is an indication of well-localized magnetic moments. The effect of spin-fluctuation scattering has been demonstrated in the RCo_2 series. Finally, the resistivity of YMn_2 is shown as an example that, although this compound crystallizes in the cubic Laves phase, its resistivity behavior is difficult to explain in the scope of a classical (Boltzmann equation) concept.

See also: Electron Systems: Strong Correlations; Electronic Configuration of 3*d*, 4*f* and 5*f* Elements: Properties and Simulations; Kondo Systems and Heavy-fermions: Transport Phenomena; Magnetoresistance: Magnetic and Nonmagnetic Intermetallics

Bibliography

Bauer E, Gratz E, Kirchmayr H, Pillmayr N, Nowotny H 1985 Electrical resistivity, thermal conductivity and thermopower of nonmagnetic REAl$_2$ compounds. *J. Less Comm. Met.* **111**, 369–73

Bauer E, Gratz E, Nowotny H 1986 Transport properties and electronic structure of nonmagnetic RAg compounds. *Z. Phys. B* **64**, 51–8

Blatt F J 1968 *Physics of Electronic Conduction in Solids.* McGraw-Hill, New York

Eriksson O, Nordström L, Brooks M S, Johansson B 1988 4f-Band magnetism in CeFe$_2$. *Phys. Rev. Lett.* **60**, 2523–6

Gratz E, Bauer E, Nowotny H, Burkov A T, Vedernikov M V 1989 Temperature dependence of the electrical resistivity of REFe$_2$ compounds. *Solid State Commun.* **69**, 1007–10

Gratz E, Bernhoeft N, Paul-Boncour V, Casalta H, Murani A 2000 Use of magnetisation density fluctuation spectra to estimate the electrical resistivity of YCo$_2$. *J. Phys. Condens. Matter* **12**, 5507–18

Gratz E, Hilscher G, Sassik H, Sechovsky V 1986 Magnetic properties and electrical resistivity of (Gd$_x$La$_{1-x}$)Ni ($0 \leqslant x \leqslant 1$). *J. Magn. Magn. Mater.* **54–7**, 459–60

Gratz E, Kottar A, Lindbaum A, Mantler M, Latroche M, Paul-Boncour V, Acet M, Barner Cl, Holzapfel W B, Pacheco V, Yvon K 1996 Temperature- and pressure-induced structural transitions in rare earth deficient R$_{1-x}$Ni$_2$ (R = Y, Sm, Gd, Tb) Laves phases. *J. Phys. Condens. Matter* **8**, 8351–61

Gratz E, Resel R, Burkov A T, Bauer E, Markosyan A S 1995 The transport properties of RECo$_2$ compounds. *J. Phys.: Condens. Matter* **7**, 6687–706

Gratz E, Sechovsky V, Wohlfarth E P, Kirchmayr H 1980 The magnetic and transport properties of the compounds (Gd,Y)$_4$Co$_3$. *J. Phys. F: Met. Phys.* **10**, 2319–29

Hasegawa A, Yanase A 1980 Fermi surface of LaAl$_2$. *J. Phys. F: Met. Phys.* **10**, 847–58

Hauser R, Bauer E, Gratz E, Rotter M, Müller H, Hilscher G, Michor H, Markosyan A 1997 Decoupling of the magnetic ordering in Er$_{1-x}$Y$_x$Co$_2$ compounds driven by Y substitution. *Physica* **B239**, 83–7

Ihrig H, Vigrin D T, Kübler J, Methfessel S 1973 Cubic-to-tetragonal transformation and susceptibility in LaAg$_{1-x}$ In$_x$ alloys. *Phys. Rev. B* **8** (10), 4525–33

Knorr K, Renker B, Assmus W, Lüthi B, Takke R, Lauter H J 1980 LaAg$_x$In$_{1-x}$: II. Phonon dispersion, elastic constants and structural instability. *Z. Physik B: Condens. Matter* **39**, 151–8

Kubo R 1959 *Lecture in Theoretical Physics.* Interscience, New York, Vol. 1

Villars D 1997 *Pearsons Handbook, Desk Edition. Crystallographic Data for Intermetallic Phases.* ASM International, Materials Park, OH, Vols. 1 and 2

Yeh C T, Reichardt W, Renker B, Nuecker N, Loewenhaupt M 1981 Lattice dynamics of YAl$_2$ and LaAl$_2$—a further contribution to the La–Y puzzle. *J. de Phys.* **C6** (12), 371–3

E. Gratz
Vienna University of Technology, Austria

Intermetallics: Hall Effect

The basic theories and experiments on the Hall effect are first described, and then typical Hall effect results in *f*-electron intermetallic compounds are presented.
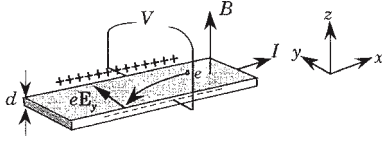
Figure 1
Experimental geometry for measurement of the Hall effect.

1. What is the Hall Effect?

In isotropic metals and alloys, a resistive voltage develops only along the current direction (x) in a zero magnetic field. Under a magnetic field **B** applied normal (z) to the current direction (density = **j**) (Fig. 1), there appears a transverse field:

$$E_y = R_H \mathbf{B} \times \mathbf{j} \tag{1}$$

which is known as the Hall effect, and R_H is defined as the Hall coefficient (Hurd 1972, 1980). Experimentally, R_H measured on a thin plate with a thickness of d can be determined as:

$$R_H = V_y d / IB \tag{2}$$

where V_y is the transverse voltage, I is the current, and B is the magnetic field strength.

Empirically, the general expression for the Hall resistivity in magnetic materials is given as:

$$\rho_H = R_{H0} B + R_S M \tag{3}$$

The origin of the first term is a Lorenz force $-e\mathbf{v}_d \times \mathbf{B}$ experienced by the conduction electrons with a drift velocity of $\mathbf{v}_d$, which is balanced by the force from the Hall field $e\mathbf{E}_y$ in a steady state:

$$-e\mathbf{v} \times \mathbf{B} = e\mathbf{E}_y \tag{4}$$

as shown in Fig. 1. R_{H0} is called the normal Hall coefficient. The second term in Eqn. (3) is the anomalous Hall resistivity, resulting from the asymmetric scattering of conduction electrons at magnetic ions, which often dominates in magnetic materials.

In the analysis of the Hall effect in magnetic intermetallics, special care should be paid to separate the various contributions to the Hall voltages. The temperature dependence of R_H in magnetic materials has often been ascribed wholly to the anomalous Hall effect. However, several other possibilities should be taken into account. One is the change in carrier number resulting from the Fermi surface reconstruction, if the system exhibits phase transitions. More importantly, the variation of the wave vector dependence of the conduction electron relaxation time $\tau(\mathbf{k})$ with temperatures (e.g., for scattering by phonons) changes from isotropic large angle scattering at

high temperatures to smaller angle scattering at lower temperatures. This should not be ignored, because it leads to the temperature dependence of R_{H0}. In fact, even in normal metals, an apparent temperature dependence of R_{H0} resulting from the temperature dependence of anisotropy in $\tau(\mathbf{k})$ was reported (Hurd 1972). Furthermore, the low-field/high-field transition in the cyclotron motion should be taken into account, especially in samples having a low residual resistivity.

2. Brief Summary of the Theories

2.1 Normal Hall Effect

In the free electron model, the current density can be written in terms of the carrier density n as:

$$\mathbf{j} = ne\mathbf{v}_d \tag{5}$$

Substituting Eqns. (4) and (5) into Eqn. (1), we obtain:

$$R_H = 1/ne \tag{6}$$

Thus, the measurement of R_H allows us to determine the carrier density n. For simple metals at room temperature R_H, calculated from the free electron density, agrees with experimental results. For instance, the experimental value of $R_H = -3.4(\pm 0.1) \times 10^{-11}$ $\mathrm{m^3\,C^{-1}}$ in aluminum agrees well with the estimated value of $-3.45 \times 10^{-11}\,\mathrm{m^3\,C^{-1}}$ from Eqn. (6) assuming three conduction electrons per ion. However, such an agreement is accidental except for the simple (alkaline) metals. In general, the Hall coefficient depends on the magnetic field direction. Even for metals with the cubic crystal structure, the Hall coefficient is field- and temperature-dependent, reflecting a non-spherical Fermi surface. All these behaviors are beyond the free electron model.

For cubic metals and low field condition, a general formula was given by Tsuji (1985) as:

$$R_H = \left(\frac{12\pi^3}{e}\right) \frac{\int \tau(\mathbf{k})^2 \mathbf{v}(\mathbf{k})^2 \rho(\mathbf{k})^{-1} dS}{\left(\int \tau(\mathbf{k})\mathbf{v}(\mathbf{k}) dS\right)2} \tag{7}$$

where $\tau(\mathbf{k})$, $\mathbf{v}(\mathbf{k})$ and $\rho(\mathbf{k})^{-1}$ are the relaxation time, velocity and mean local curvature of the Fermi surface at $\mathbf{k}$. This formula shows that, even for the cubic metals, the Hall coefficient can be temperature-dependent through the temperature dependence of $\tau(\mathbf{k})$. The sign of local mean curvature $\rho^{-1}(\mathbf{k})$ on the Fermi surface in the numerator determines the sign of the Hall coefficient through the Fermi surface integral in the numerator with weight factor $\tau(\mathbf{k})$.

The two-carrier model, the simplest possible approach to explain the temperature and field dependences, is derived from the Tsuji formula by dividing the Fermi surface integral into integrals over two

spherical Fermi spheres. In the model, we assume that the two Fermi spheres have different charges, q_e ($=e<0$) and q_h ($=|e|$), different carrier numbers n_e and n_h, different effective masses m_e and m_h and different relaxation times τ_e and τ_h. The two Fermi spheres carry the electrical current in parallel; i.e., the total conductivity is written as the sum of the contributions from the two spheres as:

$$\sigma_0 = \sigma_{0e} + \sigma_{0h} \tag{8a}$$

$$\sigma_{0\xi} = n_\xi q_\xi^2 \tau_\xi / m_\xi (\xi : \text{electron or hole}) \tag{8b}$$

In the low field condition ($\omega_c \tau \ll 1$), the Hall coefficient is written as:

$$R_H = [\sigma_e q_e \tau_e / m_e + \sigma_h q_h \tau_h / m_h] / \sigma_0^2 \tag{9}$$

Even in this simplest model, R_H possibly varies with temperature, if τ_e and τ_h have different temperature dependences.

2.2 Extraordinary Hall Effect

(a) Skew scattering and side jump mechanisms

In magnetic materials, the second term in Eqn. (3), resulting from the magnetic scattering of conduction electrons, often dominates (Fert and Hamzic 1980, Berger and Bergmann 1980).

The origin of the anomalous Hall voltage can be described as follows. There remains a net unbalance between the scattering probabilities, from the same incident wave vector of $\mathbf{k}$, to the right (state $\mathbf{k}^r$) and to the left (state $\mathbf{k}^l$) with the y-component of different sign ($k_y^r = -k_y^l$):

$$W_{\mathbf{k}^r,\mathbf{k}} \neq W_{\mathbf{k}^l,\mathbf{k}} \tag{10}$$

For simplicity, we assume the magnetic field (magnetization) and the current directions as z- and x-axes, respectively. More generally, the breakdown of reversal symmetry in the transition probability $W_{\mathbf{k},\mathbf{k}'}$ (i.e., $W_{\mathbf{k},\mathbf{k}'} \neq W_{\mathbf{k}',\mathbf{k}}$) generates a current along the y-direction which is compensated by the anomalous Hall voltage along the y-direction.

More intuitively, an example to produce such an asymmetry in the scattering probability is shown in Fig. 2, where the asymmetry is caused by the coupling
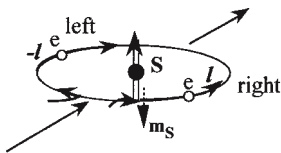
Figure 2
An example of conduction electron orbital motion leading to asymmetric scattering.

of an orbital motion (represented by the angular momentum l) of conduction electrons with an ion's spin $\mathbf{S}$. The pass along the left-hand half circle is preferred, since the energy is lower for $\mathbf{S}//\text{-}\mathbf{l}$. If the conduction electron spins ($\mathbf{s}$) are polarized as in 3d-ferromagnetic metals, even for the nonmagnetic scattering centers, the intrinsic spin–orbit interaction ($\mathbf{s}\cdot\mathbf{l}$) leads to the asymmetric scattering of conduction electrons (Hurd 1972).

The magnetic conductors are classified roughly into two categories, depending on whether the electrons responsible for magnetism are itinerant or localized. Several theories based on the itinerant magnetic electrons have been reported, and were successfully applied to 3d-magnetic systems (Hurd 1972). However, such theories are not suitable for rare-earth intermetallics with highly localized 4f electrons. Here we briefly summarize mechanisms that are more suitable for systems containing localized magnetic electrons.

The origin of the left–right asymmetric scattering, the orbital exchange interaction, is introduced (Kondo 1962) via the relation:

$$H_{\text{O.Ex}} \approx \xi(2 - g_J)\mathbf{l} \cdot \mathbf{J}, \tag{11}$$

where g_J and $\mathbf{J}$ are the Landé g-factor and the total angular momentum of the localized electrons (ions), respectively. However, the orbital exchange term is apparently not enough to explain the experimental results in 4f-electron systems, since gadolinium-containing materials, where the orbital angular momentum is absent ($g_J = 2$), also show a large anomalous Hall effect. It is understood as a combined effect of the spin exchange scattering ($\sim\mathbf{s}\cdot\mathbf{J}$) and the spin–orbit scattering (due to the intrinsic spin–orbit coupling $\sim\mathbf{s}\cdot\mathbf{l}$) (Fert and Hamzic 1980). The combination of the two mechanisms (the orbital exchange and the spin–orbit coupled spin exchange scattering) well explains the experimental results, both for dilute rare-earth impurities in noble metals and for rare-earth intermetallic compounds, though several additional mechanisms have been proposed.

In the ferromagnetic state with a large magnetic scattering, the field dependence of R_H mimics that of the magnetization, since the second term in Eqn. (3) prevails in R_H. Figure 3 shows how to decompose the normal and anomalous Hall components in the field-dependent Hall resistivity for ferromagnetic metal thin plates based on Eqn. (2). ρ_H shows a tendency to saturate around a demagnetization field B_d (the demagnetizing coefficient is ~1 for thin plates). The slope above B_d gives the normal part of the Hall coefficient R_{H0}, while the intercept of the extrapolated line of the slope with the vertical axis gives $R_S M_S$.

The anomalous Hall term can be further decomposed into so-called skew-scattering and side jump mechanisms. Another possible mechanism (spin-effect, Fert *et al.* 1981), originating from the difference in the relaxation time between the split up- and
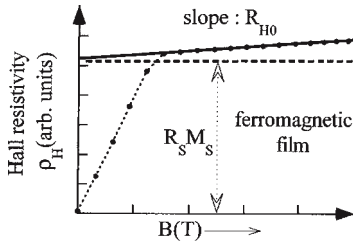
Figure 3
A typical example of Hall resistivity in a ferromagnetic thin plate.
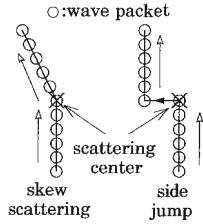
Figure 4
Schematic comparison of skew-scattering and side-jump scattering.

down-spin bands, can be neglected under ordinary conditions (at least at low fields). Note that the spin component could be basically viewed as arising from the two-carrier (up- and down-spin carriers) model with different relaxation times described above. The skew scattering mechanism can be understood within the classical picture as a deflection of the electron trajectory by an angle θ after the scattering through spin–orbit coupling. The side jump mechanism is basically a quantum effect, which can be viewed as a side step of the center of gravity of a wave packet, as shown in Fig. 4, as an analogy.

The difference in the two mechanisms is reflected in the dependence of each term on the resistivity ρ (Hurd 1972): the anomalous Hall coefficient R_S is the sum of the skew scattering term proportional to ρ and the side-jump term proportional to ρ^2:

$$R_S = a\rho + b\rho^2 \tag{12}$$

The electron scattering on only static imperfections (like impurities) was initially considered as the origin of the anomalous Hall effect in measurements of the impurity concentration dependence of R_H, where the residual resistivity ρ_0 is employed in Eqn. (12).

Later on, it has been extended to the scattering by thermal spin disorder and/or by phonons, both experimentally and theoretically (Irkhin and Shavrov 1962, Kondorskii 1965). In most theories, the magnetic part of the resistivity ρ_{mag} is assumed to be

inserted in Eqn. (12), although it is not always easy to separate the nonmagnetic contribution from the total resistivity. In rare-earth intermetallic compounds, ρ_{mag} is usually obtained by subtracting the resistivity $\rho_{ref}(T)$ of nonmagnetic reference compound from the total resistivity $\rho_{tot}(T)$ as:

$$\rho_{mag}(T) = \rho_{tot}(T) - \rho_{ref}(T) \tag{13}$$

It should be noted, however, that for the itinerant magnetic electrons model, the relation, $R_S \sim \rho_{tot}^2$, was theoretically reported for the thermal phonon or spin disorder scattering at elevated temperatures (Hurd 1972).

(b) Kondo systems
The skew scattering theory based on the Coqblin–Schrieffer model (1969) was first proposed by Fert (1973), and was successfully applied to explain the Hall effect in dilute lanthanum–cerium alloys. For cerium compounds, Coleman *et al.* (1985) have given an explanation of the large anomalous Hall constant in terms of skew scattering by impurities, based on the resonance-level model assuming a strong spin–orbit coupling in the two limits of $T \gg T_K$ and $T \ll T_K$. Later, Fert and Levy (1987) formulated the more generalized form, which describes experiments reasonably well in a wider temperature range from $T > T_K$ to $T \ll T_K$. The Hall coefficient from the intrinsic skew scattering was given by the following general expression:

$$R_S(T) = \gamma\chi_{red}(T)\rho_r(T) \tag{14}$$

where $\chi_{red}(T)$ $\{= 3k_B\chi/(g\mu_B)^2 j(j+1)\}$ is the reduced susceptibility, $\rho_r(T)$ is the resistivity due to the resonant scattering. The coefficient γ takes different values γ_1 and γ_2 above and below T_K, related to the phase shifts δ_l for channel l:

$$\gamma_1 = (-5/7)g\mu_B k_B^{-1}\sin\delta_2\cos\delta_2 \tag{15a}$$

for $T \gg T_K$, and

$$\gamma_2 = (-5\pi/21)g\mu_B k_B^{-1}\sin(2\delta_3 - \delta_2)\sin\delta_2/\sin^2\delta_3 \tag{15b}$$

for $T \gg T_K$.

Fert and Levy (1987) have succeeded in reproducing the experimental temperature dependence of R_H in typical heavy-Fermion compounds such as $CeAl_3$ and $CeCu_6$. Even for the coherent state, they found that Eqn. (14) accounts for the main features of the Hall effect.

For the coherent state, Kontani and Yamada (1994) first derived a formula for the anomalous Hall coefficient, based on the Fermi liquid theory. The anomalous part of the Hall coefficient is described as:

$$R_S = C\chi_{enh}\rho^2 \tag{16}$$

where the electrical resistivity follows $\rho = \rho_0 + AT^2$ and χ_{enh} is the enhancement factor proportional to the magnetic susceptibility (see *Electron Systems: Strong Correlations*).

3. Typical Experimental Results

Firstly, the most important factors for analyzing the temperature dependence of Hall coefficient in Kondo systems can be summarized as follows.

From the viewpoint of reliability of the analysis, $R_H(T)$, $\chi(T)$, and $\rho(T)$ should be measured on the same sample and with the same geometry, which reduces the errors due to unknown sources. For compounds with an anisotropic crystal structure, measurements on single crystals are essential. The magnetic contribution to the measured resistivity $\rho_{exp}(T)$ could be estimated by subtracting the resistivity $\rho_{ref}(T)$ of a proper reference compound (for example, a lanthanum analog for a cerium compound) as:

$$\rho_{mag}(T) = \rho_{exp}(T) - \rho_{ref}(T) \qquad (17)$$

Using $\rho_{mag}(T)$ thus obtained, $R_H(T)$ is plotted against $\chi(T) \times \rho_{mag}(T)$ as shown in Fig. 5. The slopes in the two linear regions above T_K and below T_K give γ_1 and γ_2 in Eqns. (15a) and (15b).

3.1 Well-localized 4f Compounds

The series $RECu_6$ (RE: La, Pr, Nd, and Sm) was selected as a typical example for the well-localized system. Fig. 6 shows the temperature dependence of R_H in $RECu_6$ for the light rare-earth elements (Ōnuki *et al.* 1989). At high temperatures, R_H is only weakly temperature-dependent for all the compounds except $CeCu_6$. For all the compounds, R_H is approaching -5×10^{-10} m^3 C^{-1}, which should be the normal part
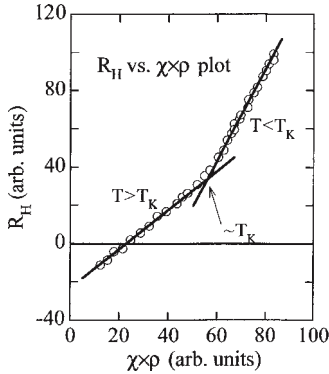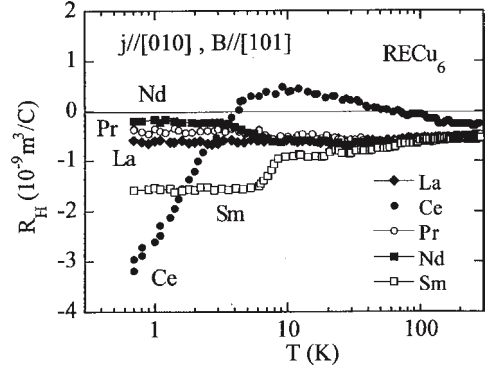
Figure 6
Temperature dependence of R_H in $RECu_6$.

of the Hall coefficient. The negative sign of R_H suggests that the relaxation time for the carriers with electron-like Fermi surface curvatures, positive ρ^{-1} in Eqn. (7), is larger than that for the hole-like Fermi surface curvatures, since $RECu_6$ is a compensated metal with the same volume for both electron-like and hole-like Fermi surfaces.

R_H for $NdCu_6$ and $SmCu_6$ shows a clear change at the corresponding Néel temperatures T_N of 6 K and 9 K, respectively. At T_N, two possible contributions coexist; namely the change in the carrier concentration resulting from the AF super-zone gap formation, and the change in anisotropy in the relaxation time. For $SmCu_6$, taking into account the fact that the change in R_H is steep, while that in ρ is gradual, the two contributions compete in ρ and cooperate in R_H.

The unique behavior in $CeCu_6$ results from the dominant Kondo scattering in this compound, which will be discussed below.

3.2 Cerium–Kondo Systems at Higher Temperatures ($Ce_xLa_{1-x}Cu_6$, $CeRu_2Si_2$, etc.)

Among the rare-earth intermetallic compounds, the works on the Hall effect were rather limited to the Kondo or heavy-Fermion compounds, mainly cerium and ytterbium compounds (Cattaneo 1985, Ōnuki *et al.* 1993). Here, we concentrate on the current understanding of the Hall effect in cerium compounds, based on typical examples in correlation with the reported theories.

To start with, the Hall coefficient of $Ce_xLa_{1-x}Cu_6$, which has been the most systematically investigated, is best suited for comparison with the skew scattering theory. Figure 7 shows the comparison of the temperature dependences of R_H in the experiment with Eqn. (14) for selected values of cerium concentration. Here, the magnetic contribution to the resistivity, $\rho_m(T)$, has been estimated by subtracting the resistivity $\rho_{nm}(T)$ of a $LaCu_6$ sample from the

Figure 5
Schematic figure showing how to estimate γ_1 and γ_2 from the experimental R_H.
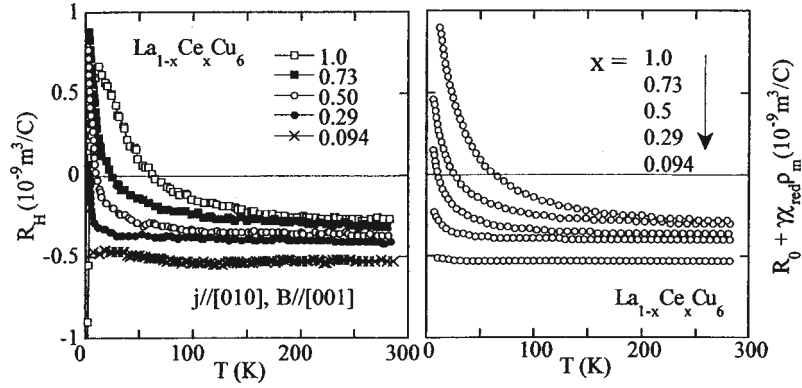
Figure 7
Comparison of R_H in the experiment with Eqn. (14) for $La_{1-x}Ce_xCu_6$.

experimental one: $\rho_{exp}(T)$; $\rho_m(T) = \rho_{exp}(T) - \rho_{nm}(T)$. $\chi_{red} = \chi/C$ is estimated by using the experimental value of χ. It should be noted that the experimental curves could be fitted by almost the same value of the phase shift $\delta_2 \approx -0.02$ for all cerium concentrations. The agreement is quite good over a wide temperature range. Even for pure $CeCu_6$, the agreement is satisfactory above ~ 20 K, below which the development of the coherent state naturally leads to a different conduction electron state. However, it is not easy to separate the intrinsic skew scattering contribution only from this figure, since a large anisotropy in R_H at low temperatures could be expected.

For the coherent state, the scaling relation Eqn. (16) has been tested in selected heavy-Fermion systems. The results for $CeCu_6$ and $CeRu_2Si_2$ are shown in Fig. 8, where the linearity is reasonably good for the lowest temperatures (Ōnuki *et al.* 1993).

For $CeRu_2Si_2$, there has been a controversy over the difference in the anisotropy between the anomalous Hall coefficient and the magnetic susceptibility: the anisotropy in R_H is small in contrast to the large anisotropy in χ, reflecting the crystalline electric field (CEF) of the 4f levels. This fact opens the question of whether the temperature dependence of R_H is caused by the skew scattering contribution to the anomalous Hall effect or not. Kontani *et al.* have explained the difference in the anisotropy as being due to the different contribution from the higher excited CEF levels to χ and R_H (Kontani *et al.* 1997). However, in order to fully understand the heavy-Fermion state, more systematic investigations on high-quality single crystals are necessary.

3.3 Uranium Intermetallic Compounds (UNiGa, UCoAl, UPd₃)

UNiGa is one of the typical compounds whose Hall effect has been successfully utilized to solve
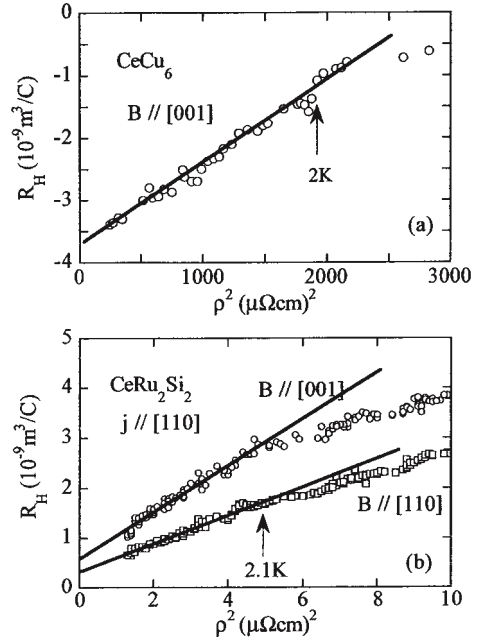
Figure 8
R_H versus ρ^2 plots for $CeCu_6$ and $CeRu_2Si_2$ at low temperatures.

important issues (Kobayashi *et al.* 1996). At low temperatures, uranium moments order ferromagnetically within the basal plane sheets with a strong uniaxial anisotropy along the c-axis. An antiferromagnetic (AF) structure, characterized by c-axis stacking of the type ($\uparrow\uparrow\downarrow\uparrow\downarrow\downarrow$), is stabilized.

A magnetic field applied along the c-axis induces a first-order type metamagnetic transition leading to a ferromagnetic (F) stacking, accompanied by a large resistance change across the metamagnetic transition

(Sechovsky *et al.* 1991). Spin-dependent scattering was initially thought to be the origin of the large magnetoresistance, since it bears a geometrical resemblance to the giant magnetoresistance (GMR) in artificial magnetic superlattices.

Another plausible explanation of the large magnetoresistance is based on the Fermi surface reconstruction due to the disappearance of the AF super-zone gap. This was initially rejected from results of specific heat measurements (Sechovsky *et al.* 1993), where no clear change in C/T was observed across the metamagnetic transition.

The measurement of Hall effect has been used as a powerful tool to judge the origin of the large magnetoresistance (Kobayashi *et al.* 1996). Figure 9 shows the field dependence of R_H across the metamagnetic transition at 4.2 K, along with the magnetization and magnetoresistance measured on the same sample in the same geometry. Fortunately, R_S is practically field-independent at low and high fields, except close to the metamagnetic transition, since both M and ρ are almost constant due to the strong uniaxial anisotropy. Therefore, the normal Hall

coefficient R_{H0} below and above the metamagnetic transition can be determined from the slopes in the two regions. R_{H0} changes from $-2.9 \times 10^{-9} \, \text{m}^3 \, \text{C}^{-1}$ in the AF state to $-1.7 \times 10^{-9} \, \text{m}^3 \, \text{C}^{-1}$ in the F state, which gives evidence of a Fermi surface change across the metamagnetic transition. Based on this fact, the specific heat was remeasured, and a clear change of the γ value was found from 43 mJ K^{-2} mol^{-1} below to 48 mJ K^{-2} mol^{-1} above the metamagnetic transition. This corroborates the scenario of the Fermi surface reconstruction across the metamagnetic transition.

Another important issue on this material is the itinerancy of 5*f* electrons. The temperature dependence of R_H for UNiGa is shown in Fig. 10, along with those of $\rho(T)$ and $M(T)$.

It is meaningful to compare this result with those obtained on UPd$_3$. The latter compound was confirmed to be a typical 5*f*-localized system, based on an inelastic neutron scattering experiment. The temperature dependences of R_H for $B \| [0001]$ and [1010] are shown in Fig. 11 (Ōnuki *et al.* 1993). One prominent feature of these figures is the large difference in the temperature-dependent part of R_H between the two compounds. That in UNiGa is about two orders of magnitude larger than that in UPd$_3$. This fact strongly suggests that the 5*f* electrons responsible for the magnetism are itinerant in UNiGa, while they are localized in UPd$_3$.

Figure 9
Field dependence of ρ_H, ρ, and M in UNiGa at 4.2 K.
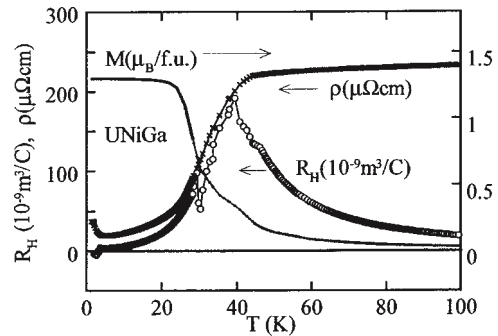
Figure 10
Temperature dependence of ρ, R_H and M in UNiGa.
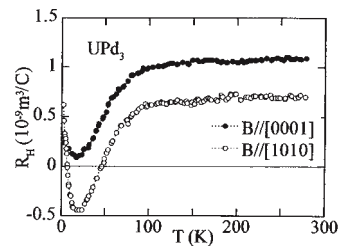
Figure 11
Temperature dependence of R_H in UPd$_3$.

In the paramagnetic state, R_H for UNiGa varies linearly as ρM, as expected from Eqn. (14), while in the ferromagnetically aligned state at low temperatures, R_S/ρ is linear, passing through zero as a function of ρ (Fig. 12). Namely, in the high field state, the side jump scattering in Eqn. (12) dominates, resembling $3d$ ferromagnetic materials with a strong electron scattering. It should be also noted that such good linear relations were found experimentally by using the total resistivity, as was theoretically obtained for the itinerant magnetic system (Irkhin and Shavrov 1962), in many uranium compounds (without subtracting the nonmagnetic component).

In contrast, no simple correlation was found between R_H, χ, and ρ for UPd$_3$, as shown in Fig. 13,
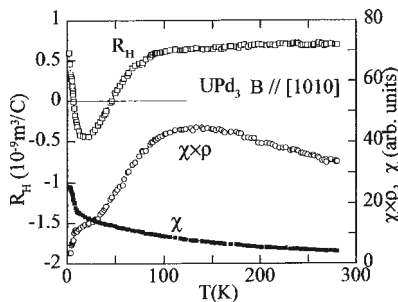
which can be understood if the contribution from the temperature-dependent anisotropic relaxation time masks a small skew scattering contribution. This fact is another evidence of the localized character of the $5f$ electrons (at least there is only very little hybridization) in this compound.

Another example of $5f$-itinerant compounds is UCoAl (Sato *et al.* 1998), which is a rare example exhibiting a metamagnetic transition from the paramagnetic ground state. The mechanism of the metamagnetic transition in typical $3d$ metamagnets, such as YCo$_2$ and LuCo$_2$, is well understood in terms of itinerant-electron metamagnetism resulting from the high $3d$-band density of states near the Fermi level (Goto *et al.* 1994). A close resemblance of UCoAl to the $3d$-itinerant metamagnets has been invoked, based on intensive studies of the effect of alloying and pressure on the metamagnetic transition. Figure 14 shows the temperature dependence of R_H for two different values of the magnetic field. The inset shows M/B measured on a same sample. The temperature dependences of the two properties resemble each other, which becomes more apparent in the R_H vs. $\chi\rho$ plot in Fig. 15. In the wide temperature range above 60 K, R_H is linear against $\chi\rho$, as expected for the skew

Figure 12
(a) R_H versus ρM plot and (b) R_S/ρ versus ρ plot for UNiGa.
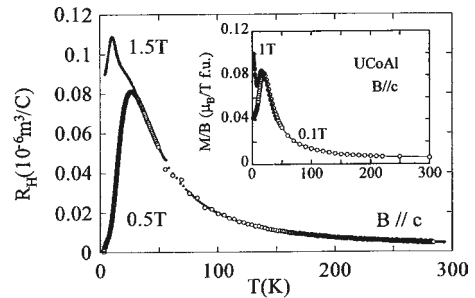
Figure 14
Temperature dependence of R_H in UCoAl.

Figure 13
Temperature dependences of R_H, χ, $\chi\rho$ in UPd$_3$.
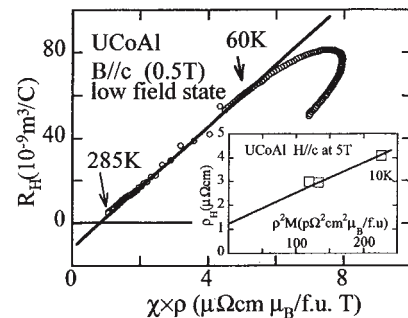
Figure 15
R_H versus $\chi\rho$ plot for UCoAl. The inset shows ρ_H versus $\rho^2 M$ plot at high fields.
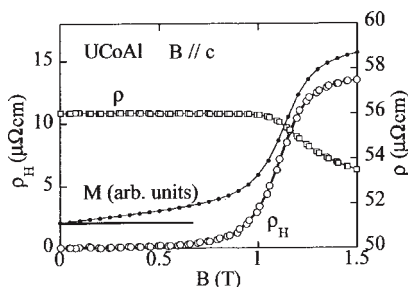
Figure 16
Field dependence of ρ, ρ_H, and M in UCoAl at 4.2 K.

scattering mechanism. This fact, as well as the large magnitude of R_H, suggests the 5f electrons to be itinerant.

The field dependence at low temperatures in Fig. 14 reflects the metamagnetic transition. Figure 16 shows the field dependence of resistance, Hall resistivity and magnetization for UCoAl on the same sample and under the same conditions. We note an apparent resemblance between the Hall resistivity and the magnetization curves. Note that in the field-induced ferromagnetic state, ρ_H varies as ρ^2 (the inset of Fig. 15). Across the metamagnetic transition field, the transverse magnetoresistance shows a clear decrease with increasing field, while an increase in the resistivity has been reported for the longitudinal geometry. This can be understood to be a so-called anisotropic magnetoresistance resulting from the anisotropy in the spin–orbit coupling, which is common in 3d-ferromagnetic metals and alloys. This fact also suggests that UCoAl is in a 5f-band split ferromagnetic state above the metamagnetic transition field. The change in the density of states due to the band splitting was further manifested in the field dependence of specific heat as a decrease of C/T (Matsuda *et al.* 1999).

4. Concluding Remarks

The Hall effect in intermetallics is not always analyzed straightforwardly. However, depending on the system, it has the potential to give important information on the electronic structure, which can hardly be extracted by other experimental techniques. In order to accomplish this, a proper analysis including the separation of different contributions, e.g., either normal or anomalous, is essential.

See also: 5f Electron Systems: Magnetic Properties; Heavy-fermion Systems; Intermediate Valence Systems; Kondo Systems and Heavy-fermions: Transport Phenomena

Bibliography

Berger L, Bergmann G 1980 The Hall effect of ferromagnets. In: Chien C L, Westgate C R (eds.) *The Hall Effect and its Applications*. Plenum, New York, pp. 55–76

Cattaneo E 1985 Hall effect of some intermediate-valent Ce and Yb compounds. *Z. Phys.* **47/48**, 529–31

Chambers R G 1976 Transport properties: surface and size effect. In: Ziman J M (ed.) *The Physics of Metals*. Cambridge University Press, London, pp. 175

Coleman P, Anderson P W, Ramakrishnan T V 1985 Theory for the anomalous Hall constant of mixed-valence systems. *Phys. Rev. Lett.* **55**, 414–7

Coqblin B, Schrieffer J R 1969 Exchange interaction in alloys with cerium impurities. *Phys Rev.* **185**, 847–53

Fert A 1973 Skew scattering in alloys with cerium impurities. *J. Phys. F: Met. Phys.* **3**, 2126–42

Fert A, Friederic A, Hamzic A 1981 Hall effect in dilute magnetic alloys. *J. Magn. Magn. Mater.* **24**, 231–57

Fert A, Hamzic A 1980 Hall effect from skew scattering by magnetic impurities. In: Chien C L, Westgate C R (eds.) *The Hall Effect and its Applications*. Plenum, New York, pp. 77–98

Fert A, Levy P M 1987 Theory of the Hall effect in heavy-fermion compounds. *Phys. Rev. B* **36**, 1907–16

Goto T, Aruga Katori H, Sakakibara T, Mitamura H, Fukamichi K, Murata K 1994 Itinerant electron metamagnetism and related phenomena in Co-based intermetallic compounds. *J. Appl. Phys.* **76**, 6682–7

Hurd C M 1972 *The Hall Effect in Metals and Alloys*. Plenum, New York

Hurd C M 1980 "Pressing electricity": a hundred years of Hall effect in crystalline metals and alloys. In: Chien C L, Westgate C R (eds.) *The Hall Effect and Its Applications*. Plenum, New York, pp. 1–54

Irkhin Yu P, Shavrov V G 1962 Theory of the spontaneous Hall effect in ferromagnets. *Sov. Phys. JETP* **15**, 854–8

Kobayashi Y, Aoki Y, Sugawara H, Sato H, Sechovsky V, Havela L, Prokes K, Mihalik M, Menovsky A 1996 Hall effect and thermoelectric power in UNiGa. *Phys. Rev. B* **54**, 15330–4

Kondo J 1962 Anomalous Hall effect and magnetoresistance of ferromagnetic metals. *Prog. Theor. Phys.* **27**, 772–90

Kondorskii E I 1965 Role of electron scattering by phonons and magnetic inhomogeneities in the Hall effect in ferromagnetic metals. *Sov. Phys. JETP* **21**, 337–41

Kontani H, Miyazawa M, Yamada K 1997 Theory of anomalous Hall effect in a heavy-fermion system with a strong anisotropic crystal field. *J. Phys. Soc. Jpn.* **66**, 2252–5

Kontani H, Yamada K 1994 Theory of anomalous Hall effect in heavy-fermion system. *J. Phys. Soc. Jpn.* **63**, 2627–52

Matsuda T D, Aoki Y, Sugawara H, Sato H, Andreev A V, Sechovsky V 1999 Specific heat anomaly around metamagnetic transition in UCoAl. *J. Phys. Soc. Jpn.* **68**, 3922–6

Ōnuki Y, Yamazaki T, Ukon I, Komatsubara T, Umezawa A, Kwok W K, Crabtree G W, Hinks D G 1989 Anomalous Hall coefficient in the f-electron systems—U compounds. *J. Phys. Soc. Jpn.* **58**, 2119–25

Ōnuki Y, Yun S W, Satoh K, Sugawara H, Sato H 1993 Anomalous Hall coefficient in the f-electron system. In: Oomi G, Fujii H, Fujita T (eds.) *Transport and Thermal Properties of f-Electron Systems*. Plenum, New York, pp. 103–11

Sato H, Aoki Y, Matsuda T D, Sugawara H, Kobayashi Y, Andreev A V, Sechovský V, Havela V, Settai R, Ōnuki Y 1998 Transport and thermal properties across phase

transitions in f-electron systems. In: Kazimierski M (ed.) *11th Sem. Phase Transitions and Critical Phenomena*. Polish Academy of Sciences, Wroclaw, Poland, pp. 23–33

Sechovský V, Havela L, de Boer F R, Brück E, Suzuki T, Ikeda S, Nishigori S, Fujita T 1993 Specific heat and magnetocaloric effect in UNiGa. *Physica B* **186–8**, 775–7

Sechovský V, Havela L, Jirman L, Ye W, Takabatake T, Fujii H, Brück E, de Boer R, Nakotte H 1991 Giant magnetoresistance effects in UNiGa. *J. Appl. Phys.* **70**, 5794–6

Tsuji M 1958 The thermoelectric, galvanomagnetic and thermomagnetic effects of monovalent metals. III. The galvanomagnetic and thermomagnetic effects for anisotropic media. *J. Phys. Soc. Jpn.* **13**, 979–86

H. Sato
Tokyo Metropolitan University, Japan

Y. Ōnuki
Osaka University, Japan

Invar Materials: Phenomena

In the search for a cheaper length standard than the meter made of Pt–Ir, the Swiss physicist Charles Guillaume in 1897 discovered "Invar," a ferromagnetic (FM) f.c.c. alloy of 65 at.% iron and 35 at.% nickel with small and almost temperature-independent—"invariant"—thermal expansion. After discovering "Elinvar," a FM f.c.c. Fe–Ni–Cr alloy with constant elastic behavior, Guillaume was awarded the Nobel Price for physics in 1920, not the least because of the technical importance of his findings. The understanding of Invar remained a problem (Wassermann 1990, Wittenauer 1997) before *ab initio* calculations (Entel *et al.* 1993) gave basic insights into the relations between lattice structure, atomic volume, and magnetic properties, and brought to light "anti-Invar" and how it relates to martensite, the long-known structural f.c.c.–b.c.c. transformation of iron and iron-rich alloys (Wassermann *et al.* 1999).

1. Basic Physical Properties and Definitions

Invar- and often also Elinvar-like behavior is found in transition metal alloy systems with different lattice structures (see Table 1), most with iron as a component. Figure 1 shows schematically the most typical features. The temperature dependence of the thermal expansion coefficient α (Fig. 1(a)) in the FM ordered range $T < T_C$ (where T_C is the Curie temperature) of Invar is reduced relative to a nonmagnetic reference, for which $\alpha(T)$ is given by the classical Grüneisen theory. Analogous behavior is found in antiferromagnetic (AF) Invar alloys such as $Fe_{40}Mn_{60}$ in the range $T < T_N$ (where T_N is the Néel temperature). Figure 1(b) shows that relative to the Grüneisen

Table 1
Invar and Elinvar systems.

F.c.c. structure
Fe–Ni
Fe–Pt (ordered)
Fe–Pt (disordered)
Fe–Pd
Fe–Mn
Co–Mn
Fe–Ni–Mn
Fe–Ni–Cr
Fe–Ni–Co
Fe–Ni–Pt, Pd
B.c.c. structure
Cr–Fe
Cr–Mn
Fe–Cr–Mn
Hexagonal structure
Co–Cr
Amorphous
Fe–B, P
Fe–TM (TM = Sc, Y, Zr, Hf)
(Fe–TM)Gl (TM = Mn, Co, Ni; Gl = Si, B, P)
Laves phases, compounds
ETFe$_2$ (ET = Ti, Zr)
RECo$_2$ (RE = all except Eu)
RE$_2$Fe$_{17}$ (RE = Y, Dy, La)
Dy$_2$(FeCo)$_{17}$
Fe$_3$C
Fe$_{14}$Nd$_2$B

reference the volume in a FM or an AF Invar alloy in the range $T \leqslant T_{C,N}$ is enhanced. This spontaneous volume magnetostriction, ω_s, has a maximum value at zero temperature, $\omega_{s0} = (\Delta V/V)_{T=0}$, corresponding to the area between the data and the reference curve in Fig. 1(a). Figure 1(c) shows that the shear modulus, G, starts to soften at T_C and then displays the temperature-independent Elinvar behavior. Figure 1(d) shows that the bulk modulus, $B(T)$, softens much above T_C in FM Invar alloys, different from that observed in AF Invar alloys (Wassermann 1990).

For $e/a < 8.5$ (the number of valence electrons per atom) in f.c.c. iron-based systems, there is also *anti-Invar* behavior (Acet *et al.* 1994), the opposite of Invar. Anti-Invar behavior describes the increase of the volume and the enhancement of the thermal expansion relative to a reference in the high-temperature *paramagnetic* range. The relative volume increase, $\Delta V/V$, can be determined quantitatively by plotting $\alpha T_m = f(T/T_m)$, where T_m is the melting temperature. For "normal" metals and alloys without magnetovolume anomalies such a plot results in an almost universal expansion curve, giving the average lattice curve $\alpha_{lat} T_m(T)$, which can be used as a general Grüneisen-like reference for $\alpha(T)$ of Invar
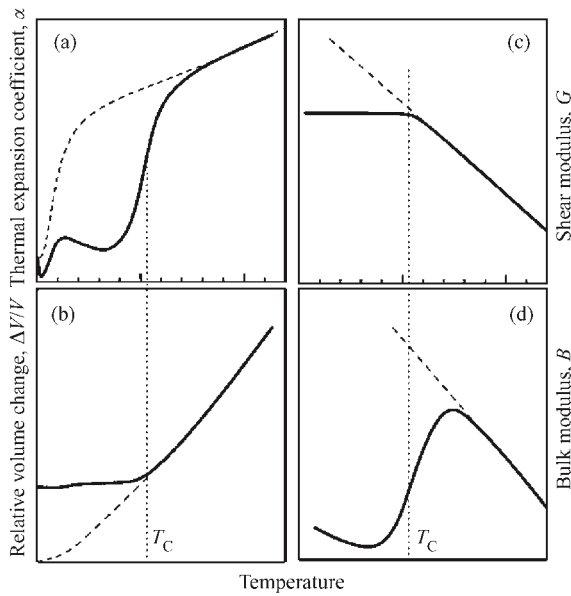
Figure 1
Schematic representation of the temperature dependence of (a) the thermal expansion coefficient α, (b) the relative volume change $\Delta V/V$, (c) the shear modulus G, and (d) the bulk modulus B for an Invar alloy. The dashed curves are the nonmagnetic Grüneisen reference.

Figure 2
Thermal expansion coefficient α multiplied by the melting temperature T_m vs. T/T_m for f.c.c. Fe–Ni alloys and f.c.c. γ-iron. The upward pointing arrows indicate the Curie temperatures T_c. The curves for $70 \leqslant x \leqslant 100$ are measured down to their corresponding martensite start temperatures M_s. The solid curve is the nonmagnetic Grüneisen-like lattice reference. Inset: $\alpha T_m(T/T_m)$ for $Fe_{50}Ni_{25}Mn_{25}$ anti-Invar, f.c.c. stable to 0 K.

and anti-Invar alloys. A plot of $\alpha T_m = f(T/T_m)$ for Fe_xNi_{100-x} alloys and elemental iron in the f.c.c. stability range shown in Fig. 2 reveals the continuous transition from FM Invar behavior in $Fe_{65}Ni_{35}$ ($e/a = 8.7$) to anti-Invar behavior in iron-rich samples and f.c.c. iron. In $Fe_{70}Ni_{30}$ ($e/a = 8.6$) both effects are observed, i.e., Invar behavior for $T < T_C/T_m$ and anti-Invar behavior for $T > T_C/T_m$. For $x > 75$ ($e/a < 8.5$) one encounters only anti-Invar behavior, for which an example is given in the inset of Fig. 2, showing $\alpha(T)$ of $Fe_{50}Ni_{25}Mn_{25}$, a paramagnetic alloy with f.c.c. stability to 0 k. With decreasing temperature the anti-Invar behavior terminates at the martensite start temperature, M_s, where the f.c.c.–b.c.c. transition takes place.

Figure 3 shows absolute values of the relative volume increase, $|\Delta V/V|$, vs. the composition (e/a) caused by the FM and AF Invar effects and the anti-Invar effect in different f.c.c. alloys. The volume increases shown occur *in addition* to the $\sim 7.5\%$ increase any metal or alloy experiences in the range $0 \leqslant T \leqslant T_m$ because of the "normal" thermal expansion due to anharmonic lattice potential (Grüneisen behavior). FM Invar behavior occurs only for $e/a > 8.5$, while for $e/a < 8.5$ one finds either anti-Invar behavior at high temperatures and AF Invar behavior at low temperatures, or anti-Invar behavior at high temperatures and martensite at low temperatures, if the f.c.c. stability is limited.

2. Microscopic Understanding

The present understanding of Invar and anti-Invar behavior stems from ground state properties as determined in *ab initio* calculations (Entel *et al.* 1993, Herper *et al.* 1999). A simplified picture is given in Fig. 4, showing for Invar and anti-Invar the volume dependence of the total energy $E(V)$ (Figs. 4(a) and (b)) and the magnetic moments (Figs. 4(c) and (d)). V_0 denotes the equilibrium and V_c the critical volume, where the equilibrium state becomes energetically unfavorable. In anti-Invar (Fig. 4(a)) the ground state at V_0 is a low-spin (LS) state with a small magnetic moment (Fig. 4(c)) relative to the FM high-spin (HS) state at larger volumes, causing an enhanced anharmonicity of the lattice towards *larger* volumes $V > V_c$ in $E(V)$. Invar (Fig. 4(b)) is just the opposite, because the ground state at V_0 is a FM HS state and the enhanced anharmonicity in $E(V)$ is towards *smaller* volumes $V < V_c$, caused by the LS state.
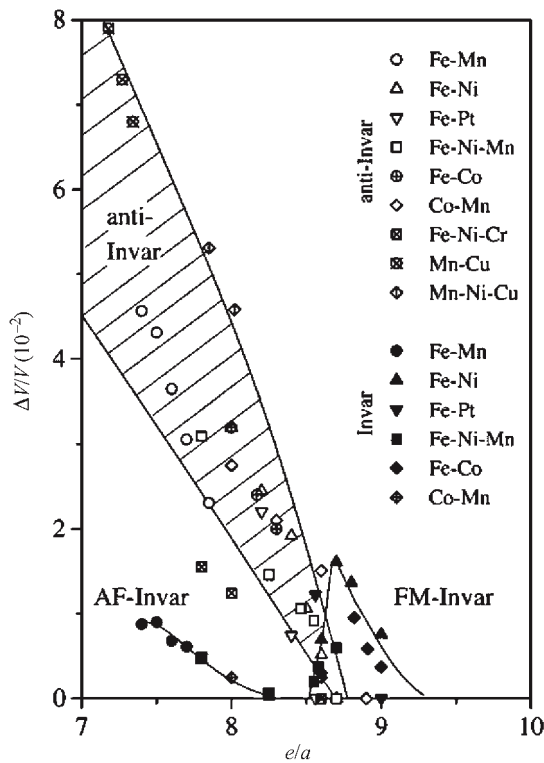
Figure 3
Relative volume enhancement $|\Delta V/V|$ through FM Invar, AF Invar, and anti-Invar effect vs. composition in electrons per atom (e/a) for different f.c.c. alloy systems.

The presence of these moment–volume instabilities in Fe–Ni and Fe–Pt Invar alloys has been demonstrated experimentally in Mössbauer experiments at 4.2 K, showing HS to LS transitions to occur when the lattice constant is reduced by high pressure (Abd-Elmeguid and Micklitz 1989). The *ab initio* calculations also corroborate the systematic behavior shown in Fig. 3. With increasing e/a anti-Invar behavior progressively transforms to FM Invar behavior as ΔE, the energetic difference between the HS and the LS states, decreases, goes through zero (so that LS and HS states are degenerate) near $e/a \sim 8.3$, and then increases again with the HS state becoming lower in energy.

Concerning the behavior at finite temperatures, the key point is that ΔE is of the order of milli-Rydbergs (1 mRy $\sim$ 150 K), so that transitions from the ground state to the energetically elevated state are possible by raising the temperature. Thus, as indicated with the arrows in Fig. 4, in anti-Invar LS–HS and in Invar HS–LS transitions occur, and the magnetic moment increases (Fig. 4(c)) or decreases (Fig. 4(d)), respectively. This is confirmed by high-temperature neutron investigations on the paramagnetic spin fluctuations
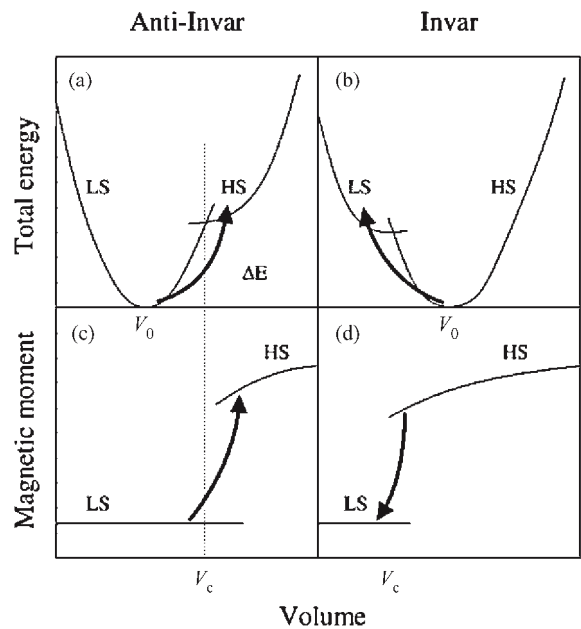
Figure 4
Schematic representation of volume dependence of (a, b) the total energy and (c, d) the magnetic moment of Invar and anti-Invar. V_0, equilibrium volume; V_c, critical volume for the transition from the LS to the HS state. Arrows indicate the direction of response of the system to increasing temperature.

of Fe_xNi_{100-x} alloys within the f.c.c. stability range (Acet *et al.* 1997). Figure 5 shows the results in a plot of the average magnetic moment, μ, vs. the temperature for compositions between $x = 65$ Invar (dashed curve) and pure γ-iron. With increasing iron concentration the slope of the $\mu(T)$ curves changes sign, in accordance with a change from a HS–LS transition for $Fe_{65}Ni_{35}$ Invar to a LS–HS transition in $Fe_{90}Ni_{10}$ anti-Invar or $Fe_{77}Ni_{13}Mn_7C_3$, an anti-Invar material with f.c.c. stability to 0 K. The high-temperature spin fluctuations in Fe–Ni alloys and in f.c.c. iron are always FM, although at low temperatures AF correlations occur, even AF long-range order in f.c.c. iron for $T_N < 70$ K. There is evidence from first principles calculations (van Schilfgaarde *et al.* 1999) that non-collinear magnetic moments and AF short-range order cause additional lattice softening and negative anharmonicity in Fe–Ni Invar.

Deeper insight into the microscopic background is gained from calculations resolving the properties of the d electrons in the vicinity of the Fermi energy E_F (Entel *et al.* 1993) with respect to their orbital symmetry (t_{2g}, e_g) and their antibonding (AB), nonbonding (NB), or bonding (B) character. The respective electronic density of states (DOS) curves in the LS and HS state are shown schematically in Fig. 6. The
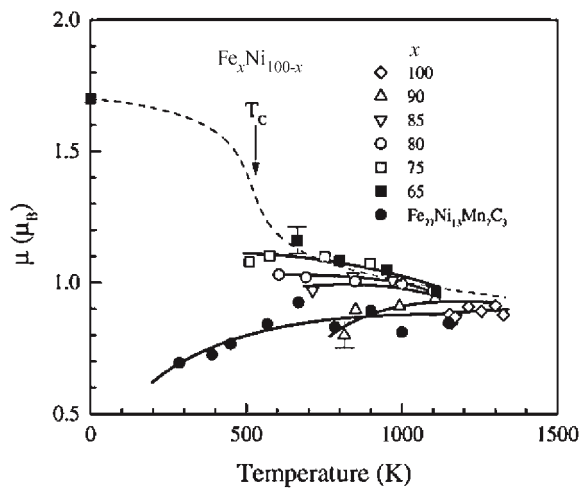
Figure 5
Average magnetic moment vs. temperature for
Fe_xNi_{100-x} alloys with different x as indicated and pure
γ-iron, all within the range of the stability of the f.c.c.
structure. The dashed line is $\mu(T)$ for $Fe_{65}Ni_{35}$ Invar with
f.c.c. stability to 0 K. The solid curve and the filled circles
are for $Fe_{77}Ni_{13}Mn_7C_3$ anti-Invar f.c.c. stable to 0 K.
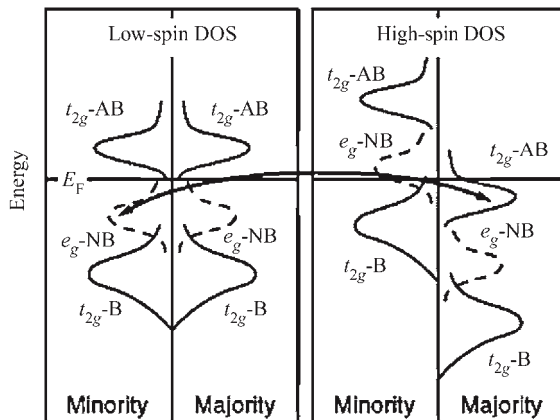
Figure 6
Schematic representation of the spin split DOS for a
system with moment–volume instability. DOS in the LS
state (left) and in the HS state (right). The arrow marks
the electronic transitions near the Fermi energy E_F from
the AB t_{2g} majority-spin states to NB e_g minority-spin
states (arrow from right to left) corresponding to a
HS–LS transition in Invar, and in the reverse direction
for a LS–HS transition in anti-Invar with increasing
temperature.

t_{2g} orbitals have a maximum charge density in the
[110] direction and thus in an f.c.c. lattice form strong
$dd\sigma$ bonds with nearest neighbors. The t_{2g} DOS is
therefore split and shows an energetically high-lying

peak with AB character and an energetically low-
lying one with B character. The e_g orbitals have max-
imum charge densities in the [100] direction and in an
f.c.c. lattice form $dd\pi$ bonds with the next nearest
neighbors. They are NB and found between the two
t_{2g} peaks in the f.c.c. DOS. The position of the Fermi
energy, E_F, relative to these levels, which depends on
the electron concentration, the atomic volume, and
the temperature, determines which type of transition
occurs between these levels, to lead to Invar, anti-
Invar, or to a martensitic transformation.

The arrow in Fig. 6 indicates the possible excita-
tions with increasing temperature. For anti-Invar
with a LS ground state the arrow reads from left to
right, because there is a charge transfer from NB mi-
nority-spin e_g orbitals to AB majority-spin t_{2g} orbit-
als. These excitations lead to a band splitting and
finally the HS state with a large volume caused by the
AB character of the t_{2g} majority-spin states. In Invar
the arrow in Fig. 6 reads from right to left, because
the HS state is the ground state and the charge trans-
fer is from AB t_{2g} majority-spin states to NB e_g mi-
nority-spin states when the temperature is increased.
This reduces the band splitting, corresponding to a
HS to LS transition.

In summary, more than 100 years after the find-
ing by Guillaume, through to the t_{2g}–e_g scenario, the
microscopic background of Invar, Elinvar, and anti-
Invar and also the relationship to the martensite in
iron-based systems is basically understood. However,
the true solution of the Invar problem will be found
when a first principles calculation reproduces cor-
rectly the archetypical property of Invar, i.e., the
anomalous temperature dependence of the thermal
expansion coefficient. To reach this goal a substantial
amount of research is still necessary.

See also: Magnetoelastic Phenomena

Bibliography

Abd-Elmeguid M M, Micklitz H 1989 Magnetism at high pres-
sure in f.c.c. Fe-based alloys. *Physica B* **161**, 17–21
Acet M, Wassermann E F, Andersen K, Murani A, Schärpff O
1997 The anomalous temperature dependence of the para-
magnetic response of Fe-rich f.c.c. Fe–Ni. *Europhys. Lett.* **40**,
93–8
Acet M, Zähres H, Wassermann E F, Pepperhoff W 1994
High-temperature moment–volume instability and anti-Invar
of γ-Fe. *Phys. Rev. B* **49**, 6012–7
Entel P, Hoffmann E, Mohn P, Schwarz K, Moruzzi V L 1993
First-principles calculations of the instability leading to the
Invar effect. *Phys. Rev. B* **47**, 8706–20
Herper H C, Hoffmann E, Entel P 1999 *Ab initio* full-potential
study of the structural and magnetic phase stability of iron.
Phys. Rev. B **60**, 3839–48
Van Schilfgaarde M, Abrikosov I A, Johansson B 1999 Origin
of the Invar effect in iron–nickel alloys. *Nature* **400**, 46–9
Wassermann E F 1990 Invar: moment–volume instabilities in
transition metal alloys. In: Buschow K H J, Wohlfahrt E P

(eds.) *Ferromagnetic Materials*. Elsevier, Amsterdam, Vol. 5, pp. 238–322

Wassermann E F, Acet M, Entel P, Pepperhoff W 1999 Basic understanding of the relations between Invar, anti-Invar and martensite in Fe-based alloys. *J. Magn. Soc. Jpn.* **23**, 385–90

Weiss R J 1963 The origin of the Invar effect. *Proc. Phys. Soc. London* **82**, 281–8

Wittenauer J (ed.) 1997 *The Invar Effect: A Centennial Symposium*. Mineral, Metals and Materials Society, Warrendale, PA, pp. 51–62

E. F. Wassermann
Gerhard-Mercator-Universität, Duisburg, Germany

Itinerant Electron Systems: Magnetism (Ferromagnetism)

The development of the electron band model (Bloch 1929) paved the way for an understanding of the magnetism of "itinerant" electrons. The first attempts to understand the metallic state were based on the free electron gas model and Pauli (1927) showed that the quenching of the spin can be explained if it is assumed that all the electrons in open shells (conduction electrons) are at least partially free. The Pauli exclusion principle requires that two electrons have to be different in at least one quantum number. For free electrons the only relevant quantum numbers are the spin and the electron momentum k. Since any state with quantum number k can accommodate two electrons, these electrons must have opposite spin so that all spins appear to be compensated. For the susceptibility of the noninteracting (no exchange) gas of free electrons Pauli developed his well-known expression:

$$\chi_P = 2\mu_B^2 N(\varepsilon_F) \qquad (1)$$

which relates the paramagnetism of the free electrons to the density of states at the Fermi energy $N(\varepsilon_F)$. Formally this relation resembles the result for the specific heat of the free electron gas which also depends on the density of states at the Fermi energy.

These ideas about the metallic state described as an electron gas were further developed by Mott (1935) and Slater (1936a, 1936b), who introduced more realistic models for the bandstructure and finally by Stoner (1936, 1938), who succeeded to formulate a phenomenological "molecular field" model (analogous to the Weiss model) by employing the electronic bandstructure instead of the discrete angular momentum levels. This model of itinerant electron magnetism accounts for noninteger magnetic moments in terms of a band filling of the narrow d band and by taking into account the interaction of the s and d electrons of the valence band. Within the framework of the Stoner model, the susceptibility of the interacting (including exchange) gas of free electrons

becomes enhanced by the exchange interaction and reads:

$$\chi_S = \frac{2\mu_B^2 N(\varepsilon_F)}{1 - IN(\varepsilon_F)} \qquad (2)$$

The quantity I in Eqn. (2) is the Stoner exchange factor, which is a slowly varying atomic quantity through the periodic table. The denominator allows the formulation of a criterion for the spontaneous onset of magnetism. If, in the nonmagnetic state the denominator is negative, the resulting negative susceptibility means that the paramagnetic state is not at a total energy minimum but at a maximum, so that any magnetic state must have a lower total energy. This is the famous Stoner criterion which is usually formulated such, that magnetism occurs if the inequality holds:

$$IN(\varepsilon_F) \geqslant 1 \qquad (3)$$

An attempt to clarify the role of the exchange interaction in metals was made by performing Hartree–Fock calculations for the free electron gas in comparison to tight binding calculations for the valence electrons (see review by Wohlfarth (1953)).

A crucial step towards the understanding and practicability of quantum mechanical calculations of the metallic state was done by Slater (1951). He suggested that the exchange interaction could be approximated by an averaged potential over the occupied states of a homogenous electron gas, which is no longer a nonlocal quantity but depends only on the local electron density at the point r:

$$v_s(r) = -3e^2 \left(\frac{3}{8\pi}\right)^{1/3} \rho(r)^{1/3} \qquad (4)$$

A significant improvement to the Slater exchange occurred with the introduction of the Xα method where the Slater exchange potential $v_s(r)$ is multiplied by a factor α, which is determined from the requirement that the total energy of an isolated atom calculated from the Xα-potential equals the respective Hartree–Fock value (Schwarz 1972).

The next major step towards an understanding of the electronic structure of solids and subsequently of their magnetism was the density functional formalism introduced by Hohenberg and Kohn (1964). They showed that the ground state energy can be expressed in terms of a universal functional of the electron density (for details on this subject area see *Density Functional Theory: Magnetism*). The variation of the energy with respect to the electron density leads to effective one-electron Schrödinger type equations (Kohn and Sham 1965). In these equations the exchange-correlation potential $v_{xc}(r)$ enters additively to the Coulomb part, allowing straightforward use of independent interpolation formulae to approximate

Table 1
Exchange splitting ΔE and Stoner factor I for closed packed cobalt for various models of the LSDA for exchange and correlation.

	exp[a]	$X\alpha$[b]	LA[c]	HL[d]	vBH[e]
ΔE (eV)	1.05	2.05	1.23	1.40	1.49
I (eV/μ_B)	0.65	1.21	0.72	0.93	0.96

a–e See text for details.

$v_{xc}(r)$. This treatment is called the "local spin density approximation" (LSDA) for exchange and correlation (Hedin and Lundquist 1971, von Barth and Hedin 1972, Parr and Yang 1989).

Table 1 compares the values for ΔE and I for h.c.p. (f.c.c.) cobalt for some commonly used models of the LSDA. Table 1 shows that most of the usual models yield too large a band splitting and Stoner factor. This shortcoming is due to an incomplete description of correlation effects. Only in case (c), where a special treatment is used to improve the correlation, do the calculated values come closer to the experimental estimates. Despite the large scattering found for ΔE and I the calculated magnetic moments are all between 1.55 and 1.7 μ_B (exp: 1.62 μ_B). The data given in Table 1 are taken from: (a) best value from experiments (h.c.p. cobalt) given by Wohlfarth (1980), (b) $X\alpha$ result for f.c.c. cobalt given by Wakoh and Yamashita (1970), (c) to obtain an improved description of the correlation effects Oles and Stollhoff (1986) introduced their local approach (LA) (f.c.c. cobalt), and (d) and (e) are values taken from Mohn and Schwarz (1993) for h.c.p. cobalt employing the Hedin–Lundquist (HL) and the von Barth–Hedin (vBH) exchange potential.

Parallel to the development of bandstructure theory there was a search for "simple" toy models to explain solid state magnetism. The most prominent of these models was introduced by Hubbard (1963), who tried to describe transition metal oxides with their narrow d bands and their strong correlation. These models resemble the main features of electrons in a solid which are the bonding to a certain site and the Coulomb repulsion of electrons at the same site.

With these tools at hand it became possible to calculate the ground state properties with high reliability and also to understand the complex mechanisms occurring in solids. Among the remaining problems the most crucial one was the temperature dependence of solid state magnetism. While for the localized moment models the finite temperature effects became reasonably clear at a very early stage, this development took some time for metals.

For the free electron gas the temperature dependence of the susceptibility was calculated from the finite temperature properties of the Fermi–Dirac distribution (Sommerfeld expansion). Stoner applied the same ideas to introduce finite temperatures into the itinerant electron model. Unfortunately, the respective Curie temperatures T_c came out too large by a factor of 4–8 and the inverse susceptibility above T_c showed a T^2 rather than a linear T dependence (as observed experimentally). After years of persistent struggle to salvage the finite temperature Stoner model, it finally became clear that the single particle excitations are not (or only to a small amount) responsible for the finite temperature behavior of metallic magnetism.

These results suggest that two extreme limits must be considered:
(i) the localized limit for which the magnetic moments and their fluctuations are localized in space (delocalized in k space), with their amplitudes being large and fixed.
(ii) the itinerant (or weak ferromagnetic) limit for which the moments and their fluctuations are localized in k space (delocalized in real space), with their amplitudes being temperature dependent.

A Curie–Weiss law is observed in both cases but its physical origin and the corresponding value of the Curie constant is different.

To solve these inconsistencies, Moriya and Kawabata (1973) tried to include thermally induced collective excitations of the spins (as they were already known for localized spins) in order to formulate an unified picture of magnetism (for a review see Moriya 1985). A similar approach was introduced by Murata and Doniach (1972), who introduced local and random classical fluctuations of the spin density (spin fluctuations) which should be excited thermally. Both of the latter two models become equivalent at high temperatures and lead to a Curie–Weiss law. Although the Murata–Doniach approach runs into trouble at $T = 0\,K$ (the classical fluctuations violate of the third law of thermodynamics), it has successfully been applied to calculate T_c from data derived from de Haas–van Alphen measurements (Lonzarich and Taillefer 1985) and to formulate a simple model for T_c of metallic solids (Mohn and Wohlfarth 1986) which gives much better results than the Stoner model.

1. Models for Delocalized Moments

The magnetism of the delocalized (itinerant) band electrons represents an extreme limit of solid state magnetism. For these electrons the angular quantum number is no longer a sufficient description of their quantum state since their properties are described by a new quantum number, the electron momentum k. Together with the symmetry breaking due to the crystal field, it is also this quantum number which is responsible for the quenching of the angular momentum. Each electronic state, which is now represented by a certain value of k, is occupied with electrons which differ pairwise in all their other quantum

numbers so that the total angular momenta are always close to zero. In this situation the discrete energy levels, which were characterized by their magnetic quantum number m_J and integer occupation numbers, which appeared in the Weiss model, have now to be replaced by quasi-continuous energy levels. These are characterized by the respective k vector and a no longer integer occupation number given by the density of states. Since the electron states are given by plane waves (Bloch states) they extend over the whole crystal. A possible magnetic moment created by these electrons is no longer localized at a certain atomic site but appears to be smeared out (delocalized) over the whole crystal. In the limit of the free electron gas the electron density is constant in real space, so that a magnetic moment (which would better be described by the spin density) is also constant everywhere in space.

The magnetic behavior of the delocalized electrons can be described by transforming the real-space properties of the localized moments into k space. The delocalized electrons are localized in k space, the intra-atomic exchange interaction (localized in real space), which was responsible for the formation of a localized moment, is now an interatomic-like exchange interaction localized in k space. Also the energetic localization of the atomic-like energy states is now broadened to a band state and appears to be energetically delocalized.

This extreme point of view is of course only valid for a quasi-free electron description of metallic solids. If a metal can be described by considering a quasi-free electron behavior only, its paramagnetic susceptibility should be given by the Pauli susceptibility (Eqn. (1)). However, even for simple metals like the alkalines the Pauli values are too low compared to experimental values. The reason for this discrepancy is the relatively high electron density in solids (even in simple metals such as sodium) which leads to a non-negligible exchange interaction (c.f. Eqn. (4)). In extreme cases like f.c.c. palladium, the Pauli susceptibility is too low by a factor of 9–10. Although d electron systems like palladium (but also iron, cobalt, and nickel) are far from showing a "free electron-like" behavior, since the d electron band width is much smaller than that of the s band, their magnetism can be described along similar lines. This is due to the fact that for a fermion system all excitations (either thermally or due to an external field) occur in a narrow energy range around the Fermi surface so that only the properties at the Fermi energy are relevant.

1.1 The Stoner Model of Itinerant Electron Magnetism

Stoner (1936, 1938) formulated his model of itinerant electron magnetism which can be seen as a transcription of the Weiss model for metallic solids. Stoner replaced the local "free atom-like" energy

levels in the Weiss model, which are characterized by their respective magnetic quantum number, by the electronic bandstructure. Due to the crystal field interaction in solids the angular momentum appears to be quenched (angular quantum numbers are no longer relevant), so that only the k vector and the spin of the valence electrons remains in describing the state of the electrons. The model is based on the following three postulates: (i) the carriers of magnetism are the electrons in the d band, (ii) effects of exchange and correlation are treated within a molecular field term, and (iii) it must conform to Fermi statistics.

It is assumed that for an applied magnetic field, which is the molecular field (eventually including an external field H_{ex}) the Fermi energy of the paramagnetic state is shifted to new values ε_f^+ for spin-up and ε_f^- for spin-down which leads to new occupation numbers n^+ and n^- (Fig. 1, left panel). This picture is identical to the actual shifting of the two spin-dependent bands by the spin splitting ΔE (Fig. 1, right panel).

Since the Fermi energy is the energy of the highest occupied state it is equal to the chemical potential μ; and consequently the new Fermi energies, caused by the field, can be seen as chemical potentials for spin-up ($+$) and spin-down ($-$) as μ^+ and μ^-. The Stoner equations can now be formulated:

$$n^{\pm} = \int_0^{\infty} N(\varepsilon) \frac{1}{\exp\left(\dfrac{\varepsilon}{k_B T} - \eta^{\pm}\right) + 1}\, d\varepsilon \qquad (5)$$

$$k_B T \eta^{\pm} = k_B T \eta \pm \frac{IM}{2} \pm \mu_B H_{ex} \quad \text{with} \quad \eta = \frac{\mu}{K_B T}$$
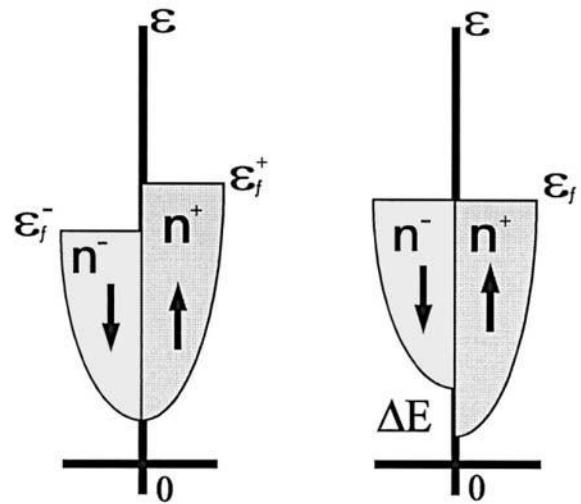
Figure 1
Magnetic splitting of the spin resolved density of states as assumed in the Stoner model of itinerant magnetism.

The number of spin-up and spin-down electrons $n^{\pm}$ is given by the integral over all occupied states, where for $T = 0\,\text{K}$ the upper limit can be taken as the Fermi energy ε_F. In its original formulation, Stoner assumed that the spin-up and spin-down bandstructure were equal so that the density of states $N(\varepsilon)$ are the same for both spin directions. This treatment is referred to as the rigid band picture, which assumes that during the transition from a nonmagnetic to a ferromagnetic state the spin-up and spin-down bands do not change their shape and that they only become shifted energetically by the spin splitting ΔE (c.f. Table 1) given by:

$$\Delta E = IM = I(n^+ - n^-) \tag{6}$$

In Eqns. (5) and (6), the quantity I is the Stoner exchange factor and M is the magnetic moment. From the Stoner equations the susceptibility can be calculated which becomes:

$$\chi = \frac{M}{H} = \frac{2\mu_B^2 \int_0^\infty N(\varepsilon)\left|\frac{df}{d\varepsilon}\right|d\varepsilon}{1 - I \int_0^\infty N(\varepsilon)\left|\frac{df}{d\varepsilon}\right|d\varepsilon} \tag{7}$$

where $df/d\varepsilon$ is the energy derivative of the Fermi–Dirac distribution. Equation (7) is the most general form of the Stoner susceptibility which for $T = 0\,\text{K}$ reduces to:

$$\chi = \frac{2\mu_B^2 N(\varepsilon_F)}{1 - IN(\varepsilon_F)} = 2\mu_B^2 N(\varepsilon_F)S \tag{8}$$

which is the Pauli susceptibility $2\mu_B^2 N(\varepsilon_F)$ enhanced by the exchange interaction via a factor S (Stoner enhancement factor). If the term $IN(\varepsilon_F)$ becomes larger than 1, χ becomes negative, which means that the interacting electron gas is unstable against the formation of a magnetic moment (spontaneous magnetic order). This gives rise to the formulation of the famous Stoner criterion for the onset of magnetism which happens if:

$$IN(\varepsilon_F) \geqslant 1 \tag{9}$$

Since the Stoner exchange factor I is an atom specific constant, a possible transition to a magnetic state depends only on the density of states at the Fermi energy $N(\varepsilon_F)$. This in turn means that bands are needed which are narrow enough to create a large density of states. This is not only the explanation why band magnetism occurs only in the $3d$ transition metals (Cr, Mn, Fe, Co, and Ni) and the $5f$-actinides starting with curium. The band width of the $4d$ and $5d$ series is already too large, which implies that a certain degree of *localization* is necessary.

If a system fulfills the Stoner criterion and thus has a magnetic ground state, Eqn. (7) also allows to calculate the Curie temperature by requiring that T_c

is given by the temperature for which the denominator of Eqn. (7) becomes zero:

$$I \int_0^\infty N(\varepsilon)\left|\frac{df}{d\varepsilon}\right|d\varepsilon = 1 \tag{10}$$

Eqn. (10) is a temperature dependent Stoner criterion. Due to the convolution with the function $df/d\varepsilon$, the effective density of states becomes progressively smaller when the temperature rises until the relation given above is fulfilled. Once this happens, the Stoner theory does no longer see any magnetic moment so that the paramagnetic state (the state above T_c) is the nonmagnetic state. This is a new mechanism compared to the Weiss model, where the paramagnetic state was given by complete disorder of the local moments, or to the Heisenberg model within the mean field approximation, where the thermal agitation leads to a breakdown of the interaction aligning neighboring spins. Unfortunately the Curie temperatures calculated within the Stoner model are too high by a factor of 4–8 (Gunnarsson 1976). The thermal excitation mechanism is called single-particle excitations or simply Stoner excitations. At $T = 0\,\text{K}$ all states below the Fermi energy are occupied and all states above are empty. With rising temperature the softening of the Fermi–Dirac distribution creates holes below the ($T = 0\,\text{K}$) Fermi energy and creates occupied states above.

This is the typical case of an electron-hole excitation or exciton, however, only excitations which are connected with a spin flip are able to reduce the bulk magnetic moment. The energy scale on which these single particle excitations occur is set by the $T = 0\,\text{K}$ Fermi energy via the effective Fermi degeneracy temperature T_F:

$$T_F^{-2} = \left| \frac{\pi^2 k_B^2}{6}\left[\frac{N(\varepsilon_F)''}{N(\varepsilon_F)} - \left(\frac{N(\varepsilon_F)'}{N(\varepsilon_F)}\right)^2 \right] \right| \tag{11}$$

which depends on the local structure of the density of states at the Fermi energy via its first and second energy derivative (Sommerfeld expansion). For most systems this temperature is $5000\,\text{K}$ to $10000\,\text{K}$ so that T_c within the Stoner model hardly ever reaches a reasonable order of magnitude. With the definition of T_F (which is basically the expansion of the integrand of Eqn. (10)), T_c can be written as:

$$T_c^2 = T_F^2(IN(\varepsilon_F) - 1) \tag{12}$$

It is easy to see that T_c only becomes considerably smaller than T_F if $IN(\varepsilon_F)$ is only slightly larger than one, which is the condition for the very weak itinerant electron magnetism (Edwards and Wohlfarth 1968).

Systems under this class are supposed to have a very low saturation magnetization and also a very low T_c. The progress in metallurgy and solid state

Itinerant Electron Systems: Magnetism (Ferromagnetism)

chemistry during the 1960s, mostly due to the search for BCS-superconductors, led to the discovery of a few candidates like $ZrZn_2$, Sc_3In, and Ni_3Al. Although their behavior below T_c can be described within the theory of weak itinerant ferromagnets, for $T > T_c$ all three systems show a Curie–Weiss behavior which is not consistent with the Stoner model.

Within the Stoner model the finite temperature behavior of the susceptibility and the magnetic moment are described by the equation for the magnetic isotherms of weakly itinerant systems:

$$\left(\frac{M(H,T)}{M(0,0)}\right)^3 - \frac{M(H,T)}{M(0,0)}\left(1 - \frac{T^2}{T_c^2}\right) = \frac{2\chi_0 H}{M(0,0)} \quad (13)$$

which represents the linear Arrott plots found also experimentally. Explicitly the temperature dependence of the magnetic moment is given by:

$$\frac{M}{M_0} = \left(1 - \frac{T^2}{T_c^2}\right)^{1/2} \quad (14)$$

which for $T \to T_c$ shows the expected mean field behavior with a critical exponent $\beta = \frac{1}{2}$.

Eqn. (13) is equivalent to the Landau expansion of the free energy of a ferromagnet which reads:

$$F(M) = \frac{A}{2}M^2 + \frac{B}{4}M^4 - MH \quad (15)$$

The respective values of the coefficients A and B can easily be determined and become:

$$A = -\frac{1}{2\chi_0}\left(1 - \frac{T^2}{T_c^2}\right) \quad \text{and} \quad B = \frac{1}{2x_0 M_0^2} \quad (16)$$

where χ_0 and M_0 are the susceptibility and magnetic moment at the equilibrium, respectively.

The temperature dependence of the susceptibility is a subject on its own. The functional dependence above T_c can easily be calculated from Eqn. (13) if one considers, that for $T > T_c$ the magnetic moment $M(0, T)$ vanishes. The respective result is:

$$\chi = 2\chi_0\left(\frac{T^2}{T_c^2} - 1\right)^{-1} \quad \text{for } T > T_c \quad (17)$$

which allows to calculate the Curie constant C defined as:

$$C = \frac{d(\chi^{-1})}{dT} = \frac{T}{\chi_0 T_c^2} \quad (18)$$

which for the Stoner model varies linear in T rather than being a "constant."

For temperatures below T_c one has to consider the additional temperature dependence of the magnetic

moment, so that the susceptibility becomes:

$$\chi = \chi_0\left(1 - \frac{T^2}{T_c^2}\right)^{-1} \quad \text{for } T \leqslant T_c \quad (19)$$

The reason for the surprising result that the susceptibility changes by a factor of two is not an artifact of the Stoner model, but is a general feature. The reason for it lies in the fact that the susceptibility simply measures the amount of magnetic moment produced by an applied field. The result means that it is twice as easy to create the same moment from a nonmagnetic spin system than from a magnetic spin system, where the applied field has to work against an already magnetized ensemble. In both temperature ranges, however, the inverse susceptibility does not show a Curie–Weiss law, but always a T^2 behavior.

Although the Stoner model gives a very good description of the $T = 0\,K$ ground state properties, its finite temperature behavior fails completely. The electron-hole excitations considered are not able to yield reasonable values for T_c and also lead to the wrong power law for the χ versus T dependence.

1.2 The Hubbard Model

Parallel to the development of bandstructure theory there was a search for "simple" toy models to explain solid state magnetism. The Hubbard model combines electron hopping between neighboring sites and the Coulomb repulsion of electrons at the same site. These features are combined within the Hubbard Hamiltonian (Hubbard 1963), which in its simplest form reads:

$$H = \sum_{ij\sigma} t_{ij} c_{i\sigma}^+ c_{j\sigma} + U \sum_i n_{i\uparrow} n_{i\downarrow} \quad (20)$$

The electron hopping is controlled by the parameter t_{ij}, U models the Coulomb interaction. $c_{i\sigma}^+$, $c_{i\sigma}$ are the fermion creation and annihilation operators for an electron with spin σ on site i and $n_{i\sigma} = c_{i\sigma}^+ c_{i\sigma}$ is the related ladder operator counting the occupation on site i. These fermion operators obey the following anticommutator rules:

$$[c_{i\sigma}^+, \ c_{j\sigma'}] = \partial_{ij}\partial_{\sigma\sigma'} \ [c_{i\sigma}^+, \ c_{j\sigma'}^+] = [c_{i\sigma}, \ c_{j\sigma'}] = 0 \quad (21)$$

Depending on the sign of U the Hubbard Hamiltonian describes various phases, i.e., (i) $U > 0$ (repulsive) paramagnetic metallic, ferromagnetic metallic, and antiferromagnetic insulating; and (ii) $U < 0$ (attractive) normal Fermi liquid, superconducting, charge density wave (insulator), and normal Bose liquid (insulator).

U is, however, not the only parameter. There exists also the strength of the electron hopping t_{ij} and the temperature T. Further "hidden" variables are the dimensionality of the system and the structure of

the crystal lattice. Since the band filling (thus the number of electrons) plays an important role also the electron density $n = n_\uparrow + n_\downarrow$ can be regarded as a parameter of the Hubbard Hamiltonian. Since the Pauli principle avoids that two electrons with like spin occupy the same lattice site then $n_\sigma \leqslant 1$ for $\sigma = \uparrow, \downarrow$ and thus $n \leqslant 2$. The special case $n = 1$ describes the half-filled band (antiferromagnetism).

A straightforward solution can be found in the unperturbed case $U = 0$. The solution is found by the Fourier transform of the respective operator. In the time dependent form

$$\hbar \dot{c}_{i\sigma} = -\sum_j t_{ij} c_{j\sigma} \Rightarrow c_{i\sigma} = \frac{1}{\sqrt{N}} \sum_{\mathbf{k}} e^{i\mathbf{k}\mathbf{R}_i} c_{\vec{k}\,\sigma} \quad (22)$$

$$\hbar \dot{c}_{\mathbf{k}\sigma}(t) = \varepsilon_{\mathbf{k}}^0 c_{\mathbf{k}\sigma}(t) \Rightarrow c_{\mathbf{k}\sigma}(t) = e^{-\frac{i}{\hbar}\varepsilon_{\mathbf{k}}^0 t} c_{\mathbf{k}\sigma}(0) \quad (23)$$

which as a solution describes a single electronic band in the tight binding limit:

$$\varepsilon_{\mathbf{k}}^0 = \varepsilon_0 - \sum_{j \neq i} t_{ij} e^{i\mathbf{k}(\mathbf{R}_i - \mathbf{R}_j)} \quad (24)$$

For a $2d$ square lattice $\varepsilon_k^0 = -2t(\cos(k_x a) + \cos(k_y a))$ leading to a bandwidth $W = 4t$.

In a similar way one treats the case for $U \neq 0$ in the Hartree–Fock approximation where the Hubbard interaction $n_{i\uparrow} n_{i\downarrow}$ is replaced by $\bar{n}_{i\uparrow} n_{i\downarrow} + n_{i\uparrow} \bar{n}_{i\downarrow} - \bar{n}_{i\uparrow} \bar{n}_{i\downarrow}$. The entities $\bar{n}_{i\sigma}$ are thermodynamical averages which have to be determined self-consistently. The physical interpretation of the Hartree–Fock approximation is that fluctuations in the double occupancy $n_{i\uparrow} n_{i\downarrow}$ are suppressed. The respective time-dependent Schrödinger equations reads:

$$\left(i\hbar \frac{\mathrm{d}}{\mathrm{d}t} - \varepsilon_0 - U\bar{n}_{i-\sigma} \right) c_{i\sigma} = -\sum_j t_{ij} c_{j\sigma} \quad (25)$$

The solutions are two bands split by the Hubbard interaction U:

$$\varepsilon_{\mathbf{k}}^\uparrow = \varepsilon_{\mathbf{k}}^0 + \tfrac{1}{2} U(\bar{n} + m), \ \varepsilon_{\mathbf{k}}^\downarrow = \varepsilon_{\mathbf{k}}^0 + \tfrac{1}{2} U(\bar{n} - m) \quad (26)$$

$$\text{with} \quad \bar{n}_\uparrow = \tfrac{1}{2}(\bar{n} + m), \ \bar{n}_\downarrow = \tfrac{1}{2}(\bar{n} - m) \quad (27)$$

The respective band splitting is thus given by $\Delta E = Um = \varepsilon_{\mathbf{k}}^\uparrow - \varepsilon_{\mathbf{k}}^\downarrow$, which can directly be compared to the result obtained from the Stoner model (Eqn. (6)). In complete analogy to the Stoner model one also arrives at a criterion for magnetic ground state which is fulfilled if $UN(\varepsilon_F) \geqslant 1$ (c.f. Eqn. (9)).

It is found that within the Hartree–Fock approximation the Hubbard model and the Stoner model become equivalent. The suppression of fluctuations in the double occupancy leads to an effective mean field treatment where Um represents the resulting self-consistent molecular field.

The missing physics is again the orientational disorder. This is well described by the Heisenberg model but hard to see for itinerant electrons where in the Hartree–Fock approximation the paramagnetic state becomes the nonmagnetic state. However, what is required for the paramagnetic state is that the average over the magnetic moments vanishes:

$$\left\langle \sum_i m_i \right\rangle = \left\langle \sum_i (n_{i\uparrow} - n_{i\downarrow}) \right\rangle \quad (28)$$

but the individual moment at site i remains, so that $m_i = n_{i\uparrow} - n_{i\downarrow} \neq 0$ for times τ such that

$$\frac{\hbar}{W} \leqslant \tau \leqslant \frac{\hbar}{k_B T}$$

1.3 Spin Fluctuations

From the preceding discussion it becomes clear that also in itinerant systems collective excitations of the spin system govern the finite-temperature properties. In the mid-1970s the first self-consistent spin polarized bandstructure calculations of the ground state of transition metals were performed using the LSDA to treat exchange and correlation effects. These calculations yielded satisfactory values for the magnetic moment, the exchange splitting, the cohesive energy, and a magnetic ground state which could be explained within the Stoner model. However, any attempt to explain the finite temperature behavior from these results failed. In the light of the previous discussion this failure is nowadays no longer surprising. Although these calculations contain all the many-body interactions via the density functional formalism, they still lack the ability to describe an excitation spectrum beyond the single particle picture. It has become clear (see review Shimizu 1981), that the problem is caused by imposing the translational symmetry of the spin density, an assumption which becomes violated by the collective excitations for $T > 0$ K. This breakdown of the conventional band picture has led to three main directions to go beyond it.

(i) In the Murata and Doniach (1972) approach the properties of the magnetic systems are described via a Landau–Ginzburg expansion of the free energy. The effect of spin fluctuations is formulated via randomly fluctuating local magnetic moments which couple to the bulk magnetization. Although these local moments $m(r)$ are vectors, the averaging process using Gaussian statistics leads to scalar quantities $\langle m(r)^2 \rangle$, which simply renormalize the original Landau expansion for a ferromagnet (Eqn. (15)). This scheme was successfully applied by Lonzarich and Taillefer (1985) to ferromagnetic and nearly ferromagnetic metals.

(ii) In the disordered local moment approach, the magnetic moments on individual atoms are allowed

to have random orientations in the sense described by Herring (1952a, 1952b) and later by Hubbard (1979a, 1979b) and Hasegawa (1980). Pindor *et al.* (1983) implemented this model in a self-consistent Korringa–Kohn–Rostoker (KKR) Coherent-Potential-Approximation (CPA) calculation to simulate the magnetic properties of the transition metals at finite temperature. Within this formalism Staunton *et al.* (1984) calculated the temperature dependent spin density and the wave vector-dependent susceptibility $\chi(q)$. With this model T_c values of 1260 K and 225 K for iron and nickel were obtained, which should be compared to experimental values of 1043 K and 630 K, respectively. The discrepancy between theoretical and experimental values could be due to the assumption that directional disorder is complete above T_c, so that effects of short range order are neglected which could be important as suggested by Prange and Korenman (1979a, 1979b) and Capellmann (1979). However, what these CPA calculations have clearly shown is that the density of states (and thus all related macroscopic quantities) remain virtually unchanged up to temperatures well above the Curie point.

(iii) Later Nolting *et al.* (1995) proposed a new approach where the LSDA ground state bandstructure is fitted to a tight-binding model which enters a Hubbard Hamiltonian. The idea of this treatment is to start from the best quantum mechanical ground state available and to use it as a basis for a many particle treatment within the Hubbard model, which also allows correction for the too small correlation in the usual LSDA schemes. The calculated T_c values for Fe, Co, and Ni are in excellent agreement with experimental values. What makes this approach even more promising is the fact that it explains the experimental photo-electron spectra which could not be related to the bare LSDA bandstructure results.

1.4 Fluctuations of the Magnetic Moment

The idea of the introduction of fluctuations is to account for the shortcoming of the Stoner model, which does not allow for any tilting of the spins. In addition, these fluctuating moments which are induced by temperature should give rise to a Curie–Weiss behavior of the susceptibility. Such a fluctuation is shown in Fig. 2.

For the gas of free electrons the eigenfunctions are plane waves and the charge and spin density are constant in space. A local fluctuation (here it is only a parallel component) can be seen as a perturbation of the ground state spin density with a finite lifetime well below the characteristic time for electron hopping. It can also be assumed that the spatial extension of the fluctuation is larger than the range of interaction in the system, which means that fluctuations are treated in the limit of long wavelength.
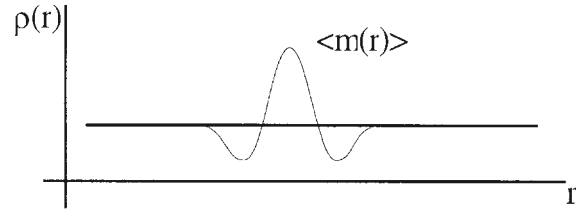
Figure 2
Schematic depiction of a local, longitudinal fluctuation of the spin density $\rho(r)$ (thick horizontal line) of the electron gas.

In the framework of the Landau theory of phase transitions the bulk magnetic moment M was introduced as the order parameter for the free energy (Eqn. (15)). With this choice it was assumed that any vector properties of M were irrelevant for the results, since time reversal symmetry requires that only even powers of M enter the free energy. Introducing local fluctuations of the magnetic moment one has to recognize the vector properties of both the magnetic moment M and its fluctuation $m(r)$. Consequently one has to distinguish fluctuations which are parallel and which are perpendicular to the direction of M. In the fluctuation treatment one replaces the order parameter M in Eqn. (15) by a new quantity which, in addition, contains the fluctuating magnetic moment:

$$M^{2n} \to \left\langle \left(M + \sum m_i\right)^{2n}\right\rangle \qquad (29)$$

The bracket $\langle \cdots \rangle$ denotes the Gaussian average and the index of m represents the three components of the fluctuation in the local coordinate system of M. Unambiguously it can be assumed that M points into the z direction, which (for an isotropic system) leads to two components of the fluctuation which are perpendicular to M, namely m_x and m_y, and one parallel component, m_z. To simplify the legibility the obvious r dependence of $m(r)$ is omitted. As an example the square of the order parameter is given in:

$$\left\langle \left(M + \sum m_i\right)^{2n}\right\rangle = \left\langle M^2 + 2M\sum m_i + \sum\sum m_i m_j\right\rangle$$
$$M^2 + 2\langle m_\perp^2\rangle + \langle m_{||}^2\rangle \qquad (30)$$

When averaged the mixed term vanishes because m_i always appears with an odd power. From the term $m_i m_j$, for the same reason, only the diagonal elements remain. In the resulting relation the subscripts were replaced by symbols denoting the perpendicular components m_x and $m_y \Rightarrow m_\perp$ and the parallel component $m_z \Rightarrow m_{||}$.

One now replaces the order parameter M^{2n} in the free energy expression (Eqn. (15)) by the respective new order parameter $\left\langle \left(M + \sum m_i\right)^{2n}\right\rangle$ and obtains

the "dynamical" form for the free energy F:

$$F = \frac{A}{2}(M^2 + 2\langle m_\perp^2 \rangle + \langle m_\parallel^2 \rangle)$$
$$+ \frac{B}{4}(M^4 + M^2(6\langle m_\parallel^2 \rangle + 4\langle m_\perp^2 \rangle)$$
$$+ 8\langle m_\parallel^2 \rangle^2 + 3\langle m_\perp^2 \rangle^2 + 4\langle m_\parallel^2 \rangle\langle m_\perp^2 \rangle) \quad (31)$$

The original static form of F has just been extended by the fluctuations. For $T = 0\,\text{K}$, the fluctuations vanish and Eqn. (31) reduces to Eqn. (15). Since the fluctuations only renormalize the original Landau coefficients, the physical meaning and definition of both A and B are the same as before. What can be seen immediately is that even when the bulk magnetization M vanishes, the fluctuations are present at all temperatures since they represent thermally induced local magnetic moments so that the paramagnetic state (for $T > T_c$) is no longer the nonmagnetic state as in the Stoner model.

This expression for the free energy can now be used to derive important properties of the fluctuating moments. Since T_c is given by the temperature where the susceptibility diverges under the condition that the bulk magnetic moment M vanishes, one can calculate the amplitude of the fluctuations at $T = T_c$:

$$\frac{\partial^2 F}{\partial M^2} = \chi^{-1} = A + \frac{B}{2}(10\langle m^2 \rangle) = 0 \quad \text{for} \quad T = T_c \quad (32)$$

In Eqn. (32) the subscripts for the parallel and perpendicular component disappear, since when M vanishes a distinction between directions parallel and perpendicular to M no longer has any meaning. Using Eqn. (16) the "Moriya formula" is recovered:

$$\langle m^2 \rangle = \frac{M_0^2}{5} \text{ at } T = T_c \quad (33)$$

which demonstrates that the mean square amplitude of the fluctuation at T_c is a ground state property.

Based on these results and inspired by the work of Lonzarich and Taillefer (1985), Mohn and Wohlfarth (1986) derived a simple model for the Curie temperature in weakly itinerant systems which reads:

$$T_c \propto T_{SF} = \frac{M_0^2}{10\chi_0 k_B} \quad (34)$$

Here T_{SF} is the Curie temperature caused by the spin fluctuations. Eqn. (34) describes the long wavelength limit ($q \to 0$) for weakly itinerant magnets and is thus an approximation which is based on the assumption of an effective cut-off for the collective excitations which should be fairly constant. In the present literature this approach in known as the Mohn–Wohlfarth model and has triggered considerable interest in the application of spin fluctuation theory. Although the approach can be expected to break down for strong ferromagnets (Qi *et al.* 1994) it

can still be used to describe the relative change of T_c (Jaswal 1993), e.g., for different concentrations in an alloy system.

From the dynamical form of the free energy (Eqn. (31)) it is straightforward to calculate the specific heat and its discontinuity at T_c (Mohn and Hilscher 1989a). The specific heat becomes linear in temperature and that the discontinuity at T_c is reduced by a factor of four with respect to the Stoner result, which is due to the fact that the paramagnetic state (above T_c) is no longer the nonmagnetic state:

$$\Delta c_m = \frac{M_0^2}{4\chi_0 T_c} \quad (35)$$

As for the specific heat, spin fluctuations also have a major impact on the magnetomechanical properties and it has been shown that their presence not only reduces the spontaneous magnetostriction with respect to the Stoner model in the desired way, but also leads to a different (linear) pressure dependence of T_c (Mohn *et al.* 1987):

$$\frac{T_c(P)}{T_c(P = 0)} = \left(1 - \frac{P}{P_c}\right) \quad (36)$$

where P_c is the critical pressure for the disappearance of magnetism.

In addition, the temperature dependence of the bulk magnetization differs from the Stoner result (Eqn. (14)) and reads:

$$\frac{M}{M_0} = \left(1 - \frac{T}{T_c}\right)^{1/2} \quad (37)$$

For low temperatures the reduction of the magnetic moment is stronger than in the Stoner model. The reason is the same as for the comparison of the Weiss and Heisenberg models, i.e., the collective modes described by the spin fluctuations can readily be excited at low temperature, where the Stoner excitations are still very small.

About at the same time Entel and Schröter (1988, 1989), Mohn *et al.* (1989b), and Wagner (1989) showed how bandstructure results derived from the "fixed spin moment" (FSM) method (Schwarz and Mohn 1984) can be implemented into the spin fluctuation theory. An explicit expression for the fluctuating magnetic moment can be derived from a Landau–Ginzburg expansion for the free energy, which also contains a gradient term to describe the local variation of the fluctuations:

$$H = \frac{1}{V} \int \text{d}r[E(M + m(r))] + \frac{K}{2}\sum_{ij}(\nabla_j m_i)^2 \quad (38)$$

$E(M + m(r))$ is the dynamical form of the free energy as given by Eqn. (31). In addition, a quadratic gradient term is added containing a new coefficient K,

which measures the strength of the spin fluctuations. It should be noted that K is analogous to the spin wave stiffness constant which appears in the Heisenberg model.

To calculate the free energy the partition function must be evaluated by integrating over all fluctuation variables. Since this integration cannot be carried out analytically for the assumed Hamiltonian one approximates the result by using the Peierls–Feynman (Peierls 1936, Feynman 1955) inequality which represents an effective mean-field treatment:

$$F \leqslant F_0 + \langle H - H_0 \rangle_0 \qquad (39)$$

For the trial Hamiltonian the lowest order translationally invariant quadratic form in the fluctuations $m(r)$ is chosen:

$$H_0 = \frac{1}{V}\sum_{i=1}^{3} \int d^3r \int d^3r' \Omega_i(r-r')m_i(r)m_i(r') \qquad (40)$$

where $\Omega_i(r-r')$ is used as a variational parameter to determine the optimal solution. It should be noted that the form used in Eqn. (40) resembles the Heisenberg–Hamiltonian, where the localized spins on the lattice sites i and j are replaced by fluctuating moments located on positions r and r'. For the temperature dependence of the fluctuating moment:

$$\langle m_i^2 \rangle = \frac{k_B T}{2}\frac{V}{8\pi^3}\int_0^{k_c} \frac{4\pi k^2}{\frac{C}{2}k^2 + \frac{\partial\phi}{\partial\langle m_i^2 \rangle}}\, dk \qquad (41)$$

The function φ is that part of the energy functional which depends on the fluctuations:

$$\phi = \frac{1}{V}\int d^3r \langle E(M+m(r)) - E(M)\rangle \qquad (42)$$

In Eqn. (41) there appear two unknown parameters: the "spin wave stiffness" K and the cut-off wave vector k_c. The latter quantity must be introduced, since the Ornstein–Zernicke correlation function, which appears in the integrand, leads to a divergence if the integration is carried out to $k \to \infty$. A physical justification for the introduction of this cut-off may be found in the strong damping of the spin fluctuations by the single particle excitations for k vectors larger than a critical value. From the zero-temperature properties of the derivative of in φ the integrand of Eqn. (41) the spin wave stiffness constant K by ξ^2/χ_0 where ξ is the correlation length and χ_0 is the susceptibility can be replaced. Since $\partial\varphi/\partial\langle m_i^2 \rangle$ must vanish at $T = T_c$, integration at T_c obtains a result similar to the Mohn–Wohlfarth model:

$$T_c = \frac{M_0^2}{10\chi_0 k_B}\frac{4\pi^2 \xi^2}{Vk_c} \qquad (43)$$

In addition to Eqn. (34), here also the finite wavelength dependencies of the fluctuations are included which should lead to a wider applicability.

2. Examples

Historically it is assumed that the 3d transition metals are the prototypical representatives of itinerant electron magnets. They have noninteger magnetic moments and thus cannot be explained on the basis of any local moment model. However, the ideal "Stoner system" would rather be free electron like. This is somehow realized in the simple metals, which, due to the large bandwidth of the s electrons, are unfortunately all nonmagnetic. The key magnetic properties of the magnetic 3d transition metals are given in Table 2.

Phenomenologically one distinguishes between two classes of itinerant electron magnetic systems named weak- and strong ferromagnets. Their major properties are described as follows:

(i) Weak itinerant ferromagnets: majority carrier (spin up electrons) bands are not completely filled; minority bands often empty, unsaturated magnetic moments, large susceptibility, strong pressure dependence of the magnetic moment and the Curie temperature (alloys of iron with metals and metalloids with less than half-filled valence bands such as Fe–V, Fe–Cr, Y–Fe, Zr–Fe, etc. b.c.c. Fe).

(ii) Strong itinerant ferromagnets: majority carrier bands completely filled; minority bands partially filled, saturated magnetic moments, small susceptibility, small (often vanishing) pressure dependence of the magnetic moment and the Curie temperature (alloys of iron, cobalt, and nickel with metals and metalloids with more than half-filled valence band such as Fe–Co, Fe–Ni, Ni–Co, Ni–Cu, Ni–Zn, etc., h.c.p. Co, f.c.c. Ni, and f.c.c. Fe).

An example for the first group of weak itinerant electron magnets is given in Fig. 3, where the spin resolved density of states (DOS) of b.c.c. iron is shown. For the spin-polarized case (full line) the Fermi energy ε_F intersects the majority band just before the upper edge of the d band. For the minority band ε_F is located in a minimum of the DOS, a

Table 2
Magnetic moment M in emu/g and in multiples of μ_B and the T_c values for the ferromagnetic 3d transition metals Fe, Co, and Ni.

	M (emu g^{-1})	M (μ_B)	T_c (K)
Fe	222	2.22	1039
Co	163	1.65	1390
Ni	58	0.62	630
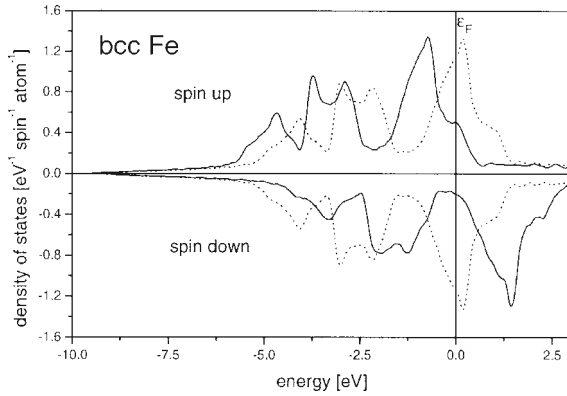
Figure 3
Spin resolved density of states for the spin polarized (solid line) and the nonmagnetic case (dotted line) for b.c.c. Fe.

Figure 4
Spin resolved density of states for the strongly itinerant ferromagnet h.c.p. Co.

Figure 5
Spin and atom resolved density of states for FeCo (CsCl structure). Fe DOS (solid line), Co DOS (dotted line).

position which is highly favorable in energy. Thus b.c.c. iron is an example for a system with an unsaturated magnetic moment. The dotted line shows the DOS for the hypothetical nonmagnetic state (majority and minority DOS are equal). The Fermi energy ε_F lies in a region of rather large DOS, which is a prerequisite to fulfill the condition given by the Stoner criterion (Eqn. (12)). An example for the strong itinerant case is found in Fig. 4 for h.c.p. cobalt. The additional valence electron saturates the majority band, so that ε_F lies above the spin up d band. This is the typical result for this class of itinerant ferromagnets, the resulting low DOS at ε_F causes the small susceptibility observed. For both b.c.c. iron and h.c.p. cobalt, it can be observed that the shape of the majority and minority DOS is almost equal. For these monoatomic solids spin polarization only produces a mutual shift between the spin up and spin down bands (see Fig. 1) an effect which is known as the rigid band picture. The resulting spin splitting can, for example, be measured from the energy difference of the respective DOS peaks in the middle of the d bands. The respective value for ΔE is 1.49 eV, which according to Eqn. (6) yields a Stoner exchange factor, I, of 0.98 eV.

In the case of magnetic alloys the rigid band picture breaks down. As an example the DOS for FeCo (in the CsCl structure) is shown in Fig. 5.

From the completely filled majority band it is obvious that FeCo is a strong ferromagnet. Due to the interaction with the neighboring cobalt atoms, the magnetic moment of iron is increased to 2.6 μ_B making iron a strong ferromagnet (in contrast to b.c.c. iron). The moment per cobalt atom is 1.7 μ_B which is only a minor increase compared to h.c.p. cobalt which already shows strong ferromagnetism. The density of states also nicely shows the influence of the spin splitting on the binding mechanism. For the majority spin both the iron and the cobalt d band are very much alike. For both constituents the spin up d band is filled and between the two atomic species a so-called *common band* is formed. In the minority band strong differences in the height of the iron and cobalt DOS are visible. Below ε_F the cobalt DOS is larger than the iron DOS and vice versa above ε_F. This behavior is needed to accommodate the additional electron of cobalt. In general this kind of spin dependent interaction has been described as *covalent magnetism* (Williams *et al.* 1982).

As a general feature it must be mentioned that pure itinerant electron magnetism hardly ever occurs. The most prominent candidates for this extreme model are $ZrZn_2$ and Ni_3Al, both having very small magnetic moments and very large susceptibilities leading to small T_c values. In most other magnetic transition

metal alloys the narrow 3*d* band leads to a certain degree of localization, which has to be taken into account. Examples for this latter behavior are most Mn compounds in particular the Mn containing Heusler alloys whose finite temperature magnetic properties have successfully be described on the basis of a Heisenberg model (Kübler *et al.* 1983).

See also: Density Fluctuational Theory: Magnetism; Magnetism in Solids: General Introduction; Phase Transitions, Landau Theory of; Spin Fluctuations

Bibliography

Bloch F 1929 Bemerkungen zur Elektronentheorie des Ferromagnetismus und der elektrischen Leitfähigheit. *Z. Phys.* **57**, 545–55

Capellmann H 1979 Theory of itinerant ferromagnetism in the 3*d* transition metals. *Z. Phys. B* **34**, 29–35

Entel P, Schröter M 1988 Landau description of volume instabilities in itinerant magnetic systems. *J. Phys.* **49**, 293–4

Entel P, Schröter M 1989 A novel theoretical description of volume instabilities in itinerant magnetic systems. *Physica B* **161**, 153–4

Edwards D M, Wohlfarth P W 1968 Magnetic isotherms in the band model of ferromagnetism. *Proc. R. Soc. A* **303**, 127–37

Feynman R P 1955 Slow electrons in a polar crystal. *Phys. Rev.* **97**, 660–5

Gunnarsson O 1976 Band model for magnetism of transition metals in the spin density functional formalism. *J. Phys. F. Met. Phys.* **6**, 587–606

Hasegawa H 1980 Single site spin fluctuation theory of itinerant electron systems with narrow bands. II. Iron and nickel. *J. Phys. Soc. Jpn.* **49**, 963–71

Hedin L, Lundquist B L 1971 Explicit local exchange correlation potentials. *J. Phys. Condens. Matter* **4**, 2064–83

Herring C 1952a Energy of a Bloch wall on the band picture. I. Spiral approach. *Phys. Rev.* **85**, 1003–12

Herring C 1952b Energy of a Bloch wall on the band picture. II. Perturbation approach. *Phys. Rev.* **87**, 60–73

Hohenberg P, Kohn W 1964 Inhomogeneous electron gas. *Phys. Rev.* **136**, 864–71

Hubbard J 1963 Electron correlations in narrow energy bands. *Proc. R. Soc. A* **276**, 238–57

Hubbard J 1979a The magnetism of iron. *Phys. Rev. B* **19**, 2626–36

Hubbard J 1979b Magnetism of iron: II. *Phys. Rev. B* **20**, 4584–95

Jaswal S S 1993 Electronic structure and properties of a permanent magnet material: $NdFe_{11}TiN_x$. *Phys. Rev. B* **48**, 6156–8

Kohn W, Sham L J 1965 Self-consistent equations including exchange and correlation effects. *Phys. Rev.* **140**, 1133–8

Kübler J, Williams A R, Sommers C B 1983 Formation and coupling of magnetic moments in Heusler alloys. *Phys. Rev. B* **28**, 1745–55

Lonzarich G G, Taillefer L 1985 Effect of spin fluctuations on the equation of state of nearly ferromagnetic materials. *J. Phys. C* **18**, 4339–71

Mohn P, Hilscher G 1989a The influence of spin fluctuations on the specific heat and entropy of weakly itinerant systems. *Phys. Rev. B* **40**, 9126–34

Mohn P, Schwarz K, Wagner D 1989b Magnetovolume effects in Fe–Ni Invar: a first principles theory. *Physica B* **161**, 153–6

Mohn P, Schwarz K 1993 Itinerant magnetism in solids. In: *Physics of Transition Metals*. World Scientific, Singapore, New Jersey, London, Hong Kong, pp. 597–684

Mohn P, Wagner D, Wohlfarth E P 1987 Magnetoelastic anomalies due to spin fluctuations in weakly itinerant ferromagnetic systems. *J. Phys. F. Met. Phys.* **17**, L13–8

Mohn P, Wohlfarth E P 1986 The Curie temperatures of the ferromagnetic transition metals and their compounds. *J. Phys. F. Met. Phys.* **17**, 2421–30

Moriya T 1978 Spin fluctuation theory of itinerant electron ferromagnetism—a unified picture. *J. Phys. Soc. Jpn.* **45**, 397–408

Moriya T 1985 Spin fluctuations in itinerant electron magnetism. Springer Series in Solid-State Sciences **56**. Springer, Berlin

Moriya T, Kawabata A 1973 Effect of spin fluctuations on itinerant electron ferromagnetism. *J. Phys. Soc. Jpn.* **35**, 69–76

Mott N F 1935 A discussion of the transition metals on the basis of quantum mechanics. *Proc. Phys. Soc.* **47**, 571–88

Murata P P, Doniach S 1972 Theory of magnetic fluctuations in itinerant ferromagnets. *Phys. Rev. Lett.* **29**, 285–8

Nolting W, Borstel G, Dambeck T, Fauster T, Vega A 1995 Temperature dependent electronic structure of Ni, Fe and Gd. *J. Magn. Magn. Mater.* **140–4**, 55–6

Oles A M, Stollhoff G 1986 Magnetic correlations in the paramagnetic state of 3*d* transition metals. *J. Magn. Magn. Mater.* **54–57**, 1045

Parr R G, Yang W 1989 *Density Functional Theory of Atoms and Molecules.* Oxford University Press, New York

Pauli W 1927 Über Gasentartung und Paramagnetismus. *Z. Phys.* **41**, 81–102

Peierls R 1938 On a minimum property of the free energy. *Phys. Rev.* **54**, 918–9

Pindor A J, Staunton J, Stocks G M, Winter H 1983 Disordered local moment state of transition metals: a self-consistent KKR-CPA calculation. *J. Phys. F. Met. Phys.* **13**, 979–89

Prange R E, Korenman V 1979a Local band theory of itinerant ferromagnetism. IV Equivalent Heisenberg model. *Phys. Rev. B* **19**, 4691–7

Prange R E, Korenman V 1979b Local band theory of itinerant ferromagnetism. V Statistical mechanics of spin waves. *Phys. Rev. B* **19**, 4698–702

Qi Q, Skomski R, Coey J M 1994 Strong ferromagnets: Curie temperature and density of states. *J. Phys. Condens. Matter* **6**, 3245–51

Schwarz K 1972 Optimization of the statistical exchange parameter α for the free atoms H through Nb. *Phys. Rev. B* **5**, 2466–8

Schwarz K, Mohn P 1984 Itinerant metamagnetism in YCo_2. *J. Phys. F Met. Phys.* **14**, L129–34

Shimizu M 1981 Itinerant electron magnetism. *Rep. Prog. Phys.* **44**, 329–409

Slater J C 1936a The ferromagnetism of nickel. *Phys. Rev.* **49**, 537–45

Slater J C 1936b The ferromagnetism of nickel: II Temperature effects. *Phys. Rev.* **49**, 931–7

Slater J C 1951 Magnetic effects and the Hartree–Fock equation. *Phys. Rev.* **82**, 538–41

Staunton J, Gyorffy B L, Pindor A J, Stocks G M, Winter H 1984 The "disordered local moment" picture of magnetism at finite temperatures. *J. Magn. Magn. Mater.* **45**, 15–22

Stoner E C 1936 Collective electron specific heat and spin paramagnetism in metals. *Proc. Roy. Soc. A* **154**, 656–78

Stoner E C 1938 Collective electron ferromagnetism. *Proc. Roy. Soc. A* **165**, 372–414

von Barth U, Hedin L 1972 A local exchange-correlation potential for the spin-polarized case: I. *J. Phys. Condens. Matter* **5**, 1629–42

Wagner D 1989 Fixed spin moment method and fluctuations. *J. Phys. Condens. Matter* **1**, 4635–40

Wakoh S, Yamashita J 1970 Band structure of cobalt by a self-consistent procedure. *J. Phys. Soc. Jpn.* **28**, 1151–6

Williams A R, Moruzzi V L, Gelatt C D Jr., Kübler J, Schwarz K 1982 Aspects of transition metal magnetism. *Appl. Phys.* **53**, 2219–23

Wohlfarth E P 1953 The theoretical and experimental status of the collective electron theory of ferromagnetism. *Rev. Mod. Phys.* **25**, 211–9

Wohlfarth E P 1980 In: Wohlfarth E P (ed.) *Iron, Cobalt and Nickel Ferromagnetic Materials*. Vol. 1, North-Holland, Amsterdam, pp. 1–70

P. Mohn
Technische Universität Wien, Austria

This page intentionally left blank

J

Josephson Junctions: High-T_c

With the advent of ceramic superconductors, attempts were very quickly made to translate the techniques known from classical superconducting electronics to this new class of materials. In classical superconductivity, Josephson junctions are generally fabricated in a multilayer technology, incorporating at least two superconducting layers (niobium or NbN) and between them either insulating layers for tunnel junctions (Al_2O_3, MgO, AlN, etc.) or normal conducting layers for proximity effect devices or combinations thereof for special junction types, e.g., SINIS junctions. For high-T_c devices this concept turned out to be very difficult with the materials preparation techniques available at that time and with the very short coherence length of the high-T_c superconductors (HTSs). It was recognized very early that grain boundaries in HTSs behave like Josephson junctions. Much research was done on how to prepare grain boundaries in HTSs in a controlled manner and to elucidate the relationship between grain boundary structure and critical current density, j_c, for the supercurrent. This led to the experimental verification of the prediction for a d-wave symmetry of the wave functions describing the superconducting state in a HTS. The results also made clear that grain boundary junctions are unlikely to create the necessary reproducibility needed for superconducting electronic devices. Nevertheless, as a research tool or for devices with a very small number of junctions like SQUIDs, the grain boundary junctions are very valuable.

Subsequently a new junction type has been demonstrated, which makes use of the high critical current densities in the *ab*-planes of the HTS and the epitaxial growth of homologous perovskite materials onto a ramp, cut into the superconductor under a flat angle. Even though the fabrication process is more complicated, the reproducibility and controllability of these junctions is much better than that of grain boundary junctions. Circuits of some tens of junctions can be realized with reasonable chance of success. In various forms, this junction type is the standard in research laboratories and industry for circuits with about 10 junctions or more.

The $I_c R_n$ product of HTS Josephson junctions strongly influences the switching speed and maximum frequency in digital circuits and oscillators and the modulation voltage for SQUIDs. Whereas at low temperatures $I_c R_n$ products of 30 mV or more were originally expected for YBaCuO Josephson junctions, the maximum values reached are about 9 mV. Most junctions, however, only show an $I_c R_n$ product of a few hundred microvolts at their operation temperature. It is clear that interfaces between electrode and barriers of the Josephson junctions play an important role. It has been shown that band bending effects at these interfaces probably play an important role in decreasing their transparency. There are strong indications that calcium doping near the interface might decrease the band bending.

1. Grain Boundary Junctions

The first HTS Josephson junctions were based on the naturally occurring grain boundaries in sintered bulk materials or in polycrystalline films prepared by the two-step method. It was possible to demonstrate the Josephson effect and SQUID operation with these junctions, but a controlled preparation was impossible. After the epitaxial growth of YBCO on $SrTiO_3$ was demonstrated, Dimos *et al.* (1990) used this technique to prepare the first controlled grain boundaries on a $SrTiO_3$ bicrystal: two crystals of $SrTiO_3$ with different orientation of the crystal axes are glued together, so that an artificial grain boundary is created.

YBCO films epitaxially grown on top of the bicrystal have the same orientation as the substrate and form a grain boundary with the same angle as the bicrystal at the bicrystal interface (see Fig. 1(a)). By changing the angle of the bicrystal, grain boundaries in the YBCO films with different angles can be created. In this way more complicated grain boundary structures can also be created such as tri-ray and multiple parallel structures.

The electrical transport through such a grain boundary shows Josephson behavior, which can be described by an RSJ model with some capacitive loading. The normal resistance and the critical current density of the grain boundary junction depend on the grain boundary angle (see Fig. 1(b)).

Whereas the electrical transport can be described by simple models, the magnetic field dependence of the critical current density is complicated and shows only a vague resemblance to the Fraunhofer pattern found for classical Josephson junctions. This behavior was for long attributed to inhomogeneities in the grain boundary. Subsequent work has shown instead that the magnetic field dependence can be explained by a d-wave symmetry of the wave function describing the state of the superconductor.

The local structure of the grain boundary leads to locally back-flowing currents and thus to a mixture of positive and negative current densities along the junction. Simulations assuming d-wave symmetry yield good agreement with measured results for the magnetic field dependence. In contrast to the well-known flux lines containing $\Phi_0 = h/2e$, flux lines
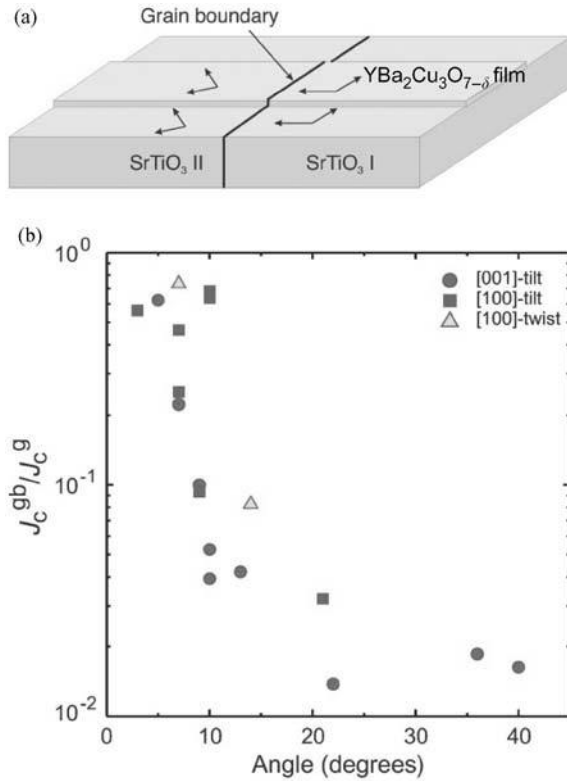
containing $\Phi_0/2$ can spontaneously occur at interfaces. Tsuei and Kirtley (2000) predicted the d-wave symmetry and showed experimentally using a tricrystal grain boundary ring structure (see Fig. 2) that the predicted flux lines with half-integer flux quanta exist.

In this geometry two of the three junctions are normal Josephson junctions, the third is a Josephson π-junction, in which an additional phase shift of π occurs owing to the symmetry of the d-wave function:

$$J = J_0 \, \sin\varphi \, (\text{normal Josephson junction})$$

$$J = J_0 \, \sin\varphi + \pi = -J_0 \, \sin\varphi \, (\text{Josephson } \pi\text{-junction})$$

The Josephson π-junction is unique to HTSs. It can simplify the design of superconducting electronics circuits and it opens opportunities for new applications, e.g., qubits for quantum computing.

In addition to the bicrystal method, a number of other methods exist for creating artificial grain boundaries. The two principal ones are seed layer junctions and step edge junctions (Fig. 3). Seed layer junctions make use of the fact that some oxide layers
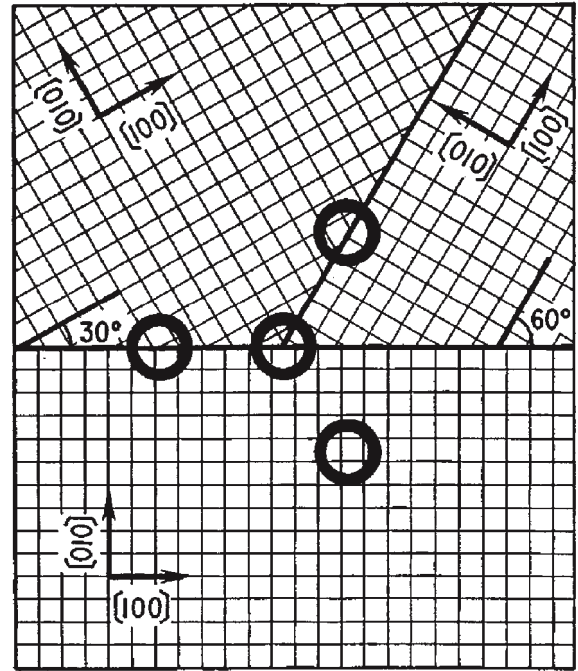
Figure 2
Experimental configuration for the π-ring tricrystal experiment of Tsui and Kirtley (2000).
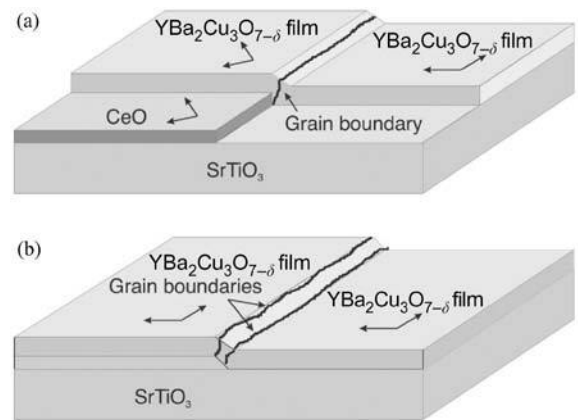
Figure 3
(a) Seed layer and (b) step edge Josephson junctions.

grow on top of each other epitaxially, but rotated in their crystal axes by a certain angle owing to a mismatch of the lattice parameters. The complicated grain boundary structures result in poor Josephson behavior and bad reproducibility. Step edge junctions in contrast can yield junctions of high quality, although this technique is also not very reproducible.

For fabrication one has to prepare a step on a substrate surface, which is either done by etching away part of the substrate or by locally adding (homo)epitaxially a layer on top of the substrate. Step height and angle are critical. Deposition of a thin film of a HTS on top results in the formation of grain boundaries at the top and the bottom edge of the step. A step edge Josephson junction thus consists of two series-connected closely coupled Josephson junctions. In general some roughening owing to the etching or lithographic process occurs along the step resulting in complicated grain boundary structures along the edge. For a small number of Josephson junctions next to each other as needed in SQUID applications, these junctions are quite similar in general. High-quality step edge junctions have successfully been fabricated and incorporated in SQUID structures.

2. *Josephson Junctions with Artificial Barriers*

Two advantages of classical planar Josephson junctions are the ability to fabricate it anywhere on a substrate and to change its transport properties in a controlled way, e.g., engineer the composition of the barrier down to the atomic level by thin-film deposition techniques. For high-T_c Josephson junctions one would also like to adjust the barrier transparency and its height and fabricate the junction in places where it would be needed from circuit design requirements and not vice versa. In this sense planar high-T_c Josephson junctions would be ideal. Not only is the circuit design and layout well known from classical superconductivity, but also barrier material and barrier thickness could be varied or even complex barrier structures realized.

2.1 *Planar Junctions*

HTSs are strongly anisotropic with significantly higher critical current densities in the Cu–O *ab*-planes than for transport along the *c*-axis. The quasi two-dimensional behavior leads to the possibility of building junctions by layer-by-layer engineering, choosing layer compositions that enable epitaxial growth on one side that modify the transport properties from superconducting to normal conducting or insulating behavior over a length scale of one or very few perovskite building blocks on the other side.

Such work requires extreme growth control of the materials and is practically only possible in oxide-MBE machines or pulsed laser deposition systems with similar controls. Bozovic and Eckstein (1997) have done pioneering work especially by applying MBE to the growth of bismuth compounds and to the modification of transport properties in the *c*-axis direction (see Fig. 4). Even though the critical current densities are still quite low, MBE seems to be the way towards a reproducible fabrication of large numbers of high-T_c Josephson junctions.
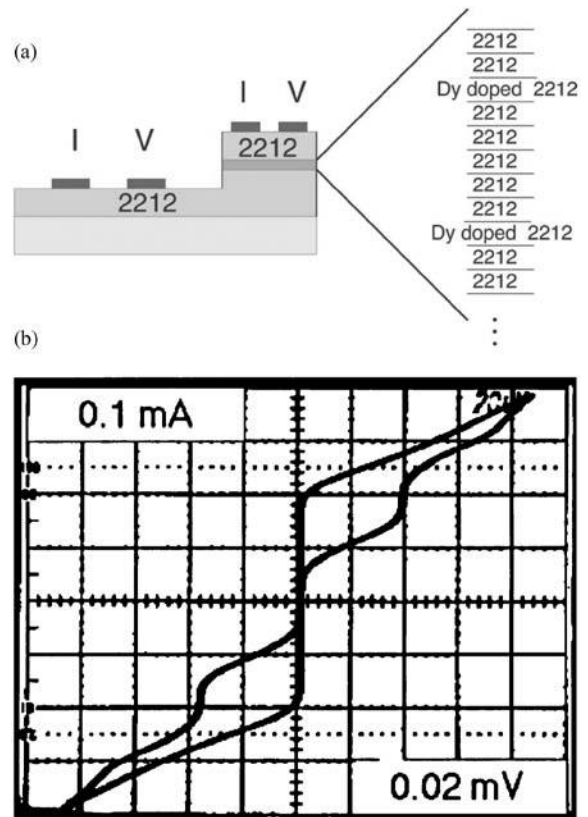
Figure 4
Layer-by-layer engineering of bismuth compounds for HTS Josephson junctions: (a) cross-section through a sandwich; (b) *I*–*V* characteristics of the resulting Josephson junction.

The fabrication of planar Josephson junctions has been tried in a number of ways. Attempts to isolate natural tunnel junctions from bismuth compounds (transport in the *c*-axis direction) have been successful. These junctions show interesting characteristics, but have only little practical impact. Attempts to make use of the *c*-axis coupling in YBaCuO or to grow sandwich structures on *a*-axis-oriented YBaCuO results in irreproducible Josephson junction behavior, with very unrealistic decay length for the transport through the structures. Sandwich junctions on 103-oriented YBaCuO have shown some success, these junctions showing reproducibility comparable to other high-T_c Josephson junctions.

2.2 *Ramp-type Josephson Junctions*

Ramp-type Josephson junctions form the basis for most applications in which 10 or more junctions are needed. They are based on the idea that the barrier

for Josephson operation should separate the CuO planes capable of carrying high current densities and transporting the supercurrents to the barrier. A schematic cross-section is depicted in Fig. 5(a). The most critical step is the cut through the base sandwich under a flat angle without destroying the surface of the ramp for subsequent epitaxial growth of the barrier and counter-electrode. Depending on the type of
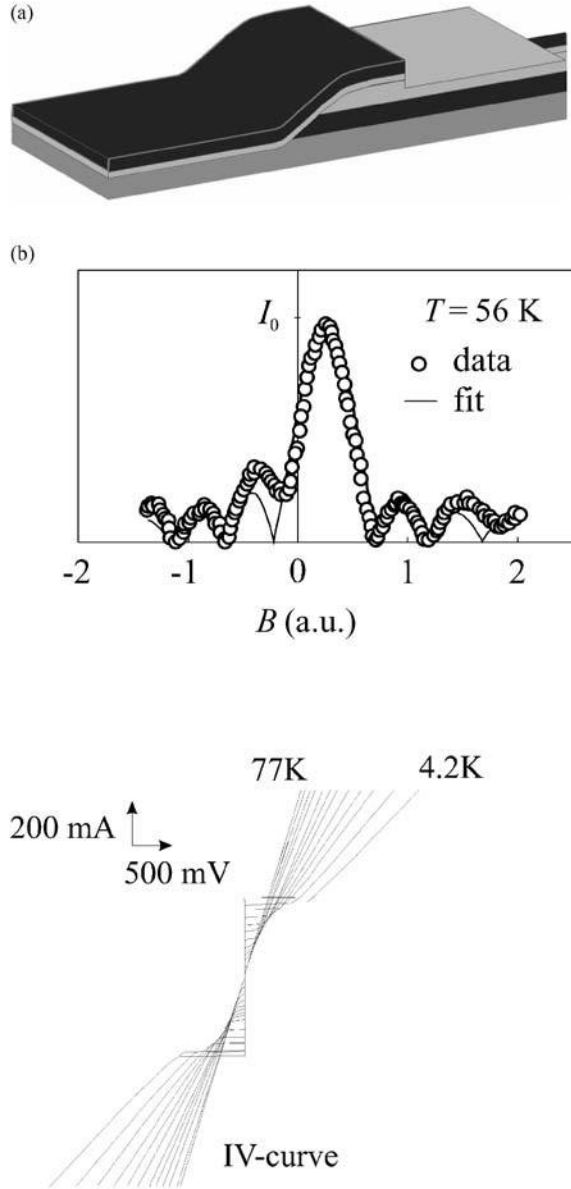
Figure 5
(a) Schematic and (b) magnetic field dependence and *I*–*V* characteristics of a typical ramp-type junction.
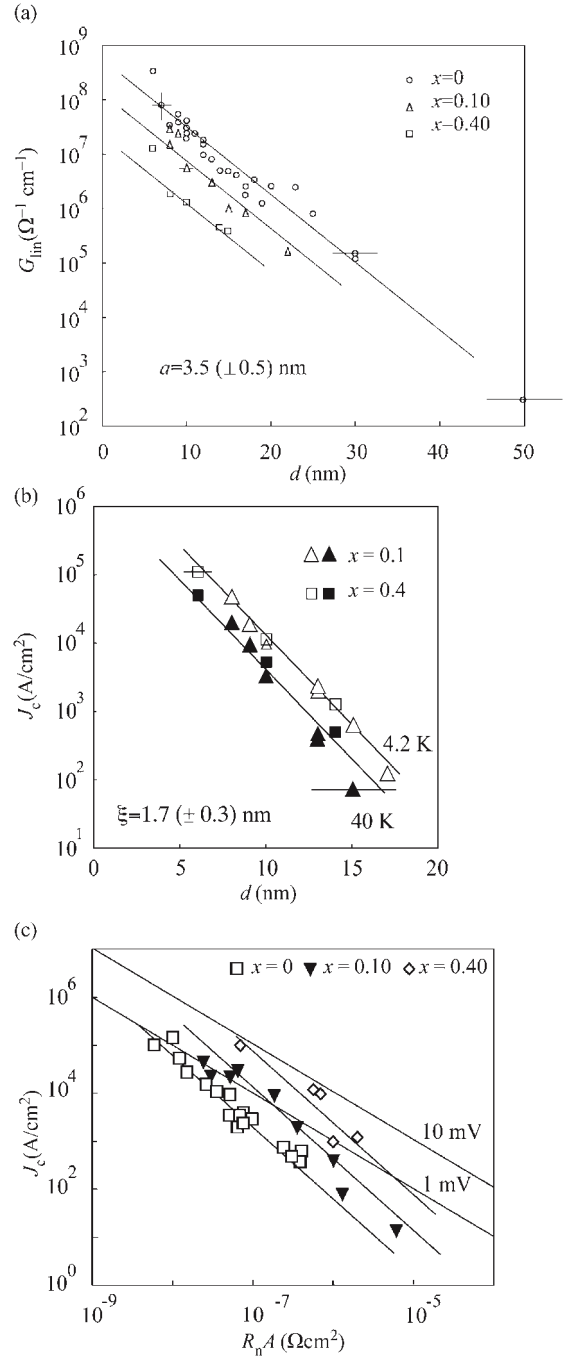
Figure 6
Dependence of (a) normal state conductance and (b) critical current density on the barrier thickness for gallium-doped PrBaCuO for different doping levels. (c) Relationship between critical current density and specific resistance with lines of constant $I_c R_n$ product.

barrier and thickness, the critical current density and the normal resistance of the junction can be adjusted.

The most promising barrier for operation at 77 K is cobalt-doped YBaCuO. Also "interface engineered" junctions have received a lot of attention because of their slightly better reproducibility. For operation at temperatures below 50 K, e.g., for digital applications, PrBaCuO barriers are very attractive. With this barrier material the critical current density and the normal resistance can be adjusted independently (see Fig. 6(a))—the critical current density via the thickness of the barrier and the normal resistance via the amount of gallium doping, which enhances the specific resistance with increasing gallium content.

2.3 High-T_c–Low-T_c Junctions

In an effort to combine high-T_c and low-T_c junctions on the same chip, high critical current density transitions between high-T_c and low-T_c superconductors have been developed in the form of ramp-type junctions with YBaCuO base electrode, gold barrier, and niobium counter-electrode. These junctions show excellent Josephson characteristics (see Figs. 7(a) and (b)) with little parameter spread. In addition, these junctions can be prepared on ramps with an orientation in different crystallographic directions, thus yielding junctions with 0- to π-junction characteristics. Such junctions combine the reproducibility of

Figure 7
YBaCuO/Au/Nb ramp-type junction: (a) cross-section; (b) *I–V* characteristics.

the low-T_c junctions with the high I_cR_n product and the unique d-wave characteristics of HTSs.

2.4 Electron Beam and Ion Beam Josephson Junctions

Oxygen-deficient or structurally damaged regions of HTSs have a lower T_c or become normally conducting or even insulating. Such damage can be introduced locally by high-energy bombardment with electrons or with ions. In this way a Josephson junction can be "written" into a thin film of YBaCuO. The resulting junctions show good nonhysteretic Josephson behavior. For electron beam writing, electron microscopes with an acceleration voltage of about 400 keV are needed; for ion beam writing, focused ion beam (FIB) etchers are applied with an acceleration voltage of about 30 keV. Quite high radiation doses are needed to prepare the barrier, so that the writing speed is quite low. In addition, the junction parameters cannot easily be modified. Nevertheless, electron beam and FIB writing is attractive for the prototyping of simple superconducting circuits but cannot be considered as a production-type technique.

3. Conclusion

The availability of reliable and reproducible high-T_c Josephson junctions depends strongly on advances in materials research in the area of perovskites and the refined control of the deposition of these materials, both for composition and structure. The techniques for the preparation of high-T_c Josephson junctions are sufficient for small electronics circuits with about 10–50 Josephson junctions. For applications with a larger number of junctions, the knowledge of fabrication and understanding of these materials has to be improved significantly in order to reach the required reproducibility.

See also: Josephson Junctions: Low-T_c
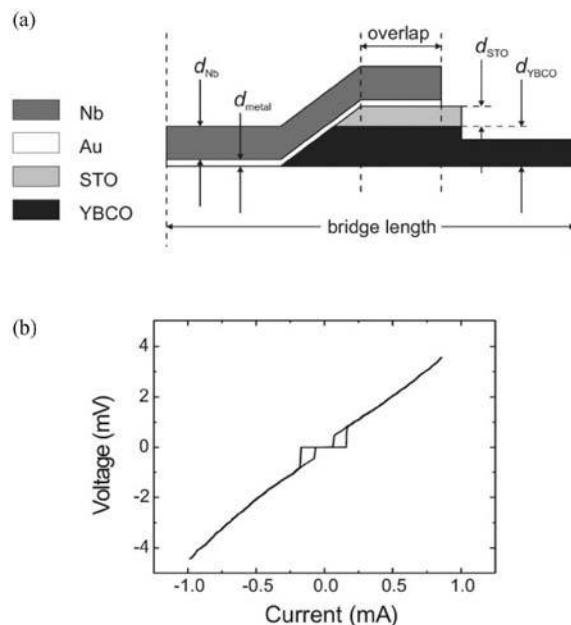
Bibliography

Bozovic I, Eckstein J N 1997 Atomic-level engineering of cuprates and manganites. *Appl. Surf. Sci.* **114**, 189–97
Bozovic I, Eckstein J N, Virshup G F 1994 Superconducting oxide multilayers and superlattices—physics, chemistry and nanoengineering. *Physica C* **235**, 178–81
Char K, Antognazza L, Geballe T H 1994 Properties of YBa$_2$Cu$_3$O$_{7-x}$/YBa$_2$Cu$_{2.79}$Co$_{0.21}$O$_{7-x}$/YBa$_2$Cu$_3$O$_{7-x}$ edge junctions. *Appl. Phys. Lett.* **65**, 904–6
Dimos D, Chaudhari P, Mannhart J 1990 Superconducting transport properties of grain boundaries in YBa$_2$Cu$_3$O$_7$ bicrystals. *Phys. Rev. B* **41**, 4038
Dimos D, Chaudhari P, Mannhart J, LeGoues F K 1988 Orientation dependence of grain-boundary critical currents in YBa$_2$Cu$_3$O$_{7-\delta}$ bicrystals. *Phys. Rev. Lett.* **61**, 219–22

Gao J, Aarnink W A M, Gerritsma G J, Rogalla H 1990 Controlled preparation of all high-T_c SNS-type edge junctions and d.c. SQUIDs. *Physica C* **171**, 126–30

Golubov A A, Kuprianov M Y 1988 Theoretical investigation of Josephson tunnel junctions with spatially inhomogeneous superconducting electrodes. *J. Low-Temp. Phys.* **70**, 83–130

Hilgenkamp H, Mannhart J 1998 Superconducting and normal-state properties of YBa$_2$Cu$_3$O$_{7-\delta}$ bicrystal grain boundary junctions in thin films. *Appl. Phys. Lett.* **73**, 265–7

Hilgenkamp H, Mannhart J, Mayer B 1996 Implications of d$_{x2-y2}$ symmetry and faceting for the transport properties of grain boundaries in high-T_c superconductors. *Phys. Rev. B* **53**, 14586–93

Katz A S, Woods S I, Dynes R C, Sun A G 1999 Stability and uniformity of planar high-temperature Josephson junctions fabricated using nanolithography and ion damage. *IEEE Trans. Appl. Supercond.* **9**, 3005–7

Koch R H, Umbach C P, Clark G J, Chaudhari P, Laibowitz R B 1987 Quantum interference devices made from superconducting oxide thin films. *Appl. Phys. Lett.* **51**, 200–2

Moeckly B H, Char K 1997 Properties of interface-engineered high-T_c Josephson junctions. *Appl. Phys. Lett.* **71**, 2526–8

Pauza A J, Moore D F, Campbell A M, Broers A N, Char K 1995 Electron-damaged high-T_c junctions—stability, reproducibility and scaling laws. *IEEE Trans. Appl. Supercond.* **5**, 3410–3

Rijnders G J H M, Koster G, Blank D H A, Rogalla H 1997 *In situ* monitoring during pulsed laser deposition of complex oxides using reflection high energy electron diffraction under high oxygen pressure. *Appl. Phys. Lett.* **70**, 1888–90

Smilde H J H, Hilgenkamp H, Gerritsma G J, Blank D H A, Rogalla H 2001 Y–Ba–Cu–O/Au/Nb ramp-type Josephson junctions. *IEEE Trans. Appl. Supercond.* **11**, 501–4

Tsuchiya R, Kawasaki M, Kubota H, Nishino J, Sato H, Akoh H, Koinuma H 1997 YBa$_2$Cu$_3$O$_{7-\delta}$ trilayer junction with nm thick PrGaO$_3$ barrier. *Appl. Phys. Lett.* **71**, 1570–2

Tsuei C C, Kirtley J R 2000 Pairing symmetry in cuprate superconductors. *Rev. Mod. Phys.* **72**, 969–1016

Verhoeven M A J, Gerritsma G J, Rogalla H, Golubov A A 1996 Ramp-type junction parameter control by Ga doping of PrBa$_2$Cu$_3$O$_{7-\delta}$ barriers. *Appl. Phys. Lett.* **69**, 848–50

H. Rogalla
University of Twente, Enschede, The Netherlands

Josephson Junctions: Low-T_c

In the field of superconducting electronics, Josephson junctions with electrodes made of niobium thin films ($T_c = 9.0$–9.3 K) or niobium nitride (NbN) thin films ($T_c = 14$–17 K) play an important role. For example, Josephson junctions with niobium thin films as electrodes and very thin aluminum oxide layers as barriers (Nb/AlO$_x$/Nb junctions) are widely used for implementing practical superconducting devices, e.g., superconducting quantum interference devices (SQUIDs) for biomedical applications (see *SQUIDs: Biomedical Applications*), superconductor–insulator–superconductor (SIS) mixers for radio astronomy,

and Josephson junction devices for voltage standards (see *Josephson Voltage Standard*). Also, Nb/AlO$_x$/Nb junctions are used for demonstrating the performance of various digital and analog circuits that are operated based on Josephson effects. This is because Nb/AlO$_x$/Nb junctions are extremely stable with respect to thermal cycling and storage in air, have high-quality tunneling characteristics, and can be fabricated with good run-to-run reproducibility. Josephson junctions with NbN thin films as electrodes are used for fabricating superconducting devices with unique performance, e.g., an SIS mixer having low noise temperatures at a frequency range over 700 GHz and an analog-to-digital converter operated at 10 K.

This article describes the fabrication, electrical characteristics, and stability of Nb/AlO$_x$/Nb junctions and NbN Josephson junctions.

1. Nb/AlO$_x$/Nb Junctions

1.1 Fabrication

The first successful fabrication of Nb/AlO$_x$/Nb junctions was reported by Gurvitch *et al.* (1983), followed by a large number of reports on the characterization of junctions and the development of technologies for fabricating junctions with high yield, high uniformity, and high reproducibility. The adoption of aluminum as a barrier material for Josephson junctions with niobium electrodes was motivated by the fact that aluminum shows a suitable wettability on fresh surfaces of niobium. Because of the affinity of aluminum to niobium, an aluminum layer deposited on a niobium base electrode well covers the surface of the electrode even when the thickness of the overlayer is very small (<10 nm). This enables the formation of a uniform and pinhole-free tunnel barrier by thermally oxidizing an aluminum layer on a niobium electrode, resulting in the fabrication of a high-quality junction. However, there exist several causes that induce deterioration of junction characteristics. For example, Huggins and Gurvitch (1985) emphasized that heat sinking of the substrate to a water-cooled table during the junction preparation is crucial for obtaining a high yield of high-quality samples. Experimental results suggest that without heat sinking of the substrate, diffusion of oxygen atoms in the barrier into the electrodes occurs by elevation of the substrate temperature during the deposition of the counter electrodes. Kuroda and Yuda (1988) have claimed that relaxation of stress in sputter-deposited niobium films with etching of the films causes deformation of the electrodes, resulting in large leakage currents in junctions.

Fabrication of Nb/AlO$_x$/Nb junctions is generally carried out in a sputtering system with a stainless steel chamber (or chambers), a water-cooled substrate holder (or holders), sputtering targets of niobium and aluminum, and a vacuum pump (or pumps)
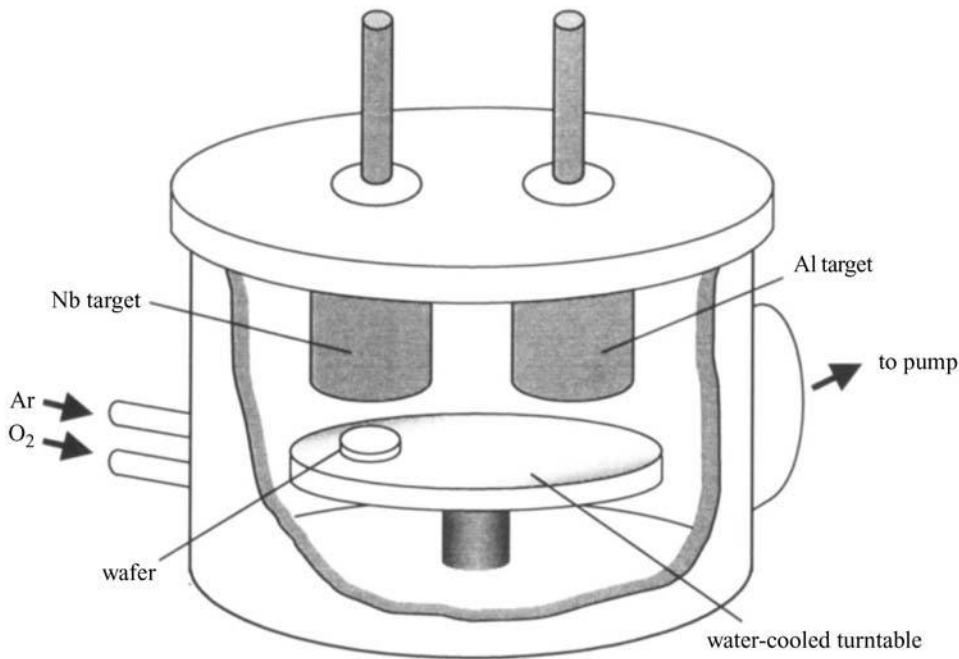
Figure 1
Schematic of a sputtering system used for fabricating $Nb/AlO_x/Nb$ junctions.

(see Fig. 1). A wafer (usually a single crystal of silicon) with a mirror polished surface is set on the substrate holder (the turntable in Fig. 1) with a good thermal contact. After filling the chamber with research-purity argon up to a pressure of 1–2 Pa, a niobium film (100–200 nm) is deposited on the wafer by sputtering the niobium target. A very thin aluminum layer (5–10 nm) is then deposited on top of the niobium film by sputtering the aluminum target. The formation of a tunnel barrier is achieved by oxidizing the aluminum layer in a static atmosphere of pure oxygen. The pressure of oxygen gas and oxidation time are set so as to obtain a targeted critical current density, J_c, for the junctions (Miller *et al*. 1993). After finishing the formation of a tunnel barrier, a niobium film (100–200 nm) for the counter electrodes of the junctions is deposited in an argon atmosphere, resulting in the formation of a junction sandwich on the wafer (Fig. 2(a)).

Definition of individual junctions from the junction sandwich is performed using photolithography and etching techniques. After taking the wafer out of the sputtering system, the wafer is covered with a photoresist pattern that defines the base electrodes of the junctions. Multilayers unprotected by the photoresist pattern are then removed by wet etching or dry etching (Fig. 2(b)). The definition of individual junctions is performed by trimming the counter niobium film in a reactive gas using another photoresist

pattern as a mask (Fig. 2(c)). Next, an insulation film (usually a sputtered SiO_2 film) is deposited onto the sample to protect the exposed surface of the base electrodes (Fig. 2(d)). Via holes for making contacts to junctions are then fabricated by locally etching the insulation film in a reactive gas (Fig. 2(e)). Finally, wiring electrodes are fabricated by depositing a niobium film on the sample and trimming with a reactive gas (Fig. 2(f)).

The process used for fabricating $Nb/AlO_x/Nb$ junctions is called a ''whole-wafer'' process because a junction sandwich is formed on the whole surface of a wafer prior to the lithographic processes. The advantage of the ''whole-wafer'' process is that all wet processes are excluded from the formation of the junction sandwich, enabling fabrication of junctions with good run-to-run reproducibility. The concept of the ''whole-wafer'' process was first demonstrated by Kroger *et al*. (1981) in the fabrication of Nb/Si:H/Nb junctions.

1.2 Electrical Characteristics

Measurement of current–voltage (*I–V*) characteristics for $Nb/AlO_x/Nb$ junctions is, in general, carried out while immersing the sample in liquid helium since all devices fabricated using $Nb/AlO_x/Nb$ junctions are operated at liquid helium temperature (4.2 K), with a
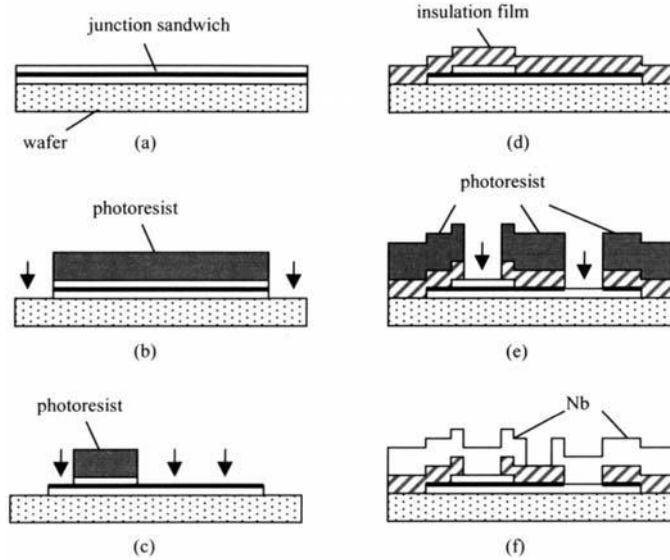
Figure 2
Fabrication process of a Nb/AlO$_x$/Nb junction.
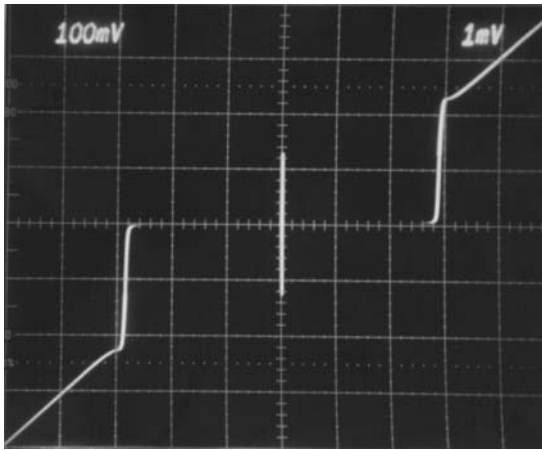
Figure 3
I–V characteristic for a Nb/AlO$_x$/Nb junction at 4.2 K (vertical axis: 1 mA per division; horizontal axis: 1 mV per division).

few exceptions. During the measurement of *I–V* characteristics, the sample is surrounded with μ-metal or niobium cans to minimize the influence of external magnetic fields, e.g., the terrestrial magnetic field. An *I–V* characteristic measured for a Nb/AlO$_x$/Nb junction at 4.2 K is shown in Fig. 3. Like this example, at 4.2 K Nb/AlO$_x$/Nb junctions typically show high-quality tunneling characteristics with a well-defined gap and very small subgap leakage currents.

The gap voltage, V_g, which is defined as the voltage at which the slope of the *I–V* curve becomes a maximum, is 2.9 mV for the junction in Fig. 3, very close to the theoretical value (3.0 mV) calculated for a Josephson tunnel junction with niobium base and counter electrodes. This means that the superconducting properties in the base and counterelectrodes of the junction are as good as that for bulk niobium. The relative amplitude of leakage currents for a Josephson tunnel junction can be evaluated by a ratio of a static resistance measured below V_g (typically at a voltage near half of V_g) and a static resistance measured above V_g (typically at a voltage more than twice V_g).

The former is called the subgap resistance, R_{sg} and the latter the normal resistance, R_n. Nb/AlO$_x$/Nb junctions typically have R_{sg}/R_n values exceeding 10 unless their critical current density is extremely high. The specific capacitance, C_s, i.e., a capacitance per unit area, for a Josephson tunnel junction is an important parameter in the design of SQUIDs, SIS mixers, etc. C_s values for Nb/AlO$_x$/Nb junctions have been estimated from measurement of Fiske modes for junctions (van der Zant *et al*. 1994) and measurement of resonant voltages for SQUIDs (Maezawa *et al*. 1995).

1.3 Stability

The stability of Nb/AlO$_x$/Nb junctions against thermal cycling, aging at room temperature, and annealing at an elevated temperature has been examined. In

one study (Gates *et al.* 1984) 400 Nb/AlO$_x$/Nb junctions were cycled 4880 times between room temperature and 6 K, resulting in no failures due to shorts and no change in the average critical currents. The same junctions were then aged in a nitrogen atmosphere at room temperature for two months, resulting in no change in the average critical currents. Finally, the junctions were annealed at 100 °C for 2 h in a helium atmosphere, again resulting in no change in the average critical currents. A finite change (reduction) in the critical currents was observed after the junctions had been annealed at 150 °C.

2. NbN Josephson Junctions

2.1 Fabrication

Fabrication of Josephson junctions with NbN films as base and counter electrodes was first reported by Shinoki *et al.* (1981). Reactively sputter-deposited NbN films were used as electrodes and amorphous silicon (a-Si) films that had been produced by glow discharge decomposition of silane (5% SiH$_4$ and 95% argon) as tunnel barriers. The NbN/a-Si/NbN junctions showed good tunneling characteristics with small subgap leakage currents. However, their gap voltages remained at 4.2 mV, much lower than the theoretical gap voltage (>6 mV) for a Josephson tunnel junction with NbN base and counter electrodes. Improvement of the gap voltage for NbN junctions was made by Shoji *et al.* (1985) by introducing very thin MgO films (<1 nm) as tunnel barriers and a "whole-wafer" process to the junction fabrication. MgO is employed as a barrier material for NbN junctions since it has the same structure (B1: f.c.c., NaCl type) as NbN and a lattice parameter close to that of NbN. Wang *et al.* (1997) reported NbN junctions with reactively sputter-deposited aluminum nitride (AlN) barriers had gap voltages as large as those for NbN/MgO/NbN junctions. AlN also has B1 structure and a lattice parameter close to that of NbN.

2.2 Electrical Characteristics

An *I–V* characteristic measured for a NbN/MgO/NbN junction at 4.2 K is shown in Fig. 4. Like this example, NbN/MgO/NbN junctions typically show good *I–V* characteristics at 4.2 K with gap voltages greater than 5 mV and small subgap leakage currents. This is the same as for the case of NbN/AlN/NbN junctions. The V_g values for NbN/MgO/NbN and NbN/AlN/NbN junctions are roughly twice those for Nb/AlO$_x$/Nb junctions, but are still smaller than the theoretical V_g value for all-NbN junctions. The reduction of experimental V_g values from the theoretical value mainly arises from lower superconducting energy gaps in counter electrodes than in base electrodes. The relative
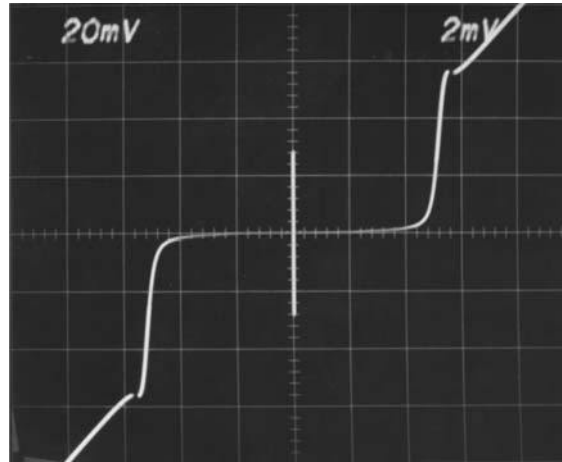
Figure 4
I–V characteristic for a NbN/MgO/NbN junction at 4.2 K (vertical axis: 0.2 mA per division; horizontal axis: 2 mV per division).
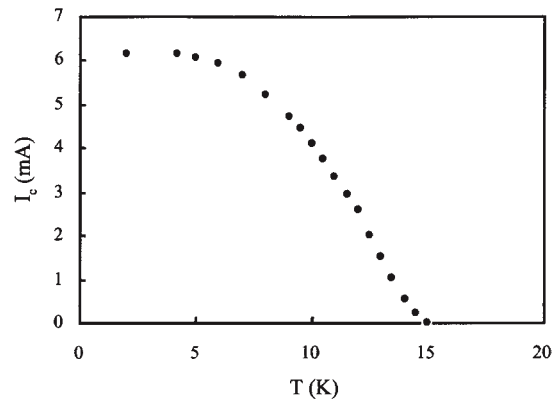
Figure 5
Temperature dependence of critical current for a NbN/MgO/NbN junction.

amplitude of leakage currents for NbN/MgO/NbN and NbN/AlN/NbN junctions depends strongly on their critical current density. For example, NbN/MgO/NbN junctions with $J_c < 1$ kAcm^{-2} typically have $R_{sg}/R_n > 10$, while junctions with $J_c > 1$ kA cm^{-2} have $R_{sg}/R_n < 10$. A theoretical explanation for the reduction of R_{sg}/R_n values with increase in critical current density has not been given. C_s values for NbN/MgO/NbN and NbN/AlN/NbN junctions have been estimated from measurement of Fiske modes (Shoji *et al.* 1985) and measurement of resonant voltages for SQUIDs (Wang *et al.* 1997), respectively.

Critical currents for a NbN/MgO/NbN junction measured at 2 K and higher temperatures are plotted in Fig. 5. As can be seen, owing to high superconducting

critical temperature (14–17 K) in NbN electrodes, critical currents of NbN Josephson junctions at 10 K are more than 60% of those at 4.2 K. This has stimulated development of Josephson devices that are operated at 10 K with a compact closed-cycle refrigeration system.

2.3 Stability

As is the case for Nb/AlO$_x$/Nb junctions, Josephson junctions having NbN electrodes show extremely high stability with respect to thermal cycling and storage in air. Furthermore, because NbN is less chemically active, Josephson junctions with NbN electrodes can withstand a higher processing temperature than those with niobium electrodes.

3. Summary

Fabrication of high-quality Josephson junctions with sputter-deposited niobium films or reactively sputter-deposited NbN films as electrodes has been achieved by the use of barrier materials fit to the electrodes and the introduction of a "whole-wafer" process. In the case of Josephson junctions with niobium electrodes, aluminum is employed as a barrier material since it shows suitable wetting on a fresh surface of niobium. Because of the affinity of aluminum to niobium, an aluminum layer deposited on a niobium electrode covers the surface of the electrode well, resulting in the formation of a uniform and pinhole-free tunnel barrier by thermal oxidation of the aluminum layer. The introduction of a "whole-wafer" process enables junctions to be fabricated with good run-to-run reproducibility. In the case of Josephson junctions with NbN electrodes, high-quality tunneling characteristics with gap voltages greater than 5 mV and small subgap leakage currents have been achieved by the use of very thin MgO or AlN films as tunnel barriers. Both materials have the same structure as NbN and lattice parameters close to that of NbN, which must be the origin of the improved junction characteristics.

See also: Josephson Junctions: High-T_c

Bibliography

Gates J V, Washington M A, Gurvitch M 1984 Critical current uniformity and stability of Nb/Al–oxide–Nb Josephson junctions. *J. Appl. Phys.* **55**, 1419–21

Gurvitch M, Washington M A, Huggins H A 1983 High quality refractory Josephson tunnel junctions utilizing thin aluminum layers. *Appl. Phys. Lett.* **42**, 472–4

Huggins H A, Gurvitch M 1985 Preparation and characteristics of Nb/Al–oxide–Nb tunnel junctions. *J. Appl. Phys.* **57**, 2103–9

Kroger H, Smith L N, Jillie D W 1981 Selective niobium anodization process for fabricating Josephson tunnel junctions. *Appl. Phys. Lett.* **39**, 280–2

Kuroda K, Yuda M 1988 Niobium-stress influence on Nb/Al-oxide/Nb Josephson junctions. *J. Appl. Phys.* **63**, 2352–7

Maezawa M, Aoyagi M, Nakagawa H, Kurosawa I 1995 Specific capacitance of Nb/AlO$_x$/Nb Josephson junctions with critical current densities in the range of 0.1–18 kA/cm^2. *Appl. Phys. Lett.* **66**, 2134–6

Miller R E, Mallison W H, Kleinsasser A W, Delin K A, Macedo E M 1993 Niobium trilayer Josephson tunnel junctions with ultrahigh critical current densities. *Appl. Phys. Lett.* **63**, 1423–5

Shinoki F, Shoji A, Kosaka S, Takada S, Hayakawa H 1981 Niobium nitride Josephson tunnel junctions with oxidized amorphous silicon barriers. *Appl. Phys. Lett.* **38**, 285–6

Shoji A, Aoyagi M, Kosaka S, Shinoki F, Hayakawa H 1985 Niobium nitride Josephson tunnel junctions with magnesium oxide barriers. *Appl. Phys. Lett.* **46**, 1098–100

Van der Zant H S J, Receveur R A M, Orlando T P 1994 One-dimensional parallel Josephson junction arrays as a tool for diagnostics. *Appl. Phys. Lett.* **65**, 2102–4

Wang Z, Uzawa Y, Kawakami A 1997 High critical current density NbN/AlN/NbN tunnel junctions for submillimeter wave SIS mixers. *IEEE Trans. Appl. Supercond.* **7**, 2797–800

A. Shoji
Electrotechnical Laboratory, Tsukuba, Japan

Josephson Voltage Standard

The electronic system of a macroscopic superconductor is characterized by the formation of electron pairs, so-called Cooper pairs (Bardeen *et al.* 1947), which carry d.c. currents without these being dissipated. The Cooper pair system of two separated superconductors can be described by two independent single macroscopic order parameters $\psi_{1,2} = |\psi_{1,2}|\exp(i\varphi_{1,2})$, the time evolution of which is expressed by the Schrödinger equation $\partial\psi_{1,2}/\partial t = (-i/\hbar)E_{1,2}\psi_{1,2}$. $E_{1,2}$ are the energies of the Cooper pair systems and $|\psi_{1,2}| = (n_{1,2})^{1/2}$ denotes the Cooper pair densities $n_{1,2}$. In 1962 Josephson described the phenomenon of Cooper pair transport between two weakly coupled superconductors by two equations:

$$I_J = I_c\sin\varphi \text{ and } V(t) = (\hbar/2e)\mathrm{d}\varphi/\mathrm{d}t$$

The first Josephson equation denotes the superconducting d.c. Cooper pair current across the barrier dependent on the phase difference $\varphi_2 - \varphi_1 = \varphi$ of the order parameters of the two weakly coupled superconductors: a Josephson junction. I_c is the maximum possible supercurrent. The second equation shows that the voltage across a Josephson junction is proportional to the time derivative of the phase difference (see *Josephson Junctions: Low-T_c, Josephson Junctions: High-T_c*). If the Josephson junction is biased by a constant voltage, $V(t)$ in the second Josephson equation is replaced by the constant value V. Integrating

the equation and introducing the result $\varphi = \varphi_0 + (2e/\hbar)Vt$ into the current equation, one obtains $I = I_c\sin(\omega t + \varphi_0)$, which describes an alternating supercurrent with frequency $f = \omega/2\pi = 2e/V$. The Josephson junction is a high-frequency oscillator that converts a frequency into a voltage: $V = (h/2e)f = \varphi_0 f$.

The parameter φ_0 denotes the flux quantum. The d.c. voltage across a Josephson junction is the rate of flux quanta transferred across the junction. If the Josephson oscillator is phase locked to an external microwave oscillator with a well-known frequency, f_e, constant voltage steps appear at $V_n = n\varphi_0 f_e$ ($n = 1, 2, 3 \ldots$) in the nonlinear d.c. characteristic of the junction (Shapiro 1963). For the nth harmonic the current range, ΔI_n, over which the junction oscillator is phase locked to the external oscillator is described by $\Delta I_n = 2I_c|J_n(2eV_{rf}/\hbar\omega_e)|$, where V_{rf} is the radio-frequency (RF) voltage amplitude across the junction. The precision of the voltage steps is determined only by the uncertainty of f_e, which can be kept smaller than 10^{-11} by means of modern frequency standards like atomic cesium clocks. This makes the voltage steps ideal reference voltages for standard voltage measurements. The maximum step voltage (e.g., $V_1 \approx 145\,\mu V$ for $f_e = 70\,GHz$) is limited by the energy gap voltage of the superconducting electrodes (e.g., $2.5\,mV$ for niobium).

In contrast to the ideal Josephson contact described above, a real junction is a parallel connection of the external current source $I(t) = I_0 + I_1\sin\omega_e t$, the junction normal-state resistance R_n, the junction capacitance C, and the ideal Josephson inductance $I = I_c\sin\varphi$. If the currents are distributed homogeneously across the junction area A, this circuit is described by

$$I_0 + I_1\sin\omega_e t = I_c\sin\varphi + V(t)/R_n + CdV(t)/dt$$

(Stewart 1968, McCumber 1969, Kautz 1981). With $V(t) = (\hbar/2e)d\varphi/dt$, $i_0 = I_0/I_c$, $i_1 = I_1/I_c$, $\Omega = \hbar\omega_e/2eI_cR_n$, $t' = \hbar t/2eI_cR_n$, and $\beta = 2eI_cR_n^1C/\hbar$, one obtains a dimensionless differential equation for a damped driven oscillator:

$$\beta d^2\varphi/dt^2 + d\varphi/dt + \sin\varphi = i_0 + i_1\sin(\Omega t')$$

where $\beta^{1/2}$ is the quality factor for the LC Josephson resonator and characterizes the damping of the Josephson oscillator.

Large values of R_n and C lead to low junction damping and thus to a hysteresis in the d.c. characteristic. Particularly, superconductor–insulator–superconductor (SIS) tunnel junctions provide very low damping and a strong hysteresis in the d.c. characteristic (Fig. 1(a)). Moreover, in this case, the quasiparticle branch of the d.c. characteristic more or less follows the voltage axis at nearly zero current for voltages smaller than the gap voltage. Therefore, the constant voltage steps may cross the voltage axis with the effect that reference voltages are generated without any current flowing across the junctions (Fig. 1(b)). The zero current steps generally are multivalued: up to about seven defined voltage steps per junction for $f_e = 70\,GHz$. Other junction types made of super-conductor–normal metal–superconductor (SNS) sandwiches or superconductor–insulator–normal metal–insulator–superconductor (SINIS) sandwiches (Maezawa and Shoji 1997, Sugiyama *et al.* 1997, Kupriyanov *et al.* 1999) show much higher damping and thus no hysteresis in the d.c. characteristic (Fig. 1(c)).

There is only one reference voltage step at a certain bias current (Fig. 1(d)), which makes the reference voltage single valued but also results in an arbitrarily lower maximum output reference voltage per single junction at a given frequency. Typical junction data are given in Table 1.

1. Conventional SIS Voltage Standard

Figure 1 shows that a single Josephson junction generates reference voltages not much higher than about $1\,mV$. Early voltage standards on the basis of a single junction, together with a conventional voltage divider, provided an output voltage of $1\,V$ with an uncertainty of about $5 \times 10^{-8}\,V$ (Kose 1974). The accuracy of these instruments was finally limited by the complex calibration procedure for the voltage divider. Further improvement could therefore be achieved only by an increase in the Josephson reference voltage from a few millivolts to values of $1\,V$ or more by means of large series arrays of Josephson junctions. To realize such a series array voltage standard, the use of underdamped SIS tunnel junctions has been suggested (Levinsen *et al.* 1977), because for zero current steps it would not be necessary to have a small junction parameter spread. In the zero current mode a parasitic series resistance would not create errors and the maximum output reference voltage of about $1\,mV$ per junction in the case of niobium electrodes would limit the junction number to a technologically acceptable value (about 1000 junctions for $1\,V$). In addition, a large number of quantized voltages between zero and the maximum output voltage for convenient nonlinearity or voltage ratio measurements can be adjusted.

To operate successfully such a series array of underdamped tunnel junctions, two problems must be solved.

(i) The single junction is a nonlinear, underdamped oscillator that has to be coupled to the external oscillator without creating chaos (for an overview see Kautz 1996). To reach the goal of a stable phase lock with the external oscillator, the resonance frequency of the Josephson oscillator, $\omega_p = (2eI_c/\hbar C)^{1/2}$, should be kept lower than the frequency of the external drive, ω_e. Moreover, the
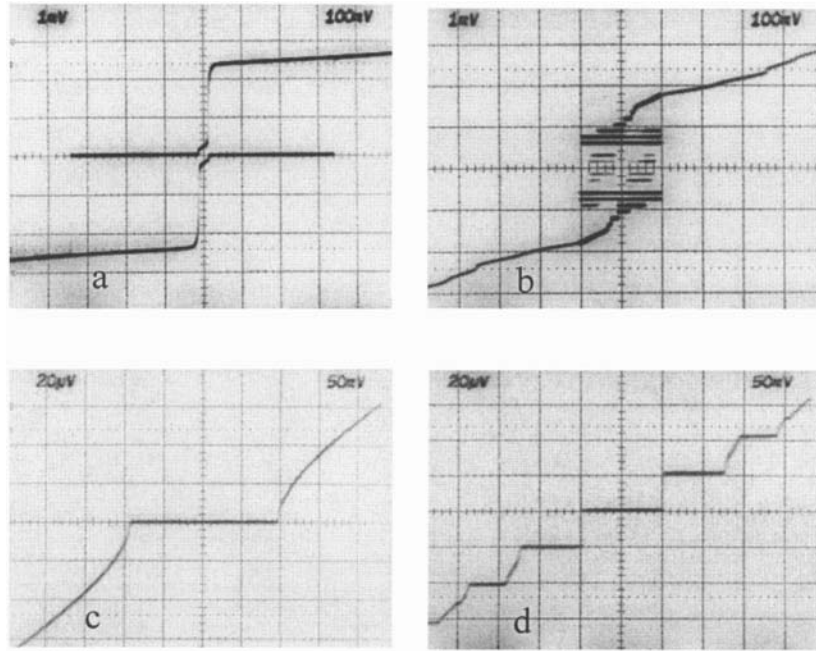
Figure 1
d.c. characteristic of (a) Nb–Al$_2$O$_3$–Nb tunnel junction (vertical: 1 mV per division; horizontal: 0.125 mA per division); (b) Nb–Al$_2$O$_3$–Nb tunnel junction under 70 GHz microwave radiation (vertical: 1 mV per division; horizontal: 0.125 mA per division); (c) Nb–PdAu–Nb junction (vertical: 20 µV per division; horizontal: 0.4 mA per division); (d) Nb–PdAu–Nb junction under 10 GHz microwave radiation (vertical: 20 µV per division; horizontal: 0.4 mA per division).

Table 1
Typical junction parameters for SIS, SNS, and SINIS junctions.

Parameter	SIS	SNS	SINIS
β_c	10^5	$\to 0$	1
$I_c R_n$	1 mV	20 µV	100 µV
$\omega_e/2\pi$	70 GHz	10 GHz	70 GHz
R_n	100 Ω	0.003 Ω	0.1 mΩ
$(\omega_e C)^{-1}$	0.06 Ω	$\to \infty$	0.06 Ω
A	20 µm × 50 µm	2 µm × 2 µm	20 µm × 50 µm

distribution of the phase difference across the junction area should be homogeneous. These restrictions lead to a limitation of the critical current and thus to a finite current width of the step. With an external drive frequency of $f_e = 70$ GHz, a sufficient step width and a stable phase lock are obtained for critical currents of about 150 µA and junction areas of about 20 µm × 50 µm in the case of Nb–Al$_2$O$_3$–Nb junctions.

(ii) As the stable phase lock of the junctions to the external microwave is also dependent on the incident microwave power, the array must be integrated into a microwave circuit that homogeneously distributes the microwave power to all junctions (Niemeyer *et al.* 1984, 1985). The series array is therefore arranged as a part of a periodic low-impedance (5 Ω) superconducting microstripline. In the case of the SIS junction array, the RF currents are mainly capacitive and the impedance mismatch between the stripline impedance and R_n is large. This prevents an effective RF power dissipation in a single junction of the array. As only a very small fraction of the RF power is transferred to the single junction, the distribution of the power along the stripline is homogeneous enough to integrate up to about 3500 junctions into a continuous stripline. For larger arrays the stripline configuration is divided into four or eight parallel microwave paths that are terminated by matched loads and separated by d.c. blocks from the RF distribution network (cf. Fig. 2).

This RF design has proved so effective that it can be applied to circuits with up to 2×10^4 junctions and output voltages of more than 10 V (Hamilton *et al.*
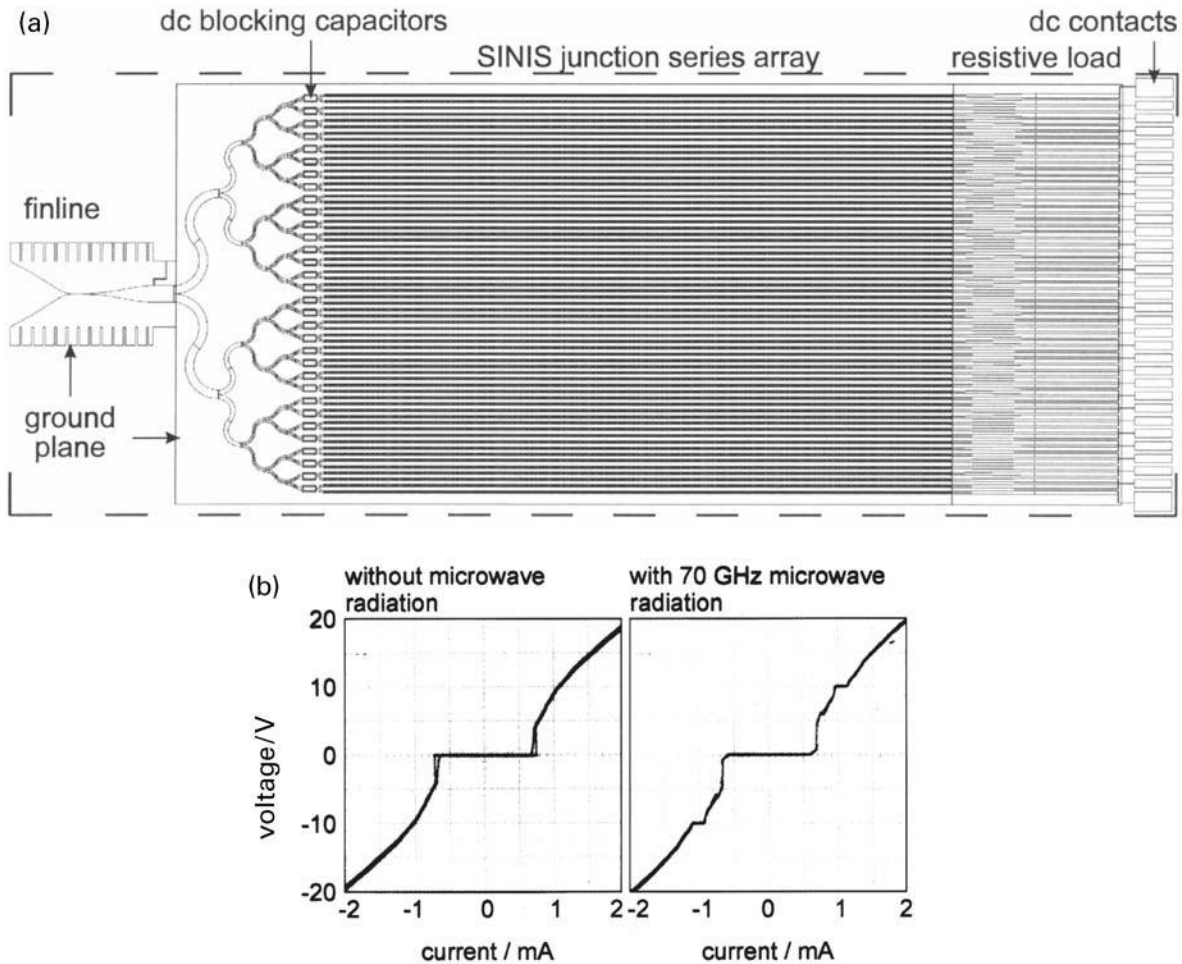
Figure 2
(a) Design of a 10 V SINIS array with 69 120 Nb–Al$_2$O$_3$–Al–Al$_2$–Al$_2$O$_3$–Nb junctions. Chip size: 28 mm × 10.5 mm. (b) d.c. characteristic of the array without and with 70 GHz microwave radiation.

1989). Further increases in the circuit reliability can be achieved by the wafer technology on the basis of Nb–Al$_2$O$_3$–Nb (Gurvitch *et al*. 1983, Niemeyer *et al*. 1989, Müller *et al*. 1997).

Since 1990 the Josephson constant, K_{J90} η $2e/h$, has been officially defined as a practical unit to the value of 483597.9 GHzV^{-1} for the reproduction of the unit of volts. This value was chosen as close as possible to the SI value but is not identical to it because an instrument as precise as a Josephson series array voltage standard does not exist. Only direct comparisons between Josephson voltage standards may allow one to define their practical precision, which normally is limited by the room temperature zero instrument and the drift of the thermal e.m.f. differences in the voltage leads. Key comparisons of the PTB standard with

that of the BIPM reveal uncertainties of 5×10^{-11} related to 10 V.

2. Programmable Voltage Standards

In the case of the conventional SIS voltage standard, the use of zero-current voltage steps implies a difficult stability problem: as the reference voltages completely overlap the system does not automatically return to the adjusted voltage if the phase lock is lost owing to an external disturbance. Readjustment of the standard is time consuming and thus prevents rapid programmable selection of certain reference voltages. Especially, the synthesis of a.c. voltages for D/A conversion with fundamental precision seems to be

impossible. Therefore, using highly damped junctions (cf. Fig. 1(c) and (d)) in series arrays to avoid the reference voltage being multivalued has been suggested (Hamilton *et al.* 1995). If such an array is biased on a constant voltage step, it will remain at the adjusted value even if the phase lock is lost for a short moment. Besides zero voltage, an individual junction contributes an exactly defined number of constant voltage steps to the total reference voltage: in modern designs the steps are $\pm V_1$. In this case, an array of N junctions provides only one reference voltage: NV_1. To adjust rapidly any voltage between zero and NV_1, new circuit designs have been suggested, which are described below.

2.1 Binary Arrays

For the rapid selection of d.c. reference voltages it has been suggested to divide an array of highly damped Josephson junctions into a series of binary sections that allow the reference voltage to be defined by combining a certain fraction of the binary sections in such a way that the desired reference voltage is obtained (Benz *et al.* 1997). Binary divided SNS arrays of 32768 Nb–PdAu–Nb junctions have been successfully operated at 16 GHz and generate RF-induced reference voltages of 1 V. As the junction capacitance approaches zero (Table 1), the RF currents are resistive. The array is part of a coplanar stripline configuration of eight parallel lines, with a line impedance of about 50 Ω, so that a large impedance mismatch between junctions and stripline allows homogeneous microwave coupling to all junctions.

The small product of $I_c R_n$ of 10–40 μV is tolerable for voltage standards with relatively low drive frequencies and maximum output voltages not larger than 1 V. But it would be advantageous to increase $I_c R_n$ to values that would make possible drive frequencies of 70 GHz and thus a reduction of the junction number for a given maximum output voltage.

Large products of $I_c R_n$ are obtained in series arrays of Nb–Al$_2$O$_3$–Al–Al$_2$O$_3$–Nb SINIS junction (Schulze *et al.* 1998). Here the transparency of the junction barriers can be adjusted over a wide range by the fabrication parameters. This allows SINIS arrays to be operated over a frequency range of at least 10–100 GHz. Typical junction parameters are listed in Table 1. An 8192-junction array divided into binary subarrays is, therefore, large enough to reach a maximum output voltage of 1 V. Moreover, the microwave supply to the conventional voltage standard can be used for this type of programmable voltage standard. Direct comparisons of the 1 V output voltages of SIS and SINIS arrays show no deviation within a standard uncertainty of 1.6×10^{-10} (Behr *et al.* 1999). Rapid calibration of Zener references has been realized with a standard deviation of less than 10 nV. With a two-array system fully automated

calibrations of the ratio of a 1 Ω/10 Ω resistive voltage divider have been performed with an uncertainty of five parts in 10^9 (Behr *et al.* 2000). A 7492-junction SINIS array has been used to determine the fast reverse d.c. to d.c. transfer difference of a multijunction thermal converter (Funck *et al.* 2000).

The SINIS arrays are integrated into a low-impedance microstripline comparable to that for the SIS arrays. However, in contrast to the SIS junctions, an arbitrary part of dissipative RF current here flows over the junction resistance because R_n is comparable to the stripline impedance. This impedance matching allows RF power from the individual junction oscillator to be transferred to the stripline to an amount large enough for the phase locking of adjacent junctions. If the junction number is large enough, the array will act as a coherent microwave oscillator whose output power is added to the RF power of the external oscillator that is locked to the first junctions in the array (Schulze *et al.* 1999). It is, therefore, possible to generate constant voltage steps in very long arrays, although the attenuation of the stripline is rather high (about 0.05 dB per stripline period or 1 dB mm^{-1}).

As a result of the microwave contribution from the active stripline, the microwave power required to generate a certain reference voltage is about 10 times smaller than that needed to reach comparable output voltages by means of a conventional SIS array with much fewer junctions. The coherent operation of the SINIS array makes it possible to generate maximum reference voltages of 10 V with a 69120-junction array under 70 GHz radiation with an RF power of less than 1 mW at the circuit antenna (Fig. 2) (Schulze *et al.* 2000, Kohlmann *et al.* 2000).

The binary arrays described reach a minimum switching time between different reference voltages of about 1 μs. This makes them ideal programmable d.c. quantum voltmeters. However, while array sections are switched from the step voltage to zero voltage, undefined voltage states of the transients between the voltage steps contribute to the reference voltage. This makes it difficult to achieve an accuracy sufficient for synthesizing fast a.c. voltages.

2.2 Digital-to-Analog Converter

To overcome the difficulties with the switching transients in the case of binary arrays, it has been suggested using an RF pulse drive instead of a sinusoidal microwave drive, which allows the reference voltage to be adjusted by controlling the repetition rate of the drive over a wide range (Benz and Hamilton 1996, Benz *et al.* 1998). By the restriction to single polarity pulses the system generates unipolar waveforms only. A unipolar 23.4 MHz sine wave with a peak-to-peak amplitude of 4.3 mV with an error of five parts in 10^8 has been verified in experiments (Benz *et al.* 1998). Bipolar waveforms can be synthesized by biasing of

an array of overdamped junctions with a signal composed of a conventional sinusoidal drive and a two-level broadband digital code. This allows a controlled sequence of negative and positive pulses to be generated. Reference voltages between $-NV_1$ and $+NV_1$ are obtained by time averaging of periodic sequences of pulses with an appropriate number and polarity (Benz *et al.* 1999). A synthesis of a sine wave with an amplitude of $\pm 18\,mV$ at $5\,kHz$ has been verified. All pulse-driven D/A converters need a perfect broadband transmission line without dispersion for fast signal propagation. In practice this is very difficult to achieve for large arrays with an output voltage amplitude of $1\,V$ or more.

In principle, the use of rapid single-flux quantum (RSFQ) voltage multipliers would overcome the difficulties with the broadband transmission lines of the pulse-driven systems (Semenov 1993, Semenov *et al.* 1997, Sasaki *et al.* 1999). These complex digital circuits amplify the voltage with integer gain by multiplication of SFQ pulses. An RSFQ D/A converter contains a certain number of voltage multipliers in series connection that are independently controlled by the generation of a train of pulses with a repetition rate proportional to the input code. With a 2500-junction circuit an output voltage of $5\,mV$ has been verified. Higher voltages can basically be achieved by hybrid integration of such circuits.

See also: Electrodynamics of Superconductors: Flux Properties; Electrodynamics of Superconductors: Weakly Coupled; Metrology: Superconducting Cryogenic Current Comparators

Bibliography

Bardeen J, Cooper C N, Schrieffer J R 1947 Theory of superconductivity. *Phys. Rev.* **108**, 1175–204

Behr R, Grimm L, Funck T, Kohlmann J, Schulze H, Müller F, Schumacher B, Warnecke P, Niemeyer J 2001 Application of Josephson series arrays to a DC quantum voltmeter. *IEEE Instrum. Meas.* **50**, 185–7

Behr R, Schulze H, Müller F, Kohlmann J, Niemeyer J 1999 Josephson arrays at 70 GHz for conventional and programmable voltage standards. *IEEE Trans. Instrum. Meas.* **48**, 270–3

Benz S P, Hamilton C A 1996 A pulse-driven programmable Josephson voltage standard. *Appl. Phys. Lett.* **68**, 3171–3

Benz S P, Hamilton C A, Burroughs C J, Harvey T E 1997 Stable 1 volt programmable voltage standard. *Appl. Phys. Lett.* **71**, 1866–8

Benz S P, Hamilton C A, Burroughs C J, Harvey T E 1999 AC and DC bipolar voltage source using quantized pulses. *IEEE Trans. Instrum. Meas.* **48**, 266–9

Benz S P, Hamilton C A, Burroughs C J, Harvey T E, Christian L A, Przybysz J E 1998 Pulse-driven Josephson digital/analog converter. *IEEE Trans. Appl. Supercond.* **8**, 42–7

Funck T, Behr R, Klonz M 2000 Fast reversed DC measurements on thermal converters using a SINIS Josephson junction array. *IEEE Instrum. Meas.* in press

Gurvitch M, Washington M A, Huggins H A, Rowell T M 1983 High quality refractory Josephson tunnel junctions utilizing thin aluminum layers. *IEEE Trans. Magn.* **19**, 791–4

Hamilton C A, Burroughs C J, Kautz R L 1995 Josephson D/A converter with fundamental accuracy. *IEEE Trans. Instrum. Meas.* **44**, 233–4

Hamilton C A, Lloyd F L, Chie K, Goeke W C 1989 A 10-V Josephson voltage standard. *IEEE Trans. Instrum. Meas.* **IM-38**, 314–6

Josephson B D 1962 Possible new effects in superconductive tunneling. *Phys. Lett.* **1**, 251–3

Kautz R L 1981 The a.c. Josephson effect in hysteretic junctions: range and stability of phase lock. *J. Appl. Phys.* **52**, 3528–41

Kautz R L 1996 Noise, chaos and the Josephson voltage standard. *Rep. Prog. Phys.* **59**, 935–92

Kohlmann J, Schulze H, Behr R, Müller F, Niemeyer J 2000 10 V SINIS Josephson junction series arrays for programmable voltage standards. *IEEE Instrum. Meas.* in press

Kose V 1974 Maintaining the unit of voltage at PTB via the Josephson effect. *IEEE Trans. Instrum. Meas.* **IM-23**, 271–5

Kupriyanov MYu, Brinkman A, Golubov A A, Siegel M, Rogalla H 1999 Double barrier Josephson structures as the novel elements for superconducting large scale integrated circuits. *Physica C* **326–327**, 16–45

Levinsen M T, Chiao R Y, Feldman M J, Tucker B A 1977 An inverse a.c. Josephson effect voltage standard. *Appl. Phys. Lett.* **31**, 776–8

Maezawa M, Shoji A 1997 Overdamped Josephson junctions with Nb/Al/Al$_x$O$_y$/Al/Al$_x$O$_y$/Nb structure for integrated circuit application. *Appl. Phys. Lett.* **70**, 3603–5

McCumber D E 1969 Effect of AC impedance on DC voltage current characteristics of superconductor weak link junctions. *J. Appl. Phys.* **39**, 3113–8

Müller F, Pöpel R, Kohlmann J, Niemeyer J, Meier W, Weimann T, Grimm L, Dünschede F, Gutmann P 1997 Optimized 1 V and 10 V Josephson series arrays. *IEEE Trans. Instrum. Meas.* **46**, 229–32

Niemeyer J, Grimm L, Meier W, Hinken J H, Vollmer E 1985 A stable Josephson reference voltage between 0.1 and 1.3 V for high-precision voltage standards. *Appl. Phys. Lett.* **47**, 1222–3

Niemeyer J, Hinken J H, Kautz R L 1984 Microwave-induced constant-voltage steps at one volt from a series array of Josephson junctions. *Appl. Phys. Lett.* **45**, 478–80

Niemeyer J, Sakamoto Y, Vollmer E, Hinken J H, Shoji A, Nakagawa H, Takada S, Kosaka S 1989 Nb/Al-oxide/Nb and NbN/MgO/NbN tunnel junctions in large series arrays for voltage standards. *Jpn. J. Appl. Phys.* **25**, L343–5

Sasaki H, Kiryu S, Hirayama F, Kikuchi T, Maezawa M, Shoji A 1999 RSFQ-based D/A converter for AC voltage standard. *IEEE Trans. Appl. Supercond.* **9** (2), 3561–4

Schulze H, Behr R, Kohlmann J, Müller F, Niemeyer J 2000 Design and fabrication of 10 V SINIS Josephson arrays for programmable voltage standards. *Supercond. Sci. Technol.* **9**, 1293–5

Schulze H, Behr R, Müller F, Niemeyer J 1998 Nb/Al/Al$_x$O$_y$/Al/Al$_x$O$_y$/Nb Josephson junctions for programmable voltage standards. *Appl. Phys. Lett.* **73**, 996–8

Schulze H, Müller F, Behr R, Kohlmann J, Niemeyer J, Balashov D 1999 SINIS Josephson junctions for programmable Josephson voltage standard circuits. *IEEE Trans. Appl. Supercond.* **9**, 4241–4

Semenov V K 1993 Digital to analog conversion based on processing of the SFQ pulses. *IEEE Trans. Appl. Supercond.* **3**, 2637–40

Semenov V K, Shevchenko P N, Polyakov A 1997 Digital-to-analog converter based on processing of SFQ pulses. *Ext. Abstr. ISEC '97* **2**, 320–2

Shapiro S 1963 Josephson currents in superconducting tunnelling. The effect of microwaves and other observations. *Phys. Rev. Lett.* **11**, 80–2

Stewart W C 1968 Current–voltage characteristics of Josephson junctions. *Appl. Phys. Lett.* **12**, 277–80

Sugiyama H, Yanada A, Ota M, Fujimaki A, Hayakawa H 1997 Characteristics of Nb/Al/Al$_x$O$_y$/Al/Al$_x$O$_y$/Nb junctions based on the proximity effect. *Jpn. J. Appl. Phys.* **36**, L1157–60

J. Niemeyer
Physikalisch-Technische Bundesanstalt, Braunschweig Germany

K

Kerr Microscopy

Kerr microscopy allows the imaging of magnetic domains and magnetization processes in an optical polarization microscope. The method is based on the magnetooptical Kerr effect, i.e., the rotation of plane polarized light in dependence of the magnetization direction on reflection from a nontransparent sample.

In this article some fundamentals and possibilities of Kerr microscopy will be presented. Examples of domain images obtained by the method from a variety of materials can be found in *Magnets, Soft and Hard: Domains*. For a comparison with other imaging techniques (see *Magnetic Materials: Transmission Electron Microscopy* and *Magnetic Force Microscopy*). A comprehensive review on domain imaging with emphasis on Kerr microscopy is given by Hubert and Schäfer (1998) where also an extended bibliography can be found.

1. Kerr Microscope

Domain observations with a lateral resolution down to the limit of optical microscopy (about 300 nm) are possible in a conventional polarizing microscope (Fig. 1). The domain contrast is optimized by the rotation of an analyzer and compensator. The aperture diaphragm, controlling the illumination, has to be adjustable so that the angle and plane of incidence can be chosen, allowing optimization of the Kerr sensitivity to in- or out-of-plane magnetization configurations (see Sect. 2). The application of fields up to 1 T is possible using an electromagnet with proper pole-tip geometry. The often weak domain contrasts require image processing for enhancement (see Sect. 3).

2. Kerr Effect and Contrast

For the Kerr effect the magnetooptical interaction between light and magnetization m is phenomenologically described by a dielectric law

$$D = \varepsilon(E + iQm \times E) \tag{1}$$

in which a displacement vector D, representing the magnetooptically generated light amplitude, is connected to the electric vector E of the illuminating plane light wave (ε is the dielectric constant and Q is a complex material constant). Accordingly, the Kerr effect is linear in magnetization.

The cross-product in Eqn. (1) reveals the gyroelectric nature of the Kerr effect. Its symmetry can be derived by using the concept of a Lorentz force ($m \times E$) acting on light-agitated electrons (Fig. 2(a)). The Lorentz motion v_{Lor} (parallel to D) creates a
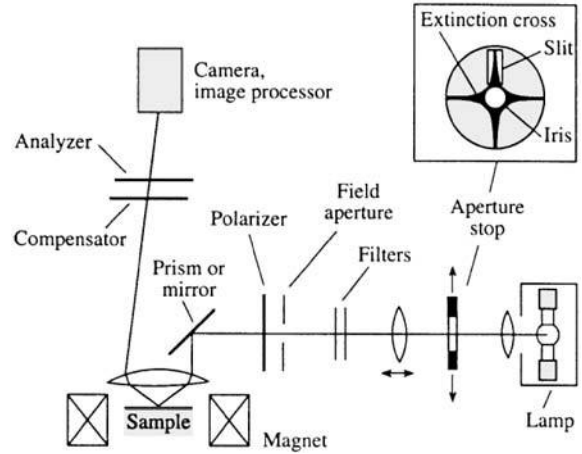
Figure 1
The essential components of a Kerr microscope. The inset shows the diffraction plane of the microscope where the illumination diaphragm can be viewed and adjusted. To obtain best contrast conditions the illumination should be restricted to the zone of maximum extinction that is cross-shaped at crossed polarizers due to depolarization effects. For perpendicular incidence an aperture iris has to be centered, while for oblique incidence an off-centered slit aperture is preferred.
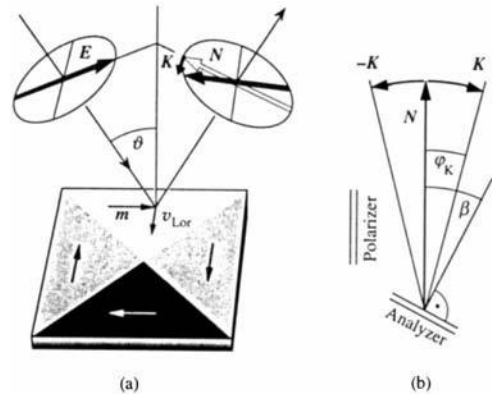
Figure 2
(a) Schematic diagram of the (longitudinal) Kerr effect. The interaction of the incident light E-vector with the magnetization m generates the "Lorentz velocity" v_{Lor}. The regularly reflected amplitude N is modified by the magnetization-dependent amplitude K, leading to a rotation of the E-vector in reflection by a small angle φ_K; (b) the analyzer should be set at the angle $\beta > \varphi_K$ to achieve optimum contrast conditions.

369

magnetic contribution **K** (Kerr amplitude) to the re-flected amplitude, which is polarized perpendicular to the regularly reflected amplitude **N**. By interference of **K** and **N** the resulting vector is rotated by the (small) angle $\varphi_K = K/N$. For two domains with opposite magnetization the Kerr amplitudes differ in sign. A domain contrast is obtained by extinguishing the light of one domain by the proper setting of the analyzer (Fig. 2(b)). If **K** and **N** differ in phase, the rotation is connected with some ellipticity. In this case the ellipticity of the darker domains should be removed by a phase-shifting compensator (such as a rotatable quarter-wave plate) to improve the contrast.

For every magnetization configuration the light incidence has to be properly chosen to generate a Lorentz motion that results in a detectable rotation. It turns out that the Kerr rotation is proportional to the magnetization component parallel to the reflected light beam. This rule immediately shows that do-mains magnetized parallel to the surface require ob-lique illumination with the plane of incidence parallel to the magnetization axis for maximum contrast (*longitudinal* Kerr effect), while the contrast of per-pendicularly magnetized domains becomes strongest at perpendicular incidence ($\varphi = 0$, *polar* Kerr effect). The separation of polar and in-plane magnetization components is possible by different microscope set-tings as demonstrated in Fig. 3.

Important for good domain visibility is the size of the usable signal and this also determines the signal-to-noise ratio in video systems. The relative signal *S*, i.e., the difference between the intensities of bright

Figure 4
Effect of a dielectric antireflection coating on the Kerr contrast, demonstrated for an amorphous ribbon with and without a ZnS interference layer.

and dark domains, is derived (Hubert and Schäfer 1998) as

$$S \approx 4\beta KN \qquad (2)$$

Three important properties should be noted: (i) the Kerr signal is a linear function of the Kerr amplitude *K* and therefore of the respective magnetization com-ponents according to Eqn. (1); (ii) the (often weak) Kerr signal can be enhanced by increasing the anal-yzer angle β beyond φ_K, allowing an increase in the signal-to-noise ratio and adjusting the sensitivity of the detector; and (iii) the "visibility" of domains is determined by the Kerr *amplitude* and not by the Kerr rotation.

Although *K* depends on material constants, it can be enhanced in materials where the incoming light is not completely absorbed by magnetooptical interac-tion but "uselessly" reflected to some extent. Antire-flection coatings increase the absorbed intensity (based on interference effects), proportionally raising *K* and thus the useful signal (Fig. 4). Effective di-electric coatings are ZnS for metals and MgF_2 for oxides. As the Kerr effect is generally weak, this gain should not be relinquished even if digital image processing is applied.

3. Contrast Enhancement by Image Processing

A significant enhancement of magnetic contrast is possible by video microscopy and digital image processing. The standard procedure (Fig. 5) starts with a digitized image of the magnetically saturated state, where in an external a.c. or d.c. magnetic field all domains are eliminated. This background (refer-ence) image is subtracted from a state containing domain information, so that in the difference image a

Figure 3
Domains in a coarse-grained NdFeB crystal in which the magnetization axes of the different grains are misaligned relative to the surface as sketched in (c); (a) the magnetization components perpendicular to the surface (polar components) can be imaged separately at perpendicular incidence. At oblique incidence polar and in-plane components show up simultaneously. When the illumination direction is rotated by 180°, the polar Kerr effect does not change sign, whereas the longitudinal effect does. By forming the image difference the polar contrast disappears, leaving just in-plane contrast as shown in (b).

Figure 5
The difference technique for contrast enhancement. Stress-induced domains on an iron-rich metallic glass in the longitudinal Kerr effect are shown.
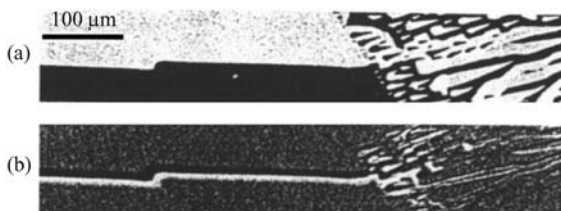
Figure 6
The kinetics of a domain pattern in a transformer sheet: the starting configuration (a) is subtracted from the image of a state in which the sample is subjected to an alternating magnetic field. The moving domain walls become visible by a black and white contrast in the dynamically averaged difference image (b).

Figure 7
Quantitative Kerr microscopy: by imaging a domain pattern under two complementary Kerr sensitivities and comparing its intensities with the corresponding calibration functions, the magnetization vector field can be quantitatively measured. The example shows domains on an amorphous ribbon. A vector plot and color code can be used for presentation.

clear micrograph of the domain pattern is obtained which can be digitally enhanced, free of topographic structures.

The difference technique opens further experimental possibilities. For example, in Fig. 6 a domain image (Fig. 6(a)) is subtracted from an image where changes in the pattern are induced by a magnetic field. In the difference image (Fig. 6(b)) only those areas where the changes occur show a contrast. Such observations give hints as to the local variation of coercivity or to the amplitude of domain wall motion.

4. Quantitative Kerr Microscopy

Due to its linearity and direct sensitivity to m, the Kerr effect can be used for quantitative determination of the magnetization direction (Rave *et al*. 1987). The Kerr intensity has a sinusoidal dependence on the direction of the magnetization vector (Fig. 7). This sensitivity function is obtained by measuring the intensity of well-defined domains or saturated states. The intensity of unknown domains can then be compared with the calibration function and so the angle of m in the surface can be measured. The problem is that due to the sinusoidal dependence there are two possible angles for a given domain intensity. To resolve this ambiguity, the domain pattern of interest has to be imaged twice under different sensitivity conditions that should be shifted by $90°$ (e.g., by choosing two orthogonal planes of incidence). The method can only be applied to soft magnetic materials for which no polar magnetization components are present at the surface.

5. Depth-selective Microscopy

The magnetic information depth of the Kerr effect is about 20 nm in metals. A quantification of this depth sensitivity has to consider the *phase* of the magnetooptic amplitude (Träger *et al*. 1992). The total magnetooptical signal can be seen as a superposition of contributions from different depths,
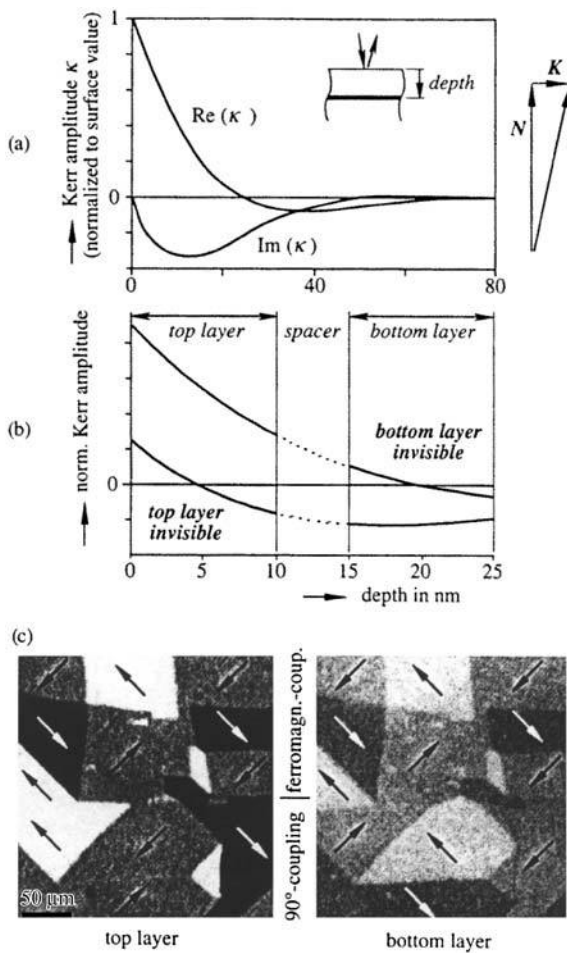
Figure 8
(a) Depth-sensitivity of the Kerr amplitude in iron. The relative phase of K and N was selected so that N is allowed to interfere with the K generated right at the surface; (b) proper phase selection allows layer-selective Kerr imaging on thin-film sandwiches; (c) a (100)-oriented Fe (10)–Cr (≈ 0.5)–Fe (10 nm) trilayer, showing ferromagnetic and biquadratic (90°) coupling in one image. Note that the contrast of the bottom layer is reduced due to absorption.

which are damped exponentially and which differ in phase according to a complex amplitude penetration function (Fig. 8(a)).

These phase differences can be exploited in Kerr microscopy. Using a rotatable compensator, the phase of the Kerr amplitude, generated at a certain depth, can be adjusted relative to the regularly reflected light amplitude (note that a detectable Kerr rotation is only possible if K and N are in-phase). In this way light from selected depth zones can be made invisible if their Kerr amplitude is adjusted out-of-phase

with respect to the regular light. In sandwich films, consisting of ferromagnetic layers that are interspaced by nonmagnetic layers, the zero of the information depth can be put somewhere into the middle of one layer such that the integral contributions of this layer just cancel, leaving only contrast from the other layer (Fig. 8(b)). This kind of layer-selective Kerr microscopy is demonstrated in Fig. 8(c) for an Fe–Cr–Fe sandwich sample (see also (Schäfer 1995)).

6. Other Magnetooptical Effects

Two other magnetooptical effects can be used in a Kerr microscope: the Voigt effect and the gradient effect (Schäfer and Hubert 1990). Both effects appear at perpendicular incidence (where a Kerr contrast of in-plane domains is not possible) and require a compensator for adjustment. The Voigt effect is quadratic in the magnetization components, so that only domains magnetized along different axes show a contrast, while the gradient effect is a birefringence effect that depends linearly on magnetization gradients. Both effects (in combination with the Kerr effect) are helpful in the analysis of domains in cubic materials such as epitaxial thin-film systems by considering their contrast laws and depth sensitivities (see (Schäfer 1995) for an overview). The gradient effect can also favorably be applied to image fine transitions and domain modulations.

7. Dynamic Domain Imaging

Domain dynamics can be observed visually as fast as the eye can follow. Recording periodic processes with long exposure times yields zones of intermediate contrast that may give valuable information at least on the amplitudes of wall motion (see Fig. 6).

Periodic magnetization processes can be observed stroboscopically either by a triggered video camera or by a pulsed light source. Triggering the light or camera pulses with precise timing relative to a field pulse and sweeping the delay time yields a series of corresponding pictures of periodic or quasi-periodic processes (Petek *et al.* 1990).

8. Conclusions

Kerr microscopy is a versatile method for the experimental analysis of magnetic microstructures, only limited by resolution down to a few tenths of a micrometer. Enhanced by image processing, magnetic domains on virtually all relevant materials can be imaged. The dynamic capability and the compatibility with arbitrary applied fields make Kerr microscopy ideally suited for the investigation of magnetization processes. Due to the direct sensitivity and linear

dependence on the magnetic polarization, the method allows the quantitative determination of magnetization vector fields at the surface of soft magnets by calibrating the contrast. In favorable sandwich structures, layer-selective imaging is possible within a depth-sensitivity range of about 20 nm in metals. On bulk materials, however, it is just the surface region that can be seen (like in most other domain observation techniques). Here often theoretical arguments combined with domain studies in magnetic fields are required to obtain a three-dimensional understanding of the magnetic microstructure.

See also: Magneto-optics: Inter- and Intraband Transitions, Microscopic

Bibliography

Hubert A, Schäfer R 1998 *Magnetic Domains. The Analysis of Magnetic Microstructures*. Springer, Berlin

Petek B, Trouilloud P L, Argyle B E 1990 Time-resolved domain dynamics in thin-film heads. *IEEE Trans. Magn.* **26**, 1328–30

Rave W, Schäfer R, Hubert A 1987 Quantitative observation of magnetic domains with the magneto-optical Kerr effect. *J. Magn. Magn. Mater.* **65**, 7–14

Schäfer R 1995 Magneto-optical domain studies in coupled magnetic multilayers. *J. Magn. Magn. Mater.* **148**, 226–31

Schäfer R, Hubert A 1990 A new magnetooptic effect related to non-uniform magnetization on the surface of a ferromagnet. *Phys. Status Solidi A* **118**, 271–88

Träger G, Wenzel L, Hubert A 1992 Computer experiments on the information depth and the figure of merit in magneto-optics. *Phys. Status Solidi A* **131**, 201–27

R. Schäfer
IFW-Dresden, Germany

Kondo Systems and Heavy Fermions: Transport Phenomena

The proximity of the $4f$ or $5f$ shell of certain lanthanide and actinide elements to the Fermi level gives rise to numerous unusual physical properties at low temperature. Among them are heavy fermion behavior and superconductivity, intermediate valence, Fermi- and non-Fermi-liquid as well as reduced magnetic moments in a magnetically ordered ground state. The outweighing number of such phenomena is attributed to a particular interaction of the conduction electron spin $\vec{s}$ with the total angular momentum $\vec{j}$ of the rare earth elements, known as the Kondo effect (Kondo 1964). Here, $\vec{s}-\vec{j}$ scattering causes an intermediate stage and as a consequence thereof a spin-flip process. One manifestation of this effect has been known since the early 1930s from a $-\ln T$

contribution to the electrical resistivity $\rho(T)$, observed for $3d$ magnetic impurities diluted in a nonmagnetic host. When this term is added to the phonon contribution of such a system, it is sufficient to explain the well-known minimum in $\rho(T)$.

1. Basic Features of Transport Phenomena in Kondo Systems and Heavy Fermions

The physics of Kondo systems and heavy fermions is usually accounted for in terms of the Anderson model (Anderson 1961)

$$H = \sum_{k,\sigma} \varepsilon_k c_{k,\sigma}^+ c_{k,\sigma} + \sum_{i,\sigma} E_0 f_{i,\sigma}^+ f_{i,\sigma}$$
$$+ V \sum_{i,\sigma} (c_{i,\sigma}^+ f_{i,\sigma} + c.c.) + U \sum_{i,\sigma} n_{f,i}^\uparrow n_{f,i}^\downarrow \quad (1)$$

where $n_{f,i}^\sigma = f_{i,\sigma}^+ f_{i,\sigma}$. It describes the conduction electrons $c_{k,\sigma}$ with dispersion ε_k and width W which hybridize with the localized electrons of energy E_0. The hybridization matrix element is usually approximated by a constant V. U represents the on-site Coulomb repulsion of the $d(f)$ electrons. For large Coulomb repulsion U the $d(f)$ spectral weight is split into two parts at E_f and $E_f + U$, having a width $\Delta \approx V^2/W$.

The Anderson model exhibits various parameter regimes. (i) $E_0 + U \gg E_F$, $E_0 \ll E_F$ with $|E_0 + U - E_F|$, $|E_F - E_0| \gg \Delta$. For such parameters local magnetic moments exist which interact antiferromagnetically with the conduction electrons. (ii) If E_0 or $E_0 + U$ approach the Fermi energy so that $E_0 - E_F$ or $E_0 + U - E_F$ become comparable with Δ, or even smaller, the charge fluctuations of the impurity become important. This regime is known as the intermediate valence regime. (iii) In the case of only small admixtures of localized and delocalized electrons, the Schrieffer–Wolff transformation allow transformation of the hybridization matrix element V of Eqn. (1) into an effective exchange coupling J, equivalent to the Heisenberg $s-d$ model, $H = J\vec{s}\vec{S}$.

The Anderson Hamiltonian is then led over into the Coqblin–Schrieffer model (Coqblin and Schrieffer 1969), which is used for practical reasons in most of the theoretical treatments of Kondo physics. The most powerful methods to diagonalize the Anderson, and in particular the Coqblin–Schrieffer Hamiltonian are the renormalization group calculations, the exact Bethe-ansatz solution and the large-N approximation. Perturbation-type calculations and Fermi-liquid theories are also used. An excellent review of these subjects can be found in Hewson's textbook (Hewson 1993) (see *Electron Systems: Strong Correlations*).

1.1 Transport Coefficients

In a general treatment of transport phenomena, the linearized Boltzmann equation yields the following

transport coefficients (Ziman 1964):

$$\sigma \equiv 1/\rho = e^2 K_0 \qquad (2)$$

$$S = -\frac{K_1}{|e| T K_0} \qquad (3)$$

$$\lambda = \frac{1}{T}\left(K_2 - \frac{K_1^2}{K_0}\right) \qquad (4)$$

where σ is the electrical conductivity, ρ is the electrical resistivity, S the Seebeck coefficient and λ the thermal conductivity. In simple metallic systems, the second term of Eqn. (4) is usually neglected. The transport integrals K_n are given by:

$$K_n = \frac{k_F^3}{3\pi^2 m} \int \varepsilon_k^n \tau(\varepsilon_k)\, \mathrm{d}\varepsilon_k \left(-\frac{\mathrm{d}f_k}{\mathrm{d}\varepsilon}\right) \qquad (5)$$

where k_F is the Fermi wave vector, m is the carrier mass, ε_k is the carrier energy and f_k is the Fermi–Dirac distribution function.

The key magnitude of the transport integrals is the relaxation time $\tau(\varepsilon_k)$. Since conduction electrons are scattered in and out of the d or f impurity orbitals, the density of states (DOS) of such impurities, $\rho_{d(f)}(\varepsilon)$, determines the scattering rate. Formally, the energy- and temperature-dependent scattering rate is given per unit impurity concentration c_{imp} by (Hewson 1993):

$$\tau^{-1}(\varepsilon_k) = 2\pi c_{\mathrm{imp}} |V|^2 \rho_{f(d)}(\varepsilon) \qquad (6)$$

Once $\tau(\varepsilon_k)$ is known for particular interaction processes, all the transport coefficients can be calculated.

1.2 Electrical Resistivity

(a) Single impurity Kondo systems

If $3d$ elements such as iron or manganese, or f elements such as cerium, ytterbium or uranium, are dissolved in a nonmagnetic host such as copper, aluminum or LaAl$_2$, spin-flip scattering occurs, responsible for the generation of a spin-compensating cloud of conduction electrons around the impurity. As a result, the impurity magnetic moment becomes screened, thus forming a singlet ground state. In order to take account of the removed spin and orbital degrees of freedom, a narrow many-body resonance develops close to the Fermi energy (Kondo resonance), which is responsible for extraordinary low temperature features of physical quantities. In particular, enhanced scattering of conduction electrons at low temperatures affects transport coefficients, owing to an increased density of low energy excitations in the Kondo resonance near to E_F, and the large DOS at E_F owing to the Kondo resonance is synonymous with extraordinarily enhanced effective masses of the carriers.

The first successful ansatz to account for the observed anomalous behavior of such systems dates back to Kondo (1964), who assumed that a local magnetic moment with a spin $\vec{S}$ is coupled via an exchange interaction J with the conduction electron spin $\vec{s}$, i.e., $H = J\vec{s}\vec{S}$. Using a third-order perturbation-type calculation in J leads to singular scattering of the delocalized electrons near to E_F and to a $-\ln T$ contribution to the electrical resistivity $\rho(T)$, i.e.,

$$\rho_{\mathrm{imp}} = \rho_B\left[1 - 2JN(E_F)\ln\left(\frac{2\gamma}{\pi}\frac{D}{k_B T}\right)\right] \qquad (7)$$

with

$$\rho_B = \frac{\pi m c_{\mathrm{imp}} N(E_F)}{e^2 \hbar} J^2 S(S+1) \qquad (8)$$

where $2\gamma/\pi = 1.13$, D is a cut-off parameter and $N(E_F)$ is the electronic density of states at the Fermi energy E_F.

For antiferromagnetic $s-d$ coupling, $(J < 0)$, $\rho_{\mathrm{imp}}(T)$ increases logarithmically with decreasing temperature. However, since the $\ln T$ term diverges for $T \to 0$, Kondo's calculation becomes invalid at low temperatures. If the leading-order logarithmic terms are summed up, a divergence is obtained for $J < 0$ at a finite temperature T_K, known as the Kondo temperature (Hewson 1993). The electrical resistivity then reads:

$$\rho_{\mathrm{imp}} = \rho_B \frac{1}{\left[1 + JN(E_F)\ln\left(\frac{2\gamma}{\pi}\frac{D}{k_B T}\right)\right]^2} \qquad (9)$$

and the characteristic temperature T_K is given by

$$k_B T_K = \frac{2\gamma}{\pi} D e^{-1/(|J|N(E_F))} \qquad (10)$$

The divergence of physical properties at $T = T_K$ is unphysical since a supposed phase transition is suppressed from very strong fluctuations. Besides, this temperature marks the breakdown of the validity of perturbation-type calculations as many-body interactions become dominant.

Owing to the screening of magnetic moments by the conduction electron spin density within a sphere of radius $\xi \sim (W/k_F)T_K$, $W \ldots$ bandwidth, (Schlottmann 1989), magnetic scattering processes die out for $T \ll T_K$ and the resulting singlet object acts entirely like a simple potential scatterer. Hence, Fermi-liquid (FL) results are applicable. In the scope of the n-channel Kondo model ($n = 2S$) ρ_{imp} is expressed as (Schlottmann and Sacraqmento 1993):

$$\rho_{\mathrm{imp}} = \rho_{\mathrm{imp}}(0)\left[1 - c_2\left(\frac{T}{T_K}\right)^2\right]$$
$$\text{with } c_2 = \frac{1}{8}\left(\frac{5\pi}{n+2}\right)^2 \qquad (11)$$
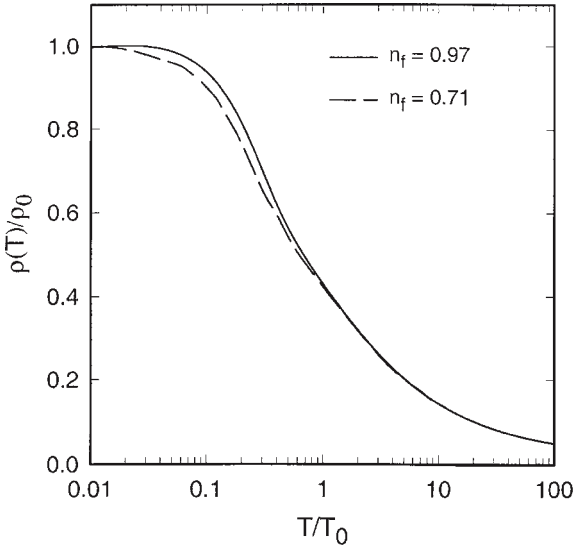
Figure 1
Temperature variation of the scaled resistivity $\rho(T)/\rho_0$ calculated in the scope of the noncrossing approximation for various values of n_f.

where $n = 2$ represents the ordinary Kondo effect. A model calculation for ρ_{imp} over the full temperature range requires knowledge of the density of states over the low frequency range at all temperatures (Hewson 1993). By applying the noncrossing approximation (NCA) to the Anderson model (Bickers *et al.* 1987), resistivity results were derived for $N = 6$ ($N = 2j + 1$). Results are shown in Fig. 1 for various values of the f occupation number n_f.

The NCA data exhibit an almost universal behavior over a significant temperature range when plotted as a function of T/T_0, where $T_0 = wT_K$. w is Wilson number (Hewson 1993) and T_0 can be associated with the position of the Kondo resonance with respect to the Fermi energy. Good overall agreement is found from this model with experimental data of, for example, cerium diluted in LaB_6 or Fe**Cu** (Schlottmann and Sacramento 1993). The resistivity is roughly logarithmic in T near T_0; at low temperatures $\rho(T)$ saturates quadratically, in agreement with the Fermi-liquid theory (Eqn. (11)). Based on an approximation scheme (Fulde *et al.* 1993), a simple analytical expression is available for the transport coefficients, applicable over an extended temperature range.

For $N = 2$, corresponding to $j = 1/2$ or to a doublet as ground state, the NCA calculations can no longer be used. Instead, Costi and Hewson (Hewson 1993) adopted the numerical renormalization group method to account for the temperature dependence of the dynamic response function, which allows derivation of appropriate results for the resistivity, at least in the crossover regime.

(b)   Kondo impurity versus concentrated Kondo systems

The above-outlined features primarily trace the temperature dependence of the electrical resistivity of impurity systems, that is, alloys where a statistically small amount of $3d$, $4f$ or $5f$ elements are dissolved in a nonmagnetic host such as gold, silver or copper. Since in such a case the d or f wave-functions do not overlap, the system will not order magnetically. In f systems, however, it is possible to increase the number of magnetic impurities up to a level where, for example, cerium, ytterbium, or uranium build up a fully ordered sublattice in the compound without losing those appearances associated with the Kondo effect. Basically, two features make a lattice different from an impurity system: (i) intersite interactions between the magnetic moments on the various lattice sites may no longer be negligible, and (ii) coherent scattering of the conduction electrons with the periodically arranged $4f$ and $5f$ magnetic moments is responsible for dramatic change of $\rho(T)$ on lowering the temperature.

The definition of coherence corresponds simply to Bloch's theorem: at zero temperature and excitation energy, inelastic scattering is frozen out so that translational invariance of a perfect sublattice of the magnetic ions requires zero resistance (Cox and Grewe 1988). This coherent ground state of the 10^{23} particles is most likely caused from the development of antiferromagnetic correlations, as is proven from neutron inelastic scattering, nuclear magnetic resonance, and muon-spin relaxation (Thompson and Lawrence 1994). While in the impurity case the resistivity grows continuously, reaching the unitarity limit for $T \rightarrow 0$ (associated with a phase shift $\eta = \pi/2$), coherence causes for a lattice of Kondo scatterers a substantial decrease of $\rho(T)$ upon a temperature decrease and the occurrence of a maximum at $T \approx T_0 \propto T_K$. In the low temperature limit, the frequently observed power law $\rho = \rho_0 + AT^2$ evidences electron-electron scattering in a FL state with $A \propto N(E_F)^2$.

Cox and Grewe (1988) calculated the temperature-dependent resistivity for both circumstances by applying the self-consistent NCA (Bickers *et al.* 1987) to the periodic Anderson lattice, where they explicitly included coherence, but intersite interactions are neglected. Results are shown in Fig. 2, matching the expected features almost perfectly. If intersite interactions of the RKKY type gain weight with respect to the Kondo interaction, the system is able to order magnetically below a certain transition temperature T_{mag}. Both the magnitude of the ordered moments as well as T_{mag}, however, can significantly be reduced when compared to a system without the Kondo effect. Such a transition into a magnetically ordered ground state will modify the low-temperature behavior of transport coefficients.
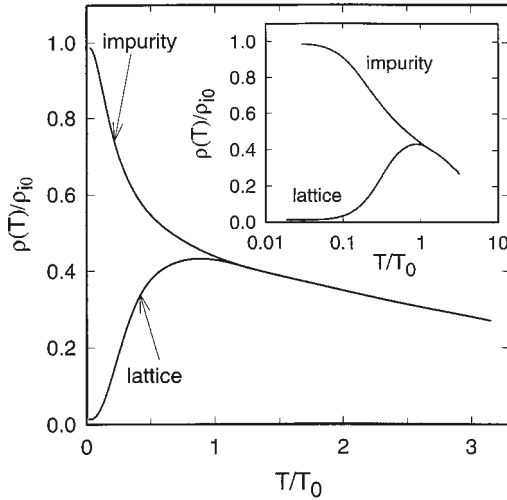
Figure 2
Normalized resistivity $\rho(T)/\rho_{i0}$ of the six-fold degenerate Anderson lattice calculated in the scope of the noncrossing approximation. For comparison, the full temperature dependence of the impurity resistivity is shown. ρ_{i0} is the zero temperature resistivity per ion in the dilute limit.

(c) Fermi- and non-Fermi-liquids
Although a large number of Kondo systems at low temperature may be accounted for in terms of the FL model, an increasing number of alloys and compounds are already known, showing striking deviations from the simple temperature dependencies of an FL (see *Non-Fermi Liquid Behavior: Quantum Phase Transitions*). This new class of materials was termed non-Fermi-liquid (NFL). In most cases, NFLs are characterized by a transition into an anti-ferromagnetically ordered ground state at $T = 0$, which behaves as a quantum critical point (QCP). Different scenarios were proposed to account for the NFL behavior near to a QCP (Rosch 2000). Among them are: (i) scattering of FL quasiparticles by strong spin fluctuations near the spin-density-wave instability, (ii) breakdown of the Kondo effect, owing to competition with the RKKY inter-action, and (iii) the formation of magnetic regions, owing to rare configurations (Griffith phase) of the disorder.

With respect to transport properties, the self-con-sistent renormalization theory (SCR) of spin fluctu-ations (Hatatani and Moriya 1995) was successfully applied for ferromagnetic and antiferromagnetic heavy fermion systems around their magnetic insta-bility. Depending on the nature of the interaction and its dimensionality, the calculated resistivity clearly deviates from the FL prediction $\rho \sim T^2$. Some of the results are listed in Table 1.

Table 1
Critical behavior of the electrical resistivity just at the magnetic instability of two- and three-dimensional ferro- and antiferromagnets.

	Two-dimensional	Three-dimensional
Ferromagnetic spin fluctuations	$\rho(T) \sim T^{4/3}$	$\rho(T) \sim T^{5/3}$
Antiferromag-netic spin fluctuations	$\rho(T) \sim T$	$\rho(T) \sim T^{3/2}$

(d) Magnetoresistivity
The application of a magnetic field to Kondo systems influences details of the DOS in the proximity of the Fermi energy. Hence, properties depending on the DOS are modified. The effect of a magnetic field on the electrical resistivity is described by $\rho(B)/\rho(0)$, where $\rho(B)$ and $\rho(0)$ are the field and zero-field resistivities, respectively.

At $T = 0$, the magnetoresistance can be derived from the Friedel sum rule. In the scope of the Coqblin–Schrieffer model (Coqblin and Schrieffer 1969) with N-fold degenerate total angular momen-tum states, the Friedel sum rule yields:

$$\frac{\rho_{imp}(B)}{\rho_{imp}(0)} = \left[\frac{\sin^2(\pi/N)}{N} \sum_m \frac{1}{\sin^2(\pi n_m(B))} \right]^{-1} \quad (12)$$

where n_m is the occupation number of the $N = 2j + 1$ channels derived from Zeeman splitting. The occupa-tion numbers can be calculated using the Bethe ansatz solution (Schlottmann and Sacramento 1989). Results of model calculations are shown in Fig. 3 for j-values ranging from 1/2 to 5/2. The single impurity nature is reflected from the scaling behavior of this quantity.

For large magnetic fields the magnetoresistivity shows Kondo logarithms, which are characteristics of asymptotic freedom and $\rho_{imp}(B)$ falls off as $\ln^{-2}(B/T_K)$. There are some qualitative differences of the magnetoresistivity results for the different total an-gular momenta, since for $j = 1/2$ the Kondo peak is on-resonance with the Fermi level but is above the Fermi level for all other values of j. A magnetic field causes, then, a decrease of the impurity density of states for $j = 1/2$ but an increase for $j \geqslant 3/2$.

For $N = 2$, the magnetoresistance can also be expressed in terms of the impurity magnetization (Hewson 1993):

$$\rho_{imp}(B) = \rho_{imp}(0) \cos^2\left(\frac{\pi M_{imp}}{g\mu_B} \right) \quad (13)$$

where M_{imp} is the magnetization and g is the Landé factor.
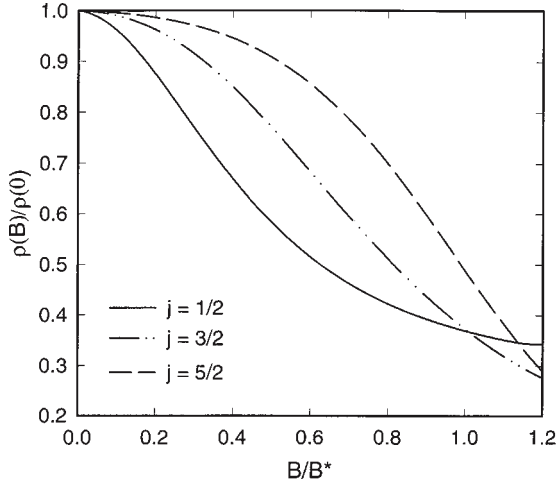
Figure 3
Magnetoresistance $\rho(B)/\rho(0)$ versus B/B^* for the $j=1/2$ to $j=5/2$ Coqblin-Schrieffer model. B is the magnetic field and B^* is the characteristic field, closely related to T_K.

Figure 4
Temperature-dependent behavior of (a) the spin-disorder resistivity R_s, (b) the total resistivity ρ and (c) the relative Kondo perturbation. The relevant parameters are: cubic symmetry, $\Delta = 100\,K$, $D = 400\,K$, $J = -0.095\,eV$, $V = 0.07\,eV$, $\bar{V} = 0.05\,eV$, $N(E_F) = 0.5$ states/eV, $\alpha_1 = 2$ and $\alpha_2 = 4$.

(e) Crystal field effects

In 4f systems based on cerium or ytterbium, crystal field (CF) effects can no longer be neglected. The thermal population of the various CF levels with increasing temperature changes most of the physical properties, and moreover, the Kondo effect itself changes.

In the scope of a third-order perturbation-type calculation in $JN(E_F)$, Cornut and Coqblin (1972) derived the cumulative effect of Kondo interaction in the presence of crystal field splitting. Results of their calculations have been applied to numerous compounds such as CeAl$_2$ or CeAl$_3$. The relaxation time τ_k for the above model is obtained as

$$\frac{1}{\tau_k} = \frac{mkV_0 c_{imp}}{\pi \hbar^3 (2j+1)} (R_k + S_k) \qquad (14)$$

where k is the wave vector and V_0 the sample volume. R_K describes second-order terms (direct scattering from the initial to the final state) and is proportional to J^2, while S_K accounts for third-order terms (spin-flip processes) which are proportional to J^3. Direct and resonant (Kondo) scattering yield the following magnetic contribution to the electrical resistivity:

$$\rho_{mag}(T) = AN(E_F) \left[\bar{V}^2 + \frac{\lambda_n^2 - 1}{\lambda_n(2j+1)} J^2 \right]$$
$$+ AN(E_F) \left[J^3 N(E_F) \frac{\lambda_n^2 - 1}{2j+1} \ln\left(\frac{k_B T}{D_n}\right) \right] \quad (15)$$

Here, A is a constant, V is the direct interaction strength, and D_n is a cut-off parameter. $\lambda_n = \sum_{i=0}^{n} \alpha_i$, where α_i is the degeneracy of the ith CF level with energy Δ_i. The second term describes the usual spin disorder resistivity (second-order perturbation theory). The temperature dependence of this contribution results from the thermal population of the various CF levels. The third term is the Kondo resistivity. The resistivity according to Eqn. (15) is plotted in Fig. 4 for a typical set of parameters which roughly accounts for the case of CeAl$_2$.

1.3 Thermal Conductivity

In metallic systems, the thermal conductivity λ consists of a lattice contribution λ_l and of an electronic contribution λ_e, i.e., $\lambda = \lambda_l + \lambda_e$. According to Matthiessens's rule, the thermal resistivity $W_{l(e)} \equiv 1/\lambda_{l(e)}$ is given by a sum resulting from different scattering events, like electron–phonon scattering or scattering of electrons or phonons on static imperfections. Thus, $W_{l(e)} = \Sigma_i W_{l(e), i}$. The temperature dependence of λ follows from Eqn. (4), using the appropriate relaxation time. Thermal conductivity limited by magnetic scattering processes in the presence of CF splitting is then derived from Eqn. (14) as (Bhattacharjee and Coqblin 1988)

$$\lambda_{e,mag}(T) = \frac{(2j+1)\hbar^3 k_F^2}{3\pi m^2 v_0 c} \frac{1}{T} (W_2 - W_3) \qquad (16)$$

with

$$W_2 = \int \varepsilon_k^2 \left(-\frac{df_k}{d\varepsilon_k} \right) \frac{d\varepsilon_k}{R_K} \tag{17}$$

and

$$W_3 = \int \varepsilon_k^2 \left(-\frac{df_k}{d\varepsilon_k} \right) \frac{S_K}{R_K^2} \, d\varepsilon_k \tag{18}$$

$\lambda_{e,mag}(T)$ is plotted in Fig. 5 for a set of typical parameters. It is interesting to note that there are no typical features evidencing Kondo interaction; however, CF effects seem to be of importance.

Experimental data, however, clearly indicates Kondo interaction in the presence of crystal field splitting, when plotted as $W_{e,mag}T$ where $W_{e,mag} = 1/\lambda_{e,mag}$. Figure 6 shows $W_{e,mag}T$ of CeAl$_2$ displayed on a logarithmic temperature scale. For purpose of comparison, $\rho_{mag}(T)$ of CeAl$_2$ is added, also. Such a representation of the data exhibits negative logarithmic ranges and a maximum, very similar to that of $\rho_{mag}(T)$. This particular behavior can theoretically be accounted for by (Bauer *et al.* 1993a)

$$W_{e,mag}T = \frac{R}{L_0} \left[\bar{V}^2 + \frac{(\lambda^2 - 1)}{(2j+1)\lambda} J^2 \right]$$
$$+ 2 \frac{R}{L_0} N(E_F) J^3 \frac{(\lambda^2 - 1)}{2j+1} \ln\left(\frac{k_B T}{D} \right) \tag{19}$$

0.3

——	1
----	2
-- --	3
-·-	4

0.2

$\lambda_{e,mag}$ [W/cmK]

0.1

0.0

0   50   100   150   200

T [K]
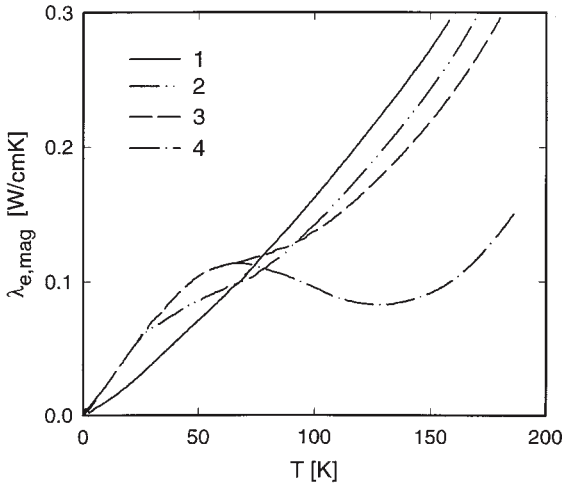
Figure 5
Temperature-dependent thermal conductivity λ_{mag} caused by spin-dependent scattering according to Eqn. (16): (1) cubic field with Γ_8 as ground state and $\Delta = 200$ K; (2) hexagonal field with three equidistant doublets at 0, 100 and 200 K; (3) cubic field with Γ_7 as ground state and $\Delta = 200$ K. (4) hexagonal field with three doublets at 0, 200 and 400 K. Additional parameters are $D = 850$ K, $V = 700$ K, $J = -0.1$ eV, $\bar{V} = -0.25$ eV, $N(E_F) = 2$ states/eV.
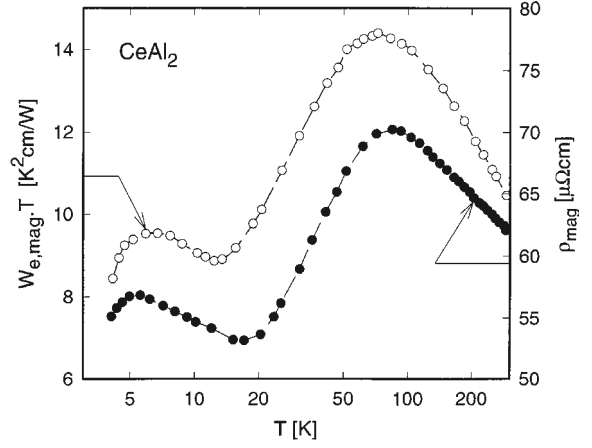
Figure 6
Left axis: temperature-dependent magnetic contribution to the thermal resistivity of CeAl$_2$, plotted as $W_{e,mag}T$ versus $\ln T$. Right axis: temperature-dependent magnetic contribution to the electrical resistivity ρ_{mag} of CeAl$_2$. LaAl$_2$ was used in both cases to define the electron–phonon interaction.

where $R = (3m\pi v_0 c)/(e^2 h k_F^2)$, and $L_0 = (\pi^2 k_B^2)/(3e^2)$ is the Sommerfeld value of the Lorenz number.

Equation (19) allows various conclusions to be drawn. (i) There are negative logarithmic ranges for $W_{e,mag}T$ at temperatures $T \gg \Delta_i/k_B$ and $T \ll \Delta_i/k_B$. (ii) $W_{e,mag}T$ shows maxima in the vicinity of each crystal field level if they are well separated. (iii) The ratio of the logarithmic slopes of $W_{e,mag}T$ reflects the degeneracy of the crystal field levels involved.

1.4 Thermopower

The temperature-dependent thermopower $S(T)$ can be evaluated from

$$S = -\frac{K_1}{|e|TK_0} = -\frac{1}{eT} \left[\frac{\int_{-\infty}^{+\infty} \varepsilon_k \tau_k \left(-\frac{df_k}{d\varepsilon} \right) d\varepsilon_k}{\int_{-\infty}^{+\infty} \tau_k \left(-\frac{df_k}{d\varepsilon} \right) d\varepsilon_k} \right] \tag{20}$$

Owing to strong energy-dependent scattering processes, the Kondo effect sensitively influences the overall shape of $S(T)$, which is calculated from:

$$S = \frac{1}{eT} \frac{1}{\sigma^{(2)}} \int_{-\infty}^{+\infty} \frac{S_k}{R_k^2} \left(-\frac{df_k}{d\varepsilon_k} \right) d\varepsilon_k \tag{21}$$

with $e > 0$ (Bhattacharjee and Coqblin 1976). R_k and S_k are again contributions from the second and third order perturbation type calculations; $\sigma^{(2)}$ is a
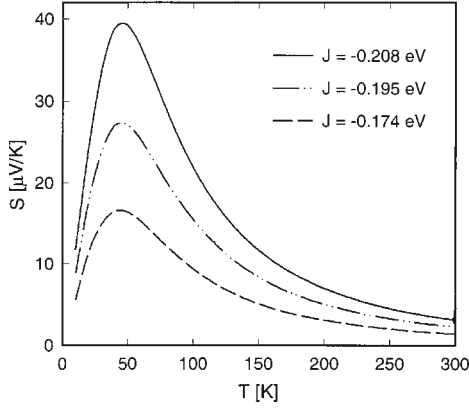
Figure 7
Temperature-dependent thermopower for a three-level system according to Eqn. (21) for various values of the exchange constant J. The following parameters are used: $\Delta_1 = 87\,\text{K}$, $\Delta_2 = 210\,\text{K}$, $D = 850\,\text{K}$, $\bar{V} = -1.5\,\text{eV}$, $N(E_F) = 2.2$ states/eV, $\alpha_1 = \alpha_2 = \alpha_3 = 2$.

characteristic function:

$$\sigma^{(2)} = \int_{-\infty}^{+\infty} \frac{1}{R_k^2}\left(-\frac{\mathrm{d}f_k}{\mathrm{d}\varepsilon_k}\right)\mathrm{d}\varepsilon_k \qquad (22)$$

In the absence of CF splitting, Kondo scattering is responsible for unusually large thermopower values ($\approx 100\ \mu\text{VK}^{-1}$) with a maximum in the vicinity of $T \approx T_K$. In real compounds and alloys, CF effects cause a modification of that universal behavior. The maximum in $S(T)$ is then no longer at $T \approx T_K$, rather, a renormalization of $T_S^{\max}$ takes place with $T_S^{\max} \approx (1/3 - 1/6)\Delta_{\text{CF}}$, where Δ_{CF} is the overall crystal field splitting of the system. Results derived from Eqn. (21) are shown in Fig. 7.

2. Temperature-, Pressure-, and Field-dependent Transport Coefficients of Kondo and Heavy Fermion Systems

In order to demonstrate the various interaction mechanisms which generally occur in Kondo and heavy fermion systems, as well as their mutual interplay, the temperature-dependent resistivity of YbCu$_4$M, with M = Ag, Au and Pd, is shown in Fig. 8 (Bauer *et al.* 1993b, 1994). The compounds are isoelectronic and isostructural and crystallize in an ordered variant of the cubic AuBe$_5$ structure. Different dominating interaction mechanisms cause distinct features for each particular compound.

2.1 YbCu$_4$Ag

This crystallographic fully ordered ternary compound represents a typical Kondo lattice. At high

Figure 8
Temperature-dependent resistivity ρ of YbCu$_4$M with M = Au, Ag, Pd.

temperatures, the negative logarithmic contribution to the total electrical resistivity leads to single impurity Kondo interaction of the conduction electrons with the almost localized Yb-4f moments. At low temperatures, however, the ordered ytterbium sublattice allows a Bloch-like motion of the conduction electrons, and consequently the resistivity falls. Both regimes are separated by a smooth maximum near 100 K with $T_\rho^{\max} \propto T_K$ (Cox and Grewe 1988). Therefore, YbCu$_4$Ag represents a Kondo lattice with a relatively high Kondo temperature.

This provokes a couple of important consequences for physical properties: because T_K of YbCu$_4$Ag is large, the associated hybridization prevents pronounced CF effects and the eight-fold degenerate state of the Yb ion ($j = 7/2$) dominates the whole temperature range. Moreover, as $T_K \gg T_{\text{RKKY}}$, long-range magnetic order is unlikely and the system remains paramagnetic down to the mK range. Below 10 K the T^2 behavior of $\rho(T)$ refers to a FL behavior and the large coefficient $A = 8\ \text{n}\Omega\,\text{cm/K}^2$ (Bauer *et al.* 1993b) results from interactions with the heavy quasiparticle bands. The overall $\rho(T)$ behavior matches almost perfectly the theoretical predictions of Cox and Grewe (1988).

2.2 YbCu$_4$Au

Although YbCu$_4$Au is isoelectronic with YbCu$_4$Ag, the ground state properties behave significantly differently. While the latter is nonmagnetic, the former orders antiferromagnetically below $T_N \approx 0.6\,\text{K}$ (see inset, Fig. 8) with a wave vector $\vec{k} = [0.553, 0.415, 0.303]$ and an ordered moment $\mu = 0.85\ \mu_B/\text{Yb}$ (Bauer *et al.* 1997). A comparison with YbCu$_4$Ag shows that primarily the low value of the Kondo temperature

$(T_K \approx 2\,\text{K})$ is responsible for the appearance of long range magnetic order as $T_{RKKY} \approx T_K$. Additionally, since $T_K \ll \Delta_{CF}$ the eight-fold degenerate ground state is lifted into a doublet, a quartet at about 40 K above and as the uppermost level, a doublet centered at about 80 K (Severing *et al.* 1990).

Owing to these well-separated crystal field levels, Kondo interaction is observed from negative logarithmic resistivity contributions in the various temperature ranges. These ranges are disjoined by a pronounced maximum, thus precisely coinciding with the predictions of Cornut and Coqblin (1972). In the low temperature range the resistivity increase marks Kondo scattering in the CF ground state followed by the development of coherence below 1 K. On further temperature decrease, magnetic ordering occurs below 0.6 K, observed by a distinct change of $d\rho/dT$.

2.3 YbCu₄Pd

Different from YbCu₄Au, YbCu₄Pd orders ferromagnetically below $T_C \approx 0.8\,\text{K}$ with an ordered moment $\mu_{ord} = 0.4\mu_B/\text{Yb}$ (Bauer *et al.* 1997). The $\rho(T)$ of YbCu₄Pd shows a minimum around 50 K and above 100 K $\rho(T)$ is simply described by a linear dependence up to 300 K. The upturn in $\rho(T)$ below 15 K is well accounted for by the Kondo $-\ln T$ term together with an appropriate phonon contribution. A maximum is reached at 0.8 K and the resistivity drop below this can partly be attributed to the onset of long-range magnetic order. Distinct features of crystal field splitting are not obvious from this data. Such a peculiarity is also derived from neutron inelastic scattering where clear inelastic excitations are observed for YbCu₄Au, while the INS data of YbCu₄Pd do not exhibit typical features of CF excitations (Severing *et al.* 1990).

To trace in some detail the pressure response of Kondo compounds, two typical members are selected: CeCu₆ and YbCu₄Ag. The behavior of the latter has already been discussed for ambient pressure values. CeCu₆ also stays paramagnetic down to the mK range. The electrical resistivity is displayed in Fig. 9 for various values of applied pressure (Kagayama and Oomi 1993). At ambient pressure, CeCu₆ exhibits the well-known behavior of a Kondo lattice, i.e., at high temperatures ($T > 50\,\text{K}$), $\rho(T)$ shows a logarithmic contribution from independently acting Kondo scatterers, followed by a maximum at $\approx 12\,\text{K}$ with $T_\rho^{max} \propto T_K$. Well below this maximum, CeCu₆ enters its coherent ground state, reflected from a T^2 behavior in $\rho(T) = \rho_0 + AT^2$ where the huge coefficient $A \approx 110\,\mu\Omega\,\text{cm}\,\text{K}^{-2}$ results from the significantly enhanced quasi-particle density of states at the Fermi energy.

Increasing values of pressure cause different responses. (i) T_ρ^{max} substantially grows, thus reflecting an increase of T_K which is derived from a growing
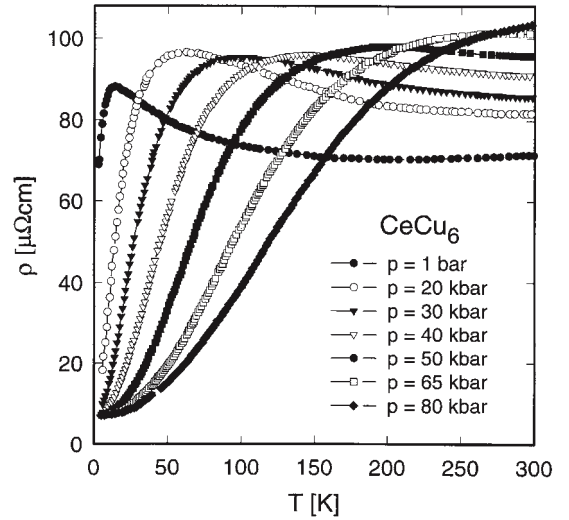
Figure 9
Temperature- and pressure-dependent resistivity ρ of CeCu₆.
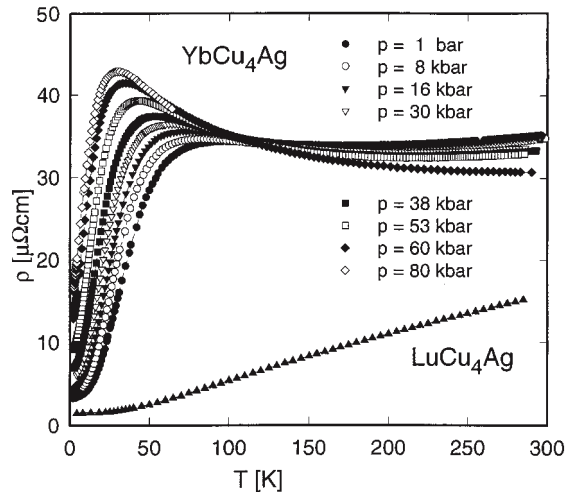
Figure 10
Temperature- and pressure-dependent resistivity ρ of YbCu₄Ag.

hybridization of the almost localized $4f$ electrons with the delocalized conduction electrons. (ii) The coefficient A decreases, which is associated with a decrease of the density of states at $E = E_F$. The overall effect of pressure on cerium systems basically is the destabilization of the magnetic $4f^1$ state, since the cerium $4f^1$ electron becomes progressively squeezed out of the $4f$ shell.

An opposite "mirror-like" behavior is found for YbCu₄Ag (Fig. 10), representing a typical Yb-based

Kondo lattice: pressure causes both a decrease of T_ρ^{max} and a significant increase of A. Now, the former indicates a lowering of T_K and the latter reflects a growing DOS at the Fermi energy. The total effect of pressure applied to ytterbium systems is therefore a reduction of the hybridization and a stabilization of the ytterbium magnetic moments.

Basically, this "mirror-like" behavior can be understood from an electron-hole analogy of the electronic configurations (EC) of cerium and ytterbium, where the magnetic and the nonmagnetic states depend on the respective volumes. In the case of cerium, the magnetic state $4f^1$ gives rise to the larger volume. Pressure applied to cerium ions will reduce the atomic volume by squeezing out the $4f^1$ electron. Hence, the nonmagnetic small-volume EC $4f^0$ is progressively attained. In the case of ytterbium, the EC with the larger volume is the nonmagnetic $4f^{14}$. Again, pressure will reduce the available volume by squeezing out one electron, which is synonymous with the creation of a hole in the f-shell as the small-volume magnetic $4f^{13}$ state is approached.

Magnetic fields applied to systems dominated by the Kondo effect, long-range magnetic order and crystal field splitting can dramatically modify the ground-state properties. This is owing to a possible suppression of Kondo interactions by magnetic fields, a suppression of long-range magnetic order in the case of antiferromagnetism, the quenching of spin fluctuations, or the complete removal of the degeneracy of the CF split levels.

Such a pronounced effect of a magnetic field is obtained in the case of ternary $YbRh_2Si_2$, which crystallizes in the tetragonal $ThCr_2Si_2$ type of structure. Magnetic order is absent down to a few hundred mK (Trovarelli *et al.* 2000). At ambient pressure and at zero field, $\rho(T)$ shows typical Kondo lattice properties and T_ρ^{max} decreases with growing pressure (Fig. 11). However, a T^2 behavior is not resolved for $T \to 0$, which would characterize a FL. Rather, in a range up to 10 K, the resistivity is accounted for by $\rho(T) = \rho_0 + BT^n$ with $n \approx 1$ (Trovarelli *et al.* 2000). Such an exponent may point out a NFL, originating from two-dimensional antiferromagnetic spin fluctuations above the QCP (Hatatani and Moriya 1995). Two-dimensionality seems to be possible in this compound owing to the peculiarities of the $ThCr_2Si_2$ crystal structure. Magnetic fields can suppress such fluctuations and as a result, a FL is recovered with $\rho \propto T^2$, which, in fact, is found for $YbRh_2Si_2$ for $H > 6T$ (inset, Fig. 11).

Figure 11
Temperature-, pressure- and field-dependent resistivity ρ of $YbRh_2Si_2$.

simple metals. The most well-known is a $-\ln T$ contribution to the electrical resistivity, found both in theory and in experiment.

Depending on a single impurity or a lattice scenario, the conduction electrons are scattered incoherently or coherently at low temperatures, respectively. In the former case the resistivity increases on a reduction of the temperature, eventually reaching the unitarity limit for $T \to 0$. In the latter case a decrease of the resistivity is observed for $T \to 0$ owing to the lattice periodicity of the magnetic ions, which serve as Kondo scatterers.

The particular temperature dependence of transport coefficients is significantly modified if RKKY interactions or CF effects are of equal or larger strength compared with the Kondo scale. A number of control parameters such as appropriate substitution, hydrostatic pressure or magnetic fields are able to tune the most important mutual interactions present in such systems; thus, substantial changes of the ground state properties may become evident.

See also: Boltzmann Equation and Scattering Mechanisms; Heavy-fermion Systems; Intermediate Valence Systems; Rare Earth Intermetallics: Thermopower of Cerium, Samarium and Europium Compounds

3. Summary

The narrow many-body resonance in the proximity of the Fermi energy of Kondo and heavy fermion systems causes significant changes in temperature-dependent transport coefficients when compared with

Bibliography

Anderson P W 1961 Localized magnetic states in metals. *Phys. Rev.* **124** (1), 41–52

Bauer E, Fischer P, Marabelli F, Ellerby M, McEwen K A, Roessli-B, Fernandes-Dias M T 1997 Magnetic structures

and bulk magnetic properties of $YbCu_4M$, $M = Au$, Pd. *Physica B* **234–236**, 676–8

Bauer E, Gratz E, Hauser R, Galatanu A, Kottar A, Michor H, Perthold W, Kagayama T, Oomi G, Ichimiaya N, Endo S 1994 Pressure- and field-dependent behavior of $YbCu_4Au$. *Phys. Rev. B* **50** (13), 9300

Bauer E, Gratz E, Hutflesz G, Bhattacharjee A K, Coqblin B 1993a Thermal conductivity of Ce-based Kondo compounds. *J. Magn. Magn. Mater.* **108** (1), 159–60

Bauer E, Hauser R, Gratz E, Payer K, Oomi G, Kagayama T 1993b Pressure dependence of the electrical resistivity of $YbCu_4Ag$. *Phys. Rev. B* **48** (21), 15873

Bickers N E, Cox D L, Wilkins J W 1987 Self-consistent large-N expansion for normal-state properties of dilute magnetic alloys. *Phys. Rev. B* **36** (4), 2036–79

Bhattacharjee A K, Coqblin B 1976 Thermoelectric power of compounds with cerium: influence of the crystalline field on the Kondo effect. *Phys. Rev. B* **13** (8), 3441–51

Bhattacharjee A K, Coqblin B 1988 Thermal conductivity of cerium compounds. *Phys. Rev. B* **38** (1), 338–44

Coqblin B, Schrieffer J R 1969 Exchange interaction in alloys with cerium impurities. *Phys. Rev.* **185** (2), 847–53

Cornut B, Coqblin B 1972 Influence of the crystalline field on the Kondo effect of alloys and compounds with cerium impurities. *Phys. Rev. B* **5** (11), 4541–61

Cox D L, Grewe N 1988 Transport properties of the Anderson lattice. *Z. Phys. B–Condensed Matter* **71**, 321–40

Fulde P, Pulst U, Zwicknagl G 1993 Quasiparticles in heavy fermion systems below and above the coherence temperature. In: Oomi G, Fujii H, Fujita T (eds.) 1993 *Transport and Thermal Properties of f-Electron Systems*. Plenum Press, New York, pp. 227–35

Hatatani M, Moriya T 1995 Ferromagnetic spin fluctuations in two-dimensional metals. *J. Phys. Soc. Japan* **64** (9), 3434–41

Hewson A C 1993 The Kondo problem to heavy fermions. Cambridge Studies in Magnetism. Cambridge University Press, Cambridge, Vol. 2

Kagayama T, Oomi G 1993 Collapse of the heavy fermion state under high pressure. In: Oomi G, Fujii H, Fujita T (eds.) *Transport and Thermal Properties of f-Electron Systems*. Plenum Press, New York, pp. 155–64

Kondo J 1964 Resistance minimum in dilute magnetic alloys. *Prog. Theor. Phys.* **32** (1), 37–49

Rosch A 2000 Disorder effects on transport near AFM quantum phase transitions. Physica B, **280**, 341–6

Schlottmann P 1989 Some exact results for dilute mixed-valent and heavy-fermion systems. *Phys. Rep.* **181** (1/2), 1–119

Schlottmann P, Sacramento P D 1993 Multichannel Kondo problem and some applications. *Adv. Phys.* **42** (6), 641–82

Severing A, Murani A P, Thompson J D, Fisk Z, Loong C K 1990 Neutron scattering experiments on $YbXCu_4$ and $ErXCu_4$ (X = Au, Pd, and Ag). *Phys. Rev. B* **41** (4), 1739–49

Thompson J D, Lawrence J M 1994 High pressure studies–physical properties of anomalous Ce, Yb and U compounds. In: Gschneidner K A Jr., Eyring L, Lander G H, Choppin G R (eds.) Elsevier Science, Amsterdam, pp. 383–478

Trovarelli O, Geibel C, Steglich F 2000 Low temperature properties of $YbRh_2Si_2$. *Physica B* **284–288**, 1507–8

Ziman J M 1964 *Principles of the Theory of Solids*. Cambridge University Press, London

E. Bauer
Institut für Experimentalphysik, Wien, Austria

L

Localized 4*f* and 5*f* Moments: Magnetism

An atom (ion) in a solid has a net magnetic moment in cases when an inner *d* or *f* electron shell is incomplete so that the individual electronic moments do not cancel completely. In the periodic table, there are five groups of elements in which this incomplete cancellation occurs: the iron group (3*d*), the palladium group (4*d*), the rare earth (or lanthanide) group (4*f*), the platinum group (5*d*), and the actinide group (5*f*). Note that the 4*d* and 5*d* shells are rather delocalized and their contribution to magnetism is in general very weak. This article focuses on the 4*f* and 5*f* groups. The magnetism of systems containing both 4*f* and 3*d* elements is treated elsewhere (see *Alloys of 4f (R) and 3d (T) Elements: Magnetism*; *Transition Metal Oxides: Magnetism*).

A magnetic rare earth (RE) or actinide (An) ion when placed in a solid is subject to numerous forces, absent in free ions, which in general significantly influence the magnetic properties of a given system. Leaving aside the cases of fluctuating valence (see *Intermediate Valence Systems*) and heavy fermion 4*f* and 5*f* electron systems (see *Electron Systems: Strong Correlations*; *Heavy-fermion Systems*), these forces represent merely a perturbation of the free-ion *f* shell state and the ionic magnetic moment can be considered as well localized.

Two of these perturbations which are particularly important are treated in this article. One is an interaction of the incomplete *f*-shell electrons with the crystal field (CF) produced by the neighboring core charges and valence electronic charge density. The other is the magnetic coupling with neighboring ionic moments which can result in cooperative effects. The magnetic behavior of *f*-electron systems is described using microscopic Hamiltonians reflecting general symmetry properties of the system under consideration. Parameters of these Hamiltonians are either determined from experiment or calculated using various theoretical models. This article mainly focuses on trivalent *f* ions. This oxidation state strongly dominates in the rare earth elements. However, a multiplicity of oxidation states is displayed by many actinides (Wybourne 1965, Fournier 1985).

1. Free Ion Interactions

The starting point for understanding of the magnetism of RE and An compounds is the quantum mechanical description of an unperturbed many-electron ion. Assuming that the nucleus of an ion is at rest, the generic nonrelativistic Hamiltonian can be taken as:

$$H = -\frac{\hbar^2}{2m}\sum_{i=1}\nabla_i^2 - Ze^2\sum_{i=1}\frac{1}{r_i} + e^2\sum_{j>i=1}\frac{1}{|\mathbf{r}_i - \mathbf{r}_j|} \quad (1)$$

where Ze is the nuclear charge and summations are over the coordinates of all the electrons. Individual terms describe the kinetic energy of electrons, the Coulomb potential due to the nuclear attraction, and the Coulomb repulsion between the pairs of electrons. No exact solution for the Schrödinger equation of the Hamiltonian of Eqn. (1) is known for a system containing more than one electron.

Fortunately the electrons occupying closed shells can be separated and the corresponding electronic structure can be described (Cai *et al.* 1992, Eliav *et al.* 1995).

The electrons from the outer 6*s*5*d* shell in RE atoms (7*s*6*d* shell in An atoms) participate in the chemical bonding. It follows from *ab initio* calculations that the asphericity in the charge density of these electrons influences significantly the CF splitting of the *f*-electron states (see below). The standard description of the outer electron states is based on the effective one-electron Hamiltonian which contains kinetic and potential energies describing the interaction with the ionic cores and charge density of the remaining valence electrons involved in the bonding of condensed matter. The effective one-electron approach can be formulated using Hartree–Fock (HF) (Freeman and Watson 1962) or density functional theory (DFT) (see *Density Functional Theory: Magnetism*).

1.1 Central Field Approximation

The so-called central field approximation is commonly used to calculate the electronic structure of N electrons in an *f* shell, where each *f* electron is assumed to move independently in a spherically symmetric effective potential, $-U(r_i)/e$:

$$H_0 = -\sum_i^N \left[\frac{-\hbar^2}{2m}\nabla_i + U(r_i)\right] \quad (2)$$

The sum is over the electrons in the f^N shell, i.e., contributions involving electrons in closed shells are neglected. In the HF or DFT method the one-electron eigenfunctions of the Hamiltonian of Eqn. (2) are of the form:

$$\psi_{nlm_lm_s}(\mathbf{r},\sigma) = R_{nl}(r)Y_{lm_l}(\theta,\phi)\chi_{m_s} \quad (3)$$

where $R_{nl}(r)$ is the radial wave function $n = 4, 5$ is the principal quantum number, the quantum numbers
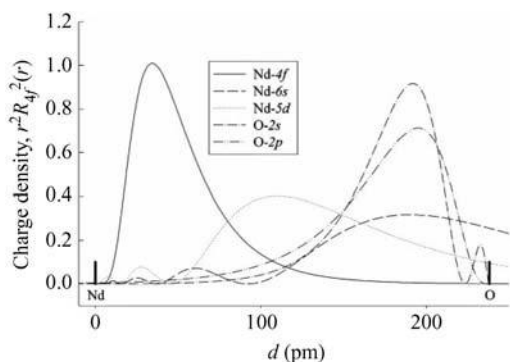
Figure 1
Radial $4f$, $6s$, and $5d$ charge density of the neodymium atom, and $2s$ and $2p$ density of the oxygen atom. The typical nearest-neighbor distance $d = 0.238$ nm in crystals was used for Nd–O pair.

$l = 3$ and m_l characterize the orbital angular momentum, χ_{m_s} is the one-electron spinor function, and m_s is the spin quantum number. The angular part of the one-electron eigenfunction can be written exactly using spherical harmonics as $Y_{lm_l}(\theta, \phi)$, while the radial part depends on the form of the potential $U(r)$ (Fig. 1). The quantum numbers n, l define an f-electron *configuration*, entirely degenerate within the central field approximation. For the nf^N configuration the degeneracies are given by the binomial coefficients $\binom{4l+2}{N}$ which are 1, 14, 91, 364, 1001, 2002, 3003, 3432 for $N = 0$–7. For the second half of the nf series, the degeneracies are the same as in the first half but in the opposite order.

The degeneracy of the nf^N configuration is lifted by interactions which cannot be accounted for in the central field approximation. The calculation of the matrix elements of the related Hamiltonians is facilitated by the defining of a complete set of many-electron basis states in some well-defined coupling scheme. In the frequently used Russell–Saunders (LS) coupling, the orbital angular momentums of the electrons are vectorially coupled to give a total orbital angular L and the spins are coupled to give a total spin S. These angular momentums are then coupled to give total angular momentum J. The numbers L and S are said to define a *term* (^{2S+1}L) of the configuration, J defines a *multiplet* ($^{2S+1}L_J$) of the term. Group-theoretical methods are used to classify terms having the same L and S values (Wybourne 1965). According to Hund's rules (see *Density Functional Theory: Magnetism*) the lowest energy term has, first, S with maximum value compatible with the Pauli principle and then L with maximum value compatible with the S value. The spin–orbit coupling (see Sect. 1.3) lifts the degeneracy of the ^{2S+1}L terms producing the $(2J+1)$-fold degenerate $^{2S+1}L_J$ multiplets. The lowest energy multiplet is such that $J = |L - S|$ if the nf

shell is less than half full and $J = L + S$ in the other case. For instance, in the f^2 configuration, the ^3H term splits into the $^3H_4$, $^3H_5$ and $^3H_6$ levels, where $^3H_4$ is the ground state.

1.2 Coulomb Interaction

The strongest perturbation, splitting the nf^N configuration into the terms, arises from the Coulomb repulsion between the f electrons, described by the third term in Eqn. (1). As a result of expanding this interaction in Legendre polynomials, the corresponding Hamiltonian, H_1, can be written as:

$$H_1 = \sum_i^3 E^i \mathbf{e}_i \qquad (4)$$

where $\mathbf{e}_i$ are operators that transform according to definite irreducible representations of the groups G_2 and R_7 (Racah 1949) and represent the angular part of the interaction. Matrix elements of the $\mathbf{e}_i$ operators have been tabulated for all states of the f^N configuration (Nielson and Koster 1963). E^i are linear combinations of Slater integrals $F^{(k)}$. In the case of f electrons ($l = 3$), only the integrals, $k = 2$, 4, and 6 need be considered.

Their definition is:

$$F^{(k)} = e^2 \int_0^\infty \int_0^\infty \frac{r_<^k}{r_>^{k+1}} R_{nl}^2(r_i) \, R_{nl}^2(r_j) r_i^2 r_j^2 \, dr_i dr_j \quad (5)$$

where $r_<$ and $r_>$ are, respectively, the lesser and greater of r_i and r_j. Estimates of Slater integrals can be obtained by *ab initio* calculations. Both nonrelativistic and relativistic HF calculations substantially overestimate their values (Freeman and Watson 1962, Freeman 1979). When $F^{(2)}$, $F^{(4)}$ and $F^{(6)}$ are treated as phenomenological parameters fitted to the observed energy levels, they are found to be some 30–40% below the *ab initio* estimates. This discrepancy is ascribed to a screening mechanism within the free ion. The screening is ascribed to an admixture of higher lying electronic configurations into the nf^N configuration causing the f electrons spend part of their time in more delocalized states, so effectively weakening their repulsion. Although the predominant screening mechanism is present in the free ion, there is an additional reduction of the values of the Slater integrals in ionic solids. The underlying mechanism is the hybridization of f-electron wave functions with the ligand orbitals. Even greater screening-induced reduction of $F^{(k)}$ is revealed in metallic systems (see *Density Functional Theory: Magnetism*).

1.3 Spin–Orbit Interaction

The free-ion Hamiltonian contains, besides the electrostatic interactions, magnetic interactions. Among

these, the spin–orbit interaction is by far the predominant interaction, given by:

$$H_2 = \sum_{i=1}^{N} \xi(r_i)(\mathbf{s}_i \cdot \mathbf{l}_i) \qquad (6)$$

where r_i is the radial coordinate, $\mathbf{s}_i$ the spin, and $\mathbf{l}_i$ the orbital angular momentum of the ith electron. Note that the spin–orbit interaction influences the nl radial charge density distribution and Eqn. (3) should be modified to satisfy the relativistic Dirac–Fock Hamiltonian (see *Density Functional Theory: Magnetism*). The spin–orbit parameter $\xi(r)$ is then given by:

$$\xi(r_i) = \frac{\hbar^2}{2m_e^2 c^2} \frac{1}{r_i} \frac{dU}{dr_i} \qquad (7)$$

The Hamiltonian of Eqn. (6) can be conveniently rewritten in the form appropriate for matrix elements between nf^N states as follows:

$$H_2 = 2\zeta_{nl}\sqrt{21} \cdot \sum_{\mu} (-1)V^{11}_{\mu,-\mu} \qquad (8)$$

where ζ_{nl} is the spin–orbit radial integral which is a constant for the states of a given configuration and is defined as (Condon and Shortley 1967):

$$\zeta_{nl} = \int_0^{\infty} R_{nl}^2 \xi(r) r^2 \, dr \qquad (9)$$

and $V^{(11)}$ is the unit double tensor (Wybourne 1965).

The matrix elements on the right-hand side of Eqn. (8) can be calculated using available formulas (Wybourne 1965) and tables (Nielson and Koster 1963).

Within the LS coupling scheme, the spin–orbit coupling can be represented by the simple formula:

$$H_2 = \lambda(\mathbf{L} \cdot \mathbf{S}) \qquad (10)$$

where λ is a constant for a given LS state. This equation leads to the *Landé interval rule* that causes separation between levels differing by unity in their J values:

$$E_J - E_{J-1} = \lambda J \qquad (11)$$

Departures from the Landé interval rule give a measure of the breakdown of Russell–Saunders coupling owing to the spin–orbit interaction (Wybourne 1965). As this interaction is large enough in RE and An compounds it is usual to perform an "intermediate coupling" calculation, where the perturbation matrix containing both Coulomb and spin–orbit interactions is diagonalized. The spin–orbit interaction mixes different ^{2S+1}L levels with the same J which means that L and S are no longer good quantum numbers. In some cases, it can be difficult to assign a meaningful $^{2S+1}L_J$ label to a particular level, since several terms

make nearly equal contributions (Dieke 1968). This is not a serious problem for the lowest lying multiplets of interest for magnetic properties, most of which have a dominant component from one ^{2S+1}L term.

There is a considerable increase in ζ_{nl} with increasing atomic number and ζ_{nl} is considerably greater in An ions than in the corresponding RE ions. Like the Coulomb interaction (see Sect. 1.2), the spin–orbit interaction ζ_{nl} is also overestimated in usual *ab initio* calculations, although the discrepancy is smaller, less than 10% (see *Density Functional Theory: Magnetism*). In comparison with the Coulomb interaction, the spin–orbit interaction is much less sensitive to the local environment.

The f^N configuration may have several hundred levels and is of the order of 10^5cm^{-1} (K) wide (Dieke 1968). When Eqns. (4) and (9), containing respectively three Slater integrals $F^{(k)}$ and spin–orbit parameter ζ_f are used, discrepancies of up to a few hundred cm^{-1} (K) remain between the calculated and experimental energy levels. A more complete free-ion Hamiltonian contains several additional interactions arising from the effect of configuration interactions and the couplings of the orbital and spin angular moments on different electrons (orbit–orbit, spin–spin, spin–other orbit). Such a Hamiltonian typically contains 19 parameters. As none of them can, in the majority of cases, be calculated theoretically with sufficient precision, they are usually determined along with the appropriate set of CF parameters (see Sect. 2) in a least-squares fitting to experimental energy spectra (Morrison and Leavitt 1982). Note that more sophisticated large-scale multiconfigurational Dirac–Fock (Cai *et al.* 1992) and coupled cluster methods (Eliav *et al.* 1995) allow one to calculate the multiplet energies of $4f^2(Pr^{3+})$ and $5f^2(U^{4+})$ configurations with very good accuracy.

In general, an understanding of the free-ion Hamiltonian is an important prerequisite for CF study (see Sect. 2).

2. Crystal Field Interactions

The $(2J+1)$-fold degenerate energy levels of $4f$ or $5f$ ions in a compound are split by the CF interaction. Its impact on the magnetic properties is important. It "quenches" the orbital contribution to ionic magnetic moments (see Sect. 3) and in combination with the spin–orbit coupling (see Sect. 1.3) it is the principal source of magnetic anisotropy, i.e., of the dependence of magnetic properties on direction in the compound (see *Alloys of 4f (R) and 3d (T) Elements: Magnetism* and *Transition Metal Oxides: Magnetism*). Further physical properties influenced by the CF interaction include the magnetoelastic properties (see *Magnetoelastic Phenomena*) (Häfner *et al.* 1981), specific heat (Luong and Franse 1995, Purwins and Leson 1990), and transport properties (Gratz and Zuckermann 1982).

2.1 Hamiltonian

The interaction Hamiltonian H_{CF} of f electrons with the CF potential can always be written in terms of one-electron irreducible tensor operators as:

$$
\begin{aligned}
H_{CF} &= \sum_{k,q,i} B_{kq}[c_q^{(k)}(i) + c_{-q}^{(k)}(i)] \\
&= \sum_{k,q} B_{kq} \sum_i c_q^{(k)}(i) + c_{-q}^{(k)}(i) \\
&= \sum_{k,q} B_{kq}[C_q^{(k)} + C_{-q}^{(k)}]
\end{aligned}
\qquad (12)
$$

where $C_q^{(k)}$ transform as tensor operators (Racah 1949, Wybourne 1965, Judd 1979) under simultaneous rotations of the coordinates of all the f electrons. The B_{kq} are so-called CF parameters characterizing the CF interaction in a given compound. Once these parameters are available, the matrix representation of H_{CF} can be constructed. The eigenvalues and eigenstates of the operator H_{CF} are obtained from the standard secular equation. The matrix elements of $C_q^{(k)}$ with respect to states of a nf^N configuration characterized by quantum numbers $\alpha SLJJ_z$, where α represents the set of quantum numbers necessary to distinguish states of the same L and S, are diagonal in the spin S and may be calculated using the *Wigner–Eckart theorem* (Wybourne 1965):

$$
\begin{aligned}
&(nf^N \alpha SLJJ_z | C_q^{(k)} | nf^N \alpha' SL'J'J'_z) \\
&= (-1)^{J-J_z} (f \| \mathbf{C}^{(k)} \| f)(nf^N \alpha SLJ \| U^{(k)} \| nf^N \alpha' SL'J') \\
&\times \begin{pmatrix} J & k & J' \\ -J_z & q & J'_z \end{pmatrix}
\end{aligned}
\qquad (13)
$$

where $U^{(k)}$ is a unit tensor operator. The last factor in Eqn. (13) is a 3-j symbol. The matrix elements on the right-hand side of Eqn. (13), indicated by the double modulus rules around the tensor operator, are called the *reduced matrix elements*. They can be calculated from available formulas (Wybourne 1965) and tables (Nielson and Koster 1963).

In practice the CF parameters are either determined from experimental data or calculated from a semiphenomenological or *ab initio* theory (see Sect. 2.3).

The splitting of the J multiplets by the CF is of the order of 10^2–$10^3 \mathrm{cm}^{-1}$ (K). The *crystal field strength parameter*, defined as follows (Kibler 1983):

$$
s = (2l+1)\left[\sum_{kq} \frac{1}{2n+1} \begin{pmatrix} l & k & l \\ 0 & 0 & 0 \end{pmatrix}^2 |B_{kq}|^2 \right]^{1/2}
\qquad (14)
$$

is a quantitative measure of the strength of the CF interaction of a particular f-electron ion with a particular host crystal.

Especially in older literature one can find alternative parameterization schemes for the CF interaction of Eqn. (12). This led to a degree of confusion between the meanings of similar or identical symbols used by different authors (Dieke 1968). Widely used is a formula arising from the theory of equivalent operators (Abragam and Bleaney 1970, Stevens 1997). The main disadvantage of this method is that it does not take into account the J mixing, i.e., the mixing of different free-ion levels by the CF interaction. Consequently, the use of this method can lead to considerable error in analysis of optical spectra (Morrison and Leavitt 1982).

In the great majority of cases the single-ion Hamiltonian (Eqn. (12)) is adequate to account for observed CF spectra of f ions in solids. There are, however, a few exceptions. The $^1D_2$ multiplet of the $4f^2$ configuration in Pr^{3+} can serve as an example, where large errors remain in the description of the experimental data. The terms in the CF Hamiltonian involving two-electron interaction ("correlation crystal field") have to be considered in such cases (Judd 1979). Note that attempts to fit the experimental data by the Hamiltonian represented by Eqn. (12) in cases where two-electron effects are significant will lead to a term dependence of the CF parameters (Morrison and Leavitt 1982).

2.2 Symmetry

A restriction on the number of nonvanishing parameters B_{kq} in Eqn. (12) arises from symmetry considerations. It follows from the hermiticity and time-reversal invariance of H_{CF} that k must be even. In addition, if only f electrons are involved, only the terms with $0 \leqslant k \leqslant 6$ are nonzero. Moreover, B_{kq} for $q<0$ are related to those for $q>0$ by:

$$
B_{kq} = (-1)^q \cdot B_{kq}^*
\qquad (15)
$$

The first term in the expansion given in Eqn. (12), $k=q=0$, is spherically symmetric. Although this term is by far the largest term in the expansion it gives a uniform shift to all the levels of the configuration and may be ignored as far as the CF splitting is concerned. A further restriction arises from the requirement of invariance under the point group operations. B_{kq} are real in any symmetry group that contains a rotation about the y-axis by π or a reflection through the x–z plane, otherwise they are complex.

The 32 point groups are listed in sets in Table 1, each of which has the same nonvanishing B_{kq}. An example is given for each set.

Depending on the site symmetry, the CF removes partly or entirely the $(2J+1)$-fold degeneracy of the free-ion J multiplets. There are two important theorems concerning the degeneracy of the CF energy levels:

Table 1
Independent nonvanishing B_{kq} for the 32 point groups.

Group	Nonvanishing B_{kq}	Example
C_1, C_I	All B_{kq} (B_{21} real)	NdP_5O_{14}
C_2, C_S (C_{1h}), C_{2h}	B_{20}, ReB_{22}, B_{40}, B_{42}, B_{44}, B_{60}, B_{62}, B_{64}, B_{66}	LaF_3
D_2, C_{2v}, D_{2h}	B_{20}, ReB_{22}, B_{40}, ReB_{42}, ReB_{44}, B_{60}, ReB_{62}, ReB_{64}, ReB_{66}	$Y_3Al_5O_{12}$, $NdCu_2$, $NdBa_2Cu_3O_7$
C_4, S_4, C_{4h}	B_{20}, B_{40}, ReB_{44}, B_{60}, B_{64}	$CaWO_4$
D_4, C_{4v}, D_{2d}, D_{4h}	B_{20}, B_{40}, ReB_{44}, B_{60}, ReB_{64}	YVO_4, Nd_2CuO_4, $NdCu_2Si_2$
C_3, S_6	B_{20}, B_{40}, ReB_{43}, B_{60}, B_{63}, B_{66}	$LiNbO_3$
D_3, C_{3v}, D_{3d}	B_{20}, B_{40}, ReB_{43}, B_{60}, ReB_{63}, ReB_{66}	Y_2O_2S
C_6, C_{3h}, C_{6h}, D_6, C_{6v}, D_{3h}, D_{6h}	B_{20}, B_{40}, B_{60}, ReB_{66}	$LaCl_3$, $ErGa_2$
T, T_d, T_h, O, O_h	B_{20}, ReB_{44}, B_{60}, ReB_{64}	$ErAl_2$, PrO_2, UO_2

Kramers' theorem. This states that for odd-electron systems—Kramers ions—there is a remaining two-fold degeneracy which cannot be removed by any electric fields. It is interesting to note that the entropy of a Kramers ion is at least $S = k_B \ln2$ at temperatures approaching absolute zero. This degeneracy thus must necessarily be removed by some mechanism if the third law of thermodynamics is to retain its validity.

The Jahn–Teller theorem. This states that any atom in a solid with ground state degeneracy of non-Kramers type lifts this degeneracy by lowering its symmetry (see *Transition Metal Oxides: Magnetism*). Such a lowering occurs in many *f*-electron compounds (Gehring and Gehring 1975, Aminov *et al.* 1996).

2.3 Crystal Field Parameters

A principal aim of most CF studies is to find a complete and reliable set of the CF parameters in a given compound. The methods used to this end are described in the following.

(a) Determination of CF parameters from experimental data

Given the CF energy levels, i.e., the eigenvalues of the secular equation of H_{CF}, one can calculate the unknown parameters B_{kq}, determining the elements of the matrix H_{CF}, solving numerically the *inverse secular problem*. Symmetry of an *f* ion site must to be known from the x-ray or neutron scattering data or assumed before the CF calculation is initiated.

The most straightforward and extensive experimental information on CF energy levels is provided by optical and neutron scattering spectra (see *Crystal Field Effects in Intermetallic Compounds: Inelastic Neutron Scattering Results*). The peaks in these spectra are present owing to electric and magnetic dipole *f–f* transitions, respectively (Dieke 1968, Marshall and Lovesey 1971). Optical methods, including absorption, fluorescence, and Raman scattering measurements, are used for transparent insulators and semiconductors. In general, a combination of several experimental methods allows the determination of a sufficiently complete CF spectrum of an nf^N configuration. The number of experimental CF energy levels then usually exceeds considerably the number of fitted CF parameters that guarantees their reliability (Dieke 1968, Hüfner 1978, Morrison and Leavitt 1982). The cuprate Nd_2CuO_4 can serve as an example of a compound studied by optical absorption as well as by inelastic neutron and Raman scattering (Jones *et al.* 1992, Muzichka *et al.* 1992, Jandl *et al.* 1995, 1998). Very sensitive optical absorption techniques also allowed one to detect sharp *f–f* transitions in some metals. Measurement of CF transitions in the superconductor $(Nd,Ce)_2$ CuO_{4-x}, metallic above $T_C \approx 20$–24K, can serve as an example (Jones *et al.* 1992). There is one earlier example of a metallic system, CeB_6, which has been studied by Raman scattering (Zirngiebl *et al.* 1985).

Various techniques are used to circumvent experimental difficulties. For example, instead of in nearly opaque ferrimagnetic iron garnets (see *Transition Metal Oxides: Magnetism*) the CF spectra of RE ions are measured in optically transparent, structurally very similar gallium and aluminum garnets (Winkler 1981). Similarly, to obtain the "CF only" spectra in RE metals one can decrease the magnetic interaction by dilution with nonmagnetic ions (Fulde and Loewenhaupt 1986). Trivalent ions are preferably replaced by scandium, yttrium, lanthanum, or lutetium.

Besides transition energies, relative transition intensities can also be used as input data in the best-fit search of the CF parameters. This is advantageous in the case of Raman and neutron measurements where calculation of matrix elements of electric dipole and magnetic dipole moments, respectively, determining

the transition probability between two CF states, is straightforward (Nekvasil 1982, Hilscher *et al*. 1994). Calculation of relevant matrix elements in the case of optical absorption or emission is more complicated owing to the necessity of considering mixing of opposite-parity configurations by odd-parity components of the CF (Dieke 1968).

Phenomenological CF parameters for *f*-electron ions in various host crystals are widely available in the literature. Mentioned here are the reviews for RE ions in nonmetallic compounds (Morrison and Leavitt 1982, Aminov *et al*. 1996), metallic compounds (Moze 1998), and cuprates (Nekvasil *et al*. 1995, Staub and Soderholm 2000). For actinides CF parameters are also available (Gajek 1995). The precision of the CF values quoted in the literature depends on the number and reliability of the underlying experimental data as well as on their numerical and quantum mechanical processing. In general, the most favorable situation in fitting the experimental data is the diagonalization of the many parameter free-ion Hamiltonian (see Sect. 1), together with the CF Hamiltonian, in a basis that spans the entire f^N configuration. Unfortunately a large quantity of experimental data is required to ensure its success. Therefore, CF data are often obtained by using various approximations. There is a long list of problems that may occur in interpreting the CF values available in the literature (Morrison and Leavitt 1982).

(b) Semiempirical models

The superposition model (SM) was introduced to separate the geometrical and physical information contained in the CF parameters (Newman and Ng 1989). The SM is based on several postulates:

(i) The total CF acting on the open-shell electrons of a paramagnetic ion is the sum of the contributions coming from neighboring ions (commonly referred to as ligands) forming the coordination polyhedron.

(ii) Each ligand contribution to the sum is axially symmetric about the line joining its center to that of the paramagnetic ion. Frequently a third, transferability, postulate is invoked:

(iii) Single-ligand contributions depend only on the nature of the ligand and its distance from the paramagnetic ion, and do not depend on other properties of the host crystal.

Postulates (i) and (ii) allow one to describe each individual contribution by "intrinsic (i.e., geometry-independent) CF parameters" $b_k(R)$ where R denotes the distance between the RE and ligand ion. The CF parameters B_{kq} in Eqn. (13) and intrinsic parameters $b_k(R)$ are related as:

$$B_{kq} = \sum_i S_{kq}(i) \cdot b_k(R_i) \qquad (16)$$

where $S_{kq}(i)$ is the geometrical factor determined by angular coordinates of ligands at the same distance R_i.

These structural data can be determined with sufficient precision from x-ray or neutron scattering data. Note that independent of the mechanism of interaction between the paramagnetic ion and ligand, the relation B_{kq}/B_{k0} only depends on the geometry of the coordination polyhedron. This explains why in some cases the relation B_{kq}/B_{k0} calculated using the unrealistic standard point charge model provides a useful prediction. The SM does not apply for the $k = 2$ parameters where the long-range electrostatic contribution appears to dominate, which causes a breakdown of postulate (i) of the SM.

A convenient way of expressing the distance dependence of the intrinsic parameters is to assume the power law dependence:

$$b_k = b_k(R_0) \cdot (R_0/R)^{t_k} \qquad (17)$$

where R_0 is some arbitrarily fixed "standard" paramagnetic ion–ligand distance. For each value of k, the values up to $2k + 1$, in general complex, CF parameters B_{kq} are determined by just two real SM parameters, $b_k(R_0)$ and t_k. In the case of low-symmetry sites an application of the SM thus means a significant reduction of the number of independent parameters required to describe the CF interaction.

The intrinsic parameters and power law exponents have been extracted from the phenomenological CF parameters B_{kq} available for various nonmetallic materials. These include di- and trivalent RE ions with fluorine, oxygen, and chlorine ligands as well as tri-, tetra-, and pentavalent actinides with oxygen and halide ligands. These data confirm the general validity of the SM (Newman and Ng 1989). In particular, having available the intrinsic parameters and power law exponents for a given paramagnetic ion in one host system, postulate (iii) of the SM model makes possible the prediction of the CF interaction for the same paramagnetic ion in other host systems with the same ligand. As an example of such a prediction the CF splitting of the lowest J multiplets of trivalent RE ions in $REBa_2Cu_3O_7$ (RE = Ho, Er), compared to later experimental data in Fig. 2, may serve. It is seen in Fig. 2 that, despite the uncertainty in the values of the second-order CF parameters, the SM calculation using the available structural data and the model parameters available in garnets predicts successfully the main features of the CF spectra.

In metallic systems, applications of the SM are rather scarce. The available data for a few RE binary (Newman and Ng 1989, Diviš 1991) and ternary (Goremychkin *et al*. 1994) intermetallics indicate that, while the model provides qualitative interpretation of the main features of the phenomenological CF data, its general validity has yet to be confirmed in these systems. A useful tool allowing one to examine the model postulates is provided by first principle calculations (see below). It follows from these calculations that in the case of fourth-order CF parameters
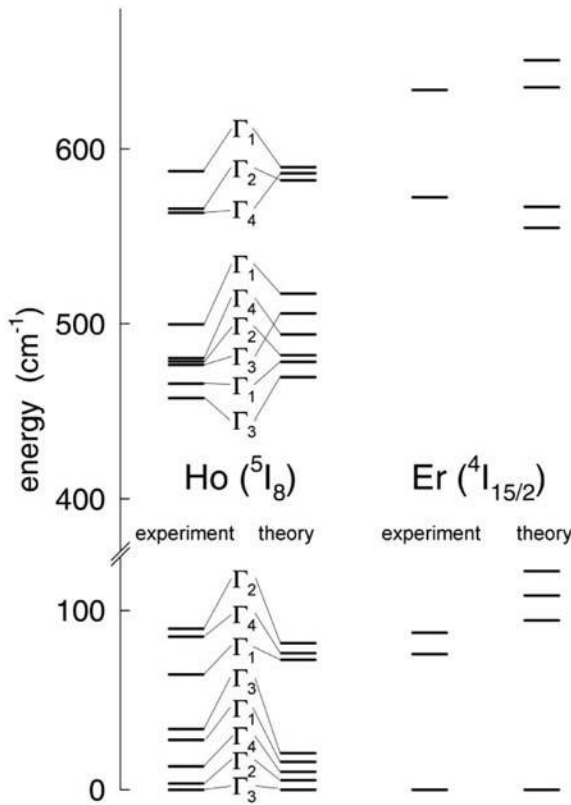
Figure 2
Predicted and experimentally measured CF levels of
$HoBa_2Cu_3O_7$ ($J = 8$) and $ErBa_2Cu_3O_7$ ($J = 15/2$). Γ_i
denote the irreducible representation (point group
symmetry) of particular CF eigenstates (Nekvasil *et al.*
1988 and references therein).

the contribution of the charge density from the region
of the next nearest neighbor is significant, which
throws some doubt on the validity of postulate (i) of
the model. This contribution is smaller in the case of
sixth-order CF parameters (Diviš *et al.* 1997).

The point charge model (PCM), often used for the
charge distribution, can be considered as a special
case of the SM. Note the PCM values of the power
law exponents, $t_4 = 5$ and $t_6 = 7$. Comparison with
the SM values $t_4 = 9.9$ and $t_6 = 3.9$, obtained by a
detailed analysis of 14 sets of reliable phenomeno-
logical CF parameters available in RE garnets,
strongly indicates that the nonelectrostatic contribu-
tions including overlap, exchange, and charge pene-
tration contributions to the CF, none accounted for
by the PCM, dominate (Nekvasil 1979).

The angular overlap model parameterizes the CF
pair interaction in a formally similar way to the SM,
where the intrinsic parameters are replaced by quan-
tities which are functions of the overlap integral of *f*

and ligand wave functions. The angular overlap
model can be considered as the semiempirical version
of the many-body perturbation theory (Newman and
Ng 1989).

(c) Ab initio calculations
Ab initio calculations of the CF interaction in *f*-elec-
tron compounds are usually based either on the DFT
or on the many-body perturbation theory (MBPT).
These calculations naturally include the contributions
from bonding $6s5d$ ($7s6d$) electrons and the aspherical
shielding effects originating from $5s5p$ ($6s6p$) elec-
trons of a RE (An) ion in a crystalline environment.

Within the DFT the parameters B_{kq} of the CF
Hamiltonian (Eqn. (12)) originating from the effec-
tive potential V inside the crystal, are written as:

$$B_{kq} = a_k^q \int_0^\infty |R_{nl}(r)|^2 \, V_k^q(r) r^2 \, dr \qquad (18)$$

where nonspherical components $V_k^q(r)$ reflect, besides
the nuclear potentials and Hartree part of the inter-
electronic interaction, also the exchange correlation
(XC) term which accounts for many-particle effects.

The key task of *ab initio* methods is to calculate the
components $V_k^q(r)$. Within the linear augmented
plane wave method (LAPW), Eqn. (18) is written as
a sum of two contributions:

$$B_{kq} = a_k^q \left(\int_0^{R_{MT}} |R_{nl}(r)|^2 U_k^q(r) r^2 \, dr \right.$$
$$\left. + \int_{R_{MT}}^\infty |R_{nl}(r)|^2 W_k^q(r) r^2 \, dr \right) \qquad (19)$$

where $U_k^q(r)$ and $W_k^q(r)$ are, respectively, the compo-
nents of the effective potential inside the atomic
sphere with radius R_{MT} and in the interstitial region.
The conversion factor a_k^q (Novák 1996, Dieke 1968)
establishes the relationship between the LAPW sym-
metrized spherical harmonic and the real Tesseral
harmonics. A comprehensive survey of the computa-
tional techniques used in the framework of DFT
calculations is available (Richter 1998).

In comparison with LAPW, the OLCAO method
combines the advantage of a fast computational
scheme with a sufficiently accurate representation of
the effective potential V. The latter method provides
a significant insight into the physical origin of the CF
interaction. In particular, it allows the determination
of where in space the CF creating charges are situ-
ated. It turns out that, roughly, a neighborhood ex-
tending to 0.7nm (containing ~ 70 atoms in typical
intermetallics) is responsible for the second-order CF
parameters, whereas fourth- and sixth-order para-
meters are created within 0.5nm (~ 30 atoms) and
0.4nm (~ 20 atoms), respectively.

The second important quantity of Eqn. (18) is
the radial *f* wave function R_{nl}. Its atomic value,

Table 2
CF parameters, B_{kq} (in cm^{-1}), of SmCo$_5$ (1cm^{-1} = 0.123 meV).

	B_{20}	B_{40}	B_{60}	B_{66}
Experiment	−250 to −584	−78	+100	+168
Novák 96	−485	−205	+79	+231
Hummler 96	−706	−111	+21	(−)40
Daalderop 96	−1061	−150	+40	+72
Richter 95	−1056	−206	+122	+212

Source: Richter (1998).

determined by Dirac–Fock-type calculations, has to be replaced by the value reflecting the self-consistent DFT crystal potential.

DFT-based methods have been used to calculate the CF parameters in many metallic RE and An systems. As is shown in Table 2 this method interprets well the experimentally observed influence of the chemical composition on magnetic properties (Richter 1998).

The only DFT-based CF data available in insulators are those for cuprates (Diviš *et al.* 1998). It appears that while the sign and magnitude of second-order CF parameters are obtained correctly, those of fourth- and sixth-order CF parameters are only poorly described. This inadequacy is tentatively associated with the underestimation of the strong correlation effects related to the local approximation for the exchange correlation part of the effective crystal potential (see *Density Functional Theory: Magnetism*).

Ab initio calculations of CF parameters can also be performed by using a many-body approach (Newman 1971). Its principal idea is to confine all the interactions in a many-electron system to the effective, one-electron potentials by using standard renormalization and averaging procedures within MBPT. The most important assumptions associated with these procedures are (Gajek 1995):

(i) The many-electron wave functions are replaced by determinants built from free-ion orbitals. Only the electrons from outer shells are considered. For instance, in the case of PrCl$_3$ the 4f, 5s, and 5p orbitals of the Pr^{3+} ion as well as the 3s and 3p orbitals of the six Cl$^-$ ions are taken into account.

(ii) The corrections due to the nonorthogonality of RE (An) and ligand orbitals and configuration interaction effects are described by the second order of the perturbation series.

(iii) The Hamiltonian describing the interactions in the crystal lattice is divided into two parts. The first part represents the interactions within the cluster formed by the central f ion and ligands; the second part corresponds to the interactions with the rest of the crystal lattice. It is usually assumed that the interactions within a cluster can be regarded as a sum of axially symmetric interactions calculated for the individual paramagnetic ion–ligand pairs. This simplification, identical with postulates (i) and (ii) of the SM (see above), allows one to neglect the polarization effects. The interaction with the rest of the crystal lattice is approximated by the Madelung-like potential.

In contrast with DFT methods, applied mainly to metallic compounds, the MBPT in its form described above is suitable for f ions in insulators (Gajek 1995).

3. Ions in Applied Magnetic Fields

3.1 Zeeman Effect

The CF-split f-electron spectra of the ionic or atomic J multiplets may be further perturbed by applying an external magnetic field, H^a. Such a perturbation, called the *Zeeman effect*, can be described by the Hamiltonian H_{Zeem}:

$$H_{\text{Zeem}} = -\boldsymbol{\mu} \cdot \mathbf{H}^a \qquad (20)$$

where

$$\boldsymbol{\mu} = \mu_B(g_l\mathbf{L} + g_s\mathbf{S}) \qquad (21)$$

is the magnetic moment and g_l and g_s are the orbital ($=1$) and spin ($=2.0023$) gyromagnetic factors. For the calculation of the matrix elements of the Zeeman term (Eqn. (20)), it is useful to express $\boldsymbol{\mu}$ by means of the tensor operator $T^{(1)}$ (Wybourne 1965):

$$T^{(1)}_{\pm 1} = \frac{\mp 1}{\sqrt{2}}[(L_x + 2S_x) \pm i(L_y + 2S_y)]$$
$$T^{(1)}_0 = L_z + 2S_z \qquad (22)$$

$$\langle SLJJ_z | T^{(1)}_q | SLJ'J'_z \rangle =$$
$$(-1)^{J-J_z} \begin{pmatrix} J & 1 & J' \\ -J_z & q & J'_z \end{pmatrix} \langle SLSJ \, \| T^{(1)} \| \, SLJ' \rangle$$

The reduced matrix elements of $T^{(1)}$ can be obtained by the tensor operator method (Wybourne 1965). Within a given J multiplet one can write:

$$\mathbf{L} + g_s\mathbf{S} = g_J\mathbf{J} \qquad (23)$$

$$H_{\text{Zeem}} = -g_J\mu_B\mathbf{J} \cdot \mathbf{H}^a \qquad (24)$$

where $g_J = 1 + (g_s - 1)[J(J+1) + S(S+1) - L(L+1)]/2J(J+1)$ is the *Landé factor*.

Note that in the absence of the CF the J multiplet is split by a magnetic field into $2J+1$ equidistant levels each corresponding to a different value of J_z, where z is the direction of the applied magnetic field. Two neighboring levels are separated by the energy gap $\mu_B g_J H_z$.

3.2 Paramagnetism

A paramagnetic system can be treated as an assembly of N noninteracting f-electron ions in magnetic field H^a. The thermal average of ionic magnetic moments is given by the Boltzmann statistics formula:

$$\mathbf{M} = (1/Z) \sum_i \boldsymbol{\mu}_i \exp(-E_i/k_B T) \qquad (25)$$

where $\boldsymbol{\mu}_i$ is the magnetic moment of the ith energy level:

$$\boldsymbol{\mu}_i = -\mu_B \langle i | \mathbf{L} + g_s \mathbf{S} | i \rangle \qquad (26)$$

and where Z is the partition function:

$$Z = \sum_i \exp(-E_i/k_B T) \qquad (27)$$

E_i and $|i\rangle$ are, respectively, eigenvalues and eigenvectors of the total perturbation Hamiltonian H_R which includes the CF (Eqn. (12)) and Zeeman terms (Eqn. (20)):

$$H_R = \sum_{kq} B_{kq} C_q^{(k)} - \boldsymbol{\mu} \cdot \mathbf{H}^a \qquad (28)$$

Note that E_i denotes the energy of the levels with respect to the ground state.

The calculation of the magnetic moment using Eqns. (25)–(28) is straightforward provided that the CF parameters for the given compound are known. The magnetic moment is in general anisotropic, as besides the magnitude of H^a it also depends on its orientation with respect to the crystallographic axes (see Fig. 3). In the absence of the CF and neglecting the higher excited multiplets, the right-hand side of Eqn. (25) can be expressed in terms of the Brillouin function (Gignoux 1991).

The tensor of magnetic susceptibility $\boldsymbol{\chi}$ is given by the formula:

$$\chi_{\alpha\beta} = \left(\frac{\delta M_\alpha}{\delta H_\beta^\alpha} \right)_{H^\alpha \to 0} \qquad (29)$$

An alternative perturbation approach to the Zeeman effect allows one to write the susceptibility per ion along the principal axes ($\alpha = \beta = a, b, c$) as (Luong and Franse 1995):

$$\chi^\alpha = \frac{g_J^2 \mu_B^2}{Z} \sum_i$$
$$\times \left\{ \frac{1}{kT} |\langle i | J_\alpha | i \rangle|^2 + 2 \sum_{j \neq i} \frac{|\langle j | J_\alpha | i \rangle|^2}{E_j - E_i} \right\} \exp(-E_i/k_B T) \qquad (30)$$

where the first term in the braces, temperature dependent, is called the Curie term and the second,
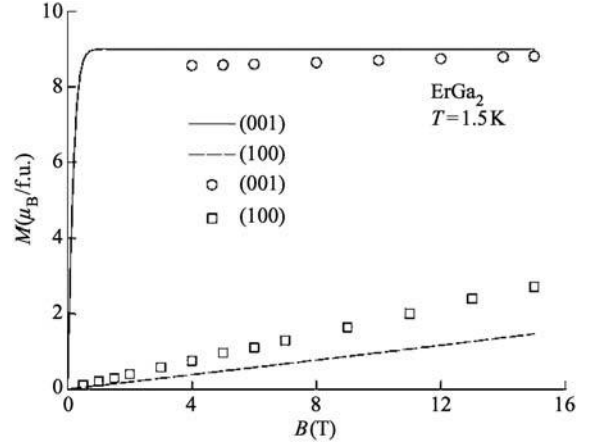
Figure 3
Magnetization of ErGa$_2$ as a function of the external magnetic field. In (001) direction, only data for $B > 4$T are shown since data below 4T are strongly influenced by exchange interaction inducing two metamagnetic transitions. The lines are obtained from calculations based on CF and Zeeman Hamiltonian (Eqn. (28)), with CF parameters obtained from density functional theory (Diviš *et al.* 1997).

temperature independent, is the Van Vleck term. For a polycrystalline sample the susceptibility $\chi^{(p)}$ is obtained by the approximation:

$$\chi^{(p)} = (\chi^{(a)} + \chi^{(b)} + \chi^{(c)})/3 \qquad (31)$$

From symmetry considerations it follows that: (a) χ is isotropic in cubic compounds; (b) $\chi^{(c)} \neq \chi_{\perp c}$ in hexagonal and tetragonal systems; and (c) $\chi^{(a)} \neq \chi^{(b)} \neq \chi^{(c)}$ in orthorhombic systems. At high temperatures the inverse susceptibility along each axis tends to be linear with the same slope, giving rise to the same effective moment $g_J \mu_B \sqrt{(J(J+1))}$. For a noncubic compound, the shifts between the high-temperature susceptibilities are proportional to the second-order CF parameters. The low-temperature behavior of the susceptibility is strongly influenced by the CF. In particular the Van Vleck contribution to the susceptibility tends to dominate in the case of non-Kramers ions in which the lowest energy state is a singlet or nonmagnetic doublet. Such compounds are called Van Vleck paramagnets (Gignoux 1991, Aminov *et al.* 1996). As an example of such system the susceptibility of the Pr^{3+} ion in a cubic CF is shown in Fig. 4.

4. Cooperative Effects

A magnetic state arising from localized moments in a solid is the net effect of competing influences: the
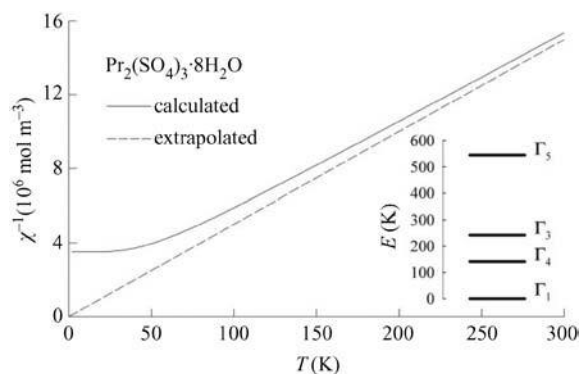
Figure 4
Splitting of the ground state multiplet ($J = 4$) of the Pr^{3+} ion in $Pr_2(SO_4)_3 \cdot 8H_2O$ (inset). The susceptibility is determined by the temperature independent Van Vleck term in Eqn. (30) (full lines) at low temperatures. The dashed line is the high-temperature asymptote of the thermal variation of the reciprocal susceptibility.

ordering resulting from a magnetic coupling is perturbed by the thermal energy which tends to randomize the orientation of each moment. The cooperative effects are primarily due to pair exchange coupling, derived from the influence of the Pauli principle on the Coulomb repulsion between electrons. One can distinguish two classes of exchange coupling (Hurd 1982). *Direct exchange* operates between moments on ions whose magnetic orbitals have significant overlap. Such interaction, which occurs in 3*d* intermetallic compounds and is responsible for the high ordering temperatures in ferromagnets used for technical applications, gives a strong but short-range coupling (see *Itinerant Electron Systems: Magnetism (Ferromagnetism)*). Weaker, *indirect exchange*, coupling moments over relatively large distances, occurs in *f*-electron compounds. It is mediated by itinerant electrons in metals and by nonmagnetic ions (ligands) in insulators. These couplings are known as the RKKY (after Ruderman, Kittel, Kasuya, and Yosida) and *superexchange* effects, respectively. The physical interaction mechanisms which occur in *f*-electron compounds also include *electric multipole interactions* and *magnetic dipole–dipole coupling* (Wolf 1971, Aminov *et al.* 1996, Jensen and Mackintosh 1991).

4.1 Form of Interaction Hamiltonian

The exchange interaction between two *S* state ions (orbitally nondegenerate) *i* and *j*, having spins $\mathbf{S}_i$ and $\mathbf{S}_j$, respectively, can be described by an isotropic Heisenberg Hamiltonian:

$$H_{ij} = -J_{ij}\mathbf{S}_i\mathbf{S}_j \qquad (32)$$

where J_{ij} is called the exchange parameter which can be positive (ferromagnetism), negative (antiferromagnetism), or oscillatory (e.g., helical structures) as in the case of an RKKY-type interaction. Within the ground state multiplet it is often convenient to express H_{ij} in terms of **J** rather than **S** (see Sect. 3.1):

$$H_{ij} = -J_{ij}(g_J - 1)^2 \mathbf{J}_i\mathbf{J}_j \qquad (33)$$

In systems containing *f*-electron ions the isotropic exchange operator (Eqns. (32) and (33)) has to be in general extended by *anisotropic* terms. The anisotropy of the coupling is associated with the orbital moment of the electrons involved. The exchange Hamiltonian then takes the form (Wolf 1971, Baker 1971, Levy 1975, Jensen and Mackintosh 1991):

$$H_{ij} = \sum_{ll'mm'} K_{ll'}^{mm'}(ij) T_l^{(m)}(\mathbf{J}_i) T_{l'}^{(m')}(\mathbf{J}_j) \qquad (34)$$

where the terms that appear in the sum are restricted by symmetry, but otherwise may exhibit a large variety, depending on their origin. The matrix elements of the operator (Eqn. (34)) can be calculated using the methods of Racah algebra (Levy 1975). The general exchange operator (Eqn. (34)) contains, besides the bilinear isotropic term (Eqn. (32)), also higher order isotropic interactions and all types of anisotropic exchange, e.g., the pseudodipole exchange and the antisymmetric Dzyaloshinskii–Moriya exchange (see *Transition Metal Oxides: Magnetism*). The effective spin–spin coupling due to the electric multipole interaction produced by aspherical charge distributions in solids can be also written like Eqn. (34) (Wolf and Birgeneau 1968, Levy 1975). For *f* electrons there are up to 4096 exchange parameters $K_{ll'}^{mm}$ of which 1954 are independent.

These numbers further increase in cases when the interacting RE ions are not identical (Levy 1975). The exchange anisotropy may be very pronounced: there are systems in which the isotropic Heisenberg-type exchange (Eqn. (32)) alone appears to be completely incapable of explaining the observations (Cone and Wolf 1978, Jandl *et al.* 1999, Nugroho *et al.* 2001). Consequently, it is meaningless to apply the operator (Eqn. (34)) in an arbitrarily simplified form. One of the most important practical roles of the theory is thus the identification of special cases where the real interaction can be described by only a few parameters. This is the case, for example, in the interaction of Er^{3+} impurities with the Tb^{3+} magnetic sublattice in $Tb(OH)_3$ where the number of parameters $K_{ll'}^{mm'}$ can be reduced from the very large number of 21 736 to 8 (Cone and Wolf 1978). In some cases, one can lower the number of parameters required to describe the anisotropic exchange coupling by projection of the operator (Eqn. (34)) onto the states of an *effective* total angular momentum (fictitious spin) *s'*.

The most general operator H_{ij} coupling two $s' = 1/2$ (Kramers) systems is:

$$H'_{ij} = \sum_{\alpha\beta} s'_{i\alpha} \mathbf{K}_{\alpha\beta} s'_{jb} \qquad (35)$$

where the second-order tensor $\mathbf{K}$ has only nine constants. This number can usually be further reduced. For example, a special nature of low-lying $4f$ states imprinted by the CF can reduce Eqn. (35) to an Ising-like form, determined by a single exchange parameter K_{zz}. Magnetic properties of several dysprosium, terbium, and holmium compounds have been analyzed using the Ising-like effective spin Hamiltonian (Wolf 1971, Nekvasil and Veltruský 1994).

Data allowing one to determine a fairly large number of unrelated parameters in Eqn. (34) are obtained using various spectroscopic methods including EPR, optical absorption, and inelastic neutron scattering as well as by measurements of macroscopic properties such as susceptibility and specific heat (Wolf 1971, Jensen and Mackintosh 1991).

Note that although investigators are usually aware of the anisotropic exchange effects, the simple isotropic form of Eqn. (33) is usually used to examine the magnetic structures described in the following.

4.2 Magnetic Structures

The magnetic structures assumed by f-electron compounds are usually examined within the *mean field theory*. The essential feature of this conceptually simple method is the approximation of the two-ion interaction (Eqn. (33)) by effective single-ion terms in which the instantaneous values of the $\mathbf{J}$ operators in the surroundings of any particular ion are replaced by their expectation values (Jensen and Mackintosh 1991). The exchange term then can be written in the Zeeman-like form:

$$H_{\text{ex}} = -\mathbf{\mu} \cdot \mathbf{H}^m \qquad (36)$$

where the applied field $\mathbf{H}^a$ appearing in Eqn. (20) is replaced by a *molecular field* $\mathbf{H}^m$:

$$\mathbf{H}^m = -\lambda_m g_J \mu_B \langle \mathbf{J} \rangle \qquad (37)$$

where the molecular field constant λ_m is determined by the strength of the exchange interaction and is calculated from the divergence of magnetic susceptibility $\chi(T)$ at the ordering temperature T_C. According to the Curie–Weiss law:

$$\frac{1}{\chi(T)} = \frac{1}{\chi_0(T)} - \lambda_m \qquad (38)$$

leading to:

$$\lambda_m = \chi_0^{-1}(\{B_{kq}\}, T_C) \qquad (39)$$

where $\chi_0(T)$ is the component of the single-ion susceptibility parallel to $\mathbf{H}^m$ (Wang and Cooper 1970):

$$\chi_0(T) = \frac{g_J^2 \mu_B^2}{KT} \left[\sum_n |\langle n|J_z|n \rangle|^2 \frac{\exp(-E_n/k_B T)}{Z} \right.$$
$$\left. - \left(\sum_n |\langle n|J_z|n \rangle| \frac{\exp(-E_n/k_B T)}{Z} \right)^2 \right]$$
$$+ 2g_J^2 \mu_B^2 \sum_{n \neq m} \frac{|\langle n|J_z|n \rangle|^2}{E_n - E_m} \cdot \frac{\exp(-E_n/k_B T)}{Z}$$
$$(40)$$

where E_n and $|n\rangle$ are, respectively, eigenvalues and eigenvectors of the Hamiltonian of the form of Eqn. (28), in which the Zeeman term has been replaced by the exchange term (Eqn. (36)).

The complete Hamiltonian within the ground state multiplet is

$$H'_R = \sum_{kq} B_{kq} C_q^{(k)} - \mathbf{\mu} \cdot (\mathbf{H}^m + \mathbf{H}^a) \qquad (41)$$

where the only unknowns are the CF parameters B_{kq} and the molecular field constant λ_m.

Equation (41) is adequate in explaining the occurrence of most observed magnetic structures (Jensen and Mackintosh 1991) as well as various physical properties associated with the f electrons (see Sect. 2).

(a) Nonmetallic compounds

Nonmetallic RE compounds are ferro- or antiferromagnets (see *Magnetism in Solids: General Introduction*) in which the magnetic ordering occurs owing to the superexchange, the electric multipole, and the classical dipole–dipole interactions. The ordering temperatures are typically of the order of 1K. The magnetic properties have been systematically studied in number of compounds including RE ethylsulfates, tetrafluorides $LiREF_4$ with scheelite structure, $REMO_4$ crystals having zircon structure (M = V, P, As), trifluorides REF_3, RE elpasolites, and RE cuprates. The highest value among trivalent RE compounds of 17.9K was reported for the antiferromagnetic cuprate $PrBa_2Cu_3O_7$. An even higher ordering temperature of 34K occurs in the antiferromagnetic perovskite $TbBaO_3$, where the terbium ions are tetravalent. The CF ground state in the above-mentioned magnetically ordered RE compounds is usually the Kramers doublet or non-Kramers (quasi)doublet or (quasi)triplet (for a survey of magnetic ordering data see Aminov *et al.* 1996).

An example of localized magnetism in An compounds is UO_2 (Fournier 1985). In this semiconductor the special nature of the band structure ensures good localization of the $5f$ electrons (Kelly and Brooks 1980, Amoretti *et al.* 1989, Diviš *et al.* 1996).

UO_2 orders antiferromagnetically at $T_N = 31K$. Another example is UCl_3, an antiferromagnet with $T_N = 6.5K$ (Fournier 1985) (see also *5f Electron Systems: Magnetic Properties*).

(b) Metallic compounds

In general, the magnetic ordering temperatures in metallic compounds are lower than room temperature. The most important contribution to the magnetic coupling is provided by indirect exchange. Its origin is due to the polarization of the conduction-electron gas by the spin on one ion, which influences the spin of a second ion.

In the widely used isotropic approximation the exchange parameter in Eqn. (33) takes the Fourier transform form (Jensen and Mackintosh 1991):

$$J_{ij} = \frac{1}{N} \sum_q J(\mathbf{q}) e^{iq(\mathbf{R}_i - \mathbf{R}_j)} \qquad (42)$$

where N is the number of ions and

$$J(\mathbf{q}) = (g_J - 1)^2 \left[J_S(\mathbf{q}) - \frac{1}{N} \sum_{\mathbf{q'}} J_S(\mathbf{q'}) \right] \qquad (43)$$

and

$$J_S(\mathbf{q}) = \frac{V}{N\mu_B^2} |I(\mathbf{q})|^2 \chi(\mathbf{q}) \qquad (44)$$

where $I(\mathbf{q})$ and $\chi(\mathbf{q})$ are, respectively, Fourier transforms of the exchange parameter between a conduction-electron spin and the f spins and magnetic conduction-electron susceptibility, and V is the volume. The Fourier transform $[J(\mathbf{q}) - J(\mathbf{0})]$ can be extracted from elastic neutron scattering data. The position of maximum on a $[J(\mathbf{q}) - J(\mathbf{0})]$ vs. $\mathbf{q}$ curve, which in general occurs at nonzero $\mathbf{q}$, determines the type of magnetic order (see below).

The susceptibility $\chi(\mathbf{q})$ is given by:

$$\chi(\mathbf{q}) = \frac{2\mu_B^2}{V} \sum_{nn'k} \frac{f_{nk} - f_{n'k-q}}{\varepsilon_{n'}(\mathbf{k} - \mathbf{q}) - \varepsilon_n(\mathbf{k})} \qquad (45)$$

where f_{nk} is the Fermi–Dirac distribution function. A large contribution to the sum is made by pairs of electronic states, separated by $\mathbf{q}$, one of which is occupied and the other empty, and both of which have energies very close to the Fermi level. Parallel or nesting regions of the Fermi surface tend to produce peaks at the wave vector $\mathbf{Q}$ which separates them. Such peaks are known as Kohn anomalies. The Kohn anomalies in $J(\mathbf{q})$ Fourier transform into Friedl oscillations in $J(\mathbf{R})$. First-principle calculations of $J(\mathbf{q})$ have not been very successful. While the calculated $\chi(\mathbf{q})$ exhibits the expected peaks, the matrix elements determining $I(\mathbf{q})$ are much less tractable.

A simple mean field calculation shows that spontaneous ordering occurs at the wave vector $\mathbf{Q}$ for which $J(\mathbf{q})$ has its maximum value and the Néel temperature T_N is

$$T_N = \frac{J(\mathbf{Q})J \cdot (J+1)}{3k_B} \qquad (46)$$

Considering Eqn. (46) one finds that T_N is proportional to the de Gennes factor $(g_J - 1)^2 J(J+1)$, provided that the susceptibility of the conduction-electron gas is constant. As a representative example of this frequently used approach, the values of T_N for antiferromagnetic RCu_2 displayed in Fig. 5 may serve. The remaining discrepancy between the experimental and calculated data in Fig. 5 can be ascribed to variation of $J_S(\mathbf{q})$ across the isostructural series and neglecting of the CF as well as of the anisotropic part of the exchange interaction (Jensen and Mackintosh 1991).

The long-range and oscillatory indirect exchange gives arise to large variety of magnetic structures in RE metals and intermetallic compounds. A compound is ferromagnetic if a maximum on $(\mathbf{q})$ occurs at $\mathbf{Q} = 0$
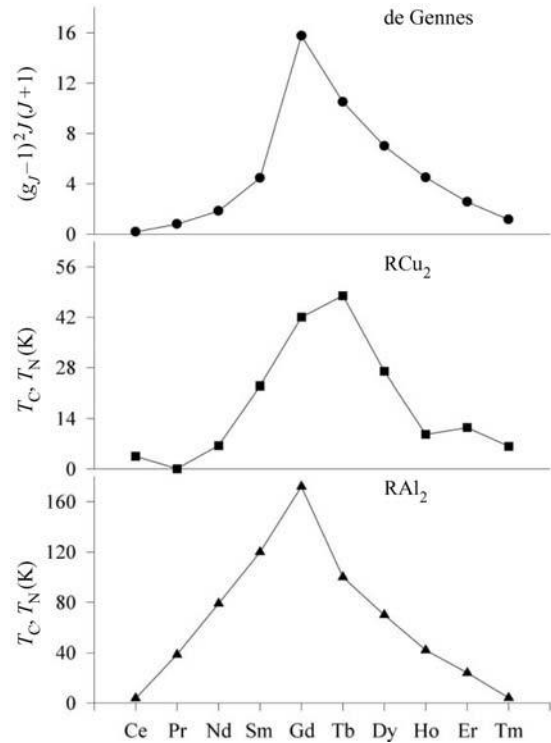
Figure 5
Values of the Curie (Néel) temperature in the RCu_2 and RAl_2 series and values of the de Gennes factor $(g_J - 1)^2 J(J+1)$ across the 4f series. The values shown are for R^{3+} ions.
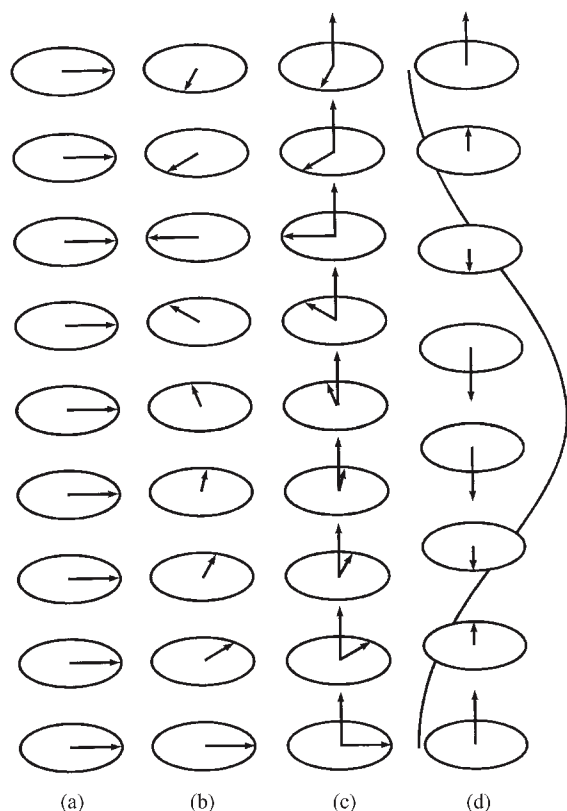
Figure 6

Magnetic structures of heavy rare earth metals. (a) In the basal-plane ferromagnet all moments are aligned along the direction of magnetization. (b) The moments in the helix rotate by a specific angle between neighboring planes. (c) The cone is a combination of a helix and an axial ferromagnetic component, so that the total moment rotates on the surface of a cone. (d) In the longitudinal wave structure the c-axis component varies sinusoidally, while in the basal plane it is disordered.

and simple antiferromagnetic at the reduced propagation vector $\mathbf{Q} = 1/2$ (0,0,1). Such structures occur, for example, in metallic gadolinium and most of the REAl$_2$ compounds. For $0 < \mathbf{Q} < 1/2$ (0,0,1) different types of magnetic structure occur including the helix, the cone, and the longitudinal wave structures (see Fig. 6). In general, the magnetic easy axis may change from one RE to another owing to the CF interaction.

5. Summary

This article has considered f-electron compounds in which the RE or An ions are assumed to be present in well-defined ionic states. Most of the magnetic properties of these compounds can be described in terms of two microscopic interactions involving the

f electrons: the CF interaction and the exchange interaction. Various theoretical and experimental methods used to study and describe these interactions have been discussed. These methods can be also applied to 3d–4f alloys (see *Alloys of 4f (R) and 3d (T) Elements: Magnetism, Magnetoelastic Phenomena*, and *Magnetic Systems: External Pressure-induced Phenomena*) and compounds (see *Transition Metal Oxides: Magnetism*).

See also: Crystal Field and Magnetic Properties, Relationship between

Bibliography

Abragam A, Bleaney B 1970 *Electron Paramagnetic Resonance of Transition Ions*. Clarendon, Oxford

Aminov L K, Malkin B Z, Teplov M A 1996 Magnetic properties of nonmetallic lanthanide compounds. In: Gschneidner K A Jr., Eyring L R (eds.) *Handbook on the Physics and Chemistry of Rare Earths*. Elsevier, Amsterdam, Vol. 22

Amoretti G, Blaise A, Caciuffo R, Fournier J M, Hutchings M T, Osborn R, Taylor A D 1989 5f-electron states in uranium dioxide investigated using high-resolution neutron spectroscopy. *Phys. Rev. B* **40**, 1856–70

Baker J M 1971 Interactions between ions with orbital angular momentum in insulators. *Prog. Phys.* **34**, 109–73

Cai Z, Meiser Umar V M, Fischer C F 1992 Large-scale relativistic correlation calculation: levels of Pr^{3+}. *Phys. Rev. Lett.* **68**, 297–300

Condon E U, Shortley G H 1967 *The Theory of Atomic Spectra*. University Press, Cambridge

Cone R L, Wolf W P 1978 Anisotropic exchange effects in optical spectra: Er^{3+} in ferromagnetic Tb(OH)$_3$. *Phys. Rev. B* **17**, 4162–80

Dieke G H 1968 In: Crosswhite H M, Crosswhite H (eds.) *Spectra and Energy Levels of Rare Earth Ions in Crystals*. Interscience, New York

Diviš M 1991 Crystal field in some rare earth intermetallics analysed in terms of the superposition model. *Phys. Stat. Sol. (b)* **164**, 227–34

Diviš M, Kuriplach J, Richter M, Steinbeck A 1996 First-principles calculation of crystal field in dioxides. *Acta Phys. Slov.* **46**, 95–9; *Czechoslovak J. Phys.* **46**, 1929–30

Diviš M, Nekvasil V, Kuriplach J 1998 Density functional calculation of the crystal field interaction in rare earth cuprates. *Physica C* **301**, 23–8

Diviš M, Richter M, Forstreuter J, Koepernik K, Eschrig H 1997 Crystal-field and magnetism of RGa$_2$ (R = Ce, Er) compounds derived from density-functional calculations. *J. Magn. Magn. Mater.* **176**, L81–8

Eliav E, Kaldor U, Ishikawa Y 1995 Relativistic coupled-cluster method: intrashell excitations in the f^2 shells of Pr^{3+} and U^{4+}. *Phys. Rev. A* **51**, 225–30

Fournier J M 1985 Magnetic properties of actinide solids. In: Manes L (ed.) *Actinides—Chemistry and Physical Properties*. Springer, Berlin

Freeman A J 1979 Dirac–Fock studies of some electronic properties of rare-earth ions. *J. Magn. Magn. Mater.* **12**, 11–21

Freeman A J, Watson R E 1962 Theoretical investigation of some magnetic and spectroscopic properties of rare-earth ions. *Phys. Rev.* **127**, 2058–75

Fulde P, Loewenhaupt M 1986 Magnetic excitations in crystal-field split 4f systems. *Adv. Phys.* **34**, 589–661

Gajek Z 1995 Reliability of conventional crystal field models on f-electron systems. *J. Alloys Compounds.* **219**, 238–43

Gehring G A, Gehring K A 1975 Co-operative Jahn–Teller effects. *Rep. Prog. Phys.* **38**, 1–89

Gignoux D 1991 Magnetic properties of metallic systems. In: Buschow J (ed.) *Electronic and Magnetic Properties of Metals and Ceramics.* VCH, Weinheim, Germany, Vol. 3A

Goremychkin E A, Osborn R, Yu A, Muzychka A, Yu 1994 Crystal-field effects in PrCu$_2$Si$_2$: an evaluation of evidence for heavy-fermion behaviour. *Phys. Rev. B* **50**, 13863–6

Gratz E, Zuckermann M J 1982 Transport properties (electrical resistivity, thermoelectric power and thermal conductivity) of rare earth intermetallic compounds. In: Gschneidner K A Jr., Eyring L R (eds.) *Handbook on the Physics and Chemistry of Rare Earths.* Elsevier, Amsterdam, Vol. 5

Häfner H U, Ludwigs H-W, Nicholson K, Wohlleben D 1981 Low temperature magnetostriction and magnetization of RE$_x$Y$_{1-x}$Pd$_3$ alloys. *Z. Phys. B* **42**, 219–30

Hilscher G, Holland-Moritz E, Holubar T, Jostarndt H-D, Nekvasil V, Schaudy G, Walter U, Fillion G 1994 Valence of praseodymium in Pr$_x$Y$_{1-x}$Ba$_2$Cu$_3$O$_{7-\delta}$: inelastic neutron scattering, specific heat, and susceptibility study. *Phys. Rev. B* **49**, 535–50

Hüfner S 1978 *Optical Spectra of Transparent Rare Earth Compounds.* Academic Press, New York

Hurd C M 1982 Varieties of magnetic order in solids. *Contemp. Phys.* **23**, 469–93

Jandl S, Dufour P, Richard P, Nekvasil V, Zhigunov D I, Barilo S A, Shiryaev S V 1998 Infrared study of crystal field excitations in Nd$_2$CuO$_4$. *J. Lumin.* **78**, 197–203

Jandl S, Dufour P, Strach T, Ruf T, Cardona M, Nekvasil V, Chen C, Wanklyn B M 1995 Raman study of intermultiplet crystal-field excitations in Nd$_2$CuO$_4$. *Phys. Rev. B* **52**, 15558–64

Jandl S, Richard P, Nekvasil V, Zhigunov D I, Barilo S N, Shiryaev S V 1999 Infrared study of neodymium–copper exchange interaction in Nd$_2$CuO$_4$. *Physica C* **314**, 189–95

Jensen J, Mackintosh A R 1991 *Rare Earth Magnetism.* Clarendon, Oxford

Jones M L, Shortt D W, Sterling B W, Schawlow A L, Macfarlane R M 1992 Optical line spectra in metallic (Nd,Ce)$_2$CuO$_{4-x}$. *Phys. Rev. B* **46**, 611–7

Judd B R 1979 Correlation crystal fields for rare earths and actinides. *J. Lumin* **18/19**, 604–8

Kelly P J, Brooks M S S 1980 Cohesive properties of uranium dioxide. *J. Physica* **102B**, 81–3

Kern S, Robinson R A, Nakotte H, Lander G H, Cort B, Watson P, Vigil F A 1999 Crystal-field transition in PuO$_2$. *Phys. Rev. B* **59**, 104–6

Kibler M 1983 An alternative crystal-field strength parameter and its relation with the parameters N$_v$ and S. *Phys. Lett.* **98A**, 343–5

Levy P M 1975 Exchange. In: Craik D J (ed.) *Magnetic Oxides.* Wiley, London Part 1

Luong N H, Franse J J M 1995 Magnetic properties of rare earth–Cu$_2$ compounds. In: Buschow K H J (ed.) *Handbook of Magnetic Materials.* Elsevier, Amsterdam, Vol. 8

Marshall W, Lovesey S W 1971 *Theory of Thermal Neutron Scattering.* Oxford University Press, Oxford

Morrison C A, Leavitt R P 1982 Spectroscopic properties of triply ionized lanthanides in transparent host crystals. In: Gschneidner K A Jr., Eyring L R (eds.) *Handbook of the Physics and Chemistry of Rare Earths.* North-Holland, Amsterdam, Vol. 5

Moze O 1998 Crystal field effects in intermetallic compounds studied by inelastic neutron scattering. In: Buschow K H J (ed.) *Handbook of Magnetic Materials.* Elsevier, Amsterdam, Vol. 11

Muzichka Y U, Goremychkin E A, Sashin I V, Diviš M, Nekvasil V, Nevřiva M, Fillion G 1992 Crystal field in Nd$_2$CuO$_4$. *Solid State Commun.* **82**, 461–4

Nekvasil V 1979 Dependence of crystal field in rare earth garnets on the structure of coordination dodecahedron. *Czech. J. Phys.* **B29**, 785–96

Nekvasil V 1982 Crystal field analysis of electronic Raman scattering data in YbAG and YbGG. *Phys. Stat. Sol. (b)* **109**, 67–74

Nekvasil V, Diviš M, Hilscher G, Holland-Moritz E 1995 Crystal field phenomena in rare earth cuprates. *J. Alloys Compounds* **225**, 578–85

Nekvasil V, Stehno J, Šebek J, Havela L, Sechovský V, Svoboda P 1988 Crystal-field effects in REBa$_2$Cu$_3$O$_7$. *J. Phys. Colloq. C8* **49**, 2177–8

Nekvaskil V, Veltrusky I 1994 Ising-like magnetism in rare-earth cuprates. *Physica C* **235–40**, 1549–50

Newman D J 1971 Theory of lanthanide crystal fields. *Adv. Phys.* **20**, 197–256

Newman D J, Ng B 1989 The superposition model of crystal fields. *Rep. Prog. Phys.* **52**, 699–763

Nielson C W, Koster G F 1963 *Spectroscopic Coefficients for p^n, d^n and f^n Configurations.* MIT Press, Cambridge, MA

Novák P 1996 Calculated crystal field parameters in RCo$_5$ and RNi$_5$ systems. *Phys. Stat. Sol. (b)* **198**, 729–40

Nugroho A A, Nekvasil N, Veltrusky I, Jandl S, Richard P, Menovsky A A, de Boer F R, Granse J J M 2001 Anisotropy of the neodymium–copper exchange interaction in Nd$_2$CuO$_4$. *J. Magn. Magn. Mater*, in press

Purwins H-G, Leson A 1990 Magnetic properties of (rare earth)Al$_2$ intermetallic compounds. *Adv. Phys.* **39**, 309–403

Racah G 1949 Theory of complex spectra. IV. *Phys. Rev.* **76**, 1352–65

Richter M J 1998 Band structure theory of magnetism in 3d–4f compounds. *J. Phys. D: Appl. Phys.* **31**, 1017–48

Staub U, Soderholm L 2000 Electronic 4f state splittings in cuprates. In: Gschneidner K A Jr., Eyring L R (eds.) *Handbook on the Physics and Chemistry of Rare Earths.* North-Holland, Amsterdam in press

Stevens K W H 1997 *Magnetic Ions in Crystals.* Princeton University Press, Princeton, NJ

Wang Y-L, Cooper B R 1970 Crystal-field effects and anomalous susceptibility of antiferromagnets: application to Ce-group-V compounds. *Phys. Rev. B* **2**, 2607–9

Winkler G 1981 *Magnetic Garnets.* Vieweg, Braunschweig, Germany

Wolf W P 1971 Anisotropic interactions between magnetic ions. *J. Phys. (Paris)* **32**, C1–26

Wolf W P, Birgeneau R J 1968 Electric multipole interactions between rare earth ions. *Phys. Rev.* **166**, 376–82

Wybourne B G 1965 *Spectroscopic Properties of Rare Earths.* Interscience, New York

Zirngiebl E, Blumenroeder S, Güntherodt G, Assmus W 1985 Inelastic electronic excitations in CePd$_3$ observed by Raman scattering and luminescence emission. *J. Magn. Magn. Mater.* **47/48**, 72–4

V. Nekvasil
Institute of Physics, ASCR, Prague, Czech Republic

M. Diviš
Charles University, Czech Republic

Longitudinal and Perpendicular Recording: Thermal Stability

The magnetization, coercivity, and recorded signal of longitudinal and perpendicular media decrease with time due to thermal effects. In this section, the effects of material parameters (average grain size, film thickness, grain size dispersion, anisotropy energy constant, exchange energy constant between adjacent grains) and recording density on thermal stability of longitudinal and single-layer perpendicular media will be reported. Most of the results were obtained using computer simulation, because it is not easy to change the parameters except film thickness independently in an experiment.

1. Thermal Stability of Magnetization of Small Particles

The stability of the magnetization of small particles or grains, as used in magnetic recording media, is affected by thermal energy, which causes transitions over the energy barriers which give rise to the hysteresis. The stability of the magnetization (and consequently the recorded signal) is dependent on the ratio $K_u V/kT$. Here, K_u is the uniaxial anisotropy constant (including shape anisotropy constant), V is the volume of the particle, k is the Boltzmann constant, and T is the absolute temperature. Therefore, not only the magnetic properties (magnetization, coercivity, squareness, etc.) but also the recorded signal of magnetic recording media may change a long time after recording.

Suppose that a field is applied to a particle. If the field is not large ($<H_k$ if the field direction coincides with the easy direction), the particle has two minimum energy states, state 1 and state 2, and there is an energy barrier between the states 1 and 2. Say that the barrier height from the state 1 is ΔE_1 and that from the state 2 is ΔE_2.

The changing rate of the probability, N_1, in which a particle exists in the state 1, is given by

$$\frac{dN_1}{dt} = -f_0 \left[N_1 \exp\left(-\frac{\Delta E_1}{kT}\right) - N_2 \exp\left(-\frac{\Delta E_2}{kT}\right) \right] \quad (1)$$

where N_2 is the probability in which the particle exists in the state 2. Suppose that $\Delta E_2 \gg \Delta E_1$, then we have

$$\frac{dN_1}{dt} = -\frac{1}{\tau} N_1 \quad (2)$$

where

$$\tau = \frac{1}{f_0} \exp\left(\frac{\Delta E}{kT}\right) \quad (3)$$

These relations are called the Arrhenius–Néel law (Néel 1955). The stability of the magnetization can be quantified by comparing the relaxation time with the characteristic time of measurement t. Setting $t/\tau = 1$ gives a critical volume in zero field $V_c = kT \ln(f_0 t)/K$. Because of the rapid variation of τ with V, to a good approximation for $V > V_c$, $t \ll \tau$ and the behavior is thermally stable. However, for $V < V_c$, $t \gg \tau$, and the behavior is referred to as "superparamagnetic." Such grains have zero remanence and cannot be used to store information. Clearly there is a minimum grain size for magnetic recording. Although this is easy to estimate for isolated (noninteracting) grains, it becomes much more difficult for real media where intergranular interactions (exchange and magnetostatic) can be very strong. This problem is in the realm of computer simulation, to which this article is devoted.

2. Time Dependence of Squareness, Coercivity, and Output Signal

Figures 1 and 2 show time dependence of squareness S, coercivity H_c, and output signal of longitudinal
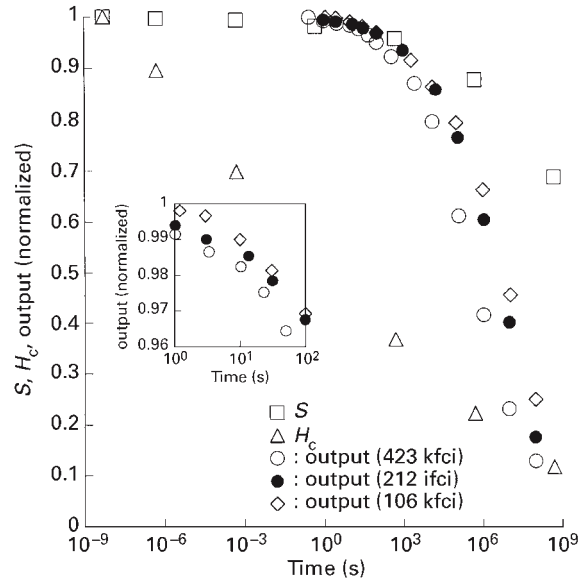
Figure 1
Time dependence of squareness, coercivity, and output signal of a longitudinal medium. An enlarged figure for $t = 1$–100 s and output $= 0.96$–1 is also shown. The physical parameters of the medium is as follows;
$K_u = 2 \times 10^6$ erg cm^{-3} (2×10^5 J m^{-3}),
$V = 10 \times 10 \times 10$ nm^3, Ms $= 400$ emu cm^{-3}
(4×10^5 A m^{-1}), $T = 350$ K. This is a revised version of Fig. 6 in Uesaka *et al.* (1997).
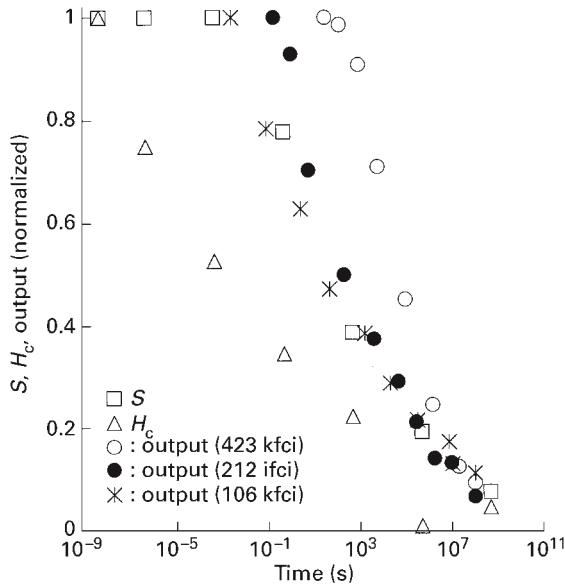
Figure 2
Time dependence of squareness, coercivity, and output signal of a perpendicular medium. The physical parameters of the medium is as follows;
$K_u = 2 \times 10^6 \, \mathrm{erg \, cm}^{-3}$ ($2 \times 10^5 \, \mathrm{J \, m}^{-3}$),
$V = 10 \times 10 \times 10 \, \mathrm{nm}^3$, $Ms = 400 \, \mathrm{emu \, cm}^{-3}$
($4 \times 10^5 \, \mathrm{A \, m}^{-1}$), $T = 350 \, \mathrm{K}$. This is a revised version of Fig. 7 in Uesaka *et al.* (1997).

and perpendicular media. The vertical axes are the values normalized by those just after recording. The horizontal axes for S and H_c mean half of the time to measure a M–H loop. The results in the figures are simulation results at 350 K for 2 D random films with uniform rectangular grains with uniaxial anisotropy energy constant $K_u = 2 \times 10^6 \, \mathrm{erg \, cm}^{-3}$ ($2 \times 10^5 \, \mathrm{J \, m}^{-3}$), volume $V = 10 \times 10 \times 10 \, \mathrm{nm}^3$, frequency factor $f_0 = 1 \times 10^9 \mathrm{s}^{-1}$, Gilbert's damping constant $\alpha = 1$. In both figures, the decrease of output signal is not similar to that of H_c, but rather to that of S.

It has been reported that the H_c of a longitudinal medium changes according to the following equation

(Sharrock 1984);

$$H_c/H_{c0} = 1 - [kT \ln(f_0 t)/(K_u V)]^n \qquad (4)$$

Here, kT is the thermal energy, f_0 is a frequency factor of the order of 10^9–$10^{11} \, \mathrm{s}^{-1}$, K_u is the anisotropy energy constant of a particle (or a grain) in the medium, and V is the volume of the particle. Several n values have been reported. They are listed in Table 1. The time dependence of H_c in Fig. 1 coincides well with $n = 0.735$ case which He *et al.* (1995) reported for the 2D random case.

3. Recording Density Dependence of Output Signal

A figure with enlarged time and output scales is inserted in Fig. 1. It is seen from this enlarged figure and from Fig. 2 that the rate of decay of the output signal increases with recording density in the longitudinal medium, whereas the opposite is true in the perpendicular medium. This was in agreement with experiment (Hirayama *et al.* 1996, Sato *et al.* 1997). Figure 3 shows linear recording density dependence of signal output during a time span of 17 h measured for perpendicular (CoCrPt and CoCrTa) and longitudinal (CoCrPt) media (Hirayama *et al.* 1996). This result arises from the fact that switching begins near the transition region in a longitudinal recording medium, though it begins in the saturation region in a perpendicular recording medium, as shown in Figs. 4 and 5. The improved thermal stability of perpendicular recording at high densities is the reason for its continued development.

4. Grain Size and Height of a Grain

Figure 6 shows the dependence of the thermal stability of longitudinal and perpendicular media on $K_u V/kT$ obtained using computer simulation. The anisotropy energy constant K_u was fixed at $2 \times 10^6 \, \mathrm{erg \, cm}^{-3}$ ($2 \times 10^5 \, \mathrm{J \, m}^{-3}$) and the grain size or height of the magnetic layer of the media was varied ("long., grain size" in the figure means that the grain size of the longitudinal media was varied, "long., height" means

Table 1
Value of n in Eqn. 4 obtained by various conditions.

Value of n	Conditions	Method	References
0.5	γ-Fe$_2$O$_3$ tape	experiment	Flanders and Sharrock (1987)
0.5	γ-Fe$_2$O$_3$, CrO$_2$, BaFe tapes	experiment	He *et al.* (1995)
0.667	distributed easy axis orientation	analytical calculation	Victora (1989)
0.667	cubic anisotropy paricles	analytical calculation	Sharrock (1984)
0.735	2 D random	computer simulation	Lu and Charap (1995)
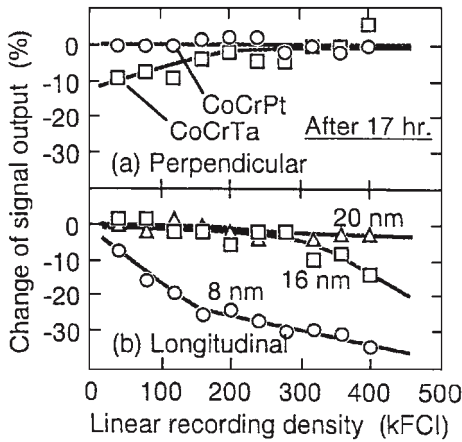
Figure 3
Linear recording density dependence of output signal during time span of 17 h measured for longitudinal and perpendicular media after Hirayama *et al.* (1996).

that the height of the longitudinal media was varied, and so on). The standard values of the grain size and height of a grain were 10 nm. The vertical axis is the time when the output signal decreases 5% from that just after recording.

This figure shows that increasing grain size in longitudinal media and increasing height in perpendicular media give larger thermal stability than the other two cases. However, increasing the grain size gives larger noise. Therefore, if much thicker films can be used in perpendicular recording than the films in longitudinal recording, perpendicular recording will be superior to longitudinal recording from a thermal stability point of view.

Abarra *et al.* (1997) and Yu *et al.* (1998) investigated longitudinal recording films with various thicknesses and found that thermal stability increases with increasing thickness.

5. Grain Size Dispersion

Figures 7 and 8 show time dependence of signal outputs of longitudinal and perpendicular recording media with various grain size dispersions. The output signal of both media decreases faster with increasing grain size dispersion. This is because the magnetic moments of small grains switch faster than those of large grains. This suggests that reducing the number of small grains will increase the thermal stability of longitudinal and perpendicular recording media.

6. Exchange Interaction Between Adjacent Grains

Figure 9 shows the grain size for which the output signal after three years decreases to 90% of that just
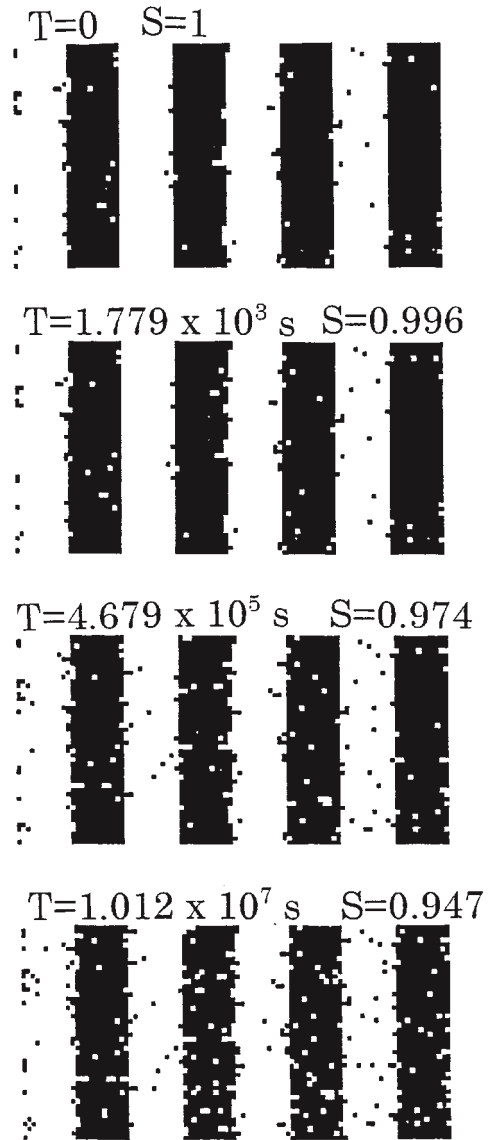
Figure 4
Magnetization state of a longitudinal medium after recording. T is elapsed time, and S is normalized output signal. The initial state ($T = 0$, $S = 1.0$) was obtained from the ideally recorded state using a micromagnetic simulation (Nakatani *et al.* 1979). A white circle indicates that the track direction component of the magnetic moment (M_x) of the corresponding grain is positive, and a black circle means M_x is negative. $K_u = 2 \times 10^6 \, \text{erg cm}^{-3}$ ($2 \times 10^5 \, \text{J m}^{-3}$), $V = 10 \times 10 \times 15 \, \text{nm}^3$, $\text{Ms} = 400 \, \text{emu cm}^{-3}$ ($4 \times 10^5 \, \text{A m}^{-1}$), $T = 350 \, \text{K}$. This is a revised version of Fig. 8 in Uesaka *et al.* (1997).
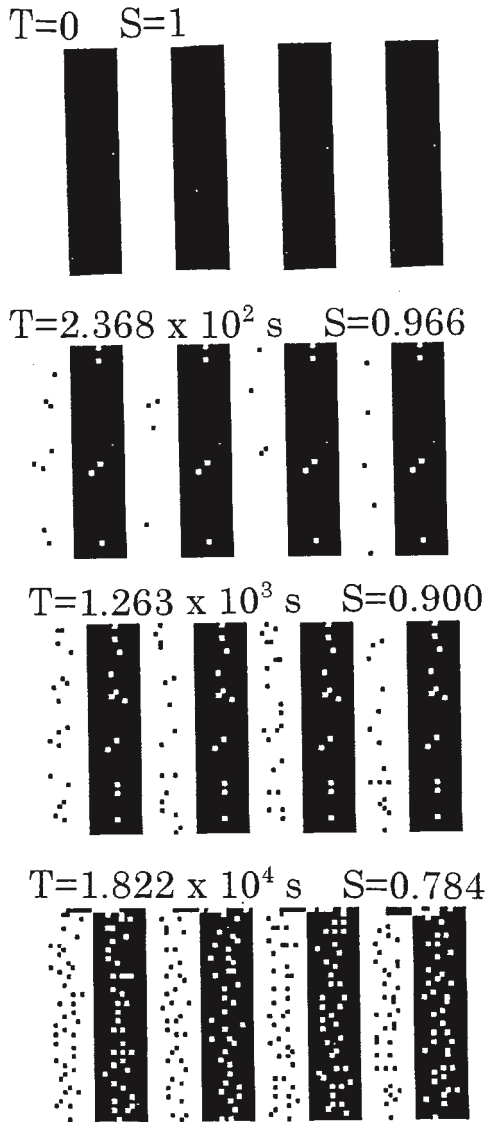
Figure 5
Magnetization state of a perpendicular medium after recording. T is elapsed time, and S is normalized output signal. The initial state ($T=0$, $S=1.0$) was obtained from the ideally recorded state using a micromagnetic simulation (Nakatani *et al.* 1979). A white circle indicates that the perpendicular component of the magnetic moment (M_z) of the corresponding grain is positive, and a black circle means that M_z is negative. $K_u = 2 \times 10^6\,\mathrm{erg\,cm^{-3}}$ ($2 \times 10^5\,\mathrm{J\,m^{-3}}$), $V = 10 \times 10 \times 15\,\mathrm{nm^3}$, $M_s = 400\,\mathrm{emu\,cm^{-3}}$ ($4 \times 10^5\,\mathrm{A\,m^{-1}}$), $T = 350\,\mathrm{K}$. This is a revised version of Fig. 9 in Uesaka *et al.* (1997).
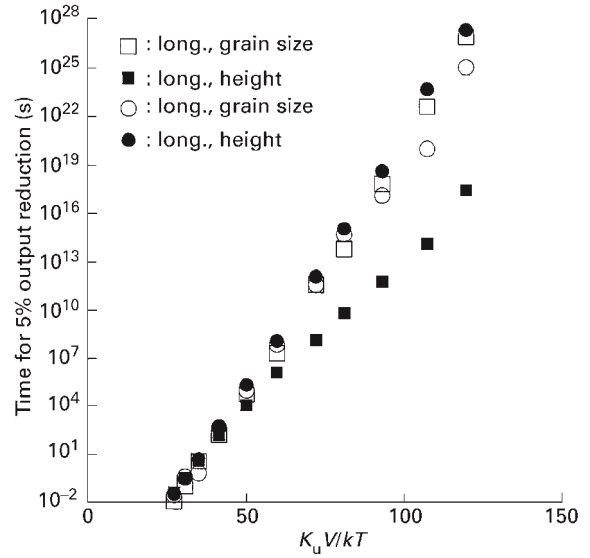
Figure 6
Effect of $K_u V/kT$ on the thermal stability of longitudinal and perpendicular media. $K_u = 2 \times 10^6\,\mathrm{erg\,cm^{-3}}$ ($2 \times 10^5\,\mathrm{J\,m^{-3}}$). The linear recording density was 423 kfci for both media. Grain size or thickness of the film was varied.
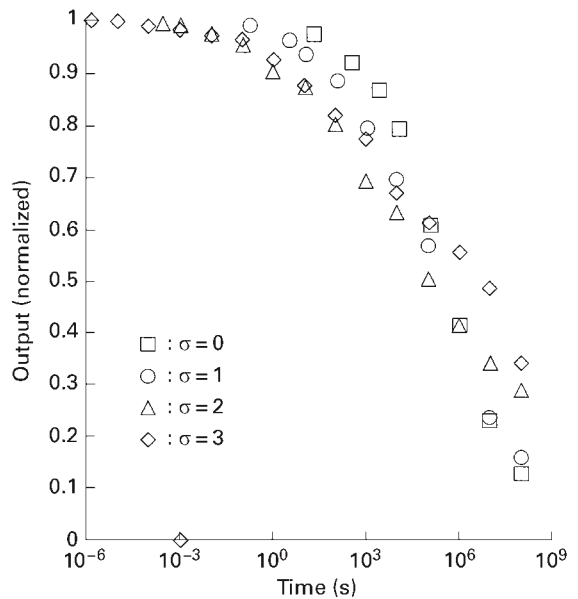
Figure 7
Time dependence of output signal of longitudinal media with various grain size dispersion σ (nm). This is a revised version of Fig. 3 in Nakatani *et al.* (1998).
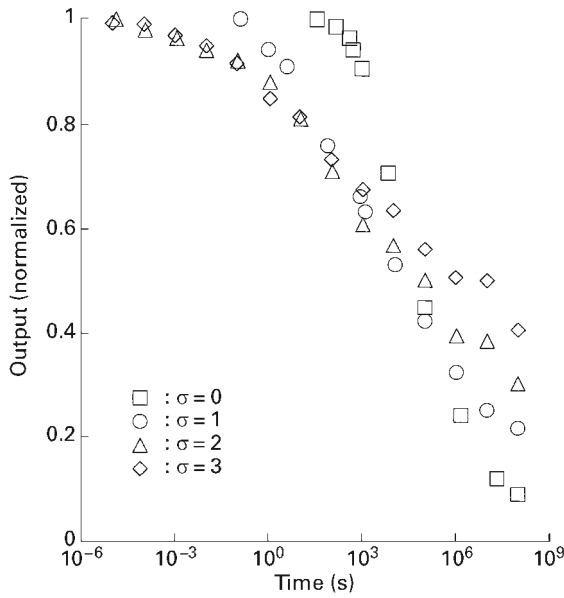
Figure 8
Time dependence of output signal of perpendicular media with various grain size dispersion σ (nm). This is a revised version of Fig. 5 in Nakatani *et al.* (1998).

Figure 9
Effect of intergranular exchange constant A on boundary grain size in which output signal decreases by 10% after three years' decay. $K_u = 2 \times 10^6$ erg cm^{-3} (2×10^5 J m^{-3}), $V = 10 \times 10 \times 10$ nm^3, Ms = 400 emu cm^{-3} (4×10^5 A m^{-1}), $T = 350$ K. This is a revised version of Fig. 6 in Nakatani *et al.* (1999).

after recording, as a function of the intergranular exchange constant A. The thermal stability of longitudinal recording media is degraded with increasing A. On the other hand, the thermal stability of perpendicular recording media is improved as A is increased. The reason for these results is understood as follows: Because the intergranular exchange interaction tends to align the magnetization, it tends to destroy the magnetization structure in the transition region and to support the structure in the saturation region. Therefore, thermal magnetization change is accelerated in longitudinal recording media and suppressed in perpendicular recording media by the introduction of exchange coupling between grains.

7. Simulation Model

Lyberatos *et al.* developed a Monte Carlo simulation method to investigate the thermal stability problem of magnetic materials (Lyberatos *et al.* 1985), and Lu and Charap used it to investigate the problem of longitudinal recording media (Lu and Charap 1994, 1995). In the simulations, the frequency factor f_0 was fixed at 10^9 s^{-1}. The simulation results mentioned above also used this value. This is appropriate for a magnetic recording medium when the field (magnetostatic, and exchange field) is small and parallel to the easy direction.

However, f_0 with the field applied to a different direction from the easy direction is smaller ($1 \sim 1/1000$)

than f_0 with the field applied parallel to the easy direction Coffey *et al.* (1998). In a perpendicular recording medium, the easy direction of a grain is almost aligned in the direction perpendicular to the film plane and the magnetostatic field is also applied in this direction, but in a longitudinal recording medium the direction of the magnetostatic and/or exchange field in a grain does not necessarily coincide with the easy direction. Therefore, the thermal stability of longitudinal media could be larger than the values stated above.

The simulation results mentioned above were obtained assuming coherent rotation of the magnetic moment of a grain. However, H_c and S of a perpendicular medium obtained using this model are larger than the values obtained experimentally. This may suggest that each grain does not rotate coherently and that the thermal stability of a perpendicular medium is worse than that stated above.

8. Conclusion

Thermal stability of longitudinal recording media was compared with that of perpendicular recording media. The decrease of output signal is not similar to

that of H_c but rather to that of S. The output signal of higher recording density (higher frequency) decreases faster than that of lower recording density in the longitudinal medium, but it is opposite in the perpendicular medium. H_c of a longitudinal medium changes according to the following equation with $n = 0.5 \sim 0.735$;

$$H_c/H_{c0} = 1 - [kT \ln(f_0 t)/(K_u V)]^n \qquad (5)$$

Perpendicular recording will be superior to longitudinal recording from a thermal stability point of view if much thicker film can be used. Reducing the number of small grains will increase the thermal stability of longitudinal and perpendicular recording media. Thermal stability of longitudinal recording media is degraded with increasing intergranular exchange A, but that of perpendicular recording media is improved as A is increased.

See also: Longitudinal Media: Fast Switching; Magnetic Recording: Rigid Media, Recording Properties; Magnetic Recording Media: Advanced; Magnetic Recording Technologies: Overview; Metal Particle versus Metal Evaporated Tape; Micromagnetics: Basic Principles

Bibliography

Abarra E N, Phillips G N, Okamoto I, Suzuki T 1997 Magnetic force microscopy analysis of thermal stability in 8 Gbits/in^2 longitudinal recording media. *J. Magn. Soc. Jpn.* **21** (S2), 291–6

Coffey W T, Crothers D S F, Dormann J L, Geoghegan L J, Kennedy E C 1998 Effects of an oblique magnetic field on superparamagnetic relaxation time. II. Influence of the gyromagnetic term. *Phys. Rev. B.* **58** (6), 3249–66

Flanders P J, Sharrock M P 1987 An analysis of time-dependent magnetization and coercivity and of their relationship to print-through in recording tapes. *J. Appl. Phys.* **62** (7), 2918–28

He L, Wang D, Doyle W D 1995 Remanence coercivity of recording media in the high-speed regime. *IEEE Trans. Magn.* **31** (6), 2892–4

Hirayama Y, Itoh K, Honda Y, Inaba N, Futamoto M 1996 Thermal stability of CoCr-alloy perpendicular magnetic recording media. *J. Magn. Magn. Mater.* **193**, 253–7

Lu P, Charap S H 1994 Thermal instability at 10 Gbits/in^2 magnetic recording. *IEEE Trans. Magn.* **30** (6), 4230–2

Lu P, Charap S H 1995 High-density magnetic recording media design and identification: susceptibility to thermal decay. *IEEE Trans. Magn.* **31** (6), 2767–9

Lyberatos A, Wohlfarth E P, Chantrell R W 1985 Simulated annealing: an application in fine particle magnetism. *IEEE Trans. Magn* **MAG-21** (4), 1277–82

Nakatani Y, Uesaka Y, Hayashi N 1979 Direct solution of the Landau–Lifshitz–Gilbert equations for micromagnetics. *Jpn. J. Appl. Phys.* **28** (12), 2485–507

Nakatani Y, Hayashi N, Uesaka Y, Fukushima H 1998 Effect of grain-size dispersion on read/write properties in thin film recording media affected by thermal fluctuation. *IEEE Trans Magn.* **34** (4), 1618–20

Nakatani Y, Hayashi N, Uesaka Y, Fukushima H 1999 Effect of inter-granular exchange coupling on read/write properties in thin film recording media affected by thermal fluctuation. *J. Appl. Phys.* **85** (8), Part 2, 4726–8

Néel L 1955 Some theoretical aspects of rock magnetism. *Adv. Phys.* **4**, 191

Sato K, Yoshida Y, Okuyama C, Okamoto I, Shinohara M 1997 Thermal stability of perpendicular and longitudinal recorded information. *J. Magn. Soc. Jpn.* **21**(S2), 321–4

Sharrock M P 1984 Particle-size effects on the switching behavior of uniaxial and multiaxial recording materials. *IEEE Trans. Magn.* **MAG-20**(5), 754–6

Uesaka Y, Takahashi Y, Nakatani Y, Hayashi N, Fukushima H 1997 Monte Carlo simulation of thermal fluctuation in magnetization of longitudinal and perpendicular recording media. *J. Magn. Magn. Mater.* **174**, 203–18

Victora R H 1989 Predicted time dependence of the switching field for magnetic materials. *Phys. Rev. Lett.* **63** (4), 457–60

Yoshida K, Hirayama Y, Igarashi M, Futamoto M, Sugita Y 1999 Switching mechanism of a perpendicular magnetic recording medium at very low temperature. *J. Magn. Magn. Mater.* **193**, 462–5

Yu M, Doener M F, Sellmyer D J 1998 Thermal stability and nanostructure of CoCrPt longitudinal recording media. *IEEE Trans. Magn.* **34** (4), 1534–6

Y. Uesaka
Nihon University, Fukushima, Japan

Y. Nakatani, N. Hayashi
University of Electrocommunications, Tokyo, Japan

H. Fukushima
Honda-cho, Chiba, Japan

Longitudinal Media: Fast Switching

Every modern computer has several devices that permanently store information. Of particular interest are those storage devices that enable the user not only to read back information but also to write information. In general, useful storage devices must have sufficient storage capacity with short access time. For fast and nonvolatile mass data storage, as is required in a personal computer or in a server system, magnetic hard disk recording is exclusively in use.

From a practical point of view, it is highly desirable that the data transfer rate is increased together with the storage capacity. Increasing the linear bit density in a hard drive (i.e., the number of bits per unit length in the down-track direction) has the desired effect of increasing storage density and transfer rate. However, the performance of a hard disk drive not only depends on the maximum transfer rate but also on access time. Since the access time includes the latency until the transducer reads a specific sector of

a track, it is controlled by the rotational speed. For high-performance drives, therefore, very high rotational speeds become attractive. Disk drives spinning the disk as fast as 15000 rpm are commercially available.

The practically realizable writing speed depends on the design of the writing head and the driving electronics. Traditionally, the contribution of the medium to the speed of recording has been neglected. For modern high-performance drives, however, the contributions of the media can no longer be disregarded. This article reviews the fundamental parts of the theory of fast switching in media as well as experimental information available in the literature.

1. The Different Time Regimes in Magnetization Reversal

Figure 1 shows the time axis involved in magnetic recording. For "long times," referred to as "viscosity regime", say at times larger than 100 ns, the magnetization reversal behavior is adequately described by the theory of thermally activated magnetization reversal over finite energy barriers (Arrhenius–Néel formalism, see Sect. 1.1). At very short times, intrinsic dynamics lead to precessional motion that determines the reversal behavior, which is reviewed in Sect. 1.2. As a numerical example, consider magnetic recording in a hard disk drive of relatively low performance (1999). Assuming a bit length of 200 nm at a speed of $10\,\mathrm{ms}^{-1}$, the time for one bit is roughly 20 ns. In order to achieve high recording performance, the switching process needs to be completed within a small enough fraction of the bit cell duration, e.g., 4–5 ns. As Fig. 1 illustrates, this time falls between the viscosity regime and the precessional regime, in a timescale in which the dynamic behavior is extremely complex.

1.1 Switching in the "Viscosity Regime"

The theory of thermally activated magnetization reversal is now reviewed. At first sight, thermally activated magnetization reversal does not seem to be related to the switching speed at all, but a closer examination shows that this is not true.

Street and Woolley (1949) first discussed thermally activated magnetization reversal and pointed out that every magnetization reversal process is initiated by the thermal energy k_BT (k_B = Boltzmann's constant = $1.38 \times 10^{-23}\,\mathrm{JK}^{-1}$, T = temperature in K). Néel (1949) expressed the probability of magnetization reversal as

$$r = f_0 \exp\left(-\frac{\Delta E}{k_B T}\right) \quad (1)$$

where r is the reversal rate, ΔE is the magnetic energy barrier to be surmounted, and f_0 is a frequency factor of the order of 10^{10} Hz. Equation (1) has the same form as it appears in the theory of semiconductors; therefore, it is also referred to as the "Arrhenius–Néel" approach. In a simple phenomenological interpretation, Eqn. (1) means that the thermal energy makes f_0 trials per second to reverse the magnetization. The magnetic energy, ΔE, and the thermal energy, k_BT, determine the probability of success of these trials; for $\Delta E \gg k_BT$, the probability of success is virtually zero, while it is large for $\Delta E \ll k_BT$. Thus, Eqn. (1) predicts a time-dependent magnetization. Clearly, the concept breaks down when f_0 is approached.

Magnetic recording media consist of very fine grains or particles. In this case, the (short-range) quantum mechanical exchange forces are sufficiently strong to keep the magnetization in these particles uniform (Brown 1969).

For the case of a single-domain particle, the energy barrier entering in Eqn. (1) can be evaluated easily using the model of coherent rotation (Stoner and Wohlfarth 1948). Consider a single-domain particle with uniaxial anisotropy that can be either of shape or magnetocrystalline origin. As indicated in Fig. 2, the easy axis (dashed line) forms an angle θ_0 with the applied field, $\vec{H}$. The magnetization, $\vec{M}$, makes an angle θ with the field axis. The magnetic energy, $E(\theta)$, of the particle in the applied field is then given by
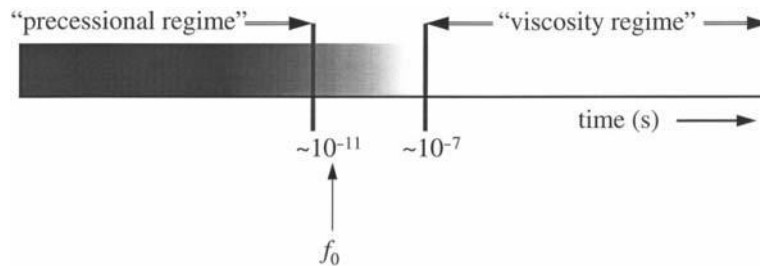
Figure 1
Time axis in magnetic recording. For long times ($\geqslant 10^{-7}$ s) the magnetization reversal is governed by thermally activated reversal, while at short times ($\leqslant 10^{-11}$ s) it is governed by spin precession dynamics.
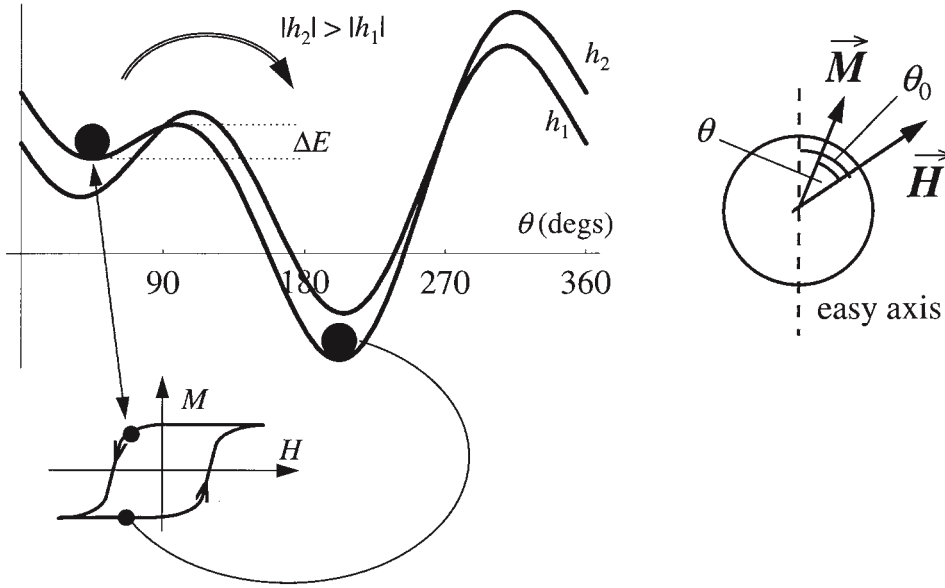
Figure 2
Thermally activated magnetization reversal. In the general case, the magnetization can have two local energy minima. The thermal energy can push the magnetization over the energy barrier ΔE.

(assuming uniaxial anisotropy)

$$E(\theta) = -\mu_0 M_s H V \cos\theta + K_1 V \sin^2(\theta - \theta_0) \qquad (2)$$

where M_s is the saturation magnetization of the material, K_1 is the anisotropy constant, V is the particle volume, and $\mu_0 = 4\pi \times 10^{-7}\,\mathrm{Vs\,A^{-1}m^{-1}}$. From the anisotropy constant, the anisotropy field, H_A, can be derived as $H_A = 2K_1/\mu_0 M_s$. The free parameter of the system is the angle θ between magnetization and field. As Fig. 2 illustrates, there are two local energy minima in the general case. The local minimum having the lower energy corresponds to the case of alignment between the magnetization and the applied field, whereas the other minimum represents opposing magnetization and field. The latter state is stable if the energy barrier, ΔE, which has to be overcome at magnetization reversal is larger than zero. Note that the energy barrier is field dependent, as illustrated in Fig. 2. The field strength at which the energy barrier becomes zero is the maximum attainable switching field (Stoner and Wohlfarth 1948):

$$|h_{SW}(\theta_0)| = \frac{1}{(\cos^{2/3}(\theta_0) + \sin^{2/3}(\theta_0))^{3/2}} \qquad (3)$$

Most theoretical analyses have considered the case $\theta_0 = 0$, i.e., alignment of the applied field with the easy axis. The energy barrier then simplifies to

$$\Delta E(\theta_0 = 0, h) = K_1 V (1 + h)^2 \qquad (4)$$

If there are N_0 grains, the number of grains not yet switched, $n(t)$, is given by the exponential $n(t) = N_0 \exp(-rt)$. Together with the rate equation (Eqn. (1)) and the condition that $n(t) = N_0/2$ at remanent coercivity (the remanent coercivity is the field which switches 50% of the magnetization), one can derive (Kneller and Luborsky 1963, Sharrock and McKinney 1981) the following:

$$|H_r(\theta_0 = 0, t)| = H_A \left(1 - \sqrt{\frac{k_B T}{K_1 V} \ln \frac{f_0 t}{\ln 2}}\right) \qquad (5)$$

Equation (5) gives the field that is required to reverse 50% of the magnetization of a previously saturated magnetic sample subjected to a field pulse of duration t.

For thin-film media, the grains are oriented at random in the film plane, so that the case of a magnetically easy axis aligned with the field is highly exceptional. Victora (1989) gave an approximation for the energy barrier for the general case $\theta = 0$:

$$\Delta E(\theta_0, h) \cong 2K_1 V \left(\frac{2}{3}\right)^{3/2} \left(1 + \frac{h}{h_{SW}(\theta_0)}\right)^{3/2}$$
$$\sin[2(\theta_{SW}(\theta_0) - \theta_0)] \qquad (6)$$

where $\theta_{SW}(\theta_0) = \theta_0 + \tan^{-1}(\sqrt[3]{\tan\theta_0})$.

Bertram and Richter (1999) and Richter and Ranjan (1999) have shown that for thin-film media consisting of noninteracting grains with their easy

404
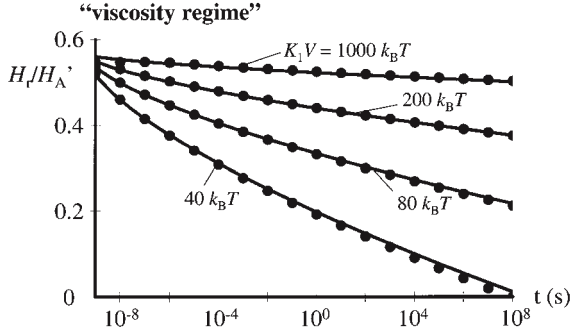
"viscosity regime"

Figure 3
Time-dependent coercivity in the "viscosity regime."
The curves hold for an assembly of single-domain
particles with their easy axes in plane. The lines are
calculated using Eqn. (7) and the dots are exact solutions
for the entire particle assembly.

axes oriented at random in the plane, the time-
dependent coercivity of the entire film can be appro-
ximated by

$$|H_r(t)| = 0.566 H_A \left(1 - 0.977 \left[\frac{k_B T}{K_1 V} \ln \frac{f_0 t}{\ln 2}\right]^{2/3}\right) \quad (7)$$

Equation (7) assumes that there is no magnetic in-
teraction between the grains. Figure 3 illustrates the
time dependence of the remanent coercivity for a two-
dimensional, isotropic, noninteracting particle en-
semble. As can be seen, for low values of the ratio
$K_1 V/k_B T$, the coercivity at long times (storage) is
significantly lower than at short times (writing). Since
very small grains are required to achieve high signal-
to-noise ratios (Richter 1999), it is important to
note that, especially in high-density recording, the
coercivity obtained for typical magnetometer meas-
urements is considerably lower than that relevant for
the writing process.

1.2 Precession Dynamics

According to quantum theory, a magnetic moment,
$\vec{\mu}$, is accompanied by an angular momentum, $\vec{L}$. The
ratio between the magnetic moment and the angular
momentum is called the gyromagnetic ratio, γ:

$$\vec{\mu} = \gamma \vec{L} \quad (8)$$

where $\gamma = -1.761 \times 10^{11} \text{m}^2 \text{ V}^{-1} \text{s}^{-2}$.

Since magnetization is created by electrons that
have the electrical charge $-e$, γ in Eqn. (8) is written
as a negative value. If the magnetic dipole is subjected
to a homogeneous magnetic field, $\vec{H}$, it experiences a
torque, $\vec{T}_M$, which seeks to orient it with the field
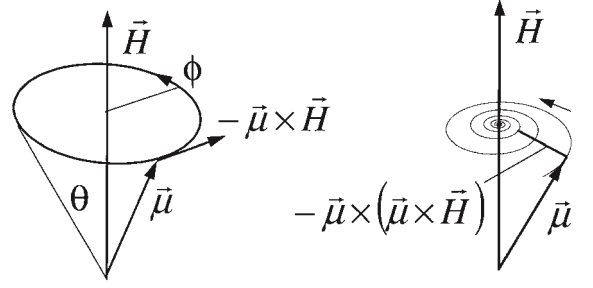
Figure 4
Precession. An undamped system would precess forever,
while in a damped system (right) the magnetization
approaches equilibrium asymptotically.

direction:

$$\vec{T}_M = \mu_0 \left(\vec{\mu} \times \vec{H}\right) \quad (9)$$

Since $\vec{T}_M = d\vec{L}/dt$, Eqns. (8) and (9) give

$$\frac{d\vec{\mu}}{dt} = -\mu_0 |\gamma| (\vec{\mu} \times \vec{H}) \quad (10)$$

Equation (10) is the magnetic torque equation and
means that the magnetization precesses counterclock-
wise around the direction of the field, as illustrated in
Fig. 4. Since there is no damping considered, the
precession lasts forever.

The inclusion of damping leads to the Landau–
Lifshitz equation (Landau and Lifshitz 1935), which
was later modified by Gilbert (1955). The *Landau–
Lifshitz–Gilbert equation* for the magnetization is

$$\frac{d\vec{M}}{dt} = -\mu_0 |\gamma| (\vec{M} \times \vec{H}) + \frac{\alpha}{M}\left[\vec{M} \times \frac{d\vec{M}}{dt}\right] \quad (11)$$

where α is a dimensionless phenomenological damp-
ing constant. Landau and Lifshitz (1935) considered
only very small damping and gave an expression that
can be written as

$$\frac{d\vec{M}}{dt} = -\frac{\mu_0 |\gamma|}{1+\alpha^2}(\vec{M} \times \vec{H}) - \frac{\mu_0 |\gamma| \alpha}{(1+\alpha^2)M}[\vec{M} \times (\vec{M} \times \vec{H})]$$
$$= -\mu_0 |\gamma'| (\vec{M} \times \vec{H}) - \mu_0 \lambda [\vec{M} \times (\vec{M} \times \vec{H})] \quad (12)$$

It is customary to write the Landau–Lifshitz equa-
tion in the form given on the right-hand side of Eqn.
(12). As shown in Fig. 4(b), the vector $-\vec{\mu} \times (\vec{\mu} \times \vec{H})$
(or $-\vec{M} \times (\vec{M} \times \vec{H})$, respectively) points towards the
direction of $\vec{H}$ (as it should) and the magnetization
aligns with the field for $t \to \infty$. However, Eqn. (12)
implies that only the precessional part of the motion
of the magnetization vector, namely $(\vec{M} \times \vec{H})$,

experiences damping. This means that losses owing to any nonprecessional magnetization changes are neglected—which is only true for small damping.

Although the two equations can formally be transferred into one another, they describe different physics and the Gilbert form should be preferred (Kikuchi 1956, Mallinson 1987). Safonov has since pointed out that both the Landau–Lifshitz as well as the Gilbert form are compatible with thermodynamics only for very small damping (Safonov 1999).

In the following, the magnetization reversal of a single spin, or, alternatively, that of a homogeneously magnetized single-domain particle is considered. For many applications, it is useful to write the Landau–Lifshitz–Gilbert equation in a parametric form in which the magnetization vector is described by the polar angle $\theta(t)$ and the azimuth angle $\phi(t)$, as indicated in Fig. 4. In this case, the following pair of equations has to be solved (Bertram and Mallinson 1970):

$$\frac{d\theta}{dt} = \frac{-|\gamma|}{M_s V(1+\alpha^2)}\left(\alpha\frac{\partial E}{\partial\theta} - \frac{1}{\sin\theta}\frac{\partial E}{\partial\phi}\right) \quad (13a)$$

$$\frac{d\phi}{dt} = \frac{-|\gamma|}{M_s V(1+\alpha^2)}\left(\frac{1}{\sin\theta}\frac{\partial E}{\partial\theta} + \frac{\alpha}{\sin^2\theta}\frac{\partial E}{\partial\phi}\right) \quad (13b)$$

Evaluation of the partial derivatives of the magnetic energy, E, yields

$$\frac{d\theta}{dt} = \frac{-|\gamma|\mu_0 H_A \alpha}{1+\alpha^2}$$
$$\times \left[\begin{array}{c} h(\cos\theta_0\sin\theta - \sin\theta_0\cos\theta\cos\phi) \\ +\sin\theta\cos\theta - \dfrac{h}{\alpha}\sin\theta_0\sin\phi \end{array}\right] \quad (14a)$$

$$\frac{d\phi}{dt} = \frac{-|\gamma|\mu_0 H_A \alpha}{1+\alpha^2}\left[\frac{h}{\alpha}(\cos\theta_0 - \sin\theta_0\cot\theta\cos\phi)\right.$$
$$\left. + \frac{\cos\theta}{\alpha} + h\sin\theta_0\frac{\sin\phi}{\sin\theta}\right] \quad (14b)$$

It is useful to define the natural precession frequency, f_{nat} (Hempel 1962):

$$f_{nat} = \frac{\Omega_{nat}}{2\pi} = \frac{|\gamma|\mu_0 H_A}{2\pi} \quad (15)$$

At zero applied field, the precession of the magnetization is driven only by the anisotropy field which gives f_{nat} its name. For modern hard disk media, $H_A \approx 800\,\text{kA}\,\text{m}^{-1}$ (10 kOe) and $f_{nat} \approx 28\,\text{GHz}$.

For $\theta_0 = 0$, which represents alignment of the easy axis with the applied field, Eqns. ((14a) and (14b)) become

$$\frac{d\theta}{dt} = \Omega_{nat}\frac{\alpha}{1+\alpha^2}\sin\theta(h+\cos\theta) \quad (16a)$$

$$\frac{d\phi}{dt} = \Omega_{nat}\frac{1}{1+\alpha^2}(h+\cos\theta) \quad (16b)$$
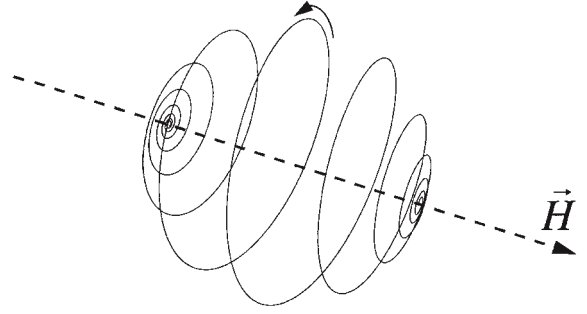
Figure 5
Trajectory of the tip of the magnetization vector during reversal. The field is applied along the easy axis.

Consider first the case of vanishing damping, $\alpha \to 0$. According to Eqns. (16a) and (16b), the polar angle θ remains constant and the magnetization continues with its precession movement—regardless of the applied field value. The magnetization cannot switch, because there is no mechanism by which the spin system can transport energy to the lattice. For small damping, however, the polar angle of the magnetization can change with time and the applied field can switch the magnetization (see Fig. 5). Equations (16a) and (16b) show that for small damping the precession movement, $d\phi/dt$, depends only very weakly on the damping, but the rate of change of the polar angle, $d\theta/dt$, is directly proportional to the damping constant. Larger damping therefore accelerates the switching speed, as long as the system does not become critically damped. Kikuchi (1956) first analyzed the switching problem and showed that the switching time is proportional to $(1+\alpha^2)/\alpha$. The switching time is therefore minimized for $\alpha = 1$, which corresponds to the critically damped case.

For the case of alignment of the easy axis with the field ($\theta_0 = 0$, see Eqns. (16a) and (16b)), the differential equation for the polar angle θ can be solved analytically:

$$t = -\frac{1+\alpha^2}{\alpha\Omega_{nat}}\left\{\begin{array}{c} \dfrac{\ln\left(\dfrac{\cos(\theta(t)/2)}{\cos(\theta(0)/2)}\right)}{1-h} \\[3ex] +\dfrac{\ln\left(\dfrac{h+\cos\theta(t)}{h+\cos\theta(0)}\right)}{h^2-1} \\[3ex] +\dfrac{\ln\left(\dfrac{\sin(\theta(t)/2)}{\sin(\theta(0)/2)}\right)}{1+h} \end{array}\right\} \quad (17)$$

Note that the initial value of the polar angle, $\theta(0)$, determines the reversal time. For $\theta(0) = 0$, the solution degenerates and the magnetization never switches. In order to reverse, the magnetization needs an "initial

kick" away from the metastable orientation $\theta = 0$, which can, for instance, be provided thermally. In Sect. 1.3, the combination of thermal activation and precession dynamics is discussed.

1.3 Transition between Viscosity and Precession Regime

In Sect. 1.1, the rate equation (Eqn. (1)) is introduced phenomenologically. Brown (1963) first treated thermal fluctuations of a single-domain particle in depth and derived the rate equation as well as an expression for the frequency factor, f_0. Brown treated the problem in an analogous way to that of a particle undergoing Brownian motion. This approximation is valid, because the correlation time of the thermal energy ($\approx 10^{-13}\,\mathrm{s}$) is much shorter than the response time of a spin system ($\approx 1/\Omega_{\mathrm{nat}} \approx 10^{-11}\,\mathrm{s}$).

The starting point for further calculation is the Landau–Lifshitz–Gilbert equation (Eqn. (11)) in which the thermal forces are considered by adding a random field term to the effective field. This extra field term has a statistical average of zero and is normally distributed with a variance given by the fluctuation dissipation theorem (Brown 1963). The modified Landau–Lifshitz–Gilbert equation is called the "Langevin equation". For the simplest case in which the easy axis is aligned with the field, Brown solved the Langevin equation and obtained a relaxation rate of the form given in Eqn. (1). An expression was obtained for the frequency, f_0, which typically yields values of the order of $10^{10}\,\mathrm{Hz}$. During the derivation, Brown used the approximation that the magnetic energy barrier is much greater than the thermal energy. Note that the energy barrier is field dependent and that large reverse fields inevitably make the energy barrier so small that the assumption $\Delta E \gg k_{\mathrm{B}} T$ is no longer valid.

The general solution for the aligned case including energy barriers of arbitrary height has been obtained (Safonov 1999, Safonov and Bertram 2000). When the assumption $\Delta E \gg k_{\mathrm{B}} T$ is dropped it is not legitimate to neglect the occupancies of the magnetization states away from the energy minimum. Therefore, one deals with a variety of magnetization orientations in each state as opposed to a discrete orientation model.

In the classical Arrhenius–Néel case, the relaxation time, τ_1, is governed by the time that it takes the magnetization to find its way to the top of the energy barrier. For the general case, however, the time that the magnetization needs to reach the lower energy minimum, τ_2, cannot be neglected. In addition, one has to consider a third relaxation time, τ_{12}, which reflects that the magnetization does not necessarily switch to a new state once it has reached the energy maximum; it can also fall back into its original state. The three relaxation times add up to the total
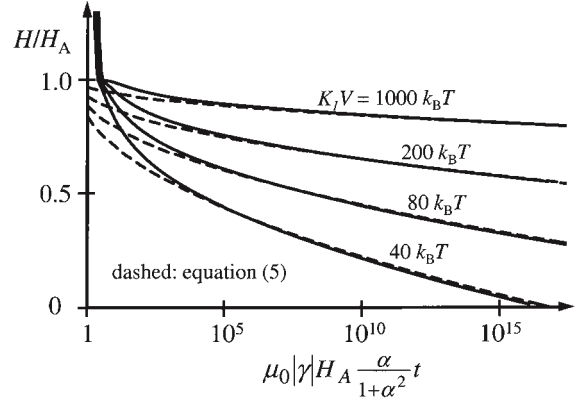
Figure 6
Time dependence of coercivity for various energy barriers $K_1 V$. The solid lines give the exact solutions. The dashed lines correspond to purely thermal reversal.

relaxation time, τ (Safonov and Bertram 2000):

$$\tau = \tau_1 + \tau_2 + \tau_{12} \qquad (18)$$

Therefore, the relaxation time is longer than that from the simple Arrhenius–Néel theory, or, equivalently, the faster one desires to switch the magnetization, the higher the required field. Figure 6 compares the time dependence of the coercivity for Arrhenius–Néel behavior with the exact solution, whereby the frequency, f_0, (Safonov and Bertram 2000)

$$f_0 = 2\sqrt{\frac{2}{\pi}} \frac{\alpha}{1+\alpha^2} \sqrt{\frac{K_1 V}{k_{\mathrm{B}} T}} \mu_0 |\gamma| H_{\mathrm{A}} \qquad (19)$$

It is important to realize that the precession frequency of the magnetization changes as a function of magnetization orientation. When the magnetization moves from one energy minimum to another, the precession frequency first decreases, then becomes zero at the energy maximum, and finally starts to precess again in the opposite sense. Owing to the low precession frequencies, the magnetization behaves "sluggishly," which explains that deviations from Eqn. (5) are observed at surprisingly long times $\approx 100/f_0 \ldots 1000/f_0$. The problem can be regarded as a "random walk" of a nonlinear oscillator (Safonov 1999). For a typical anisotropy field of a recording medium, $H_{\mathrm{A}} = 800\,\mathrm{kA\,m^{-1}}$ (10 k Oe), one finds $f_0 \approx 100\,\mathrm{GHz}$ ($\alpha = 0.04$). The steep increase of coercivity is found at $t \approx 1/f_0$, which then amounts to 0.01 ns. The phenomenological damping parameter, α, which has been set to 0.04 without further consideration, is discussed below.

407

1.4 Switching Dynamics of Recording Media

The previous sections have dealt with simple systems. Real recording media consist of particle systems, which are magnetically coupled by intergranular exchange and magnetostatic forces. Real systems also show a high degree of disorder. The interactions and the degree of disorder control the details of the switching process.

So far, the damping has been treated on a phenomenological basis. Using ferromagnetic resonance, the damping parameter has been determined to be around 0.02 for cobalt-based recording media (Inaba *et al.* 1997). The damping parameter describes how effectively energy can be transported away from the spin system into the lattice, where it is eventually dissipated and transformed into heat. Peng and Bertram (1998) modeled the switching behavior of a two-dimensional isotropic recording medium using a regular array of hexagons. They solved the full Langevin equation and calculated coercivity as function of field pulse time. The result obtained is similar to that shown in Fig. 6; it also agrees well with the simple formula of Eqn. (7) for times longer than ~ 100–$1000 \times f_0^{-1}$ (Bertram and Richter 1999).

In complex interacting systems, such as recording media, the spin system does not only perform a simple precession in unison as discussed above. The spin system can be excited in various modes or "spin waves" (Chantrell *et al.* 1998). Irregularities or non-uniform grain size distributions, which are present in real recording media, can disturb regular precession patterns of the magnetization. This means that the energy inherent in the spin system is transported first into complicated magnetization modes before it is finally dissipated in the lattice. Effectively, this increases the damping parameter, and the overall response time of the spin system to an external field is reduced (Hannay *et al.* 1999). For a discussion of the physical origin of damping see Suhl (1998).

The role of disorder in the switching response of a polycrystalline magnetic film to field pulses of varying duration was investigated in the experimental work of Rizzo *et al.* (1999). Their magnetization data as a function of time show a distinct kink at 10 ns, indicating a shift from an exponential to a logarithmic time dependence of the magnetization. Using concepts of statistical physics, they distinguished two regimes, a thermal regime characterized by statistical relaxation between states of metastable equilibrium and a nonequilibrium regime described by the driven response to the applied field. The time constant assigned to the transition between the two regimes is 5 ns. The media used for this experiment had a very low coercivity; in a subsequent experiment, however, no such kink was found for a medium with higher coercivity down to field pulses of 1 ns (Rizzo *et al.* 2000).

2. Experimental Techniques and Data

The first experimental investigation of switching speed in recording media was by Thornley (1975). Particulate tapes with low coercivity were subjected to subnanosecond field pulses. These field pulses were created using a recording head equipped with a microstrip-line. Switching speed values of the order of 2×10^{-5} A s m^{-1} were assigned to the various media. Since then switching speed measurements have been reconsidered and more comprehensive measurements have been performed (Doyle and He 1993, He *et al.* 1995, He *et al.* 1996). It was found—consistent with Thornley's early results—that oxide media such as γ-Fe$_2$O$_3$, CrO$_2$, and barium ferrite switch more slowly than the more advanced metallic particles and metal-evaporated tape. Since the field created by the strip-line is insufficient to switch high coercivity media, such as metallic particles, it is inevitable to use an additional bias field to assist the switching process. It has also been reported that the damping constant measured using FMR is inversely correlated with the switching speed observed (Yu and Harrell 1996).

Microstrip-line measurements have been extended to thin-film media (Stinnett *et al.* 1998). In order to achieve higher pulse fields, the minimum achievable pulse time is compromised to about 10 ns. The switching behavior of the thin-film media is found to be similar to that of the particulate media investigated before.

Apart from microstrip techniques, alternative techniques using spin-stands have been suggested to measure the time dependence of coercivity (Rubin *et al.* 1998, Moser *et al.* 1999). Di-bits have been written with pulsed fields from a recording head. The coercivity is identified with the current needed to achieve 50% of the maximum di-bit signal. The data obtained have to be corrected for the dynamic behavior of the head as well for the demagnetizing field associated with the di-bit. A different spin-stand technique uses the idea that each pass of a d.c. excited head presents a field pulse of duration $\Delta t \approx g/v$ to the media, where v is the linear velocity and g is the gap length of the writer (Richter *et al.* 1998). Longer times can be realized by passing the head repeatedly over the media, resulting in a longer exposure of the media to the head field. It has been argued that the repetitive application of a short pulse ("reptation") is very close to exposing the media only once with a correspondingly longer pulse.

This technique breaks down for very short-time pulses for which the magnetization reversal process is dominated by precession dynamics. The magnetic state is characterized by the integrated noise, whereby the noise is at a maximum when the medium is demagnetized; i.e., it is in the remanent coercive state. Wachenschwanz and Alex (1999) suggested a modification of the "reptation technique" where the
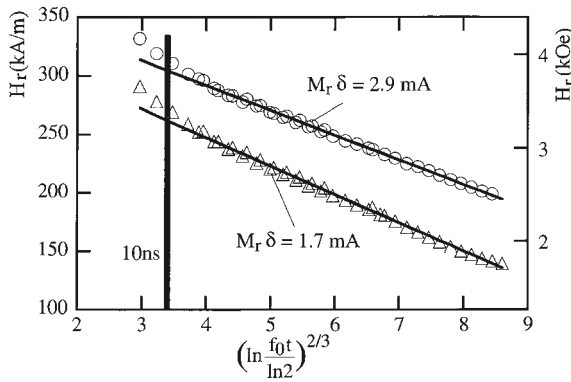
Figure 7
Measured time dependence of coercivity for thin-film media (reproduced by permission of IEEE from *IEEE Trans. Magn.*, 1999, **35**, 2790–5).

amount of erasure of a long wavelength square-wave recording rather than the d.c. erased noise is used as an indicator of the magnetization state. Although this modification has practical advantages, the effect of the demagnetizing field associated with the transitions as well as head nonlinearities can alter the result.

Figure 7 shows dynamic coercivity data obtained using the reptation technique for about eight orders of magnitude in time (Richter 1999). As Eqn. (7) suggests, the data should follow a straight line when plotted vs. $[\ln(f_0 t/\ln 2)]^{2/3}$. Deviations are seen for $[\ln(f_0 t/\ln 2)]^{2/3} \leqslant 3.5$, corresponding to $t \leqslant 500/f_0$, which is roughly consistent with the results of Sect. 1.3. On the other hand, these deviations are, at least partially, due to a demagnetization effect inherent to the measurement. The slope can be used to estimate the value for $K_1 V/k_B T$.

The Landau–Lifshitz equation predicts that the media can, in principle, be switched infinitely fast for a sufficiently large driving field. Such an experiment has indeed been done and it is confirmed that the magnetization can be switched with field pulses as small as 6 ps (Siegmann *et al.* 1995), consistent with the Landau–Lifshitz equation (He and Doyle 1996).

More experiments of this kind have shown that the damping for recording media is surprisingly high and can be close to 1, whereas that of perpendicular media is somewhat smaller, about 0.3 (Tudosa *et al.* 2004). In these experiments, the spins inside the grains are excited in a non-uniform manner and the damping so obtained cannot be compared directly with that of traditional FMR experiments in which the magnetization precesses uniformly around the equilibrium orientation.

The high speed experiments have also revealed that the ultimate speed limit for the switching of recording media is of the order of a few pico-seconds which is slower than previously expected (Tudosa *et al.* 2004).

For practical applications, this ultimate limit has no consequence, because the linear densities and spinning speeds that would lead to such high data rates cannot be achieved. Moreover, the driving fields used in these experiments are higher than those that can be obtained in disk drives.

3. Recording Considerations

The switching speed under recording conditions has only been addressed theoretically so far. The switching speed in the dynamical regime (no thermal activation included) has been calculated (Fang and Zhu 1996, Peng and Bertram 1997). Similarly to the considerations for single grains, small damping parameters—which are likely to be applicable to thin-film media—have been reported to increase the switching time.

The switching speed of longitudinal recording media has been compared theoretically with that of vertically oriented media (Peng and Bertram 1997). Media were compared with equal coercivities, whereby the longitudinal media were subjected to a ring head field and the vertical media were subjected to a field created by a probe head in conjunction with a magnetically soft underlayer. Longitudinal media were found to switch faster, which is fundamentally owing to the effect of the film-demagnetizing field. For longitudinal media, the film-demagnetizing field is perpendicular to the reversal direction and thus creates an extra torque on the magnetization. In the case of vertical media, there is no extra torque, because the demagnetizing field is parallel to the reversal direction.

4. Summary

Data rates in magnetic recording begin to approach the intrinsic switching speed limits of recording media. It is thought that precession dynamics limit the switching speed of longitudinal recording media to times of the order of 0.1 ns in practice. For times longer than ~100 ns, dynamical effects are described well by the Arrhenius–Néel formalism. The theoretical understanding of the transition between the viscosity regime and the precessional regime is not fully developed.

See also: Magnetic Recording Technologies: Overview; Magnetic Recording: Rigid Media, Recording Properties; Magnetization Reversal Dynamics; Magnetic Viscosity; Micromagnetics: Basic Principles

Bibliography

Bertram H N, Mallinson J C 1970 Switching dynamics for an interacting anisotropic dipole pair of arbitrary bond angle. *J. Appl. Phys.* **41**, 1102–4

Bertram H N, Richter H J 1999 Arrhenius–Néel thermal decay in polycrystalline thin-film media. *J. Appl. Phys.* **85**, 4991–3

Brown W F Jr. 1963 Thermal fluctuations of a single-domain particle. *Phys. Rev.* **130**, 1677–86

Brown W F Jr. 1969 The fundamental theorem of the theory of fine ferromagnetic particles. *Ann. New York Acad. Sci.* **147**, 461–88

Chantrell R W, Hannay J D, Wongsam M, Schrefl T, Richter H J 1998 Computational approaches to thermally activated fast relaxation. *IEEE Trans. Magn.* **34**, 1839–44

Doyle W D, He L 1993 Measurement of the switching speed limit in high coercivity magnetic media. *IEEE Trans. Magn.* **29**, 3634–6

Fang h, Zhu J G 1996 Switching speed of longitudinal thin-film recording media. *IEEE Trans. Magn.* **32**, 3584–6

Gilbert T L 1955 A Lagrangian formulation of the gyromagnetic equation of the magnetization field. *Phys. Rev.* **100**, 1243

Hannay J D, Chantrell R W, Richter H J 1999 Simulations of fast switching in exchange coupled longitudinal thin-film media. *J. Appl. Phys.* **85**, 5012–4

He L, Doyle W D 1996 A theoretical description of magnetic switching experiments in picosecond field pulses. *J. Appl. Phys.* **79**, 6489–91

He L, Doyle W D, Varga L, Fujiwara H, Flanders P J 1996 High-speed switching in magnetic recording media. *J. Magn. Magn. Mater.* **155**, 6–12

He L, Wang D, Doyle W D 1995 Remanence coercivity of recording media in the high speed regime. *IEEE Trans. Magn.* **31**, 2892–4

Hempel K A 1962 Über die ferrimagnetische Resonanz in polykristallinen Ferriten mit hexagonaler Anisotropie. *Z. Angew. Physik.* **14** (9), 488–95

Inaba N, Uesaka Y, Nakamura A, Futamoto M, Sugita Y 1997 Damping constants of Co–Cr–Ta and Co–Cr–Pt thin films. *IEEE Trans. Magn.* **33**, 2989–91

Kikuchi R 1956 On the minimum of magnetization reversal time. *J. Appl. Phys.* **27**, 1352–7

Kneller E F, Luborsky F E 1963 Particle size dependence of coercivity and remanence of single domain particles. *J. Appl. Phys.* **34**, 656–8

Landau L, Lifshitz E 1935 On the theory of the dispersion of magnetic permeability in ferromagnetic bodies. *Phys. Z. Sowjet.* **8**, 153–69

Mallinson J C 1987 On damped gyromagnetic precession. *IEEE Trans. Magn.* **23**, 2003–4

Moser A, Weller D, Best M E, Doerner M F 1999 Dynamic coercivity measurements in thin-film recording media using a contact write/read tester. *J. Appl. Phys.* **85**, 5018–20

Néel L 1949 Influence des fluctuations thermiques sur l'aimantation de grains ferromagnétique trés fins. *C. R. Acad. Sci. Paris* **228**, 664–6

Peng Q, Bertram H N 1997 Micromagnetic studies of switching speed in longitudinal and perpendicular polycrystalline thin-film recording media. *J. Appl. Phys.* **81**, 4384–6

Peng Q, Bertram H N 1998 Numerical simulations of the effect of record field pulse on medium coercivity at finite temperatures. *IEEE Trans. Magn.* **34**, 1543–5

Richter H J 1999 Longitudinal recording at 10 to 20 Gbit/inch^2 and beyond. *IEEE Trans. Magn.* **35**, 2790–5

Richter H J, Ranjan R Y 1999 Relaxation effects in thin-film media and their consequences. *J. Magn. Magn. Mater.* **193**, 213–9

Richter H J, Wu S Z, Malmhäll R K 1998 Dynamic coercivity effects in thin-film media. *IEEE Trans. Magn.* **34**, 1540–2

Rizzo N D, Silva T J, Kos A B 1999 Relaxation times for magnetization reversal in a high coercivity magnetic thin film. *Phys. Rev. Lett.* **83**, 4876–9

Rizzo N, Silva T J, Kos A B 2000 Nanosecond magnetization reversal in high coercivity thin films. *IEEE Trans. Magn.* **36**, 159–65

Rubin K, Goldberg J S, Rosen H, Marinero E, Doerner M, Schabes M 1998 Dynamic coercivity and thermal decay of magnetic media. *Mater. Res. Soc. Proc.* **517**, 261–6

Safonov V L 1999 Thermal reversal of magnetization as "random walk" dynamics of a nonlinear oscillator. *J. Appl. Phys.* **85**, 4370–2

Safonov V L, Bertram H N 2000 Dynamic-thermal reversal in a fine micromagnetic grain: time dependence of coercivity. *J. Appl. Phys.* **87**, 5681–3

Sharrock M P, McKinney J T 1981 Kinetic effects in coercivity measurements. *IEEE Trans. Magn.* **17**, 3020–2

Siegmann H C, Garwin E L, Prescott C Y, Heidmann J, Mauri D, Weller D, Allenspach R, Weber W 1995 Magnetism with picosecond field pulses. *J. Magn. Magn. Mater.* **151**, L8–12

Stinnett S M, Doyle W D, Flanders P J, Dawson C 1998 High speed switching measurements in thin-film disk media. *IEEE Trans. Magn.* **34**, 1828–30

Stoner E C, Wohlfarth E P 1948 A mechanism of magnetic hysteresis in heterogeneous alloys. *Philos. Trans. R. Soc.* **A240**, 599–642

Street R, Woolley J C 1949 A study of magnetic viscosity. *Proc. R. Soc.* **A62**, 562–72

Suhl H 1998 Theory of the magnetic damping constant. *IEEE Trans. Magn.* **34**, 1834–8

Thornley R F M 1975 Pulse response of recording media. *IEEE Trans. Magn.* **11**, 1197–9

Tudosa L, Stamm C, Kashuba A B, King F, Siegmann H C, Stöhr J, Ju G, Lu B, Weller D 2004 The ultimate speed of magnetic switching in granular recording media. *Nature* **428**, 831–3

Victora R H 1989 Predicted time dependence of the switching field for magnetic materials. *Phys. Rev. Lett.* **63**, 457–60

Wachenschwanz D, Alex M 1999 The effect of switching rate dependence of coercivity on recording performance. *J. Appl. Phys.* **85**, 5312–4

Yu Y, Harrell J W 1996 FMR determination of damping constants in magnetic tapes. *J. Magn. Magn. Mater.* **155**, 126–8

H. J. Richter
*Seagate Recording Media, Fremont, California
USA*

M

Magnetic Anisotropy

"Magnetic anisotropy" is an ambiguous term. Since a magnetic field is a vector quantity, it implies by definition direction dependence. In 1821 Poisson assumed an interplay of magnetism with crystallinity. After 1850 the "magnetism of crystals" was experimentally investigated. Since then it has been known that diamagnetism, paramagnetism, and natural ferromagnetism all depend on the properties of the different materials, especially on the crystallographic properties.

Any dependence of the magnetic properties of a material on the direction can be termed magnetic anisotropy. It can be described by a dimensionless "anisotropy function," and it is closely related to space-dependent magnetization patterns, yielding a total (direction-dependent) magnetic free energy. Usually, however, only the magnetic properties of solids in the magnetically ordered state are characterized by magnetic anisotropy.

Several different origins and manifestations of magnetic anisotropy can be distinguished, namely shape anisotropy, exchange anisotropy, stress aniso tropy, surface anisotropy, anisotropy induced by a magnetic field, and, last but not least, magnetocrystalline anisotropy. The last is the most important for modern hard magnetic materials and permanent magnets.

1. Definitions of Magnetic Anisotropy

The term "magnetic anisotropy" is not a primary unit (see *Magnetic Units*), although magnetic anisotropy is of utmost importance for soft and especially hard magnetic materials.

For soft magnetic materials (see *Magnetic Losses*) the smallest possible coercivity $_MH_C$ or $_BH_C$ is a primary goal. It can be deduced from the hysteresis loop in the M–H or B–H representation, respectively. Since the magnetic anisotropy is linked to coercivity, usually the magnetic anisotropy of any origin is minimized in soft magnetic materials. Medium-soft magnetic materials, especially magnetic recording materials, rely on a sufficiently large (because of long-term stability) but sufficiently small (because of the necessity of frequent remagnetization) coercivity, and is usually in the range of 10^4–10^5 Am^{-1} (ca. 100–1000 Oe). For such applications materials with shape anisotropy (e.g., Fe_2O_3 needles), surface anisotropy (thin films), or magnetocrystalline anisotropy are needed. A clear-cut distinction of the nature of magnetic anisotropy is rarely possible.

Shape anisotropy is nearly always present, since the magnetic medium is never an ideal sphere. The origin of shape anisotropy is the magnetostatic energy. Shape anisotropy can be used to prepare permanent magnets. (In the 1950s elongated single domain magnets were fabricated from pure cubic iron in the shape of needles). Shape anisotropy also plays an important role in the anisotropy of Alnico magnets (see *Alnicos and Hexaferrites*).

Stress anisotropy is the counterpart to magnetostriction. It is observed if an external stress, via magnetoelastic coupling, favors energetically some magnetization directions. The already mentioned surface anisotropy is always present in thin layers or if extended surfaces are present in the material, e.g., nanocrystalline samples (see, e.g., *Amorphous and Nanocrystalline Materials*).

In this article mainly the subject of magnetocrystalline anisotropy (MCA) will be treated in more detail, since it is the basis of modern permanent magnets.

2. Experimental Determination of Magnetic Anisotropy

In principle the measurement of magnetic properties (see *Magnetic Measurements: Quasistatic and ac*) can be performed as a function of the crystallographic directions of the sample and/or an applied magnetic field. From these results frequently information about the magnetic anisotropy can be deduced. Some methods especially suited to probe magnetic anisotropy, however, are mentioned here. If a single crystal of the magnetic material is available, the magnetic anisotropy and the anisotropy coefficients K, etc., are obtained by, e.g., a torque magnetometer. An aligned ensemble of powders can be used instead of a single crystal but with reduced accuracy.

Due to the magnetic moment of the neutron, elastic and inelastic neutron scattering (see *Magnetic Excitations in Solids*) is a primary tool to establish the spin structure of magnetic materials and also the magnetic excitations. Since these measurements can be performed at different magnetic fields and at variable temperatures, many magnetic parameters, including the magnetic anisotropy, can be deduced from neutron experiments. By rotating a sample in a magnetic field and detecting the transverse susceptibility the pinning field, which is directly linked to the magnetic anisotropy, can be measured (Elk and Hermann 1992).

"Free moving" particles studied for magnetization at high (pulsed) fields allow an analysis of the coupling of different magnetic sublattices and the associated magnetic anisotropy (Franse and Radwanski 1996).

In their classical measurement of the magnetization of a YCo_5 single crystal in two perpendicular

directions Hoffer and Strnat (1966) detected a huge anisotropy field of approximately 13 T (130 kOe) and opened up the area of rare-earth permanent magnets (see *Rare Earth Magnets: Materials*).

3. Magnetocrystalline Anisotropy

Disregarding the microscopic origin of MCA this property can be measured and analyzed. It can be described in the following manner (Kirchmayr 1991). Since hexagonal and tetragonal crystal structures are the most important structures for modern permanent magnets, only these two are discussed here. The mean magnetic moment of a ferro- or ferrimagnetic substance is directed, in the absence of an external magnetic field, in the crystallographic direction in which the absolute minimum free energy, F, is achieved.

This direction is called the "easy magnetization direction" or "easy axis." A part of the total free energy, therefore, depends on the direction of magnetization with respect to the different crystallographic directions and is called the magnetocrystalline free energy, F_a or the MCA. Usually, F_a is expressed in terms of simple sine or cosine functions. For hexagonal crystals,

$$F_a = K_1\sin^2\theta + K_2\sin^4\theta + K_3\sin^6\theta + K_3'\sin^6\theta\cos6\phi$$

and for tetragonal crystals,

$$F_a = K_1\sin^2\theta + K_2\sin^4\theta + K_3\sin^4\theta\cos4\phi$$

where θ is the angle between the c axis and the vector of magnetization, ϕ is the angle between the projection of the magnetization vector in the basal plane of the crystal and one of the a axes, and K_1, K_2, K_3, and K_3' are the coefficients of anisotropy, expressed in J m^{-3} or in GOe; 1 MGOe = 7.9577 kJm^{-3}.

The anisotropy constants reflect the magnetic anisotropy only phenomenologically and have no direct connection with the physical origin of magnetic anisotropy.

If an external magnetic field H is applied to a crystal, an additional term appears in the free energy, F, which is given by

$$F = F_a - M_s H\cos(\theta - \beta)$$

where M_s is the saturation magnetization, β is the angle between H and the c axis, and $(\theta-\beta)$ is the angle between M_s and H. In this equation the stray field energy, which depends on the size and the shape of the sample, has been neglected. Equilibrium is achieved when F reaches a minimum, hence

$$\delta F/\delta\theta = \delta F_a/\delta\theta + \mu_0 M_s H\sin(\theta - \beta) = 0$$

or

$$-\delta F/\delta\theta = \mu_0 M_s H\sin(\theta - \beta) = \mu_0\left|M \times H\right|$$

where $\mu_0\left|M \times H\right|$ is the torque exerted by the crystal anisotropy and is counterbalanced by the external field. For small deviations from the easy axis, $\Delta\theta = 0$, the term

$$(1/\mu_0 M_s).(\delta^2 F_a/\delta\theta^2)\big|_{\Delta\beta=0} = H = H_A$$

is equivalent to a field, called the anisotropy field, H_A.

As can be seen from the above discussion, H_A is deduced from small deviations from the easy axis and is therefore defined for small applied fields. It must be distinguished from the anisotropy field, H_A^*, which can be measured directly by the singular point detection method, i.e., at high magnetic fields above H_A. This method has its merits because it may be applied to polycrystalline samples and in pulsed fields (see *Magnetic Measurements: Pulsed Field*). It yields directly the anisotropy field H_A^*.

The magnetic anisotropy can therefore be given by the anisotropy constants K_1, K_2, and K_3 or by the anisotropy field H_A resp. H_A^*. (K_3 is usually neglected.) The anisotropy field can be measured directly on polycrystalline samples, in contrast to K_1, K_2, and K_3 which are usually not directly accessible but can be determined on single crystals by torque measurements. However, because of the problem of achieving well-developed single crystals with different compositions and because of technical problems to measure the torque at different temperatures, the classical determination of the magnetic anisotropy constants by means of torque measurements is of limited practical use.

4. Microscopic Origin of Magnetocrystalline Anisotropy

Long-range spin ordering over macroscopic distances is the result of exchange, i. e., the combination of the electrostatic coupling between electron orbitals and the Pauli exclusion principle. The nature of this exchange is isotropic. Anisotropy, however, is the result of the interaction of the electron orbitals with the potentials of the lattice. The lattice symmetry is therefore responsible for the MCA. A rigorous calculation of the MCA from first principles is at present not possible. A simplified approach is the molecular field calculation. In the case of RE–3d (RE = rare-earth) intermetallics a phenomenological separation into the contributions of the RE and the 3d sublattice is often meaningful. Micromagnetism tries to discuss the behavior of magnetic materials without detailed knowledge of the basic origin of magnetic ordering and anisotropy. Much progress has been achieved by this approach, especially by Kronmüller *et al.* (1994); (see *Coercivity Mechanisms*).

There are three different types of permanent magnetic materials, namely RECo$_5$ and RE$_2$Co$_{17}$, which

are both hexagonal, and $RE_2Fe_{14}B$ which is tetragonal (Kirchmayr 1996). The basis of the magnetic ordering and the magnetic anisotropy in metallic compounds of RE metals with transition metals (T) are the RE–RE, T–T, and RE–T interactions. (For a review of the phases, crystal structures, and magnetic properties of RE–$3d$ intermetallics see Kirchmayr and Burzo 1990). In the $RE_2Fe_{14}B$ compounds the situation is even more complex because of the presence of a third element. Naturally, in a metallic system most of the interactions are mediated by the electrons, especially the conduction electrons, which means that the fullband structure has to be taken into account. While the RE anisotropy is a single-ion anisotropy mainly governed by crystal field effects, the T anisotropy is complex and less well understood. All these interactions plus sublattice anisotropies are responsible for various types of magnetic transitions and peculiarities, such as first-order magnetization processes, critical fields, noncollinarity of ferrimagnetic structures, etc. (see also *Localized 4f and 5f Moments: Magnetism* and *Alloys of 4f (R) and 3d (T) Elements: Magnetism*).

5. Magnetocrystalline Anisotropy as a Basis for Modern Permanent Magnets

In Table 1 some basic data for hard magnetic materials are summarized (for the temperature dependence of K_1 and K_2 of these compounds see also Kirchmayr and Burzo 1990). A comparison of the anisotropy field H_A and the coercivity $_MH_c$ shows a large discrepancy. H_A serves as an upper limit for $_MH_c$ and is a necessary prerequisite for a good modern permanent magnet with large saturation and coercivity and therefore energy product (see *Hard Magnetic Materials, Basic Principles of*). In practice the B–H representation of the hysteresis loop is used. In this case $_BH_c > M_s$ is sufficient to achieve a linear demagnetization curve in the second quadrant. Since the coercivity decreases with increasing temperature, even at the operating temperature $_BH_c > M_s$ should be valid. This condition is usually met by modern permanent magnets. In the future a further increase in the energy product seems therefore to be feasible only by increasing the saturation, but not by increasing the coercivity or the magnetic anisotropy.

Table 1
Basic data for hard magnetic materials.

Compound	T_c (K)	μ_0H_a (T)	$(K)_1$ (MJ m^{-3})	μ_0M_s (T)
$SmCo_5$	993	40	17	1.05
Sm_2Co_{17}	1100	6.5	3.3	1.30
$Nd_2Fe_{14}B$	585	6.7	5	1.60

Source: Gutfleisch (2000).

6. Summary and Conclusions

Anisotropy is a basic property of all crystalline materials. Even in nanocrystals and amorphous solids, e.g., metallic glasses, anisotropy is present on an atomic level. Therefore magnetic anisotropy is an intrinsic property of magnetization in general.

In the last decades MCA made possible the development of better and stronger permanent magnets, characterized by a higher coercivity and an ever increasing energy product. This fast development, however, may reach a natural boundary, because the coercivity has reached a value which is sufficient to make full use of the possibilities of modern permanent magnet materials. Any further progress in energy product cannot be achieved by an increase in magnetic anisotropy, but only by the development of materials with larger saturation magnetization while maintaining sufficiently high coercivity. The development of materials with large magnetocrystalline anisotropy attempts to retain this property also at elevated temperature.

From the viewpoint of basic research, the understanding and calculation of magnetic anisotropy from first principles is still in its infancy. Therefore, studies of the magnetic anisotropy will continue to be a fascinating area of basic and applied research for the time to come.

Bibliography

Coey J M D (ed.) 1996 *Rare-earth Iron Permanent Magnets.* Clarendon Press, Oxford

Elk K, Hermann R 1992 The transverse susceptibility of texturized polycrystals. *J. Magn. Magn. Mater.* **117**, 359–67

Franse J J M, Radwanski R F 1996 Intrinsic magnetic properties. In: Coey J M D (ed.) *Rare-earth Iron Permanent Magnets.* Clarendon Press, Oxford

Gutfleisch O 2000 Controlling the properties of high energy density permanent magnetic materials by different processing routes. *J. Phys. D: Appl. Phys.* **33**, R157–72

Hoffer G, Strnat K J 1966 Magnetocrystalline anisotropy of YCo_5 and Y_2Co_{17}. *IEEE Trans. MAG.* **2**, 487–9

Kirchmayr H 1991 Determination of the anisotropy field by the singular point detection method. In: Long G J, Grandjean F (eds.) *Supermagnets, Hard Magnetic Materials.* Kluwer Academic Publishers, The Netherlands, pp. 449–60

Kirchmayr H R 1996 Permanent magnets and hard magnetic materials. *J. Phys. D: Appl. Phys.* **29**, 2763–78

Kirchmayr H R, Burzo E 1990 Magnetic properties of rare earth compounds with 3d elements. In: *Crystal and Solid State Physics, Magnetic Properties of Metals; Subvolume d2. Compounds Between Rare Earth Elements and 3d, 4d or 5d Elements.* Landolt–Börnstein New Series Group III, Springer, Berlin, vol. 19, Chap. 2.4, pp. 1–468

Kronmüller H, Schrefl T, Fischer R, Fidler J 1994 Micromagnetic analysis of coercivity of rare earth–transition metal intermetallics and interstitial compounds. *Proc. 8th Symp. on Magnetic Anisotropy and Coercivity in RE–TM Alloys*, Birmingham, pp. 1–20

H. Kirchmayr
Vienna University of Technology, Austria

Magnetic Excitations in Solids

This article is focused on the discussion of one important experimental method for measurements of magnetic excitations in solids, i.e., inelastic neutron scattering (INS): a method that has been in the past and that will be in the future the method of choice in this field.

In the first part, an overview is given on magnetic neutron cross-sections, on the range of experimentally accessible transfers of momentum and energy ($(\boldsymbol{Q}, \omega)$-range), and on important types of neutron spectrometers that are used for the measurements of magnetic excitations.

In the second part, the hierarchy of relevant solid-state interactions and the involved energy scales will be discussed for compounds containing the magnetic elements with $3d$-, $4f$-, and $5f$-electrons in open atomic shells.

In the third and last part, elementary magnetic excitations like those from spin waves, crystal-field transitions, inter-multiplet transitions, and spin fluctuations will be presented in relation to their occurrence in bulk magnetic materials containing the elements with $3d$-, $4f$-, and $5f$-electrons.

An early review on magnetic excitations was given by (Stirling and McEwen 1986).

1. Magnetic Neutron Cross-sections

The interaction of thermal neutrons with matter is twofold: the nuclear interaction with the atomic nuclei and the magnetic interaction of the neutron's magnetic dipole moment with the magnetic field $\boldsymbol{B}$ created by the unpaired electrons in the sample. A comprehensive theoretical treatment is given in the two volumes of the book by Lovesey (1984). Focusing on magnetic scattering we give as an example the scattering cross-section for unpolarized neutrons (Böni and Furrer (1998); for meaning of symbols look up the cited article):

$$\left(\frac{d\sigma}{d\Omega\, dE_f}\right)_{\text{mag}} = \frac{k_f}{k_i}\left(\gamma r_0 \frac{g}{2} F(\boldsymbol{Q})\right)^2$$
$$\times \sum_{\alpha\beta}\left(\delta_{\alpha\beta} - \hat{Q}_\alpha \hat{Q}_\beta\right) S^{\alpha\beta}(\boldsymbol{Q}, \omega) \quad (1)$$

where $S^{\alpha\beta}(\boldsymbol{Q}, \omega)$ is the van Hove magnetic scattering function:

$$S^{\alpha\beta}(\boldsymbol{Q}, \omega) = \frac{1}{2\pi\hbar}\int \sum_{jj'}\left\langle S_{j'\alpha}(0) S_{j\beta}(t)\right\rangle$$
$$\times \left\langle \exp\left(-i\boldsymbol{Q}\cdot\boldsymbol{r}_{j'}(0)\right)\exp\left(+i\boldsymbol{Q}\cdot\boldsymbol{r}_j(t)\right)\right\rangle$$
$$\times \exp(-i\omega t)\, dt \quad (2)$$

$S^{\alpha\beta}(\boldsymbol{Q}, \omega)$ corresponds to the Fourier transform of the magnetic pair correlation function that gives the

probability to find a magnetic spin at position $\mathbf{r}_j$ at time t with component $S_{j\beta}(t)$ and a spin at position $\mathbf{r}_{j'}$ at time $t = 0$ with a component $S_{j'\alpha}(0)$. Therefore, the magnetic cross-section depends on magnetic as well as on lattice vibrational degrees of freedom. This is usually taken into account by a Debye–Waller factor, $\exp(-2W(\boldsymbol{Q}))$; in the following this factor has been omitted.

In Eqn. (2), $S^{\alpha\beta}(\boldsymbol{Q}, \omega)$ is expressed in terms of expectation values of time-dependent operators (Heisenberg picture). Equivalently, the scattering function can be written in terms of time-independent operators (Schrödinger picture) by replacing the integral over time by a δ-function in energy obtaining

$$S^{\alpha\beta}(\boldsymbol{Q}, \omega) = \sum_{jj'}\exp(i\boldsymbol{Q}\cdot(\boldsymbol{r}_j - \boldsymbol{r}_{j'}))\sum_{\lambda_i\lambda_f} p_{\lambda_i}\left\langle \lambda_i|\hat{S}_{j'}^\alpha|\lambda_f\right\rangle$$
$$\times \left\langle \lambda_f|\hat{S}_j^\beta|\lambda_i\right\rangle \delta(E_{\lambda_i} - E_{\lambda_f} + \hbar\omega) \quad (3)$$

The magnetic scattering function is also directly related to the imaginary part of the wavevector and frequency-dependent susceptibility via the fluctuation–dissipation theorem by

$$S^{\alpha\beta}(\boldsymbol{Q}, \omega) = \frac{\hbar}{\pi}\frac{1}{1 - \exp(-\hbar\omega/k_B T)}\text{Im}\,\chi^{\alpha\beta}(\boldsymbol{Q}, \omega) \quad (4)$$

This theorem implies that the magnetic moment of the neutron acts on the sample as a frequency- and wavevector-dependent magnetic field $\boldsymbol{B}(\boldsymbol{Q}, \omega)$, monitoring the magnetic response $\boldsymbol{M}(\boldsymbol{Q}, \omega)$ of the sample with

$$M^\alpha(\boldsymbol{Q}, \omega) = \sum_\beta \chi^{\alpha\beta}(\boldsymbol{Q}, \omega) B_\beta(\boldsymbol{Q}, \omega) \quad (5)$$

where $\chi^{\alpha\beta}(\boldsymbol{Q}, \omega)$ is the generalized susceptibility tensor. The fluctuation–dissipation theorem allows direct comparisons of $\chi^{\alpha\beta}$ as obtained by neutron scattering with bulk measurements of χ using the Kramers–Kronig relation (see text books on solid-state physics).

For the discussion of the polarization dependence of the neutron cross-section, we refer the reader to the book of (Williams 1988). Here it is sufficient to state that a polarization analysis allows us to separate unambiguously nuclear and magnetic scattering though a loss of overall intensity has to be taken into account. Furthermore, it is possible to determine, for example, individual matrix elements of the spin operators between crystal-field states ($|\langle \lambda_i|\hat{S}_j^\alpha|\lambda_f\rangle|^2$).

2. Accessible $(\boldsymbol{Q}, \omega)$-range

The magnetic scattering functions $S^{\alpha\beta}(\boldsymbol{Q}, \omega)$ as given in the previous section depend only on the *transfer* of energy ($\hbar\omega = E_i - E_f$) and momentum ($Q = \boldsymbol{k}_i - \boldsymbol{k}_f$)
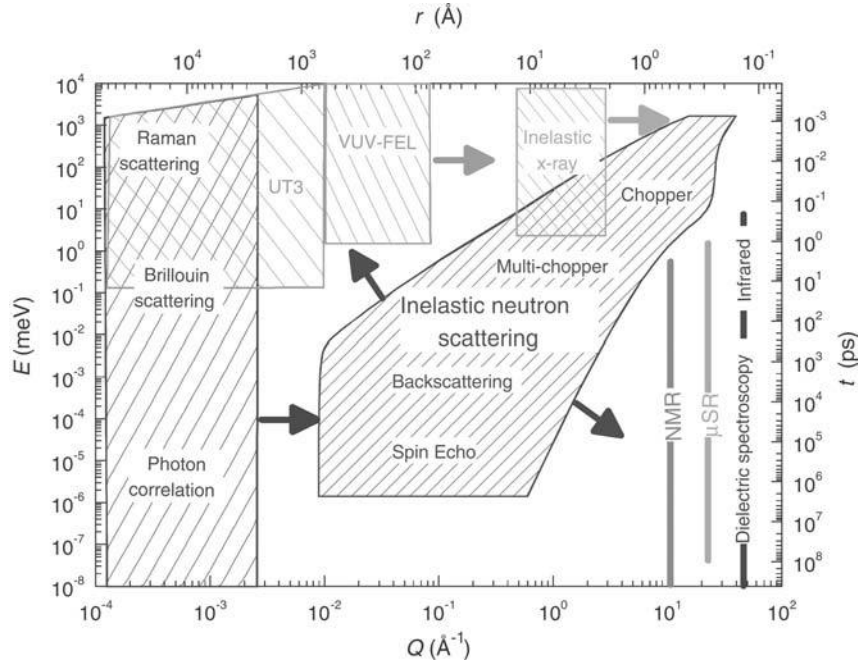
Figure 1
Accessible range of transfer in energy ($\hbar\omega$ in meV) and of the modulus of the momentum Q (in Å^{-1}) for neutron scattering in comparison to other experimental methods. Also indicated is the corresponding range in time (in ps) and real space (in Å) (from ESS 2003).

from the neutron to the sample. E_i (k_i) and E_f (k_f) refer to the initial and final energy (wavevector) of the neutron, respectively. The different formulations of the scattering function (Eqns. (2)–(4)) allow for a straightforward interpretation of the measured cross-sections in meaningful theoretical concepts, i.e., spin–spin correlation functions (Eqn. (2)), transition matrix elements (Eqn. (3)), or as generalized susceptibility tensor (Eqn. (4)). The presently accessible range of energy and momentum transfer by neutrons is shown in Fig. 1 (ESS 2003). Also indicated by arrows are its extension for neutron sources of the next generation and the corresponding range of complementary measuring techniques such as x-rays, free-electron-lasers (FEL), NMR, etc.

3. Neutron Spectrometers

Since the first neutron instrumentation at research reactors in the 1950s and at accelerator-based neutron spallation sources in the 1980s, a large variety of neutron spectrometers has been developed. The two main types of spectrometers for the investigation of excitations in solids depend on the different way the neutron wavevector is determined before and after the scattering process: by reflection from a single crystal or by measuring the neutron time-of-flight.

In a triple-axis spectrometer (Brockhouse 1955, Shirane *et al*. 2002), the reflection from a single crystal (monochromator) selects a well-defined wavevector k_i from the white spectrum of the neutron source (first axis). The monochromatic beam is scattered from the sample (scattering angle = second axis). The scattered beam is reflected from the analyzer crystal (third axis) onto the detector, thus defining the final neutron wavevector k_f and the energy transfer $\hbar\omega$ as well. A schematic view is shown in Fig. 2 (IN1, ILL 2003). Data are taken point-by-point in reciprocal space either with fixed momentum transfer Q (to obtain an energy spectrum) or with fixed energy transfer $\hbar\omega$. This method is typically used for the determination of dispersion relations using single crystalline samples.

Time-of-flight methods are preferentially used for the investigation of polycrystalline samples and at neutron spallation sources taking advantage of the pulsed character of the neutron production in the target. As an example the layout of the MERLIN spectrometer at the ISIS Facility is shown in Fig. 3 (ISIS 2003). The pulsed beam is monochromatized by the (Fermi-) chopper in front of the sample by phasing the chopper opening with the neutron production in the target (spallation target and moderator at upper right side, not shown in the figure). A background chopper additionally suppresses unwanted neutrons

415
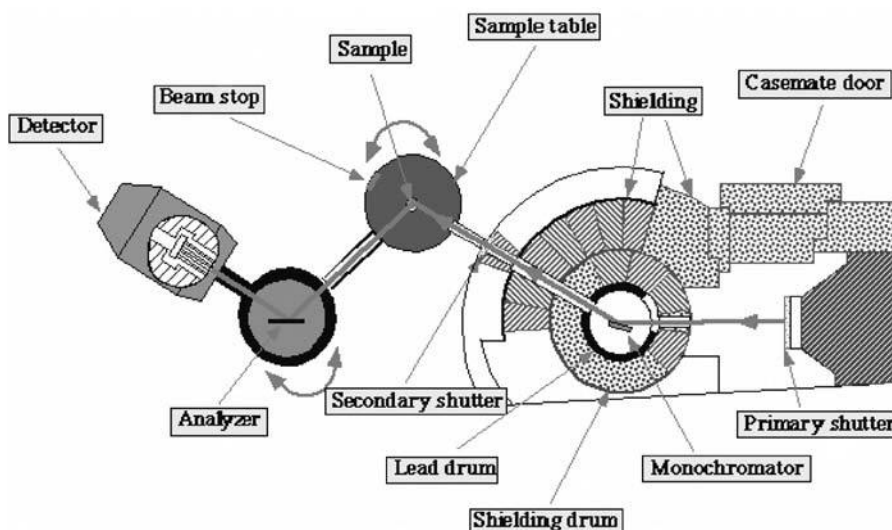
Figure 2
Scheme of a neutron triple-axis spectrometer at a neutron reactor (IN1 at the Institute Laue-Langevin, ILL, Grenoble) (from ILL 2003).
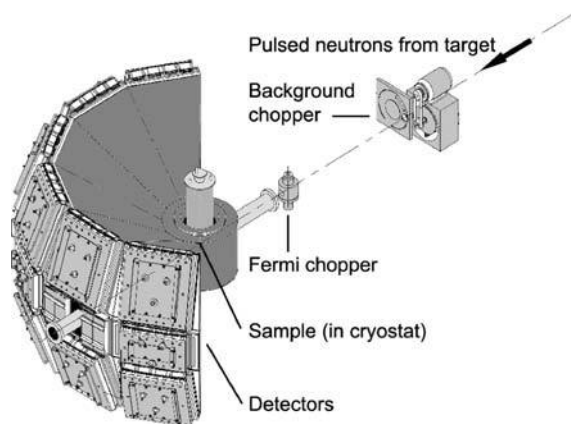
Figure 3
Schematic view of a neutron time-of-flight spectrometer at a neutron spallation source (MERLIN at the ISIS Facility, Rutherford Appleton Laboratory) (from ISIS 2003).

from the source. A large array of detectors covers a large solid angle and allows for the simultaneous measurement of a large range in energy transfer and of the modulus of the momentum transfer.

4. Magnetic Interactions in Solids

When elements with partly filled shells containing 3d-, 4f-, and 5f-electrons are condensed into the solid state (either as pure elements, intermetallic compounds, semiconductors, or insulators), they often preserve their magnetic properties. As the 4f-electrons (elements of the Lanthanide series) occupy inner spatial regions of the atom, they lose only little of their magnetism when embedded in a solid (see *Localized 4f and 5f Moments: Magnetism*). The magnetic ground state is determined by taking into account all three Hund's rules (see textbooks on solid-state physics). The interaction with the crystalline electric field (CF) that surrounds the 4f-ion (single-ion interaction) and the magnetic interaction with the magnetic moments of neighboring atoms (two-ion interaction) leads to a (CF-) splitting of the ground-state multiplet and to a dispersion of the magnetic excitations, respectively. Both interaction strengths can be of the same order of magnitude (1–100 meV). In compounds containing 3d-elements the interaction leading to the third Hund's rule (the spin–orbit interaction) is much weaker than the CF-interaction (see *Magnetism in Solids: General Introduction*) resulting in a different scenario for the description of the magnetic ground-state (band-type electronic wave functions of e_g and t_{2g} character). In metallic systems this leads to a "quenching" of the orbital moments resulting in a description of the magnetic properties as spin-only moments dominated by the collective magnetic interactions. 3d-Insulators will not be considered here (a decoupling of spin, charge, and orbital degrees of freedom is presently discussed in connection with metal–insulator transitions). The situation in systems with 5f-elements (elements of the actinide series) is between that of 4f-systems (localized) and that of 3d-systems (itinerant) and thus rather complicated.

5. Spin Waves, Crystal-field and Inter-multiplet Transitions

Spin waves (magnons) are the low-energy collective excitations of a magnetically ordered system. For an isotropic Heisenberg interaction of localized magnetic moments, the textbooks on solid-state physics yield for a ferromagnet for small $|q|$ a quadratic dispersion in $|q| = |Q − G|$, with G being a reciprocal lattice vector of the (ferromagnetic) lattice. For an antiferromagnet the dispersion is linear in $|q|$ in the neighborhood of the antiferromagnetic reciprocal lattice vector. The magnetic excitations of the elementary magnets like Fe and Ni have been investigated over many decades resulting in an isotropic and gap-less spin wave-like spectrum in the low-energy region but with drastic modifications when following the dispersion towards the zone boundary. The latter findings have been analyzed in the light of electronic band structure effects or by saying that the sharp collective spin waves interfere with single-particle excitations of the $3d$-electrons (exhibiting a Stoner continuum) giving rise to strong damping effects (Lovesey 1984, Mook 1988).

Spin waves in the presence of CF-interactions are discussed experimentally and theoretically for the rare earth elements by Jensen and Mackintosh (1991). The excitation spectra of rare earths diluted in nonmagnetic metals and intermetallic compounds are discussed by Fulde and Loewenhaupt (1985, 1988) and for rare earth intermetallic compounds including rare earth-transition metal compounds by Moze (1998). The latter compounds are the base materials for novel permanent magnet production. The types of excitations in a rare earth compound accessible by inelastic neutron scattering are shown exemplarily in Fig. 4. In this case the hierarchy of energies yields a spin wave spectrum in the very low energy part (due to the low magnetic ordering temperature of typical several K), transitions to excited CF-levels (several meV; 1 meV corresponds to 11.6 K), and inter-multiplet transitions (several hundredth of meV). The advent of neutron spallation sources made it possible to investigate also the high-energy region of the magnetic excitation spectra, e.g., inter-multiplet transitions, an area that was usually restricted to light scattering (Hüfner 1978). An early documentation of the possibilities of neutron scattering in the field of investigating inter-multiplet transitions is given by Osborn *et al.* (1991).

To determine the magnetic excitation spectra of an intermetallic rare earth compound (as an example we show the results for orthorhombic $NdCu_2$), time-of-flight spectroscopy on a polycrystalline sample is performed as a first step. In Fig. 5 the CF-transitions from the ground-state doublet to the four excited-state doublets of Nd^{3+} (having the angular momentum quantum number $J = 9/2$ and hence five doublets due to the CF-interaction and Kramers degeneracy)
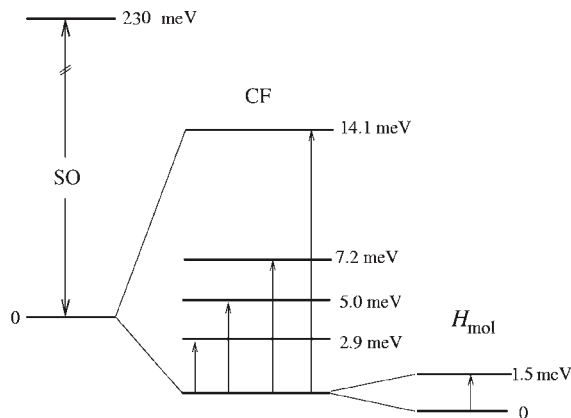
Figure 4
Typical splitting of levels in a rare earth system due to spin–orbit (SO), crystal-field (CF), and exchange interaction (H_{mol}). Scheme reproducing approximately the situation of Nd^{3+} ions in $NdCu_2$.

can clearly be identified. While the spectrum of Fig. 5 was taken in the magnetically disordered state at 10 K, the spectrum at 2 K in the magnetically ordered state is shown in Fig. 6. The main difference is that in the ordered state a molecular field is present in addition to the CF. This yields a splitting of the doublets and a modification of the transition matrix elements. The transitions within the split ground-state doublet are shown with increased resolution in the inset of Fig. 6. The structure of this part of the excitation spectrum reflects the dispersive nature of the splitting with its intensity being proportional to the magnon density-of-states. To show the power of inelastic neutron scattering on this very low energy side of the range of excitations in $4f$-systems, we present in Fig. 7 the spin wave dispersion curves measured on a single crystal of $NdCu_2$ in the ferromagnetically induced state in a field of 3 T on a triple-axis-spectrometer employing cold neutrons (Rotter *et al.* 2000). The spin waves have been analyzed by a mean-field model in random-phase approximation (MF-RPA; see, e.g., Jensen and Mackintosh 1991) allowing for anisotropic effects due to the single-ion CF-interaction and also for anisotropic two-ion exchange interactions. From the interpretation of the magnetic-phase diagrams (Rotter 2003), the dispersion relations and the CF-excitation spectra of one compound ($NdCu_2$) predictions could be made for the magnetic properties of the whole series RCu_2 with R being any rare earth element.

In general, elementary excitations in solids such as CF-transitions and lattice vibrations (phonons) are considered decoupled and the determination and interpretation of the measured spectra of the two phenomena, i.e., the CF level schemes and the phonon
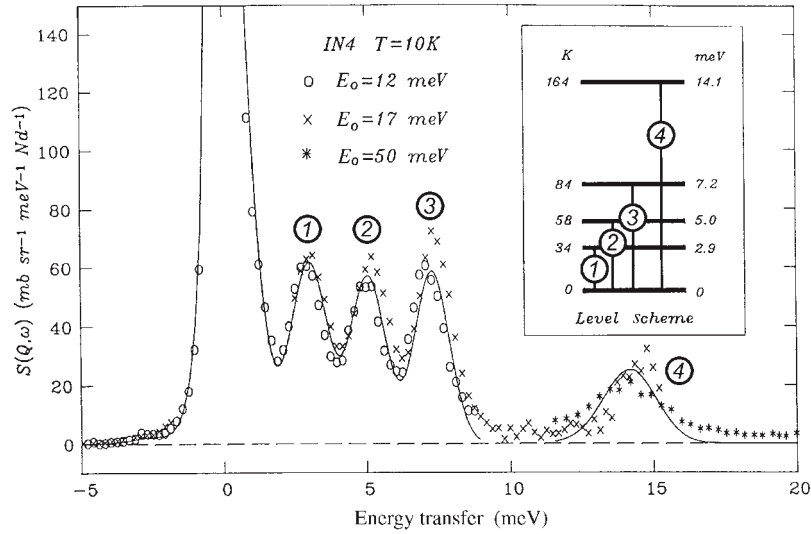
Figure 5
CF-transitions from the ground-state doublet to the four excited-state doublets in NdCu$_2$ measured on a time-of-flight spectrometer (IN4, ILL) in the magnetically disordered state at $T = 10\,$K and zero external field. Inset shows the CF-level scheme (from Gratz *et al.* 1991).
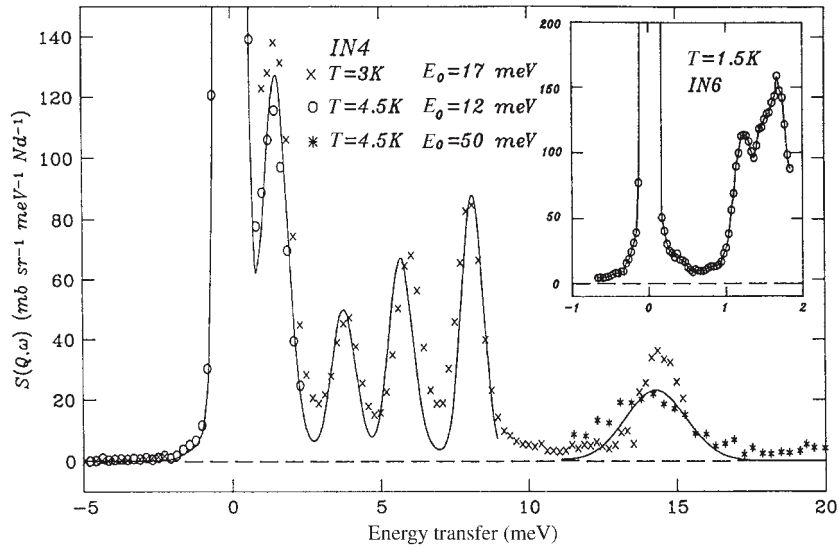
Figure 6
CF-transitions and magnon density-of-states (shown on an enlarged scale in the inset) in the magnetically ordered state of NdCu$_2$ at $T = 2\,$K ($T_N = 6.5\,$K) and zero external field measured on time-of-flight spectrometers (IN4 and IN6, ILL) (from Gratz *et al.* 1991).

dispersion relations, are performed independently of each other. A survey on coupling effects between both phenomena as investigated by INS is given by Loewenhaupt and Witte (2003).

6. Spin Fluctuations

Spin wave theory in MF-RPA neglects spin quantum fluctuations. However, fluctuations become important
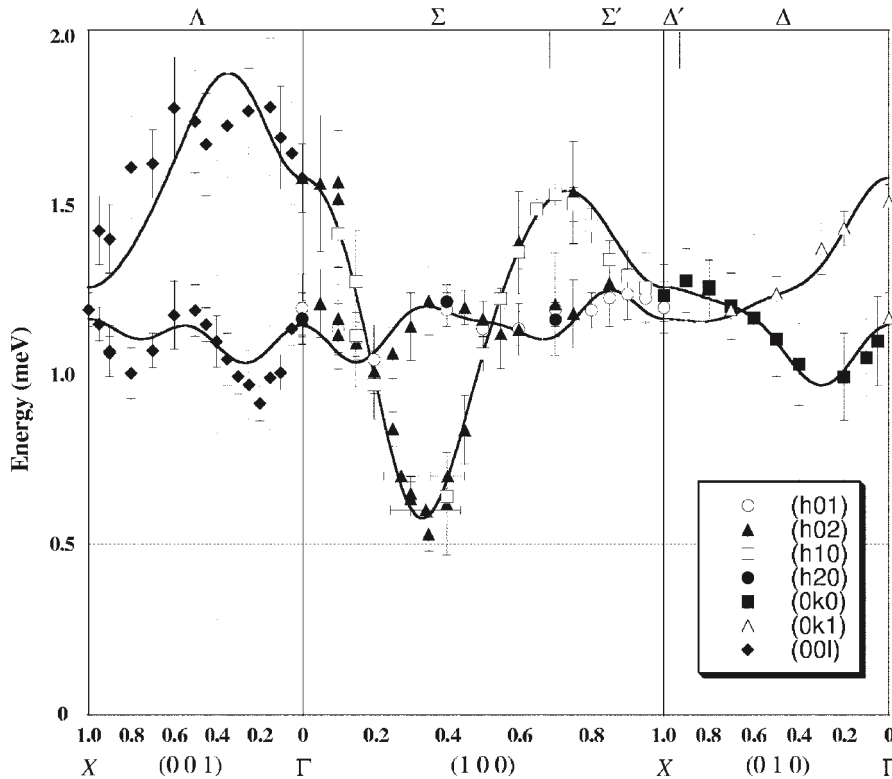
Figure 7
Spin waves in $NdCu_2$ measured in the ferromagnetically induced phase at $T = 2\,K$ and with magnetic field of 3 T applied along the crystallographic *b*-direction measured on a triple-axis spectrometer (IN12, ILL) (from Rotter *et al.* 2000).

for low-dimensional systems and low spin- quantum numbers (see *Non-Fermi Liquid Behavior: Quantum Phase Transitions*). The new phenomena observed in such systems are presently discussed in a wide context from one-dimensional antiferromagnets (Cowley 1998, 2002, Mikeska 2002) via heavy-fermion superconductors (Bernhoeft *et al.* 1998, Thalmeier 2002) to high-temperature superconductors (Bourges *et al.* 2000).

Classical examples of three-dimensional systems exhibiting also strong spin fluctuations are mixed-valent and heavy-fermion compounds (see *Intermediate Valence Systems; Heavy-fermion Systems*). Reviews on the lanthanides (Loewenhaupt and Fischer 1993, Aeppli and Broholm 1994) and actinides (Holland-Moritz and Lander 1994) make the strong coupling between the localized *f*-electrons and the delocalized conduction electrons responsible for the observed magnetic instabilities. Detailed INS measurements were reported for single crystalline samples of the series $CeCu_{6-x}Au_x$ where the variation of *x* drives the system from Fermi-liquid behavior ($x = 0$) via a quantum critical point ($x = 0.1$) to a magnetically

ordered ($x = 1$) system (Schröder *et al.* 1997, Stockert *et al.* 1997).

See also: Crystal Field Effects in Intermetallic Compounds: Inelastic Neutron Scattering Results; Magnetism: Applications of Synchrotron Radiation; Permanent Magnet Materials: Neutron Experiments

Bibliography

Aeppli G, Broholm C 1994 Magnetic correlations in heavy fermion systems: neutron scattering from single crystals. In: Gschneidner K A, Jr., Eyring L, Lander G H, Choppin G R (eds.) *Handbook on the Physics and Chemistry of Rare Earths.* Elsevier, Vol. 19, Chap. 131, pp. 123–75

Bernhoeft N, Sato N, Roessli B, Aso N, Hiess A, Lander G H, Endoh Y, Komatsubara T 1998 Enhancement of magnetic fluctuations on passing below T_C in the heavy fermion superconductor UPd_2Al_3. *Phys. Rev. Lett.* **81**, 4244–7

Böni P, Furrer A 1998 Introduction to neutron scattering. In: Furrer A (ed.) *Neutron Scattering in Layered Copper-oxide Superconductors.* Kluwer, Dordrecht, pp. 1–22

Bourges P, Sidis Y, Fong H F, Regnault L P, Bossy J, Ivanov A, Keimer B 2000 The spin excitation spectrum in superconducting YBa$_2$Cu$_3$O$_{6.85}$. *Science* **288**, 1234–7

Brockhouse B N 1955 *Can. J. Phys.* **33**, 889

Cowley R A 1998 The excitations of one-dimensional spin 1/2 antiferromagnets. In: Skjeltorp A K, Sherrington D (eds.) *Dynamical Properties of Unconventional Magnetic Systems.* Kluwer, Dordrecht, pp. 5–27

Cowley R A 2002 Low dimensional systems: experimental studies of antiferromagnets. In: *Magnetism, Lecture Notes of the 1st PSI Summer School on Condensed Matter Research*, Zuoz, pp. 167–80

ESS 2003 http://essnets.ess.kfa-juelich.de/TheESSProject/additional_information/F8.pdf

Fulde P, Loewenhaupt M 1985 Magnetic excitations in crystal-field split 4*f* systems. *Adv. Phys.* **34**, 589–661

Fulde P, Loewenhaupt M 1988 4*f*-Moments and their interaction with conduction electrons. In: Borovik-Romanov A S, Sinha S K (eds.) *Spin Waves and Magnetic Excitations.* Elsevier, Amsterdam, Vol. 22.1, Chap. 6, pp. 367–423

Gratz E, Loewenhaupt M, Divis M, Steiner W, Bauer E, Pillmayr N, Müller H, Nowotny H, Frick B 1991 Structural, magnetic, electronic, and transport properties of NdCu$_2$. *J. Phys.: Condens. Matter* **3**, 9297–318

Holland-Moritz E, Lander G H 1994 Neutron inelastic scattering from actinides and anomalous lanthanides. In: Gschneidner K A, Jr. Eyring L, Lander G H, Choppin G R (eds.) *Handbook on the Physics and Chemistry of Rare Earths.* Elsevier, Vol. 19, Chap. 130, pp. 1–121

Hüfner S 1978 *Optical Spectra of Transparent Rare Earth Compounds.* Academic Press, New York

ILL 2003 http://www.ill.fr/YellowBook/IN1

ISIS 2003 http://www.isis.rl.ac.uk/excitations

Jensen J, Mackintosh A R 1991 *Rare Earth Magnetism (Structures and Excitations).* Clarendon Press, Oxford

Loewenhaupt M, Fischer K 1993 Valence-fluctuation and heavy-fermion 4*f* systems. In: Gschneidner K A, Jr., Eyring L (eds.) *Handbook on the Physics and Chemistry of Rare Earths.* Elsevier, Amsterdam, Vol. 16, Chap. 105, pp. 1–105

Loewenhaupt M, Witte U 2003 Coupling between electronic and lattice degrees of freedom in 4*f*-electron systems investigated by inelastic neutron scattering. *J. Phys.: Condens. Matter* **15**, S519–36

Lovesey S W 1984 *Theory of Neutron Scattering from Condensed Matter (Vol. 1: Nuclear Scattering, Vol. 2: Polarization Effects and Magnetic Scattering).* Clarendon Press, Oxford

Mikeska H -J 2002 Low dimensional systems: theory. In: *Magnetism, Lecture Notes of the 1st PSI Summer School on Condensed Matter Research*, Zuoz, pp. 147–66

Mook H A 1988 Neutron scattering studies of magnetic excitations in itinerant magnets. In: Borovik-Romanov A S, Sinha S K (eds.) *Spin Waves and Magnetic Excitations.* Elsevier, Amsterdam, Vol. 22.1, Chap. 7, pp. 425–78

Moze O 1998 Crystal field effects in intermetallic compounds studied by inelastic neutron scattering. In: Buschow K H J (ed.) *Handbook of Magnetic Materials.* Elsevier, Amsterdam, Vol. 11, Chap. 4, pp. 494–624

Osborn R, Lovesey S W, Taylor A D, Balcar E 1991 Inter-multiplet transitions using neutron spectroscopy. In: Gschneidner K A, Jr., Eyring L (eds.) *Handbook on the Physics and Chemistry of Rare Earths.* Elsevier, Amsterdam, Vol. 14, Chap. 93, pp. 1–61

Rotter 2003 http://www.mcphase.de

Rotter M, Loewenhaupt M, Kramp S, Reif T, Pyka N M, Schmidt W, van de Kamp R 2000 Anisotropic magnetic exchange in orthorhombic RCu$_2$ compounds (R = rare earth). *Eur. Phys. J. B* **14**, 29–42

Schröder A, Aeppli G, Bucher E, Ramazashvili R, Coleman P 1997 Scaling of magnetic fluctuations near a quantum-phase transition. *Phys. Rev. Lett.* **80**, 5623–6

Shirane G, Shapiro S M, Tranquada J M 2002 *Neutron Scattering with a Triple-axis Spectrometer: Basic Techniques.* Cambridge University Press

Stirling W G, McEwen K A 1986 Magnetic excitations. In: Sköld K, Price D L (eds.) *Methods of Experimental Physics: Neutron Scattering.* Academic Press, New York, Vol. 23, Part C, Chap. 20, p. 159

Stockert O, von Löhneysen H, Rosch A, Pyka N M, Loewenhaupt M 1997 Two-dimensional fluctuations at the quantum critical point of CeCu$_{6-x}$Au$_x$. *Phys. Rev. Lett.* **80**, 5627–30

Thalmeier P 2002 Dual model for magnetic excitations and superconductivity in UPd$_2$Al$_3$. *Eur. Phys. J. B* **27**, 29–48

Williams W G 1988 *Polarized Neutrons.* Clarendon Press, Oxford

M. Loewenhaupt

IAPD, Dresden, Germany

Magnetic Fields: Thermoelectric Power

The coefficient of the thermoelectric power (S) measured in variable magnetic fields (B) is called magnetothermopower. This physical quantity can provide very valuable complementary information concerning details of electronic band structure. In comparison with the magnetoresistivity, the magnetothermopower is not sensitive to a uniform change of mobility of conduction electrons by the Lorentz force. The magnetothermopower of metallic materials basically depends on a relative change of the mobility of conduction electrons with different energy near the Fermi surface.

The effect of magnetic fields on thermopower is important also from a practical point of view. Thermocouples are widely used as temperature sensors. Therefore, in low-temperature thermometry in equipment with strong magnetic fields, such as research cryostats with superconducting magnets, a knowledge of the sensitivity of a thermocouple to the magnetic field is essential. Another significant and expanding field for the application of thermoelectric phenomena is thermoelectric heat–energy conversion and thermoelectric cooling. It is known that the thermoelectric efficiency of some materials can be considerably enhanced in a magnetic field (examples are bismuth-based alloys which are used for low-temperature refrigeration).

1. Theoretical Aspects of Magnetothermopower

The thermopower, or Seebeck, coefficient S is defined as the coefficient in the relation: $\mathbf{E} = S\nabla T$ between

the temperature gradient ∇T and the electrical field $\mathbf{E}$ in a conducting material, where the net current through the sample is zero (see *Boltzmann Equation and Scattering Mechanisms*). There are two other thermoelectric phenomena: the Peltier heat (characterized by the coefficient Π) and the Thomson heat (characterized by the coefficient μ_T), which can be observed under different conditions. However, these three coefficients S, Π, and μ_T are not independent; they are connected to each other by the Thomson relations. For an isotropic medium, without a magnetic field, the relations read: $\Pi = TS$ and $\mu_T = T\mathrm{d}S/\mathrm{d}T$ (Barnard 1972). In a general case, S, Π, and μ_T are tensors of second rank, which can have as many as nine independent components. The most general form of the Thomson relation is given by the expression: $\Pi_{ik}(B) = TS_{ki}(-B)$ (Landau and Lifshitz 1977).

If there is, in addition to the temperature gradient, an external magnetic field applied to the sample, the thermoelectric field can be written as: $\mathbf{E} = S\nabla T + N\mathbf{B} \times \nabla T$ (Abrikosov 1972). The second term in this equation is the so called Nernst–Ettingshausen (N–E) effect, with N the Nernst–Ettingshausen coefficient. However, apart from the N–E effect, the coefficient S can also be dependent on the magnetic field. The change of S in an external magnetic field is called magnetothermopower: $\Delta S = S(B, T) - S(0, T)$. In the weak field limit, this dependence is a second-order correction of the thermoelectric field $\mathbf{E}$ in the presence of a magnetic field.

With respect to experimental conditions, two different situations are possible, depending on the mutual orientation of the magnetic field and the temperature gradient: the magnetic field parallel to the temperature gradient, and the magnetic field perpendicular to the temperature gradient. One distinguishes, respectively, longitudinal magnetothermopower ΔS_L and transversal magnetothermopower ΔS_T. In the case of anisotropic materials, special care should be taken to separate ΔS_T and the influence of the Nernst–Ettingshausen effect. According to the mechanism of the change of thermopower in a magnetic field, the effect can be subdivided into two main categories. In the first category, the effect is connected to the orbital motion of the conduction electrons in a magnetic field caused by the Lorentz force. In the second category, the effect is related to a change in the electronic structure and/or scattering mechanism in a magnetic field.

With regard to the Lorentz force-driven magnetothermopower, two different regimes are distinguishable, depending on the strength of the magnetic field. This field strength can be characterized by the product $\omega_c\tau$, where $\omega_c = eB/m^*c$ is the classical cyclotron frequency, τ is the average time between collisions of a conduction electron with scattering centers, m^* is the effective electron mass, and c is the speed of light. The low-field regime corresponds to $\omega_c\tau \ll 1$, while

$\omega_c\tau \geqslant 1$ is the condition for the high-field range. From a theoretical point of view, the high-field case has been much better understood than the low-field one. In the high-field regime, the scattering processes become unimportant, and galvano- and thermomagnetic phenomena are determined by the topological properties of the Fermi surface. In the high-field limit $\omega_c\tau \gg 1$, the longitudinal magnetothermopower ΔS_L is independent of the magnetic field for any Fermi surface geometry.

The transversal magnetothermopower ΔS_T is proportional to B for closed electron orbits in compensated metals, and is independent of the field in other cases (Blatt *et al.* 1976). A special case of the high-field regime is realized under the additional condition $\hbar\omega_c > k_BT$ ($k_B = 1.3806568 \times 10^{-23}\,\mathrm{JK}^{-1}$ is the Boltzmann constant, $\hbar = 1.05457266 \times 10^{-34}\,\mathrm{Js}$ is the Planck constant). Under this condition, Landau quantization of the orbital motion of the conduction electrons in the plane, normal to the magnetic field, becomes important and all electronic properties of metals, including thermopower, show an oscillatory dependence on B^{-1} with a period ΔB^{-1}. The period depends on the extreme cross-sectional area A_e of the Fermi surface in a plane normal to the magnetic field: $\Delta B^{-1} = (2\pi e/\hbar c)(1/A_e)$ (Landau and Lifshitz 1977). These oscillations can best be observed in a very pure single crystal at low temperatures: $T < (\hbar e/m^*ck_B)B \approx 1.34B$, where B is the field in teslas.

In the low-field regime, the scattering mechanism is essential and this makes a theoretical description extremely difficult. Within this limit, the Lorentz force driven magnetothermopower is expected to be proportional to B^2 (Abrikosov 1972, Landau and Lifshitz 1977, Ri *et al.* 1994).

The magnetothermopower due to a change of electronic structure can be dominant in non-simple metals, magnetic or nearly magnetic materials, strongly correlated systems, and in conductors with magnetic impurities. The effect essentially depends on details of the electronic structure of a particular system. No general theory has been developed up to now. The influence of a magnetic ordering on the thermopower has been discussed and investigated both theoretically and experimentally. On a qualitative level, the variation of thermopower of itinerant ferromagnets in the vicinity of Curie temperature has been explained by Mott, based on his *s–d* scattering model (Blatt *et al.* 1976). A summary of theoretical and experimental results can be found in Blatt *et al.* 1976, and in Yagasaki *et al.* 1996.

A somewhat special field represents the thermomagnetic phenomena in superconductors. This field has experienced a burst of theoretical and experimental activities in connection with the discovery of high-temperature superconductors. Large thermomagnetic effects were observed in the mixed state of high-T_c materials. These effects are related to the magnetic flux flow driven by a temperature gradient.

For a review, see Huebener (1979) and Ri *et al.* (1994).

A review of the theory of galvanomagnetic and thermomagnetic effects in metals and of experimental results prior to 1957 is given in Jan (1957).

2. Details of the Measurement

Compared to measurements of the thermopower without a magnetic field, magnetothermopower measurements require several additional considerations:

(i) In the high-field limit, thermopower can be anisotropic even for crystals of cubic symmetry.

(ii) Contributions from galvano- and thermomagnetic effects, different from thermopower, should be carefully eliminated (the Nernst–Ettingshausen effect particularly).

(iii) Calibration of temperature sensors and reference electrodes in a magnetic field is important.

(iv) Care should be taken to avoid a magnetic field gradient.

Several different designs have been introduced for measurements of magnetothermopower. As an example, we mention the apparatus described by Resel *et al.* (1996). With this setup, the thermopower can be measured in magnetic fields from 0 T to 17 T in the temperature range from 3 K to 300 K. The main part of the sample holder is shown in Fig. 1. A special modulation technique for the temperature gradient is used in this setup to eliminate spurious voltages. Two gradient heaters working in opposite directions are utilized to generate an alternating temperature gradient in the sample. The total heating power produced by the two heaters is constant. Therefore, the average temperature of the sample is not affected by the gradient modulation. In order to avoid the N–E effect contribution, a parallel alignment of the temperature gradient and magnetic field direction is chosen. The temperature difference across the sample is measured with the help of two Chromel–Constantan thermocouples.

The sensitivity of this thermocouple is independent of the magnetic field within an error of 5%, in the field range from 0 T to 17 T at temperatures from 3 K to 300 K. For the reference electrode a Chromel wire is used, since the thermopower of this alloy has a comparatively weak and simple dependence on the external magnetic field and the temperature. However, for precise measurements of magnetothermopower of metals, where the effect is small, it is necessary to make corrections in the thermopower of Chromel, so that $S_{Ch}(B, T) = S_{Ch}(0, T) + \Delta S(B, T)$. It was found that $\Delta S(B, T)$ can be approximated by an empirical function $f(B, T)$ with an accuracy of $0.1\,\mu VK^{-1}$. This function reads:

$$f(B, T) = aT \exp(bT^2) + cT^2 \exp(dT)$$
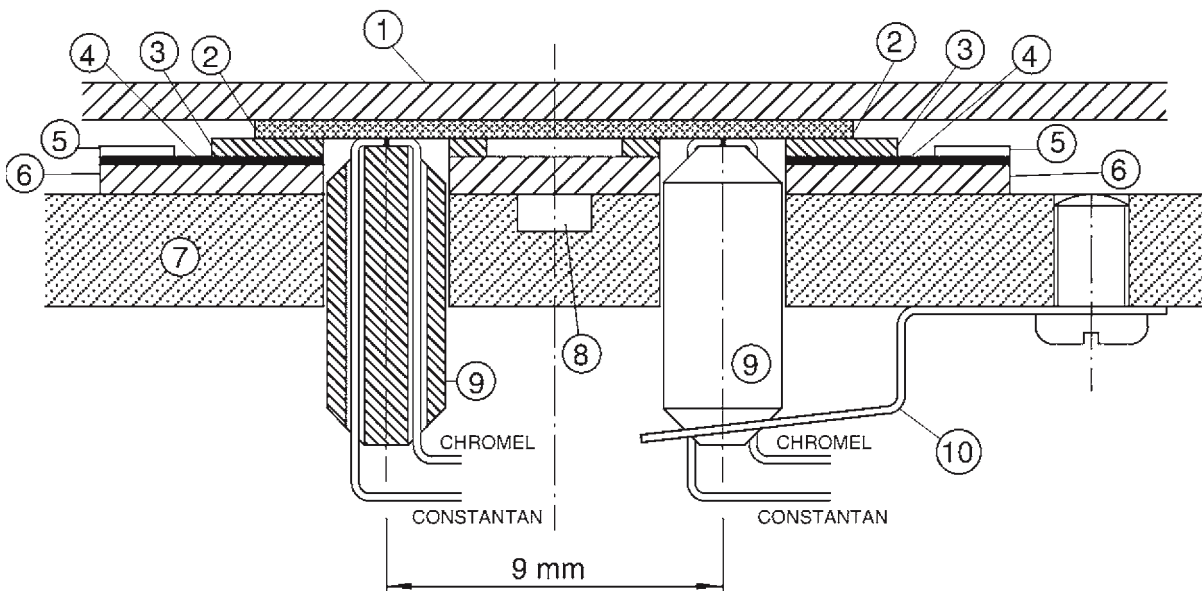
Figure 1

A part of the sample holder for thermopower measurement in a magnetic field. (1) and (6) sample-pressing and sample-supporting plates (glass epoxy); (2) sample; (3) AlN plates; (4) copper layers; (5) gradient heater; (7) heat sink (copper-beryllium bronze); (8) temperature sensor; 9) Al_2O_3 tubes holding thermocouples; (10) spring (copper–beryllium bronze).
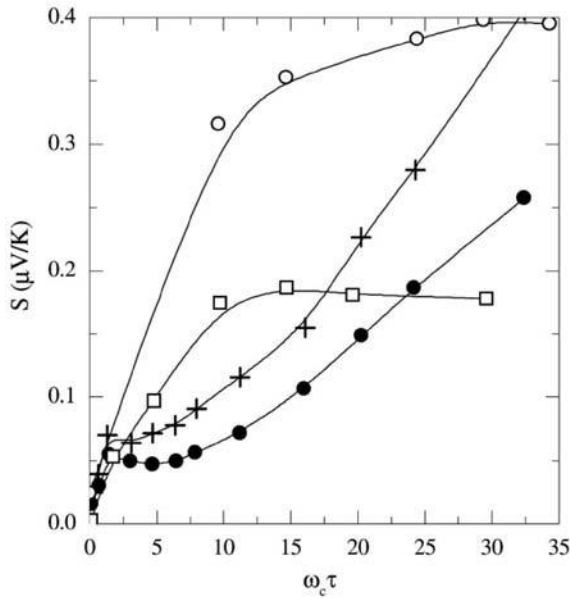
Figure 2
Magnetothermopower of silver against a magnetic field
(Stanley 1974). Results for single crystal specimens of
silver of different purity and crystallographic orientation
are shown. Thermopower was measured with the
longitudinal orientation of the magnetic field with
respect to the temperature gradient. $\square$: RRR = 1380,
along [741] crystallographic direction, $T = 2.5$ K; $\bigcirc$: the
same sample, $T = 4.4$ K; $\bullet$: RRR = 2280, along [111],
$T = 4.9$ K; and $+$: the same sample at $T = 6.2$ K.
RRR$\equiv\rho(300)/\rho(4.2)$.

where

$$a = \frac{2.1 \ 10^{-2}B}{-51.4 + 49.1 \exp(-2.91 \times 10^{-2}B)}$$

$$b = -2.2 \times 10^{-4} - 1.02 \times 10^{-5} \exp(0.187B)$$

$$c = -4.18 \times 10^{-5}B$$

$$d = -7.47 \times 10^{-5}B^2 + 2.33 \times 10^{-3}B - 4.38 \times 10^{-2}$$

(where B is the magnetic field in teslas).

3. Experimental Results

Most systematic and comprehensive investigations of
the magnetothermopower have been performed for
simple monovalent and divalent metals as well as for
noble metals. It was found that in many cases
$\Delta S = S(B, T) - S(0, T)$ is large at low temperatures.
In noble and divalent metals, a large contribution to
ΔS is referred to as an increase of the phonon drag
thermopower in a magnetic field. A summary of these
studies is given in Blatt *et al.* (1976). A comprehensive
investigation of ΔS in the high-field regime was made
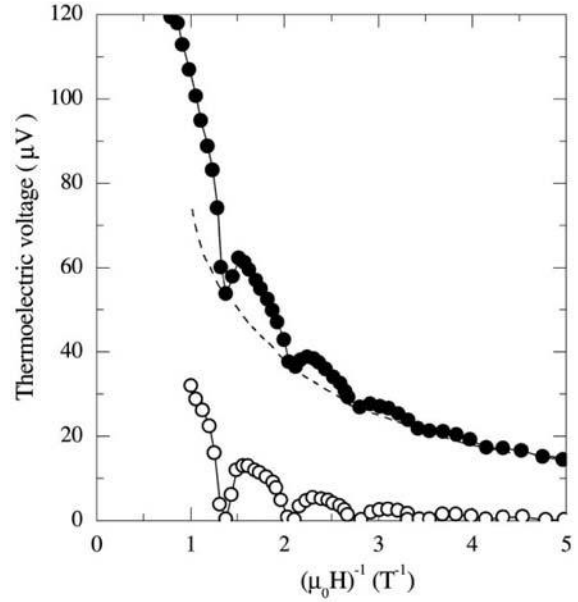
Figure 3
Quantum oscillations of the thermoelectric voltage
versus the inverse magnetic field for Bi are shown. $\bullet$:
total thermoelectric voltage; $\bigcirc$: oscillating part (broken
line shows the envelope curve).
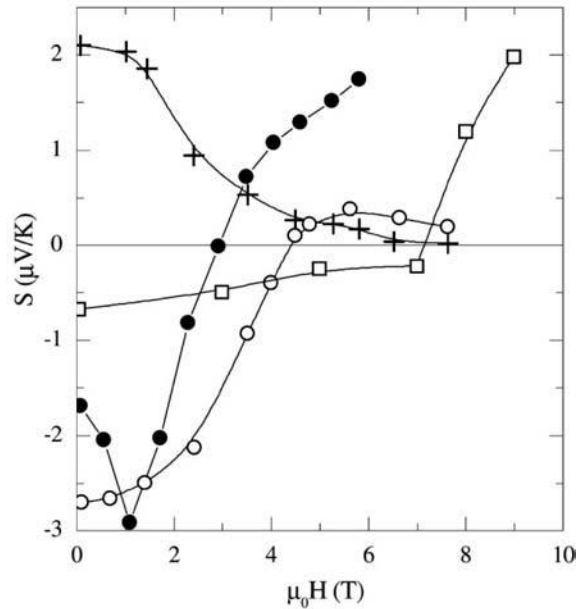
Figure 4
Thermopower of heavy-fermion compounds against a
magnetic field (Marcenat *et al.* 1990). $\bigcirc$: CeAl$_2$ at
$T = 0.58$ K; $\bullet$: CeAl$_3$ at $T = 0.5$ K; $+$: (*La*Ce)Al$_2$ at
$T = 0.58$ K; $\square$: CeRu$_2$Si$_2$ at $T = 1.5$ K.
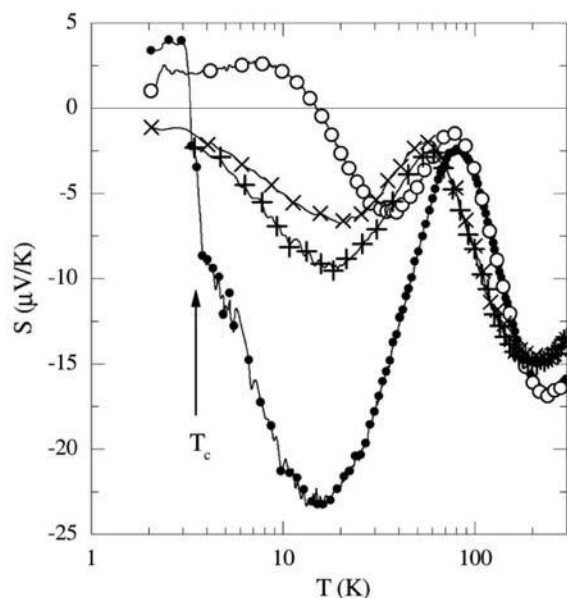
Figure 5
Thermopower of a nearly magnetic YCo_2 and of a ferromagnet $TmCo_2$ against temperature. ●: $TmCo_2$, $\mu_0 H = 0\,T$; ○: $TmCo_2$, $\mu_0 H = 15\,T$; +: YCo_2, $\mu_0 H = 0\,T$; ×: YCo_2, $\mu_0 H = 15\,T$. The arrow indicates Curie temperature of $TmCo_2$.

for silver (Stanley 1974). Some results for single silver crystals are presented in Fig. 2.

The quantum oscillations of the magnetothermopower and the Peltier coefficient were measured for bismuth, tin, antimony, aluminum, and zinc single crystals. The results of these studies are summarized by Blatt *et al*. (1976). The quantum oscillations of the thermoelectric voltage versus the inverse magnetic field at $T = 4.2\,K$ for bismuth are presented in Fig. 3.

Very little has been done with respect to the magnetothermopower of magnetic materials and intermetallic compounds. Some results on ΔS of heavy-fermion compounds can be found in Marcenat (1990): see Fig. 4. Results for magnetic and nearly magnetic compounds are shown in Fig. 5.

Applications of thermomagnetic effects for thermoelectric energy conversion form a separate and large field. Semimetals and heavily doped semiconductors have mainly been used in these applications. Theoretical basics and a review of important experimental results can be found in Hartman and Honig (1967).

See also: Rare Earth Intermetallics: Thermopower of Cerium, Samarium, and Europium Compounds

Bibliography

Abrikosov A A 1972 *Introduction to the Theory of Normal Metals*. Academic Press, New York

Barnard R D 1972 *Thermoelectricity in Metals and Alloys*. Taylor and Francis, London

Blatt F J, Schroeder P A, Foiles C L 1976 *Thermoelectric Power of Metals*. Plenum, New York

Foiles C L 1985 *Thermopower of Pure Metals* In: Hellwege K-H, Olsen J L (eds.) *Landolt-Börnstein. Numerical Data and Functional Relationships in Science and Technology: new series, Group III–Crystal and Solid State Physics. Metals: Electronic Transport Phenomena*. Subvolume b. Springer, Berlin, Vol. 15., pp. 48–104

Hartman T C, Honig J M 1967 *Thermoelectric and Thermomagnetic Effects and Applications*. McGraw-Hill, New York

Huebener R P 1979 *Magnetic Flux Structures in Superconductors*. Springer, Berlin

Jan J-P 1957 *Galvanomagnetic and Thermomagnetic Effects in Metals*. In: Seitz F, Turnbull D 1957 (eds.) *Solid State Physics. Vol. 5*. Academic Press, New York, pp. 1–96

Landau L D, Lifshitz E M 1977 In: *Course of Theoretical Physics: Quantum Mechanics*. (3rd edn) Pergamon, Oxford, Vol. 3

Marcenat C, Jaccard D, Sierro J, Flouquet J, Onuki Y, Komatsubahara T 1990 Extended transport measurements on high-purity CeB_6. *Journal of Low Temperature Physics* **78**, 261–85

Resel R, Gratz E, Burkov A T, Nakama T, Higa M, Yagasaki K 1996 Thermopower measurements in magnetic fields up to 17 tesla using the toggled heating method. *Rev. Sci. Instrum.* **67**, 1970–5

Ri H-C, Gross R, Gollnik F, Beck A, Huebener R P 1994 Nernst, Seebeck, and Hall effects in the mixed state of $YBa_2Cu_3O_{7-\delta}$ and $Bi_2Sr_2CaCu_2O_{8+x}$ thin films: a comparative study. *Phys. Rev. B* **50**, 3312–29

Stanley D J 1974 Low-temperature magnetothermopower of silver. *Proc. R. Soc. London A* **339**, 97–117

Yagasaki K, Nakama T, Higa M, Sakai E, Burkov A T, Gratz E, Resel R 1996 Thermopower of $GdAl_2$ with see-saw heating system. *J. Phys. Soc. Jpn.* **65** Suppl. B, 181–7

K. Yagasaki
University of the Ryukyus, Okinawa, Japan

A. T. Burkov
Russian Academy of Sciences, St Petersburg, Russia

Magnetic Films: Anisotropy

Magnetic anisotropy is the coupling of the magnetization of a material to particular directions, either at a local or a macroscopic level. It means that the measured magnetic properties depend on the direction in which the magnetic field is applied, and that in zero applied field, the magnetization will lie along preferred direction(s). Without magnetic anisotropy, there can be no coercivity and no remanent magnetic moment and hence no permanent magnets or magnetic recording media. For these technologies, high anisotropy is generally advantageous, as it causes the moment to remain fixed in some desired direction.

For magneto-optic recording and proposed perpendicular recording media, perpendicular anisotropy is essential. For present-day longitudinal magnetic recording media, an anisotropy axis along the track direction allows greater thermal stability of magnetic bits, and hence smaller bit sizes. Minimizing anisotropy is equally important for technologies that require high susceptibility, such as transformers. Understanding what causes anisotropy and how to control it is thus crucial to the technological use of nearly all magnetic materials including films.

There are many sources of magnetic anisotropy in solids; for a description (see *Magnetism in Solids: General Introduction*; *Localized 4f and 5f Moments: Magnetism*; *Transition Metal Oxides: Magnetism*; and *Density Functional Theory: Magnetism*). All sources of anisotropy are fundamentally linked to the structure of the material, and therefore must have the symmetry of that structure. However, the symmetry as measured, for instance, by x rays is not necessarily the same as the local symmetry, and some substantial and technologically important anisotropy is found in films that superficially seem to be of a different symmetry. In this case, the material must have a subtle structural anisotropy that is detectable only by the most careful measurements, if at all. Much effort has been devoted to creating anisotropy in films by deliberating making materials whose structure has the desired symmetry, such as multilayers or hexagonal or tetragonal structures with c-axes either perpendicular to or along a particular in-plane direction. However, the growth process itself creates in many cases quite a large perpendicular or in-plane axis anisotropy even in amorphous and in structurally cubic materials.

While there can be a wide variety of symmetries, the most important for technologically interesting films are uniaxial and cubic. In all cases, we speak of an easy axis or axes along which the magnetization lies in zero field; it is also possible to have an easy

plane of magnetization, which is equivalent to a hard magnetic axis for which the energy would be high if the magnetization were forced in that direction. Films of a wide variety of materials, as well as bulk hexagonal and tetragonal materials, can be approximated quite well with a uniaxial anisotropy. The anisotropy energy density E_{an} in a uniaxial material is written as

$$E_{an} = K_u \sin^2\theta + K_2 \sin^4\theta + \dots \quad (1)$$

where θ is the angle between the magnetization and the easy axis and K_u is the anisotropy constant for the material in ergs cm^{-3} (J m^{-3}), and depends on temperature. Often the higher order terms (K_2) can be neglected. Figure 1 shows classical magnetic hysteresis curves $M(H)$ for uniaxial magnetic films, one with $K_u < 0$ and one with $K_u > 0$ (and substantial coercivity).

For a film with a perpendicular easy axis, θ would be measured with respect to the perpendicular and K_u would be >0. In zero applied field, for a uniaxial material, if there were no dipolar coupling, the sample would be completely magnetized with M lying along the perpendicular, either up or down. The long-range nature of magnetic dipolar coupling causes a mixture of up and down domains to form in films with perpendicular anisotropy in the equilibrium state; this state is easily imaged in MFM (see *Magnetic Force Microscopy*) and has a classical stripe domain pattern. Like any other magnetic domain structure, hysteresis is important, so that remanent states with a single domain structure can be created following application of a saturating magnetic field (see Fig. 1(b)), essential to most technological uses (e.g., magnetic and magneto-optic recording). Equation (1) assumes isotropy relative to other directions, e.g., that for $\theta = 90°$, the energy is equal in all directions in plane; this is not always a good assumption.

The anisotropy energy density in a material with cubic symmetry requires two constants and more
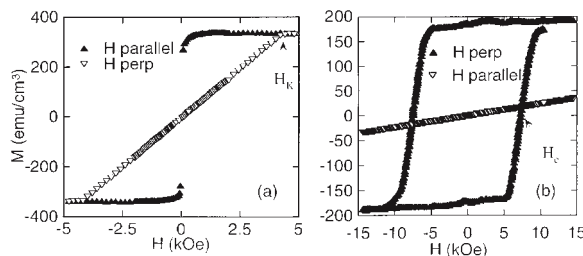
Figure 1
$M(H)$ curves for films with (a) a hard perpendicular axis, i.e., easy plane, owing to shape anisotropy; (b) easy perpendicular axis owing to growth-induced anisotropy. $M(H)$ is shown for H applied parallel and perpendicular to the plane of the film. $H_K = 4\pi M_s = 2K_u/M_s$ is shown in (a); for (b), $H_K > 80$ kOe (8 T). In (b), the large coercive field H_c is shown; for (a) $H_c = 25$ Oe. The film in (a) is f.c.c. (111) CoPt$_3$ grown at 800 °C; (b) is amorphous TbFe$_2$ film grown at 45 °C, both by e-beam co-evaporation. Data taken at room temperature.

angles to describe it:

$$E_{an} = K_1(\alpha_1^2\alpha_2^2 + \alpha_2^2\alpha_3^2 + \alpha_3^2\alpha_1^2) + K_2(\alpha_1^2\alpha_2^2\alpha_3^2) + \dots \quad (2)$$

where K_1 and K_2 are constants for the material, dependent on temperature, and α_i are the cosines of the angles M makes with the crystal axes. Often, $K_2 \approx 0$. In this case, if $K_1 > 0$ (as in bulk b.c.c. iron), the set of $\langle 100 \rangle$ directions are the easy axes, the set of $\langle 111 \rangle$ directions are the hard axes, and the $\langle 110 \rangle$ are intermediate. If $K_1 < 0$ (as in bulk f.c.c. nickel), the $\langle 111 \rangle$ are easy directions and the $\langle 100 \rangle$ hard. When $K_2 \neq 0$, the easy axes depend on the K_1/K_2 ratio.

1. Anisotropy in Films

Starting from the basic principles of anisotropy, it is possible to distinguish a number of different contributions in films, at least theoretically. In addition to the magnetocrystalline anisotropy expected from measurements on equivalent bulk materials, there are a number of contributions that are unique to films. The simplest to understand is shape anisotropy, which is due to the difference in demagnetization factor in the directions parallel and perpendicular to the film plane. This contribution causes a hard perpendicular axis (an easy plane). Other contributions result from the modified nature of the atomic arrangements in films. The broken/altered bonds at the top and bottom surfaces of a film or interface in a multilayer cause a change in the crystal fields and dipole energies of the atoms/ions at these surfaces and interfaces.

These interfaces will usually result in uniaxial anisotropy, which may have K_u greater or less than 0 (easy perpendicular axis or easy plane). In addition, surfaces and interfaces may cause reconstructions and relaxations of the atomic arrangement such that the atomic structure at top and/or bottom may be quite different from a simple termination of the bulk structure, leading to additional anisotropy. Strain in a material due to intrinsic growth phenomena, epitaxy, or differential thermal contraction will generally give rise to a uniaxial anisotropy.

Experimentally, it is not always easy to separate these contributions. For films with uniaxial anisotropy (the most common), K_u is usually written as a sum of the various contributions (discussed in more detail below):

$$K_u = -2\pi M_s^2 + K_{u\sigma} + K_{ui} + K_s/t \quad (3)$$

where $-2\pi M_s^2$ is the shape contribution, $K_{u\sigma}$ is the stress-induced contribution, K_{ui} the growth-induced or intrinsic magnetocrystalline term for uniaxial symmetry materials, and K_s/t due to the surfaces, where t is the film or layer thickness. If cubic terms are needed, or if the angles about which the uniaxial anisotropy occurs for each contribution (e.g., growth

induced terms can be tilted away from the film normal due to incident atomic beam effects, while shape anisotropy is strictly relative to the film plane), care must be taken to add these contributions more carefully (see, e.g., Hellman *et al.* 1989).

In addition, many magnetic materials of interest are multi-component alloys, amorphous, or nanocrystalline composites. In such materials, local magnetic anisotropy may be large but is expected to be randomly oriented at different sites, possibly giving rise to coercivity but no net macroscopic anisotropy. However, for films made from these materials, strain or local chemical or structural ordering can lead to an alignment of the local anisotropy axes, causing large macroscopic anisotropy. The source of this seemingly extrinsic anisotropy may be quite fundamental: e.g., the growth process of a film, or the epitaxial strain of the magnetic layer on a substrate.

1.1 Shape Anisotropy

The source of shape anisotropy lies in the difference in demagnetization factors in the directions parallel and perpendicular to the film plane; this energy is fundamentally a summation of the magnetic dipole–dipole coupling of all the moments in the film. For a film whose thickness is much less than its other dimensions, shape anisotropy gives an easy plane, which is equivalent to a hard perpendicular axis: $K_u = -2\pi M_s^2$ ($-\mu_0 M_s^2/2$ in SI units) for films with thickness that is small compared to their other two dimensions. Uniaxial shape anisotropy (or other film-related uniaxial contributions) often dominate an intrinsic cubic magnetocrystalline anisotropy, as in Fig. 1(a) for f.c.c. $CoPt_3$. There is also a small contribution for antiferromagnets; here the dipolar interaction causes the moments to align side-by-side, which, summed up over the moments in a thin film, means $K_u > 0$. This K_u is however small (compared to $2\pi M_{sa}^2$ where M_{sa} refers to a sublattice magnetization) and is in essence a surface contribution, hence it varies inversely with film thickness.

Columnar microstructures are often found in films. It is important to note that unless the areal density of columns in a film is extremely low (less than 0.5 filling), the shape anisotropy of these columns alone will not produce a net perpendicular anisotropy (Yafet *et al.* 1986). However, effects such as oxidation and the broken/altered bonds at the surfaces of these columns, like the surfaces and interfaces of films discussed below, could lead to anisotropy via the other mechanisms described in this article.

1.2 Intrinsic Magnetocrystalline Anisotropy

If the lattice constant and structure of a material is the same for a film as for a bulk material, the intrinsic magnetocrystalline anisotropy is the same. By

manipulating the growth conditions, different types of anisotropy can be created, even for the same crystal structure. Examples of this are growth of h.c.p. cobalt with its *c* axis perpendicular, or using epitaxial relationships to cause the *c*-axis of tetragonal CoPt or FePt to grow along a particular in-plane direction (Coffey *et al.* 1995, Farrow *et al.* 1996). In each case, the easy magnetic axis will lie along the *c*-axis, but the net effect will be perpendicular or in-plane anisotropy. This contribution to anisotropy is independent of thickness as long as the crystal quality is maintained and strain is not a factor.

1.3 Strain-induced Anisotropy

In general, films prepared by vapor deposition processes are not structurally identical to their bulk counterparts. It is of course possible to create structures not observed in bulk materials, e.g., f.c.c. cobalt, which then have the symmetry of this new material. But even if the structure is nominally the same as a known bulk material, vapor deposition produces strains and defects that influence the magnetic properties. There are many sources of strain in vapor-deposited materials, discussed more completely in *Stress Coupled Phenomena: Magnetostriction* and *Magnetoelasticity in Nanoscale Heterogenous Materials*. Differential thermal contraction and epitaxy with a substrate of a different lattice constant are sources of stress produced by the substrate (or by an overlayer, although these are usually thin and hence produce less strain in the film than the substrate). There are also a number of sources of stress intrinsic to the growth process, e.g., bombardment by energetic ions/atoms in sputtering tends to produce compressive strain; early stage coalescence phenomena tend to produce tensile strain. These types of strain tend to be uniaxial relative to the film plane and can be either compressive or tensile.

The link between strain and anisotropy is through magnetostriction. Magnetostriction is fundamentally linked to spin-orbit coupling and to crystal fields as discussed in *Magnetism in Solids: General Introduction* and *Electron Systems: Strong Correlations*. Strain could in fact be regarded to result in anisotropy by simply being magnetocrystalline anisotropy but for an e.g., tetragonal structure instead of the intrinsic cubic structure. However, it is not usually calculated in this way, in part because the strain and hence the tetragonal distortion is typically a few parts in 10^5. Instead it is treated as a separate contribution to the anisotropy. A uniaxial strain in an isotropic (or nearly isotropic) material results in a uniaxial contribution to the anisotropy:

$$K_{u\sigma} = -3\lambda\sigma/2 \qquad (4)$$

where λ is the magnetostrictive constant and σ is the strain. The sign convention for strain is $\sigma > 0$ is tensile, and $\sigma < 0$ is compressive.

For materials with positive magnetostrictive constant λ, this means compressive strain causes a perpendicular easy axis. For cubic materials, or even hexagonal materials since the plane cannot be assumed to be isotropic, the anisotropy produced by various types of strain is more complex (see, e.g., Cullity 1972, p. 250 forward). Magnetostriction is typically measured by measuring the lattice distortion on applying a magnetic field, which eliminates domains. Since most films are on substrates, this is most easily done by measuring deflection (i.e., bending) of the substrate/film combination on magnetizing the film. In this case, a knowledge of the mechanical properties of substrate and film (specifically, Young's modulus and Poisson's ratio) is needed to make quantitative calculations.

An example of strain-induced anisotropy in a film of an otherwise cubic material is strained Laves phase TbFe$_2$, which may be useful for giant magnetostrictive devices (Wang *et al.* 1996).

1.4 Growth-induced Anisotropy

This contribution fundamentally comes from the same sources as magnetocrystalline anisotropy but arises in structures where the underlying symmetry is apparently cubic or isotropic. It is a separate contribution from strain-induced anisotropy, and can be identified in films with extremely low strain, or where the sign of the strain can be changed with no significant change in anisotropy. It originates intrinsically from the growth process producing a subtle anisotropy in short-range order, which can be either structural or chemical or both. The structural or chemical anisotropy in turn produces a magnetic anisotropy, either via crystal field effects (often known as single-ion anisotropy) or via dipolar coupling (sometimes called pair anisotropy). The latter is generally significant only when the crystal field contribution is small, e.g., for $L = 0$ ions such as gadolinium.

The current magneto-optic recording media, quaternary alloys related to amorphous Tb–Fe, rely completely on this source of anisotropy to give a perpendicular easy axis, as in Fig. 1(b) (see, e.g., Hellman and Gyorgy 1992 and references given there). Seemingly cubic (f.c.c.) Co–Pt alloys grown by vapor co-deposition at deposition temperatures near 400 °C have anisotropies nearly 10% of that found in the best Co/Pt multilayers; this effect has been attributed to growth-induced cobalt clustering into platelets within a platinum-rich matrix, much like an incoherent local multilayer (see, e.g., Weller *et al.* 1992, Shapiro *et al.* 1999, and references therein). For both *a*-Tb–Fe and f.c.c. Co–Pt, EXAFS has shown signs of anisotropic local structure (e.g., Harris *et al.* 1992, Tyson *et al.* 1996). The characteristic feature of this source of anisotropy is that it is produced by the vapor deposition process and
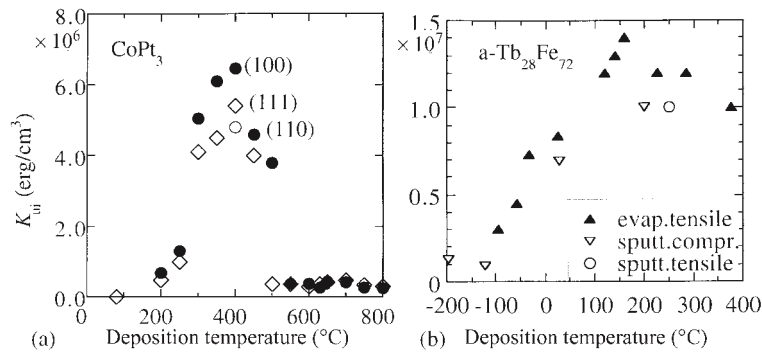
Figure 2
Dependence of growth-induced anisotropy K_{ui} (shape contribution $-2\pi M_s^2$ removed) on growth temperature for (a) f.c.c. (as measured by x ray and TEM) $CoPt_3$ and (b) amorphous $TbFe_2$, prepared under various growth conditions (e.g., different epitaxial orientations, sputtered, e-beam co-evaporated, under tensile or compressive strain as grown). In (a), annealing at $450\,^{\circ}C$ eliminates K_{ui} for all samples; in (b), annealing eliminates K_{ui}, but higher annealing temperatures are required for films grown at higher temperatures (see Hellman *et al.* 1999, Hellman and Gyorgy 1992, and Shapiro *et al.* 1999 for details). Data taken at room temperature.

vanishes upon annealing of the material, even at temperatures that produce no obvious structural change. It is largely deduced by experimentally ruling out other sources of anisotropy, e.g., strain, surface, and intrinsic magnetocrystalline anisotropies.

The growth process can break the symmetry of the structure by several quite distinct means. First, there can be a chemical or structural memory of the incident atomic beam directions. This effect is dominant at low growth temperatures, where growth phenomena such as kinetic roughening are important. Columnar microstructure tilted at an angle intermediate to the incident beam direction and the film normal are an obvious structural manifestation of this effect; such shadowing-related effects are much studied in growth simulations. Even in materials where this obvious structure is not seen, the magnetic anisotropy can still reflect the effect of the incident beam angle (e.g., Hellman *et al.* 1987). This effect of the incident beams on anisotropy (and in turn on coercivity) is quite pervasive, and is seen in nearly all alloys, particularly those grown at room temperature and below. In some cases, it may be used to advantage, by giving a preferred in-plane axis, but it can also be detrimental to desired low coercivity materials.

At higher growth temperature, adatom surface mobility typically erases this memory of the incident beam direction(s). However, an even stronger source of growth-induced anisotropy occurs in this growth regime. Here, at intermediate growth temperatures, surface adatom mobility is extremely high compared to bulk mobility (typical root mean square diffusion lengths are tens to hundreds of nanometers during the lifetime of the adatom before it is buried by the next layer of adatoms at typical growth rates, while

typical r.m.s. diffusion lengths for an atom once buried in the bulk of the film for the duration of a typical deposition are less than an atomic spacing). As a result, in this intermediate growth regime, an as-deposited film is really a sequence of surface layers, trapped in. At still higher temperatures, typically above approximately one-third of the materials' melting temperature T_m, bulk atomic diffusion becomes important and the equilibrium structures are found. The result (shown in Fig. 2) is that for both amorphous Tb–Fe and crystalline f.c.c. Co–Pt films, anisotropy increases with increasing growth temperature up to the onset of appreciable bulk atomic mobility (Hellman *et al.* 1999).

Defects also affect the anisotropy, although if they are point defects randomly distributed, their effect will not add up to a net macroscopic anisotropy. However, the local anisotropy associated with stacking faults, dislocation layers, and internal interfaces in a columnar growth structure can, at least in theory, produce macroscopic anisotropy.

1.5 Surfaces of Ultrathin Films

The broken bonds of the surface of the film (and the bottom of the film, next to the substrate) lead to a uniaxial anisotropy which can be of either sign, as originally described by Néel in 1954. This topic is discussed in *Monolayer Films: Magnetism*, and will be touched on only briefly here. This contribution arises fundamentally from the same sources as cause bulk magnetocrystalline anisotropy. A good example is that f.c.c. cobalt films a few monolayers thick have a perpendicular easy axis, which drops into the plane as

the film thickness increases. This anisotropy is extremely dependent on the details of the surface structure, and hence is affected by impurity adsorption, surface reconstruction, relaxation, segregation, and other properties well known to surface scientists. To the extent that the film structure can be assumed to remain constant, independent of thickness, this contribution to the total anisotropy will fall off as inverse thickness, i.e., $K_u = K_s/t$ where K_s is a surface anisotropy in ergs cm^{-2} (J m^{-2}) and t is the film thickness.

1.6 Interfaces in Multilayers and Nanocrystalline Films

This contribution is fundamentally the same as the preceding one for surfaces, except that instead of broken bonds at a vacuum interface, there are bonds to a neighboring layer. The anisotropy in multilayers is generally uniaxial, often quite sizable, and can be of technological significance (e.g., optimized Co/Pt multilayers of particular thickness for each layer have $K_u > 2 \times 10^8$ ergs cm^{-3} (2×10^7 J m^{-3}), making them possible future perpendicular recording or magneto-optic recording media; see, e.g., Weller *et al.* 1993). Figure 3 shows the dependence of anisotropy on cobalt layer thickness for different orientations. In general, there are contributions both from the strain induced by the lattice mismatch of the two (or more) materials, and from an intrinsic interface contribution, as well as the intrinsic magnetocrystalline anisotropy, which may also be uniaxial. In principle, these can be separated by measuring the dependence of the anisotropy on layer thickness, as in Fig. 3, since the interface contribution to the total anisotropy should drop off as inverse thickness, while the others may remain constant. However, there are dangers in

the interpretation of this data since both strain and interface structure may depend on thickness (see *Monolayer Films: Magnetism*).

In nanocrystalline films, internal interfaces between magnetic and nonmagnetic (or other magnetic) materials can also lead to local anisotropy, although it will tend to be randomly oriented and therefore not lead to a net macroscopic anisotropy. However, any alignment of the nanocrystal axes by growth effects would lead to net anisotropy.

1.7 Unidirectional Anisotropy

In principle, the lowest order symmetry possible for anisotropy is uniaxial, which has 180° symmetry. It was however realized many years ago that by taking advantage of exchange coupling between the magnetic material of interest and an antiferromagnet with substantial anisotropy, such as in a bilayer or multilayer, a unidirectional anisotropy could be created (see, e.g., review by Nogues and Schuller 1999). This effect is technologically important for biasing of magnetoresistive read heads or other sensors. The fundamental source of this symmetry breaking is the alignment of the antiferromagnet's Néel vector, most commonly by cooling through the Néel temperature of the antiferromagnet while applying a field sufficient to align the ferromagnet. Exchange coupling then forces the Néel vector and hence one sublattice to lie along a direction set by the cooling field. Subsequent application of a field in another direction is insufficient to reverse the antiferromagnet, owing to its high magnetocrystalline anisotropy and low net moment.

The ferromagnet is exchange coupled to the antiferromagnet and hence does not reverse in low fields. The detailed nature of this exchange biasing becomes
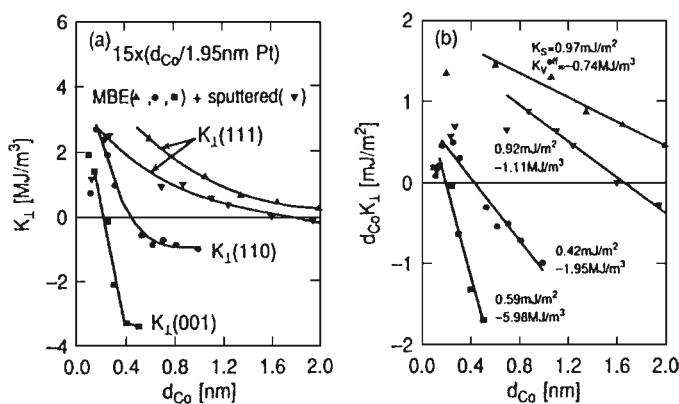
Figure 3
(a) $K_\perp$ (i.e., K_u with shape contribution $-2\pi M_s^2$ removed) and (b) $d_{Co} \times K_\perp$ for epitaxial and sputtered Co/Pt multilayers versus cobalt layer thickness d_{Co}. Data taken at room temperature (reproduced by permission of the Materials Research Society from *MRS Symp. Proc.*, 1993, **313**, 791–7).

quite complex, owing to the possibilities of canting, antiferromagnetic domains, compensated and uncompensated planes, and surface roughness in the antiferromagnet; the result is that the underlying source is not well understood. It is clear that it is not necessary for a single sublattice defined over the macroscopic dimensions of the antiferromagnet to be aligned, but instead there can be alignment within domains of the locally defined sublattice physically most near the ferromagnet. It is also possible to use ferrimagnets instead of antiferromagnets, or even ferromagnets if their anisotropy is high enough to prevent switching in the low fields used to switch the primary ferromagnetic material (e.g., Hellman *et al*. 1987).

2. Measurements of Anisotropy

The first and often most important step is simply to determine the anisotropy symmetry, i.e., cubic or uniaxial, perpendicular easy or hard axis. This may be done in a variety of ways, including $M(H)$ curves, torque magnetometry, Kerr or Faraday rotation observations, magnetic force microscopy, even magnetoresistance with H applied along different directions. The simplest way to measure anisotropy energy is by torque magnetometry. The first step is to technically saturate the magnetization of the film by applying a field **H** along an easy axis which is strong enough to eliminate magnetic domains ($H > H_c$, where H_c is the coercive field). Figure 4 shows the geometry for a film with uniaxial anisotropy. Then the direction α of the magnetic field is rotated; for high anisotropy materials, Miyajima's $\alpha = 45°$ method is often used (if $H_c < H < H_K$, we are not in the high field limit often assumed, e.g., by Cullity 1972, p. 215).

The minimum energy would be if the moment **M** could follow the direction of the field, by physically rotating the sample so that its easy axis direction remained along the direction of the rotating field. If the sample is physically constrained from doing this, then it will exert a torque **T** on the constraint. The energy of this arrangement can be written as

$$E = -\mathbf{M} \cdot \mathbf{H} + E_{an} = -MH\cos(\alpha - \theta) + K_u\sin^2\theta \qquad (5)$$

for a simple uniaxial anisotropy, where θ and α are the angles **M** and **H** make with respect to the easy axis, α is fixed, but θ will adjust to minimize the energy, so

easy axis α θ $\vec{M}$ $\vec{H}$
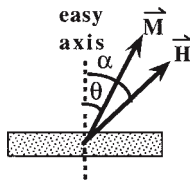
Figure 4
Geometry of torque measurement for uniaxial anisotropy film.

$\delta E/\delta\theta = 0$. The torque exerted by the sample on the constraint $\mathbf{T} = \mathbf{M} \times \mathbf{H} = MH\sin(\alpha-\theta)$ is measured using one of several techniques. This then effectively gives θ, and hence E_{an} (see, e.g., Hellman *et al*. 1989 for more details).

It is sometimes possible to make a direct measurement of θ by measuring the component of M perpendicular to the applied field, using for example quadrature pick-up coils. This is more difficult than measuring torque, because the perpendicular component and θ become quite small for large H, while the torque $\mathbf{M} \times \mathbf{H}$ remains large. There are also specialized techniques used, e.g., *in situ* in a vacuum deposition system where a Kerr measurement can be used to infer the perpendicular component of **M** and hence the anisotropy.

Magnetic resonance is another powerful technique for determining anisotropy. The constant applied field is applied usually along an easy axis. For a uniaxial sample, the resonance condition is then given by the sum of the applied field and the anisotropy field $H_K = 2K_u/M_s$. For cubic systems, K_1 and K_2 can be determined by measuring with H applied along various axes.

In limited cases, magnetic hysteresis curves can also be used. Here, the applied field is usually applied along a hard axis, causing magnetization to rotate. In the limit that there is no domain motion, only rotation, for example in a uniaxial material, the magnetization saturates at M_s for a well defined field $H_K = 2K_u/M_s$ (see, e.g., Fig. 1). Alternatively, the difference in areas between the hard and easy axis curves is proportional to the anisotropy energy.

3. Summary and Future Directions

Anisotropy in films is a sum of contributions from the intrinsic magnetocrystalline anisotropy expected from the bulk equivalent material and a number of effects linked to the fact that the structure of a film is for many reasons not equivalent to the bulk. There are many sources of these differences, connected both to the fact that a film is grown on a substrate and has a top and bottom surface whose properties, both structural and magnetic, are not simply related to the properties of the bulk material, and to intrinsic effects of the growth processes used to prepare films which cause a memory of the growth direction to be trapped into the structure. At present, there is almost no way to predict the anisotropy of a film of a new material; there are many contributions and it is difficult to know in advance which effects will dominate.

Experimental efforts to find improved materials often center on taking advantage of the bulk magnetocrystalline anisotropy, or on deliberately prepared multilayers, but in fact growth-induced effects and other less predictable contributions often dominate, certainly for materials presently used for practical applications.

See also: Magnetic Films: Hard; Metal Evaporated Tape; Monolayer Films: Magnetism; Multilayers: Interlayer Coupling; Thin Films: Domain Formation; Thin Films: Stresses

Bibliography

Coffey K R, Parker M A, Howard J K 1995 High anisotropy $L1_0$ thin films for longitudinal recording. *IEEE Trans. Magn.* **31**, 2737–9

Cullity B D 1972 *Introduction to Magnetic Materials*. Addison-Wesley, Reading, MA

Farrow R F C, Weller D, Marks R F, Toney M F, Cebollada A, Harp G R 1996 Control of the axis of chemical ordering and magnetic anisotropy in epitaxial FePt films. *J. Appl. Phys.* **79**, 5967–9

Harris V G, Aylesworth K D, Das B N, Elam W T, Koon N C 1992 Structural origins of magnetic anisotropy in sputtered amorphous Tb-Fe films. *Phys. Rev. Lett.* **69**, 1939–42

Hellman F, Gyorgy E M 1992 Growth-induced magnetic anisotropy in amorphous Tb-Fe. *Phys. Rev. Lett.* **68**, 1391–4

Hellman F, Shapiro A L, Abarra E N, Rooney P W, Tran M Q 1999 Magnetic anisotropy and coercivity in magneto-optical recording materials. In: (eds.) *MORIS '99 Conf. Proc. J. Magn. Soc. Jpn.* **23**(Suppl. S1), 79–84

Hellman F, van Dover R B, Gyorgy E M 1987 Unexpected unidirectional anisotropy in amorphous Tb-Fe/Ni-Fe-Mo bilayer films. *Appl. Phys. Lett.* **50**, 296–8

Hellman F, van Dover R B, Nakahara S, Gyorgy E M 1989 Magnetic and structural investigation of the composition dependence of the local order in amorphous Tb-Fe. *Phys. Rev. B* **39**, 10591–605

Nogues J, Schuller I K 1999 Exchange bias. *J. Magn. Magn. Mater.* **192**, 203–32

Shapiro A L, Rooney P W, Tran M Q, Hellman F, Ring K M, Kavanagh K L, Rellinghaus B, Weller D 1999 Growth-induced magnetic anisotropy and clustering in vapor-deposited Co-Pt alloy films. *Phys. Rev. B* **60**, 12826–36

Tyson T A, Conradson S D, Farrow R F C, Jones B A 1996 Observation of internal interfaces in $Pt_xCo_{1-x}(x \approx 0.7)$ alloy films: a likely cause of perpendicular magnetic anisotropy. *Phys. Rev. B* **54**, R3702–5

Victora R H, MacLaren J M 1993 Theory of magnetic interface anisotropy. *Phys. Rev. B* **47**, 11583–6

Wang C T, Clemens B M, White R L 1996 Effects of substrate on the magnetic properties of epitaxial $TbFe_2$ (111) films. *IEEE Trans. Magn.* **32**, 4752–4

Weller D, Brandle H, Gorman G, Lin C-J, Notarys H 1992 Magnetic and magneto-optical properties of cobalt–platinum alloys with perpendicular magnetic anisotropy. *Appl. Phys. Lett.* **61**, 2726–8

Weller D, Farrow R F C, Marks R F, Harp G R, Notarys H, Gorman G 1993 Interface and volume anisotropy of MBE-grown Co/Pt(111), (110) and (001) and sputtered Co/Pt multilayers. *Mater. Res. Soc. Symp. Proc.* **313**, 791–7

Yafet Y, Gyorgy E M, Walker L R 1986 Directional dependence of the demagnetizing energy in imperfect thin magnetic films. *J. Appl. Phys.* **60**, 4236–9

F. Hellman
*University of California, San Diego
California, USA*

Magnetic Films: Hard

The scope of this article is to provide a general introduction to hard magnetic films. It discusses application-relevant extrinsic magnetic properties and focuses on a specific hard magnetic material ($Nd_2Fe_{14}B$) to demonstrate the interplay between the film-related microstructure and the magnetic performance. The article by (Kruusing 1999) is a good addendum, as he reviews $Nd_2Fe_{14}B$ thin films and describes preparation-specific topics.

1. Applications

One area for application of hard magnetic films are microsystem techniques, especially microelectromechanical systems (MEMS). These devices are prepared from relatively thick films (1–5 µm) and the high-energy product of the rare earth magnets promises smaller lateral device sizes. Until now, however, only a few systems have been realized, for example a sub-millimeter electric motor (Yamashita *et al.* 1991), and a stepper motor (Belmans and Hameyer 1998). The challenge facing rare earth magnets in this field is their high corrosion rate when exposing a large surface after structuring. Another potential application is in monolithic microwave integrated circuits (MMICs) (Levy *et al.* 1996) using thin hard magnetic layers to create bias fields for ferrite devices. Although an optical isolator could be realized this way, this technology has to compete with the conventional technology, which is not based on ferrites.

The largest market for hard magnetic films is in magnetic data storage on computer hard disks. While the bit density increases by about 60% each year, the conventional materials (e.g., CoPtCr, CoCrTa) are expected to reach the superparamagnetic limit by around 2005, where the small magnetic dots used to store the information tend to become thermally unstable. In order to exceed densities of 100 Gbit in^{-2}, materials with a higher uniaxial magnetic anisotropy are of interest (see *Magnetic Anisotropy*). The high perpendicular magnetic anisotropy of $Nd_2Fe_{14}B$ thin films presents the additional possibility of packing bits closer together using perpendicular recording, where the spins representing the bits are oriented perpendicular to the substrate. Compared to other applications, the required film thickness is small (20–50 nm).

2. Structure Formation

The $Nd_2Fe_{14}B$ phase providing the desired intrinsic magnetic properties has a tetragonal unit cell ($a = 8.805$ Å, $c = 12,203$ Å) comprising 68 atoms (see *Rare Earth Magnets: Materials*). At room temperature

the magnetic easy axis is along the *c*-axis. When depositing films on heated substrates below temperatures of 500–675 °C, x-ray diffraction patterns reveal only amorphous spectra and the films are soft magnetic. However, using transmission electron microscopy, Mapps *et al.* (1997) observed small inclusions of the $Nd_2Fe_{14}B$ phase with grain sizes below 10 nm (which are invisible to x-ray diffraction) already on films deposited at room temperature. At higher temperatures a significant amount of the hard magnetic $Nd_2Fe_{14}B$ phase forms, but even at temperatures above 650 °C part of the material can remain in the amorphous state (Shima *et al.* 1998).

3. Coercivity Mechanism

Magnetization reversal can be inhibited by two different mechanisms (see *Coercivity Mechanisms*). In the nucleation type magnets, domain wall motion inside almost perfect grains is easy, but the nucleation field necessary to create new Bloch walls is high, as no extended defects lower the Bloch wall energy. When magnetizing this type of material in a field below the saturation field, the remaining domain walls cause a lower remanence than when magnetizing by a field strong enough to remove all domain walls. This coercivity mechanism is usually valid when relatively large and perfect grains exist and can be used to describe annealed $Nd_2Fe_{14}B$ films on Ta/Si(111) (Tsai *et al.* 1998) (a system showing no intermixing) and films grown on heated W/Si(111) (Tsai *et al.* 1999a) where only few neodymium-rich precipitates are observed.

In pinning type magnets, the nucleation of reversed domains is not inhibited, but a lot of defects exist—preferably with a size comparable to the Bloch wall thickness—where the domain walls are pinned. Magnetization reversal occurs when the force exerted on the domain wall (pinned at the inhomogeneities) becomes sufficiently strong. In $Nd_2Fe_{14}B$ films deposited on heated Pt/Si(111) (Tsai *et al.* 1999a) and in annealed samples on silicon (Tsai *et al.* 1998) pinning seems to control the coercivity.

4. Grain and Domain Size

A very effective way to increase coercivity is to reduce the grain size below the single domain particle size. This is often found in NdFeB films where the domain size is even larger than the lateral grain size (Gouteff *et al.* 1998, Lemke *et al.* 1997). Here exchange coupling between neighboring grains leads to the occurrence of interaction domains. Generally the domain walls follow the grain boundaries, demonstrating their pinning effect. Therefore the coercivity typically increases with decreasing grain size and with decoupling of neighboring grains.

The key parameters for controlling grain growth are the annealing temperature and the annealing time. When the films are deposited at room temperature and annealed afterwards, both parameters can be controlled but the annealed samples are isotropic, eliminating the possibility of preparing textured films (having perpendicular anisotropy with respect to the surface). The crystallization develops via intermediate stages depending on the composition (Linetsky *et al.* 1992). With rapid thermal annealing of 60 s at 500 °C it is possible to obtain grain sizes of 50 nm and a coercive field H_c up to 20 kOe—a two-fold improvement compared to annealing times in the ten minute range (Yu *et al.* 1998).

To achieve a *c*-axis texture (see below), however, structure formation is necessary already during deposition, which requires a substrate temperature above 500 °C. Parhofer (1997) observed an increase in the perpendicular grain size with increasing substrate temperature but as a variation in temperature also influences the phase formation, texture, etc., no systematic examination of the perpendicular and lateral grain size and their influence on the magnetic properties yet exists.

The deposition method also seems to influence the grain size. While sputtered films usually have grain sizes of about 100 nm (Gouteff *et al.* 1998, Tsai *et al.* 1998, 1999c), films prepared by pulsed laser deposition (PLD) have smaller grain sizes (down to 12–20 nm) (e.g., Lemke *et al.* 1997). This is a known effect originating from the significantly higher kinetic energy of the deposited particles during PLD compared to other deposition methods (Fähler and Krebs 1996). The ions are implanted into the topmost monolayers ("subsurface growth") (Fähler *et al.* 2000) reducing their mobility and the grain size of laser deposited metallic films is usually smaller. On the other hand, this implantation can cause defects which reduce the magnetic order and this may be the reason why the magnetic properties of the PLD films are not improved as expected.

A sharp grain size distribution leads to a simultaneous switching of the grains and a more square magnetization curve. For magnetic recording, a broad grain size distribution can result in the undesirable failure of some bits. A smooth, round grain surface is also favored as at asperities the enhanced stray field favors the nucleation of reversed domains.

5. Influence of Composition

The $Nd_2Fe_{14}B$ phase shows only a small existence region so that variations in the concentration result in an inhomogeneous microstructure with additional phases which can be used to improve the magnetic properties. Similar results can be achieved with additives in most magnetic systems, but when additives are solved partly in the main magnetic phase it is difficult to distinguish between changes in the intrinsic and extrinsic properties.

Adding a paramagnetic component such as neodymium in NdFeB forms a neodymium-rich intergranular paramagnetic phase decoupling the ferromagnetic $Nd_2Fe_{14}B$ grains. The decoupling prevents domain nucleation induced by neighboring grains and increases the coercivity. With increasing neodymium content the *c*-axis texture is lost but the grain size is reduced and the energy product can be optimized with neodymium concentrations slightly higher than the stoichiometric composition (Piramanayagam *et al.* 1998).

It has been observed that increasing boron content up to 17 at.% leads to an increase in the *c*-axis texture and increases the perpendicular coercivity significantly (Araki *et al.* 1999). Due to the excess boron a soft magnetic amorphous phase is formed between the columnar $Nd_2Fe_{14}B$ grains. This fine microstructure should be exchange coupled and the authors suggest that the observed sharp interfaces prevent domain nucleation. Boron contents above 17 at.% reduce the coercivity as the amount of the soft magnetic amorphous phase increases.

Of different intention is the addition of a second phase with a higher saturation magnetization M_s by increasing the iron content above the stoichiometric value. Such a composite material can possess a higher saturation magnetization and also a higher remanent magnetization, provided the soft iron phase is coupled to the hard magnetic $Nd_2Fe_{14}B$ phase. Accordingly, in NdFeB films an increase in M_s with the iron content has been observed (Piramanayagam *et al.* 1998). Additionally, the iron content can improve the *c*-axis texture. Both factors should contribute to the observed increase in remanence.

However, as large soft iron grains can act as a nucleus during the magnetic reversal and significantly reduce the coercivity, it is important for a composite film to limit the iron grain size so that the complete iron grains are coupled to the hard $Nd_2Fe_{14}B$ grains (grain size less than $\sim 10\,nm$—twice the Bloch wall width). Films sputtered at $650\,°C$ show iron grain sizes of $\sim 10\,nm$, and up to 17 vol. % Fe the coercivity decreases only slowly (Tsai *et al.* 1999b).

6. Multilayers

The well-defined preparation of alternating soft and hard magnetic layers should enable the testing of the micromagnetic models of exchange coupling (see Magnets: Remanence-enhanced). Parhofer *et al.* (1996) showed that iron layers below 30 nm are fully coupled to the $Nd_2Fe_{14}B$ layers and the reduced remanence $R = J_R/J_S$ increases significantly when the iron thickness is reduced to this value. He confirmed that the saturation magnetization can be calculated from the volume-weighted sum of both magnetizations, indicating that at the interface no significant structural deterioration occurs.

In nanocomposite magnets, for optimum BH_{max} the following considerations hold: To make use of the high M_S of the soft magnetic phase, its fraction should be increased. On the other hand the nucleation field for magnetization reversal (and consequently H_C) is lowered as the thickness of the soft magnetic phase becomes larger. So in order to keep a high fraction of the soft phase, also the thickness of the hard phase must be reduced. But this reduction is limited as the coercivity of the hard magnetic phase is lost if its thickness reaches the same order of magnitude as the domain wall width. Shindo *et al.* (1997) confirmed this trend in experiment and found a good agreement with a micromagnetic calculation when using an interlayer exchange-coupling strength of about 10% of the intralayer couplings. They also confirmed the exchange-spring effect by measuring reversible minor magnetization curves.

In spite of these advantages, such multilayers tend to lose the *c*-axis texture (Parhofer 1997), their crystallinity can be reduced, they show a significant increase in roughness, and intermixing in the range of 10 nm can occur (Shindo *et al.* 1997).

Multilayers of $Nd_2Fe_{14}B$ and a nonmagnetic material should also allow decoupling of the magnetic layers. While experiments with silver failed due to the reaction to form NdAg (Aylesworth *et al.* 1989), multilayers with tunsgten (Panagiotopoulos *et al.* 1997) only break their layered structure during annealing. With an appropriate $Nd_2Fe_{14}B$ thickness of about 5 nm, the resulting microstructure consists of separated isotropic $Nd_2Fe_{14}B$ grains (grain size $\sim 10\,nm$) in a tungsten matrix and H_C is improved up to 20 kOe.

7. Texture

The aim of having a textured film is to use the microscopic anisotropy for an application with a macroscopic anisotropy and to increase M_R/M_S above the limit of 0.5 for a randomly-oriented film. While films deposited at room temperature and subsequently annealed are isotropic, films on heated substrates can be grown with a *c*-axis texture, so that the hard magnetic axis is oriented perpendicular to the substrate. (In contrast to CoSm, the substrate temperature is usually above T_C, therefore no stray field forces the *c*-axis to lie within the film surface.) As an explanation for the *c*-axis texture, Cadieu (1987) suggested that a high ion flux onto the substrate (usually obtained at low deposition rates during sputtering) should prevent the formation of long ordered repeat distances parallel to the substrate plane, and materials having a longer *c*-axis (as $Nd_2Fe_{14}B$) should, therefore, favor a *c*-axis texture. In agreement with this, he observed a decrease in the *c*-axis texture with increasing deposition rate.

Another reason for this texture can be the anisotropic growth velocity known from bulk material, which forms longer *c*-surfaces than *a* and *b*. Starting with an isotropic texture, the *c*-axis oriented grains grow faster and cover more and more of the substrate resulting in *c*-axis texture. In agreement with this, films with a rough surface and grown at higher temperatures above 650–700 °C (leading to a stronger reaction with the substrate) lose the *c*-axis texture. Also the film composition can influence the texture: a high iron content (Piramanayagam *et al.* 1998) or boron content (Araki *et al.* 1999) improves the *c*-axis texture.

A buffer also provides the possibility to modify film texture. While films on tantalum and titanium generally obtain a (001) *c*-axis texture, a tungsten or molybdenum buffer can change the texture towards (105), whereas on platinum no texture was observed. With a chromium buffer different textures were observed. Also the grain size and roughness is influenced by different buffers (Piramanayagam *et al.* 1998, Shima *et al.* 1998, Shindo *et al.* 1997, Tsai *et al.* 1998, Tsai *et al.* 1999c, Parhofer *et al.* 1998).

In spite of the reactivity with a silicon substrate, it seems to be possible to deposit epitaxial $Nd_2Fe_{14}B$ films on Si(111) with the *c*-axis lying in plane (Kruusing 1999), while approaches to prepare epitaxial films on Mo(001) with the *c*-axis perpendicular to the substrate have not been successful: here a different, unidentified, phase grows epitaxially at the beginning (Keavney *et al.* 1997).

Since in all the experiments the texture could not be controlled without changing other parameters such as the grain size or composition, it is difficult to deduce the effect of texture on the magnetic properties. However, it occurs, as a general tendency, that the films with the best magnetic properties do not possess the best *c*-axis texture (Parhofer 1998). With a strong *c*-axis texture the angle between the spins in neighboring grains is small and the grain boundaries seem not to provide effective pinning. This effect is described by the coercivity model of Kronmüller (see *Coercivity Mechanisms*) where the microstructural parameter for pinning efficiency increases with stronger grain misalignment. Here it would be useful to separate the grains magnetically while retaining the *c*-axis texture.

8. Roughness

Films grown at higher temperatures show an increased film roughness. In general, films with a rough surface exhibit a higher H_C than smooth films. This is attributed to pinning of the magnetic domains at the asperities. But since applications such as microstructuring or hard disks need a smooth surface (danger of head crashes or a too large read/write distance), an increased roughness is not suitable.

9. Stability and Thickness

Oxide and silicon substrates react strongly with NdFeB and destroy the magnetic properties—a general problem with rare earth components. Also some metals show interdiffusion: silver (Aylesworth *et al.* 1989); molybdenum (Tsai *et al.* 1999c), tungsten (Tsai *et al.* 1999c, Panagiotopoulos *et al.* 1997). In order to keep the intrinsic properties, inert substrates or buffers such as chromium (Parhofer *et al.* 1998), platinum (Tsai *et al.* 1999c) or tantalum (Piramanayagam *et al.* 1998, Aylesworth *et al.* 1989) can be used.

Though Parhofer *et al.* (1998) showed that a chromium protection layer of 20 nm can limit the decay of H_C below about 10% per year, this is not sufficient for a device lifetime of 10 years and also for use in a hard disk the protection layer thickness must be significantly reduced. Therefore long-term stability will remain a challenge for this material.

With decreasing thickness also the grain size can decrease and a two-fold increase in H_C has been observed when reducing the thickness from some 100 nm to 25 nm (Parhofer *et al.* 1998), a thickness appropriate for a storage material. It should be noted that for NdFeB films deposited directly on quartz (without a chromium buffer) H_C vanishes below 100 nm, interdiffusion seems to destroy the intrinsic properties. Otherwise films on tantalum show an increase of H_C up to a thickness of 500 nm (Piramanayagam *et al.* 1997).

10. Conclusions and Perspectives

$Nd_2Fe_{14}B$ thin films show a good example of the application of hard magnetic concepts in thin films and of the possibilities of thin film methods to influence the microstructure. As in bulk material, controlling the microstructure is the key to optimizing the magnetic properties. For thin films an appropriate buffer can control the microstructure in addition to interdiffusion or texture. As a growing film tends to replicate the grain size of the existing film, for example the selection of a binary system (NiAl) instead of chromium could cut the grain size of the buffer and of the conventional magnetic film in half (Feng *et al.* 1994). Another approach is to use the chemical segregation observed for instance in the Cr–Co system. In this system chromium segregates into the grain boundaries which reduce the exchange-coupling between the cobalt-rich grains (Wittig *et al.* 1998). Using similar systems as buffer and replicating this microstructure should allow modification of the microstructure while conserving the intrinsic properties of $Nd_2Fe_{14}B$. These two examples show the potential of binary buffers and their application.

Structuring the films to prepare separate magnetic dots is a potential path for producing magnetic

recording media. The achieved structural size of $0.5 \times 0.5\,\mu m$ (Kubota *et al.* 2000) opens the perspective that the noise caused by a statistical grain ensemble is reduced by a structured media.

See also: Magnetic Films: Anisotropy; Magnetic Layers: Anisotropy

Bibliography

Araki T, Nakanishi T, Umemura T 1999 Texture of Nd–Fe–B thin-films prepared by magnetron sputtering. *J. Appl. Phys.* **85** (8), 4877–9

Aylesworth K D, Zhao Z R, Sellmyer D J, Hadjipanayis G C 1989 Growth and control of the microstruture and magnetic properties of sputtered $Nd_2Fe_{14}B$ films and multilayers. *J. Magn. Magn. Mater.* **82**, 46–56

Belmans R, Hameyer K 1998 Electromagnetic and design aspects of magnetic mini-actuators. *Proc. 6th Int. Conf. New Actuators.* Bremen, Germany pp. 537–40

Cadieu F J 1987 High coercive force and large remanent moment magnetic films with special anisotropies. *J. Appl. Phys.* **61** (8), 4105–10

Fähler S, Kahl S, Weisheit M, Sturm K, Krebs H U 2000 The interface of laser deposited Cu/Ag multilayers: evidence of the ''subsurface growth mode'' during pulsed laser deposition. *Appl. Surf. Sci.* **154–5**, 419–23

Fähler S, Krebs H U 1996 Calculations and experiments of material removal and kinetic energy during pulsed laser ablation of metals. *Appl. Surf. Sci.* **96–8**, 61–5

Feng Y C, Laughlin D E, Lambeth D N 1994 Interdiffusion and grain isolation in Co/Cr thin films. *IEEE Trans. Magn.* **30** (6), 3948–50

Gouteff P C, Folks L, Street R 1998 MFM study of NdFeB and NdFeB/Fe/NdFeB thin films. *J. Mag. Mag. Mater.* **177** (2), 1241–2

Keavney D J, Fullerton E E, Pearson J E, Bader S D 1997 High-coercivity, *c*-axis oriented $Nd_2Fe_{14}B$ films grown by molecular-beam epitaxy. *J. Appl. Phys.* **81** (8), 4441–3

Kruusing A 1999 Nd–Fe–B films and microstructures. *Int. Mater. Rev.* **44** (4), 121–40

Kubota H, Ikari T, Ando Y, Kato H, Miyazaki T 2000 Effect of particle size on the magnetization process in lightographic arrays of $Nd_2Fe_{14}B$. *J. Appl. Phys.* **87** (9), 6325–7

Lemke H, Thomas G, Medlin D L 1997 Magnetic properties of Nd–Fe–B films analyzed by Lorentz microscopy. *Nanostruct. Mater.* **9** (1–8), 371–4

Levy M, Osgood R M Jr, Hedge H, Cadieu F J, Wolfe R, Fratello V J 1996 Integrated optical isolators with sputter-deposited thin-film magnets. *IEEE Photon. Tech. Lett.* **8** (7), 903–5

Linetsky Y L, Raigorodsky V M, Tsvetkov V Y 1992 Phase-transformations in sputtered Nd–Fe–B alloys. *J. Alloys Compounds* **184** (1), 35–42

Mapps D J, Chandrasekhar R, O'Grady K, Cambridge J, Petford L A, Doole R 1997 Magnetic properties of NdFeB thin-films on platinum underlayers. *IEEE Trans. Magn.* **33** (5), 3007–9

Panagiotopoulos I, Mengburany X, Hadjipanayis G C 1997 Granular $Nd_2Fe_{14}B/W$ thin films. *J. Magn. Magn. Mater.* **172** (3), 225–8

Parhofer S M 1997 Hartmagnetische Nd–Fe–B–Dünnfilme (Hard magnetic Nd–Fe–B thin films). Ph. D. thesis, Technical University of Dresden, Verlag Mainz, Aachen, Germany

Parhofer S, Gieres G, Wecker J, Schultz L 1996 Growth characteristics and magnetic properties of sputtered Nd–Fe–B thin-films. *J. Magn. Magn. Mater.* **163** (1–2), 32–8

Parhofer S, Kuhrt C, Wecker J, Gieres G, Schultz L 1998 Magnetic properties and growth texture of high-coercive Nd–Fe–B thin films. *J. Appl. Phys.* **83** (5), 2735–41

Parhofer S M, Wecker J, Kuhrt C, Gieres G, Schultz L 1996 Remanence enhancement due to exchange coupling in multilayers of hardmagnetic and softmagnetic phases. *IEEE Trans. Magn.* **32** (5), 4437–9

Piramanayagam S N, Matsumoto M, Morisako A, Takei S 1997 Synthesis of Nd–Fe–B thinfilms with high coercive force by cosputtering. *IEEE Trans. Magn.* **33** (5), 3643–5

Piramanayagam S N, Matsumoto M, Morisako A, Takei S 1998 Studies on NdFeB thin films over a wide composition range. *J. Alloys Compounds* **281** (1), 27–31

Shima T, Kamegawa A, Aoyagi E, Hayasaka Y, Fujimori H 1998 Magnetic properties and structure of Nd–Fe–B thin films with Cr and Ti underlayers. *J. Magn. Magn. Mater.* **177** (2), 911–2

Shindo M, Ishizone M, Sakuma A, Kato H, Miyazaki T 1997 Magnetic properties of exchange-coupled α-Fe/Nd–Fe–B multilayer thin-film magnets. *J. Appl. Phys.* **81** (8), 4444–6

Tsai J L, Chin T S, Chen S K 1999a Coercivity mechanism and microstructure study of sputtered Nd–Fe–B/X/Si(111) (X = W, Pt) films. *Jpn. J. Appl. Phys.* **38** (1, 10), 5879–84

Tsai J L, Chin T S, Chen S K, Shih J C 1999c Magnetic properties and growth behaviour of Nd–Fe–B films on Si(111). *Jpn. J. Appl. Phys.* **38**, 4051–5

Tsai J L, Chin T S, Huang E Y, Chen S K 1998 Magnetization reversal of Nd(Dy)–Fe–B thin films on Si(111) or Ta/Si(111). *J. Appl. Phys.* **83** (11), 6241–7

Tsai J L, Chin T S, Shih J C, Chen S K 1999b Magnetic properties of nanocomposite $Nd_2Fe_{14}B$–Fe films. *IEEE Trans. Magn.* **35** (5), 3337–9

Wittig J E, Nolan T P, Ross C A, Schabes M E, Tang K, Sinclair R, Bentley J 1998 Chromium segregation in CoCrTa/Cr and CoCrPt/Cr thin films for longitudinal recording media. *IEEE Trans. Magn.* **34**, 1564–6

Yamashita S, Yamasaki J, Ikeda M, Iwabuchi N 1991 Anisotropic Nd–Fe–B thin-film magnets for milli-size motor. *J. Appl. Phys.* **70**, 6627–9

Yu M, Liu Y, Liou S H, Sellmyer D J 1998 Nanostructured NdFeB films processed by rapid thermal annealing. *J. Appl. Phys.* **83** (11, 2), 6611–3

S. Fähler and L. Schultz
IFW Dresden, Germany

Magnetic Force Microscopy

Magnetic force microscopy (MFM) (Martin and Wickramasinghe 1987, Grütter *et al.* 1992) is a slow-scan, raster-type imaging technique that maps a signal issued from the interaction of a tiny magnetic probe, or tip, with the magnetization distribution within the observed sample. The technique has been demonstrated to yield a resolution below some 20 nm in favorable cases with minimal or even no sample preparation. A magnetic force microscope may be

operated under ambient conditions or ultrahigh vacuum, allowing the study of clean magnetic surfaces and the link between growth and magnetic properties. Static magnetic fields may be applied to the sample during image acquisition, a necessary condition for correlating magnetic microstructures and hysteresis cycles. Because MFM relies on the interaction of two magnetic bodies, the probe and the sample, MFM is an indirect imaging method. It is potentially perturbative and, thus, may not be termed noninvasive.

1. Operation Principle

A magnetic force microscope (Fig. 1) may be described as composed of a force transducer, a microfabricated cantilever coated with a magnetic thin layer (Grütter *et al.* 1990), an *x,y,z* set of translation actuators, and a signal processing and feedback unit. Various types of forces may act on the tip located at the extremity of the cantilever, among them van der Waals forces when the tip and sample surfaces are brought into close contact, capillary forces owing to an adsorbed water layer when the microscope is operated under ambient conditions, electrostatic forces, and magnetostatic forces if both the probing tip and sample are magnetic. Magnetostatic forces are those forces that govern the interactions of, for example, two bar magnets or allow a hard magnetic material body to attract soft magnetic elements. A magnetic force microscope should be operated under such conditions that long-range dipolar-type forces become prominent (Schönenberger *et al.* 1990).

In the static mode or force detection scheme, the restoring force constant of the cantilever opposes the magnetically induced cantilever deflection, thus

Figure 1
Schematic representation of a force microscope (not to scale). S is the sample.

establishing equilibrium. Although different methods have been developed to monitor the cantilever deflection, optical means now dominate. Interferometric techniques have been used to measure precisely the distance between the cantilever end and a fixed point in space (e.g., Rugar *et al.* 1988). In Fig. 1 a laser beam is reflected from the upper surface of the cantilever into a quadrant detector. Signal combinations $(A+B)-(C+D)$ and $(A+D)-(B+C)$ are proportional to the deflection and torsion of the cantilever, respectively (Meyer and Amer 1990).

In a second operating mode, the dynamic or a.c. mode (Martin and Wickramasinghe 1987, Hobbs *et al.* 1989), a piezoactuator induces forced oscillations of the cantilever. In the limit of small amplitude oscillations along the *z* direction and an assumed harmonic oscillator behavior, the resonance frequency of the cantilever varies with the force gradient as

$$\omega = \omega_0 \sqrt{1 - \frac{1}{k}\frac{\partial F}{\partial z}} \qquad (1)$$

where ω_0 is the free oscillation cantilever resonance frequency and k is the cantilever restoring force constant. It has been recognized (Albrecht *et al.* 1991) that frequency detection is preferable to amplitude detection because of the long characteristic response time of the latter to a pulse-like change in the force gradient.

An MFM image is therefore a mapping of the position-dependent force or force gradient exerted by the sample on a magnetic tip moving at a given distance from the sample surface. If the distance is too short, van der Waals-type forces may dominate, whereas spatial resolution is bound to decrease with increasing distance. In practice, working (often referred to as "lift") distances between a few nanometers and a few tens of nanometers are used. Since the strength of the force and/or force gradient rapidly decays with distance from the surface, surface relief needs to be compensated for (Schönenberger *et al.* 1990). This may be achieved through three point landmark interpolation for smooth surfaces (Hug *et al.* 1993) or a more advanced protocol including topography monitoring followed by force or force gradient detection at a preset lift height z_{lift} (Fig. 2) (Babcock *et al.* 1995). Whereas forces as low as 1 pN (10^{-12} N) may be detected with a good signal-to-noise ratio (SNR) in state-of-the-art static experiments (Hug *et al.* 1998), the minimal detectable force gradient against thermal noise (Albrecht *et al.* 1991) is given by

$$\left|\frac{\delta F_{\min}}{\delta z}\right| = 2k\frac{\delta\omega}{\omega_0} = \frac{2}{A}\sqrt{\frac{kk_B T\Delta\nu}{Q\omega_0}} \qquad (2)$$

where A, k_B, T, $\Delta\nu$, and Q are the cantilever oscillation amplitude, Boltzmann constant, temperature, detector bandwidth, and cantilever resonance quality factor, respectively. Under ambient conditions
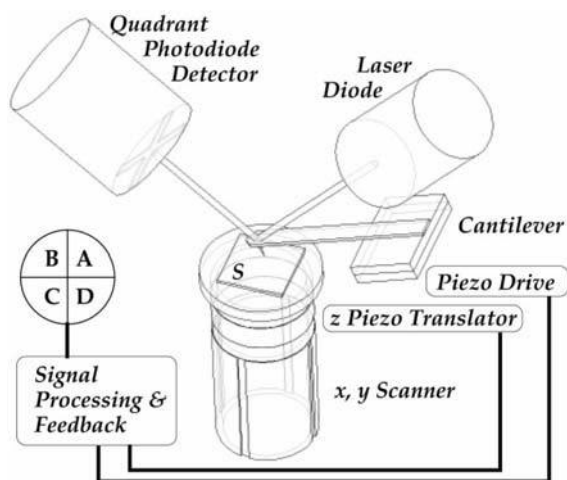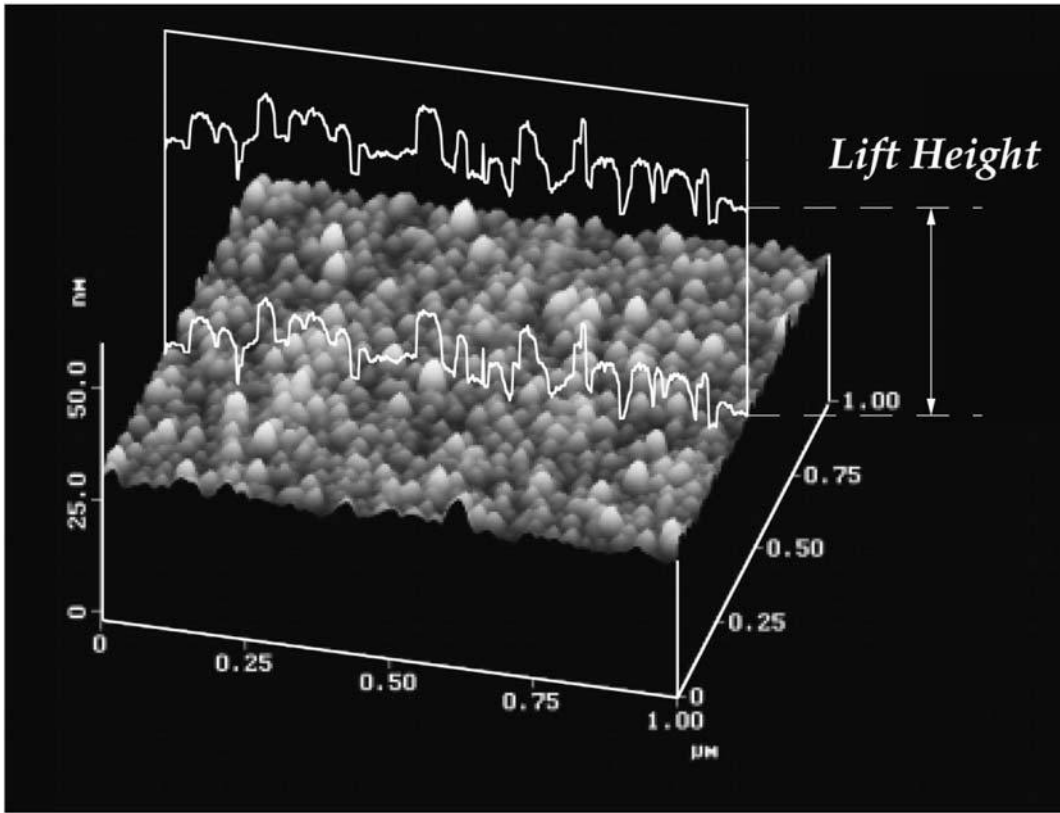
Figure 2
MFM operating mode: the influence of the sample topography (here, grains in a NiFe thin film deposited on a sputter deposited NiO underlayer (courtesy of P. Gogol)) is minimized by measuring the frequency shift due to the interaction between the magnetized probe and the sample at a fixed "lift" height above the sample along each line scan. Usual "lift" heights are in the range 20–50 nm.

($Q \sim 100$–150), force gradients as low as 10^{-5} N m^{-1} are routinely measured.

2. Image Formation

Central to the understanding of MFM is the magnetostatic equivalent to Coulomb's law expressing the force between two magnetic "monopoles" (Fig. 3):

$$\vec{F} = -\vec{F} = \left(\frac{1}{4\pi\mu_0}\right)\frac{pp'}{|r - r'|^3}(\vec{r} - \vec{r}') \qquad (3)$$

In a ferro- or ferrimagnetic body, magnetic charge densities may be defined and related to the magnetization distribution $\vec{M}(\vec{r}) = M_S \vec{m}(\vec{r})$, $m^2 = 1$, through the relationships

$$\lambda_V = -\mu_0 M_S \text{div } (\vec{m}) \text{ in the volume}$$
$$\qquad (4)$$
$$\sigma_S = +\mu_0 M_S (\vec{m} \cdot \vec{n}) \text{ at free surfaces}$$
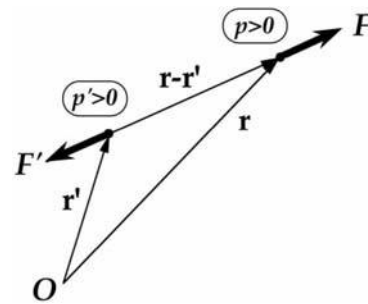
Figure 3
(Central) forces between two magnetic point-like charges.

It follows that MFM neither directly maps the magnetization distribution (the unknown in a magnetic imaging experiment) nor the magnetic induction.

In order to improve understanding of image formation processes, the demagnetizing or stray field

$\vec{H}_D(\vec{r})$ arising from volume or surface charge densities located at $\vec{r}'$ is introduced. According to standard electromagnetic theory, it derives from the scalar potential $\Phi_D(\vec{r})$ owing to:

$$\vec{H}_D(\vec{r}) = -\text{grad}[\Phi_D(\vec{r})] \qquad (5)$$

with

$$\Phi_D(\vec{r}) = \frac{1}{4\pi\mu_0}$$
$$\times \left[\iiint_{V'} \frac{\lambda_V(r^{\to\prime})}{|r^{\to} - r^{\to\prime}|}\,\mathrm{d}^3r' + \iint_S \frac{\sigma_S(r^{\to\prime})}{|r^{\to} - r^{\to\prime}|}\,\mathrm{d}^2r'\right]$$
$$(6)$$

For instance, volume and surface charges pertaining to the tip are the source of a demagnetizing field inside the tip itself and a (localized) stray field $\vec{H}_D^{\text{tip}}$ acting on the sample. It proves convenient at this point to assume that the magnetization distribution within the tip remains fixed (say pinned) during image acquisition. Let the magnetization within the sample reach its equilibrium configuration as the result of exchange interactions, anisotropy, demagnetizing field distribution (represented by the constants A, K, and vector field $\vec{H}_D^{\text{sample}}$, respectively), and tip-induced stray field $\vec{H}_D^{\text{tip}}$ for a given lift height:

$$\vec{m}^{\text{sample}} = \vec{m}[A, K,\ \vec{H}_D^{\text{sample}},\ \vec{H}_D^{\text{tip}}(\vec{r},\ z_{\text{lift}})] \qquad (7)$$

Now assume an infinitesimal variation δz of the tip to sample distance. Precisely because $\vec{m}$ has reached its equilibrium configuration, the virtual work done by $\vec{m}$ simply reads

$$\delta E = -\mu_0 M_S^{\text{sample}}$$
$$\times \iiint_{\text{sample}} [\text{grad}(\vec{H}_D^{\text{tip}}) \cdot \vec{m}^{\text{sample}}]\mathrm{d}^3r]\delta z_{\text{lift}} \quad (8)$$

It follows directly that the force acting on the tip is given by

$$F_Z = \mu_0 M_S^{\text{sample}} \iiint_{\text{sample}} \left[\frac{\partial H_D^{\to\,\text{tip}}}{\partial z} \cdot \vec{m}^{\text{sample}}\right]\mathrm{d}^3r \quad (9)$$

Similarly, the force gradient reads

$$\frac{\delta F_Z}{\delta z_{\text{lift}}} = \mu_0 M_S \left\{\iiint_{\text{sample}} \left[\frac{\partial^2 H_D^{\to\,\text{tip}}}{\partial z^2} \cdot \vec{m}^{\text{sample}}\right]\mathrm{d}^3r\right.$$
$$\left. + \iiint_{\text{sample}} \left[\frac{\partial H_D^{\to\,\text{tip}}}{\partial z} \cdot \frac{\delta m^{\to\,\text{sample}}}{\delta z_{\text{lift}}}\right]\mathrm{d}^3r\right\} \qquad (10)$$

In Eqns. (9) and (10), the first and second derivatives of the tip stray field may, for a given tip, be experimentally determined. In view of Eqn. (5), integration

by parts of Eqn. (9) leads to the following important result:

$$F_Z = -\left(\iiint \lambda_V \frac{\partial \Phi_D^{\text{tip}}}{\partial z}\,\mathrm{d}^3r + \iint \sigma_S \frac{\partial \Phi_D^{\text{tip}}}{\partial z}\,\mathrm{d}^2r\right)$$
$$= \iiint \lambda_V H_{D,z}^{\text{tip}}\mathrm{d}^3r + \iint \sigma_S H_{D,z}^{\text{tip}}\mathrm{d}^2r \qquad (11)$$

Equation (11) shows that the force acting on the tip is the convolution product of the charge distribution and the component along the tip displacement direction of the tip stray field. In this sense, MFM may be viewed as a microscopy of the charge distribution within and at the free surfaces of the sample, a result first established by experiments (Rave *et al.* 1994) and derived in the case of the tip stray field not influencing the magnetization distribution in the sample (Hubert *et al.* 1997). It ought to be stressed that the charge densities in Eqn. (11) do include potential perturbations of the sample charge distribution under the influence of the tip stray field.

Since the force exerted by the sample on the tip is necessarily equal and opposite to the force exerted by the tip on the sample, the subscripts "sample" and "tip" may be interchanged in Eqns. (9)–(11). If the tip is to be viewed as a monopole or a point dipole, then the force and force derivative read

Monopole : $F_Z = \rho^{\text{tip}}H_{D,Z}^{\text{sample}}; \dfrac{\partial F_Z}{\partial z} = \rho^{\text{tip}}\dfrac{\partial H_{D,Z}^{\text{sample}}}{\partial z}$

Point dipole : $F_Z = \vec{\mu}^{\text{tip}} \cdot \dfrac{\partial H_D^{\to\,\text{sample}}}{\partial z}; \dfrac{\partial F_Z}{\partial z} = \vec{\mu}^{\text{tip}} \cdot \dfrac{\partial^2 H_D^{\to\,\text{sample}}}{\partial z^2}$
$$(12)$$

where ρ^{tip} and $\vec{\mu}^{\text{tip}}$ are the monopole strength and tip moment, respectively. Equations (12), neglecting altogether perturbations, have provided and still provide a simple although inaccurate interpretation tool for MFM image analysis.

In spite of their concise form, neither Eqn. (9) nor Eqn. (11), notwithstanding Eqns. (12), provide any means of solving the inverse problem, namely finding the magnetization distribution knowing the force map, except if accepting extremely constraining assumptions such as the existence of only two magnetization directions, say, up and down (Hug *et al.* 1998). Rather, MFM image interpretation will in most cases need to rely on a highest likelihood basis and/or estimation of a magnetization distribution and, knowing tip characteristics, simulating the MFM image. Several iterations might prove necessary before a reasonable agreement between experimental data and simulations is achieved.

3. Probes

Integrated silicon cantilever and pyramid assemblies (Grütter *et al.* 1990) now form the largest basis for

MFM probes. The pyramid (and cantilever, usually) is sputter coated with a suitable magnetic alloy (e.g., CoCr) with thickness up to a few tens of nanometers (Fig. 4). Tip stray fields are by no means small (Thiaville *et al*. 1997, McVitie *et al*. 1997, Lohau *et al*. 1999), typically ranging from 10 mT to 50 mT (Fig. 5). If uniform, such high-amplitude external fields would prove sufficient to saturate low to medium coercivity samples. MFM thus relies on the fact that the lateral extension of the tip stray field remains small. The aspect ratio of tips may be improved either via the growth of carbon needles at the extremity of standard silicon pyramids (Rührig *et al*. 1994) or via micromachining techniques such as focused ion beam etching. Through directional evaporation and shadowing, the amount of magnetic material deposited on the tips may be greatly reduced. The stray field, however, cannot be reduced beyond figures quoted above
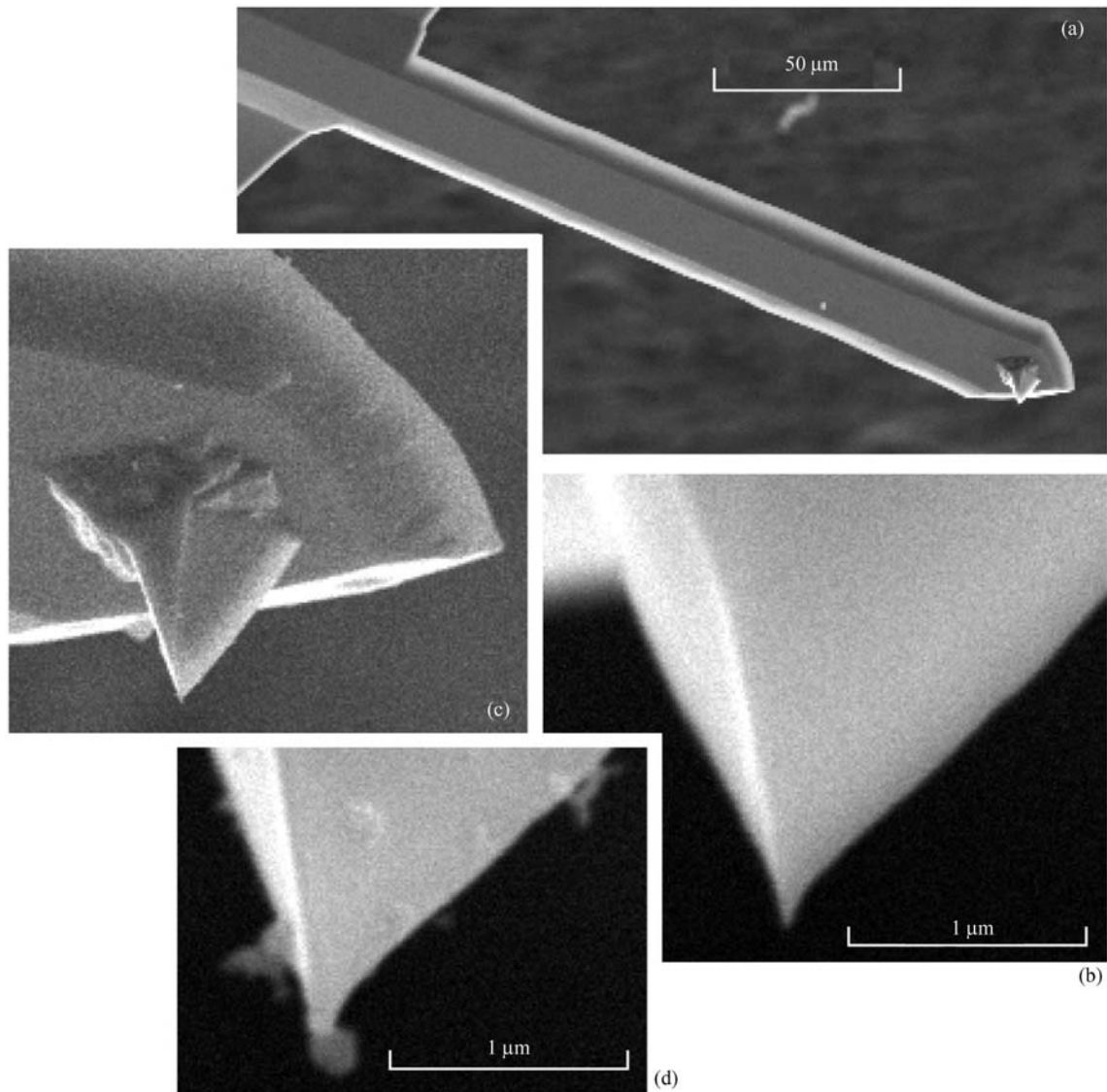
Figure 4
Scanning electron microscopy images of microfabricated cantilever tip assemblies (NANO*SENSORS*) (a, b) prior to magnetic film deposition, and (c, d) after deposition and intensive MFM imaging. Note the sharpened pyramid apex in (b) and a similar profile in (d) in spite of a 35 nm CoCr layer sputter coated on the silicon tip and the collection of nanometer debris after use.
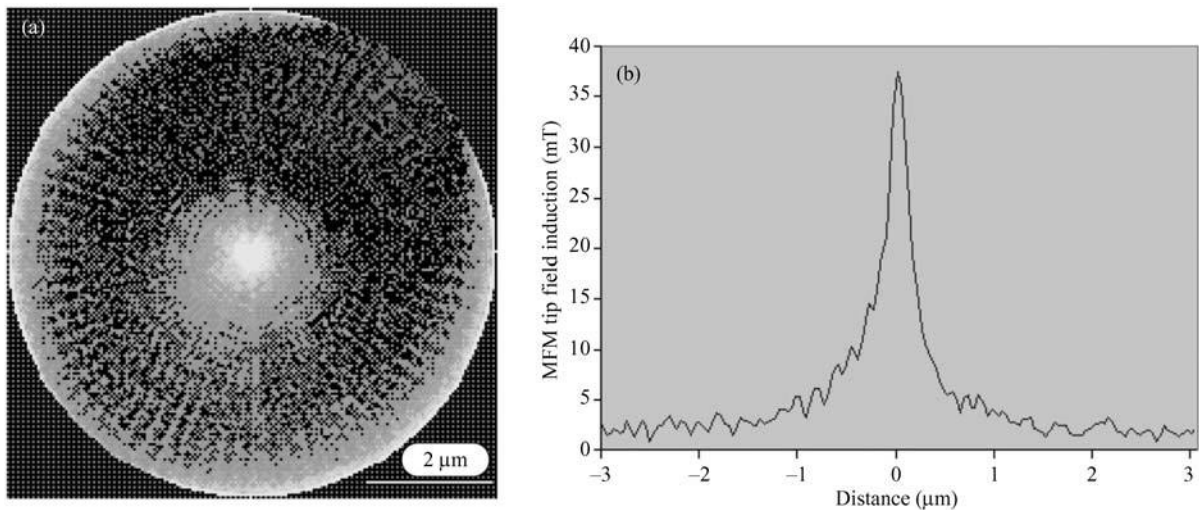
Figure 5
Field distribution in a plane perpendicular to the tip axis and about 50 nm away from the tip apex as measured by means of electron tomography (courtesy of S. McVitie).

since it is essential in order to provide a fair SNR. However, a higher aspect ratio helps in reducing the stray field lateral extension. Image interpretation can indeed be greatly simplified if tip stray fields may be approximated by a monopole or well-defined extended dipole for the operating lift height.

Alternatively, extremely soft, or even paramagnetic, coatings may be used (Hopkins *et al.* 1996). The interaction between the sample and the tip is then mostly if not solely attractive. A point-like paramagnetic tip probes the square modulus of the stray field generated by the sample and allows for an accurate stray field mapping under specific conditions (Proksch *et al.* 1996).

4. Applications of MFM

The need for fast observations of recorded bit patterns fostered the development of MFM. Perpendicular media have been widely studied. Figure 6 shows an example of dense periodical flux changes in a CoPtCrO(12nm)/RuCr(4nm)/CoPtCrO(12nm) granular-type perpendicular recording medium, which demonstrates a recording performance of 4 Gbit cm^{-2} (26 Gbit in^{-2}). Atomically ordered alloys with an L1$_0$ type phase, such as FePd or FePt, are known to exhibit an abnormally large uniaxial anisotropy with a perpendicular to the plane easy axis. Over a wide thickness range, a stripe pattern develops (Fig. 7(a)) with domains magnetized alternately up and down.
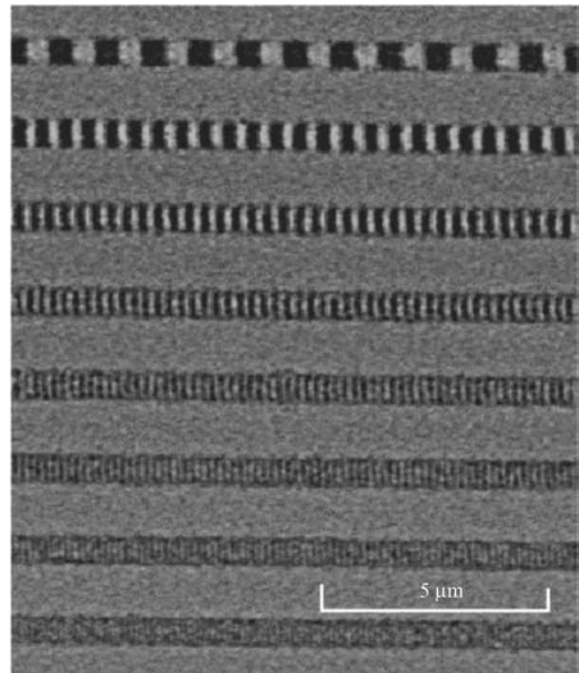
Figure 6
Recorded bits in a granular-type perpendicular recording medium along tracks with densities ranging from 50 kfci (kilo flux change per inch) to 400 kfci in steps of 50 kfci (courtesy of Takao Suzuki and A. Ehsan, Toyota Technological Institute).
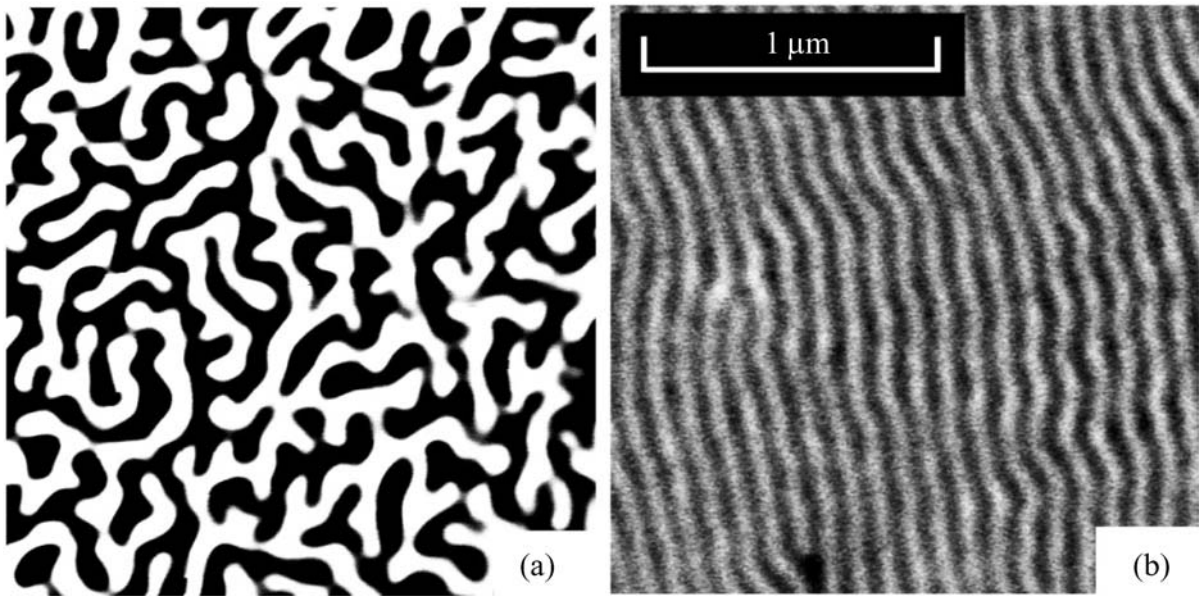
Figure 7
MFM images of (a) (fragmented) "strong" and (b) "weak" stripes in chemically ordered FePd alloy thin films. Domain widths as low as ~ 35 nm have been observed in such materials (courtesy of Y. Samson).

As the thickness increases, the stripe width first sharply decreases and then slowly increases as the result of the competition between wall and demagnetizing field energies. In samples grown at room temperature the chemical ordering is imperfect resulting in a reduced perpendicular anisotropy. So-called "weak" stripe domains (Fig. 7(b)) as narrow as ~ 35 nm have been observed for such samples (Samson *et al.* 1999) thereby setting an upper limit to MFM resolution in the favorable case of a periodic domain pattern. MFM also proves sensitive as clear initial domain pattern observations in cobalt layers as thin as three monolayers with the smallest features in the 400 nm range have been reported.

Patterned magnetic layers are viewed as possible future high-density recording media. Shape anisotropy now relays growth or chemical ordering-induced anisotropy. Figure 8 shows a partially demagnetized array of iron pillars with a large height-to-diameter aspect ratio, fabricated by scanning tunneling microscopy-assisted chemical vapor deposition (Wirth *et al.* 1999). In this study, the smallest periodicity of particles was 80 nm corresponding to a data storage density of ~ 15 Gbit cm^{-2} (~ 100 Gbit in^{-2}). As a prerequisite to applications, a precise physical understanding of reversal processes in nanometer-scale particles proves necessary, such as the size threshold between a pure thermally activated Stoner–Wohlfarth-type behavior in weakly interacting particles and the emergence of more complex nucleation modes.
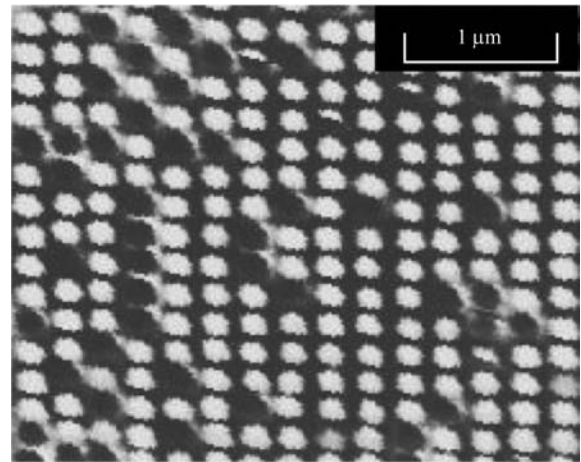
Figure 8
MFM image of part of an array of iron pillars grown on gold. A pulsed field of 66 mT has caused reversal of some of the pillars (color change from bright to black) (courtesy of S. Wirth).

Because of its ability to handle complex topographies and of its spatial resolution and sensitivity, MFM appears, in this context, singular among magnetic imaging techniques. Similar arguments prevail in the observation of magnetic nanowires. One of the most illustrative observations in 80 nm diameter

nanowires is shown in Fig. 9 (Belliard *et al*. 1998). In spite of a rather unpromising geometry, submicro-meter-size domains are clearly revealed. Image analysis leads to the picture of axially magnetized wire segments separated by off-axis magnetized domains, in agreement with knowledge of the growth properties of such wires. As the diameter is reduced to ~ 30 nm, the magnetization distribution remains axial owing to shape anisotropy, with, because of magnetic history, the possible occurrence of head-to-head or tail-to-tail charged walls (Ebels *et al*. 2000).

If MFM offers unprecedented imaging capabilities in systems displaying localized charge densities, it proves much less efficient in the high-resolution observation of soft magnetic materials, owing to their very specific ability to screen and/or spread magnetic charges. In low saturation magnetization soft magnetic materials such as Permalloy ($Ni_{80}Fe_{20}$),
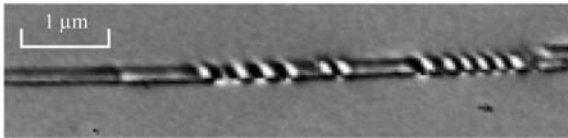
Figure 9
MFM image of a ~ 80 nm diameter magnetic nanowire showing regions of axial (long sections) and off-axis (short sections with alternate contrast) magnetization directions (courtesy of L. Belliard).

the domain wall contrast in micrometer-size elements proves diffuse, as shown in Fig. 10 (Gomez *et al*. 1999), whereas large wall distortions are commonly observed in larger-size elements. Numerical simulations shed light on the underlying physical phenomena (Fig. 11): magnetic charges gather in the soft material under the influence of the tip stray field. Their associated demagnetizing field opposes the tip field (screening). Tip-induced charges interact with charges already present in the soft magnetic material along walls, for instance, thereby modifying the shape of the wall (Fig. 11(a)). As the tip moves above the surface of the element, the overall charge pattern evolves and so does the tip–sample interaction energy, hence the force or force gradient acting on the tip (Eqns. (7), (9), and (10)).

If MFM was mapping the charge distribution inside the sample without perturbation, then the image would mirror perfectly the wall symmetry, here a set of four 90° walls building a perfect flux closure (Landau–Lifshitz) pattern (Fig. 11(b)). When tip perturbations are duly accounted for, the MFM image resembles that of distorted walls (Fig. 11(c)) although it is the result of a complex convolution process. Simulations performed with realistic tip field distributions properly predict the existence of a global attractive force between the tip and the soft element as well as the right order of magnitude for "wall contrast." Interestingly enough, noticeably stable images of naturally pinned magnetic structures such as 360° walls have been produced in a number of laboratories (e.g., Cho *et al*. 1999).
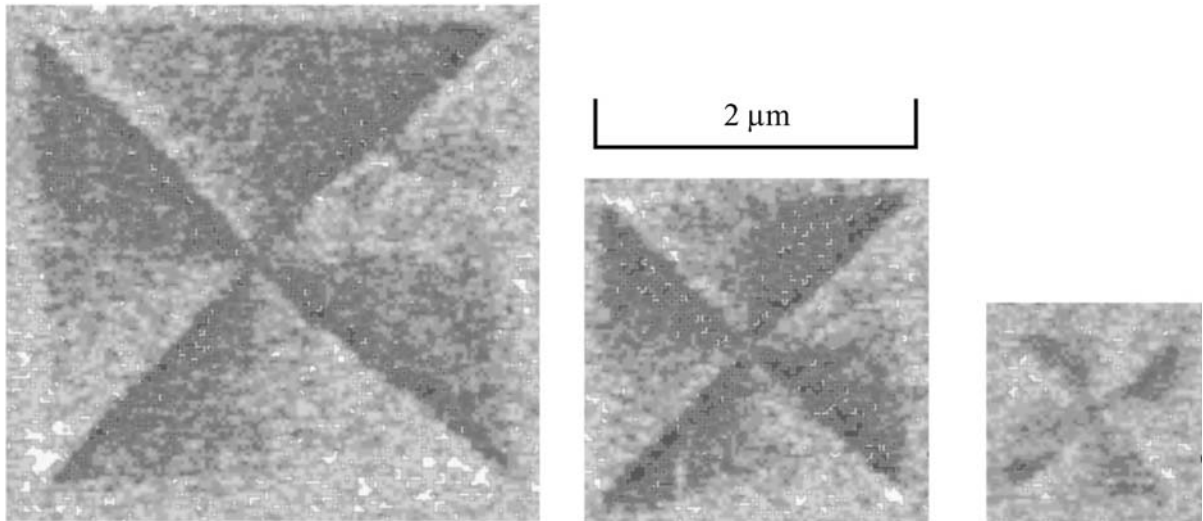
Figure 10
MFM images of flux closure domain patterns in Permalloy square elements imaged with a "low moment" tip. From left to right (μm): 3×3, 2×2, 1×1; thickness 28 nm (courtesy of R. D. Gomez).
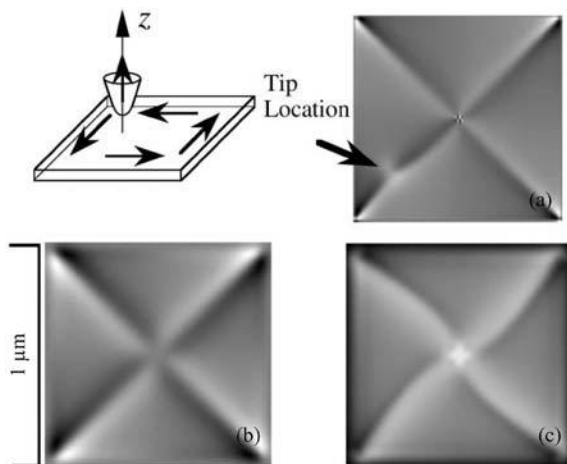
Figure 11
Numerical simulations: (a) local perturbation in a Permalloy platelet (size 1 μm × 1 μm) under the action of a tip representative of standard MFM probes; (b) simulated MFM image in the "no perturbation" limit; (c) simulated MFM image taking account of tip on sample perturbations.

5. Outlook and Perspectives

Further development of MFM needs to include better magnetic tip calibration and repeatability as well as environment cells (e.g., temperature and field). Modulation techniques allow the analysis of phenomena occurring at a time scale much shorter than the resonance period of cantilevers (Proksch *et al.* 1999b). Besides, a finer interpretation of the mechanics of force microscopes is also highly desirable: an independent monitoring of both the frequency shift and the cantilever motion amplitude vs. position are key factors towards a full analysis of dissipation (Proksch *et al.* 1999a) and nonlinear oscillations in the high Q regime (Aimé *et al.* 1999).

See also: Magnetic Materials: Transmission Electron Microscopy; Magnets, Soft and Hard: Domains

Bibliography

Aimé J P, Boisgard R, Nony L, Couturier G 1999 Nonlinear dynamic behavior of an oscillating tip-microlever system and contrast at the atomic scale. *Phys. Rev. Lett.* **82**, 3388–91

Albrecht T R, Grütter P, Horne D, Rugar D 1991 Frequency modulation detection using high-Q cantilevers for enhanced force microscope sensitivity. *J. Appl. Phys.* **69**, 668–73

Babcock K, Dugas M, Manalis S, Elings V 1995 Magnetic force microscopy: recent advances and applications. *Mater. Res. Soc. Symp. Proc.* **355**, 311–22

Belliard L, Miltat J, Thiaville A, Dubois S, Duvail J L, Piraux L 1998 Observing magnetic nanowires by means of magnetic force microscopy. *J. Magn. Magn. Mater.* **190**, 1–16

Cho H S, Hou C, Sun M, Fujiwara H 1999 Characteristics of 360°-domain walls observed by magnetic force microscope in exchange-biased NiFe films. *J. Appl. Phys.* **85**, 5160–2

Ebels U, Radulescu A, Henry Y, Piraux L, Ounadjela K 2000 Spin accumulation and domain wall magnetoresistance in 35 nm Co wires. *Phys. Rev. Lett.* **84**, 983–6

Gomez R D, Luu T V, Pak A O, Kirk K J, Chapman J N 1999 Domain configurations of nanostructured Permalloy elements. *J. Appl. Phys.* **85**, 6163–5

Grütter P, Mamin H J, Rugar D 1992 Magnetic force microscopy. In: Wiesendanger R, Güntherodt H-J (eds.) *Scanning Tunneling Microscopy*. Springer-Verlag, Berlin, Vol. II, pp. 151–207

Grütter P, Rugar D, Mamin H J, Castillo G, Lambert S E, Lin C -J, Valetta R M, Wolter O, Bayer T, Greschner J 1990 Batch fabricated sensors for magnetic force microscopy. *Appl. Phys. Lett.* **57**, 1820–2

Hobbs P C D, Abraham D W, Wickramasinghe H K 1989 Magnetic force microscopy with 25 nm resolution. *Appl. Phys. Lett.* **55**, 2357–9

Hopkins P F, Moreland J, Malhotra S S, Liou S H 1996 Superparamagnetic magnetic force microscope tips. *J. Appl. Phys.* **79**, 6448–50

Hubert A, Rave W, Tomlinson S 1997 Imaging magnetic charges with magnetic force microscopy. *Phys. Stat. Sol. B* **204**, 817–28

Hug H J, Moser A, Jung Th, Fritz O, Wadas A, Parashikov I, Güntherodt H-J 1993 Low temperature magnetic force microscopy. *Rev. Sci. Instrum.* **64**, 2920–5

Hug H J, Stiefel B, van Schendel P J A, Moser A, Hofer R, Martin S, Güntherodt H-J, Porthun S, Abelmann L, Lodder J C, Bochi G, O'Handley R C 1998 Quantitative magnetic force microscopy on perpendicularly magnetized samples. *J. Appl. Phys.* **83**, 5609–20

Lohau J, Kirsch S, Carl A, Dumpich G, Wassermann E F 1999 Quantitative determination of effective dipole and monopole moments of magnetic force microscopy tips. *J. Appl. Phys.* **86**, 3410–7

Martin Y, Wickramasinghe H K 1987 Magnetic imaging by "force microscopy" with 1000 Å resolution. *Appl. Phys. Lett.* **50**, 1455–7

McVitie S, Ferrier R P, Nicholson W A P 1997 Absolute field strength determination of magnetic force microscope tip stray fields. *Inst. Phys. Conf. Ser.* **153**, 201–4

Meyer G, Amer N M 1990 Simultaneous measurement of lateral and normal forces with an optical-beam-deflection atomic force microscope. *Appl. Phys. Lett.* **57**, 2089–91

Proksch R, Babcock K, Cleveland J 1999a Magnetic dissipation microscopy in ambient conditions. *Appl. Phys. Lett.* **74**, 419–21

Proksch R, Neilson P, Austvold S, Schmidt J J 1999b Measuring the gigahertz response of recording heads with the magnetic force microscope. *Appl. Phys. Lett.* **74**, 1308–10

Proksch R, Skidmore G D, Dahlberg D E, Foss S, Schmidt J J, Merton C, Walsch B, Dugas M 1996 Quantitative magnetic field measurements with the magnetic force microscope. *Appl. Phys. Lett.* **69**, 2599–601

Rave W, Belliard L, Labrune M, Thiaville A, Miltat J 1994 Magnetic force microscopy analysis of soft thin film elements. *IEEE Trans. Magn.* **30**, 4473–8

Rugar D, Mamin H J, Erlandsson R, Stern J E, Terris B D 1988 Force microscope using a fiber-optic displacement sensor. *Rev. Sci. Instrum.* **59**, 2337–40

Rührig M, Porthun S, Lodder J C 1994 Magnetic force microscopy using electron-beam fabricated tips. *Rev. Sci. Instrum.* **65**, 3224–8

Samson Y, Marty A, Hoffmann R, Gehanno V, Gilles B 1999 Magnetic domains in thin films with perpendicular anisotropy: an extensive study. *J. Appl. Phys.* **85**, 4604–6

Schönenberger C, Alvarado S F, Lambert S E, Sanders I L 1990 Separation of magnetic and topographic effects in force microscopy. *J. Appl. Phys.* **67**, 7278–80

Thiaville A, Belliard L, Majer D, Zeldov E, Miltat J 1997 Measurement of the stray field emanating from magnetic force microscope tips by Hall effect microsensors. *J. Appl. Phys.* **82**, 3182–91

Wirth S, von Molnar S, Field M, Awschalom D D 1999 Magnetism of nanometer-scale iron particle arrays. *J. Appl. Phys.* **85**, 5249–54

J. Miltat and A. Thiaville
Université Paris-Sud, Orsay, France

Magnetic Hysteresis

When a magnetic field acts on a demagnetized ferromagnetic body, the component of the macroscopic magnetization along the field direction increases nonlinearly. In general, the increase takes place with a low initial slope, a drastic increase of this slope at intermediate fields, and a new decrease at higher fields up to the technical saturation (total saturation requires 0 K or applied fields with strength tending to infinity). When the field is removed, the macroscopic magnetization decreases along a curve located well above the initial magnetization curve. For zero field a noticeable magnetization generally remains that is called remanence or remanent magnetization, M_r. After reversal of the field, the magnetization drops and vanishes for a reversal field known as coercive field, H_c. Further increase of the field leads to the saturation. When the field is cyclically applied, the magnetization curve is a hysteresis loop as that shown in Fig. 1. If the maximum applied field is not high enough to get saturation, the loop is called a minor loop.

The coercive field permits the scaling of the applied fields as weak, lower than H_c, intermediate, those of the order of H_c, and high fields, stronger than H_c. If superimposed to a constant field, a cyclically varying field is applied, and we obtain a hysteresis loop around a point of the hysteresis loop, generally known as a shifted loop. It is important to remark that the field acting on a magnetized sample is the sum of the externally applied field and the demagnetizing field due to the magnetization itself. As the demagnetizing field can be roughly approximated by $-NM$, where the demagnetizing factor, N, is geometry dependent, the shape of the hysteresis loop of any material depends on its geometry. Customarily, it has been well established in the textbooks that the ideal shape of a magnetic sample is either toroidal or a
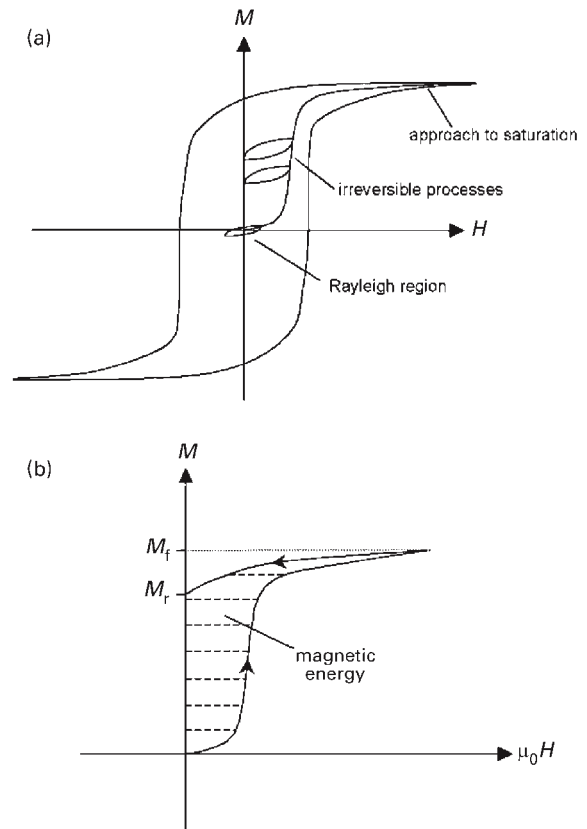
Figure 1

(a) Hysteresis loop and initial magnetization curve showing some characteristic regions: the Rayleigh region, minor loops at the irreversible region and the approach to saturation region. (b) Magnetic energy stored in a ferromagnetic material after being magnetized up to M_f.

long narrow bar, both exhibiting negligible demagnetizing factors. For a more detailed discussion of the hysteresis in ferromagnetic materials the reader is referred to the book of Bertotti (1998).

1. Technical and Fundamental Importance of the Magnetization Curve

Ferromagnetic materials are used for two main technological applications: (i) as flux multipliers forming the nucleus of electromagnetic machines, and (ii) as stores of either energy (magnets) or information (magnetic recording). The technical requirements to improve the material performance for both functions are related to the characteristics of the hysteresis loop and magnetization process. Flux multiplication requires high permeability and narrow hysteresis loop or low

coercivity, $\mu_0 H_c$. These properties are characteristic of the so-called "soft" magnetic materials. Storage requires high remanence and wide hysteresis loop in order to prevent demagnetization. Both properties are characteristic of "hard" magnetic materials.

Even though for all types of applications the higher the spontaneous magnetization, M_s, the better the performance, the difficulty of increasing M_s artificially yields coercivity as the key parameter to be controlled by the material scientist. In fact, the history of the magnetic material research is the history of the progressive increase of the available coercivity spectrum. The maximum spontaneous magnetization is that corresponding to 0 K and it is known as saturation magnetization; its value is roughly given by the atomic magnetic moment, of the order of Bohr magneton, 10^{-23} J T^{-1}, times the number of atoms per unit volume, typically 10^{29}, that leads to $\mu_0 M_s$ of the order of 1 T. At the beginning of the twentieth century, just as in Plato's time, the harder material, "hard steels," had a coercivity $\mu_0 H_c = 10^{-2}$ T, only two orders of magnitude larger than that of the known softer material, "purified iron." At the beginning of the twenty-first century, the softer material is nanocrystalline $Fe_{84}Zr_7B_9$ with coercivity $\mu_0 H_c = 10^{-7}$ T whereas the harder material is nanocrystalline $Fe_{84}Nd_7B_9$ with coercivity $\mu_0 H_c = 1$ T.

Seven orders of magnitude separate the coercivity from the harder to the softer ferromagnetic material which compositionally differs only in 7 at.% of atoms, zirconium for the softer and neodymium for the harder. This result summarizes the best achievement of the science of magnetic materials. It has been the control of the magnetization curve, made possible from the deep understanding of its governing parameter, anisotropy, which has allowed the outstanding enhancement of the required properties. Anisotropy can be tailored through both composition and microstructure. Since $\mu_0 M$ and $\mu_0 H$ have the same units it is possible to compare the hysteresis loops of soft and hard materials, taking into account that the height of the loop of soft materials is seven orders of magnitude larger than its width, whereas the hysteresis loop of the best hard materials are square, exhibiting the same height as width, typically 1 T.

The central characteristics of ferromagnetic materials, the magnetization curve and the hysteresis loop, depend on the macroscopic magnetization measured along the direction of the applied field as a function of the field strength. We have seen that magnetization curve features are of maximum relevance for material application. From the fundamental point of view, the problems involved in the physical processes underlying hysteresis, such as relaxation, nonlinearity, metastability, energy dissipation, irreversibility, domain wall nucleation and propagation, coherent rotation, or incoherent modes, are the more attractive issues for basic scientists.

2. Magnetization Processes

Ferromagnetic materials do not generally exhibit macroscopic magnetization. Even though exchange interactions tend to align all spins along the same direction, the minimization of the magnetostatic energy tends to break the spin directional order achieving a demagnetized macroscopic state. As crystalline ferromagnets contain a discrete set of easy directions for the magnetization, the more common spin configuration minimizing the sum of exchange, magnetostatic, and anisotropy energies becomes the domain structure, as that schematically illustrated by Fig. 2. Domains, within which the spontaneous magnetization, M_s, is oriented along an easy axis, are separated by domain walls with thickness δ corresponding to the exchange correlation length. δ is of the order of $(A/k)^{1/2}$ where k is the anisotropy constant and A is the exchange constant $A = 2JS^2/a$, J being the exchange interaction between two adjacent magnetic moments, S the spin value in h units and a the interatomic distance (see Magnets, Soft and Hard: Domains). In general, A is around 10^{-11} J m^{-1}. Since k varies from 10^7 to 10^2 Jm^{-3}, δ ranges from 1 nm to a few micrometers (Cullity 1972 pp. 290). The energy of the configuration, anisotropy and exchange, is stored in the walls with a surface density $\gamma = (Ak)^{1/2}$. However, in sufficiently small ferromagnetic particles the minimum energy corresponds to the single domain structure. This fact is due to the different geometrical dependence of the magnetostatic energy that increases with the sample volume, compared to the wall energy that increases with the wall area. In the following case of multidomain structures will be analyzed.

In multidomain samples each domain is a magnetic moment. At the demagnetized state the vectorial sum of the magnetic moments corresponding to each domain vanishes. When an external magnetic field, H, is applied along the positive z-direction the Zeeman energy of the ith domain becomes $\mu_0 M_s H v_i \cos \theta_i$, where v_i is the volume of the ith domain and θ_i the angle formed by M_s of the ith domain with the z-axis,
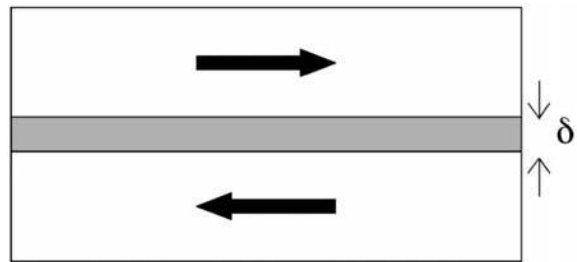
Figure 2
Schematic representation of two magnetic domains separated by a domain wall of width δ.

respectively. Since the Zeeman energy changes from domain to domain there is an energy gradient through the walls and, therefore, a pressure exerted on them. On the other hand, under the torque $\mu_0 M_s H v_i \sin\theta_i$ the magnetization tends to rotate from the easy axis to the field direction. Under the field effect, if the temperature is above 0 K, there is also a tendency to increase the spontaneous magnetization. This is the so-called para-effect that is observable in the approach to saturation. Therefore, the changes in the macroscopic magnetization, ΔM, can generally be expressed in the following schematic way

$$\Delta M = M_s \cos\theta_i \Delta v_i + M_s v_i \Delta\cos\theta_i + \cos\theta_i v_i \Delta M_s \quad (1)$$

The first term is known as domain wall motion contribution, the second corresponds to rotations of the spontaneous magnetization, and the third describes the para-effect or increase of the spontaneous magnetization strength induced by the field against the disordering thermal effect. It has been customarily assumed that domain wall motion takes place at lower fields whereas rotations seemed to require higher applied fields. In fact, one of the historically more attractive objectives of researchers in order to increase coercivity was the production of single domains to avoid the wall motion contribution to the magnetization process. The subsequent development of materials and experimental techniques pointed out that domain wall motion in high anisotropy samples could require field strengths as large as that required for magnetization rotation (Becker 1970). However, it can be accepted that generally domain wall motion is the main magnetization process at low fields, whereas rotations become preponderant for higher fields. As stated above, the character of "low" or "high" fields should be related to the coercivity and, therefore, depends on the nature of each sample. As shown in Fig. 1, the initial region of the initial magnetization curve, the Rayleigh region, corresponds to applied fields much smaller than the coercivity and is due to almost reversible processes. For applied fields of the order of coercivity the maximum contribution of irreversible processes takes place. Finally for applied fields higher than coercivity that region known as "approach to saturation" is reached.

For a given pressure exerted by the field on the wall, the wall displacement depends on the resistance that the solid presents to such displacement. Let p be the pressure acting on a wall initially located at x_0, that for a 180° domain wall with the field parallel to one domain is of the order of $2\mu_0 M_s$. Under a pressure p the wall moves to a new position x at which the pressure exerted by the solid that is due to the position dependence of the wall energy, $d\gamma/dx$, exactly counterbalances p. Many models have tried to account for the spatial dependence of the wall energy density γ. Fluctuations due to modulation of residual stresses, point defects, dislocations, and grain boundaries

affecting either A or k have been invoked and many times evidenced as sources of discontinuities in the domain wall displacement (Néel 1978). Nevertheless, it should be emphasized as the more relevant fact that the correlation length of the fluctuation, l, must be scaled to the domain wall width. When $l < \delta$ the wall energy does not depend on position and therefore the hindrance to displacement disappears.

This is the case for amorphous materials for which the structural or topological disorder has a typical correlation length shorter than δ and therefore the energy of the wall, though high, does not depend on position. Note that at any relative equilibrium position x_i of the wall at $H = 0$ it is verified $(d\gamma/dx)_{x_i} = 0$. Around x_i, γ allows a quadratic Taylor expansion that yields to a reversible linear displacement for sufficiently low fields. When the field rises leading to an effective pressure p that overcomes the maximum $(d\gamma/dx)$ the wall undergoes an irreversible jump and disappears and provides an order of magnitude for the coercivity. But note that the derivative $d\gamma/dx$ has only sense for $dx > \delta$, therefore the maximum $d\gamma/dx$ means the maximum $\Delta\gamma/\delta$ which is of the order of $(Ak)^{1/2}/(A/k)^{1/2}$, a ratio that becomes proportional to k. In other words H_c in this case should increase proportionally to k. Figure 3 illustrates a typical dependence of the wall energy density with position.

The rotation process has also reversible and irreversible steps. Consider a uniaxial anisotropy, of constant k, that in first order can be described by an energy density term $F_k = k(\cos^2\varphi - 1/3)$, where φ is the angle formed by the spontaneous magnetization and the easy axis, see Fig. 4. As the easy axis forms an angle θ_i with the applied field the magnetization
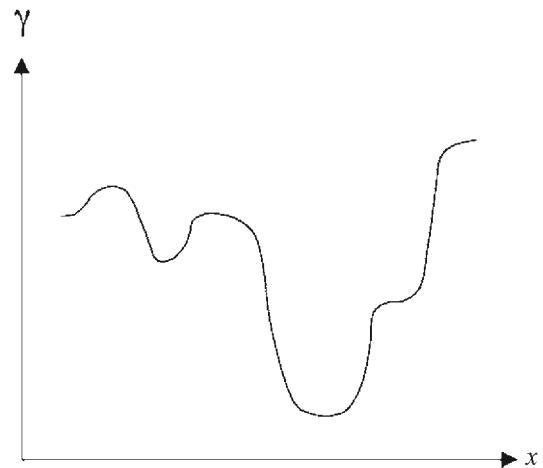
Figure 3
Typical dependence of the wall energy density (γ) with position (x).

Figure 4
Rotation of the magnetization from the easy axis under the influence of an external magnetic field.

would rotate by an angle φ_i, from the easy axis towards the field direction, for which the sum of the anisotropy and Zeeman energy densities vanishes. Therefore, at the stable equilibrium position, the total energy should be a minimum and thereby, it is verified for the first derivative

$$\left[\frac{d}{d\phi_i}\right][k(\cos^2\phi_i - \tfrac{1}{3}) - \mu_0 M_s H \cos(\theta_i - \phi_i)] = 0 \quad (2)$$

and for the second derivative

$$\left[\frac{d^2}{d\phi_i^2}\right][k(\cos^2\phi_i - \tfrac{1}{3}) - \mu_0 M_s H \cos(\theta_i - \phi_i)] > 0 \quad (2a)$$

The component of the magnetization along the field direction M_z, that initially at zero field was $M_s\cos\theta_i$, increases with H to $M_s\cos(\theta_i - \varphi_i)$. The dependence of $M_s\cos(\theta_i - \varphi_i)$ with H can be obtained from relations (2) and (2a). The solutions are known as Stoner–Wohlfarth model for coherent rotation in uniaxial materials (Stoner and Wohlfarth 1948). Figure 5 summarizes some of the corresponding hysteresis loops. It is worth noting that the hysteresis depends on θ_i being maximum for the $\theta_i = \pi$ case for which only two stable or metastable states corresponding to $\varphi_i = 0$ or $\varphi_i = \pi$ are allowed and the coercivity corresponds to the so-called anisotropy field $\mu_0 H_c = 2k/M_s$. In contrast, for $\theta_i = \pi/2$ the magnetization curve is reversible and linear with slope $M_s^2/2k$ for applied fields smaller than the anisotropy field, i.e., the field at which the magnetization finishes its rotation reaching the applied field direction. For a random distribution of the easy axes orientation the coercivity increases with k as well as the field required to reach saturation.
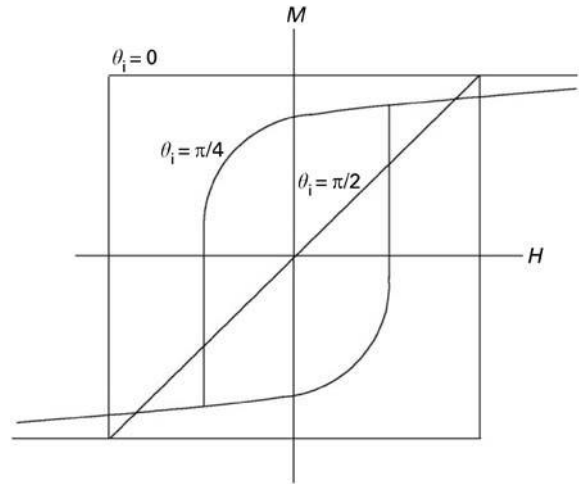
Figure 5
Schematic representation of the hysteresis loops of a uniaxial material according to the Stoner–Wohlfarth model for coherent rotation. θ_i is the angle between the easy axis and the external magnetic field.

3. Dissipation and Irreversible Processes

One of the more important features of the magnetization process is its irreversibility due to the fact that for a given field there exist many wall positions for which the energy is a relative minimum. In other words, for a given applied field the macroscopic magnetization is not a single-valued function of the applied field. For rotation processes also the anisotropy barrier that should be overcome in order to reverse magnetization yields irreversible jumps and hysteresis. Note that the magnetization energy or work supplied in an adiabatic magnetization process during which, under the action of an increasing applied field, M increases from zero to M_f is given by the integral between zero and M_f of $\mu_0 H dM$ (see Fig. 1). If after removing the field the magnetization evolves to the remanent state the expended energy has not been restored and the process of increasing and decreasing the applied field had the energy cost indicated in Fig. 1.

During a complete hysteresis loop the energy irreversibly lost is that given by the area enclosed by the loop (see *Magnetic Losses*). This energy, according to the M and H scales indicated above, ranges from 10^6 Jm^{-3} to 10^{-1} Jm^{-3} for hard and soft materials, respectively. The magnetic energy that a magnet can store is of the order of the energy dissipated during a complete hysteresis loop. Where does the electromagnetic energy go? It is dissipated as heat. Suppose that the magnetization process of a metallic ferromagnet is completely reversible at very low frequency

of the applied field. As the field frequency increases the electric field as well as the eddy currents induced through the Faraday law rise. The increase of frequency leads to a dissipation of Joule energy as heat and to the appearance of hysteresis or phase shifts between field and macroscopic magnetization. These types of losses are known as eddy current losses. Suppose now that the frequency of the applied field is almost zero. The losses now result only from the hysteresis of the macroscopic magnetization. In metallic materials the main source of hysteresis losses is that of the eddy currents.

The walls are locally pinned and suddenly jump as the field varies producing local eddy currents associated to these processes known as Barkhausen jumps (Barkhausen 1919). Local or microscopic eddy currents located around the pinning centre are induced. Structural relaxation, driven by motion and rearrangement of atoms, and magnetization relaxation through interaction between the spin and lattice systems also contribute to introduce delays between magnetization and field. All these considerations outline the complexity of the magnetization process as a thermodynamic transformation far from equilibrium, with time-dependent behavior and irreversible steps leading to energy dissipation.

4. Anisotropy as the More Important Factor Determining Hysteresis

From the point of view of the material physicist, the important conclusion of this overview is the importance of the anisotropy in the control of coercivity (see *Coercivity Mechanisms*). Anisotropy is related to technical magnetism, magnetization process and hysteresis loop just as exchange is to basic magnetism and magnetic structures. The structural anisotropy is due to the combined effect of the spin–orbit coupling and the non-spherical charge distribution around the magnetic atom. Thus, anisotropy can be increased by introducing magnetic atoms with large atomic weight, as rare earth elements. Nowadays, we know that the average or macroscopic anisotropy can be controlled from the local or structural anisotropy through the control of the nanostructure. In particular, for nanostructured multiphase random anisotropy systems, with the exchange correlation length larger than the structural fluctuation, the macroscopic anisotropy undergoes a noticeable reduction with respect to the local anisotropy by the smoothing effect of the exchange energy (Herzer 1989). The importance of the anisotropy on the coercivity is illustrated by taking into account that different theories of coercivity lead to the expression

$$H_c = \alpha \left(\frac{2k}{\mu_0 M_s} \right) - \beta M_s \qquad (3)$$

where the meaning of the α parameters depend on the particular theory and magnetization process (Kronmüller *et al.* 1988, Givord *et al.* 1991) and β is a local demagnetizing factor.

5. Single Domains

An important question rises in the case of single domains corresponding to saturated multidomains as well as in the case of stable single domains; that is, how can the magnetization reversal take place when no wall exists over the sample? This is a fundamental question for the understanding of magnetization reversal. Let us suppose that a sample is completely saturated under an applied field along the positive z-axis that is an easy axis. If after removing the field the macroscopic magnetization decreases, it is because some domains oriented along the negative z-axis have been formed. But to nucleate a reversed seed a field of the order of the anisotropy field is required. Therefore the demagnetizing field acting on the sample when the applied field is removed should be higher than the anisotropy field. It is well known that coercivity is generally much lower than that expected from the value of the anisotropy field. This fact, known as Brown's paradox, has been interpreted by using two types of main arguments. (i) Existence of defects yielding local anisotropy effective constant fluctuations. Such fluctuations would decrease at some regions the reversal barrier height. (ii) The saturated state is not a completely saturated state but it contains a few very small domains oriented along the negative z-axis.

These domains, as observed in Fig. 6 in a saturated Co–Ni multilayer (González *et al.* 1999), would grow under the reversal field up to a critical size (reached at the growing field) and then propagate through the whole sample. For this case the nucleation of reversed domains is not necessary for the magnetization reversal. There are two important fields, nucleation and propagation fields, governing the shape of the hysteresis loop. The concept of nucleation field is generalized to that of growing field, when reversed domains are frozen. The hysteresis shape is smoothed if the propagation field is higher than the nucleation one. On the other hand, the hysteresis loop is rectangular when the propagation field is smaller than the nucleation, which is a condition of bistability. This property allowed Sixtus and Tonks (1931) to evidence the contribution of domain wall motion to the magnetization reversal. A nice example is shown in the experiment described by Fig. 7. A positive magnetostriction amorphous wire keeps closure domains at its end in the saturated state.

If a uniform field larger than the propagation field is applied along the direction opposite to M_s and an extra field located at one end is superimposed in such
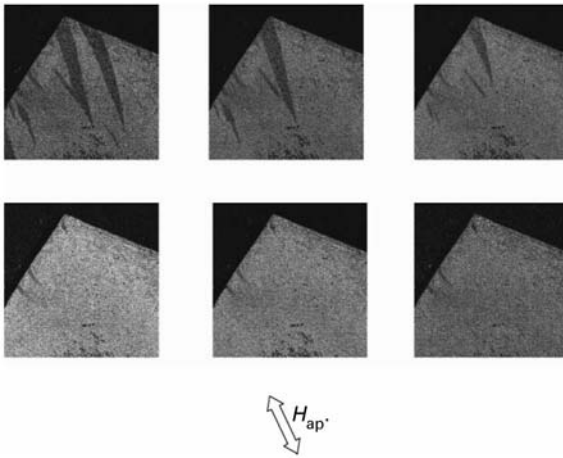
Figure 6
Magnetic domain structure of a Co–Ni multilayer obtained by magneto-optical Kerr effect. The sequence shows the approach to saturation by increasing the applied magnetic field. Notice the existence in the saturated state (last image) of domains with the magnetization opposite to the field.
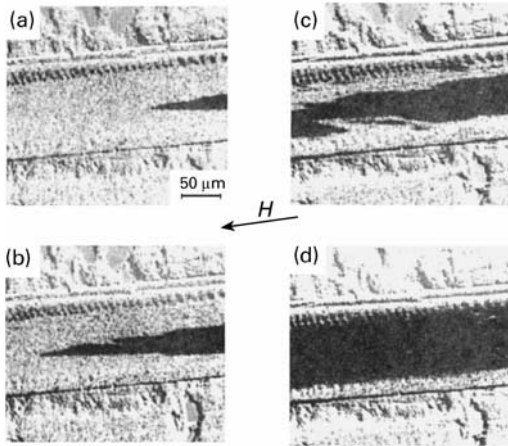
Figure 7
(a)–(d) Magnetic domain structure of an amorphous wire obtained by magneto-optical Kerr effect showing the domain wall motion (see text).

a way that at this end the field is higher than the growing field, the wall propagates (Reininger *et al.* 1993). As in the classic Sixtus and Tonks experiment, two small pick-up coils, separated by z along the axial direction z will collect the induced voltage due to the magnetization reversal with a relative delay, $t = z/v$, where v is the wall speed during its propagation.

When the length of the wire becomes short enough to allow overlapping of the closure domains the bistability disappears since the growing field decreases below the propagation field. Nowadays theoreticians and experimentalists proceed the research on magnetization reversal mechanisms that form an open framework for the technical magnetism.

Let us now take into account the case of single domains. If we focus our interest on small ferromagnetic particles the nonequilibrium character of the hysteresis loop can be easily illustrated. Suppose a set of N uniaxial single domains with their easy axis perfectly oriented along the z-direction. If this assembly has been saturated under a field applied along the positive z-direction, the system is expected to remain saturated just immediately after the field was removed. If we call $N^+(t)$ and $N^-(t)$ the number of particles with the magnetization oriented along the positive or negative z axis respectively, the condition at $t = 0$ is $N^+(0) = N$. This configuration corresponds to an equilibrium situation only at $T = 0$ K. For T above 0 K any remanent magnetization at equilibrium is zero. The free energy ($F = U - TS$) minimization requires minimum energy and maximum entropy. If we assume the magnetization to lie along either the positive or negative z-direction the energy at zero applied field is minimum for both cases, since only anisotropy energy contributes. Therefore, we have to consider only maximum entropy as equilibrium condition. The maximum entropy clearly corresponds to $N^+ = N^- = N/2$. To reach this equilibrium configuration it takes a time, which is typically the relaxation time of the system (see *Magnetic Viscosity*).

Conceptually speaking it is important to remark that remanence is always relaxing to demagnetized state. The hysteresis is due to the fact that the measuring time is much smaller than the relaxation time. As the relaxation time of a particle of volume v and anisotropy constant k is of the order of one minute for $kv = 25K_B T$, K_B being the Boltzmann constant, it is inferred that a system of particles with kv lower that $25K_B T$ should behave as a paramagnetic (superparamagnetic) material without exhibiting any hysteresis in the field dependence of magnetization (Cullity 1972 pp. 410–18). However, by decreasing the temperature the relaxation time exponentially increases and the system becomes ferromagnetic exhibiting hysteresis. The magnetic field acts on the magnetization by increasing or decreasing the macroscopic magnetization in times smaller than the relaxation time, whereas the thermal motion tends to demagnetize the sample overcoming the anisotropy barriers and eliminating the hysteresis phenomena. Therefore, for systems formed by small particles for which, at reasonable temperatures, it may be verified from $kv = 25K_B T$—for usual k values of the size of a few nanometers—a

new term should be included in the general expression of the coercivity (3) that becomes

$$H_c = \alpha \left[\frac{2k}{\mu_0 M_s} \right] \left[1 - \left(\frac{25 K_B T}{kv} \right)^{1/2} \right] - \beta M_s \quad (4)$$

The thermal term tends to decrease coercivity by decreasing the relaxation time. Superparamagnetism or disappearance of the hysteresis was a surprising and amazing experimental observation found by Bean and Livingston (1959) just while they tried to decrease the particle size in order to prevent domain wall contribution for "improving" hard properties (Jacobs and Bean 1963). In 1949, Néel had predicted superparamagnetism (Néel 1949). Nowadays, the nanostructures formed by different amorphous and nanocrystalline phases with different Curie temperatures have lifted superparamagnetism and, in general, relaxation processes (García del Muro *et al.* 1997) to an outstanding position of interest.

6. Effect of the Nanostructure

Finally, three examples, based on fairly recent experiments and illustrative of the influence of the nanostructure on the magnetization curve are summarized.

Nanocrystalline materials, composed of ferromagnetic Fe(Si) nanograins embedded in an amorphous matrix with lower Curie temperature, T_c^{am}, exhibit a noticeable thermal dependence of magnetization as shown in Fig. 8 (Hernando and Kulik 1994). For $T < T_c^{am}$ the coercivity is very low due to the exchange coupling between the crystallites transmitted by the matrix. As the temperature rises the magnetization of the matrix drops and the grains are less coupled giving rise to a progressive increase of the coercivity that

reaches an abrupt maximum at T_c^{am}, since at this temperature the grains behave as single domains. Further increase of the temperature leads to a superparamagnetic transition and the coercivity falls to zero.

An example of the influence of the domain wall width, δ, on the coercivity and magnetization curve is illustrated by Fig. 9 (Arcas *et al.* 2000). In a sample composed of iron nanocrystallites embedded in a FeZr amorphous matrix, δ depends on the number of crystallites. The influence on δ of the exchange
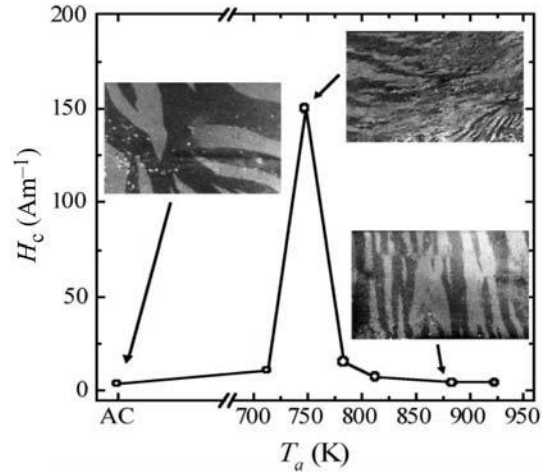
Figure 9
Coercive field and domain patterns of a FeZrBCu amorphous alloy as a function of the annealing temperature.

Figure 8
Temperature dependence of the coercive field for a nanocrystalline material. Notice the drastic increase of the coercive field as we approach the Curie temperature of the amorphous matrix ($T_c^{am} \approx 370\,°C$).
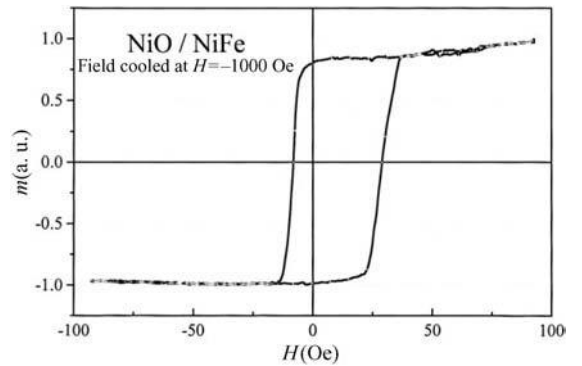
Figure 10
Shifted hysteresis loop, obtained by Kerr effect, corresponding to an exchange coupled NiO/NiFe thin film system. The sample was cooled under an applied field of $H = -1000$ Oe from 370 K down to room temperature.

coupling between the grains analyzed by Herzer (see *Amorphous and Nanocrystalline Materials*) is reflected in the coercivity.

Finally an example of minor hysteresis loops obtained around a fixed point of the hysteresis loop, shifted loops, is outlined. Spin–valve systems allow the shift of the hysteresis loop through the coupling between an antiferromagnetic (hard) layer and a ferromagnetic (soft) layer. Figure 10 shows a typical shifted hysteresis loop (Dimitrov *et al.* 1998). The minor loop corresponding to the reversal of the magnetization at the soft layer takes place under the effective exchange field exerted by the hard layer.

Bibliography

Arcas J, Hernando A, Gómez-Polo C, Castaño F J, Vázquez M, Neuweiler A, Kronmüller H 2000 Exchange interaction through amorphous intergranular layers in a two-phase system. *J. Phys.: Condens. Matter* **12**, 3255–65

Barkhausen H 1919 Two phenomena uncovered with help of new amplifiers. *Phys. Z* **20**, 401–3

Bean C P, Livingston J D 1959 Superparamagnetism. *J. Appl. Phys.* **30**, 120-9S

Becker J J 1970 Rare-earth compound magnets. *J. Appl. Phys.* **41**, 1055–64

Bertotti G 1998 *Hysteresis in Magnetism.* Academic Press, New York

Cullity B D 1972 *Introduction to Magnetic Materials.* Addison-Wesley, Reading, MA

Dimitrov D V, Prados C, Ni C Y, Hadjipanayis G C, Xiao J Q 1998 Magnetoresistance in NiCoO/Py/Cu/Py. *J. Magn. Magn. Mater.* **189**, 25–31

García del Muro M, Batle X, Labarta A, González J M, Montero M I 1997 The effect of magnetic interaction in barium hexaferrite particles. *J. Appl. Phys.* **81**, 3812–4

Givord D, Lu Q, Rossignol M F 1991 Coercivity in hard magnetic materials. In: Hadjipanayis G C, Prinz G A (eds.) *Science and Technology of Nanostructured Magnetic Materials.* Plenum, New York, pp. 635–56

González J M, Salcedo A, Cebollada F, Freijo J J, Muñoz J L, Hernando A 1999 Thermally activated demagnetization in Co/Ni multilayers involving discrete identifiable stages. *Appl. Phys. Lett.* **75**, 847–9

Hernando A, Kulik T 1994 Exchange interactions through amorphous paramagnetic layers in ferromagnetic nanocrystals. *Phys. Rev. B* **49**, 7064–7

Herzer G 1989 Grain structure and magnetism of nanocrystalline ferromagnets. *IEEE Trans. Magn.* **25**, 3327–9

Jacobs I S, Bean C P 1963 Fine particles, thin films and exchange anisotropy. In: Rado G T, Suhl H (eds.) *Magnetism.* Academic Press, New York, Vol. III, pp. 271–350

Kronmüller H, Durst K-D, Sagawa M 1988 Analysis of the magnetic hardening mechanism in RE-FeB permanent magnets. *J . Magn. Magn. Mater.* **74**, 291–302

Néel L 1949 Influence des fluctuations thermiques sur l'aimantation des grains ferromagnétiques trés fins. *Comp. Rend.* **228**, 664–6

Néel L 1978 *Oeuvres Scientifiques de Louis Néel.* Editions du CNRS, Paris

Reininga T, Kronmüller H, Gómez-Polo C, Vázquez M 1993 Magnetic domain observation in amorphous wires. *J. Appl. Phys.* **73**, 5357–9

Sixtus K J, Tonks L 1931 Propagation of large Barkhausen discontinuities. *Phys. Rev.* **37**, 930–58

Stoner E C, Wohlfarth E P 1948 A mechanism of magnetic hysteresis in heterogeneous alloys. *Philos. Trans. R. Soc. A* **240**, 599–642

A. Hernando, P. Crespo, P. Marín, and A. González
Instituto de Magnetismo Aplicado, Universidad Complutense de Madrid-RENFE Spain

Magnetic Layers: Anisotropy

A dictionary definition of anisotropy is "a difference of property or of effect in different directions." Magnetic anisotropy in materials is concerned with the observation that the magnetization prefers to point parallel or antiparallel to a particular direction or axis. A detailed treatment of the fundamentals of magnetic anisotropy is given by Chikazumi (1997).

Anisotropy can be related to the crystal structure of the material and, in the case of thin-film materials, to the form of the material, to the importance of the break of symmetry at the surfaces of the thin layer, to any strain in the thin film, to the morphology of the microstructural units making up the film, to any directional atomic ordering in the film, and to any other interface atomic effects at the junction of overlaid films. It is clear that perpendicular anisotropy, i.e., anisotropy favoring an orientation of the magnetization normal to the plane of the film, is one of the most important materials requirements in MO recording technology.

To a sufficient approximation the effective anisotropy, K_{EFF}, can be written phenomenologically in terms of a volume term, K_V, and a surface term, K_S:

$$K_{EFF} = K_V + 2K_S/t_F \tag{1}$$

where t_F is the thickness of the magnetic element. K_V necessarily contains a magnetocrystalline anisotropy term, any stress term, any shape anisotropy term, any growth-induced anisotropy term, and any other volume sources of anisotropy. The demagnetizing energy for a film magnetized normal to its surface is also included as the last term:

$$K_V = (K_{MC} + K_{ST} + K_{SH} + K_G \cdots - \mu_0 M_S^2/2) \tag{2}$$

In the case of a thin film the surface term, which accounts for the two surfaces, is only of significance if t_F is of nanometer dimensions. This can occur practically in multilayer systems. K_{EFF} is positive for perpendicular magnetization.

1. Magnetocrystalline Anisotropy

The microscopic origin of this anisotropy is related to the spin state of the magnetic moments and by the symmetry of their arrangement in the crystal lattice that involves spin–lattice coupling. It occurs in all crystalline ferro- and ferrimagnetic materials.

The anisotropy can be describe phenomenologically in terms of the direction cosines of the magnetization with respect to rectangular coordinate axes or in terms of spherical harmonics. Any perpendicular magnetization will realistically occur in an effectively uniaxial system. The latter representation gives, for a simple hexagonal symmetry:

$$E_{MC} = K_1 \sin^2\theta + K_2 \sin^4\theta + \cdots + K_4 \sin^6\theta \cos 6\varphi \tag{3}$$

in terms of the anisotropy constant K_i and the polar and azimuthal angles θ and φ between the magnetization and the c- and a-axes. In an oriented film with an easy axis normal or close to normal to the surface of the film, perpendicular magnetization can be achieved, in the absence of any other sources of anisotropy, if the magnetocrystalline anisotropy energy is greater than the demagnetizing energy. This requires, following Eqn. (2), to a sufficient approximation neglecting higher terms $K_1 > \mu_0 M_S^2/2$.

2. Stress Anisotropy

This anisotropy comes from stresses produced in the film by the deposition process or by thermal expansion differences between the substrate and the magnetic film. The magnetoelastic energy produced by a stress σ is essentially the product of this stress and the resulting value of magnetic strain or magnetostriction, λ. Again, assuming a uniaxial system the volume magnetoelastic energy is given by

$$E_{ML} = -3\sigma\lambda_S \cos^2\theta/2 \tag{4}$$

where λ_S is an isotropic magnetostriction coefficient and θ is the angle between the magnetization M_S and σ. Stress can therefore create uniaxial anisotropy with a relevant stress-induced anisotropy constant given by

$$K_{ST} = 3\sigma\lambda_S/2 \tag{5}$$

The stress axis is an easy direction of magnetization if $\sigma\lambda_S > 0$, i.e., positive magnetostriction will promote perpendicular magnetization for a compressive stress in the film while a negative constant requires a tensile stress.

3. Shape Anisotropy

In general magnetostatic energy in a thin film acts to orient the magnetization in the plane of the film as suggested above. However, many deposited films can contain microstructural units that by their shape and orientation favor magnetization normal to the film. This is very possible in films that contain columnar grains or directional voids. In a prolate spheroid the magnetostatic energy can be written as

$$E_{ME} = \mu_0 (N_a - N_c) M_S^2 \sin^2\theta/2 \tag{6}$$

where N_a and N_c are constant factors known as demagnetizing factors related to the semiminor and semimajor axes, respectively, and θ is the angle between M_S and the c-axis. In analogy to the case of stress, a shape anisotropy constant can be written as

$$K_S = \mu_0 (N_a - N_c) M_S^2/2 \tag{7}$$

If $N_a < N_c$ then the shape anisotropy is a minimum with M_S along the c-axis.

4. Growth-induced Anisotropy

Thin films essentially condense and grow in a unidirectional manner from the substrate surface. This can lead to particular growth morphologies and also directional ordering of atoms and a so-called growth-induced anisotropy. This source of anisotropy is important in ferrite and garnet films and in amorphous alloy films.

In amorphous films single magnetic ions may have a particular atomic coordination, say in the plane of the film, which gives rise to a directional magnetic coupling and perpendicular anisotropy. Also, atom pairs may order preferentially parallel or normal to the surface, and in mixed oxide crystalline films atoms may occupy lattice sites in a preferential manner, so reducing the magnetic symmetry of the system. The anisotropy may be represented phenomenologically in terms of the direction cosines of the magnetization with respect to any lattice and the normal to the growth surface. Again, for a uniaxial system

$$E_G = K_G \sin^2\theta \tag{8}$$

where θ is the angle between the growth direction and the magnetization.

5. Surface or Interface Anisotropy

Interface or surface anisotropy is related to the reduced symmetry, lower coordination numbers, the presence of localized near-surface and interface states, and other effects at a surface (Bayreuther 1989). The reduced symmetry at the surface modifies the magnetocrystalline anisotropy and this contribution can, in fact, be positive or negative encouraging out-of-plane and in-plane magnetization. There can also be a contribution to the interface anisotropy that is magnetoelastic in origin. This is related to stress

relief by defect formation at interfaces. It is inversely related to the layer thickness and may therefore be significant at small thicknesses.

Phenomenologically the effect of surface anisotropy can be represented by a term K_S added to the volume anisotropy in an equation for the total anisotropy, as shown in Eqn. (1). Conventionally, a positive K_{EFF} signifies a perpendicular anisotropy and a plot of $K_{EFF}t_F$ against t_F gives a slope of K_V and an intercept of $2K_S$.

There is one further anisotropy that will be mentioned only briefly as it is not important here: exchange anisotropy. This effect is unidirectional and involves the pinning of moments in a ferromagnet layer by an adjacent antiferromagnet layer on cooling through the Néel temperature of the antiferromagnet in an applied field. Exchange anisotropy is of growing importance in several magnetic thin-film devices such as giant magnetoresistance sensors.

6. Materials

6.1 Rare Earth–Transition Metal Alloy Films

The generic materials that form the various layers in the storage medium in MO recording are amorphous rare earth–transition metal alloy (RE–TM) films. RE–TM films are treated in a review by Grundy (1994). In brief, the deposition and alloying of the heavy rare earths gadolinium, terbium, and dysprosium with cobalt and/or iron produces thin ferrimagnetic films with the necessary magnetic coercivity, in relation to the compensation phenomenon, and perpendicular anisotropy to store stable magneto-optically written bits in the memory layer. The perpendicular anisotropy is composition dependent and, more than any other magnetic parameter, it can be strongly dependent on fabrication conditions and microstructure. For example, early measurements showed that $K_{EFF} > 0$ for bias sputtered GdCo and evaporated GdFe films, whereas $K_{EFF} < 0$ for evaporated and zero-bias sputtered GdCo and GdFe sputtered at relatively high biases. In most situations several sources of anisotropy may be active. Measured values of the principal perpendicular anisotropy constant for compositions of interest are of the order of 5×10^5 J m^{-3}.

Magnetocrystalline anisotropy is not relevant in amorphous films and the potential sources of anisotropy therefore come from any growth-induced structural anisotropy, atomic ordering, stress, or shape effects. The first growth-induced anisotropy to be considered is single-ion anisotropy (Suzuki *et al.* 1987) that may be present with non-S state ions such as terbium and with dysprosium but not with gadolinium. An anisotropic distribution of atoms is assumed with more nearest neighbors in the plane of the film. Interactions such as that between the RE 4f electrons and the surrounding ions give perpendicular

anisotropy in such a "bond-order" anisotropy (Prados *et al.* 1997).

The second ordering effect, that of pair ordering (Mizoguchi and Cargill 1979), has also found favor in explaining the perpendicular anisotropy in RE–TM alloy films. The atomic arrangement in amorphous films is only pseudorandom and may include slight chemical order in which some TM–TM or RE–TM pairs are oriented parallel or normal to the plane of the film. There appears to be experimental evidence for such an arrangement in TbFe films (Hufnagel *et al.* 1995) and good correlation between modifications of such an anisotropic local atomic arrangement on annealing with loss of magnetic anisotropy (Harris *et al.* 1993). Calculations of anisotropy from such arrangements suggest that only a few percent of atoms need be coupled in this way to promote perpendicular magnetization. The large anisotropies observed in some substituted TbREFe alloys may only be explained by a pair ordering mechanism, but the complete picture is not always clear.

Stress in thin films is related to the deposition process and deposition conditions, e.g., the argon pressure during sputtering and the substrate temperature. A change from compressive to tensile stress with increasing argon pressure has been observed in sputter-deposited RE–Fe. In general, RE–TM films deposited at ambient temperatures should not suffer much thermal stress due to mismatch of the expansion coefficients for the film and the substrate. Any residual stress will couple with magnetostriction and produce stress-induced anisotropy. Magnetostriction in Gd–TM alloys is relatively small at $\sim 10^{-6}$–10^{-5}, whereas measurements for TbFe and TbFeCo and TbDyFe films find values of $\sim 2 \times 10^{-4}$–7.5×10^{-4} (Williams and Grundy 1994). Clearly, in terbium-based alloys magnetostriction can play a significant role in providing stress-induced perpendicular anisotropy (Prados *et al.* 1997) and residual values of the order of 3×10^4 J m^{-3} have been measured (Cheng *et al.* 1989).

PVD techniques, particularly sputter deposition, can create anisotropic microstructures in thin films, e.g., the well-known columnar structure, which are dependent on factors such as surface mobility in the growing film and the inclusion of sputtering gas. These factors appear to be mainly dependent on the argon pressure and substrate temperature during deposition and on any target bias. Thermalization of the sputtering process at higher pressures, the use of heavier sputtering gases, and reduced bombardment of the growing film lead to coarser microstructures. The maximum possible value for shape-induced anisotropy would be $0.5\mu_0 M_S^2$ or typically 10^3–10^4 J m^{-3}, and in general this is not sufficient to support perpendicular magnetization. This model of anisotropy also does not fit with observations that the anisotropy can vary smoothly through the compensation point, where M_S is zero or at least very small,

and that it reaches its largest values in dense, microstructurally featureless films.

6.2 Magnetic Oxides

Other candidates for MO recording that have been investigated are garnet and uniaxial ferrite films. In most cases films prepared on ambient temperature substrates are amorphous and must be crystallized to produce the magnetic mixed oxide. The deposition conditions and the subsequent nucleation and growth process on annealing affect the microstructure and magnetic properties of the film. Magnetic properties can also be tailored in cubic $RE_3Fe_2Fe_3O_{12}$ garnet films by substitution with particular ions; dysprosium typically enhances perpendicular anisotropy and bismuth and cerium substitutions improve the magneto-optic interaction.

Any perpendicular anisotropy in polycrystalline cubic films must originate in stress, growth-induced ordering, or microstructural inhomogeneities. Measured K_{EFF} values for substituted garnet films can reach $\sim 5 \times 10^3 \, \mathrm{J \, m^{-3}}$ at the compensation temperature. Calculations of any stress-induced anisotropy from the thermal mismatch between film and substrate give values of this order. Such anisotropy values are relatively low but, coupled with reduced magnetization values near compensation, are sufficient to support perpendicular magnetization and reasonable coercivities.

Cubic and hexagonal ferrite films also have useful magneto-optic properties and can be prepared with perpendicular anisotropy. The intrinsic uniaxial magnetocrystalline anisotropy in hexagonal Ba,Sr–$Fe_{12}O_{19}$ ferrites of the order $5 \times 10^6 \, \mathrm{J \, m^{-3}}$ is sufficient to ensure $K_{EFF} > 0$ in (0001) textured polycrystalline films. The high anisotropy ensures high coercivities in films in which the value of M_S can be controlled by substitution, typically cobalt, titanium, lanthanum, or zinc (e.g., Atkinson *et al.* 1994, Ogata *et al.* 1999). Cubic ferrites, e.g., $CoOFe_2O_3$ also have large intrinsic anisotropies that are a disadvantage in attempts to create a stress-induced preferred direction normal to the film plane.

6.3 Multilayer Films

In nanoscaled multilayered thin films the contribution of any surface anisotropy to the total anisotropy can become significant. Typical systems in which this is the case are Co,CoNi/X, where X can be Ni, Cu, Ru, Pd, V, Pt, and Au, and RE/TM multilayers such as Tb/Fe.

In the first group attention has focused on Co,CoNi/Pt,Pd multilayers for MO recording investigations. These systems have increased Kerr rotations at short wavelengths. A rough calculation for a Co/Pt multilayer using the values of K_{MC} for f.c.c. cobalt (the cobalt layers in these systems are in the

cubic phase), a value of $1400 \, \mathrm{kA \, m^{-1}}$ for M_S and a typical value of K_S of $0.5 \, \mathrm{mJ \, m^{-2}}$ in Eqn. (1) shows that the cobalt layers should be less than about 1 nm thick. A plot of any experimentally determined $K_{EFF}t_{Co}$ against t_{Co} gives an intercept at $t_{Co} = 0$ of the surface anisotropy and the slope gives the volume contribution. Several sources of anisotropy may be present and it has been shown that magnetostrictive stress-induced anisotropy makes a significant contribution to the volume anisotropy in Co/Pd multilayers but not in Co/Pt multilayers (Umeda *et al.* 1996). In practice the cobalt layer is maintained below $\sim 0.4 \, \mathrm{nm}$ in the multilayers whereas the thickness of the platinum layer is not critical in affecting the effective anisotropy but values below 2 nm are usual.

The effective anisotropy of the multilayer can be affected by the growth conditions. The use of different substrates, the inclusion of underlayers, the use of different sputtering gases at different pressures, and different substrate temperatures have all been shown to affect the microstructure of multilayer films. A volume contribution can be obtained by a preferred texture, which is usually $\langle 111 \rangle$ in polycrystalline cubic films, and the surface contribution is dependent on the form and sharpness of the interfaces in the system. This fits well with the observation of improved $\langle 111 \rangle$ texture with underlayer thickness. Investigations of the effects of the sputtering gas show that thermalization of the deposition process and the reduction in bombardment of the growing film can increase interface roughness but lead to increased interface anisotropy (Carcia *et al.* 1993).

Other multilayer films explored for their anisotropic properties and their potential for MO recording investigations are RE/TM systems with the basic compositions Gd,Tb/Fe,Co (e.g., Jamet *et al.* 1996). For example, perpendicular anisotropy is observed in sputter-deposited Tb/Fe and Tb/Co multilayers, as in Co/Pt systems, when the thickness of the layers is below 1 nm or 2 nm. Again, the value of K_{EFF} depends on the thickness of the TM layers and indicates the presence of a significant surface anisotropy. Typical values of K_{EFF} can vary between $5 \times 10^4 \, \mathrm{J \, m^{-3}}$ for Tb/Co multilayers and $10^6 \, \mathrm{J \, m^{-3}}$ for Tb/FeCo.

However, these values can be dependent on the details of the coupling between the RE and TM layers and an additional property of these systems is that they can show antiferromagnetic coupling and ferrimagnetic ordering and a compensation temperature. This behavior can be tuned by varying the relative thicknesses of the two layers and also in proportion to the composition of the equivalent alloy. Magnetic spin reorientation effects also occur as a function of temperature, in which the system is dominated by the RE and TM magnetization in different temperature ranges as in homogeneous alloys. The crystal structure of the layers is also unusual in that for the thinner layers the RE and TM are amorphous but for thicker layers the TM is crystalline.

Exchange coupled layers are the basis of media for super-resolution MO storage techniques. Although not multilayers in the usual sense, temperature-dependent spin reorientations occur also in these bi- or trilayer structures that are used in the read-out process (e.g., Nishimura *et al.* 1996). The perpendicular anisotropy in the memory layer, e.g., TbFeCo, the mediating effect on exchange coupling of any intermediate layer, and the in-plane anisotropy in the read-out layer, e.g., GdFeCo, can clearly be controlled by adjustment of compositions for the required temperatures (Stavrou *et al.* 2000) (see also *Magneto-optic Recording: Overwrite and Associated Problems*).

6.4 Other Materials

The first requirement of a thin-film material for MO recording is significant magneto-optic activity at wavelengths of interest. As already made clear, the second requirement is perpendicular anisotropy that is sufficiently strong to maintain magnetization normal to the plane of the film. This first property has been the trigger for successful investigations of many metallic alloys, oxides, and composite materials but the second property has often not been realized. Several materials of the many that have been investigated can be addressed.

The relatively high Kerr rotations observed for CoPt alloys, rather than multilayers, has suggested their possible use as MO recording media. Growth on oriented platinum underlayers at temperatures ~ 200–$500\,^{\circ}$C can result in films with a perpendicular K_{EFF} greater than $10^6\,\mathrm{J\,m^{-3}}$ (Lin and Gorman 1992). Equiatomic CoPt films grown at $\sim 500\,^{\circ}$C show ordered face-centered tetragonal (f.c.t.) and disordered cubic phases with $\langle 111 \rangle$ and $\langle 200 \rangle$ preferred orientations and $CoPt_3$ films grown at $\sim 200\,^{\circ}$C are also f.c.t. The large effective anisotropies have been associated with the large K_{MC} along the tetragonal c-axis that is oriented normal to the film plane (Iwata *et al.* 1999).

Alloys related to the Heusler alloys have very interesting MO properties. PtMnSb, with the $C1_b$ structure has a very large Kerr rotation of $\sim 2^{\circ}$ at 633 nm. This is related to its semimetallic nature and unusual band structure. Unfortunately the compounds have cubic symmetry and deposited films show in-plane anisotropy and low coercivities (Attaran and Grundy 1989, Carey *et al.* 1993). MnBi, MnSb, and related compounds, such as MnGaGe, have also been investigated for MO applications over many years but have not been adopted because, although their magneto-optic properties are very attractive, difficulties in thin-film fabrication and magnetic and structural instabilities make them unsuitable.

See also: Magnetic Films: Anisotropy; Monolayer Films: Magnetism; Magneto-optic Recording Materials: Chemical Stability and Life Time; Magneto-optic Recording: Total Film Stack, Layer Configuration; Magneto-optic Multilayers

Bibliography

Atkinson R, Papakonstantinou P, Salter I W, Gerber R 1994 Optical and magneto-optical properties of Co–Ti substituted Ba-hexaferrite single crystals and thin films produced by laser ablation. *J. Magn. Magn. Mater.* **138**, 222–31

Attarar E, Grundy P J 1989 The magnetic magneto-optical and structural properties of PtMnSb thin films. *J. Magn. Mater.* **78**, 51–5

Bayreuther G 1989 Magnetic surfaces. *Hyperfine Interact.* **47**, 237–49

Carcia P F, Li Z G, Zeper W B 1993 Effect of sputter-deposition processes on the microstructure and magnetic properties of Pt/Co multilayers. *J. Magn. Magn. Mater.* **121**, 452–60

Carey R, Jenniches H, Newman D M, Thomas B W J 1993 PtMnSb films prepared by rapid thermal annealing. *J. Magn. Soc. Jpn.* **17**, 290–3

Cheng S-C N, Kryder M H, Mathur M C A 1989 Stress related anisotropy studies in d.c.-magnetron sputtered TbCo and Tb films. *IEEE Trans. Magn.* **25**, 4018–20

Chikazumi S 1997 *Physics of Ferromagnetism*. Clarendon Press, Oxford

Grundy P J 1994 High density magneto-optical recording materials. In: Buschow K H J, Cahn R W, Haasen P, Kramer E J (eds.) *Materials Science and Technology*. VCH, Weinheim, Germany, Vol. 3B, pp. 567–710

Harris V G, Elam W T, Koon N C 1993 Correlation of magnetic and structural anisotropy in amorphous TbFe via EXAFS. *J. Magn. Soc. Jpn.* **17**, 267–71

Hufnagel T C, Brennan S, Clemens B M 1995 Pair ordering anisotropy in amorphous TbFe films. *Mater. Res. Symp. Proc.* **384**, 239–44

Iwata S, Yamashita S, Tsunashima S 1999 Structure and perpendicular anisotropy of MBE grown PtCo alloy films. *J. Magn. Magn. Mater.* **198**, 481–3

Jamet J P, Meyer P, Grolier V, Ferre J 1996 Thermomagnetic writing and time resolved imaging in a Tb/Fe multilayer. *J. Magn. Soc. Jpn.* **20**, 217–22

Lin C J, Gorman G L 1992 Evaporated CoPt alloy films with strong perpendicular anisotropy. *Appl. Phys. Lett.* **61**, 1600–3

Mizoguchi T, Cargill G S III 1979 Magnetic anisotropy from dipolar interactions in amorphous ferrimagnetic alloys. *J. Appl. Phys.* **50**, 3570–82

Nishimura N, Hiroki T, Okada T, Tsunashima S 1996 Transition from in-plane to perpendicular magnetization in MSR magneto-optical disks. *J. Appl. Phys.* **79**, 5683–5

Ogata Y, Kubota Y, Takami T, Tonunaga M, Shinohara T 1999 Improvement of magnetic properties of Sr ferrite magnets by substitution of La and Co. *IEEE Trans. Magn.* **35**, 3334–6

Prados C, Marinero E, Hernando A 1997 Magnetic interactions and anisotropy in amorphous TbFe films. *J. Magn. Magn. Mater.* **165**, 414–6

Stavrou E, Sbiaa R, Suzuki T 2000 Different mechanisms of spin reorientation in exchange coupled double Re–Tm layers. *J. Appl. Phys.* **87**, 6893–5

Suzuki Y, Takayama S, Kirino F, Ohta N 1987 Single ion model for perpendicular magnetic anisotropy in RE–TM films. *IEEE Trans. Magn.* **23** (5), 2275–7

Umeda K, Fujiwara Y, Matsumoto T, Nakagawa N, Itoh A 1996 Contribution of stress-induced magnetic anisotropy to the perpendicular anisotropy of Co/Pd and Co/Pt multilayers. *J. Magn. Magn. Mater.* **156**, 75–6

Williams P I, Grundy P J 1994 Magnetic and magnetostrictive properties of rare earth–transition metal alloy films. *J. Phys. D: Appl. Phys.* **27**, 897–901

P. J. Grundy
University of Salford, Manchester, UK

Magnetic Levitation: Materials and Processes

Magnetic levitation is one of the most outstanding properties of superconductors, which in addition has launched the development of several electromechanical systems. The simplest experiment consists of a single permanent magnet levitating in a stable position over a superconducting pellet refrigerated with liquid nitrogen.

It is indeed the characteristic of stable levitation that gives rise to great interest in devices such as magnetic bearings, rotating machinery, linear transport systems, etc.

The axial vertical force of a permanent magnet over a superconductor stems from the flux exclusion associated with materials with high critical currents (Moon 1994). In this case, the following can be written:

$$\vec{F} = \int_V (\vec{M} \cdot \vec{\nabla}) \cdot \vec{B}_{ext} \, dV$$

where M is the magnetization of the superconductor, B_{ext} is the magnetic field generated by the permanent magnet, and the integral is extended over the whole volume of the superconductor.

Therefore a body may magnetically levitate if the vertical gradient of the magnetic induction displays a positive F_z component, which eventually overcomes the weight of the permanent magnet. From the superconducting material point of view, the generation of a large magnetization requires current loops shielding the magnetic field generated by the permanent magnet. According to the critical state model, a partial flux penetration occurs in which the flux gradient obeys the Ampere law $rot\mathbf{B} = \mu_0\mathbf{J}_c$, where $\mathbf{J}_c$ is the critical current of the superconductor. Hence, the magnetization of the superconductor increases only if $|\mathbf{J}_c|$ or the area of the corresponding current loop increases.

Consequently, applications based on the magnetic levitation phenomenon require large quasisingle-crystalline superconducting materials with high critical currents.
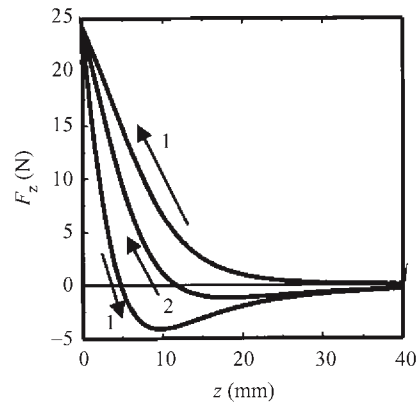
Figure 1
Hysteretic levitation force measured when a permanent magnet approaches a superconductor in a zero-field cooling process (1) for the first time and (2) after a whole cycle when some flux has been trapped in the superconductor.

An additional advantage of the high critical current density is the enhanced lateral and vertical stability, since magnetic stiffness is proportional to the pinning capability of the vortices penetrated within the superconductor. It must also be noted that because of the hysteretic nature of the magnetization of hard superconductors the magnetic levitation force will also be history dependent (Fig. 1). For instance, if the cooling of the superconductor is performed with the permanent magnet in close contact with the superconductor (field cooling procedure), an attractive force will be generated when retrieving it and, hence, the phenomenon of a stable magnetic suspension may also be obtained.

1. Superconducting Materials

The development of practical applications based on magnetically levitating systems working at liquid nitrogen temperature requires the use of superconducting materials with high critical currents at the magnetic fields generated by high-power NdFeB or SmCo magnets ($B_r \approx 1$ T; see *Magnets: Sintered*).

Among the different high-temperature superconducting phases, that presenting the highest J_c at 77 K is $YBa_2Cu_3O_7$ (Y-123), which displays an irreversibility line (the magnetic field where $J_c \approx 0$) at 77 K around 5–7 T. Also the isomorphous systems Re-123 (Re = Nd, Sm), which may have irreversibility lines as high as 10 T at 77 K, should be considered.

Also to be taken into account is the fact that the critical currents of cuprate superconductors are strongly anisotropic, the highest being those flowing within the *ab*-planes. For this reason, an optimized

material for magnetic levitation should have the *ab*-planes perpendicular to the vertical component of the magnetic field of the permanent magnet. In conclusion, the most appropriate materials for magnetic levitation are bulk quasisingle-crystalline $ReBa_2Cu_3O_7$ (Re = Y, Nd, Sm) pellets with *ab*-planes oriented parallel to the basal surface.

2. Processing of Bulk $ReBa_2Cu_3O_7$ (Re = Y, Nd, Sm)

The preparation of large-grain Y-123 ceramics is based on melt texturing processes. Essentially these techniques rely on a controlled crystallization from a semisolid state following the peritectic reaction $Y_2BaCuO_5(s) + 3BaCuO_2(l) + 2CuO(l) \rightarrow 2YBa_2Cu_3O_7$. The peritectic decomposition temperature of Y-123 occurs at $T_p \approx 1010\,^{\circ}C$, thus melt processing requires heating the samples at temperatures above T_p, typically 1040–1110 $^{\circ}C$, and cooling them at a typical rate of 1 mmh^{-1} in such a way that a single large grain may be grown.

The generation of single-grain Y-123 materials requires carrying out a directional solidification process where a selection of the nucleation centers is done and the conditions of a plane growth front are still maintained. Two techniques have been used successfully for this purpose: the Bridgman growth method where a temperature gradient is imposed (typically 10 $^{\circ}Ccm^{-1}$) and the top seeding growth (TSG) technique where the nucleation is generated at a crystalline seed while the homogeneous nucleation is avoided through a limitation of the degree of undercooling of the liquid.

The Bridgman technique appears to be more adapted to long ceramic shapes while the TSG technique enables one to grow large-diameter samples having the *ab*-planes oriented parallel to the basal surface. Thus, the TSG technique is the most suitable for preparing samples for magnetic levitation applications. The seeds that have been found to be chemically and structurally compatible with the high-temperature semisolid state are MgO and $ReBa_2Cu_3O_7$ (Re = Nd, Sm) single crystals. Re-123 crystals are preferred because they have a crystalline structure closer to that of the Y-123 phase. However, they have peritectic decomposition temperatures only 30–50 $^{\circ}C$ above that of Y-123 and thus they may display some solubility that has to be controlled.

Single-grain cylindrical materials with diameters up to 10 cm and the *ab*-planes oriented parallel to the basal plane have been grown based on this methodology. Levitation forces greater than 1676 N can be reached with a single SmCo permanent magnet with $B_r = 0.4\,T$, which corresponds to a magnetic pressure greater than $2.2 \times 10^{-3}\,m^2$ (Sawamura 1999).

In order to grow large domains it is essential to select a narrow temperature window where crystallization
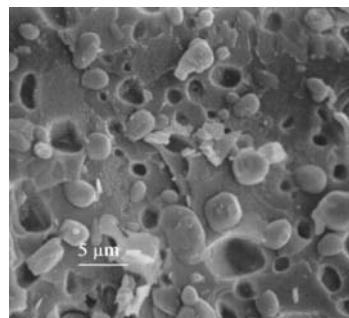
Figure 2
Scanning electron microscopy image of a $YBa_2Cu_3O_7/Y_2BaCuO_5$ composite where the Y-211 precipitates imbedded in the superconducting matrix can be observed.

is initiated only at the seed and still providing enough driving force to the growth front. *In situ* optical observation of the growth process shows that a progressive decrease of the growth rate may occur, probably because of a change of the liquid composition (Gautier-Picard *et al.* 1997).

Analysis and control of the microstructure of the single-domain material is essential, both to understand the growth process and to optimize the superconducting performance. Several additives are included in the green pellets to minimize the liquid loss and refine the final size of the Y-211 precipitates, which remain embedded in the matrix as a consequence of the sluggish character of the peritectic reaction. Platinum and CeO_2 particles are found to fulfill perfectly this second requirement by keeping the Y-211 particles in the submicrometer range, thus avoiding the coarsening of Y-211 particles in the semisolid state (Fig. 2).

The beneficial effects of the Y-211 precipitates are twofold: they increase the mechanical toughness and they enhance the critical currents that rise typically to $5 \times 10^4\,A\,cm^{-2}$ at 77 K and null field. A typical optimal composition of Y-123/211 ceramic tiles used for magnetic levitation would be 64% $YBa_2Cu_3O_7$ + 35% Y_2BaCuO_5 + 1% CeO_2.

Large batch processes of up to 30 samples having diameters of 40 mm have been demonstrated using quasi-isothermal furnaces with a good reproducibility of their performance. Thus there is no major limitation to scale-up of the TSG process to industrial production (Cardwell *et al.* 1998, p. 75, Ullrich *et al.* 1999).

Additionally, it is well known that the superconducting properties of the Y-123/211 composites may be strongly modified through changes of the microstructure (Sandiumenge *et al.* 1997). Postprocessing methodologies, such as oxygenation, isostatic pressing, or irradiation, show strong modification of the critical currents of Y-123/211 melt textured ceramics. For instance, an enhanced pinning capability with

$J_c \approx 10^5 \, \mathrm{Acm}^{-2}$ at 77 K has been demonstrated through a cold isostatic pressing postprocessing treatment at 300 °C under 2 kbar of argon (Martinez *et al.* 1999). This process generates nanometric stacking fault loops that are very effective vortex pinning centers. Its potential relies in the enhanced levitation force that can be obtained in large-scale ceramic fabrication.

New effective flux pinning centers have also been generated in Re-123 (Re = Nd, Sm) materials displaying a large fishtail effect at 77 K. Actually, these materials form a solid solution, $\mathrm{Re}_{1+x}\mathrm{Ba}_{2-x}\mathrm{Cu}_3\mathrm{O}_{7+\delta}$, and the degree of Re substitution at the barium sites can be controlled through processing. When a small excess, in the region $x \approx 0.05$, is included there is a tendency to the formation of nanometric clusters where the local oxygen content is higher. These nanometric clusters have a decreased superconducting order parameter and consequently they become normal when a magnetic field is applied, thus becoming flux pinning centers at intermediate fields. The final concentration of neodymium excess and its pinning effectiveness is found to depend on the oxygenation pressure during the growth and postprocessing treatment (Puig *et al.* 1998).
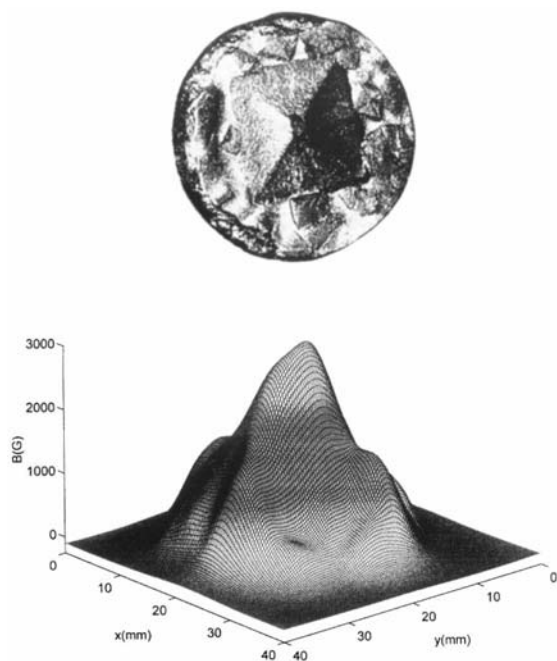
Figure 3
Micrograph of a $\mathrm{YBa}_2\mathrm{Cu}_3\mathrm{O}_7$ pellet prepared by TSG and flux remanence profile of the superconducting cylinder after a partial penetration of magnetic flux in a zero-field cooling process. The observed asymmetries correspond to subgrain boundaries within a single domain.

The potential of Re-123 ceramic tiles for use in magnetic levitation or as trapped-field magnets appears to be very high; however, owing to the complexity of their phase diagrams the preparation process must be tightly controlled (Murakami 1998).

The most successful nondestructive testing methodologies of the final superconducting tiles are the measurement of the levitation force, which may be considered as an integral process, or the determination of the magnetic remanence flux profiles by means of Hall effect microprobes. In the latter case, it appears very easy to detect any remaining grain boundary or even subgrain boundaries and macroscopic compositional inhomogeneities (Fig. 3).

Demonstrations that bulk melt textured tiles may be integrated in real systems such as magnetic bearings, motors, flywheels, etc., continue. In this respect, the feasibility appears very promising of cutting, assembling, or even welding these materials for large-diameter rotors or the buildup of more complex shapes (Cardwell *et al.* 1998).

See also: Magnetic Levitation: Superconducting Bearings; Superconducting Permanent Magnets: Potential Applications; Superconducting Permanent Magnets: Principles and Results

Bibliography

Cardwell D A, Murakami M, Salama K 1998 Processing and applications of superconducting (Re)BCO large grain materials. *Mater. Sci. Eng.* **B53**, 1–237

Gautier-Picard P, Beaugnon E, Tournier R 1997 In-situ $\mathrm{YBa}_2\mathrm{Cu}_3\mathrm{O}_x$ growth analysis. *Physica C* **276**, 35–41

Martínez B, Richard L, Sandiumenge F, Puig T, Rabier J, Obradors X 1999 Enhanced critical currents in melt textured $\mathrm{YBa}_2\mathrm{Cu}_3\mathrm{O}_7$ by cold isostatic pressing. *Appl. Phys. Lett.* **74**, 73–5

Moon F C 1994 *Superconducting Levitation*. Wiley, New York

Murakami M 1998 Key issues for the characterization of Re–Ba–Cu–O systems (Re: Nd, Sm, Eu, Gd). *Appl. Supercond.* **6**, 51–9

Sandiumenge F, Martínez B, Obradors X 1997 Tailoring of microstructure and critical currents in directionally solidified $\mathrm{YBa}_2\mathrm{Cu}_3\mathrm{O}_7$. *Supercond. Sci. Technol.* **10**, A93–119

Puig T, Obradors X, Martínez B, Alonso J A 1998 Enhanced interface and aging by high pressure oxygenation of melt textured $\mathrm{Nd}_{1+x}\mathrm{Ba}_{2-x}\mathrm{Cu}_3\mathrm{O}_{7-\delta}$. *Physica C* **308**, 115–22

Sawamura M 1999 *Recent activity of bulk material development and application. Workshop on Bulk High Temperature Superconductors and their Applications*. Argonne National Laboratory, Argonne, IL

Ullrich M, Walter H, Leenders A, Freyhardt H C 1999 Batch production of high-quality customized-shaped monolithic HTSC. *Physica C* **311**, 86–92

X. Obradors and T. Puig
Institut de Ciéncia de Materials de Barcelona
Spain

Magnetic Levitation: Superconducting Bearings

Passive superconducting bearings are based on the stable levitation of a permanent magnet over a bulk superconductor. This stable levitation is due to the pinning of magnetic flux surrounding the permanent magnet on defects within the superconductor. The interest in superconducting bearings strongly increased since bulk, melt-textured $YBa_2Cu_3O_{7-x}$ (YBCO) is available, because this high-temperature superconductor exhibits large critical current densities at liquid nitrogen temperatures. Superconducting bearings can be used for rotating machines and for linear transportation systems. The main parameters of superconducting bearings as the levitation force and the magnetic stiffness will be discussed.

1. Levitation and Superconducting Magnetic Bearings

One of the most promising applications of bulk high-T_c superconductors is the superconducting levitation which can be used in rotating superconducting magnetic bearings and in noncontact linear transportation. The advantage of superconducting magnetic bearings is that the levitation of a ferromagnetic permanent magnet over a bulk YBCO sample is completely passive. Contrary to this, no stable levitation is possible for two permanent magnets which interact via a $1/r^2$ force law the Earnshaw's theorem (Earnshaw 1842). Such an inverse square law is governed by the Laplace equation and allows only saddle-type equilibria resulting in unstable levitation. Therefore, conventional magnetic bearings composed of ferromagnetic permanent magnets require an active feedback control in order to stabilize the levitation. Inherently stable levitation can be achieved by introducing diamagnetic materials such as superconductors (Braunbeck 1939). The first superconducting bearing was developed for a small motor (Buchhold 1960) using low-temperature superconductors cooled with liquid helium. The interest in superconducting bearings strongly increased after the discovery of high-T_c superconductors (HTSs), when levitation experiments could be done in open styrofoam containers filled with liquid nitrogen. Rotating HTS bearings are particularly interesting for cryogenic turbopumps, superconducting motors, high-speed centrifuges, and for flywheel energy storage systems, whereas linear HTS bearings can advantageously used for noncontact transport systems in clean rooms of microelectronic factories.

2. Materials Aspects: Bulk YBCO Superconductors

The material of choice for superconducting bearings is bulk YBCO. YBCO has a superconducting transition temperature of 92 K and a relatively high irreversibility field of $H_{irr} \sim 7\,T$ at 77 K for magnetic fields oriented parallel to the crystallographic c-axis. Applications are restricted to magnetic fields below H_{irr}, because the critical current density disappears at the irreversibility field $H_{irr} < H_{c2}$ with H_{c2} as the upper critical field.

The levitation force of a superconducting bearing is proportional to the magnetization M of the bulk superconductor which is given by $M = Aj_c d$, where A is a constant, j_c is the critical current density, and d is the grain diameter. The trapped field properties and the critical current density of bulk, polycrystalline YBCO material with randomly oriented grains are strongly limited by its pronounced weak link behavior. Only very small currents are able to flow across the grain boundaries, especially if a magnetic field is applied. Weak links can be avoided by growing large grains using melt processing techniques. Several techniques have been found to be suitable for the growth of large single-domain YBCO material without high-angle grain boundaries (Murakami 1993, Krabbes *et al.* 1997).

In most cases, seed crystals (Sm-123 or MgO) are used in order to orientate the c-axis of the YBCO sample perpendicular to the plane surface of the sample. Large superconducting domains with a c-axis texture can be produced in this way. In the present state of the art, bulk, single-domain YBCO samples with diameters up to 10 cm can be produced.

3. Levitation Force

The most important feature of superconducting bearings is the levitation force between the superconductor and the permanent magnet. Other relevant properties of superconducting bearings are their stiffness and dynamic performance. Several reviews are available describing levitation forces and the application of superconducting bearings (Moon 1994, Hull 2000).

Stable levitation of a YBCO disk above a permanent magnet (see Fig. 1) can be achieved both from diamagnetic and flux pinning properties of the superconductor. The diamagnetic repulsive levitation is based on the flux exclusion and can be realized by cooling the superconductor below the superconducting transition temperature in a large distance from the permanent magnet. This is called zero-field cooling. In the case of YBCO, it is convenient to use liquid nitrogen as coolant. By reducing the distance between superconductor and permanent magnet, a
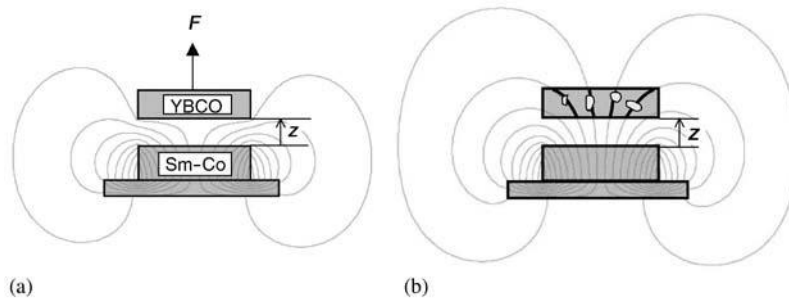
Figure 1
Superconducting magnetic bearing consisting of a YBCO disk and a permanent magnet. The iron plate below the permanent magnet is used to focus the magnetic flux on the superconductor. (a) Cooling of the YBCO disk in a large distance from the permanent magnet (zero-field cooling). If the distance is reduced, a repulsive force develops due to the diamagnetism of the superconductor. No magnetic flux penetrates the superconductor as shown by the magnetic field lines. (b) Cooling of the YBCO disk in a small distance from the permanent magnet (field cooling). The levitation force is based on the pinning of flux lines, i.e., by their interaction with defects within the superconductor.
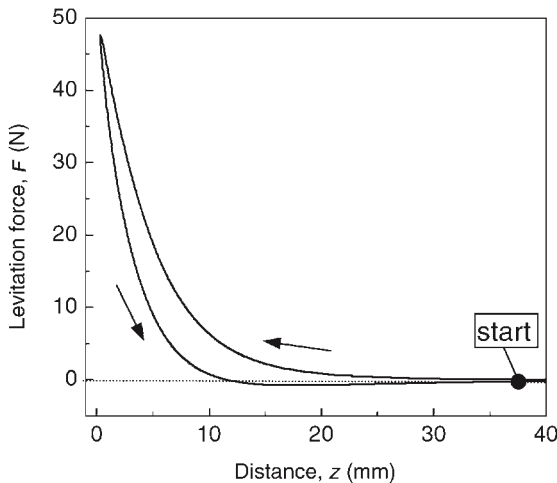
Figure 2
Vertical levitation force between a YBCO disk (diameter 25 mm) and an Sm–Co permanent magnet (diameter 25 mm) in dependence on the distance between superconductor and permanent magnet after zero-field cooling. The force is mainly repulsive. A very small attractive levitation force is observed only for increasing distance.

repulsive force develops. In Fig. 2, the vertical force between a YBCO disk (diameter 25 mm) and an Sm–Co permanent magnet (diameter 25 mm) is plotted against the vertical distance. The repulsive force increases as the magnet approaches the superconductor and reaches a maximum value for a small distance. The force at a given distance becomes smaller when the magnet is moved away from the superconductor.

This hysteretic behavior can be explained by the penetration of magnetic flux into the superconductor. A small attractive force component develops due to flux pinning and reduces the repulsive force for increasing distance between superconductor and magnet.

The case of zero-field cooling is impractical for superconducting bearings in which superconductors and permanent magnets are assembled at 300 K. In this case, the superconductors are cooled to below T_c in the presence of the magnetic field of the permanent magnets (field cooling). In type II superconductors discrete structures in the material, so-called flux lines, create paths for the magnetic flux. The motion of flux lines is prevented by their interaction with defects in the superconductor. Therefore, the field distribution of the permanent magnets is frozen within the superconductor. The pinning-assisted levitation after field cooling is generally more stable against displacements in the horizontal direction than the levitation after zero-field cooling. An example for the vertical force versus distance relation after field cooling is shown in Fig. 3. The force which is almost zero after field cooling becomes negative as the permanent magnet is moved away from the superconductor. This attractive force can be used for stable levitation via suspension, i.e., with the permanent magnet below the superconductor.

4. Upper Limit for the Bearing Pressure

The levitation force of a superconducting bearing is enhanced with increasing magnetization of the superconductor, the latter being proportional to the critical current density j_c and the diameter of a single-domain YBCO sample (see Sect. 2). The strong increase of the critical current density with decreasing temperature can be used to reach higher levitation
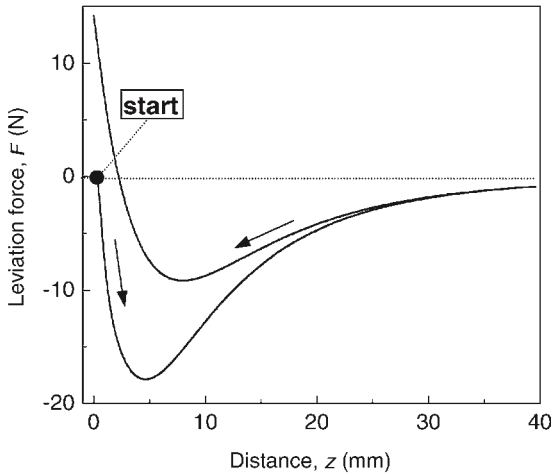
Figure 3
Vertical levitation force between a YBCO disk (diameter 25 mm) and an Sm–Co permanent magnet (diameter 25 mm) in dependence on the distance between superconductor and permanent magnet after field cooling. The levitation force is mainly attractive.

forces than at 77 K. However, the magnetization of the superconductor cannot exceed the magnetization value that is necessary to produce a diamagnetic image of the permanent magnet for zero-field cooling. The upper limit of the levitation force achievable for a given permanent magnet would be obtained for an ideal superconductor of infinite site and infinitely large critical current density that would perfectly shield the magnetic field of the permanent magnet. The resulting levitation force is equivalent to the interaction between the permanent magnet and its mirror magnet at zero gap and is given by (Teshima *et al.* 1996)

$$F_{\max} = AB_s^2/(2\mu_0) \tag{1}$$

where A is the magnet pole face and B_s is the surface field on the magnet face. By dividing this force by A one obtains the bearing pressure

$$F_{\max}/A = B_s^2/(2\mu_0) \tag{2}$$

For a maximum field strength of $B_s = 0.5$ T, which is typical for good rare earth magnets, the maximum achievable bearing pressure is $F_{\max}/A = B_s^2/(2\mu_0) \approx 31$ N cm^2. The experimental values for YBCO samples mentioned above achieve up to 70% of this upper limit. Much larger bearing pressures up to 5000 N cm^{-2} are expected if a superconducting permanent magnet with a trapped fields as high as 11 T would be used instead of a conventional permanent magnet. Such high trapped fields are available in bulk

YBCO at temperatures ~ 30 K (Gruss *et al.* 2001, Gonzales-Arrabal *et al.* 2002). The most important problem which has to be solved in order to utilize YBCO magnets for applications at temperatures lower than 77 K is to magnetize the superconductor. Pulsed magnetic fields can be used for magnetizing YBCO disks. However, large viscous forces act on the penetrating magnetic flux, especially in the case of short rise times (~ 1 ms) of the pulsed field. The heat generated by the rapid motion of magnetic flux strongly reduces the trapped field achievable at temperatures lower than 77 K. One possibility to overcome this problem is to increase the rise time of the pulsed field.

5. Rotating HTS Bearings

Simply designed thrust bearings (see Fig. 1) have an axial geometry, i.e., the bulk YBCO is assembled as a plane stator sandwiched by a permanent ring magnet which is connected to the rotor. However, the axial-type superconducting bearing has limitations with regard to the vertical levitation force F_z and magnetic stiffness. The stiffness is defined as the change of the force for a small displacement of the permanent magnet from its initial position. In order to improve the stiffness one can replace the permanent magnet in Fig. 1 by a set of concentric permanent ring magnets. Nevertheless, especially the horizontal stiffness dF_x/dx (for a displacement of the permanent magnet parallel to the superconductor) remains relatively small. In order to overcome these limitations, journal-type bearings have been developed (Kummeth *et al.* 2002, Schultz *et al.* 2002) in which a special arrangement of permanent magnets and iron disks leads to high magnetic gradients both in axial and radial direction. The bearing shown schematically in Fig. 4 consists of a YBCO hollow cylinder and stacks of permanent magnets and iron disks. Neighboring magnets in the YBCO hollow cylinder of the radial bearing are polarized in the opposite direction and separated by iron disks. In this way, the magnetic flux is focused on the gap between the magnets and guided in radial direction, generating a highly inhomogeneous field distribution within the superconductor. The large magnetic gradients obtained with such configurations result in high values of both radial and axial stiffness provided that the interface between the superconductor and the stack of magnets and iron disks is large enough. A radial stiffness of 160 N mm^{-1} was reported for such a bearing in which the YBCO hollow cylinder was 9 cm long and had an inner diameter of 4 cm (Schultz *et al.* 2002). The radial stiffness can be easily scaled up by increasing the radial dimension of the superconducting bearing. It is noteworthy that, independent of the bearing type, the horizontal stiffness dF_x/dx after field-cooling is exactly half the vertical stiffness dF_z/dz.

461
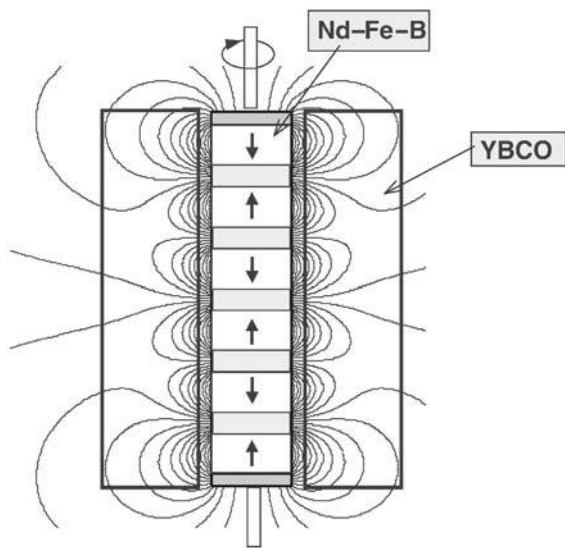
Figure 4
Schematic view of a superconducting magnetic bearing consisting of a YBCO hollow cylinder and a stack of Nd–Fe–B permanent magnets and iron disks (for details see text). The field distribution in the superconducting hollow cylinder after field cooling is shown. For the application in a rotating machine the YBCO hollow cylinder is held stationary, whereas the inner part with the magnets and iron disks is connected with the rotor of the machine.

6. Applications of HTS Bearings

Promising applications of rotating HTS bearings are cryogenic turbopumps, because in this case the cryogenic environment already exists. HTS bearings could replace the mechanical bearings of turbopumps which have very poor tribological properties at cryogenic temperatures. Of special interest are turbopumps (with HTS bearings) for liquid hydrogen which is considered as the fuel of the future. Another applications for which a cryogenic environment exists are superconducting reluctance motors in which large bulk YBCO pellets are used in the rotor in order to increase the energy density up to a factor of 2 (Oswald *et al.* 2003). High-speed centrifuges are another attractive application of HTS bearings. Prototype centrifuges designed with HTS bearings were successfully tested up to 30 000 rpm (Werfel *et al.* 2001). HTS bearings have a great potential to improve the performance of flywheels for energy storage. With HTS bearings the high-speed idling losses of flywheels can be drastically reduced to values of 0.1% per hour compared to 1% per hour for flywheels with conventional bearings. This would allow to construct flywheels with a 90% diurnal storage efficiency. In flywheels prototypes with HTS

bearings, energies in the range of more than 1 kWh have already been stored (Nagaya *et al.* 2001).

Promising applications of linear HTS bearings are noncontact transport systems in clean-room environments of microelectronic factories, where the contactless motion would not create any wear debris, in track-bound individual traffic systems, or in elevators (Schultz *et al.* 2002).

7. Summary

The most promising application of bulk HTS is the development of HTS bearings utilizing the inherently stable levitation between the bulk HTS and permanent magnets. The main parameters of HTS bearings as the levitation forces and magnetic stiffness depend on the properties of superconductor and permanent magnet. Large melt-textured YBCO with high critical current densities are now available. As a result of the large progress in this field, the bearing pressure of modern HTS bearings, i.e., the levitation force divided by the area of the permanent magnet, is mainly limited by the surface field of the permanent magnet. HTS bearings operating at 77 K can be used in order to realize frictionless support in rotating machines (as flywheels for energy storage, superconducting motors, cryogenic pumps, high-speed centrifuges), and for frictionless linear transportation. The latter should allow transportation of extremely heavy objects which can no longer be moved by wheel systems, like concrete ports or moving bridges. Moreover, contactless transportation which does not create any wear debris can advantageously be used in clean rooms in the microelectronics industry.

See also: Magnetic Levitation: Materials and Processes; Superconducting Machines: Energy Storage; Superconducting Permanent Magnets: Potential Applications; Superconducting Permanent Magnets: Principles and Results

Bibliography

Braunbeck W 1939 Freies Schweben diamagnetischer Körper im Magnetfeld. *Z. Physik.* **112**, 764–79
Buchhold T A 1960 Applications of superconductivity. *Sci. Am.* **202** (3), 74
Earnshaw S 1842 On the nature of molecular forces which regulate the constitution of luminiferous ether. *Trans. Cambridge Phil. Soc.* **7**, 97–112
Gonzales-Arrabal R, Eisterer M, Weber H W, Fuchs G, Verges P, Krabbes G 2002 Very high trapped fields in neutron irradiated and reinforced $YBa_2Cu_3O_{7-\delta}$ melt-textured superconductors. *Appl. Phys. Lett.* **81**, 868–70
Gruss S, Fuchs G, Krabbes G, Verges P, Stöver G, Müller K H, Fink J, Schultz L 2001 Superconducting bulk magnets: very high trapped fields and cracking. *Appl. Phys. Lett.* **79**, 3131–3
Hull J R 2000 Superconducting bearings. *Supercond. Sci. Technol.* **13**, R1–15

Krabbes G, Schätzle P, Bieger W, Fuchs G, Wiesner U, Stöver G 1997 Thermodynamically controlled melt processing to improve bulk materials. *IEEE Trans. Appl. Supercond.* **7**, 1735–8

Kummeth P, Nick W, Ries G, Neumüller H W 2002 Development of superconducting magnetic bearings. *Physica C* **372–376**, 1470–3

Moon F C 1994 *Superconducting Levitation*. Wiley, New York

Murakami M 1992 Processing of bulk YBaCuO. *Supercond. Sci. Technol.* **5**, 185–203

Nagaya S, Kashima N, Minami M, Kawashima H, Unisuga S, Kakiuchi Y, Ishigaki H 2001 Study on characteristics of high temperature superconducting magnetic trust bearing for 25 kWh flywheel. *Physica C* **357–360**, 866–9

Oswald B, Krone M, Strasser T, Best K J, Soell M, Gawalek W, Gutt H J, Kovalev L, Fisher L, Fuchs G, Krabbes G, Freyhardt H C 2003 Design of HTS reluctance motors up to several hundred kW. *Physica C* **372–376**, 1513–6

Schultz L, Krabbes G, Fuchs G, Pfeiffer W, Müller K H 2002 Superconducting permanent magnets and their application in magnetic levitation. *Z. Metallkd.* **93**, 1057–64

Teshima H, Morita M, Hashimoto M 1996 Comparison of the levitation forces of melt-proessed YBaCuO superconductors for different magnets. *Physica C* **269**, 15–21

Werfel F N, Flögel-Delor U, Rothfeld R, Wippich D, Riedel T 2001 Centrifuge advances using HTS magnetic bearings. *Physica C* **354**, 13–7

G. Fuchs
IFW, Dresden, Germany

Magnetic Losses

The term magnetic losses generically refers to the various energy dissipation mechanisms taking place when a magnetic material is subject to a time-varying external field $H(t)$. As a consequence of the inherent irreversible nature of magnetization processes, part of the energy injected into the system by the external field is irrevocably transformed into heat. A case of particular interest is the one where the material is subject to a cyclic field of frequency f, with the field and the average magnetic induction B in the material remaining colinear during the process.

Then the time integral

$$W = \int H \frac{dB}{dt}\, dt \qquad (1)$$

over one magnetization cycle gives the energy per unit volume transformed into heat in the cycle. This integral is usually termed *loss per cycle*, whereas the term *power loss* is used to denote the loss per unit time $P = fW$.

Simple expressions can be derived for W when the equilibrium relationship between field and induction in the material is linear, $B = \mu H$, and the delayed response to time variations of the field is characterized

by the single time constant τ. Then, the loss per cycle under sinusoidal field can be expressed as

$$W = \frac{2\pi^2 \tau}{\mu} B^2 f \qquad (2)$$

where B represents the induction peak value in the cycle. Under these conditions: (i) hysteresis loops are elliptical—that is, the system response to the sinusoidal field is sinusoidal; and (ii) the loss per cycle is proportional to the frequency.

When the system is still linear but the dynamic response is controlled by multiple time constants, Eqn. (2) takes the more general form

$$W = \frac{\pi}{\mu} B^2 \mathrm{tg}\phi \qquad (3)$$

where the parameter ϕ, the so-called *loss angle*, measures the lag of the induction with respect to the field. The loss behavior is governed by the dependence of ϕ on frequency. In general, $\phi \to 0$ when $f \to 0$, i.e., the loss vanishes under quasi-static excitation, where the material response must reduce to the dissipationless linear law $B = \mu H$. In the particular case of Eqn. (2), $\mathrm{tg}\phi = 2\pi f\tau$.

Magnetic materials are inherently nonlinear hysteretic systems where strong deviations from the behavior described by Eqns. (2) and (3) are observed. The loss per cycle is a nonlinear function of frequency and the response to a sinusoidal excitation is usually heavily distorted. In addition, the loss depends not only on the magnetization frequency f and the peak induction B, but also on the induction wave-shape, which means that losses under sinusoidal induction are in general different from losses under triangular induction at the same peak induction and frequency. International standards require that magnetic losses be measured under controlled sinusoidal induction rate and give detailed prescriptions about admitted methods and tolerances in the realization of the appropriate test conditions.

Various mechanisms are active during the magnetization process and can contribute to magnetic losses. Examples are the generation and decay of spin waves or acoustic waves, and, in metals, the decay by the Joule effect of the electric currents (eddy currents) induced by the induction changes in the material. These mechanisms are all activated by the motion of the domain walls separating different magnetic domains or by the large-scale instabilities accompanying the nucleation and annihilation of magnetic domains (see also *Magnets, Soft and Hard: Domains*). The chief problem in the study and application of magnetic materials is the prediction of the complex loss behavior observed in experiments in terms of these mechanisms.

Eddy current effects are dominant in metallic soft magnetic materials, where the principal magnetization process is just the eddy-current-damped motion

of magnetic domain walls. The loss figure is the fundamental quality parameter used to monitor material production and to select the materials best suited to particular applications. In the following sections, attention will be mainly focused on magnetic losses in metallic materials. Other loss aspects not discussed in this article arise in relation to magnetic after-effects (see *Magnetic Viscosity*) and resonance phenomena (see *Nuclear Magnetic Resonance Spectrometry*).

1. Loss Separation

The typical behavior of dynamic hysteresis loops and magnetic losses in a metallic soft magnetic material is shown in Figs. 1 and 2. The following points should be noted:

- the dynamic loops are far from elliptical, with shapes strongly dependent on frequency, peak induction, and material microstructure;
- the loop area W is a nonlinear function of f, the nonlinearity being more pronounced at low frequency;
- the loop area W tends toward a nonzero limit when the magnetization frequency is reduced toward zero: this value is referred to as (quasi-)static loss or hysteresis loss;
- the loss significantly increases above the quasi-static limit already at frequencies of a few Hz.

The physical picture underlying this complex behavior is clear in principle (Cullity 1972). A change of induction always accompanies the motion of a domain wall. Because of Faraday's law, this change gives rise to a rotational electric field **E** around the
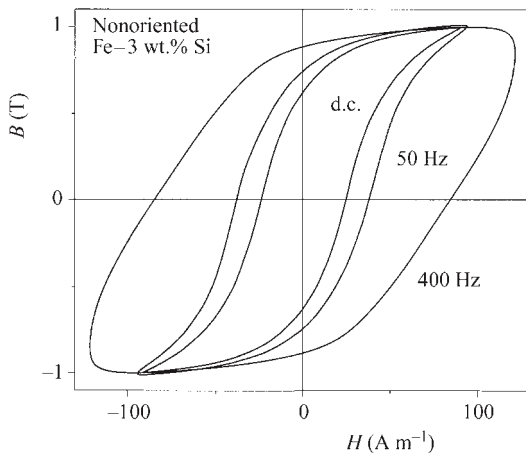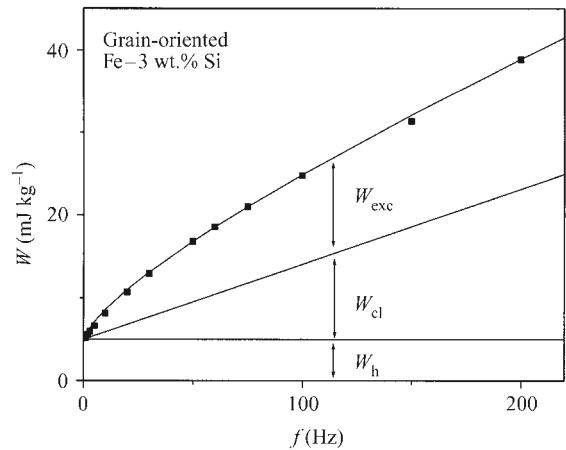
Figure 2
Loss per cycle and per unit mass as a function of frequency for a grain-oriented Fe–3 wt.% Si lamination 0.30 mm thick. The hysteresis (W_h), classical (W_{cl}), and excess (W_{exc}) loss components involved in loss separation are indicated (courtesy of Luciano Rocchino).

moving wall and consequently to an electric current density $\mathbf{j} = \sigma \mathbf{E}$ (eddy current), where σ is the electrical conductivity of the material. Therefore, in any elementary volume Δv of the material, the power $(|\mathbf{j}|^2/\sigma)\Delta v$ is dissipated through the Joule effect. The total loss is obtained by summing up these contributions over all elementary volumes. The result will depend on the space–time details of the eddy-current density $\mathbf{j}(\mathbf{r},t)$. This function will be as complicated as typical magnetic domain structures are, and a straightforward calculation of the loss by direct integration is impossible in the majority of cases.

Given the complexity of the problem, in practice one looks for phenomenological laws summarizing in simple terms the regularities observed in experiments. Most useful in this respect is the concept of *loss separation*, according to which the total power loss P at frequency f is decomposed into the sum of three contributions, P_h, P_{cl}, and P_{exc}, termed *hysteresis loss, classical loss*, and *excess loss*, respectively (see Fig. 2), such that

$$P = P_h + P_{cl} + P_{exc} \tag{4}$$

This deconvolution reflects the existence of three scales in the magnetization process: the scale set by the specimen geometry (classical loss), the scale of domain wall-pinning mechanisms (hysteresis loss), and the scale of magnetic domains (excess loss). Given the complex, strongly nonlinear character of the magnetization process, there is no obvious reason why the superposition law expressed by Eqn. (4) should hold true under broad conditions. In fact, it is

Figure 1
Typical dynamic hysteresis loops for a nonoriented Fe–3 wt.% Si lamination 0.35 mm thick, measured under controlled sinusoidal induction rate at a peak induction of 1 T and at different frequencies (quasi-static (d.c.), 50 Hz, 400 Hz).

only by applying statistical methods to the analysis of stochastic magnetization processes that one is able to show that the three scales just mentioned affect the loss in an approximately statistically independent way (Bertotti 1998).

1.1 Classical Loss

The classical loss is the loss calculated from Maxwell equations for a perfectly homogeneous conducting medium, that is, with no structural inhomogeneities and no magnetic domains (Bozorth 1993). The scale relevant to the classical loss is the scale set by the system geometry—for example, in a lamination, the slab thickness d. This scale controls the boundary conditions for Maxwell equations, which in turn determine the distribution of eddy currents in the specimen cross-section and the ensuing Joule dissipation. The classical loss acts as a sort of background loss, present under all circumstances, to which other contributions are added when structural disorder and magnetic domains play a role. By solving Maxwell equations, one finds that the classical loss takes the form

$$P_{cl} = \frac{\pi^2 \sigma d^2}{6} (Bf)^2 \quad (\mathrm{W\,m^{-3}}) \tag{5}$$

when it is calculated for a lamination of thickness d and electrical conductivity σ, magnetized at the frequency f and at the peak induction B. As mentioned before, the loss does depend on the induction waveform even when f and B are fixed. Equation (5) is valid under sinusoidal induction. The minimum loss is attained under triangular induction (i.e., constant dB/dt in each magnetization half-cycle). In that case, the coefficient $\pi^2/6$ is reduced to $4/3$.

Equation (5) contains no parameter describing the magnetization law of the material. All materials behave in the same way if their geometry and their electric properties are the same. This remarkable simplification derives from the fact that Eqn. (5) is actually a low-frequency limit, valid only when the induction rate dB/dt is approximately uniform throughout the lamination thickness. With increasing frequency, this is no longer the case. The magnetic field produced by eddy currents, being opposed to the external field, tends to inhibit magnetization reversal in the interior of the lamination. This eddy-current shielding effect yields deviations from Eqn. (5) that depend on the magnetization law of the material (Mayergoyz 1998). In the case of a linear magnetization law, $B = \mu H$ and in the limit of heavy shielding, i.e., $\sigma \mu d^2 f \gg 1$, instead of Eqn. (5) one obtains

$$P_{cl} = \frac{\pi^{3/2}}{2} \sqrt{\frac{\sigma d^2}{\mu}} B^2 f^{3/2} (\mathrm{W\,m^{-3}}) \tag{6}$$

In a silicon steel lamination with $\sigma \cong 2 \times 10^{-6} \Omega^{-1} \mathrm{m^{-1}}$, $\mu/\mu_0 \cong 2 \times 10^3$ ($\mu_0 = 4\pi \times 10^{-7} \mathrm{TmA^{-1}}$ is the permeability of the vacuum), and $d \cong 3 \times 10^{-4}$ m, one finds that $\sigma \mu d^2 f \cong 1$ at frequencies $f \cong 2$ kHz. Conversely, whenever field amplitudes much larger than the material coercive field are involved, it may be appropriate to approximate the magnetization law of the material by a step function, jumping between opposite values of maximum induction when the field changes sign. Under these conditions, the loss takes the value

$$P_{cl} = \frac{\pi^2 \sigma d^2}{4} (Bf)^2 \quad (\mathrm{W\,m^{-3}}) \tag{7}$$

This expression is simply 3/2 times the low-frequency limit of Eqn. (5).

1.2 Hysteresis Loss

Hysteresis losses are the consequence of the fact that on the microscopic scale the magnetization process proceeds through sudden jumps of the magnetic domain walls that are unpinned from defects or other obstacles by the pressure of the external field (see also *Magnetic Hysteresis*). The local eddy currents induced by the induction change accompanying the wall jump dissipate a finite amount of energy through the Joule effect.

The sum over all jumps gives the hysteresis loss associated with the jump sequence. The jumps are so short (of the order of 10^{-8}–10^{-9} s) that the external field is unable to influence the internal jump dynamics. The only effect of the field is to compress or expand the time interval between subsequent jumps in inverse proportion to the field rate of change, which yields a number of jumps per unit time and an amount of energy dissipated per unit time proportional to the magnetization frequency. Therefore, for the hysteresis loss in a loop of peak induction B, one obtains the typical expression

$$P_h = 4k_{hyst}B^{\alpha}f \tag{8}$$

The loss per cycle $W_h = P_h/f$ is thus independent of frequency (see Fig. 2). The parameter k_{hyst} and the exponent α include the structural aspects affecting domain wall pinning and magnetization reversal. Their value will differ from material to material. The rule $\alpha = 1.6$ has been claimed to have some general validity and is known in the literature as Steinmetz law (Bozorth 1993).

The hysteresis loss is intimately related to the structural disorder in the material. Possible sources of domain wall pinning are interstitials, nonmagnetic or less-magnetic inclusions, voids, or dislocations. At a higher level of complexity, dislocation tangles and grain boundaries play a role. In amorphous alloys, fluctuations of local exchange and anisotropy should be taken into account, but often, in all cases where magnetostriction is not negligible, magnetoelastic coupling to randomly distributed internal stresses

dominates. Finally, in thin ribbons, surface roughness may be a substantial source of pinning effects.

1.3 Excess Loss

Excess losses arise from the existence of a third relevant scale in the magnetization process, the scale of magnetic domains. The excess loss results from the smooth, large-scale motion of domain walls across the specimen cross-section, when the fine-scale jumps responsible for the hysteresis loss are disregarded. Eddy currents tend to concentrate around the moving domain walls, a fact that gives rise to losses higher than the classical ones because of the quadratic dependence of the local loss $(|\mathbf{j}|^2/\sigma)\Delta v$ on the intensity of the eddy-current density (Williams *et al.* 1950, Pry and Bean 1958).

According to the picture just described, excess losses are expected to be as ubiquitous as the presence of magnetic domains. However, the importance of excess losses in comparison with classical and hysteresis losses will substantially depend on the size and arrangement of magnetic domains. As a general rule, the finer the domain structure, the smaller the excess loss contribution. This conclusion can be given a precise quantitative measure in the case of a lamination of thickness d containing longitudinal bar-like magnetic domains of random width (Bishop 1976). In this case, Maxwell equations can be exactly solved, giving the result

$$P_{exc} = \left(\frac{48}{\pi^3} \sum_{odd\ n} \frac{1}{n^3}\right)\frac{2L}{d}\ P_{cl} \cong 1.63\ \frac{2L}{d}\ P_{cl} \qquad (9)$$

where $2L$ represents the average domain width and P_{cl} is given by Eqn. (5). Equation (9) identifies the ratio $2L/d$ as the relevant parameter of the problem. The excess loss is proportional to $2L/d$ and becomes negligible with respect to the classical loss when the domain width is much smaller than the lamination thickness.

This prediction is helpful in the interpretation of losses in grain-oriented silicon steels, where domain structures are often not far from the one assumed in the model. However, one should not forget that the regular arrangement of longitudinal domains assumed in the model can be far from the conditions encountered in ordinary materials. In many cases, the domain size is no longer itself the important parameter, because microstructural features introduce additional characteristic lengths (e.g., grain size, fluctuation wavelength of residual stresses, etc.) that tend to control the loss problem.

In these more complex cases, the excess loss approximately follows a law of the type (Bertotti 1998)

$$P_{exc} = k_{exc}\sqrt{\sigma}(Bf)^{3/2} \quad [\text{W m}^{-3}] \qquad (10)$$

where the parameter k_{exc} includes the effect of the various relevant microstructural factors. Equation (10) applies to grain-oriented silicon steels too, a fact that should not be interpreted as a contradiction with respect to Eqn. (9). The point is that the ratio $2L/d$ in Eqn. (9) is unknown. In particular, there is no reason why this ratio should be a constant of the material. In fact, one finds that the average magnetic domain size decreases when the magnetization frequency is increased, through the nucleation of additional domains. This domain multiplication process, together with other dynamic effects—particularly domain wall bowing (Carr 1976)—makes the dependence of losses on frequency weaker than the quadratic one of Eqn.(9) and eventually yields a loss law of the form of Eqn. (10).

1.4 Factors Affecting the Total Loss

According to the previous analysis, an approximate expression for the total power loss, valid at frequencies low enough to avoid the onset of important eddy-current shielding, is

$$P \cong 4k_{hyst}B^{\alpha}f + \frac{\pi^2\sigma d^2}{6}(Bf)^2$$
$$+ k_{exc}\sqrt{\sigma}(Bf)^{3/2} \quad (\text{W m}^{-3}) \qquad (11)$$

Classical losses depend on the combination σd^2, which shows that the losses are smaller the smaller the electrical conductivity and the lamination thickness. Magnetic cores of machines and devices are never made of bulk material for this reason. On the other hand, one of the factors that favored the introduction of silicon steels was just the fact that the addition of a few percent of silicon strongly reduces the electrical conductivity without substantially changing the other magnetic properties.

The hysteresis loss is independent of the electrical conductivity σ. The amount of energy dissipated in individual wall jumps is determined by the height of the energy barrier created by the pinning obstacle. A change in the conductivity would alter the typical velocity attained by the domain wall during the jump, but not the amount of energy eventually dissipated as heat. The hysteresis loss is also expected to be fairly independent of the lamination thickness when pinning effects are volume effects. The situation is different when the surface of the lamination also acts as a relevant pinning source. In this case, the hysteresis loss increases when the lamination thickness is reduced.

Equation (11) applies to the particular case of a material magnetized under controlled sinusoidal induction rate. However, there are several situations where magnetic materials operate under distorted flux conditions, for which a generalization of Eqn. (11) is needed. This generalization is obtained

by calculating the instantaneous power loss at individual points of the magnetization cycle and then by carrying out the time average over the particular wave-shape involved. This more general expression reads (Fiorillo and Novikov 1990)

$$P \cong P_h + \frac{\sigma d^2}{12}\overline{\left[\frac{dB}{dt}\right]}^2 + k'_{exc}\sqrt{\sigma}\overline{\left|\frac{dB}{dt}\right|}^{3/2} [\text{W m}^{-3}] \quad (12)$$

where the bars indicate time averaging over the magnetization cycle. The hysteresis loss is independent of the induction wave-shape, provided the induction is monotone in each magnetization half-cycle (no generation of inner hysteresis loops during the cycle).

2. Loss Behavior in Different Magnetic Materials

The dependence of losses on frequency and induction results from the combination of the three terms of Eqn. (11). The final behavior can be rather different from material to material, depending on the relative contribution of the various loss components to the total loss (Bertotti 1988) (see Fig. 3). When the objective is loss reduction, it is vital to identify the loss term giving the dominant contribution under the working conditions of interest and then to develop optimization strategies for the magnetization scale associated with that term. Metallurgical factors, structural optimization, and control of domain structures play a role in these optimization strategies.
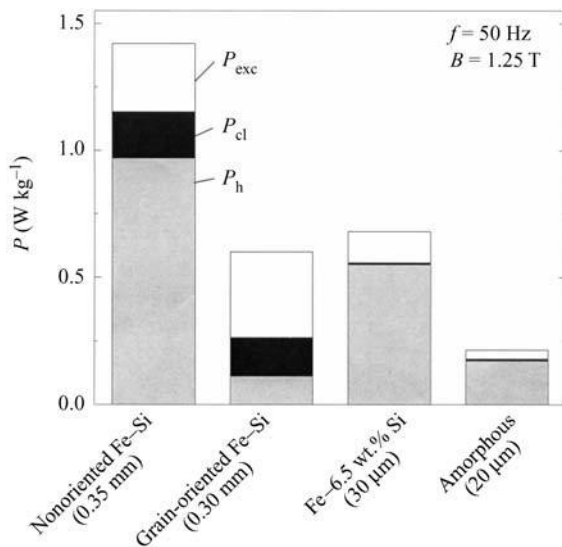
Figure 3
Examples of loss separation in different classes of soft magnetic materials, at 50 Hz magnetization frequency and 1.25 T peak induction.

2.1 Iron and Low-carbon Steels

Low-carbon steels, with a typical carbon content from 0.005 to 0.1 wt.%, are used as low-grade, low-cost materials for magnetic cores where magnetic losses are not the major concern and acceptable performance at low price is the main goal. This is reflected in the fact that these materials are usually produced as fairly thick laminations (typical thickness ranges from 0.5 to 0.85 mm) which causes substantial classical losses. The presence of carbon yields important aging effects, i.e., a progressive increase of the hysteresis loss over time. This is due to the formation of cementite precipitates, which act as additional domain wall pinning centers. Materials with improved loss properties are obtained by purification processes, which reduce the carbon, nitrogen, and sulfur content, or by the introduction of some silicon (up to 1 wt.%). When no particular purification processes are carried out and the silicon content is negligible, total losses take values of the order of 15 W kg^{-1} at 1.5 T and 60 Hz in laminations 0.5 mm thick. The addition of about 1 wt.% Si accompanied by better composition control can lower the loss to less than 8 W kg^{-1}. Very clean ultra-low-carbon steels can reach loss figures as low as 4 W kg^{-1} at 1.5 T and 50 Hz in 0.5 mm laminations.

2.2 Silicon Steels

Silicon steels are iron-based materials where a few percent of soluble elements, like silicon or aluminum, are deliberately introduced. The addition of silicon causes a substantial increase in the electrical resistivity, with a consequent decrease in classical and excess losses. In addition, silicon alloying yields a decrease in the magnetocrystalline anisotropy constant, which results in a decrease in the hysteresis loss. The main limitation to excessive addition of silicon comes from the progressive reduction of the saturation magnetization and the increase in brittleness of the material (see also *Steels, Silicon Iron-based: Magnetic Properties*).

Silicon steels are divided into two main categories: nonoriented steels and grain-oriented steels. Nonoriented steels are characterized by an approximate isotropic grain structure. This makes them suitable for all those applications where fairly isotropic magnetic properties are needed. The silicon concentration ranges from about 1 to 3.7 wt.%. Some aluminum and manganese is also added to achieve higher electrical resistivity with no detrimental effects on the mechanical properties. The top-grade materials have about 4 wt.% Si + Al and exhibit losses of 2.1–2.3 W kg^{-1} at 1.5 T and 50 Hz in laminations 0.35–0.50 mm thick. Materials with improved losses are developed by a careful control of impurity content, grain size, crystallographic texture, surface state, and residual stresses. Impurities like carbon,

nitrogen, sulfur, and oxygen contribute to increasing hysteresis losses, because they form precipitates that act as pinning centers on moving domain walls. They also have an indirect detrimental effect, because they hinder grain growth and negatively affect the formation of favorable textures. Finally, the control of grain size is important. The hysteresis loss is a decreasing function of the average grain size s, and usually follows a law of the type $P_h \cong a + b/s$, where a and b are material-dependent constants. Conversely, the excess loss is an increasing function of s, of the type $P_{exc} \cong ks^{\beta}$, with $\beta \sim 1/2$. As a result, the total loss has a minimum for a particular grain size. Material manufacturers try to obtain materials with optimal loss performance by appropriate grain-growth treatments. The optimal grain size is of the order of 150 μm at 1.5 T and 50 Hz.

Contrary to nonoriented steels, grain-oriented steels are characterized by strongly anisotropic properties. These materials contain between 2.9 and 3.2 wt.% Si. As the result of highly sophisticated metallurgical processes of selective grain growth, a grain-oriented lamination is characterized by a particular texture, known as Goss texture, in which all the crystal grains have one of their [001] axes close to the lamination rolling direction. This fact, together with the large grain size of these materials (in the millimeter–centimeter range) and the low impurity content yields hysteresis losses about one order of magnitude lower than those typical of nonoriented steels, when the lamination is magnetized along the rolling direction. Grain-oriented steels are further subdivided into conventional grain-oriented (CGO) and high-permeability grain-oriented (HGO) materials.

The main difference is the more accurate texture control realized in HGO materials which yields better loss performance. In CGO steels, the lamination thickness ranges from 0.35 to 0.23 mm and the loss accordingly ranges from 1.4 to 1.15 Wkg^{-1} at 1.7 T and 50 Hz. In HGO steels, the lamination thickness ranges from 0.30 to 0.23 mm and the loss from 1.05 to 0.80 Wkg^{-1} at 1.7 T and 50 Hz. The more refined texture control of HGO materials is reflected in the magnetic domain structure. In fact, the nearly perfect grain orientation yields very regular structures of wide longitudinal bar-like domains, quite similar to the ones assumed in the calculation of Eqn. (9). The regularity of the domain structure and the material perfection (very low impurity content and lack of grain boundary effects because of the large grain size) give a very low hysteresis loss. However, as shown by Eqn. (9), the excess loss may attain substantial values when wide domains are present ($2L/d \gg 1$).

For this reason, methods aimed at artificially reducing the domain size without altering the hysteresis loss have been developed. Two of them are of particular interest:

- deposition of a coating on the lamination surface that exerts a tensile stress of 2–10 MPa on the material. The stress introduces a magnetoelastic energy contribution that alters the energy balance in the material and favors the formation of smaller magnetic domains;
- scribing of the lamination surface by one among many possible techniques (mechanical scratching, laser irradiation, plasma jet scribing, or etch pitting). Scribing alters the magnetoelastic and magnetostatic energy content of the lamination in a way that again favors the formation of smaller domains.

The power loss at 1.7 T and 50 Hz is as low as 0.80 Wkg^{-1} in coated, scribed laminations of 0.23 mm thickness.

2.3 Rapidly Solidified Materials

Soft magnetic materials can be prepared as very thin ribbons by means of rapid solidification methods, in particular by planar-flow-casting. The resulting ribbons have variable width (up to 20 cm and more) and a thickness of 10–100 μm. The reduced thickness inhibits classical losses (see Fig. 3) and makes these materials suited to high-frequency applications, where classical losses play the most detrimental role. On the other hand, rapid solidification permits the preparation of materials in a variety of quenched metastable states not present in the equilibrium phase diagram, which display a broad range of interesting magnetic and mechanical properties.

Amorphous ribbons, lacking long-range atomic order, are prepared by rapid solidification of alloys containing around 80 at.% transition metals and 20 at.% metalloids (B, Si, P, C). The lack of atomic order yields electrical resistivities two to three times larger than the corresponding crystalline alloy (typical values are in the range 120–140 10^{-8} Ωm), with important benefits for losses. At the same time, atomic disorder leads to a random distribution of local magnetic anisotropy, which is averaged to zero over the typical distances involved in magnetization processes, a fact that yields magnetic softness and low hysteresis loss. Magnetic softness is further enhanced in materials with vanishing magnetostriction, because the absence of magnetoelastic coupling eliminates the pinning action of internal stresses. In $Fe_{78}B_{13}Si_9$ amorphous ribbons 25 μm thick, power losses attain values around 0.25 Wkg^{-1} at 1.4 T and 50 Hz. Of this, the main contribution comes from the hysteresis component (compare Fig. 3). A similar behavior is exhibited by nanocrystalline materials (grain dimension of the order of 10 nm) obtained by suitable annealing of amorphous materials of appropriate composition ($Fe_{73.5}Cu_1Nb_3Si_{13.5}B_9$ in so-called Finemet materials) (see also *Amorphous and Nanocrystalline Materials*).

Rapidly solidified Fe–6.5 wt.% Si materials exhibit a favorable combination of high resistivity, low magnetocrystalline anisotropy, and vanishing magnetostriction, which contribute to lowering losses. Materials

with this composition cannot be prepared by rolling techniques because of material brittleness. This drawback is circumvented by rapid solidification. Ribbons with thicknesses between 30 and 100 μm can be prepared. Power losses are lower than $15\,\mathrm{Wkg^{-1}}$ at 1 T and 1 kHz, which compares favorably with other materials for medium-frequency applications.

2.4 Nickel–Iron Alloys

Nickel–iron alloys are of particular interest because a broad variety of qualitatively different magnetic properties can be obtained by adjusting the composition and the preparation process. There are no restraints to rolling so it is possible to obtain good laminations with thickness down to 10–20 μm, with great benefits for classical losses. Both the crystal anisotropy and the magnetostriction cross the zero value for compositions around 80 wt.% Ni. Treatments on materials with approximately this composition (and the deliberate introduction of other elements like Mo, Cu, and Cr) yield materials with extremely low hysteresis losses (coercive field less than $1\,\mathrm{Am^{-1}}$), and a variety of hysteresis loop shapes controlled by induced anisotropy. The combination of low hysteresis losses and low classical losses makes these materials most suited to applications at high frequencies.

2.5 Soft Ferrites for High-frequency Applications

Most applications at high frequency, up to the 100 MHz region, make use of soft ferrites, because their nonmetallic nature precludes eddy current dissipation. In most applications, mixed Mn–Zn or Ni–Zn ferrites are employed, in which it is possible to tailor the material properties to specific applications by tuning the concentration of the component atoms. The electrical resistivity is of the order of $10^7\,\Omega\mathrm{m}$ in Ni–Zn ferrites and 10^{-2}–$10\,\Omega\mathrm{m}$ in Mn–Zn ferrites. The initial susceptibility is constant and the loss angle (see Eqn. (3)) is negligible up to frequencies of some MHz for Mn–Zn ferrites and 100 MHz for Ni–Zn ferrites (see also *Ferrites*).

3. Conclusions

In metallic materials, magnetic losses exhibit a remarkably complex phenomenology. Although the physical loss mechanism is in principle clear (Joule effect associated with the eddy currents induced by domain wall motion), the details depend on the space–time eddy current distribution $\mathbf{j}(\mathbf{r}, t)$, which is as complicated as typical magnetic domain structures are in ordinary materials. Of central importance to the treatment of the loss behavior is the concept of loss separation, according to which the total loss is broken down into the sum of three distinct contributions:

classical, hysteresis, and excess loss. Each of these contributions is related to processes occurring in different spatial scales and has a distinct dependence on magnetization frequency, peak induction, and microstructure. Therefore, the crucial step in any loss optimization strategy is to clarify which of the three loss terms gives the dominant contribution and modify appropriately the microstructural or geometrical conditions affecting the magnetization process on that particular scale.

See also: Amorphous Intermetallic Alloys: Resistivity; Ferrite Ceramics at Microwave Frequencies

Bibliography

Bertotti G 1988 General properties of power losses in soft ferromagnetic materials. *IEEE Trans. Magn.* **24**, 621–30
Bertotti G 1998 *Hysteresis in Magnetism*. Academic Press, Boston, MA
Bishop J E L 1976 The influence of a random domain size distribution on the eddy-current contribution to hysteresis in transformer steel. *J. Phys. D: Appl. Phys.* **9**, 1367–77
Bozorth R M 1993 *Ferromagnetism*. IEEE Press, New York
Carr W J Jr. 1976 Magnetic domain wall bowing in a perfect metallic crystal. *J. Appl. Phys.* **47**, 4176–81
Chikazumi S 1964 *Physics of Magnetism*. Wiley, New York
Cullity B D 1972 *Introduction to Magnetic Materials*. Addison-Wesley, Reading, UK
Fiorillo F, Novikov A 1990 An improved approach to power losses in magnetic laminations under nonsinusoidal induction waveform. *IEEE Trans. Magn.* **26**, 2904–10
Hadjipanayis G (ed.) 1997 *Magnetic Hysteresis in Novel Magnetic Materials*. Kluwer, Dordrecht, The Netherlands
Mayergoyz I D 1998 *Nonlinear Diffusion of Electromagnetic Fields*. Academic Press, Boston, MA
Pry R H, Bean C P 1958 Calculation of the energy loss in magnetic sheet materials using a domain model. *J. Appl. Phys.* **29**, 532–3
Williams H J, Shockley W, Kittel C 1950 Studies of the propagation velocity of a ferromagnetic domain wall boundary. *Phys. Rev.* **80**, 1090–4
Wohlfarth E P, Buschow H K J 1980–1996 *Handbook of Ferromagnetic Materials*. North-Holland, Amsterdam

G. Bertotti
Istituto Elettrotecnico Nazionale Galileo Ferraris
Turin, Italy

Magnetic Materials: Domestic Applications

Hard magnetic materials or permanent magnets, and soft magnetic materials are fundamental to the technological success of many devices and products, in particular electric machines and related devices (see Fig. 1). In modern industrialized western economies
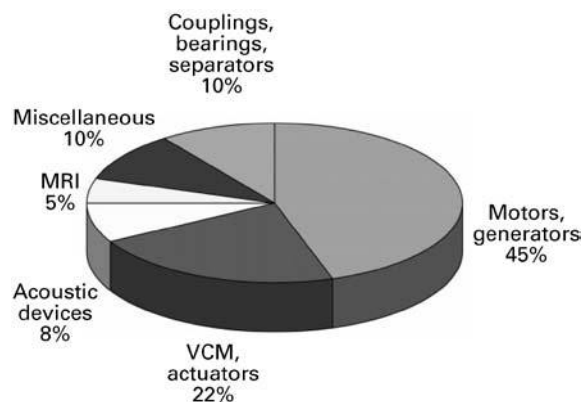
Figure 1
Expected application of $Nd_2Fe_{14}B$ in Europe for 1995 (Krebs 1995).

the electric motor is ubiquitous and consumes 40–45% of all electrical energy generated. Most of this energy is consumed by large industrial electric drives, but nonetheless an increasing proportion is consumed by small electric motors used in domestic appliances, for example, in refrigerators which operate continuously. Regardless of the motor application there is pressure to improve electric motor efficiency as people and governments become more aware of the consequences of global warming, due to the emission of the greenhouse gas, CO_2, from large coal-fired power stations.

Electric motors are present in many household products (for the purposes of this section "domestic" is defined as any product that is found in the home). Products containing electric motors can be grouped according to their domestic application area and a list, by no means exhaustive, includes: laundry—washing machine and clothes dryer; kitchen–dishwasher, microwave oven, fan-forced convection oven, refrigerator, food blender, electric knife, garbage disposal unit, mixmaster, etc; bathroom—hairdryer, electric tooth brush, hair clippers, electric shaver, etc; entertainment—videorecorder, CD player, hi-fi system, camcorder, walkman, camera, etc; home study—personal computer, printer, photocopier, facsimile machine, etc; general household—vacuum cleaner, exhaust fans, ceiling fans, swimming pool and spa pumps, air-conditioner, fans in gas and electric heating systems, etc; and garage—electric drills, saws, routers and grinders, electric screwdriver, electric lawn mower, edge clipper, garden shears, garage door/gate opener, etc.

Some products or appliances may contain as many as four or five individual motors, for example, a camcorder, and where there is a motor there is likely to be power and control electronics, for example, a switch-mode power supply that incorporates magnetic components. Not included in domestic appliances is the family automobile, which may contain up to 40 or even more electric motors. The use of magnetic materials is not just confined to motors, as they are used in speakers in televisions and hi-fi systems, holding devices, water-meters, watt-hour meters and fluorescent lighting ballasts.

1. Motor Technology

A conventional brushed d.c. electric motor can be viewed as having three key components: a field system, which usually consists of a winding around teeth on a stator yoke; an armature, consisting of a series of coils wound in slots on a rotor; and a commutator, for making the electrical connection to the armature coils (Hamdi 1994). The stator and armature laminations are made from a soft magnetic material, usually low-loss silicon steel laminations, and are part of the magnetic circuit which carries and guides the magnetic flux in the machine. In a permanent magnet machine the field system uses permanent magnets rather than producing the field by passing current through coils.

The replacement of the wound field system by permanent magnets results in a significant improvement in motor efficiency, as no electrical energy is used in field production. The motor can then be turned inside-out with the field magnets being attached to the rotor, a multiphase armature winding on the stator, and the commutator replaced by electronic switching devices which switch the current through the stator windings (see Fig. 2). This configuration has the advantage of improved thermal performance, as improved cooling is obtained by having the high-current stator winding in good thermal contact with the motor case. Motors of this type are known as permanent magnet brushless d.c. motors or just brushless d.c. motors (Hughes 1993, Gieras and Wing 1997).

Modern permanent magnet brushless d.c. motors have the advantages of high torque or power per unit volume, improved efficiency, better dynamic response (due to the low inertia of the rotor), reduced volume, reduced weight, mechanical simplicity and reliability (as there are no brushes or commutator), and quiet operation (Hanitsch 1989). These improvements did not happen overnight, but are the result of advances in materials science over the past 30 years, particularly the development of rare-earth permanent magnets (Sm_2Co_{17} and $Nd_2Fe_{14}B$) (see *Rare Earth Magnets: Materials*), and new soft magnetic materials, such as amorphous or glassy metals (see *Amorphous and Nanocrystalline Materials*). In parallel with these developments in materials science there have been major advances in magnetic circuit design, using computational methods based on finite-element techniques, and a revolution in semiconductors, resulting in low-cost microprocessors and digital signal
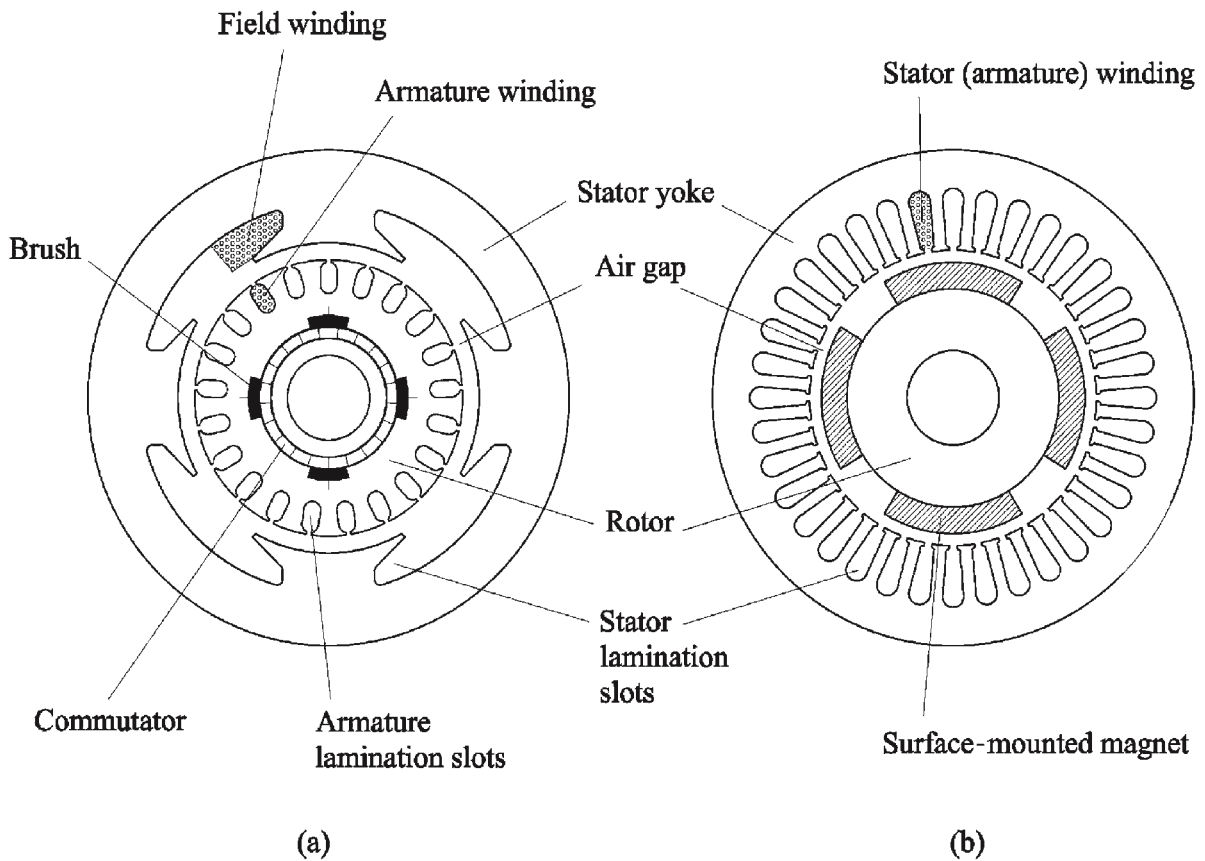
Figure 2
Schematic showing (a) a wound field brushed DC motor and (b) a brushless permanent magnet motor.

processors for motor control, and high-power switching devices.

Losses in electric motors have three main sources:

- copper losses or I^2R losses, which are due to the finite electrical resistance of the copper wire used in the windings (in a brushed machine this also includes losses from brush contact resistance);
- magnetic or iron losses from both magnetic hysteresis losses in the soft magnetic components and eddy currents; and
- friction and windage losses from bearing friction, brushes, if present, and the rotor peripheral speed (Hamdi 1994).

The design of a high-efficiency motor requires minimization of the losses, and may be achieved by the use of novel motor topologies, good magnetic circuit design, and judicious choice of materials, for example, low-loss electrical steels. Innovative motor designs may not use any iron at all; an example is an axial flux in-wheel motor developed for a solar powered car that has an efficiency of 98% (Ramsden 1998).

Motors used in domestic applications range in power from a fraction of a watt, or a few watts, to about 2 kW, have an output torque in the range from a few mNm to about 10 Nm, an efficiency of 60 to 70%, and an operational speed from a few rpm to 25 000 or 30 000 rpm. No one motor type satisfies all these power, torque, and speed requirements. A variety of motor types is used, each with performance characteristics to match the application. For example, a vacuum cleaner motor is required to operate at high speed, and may be only used for an hour per week.

With this intermittent operation there is no great need for high reliability or high efficiency; rather, manufacturers aim for a motor of minimum cost. The situation is somewhat different with a washing machine. Here the motor has two extremes of operation; it is required to operate at low speed with high torque for the wash cycle and high speed with low torque

471

during the spin cycle, to remove water from the clothes. On the other hand, for a refrigerator that operates continuously or a battery-powered hand-held drill there is an advantage in having a motor of high efficiency as this will minimize energy consumption, and for the drill it will give a longer period of use between battery charges.

Generally most domestic appliances are low-cost items, and the motor is usually chosen with this in mind. A common motor type used in intermittently operated hand-held appliances is the brushed universal motor (it has the same configuration as a brushed d.c. motor). Universal motors are made in a variety of sizes, are very low cost, and have the advantage of a simple controller for variable speed operation, though they are noisy at high speeds. Universal motors are used in hair-dryers, food blenders, vacuum cleaners, electric drills, saws and routers, mixmasters, etc. Induction motors tend to be favored in constant-speed continuous operation situations, for low noise and for their low-cost: for example, in fans, compressors in air-conditioners and refrigerators, clothes dryers, pool and spa pumps, etc.

Permanent magnet motors may use either hard-ferrite or rare-earth permanent magnets (very rarely AlNiCo), with the former often used in small pumps in washing machines and dishwashers, and in compact low-noise fans and the latter where the features of high efficiency and high power/torque per unit volume are required, e.g., video-recorders, computer disk drives, CD players, camcorders, cameras, facsimile machines, battery-powered screw drivers, and drills. The situation with washing machines is interesting and reflects market diversity. In Europe frontloading washing machines dominate and tend to use brushed universal motors, while in the USA front-loaders may use a switched reluctance motor. For toploading machines, which are popular in the USA and Australia, both induction motors and direct-drive ferrite permanent magnet motors are used.

In domestic applications hard ferrite magnets dominate, with only limited use of rare-earth permanent magnet motors. More widespread use of rare-earth permanent magnet motors will occur when some, or all, of their advantages of compactness, high efficiency, high torque/power per unit volume, and improved dynamic response are required by the particular product. Domestic applications are highly cost-sensitive, and manufacturers are constantly seeking the lowest cost solution, which inhibits the take-up of motors using rare-earth permanent magnets as they are often of higher cost compared with competing motor types. This is changing as rare-earth magnet prices decrease, motor numbers increase, and the technical advantages of rare-earth permanent motors in particular applications become more apparent.

2. Soft Magnetic Materials

In an electrical machine, the magnetic losses or core losses are due to the soft magnetic material operating in a time-varying magnetic field. Core losses (see *Magnetic Losses*) are made up of eddy current losses that arise from circulating electrical currents induced in conducting materials (the electrical steel used in the stator and copper used in the motor windings) and magnetic hysteresis losses which are proportional to the enclosed area of the B–H loop of the particular material. The characteristics required of the soft magnetic material are:

● high saturation induction to minimize weight and volume of the iron parts;

● high permeability for design of a low reluctance magnetic circuit;

● low coercivity to minimize hysteresis losses; and

● high resistivity to minimize eddy current losses (minimization of eddy currents is also achieved by using thin laminations that are covered by a thin insulating layer to provide interlaminar insulation).

These desirable magnetic properties are not found in one material, as there are many factors that affect the magnetic properties. The magnetic properties of a material may be tailored by the addition of chemical elements, mechanical working of the material, and heat treatment. The characteristics of a range of soft magnetic materials are shown in Fig. 3 and Table 1 (for reference data see Warlimont 1990 and Clegg *et al.* 1993).

2.1 Silicon–Iron Electrical Steels

The most common soft magnetic material used in electrical machines is silicon–iron electrical steel (see *Steels, Silicon Iron-based: Magnetic Properties*) in the form of thin laminations. The addition of silicon to soft iron results in a significant decrease in coercivity,
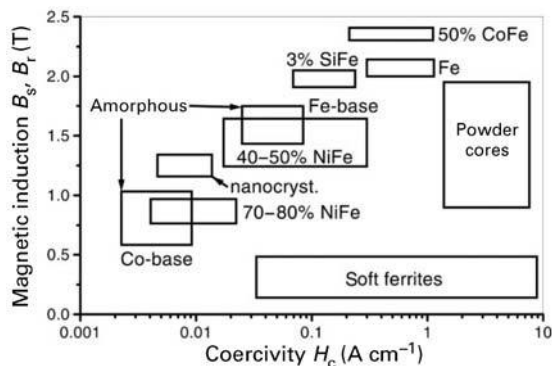
Figure 3
Typical property ranges of soft magnetic materials.

Table 1
Properties of some common soft magnetic materials.

Grade	Thickness (mm)	Nominal silicon content (%)	Resistivity (μΩ m)	Core loss at 1.5 T and 50 Hz (Wkg^{-1})
Low-loss Si–Fe steel, nonoriented				
Transil 300-35-A5	0.35	2.9	0.48	2.95
Losil 400-50-A5	0.50	2.4	0.44	3.60
Losil 800-65-A5	0.65	1.3	0.29	6.5
Low-loss Si–Fe steel, oriented				
Unisil 35M6	0.35	3.1	0.48	1.00
Permendur 49 (Co49/Fe49/V2)	0.35	NA	0.40	3.0
METGLAS 2605SA1	0.025	NA	1.3	0.16[a]
SMC (iron powder)	NA	NA	NA	10

a Measured at 1.4 T.

a slight decrease in saturation magnetization, and an increase in resistivity. There are two distinct categories of electrical steels: nonoriented isotropic products with silicon contents in the range 1–3.5%, and grain-oriented anisotropic products which contain 2.9–3.15% Si ($+$Al). Silicon levels above 3.5% result in the steel becoming very brittle and hard to work. Oriented steels have the lowest core loss (see Table 1) and are used in transformers, whereas nonoriented steel is used in electrical machines as there are varying flux directions.

Domestic appliances are dominated by low-cost universal and induction motors, with efficiencies of 60–70%. The quest for low cost results in motors that use lower-quality nonoriented electrical steels and thicker laminations (typically 0.65 mm), the latter resulting in a reduction in the number of stamping operations necessary to produce the stator lamination stack.

2.2 Iron–Cobalt Alloys

Iron–cobalt alloys (such as Permendur 49, 49Co–49Fe–2 V) have the highest saturation magnetization of all the soft magnetic materials (see Fig. 3). They have the disadvantage of a much higher cost than silicon–iron steels, but are used in applications where it is advantageous to reduce size and weight. Iron–cobalt alloys are used in aircraft generators, some 400 Hz motors, and active magnetic bearings.

2.3 Amorphous or Glassy Metals

Amorphous metals (see *Amorphous and Nanocrystalline Materials*) are made from alloys whose constituents may include Fe, Ni, and Co and a metalloid or glass former such as silicon, boron, or carbon. A typical amorphous metal, offered for sale by Allied-Signal Inc, USA, is METGLAS 2826, which has the

composition $Fe_{40}Ni_{40}P_{14}B_6$. Amorphous metals are very thin, of the order of 0.025 to 0.04 mm. They have the lowest coercivity of all the soft magnetic materials and a higher resistivity than electrical steels, resulting in a material with the lowest core loss (see Table 1).

There is a number of issues regarding the use of amorphous metals in electrical machines. The very desirable feature of low coercivity is counterbalanced by the lower saturation magnetization, ≈ 1.5 T compared with ≈ 2 T in silicon–iron steels. The cutting and forming of amorphous metal laminations is expensive due to increased tool wear from their hardness (over C-80 Rockwell), and being very thin there is a greater number of stamping operations, and the material does not stack as well. Amorphous metals have been used in electrical motors where high efficiency is all-important ($>94\%$), but it is in distribution transformers where the material is proving most beneficial (DeCristofaro 1998).

2.4 Soft Magnetic Composites

Soft magnetic composite (SMC) materials are made from bonded iron powders. The iron powder is coated with an insulating layer and pressed into a solid material using a die before final heat treatment to cure the bond. It is not a powder metallurgy process where sintering is used. SMC materials are rather new and have a number of advantages. The material is isotropic, enabling the design of magnetic circuits that have three-dimensional flux paths, and since there is an insulating layer between the iron powder particles, losses due to eddy currents are minimized.

The material can be used at frequencies up to 100 kHz, and the cross-over point for core loss for it and 3% silicon steel (0.5 mm thick) is about 400 Hz, where at 1.5 T the loss for both materials is about 90 W kg^{-1}. The main advantage of the material may

be in low-cost manufacture, as parts can be made to net shape, using highly-automated mass production methods. The main disadvantage of the material is its high core loss at 50 Hz when compared with silicon–iron electrical steels. Nonetheless, a number of prototype transverse flux and claw-pole electrical machines have been made using SMCs (Jack 1998).

2.5 Soft Ferrites

The magnetically soft ferrites (see *Ferrites*) have the general chemical formula $MeFe_2O_4$, where Me is most commonly MnZn (MnZn ferrite) or NiZn (NiZn ferrite), and have the cubic structure of the mineral spinel. The properties of the soft ferrite may be further adjusted by additions of Mg, Cu, or Co, or a mixture of these. The soft ferrites have the general characteristics of low coercivity, high permeability, and high resistivity.

The high resistivity results in negligible losses due to eddy currents, enabling the material to be used at high frequencies ($\gg 1$ MHz). Generally the NiZn ferrites have a higher resistivity than the MnZn ferrites, but a lower saturation induction. The soft ferrites are manufactured in a range of core shapes, rings, pots, and E and C cores, for use in inductors and transformers. Their use is primarily in compact electronic power supplies and telecommunication components. Their relatively low saturation induction makes them unsuitable for use in power or high-flux transformers.

Another class of soft ferrites, the iron garnets with the general formula $R_3Fe_5O_{12}$, where R is a rare-earth, usually yttrium, is used in specialized microwave devices.

3. Hard Magnetic Materials

The role of hard magnetic materials, in particular high-energy permanent magnets, in electric motors is replacement of the field winding. In any application, including motors, there is a multitude of factors that require consideration to ensure that the optimum magnet material is selected (Coey 1996a, Kirchmayr 1996). Of importance are:

● magnetic parameters: remanence, intrinsic coercivity, and magnetic energy product, BH_{max};
● temperature stability of the magnetic parameters;
● ease of magnetizing the material;
● ease of forming the magnet into the desired shape;
● environmental factors, such as resistance to corrosion; and
● cost (cost can be treated in a variety of ways, and includes material cost, cost per unit of magnetic energy product, and the cost of forming the material into the desired shape and its magnetization).

Selection of the permanent magnet material impacts on the motor design; for example, a motor using a hard ferrite has narrow stator teeth, compared to the wider teeth in a machine using rare-earth permanent magnets, where the magnetic flux density is much higher. It is also desirable for motors that the magnet material has a linear *B–H* curve in the second, or demagnetizing, quadrant of the hysteresis loop. Both hard ferrite and rare-earth magnets have this characteristic, whereas AlNiCo differs by exhibiting a highly nonlinear demagnetization behavior.

For the motor designer rare-earth permanent magnets offer the advantages of a high BH_{max}, which reduces the amount of magnet material required, and high-intrinsic coercivity, which is important if the motor is to withstand high armature currents, which could lead to demagnetization of the magnets. Typical properties for a range of permanent magnet materials are given in Tables 2 and 3. For detailed information on magnet types see McCaig and Clegg (1987) and Coey (1996b); see also Hard Magnetic Materials, Basic Principles of).

The use of any permanent magnet material in a particular application is not only governed by the

Table 2
Typical properties of some common permanent magnet materials.

Material	Remanence (T)	Intrinsic coercivity (kAm^{-1})	Energy product (kJm^{-3})
Sintered $Nd_2Fe_{14}B$	1–1.4	3200–1000	190–380
Sintered Sm_2Co_{17}	1.04–1.12	2070–800	200–240
Sintered $SmCo_5$	0.90–1.01	2400–1500	160–200
Anisotropic bonded HDDR $Nd_2Fe_{14}B$	0.81–0.87	915–1154	123
Isotropic plastic bonded $Nd_2Fe_{14}B$	0.4–0.7	1000–600	30–76
Sintered anisotropic AlNiCo	0.72–1.26	1920–610	20–44
Sintered isotropic AlNiCo	0.62–0.84	1190–125	4–18
Hard ferrite, anisotropic	0.36–0.40	180–270	25–31
Hard ferrite plastic bonded anisotropic	0.22–0.30	240–190	15–18
Hard ferrite isotropic	0.22–0.28	230–300	8.5–10
Hard ferrite plastic bonded isotropic	0.1–0.15	180–230	2–4

Table 3

Thermal characteristics for some permanent magnet materials (α is the reversible temperature coefficient of the remanence and β is the reversible temperature coefficient of the intrinsic coercivity).

Material	α (%K^{-1})	β (%K^{-1})	Max. operating temperature (°C)	Curie temperature (°C)
Sintered $Nd_2Fe_{14}B$	-0.13	$-(0.5\text{--}0.65)$	200	310
Sintered $SmCo_5$	-0.045	$-(0.2\text{--}0.3)$	250	720
Sintered Sm_2Co_{17}	-0.03	-0.19	350	825
AlNiCo	$-(0.01\text{--}0.02)$	$0.01\text{--}0.03$	500	830
Ferrites	-0.2	$0.3\text{--}0.4$	300	450

Table 4

World permanent magnet market in 1994 and current prices.

Material	Market 1994 (US$ Millions)	Price ($USkg^{-1})
Bonded $Nd_2Fe_{14}B$	194	30–100
Sintered $Nd_2Fe_{14}B$	603	30–150
Bonded ferrite	673	2.50–6
Bonded rare-earth cobalt	30	230
Sintered ferrite	1244	2.50–5
Sintered rare-earth cobalt	218	250–300
Other (including AlNiCo)	248	50–80[a]
Total	3210	

a For cast/sintered AlNiCo.

magnetic, physical, and chemical parameters, but also by the cost of the material. Applications and products are driven by markets, and the success or failure of a product in a particular market is driven by cost. The world market for various magnet types is given in Table 4 (Ormerod and Constantinides 1997), and it shows that the market is dominated by the low-cost hard ferrites. Included in Table 4 is the price per kilogram for various magnet materials. These prices are at best estimates, and are based on information from a variety of sources, including Abraham (1995) and material presented at the 1999 Gorham/Intertech NdFeB '99 Meeting (Gorham/Intertech Consulting, Portland, ME, USA). It is difficult to give accurate pricing, as this information is often kept confidential by manufacturers, can be very dependent on quantity and complexity of the magnet shape, and subject to market volatility. For example, the advent of low-cost $Nd_2Fe_{14}B$ from the Far-East has had a considerable impact. Nonetheless, Table 4 does give a guide to the relative prices. In terms of cost per unit of energy, both sintered hard ferrite and sintered $Nd_2Fe_{14}B$ are approaching parity (hard ferrite of $27\,kJm^{-3}$, $2.50–3.00\,kg^{-1}$, $\approx$\$0.10 $(kJm^{-3})^{-1}$ and $Nd_2Fe_{14}B$ of $250\,kJm^{-3}$, \$30 kg^{-1}, $\approx$\$0.12 $(kJm^{-3})^{-1}$). In recent years, both sintered and bonded $Nd_2Fe_{14}B$ have decreased in price, and it appears this trend will

continue as market share increases and $Nd_2Fe_{14}B$ becomes cost-effective in new applications and replaces existing magnet materials in current applications.

3.1 Rare-earth Cobalt Magnets

Sintered and polymer-bonded magnets based on both the $SmCo_5$ and Sm_2Co_{17} alloy composition are available from a variety of manufacturers. The main advantage of Sm–Co-based magnets is their high Curie temperature, making them suitable for use in applications at elevated temperatures, but they suffer from the disadvantage of high cost. The sintered material tends to be somewhat harder and more brittle than $Nd_2Fe_{14}B$, but it has excellent corrosion resistance. Sintered Sm–Co magnets are used in applications where arduous conditions apply, for example, in motors that are used in oil-wells, high-temperature automotive sensors, and microwave switches in telecommunication satellites.

3.2 Neodymium–Iron–Boron (Nd₂Fe₁₄B) Magnets

$Nd_2Fe_{14}B$ magnets are commercially available in a number of forms—anisotropic sintered and anisotropic

and isotropic powders for polymer bonded magnets. Isotropic powders are prepared using a rapid solidification method and anisotropic powders by the HDDR (hydrogenation, desorption, disproportionation, recombination) process (Kirchmayr 1996). Projections suggest a cost of $30 kg^{-1} for isotropic powder by 2001. Polymer-bonded magnets are formed by either compression or injection molding, and binders include nylon 6/6. The great advantage of polymer-bonded magnets is that complicated shapes and geometries can be prepared to near-net or net shape using very low-cost production processes.

For applications requiring magnets of the highest possible energy product, sintered $Nd_2Fe_{14}B$ is the magnet of choice (see Magnets: Sintered). The thermal stability of sintered $Nd_2Fe_{14}B$ magnets has improved, with operating temperatures of 200 °C now attainable. Similar advances have been made in corrosion resistance with the addition of cobalt and other alloying components. Sintered magnets find uses in applications that require the best possible performance, for example, servomotors in machine tools.

Polymer-bonded magnets are the most rapidly growing section of the permanent magnet market. The reason for this rapid expansion is the demand for magnets for computer disk drives. Currently more than 50% of rare-earth magnets produced in Japan are used in computer disk drives, and the world market for computer disk drives is expected to exceed 250 million units by 2002. There is also considerable demand for polymer-bonded magnets for small motors in video recorders, camcorders, printers, facsimile machines, office automation, automotive, and portable drills (Ormerod and Constantinides 1997).

3.3 Aluminum–Nickel–Cobalt (AlNiCo) Magnets

AlNiCo magnets are manufactured by a powder metallurgy process or by casting, and are available in both isotropic and anisotropic forms. They tend to be expensive due to the cost of the raw materials, but they have good corrosion resistance and a very respectable remanence, 1.26 T, when compared with the value of 1–1.4 T for $Nd_2Fe_{14}B$. The major disadvantage of AlNiCo is its low coercivity, which creates problems in handling and its use in electric motors. For example, removal of AlNiCo magnets from the magnetic circuit in a small electric motor often results in their partial, or complete, self-demagnetization. A consequence of this is that it is usually necessary to magnetize AlNiCo magnets *in situ*.

The advantage that AlNiCo has compared with other commonly used permanent magnets is its excellent temperature stability. It has a reversible temperature coefficient of remanence of −0.01 to −0.02%K^{-1}, compared with −0.13%K^{-1} for $Nd_2Fe_{14}B$. The excellent temperature stability of AlNiCo makes it the

magnet of choice for watt-hour meters, ammeters, and voltmeters. Additionally, AlNiCo magnets are frequently used in small servomotors in aircraft and military hardware (see also *Alnicos and Hexaferrites*).

3.4 Hard Ferrite Magnets

In terms of the global permanent magnet market hard ferrite magnets still dominate. Ferrite magnets have the stoichiometry $BaFe_{12}O_{19}$ or $SrFe_{12}O_{19}$, the latter being increasingly used due to its higher coercivity. They are very cheap, as the raw materials from which they are made are abundant. A further advantage is their resistance to many chemicals, and being an oxide they are ideal for use in damp or wet environments. Isotropic and anisotropic sintered magnets, and polymer-bonded magnets formed from the milled powder, are widely available and used extensively.

The temperature coefficient of the intrinsic coercivity is positive for the hard ferrites, in contrast to rare-earth permanent magnets, and consequently there is a risk of demagnetization if the hard ferrite magnet is exposed to too low a temperature. Hard ferrite magnets are found in applications ranging from door seals in refrigerators to small electric motors used in dishwashers and washing machines (see also *Alnicos and Hexaferrites*).

4. Selected Applications

4.1 Computer Disk Drives

Computer disk drives are a prime example of where performance enhancements are traceable to improvements in permanent magnets. In a fixed disk drive permanent magnets are used in the spindle motor, in the actuator that drives the read/write heads (generally termed the voice coil motor (VCM)), and the latch assembly (see Fig. 4). Disk drives nowadays have a 2.5, 3, or 3.5 inch form factor, as emphasis has switched from miniaturization to making the storage capacity of the drive as large as possible.

The availability of high-remanence rare-earth magnets has enabled the disk drive designer to reduce dramatically the size of the VCM, as only a small volume of magnet material is required, and to decrease access times. Disk drives of >1–2 GB capacity use a high-grade sintered $Nd_2Fe_{14}B$, showing typically a remanence of 1.4 T, an intrinsic coercivity of 1,190 kAm^{-1}, and an energy product of 360 kJm^{-3}. One or two magnets may be employed, with a total weight of 15.5 g, and return poles are made of low-carbon steel. Spindle motors may use sintered or polymer-bonded material, with the latter often favored as it can be easily molded to shape. Spindle motor speed is important as the higher the speed the shorter the seek time. High-capacity drives found in file-servers
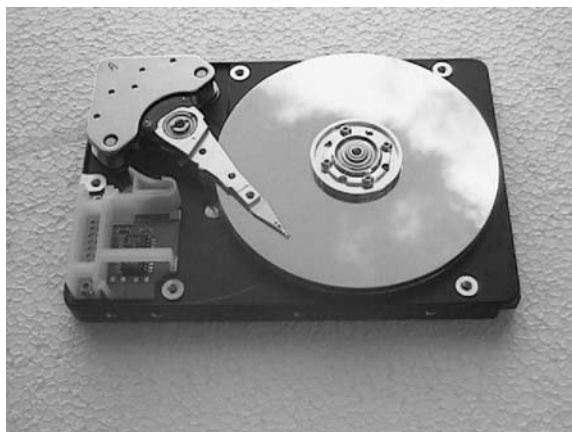
Figure 4
Hard disk drive unit; the VCM actuator can be seen in the top left hand corner.

have a spindle speed of 10 000 rpm, while drives used in desktops and notebooks have speeds of 7200 rpm and 5400 rpm, respectively. Removable cartridge drives of 100 to 250 MB capacity use linear motors and polymer-bonded $Nd_2Fe_{14}B$, to keep their cost down. On the horizon are compact disk drives for use in digital cameras. IBM is building a 1-inch 340 MB hard drive for that application that uses $Nd_2Fe_{14}B$ magnets.

4.2 White Goods

The domestic appliances most often associated with motors are refrigerators, washing machines, and dish washers. On the whole these products appear to have changed little over the years, but there is increasing pressure to improve their energy efficiency. In the USA the Department of Energy mandated a 30% reduction in energy use for refrigerators manufactured after July 2001. An energy-efficient refrigerator has been developed in the USA that uses $1.16 \, kWhd^{-1}$, and part of this efficiency improvement comes from the use of DC brushless motors (Braham 1997).

A permanent magnet brushless motor of innovative design is used in a top-loading washing machine made by Fisher & Paykel, New Zealand, and is shown in Fig. 5. The motor is of an axially compact design, approximately 270 mm diameter and 65 mm long, and uses an outer rotor with hard ferrite permanent magnets. The agitator is coupled directly to the motor. This simplifies the design of the washing machine, as the gearbox or belt-drive reduction is eliminated. Fisher & Paykel also make a low-profile pump motor for use in dishwashers (Fig. 6). Again, this is a hard ferrite brushless permanent magnet
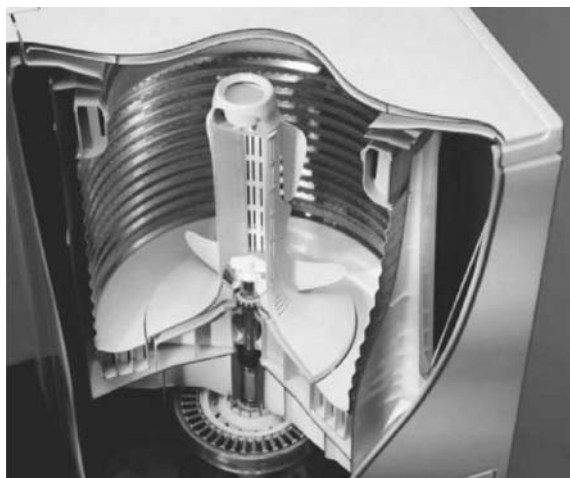
Figure 5
Cutaway showing direct-drive permanent magnet washing machine motor. (Photograph courtesy of Fisher & Paykel, New Zealand).
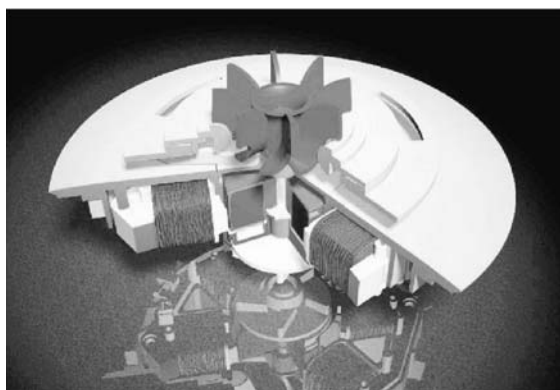
Figure 6
View of a hard-ferrite permanent magnet motor used in dishwashers. (Photograph courtesy of Fisher & Paykel, New Zealand).

motor. The magnets are located on the rotor, and the rotor runs in contact with the water detergent mix of the dishwasher. This is possible due to the excellent resistance of ferrite to chemical attack.

5. The Future

Hard and soft magnetic materials will continue to be fundamental to many domestic applications, and as improvements are made in their physical, chemical, and magnetic properties there will be corresponding product improvements. In the future one can foresee

the "plastic" motor which will be constructed from an injection or compression-molded soft magnetic composite stator and polymer-bonded magnets, bonded directly on the rotor. The great attraction of such a motor will be its excellent performance and low cost, as its key components can be manufactured using low-cost plastic molding methods.

See also: Magnetocaloric Effect: From Theory to Practice; Magnetic Refrigeration at Room Temperature; Permanent Magnets: Sensor Applications; Permanent Magnet Assemblies

Bibliography

Abraham T 1995 Magnets and magnetic materials: a technical economic analysis. *Int. J. Powder Metall.* **31**, 133–6

Braham J 1997 Energy efficiency sends appliance designers into a spin. *Machine Des.* 40–6

Clegg A G, Beckley P, Snelling E C, Major R V 1993 Magnetic materials. In: Jones G R, Laughton M A, Say M G (eds.) *Electrical Engineers Reference Book, Fifteenth Edition*. Butterworth Heinemann, Oxford, UK, Chap. 14

Coey J M D 1996a Industrial applications of permanent magnetism. *Phys. Scr.* **T66**, 60–9

Coey J M D 1996b *Rare-earth Iron Permanent Magnets*. Clarendon Press, Oxford, UK

DeCristofaro N 1998 Amorphous metals in electric-power distribution applications. *MRS Bull*, **(May)**, 50–6

Gieras J F, Wing M 1997 *Permanent Magnet Motor Technology*. Marcel Dekker, New York

Hamdi E S 1994 *Design of Small Electrical Machines*. Wiley, Chichester, UK

Hanitsch R 1989 Electromagnetic machines with Nd–Fe–B magnets. *J. Magn. Magn. Mater.* **80**, 119–30

Hughes A 1993 *Electric Motors and Drives*. Newnes, Oxford, UK

Jack A G 1998 Experience with the use of soft magnetic composites in electrical machines. In: Ertan B, Üctu Y (eds.) *Proc. Int. Conf. on Electrical Machines*. Middle East Technical University, Ankara, Turkey, pp. 1441–8

Kirchmayr H R 1996 Permanent magnets and hard magnetic materials. *J. Phys. D: Appl. Phys.* **29**, 2763–78

Krebs J 1995 Hot pressed and die-upset forged magnets. *Magnews* 19–21

McCaig M, Clegg A G 1987 *Permanent Magnets in Theory and Practice*, 2nd edn. Pentech Press, London

Ormerod J, Constantinides S 1997 Bonded permanent magnets: current status and future opportunities. *J. Appl. Phys.* **81**, 4816–20

Ramsden V S 1998 Application of rare-earth magnets in high-performance electric machines. In: Schultz L, Müller K-H (eds.) *Proc. 15th Int. Workshop on Rare-earth Magnets and their Applications*. Werkstofi-Informationsgesellschaft mbH, Frankfurt, Germany, pp. 623–42

Warlimont H 1990 Magnetic property assessment: between physical maximum and economic optimum. *IEEE Trans. Magn.* **26**, 1313–21

S. J. Collocott
CSIRO Telecommunications and Industrial Physics
Lindfield, Australia

Magnetic Materials: Hard

The prerequisite for permanent magnet materials that owe their hard magnetic properties to the presence of magnetocrystalline anisotropy is a crystal structure of less than cubic symmetry. The tetragonal structure of the AuCu type ($L1_0$) is a well-known example able to generate uniaxial magnetic anisotropy in compounds in which the magnetic moments are carried by cobalt, iron, or manganese atoms. As illustrated in the left-hand (or right-hand) part of Fig. 1, the unit cell of this structure can be obtained by atomic ordering of the two components (filled and open circles), an atomic ordering that leads to a small contraction of the *c*-axis. As discussed below, the attainment of this tetragonal structure for CoPt and FePt alloys is metallurgically different from that for MnAl alloys. The permanent magnets based on compounds of this tetragonal crystal structure are rather expensive for CoPt and FePt owing to the high price of platinum metal. The application of the latter magnets is therefore a restricted one. The MnAl magnets are low-cost, low-performance magnets, but their widespread application suffers from the competition of hard ferrite magnets (see *Alnicos and Hexaferrites*).

1. Permanent Magnets based on Noble Metal Compounds

At high temperatures the platinum–cobalt phase diagram is characterized by a range of complete solid solubility. The crystal structure is a disordered f.c.c. structure over the whole solid solubility range, in which cobalt and platinum atoms statistically occupy the crystallographic sites. This high-temperature phase is practically useless for permanent magnet applications because it does not show a sufficiently high magnetic anisotropy. Structural transformations take place, however, when the rapidly cooled solid solution $Co_{1-x}Pt_x$ alloys are annealed at lower temperatures. The f.c.c. phase gives rise to a disorder–order transformation for comparatively high platinum concentrations ($x > 0.75$) whereas for
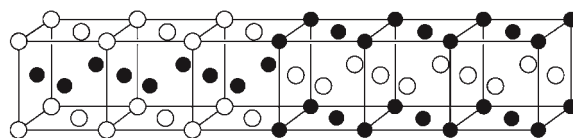
Figure 1
Schematic representation of an array of unit cells of the tetragonal AuCu structure type in which one component occupies the basal plane positions and the other component the equatorial plane positions. Switching of positions can lead to an antiphase boundary visible in the central part.

relatively low platinum concentrations ($x < 0.23$) it transforms into a h.c.p. structure. The applicability of $Co_{1-x}Pt_x$ alloys as permanent magnet materials is based on the transformation of the disordered f.c.c. phase to an ordered face-centered tetragonal (f.c.t.) phase occurring for alloys in the intermediate concentration range ($40 < x < 75$). Only the latter phase has a sufficiently high uniaxial magnetic anisotropy, the easy magnetization direction being along the tetragonal *c*-axis.

The origin of the magnetic anisotropy and the role played by the orbital moment in transition metal compounds in CoPt has been explained by means of first principles band structure calculations using the local spin density approximation. For a more detailed discussion of this topic the reader is referred to the review by Buschow (1997). The Curie temperature of these materials is around 500 °C for the equiatomic composition and slightly decreases with platinum concentration.

The maximum of the magnetic anisotropy energy $E_A = K_1 + 2K_2$ is found at the equiatomic composition, although the maximum of the anisotropy field $H_A = (2K_1 + 4K_2)/M_s$ is located at slightly higher x values because of the fairly strong decrease of the saturation magnetization, M_s, with x. For obtaining optimum values for the coercivity slightly higher platinum concentrations than the equiatomic composition are desirable because it is the anisotropy field rather than the anisotropy energy that determines the coercivity (see *Coercivity Mechanisms*). However, the energy product depends very strongly on the magnetization. For this reason, concentrations close to the equiatomic composition are generally chosen for practical applications in permanent magnets.

As described in detail elsewhere (see *Coercivity Mechanisms*) high coercivities are usually obtained in magnet bodies composed of an assembly of sufficiently fine particles. CoPt alloys are known to have outstanding mechanical strength and for this reason the powder metallurgical route commonly used for the attainment of high coercivities in many other permanent magnet materials (see *Magnets: Sintered*) is not applicable here. In these alloys one may profit, however, from particulars of the phase diagram because the presence of the f.c.c.-to-f.c.t. phase transition provides ample means of obtaining sufficiently small f.c.t. particles. This is the reason that the generation of coercivity in CoPt alloys is a matter of controlling the nucleation and growth of f.c.t. particles during the phase transformation. This process involves heat treatments of the ingots under carefully selected conditions.

Kaneko *et al.* (1968) have shown that the coercivity passes through a maximum when CoPt alloys are heat treated for variable aging times at temperatures sufficiently below the f.c.c.–f.c.t. transformation temperature, the optimum annealing temperature being around 680 °C. Furthermore, it has been found that

even better results are obtained when the first aging step is followed by a second aging step, provided the first aging step is kept sufficiently short to prevent overaging. The first annealing step is regarded as leading to the formation of a fine precipitate of the f.c.t. phase in the f.c.c. matrix, whereas the second step is held responsible for an increase of the magnetocrystalline anisotropy of the f.c.t. phase. This increase is probably associated with a more perfect atomic ordering of the cobalt and platinum atoms in the f.c.t. grains. By applying this two-step annealing process, coercivities can be obtained of greater than $700 \, kAm^{-1}$ for alloys annealed first at 680 °C and subsequently at 600 °C for variable times. The corresponding energy products of the ingot magnets can reach values around $100 \, kJm^{-3}$.

The origin of the coercivity in f.c.t. CoPt alloys has been studied (Zhang and Soffa 1994) by means of Lorentz microscopy. It has been shown that the occurrence of antiphase boundaries (APB) is essential for the understanding of the coercivity in these materials. It is mentioned above that the f.c.t. phase precipitates from a disordered f.c.c. matrix phase on annealing. This phase transformation proceeds by means of a nucleation and growth mechanism, starting at a multitude of different locations in the alloy. The coalescence of the ordered regions during the growth process invariably leads to the occurrence of a large number of APBs. The atomic arrangement at APBs is shown schematically in Fig. 1. Zhang and Soffa (1994) showed by means of electron microscopy that the microstructure of fully ordered alloys can be characterized by profuse micro- and macrotwinning, leading to a dense net of APBs within the micro- and macrotwins. It is assumed that the coercivity is controlled by domain wall pinning at APBs and stacking faults.

Behavior fairly similar to that described above for $Co_{1-x}Pt_x$ alloys is found also for $Fe_{1-x}Pt_x$ alloys. High coercivities for $Fe_{1-x}Pt_x$ alloys are obtained when alloys around the equiatomic composition are first homogenized at high temperatures and subsequently annealed at temperatures below the order–disorder transition temperature. Tanaka *et al.* (1997) made a fairly detailed investigation of the microstructures of heat-treated $Fe_{1-x}Pt_x$ alloys and the resulting coercivities. It was shown that composition control is essential for the attainment of high coercivities. In as-quenched alloys optimum coercivities are reached for 39.5 at.% platinum because the disordered f.c.c. phase disappears during quenching and can no longer act as nucleation centers for domain walls. Tanaka *et al.* (1997) further showed that alloys with optimum coercivities are reached after heat treatments in which the local stress associated with the cubic-to-tetragonal transformation is not yet released by twin formation, and the f.c.t. phase is still present in the form of nanoscale antiphase domains. The antiphase domain boundaries between the single-domain particles act as

pinning sites for domain wall motion and in this way generate high coercivities. An overlong aging treatment leads to particle growth so that these are no longer single-domain particles. Consequently, the coercivity is reduced.

Investigations by Watanabe (1991) have made it clear that permanent magnets with hard magnetic properties even superior to those of CoPt alloys can be obtained for FePt alloys to which a small amount of niobium is added. The corresponding ingots are first homogenized at 1325 °C and then quenched in water. The desired high coercivity is obtained after a subsequent isothermal annealing treatment performed in a temperature range of 600–700 °C. The iron moments are somewhat higher than the cobalt moments in the iron alloys. This implies also that the remanences in the iron alloys are higher than in the cobalt alloys. This, in turn, leads to larger maximum energy products with $(BH)_{max}$ values higher than $160 \, kJm^{-3}$.

The platinum-based magnets are extremely expensive owing to the fact that they consist of roughly 75 wt.% platinum. Advantages of these magnets are that they can be produced as ingot magnets, avoiding the complicated powder metallurgical manufacturing route. The magnets are of high mechanical strength and of unequalled corrosion resistance. Because of price considerations they are produced only in small quantities and are mainly used for medical implants. Investigations (Liu *et al.* 1998) have shown that PtFe-type permanent magnets can also be obtained in the form of thin films by combining Fe/Pt multilayering and rapid thermal processing. Energy products as high as $318 \, kJm^{-3}$ (40 MGOe) have been reached and attributed to the presence of exchange coupling between the hard magnetic f.c.t. phase and soft magnetic f.c.c. phase. A detailed description of the exchange coupling mechanism and the concomitant remanence enhancement in nanostructured microstructures can be found in *Magnets: Remanence-enhanced*.

When comparing the manufacturing routes of Alnico magnets (see *Alnicos and Hexaferrites*) and platinum alloy magnets one may notice that there is a striking similarity. In both cases the manufacturing benefits from the fact that an extended range of solid solubility exists at high temperatures and that on cooling this solid solution becomes supersaturated and leads to the precipitation of new phases. In both cases the decomposition of the supersaturated solid solution has to be performed at sufficiently low temperatures so that the resulting microstructure consists of fine grains and exhibits magnetic hardness.

Interestingly, neither of the two parent solid solutions has a magnetic anisotropy of any significance. In the case of the platinum alloys the required magnetic anisotropy is obtained by the formation at low temperatures of a phase of lower symmetry (f.c.t.) than the parent phase (f.c.c.). In contrast to the latter, the former phase exhibits a fairly strong magnetocrystalline anisotropy. Both phases have the same composition and the particle size is not very critical for the generation of anisotropy. Roughly speaking it can be said, therefore, that the main goal of finding optimum annealing treatments is to generate microstructures with grain sizes sufficiently small for generating coercivity. By contrast, the main goal of finding optimum annealing treatments in the case of Alnico alloys is to produce microstructures where not only the size but also the shape of the precipitated particles is at a premium, because not only coercivity but also shape anisotropy has to be generated owing to the absence of magnetocrystalline anisotropy.

2. MnAl Permanent Magnets

Permanent magnets based on MnAl alloys owe their hard magnetic properties to the so-called τ-phase. This is an intermetallic compound with an f.c.t. structure (CuAu-type superstructure). It occurs in the composition range 51–58 at.% (67—73 wt.%) manganese. The manganese atoms are located predominantly at the 1a and 1c positions at $(0, 0, 0)$ and $(\frac{1}{2}, \frac{1}{2}, 0)$, respectively. The aluminum atoms occupy mainly the 2e positions at $(0, \frac{1}{2}, \frac{1}{2})$ in this crystal structure. Owing to the fact that the composition is richer in manganese than the equiatomic composition, not all the manganese atoms can occupy the former two sites. This has as a consequence in that the excess manganese atoms must be accommodated at the $(0, \frac{1}{2}, \frac{1}{2})$ positions, which they share with the aluminium atoms. Neutron diffraction results indicate that deviations from the ideal site occupancy in this type of MnAl alloy can lead to antiferromagnetic coupling between the manganese moments. This unfavorable feature has important consequences for the saturation magnetization and for the hard magnetic properties of permanent magnets based on MnAl alloys.

A second difficulty associated with MnAl alloys is the metastable nature of the τ-phase. In fact, this phase is not found in the Mn–Al phase diagram (see Fig. 2). It can be obtained by starting from the high-temperature equilibrium ε-phase occurring in this concentration range, which has an h.c.p. structure. However, the preparation of the f.c.t. τ-phase from the h.c.p. ε-phase is not easy. Formerly it was believed that the τ-phase forms from the ε-phase via an intermediate phase, ε', of orthorhombic structure (B19) by means of the reaction scheme

$$h.c.p.(\varepsilon) \rightarrow B19(\varepsilon') \rightarrow f.c.t.(\tau)$$
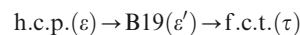
where the h.c.p. structure (ε) transforms first into the orthorhombic ε'-phase by an atomic ordering reaction. Subsequently, the metastable f.c.t. ferromagnetic τ-phase is formed by way of shear transformation. However, this reaction scheme is rather unlikely in
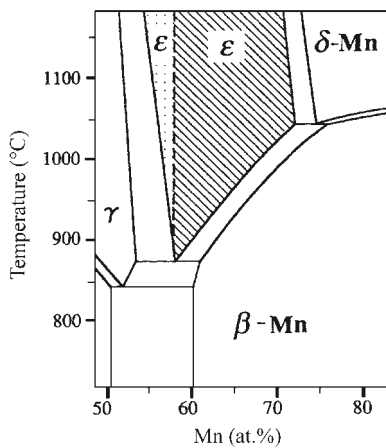
Figure 2
Central portion of the Mn–Al phase diagram as reported by Liu *et al*. (1996). The shaded area of the homogeneity region of the β-phase corresponds to alloys that transform into β-Mn on quenching.

Figure 3
Schematic representation of an antiphase boundary and the corresponding reversal in magnetization direction across the boundary.

view of the observation by electron microscopy that precipitates of the ε′-phase in undercooled ε do not act as nucleation centers for τ.

The occurrence of a massive transformation has been proposed by Hoydick *et al*. (1997). It is furthermore important to realize that the metastable τ-phase, after an annealing time that depends on alloy composition and the annealing temperature, tends to decompose into the two stable phases with β-Mn (β) and Cr_5Al_8 type structure (γ₂). For this reason, the annealing time has to be chosen carefully.

Various heat treatments have been proposed to obtain and preserve the τ-phase, as discussed in more detail in the review of Müller *et al*. (1996). In several investigations (Otani *et al*. 1977, Pareti *et al*. 1986) it has been shown that doping with carbon can lead to significant improvements in the kinetics associated with the formation and decomposition of the τ-phase. In the carbon-doped alloys, an incubation period is involved with the formation of the τ-phase. The equilibrium phases β and γ₂ do not form simultaneously with the τ-phase, but form subsequently. The upshot is that the retardation of the formation allows for better process control because it also delays the formation of the undesirable β- and γ₂-phases. Carbon doping has, furthermore, a beneficial effect on the saturation magnetization, although there is a substantial decrease in Curie temperature.

The partial occupation of aluminum sites by manganese atoms at $(0, \frac{1}{2}, \frac{1}{2})$ implies that many antiphase domain boundaries occur in the crystal lattice of the τ-phase. As shown in Fig. 3, these antiphase domain boundaries can act as nucleation sites for Bloch walls, which leads to a relatively easy magnetization

reversal and hence to low values of the coercivity and remanence.

The magnetic properties of the τ-phase in the concentration range 67–73 wt.% manganese have been investigated by Pareti *et al*. (1986). It has been shown that an increasing manganese concentration in the homogeneity range of the τ-phase leads to an increase in the Curie temperature but it lowers the saturation magnetization. The increase of T_C is the result of a general increase of the exchange interaction when magnetic manganese replaces nonmagnetic aluminum. The decrease of the saturation magnetization originates from the excess manganese atoms occupying former aluminum sites. These manganese moments, when coupled antiparallel to those of the main lattice, can cause a reduction in the net saturation moment. The anisotropy field shows a slight increase with manganese content. According to Pareti *et al*. (1986) this increase in H_A is not a real increase in anisotropy but merely reflects the fact that the anisotropy constant, $K_1 = M_s H_A / 2$, remains approximately constant since M_s decreases with manganese concentration. The effect of carbon addition and aluminum concentration on the anisotropy field is shown in Fig. 4.

An important improvement in the magnet manufacturing is due to Otani *et al*. (1977). They have shown that the hard magnetic properties can be significantly enhanced when using a high-temperature extrusion process. In this process microstructures are realized consisting of very fine grains while also the number of antiphase boundaries is strongly reduced. The manufacturing route involves the following steps. The alloys (typically 70.0 wt.% Mn, 29.5 wt.% Al,
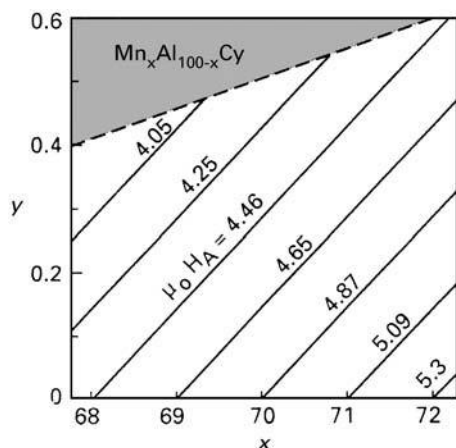
Figure 4
Dependence of the room temperature anisotropy field, H_A, on carbon and manganese content in $Mn_xAl_{100-x}C_y$ with $68 < x < 72$ wt.% and $0 < y < 0.6$ wt.%. Constant anisotropy field values are represented by solid lines. The shaded area corresponds to alloys above the carbon solubility limit (after Pareti *et al*. 1986).

0.5 wt.% C) are given a homogenizing treatment at 1100 °C for 1 h. After quenching the ingots to 500 °C they are annealed at 600 °C for 30 min. The hot extrusion is performed at 700 °C with a pressure of 80 kgmm^{-2}. Finally, the extruded material is aged at 700 °C for 10 min. The energy product can reach values close to 56 kJm^{-3} (7 MGOe). Compared with the energy products reached in rare earth-based magnets (see *Rare Earth Magnets: Materials*) these values are very low. However, one has to take into consideration that the raw materials costs are much lower. Moreover, the production cost is much lower because the whole processing route can be performed in air.

See also: Ferrite Magnets: Improved Performance; Hard Magnetic Materials, Basic Principles of

Bibliography

Buschow K H J 1997 Magnetism and processing of permanent magnet materials. In: Buschow K H J (ed.) *Handbook of Magnetic Materials*. Elsevier, Amsterdam, Vol. 10, Chap. 4
Hoydick D P, Palmiere E J, Soffa W A 1997 Microstructural development in Mn–Al base permanent magnet materials: new perspectives. *J. Appl. Phys*. **81**, 5624–6
Kaneko H, Homma M, Suzuki K 1968 A new heat treatment of Pt–Co alloys of high-grade magnetic properties. *Trans. JIM* **9**, 124–9
Liu J P, Luo C P, Liu Y, Sellmyer D J 1998 High energy products in rapidly annealed nanoscale Fe/Pt multilayers. *Appl. Phys. Lett*. **72**, 483–5

Liu X J, Kainuma R, Ohtani H, Ishida K 1996 Phase equilibria in the Mn-rich portion of the binary system Mn–Al. *J. Alloys Compds*. **235**, 256–61
Müller Ch, Stadelmaier H H, Reinsch B, Petzow G 1996 Metallurgy of the magnetic τ-phase in Mn–Al and Mn–Al–C. *Z. Metallkd*. **87**, 594–7
Otani T, Kato N, Kojima S, Kojima K, Sakomoto Y, Konno I, Tsukahara M, Kubo T 1977 Magnetic properties of Mn–Al–C permanent magnets. *IEEE Trans. Magn*. **MAG-13**, 1328–30
Pareti L, Bolzoni F, Leccabue F, Ermakov A E 1986 Magnetic anisotropy of MnAl and MnAlC permanent magnets. *J. Appl. Phys*. **59**, 3824–8
Tanaka Y, Kimura N, Hono K, Yasuda K, Sakurai T 1997 Microstructure and magnetic properties of Fe–Pt permanent magnets. *J. Magn. Magn. Mater*. **170**, 289–97
Watanabe K 1991 Permanent magnetic properties and their temperature dependence in the Fe–Pt–Nb alloy system. *Mater. Trans. JIM* **32**, 292–8
Zhang B, Soffa W A 1994 The structure and properties of L1$_0$ ordered ferromagnetic Co–Pt, Fe–Pt, Fe–Pd and Mn–Al. *Scr. Metall*. **30**, 683–8

K. H. J. Buschow
University of Amsterdam, The Netherlands

Magnetic Materials: Transmission Electron Microscopy

The application potential of many advanced magnetic materials depends on a combination of the intrinsic and extrinsic properties of the materials in question. Hence a detailed knowledge of both the physical and magnetic microstructure is essential if the structure–property relation is to be understood and materials with optimized properties produced. Most of the materials of interest today are markedly inhomogeneous with features requiring resolution on a sub-50 nm scale for their detailed investigation. Transmission electron microscopy (TEM) has two primary attractions. It offers very high spatial resolution and, because of the large number of interactions that take place when a beam of fast electrons hits a thin solid specimen, detailed insight into compositional, electronic, as well as structural and magnetic, properties. The resolution that is achievable depends largely on the information sought and may well be limited by the specimen itself. Typical resolutions achievable for structural imaging are 0.2–1.0 nm, for extraction of compositional information 0.5–3.0 nm, and for magnetic imaging 2–20 nm.

Although TEM is used extensively for both microstructural and micromagnetic studies it is only the latter that are considered in this chapter. It begins with a description of the basic interaction, which allows magnetic domains to be revealed. Thereafter a

brief description is given of the most widely used imaging modes together with the performance expectation of each. Studies can be made of specimens in their as-prepared states, in remanent states and in the presence of applied fields. From these can be derived basic micromagnetic information, the nature of domain walls, where nucleation occurs, and the importance or otherwise of domain wall pinning and many other related phenomena. It is only recently that extensive *in situ* magnetizing experiments have been undertaken and there is a short discussion of the various ways of implementing them. In the final section, examples of the application of TEM to magnetic materials are given. As TEM is essentially restricted to viewing material sections $<200\,$nm thick, it is ideally suited to the study of thin films. Illustrative examples for both hard and soft films are presented. However, useful information on bulk magnetic material can also be determined and the use of TEM in this area is discussed briefly.

1. Imaging Magnetic Structures by TEM

The principal difficulty encountered when using a TEM to study magnetic materials is that the lenses are essentially electromagnets and the specimen is usually immersed in the high magnetic field (typically $>0.6\,$T) of the objective lens. This is sufficient to completely eradicate or severely distort most domain structures of interest. A number of strategies have been devised to overcome the problem of the high field in the specimen region (McFadyen and Chapman 1992). These include (i) simply switching off the standard objective lens, (ii) changing the position of the specimen so that it is no longer immersed in the objective lens field, (iii) retaining the specimen in its standard position but changing the pole-pieces, once again to provide a non-immersion environment, or (iv) adding super mini-lenses in addition to the standard objective lens which is once again switched off. The last named is the preferred option as it offers both high performance and minimum disruption to the other microscope functions.

Magnetic structures are most commonly revealed in the TEM using one of the modes of Lorentz microscopy. This generic name is used to describe all imaging modes in which contrast is generated as a result of the deflection experienced by electrons as they pass through a region of magnetic induction (Hale *et al.* 1959). The Lorentz deflection angle $\boldsymbol{\beta}_{\mathrm{L}}$ is given by

$$\boldsymbol{\beta}_{\mathrm{L}} = e\lambda t(\mathbf{B}\cdot\mathbf{n})/h \qquad (1)$$

where $\mathbf{B}$ is the induction averaged along an electron trajectory, $\mathbf{n}$ is a unit vector parallel to the incident beam, t is the specimen thickness, and λ is the electron wavelength. Substituting typical values into Eqn. (1) shows that β_{L} rarely exceeds $100\,\mu$rad. Given the

small magnitude of β_{L} there is no danger of confusing magnetic scattering with the more familiar Bragg scattering where angles are typically in the range $1–10\,$mrad.

The description given so far is classical and much of Lorentz imaging can be understood in these terms. However, for certain imaging modes and, more generally if a full quantitative description of the spatial variation of induction is sought, a quantum mechanical description of the beam-specimen interaction must be sought (Aharanov and Bohm 1959). Using this approach the magnetic film should be considered as a phase modulator of the incident electron wave, the phase gradient $\boldsymbol{\nabla}\varphi$ of the specimen transmittance being given by

$$\boldsymbol{\nabla}\varphi = 2\pi et(\mathbf{B}\cdot\mathbf{n})/h \qquad (2)$$

where e and h are the electronic charge and Planck's constant respectively. Substituting typical numerical values shows that magnetic films should normally be regarded as strong, albeit slowly varying, phase objects. For example, the phase change involved in crossing a domain wall usually exceeds π rad.

2. Imaging Modes in Lorentz Microscopy

Magnetic imaging can be performed in either fixed-beam or conventional (C)TEMs or in scanning (S)TEMs. Examples of each along with their associated advantages and drawbacks are given below. Fuller details on the techniques can be found in Reimer (1984), Jakubovics (1994), Chapman (1984), and Chapman and Scheinfein (1999).

2.1 Fresnel and Foucault Imaging

The most commonly used techniques for revealing magnetic domain structures are the Fresnel (or defocus) and Foucault imaging modes. Both are normally practiced in a CTEM. Schematics of how magnetic contrast is generated are shown in Fig. 1. For the purpose of illustration, a simple specimen comprising three domains separated by two $180°$ domain walls is assumed. In Fresnel microscopy the imaging lens is simply defocused so that the object plane is no longer coincident with the specimen. Narrow dark and bright bands, delineating the positions of the domain walls, can then be seen in an otherwise contrast-free image. For Foucault microscopy, a contrast-forming aperture must be present in the plane of the diffraction pattern and this is used to obstruct one of the two components into which the central diffraction spot is split due to the deflections suffered as the electrons pass through the specimen. Note that in general, the splitting of the central spot is more complex than for the simple case considered here. As a result of the partial obstruction of the diffraction
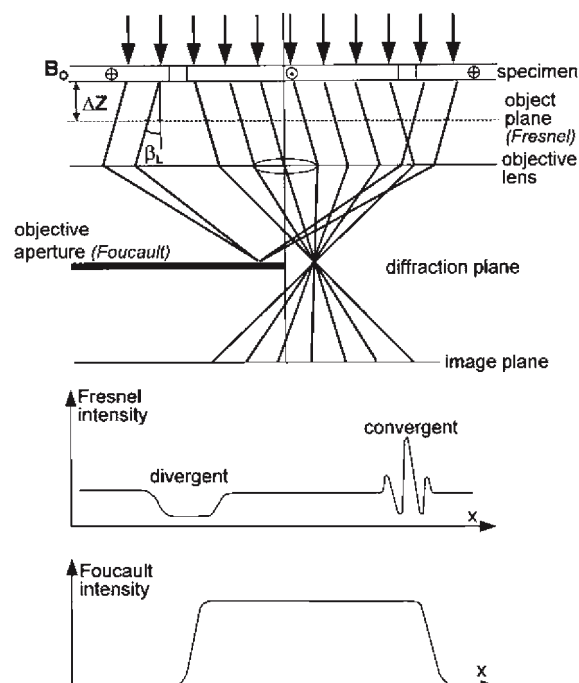
Figure 1
Schematic of magnetic contrast generation in the Fresnel and Foucault imaging modes.

spot, domain contrast can be seen in the image. Bright areas correspond to domains where the magnetization orientation is such that electrons are deflected through the aperture and dark areas to those where the orientation of magnetization is oppositely directed.

The principal advantages of Fresnel and Foucault microscopy together are that they are fairly simple to implement and they provide a clear picture of the overall domain geometry and a useful indication of the directions of magnetization in (at least) the larger domains. Such attributes make them the preferred techniques for *in situ* experimentation (see Sect. 3). However, a significant drawback of the Fresnel mode is that no information is directly available about the direction of magnetization within any single domain, whilst reproducible positioning of the contrast-forming aperture in the Foucault mode is difficult. Moreover, both imaging modes suffer from the disadvantage that the relation between image contrast and the spatial variation of magnetic induction is usually nonlinear. Thus extraction of reliable quantitative data, especially from regions where the induction varies rapidly, is problematic.

Part solutions to these problems have very recently been provided. Whilst the statements made above stand if a single Fresnel image is considered, a novel

development (proposed by Paganin and Nugent (1998)) is to make use of two images of exactly the same area recorded with the same values of under- and over-focus. By combining the images in different ways maps of the two orthogonal components of magnetic induction perpendicular to the direction of electron travel can be obtained. Initial results look very promising but it remains to be seen down to what level reliable information can be extracted. A variant on standard Foucault microscopy—coherent Foucault imaging—has been introduced by Johnston and Chapman (1995). Here the standard objective aperture is replaced by a thin film aperture, which instead of obscuring part of the central diffraction spot simply phase shifts those parts passing through the film. Provided there is a region of free space close to the magnetic specimen and the thin film aperture is positioned to cut the (undeflected) diffraction spot arising from the free space area, the image takes the form of a magnetic interferogram corresponding to the lines of flux running through the magnetic specimen. Similar interferograms are generated using electron holography and further discussion is delayed until Sect. 2.4.

2.2 Low Angle Diffraction

An alternative approach towards determining quantitative data from the TEM is by directly observing the form of the split central diffraction spot. The main requirement for low angle diffraction (LAD) is that the magnification of the intermediate and projector lenses of the microscope is sufficient to render visible the small Lorentz deflections. Camera constants (defined as the ratio of the displacement of the beam in the observation plane to the deflection angle itself) in the range 30–100 m are typically required. Furthermore, high spatial coherence in the illumination system is essential if the detailed form of the low angle diffraction pattern is not to be obscured. In practice this necessitates the angle subtended by the illuminating radiation at the specimen to be considerably smaller than the Lorentz angle of interest. The latter condition is particularly easy to fulfil in a TEM equipped with a field emission gun (FEG). Thus whilst LAD moves some way to supplementing the deficiencies of standard Fresnel and Foucault imaging, the fact that it provides global information from the whole of the illuminated specimen area rather than local information means that alternative imaging techniques are still desirable.

2.3 Differential Phase Contrast Imaging

Differential phase contrast (DPC) microscopy (Dekkers and de Lang 1974, Chapman *et al.* 1990) overcomes many of the deficiencies of the imaging modes discussed above. Its normal implementation
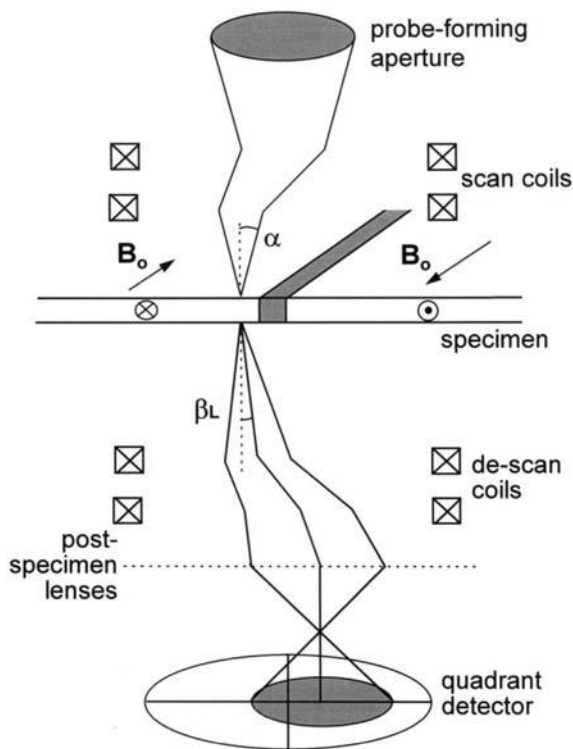
Figure 2
Schematic of magnetic contrast generation in the DPC imaging mode.

requires a STEM. It can usefully be thought of as a local area LAD technique using a focused probe; Fig. 2 shows a schematic of how contrast is generated. In DPC imaging the local Lorentz deflection at the position about which the probe is centered is determined using a segmented detector sited in the far field. Of specific interest are the difference signals from opposite segments of a quadrant detector as these provide a direct measure of the two components of β_L. By monitoring the difference signals as the probe is scanned in a regular raster across the specimen, directly quantifiable images with a resolution approximately equal to the electron probe size are obtained. Providing a FEG microscope is used, probe sizes $<10\,nm$ can be achieved with the specimen located in field-free space. A full wave-optical analysis of the image formation process confirms the validity of the simple geometric optics argument outlined above for experimentally realizable conditions. The main disadvantage against which this must be set is the undoubted increase in instrumental complexity and operational difficulty compared with the fixed-beam imaging modes.

The two difference-signal images are collected simultaneously and are therefore in perfect registration. From them a map of the component of

magnetic induction perpendicular to the electron beam can be constructed. In addition a third image formed by the total signal falling on the detector can be formed. Such an image contains no magnetic information (the latter being dependent only on variations in the position of the bright field diffraction disk in the detector plane) but is a standard incoherent bright field image as would be obtained using an undivided spot detector. Thus a perfectly registered structural image can be built up at the same time as the two magnetic images, a further distinct advantage of DPC imaging. However, at this point it is important to recognize one of the primary difficulties encountered in all Lorentz microscopy modes. The simple analyses given above have assumed that image contrast arises solely as a result of the magnetic induction/electron beam interaction whereas, in reality, contrast arising from the physical microstructure is present virtually always as well. Moreover, it is frequently stronger than that of magnetic origin with the result that the resolution at which useful magnetic information is extracted is often limited by the specimen rather than the inherent instrumental capability.

Although the presence of unwanted contrast of structural origin is serious, its effect can be ameliorated to some extent by suitable choice of operating conditions or modification of the techniques themselves. It is frequently (but not always!) the case that the physical microstructure is on a significantly smaller scale than its magnetic counterpart. If this is so, the influence of high spatial frequency components in the image can be reduced by substitution of the solid quadrant detector by its annular counterpart (Chapman *et al.* 1990). Indeed, in the latter case, not only is the unwanted signal component suppressed considerably but the signal-to-noise ratio in the magnetic component is significantly enhanced.

2.4 Electron Holography

Whilst DPC imaging can provide high spatial resolution induction maps and direct information on domain wall structures, difficulties still remain when absolute values of β_L, rather than relative variations, are sought. A final class of techniques, involving electron holography, go some way to overcoming this problem. Here the electron wave, phase-shifted after passing through the specimen in accordance with Eqn. (2), is mixed with a reference wave and the resulting interference pattern is analyzed to yield a full quantitative description of the averaged induction perpendicular to the electron trajectory. Several distinct strategies exist for mixing the specimen and reference waves and for realizing an interpretable image. In off-axis holographic techniques, a charged wire acts as a biprism, which is located before the specimen in scanning TEMs (Mankos *et al.* 1994) and after it in fixed-beam instruments (Tonomura 1987,
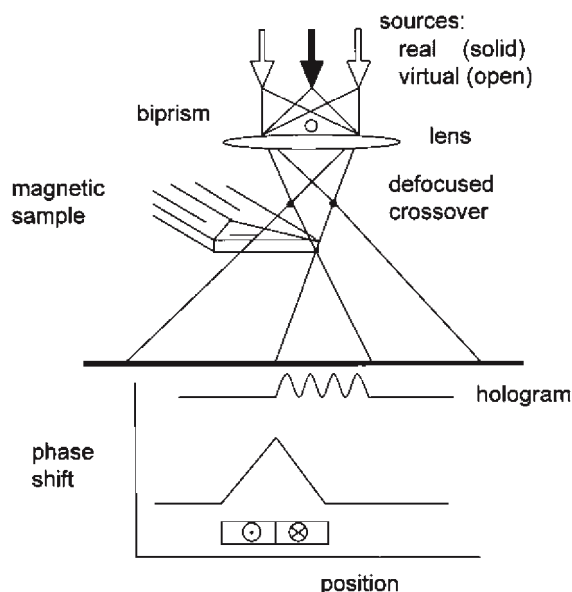
Figure 3
Schematic of how electron holography is implemented in a scanning instrument.

Dunin-Borkowski *et al.* 1998). Figure 3 shows a schematic relating to the former case. Images generated by holography are frequently in the form of magnetic interferograms which can be produced directly or by computer- or optical-processing of recorded holograms. The flux enclosed between adjacent fringes in the interferograms is h/e and so absolute values of the induction integrated along an electron trajectory can be determined. Difficulties with holographic techniques are the high level of instrumental sophistication (a FEG is essential and other instrumental modifications are usually mandatory), the difficulty of imaging away from specimen edges where suitable reference beams are inaccessible, the rapid deterioration in performance with increasing inelastic scattering (severely restricting maximum specimen thicknesses accessible) and excessive fringe separations when very thin specimens are under investigation. Thus, whilst a very powerful addition to the available techniques of Lorentz microscopy, holography brings with it its own associated problems and limitations.

3. *In Situ Studies of Magnetization Reversal by TEM*

One of the major attributes of TEM is the ability to change the magnetic state of the specimen *in situ*. To observe how magnetic structures evolve as a function of temperature is particularly straightforward, and

simply involves mounting the specimen in a variable temperature holder. The use of a small furnace built into a holder allows temperatures to be raised from room temperature to temperatures in excess of 1200 K, which is beyond the Curie temperature of essentially all magnetic materials of interest. Alternatively, cooling holders can be used in which case the temperatures attained depend on whether liquid nitrogen or helium is the coolant employed. In these cases, the minimum temperatures at the points of observation are usually significantly greater than the liquefaction temperatures of the coolants involved. Realistic temperatures achievable at the center of a thin film specimen are 110 K and 20 K for liquid nitrogen and liquid helium respectively. Lower temperatures are difficult to achieve mainly as a result of poor thermal paths rather than because of significant heating in the electron beam itself. The energy deposited, and hence the consequent temperature rise, is generally very small in a thin film sample.

For magnetic specimens, *in situ* observations of the magnetization reversal process itself are crucial if, for example, hysteresis is to be understood at a microscopic level. There are two different approaches to subjecting the specimen to varying magnetic fields in a TEM. In the first a magnetizing stage is used which generates a horizontal field in the plane of the specimen. Two variants are possible. A magnetizing stage can be built into the specimen mounting rod (Hefferman *et al.* 1990) or, if spare ports are available at appropriate positions in the microscope column, one can be introduced as a separate entity. As the maximum available field relates strongly to the volume of the exciting coils and the nature of the magnetic circuit, greater fields can usually be generated using an independent stage. However, irrespective of which variation is adopted, the presence of a horizontal field over a vertical distance many times greater than the specimen thickness results in the electron beam being deflected through an angle orders of magnitude greater than typical Lorentz angles. Under these conditions the illumination normally disappears from the field of view and can only be restored using compensating coils. This introduces an additional element of complexity and the inevitable result is that in such experiments there is limited opportunity to observe changes as they occur; rather the changes that took place due to a change of field are normally observed some time after the event.

An alternative approach, which can be used in instruments where super mini-lenses are present as well as the standard objective lens, is to use the latter as a source of magnetic field given that the specimen remains located somewhere close to its center (Chapman *et al.* 1995, McVitie *et al.* 1995). The objective lens now acts as a source of vertical field whose excitation is under the control of the experimenter. Variation in the excitation of the mini-lenses compensates for the additional focusing effect

introduced. As the field of the objective lens is parallel to the optic axis, it is clearly suitable for studying magnetization processes in perpendicular magnetic materials. However, by tilting the specimen, a component of field in the plane of the specimen can also be introduced. Furthermore, given that demagnetizing effects perpendicular to the plane of a thin film are very large, the presence of even moderately large perpendicular fields can often be ignored and it is the smaller fields in the plane of the specimen that are of interest. When this is the case the objective is set to an appropriate fixed excitation giving a constant vertical field and the sample is simply tilted from a positive angle to a negative one and back again to take it through a magnetization cycle. The principal attraction of the second approach is that the electron optical conditions do not vary during the experiment. Hence, the specimen can be observed throughout and the experimenter can devote full attention to the changing magnetization distribution. It is this approach, which has been used primarily to obtain the results described in the following section.

4. Illustrative Examples of the Use of TEM to Study Soft and Hard Magnetic Materials

In this section the use of TEM is illustrated with reference to some materials systems of current magnetic interest. Soft and hard magnetic films, as well as displaying many fascinating scientific properties are also of major technological importance. Soft magnetic films are used extensively as sensors whilst hard magnetic films are the material of choice for storing information in hard disks and other recording systems. As an example of the former, some magnetic images from spin-valves are presented (Sect. 4.1) whilst domain studies in thin CoPt films serve to show the kind of small-scale domain structure found in magnetically hard films (Sect. 4.2). TEM is also used to study bulk materials such as hard magnetic alloys used in permanent magnets. However, unlike the case with thin films where specimen preparation is at most restricted to the removal of an underlying substrate, here the magnetic material itself must be thinned. Once thinning is undertaken, particularly to the extent required for TEM, the macroscopic magnetic properties themselves change markedly. Thus, taking sintered NdFeB as an example, the grain size is likely to be in the range of 5–10 μm so that the domain structure existing in such a grain situated in the bulk of the material will be quite different from that in a 100 nm thick section of the material as typically used in TEM. This arises primarily as a consequence of the increased importance of the magnetostatic contribution to the total energy in the latter case. Hence extreme care must be taken in making deductions from TEM domain images. Despite this, useful information can be extracted on, for example, magnetic coupling across grain boundaries. Typical results are presented in Sect. 4.3.

4.1 Domain Structures in Spin-valves

Reduced to its simplest form a spin-valve comprises four thin layers (Dieny 1994, Kools 1996). Two are ferromagnetic films, frequently permalloy, which are separated by a thin non-magnetic spacer, usually copper. On top of one of the ferromagnetic layers is deposited an antiferromagnetic film, which serves to "pin" the magnetization of that layer. Changes in resistance occur when the magnetization orientation of the other magnetic layer—the so-called "free" layer—changes under the influence of a small magnetic field. In the absence of any applied field the orientation of the free layer magnetization is generally parallel to that in the pinned layer due to weak magnetostatic coupling between the layers. A magnetic field of 5–30 Oe is often all that is required to completely reverse the magnetization in the free layer. Under such small fields there is no change in the orientation of the pinned layer magnetization. To overcome the exchange-biasing between the pinned layer and the antiferromagnet and so effect a reversal of the magnetization here, fields well in excess of 100 Oe are the norm. For optimized sensor performance it is important to know the mechanism by which each of the two layers reverses and it is here that Lorentz microscopy has a very important role to play.

Figure 4 shows Fresnel images of a spin-valve taken under different applied fields. Initially both layers are uniformly magnetized and no contrast is seen (Fig. 4(a)). As the field increases, magnetization ripple becomes apparent (Fig. 4(b)) after which a number of domain walls appear (Figs. 4(c, d)) and it is clear that reversal is by domain propagation. The walls are not particularly straight nor are they as mobile as in a single isolated ferromagnetic permalloy layer (Gillies *et al.* 1995). Another feature to notice is that black-white walls form and these can be identified as 360° structures (Figs. 4(e, f)); these have an enhanced stability and do not disappear at the same field as the other walls. Once they have been annihilated the reversal of the free layer is complete and no further contrast changes are seen until much higher fields are applied. If information on the nature of the walls themselves is required, the DPC mode is appropriate. Figure 5 shows an image pair, sensitive to orthogonal in-plane induction components, from some 360° walls formed during the reversal of the free layer. These images, recorded at much higher magnification give direct information of the profile of this complex domain structure.

At higher fields magnetic contrast again appears as the reversal of the pinned layer commences. Figure 6 shows examples of the kind of domain structure that occurs in pinned or exchange-biased layers. The most
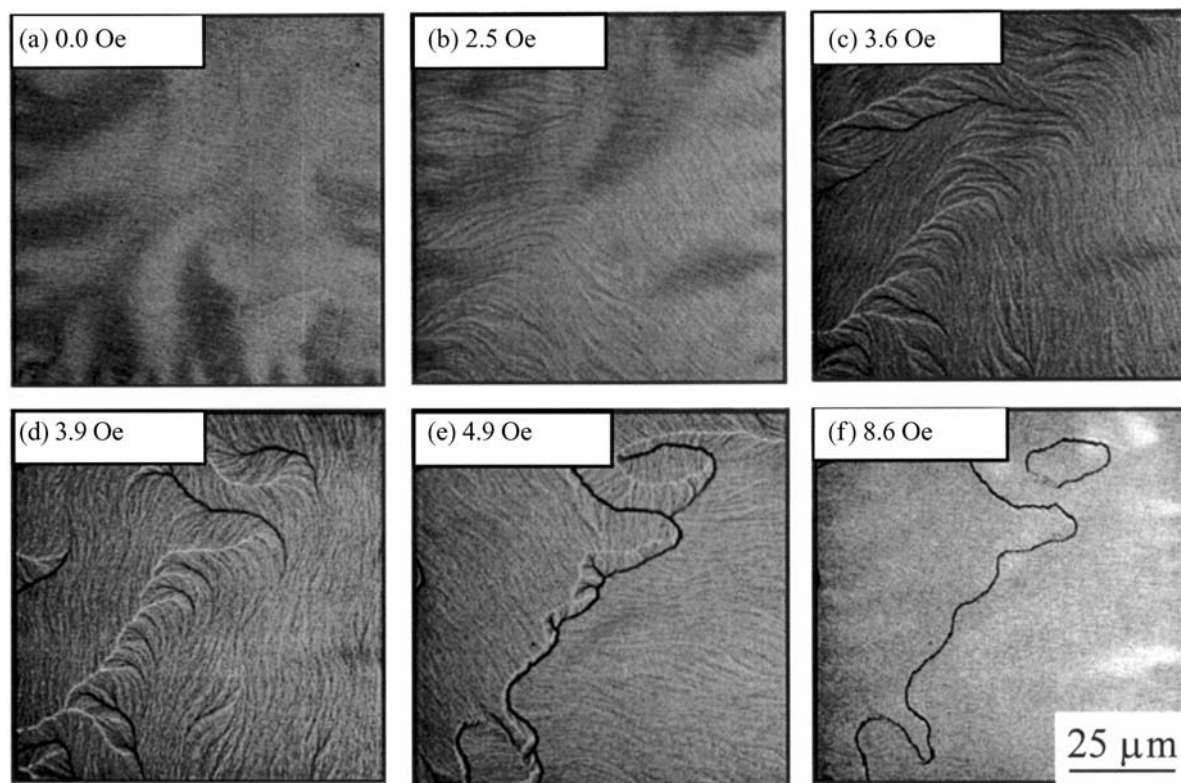
Figure 4
(a)–(f) Fresnel image sequence showing magnetization reversal of the free layer in a spin-valve. Fields at which each image was recorded are shown in the insets.
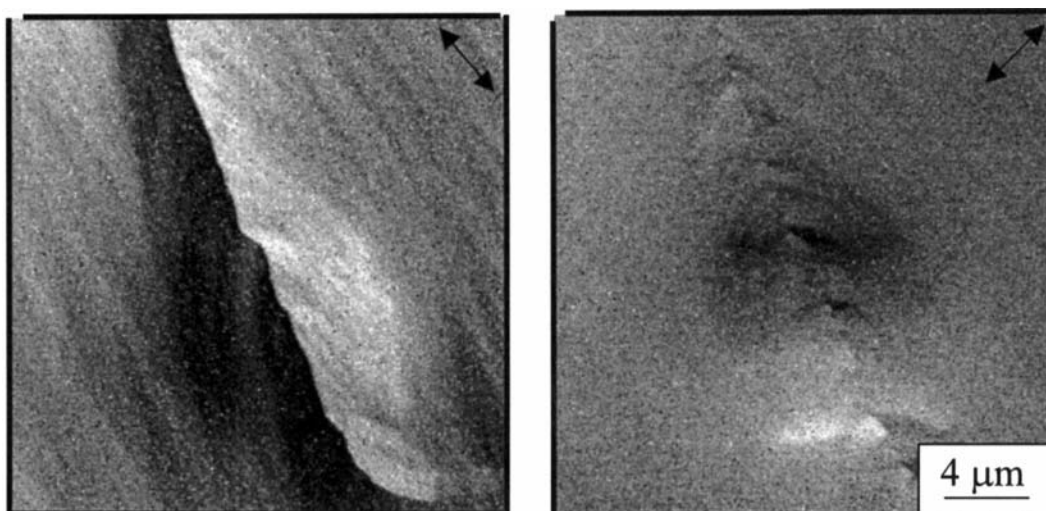
Figure 5
DPC images of a 360° wall segment in the free layer of a spin-valve. The arrows denote the direction of induction mapped in each image.
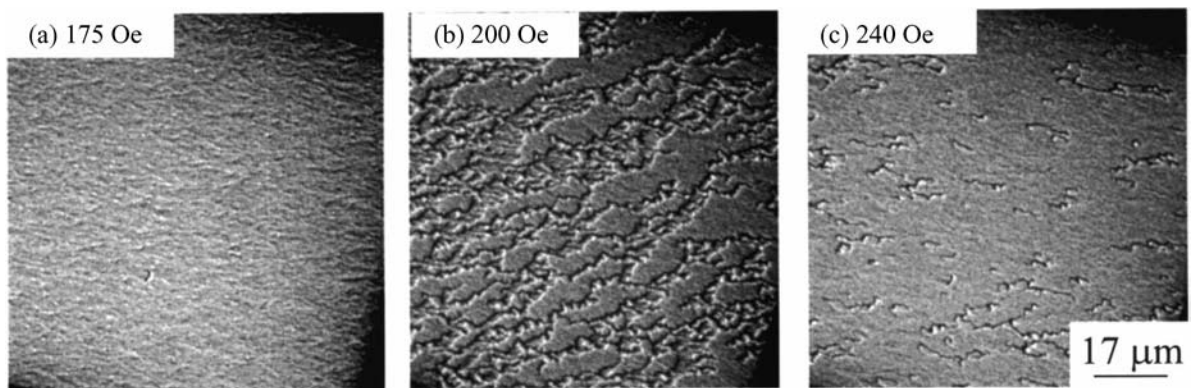
Figure 6
(a)–(c) Fresnel image sequence showing magnetization reversal of an exchange-biased layer. Fields at which each image was recorded are shown in the insets.

important point to note is that whilst reversal is again primarily by domain processes, the geometry and scale of the resulting domains are completely different from those observed in the free layer.

4.2 Domain Structures in CoPt Films with in-plane Magnetization

The storage layer in a hard disk is almost universally a thin film with a granular structure (Richter 1999). Most usually the main constituent is cobalt but up to four additional elements can be present in commercial hard disk media, the most important additions being chromium and/or platinum. The films themselves are generally produced by sputtering and have a mean grain size in the 10–15 nm range. The roles of the additional elements are to achieve very small grains with a tight size distribution and to reduce substantially the exchange coupling between individual grains. The latter is of the utmost importance if the medium is to support small domains and this, in turn, is necessary if information is to be stored at high density. If the medium does not support small domains, or if the stability of these domains is low, then the bit pattern, written by the recording head, changes with consequent loss of information. To avoid accidental erasure and to minimize the effect of thermal demagnetization, the coercivity of the cobalt alloys must be high. Hence, if Lorentz microscopy is to be used effectively to study domain processes in hard cobalt alloy films it is necessary to be able to subject the specimen to changing fields in the range 1–3 kOe. Whilst observation in these fields may also be desirable, it is frequently not necessary as it is irreversible changes in the magnetization distribution that are of the greatest interest here. Hence observations can be made, for example, of a remanence as opposed to a

hysteresis cycle. Figure 7 shows Foucault images and their associated LAD patterns at different stages in a remanence cycle. Fresnel imaging is not appropriate here as the wall contrast simply does not stand out against the relatively high crystallographic contrast present. From the Foucault images, it is clear that the film does support small domains (linear dimensions of the smallest domains ⩽100 nm); from the LAD patterns, the overall dispersion of the magnetization in the corresponding states can be assessed from the variation in circumferential intensity around the arcs.

4.3 Domain Structures in Thin Sections of NdFeB-type Alloys

As noted in the introduction to this section, the information obtainable from bulk specimens using Lorentz microscopy is more limited than that from magnetic thin films. Nonetheless much useful information can be gleaned and this is illustrated by reference to studies on NdFeB-type alloys. These alloys are used extensively as high-energy product permanent magnets and derive their attractive properties from a combination of intrinsic and extrinsic properties, the latter depending on the processing to which the materials are subjected (Gutfleisch and Harris 1996, Buschow 1998). TEM is thus needed to characterise both the physical and magnetic microstructures although it is only the latter, which is of interest here. At comparatively low magnifications and in an unmagnetized specimen, Foucault imaging reveals the domain geometry and allows the orientation of the magnetization in the domains to be determined. Mismatches between orientations in nearby grains relate to the overall anisotropy or lack of it in the sample. Furthermore, in some instances estimates can be made of the domain wall energy from studies of wall spacings in grains whose
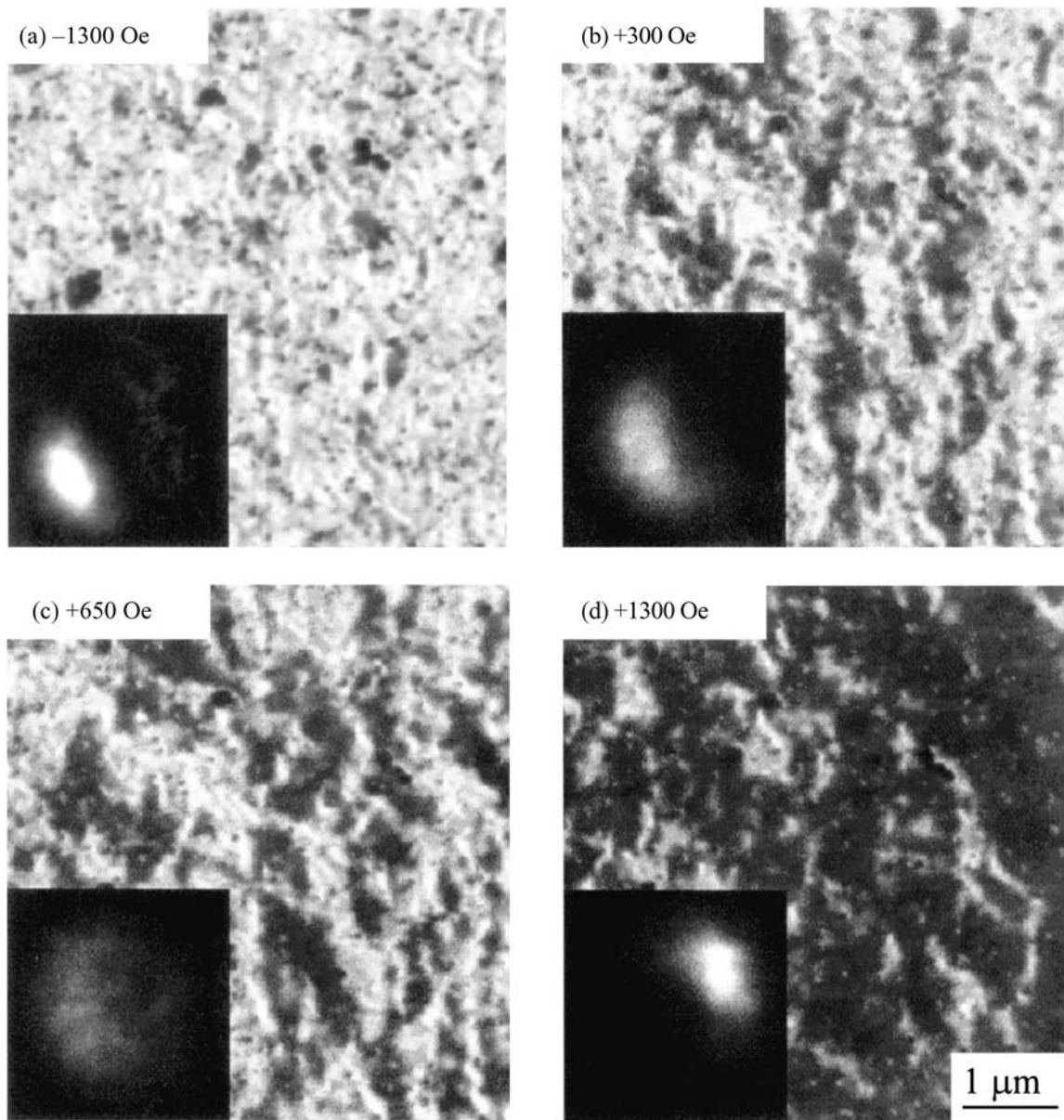
Figure 7
(a)–(d) Foucault images and accompanying LAD patterns from a CoPt film in different remanence states following application of the fields shown in the insets.

physical size is much larger than the mean wall separation (Young and Chapman 1993). At higher magnification attention shifts to the boundaries between adjacent grains, as shown in Fig. 8. The Foucault image here shows how the domain structures distort as walls approach the boundaries. Continuity or otherwise across a boundary then provides important information as to whether there is exchange coupling across boundaries or if interactions between grains are primarily magnetostatic in nature.
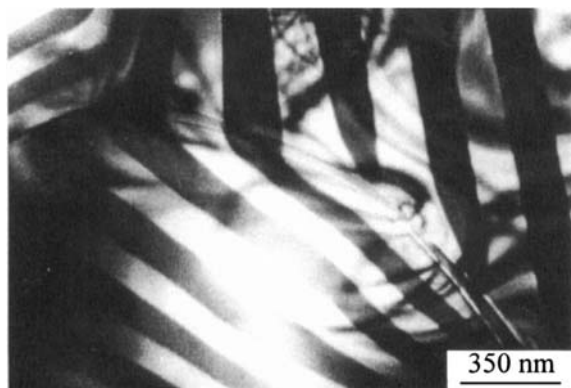
Figure 8
Foucault image of the boundary regions between grains in a thinned section of a NdFeB-type alloy.

5. Conclusions

The techniques of Lorentz microscopy provide a powerful and direct means of obtaining experimental micromagnetic information from magnetic films and, to a slightly lesser extent, from thinned sections of bulk magnetic materials. Many of the techniques possess complementary advantages. The experimenter can choose between an imaging mode that is easy to implement and which is suitable for rapid specimen assessment and real-time studies, or one which yields a detailed quantitative description of the distribution of induction at very high spatial resolution. It is noteworthy that the phenomenon of magnetization reversal varies markedly in different material systems. Hence, the ability to observe directly how reversal proceeds, and to study the nature of domain walls involved, provides invaluable insight into the overall magnetic behavior.

6. Acknowledgments

See also: Kerr Microscopy; Magnetic Force Microscopy; SQUIDs: Magnetic Microscopy

Bibliography

Aharanov Y, Bohm D 1959 *Phys. Rev.* **115**, 485
Buschow K H J 1998 *Permanent-magnet Materials and Their Application*. Transtec, Zurich, Switzerland p. 22
Chapman J N 1984 The investigation of magnetic domain structures in thin foils by electron microscopy. *J. Phys. D Appl. Phys.* **17**, 623–47
Chapman J N, Heyderman L J, McVitie S, Nicholson W A P 1995 Direct observation of magnetic domain structures by field emission Lorentz microscopy. In: Bando Y, Kamo M, Haneda H, Aizawa T (eds.) *Proc. 2nd NIRIM Int. Symp. Advanced Materials*. NIRIM, Japan, pp. 123–30
Chapman J N, McFadyen I R, McVitie S 1990 Modified differential phase contrast Lorentz microscopy for improved imaging of magnetic structures. *IEEE Trans. Magn.* **26**, 1506–11
Chapman J N, Scheinfein M R 1999 Transmission electron microscopies of magnetic microstructures. *J. Magn. Magn. Mater.* **200**, 729–40
Dekkers N H, de Lang H 1974 *Optik*. **41**, 452
Dieny B 1994 Giant magnetoresistance in spin-valve multilayers. *J. Magn. Magn. Mater.* **136**, 335–59
Dunin-Borkowski R E, McCartney M R, Kardynal B, Smith D J 1998 *J. Appl. Phys.* **84**, 374
Gillies M F, Chapman J N, Kools J C S 1995 Magnetization reversal mechanisms in NiFe/Cu/NiFe/FeMn spin-valve structures. *J. Appl. Phys.* **78**, 5554–62
Gutfleisch O, Harris I R 1996 Fundamental and practical aspects of the hydrogenation, disproportionation, desorption and recombination process. *J. Phys. D* **29**, 2255–65
Hale M E, Fuller H W, Rubinstein H 1959 *J. Appl. Phys.* **30**, 789
Hefferman S J, Chapman J N, McVitie S 1990 In situ magnetizing experiments on small regular particles fabricated by electron beam lithography. *J. Magn. Magn. Mater.* **83**, 223–4
Jakubovics J P 1994 *Magnetism and Magnetic Materials*, 2nd edn. Institute of Materials, London
Johnston A B, Chapman J N 1995 The development of coherent Foucault imaging to investigate magnetic microstructure. *J. Microsc.* **179**, 119–28
Kools J C S 1996 Exchange-biased spin-valves for magnetic storage. *IEEE Trans. Magn.* **32**, 3165–84
Mankos M, Scheinfein M R, Cowley J M 1994 *J. Appl. Phys.* **75**, 7418
McFadyen I R, Chapman J N 1992 Electron microscopy of magnetic materials. *EMSA Bull.* **22**, 64–75
McVitie S, Chapman J N, Zhou L, Heyderman L J, Nicholson W A P 1995 *In situ* magnetizing experiments using coherent magnetic imaging in TEM. *J. Magn. Magn. Mater.* **148**, 232–6
Paganin D, Nugent K A 1998 Noninterferometric phase imaging with partially coherent light. *Phys. Rev. Lett.* **80**, 2586–9
Reimer L 1984 *Springer Series in Optical Sciences,* Vol. 36. Springer, Berlin
Richter H J 1999 Longitudinal recording at 10 to 20 Gbit/inch^2 and beyond. *IEEE Trans. Magn.* **35**, 2790–5
Tonomura A 1987 *Rev. Mod. Phys.* **59**, 639
Young S, Chapman J N 1993 An investigation of domains and walls in two NdFeB alloys by transmission electron microscopy. *IEEE Trans. Magn.* **29**, 2779–82

J. N. Chapman
University of Glasgow, UK

Magnetic Measurements: Pulsed Field

Pulsed high field systems are important for studying physical properties in high magnetic fields. A large variety of experiments is possible here. Therefore, generation and permanent increase of the available

fields is an important topic. The production of high magnetic fields dates back to 1924 where fields up to 200 kOe were produced by discharging a large number of accumulators (Kapitza 1924). Later, as a most common technique, the discharge of large condenser batteries was used in order to achieve fields up to 1 MOe (100 T), but for a short time period, typically several microseconds (Foner and Fisher 1967).

Static fields are nowadays generated using superconducting solenoids. With this technology, fields up to 21 T are available (Brown *et al.* 1996, Kiyoshi *et al.* 1996). Higher static fields can be produced using resistive magnets with a huge power supply of about 10 MW in a polyhelix (Schneider-Muntau 1989) and with 13.5 MW in a combined system using a bitter magnet with a polybitter-type helix, which allows static fields up to 27 T (Bird *et al.* 1996). Hybrid systems combining a superconducting magnet with a resistive magnet generate static fields up to about 40 T. Such machines were constructed at the High Magnetic Field Laboratory (HMFL) in Grenoble, at the National High Magnetic Field Laboratory (NHMFL) in Tallahassee, and also in Japan (Sendai and Tsukuba); for a review see Herlach and Perenboom (1995). Beyond 40 T, transient fields are used. One can differentiate between reproducibly—non destructive—methods and single-shot experiments.

Using a condenser battery in connection with a reinforced and well-optimized wire wound magnet, pulsed fields between 53.6 T (Asano *et al.* 1995) and 72.6 T are reproducibly achieved (Herlach 1994). The typical pulse duration is of the order of 5–10 ms, the amplitude of the produced field is limited by the mechanical properties of the conductors, such as Cu–Ag, Cu–SS (SS: stainless steel), Cu–Nb, etc. (Dupouy *et al.* 1995, Frings and van Bockstal 1995, Foner *et al.* 1988). Fields up to 200 T are produced in single-turn coils (von Ortenberg *et al.* 1996) and up to 550 T by flux compression (Miura *et al.* 1996). These are single-shot experiments with a typical pulse duration of 10 µs. A pulse duration below 1 ms is, for metallic samples, generally too short to obtain reliable results. A survey of the magnet laboratories worldwide using nondestructive pulsed fields is given by Herlach and Perenboom (1995).

The disadvantages of short pulsed fields are eddy currents, which limit the experimental studies of metallic samples. In order to overcome this problem, in several laboratories, systems with quasi-static field pulses (100 ms to 1 s) were built. Examples of such high field facilities are located at the University of Amsterdam (Roeland *et al.* 1989, Gersdorf *et al.* 1965), the new installation at the Technical University of Vienna (Grössinger *et al.* 1999), and the CNRS in Toulouse (Askenazy *et al.* 1989). In these systems quasi-static fields between 40 T and 60 T are achieved. The systems of Amsterdam and Vienna use a regulated current supply, which is directly connected to the line delivering 5.4 MW and 10 MW respectively,

at times up to 1 s. In Toulouse a huge condenser battery of 1 MJ is in operation. A larger battery of 12 MJ is just under installation. A new high quasi-static field center is under construction in Dresden. A condenser battery of 1 MJ is used to produce fields up to 50 T in a wire-wound magnet. Additionally, a larger installation with a condenser battery of 30 MJ is expected to allow fields up to 100 T.

1. Applications of High Magnetic Fields to Magnetism

Experiments that need high magnetic fields cover areas from semiconductor physics (e.g., quantum dots) and superconductivity (organic superconductors, high-T_c super-conductors) to magnetism (phase diagram of rare earth 3d compounds, study of actinide compounds, organic ferromagnets, etc.). A comprehensive survey of applications of high magnetic fields has been compiled (*MRS Bulletin* 1993). In the area of magnetism and magnetic materials, there are many publications with open questions, owing to the necessity for experiments with magnetic fields higher than those available. Some examples are: field-induced magnetism, e.g., in YCo_2 and similar compounds (Misawa 1995, Yamada 1995); field-induced changes of the spin structure, e.g., in the R_2Co_{17} and R_2Fe_{17} based materials (Sinnema *et al.* 1986); and also topics related to the application of hard magnetic materials such as the study of the magnetocrystalline anisotropy covering a broad temperature range, e.g., the Sm_2Co_{17} based permanent magnets (Tellez-Blanco *et al.* 1996), $R_2Fe_{14}B$ (Grössinger *et al.* 1985), $R(Fe,Ti)_{12}$ (Kou *et al.* 1993, Grössinger *et al.* 1994) and other materials with high anisotropy.

2. Set-up for a High Field System

2.1 Block Diagram

Figure 1 shows the block diagram of a high field system based on a condenser discharge. It consists of a charging unit, a condenser battery, a discharge switch (e.g., thyristors + diode), a pulse magnet, a measuring system and some measuring electronics. The stored energy (units J or Ws) is given by $C \cdot U^2/2$. In other words, the power (W) can be varied by changing the pulse time. The pulse duration is determined by the design of the magnet, which also determines the volume where the field is available and the maximum achievable field. The pulsed field technique can be used for measurements of magneto-resistance, magnetization, magnetostriction and also for more sophisticated techniques such as de Haas–van Alphen or Schubnikov–de Haas effect but also for the determination of elastic constants in high magnetic fields using an ultrasonic method.
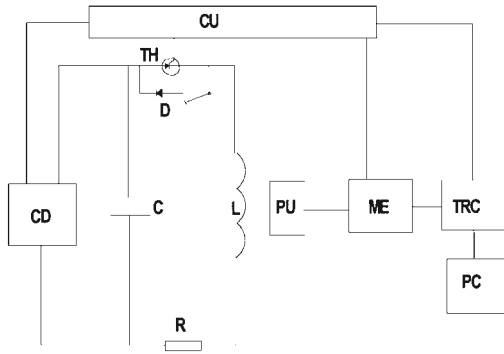
Figure 1
Block diagram of a high pulsed field system (CD, charge device; CU, control unit; PU, pick-up system; ME, measuring electronics including amplifier, integrator, differentiator and input protector; TRC, transient recorder; PC, personal computer; R, resistance from wire; C, condenser battery; L, field generating coil "Magnet"; D, diode, TH, thyristor).

2.2 The Magnet

High field magnets need high current densities. They are limited mainly by two factors: the heating of the magnet and stresses in the magnet windings.

The adiabatic heating can be calculated from:

$$\int j^2(t)\mathrm{d}t = \int_{T_1}^{T_2} \frac{D \cdot c(T)}{\rho(T)}\, \mathrm{d}T = \Gamma \qquad (1)$$

where $j(t)$ is the current density, D is the density of the conductor, $c(T)$ is the specific heat and $\rho(T)$ is the specific resistivity of the conductor. The temperature rise of a pulse magnet can be calculated assuming that thermal conductivity within the short time of the high-field experiment can be neglected (adiabatic condition). The right-hand side of Eqn. (1) shows that the heating of the magnet is determined only by material parameters of the conductor such as D, $c(T)$ and $\rho(T)$. This expression is called the current carrying capability function ("action integral") Γ (van Bockstal 1994). The magnet is generally cooled with liquid nitrogen (77 K) in order to reduce the Joule losses.

However, the more serious limiting factor is the stress in the magnet, which is caused by the Lorentz forces. The stress equilibrium condition of the magnet is given by the derivative of the stress in the radial direction:

$$\frac{\partial \sigma_r}{\partial r} = \frac{\sigma_\theta - \sigma_r}{r} - \lambda \cdot F_r \approx \frac{\sigma_C}{r} - \lambda \cdot j \cdot B_z(r) \qquad (2)$$

where σ_r, σ_θ, and σ_z are the stress components in cylindrical coordinates, σ_C is the yield strength of the wire material, λ is the filling factor, r is the distance

from the axis, and $F_r = j \cdot B_z$ is the radial body force. Solving this differential equation including boundary conditions (reinforcement, etc.) leads to stress in the $z = 0$ plane, which allows a decision about the mechanical stability of the magnets to be made. Additionally, for stability of the magnets the plastic deformation of the wire material as well as the reinforcement must be considered (Gersdorf and Frings 1995, Liang and Herlach 1995).

The maximum achievable field using a certain conductor material is determined, therefore, by considering both the stresses and the "action integral" Γ (Bockstal 1994). So far, the maximum field that can be achieved using standard copper conductors is 40 T. However, it is possible to obtain higher fields when a conductor with a higher yield strength, and/or a stress-adjusted reinforcement of each layer (Askenazy 1995) and/or a variation of the current densities in each layer (Askenazy 1996, Gersdorf and Frings 1995) are realized.

3. Magnetization Measurements

For magnetization measurements three main methods exist which can be used in high pulsed fields:

(i) Measurement of the force acting on a magnetic dipole

(ii) Magnetization measurement using the law of induction

(iii) Magneto-optical methods

The first two methods are focused on here.

3.1 Force Method

A magnetic dipole recognizes a force in an inhomogeneous field. For static magnetization measurements this method is commonly known as the Faraday balance. In fast-pulsed high magnetic fields, the measurement of magnetic forces is technically difficult, owing to the occurrence of mechanic resonances. However, for long pulsed fields a so-called cantilever method has been developed (Naugthon *et al.* 1998). A small sample is mounted on a semiconducting cantilever, which bends owing to the magnetic force. The bending of this cantilever is proportional to the force on the magnetic dipole. The bending is determined using integrated sensor electronics. In the case of a high magnetic field system, the signal is relatively large, owing to the amplification factor of high fields.

3.2 Induction Method

Generally, magnetization is measured using a compensated pick-up coil system, in order to measure the magnetization M instead of the inductance B. For this purpose different arrangements of pick-up coils are used. The general idea is always to get a signal which is proportional to $\mathrm{d}M/\mathrm{d}t$. Such systems consist at least of two coils.

The induction voltage in such coils can be given by:

$$u_1(t) = -\mu_0 N_1 K_1 \pi R_1^2 \left(\frac{dH}{dt} + \frac{dM}{dt} \right)$$

$$u_2(t) = \mu_0 N_2 K_2 \pi r_2^2 \left(\frac{dH}{dt} \right)$$

$$u_s(t) = u_1(t) + u_2(t) \qquad (3)$$

where dH/dt is the applied field rate, u_i, N_i, K_i, r_i ($i = 1, 2$) are induction voltage, number of windings, coupling factor or radius of the outer ($i = 1$) and inner ($i = 2$) pick up coil, respectively. The addition of $u_1(t)$ and $u_2(t)$ shall be performed in such a way that $u_s(t)$ is proportional to dM/dt. One can get this condition in the following cases:

(i) An axial two-coils system N–N: two identical coils are wound on the same diameter, then we may have $N_1 = N_2$; $r_1 = r_2$ and $K_1 = K_2$ (see Fig. 2). This system is sensitive to the local position and therefore sensitive to vibrations.

(ii) An axial three-coils system $\frac{N}{2}/N/\frac{N}{2}$: compensating coils, $u_2(t)$, are formed by two $N/2$ coils. In this case we have: $N_1 = N$; $N_2 = N/2$; $r_1 = r_2$; and $K_1 = K_2$ (see Fig. 2(b)). This system needs a long homogeneous field.

(iii) A coaxial system where $N_1 \neq N_2$; $r_1 \neq r_2$; $K_1 \approx K_2$ (see Fig. 2(c)). The coaxial systems, which are based on Maxwell coils (a centric spherical coil system) are best suited (Gersdorf *et al.* 1967). The requirement of a larger volume is one of the disadvantages of this system. In the compensated system, from Eqn. (3), we can get:

$$N_1 r_1^2 = N_2 r_2^2 \qquad (4)$$

(a)

(b)

(c)
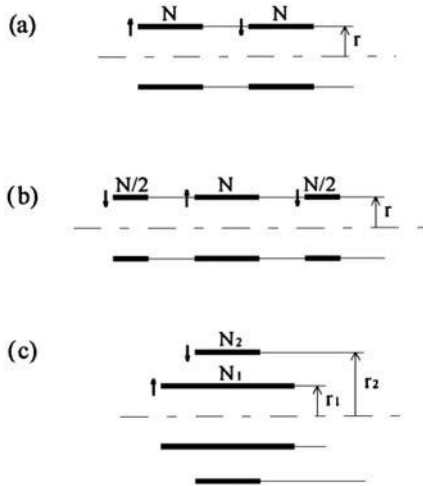
Figure 2
Scheme of the different types of pick-up systems for magnetization measurements. See text for details.

In order to achieve an optimum pick-up geometry (length) for a given experiment, also cancelling of the quadrupolar contribution, the homogeneity field range according to the size of the sample and the inductivity of the two coils has to be considered. Finally, a good degree of compensation of the field, which also holds for higher frequency components, should be achieved. However, the compensation is very sensitive to deviations of the radii or lengths of the induction coils. Therefore, all dimensions of the pick-up coil have to be of the highest possible accuracy (≈ 0.001 mm). The sensitivity of measuring magnetization is limited by the remaining unbalance of the pick-up system. It is worth noting that for measuring paramagnetic substances a compensation of 1×10^6 is desired! The dynamic behavior of such systems is described by the transfer function. Especially in this case, possible resonance peaks have to be avoided.

It should be mentioned that the degree of compensation changes with temperature, owing to the thermal expansion of the supporting materials. Therefore, in this case, the use of supporting materials with a very low thermal expansion (as, e.g., quartz glass, ceramics) or additional position coils which allow a readjustment of the system at each temperature, is suggested. Below 20 K, the magneto-resistance effect of the wire, which may change the calibration constant of the pick-up coils, must be considered.

The magnetization of the magnetic materials is obtained by integrating dM/dt. Generally, in quasi-static systems, owing to the low frequency integration, this method presents a bad signal-to-noise ratio, resulting in low sensitivity. To improve the signal-to-noise ratio, two different methods for measuring the magnetization are proposed: modulation and vibration techniques. In the first method, the field pulse $H(t)$ will be modulated by a small a.c. field of the type $H_{ac} = H_0 \sin \omega t$ (with $H_0 \ll H$ and $T \ll \tau$; where T is the period of a.c. field and τ is the pulse duration). The disadvantage of this method is that the technique of modulating a high field pulse is very complicated. In the second method, the sample can be mounted on a vibrating piezoelectric actuator. The frequency is chosen according to the characteristics of the quasi-static pulse field system. For example, 100 kHz is sufficient for a 100 ms to 1 s quasi-static system. However, generally the amplitude of a piezoelectric system decreases with increasing frequency.

In both cases a periodic induction voltage is produced in pick-up coils, allowing use of a lock-in technique which combines a high Q band pass with a phase-locking method, improving the signal-to-noise ratio drastically. However, for fast a.c. field measurements of a metallic sample in a short pulse magnetic field, the skin effect (penetration of the magnetic field into the material) has to be considered.

Table 1
Skin depth of conducting materials.

Frequency	δ_{Cu} (mm)	$\delta_{Nd-Fe-B}$ (mm)
100 Hz	11	69
100 kHz	0.35	2.2

The skin depth, δ, is given by:

$$\delta = \sqrt{\frac{2}{\omega \cdot \mu_r \cdot \mu_0 \cdot \sigma}} \qquad (5)$$

where μ_r is the relative permeability, μ_0 is the vacuum permeability and σ is the conductivity of the material. To compare the skin depth values between good and bad conductors (Cu: $1/\sigma = 5 \times 10^{-8}\,\Omega m$; Nd–Fe–B: $1/\sigma = 200 \times 10^{-8}\,\Omega m$) Table 1 shows δ values obtained for a pulse duration of 10 ms and for a modulating frequency of 100 Hz and 100 kHz.

Two factors are extremely important for an accurate magnetization measurement in a pulsed high-field magnetometer, namely: (a) field and magnetization calibration of the magnetometer and (b) eddy current effect in conducting magnetic materials.

(a) Calibration of pulsed field magnetometer

In a magnetometer the field and the magnetization have to be calibrated. For pulsed magnetic high-field calibration, the "calibration sample" method is often used. For low temperature magnetization measurements, samples with well known critical fields at which a magnetic transition occurs are chosen for the field calibration. One example is the anti-ferromagnetic MnF_2 where at a field of 9.2 T a spin-flop transition occurs at 4.2 K. For high temperatures, the field is usually calibrated to the internal anisotropy field, H_A, of barium ferrite ($H_A = 1.65$ T, at room temperature). This material is chosen because H_A changes only slightly around room temperature (Kojima 1982). The magnetization M is usually calibrated using the $M(H)$ of pure nickel or iron.

The reliability of pulsed field measurements was tested by comparison with static measurements performed at the CNRS in Grenoble. Figure 3 shows hysteresis loops measured on an isotropic barium ferrite sample obtained in the static system of Grenoble and that measured in a well-calibrated pulsed field system (TU Vienna). The use of barium ferrite has the advantage that there are no eddy currents, because this material is insulating. The difference is within the line thickness.

(b) Eddy current effect

The effect of eddy currents in the sample depends on the sample geometrical dimensions and the pulse
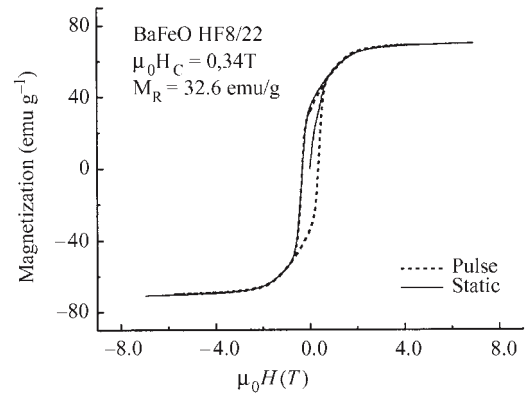
Figure 3
Hysteresis loop measured on the isotropic BaFeO HF 8/22 spherical sample.
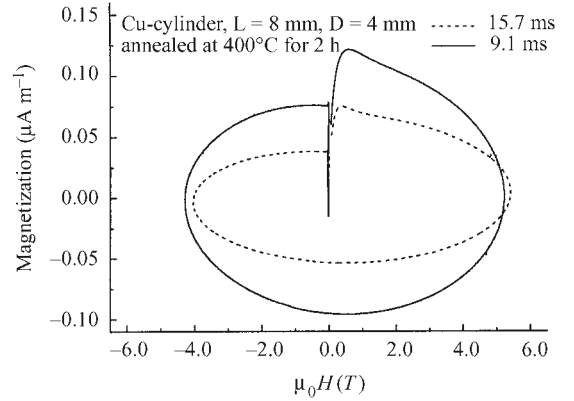
Figure 4
Hysteresis loops measured on a cylindrical copper sample with $\mu_0 H_{max} = \pm 5.7$ T and two different pulse durations of 9.1 ms and 15.7 ms.

time. For a cylinder of nickel of about 4 mm in diameter and a pulse time of about 15 ms the eddy current effect in the magnetization is about 2%. Theoretically, for a well defined sample geometry, it is possible to correct the eddy current effect to the magnetization, but use of a nonconducting soft magnetic calibration is preferred (Grössinger *et al.* 1999). For this type of calibration, material such as Fe_3O_4 is proposed.

In pulsed field measurements, the effect of eddy currents that occur in a metallic sample is shown by measuring the mean magnetization that is generated by these currents. Figure 4 shows, as an example, the magnetization curve measured on a cylindrical copper sample at room temperature applying a field pulse with $\mu_0 H_{max} = \pm 5.7$ T at two different pulse

durations, namely 9.1 ms and 15.7 ms. The increase of the eddy current moment with decreasing pulse duration is clearly visible. The phase shift between magnetization and field is approximately 90°. The experimentally determined eddy currents agree well with a Finite Element calculation. It was shown that plotting the eddy current magnetization versus dH/dt delivers a linear relation which can also be explained theoretically (Grössinger *et al*. 1999).

4. The SPD method

A very important magnetic property of hard magnetic materials is the magneto-crystalline anisotropy (see *Magnetic Anisotropy*). Generally, to investigate this anisotropy a direction-dependent study of single crystals is needed. In many cases such single crystals of technically relevant materials are not available. Often, hard magnetic materials cannot be aligned, owing to special preparation methods. In this case the so-called SPD method (Asti and Rinaldi 1974) is a unique technique for determining the anisotropy.

The SPD method is based on the idea that in higher derivatives of the magnetization with respect to the field, $d^n M/dH^n$, a singularity appears just at that field where $H_{ext} = H_A$. In the case of a uniaxial material the second derivative of the magnetization is already sufficient. The amplitude of the singularity is proportional to the ratio of anisotropy constants K_2/K_1 and also proportional to the distribution function of the crystallites. Additionally, the amplitude is determined by $\omega^2 (H_{max}^2 - H_A^2)$. This means that a maximum external field sufficiently higher than the anisotropy field is necessary. Moreover, the pulse time τ ($\omega \approx 2\pi/\tau$) should be as short as possible taking into account that the scaling is proportional to ω^2 and that the noise is reduced with increasing frequency. An example of the use of the SPD method is shown in Fig. 5. It shows singularities obtained by measurement (a) and by calculation (b) for the polycrystalline Sm_2Co_{17} at room temperature. Although the theoretical peak is sharper than that obtained by

experiment, an excellent agreement in the peak position is observed.

The SPD method delivers the physically real anisotropy field, H_A, from which, knowing the saturation magnetization, the technically relevant anisotropy energy can be obtained.

See also: Magnetism: High-field; Magnetic Measurements: Quasistatic and ac

Figure 5
Measured (a) and theoretically calculated (b) singularity of polycrystalline Sm_2Co_{17} at $T = 300$ K.

Bibliography

Asano T, Sakai Y, Kido G, Inoue K, Maeda H 1995 Development of wire wound pulsed magnet. *Physica B* **211**, 46–9

Askenazy S 1995 Analytical solution for pulsed field coils placed in a magnetic field. *Physica B* **211**, 56–64

Askenazy S 1996 Coilin and Coilex: A route for 100 T non-destructive magnets. *Physica B* **216**, 221–5

Askenazy S, Marquez J, Ricart D 1989 Non-destructive quasi-static pulsed magnetic fields at Toulouse. *Physica B.* **155**, 55–7

Asti G, Rinaldi S 1974 Singular points in the magnetization curve of a polycrystalline ferromagnet. *J. Appl. Phys.* **45**, 3600–10

Bird M D, Bole S, Eyssa Y M, Gao B J, Schneider-Muntau H J 1996 Resistive magnets at the national high magnetic field laboratory: design and operation, 27–33 T. *Physica B* **216**, 193–5

Brown F J, Kerley N M, Knox R B, Timms K W 1996 Review of high field superconducting magnet development at Oxford Instruments. *Physica B* **216**, 203–8

Dupouy F, Askenazy S, Peyrade J P, Legat D 1995 Composite conductors for high pulsed magnetic fields. *Physica B* **211**, 43–5

Foner S, Fisher W G 1967 Solid helix magnets for large volume pulsed high fields. *Rev. Sci. Instr.* **38**, 440–2

Foner S, Bobrov E, Renaud C, Gregory E, Wong J 1988 68.4 T pulsed magnet with a wire-wound metal-matrix Cu/Nb microcomposite. *IEEE Trans. Magn.* **24**, 1059–62

Frings P H, van Bockstal L 1995 Strength versus conductivity. *Physica B* **211**, 73–6

Gersdorf R, Frings P H 1995 Optimisation of coils for semi-continuous magnetic fields. *Physica B* **205**, 133–41

Gersdorf R, Muller F A, Roeland L W 1965 Design of high field magnet coils for long pulses. *Rev. Sci. Instrum.* **36**, 1100–9

Gersdorf R, Muller F A, Roeland L W 1967 Pick-up coil system for measuring magnetization in high fields. *Col. Int. CNRS.* No. 166

Grössinger R, Kirchmayr H, Sassik H, Schwetz M, Taraba M, Frings P, Kaspar G, Raithmayr W 1999 Austromag – a new high-field facility. *J. Magn. Magn. Mater.* **196–7**, 927–9

Grössinger R, Kou X C, Wiesinger G 1994 Magnetic anisotropy and magnetic phase transitions of RFe$_{12-x}$M$_x$ (M = Ti or V). *IEEE Trans. Magn.* **30**, 1018–20

Grössinger R, Sun X K, Eibler R, Buschow K H J, Kirchmayr H 1985 The temperature dependence of the anisotropy field in R$_2$Fe$_{14}$B Compounds (R = Y, La, Ce, Pr, Nd, Gd, Ho, Lu). *J. Phys.* **46**, C6–221–4

Grössinger R, Wittig E, Küpferling M, Taraba M, Reyne G, Golovanov C, Enzberg-Mahlke B, Fernengel W, Lethuillier P, Dudding J 1999 Large bore pulsed field magnetometer for characterizing permanent magnets. *IEEE Trans. Magn.* **35** (5), 3871–3

Herlach F 1994 Pulsed magnetic fields. In: Challis L, Frause J, Herlach F, Wyder P (eds.) *Proc. 2nd European Workshop on Science in 100 T*, Leuven, pp. 31–46
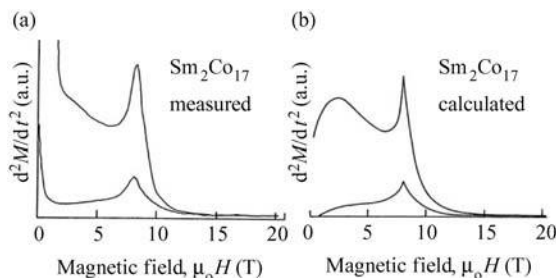
Herlach F, Perenboom A A J 1995 Magnet laboratory facilities worldwide—an update. *Physica B* **211**, 1–16

Kapitza L P 1924 A method of producing strong magnetic fields. *Proc. Royal Soc. London A* **105**, 691–710

Kiyoshi T, Kosuge M, Inoue K, Maeda H 1996 21 T superconducting magnet system at TML. *Physica B* **216**, 196–9

Kojima H 1982 Fundamental properties of hexagonal ferrites with magnetoplumbite structure. In: Wohlfarth E P (ed.) *Ferromagnetic Materials*. North-Holland, Amsterdam, Vol. 3, Chap. 5, pp. 305–91

Kou X C, Zhao T S, Grössinger R, Kirchmayr H, Li X, de Boer F R 1993 Magnetic phase transitions, magnetocrystalline anisotropy, and crystal-field interactions in the $RFe_{11}Ti$ series (where R = Y, Pr, Nd, Sm, Gd, Tb, Dy, Ho, Er, or Tm). *Phys. Rev.* **47** (6), 3231–42

Liang L, Herlach F 1995 Deformation analysis of pulsed magnets with internal and external reinforcement. *Meas. Sci. Technol.* **6**, 1035–42

Misawa S 1995 Fermi liquid description for metamagnetic transition and high field magnetization in $Y(Co,Al)_2$. *Physica B* **211**, 158–60

Miura N, Nojiri H 1996 Recent advances in megagauss physics. *Physica B* **216**, 153–7

MRS Bulletin 1993 *Material Science in High Magnetic Fields* **XVIII** (8), 17–63

Naugthon M J, Ulmet J P, Narjis A, Askenazy S, Chaparala M V, Richter R 1998 Demonstration of cantilever magnetometry in pulsed magnetic fields. *Physica B* **246–7**, 125–8

Roeland L W, Gersdorf R, Mattens W C M 1989 The 40T facility of the university of Amsterdam. *Physica B* **155**, 58–60

Schneider-Muntau H J 1989 D.C. laboratory electromagnets. *Physica B* **155**, 3–9

Sinnema S, Franse J J M, Menovsky A, Radwanski R J 1986 High field magnetization studies on single crystalline Dy_2Co_{17}. *J. Magn. Magn. Mater.* **54–7**, 1639–40

Tellez-Blanco J C, Kou X C, Grössinger R, Estevez-Rams E, Fidler J, Ma B M 1996 Study of coercivity and magnetic anisotropy of sintered Sm_2Co_{17} type permanent magnets in the temperature range from 4.2 K to 1000 K. In: Missel F P, Villas-Boas V, Rechenberg H R, Landgraf F J G (eds.) *Proc. 14th Int. Workshop on Rare-Earth Magnets and their Applications*. World Scientific, Sao Paulo, Brazil, pp. 707–16

van Bockstal L 1994 Wire wound coils for 100 T. In: Challis L, Frause J, Herlach F, Wyder P (eds.) *Proc. 2nd European Workshop on Science in 100 T*, Leuven, pp. 75–98

von Ortenberg M, Portugall O, Puhlmann N, Mueller H U, Barczewski M, Machel G, Thiede M 1996 The Megagauss facility of the HUMBOLDT high magnetic field center in Berlin. *Physica B* **216**, 158–60

Yamada H 1995 Pressure effect of metamagnetic transition in YCo_2 and $LuCo_2$. *Physica B* **211**, 161–4

R. Grössinger
Technische Universität Wien, Vienna, Austria

Magnetic Measurements: Quasistatic and ac

It is of great importance to develop and to improve measurement systems for groups of magnetically ordered materials, which have special demands with respect to typical sample shapes and also to the field range. A magnetically ordered material is characterized by its critical temperature, the Curie temperature T_C, which is proportional to the exchange energy. In rare earth–3d based materials at low temperatures a spin reorientation may occur due to the interplay between the different sub-lattice magnetization or because of the crystal electric field (see, e.g., Kou *et al.* 1993, 1995a, 1998, Grössinger *et al.* 1996). One of the usual methods determining these critical temperatures is the measurement of a.c. susceptibility in low fields as a function of temperature.

The most important technique to characterize magnetic materials is the measurement of their hysteresis loop (see *Magnetic Viscosity*). Figure 1 shows a typical hysteresis loop of a ferromagnetic material with all the significant parts and points of the loop. A loop like this is obtained by applying a cycle of magnetic field H to a magnetic material and by recording the change of the magnetization M or of the magnetic induction B along the field direction. Hysteresis loops may take many different shapes and are important for obtaining parameters that give a first characterization of loop properties such as the coercive field H_c, and the remanence M_r. The technically relevant materials differ only in the special properties of the loop (see Table 1). For hard magnetic materials the coercive field lies between 80 and 1600 kAm^{-1}, whereas for soft magnetic materials the coercive field is below 100 Am^{-1}.

An additional parameter of basic importance in the characterization of soft magnetic materials is the power loss, which is proportional to the area of the hysteresis loop. The most important parameter characterizing the strength of a hard magnetic material is the maximum energy product, which gives a measure of the energy density available in the magnet for external work. The coercive fields of magnetic recording materials lie somewhere between those of hard and soft materials. In both cases the saturation magnetization, M_s, should be as high as possible. Generally,
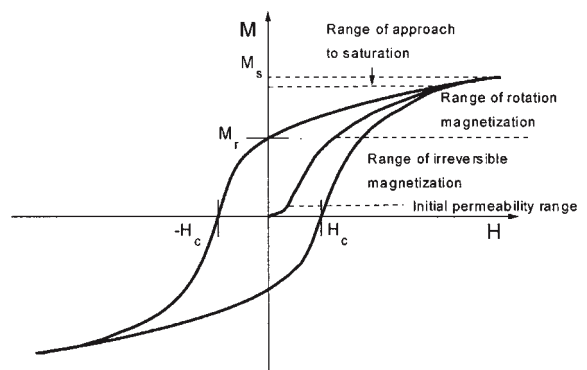
Figure 1
Hysteresis curve of a ferromagnetic material.

Table 1
Comparison of important magnetic properties between soft and hard magnetic materials.

	Soft magnetic material	Hard magnetic material
Saturation magnetization	As high as possible (0.8–2 T)	As high as possible (0.2–1.5 T)
Coercive force	As low as possible ($<100\,\mathrm{Am^{-1}}$)	As high as possible (80–$400\,\mathrm{kAm^{-1}}$)
Permeability	As high as possible 10 000–200 000	Not important
Losses	As low as possible, frequency-dependent	Area of loop $\cong$ stored energy as high as possible
Shape of loop	Important because it determines application	Important and should be rectangular
Remanence	Not important	As high as possible
Conductivity	Determines a.c. losses	Important for magnetizing procedure

for obtaining the "true" saturation magnetization the law of approach to saturation extrapolating for $H \to \infty$ or fitting the $M(H)$ curve (Akulov 1931, Gans 1932, Grössinger 1981) may be applied.

In addition, the loop itself as well as parts of the hysteresis (initial curve, minor loops, recoil curves) is used for modeling, and this yields an understanding of the magnetization process (Mayergoyz 1991, Bertotti 1996, Hauser 1994).

A hysteresis loop can be created in terms of $B(H)$ or of $M(H)$, where $\mathbf{B} = \mu_0(\mathbf{H} + \mathbf{M})$. For technical applications $B(H)$ is more important whereas for scientific investigations $M(H)$ is generally used. In contrast to hard materials where H and M have comparable orders of magnitude, in a soft material (for low H) plotting $B(H)$ or $M(H)$ makes no difference due to a very good approximation, $\mathbf{B} \cong \mu_0 \mathbf{M}$. In hard magnetic materials $_\mathrm{I}H_\mathrm{C} > _\mathrm{B}H_\mathrm{C}$, whereas in soft magnetic materials both coercivities are equal ($_\mathrm{I}H_\mathrm{C}$ is coercivity where $\mathbf{I} = \mu_0 \mathbf{M} = 0$, $_\mathrm{B}H_\mathrm{C}$ is coercivity where $\mathbf{B} = 0$). Therefore a hysteresigraph for soft magnetic materials is technically different from that of a system suited for hard magnetic materials or for recording materials.

Consequently, within this contribution two groups of measurements will be proposed which are important for characterizing hard and soft magnetic materials:

A.c. susceptibility. The temperature dependence of the susceptibility yields the Curie temperature, spin reorientation temperature, freezing temperature for spin glasses, magnetic relaxation, etc. and also domain parameters such as the Rayleigh constant and the pinning field;

Magnetization and hysteresis loop. This delivers the coercive force, remanence, saturation magnetization, and energy losses (or stored energy) and also gives information about the magnetization process. A special type of instrument used here is a torque magnetometer which allows determination of the anisotropy constants.

1. Susceptibility Measurements

1.1 Theoretical Considerations

Starting from a demagnetized state of the hysteresis loop, the inclination of the initial curve is called the initial susceptibility χ_i (if one considers $M = \chi_\mathrm{i}H$) or the initial permeability μ_i (if one considers $B = \mu_\mathrm{i}H$). For a soft magnetic material the initial susceptibility is very high and $\mu_\mathrm{i} \approx \chi_\mathrm{i}$.

In randomly oriented particle systems, polycrystalline bulk materials where due to the presence of differently oriented crystal grains a random variation of anisotropies exists, or in magnetically soft materials where a fluctuating internal stress couples magnetoelastically to the magnetization, the response to small fields is mainly controlled by the local anisotropy fields. In this simple case the initial susceptibility can be written as:

$$\chi_\mathrm{i} = \frac{\mu_0 M_\mathrm{s}^2}{cK} \qquad (1)$$

where K stands for all kinds of anisotropy energies including the magnetoelastic energy and c is a dimensionless factor dependent on the specific distribution of the anisotropy axes of anisotropy constants. Very often an additional contribution comes from the actual microstructure. However, this is very difficult to estimate.

With increasing fields the first irreversible losses have to be considered. If local inhomogeneities (local stress centers, etc.) occur a well-defined pinning field can be observed as will be discussed below. The different field dependencies of the permeability are shown in Fig. 2. The hysteresis loop of low fields, where the maximum fields involved are much smaller than the coercive field, can be described by the Rayleigh law (Fig. 2(a); see, e.g., Jordan 1922 or Chikazumi 1964). Within the Rayleigh law, under small but finite fields, the permeability consists of two contributions: the reversible magnetization is
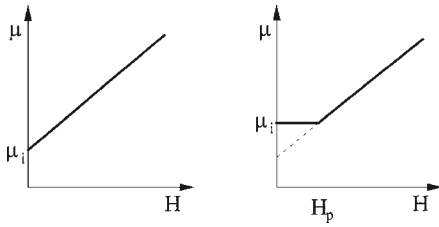
Figure 2
Field dependence of the permeability: (a) assuming the Rayleigh law; (b) showing an initial range below H_p.

described by the first term (initial permeability μ_i) and the irreversible part that depends on the square of the field:

$$B = \mu_i H + \nu H^2 \tag{2}$$

where ν is the Rayleigh constant. This law is important in principle as a description of the initial steps of irreversibility.

If a magnetic material is magnetized by an a.c. field $H = H_0 e^{i\omega t}$, the magnetic flux density B is delayed by the phase angle δ because of the presence of losses and is then expressed as $B = B_0 e^{i(\omega t - \delta)}$. The permeability is given by:

$$\mu_r = \frac{B}{\mu_0 H} = \frac{B_0 e^{i(\omega t - \delta)}}{\mu_0 H_0 e^{i\omega t}} = \frac{B_0}{\mu_0 H_0} e^{-i\delta} = \mu' - i\mu'' \tag{3}$$

where the real part is $\mu' = (B_0/\mu_0 H_0)\cos\delta$ and the imaginary part $\mu' = (B_0/\mu_0)\sin\delta$. The imaginary part is related to the losses. Another important loss contribution for ferromagnetic metals and alloys is the eddy current loss. Since a power loss of this type increases proportionally to the square of the frequency, it plays an important role in the high-frequency range.

Generally in soft magnetic materials due to the existence of well-defined local pinning centers a critical field, the pinning field H_p, is often observed (see Fig. 2(b)). Up to H_p the permeability is constant and for an applied field higher than H_p the permeability increases. If a linear behavior is observed the permeability can be described by a modified Rayleigh law:

$$\mu = \frac{B}{H} = \mu_i + \nu(H - H_p) \tag{4}$$

If one considers now the magnetization curves in more ordinary materials where the presence of structural defects or disorder plays a dominant role under most circumstances, the measurement of the a.c. susceptibility is one of the techniques to characterize these materials. In hard magnetic materials the shape of the virgin magnetization curve as well as the shape of the loop with increasing external field is used to determine roughly the different types of

magnetization processes (nucleation or pinning controlled) (Becker 1976).

1.2 Experimental Determination of the a.c. Susceptibility

As shown above the measurement of the initial susceptibility (in a field which should be small compared with the coercivity) as a function of temperature is important. Because the susceptibility is roughly proportional to $1/K$ (Eqn. (1)) it shows a dramatic change at any spin reorientation temperature, crystallization temperature, or the Curie temperature, because the anisotropy goes much faster to zero than M_s. For this purpose a small a.c. field is applied to a sample which is surrounded by a pick-up coil. In principle the a.c. susceptibility can be measured in most hysteresigraph systems (using an air coil), where one has just to drive the magnet with a low a.c. field. The pick-up coil system is then connected to a lock-in amplifier which can measure the real and imaginary parts of the susceptibility simultaneously. A block diagram suitable for soft magnetic ribbons is shown in Fig. 3. In this device an external stress can also be applied to the sample which additionally causes an effect on the domain configuration (Holzer 1998). In the case of a hard magnetic material the ribbon is replaced by a (spherical) sample inside a compensated pick-up system.
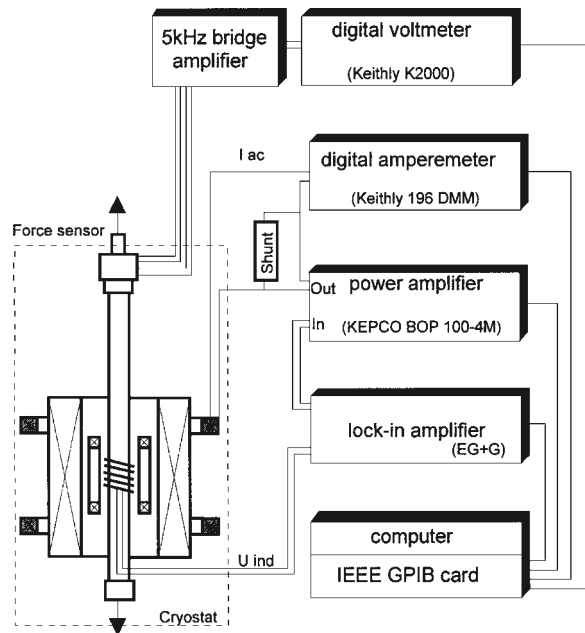
Figure 3
Setup for a.c. susceptibility measurements (after Holzer 1998).

The temperature of the sample can be varied by using either a furnace or a cryostat. The susceptibility deduced for a lock-in amplifier ($U_{ac} = $ RMS value of the signal) is given by:

$$\chi = \frac{U_{ac}}{N_{pick}\mu_0 2\pi f k I_{ac} X} = \mu - 1 \qquad (5)$$

where N_{pick} is the number of turns of the pick-up coil, f is the frequency of the a.c. current, and k is the calibration factor of the field coil. For a ribbon $X = A_{rib}$ (cross-section of the sample) because the ribbon is much longer than the pick-up coils. For a small sample, X takes the value of the area of the cross-section of the pick-up coil (e.g., a hard magnetic spherical specimen). The voltage U_{ac} is in any case proportional to the mass of the sample—the calibration factor has to be determined experimentally.

For an absolute value of the measured susceptibility, the following points have to be considered. In the case of thin long samples such as amorphous ribbons one can measure on toroid and open ribbons:

Toroid ribbon: this is a magnetically closed circuit, which means the demagnetizing factor is zero. The disadvantage is that in the case of a soft magnetic thin ribbon this is not a stress-free state. Also stress-dependent measurements are not possible on a toroid. It should be mentioned that the domain structure of soft magnetic materials is strongly stress-dependent (Badurek *et al.* 1988, Veider *et al.* 1986);

Straight ribbon: this is not a closed magnetic circuit. Therefore, the measurements in low fields are very sensitive to external fluctuating fields. Either a very effective shielding or an accurate earth field compensation is essential for soft magnetic materials. Additionally the demagnetizing factor N may be considered. The effective susceptibility with the internal field H_{int} can be described as:

$$\chi = \frac{M}{H_{int}} = \frac{M}{H - NM} = \frac{\chi_{meas}}{1 - N\chi_{meas}} = \frac{1}{(1/\chi_{meas}) - N} \qquad (6)$$

For a soft magnetic material χ is large which means that the measured χ is proportional to $1/N$. Therefore the samples should be very long compared with the cross-section in order to reduce N. For hard magnetic materials χ is small and proportional to $1/K$.

2. Magnetization Measurements

There are many techniques for measuring hysteresis loops and magnetization. The majority of them is based on the law of induction. Besides this, devices exist where the magnetization is measured via the force of a dipole in an inhomogeneous field (Faraday balance) or even magneto-optically by measuring the Faraday rotation due to the magnetization. The latter method is, of course, important for recording
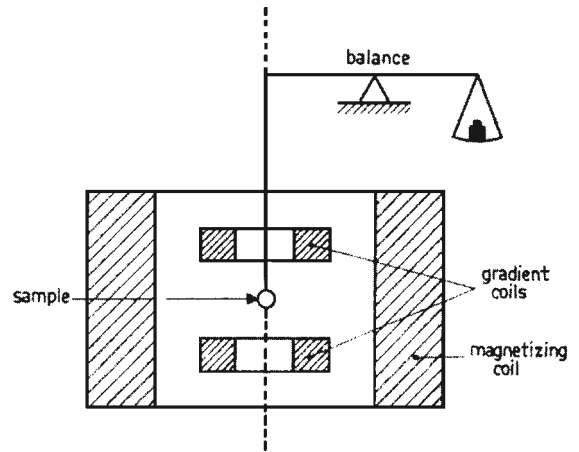
Figure 4
Sketch of a Faraday balance arranged in a solenoid.

materials. Figure 4 shows a sketch of the Faraday method. The field can be produced using a solenoid which can be also superconducting or have an iron-yoke. In the case of an electromagnet the specially shaped pole pieces generate a field gradient in the air gap. The force can be measured by all kinds of force sensors such as strain gauges or piezoelectric sensors. Also torque magnetometers, in which a single crystalline sample feels a torque $\mathbf{L} = \mathbf{m} \times \mathbf{H}$ in a magnetic field, are based on similar principles. These systems are very important for studying magnetocrystalline anisotropy.

One can consider two main possibilities for induction-based methods.

The first is that one can integrate the induction voltage which is proportional to dB/dt and consequently to dM/dt during the variation of the field. Generally this method is a d.c. technique because the variation of the field, which is produced by an electromagnet or by a superconducting magnet, is performed slowly. This technique needs a very stable integrator. The sensitivity is limited principally by the thermal drift of the system as well as by the $1/f$ noise.

The second method uses a type of modulating method either by vibrating the sample or by slowly modulating the varying field. This technique overcomes the drift problem. In this case the induced voltage u is a periodic signal which is proportional to $dM/dt \sin(\omega t + \delta)$. Normally in this technique a lock-in amplifier is used which provides a drastically enhanced signal-to-noise ratio due to reduction of the bandwidth of the system. In metallic samples the frequency is chosen such that eddy current effects can be avoided. Consequently the frequency is rather low (< 82 Hz), so drift problems can be overcome but the $1/f$ noise problem cannot be solved completely.

2.1 Vibrating Sample Magnetometer

A vibrating sample magnetometer (VSM) is a state-of-the-art device for magnetization measurements. There exist several commercial VSMs which operate from very low temperatures up to about 1000 K. In a VSM the sample is driven by a mechanically vibrating system and the signal is measured by a pick-up system. The first working model of a VSM was assembled by Foner (1956) using a reduced-amplitude 60 Hz line excitation of a loudspeaker. The sample vibrates perpendicularly to the applied field. Small permanent magnets were used to generate a reference signal in order to stabilize the movement of the loudspeaker. Field modulation combined with lock-in amplification was used for signal processing and a lock-in amplifier was used to enhance the signal-to-noise ratio. Later, Foner (1959) described a more standard version of a VSM in a comprehensive paper. In the first system electromagnets generated the external field. With the development of high-field superconductors, superconducting solenoids were introduced into the VSM, producing fields up to about 20 T. These systems are commercially available for measurements from low temperatures up to furnace systems. The principal setup of a VSM is shown in Fig. 5.

2.2 SQUID Magnetometer

SQUID (superconducting quantum interference device) magnetometers are generally used to measure the magnetization of very small samples (e.g., thin films) or systems that are just on the limit of magnetic order. Therefore, SQUID magnetometers are mainly applied to scientific investigations. Measuring materials with a high magnetization requires the use of an attenuator, but due to their very great sensitivity geological, biological, and medical applications are increasing. The operation of a SQUID magnetometer is based on two effects: flux quantization and the Josephson effect.

The classical Josephson junction consists of an insulating barrier between two superconductors thin enough to couple "weakly." This allows an electron pair tunneling via the barrier. The flux Φ_0 in the superconducting state is quantized in steps of $\Phi_0 = h/2e = 2.07 \times 10^{-15}$ Wb, where h is Planck's constant and e is the electron charge. Due to the different types of electronic readout, a SQUID consists basically of a superconducting ring interrupted at one or two positions by a Josephson junction. SQUIDs with one junction are RF-SQUIDs (radio-frequency) and those with two junctions are d.c.-SQUIDs (see *SQUIDs: The Instrument*).

Figure 6 shows the basic electronic circuit of a RF-SQUID. The peak value of the voltage drop V_{rf} across the tank circuit is measured by a RF amplifier together with a detector. This signal has to be set in relation to the RF signal at a power P_{rf} applied to the tank circuit. The value of V_{rf} depends on the low-frequency input signal, i.e., the flux Φ_{ext} is applied to the SQUID ring via the inductively coupled input coil. The advantage of a RF-SQUID is that the use of a high-frequency a.c. signal allows the application of a.c. techniques which improve the signal-to-noise ratio. Unlike the inductive detector VSM, whose output is proportional to frequency, the output of the SQUID detector is independent of frequency.

The SQUID generally operates at 4.2 K since the critical temperature of superconductors is low. High-T_C superconductors allow systems to operate at temperatures up to 77 K. Since the SQUID is an extremely sensitive flux detector it must be carefully

Figure 5
Principal setup of a VSM.
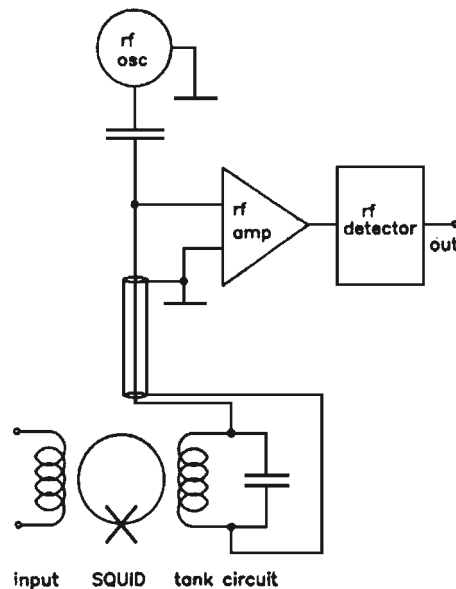
Figure 6
Block diagram of a RF-SQUID.

501

shielded. But the high sensitivity means it can be used to measure very small fields. There are SQUID magnetometers which operate in external fields up to 6 T. They can also be used for medical applications such as measuring brain currents. A good survey of this field is given by Koch (1991).

2.3 Pulsed Field Magnetometer

Generally, pulsed field systems are used for measurements in high external fields which are above those which are available as static fields. This means that such magnetometers are used in fields up to 100 T (Herlach 1994) and higher. However, there are also technical applications which are interesting because here the easy-to-handle factor and fast measurement becomes important. Modern high-quality permanent magnets, such as Sm–Co- or Nd–Fe–B-based materials, need rather high magnetic fields in order to measure the hysteresis loop. Static fields such as those available with Fe-yokes (up to about 2 T) are not sufficient here. Additionally, static hysteresis measurements take too much time for an industrial production control. Using pulsed field magnetometry full hysteresis loops $M(H)$ of a hard magnetic material can be measured very quickly and with an accuracy of 1% at room temperature (for details see *Magnetic Measurements: Pulsed Field*).

3. Characterization of Soft Magnetic Materials

Soft magnetic materials (see *Magnets, Soft and Hard: Magnetic Domains*), such as Fe–Si strips, amorphous ribbons, or nanocrystalline materials, exhibit a special geometry. Because of its technical importance Fe–Si needs a very accurate and standardized determination of the hysteresis properties. For measuring the losses as well as the permeability in fields that are not too high the so-called Epstein frame (Epstein 1900) is well established (see *Magnetic Hysteresis*).

New kinds of soft magnetic materials such as amorphous ribbons based on a 3*d* metal (Fe, Co)–metalloid (B, Si, C) compound (see, e.g., Luborsky 1983) are thin ribbons (typical thickness 20–50 μm, width 1–15 mm) produced by rapid quenching through melt spinning. Some of them can be transformed after special heat treatment into the nanocrystalline state and they also exhibit excellent soft magnetic properties (Yoshizawa *et al*. 1988, Herzer 1990) (see also *Amorphous and Nanocrystalline Materials*). The ribbon-like geometry requires special equipment. Due to their very low coercive field (typically between 1 and 20 Am^{-1}) standard magnetometers using either an electromagnet or a superconducting solenoid cannot be used, since the lowest achievable field is determined by the remanence of the system which is in the order of 10 kAm^{-1}.
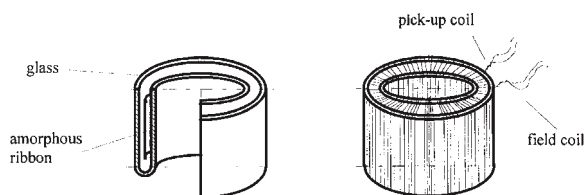
Figure 7
Example of a toroidal measurement facility suited for use in a furnace: glass toroid, sample, and coils.

Additionally, at very low fields, the electromagnetic noise of the surroundings is a limiting factor. As examples, two systems suitable for scientific applications are described which allow measurements at both low and elevated temperatures.

The magnetic properties of soft ferromagnetic ribbons (hysteresis loop, susceptibility) can be measured either on toroidal samples or on single strips. The toroidal sample (see Fig. 7) has the advantage that, to the first order, the demagnetizing field can be neglected, which is important especially for permeability and loss measurements such as in an Epstein frame. However, for determining the saturation magnetization, this shape is no more advantageous due to the increase in the stray field of the system with the increase of the applied field, which causes an undefined error.

3.1 Low-temperature Hysteresis Loops

Low-temperature measurements are generally important in order to test the validity of theoretical predictions such as the Bloch law (Bloch 1930) or the $l(l+1)$ power law for the anisotropy and magnetostriction (Callen and Callen 1966). For the system that will be described here (see Fig. 8) the temperature dependence of the hysteresis loops can be measured on wires, single ribbons, or thin sheets. Due to the special geometry of the setup, an external stress can also be applied which is very useful for studying the effect of the magnetoelastic energy on the hysteresis. This effect is especially important for sensor applications.

Figure 8 shows a system that measures hysteresis loops between 4.2 K and room temperature. The facilities necessary for measuring the hysteresis loop are field coils (cylindrical coil + Helmholtz coil), a compensated pick-up coil, a current source, an amperemeter, and an integrator (fluxmeter). The devices can be connected and controlled by a data acquisition and control unit forming a fully automatic hysteresis loop system. The external stress is measured by a strain gauge bridge. To avoid the influence of eddy currents and magnetic relaxation effects measurements are performed quasi-statically (0.05–0.03 Hz).
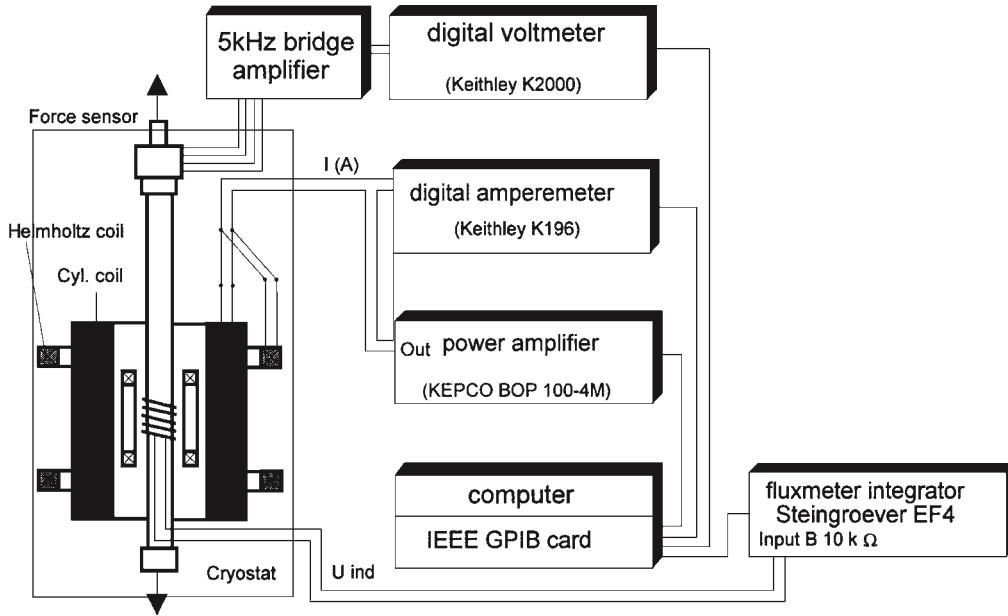
Figure 8
Hysteresigraph for quasi-static hysteresis measurements and device for force measurements (Polak 1992, Holzer 1998).

In this case the measurement of one hysteresis loop takes 20–30 s. The magnetic field is deduced from the current measured by the amperemeter and the induction from the magnetic flux is measured by the integrator. Since the change of the induction voltage is slow, a very stable industrial integrator (e.g., Fluxmeter Steingroever EF4) is required. Effectively it is a d.c. method where the drift is a limiting factor.

When a time-dependent magnetic field is applied, the induction signal in the pick-up coil is:

$$u_{\text{pick-up}} = -N_{\text{pick}}\frac{\mathrm{d}\Phi_{\text{pick-up}}}{\mathrm{d}t}$$
$$= -N_{\text{pick}}\mu_0\left(A_{\text{rib}}\frac{\mathrm{d}M}{\mathrm{d}t} + A_{\text{pick}}\frac{\mathrm{d}H}{\mathrm{d}t}\right) \quad (7)$$

and the induction signal in the compensation coil is:

$$u_{\text{comp}} = -N_{\text{comp}}\frac{\mathrm{d}\Phi_{\text{comp}}}{\mathrm{d}t} = -N_{\text{comp}}\mu_0 A_{\text{comp}}\frac{\mathrm{d}H}{\mathrm{d}t} \quad (8)$$

Then in the compensated system the signal is:

$$u_{\text{ind}} = u_{\text{pick-up}} - u_{\text{comp}} = -N_{\text{pick}}\mu_0 A_{\text{rib}}\frac{\mathrm{d}M}{\mathrm{d}t} \quad (9)$$

For this measurement system there are three important points.

The resistance of the pick-up system is temperature-dependent for low-temperature measurements. The resistance of a pick-up system with many windings can be several hundreds of Ohms at room temperature, which can change by a factor of 7 to 10 when it is cooled down to 4.2 K. Generally, the input resistance of a fluxmeter is not very high (typically 10 kΩ); therefore, this has to be taken into consideration in the calibration procedure.

A zero-signal must be subtracted. This is necessary because the compensation changes with temperature.

Equation (9) contains also the cross-section A_{rib} of the ribbon. Therefore, it is very difficult to obtain an accurate value of A_{rib} of amorphous or nanocrystalline ribbons due to fluctuations in thickness as well as in the width. This often limits the accuracy of the determined magnetization values.

3.2 High-temperature Hysteresis Loops

For the study of magnetic properties at high temperature, generally three aspects are considered: (i) the temperature range up to 100 °C is technically relevant for many applications; (ii) investigations up to T_C are important to study the break-down of the ordering process or phase transition; and (iii) higher temperature ranges are necessary to determine the susceptibility above T_C from which the effective paramagnetic moment can be deduced. They are also used for the study of metastable materials. As examples, investigations of relaxation effects in the amorphous state (Grössinger *et al.* 1996) or of the

onset of crystallization *in situ* to obtain nanocrystalline materials (Grössinger *et al.* 1995, Schwetz *et al.* 1998) can be cited. Additionally, the thermal stability investigation in metastable hard magnetic materials such as $Sm_2Fe_{17}N$ (Kou *et al.* 1995b) should be mentioned here. However, a complete experimental curve of $M_S(T)$ is of great importance because, by analyzing this curve, important magnetic parameters such as the exchange constant or critical exponents can be obtained.

The setup for high-temperature hysteresis loop measurements is similar to that of Fig. 8 when the cryostat is replaced by a furnace. One of the technical difficulties of the construction of high-temperature systems is to obtain a sensitive and well compensated pick-up system that survives higher temperatures.

One other very useful high-temperature hysteresigraph is the system described in Fig. 9, which uses the technically relevant line frequency of 50 Hz (Schwetz *et al.* 1998). The basic idea of this system is the use of one or two periods of the main line to generate a reasonable high field in an air coil. The apparatus consists of:

A field-generating coil with a high-power transformer which is connected on the primary side to the line as power supply;

A pick-up system which is placed inside the inner diameter of the field generating coil;

1. ...Pick-up coil
2. ...Transformer (220V prim.-33V sec.)
3. ...Relais (HRS 240 D45)
4. ...Shunts (Arcol, 5 x 100 W, 0.1 Ohm)
5. ...Storage Oscilloscope
6. ...Heating- (Powersupply 60W) and Cooling Device
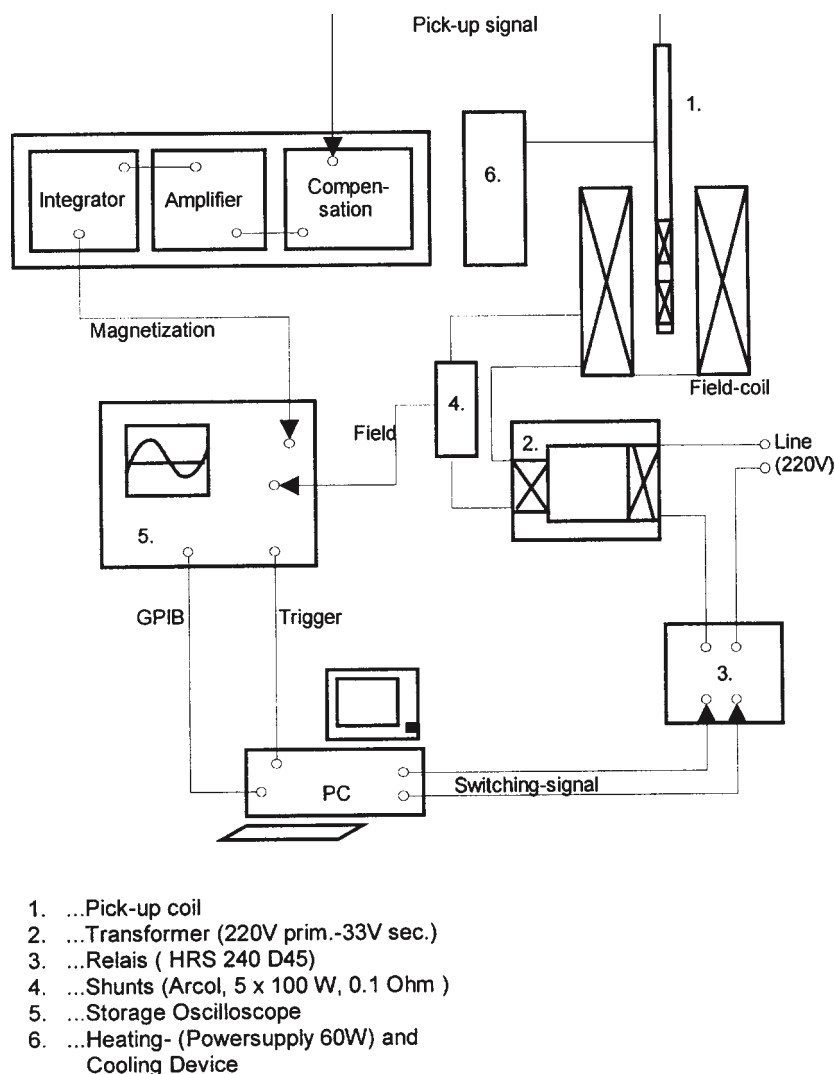
Figure 9
High-temperature hysteresis measurement system.

A switching unit with a solid-state, high-current switch;

Electronic devices to compensate, amplify, and integrate the signal induced in the pick-up system;

A storage oscilloscope and a personal computer (PC);

A heating system employing a bifilar wound heater in order to avoid a field due to the heating current.

For producing the field a current (several cycles of 50 Hz) is applied to the field-generating coil which will induce a signal in the pick-up system. This signal is compensated, amplified, integrated, and then saved in the memory of a storage oscilloscope. The field-producing current is measured by shunts and stored also in the oscilloscope. Afterwards the measured data are transferred to the PC. The switching and heating procedures, the oscilloscope, and the electronic devices are controlled by a PC.

This a.c. method system is very easy to realize. However, very close to application, due to possible 50 Hz noise, the accuracy is rather limited. With this system many interesting *in situ* high-temperature studies can be performed (Schwetz *et al.* 1998). Due to the high intensity of the applied field (maximum field of $300 \, \text{kAm}^{-1}$), this system can be used to investigate the semihard magnetic materials.

These are only two examples of high-temperature systems. There are many other possibilities to realize a high-temperature magnetometer that works in the gap of an electromagnet or in the temperature-isolated hole of a superconducting solenoid. Here, various methods such as the integration of the induction voltage in a pick-up system or the detection of an a.c. voltage (of a VSM) can be used.

4. Characterization of Hard Magnetic Materials

The magnetic methods characterizing hard magnetic materials (see *Hard Magnetic Materials, Basic Principles of*) differ slightly from those of soft magnetic materials. In hard magnetic materials the shape of the initial curve, minor loops as well as recoil curves, is important for studying the magnetization process.

Hard magnetic materials have a high coercive field (typically between $240 \, \text{kAm}^{-1}$ and $1600 \, \text{kAm}^{-1}$) where the origin is a high magnetocrystalline anisotropy. Therefore, high external fields are necessary for studying these types of materials. A standard tool for studying permanent magnet materials is an electromagnet as shown in Fig. 10. The field is generated by the electromagnet and the sample is in the air gap of pole pieces. In the case of room-temperature measurements the sample should have polished and plane surfaces in order to avoid undefined air gaps which cause stray field errors. The magnetization can be measured by pick-up coils and the actual field by a magnetic potentiometer or by Hall probes. The signal is then integrated using a fluxmeter. Such a system is
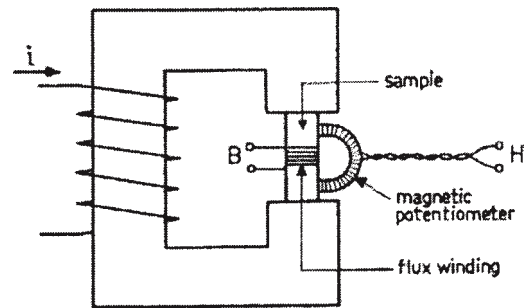
Figure 10
Sketch of magnetic measurement in an electromagnet.

well suited for measuring minor loops and recoil curves; however, for determining the full loop or the saturation magnetization, the achievable external field, which is about $800 \, \text{kAm}^{-1}$, is not sufficient. Additionally, a determination of H_c for high coercive field materials is also limited by the insufficiently low external field. Because an electromagnet has a high induction the change of field with time is slow. Therefore, the measurement usually takes seconds and the sensitivity of the system is limited by drift problems as well as by noise.

If measurements at variable temperatures are to be performed this system loses its advantage (magnetically closed system) because the use of a furnace or a cryostat causes an air gap, which means that the demagnetizing field of the sample has to be considered. Generally, the available field in the air gap of an electromagnet is too low ($800–1200 \, \text{kAm}^{-1}$) for modern hard magnetic materials. This situation can be improved using a superconducting solenoid which allows the field range to be extended such that fields up to about 20 T become available.

5. Conclusions

The main techniques to characterize hard magnetic materials besides the a.c. susceptibility measurements are magnetometers as described in Sect. 2. In short, the advantage of a VSM is that it gives good accuracy in reasonablly high fields covering a wide field and temperature range. A SQUID is an extremely sensitive device where a magnetic field resolution in the order of femtoteslas can be achieved.

See also: Magnetic Units; Magnetism: High Field

Bibliography

Akulov N 1931 Theories of magnetization curve of single crystals. *Z. Phys.* **69**, 78–99

Badurek G, Giersig R, Grössinger R, Veider A, Weinfurter H 1988 Domain structure studies of hard magnetic materials by neutron depolarisation. *J. Phys.* **49**, C8-665–6

Becker J J 1976 Reversal mechanism in copper modified cobalt rare earths. *IEEE Trans. Magn.* **12**, 965–7

Becker R, Kersten M 1930 Magnetization of Ni wire under large stress. *Z. Phys.* **64**, 660–81

Bertotti G 1996 Energetic and thermodynamic aspects of hysteresis. *Phys. Rev. Lett.* **76**, 1739–42

Bloch F 1930 Zur Theorie des Ferromagnetismus. *Z. Phys.* **61**, 206–19

Callen H B, Callen E 1966 The present status of the temperature dependence of magnetocrystalline anisotropy and the $l(l+1)$ power law. *J. Phys. Chem. Solids* **27**, 1271–85

Chikazumi S 1964 *Physics of Magnetism*. Chaps. 7, 16

Epstein J 1900 Magnetic testing of iron sheet. *Z. Elektrotech.* **21**, 303–7

Foner S 1956 Vibrating sample magnetometer. *Rev. Sci. Instrum.* **27**, 548–53

Foner S 1959 Versatile and sensitive vibrating sample magnetometer. *Rev. Sci. Instrum.* **30**, 548–57

Gans R 1932 On the magnetic properties of isotropic magnetic materials. *Ann. Phys.* **15**, 28–44

Grössinger R 1981 A critical examination of the law of approach to saturation: I. Fit procedure. *Phys. Stat. Solidi A* **66**, 665–74

Grössinger R, Holzer D, Kussbach C, Sassik H, Sato Turtelli R, Sinnecker J P, Wittig E 1995 High temperature behaviour of FINEMET ribbons in the amorphous and in the nanocrystalline state. *IEEE Trans. Magn.* **31**, 3883–5

Grössinger R, Kou X C 1996 Magnetic phase transition and magnetocrystalline anisotropy of rare-earth transition metal alloys. In: Leccabue F, Sagredo V (eds.) *Proc. III Latin American Workshop*. World Scientific, Singapore, pp. 55–68

Grössinger R, Sato Turtelli R, Hong Duong Vo, Kuss C 1996 High temperature behaviour of amorphous and nanocrystalline soft magnetic materials. In: Leccabue F, Sagredo V (eds.) *Proc. III Latin American Workshop*. World Scientific, Singapore, pp. 202–15

Grössinger R, Wittig E, Küpferling M, Taraba M, Reyne G, Golovanov C, Enzberg-Mahlke B, Fernegel W, Lethuillier P, Dudding J 1999 Large bore pulsed field magnetometer for characterizing permanent magnets. *IEEE Trans. Magn.* **35**, 3871–3

Hauser H 1994 Energetic model of ferromagnetic hysteresis. *J. Appl. Phys.* **75**, 2584–97

Herlach F 1994 Pulsed magnetic fields. In: *Proc. 2nd European Workshop on Science in 100T*, Leuven, p. 1

Herzer G 1990 Grain size dependence of coercivity and permeability in nanocrystalline ferromagnets. *IEEE Trans. Magn.* **26**, 1397–402

Holzer D 1998 Low temperature properties of soft magnetic materials. PhD Thesis, Technical University of Vienna

Jewell G W, Howe D, Schotzko C, Grössinger R 1992 A method for assessing eddy current effects in pulsed magnetometry. *IEEE Trans. Magn.* **28**, 3114–6

Jordan H 1927 *Elektr. Nachr. Technik.* **1**, pp. 489, 781, 788, 796

Koch H 1991 SQUID sensors. In: Göpel W, Hesse J, Zemel J N (eds.) *Sensor*. VCH, Weinheim, Germany, Vol. 5, Chap. 10

Kou X C, de Boer F R, Grössinger R, Wiesinger G, Suzuki H, Kitazawa H, Takamasu T, Kido G 1998 Magnetic anisotropy and magnetic phase transitions in R_2Fe_{17} with R = Y, Ce, Pr, Nd, Sm, Gd, Tb, Dy, Ho, Er, Tm and Lu. *J. Magn. Magn. Mater.* **177–181**, 1002–7

Kou X C, Grössinger R, Wiesinger G, Liu J P, de Boer F R, Kleinschroth J, Kronmüller H 1995a Intrinsic magnetic properties of $RFe_{10}Mo_2$ compounds (R = Y, Pr, Nd, Sm, Gd, Tb, Dy, Ho, Er, or Tm). *Phys. Rev. B* **51**, 8254–65

Kou X C, Sinnecker E H C P, Grössinger R, Wendhausen P A P, Müller K H 1995b Coercivity mechanism of Zn-bonded isotropic $Sm_2Fe_{17}N_x$ permanent magnets prepared by HDDR. *IEEE Trans. Magn.* **31**, 3638–40

Kou X C, Zhao T S, Grössinger R, Kirchmayr H, Li X, de Boer F R 1993 Magnetic phase transitions, magnetocrystalline anisotropy, and crystal-field interactions in the $RFe_{11}Ti$ series (R = Y, Pr, Nd, Sm, Gd, Tb, Dy, Ho, Er, or Tm). *Phys. Rev.* **47**, 3231–42

Mayergoyz I D 1991 *Mathematical Models of Hysteresis*. Springer, Berlin

O'Handley R C 1983 Fundamental magnetic properties. In: Lubovsky F E (ed.) *Amorphous Metallic Alloys*. Butterworths, London, Chap. 14, p. 257

Polak C 1992 Hysteresis and magnetostriction of iron- and cobalt-based soft magnetic alloys. PhD Thesis, Technical University of Vienna

Schwetz M, Sato R, Turtelli R, Grössinger R, Sassik H 1998 Crystallization behavior in Fe–Zr–Cu–B. In: Rivas J, Lopez-Quintela M A (eds.) *Non-crystalline and Nanoscale Materials*. World Scientific, Singapore, pp. 329–36

Van Oosterhout G W 1955 A rapid method for measuring coercive force and other ferromagnetic properties of very small samples. *Appl. Sci. Res.* **B6**, 101–4

Veider A, Grössinger R, Badurek G, Kronmüller H 1986 Optical and neutron domain structure studies of amorphous ribbons. *J. Magn. Magn. Mater.* **60**, 182–94

Yoshizawa Y, Oguma S, Yamauchi K 1988 New Fe-based soft magnetic alloys. *J. Appl. Phys.* **64**, 6044–6

R. Grössinger and R. Sato
Technische Universität Wien, Vienna, Austria

Magnetic Micro-actuators (MAGMAS)

Magnetic micro-actuators and systems (MAGMAS; also called "MAG-MEMS," (micro-electromechanical systems)) present outstanding performance for powerful integrated conversion from electrical to mechanical energy. MAGMAS, due to available forces and energies, belong to the recently appearing "Power-MEMS" family. Besides, the diversity of structures and the range of possible applications, including distance and remote-controlled actuation, explains the many recent publications and the large scope of research in this field. The topics addressed range from power energy microsources, to micromotors, micro-actuators, microswitches, levitation and remote-controlled magnetic micro-objects. The corresponding devices comprise optical, electrical, radiofrequency (RF), biomedical, and fluid dynamics applications.

MEMS are presently diversifying towards different principles of actuation, either electrostatic, magnetic, piezoelectric, or thermal, or actuation based on

shape memory alloys. Each principle presents specific properties so as to cover a wider range of possibilities and applications. MAGMAS' development is recent, rapid, and promising as most specific and limiting technological problems are progressively being solved. It combines magnetic materials now available on silicon: microcoils, soft magnetic materials, micromagnets, magnetostrictive thick layers, etc., with either an integrated or remote-control field resulting in numerous possibilities. MAGMAS deserve more credence and attention from MEMS designers, and materials scientists should continue to develop better thick-film patterned permanent magnets compatible with microsystem technologies.

Stress will be put on downscaling laws. Due to both new available materials and the impressive increase of current density in microcoils, it is demonstrated that downscaling actually results in more effective electromagnetic converters. That magnetic interactions actually improve on downscaling is quite new and revolutionary.

1. A Brief History of MEMS and Magnetism

Developments in microelectronics led to MEMS, where the first actuations of thin beams employed were electrostatic, aluminum conductors and electrodes being standard. Thermal bimorph actuation came later. Development of other actuation principles (electromagnetism, piezoelectricity, magnetostriction, shape memory, etc.) has been slower because basic components and specific materials are not standard.

Early on, it was felt strongly that electromagnetism would not be very relevant for MEMS. Based on the simplified interactions between conductors in air or between a conductor in air and a piece of iron, but no effective electromagnetic power conversion, downscaling is catastrophic! This is even more so when drastic changes of essential parameters such as gradients or current densities were not considered when downscaling! Obviously, many recently published "downscaling laws" still favor electrostatics considering electromagnetism in its less appropriate and less downscalable configuration. These theories did not consider direct and homothetic scale reduction of the familiar electrical machines in daily use.

Generally, the perspectives for downscaling of different types of actuation for MEMS were neutral or pessimistic for magnetism, whereas a rigorous electrical engineering approach led to very positive conclusions (Jufer 1994). In the late 1980s, the first teams designed and promoted magnetic micro-actuators (Wagner and Benecke 1990, Guckel *et al.* 1991, Benecke 1994). They wisely remarked that permanent magnets are vital to magnetic actuation but that unfortunately their integration needs to be mastered (Guckel 1996). This is still a bottleneck. Many other works deserve to be read (Nami *et al.* 1996,

Busch-Vishniac 1992). More details on MAGMAS, principles, materials, and applications have been collected in the book of Cugat (2002). The reader is also referred to the Feynman (1992, 1993) articles for perspectives in the early 1990s.

2. Magnetic Interactions and Downscaling at Constant Current Density δ

For simple energy considerations, electrical engineering clearly indicates that macroscopic devices (electrical engines and actuators that dominate the macroscopic world) are mainly composed of ferromagnetic materials (either soft magnetic materials or permanent magnets). Hence, the focus is on laws of scale reduction applied to such structures.

2.1 Magnetic Field of Magnets

A magnet of volume v_1 and magnetic polarization J_1 generates a scalar potential V at any point P located at a distance r from the magnet. The magnetic field H is the local gradient of the scalar potential V:

$$V(P) = \frac{v_1}{4\pi\mu_0} \frac{\boldsymbol{J} \cdot \boldsymbol{r}}{r^3}, \qquad \boldsymbol{H} = \nabla V \qquad (1)$$

Homothetic miniaturization (all dimensions reduced by the same factor $k = 10, 100, 1000, \ldots$) of a given magnet (homogeneous material and constant polarization J_1) generates a constant magnetic field H, whereas the scalar potential $V(P)$ is divided by k. The relative geometry and magnitude of the field map around a magnet remain unchanged after scale reduction (Fig. 1). A direct and remarkable consequence is that the field gradients are multiplied by k. This has a tremendous impact on the interaction forces.
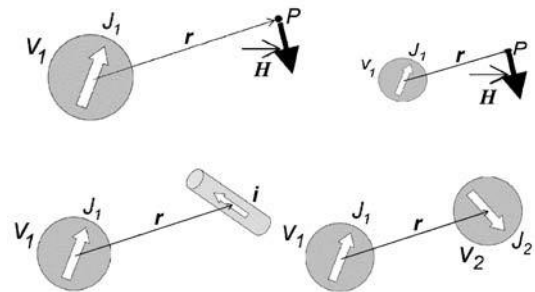
Figure 1
Top: Magnet—magnetic field unchanged with scale.
Bottom: Interactions—magnet–current and magnet–magnet.

2.2 Interactions between Magnets and Current-Carrying Conductors

Intuitively, one considers the forces of magnets on current-carrying conductors. Homothetical downscaling of the magnetic field maps due to the magnets leaves the Lorentz forces on conductors unchanged.

Obviously it is equivalent to consider the forces exerted by the conductors on the magnets. The Biot–Savart law states that the magnetic field H created in point P by a conductor of length dl and cross-sectional area S, carrying a current density δ (current $I = \delta \cdot S$), is

$$H(P) = \frac{1}{4\pi} \frac{\delta \cdot S \cdot dl \times r}{r^3} \qquad (2)$$

Hence, scale reduction by a factor of $1/k$ decreases the fields H due to the conductors by a factor of k. The magnetic force F on the magnet derives from their mutual magnetic interaction energy W_i:

$$W_i = -J \cdot \text{v} \cdot H, \qquad F = -\nabla W_i \qquad (3)$$

Scale reduction by a factor k reduces the energy W_i by a factor $1/k^4$, F by a factor $1/k^3$, and the force-to-weight (or force-to-volume) ratio does not change.

2.3 Torque on a Magnet Due to External Field

The torque experienced by a magnet of polarization J and volume v immersed in a homogeneous field H is proportional to M and H (where the magnetic moment equals $M = vJ$). During the homothetic $1/k$ reduction, both H and J remain constant, thus the torque-to-volume ratio also remains constant.

2.4 Magnet–Magnet and Magnet–Iron Interactions

Once again, the magnetic field of magnets remains unchanged upon downscaling. Hence, for magnet–magnet or magnet–iron interactions, Eqn. (3) shows a decrease of W_i by a factor $1/k^3$, F by a factor $1/k^2$ and an increase by k of the force-to-volume ratio.

Not only are macroscopic magnetic systems the most performing electric-to-mechanical converters but their scale reduction by $1/k$ can increase the force-to-weight ratio by k, allowing MAGMAS to provide large forces exactly as an ant can carry much heavier charges relative to its own weight than can an elephant.

2.5 Scale-reduction Laws on Magnetic Interactions

Similar calculations can be done for the magnetic interactions involving soft ferromagnetic materials combined to currents, and time-variation-induced currents (Cugat 2002, see chapter 2); see Fig. 2.

Figure 2
Effect of scale reduction $1/k$ on volume force for basic magnetic interactions, for a constant current density.

For a constant current density δ, the following conclusions can be drawn:
• The main magnetic interactions benefit from scale reduction.
• The most efficient magnetic interactions in devices of small dimensions involve permanent magnets.
• The forces between two magnets or between a magnet and a soft iron core increase by a factor k upon scale reduction by a factor $1/k$.
• The forces between a magnet and current-carrying conductors, when effective on a macroscopic scale, remain as effective once miniaturized.
• Inductive effects are to be avoided.

3. Permanent Magnets for MAGMAS

The application of MAGMAS requires the integration of small but high-quality magnets. Material researchers are addressing this bottleneck and new results are presently being reported. Large availability of thick high-quality magnets in microtechnology will boost the performance of electrical-to-mechanical conversion and, more generally, of MEMS.

3.1 Micromagnet Fabrication Techniques

The most common and most powerful micromagnets currently used in MAGMAS are those individually micromachined from bulk rare-earth permanent magnets (REPMs) such as Nd–Fe–B or Sm–Co magnets (see *Magnets: Sintered*), generally using machining by spark cutting. However, this method is hardly compatible with full integration or batch fabrication.

Many other ways to obtain micromagnets for MAGMAS are being developed (see *Magnetic Films: Hard*). These methods all provide good results but each suffers from a moderate or major drawback (Cugat 2002, chapter 5). Some techniques are well adapted to microfabrication (electroplating of Co–Pt, screen printing of bonded powders) but the resulting magnetic properties are relatively poor compared to

bulk REPMs (Zangari *et al.* 1996). Other techniques giving excellent magnetic properties are sputtering (Linetsky and Kornilov 1995), pulsed laser deposition (Cadieu *et al.* 1998), low-pressure plasma spraying (Rieger *et al.* 2000), or direct sintering (Yamashita *et al.* 2002). But either the thickness of the deposited layer is too thin, or it is difficult to adapt the process to microtechnology and batch fabrication (high deposition temperature, chemical pollution, slow deposition rate, small deposition surface). An important aspect currently emerging is the patterning of thick magnet films (Budde and Gatzen 2002). Optimal magnetic orientation of micromagnets is also studied (Kruusing 2002). The perspectives of achievements with low-temperature electroplated high-quality REPMs are discussed by Schwartz *et al.* (1998).

The large impact of the expected results justifies the increasing number of research efforts made in this field. However, perfect candidates for cheap, compatible, and fast integration of thick patterned layers of good-quality micromagnets remain to be found. Recently, technologies have improved rapidly and breakthroughs in this critical field are likely.

3.2 Equivalence between a Permanent Magnet and a Current-carrying Coil

A magnet is equivalent to a current-carrying coil (current density i, radius r) whose circumferential current density ($i/2\pi r$) remains constant (Amperian current model). This means that the equivalent volume current density increases by k when the magnet (or the equivalent coil) is downscaled by $1/k$.

4. Current Density in Microcoils

Magnetic sensors use microcoils and MAGMAS require them for variable fields and forces. Microcoils of various shapes and sizes can stand very high current densities. In macro-applications, the limitation to 3–5 A mm^{-2} is mainly due to thermal overheating. In micro-applications, thermal downscaling laws allow densities of 10^3–10^4 A mm^{-2}. While Joule conduction losses are volume related, the heat flow (for cooling) is proportional to the cross-section and inversely proportional to the thickness the heat flows through. Hence, heating scales as k^3, whereas heat flow dissipated by conduction scales as k. For the same temperature, Joule losses can increase by $k^3/k = k^2$. These Joule losses being proportional to the square of the current density, the current density can increase as k. Hence microcoil downscaling by $1/k$ can be done with the current density increasing by a factor of k. This is equivalent to a constant surface current density or, in other words, magnets and actual microcoils downscale in the same way. As forces and energies are proportional either to that current density or to the square of that density, this deeply boosts scale reduction laws.

The small volume-to-surface ratio of microcoils (planar geometry) and the direct contact with good heat-conducting substrates (e.g., Si), allows even higher DC currents, not to speak of pulsed currents (Cugat 2002, chapters 3 and 4, MacKay *et al.* 2000). However, it cannot be avoided that such increases in current densities and the concomitant increases of thermal losses in conductors can reduce both the efficiency and the autonomy (if used on batteries), and needs adapted heat sinks. These side-effects are practical limiting parameters for real design of MAGMAS.

5. Optimal Downscaling Laws ($\delta \sim k$)

With good magnets and current densities increasing as k, the downscaling laws can become significantly modified (Fig. 3).

One can draw the following outstanding conclusions (see Table 1):
- All magnetic interactions benefit from scale reduction.
- Magnet–magnet or magnet–iron core forces increase as k.
- Current volume forces increase the same way and possibly faster (pulses). It depends on the specific characteristics of the application and the associated side-effects stated earlier.
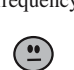
Figure 3
Effect of scale reduction $1/k$ on basic magnetic interactions, with current density increasing as k (constant temperature).

Table 1
Optimal downscaling laws.

Downscaling	$1/k$
Volume, mass, or gravity force	$1/k^3$
Heat flow dissipated by conduction	$1/k$
Electrostatic forces	$1/k^2$
Current density (constant temperature)	k
Most magnetic interactions ($1/k^2$)	$1/k^2$
Force/volume for most magnetic interactions	k

- Magnetic forces downscale as electrostatic forces. Here one has to bear in mind that magnetic forces largely dominate in the macroscopic world.
- Inductive effects could benefit from the increase of frequencies when downscaling. The smaller the object, the faster are thermal, mechanical, or electrical effects. However, size reduction increases resistances and decreases inductances, thus handicapping inductive effects.

6. Additional Characteristics of MAGMAS

In addition to high energy densities and forces, electromagnetic interactions present other advantages, but also drawbacks for the actuation of microscopic systems (Reyne 2002).

6.1 Permanent Forces, Bistability, and Suspensions

Permanent magnets provide constant magnetic fields. Hence, simple latching or bistability is achievable without supply. This ensures energy savings or guarantees excellent safety in case of power failure (Fisher *et al.* 2001, Ruan *et al.* 2001). Bistability combines particularly well with pulsed-switching currents. Such permanent forces can also be implemented into passive magnetic suspensions/bearings, providing an elegant solution to the problem of friction in MEMS (Klöpzig 1998, Cugat *et al.* 1996).

6.2 Long-range, Remote, or Wireless Actuation

- Magnetic fields and gradients can be effective over long distances relative to the size of MEMS. This allows integrated large-throw and/or wide-angular actuators.
- Contactless magnetic interaction allows remote actuation through sealed interfaces allowing wireless actuation or vacuum packaging of resonant systems for high Q factors (no air viscosity dampening). Furthermore, remote actuation through sealed interfaces makes magnetic actuators very well suited to harsh environment (e.g., ABS sensors).
- External magnets or macrocoils can be added to power the microsystem thus avoiding integration of supply and most side-effects. It considerably simplifies fabrication. This characteristic is unique and deserves to be used for medical applications with implanted wireless MAGMAS actuated by distance external fields.

6.3 Possible Future Actuation Modes for MAGMAS

Major drawbacks of magnetic actuation are side-effects of Joule losses in conductors. One might overcome this problem by exploring new ways to modify magnetic fields:

- thermal demagnetization of a thermomagnetic material,
- magnetic "reprogramming" of semi-hard materials by demagnetization and remagnetization,
- strain-induced modulation of the magnetization of a magnetostrictive material (see *Magnetoelasticity in Nanoscale Heterogeneous Materials*) by hybridization with a voltage-actuated piezoelectric element, and superconducting films can be used for levitation (see *Magnetic Levitation: Superconducting Bearings*) and high-temperature superconductivity may be a future possible solution for magnetizing MAGMAS for specific applications (space, cryogenic systems, etc.).

6.4 Power Supplies, Control, and Coolers

Electrostatic actuators use high voltages and low currents, whereas MAGMAS require high currents and low voltages. Current pulses, if used, need faster command and control. Hence, final performances strongly rely on working conditions and development of appropriate integrated supplies and coolers.

7. Applications

Magnetic sensors are already well established in commercial products (HDD read-heads, fluxgates, transmission coils, ABS sensors, etc.). However, few MAGMAS have, so far, reached industrial production. Laboratory-developed prototypes include radio frequency μ-switches for mobile phones, read/write heads and μ-positionners, matrixes of optical μ-commutators for fiber optic networks, μ-motors for noninvasive surgery and μ-robotics, μ-pumps, and μ-valves for lab-on-chip and μ-fluidic devices, electrical μ-generators for autonomous power supplies, μ-mirrors for adaptive optics, magnetic suspensions for hard disk drives, etc.

8. Conclusion

Electromagnetic interactions deserve a larger interest from the MEMS community. MAGMAS offer large forces, large strokes, remote or distance control, bistability, and high robustness, all these properties offering great opportunities for new devices in many applications. The large current densities available at small scales, together with the development of magnetic thick films, specific supplies, and coolers should soon greatly promote the development of MAGMAS.

See also: Magnetic Films: Hard; Permanent Magnets: Sensor Applications; Rare Earth Magnets: Materials

Bibliography

Benecke W 1994 Scaling behavior of microactuators. *Proc. ACTUATOR* **94**, Bremen, 19–24

Budde T, Gatzen H H 2002 Patterned sputter deposited Sm-Co films for MEMS applications. *J. Magn. Magn. Mater.* **April**

Busch-Vishniac I J 1992 The case for magnetically-driven micro-actuators. *Sensors & Actuators* **A33**, 207–20

Cadieu F J, Rani R, Quian X R, Chen L 1998 High coercivity Sm-Co based films made by pulsed laser deposition. *J. Appl. Phys.* **83–11**, 6247–9

Cugat O, Fernandez V, Roy D, Reyne G, Delamare J 1996 Miniature permanent magnet bearings: application to planar micromotors. *Proc. Europe-Asia Conference MECATRO-NICS* **96**

Cugat O 2002 Microactionneurs electromagnétiques – MAG-MAS. *Hermés-Science/Lavoisier ISBN 2-7462-0449-5*, 340pp

Feynman R P 1992 & 1993 There's plenty of room at the bottom. 1959 Infinitesimal machinery. 1983 reprinted *J. MEMS* **1**(1), 60–66 & *J. MEMS* **2**, 4–14

Fisher K, *et al.* 2001 A latching bistable optical fiber switch combining LIGA technology with micro-machined permanent magnets. *Transducers* **01**

Guckel H, *et al.* 1991 Fabrication and testing of the planar magnetic micromotor. *J. Micromech. Microeng.* **1**, 135–8

Guckel H 1996 Progress in electromagnetic actuators. *Proc. ACTUATOR* **96**, Bremen, 45–8

Jufer M 1994 Size limits and characteristic influence of electromagnetic actuators. *Proc. 4th International Conference on New Actuators*, 390–3

Klöpzig M 1998 A novel linear micromachined electromagnetic actuator including magnetic suspension. *Proc. ACTUATOR* **98**, 548–51

Kruusing A 2002 Actuators with permanent magnets having variable in space orientation of magnetization. *Sens. & Act.* **A101**, 168–74

Linetsky Y L, Kornilov N V 1995 Structure and magnetic properties of sputtered Nd–Fe–B alloys. *J. Mat. Eng. and Performance* **4–2**, 188–95

MacKay K, Bonfirm M, Givord D, Fontaine A 2000 50 T pulsed magnetic fields in microcoils. *J. Appl. Phys.* **87–4**, 1996–2002

Nami Z, Ahn C, Allen M G 1996 An energy-based design criterion for magnetic micro-actuators. *J. Micromech. Microeng.* **6**, 337–44

Reyne, G., 2002. Electromagnetic actuation for MOEMS, examples, advantages and drawbacks of MAGMAS. *MMM Journal of Magnetism and Magnetic Materials, Elsevier* **242–245**, **Part II**, 1119–25

Rieger G, Wecker J, Rodewald W, Sattler W, Bach Fr-W, Duda T, Unterberg W 2000 Nd–Fe–B permanent magnet (thick films) produced by a vacuum-plasma-spraying process. *J. Appl. Phys.* **87–9**, 5329–31

Ruan M, Shen J, Wheeler C B 2001 Latching micromagnetic relays. *J. MEMS* **10–4**, 511–7

Schwartz M, *et al.* 1998 Thin film alloy electrodeposits of transition rare-earth metals from aqueous media. *Electrochemical Society Proc.* **98–20**, 646–59

Wagner B, Benecke W. 1990 Magnetically driven micro-actuators: design considerations. Microsystem Technologies. Springer Verlag, Vol. 90, 838pp

Yamashita F, *et al.* 2002 Preparation of thick-film Nd–Fe–B magnets by direct Joule heating. *Proc. REM* **XVII**, 668–74

Zangari G, Bucher P, Lecis N, Cavallotti P L, Callegaro L, Puppin E 1996 Magnetic properties of electroplated Co-Pt films. *J. Mag. Mag. Mat.* **157/158**, 256–7

G. Reyne
Laboratoire d'Electrotechnique INPG BP 46 F-38402 Saint Martin d'Heres Grenoble Cedex France

J. Delamare, and O. Cugat
Laboratoire d'Electrotechnique de Grenoble UMR 5529 INPG/UJF – CNRS ENSIEG – BP 46 F-38402 Saint-Martin-d'Heres Cedex France

Magnetic Microwires: Manufacture, Properties, and Applications

Amorphous metallic materials take a prominent position among metallic materials due to their unique and favorable association of physical properties related to the absence of long-range order. These materials possess superior mechanical, electrical, magnetic, and chemical properties (see *Amorphous Intermetallic Alloys: Resistivity*, and *Amorphous and Nanocrystalline Materials*). The use of preparation methods that allow rapid condensation of atoms or rapid solidification of liquid metallic melts in order to avoid crystallization is necessary to achieve the energetically metastable amorphous state. The formation of the amorphous state depends on the alloy composition as well as on the process conditions. Presently known amorphous metallic materials have been obtained in shapes like thin films (Cahn 1993), ribbons (Boll *et al.* 1983), wires (Hagiwara and Inoue 1993), powders (Yagi *et al.* 2000), and very recently bulk materials with dimensions in the range of millimeters (Inoue 2000). Amorphous metallic materials are used in applications based on their outstanding properties, but the most important are those based on magnetic properties, their soft magnetic behavior leading to high permeability and low coercivity.

Amorphous ribbons have been used in transformer cores, magnetic recording heads, and in sensing elements. The amorphous metallic wires have attracted much interest due to their more convenient shape, dimensions, and specific properties emerging from their degree of symmetry. Amorphous metallic wires with diameters ranging between 80 µm and 160 µm are obtained by the so-called in-rotating-water quenching technique (Ogasawara and Ueno 1995). This procedure implies a very high cooling rate from the molten alloy and gives rise to local magnetoelastic anisotropies from the coupling between internal stresses and magnetostriction. These internal stresses originate from the thermal gradient present during the quenching, and their order of magnitude, $\sim 10^2$ MPa, is determined by Young's modulus, the

Poisson coefficient, and the average temperature during fabrication.

The main interest of amorphous wires is related with the cylindrical geometry and magnetostriction constant. In the latter case, in Fe-rich alloys, the magnetization process is characterized by a single Barkhausen jump (Vázquez and Chen 1995) associated with a square hysteresis loop. This behavior, that it is observed above a critical length of $\sim 7\,cm$, is determined by a particular domain structure originating from stresses induced in the wire during the fabrication procedure. Current and voltage transformers and magnetic sensors have been developed based on this effect (Mohri *et al.* 1984). On the other hand, Co-rich alloys exhibit vanishing magnetostriction and do not show bistability (Gómez-Polo and Vázquez 1993). Although the saturation magnetization is low, the outstanding properties of this material are related with a high initial susceptibility and with another effect, strongly connected with the geometrical shape, known as magneto-impedance effect. The latter induces wire impedance variations by magnetic field application (Beach and Berkowitz 1994, Panina and Mohri 1994). This effect can be used in magnetic sensors for detecting magnetic fields.

In contrast, glass-coated microwires are obtained by an extracting melt-spinning technique, based on Taylor's classical method (Taylor 1924). The tiny dimensions and the outstanding magnetic behaviors at low-, medium-, and high-frequency magnetic fields make them very useful for practical purposes.

1. Material Preparation: Production Technique of Amorphous Glass-covered Metallic Microwires

The production of glass-covered metallic microwires is presently achieved by the glass-coated extracting melt-spinning method. The basic idea of this method was initially proposed by Taylor (1924) and improved by Ulitovsky (1932) and Parkhachev (1966). Figure 1 shows a schematic diagram of the method. It consists in the rapid drawing of a softened glass capillary in which the molten metal is entrapped. The capillary is drawn from the end of a glass tube containing the molten alloy. Previously, a metallic pellet of the master alloy, prepared by induction melting of pure elements, has been placed inside the sealed end glass tube and then the alloy is melted by a high-frequency field of an inductive coil and the end of the glass tube is softened. Hence, around the molten metal drop, there is a softened glass cover which allows the drawing of the capillary. A low level of vacuum (~ 50–$200\,Pa$ of an inert gas atmosphere) within the glass tube prevents metal oxidation. It also assures stable melt-drawing conditions, in conjunction with induction heating, employing the levitation principle. In order to ensure continuity of the process, there is a glass tube displacement with a uniform feed-in speed
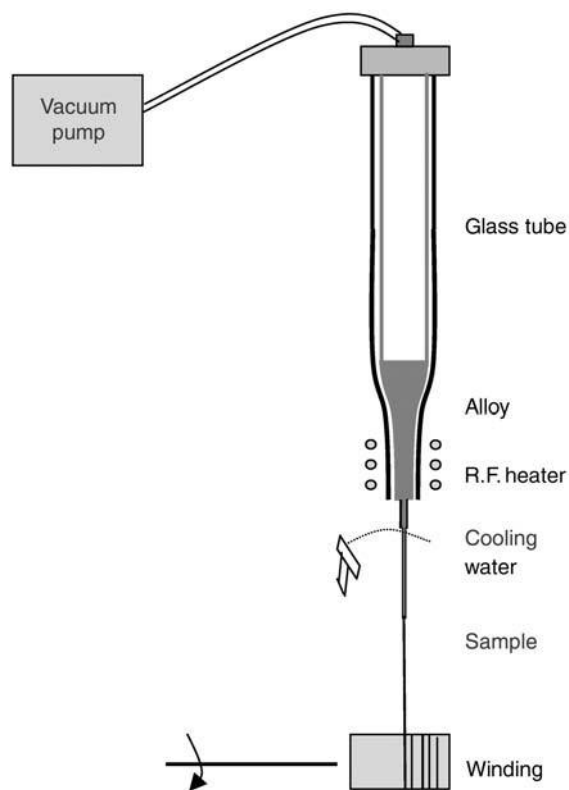
Figure 1
Schematic diagram of the glass-coated melt spinning method.

between $0.5\,mm\,min^{-1}$ and $10\,mm\,min^{-1}$. The rapid cooling rate required to obtain an amorphous structure, between $10^5\,K\,s^{-1}$ and $10^6\,K\,s^{-1}$, is reached by cooling the as-formed wire by a water jet at $\sim 1\,cm$ under the high-frequency induction coil.

It is clear both intuitively and from the available literature (Donald 1987) that the successful production of high-quality, continuous filaments of given dimensions by the Taylor-wire technique is dependent on a number of critical materials and process factors. These are summarized below.

The materials selection is crucial in order to be successful. In the case of amorphous metallic alloys the composition chosen should be that, of a glass former. It is well known (Chiriac and Óvári 1997) that glass formation is favored at compositions for which the liquid is relatively stable compared to crystalline phases. This relative stability also correlates with the sizes of the atomic species in the alloy.

Once the alloy composition is chosen, the glass should be well selected in order to allow a properly glass-coated fabrication. It must be compatible with the metal or alloy at the drawing temperature to

avoid, as much as possible, chemical reaction between glass and metal. Its working (drawing) temperature must be higher than the melting point of the metal or alloy employed, but below its boiling point and below the temperature at which the metal vapor pressure becomes high enough to disrupt the process. The viscosity–temperature behavior of the glass must allow easy fiber drawing in the temperature range of interest and its crystallization temperature should be higher than the working temperature.

The thermal expansion coefficient of the glass should be matched to, or be slightly less than, that of the metal or alloy of interest. The viscosity of the glass coating must attain a high enough value, where further extension during drawing cannot occur before the metal core has solidified. Otherwise, if the core is solid and the coating continues to extend, metal core fracture will be initiated and a discontinuous product will be obtained.

In practice, because glass is used in the form of tubes of uniform dimensions in the Taylor-wire process, the choice of specific glass compositions is severely restricted due to the limited range of commercial offers. This restricts the choice to Pyrex-type borosilicate compositions or to fused silica.

As it will be reported later, two main factors are predominantly responsible for the microwire magnetic behavior, i.e., the metallic core microstructure and the ratio of the metallic core radius to the total radius of the microwire $\rho = R_m/R$ (Chiriac and Óvári 1997). These microstructural and geometrical factors can be controlled by process conditions. A good control of melting temperature allows the obtention of amorphous and partially nanocrystallized samples. The most important factor governing the core diameter of the filament seems to be the take-up speed; the higher the speed, the smaller the fiber dimensions obtained. Another important factor is the vacuum level. In practice, the metal thickness is indirectly controlled by a measurement device based on emission and reception antennas that acts on the vacuum pump when the metal diameter deviations are detected. The thickness of glass coating depends mainly on the feed-in rate of the glass tube, but also depends, to a lesser degree, on the thickness of the glass tube employed, and the take-up speed.

Figure 2 shows a photograph corresponding to a microwire scanning electron microscope (SEM) image. The composition is $(Fe_{30}Co_{70})_{72.5}Si_{12.5}B_{15}$ and corresponding dimensions are a total diameter D of 12 μm and a metal nuclei diameter D_m of 3.5 μm.

2. Magnetic Properties

A large variety of magnetic alloys (Hernando and Vázquez 1993) can be fabricated mainly based on iron and cobalt. The high mechanical strength and the ferromagnetic character make them attractive as
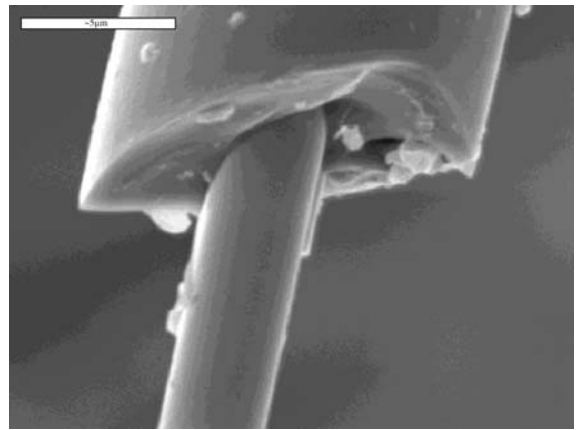
Figure 2
SEM photograph of an $(Fe_{30}Co_{70})_{72.5}Si_{12.5}B_{15}$ amorphous magnetic microwire with total diameter $D = 12$ μm and metal core diameter $D_m = 12$ μm (photograph courtesy of H. García-Miquel, UPV Valencia, Spain).

reduced size components in electronics, for magnetic recording, biomedical implantations, etc. Their high-frequency behavior can also be exploited in devices for electromagnetic power absorption.

2.1 Magnetic Domains and Low-frequency Axial Hysteresis Loop

The hysteresis loop shape is strongly dependent on the composition of the metallic core. The magnetization process is strongly dependent on the magnetostriction constant and the magnetoelastic anisotropy induced by internal stresses (Vázquez *et al.* 1996). Glass coating induces an extra radial internal stress due to the different thermal expansion coefficients of the nucleus and the glass. Besides, the extraction tensile stress induces an axial internal anisotropy. The coupling determines the domain structure, an inner axial single domain, and the outer shell.

As shown in Fig. 3, in positive magnetostrictive microwires (Fe-rich), the inner core has an easy magnetization direction along the axis and the outer-shell easy direction is perpendicular to the axis. In negative magnetostrictive microwires (Co-rich), the inner-core easy magnetization is perpendicular to the axis direction while the external shell adopts circular directions. Magnetic microwire behavior is determined by this type of domain structure.

Positive magnetostrictive microwires show a square hysteresis loop with large Barkhausen jump. This effect results from the magnetization reversal in the inner core at a given value of the axial magnetic field, called switching field, H^*. The value of the
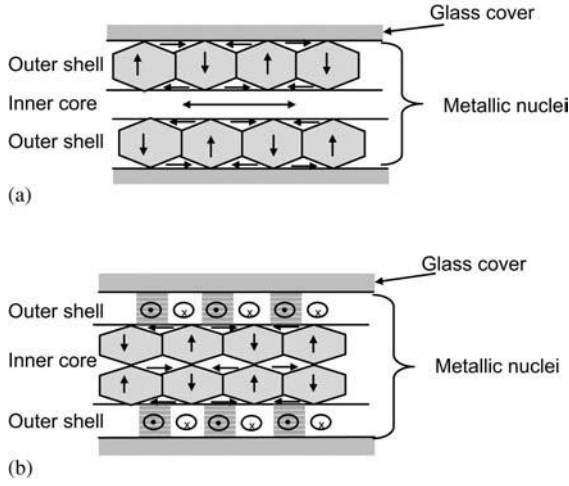
Figure 3
Schematic diagram of the estimated domain structure in positive (a) and negative (b) magnetostrictive amorphous glass-coated microwires (Chiriac *et al.* 1997).

switching field depends on the average value of the uniaxial anisotropy constant of the inner core, and consequently on the level of the internal stresses. These thermoelastic internal stresses depend on the mechanical, thermal properties and the cross-sectional ratio of glass and metal (Baranov 2001), $x = (R/R_m)^2 - 1 = (1/\rho^2) - 1$.

The general equation describing the internal stresses can be simplified, considering $n_1 = n_2 = \frac{1}{3}$ where n_i are the Poisson coefficients of crystal and metal, respectively. They can be expressed as follows in a cylindrical coordinate system:

$$\sigma_z = \sigma_0 \frac{kx}{kx+1} \frac{(k+1)x+1}{(k/3+1)x+4/3} \qquad (1)$$

$$\sigma_r = \sigma_\phi = \sigma_0 \frac{kx}{(k/3+1)x+4/3} \qquad (2)$$

where $\sigma_0 = E_1(a_1 - a_2)(T^* - T)$, k is the ratio of the Young's moduli $k = E_2/E_1 = 0.3-0.6$.

The internal stresses cause the appearance of magnetoelastic anisotropy, corresponding to a magnetic field:

$$H_a = \frac{\lambda \sigma_0}{M} \frac{Kx}{Kx+1} F(k,x) \qquad (3)$$

were $F(k,x)$ is a slowly varying function of k and x.

Figure 4 shows the composition dependence of microwire hysteresis loops. Figures 4(a) and 4(b) are for microwires of the compositions $Fe_{70}Si_{10}B_{15}C_5$ and $Co_{60}Fe_{15}Si_{15}B_{10}$, respectively. Magnetic bistability is clearly observed in both cases. In turn, Fig. 4(c)
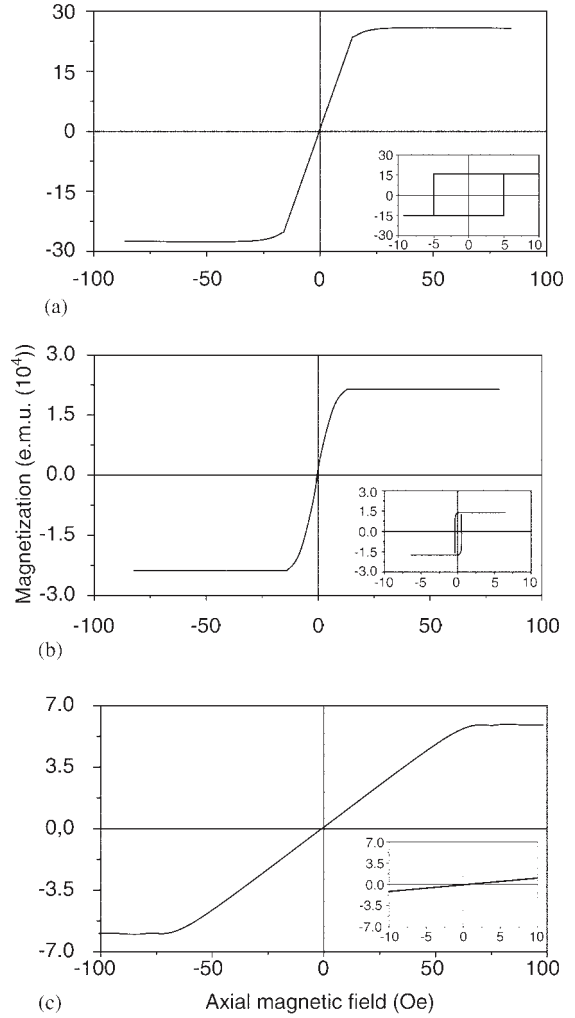
Figure 4
Low-field (inset) and high-field hysteresis loops for microwires of $Fe_{70}Si_{10}B_{15}C_5$ (a), $Co_{60}Fe_{15}Si_{15}B_{10}$ (b), and $Co_{68.5}Si_{14.5}B_{14.5}Y_{2.5}$ (c) alloys.

shows a nonbistable loop for a $Co_{68.5}Si_{14.5}B_{14.5}Y_{2.5}$ alloy microwire. The main difference derived from the various compositions of the three microwires is the magnetostriction constant, λ_s. The corresponding values for Figs. 4(a)–(c) are 2×10^{-5}, 1×10^{-7}, and -2×10^{-6}, respectively. Accordingly, microwires with large and positive λ_s show magnetic bistability, whereas those having intermediate negative λ_s do not show that behavior. The microwire with nearly zero but positive λ_s (Fig. 4(b)) also shows bistable behavior. In fact, as reported by Baranov *et al.* (1995), the bistability disappears when λ_s changes its sign from positive to negative.
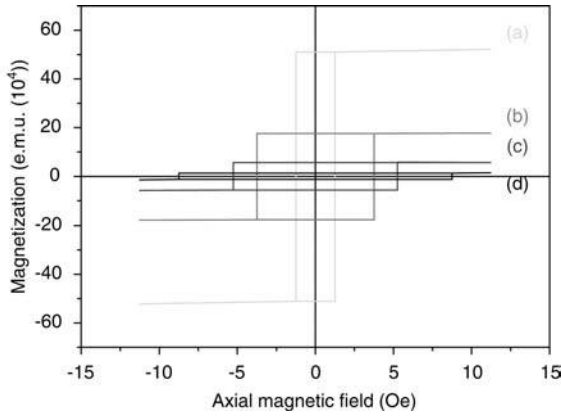
Figure 5
Hysteresis loops for $Fe_{89}Si_3B_1C_3Mn_4$ microwires with different ratio $\rho = R_m/R$ between the radius of the metallic core, R_m, and the radius of the microwire, R, for $\rho = 0.6$ (a), $\rho = 0.28$ (b), $\rho = 0.25$ (c), and $\rho = 0.2$ (d).

On the other hand, the ratio $\rho = R_m/R$ between the radius of the metallic core, R_m, and the total radius, R, of the microwire plays an important role in determining the parameters of the hysteresis loop. Figure 5 shows the bistable loops as a function of ρ. A higher longitudinal anisotropy due to thinner inner core is associated with a higher anisotropy field, H_k, and lower remanence.

The hysteresis loop behavior can be tailored by means of annealing. Amorphous structural relaxation and nanocrystallization (Vázquez et al. 1999, Marín et al. 1997) can change the microwire anisotropy field leading to a broad spectrum of magnetic behaviors with different hysteresis loops which is very interesting from the applications point of view.

2.2 High Magneto-impedance Effect

The magneto-impedance effect has been recently discovered in soft amorphous wires with very high circular permeability (Beach and Berkowitz 1994, Panina and Mohri 1994). It consists of a large relative change (up to $\sim 400\%$) of the impedance (both real and imaginary parts) upon application of a d.c. magnetic field or stress. In order to measure the impedance, typically a low-density current flows along the sample having a frequency in the range of MHz. This effect has been detected in nearly zero magnetostriction Co-base samples of the shape of a wire, ribbon, or thin film. It has been interpreted as arising from the classical skin effect, the penetration depth of which is defined as

$$\delta = (\rho/\pi\mu f)^{1/2} \tag{4}$$

ρ being the electrical resistivity, f the frequency, and μ the transverse permeability.

Upon application of a d.c. field, the permeability decreases, and accordingly δ increases until it reaches the radius of the wire which finally results in an effective change of the impedance, Z, considered for a magnetic conductor given by

$$Z = R_{dc}(kR)J_0(kR)/2J_1(kR) \tag{5}$$

with $k = (1+j)/\delta$ where J_0 and J_1 are the Bessel functions and R the radius of the microwire (Chen et al. 1998).

Amorphous microwires show also magneto-impedance effects and they are found to be more promising for several applications compared to wires and ribbons because of their tiny dimensions and protective glass coating. The influence of domain structure on this effect has been observed for vanishing negative (Vázquez et al. 1998) and positive (Mandal et al. 2000) magnetostrictive microwires.

Figure 6 (Vázquez et al. 1998) shows the magneto-impedance effect for $Co_{68.5}Mn_{6.5}Si_{10}B_{15}$ microwires with a metallic diameter of $\sim 14\,\mu m$ and an insulating glass coating thickness of $5\,\mu m$. The wire displays a nonbistable hysteresis loop similar to that shown in Fig. 4(c) associated with a very low and negative magnetostriction constant $(\lambda_s \sim 10^{-7})$. The negative nature of λ_s is deduced from the increase of the anisotropy field upon application of a tensile stress. A bamboo-like domain structure can be assumed, as in the case of negative magnetostriction amorphous wires obtained by the in-rotating-water quenching technique (Yamasaki 1992).

The existence of $(\Delta Z/Z)_m$ for a given H_m has been reported for samples heated in the presence of a transverse magnetic field (Sommer and Chien 1996) or tensile stress (Tejedor et al. 1996) where a circular magnetic anisotropy is deliberately induced. In the present case such anisotropy spontaneously appears from the coupling between internal stress and magnetostriction. Then it seems likely that the appearance of $(\Delta Z/Z)_m$ is associated with the existence of a transverse circular anisotropy. In fact, the maxima in Fig. 6 should be ascribed to the maximum value of the circular permeability, where according to Eqn. (4) the penetration depth reaches a minimum.

The effect of applying an increasing axial field, H, is to balance the anisotropy field H_k. Consequently, $(\Delta Z/Z)_m$ is observed for $H = H_k$. Further increase of H gives rise to reduction of the circular permeability and to a final decrease of impedance. The increase of $(\Delta Z/Z)_m$ with frequency (see inset of Fig. 6(a)) should be, in principle, ascribed to a stronger skin effect (Eqn. (4)).

The magneto-impedance effect has also been observed for very low and positive magnetostriction in a $Co_{83.2}Mn_{7.6}Si_{5.8}B_{3.3}$ microwire having a hysteresis loop similar to Fig. 4(b). As shown in Fig. 6(b)
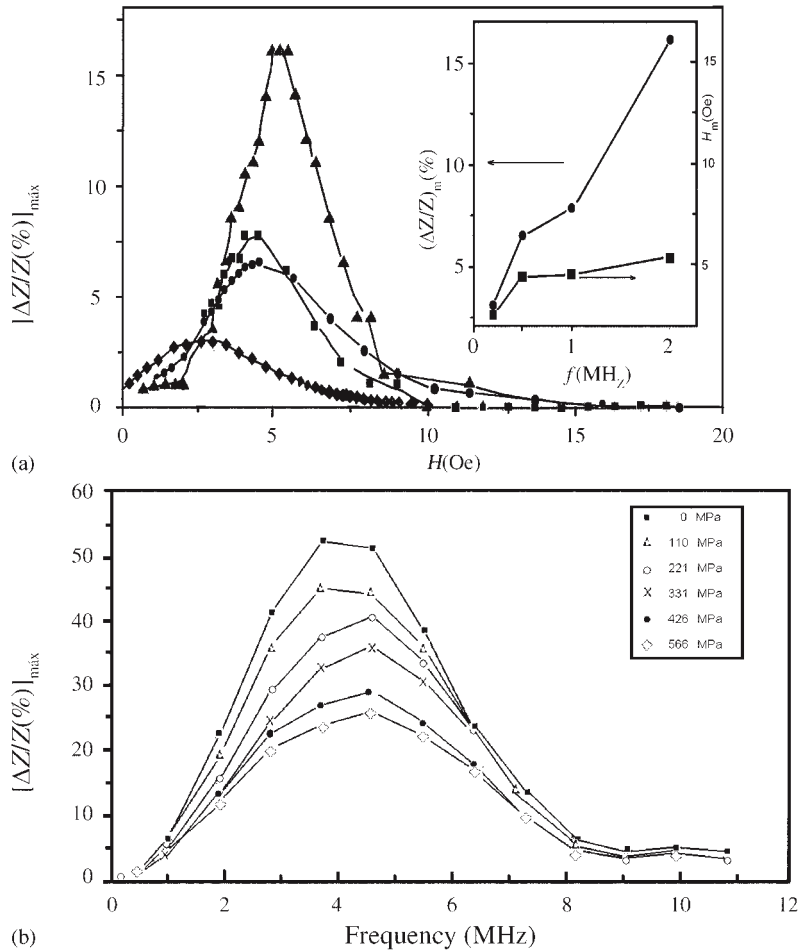
Figure 6
(a) Magneto-impedance effect of an as-prepared $Co_{68}Mn_7Si_{10}B_{15}$ sample at different frequencies ($I = 2.9\,mA$) of a.c. current: 0.2 MHz ($\blacklozenge$), 0.5 MHz ($\bullet$), 1 MHz ($\blacksquare$), 2 MHz ($\blacktriangle$). The inset shows the dependences $(\Delta Z/Z)_m$ and H_m on frequency of a.c. current (reproduced by permission of Vázquez *et al.* (1998) from *IEEE Trans. Magn.* **34**, 724–8; © IEEE). (b) The variation of maximum percentage change in magneto-impedance (i.e., the peak value of giant magneto-impedance), $(\Delta Z/Z)_m$ with frequency under different axial tensile stresses with 1 mA a.c. current through the sample (reproduced by permission of Mandal *et al.* (2000) from *Phys. Rev. B* **62**, 6598–602; © American Physical Society).

(Vázquez *et al.* 1998) a change of more than 50% in magneto-impedance has been observed for this sample. It has been obtained for a 140 Oe d.c. magnetic field along the length of the microwire. The application of external stress can change the magneto-impedance magnitude to a large extent, which opens the possible application of microwires as stress sensors.

In this case, the giant magneto-impedance can be explained by considering the change in penetration depth, δ, due to the change in circular permeability according to Eqn. (4) caused by the application of a magnetic field. The applied d.c. magnetic field nearly compensates the axial magnetic anisotropy when it

reaches the switching field of the sample. At this field, the quasi-free magnetization responds quickly to the external oscillating magnetic field and gives rise to a large circular permeability. As the switching field of our low-magnetostrictive sample is very small, a few mOe, the maximum value of the giant magneto-impedance is observed close to $H_{dc} = 0$. When the external d.c. field is increased beyond the switching field, the circular permeability decreases owing to the unidirectional magnetostatic anisotropy caused by H_{dc}. Therefore, with the increase of a d.c. magnetic field, the increase in penetration depth, δ, results in a decrease in magneto-impedance.

The applied tensile stress generates a uniaxial anisotropy along the axis of the wire and increases the volume of the inner-core domain. As a result of it, the circular permeability and hence the value of magneto-impedance decreases with the increase of stress (Fig. 6(b)).

2.3 Ferromagnetic and Natural Ferromagnetic Resonance

Technologically, the study of microwave properties is also very promising. In the microwave region (approaching GHz range), ferromagnetic resonance occurs, which is accompanied by absorption of energy at the resonance frequency.

Using the equation of Kittel for a plane (Kittel 1948), the resonance frequency f_r can be calculated by means of

$$f_r = \frac{g}{2\pi}\sqrt{(H_a + 4\pi M)(H_a + H)} \quad (6)$$

Here H_a is the anisotropy field, M the magnetization, g the gyromagnetic ratio, and H the external applied magnetic field. At that frequency, the permeability increases dramatically and the skin depth is very small (less than $1\,\mu m$). Ferromagnetic resonance (FMR) is connected with spin precession about the magnetization vector due to the effect of a high-frequency electromagnetic field applied such that the magnetic component is perpendicular to the magnetization vector (Antonenko *et al.* 1997). As a rule, the observation of FMR needs the application of an external d.c. magnetic field which provides a uniform magnetization of the examined sample.

One of the most interesting phenomena observed in amorphous ferromagnetic cast microwire is natural ferromagnetic resonance (NFMR) (Kraus *et al.* 1981, Baranov 1988). The NFMR was observed in ferrite without the application of an external magnetic field. The cause of NFMR is the internal magnetic anisotropy. The frequency depends on the value of the magnetic anisotropy. In known materials, the NFMR frequency is less than 1 GHz.

The appearance of NFMR, in positive magnetostrictive microwires, characterized by a single well-distinguished line in the range 2–10 GHz indicates the existence of a large magnetic anisotropy. Generally, the magnetic component of the a.c. field is perpendicular to the microwire axis, so the internal magnetic anisotropy causes the microwire to be magnetized along its axis. This conclusion agrees with the axial magnetization presented by positive magnetostrictive microwires associated with bistable magnetic behavior.

Due to the high resonance frequency (up to 10 GHz) and the extremely large magnitude of the permeability ($\mu'' > 100$), microwires are of great importance for utilization as radio-frequency absorbing materials. The NFMR in the range from 2 GHz to 10 GHz is observed in all amorphous microwires with positive magnetostriction constant.

The NFMR frequency can be calculated by taking into account that the depth of the skin layer, δ, is smaller than the radius of the microwire, r. Using Kittel's equation (Eqn. (6)) for plane and considering $H = 0$, one finds

$$f_r = \frac{g}{2\pi}\sqrt{(H_a + 4\pi M)H_a} \quad (7)$$

If $H_a \ll 4\pi M$, Eqn. (5) can be written as

$$f_r = \left(\frac{g^2 M H_a}{\pi}\right)^{1/2} \quad (8)$$

Considering H_a as given by Eqn. (3) the resonance frequency can be given as

$$f_r = \left(\frac{\lambda \sigma_0 g^2}{\pi} \frac{kx}{kx+1} F(k,x)\right)^{1/2} \quad (9)$$

Equation (8) shows that there is a strong dependence of the resonance frequency on composition, through the magnetostriction constant, and on fabrication conditions, through x and σ_0. Figure 7 illustrates the dependence of the anisotropy field, H_k, and the natural ferromagnetic resonance frequency on the ratio $\rho = R_m/R$ for the $Fe_{89}Si_3B_1C_3Mn_4$ microwires shown in Fig. 5.

3. Applications

A broad number of applications can be developed using amorphous magnetic microwires (Marín *et al.* 1997) that are based on the magnetic properties
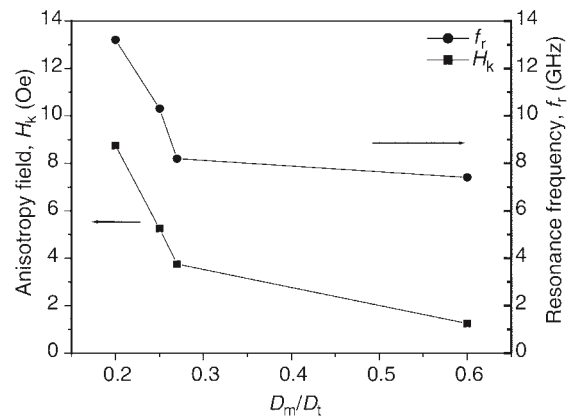
Figure 7
Dependence of anisotropy field, H_k, and natural ferromagnetic resonance on the ratio $\rho = R_m/R = D_m/D_t$ of $Fe_{89}Si_3B_1C_3Mn_4$ microwires shown in Fig. 5.

discussed above. Magnetic tags and magnetic detectors based on the bistable magnetic behavior or on the high magnetic susceptibility can be developed to work at low frequencies. Stress, current, position, liquid level or pressure sensors, and magnetic field detectors are based on giant magneto-impedance effect and would work at medium frequency. This type is employed in technologies such as car traffic monitoring, quality control of steels, vibrational detection of earthquakes, or biomagnetic sensors. Ferromagnetic resonance can be used to develop tags for article electronic surveillance and for electromagnetic wave shielding. In the following sections two particular applications are described.

3.1 Magnetic Tag

One of the applications consists in the use of several Fe-based magnetostrictive microwires for sensing elements in magnetic tags. The tag contains several microwires with well-differentiated coercivity, all of them characterized by a bistable magnetic loop. Once the magnetic tag is submitted to an increasing magnetic field, each particular microwire reverses its magnetization resulting in an electrical signal on a coil system (Vázquez and Zhukov 1996). Figure 8 shows the schematic representation for a working system of a magnetic tag as described here.

3.2 Wireless Stress Sensor for Vehicle Tires

This application is based on the stress dependence of the magneto-impedance effect. The sensor system
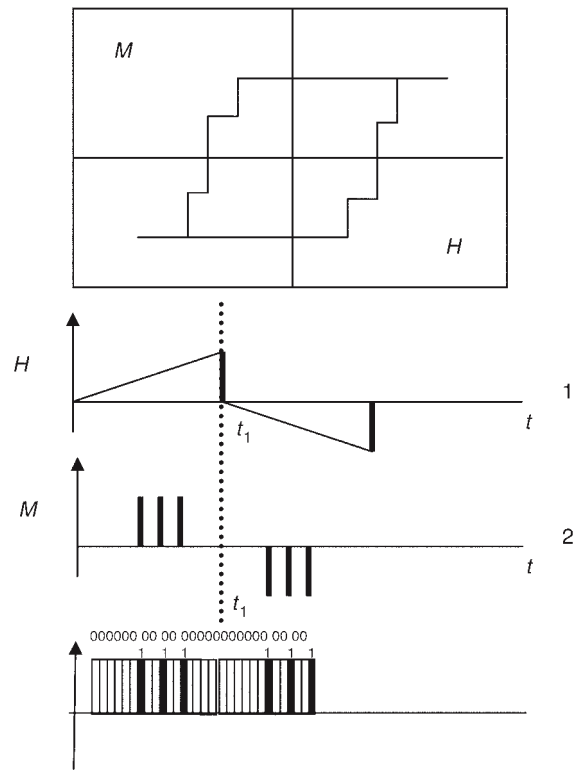
Figure 8
Schematic representation of the working system of a magnetic tag as described in the text (Vázquez *et al.* 1996).
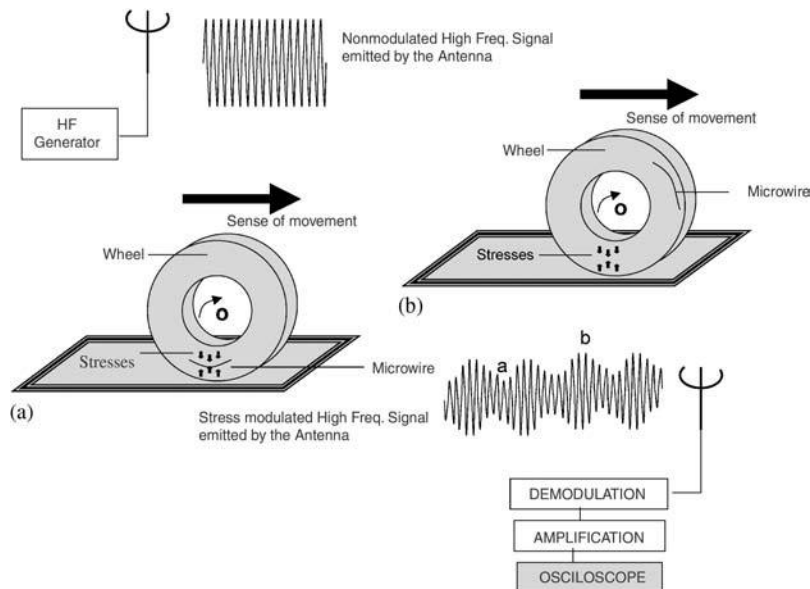
Figure 9
Schematic representation of a wireless stress sensors for vehicle tires.

518

monitors the frictional conditions between the tire and the roadway in order to enhance vehicle safety.

It has been shown that the stress measured at suitable positions in a car tire can be analyzed to give information on the frictional coefficient, the roadway conditions, and the tire inflation. The sensor proposed here (Tyren *et al.* 2000) is based on a combination of magnetostriction and magneto-impedance. The stress produces a change in the permeability in the magnetoelastic microwire. Thus, the skin depth of this element is altered leading to a change in its electrical impedance. This results in amplitude variations measured by a radio-frequency link between the sensor and stationary antenna. Figure 9 shows a scheme of the basic principles of the sensor.

See also: Magneto-impedance Effects in Metallic Multilayers; Magnetoelasticity in Nanoscale Heterogeneous Materials

Bibliography

Antonenko A N, Baranov S A, Larin V S, Torkunov A V 1997 Natural ferromagnetic resonance in cast microwires covered by glass insulation. *J. Mater. Sci. Eng.* **A248**, 248–50

Baranov S A 1988 Magnetic properties of amorphous microwire in the microwave range. *Zh. Teor. Fiz.* **68** (1), 136–7

Baranov A S, Larin V S, Torkunov A V, Zhukov A P, Vázquez M 1995 Magnetic properties of glass insulated amorphous microwires. In: Vázquez M, Hernando A (eds.) *Nanocrystalline and Non-crystalline Materials*. World Scientific, Singapore, pp. 567–71

Baranov S A 2001 Evaluation of the distribution of residual stresses in the cord of amorphous microwire. *Metal Sci. Heat Treat.* **43** (3–4), 167–8

Beach R S, Berkowitz A E 1994 Giant magnetic field dependent impedance of amorphous FeCoSiB wire. *Appl. Phys. Lett.* **64**, 3652–4

Boll R, Hilizinger H R, Warlimont H 1983 Magnetic material properties and applications of metallic glasses. In: Hasegawa R (ed.) *The Magnetic, Chemical and Structural Properties of Glassy Metallic Alloys*. CRC Press, Boca Raton, FL, pp. 183–201

Chan R W 1993 Background to rapid solidification processing. In: Liebermann H H (ed.) *Rapidly Solidified Alloys, Materials Engineering Series*. Dekker, Parsippany, NJ, Vol. 3, pp. 1–15

Chen D X, Muñoz J L, Hernando A, Vázquez M 1998 Magnetoimpedance of metallic ferromagnetic wires. *Phys. Rev. B* **57** (17), 10699–704

Chiriac H, Óvári T A 1997 Amorphous glass-covered magnetic wires: preparation, properties, applications. In: *Progress in Materials Science*. Elsevier, Great Britain, Vol. 4, pp. 333–407

Donald I W 1987 Production, properties and applications of microwire and related products. *J. Mater. Sci.* **22**, 2661–79

Gómez-Polo C, Vázquez M 1993 Structural relaxation and magnetic properties of Co-rich amorphous wire. *J. Magn. Magn. Mater.* **118**, 86–92

Hagiwara M, Inoue A 1993 Production techniques of alloy wires by rapid solidification. In: Liebermann H H (ed.) *Rapidly Solidified Alloys*. Dekker, New York, pp. 141

Hernando A, Vázquez M 1993 Engineering magnetic properties of rapidly solidified alloys. In: Liebermann H H (ed.) *Rapidly Solidified Alloys, Materials Engineering Series*. Dekker, Parsippany, NJ, Vol. 3, pp. 553–89

Inoue A 2000 Stabilization of metallic supercooled liquid and bulk amorphous alloys. *Acta Mater.* **48**, 279–306

Kittel C 1948 On the theory of ferromagnetic resonant absorption. *Phys. Rev.* **73**, 155–61

Kraus L, Frait Z, Schneider I 1981 Ferromagnetic resonance in amorphous $(FeNi)_{80}P_{10}B_{10}$ alloys. *Phys. Stat. Sol. (a)* **63**, 669–75

Mandal K, Puerta S, Vázquez M, Hernando A 2000 Giant magnetoimpedance in amorphous $Co_{83.2}Mn_{7.6}Si_{5.8}B_{3.3}$. *Phys. Rev. B* **62** (10), 6598–602

Marín P, Arcas J, Zhukov A, Vázquez M, Hernando A 1997 Evolution of magnetic properties with annealing temperature for CoMnSiB microwires. In: Hadjipanayis G C (ed.) *Magnetic Hysteresis in Novel Magnetic Materials*. Kluwer Academic, The Netherlands, pp. 743–8

Marín P, Hernando A 2000 Application of amorphous and nanocrystalline magnetic materials. *J. Magn. Magn. Mater.* **215–216**, 729–34

Mohri K, Humphrey F B, Yamasaki J, Okamura K 1984 Jitterless pulse generator elements using amorphous bistable wire. *IEEE Trans. Magn.* **MAG-20**, 1409–11

Ogasawara I, Ueno S 1995 Preparation and properties of amorphous wires. *IEEE Trans. Magn.* **31**, 1219–123

Panina L, Mohri K 1994 Magnetic-impedance effect in amorphous wires. *Appl. Phys. Lett.* **65**, 1189–91

Parkhachev V N 1966 Installation for production of glass insulated microwire directly from liquid metal. *US Patent* 3,256,584

Sommer R L, Chien C L 1996 Giant magneto-impedance effects in metglas 2705M. *J. Appl. Phys.* **79** (8), 5140–3

Tejedor M, Hernando B, Sánchez M L, García-Arribas A 1996 Influence of induced anisotropy on magneto-impedance in Co-rich metallic glasses. *J. Magn. Magn. Mater.* **157/158**, 141–2

Taylor G F 1924 A method for drawing metallic filaments and discussion of their properties and uses. *Phys. Rev.* **24**, 6555–60

Tyren C, Vázquez M, Hernando A, Quiñónez C 2000 Stress-wire sensor. *Patent* WO00/57147

Ulitovsky A 1932 Electrical adjustable resistance. *US Patent* 369,646

Vázquez M, Chen D X 1995 The magnetization reversal in amorphous wires. *IEEE Trans. Magn.* **31**, 1229–38

Vázquez M, Zhukov A P, Antonenko A, Larin V, Torkunov A 1996 Método de codificación y marcado magnético de objetos. *ES Patent* P9601993

Vázquez M, Zhukov A P 1996 Magnetic properties of glass-coated amorphous and nanocrystalline wires. *J. Magn. Magn. Mater.* **160**, 223–8

Vázquez M, Zhukov A P, Aragoneses P, Arcas J, García-Beneytez J M, Marín P, Hernando A 1998 Magneto-impedance in glass-coated amorphous microwires. *IEEE Trans. Magn.* **34**, 724–8

Vázquez M, Marín P, Arcas J, Hernando A, Zhukov A P, González J 1999 Influence of nanocrystalline structure on the magnetic properties of wires and microwires. *Textur. Microstruct.* **32**, 245–67

Yagi M, Endo I, Otsuka I, Yamamoto H, Okuno R, Koshimoto H, Shintani A 2000 Magnetic properties of Fe-based amorphous powder cores produced by a hot-pressing method. *J. Magn. Magn. Mater.* **215–216**, 284–7

Yamasaki J 1992 Sensing function and amorphous magnetic materials. *J. Magn. Soc. Japan* **16**, 14–26

A. Hernando and P. Marín
Instituto de Magnetismo Aplicado, Madrid, Spain

Magnetic Phase Transitions: Field-induced (Order to Order)

This article is concerned with high magnetic field magnetization processes in ferrimagnets which are connected to the variation of mutual orientation of their magnetic sublattices and which reveal themselves through characteristic kinks and jumps in the magnetization curves. The magnetic symmetry of a crystal changes when the orientation of the magnetic sublattices spontaneously varies. In other words, a phase transition accompanied by a change of the magnetic symmetry takes place. In the present terminology such phase transitions are referred to as field-induced phase transitions (FIPTs), which may be of first or second order. It is evident that such phase transitions are accompanied by anomalous behavior of some physical properties and characteristics of the ferrimagnets (susceptibility, thermal properties, magnetostriction, magnetoelastic anomalies, Hall effect and magnetoresistance, magneto-optic phenomena, etc.). Comprehensive data and bibliography have been detailed in the survey of Zvezdin (1995).

FIPTs are traditional subjects in the physics of magnetic phenomena. The first examples attracting considerable attention were spin-flop transitions. The concept of these transitions was proposed by Néel in 1936, and they were found later in $CuCl_2 \cdot H_2O$ by Poulis and co-workers in 1951. In these transitions a collinear phase turns into a canted phase and further into a ferromagnetic one in an increasing field. A distinctive feature of the spin-flop transition in an ideal Néel antiferromagnet is that the differential susceptibility of the material in the angular phase is not dependent on the magnetic field or temperature. Later, similar phase transitions were investigated in ferrimagnets whose behavior turned out to be more sophisticated and interesting. The latter materials form typical examples to illustrate the general features of FIPTs.

That noncollinear magnetic structures may exist was first demonstrated theoretically by Tyablikov in 1956. He also defined the conditions of their existence in the case of isotropic ferrimagnets and calculated anomalies of the magnetization arising in the vicinity of such transitions. Perhaps the first experimental manifestations of these phenomena were observed in rare earth iron garnets by Rode and Vedyaev in 1963.

1. Magnetic Materials and H–T Diagrams

To comprehend FIPTs in a ferrimagnet and to obtain its phase diagrams, it is of prime importance to take the real magnetic anisotropy of the material into account. Consequently, various interesting phase diagrams result for ferrimagnets close to the compensation temperature. They include lines of first- and second-order phase transitions, critical points of the liquid–vapor type, and tricritical points, where the first-order phase transition line goes over to the second-order one on the line separating the phases, etc. (e.g., see Fig. 1).

1.1 Rare Earth Ferrite Garnets

FIPTs have been investigated rather closely in rare earth ferrite garnets where the critical fields of the transitions into the canted phase are not too large. Gadolinium iron garnet has been studied in much detail owing to the fact that application of the Néel model is well justified since the Gd^{3+} ion, whose ground state is an orbital singlet ^8S, has a comparatively small magnetic anisotropy (Fig. 2). The rare-earth sublattices in other rare earth ferrite garnets possess substantial magnetic anisotropy. The phase diagrams and the character of the phase transitions differ essentially from those of Néel ferrimagnets.

1.2 Intermetallic Compounds

Considerable attention has been devoted to intermetallic compounds R–TM, where R = rare earth and TM = transition metal (e.g., RCo_5, R_2Fe_{17}, R_2Co_{17}, $R_2Fe_{14}B$, RFe_2 etc.) (see *Alloys of 4f(R) and 3d(T) Elements: Magnetism*) (Fig. 3).

One of the various interesting phenomena inherent in these materials is the FIPT. Polycrystalline and powder samples have been the main objects for measurements. With the progress in both single-crystal growth and strong magnetic field production, crystal field effects and the role of magnetic anisotropy have become obviously of particular interest.

1.3 Free-powder Samples

Single crystals are not always available for the study of FIPTs and intrinsic magnetic properties. Free-powder samples are a good alternative. Verhoef *et al.* (1989, 1990a, 1990b) and de Boer and Buschow (1992) reported the elegant high-field free-powder method, which has been used to determine the inter-sublattice coupling strength in a fairly large number of intermetallic compounds. The particles of the free-powder sample, having a size of about 40 μm, are assumed to be small enough to be regarded as single crystalline and are free to rotate in the sample holder during the magnetization process, so that they will be oriented by the applied field with their magnetic moment in the field direction.

Verhoef *et al.* (1989) analyzed magnetization curves of $Er_2Fe_{14-x}Mn_xC$ compounds. These magnetization curves are the same as in the isotropic case. Only if both sublattices display magnetic anisotropy can an influence on the free-powder magnetization be observed. Figure 4 shows the free-powder
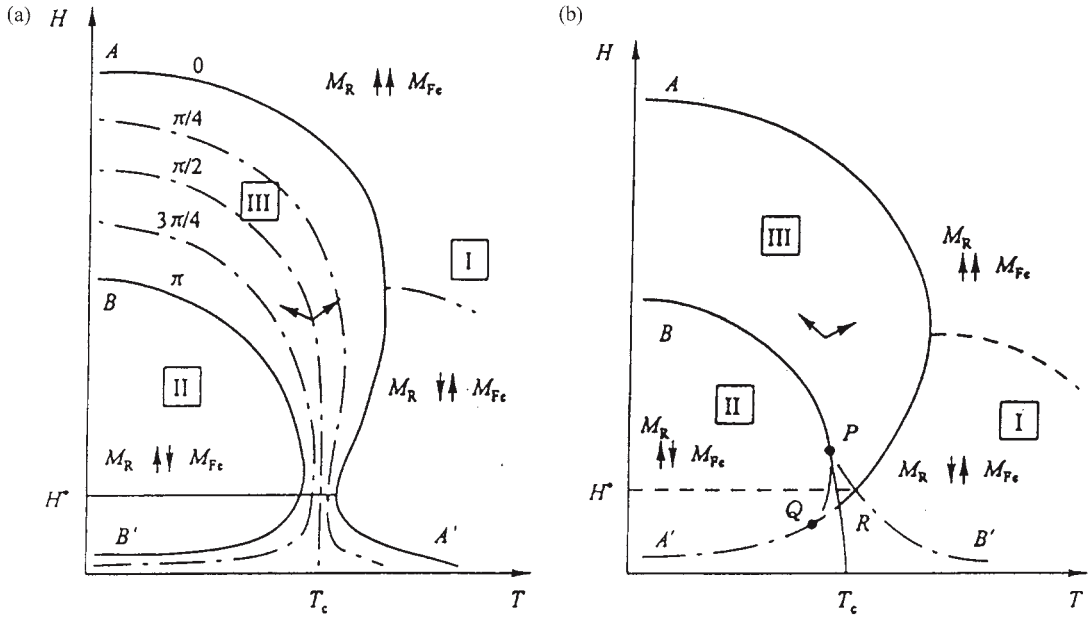
Figure 1
Phase diagram of a uniaxial ferrimagnet in a field (a) perpendicular and (b) parallel to the easy axis. In (a) the dashed curves are isoclines $\theta = \theta(H,T)$. The solid curves pertain to second-order phase transitions. In (b) BP and AR are curves of the second kind of phase transition, and A′R and PB′ are curves representing the loss of the collinear phase stability. PQ is a curve representing the loss of metastable canted phase stability, PRT$_c$ is a curve describing the first kind of phase transition, and P is the tricritical point (Zvezdin and Matveev 1972).
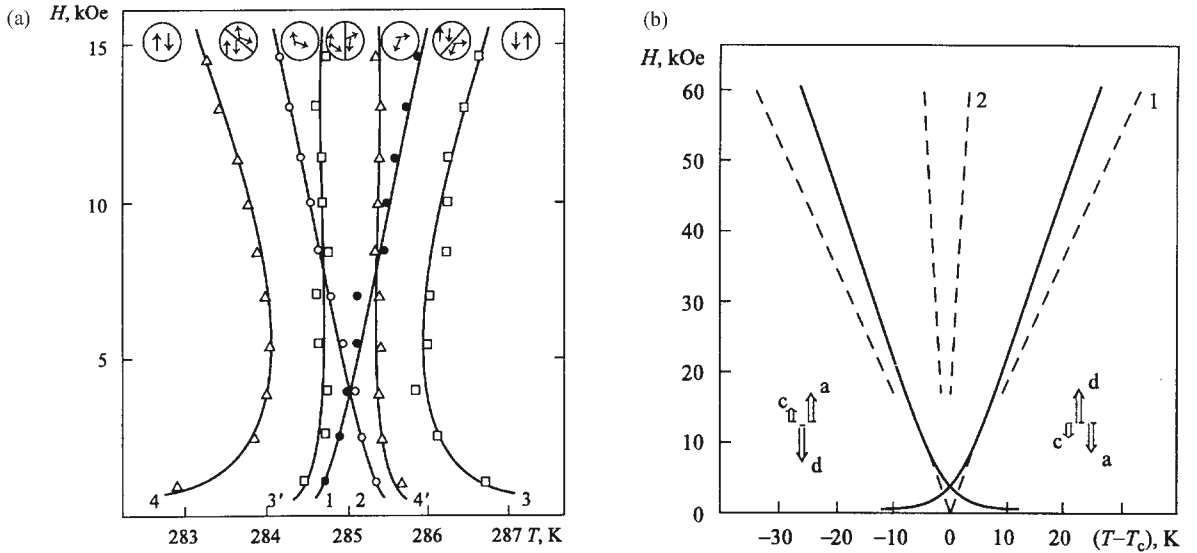
Figure 2
(a) Phase diagram of gadolinium ferrite garnet for $H^{\rightarrow} \psi$ [111] (Kharchenko *et al.* 1975a) and (b) the "reconstructed" high-field phase diagram of the epitaxial film $Y_{2.6}Gd_{0.4}Fe_{3.9}Ga_{1.1}O_{12}$ with $T_c = 183$ K (Gnatchenko *et al.* 1977).

Figure 4
Free-powder magnetization curves of $DyCo_{12}B_6$ measured at 4.2 K. The circles represent measurements in a quasi-continuous field and the dotted lines represent a measurement in a field varying linearly with time (Zhou *et al.* 1992a).

Figure 3
Experimental and theoretical phase diagrams of $DyCo_{5.3}$ in a field directed along the easy axis a and along the hard axis b in the basal plane: $\bigcirc$, experimental critical field (H'_{cr}) and anisotropy field during increase of the external field; $\bullet$, critical field (H''_{cr}) during decrease of the external field; $<$, critical fields coincide. The heavy lines are experimental phase diagrams, the thin solid lines are theoretical lines of phase transitions of the second kind, the dotted lines are theoretical stability curves of the collinear phase, and the dashed–dotted curves those of the noncollinear (high-field) phase (Berezin *et al.* 1980).

magnetization for $DyCo_{12}B_6$ at 4.2 K. This is a good example of the complete bending process in a ferromagnet. The magnetization curve in the canted phase is nearly linear indicating that the dysprosium sublattice anisotropy is much larger than that of the cobalt sublattice. It is seen that the effect of the magnetic anisotropy of the cobalt sublattice is rather small.

2. Some General Features of FIPTs

The phase transitions considered above are typical transitions with a magnetic symmetry change. For

instance, during the I–III transition (Fig. 1) the symmetry is relative to a rotation around the z-axis (i.e., parallel to the external magnetic field) with an angle π (symmetry element C_2^z). This symmetry element is absent in phase III but double the number of equilibrium states in comparison with phase I are present here, which are transferred from one to the other by the "broken" symmetry element. Identical values of the free energy ("degeneration") correspond to these two states. It is accompanied by a division of the sample into domains of a low-symmetry phase.

There are peculiarities in the behavior of many physical properties near the transition point:

(i) The susceptibility goes to infinity. In this case the susceptibility describes the response of an order parameter to the thermodynamically conjugated field.

(ii) The occurrence of anomalies of thermodynamic quantities such as kinks, jumps, and λ-curves (the specific heat, magnetocaloric effect, Young's modulus and sound velocity, magnetostriction, and magnetooptical phenomena).

(iii) The conversion of the order parameter oscillation frequency to zero (soft mode) and the hindering of its relaxation.

(iv) The increasing order parameter fluctuations and their correlation radius.

(v) The expansion of domain walls and the rearrangement of domain structure in the sample.

Many theoretical studies devoted to FIPTs have been carried out using the mean field theory (or using equivalent approximations such as the Landau theory). These theories when constructing the free

energy of a system neglect, to some extent, the fluctuations of the order parameter. In the region of the transition temperature, i.e., in the region where the system stability is lost, the fluctuations increase strongly and these theories become inapplicable. A characteristic feature of the phase transitions studied is the fact that the Landau theory can be used for their description with practically no limitations. The region of inapplicability becomes extremely narrow: $\Delta T \approx 10^{-6}$– 10^{-8} K. This is a consequence of the fact that the fluctuations that occur in the region of the transition have a very large value of correlation radius.

3. Physical Anomalies Near FIPTs

3.1 Magnetization and Susceptibility

The magnetization isotherms $M_T(H)$ show a kink and the longitudinal susceptibility shows a jump at the transition into a noncollinear phase. This fact can be employed for the experimental determination of the critical fields. The field dependence of the magnetization in ferrite garnets of dysprosium, holmium, and erbium is shown in Fig. 5(a). The linear parts of $M_T(H)$ describe the magnetization in the collinear phase and the curved parts describe the
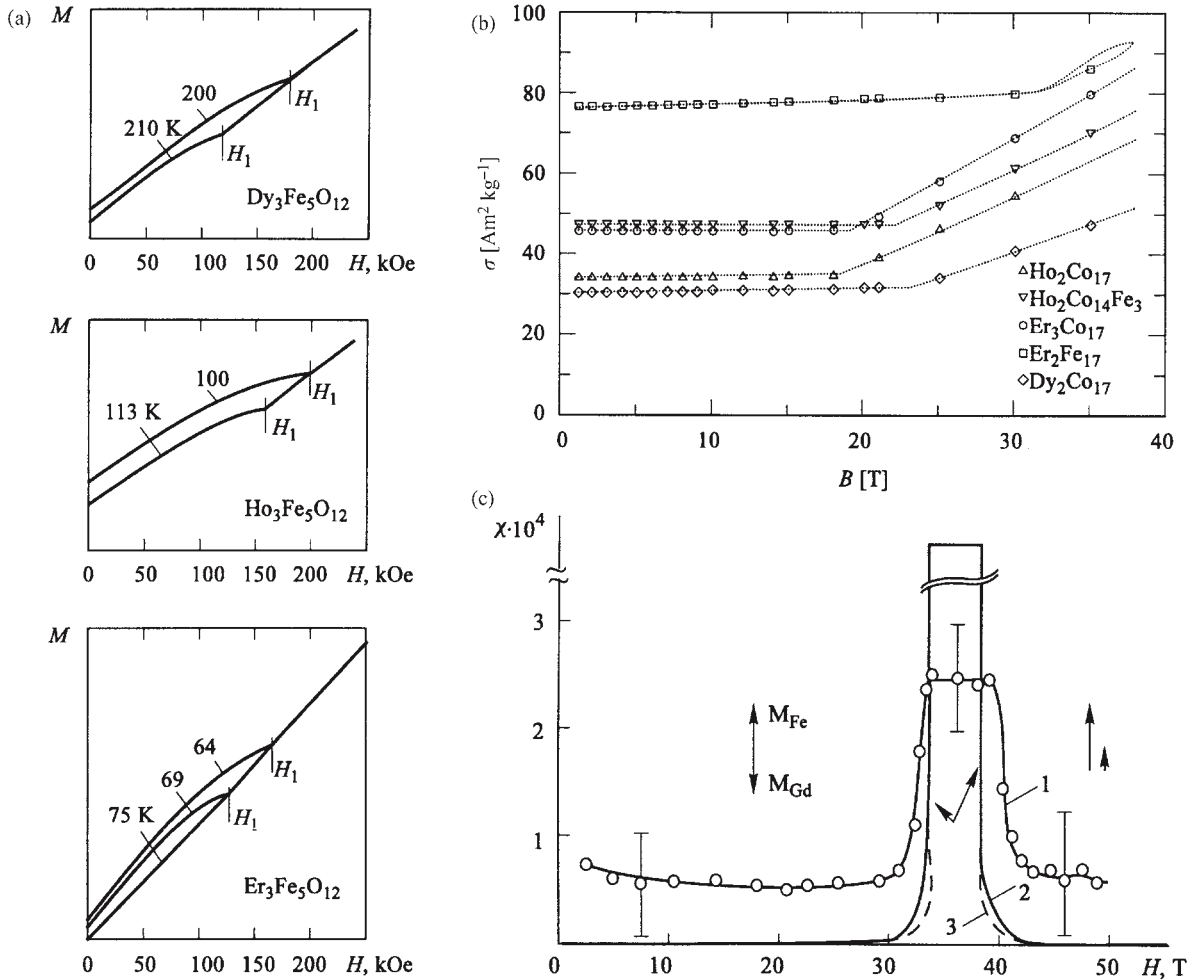
Figure 5
Field dependences of (a) the magnetization in ferrite garnets of dysprosium, holmium, and erbium (Levitin and Popov 1975), (b) high-field magnetization at 4.2 K of several R_2M_{17} single-crystalline spheres that are free to orient themselves in the applied magnetic field (Verhoef 1990), and (c) differential susceptibility of $(GdY)_3Fe_5O_{12}$ iron garnet; $\bigcirc$, experiment; (– – –), theory (Gurtovoy *et al.* 1980).

magnetization in the noncollinear phase. Bend points (or the kinks) in the magnetization curves determine the values of the transition fields from collinear into the noncollinear phases. Much research has been devoted to the high-field magnetization of ferrimagnetic

f–d intermetallic compounds. Many results have been obtained on oriented-powder samples. Figure 5(b) shows, for example, the typical curves for several 2–17 compounds clearly displaying the transitions from the collinear into the canted phase.

The effect of anisotropy on the M_T and especially on the χ_d (differential susceptibility) behavior can be essential in the low-field part of phase diagrams and can give rise to additional anomalies. The region of canted phase narrowing (the ''narrow throat'' of the phase diagram, e.g., see Fig. 1) has to be taken as most ''dangerous'' on that count. In this area the angle rapidly changes with variation of the field and temperature, which results in anomalies in χ_d.

The anomalous behavior of *the differential susceptibility* in the vicinity of the compensation point is attributed to the noncollinear structures in the field. Figure 5(c) illustrates the typical behavior of the differential susceptibility.

A *temperature hysteresis* of various physical quantities may arise during a transition into the non-collinear phase in the vicinity of the FIPTs. Butterfly-like temperature hysteresis loops as shown in Fig. 6 have been observed experimentally in the temperature dependence of the remanent magnetization in ErFe$_2$ near T_c.

The hysteresis of the magnetization vector in ferri-magnets near the compensation point leads to many anomalies in the behavior of other physical quantities, e.g., of kinetic effects. This concerns *galvano-magnetic* and *magneto-optical phenomena* (Hall effect

Figure 6
Temperature dependence of the magnetization of ErFe$_2$ in the vicinity of the compensation temperature (Belov *et al.* 1979).
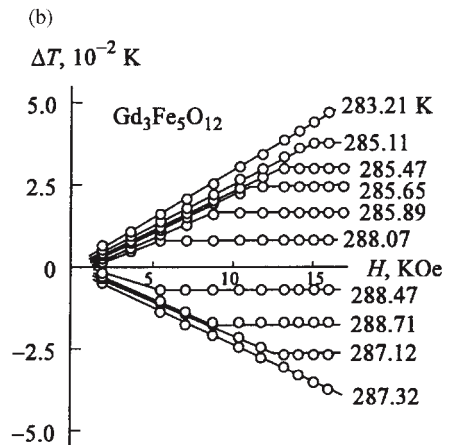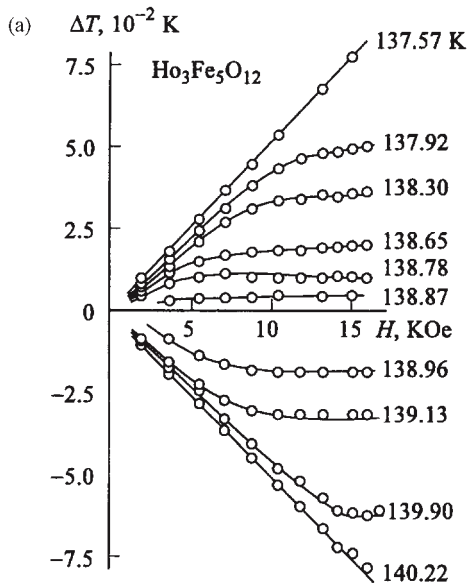
Figure 7
Magnetocaloric effect in (a) Dy$_3$Fe$_5$O$_{12}$ and (b) Ho$_3$Fe$_5$O$_{12}$ in the vicinity of the compensation temperature (Belov *et al.* 1979).

and magnetoresistence, Faraday effect) in the vicinity of the compensation point. These effects have been studied in ferrites, in amorphous R–Co (Fe) alloys, in the intermetallic compound Mn_5Ge_2, and in amorphous Dy–Co films.

3.2 Thermal Properties, Specific Heat, Magnetocaloric Effect

A characteristic property of the second-order phase transition is the kink in the isotropic curve, i.e., the jump of $(dT/dH)_S$ at the boundary between the phases. Experimental data for some compounds are shown in Fig. 7. It is seen that $(dT/dH)_S = 0$ with good accuracy in some phases of the gadolinium ferrite garnets. This value perceptibly differs from zero in the noncollinear phase of holmium and dysprosium ferrite garnets. This is attributed to the large value of the anisotropy energy inherent in these materials.

There are also specific phenomena in the context of FIPTs related to magnetostriction, the thermal expansion coefficient, domain structure, and magnetic structure at the local defect (Zvezdin 1995).

4. Concluding Remarks

Turning back to the question regarding the term "field-induced phase transition" let us note that a broader class of phase transition is described by this term:

(i) Ferrimagnetic–canted–ferromagnetic transitions, which are under consideration here. Occasionally these are referred to as spin-flop transitions by analogy with antiferromagnets.

(ii) Metamagnetic transitions in itinerant ferrimagnets of YCo_2 or RCo_2 type.

(iii) Crossover level transitions, which may be due to a field–induced crossing of the ground state levels of the f or d ions. It should be stressed that this crossing is accompanied by transformation of the magnetic structure of the crystal, i.e., a magnetic analog of the Jahn–Teller effect takes place.

(iv) First-order magnetic processes (FOMPs), which can be due to a competition between crystal field contributions of different order from the free energy.

It should be emphasized that there are no distinct boundaries between these FIPTs. Moreover, it is often possible to find some features inherent in one type of transition than in the others. For example, the mechanism of the spin-flop transitions considered in this survey is closely connected to the crossover-type transitions. Such inter-relations of different mechanisms of FIPTs are of great significance for strongly anisotropic ferrimagnets.

See also: Magnetic Refrigeration at Room Temperature; Magnetic Systems: Specific Heat; Magnetism in Solids: General Introduction; Magnetocaloric Effect: From Theory to Practice; Transition Metal Oxides: Magnetism

Bibliography

Belov K P, Zvezdin A K, Kadomtseva A M, Levitin R Z 1979 *Orientational Transitions in Rare-Earth Magnets*. Science, Moscow

Berezin A G, Levitin R Z, Popov Yu F 1980 Appearance of noncollinear magnetic structures in $DyCo_{5.3}$ near the compensation temperature in strong magnetic fields. *Zh. Eksp. Teor. Fiz. (Sov. Phys. JETP)* **79**, 268–80

De Boer F R, Buschow K H J 1992 High-field properties of 3d–4f intermetallic compounds. *Physica B* **177**, 199–206

Gnatchenko S L, Kharchenko N F, Konovalov O M, Pusikov V M 1977 Magnetic phase diagram of uniaxial epitaxial (magnetooptic and visual studies). *Ukraine Fiz. Zhurnal* **22**, 555–64

Gurtovoy K G, Lagutin A S, Ozhogin V I 1980 Magnetic phase diagram of iron garnets of the $Y_{3-x}Gd_xFe_5O_{12}$ system in fields up to 50 T. *Zh. Eksp. Theor. Phys. (Sov. JETP)* **78**, 847–54

Kharchenko N F, Eremenko V V, Gnatchenko S L 1975a Magnetooptical investigation of the noncollinear magnetic structure of gadolinium iron garnet. *Zh. Eksp. Teor. Fiz. (Sov. Phys. JETP)* **68**, 1073–90

Kharchenko N F, Eremenko V V, Gnatchenko S L, Belyi L I, Kabanova E M 1975b Investigation of orientation transitions and coexistence of magnetic phases in cubic ferromagnetic GdIG. *Zh. Eksp. Teor. Fiz. (Sov. Phys. JETP)* **69**, 1697–709

Levitin R Z, Popov Yu F 1975 In: Belov K P (ed.) *Ferrimagnetism*. Moscow State University, Moscow

Verhoef R 1990 Magnetic interactions in $R_2Fe_{14}B$ and some other R–T intermetallics. Thesis, University of Amsterdam

Verhoef R, de Boer F R, Franse J J M, Denissen C J M, Jacobs T H, Buschow K H J 1989 Magnetic properties of $Er_2Fe_{14-x}Mn_xC$. *J. Magn. Magn. Mater.* **80**, 41–4

Verhoef R, Quang P H, Franse J J M, Radwanski R J 1990a The strength of the R–T exchange coupling in $R_2Fe_{14}B$ compounds. *J. Magn. Magn. Mater.* **83**, 139–41

Verhoef R, Radwanski R J, Franse J J M 1990b Strength of the rare earth–transition metal exchange coupling in hard magnetic materials and experimental approach based on high-field magnetization measurements: application to $Er_2Fe_{14}B$. *J. Magn. Magn. Mater.* **89**, 176–84

Zhou G F, Li X, de Boer F R, Buschow K H J 1992a Magnetic coupling in rare-earth compounds of the type $RCo_{12}B_6$. *J. Magn. Magn. Mater.* **109**, 265–70

Zhou G F, Li X, de Boer F R, Buschow K H J 1992b Magnetic coupling in rare earth–nickel compounds of the type R_2Ni_7. *J. Alloys Comp.* **187**, 299–304

Zvezdin A K 1995 Field induced phase transitions. In: Buschow K H J (ed.) *Handbook of Magnetic Materials*. Elsevier, Amsterdam

Zvezdin A K, Matveev V M 1972 Some features of the physical properties of rare-earth ferrite garnets near the compensation temperature. *Zh. Eksp. Teor. Fiz. (Sov. Phys. JETP)* **62**, 260–71

A. K. Zvezdin
Russian Academy of Sciences, Moscow, Russia

Magnetic Properties of Dislocations

Magnetic properties originate from spin, orbital, and free motion of electrons, as well as from the nuclear magnetic moment. The existence of an angular momentum due to the orbital motion and to the spin of electrons was first identified based on the normal and anomalous Zeeman effects. In crystals, symmetry, periodicity, and ordering play an important role in determining the magnetic properties, which are therefore affected by crystal defects such as dislocations. Whereas the question of magnetism, directly or indirectly related to dislocations, has gained much attention in the past century, it is only in the recent years that a clear and straightforward explanation has been given to deformation-dependent magnetization, and this is largely due to electron microscopy studies.

1. Magnetisms

1.1 Fundamental Properties

According to the Einstein's special theory of relativity, de Broglie has shown that an electron can be equally regarded as a particle and as a wave packet consisting of the so-called de Broglie waves. The energy and momentum of an electron are given by

$$E = h\nu = mc^2(1 - v^2/c^2)^{-1/2} \qquad (1a)$$

and

$$P = h/\lambda = mv(1 - v^2/c^2)^{-1/2} \qquad (1b)$$

where h is the Planck's constant having the dimension of action equal to energy multiplied by time. Then, the phase velocity of the de Broglie wave ($u = \lambda\nu$) is obtained by dividing Eqn. (1a) by Eqn. (1b) as

$$u = \lambda\nu = c^2/v = c(c/v) > c \qquad (2a)$$

The inequality comes from a principle that the electron velocity v never exceeds that of light c. Since the velocity of the wave packet is given by $d\nu/d(1/\lambda) = dE/dP$, it follows from Eqns. (1a) and (1b) that

$$dE/dP = (dE/dv)/(dP/dv) = v \qquad (2b)$$

(see Yukawa and Toyoda 1977). An electron is, thus, shown to move at the velocity of a wave packet consisting of de Broglie waves. The motion of an electron engenders a magnetic moment that interacts with external and internal fields of electronic and magnetic origins. These interactions are accounted for by quantum mechanics (Schiff 1955, Dirac 1963, Raimes 1967, Kittel 1971, Bullett *et al.* 1980).

When a material is magnetized under an external magnetic field $\boldsymbol{H}$, the magnetization $\boldsymbol{M}$ is written as

$$\{\boldsymbol{M}\} = \chi\{\boldsymbol{H}\} = (\mu - \mu_0)\{\boldsymbol{H}\} \qquad (3)$$

where χ and μ are the magnetic *susceptibility* and *permeability* of the materials, and μ_0 the *permeability in vacuum*.

Equation (3) defines the magnetic properties of materials, which are classified into the following.

(i) *Ferromagnetism*. A strong magnetization due to electron spins all aligned within a magnetic domain sufficiently below the Curie temperature. The resistance from the crystal to the motion of domain walls induces some hysteresis on a magnetization curve as shown in Fig. 1. χ_I is the initial susceptibility and χ_E is that measured under a high magnetic field, and H_C is the cohesive force.

(ii) *Antiferromagnetism*. A weak magnetization induced by application of a magnetic field due to spins which are aligned antiparallel by superexchange interaction in absence of the applied field (Anderson 1950). χ^{-1} decreases with T below the Néel temperature (Néel 1948).

(iii) *Ferrimagnetism*. A magnetization due to antiparallel electron spins as for *antiferromagnetism*, but with different strength for opposite spins. It was found in a magnetite $FeO \cdot Fe_3O_4$ composed of ferrous ions (Fe^{2+}) with *ferromagnetism* and ferric ions (Fe^{3+}) with *antiferromagnetism* (Néel 1948).

(iv) *Paramagnetism*. A weak magnetization proportional to a magnetic field with χ^{-1} increasing with T in the absence of interaction among spins (Langevin *paramagnetism*), or by spin bands near the Fermi
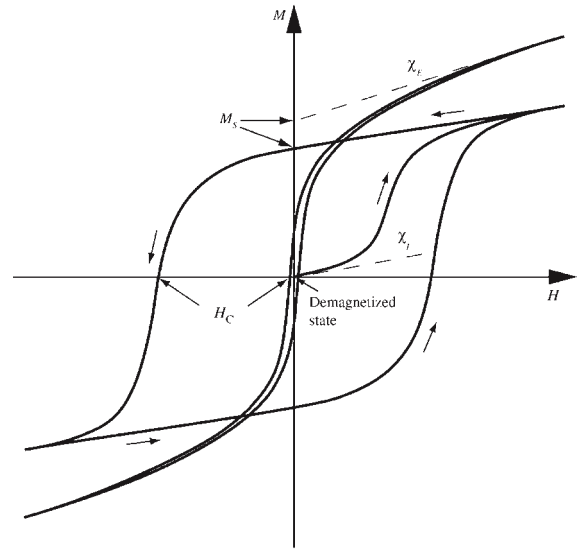
Figure 1
Magnetization curves of ferromagnetic samples with large and small H_C. M_S is defined at $H = 0$ by linear interpolation from large H. χ_I and χ_E are the susceptibilities at initial and high magnetic field (Izumi 2003).

surface due to the splitting of energy levels for opposite spins under a magnetic field (Pauli *paramagnetism*). Transition metals showing no spontaneous magnetization belong to this category (Kittel 1971). A material comprised of extremely small ferromagnetic domains may also show Langevin-type behavior (*superparamagnetism*).

(v) *Diamagnetism*. A weak magnetization characterized by a negative value of χ and observed in metals and organic materials without spin (feeble *diamagnetism*). When $\chi/\mu_0 = -1$, the transition from *paramagnetism* to perfect *diamagnetism* causes superconductivity, leading to the expulsion of the magnetic field and known as the Meissner effect (Meissner and Ochsenfeld 1933).

1.2 Magnetic Measurements

(i) *Electromagnetic induction*. An induction coil is used to detect magnetization. For example, a vibrating sample magnetometer (VSM), which uses a secondary coil placed around a sample, is designed to detect an alternating voltage induced by a vibrating sample magnetized in an applied magnetic field.

(ii) *Electron spin resonance* (ESR). The momentum J or equivalently the magnetization M of an electron is detected by resonant absorption. The application of a magnetic field forces J to undergo Larmor precession, and this is amplified by superimposition of an electromagnetic wave with appropriate frequency. The spectrum and intensity of the absorption peaks provide useful information about M. ESR is alternatively called *electron paramagnetic resonance* (Bowers and Owen 1955, Ingram 1968, Wertz 1968).

(iii) *Nuclear magnetic resonance (NMR)*. Resonance arising from the magnetic spin in the nucleus. This method picks up nuclear magneton as small as 1/1840 of the Bohr magneton. The shift of a resonance peak (Knight shift) in NMR provides detailed information about the behavior of electrons in metallic and nonmetallic crystals including Heusler alloys (Khoi *et al.* 1978). NMR is also applied to visualize a biologic organ by construction of a three-dimensional image (Gadian 1982) and to analyze the structures of proteins, nucleic acids, DNA fragments, etc. (Sarkar 1996).

(iv) *Mössbauer effect*. γ-rays with variable wavelength are generated by Doppler effect and utilized to detect by resonance small energy gaps induced by nuclear spins. The magnetic states of atoms can be analyzed by Mössbauer (1958) spectroscopy. Since the gaps are closely related to the motion of outer shell electrons, it can, for example, differentiate between Fe^{2+} and Fe^{3+}. It has also permitted to identify a transition from *ferromagnetism* to *superparamagnetism* induced in Cu–Co by cold rolling (Nasu *et al.* 1968).

(v) *Diffraction*. Crystal structures and ordering are commonly examined by x-ray, electron, and neutron diffractions. Neutron diffraction provides direct information about electron spins interacting with nuclear magnetic moments. It has been used, for example, to analyze dislocation arrangements in deformed Fe (Göltz *et al.* 1986) and to discriminate between *ferromagnetic* and *antiferromagnetic* properties of Heusler alloys (Natera *et al.* 1970).

1.3 Observation of Magnetic Structures

Electrons accelerated at high voltages are commonly employed to observe microstructures and to analyze physical and chemical properties. Various types of electron microscopes (EMs) or of electron microscopy modes have been developed in the last several decades, in particular, transmission EM (TEM), scanning EM (SEM), reflection EM (REM), scanning TEM (STEM), high-voltage EM (HVEM), high-resolution TEM (HRTEM), convergent beam electron diffraction TEM (CBEDTEM), Lorentz TEM (LTEM), and analytical TEM.

Electrons have both particle- and wave-like properties as described in Sect. 1.1. They are deflected mainly by protons and this is at the origin of a contrast in EM images and of diffraction patterns in the case of crystals as well as quasicrystals. During electron deflection, atoms may behave as secondary sources of signals such as x-rays, secondary electrons, Auger electrons, and inelastically scattered electrons. These signals serve to derive three-dimensional information, and of even higher order in the case of a quasicrystal, on local physical and chemical properties of the material. Image and diffraction properties are analyzed by electron wave mechanics (Thomas 1966, Hirsch *et al.* 1971, Williams and Carter 1998, Fultz and Howe 2002).

The TEM method utilized to visualize magnetic domains and domain walls is called Lorentz microscopy or LTEM. The magnetic domains appear upon defocusing of electron beams diffracted from different domains (Fuller and Hale 1960, Hirsch *et al.* 1971, Williams and Carter 1998, Graef and Zhu 2001). It differs from the optical methods achieved by Fe_3O_4 colloid or by using magneto-optical Kerr effect (Fowler and Fryer 1954), since the accelerated electrons are capable of penetrating through thin crystals. For example, LTEM is used to visualize Néel (1954) walls in a thin foil: the fine structure called crosstie walls in a Permalloy foil: (Huber *et al.* 1958) and the fine ripples introduced by thinning of Fe, Ni, Co and their alloys (Tsukahara 1967).

2. Dislocations

2.1 General Remarks

Dislocation is a line defect defined along the periphery of a surface, which is cut, displaced uniformly,

and then glued in an elastic continuum. The uniform displacement, called the Burgers vector, reflects crystal properties of periodicity, symmetry, and ordering. Atomic displacements around a dislocation and rearrangements of atoms carried by dislocation motion disturb the crystal properties mentioned above and therefore affect magnetic properties. There are excellent textbooks of elementary and advanced theories of dislocations (Read 1953, Friedel 1964, J. Weertman and J.R. Weertman 1967, Nabarro 1967, Hirth and Lothe 1968, Mura and Mori 1976, Mura 1987).

2.2 Stress and Strain around a Dislocation

The Burgers vector comes into an expression of eigendistortion β_{ij}^* defined in the half plane (Mura and Mori 1976, Mura 1987) as

$$\beta_{23}^*(\{x\}) = bH(-x_1)\delta(x_2) \quad \text{for a screw dislocation}$$

(4a)

and

$$\beta_{21}^*(\{x\}) = bH(-x_1)\delta(x_2) \quad \text{for an edge dislocaiton}$$

(4b)

Other β_{ij}^* are zero and b is the magnitude of the Burgers vector b. Displacements due to a screw and an edge dislocation are shown in Figs. 2(a) and 2(b) where the dislocation line is taken along the x_3-axis. $H(-x_1)$ and $\delta(x_2)$ are the Heaviside step function and the delta function, respectively, defined by

$$H(-x_1) = \begin{cases} 1, & x_1 < 0 \\ 0, & x_1 > 0 \end{cases}$$

(5)

and

$$\delta(x_2) = \begin{cases} 0, & x_2 \neq 0 \\ \infty, & x_2 = 0 \end{cases}$$

(6)

When b is an integer multiple of the crystal periodicity, the dislocation is called perfect and if not, imperfect or partial. The Hooke's law is written as (see Mura and Mori 1976, Mura 1987)

$$\sigma_{ij} = C_{ijkl}(u_{k,l} - \beta_{lk}^*)$$

(7)

Here, commas denote partial derivatives of the displacements and Einstein's summation rule is adopted for the repeated subscripts. C_{ijkl} are the elastic constants given for a cubic crystal by

$$C_{ijkl} = \lambda\delta_{ij}\delta_{kl} + \mu\delta_{il}\delta_{jk} + \mu\delta_{ik}\delta_{jl} + \mu'\delta_{ijkl}$$

(8)

where δ_{ij} and δ_{ijkl} are the Kronecker delta and λ and μ are the Lame constants. Crystal anisotropy can be defined by $A = 2C_{2323}/(C_{1111} - C_{1122}) = 2\mu/(2\mu + \mu')$, with $\mu' = 0$ for an isotropic material. By solving the equations of static equilibrium given by

$$\sigma_{ij,j} = 0 \quad (i = 1, 2, 3)$$

(9)

one obtains $u_i(\{x\})$ and $\sigma_{ij}(\{x\})$ around a dislocation at rest. For a mixed dislocation $u_i(x)$ and $\sigma_{ij}(\{x\})$ are given by superposition of its screw and edge components.

2.3 Dislocation Cores

Core configurations are usually determined by displacement of atoms from the positions determined by elasticity in the immediate vicinity of the dislocation center so as to minimize the total energy iteratively.

(a)   (b)

Figure 2
Schematic illustrations of (a) a screw and (b) an edge dislocations. See text for the explanation of u_i and β_{ij}^*.

Dislocation core energy is an important factor but its evaluation by means of atomic simulations is somewhat ambiguous for the results are often affected by boundary conditions. It is nevertheless established that the energy stored in the dislocation core is usually smaller by an order of magnitude than the total energy of a dislocation. Elastic anisotropy must be taken into account upon setting boundary conditions for the computer simulations of dislocation cores when $|\mu'|$ is large. According to Yoo (1987), μ' contributes to the strength of intermetallic compounds notably in conjunction with the cross-slip from {111} to {001} in L1$_2$ ordered alloys. Dislocations in ordered intermetallics have been studied by many researchers and reviewed, for example, by Yamaguchi and Umakoshi (1990) and by Vitek (1998).

3. Magnetic Properties Affected by Plastic Deformation

3.1 General Remarks

Historically, studies of the effects of plastic deformation on magnetic properties were initiated in the early 1900s with no knowledge of the existence of dislocations (Rhoads 1901, Nagaoka and Honda 1902). These studies were focused on the "Permalloy problem" and "Isoperm problem" in 1930–40. The high *permeability* of a Permalloy (Arnold and Elmen 1923) is closely related to ordering (Dahl 1936) and disordering (Kaya 1938). Anisotropy in the magnetization arises from the alloy crystallinity as demonstrated by Honda and Kaya (1926). The "Isoperm problem" was raised in the course of the development of a permanent magnet with high H_C. Magnetization is also affected by a magnetic field applied during heat treatments (Dillinger and Bozorth 1935, Oliver and Shedden 1938, Tomono 1948, Chikazumi 1950). Typical permanent magnets with high H_C are KS steel, MK steel, Alnico 5, Cunife, Cunico, Silmanal, and RCo$_5$. For example, fine rods of ordered precipitates aligned along $\langle 100 \rangle$ are responsible for the magnetic anisotropy in Alnico 5 (Heidenreich and Nesbitt 1952).

The basic studies on the crystalline nature, electron motion, and magnetostriction, which were rather advanced before 1950 in spite of several years of interruption, have contributed greatly to the recent understanding of the magnetic properties of dislocations. Some of the pioneering researches will be found in the Bibliography section (Rhoads 1901, Nagaoka and Honda 1902, Einstein 1905, Volterra 1907, Ewald 1917, Laue 1918, Arnold and Elmen 1923, de Broglie 1925, Pauli 1925, Schrödinger 1925, 1926, Dirac 1927, Fermi 1928, Heisenberg 1928, Bloch 1929, Fock 1930, Wigner and Seitz 1933, Kramers 1934, Dillinger and Bozorth 1935, Dahl 1936, Van Vleck 1937, Oliver and Shedden 1938, Kaya 1938, Brown 1940, 1941, Ralhenau and Snoeck 1941, Néel 1948, Chikazumi 1950, Anderson 1950).

Investigations of the effects of dislocations on magnetic properties have focused on the subjects of initial and high-field magnetization in ferromagnetic materials. In his pioneering work, Brown (1940, 1941) has given evidence that the displacements of atoms around a dislocation (Taylor 1934, Sect. 2.2) forces spin axes to rotate, influencing ferromagnetic properties. Although the effect of an isolated dislocation is small, a high density of dislocations introduced by plastic deformation affects the magnetic properties quite significantly (Seeger and Kronmüller 1960, Kronmüller and Seeger 1961, Kronmüller 1967, Umakoshi and Kronmüller 1981a). Therefore, in cyclic deformation less dominant effect appears on the magnetic anisotropy due to reversible motion of dislocations slowing down their accumulation (Mughrabi *et al.* 1976). Aspects related to the stress $\sigma_{ij}(\{\boldsymbol{x}\})$ around a dislocation will be described in more detail in Sect. 3.2.

Another important effect is that caused by dislocation motion. A strong magnetization asymmetry was found in cold-rolled Ni$_3$Fe (Ralhenau and Snoeck 1941, Chikazumi 1950, Chikazumi *et al.* 1957), in cold-rolled Ni$_3$Mn (Taoka *et al.* 1959), and in filed powder of Pt$_3$Fe (Bacon *et al.* 1963). These properties are related to the changes in atomic ordering as described in Sect.3.3 and cyclic deformation amplifies the magnetic effects markedly in ordered alloys (Yasuda *et al.* 2000, 2003, Yamamoto *et al.* 2003, Izumi 2003), at variance from the above-mentioned observations in pure Fe (Mughrabi *et al.* 1976).

3.2 Role of Stress-fields around Dislocations

Magnetic measurements are useful in analyzing the dislocation structures in deformed crystals by nondestructive testing. In measuring χ_I, χ_E, H_C, and M_S (Fig. 1) one should take the geometry of $\boldsymbol{b}$ and $\boldsymbol{t}$ into account and then compare to corresponding theoretical values (Brown 1940, 1941, Seeger and Kronmüller 1960, Kronmüller and Seeger 1961, Kronmüller 1967, Gessinger 1970, Willke 1972, Schroeder 1978, Umakoshi and Kronmüller 1981a). The magnetic energy arises from the exchange interaction between the spins (ϕ_A), the magnetocrystalline anisotropy (ϕ_K), the magnetization in the applied field (ϕ_H), the long-range stray-field interaction coming from divergences of magnetization (ϕ_S), and the magnetoelastic coupling (ϕ_M). The last term describes the interaction between the spontaneous magnetization and the stress field around a dislocation.

For a cubic crystal, the magnetoelastic coupling energy ϕ_M depends on the direction cosines $\gamma_i(\{\boldsymbol{x}\})$ of the spontaneous magnetization as

$$\phi_M = -\frac{3}{2}[(\lambda_{100} - \lambda_{111})\delta_{ijkl}\gamma_k(\boldsymbol{x})\gamma_1(\boldsymbol{x}) + \lambda_{111}\gamma_i(\boldsymbol{x})\gamma_j(\boldsymbol{x})]\sigma_{ij}(\{\boldsymbol{x}\}) \tag{10}$$

where λ_{100} and λ_{111} are the magnetostriction constants reflecting the elastic property of λ, μ, and μ'. Here, Einstein's summation rule is adopted for the repeated subscripts as in Sect. 2.1. In order to determine $\gamma_i(x)$, the total energy must be minimized and this is written as

$$\delta \int [\phi_A + \phi_K + \phi_H + \phi_S + \phi_M] \mathrm{d}v = 0 \qquad (11)$$

where the integration is taken over the specimen. Under a high field of near saturation, since directions of the M_S are nearly parallel to applied magnetic field, the partial differential equations derived from Eqn. (11) can be solved by means of Fourier transformation under a linear approximation (Seeger and Kronmüller 1960, Kronmüller and Seeger 1961, Umakoshi and Kronmüller 1981a). The spin distribution, $\gamma_i(\{x\})$, is most conveniently visualized in the dislocation coordinates (Seeger and Kronmüller 1960, Kronmüller and Seeger 1961, Kronmüller 1967, Gessinger 1970, Umakoshi and Kronmüller 1981a, Yasuda et al. 2000). This is exemplified in Fig. 3 for an edge dislocation (after Kronmüller 1967). Here, the deviation of $\gamma_i(\{x\})$ from the direction of the magnetic field applied along b is shown by arrows.

$$l_H = \kappa_H^{-1} = \left(\frac{2A}{Hl_s}\right)^{\frac{1}{2}}$$
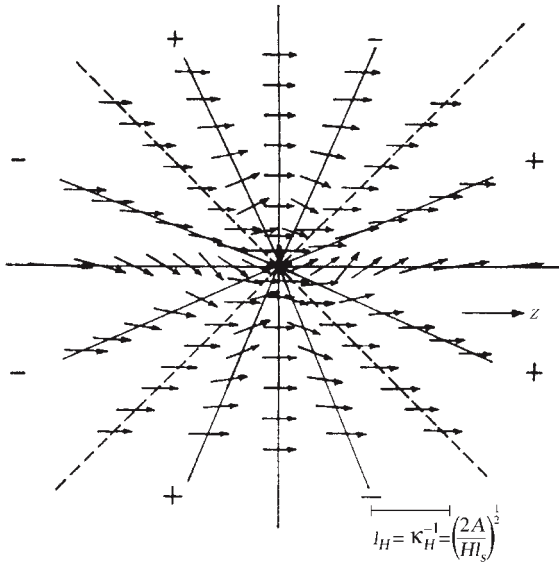
Figure 3
Distribution of the spontaneous magnetization (spins) around an edge dislocation in Ni. The magnetic field of $H = 100\,\mathrm{Oe}$ is parallel to the Burgers vector. The arrows indicate directions magnified along the vertical axis by a factor of 5 (Kronmüller and Seeger 1961) (reproduced by permission of Kronmüller (1967) from *Can. J. Phys.* **45**, 633).

A method to obtain $u_i(\{x\})$ and $\sigma_{ij}(\{x\})$ around a dislocation in an anisotropic material is given in the literature (Stroh 1958, Nabarro 1967, Hirth and Lothe 1968, Mura and Mori 1976, Mura 1987). For simplicity though, μ' is set to zero in most of the calculations of $\sigma_{ij}(\{x\})$ used to analyze the crystallographic characteristics of magnetism. Since dislocations may pile up against obstacles, the equilibrium of linear arrays of dislocations must be known and this problem was solved by (Eshelby *et al.* 1951).

(a)   B.c.c. Fe
Plastic deformation in b.c.c. transition metals and in some covalent crystals is controlled by the motion of screw dislocations that overcome a large Peierls–Nabarro stress (Nabarro 1967) by thermally activated nucleation of double kinks (Celli *et al.* 1963, Dorn and Rajnak 1964). Such a motion is assisted by dispersed misfit strain centers at low temperatures, whereas the motion of edge portions is opposed by the same strain centers at high temperatures (Sato *et al.* 1970, Sato and Meshii 1973). This explains why TEM observations show that the dislocation structure strongly depends on deformation temperature (Foxall and Statham 1970).

Another characteristic feature to be noted in plastic deformation is that as dislocations are generated at some multiplication sources (Read 1953), they tend to pile up against obstacles. In the b.c.c. Fe, dislocation interaction with other obstacles takes over the double kink nucleation mechanism at a higher temperature so that dislocations are introduced as groups. In general, the susceptibility under a high magnetic field is proportional to $\sim b^2 N$ where N is the total number of dislocations but this is modified by dislocation pileups as follows. In a pileup containing n dislocations, b is effectively increased to nb and N is decreased to N/n, thus changing the proportionality factor into $(nb)^2(N/n) = nb^2N$. Consequently, χ_E is increased by a factor n (Kronmüller and Seeger 1961, Kronmüller 1967, Gessinger 1970, Willke 1972, Schroeder 1978, Umakoshi and Kronmüller 1981a, Göltz *et al.* 1986).

This property has been utilized to identify the number of dislocations contained in pileups. According to the orientation dependence of the high-field χ_E measured on a disk sample cut either parallel to the slip plane or perpendicular to the Burgers vector, Schroeder (1978) showed that $n = 16-17$ for the primary dislocations and $n = 12$ for the secondary dislocations in Fe single crystals deformed to stage III at room temperature. On the other hand, isolated edge dislocations are identified to be responsible for the orientation dependence of χ_E after deformation to stage I.

Umakoshi and Kronmüller (1981a) have examined the changes of χ_E in b.c.c. Fe due to primary edge and conjugate screw dislocations at successive stages of

$b = [111]/2$ edge dislocation

$b = [111]/2$ screw dislocation

$b = [\bar{1}11]/2$ screw dislocation

(a)

(b)

Strained to

● 6%
○ 10%
▽ 18%
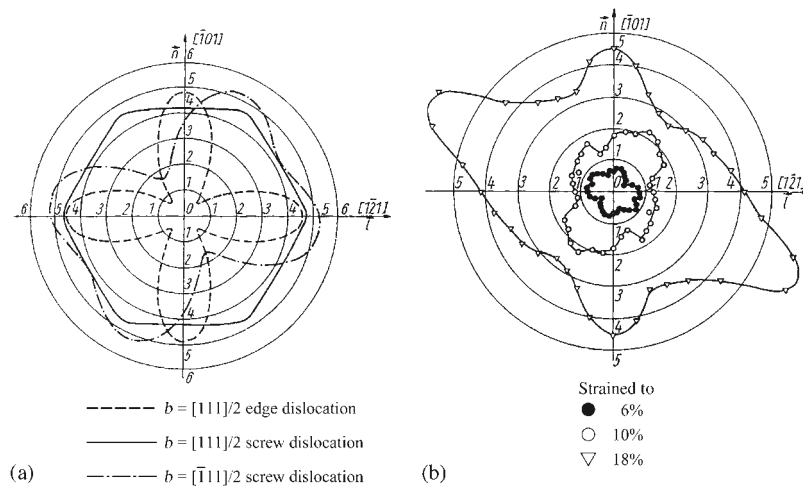
Figure 4

Comparison of the calculated (a) and measured (b) high-field χ shown by polar diagrams on a (111) plane perpendicular to the primary Burgers vector. It can be noted that χ conjugate Burgers vector $[\bar{1}11]/2$ becomes notable in addition to the contribution of the primary screw dislocations at a large strain in (b) (reproduced by permission of Umakoshi and Kronmüller (1981a) from *Phys. Stat. Sol. (a)* **66**(2), 509–520).

deformation at 77 K after pre-straining at 295 K. Figure 4 shows an example of their study. The orientation dependence of χ_E measured on a disk sample sliced perpendicular to the primary Burgers vector (after Umakoshi and Kronmüller 1981a) shows asymmetry due to introduction of conjugate screw dislocations. By comparison with the calculated contribution shown in (a), it can be seen that the measured χ_E in (b) is contributed by all dislocation characters. For a better understanding of the figure, it is required to incorporate the results of other disks sliced along different orientations (Umakoshi and Kronmüller 1981a).

Long-range internal stresses due to piled-up dislocations may alter the magnetic domain patterns. Umakoshi and Kronmüller (1981b) have examined the domain structures of Fe single crystals deformed at 77 K and 195 K by using the magneto-optical Kerr effect (Fowler and Fryer 1954). They showed that the structure is finer after deformation at 77 K than at 195 K in accordance with the operation of a double kink nucleation mechanism at low temperatures. Schroeder (1978) has examined domain patterns in Fe single crystals deformed at room temperature and explained the structure as a compromise between (i) the stray-field energy that forces spins to align parallel to each other and (ii) the Bloch wall energy that governs spin rotation in domain walls under the influence of stress field from piled-up dislocations. Magnetic measurements, thus, provide a wide range of information about dislocations introduced into ferromagnetic b.c.c. Fe by plastic deformation without damaging a sample.

(b)   F.c.c. Ni and Ni₃Fe

In 1960s, it was questioned if the forest dislocations contribute to the work hardening in f.c.c. metals. In his review on the question, Kronmüller (1967) pointed out that magnetic measurements are useful as a nondestructive testing method to delineate the dislocation arrangements and to get some insight into the work-hardening mechanism. In spite of the fact that investigations are restricted to ferromagnetic materials and that interpretation of experimental results require some solid theoretical background, several researchers have taken advantage of magnetic measurements to identify the dislocation types, densities, and their distribution in f.c.c. Ni in a wide range of plastic deformation.

According to Eqn. (11), χ_I and H_C are shown to be proportional to $N^{-1/2}$ and $N^{1/2}$, respectively (Seeger *et al.* 1964, Willke 1972). Since the work-hardening $\Delta\sigma$ is proportional to $N^{1/2}$ in a polycrystal (Taylor 1934) or in stage II of a single crystal, χ_I and H_C are proportional to $\Delta\sigma^{-1}$ and $\Delta\sigma$, respectively (Seeger *et al.* 1964), as is observed in Ni single crystals (Hayashi 1967). Hayashi (1967) also shows experimentally that χ_I^{-1} is proportional to $\Delta\sigma^{1/2}$ in stage I in agreement with the work-hardening theory (Mott 1952). Dislocation structures in deformed Ni single crystals have been studied in more details by analyzing the high field χ_E due to edge, screw, and 60° dislocations (Gessinger 1970). The information about dislocation distribution can also be obtained from the domain structure by differentiating the dislocation-induced anisotropy of ϕ_M from the magnetocrystalline anisotropy of ϕ_K on the ground of theoretical analysis of the high-field χ_E (Willke 1972).

In ordered alloys, dissociated superdislocations may also contribute to the magnetic anisotropy. In a deformed Ni$_3$Fe, the anti-phase boundary the (APB) strip alters the orientation dependence of χ_E measured on the disks sliced along the low index planes in the dislocation coordinates (Yasuda *et al.* 2000). The magnetic anisotropy induced by the APBs differs from that due to the $\sigma_{ij}(\{x\})$ around dislocations. More importantly, introduction of the APBs alters the absolute magnitude of the M_S as described below.

3.3   Role of Atomic Rearrangements

The motion of partial dislocations affects magnetic properties in various ways depending on crystal structure, chemical composition, deformation temperature, strain rate, etc. The Néel and Curie temperatures are different in deformed specimens, basically due to the change in spin–orbital interactions (Kramers 1934, Van Vleck 1937, Anderson 1950). Microscopic observations, diffraction analyses, and spectroscopy are useful in studying magnetic properties that can be strongly affected by interchanges of atoms as exemplified below for some popular intermetallics.

(a)   B.c.c.-based superlattice
There are three main types of b.c.c.-based superlattices as shown in Fig. 5. Plastic deformation increases magnetization most evidently for ~35 at.% Al in Fe–Al intermetallics (Taylor and Jones 1958, Huffman and Fisher 1967, Gengnagel *et al.* 1972, Takahashi *et al.* 1996). In this composition, although both the B2 and D0$_3$ phases coexist, dislocations generated in the B2 phase control the plastic deformation as well as magnetic properties (Yamashita *et al.* 1998). The
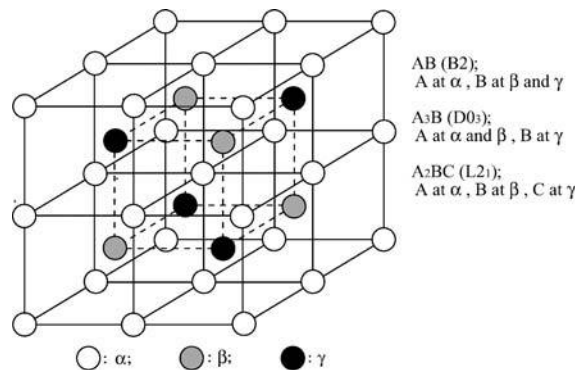
local change in ordering introduced by deformation increases the magnetization (Chikazumi *et al.* 1957, Takahashi and Umakoshi 1990, Takahashi *et al.* 1996). Mössbauer spectroscopy shows that the number of first-nearest neighbor (FNN) Fe–Fe pairs contributes to M_S (Huffman and Fisher 1967).

In contrast, plastic deformation reduces the magnetization of a Heusler alloy of L2$_1$-ordered Pd$_2$MnSi (Takahashi and Shinohara 1982), whose structure sketched in Fig. 5 was first found in a Cu–Mn–Al system (Heusler 1934). NMR analyses of various Heusler alloys show that *antiferromagnetic* and *ferromagnetic* properties come from the interaction between atoms in the second- (SNN) and the third-nearest neighbor positions (TNN), namely by B–C and B–B interactions where B is Mn (Khoi *et al.* 1978). The motion of a partial dislocation $\langle 111 \rangle /2$ on a {110} plane in the L2$_1$ structure introduces the FNN Mn–Mn pairs at the expense of the TNN Mn–Mn pairs reducing *ferromagnetism*. This is because the Mn–Mn magnetic interaction is *antiferromagnetic* when they are located close (Néel 1948) and *ferromagnetic* when they are located apart (Kasper and Roberts 1956).

(b)   F.c.c.-based superlattice
L1$_2$ and D0$_{22}$ are the most popular structures as shown in Fig. 6. The L1$_2$ structure originally found in an Au–Cu system (Johansson and Linde 1925) has gained much attention because of the good symmetry and ductility. Although slip takes place on {111} planes in general at a low temperature, limited motion of $\langle 110 \rangle /2$ superpartial dislocations on cube planes introduces D0$_{22}$ structure locally. Plastic deformation reduces the susceptibility of Pt$_3$Fe and

AB (B2);
A at α, B at β and γ

A$_3$B (D0$_3$);
A at α and β, B at γ

A$_2$BC (L2$_1$);
A at α, B at β, C at γ

$\bigcirc$: α;   ◐: β;   ●: γ

Figure 5
B2, D0$_3$, and L2$_1$ in b.c.c.-based superlattices. The figure contains eight unit cells for the B2 structure. A Heusler alloy assumes the L2$_1$ structure.

A$_3$B (L1$_2$)   A$_6$B$_2$ (D0$_{22}$)

A at $\bigcirc$, B at ●   A at $\bigcirc$, B at ●
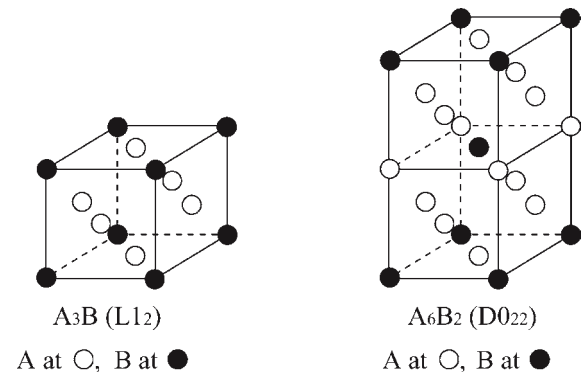
Figure 6
L1$_2$ and D0$_{22}$ in f.c.c.-based superlattices. The motion of a [110]/2 superpartial dislocation on a (001) plane induces the phase transformation L1$_2$ $\Rightarrow$ D0$_{22}$, which does not involve interchanges of the FNN atoms (Flinn 1960).

introduces spontaneous magnetization (Bacon *et al.* 1963, Takahashi and Umakoshi 1990). On the contrary, spontaneous magnetization in ferromagnetic Ni_3Mn, Ni_3Al, and Ni_3Ge disappears by plastic deformation (Taoka *et al.* 1959, Bacon *et al.* 1963, Takahashi and Ikeda 1983, Izumi 2003). This subject will be discussed more in Sect. 3.4(b).

3.4 Contribution of APB Tubes

Vidoz and Brown (1962) have introduced the concept of APB tubes to explain the work hardening in superlattices. APB tubes were then observed and discussed by many researchers in both B2 (Crawford 1976, Chou and Hirsch 1981, 1983, Yamashita *et al.* 1998, Yamamoto *et al.* 2003) and $L1_2$ alloys (Chou *et al.* 1982, Shi *et al.* 1996, Murakumo *et al.* 2000a, 2000b). The APB tubes disappear upon annealing at a relatively low temperature, thus providing a simple means to discriminate their contribution to the magnetization (Yang and Baker 1997, Yamashita *et al.* 1998, Yang *et al.* 1999) from that due to APB ribbons bound by superpartials within a dissociated superdislocation (Takahashi *et al.* 1996, Takahashi and Umakoshi 1990).

APB tubes can be formed in any given ordered alloy whenever the leading and trailing partials that belong to a perfect dislocation are forced to move on different slip planes, and this may occur locally at jogs or at kinks. It is important to notice that APB tubes are free from dislocations except at their ends. Another point to be recalled is that change in ferromagnetism is essentially determined by spin–orbital interactions (Kramers 1934, Van Vleck 1937, Anderson 1950) related strictly to the atomic elements at APB tubes and APB ribbons in the ordered intermetallics. Formation of the APB tubes is favored by high deformation rates (Murakumo *et al.* 2000b, Yoneyama 2002) as well as by cyclic deformation (Yamamoto *et al.* 2003, Yasuda *et al.* 2000, 2003, Izumi 2003). Since the latter case is regarded as heavy deformation in the sense of accumulated strain, it is speculated that APB tubes might have also been introduced at high densities in crashed Fe–Al (Gengnagel *et al.* 1972) and in filed Pt_3Fe (Bacon *et al.* 1963).

(a) APB tubes in b.c.c.-ordered superlattices
The introduction of APB tubes by plastic deformation in an Fe–Al alloy increases magnetization substantially (Yang and Baker 1997, Yamashita *et al.* 1998, Yang *et al.* 1999). Furthermore, M_S increases markedly by cyclic deformation as shown in Fig. 7 (after Yamamoto *et al.* 2003). Here, the cyclic deformation corresponds to 33.7% of accumulated strain achieved by changing the mutually orthogonal compression axes. A constraint was imposed on the side surfaces to limit the operative shear systems
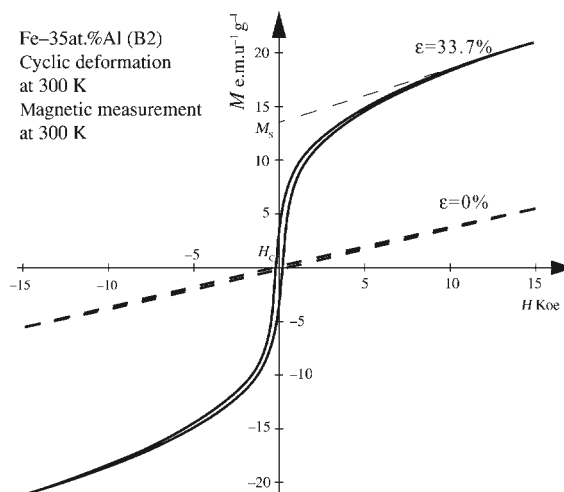
Figure 7
Strong magnetization in B2-ordered Fe–Al induced by cyclic deformation to an accumulated strain of 33.7%. Note that the small value of H_C is about the same as that in deformed and nondeformed Fe_3Ge shown later in Fig. 11 (Yamamoto *et al.* 2003).

(Murakumo *et al.* 2000a) and to hold the specimen dimension unchanged.

The observed evolution of H_C can be attributed to the introduction of APB tubes. The small value of H_C is reasonable since APB tubes are rather narrow without accompanying long-range stress. H_C is approximately the same as that in Fe_3Ge, but substantially larger than that in Ni_3Ge, as shown later in Figs. 9 and 11. The APB tube density is several times higher than the dislocation density as shown in Fig. 8 (after Yamamoto *et al.* 2003). M_S decreases by 80% after annealing at 573 K for 30 min, which, as shown by TEM observations, coincides with the disappearance of APB tubes (Yamamoto *et al.* 2003).

(b) APB tubes in f.c.c.-ordered superlattices
In contrast to what is observed in B2-ordered Fe–Al, plastic deformation reduces M_S markedly in Ni_3Ge cyclically deformed at 4.2 K as shown in Fig. 9 (after Izumi 2003). Superpartial dislocations are forced to glide on both {111} and {001} planes as a result of compression being applied along [100] and [011] axes alternatively. Generation of a high density of APB tubes by cyclic deformation is illustrated in Fig. 10, confirming that introduction of APB tubes is the main origin of the reduction in M_S (Izumi 2003).

At this point, it is interesting to compare the above result on Ni_3Ge with that on Ni_3Al (Takahashi and Ikeda 1983) that shows a similar decrease in M_S at 4.2 K. In the latter, M_S decreases proportionally to the strain in the early stages and to the square root of
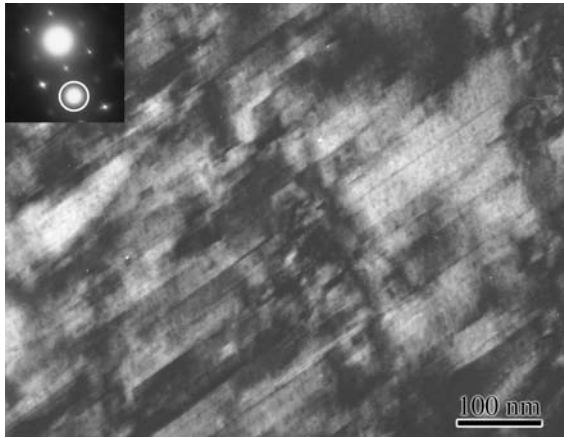
Figure 8
APB tubes introduced into the deformed Fe–Al of
Fig. 7. The beam direction is nearly along [0$\bar{1}$1] and the
dark-field image is taken under the 111 order spot
(Yamamoto *et al.* 2003).

Figure 10
APB tubes introduced into the deformed specimen of
Fig. 9. Irradiation-induced secondary defects are formed
preferentially along the APB tubes which facilitates the
visualization of the latter (Murakumo *et al.* 2000). The
inset shows the 111 ordered spot used in the dark-field
image. The beam direction is taken nearly along [0$\bar{1}$1]
(Izumi 2003).

Figure 9
The spontaneous magnetization in Ni$_3$Ge measured at
4.2 K decreases notably by cyclic deformation given at
77 K to accumulated strain of 10.0% (Izumi 2003).
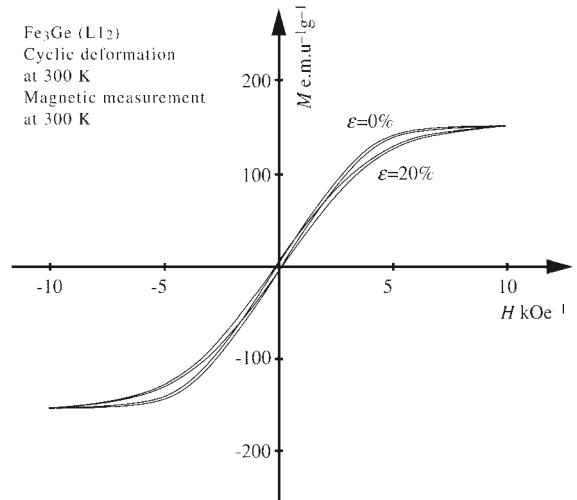
Figure 11
Magnetization curves obtained in nondeformed and
cyclically deformed Fe$_3$Ge at room temperature. Plastic
deformation at room temperature does not change
either M_S or H_C in visible amount, but it increases the
high-field χ_E notably (Taniguchi 2003).

the strain at higher strains. It is known that APB
tubes are also formed in Ni$_3$Al (Chou *et al.* 1982, Shi
et al. 1996, Murakumo *et al.* 2000b) and it is likely
that they contribute to the ferromagnetic to para-
magnetic transition through changes in environmen-
tal atoms as discussed for APB ribbons by Takahashi
and Ikeda (1983).

It should be emphasized that plastic deformation
does not reduce M_S in Fe$_3$Ge at 300 K as shown in
Fig. 11 (after Taniguchi 2003). The effect of plastic

deformation on Fe$_3$Ge, thus, differs from that ob-
served in Ni$_3$Ge and Ni$_3$Al, despite that they are all
ferromagnetic at the temperatures examined. The
origin may be ascribed to the difference in activated

slip planes. The preference for {111} versus {001} slip has been discussed and the anomalous strengthening of L1$_2$-ordered alloys is commonly attributed to the K–W locks (Kear and Wilsdorf 1962). More precise arguments are founded on the dislocation core structure (Yamaguchi *et al.* 1982, Paider *et al.* 1984, Umakoshi *et al.* 1984, Mryasov *et al.* 2002), APB energies (Flinn 1960, Saada and Veyssiére 1992, 1994), elastic anisotropy (Stroh 1958, Yoo 1987), super intrinsic stacking fault (SISF) (Fang *et al.* 1994), and complex stacking fault (CSF) (Hemker and Mills 1993, Balk *et al.* 2001).

It is interesting that Fe$_3$Ge is one of a few L1$_2$ intermetallics, which does not exhibit anomalous strengthening and this has been interpreted as a result of the operation of cube slips in a wide temperature range (Ngan *et al.* 1992). Recently, production of $\langle 110 \rangle /2$ {001} partial dislocations and their multiplication have been confirmed by semi-*in-situ* experiments of a thin foil of stoichiometric Fe$_3$Ge (Taniguchi 2003). Since the structural change from L1$_2$ to D0$_{22}$ in Fig. 6 or equivalently motion of $\langle 110 \rangle /2$ superpartial dislocations on {001} planes does not involve interchanges of the FNN pairs (Flinn 1960), it is natural that plastic deformation does not affect M_S in Fe$_3$Ge if FNN pairs are important. Concurrently, the high-field χ_E increases due to introduction of superdislocations as shown in Fig. 11.

On the other hand, plastic deformation induces spontaneous magnetization in Pt$_3$Fe (Bacon *et al.* 1963, Takahashi and Umakoshi 1990) and in Ni$_3$Fe (Yasuda *et al.* 2000) mainly by introduction of the FNN Fe–Fe pairs as evidenced in neutron diffraction study (Bacon *et al.* 1963). The spontaneous magnetization can be attributed to the introduction of APB tubes and APB ribbons as in the case of Fe–Al (Sect. 3.4.(a)). The dissimilar properties of M_S in Pt$_3$Fe and Ni$_3$Ge (Fe$_3$Ge) can be ascribed to the difference in the sites A and B occupied by ferromagnetic atoms: B for the former and A for the latter as shown in Fig. 6. Ferromagnetic FNN pairs are absent before deformation in Pt$_3$Fe and introduced by superpartial dislocation motion, whereas FNN pairs of ferromagnetic atoms are readily present in Ni$_3$Ge and Fe$_3$Ge. The FNN pairs are destroyed by {111} slip in Ni$_3$Ge but not by {001} slip in Fe$_3$Ge. The APB tubes are not found in Fe$_3$Ge, whereas $\langle 110 \rangle /2$ superpartial dislocations are found in {001} planes after both bulk and thin foil deformation (Taniguchi 2003), in support of the predominant operation of {001} slip in Fe$_3$Ge (Ngan *et al.* 1992).

3.5 Magnetic Transition Involving Large Strain

Both for practical and academic purposes, ferromagnetic shape-memory alloys (SMAs) have gained much attention in the recent years. Interest started after the discovery of a large strain in a tetragonal Ni–Mn–Ga

induced by application of a magnetic field at a low temperature (Ullako *et al.* 1996). The elongation strain becomes as large as 6% in Ni$_{50}$Mn$_{28}$Ga$_{22}$ (Murray *et al.* 2000), 0.6% in Fe$_{70}$Pd$_{30}$ (James and Watting 1998), and −2.3% in Fe$_3$Pt (Kakeshita *et al.* 2000). These values are strikingly larger than usual strain values for magnetostriction, e.g., 0.001% (Rhoads 1901, Nagaoka and Honda 1902) $\sim 0.17\%$ (Clark *et al.* 1988). The effects of a magnetic field on the cubic-to-tetragonal phase transformation have also been discussed in the presence of hydrostatic (Kurisu *et al.* 1987) and unidirectional (Muto *et al.* 1987) stresses, raising a question of a distinction between mechanical and magnetic forces.

Steuwer *et al.* (2003) have compared the energies dissipated during 6% elongation in the two experiments of Ni$_{50}$Mn$_{28}$Ga$_{22}$ (Murray *et al.* 2000), one under a stress and the other under a magnetic field. The estimated energy dissipation is markedly larger for the stress–strain closure than for the magnetic hysteresis curves. The discrepancy may result from combination of the following two factors: (i) Evolution of such a large strain may be ascribed to motion of a line defect that carries uniform displacement or uniform rotation of the tetragonal lattice. The latter line defect is called disclination for which the eigendistortion $\beta_{ij}^*(\{x\})$ is written in different manner from a dislocation (see Mura 1987). (ii) The variables controlled in the two experiments are different in terms of thermodynamics (Callen 1960); the parameter under control in the magnetic measurements is a magnetic field, H, which is intensive, whilst it is the length of the sample that is extensive, that is controlled in the mechanical tests.

Regarding the point (i), the so-called "giant magnetostriction" expressed by ϕ_M would be localized at the line defect. The large strain induced either by magnetic or mechanical force must be attributed to reorientation of the tetragonal lattice variants either from the magnetically hard to soft variants, or from the stress-free to stress-induced variants. Application of a sufficient magnetic field will move the line defect to reduce the magnetocrystalline anisotropy energy by the variant conversion, whereas application of a stress will do work to change the material dimension. These motions will accompany energy dissipation. The magnetic driving force required for the motion would be supplied by the asymmetric distribution of spins around the line defect under a high magnetic field, similar to that calculated for a dislocation (Seeger and Kronmüller 1960, Kronmüller and Seeger 1961, Seeger *et al.* 1964, Umakoshi and Kronmüller 1981a, Göltz *et al.* 1986). The point (ii) comes into the evaluation of the magnetic energy dissipated by motion of the line defect. In practice, the variant conversion takes place from one domain to another in discrete steps under a high magnetic field (Steuwer *et al.* 2003). The sudden change in the magnetic field caused by rotation of the spin direction would be

adjusted instantaneously by the power supply to maintain the magnetic field set in the experiment. Steuwer *et al.* (2003) suggest that the energy dissipation may be found only by measuring the energy consumed in the power supply that generates magnetic field.

From practical purposes, the large strain induced by a magnetic force is useful, for example, as an actuator that responds quickly by application of a magnetic field. The property differs from the usual SMA, which requires heat for the shape change. The quick response certainly comes from the characteristic properties of magnetism controlled by motion of electrons. However, it must be reminded that the shape change occurs by motion of a line defect, accompanying a friction. The energy dissipated in the shape deformation measurable on a stress–strain curve should provide useful information about the switching when such a material is used as an actuator.

4. Conclusion

Magnetic properties are affected by plastic deformation as a result of the introduction of perfect and imperfect dislocations and of the motion of these. Magnetic moments interacting with stress and strain around dislocations change χ and H_C offering a nondestructive method to investigate dislocation structures in ferromagnetic materials. The observation of APB tubes by electron microscopy shows that the large effects of plastic deformation on the magnetic properties come from the interchanges of atoms in the wake of jogs and kinks, and this is not necessarily linked to the dislocation density generated by deformation. Giant magnetostriction in a ferromagnetic SMA is a current problem whose interpretation is certainly also founded on the motion of a line defect.

Bibliography

Anderson P W 1950 Antiferromagnetism, theory of superexchange interaction. *Phys. Rev.* **79** (2), 350–6

Arnold H D, Elmen G W 1923 Permalloy, an alloy of remarkable magnetic properties. *J. Franklin Inst.* **195** (5), 621–32

Bacon G E, Harwell A E R E, Crangle J 1963 Chemical and magnetic order in platinum-rich Pt + Fe alloys. *Proc. Roy. Soc.* **272** (1350), 387–405

Balk T J, Mukul Kumar, Hemker K J 2001 Influence of Fe substitutions on the deformation behavior and fault energies of Ni_3Ge–Fe_3Ge–$L1_2$ intermetallic alloys. *Acta Mater.* **49**, 1725–36

Bloch F 1929 Über die Quantenmechanik der Elektronen in Kristallgittern. *Z. Physik* **52**, 555–600

Bloch F 1932 Zur Theorie des Austauschproblems und der Remanenzerscheinung der Ferromagnetika. *Z. Physik* **74** (5–6), 295–335

Bowers K D, Owen J 1955 Paramagnetic resonance II. *Repts. Prog. Phys.* **18**, 304–73

Brown W F 1940 Theory of the approach to magnetic saturation. *Phys. Rev.* **58**, 736–43; 1941 The effect of dislocations on magnetization near saturation. *Phys. Rev.* **60**, 139–47.

Bullett D W, Haydock R, Heine V, Kelly M J 1980 Electronic structure from the point of view of the local atomic environment (Heine). The renaissance and quantitative development of the tight-binding method (Bullet). The recursive solution of the Schrödinger equation (Haydock). Applications of the recursion method to the electronic structure from an atomic point of view (Kelly). Solid State Physics, Academic Press, New York, Vol. 35

Callen H B 1960 *Thermodynamics*. Wiley, New York, USA

Celli V, Kabler M, Ninomiya T, Thomson R 1963 Theory of dislocation mobility in semiconductors. *Phys. Rev.* **131** (1), 58–72

Chikazumi S 1950 Ferromagnetic properties and superlattice formation of iron–nickel alloys (I), (II). *J. Phys. Soc. Japan* **5** (5), 327–33

Chikazumi S, Suzuki K, Iwata H 1957 Studies on the magnetic anisotropy induced by cold rolling of ferromagnetic crystal: I. Iron–nickel alloys. *J. Phys. Soc. Japan.* **12** (11), 1259–76; 1960 II. Iron–aluminum alloys. *J. Phys. Soc. Japan* **15** (2), 250–60.

Chou C T, Hirsch P B 1981 Anti-phase domain boundary tubes in plastically deformed ordered Fe 30.5 at.% Al alloy. *Phil. Mag.* **44** (6), 1415–9 1983 Electron microscopy of antiphase domain boundary tubes in deformed ordered alloys. *Proc. Roy. Soc. Lond. A* **387**, 91–104

Chou C T, Hirsch P B, McLean M, Honddros E 1982 Antiphase domain boundary tubes in Ni_3Al. *Nature* **300** (5893), 621–3

Clark A E, Teter J P, McMaster O D 1988 Magnetostriction "jumps" in twinned $Tb_{0.3}Dy_{0.7}Fe_{1.9}$. *J. Appl. Phys.* **63** (8), 3910–2

Crawford R C 1976 Deformation of an ordered Fe–35.5 at.% Al alloy. *Phil. Mag.* **33** (3), 529–55

Dahl D 1936 Kaltverformung und Erholung bei Legierungen mit geordneter Atomverteilung. *Z. Metallk.* **28** (5), 133–8

de Broglie L 1925 Recherches sur la théorie des quanta somaire. *Ann. de Physiques* **3**, 22–128

Dillinger J F, Bozorth R M 1935 Heat treatment of magnetic materials in a magnetic field. *Physics (J. Appl. Phys.)*. **6**, 279–91

Dirac P A M 1927 The quantum theory of the emission and absorption of radiation. *Proc. Roy. Soc.* **114** (769), 243–65

Dirac P A M 1963 *Principles of Quantum Mechanics*. Clarendon Press, London

Dorn J E, Rajnak S 1964 Nucleation of kink pairs and the Peierls mechanism of plastic deformation. *Trans. Metall. Soc. AIME* **230** (5), 1052–70

Einstein A 1905 Über einen die Erzeugung und Verwandlung des Lichtes betreffenden heuristischen Gesichtspunkt. *Ann. der Physik* **17**, 132–48

Eshelby J D, Frank F C, Nabarro F R N 1951 The equilibrium of linear arrays of dislocations. *Phil. Mag.* **42**, 351–64

Ewald P P 1917 Zur Begründung der Kristalloptik. *Ann. der Physik* **54** (22), 519–56

Fang J, Schulson E M, Baker L 1994 The dislocation structure in L12 ordered alloy Ni_3Ge. *Phil. Mag.* **70** (6), 1013–25

Fermi E 1928 Ein statistische Methode zur Bestimung einiger Eigenschaften des Atoms und ihre Anwendung auf die Theorie des periodischen Systems der Elemente. *Z. Physik* **48**, 73–9

Flinn P A 1960 Theory of deformation in superlattices. *Trans. AIME* **218** (1), 145–54

Fock V 1930 Näherungsmethode zur Lösung des quanten-mechanischen Mehrkörper problems. *Z. Physik* **61**, 126–48

Fowler C A, Fryer E M 1954 Magnetic domains by the longitudinal Kerr effect. *Phys. Rev.* **94** (1), 52–6

Foxall R A, Statham C D 1970 Dislocation arrangements in deformed single crystals of niobium–molybdenum alloys and niobium–9 at.% rhenium. *Acta Met.* **18** (11), 1147–58

Friedel J 1964 *Dislocations.* Pergamon, Addison-Wesley, MA, USA

Fuller H W, Hale M E 1960 Determination of magnetization distribution in thin films using electron microscopy. *J. Appl. Phys.* **31** (2), 238–48

Fultz B, Howe J M 2002 *Transmission Electron Microscopy and Diffractometry of Metals.* Springer, Heidelberg, Germany

Gadian D G 1982 *Nuclear Magnetic Resonance and Its Applications to Living Systems.* Oxford University Press, New York

Gengnagel H, Besnus M J, Danan H 1972 Temperature and field dependence of the magnetization of Fe–Al powders in cold-worked and annealed state. **13** (2), 499–503

Gessinger H 1970 Die theoretische Deutung der magnetischen Anisotropie plastisch verformter Nickel-Einkristalle. *Phys. Stat. Sol. (a)* **39** (2), 581–98

Göltz G H, Kronmüller G, Seeger A, Scheuer H, Schmatz W 1986 Investigation of the dislocation arrangements in plastically deformed Fe single crystals using magnetic small-angle scattering of neutrons. *Phil. Mag. A* **54** (2), 213–35

Graef M D, Zhu Y 2001 Magnetic imaging and its applications to materials. In: *Experimental Methods in the Physical Sciences.* Academic Press, San Diego, CA, Vol. 36

Hayashi S 1967 Effect of dislocations on the initial susceptibility of nickel single crystals. *Trans. JIM* **8** (1), 14–8

Heidenreich R D, Nesbitt E A 1952 Physical structure and magnetic anisotropy of Alnico 5. *J. Appl. Phys.* **23** (4), 352–65

Heisenberg W 1928 Zur Theorie des Ferromagnetismus. *Z. Physik* **49**, 619–36

Hemker K J, Mills M J 1993 Measurements of antiphase boundary and complex stacking fault energies in binary and B-doped Ni₃Al by using TEM. *Phil. Mag.* **68** (2), 305–24

Heusler O 1934 Kristallstructur und Ferromagnetismus der Mangan-Aluminium-Kupferlegierungen. *Ann. Physik* **19** (5), 155–201

Hirsch P B, Howie A, Nichoson R B, Pashley D W, Whelan M J 1971 *Electron Microscopy of Thin Crystals.* Butterworth, London

Hirth J P, Lothe J 1968 *Theory of Dislocations.* McGraw-Hill, New York

Honda K, Kaya S 1926 On the magnetisation of single crystals of iron. *Sci. Rep. Tohoku Univ. Ser. 1* **15**, 721–54

Huber E E, Smith D O, Goodenough J B 1958 Domain wall structure in Permalloy films. *J. Appl. Phys.* **29** (1), 735–45

Huffman G P, Fisher R M 1967 Mössbauer studies of ordered and cold-worked Fe–Al alloys containing 30–50 at.% aluminum. *J. Appl. Phys.* **38** (2), 735–45

Ingram D J E 1968 Electron spin resonance. In: Flügge S, Wijn H P J (eds.) *Encyclopedia of Physics.* Springer, Berlin, Vol. 18, pp. 94–144

Izumi T 2003 Cyclic deformation of Ni₃Ge single crystals under constraint:dislocation structure and magnetization (Japanese). MS thesis, Tokyo Institute of Technology, Yokohama Japan

James R D, Watting M 1998 Magnetostriction of magnetic field induced redistribution of twins. *Phil. Mag. A* **77** (5), 1273–99

Johansson C H, Linde J O 1925 Röntgenographische Bestimmung der Atomanordnung in den Mischkristallihen Au–Cu und Pd–Cu. *Ann. der Physik* **78** (21), 439–60

Kakeshita T, Takauchi T, Fukuda T, Saburi T, Oshima R, Muto S, Kisho K 2000 Magnetic field induced martensitic transformation and giant magnetostriction in Fe–Ni–Co–Ti and ordered Fe₃Pt shape memory alloys. *Mater. Trans. JIM* **41** (8), 882–7

Kasper J S, Roberts B W 1956 Antiferromagnetic structure of α-manganese and a magnetic structure study of β-manganese. *Phys. Rev.* **10** (2), 537–44

Kaya S 1938 Die Überstrukturbildung in den Kickel-Eisen Legierungen und das Permalloyproblem. *J. Faculty Sci. Hokkaido Univ. Ser. 2* **2**, 29–53

Kear B H, Wilsdorf H B F 1962 Dislocation configurations in plastically deformed polycrystalline Cu₃Au alloys. *Trans. AIME* **224** (2), 382–6

Khoi L D, Veillet P, Campbell I A 1978 Hyperfine fields and magnetic interaction in Heusler alloys. *J. Phys. F: Met. Phys.* **8** (8), 1811–50

Kittel C 1971 *Introduction to Solid State Physics.* Wiley, New York, USA

Kramers H A 1934 L'interaction entre les atomes magnétogenes dans un crystal paramagnétique. *Physica.* **1**, 182–92

Kronmüller H 1967 On the mechanism of work hardening in FCC metals. *Can. J. Phys.* **45**, 631–60

Kronmüller H, Seeger A 1961 Die Einmündung in die ferromagnetische sättigung-II, Theorie des Einmündungsgesetzes in plastischverformten Kubischflächenzentrierten Einkristallen. *J. Phys. Chem. Solids* **18** (2/3), 95–115

Kurisu M, Kadomatsu H, Fujiwara H 1987 Anomalous magnetostriction in CeAg₁₋ₓInₓ. *J. Phys. Soc. Japan* **56** (7), 2279–81

Laue M V 1918 Röntgenstrahlinterferenz und Mischkristalle. *Ann. der Physik* **56** (15), 497–506

Meissner W, Ochsenfeld R 1933 Ein neuer Effekt bei Eintritt der Supraleiffähigkeit. *Natur wiss.* **21**, 787–8

Mössbauer R L 1958 Kernresonanzfluoreszenz von Gammastrahlung in Ir¹⁹¹. *Z. Physik* **151**, 124–43

Mott N F 1952 A theory of work-hardening of metal crystals. *Phil. Mag.* **43** (346), 1151–78

Mughrabi H, Kütterer R, Lubitz K, Kronmüller H 1976 Magnetic studies on cyclically deformed α-iron single crystals. *Phys. Stat. Sol. (a)* **38** (1), 261–70

Mura T 1987 *Micromechanics of Defects in Solids.* Martinus Nijhoff, Dordrecht, The Netherlands

Mura T, Mori T 1976 *Micromechanics (in Japanese).* Baifukan, Chiyodaku, Tokyo, Japan

Murakumo T, Kumai S, Sato A 2000a Effects of mechanical constraint on the strength of Ni₃Ge single crystals. *Mater. Trans. JIM* **41** (2), 279–86

Murakumo T, Ueta S, Miyahara A, Hannuki T, Sato A 2000b Irradiation induced defects in deformed Ni₃Ge and Ni₃Al single crystals. *Phil. Mag. A* **80** (4), 893–918

Murray S J, Marioni M, Allen S M, O'Handley R C 2000 6% magnetic field induced strain by twin-boundary motion in ferromagnetic Ni–Mn–Ga. *Appl. Phys. Lett.* **77** (6), 886–8

Muto S, Oshima R, Fujita F E 1987 Relation of magnetic domain structure to FCT martensite variants in Fe–Pd alloys. *Scrip. Met.* **21** (4), 465–8

Mryasov O N, Gornostyrev Yu N, Schilfgaarde M, Freeman A J 2002 Superdislocation core structure in L1₂ Ni₃Al, Ni₃Ge and Fe₃Ge: Peierls–Nabarro analysis starting from *ab initio* GSF energetics calculations. *Acta Mater.* **50**, 4545–54

Nabarro F R N 1967 *Theory of Crystal Dislocations*. Oxford University Press, Ely House, London

Nagaoka H, Honda K 1902 On the magnetostriction of steel, nickel, cobalt, and nickel-steels. *Phil. Mag.* **4**, 45–72

Nasu S, Nakamura Y, Shinjo T 1968 Mössbauer effect study in Cu–2%Co alloy. *Scrip. Met.* **2** (11), 647–52

Natera M G, Murthy M R L N, Begum R J, Murthy N S S 1970 Atomic and magnetic structure of Heusler alloys Pd_2MnGe, Pd_2MnSn, Cu_2MnIn, and Co_2MnSb. *Phys. Stat. Sol. (a)* **3** (4), 959–64

Néel M L 1948 Proprietes magnétiques des ferrites; ferrimagnétisme et antiferromagnétisme. *Ann. de Physiques*. **3**, 137–98

Néel M L 1954 Anisotropie magnétique superficielle et surstructueres d'orientation. *J. Phys. Radium* **15** (4), 225–39

Ngan A H W, Johnes I P, Smallman R E 1992 The negative temperature dependence of yield strength in the $L1_2$ compound Fe_3Ge. *Mat. Sci. Eng.* **A153**, 387–91

Oliver D A, Shedden J W 1938 Cooling of permanent magnet alloys in a constant magnetic field. *Nature* **142** (3587), 209–209

Pauli W 1925 Über Gasentartung und Paramagnetismus. *Ann. der Physik* **31**, 765–83

Paider V, Pope D P, Vitek V 1984 A theory of the anomalous yield behavior in $L1_2$ ordered alloys. *Acta Metall.* **32** (3), 435–48

Raimes S 1967M *The Wave Mechanics of Electrons in Metals*. North-Holland, Amsterdam, The Netherlands

Ralhenau G W, Snoeck J L 1941 Magnetic anisotropy phenomena in cold rolled nickel–iron. *Physica* **8** (6), 555–75

Read W T Jr. 1953 *Dislocations in Crystals*. McGraw-Hill, New York

Rhoads E 1901 Experiments on the change in dimensions caused by magnetism in iron. *Phil. Mag.* **2** (11), 463–8

Saada G, Veyssière P 1992 The dissociation of a screw superdislocation in the $L1_2$ structure. *Phil. Mag.* **66** (6), 1081–103; 1994 Motion under stress of a screw superdislocation in the $L1_2$ structure. *Phil. Mag.* **70** (6), 925–42

Sarkar S K 1996 *NMR Spectroscopy and Its Application to Biomedical Research*. Elsevier, Amsterdam

Sato A, Meshii M 1973 Solid solution softening and solid solution hardening. *Acta Met.* **21**, 753–68

Sato A, Mifune T, Meshii M 1970 Effect of electron irradiation on the strength of irradiation on iron single crystals. *2nd Int. Conf. on the Strength of Metals and Alloys*. Asilomar, CA, USA, pp. 747–751

Schiff L I 1955 *Quantum Mechanics*. McGraw-Hill, New York Translated (Japanese) by Takeshi Inoue, Maruzen, Tokyo

Schrödinger E 1925 Quantisierung als Eigenwertproblem. *Ann. der Physik* **79** (6), 489–526; 1926 **80** (13), 437–90; 1926 **81** (18), 110–39.

Schroeder G 1978 Investigation of the dislocation arrangement in plastically deformed iron single crystals by means of ferromagnetic techniques. *Phys. Stat. Sol. (a)* **47** (1), 145–56

Seeger H, Kronmüller H 1960 Die Einmündung in de ferromagnetische sättigung-I, allgemeine Theorie des Einflusses innerer Spanungen auf das Einmündungsgesetz, mit anwendungen auf Zwischengitteratome und abgeschreckte Metalle. *J. Phys. Chem. Solids* **12**, 298–313

Seeger H, Kronmüller H, Rieger H, Träuble 1964 Effect of lattice defects on the magnetization curve of ferromagnets. *J. Appl. Phys.* **35** (3), 740–8

Shi X, Saada G, Veyssiere P 1996 The formation of antiphase-boundary tubes in Ni_3Al. *Phil. Mag. A* **73** (4), 1159–71

Steuwer A, Mori T, Kato H, Wada T 2003 Energetics of variant conversion in ferromagnetic shape memory alloys by external magnetic fields. *J. Appl. Phys.* **94** (4), 2761–3

Stroh A N 1958 Dislocations and cracks in anisotropic elasticity. *Phil. Mag.* **3** (30), 625–46

Takahashi S, Ikeda K 1983 Te influence of cold-working on magnetic properties in Ni_3Al. *J. Phys. F: Met. Phys.* **13**, 2169–74

Takahashi S, Shinohara T 1982 Magnetic moment distribution in deformed Heusler alloy Pd_2MnSi. *J. Phys. F: Met. Phys.* **12** (5), 3115–22

Takahashi S, Umakoshi Y 1990 Superlattice dislocations and magnetic transition in Pt_3Fe alloy with the $L1_2$-type ordered structure. *J. Phys.: Condens. Matter* **2**, 2133–42; 1991 Fe–Al alloys with B2-type. **3**, 5805–16.

Takahashi S, Li X G, Chiba A 1996 Spin distribution in plastically deformed Fe–Al intermetallic compounds. *J. Phys.: Condens. Matter* **8**, 11243–57

Taniguchi M 2003 On the shear systems in Fe_3Ge (Japanese). M.S. thesis, Tokyo Institute of Technology, Yokohama, Japan

Taoka T, Yasukochi K, Honda R, Oyama I 1959 An experimental investigation on the mode of slip in face-centered cubic metals. *J. Phys. Soc. Japan* **14** (7), 888–92

Taylor G I 1934 The mechanism of plastic deformation of crystals. *Proc. Roy. Soc. A* **145**, 362–404

Taylor A E, Jones R M 1958 Constitution and magnetic properties of iron-rich iron–aluminum alloys. *J. Phys. Chem. Solids* **6** (1), 16–37

Thomas G 1966 *Transmission Electron Microscopy of Metals*. Wiley, New York, USA

Tomono Y 1948 Several experiments on the Permalloy problem. *J. Phys. Soc. Japan* **4** (6), 298–300

Tsukahara S 1967 Electron microscopic studies on origins of magnetization ripples in ferromagnetic thin films. *J. Phys. Soc. Japan* **23** (2), 189–204

Ullako K, Huang J K, Kantner C, O'Handley R C, Kokorin V V 1996 Large magnetic-field-induced strains in Ni_2MnGa single crystals. *Appl. Phys. Lett.* **69** (13), 1966–8

Umakoshi Y, Kronmüller H 1981a Observations of dislocations in deformed iron single crystals by means of high field susceptibility measurements. *Phys. Stat. Sol. (a)* **66** (2), 509–20 1981b On magnetic domain patterns and dislocation structures in iron single crystals deformed at 195 and 77 K. **68** (1), 159–72

Umakoshi Y, Pope D P, Vitek V 1984 The asymmetry of the flow stress in Ni_3(Al, Ta) single crystals. *Acta metall.* **32** (3), 449–56

Van Vleck H 1937 On the anisotropy of cubic ferromagnetic crystals. *Phys. Rev.* **52** (10), 1178–98

Vidoz A E, Brown L M 1962 On work hardening in ordered alloys. *Phil. Mag.* **7**, 1167–75

Vitek V 1998 Atomic structure of dislocations in intermetallics with close packed structures: a comparative study. *Intermetallics* **6** (5), 579–85

Volterra V 1907 Sur l'équilibre des corps élastiques multiplemont connexes. *Ann. Sci. de l'École Norm. Super.* **24**, 401–517

Weertman J, Weertman J R 1967 *Elementary Dislocation Theory*. Macmillan, New York, USA

Wertz J E 1968 Structural information from paramagnetic resonance. In: Flügge S, Wijn H P J (eds.) *Encyclopedia of Physics*. Springer, Berlin, Vol. 18, pp. 145–264

Wigner E, Seitz F 1933 On the constitution of metallic sodium. *Phys. Rev.* **43**, 804–10

Williams D B, Carter C B 1998 *Transmission Electron Microscopy*. Plenum, New York, USA

Willke Von H 1972 Die Bereichsstruktur von Nickeleinkristallen nach plastischer Verformung (the domain structure of nickel single crystals after plastic deformation). *Phil. Mag.* **25** (2), 397–424

Yamaguchi M, Umakoshi Y 1990 The deformation behaviour of intermetallic superlattice compounds. *Prog. Mater. Sci.* **34**, 1–148

Yamaguchi M, Paider V, Pope D P, Vitek V 1982 Dissociation and core structure of $\langle 110 \rangle$ screw dislocations in $L1_2$ ordered alloys: I. Core structure in an unstressed crystal. *Phil. Mag. A* **45** (5), 867–82

Yamamoto K, Miyazaki S, Kumai S, Sato A 2003 Strong magnetization by antiphase-boundary tubes in a cyclically deformed Fe–35 at.% Al alloy. *Phil. Mag. A* **83** (12), 1431–49

Yamashita K, Imai M, Matsuno M, Sato A 1998 Formation of antiphase-boundary tubes and magnetization in Fe–35 at.% Al by plastic deformation at 77 K. *Phil. Mag. A* **78** (2), 285–303

Yang Y, Baker I 1997 Annealing of cold-rolled Fe–40Al single crystals. *MRS Proc.* **460**, 367–71

Yang Y, Baker I, Martin P 1999 On the mechanism of the paramagnetic to ferromagnetic transition in Fe–Al. *Phil. Mag. B* **79** (3), 449–61

Yasuda H Y, Frusta D, Sasaki A, Umakoshi Y 2000 Magnetic observation of deformation substructure in cyclically deformed Ni_3Fe. *J. Appl. Phys.* **88** (10), 5909–14

Yasuda H Y, Jimba R, Umakoshi Y 2003 Quantitative analysis of anti-phase boundary tubes in cyclically deformed Fe–40 at.% Al single crystals by means of magnetic technique. *Scrip. Mater.* **48** (5), 589–92

Yoneyama N 2002 Mechanical properties and microstructures of Fe–Mn–Si, Ni_3Ge, Al–Al_3Ti and Al–Al_3Fe deformed at high strain rate. Ph.D. thesis, Tokyo Institute of Technology, Yokohama, Japan

Yoo M H 1987 Stability of superdislocations and shear faults in $L1_2$ ordered alloys. *Acta Metall.* **35** (7), 1559–69

Yukawa H, Toyoda T 1977 *Quantum Mechanics I*. Iwanami-Bookstore, Chiyodaku, Tokyo, Japan, pp. 36

A. Sato and M. Nagao
Tokyo Institute of Technology, Yokohama, Japan

Magnetic Recording Devices: Future Technologies

The ability to electronically access stored programs and data was the enabling technology in the development of general purpose computers a little over 50 years ago. One of the first practical electronic memory devices was a tank of mercury, roughly the size of an oil barrel, in which data was "stored" dynamically in the form of acoustic pulses passing through the mercury from a transmitter on one end to a receiver on the other. Less than 10 000 bits could be stored for only a few milliseconds at a cost of several dollars per bit and, of course, the data was lost when the power was shut off. Now for less than US$1000, one can obtain a desktop computer operating at 700 MHz with 128 Mbytes of high-speed semiconductor random access memory (RAM) supported by a 30 Gbyte magnetic hard drive.

This incredible improvement in performance and cost has been driven in both semiconductor and magnetic technology primarily by dimensional scaling of critical geometries, the sizes of which are now rapidly approaching fundamental limits. This article surveys new concepts which have been proposed to replace traditional magnetic disk systems. Only those which are nonvolatile are considered. These include patterned media, probe-based storage, and optical storage.

1. Storage Metrics and Recording Limits

Storage density is the most important metric driving both capacity and cost. Conventional longitudinal disk storage, for which new world records are being announced on the internet every few weeks, has been demonstrated at $> 50 \, \mathrm{Gbit \, in^{-2}}$. Recent projections (Bertram and Williams 2000) suggest limits of $100 \, \mathrm{Gbits \, in^{-2}}$ for longitudinal recording and $500 \, \mathrm{Gbits \, in^{-2}}$ for perpendicular recording. In fact, values as high as $1000 \, \mathrm{Gbits \, in^{-2}}$ seem theoretically possible for perpendicular recording (Wood 2000). At $100 \, \mathrm{Gbits \, in^{-2}}$, the bit cell size is only $80 \, \mathrm{nm^2}$. Thus, new technologies which should realistically promise factors of 10 or more greater density to justify investment must immediately confront dimensions beyond the limits of established processing technology.

Capacity is the number of bytes (8 bits) which can be accessed directly. Drives with capacities $> 70 \, \mathrm{Gby}$tes are being sold today and by extrapolation should reach capacities of $> 700 \, \mathrm{Gbytes}$. The range of capacities, however, will extend as low as $1–10 \, \mathrm{Gbytes}$ in physically smaller drives targeted for increasingly important portable applications.

The ultimate metric is the cost/byte. In 1999, the average cost per Gbyte for hard disk storage was $\sim \$20$ and by 2001 had dropped to $\sim \$4$. Again by extrapolation, the cost of disk storage will certainly be reduced to $< \$1/\mathrm{Gbyte}$ for high capacity drives.

Access time is the time required on average to reach a random bit. Because they are mechanical, even the highest performance hard drives have relatively slow access time of $> 6 \, \mathrm{ms}$. Even when rotation speeds are increased to 20 000 rpm or higher, the cost of reducing the head positioning time will probably limit access times to $\sim 4 \, \mathrm{ms}$.

The rate at which data can be either written or read is the same in hard drives but in other technologies may not be. For fundamental reasons relating to the dynamics of magnetization switching and available head materials, data rates $> 5 \, \mathrm{GHz}$ will be difficult to achieve in drives using only a single head. Multiple head systems could, of course, provide high data rates at a cost and power penalty.

Reliability will be used here to include error rate, archivability, and environmental resilience. For all technologies, corrected error rates of $\leqslant 1 \times 10^{-15}$ and a 10-year storage life are required. Resilience, e.g., shock resistance, will define market size. Hard drives have shown considerable improvement in this area and are now being considered for demanding applications such as portable cameras.

2. Patterned Magnetic Media

In conventional continuous polycrystalline thin film magnetic media, transition noise is reduced by reducing the grain size and the coupling between grains (see *Magnetic Recording Technologies: Overview*, *Micromagnetics: Basic Principles*). To circumvent superparamagnetic effects which limit the minimum grain size, it has been proposed to pattern media composed of highly coupled grains into discrete single domain-size bits. Then, the transition noise would be determined by the accuracy with which the pattern edges could be defined. In various embodiments, this concept is critical to several potential technologies discussed below. In this section, we address it in its simplest implementation as a direct replacement for continuous media in an otherwise conventional disk system.

Using direct write e-beam lithography (DWEL), magnetic circular dot arrays of 65 Gdots in^{-2} (Chou *et al.* 1994) and holes at >300 Gholes in^{-2} (Xu *et al.* 1995), close to the e-beam lithography limit, have been prepared. The highest density array in which individual elements have been characterized magnetically had only 29 Gdot in^{-2} produced by DWEL and showed a surprisingly large $\pm 58\%$ variation in coercivity (Haginoya *et al.* 1999). This is a serious problem which must be investigated further. There are, however, no convenient techniques to characterize individual elements with dimensions <50 nm, the present practical limit of magnetic force microscopy. It is also prohibitively expensive to routinely make arrays with DWEL large enough to be characterized on standard magnetometers.

In fact, the highest density array which has been examined magnetically had 65 Gdots in^{-2} (Fig. 1) over ~ 10 mm^2 and was produced by interference lithography (Ross *et al.* 1999). This is an interesting technique for producing 2D periodic patterns over large areas with a periodicity somewhat greater than half the wavelength of the illumination. Although available sources and photoresists have limited the periodicity to 100 nm, experiments are in progress to reduce this by a factor of 2–4. If a periodocity of 25 nm could be achieved, it would seem to offer a cost-effective process for producing patterned media with densities of 1000 Gbit in^{-2}. However, it is not clear how this can be done in a circular array compatible with conventional disk technology.
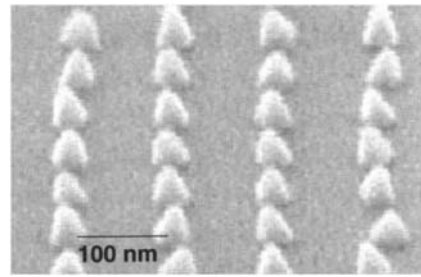
Figure 1
Electron micrograph of evaporated Ni pyramids with base 35 nm and height 40 nm. The pyramids form a 100 nm period square array, which appears foreshortened in the micrograph (from Ross *et al.* 1999).

To minimize the lithography cost, another imaginative approach is to write the desired pattern on a large area die and then use the die repeatedly to transfer the pattern by printing a masking material (Wang *et al.* 1997) or by imprinting the pattern into a masking material. Using the latter technique to form a template, Cui *et al.* (1999) were able to prepare arrays of Ni particles 70 nm in diameter at a density of 18 Gbits in^{-2} over an area of 16 cm^2. Recalling that contact lithography was plagued historically by resist pull-outs, mask damage, and nonuniform contact, considerable ingenuity will be required to obtain high yield at nanometer dimensions especially with processes which require high temperature or pressure. However, recent results (Colburn *et al.* 1999) using a photopolymerizable liquid between the substrate and the template to form the etch mask demonstrate reliable replication of features as small as 60 nm. A key feature is the release coating on the template formed from a self-assembled monolayer.

Still another clever idea is the possible use of patterned structures which can act as electron emitters in the presence of large electric fields. An additional magnetic field in combination with the electric field is used to focus the electrons onto a closely spaced resist film, thus forming an image of the pattern in the resist. This has the potential for rapidly reproducing high-resolution images over large areas. Resolution better than 50 nm has been demonstrated (Tromp 2000).

The development of a reliable head/disk interface, which allows heads to fly less than 25 nm above the media surface, is a major factor in the continuing increases in disk storage density. Providing a suitably robust surface is a challenge for patterned media which significantly complicates additive or subtractive fabrication processes. A more attractive approach in which the pattern is formed magnetically rather than geometrically has recently been demonstrated (Devolder *et al.* 1999). Ion implantation of perpendicularly oriented Co–Pt multilayers with

30 keV He$^+$ ions through a mask significantly reduced the coercivity and allowed regions as small as 50 nm to be defined in a planar film. In other experiments, the Curie temperature was also reduced, suggesting the possibility of leaving magnetic islands in a nonmagnetic matrix.

An elegant way to avoid the lithography problem would be to have the patterning done by nature through a process of self-assembly. This is now the subject of intense study across many disciplines well beyond the focus of this review. However, one very relevant scheme relates to the self-ordering of pores in alumite. It is well known that the anodization of aluminum can produce a disordered porous structure. For many years, workers used the structure as a template to study electroplated magnetic nanowires with diameters as small as 10 nm. Extended multiple anodization has been shown to produce beautifully ordered hexagonal arrays of pores (Fig. 2). This suggested immediately the possibility of self-assembled perpendicular media obtained by electroplating magnetic wires into the ordered pores.

Despite considerable efforts, however, it has not been possible to increase the size of the ordered domains to more than $100 \, \mu m^2$ and that only after lengthy anodization of up to 87 hours. In addition, conditions for ordering constrain the periodicity to ~ 100 nm (64 Gpores in^{-2}). Remarkable progress in circumventing the first of the two problems has been demonstrated, however. Ordered pores over $20 \, mm^2$ were produced by anodization of an Al surface initially decorated by imprinting with a SiC die. The highest density achieved was 64 Gpores in^{-2}, limited by the resolution of the die, patterned with DWEL. If this can be extended to higher densities and circular arrays, it would offer another route to a practical media process.

A chemical method for preparing self-assembled thin film arrays with either cubic or hexagonal symmetry of highly uniform spherical FePt single crystal particles has been described by Sun *et al.* (2000). After annealing above 500 °C to obtain the high anisotropy FCT phase, randomly oriented 4 nm particles on 6 nm centers with coercivities in excess of 4000 Oe were obtained. This exciting development has enormous potential both in the near term where a single bit in a conventional rotating disk system could include many particles and in the future where particles might be addressed individually. The latter would translate to densities in excess of 10 Tbits in^{-2}.

In summary, lithography limits are a major obstacle to producing cost-effective patterned media with densities > 100 Gbits in^{-2}. However, new developments in interference lithography, imprint technology and patterned implantation could extend this to 1000 Gbits in^{-2}. Self-assembly offers the potential for even higher densities. It is, of course, assumed that processing technology will allow heads with commensurate dimensions to be fabricated.
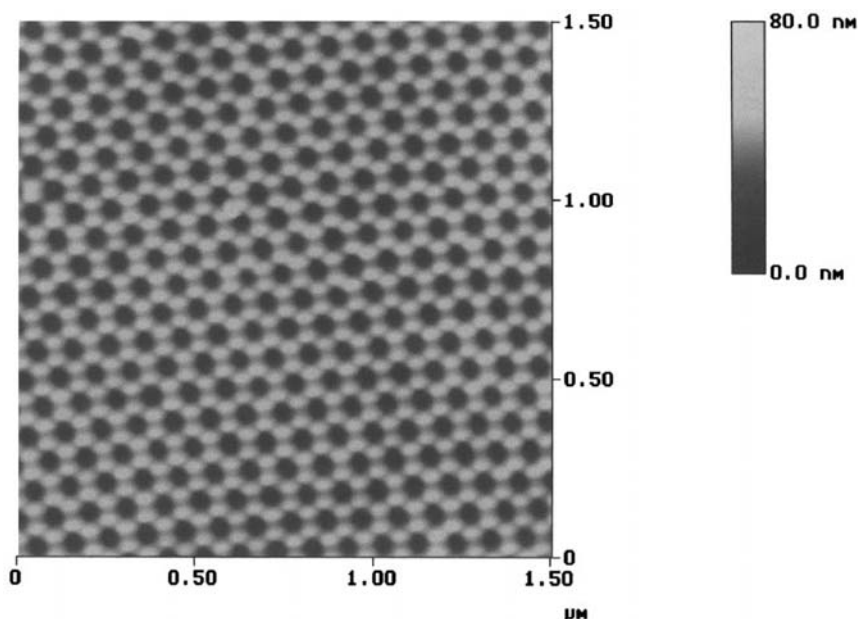
Figure 2
Atomic force micrograph ($1.5 \times 1.5 \, \mu m^2$) of ordered aluminum Al (plus Al$_2$O$_3$ formed in air) after anodizing in H$_2$C$_2$O$_4$ for 25 hours, then stripping Al$_2$O$_3$ porous film with H$_3$PO$_4$/H$_2$CrCo$_4$. The darker spots are the pore bottoms.

3. Probe-based Storage

The development in the last 15 years of scanning probe microscopy (SPM) based on precisely positioned micromechanical cantilevers has resulted in a variety of techniques for characterizing, imaging, and manipulating surface layers with resolutions and positioning accuracies ranging from 1×10^{-1}–1×10^{2} nanometers (Wiesendanger 1998). The potential application to high-density storage has been widely recognized although inherent speed limitations posed what initially appeared to be a fatal weakness. However, equally rapid developments in microelectromechanical system (MEMS) devices suggest the possibility of operating multiple probe heads in parallel to achieve acceptable data rates.

The ability to fabricate probes with tips a few nanometers in size is a key element to SPM. Furthermore, since the probes and their supporting cantilevers are usually formed by etching from a silicon wafer, it is possible to integrate active devices into the probe structure allowing a wide range of functionality based on electrical, magnetic, mechanical, optical, and thermal phenomena. Four implementations are of particular interest for storage: scanning tunneling microscopy (STM), atomic force microscopy (AFM), magnetic force microscopy (MFM), and scanning near-field optical microscopy (SNOM). In STM, the tunneling current between the probe tip and the surface is used to measure the topography and electronic characteristics of the surface with atomic resolution. In AFM, the probe tip is kept close to or in contact with the surface and the force on the tip used to detect topography. Special AFM probes have also been used to mark the surface mechanically or thermally or to make electrical contact.

Carbon nanotubes attached to probes are particularly attractive because of their size, flexibility, and electrical and magnetic characteristics. Although atomic resolution is also possible with AFM, it is typically not less than a few nanometers in the contact mode, limited by the size of the probe tip. In the most common form of MFM, the probe tip is coated with magnetic material and the force (or force gradient) measured between the tip and the stray field above the surface of the sample arising from a divergence of the magnetization in the sample (see *Magnetic Force Microscopy*). Since all the magnetic material on the probe contributes to the force, the resolution of MFM is 30–50 nm, the poorest of the four techniques. Instruments using other magnetic interactions such as magnetic resonance or torque have been developed but their applications to storage have not been discussed. In SNOM, special lenses or apertures in close proximity to a surface are used to provide resolution in the near field several times less than the wavelength of the illumination. In one configuration using interference, the resolution observed was an extraordinary $\lambda/800$ (Zenhausern et al. 1995).

While the use of STM for surface analysis has become ubiquitous, the realization of a practical storage scheme still faces enormous challenges. Although STM has the highest resolution, its extreme sensitivity to tip-to-surface spacing and the likelihood of required operation in UHV to avoid surface contamination, makes STM the least explored of the four methods at this time. One recent report (Hou et al. 1999) however, claims the record for the smallest observable induced features, 1.4 nm on 9 nm centers (10 T features in^{-2}). They were obtained in ambient conditions by applying a voltage pulse to an organic thin film which caused a local transition from insulating to metallic for reasons not yet understood. In another very beautiful piece of work, Heinze et al. (2000) used spin-polarized STM to image the antiferromagnetic superstructure on the surface of a Mn film with a periodicity < 0.5 nm. Although these demonstrations are far from a storage system, they do highlight the advantages STM has in resolution and in electronic access.

In contrast, considerable work on the utilization of AFM and MFM has been reported. Much of it has focused only on the formation of some observable array of features particularly with contact AFM. For example, Cooper et al. (1999) formed 8 nm titanium oxide dots on 20 nm centers by anodizing a titanium film through the tip of a carbon nanotube. While this remarkable achievement corresponds to 1.6 Tdots in^{-2}, it would appear to be limited to write-once applications and at the reported writing speed of 5 kHz, would require massive parallel operation. The difficulties in reducing an array of nanodots to a practical AFM storage system have been considered most completely by Mamin et al. (1999). They developed a cantilever probe (Fig. 3) which could be used both to write features thermally in a polymetric film on a rotating disk and also to read the features with an integrated piezoresistive sensor.

Successful operation was obtained with 120 nm marks written at 50 kbits s^{-1}. (It is ironic to note that thermal effects which limit magnetic storage can easily be detected in the noise spectrum at the resonant frequency of a few megahertz in these sensitive cantilevers.) The authors extended the study to a read-only system in which 100 nm marks preformed in a disk were read at 10 Mbits s^{-1} with a probe/disk velocity of 1 ms^{-1}. In another test at only 30 mms^{-1}, sufficient probe wear occurred after 148 hours to cause an observable reduction in output. The critical problem of tracking was also considered and the authors concluded that pre-written timing marks smaller than the present limit of DWEL would be required for track pitches below 100 nm.

Improvements in writing thermally have been reported by Binnig et al. (1999) who produced 40 nm pits on 40 nm centers (400 Gbits in^{-2}) (Fig. 4) in a 40 nm thick film of polymethylmethacrylate (PMMA) with 2 μs pulses (500 kbits s^{-1}). Using the
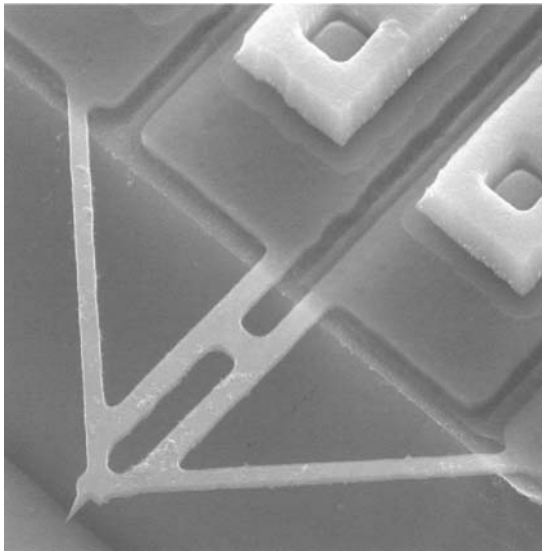
Figure 3
SEM images of a 29 μm long piezoresistive cantilever with a separate resistive heater for writing (after Mamin *et al.* 1999).
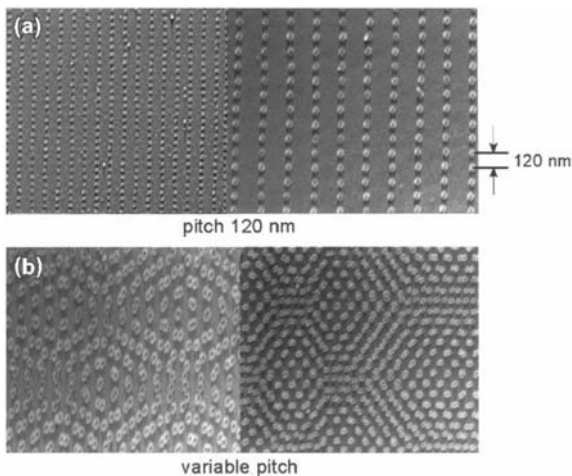
Figure 4
(a) Series of 40 nm data pits formed in a uniform array, demonstrating reliable thermal writing. (b) Different arrangement of data pits, with some pits written virtually next to each other with no merging. This results in bit areal densities of ~400 Gbits in^{-2}. All images obtained by the thermal readback technique (after Binnig *et al.* 1999)

temperature-dependent resistance of the cantilever, they were also able to read with the same probe at 100 kbit s^{-1} limited by the 10 μs thermal response time of the 1 μm thick cantilever. It was estimated

that to reduce the response time to 1 μs, levers with thicknesses measured in nanometers would be required. The possibility that repeated block erasure of the pits could be achieved by heating local regions to 150 °C for a few seconds was also demonstrated.

This concept was combined with a remarkable advancement in MEMS technology, the 1000 probe 'Millipede' (Vettiger *et al.* 2000) to test feasibility (Lutwyche *et al.* 2000). The "Millipede" (Fig. 5) is a 32×32 array of AFM probes on 92 μm centers with integrated read/write capability. Rows and columns of probes can be accessed to allow 32 probes to write and read in parallel. The array was positioned globally with respect to the polymer film medium without separately controlling the height of each probe. Data was written and read back at 1 kbits^{-1} per probe giving a total data rate of only 32 kbits s^{-1}. However, this limit was set by the test system and it is believed that higher data rates are possible. The density was varied from 15 Gbits in^{-2} with >80% of the probes operational to 300 Gbits in^{-2} with a lower probe yield. No information on erasure or reliability was given.

Electrical phenomena for probe-based storage such as charge trapping (Terris and Barrett 1995) or non-linear conduction in Langmuir-Blodgett films (Sakai *et al.* 1988) have been investigated but more recent reports are not available. One would also expect that phase change or ferroelectric materials should be candidates for probe-based media, but few results have been presented.

The conspicuous advantages of magnetic materials for re-writable storage applications makes MFM a natural choice for investigation. Indeed, most of the work on patterned magnetic media has used MFM to characterize the elements with a significant effort demonstrating that individual elements could be switched with the field from the probe tip alone and/or with an external field. Curiously, no results on prototype MFM system comparable to those available for AFM have appeared. This may reflect a combination of the difficulty described above in preparing suitable patterned media, the relatively low resolution of MFM probes, and the complexity of an integrated active bipolar probe for writing.

However, Carley *et al.* (2000) presented a comprehensive and imaginative design paper on the implementation of a small capacity (2 GB) miniature (2.5 cm^3) re-writable system with a data rate of 20 MB. It relies heavily on MEMS technology to position a media sled relative to a highly integrated array of 1000 probes in which the height of each probe is controlled individually relative to the media (Fig. 6). An important feature is the assumption of continuous perpendicular media for which it is asserted that superparamagnetic effects will be less severe than in conventional longitudinal media.

A bit size of 50 nm × 50 nm is specified which corresponds to an intrinsic density of >250 Gbits in^{-2},
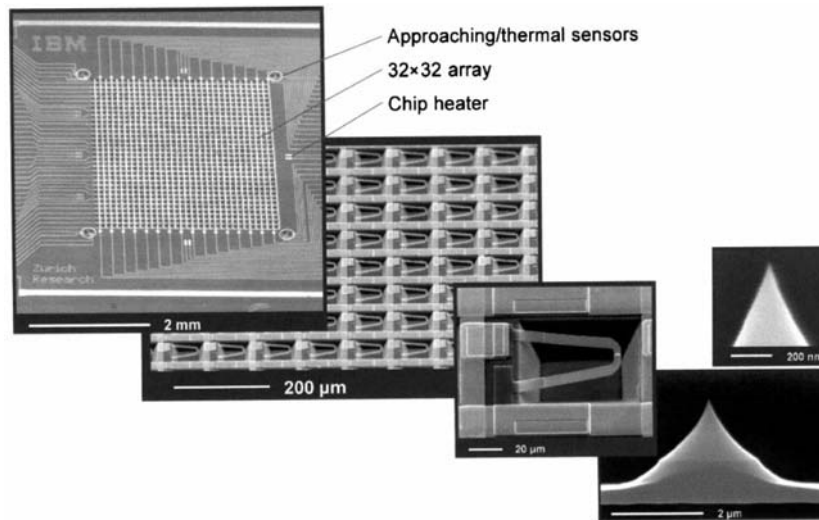
Figure 5
SEM images of the cantilever array section of the millipede with approaching and thermal sensors in the corners, array and single cantilever details, and tip apex (after Vettiger *et al.* 2000).
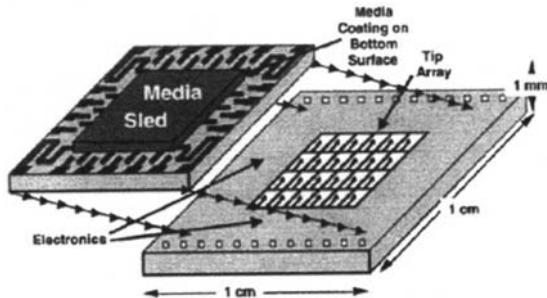
Figure 6
Conceptual diagram MEMS-actuated data storage devices with *x–y* motion of the media and *z* motion of a 4×5 array of probe tips (after Carley *et al.* 2000).

although the effective density in the system is reduced to $155\,Gbits\,in^{-2}$. The large number of probes operating in parallel increases the data rate to $>20\,MB$. It is envisioned that each probe would incorporate a write coil and a recessed GMR sensor using the magnetic material on the pole tip to guide the flux from the bit to the sensor. Calculations not presented in detail suggest that the total write power would be practical and that reasonable output signals could be obtained. No discussion of the interconnect problem which would seem quite formidable is presented.

In reflecting on the difficult technical challenges inherent in a massively parallel MFM system, it is sobering to recognize that an existing disk product announced in 1999 had a capacity of 340 MB, a data rate of 3 MB, a volume of $7.8\,cm^3$ and could be purchased off the Internet for $<\$450$. Given the evolutionary improvements expected in disk technology, it is clear that the target for future probe-based systems must be even more aggressive than that set by Carley *et al.* (2000). Furthermore, if continuous perpendicular media can be used to extend the superparamagnetic limit, it would seem that a single conventional head with no greater level of processing complexity than an array of MFM probe heads could be used in a rotating disk system to achieve higher performance at lower cost.

The use of SNOM was much heralded in several commercial ventures to offer a factor of ten improvement in density relative to conventional magnetic storage. To date this has not been realized for reasons that are best discussed elsewhere. However, the unique capability of the microscope described by Zenhausern *et al.* (1995) has been tested for a read-only application by Martin *et al.* (1997) (Fig. 7). By observing the modulation of the light scattered from a sharp probe due to the dipole–dipole coupling between the probe and the surface being scanned, a resolution of $\lambda/800$ can be achieved with visible light. The authors were able to detect 50 nm pits and estimated that it should be possible to detect 2 nm bits ($>40\,Tbits\,in^{-2}$) at 100 MHz with 50 dB SNR.

In summary, probe-based technologies allow very small features to be resolved and therefore offer the potential for storage densities of 1×10^{12}–1×10^{14} bits in^{-2}. However, while present work suggests this could be achieved in write-once systems, re-writable technologies competitive with disk storage will be
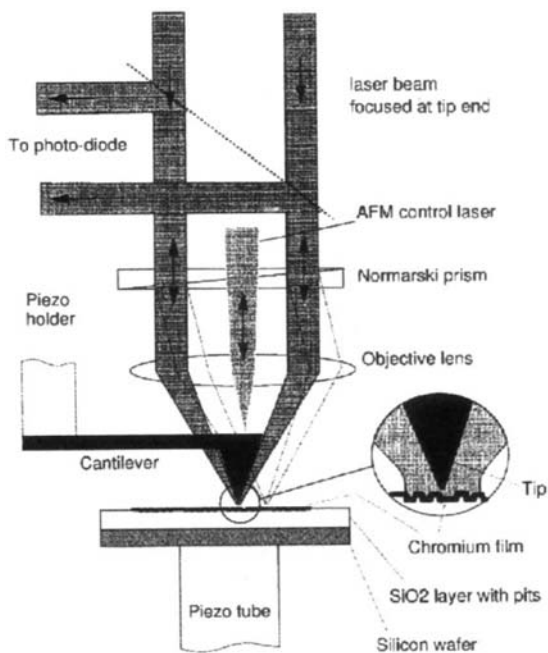
Figure 7
Principle of scanning interferometric apertureless
microscope in reflection mode (after Martin *et al.* 1997).

more difficult. In all cases, data rate remains a major
obstacle and the use of probe arrays as a solution is at
this time largely conceptual. Finally, probe systems
that require contact between the probe tip and
the media may be restricted to considerably lower
densities due to tip wear.

4. Optical Storage

The complex optical properties of many materials
offer a rich opportunity for exploitation in data stor-
age. To circumvent the constraint on areal density
imposed by the wavelength of light in conventional
optical storage, it has been proposed either to store
multiple bits in a single location using spectral hole-
burning or to store bits in three dimensions using
holography or two-photon absorption.

The possibility of using selective spectral absorp-
tion to store data has been considered for more than
20 years but after an intense but relatively unsuc-
cessful international effort to find appropriate mate-
rials, interest has declined. The basic concept, present
status and challenges have been reviewed recently by
Maniloff *et al.* (1999). In a variety of materials, so-
called *inhomogeneous absorption* occurs over a rela-
tively broad band of optical frequencies due to local
nonuniformities (Fig. 8(a)). However, selective ab-
sorption can also occur if the material is illuminated
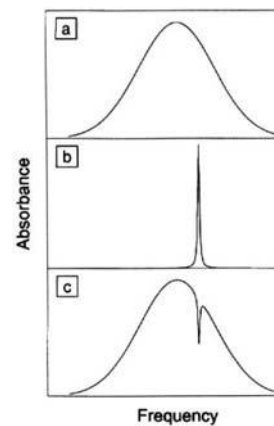
Figure 8
An illustration of a material's (a) inhomogeneous
absorption and (b) homogeneous absorption. If the
material is illuminated by narrow-band light, a spectral
hole is produced in the inhomogeneous distribution, as
shown in (c) (after Maniloff *et al.* 1999).

with narrow band light (Fig. 8(b)) which can be de-
tected later as reduced absorption referred to as a
hole at that frequency in the inhomogeneous absorp-
tion spectrum (Fig. 8(c)). This raises the possibility of
storing many bits represented by different frequencies
inside a single volume of material since the ratio
of the two bandwidths could be several orders of
magnitude.

Bulk erasure would presumably be required. Un-
fortunately, the lifetimes of the excited states are lim-
ited, ranging from milliseconds to a few hours even in
the best rare-earth doped materials and then only at
cryogenic temperatures. Also, interactions between
the excited states significantly reduces the ratio of the
bandwidths and the fast tunable lasers which would
be required are not available. The best result that
has been achieved is a few thousand bits in a
$30\,\mu m \times 30\mu m$ spot ($\sim 3\,\text{Gbits in}^{-2}$). Finally, the rate
at which data can be recorded or read is limited fun-
damentally to be less than or equal to the spectral
channel width. This has led to significantly more
complex systems using holographic spatial modula-
tion as well to write and read data blocks in parallel.
Until solutions to these fundamental problems are
found, spectral hole-burning will not pose a challenge
to disk storage.

Holography is another technology with a long
unrealized promise for data storage. The concept
(Fig. 9) is basically the same today as it was 30 years
ago. Instead of storing data as bits in a localized spot,
a 2D array of bits composed as a page is illuminated
with a laser and the holographic image caused by the
interference between the array image and a reference
beam captured in a photosensitive material. The data

545
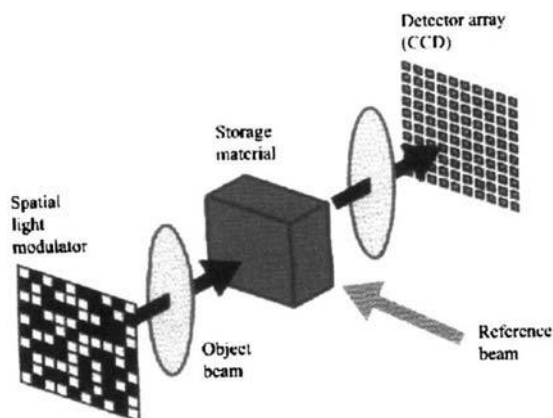
Figure 9
Basic holographic data storage system. Data are imprinted onto the object beam with a pixelated input device called a SLM. A pair of lenses image the data through the storage material onto a pixelated detector array such as a CCD. A reference beam intersects the object beam in the storage material, allowing the storage and later retrieval of holograms (after Ashley *et al.* 2000).

is read by illuminating the hologram and capturing the image of the reconstructed data on a 2D detector. Because the data is written and read in parallel, very high data rates should be possible. By varying the angle of the reference beam, multiple holograms can be stored in the same volume giving the potential for very high volume storage densities. When holographic storage was first conceptualized, every component in the system faced significant practical limitations so interest shifted to other less demanding optical schemes. However, significant improvements in laser light sources, spatial light modulators (SLMs) and charge-coupled device (CCD) light detectors led, in the last few decades, to a re-examination of holographic storage particularly by a consortium of industry and university researchers funded in part by DARPA. A comprehensive review of some of this work placed in historical context has been presented recently by Ashley *et al.* (2000).

Of the several problems still preventing the development of a practical holographic storage system, the recording material continues to be the most serious. Although other major components need further improvement, their usefulness in other applications has paced their development. One can expect smaller, higher power, lower cost solid state lasers; continued progress in displays means higher capacity, faster SLMs for page composers; newly developed CMOS detectors promise lower cost and higher performance than CCD devices. However, although new photopolymer materials with improved sensitivity are

attractive for write-once applications, no materials are known which meet the stringent characteristics required for high data rate, high-density rewritable storage competitive with hard disks.

Holographic materials capable of storing many holograms must have high optical quality in layers several millimeters thick, a large refractive index change per unit exposure measured by the sensitivity S, and a large dynamic range measured by the M-number, which is defined as the sum of the diffraction efficiency over M holograms in one location. Ashley *et al.* (2000) estimate to achieve data rates of $\sim 1\,\mathrm{Gb\,s^{-1}}$ and densities of approximately $100\,\mathrm{Gb\,in^{-2}}$ under practical conditions, values of $S \cong 20\,\mathrm{cm^2 J^{-1}}$ and $M \cong 5$ are required. They also provide values of S and M for several potential media candidates. The classic material has been bulk single crystals of photorefractive Fe-doped lithium niobate. However, its values of $S = 0.02$ and $M = 1$ fall well below the target values. In addition, since the refractive index change is linear in light intensity, data can be erased during the read operation. Photopolymers with $S = 20$ and $M = 1.5$ have recently been reported. However, their thicknesses are limited to $< 1\,\mathrm{mm}$ and they are not rewritable.

In summary, the realization of practical holographic systems will require continued improvement in all major components. The most serious problem is the storage material which, at the present time, is limited to write-once applications.

Another scheme to achieve volumetric optical storage is the so-call *two photon* process. The idea is conceptually simple and based on a well-documented effect in many materials in which the absorption of energy in the form of photons produces a measurable chemical change from an initial state A to a final state B. Then, A can be used to represent a "one" and B to represent a "zero." If the energy E_w required to write, i.e., cause the transition from A to B, is provided by two photons, each with energy $< E_\mathrm{w}$ then writing will occur only at those locations where both photons are coincident in time. Thus, writing can be made to occur at any point in a 3D matrix by steering two optical beams to the desired location. In order to read optically, the optical characteristic of A and B must be distinguishable in some way which does not disturb the stored data.

The reduction to practice of the two-photon concept has been discussed in several papers. One proposed material system was photochromic spiropyran for A, which after absorption at 350 nm (E_w) converts to merocyanine (B). For reading, the latter conveniently has an absorption peak of $\sim 550\,\mathrm{nm}$. After absorption of an incident "read" photon, it fluoresces immediately back to the ground state of B. Detection of the fluorescence identifies the site as a 'zero'. The reverse conversion from B to A is less straightforward. Since (apparently) A is a lower energy state than B, the addition of sufficient energy to B will

result in its transformation back to A. Bulk erasure by heating the storage medium may be necessary.

Very little information about the practical operating characteristics for a two-photon re-writable system have been given. The asymmetry between the A→B and B→A transitions suggests that these materials may be more suited to write-once applications. Certainly, the reliability of rewriting has not been demonstrated. No information has been given on the speed of either the write or read process or the timing margin for writing.

The problem of achieving spatial and temporal coincidences is not trivial so more recent work (Zhang *et al.* 2000) has used a single beam with variable focus depth to achieve vertical spatial resolution on a rotating disk. Data bits $3.5 \times 3.5 \times 20\,\mu m^3$ were recorded in an undefined material using a Ti:sapphire laser on 25 layers with a 75μm layer spacing. Using a continuous 532 nm laser, a CNR of 42 dB in a bandwidth of 1 kHz was achieved at a laser power of $5\,kW\,cm^{-2}$. At $20\,kW\,cm^{-2}$, significant data erasure was observed after multiple read cycles. Erasure or re-writability were not discussed.

Clearly, while the two-photon concept is elegant, the performance is severely hampered by available materials. Systems may be limited to write-once applications and are not competitive with hard disks.

5. Concluding Remarks

The continued improvement in cost and performance of magnetic hard drives poses an extremely difficult challenge for new technologies. Lithographically patterned media may offer only an incremental improvement over continuous media. 2D optical technologies face fundamental wavelength limitations and 3D concepts require materials which do not yet exist. At the present time, practical storage systems using self-assembled media addressed with multiple probe heads cannot be realized. However, enormous progress is being made both in understanding the fundamental aspects of self-assembly and in the fabrication of complex MEMS devices. Together, they may provide the next revolution in storage especially suited for the miniaturization of personal computing devices expected in the 21st century.

Acknowledgment

See also: Magnetic Recording: Patterned Media; Magnetic Recording Heads: Historical Perspective and Background; Magneto-optic Recording: Overwrite and Associated Problems; Magneto-optical Effects, Enhancement of

Bibliography

Ashley J, Bernal M P, Burr G W, Coufal H, Guenther H, Hoffnagle J A, Jefferson C M, Marcus B, MacFrlane R M, Shelby R M, Sincerbox G T 2000 Holographic data storage. *IBM J. Res. Develop.* **44**, 341–66

Bertram H N, Williams M 2000 SNR and density limit estimates: A comparison of longitudinal and perpendicular recording. *IEEE Trans. Magn.* **36**, 4–9

Binnig G, Despont M, Drechsler U, Häberle W, Lutwyche M, Vettiger P, Mamin H J, Chui S W, Kenny T W 1999 Ultrahigh-density atomic force microscopy data storage with erase capability. *Appl. Phys. Lett.* **74**, 1329–31

Carley L R, Bain J A, Fedder G K, Greve D W, Guillow D F, Lu M S C, Mukherjee T, Santhanam S, Abelnann L, Min S 2000 Single chip computers with microelectromechanical systems-based magnetic memory. *J. Appl. Phys.* **87**, 6680–5

Chou S Y, Wei M S, Krauss P R, Fischer P B 1994 Single domain magnetic pillar array of 35 nm diameter and 65 Gbits/in² density for ultrahigh density quantum magnetic storage. *J. Appl. Phys.* **75**, 6673–5

Colburn M, Johnson S, Stewart M, Damle S, Bailey T, Choi B, Wedluke M, Michaelson T, Sreenivasan S V, Willson C G 1999 Step and flash imprint lithography: A new approach to high-resolution patterning procedures. *SPIE* **3676**, 379–89

Cooper E B, Mamalis S R, Fang H, Dai H, Matsumoto K, Minne S C, Hunt T, Quate C F 1999 Terabit-per-square-inch data storage with the atomic force microscope. *Appl. Phys. Lett.* **75**, 3566–7

Cui B, Wu W, Kong L, Sun X, Chou S Y 1999 Perpendicular quantized magnetic disks with 45 Gbits on a $4 \times 4\,cm^2$ area. *J. Appl. Phys.* **85**, 5534–6

Despont M, Brugger J, Dreschler U, Durig U, Haberle W, Lutwyche M, Roithuizen H, Stutz R, Widmer R, Roher H, Binning G K, Vettiger P 1999 VLSI-MEMS chip for AFM data storage. *IEEE Int. Micro Electro Mechanical Sys.* 564–9

Devolder T, Chappert C, Chen Y, Cambril E, Bernas H, Jamet J P, Ferr E 1999 Sub-50nm planar magnetic nanostructures fabricated by ion irradiation. *Appl. Phys. Lett.* **74**, 3383–5

Haginoya C, Heike S, Ishibashi M, Nakamura K, Koike K, Yoshimura T, Yamamoto J, Hirayama Y 1999 Magnetic nanoparticle array with perpendicular crystal magnetic anisotropy. *J. Appl. Phys.* **85**, 8327–31

Heinze S, Bode M, Kubetzka A, Pietzsch O, Nie X, Blügel S, Wiesendanger R 2000 Real-space imaging of two-dimensional antiferromagnetism on the atomic scale. *Science* **288**, 1805–8

Hou S M, Zhao X Y, Yang C, Xue Z Q, Yang W J, Chen H Y 1999 Ultrahigh density data storage in an organic film with a scanning tunneling microscope. *J. Vac. Sci. Technol. B* **17**, 2467–70

Lutwyche M I, Despont M, Dreschler U, Dürig U, Häberle w, Rothuizen H, Stutz R, Widmer R, Binig G K, Vettiger P 2000 Highly parallel data storage system based on scanning probe arrays. *Appl. Phys. Lett.* **77**, 3299–301

Mamin H J, Ried R P, Terris B O, Rugar D 1999 High-density data storage based on the atomic force microscope. *Proc. IEEE* **87**, 1014–27

Maniloff E S, Johnson A E, Mossberg T W 1999 Spectral data storage using rare-earth doped crystals. *MRS Bull.* 46–50

Martin Y, Rishton S, Wickramasinghe H K 1997 Optical data storage read out at 2.56 Gbits/in^2. *Appl. Phys. Lett.* **71**, 1–3

Ross C A, Savas T A, Smith H I, Hwang M 1999 Modelling of hysteresis loops of arrays of 100 nm period nanomagnets. *IEEE Trans Magn.* **35**, 3781–3

Sakai K, Matsuda H, Kawada H, Eguchi K, Nakagiri 1988 Switching and memory phenomena in Langmuir-Blodgett films. *Appl. Phys. Lett.* **53**, 1274–6

Sun S, Murray C B, Weller D, Folks L, Moser A 2000 Mono-disperse FePt Nanoparticles and ferromagnetic FePt nano-crystal superlattices. *Science* **287**, 1989–92

Terris B D, Barrett R C 1995 Data storage in NOS: Lifetime and carrier-to-noise measurements. *IEEE Trans. Elec. Dev.* **42**, 944–9

Tromp R M 2000 Low-energy electron microscopy. *IBM J. Res. Dev.* **44**, 503–16

Vettiger P, Despont M, Drechler U, Dürug U, Häberle W, Lutwyche M I, Rothuizen H E, Stutz R, Widmer R, Bining G K 2000 The 'Millipede'—more than one thousand tips for future AFM data storage. *IBM J. Res. Dev.* **44**, 323–40

Wang D, Thomas S G, Wang K L, Xia Y, Whitesides G M 1997 Nanometer scale patterning and pattern transfer on amorphous Si, crystalline Si and SiO$_2$ surfaces using self-assembled monolayers. *Appl. Phys. Lett.* **70**, 1593–5

Weisendanger R 1998 *Scanning Probe Microscopy.* Springer-Verlag, Berlin

Wong J, Sherer A, Todorovic M, Schultz S 1999 Fabrication and characterization of high aspect ratio perpendicular pat-terned information storage media in an Al$_2$O$_3$/GaAs subst-rate. *J. Appl. Phys.* **85**, 5489–91

Wood R 2000 The feasibility of magnetic recording at a tera-byte per square inch. *IEEE Trans. Magn.* **35**, 36–42

Xu W, Wong J, Cheng C C, Johnson R, Sherer A 1995 Fab-rication of ultrasmall magnets by electroplating. *J. Vac. Sci. Technol. B* **13**, 2372–5

Zenhausern F, Martin Y, Wickramasinghe H K 1995 Scanning interferometric apertureless microscopy: Optical imaging at 10 angstrom resolution. *Science* **269**, 1083–5

Zhang H, McCormick F B, Dvornikov A S, Chapman C, Walker E P, Kim N-H 2000 Single-beam two-photon-recorded monolithic multi-layer optical disks. *Proc. SPIE* **4090**, 174–8

W. D. Doyle
The University of Alabama, Alabama, USA

Figure 1
Magnetic head slider flying over a disk surface compared with an aircraft flying over ground with a close physical spacing.

Magnetic Recording Devices: Head/Medium Interface

Magnetic storage and retrieval devices include tape, flexible disk, and rigid disk drives used for audio, video, and data processing applications. The magnetic recording process involves relative motion between a magnetic medium (tape or disk) and a stationary or rotating read/write magnetic head. For construction and materials used in magnetic head and medium components see Bhushan (1996a, 1999a, 2000). The need for ever-increasing recording densi-ties requires that surfaces should be as smooth as possible and flying height (physical separation or clearance between a head and a medium) be as low as possible. In modern tape and flexible and rigid disk drives, flying height ranges from about 25 nm to 50 nm, and roughness of the head and medium sur-faces ranges from about 1.5 nm to 5 nm r.m.s. As an analogy, a magnetic head slider flying over a disk surface with a flying height of 25 nm with a rela-tive speed of 20 ms^{-1} is equivalent to an aircraft flying 0.2 μm above the ground at 900 kmh^{-1} (Fig. 1). This is what a disk drive experiences during its operation.

The ultimate objective in magnetic storage devices is to run two surfaces in contact (with practically zero physical separation) if the tribological issues can be resolved. Smooth surfaces lead to an increase in adhesion, friction, and interface temperatures, and closer flying heights lead to occasional rubbing of high asperities and increased wear (Bhushan 1999b). Friction and wear issues are resolved by an appro-priate selection of interface materials and lubricants, by controlling the dynamics of the head and medium, and by the environment Bhushan (1996a, 1999a, 2000). A fundamental understanding of the tribology (friction, wear, and lubrication) of the magnetic head/medium interface, both on macro- and micro/nano-scales, becomes crucial for the continued growth of the more than US$80 billion a year magnetic storage industry.

In this article magnetic storage devices and com-ponents are introduced first. Results for selected tri-bological problems important for the reliability of magnetic storage devices are then presented. Finally, results are presented of micro/nanotribological stu-dies conducted using atomic force/friction force microscopy to better understand the fundamental mechanisms of friction and wear.

1. Magnetic Storage Devices and Components

Schematics of tape and rigid disk drives and the con-struction and materials used in magnetic heads and media are shown in Figs. 2 and 3. In a linear data processing IBM 3490/STK4490 tape drive as shown in Fig. 2(a), after loading the cartridge into the drive,

(a)

Threader

Head

Take-up reel

Tension transducer

Cartridge loader

(b)

Ni-Zn ferrite

Tape contact region

Inductive
write head

MR read head

(c)   ME tape structure

Liquid lubricant (< 5 nm)

DLC (8-10 nm)

Magnetic coating (0.2 μm)

Polymer film with particulates (10-25 nm)

PET film (6 μm)

Back coat (0.5 μm)

Liquid lubricant (8-10 nm)

MP tape structure

Magnetic coating (0.3 μm)

Non-magnetic coating (1.2 μm)

PET film (6.5 μm)

Back coat (0.5 μm)

Figure 2
Schematics of (a) a tape path in an IBM 3490 data processing tape drive, (b) an inductive/MR thin-film head (with a radius of cylindrical contour of 20 mm), and (c) sectional views of metal-particle (MP) and metal-evaporated (ME) magnetic tapes.

(a)

Diamondlike carbon overcoat 3.5 nm thick

Al³O³-TiC

(b)

Liquid lubricant 1-2 nm

Diamondlike cvarbon overcoat 8-10 nm

Magnetcic coating 25-75 nm

A1-Mg/10 μm Ni-P, Glass or Glass-ceramic 0.78-1.3 mm

(c)
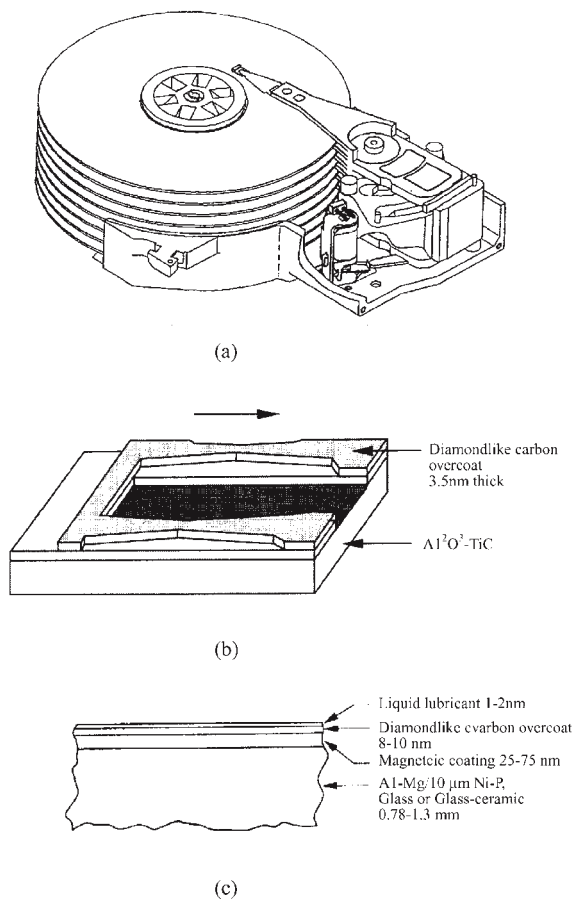
Figure 3
Schematics of (a) a rigid disk drive, (b) an inductive/MR thin-film picoslider, and (c) sectional view of a thin-film rigid disk.

the tape leader is threaded into the drive over a read/write head to the take-up reel by a pentagon threading mechanism. A decoupler column placed near the cartridge entrance decouples any tape vibrations that may occur inside the cartridge. The tension is sensed and controlled by a tension transducer. In a rigid disk drive as shown in Fig. 3(a), a stack of disks is mounted on a sealed, grease lubricated ball-bearing spindle. The disk stack is rotated by a d.c. motor at speeds ranging from a few thousand rpm to a maximum speed of about 10 000 rpm. A head slider is supplied for each disk surface. The slider suspension assembly is actuated by a stepping motor or a voice-coil motor for read/write operation (Bhushan 1996a, 2000).

Magnetic heads consist either of conventional inductive or inductive/magnetoresistive (MR) devices (Bhushan 1993, 1996a, 2000). If MR head design is used, it is only used for read purposes. Air-bearing surfaces of tape heads are generally cylindrical in shape (Fig. 2(b)). The tape is slightly underwrapped over the head surface to generate hydrodynamic lift during read/write operations. The head sliders used in rigid disk drives are either two- /three-rail, taper-flat design or two-rail, step, negative pressure design (Fig. 3(b)). The sliders are supported by a nonmagnetic steel leaf spring (flexing) suspension to allow motion along the vertical, pitch, and roll axes. The front taper or step pressurizes the air lubricant, while some air leaking over the side boundaries of the rail results in a pitch angle.

Magnetic media fall into two categories: (i) particulate flexible media, where magnetic particles are dispersed in a polymeric matrix and coated onto the polymeric substrate (Fig. 2(c)); and (ii) thin-film media, where continuous films of magnetic materials are deposited by vacuum techniques onto the polymeric substrate or flexible media (Fig. 2(c)) or onto a rigid substrate such as aluminum, glass, or glass ceramics (Fig. 3(c)) (Bhushan 1993, Miller and Bhushan 1996).

2. Macrotribology of Magnetic Storage Devices

Friction and wear of two surfaces in relative motion is governed by the real area of contact and interfacial adhesion. In addition, for wet contacts with a tiny amount of liquid present at the interface, "stiction" (or high static friction) can occur owing to meniscus/viscous effects (Fig. 4). Generally, any liquid that wets or has a small contact angle on surfaces will condense from vapor in the form of an annular-shaped capillary condensate in the contact zone. The negative (attractive) pressure of the liquid films of the capillary condensates or pre-existing film of lubricant can significantly increase the adhesion between solid bodies. Liquid-mediated adhesive forces can be divided into two components: meniscus force (F_M) owing to surface tension and a rate-dependent viscous force (F_V). The total tangential force (F) required to separate the surfaces during sliding is equal to intrinsic friction force (F_A) and stiction force (F_S, a combination of friction force owing to the meniscus

$F_A + F_S$ $W + F_M$ Direction of motion

Liquid
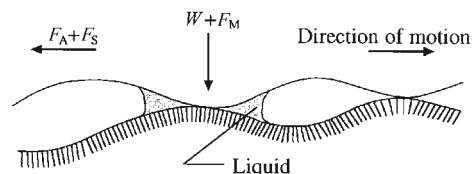
Figure 4
Schematic of a wet interface with meniscus formation, showing various forces being applied during sliding. F_M is the meniscus force, W is the normal force, and F_A and F_S are intrinsic friction and stiction forces, respectively.

effect and the peak viscous force) (Bhushan 1999b):

$$F = F_A + F_S = \mu_r(W + F_M) + F_V \qquad (1)$$

where μ_r is the "true" static coefficient of friction and W is the normal the load. It turns out that since the surfaces in magnetic storage devices are smooth and the normal load being applied is relatively low, frictional effects because of meniscus and viscous forces are significant. Optimization of surface topography of head and medium and overcoats and lubricant films needs to be achieved for long-term reliability of magnetic storage devices.

2.1 Contact Modeling

Numerical techniques are used to solve contact problems of rough surfaces under dry and wet conditions (Bhushan 1996b, 1996c, 1998, 1999b, Tian and Bhushan 1996a, 1996b, Peng and Bhushan 2001). The numerical model does not require an asperity model and makes no probabilistic assumptions such as distribution of asperity heights, slopes, and curvatures, as required in analytical models. The numerical techniques allow analysis of a large number of contact spots that go through elastic and elastic/plastic deformations. The numerical model provides useful information on the number of contact spots, their sizes and distributions, and the spacing between contacts. Furthermore, wet contact analysis for contact of rough surfaces with a liquid film can be carried out. In the wet contact analysis, elastic/plastic dry contact of rough surfaces is first analyzed. In the next step, a liquid film of known mean thickness is introduced over the deformed rough surfaces. Wetted areas are determined by selecting the area where asperities of both contacting surface touch the liquid. The total projected meniscus area is then used for the calculations of meniscus forces. The model can be used to develop optimum surface roughness distributions for the head and medium surfaces. Figure 5 shows representative contact area and meniscus area maps for a computer-generated random rough surface in contact with a smooth surface in the presence of water film. As expected, the meniscus area is larger than the contact area and the meniscus force is three times that of the normal force.

Tian and Bhushan (1996b) and Poon and Bhushan (1996) used the model to predict the effects of relative humidity and liquid film thickness on the meniscus force (see also Bhushan 1998). The effect of relative humidity on the meniscus force at an interface is shown in Fig. 6(a). The effect of liquid film thickness and interface roughness on computer-generated rough surfaces in contact with a smooth surface is shown in Fig. 6(b). An increase in either relative humidity or liquid film thickness increases the liquid present at the interface. The thicker a liquid film, the more asperities touch the liquid surface and the more

Pa = 32.8kpa

Contact area — Meniscus area

$A_r/A_2 = 1.23 \times 10^{-4}$ — $A_m/A_2 = 1.5 \times 10^{-3}$

$W/A_r = 0.32$ GPa — $F_m/A_2 = 0.10$ MPa
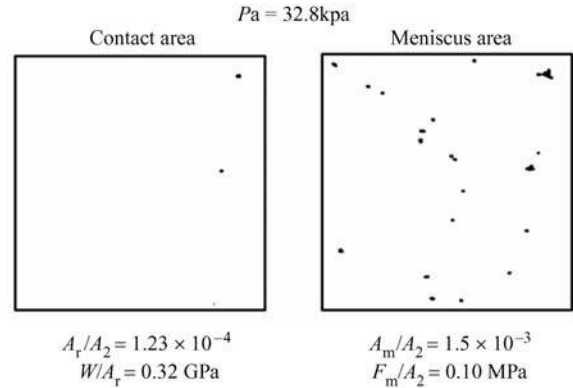
Figure 5
Contact area and meniscus area for the case of computer-generated rough surface ($\sigma = 1$ nm, $\beta^* = 0.5\,\mu$m) in contact with a smooth, flat surface with a composite elastic modulus of 100 GPa and a water film ($\gamma = 73$ dyne cm^{-1} (7.3 $\times$ 10^{-4} N cm^{-1}), $\theta = 60°$) thickness of 1 nm and meniscus height of 1 nm (after Poon and Bhushan 1996).

menisci form on a larger number of asperities. In addition, with a thicker film, a larger volume of liquid is present around the asperities resulting in a greater amount of meniscus volume accumulated at the contact interface and a greater meniscus height. These effects lead to larger meniscus forces. There is a critical film thickness for a surface with given roughness above which the meniscus force increases rapidly. The critical film thickness is of the order of three-quarters of the composite r.m.s. roughness of the mating surfaces (σ).

Bhushan and Chilamakuri (1996) and Chilamakuri and Bhushan (1998a) used the numerical model to study contact between flat rigid surfaces and non-Gaussian rough surfaces with known skewness (Sk) and kurtosis (K). Rough surfaces with different skewness and kurtosis were generated using a two-dimensional digital filter technique. Figure 7 shows the probability density functions of surfaces with various skewness and kurtosis values. Figure 8(a) shows the effect of skewness and kurtosis on the fractional real area of contact (A_r/A_a, where A_r is the contact area and A_a is the apparent area) and relative meniscus force (F_M/W) at different nominal pressures (p). A positive skewness between 0 and 0.2 at low pressure and about 0.2 at higher pressures results in the lowest real area of contact and meniscus force. Contact area and meniscus force decrease with an increase in the kurtosis. Fewer peaks present on a surface with a range of positive skewness values or high kurtosis can explain the trends. Figure 8(b) shows the variation of relative meniscus force with h/σ ratio for different skewness and kurtosis values. Note that the sensitivity of h/σ to the meniscus force decreases at a range of

(a)

(a)

(b)
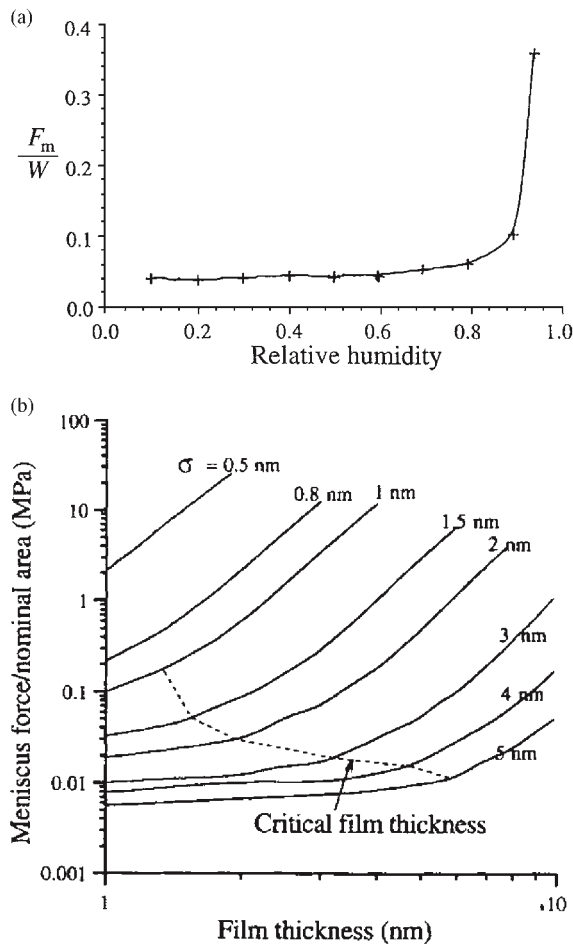
Figure 6
(a) Effect of relative humidity on the relative meniscus force for a glass/ceramic disk substrate in contact with a smooth surface (after Tian and Bhushan 1996b). (b) Effect of water film thickness and surface roughness on the relative meniscus force for computer-generated Gaussian surfaces (correlation distance $\beta^* = 0.5\,\mu m$) in contact with a smooth surface. The dotted line defines the critical film thickness for different σ (after Poon and Bhushan 1996).

Figure 7
Probability density functions for surfaces with (a) different skewness and (b) different kurtosis values (after Chilamakuri and Bhushan 1998a).

positive skewness of 0–0.2, and kurtosis of about five or larger is optimum.

Laser-textured disks are becoming increasingly popular in the design and manufacture of rigid disks. In the laser-texturing technique, discrete topographic features with either rounded, dome-like protrusions (sombrero shaped) or craters (V or W types or donut shaped) usually known as bumps are generated over the disk surface. In laser-textured disk surfaces, these microscale features are placed in the landing zone to reduce friction/stiction during the start and stop operations. Typical sombrero-, V-, and W-type bumps have about 10–15 μm rim diameter and height of about 15–25 nm with a 50 μm × 50 μm pitch. This gives of the order of 4×10^5 bumps in the landing zone of a 95 mm diameter disk. V- or W-type bumps are more commonly used because they can be reproducibly manufactured. The stiction phenomena at the head/disk interface can be controlled by controlling the size and shape of the laser bumps. Studies to identify an optimum bump shape and the relationship between the optimum number of bumps as a function of the bump geometry for a given bump shape have been conducted (Chilamakuri and Bhushan 1997, 1998b, 1999a, 1999b, Chilamakuri *et al.* 2000).

The following design methodology has been used to determine an optimum number of bumps. For a given size and shape, the meniscus force increases with an increase in the number of bumps, so it is important to minimize the number of bumps to control the stiction phenomena. However, too few bumps can result in
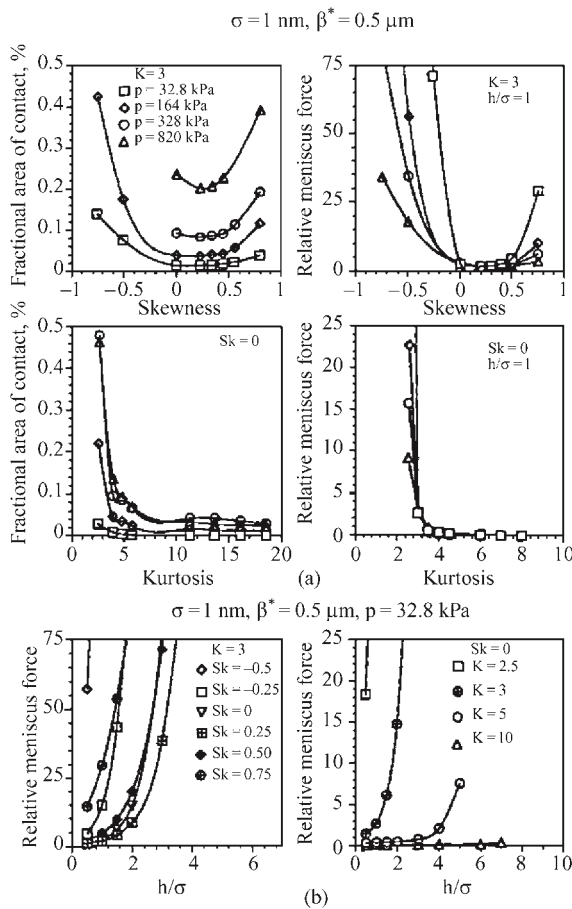
Figure 8
(a) Fractional real area of contact and relative meniscus force as a function of skewness and kurtosis at various nominal pressures, and (b) relative meniscus force as a function of h/σ for different skewness and kurtosis values, for an interface in the presence of perfluoropolyether film ($\gamma = 25\,\mathrm{dyne\,cm^{-1}}$ ($2.5 \times 10^{-4}\,\mathrm{N\,cm^{-1}}$), $\theta = 10°$) (after Chilamakuri and Bhushan 1998a).

Figure 9
Three-dimensional surface plots and two-dimensional line plots of sombrero-, V-, and W-type laser surfaces ($R_{\mathrm{rim}} = 7.5\,\mathrm{\mu m}$, $H_{\mathrm{mean}} = 25\,\mathrm{nm}$, $\sigma = 5\,\mathrm{nm}$) with a Gaussian height distribution.

the failure of the disk surface owing to plastic deformation and wear. To prevent the bumps from yielding, the number of bumps on the disk surface should be greater than a certain minimum, which would also give a lower bound for the stiction. Numerical analyses of computer-generated surfaces are used to predict an optimum number of bumps. Figure 9 shows typical computer-generated surfaces with various bump types and variable heights. The three-dimensional numerical contact model mentioned earlier is used to perform contact analysis of a computer-generated laser-textured surface against a flat

surface. Figure 10 shows an optimum number of bumps, contact area, and meniscus force as a function of yield stress at different values of coefficient of friction. As expected, the optimum number of bumps increases with an increase in the coefficient of

$R_{rim} = 7.5\ \mu m,\ H_{mean} = 25\ nm,\ \sigma = 3\ nm$
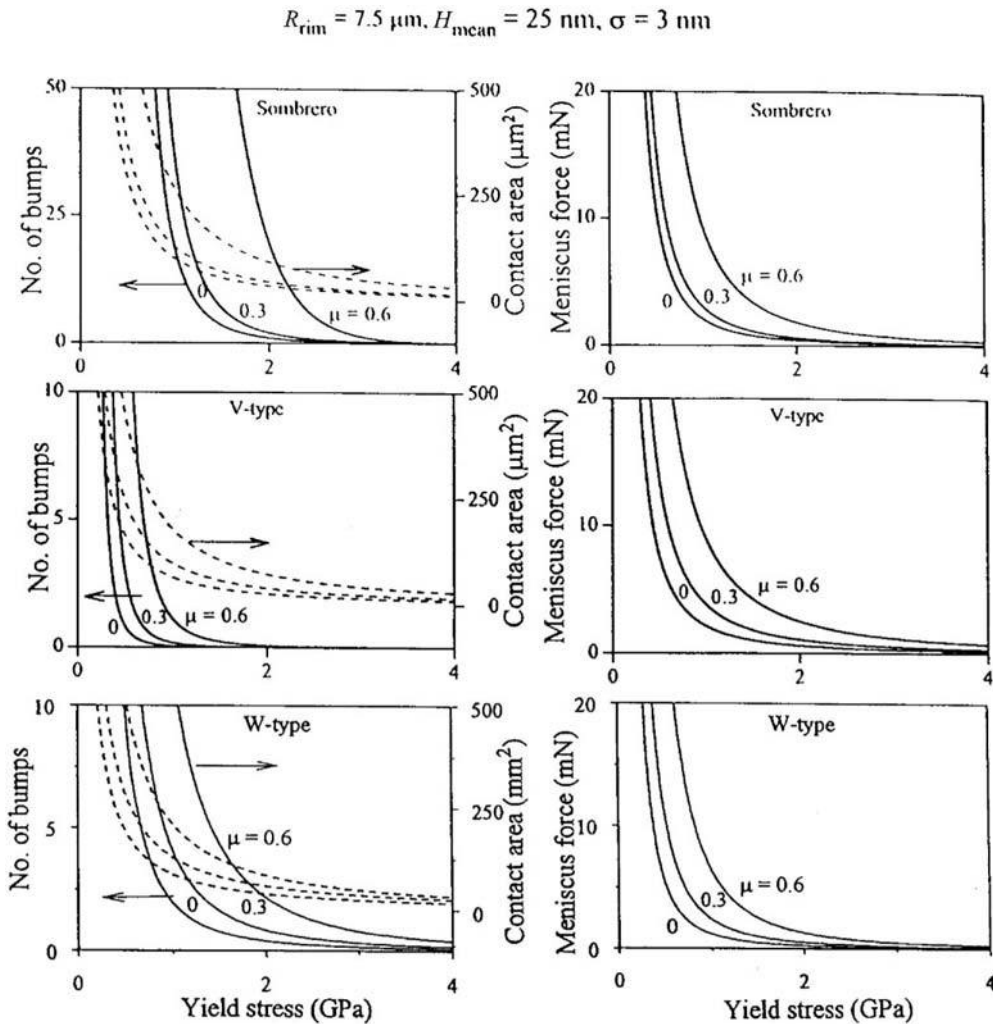
Figure 10
Effect of coefficient of friction, μ, on number of bumps, contact area, and meniscus force for sombrero-, V-, and W-type bumps at $\sigma = 3\ nm$.

friction. Contact area and meniscus force also follow similar trends. Measurements made on experimental disks verify numerical predictions (Bhushan 2000).

2.2 Overcoats and Lubricants

The carbon overcoat is almost exclusively used as an overcoat for thin-film disks and metal tapes (Bhushan 1999c). It has to be chemically active in order to attach to lubricant molecules, whereas the lubricant molecules should be hydrophobic so that they repel water from the environment. Lubricants can attach to the carbon surface by one or more of the following

mechanisms: physisorption, conformational rearrangement, and chemisorption. The type and degree of attachment depends on the molecular structure and end groups of the lubricants and surface groups on the carbon surface. A hydrogenated carbon surface is highly functional and consists of many oxygen-containing surface groups which include –C–O–C– (ether), $>C=O$ (carbonyl), –COOR (ester), –COOH (carboxyl), and –COH (hydroxyl) groups, as well as unpaired electrons (dangling bonds). Figure 11 shows schematically the adsorption of a polar perfluoropolyether (PFPE) (Z-Dol) molecule on a carbon surface at 20 °C. The $C=O$ bond and the hydroxyl groups in the case of Z-Dol interact with functional groups and dangling bonds on the carbon surface. The
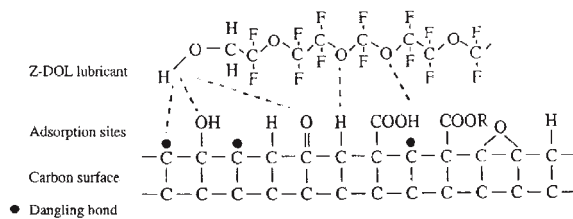
Figure 11
Schematic of Z-Dol molecules adsorbed on a carbon
surface at 20 °C.

functional groups behave as an anchor, i.e., an immobile fraction of the lubricant film. The addition of an alcohol (–OH) end group to a lubricant molecule adds an interaction energy of the order of $20\,\mathrm{kJmol^{-1}}$, even if no chemical reaction occurs with the surface. The attachment of lubricant molecules with or without functional groups is enhanced after sliding as long as the lubricant chains are exposed to the disk surface (Zhao *et al.* 1999).

The PFPE backbone mainly interacts with surfaces through van der Waals forces. The van der Waals interaction energy of PFPE molecules with a DLC surface is of the order of $2\,\mathrm{kJmol^{-1}}$ or less. This energy is sufficiently high so that molecules lie flat on the surface when the lubricant film thickness is comparable to the polymer chain diameter of 0.7 nm.

There are two approaches for chemisorption that have been shown to be successful in chemical bonding of the liquid monolayer to the overcoat. The first relies on exposure of the disk lubricated with neutral PFPE to various forms of radiation, such as low-energy x rays, electron or ion beam, nitrogen plasma, or far UV. The improved affinity of the lubricant for the surface by obtained by UV radiation is believed to result from enhanced bonding by photochemical alteration of the lubricant, the substrate, or the air-deposited organics. The PFPEs undergo dissociative electron attachment caused by photoelectrons that are generated by the interaction of the UV light with the substrate. This dissociative electron attachment results in the formation of a negative ion and a radical. It is suggested that subsequent radical propagation and termination steps cross-link the PFPE and bond it to the substrate. Another approach uses chemically active PFPE molecules through either the above-mentioned treatments or a post-thermal treatment, in which the various functional end groups offer the opportunity of strong attachments to a specific interface if a high enough temperature is applied to overcome the activity barrier (Zhao and Bhushan 1996, Zhao *et al.* 2000). The activation energy of the thermal attachment of Z-Dol to a carbon surface is of the order of $30\,\mathrm{kJmol^{-1}}$. Surface cleanliness and chemical activity of the overcoat affect the degree of bonding. The length of the thermal

treatment and the temperature for PFPE lubricants with polar end groups are important factors in determining the adsorption level of lubricants to the disk surface (Zhao and Bhushan 1996).

The lubricant film thickness (h) and composite roughness (σ) are generally known to have an opposite effect on static and kinetic friction and durability in terms of desirability, i.e., an increase in h or a decrease in σ results in an increase in the values of F_s/W, F_k/W, and durability. F_s/W, F_k/W, and durability data obtained on various disks with a lubricant C (Z-Dol) as a function of h/σ is shown in Fig. 12 (Bhushan and Zhao 1999). In Fig. 12, h represents a mobile fraction of the total lubricant film thickness in static and kinetic friction because only the mobile fraction forms menisci; h is a total film thickness in durability because both mobile and immobile fractions affect wear life. The Z-Dol lubricants used are untreated, partially bonded, and fully bonded. The normalized static friction force (F_s/W) and normalized kinetic friction force (F_k/W) increase rapidly above a critical value of h/σ ($\sim$0.7) and durability decreases above the critical film thickness. Trends in experimental results for static friction force are comparable with the results of the numerical contact model presented earlier (see Fig. 6(b)). A rapid decrease in durability above a critical film thickness occurs because of a large meniscus being formed around slider edges and the presence of the stick/slip phenomena (Bhushan and Zhao 1999).

Zhao *et al.* (2000) and Kajdas and Bhushan (1999) have presented detailed discussion of various degradation mechanisms of Z-Dol lubricant which include thermal decomposition, catalytic degradation, electron-mediated degradation, and mechanical degradation processes. Comparing various degradation mechanisms it is believed that the catalytic degradation mechanism proposed in the literature is not relevant because kinetics is slow at asperity temperatures. Based on a wide variety of experimental data it is reasonable to emphasize that anionic intermediates (negative ions and/or negative-ion/radical species) produced by low-energy electrons play an important part in both (i) the electron-mediated degradation process of PFPE lubricants, and (ii) chemical bonding of PFPE lubricant films with DLC surfaces under sliding conditions.

3. Microtribology of Magnetic Storage Devices

At most interfaces of technological relevance, contact occurs at multiple asperity contacts. Consequently, the importance of investigating single-asperity contacts in studies of the fundamental micromechanical and tribological properties of surfaces and interfaces has long been recognized. The emergence and proliferation of proximal probes, in particular tip-based microscopy (the atomic force microscope/friction

σ = 3.0 and 4.7 nm, Lubricant C

$F_s/W = 0.30 \exp(1.5\, h/\sigma)$

$F_k/W = 0.24 \exp(1.2\, h/\sigma)$
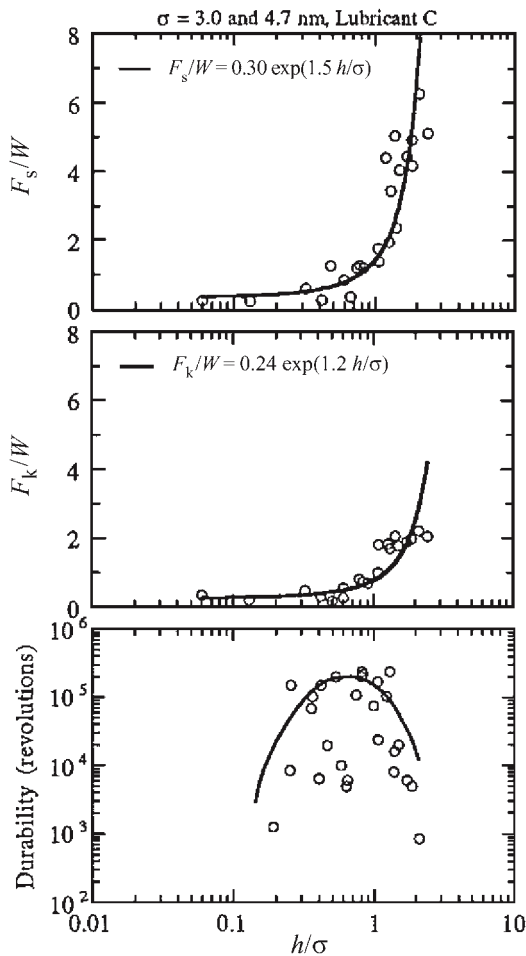
Figure 12
Normalized static and kinetic friction forces and durability in revolutions as a function of the ratio of the lubricant film thickness to composite roughness (h/σ). Data on untreated, partially bonded, and fully bonded Z-Dol lubricants are presented. For static and kinetic friction data, h used is a mobile fraction; for durability, h used is a total film thickness (after Bhushan and Zhao 1999).

microscope (AFM/FFM)), and of computer simulations of tip/surface interactions and interfacial properties, provide nanoscale realizations of single-asperity contacts, and allow systematic investigations of interfacial problems of materials with high resolution as well as ways and means for modifications and manipulations of nanoscale structures. These advances provide the impetus for intensive research endeavors aimed at fundamental understanding of the nature and consequences of the interactions between materials on the atomic scale, and guide the "rational" design of material for technological applications. The advent of these techniques and methodologies has led to the development of the field of micro/nanotribology and micro/nanomechanics (Bhushan 1999a, Bhushan *et al.* 1995). This field pertains to experimental and theoretical investigations of processes ranging from the atomic and molecular scales to the microscale, that arise as a consequence of interfacial interactions.

3.1 Friction

Friction has been measured on a microscale (Bhushan 1999a), and it has been reported that the coefficient of friction on a microscale is lower than the macrofriction. Table 1 gives typical values of coefficients of friction of metal-particle (MP) and metal-evaporated (ME) tapes, poly(ethylene terephthalate) (PET) tape substrate, and thin-film rigid disks. Friction values on the microscale are much lower than those on the macroscale, which is believed to be because of a lower plowing contribution (almost no damage on the disk surface as measured). When measured for the small contact areas and very low loads used in microscale studies, mechanical properties are higher than at the macroscale, this reduces the degree of wear. In addition, the apparent area of contact reduces the number of particles trapped at the interface, and thus minimizes the plowing contribution to the friction.

Gray-scale plots of coefficients of local friction of a thin-film disk as the FFM tip is scanned in either direction are shown in Fig. 13. Corresponding gray-scale plots of slope of roughness profiles are also shown in Fig. 13. Since the sign of the friction and the slope reverses with the change in the scanning direction, the sign of one set of images needs to be reversed before data can be compared. The left-hand sections correspond to the sample sliding from the left towards the right, the center sections correspond to the sample sliding from the right toward the left, and the right-hand sections correspond to the first set with the sign of slope and friction values reversed. We note a general correlation between the slope and friction profiles. We note that generally the points that have high friction in the left to right scan also have high friction as the sliding direction is reversed (after sign change). This relationship is not true at some locations. We observe some differences in the friction profiles that may result from the asymmetrical asperities and/or asymmetrical transfer of wipe material during manufacturing of the disk. The directionality effect in friction on a macroscale has been observed in some magnetic tapes (Bhushan 1999a).

3.2 Scratching and Wear

Microscratches made on MP tape and on an unlubricated thin-film rigid disk at various loads are

Table 1
Surface roughness (r.m.s.), microscale and macroscale friction, and nanohardness data of thin-film magnetic rigid disk, magnetic tape, and magnetic tape substrate (PET) samples.

| Sample | Roughness (r.m.s.) (nm) | | | Coefficient of microscale friction | | Coefficient of macroscale friction | | |
| | NOP[a] | AFM[b] | | | | | | |
	$250 \mu m \times$ $250 \mu m^c$	$1 \mu m \times$ $1 \mu m^c$	$10 \mu m \times$ $10 \mu m^c$	$1 \mu m \times$ $1 \mu m^c$	$10 \mu m \times$ $10 \mu m^c$	Mn–Zn ferrite	Al_2O_3– TiC	Nanohardness/normal load (GPa)/(μN)
Unlubricated disk	2.2	3.3	4.5	0.05	0.06		0.26	21/100
Lubricated disk	2.3	2.3	4.1	0.04	0.05		0.19	
Metal-particle tape	6.0	5.1	12.5	0.08	0.06	0.19		0.30/50
Metal-evaporated tape	9.3	4.7	5.1	0.05	0.03	0.18		0.7 to 4.3/75
PET tape substrate	33	5.8	7.0	0.05	0.04	0.55		0.3/20 and 1.4/20[d]

a Noncontact optical profiler. b Atomic force microscope. c Scan area. d Polymer and particulate regions, respectively.
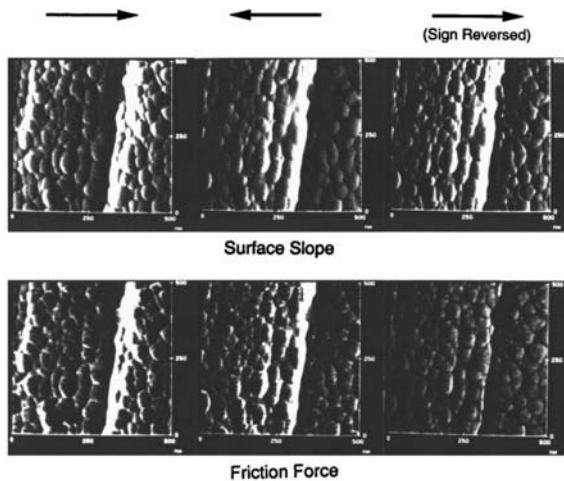
Figure 13
Gray-scale plots of the slope of the surface roughness and the friction force profiles for a lubricated disk with FFM tip sliding in different directions. Higher points are shown by lighter color (after Bhushan 1999a).

shown in Fig. 14. All scratches are made with 10 cycles. We notice that the scratch depth increases with an increase in the normal load. Figure 15 shows the microwear profiles at $20 \mu N$ load and at various cycles of an unlubricated thin-film disk. We note that wear is not uniform and is largely initiated at the texture marks present on the disk surface. This suggests that surface defects act as initiated sites for wear. Figure 16(a) shows the wear depth as a function of the number of cycles for unlubricated and lubricated thin-film disks at $10 \mu N$ and $20 \mu N$ loads. Wear
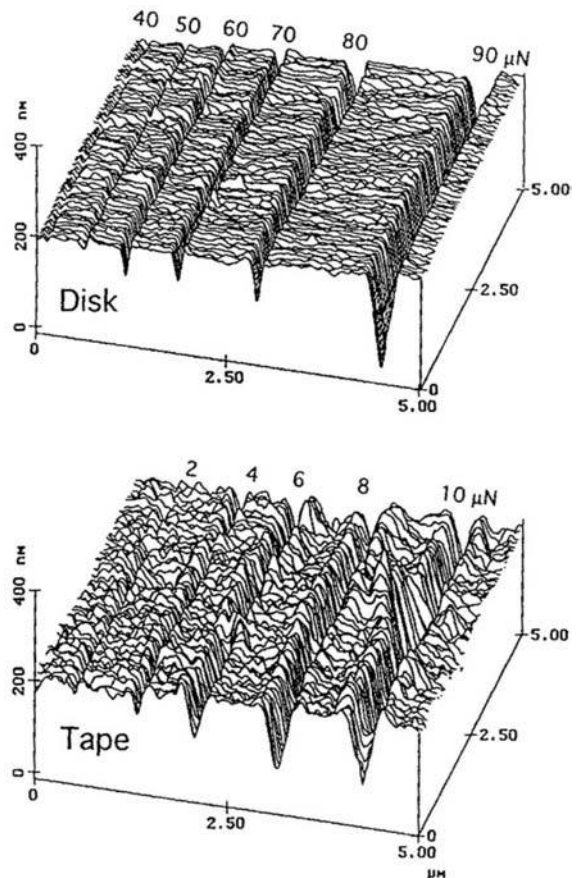
Figure 14
Surface profiles for scratched, unlubricated thin-film rigid disk and MP tape (after Bhushan 1999a).
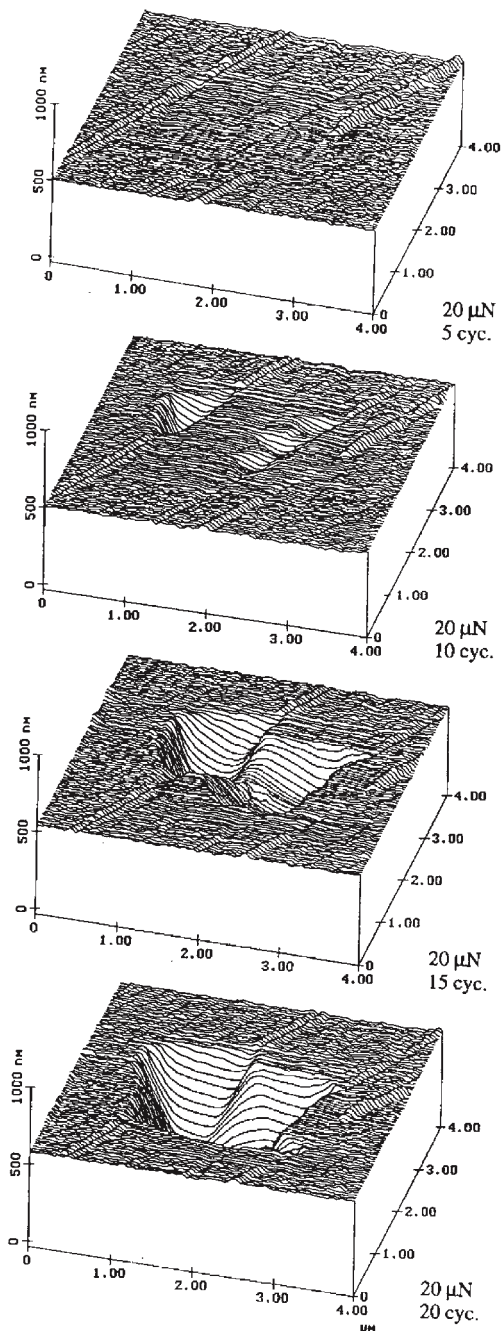
Figure 15
Surface profiles of unlubricated thin-film rigid disk showing the worn region (center $2\,\mu m \times 2\,\mu m$). The normal load and the number of test cycles are indicated (after Bhushan 1999a).
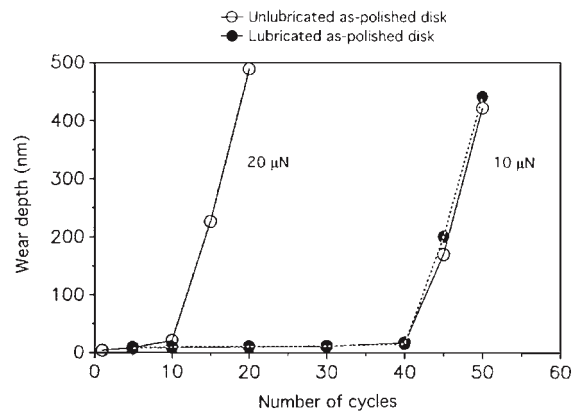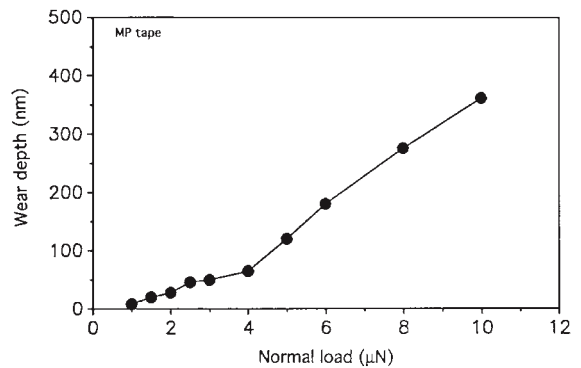
Figure 16
Wear depth as a function of number of cycles for (a) unlubricated and lubricated thin-film rigid disks at $10\,\mu N$ and $20\,\mu N$ loads, and (b) MP tape at a normal load of $2\,\mu N$ (after Bhushan 1999a).

initially takes place slowly with a sudden increase after about 40 cycles at $10\,\mu N$ and after about 10 cycles at $20\,\mu N$. The rapid increase is associated with the breakdown of the carbon coating. Similar behavior has been reported for ME tapes. Wear rates for particulate tapes (Fig. 16(b)) and PET tape substrates are approximately constant for various loads and number of cycles (Bhushan 1999a).

We note that scratches and wear profiles can be produced with very shallow depths, thus the AFM technique can be used to measure scratch resistance and wear resistance of ultrathin films.

3.3 Lubrication

To study lubricant depletion during microscale measurements, the microscale friction as a function of
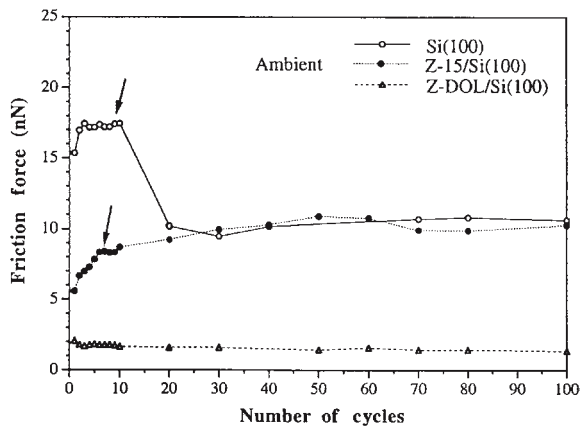
Figure 17
Friction force as a function of number of cycles for unlubricated and lubricated silicon samples (after Bhushan 1999a).

number of cycles of a virgin Si(100) surface and a silicon surface lubricated with about 2 nm thick Z-15 and Z-Dol PFPE lubricants are shown in Fig. 17. These experiments were conducted in an AFM/FFM by sliding a Si_3N_4 tip against the samples. Z-Dol is a PFPE lubricant with hydroxyl end groups. Its lubricant film was thermally bonded at 150 °C for 30 minutes and washed off with a solvent to provide a chemically bonded layer of the lubricant film. We note from Fig. 17 that the friction force in a virgin silicon surface decreases after a few cycles after the natural oxide and other contaminant film present on the silicon surface gets removed. In the case of the Z-15-coated silicon sample, the friction force is initially low and then approaches that of an unlubricated silicon surface after a few cycles. The increase in friction of the lubricated sample suggests that the lubricant film gets worn and the silicon underneath is exposed.

In the case of the Z-Dol-coated silicon sample, the friction force starts out low and remains low during the 100 cycles of the test. It suggests that Z-Dol does not get displaced/depleted as readily as Z-15. Furthermore, the initial friction value for Z-Dol is low as compared to that of Z-15. Z-15 gets displaced locally by condensed water molecules permeated through the lubricant film or condensed over exposed areas, whereas Z-Dol does not get displaced as readily by water because it is chemically bonded to the substrate. The absence of mobile lubricant and lack of water molecules minimize the possibility of formation of meniscus bridges, which is responsible for low friction in the case of Z-Dol. From this example, it is clear that AFM methods can be used to study the performance of lubricants in simulated single-asperity contacts.

4. Closure

The magnetic recording process involves relative motion between a magnetic medium and a stationary or rotating read/write magnetic head. Under steady operating conditions, a load-carrying air film is formed. There is a physical contact between the medium and the head during starting and stopping. In modern high-end computer tape and disk drives, the surfaces have roughness of the order of 2–5 nm r.m.s. and the head-to-medium separation is of the order of 25–50 nm. The need for higher recording densities requires the surfaces be as smooth as possible and the flying height be as small as possible. The very smooth surfaces and ultralow flying heights required present challenges and opportunities unparalleled in any other industry.

Analytical models and experimental data available of the tribology of the head/medium interface are plentiful. Understanding of tribology on nanoscales is beginning to emerge. Understanding of micro/nanotribology of ultrasmooth surfaces and small components in future head/medium interfaces is lacking. AFM/FFM studies are expected to play a major role in computer tribology.

See also: Magnetic Recording: Rigid Media, Tribology; Magnetic Recording Technologies: Overview

Bibliography

Bhushan B 1993 Magnetic slider/rigid disk substrate materials and disk texturing techniques—status and future outlook. *Adv. Info. Storage Syst.* **5**, 175–209
Bhushan B 1996a *Tribology and Mechanics of Magnetic Storage Devices*, 2nd edn. Springer, New York
Bhushan B 1996b Contact mechanics of rough surfaces in tribology: single asperity contact. *Appl. Mech. Rev.* **49**, 275–98
Bhushan B 1996c Methodology for roughness measurement and contact analysis for optimization of interface roughness. *IEEE Trans. Magn.* **32**, 1819–25
Bhushan B 1998 Contact mechanics of rough surfaces in tribology: multiple asperity contact. *Tribol. Lett.* **4**, 1–35
Bhushan B (ed.) 1999a *Handbook of Micro/Nanotribology* 2nd edn. CRC Press, Boca Raton, FL
Bhushan B 1999b *Principles and Applications of Tribology*. Wiley, New York
Bhushan B 1999c Chemical, mechanical and tribological characterization of ultra-thin and hard amorphous carbon coatings as thin as 3.5 nm: recent developments. *Diamond Relat. Mater.* **8**, 1985–2015
Bhushan B 2000 *Mechanics and Reliability of Flexible Magnetic Media*, 2nd edn. Springer, New York
Bhushan B, Chilamakuri S K 1996 Non-Gaussian surface roughness distribution of magnetic media for minimum friction/stiction. *J. Appl. Phys.* **79**, 5794–6
Bhushan B, Israelachvili J N, Landman U 1995 Nanotribology: friction, wear and lubrication at the atomic scale. *Nature* **374**, 607–16
Bhushan B, Zhao Z M 1999 Macroscale and microscale tribological studies of molecularly thick boundary layers of

perfluoropolyether lubricants for magnetic thin-film rigid disks. *J. Info. Storage Proc. Syst.* **1**, 1–21

Chilamakuri S K, Bhushan B 1997 Optimization of asperities for laser-textured magnetic disk surfaces. *Tribol. Trans.* **40**, 303–11

Chilamakuri S K, Bhushan B 1998a Contact analysis of non-Gaussian random surfaces. *Proc. Inst. Mech. Eng., Part J: J. Eng. Tribol.* **212**, 19–32

Chilamakuri S K, Bhushan B 1998b Design of sombrero and donut shaped bumps for optimum tribological performance. *IEEE Trans. Magn.* **34**, 1795–7

Chilamakuri S K, Bhushan B 1999a Contact analysis of laser textured disks in magnetic head–disk interface. *Wear* **230**, 11–23

Chilamakuri S K, Bhushan B 1999b Effect of peak radius on design of W-type donut shaped laser textured surfaces. *Wear* **230**, 118–23

Chilamakuri S K, Zhao X, Bhushan B 2000 Failure analysis of laser textured surfaces. *Proc. Inst. Mech. Eng., Part J: J. Eng. Tribol.* **1**, 303–20

Kajdas C, Bhushan B 1999 Mechanism of interaction and degradation of perfluoropolyethers with DLC coating in thin-film magnetic rigid disks—a critical review. *J. Info. Storage Proc. Syst.* **1**, 303–20

Miller R A, Bhushan B 1996 Substrates for magnetic hard disks for gigabit recording. *IEEE Trans. Magn.* **32**, 1805–11

Peng W, Bhushan B 2001 A numerical three-dimensional model for the contact of layered elastic/plastic solids with rough surfaces by a variational principle. *ASME J. Tribol.* in press

Poon C Y, Bhushan B 1996 Numerical contact and stiction analyses of Gaussian isotropic surface for magnetic head slider/disk contact. *Wear* **202**, 68–82

Tian X F, Bhushan B 1996a A numerical three-dimensional model for the contact of rough surfaces by variational principle. *ASME J. Tribol.* **118**, 33–42

Tian X F, Bhushan B 1996b The micro-meniscus effect of a thin liquid film on the static friction of rough surface contact. *J. Phys. D: Appl. Phys.* **29**, 163–78

Zhao Z M, Bhushan B 1996 Effect of bonded lubricant films on the tribological performance of magnetic thin-film rigid disks. *Wear* **202**, 50–9

Zhao Z M, Bhushan B, Kajdas C 1999 Effect of thermal treatment and sliding on chemical bonding of PFPE lubricant films with DLC surfaces. *J. Info. Storage Proc. Syst.* **1**, 259–64

Zhao Z M, Bhushan B, Kajdas C 2000 Lubrication studies of head–disk interfaces in a controlled environment: Part II. Degradation mechanisms of PFPE lubricants. *Proc. Inst. Mech. Eng., Part J: J. Eng. Tribol.* in press

B. Bhushan
Ohio State University, Columbus, Ohio, USA

Magnetic Recording Devices: Inductive Heads, Properties

Modern magnetic recording heads are made using the techniques of integrated circuit fabrication technology: photolithographic pattern transfer, selective thin film deposition and selective thin film etching. The use of these methods has allowed dramatic miniaturization of components and increases in recording densities and operating frequencies. The first magnetic recording heads had magnetic cores machined from ferrite and did not use thin film technology. This approach was used in both magnetic tape and disk recording until the end of the 1970s, and was the focus of much invention and miniaturization in its own right.

Then, in 1970, researchers at IBM published a description of thin film processes that could be used to fabricate recording heads (Romankiw *et al.* 1970). Further refinements led to several patented designs by IBM (Church and Jones 1980, Jones 1980) and a transition to thin film technology for head fabrication in the disk industry, allowing greater degrees of manufacturing automation and integration. Tape recording heads followed suit approximately 10 years later. While begun over two decades ago, this trend toward greater degrees of integration continues today, as merged inductive and magnetoresistive (MR) heads are integrated with secondary mechanical actuators and trace suspension assemblies. These trends in head manufacturing are likely to continue for the foreseeable future, and will be detailed in the ensuing sections of this article.

The progress in shrinking magnetic recording heads through advances in fabrication technology can be seen in Fig. 1, which shows an outline, to scale, of the various disk head sliders over the last several decades. As can be seen the technology has been shrunk by a factor of three times (in each linear dimension) since the 1970s. The dimensions given are industry standards, and are available in Hoyt (1997; see also *Magnetic Recording Heads: Historical Perspective and Background*).

1. Pre-1990s Head Fabrication Technology

1.1 Ferrite Heads

Prior to the advent of thin film head technology, magnetic recording heads for rigid disk applications were fabricated using precision machining techniques from bulk materials, typically magnetic ferrites. Ferrites are insulators, and, therefore, can be operated at high frequencies without eddy current damping. Ferrite heads were the workhorse recording heads for many years in both tape and disk drives, serving both the magnetic writing function and the inductive readback function. MnZn–ferrite and NiZn–ferrite were the main materials used.

Slider bodies were made of a nonmagnetic ceramic body to provide mechanical durability. A variation on this was a 'monolithic' head design, introduced by IBM. This name signified that the entire slider was machined and assembled from ferrite, reducing the part count and the number of assembly steps in the head fabrication. This was made possible by advances in ferrite technology which permitted them to have
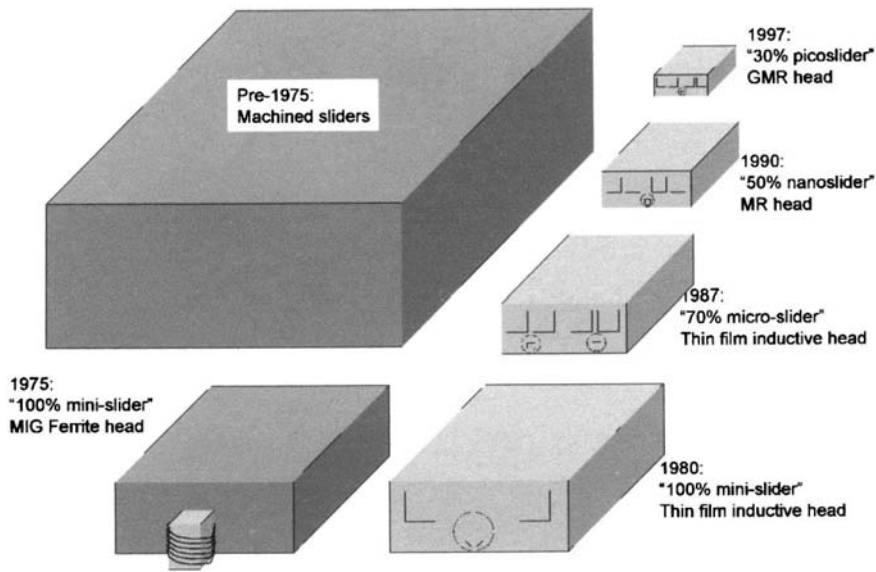
sufficient mechanical toughness to serve both a mechanical (the slider) and a magnetic function (the core). This summary is drawn from an excellent discussion of the ferrite head process in (Ashar 1997, Chap. 4).

As the demands on the recording heads became more stringent, it became difficult for ferrite to meet both the frequency requirements and the magnetic field levels required by the system. Ferrites, while conveniently insulating, have relatively low values of magnetization compared to most magnetic metals, and therefore cannot generate a very large write field. This situation gave rise to the metal-in-gap (MIG) head. The MIG design inserts a metal layer (typically sputter deposited) in the gap of the ferrite core. This allowed the use of higher induction metals, like NiFe or Sendust (FeSiAl) for generating higher writing fields, while continuing to suppress eddy currents in the large part of the magnetic yoke by continuing to make them out of ferrite.

The features of these major types of magnetic heads are illustrated in Fig. 2, which compares a composite-body head, a monolithic head, and a thin film head, which represents current (2001) technology (Ashar 1997). Also shown as an inset in Fig. 2 is a schematic cross-section of a gap of a MIG head, in which the additional metal layers are indicated. All three of these fabrication methods are compared in Table 1.

1.2 Thin Film Inductive Heads

While MIG heads offered ways to obtain both high frequency performance and reasonably high writing
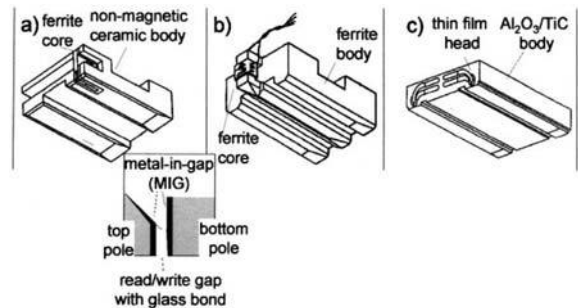
Figure 2
Types of recording head architectures: (a) monolithic, (b) composite, (c) thin film (adapted from Ashar 1997).

fields, they had some serious drawbacks. Chief among these was manufacturing costs. Most designs had some degree of hand assembly, which introduced expense and variability in device parameters. Additionally, shrinking sizes were harder to produce with traditional precision machining technology, and the allowed geometries and materials were limited. Thus, thin film technology became the preferred method of device fabrication after the first devices were introduced by IBM in 1970 (Romankiw 1970) and patented in 1978 (Church and Jones 1980, Jones 1980).

The original patented thin film head design from 1978 is shown in Fig. 3 (Church and Jones 1980). Like monolithic and composite heads, the first thin film heads were used both for writing and inductive

Table 1
Features of heads fabricated using the major fabrication techniques.

Feature	Composite	Monolithic	Thin film
Magnetic core	Machined ferrite (metal in gap)	Machined ferrite (metal in gap)	Electroplated or sputter deposited
Coil	Hand-wound or machine-wound	Hand-wound or machine-wound	Electroplated
Coil insulation	Coated wire	Coated wire	Photoresist or dielectric films
Slider body	Machined ceramic (nonmagnetic)	Machined ferrite	Alumina-TiC
Airbearing	Sawed slots	Sawed slots	Sawed slots or ion milled patterns
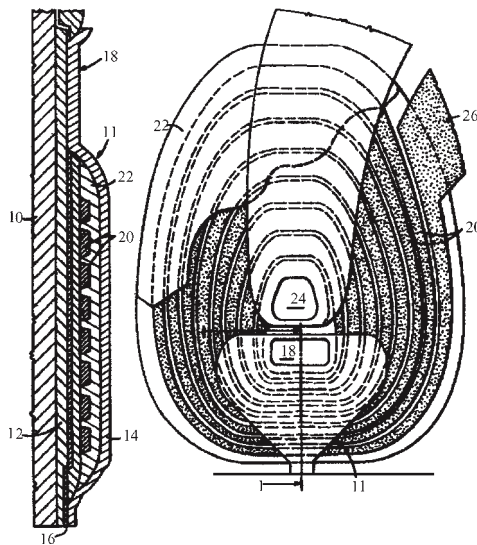
Figure 3
Original thin film inductive head from the IBM patent (Church and Jones 1980).

readback. This part of thin film write heads has not changed substantially since its inception, although dramatic shrinking has taken place. However, inductive writers have been combined with MR readback sensors in modern devices, as demonstrated first in Bajorek *et al.* (1974). These MR heads will be discussed in an ensuing section, with detail being given about the fabrication of both the read and write parts of the head. The basic structure of the thin film write head will be summarized here.

Scrutiny of Fig. 3 reveals that there are six essential layers in the fabrication of an inductive thin film head: Pole 1, Underpass, Insulator 1, Coil, Insulator 2, and Pole 2. These are labeled and shown more clearly in Fig. 4, which indicates how these layers are oriented relative to the substrate and the final device. In addition to the six layers that form the device,

there are a number of packaging and interconnect layers also indicated in Fig. 4. These include Cu studs, Al_2O_3 overcoat, and Au bond pads. All of these layers will be discussed further in the next section on merged inductive/MR heads.

While thin film inductive heads enjoyed a number of years of high volume production as the head of choice, they were eventually supplanted by heads in which MR elements were used for readback. There were a number of limitations to the inductive-only designs that eventually led to this transition.

The main driver for the obsolescence of inductive heads was the fact that one head had to serve both the write and read function. Inevitably this led to design compromises in which both read and write functions performed by the inductive core were suboptimal. For example, in deciding the number of turns within a thin film inductive design, writing speed considerations favored a small number of turns for low inductance. However, readback sensitivity favors a large number of turns for large inductance and larger readback voltage. Increasing the data rate makes this situation worse, and limits the sensitivity of an inductive readback head, such that the more sensitive MR heads eventually become necessary. A summary of the main design tradeoffs in optimizing an inductive head for both reading and writing are listed in Table 2.

The transition from inductive read/write heads to merged MR/inductive heads was delayed by a number of design and fabrication innovations with the inductive heads. These innovations mainly focused on increasing readback sensitivity, without increasing inductance. Typical of these innovations was the use of multilevel coils first reported in Tamura *et al.* (1990) and eventually extended up to a total of four levels (Daniel *et al.* 1999). This approach allowed more compact coil designs with a lower inductance and higher efficiency as compared to a design with the same number of turns, but in a single layer. New planar yoke designs have also been demonstrated, for example, the so-called *omega-head*, with as many as 120 turns (Tang *et al.* 1994).
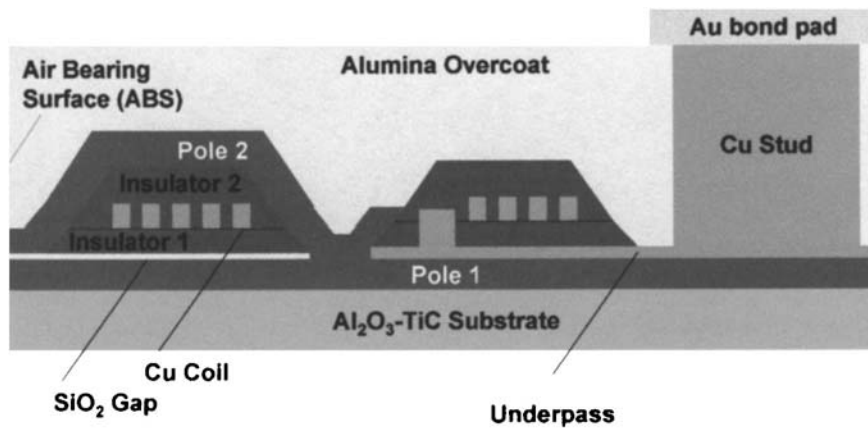
Figure 4
Basic structure of layers in early thin film inductive heads.

Table 2
Design tradeoffs in an inductive read/write head.

Wafer fabrication		Postwafer fabrication	
Major steps	Description	Major steps	Description
Bottom shield	Photolithographic patterning and electrodeposition	Rowbar slice	Precision sawing
Bottom read gap	Vapor deposition and patterning	Throat lap	Lapping with electrical feedback
MR sensor and MR thin leads	Sputter deposition and patterning with biasing elements	Airbearing pattern	Patterning and ion milling
Top MR shield/ Bottom write pole	Vapor deposition and patterning	Slider dice	Precision sawing
Thick MR leads	Vapor deposition and patterning	HGA assembly	Precision assembly and wire bonding
Write coil and insulation	Patterning and electrodeposition		
Top pole	Patterning and electrodeposition		
Leads and studs	Patterning and electrodeposition		
Alumina overcoat	Sputter deposition		
Planar lap	Lapping/polishing		
Bond pads	Patterning and electrodeposition		

To further increase efficiency, a recessed cavity design was developed. In this design, the bottom pole is deposited into a cavity, such that the same separation between the two poles can be achieved with less steep slopes in each layer (Zak *et al*. 1996). An even more novel design was proposed by Mallary and co-workers, the so-called *diamond head*, in which all the flux threads in each coil turn twice for greater output (Mallary *et al*. 1994, Mallary and Ramaswamy 1993).

2. 1990s Technology: Integrated MR Heads

2.1 Overview of the Head Fabrication Process

Since the late 1980s, the canonical recording head configuration has been an inductive writer coupled with a MR reader. As with the original thin film inductive heads, these heads are constructed using thin film fabrication techniques. MR heads are used because they give much better signal to noise performance than inductive readers, and the separation of

the two functions allows greater optimization of each one.

These types of heads are typically referred to as "*merged heads*" because the reader and writer actually share one magnetic element. This can be seen in Fig. 5, which shows a schematic of the active region a state-of-the-art magnetic head circa 2001. The magnetic film that forms both the bottom pole of the writer and the top shield of the reader is shown. The hierarchy of the steps in fabricating a merged MR head are shown in Fig. 6. Each of the following subprocesses will be discussed below: reader fabrication, writer fabrication, mechanical encapsulation, and postwafer fabrication. A tabulation of the major steps in a typical head process flow is given in Table 2.

While the merged back-of-slider architecture (e.g., Hannon 1994) represents the vast majority of commercial heads (c. 2001), a number of other inductive write/MR read head designs have been proposed and occasionally commercialized on a smaller scale. Preceding the merged head, a "piggy-back" design was commercialized in which the top MR shield
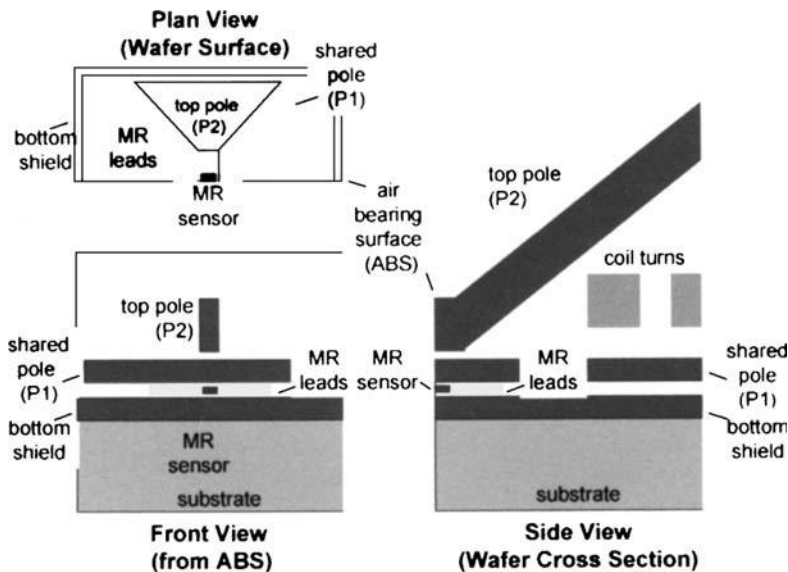
Figure 5
Structure of merged MR head (ca. 2001).
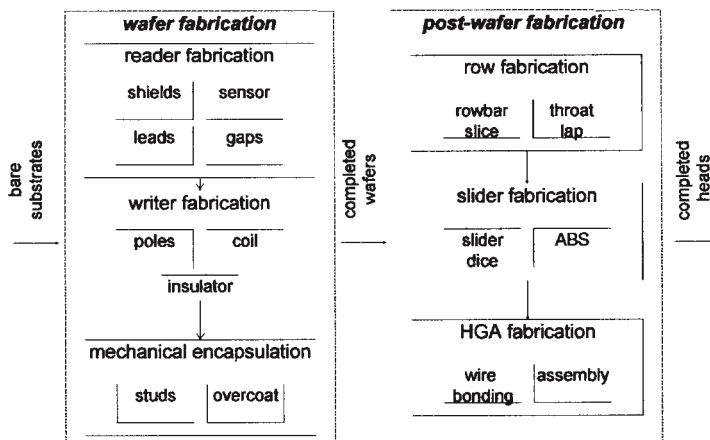
Figure 6
Hierarchy of fabrication steps in the construction of a merged MR thin film recording head.

and the bottom pole were separate layers (Bajorek *et al.* 1974, Tsang *et al.* 1990a, 1990b). Yoke heads, in which the MR head is separated from the medium surface by a flux conductor and forms part of a magnetic circuit have been commercialized. The most notable was that of the Digital Compact Cassette (DCC) tape recording system architected by Philips (Zieren 1993). Silmag, in France commercialized the planar head on a Si substrate (Lazzari 1974, 1996, 1997), and MR heads in which the current flows perpendicular to the MR sensor film plane have been proposed due to their higher giant MR (GMR) ratio in this geometry (Zhu and O'Connor 1995). All of these innovations in design required somewhat different fabrication sequences, but all were built out of the same basic set of thin film processes. The details of each of these heads will not be discussed here; rather a detailed discussion of the fabrication steps of a merged MR head will be given as representative of head fabrication in general.

An important concept in the discussion of thin film device fabrication is that of the critical dimension. This is the smallest feature that can be reliably fabricated on the wafer using a particular process. Recording heads, like semiconductor devices, have several critical dimension per device, with typically 10000 devices per wafer. Si device wafers can have billions of critical dimensions per wafer. This will have important consequences for the feasibility of certain types of high-resolution fabrication techniques that have a serial nature to them, like electron beam lithography or focused ion beam etching. These processes have some application in head fabrication, while they are expensive to implement in the semiconductor industry.

There are at least seven critical physical dimensions in a merged MR recording head. Control of these dimensions is required to get reliable performance from the fabricated device. This is accomplished though careful process design. The seven critical dimensions are as listed here, and the fabrication processes used to control them are discussed below. The read trackwidth and the write trackwidth are the only two critical dimensions controlled exclusively by lithography. The MR sensor stripe height, the write head throat height, and the head medium separation are controlled by a combination of lithography and precision mechanical machining. Finally the MR sensor thickness, MR gap thickness, write gap thickness, and the pole thicknesses are controlled by film deposition, and are not influenced by lithography.

In addition to critical dimensions in head manufacturing, there are also critical alignments. These include the read to write track alignment and the alignment of the magnetic to the electrical trackwidths of the MR sensor. Some important processing advances have been made in addressing the need to control these alignments.

Finally, in addition to mechanical dimensions and positions, the material properties of the thin films from which the heads have been fabricated must be carefully controlled. These include the sensitivity, bias point and the stability of the reader, and the permeability and switching speed of the writer core. The materials used in these devices are listed in Table 4.

2.2 MR Read Sensors

(a) Sensor materials
MR heads utilize materials whose resistance changes with applied field. These may be anisotropic magnetoresistive (AMR) materials in which the resistance versus field is given by:

$$R(\theta_{AMR}) = R_{\perp,AMR} + \Delta R_{AMR} \cos^2\theta_{AMR} \qquad (1)$$

Table 3
Major steps in the fabrication of modern magnetic recording heads.

Design feature	Desirable properties for …		Comment
	Inductive writing	Inductive reading	
Pole materials	High magnetization for high field	High permeability for sensitivity	Features are not mutually exclusive but dual optimization is restrictive
Pole thickness	Small for speed large for efficiency	Large for sensitivity	Fundamental write speed vs. read sensitivity trade-off
Number of turns	Small for speed large for high field	Small for resonance large for sensitivity	Fundamental write speed versus read sensitivity trade-off
Fly height	Small for resolution	Small for resolution	Smaller fly height is always better
Write gap	Large for overwrite small for sidewriting	Small for resolution	Fundamental overwrite versus resolution trade-off

Table 4

Thin film materials used in the fabrication of magnetic recording heads.

Component	Materials
Substrate	Al_2O_3/TiC
Poles and shields	$Ni_{80}Fe_{20}$ (permalloy) $Ni_{45}Fe_{55}$ FeXN (X = Al, Ta, Zr) (iron nitride) FeCoN (iron cobalt nitride)
Read and write gaps	SiO_2 (silicon dioxide) SiN (silicon nitride) Al_2O_3 (aluminum oxide or 'alumina') AlN (aluminum nitride)
MR sensors	$Ni_{80}Fe_{20}$ (permalloy) Spin valve stacks (e.g., NiFe/Cu/NiFe; CoFe/Cu/CoFe) Antiferromagnets (e.g., FeMn, NiMn, IrMn, PtMn, NiO, CoO)
Coil insulators	Photoresist (hardbaked) SiO_2
Leads	AlCu Cu
Studs	Cu
Bondpads	Au

Figure 7
Comparison of different MR sensor responses on the same scale (from Brug *et al*. 1996).

where $R(\theta_{AMR})$ is the resistance of the device as a function of θ_{AMR}, the angle between the current in the device and the magnetization. $R_{\perp,AMR}$ is the resistance of the device when the current and field are perpendicular to one another and ΔR_{AMR} is the amount of change in the resistance in going from a parallel configuration of magnetization to a perpendicular one. Thin films of NiFe show this effect ($\Delta R_{AMR} \sim 2\%$) and have been widely used as sensors.

The sensor materials may also be GMR materials, in which the resistance of the sensor is given by:

$$R(\theta_{GMR}) = R_{\parallel,GMR} + \Delta R_{GMR} \sin\theta_{GMR} \qquad (2)$$

where $R(\theta_{GMR})$ is the resistance of the device as a function of θ_{GMR}, the angle between the magnetization in one ferromagnetic layer and the magnetization in the other. $R_{\parallel,GMR}$ is the resistance of the device when the two magnetizations are parallel and ΔR_{GMR} is the change in resistance of the device when the two layers change from being parallel to antiparallel.

Examples of typical transfer functions for these devices are shown in Fig. 7 (Brug *et al*. 1996). It can be seen that the amplitude of the GMR effect is typically much larger than the AMR effect (hence the term 'giant'), which is the reason for the appeal of these materials. It can also be seen from this figure and from the functional forms of Eqns. (1) and (2), that the transfer functions have very different shapes, and therefore require different biasing schemes to achieve linear operation.

This biasing process is typically accomplished using soft adjacent layers (SALs) or exchange pinning with antiferromagnets. These layers are typically incorporated within the so-called *MR stack*, such that the construction of the sensor and the biasing scheme can be thought of as a single manufacturing step. This article will not dissect the stack structure and function in detail as several excellent references exist on the AMR effect (McGuire and Potter 1975), the GMR effect (White 1992), and MR head materials and technologies (Mallinson 1996, Jones *et al*. 1995). An excellent review of antiferromagnetic metallic exchange materials is also available (Lederman 1999), and developments in synthetic antiferromagnets (trilayers of Co/Ru/Co patented by IBM, Coffey *et al*. 1994) have added enormous flexibility to the MR fabrication process by eliminating most of the demagnetizing fields from the biasing layer.

While the deposition of the MR sensor layer (sensing layer plus biasing layers) can be treated like a single manufacturing step, consisting of the deposition and patterning of a composite structure, the complexity of this step and the associated tooling should not be underestimated. A typical stack of modest complexity is shown in Fig. 8. Note that this structure consists of nine layers and six different materials, and the complexity can grow to twice this for dual spin valves. Deposition tools with 1.5 m diameter chambers containing six or more 30 cm diameter targets and costing several million US dollars are needed for this process.

(b) Shields and gaps

When an acceptable sensor material candidate is identified, it must be patterned into a sensor and placed between two insulating shields, to provide resolution during the readback process. Without shields, the sensor will pick up magnetic flux from many bits and not be able to resolve single bits easily.
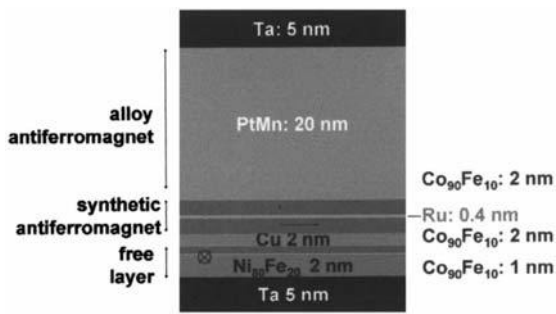
Figure 8
A typical MR stack consisting of a spin valve of modest complexity. All nine of these layers, consisting of six different materials, must be deposited in a single pumpdown.

Shields are constructed of electroplated or sputter deposited thin films, typically 1–2 μm thick, consisting of materials similar to pole materials. High permeability and magnetic stability is a higher priority in these materials than is high saturation magnetization, as the shields conduct signal flux during readback. Ductility of the shields is undesirable to prevent smearing of these layers during the mechanical lapping process (see discussion below under stripe height definition). This can cause shorting of the shields to the sensor, rendering it nonfunctional.

A functional sensor is electrically isolated from the magnetic shields (which are usually electrically conductive) by a thin insulating gap. Controling the dimension of this gap, of the order of 100 nm in thickness, is relatively straightforward, since it is set by a film thickness. This dimension determines, to a large degree, the resolution of the head. However, ensuring that no electrical shorting takes place across this gap is more challenging. While chemical vapor deposition of these layers would produce denser films with better insulation properties, these films are typically sputtered because this approach can be done at a lower substrate temperature. GMR films are particularly temperature sensitive and cannot typically survive above 250 °C.

(c) Stripe height definition
The definition of the stripe height in an MR head is accomplished not through optical lithography, but through a mechanical lapping or polishing process. Optically defined structures (lapping guides) are used, indirectly, to control this process, but the physically polished interface determines the final stripe height. This process is discussed below in the context of postwafer fabrication.

(d) Trackwidth definition
The definition of the reader trackwidth involves two critical dimensions and a critical alignment. Since the
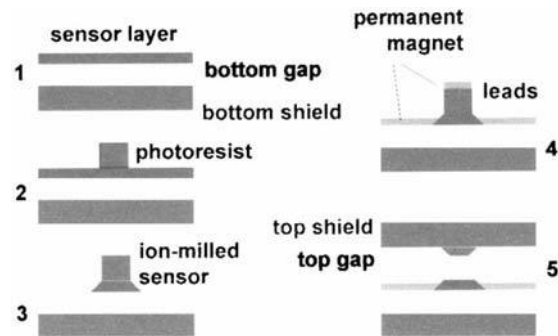
Figure 9
The self-aligned lift-off process typically used for the definition of read sensor magnetic width, electrical width, and for accomplishing the alignment of these two features.

head conducts electrical current and magnetic flux, it actually has two widths: a magnetic width and an electrical width. These are the two critical dimensions. Additionally, these two segments need to be aligned, which constitutes the critical alignment. The standard way of accomplishing this task that has emerged is the self-aligned lift-off process. This method allows two layers to be patterned with the same photoresist, making the process "self-aligning." The two layers are the sensor stripe and the electrical leads. An example of how this is accomplished is shown in Fig. 9. The permanent magnets used for longitudinal stabilization are also shown.

(e) Longitudinal stabilization
Longitudinal stabilization of MR sensors is done to prevent random, nonrepeatable domain activity in the sensor, which introduces noise into the readback channel. In today's devices it is accomplished with permanent magnet abutted junctions. These permanent magnets are typically incorporated into the self-aligned lift-off as noted in Fig. 9. This procedure was patented by IBM in 1991 (Krounbi *et al.* 1991). These magnets provide a longitudinal field that helps to keep the device in a single domain, and prevent domain wall jumps. The abutted junction is usually not ideal, and is frequently represented as trapezoidal, (as shown in Fig. 9) due to the etching profile of the sensor stripe before the permanent magnet and lead deposition step.

While a close placement of the magnetic material is good for achieving large fields, it is important to decouple (in terms of magnetic exchange) the permanent magnetic from the sensor. If they are strongly coupled, this introduces noise in the sensor, due to the nucleation of domain walls by the permanent magnet grains (Zhu and O'Connor 1996). Permanent magnet stabilization has also been implemented using

567

overlay techniques, in which an abutted junction is not formed. Both designs have been analyzed for performance (Shen *et al.* 1996) and produced commercially.

One other widely used longitudinal biasing scheme was the exchange tab. In this design, material in the wings of the sensor (outside the trackwidth) was tightly coupled to an antiferromagnetic layer in this region (Tsang and Fontana 1982). This rendered this region like a permanent magnet with the same magnetization as the active region of the sensor. This approach has at least two drawbacks. First, the wing region is not pinned rigidly, so some side reading occurred due to flux sensing in the tab region. Second, an exactly matched permanent magnet was not optimal. In fact typically, permanent magnets used for longitudinal stabilization have a greater thickness-magnetization product than the sensor they stabilize.

2.3 Inductive Write Transducer

(a) Pole materials

The thin film materials used for write head poles need to satisfy several criteria. First, they need to have sufficient saturation magnetization, as this sets the ultimate field they can generate. Second, they need to be magnetically soft, such that they produce a linear field response with current, and maintain this permeability up to high frequencies of operation. Current systems operate in the hundreds of MHz range with GHz operation frequencies on the horizon. Third, they need to be compatible with head fabrication techniques. For example, they cannot require processing temperatures above $250\,°C$. Finally, they need to be magnetically and chemically stable for a long period of reliable operation.

A list of the main candidates for thin film pole materials is given in Table 5. These materials are sorted in order of saturation magnetization, M_s, ranging from $800\,kAm^{-1}$ in permalloy to $1900\,kAm^{-1}$ in FeCoN. Steady increases in pole magnetization have made writing on higher coercivity media possible. In the right most column of Table 5 is listed the maximum coercivity of the media that a head with the given pole composition could write on. This ratio between the magnetization and the maximum longitudinal media coercivity (measured at room temperature and at long time scales) is about 4:1.

All of the materials in this list have been made in highly permeable forms. Maintaining high magnetic permeability at high frequency requires two things. First, eddy currents must be suppressed. Eddy currents occur when the skin depth of the material, δ becomes less than half the film thickness. At this point, the center of the film (most distant from the surface) is shielded from the applied current and ceases to switch. Pole permeability consequently falls off. The skin depth, δ is given by:

$$\delta = \sqrt{\frac{\rho}{2\pi f \mu_r \mu_0}} \qquad (3)$$

where ρ is the material electrical resistivity, f is the operation frequency, μ_r is the relative permeability of the material (unitless) and μ_0 is the permeability of free space (H/m). The above equation suggests that high resistivity materials are the only practical solution, as frequency is a given and a reduction of permeability is generally undesirable for magnetic functionality.

Increasing film resistivity is accomplished in one of two ways: adding elemental constituents or laminating. In either case, a reduction of the saturation magnetization, M_s, generally occurs because of the introduction of nonmagnetic material. Lamination with insulating layers (by analogy to power transformers and other $60\,Hz$ devices) is more predicable in its effects on high frequency permeability than alloying, and generally improves the magnetic domain configuration of the layers. However, it is much less compatible with electrodeposition (the preferred method of pole fabrication from a cost perspective) than alloying.

A second requirement at high frequencies is the rapid damping of magnetic precession. This ensures

Table 5
Pole materials.

Material			Media	
Composition	Name	Deposition method	Ms (kAm^{-1})	Hc Max (kAm^{-1})
Ni$_{80}$Fe$_{20}$	Permalloy	Plating, sputtering	796	199
FeAlSi	Sendust	Sputtering	955	239
Ni$_{45}$Fe$_{55}$		Plating, sputtering	1114	279
CoZrX		Sputtering	1194	298
FeXN	Fe-Nitride	Reactive sputtering	1592	398
FeCo		Plating, sputtering	1910	477

that the magnetization actually switches, rather than simply precessing at the frequency of interest. While the actual ferromagnetic resonance frequency, ϖ_{FMR}, can be pushed to higher values by proper design, increasing the damping is presently not a well-understood process. The FMR resonance frequency, ϖ_{FMR}, is given approximately by:

$$\varpi_{FMR} \approx \gamma \sqrt{\frac{M_s^2}{\mu_r}} \qquad (4)$$

where γ is the gyromagnetic constant ($HzmA^{-1}$), M_s is the saturation magnetization of the film, and μ_r is the relative permeability of the film (unitless). From this relationship, it can be seen that resonant frequency can be increased by raising M_s (desirable) or decreasing μ_r, (undesirable).

The above considerations are relevant to choices made in the head fabrication process. As seen in Table 5, the two main options for pole deposition are electroplating and sputter deposition. Plating has the advantages that it tends to have higher throughput, require lower cost tools, produce films with lower stresses, and facilitates finer line patterns, since it is an additive rather than a subtractive process. Sputtered materials have the big advantage that laminating with insulators is simple within a sputter deposition system. Until now, there has been very little commercialization of sputtered materials in disk heads. (Tape heads use them regularly for their superior wear resistance.) This is because the cost of processing and the ability to cheaply fabricate narrow tracks have dominated the tooling decisions.

(b) Trackwidth definition
Definition of the write trackwidth is perhaps the single greatest challenge of the modern writer process. This is because of the large aspect ratios of these devices. In some cases a submicron lateral dimension is needed on a 2–3 μm thick feature. As a general rule, aspect ratios of this type are difficult in planar lithographic processes. Typically, the top pole is electroplated into a photoresist mask to give a high aspect ratio, then "trimmed" after photoresist removal, to give a top and bottom pole that are close to the same width, and well-aligned. This is another self-aligning process, and is shown schematically in Fig. 10.

(c) Coil formation
The fabrication of coils in heads is typically through electrodeposition (or "plating") of Cu into photoresist dams. An electrically conductive seedlayer (50–100 nm thick) is needed, as in the electrodeposition of poles, in order to preferentially plate where the coil needs to be formed. After plating 1–2 μm of Cu into the photoresist dams, all of the turns of the
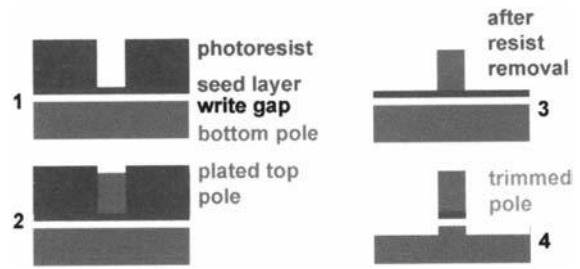
Figure 10
Electrodeposition of the top pole followed by pole trimming at the wafer level.

coil are shorted together by the seedlayer. Thus it is removed by ion milling. An insignificant amount of the coil themselves is removed in this process as well. In high performance inductive writers, there is a push toward fewer turns, short yokes, and coils that are less complicated than those used in inductive read heads. This trend allows a very low inductance head to be constructed, which has good high-speed performance.

2.4 Electrical Connection and Mechanical Encapsulation

After a head is electrically complete, it must be mechanically processed to expose the sensor at the edge of the slider. This requires that the head be encapsulated in a thick layer of electrically insulating, mechanically robust material. Typically, sputtered alumina is used, because it can be made thick with low stress and, therefore, low propensity for delamination. It is, however, a somewhat time consuming process, taking typically several hours to deposit the required 20 μm thick films.

Electrical connection through the encapsulation is necessary to contact the devices, and this is typically done with a composite stud-bond pad structure. The studs are 20 μm thick posts of Cu that are electroplated before the deposition of the alumina. A mechanical planarization process, like lapping or chemical-mechanical polishing (CMP) is used to expose the Cu after the alumina deposition. Finally, the exposed Cu contact regions are covered with Au bond pads to facilitate the connection of the head leads and to prevent Cu corrosion.

2.5 HGA Construction: Postwafer Fabrication

After the wafer is complete, it is diced into rows, and these are lapped to create the correct stripe height in the MR head and the correct throat height in the inductive writer. Since this is a single operation that sets two critical dimensions, the alignment of the zero

stripe height point of the reader to the zero throat height point of the writer is extremely critical, as only one of the layers can be used as the reference layer for lapping.

Control of the lapping process is done with some lithographically defined feature that changes in a systematic way with lap depth. In early generations of thin film head technology, optical lapping guides (OLGs) were used. These were patterned structures thick enough to be seen in cross-section from the airbearing surface during lapping. They were typically triangular in shape such that their visible width changed in a systematic way with lapping depth. Lapping was stopped when a particular dimension was reached in the visible structure.

Since this process did not lend itself easily to automation, electronic lapping guides (ELGs) became the standard. These structures were made from the same layer as the MR stripe, and were similar in shape. Their resistance increased as their stripe height was reduced in a predictable fashion and could be used as an endpoint detection for lapping. Once this process was automated, it was possible to sense variations across the row by monitoring a number of lapping sensors and to actually flex the row slightly, increasing the pressure in slow lapping points to obtain maximum uniformity during the lapping process. Absolute resistance is typically not used as a stopping criterion, as it is too susceptible to process variation. Typically a differential or ratio technique is used to make the sensors as insensitive as possible to process variations in film thickness, stripe height, etc.

Once the rows have lapped to stripe height, an airbearing contour is formed on the airbearing surface of each slider in the row. Older-style air bearings were simply machined rails, which allowed the head to be near the disk while allowing a lot of air to rush through a channel between the head and medium. Air bearings have become patterns that cannot be formed with rectilinear batch machining, and are formed through one or more steps of ion milling. This requires photolithography on the air-bearing surface, allowing air bearings of arbitrary shape. Some of these are quite complicated with negative and positive pressure regions, fly heights that are insensitive to speed, and excellent stability. State-of-the-art commercial air bearings (ca. 2001) allow head to medium spacings of $<25\,nm$, with further reductions of at least a factor of three under development. A good review of ABS technology is given in Hoyt (1997).

Once the air bearings are complete, the rows are diced or parted into sliders, again with precision sawing. Individual sliders are then mounted on stainless steel suspensions, using adhesive between the gimbal mounting point and the slider. In some advanced designs, these suspensions are active devices, incorporating secondary fine actuators that use piezoelectric, electrostatic (Kim *et al.* 1999), or electromagnetic (Lin and Ong 1999) forces to provide fine tracking. It is widely assumed that secondary actuation is required for very high track densities (Fan *et al.* 1995).

3. The Future of Recording Head Fabrication

The future of magnetic recording likely holds at least four major paradigm shifts in the coming years. Some of these will have a profound impact on head fabrication. Not all of these will become a reality, but it is almost certain that at least one that will have major effect on head architecture and fabrication will reach commercialization. These four trends are (in order of increasingly radical departure from today's head manufacturing paradigm);

- patterned media
- perpendicular or vertical recording
- thermally assisted (or hybrid) recording
- micro-array based storage

Patterned media do not in themselves require any changes in the head, although it will certainly change the system architecture, especially the channel (Nair and New 1998, Hughes 1999). It may change the head, if the required field magnitudes or rise times become radically different than they are today. If (and/or when) patterned media do become commercialized, the head changes to support it will be mainly evolutionary.

Perpendicular recording will almost certainly change the write head design, although similar steps will be used in fabrication. It is possible to record on and read from perpendicular media with a standard head for longitudinal recording, but more optimum designs are possible (Khizroev *et al.* 1997). Some kind of probe head with a relatively large gap is likely for writing. Soft underlayers in the media will be used to increase the head field. Long magnetic circuits with distant return paths must be avoided to avoid stray field sensitivity (Cain *et al.* 1996). Reading will be magnetoresistive, but whether the sensor will be at the airbearing or recessed, and the exact type of sensor, is still to be determined.

Thermally assisted recording will precipitate a radical change in the head geometry. Some source of heat, most likely light will need to be conducted to the medium by the head. At the densities where this will become necessary due to thermal stability considerations (Ruigrok *et al.* 2000), near-field optics will be necessary. This will require optical coupling and focusing elements on the head, and many new fabrication techniques.

Several research groups are currently working on microarray-based storage, including IBM and Hewlett Packard (described in Toigo and Hayashi 2000), Kionix and Carnegie Mellon (Carley *et al.* 2000). If these devices become widely commercialized, they will represent radical departures in head

fabrication technology. Heads will be tightly integrated with Si electronics, on Si substrates. They will be massively parallel, and they may employ any number of physical mechanisms to read and write including magnetic. Whether such radical architectural changes will completely replace standard disk drives is an open question. It almost certain, though, that they will at least find some niche market, and introduce some radically different designs to the data storage head.

See also: Magnetic Recording Technologies: Overview; Magnetic Recording Devices: Future Technologies; Magnetoresistive Heads: Physical Phenomena; Magnetic Recording Devices: Head/Medium Interface

Bibliography

Ashar K G 1997 *Magnetic Disk Drive Technology: Heads, Media, Channel, Interfaces and Integration*. IEEE Press, New York

Bajorek C, Krongelb S, Romankiw L T, Thompson D 1974 An integrated magnetoresistive read, inductive write high density magnetic recording head. In: *Proc. Magnetism and Magnetic Materials Conf.*

Brug J A, Anthony T C, Nickel J H 1996 Magnetic recording head materials. *MRS Bull.* **21**, 23–6

Cain W C, Payne A P, Baldwinson M, Hempstead R 1996 Challenges in the practical implementation of perpendicular magnetic recording. *IEEE Trans.* **32**, 97–102

Carley L R, Bain J A, Fedder G K, Greve D W, Guillou D F, Lu M S C, Mukherjee T, Santhanam S, Abelmann L, Min S 2000 Single chip computers with MEMS-based magnetic memory. *J. Appl. Phys.* **87**, 6680–5

Church M A, Jones R E Jr 1980 Thin film magnetic head assembly. *US Patent* 4 219 854

Coffey K R, Gurney B A, Heim B E, Lefakis H, Mauri D, Speriosu V S, Wilhoit D R 1994 Spin valve magnetoresistive sensor with self-pinned laminated layer and magnetic recording system using the sensor. *US Patent*

Daniel E D, Mee C D, Clark M H 1999 *Magnetic Recording: The First 100 Years*. IEEE Press, New York

Fan L-S, Ottesen H H, Reiley T C, Wood R W 1995 Magnetic recording-head positioning at very high track densities using a microactuator-based, two-stage servo system. *IEEE Trans. Indust. Electron.* **42**, 222–33

Guo W, Wang Z, Yao X, Huang T, Bi C 1998 A high bandwidth piezoelectric suspension for high track density magnetic data storage devices. *IEEE Trans.* **34**, 1907–9

Hannon D, Krounbi M T, Christner J 1994 Allicat magnetoresistive head design and performance. *IEEE Trans.* **30**, 298–302

Hoyt R F 1997 Head-disk interface. In: Ashar K G (ed.) *Magnetic Disk Drive Technology: Heads, Media, Channel, Interfaces and Integration*. IEEE Press, New York, Chap. 10, pp. 268–305

Hughes G F 1999 Read channels for patterned media. *IEEE Trans.* **35**, 2310–2

Jones R E Jr 1980 Thin film magnetic head. *US Patent* 4 219 855

Jones R E Jr, Mee C D, Tsang C 1995 Recording heads. In: Mee C D, Daniel E D (eds.) *Magnetic Recording Technology*. (2nd edn). McGraw-Hill, New York, Chap. 6, pp. 1–91

Khizroev S K, Bain J A, Kryder M H 1997 Considerations in the design of probe heads for 100 Gbit/in^2 recording density. *IEEE Trans.* **33**, 2893–5

Kim B-H, Park S, Kim H-C, Chun K, Cho D-I D, Lee J-W, Lee H-J, Kim S-H, Seong W-K, An Y-J 1999 MEMS fabrication of high aspect ratio track-following microactuator for hard disk drive using silicon on insulator. In: *Proc. 12th IEEE Int. Conf. on Micro Electro Mechanical Systems*. Orlando, FL, USA

Krounbi M T, Voegeli O, Wang P-K 1991 Magnetoresistive read transducer having hard magnetic bias. *US Patent* 5 018 037

Lazzari J P 1974 Integrated magnetic recording heads. Review and outlook. *Proc. AIP.* **18**, 990–1004

Lazzari J P 1996 Planar silicon head: the modern solution for the disk drive industry. *Proc. Electrochem. Soc.* **95**, 30–2

Lazzari J P 1997 Planar silicon heads for disk drive industry. In: *Transducers 97, Int. Conf. Solid-state Sens. Actuators* **2**, pp. 1077–80

Lederman M 1999 Performance of metallic antiferromagnets for use in spin-valve read sensors. *IEEE Trans.* **35**, 794–9

Lin H, Ong E H 1999 Design and optimization of a dual-stage high bandwidth piggy-back electromagnetic milli-actuator. *IEEE Trans.* **35**, 3673–5

Mallary M L, Dipalma L, Gyasi K, Sidman A L, Wu A 1994 Advanced multi-via heads. *IEEE Trans.* **30**, 287–90

Mallary M L, Ramaswamy S 1993 A new thin film head which doubles the flux through the coil. *IEEE Trans.* **29**, 3832–6

Mallinson J C 1996 *Magneto-resistive Heads: Fundamentals and Applications*. Academic Press, San Diego, CA

McGuire T R, Potter R I 1975 AMR effect review. *IEEE Trans.* **11**, 1018–38

Nair S K, New R M H 1998 Patterned media recording: noise and channel equalization. *IEEE Trans.* **34**, 1916–8

Romankiw L T, Croll I M, Hatzakis M 1970 Batch-fabricated thin-film magnetic recording heads. *IEEE Trans.* **6**, 597–601

Ruigrok J J M, Coehoorn, Cumpson S R, Kesteren H W 2000 Disk recording beyond 100 Gb/in^2: Hybrid recording? *J. Appl. Phys.* **87**, 5398–403

Shen Y, Chen W, Jensen W, Ravipati D, Retort V, Rottmayer R, Rudy S, Tan S, Yuan S 1996 Comparative study of MR head designs with abutted vs overlaid permanent magnet bias. *IEEE Trans.* **32**, 19–24

Tamura K, Nagao E, Ohdoi Y 1990 Development of a 48-turn thin-film head. *J. Appl. Phys.* **67**, 4857–9

Tang D D, Lee R E, Su J L, Chu F, Lo J, Santini H A A, Lane L, Robertson N, Ponce M, Cisneroz P, Guthmiller G 1994 Omega head—an experimental 120-turn inductive head. *J. Appl. Phys.* **75**, 6397–9

Toigo J W, Hayashi A M 2000 Avoiding a data crunch. *Sci. Am.* 58–71

Tsang C, Chen M-M, Yogi T, Ju K 1990a Performance study and analysis of dual element head on thin-film disk for gigabit-density recording. *IEEE Trans.* **26**, 2949–53

Tsang C, Chen M -M, Yogi T, Ju K 1990b Gigabit density recording using dual element MR/inductive heads on thin-film disks. *IEEE Trans.* **26**, 1689–93

Tsang C, Fontana R E Jr 1982 Fabrication and wafer testing of barber-pole and exchange-biased narrow-track MR sensors. *IEEE Trans.* **18**, 1149–51

White R L 1992 Giant magnetoresistance: a primer. *IEEE Trans.* **28**, 2482–7

Zak B, Curland N, Giusti J H, Ash K P, Cameron G P 1996 Design and performance of a recessed thin film inductive transducer. *IEEE Trans.* **32**, 74–9

Zhu J-G, O'Connor D J 1995 A new design for an ultra-high density magnetic recording head using a GMR sensor in the CPP mode. *IEEE Trans.* **31**, 2597–9

Zhu J-G, O'Connor D J 1996 Impact of microstructure on stability of permanent magnet biased magnetoresistive heads. *IEEE Trans.* **32**, 54–60

Zieren V, Somers G, Ruigrok J J M, de Jongh M, van Straalen E, Folkerts W, Draaisma E, Pronk F 1993 Design and fabrication of thin film heads for the digital compact cassette audio system. *IEEE Trans.* **29**, 3064–8

J. A. Bain
*Carnegie Mellon University, Pittsburgh
Pennsylvania, USA*

Magnetic Recording Heads: Historical Perspective and Background

Magnetic recording heads are a key enabling technology for the recording of information on magnetic media since they both write and read the magnetic transitions. The first recording heads were inductive, composed of a bulk ferromagnetic material such as iron and a coil to both magnetize the iron and to provide a means to detect the magnetic flux from a magnetic transition.

The inductive head served to both read and write in the same structure. Figure 1 shows a simplified diagram of an inductive recording head. As current flows through the coil a magnetic field flows in a circular path through the core and gap of the device. Some of the flux in the gap fringes outside of the core. It is this flux that writes the transition on the media. By a principle known as reciprocity the flux from a transition beneath the head will be picked up by the coil and sensed as voltage proportional to the change in flux under the gap; i.e., the signal is proportional to the product of the velocity of the head over the media and strength of the flux emanating from the transition.
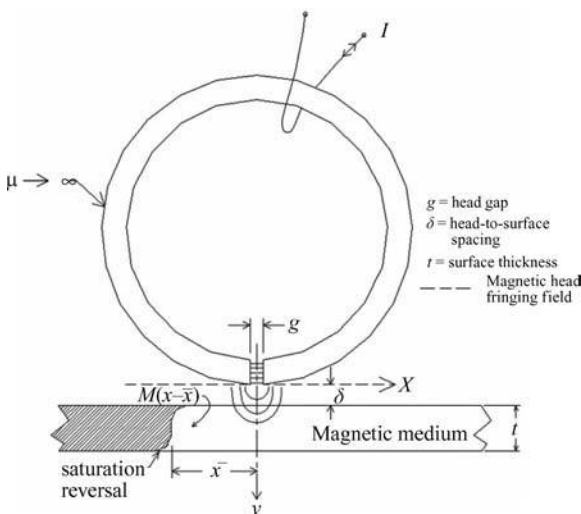
Oberlin Smith, an American, suggested the first magnetic recording head in 1888. It featured a wire recording medium with an electromagnet consisting of a coil wound around a rod of iron as shown in Fig. 2. Valdemar Poulsen of Denmark built the first functioning recorder using this head in 1898.

The wire was replaced by a steel tape in the 1930s. In Germany, the Stabltone-Bandmachine was first offered for sale in 1935. In England, the Blattnerphone was first offered for lease in 1931 and in 1933 the rights to the Blattnerphone were sold to Marconi's Wireless Telegraph Company, Ltd.

Marconi, in cooperation with Stille, one of the developers of Stabltone-Bandmachine, developed a second-generation machine. The head on this machine consisted of a dual pole head, one on each side of the tape. The flux was concentrated by tapering the tips of each pole. In 1935, Marconi modified the head design to single-pole design. It is interesting to note the pole head is favored for perpendicular recording, which has attracted a lot of attention lately in the push to higher areal densities.

In 1933, Eduard Schuller of AEG in Germany took out a patent on the ring head. At AEG, tape recorders were built using ring heads for recording, playback, and erasure. They are still used today for virtually all writing on magnetic recording media.

For five decades ring heads were used for reading and writing in most recording applications. The basic

Figure 1
Inductive ring head.
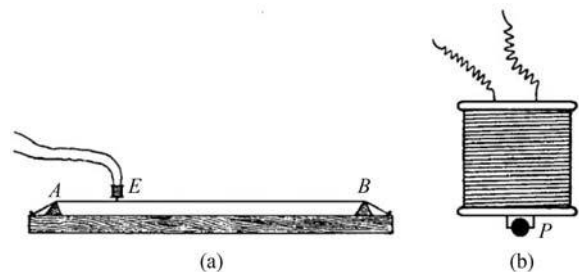
Figure 2
(a) The apparatus used by Poulsen for his first experiments. A steel wire is stretched between A and B. The electromagnet E was moved along the wire by hand to record or replay sound. In (b), the wire is shown partially surrounded by the pole piece of the electromagnet.

design remained the same but improvements in materials and the manufacture of smaller heads with tighter tolerances extended them to more advanced application. The original steel heads were replaced by mu metal and laminated mu metal. This was followed by NiZn and then MnZn ferrite. Manufacturing technology improved to allow for batch fabrication of many cores together which were then sliced up like loaves of bread to yield individual cores.

Core winding moved overseas. Epoxy and then glass was used to bond together the cores and to bond the cores into the sliders. The last evolution in this batch-fabricated technology was the MIG (metal in gap) head, which featured a ferrite core with high-moment material such as Sendust deposited in the gap.

The first commercial thin-film single-turn heads were made by Burroughs in 1975 on the B9470 head/track disk file. In 1979, IBM introduced thin film heads. These heads were made by a semiconductor-type process with hundreds and then thousands of heads fabricated on a single wafer. The wafers were then sliced up, made into sliders, and mounted on head gimbal assemblies (HGA) as shown in Fig. 3. This batch process eventually reduced the cost and

improved the performance of the magnetic recording heads until MIG ferrite heads were driven from the market place for disk drives around 1995. Ferrite heads continue to find application in floppy disks, video, and other tape recorders.

As the areal density increased in the 1980s the smaller tracks required more and more turns be put on the heads to make up for the signal lost as the track width was decreased. This was not entirely without cost since the inductance increased with the square of the number of turns and the increasing turns reduced the frequency response of the heads by increasing the resonant frequency of the coil. The thin-film heads had an advantage in this respect over the ferrite heads since their smaller size resulted in lower inductance than the larger ferrite heads.

The first IBM thin-film heads had a single-layer eight-turn coil. Two-layer coils followed these. In the early 1990s, three-layer and four-layer coils were developed. Inductive thin-film heads reached their limit with heads manufactured by Dastek Corporation consisting of four layers and 54 coil turns. The last read/write inductive head drive was shipped by Western Digital Corporation in 1995.
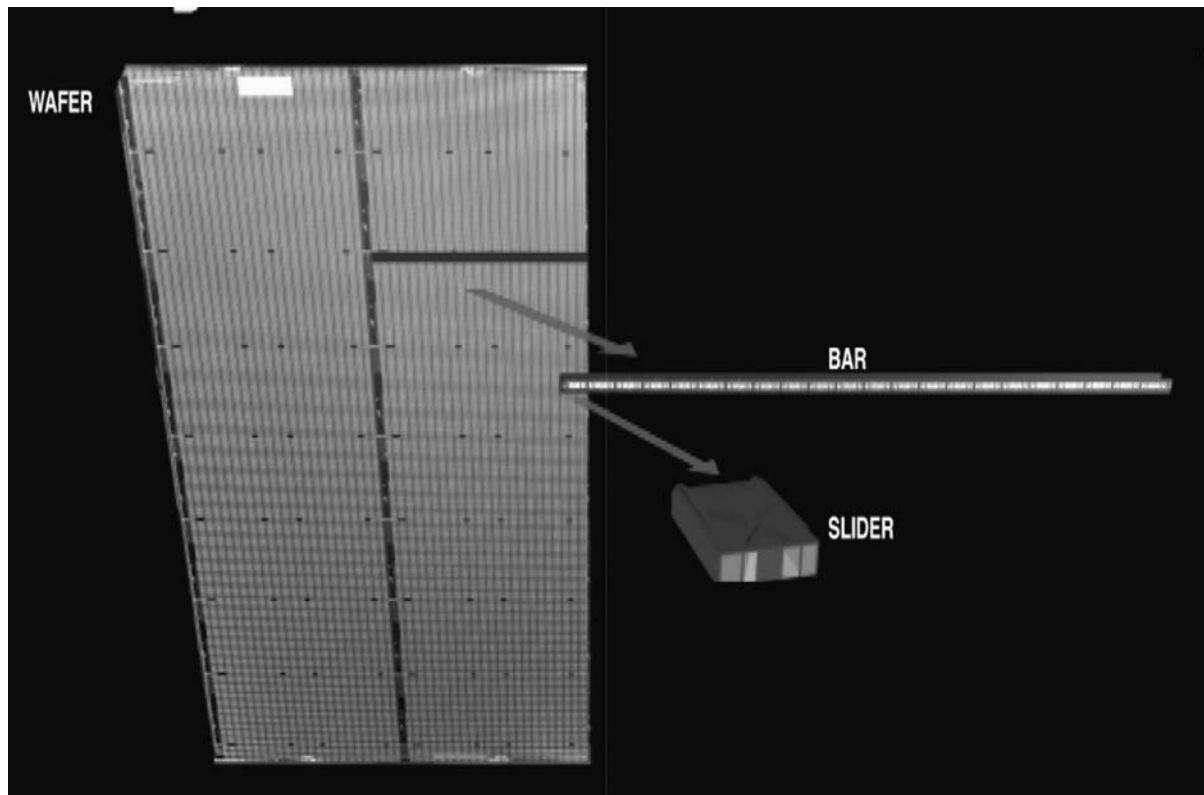
Figure 3
Thin-film head process—wafer to slider (courtesy of Seagate Technology, LLC).
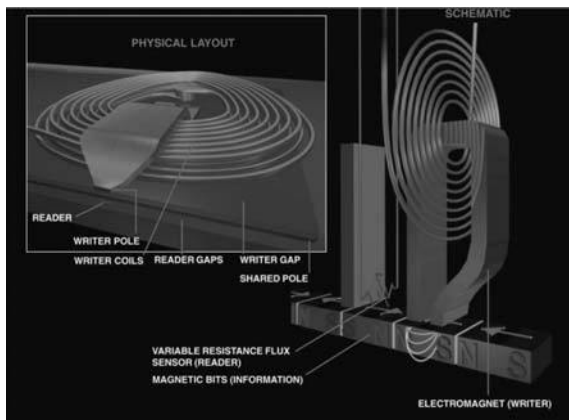
Figure 4
Merged MR head (courtesy of Seagate Technology, LLC).

In 1991 IBM introduced the MR (magneto-resistive) read head using the AMR (anisotropic magnetoresistive) effect in which the resistance of the element was determined by the angle between the sense current and the magnetization. This AMR device was coupled with an inductive write head (see Fig. 4). From this point MR and GMR heads proceeded to dominate the disk storage business within the next five years.

1. Air Bearings

Hand-in-hand with the improvements in transducers, the increases in areal density of the previous four decades were enabled by the decrease in head-to-media spacing (HMS), usual referred to as "fly height" (FH). In 1953, Bill Goddard of IBM designed and flew a hydrostatic air bearing as part of the development of the IBM RAMAC disk drive. This was an externally pressurized air bearing where the air cushion was supplied by air piped into the head assembly as shown in Fig. 5.

The heads were mounted on a gimbal spring that allowed the head to pitch and roll so that it could align with the surface of the rotating disk underneath. All subsequent flying heads used a gimbal assembly to allow alignment of the head and disk surfaces. This is referred to as a head gimbal assembly (HGA).

The first self-acting air bearing for magnetic recording was developed at IBM beginning in 1955. Jake Hagopian developed the first concept and Bill Gross, Ken Haughton, and Russ Brunner refined it. The self-acting air bearing was introduced in the IBM 1301 disk drive in 1962. This air bearing and the following ones had a cylindrical or spherical crown and featured a large mass and load pressure (several hundred grams force). The use of these cylindrical

Figure 5
RAMAC head (courtesy of IBM Corporation).

self-acting air bearings reduced the fly height from 800 μm on the RAMAC to 50 μm on the IBM 3330. They were of the load/unload type, which means they were lifted from the disk surface before the disk stopped rotating and loaded when the disk was up to speed.

In the early 1970s, IBM developed and shipped the 3340 "Winchester" disk drive which featured a two-rail taper flat air bearing with a low-low mass slider flying over a lubricated ferric oxide disk in a contact start–stop mode. The head flew at about 20 micro-inch when the disk was rotating but was in contact when the disk was stopped. At about the same time Digital Equipment Corporation designed and shipped the RS04 disk drive featuring a taper-flat, contact/start–stop, air bearing flying on a lubricated thin-film plated disk.

These taper-flat, contact/start–stop sliders were used on many drives until the introduction of the negative-pressure air bearings in 1991 by IBM in the Corsair Drive. In 1995, Read-Rite Corporation introduced the Tri-Pad air bearing featuring a pseudo-contact air bearing where the head and disk were almost in contact. This approach only worked with inductive heads due to the sensitivity of the MR and
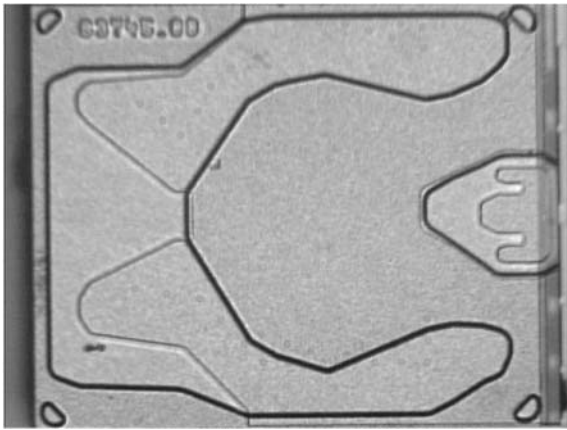
Figure 6
Negative-pressure air bearing (courtesy of Seagate Technology, LLC).

GMR heads to contact problems such as electrostatic discharge (ESD) and thermal noise due to the contact with asperities on the disk surface.

Current air bearings are of the negative-pressure type and fly below 1 microinch (25 nm). A negative-pressure air bearing has regions of both above- and below-ambient pressure as shown in Fig. 6. The resultant pressure is positive and is balanced by the head load; however the negative-pressure air bearing has the advantage of being stiffer for the same load and being amenable to designs that are insensitive to changes in pressure (altitude) and velocity (radius). The increasingly smooth surfaces needed to facilitate these low flying heights have led to a resurgence of the load/unload concept due to the wear and stiction problems associated with two very flat surfaces in contact.

The complex shapes required for negative-pressure designs are created by photopatterning after the bar is cut from the slider. The cavities are formed by ion etching of the air-bearing surface.

To be useful in a disk drive, the slider must be mounted on a HGA and assembled into a positioner in the drive as shown in Fig. 7. Basic flexure design has not fundamentally changed since the early days of disk storage. They have become less stiff and apply smaller loads as the sliders have become smaller. The discrete wires of the early heads have given way to miniature flex circuits for connecting the head to the electronics.

The higher performance of tomorrow's drives has given rise to consideration of moving the critical front end electronics closer to the head itself and even integrating the electronics with the head on the slider. The ever-increasing number of tracks per inch (tpi) has resulted in much development on microactuator designs. These are structures which move the head a

Figure 7
HGA head assembly (courtesy of Seagate Technology, LLC).

very small distance very quickly and significantly enhance the servo performance of the heads.

2. The Longitudinal Write Head

The simplest approximation to the write field from a ring head is the Karlqvist head equation published in 1954 (Karlqvist 1954) as shown in Fig. 8. It ignores the bulk of the head and concentrates on the gap area where a very high (infinite) permeability is assumed. The head is assumed to be infinitely wide, reducing the problem to two dimensions and the magnetic field in the gap region is assumed to be uniform.

In the limit of a very small gap, the equation reduces to

$$H_x = (H_g g/\pi)(y/x^2 + y^2)$$

$$H_y = (H_g g/\pi)(x/x^2 + y^2)$$

The field in the gap can be approximated by

$$H_g = (NI/g)E$$

where E is the head efficiency and I is the current in the coil. The head efficiency is a measure of how difficult it is to pass flux through the core of the head. The efficiency is dependent on the head material, head geometry and, if there is saturation, the right
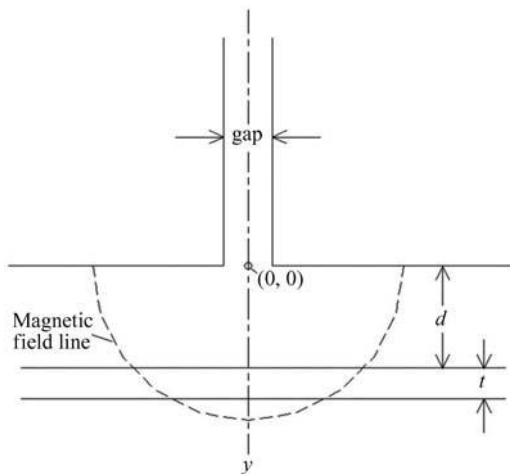
Figure 8
Karlqvist head.

current. In a good modern design, the write efficiency can vary from 40% to 80%.

The Karlqvist equation predicts that when the wavelength of the written signal, $\lambda = g/n$, where $n = 1$, 2, 3,…, then the readback will be zero. This is called the gap null. It must be considered when using the inductive head to readback but no null is created when writing at gap null wavelengths. The Karlqvist equation is an approximation and more exact calculations show that the first gap null is at 1.136 g.

In a real inductive head the magnetic fields produced by the head are complex and difficult to model because of several factors including the complicated head geometry, the nonlinear magnetic materials, and the size of the calculation to do a full micromagnetic calculation.

The important parameters that a write head designer will consider are:

- The strength of the field at the media,
- The write-field gradient at the point where the transition is written,
- The off-track writing or fringing,
- The frequency response of the head.

The head designer using a standard thin film ring head has the following parameters to work with:

(i) The gap length can be adjusted and write field and gradient traded off against fringing.

(ii) The number of turns can be adjusted and inductance traded off against write current.

(iii) The yoke can be made shorter to gain better NLTS (nonlinear transition shift) and frequency response.

(iv) The frequency response can be increased by laminations, thinner poles, higher resistivity pole material, and materials with high-frequency permeability.

(v) The field and field gradient can be increased in the head by increasing the deep gap field using higher moment materials.

The design improvements in the head show a trend to heads moving to fewer turns, shorter yokes, and a tendency to run closer to the saturation of the pole tips. Actual saturation of the pole tips can lead to very undesirable nonlinear effects.

High-resistivity materials such as CoZrTa and CoZrNb have been used in poles or in the part of the pole close to the gap. Although these materials reduce eddy currents, they have a B_s of only about 1.3 T so they can not produce the high fields of alternative materials. B_s is the saturation magnification and is the highest magnetization that can be induced in a material. Laminated materials have been used to suppress eddy currents in the yokes of heads; however, they have not been widely used.

The materials used in head poles are moving to higher saturation moments with a common composition now being $Ni_{45}Fe_{55}$ ($B_s = 1.6$ T). These alloys are in common use and are deposited by electroplating. Sputtered alloys with higher moments such as FeNX (X = tantalum, aluminum, zirconium, etc.) ($B_s = 2.0$ T) and other alloys such as FeCoX (X = zirconium, niobium, boron) ($B_s = 2.2$ T), and FeCoNi ($B_s = 2.0$ T) are also known. High-moment materials are often used with other lower-moment materials in the pole tips as shown in Fig. 9. The high-moment material is placed closed to the gap where the high flux is needed. Lower-moment material guides the flux to the gap. Generally, the lower-moment materials such as Permalloy have superior soft properties to the higher-moment materials.

The maximum B_s obtained in a bulk alloy is 2.4 T in $Fe_{65}Co_{35}$. Some materials have been reported with higher B_s such as $Fe_{16}N_2$ but never in stable phases of

High Moment Material →
(First Top Pole Plating Seedlayer)
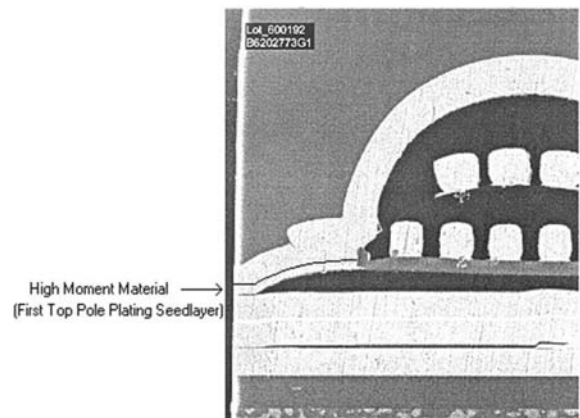
Figure 9
Dual-layer write head (courtesy of Seagate Technology, LLC).

enough material to make a pole. This lack of a soft material of high B_s places a fundamental limit on how high a coercivity can be written. The coercivity, in turn, is directly related to the stability of the grains in the media and thus the B_s of the pole material is one of the key factors in limiting the size of the grains in magnetic media.

Since smaller grains are required for higher signal-to-noise, the B_s of the pole material limits the density of magnetic recording. Researchers continue to search for higher-moment materials that have adequate soft properties, are stable over the operating temperatures of the disk drive and the processing temperatures of head manufacture, and can be made in large enough pieces for pole fabrication.

3. Perpendicular Write Heads

The longitudinal heads discussed above are limited to a field of less than $2\pi M_s$ (< 1.2 T for known materials) at the media. Perpendicular recording, on the other hand, can produce fields of almost $4\pi M_s$ (2.4 T) due to the more favorable geometry utilizing a soft underlayer (SUL) beneath the recording layer in the media. This is one of the main attractions of perpendicular magnetic recording.

Perpendicular recording utilizes a so-called pole head to write on the media as shown in Fig. 10. In this process, the vertical field from the head is used to write the media. In perpendicular recording, the SUL in the media is really part of the head flux path providing the return path for the flux from the head. As we approach the ''superparamagnetic limit,'' taking into account thermal stability and SNR in a model with a number of simplifications, Bertram (1994) has shown that perpendicular recording can have a 4–5 times advantage in areal density over longitudinal.

While there are factors other than SNR and thermal stability that may affect the relative densities of perpendicular and longitudinal recording, there has been a reawakening of interest in perpendicular recording for high densities.
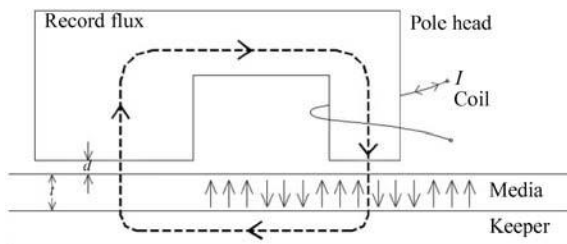
Figure 10
Perpendicular write head.
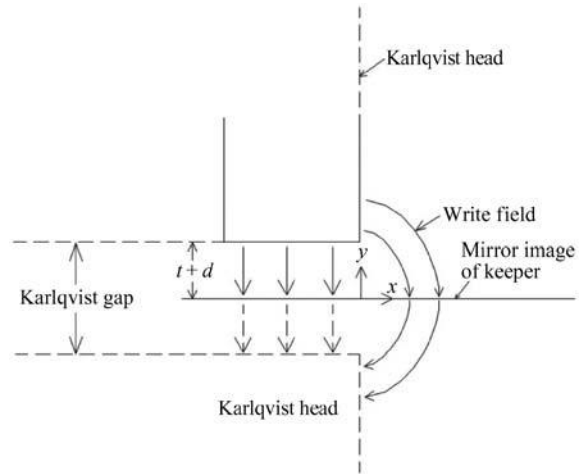
Figure 11
Karlqvist model for perpendicular.

The perpendicular recording head can be modeled by a Karlqvist head turned on its side as shown in Fig. 11. In this case, the field is given by

$$H_{\text{head}} = \frac{H_g}{\pi}\left[\tan^{-1}\left(\frac{d + t/2}{x}\right) + \tan^{-1}\left(\frac{d + 3t/2}{x}\right)\right]$$

where H_g is the deep gap field.

The considerations for designing a perpendicular write head are similar to those for a longitudinal. Frequency response can be improved by using lamination or using high-resistivity materials and by making the structure smaller. The write efficiency is generally higher in perpendicular heads so lower currents can be used for the same number of turns. Off-track writing is not affected by the gap and can be less than longitudinal in the ideal case. The fringing will, however, increase with increasing skew angle and this may be a problem for heads with finite-length pole tips. The SUL causes some unique problems since it provides the return path for the head flux and is part of the media.

Its orientation, permeability, and saturation magnetization are important. The SUL also extends far beyond the normal extent of a normal ring head and this requires careful treatment in models. The shape of the pole is important in preventing the pole from becoming magnetized when not being driven by the coil. Work in the past has also shown perpendicular heads to be more susceptible to the pick up of stray flux. Whether perpendicular recording will replace longitudinal at densities above 100 Gb/in^2 depends on overcoming these and other problems to realize the potential density increases promised by thermal stability and SNR considerations.

4. The Read Head

In 1988, the giant magnetoresistive (GMR) effect was discovered by Baibich *et al.* (1988) in Fe/Cr multilayers (see *Giant Magnetoresistance*). In this effect layers, of ferromagnetic (FM) material alternate with layers of nonmagnetic metals. These structures exhibit a large change in resistance when switched from the low-resistance state, where the FM layers are parallel to each other, to a high-resistance state, where the layers are antiparallel.

There are two types of architecture of potential use in read-head geometry, the CIP (current in plane) and CPP (current perpendicular to the plane) as shown in Fig. 12. The vast majority of today's heads are in a simple two-layer CIP configuration referred to as a spin valve.

Spin valve heads (see *Magnetic Recording Systems: Spin Valves*) have separate read and write elements as shown in Fig. 4, which allows separate optimization of the read and write function as compared to the inductive only head. These heads are also much more sensitive to flux than inductive or the MR readers. An inductive-style writer is usually built on top of a magnetoresistive reader. As shown in Figs. 13 and 14 the GMR sensor consists of several layers.

In the bottom spin valve shown here there is a seed layer, an antiferromagnetic (AF) pinning layer that holds the pinned layer magnetization in a constant direction through exchange coupling with the pinning layer which has no net moment. Between the pinned layer and the free layer is a thin layer of copper. The free layer is free to rotate under an applied field as shown in Fig. 15. The structure is protected with a capping layer.

The change in voltage of the spin valve is given by

$$\Delta V = -\tfrac{1}{2}I\Delta R\sin\Theta$$

where I is the bias current flowing through the sensor, Θ is the angle of rotation of the free layer wrt in its quiescent state and ΔR is the maximum change in resistance when the two layers change from parallel to antiparallel. The response of a spin valve to a transition on the disk is shown in Fig. 16.

In a real spin valve the magnetization is not uniform and the $\sin\Theta$ must be averaged over the active area of the spin valve.
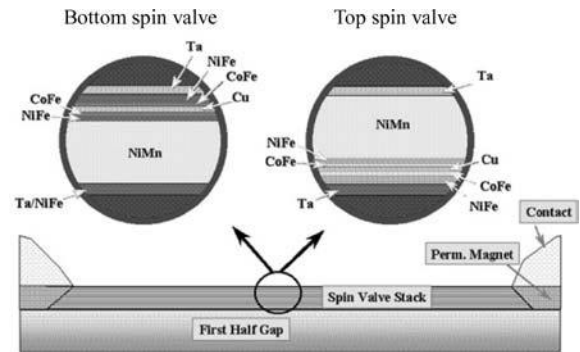
Figure 13
GMR spin valve sensor stack.
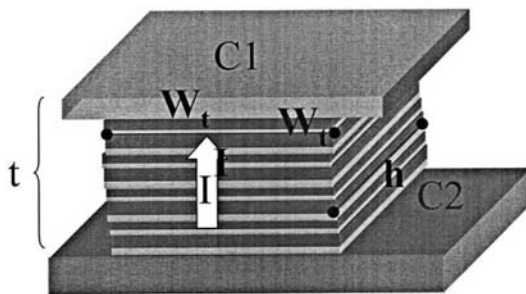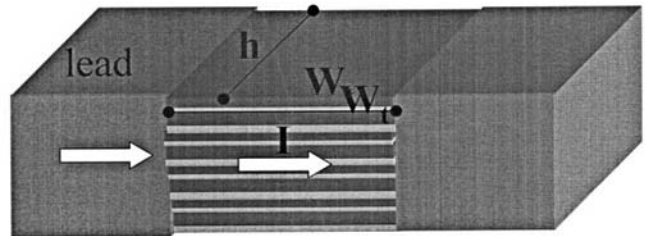
Figure 12
CPP and CIP geometries.
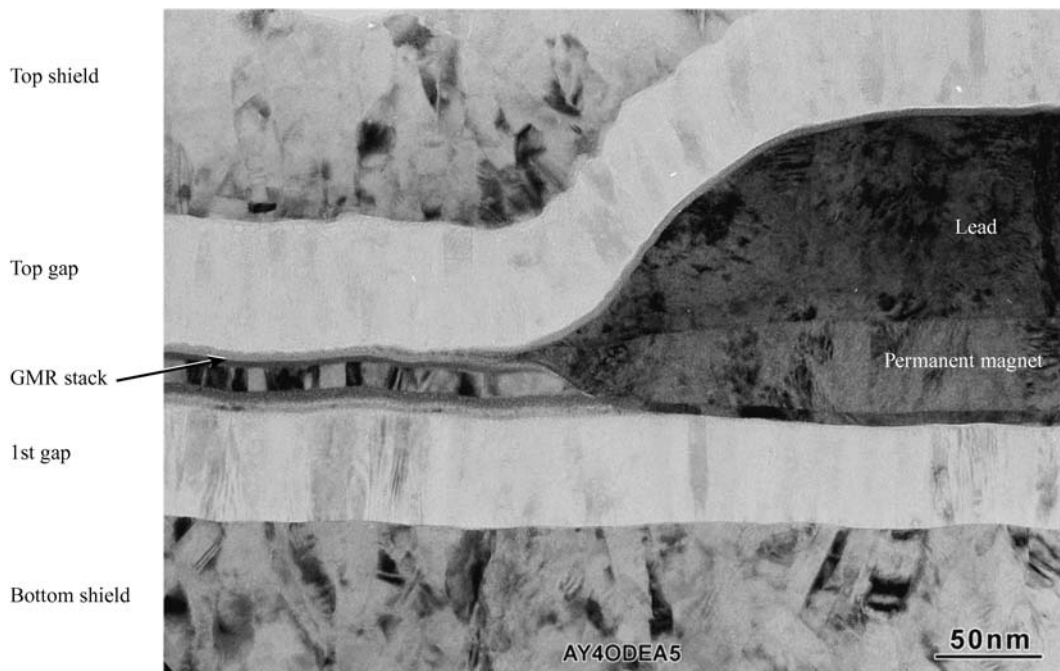
Figure 14
Cross section of a GMR reader (courtesy of Seagate Technology, LLC).
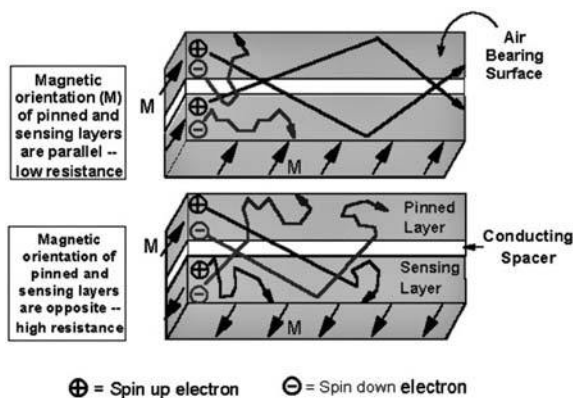
Figure 15
GMR sensor basics (courtesy of IBM Corporation).

$\Delta R/R$ values of over 20% have been observed in spin valves but values of 7–12% are typical of today's production. Typical sensor resistances are 40–50 Ω. Bias currents are typically about 5 mA. Output voltages of over 1 mV/μm have been achieved.

This spin valve structure is sandwiched between two insulating layers so that the device will not short. This structure is then placed between two soft magnetic layers called shields as shown in Fig. 14. These shields prevent the sensor from picking up flux from bits both down-track and up-track from the sensor and limit the pickup to the flux immediately under the device.

In order to remain stable under the operating conditions of disk drives, these heads require longitudinal stabilization, which keeps the magnetization in these devices more coherent and prevents the breakup into smaller domains. This function is served by attaching a permanent magnet structure (PM) to the sides of the GMR sensor and magnetizing it in a direction across the track. The PM is combined with a lead structure to bring the sense current to the device. The change in resistance is then typically read out as a change in voltage with a constant sense current.

In addition to the gap and track width, the height of the sensor is important. This is referred to as the stripe height and is accomplished by precision lapping of the sensor after it is cut from the wafer in the form of a bar. In order to precisely determine the stripe height, electronic lapping guides are formed simultaneously with the sensor and provide an exact reference to the back of the stripe.

The modern spin valve head is made up of several layers of very thin films (10–200 Å commonly) and small feature sizes (submicron track widths) (see Fig. 13). These sensors require ultraclean vacuum processing and thickness control better than 1 atomic

layer in many cases. Special precautions must be taken because of ESD (electrostatic discharge). Precise photo-processing and etch techniques are needed. In spite of these exacting requirements, spin valve heads are manufactured by the million using advanced manufacturing techniques unavailable before the end of the 1990s. It is the dominant sensor in magnetic recording.

In 1995 the concept of a head architecture using the shields as leads on the top and bottom of a sensor in the CPP mode was proposed (Rottmayer 1994, Rottmayer and Zhu 1995). This configuration can
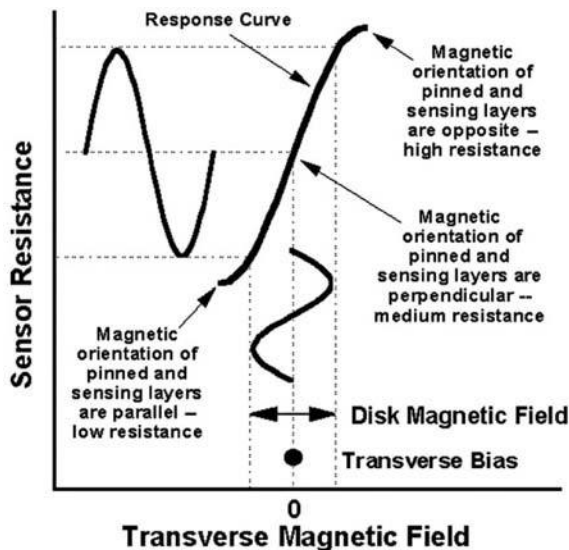
Figure 16
GMR sensor response to disk magnetic field (courtesy of IBM Corporation).

be used with both a CPP GMR multilayer or MTJ (magnetic tunnel junction) sensor.

The CPP GMR head consists of a number of layer pairs of GMR material, e.g., copper/cobalt as shown in Fig. 17. The interlayer coupling across the copper is relatively small so that the coupling is primarily magnetostatic. The GMR $\Delta R/R$ is 2–4 times the $\Delta R/R$ in the CIP direction and can be as high as 100%. The device is placed between two shields, which also serve as leads. This confers a large degree of ESD protection since all parts of the device are at approximately the same potential.

A single bias magnet is placed behind the sensor. This is an advantage over the leads and magnets that must be attached to the sides of a spin valve head since it is much easier to fabricate and control track width. The CPP GMR is a low-impedance device having a resistance of only a few ohms even at densities of $100\,\text{Gb/in}^2$. This can result in a low signal amplitude. However, the CPP GMR has the advantages that its resistance increases with the square of the track width (TW) and so as densities increase, the resistance is in a more favorable range.

The MTJ device is made by sandwiching a thin insulating layer of alumina between two ferromagnetic metal layers, one of which is pinned as in a spin valve as shown in Fig. 18. Electrons can tunnel through the thin ($<2\,\text{nm}$) barrier. Since they are spin-polarized, the current is larger when the magnetization of the two FM layers is parallel. $\Delta R/R$ ratios of more than 25% have been reported for MTJs.

In contrast to the CPP GMR head, the MTJ has a high resistance of about $1\,\text{k}\Omega$ at $100\,\text{Gb/in}^2$. The MTJ requires longitudinal stabilization with a magnetic field; however, this does not require that the magnet be in contact with the MTJ and so it enjoys the same advantages as the CPP GMR as far as ease of fabrication and track width definition. The thin barrier is
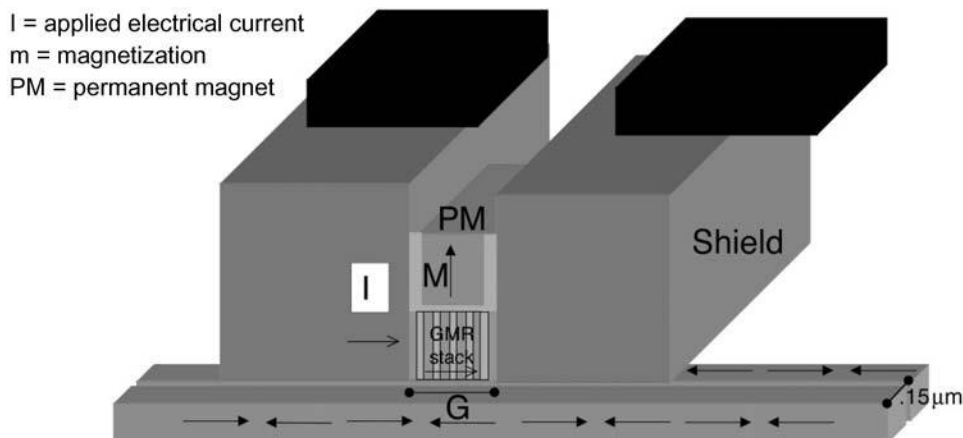
Figure 17
CPP GMR head (after Rottmayer and Zhu 1995).
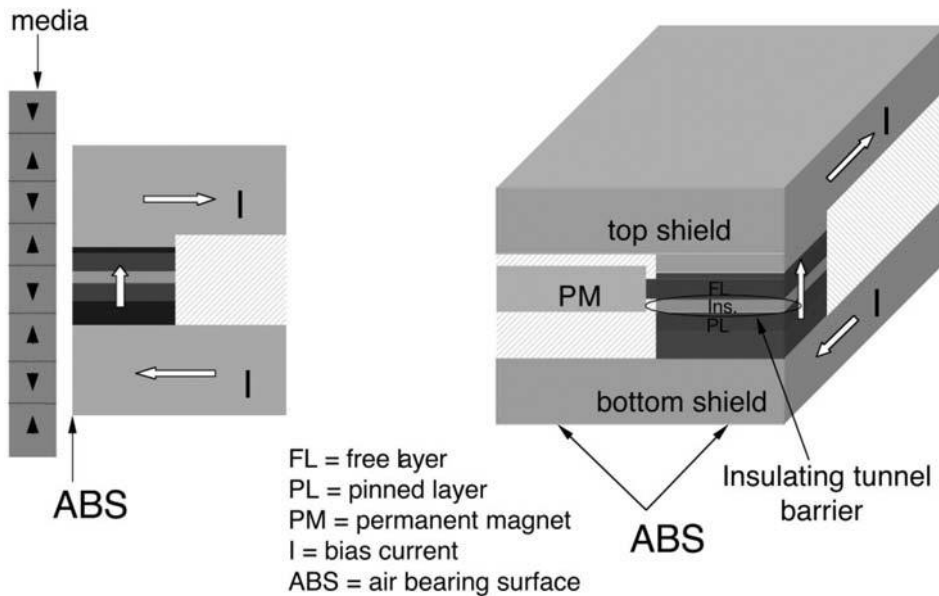
Figure 18
Magnetic tunnel junction read head.

susceptible to ESD and this will be a challenge for use in disk drives.

5. *The Future of Magnetic Recording Heads*

Magnetic recording heads have answered the challenges of the data storage market place from the IBM Ramac ($2.6\,Kb/in.^2$) to today's drives of approximately $20\,Gb/in^2$. This represents an increase in areal density of seven orders of magnitude in 45 years. This has been accomplished primarily by scaling—that is reducing the dimensions of the head, as the bits became smaller. The high leverage scaling parameters were the fly height, the gap length track width, and core size. In conjunction with this, scaling advances in materials also contributed. Most notable was the change from bulk-ferrite to thin-film magnetic materials and the development of GMR sensors for increased output. Semiconductor-like batch fabrication processes have reduced the costs while simultaneously improving performance. What does the future hold?

Head media spacing (HMS) continues to be a key parameter in increasing areal density. With today's fly heights close to 10 nm and an additional 5–7 nm of disk overcoat, head protection, and lubrication film, we are approaching a regime where we are getting close to the physical limits of the proximity of two materials. In addition, other considerations such as media thickness limit the advantage of lower fly height as we get into the nm region. So gains will be limited by HMS in the future.

In the area of head critical dimensions (CD), the acceleration of the areal density race has led to a convergence between the semiconductor line-width roadmap and the head-track-width roadmap. At the present rates of growth, the two curves will intersect early in the first decade of the twenty-first century. The head industry has traditionally relied on the semiconductor industry to develop the lithography equipment and processes.

If the track density of magnetic recording continues to outpace the line-width reduction of semiconductors then the head industry will no longer be able to depend solely on the semiconductor industry for its technology. However, there are lithographic technologies that can push track widths more than an order of magnitude from current production. There are also alternative architectures such as putting the transducer on the side of the slider and allowing the deposition thickness to determine the track width.

Gaps and sensor thicknesses are defined by deposition processes which can be extended to much higher areal densities. The most important problem at this time is thin insulating layers needed both for gap layers in SPV heads and for the tunnel barrier on MTJ heads. Both the rapid advances in deposition technology and the variety of alternative architectures mentioned above show great promise in extending head areal densities.

Sensor sensitivity can be extended by further improvement in SPV heads and the use of alternative technologies such as CPP GMR and MTJ heads. The frequency capability of the write head is now the

major problem in higher data rates. Improved materials, geometries, and architectures can extend frequency limits of the write head. The switching frequency of the head may be ultimately limited by ferromagnetic resonance in the head materials.

The biggest problem in recording-head design today is providing heads with the capability to write higher media coercivities and thus push back the superparamagnetic limit. Perpendicular recording with a soft underlayer can help overcome this problem. Also, thermally assisted magnetic recording can lower the coercivity of the media during writing thus enabling the writing of a pattern more stable at operating temperatures. Whatever the architecture used, the density can be extended by increasing the B_s of the pole materials. Thus there is much active research on materials with $B_s > 2.4\,\text{T}$. It is, however, not clear that such materials exist in a form suitable for head poles.

Even though magnetic recording is pushing some physical limits and certain fabrication limits mentioned above, there still exist many paths to increase areal density and data rates. Heads play a key role in both areas. With the many alternatives available to increase areal density and data rate, magnetic recording should continue to improve in performance with magnetic recording heads playing a key role.

See also: Magnetoresistive Heads: Physical Phenomena; Magnetic Recording Devices: Future Technologies; Magnetic Recording Devices: Inductive Heads, Properties; Magnetic Recording: Rigid Media: Overview; Magnetic Recording Technologies: Overview; Micromagnetics: Basic Principles

Bibliography

Baibich M N, Broto J M, Fert A, Nguyen Van Dau F, Petroff F, Eitenne P, Creuzet G, Friederich A, Chazelas J 1988 Giant magnetoresistance of (001) Fe/(001) Cr magnetic superlattices. *Phys. Rev. Lett.* **61**, 2472–5
Bhushan B 1999 *Micro/Nano Tribology*, 2nd edn. CRC Press, Boca Raton, FL
Betram H N 1994 *Theory of Magnetic Recording*. Cambridge University Press, Cambridge
Betram N H, Williams M 2000 SNR and density limit estimates: a comparison of longitudinal and perpendicular recording. *IEEE Trans. Magn.* **36**, 4–9
Daniel E C, Mee C D, Clark M H 1999 *Magnetic Recording: The First 100 Years*. IEEE Press, New York
Hoagland A S, Monson J E 1991 *Digital Magnetic Recording*, 2nd edn. Wiley, New York
Karlqvist O 1954 Calculation of the magnetic field in the ferromagnetic layer of a magnetic drum. *Trans. R. Inst. Technol.* **86**, 22
Mee C D, Daniel E D 1996 *Magnetic Storage Handbook*, 2nd edn. McGraw-Hill, New York
Rottmayer R, Zhu J 1995 A new design for an ultra-high density magnetic recording head using a GMR sensor in the CPP mode. *IEEE Trans. Magn.* **31** (6), 2597–9
Rottmayer R 1994 Magnetic head assembly with MR sensor. US Patent 5 446 613
Rottmayer R, Spash J L 1976 Transducer assembly for a disc drive. US Patent 3 975 570
Wang S X, Taratorin A M 1999 *Magnetic Information Storage Technology*. Academic Press, New York
White R M 1984 *Introduction to Magnetic Recording*. IEEE Press, New York

R. E. Rottmayer
Seagate Research, Pittsburgh, Pennsylvania, USA

Magnetic Recording Materials: Tape Particles, Magnetic Properties

The basic principles of magnetic recording and information storage have remained unchanged for more than a century. The initial machines used steel wire as the recording medium, but in 1928 Pfleumer patented a paper tape coated with iron filings and a magnetophone using this tape was demonstrated in the 1935 Berlin exhibition. During the World War II, plastic tapes coated with magnetic particles were developed in Germany and since then the basic structure of the modern magnetic storage tape has remained unchanged. Certainly there have been innovations, improvements in performance and properties of the media, and a range of different formats and methods of storing the information, but the basic structure of magnetic particles embedded in a non-magnetic matrix on a plastic substrate has remained the same.

When considering analog recording, it is not obvious what the fundamental properties of the magnetic medium should be. In all analog systems a linear relationship is required between the signal and the magnetization and this is usually achieved by a.c. bias to use the anhysteretic remanence properties of the magnetic components. The a.c. bias is superimposed on the signal in the case of analog audio systems, but is self biasing when frequency modulation is used in analog video recording.

The fundamental properties of the magnetic medium becomes more obvious when digital storage is considered. Here, information is stored as one of two states (in simple terms corresponding to the binary states of digital bits) and it is clear that the components used to make up the magnetic medium must also have two discrete magnetic states. If the medium is composed of particles, then these particles should be capable of being switched between two states with an easy axis which can be magnetized in either of two directions. These particles are single domain and ideally should have a square hysteresis loop. In addition, since the information must be stored indefinitely or until erased, the energy barrier between these two

states should be of sufficient height to prevent thermal decay of the information or accidental erasure.

Modern data systems require very high aerial densities of information to be written at very high rates. In order to accommodate the higher densities, there is a continual move towards thinner magnetic layers and to higher coercivitiy particles. For analog audio and video formats, magnetic layer thickness of several microns consisting of ferrite particles were adequate. For the latest advanced data storage tapes metal particles have replaced the earlier ferrites allowing coercivity to be pushed up to in excess of 2 kOe and magnetic layer thickness down to hundreds of nanometers.

Magnetic properties are also dependent on the time scale so that writing at high frequencies confronts the dynamic switching time of particles resulting in much higher coercivities than those involved in the long-term storage. This is becoming more of a problem as data rates increase. Time dependence of magnetization is, therefore, crucial to magnetic information storage properties at both ends of the time scale—at high frequencies the time to switch a particle is a limiting factor whereas for long-term archival of information, thermally activated decay of magnetization presents a problem. All these properties will be considered in this article.

1. Magnetization Reversal (the Origin of Coercivity)

1.1 Single Domain Particles

Bulk magnetic materials will divide up into domains. This has the effect of reducing the total magnetic energy contribution. However, because energy is associated with a domain wall, for small particles it is energetically preferable for the particle to remain as a single domain and, with the associated anisotropy resulting from the shape and the intrinsic crystal properties of the material, the single domain magnetization will lie in preferred directions. In the case of hexagonal or uniaxial anisotropy, there are two easy directions and the particle is said to have an easy axis. (See also *Magnets, Soft and Hard: Domains, Coercivity Mechanisms.*)

1.2 Coherent Reversal

The Stoner Wohlfarth model (Stoner and Wohlfarth 1948) was the first successful attempt to describe the hysteresis behavior of a particle. Although the predicted coercivity was much larger than that observed in experimental systems, the simplicity of the model allowed a mathematical description of the reversal and the model is still used as a means of describing particulate systems and is a good model for visualizing the reversal process. Stoner and Wohlfarth

(1948) and Cullity (1972) provide a full description of the model. In the model, reversal is regarded as a coherent process where all the individual spins rotate in unison.

The particle moment is, therefore, single valued and can rotate relative to the particle axis. Crystal and shape anisotropy of the particle will determine the energy associated with different orientations of the particle moment and result in an energy barrier between minimum energy positions. For a uniaxial system, these energy minima are opposite each other and the system has a particle easy axis and, in the absence of an external magnetic field, the energy is a minimum when the moment is pointing along the axis or in the opposite direction. At an angle θ, then the energy can be written approximately as

$$E = K_1 V \sin^2 \theta \qquad (1)$$

where K_1 is the anisotropy constant, V is the particle volume, and KV is the height of the energy barrier. Given the potential energy of interaction of the particle moment with an external field and expressing the anisotropy constant in terms of the anisotropy field as

$$K_1 = H_K M_s / 2 \qquad (2)$$

where H_K is the anisotropy field and M_s is the saturation magnetization of the particle, then the energy associated with the magnetic moment of the particle, μ, in an applied field H at an angle ϕ to the particle axis can be written as a 2D expression as

$$E = \mu[H_K \sin^2 \theta / 2 - H \cos(\theta - \phi)] \qquad (3)$$

Visualizing the reversal process for different orientations of the particle is straightforward and a number of examples are shown in Fig. 1. Figure 1(a) shows the energy of a moment as a function of angle for various fields applied in the direction of the particle easy axis. Consider the moment at $\theta = 0$ in a field H_K. The moment will be in the energy minimum at A. As the field is reduced the moment will remain at $\theta = 0$ until $H = -H_K$ when the equilibrium position becomes unstable and thermal fluctuations will switch the moment direction to $180°$ at position B. It will remain in that direction until the field is increased to $+H_K$. Thus, the particles will exhibit a square hysteresis loop (Fig. 2). Figure 1(b) shows the case where the applied field is at $45°$ to the particle easy axis. At high positive fields the particle moment will lie along the field direction.

However, note that when the field has been reduced to H_K, the energy minimum at A has moved towards the easy axis direction. As the field is reduced further, the energy minimum becomes shallower and moves towards $\theta = 0$ and at $H \sim -0.5 H_K$ it disappears so that the moment will switch to position B and then move towards the field direction as the field becomes
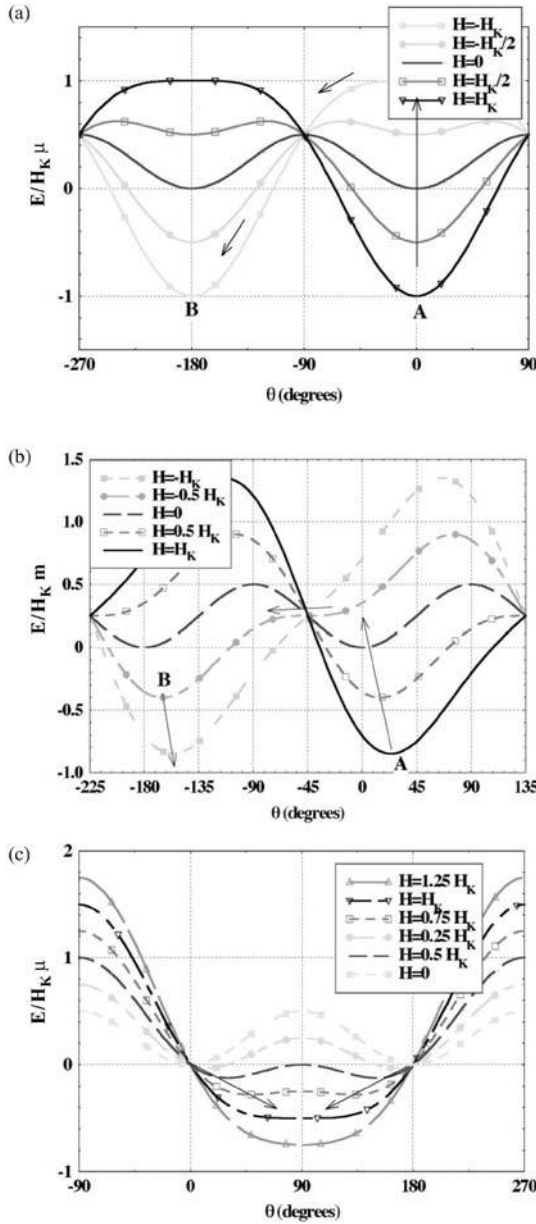
Figure 1
Energy of a particle moment as a function of angle to the easy axis direction when the magnetic field is applied in different directions: (a) along the easy axis, (b) at 45° to the easy axis, and (c) at right angles to the easy axis.

Figure 2
Hysteresis loops for a Stoner Wohlfarth particle for applied field directions of 0°, 45°, and 90° to the easy axis.

coercivity. Figure 1(c) shows the case when the field direction is at rights angles to the easy axis. In this case no switching occurs but the two energy minima merge to produce a single flat bottomed minimum at $H = H_K$. Hysteresis loops for all three conditions are shown in Fig. 2 obtained by a numerical solution of the Stoner Wohlfarth model.

1.3 Superparamagnetism

The energy barrier to reversal is proportional to the particle volume so that as the size of the particle is reduced, the height of the barrier moves into the thermal regime when the particle moment can be switched by thermal energy alone and the time for reversal, τ, is given by the Néel-Arrhenius law (Néel 1949):

$$T^{-1} = f_o \exp(-E_b/kT) \tag{4}$$

where f_o is a frequency factor usually taken as $\sim 1 \times 10^9$, k is Boltzmann's constant, and E_b is the height of the energy barrier. The particle is then said to be superparamagnetic. The onset of superparamagnetism is not only dependent on the shape and size of the particle but is also related to saturation magnetization and the anisotropy constant.

1.4 Incoherent Reversal

In practice, coherent reversal is only observed for very small particles and recording tape particles are sufficiently large that the normal reversal mode is incoherent. In this case, the energy is minimized during reversal by reducing the magneto-static energy

more negative. The whole process is reversed when the field change is in the positive direction and this produces a hysteresis loop with reversible, but field-dependent, magnetization at fields in excess of the

between individual spins through their misalignment. There are various simple models for this incoherent reversal and the two most commonly referred to are fanning and curling whose names graphically describe the particle motion during the reversal process.

1.5 Interaction Effects in Particle Systems

In recording media, magnetic properties are determined by the mean behavior of all the particles in the system. Particles will have a range of volumes and shapes which will produce a distribution of switching properties. In addition, particle orientation will be spread around an axis determined by magnetic orientation along the tape during manufacture. These will produce a switching field distribution which is further modified by the magneto-static interactions between particles due to their close proximity and the long range of the dipole–dipole interaction. A study of single particle properties from optical observation of magnetic reversal of single particles and comparison of simulated magnetic tape properties with measured properties indicated a very large shift in the switching field distribution (McConochie *et al.* 1996). Figure 3 shows results for such a system in which the displacement of the switching field distribution due to interactions can be seen.

Because of interaction effects, the switching field distribution of a system varies between processes. In Fig. 4 switching field distributions for the isothermal remanent magnetization and the d.c. demagnetization processes are shown for a cobalt modified γ-Fe_2O_3 video tape. These curves are also referred to as the *irreversible susceptibility* curves because they are measured in the remanent state so that changes are only due to irreversible switching properties. These susceptibility distributions have been normalized so

Figure 4
Switching field distributions for a cobalt-modified γ-Fe_2O_3 video tape measured for isothermal remanent magnetization and d.c.-demagnetization processes.

that the area under the curve is unity. Any magnetization state can then be represented by an integral of these distributions as

$$M(H) = \frac{\int_0^H \chi(H)\mathrm{d}H}{\int_0^\infty \chi(H)\mathrm{d}H} \tag{5}$$

where $\chi(H)$ is the susceptibility.

2. Time Dependence

The previous discussion has been in terms of static properties of media. However, thermal activation can cause moments to switch over energy barriers and will produce time-dependent changes in magnetization. This was first investigated by Street and Woolley (1949) who observed a logarithmic decay as:

$$M = \mathrm{const} - S \ln(t) \tag{6}$$

where S is the magnetic viscosity coefficient and is dependent in the applied magnetic field (see *Magnetic Viscosity*). Although this relationship does not hold over very short and very long time scales, it is found to be applicable over several decades of time and gives a reasonable description of time-dependent behavior in most cases. The magnetic viscosity coefficient is field dependent and is related to the number of moments which are in an energy minimum within the thermal range.

Intuitively it would be expected that the maximum S would occur close to the center of the switching field distribution (i.e., near to the coercive field) and that the variation of the viscosity coefficient would be closely related to the switching field distribution. This

Figure 3
Switching field distributions simulated for an ensemble of tape particles and the measured switching field distribution showing the shift in properties produced by the interaction effects.
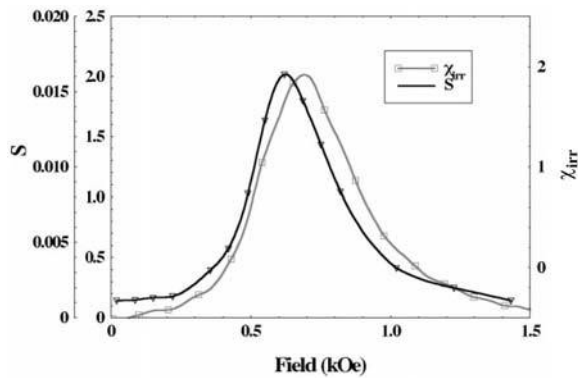
Figure 5
Variation of the magnetic viscosity coefficient for a cobalt-modified γ-Fe$_2$O$_3$ video tape showing the peak close to the coercive field value.

is indeed found to be the case and Fig. 5 shows the variation of S with field along with χ_{irr} obtained from the d.c.-demagnetization curve for the cobalt γ-Fe$_2$O$_3$ video tape. Because of the intuitive link between S and χ_{irr}, Street and Woolley proposed a parameter called the *fluctuation field*, H_{f} defined by:

$$S = \chi_{\text{irr}} H_{\text{f}} \tag{7}$$

The fluctuation field was associated with the concept of an activation volume, V_{ac} by Wohlfarth (1984) where

$$H_{\text{f}} = \frac{kT}{V_{\text{ac}} I_{\text{s}}} \tag{8}$$

and I_{s} is the saturation magnetization of the bulk material. The interpretation of the fluctuation field and activation volume is difficult as they do not relate to any physical media properties. However, the activation volume is often taken to represent the volume of the particle which is involved in the initial reversal process. This does seem to have some basis as activation volumes are generally smaller than the particle volume and can be considered as the volume of the region in which reversal is first propagated during an incoherent process. However, this is not always the case, and sometimes activation volume can exceed the particle volume which seems physically unreal.

3. Concluding Remarks

Intrinsic magnetic properties of tape particles and the recording process have remained unchanged throughout the history of magnetic recording. However, to accommodate the need for higher data densities and

faster switching there has been a move to thinner magnetic layers and higher coercivity particles. The earlier ferrite particles are now being replaced by metal particles in the high density advanced data storage systems.

See also: Magnetic Recording Media: Advanced; Magnetic Recording Technologies: Overview; Metal Particle versus Metal Evaporated Tape; Micromagnetics: Basic Principles

Bibliography

Cullity B D 1972 *Introduction to Magnetic Materials*. Addison Wesley, Reading, MA
McConochie S R, Schmidlin F, Bissell P R, Gotaas J A, Parker D A 1996 Interaction effects from reversal studies of single particles. *J. Magn. Magn. Mater*. **155**, 89–91
Néel L 1949 Théorie du trainage magnétique des ferro-magnétiques en grains fins avec application aux terres cuites. *Ann. Geophys*. **5**, 99–136
Pfleumer F 1928 German Pat. DRP 500 900
Stoner E C, Wohlfarth E P 1948 A mechanism of magnetic hysteresis in heterogeneous alloys. *Roy. Soc. Phil. Trans*. **240**, 599–642
Street R, Woolley J C 1949 A study of magnetic viscosity. *Proc. Phys. Soc. A*. **62**, 562–72
Wohlfarth E P 1984 The coefficient of magnetic viscosity. *J. Phys. F*. **14**, L155–9

P. R. Bissell
University of Central Lancashire, Preston, UK

Magnetic Recording Measurements

Magnetic recording devices use materials that exhibit spontaneous magnetization in their operating temperature range: ferromagnets and ferrimagnets (see *Magnetic Recording Technologies: Overview*). The magnetic properties of these materials can be classed into two categories: properties that are determined by composition and crystal structure, denoted intrinsic; and properties that depend on microstructural factors such as grain size and shape in a polycrystal, or particle shape and orientation in a composite, denoted extrinsic. Both intrinsic and extrinsic magnetic properties are functions of environmental factors such as electric and magnetic fields, temperature, pressure, and atmosphere.

The measurements described below depend on the scale on which they view the magnetic property to be measured. The microscopic scale focuses on a magnetic material as an arrangement of interacting atoms and interprets magnetic properties in terms of spin and orbital moments, energy levels, binding energies, spin–orbit, exchange, and superexchange

interactions, etc. The mesoscopic scale averages these microscopic interactions over small homogeneous regions (grains, particles) comprising many atoms. Averages over many such (interacting) regions constitute the macroscopic properties of the magnetic material.

An important consideration in measuring the magnetic properties of a material is its uniformity. Inhomogeneities may occur on the microscopic scale (point defects such as vacancies and interstitials, line and planar defects such as dislocations, or composition fluctuations in disordered alloys), on the mesoscopic scale (grain or particle clusters, voids, and segregations), and on the macroscopic scale, given the limits on quality control in fabrication.

1. General Measurements

In most instances, magnetic measurements described below are *extrinsic* measurements made by measuring a sample's response to an externally applied magnetic field. The measurements can depend on the sample's shape: the inhomogeneities and discontinuities of the magnetization in the sample's interior and on its surface are sources of a magnetostatic demagnetizing field that depends on the sample's shape and that affects the internal field. As the internal magnetization changes in response to applied fields, temperature, or time, the internal field will also change due to the changing demagnetizing fields. These fields can also be microstructure dependent because typical polycrystalline or particulate materials exhibit effects due to grain boundaries and particulate or grain orientation.

These measurements are also affected by the rate at which the magnetic field is changing (viscosity and eddy current effects) and how long it takes to make the measurements. Indeed, the magnetization of all materials will eventually seek the lowest energy state, if we wait long enough at any nonzero temperature. In the absence of an applied field this is always a state of demagnetization with zero net magnetization when summed over the whole sample volume, because such a demagnetized state minimizes the magnetostatic or dipolar self-energy. We conclude that the sample's coercivity, defined as the field that must be applied to a magnetized sample to reduce its magnetization to zero, is zero for infinite-time measurements! At the other end of the time scale we might try to coerce the spins in a magnetic material to change directions with a short field pulse.

We are concerned here with the magnetic properties of electron spins but, as the word implies, spins are associated with angular momentum, and exhibit the (quantum mechanical) inertial effects of angular momentum. Moreover, spins are usually coupled to each other and to their surroundings, and thus spin dynamics exhibits spring-like inertial and damping effects. Put another way, spins do not change

instantaneously but take time to alter their direction. In general, if the magnetization is to be changed a given amount (say from a magnetized to a demagnetized state) in a shorter time, this will require a larger externally applied field. Measured coercivities are larger for shorter applied field times.

Measurements then need to be described by the applied field rates of change and are generally grouped in three regimes: slowly varying fields, quickly varying fields, and pulsed fields. The fields may be localized, uniform over large areas, or changing in space (field *gradients*). The measurements can interrogate a small region of a whole or an entire large sample. (See also *Magnetic Measurements: Quasistatic and ac*.)

1.1 Vibrating Sample Magnetometry

Developed in the late 1950s by S. Foner, the vibrating sample magnetometer (VSM) continues in widespread use for measuring magnetic properties of materials including thin films and particulate media. The basic technique involves a large-scale applied field, using an electromagnet to immerse an entire small sample in a nearly uniform field (Fig. 1). The field is swept *slowly* (usually less than mTs^{-1}) and the sample is moved (vibrated) in the applied field. As described previously, the magnetic sources associated with a sample's geometry and magnetization cause internal magnetostatic fields and of course external fringing fields. Inductive pick-up coils are placed in close proximity to the sample, inside the applied field, and sensed synchronously with the motion of the sample. The assumption is made that the external fields are proportional to the net internal magnetization (modified only by the geometry of the sample, i.e., its demagnetizing factor) but since this is a large-scale measurement, internal domain structure may affect the measurement.

1.2 AGFM

Another approach to generating macroscopic magnetic parameters is the alternating gradient force magnetometer (AGFM). Its salient feature is the ability to trace a major hysteresis loop in seconds rather than minutes as with a VSM.

1.3 a.c. Hysteresis Loop Measurement

If the interrogating magnetic field is applied rapidly and repetitively, usually at 60 Hz or 1 kHz, the sample's major hysteresis loop can be detected and traced synchronously. In this method, the sample is stationary and the field changes rapidly causing the magnetization and its resulting fringing field to change at the rate of the applied field. Differential inductive pickup coils are typically employed to sense these
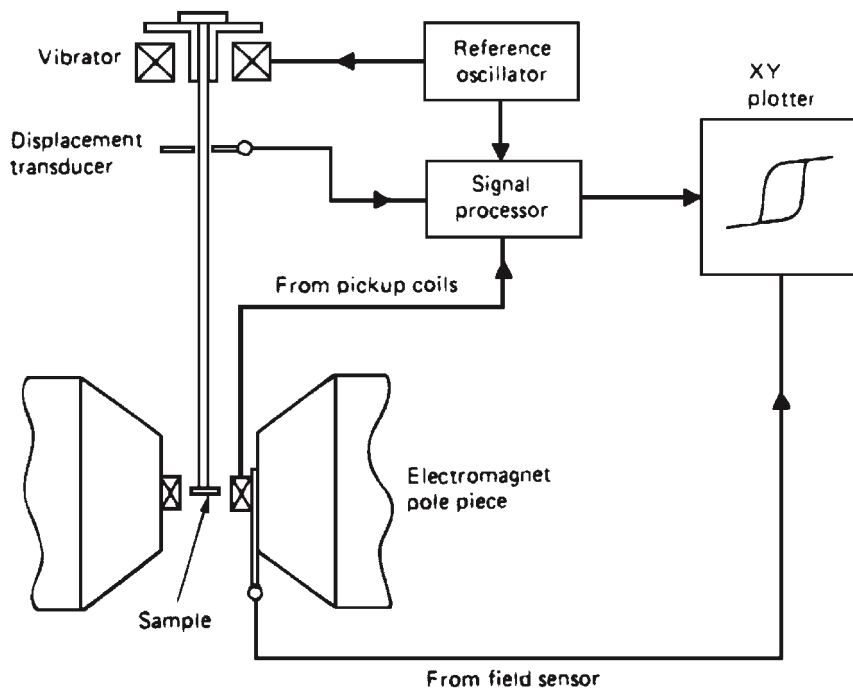
Figure 1
VSM illustration (schematic).

fringing fields and the average magnetization is assumed to be proportional to them. Measurements are made considerably faster than with a VSM. As discussed previously, these faster measurements can produce measured values of coercivity larger (by tens of percent) than those obtained from a more slowly varying VSM measurement.

1.4 Torque Magnetometry

If a sample's average magnetization is not aligned with an applied uniform magnetic field, a torque will be created on the sample through its magnetostatic energy (as described above) and its magnetocrystalline energy, the energy associated with the orientation of the spins relative to the material's crystal lattice. A material may have a preferred easy axis of magnetization, through a macroscopic shape, mesoscopic particulate or granular alignment, magnetocrystalline anisotropy, or other phenomena. To examine internal anisotropies, a large, static magnetic field is applied to a sample with uniform demagnetizing factors (ideally an ellipsoid of revolution). As the sample is rotated in this field, the magnetization does not completely align with the applied field because of its internal anisotropy. The resulting torque on the sample is measured and recorded as a function of sample rotation angle. A typical method includes suspending

the sample on a torsional wire or glass fiber, and small torsional angles are measured optically using a reflecting mirror attached to the suspension and optical lever enhancement. These data can be used to determine the form (uniaxial, cubic, or other) of the anisotropy and its magnitude as a function of applied field.

1.5 Magneto-optical Measurement

Instead of measuring the external fringing fields and inferring the average magnetization from them, the samples may be probed optically. The Faraday or Kerr effects are incorporated into these systems and very small samples or small sample areas of larger samples can be examined. These magneto-optical methods utilize the interaction of light with a magnetic material (see *Magneto-optics: Inter- and Intraband Transitions, Microscopic Models of*). The customary system measures the rotation of the plane of polarization or induced ellipticity of a light beam (often from a HeNe laser) as the linearly polarized light ray passes through (Faraday) or reflects off (Kerr) the sample. For the former, linearly polarized light passes through samples and the electric field of the light interacts with the transverse magnetization and induces an electric field orthogonal to both the planes of polarization and magnetization. This is

588

particularly effective for samples whose magnetization is collinear with the applied light. The rotation for magnetization parallel to the direction of propagation is opposite that for magnetization antiparallel to the propagation direction. To overcome the reduction in amplitude from material absorption, transparent materials or thin magnetic films need to be used for the Faraday measurement to be practical.

The Kerr effect employs a similar phenomenon associated with the interaction of the electric field with the sample's magnetization. The interaction induces a secondary electrical field that alters the light's initial polarization. In this technique, linearly polarized light is reflected from a magnetic material's surface. Since the angle of incidence is usually not normal, the *s*- and *p*-polarizations interact differently with the magnetization and by examining the rotation and ellipticity, in-plane and perpendicular (polar) magnetizations can be measured.

These magneto-optical measurements can be made at any speed with which the magnetization can be changed, from subnanoseconds to hours. The light can be spread to average large sample areas or focused to subdiffraction limited spots using near-field optics. Since microscopic measurements can be made rapidly, this technique is often employed to determine a sample's degree of uniformity.

1.6 Magnetoresistance Measurement

Transport properties of films used in magnetic recording for transducer applications are measured to predict device performance. Typically, the resistivity of unpatterned films of magnetoresistive materials is measured using a four-point probe technique. Typical four-point probes use an in-line geometry but magnetoresistance measurements are best done with a rectangular configuration with the current applied along the long side of the rectangle and the voltage measured along the other long side of the configuration. The measurements are made in a varying applied magnetic field. The output is normally expressed as the ratio of the difference of the resistivities measured with the magnetization along the current direction ($\rho_\parallel$) and transverse to it ($\rho_\perp$), to the average resistivity; i.e.,

$$\rho_{\text{ave}} = \frac{\rho_\parallel - \rho_\perp}{\frac{1}{3}\rho_\parallel + \frac{2}{3}\rho_\perp}$$

The field that saturates the film or device, the anisotropy field H_k, together with the magnetoresistance ratio, forms the figure of merit, or usefulness. The amount of resistance change *per applied field* is often the quantity of interest. A device having a 50% change in resistance at several tesla may not be as useful to a system as one that has a 2% resistance change at less than a millitesla.

1.7 Magnetostriction Measurement

As a sample's magnetization is changed the material may deform and similarly as a material is stressed the magnetization may be affected. This phenomenon of magnetostriction is important for magnetic recording media and transducer fabrication, since stresses developed in these materials during deposition or patterning, or temperature-induced stresses due to thermal expansion mismatches between materials including the substrate, can dramatically affect the properties and performance of the materials and devices. To measure these effects on films for magnetic recording applications, film samples are typically prepared on substrates that are not perfectly rigid. The sample is placed in uniform applied magnetic fields that cause the sample to bend due to differential strains of the film and substrate. These small bends can be measured effectively using optical reflection: the position of a light spot specularly reflected off the sample's surface is monitored as a function of applied field (see *Magnetoelasticity in Nanoscale Heterogeneous Materials*).

1.8 Electron Microscopy

Since the introduction of magnetic force microscopy (MFM, see below) using an electron beam for imaging magnetic structure has been rendered largely obsolete because of the difficult sample preparation necessitated by electron microscopy. To the extent that it is still used, magnetic contrast in the electron microscope can be classified into three categories: scanning electron microscope (SEM), Lorentz deflection microscopy in the transmission electron microscope (TEM), and electron holography.

There are two basic modes of magnetic contrast in the SEM, denoted as type I and type II magnetic contrast. In these modes, the electron beam interacts with the sample and the fringing magnetic field. Type I contrast comes from polar magnetization through Lorentz force effects on the secondary electrons. In one orientation, the Lorentz force will cause more electrons to drift toward the detector while the opposite magnetization will force the secondary electrons away from the detector. Type II contrast images in-plane magnetization when the sample is rotated along an axis collinear with the magnetization. This technique involves number contrast with the backscattered electrons. As the electrons come near the sample the Lorentz force due to the magnetization will cause more electrons go toward the sample for one orientation while the other magnetization direction will force the electrons out, away from the sample. For these electron beam techniques, samples need to be clean and conductive (to reduce charging) and are placed in a vacuum. Spatial resolution of 50 nm is readily achieved but a quantitative measure of magnetization is impossible to obtain.

Transmission imaging in the TEM uses Lorentz forces as the electron beam passes through the sample. This diffraction contrast method is sensitive to in-plane magnetization and uses a defocused electron beam image. Imaging domains and domain ripple are the premier application for TEM Lorentz microscopy. Since the beam needs to pass through the material, samples must be thin and conductive, and usual techniques for vacuum sample preparation need to be observed. Submicron spatial resolution for this method can be achieved but higher resolution imaging can be very difficult.

Electron holography uses the interference effects as some of the electrons pass through a perturbing fringing field. These fields may even be from a magnetized sample of an energized device such as a recording head. The Lorentz force causes the electron path, integrated along the field, to deflect it from its nominal path. (See also *Magnetic Materials: Transmission Electron Microscopy*.)

1.9 Magnetic Force Microscopy

Developed from the 1986 Physics Nobel Prize winning development of the scanning tunneling microscope (STM), magnetic force microscopy (MFM) uses a small magnetic probe tip that scans over an area of a sample's surface. The tip first measures the sample's mechanical surface detail, then retraces the surface measuring the interaction between the magnetized tip and the fringing fields emanating from the sample's surface. In contrast with the original STM that requires a vacuum, MFM is typically performed in ambient conditions. As with most of the techniques described the measurement only senses the external fields. This necessarily means that the magnetization within the sample is not known directly and can only be inferred.

In a typical measurement, a micromachined cantilever with a pyramidal tip coated with a ferromagnetic film is vibrated at resonance (Fig. 2(a)). The fringing fields from the medium interact with the ferromagnetic tip shifting the tip's resonance. This frequency change is related to the strength and direction of the fringing field and the resolution is limited by the gradient of the magnetic field and the geometry of the tip. Quantitative MFM output is still being developed. The spatial resolution of this technique is currently about 30 nm. Images take several minutes to produce and are typically less than 100 micrometers square. The images are usually taken in remanence but techniques for making measurements at applied fields have been developed and are becoming widely used.

A striking example of the power of the method is shown in the image (Fig. 2(b)) of a track written on a longitudinal medium. The image displays not only
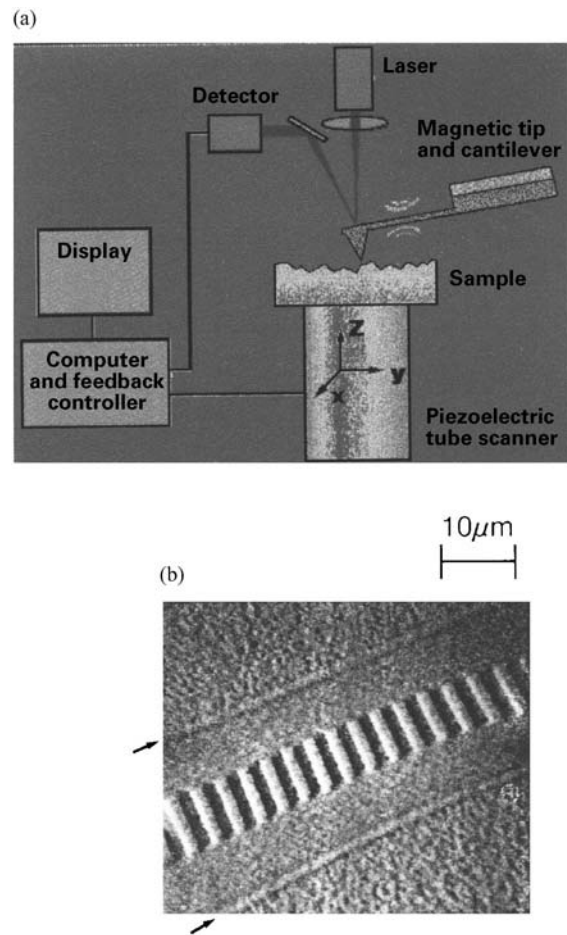
Figure 2
MFM illustration (schematic and typical output). (a) Schematic of a scanning probe microscope (MultiMode design). For magnetic imaging, the probe has a magnetic tip. The sample is moved in a raster pattern by the piezoelectric scanner, and the sample's stray fields cause shifts in the resonance of the cantilevered probe that are measured by laser detection. (Copyright © 1994 PennWell Publishing Co., Tulsa, OK. Reproduced with permission.) (b) MFM image (reproduced by permission of the American Institute of Physics from *J. Appl. Phys.*, 1990, **68**, 1169).

the written bits and the transitions between them; it also shows the contrast between the d.c.-erased region on which the track was written, a region which is at remanence with its relatively uniform magnetization, and the surrounding demagnetized region, with its randomly magnetized and hence noisier grain structure. (See also *Magnetic Force Microscopy*.)

2. General Recording

As a context for the application of magnetic measurement techniques to recording measurements, we begin with a brief outline of the various forms of the magnetic recording process. This context is necessary for an understanding of the relation between the measured macroscopic magnetic properties and the recorded signals. This includes such obvious relations as that between the amplitude of the signal and the remanence of the recording medium, or the medium coercivity and the demands on the saturation magnetization of the head, the less obvious effect of medium coercivity and saturation magnetization on the transition width in digital recording setting a bound on the bit cell size, and such subtle effects as the degree of intergrain exchange interaction on the noise properties of polycrystalline films.

2.1 Analog and Digital Recording

Analog recording still dominates consumer audio and video apparatus. In the standard audiotape cassette system, a carrier (called the a.c. bias) is amplitude modulated at the audio frequency and partially magnetizes a thick magnetic coating of the tape. The portion of the coating magnetized is linearly proportional to the audio signal. In the various video recording schemes, a frequency-modulated carrier saturates the tape, and the signal is recorded and detected in the zero crossings.

Digital magnetic recording is the standard in data storage and instrumentation recorders, is becoming so in professional audio and video recording, and has begun making inroads in consumer audio and video. In digital systems, the information is quantized and represented as a sequence of binary bits. The bits are recorded and sensed as transitions between saturated regions, usually along narrow tracks of magnetic tape or disk.

2.2 Anhysteretic Remanence

The media bearing magnetically recorded information are stored under ambient conditions. This means that their magnetic state is a remanent state from whatever magnetic history they have been subjected to, ordinarily not a state linearly related to the most recently experienced magnetic field. In saturation recording, the state is the conventional remanence, which is independent of the most recently experienced field, if that field was large enough. When linearity is required, as in analog audio recording, the linearity is provided by the a.c. bias field. In the presence of the bias field, the remanent magnetization is a function of the modulating field known as the anhysteretic remanence. The anhysteretic remanence curve is a linear function of the modulating field for small

values of that field, and the linear range is largest for bias fields near the medium coercivity.

2.3 Erasure

The virtually universal practice in saturation recording is direct overwriting. The write head field is designed to have a value several times the medium coercivity, so that any previously written information is wiped out. Incomplete erasure of track edges does present some problems, which are addressed by methods (servo, coding) discussed elsewhere.

Erasure is an essential requirement in linear audio recording, where any existing recorded signal would not be completely overwritten by the new information. The standard practice is to provide the transducer with a separate erase head. This head has a wider gap than the write or read heads, so that its field is assured of penetrating through the full thickness of the medium. The erase can be either d.c. or a.c. In d.c. erase, a large steady head field leaves the medium saturated, obliterating any existing information. In a.c. erase, a large oscillating field is gradually reduced to zero, leaving the medium demagnetized. In practice, a.c. erasure is achieved with an oscillating field of constant amplitude; the decrease of the field occurs as the tape leaves the head region.

2.4 Tape and Disk

Tape and disk storage have kept pace with increases in density and speed. Magnetic tape is polyethylene tape coated with a magnetic particulate or film medium. Signals are recorded on tape in linear, helical, or transverse tracks. The tape is stored on reels or cassettes. Magnetic disks are flexible (diskettes) or rigid. Flexible disks are made of polyethylene, usually coated with a particulate magnetic medium, and enclosed in a protective package. Rigid disks are aluminum alloy or glass, now universally coated with continuous magnetic films. Information is recorded in circular tracks.

Tape has the advantage of low cost and small volume per stored bit; disk the advantage of rapid direct access. These properties—and the scope of the competing optical storage technologies—affect the application areas of tape and disk. Tape dominates archival digital storage, and audio and video magnetic recording. Disks—including such developments as redundant arrays of inexpensive disks (RAID) are ubiquitous in storage for computers.

2.5 Particulate Recording Media

The original (and long since obsolete) recording medium was a magnetized wire. This was replaced by a plastic tape or disk coated with a medium consisting of submicron size magnetic particles in an organic

binder. The commonly used particles are iron oxide or chromium oxide or a magnetic metal or alloy; they are too small to sustain domain walls and each particle therefore is approximately uniformly magnetized. The particles typically are of elongated shape, giving each particle a preferential magnetization axis; an alternative class of particulate media use submicron barium ferrite platelets that have a very large magnetocrystalline anisotropy that aligns their magnetization along the platelet normal. In all these media the particles are spatially distributed randomly, and they can be geometrically oriented during fabrication.

In operation, each magnetized region of a particulate medium must contain a large enough number of particles to keep the noise due to number fluctuations and anisotropy distribution in bounds.

2.6 Film Media

A disadvantage of particulate media is the presence of the binder which constitutes wasted nonmagnetic volume, and the difficulty of fabricating media with magnetic volume fractions exceeding 60–70%. The disadvantage is overcome by using polycrystalline oxide, ferrite, and especially metallic alloy films whose grains can occupy very nearly the entire film volume. This also means that the medium can effectively be a single layer of grains, thus considerably thinner than a typical particulate medium. Very thin media are ideally suited for high-density longitudinal recording.

A generally undesirable consequence of close proximity is the resulting exchange coupling of the grains that leads to magnetic clustering and results in increased noise. Various metallurgical procedures have been found capable of inducing grain boundary compositional segregation that reduces the coupling and improves noise performance.

2.7 Longitudinal and Perpendicular Recording

Information is recorded by magnetizing regions of the recording medium in opposite directions either in the plane of the planar medium (longitudinal recording) or normal to the plane (perpendicular recording) (see Fig. 3). The dominant recording technology is longitudinal, but it has been argued for several decades that perpendicular recording offers advantages that will lead to its widespread adoption as recording densities increase. Longitudinal recording is favored by circumstances of history and inertia; in-plane magnetization is favored by shape anisotropy in thin planar media; longitudinal write heads are simpler; and the information is stored in the form of magnetic poles with large fringing fields. This last advantage is also a central problem of the technology, because the demagnetizing fields associated with the poles become destabilizing at high recording densities. In perpendicular recording the magnetization direction is determined by the chosen magnetocrystalline anisotropy of the material. Its greatest advantage is that oppositely magnetized adjacent regions give rise to magnetic dipoles instead of poles, and the resulting demagnetizing fields are stabilizing.

2.8 Keepered Media

Keepered media are films in which a magnetically soft film (the keeper) is deposited under the recording medium, on the side opposite the head, or on top of the recording layer (in which case the recording is done through the keeper layer) (see Fig. 4). This device addresses two of the issues raised in Sect. 2.7. In a longitudinal medium the adjacent soft magnetic film provides a low reluctance path for the demagnetizing flux, shunting it out of the medium itself. In a perpendicular medium it provides a low reluctance
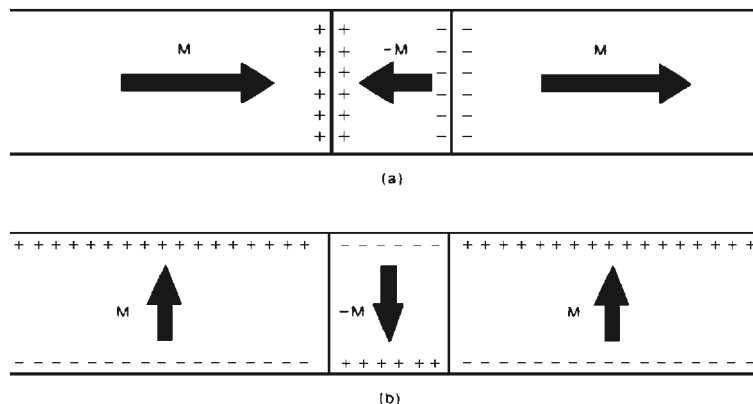
Figure 3
Longitudinal and perpendicular recording schematics (after Mee and Daniel 1990).
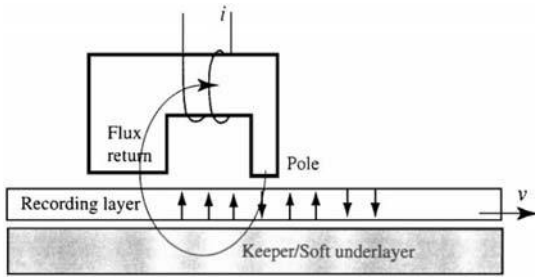
Figure 4
Perpendicular recording schematic with keepered media and probe-type head (reproduced by permission of Academic Press from *Magnetic Information Storage Technology*, 1999, p. 193).

return path for the perpendicular component of the write head flux, effectively increasing the recording layer thickness.

3.   Medium Measurements

3.1   Definitions and Measurements

Magnetization **M**: magnetic moment per unit volume, a vector quantity of magnitude M.

Hysteresis loop: a plot of magnetization M as a function of magnetic field H (Fig. 5). This is a multiple-valued function, depending on the sequence in which the time-varying field is applied. In the figure it is assumed that the measurement is made starting from a very large field in either direction.

Saturation magnetization M_s: strictly, the magnetization of a uniformly magnetized region (domain) in a homogeneous magnetic medium. This is an intrinsic property, a function of temperature, and weakly dependent on magnetic field and stress. In practice, M_s is also used for the magnetization M of any (not necessarily homogeneous) magnetic material in a large applied field.

Remanence (or remanent magnetization) M_r: the magnetization of a magnetic object that remains after it has been magnetized in a large applied field that is subsequently removed. Remanence is an extrinsic quantity that depends on microstructure, shape, and the phase of the moon (this last factor is meant to indicate the experimentalist's frustration with the sometimes apparently random fluctuations in the results of very carefully controlled measurements). A related quantity most meaningful for magnetic recording, especially with thin media, is the product of remanent magnetization and thickness $M_r t$. This quantity determines the magnetic moment associated with a bit cell of a given size, and thus the ability to detect it. $M_r t$ of a specimen of known area can be accurately measured in a VSM even if M_r and t are poorly determined.
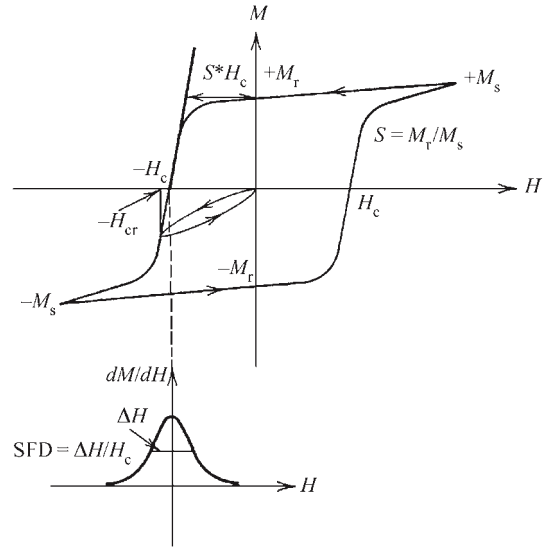
Figure 5
Schematic hysteresis loop (after Hoagland and Monson 1991).

Remanence curve $M_r(H)$: a plot of the sequence of final values of M reached when a specimen is cycled as follows: saturation by a large applied field; application of a reversing field H which is then reduced to zero; resaturation; and repetition with a different reversing field. On this curve, the remanence as defined above is $M_r(0)$.

The remanence curve of a specimen can be measured directly, for example in a VSM, by following this procedure, a time-consuming process. A fair approximation can be constructed from the hysteresis loop by drawing lines, with the slope of the loop at remanence, from the loop at several values of reversing field to the M-axis, and associating with each field value the value of M at the intersection with the axis.

The remanence curve of a recording medium can also be measured nondestructively on a spin stand by measuring the output voltage from nonsaturating transitions.

Coercivity H_c: the value of reverse applied magnetic field required to reduce the magnetization from remanence to zero in the presence of the reversing field.

Remanence coercivity H_{cr}: the value of reverse applied magnetic field required to reduce the magnetization from remanence to zero after the reversing field has been turned off.

Squareness: a measure of the degree to which the shape of a hysteresis loop is approximated by a rectangle. Two measures of squareness are in common use: the remanence squareness $S = M_r/M_s$ which measures how close the top and bottom traces of

the loop are to a horizontal; and the coercive square-ness S^* (see Fig. 5) which measures how close the tangent to the loop at H_c is to a vertical.

Anisotropy energy: energy associated with the direction of the vector magnetization **M** relative to a given set of axes. The energy is associated with the shape of the magnet and with its crystal structure. In an ellipsoidal body the shape anisotropy energy (extrinsic) is minimum when **M** lies along the longest principal axis, and higher when it lies along any other direction (for example, the magnetization of a magnetic needle tends to align along the needle, not across it). The magnetocrystalline anisotropy energy (intrinsic) K_a is the energy per unit volume associated with the direction of **M** relative to the crystal axes. For example, in a uniaxial crystal such as cobalt, $K_a = K\sin^2\varphi$, where K is the anisotropy constant and φ is the angle relative to the c-axis.

Anisotropy field H_k: a magnetic field that represents the magnetocrystalline anisotropy in the form $\mathbf{K_a} = -\mathbf{M} \cdot \mathbf{H_k}$. In a uniaxial crystal, the magnitude of H_k is $(2K/M_s)\sin 2\varphi$.

Magnetostriction: the deformation of a magnetic specimen when its magnetization **M** is varied and, conversely, the effect of a strain on **M**. The exchange and dipolar interaction energy of the atomic magnets on a crystal lattice depends on their orientation and on the bond lengths and bond angles. This energy can be represented as a magnetoelastic constant, an intrinsic property of the material, times the product of the strain tensor and the direction cosines of **M**. The equilibrium orientation and strain minimize the sum of the magnetoelastic energy, which is linear, and the elastic energy, which is quadratic in the strain (see also *Magnetoelastic Phenomena*).

Magnetic viscosity S: a measure of the thermally activated decay rate of the magnetization M. It is found experimentally that the magnetization of a magnetized body decays logarithmically over a wide range of time: $M(t) = M(0) - S\log t$. This behavior has been accounted for as being a summation of exponential Arrhenius type decays over a typical range of energy barriers. The viscosity S is a property of the magnetic material that is a function of temperature and of the applied reversing field and it is generally maximum when the reversing field is equal to the coercivity (see *Magnetic Viscosity*).

Grain size and size distribution: the most widely used media in rigid disk recording are polycrystalline films thin enough to consist of a single layer of grains. Individual grains of these films are too small to support magnetic domain walls, and therefore are approximately homogeneously magnetized. Measurements of grain size can use transmission or scanning electron microscopy. The distribution of grain sizes can affect the switching field distribution and the thermal stability.

Intergranular interactions, Henkel plots, and δM: the grain size sets the ultimate limit on the switching unit and hence on storage density. However, intergranular interactions can couple the switching behavior of neighboring grains, and contribute to medium noise. Intergranular exchange coupling can lead to the formation of grain clusters; dipolar interactions can favor parallelism (in longitudinal media) and antiparallelism (in perpendicular media) of neighboring grains.

A measure of intergranular coupling can be obtained by the use of a Henkel plot or the equivalent δM curve. The Henkel plot is generated by obtaining a curve named the isothermal remanent magnetization $M_{ri}(H)$. This curve is measured by the same procedure as $M_r(H)$ described above (in this context sometimes denoted $M_{rd}(H)$), except now the starting point of each cycle is a.c. demagnetization, with $M_{ri}(0) = 0$. It is easy to see that now, since initially half the switching units are already in the direction favored by the reversing field, only half as many will reverse with each field step. Thus one expects that $M_{rd}(H) = M_{ri}(\infty) - 2M_{ri}(H)$. This relation, however, only holds for non-interacting switching units, and deviations indicate the presence of intergranular coupling. The conventional form of representing the deviations is the Henkel plot, $M_{rd}(H)/M_{ri}(\infty) = 1 - 2M_{ri}(H)/M_{ri}(\infty) + \delta M(H)$, with δM positive for interactions favoring parallelism, negative for antiparallelism.

The measurement can be carried out on a coupon of the medium in a VSM, or nondestructively on a spin stand by measuring the output voltages from transitions written on the medium in saturated and a.c. demagnetized states.

Switching field distribution (SFD): the fraction of medium magnetization reversed per increment of reversing field range $\delta M/\delta H$. This is a function of H, peaking at or near H_c. SFD is also sometimes defined as the reversing field range required to reduce the magnetization of an initially saturated medium from $M_r/2$ to $-M_r/2$. SFD can be inferred from the remanence curve. It has also been measured by differencing MFM images and counting switching events.

Time dependence of measurements: the result of a measurement may depend on the time scale on which the measurement is carried out. The hysteresis loop of a specimen is usually measured on a VSM, on a time scale of minutes or hours, or on a *B–H* loop tracer, on a time scale of typically tens of milliseconds. Magnetization reversals in writing recording transitions take place in nanoseconds. As mentioned earlier, the medium response to a magnetic field is not instantaneous. Specifically, the coercivity of a medium depends on the time scale of the measurement, leading to the concept of a dynamic coercivity, which increases with the rate of field application. A phenomenological theory has been developed which is quite successful in accounting for such effects (Sharrock and Flanders 1990).

Orientation ratio: it is desirable in several media to have the magnetic properties along the track different from those across the track. For tape, the coercivity along the tape can be greater than that across it and for disks, the circumferential (recording direction) coercivity may be larger that the radial coercivity by tens of percent. This phenomenon is built into the material at the time of manufacture and can be controlled by the deposition conditions, especially angle of incidence and applied magnetic fields, or from anisotropy in the substrate, especially microscratching. The conventional measure of this is the ratio of the macroscopically measured recording to cross-track coercivities.

3.2 Head Measurements

The write head must generate enough flux to saturate the recording medium and must be able to operate at high enough frequency and/or with fast enough pulse response to satisfy the system requirements, and it must do these things with reasonable head efficiency and at low cost.

The earliest write heads were small electromagnets with high permeability ferromagnetic metal cores. They were satisfactory for low-frequency applications. The frequency response is limited by eddy current effects, which can be reduced by laminating the cores and pole pieces. This makes metal heads usable at high audio frequencies. Better performance at megahertz frequencies could be obtained by using high-resistivity ferrite cores. This sacrificed permeability and flux density for frequency and pulse response, but was satisfactory for writing on recording media whose coercivity was no higher than about a third of the ferrite's saturation magnetization, in the range of 1000 Oe. Ferrite heads continue to be used in video recording; these are typically single crystal structures fabricated by precision grinding, a relatively costly procedure.

Write heads for modern high-coercivity media are again fabricated from ferromagnetic metals and alloys, now in the form of high-moment, high-resistivity films thin enough to be resistant to eddy current losses. These heads, and the coils driving them, are fabricated as integrated structures by lithographic, deposition, and etching techniques similar to those used in the fabrication of integrated semiconductor circuits.

3.3 Write Head Fields

Most recording heads are inductive in nature: a soft ferromagnetic core is coupled to a conductive write coil (Figs. 6, 7). The current in the coil creates flux that flows through the magnetic pole pieces. Some of the flux squirts out of a gap in the magnetic circuit. This flux is used to magnetize regions of the magnetic
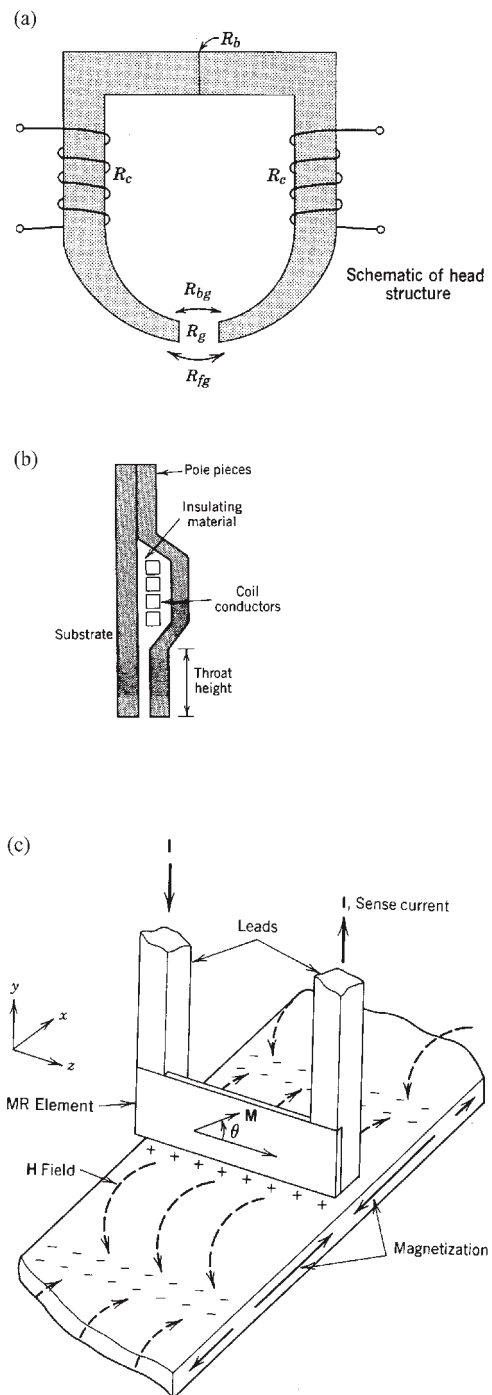
Figure 6
Recording head schematics: (a) ring-type head, (b) thin film-type head cross-section, (c) magnetoresistive (MR) head.
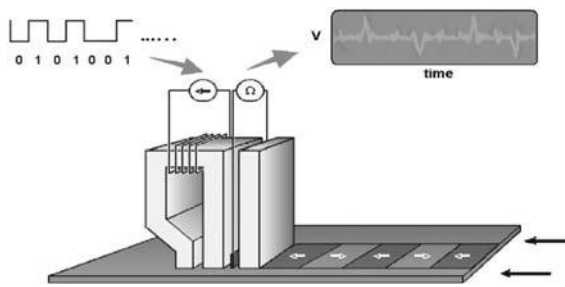
Figure 7
Recording schematic.

medium. The magnetic flux must be of sufficient strength to bring the magnetization to M_r. This field is typically much larger than the coercivity. A good rule of thumb is to supply a field about three to five times the medium's macroscopically quasistatically measured coercivity. To supply this large a field requires pole materials to have a very large effective permeability and saturation magnetization.

The pole piece saturation magnetization can be measured macroscopically in a variety of ways: VSM, a.c. hysteresis looper, etc. The effectiveness of the write field is verified easily through the saturation plot (see Sect. 4). The curve should reach and hold a maximum output, or even decrease slightly due to overwriting, for large currents. This indicates either that the medium is saturating or that the head pole material is saturating. If the head can write on higher coercivity media then saturation of the medium is differentiated from head saturation. Saturation of the pole material usually occurs first at the pole piece corners and where the coil couples with the poles. Once saturation is approached, the flux enhancement from the material's permeability is diminished.

The fabricated pole pieces typically have multi-domain structure. These domain structures can affect the writing process through speed, stability, and efficiency. Domains usually rotate faster than domain walls can move, so in multi-domain heads for high-speed applications it is desirable to have the walls pinned compelling the magnetization to rotate in response to applied fields. Domain wall jumps induce noise into the readback channel, even microseconds after writing. The direction and number of the domains also control the flux guiding property of the core.

The geometry of the writing field is controlled in large part by the geometry of the head pole pieces. The gap length controls the depth of the recording (of importance to particulate media but not for film media), the angle at which the medium sees the field, and the writing efficiency of the structure. During recording, the *gradient* of the write field is one of the most important metrics in defining good, sharply written

transitions. Optimal head design attempts to have the maximum of the field gradient occur where the field equals the medium coercivity, which is where the transition is written. In addition, the gap defines the side writing; the field that fringes from the side, creating an effective erase band but potentially erasing previously written data.

The recording head in a rigid disk or high-end tape drive may be asked to switch at nanosecond rates to accommodate data transfer rates of hundreds of megabytes per second. As with media measurements (especially the dynamic coercivity) the high-frequency character of the switching of magnetization in magnetic head structures is critical to the success of the operation of the head. a.c. hysteresis looper measurements and conventional permeameters are not able to operate in the gigahertz range. The measurements of materials for use in heads are typically done with a pulsed frequency measurement. One method involves discharging a charged capacitive structure into a narrow stripline. The current through the line induces a magnetic field around it. The presence of a magnetic material will change the impedance of the pulsed stripline structure. Pulses can produce subnanosecond fields and reach fractions of a tesla. Sophisticated recording measurements can be carried out that can separate the write field rise time effects from other system effects.

An increasing number of read transducers are not inductive but flux-based sensors. The phenomenon used most often is magnetoresistivity. The material's magnetoresistance ratio, $\Delta R/R$, and the anisotropy, H_k, control the sensitivity and ultimately the figure of merit of these transducers.

These properties may be measured on the bulk films or in the patterned sensors as described above. Domain structures, demagnetizing fields, and stresses can have a tremendous effect on ultimate device performance so it is most meaningful, but usually more difficult, to measure the properties of the transducer itself.

An important issue with system performance of these devices is stability. The write field can affect the read transducer by changing the nominal state of the films and can induce noise through changing domain states of the write head long after the write current has ceased. A biasing field, from currents or magnetic materials, is used to assist in creating a known initial state and linearizing the output. The bias design point can be inferred from the magnetoresistance transfer character measured as described previously.

The read gap, the effective separation between the shields, is the dominant factor that controls the spatial resolution of a read head and, hence, its high-frequency performance. The physical gap is usually about 10% shorter than the gap inferred from magnetic recording measurements. Magnetically inactive inner surfaces account for this increase in effective gap.

596

The read width is largely controlled by the separation between the conductive leads, although some devices exhibit sensitivity to flux from the side, known as side reading. In general, a write-wide/read-narrow configuration is desired for overall device performance. This relaxes the tolerance for servoing during a read operation, but trades off some signal output.

Flying height, the distance between the head and the medium, is important to system performance since the output decreases exponentially with this separation. For rigid media, the head is designed with an air bearing to fly over the medium. The flying height may be measured optically, using a transparent head. As the separations are nominally less than the wavelength of visible light, broadband white light interferometry is used for this determination. Capacitive measurement can also provide the flying height if the medium is conductive and the head has some conductive contact area. Since the output varies exponentially, recording measurements can be made to infer the flying height as well. In most tape systems, contact between the head and medium is assumed but it is experimentally found that high-velocity tape drives have nonzero head–medium separations.

4. Recording Measurements

4.1 Introduction

The measurements discussed above concern properties and parameters that affect the performance of the recording system, and that are measured using a variety of instrumentation. Some parameters that impact performance are significant only in the context of recording, and can be carried out only in the recording system itself, on a spin stand or using the disk or tape drive itself. This section describes such measurements.

4.2 Saturation Plot

The measurement of the recording output (voltage amplitude) as a function of write current is the saturation plot. Initially the medium is demagnetized or in uniform remanence (from d.c. saturation). The recording head is used to apply the magnetic fields. The spatial field gradients are enormous and have a huge impact on the resulting magnetization in the medium. Very small amplitude applied fields will have no effect on whatever state the medium is in. As the applied field is increased through application of larger currents, more and more of the medium will respond, in part through the SFD. If a square wave signal is applied to the head as it moves relative to the medium, the magnetization will approximate this square wave remanence

4.3 Density Plot or Rolloff Curve

The rolloff curve is a measurement of the recording (voltage amplitude) output as a function of the recording density. For longitudinal recording, low densities have larger output amplitude than the higher densities. This is a consequence of demagnetizing effects and of the finite gap length. The internal demagnetizing field stresses the remanent magnetization for these densities more than in low-density recordings. This spreads transitions and reduces the magnetization, causing a reduction in the sensed output. The finite gap length also affects the output as a function of recording density. It was shown (Wallace 1951) that the output of a single-frequency sinusoidal recording varies as a sine function of density, with the ratio of wavelength to read head gap length as the argument of the sine. For digital recording, the output tracks this phenomenon as the fundamental of the square wave recorded signal. The nulls in the sine function ("gap-nulls") correspond to an even number of transitions filling the length of the gap. D_{70} or D_{50}, the density before the first gap null at which the readback output is 70% or 50% of the low density output, are typical design values for the maximum density in a system.

4.4 Read Head Linearity, Asymmetry, and Baseline Shift

Read head output, in particular MR transducers, are characterized by their linearity and asymmetry as well as their down-track and across-track spatial resolution. The head may respond differently to upward flux from a positive magnetic transition than from downward flux arising from a negative transition (asymmetry). The output may also not respond linearly to applied flux—a stronger flux may not produce a proportionately larger output. In addition, the level the output may reach after sensing a positive transition may be different from the level seen after a negative transition (baseline shift). These asymmetric and nonlinear effects may challenge the channel demodulation and degrade system BER (bit error rate, the fraction—before any error correction—of a misread zero or one) and performance.

4.5 Noise Spectrum

One measurement of the background system perturbations is the averaged noise power. This measurement may be taken with a spectrum analyzer providing measure of the noise power over a wide band of frequencies. The measurement can be made with the medium in d.c. remanence, a.c. demagnetized, or written with a very high-frequency signal that may approximate a.c. erasure. Note that this

measurement does not account for any signal dependence of the noise.

4.6 Signal-to-noise Ratio

There are different ways of measuring a recording system's overall ability to reconstruct the written signal. In general, the system's ability to reproduce the written signal is proportional to the signal's amplitude with respect to the system's noise. It is assumed that the noise is independent of the signal and uniform over a broad frequency band (white Gaussian noise). A typical measurement of this metric is to record a single, moderate-valued frequency onto the medium, measure the signal's amplitude, and compare this output to the broadband noise. This noise may be measured from a medium that may have been erased with an a.c. or d.c. field, or may be written with a density beyond that which the system can reproduce. In a system characterized by Gaussian noise, the performance in detecting a signal is determined by the signal-to-noise ratio (SNR). Thus, the raw bit error rate is then determined by the SNR.

4.7 NLTS

When the transitions close in on one another their signal pulses begin also to overlap and interact, changing their perceived shape. For moderate recording densities, the pulses can be represented as the linear superposition of two independent pulses. Such linear phenomena are usually easy to characterize and can be effectively removed through pre- and post-compensation techniques. As the transitions move closer together, their output can no longer be represented as the linear superposition of independent pulses. This phenomenon, usually referred to as nonlinear transition shift (NLTS), may be due to magnetic interactions of one transition with another and erasure of the magnetization between the transitions, and may be caused by a combination of the writing process of the transitions and of effects after the transitions have been written. The measurement of this effect can be done in several ways: writing and reading series of di-bits, using a pseudo-random binary sequence, or measuring noise as a function of recording density of a single tone.

4.8 Track Profile and Bathtub

The ability to recover data is sensitive to the system's ability to remain on the data track during the time the transducer is reading the data. The measurement of track misalignment or track misregistration (TMR) is ever more challenging as the tracks become narrower. From a system viewpoint, the percentage of error allowed for TMR remains relatively constant. In general the head is not constantly being kept on track

but servoed intermittently for a short time and then allowed to run freely. The track profile is generally plotted as the track averaged output amplitude as a function of the distance off track. If the source for the read signal were a very narrow track the curve would trace out the read sensitivity function of the head: insensitive to signals far off to either side; increasing as the source comes closer to the head; and uniform as the source moves across the read head's width (provided that the sensor's configuration is symmetric).

Such a "micro-track" can be approximated by writing a full width track and erasing all but a very narrow region of the track. If the bit error rate is measured and plotted as a function of distance off track, the error would increase as the head moves from the track center. When plotted with the vertical axis as the log of the BER and the abscissa as a linear function off-track, the resulting curve resembles a bathtub. The base of this curve with the lowest BER (lowest probability of error) will be relatively flat for a small distance and rise along the edges as the read transducer moves further from the track center. The upper edge of the curve (bathtub edge) will be reached when the signal can no longer be determined, when the read head is completely off the written track (and cannot even read the signals from its edge).

The measured track profile includes both the read sensitivity and its width as well as the write head's write width. Typical head configurations using a magnetoresistive head for read along with an inductive writer are designed so that the written track is wider than the reader's sense width. This "write-wide/read-narrow" configuration trades off some read signal (since not all of the written magnetization's flux enters the head) for more robust tracking—the head can wander from the track-center and still be reading over the original track.

4.9 Squeeze and 747

These measurements are aimed at measuring the system's ability to reproduce recorded data in the presence of other information in adjacent tracks. After a test track has been written, adjacent tracks are written on both sides of the test track. The head is returned to the test rack center and the original data are read. Squeeze is measured as the adjacent tracks are moved in from afar. Initially the tracks have no effect, but will increasingly perturb the readback signal as they are brought in contact with the test track and then overwrite it. Eventually the test track will not be recoverable. This curve has a form something like the right side of a v-shaped valley. Due to the symmetrical approach from both sides of the over-writing tracks, it makes sense to plot only positive values.

In a more elaborate and more closely recording-like test, *old information* data tracks are first laid

down so that they extend (beyond, underneath) to the right and left of the test track (which overwrites a portion of the old information tracks). This is the worst-case situation for direct overwriting. The "747-curve" is formed as this situation is further aggravated by squeezing overwritten tracks into this situation and the original signal is measured with the head moved back on-track. Initially, when the squeeze tracks are far from the test track, no changes in the output are observed. When the squeeze tracks approach the test track, just enough so the edge of the head's erase band erases the old information but does NOT erase any part of the test track, the test signal becomes *easier* to read since all of the old information has been erased and the newly written signal is at least an erase-band's distance away. The system's off-track capability (OTC), or track misregistration (TMR) allowed to obtain a fixed BER increases slightly, proportional to the erase band of the write head. As the tracks squeeze in further, they begin to overwrite the test track reducing the OTC. These data, when plotted, modify the v-shaped valley as seen with a simple squeeze test by adding a mound to the top edge of the valley. This shape resembles the side view of a Boeing 747 aircraft: the nose rises to the hump of the cockpit that rolls off and levels out well above nose-level.

4.10   Write Width, Read Width, Side Reading, Side Writing

The physical, patterned dimensions of the head are usually not equal to the precise read and write widths as determined using recording measurements. The effects of all of these parameters are seen in any usual recording system. The read and write widths are typically wider than those measured optically. Most write elements produce fields along the edge of the head that tend to degrade or erase old information a fraction of a gap length. This effect may provide a system with a natural guardband. Likewise the reader senses flux arising from beyond the side of the head.

4.11   Pulse Shape

The shape of the voltage output is the product of the read head sensitivity function and the fringing magnetic field. The medium's magnetization controls only a part of the output pulse shape and the head's spatial extent determines the rest. The write field gradient, the medium's switching field distribution, and the demagnetizing fields at the transitions determine the sharpness of the magnetization through the transition and hence the spatial distribution of the external flux. The read head gap and the flying height define the spatial sensitivity of the sensor, analogous to the determination of spot size and resolution by the aperture in a classical optical system. The pulse shape in space determines the resolvability of a signal consisting of a set of pulses arising from closely spaced magnetic transitions. If the pulse is broad, the pulses will need to be spaced farther apart if the system is to recover the signal, as compared to a pulse whose amplitude is the same but whose width is narrower. The measurement of an isolated pulse's width is usually denoted by the width at half the amplitude height and designated as PW_{50}.

4.12   Jitter

The most critical effect in determining a digital, saturation recording system's ability to recover information is the timing of the transitions. The *mis*placement of this timing is jitter. If the transitions could be placed and sensed with unlimited precision, the amount of information stored would be boundless. In real systems, a fraction of the bit cell, denoted as the timing window, is the interval when the transitions are allowed to occur in order to be counted. If a transition falls outside of this window a raw error will occur. The timing errors can come from electronics noise, magnetic noise in the head, or from the magnetic medium (in particular its microstructure), and can manifest itself during writing, reading, and in general both. A jitter measurement quantifies the statistics of this uncertainty. A simple measurement consists of writing a single frequency square wave onto the medium and building up the histogram of the timing errors of the readback signal.

4.13   Thermal Decay

As areal recording densities steadily increase the size of the bit cells decrease proportionately. In order that the shrinking bit cells may contain sufficient grains to supply reasonable statistics, so that written signals can be easily recovered (conventionally at least hundreds of grains), grain size must shrink to accommodate these needs. The stability of the grain is a function of the volume of the grain. Thermal energy becomes comparable to the magnetic stabilization energy with grain sizes near the regime where the atoms are readily countable, roughly 100 Å on a side. In this superparamagnetic regime, the grain remains magnetized but the direction of its magnetization is changed by thermal agitation. In a recording system, this change in magnetization direction results in degradation of a recorded signal. Since this is a thermal effect, time as well as temperature is a determining factor of the amount of signal lost. Assuming Arrhenius behavior, an assembly of non-interacting particles, each having the same activation energy, displays an exponential decay of magnetization with time. A collection of non-interacting particles with a wide, uniform distribution of activation energies exhibits logarithmic time decay. Many conventional

recording media can be approximated by such a model. If a recording is stressed in time by heat or applied fields, this manifests itself as decay in the signal sensed. If the track averaged output is plotted against the logarithm of time, nearly linear decay may result and can be used to predict the signal that will remain after a given time, for a given temperature, at a given recording density (whose demagnetizing fields act to reduce the stability of the grain's magnetization).

4.14 Imaging Internal to the Drive

The scale of the magnetic features in a magnetic recording system can range from smaller than a single bit to many thousands of bits down-track or thousands of tracks wide. A millimeter long scratch, a thousandth of a millimeter wide, on a surface containing a million bits per square millimeter recorded with a bit aspect ratio of ten, may affect as many as ten thousand bits. Such a defect may be difficult to observe without taking the recording system apart. A sophisticated measurement that uses the read head as a probe of the surface and then plots the output from several adjacent tracks to build up a spatial picture of the surface can assist in the determination of systemic problems without having to disassemble the recording system. This type of functional imaging of the medium's surface can have resolution comparable to that of MFM and can be nondestructive.

See also: Longitudinal and Perpendicular Recording: Thermal Stability; Magnetic Recording Devices: Inductive Heads, Properties; Magnetic Recording Materials: Tape Particles, Magnetic Properties; Magnetic Recording Media: Particulate Dispersions

Bibliography

Aharoni A 1996 *Introduction to the Theory of Ferromagnetism*. Oxford University Press, New York
Ashar K G 1997 *Magnetic Disk Drive Technology: Heads, Media, Channel, Interfaces, and Integration*. IEEE Press, Piscataway, NJ
Bertram H N 1994 *Theory of Magnetic Recording*. Cambridge University Press, New York
Bozorth R M 1993 *Ferromagnetism*. IEEE Press, Piscataway, NJ
Brown W F 1963 *Micromagnetics*. Wiley, New York
Camras M 1988 *Magnetic Recording Handbook*. Van Nostrand Reinhold, New York
Chikazumi S 1964 *Physics of Magnetism*. Wiley, New York
Craik D J 1995 *Magnetism: Principles and Applications*. Wiley, New York
Hoagland A S, Monson K E 1991 *Digital Magnetic Recording*. Wiley, New York
Jorgensen F 1988 *The Complete Handbook of Magnetic Recording*, 3rd edn. Tab Books, Ridge Summit, PA
Jorgensen F 1996 *The Complete Handbook of Magnetic Recording*, 4th edn. McGraw-Hill, New York
Mallinson J C 1993 *The Foundations of Magnetic Recording*, 2nd edn. Academic Press, San Diego, CA
Mee C D, Daniel E D 1990 *Magnetic Recording Handbook: Technology and Applications*. McGraw-Hill, New York
Mee C D, Daniel E D 1996 *Magnetic Recording Technology*, 2nd edn. McGraw-Hill, New York
Morrish A H 2001 *The Physical Principles of Magnetism*. IEEE Press, Piscataway, NJ
O'Grady K, Chantrell R W, Popplewell J, Charles S W 1981 Time dependent magnetization of a system of fine cobalt particles. *IEEE Trans. Magn.* **17** (6), 2943–5
Sharrock M P, Flanders P J 1990 Time-dependent magnetic phenomena and particle-size effects in recording media. *IEEE Trans. Magn.* **26** (1), 193–7
Wang S X, Taratorin A M 1999 *Magnetic Information Storage Technology*. Academic Press, San Diego, CA
Wallace R L 1951 The reproduction of magnetically recorded signals. *Bell Syst. Tech. J.* **30**, 1145–73
Watkinson J 1990 *Coding for Digital Recording*. Focal Press, Stoneham, MA
White R M 1985 *Introduction to Magnetic Recording*. IEEE Press, Piscataway, NJ

R. S. Indeck and M. W. Muller
Washington University, St. Louis, Missouri, USA

Magnetic Recording Media: Advanced

The development of advanced metal particle (AMP) media was initially driven by the need to match the performance of metal evaporated (ME) media in terms of areal data density and recording performance (output, frequency response, etc.). In this article, the term 'advanced MP media' is taken to mean a magnetic recording system containing a thin magnetic layer, an underlayer, a substrate, and a back coat. A schematic representation of such a system is shown in Fig. 1. The primary role of the back coat is to act as a conductive layer to disperse any static charge that may build up on the tape. The back coat will not be addressed in this article other than to say it consists of carbon black (graphitic carbon) particles dispersed in a binder matrix with a typical layer thickness of $0.5\,\mu m$.

The technological advantage of AMP media, initially introduced by Fuji Photo Film in 1992 (Shibata *et al.* 1992) with their Advanced Thin Layer High Output Metal Media (ATOMM) and subsequently adopted by many other magnetic media companies producing advanced data recording products, is a tribute to the technical excellence of the media manufacturers. Details of the exact processes used by the media manufacturers to obtain such uniform thin magnetic coating layers remains very much proprietary information.
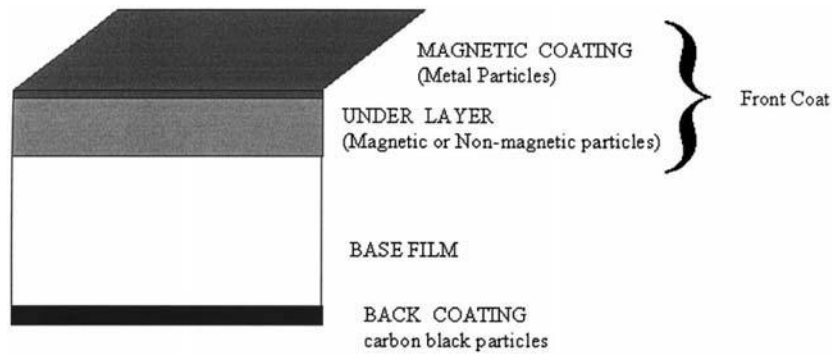
Figure 1
Schematic diagram of advanced MP media.

ATOMM technology is defined by the use of a dual layer front coating comprising a thin ($<0.25\,\mu m$) magnetic layer on top of a nonmagnetic underlayer ($<2.0\,\mu m$). The dual coat strategy confers the considerable advantages of reducing the surface roughness of the magnetic coating after post-coat calendering and improving the general durability of the media due to the design properties of the underlayer. Technological developments in the material science of metal particles, underlayer properties, and the substrate have contributed to the continued development of AMP media since the first introduction of a dual layer media product. The remainder of this article will address the development of each of these key areas, and address the impact of these developments on the recording performance of the system.

1. Metal Particle Development

The manufacture of metal particles is highly proprietary within the very few companies that have large-scale production capability. The general technology trend for the particle manufacturers is to continually evolve and improve the properties of the metal particles to meet the requirements of a two-fold data capacity increase in AMP media every 2–3 years.

The first metal particles for digital data storage, developed in the mid-1980s, had a coercivity of approximately 1500 Oe (119 kAm^{-1}), a particle length of 230 nm, aspect ratios of $>10{:}1$, and were based on a magnetic iron core protected by a passivating oxidation shell. Such a particle is shown schematically in Fig. 2. The corrosion resistance ($\Delta\sigma_s$) of these early metal particles, which measured the decrease in specific magnetization (σ_s), when subjected to 7 days storage at the environmental extremes of 60 °C and 90% relative humidity (RH), was typically around 20–25%. The loss of magnetic signal defined by $\Delta\sigma_s$ was initially a concern, as over time this corresponds to a reduction in the signal output from the tape. The
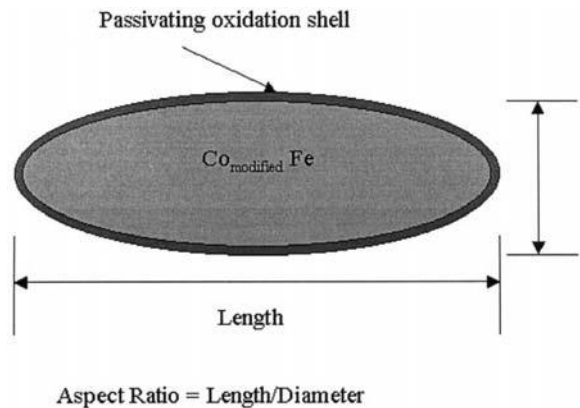
Figure 2
Schematic diagram of advanced metal particle.

early specialized surface treatments did manage to reduce this to $<10\%$, but with a corresponding loss in σ_s which compromised recording output of the media.

The incorporation of rare-earth elements in the protective oxidation shell improved the particle's corrosion resistance. The increased effectiveness of the outer shell in protecting the magnetic core from the degrading effects of oxidation allows a reduction in the average outer shell thickness. This reduction in the outer shell thickness increases the σ_s value by allowing an increase in the ratio of the volume of the magnetic core to the volume of the oxidation shell. The use of magnetic alloys, using 10–30% weight ratio cobalt alloyed with iron as the magnetic core, has also allowed an increase in coercivity from 1500 Oe to 2400 Oe (119 to 191 kAm^{-1}) for large-scale production particles. Current AMP formats such as DDS-3 and DDS-4 media use metal particles with coercivities as high as 2300 Oe (183 kAm^{-1}), particle lengths of <100 nm and aspect ratios from 4:1 to 5:1.

Table 1
Advanced media metal particle properties.

Classification	Year	Particle length (nm)	Coercivity (Oe)	σ_s (emu g^{-1})	$\Delta\sigma_s$	Particle volume (nm^3)
1st MP data type particle						
	1985	230	1500	122	20	49 000
MP+						
	1989	170	1600	121	20	38 600
MP++ AMP media						
	1993	100	1850	130	12	24 000
MP+++ AMP media						
High output	1995–1998	~100	2300	150	10–15	21 000
AMP media						
Low output	1999	~75	2400	110–140	~20	~10 000

Metal particle manufacturing technology continues to advance at a pace that addresses the requirements of high output, low noise, and acceptable $\Delta\sigma_s$ for AMP media, Okamoto *et al.* (1996). Metal particles can be customized to meet the requirements of specific applications. The current high output types have a σ_s of ~150 emu g^{-1} which is approximately 25% higher than the first metal particles introduced for digital data storage cartridges in the 1980s, such as DLTIII. This is achieved while maintaining or improving other important properties such as $\Delta\sigma_s$. The very latest metal particle types have also been reported to have particle lengths in the range of 40–60 nm to meet the requirements for low noise applications. Table 1 illustrates the evolution of the metal particle since the introduction in the 1980s to the AMP media applications.

The advantages of higher coercivity, smaller particle size, and increased σ_s gave considerable advantages in recording density and output. For example, a 'state of the art' single-coated MP data cartridge (DLTIII) of 1989 had a storage capacity of 10 GB and a transfer rate of 1.5 MBs^{-1}. This compares to a year 2000 data cartridge with 100 GB and transfer rate of ~15 MBs^{-1}. As the flexible media recording industry moves to recording systems using magneto-resistive (MR) head technologies the demand for high-output metal particles is being replaced by the need for lower noise systems, i.e., smaller particles with better dispersion properties.

As the particle size continues to reduce it becomes more difficult to maintain the coercivity and narrow switching field distribution of acicular particles, which depend upon shape anisotropy for their coercivity. The need for maintaining the higher coercivity and narrow switching field distribution of particles in the sub-30 nm size range have led researchers to investigate nano-sized spherical particles, which depend upon crystalline anisotropy for their coercivity. Examples of these spherical nano-particles, with

particle sizes of less than 20 nm, are FePt based particles (Hattori 2004) and iron-nitride based particles (Sasaki 2005).

2. Underlayer Technologies

The role of the underlayer is a crucial one for both the recording and tribological properties of AMP media. It is the underlayer in the dual coating process, which allows for the uniform thin, smooth magnetic coating required for the improved recording performance.

Saitoh *et al.* (1995) suggested that the role of the underlayer is to realize advantages in durability by replenishing the surface with lubricant from the underlayer. The head/media contact can also be adjusted by controlling the physical properties of the underlayer, and conductive agents in the underlayer can be used to control the electrical properties of the film. Initially the underlayer comprised of small, spherical TiO$_2$ particles to meet the required mechanical and durability properties. Saitoh *et al.* (1995) reported significant improvements in recording performance for the dual layer system compared to conventional single layer media.

The role of the underlayer was confirmed (Sasaki *et al.* 1997) and it was further reported that the friction coefficient of the dual layer tape could be lower than that of a single layer tape despite having a lower surface roughness. More recently, advanced non-spherical particles (nonmagnetic) have been used to control the interface between the magnetic layer and the underlayer (Inaba *et al.* 1998). The reliability/durability of recording systems using AMP media has been reported (Maness and Bradshaw 2000).

The underlayer may also be used to play a direct role in the recording properties of the media. Magnetic particles have been used in the underlayer to modify the long wavelength recording properties and

to improve the ability of the system to overwrite lower frequency signals with higher frequency signals (Veitch *et al.* 1999).

3. Substrates

The material science of substrates, or base films, has evolved with the quest for increased storage capacity per unit volume. Increasing the media length by reducing the substrate thickness has immediate advantages for increased storage capacity, provided that the transportation mechanics of the drive can handle the thinner media and that the desired conformance to the head contour (for stable head/media separation) can be satisfied. The development of linear recording formats using multiple data channels for higher transfer rate applications has led to the need for advanced substrates with very stable dimensional properties (Richards and Sharrock 1998).

3.1 Dimensional Stability

Dimensional stability is defined as the percentage change in either the transverse or the longitudinal direction when subjected to changes in temperature (thermal) or relative humidity (hygroscopic).

Polyethylene teraphthalate (PET) was the substrate material of choice for many generations of data tape, ranging in thickness from 39 μm (1960s, 9 track) to 6.2 μm (mid-1990s DLT). To achieve a 6 μm thickness in PET suitable for AMP media requires extensive processing in terms of increasing the film stiffness in either the longitudinal or transverse direction. The film process known as *tensilization* induces an orientation dependent crystallinity and increases the

mechanical stiffness (Young's modulus, creep, etc.). PET has a lower thickness limit of 6 μm and the demand for even thinner media and increased stiffness has been met by the introduction of substrate materials such as polyethylene naphthalate (PEN) and polyaramid (PA). Table 2 illustrates typical properties of AMP media substrates.

PEN and PA substrates have lower thermal and hygroscopic expansion coefficients than PET. This improves the dimensional stability when subjected to environmental extremes and is a key requirement for AMP multitrack, linear recording systems where the effects of thermal and hygroscopic expansion can cause a dimensional change both in the transverse and longitudinal direction of the substrate. For example, the transverse dimensional change has to be controlled within a tolerance that allows sufficiently accurate alignment of the recording heads with the data tracks across the operating environment of the system. This is particularly important for AMP media in a system such as LTO Ultrium, which has a total of 384 data tracks across the 12.65 mm tape width (Simmons 2000).

It can be calculated for this particular recording system that the transverse dimensional change must be limited to a maximum of 0.12% across the operating environment of the system (10–45 °C and 10–80% RH). The primary properties of the substrate are dictated by the chemistry of the substrate, but these can be influenced by the relative degree of tensilization in the longitudinal and transverse direction. This balance of tensilization, determined in the manufacturing process, is critically important in determining the final dimensional stability properties of the substrate. Table 3 illustrates the effect of tensilization on dimensional stability.

Table 2
Advanced media substrate properties.

Property	PET (tensilized in M/D)	PEN	PA
Minimum thickness AMP media	6.2 μm	5.0 μm	3.2 μm is commercially available
Creep: Load 28 MPa at 20 °C	0.7%	1.3%	0.8%
Tear strength M/D	350 gmm^{-1}	150 gmm^{-1}	200 gmm^{-1}
Heat shrinkage M/D 100 °C, 30 min	1.8%	0.1%	0%
Transverse dimensional stability	0.13%	0.09%	0.1%
Young's modulus M/D	7200 MPa	7800 MPa	11300 MPa
T/D	5800 MPa	8100 MPa	14700 MPa
Typical application	DLT IV (1996)	LTO Ultrium (2000)	DDS-3 and DDS-4 (1997 and 1999)

		PEN Substrate		
Classification		MD tensilized	MD semi-tensilized	Balanced
Young's modulus ($kg\,mm^{-2}$)	MD[1]	900	800	700
	TD[2]	600	650	730
Dimensional stability to thermal and hydroscopic expansion	MD[1]	Very good	Good	Fair
	TD[2]	Fair	Good	Very good

Note: MD = machine direction (longitudinal), TD = transverse direction.

3.2 Dual Surface Substrate

The requirement for higher and higher recording densities on thinner substrates have led the substrate manufacturers to focus on making smoother substrate surfaces to allow for a reduction in underlayer thickness. This has resulted in substrate surface roughness (R_a) decreasing from $\sim 40\,nm$ (1970s audio/video tape) to $< 10\,nm$ for the current generation of AMP media. Surface roughness is controlled by the addition of organic and inorganic filler particles with a tightly controlled particle size distribution.

These filler particles create protrusions at the surface of the substrate and a defined surface roughness, which is primarily dictated by the filler particle size. Smoother substrates ultimately give improved recording properties but smoother substrates are more difficult to transport and guide through the media manufacturing process. This presents the dilemma of satisfying the competing requirements of reducing the surface roughness for optimum recording performance while maintaining the substrates handling properties, required for the media manufacturer to precisely control the tension and winding of the substrate during a complex multistage coating operation. The major substrate manufacturers have met this challenge with the development of dual surface substrates, using their proprietary technologies that allow both of these requirements to be met.

The dual layer substrate results in an extremely smooth substrate 'front coat' surface ($R_a = 4\,nm$) and a rougher 'back coat' surface ($R_a = 9\,nm$), which aids processability of the substrate at the media manufacturer. The use of dual layer substrates, in place of single layer substrates ($R_a = 6\,nm$), may yield an output increase of up to 1.5 dB. AMP media products are beginning to migrate to the use of dual layer substrates for production of media with improved recording properties.

3.3 Other Substrate Properties

Other important substrate properties include creep and physical properties such as Young's Modulus and tear strength when subjected to load and thermal stresses typical of those the media is subjected to during normal drive winding and search operations. These properties are dominated by the polymer type but can be influenced by the processing in the same way as the dimensional stability characteristics can be customized for a particular application.

In a competitive data storage environment the substrate cost is important and undoubtedly is increasing due to the complex and evolving technology of substrate design and manufacturing.

4. Concluding Remarks

The combination of the key developments in all of these component (particles, substrate, and underlayers) technologies has enabled AMP media to match or exceed the recording performance of thin film (ME) tape media, and development continues at a rapid pace. The emergence of MR read and thin film write head technology in multitrack linear tape recording systems promises a long future of continued growth in AMP media and will require further development of smaller particles and thinner magnetic layers ($< 100\,nm$).

See also: Magnetic Recording: Particulate Media, Micromagnetic Simulations; Magnetic Recording Technologies: Overview; Metal Evaporated Tape; Metal Particle versus Metal Evaporated Tape; Micromagnetics: Basic Principles

Bibliography

Hattori Y, Waki K, Ogawa K, Furusawa G 2004 Synthesis of FePt and FePtCu nanoparticles by a reverse micelle method and studies of magnetic recording media using them. *Trans. Magn. Soc. Japan.* **4**, 85–8
Inaba A, Ejiri K, Masaki K, Kitahara T 1998 Development of an advanced metal particulate tape. *IEEE Trans. Magn.* **34**, 1666–8
Maness B, Bradshaw R 2000 Extensive testing/design features support LTO reliability/interoperability. *Data Storage* 30–3
Okamoto O, Okazaki Y, Nagai N, Uedaira S 1996 Advanced metal particles technologies for magnetic tapes. *J. Magn. Magn. Mater.* **155**, 60–6

Richards D B, Sharrock M P 1998 Key issues in the design of magnetic tapes for linear systems of high track density. *IEEE Trans. Magn.* **34**, 1878–82

Saitoh S, Inaba H, Kashiwagi A 1995 Developments and advances in thin layer particulate recording media. *IEEE Trans. Magn.* **31**, 2859–64

Sasaki Y, Nishida Y, Okamoto K, Kondo H 1997 Role of the under layer on surface smoothness and friction for double-layered particulate tape. *IEEE Trans. Magn.* **33**, 3064–6

Sasaki Y, Usuki N, Matsuo K, Kishimoto M 2005 Development of NanoCAP (Nano Compost Advanced Particles) technology for high density recording. Presented at Intermag. 2005 (paper GR-02) to be published in *IEEE Trans. Magn.*

Shibata N, Chino T, Chikamasa H 1992 Simultaneous video double layer coating technology. *Fujifilm Res. Develop.* **37**, 107–11

Simmons R 2000 HDD technologies key to Ultrium tape. *Data Storage* 25–8

Vietch R J, Ilmer A, Lenz W 1999 Improved overwrite performance of dual magnetic tape layer coatings. *IEEE Trans. Magn.* **35**, 2787–9

G. Spratt
Hewlett Packard, Boise, USA

P. Hobby
Philmore Group Limited, Monmouthshire, UK

Magnetic Recording Media: Particulate Dispersions

Magnetic particle dispersions or inks consist of magnetic particles suspended in a mixture of organic solvents by a wetting polymer (O'Grady *et al.* 1991). The particles are dispersed in a mill that applies shear forces to break apart aggregates. The wetting polymer adsorbs to the particle surface to provide a steric barrier that inhibits particle flocculation by magnetic attraction. The dispersion also contains lubricants and alumina particles to control the tribology (see *Magnetic Recording: Rigid Media, Tribology*) of the head–tape interface. Carbon black may be added to raise the conductivity of the coating, allowing the dissipation of static electricity. A polyisocyanate cross-linker is added immediately before coating. In this article we will consider the science of simple particulate dispersions that contain only magnetic particles, wetting binders, and organic solvents.

The ideal dispersion would have each particle separated from every other particle, the particles would have an adsorbed polymer layer, and the adsorbed polymer layer would be solvated by the organic solvents. The ideal dispersion of individually dispersed acicular particles is rare (Veitch *et al.* 1999) and more likely the particles are found in bundles.

1. Particle–Binder Interactions

1.1 Particle Size Distributions

The preparation of commercial iron particles is described in *Magnetic Recording: Rigid Media, Preparation*. The particles have a lognormal distribution of lengths, diameters, and aspect ratios. For particles used in high-end video tapes, our measurements found the average length was 190 nm, the average diameter was 22 nm, and the average aspect ratio was 9.8. The polydispersity of the distribution was 30.5%. The effect of this distribution on the physical properties of magnetic dispersions is not known. No one has ever prepared acicular particles with a monodisperse distribution of lengths and diameters. However, polydispersity in sizes does have an effect on the rheological properties of other colloidal systems (Roscoe 1952).

A suggestion of the effect of polydispersity in particle lengths comes from computer simulations of particle dynamics during orientation by an external magnetic field. A monodisperse distribution of sizes assembles into a smectic ordered phase consisting of layers with the particles oriented perpendicular to the layer (Visscher and Gunal 1997). When the particles have a lognormal distribution with a polydispersity of greater than 10%, the ability of the particles to form the ordered phases is suppressed (Visscher and Gunal 1998). Such ordering has never been observed in dispersions containing acicular magnetic particles. Commercial particles have a polydispersity ranging from 29% up to 53% (Inaba *et al.* 1998). It is interesting to imagine the potential benefits of highly ordered particle dispersions and the potential to achieve high degrees of orientation in the resulting magnetic coatings. One would first need to discover methods to produce monodisperse acicular magnetic particles.

1.2 Particle Surface Chemistry

Commercial iron particles have a thin oxide layer that serves three roles: (i) to prevent sintering during particle preparation, (ii) to modify the magnetic properties, and (iii) to passivate the iron surface. The thickness of the oxide layer is about 4 nm (Rosler *et al.* 1996). The oxide contains mostly aluminum, but can contain bismuth, boron, cerium, cobalt, neodymium, silicon, titanium (Gokturk and Maki 1997), or yttrium (Okamoto *et al.* 1996). Except for compositional data obtained from x-ray photoelectron spectra, little is known about the chemistry of the oxide layer.

The layer is amorphous, as one would expect, since the particles are processed at temperatures less than 500 °C. This is much lower than the crystallization temperature for alumina. If one considers the oxide layer to be a doped amorphous alumina phase, then the literature for alumina chemistry can provide

insight into the types of binding sites available for adsorbates (Henrich 1994). Alumina has both acidic and basic sites. The dopants play a role in determining the nature of the sites. Commercial iron particles are basic (Gokturk and Maki 1997, Veitch *et al.* 1999), which means there are more basic sites than acidic sites. The acid sites are coordinately unsaturated aluminum cations and the base sites are coordinately unsaturated oxygen anions (Hsaio *et al.* 1998).

1.3 Wetting Binders

The wetting binders are moderate molecular weight polymers containing anionic functional groups, e.g., carboxylates, sulfonates, or phosphonates that have a high affinity for the particle surface. The binders chemisorb to the particle surface, anchored primarily by the anionic functional groups. Other functional groups in the binder, such as alcohols, also adsorb to the particle surface. The binder also has loops and tails that extend from the anchor points away from the particle. This provides the steric stabilization of the dispersion. Early wetting binders had the wetting groups randomly distributed along the polymer chains. Subsequently the use of block copolymers has been reported (Weingart *et al.* 1996). One block is responsible for adsorption and the other block for steric stabilization.

The two most important wetting binders for MP tape have been poly(vinyl chloride) (PVC) and thermoplastic polyurethanes (TPUs). The PVC is a copolymer of vinyl chloride and vinyl acetate, where a portion of the acetate groups has been hydrolyzed to give vinyl alcohol groups. The most important PVC is MR-110 from Nippon Xenon (Jeon *et al.* 1997), which contains 0.5 wt.% vinyl alcohol. The alcohol groups have an affinity for the particle surface; however, MR-110 also contains 0.7 wt.% sulfonate groups that have a high affinity for the surface.

The weight average molecular weight (M_w) is about 26 000. On average, each polymer chain contains about one alcohol and one sulfonate wetting group. TPUs, such as Estanes from BFGoodrich or Morthanes from Morton International, have either sulfonate or phosphonate wetting groups. These are block copolymers containing polyester blocks coupled together with urethane linkages. The sulfonate groups are introduced into the polyester blocks via copolymerization of 5-sulfoisophthalic acid (Yatsuka *et al.* 1997).

1.4 Solvents

The solvents used in magnetic dispersions include ketones (methyl ethyl ketone (MEK), methyl isobutyl ketone (MIBK), or cyclohexanone), tetrahydrofuran (THF), and toluene. These are typically mixtures containing a highly volatile solvent (MEK or THF) and a less volatile solvent (MIBK, cyclohexanone, or toluene). The choice of solvent mixture is determined by dynamics of the drying process. After coating and orienting in a magnetic field, the more volatile solvent leaves the coating. This causes a large increase in viscosity that locks the particles in place. The less volatile solvent plasticizes the binder, allowing any stresses developed during drying to be relieved.

A problem with the organic solvents used in magnetic tape manufacture is their potential to cause air pollution. The US Environmental Protection Agency (EPA) has listed MEK, MIBK, and toluene as hazardous air pollutants. The regulations for the US magnetic tape industry have been published in the 1994 National Emissions Standards for Hazardous Air Pollutants (*Federal Register* 1994). In modern tape manufacturing plants the solvent vapors from the drier are recovered by use of a carbon bed adsorber. The carbon bed is stripped by steam, and the steam is condensed or put through a distillation column. This allows recovery and reuse of the individual components. Typically 93–95% of the solvents are captured and recycled. The coating operations are safe and the air emissions meet EPA standards. Considerable capital equipment is required to contain and recycle the organic solvents. With increasing worldwide concern for the environment, there will be increasing pressure to minimize or eliminate air pollution in tape coating operations.

1.5 Adsorption

Adsorption of molecular or macromolecular dispersants onto commercial iron particles follows a Langmuir isotherm behavior. The amount depends on the choice of anionic anchoring group and the solvent mixture. Adsorption of stearic acid from THF solution gives a Langmuir capacity of $52\,mg\,g^{-1}$, while adsorption from toluene solution gives a capacity of $86\,mg\,g^{-1}$ (Papirer *et al.* 1997). Clearly THF is competing with stearic acid for the surface sites.

Adsorption of bis(2-ethylhexyl) phosphate from THF solution gives a compact monolayer on the particle surface with a Langmuir capacity of $36\,mg\,g^{-1}$. THF does not compete with bis(2-ethylhexyl) phosphate for binding sites. Incorporating sulfonate groups into the polyester blocks of TPUs increases the amount of polymer adsorbed to the particle surface (Table 1). For a polymer having no sulfonate groups, adsorption from 64/36 wt.% toluene/2-butanone gives a capacity of $80\,mg\,g^{-1}$. When 2.5 mol% 5-sulfoisophthalic acid is incorporated into the polymer, the adsorption amount increases to $185\,mg\,g^{-1}$. For both polymers the amount adsorbed is significantly lower when cyclohexanone is included in the solvent mixture. Cyclohexanone is competing with the polymer for binding sites on the particles.

Table 1
Effect of the presence of sulfonate groups and the choice of solvent mixture on the adsorption capacity of thermoplastic polyurethanes.

Polymer[a]	Toluene (wt.%)	2-Butanone (wt.%)	Cyclohexanone (wt.%)	Capacity (mg g^{-1})
1	36.5	36.5	27	19
1	50	50	0	64
1	64	36	0	80
2	36.5	36.5	27	140
2	50	50	0	170
2	64	36	0	180

Source: Yatsuka *et al.* (1977).
a Polymer 1 has no 5-sulfoisophthalate groups, polymer 2 has 2.5 mol% 5-sulfoisophthalate.
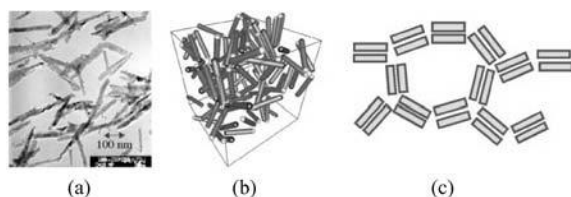
Figure 1
MP dispersion: (a) cryo-TEM photograph; (b) simulation; (c) schematic of dispersion microstructure with small bundles of particles connected in a network structure.

2. Characterization of Magnetic Inks

2.1 Microstructure of Magnetic Inks

The high concentration of magnetic particles in the ink results in strong magnetic and steric interparticle interactions. Figure 1(a) is a cryo-transmission electron microscopy (TEM) image of an MP ink (Chen and Nikles 2001). A microstructural simulation of an MP ink is shown in Fig. 1(b) (Visscher and Gunal 1997). A schematic that can be used as a model of the microstructure is shown in Fig. 1(c). Individual particles are usually held together in small bundles of particles in a side-by-side orientation of their magnetic moments. Weaker dipole–dipole magnetic attraction between the ends of these bundles link them together in a larger network or floc. The attractive magnetic interactions are countered by the steric repulsion force from the polymer adsorbed on the particle surfaces.

This microstructure determines the physical behavior of the ink and ultimately the properties of the final tape product. The interactions between aggregates determine the colloidal stability of the ink. The viscoelastic properties determine how the ink flows in the coating head and onto the web or onto an underlayer in the case of double coating. The net magnetic moment and size of the particles and aggregates and their interaction with other aggregates determines their ability to rotate in an orienting field.

These properties also affect how quickly the particles and aggregates will disorient due to elastic recovery and Brownian motion once the web moves beyond the orienting field.

2.2 Physical Properties of the Magnetic Inks

Many researchers have characterized the properties of magnetic ink using various rheological and magnetic techniques. The most common and meaningful test is to simply make a hand-drawn laboratory tape sample by spreading the ink on a plastic film or glass plate with a calibrated knife coater. When dry this sample can be observed optically with a gloss meter or microscope and tested in a VSM or BH loop tracer for magnetic properties such as coercivity, squareness, and switching field distribution. These tests are, of course, only an indirect measure of ink properties.

(a) Optical methods
It is difficult to use normal optical methods to view the ink because it is too thick to transmit light. Figure 1(a) was obtained by spreading a thin film of wet ink at its normal solids concentration onto a TEM grid with immediate quenching in liquid nitrogen to prevent the solvent from evaporating. It was kept frozen in a specialized TEM sample holder and observed at 10 000% magnification. Both the particle agglomerates and their network structure can be observed. However, one must search the TEM grid for regions thin enough to see through, leaving some doubt as to how representative any one region is. The ink can also be diluted with more solvent or other particles and dried on a TEM grid (Scholten and Felius 1990). The aggregates can be observed but their network structure is destroyed. These methods give qualitative insight into the structure of the ink.

(b) Rheology
It is common to test the rheology of the ink, especially the viscosity at high and low shear rates. In rheology
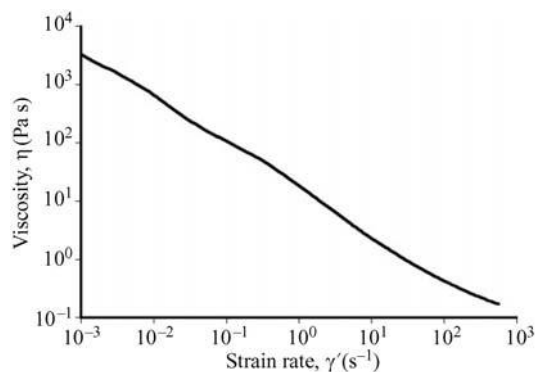
Figure 2
Viscosity as a function of shear rate for an MP
dispersion.

Figure 3
Storage (G', ▲) and loss (G'', ■) modulus as a function
of polymer concentration. G'' (●) is also shown for the
polymer solution.

measurements a force is applied to the surface of a
fluid and the rate at which it moves is measured. A
sample of ink is subjected to shear at a controlled
strain rate and the resulting stress is measured in a
controlled rate instrument or vice versa in a controlled
stress instrument. There are many variations of this
experiment with shear applied in a steady, transient,
or oscillatory fashion, at various amplitudes and fre-
quencies, in various geometries, and in the presence of
other shear and magnetic forces.

The viscosity as a function of shear rate for an MP
ink is shown in Fig. 2 (Chae, unpublished data, 2001).
The viscosity is the ratio of shear stress to shear rate
and should be constant for a Newtonian fluid. These
inks are decidedly non-Newtonian because of the in-
teractions between particles. At low shear rates the
network structure breaks and reforms on a time scale
faster than the shear rate resulting in a constant vis-
cosity. But high shear rates tear apart the structure
faster than it can reform, making the fluid easier to
move. This is called shear-thinning behavior.

The shear can be applied in a sinusoidal fashion to
obtain the storage (G') and loss modulus (G'') that
reflect the elastic and viscous nature of the ink. If the
amplitude is kept small, the particle microstructure
remains intact and can be probed. Figure 3 shows G'
and G'' of a Co–γ-Fe$_2$O$_3$ ink at various resin concen-
trations (Potanin *et al*. 1998). Magnetic inks are G'
dominant, unlike many polymer solutions. The elas-
ticity of the particle network is very strong. Further-
more, the moduli are much higher than for the resin
solution without particles, indicating that the visco-
elastic properties of the ink are largely determined by
the particle interactions. Note that the moduli under-
go a minimum at around 5 wt.% polymer concentra-
tion. At low polymer concentration, the magnetic
attraction between particles is very strong in the ab-
sence of good steric protection. At high polymer con-
centration, excess polymer builds up on the particles,
giving them a different type of elastic response.
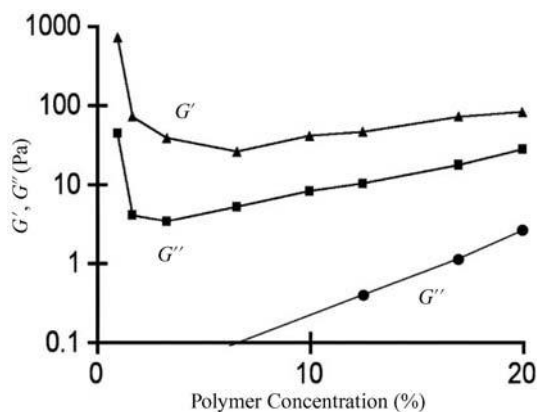
(c) Magnetic measurements

In a magnetic measurement an applied magnetic field
acts on the individual particles inside the ink. A VSM
measurement of a γ-Fe$_2$O$_3$ ink showed a "coercivity"
of 100 Oe that is due to particle rotation in the wet
ink and not magnetic switching (which can be seen as
a much smaller transition at 800 Oe) (Greaves *et al*.
1996a). The complication in interpreting magnetic
measurements of magnetic ink is that the particles
readily move, a phenomenon that does not happen
when measuring tape.

Methods have been demonstrated that effectively
prevent the particles from moving in response to the
magnetic field so that magnetic switching information
can be obtained. In one technique, the ink is frozen at
liquid nitrogen temperatures (with or without first
applying an orienting field) and kept frozen during a
VSM measurement. Figure 4 shows the interaction
parameter, δM, for a dispersion of barium ferrite
with different amounts of milling (Greaves *et al*.
1996b). The positive interactions (due to stacking of
the hexagonal platelets) decrease as the time of mill-
ing increases. In another technique, a special pulse
magnetometer is constructed to apply a field over a
period of 50 ns, too fast for the particle to physically
move, but slow enough for the magnetic moment to
switch (Greaves *et al*. 1996a).

Much information about the ink can be obtained
by observing the motion of the particles in a magne-
tic field. As with rheology there are many varia-
tions on this experiment with the field applied in
a steady (d.c.), transient, or oscillatory (a.c.) fashion,
at various amplitudes and frequencies, in various
geometries, and in the presence of other shear and
magnetic forces.

In a.c. susceptibility measurements, a low-ampli-
tude a.c. field wiggles the particles while their motion
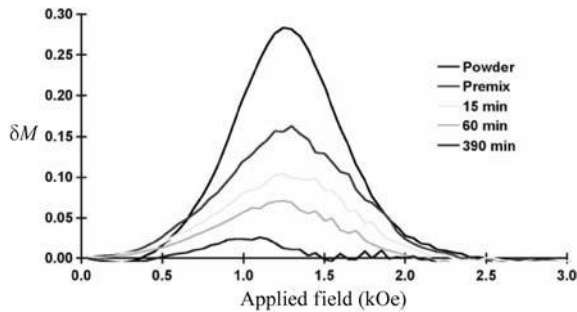
Figure 4
Interaction parameter, δM, as a function of applied d.c. field for barium ferrite inks milled for various times. The cryo-VSM technique was used to keep the ink frozen in order to eliminate particle motion.
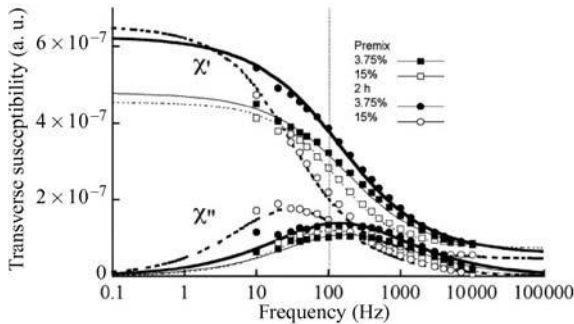
Figure 5
In-phase, χ', and out-of-phase, χ'', a.c. susceptibility of a Co–γ-Fe$_2$O$_3$ ink prepared with different resin concentrations and milling time.

is sensed by a pickup coil. If a transverse d.c. field is applied, the particles rotate perpendicular to the a.c. field, increasing the signal. This motion is presumably larger for better dispersed particles. However, in a dispersion of Co–γ-Fe$_2$O$_3$ particles with 3.75% or 15% wetting binder, the susceptibility (at an a.c. frequency of 100 Hz) improves with milling for the low-resin ink but decreases for the high-resin ink. Figure 5 shows the in-phase (χ') and out-of-phase (χ'') components of the a.c. susceptibility (with no transverse d.c. field) over a large frequency range (Peikov *et al.* 1999). The data are fit and extrapolated using a Cole–Cole model. The low-frequency a.c. susceptibility shows that both dispersions are actually improved with milling. The relaxation time, as indicated by the peak of the χ'' curve, shows a shift to longer times (lower frequencies) consistent with a buildup of polymer on the particles.

3. Conclusions

Much progress has been made in the understanding of the physical properties of magnetic inks and the underlying particle microstructure. It is still difficult, though, to determine exactly what makes a good ink become a good tape. Most techniques are demonstrated with very good and very bad dispersions (milling time, polymer concentration, solids content) and the differences are large and interpretable. But of more practical interest to industry is the difference between a very good and an excellent dispersion. This requires more fundamental research and development of a large body of experience.

See also: Magnetic Recording Technologies: Overview; Magnetic Recording Media: Advanced; Magnetic Recording Materials: Tape Particles, Magnetic Properties; Magnetic Recording: Rigid Media, Preparation; Metal Particle versus Metal Evaporated Tape

Bibliography

Chen M, Nikles D E 2001 Surface characterization of iron particles treated with a polyvinylchloride wetting binder. *IEEE Trans. Magn.* **37**, 1637

Federal Register 1994, **59** (240), 64180–612

Gokturk H, Maki K 1997 Surface properties and particle interactions of metal magnetic particles. *J. Magn. Magn. Mater.* **167**, 166–78

Greaves S J, Hancock C P, O'Grady K, Lane A M 1996a Pulse and low temperature magnetometry of γ-Fe$_2$O$_3$ dispersions. *IEEE Trans. Magn.* **32** (5), 4040–2

Greaves S J, O'Grady K, Lane A M 1996b Interaction effects in barium ferrite dispersions using low temperature magnetometry. *IEEE Trans. Magn.* **32** (5), 4046–8

Henrich V E 1994 *The Surface Science of Metal Oxides.* Cambridge University Press, London

Hsaio G S, Erley W, Ibach H 1998 Probing the surface acidity of single crystal alumina surfaces: CO adsorption as measured by infrared reflection absorption spectroscopy. *Surf. Sci.* **405**, L465–71

Inaba H, Ejiri K, Masaki K, Kitahara T 1998 Development of an advanced metal particle tape. *IEEE Trans. Magn.* **34** (4), 1666–9

Jeon K S, Shrauti S M, Arnold D W, Lane A M 1997 Transverse susceptibility and polymer adsorption of magnetic ink. *IEEE Trans. Magn.* **33**, 3067–9

O'Grady K, Gilson R G, Hobby P C 1991 Magnetic pigment dispersions (a tutorial review). *J. Magn. Magn. Mater.* **95**, 341–55

Okamoto K, Okazaki Y, Nagai N, Uedaira S 1996 Advanced metal particles technologies for magnetic tapes. *J. Magn. Magn. Mater.* **155**, 60–6

Papirer E, Walter E, Vidal A, Sifert B 1997 Adsorption of steric acid and diethylhexyl phosphate on magnetic metallic iron pigments: electrical surface charging and adsorption competition. *J. Coll. Interfac. Sci.* **187**, 529–38

Peikov V T, Jeon K S, Lane A M 1999 Characterization of magnetic inks by measurements of frequency dependence of AC susceptibility. *J. Magn. Magn. Mater.* **193**, 307

Potanin A A, Shrauti S M, Lane A M, Arnold D W 1998 Rheological probing of structure and pigment–resin interactions in dispersions of magnetic paints. *Rheol. Acta.* **37**, 1–8

Roscoe R 1952 The viscosity of suspensions of rigid spheres. *Brit. J. Appl. Phys.* **3**, 267–9

Rosler M A, Hofmeister H, Jakusch H 1996 Investigation of the oxide layer structure of iron pigments by high-resolution TEM. *J. Magn. Magn. Mater.* **162**, 377–82

Scholten P C, Felius J A P 1990 Observation of aggregates in magnetic particle lacquers. *IEEE Trans. Magn.* **26**, 1

Veitch R J, Ilmer A, Lenz W, Richter V 1999 MP technology for a new generation of magnetic tapes. *J. Magn. Magn. Mater.* **193**, 279–83

Visscher P B, Gunal Y 1997 Field-induced smectic ordering in model magnetic inks. *J. Appl. Phys.* **81**, 3827–9

Visscher P B, Gunal Y 1998 Self-assembly in model magnetic inks. *IEEE Trans. Magn.* **34**, 1687–9

Weingart F, Brodt G, Lehner A 1996 AB-block copolymers as dispersants in magnetic coating formulations. *J. Magn. Magn. Mater.* **155**, 77–9

Yatsuka T, Saimoto H, Shigemasa Y 1997 Evaluation of polyurethanes having SO_3Na group as magnetic binder: II. Two-step dispersion of magnetic particles. *Polym. J.* **29**, 358–65

A. M. Lane and D. E. Nikles
University of Alabama, Tuscaloosa, Alabama, USA

Magnetic Recording Systems: Spin Electronics

Hitherto, conventional electronics has ignored the spin of the electron. The charge carriers in ordinary electronic devices can not only have charges of different sign, they also possess spin which may be "up" or "down" with respect to a local quantization axis. However no use is made of this property.

Spin electronics is the new science and technology of electronic devices that recognizes the spin of the electron as a distinguishing label. Just as a conventional semiconductor transistor distinguishes families of electrons and holes by their opposite charge, a spin transistor divides the electrical carriers into differentially manipulated families (spin channels) which are either spin up or spin down.

Spin electronic devices function by transferring magnetic information from one part of the device to another by using nanoscale magnetic elements (mesomagnets) to encode it onto (and subsequently read it off) the spin channels. This coding may be changed by remagnetizing the mesomagnets thus enabling the creation of electronic components whose characteristics may be engineered to respond to applied magnetic fields.

The first (and simplest) spin electronic components were passive two-terminal devices—the giant magnetoresistance (GMR) trilayers that have already been adopted as the next generation read head technology in the hard-disk industry. Then followed the all-metal spin transistor, a passive three-terminal device. Its successor, the hot spin transistor, represents a very significant advance in that it is the first attempt to integrate silicon and ferromagnetic metals to make a hybrid spin-dependent electronic component.

Hybrid spin electronics (HSE) (which combine semiconductor and spin asymmetric technologies to make devices such as the hot spin transistor) is attractive because, in principle, it can offer nonvolatile memory function and sensitivity to magnetic fields in combination with the other functions generally available from semiconductors such as power gain, high input impedance, etc. Moreover, transport phenomena found only in semiconductors (such as depletion layers, diffusion currents, and the ability of junctions to screen out electric fields from adjacent material) offer a versatility of device design that is unthinkable in systems containing metals alone.

Two- and three-terminal spin-tunnel devices represent a parallel development, which has also generated two- and three-terminal memory and transistor devices with unusual characteristics. Spin tunneling would seem to have a number of advantages in terms of ease of fabrication, flexibility in design parameters, and size of output signal. Spin-tunnel devices seem set to dominate the magnetic memory market for the foreseeable future.

A development of the single electron transistor involving ferromagnetic electrodes has not been realized experimentally, but has wide potential application in information processing and electronic miniaturization.

Likewise the spin FET proposed by Datta and Das (1990) has received much attention but a working example has not yet been demonstrated.

1. Technical Basis of Spin Electronics: the Two Spin Channel Model

The basis of spin electronics was established in the 1930s with the observation that features of electrical transport in ferromagnets distinguished them from other metals. Mott (1936) explained this by postulating that the transport was effected by two independent families of carriers whose members are distinguished by their being either up-spin or down-spin. Spin flip processes are rare on the timescale of the other scattering processes that control the transport, hence these two spin channels may be regarded as being pseudo-independent.

1.1 Spin Asymmetry

The two-spin channel model is further qualified by the fact that the spin-up and spin-down electrons have different properties and this spin asymmetry

arises from the bandstructure splitting caused by the ferromagnetic exchange interaction. The splitting causes different densities of states at the Fermi energy and this in turn has two consequences: (i) the number of available carriers of a particular spin type or (in a tunneling process) the number of available final states for such carriers is different for each spin type; and (ii) owing to the different densities of final states for each spin type, they are differently affected by momentum-changing scattering processes and hence their mobilities are in general different. Most spin electronic phenomena are based on either or both of these asymmetries that have a common origin in the bandstructure splitting (Barthelemy and Fert 1991).

1.2 The Half-metallic Ferromagnet

In the extreme limit of spin asymmetry lies the half-metallic ferromagnet (HMF) (de Groot *et al.* 1984), in which the bandstructure splitting is such that only one spin band is available at the Fermi surface and hence all current must be carried by these so-called majority spins. Practical examples include chromium dioxide, lanthanum strontium manganite, magnetite, and some Heusler alloys. In reality, obtaining half-metallic spin electronic behavior is fraught with problems mainly to do with the interfaces.

1.3 Density of States Asymmetry Versus Mobility Asymmetry

The density of states asymmetry (which leads in the extreme case to half-metallic ferromagnets) and the mobility asymmetry compete with one another in spin electronics. The mobility asymmetry arises where the bandstructure at the Fermi surface contains components which have *s* and *d* character respectively. The *s*-like effective masses are small compared to the *d*-like masses and so the current is primarily mediated by *s*-electrons. However, the *d*-electrons are significantly split by the exchange interaction and present very different densities of states into which the *s*-electrons may be scattered. As a result, the *s* channel whose spin corresponds to the spin of the majority *d*-electrons suffers the most scattering and hence has lower mobility than the other *s* channel; the latter consequently carries most of the current. Thus, in a system with *s*- and *d*-like character at the Fermi surface, the tendency is for the current to be carried by the minority carriers (those with the lower density of states at the Fermi energy) whereas in a HMF clearly the current may only be carried by majority carriers.

This conflict between the two types of asymmetry is one reason why spin tunnel devices have an advantage over their competitors since they exploit only the density of states asymmetry and the mobility asymmetry has no chance to compete and reduce the overall device performance.

2. Spin Injection Across an Interface

Clearly if one carrier spin type is dominant in the electrical transport of a ferromagnet, then when a current is passed from such a ferromagnet to a paramagnetic metal such as silver or aluminum, the electrical current brings with it a net injection of spin angular momentum and hence also magnetization (Johnson and Silsbee 1985).

2.1 Spin Accumulation and Spin Diffusion Length

This magnetization that builds up in the new material is known as a spin accumulation. Its size in the paramagnetic metal is determined by a balance between the spin injection rate at the interface and the spin-flipping rate in the body of the paramagnet. The injected magnetization diffuses away from the interface and decays exponentially on a length scale called the spin diffusion length test l_{sd} given by

$$l_{sd} = \sqrt{v_F \tau_{\uparrow\downarrow} \lambda / 3}$$

where v_F is Fermi velocity, $\tau_{\uparrow\downarrow}$ is the spin flip time, and λ is the mean free path. The actual size of the spin accumulation in terms of the spin density n at distance x from the interface is given as

$$n = n_0 \exp\left(-x/l_{sd}\right)$$

where n_0, the density at the interface, is given by

$$n_0 = 3\alpha j l_{sd}/ev_F \lambda$$

where α is polarization of the ferromagnet and j is current density at the interface. Substituting typical numbers of $j = 1000$ Acm^{-2}, $\alpha = 1$, $v_F = 10^6$ ms^{-1}, $\lambda = 5$ nm, $l_{sd} = 100$ nm gives a value of spin density of 10^{22} m^{-3} as opposed to a total electron density of about 10^{28} m^{-3}.

That such small asymmetries in spin density can give rise to such huge electrical transport effects as GMR is yet one more example of the dominance of the electrons at the metal Fermi surface which is where these spins are concentrated.

Various practical methods of measuring the spin diffusion length have been described (Yang *et al.* 1994). Measuring the spin density or its associated magnetization is difficult owing to its smallness and the difficulty in distinguishing convincingly the magnetic fields associated with the accumulation itself from those caused by the current that is generating the accumulation.

An elegant analysis of the spin accumulation phenomenon (Valet and Fert 1993) proceeds by treating

it as a divergence of the electrochemical potentials for spin-up and spin-down carriers either side of the interface. This treatment shows clearly the relationship between the accumulations both sides of the interface and also how the magnitude of the accumulation depends on the relative conductivities of each metal. This has implications for spin injection into low conductivity materials such as doped semiconductors.

2.2 The Role of Impurities in Spin Electronics

From the expression above for spin diffusion length it is clear that introducing impurities into the material concerned diminishes l_{sd} rapidly for two reasons: the impurities shorten the mean free path and also the spin flip time via spin-orbit scattering (Fert *et al.* 1995). The latter may be thought of as a relativistic effect: under Lorentz transform, electric fields assume a magnetic component. To electrons at the Fermi surface which have weakly relativistic velocities, the electric fields generated by impurity atoms appear weakly magnetic. If the symmetry of the impurity site is sufficiently low, this field may Zeeman couple to the S^+, S^- operators that induce spin–flip transitions. Hence materials with point defects and low symmetry structural disorder are likely to exhibit reduced spin diffusion lengths (Dubois *et al.* 1999).

3. Two-terminal Spin Electronics

The simplest spin electronic devices are called GMR trilayers or spin valves depending on their magnetic construction, i.e., whether the layers are RKKY-coupled or exchange pinned. They have two terminals and consist of sandwiches comprising three metal films: two ferromagnetic metal films flanking a film of nonmagnetic metal. If the terminals are contacted to the two ferromagnetic films the configuration of the device is described as current perpendicular to plane (CPP). However the terminals may also be attached to opposite ends of the film stack such that the current flows through all three films to transit the device: this configuration is known as current in plane (CIP). The magnetizations of the ferromagnetic layers are engineered to lie antiparallel in zero magnetic field (by either RKKY coupling or exchange biasing), but application of an external field may align them. When this happens the electrical resistance between the device terminals drops, a phenomenon known as giant magnetoresistance. For a fuller description see *Magnetoresistance, Anisotropic*; *Giant Magnetoresistance*, *Magnetoresistance: Magnetic and Nonmagnetic Intermetallic*.

3.1 CPP GMR

CPP GMR may be explained, with recourse to the Valet/Fert model (Valet and Fert 1993), in terms of the electrochemical potential splittings at the successive interfaces. If the interfaces are separated by a distance less than a spin diffusion length, the successive spin accumulations interfere and generate additional electrochemical potential drops associated with the interfaces. These change with the magnetic configuration of the device and in turn they translate into changes in the resistance of the overall device (Lee *et al.* 1993).

3.2 The Analogy with Polarized Light

A more immediate way to understand the physical significance of this phenomenon is by analogy with crossed optical polarizers. In the extreme case in which the ferromagnets are half metallic, they accept or dispense only electrons of one spin type, for example spin-up (parallel to the magnetization). Assuming that the intermediate nonmagnetic layer is thinner than a spin diffusion length, this means that the spin emitted by one magnetic layer preserves its polarization until it meets the other layer. Whether it gains access to this second ferromagnetic layer then depends on whether the magnetizations of the two layers are parallel or antiparallel. The analogy with optical linear polarizers is exact except in that the extinction angle in the spin electronic case is $180°$ rather than $90°$. As expected from this model, the GMR varies as the cosine of the angle between magnetic layers (Dieny *et al.* 1991).

3.3 The Resistor Model of GMR

A simple parallel resistor model may thus be used to describe CPP GMR. The two parallel paths, each consisting of two series resistors, represent the respective spin channels and the first and second resistors in each path are the resistances which they experience at the first and second interfaces respectively.

If we arbitrarily assign resistance values of $1\,\Omega$ and $10\,\Omega$ to the majority and minority interface resistances, it is seen that the magnetization parallel and antiparallel configurations have overall resistance of $1.8\,\Omega$ and $5.5\,\Omega$ respectively.

3.4 CIP GMR

This was in fact the first GMR to be experimentally demonstrated, its geometry being easier to realize than the CPP geometry, which requires sophisticated nanolithography (Baibich *et al.* 1988). CIP GMR is characterized by the same drop in electrical resistance of the thin film sample when a magnetic field is applied. However the explanation is fundamentally different. Symmetry considerations show clearly that no spin accumulation is set up in this case since current flow is parallel to the layers. Instead the explanation

invokes the differential mobilities of the spin-up and spin-down electrons and relies on the nonmagnetic interlayer being sufficiently thin that a high proportion of the current carrying electrons experience successive momentum scattering events in different magnetic layers. This in turn means that if the layers are antiparallel, either spin type has high mobility since each experiences heavy scattering in one or other layer. However if the layers are parallel, one spin type is heavily scattered in both layers and the other spin type is relatively unscattered and hence its high mobility electrically short-circuits the device. The resistor model above works equally for the CIP geometry: the two parallel paths are again representative of the spin channels and the resistors represent the scattering they experience in the respective layers, assuming that their trajectories sample both layers.

3.5 Comparative Length Scales of CIP and CPP GMR

It is evident for this discussion that two quite different length scales are relevant to CIP and CPP GMR. For CPP GMR, the interlayer must be less than the spin diffusion length whereas for CIP GMR to appear the interlayer must be less than a mean free path which is a rather shorter distance. In practice typical CIP GMR multilayers use nonmagnetic spacers of the order of 10 Å or less.

3.6 Inverse GMR

In the above discussion it is assumed that the metals in the two ferromagnetic layers are similar, or at least that the sign of their polarizations is the same. That is to say that the majority spin for each ferromagnet is parallel to the magnetization (positive polarization) or antiparallel to the magnetization (negative polarization). If a combination of two ferromagnets with opposite polarizations is used to make a GMR trilayer, the GMR is inverted which means that the resistance of the device increases on application of an external magnetic field. This is because when the ferromagnets have parallel magnetizations they disagree as to which spin direction is the majority type (Renard *et al.* 1996).

3.7 Obtaining Differential Magnetization: RKKY Coupling Versus Exchange Pinning—The Spin Valve

There are two techniques used to engineer GMR systems such that the two ferromagnetic layers are differentially switchable in an externally applied field.

(a) RKKY coupling
The first technique involves making the metallic interlayer of such a thickness (of order 1 nm) that the

RKKY coupling across it between the magnetic layers is antiferromagnetic and so the layers antialign in zero applied field but are parallel in applied field (Parkin *et al.* 1990). This technique imposes constraints on the device design, which may militate against obtaining the best GMR signal.

(b) The spin valve
The other technique is to make one layer magnetically hard by exchange pinning it to an antiferromagnet on the side opposite to that which abuts the GMR device. In this case only the unpinned soft layer moves in small magnetic fields. The resulting device is termed a spin valve (Dieny *et al.* 1991).

3.8 The Artificial Antiferromagnet (AAF)

The AAF is a clever combination of the two above ideas. No RKKY coupling is used in the GMR spacer layer. However, one of the ferromagnetic electrodes is rendered magnetically hard by fabricating it from two distinct ferromagnetic layers A and B of almost identical thickness, which are RKKY-coupled such that in zero applied field they are antiparallel and hence their net moment is small. The switching field of this artificial antiferromagnet block (A + B) is thus enhanced by a so-called Q factor which is the ratio of the total magnetic moment when A and B are aligned in a high field to the net moment when A and B are antialigned (Tiusan *et al.* 1999).

3.9 GMR in Nanowires

An interesting practical realization of CPP GMR is by using electroplating technology to construct metallic nanowires in nanopores of a membrane (Piraux *et al.* 1994). With a suitable electrolyte containing a selection of ions, the material being deposited may be varied every few nanometers along the wire by switching the value of the electroplating potential, thereby creating a magnetic multilayer structure. This technique has the added convenience that the geometry of the wires is conducive to easy measurement, unlike thin evaporated films, which must be lithographed in order to obtain specimens whose resistance is high enough for practical purposes.

4. Quantum Tunneling

If two conducting layers between which a potential is applied are separated by a thin insulating film, electrical current passes between the metal electrodes by quantum mechanical tunneling of the current carriers through the insulating tunnel barrier. The tunneling rate for carriers of a particular energy is proportional to the product of the carrier densities of states at that energy each side of the barrier. Also, the thinner the

barrier and the lower the barrier height, the larger the current. This phenomenon was extensively studied in the context of superconducting thin films where it enables accurate determination of the superconducting energy gap (Giaever and Megerle 1961).

4.1 Spin Tunnel Junctions

Spin tunnel junctions are two-terminal spin electronic devices whose magnetotransport characteristics closely mirror those of CPP GMR trilayers, except that their parameters are more readily adaptable to practical applications. They consist of pairs of ferromagnetic electrodes separated by electrical insulators and they exhibit large changes in tunnel resistance depending on the relative alignment of the ferromagnetic electrode magnetizations. The thickness of the tunnel barrier must be in the low nanometer regime to obtain reasonable current densities. The effect may be understood, at least simplistically, according to a model of Julliere (1975) which was in turn inspired by the ideas of Merservey and Tedrow (1971), in which the tunnel current is proportional to the product of the densities of spin-states either side of the tunnel barrier.

In the simple case of HMF electrodes whose magnetic moments are anti-aligned, it is clear that the product of the initial and final densities of states is zero for either spin type and no current flows. However if the moments are aligned the half band of majority spins may tunnel and the device will have low resistance. It may be seen that this device is highly analogous to the CPP GMR trilayer except that it relies exclusively on asymmetry in density of states and does not invoke mobility spin asymmetry. This makes analysis cleaner and also means that in general the magnetoresistance (MR) effects are larger. Also, because tunneling and not ohmic conduction is involved, the resistance of a tunnel junction is higher than that of an all-metallic GMR system of comparable geometry and this makes spin tunnel junctions rather more easily adaptable to practical applications.

4.2 Refinements in the Understanding of Spin Tunneling

The simple Julliere tunneling theory gives good insight into the physical basis of spin tunneling but is incapable of explaining the finer experimental detail. For example, most spin tunnel junctions display a bias-dependent magnetoresistance whose explanation needs a more sophisticated treatment (Chui 1997). Moreover, simple spin tunneling theory suggests that a particular spin asymmetric material should always exhibit the same characteristic polarization for tunneling processes and that this polarization value is closely related to and predictable from its bulk bandstructure. However, experiment reveals that, on the contrary, the polarization which magnetic electrodes manifest for tunneling purposes is found to be a function of the magnetic metal/insulator combination, not just of the magnetic metal itself. The polarization of a particular spin electronic material may actually change sign depending on which insulator accompanies it (De Teresa *et al.* 1999). The explanation is thought to be that the tunneling electrons come from the first few atomic layers of the metal which are hybridized with the insulator and hence do not have the bulk bandstructure. Since spin electronic effects are almost all interface related, it is generally these interface bandstructures that are more relevant to practical device performance.

4.3 Spin Tunnel Junction Resistance and Heat Dissipation

Spin tunnel junctions are characterized by a real conductance per unit area. The associated junction resistance scales roughly exponentially (according to the very simplest theory) with thickness and barrier height. However the net dissipation associated with this tunnel resistance when a tunnel current flows is not dissipated in the junction itself but rather in the conducting material on its downstream side. Hot carriers are injected into this region from the junction insulator and thermalize rapidly owing to their being high above the Fermi surface where there is a high density of empty states into which they may scatter.

4.4 Coherent Spin Tunneling—Resonant Structures

Clearly if two separate tunnel junctions are cascaded their resistances add according to Ohm's law. However, if the junctions are sufficiently close that the wavefunction of the electrons entering the first junction is coherent with those exiting the second junction, in other words the transport is ballistic in the layer separating the junctions, the analysis is more complex. This implies that, since the electrons have at least partially preserved their phase memory, they have not been properly thermalized in the intermediate layer and the concept of single junction resistance is not valid. The entire multiple tunnel structure must then be analyzed as an entity in similar fashion to that in which optical thin film interference filters are treated. Such resonant tunnel structures are potentially useful for making spin-tunnel devices with a high back-to- front electrical transmission ratio.

5. Superparamagnetism

There are three main energy terms that govern ferromagnetic behavior: the magnetostatic energy stored in the magnetic field surrounding a ferromagnet with free magnetic poles; the exchange energy, which

varies with the cosine of the angle between adjacent spins; and the anisotropy energy, which increases if any individual spin orients itself at an angle to the easy direction in the material. Reduction of the magnetostatic energy is the reason for the existence of ferromagnetic domains. However, between any two domains is a domain wall whose width and energy are determined by a trade-off between the other two energy terms, the exchange and the anisotropy energies. The magnetostatic energy of a specimen scales as its volume V and domain wall energy as cross-sectional area. This implies that for ferromagnetic systems below a certain dimensional threshold, the energy needed to create a domain wall in the system exceeds the magnetostatic energy reduction that this would effect.

Such particles are thus single domained and termed superparamagnetic since they behave as a single giant spin. This giant spin has lowest free energy when aligned along its easy axis. If the system has uniaxial anisotropy with the easy direction on this axis, then below a certain critical temperature T_b (called the blocking temperature) given by $KV = k_B T_b$, single domain particles are trapped in one or other of the potential wells in free energy which correspond to magnetization parallel or antiparallel to the easy direction. Such a system is said to be blocked and, unlike a superparamagnet (i.e., itself at higher temperature) has a hysteretic magnetic response (Bean and Livingstone 1959).

5.1 Granular GMR Materials

When different proportions (say 20%, 80%) of two immiscible metals are cosputtered and then annealed, the initial interatomic mixture phase separates into granules of one metal in a matrix of the other. If the granules are ferromagnetic and the matrix paramagnetic, the resulting material exhibits GMR. Such materials may also be formed by mechanical alloying. The effect was first observed by Gerritson (1959) before the theory existed to explain the phenomenon. The GMR arises because in zero field the angle between adjacent magnetic granules is totally random whereas in high magnetic field the moments are virtually all aligned. Simple trigonometry shows that the GMR, which is again proportional to the cosine of these inter-grain angles, varies as the square of the sample magnetization (Barnard *et al*. 1992, Berkowitz *et al*. 1992). In the absence of significant interaction between the grains this is experimentally verified. Owing to the geometry of such granular systems, the GMR that they exhibit is a mixture of CIP and CPP and both characteristic length scales for these two phenomena are in play (see *Giant Magnetoresistance*).

5.2 Jitterbug Depolarization

Granular GMR systems comprise a spread of magnetic particle sizes whose span depends on the mode of preparation. The larger particles whose diameters are of the order of the electron mean free path contribute to the GMR. The smaller particles are insufficiently large to cause appreciable scattering but they nevertheless play a role in determining the magnetotransport by causing passing spins to precess. This spin precession causes the spin to turn through an angle, which is a function of the incident spin orientation, the particle magnetization orientation, and the particle thickness. The result is a progressive depolarization or mixing of the spin channels, which militates against the GMR. This spin mixing mechanism is called the jitterbug effect after the swing-dance of that name which the electron's successive random precessions resemble (Gehring *et al*. 1995).

6. Giant Thermal Magnetoresistance

Electrical current carriers are capable of mediating a variety of signals. These include not only electric current and magnetization but also heat. Thermal and electrical transport in metals generally are closely related, as witness the Peltier effect (using an electric current to produce cooling) and the thermoelectric effect (using a thermal difference to generate a voltage). The Wiedemann–Franz Law (see *Boltzmann Equation and Scattering Mechanisms*) also tells us that there is an intimate relationship between the thermal and electrical conductivities of metals under most circumstances. This close connection is further extended in the case of magnetoconductivity. Just as the electrical conductivity of a giant magnetoresistive material is a function of applied magnetic field, so also is the thermal conductivity, though the percentage effects may be different owing to the different way in which the thermal information is encoded onto the electrical carriers that mediate it (Daniel *et al*. 1995).

7. The Exchange Length in Spin Electronics: The Ferromagnetic Domain Wall as a Giant Magnetoresistor

Exchange length is an ambiguous term in nanomagnetism, which may be taken as the characteristic length scale defined by the exchange energy and the magnetostatic energy, or more practically by the exchange energy and the anisotropy energy. In the latter case it is closely related to the thickness of ferromagnetic domain walls.

The electrical resistivity associated with ferromagnetic metal domain walls has been a subject of intensive study for many decades (Berger 1991, Cabrera and Falicov 1974). A spin electronic interpretation of this resistance is possible which draws on the analogy between a ferromagnetic domain wall and a GMR trilayer (Gregg *et al*. 1996). When the wall is present the magnetizations either side are antiparallel and

when it is absent they are parallel. In the limit where the carrier spins traverse the wall with spin directions unaltered, the analogy with CPP transport in a GMR trilayer is complete. However, depending on the strength of the exchange field and hence the spin's pseudo-Larmor precession frequency, and also the wall thickness, the spin directions of the transiting carriers may track the magnetization rotation in the domain wall more or less adiabatically. Any mistracking gives rise to a quantum mechanical admixture of the opposite spin wavefunction which lays the spin open to momentum scattering by the normal processes which cause resistance. This model gives rise to an expression for the increase in resistivity of material in a domain wall of:

$$\delta\rho_W/\rho_0 = (\lambda^*/\lambda + \lambda/\lambda^* - 2)\langle \sin^2 (\theta/2)\rangle$$

Unlike other previous models for domain wall resistance, this model predicts a percentage resistance change for such material which is independent of impurity content.

Very large magnetotransport effects (of the order of 600%) have been observed in ferromagnetic nanocontacts between oppositely magnetized domains of half-metallic ferromagnet (magnetite) (Versluijs *et al.* 2001).

8. Three-terminal Spin Electronics: The Johnson Transistor

Three-terminal spin electronics is the logical succession to GMR and TMR devices and is realized in the simplest case by attaching a third electrode to the intermediate layer in an all-metallic GMR system (Johnson 1993).

The result is the Johnson spin transistor. Its function may be briefly understood as follows. It is assumed for simplicity that the ferromagnets are half-metallic. We denote the new connection to the paramagnetic intermediate layer of the trilayer as the "base," and the connections to the ferromagnetic layers as the "emitter" and "collector," respectively. The device is biased by pumping an electron current through from emitter to base, thereby establishing a spin accumulation in the base, which extends to meet the base–collector interface. If the collector is left electrically floating, i.e., its potential is monitored by a high impedance voltmeter, which draws from it no current. Since the collector is capable of accepting only one spin type, it floats at a potential which equalizes its electrochemical potential with that of the corresponding spin type in the base. Since the base has a spin accumulation, this implies that its spin-up and spin-down electrochemical potentials are different and hence that the floating potential of the collector will alter by this differential if the magnetization of the collector (of the emitter spin injector) is

reversed. Thus, we have the embodiment of a three-terminal spin electronic device: electrical characteristics of the third electrode determined by the relative conditions at the other two and in addition the capability of changing this dependence by applying a magnetic field.

9. Power Gain and Noise Considerations in All-metallic Spin Electronics

The Johnson transistor is an all-metal device that obeys Ohm's law and as such it cannot deliver signal power gain without further modification. This might take the form of additional terminals or a change to the internal structure. Moreover, the source impedances of such devices are small, particularly those with perpendicular structures. Optimizing noise figure when matching small source impedances to conventional electronics is difficult and requires impedance transformation, which is frequently bulky and impractical.

10. Hybrid Spin Electronics

A potential solution to these technical problems is found in hybrid spin electronics. This is the combination of spin-asymmetric materials with conventional semiconductors. It releases to the spin electronic designer a variety of constructional options such as deployment of reverse biased junctions with minimal admittance, depletion layers to screen regions of the device, and diffusive carrier transport.

10.1 The Monsma Transistor

The first hybrid spin electronic device was the Monsma transistor produced by the University of Twente which was fabricated by sandwiching a traditional spin valve device between two layers of silicon (Monsma *et al.* 1995). Three electrical contacts are made to the spin-valve base layer and the respective silicon layers. The spin valve is more sophisticated than that discussed above and comprises multiple magnetic/nonmagnetic bilayers, but the operating principle is the same. Schottky barriers form at the interfaces between the silicon and the metal structure and these absorb the bias voltages applied between pairs of terminals. The collector Schottky barrier is back biased and the emitter Schottky is forward biased. This has the effect of injecting (unpolarized) hot electrons from the semiconductor emitter into the metallic base high above its Fermi energy. The question now is whether the hot electrons can travel across the thickness of the base and retain enough energy to surmount the collector Schottky barrier. If not they remain in the base and get swept out the base connection.

By varying the magnetic configuration of the base magnetic multilayer the operator can determine how

much energy the hot electrons lose in their passage across the base. If the magnetic layers are antiferromagnetically aligned in the multilayer then both spin types experience heavy scattering in one or other magnetic layer orientation, so the average energy of both spin types decays rapidly as a function of distance. On the other hand, if the magnetic multilayer is in an applied field and its layers are all aligned, one spin class gets scattered heavily in every magnetic layer, whereas the other class is lightly scattered everywhere and hence retains its "hot" status over a longer distance. Thus, for parallel magnetic alignment, spins with higher average energy impinge on the collector barrier and the collected current is correspondingly higher. Once again we have a transistor whose electrical characteristics are magnetically tunable. This time, however, the current gain and the magnetic sensitivity are sufficiently large that, with help from some conventional electronics, this is a candidate for a practical working device.

Evidently, there is a tradeoff to be made in determining the optimum base thickness. A thin base allows a large collector current harvest but affords little magnetic discrimination. A thick base on the other hand means a large factor between the collector currents corresponding to the two magnetic states of the multilayer but an abysmally small current gain. (The low current gain has always been the Achilles heel of metal base transistors, and is probably the main reason for their fall from favor as practical devices despite their good high frequency performance owing to the absence of base charge storage.)

An interesting feature of the Monsma transistor is that the transmission selection at the collector barrier is done on the basis of energy. Thus, the scattering processes in the base that determine collected current are the inelastic ones. Elastic collisions that change momentum but not energy are of less significance. This contrasts with the functioning of a spin valve-type system in which all momentum changing collision processes have the same status in determining device performance.

10.2 Spin Transport in Semiconductors

The Monsma transistor represents a very important step in the evolution of spin electronics. It is the first combination of spin-selective materials with semiconductor. However, as yet, the semiconductor is used only to generate barriers and shield the spin-dependent part of the device from electric fields. To release the full potential of hybrid spin electronics we need to make devices that exploit spin-dependent transport in the semiconductor itself.

10.3 The SPICE Transistor

The current gain of a conventional bipolar transistor is in part due to the screening action of the junctions either side of the base, which absorb the bias voltages and leave the base region relatively free of electric fields. The current which diffuses across the base is primarily driven by carrier concentration gradient and to a rather lesser extent by electric field and the randomness associated with concentration driven current flow helps to improve the current gain. The carriers injected by the emitter are forced to wander towards the base along the top of an extended cliff in voltage, at the bottom of which lies the collector. For example, 99% of the carriers stumble over the cliff and are swept out the collector and the remaining 1% make it to the base connection; this gives a very satisfactory current gain $\beta = I_c/I_b$ of 99.

Implementing spin-polarized current transport in a semiconductor enables a new concept in spin transistor design—the spin-polarized injection current emitter device (SPICE) (Gregg *et al.* 1997) in which the emitter launches a spin-polarized current into the electric field screened region and a spin-selective guard-rail along the top of the cliff determines whether these polarized carriers are allowed to fall into the collector. Thus, we have a device with a respectable current gain from which power-gain may easily be derived, but whose characteristics may again be switched by manipulating the magnetic guard rail via an externally applied magnetic field. A wide variety of designs are possible which answer to this general principle. For example the emitter and collector interfaces may be realized by *p–n* junctions, Schottky barriers, or spin tunnel junctions and the geometry of the device may be adjusted to allow a greater or lesser degree of electric field driving component to the diffusion current in the base depending on the application.

10.4 Measuring Spin Decoherence in Semiconductors

The crucial question which needs to be answered in order to realize this kind of spin transistor is whether spin transport is possible at all in semiconductors, and, if so, whether it is possible over the sort of physical dimensions on which a typical transistor is built. In other words, we need an estimate of the spin diffusion length in a typical semiconductor. A subsidiary question concerns the role of dopants in the semiconductor and whether they introduce spin-orbit scattering, which militates against the spin transport by reducing the spin flip times. Some consideration has been given to allowed nonequilibrium spin configurations in a semiconductor (Flatte and Byers 2000).

10.5 Direct Spin Injection from Metals to Semiconductors

Experiments have been performed (Gregg *et al.* 1997, Jia *et al.* 1996) in which ferromagnetic contacts

perform direct spin-injection into a semiconductor and analyze the polarization of the current that emerges on the other side. Transport results are observed which are insensitive to magnetic field direction, have even symmetry (thereby eliminating AMR and Hall effect as a possible cause) and they are compatible with the observed domain magnetization processes for the cobalt pads. They appear to correspond to spin transport through the semiconductor. However the spin transport effects are of the order of a few percent at best, yet the effect decays only very slightly with silicon channel length and was still well observable for 64 μm channels. This suggests that the spin diffusion length in silicon is many tens of microns at the least, but that the spin injection process at the metal/silicon interface is highly inefficient. Clearly the process is highly preparation sensitive as witnessed by the null results with evaporated silicon (Loraine *et al.* 2000).

This direct injection inefficiency is being widely observed and its cause is still hotly debated. It may arise from spin depolarization by surface states, or it may be explainable by the Valet/Fert model (Valet and Fert 1993) in which spin injection is less efficient for materials of very different conductivities. The discussion below in connection with spin tunneling concerning hybridization at the interface with the spin selective injector is no doubt relevant in this context also. It may also be because the spin injection is not being implemented at the optimum point in the semiconductor bandstructure. From the latter point of view, spin tunnel injection into semiconductors is a more versatile technique, since, for a given injected tunnel-current density, the necessary bias (and hence the point in the band-structure where injection occurs) may be tuned by varying the thickness and/or the tunnel barrier height.

10.6   Optical Polarized Carrier Generation

A direct measurement of semiconductor spin diffusion length has been made by decoupling from the spin injection problem and generating the spin-polarized carriers in the semiconductor itself (Hagele *et al.* 1998, Kikkawa and Awschalom 1999). Gallium arsenide was used as the host that has the property that, when pumped with circularly polarized light, the selection rules are such as to populate the conduction band with predominantly one spin type. These spins can be made to precess by application of a small magnetic field. The resulting precessing magnetization is then detected using optical Faraday rotation using a probe beam from the same optics as provides the pump. The magnetization drifts under the application of a driving electric field and the spatial decay in precession signal gives a measure of the spin diffusion length. The results are of the order of many tens of microns, in accordance with the silicon direct injection experiment discussed above.

Thus, it would seem beyond doubt that the spin diffusion length in semiconductors is adequate for the design and realization of SPICE-type transistor structures—so long as means are provided for efficient delivery of the initial spin-polarized current.

10.7   Spin Injection from Magnetic Semiconductors

An alternative method of generating spin-polarized carriers in a semiconductor is by injection from a magnetic semiconductor (Fiederling *et al.* 1999, Ohno *et al.* 1999). Striking results are obtained by injecting spin-polarized carriers from a magnetic semiconductor into a normal semiconductor light emitting diode structure. The polarization of the injected carriers is dependent on the magnetization direction of the magnetic semiconductor that supplies them. This is reflected in the polarization of the light emitted by the LED—its polarization is related to the spin of the electrons which cause it via the same selection rules as discussed above in the Awschalom experiment (Hagele *et al.* 1998, Kikkawa and Awschalom 1999). The polarization of the light emitted correlates well with the hysteresis loop for the magnetic semiconductor and decays with temperature exactly as the magnetic moment of the magnetic semiconductor, leaving little doubt that successful spin injection has been achieved. The percentage injection achieved here is more favorable than has been possible by direct injection from metals and it may be that magnetic semiconductors have an important role to play in future spin electronics development, notwithstanding the non-negligible materials problems which they pose.

Spin-tunnel injection into semiconductors is also a promising technique which offers higher injection efficiency than direct spin-injection (Prins *et al.* 1996).

11.   The Rashba Effect

The Lorentz transformation indicates that to a relativistic observer traveling with respect to the source of an electric field, it appears to have a magnetic component whose orientation depends on the geometry of the observer's travel relative to the field axis. If the electric field in question originates from crystal field effects or from the depletion layer in a semiconductor structure, then the magnetic component that appears to relativistic electrical carriers is capable of spin-splitting the conduction band if it is diagonal and of causing spin precession if it is off-diagonal. This is the Rashba effect.

11.1   The Datta–Das Transistor or Spin FET

The Rashba effect gives rise to a novel spin electronic device concept proposed by Datta and Das (Datta and Das 1990), but not realized experimentally. The device has the construction similar to that of a

conventional field effect transistor with source and drain electrodes made in ferromagnetic metals and a semiconductor channel which is subject to a transverse electric field whose magnitude may be tuned by applying a gate voltage. Spin-polarized carriers leave the source with their spins parallel to the source magnetization and precess in transit through the channel owing to the Rashba effect. If the drain magnetization is parallel to that of the source and the carriers perform an integral number of precessions in transit, then the device conductance is high. However, slight modification to the gate voltage changes the precession rate and if the spins now execute $N + 1/2$ precessions in transit, the device conductance is minimized. The resulting device thus behaves like a normal FET with the additional feature that the differential magnetization of its electrodes (and hence its electrical characteristics) are sensitive to externally applied magnetic field.

Although the device has not been realized, much groundwork on the materials properties and principles exist in the literature and spin-valve effects have apparently been observed in experiments involving two-dimensional electron gases in which spin-polarized carriers are injected from a permalloy contact into an AlSb/InAs quantum well and analyzed by a second permalloy contact with a different switching field (Hammar *et al.* 1999).

However some skepticism has been voiced by other workers on the spin FET problem (van Wees *et al.* 2000), and theoretical signposts have been placed to spin precession-type data which will unambiguously confirm that Datta–Das-type device function has been observed (Tang *et al.* 2000). This is clearly an exciting topic which will continue to attract attention and research activity for the foreseeable future.

12. Coulomb Effects: Coulomb Blockade and the Single Electron Transistor

The electrostatic energy of a charged capacitor is $\frac{1}{2}Q^2/C$. If C is sufficiently small, this energy can compete with thermal quanta of size k_BT, even for $Q = e$, the electronic charge. Small metallic spheres or pads with physical dimensions in the nanometer range have capacitances in the right ballpark for this condition to be obtained. If such a metallic island is sandwiched between two physically close metallic electrodes (the source and the drain), a single electron transistor (SET) is formed (Devoret and Grabert 1992). A third electrode (the gate) which is capacitatively coupled to the metallic island is biased in order to pass current or to coulomb blockade the SET.

The physics involved is a competition between three energy terms; the electrostatic energy, E_i, of the island due to the presence on it of just one electron, the thermal quantum k_BT, and the energy eV_b gained

by an electron in falling through the bias voltage V_b. The first electron which arrives on the island from the source electrode charges it to a potential which is sufficient to prevent any further electrons hopping to the island until the first electron has left via the drain electrode. The charges are encouraged to jump from the island to the drain (and hence make room for more charges to arrive from the source) by appropriate bias on the gate electrode. If the thermal quantum size is arranged to be small compared with the electrostatic energies in play, the risk of random thermal interference with the current control is negligible.

12.1 The Ferromagnetic Single Electron Transistor

In a spin transistor, there is a fourth energy term which we can now introduce into the problem, namely the electrochemical potential difference for spin-up and spin-down electrons associated with a spin accumulation. In practice this is achieved by making the electrodes and/or the island from ferromagnetic material. A ferromagnetic source electrode will in principle produce a spin accumulation on a nonmagnetic island and, under certain bias conditions, the associated electrochemical potential holds the balance of power between the main energy terms and hence has a large degree of control over the current flow to the ferromagnetic drain. Other configurations are possible in which the island also is magnetic. Fert and Barnas have made extensive calculations for various temperature regimes of the various possible modes of behavior of such devices which are called ferromagnetic single electron transistors (FSETs) or spin SETs (Barnas and Fert 1998).

12.2 Spin Blockade

Another possibility which arises also if the magnetic island is itself a ferromagnet is that of a spin-blockaded system in which electrical transport across the device is switched by magnetizing the island (Sirisathitkul *et al.* 2001a). An example is a Schottky barrier on the edge of which has been placed a series of magnetic islands which are antiferromagnetically coupled (and hence blockaded) in zero applied magnetic field. Applying a field orients these superparamagnetic particles and the resistance of the structure decreases owing to a tunnel-hopping current between adjacent islands. Exposure to light increases the resistance of the structure owing to photon-promotion of electrons from the islands to the large density of adjacent surface states. The geometry of this system is not unlike that of a high electron mobility transistor (HEMT) in which the performance of the main current channel is controlled by localized states in a physically distinct nearby region of the device.

13. Three-terminal Spin Electronic Device Variants

Ounadjela and Tiusan (1999) have proposed a neat and versatile metallic spin-tunnel transistor with particular relevance to three-terminal spin-tunnel MRAM application. The device has two tunnel barriers between emitter/base and base/collector respectively. It operates on the SPICE principle and has numerous variants which differ in respect of the precise location of the encoder and decoder electrodes relative to the collector structure.

Mizushima *et al.* (1998, 1999) have also produced a variety of interesting tunnel transistor designs, again operating on the SPICE principle but, unlike the Ounadjela/Tiusan device they comprise semiconductor collector elements.

14. Spin Electronics in Carbon Nanotubes

An unusual but prophetic venture in spin electronics is the use of single-wall carbon nanotubes as spin conductors (Alphenaar *et al.* 2000). Surprisingly it is discovered that the spin diffusion lengths in such tubes are many tens of nanometers and their future application looks promising.

15. Voltage-induced Switching

Interesting predictions have been made with respect to the simple RKKY-coupled GMR trilayer structure to the effect that the interlayer magnetic coupling could be changed in sign by application of sufficient voltage across the structure (You and Bader 1999). The object of such endeavor is to produce a magnetic memory element or switch whose transport in one dimension may be altered by magnetic switching which is induced not by external magnetic fields but rather by an electric potential in *n* orthogonal direction. This remains to be demonstrated experimentally.

16. Current-induced Switching

Current-induced switching of a spin electronic structure has also been predicted and experimental results are available which appear to confirm it. The principle harks back to an idea of Luc Berger (Myers *et al.* 1999) in which he examines the relationship between current density and the torque/force on a ferromagnetic domain wall. If a sufficiently large spin-polarized current is incident normally on a domain wall, the spin angular momentum exerts a torque which twists the spins and hence effectively causes the wall to move. When implemented in ferromagnetic nanocontacts, the effect is attractive as an operating principle for simple MRAM memory elements (Coey 2001).

17. Quantized Conductance

When a point contact with dimensions of atomic size is made between two metallic nanowires, the lateral confinement causes mutual distancing of the k-states in a plane perpendicular to the direction of current flow (Ott *et al.* 1998). This means that only a small number of conductance channels are below the metal Fermi surface. By varying the contact width, the individual conductance quanta may be observed. Simple theory suggests that in the case of spin asymmetric contacts, the quanta should be halved, but so far this effect has eluded observation.

18. Measuring Spin Asymmetry

Various techniques are used for estimating the spin asymmetry of spin electronic materials. They include spin-resolved photoemission (Park *et al.* 1998), Andreev reflection (Soulen *et al.* 1998), measurement of the Zeeman effect of chemical potential (Sirisathitkul *et al.* 2001b), and by spin tunneling to a material with 100% polarization (de Teresa *et al.* 1999). The last tunneling technique relies on the control electrode genuinely behaving as if it is 100% polarized. Merely because its bulk bandstructure is fully polarized is no guarantee of this. As discussed above, the polarization which magnetic electrodes manifest for tunneling purposes is found to be a function of the magnetic metal/insulator combination, not just of the magnetic metal itself. Thus, it is important that the control electrode is always accompanied by the same insulator. This casts a new light also on the other measurement techniques for measuring spin polarization and shows not only the importance of establishing exactly what they are measuring, but it also begs the question as to what we really should be trying to measure for practical purposes.

19. Competing Magnetotransport Phenomena

There exists a large number of magnetotransport effects which are not strictly spin electronic in origin but which nonetheless can display similar characteristics. They include anisotropic magnetoresistance, Hall effect and anomalous Hall effect.

In this category, an interesting and potentially useful giant magnetotransport effect has been observed in a ferromagnet/semiconductor structure in which arrays of submicron ferromagnets are fabricated on a heterostructure containing a near surface two-dimensional electron gas. The magnetoresistance arises from electrons propagating in open orbits along lines of zero magnetic field (Nogaret *et al.* 1997).

20. Measurement Artefacts

In spin electronics the currents and voltages measured are frequently small and this heightens the need

for vigilance against interference from rival transport effect and spurious artefacts. The most obvious sources of such trouble are radiated electrical noise and earth loops. However there is also a more subtle artefact which may occur in a.c. transport measurements in applied magnetic field if the flying leads to the sample are free to move. The current carrying wires are subject to a harmonic torque in a magnetic field and if they are capable of mechanical displacement this leads to a harmonic flux variation. The result is a parasitic voltage and hence an apparent resistance which is proportional to the square of the magnetic field.

21. *Applications of Spin Electronics*

Applications to date of spin electronics include hard disk read heads, advanced high density tape heads, and various position and motion sensors based on GMR and high frequency properties of spin electronic materials. Although not yet commercialized, spin tunnel MRAM is at an advanced stage of development also. More speculative uses with future potential include applications of spin FETS to quantum information processing and the radiofrequency ferromagnetic single electron transistor.

Bibliography

Alphenaar B W, Tsukagoshi K, Ago H 2000 Spin electronics using carbon nanotubes. *Physica E* **6**, 848–51

Baibich M N, Broto J M, Fert A, Nguyen Van Dau F, Petroff F, Etienne P, Creuzet G, Friederich A, Chazelas J 1988 Giant magnetoresistance of (001)Fe/(001)Cr magnetic superlattices. *Phys. Rev. Lett.* **61**, 2472–5

Barnard J A, Waknis A, Tan M, Haftek E, Parker M R, Watson M L 1992 Giant magnetoresistance observed in single layer Co–Ag alloy films. *J. Magn. Magn. Mater.* **114**, L230–4

Barnas J, Fert A 1998 Effects of spin accumulation on single-electron tunneling in a double ferromagnetic microjunction. *Europhys. Lett.* **44**, 85–90

Barthelemy A, Fert A 1991 Theory of the magnetoresistance in magnetic multilayers analytical expressions from a semiclassical approach. *Phys. Rev. B* **43**, 3124–9

Bean C P, Livingstone J D 1959 *J. Appl. Phys.* **30**, 120

Berger L 1991 Galvanomagnetic voltages in the vicinity of a domain wall in ferromagnetic thin films. *J. Appl. Phys.* **69** (3), 1550–5

Berkowitz A E, Mitchell J R, Carey M J, Young A P, Zhang S, Spada F E, Parker F T, Hutten A, Thomas G 1992 Giant magnetoresistance in heterogeneous Cu–Co alloys. *Phys. Rev. Lett.* **68**, 3745–8

Cabrera G G, Falicov L M 1974 *Phys. Stat. Sol. (b)* **61**, 539

Chui S T 1997 Bias dependence in spin-polarised tunneling. *Phys. Rev. B* **55** (9), 5600–3

Coey J M D 2001 Magnetic peanut memory device. Irish Patent filing

Daniel D, Gregg J F, Thompson S M, Coey J M D, Fagan A, Ounadjela K, Fermon C, Saux G 1995 Giant magnetothermal resistance. *J. Magn. Magn. Mater.* **1404**, 493–4

Datta S, Das B 1990 Electronic analog of the electrooptic modulator. *Appl. Phys. Lett.* **56**, 665–7

de Groot R A, Mueller F M, van Engen P G, Buschow K H J 1984 Half-metallic ferromagnets and their magneto-optical properties. *J. Appl. Phys.* **55** (6), 2151–4

De Teresa J M, Barthelemy A, Fert A, Contour J P, Montaigne F, Seneor P 1999 Role of metal-oxide interface in determining the spin polarisation of magnetic tunnel junctions. *Science* **286**, 507–9

Devoret M H, Grabert H 1992 *Single Charge Tunneling*. Plenum, New York

Dieny B, Speriosu V S, Parkin S S P, Gurney B A, Wilhoit D R, Mauri D 1991 Giant magnetoresistance in soft ferromagnetic multilayers. *Phys. Rev. B* **43**, 1297–300

Dubois S, Piraux L, George J M, Ounadjela K, Duvail J L, Fert A 1999 Evidence for a short spin diffusion length in permalloy from the giant magnetoresistance of multilayered nanowires. *Phys. Rev. B* **60** (1), 477–83

Fert A, Duvail J-L, Valet T 1995 Spin relaxation effects in the perpendicular magnetoresistance of magnetic multilayers. *Phys. Rev. B* **52**, 6513–21

Fiederling R, Keim M, Reuscher G, Ossau W, Schmidt G, Waag A, Molenkamp L W 1999 Injection and detection of a spin polarised current in a light emitting diode. *Nature* **402**, 787–90

Flatte M E, Byers J M 2000 Spin diffusion in semiconductors. *Phys. Rev. Lett.* **84** (18), 4220–3

Gehring G A, Gregg J F, Thompson S M, Watson M L 1995 Electron spin depolarisation in granular magnetic systems. *J. Magn. Magn. Mater.* **1404**, 501–2

Gerritsen A N 1959 *Physica* **25**, 489–502

Giaever I, Megerle K 1961 *Phys. Rev.* **122** (4), 1101

Gregg J F, Allen W, Ounadjela K, Viret M, Hehn M, Thompson S M, Coey J M D 1996 Giant magnetoresistive effects in a single element magnetic thin film. *Phys. Rev. Lett.* **77** (8), 1580–3

Gregg J F, Allen W D, Viart N, Kirschmann R, Sirisathitkul C, Schille J-P, Gester M, Thompson S M, Sparks P, da Costa V, Ounadjela K, Skvarla M 1997 *J. Magn. Mater.* **175**, 1–9

Hagele D, Oestreich M, Ruhle W W, Nestle N, Ebert K 1998 Spin transport in GaAs. *Appl. Phys. Lett.* **73** (11), 1580–2

Hammar P R, Bennett B R, Yang M J, Johnson M 1999 Observation of spin injection at a ferromagnet–semiconductor interface. *Phys. Rev. Lett.* **83** (1), 203–6

Jia Y Q, Shi R C, Chou S Y 1996 Spin-valve effects in nickel/silicon/nickel junctions. *IEEE Trans. Magn.* **32** (5),

Johnson M 1993 Bipolar spin switch. *Science* **260** (5106), 320–3

Johnson M, Silsbee R H 1985 Interfacial charge-spin coupling: injection and detection of spin magnetisation in metals. *Phys. Rev. Lett.* **55** (17), 1790–3

Julliere M 1975 *Phys. Lett. A* **54**, 225

Kikkawa J M, Awschalom D D 1999 Lateral drag of spin coherence in gallium arsenide. *Nature* **397**, 139–41

Lee S F, Pratt W P, Yang Q, Holody P, Lololee R, Schroeder P A, Bass J 1993 2-Channel analysis of CPP-MR data for Ag/Co and AgSn/Co multilayers. *J. Magn. Magn. Mater.* **118**, L1–5

Loraine D R, Pugh D I, Jenniches H, Kirschman R, Thompson S M, Allen W, Sirisathitkul C, Gregg J F 2000 Effect of silicon crystal structure on spin transmission through spin electronic devices. *J. Appl. Phys.* **87** (9), 5161–3

Mizushima K *et al.* 1998 US Patent 5747859

Mizushima K *et al.* 1999 US Patent 5973334

Monsma D J, Lodder J C, Popma J A, Dieny B 1995 Perpendicular hot-electron spin-valve effect in a new magnetic field

sensor the spin-valve transistor. *Phys. Rev. Lett.* **74** (26), 5260–3

Mott N F 1936 *Proc. R. Soc.* **153**, 69

Myers E B, Ralph D C, Katine J A, Louie R N, Buhrman R A Current-induced switching of domains in magnetic multi-layer devices. *Science* **285** (5429), 867–70

Nogaret A, Carlton S, Gallagher B L, Main P C, Henini M, Wirtz R, Newbury R, Howson M A, Beaumont S P 1997 Observation of giant magnetoresistance due to open orbits in hybrid semiconductor/ferromagnet devices. *Phys. Rev. B* **55** (24), R16037–40

Ohno Y, Young D K, Beschoten B, Matsukura F, Ohno H, Awschalom D D 1999 Electrical spin injection in a ferro-magnetic semiconductor heterostructure. *Nature* **402**, 790–2

Ott F, Barberan S, Lunney J G, Coey J M D, Berthet P, de Leon-Guevara A M, Revcolevschi A 1998 Quantised con-ductance in a contact between metallic oxide crystals. *Phys. Rev. B* **58** (8), 4656–9

Ounadjela K, Tiusan C 1999 Dispositif microelectronique a jonctions tunnel et reseau de memoires et capteur compren-ant de tels dispositifs. Demande de brevet Francais 9904227

Park J-H, Vescovo E, Kim H -J, Kwon C, Ramesh R, Venk-atesan T 1998 Direct evidence for a half-metallic ferromag-net. *Nature* **392**, 7946

Parkin S S P, More N, Roche K P 1990 Oscillations in exchange coupling and magnetoresistance in metallic superlattice structures: Co/Ru, Co/Cr and Fe/Cr. *Phys. Rev. Lett.* **64**, 23047

Piraux L, George J M, Despres J F, Leroy C, Ferain E, Legras R, Ounadjela K, Fert A 1994 Giant magnetoresistance in magnetic multilayered nanowires. *Appl. Phys. Lett.* **65** (19), 1–3

Prins M W J, Jansen R, van Kempen H 1996 Spin-polarised tunneling with GaAs tips in scanning tunneling microscopy. *Phys. Rev. B* **53** (12), 8105–13

Renard J P, Bruno P, Megy R, Bartenlian B, Beauvillain P, Chappert C, Dupas C, Kolb E, Mulloy M, Prieur J, Veillet P, Velu E 1996 *J. Appl. Phys.* **79** (8), 5270–5

Sirisathitkul C, Allen W D, Gregg J F, Sparks P D, Coey J M D, Kirschman R, Thompson S M 2001a Spin blockaded silicon Schottky barrier. (In preparation)

Sirisathitkul C, Allen W D, Gregg J F, Sparks P D, Coey J M D, Kirschman R, Thompson S M 2001b Measuring spin asymmetry via the chemical potential Zeeman shift. (In prep-aration)

Soulen R J, Byers J M, Osofsky M S, Nadgorny B, Ambrose T, Cheng S F, Broussard P R, Tanaka C T, Nowak J, Moodera J S, Barry A, Coey J M D 1998 Measuring the spin polar-isation of a metal with a superconducting point contact. *Science* **282**, 85–8

Tang H X, Monzon F G, Lifshitz R, Cross M C, Roukes M L 2000 Ballistic spin transport in a two dimensional electron gas. *Phys. Rev. B* **61** (7), 4437–40

Tedrov P M, Merservey R 1971 *Phys. Rev. Lett.* **26**, 192

Tiusan C, Hehn M, Ounadjela K, Henry Y, Hommet J, Meny C, van den Berg H, Baer L, Kinder R 1999 Artificial antif-erromagnetic tunnel junction sensors based on Co/Ru/Co sandwiches. *J. Appl. Phys.* **85**,

Valet T, Fert A 1993 Theory of the perpendicular magnetore-sistance in magnetic multilayers. *Phys. Rev. B* **48**, 7099–113

van Wees B J, *et al.* 2000 Comment on observation of spin injection at a ferromagnet–semiconductor interface. *Phys. Rev. Lett.* **84** (21), 5022

Versluijs J J, Bari M A, Coey J M D 2001 Magnetoresistance of half-metallic oxide nanocontacts. in press

Yang Q, Lee S F, Henry L L, Lololee R, Schroeder P A, Pratt W P, Bass J 1994 Diffusion length and giant magnetoresist-ance at low temperatures. *Phys. Rev. Lett.* **72**, 3274–7

You C-Y, Bader S D 1999 Prediction of switching/rotation of the magnetisation direction with applied voltage in a con-trollable interlayer exchange coupled system. *J. Magn. Magn. Mater.* **195**, 488–500

J. Gregg
University of Oxford, Oxford, UK

Magnetic Recording Systems: Spin Valves

The rapid increase in information storage density in magnetic recording systems over recent years has been made possible in part by the development of spin-valve (SV) read heads. These rely on the phe-nomenon of giant magnetoresistance (GMR), in which a change in resistance is observed on applica-tion of a magnetic field (see *Giant Magnetoresist-ance*). This article discusses the GMR effect on which the devices are based, and also the parameters that are important in consideration of the design of spin-valve structures, such as the choice of materials for the various layers in the device, and thermal stability. The effect of microstructure and of magnetization reversal on device operation are also discussed.

1. Introduction

A change in resistance on application of a magnetic field in magnetic materials gives rise to a tremendous number of applications in the electronics industry. One of the most spectacular examples is the applica-tion of giant magnetoresistance in ultrahigh-density magnetic recording technology, and one of the de-vices based on this phenomenon is the SV structure that has applications as read heads (Brug *et al.* 1996) in hard disk storage systems or as magnetoresistive random access memory (MRAM) elements (Daugh-ton 1997). The rapid increase in interest in these de-vices has been motivated by the high demand for improvement in information storage density and per-formance, mainly for graphics-intensive applications.

Improvements in signal processing and disk media, plus the development of SV read heads, have allowed the density to be increased to $50\,\text{Gb/in}^2$ with a pro-jected obtainable density of $80–100\,\text{Gbits/in}^2$. The limits on memory density that can be achieved using solid-state memory (for example DRAM) means that there has been renewed interest in the development of magnetic memory based on the GMR effect, namely MRAM. In addition, MRAM would be nonvolatile.

2. The GMR Effect

GMR is observed in films consisting of alternate ferromagnetic (FM) and nonmagnetic layers, as a

large change in resistance with applied magnetic field. The resistance is a function of the relative alignment of the magnetization in the magnetic layers, and thus of spin-dependent scattering of the conduction electrons. It was first observed for Fe/Cr multilayers with thicknesses of a few nanometers.

(For a general description of GMR the reader is referred to a number of review papers, for example Dieny (1994).) The GMR ratio is defined as:

$$\Delta R/R = (R - R_P)/R_P \qquad (1)$$

where R_P is the resistance for parallel alignment of the FM layer magnetization directions. The maximum GMR ratio is observed when

$$R = R_{AP} \qquad (2)$$

where R_{AP} is the resistance of the antiparallel magnetization configuration.

3. The Spin Valve Structure

SV structures (see, for example, review of SV structures in Portier and Petford-Long (1999), however, offer greater possibilities for development for real applications than multilayer structures. In their simplest form, a SV consists of two ferromagnetic layers separated by a nonmagnetic spacer layer. The magnetization direction (easy axis) of one FM layer is fixed by an adjacent antiferromagnetic (AF) layer (pinning layer) through exchange coupling (see *Multilayers: Interlayer Coupling*). The magnetization direction of the other FM layer (sense layer) can be rotated by applying a small external magnetic field (of the order of a few oersteds) in the plane of the layers. A schematic illustrating the structure of a simple SV is shown in Fig. 1(a).

In a spin valve, unlike in a GMR exchange coupling of the two FM layers across it is small. For a spin valve, the GMR is linearly dependent on $(\cos\theta)$ where θ is the angle between the sense and pinned layer magnetizations:

$$R(\theta) = R_P + (R_{AP} - R_P)(1 - \cos\theta)/2 \qquad (3)$$

When applying the external field perpendicular to the easy axis, the change in resistance is linear with low coercivity and a sense layer magnetization reversal characterized by coherent rotation (see Fig. 1(b)). This configuration is used for sensors. The second commonly used configuration is to apply the external field along the easy axis direction. In this case, two remanent states can be stabilized with either parallel (P) or antiparallel (AP) alignment of the magnetization of the pinned and sense layers. The magnetization reversal is then a hysteretic reversal process, with the P and AP states corresponding to the minimum and maximum resistance values,
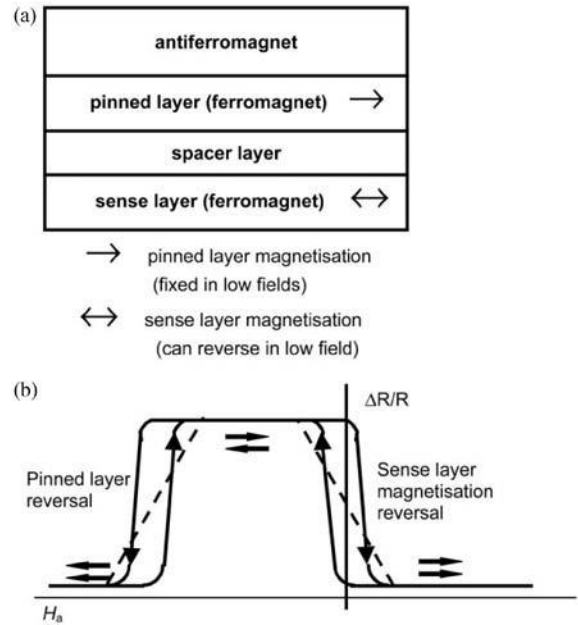
Figure 1
(a) schematic cross-section through a simple SV structure, (b) schematic GMR curve for a SV with the external field applied perpendicular to the easy axis of magnetization in the pinned layer (- - - - -) and with the external field applied parallel to the easy axis of magnetization in the pinned layer (——).

respectively. This is suitable for MRAM devices (high and low resistance could correspond to "1" and "0" bit states). A GMR ratio of up to 23.4% has been obtained for a SV structure at room temperature.

Despite the fact that SV materials have been introduced commercially as read heads in the latest generations of hard disk drives, a number of problems remain to be solved. These include magnetostatic coupling of the pinned and sense layers, which leads to an offset of the GMR curve with respect to remanence, and thus to a need for a higher operating magnetic field, low exchange coupling between the pinned and pinning layer for some configurations, and a reduction in GMR after lithographic processing. Solving these problems requires understanding the microstructure and local magnetic structure of the SV films.

3.1 Microstructure

To enhance the GMR ratio, several different SV structures have been proposed, for example the "top" SV (see Fig. 1(a)) and the "bottom" SV in which the layer order is reversed. Changing the deposition order changes both the crystallographic texture of the film
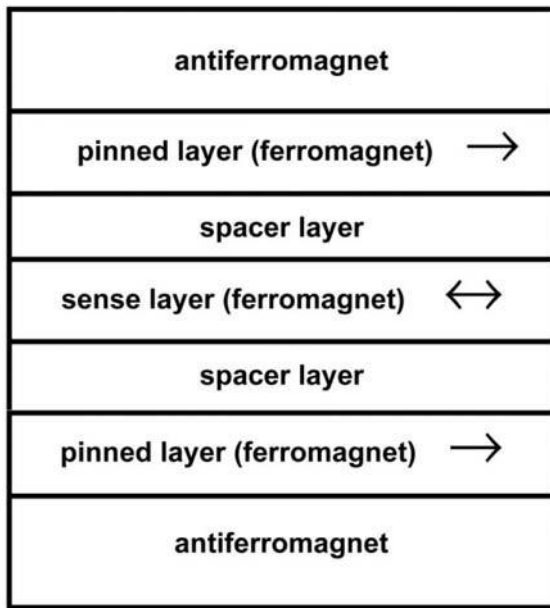
Figure 2
Schematic of dual SV structure.

and the interfacial roughness, which are of crucial importance in controlling the GMR. Figure 2 shows a schematic of the dual, or symmetric, SV, which contains one central FM sense layer and two biased FM layers. This structure has been found to increase the GMR ratio up to 23.4% compared with a top SV made with the same materials which gives only a 10% GMR ratio. In all cases, the FM material used for the pinned and sense layers can be either the same or different, depending on the properties required. The structures are usually protected from oxidation by a cap layer.

One of the important requirements in operating SV structures is to be able to reverse the magnetization of the sense layer in a low external magnetic field, hence the use of soft magnetic materials such as Permalloy ($Ni_{80}Fe_{20}$). Cobalt is also widely used and has a higher saturation magnetization, coercivity, and magnetocrystalline anisotropy, particularly for the h.c.p. structure, which tends to form for layer thicknesses greater than 4 nm. Sense layer *thickness* is also important, with an increase in thickness leading to a larger grain size and decrease in coercivity. A typical grain size is about 20 nm for an 8 nm-thick NiFe sense layer, which gives an optimal GMR ratio.

Another alternative for the pinned layer is to use an artificial antiferromagnet (AAF) such as Co/Ru/ Co, in which the cobalt layers are antiferromagnetically exchange-coupled across the ruthenium, and one of the cobalt layers is pinned by an adjacent AFM material. The net magnetization of the pinned layer is then close to zero. SVs containing an AAF show good sensitivity to an external magnetic field because stray-field coupling between the pinned and sense layers in lithographically defined elements is very much reduced.

The spacer layer needs to be very conductive to reduce spin-independent scattering of the conduction electrons and is commonly copper, silver, or gold. Copper is most widely used as its structure matches well (1.85% mismatch) with those of cobalt or $Ni_{80}Fe_{20}$. Intermixing between NiFe and copper can lead to the formation of a paramagnetic interfacial alloy layer, resulting in spin-flip scattering and loss of GMR, but this can largely be avoided by inserting a thin cobalt layer at the NiFe/Cu interface. The GMR properties of SVs are very dependent on the nature of the interfaces between the layers, and three different types of interlayer coupling can arise across the FM/NM/FM interfaces:

• FM exchange coupling between the FM layers through pinholes in the spacer, although this is largely avoidable for spacer layers thicker than about 1.5 nm.

• Magnetostatic "orange-peel" coupling which arises because of the waviness of the FM layer/spacer layer interface leading to free magnetic poles of opposite sign across the spacer layer, for which Néel proposed a model relating the period and the amplitude of the waviness to the coupling strength.

• An oscillatory Ruderman-Kittel-Kasuya-Yosida (RKKY-like) coupling which is dependent on the spacer layer thickness and decays with increasing thickness in an oscillatory manner between FM and AFM coupling. The spacer layer thickness is usually chosen to be high enough that the RKKY coupling is negligible, but if it is too high, increased spin-independent scattering of the conduction electrons and increasing shunting of the current through the spacer layer lead to a decrease in GMR. The optimum thickness has been found to be ~ 2.5–3 nm.

One of the key parameters for a SV device is the strength of the exchange coupling ($\mathbf{H_{ex}}$) between the antiferromagnetic (pinning) and pinned layers (see Nogués and Schuller 1999) for a review of exchange-biasing effects). The exchange field is set by applying a magnetic field during deposition or postdeposition anealing in order to align the magnetization of the first monolayer of the AFM material with that of the adjacent FM layer. The coupling strength depends on the AFM material used and on its microstructure, with the most commonly used materials being FeMn, NiMn, and IrMn, although other materials such as CoO, NiO, TbCo, α-Fe_2O_3, and other manganese alloys are being considered. An increase in $\mathbf{H_{ex}}$ and in the pinned-layer coercivity are observed when reducing the thickness of the FM material, and an increase of $\mathbf{H_{ex}}$ and of the blocking temperature (the temperature above which no exchange field is observed) have been linked to an increase in grain size.

The surface topology is also important since a smoother interface between the pinning and pinned layers tends to improve H_{ex}.

The first systems to be studied used FeMn because it is structurally very similar to the FM and spacer layers. However, H_{ex} (~ 150 Oe) and the blocking temperature ($\sim 150\,^{\circ}$C) are relatively low and its corrosion resistance is not very high (this can be improved by adding chromium, iridium, platinum, rhodium, or ruthenium during deposition). The most promising AFM material to date is MnNi with H_{ex} up to 500 Oe after annealing, a blocking temperature of $\sim 380\,^{\circ}$C, a reasonable corrosion resistance, and very good thermal stability. The as-grown MnNi is cubic and nonmagnetic, but an anneal at about $220\,^{\circ}$C for 1 hour leads to a phase transformation to the antiferromagnetic face-centred-tetragonal (f.c.t.) phase. A difficult task is to determine the real proportion of MnNi grains with the f.c.t. structure compared to those still with the f.c.c. structure.

The most common deposition techniques used for fabricating SVs are ion-beam deposition (IBD), DC magnetron sputtering, and MBE. MBE-grown films tend to be epitaxial and single crystal, whereas the sputtered films are polycrystalline. Films grown by IBD usually have higher resistivities and lower GMR than DC magnetron-sputtered films because of greater intermixing between the layers. Polycrystalline films tend to show better GMR properties than MBE-grown films, but a good $\langle 111 \rangle$ texture between the pinning and the pinned layers is preferable for a strong pinning effect. In addition, the coercivity of the sense layer is lower for a well-textured film, which enables a rapid transition between the P and AP states for MRAM applications.

To increase the grain size and degree of texture in the film, a seed layer such as niobium, tantalum, titanium, or zirconium is commonly used. Tantalum is the most widely used, as it induces the $\langle 111 \rangle$ texture for most of the various FM materials used as the sense layer resulting in a columnar growth from bottom to top in the SV structure. In addition, the tantalum/FM layer interface usually has a good thermal stability. However, an intermixed, magnetically "dead" layer of a few monolayers is often observed between the seed and the FM layer. Note that for bottom SV structures it is sometimes necessary to deposit a thin FM layer below the AFM material to obtain a good crystallographic texture.

4. Thermal Stability

The GMR amplitude decreases linearly with temperature by a factor of about three from 4 K to room temperature. The main effect is magnon scattering of the conduction electrons in the bulk of the FM layers which has been correlated to the Curie temperature of the FM material, but another contribution will be

phonon scattering in the NM layer preventing the exchange of conduction electrons between the sense and pinned layers. Operating a SV structure at elevated temperatures thus leads to a decrease of the GMR effect, but the critical temperature above which the linear dependence is lost depends strongly on the structure used.

The critical temperatures are much lower than in bulk materials because of the numerous grain boundaries whose diffusion coefficients are much higher than the bulk values, favoring layer interdiffusion at lower temperatures. In addition, changes to the interface between the seed layer and the sense layer can degrade the GMR effect following annealing, because of the formation of a high-resistivity alloy at the seed layer/ FM interface. The cobalt/copper system is more thermally stable than other systems such as NiFe/ copper, for example, because cobalt/copper is a phase-separating system and, because the Curie temperature of cobalt is high in comparison with NiFe, although the GMR properties are not as good.

5. Micromagnetic Considerations

5.1 Sense-layer Reversal

One of the important parameters for the operation of a SV is the magnetization-reversal mechanism of the sense layer, because of its influence on the GMR response of the SV. If the applied field is along the easy axis direction, the reversal of the sense layer magnetization occurs via domain wall motion for NiFe, and by magnetization rotation mechanisms for cobalt, with a higher reversal field for the cobalt-based SVs. This is expected because of the higher saturation magnetization and magnetocrystalline anisotropy of cobalt. However, some other features can be seen, which are directly attributable to the FM interlayer coupling. First, the domain structure for a NiFe-based SV is more complex than for a single NiFe film. In addition, domain walls are observed to lie at an angle with respect to the easy axis direction because of the residual torque associated with coupling to the pinned layer.

Third, the P–AP and AP–P reversal are not symmetric, with more magnetization rotation observed for the AP–P reversal. This is a result of the combination of the unidirectional anisotropy imposed by the exchange field of the AFM layer on the pinned FM layer and the FM "orange-peel" magnetostatic coupling between the pinned and sense layers.

A further important feature is that the hysteresis loop is shifted with respect to zero field, and there are a number of terms that contribute to this effect. The first of these is the orange-peel coupling (H_{FM}), which is FM in nature. Second, there is a magnetic field induced by the current passing through the device (H_I), whose effect depends on the direction of current flow and its magnitude.

A simple model based on Ampere's law:

$$\mathbf{H_I} = 0.75I(4\pi \times 10^{-3})/2h \qquad (4)$$

where I is the current and h is the height (width) of the element, provides good agreement with experimental observations. Third, magnetostatic stray-field coupling occurs at the edges of a lithographically defined SV element because of the demagnetizing field ($\mathbf{H_d}$) between the pinned and sense layers. This phenomenon becomes of primary importance as the element size is reduced and is strongly dependent on element size and shape. The stray-field coupling is AFM in nature, and $\mathbf{H_d}$ can be simply estimated using:

$$\mathbf{H_d} = -(4\pi Mt/h)u_y \qquad (5)$$

where M and t are the saturation magnetization and thickness of the sense layer, respectively, h is the width of the element, and u_y is a unit vector in the easy axis direction. A possible expression for the offset field ($\mathbf{H_{off}}$), by which the GMR curve is displaced from zero, can then be given as:

$$\mathbf{H_{off}} = \mathbf{H_{FM}} + \mathbf{H_I} + \mathbf{H_d} \qquad (6)$$

As mentioned previously, a decrease in sense-layer thickness and/or the use of an AAF as the pinned layer lead to a substantial reduction of the stray field coupling. Flattening the FM/NM/FM layer interfaces, for example by the use of a surfactant such as indium, can reduce the orange peel coupling. $\mathbf{H_{off}}$ should be kept as low as possible to reduce the external field that must be applied to reverse the sense layer magnetization.

Finally, 360° domain walls are often observed, mainly at the end of the P–AP transition, which consist of a pair of very close domain walls separated by a very narrow region of film in which the magnetization in the two FM layers is still in the P configuration.

These defects remain up to a much higher applied field value and act as domain nucleation sites for the opposite reversal, which can result in differences in reversal field for different devices with nominally exactly the same structure. Applying an external field perpendicular to the easy axis results in a magnetization reversal of the sense layer via coherent magnetization rotation with a single domain behavior.

Assuming that the magnetization of the pinned layer remains parallel to the easy axis during the reversal, the change in resistance is only due to the change in magnetization direction in the sense layer. This assumption is based on the fact that the exchange bias field is usually much higher than the reversal field of the sense layer. An important issue is thus the uniformity of the pinned layer magnetization. Nonuniformity can result in different responses

from nominally identical devices, since the GMR is determined by the misorientation between the magnetization directions of the FM layers, and can be caused by variations in the exchange coupling imposed by the adjacent AFM layer, for example because of incomplete transformation to the f.c.t. phase for MnNi.

The operating temperature of devices such as read heads in hard-disk systems can be of the order of 150 °C, so the thermal behavior of SV films is an important issue. An increase in temperature results in a reduction in both the field value and the field range over which the sense layer magnetization reverses. This is believed to be a result of the increase in thermal energy which compensates the effect of the FM interlayer coupling. If the temperature becomes too close to the blocking temperature, then $\mathbf{H_{ex}}$ becomes zero, leading to simultaneous magnetization reversal of the two FM layers and loss of the GMR effect.

Current density through the SV is an important parameter in operating SV elements since it imposes the amplitude of the signal to be read for distinguishing the P and AP remanent states. A typical value is of the multilayer, the spacer layer thickness is such that the order of 10^7 Acm^{-2} and a decrease in GMR and in coercivity are usually observed with increasing current density. The current can also have a more subtle effect on the sense layer magnetization reversal because the increase in thermal energy supplied to the device can counteract the coupling between the sense and pinned layers. There will also be a current density limit above which the film resistance increases dramatically and, consequently, above which the element begins to be damaged by heating effects. The critical current density depends on the size and shape of the element.

See also: Magnetic Recording Heads: Historical Perspective and Background; Magnetoresistive Heads: Physical Phenomena; Thin Films: Domain Formation

Bibliography

Brug J A, Anthony T C, Nickel J H 1996 Magnetic recording head materials. *MRS Bull.* **21** (9), 23–8
Daughton J M 1997 Magnetic tunneling applied to memory. *J. Appl. Phys.* **81** (8), 3758–63
Dieny B 1994 Giant magnetoresistance in spin-valve multilayers. *J. Magn. Magn. Mater.* **136**, 335–59
Nogués J, Schuller I K 1999 Exchange bias. *J. Magn. Magn. Mater.* **136**, 203–32
Portier X, Petford-Long A K 1999 Electron microscopy studies of spin-valve structures. *J. Phys. D: Appl. Phys.* **32**, R89–108

A. K. Petford-Long
University of Oxford, Oxford, UK

Magnetic Recording Technologies: Overview

Magnetic recording technology is the key element of large-scale information storage and retrieval. In addition to its obvious importance in science and engineering, it has become indispensable to our daily lives. When we make a bank transaction, reserve an airplane ticket, use a credit card, or watch a movie from a videotape, we are using the technology of magnetic recording. The general requirements for data storage are information integrity, fast access, and low cost. In its simplest form, a magnetic recording system consists of a magnetic head and a magnetic medium, as schematically shown in Fig. 1. The head is made of a piece of magnetic material in a ring shape, with a small gap facing the medium and a coil away from the medium.

The head records and reproduces information, while the medium stores the information. The recording process is based on the phenomenon that an electric current i generates a magnetic flux φ as described by Ampere's law. The flux φ leaks out of the head core at the gap, and magnetizes the magnetic medium. The orientation of the magnetization is determined by the current direction. As the medium moves from left to right with a velocity V under the head gap, magnetization is retained in the medium at different locations.

There are two types of head used in reproducing. One senses magnetic flux change rate, and the other senses the magnetic flux. During the reproduction process, a magnetized medium is placed under the head gap. A part of the flux coming out of the medium surface enters the head through the gap. As the medium moves, the prerecorded information is reproduced by the head.

The distance between two closest transitions in the medium is the flux change length B, and the distance between two adjacent data tracks is the track pitch
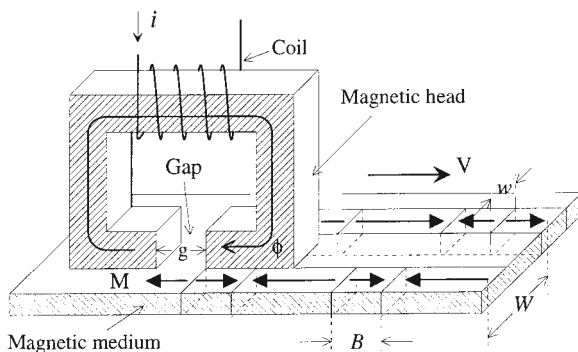
Figure 1
Conceptual diagram of a magnetic medium and an inductive head.

W, which is wider than the data track width w. The flux change length can be directly converted into bit length with the proper coding scheme. The reciprocals of the bit length and the track pitch are termed the linear density and the track density, respectively. Their product yields the areal density of the information stored in the medium. This areal density is a figure of merit for a recording system.

The research and development efforts of the magnetic recording industry have been focused on increasing the areal density. During the 1990s, the areal density was increasing at 60% annual rate. More recently, the rate has been accelerated to more than 100%. At present, hard disk drives used in desktop computers feature areal densities of more than $30\,\mathrm{Mb\,mm^{-2}}$ ($B < 0.06\,\mu\mathrm{m}$ and $W < 0.6\,\mu\mathrm{m}$). This yields a total storage capacity of more than $30\,\mathrm{Gb}$ for a disk of 95 mm diameter.

1. Magnetic Media and Magnetic Heads

Magnetism is the result of uncompensated electron spin motions in an atom. Only transition elements exhibit this property, and nearly all practical interest in magnetism centers on the first transition group of elements (manganese, iron, nickel, and cobalt) and the rare earth elements (gadolinium, and terbium). While the first transition group of elements and their alloys are the materials used in magnetic recording, amorphous rare earth-transition metal alloys are the only commercially used magneto-optical storage medium. The strength of magnetism is represented by magnetization M, and is related to magnetic field H and magnetic flux density B by

$$B = \mu_0(H + M) \tag{1}$$

where μ_0 is the permeability of vacuum. The ratio of B with and without a magnetic material is the relative permeability μ of that magnetic material.

When a magnetic field H is applied to a piece of demagnetized magnetic material, the magnetization M starts increasing with H from zero. The rate of increase gradually slows down and M asymptotically approaches a value M_s. If H is reduced to zero, M follows to a lower value M_r. Further reduction of H to a very high negative value will magnetize the material to $-M_s$. In order to bring the material to the demagnetized state, a positive field H_c is required. Continuous increase in H field will bring the trace of M to a closed loop. This loop is the major hysteresis loop, as illustrated in Fig. 2.

The hysteresis loop shows that magnetic material has memory. It is this memory that is used in the medium for storing information. H_c is the coercivity, indicating the strength of magnetic field required to erase the memory of a magnetic material. Magnetic materials with high H_c are "hard" magnets, and are
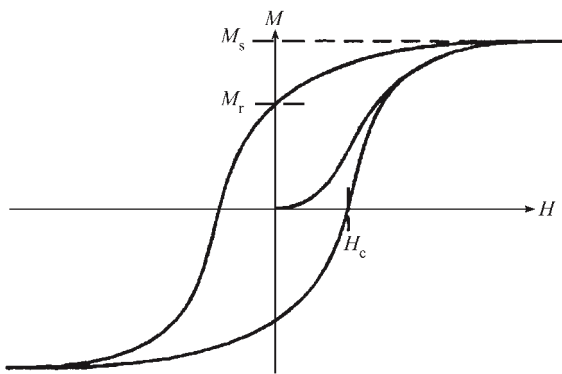
Figure 2
Hysteresis loop of a magnetic material.

Figure 3
Cross-sections of a particulate magnetic tape (top) and a thin-film hard disk (bottom).

suitable for recording media applications if they also have high M_r. On the other hand, magnetic materials with low H_c are "soft" magnets, and are candidates for head core materials if they also have high M_s and high μ. M_r and M_s are the remanent and saturation magnetization, respectively, and their ratio is the remanent squareness.

There are two groups of magnetic media. The first group is called particulate media because the magnetic materials are in the form of particles. This group includes oxide (γ-Fe_2O_3), cobalt-modified iron oxide (γ-Fe_2O_3 + Co), metal particles, and barium ferrite ($BaFe_{12}O_{19}$). Some of these have been used in magnetic recording for several decades. The other group of media is called the thin-film media, because the magnetic layer can be deposited as a continuous thin film. Most materials in this group are cobalt-based alloys. Compared with particulate media, the thin-film media usually have a higher coercivity H_c and a higher remanence M_r, and are suitable for high areal density applications.

Magnetic media can be classified into three general forms of applications. Tape is the oldest form and remains an important medium today. It is central to most audio, video, and instrumentation recording, although it is also used in the computer industry for archival storage. It is economical and has a large capacity, but suffers slow access time. Hard disk is traditionally the primary storage unit inside a computer, and is just being introduced in the consumer market (audio/video box). It provides the user with fast data access, but has poor transportability. Flexible disk is designed for easy data removability, but is limited in capacity. Besides these three general forms of applications, a hybrid of flexible medium and hard disk has appeared recently. It is a removable rigid disk capable of holding up to several gigabytes of digital data. In addition, magnetic stripes are getting widely used in various forms of cards.

The magnetic layer alone cannot be used as a medium. It needs additional components to improve its chemical and mechanical durability. Typical cross sections of a particulate magnetic tape and a thin-film hard disk are shown in Fig. 3. In the case of tape application, iron particles with a typical size of 0.5 μm long and 0.1 μm wide are dispersed in a polymeric binder, together with solvents, lubricants, and other fillers to improve magnetic and mechanical durability. This dispersed material is then coated on a biaxially oriented polyethylene terephthalate substrate. An optional back coat may also be applied to the other side of the substrate. The cross section of a hard disk is more complex. A high-purity aluminum–magnesium (5 wt.%) substrate is diamond-turned to a fine surface finish, and then electrolessly plated with a nonmagnetic nickel–phosphorus (10 at.%) undercoat.
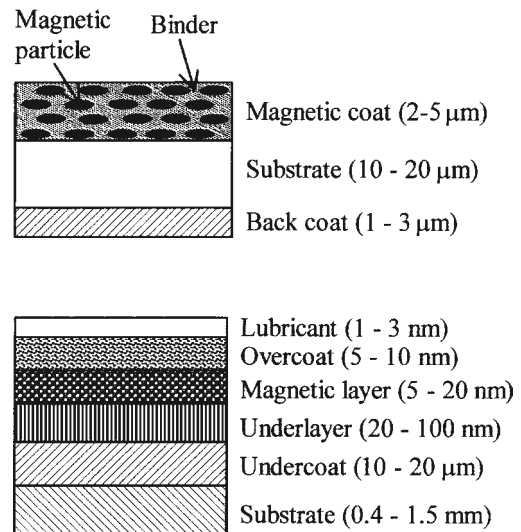
This layer is used to increase the hardness, reduce the defects, and improve the finish of the aluminum–magnesium alloy, and is polished to a super surface finish. Next, an underlayer of chromium is sputtered to control the properties of the magnetic film, followed by sputtering the magnetic film. Finally, a layer of hydrogenated or nitrogenated carbon is overcoated on the magnetic film, and an ultrathin layer of perfluorinated hydrocarbon liquid lubricate is applied on top. The carbon and lubricant layers are used to improve the corrosion and mechanical resistance of the disk. To achieve high shock resistance, glass disk is sometimes used, especially in mobile applications. For a 95 mm disk, the finished product should have a surface flatness better than 8 μm and an arithmetic average roughness (R_a) of less than 0.3 nm.

Magnetic heads serve three functions: recording, reproducing, and erasing. Two groups of head are employed to carry out these three functions. The

first group is the inductive heads, as schematically illustrated in Fig. 1. The evolution of the inductive head follows the selection of core materials, as shown in Fig. 4. Early heads used laminated molybdenum Permalloy (Ni–Fe–Mo, 79–17–4 wt. %). The primary drawbacks are frequency limitation, gap dimension inaccuracy, mechanical softness, and frequency limitation caused by eddy current loss. One way to reduce eddy current loss is to increase core material electric resistivity. Two types of ferrite material have high resistivity (four to nine orders higher than Permalloy) and reasonable magnetic properties: nickel–zinc and manganese–zinc.

These materials are also very hard, providing greater head durability during head/medium contacts. The major deficiency of ferrite materials is their low B_s values. In order to record in high H_c media, high flux density B is needed in the head core. When the flux density in the core material reaches its saturation B_s, it will not increase despite the increase of recording current or coil turns. This saturation starts from the corners of the gap due to its geometry. To remedy this deficiency, a layer of metallic alloy material with much higher B_s is deposited on the gap faces. This type of head is called the metal-in-gap (MIG) head.

(a)

(b)

(c)

Figure 4
Various inductive head structures: (a) laminated, (b) MIG, and (c) thin film.

Thin-film heads capitalize on semiconductor-like processing technology to reduce the customized fabrication steps for individual heads. The core, coil, gap, and insulator layers are all fabricated by electroplating, sputtering, or evaporation. Due to the nature of the semiconductor process, the fabrication is more accurate for small dimensions. Small gap dimensions are suitable for high linear and track density, and small core dimensions allow the use of high B_s Permalloy material (nickel–iron, 80–20 wt. %) as a core with low inductance for high data-rate applications. The high cost of the semiconductor-like process is offset by high throughput: a 150 mm × 150 mm wafer can produce 40 000 pico-slider heads (1.25 × 1.00 × 0.30 mm). One disadvantage is the limited band-recording capability because the small pole length limits low-frequency response. A second disadvantage is the Barkhausen noise, which is characterized as the sudden jump of magnetic flux flowing around the head, and is caused by the relatively small number of magnetic domains in the core.

The recording and erasing functions are performed by an inductive head in all magnetic recording devices. The reproducing function, however, can be carried out either by an inductive head or by a magnetoresistive (MR) head. The reproducing performance of an inductive head is described by Faraday's equation:

$$v = -nV \frac{\mathrm{d}\phi}{\mathrm{d}x} \tag{2}$$

where v is the output electric voltage from the head, n is the number of the coil turns, V is the medium moving velocity, and $\mathrm{d}\varphi/\mathrm{d}x$ is the derivative of the magnetic flux with respect to medium moving direction.

When an inductive head is used for reproducing, this head is usually also used for recording and erasing. The optimal performance cannot be achieved because recording and reproducing have contradictory requirements for head design. To solve this problem, a new reproduction head was introduced in the 1990s. This is the MR head. An MR head is always integrated together with an inductive head in such a way that the MR head performs the reproducing and the inductive head carries out the recording and erasing.

The first generation of MR head introduced in 1990 is the anisotropic type (AMR). As shown in Fig. 5, conceptually, an AMR head has a magnetoresistive element (MRE) and two electric leads. The MRE is a Permalloy stripe (nickel–iron, 80–20 wt.%), with thickness t, width w, and height h. An electric current, with density J, passes through the MRE through the leads. The electric resistivity of the MRE is a function of the angle θ between J and MRE magnetization M:

$$\rho_\theta = \rho \left(1 + \frac{\Delta\rho}{\rho} \cos^2 \theta \right) \tag{3}$$
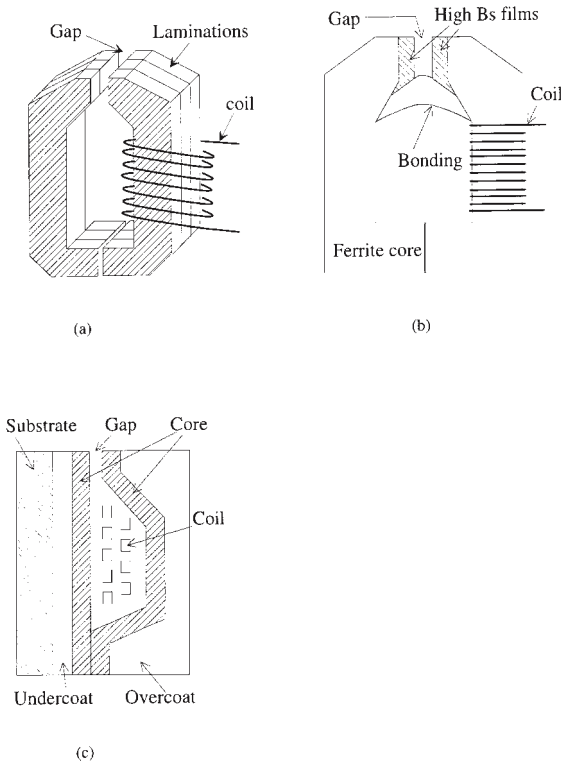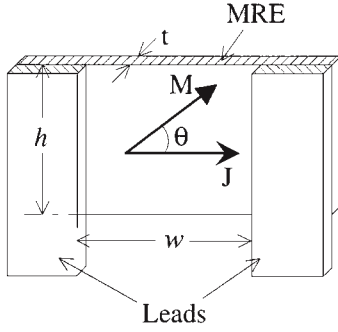
Figure 5
Conceptual diagram of an AMR head.

Figure 6
Conceptual diagram of a GMR head.

where ρ_θ is the resistivity at θ, ρ is the resistivity at $\theta = 90°$, and $\Delta\rho$ is the resistivity difference between $\theta = 0°$ and $\theta = 90°$. $\Delta\rho/\rho$ is the anisotropic magneto-resistive ratio of the MRE. Usually a transverse magnetic field is applied to the MRE so that $\theta = \theta_0$ when the head is not reading a magnetic signal.

Assume that a magnetic signal from the medium rotates M from θ_0 to θ, then an electric voltage change v will be detected across the MRE as the output signal:

$$v = Jw\rho\frac{\Delta\rho}{\rho}(\sin^2\theta_0 - \sin^2\theta) \qquad (4)$$

where θ_0 is the bias angle and is set to $45°$ for good linearity. Equations (3) and (4) tell us that while inductive head output is proportional to medium velocity and not suitable for low-velocity applications, the MR head can be used for either high- or low-velocity applications.

The second generation of MR head introduced recently is the Giant Magnetoresistive (GMR) head (see *Giant Magnetoresistance*). The most commonly used implementation of the GMR head is the spin valve configuration. As depicted in Fig. 6, it has four basic layers. The antiferromagnetic material (AFM) provides an exchange field to pin the magnetization of the adjacent (pinned) layer to the direction $90°$ from the medium surface. A nonmagnetic spacer (typically copper) separates the magnetic free layer from the pinned layer. When there is no magnetic field from the medium, the magnetization of the free layer parallels with the medium surface.

When a magnetic field is applied from the medium, the magnetization of the free layer rotates an angle θ from its original direction. θ is a function of the strength and direction of the magnetic field. Similar to the AMR head, the resistivity of the MRE changes with magnetic field, yielding

$$v = \frac{1}{2}Jw\Delta\rho\sin\theta \qquad (5)$$

Compared with the AMR head, the GMR head has higher sensitivity, better linearity, and needs no bias.

With some modifications and enhancements, the GMR head may be able to achieve an areal density around $100\,\text{Mbits mm}^{-2}$. Engineers and scientists in the magnetic recording industry and universities are exploring new reproducing heads to extend the areal density beyond that limit. A promising technique is the tunneling magnetoresistive (TMR) head. It is composed of two ferromagnetic layers separated by a thin insulating layer. The electric current flows in the direction perpendicular to the layers, in contrast with the GMR head where the current flows in the direction parallel to the layers. The TMR head promises to deliver higher linear density (smaller bit length B) and higher signal amplitude, but has the disadvantage of very high impedance.

2. Recording and Reproducing Process

Due to the nonlinear nature of the hysteresis loop, the recording process is complex and we need to adopt some approximation to simplify the analysis. If we set the origin of a coordinate system at the center of the gap with the x-axis on the head surface and the y-axis pointing away from the head, then the longitudinal magnetic field H_x of this head can be expressed by the Karlqvist approximation:

$$H_x = \frac{ni}{\pi(g + lA_g/\mu A_c)}\tan^{-1}\left[\frac{yg}{x^2 + y^2 - (g^2/4)}\right] \qquad (6)$$

where n is the number of coil turns, i is the current in the coil, g is the gap length, l is the core length, A_g is the core cross-sectional area, μ is the relative permeability of core material, and A_c is the gap cross-sectional area. Equation (6) shows that the contours of constant H_x field are circles nesting on the two gap corners, as shown in Fig. 7. The greater the diameter of the circle, the weaker the magnetic field.
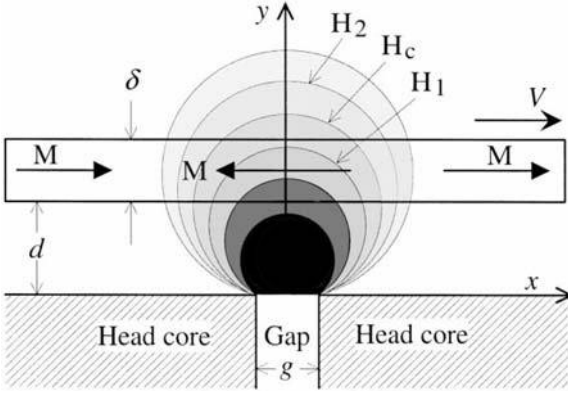
Figure 7
The contour of a longitudinal magnetic field from the Karlqvist approximation.

Figure 8
An isolated arctangent magnetization transition from negative M_r to positive M_r.

Assume a magnetic medium, moving from left to right with a distance d above the head, has a thickness δ and a magnetization M pointing to the right. At some instant the recording current turns on and generates the magnetic field H_x above the gap as depicted in Fig. 7. On the circumference of $H_x = H_c$, half of the medium material has its magnetization reversed and half remains the same, resulting in zero total magnetization. Since H_x has a gradient, the medium closer to the gap (inside a smaller circle) gets its magnetization reversed more completely than the medium further away from the gap (outside a bigger circle). Therefore, magnetic transition is gradual in the medium even if the change of recording current follows a step function.

Assume the original magnetization is M and the completely reversed magnetization is $-M_r$, this gradual change of magnetization for an isolated transition can be modeled by:

$$M = \frac{2}{\pi} M_r \tan^{-1}\frac{x}{a} \qquad (7)$$

where x is the distance from the center of transition, and a is a parameter characterizing the sharpness of the transition as shown in Fig. 8. For a thin-film medium, a is found to be

$$a = \frac{(1 - S^*)(d + \delta/2)}{\pi Q}$$
$$+ \sqrt{\left(\left[\frac{(1 - S^*)(d + \delta/2)}{\pi Q}\right]^2 + \frac{M_r\delta(d + \delta/2)}{\pi Q H_c}\right)} \qquad (8)$$

where S^* is the medium loop squareness, and Q is the head-field gradient factor. For a reasonably well-designed head, $Q \approx 0.8$. It is obvious that we want to make parameter a as small as possible so that we can record more transitions for a unit medium length. If

the head gap length g and medium thickness δ are small compared with head/medium separation d, and the medium has a squareness of one, then the minimum possible value of a is:

$$a_m = \begin{cases} \dfrac{M_r\delta}{2\pi H_c} & \text{for } \dfrac{M_r\delta}{4\pi H_c d} \geqslant 1 \\[3mm] \sqrt{\dfrac{M_r\delta d}{\pi H_c}} & \text{for } \dfrac{M_r\delta}{4\pi H_c d} < 1 \end{cases} \qquad (9)$$

In order to decrease the value of a and therefore increase areal density, we need to reduce the medium remanence M_r, thickness δ, head/medium separation d, and to increase the coercivity H_c.

In contrast to the recording process, the reproducing process is well understood. The flux density induced in the head core is small, yielding a linear process easier for mathematical treatment. The goals for higher areal density in magnetic recording are to reduce the pulse width (PW_{50}) and to increase the reproducing amplitude. The effect of various head parameters on pulse shape can be comprehended by studying the head reproducing voltage over an isolated transition (Fig. 8) with a thin magnetic layer. For an inductive head the output voltage is:

$$v(x) = \frac{-2\mu_0 V w M_r \delta n}{\pi(g + lA_g/\mu A_c)}$$
$$\times \left[\tan^{-1}\left(\frac{g/2 + x}{a + d}\right) + \tan^{-1}\left(\frac{g/2 - x}{a + d}\right)\right] \qquad (10)$$

where x is the distance between the center of the head gap and the center of the transition, μ is the relative permeability of the core, n is the number of coil turns, g is the head gap length, d is the head/medium separation, and x is the distance between the center of the medium transition and the center of the head gap.

The term $lA_g/\mu A_c$ is closely related to g for head efficiency. When an MR head is used for reproducing,

the sensor is usually sandwiched between two magnetic shields to increase its spatial resolution to medium signals. For an AMR head with small gap and 45° bias angle, it becomes:

$$v(x) = -\frac{2\sqrt{2}EJw\Delta\rho M_r\delta}{\pi t M_{fs}}\frac{g+t}{g}$$
$$\times\left[\tan^{-1}\left(\frac{g/2+x}{a+d}\right)+\tan^{-1}\left(\frac{g/2-x}{a+d}\right)\right] \quad (11)$$

where E is the head efficiency, J is the current density, t is the AMR film thickness, g is the gap length (the distance between the MRE and the shield), and M_{fs} is the saturation magnetization of the MR film. For a GMR head, the output is

$$v(x) = -\frac{EJw\Delta\rho M_r\delta}{\pi t M_{fs}}\frac{g+t}{g}$$
$$\times\left[\tan^{-1}\left(\frac{g/2+x}{a+d}\right)+\tan^{-1}\left(\frac{g/2-x}{a+d}\right)\right] \quad (12)$$

It is clear from Eqns. (10) and (12) that the pulse shape versus x is similar for an inductive, an AMR, and a GMR head. Since the MR film thickness t is typically one order of magnitude smaller than the gap length g, the term $(g+t)/g$ is approximately a constant. This indicates that g, a, and d affect pulse shape similarly for all three types of head, provided half of the gap length needs to be used for an MR head while the full gap length has to be used for an inductive head. In fact, the PW_{50} can be derived as

$$PW_{50} \approx \sqrt{g^2 + 4(a+d)^2} \quad (13)$$

for all three types of heads. To increase linear density, we need to reduce gap length g, transition parameter a, and head-to-medium separation d.

The amplitude of a reproducing pulse is adversely affected by adjacent transitions because of the opposite polarity of the adjacent magnetizations. At high linear density, the magnetization variation in the medium approaches a sinusoidal wave,

$$M(x) = M_r\sin\frac{2\pi}{\lambda}x \quad (14)$$

where λ is the wavelength. The reproducing voltage in an inductive head becomes:

$$v(x) = \frac{-\mu_0 VwM_rng}{g+lA_g/\mu A_c}(e^{-\frac{2\pi}{\lambda}d})$$
$$\times(1-e^{-\frac{2\pi}{\lambda}\delta})\left(\frac{\sin\frac{\pi g}{\lambda}}{\pi g/\lambda}\right)\cos\frac{2\pi}{\lambda}x \quad (15)$$

This equation presents all the important features of the high linear density reproducing process. The term $\exp(-2\pi d/\lambda)$ is the spacing loss. It shows that
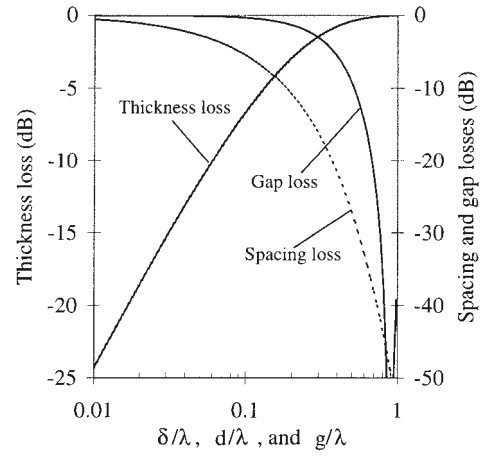
Figure 9
The spacing loss, thickness loss, and gap loss for high linear-density recording.

the reproducing voltage falls exponentially with the ratio of head/medium spacing to wavelength. The second term $1-\exp(-2\pi\delta/\lambda)$ is the thickness loss.

The name of this term is misleading because its value increases with a greater medium thickness. However, the rate of increase diminishes for a thicker medium. In fact, 80% of the maximum possible value is achieved by a medium thickness of 0.25 λ. The last term $\sin(\pi g/\lambda)/(\pi g/\lambda)$ is the gap loss. This term is based on the Karlqvist approximation. If a more accurate head fringe field is used, this term is modified to $\sin(\pi g/\lambda)/(\pi g/\lambda)$ $(1.25\ g^2-\lambda^2)/(g^2-\lambda^2)$. It shows a gap null at $\lambda = 1.12\ g$, and limits the shortest wavelength producible. These three terms are plotted in Fig. 9. The most significant loss comes from the spacing loss term, which is 54.6 dB for $d=\lambda$. Therefore, one of the biggest efforts spent on magnetic recording is to reduce the head/medium spacing as much as possible without causing mechanical reliability issues. The effects are similar for an MR head.

3. The Challenge for High Areal Density

Since areal density is the product of linear density and track density, the increase in areal density translates into the reductions in pulse width and track width. Both magnetic media and heads play important roles in these areas. One of the most prominent parameters affecting pulse width is the transition parameter a. Equations (7) to (12) indicate that it affects both the recorded transition length and reproducing pulse width. From the medium viewpoint, we can reduce a by increasing coercivity H_c, reducing $M_r\delta$, or reducing S^*. Since 1990, H_c has been increased from around 1000 Oe to 3800 Oe. The primary limitation to higher H_c is the recording head. Presently it is

difficult for a head to generate a magnitude field with the required gradient for recording on a medium with H_c over 4000 Oe, especially at high frequency.

This is described by Sharrock's law:

$$H_c(t) = H_0\left\{1 - \left[\frac{kT}{K_u V}\ln\left(\frac{f_0 t}{0.693}\right)\right]^n\right\} \quad (16)$$

where t is time, T is absolute temperature, k is the Boltzman's constant, K_u is the uniaxial anisotropy energy per unit volume, v is the grain volume of the magnetic particle, and f_0 is the Larmor frequency. If we reduce $M_r\delta$, we will sacrifice amplitude. In addition, it is more difficult to produce a uniform thin film than a thick film.

Magnetic medium noise has three components: transition noise, particulate noise, and modulation noise. While both particulate noise and modulation noise are independent of or decrease with linear density, transition noise generally increases with linear density. Consequently, reduction of transition noise becomes necessary for high areal density application. The signal-to-transition-noise ratio is

$$\text{SNR} \approx \frac{D_c B^2 w}{2\pi D^3} \quad (17)$$

where D_c is the channel density, and D is the grain diameter.

Obviously we need to reduce the grain size to achieve adequate SNR if we reduce B or w to increase areal density. A major obstacle to the reduction of grain size is the superparamagnetic limit, which indicates the thermal instability of magnetization if the grain size is smaller than a critical volume v_p:

$$v_p = \ln(2tf_0)\frac{2kT}{\mu_0 M_s H_a} \quad (18)$$

where H_a is the total anisotropy field. First-order calculation shows that a grain diameter of 10–12 nm is required for ten-year data retention.

Although we can increase either track density or linear density to increase areal density, it is more advantageous for us to increase track density from the balance of SNR and thermal stability. This is because higher linear density requires a thinner magnetic layer, resulting in shorter grains with smaller volume and lower thermal stability, whereas a higher track density allows us to keep the same magnetic layer thickness, leading to higher areal density for the same thermal stability. Consequently, the aspect ratio (w/B) needs to reach 4 for 100 Gb in^{-2}, which is presently around 8 in the 50 Gb in^{-2} demonstration and was about 20 at 100 Mb in^{-2}.

When two transitions are recorded very close, the demagnetization field from one transition affects the transition position of the other. This shift in transition position can cause difficulty in channel detection, and is termed nonlinear transition shift (NLTS). As linear density gets higher and higher, NLTS will become more of a problem.

From the recording head viewpoint, the challenge lies in writability and high frequency response. Writability is usually expressed as overwrite, which is a measurement of a head's capability to write over a preexisting signal on the medium. With the increase in medium coercivity, the recording field needs to be increased accordingly. However, the magnetic material at the corners of the recording head gap may get saturated before the required fringe field is achieved. This saturation will deteriorate the field gradient, leading to poor recording. To prevent this from happening, a high Bs layer magnetic material is deposited on the inside surfaces of the gap, similar to the MIG head in Fig. 2. The challenge is to find a material that has both high B values and high corrosion resistance. Commonly used materials are iron and cobalt alloys.

We have implied in our analysis that the recording field responds instantaneously to recording voltage pulse. In other words, the recording field has perfect square waves in time domain. When we deal with low frequency, this assumption is valid. However, when the frequency is high, it is not valid because the head has both an inductance and the core material needs finite time to rotate its magnetization. If the field rise time τ is too large compared with transition time T, then additional NLTS will be introduced. τ is typically between 1 and 5 ns, indicating frequency limitation occurs around 1 Gb s^{-1}. To reduce τ, we need short and thin magnetic yokes with high B and high electric resistance.

From the reproducing head viewpoint, the major amount of research and development emphasis has been placed in the areas of signal sensitivity and stability. With narrower track width and shorter flux change length for higher areal density, the recording head picks up less magnetic flux from each transition. To ensure adequate SNR, the recording head needs to have a higher sensitivity to the magnetic flux from the recorded signal. The change from inductive head to AMR head then to GMR head and maybe to TMR head is to achieve high SNR.

The reproduced signal must be stable for the channel to detect. This requires a stable magnetic domain in the MR film. A hard magnetic material (hard bias) is deposited adjacent to the leads along the MRE width direction to stabilize the magnetic domain and reduce large Barkhausen noise. If the strength of the hard bias field is not enough, the reproduced signal may experience jumps. This phenomenon is called baseline shift. However, if the field is too great, the head will suffer poor sensitivity. The head stability can also be a result of the change of the pinned magnetization, and the loss of exchange field of the AFM.

To address these concerns, synthetic antiferromagnetic (SAF) pinned layers are used. The SAF layer, consisting of two ferromagnetic layers separated by a thin ruthenium layer, provides a more
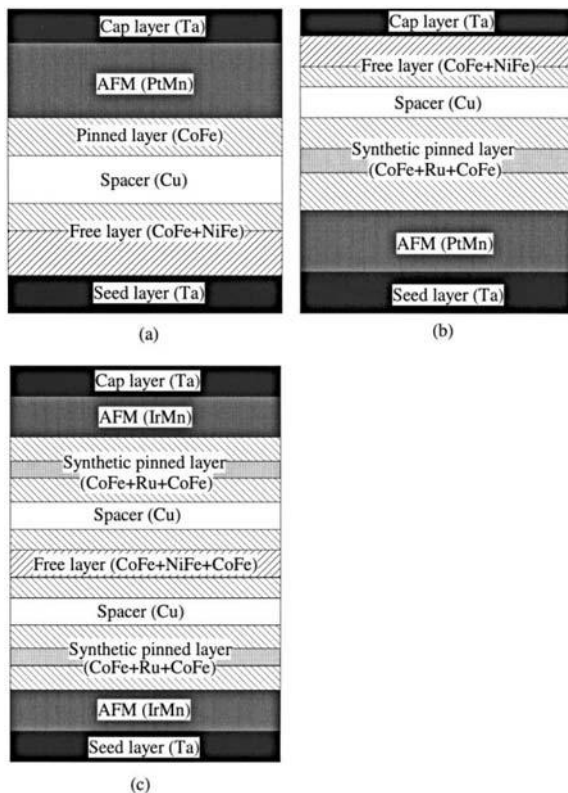
Figure 10
Sectional views of various spin-valve structures:
(a) standard, (b) bottom synthetic, and (c) dual
synthetic.

stable pinned magnetic field, as depicted in Fig. 10.
Various AFM materials have been employed to in-
crease its block temperature and pinning field. In ad-
dition to sensitivity and stability, manufacturability
and durability are important. Practical issues such as
dimension control, ESD safety, and corrosion resist-
ance all need to be resolved.

Both Eqn. (13) and Eqn. (15) show the importance
of head-to-medium spacing d. To reduce PW_{50} and
increase amplitude, we need to minimize d. If d is too
small, however, mechanical interactions will occur on
the head and/or the medium, leading to severe dam-
age. The science and art for the balance between areal
density and head/medium interface durability be-
longs to the field of tribology. For low duty-cycle
applications such as in a floppy drive, the head is in
contact with the medium surface. For high duty-cycle
applications such as in a hard drive, the head flies
over the disk surface during operation. The flying
height is between 10 and 20 nm. This small and stable
flying height is achieved by using an air-bearing
surface on the head, a flat and smooth surface on
the disk, and a pressurized air film in between. The

scientific and engineering foundation is the hydro-
dynamic lubrication, governed by the Reynolds
equation.

See also: Magnetic Recording Devices: Head/Medi-
um Interface; Magnetic Recording: Rigid Media,
Tribology; Magnetic Recording: Rigid Media,
Recording Properties

Bibliography

Bertram H N 1994 *Theory of Magnetic Recording*. Cambridge
University Press, Cambridge
Fan G J 1961 A study of the playback process of a magnetic
ring head. *IBM J. Res. Dev.* **5**, 321–5
Karlqvist O 1954 Calculation of the magnetic field in the ferro-
magnetic layer of a magnetic drum. *Trans. R. Inst. Technol.
(Stockholm)* **86**, 3–28
Maller V A J, Middleton B K 1973 A simplified model of the
writing process in saturation magnetic recording. *IERE Conf.
Proc.* **26**, 137–47
Mallinson J C 1993 *The Foundations of Magnetic Recording*.
Academic Press, San Diego, CA 2nd edn
Mee C D, Daniel E D (eds.) 1996 *Magnetic Storage Handbook*
(2nd edn). McGraw-Hill, New York
Miyata J J, Tartel R R 1959 The recording and reproduction of
signals on magnetic medium using saturation-type recording.
IRE Trans. Elec. Comp **EC-8**, 159–69
Potter R 1974 Digital magnetic recording theory. *IEEE Trans.
Magn* **MAG-10**, 502–8
Wang S, Taratorin A M 1999 *Magnetic Information Storage
Technology*. Academic Press, New York
Watkinson J 1994 *The Art of Data Recording*. Focal Press,
Oxford
Webster J G (ed.) 1999 *The Measurement, Instrumentation and
Sensors Handbook*. CRC Press, Boca Raton, FL
Westmijze W K 1953 Studies on magnetic recording. *Philips
Res. Rep.* **8**, 161–83
Williams M L, Comstock R L 1972 An analytical model of the
write process in digital magnetic recording. *AIP Conf. Proc.*
5, 38–42

Y. Li and A. K. Menon
Read-Rite Corporation, Fremont, California, USA

Magnetic Recording: Flexible Media, Tribology

The data densities demanded of magnetic media have
increased monotonically and much work has been
done to respond to these demands. The tribology of
these systems has, however, been largely neglected
and problems which occurred were solved largely by
a combination of good design, lower contact pres-
sures, better lubricants, better materials for heads and
media, and by mature use of natural tribological
laws. Thus by a combination of good system design,

exploitation of materials technology, and good fortune, the tribology of the systems has, until recently, seldom been a limiting factor in their development. Good fortune can no longer be relied upon and there is an urgent need for more effort to be made in understanding the basic mechanisms of contact in these very complex systems.

As recording densities increase, recording wavelength is reduced and the trend is to thinner magnetic coatings, two or more layered structures, thinner polymer substrates, zero head/media spacing, and smaller head dimensions. Magneto-resistive (MR) read head elements are employed which may run at temperatures of 70 °C or more. In future, giant magneto-resistive (GMR) heads will probably be used which will necessitate the use of ultrathin head coatings. In particulate media this necessitates the use of magnetic layers of different structure, with different resin binders with higher glass transition temperatures and new, more effective lubricants and lubrication systems. In addition, magnetic particle loadings must increase and particle size must be reduced. All of these factors produce acute tribological contact problems and are now significant limiting factors in the development of dynamic magnetic storage technology, and will be so increasingly in the future.

With the miniaturization of components and the consequential changes detailed above, any factor which adversely affects the intensity of the output recorded signal or which produces recording errors becomes of prime importance. For example, any process or mechanism which introduces spacing between the media and the recording head or which leads to the physical removal of material from the magnetic media must be understood and its effects eliminated. The signal falls exponentially with an increase in this spacing.

The materials aspects of the problem will be discussed later, but it is worth considering some basic tribological laws which have aided the magnetic media cause. A simple law describing the wear of materials under a wide variety of conditions is the Archard wear law:

$$\omega = kW/P_{\mathrm{m}} \qquad (1)$$

where ω is the volume of material removed per unit distance of sliding, the wear rate; W is the applied load; and P_{m} is the material flow pressure, or hardness.

From this simple law one can see that increasing head and media hardness will decrease wear, as will reduction in head loads. Here, however, the industry is further helped by nature, in that k does not remain constant, but can fall by almost an order of magnitude for a ceramic head vs. a γ-Fe_2O_3 media at low load. However, the friction coefficient increases at low pressures, particularly with very smooth surfaces. As a consequence of this effect, dynamic and static

friction problems arise under low-load conditions, which are not noticed at higher loads.

1. The Media

Flexible magnetic media consist of a thin magnetic coating applied to a polymeric substrate carrier film. The magnetic coating may be applied as a slurry containing magnetic particles (particulate media) or as an evaporated magnetic metal film (metal evaporated media). In addition to the magnetic side of the media there is often a backside coating applied to tape to give desired mechanical and tribological properties, to prevent adhesion when rolled, and to give antistatic protection. Traditionally, the base coat has been produced from polyethylene teraphthalate, but for the very thin substrates used in the continued drive towards miniaturization, materials with higher elastic modulus such as polyaramide and polyethylene naphthalate are required.

1.1 Particulate Media

In particulate media, the magnetic coating consists essentially of acicular magnetic particles bound together by means of a polymeric resin. Thus the magnetic layer in contact with the read/write heads will have the tribological properties of a filled polymer. This consists not only of the magnetic pigment (at up to 80% by weight, 50% by volume) and the polymer binder, but also a head-cleaning agent (HCA) (typically 4–8% by weight of a relatively large abrasive particle such as Al or Zr oxide) and a possible combination of wetting agents, cross-linking agents, solvents, antifungal agents, carbon black (to prevent surface charging), and the essential lubricant (typically fatty acid/fatty acid esters). Until recently, oxide magnetic pigment (Co doped γ-Fe_2O_3) was used in flexible recording media. The necessity for higher coercivity and squareness has meant that current development is concentrated on passivated metal (Fe) acicular particles (MP media) with a secondary interest in barium ferrite hexagonal platelets.

Magnetic constraints demand that particle sizes and layer thicknesses are continually decreasing with particles now being produced of about 70 nm in length (4:1 acicular ratio) with projected layer thicknesses of about 10 particles. The mechanical integrity of such a layer would not provide sufficient durability and hence tapes must be produced where the magnetic layer is formed on a thicker nonmagnetic undercoat. The most popular current method of providing lubrication in particulate media is to incorporate the lubricant in the magnetic layer. However, as layers become thinner the volume of lubricant may not be sufficient to provide the required durability over the projected lifetime of the media. Hence lubricant is incorporated into the undercoat and reaches the surface through pores in the magnetic layer.

Considering the tribology of this system, the most important part of the contact layer is the binder which must have the ability to accept high magnetic particle loading, provide good wear resistance, good substrate and particle adhesion, low surface energy (low friction), be resistant to temperature and humidity effects, and exhibit sufficient flexibility for the continual deformation required of a tape or floppy disk. To satisfy these requirements the polymeric binders consist of at least two phases, a ''hard'' glassy phase to give the system mechanical integrity and a ''soft'' rubbery phase to provide the flexibility required. The blend is cross-linked to increase phase separation and to ensure that the glass transition temperature is below the operating temperature of the media. Many present polymer blends use a dispersing or wetting agent to ensure polymer–particle adhesion and homogeneous dispersion, but dispersing binders are being developed with modified functional end groups. This results in better binder particle bonding, higher cohesive strength, higher particle loading, and better wear properties. One disadvantage may be that such binders are more polar and this may increase the adhesive forces between heads and media.

1.2 Metal Evaporated Media

In order to satisfy high areal recording density requirements, thin metal films such as Ni–Co alloys evaporated under vacuum onto a flexible polymer substrate were introduced. This media has potentially more effective magnetization than particulate media due to the increased grain density. The media consists of single, or possibly, multilayers of evaporated metal magnetic layers on a polymer substrate, covered by a protective carbon overcoat which is in turn topically lubricated. Tribologically the system is inherently simpler than the particulate media, but presents its own unique problems. Major among these is that, unlike particulate media, surface coverage of the lubricant must be complete, must remain so for the projected lifetime of the media, must afford complete corrosion protection, and should not be more than about 5 nm thick in order that spacing losses are not excessive. Metal evaporated (ME) thin film flexible media has the advantages of the porosity and surface chemistry of the particulate media, thus the demands on the lubricant present a severe challenge. The lubricants are the perfluoropolyethers, often with end group modifications. It should also be borne in mind that these thin metal films are far less compliant than particulate-filled polymer films and should not be subject to excessive strain if cracking and catastrophic failure are to be avoided.

2. Contact and Forces at Head–Media Interfaces

When two surfaces interact, the real area of contact is dependent on the physical properties of the surface,

but is generally lower than the apparent area of contact. This is because contact will only occur at asperity tips. When contact occurs, these asperities may deform either plastically or elastically and it is important to know the mode of deformation before wear and friction can be understood. Bhushan (1984) adapted the work of Greenwood and Williamson (1966) and defined a plasticity index ψ for such that:

$$\psi = \frac{E^*}{Y\left(\dfrac{\sigma}{r_a}\right)^{1/2}} \qquad (2)$$

where E^* is the complex modulus of elasticity, Y is the yield strength or hardness, σ is the standard deviation of asperity heights, and r_a is the mean radius of those asperity peaks. He suggested that for polymers if $\psi < 1.8$ the contact is elastic, and if $\psi > 2.6$ the contact is plastic. Consideration of particulate media reveals that most contacts are elastic. From the above relationship, therefore, the real area of contact, A_r, can be calculated for elastic contact from:

$$A_r \approx 3.2 \frac{W}{\psi Y} \qquad (3)$$

The classical analysis of Halliday (1955) also shows that the contact must be almost entirely elastic for particulate media and elastic/plastic for metal evaporated media.

Thus for particulate media, the forces generated when contact occurs are largely adhesive and the real areas of contact are governed by the elastic properties of the media. For metal evaporated media the contact is more complex, but, considering the elastic/plastic combination, adhesive forces probably still dominate contact.

3. Surface and Contact Temperatures

Surface and contact temperatures can have a substantial effect on the nature and magnitude of wear and friction processes. There have been many attempts to measure and calculate surface temperatures. Bhushan (1987) reported a detailed thermal analysis in which he predicted contact temperature rises for typical head–tape contacts of 7–10 °C, although he concedes that if magnetic particles are exposed the contact temperatures can be very much higher at 600–900 °C. There is some correlation of these results with IR measurements made on a simulated head/tape interface by Gulino *et al.* (1987). Our calculations, however, suggest that contact or hot spot temperatures much higher than Bhushan's figures can occur in practice.

In this model the heat generated due to friction is equated to the sum of the heat lost due to conduction into the head surface, conduction into neighboring

asperities, and that due to forced convection to the air. Taking atomic force micrographs of the surface as a basis for a realistic model, the surface was modeled into a network of nodes, each node representing an asperity. It was assumed that the asperities were subject to random Raleigh distribution of volumes and base radii. On the basis of this model, maximum contact temperatures for a typical linear tape system were calculated to be over $100\,^{\circ}$C, although the mean surface temperature was low. If it is assumed that all the load is carried by one asperity, and we have evidence to show that this may occasionally occur, then very high temperatures are predicted.

4. Friction

Friction is an important parameter in the design of magnetic recording systems. With the continual move towards miniaturization and the use of low power drives, friction which is too high can cause speed variations, high interfacial temperatures, or, ultimately, failure of drive motors. In tape systems, it is not only head–media friction which must be considered, but the tape has to negotiate a complex transport system and backcoat friction can lead to problems. Dynamic friction must therefore be understood and controlled, but equally as important is the static or "start-up" friction.

4.1 Dynamic Friction

The frictional force, F, consists of an adhesive component, F_A, plus a deformation component, F_D, which in turn consists of a plastic deformation or ploughing term and a hysteresis loss term, hence, $F = F_A + F_D$. Considering the viscoelastic nature of the magnetic layer, the nature of the contact, and the surface topography, then, except at very low speeds and at high temperatures, the deformation term in the friction equation is negligible. Hence friction may be regarded to a first approximation as being due to adhesion. All the frictional energy is dissipated in the contact region and the frictional force may be written as:

$$F \approx F_A = \tau A_r \tag{4}$$

where τ is the interfacial shear stress. τ is not constant, but will increase with pressure and will, in general, fall with increased temperature within the operating range of the media. Friction will also be speed dependent due to the time dependence of the elastic properties of the polymer and the increase in temperature with increase in velocity.

With particulate media, a fatty acid/fatty acid ester type lubricant is normally incorporated into the bulk of the magnetic coating. The coating thus acts as a reservoir to replenish lubricant molecules removed by wear. Using angle resolved x-ray photoelectron spectroscopy (XPS) we have measured the thickness and areal coverage of lubricants on a wide variety of tape and diskette surfaces and found current lubricants to be about two or three molecular layers thick, with coverages as low as 10% of the total surface area. Taking into account the presence of the lubricant, the frictional force can be written as:

$$F = A_r\{\tau(1 - \alpha) + \tau_1\}\alpha \tag{5}$$

where τ_1 is the shear stress in the lubricant and α is the fractional areal coverage of the lubricant. The lubricant provides an easily sheared layer separating the two surfaces and will also produce some plasticization at the surface of the polymer.

Polymer surfaces have low surface energy and this together with the low areal coverage means that the frictional force will not change substantially with lubrication, but the presence of this lubricant is essential to reduce wear. Since the lubricant film will not affect the frictional force, this force must be governed by the properties of the magnetic layer. Thus a high hardness, high complex modulus material should be used to reduce friction, with due regard to a suitable glass transition temperature and toughness. Rougher surfaces produce lower frictional forces; however, due to the need for minimum spacing loss, surfaces need to be as smooth as possible.

Friction increases with time of running, at least over the first few passes. This is to some extent due to the surface becoming smoother, but this is not entirely consistent with the assumptions that contact is elastic. Our findings indicate that the outer layers also change chemically. The chemical changes are confined to the outer polymer covering on the magnetic particles. Assuming the contacts to be mainly adhesive, the changes may be sufficient to influence the frictional force.

In the case of ME media, the lubricant layer coverage is complete and hence $\alpha = 1$. This is a case of classical boundary lubrication, where the friction force is wholly determined by the shear stress of the lubricant/head interface. Here, the deformation component of friction is negligible. If lubrication fails, however, friction forces can become catastrophically high.

4.2 Static Friction—Stiction

In all materials there is a distinction between dynamic and static friction, with the force required to initiate motion, static friction, being higher than that required to maintain it, dynamic friction. In magnetic recording systems where the head is often parked in contact with the media, this difference can be particularly pronounced and can lead to acute start-up problems. This results in a jerky and uneven motion of the tape or disk. There are a number of reasons for this high initial friction. As mentioned before the

filled polymer magnetic layer is in a viscoelastic state at normal operating temperatures. In this state the strain is rate dependent. This means that the real area of contact increases with time and increasing static friction. In addition to this, van der Waals forces operate between the smooth surfaces of the magnetic layer and the head and these will increase the surface area above that predicted by theory. There is some controversy over the importance of electrostatic forces, but it is likely that they account for increases in friction at very low loads.

Very high static friction forces are most apparent under conditions of high humidity. This may be due to a meniscus effect at the head–media interface or the effect of water plasticization of the polymer in the contact zone. Meniscus effects are possible since high friction is also observed if too much lubricant is present; it is more likely, however, that increased moisture levels instigate hydrolysis and plasticization takes place. To overcome these problems similar polymer properties of high complex modulus and high hardness are required with an additional requirement for the binder to be hydrophobic.

5. Wear at the Head–Media Interface

Although the ultimate life of head and tape are of importance and determined by absolute wear, the actual wear rates are, in engineering terms, very small indeed and in general it is the effect of wear on signal performance that has a greater influence on useful life than material removal rates. Any effect which introduces a spacing between the magnetic media and the read/write sensors or which results in loss of data is of prime importance. Thus media degradation and wear, head wear, differential wear, head surface modifications, and transfer film formation must all be considered. Wear is classified as adhesive, fatigue, abrasive, corrosive, or erosive. Although it is clear that the contact is largely adhesive in head–media contact, it is probable that most of these forms of wear apply at some time.

5.1 Particulate Media

(a) Transfer film—head stain

The first stage of wear usually consists of material transfer from media to head. Our x-ray spectroscopic measurements show that at the surface the magnetic particles are covered with polymeric resin to a depth of about 5 nm. Thus the initial head–media contact is between head and the polymer surface of the media. The adhesive forces formed at this contact may be either physical, involving van der Waal bonds, or chemical, involving electrostatic, ionic, or covalent bonding. Typical van der Waal bond strengths indicate that their contribution is not significant. The chemical bonds are probably more significant and

these will depend on the nature of the head material. For polymer/metal contacts covalent bonding occurs and for polymer/ceramic contact, ion-dipole bonds are formed. Each of these bond types will give strong adhesive junctions.

Within the polymer binder, atoms are covalently bound (bond strengths up to about $10\,eVatom^{-1}$) and chains bound together via dipole–dipole interactions. Dipole–dipole interactions are typically a few tenths of an $eVatom^{-1}$, although interchain bond strengths approach those of the covalent bonds due to cross-linking. Bond strengths of the adhesive junctions formed at the various polymer/head interfaces can be greater than those of the binder/particle interfaces within the magnetic layer and this, if the conditions are right, leads to adhesive transfer from media to head. (Transfer is not observed for relative humidities above about 45–60%, where water saturation of active sites on the head material surfaces prevents the formation of adhesive junctions.) Transfer is particularly evident on MR metal elements due to high temperature enhancement of covalent bond formation and reduction of surface saturation due to expulsion of water vapor and other contaminants. Thus transfer films occur readily between polymer/metal and polymer/ceramic surfaces and these can substantially affect wear properties of the junctions and may introduce spacing losses. This phenomenon is known as "head stain."

Transfer does not occur in homogeneous layers, but as a discontinuous lumpy film, with thicknesses corresponding to one magnetic particle. The thickness of these layers indicates that the depth of material removed from the media in this early phase of wear is not sufficient to produce data errors in current media.

These transfer films have been variously described as friction polymer, brown, blue, or white stain. In XPS and Auger electron spectroscopic studies we have found no friction polymers. Our XPS analysis (careful measurement of Fe $2p$ binding energies) indicates that the layer consists of magnetic pigment from the media and we conclude that color is determined by thickness and substrate.

These results are entirely consistent with the mechanisms where the thin surface polymer is adhesively bound to the head. This results in cohesive failure within the media and laminae of media that are one particle thick transferring and adhering to the head surface. Once the film has been formed contact is between it and the media, although one would expect the situation to be dynamic with continual removal and replacement of the stain. After formation, the junction strength between load bearing surfaces of the transfer film and the polymeric media is not sufficient to duplicate the transfer process and hence films will not normally increase in thickness. In tribological terms, the formation of a transfer layer is beneficial in reducing wear. However, the layer may

introduce unacceptable spacing losses and may, under certain circumstances, short out MR elements and shields. A function of the head-cleaning agent added to the magnetic layer is to limit the thickness of this stain and to reduce spacing losses. (Another and perhaps less well understood function of the head cleaning agent is to act as a bearing surface and effectively protect the soft media against wear.) During this phase of wear, surfaces of the particulate media generally become smoother and errors are reduced (Hempstock *et al.* 1998).

(b)   Delaminative wear and head clogging

The second stage of wear of particulate media is due to fatigue and results from continuous cyclic stressing of the media by contact with the head. When two solids are in sliding contact, the maximum stress occurs not at the asperity junction, but below this surface. When an asperity approaches an opposing asperity the subsurface is in compression; as the asperities separate the subsurface is in tension. Hence for repeated contact the subsurface immediately below the asperity contacts is subject to cyclic stressing. This leads to the initiation of subsurface fatigue cracks which grow to the surface and produce delaminative removal of particles, which leave crater-like recesses behind (Hempstock and Sullivan 1998). This delaminative particle removal process is analogous to that described by Suh (1986) for metals. For fatigue-induced crack initiation there needs to be defects in the matrix. Stress concentrations at these defects will then enhance crack initiation and propagation. There are three possible candidates for this: the boundary between hard and soft phases of the copolymer binder, the boundary between head cleaning agent particles and binder, or the boundary between acicular magnetic particles or agglomerates of these particles and the binder.

Although this wear phase is relative rare, it has many effects on signal performance and error growth. The removal of delaminative wear particles from the media can result in loss of bits of information. Hempstock and Sullivan (1997) have observed a correlation between such surface damage and increase in dropouts (hard errors). The released debris then forms third body particles which may damage head and media and lead to head clogging. Head clogging is due to loose debris expelled from the contact area agglomerating on the exit side of the head. The agglomerates are then picked up by the tape and eventually transferred to the head where they accumulate in the gap region, leading to spacing losses with a consequent decrease in the reproduced signal. Head clogging can produce a transfer film which is somewhat like the "stain" described above. The differences are that the film is very much thicker, more easily removed by wiping with solvents, and is more likely to be produced at high humidity, the latter probably due to water assisted breakdown within the magnetic layer, due to a chain scission mechanism. We have also seen such an effect and have shown that this can also cause gap damage which affects the high-frequency response of the system. The wear phase eventually leads to the production of more debris and an avalanche catastrophic failure mode observed by ourselves and others.

It should be noted here that increasing the magnetic particle loading to a figure of about 50% by volume leads to an increase in complex modulus and decrease in wear. Increasing loading beyond this level, however, will reduce the modulus and increase wear.

(c)   Abrasive wear

There are two forms of abrasive wear. Two-body abrasion occurs when a hard, rough surface slides over a softer one resulting in ploughing action and removal of material. Three-body abrasion occurs when hard particles become entrapped between two sliding bodies, resulting in the same effect. An essential requirement for abrasive wear is that plastic deformation should occur beneath a penetrating asperity or abrasive particle. Our calculations indicate that localized contact temperatures can be quite high and could lead to softening of the polymer matrix, thus aiding plastic flow, but reference to plasticity criteria (Greenwood and Williamson 1966) reveals that with current surface roughnesses two-body abrasive wear should not occur either in the media or at the head.

However, agglomerates of wear debris entrapped between head and media may be of sufficient size to give rise to three-body abrasion. This is almost certainly the origin of scratches seen on tape and diskette surfaces after wear. For polymeric materials the abrasive wear rate is proportional to $S^{-1} e^{-1}$, where S is the breaking strength of the material and e the elongation to break. The addition of magnetic particles will increase S, but reduce e and hence the filled polymer is no more resistant to abrasion than the polymer itself. This is not true of other forms of wear where the increased hardness and elastic modulus may reduce wear. In general, abrasive wear of the media is not too important when considering loss of signal, but may cause errors. The same cannot be said when considering the head.

(d)   Effect of lubricants

Wear of media and heads is reduced by introducing a boundary lubricant between the opposing surfaces and by reducing the polar molecule content of the binder. Sullivan and Sharma (1992) found lifetimes reduced by two orders of magnitude in the media without lubricant. Friction values were relatively unaffected. Our angle-resolved XPS measurements have shown areal coverages between 10% and 40%, and the thickness of the polymer/lubricant covering the

magnetic pigment is between 4 nm and 8 nm, depending on tape manufacturer and media type (this could represent a signal loss of something less than 1 dB). The coverage is sufficient to protect the media surfaces against premature failure, although durability increased with coverage.

Other forms of wear, if they occur, have negligible effects on signal, although polymer interaction with water vapor may have an effect on adhesion, abrasion, and fatigue. Our examinations of heads produce some circumstantial evidence that Cl from degeneration of Cl-containing polymeric binders may under some circumstances produce corrosion. In general, high humidity reduces wear and increases durability of particulate media, but adversely affects the head and reduces signal through this route.

6. Metal Evaporated Media

ME media relies on a complete boundary lubricant film, about 2–3 nm thick, and operates under pseudo-classical boundary lubrication conditions. The surface of the evaporated metal film is oxidized and sometimes carbon coated to give additional protection in the case of a momentary breakdown of the boundary lubricant. This provides a low surface energy contact which can survive occasional head/media asperity interaction, but the lubricant must be capable of self-healing any breach if high wear is not to ensue.

The lubricants used are usually perfluoropolyethers with suitable functional end groups to anchor to either a carbon overlayer or a metal oxide. Ideally there should also be a semi-mobile component in the lubricant layer to satisfy the self-healing requirement. These lubricants are chosen for their good affinity to the surface, good viscosity range, low volatility, and good chemical and thermal stability. More traditional metal boundary or antiwear additives, such as triaryl and trialkyl phosphites, may provide improved tribological performance, but probably do not satisfy anticorrosion requirements.

The asperity contacts on the tape will be mainly elastic, with a small plastic component. This takes into account the effect of the substrate-generated texture included to prevent adhesion of the very smooth surfaces. If lubricant breakdown does occur then this can lead to transfer of material from media to head. The roughening of the head can then lead to abrasive grooving of the media and the possibility of errors due to material removal. In the absence of lubricant breakdown, the dominant wear mechanism, however, is one due to fatigue.

Hempstock and Sullivan (1998) have studied the wear of commercial ME Hi-8 video tape and correlated this to signal performance. Single and double magnetic layer structures were studied in this investigation and signal degradation and error growth were monitored as functions of running time. Scanning electron microscope (SEM) examination of the surfaces clearly identified the wear mechanism. In the initial stages of wear little change occurred at the surface and few wear particles were produced. As contact continued, delaminative removal of material was observed in the media surface and consequent micron-sized wear particles appeared. The increase in delaminative craters on the surface correlated exactly to an increase in measured signal errors. The thickness of laminar particles removed from the tape was less than the thickness on the ME layer, except when the process proceeded until catastrophic fatigue, cracking, and delaminative failure of the film occurred at the ME substrate interface.

The single layered structures proved to be the most durable. Here, the failure of the media corresponds to the depletion of lubricant in the area of the scar. In the case of the dual layer media both error growth and ultimate failure occurred at an earlier stage (corresponding, for example, to 6–8 hours pause motion in helical scan mode, compared to 10–12 hours for the single layer tape). XPS analysis of dual layer media showed that substantial delamination and ultimate failure of the media both occurred before the lubricant film showed significant signs of failure.

In both types of ME media the mechanism of wear is classic Suh delamination (Jahanmir and Suh 1977), where subsurface changes and fatigue lead to the production of an immediate subsurface discontinuity which acts to concentrate fatigue cracks. This then leads to delaminative removal of material. In the case of the single layer film, gradual breakdown of the lubricant film allows more head–tape contact to occur and this will greatly accelerate fatigue-induced crack formation and propagation, since under these circumstances more energy will be dissipated in the ME layer, and less in the lubricant film. In the case of the dual layered films a discontinuity already exists at the boundary between the two layers and this concentrates subsurface stresses and provides a location for crack formation and propagation. Thus delamination takes place at an earlier stage in this media before substantial amounts of lubricant layer have been removed from the surface. Thus although dual layers may have magnetic advantages, such media are inherently less durable than single layers.

Tape drive components and tape magnetic side/back side contacts must also be taken into account. In general, the wear mechanisms outlined above are also evident in these situations with similar consequences for signal loss.

7. Read Write Heads: Wear

7.1 General Wear

There are many types of recording heads for tape systems, including ferrite, metal in gap and sandwich

heads for helical scan, and inductive write/MR read based heads for linear recording formats. All are similar in that they are multicomponent and are constructed from materials which are hard. With current thin film head constructions the allowable wear is very small, being perhaps less than a micron over the life of the component. The tribology of these hard materials is still at a very immature stage. The materials generally have high elastic modulus, high fracture strength, high chemical stability, and high thermal stability, but because of the ionic and/or covalent nature of their bonds, they are also brittle. The high chemical stability means that interfacial adhesion and the shear strength of the junction are low compared with bulk cohesive forces, hence adhesive transfer from head to tape does not occur.

The surface roughnesses and particle sizes associated with current tape formats ensure that conventional two-body abrasive wear cannot take place. The materials are not ideally brittle, however, and plastic flow and hence abrasion can occur with large third-body particles. Polishing (a form of adhesive at the nanoscale), however, can take place. Here, the hardness of the tape particles need to fulfil the Richardson (1967) criteria, but can be relatively low. Conventional polishing normally occurs when small hard particles imbedded into an elastic backing medium are passed at high speed and low load over the surface to be treated. This is exactly the situation which occurs in head/ particulate media contact. Polishing has been described by Suh (1986) in terms of microdelamination of the wearing surface. The soft magnetic materials, for example NiFe, CoZrTa alloys, used in MIG and sandwich heads, and the MR elements and shields in linear recording heads, are of similar hardness to the ceramics and exhibit similar wear mechanisms.

Reaves and Sullivan (1992) showed that this form of wear was the dominant mechanism in ferrite video heads, Harrison *et al.* (1999) and Bijker *et al.* (2000) have shown that it is also the dominant mechanism in terms of volume of material removed in sandwich heads and linear recording heads, respectively. In none of the cases, however, was it the most important mechanism in terms of signal degradation. In the case of the ferrite head, signal degradation was caused by gap damage due to third bodies becoming entrapped between head and tape, and in the case of the sandwich and linear heads was caused by pole tip recession. This mechanism is operative in glass, ceramics, and ferrites. With ferrite single crystals, however, there is the additional effect of crystal orientation. It is far more pronounced in some iron oxide or metal particle media than it is in chromium dioxide media and this may be explained in terms of plastic deformation in the ferrite crystal. This effect must be taken into consideration when, for magnetic reasons, the two halves of a head are aligned in different directions. In this case the different wear rates

lead to pole piece height differences which result in spacing loss.

Although abrasive wear should not be possible in these systems, relatively deep scratches are observed on heads and these are obviously caused by three-body abrasion, possibly as a result of agglomerate debris from the tape becoming entrapped between head and media. Such scratches not only change the surface topography, which may effect spacing, but may also destroy MR elements. If the loading in particulate tape becomes too high and the complex modulus falls, more such third bodies will be formed. Third-body abrasion will be even more important in GMR heads, when the damage could have catastrophic consequences for head performance.

7.2 Differential Wear and Pole Tip Recession

In terms of signal loss, differential wear is of greater importance than absolute wear, since this introduces spacing between media and the active areas of the head. When using a combination of different materials in the recording head, it is very difficult to exactly match wear rates. Since there is poor correlation between static measurements of elastic/plastic properties and wear over a range of different materials, model experiments must be devised, but even then it is not certain that the modes of wear measured in these experiments are appropriate in practice. The choice of materials is a compromise and the best individual material may not be suitable for use in a given head application because of mismatch in wear properties. This is the reason that a number of two-phase ceramics are used in head applications. Even with careful choice of materials, differential wear still occurs and is a major cause of spacing loss.

Harrison *et al.* (1999) have studied pole tip recession in sandwich video heads, where the recession is caused by differential wear. The soft magnetic metal sandwich is worn at a greater rate than the surrounding ceramic. In many circumstances this results in hollowing out the metal to a depth where contact with the media cannot occur. In these heads the soft magnetic materials and ceramic body have comparable wear rates, measured by simulation tests. Harrison *et al.* (1999) found that the major material removal mechanism for soft magnetic materials and ceramics was nanoadhesion (polishing), but this could not account for the recession. This was the result of two separate effects: fatigue wear of the ceramics, which resulted in the plucking out of laminar crystallite-sized particles from the surface, and the entrapment of these particles in the soft magnetic sandwich region, which produced erosive wear. The ensuing pole tip recession was then a function of the relative fracture toughness rather than hardness. The production of fatigue ''pull outs'' from the ceramic is probably increased for multiphase ceramics.

The pole tip recession observed in these heads was greatest for ME media because the material removed by nanoadhesion was far less than that removed in the case of the aggressive MP media. Thus smoother, more compliant ME tape allowed more fatigue-induced particles to form than in the case of MP tape, where the surface was being removed at a greater rate, thus removing fatigue cracks.

This form of wear has also been shown to be responsible for pole tip recession in other systems. Hempstock *et al.* (2000) have shown similar mechanisms in different linear recording systems. In these systems it is found that pole tip recession is most pronounced under conditions of high humidity. The effect of humidity on ceramics is a very complex problem. In many ceramics there is a tribo-chemical reaction at the wearing surface which generally produces hydroxides. This effect can either reduce wear by providing an easily sheared, low surface energy film at the surface, or, if the film is removed too rapidly due to the wearing conditions, can increase wear. If chemical interaction does not occur, mechanical process due to water molecule ingress may be responsible for wear. This effect is well known in the pitting of metals. Sintered ceramic materials are always porous. Water under hydrostatic pressure can enhance crack formation and propagation within individual ceramic grains within the surface.

The crack depth relates to the region of maximum stress and may be calculated from Hertzian analysis of the subsurface stresses within the ceramic surface. This can lead to two possible effects: (i) increased rates of removal of the surface due to microfatigue which enhances polishing wear, and (ii) fatigue-induced granular delamination which can lead to the formation of "third body" abrasive particles. Those particles are then fragmented and result in pole tip recession. In the case of the most popular ceramic used in linear heads, that is Al_2O_3/TiC, delaminative wear occurs preferentially at the TiC phase. In the cases cited above simple wear ranking experiments would not be expected to predict the differential wear observed in the final product.

8. Coatings

Most differential wear problems could be reduced either by using more abrasive tapes and suffering higher overall wear or by using coatings on the head. The first of these solutions is not acceptable in modern media. The second is the only viable solution and much effort needs to be expended in the development of an ultrathin surface coating. This is particularly true if GMR sensors are to be used in future generation heads, where coatings will be necessary, not only for wear protection, but also as an essential corrosion barrier. The most likely candidates for such a film are diamond-like carbon (DLC) or chromium oxide based films such as those developed by Philips/Onstream, but the challenges here are enormous. The coatings must be no more than about 7 nm thick and be capable of lasting the life of the head in continuous contact with tape.

There are two modes of wear with such thin coatings, one due to the microadhesions/microabrasions detailed in previous sections and one due to delamination. In order to survive the first of these modes with conventional advanced MP tape containing head-cleaning agents (HCA), the coatings should have a hardness (determined by the Richardson criteria) of about twice that of the HCA particles, that is about 50 GPa. Filtered cathodic arc deposition of DLC films is probably the favored process for the production of such a film. An alternative solution may be to substantially reduce the hardness of the HCA in the tape, but results of this change on transfer film formation (head stain) are difficult to predict. Similarly, the effects on tape durability cannot be predicted, since a major function of HCA is to act as a bearing surface and give the tape mechanical stability.

If other forms of wear can be eliminated, fatigue-induced delamination at the film/substrate interface will still present a major problem which may only be solved by the formation of very high strength adhesive junctions. Such junctions have not been developed at this time.

9. Altered Layers

A further consequence of wear, particularly at ferrite heads, is the production of a work-hardened amorphous magnetic dead layer, or Beilby layer, at the surface of the crystalline ferrite. Such a layer might also be present in metal elements of linear heads. These layers have been identified and measurements of thickness attempted using magneto-optic Kerr effect measurements, but the evidence so far only confirms the possible presence of Beilby layers at thicknesses of less than 100 nm. Some reliable method needs to be developed for these measurements before the effect on signal spacing loss can be properly assessed.

10. Conclusion

This is a brief review of the tribology of flexible magnetic recording media, and the effect on signal performance. Where possible, original tribological source material has been quoted. The review shows that much of the pioneering work in tribology may be used to elucidate mechanisms of wear in these systems, with the proviso that scale effects must be taken into account. The contact between media and heads is complex, but is largely elastic in nature. Fatigue-induced delamination is the major wear mechanism

in media. Microabrasion is the major wear mechanism in head materials, although other mechanisms such as delamination, three-body wear, and erosion may be more important in terms of signal degradation. Hence the major mechanisms of material removal do not necessarily have the greatest effect on signal output performance.

See also: Magnetic Recording Materials: Tape Particles, Magnetic Properties; Metal Evaporated Tape; Magnetic Recording: VHS Tapes; Magnetic Recording Technologies: Overview

Bibliography

Bhushan B 1984 Analysis of the real area of contact between a polymeric magnetic medium and a rigid surface. *J. Trib. Trans. ASME* **106**, 26–34

Bhushan B J 1987 Magnetic head-media interface temperatures. 1: Analysis. *Trib.-Trans. ASME* **109**, 243–56

Bijker M D, Draausna E A, Eisenberg M, Jansen J, Peersat N, Sourty E 2000 Future directions in advanced digital recording technology. *Tribol. Int.* **33**, 383–90

Greenwood J A, Williamson J B P 1966 Contact of normally flat surfaces. *Proc. Roy. Soc.* **A292**, 300

Gulino R, Blair S, Winer W O, Bushan B J 1987 Temperature-measurement of microscopic areas within a simulated head tape using infrared radiometric technique. *J. Trib. Trans. ASME* **108**, 29–34

Halliday J S 1955 Surface examinations by reflection electron microscopy. *Proc. Inst. Mech. Eng.* **169**, 221–35

Harrison M, Sullivan J L, Theunissen G A S 1999 Pole tip recession in sandwich heads incorporating a FeTaN magnetic track. *Tribol. Int.* **31** (9), 491–500

Hempstock M S, Sullivan J L 1997 The durability and signal performance of metal evaporated and metal particle tape. *IEEE Trans. Magnetics* **322**, 3723–32

Hempstock M S, Sullivan J L 1998 Characterisation of surface changes to metal evaporated and metal particle media following durability tests helical scan Hi-8 recorders at ambient and high humidity conditions. *Tribol. Int.* **31** (8), 419–24

Hempstock M S, Wild M, Sullivan J L 2000 Interactions of head-tape interface of a linear tape system. *Tribol. Int.* **33**, 391–9

Hempstock M S, Wild M A, Sullivan J L, May P I 1998 A study of the durability of flexible magnetic media in linear tape systems. *Tribol. Int.* **31** (8), 435–41

Jahanmir S, Suh N P 1977 Surface topography and integrity effects on sliding wear. *Wear* **44**, 87–99

Reaves L M, Sullivan J L 1992 The effect of head cleaning agents on the wear mechanism of video heads. *J. Phys. D. (Appl. Phys.)* **25**, 328–34

Richardson R D C 1967 Abrasive wear and relative hardness. *Proc. Inst. Mech. Eng.* **182**, 410–8

Suh N P 1986 *Tribophysics*. Prentice-Hall, NJ, Chap. 7

Sullivan J L, Sharma P J 1992 Factors affecting the durability of repeatedly stressed flexible magnetic recording media. *J. Phys. D. (Appl. Phys.)* **25**, 321–8

J. L. Sullivan
Aston University, Birmingham, UK

Magnetic Recording: Particulate Media, Micromagnetic Simulations

Colloidal magnetic dispersions of submicron acicular magnetic particles have been used for many years as precursors of particulate storage media. Advances in the production of the advanced metal particle (MP), Okamoto *et al.* (1996), and its use in the production of advanced ultra-thin media, Richter and Veitch (1996), mean that particulate media remain technologically competitive for a number of applications, including tapes for digital video and back-up applications. In order to understand and optimize particulate recording media for these high-density storage applications, it is necessary to understand the microstructure of the media that ultimately has its origins in the behavior of the dispersion itself.

A magnetic colloidal dispersion is a careful blend of fine magnetic particles, surface-active agents to provide stability against aggregation via short-range forces, secondary pigments, resins, and other additions such as lubricants. These are generally dispersed in a mixture of one or more solvents. Generally speaking, the resin system is the critical element in the dispersion since it is used to separate the particles in the final coating as well as for binding them together. Thus, dispersions are a very complex physical system in which the magnetic particles are merely one component, albeit an important one. A prerequisite to understanding storage media is an understanding of the magnetostatic interaction between particles and its influence on the magnetic and physical properties of the dispersion. The overall properties of dispersions have been reviewed by O'Grady *et al.* (1991) and show a rich variety of phenomena of physical interest and technical importance.

The complexity of the interaction problem requires that realistic theoretical approaches must be based on computational solutions. The microstructure of the dispersion and the magnetic media is sensitive to physical and magnetic history, therefore particular attention must be given to the generation of realistic microstructure in micromagnetic studies of particulate media.

A computer model of particulate media was proposed by Voss *et al.* (1993), treating the particles as single spins exhibiting coherent rotation, but taking into account interparticle interactions. More recently, Bertram and Seberino (1999) produced simulations taking into account incoherent reversals by representing individual particles as chains of spheres. Both these approaches suffer from the disadvantage that the microstructure of the system studied is nonrealistic, though gross features such as particle alignment can be simulated. The model and simulation described below is a first attempt to simulate the physical and magnetic properties of Advanced MP media from first principles.

The starting point for the simulation of magnetic media is a dispersion model. A model is usually based around a specific dispersion where, in an effort to maximize the available computer facilities, only the relevant physical properties of the particulate and continuum phase are taken into account. From these considerations, a choice of the most appropriate simulation method must then be made. A useful and practical introduction to simulation methods can be found in Allen and Tildesley (1990). One of the first simulations undertaken with elongated magnetic pigment in viscous medium was that of Deymier *et al.* (1994) using a Stokesian dynamic method.

The calculation of the long-range magnetostatic interaction is always problematic due to its computation demand, particularly for large systems. An approach to the development of an efficient computational algorithm can be found in the Brownian dynamic simulation of colloid aggregation made by Gunal and Visscher (1996). It is pertinent to note here that the choice of the micromagnetic model employed for the interaction calculation, and its relation to particle geometry, has been shown by Visscher and Gunal (1997, 1998) to be an important influence on the simulation predictions.

The basis of the multistage model described below is an Advanced Metal Particle Molecular Dynamic model developed by Coverdale *et al.* (1997, 1998). It has been designed to simulate dynamic particle behavior in a Newtonian fluid arising from particle interactions, surface interactions, simple shear, and a uniform magnetic field.

The model is first used to investigate the influence of shear and magnetic field on the microstructure of a magnetic pigment dispersion. It is then used in a multistage simulation of the production of magnetic media. Each stage of media production has been simulated by modeling the process assumed to be the dominant influence on the determination of the microstructure. The stages employed in the model are summarized as follows. A rectangular slab of dispersion in magnetostatic equilibrium is generated. The computation cell is $0.8\mu \times 0.8\mu \times 0.4\mu$ with a particle volume packing fraction (VPF) of 20%. The microstructure of the initial coating is modeled by shearing for 5×10^{-4} ms at a shear rate of 5×10^{6} s^{-1}, being analogous to a model line speed of 120 m min^{-1}. The dispersion is allowed to relax towards equilibrium for 1 ms after shearing. The dispersion is then field-oriented at 2000 Oe for 4 ms and dried to yield a 0.2μ coating at a VPF of 40%.

1. Molecular Dynamic Model of a Particulate Dispersion

Several of the more common algorithms used for molecular dynamics are unsuitable for a viscous system because they have a tendency to overestimate the particle velocity during a given time-step, and as a result cause problems with the estimation of the velocity-dependent viscous forces and torques. Rather than accept an unreasonably small time-step as a possible solution in order to stabilize an algorithm, it is better to choose a less sophisticated algorithm with the advantage of being more rugged and simpler to implement for a strongly interacting system.

The modeling of the motion of a particle ensemble in a viscous medium would require a full hydrodynamic description to take account of regions of flow induced by a disturbance, for example a rotation, in the neighborhood of a particle. As of 2001, it is only reasonable to address a simple case where the constraint on particle motion due to the viscous medium is approximated via the forces and torques resulting from the motion of an isolated particle in a Newtonian fluid.

The assumption is also made that the motion of a particle over a computation time-step is predominately determined by a "terminal velocity" and a "terminal angular velocity" which is a consequence of the forces acting on the body being balanced by the forces of resistance to the motion. This gives rise to a motion of constant velocity and a constant angular velocity over each computation time-step.

2. Translational Motion

The equations of translational motion of a particle of mass M subject to a resultant force F due to the magnetostatic and surface interactions is given by, $M\vec{\dot{v}} = \vec{F} - N\vec{\dot{v}}$, where the viscous "drag" $-N\vec{v}$ on the particle is proportional to the velocity.

Motion parallel, //, to the particle axis can be expected to give rise to less drag than motion perpendicular, $+$, to the axis and so the velocity must be resolved into the appropriate components. The term N is therefore written,

$$N\vec{v} = R_{+}(\vec{e} \times \vec{v}) \times \vec{e} + R_{//}(\vec{v} \cdot \vec{e})\vec{e}$$

where $\vec{e}$ is a unit vector in the direction of the particle axis. The terms R_{+} and $R_{//}$ provide the essential hydrodynamic terms and have been employed following Newman and Yarbrough (1969). These terms depend on the individual particle dimensions and the viscosity of the medium.

In order to derive a computation algorithm, this equation is put in a form with dependence directly on the velocity components,

$$N\vec{v} = R_{+}N^{B}\vec{v}_{+} + R_{//}N^{A}\vec{v}_{//}$$

The term N^{B} will now be derived. Employing an intermediary matrix,

$$\mathscr{B} = \vec{e} \times \vec{v} = \begin{pmatrix} \vec{x} & \vec{y} & \vec{z} \\ e^{x} & e^{y} & e^{z} \\ v^{x} & v^{y} & v^{z} \end{pmatrix}$$

the components of the corresponding vector are extracted as,

$$\mathscr{B}^x = (e^y v^z - e^z v^y)$$

$$\mathscr{B}^y = (e^z v^y - e^y v^z)$$

$$\mathscr{B}^z = (e^x v^y - e^y v^x)$$

The expression may now be derived,

$$N^B \vec{v} = B \times \vec{e}$$

$$= \begin{pmatrix} \vec{x} & \vec{y} & \vec{z} \\ (e^y v^z - e^z v^y) & (e^z v^x - e^x v^z) & (e^x v^y - e^y v^x) \\ e^x & e^y & e^z \end{pmatrix}$$

Expansion and manipulation yields,

$$R_+ N^B \vec{v}_+$$

$$= R_+ \begin{pmatrix} (e^z e^z + e^y e^y) & -e^y e^x & -e^x e^z \\ -e^x e^y & (e^x e^x + e^z e^z) & -e^y e^z \\ -e^x e^z & -e^y e^z & (e^y e^y + e^x e^x) \end{pmatrix}$$

$$\begin{pmatrix} v_+^x \\ v_+^y \\ v_+^z \end{pmatrix}$$

Now considering the right-hand vector term and following a similar method:

$$R_{//} N^A \vec{v}_{//} = R_{//} (\vec{e} \cdot \vec{v}) \vec{e} = (v^x e^x + v^y e^y + v^z e^z) \begin{pmatrix} e^x \\ e^y \\ e^z \end{pmatrix}$$

Therefore:

$$R_- N^A \vec{v}_{//} = R_{//} \begin{pmatrix} e^x e^x & e^y e^x & e^x e^z \\ e^x e^y & e^y e^y & e^y e^z \\ e^x e^z & e^y e^z & e^z e^z \end{pmatrix} \begin{pmatrix} v_{//}^x \\ v_{//}^y \\ v_{//}^z \end{pmatrix}$$

For the translational motion, with the equilibrium condition $M \vec{v} = 0$,

$$F = R_+ N^B \vec{v}_+ + R_{//} N^A \vec{v}_{//}$$

The velocity of a particle during each time-step may now be derived from the resultant force acting on a single particle.

3. Rotational Motion

The angular velocity $\vec{\omega}$ is not used in the formulation of the rotational motion but the unit vector in the direction of the particle axis $\vec{e}$ and the velocity $\vec{u}$ of the axis vector, after Fincham (1993), where

$$\dot{\vec{e}} = \vec{u}$$

and

$$\dot{\vec{u}} = \vec{G} - N \vec{u} - (\vec{u} \cdot \vec{u}) \vec{e}$$

First, the torque T^{mag} due to the magnetostatic forces is considered,

$$T^{\text{mag}} = \sum_i \vec{r}_i \times \vec{f}_i = \vec{e} \times \sum_i d_i \vec{f}_i = \vec{e} \times \vec{g}$$

It is convenient to resolve only the perpendicular component:

$$g_p = \vec{g} - \vec{e}(\vec{e} \cdot \vec{g})$$

Thus:

$$\vec{T}^{\text{mag}} = \vec{e} \times \vec{g}_p$$

The torque due to rotational viscosity is proportional to the angular velocity,

$$\vec{T}^\eta = R_\phi \vec{\omega}$$

The term $R\phi$ is the hydrodynamic term and has been employed following Newman and Yarbrough (1969).

The rate of change of angular velocity may now be written,

$$\dot{\vec{\omega}} = I^{-1}(\vec{T}^{\text{mag}} - \vec{T}^\eta)$$

Employing,

$$\vec{u} = \dot{\vec{e}} = \vec{\omega} \times \vec{e}$$

and differentiating with respect to time,

$$\dot{\vec{u}} = \dot{\vec{\omega}} \times \vec{e} + \vec{\omega} + \dot{\vec{e}}$$

Therefore,

$$\dot{\vec{u}} = I^{-1}(T^{\text{mag}} - \vec{T}^\eta) \times \vec{e} + \vec{\omega} \times (\vec{\omega} \times \vec{e})$$

to yield the second equation of motion,

$$\dot{\vec{u}} = I^{-1} g_p - I^{-1} R_\phi \vec{u} - (\vec{u} \cdot \vec{u}) \vec{e}$$

Note that the term $-(\vec{u} \cdot \vec{u}) \vec{e}$ is the centripetal force that is necessary to maintain the constant length of the axis vector by balancing the force generated by the rotation.

The rotational motion is dealt with in a similar way to the translational motion but first the centripetal term is removed. The effect of this term is then

replaced by a normalization of the unit vector $\vec{e}$ after each time-step, together with the condition that the time-step, thus the displacement, is kept small.

For the translational motion, with the condition $\dot{\vec{u}} = 0$,

$$I^{-1}g_{\mathrm{p}} = I^{-1}R_\phi \, \vec{u}$$

The velocity of the axis vector during each time-step may now be derived from the torque.

4. The Microstructure of a Magnetic Dispersion

Study of the dispersion is made to clarify the influences that determine the behavior of the microstructure.

The dispersion simulation is based on an advanced metal particle dispersion with a volume packing fraction of 3.8%. Simulations of the zero-field equilibrium state show that the microstructure consisted of a "honeycomb" structure brought about under the influence of the magnetostatic interactions (Fig. 1). This equilibrium state was used as the starting point for all the dispersion simulations that follow. Any change in microstructure must be brought about by overcoming the magnetostatic interaction energy that gives rise to this low-energy state.

A well-defined structure is also found in a strong magnetic field, which has the characteristic structure of long filaments of particles aligned in the field direction. The formation of filaments, viewed transverse to the field direction in Fig. 2(a), gives rise to a

(a)

(b)

Figure 2
(a) Field equilibrium, view transverse to field direction.
(b) Field equilibrium, view along field direction.

Figure 1
Zero-field equilibrium.

network of open channels, viewed along the field direction in Fig. 2(b).

The molecular dynamic (MD) method will allow the introduction of a velocity gradient and thus simulate the dynamic behavior of the particles, i.e., the microstructure, in a shear flow. In the absence of an applied field, the simulations predict that for a

Figure 3
Zero-field shear flow, low shear breaking up equilibrium structure.

relatively low shear rate, $1000\,\mathrm{s}^{-1}$, the magnetostatic interactions give rise to localized structure within the flow (Fig. 3). The structures are continuously breaking up and reforming under the influence of the velocity gradient but structure is observed at each time-step.

The microstructure may be investigated both in the shear flow alone and in a shear flow subjected to a magnetic field, thus the simulation may be used to model shear magnetometry experiments (Veitch 1996). There are two directions in which a field may be applied so that it is transverse to the direction of particle flow. The simulated effect of shearing the dispersion is modeled between two parallel plates aligned in the x–y plane moving with equal and opposite velocity in the y direction. In this configuration, a transverse field may be applied along the x-axis or the z-axis. The more common configuration used in a shear magnetometer employing a rotating cylinder is the transverse x direction.

The model has been employed to predict the microstructure for shear flow in the two transverse directions for a relatively strong applied field of 2000 Oe. When the applied field is in the transverse x direction, the particles orient into the field direction and thus lie transverse to the flow field. A typical particle configuration to be found at each time-step is shown in the two views of Fig. 4(a) and Fig. 4(b). Although the particles are strongly orientated in the field direction, they do not exhibit a tendency to form filament structures that are characteristic of zero-shear simulations.
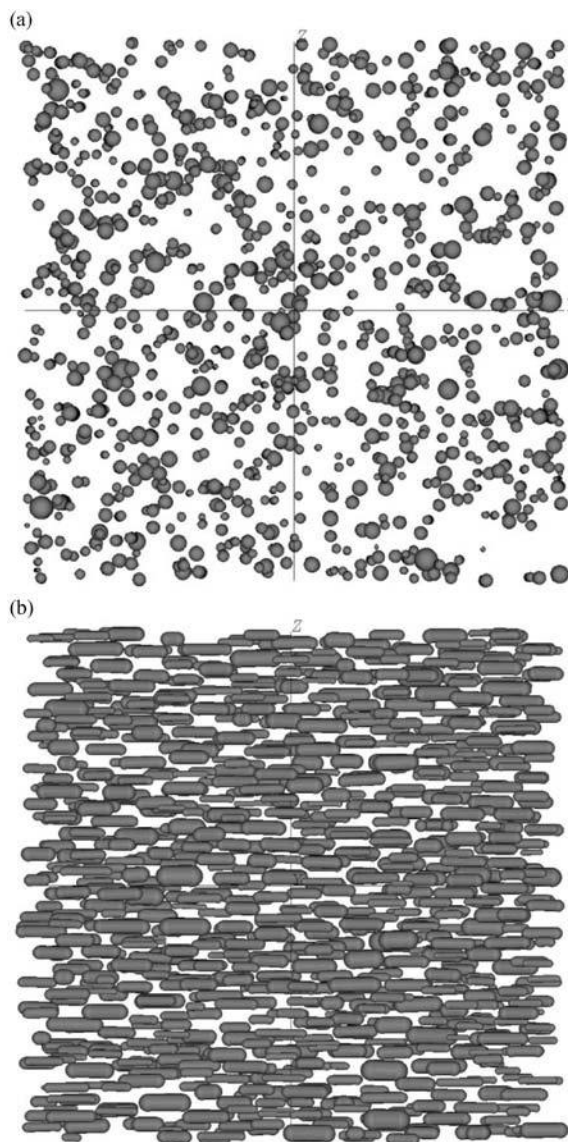
Figure 4
(a) Transverse field x-direction, high shear, transverse to field view. (b) Transverse field x-direction, high shear, flow direction view.

A very different response for the same field magnitude and shear rate is predicted when the field is applied in the transverse z direction, shown in the two views of Fig. 5(a) and Fig. 5(b). It can be seen that a very well-defined microstructure has been developed, which may be described as curtains of particles arranged parallel to the flow direction and magnetically orientated in the field direction.
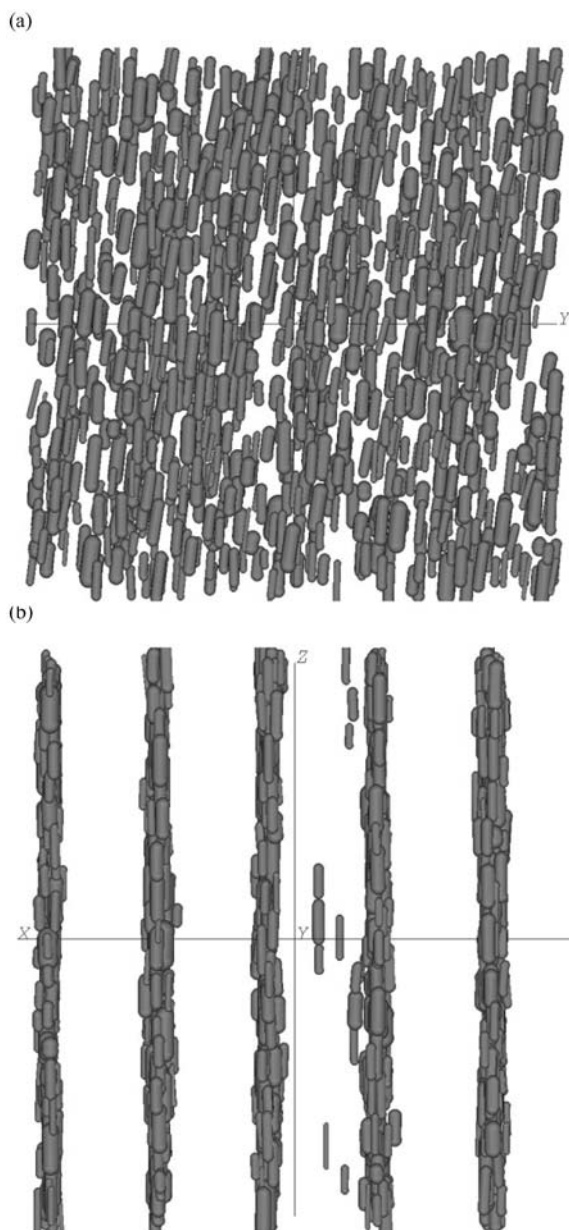
Figure 5
(a) Transverse field *z*-direction, high shear, transverse to field view. (b) Transverse field *z*-direction, high shear, flow direction view.

Thus, enhanced magnetization in shear magnetometry experiments, at least in systems of highly elongated particles, can be partially interpreted in terms of a combination of mechanical orientation due to the shear flow as well as the aligning torque of the magnetic field. The structures appear to retain their

form in conditions of medium shear rate of around $10000\,s^{-1}$, but become less well defined at the very high shear rates.

5. The Drying Process

The drying algorithm, used to model the transition from the dispersion to the media, is an important stage in the simulation of media with realistic microstructure. This is because the microstructure of the dispersion is retained as a "memory" and acts as a significant influence on the microstructure of the media.

The drying process is difficult to model because the dispersion undergoes rapid solvent loss, which may give rise to local chaotic behavior, while at the same time the resins are cross-linking to form long-chain polymer molecules that tend to inhibit particle mobility. As a result of these processes, there is expected to be a large variation in media viscosity on the local scale during drying.

For these reasons, a phenomenological approach to the drying model is taken whilst attempting to retain some of the important physical properties. The drying simulation is based on the MD-dispersion simulation with the additional feature of a forced-settling algorithm that acts as the volume-reducing scheme.

The model employed here assumes that the particle environment remains at a constant viscosity of 1 P throughout the simulated drying, although in reality the viscosity increases dramatically as the solvent escapes and the resins tend to cross-link. At each MD time-step, the height *z* of each particle above the base of the media is reduced by an amount $dz = z\Delta(t)$ proportional to *z*. The parameter Δ is a function of the drying time *t* and is calculated so that the reduction in coating thickness occurs at a rate proportional to $\log(t)$. This is in keeping with observations made on solvent loss in particulate media by Gilson (1993), Fig. 6.

6. Magnetization Modeling

The magnetic behavior of the dispersion in the coating and drying stages has been modeled via a pole–pole interaction model. This scheme is assumed to be a good approximation for the high-coercivity particles while they exhibit reasonable mobility. Magnetization modeling of the media has been carried out using a chain-of-spheres model in order that nonuniform magnetic states of a particle may be taken into account. The behavior of a particle moment is determined by a Landau-Lifshitz equation with the addition of a stochastic field term after Chantrell *et al.* 1998. This method employs estimations of the usual anisotropy, exchange, dipole and interaction field terms together with the behavior associated with thermal effects.
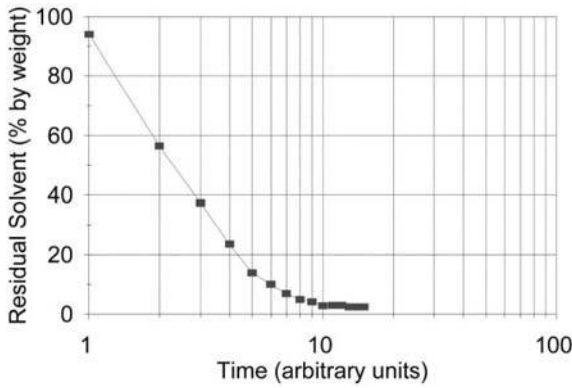
Figure 6
A typical drying curve from production of a modern data tape product, indicating the presence of three regimes.

The Landau-Lifshitz equation, describing the motion of a unit vector $\vec{m}_i$ in the magnetization direction $\vec{M} = \vec{m} M_s V_i$, of volume element V_i may be written,

$$\frac{\mathrm{d}\vec{m}_i}{\mathrm{d}t} = \frac{\gamma}{1 + \alpha^2} \vec{m}_i \times \vec{H} - \frac{\alpha\gamma}{M_s V_i(1 + \alpha^2)} \vec{m}_i \times (\vec{m}_i \times \vec{H})$$

where γ is the gyromagnetic constant, α is a damping constant.

The total local field H experienced by a moment i is the sum of contributions from the dipole field,

$$\sum_j V_j M_s \left(\frac{(\vec{m}_j \vec{r}_{ij}) \vec{r}_{ij}}{r_{ij}^3} - \frac{\vec{m}_j}{r_{ij}^3} \right)$$

where V_j is the volume of volume element J, and r_{ij} is the unit vector from element to j to i. The exchange field derived from moments in the same particle,

$$\frac{2A}{M_s} \sum_j \frac{\vec{m}_j}{d_{ij}^2}$$

where A is the exchange constant between elements in the same particle, and d_{ij} is the distance between elements of the same particle.

The anisotropy field is representative of the crystalline and shape anisotropy,

$$\frac{2K}{M_s}(\vec{e} \cdot \vec{m}) \, \vec{e}$$

where K is the anisotropy constant, and $\vec{e}$ is the unit vector in the direction of the anisotropy axis.

The thermal fluctuation field is implemented in the computation algorithm so that after a large number of statistical samplings it will exhibit a Gaussian distribution with variance according to Brown (1979) as

$$\frac{k_B T \alpha}{K V_i(1 + \alpha^2) \cdot \Delta\tau}$$

where k_B is the Boltzman constant, T is the temperature, and $\Delta\tau$ is the integration time-step. Finally, there is the applied field term.

7. The Microstructure of Magnetic Media

This study of the effect of the coating process on the bulk magnetization properties of coated media represents first-principle micromagnetic calculations since the microstructure has been realistically derived at the microscopic level.

Starting from a "wet" precursor with a VPF of around 20%, the model has been employed to study two extreme cases of drying, which yield the two extreme values of hysteresis properties for media, 40% vpf. The two cases being (i) drying without an orienting field (Fig. 7(a)), and (ii) drying in a strong orienting field (Fig. 7(b)). Both the sections shown are $0.8\,\mu \times 0.8\,\mu \times 0.2\,\mu$ in cross section.

Three fine 3D sections of the simulated microstructure are shown in Fig. 7(c). The top view of Fig. 7(c) is a $0.8\,\mu \times 0.2\,\mu \times 0.1\,\mu$ cross section, taken along the web direction of media dried in zero field which clearly shows the poor orientation of the particles. The middle view is the corresponding section of field-dried media (Fig. 7(b)), which shows very strong alignment in the web/field direction. The lower view is a finer section of the middle view showing more clearly the lack of homogeneity in the distribution of particles. The microstructure of the field-dried media contains small voids predominantly aligned in the field direction. These voids can be traced back to open regions in the dispersion microstructure. They are predicted to act as "drying channels" through which the solvent can evaporate. It has been proposed by Gilson (1993) that channels are necessary to allow the coating to dry rapidly enough and so it would appear that voids in the final coated medium are an unavoidable consequence of the drying process itself.

Particle orientation is an important property of media and may be characterized for study by a suitable correlation function. The function employed here correlates particle alignment with respect to the plane of the medium web, the x–y plane, with the plane perpendicular to the media web aligned along the web, the y–z plane. (Certain correlations are seen to be physically forbidden, such as, for example, a particle lying perpendicular to both planes.) The correlation function of the zero-field media made from nonsheared coating is shown in Fig. 8. The dispersion does not exhibit any preferential alignment but the drying process tends to alignment in the plane of the media; the x–y plane.

Strong shearing of the dispersion tends to align the particles in the shear direction but the drying process disrupts and weakens this strong orientation. The strong particle alignment seen in the dispersion

Figure 8
Correlation function of the zero-field media made from nonsheared coating.
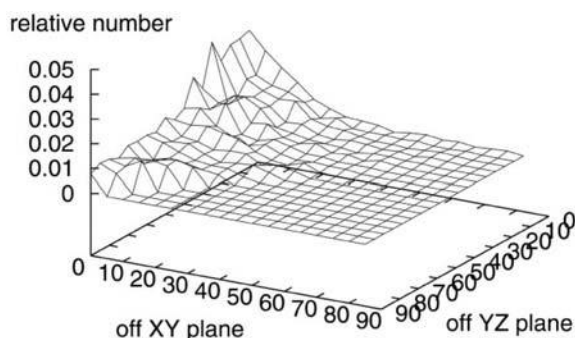
Figure 9
Correlation function of the zero-field media made from sheared coating.

Figure 7
(a) View of a zero-field media made from sheared coating. (b) View of a field-dried media made from sheared coating. (c) Cross-sections of zero-field media, field-dried media, and field-dried media showing channels.

coating is lost during the simulated drying but the media nevertheless exhibits a tendency for particle alignment in both the plane of the web and along the web direction. The correlation function for this medium is shown in the Fig 9.

In contrast, the media made by drying the dispersion in a strong magnetic field exhibits very strong alignment in the field direction, shown in Fig. 10. The predicted alignment is expected to overestimate particle orientation as the model is not able to include the disruptive effects arising from the high rate of solvent loss. This strong alignment is necessary for the production of good-quality magnetic storage media.

8. Magnetic Properties of Magnetic Media

Two hysteresis curves, one for an interacting and the other for a noninteracting system, have been calculated from an initial saturated state for the zero-field media (Fig. 7(a)) and the field-dried media (Fig. 7(b)). The results for the interacting and noninteracting
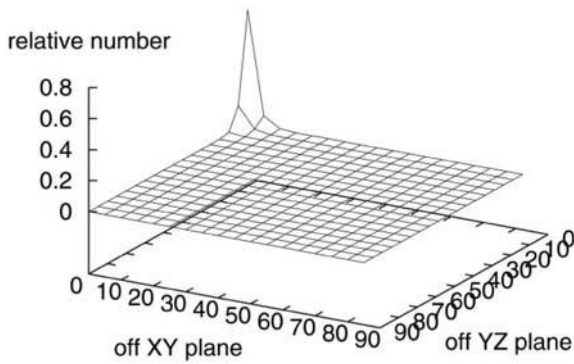
Figure 10
Correlation function of the field-dried media made from sheared coating.

Figure 12
Hysteresis curve with and without interactions for field-dried media.

Figure 11
Hysteresis curve with and without interactions for zero-field media.
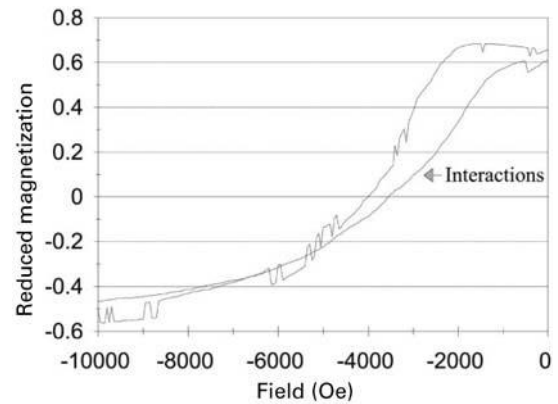
Figure 13
D.c. Demagnetization curve with and without interactions for the zero-field media.

cases have been calculated using the same simulated microstructure, therefore a direct comparison of effects may be made.

The hysteresis curve for the zero-field media (Fig. 11) shows a relatively high squareness seen in the noninteracting case and is indicative of the partial alignment during the coating process. As expected, the interparticle interactions give rise to a reduced remanence and coercivity. Although the coercivity of the medium is reasonable in comparison with experiment, the remanence is rather low. The hysteresis curve for the field-dried media is shown in Fig. 12. The coercivity is rather large, however the remanent squareness is larger than the experimental result of 0.85–0.9. It would appear therefore that these two cases represent extreme bounds with the properties of real media lying somewhere between.

The d.c. demagnetization remanence curves have also been calculated, from which the switching field distribution has be derived. For the well-aligned field-dried media, the magnetization was found to be essentially perfectly irreversible with no significant difference between the hysteresis loop and d.c. demagnetization curve. The d.c. demagnetization curves for the poorly aligned zero-field media are shown in Fig. 13.

The effect of interactions is to lower the remanence and coercivity, which is to be expected and is normally observed experimentally. A second effect is also clear, this being a dramatic increase of the initial shape of the remanence curve in small fields. This is accompanied by an increase in the width of the switching field distribution, (SFD), shown in Figs. 14 and 15, which presumably reflects a dispersion of the local interaction field, which seems reasonable.

In terms of recording properties, the increase in the initial remanence shape due to interactions is significant. It might be expected, for example, to lead to
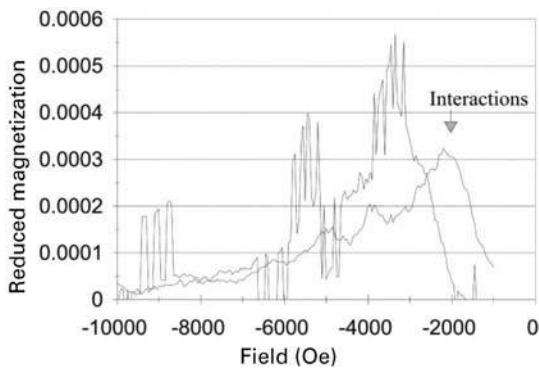
Figure 14
Switching field distribution with and without
interactions for zero-field media.
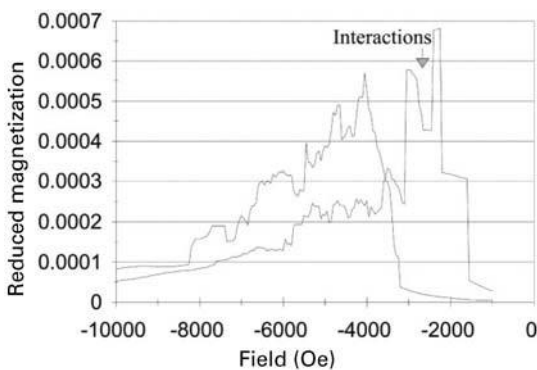
Figure 15
Switching field distribution with and without
interactions for field-dried media.

transition broadening given that the increased re-
manence shape represents a reduced stability against
demagnetization. A further factor in this respect is
the relationship between the irreversible susculibi-
bility χ_{irr} and the time-dependent magnetization, i.e.,
$S_v = \chi_{irr}H_f$, where S_v is the coefficient of magnetic
viscosity and H_f is the fluctuation field. The differ-
entiation of the remanence curve (equivalent to the
SFD) is an experimental approximation to χ_{irr}.
Hence, an increase in the SFD fields of the order of
those occurring in magnetization transitions must be
expected to lead to an increase in the magnetic vis-
cosity and a consequent reduction in the thermal sta-
bility of stored information. This effect is crucial to
the potential degradation of the data during the long-
term storage of magnetic media.

9. Conclusion

"First principles" calculations of the magnetic prop-
erties of the coated medium, i.e., one without *ad hoc*

assumptions relating to the physical microstructure,
have been made by employing a micromagnetic mod-
el of coated particulate media used in conjunction
with a molecular dynamic simulation of the medium
microstructure.

The calculations give good qualitative agreement
with experiment and demonstrate a strong depend-
ence of the magnetic properties on the detail of the
coating and orientation process, as is to be expected.
Detailed comparisons with experimental data are dif-
ficult because of the proprietary nature of informa-
tion relating to the coating process. However, this
approach could form the basis of a systematic exper-
imental investigation which would be of great benefit
in understanding both the magnetization processes of
coated media and the effects of the coating process on
magnetic and recording properties.

See also: Magnetic Recording Media: Tape Particles,
Magnetic Properties; Magnetic Recording Technolo-
gies: Overview

Bibliography

Allen M P, Tildesley D J 1990 *Computer Simulation of Liquids*.
Oxford Science Publications, Oxford
Bertram H N, Seberino C 1999 Numerical simulations of hys-
teresis in longitudinal magnetic tape. *J. Magn. Magn. Mater*.
193, 388–94
Brown W F Jr. 1979 Thermal fluctuations of fine ferromagnetic
particles. *IEEE Trans. Magn*. **15**, 1196–208
Chantrell R W, Wongsam M, Hannay J D, Schrefl T, Richter H
J 1998 Computational approaches to thermally activated fast
relaxation. *IEEE Trans. Magn*. **34**, 1839–45
Coverdale G N, Chantrell R W, Satoh A, Chang C -R 1998 A
molecular-dynamics model of the magnetic properties and
microstructure of strongly interacting colloidal dispersions.
IEEE Trans. Magn. **34**, 378–80
Coverdale G N, Chantrell R W, Satoh A, Veich R J 1997
A molecular dynamics model of the magnetic properties
and microstructure of advanced metal particle dispersions.
J. Appl. Phys. **81**, 3818–20
Deymier P A, Jung C, Raghaven S 1994 Molecular dynamics of
magnetic particulate dispersions. *J. Appl. Phys*. **75**, 5571–3
Fincham D 1993 Leapfrog rotational algorithms for linear
molecules. *Mol. Simul*. **11**, 79–89
Gilson R G 1993 Drying of particulate media coatings.
J. Magn. Magn. Mater. **120**, 97–9
Gunal Y, Visscher P B 1996 Brownian dynamics simulation of
magnetic colloid aggregation. *IEEE Trans. Magn*. **32**, 4049–
51
Newman J J, Yarbrough R B 1969 Theory of the motions of a
fine magnetic particles in a Newtonian fluid. *IEEE Trans*.
Magn. **5**, 320–4
O'Grady K, Gilson R G, Hobby P C 1991 Magnetic pigment
dispersions (a tutorial review). *J. Magn. Magn. Mater*. **95** (3),
341–55
Okamoto K, Okazaki Y, Nagai N, Uedaira S 1996 Advanced
metal particles technologies for magnetic tapes. *J. Magn*.
Magn. Mater. **155** (1–3), 60–6
Richter H J, Veitch R J 1996 MP tape for high-density digital
recording. *J. Magn. Magn. Mater*. **155** (1–3), 80–2

Veitch R J 1996 Shear magnetometry for the analysis of magnetic tape dispersions. *IEEE Trans. Magn.* **32** (5), 4028–33

Visscher P B, Gunal Y 1997 Field-induced smectic ordering in model magnetic inks. *J. Appl. Phys.* **18**, 3827–9

Visscher P B, Gunal Y 1998 Self assembly in model magnetic inks. *IEEE Trans. Magn.* **34**, 1687–9

Voss M J, Booth R L, Zhu J G, Carlson L W 1993 Computed hysteresis behavior and interaction effects in spheroidal particle ensembles. *IEEE Trans. Magn.* **29**, 3652–7

G. N. Coverdale
University of Durham, County Durham, UK

Magnetic Recording: Patterned Media

The term "patterned media" refers to the storage of data in arrays of discrete magnetic elements, such as small, lithographically patterned pillars or bars. The direction of magnetization in each element represents a binary one or zero. This differs from data storage in conventional hard disk or flexible media, in which regions of a magnetic film are magnetized to represent the stored data. Patterned media systems are in their infancy, but have excited great interest because they should in principle be capable of storing data at much higher density than is possible with conventional media.

In conventional hard disks, data are stored as magnetization patterns written onto a continuous thin film (Fig. 1(a)). The film consists of small grains of an alloy such as CoCrTaPt, 10–15 nm in diameter. The grains are exchange-decoupled due to segregation of nonmagnetic elements at the grain boundaries. Each bit written onto the medium covers an area (cell) of hundreds of grains. As recording densities increase, it is desirable to reduce the grain size in order to maintain a large number of grains per bit cell and thus to obtain a good signal-to-noise ratio. However, as grain sizes are decreased, the magnetization of the grains become thermally unstable, leading to the decay of recorded data patterns. This occurs when thermal energy, kT, is sufficient to cause reversal of the magnetization within individual grains. Here k is Boltzmann's constant and T is the temperature. This superparamagnetic behavior occurs when $KV < 60\,kT$ (Lu and Charap 1994), where K is the magnetic anisotropy energy per unit volume of the material and V is the grain volume. This behavior sets a lower limit on the grain size of the medium, and therefore limits the achievable signal-to-noise ratio of the media. Increasing the anisotropy K allows V to be decreased, but for high K it becomes difficult to write data patterns on the medium because unreasonably large write fields would be required. An upper limit for recording density on conventional media of $40\,\mathrm{Gbin}^{-2}$ was suggested (Charap

et al. 1997). However these predictions have proven to be pessimistic, and improvements in longitudinal and perpendicular media have continued. In 2005, for example, Hitachi demonstrated $230\,\mathrm{Gb/in}^2$ recording. Any practical patterned media will need to support densities well above those achievable with continuous thin film media in order to be economically viable.

Patterned media have been suggested as a means of increasing storage density beyond that achievable with thin film media. A patterned medium (Fig. 1(b) and 1(c)) consists of an array of nanoscale magnets, each of which can store one bit of information depending on its magnetization state. It is important that each element behaves as a single magnetic domain, whether it is single crystal or polycrystalline. The elements in patterned media are still subject to thermal instability, but now the volume V can be as large as the entire volume of the element instead of equal to the grain volume. The elements could be as small as 10 nm, potentially representing an increase in density of 1000 times over thin film media. The difficulties inherent in patterned media storage schemes concern the fabrication of large-area, uniform arrays of magnetic particles, and developing methods for reading and writing the arrays. This article will discuss how arrays can be made, what magnetic properties are desirable in a patterned medium, and what schemes have been proposed for incorporating patterned media into practical storage devices.

1. Fabrication of Magnetic Media

The concept of patterning a hard disk using lithography was first proposed as a means of improving tracking and signal-to-noise ratio (Lambert *et al.* 1991). However, as thermal instability limitations in conventional media became more apparent, patterned media appeared to offer a route to higher density recording. Despite this promise, significant development of patterned media did not occur until the 1990s when high resolution lithography became widely available for fabrication of arrays of magnetic elements (Chou *et al.* 1994, Chou 1997, White *et al.* 1997).

The fabrication requirements for patterned media are challenging. To make a structure consisting of 250 G particles in^{-2}, an array of elements with a period below 50 nm is needed. The lithography method used must therefore be capable of resolving 25 nm features or better over an area several centimeters or greater in diameter. This is well beyond the capabilities of the optical lithography currently used in semiconductor device fabrication, so higher resolution patterning techniques are necessary. Early studies of small, patterned structures used optical lithography to make arrays with micron-scale features, but the most common method now used to make submicron arrays with features of 10 nm and above is electron-beam
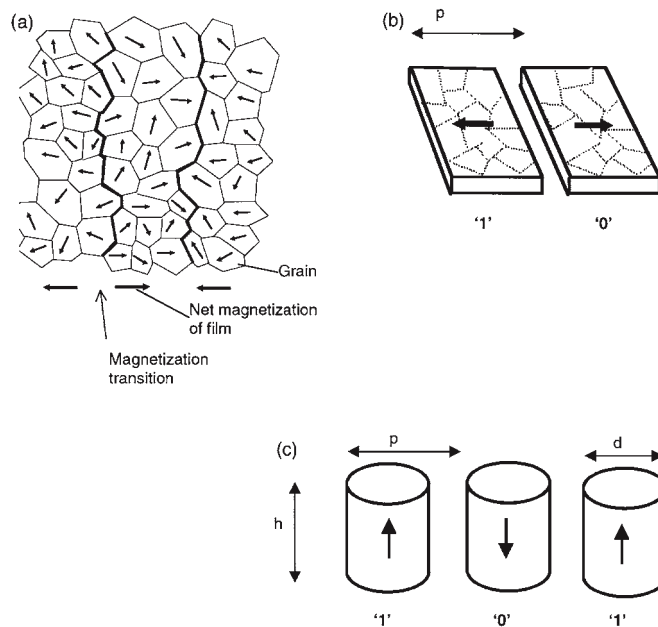
Figure 1
Schematic of (a) conventional thin film medium, consisting of single-domain grains. Bits are represented as transitions between regions of opposite net magnetization. Each bit occupies an area of tens to hundreds of grains. (b) Patterned medium with in-plane magnetization. Now the bits are defined lithographically and have period *p*. The bits can be polycrystalline (indicated by dotted lines) or single crystal, but magnetically they act as single domains. (c) Patterned medium with out-of-plane magnetization. The period is *p*, height *h* and diameter *d*. Binary one and zero are indicated. (Reprinted with permission *J. Vac. Sci. Technol. B***17**, 3168; © American Institute of Physics 1999.)

lithography (e.g., Chou *et al*. 1994, New *et al*. 1996, O'Barr *et al*. 1997). However, this is a serial method in which each element is exposed sequentially, so it is too slow for economic patterning of large areas. Other lithography methods have therefore been explored, including x-ray nanolithography (Rousseaux *et al*. 1995), nano-imprint lithography (Wu *et al*. 1998), and interference lithography (Fernandez *et al*. 1996, Haast *et al*. 1998, Ross *et al*. 1999), all of which are capable of patterning large areas. Self-assembly processes have been proposed as an alternative patterning route. In these methods, the self-assembly of, for instance, pores in anodized alumina (Bao *et al*. 1996) or domains in block copolymers (Zhu *et al*. 1997, Cheng *et al*. 2001) are used as templates for the patterning of magnetic arrays. Magnetic particles can also be made by chemical synthesis and assembled onto a surface to form a regular array (Sun and Murray 1999). Self-assembly techniques can pattern large area structures with good short-range order, but have the drawback that long-range order is often poor. High resolution lithography processes and self-assembly methods have been successfully used to make large area magnetic arrays on a laboratory scale for media prototypes, and scaling up of many of these methods is under development. A promising avenue for patterned media formation is the combination of top-down lithography with self-assembly (Naito *et al*. 2002, Cheng *et al*. 2004).

The magnetic materials themselves are formed using a variety of methods. Commonly, a mask is defined by lithography or self-assembly processes, consisting of an array of holes in a layer made of photoresist or other material. Magnetic material is then electrodeposited through the mask to form an array of pillars, or evaporated over the mask followed by a lift-off process to leave an array of cones or pillars. Alternatively, a film of magnetic material can be initially deposited onto a substrate, then a template or etch mask is defined on top of the magnetic film by lithography. The exposed magnetic material is then etched away to leave an array of magnetic dots. Thin films can also be patterned using a focussed ion beam or other direct writing technique, or by imprint lithography (Lohau *et al*. 2001, Mc Clelland *et al*. 2002). A further method relies on the self-assembly of pre-formed magnetic particles on a surface. Examples of some of these structures are shown in Fig. 2. Each deposition method has its advantages. Electrodeposition is ideal for making
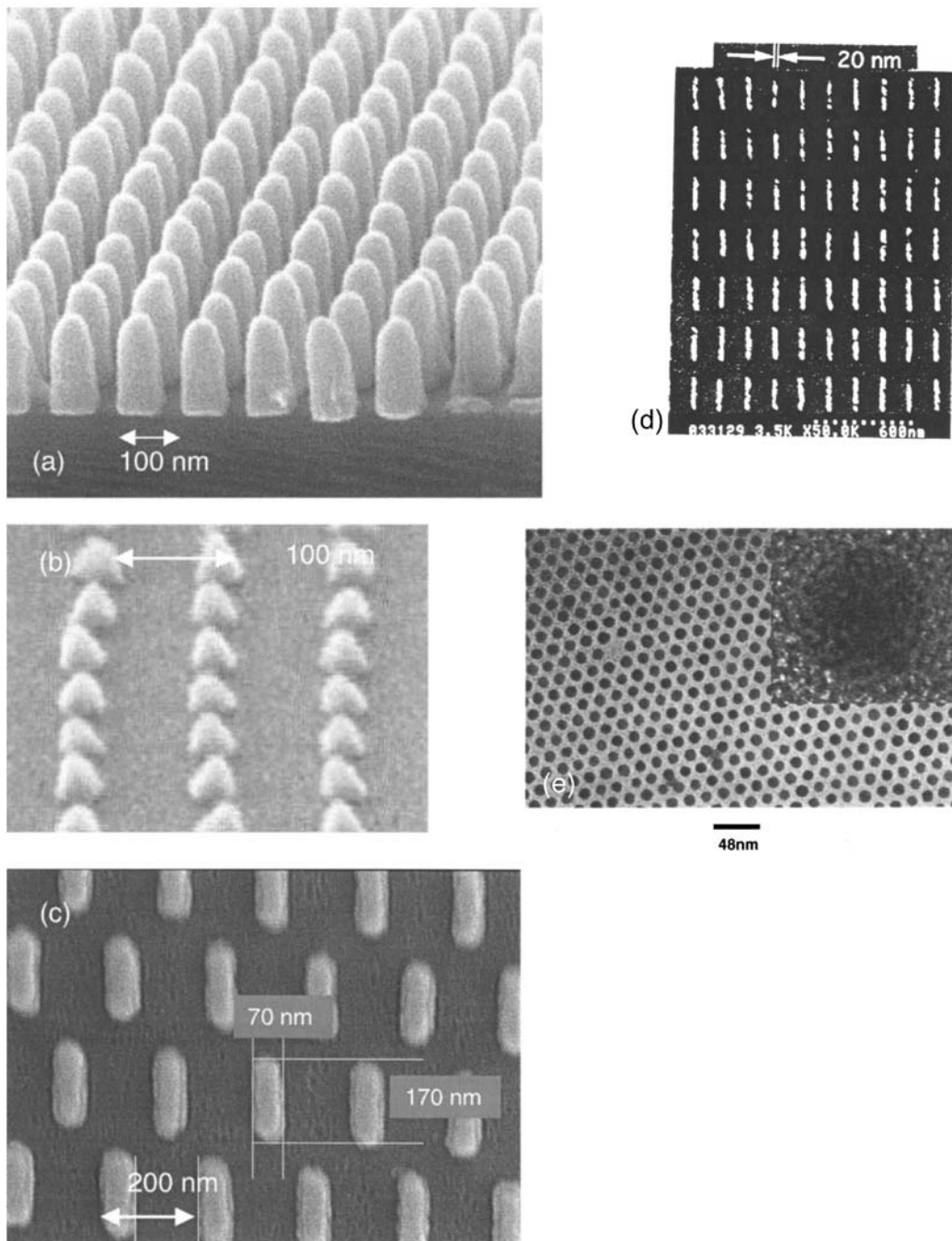
Figure 2
Examples of arrays of patterned elements. (a) An array of electrodeposited nickel pillars, height 115 nm, diameter 57 nm, period 100 nm. (b) An array of evaporated Ni pyramids, 30 nm diameter, with 100 nm period. (c) An array of etched bars made from a Co/Cu/Co multilayer, 170 nm long, 70 nm wide, 5 nm thick. (d) An array of Ni bars made by evaporation and liftoff, 20 nm wide, 200 nm long and 35 nm thick. (e) Electron micrograph of a two-dimensional self-assembled layer of 9 nm diameter Co particles. Inset: high-resolution image of a single particle. (Reprinted with permission from: (a–c) *J. Vac. Sci. Technol. B* **17** 3168; © American Institute of Physics 1999; (d) *Proc. IEEE* **85**, 652; © IEEE 1997; (e) *J. Appl. Phys.* **85**, 4325; © American Institute of Physics 1999.)

features with a large aspect ratio, but it is restricted to certain compositions. Evaporation and liftoff is convenient for flat or conical shapes but is also restricted in composition. Deposition of a film or multilayer structure by sputtering followed by etching offers the greatest range of compositions and magnetic properties, but etching of the material into dots is often difficult and the thickness of the films is limited. The methods chosen will depend on the desired geometry and composition of the array.

2. Magnetic Properties of Patterned Media

The optimum magnetic properties of patterned media (the magnetic anisotropy, coercivity or switching field, and magnetic moment) are not as clearly understood as the properties of hard disk or flexible media, and will depend on the specific recording device in which the medium is incorporated. However, some general considerations apply to all patterned media. Most importantly, the elements need to be single-domain particles with a number (usually two) of well-defined stable magnetization states to represent the data bits. For common ferromagnetic materials, single-domain behavior occurs in sub-100 nm particles because it is energetically unfavorable for domain walls to form in very small particles. Hence for a practical patterned medium with sub-100 nm period, the elements will automatically be single-domain as depicted in Fig. 1(b) and Fig 1(c).

A single-domain particle can be characterized by its total magnetic anisotropy K, its switching field H_{sw}, and its saturation magnetization M_s. The anisotropy K controls the direction and number of the preferred magnetization axes. A uniaxial anisotropy defines a single preferred magnetization direction. K includes two major contributions, one arising from the particle shape, K_s, and the other from its magnetocrystalline anisotropy, K_c (Cullity 1972). Needle-shaped particles have a uniaxial K_s with magnitude that increases with the particle aspect ratio and with M_s; the preferred magnetization direction is parallel to the long axis of the particle. K_s can therefore be controlled by choice of particle shape. In contrast, the magnetocrystalline anisotropy K_c depends on the material composition and crystal structure, and quantifies the preference for the magnetization to lie parallel to certain crystallographic directions within the crystal. Some materials such as cobalt have a strong K_c, which in cobalt causes the magnetization to lie parallel to the [0001] direction. By choice of materials, microstructure (amorphous, polycrystalline, or single crystal) and particle shapes, the total anisotropy can therefore be controlled over a wide range. Most patterned media structures rely on shape anisotropy, though magnetocrystalline anisotropy has been used to control magnetization in arrays of iron rectangles (New *et al.* 1996).

The total anisotropy K is important because it governs the switching field H_{sw}, which is the magnetic field required to change the magnetization of an element from one direction to the other. This is the most important magnetic parameter in terms of the writing process because the recording system must apply a field of at least H_{sw} to write data on the medium. H_{sw} is determined both by K and by the mechanism of magnetization reversal. In the simplest case, the magnetization of a single domain particle reverses in a uniform manner known as coherent reversal (Stoner and Wohlfarth 1948) and the switching field is simply given by $H_{sw} = 2K/M_s$ when the field is applied parallel to the anisotropy axis. However, measured switching fields are often smaller than this due to nonuniform magnetization reversal processes in which the magnetization reversal might occur by curling (Frei *et al.* 1957), or it might start in one region and propagate through the entire particle (Fredkin *et al.* 1991, Gibson and Schultz 1993, Seberino and Bertram 1997). The switching field for nonuniform reversal depends on particle size and shape, but as the particles become smaller, coherent switching becomes the dominant reversal mode and the switching fields of particles increase (e.g., Chou 1997). Clearly, a lower H_{sw} will make the medium easier to write, but it will also make it more vulnerable to thermal instability (superparamagnetism) and to accidental erasure. Most patterned media prototypes have switching fields of several hundred of oersteds.

In terms of reading data back from the medium, most recording devices are designed to detect the magnetic field surrounding each element. For single domain particles, the field approximates to a dipole field whose magnitude is proportional to M_s and to the particle volume (Cullity 1972). This field decreases as the inverse cube of the distance from the element. A stronger field will make detection of the magnetization state of the element easier. However, if the field from an element is too strong, it may cause inadvertent reversal (writing) of neighboring particles, which is undesirable. If the nearest-neighbor interaction field is H_i, then in a square array of perpendicular magnetic dipoles, the maximum field experienced by one element due to all of its neighbors is $9H_i$. Thus a criterion for arrays such as Fig. 1(c) to support stable magnetization patterns is that H_{sw} must exceed $9H_i$ (Ross *et al.* 1999). This limits how close together the elements can be placed. Arrays in which the element separation is similar to the element diameter are usually found to be stable.

3. Recording Systems

We have seen that a patterned medium can be designed by choosing the particle size, shape, and material to determine the switching field of the elements
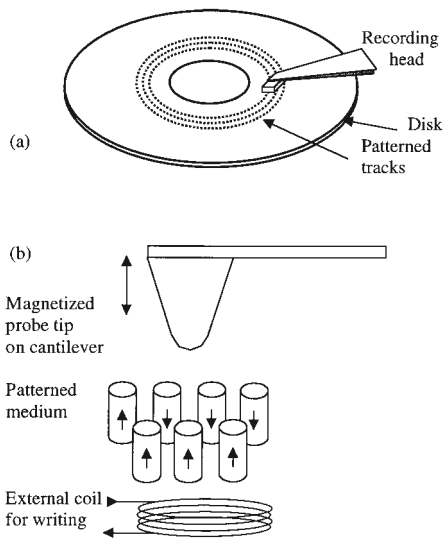
Figure 3
Recording schemes using patterned media. (a) A spinning disk. The disk is patterned with elements arranged in circumferential tracks. The medium is written and read using an ultra-narrow recording head. (b) A scanning probe. A probe tip detects the magnetic field from perpendicular patterned elements. An external field, plus the field from the probe tip, is used to write data.

Figure 4
A set of images taken using a magnetoresistive recording head which was dragged across an array of nickel pillars with 2-μm spacing. The white and dark images represent up and down magnetizations of the pillars and the linescans show the readback signal from the head. Several different patterns have been written and read back. (Reprinted with permission from *Appl. Phys. Lett.* **74**, 2516; © American Institute of Physics 1999.)

and by choosing the array geometry so that the elements do not interact too strongly. A variety of lithographic and self-assembly processes combined with deposition and etching processes have been developed to make arrays with period of 100 nm and smaller. However, the development of practical recording systems has lagged behind the development of the media.

Development of patterned recording systems has followed two distinct paths as illustrated in Fig. 3. The first is a spinning-disk system, similar to a conventional hard disk system but using a patterned instead of a continuous hard disk medium. This has the advantage that much of the existing hard drive technology is applicable, including the basic design of the drive, actuators and other mechanical components, and signal detection circuitry. The major challenges for this device are to produce heads with extremely narrow widths, to follow accurately the lithographically-defined tracks, and to synchronize the writing process with the physical location of the lithographically-defined bits. In such a scheme the patterned elements may be designed with in-plane (longitudinal) magnetization directions such as Fig. 1(b), similar to a conventional hard disk, or alternatively the elements can have out-of-plane (perpendicular) magnetization directions such as Fig. 1(c). Modeling of the readback response of both types of media has

been carried out (Nair and New 1998, Boerner *et al.* 1999), and the reading and writing of patterned media has been demonstrated (Todorovic *et al.* 1999, Zhu *et al.* 2000, Albrecht *et al.* 2003) as shown in Fig. 4, but a practical spinning-disk system has not been made.

A more radical departure from conventional recording is a probe-based system (Ohkubo *et al.* 1991, Mamin *et al.* 1995). In this case, a scanning probe tip similar to an atomic force microscope addresses an array of elements. The elements are perpendicularly magnetized as shown in Fig. 3(b). The probe tip is magnetic and is mounted on the end of a flexible cantilever. The probe detects the magnetization state of each element by responding to the force gradient exerted by the magnetic field emanating from the element, which causes a change in the resonant frequency of the cantilever. This is the same as the operation of a magnetic force microscope. To write data patterns on the medium, a magnetic field less than H_{sw} is applied to all the elements using an external coil. The magnetic probe tip is then moved close to the target element, so that the sum of the field from the probe tip plus the external field is sufficient to reverse that one element but not its neighbors (Gibson and Schultz 1993, Kleiber *et al.* 1998). Variations on this theme are also possible, for instance using a separate tip for reading and writing (Chou 1997, Kong *et al.* 1997). An example of an array with written features is shown in Fig. 5.

These probe-based systems are inherently slow because they rely on moving the probe tip to specific
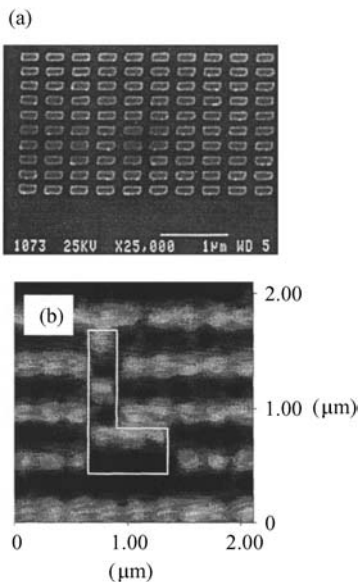
Figure 5
(a) An array of nickel bars formed by evaporation and liftoff, (b) magnetic image of sample after several bars have been reversed to delineate the letter L, using a magnetic probe tip. (Reprinted with permission from *IEEE Trans. Mag.* **33**, 3019; © IEEE 1997.)

locations in the patterned medium. To increase the data rate, a large number of probe tips working in parallel is necessary (Pohl 1995, Minne *et al.* 1996, Binnig *et al.* 1999). In these devices, the challenges are to make the device compact and mechanically robust, and to design a reliable method for writing the underlying patterned magnetic media.

One other storage scheme that should be mentioned in relation to patterned media is the magnetic random access memory (MRAM) (e.g., Tehrani *et al.* 1999), which is described in more detail in the article *Random Access Memories: Magnetic*. These devices consist of an array of magnetoresistive elements, connected together by conductor lines. Each element stores one data bit, as in the patterned media systems described above, but the elements in a MRAM consist of more complex, multilayer films such as spin-valve or spin-tunneling structures such as the sample shown in Fig. 2(c). Many of the issues of inter-element interactions, thermal stability, and switching behavior, as well as the need for high resolution lithographic patterning, are common to both MRAM elements and patterned media.

4. Summary

The onset of thermal instability (superparamagnetism) in conventional hard-disk media is driving the development of patterned media systems for areal densities exceeding hundreds of $Gbin^{-2}$. Patterned medium structures have already been fabricated using a range of lithographic and deposition techniques, and the switching field and interactions between the elements can be controlled by the choice of materials and array geometry. The development of practical storage schemes has lagged behind the development of media, but prototype systems have been demonstrated. Patterned media will most likely first appear in a spinning-disk system, but probe-based systems have also been explored.

See also: Longitudinal and Perpendicular Recording: Thermal Stability; Magnetic Recording Devices: Future Technologies; Magnetic Recording Media: Advanced; Magnetic Recording Technologies: Overview; Random Access Memories: Magnetic

Bibliography

Albrecht M, Rettner C T, Best M E, Terris B D 2003 Magnetic coercivity patterns for magnetic recording on patterned media. *Appl. Phys. Lett.* **83**, 4363
Bao X H, Li F Y, Metzger R M 1996 Synthesis and magnetic properties of electrodeposited metal particles on anodic alumite film. *J. Appl. Phys.* **79**, 4866–8
Binnig G, Despont M, Drechsler U, Haberle W, Lutwyche M, Vettinger P, Mamin H J, Chui B W, Kenny T W 1999 Ultrahigh density atomic force microscopy data storage with erase capability. *Appl. Phys. Lett.* **74**, 1329–31
Boerner E D, Bertram H N, Hughes G F 1999 Writing on perpendicular patterned media at high density and data rate. *J. Appl. Phys.* **85**, 5318–20
Charap S H, Lu P L, He Y 1997 Thermal stability of recorded information at high densities. *IEEE Trans. Magn.* **33**, 978–83
Cheng J Y, Ross C A, Chan V Z H, Thomas E L, Lammertinck R G H, Vancso G J 2001 Formation of a cobalt magnetic dot array via block copolymer lithography. *Advanced Materials* **13**, 1174
Cheng J Y, Mayes A M, Ross C A 2004 Nanostructure engineering by templated self-assembly of block copolymers. *Nature Materials* **3**, 823
Chou S Y 1997 Patterned magnetic nanostructures and quantized magnetic disks. *Proc. IEEE.* **85**, 652–71
Chou S Y, Wei M, Krauss P R, Fisher P B 1994 Study of nanoscale magnetic structures fabricated using electron-beam lithography and quantum magnetic disk. *J. Vac. Sci. Technol.* **B12**, 3695–8
Cullity B D 1972 *Introduction to Magnetic Materials*. Addison-Wesley, Reading, MA
Fernandez A, Bedrossian P J, Baker S L, Vernon S P, Kania D R 1996 Magnetic force microscopy of single-domain cobalt dots patterned using interference lithography. *IEEE Trans. Magn.* **32**, 4472–4
Fredkin D R, Koehler T R, Smyth J F, Schultz S 1991 Magnetization reversal in permalloy particles: micromagnetic computations. *J. Appl. Phys.* **69**, 5276–8
Frei E H, Shtrickman S, Treves D 1957 Critical size and nucleation field of ideal ferromagnetic particles. *Phys. Rev.* **106**, 446

Gibson G A, Schultz S 1993 Magnetic force microscope study of the micromagnetics of submicrometer magnetic particles. *J. Appl. Phys.* **73**, 4516–21

Haast M A M, Schuirhuis S, Abelmann L, Lodder J C, Popma Th J 1998 Reversal mechanism of submicron patterned CoNi/Pt multilayers. *IEEE Trans. Magn.* **34**, 1006–8

Kleiber M, Kummerlen F, Lohndorf M, Wadas A, Weiss D, Wiesendanger R 1998 Magnetization switching of submicrometer Co dots influenced by a magnetic force microscope tip. *Phys. Rev. B* **58**, 5563–7

Kong L S, Zhuang L, Chou S Y 1997 Writing and reading on 7.5 Gb/in^2 longitudinal quantized magnetic disk using magnetic force microscope tips. *IEEE Trans. Magn.* **33**, 3019–21

Lambert S E, Saunders I L, Patlach A M, Krounbi M T, Hetzler S R 1991 Beyond discrete tracks: other aspects of patterned media. *J. Appl. Phys.* **69**, 4724–6

Lohau J, Moser A, Rettner C T, Best M E, Terris B D 2001 Writing and reading perpendicular magnetic recording media patterned by a focused ion beam. *Appl. Phys. Lett.* **78**, 990

Lu P L, Charap S H 1994 Magnetic viscosity in high density recording 1994. *J. Appl. Phys.* **75**, 5768–70

Mamin H J, Terris B D, Fan L S, Hoen S, Barrett R C, Rugar D 1995 High density storage using proximal probe techniques. *IBM J. Res. Dev.* **39**, 681–99

Mc Clelland G M, Hart M W, Rettner C T, Best M E, Carter K R, Terris B D 2002 Nanoscale patterning of magnetic islands by imprint lithography using a flexible mold. *Appl. Phys. Lett.* **81**, 1483

Minne S C, Manalis S R, Atalar A, Quate C F 1996 Independent parallel lithography using the atomic force microscope. *J. Vac. Sci. Technol. B* **14**, 2456–61

Nair S K, New R M H 1998 Patterned media recording: noise and channel equalization. *IEEE Trans. Magn.* **34**, 1916–8

Naito K, Hieda H, Sakurai M, Kamata Y, Asakawa K 2002 2.5-inch disk patterned media prepared by an artificially assisted self-assembling method. *IEEE Trans. Magn.* **38**, 1949

New R M H, Pease R F W, White R L, Osgood R M, Babcock K 1996 Magnetic force microscopy of single-domain single-crystal iron particles with uniaxial surface anisotropy. *J. Appl. Phys.* **79**, 5851–3

O'Barr R, Yamamoto S, Schultz S, Xu W, Scherer A 1997 Fabrication and characterization of nanoscale arrays of nickel columns. *J. Appl. Phys.* **81**, 4730–2

Ohkubo T, Kishigami J, Yanagisawa K, Kaneko R 1991 Submicron magnetizing and its detection based on the point magnetic recording concept. *IEEE Trans. Magn.* **27**, 5286–8

Pohl D W 1995 Some thoughts about scanning probe microscopy, micromechanics and storage. *IBM J. Res. Dev.* **39**, 701–11

Ross C A, Smith H I, Savas T, Schattenburg M, Farhoud M, Hwang M, Walsh M, Abraham M C, Ram R J 1999 Fabrication of patterned media for high-density magnetic storage. *J. Vac. Sci. Technol. B* **17**, 3168–76

Rousseaux F, Decanini D, Carcenac F, Cambril E, Ravet M F, Chappert C, Bardou N, Bartenlian B, Veillet P 1995 Study of large area high-density magnetic dot arrays fabricated using synchrotron radiation-based x-ray lithography. *J. Vac. Sci. Technol. B* **13**, 2787–91

Seberino C, Bertram H N 1997 Micromagnetics of long ferromagnetic particles. *IEEE Trans. Magn.* **33**, 3055–7

Stoner E C, Wohlfarth E P 1948 A mechanism of magnetic hysteresis in heterogeneous alloys. *Philos. Trans. R. Soc. London* **A240**, 599

Sun S H, Murray C B 1999 Synthesis of monodisperse cobalt nanocrystals and their assembly into magnetic superlattices. *J. Appl. Phys.* **85**, 4325–30

Tehrani S, Chen E, Durlam M, DeHerrera M, Slaughter J M, Shi J, Kerszykowski E 1999 High-density submicron magnetoresistive random access memory. *J. Appl. Phys.* **85**, 5822–7

Todorovic M, Schultz S, Wong J, Scherer A 1999 Writing and reading of single magnetic domain per bit perpendicular patterned media. *Appl. Phys. Lett.* **74**, 2516–8

White R L, New R M H, Pease R F W 1997 Patterned media: a viable route to 50 Gb/in^2 and up for magnetic recording? *IEEE Trans. Magn.* **33**, 990–5

Wu W, Cui B, Sun X, Zhang W, Zhuan L, Kong L, Chou S Y 1998 Large-area high-density quantized magnetic disks fabricated using nanoimprintlithography. *J. Vac. Sci. Technol.* **B16**, 3825–9

Zhu J G, Lin X, Guan L, Messner W 2000 Recording, noise and servo characteristics of patterned thin film media. *IEEE Trans. Magn.* **36**, 23–9

Zhu S, Gambino R J, Rafailovich M N, Sokolov J, Schwarz S A, Gomez R D 1997 Microscopic magnetic characterization of submicron cobalt islands prepared using self-assembled polymer masking technique. *IEEE Trans. Magn.* **33**, 3022–4

C. A. Ross
Massachusetts Institute of Technology, Cambridge Massachusetts, USA

Magnetic Recording: Rigid Media, Preparation

Hard disks have various formats with diameters varying from 3.5 in (8.9 cm) for PCs to 2.5 in (6.4 cm) and to 1.8 in (4.6 cm) for laptop and notebook computer drives. The disk has a central hole for location on the spindle of the disk drive motor. The rotating disk is addressed by read/write head(s) "flying" within tens of nanometers of its surface. The disk substrate, on which the magnetic film is deposited, varies in thickness from about 1.25 mm for 3.5 in disks to 0.5 mm for the smaller format disks. Rotation speeds for the disk are continually increasing to decrease access times, and speeds approaching 10000 rpm are now used.

A cross-section of the structure on one side of a conventional disk is shown in Fig. 1. The first layer is often a thick, mechanically hard and nonmagnetic film on which is deposited one or more underlayers or seed layers that encourage a preferred microstructure and crystallographic texture in the magnetic layer. It can be seen that the magnetic film is relatively thin. The hard coating and the lubricating layer at the head/disk interface protect the magnetic storage layer in any contact stop–start phase of the head slider flight and also assist in that flight.

1. The Substrate

The most common disk substrate material is an Al–4% Mg alloy. The disk is prepared by stamping, and

Head/Slider

Flying height

~ 10nm

Lubrication	
Protective overlayer	~ 5-10nm
Magnetic film	~ 10-20nm
Underlayer (Cr ?)	~ 50nm
NiP layer (if present)	~ 10μm
Disk substrate	
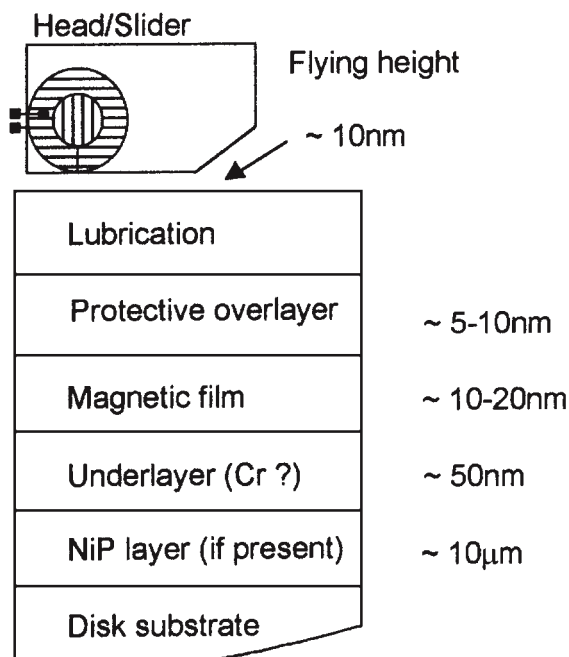
Figure 1
Schematic diagram showing a cross-section of one side
of a typical thin-film hard disk.

a first coating is generally prepared by chemically
plating the aluminum alloy disk with about $10\,\mu m$ of
a structurally amorphous and mechanically hard NiP
alloy. This layer is then often mechanically textured
on the micrometer scale and the resulting uneven
surface of the finished disk reduces problems with
stiction in the start and stop phases of the head slider
flight in systems in which the head is ''parked'' on the
disk at rest. However, the move to higher and higher
storage densities requires smaller and smaller
($\sim 10\,nm$) flying heights.

This is leading to smoother finishes on the disk and
the adoption of procedures such as locally focused
ion beam and laser etching to produce relatively
rough areas on which to land and park the head.
Faster rotation rates, essential to reduce access times
and increase data rates, require stronger, harder,
stiffer, and lighter substrate materials. These are usu-
ally nonmetallic to avoid mechanically induced dis-
tortion and glass, glass ceramic, aluminum, boron,
and silicon carbides, and silicon are being used or are
being explored. However, the substrate material must
be thermally stable and also process compatible. Al-
so, the nucleation and growth of the several layers
on the disk may very well depend on the substrate
material.

The various layers, apart from the NiP layer, are
now without exception put down by physical vapor

deposition (PVD) methods, nearly always sputter
deposition, at fairly fast rates of $\sim 10\,nms^{-1}$ onto
variable temperature substrates. The use of PVD
techniques offers the necessary control and repro-
ducibility in the deposition process. The different
forms of magnetron sputtering that may be used are
variations on a technique that offers excellent control
of deposition rate, film thickness, alloy composition,
substrate conditions and environment, and efficient
use of the target material.

2. The Underlayer

The magnetic layer is deposited on one or more chosen
underlayers or ''seed'' layers (Figs. 1 and 2). The usual
role of the underlayer(s) is to promote the growth of a
particular crystallographic texture and grain size and
morphology in the magnetic layer. The magnetic layer
is, without exception, a polycrystalline, cobalt-based
alloy film, typically CoCrTa,Pt that crystallizes with
a hexagonal crystal structure. The magnetically pre-
ferred orientation of the grains is with their [001] *c*-axis
in the plane of the film. As discussed below, there is an
exception to this in media designed for the perpendic-
ular recording mode in which the *c*-axis should be
perpendicular to the film plane. However, commercial
drives use ''longitudinal'' recording and in-plane mag-
netization is required.
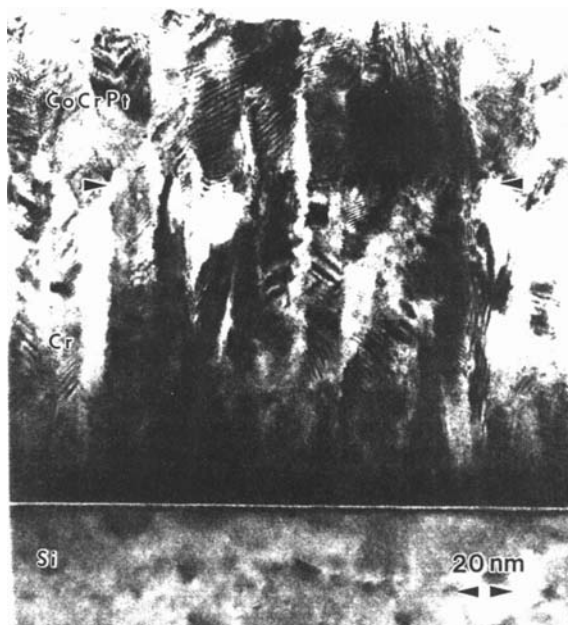
Figure 2
High-resolution transmission electron micrograph of a
cross-sectional sample prepared from an experimental
thin-film disk showing the silicon substrate, the
chromium underlayer, and the CoCrPt magnetic layer.

The heteroepitaxy between the underlayer(s) and the magnetic layer, which is so apparently beneficial to recording performance, clearly must depend on the lattice spacings of the layers as well as their crystal structures. Important additions to the basic CoCr alloy in the magnetic layer are tantalum and platinum. The alloy is still hexagonally packed but there are subtle changes in the c/a ratio on alloying. Chromium has been the usual underlayer but b.c.c. alloys based on chromium, such as CrV and CrTi, can be used (Shiroishi *et al.* 1993) to improve the crystallographic fit and perhaps also to produce elastic distortions in the magnetic layer that in turn may increase anisotropy and coercivity. Growth orientations of the cobalt alloy layer on the immediate underlayer that have been identified (Lee *et al.* 1995, Grundy 1998) are typically $(10.0)Co//(112)Cr$, $(11.0)Co//(100)Cr$.

The crystallographic texture, grain size, and morphology developed in the underlayer depend on the substrate type and process conditions. Important process conditions are base vacuum, substrate temperature, deposition rate, sputter gas pressure, and film thickness. Various strategies are used to promote oriented chromium or chromium alloy layers on glass and other substrates, including the initial deposition of special seed layers such as NiAl (Lee *et al.* 1995) under the chromium.

The requirements for the magnetic layer are that it has optimized magnetic properties and also that it provides the recording and replay performance required from the finished disk. The microstructure and many magnetic properties, such as magnetocrystalline and shape anisotropies and intergranular exchange, of the overlying magnetic layer depend on the microstructure of the underlayer(s) (Grundy 1998). Their crystallographic orientation, grain structure, crystal lattice parameters, and thermal and chemical properties control the growth of the magnetic layer. It is found that conditions restricting adatom mobility, such as low substrate temperature and high sputtering pressures ($\geqslant 1\,Pa$), encourage unoriented films with a rough surface. Low deposition pressures and higher substrate temperatures ($\sim 200\,°C$) favor increased mobility and oriented and smoother chromium and chromium alloy deposits.

3. The Magnetic Layer

The improved recording and replay performance required of magnetic disks has led to the development of CoCr-based ternary alloys, such as CoCrTa,Pt, quaternary, and, indeed, quinternary alloys and the deposition of polycrystalline films with small (20–50 nm), oriented but segregated grains (Fig. 2). The size distribution of the grains should be narrow, with a mean size as small as possible, but one that is greater than the so-called superparamagnetic limit so that the recorded signal is stable.

It is known that media noise, the dominant noise limiting recoverable signals in replay, is reduced when the magnetic medium is subdivided into isolated, noninteracting particles. However, smaller particles require a larger value of magnetic anisotropy for stability (Lu and Charap 1994). To satisfy this need, media with increased magnetocrystalline anisotropy are required.

Chromium was originally used to improve the corrosion properties of cobalt films but it was also found to help in increasing coercivity and reducing replay noise. This is achieved by segregation of chromium at the grain boundaries producing a nonmagnetic layer that interrupts exchange interactions between grains or clusters of grains (Doerner *et al.* 1993). There is also evidence that compositional gradients exist within grains (Hono *et al.* 1995). The tantalum and platinum additions substitute into the majority cobalt lattice and increase the magnetocrystalline anisotropy with a concomitant increase in coercivity. However, cobalt and its alloys can exist in other crystalline forms, notably a f.c.c. structure. The magnetization of the f.c.c. form of cobalt is not very different from that of the hexagonal phase but it has four easy axes of magnetization along the $\langle 111 \rangle$ directions and the magnetocrystalline anisotropy is much less than that of the h.c.p. phase. Cubic grains would have a deleterious effect on the recording behavior of the film (Dova *et al.* 1999).

In efforts to increase coercivity even further, what might be called the confusion principle is being applied in the investigation of even more complex quaternary and quinternary alloys such as CoCrPtXY (Akimoto and Shinohara 1998), where X and Y are tantalum, niobium, silicon, or boron. Boron enters the lattice interstitially and changes the c/a ratio, as do the substitutional solutes. It is therefore probable that anisotropy will be changed and segregation effects made more complex.

4. Overlayers

The integrity of the thin-film disk in the drive is preserved by the application of a mechanically hard overlayer. This prevents wear of the magnetic layer in any stop–start action. Such wear would involve loss of the storage medium and the information it contains and it would also introduce debris into the drive mechanisms. Low friction in the system is ensured by a final coating of a high molecular weight polymer.

The most common hard overlayer is a thin (5–10 nm) film of modified carbon. Sputter or plasma beam deposition of carbon in atmospheres containing hydrogen or hydrocarbons can result in so-called diamond-like carbon (DLC) films (Cord and Scherer 2000). The presence of hydrogen in the films favors the formation of sp^3 bond orbitals at the expense of sp^2 orbitals that are characteristic of graphitic

bonding. The resultant density and hardness of the films is a function of the hydrogen content of the films and the relative proportion of sp^3/sp^2 bonding. Values in the literature are in the range 5–20 GPa. This compares with the hardness of, for example, tungsten carbide, WC, at 3 GPa.

Typical lubricants are the perfluoropolyethers, such as Fomblin, with molecular weights of 2000 and more. These lubricants have the necessary properties of thermal and chemical stability, low vapor pressure, and low surface tension (Bushan 1990). The coating is at a monolayer thickness and binds to the carbon overcoat by interactions between end groups in the linear polymer and the carbon surface. The strong binding ensures that lubricant remains between the head slider and the disk where contact occurs and also that it does not leave the disk when it spins at high speed. However, some mobility is needed so that areas from where lubricant is lost can be recovered.

5. Perpendicular Recording Media

The thin-film media discussed so far have in-plane magnetization and record information in the longitudinal mode. A second mode of recording has been proposed (Iwasaki and Nakamura 1977) in which the transitions separate regions magnetized perpendicularly to the film surface. This situation requires a magnetically uniaxial film in which a strong, perpendicular anisotropy, K_p, outweighs the demagnetizing energy, i.e., $K_p > \mu_0 M_s^2/2$, and supports magnetization normal to the film. Several types of material have been investigated, including particulate barium ferrite films and sputter-deposited crystalline films of cobalt alloyed with transition metals (Grundy and Ali 1983).

The media investigated mostly so far are cobalt alloyed with chromium at compositions round $Co_{81}Cr_{19}$ (Wright *et al.* 1985) A well oriented, columnar or equiaxed microstructure can be obtained by growth on a variety of substrates; including rigid substrates, such as glass, and glass coated with f.c.c. crystalline underlayers and NiFe (the NiFe acts as a magnetic closure layer) and amorphous underlayers such as germanium, and flexible substrates such as polyimide and melinex. The metallic underlayers are preferentially oriented with a $\langle 111 \rangle$ fiber texture, which encourages heteroepitaxy in the CoCr layer, whereas the amorphous plastics and germanium presumably favor the nucleation of the high surface energy basal planes in the cobalt alloy. The main advantage of the perpendicular scheme is that, in principle, the recording transition width is narrower than for the longitudinal mode and hence higher bit densities are possible. At the same time, the magnetic structure is resistant to demagnetization, even at high packing densities.

There is as yet no perpendicular recording disk drive on the market. There is no doubt of the potential of the scheme for very high storage densities. Calculations (Bertram and Williams 2000) have suggested that, although acceptable limits for longitudinal recording may be upgraded to ~ 100 Gbits in^{-2} (15 Gbits cm^{-2}), perpendicular recording may support ~ 500 Gbits in^{-2} (75 Gbits cm^{-2}). There have been problems in developing a fully integrated system, and the very rapid improvements in longitudinal media and associated GMR heads are providing strong competition. However, the great potential of the perpendicular mode in resisting demagnetization and thermal instability is rekindling a great deal of activity in the development of this technology. It may yet provide the transitional mode of magnetic storage between the longitudinal scheme and patterned media.

6. Fabrication

Commercial deposition equipment attempts to reproduce the precision of laboratory systems and yet operate with the cost effectiveness and reproducibility of mass production methods. They usually take one of two forms. The first is the in-line coater in which disks are unloaded from a cassette in a load-lock chamber and progress through a series of in-line process chambers in which the various layers are sequentially deposited onto the disk.

In this type of coater, such as the Leybold A400 system (Leybold AG, Hanau, Germany), the individual deposition chambers for, say, chromium, CoCrTa,Pt, and carbon depositions are separated by individually pumped buffer chambers with narrow-aperture slit load locks that allow continuous passage of the palates loaded with disks between large rectangular magnetron cathodes. The second system is the single-station system where most of the layers are deposited onto the disk from a cluster set of circular magnetrons. The Balzers CIRCULUS M12 or M14 (Balzers Process Systems, Balzers, Liechtenstein), have 12 or 14 process stations in a circular layout (Fig. 3). Each disk progresses round the circle of magnetrons from the input station to a holding cassette at the output. Each station is isolated and has its own pumping and cold trap system, gas supply, and measurement devices.

In both systems rapid processing demands sputter deposition at rates greater than 10 nm s^{-1}, and substrate heating and cooling for the various deposition regimes. Layers are deposited with little interruption to avoid contamination and to achieve reproducibility. Uniformity across the disk can in principle be enhanced by using magnetrons with on-line adjustable magnet fields. The base vacuum standard in both systems is that of conventional high vacuum, i.e., $\leqslant 10^{-5}$ Pa, with partial pressures of $< 10^{-4}$ Pa, of H_2O and $< 5 \times 10^{-5}$ Pa of N_2 and O_2, respectively. Disk production demands, of course, a clean room environment up to semiconductor fabrication
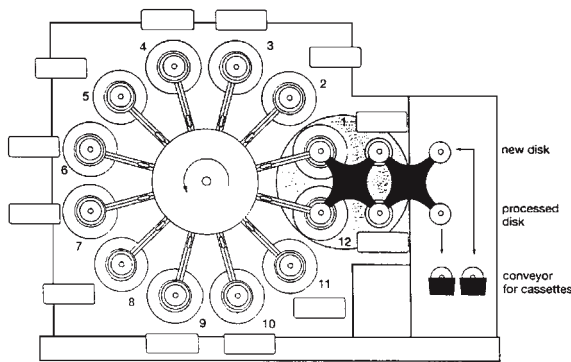
Figure 3
Schematic plan of the Balzers CIRCULUS M12 deposition system showing the disk input and output stage and the 12 magnetron positions.

standards in the initial presentation of the disks and in any subsequent testing and in packaging after fabrication. Commercial deposition systems can now produce fully coated disks at rates approaching 1000 per hour.

There are continuing efforts to improve processing procedures and to introduce new technologies in disk fabrication (Cord and Scherer 2000). For instance, research (Takahashi *et al.* 1997) has shown that improved properties, including larger magnetic coercivity, can be obtained in samples deposited in systems which have ultrahigh vacuum base pressures ($<5 \times 10^{-7}$ Pa) and use very pure target materials and sputtering gas. This is thought to produce uncontaminated thin films with grains that are less faulted, which for a given composition should have an increased anisotropy field and greater coercivity. Any moves to adopt such preparation standards commercially will need to take account of increased costs of fabrication, although investment in plant is essentially a one-off expenditure. However, the required increases in storage densities discussed above will probably lead to more demanding standards in disk fabrication.

See also: Magnetic Recording: Rigid Media, Recording Properties; Magnetic Recording: Rigid Media, Tribology; Magnetic Recording Devices: Head/Medium Interface; Magnetic Recording Media: Advanced; Magnetic Recording Technologies: Overview; Micromagnetics: Basic Principles

Bibliography

Akimoto H, Shinohara M 1998 Magnetic interaction in Co-CrPtTaNb media—utilization of micromagnetic simulation. *IEEE Trans. Magn.* **34**, 1597–9

Bertram H N, Williams M 2000 SNR and density limit estimates: a comparison of longitudinal and perpendicular recording. *IEEE Trans. Magn.* **36**, 4–9

Bushan B 1990 *Tribology and Mechanics of Magnetic Storage Devices.* Springer, New York

Cord B, Scherer J 2000 Future media manufacturing—more than just conventional sputtering. *IEEE Trans. Magn.* **36**, 67–72

Doerner M F, Yogi T, Parker D S, Lambert S, Hermsmeier B, Allegranza O C, Nguyen T 1993 Composition effects in high density CoPtCr media. *IEEE Trans. Magn.* **29**, 3667–9

Dova P, Laidler H, O'Grady K, Toney M F, Doerner M F 1999 Effects of stacking faults on magnetic viscosity in thin film magnetic recording. *J. Appl. Phys.* **85**, 2775–81

Grundy P J 1998 Thin film magnetic recording media. *J. Phys. D: Appl. Phys.* **31**, 2975–90

Grundy P J, Ali M 1983 The magnetic and microstructural properties of CoCr thin films with perpendicular anisotropy. *J. Magn. Magn. Mater.* **40**, 154–62

Hono K, Yeh K, Maeda Y, Sakurai T 1995 Three dimensional atom probe analysis of a sputter-deposited CoCr thin film. *Appl. Phys. Lett.* **66**, 1686–8

Iwasaki S, Nakamura Y 1977 An analysis for the magnetization mode for high density magnetic recording. *IEEE Trans. Magn.* **13**, 1272–7

Lee L L, Laughlin D E, Fang L, Lambeth D N 1995 Effects of Cr intermediate layers on CoCrPt thin film media on NiAl underlayers. *IEEE Trans. Magn.* **31**, 2728–30

Lu P, Charap S H 1994 Magnetic viscosity in high density recording. *J. Appl. Phys.* **75**, 5768–70

Shiroishi Y, Hosoe Y, Ishikawa A, Sugita Y, Ohno T, Ohura M 1993 Magnetic properties and read/write characteristics of CoCr(Pt,Ta)/(CrTi,Cr) thin film media. *J. Appl. Phys.* **73**, 5569–71

Takahashi M, Kikuchi A, Kawakita S 1997 The ultra-clean sputtering process and high density magnetic recording media. *IEEE Trans. Magn.* **33**, 2938–43

Wright C D, Lacey E T M, Grundy P J 1985 Optimisation of the magnetic properties of CoCr films for perpendicular recording applications. *J. de Phys.* **46**, C6-101–4

P. J. Grundy
University of Salford, Manchester, UK

Magnetic Recording: Rigid Media, Recording Properties

Rigid disk drive performances are being pushed ahead at such an enormous rate that disk recording has become the flagship for state of the art developments in digital recording. Other applications of recording benefit from and follow this lead but at a lesser pace. This article will describe briefly the theoretical background to digital recording and identify which properties of the recording media are important.

Recording media used in rigid disk drives are without exception of high coercivity and very thin. These requirements have been known for many years and have grown to be accepted as a result of early experimental and theoretical work completed largely in the
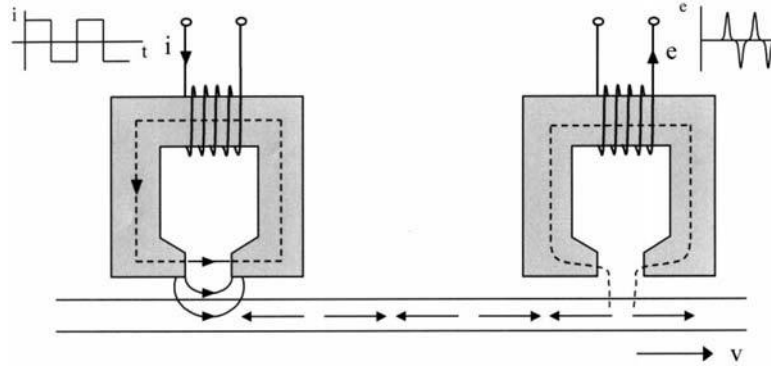
Figure 1
Schematic of the record and replay processes.

1960s and 1970s (e.g., Bertram 1994, Comstock 1999, Hoagland 1963, Hoagland and Monson 1998, Middleton 1987, Middleton 1989, Richter 1999). Since then, technology has marched ahead and so has the understanding of the nature of the record and replay processes. The values of the parameters involved have also changed dramatically but the basic requirements remain for thin media of high coercivity.

Figure 1 shows a simple diagram illustrating the complete digital record–replay cycle. A current into the record head is magnetizing a section of the medium to the right, whereas previously a current of the opposite polarity caused a magnetization to be written to the left. The magnetization transition between these states is used to represent a bit of stored information and a sequence of recorded transitions, or absences of them at particular locations along the track, is used to represent the recorded data. The width of a transition is indicative of the space needed to store a bit of information and so this is an important parameter ultimately determining the density at which bits are stored. When a transition moves under the replay head the stray field arising from its divergent magnetization couples into the head structure and generates an output voltage pulse. This article considers the nature of the recorded magnetization transitions and the corresponding output waveforms, and draws conclusions about the requirements for high-density recording.

1. The Recording of a Transition

In this theory (Middleton 1987, Middleton 1989), only components of magnetization in the plane of the recording medium, which have been assumed to arise from the influence of the planar components of the head field, will be considered. Figure 2 shows detail of how the head field magnetizes a medium to the right which had previously been magnetized to the left. The magnetization variation in the transition is determined
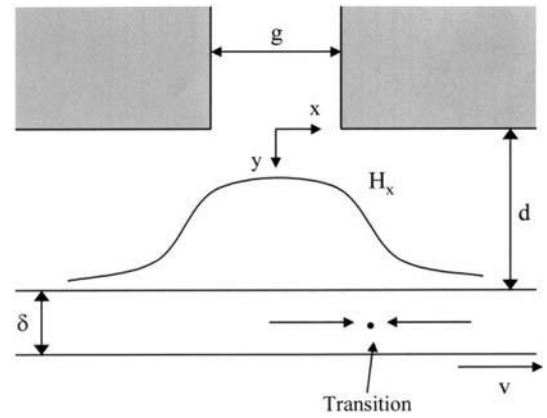
Figure 2
Close up of the head gap, the field distribution, and the recorded transition to the right of the gap.

by the hysteresis loop $M(H_t)$ of the medium and the total field H_t it experiences. The latter is made up of head field H_x plus any demagnetising field H_d produced by the medium. The head field is given by:

$$H_x = \frac{H_g}{\pi}\left(|\tan^{-1}|\left(\frac{g/2+x}{y}\right) + |\tan^{-1}|\left(\frac{g/2-x}{y}\right)\right) \quad (1)$$

where $H_g = ni\eta/g$ is the field along the surface of the head ($y = 0$) where n is the number of turns, η the head efficiency, i the record current, g the gap length, and x and y are defined in Fig. 2.

The recorded magnetization in the transition is assumed, for simplicity, to take the form:

$$M = -\frac{2}{\pi}M_r \tan^{-1}\left(\frac{x-x_o}{a}\right) \quad (2)$$

where the center of the transition is at $x = x_o$, near to the trailing edge of the gap, and the magnetization varies smoothly from a value of $+M_r$ on one side to

$-M_r$ on the other. M_r is the remanent magnetization of the medium and a is proportional to the transition width and is known as the transition width parameter. Using Eqn. (2) the demagnetizing field arising from a thin medium of thickness δ is:

$$H_d = \frac{M_r \delta (x - x_o)}{\pi((x - x_o)^2 + a^2)} \qquad (3)$$

The gradient of the magnetization in the transition is given by:

$$\frac{dM}{dx} = \frac{dM(H_t)}{dH_t}\frac{dH_t}{dx} = \frac{dM(H_t)}{dH_t}\frac{d(H_x + H_d)}{dx} \qquad (4)$$

where $dM(H)/dH$ is the slope of the hysteresis loop and dH_t/dx is the total field gradient. The head field gradient in a medium spaced $y = d$ from the head is given by $dH_x/dx = \alpha H_c/d$ where the quantity α has values, in the literature, ranging from $(2/\pi)$ to 1 depending on the size of the head gap and the magnitude of the head current. Here $\alpha = \sqrt{3}/2$ corresponds to maximization of head field gradient for a narrow gap head. At the center of the transition, where $x = x_o$, $M = 0$, and $H_t = H_c$, the slope of the hysteresis loop is χ and so, using Eqns. (3) and (4), it is easily shown that:

$$\frac{2M_r}{\pi a} = \chi\left(\frac{\sqrt{3}H_c}{2d} - \frac{M_r\delta}{\pi a^2}\right) \qquad (5)$$

Solving this equation leads to a transition width of:

$$a = \left(\frac{2M_r d}{\sqrt{3}\pi\chi H_c}\right) + \sqrt{\left(\frac{2M_r d}{\sqrt{3}\pi\chi H_c}\right)^2 + \frac{2M_r\delta d}{\sqrt{3}\pi H_c}} \qquad (6a)$$

When the hysteresis loop is steep sided and χ is large:

$$a = \sqrt{\frac{2M_r\delta d}{\sqrt{3}\pi H_c}} \qquad (6b)$$

This is the transition width in the presence of the head field but as the medium moves away from the record head, and the influence of its field wanes, the transition demagnetizes to a greater width. When the transition then moves to the vicinity of the replay head it induces within it magnetic charges which image those within the medium. The net reduced pole strength reduces the demagnetizing fields and narrows the transition widths to values approaching those given by Eqn. (6). Thus Eqn. (6) is a reasonable first approximation of the final transition width.

When the head field gradient is large, it can, according to Eqns. (6) and (3), lead to a transition sufficiently narrow as to give rise to a demagnetizing field which is larger than the coercivity of the recording medium. Such a field cannot be consistent with a hysteresis loop and so the transition widens to reduce
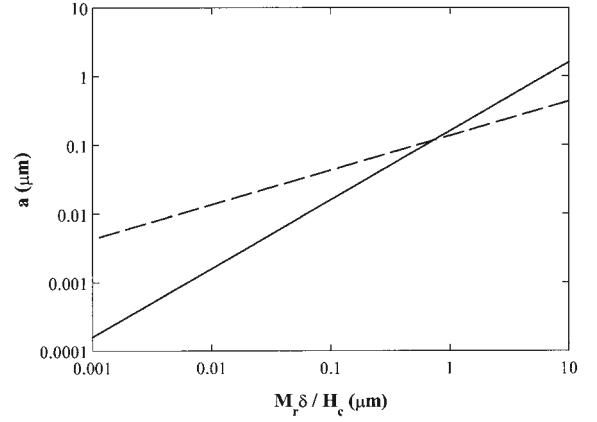
Figure 3
The broken line shows the write limited transition width, from Eqn. (6b) with $d = 40$ nm and $\chi = \infty$, while the solid line shows the demagnetizing limited case from Eqn. (7).

the field to less than or equal to the coercivity. The minimum possible transition width is when the demagnetizing field is equal to the coercivity. Thus equating the maximum of the demagnetizing field, given by Eqn. (3) at $(x - x_o) = a$, to the coercivity, the minimum value for the transition width is:

$$a = \frac{M_r\delta}{2\pi H_c} \qquad (7)$$

This is sometimes known as the self-demagnetizing limited transition width.

The transition width occurring in a recording medium is the larger of the write- or self-demagnetizing limited values given, respectively, by Eqns. (6) or (7), and these are plotted in Fig. 3 as a function of $(M_r\delta/H_c)$. Experimental results confirm these relationships and in each case the important ratio in determining recording performance is $(M_r\delta/H_c)$ which should, obviously, be kept small.

2. The Replay Process

During the replay process (Middleton 1987, Middleton 1989) transitions pass under the replay head which is sensitive to their presence. The variation of sensitivity with position under the head can be represented by a sensitivity function which has the same mathematical form as the field distribution per unit current, H'_x, obtained from Eqn. (1). The replay head voltage generated as the magnetization gradient moves through the sensitive region of the head is:

$$e(\bar{x}) = -\mu_o vw\delta \int_{-\infty}^{+\infty} \frac{dM_x(x - \bar{x})}{d\bar{x}} H'_x(x, d)dx \qquad (8)$$

where μ_o is the permeability of free space, v the medium velocity, w the track width, $\bar{x} = vt$ and t is time. Substitution of Eqn. (1) for the head sensitivity function along with the magnetization from Eqn. (2), into Eqn. (8) and evaluation leads to the output pulse shape:

$$e(\bar{x}) = \frac{-2\mu_o vwn\eta M_r \delta}{\pi}\left(|\tan^{-1}|\left(\frac{g/2 - \bar{x}}{d + a}\right) + |\tan^{-1}|\left(\frac{g/2 - \bar{x}}{d + a}\right)\right) \quad (9)$$

This pulse shape is identical to that of the sensitivity function of the head except that the spacing d is replayed by $(d + a)$. Three pulse shapes are shown in the inset of Fig. 4, where the amplitude $e(0)$ and width p_{50} are shown on one of them. From Eqn. (9) these quantities are given by:

$$e(0) = \frac{-4\mu_o vwn\eta M_r \delta}{\pi}\,|\tan^{-1}|\left(\frac{g/2}{d + a}\right) \quad (10a)$$

and

$$p_{50} = 2\sqrt{(a + d)^2 + (g/2)^2} \quad (10b)$$

It is easily seen from Eqns. (10a) and (10b) that maintaining a narrow transition width keeps the pulse amplitudes high and the pulse widths narrow, in line with the requirement for high density recording.

At high densities when the transitions are close together, the total voltage can be predicted using linear superposition. This says that the total waveform $e_t(\bar{x})$ arising from a sequence of transitions is given by the sum of the isolated pulse shapes as:

$$e_t(\bar{x}) = \sum_{n=-\infty}^{n=+\infty} (-1)^n e(\bar{x} - n\lambda/2) \quad (11)$$

where $\lambda/2$ is the spacing between the transitions.

Figure 4, inset, shows three overlapping pulses, their sum, and the consequent reduction of output. The variation of normalized output voltage with packing density, for a long sequence of pulses, is shown in Fig. 5 for a typical thin-film recording medium. This type of graph is often referred to as a roll-off curve and is one of the standard measurements of recording performance. The full line represents theoretical predictions and the points represent experimental values. Their coincidence shows the validity of linear superposition but such agreement is not found in all circumstances (Richter 1999) because intertransition interactions can cause their widths and/or shapes to change with a consequent loss of agreement.

The summation, Eqn. (11), of pulse shapes, Eqn. (9), can be represented in closed form and at short wavelengths approximates to:

$$e_t(0) \propto e^{-2\pi(a+d)/\lambda} \quad (12)$$

Now the transition width appears in an exponential term and its role in causing a fall of output becomes very strong. This re-emphasizes the need to keep a, and therefore $(M_r\delta/H_c)$, small so as to keep the output high at high recording densities.

The simplified recording theory given here has, in its full exposition, had much success in explaining

Figure 4
Inset: overlapping pulses and their sum showing a reduction of output and the occurrence of peak shift. Main graph: peak shift as a function of packing density for pulses calculated using Eqn. (9) with $a = 50$ nm, $d = 40$ nm, and $g = 220$ nm.
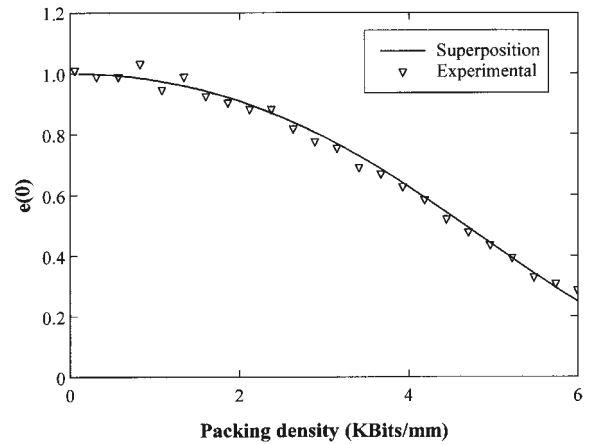
Figure 5
A roll-off curve showing normalized output voltage as a function of packing density. The solid theoretical curve is by linear superposition and the points are for a thin film medium with $M_r\delta = 20$ mA, $H_c = 159$ kA m^{-1}, $a = 50$ nm, and with $d = 40$ nm and $g = 220$ nm.

practical experience and guiding the way forward with prediction of future performances. While this theory has shortcomings with the simplicity of its basic assumptions and analysis, more sophisticated numerical modeling has not altered the basic media requirements.

The requirement for narrow transitions for high density operation has led to the widespread adoption of thin film media with high coercivity. Other requirements include media with steep sided hysteresis loops, small to medium head spacings and heads with narrow gaps. Practical media satisfying these requirements are now around 20 nm or less in thickness, and are reaching over $250 \, \text{kA m}^{-1}$ in coercivity. They are invariably of alloys of cobalt or cobalt–nickel with small additions of tungsten, platinum, or other metals. Future media suitable for the predicted very high storage densities are expected to rise to around $400 \, \text{kA m}^{-1}$.

3. Recorded Magnetization Transitions

Direct observation of recorded magnetization distributions in thin media obtained by either bitter colloid techniques or electron microscopy reveal, in plan view, a transition structure which varies in the cross track direction as shown in Fig. 6. This is known as a "saw-tooth" pattern whose nature is not indicated by Eqn. (2). Early interpretations of these patterns were that they came about to spread the magnetic poles over longer transitions, thereby reducing demagnetizing fields and self-demagnetizing energies. This may be so in wider transitions where bitter colloids have shown the presence of demagnetizing fields around the saw-teeth, and some record theories have followed this interpretation.

However, micromagnetic modeling of narrow transitions in higher coercivity films has shown that the saw-tooth like structures arise as a result of part of the magnetization distributions forming flux closure patterns. These do not contribute fields which influence the recording process, and subtraction of them from the total magnetization shows the resulting charge carrying transition to have little cross track

structure, not unreasonably represented by Eqn. (2). Indeed, micromagnetic calculations carried out on self-demagnetization limited transitions found that cross track average magnetizations, where flux closure components sum to zero, have distributions not unlike Eqn. (2) and transition widths which are close to Eqn. (7). This goes some way to explaining why record theory based on such simple assumptions, as used here, continues to apply even when the detailed structures of transitions appear so complicated.

4. Practical High Density Recording

It has been shown above that at high densities the output voltage is significantly reduced and therefore so is the signal to noise ratio. At high densities there is also a loss of timing accuracy in the replayed waveforms because the superposition of pulses leads to a total waveform where the peaks are shifted in position. This phenomenon, known as peak shift, increases rapidly as densities increase and this is illustrated in Fig. 4. These timing shifts, in concert with the reduced signal to noise ratios, lead to increased error rates in the recovered data.

5. Conclusions

This chapter has concerned itself with basic record theory to identify those properties of recording media, thinness and high coercivity, which are needed to allow high-density recording to take place. It has discussed these findings in view of the rather complicated magnetization distributions which are found in practice, and which appear at first sight not to be consistent with the theory quoted.

See also: Magnetic Recording: Rigid Media, Tribology; Magnetic Recording Devices: Head/Medium Interface; Magnetic Recording Measurements; Magnetic Recording Technologies: Overview; Micromagnetics: Basic Principles; Micromagnetics: Finite Element Approach

Figure 6
Diagrammatic representation of the plan view of the appearance of a "saw-tooth" transition.

Bibliography

Bertram H N 1994 *Theory of Magnetic Recording*. Cambridge University Press, Cambridge
Comstock R L 1999 *Introduction to Magnetism and Magnetic Recording*. Wiley, New York
Hoagland A S 1963 *Digital Magnetic Recording*. Wiley, New York
Hoagland A S, Monson J E 1998 *Digital Magnetic Recording*, 2nd edn. Krieger
Middleton B K 1987 The recording and reproducing processes. In: Mee C D, Daniel E D (eds.) *Magnetic Recording: Technology*. McGraw-Hill, New York, Vol. 1, Chap. 2, pp. 22–97

Middleton B K 1989 The recording and reproducing processes. In: Mee C D, Daniel E D (eds.) *The Magnetic Recording Handbook: Technology and Applications*. McGraw-Hill, New York, Chap. 2, pp. 24–100

Richter H J 1999 Recent advances in the recording physics of thin media. *J. Phys. D: Appl. Phys.* **32**, 147–68

B. K. Middleton and M. M. Aziz
University of Manchester, Manchester, UK

Magnetic Recording: Rigid Media, Tribology

Magnetic recording disk drives are generally designed so that the slider flies over the disk during steady-state operation of the drive. The flying of the slider is based on the formation of a thin air bearing which separates the slider and the disk. If the disk drive is shut down, the slider is in contact with the surface of the disk. During start/stop of the drive, sliding motion between the slider and the disk occurs until the air bearing is formed and the slider is supported completely by hydrodynamic pressure forces.

The design of a magnetic recording slider during steady-state operation is a problem of hydrodynamic lubrication, requiring the solution of the compressible Reynolds equation. However, during start/stop of a drive, contacts between the slider and the disk occur, requiring the understanding of boundary lubrication and wear. Since a magnetic disk drive may be turned on and off more than 50 000 times during its life, great care has to be taken in the design and implementation of the head/disk interface in order to guarantee reliable operation of the disk drive.

In order to obtain maximum signal resolution and highest recording density, it is important that the spacing between the slider and the disk be as small as possible. In fact, from a magnetics point of view, the spacing between disk and slider (or "head") should be zero. This situation, generally described as "contact recording", causes problems with friction and wear. Thus, a compromise must be made so that the spacing between the slider and the disk is small enough to give adequate signal strength, but is large enough to establish a strong air bearing to enable flying of the slider over the disk. Flying heights of typical magnetic recording sliders are of the order of 20 nm.

1. Reynolds Equation

The equation governing the hydrodynamic flying of a magnetic recording slider is the compressible Reynolds equation, given by

$$\frac{\partial}{\partial x}\left(Q(Kn)ph^3\frac{\partial ph}{\partial x}\right) + \frac{\partial}{\partial y}\left(Q(Kn)ph^3\frac{\partial ph}{\partial y}\right)$$
$$= 6\mu U\frac{\partial ph}{\partial x} + 6\mu V\frac{\partial ph}{\partial y} + 12\mu\frac{\partial ph}{\partial t} \qquad (1)$$

where p is the pressure, h is the spacing between slider and disk, μ is the viscosity of the lubricant film, and U and V are the disk velocity components in the x- and y-direction, respectively. The factor Q is a function of the local Knudsen number, Kn (ratio of mean free path and local spacing), and is an indication of the deviation of the air flow between slider and disk from continuum flow theory.

The Reynolds equation is a nonlinear partial differential equation which can be solved numerically using finite difference and finite element methods (Hu and Bogy 1996, Wahl *et al.* 1996). Two of the most important considerations in the design of magnetic recording sliders are the requirements for a slider to fly at constant flying height from the inner to the outer disk radius, and the need of a slider to be independent of altitude changes.

2. Slider Design

A typical air bearing slider is shown in Fig. 1(a). The slider consists of two side rails, a leading edge bridge, and a subambient cavity. Also shown is the positive pressure buildup over the slider rails and the subambient pressure region over the cavity portion (Fig. 1(b)).

3. Disk Characteristics

For flying heights of the order of 20 nm, the roughness of a disk has to be well controlled. The peak-to-valley roughness of a typical disk is of the order of
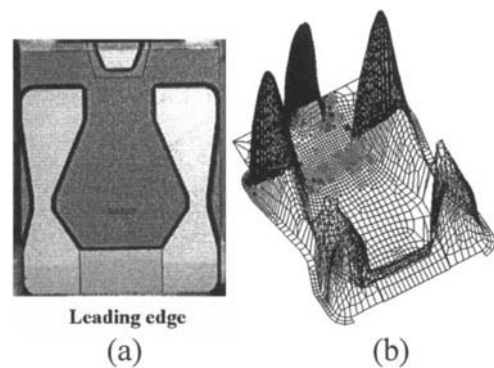
Figure 1
(a) Typical magnetic recording subambient pressure slider and (b) the pressure distribution over the slider.
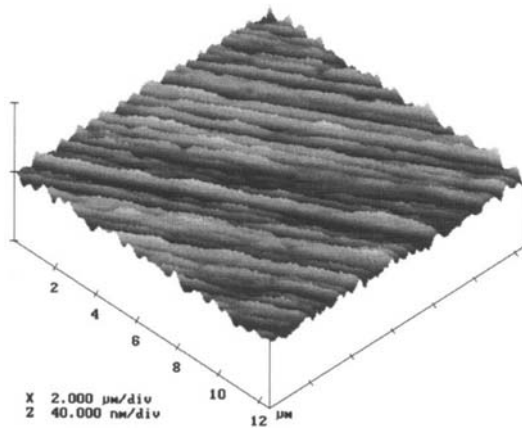
Figure 2
Surface roughness of hard disk measured with atomic force microscopy.

Figure 3
Coefficient of friction as a function of contact start/stop cycles.

10–20 nm. A roughness plot for a hard disk measured by atomic force microscopy is shown in Fig. 2. The substrate of choice for 65 mm laptop disk drives is glass, while the substrate for 95 mm disk drives is aluminum. In the case of aluminum substrates, a 10–15 μm thick layer of nickel phosphorous is first deposited on the disk, followed by a 10–50 nm thick layer of magnetic alloy. On top of the alloy is a thin carbon film that, in turn, is coated with a 1–2 nm thick lubricant film.

4. Tribology of the Head/Disk Interface

4.1 Friction and Stiction

During shutdown and startup of a disk drive the slider is in contact with the disk, resulting in friction and wear at the interface. The variation of the coefficient of friction is shown in Fig. 3 as a function of the number of start/stop cycles (CSS) between slider and disk. In general, the coefficient of friction is found to increase with the number of start/stop cycles and is influenced by environmental conditions such as temperature and humidity (Zhao and Talke 1999a).

The coefficient of friction shows, in general, a sharp increase during startup with a well-defined peak approximately 100–200 ms after motion starts. This peak in the friction force is generally described as "stiction".

The stiction force, F_s, encountered at the startup of a disk can be expressed as follows:

$$F_s = \mu(W_s + F_m) + F_v \qquad (2)$$

where μ is the coefficient of friction, W_s is the suspension load of the slider, F_m is the meniscus force, and F_v is the viscous force in the lubricant film.

Figure 4
Crater-shaped laser bump.

The meniscus force, F_m, is related to the presence of lubricant films or adsorbed water films on the disk surface. A number of models have been developed to predict stiction as a function of design parameters and environmental conditions (Gui and Marchon 1995, Zhao and Talke 1999b).

4.2 Laser Zone Texturing of Disks

A large stiction force can prevent the motor from starting the disk drive after shutdown of the drive. In order to prevent failure of the head/disk interface owing to excessive stiction, texturing of the disk surface in the start/stop region of a magnetic disk has been implemented using laser texturing. Laser texturing is performed by focusing a laser beam onto the disk surface and creating a number of small and evenly spaced "bumps" in the "landing" zone of the disk by localized melting of the disk surface (Fig. 4). The height and size of the individual laser "bumps"
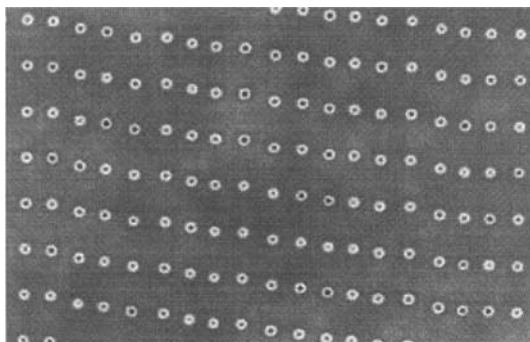
Figure 5
Array of laser bumps with bump spacing between rows of 40 μm.

Figure 6
Ramp load/unload mechanism.

can be adjusted by the energy level and pulse duration of the laser pulse, resulting in a well-controlled surface roughness of the landing zone (Baumgart *et al.* 1995). During contact of the slider on this landing zone, the formation of meniscus areas is restricted to the areas around the "bumps." Thus, the stiction force is controlled by the number and shape of the laser bumps. Because of this, stiction of laser-textured disks is much less sensitive to changes in the environmental conditions or the number of CSS cycles. An array of laser bumps with a pitch distance of approximately 40 μm between rows is shown in Fig. 5.

4.3 Load/Unload

Laser zone texturing becomes ineffective if the height of the laser bumps is required to decrease to less than 10 nm. To avoid high stiction of the head/disk interface in the latter case, ramp load/unload has been introduced as an alternative to laser texturing. In the case of ramp load/unload, the slider is loaded onto the disk during startup of the drive using the ramp mechanism shown in Fig. 6. During shutdown of the drive, the slider is lifted from the disk surface using the ramp mechanism. The use of a ramp load mechanism avoids stiction completely during start/stop. Ramp load/unload is difficult to implement, however, because of severe tolerance requirements during assembly. Ramp load/unload mechanisms are used mainly in laptop computers, but have begun to appear also in 95 mm hard disk drives.

5. Wear

Wear of the head/disk interface occurs on both the slider and the disk as the result of head/disk interactions during CSS or steady-state operation. Wear of sliders and rigid disks can occur as adhesive wear,

abrasive wear, impact wear, or tribochemical wear. Intermittent slider/disk impacts during steady-state operation lead to impact wear. In addition, tribochemical wear occurs if oxygen from the atmosphere absorbs chemically on the surface of the carbon layer, leading to the formation of surface oxides. Thermal desorption of these species leads to the formation of CO and CO_2, which depletes the surface of carbon. For lubricated disks, the lubricant film tends to act as a chemical barrier, thereby reducing the occurrence of tribochemical wear in favor of other types of wear (Talke 1995).

Disks and sliders are typically coated with a thin layer of carbon to protect the magnetic materials from wear and corrosion. Carbon overcoats used for rigid disks and sliders are typically diamond-like carbon (DLC), amorphous DLC (a-C), hydrogenated DLC (a-C:H), and nitrogenated DLC (a:CN$_x$) (Grill 1997). Hydrogenated carbon films (a-C:H) show generally improved wear performance over a-C films. The hardness and the elastic modulus of DLC increase with hydrogen concentration in the DLC because hydrogen tends to increase sp^3 bonds in DLC (Lee *et al.* 1992). Incorporation of nitrogen in DLC also improves the wear resistance of DLC films. Nitrogenated films have gained wide application as thin-film disk and slider overcoats.

6. Lubricants and Additives

In general, perfluorinated polyethers (PFPE) are used for disk lubrication since they have good load carrying capability and exhibit a very low vapor pressure. Sliding contact between a slider and a disk tends to remove the lubricant in the sliding track. To prevent lubricant depletion, a disk lubricant should have good mobility so that it can recoat areas of the disk depleted from lubricant. However, since high mobility

Table 1
Molecular structures of typical commercial disk lubricants.

Tradename	Molecular structure	End group
Fomblin Y	$CF_3O[CF(CF_3)CF_2O]_n–(CF_2O)_m–CF_3$	$–CF_3$
Krytox AD	$F–[CF(CF_3)CF_2O]_m–CF_2CF_3$	$–F, –CF_3$
Fomblin Z	$CF_3O(CF_2CF_2O)_n–(CF_2O)_m–CF_3$	$–CF_3$
Demnum	$F–(CF_2CF_2CF_2O)_n–CF_2CF_3$	$–F, –CF_3$
Fomblin Z-DOL	$HO–CH_2CF_2O–(CF_2CF_2O)_n–(CF_2O)_m–CF_2CH_2–OH$	$–OH$
Fomblin AM2001	$P–CH_2OCH_2CF_2–(CF_2CF_2O)_n–(CF_2O)_m–CF_2CH_2OCH_2–P$	$–CH_2–phe=(O)_2=CH_2$

increases lubricant spin-off, a compromise must be made between mobility and bonding. A number of commonly used disk lubricants is shown in Table 1 (Homola 1996).

Most disk lubricants exhibit thermal degradation problems when exposed to elevated temperatures. Furthermore, PFPE are susceptible to catalytic decomposition when in contact with Al_2O_3, a common slider material component. To reduce the degradation of disk lubricants caused by Al_2O_3 it is customary to eliminate the exposure of disk lubricants to Al_2O_3 by coating the slider surface with a thin carbon film. Another option is to use additives in the lubricant such as X-1P (Perettie *et al.* 1999). However, difficulties with phase separation have been observed with phosphazine additives at high temperature and humidity owing to the fact that these additives are insoluble in PFPE-based oils (Kang *et al.* 1999).

7. Future Trends in Tribology of Rigid Media

To increase the recording density to $100\,Gbits\,in^{-2}$ ($15.5\,Gbits\,cm^{-2}$), it is anticipated that the flying height of the slider must be of the order of 5 nm, that the carbon overcoat on the slider and the disk should be reduced to less than 2–3 nm, and that the root mean square surface roughness be approximately 0.2 nm.

Owing to the complexity of these requirements, the question arises as to whether it would not be better to implement contact recording, in which case the air bearing between the slider and the disk would be eliminated completely. Although the latter situation is highly desirable, contact recording would require an extremely lightly loaded slider/disk interface in order to keep wear of the slider and the disk within acceptable limits (Talke 1995). Furthermore, a lightly loaded interface is prone to stick/slip and friction-induced vibration, making this approach all but technically unfeasible. However, the trend towards reduced flying heights will continue and lower and lower flying heights will be implemented in future disk-drive products. Thus, even more difficult tribology problems will be encountered.

See also: Magnetic Recording: Rigid Media, Preparation; Magnetic Recording Devices: Head/Medium Interface; Magnetic Recording Rigid Media, Recording Properties; Magnetic Recording Technologies: Overview

Bibliography

Baumgart P, Krajnovich D J, Nguyen T A, Tam A C 1995 A new laser texturing technique for high performance magnetic disk devices. *IEEE Trans. Magn.* **31**, 2946–51

Grill A 1997 Tribology of diamondlike carbon and related materials: an updated review. *Wear* **94–95**, 507–13

Gui J, Marchon B 1995 A stiction model for a head–disk interface of a rigid disc drive. *J Appl. Phys.* **78**, 4206–17

Homola A M 1996 Lubrication issue in magnetic disk storage devices. *IEEE Trans. Magn.* **32**, 1812–8

Hu Y, Bogy D B 1996 Dynamic stability and spacing modulation of sub-25 nm fly height sliders. *ASME J. Trib.* **119**, 646–52

Kang H J, Perettie D J, Talke F E 1999 A study of phase separation characteristics of perfluoropolyethers/phosphazene (x-1p) lubricant mixtures on hard disk surfaces. *IEEE Trans. Magn.* **35**, 52385–7

Lee H J, Lee J K, Zubeck R, Smallen M, Hollars D 1992 Properties of sputtered-deposited hydrogenated carbon films as a tribological overcoat used in rigid magnetic disks. *Surf. Coat. Technol.* **54–55**, 552–6

Perettie D J, Morgan T A, Zhao Q, Kang H J, Talke F E 1999 The use of phosphazene additives to enhance the performance of PFPAE lubricants. *J. MMM* **193**, 318–21

Talke F E 1995 On tribological problems in magnetic disk recording technology. *Wear* **190**, 232–8

Wahl M H, Lee P, Talke F E 1996 An efficient finite element-based air bearing simulator for pivoted slider using bi-conjugate gradient algorithms. *Trib. Trans.* **39**, 130–8

Zhao Q, Talke F E 1999a Effect of environmental conditions on the stiction behavior of laser textured hard disk media. *Trib. Int.* **33**, 281–7

Zhao Q, Talke F E 1999b Stiction and deformation analysis of laser textured media with crater-shaped laser bumps. *Trib. Trans.* **43** (1), 1–8

F. E. Talke
University of California, San Diego, La Jolla California, USA

Magnetic Recording: VHS Tapes

The home video market is massive and is the dominant form of magnetic media sold in the world market. Estimated world sales for VHS (Video Home System) media for 1988 were equivalent to 2686 million E180 cassettes shipped at a total factory gate price of $3335 million. Figure 1 shows a comparison of VHS sales to other media. Originally used primarily for recording of TV programs for later viewing, use has now extended to home viewing of pre-recorded film, camcorder applications, and is making inroads into multimedia PC programs.

Although VHS is the most popular video system, its technology has been overtaken by other formats. However, because of the large number of video machines in homes and the considerable investment in prerecorded film for sale and rental, it is likely to remain the dominant system until replaced by digital technology. There have been some additions to the
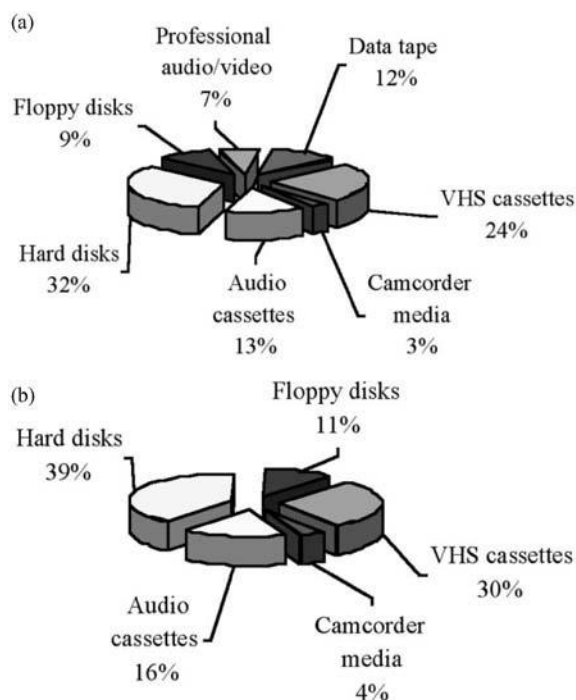
Figure 1
Chart of total sales of VHS media compared to other major magnetic storage media for 1988. Because some sales are in the form of prerecorded tape, estimates of VHS sales have been converted into the form of E180 cassettes (estimates by the Magnetic Media Information Service). (a) Total sales for 1998 as a percentage of total value ($13.833 billion.) (b) Total sales for 1998 as a percentage of total units (10.627 billion units.)

format that allow stereo sound to be recorded, a long-play facility with slower tape speed, a compact cassette version for use in camcorders which can then be played in a standard video cassette recorder (VCR) using an adapter, and a super VHS (S-VHS) with improved performance quality. S-VHS requires a special machine and tapes to take advantage of the improved quality but is backward compatible with standard VHS tapes.

VHS tape sales are very competitive and prices have fallen dramatically over time. This has reduced profit margins so that many of the large media producers have withdrawn from the business to concentrate on more profitable "high-tech" media applications or have transferred production to low-cost regions of the world such as China and the East Asian Pacific Rim countries.

1. The VHS Format

VHS is a helical scan system with the record/replay heads mounted on a drum that rotates at an angle to the tape transport direction. This produces recorded data tracks at an angle to the tape direction. This angle is dependent on the TV format and allows a relatively high head speed across the tape surface at a slow tape speed producing an efficient use of the recording area for the serially recorded signals (for the 625 line–50 field TV system, the angle of scan is $5° 57' 50.3''$ at a head speed of $3.92 \, \mathrm{ms}^{-1}$ and a tape speed of $23.39 \, \mathrm{mms}^{-1}$ (EN 60774 1994)). For a detailed description of helical scan recording see Mee and Daniel (1996).

With all removable media systems it is important that exact standards are applied to the media to allow writing and replay in different machines and maintenance of replay quality under a range of changing conditions. Standards were originally established by JVC, the manufacturer who developed VHS, but detailed specifications are now incorporated into international standards (e.g., European Standard EN60774-1). Many of the details are mechanical, such as the dimensions of the cassette (104 mm × 188 mm × 25 mm), the reel dimensions (62 mm diameter), and the tape winding path and its control. The tape has a specified width of $12.65 \, \mathrm{mm} \pm 0.01 \, \mathrm{mm}$ (0.5 in) and a maximum thickness of 20.0 μm including the magnetic coating. Playing times are specified as 30 min, 60 min, 90 min, 120 min, and 180 min, which are determined by the length of tape in the cassette. Modern VCRs usually have a long-play facility that doubles the playing time by reducing the tape speed. This does produce some loss of quality but modern head technology minimizes noise levels.

The magnetic coating has to be of a high resolution, longitudinally oriented, and with a coercivity of approximately $50 \times 10^3 \, \mathrm{Am}^{-1}$ (628 Oe). Invariably the magnetic coating consists of acicular oxide

particles, usually cobalt-modified iron oxide (γ-Fe$_2$O$_3$) although chrome dioxide (CrO$_2$) can be used. The latter is reputed to have a better high-frequency response, but the cost is generally higher than for iron oxide. Most CrO$_2$ tapes on the market now contain a mixture of CrO$_2$ and cobalt γ-Fe$_2$O$_3$ to limit price.

2. *Magnetic Particles*

The properties of magnetic particles determine the final magnetic properties of the manufactured tape. Magnetostatic interactions between particles play an important role in determining properties such as coercivity, and the measured values for individual particles, pigments, and tapes can be very different (McConochie *et al.* 1996). Magnetic properties of particles are described in detail in *Magnetic Recording Materials: Tape Particles, Magnetic Properties*. Ideally all particles should be single domain with identical magnetic properties. In practice this is not possible, but particles are manufactured so that parameters such as volume and aspect ratio have as narrow a distribution as possible. Typically particles have a length of about 600 nm and an aspect ratio of 6:1. Ferric oxide particles are the most commonly used, but basic γ-Fe$_2$O$_3$ has a coercivity controlled primarily by shape anisotropy and can only be used to make tapes with coercivities up to about 25×10^3 Am^{-1} ($\sim$300 Oe). To increase this further, particles are surface doped with cobalt. CrO$_2$ has a higher intrinsic coercivity partly associated with crystal anisotropy and is suitable for VHS applications in its basic form.

3. *Media Production*

The magnetic tape coating consists of small magnetic particles dispersed in a nonmagnetic polymer matrix with additional nonmagnetic particles for other important functions. A wet dispersion of all the components is produced which is then coated onto plastic film and dried. The tape formulation is proprietary and each tape manufacturer will have its own choice of components. Manufacturers of precursors often have test formulations that are freely available to customers and produce an acceptable final product. All dispersions have essentially the same components that serve the same specific general functions as follows:

(i) Magnetic particles—see above.

(ii) Wetting agents—usually a surfactant whose function is to coat the magnetic particles and prevent agglomeration after dispersion. Some part at least can be replaced by "wetting" polymer resins, which have functional groups effective in wetting. This reduces the final wetting agent content of the tape to the advantage of wear and friction. Although originally developed for advanced particulate media manufacture, they are in common use for commodity products such as VHS.

(iii) Polymer resins—to produce the final solid matrix and generally comprising a mixture of several types which can be classified as soft, such as polyurethane, and hard, such as vinyl. The correct combination determines the final mechanical properties of the tape, e.g., stiffness and temperature resistance characteristics, which are important for controlling properties such as magnetostriction associated with changing magnetic properties, as particles are stressed and the matrix is strained during tape flexure.

(iv) Cross-linking agents—added just before final coating of the tape to strengthen the polymer matrix and to ensure that particles are strongly bound.

(v) Solvents—to dissolve the resins and the wetting agents.

(vi) Carbon black—to reduce static electricity in the tape.

(vii) Lubricants—additional surfactants and other lubricants which are incorporated into the matrix. These leach out during the life of the tape to lubricate the surface and ensure smooth transit across the heads and guides during record and replay.

(viii) Abrasives—such as aluminum oxide particles, which help to clean debris and deposits from heads and other parts in contact with the tape during use.

Magnetic particles are supplied by pigment manufacturers in a clustered form to aid handling of what, individually, would be a very fine and hazardous powder of particles with the dimensions of smoke grains. The main function of the wet dispersion process is to separate these particles without damaging them to produce a slurry of monodispersed magnetic particles which can be coated and oriented. This dispersion is very important in determining the final quality of the tape. Not only does it affect the ability of particles to be oriented by application of a magnetic field during production, but poorly dispersed particles will increase the roughness of the tape surface and affect noise characteristics (Clarke *et al.* 1991). A detailed discussion of wet dispersions can be found in *Magnetic Recording Media: Particulate Dispersions* but the essential processes of tape manufacture are as follows:

(i) Premixing—some of the components including the magnetic particles, wetting agents, and a portion of the solvents are mixed at high shear to wet the particle surfaces and exclude any water adsorbed on the surfaces.

(ii) Milling—the components are mixed in a bead mill or similar device to generate shear and separate particles. Milling times and rates are important as "over milling" generates broken particles whereas "under milling" leaves agglomerates in the system. Broken particles will have a low switching field or may be superparamagnetic and are detrimental to the recording properties of the tape resulting in "print through" and a lower saturation remanence.

Agglomerates will cause an increase in the tape noise and poor orientation.

(iii) Let down—additional solvents are added to control the final viscosity of the slurry ready for coating. This stage has to be completed carefully to prevent solvent shock, which can cause flocculation of the particles.

(iv) Filtering—any remaining agglomerates or oversized particles are removed by passing through a fine mesh filter.

(v) Coating—the final wet dispersion is applied to a plastic substrate using a knife coater or gravure roller. This is part of the mass-production process. Coating is at high speed onto wide plastic webs.

(vi) Orientation—immediately after coating and before the film has dried, the web is passed through an arrangement of magnets that increases particle alignment along the tape axis.

(vii) Drying—the web is then passed through an oven where the solvents are driven off and collected for recycling. The dried web is then wound onto rolls and stored to allow further curing of the polymers.

(viii) Calendaring—the web is passed between heated rollers that have specially prepared paper-coated surfaces. High pressure is applied so that the combination of heat and pressure produces a smooth tape surface. This is important in maintaining a good head/tape contact in the record and replay processes to minimize asphericity and surface roughness noise.

(ix) Back coating—a nonmagnetic layer containing carbon black is coated onto the back surface of the web. This prevents slippage during use and also reduces buildup of electrostatic charge.

The large rolls of completed media, referred to as jumbos, are then slit to the final tape width, slitting debris is removed, and the tape is wound onto individual reels, called pancakes. In a separate process, tape is spliced to plastic leader tapes already attached to reels in cassettes and the appropriate length of tape is loaded ready for final labeling and packaging of the cassettes.

4. Media Properties

The performance of a tape is defined in terms of its recording and replay properties, and characteristics such as signal to noise ratio. These are specified in the international standards and comparison is made to a reference tape VRT-2, which can be provided by JVC. In practice, having established particle supply and the tape production process, quality can be controlled by static magnetic measurements using a vibrating sample magnetometer. The only static magnetic property identified in the standards is the approximate coercivity ($50 \times 10^3 \, \text{Am}^{-1}$). However, in general all tapes have very similar major hysteresis loop shape and characteristics. Figure 2 shows the major hysteresis loop for a typical proprietary VHS tape, measured in the tape direction and transverse to
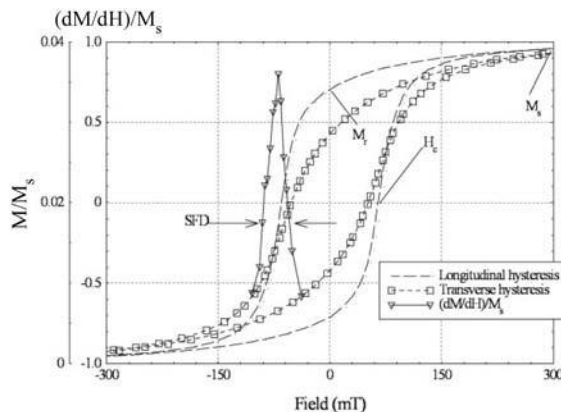
Figure 2
Hysteresis loops for a cobalt γ-Fe$_2$O$_3$ VHS tape measured along the tape axis direction and transverse to it. The differential of the hysteresis is also shown and indicates the switching field distribution measured at half height.

it. The effect of particle orientation can be clearly seen by comparison of the shape of the two loops. Listed below are some parameters that have been devised to characterize recording media and values measured for this sample.

(i) Coercivity, H_c ($52 \, \text{kAm}^{-1}$ ($648 \, \text{Oe}$))

(ii) Saturation magnetization, M_s, usually expressed as a moment per unit area ($490 \, \text{Am}^{-3}$ ($49 \, \text{memucm}^{-2}$))

(iii) Remanent magnetization, M_r ($370 \, \text{Am}^{-3}$ ($37 \, \text{memucm}^{-2}$))

(iv) Squareness, M_r/M_s (0.76)

(v) Orientation ratio, $M_{r[\text{in tape direction}]}:M_{r[\text{transverse}]}$ (1.67)

(vi) Switching field distribution (SFD), obtained by differentiating the hysteresis loop. This produces a peak around the coercivity. The SFD is defined as the peak width at half height ($27 \, \text{kAm}^{-1}$ ($340 \, \text{Oe}$))

(vii) Coercivity squareness, S^*, a measure of the steepness of the loop at the crossing point (0.68). It is defined by (Köster 1984):

$$\left(\frac{\text{d}M}{\text{d}H}\right)_{M=0} = \frac{M_r}{H_c(1 - S^*)}$$

5. Camcorder Applications

A major use of video tape is for camcorder recording. The standard VHS tape is far too cumbersome for this application and so a compact VHS cassette has been developed. This uses the standard 12.65 mm tape but in a cassette measuring $59 \, \text{mm} \times 92 \, \text{mm} \times 22.5 \, \text{mm}$, which is about a quarter of the volume of a standard cassette. The compact cassette can be inserted into an

adapter, which then allows it to be replayed or edited in a standard VHS VCR. There are rivals for analogue camcorders, the most notable being the 8 mm system, which like the later development of Hi8 use 8 mm wide tape in a much more compact cassette and an increased coercivity. The 8 mm tapes are based on metal particles, usually passivated iron, and the Hi8 uses either metal evaporated tape or advanced metal particles. The 8 mm systems have an improved response over VHS. However, in spite of taking a large part of the camcorder market, 8 mm VCR machines have failed to make much impact on the television-related use for time shifting and replay of prerecorded "videos." Digital camcorders are now available and these will replace the older VHS and 8 mm analogue systems very rapidly.

6. Prerecorded Tape

Much of the tape that is produced is sold with prerecorded films and other entertainment material. Making copies used to involve playing a master tape on one VCR that was re-recorded on a number of copy machines. This process is very slow, equipment intensive, and is not cost effective. A process of anhysteretic duplication has been developed that produces a magnetic image of a master tape in a high-speed process.

The principles of the technique are based on anhysteretic remanence. This process involves the application of a small d.c. bias magnetic field to a magnetic sample subjected to a saturating a.c. field which is then slowly removed. The d.c. bias field is then removed and a remanent magnetization is left. Figure 3 shows the anhysteretic remanent magnetization (ARM) as a function of d.c. bias field for a typical VHS tape.
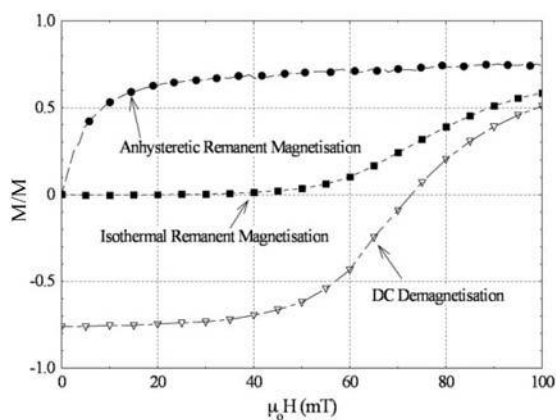
Figure 3
ARM for a cobalt γ-Fe_2O_3 VHS tape. Isothermal remanent magnetization and d.c. demagnetization curves are included for comparison.

For comparison, the isothermal remanence (IRM) and the d.c. demagnetization remanence (DCD) are also shown. The IRM curve is a plot of the remanence produced by the application of a d.c. magnetic field to an initially a.c. demagnetized specimen while the DCD curve is a plot of the remanence produced in an initially negatively saturated sample. The IRM and DCD curves are used extensively as an indication of the nature of interactions in recording media (Spratt *et al*. 1988, Kelly *et al*. 1989). The steep slope of the initial anhysteretic curve is evident in Fig. 3.

In anhysteretic duplication, a mirror image of the required video tape is produced on a master tape. When placed in contact with a blank VHS tape (magnetic surfaces together) and subjected to an a.c. field, the stray fields from the master tape magnetic recording are sufficient to produce an anhysteretic magnetic image imprinted on the VHS tape. It is clear that if the master tape is to withstand demagnetization in the process, the a.c. field must be sufficient to saturate the VHS tape but small enough so as not demagnetize the master tape, which must have a high coercivity (typically $160 \times 10^3 \, Am^{-1}$ (2 kOe)).

7. Signal Loss and Archival Problems

Tape replay is a dynamic process involving a magnetic interaction between the tape and the replay head. This produces a change in the magnetization of the tape that has to be reversible if the recorded signal is to remain unchanged. Magnetic changes do not affect the basic structure of the tape, unlike mechanical deterioration, which can result from replay in poorly maintained VCRs. Magnetic deterioration is not evident from visual inspection and re-recording restores the good quality video signal. First generation tapes did exhibit a signal loss with replay that was identified as being related to magnetostriction effects (Flanders 1976, Flanders *et al*. 1979). However, changes in formulation to reduce particle stresses improved tape performance. This effect was not evident in later generations of particles and this type of signal loss is no longer regarded as a problem in commercial tapes. However, some problems do still exist. All tapes are subject to dropouts associated with localized physical or magnetic defects where the recorded signal is defective or unstable. With replay, these dropouts increase in number resulting in a "snowy" TV image. Magnetic debris trapped on guides and heads can also cause signal loss, which is evident as missing lines on the TV image. With continual replay these can merge into bands and are referred to as magnetic scratching (S-Ararghi *et al*. 1992). Replay can also lead to a general increase in noise levels (McCann *et al*. 1999). This is believed to be a result of magnetostriction as identified in the signal loss of first generation tapes but at a much lower level so that it is only observed in the noise signal.

8. Conclusions

The VHS system has to be regarded as a commercial success story. Having been adopted as the preferred home video system, production of VCRs and video tape has produced one of the major volume storage media products. Although the technology has been surpassed by other systems, there is a tremendous inertia to change generated by the high domestic investment in machines and availability of prerecorded tapes. The VHS system is likely to remain the preferred medium for some time and will only be replaced with the move to digital recording.

See also: Magnetic Recording Materials: Tape Particles, Magnetic Properties; Magnetic Recording Media: Particulate Dispersions; Magnetic Recording Devices: Inductive Heads, Properties; Magnetic Recording Technologies: Overview

Bibliography

Clarke M D, Bissell P R, Chantrell R W, Gilson R G 1991 Experimental studies of particulate recording media noise. *J. Magn. Magn. Mater.* **95**, 17–26
EN 60774-1 Part 1 1994 VHS and compact VHS video cassette system. *European Standard*. European Committee For Electrotechnical Standardization
Flanders P J 1976 Changes in recording tape magnetization produced by stress. *IEEE Trans. Magn.* **MAG-12**, 348–55
Flanders P J, Kaganowicz G, Takei Y 1979 Magnetostriction and stress-induced playback loss in magnetic tapes. *IEEE Trans. Magn.* **MAG-15**, 1065–8
Kelly P E, O'Grady K, Mayo P I, Chantrell R W 1989 Switching mechanisms in cobalt–phosphorus thin films. *IEEE Trans. Magn.* **25**, 3880–3
Köster E 1984 Recommendation of a simple and universally applicable method for measuring the switching field distribution of magnetic recording media. *IEEE Trans. Magn.* **20**, 81–3
McCann S M, Bissell P R, Onions T, Gilson R G 1999 Effects of playback on saturation remanent state noise. *J. Magn. Magn. Mater.* **193**, 362–5
McConochie S R, Schmidlin F, Bissell P R, Gotaas J A, Parker D A 1996 Interaction effects from reversal studies of single particles. *J. Magn. Magn. Mater.* **155**, 89–91
Mee C D, Daniel E D 1996 *Magnetic Storage Handbook*, 2nd edn. McGraw Hill, New York
S-Araghi M, Bissell P R, Chantrell R W, Loyd R A 1992 Reptation effects as a mechanism for localized demagnetization in video tapes. *J. Magn. Magn. Mater.* **5**, 160–3
Spratt G W D, Bissell P R, Chantrell R W, Wohlfarth E P 1988 Static and dynamic experimental studies of particulate recording media. *J. Magn. Magn. Mater.* **75**, 309–18

Magnetic Refrigeration at Room Temperature

Magnetic refrigeration, based on the magnetocaloric effect (MCE), has recently received increased attention as an alternative to the well-established compression–evaporation cycle for room-temperature applications. In the magnetic refrigeration cycle, depicted in Fig. 1, initially randomly oriented magnetic moments are aligned by a magnetic field, resulting in heating of the magnetic material. This heat is removed from the material to the ambient by heat transfer. On removing the field, the magnetic moments randomize, which leads to cooling of the material below ambient temperature. Heat from the system to be cooled can then be extracted using a heat-transfer medium. Depending on the operating temperature, the heat-transfer medium may be water (with antifreeze) or air, and for very low temperatures helium. Therefore, magnetic refrigeration is an environmentally friendly cooling technology. It does not use ozone depleting chemicals (CFCs), hazardous chemicals (NH_3), or greenhouse gases (HCFCs and HFCs). Another key difference between vapor-cycle refrigerators and magnetic refrigerators is the amount of energy loss incurred during the refrigeration cycle. The cooling efficiency in magnetic refrigerators working with gadolinium has been shown (Zimm *et al.* 1998) to reach 60% of the theoretical limit, compared to only $\sim 40\%$ in the best gas-compression refrigerators. This higher energy efficiency will also result in a reduced CO_2 release. However, with most magnetic materials, this high efficiency is only realized in high magnetic fields, 5 T. Therefore current research aims at new magnetic materials displaying larger magnetocaloric effects, which then can be operated in lower fields, ~ 2 T, that can be generated by permanent magnets.

The heating and cooling described above is proportional to the size of the magnetic moments and the
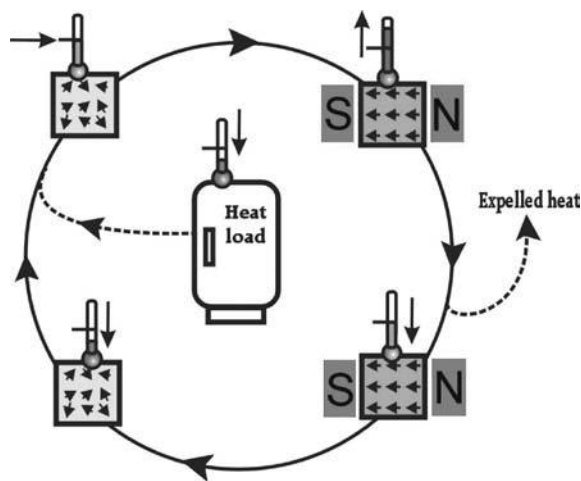
Figure 1
Schematic representation of a magnetic-refrigeration cycle, that transports heat from the heat load to the ambient. The lighter- and darker-shaded square containers depict material in low and high magnetic field, respectively.

applied magnetic field. This is the reason that, now-adays, research in magnetic refrigeration is almost exclusively conducted on super-paramagnetic materials and on rare-earth compounds (Tishin 1999). For room-temperature applications like refrigerators and air-conditioners, compounds containing manganese should be a good alternative. Manganese is a transition metal with high abundance. Also, there exist in contrast to rare-earth compounds, an almost unlimited number of manganese compounds with critical temperatures near room temperature. However, the magnetic moment of manganese generally is only about half the size of heavy rare-earth elements. Enhancement of the caloric effects associated with magnetic moment alignment may be achieved through the induction of a first order phase-transition or better, a very rapid change of magnetization at the critical temperature, which will bring along a much higher efficiency of the magnetic refrigerator. In combination with currently available permanent magnets, this will open the path to the development of small-scale magnetic refrigerators, which no more rely on rather costly and service-intensive superconducting magnets. Another prominent advantage of magnetocaloric refrigerators is that the cooling power can be varied by scaling from milliwatt to a few hundred watts.

Following the discovery of a sub-room-temperature giant-MCE in the ternary compound $Gd_5(Ge_{1-x}Si_x)_4$ $(0.2 \leqslant x \leqslant 0.5)$ (Pecharsky and Gschneidner 1997), there is a strongly increased interest from both fundamental and practical points of view to study the MCE in Gd-based materials (Choe *et al.* 2000, Morellon *et al.* 2000). The common feature of these compounds is that they undergo a first-order structural and magnetic phase transition, which leads to a giant magnetic field-induced entropy change, across their ordering temperature. Many other materials have been studied with respect to their (magneto-caloric) properties, here we will mention only a few of them. The lanthanum–manganese–perovskite oxides $La_{1-x}Ca_xMnO_3$ show considerable MCE values (Zhang *et al.* 1996, Hueso *et al.* 2002). Transition metal pnictides such as $MnP_{1-x}As_x$ (Krokozinsky *et al.* 1982) and chalcogenites such as Cr_3Te_4 (Hashimoto 1981) have been studied. The nearly equiatomic alloy FeRh undergoes a magnetic and structural order–order transformation and exhibits giant MCE between 296 K and 316 K but its MCE is irreversible and disappears after the first application of the magnetic field (Annaorazov *et al.* 1992, 2002). The Heusler alloys Ni–Mn–Ga show large magnetic-entropy changes that are due to an abrupt change of the magnetization near the martensite–to–austenite structural transition (Hu *et al.* 2000, 2001a). The compound $La(Fe,Co)_{11.83}Al_{1.17}$ with a very low rare-earth content, also shows a considerable magnetocaloric effect (Hu *et al.* 2001b). The MCEs in most transition-metal-based alloys are lower than those in lanthanide-based alloys for the same

temperature range, especially if one takes into account the fact that ΔT also depends on the specific heat of the compound (Pecharsky *et al.* 2001). This makes them unlikely candidates for use as magnetic refrigerant materials below room temperature. However, above room temperature there exist only a very limited number of rare-earth compounds exhibiting magnetic ordering, a prerequisite for showing large magnetocaloric effects. Fortunately, there exist many manganese compounds, such as MnAs (Pytlik and Zieba 1985), which display a variety of structural and magnetic phase transitions in the relevant temperature range. For a working material in a magnetic refrigerator it is however essential that the phase transition is also reversible.

1. Theoretical Considerations

When a material is magnetized in an applied magnetic field, the entropy associated with the magnetic degrees of freedom, the so-called magnetic entropy S_m, is changed as the field changes the magnetic order of the material. Under adiabatic conditions, ΔS_m must be compensated by an equal but opposite change of the entropy associated with the lattice, resulting in a change in temperature of the material. This temperature change, ΔT_{ad}, is usually called the magnetocaloric effect. It is related to the magnetic properties of the material through the thermodynamic Maxwell relation

$$\left(\frac{\partial S}{\partial B}\right)_T = \left(\frac{\partial M}{\partial T}\right)_B \quad (1)$$

For magnetization measurements made at discrete temperature intervals, ΔS_m can be calculated by means of

$$\Delta S_m(T, B) = \sum_i \frac{M_{i+1}(T_{i+1}, B) - M_i(T_i, B)}{T_{i+1} - T_i} \Delta B \quad (2)$$

where $M_{i+1}(T_{i+1}, B)$ and $M_i(T_i, B)$ represent the values of the magnetization in a magnetic field B at the temperatures T_{i+1} and T_i, respectively. On the other hand, the magnetic entropy change can be obtained more directly from a calorimetric measurement of the field dependence of the heat capacity by integration:

$$\Delta S_m(T, B) = \int_0^T \frac{C(T', B) - C(T', 0)}{T'} dT' \quad (3)$$

where $C(T, B)$ and $C(T, 0)$ are the values of the heat capacity measured in a field B and in zero field, respectively. It has been confirmed that the values of $\Delta S_m(T, B)$ derived from the magnetization measurement coincide with the values from calorimetric measurement (Gschneidner *et al.* 1999, Tegus *et al.* 2002b).

The adiabatic temperature change can be integrated numerically using the experimentally measured or theoretically predicted magnetization and heat capacity:

$$\Delta T_{ad}(T, B) = - \int_0^B \frac{T}{C(T, B')} \left(\frac{\partial M}{\partial T}\right)_B dB' \qquad (4)$$

Obviously, the MCE is large when $\left(\frac{\partial M}{\partial T}\right)_B$ is large and $C(T, B)$ is small at the same temperature. Since $\left(\frac{\partial M}{\partial T}\right)_B$ peaks at the magnetic ordering temperature, a large MCE is expected close to this magnetic phase transition.

Recently we discovered that $MnFeP_{1-x}As_x$ compounds exhibit a large magnetic entropy change (Tegus *et al.* 2002a), of a similar magnitude as the so-called giant MCE material $Gd_5Ge_2Si_2$, but whose optimum use temperature is at and above room temperature. This result is of significant practical importance, because it makes these compounds excellent working materials for magnetic refrigeration in household refrigerators or air-conditioning.

In the intermediate composition range ($0.15 \leqslant x \leqslant 0.66$), compounds in the $MnFeP_{1-x}As_x$ system crystallize in the hexagonal Fe_2P-type of structure. They have most interesting magnetic properties including a field-induced first-order magnetic transition (Zach *et al.* 1990). Polycrystalline samples can be synthesized starting from the binary Fe_2P and $FeAs_2$

compounds, Mn chips and P powder mixed in the appropriate proportions by ball milling under a protective atmosphere. After this mechanical alloying process one obtains amorphous powder. To obtain dense material of the crystalline phase, the powders are pressed to pellets and sealed in molybdenum tubes under an argon atmosphere. These are heated at 1273 K for 120 h, followed by a homogenization process at 923 K for 120 h and finally by slow cooling to ambient conditions. The powder x-ray diffraction patterns show that the compound crystallizes in the hexagonal Fe_2P-type structure. In this structure the Mn atoms occupy the three(g) sites, the Fe atoms occupy the three(f) sites and the P and the As atoms occupy two(c) and one(b) sites statistically (Bacmann *et al.* 1994). From the broadening of the x-ray diffraction reflections, the average grain size is estimated to be ~ 100 nm.

Figure 2 shows the change in critical temperature on the application of a magnetic field. As pointed out by Pecharsky *et al.* (2001), this change in critical temperature is a good indication for the temperature change induced by the application of a magnetic field. The inset of Fig. 2 shows the temperature dependence of the magnetization near room temperature of $MnFeP_{0.45}As_{0.55}$ and Gd (Alfa Aesar3N) as determined in an applied magnetic field of 1 T. It is obvious that the change in magnetization in $(Mn,Fe)_2$ (P,As) compounds at the ordering temperature T_c is much larger, despite the fact that the magnetic
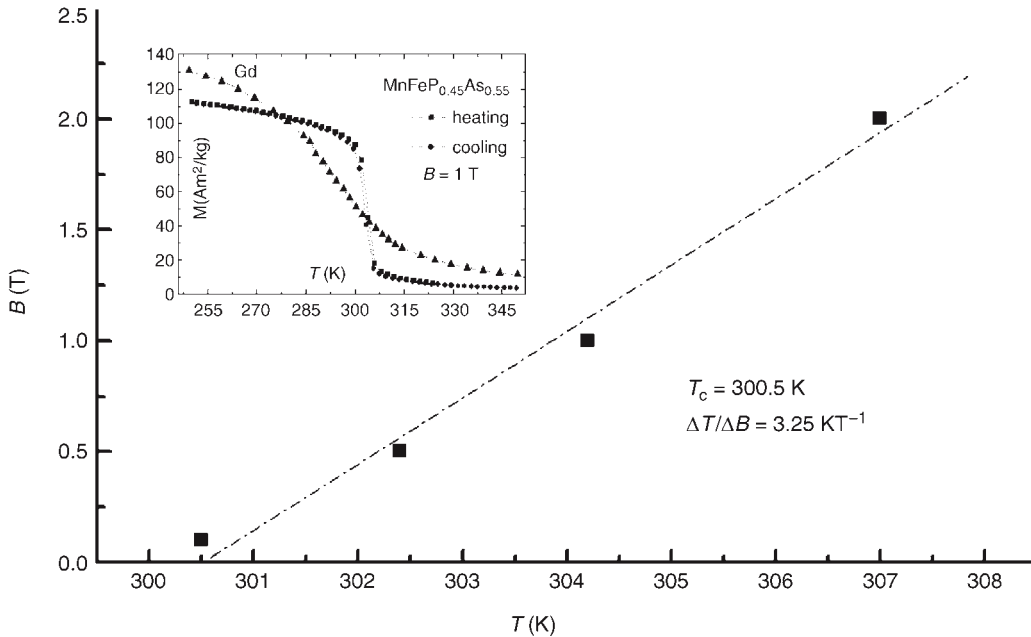
Figure 2
Variation of critical temperature with applied magnetic field, the line is a least square fit of the data. Inset: Temperature dependence of the magnetization for $MnFeP_{0.45}As_{0.55}$ and Gd measured with increasing (heating) and decreasing (cooling) temperature in a field of 1 T.

moment of Gd is much larger at low temperatures 248 Am^2kg^{-1} compared to 125 Am^2kg^{-1}. Variation of the P/As ratio between 3/2 and 1/2 makes it possible to tune T_c and the optimal operating temperature between 200 K and 350 K ($-70\,°C$ and $80\,°C$), without losing the large magnetocaloric effect. The inset shows the temperature dependence of the magnetization measured with increasing and decreasing temperature in an applied field of 1 T. The thermal hysteresis is signature of a first-order phase transition. Because of the small size of the thermal hysteresis (<1 K), the magnetization process can be considered as being reversible in temperature. From the magnetization curve at 5 K, the saturation magnetization was determined as 3.9 μ_B/f.u. This high magnetization originates from the parallel alignment of the Mn and Fe moments, though the moments of Mn are much larger than those of Fe (Beckmann and Lundgren 1991). Variation of the Mn/Fe ratio may also be used to further improve the magnetocaloric effect.

We calculated the magnetic-entropy changes, ΔS_m, from magnetization data by means of the Eqn. (2). The results are shown in Fig. 3. The calculated maximum values of the magnetic entropy change is 14.5 J $kg^{-1}K^{-1}$ for a field change from 0 T to 2 T. The maximum magnetic entropy in 3d materials depends on the spin moment S. Because there are two magnetic ions per formula unit, one has $S_m = 2R\ln(2S+1)$, where R is the universal gas constant. From the saturation magnetic moment, we estimate the average S value of the magnetic ions to be equal to $S = 1$ thus $S_m = 18.3$ J mol^{-1} K = 117 J kg^{-1} K, which is about six times larger than the value

obtained from the magnetization measurements. For comparison, the magnetic-entropy change of the compound $Gd_5Ge_2Si_2$ and Gd is also shown in the Fig. 3. It is evident that the MCE in $MnFeP_{1-x}As_x$ compounds is comparable with that of $Gd_5Ge_2Si_2$ though the Gd compound has a larger magnetic moment at 5 K. The origin of the large magnetic-entropy change should be attributed to the comparatively high three moments and the rapid change of the magnetization in the field-induced magnetic phase transition. In rare-earth materials, the magnetic moment fully develops only at low temperatures and therefore the entropy change near room temperature is only a fraction of their potential. In 3d compounds, the strong magneto-crystalline coupling results in competing intra- and inter-atomic interactions and leads to a modification of metal–metal distances which may change the iron and manganese magnetic moment and favors the spin ordering.

Bearing in mind the use of these materials in magnetic refrigerators, next to the magnetocaloric properties also the electrical and heat conductivity is of utmost importance. There is hardly any information on the electrical-transport properties of this system. The electrical resistance can also be useful for a more detailed investigation of the magnetic phase transition because it is very sensitive to changes in the interactions between magnetic ions. The availability of electrical-resistance data would make it possible to compare the critical magnetic fields derived from magnetic and electrical measurements and to understand the role of the electron–phonon and electron–magnon interactions in the magnetic phase transitions. The temperature dependence of the electrical
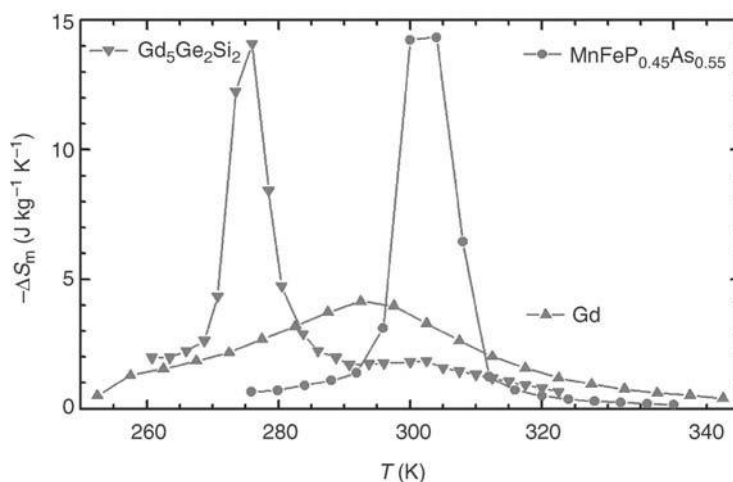
Figure 3
Magnetic-entropy changes of $MnFeP_{0.45}As_{0.55}$ for external magnetic field changes of 0–2 calculated from the magnetization data, in comparison with those of Gd (▲) and $Gd_5Ge_2Si_2$ (▼).
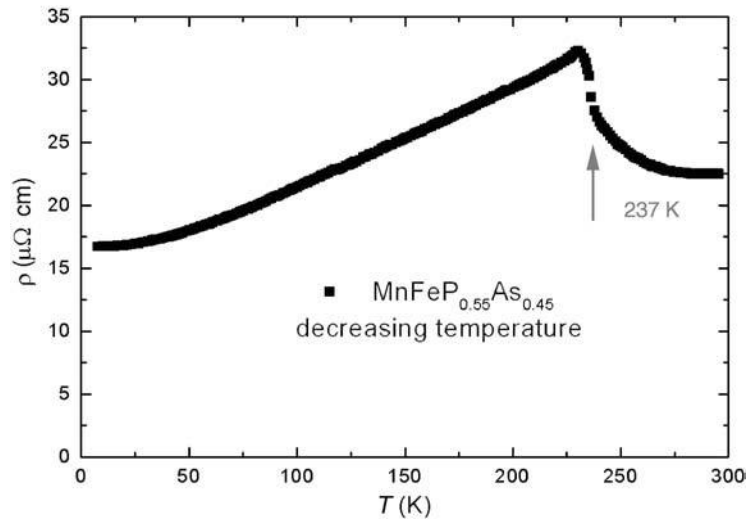
Figure 4
Temperature dependence of the electrical resistivity of $MnFeP_{0.55}As_{0.45}$, measured with decreasing temperature.

resistance of $MnFeP_{0.55}As_{0.45}$, measured during cooling of the sample, is presented in Fig. 4. It can be seen that there is an anomaly in the temperature dependence of the electrical resistance at $T_{cr} = 231$ K. Below T_{cr}, the electrical resistance increases with increasing temperature and has metallic character but, above T_{cr}, it decreases dramatically in a narrow temperature range and then recovers the metal-like dependence on temperature. The total contribution from both the electron–phonon scattering and the electron–magnon scattering in the paramagnetic (PM) phase is smaller than in the ferromagnetic (FM) phase which is contrary to normal ferromagnetic metallic materials. It is interesting to note that the transition at T_{cr} is accompanied by a change in the c/a ratio (Beckmann and Lundgren 1991), which may lead to a change in the Fermi-surface topology and may affect the electron–phonon scattering. Preliminary band-structure calculations indicate a strong shift of the Fermi level associated with the phase-transition (A. V. Antropov personal communication 2002).

The isothermal magnetic-field-dependent hysteresis loops of the magnetoresistance, defined as $\Delta\rho/\rho_0 = (R(B,T) - R(0,T))/R(0,T)$, in the temperature interval from 243 K to 265 K are shown in Fig. 5. The isothermal increase of the magnetic field leads to an increase of the electrical resistance of $MnFeP_{0.55}As_{0.45}$ beginning at a critical field B_{cr1} and ending at B_{cr2}. Hence, between 243 K and 265 K in zero-field the sample is PM but application of a magnetic field exceeding B_{cr1} brings it into the FM state. The field-induced PM–FM transition ends at B_{cr2}. During the reduction of the magnetic field, the reversible FM–PM transition begins at B_{cr3} and ends at B_{cr4}.

The behavior of the electrical resistance in a magnetic field reflects the presence of magnetic-field hysteresis for the complete PM–FM transition, which indicates that also the field-induced transition is first-order. Thus, the temperature and field dependence of the electrical resistance of $MnFeP_{0.55}As_{0.45}$ indicate that a PM–FM phase transition can be induced both by temperature and by magnetic field. The former type of transition takes place from a high-resistance ferromagnetic state at low temperature to a low-resistance paramagnetic state at high temperature. The latter type of transition leads to a positive magnetoresistance peak above T_c. The critical-magnetic-field diagram based on the electrical-resistance data shows that the FM–PM transition has a hysteresis of ~ 1 T.

In summary, we have observed a surprisingly large magnetocaloric effect in the compound $MnFeP_{0.45}As_{0.55}$, which is comparable with that of the giant-MCE material $Gd_5Ge_2Si_2$. The large MCE observed in $MnFeP_{1-x}As_x$ compounds originates from a field-induced first-order magnetic phase transition. The magnetization is reversible in temperature and in alternating magnetic field. The refrigerant capacity (Gschneidner and Pecharsky 1999) of the compound $MnFeP_{0.45}As_{0.55}$, calculated for a temperature span of 50 K, is larger than that of the well-known magnetocaloric material Gd and the ordering temperature of $MnFeP_{1-x}As_x$ compounds is tunable over a wide temperature interval (200–350 K). The excellent magnetocaloric features of the compound $MnFeP_{0.45}As_{0.55}$, in addition to the very low material costs, make it an attractive candidate material for a commercial magnetic refrigerator.
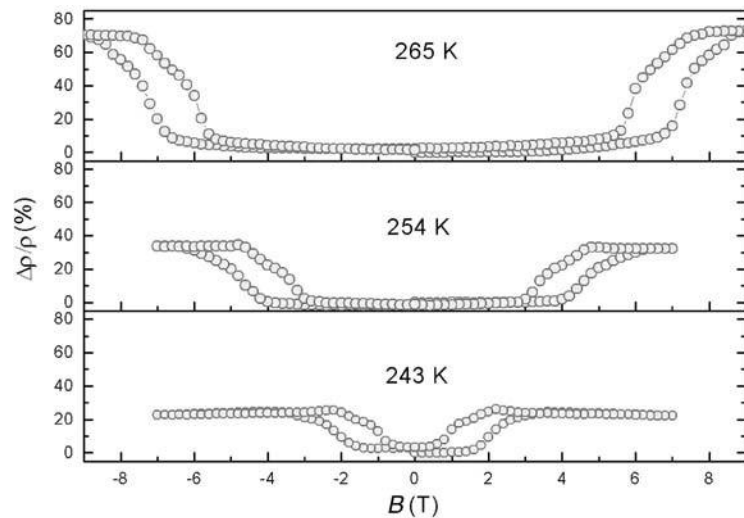
Figure 5
Magnetoresistance of MnFeP$_{0.55}$As$_{0.45}$, measured near the critical temperature.

See also: Demagnetization: Nuclear and Adiabatic; Magnetic Systems: Specific Heat; Magnetocaloric Effect: From Theory to Practice

Bibliography

Annaorazov M P, Asatryan K A, Myalikgulyev G, Nikitin S A, Tishin A M, Tyurin A L 1992 Alloys of the Fe–Rh system as a new class of working material for magnetic refrigerators. *Cryogenics* **32**, 866–72

Annaorazov M P, Ünal M, Nikitin S A, Tyurin A L, Asatryan K A 2002 Magnetocaloric heat-pump cycles based on the AF–F transition in Fe–Rh alloys. *J. Magn. Magn. Mater.* (in press online available August 21, 2002)

Bacmann M, Soubeyroux J L, Barrett R, Fruchart D, Zach R, Niziol S, Fruchart R 1994 Magnetoelastic transition and antiferro–ferromagnetic ordering in the system MnFeP$_{1-y}$As$_y$. *J. Magn. Magn. Mater.* **134**, 59–67

Beckmann O, Lundgren L 1991 Compounds of transition elements with nonmetals. In: *Handbook of Magnetic Materials*, Vol. 6, North-Holland, Amsterdam

Choe W, Pecharsky V K, Pecharsky A O, Gschneidner K A Jr., Young V G, Miller G J 2000 Making and breaking covalent bonds across the magnetic transition in the giant magnetocaloric material Gd$_5$Si$_2$Ge$_2$. *Phys. Rev. Lett.* **84**, 4617–20

Gschneidner K A Jr., Pecharsky V K 1999 Magnetic refrigeration materials (invited). *J. Appl. Phys.* **85**, 5365–8

Gschneidner K A Jr., Pecharsky V K, Pecharsky A O, Zimm O A 1999 Recent developments in magnetic refrigeration. *Mater. Sci. Forum* **315–317**, 69–76

Hashimoto T, Numazawa T, Shino M, Okada T 1981 *Cryogenics* **21**, 647

Hu F X, Shen B G, Sun J R 2000 Magnetic entropy change in Ni$_{51.5}$Mn$_{22.7}$Ga$_{25.8}$ alloy. *Appl. Phys. Lett.* **76**, 3460–2

Hu F X, Shen B G, Sun J R, Wu G H 2001a Large magnetic entropy change in a Heusler alloy Ni$_{52.6}$Mn$_{23.1}$Ga$_{24.3}$ single crystal. *Phys. Rev. B* **64**, 132412

Hu F X, Shen B G, Sun J R, Cheng Z H 2001b Large magnetic entropy change in La(Fe,Co)$_{11.83}$Al$_{1.17}$. *Phys. Rev. B* **64**, 012409

Hueso L E, Sande P, Miguens D R, Rivas J, Rivadulla F, Lopez-Quintela M A 2002 Tuning of the magnetocaloric effect in La$_{0.67}$Ca$_{0.33}$MnO$_{3-\delta}$ nanoparticles synthesized by sol-gel techniques. *J. Appl. Phys.* **91**, 9943–7

Krokozinsky H J, Santandrea C, Gmelin E, Barner K 1982 Specific heat anomaly connected with a high-spin–low-spin transition in metallic MnAs$_{1-x}$P$_x$ crystals. *Phys. Stat. Sol. (b)* **113**, 185–95

Morellon L, Blasco J, Algarabel P A, Ibarra M R 2000 Nature of the first-order antiferromagnetic–ferromagnetic transition in the Ge-rich magnetocaloric compounds Gd$_5$(Si$_x$Ge$_{1-x}$)$_4$. *Phys. Rev. B* **62**, 1022–6

Pecharsky V K, Gschneidner K A Jr. 1997 Giant magnetocaloric effect in Gd$_5$(Si$_2$Ge$_2$). *Phys. Rev. Lett.* **78**, 4494–7

Pecharsky V K, Gschneider K A Jr., Pecharsky A O, Tishin A M 2001 Thermodynamics of the magnetocaloric effect. *Phys. Rev. B* **64**, art. no. 144406

Pytlik L, Zieba A 1985 Magnetic phase diagram of MnAs. *J. Magn. Magn. Mater.* **51**, 199–210

Tegus O, Brück E, Buschow K H J, de Boer F R 2002a Transition-metal-based magnetic refrigerants for room-temperature applications. *Nature* **415**, 150–2

Tegus O, Duong N P, Dagula W, Zhang L, Brück E, Buschow K H J, de Boer F R 2002b Magnetocaloric effect in GdRu$_2$Ge$_2$. *J. Appl. Phys.* **91**, 8528–30

Tishin A M 1999 Magnetocaloric effect in the vicinity of phase transitions. In: Buschow K H J (ed.) *Handbook of Magnetic Materials*, Vol. 12, pp. 395–524

Zach R, Guillot M, Fruchart R 1990 The influence of high magnetic fields on the first order magneto-elastic transition in MnFe(P$_{1-y}$As$_y$) systems. *J. Magn. Magn. Mater.* **89**, 221–8

Zhang X X, Tejada J, Xin Y, Sun G F, Wong K W, Bohigas X 1996 Magnetocaloric effect in La$_{0.67}$Ca$_{0.33}$MnO$_\delta$ and La$_{0.60}$Y$_{0.07}$Ca$_{0.33}$MnO$_\delta$ bulk materials. *Appl. Phys. Lett.* **69**, 3596–8

Zimm C, Jastrab A, Sternberg A, Pecharsky V, Geschneidner K Jr. 1998 Description and performance of a near-room temperature magnetic refrigerator. *Adv. Cryog. Eng.* **43**, 1759–66

E. Brück
University van Amsterdam, Amsterdam
The Netherlands

Magnetic Steels

Iron is a major constituent in many ferromagnetic materials. Iron is abundant, cheap, and it has the largest elemental magnetic dipole moment, of 2.2 Bohr magnetons (μ_B). Two defining intrinsic magnetic properties of a ferromagnet are (i) the *saturation magnetic induction* associated with the former, and (ii) the *Curie temperature*. Magnetic induction is the magnetic response to an applied magnetic field; magnetic exchange coupling persists to the Curie temperature. With few exceptions the average magnetic dipole moment and Curie temperature, T_C, of ferrous alloys are reduced as compared to elemental iron (Bozorth 1951) and most alloying additions are made to alter properties other than exchange and dipole moment. The distinction between *magnetically soft* and *hard materials* is understood in terms of the magnetic hysteresis curve, **B(H)**, as discussed in *Magnetic Hysteresis*. *Magnetic Hysteresis* represents the energy consumed in cycling a *soft magnetic material* between a field **H** and −**H** and back (for a material with a square hysteresis loop this loss is equal to the saturation induction multiplied by the coercive field, **H**$_C$) as well as the stored energy in a *hard* or *permanent magnetic material*.

1. Magnetically Soft Materials

Technical properties of interest for soft magnets include: (i) *high permeability* ($\mu = \mathbf{B}/\mathbf{H}$); (ii) *low hysteresis loss*, and (iii) *low eddy current* and *anomalous losses*. For soft magnets a small magnetic anisotropy (the barrier to switching the magnetization) is desired to minimize the hysteretic losses and maximize the permeability. A desire for small magnetocrystalline anisotropy guides the choice of cubic crystalline phases of iron, cobalt, nickel or alloys (FeCo, FeNi, etc., with small values of K_1) (Jiles 1991). In crystalline alloys, such as Fe–Ni, permalloy, or Hiperco, FeCo, alloy chemistry is varied so that the first-order magnetocrystalline anisotropy energy density, K_1, is minimized. Figures of merit for magnetically soft materials include the magnetic permeability and induction, as illustrated for premier soft materials in Fig. 1. Silicon steels, amorphous and nanocrystalline soft magnetic materials are discussed in *Nanocrystal-*
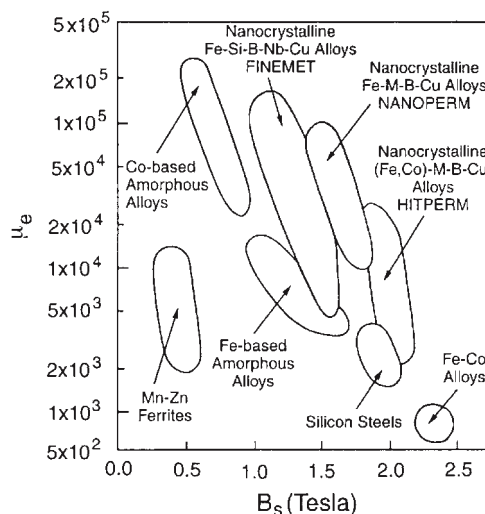
Figure 1
(a) Relationship between permeability, μ_e (at 1 kHz) and saturation polarization for soft magnetic materials (McHenry *et al.* 1999, reproduced by permission of from *Progress in Materials Science*, 1999, **44**, 291).

line Materials: Magnetism. Among other soft magnetic steels FeCo is prominent for its high induction and Curie temperature and FeNi (permalloy) for its large permeability.

FeCo soft magnetic steels (Chen 1986) have evolved under the tradenames Permendur, Supermendur and Hiperco (Hiperco50 is a tradename of CarpenterTechnology). Fe–Co alloys exhibit the largest magnetic induction of any material, at composition near the peak in the well-known Slater–Pauling curve. Alloys near the equiatomic composition exhibit large permeabilities (Pfeifer and Radeloff 1980, Rajkovic and Buckley 1981, Boll 1994). This magnetic softness is rooted in a zero crossing of the first-order magnetic anisotropy constant, K_1, near this composition. Vanadium additions are made for metallurgical reasons and to increase alloy resistivity and decrease eddy current losses. The Fe–Co alloys undergo an order–disorder transformation at a maximum temperature of 725 °C at the composition $Fe_{50}Co_{50}$, with a change in structure from the disordered b.c.c.(A1) to the ordered CsCl(B2)-type structure. This ordering is important to the mechanical properties of this alloy and influences intrinsic magnetic properties slightly.

Permalloy refers to FeNi soft magnetic alloys of which three compositions are of technical interest (O'Handley 2000). These are a 78% nickel permalloy called supermalloy (Mumetal, Hi-mu 80), a 65% nickel permalloy and a 50% nickel permalloy (Deltamax). These are based on f.c.c. Fe–Ni with Curie

temperatures in excess of 400 °C. Owing to Fe–Ni pair ordering, these materials are quite responsive to field annealing, which is used to shape their hysteresis loops and to increase permeability.

2. Magnetically Hard Materials

Magnetically hard materials or permanent magnets are ubiquitous. Among the many applications of permanent magnets are small motors, loudspeakers, communications, electronic tubes and mechanical work devices. For a permanent magnet material, large amounts of magnetic hysteresis are desired, with figures of merit including the coercive force, the remnant magnetization and the energy product, $(\mathbf{BH})_{max}$. The remnant magnetization, $\mathbf{M_r}$, or induction, $\mathbf{B_r}$, represents the largest amount of magnetization possible in the absence of a field. The coercive field, $\mathbf{H_c}$, represents the amount of reverse field required to reduce the magnetization to zero after being saturated in the forward direction. For a material with a square hysteresis loop, the energy product, $(\mathbf{BH})_{max}$, is defined at the maximum demagnetizing field, in the demagnetizing quadrant of a hysteresis loop (Fig. 2(a)) (O'Handley 2000). The energy product is the most commonly used figure of merit for permanent magnet materials. (See *Hard Magnetic Materials, Basic Principles of*.)

There are a large number of iron-based and iron oxide-based permanent magnet alloys. Magnetite, Fe_2O_3, is named after the district in which it was first discovered, Magnesia in ancient Greece. Lodestone (magnetite) was mentioned in the writing of Greek philosophers and used in compasses guiding ancient mariners (Parker 1990). Technology for developing steel wires for compass needles (Coey 1996) was developed during the Sung period (960–1279) in China. Prior to 1917, permanent magnets made of plain carbon steels were weak and unstable with respect to demagnetization by self-fields. This led to geometric constraints (i.e., the horseshoe magnet) to exploiting these materials as permanent magnets. Steel magnets used prior to 1917 included plain carbon, tungsten and chrome steels (Cullity 1972).

A figure of merit for permanent magnet materials is their *energy product* defined above. Modern permanent magnets have progressed in several notable steps. In 1917 cobalt steels were discovered in Japan (see Honda and Saito 1920). This evolution continued with the later development of AlNiCo magnets. AlNiCo is a permanent magnet derived from the intermetallic Fe_2NiAl Heusler alloy. AlNiCo magnets (see McCurrie 1994) derive their magnetic hardness from the shape of iron-rich particles which form on spinodal decomposition of the Heusler alloy into α-Fe and α'-NiAl phases. AlNiCo magnets are currently still a significant fraction of the permanent magnet market. Phases in the FePt and CoPt system were studied as early as 1936 by Jellinghaus, who observed them to have the highest energy products of any alloys known at that time (see Bozorth 1993). Important among these phases is the equiatomic FePt and CoPt, possessing the tetragonal $L1_0$ crystal structure. The specialty magnet, MnAlC, also has a tetragonal $L1_0$ crystal structure. (See *Magnetic Materials: Hard*).

Powdered iron and cobalt oxide magnets discovered in Japan by Kato and Takei (1933), and commercialized under the name Vectolite, were the forerunners of modern ferrite magnets. Synthetic hard hexagonal ferrites were developed by Philips
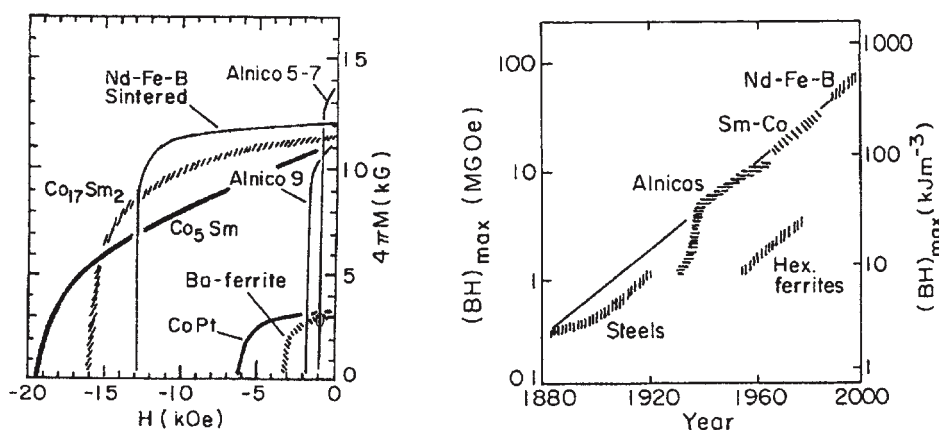
Figure 2
(a) Demagnetization curves for several premier hard magnetic materials and (b) historical progression of the magnetic energy product figure of merit for hard magnets (O'Handley 2000, reproduced by permission of Wiley from 'Modern Magnetic Materials, Principles and Applications,' 2000).

laboratories in the Netherlands during the 1950s. Went *et al.* (1952) first reported on isotropic barium hexaferrite magnets and Stuijts *et al.* (1954) reported on anisotropic strontium hexaferrites. While ferrite magnets have never held record energy products, because of their relatively inexpensive components and ease of fabrication, they constitute a large fraction of the permanent magnet market. (See *Permanent Magnets: Bonded*.)

A major development in the evolution of high energy permanent magnet materials has been the discovery of rare earth permanent magnet materials, REPMs. These materials are notable for their large magnetocrystalline anisotropies that are at the root of their large coercivities. Appropriate choice of the rare earth to transition metal ratios in REPMs results in large remnant and saturation magnetizations. The hexagonal, P6/mmm, structure of $CaCu_5$ is the prototype for the important permanent magnet material $SmCo_5$. $SmCo_5$ was first synthesized by Nassau, Cherri, and Wallace (1960), and Strnat and Hoffer (1966) are credited with first calling attention to its potential use as a permanent magnet material. It still has the highest uniaxial magnetic anisotropy ($K_u = 10^7$ J m^{-3}) of any known material. REPMs have evolved over the years and presently two families of permanent magnets have found commercial importance. The first of these are the Sm_2Co_{17} (2:17) and the second the $Fe_{14}Nd_2B$ (2:14:1)-based permanent magnets. (See *Rare Earth Magnets: Materials*.)

The 2:17 materials have favorable intrinsic properties: remanent induction $\mathbf{B}_r = 1.2$ T (25 °C), intrinsic coercivity, $_i\mathbf{H}_c = 1.2$ T (25 °C) and $T_c = 920$ °C (e.g., in comparison to 750 °C for $SmCo_5$) . Higher 3d metal content leads to higher T_c values. The 2:17 magnets currently in commercial production have a composition $Sm(CoFeCuM)_{7.5}$. Iron additions are made to increase the remanent induction (Huang *et al.* 1994); copper and M (zirconium, hafnium, or titanium) additions are made to influence precipitation hardening. Typical 2:17 Sm–Co magnets with large $\mathbf{H}_c$ are obtained through a low temperature heat treatment used to develop a cellular microstructure. Small cells of the 2:17 matrix phase are separated (and usually completely surrounded) by a thin layer of the harder 1:5 phase. The cell interior contains both a heavily twinned rhombohedral modification of the 2:17 phase and coherent platelets of the so-called z-phase (Fidler and Skalicky 1982), which is rich in iron and M and has the hexagonal 2:17 structure. Typical microstructures have a 50–100 nm cellular structure, with 5–20 nm thick cell walls.

Iron-based rare-earth intermetallic compounds were investigated by Das and Koon (1981), Croat (1981), and Hadjipaynias *et al.* (1983). Commercial $Fe_{14}Nd_2B$ permanent magnets were first synthesized in 1984 by sintering by a group at Sumitoma Metals (Sagawa *et al.* 1984) and by rapid solidification processing by a group at General Motors (Croat *et al.*

1984). Uniaxial magnetocrystalline anisotropy ($K_u = 10^7$ J m^{-3}) in these materials results from their tetragonal crystal structure. These materials are based on the cheaper more abundant iron transition metal. They have the largest room temperature energy products of any materials synthesized to date but their lower Curie temperatures as compared with Co-based magnets makes them unsuitable for high temperature applications.

See also: Alnicos and Hexaferrites; Ferrite Magnets: Improved Performance; Magnets: Sintered

Bibliography

Boll R 1994 Soft magnetic metals and alloys. In: Buschow K H J (ed.) *Materials Science and Technology, A Comprehensive Treatment*. VCH, Weinheim, Vol. 3B, Chap. 14, pp. 399–451

Bozorth R M 1951 *Ferromagnetism*. Van Nostrand, New York

Bozorth R M 1993 *Ferromagnetism*. IEEE Press, New York

Chen C W 1986 *Magnetism and Metallurgy of Soft Magnetic Materials*. Dover Publications, New York

Coey J M D 1996 *Rare Earth Iron Permanent Magnets*. Clarendon, Oxford

Croat J J 1981 Observation of large room-temperature coercivity in melt-spun $Nd_{0.4}Fe_{0.6}$. *Appl. Phys. Lett*. **39**, 357–8

Croat J, Herbst J F, Lee R W, Pinkerton F E 1984 Pr-Fe and Nd-Fe-based materials–a new class of high performance permanent magnets. *J. Appl. Phys*. **55**, 2078

Cullity B D 1972 *Introduction to Magnetic Materials*. Addison-Wesley, Reading, MA

Das B N, Koon N C 1983 Correlation between microstructure and coercivity of amorphous $(Fe_{0.82}B_{0.18})_{0.90}Tb_{0.05}Ca_{0.05}$ alloy ribbons. *Metall. Trans*. **14A**, 953–61

Fidler J, Skalicky P 1982 Microstructure of precipitation hardened cobalt rare earth permanent magnets. *J. Magn. Magn. Mater*. **27**, 127–34

Hadjipaynias G, Hazelton R, Lawless K R 1983 New iron–rare earth based permanent magnet materials. *Appl. Phys. Lett*. **43**, 797–9

Honda K, Saito S 1920 On K-S magnet steel. *Sci. Rep. Tohoku Imp. Univ*. **9**, 417–22

Huang M Q, Zheng Y, Wallace W E 1994 SmCo (2:17-type) magnets with high contents of Fe and light rare earths. *J. Appl. Phys*. **75**, 6280–2

Jellinghaus W 1936 New alloys with high coercive force. *Z. Tech. Phys*. **17**, 33–6

Jiles D 1991 *Introduction to Magnetism and Magnetic Materials*. Chapman and Hall, London

Kato Y, Takei T 1933 Permanent oxide magnet and its characteristics. *J. Inst. Elect. Engrs. (Jpn.)* **53**, 408–12

McCurrie R A 1994 *Ferromagnetic Materials: Structure and Properties*. Academic Press, London

McHenry M E, Willard M A, Laughlin D E 1999 Amorphous and nanocrystalline materials for applications as soft magnets. *Prog. Mat. Sci*. **44**, 291–441

Nassau K, Cherri L V, Wallace W E 1960 Intermetallic compounds between lanthonons and transition metals of the first long period. 1. Preparation, existence and structural studies. *J. Phys. Chem. Sol*. **16**, 123–30

O'Handley R C 2000 *Modern Magnetic Materials, Principles and Applications*. Wiley, New York

Parker R J 1990 *Advances in Permanent Magnetism*. Wiley, New York

Pfeifer F, Radeloff C 1980 *J. Magn. Magn. Mater.* **19**, 190

Rajkovic M, Buckley R A 1981 *Metal Sci.* **21**

Sagawa M, Fujimura S, Togawa N, Yamamoto H, Matsuura Y 1984 New material for permant magnets on a base of Nd and Fe. *J. Appl. Phys.* **55**, 2083–7

Strnat J, Hoffer G 1966 In: *USAF Materials Lab. Report AFML TR-65*, p. 446

Stuijts A, Ratheneau G, Weber G 1954 *Philips Tech. Rev.* **16**, 141

Went J, Ratheneau G, Gorter E, Van Ooosterhaut G 1952 *Philips Tech. Rev.* **13**, 194

M. E. McHenry

Carnegie Mellon University, Pittsburgh
Pennsylvania, USA

Magnetic Systems: De Haas–van Alphen Studies of Fermi Surface

Strongly correlated electron systems such as high-T_c cuprates, cerium, and uranium compounds have attracted strong interest with respect to the non-BCS superconducting property. The f-electron systems of the rare-earth and uranium compounds have been studied in the context of Kondo lattice, heavy fermion, Kondo insulator, anisotropic superconductivity, RKKY interaction, and quadrupolar ordering. These are based on the hybridization effect between the conduction electrons with a wide energy band and the almost localized f-electrons. The Kondo effect, especially, is a basic phenomenon in the cerium and uranium compounds, consequently yielding a large electronic specific heat coefficient γ of the conduction electron with an extremely large effective mass (Ōnuki *et al*. 1991, Ōnuki and Komatsubara 1987). It is a challenging study to detect the heavy conduction electron via the standard de Haas–van Alphen (dHvA) experiment.

1. De Haas–van Alphen Effect

The dHvA effect is caused when the Landau levels cross the Fermi energy as the magnetic field is increased. It provides a powerful tool for determining the topology of the Fermi surface, the cyclotron effective mass m_{c^*} and the scattering lifetime τ of the conduction electron. This method of dHvA measurement is illustrated in this article with the strongly correlated electron systems of the transition, rare-earth and uranium compounds (Ōnuki *et al*. 1991, Ōnuki and Hasegawa 1995).

The dHvA voltage V_{osc} is obtained in so-called 2ω detection of the field modulation method:

$$V_{osc} = A\sin\left(\frac{2\pi F}{H} + \phi\right) \tag{1}$$

$$A \propto J_2(x)TH^{-1/2}\left|\frac{\partial^2 S}{\partial k_H^2}\right|^{-1/2}\frac{\exp(-\alpha m_c^* T_D/H)}{\sinh(\alpha m_c^* T/H)}$$

$$\times \cos\left(\frac{\pi g m_c^*}{2m_0}\right) \tag{2}$$

$$\alpha = \frac{2\pi^2 k_B}{e\hbar} \tag{3}$$

and

$$x = \frac{2\pi F h}{H^2} \tag{4}$$

where $J_2(x)$ is the Bessel function, which depends on the dHvA frequency F, the modulation field h, and the magnetic field strength H. The dHvA frequency F ($= (\hbar/2\pi e)S_F$) is proportional to the extremal (maximum or minimum) cross-sectional area S_F of the Fermi surface, and T_D ($= (\hbar/2\pi k_B)\tau^{-1}$) is the Dingle temperature, which is inversely proportional to τ. The quantity $|\partial^2 S/\partial k_H^2|^{-1/2}$ is the inverse square root of the curvature factor $\partial^2 S/\partial k_H^2$. A rapid change of the cross-sectional area along the field direction diminishes the dHvA amplitude for this extremal area. The term $\cos(\pi g m_c^*/2m_0)$ is called the spin factor. When $g = 2$ (free electron value) and $m_c^* = 0.5\,m_0$, this term becomes zero for the fundamental oscillation, and the dHvA oscillation vanishes for all values of the magnetic field.

This is called the zero spin-splitting situation, in which the up and down spin contributions to the oscillation cancel out. The cyclotron mass is determined from the temperature dependence of the dHvA amplitude A under a constant field, namely from the slope of a plot of $\ln A[1-\exp(-2\alpha m_c^* T/H)]/T$ vs T at constant H and h, by using a method of successive approximations. The Dingle temperature is also determined from the field dependence of the dHvA amplitude at constant temperature, namely from the slope of a plot of $\ln[AH^{1/2}\sinh(\alpha m_c^* T/H)/J_2(x)]$ vs H^{-1} at constant temperature.

Three typical compounds Sr_2RuO_4, $CeRu_2Si_2$, and UPt_3, with extremely large cyclotron masses, will be discussed to demonstrate the use of dHvA effect studies.

2. Cylindrical Fermi Surfaces in Sr₂RuO₄

Sr_2RuO_4, with the same tetragonal crystal structure as the high-T_c superconductor $La_{2-x}Sr_xCuO_4$, is a
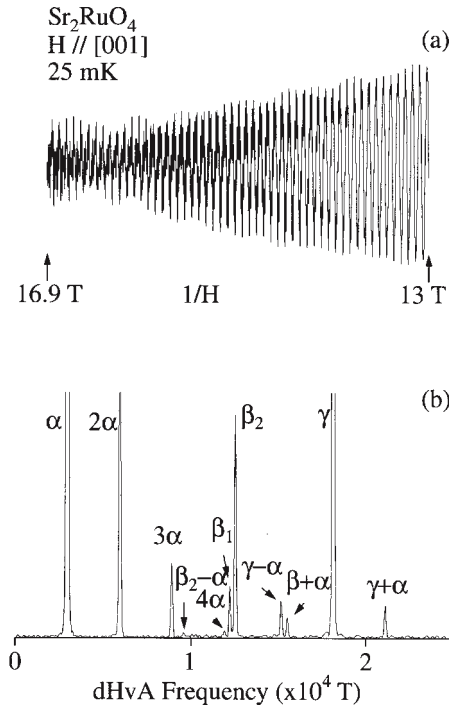
Figure 1
(a) De Haas–van Alphen oscillation; (b) its FFT spectrum in Sr_2RuO_4.

Figure 2
Angular dependence of the dHvA frequency in Sr_2RuO_4. The solid lines indicate the $1/\cos\theta$-dependence.

possible candidate for a *p*-wave (odd parity) pairing state (Ishida *et al*. 1997). The superconducting transition temperature T_c is 1.5 K in Sr_2RuO_4, in contrast to 40 K in $La_{2-x}Sr_xCuO_4$ with a *d*-wave (even parity) pairing state, where the quasi-two-dimensional network of the CuO_2 plane is replaced by the RuO_2 one.

The electronic state is two-dimensional, reflecting the crystal structure; this was clarified by the dHvA measurement and the result of energy band structure calculations (Yoshida *et al*. 1999). Figure 1 shows the typical dHvA oscillation and its fast Fourier transform (FFT) spectrum for the magnetic field along the tetragonal [001] direction, or the c-axis. Three fundamental dHvA branches, named α, $\beta(\beta_1$ and $\beta_2)$, and γ, as well as higher harmonics of α, namely 2α, 3α, 4α, and the combined harmonics ($\beta_2 \pm \alpha$ and $\gamma \pm \alpha$), are presented in Fig. 1(b).

Figure 2 shows the angular dependence of the dHvA frequency. The solid curves for the fundamental branches represent the $1/\cos\theta$-dependence, where θ is a tilt angle from [001] to [100]. The $1/\cos\theta$-dependence means a cylindrical Fermi surface. For example, branch β splits into two branches around [001], denoted by β_1 and β_2, which merge into one at $\theta \approx 30°$. This angle corresponds to a so-called Yamaji angle, where all orbits on the cylindrical but slightly

corrugated Fermi surface have the same cross-sectional area. The theoretical Fermi surfaces for branches α, β and γ are shown in Fig. 3. They are mainly due to hybridized orbitals of Ru(4*d*) and O(2*p*).

From the temperature dependence of the dHvA amplitude A, namely the magnitude of the FFT spectrum in Fig. 1(b), we can determine the cyclotron effective mass m_c^* for each Fermi surface. The cyclotron mass is 3.3 m_0 for branch α, 6.9 m_0 for β, and 17 m_0 for γ. It is noted that the corresponding band masses are 1.0, 1.9, and 2.8 m_0, respectively. The largest cyclotron mass of branch γ is six times larger than the band mass. The corresponding electronic specific heat coefficient is easily calculated, being 4.9, 10, and 25 $mJK^{-2}mol^{-1}$, respectively. The total γ-value is 40 $mJK^{-2}mol^{-1}$, which is in good agreement with the measured γ-value of 39.8 $mJK^{-2}mol^{-1}$ (Yoshida *et al*. 1999).

3. Heavy Conduction Electrons in CeRu$_2$Si$_2$ Based on the Kondo Effect

$CeRu_2Si_2$ possesses tetragonal crystal structure, with one molecule per primitive cell. Important properties of this compound are described in *Heavy-fermion Systems*. Figure 4 shows the typical dHvA oscillation for the field along the [100] direction and its FFT spectrum. Four dHvA branches named β, γ, ψ^*, and ψ, as well as their harmonics, are presented in Fig. 4(b).
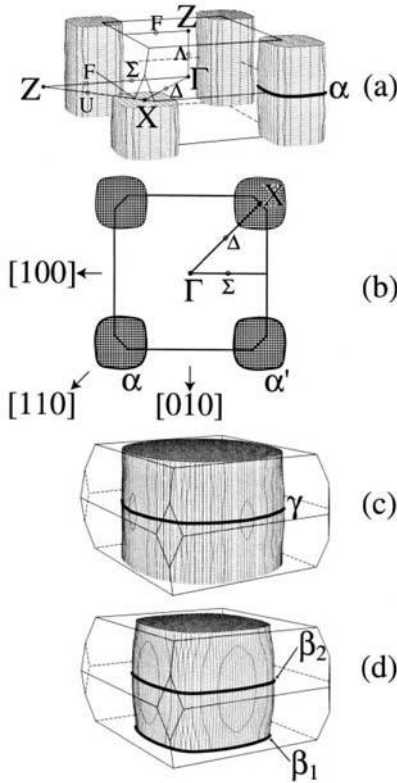
Figure 3
Fermi surfaces of (a) and (b) band-17 hole; (c) band-18 electron; (d) band-19 electron in Sr_2RuO_4.

Figure 4
(a) De Haas–van Alphen oscillation and (b) its FFT spectrum in $CeRu_2Si_2$.

Figure 5 shows the angular dependence of the dHvA frequency (Takashita *et al*. 1996) and the result of energy band calculations (Yamagami and Hasegawa 1993). All dHvA branches are characterized as follows:

- branches ψ and $\psi*$: band-14 hole
- branches κ, ε, and α: band-15 electron
- branch γ: band-13 hole
- branch β: band-12 hole.

The theoretical Fermi surfaces are shown in Fig. 6. These Fermi surfaces are calculated by a relativistic augmented plane wave (APW) method with a local-density approximation (LDA), under the assumption that 4*f*-electrons are itinerant. The experimental result is in good agreement with the 4*f*-itinerant band model, although the calculated Fermi surface has a slightly larger volume than the experimental one.

On the other hand, the cyclotron effective mass, which was determined from the temperature dependence of the dHvA amplitude, is very different from the band mass, because the many-body Kondo effect is not included in the conventional band theory. The cyclotron mass of the branch ψ is extremely large, 120

Figure 5
(a) Angular dependence of the detected dHvA frequency and (b) the result of 4*f*-itinerant band calculations in $CeRu_2Si_2$.

m_0 for the field along [100]. The corresponding band mass is 1.93 m_0. The experimental mass is about 60 times larger than the band mass. The dHvA branches ψ and $\psi*$ are not observed around [001]. This is because the metamagnetic transition occurs at about 8 T and the cyclotron effective mass is expected to
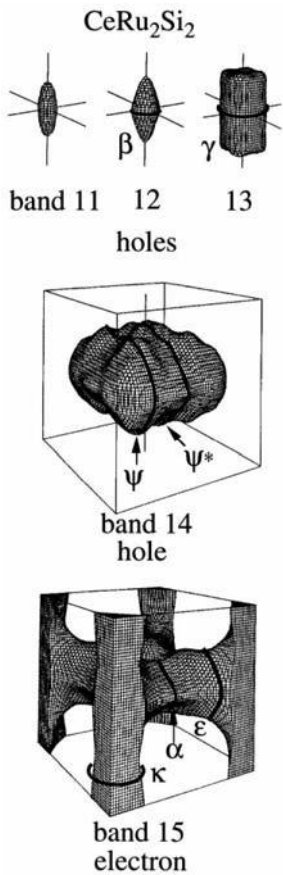
Figure 6
Theoretical Fermi surfaces in $CeRu_2Si_2$ (after Yamagami and Hasegawa 1993).

Figure 7
Angular dependence of the dHvA frequency in UPt_3. Solid lines indicate the result of 5*f*-itinerant band calculations.

become much larger than 120 m_0. This transition is confirmed to be not of the first order (Sakakibara *et al.* 1995). The electronic state in fields above the metamagnetic transition is still under study.

In conclusion, the 4*f*-electrons in $CeRu_2Si_2$ are confirmed by the dHvA study to become itinerant at low temperatures. The conduction electrons, including the 4*f*-electrons, form a so-called "large Fermi surface." This Fermi surface is very different from the corresponding small Fermi surface of $LaRu_2Si_2$, in which the 4*f*-levels are far above the Fermi energy and do not contribute to the conduction electron states.

4. Itinerant 5*f*-electrons in UPt₃

UPt_3, with hexagonal structure, is a prime candidate for the unconventional pairing state to be realized (Tou *et al.* 1998). Superconductivity in UPt_3 coexists with antiferromagnetic ordering, with a Néel temperature of about 5 K. This ordering is, however, not static but

dynamic. To understand the 5*f*-electron nature, it is vitally important to clarify the Fermi surface property (Kimura *et al.* 1998).

Figure 7 shows the angular dependence of the dHvA frequency. The origin of the detected dHvA branches will be identified on the basis of the 5*f*-itinerant band model. Figure 8 shows the theoretical Fermi surfaces. The branches are as follows:

- branch ω: band-37 electron
- branch τ, σ, ρ, λ, ε, and α: band-36 hole
- branch δ: band-35 hole.

The dHvA frequencies, shown by circles in Fig. 7, are in good agreement with theoretical results (the solid lines) of the 5*f*-itinerant band model. The branch ω possesses the largest cross-sectional area and cyclotron mass. The mass is determined as 80 m_0 in the field range of 15 to 17.5 T for the field along [0001], 105 m_0 in the field range of 18.2 to 19.6 T for [10$\bar{1}$0], and 90 m_0 in the field range of 17 to 19.6 T for [11$\bar{2}$0]. The corresponding band masses are 5.09, 6.84, and 5.79 m_0. The cyclotron masses are about 15 times larger than the corresponding band masses. It should be noted that all bands contain an *f*-electron component of about 70% and are flat in the dispersion.

respectively. These are necessary conditions to detect a conduction electron with a large mass of 100 m_0 in the dHvA experiment for $CeRu_2Si_2$ and UPt_3. Moreover, a high-quality sample is vitally important: the band-37 electron with 100 m_0 in UPt_3 was not observed for the sample of the residual resistivity ratio ($RRR = \rho_{RT}/\rho_0$) of 300–400, but was observed for $RRR = 600$–700, where ρ_{RT} and ρ_0 are the electrical resistivity at room temperature and the residual resistivity, respectively.

The topology of the detected Fermi surface is well explained by energy band calculations based on the density functional theory in LDA. The cyclotron mass is, however, very different from the corresponding band mass, because the many-body Kondo effect is not included in the conventional band theory. These Fermi surface properties should shed light on the basic understanding of strongly correlated magnetic materials.

See also: Electron Systems: Strong Correlations; Heavy-fermion Systems; Non-Fermi Liquid Behavior: Quantum Phase Transitions

Figure 8
Theoretical Fermi surfaces in UPt_3: (a) band-35 (hole), (b) band-36 (hole), (c) band-37 (electron).

In theory, nearly spherical Fermi surfaces of a band-37 electron centered at the K point in the Brillouin zone, and band-38 and -39 electrons at the Γ point are present, but they are not observed experimentally. We suppose that they are not present. If these electrons are not present, the main Fermi surface named ω has to become larger than that in Fig. 8(c). In fact, the experimentally determined cross-section is larger than the theoretical one, as shown in Fig. 7.

Thus it can be concluded that the 5f-electrons in UPt_3 are of itinerant nature. Namely, the dHvA results are well explained by the 5f-itinerant band model, although a slight alteration is necessary. All branches are heavy, with cyclotron masses of 15–105 m_0, i.e., 10 to 20 times larger than the corresponding band masses. The mass enhancement is caused by magnetic fluctuations, where the freedom of charge transfer of the 5f-electrons appears in the form of the 5f-itinerant band, but the freedom of spin fluctuation of the same 5f-electrons reveals an unusual magnetic ordering and enhances the effective mass as in the many-body Kondo effect. These heavy conduction electrons, or quasiparticles, condense into Cooper pairs. To avoid a large overlap of the wave functions of the paired particles, the heavy-fermion state would rather choose an anisotropic channel, like a p-wave spin triplet, to form Cooper pairs in UPt_3.

5. Conclusion

We presented dHvA studies on the strongly correlated electron systems of Sr_2RuO_4, $CeRu_2Si_2$, and UPt_3. A low temperature of 20 mK and a high magnetic field of 20 T can be obtained with a commercial dilution refrigerator and a superconducting magnet,

Bibliography

Ishida K, Mukuda H, Kitaoka Y, Asayama K, Mao Z Q, Mori Y, Maeno Y 1998 Spin-triplet superconductivity in Sr_2RuO_4 identified by ^{17}O Knight shift. *Nature* **396**, 658–60

Kimura N, Komatsubara T, Aoki D, Ōnuki Y, Haga Y, Yamamoto E, Aoki H, Harima H 1998 Observation of a main Fermi surface in UPt_3. *J. Phys. Soc. Jpn.* **67**, 2185–8

Ōnuki Y, Goto T, Kasuya T 1991 Fermi surfaces in strongly correlated electron systems. In: Buschow K H J (ed.) *Materials Science and Technology*. VCH, Weinheim, Germany, Vol. 3A, pp. 545–626

Ōnuki Y, Hasegawa A 1995 Fermi surfaces of intermetallic compounds. In: Gschneidner Jr. K A, Eyring L (eds.) *Handbook on the Physics and Chemistry of Rare Earths*. Elsevier, Amsterdam, Vol. 20, pp. 1–103

Ōnuki Y, Komatsubara T 1987 Heavy fermion state in $CeCu_6$. *J. Magn. Magn. Mater.* **63–4**, 281–8

Sakakibara T, Tayama T, Matsuhira K, Mitamura H, Amitsuka H, Maezawa K, Ōnuki Y 1995 Absence of a first-order metamagnetic transition in $CeRu_2Si_2$. *Phys. Rev. B* **51**, 12030–33

Takashita M, Settai R, Ōnuki Y 1996 dHvA effect of metamagnetic transition in $CeRu_2Si_2$ II—the state above the metamagnetic transition. *J. Phys. Soc. Jpn.* **65**, 515–24

Tou H, Kitaoka Y, Ishida K, Asayama K, Kimura N, Ōnuki Y, Yamamoto E, Haga Y, Maezawa K 1998 Nonunitary spin-triplet superconductivity in UPt_3: evidence from ^{195}Pt Knight shift study. *Phys. Rev. Lett.* **80**, 3129–32

Yamagami H, Hasegawa A 1993 A local-density band theory for the Fermi surface of the heavy-electron compound $CeRu_2Si_2$. *J. Phys. Soc. Jpn.* **62**, 592–603

Yoshida Y, Mukai A, Settai R, Miyake K, Inada Y, Ōnuki Y, Betsuyaku K, Harima H, Matsuda T D, Aoki Y, Sato H 1999 Fermi surface properties in Sr_2RuO_4. *J. Phys. Soc. Jpn.* **68**, 3041–53

Y. Ōnuki
Osaka University, Japan

Magnetic Systems: Disordered

All real magnetic materials are imperfect to some extent; there are static structural imperfections either on the atomic level (impurity atoms substituted on host sites in an otherwise perfect lattice) or in the form of extended defects (dislocations, grain boundaries, or rough surfaces). The degree of imperfection can be very low, as in high-quality magnetic monocrystals or films, or it can be very high, as in certain concentrated alloys or in amorphous materials. "Disorder" in the present context can mean a wide distribution of magnetic couplings between local moments because of random environments. It can also mean random local crystal fields—broadly, the interaction between the effective electric charges on the atoms surrounding a magnetic site and the nonspherical charge distribution of the electrons on the site. Moderate disorder in ferromagnets has an essential influence on the hysteresis effects that are intrinsic to the technologically vital hard ferromagnets and magnetic memory materials.

Here we will first consider the limit of strong coupling disorder, which leads to behavior where the standard ferromagnetism or antiferromagnetism is replaced by "spin glass" ordering, with totally novel behavior. Such strongly disordered magnetic systems have no direct practical applications but they show fascinating thermodynamic behavior which poses conceptually tough problems. The models that have been developed to understand strongly disordered magnetism have been widely extended to provide paradigms for complex systems of all types–structural, biological, or sociological. Spin-offs resulting directly from the ideas arising from the magnetic problems include sophisticated numerical optimization methods and neural network computers.

1. Spin Glass Materials

Historically, the spin glass phenomenon was first discovered in the magnetism of dilute alloys; it is characterized by remarkable magnetic irreversibility and relaxation properties. In certain alloys such as AuFe or CuMn the transition metal atoms are distributed at random and have localized magnetic moments down to very low concentrations (van den Berg 1961). In these alloys the magnetic interactions between the local spins are through the Ruderman–Kittel (RKKY) polarization of the conduction electron band (for RKKY interaction see *Magnetism in Solids: General Introduction*). This polarization oscillates in sign as a function of the distance between the spins, so in a random dilute alloy some pairs of spins will be coupled ferromagnetically and others antiferromagnetically, meaning that the interactions are quasi-random with both signs present. There is therefore strong disorder in the couplings. If a sample of a
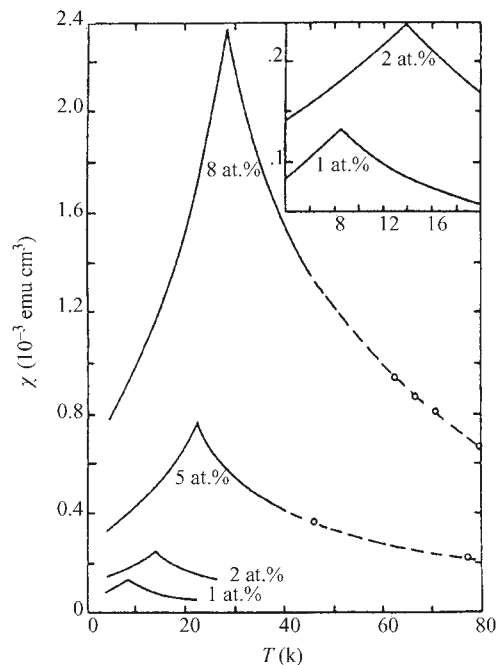
Figure 1
Low-field a.c. susceptibility of AuFe alloys 1–8 at.% Fe in a 5 gauss field at $\approx 100\,\text{Hz}$ frequency. The cusps are clearly defined. (Reproduced by permission of American Physical Society from *Phys. Rev. B* 1972, **6**, 4220.)

few percent concentration of magnetic sites is cooled slowly and the low-field a.c. susceptibility is measured, there is a well defined sharp susceptibility cusp as a function of temperature at a critical temperature T_g, (Cannella and Mydosh 1972) (Fig. 1), while paradoxically there is no sign of any singularity anywhere in the specific heat (Keesom and Wegner 1976) (Fig. 2).

If the same sample is cooled slowly in a constant low magnetic field H (field-cooled, FC), a temperature-independent magnetization plateau develops below T_g. If, instead, the sample is first cooled in zero field down to a low temperature (zero-field-cooled, ZFC), after which the same low field H is applied as before and then the temperature is raised slowly, the magnetization is lower than the FC case until the two curves meet at T_g. Typically T_g is of the order of 10 K for a sample with 1% magnetic impurities and is roughly proportional to the magnetic site concentration.

2. Dynamics and Critical Behavior

Over the whole range of temperatures above T_g relaxation is paramagnetic; the sample has an induced magnetization in an applied field, and when the field
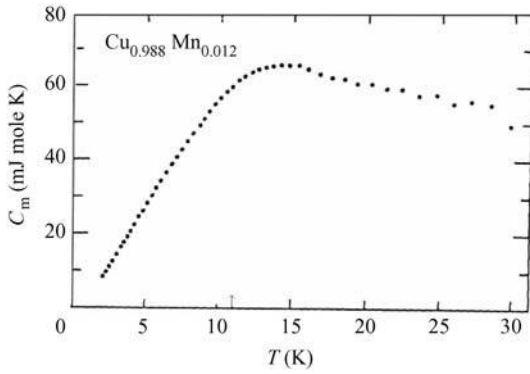
Figure 2
Magnetic specific heat for a Cu–1.2 at.% Mn alloy. The arrow at about 11 K indicates the susceptibility cusp temperature; there is no sign of any accompanying specific heat anomaly. (Reproduced by permission of American Physical Society from *Phys. Rev. B* 1976, **13**, 4053.)

is cut off the magnetization drops to zero in a short but finite time. The form of the relaxation decay becomes strongly nonexponential as T_g is approached, and the relaxation times, while still much shorter than a second, become very long compared with atomic relaxation timescales which are of the order of a picosecond (Mezei and Murani 1979).

Things are very different below T_g. If the sample is cooled in field to a temperature T below T_g and the field is then cut off, there is a residual magnetization M which decays slowly and quasi-logarithmically with time t, i.e.,

$$M(t) \sim M(0) - S \log(t) \qquad (1)$$

over many decades in t (Guy 1978). This "magnetic creep" signifies that as time passes the relaxation becomes slower, and on all practical time scales (maybe even to millions of years) the residual magnetization will never decay to zero.

The difference between behavior above T_g and below T_g is dramatic. Just above T_g relaxation is measured in microseconds while below T_g there is a huge range of effective time scales, extending through years to infinity.

In fact, quasi-logarithmic relaxation below T_g is simply a convenient approximation. S is not a constant, and the form of the relaxation expressed in terms of $S(t)$ has been studied in great detail. There are striking aging effects in the low-temperature relaxation (Lundgren *et al.* 1983): if the sample is field-cooled to T and then held at constant temperature for a "waiting time" t_w before the field is cut off (or alternatively if the sample is zero-field-cooled and then a field is applied) the relaxation of the magnetization depends on how long the waiting time is, as
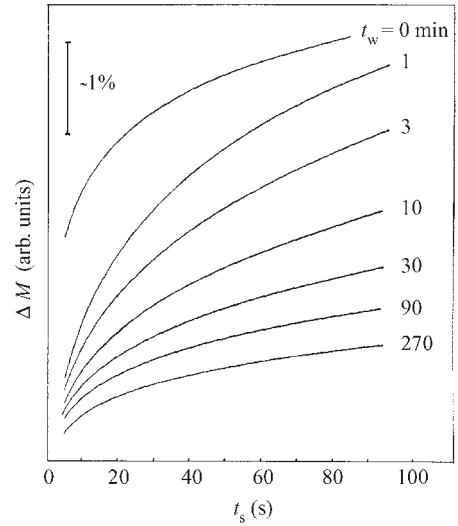
Figure 3
Relaxation in the frozen state of Cu–4 at.% Mn alloy. After cooling the sample in zero field to a temperature of 0.88 times the freezing temperature, a small field (1 gauss) is applied following a waiting time t_w. The relaxation of the resulting magnetization is measured for 100 sec after switching on the field. It can be seen that there is always a slow creep-like relaxation, and that this relaxation changes dramatically with the waiting time. (Reproduced by permission of American Physical Society from *Phys. Rev. Lett.* 1983, **51**, 911.)

shown in Fig. 3. There is a cryptic reorganization of the spins during the waiting. A related measurement is magnetic torque; if the sample is field-cooled to T and then the field is rotated by a small angle, the magnetization does not follow the field but a torque signal appears. (A torque signal is equal to the vector product of magnetization and field). The origin of this torque is closely related to a local anisotropy, a specific spin glass characteristic. The fact that torque is observed is again a consequence of the memory of the spin system; if the spins could reorganize freely there would be zero torque.

Accurate measurements of the a.c. susceptibility in the region of the cusp show slight frequency-dependent effects: the smaller the frequency the lower the apparent cusp temperature. (Typically the change in the apparent T_g is 0.1% for a decade change in excitation frequency, so this is a small effect). The change in T_g could suggest that the cusp is not the signature of an onset of ordering but just an artifact related to a continuous and gradual slowing down of relaxation. However, careful experiments have shown that the static magnetization of the spin glasses has a critical behavior with well-characterized exponents (Bouchiat and Monod 1983, Lévy 1988), as in
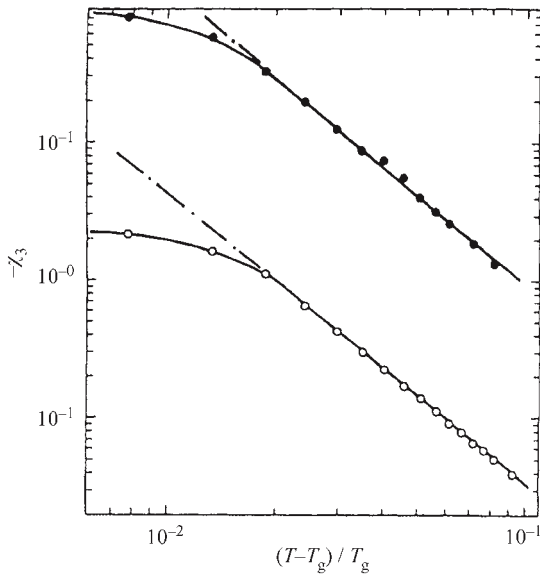
Figure 4
Temperature dependence of the nonlinear susceptibility χ_3 in a AgMn–0.5 at.% sample above the freezing temperature. Measurements made at 0.01 Hz. Open symbols: zero static applied field; closed symbols: 90 gauss static applied field. The straight line on the log–log plot is the canonical signature of critical behavior at the approach to a transition temperature. The bend over very close to the ordering temperature is a critical slowing down effect. (Reproduced by permission of American Physical Society from *Phys. Rev. B* 1988, **38**, 4983.)

standard econd-order transitions (Fig. 4). Suppose we measure the reversible magnetization above T_g and write the magnetization M as a function of applied field H in a Taylor expansion where there are only odd terms because of time reverse symmetry, the following expression is obtained:

$$M(T, H) = \chi_1(T)H + \chi_3(T)H^3 + \ldots \quad (2)$$

Then the linear susceptibility $\chi_1(T)$ does not diverge at T_g while the nonlinear susceptibility $\chi_3(T)$ does diverge, as $1/(T - T_g)^\gamma$. This important observation (where no time dependence is involved) demonstrates that T_g is a bona fide thermodynamic transition temperature and not just a crossover temperature separating a rapid relaxation regime from a slow relaxation regime. The time dependencies observed in a.c. measurements arise because the response of the sample to a change of field has a very wide range of characteristic timescales when the temperature is close to the ordering temperature.

A remarkable fact is that despite the structural randomness (which implies that the effective

concentration changes from one microscopic region to another) the freezing transition is sharp and therefore must be a long-range cooperative phenomenon.

The numerical values of the critical exponents (such as γ) are quite different from those seen at second-order transitions, magnetic or otherwise, in regular materials. Two examples are the critical exponent α for the specific heat, and the dynamic exponent z. In regular materials α is usually very near zero, which corresponds to a sharp maximum (or even a divergence) in the specific heat as the transition temperature is passed. In the spin glasses α is typically -2, which corresponds to a complete lack of singularity in the specific heat at the transition. Concerning the dynamics, in canonical systems $z \approx 2$ while in spin glasses $z \approx 6$. This means that there is an exceptionally wide regime of temperature above the transition in spin glasses where the dynamics are slowing down.

What is the physics behind the spin glass behavior? Because there is long time irreversibility below T_g the material appears to be in an "ordered" state, as a paramagnetic state only has reversible behavior by definition. The question is: What does "ordered" mean? The spin glass ordering represents a freezing of the spins into a cooperative configuration that optimizes the overall energy by satisfying as many individual pair interactions as possible. Because there are many configurations which minimize global energy almost equally well, we have all the complicated dynamics both above and below the ordering temperature. The necessary condition for spin glass order to exist would appear to be a combination of a certain degree of randomness (the random positions of the spins in the dilute alloy case) and conflicting interactions (here due to the RKKY oscillations).

In practice the conditions of randomness and conflict appear to be quite commonplace in magnetic materials, as many hundreds of experimental materials, both metallic and insulating, show the same canonical behavior. As well as the dilute alloys AuFe, CuMn, AgMn, AuCr, or AlGd there are other alloys such as NiMn over an intermediate range of concentration, Eu_xSr_{1-x}, amorphous alloys such as NiFe(P-BAl) or FeMnP, insulators such as $CdCr_{1.7}In_{0.3}S_4$, or semiconductors such as Cd(Mn)Te. Common signatures characteristic of all spin glasses are the magnetic irreversibility onset below T_g, a lack of any singular feature in the specific heat at T_g, and slow nonexponential relaxation of the residual magnetization, with aging, below T_g (Mydosh 1993).

To understand what is happening it is useful to compare the results in model systems.

3. Model Systems

The simplest of all model systems for magnetic ordering is the pure Ising ferromagnet, originally studied

by Ising in his thesis in 1925, and solved exactly in dimension two by Onsager 15 years later (for the Ising model see *Magnetism in Solids: General Introduction*). Ising spins (the spin directions are restricted to be only up or down) are placed on a regular lattice with interactions of strength $-J$ between each pair of near neighbors. In the paramagnetic state the spins flip from up to down and there is no global magnetization. When the temperature is lowered through a critical temperature T_c there is a spontaneous "symmetry breaking"; the spins all conspire to choose an overall magnetization direction, with a majority of spins pointing either up or down. When the same system is cooled down a number of times it chooses up or down at random each time, but for temperatures less than T_c, once the magnetization direction is decided after a given cooling it stays fixed. Temporary correlated clusters of spins of the same sign form and grow as T_c is approached from above, and the timescale for magnetization fluctuations diverges as the temperature tends towards the critical temperature. All the thermodynamic and statistical properties of this system are now extremely well understood thanks to the renormalization group theory (Wilson 1975).

This is a pure ferromagnetic Ising system. But what about disorder? The simplest type of disorder that can be introduced is dilution. Suppose that some of the spins are taken away at random, leaving a fraction p of occupied sites. It turns out that this does not affect the system in a very fundamental way. As could be expected the ordering temperature $T_c(p)$ drops as p decreases, tending to zero at a critical value p_c; this corresponds to a "percolation" limit. When there is no longer a giant cluster of spins all linked together by near-neighbor interactions there will no longer be an ordered state even at zero temperature. However, the properties at the transition, such as the peak in the specific heat and the divergence of the susceptibility at T_c, remain very similar to those in the pure system from $p = 1$ down to $p = p_c$.

Instead of dilution, the spin glass situation with both ferro and antiferro interactions can be mimicked by a regular lattice of Ising spins where the near-neighbor interactions are chosen randomly to be positive or negative ($-J$ or $+J$). This is much more drastic, as now half the pairs of spins want to be aligned parallel to each other and half antiparallel, giving strong frustration. It turns out that this model, the Edwards–Anderson model (Edwards and Anderson 1975), defined in a couple of lines, is extremely hard to solve theoretically, and for dimension three most of what is known comes from large-scale numerical simulations. (It is interesting to compare with the Japanese game of *Go*, which has trivially simple rules involving black and white pieces like up and down spins, and which is also of extreme complexity.)

The mean field limit (corresponding to an infinite space dimension where all spins are neighbors to all other spins) has been solved by Parisi (1983) thanks

to a mathematical *tour de force*. It turns out that there is a huge number of inequivalent ground states, so the system must choose not just between two alternatives (global magnetization up or down) as in the ferromagnet case but between very many inequivalent complex arrangements of spins, all of which manage to minimize the total energy.

For spin glasses in finite dimensions (such as the real-world dimension three) it is still not clear if the physics is strictly the same as in the mean-field situation, but there are certainly huge numbers of either ground states or very long-lived metastable states, which are almost the same for practical purposes. The numerical data show that there is an ordered low-temperature state as in the experimental spin glass, where the word "ordered" has a special sense. In a standard ferromagnet or antiferromagnet the order parameter is the overall magnetization or staggered magnetization, respectively; for the spin glass there is no equivalent.

The order parameter is defined as the memory function averaged over time and over the spins:

$$q_{EA} = [\langle S_i(t) S_i(t') \rangle] \qquad (3)$$

where $\langle \dots \rangle$ means a time average for spin S_i and [...] means an average over all spins. The difference between times t and t' is chosen to be arbitrarily long and the system contains many spins. If globally the spins have an infinitely long memory time for their individual orientations, at time t' each spin i has a probability of > 0.5 to have the same orientation as it had at time t, however long is $[t'-t]$. The spins "remember"; this defines the system as being frozen and so "ordered", and $q_{EA} \neq 0$. The name "spin glass" coined in 1970 by Coles and Anderson (Anderson 1970) expresses the fact that the difference between the paramagnetic state and the ordered state is basically one of timescale, just as the difference between a liquid and a structural glass cannot be seen from the atomic position (there is no long-range atomic order in either case) but from the timescale of the atomic movements which is short in the liquid and infinitely long in the glass. This does not imply that the change in timescale is continuous as a function of temperature; at the ordering temperature the autocorrelation timescale diverges.

A great deal of information can be obtained from the numerical simulations, which are well adapted to the problem as Ising spins are good binary objects. As the spin ensemble is cooled down (according to standard numerical procedures) relaxation becomes slow and highly nonexponential, meaning that there is a very wide range of effective relaxation times (Ogielski 1985). The transition temperature can be defined by the divergence of the mean relaxation time, or through techniques using scaling rules applied to numerical samples of finite but progressively increasing size. Like in the experimental case there is

a well-defined transition with critical behavior, and again as for the experimental materials no visible singularity in the specific heat is observed at the transition. The frustration reduces the ordering temperature compared with the ferromagnetic case; for a three-dimensional ferromagnetic system with interaction strength $-J$ the ordering temperature is 4.51 kJ. For a spin glass on the same lattice with interactions randomly $+J$ and $-J$, the freezing temperature is near 1.2 kJ. In dimension two, the ferromagnetic ordering temperature is 2.27 kJ (Onsager 1944) while the spin glass does not order until zero temperature (Binder and Young 1986).

There are several experimental materials that are quasi-Ising. These systems have dilute, randomly distributed magnetic sites in a crystal structure with an axial symmetry such that there are strong local crystal fields acting on the spins, all parallel to the symmetry axis. If the local moments are all constrained to be parallel or antiparallel to the axis, then the material behaves essentially as an Ising spin glass. Examples are the three-dimensional mixed compound $Fe_{0.5}Mn_{0.5}TiO_3$ (Ito *et al.* 1986) and the two-dimensional layer compound $Rb_2Cu_{1-x}Co_xF_4$ (Dekker *et al.* 1988). Numerical and experimental values for properties such as the critical exponents can be compared, and good agreement has been found.

All the major features of the behavior of the experimental spin glasses are reproduced by the numerical simulations. For instance, the relaxation behaviors observed experimentally below and above T_g are seen with essentially the same form in the simulations. The agreement between the experiments and the simulations (which, it must be remembered, are done on very simplified model systems) and the fact that experimental systems behave similarly to each other means that all these phenomena are intrinsic to the glassy type of ordering, and that the details of the interactions, the types of spins, and so on are fairly irrelevant. The numerical work can give access to parameters that are very hard to see experimentally such as the particular microscopic configuration taken up by the spins. Most remarkably, each time a large system is cooled down, it ends up in a microscopically different frozen state. There indeed appears to be a quasi-infinity of low-temperature configurations by which the spin ensemble can satisfy the frustrated interactions almost equally well. Instead of the system breaking symmetry by choosing between up and down global magnetization as in the ferromagnetic case, it breaks it in a fundamentally different way by choosing from among an enormous number of alternative complex inequivalent configurations.

Numerical studies of spin glasses are extremely time-consuming because of the long relaxations, and subtle difficulties appear. As a result, the ordering temperatures of the canonical models in dimension three are still not accurately determined even after more than 20 years of intensive numerical effort, and the correct description of the ordering process in finite dimensional spin glasses is still a hotly debated topic.

Finally, in the vast majority of experimental spin glass materials, the spins are Heisenberg (for a description of the Heisenberg model see *Magnetism in Solids: General Introduction*) rather than Ising, which means that the spin can take any orientation in space, not just up and down. Numerical simulations with this type of spin indicate clearly that if the mechanism of the ordering were the same as for Ising spins, then T_g should be zero in dimension three. The most plausible explanation for this paradox (we certainly know from experiment that spin glasses with finite ordering temperatures exist in real-life three-dimensional materials) is that the ordering is fundamentally "chiral," which corresponds to a three-spin correlation function for Heisenberg spins rather than a two-spin exchange interaction. The numerous consequences of this model (Kawamura 1992) are still being studied.

The spin glass is not simply a thermodynamic curiosity. It should provide the most tractable example of the vast family of complex systems with disorder and frustration, which includes glasses of all kinds, and optimization problems such as the famous travelling salesman problem. Neural computing techniques are directly inspired by spin glass work. The spin glass has become a paradigm for the behavior of complex cooperative systems in general, from the stock market to the genetic code; however, it turns out that the physics of even the simplest model spin glass is extremely subtle and is not yet fully understood. An enormous experimental and theoretical effort has gone into the study of spin glasses over the last 30 years, but only a few definitive answers have been given in response to the many questions that arise.

4. Reentrant Magnetism

In certain alloy series, the nature of the ordering changes from ferromagnetic to spin glass as a function of concentration. AuFe alloys are ferromagnetic from pure Fe down to 15% Fe concentration, while for lower Fe concentrations they order as spin glasses. Clearly this behavior corresponds to a conflict between a ferromagnetic ordering tendency when the near-neighbor ferromagnetic interactions dominate and the random interaction spin glass case for dilute spins. There are many other experimental examples of this behavior (e.g., (Campbell and Senoussi 1992)).

Very early on in the model calculations, the Ising system with near-neighbor interactions was studied for a fraction p of ferromagnetic interactions and $(1-p)$ antiferromagnetic interactions ($p = 0.5$ is of course the standard spin glass that is discussed

above). At a critical intermediate concentration p_n the order passes abruptly from spin glass to ferromagnetic, much as in the experiments. However, the behavior seen in real materials where the spins are Heisenberg rather than Ising is subtler. There is again a critical concentration p_n but on the ferromagnetic side of p_n "reentrant" behavior is found. Suppose we have a sample on the ferromagnetic side of p_n. We cool it down slowly starting from high temperatures. We will first encounter an ordering temperature T_c below which the order is conventional ferromagnetism. However, at some lower temperature T_k "canting" sets in; i.e., each spin has a frozen component M_z along the overall magnetization axis as in a ferromagnet, but it also has frozen components M_x and M_y in the plane perpendicular to the z axis.

These perpendicular components are quasi-random, so the spin system has found a compromise between ferromagnetism and spin glass ordering by having a novel type of magnetic structure where ordering of both types is superimposed. In a sense the spins are ferromagnetic as far as their z components are concerned but spin glass for their x,y components. The onset of the canted state has important consequences for the macroscopic magnetic properties of the sample. The a.c. susceptibility can be high between T_c and T_k but drops drastically at temperatures below T_k because the canting induces a blocking of the domain wall movements.

5. Random Anisotropy

Local magnetic moments are influenced not only by the exchange interactions with their neighbors but also by local effective crystal fields if their magnetism has an orbital component. In a perfect lattice there are already global anisotropies due to local crystal fields with the point symmetry of the lattice site (for crystal field and anisotropy see *Magnetism in Solids: General Introduction*, *Localized 4f and 5f Moments: Magnetism*). For instance, in a hexagonal site a local moment will generally prefer to align either parallel or antiparallel to the hexagonal axis, while in a cubic site there are higher-order anisotropy terms which favor specific crystal axes, for instance $\langle 111 \rangle$. If the crystal is made up of a random alloy of atoms A and B, individual atoms will have different local environments depending on how many of each type of neighbors it has and what neighbor sites they occupy. Atoms A and B have different effective charges, so each magnetic lattice site will have a local low-symmetry crystal field in addition to the regular crystal field arising from the crystal structure.

The orientation and strength of this local crystal field depends on the exact local environment created by the neighboring atoms; this situation is referred to as "random anisotropy." A given atomic moment can prefer to align along one space direction while another atom prefers a different direction. These anisotropy terms can be strong or weak, depending mainly on the type of magnetic atom as well as on the degree of disorder of the environment. Atoms such as Gd or Mn which have very small orbital moments are hardly influenced by the crystal fields, while other rare-earth atoms with strong orbital magnetism may be strongly affected in the same system. For a ferromagnetic alloy in presence of these random anisotropies, the local magnetic moments will be submitted to contradictory influences—the exchange interactions with the neighbors will tend to align the moments all the same way while the random anisotropies will try to force each moment to remain pointed along its local anisotropy axis.

Extreme cases are provided by amorphous alloys of rare earths. Because of the surrounding amorphous structure, rare-earth environments have very low symmetry. To a good approximation each rare-earth atom is submitted to a strong axial crystal field with the directions of the axes varying randomly from site to site. (The fact that the effective local crystal field is axial rather than planar can be shown to be a consequence of the high spins of the rare earths). When the exchange interactions between the magnetic sites are ferromagnetic, the moments freeze below an ordering temperature to form a "speromagnetic" structure: instead of all moments being aligned parallel, the moment directions fan out over a hemisphere (see *Amorphous and Nanocrystalline Materials*).

6. Random Fields

Model systems have been studied where each site is submitted to a random local magnetic field instead of a random anisotropy. A random local field does not have the same effect as a random axial anisotropy. With the latter the local moment has two equally favorable low-energy configurations, along the axis in the up or down direction. A random field favors one particular direction only. In the Random Field Ising Model (RFIM) (Imry and Ma 1975, Young 1997) random local fields of strength $+/-h$ act on each spin in an Ising ferromagnet. We know that Ising spins with ferromagnetic interactions on a two-dimensional lattice order ferromagnetically with a finite T_c. It can be demonstrated that for a large sample in dimension two, with ferromagnetic exchange interactions and random magnetic fields, the overall ferromagnetic order is destroyed even for weak h, as it is always energetically favorable for the system to break up into domains which organize themselves in such a way as to maximize the gain in energy from interaction with the field. For dimension three, ferromagnetism persists for small h, but is destroyed when h/J passes a critical value. (It is clear that when the random field term is much stronger than the

spin–spin interaction term each spin will tend to align along its local field direction and so ferromagnetic order will be destroyed.) Extensive model calculations have been made on the dynamics of the RFIM.

At first sight it is not obvious that there is any physical system which could be considered to be of a random field nature, as it is not possible to apply external magnetic fields which change from up to down on an atomic scale. In practice a physical equivalent of the model is provided by a diluted Ising-like antiferromagnet in a uniform applied field. The canonical example is $Fe_xZn_{1-x}F_2$ (King *et al.* 1986). In the pure compound FeF_2 a large crystal field anisotropy means that the magnetic Fe moments have quasi-Ising character; they can point only up or down in the crystal field direction and the ordering is antiferromagnetic. When the system is diluted by the nonmagnetic Zn, in zero field its properties stay very much the same. However, when a uniform magnetic field is applied along the crystal field axis, because of the distribution of local exchange strengths, this leads physically to a situation which can be mapped precisely on to that of a ferromagnet in a random field. The critical behavior has been very carefully studied by a variety of techniques to check the RFIM predictions. As in spin glasses the critical dynamics at the RFIM are extremely slow, and in the ordered state are governed by pinning from the random field fluctuations or by vacancies.

7. Disorder in Ferromagnets and Hard Magnetism

In the previous sections the discussion has centered on the effects of very strong disorder, which tends to produce new classes of ordering. Weaker disorder also has important implications for the magnetic properties of the ferromagnets that are of extreme importance in today's technologies.

In zero magnetic field it has been considered above that a ferromagnet sample will order with all its spins parallel, either up or down. This is an idealized picture as a number of ingredients have been left out. An ideal theoretician's ferromagnet has only exchange interactions between spins and geometrical effects do not play a role; for a real-life ferromagnet it is important for instance also to take into account classical dipole energy terms. Although these are many orders of magnitude weaker than the exchange terms, they are long-range and strongly influence the overall magnetization arrangements in all but nanoscopic ferromagnetic samples. For general sample geometries the minimum energy magnetic configuration has a domain structure with domains of parallel spins having domain walls separating them.

The width of the domain wall depends on the interplay between exchange terms and anisotropy or magnetostriction terms. Consider a ferromagnetic monocrystal. Because of anisotropy (and to some extent magnetostriction) there are preferential crystal directions for the domain axes. We will discuss a particularly simple case. Imagine we have a single crystal with axial symmetry (e.g., hexagonal) and with the macroscopic anisotropy favoring magnetization either parallel or antiparallel to the z axis. A typical magnetic configuration could be an up domain ($+z$ orientation) and a down domain ($-z$ orientation) separated by a single domain wall perpendicular to the z axis. Within the domain wall the spin directions will turn progressively from $+z$ to $-z$, swinging through some direction in the x,y plane at the center of the wall.

The width of the domain wall will depend on the ratio of anisotropy to exchange. When anisotropy is weak, the local magnetization direction can turn gradually so as to minimize the cost in exchange energy (neighboring spins within the domain wall will not be at a large angle with respect to each other if the wall is wide). We will have very broad domain walls, many hundreds of atoms thick. On the contrary, when the anisotropy is strong, the domain wall must stay narrow; the spins must turn within a short distance so as to incur as small a cost as possible in the anisotropy energy corresponding to the spins in the center of the wall which are necessarily oriented in the x,y plane, the unfavorable direction with respect to the anisotropy. The domain wall will be narrow, in extreme cases only a few atomic layers thick.

Now if a magnetic field is applied, the domain wall will tend to move so that the domain with its magnetization parallel to the field can grow. When the domain wall is wide, any local defects will have little effect as it is the average energy over the whole wall that counts, so the energy of the wall will depend little on its exact position. Local disorder on the atomic scale will have little influence on such a broad domain wall, as any energy terms will be averaged over the whole width of the wall. Soft magnetic alloy materials, with carefully tailored compositions chosen to minimize hysteresis, can be concentrated alloys (such as mumetal) or amorphous transition-metal ferromagnets, without the strong local disorder reducing significantly their high domain wall mobilities because it is a homogeneous disorder.

Mobility is reduced and the soft magnetic properties are adversely affected by more macroscopic forms of disorder such as dislocations, which can pin the domain wall efficiently as they influence the wall energy on a much larger spatial scale. As a consequence, structural damage (such as cold work) can spectacularly diminish the high permeability of soft magnetic materials.

However, when the wall is narrow a few defects (even very local defects such as vacancies) can have a strong influence on the wall energy. In a matrix with defects there will be optimal positions for the wall, or in other words the wall will tend to be "pinned." For a sample with wide walls that can move easily the

response to the applied field is almost reversible; the materials are magnetically soft, with low hysteresis and high permeability. On the other hand, when walls are narrow and can be easily pinned the material will have high hysteresis and a strong residual moment. These are just the characteristics required for permanent magnets, i.e., for "hard" magnetic materials.

The conditions of high anisotropy-to-exchange ratios and strong pinning are particularly favorable in rare-earth compounds. The rare earths (except for Gd) have exceptionally strong orbital moments, and excellent hard magnetic materials are formed by many rare-earth–transition-metal compounds, with interstitial atoms introduced so as to give extra local crystal fields and to dilate the lattice, which has the effect of increasing the ordering temperatures. Special metallurgical techniques are used to produce materials with small grains and high dislocation densities, all in order to enhance pinning. Of course for engineering applications these materials have to satisfy many other criteria as well; for example, they must have a Curie temperature that is as high possible so as to have useful magnetizations at room temperature, and they must not corrode.

See also: Magnets Soft and Hard: Magnetic Domains; Coercivity Mechanisms; Magnetic Systems: Lattice Geometry-oriented Frustration; Nanosized Particle Systems, Magnetometry on

Bibliography

Anderson P W 1970 Localization theory and the Cu–Mn problem: spin glasses. *Mater. Res. Bull.* **5**, 549–54
Binder K, Young A P 1986 Spin glasses: experimental facts, theoretical concepts and open questions. *Rev. Mod. Phys.* **58**, 801–976
Bouchiat H, Monod P 1983 Remanent magnetisation properties of the spin glass phase. *J. Magn. Magn. Mater.* **30**, 175–91
Campbell I A, Senoussi S 1992 Re-entrant systems: a compromise between spin glass and ferromagnetic order. *Phil. Mag.* **65**, 1267–74
Canella V, Mydosh J A 1972 Magnetic ordering in gold–iron alloys (susceptibility and thermopower studies). *Phys. Rev. B* **6**, 4220–37
Dekker C, Arts A F M, de Wijn H W, van Duynveldt A J, Mydosh J A 1988 Activated dynamics in the two-dimensional spin glass $Rb_2Cu_{1-x}Co_xF_4$. *Phys. Rev. Lett.* **61**, 1780
Edwards S F, Anderson P W 1975 Theory of spin glasses. *J. Phys. F* **5**, 965
Fischer K H, Hertz J A 1991 *Spin Glasses*. Cambridge University Press, Cambridge
Guy C N 1978 Spin glasses in low dc fields II: magnetic viscosity. *J. Phys. F* **8**, 1309–19
Imry Y, Ma S 1975 Random field instability of the ordered state of continuous symmetry. *Phys. Rev. Lett.* **35**, 1399–1401
Ito A, Aruga H, Torikai E, Kikuchi M, Syono Y, Takei H 1986 Time dependent phenomena in a short range Ising spin glass, $Fe_{0.5}Mn_{0.5}TiO_3$. *Phys. Rev. Lett.* **57**, 483–6
Kawamura H 1992 Chiral ordering in Heisenberg spin glasses in two and three dimensions. *Phys. Rev. Lett.* **68**, 3785–8
Keesom P H, Wegner L E 1976 Calorimetric investigation of a spin glass alloy: CuMn. *Phys. Rev. B* **13**, 4053–9
King A R, Mydosh J A, Jaccarino V 1986 AC susceptibility study of the $D = 3$ random field critical dynamics. *Phys. Rev. Lett.* **56**, 2525–8
Lévy L P 1988 Critical dynamics of metallic spin glasses. *Phys. Rev. B* **38**, 4963–73
Lundgren L, Svedlindh P, Nordblad P, Beckman O 1983 Dynamics of the relaxation time spectrum in a CuMn spin glass. *Phys. Rev. Lett.* **51**, 911–4
Mezei F, Murani A P 1979 Combined three dimensional polarization analysis and spin echo study of spin glass dynamics. *J. Magn. Magn. Mater.* **14**, 211–4
Mydosh J A 1993 *Spin Glasses*. Taylor and Francis, London
Ogielski A T 1985 Dynamics of three-dimensional Ising spin glasses in thermal equilibrium. *Phys. Rev. B* **32**, 7384–98
Onsager L 1944 Crystal statistics. I. A two dimensional model with an order-disorder transition. *Phys. Rev.* **6**, 117–49
Parisi G 1983 Order parameter for spin glasses. *Phys. Rev. Lett.* **50**, 1946–8
van den Berg G J 1961 In: Graham G M, Hollis-Hallett A C (eds.), Proc. Int. Conf. Low Temperature Physics. University of Toronto Press
Wilson K G 1975 The renormalization group: criticlal phenomena and the Kondo problem. *Rev. Mod. Phys.* **47**, 773–840
Young A P 1997 *Spin Glasses and Random Fields*. World Scientific, Singapore

I. Campbell
Université Paris Sud, Orsay, France

Magnetic Systems: External Pressure-induced Phenomena

Most elements having magnetic moments as free atoms lose the moment after condensation into solids; magnetism is retained only in a few rare cases. In the competition between cohesive and magnetic interactions, the first one wins. Application of high external pressure to magnetic solids leads to a further decrease in interatomic distances and generally to a depression of magnetism. However, under a sufficiently high pressure, some electrons can be removed from a filled inner atomic shell and an appearance of new magnetism can reflect a momentary state of the electronic configuration. A good example of this phenomenon is metallic ytterbium, which only becomes magnetic under high pressure, when one electron is removed from the originally filled $4f$ shell (see *Intermediate Valence Systems*).

All interactions responsible for magnetism in solids are sensitive to interatomic distances. Application of an external pressure leads to variations in these distances and therefore offers a unique possibility to study these aspects of magnetism. Experiments

performed under external pressure provide intrinsic results. These results are not contaminated by parasitic effects accompanying the chemical substitutions, which are widely used to vary the interatomic distances. The changes of magnetic moments, their arrangement, and the magnetocrystalline anisotropy induced under pressure are very informative phenomena for both applied and basic studies in solid-state physics.

1. Theory and Experiments

1.1 Thermodynamic Relations

From the phenomenological point of view, the pressure-induced changes of magnetic properties can be considered as an inverse effect to the magnetostriction (see also *Magnetoelastic Phenomena*). Considering only the isotropic effects, the basic relations can be derived from the differential of the Gibbs function:

$$\mathrm{d}G = -S\mathrm{d}T - M\mathrm{d}H + V\mathrm{d}p \qquad (1)$$

where M is the saturated magnetization of sample of volume V, parallel to the magnetic field H.

The relation between the magnetostriction and the pressure changes of the magnetization

$$\mathrm{d}M/\mathrm{d}p = -\mathrm{d}V/\mathrm{d}H \qquad (2)$$

directly follows from the exact differential $\mathrm{d}G$. Considering $M(T,p) = M_0(0,p)[f(T/T_C)]$, the pressure dependence of magnetization can be derived as

$$\mathrm{dln}M/\mathrm{d}p = \frac{[\mathrm{dln}M_0/\mathrm{d}p - T(\mathrm{dln}M/\mathrm{d}T)(\mathrm{dln}T_C/\mathrm{d}p)]}{[1 + 3(\alpha/\kappa)(\mathrm{dln}T_C/\mathrm{d}p)]} \quad (3)$$

where α is the linear thermal expansion coefficient, κ is compressibility and T_C is the Curie temperature. Using $\mathrm{dln}V = -\kappa\mathrm{d}p$ and the magnetic Grüneisen coefficient $\Gamma = \mathrm{dln}T_C/\mathrm{dln}V$, the critical pressure P_C for the disappearance of the magnetic state in solids is given by the simple relation

$$P_C \approx -T_C(\mathrm{d}T_C/\mathrm{d}p)^{-1} = (\kappa\Gamma)^{-1} \qquad (4)$$

To estimate the compressibility in the magnetically ordered state, the paramagnetic compressibility κ, as a material property connecting the theory and the experiment, has to be modified by a magnetic contribution κ_m depending on spontaneous magnetostriction ω_S:

$$\kappa_f = \kappa + \kappa_m \approx \kappa + \omega_S/P_C = \kappa(1 + \omega_S\Gamma) \qquad (5)$$

Nonlinear effects can indeed be expected under conditions critical for the existence of magnetism where the simple linear approximations will not be valid.

1.2 Theoretical Models

The theoretical treatment of pressure effects on magnetic properties of solids has been performed within models of both localized and band magnetism (see also *Localized 4f and 5f Moments: Magnetism* and *Itinerant Electron Systems: Magnetism (Ferromagnetism)*).

The systems with localized magnetic moments are very stable and almost insensitive to a compression up to pressures that are capable of changing the electron occupation of the nonfilled inner atomic shells (e.g., in thulium) or of delocalizing the magnetic electrons (e.g., in cerium). Where the localized electrons occupy sharp atomic energy levels, the atomic spin moments S are well defined and their interaction has been successfully described by the molecular field model with the Heisenberg exchange interaction. In the framework of this model, the Curie or Néel temperatures T_C, T_N, respectively, of many simple ferro-, ferri-, or antiferro-spin arrangements in solids have been explained as a function of the moment and the exchange interaction integral J, where $|J| = 3kT_{C,N}/2zS(S+1)$, k is the Boltzmann constant and z is the coordination number, i.e., the number of nearest neighbors (see also *Magnetism in Solids: General Introduction*). Pressure-induced changes of T_C or T_N are mainly a result of the pressure effect on the exchange interaction integral J. A simple relation can be derived for this class of magnetic solids:

$$\mathrm{dln}J/\mathrm{dln}V = \mathrm{dln}T_{C,N}/\mathrm{dln}V = \Gamma \qquad (6)$$

Nonintegral values of the atomic moments characterize a magnetic state in metallic systems with itinerant electrons. These partially delocalized electrons participate on magnetic as well as on transport—electric and thermal—properties of metals. The effective electron–electron interaction J_f and the density of states on the Fermi level $N(E_F)$ play a dominant role in the magnetism of itinerant electrons. Both, J_f and $N(E_F)$, are very sensitive to interatomic distances. In general, a decrease in distances between atoms in solids leads to an increase of both the electron interactions and the width W of the electron energy band. However, the effects of an increase in J_f and a decrease in $N(E_F) \sim 1/W$ under pressure can compensate each other in the Stoner factor $S_f = [1 - J_f N(E_F)]^{-1}$; this factor is crucial for the appearance of a magnetic state. Pressure derivatives of both J_f and $N(E_F)$ are strongly affected by many factors: by the crystal lattice symmetry and the coordination number or by the short-range order of atoms (namely in the case of amorphous metals and disordered alloys). In this respect, a variety of pressure effects on the itinerant electron magnets may be expected.

The models of band (itinerant electron) magnetism enable pressure-induced changes of T_C to be derived

in a form suitable for further characterization of the itinerant electron magnets. When T_C is basically determined by the Stoner relation, then

$$T_C^2 = T_F^2[J_f N(E_F) - 1] \qquad (7)$$

where T_F is the degeneracy temperature (usually $T_F \gg T_C$) which depends on a fine structure of the single particle density of states $N(E)$ curve. Taking into account effects of electron correlation, the effective electron interaction J_f in transition metals with a narrow energy d-band can be expressed by the relation

$$J_f = U/(1 - U/\gamma W) \qquad (8)$$

where U is the intra-atomic Coulomb energy of d-electrons and γ is a constant (Kanamori 1963). Using the relations $d\ln W/d\ln V = -\lambda$ and $d\ln J_f/d\ln V = -\lambda(J_f/\gamma W) = -\lambda R$, the volume (or pressure) derivative of Eqn. (7) raises the possibility of two limiting cases of pressure dependence of T_C in the transition-metal ferromagnets (Wohlfarth 1981). In the "strong itinerant ferromagnets" the effective electron interaction J_f is comparable with the band width, $J_f \to \gamma W$, $R \to 1$, and T_C increases with pressure. The parameter dT_C/dp is proportional to

$$dT_C/dp \sim \lambda \kappa T_C \text{ and } \Gamma \sim -\lambda \qquad (9)$$

The linear relation between dT_C/dp and T_C has also been derived on the basis of detailed theoretical calculations for crystalline NiCu alloys (Lang and Ehrenreich 1968). In the "very weak itinerant ferromagnets" with $J_f \ll \gamma W$, R goes to zero and the pronounced decrease of T_C with pressure is described by the well known Wohlfarth relation

$$dT_C/dp \sim -A_w/T_C \text{ and } \Gamma \sim +\lambda S_f \qquad (10)$$

where A_w is the Wohlfarth constant proportional to $+\lambda \kappa T_F^2$.

Calculations of the s–d interaction in transition metals are able to describe the volume dependence of the d-band width as $W \sim R^{-5}$ which leads to $\lambda = 5/3$ (Heine 1967). The pressure (volume) dependence of the band width W given by the parameter λ controls all the pressure-induced changes of the magnetic characteristics of the transition metal ferromagnets in the theoretical concept, where only single-particle excitations have been taken into consideration.

Since the late 1980s the band calculations based on the local spin density approximation (LSDA) (see *Density Functional Theory: Magnetism*) have revealed the instabilities of the transition-metal moments in the volume instability ranges (Moruzzi and Marcus 1988). The theoretically predicted existence of two ferromagnetic states, very close in energy, for iron in the f.c.c. crystal structure, and the verification of the Fe-moment stability in the more open b.c.c. crystal structure, explains the anomalous magnetovolume effects in Invar alloys (f.c.c.) as well as the almost total insensitivity of the b.c.c.-Fe to external pressures (see *Invar Materials: Phenomena* and references therein).

1.3 High-pressure Techniques

Hydrostatic pressure enables the variation of interatomic distances in compressed matter to an extent similar to that achieved in the more widely used chemical substitution, but it retains the composition, purity, and shape of the sample. The pressure-induced volume and energy changes are dependent on the compressibility of a particular sample. Hence, the high pressures comparable in magnitude with the bulk modulus should be applied to obtain a sufficient effect. Routinely, volume changes of up to $\sim$1–5% per 1 GPa can be produced by hydrostatic pressure. (The pressure unit $Pa = Nm^{-2}$ is too small for this purpose, so the unit $GPa = 10^9 Pa$ ($\sim$10000 atm) will be used in this article.)

An example of the hydrostatic high pressure cell used for measurements of magnetization is presented in Fig. 1. The cell is filled by a liquid pressure medium (mixture of oils, Fluorinert) which transmits pressure on to a sample (fixed on the plug) without shear stresses even during cooling of the cell down to liquid helium temperature. The pressure inside the cell can be increased easily up to 1.5 GPa by a piston pushed inside by a clamping bolt. The miniature pressure cell is made from nonmagnetic CuBe bronze and can be used inside a standard SQUID magnetometer. The applied pressure can be measured inside the cell using the known pressure-induced shift of the critical temperature of the transition to the superconducting state of lead (Garfinkel and Mapother 1961).

Hydrostatic CuBe cells of larger dimensions (with an inner diameter of up to 12 mm) are widely used for measurements of magnetoresistance, magnetostriction, or magneto-optical properties of solids under
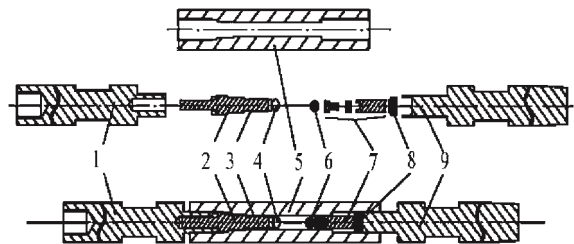
Figure 1
High pressure CuBe microcell for magnetic studies in a SQUID magnetometer, with inner diameter 2.5 mm: **1, 9**—upper and lower pressure clamping bolts; **2**—plug; **3**—sealing; **4**—sample; **5**—pressure cell; **6**—Pb pressure sensor; **7**—piston; **8**—piston backup.

pressure up to 2.5 GPa in a wide temperature range from 4 K up to 400 K. In the vicinity of room temperature, accurate measurements of the pressures applied inside the cells are usually performed by Manganin pressure sensors (Bridgman 1958). A high-pressure diamond anvil cell (DAC) has been modified for magnetization and magneto-optical measurements in high and steady as well as in pulsed magnetic fields (Yamamoto *et al.* 1991). Extremely high pressures of up to 100 GPa can be reached using the DAC; however, the sample space in the DAC is extremely small, up to 10^{-3} mm^3. Detailed information on the high-pressure techniques and methods of measurements of material properties under pressure can be found in Bridgman (1958), Sherman and Stadtmuller (1987), or Eremets (1996).

2. Magnetic Properties Under Pressure

Extended experimental data on magnetic properties of solids under pressure are presented in several reviews (Bloch and Pavlovic 1969, Schilling 1981, Wohlfarth 1981). In the tables and figures below, typical and characteristic examples of the pressure changes of the magnetization, magnetocrystalline anisotropy, and temperatures of the magnetic transitions are presented.

2.1 Magnetic Moment

Direct measurements of the effect of high pressure on atomic moments μ have been very rare. The magnetostriction experiments and Eqns. (2) and (3) have been frequently used to determine the pressure parameter $d\ln\mu_0/dp$ at low temperatures. Using SQUID magnetometers and the pressure cells mentioned above, accurate values of the saturation magnetization M_0 at low temperature and under high pressure can be obtained (see, e.g., Mikulina *et al.* 1999). The

data presented in Table 1 provide evidence of general trends.

In accordance with the discussion above, all three ferromagnetic transition elements iron, cobalt, and nickel with b.c.c., h.c.p., and f.c.c. crystal structures, respectively, exhibit a very stable magnetic moment with respect to the atomic volume. This is in good agreement with *ab initio* calculations (Moruzzi and Marcus 1988, Entel *et al.* 2000). On the other hand, a very pronounced decrease in the Fe-moment was observed under pressure in the Invar alloys Fe_xNi_{1-x} $(0.7 \geqslant x \geqslant 0.6)$ with f.c.c. crystal structure (see Table 1). This effect belongs to the Invar anomalies together with zero thermal expansion and the large spontaneous magnetostriction below T_C. This resolving effect of the crystal structure on the pressure-induced decrease of the Fe-moment correlates well with the theoretically described moment–volume instabilities in the iron-based alloys with f.c.c. crystal structure (for more details see *Invar Materials: Phenomena*).

The Invar-like magnetovolume phenomena were also observed in iron-rich RE–Fe intermetallics of the types RE_2Fe_{17} and $REFe_{11}TM$, where RE is yttrium or a rare earth element and TM is a transition metal, e.g., titanium, vanadium, or molybdenum (Givord and Lemaire 1974, Buschow 1988). A much higher value of the pressure parameter $d\ln\mu_0/dp$ in Y_2Fe_{17} than in $YFe_{11}Ti$ was predicted theoretically (Sabiryanov and Jaswal 1998) and observed experimentally (Mikulina *et al.* 1999) (see Table 1). The Y_2Fe_{17} compound has a rhombohedral crystal structure, but the nearest neighbors of the iron atoms (and the calculated density of state curve) exhibit features of f.c.c.-iron. Thus, not only global but also local properties play a role in the magnetovolume effects. The pressure-induced decreases of Fe-moment in the individual RE_2Fe_{17} intermetallics at 5 K differ from each other depending on the RE elements (see Fig. 2). However, a tendency of the parameter $d\ln M/dp$ to diverge in the vicinity of T_C due to the relation in

Table 1

Magnetic moments μ_0 of transition metals TM, rare-earth RE, and uranium atoms and the magnetocrystalline anisotropy constant K_1 in selected ferromagnetic materials under pressure.

Material	Moment μ_0 μ_B/at.(TM,RE,U)	$d\ln\mu_0/dp$ GPa^{-1}	K_1^{77K} K/f.u.	$d\ln K_1/dp$ GPa^{-1}
Ni[a]	0.61	-0.24×10^{-2}	-0.06	-2×10^{-2}
Co[a]	1.72	-0.22×10^{-2}	0.34	-3.5×10^{-2}
Fe[a]	2.22	-0.25×10^{-2}	0.05	-5×10^{-2}
$Fe_{65}Ni_{35}$[b]	1.73	-4.7×10^{-2}	—	—
$YFe_{11}Ti$[c]	1.73	-3.4×10^{-2}	21.5	-3.7×10^{-2}
Y_2Fe_{17}[c]	2.15	-8.2×10^{-2}	-46	-17×10^{-2}
Gd[a]	7.63	-0.11×10^{-2}	-0.2	—
Dy[a]	10.2	-0.15×10^{-2}	4.3	—
UGe_2[d]	1.4	-2.4×10^{-2}	—	—
UGa_2[d]	2.4	-16×10^{-2}	—	—

[a]Bloch and Pavlovic (1969). [b]Hayashi and Mori (1981). [c]Mikulina *et al.* (1999). [d]Franse *et al.* (1985).
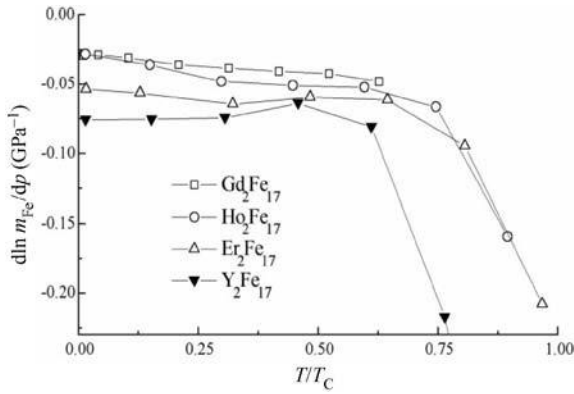
Figure 2
Temperature dependence of the pressure-induced changes of the Fe-moment m_{Fe} in the R_2Fe_{17} intermetallic compounds.

Eqn. (3) smoothes down these differences with increasing temperature (see Fig. 2) (Kamarad *et al.* 1999).

The localized moments in rare-earth elements have been observed to be pressure-independent. The pressure effect on the contribution of $5d$-electrons to the RE-moment can be considered to be responsible for the very low values of $d\ln\mu_0/dp$ in gadolinium and dysprosium, presented in Table 1 (Bloch and Pavlovic 1969). The $5f$ electrons responsible for magnetism in the actinide metals are localized in the heavy actinide elements only. Their further delocalization can be enhanced by the effect of relatively moderate external pressures. Not only the magnetic but also the structural state of actinide metals and compounds are thus strongly affected by pressure (see Sechovsky and Havela 1988 and references therein). As an example, a very pronounced decrease in the U-moment in UGe_2 and UGa_2 intermetallics is presented in Table 1. Both the $5f$–$5f$ overlap and the $5f$–ligand hybridization can be enhanced by external pressure. This leads to a very complex response in the magnetic properties of the uranium-based intermetallics—see the large initial decrease of the U-moment in UGa_2 accompanied by an increase in T_C under pressure (Franse *et al.* 1985) in Table 2.

2.2 Magnetocrystalline Anisotropy

In magnetically ordered solids, atomic moments and the resulting magnetization M are preferentially oriented into specific crystal lattice directions—easy magnetization directions (EMD)—due to magnetocrystalline anisotropy (see also *Localized 4f and 5f Moments: Magnetism*). Changes in the orientation of M relative to the EMD by an external magnetic field are connected with relevant changes in the magnetocrystalline anisotropy energy. This energy G_A can be expressed in uniaxial (hexagonal or tetragonal) crystals as

$$G_A = K_1\sin^2\theta + K_2\sin^4\theta + \cdots \quad (11)$$

where θ is the angle between M and the c axis and K_1, K_2, … are the magnetocrystalline anisotropy constants. The materials listed in Table 1 represent ferromagnets with both axial (EMD along the c-axis, $K_1 > 0$) and planar (EMD in the plane perpendicular to the c-axis, $K_1 < 0$) magnetocrystalline anisotropy. A decrease in $|K_1|$ under pressure was observed for both types of magnetocrystalline anisotropy (Bloch and Pavlovic 1969, Mikulina *et al.* 1999). The effect of pressure on the magnetocrystalline anisotropy constant K_1 in the Y_2Fe_{17} and the $YFe_{11}Ti$ intermetallics ($K_1 \gg K_2$) reflects the different local nearest-neighbor environment of the iron atoms and the difference in the parameters $d\ln\mu_0/dp$ in both intermetallics (see Fig. 3).

2.3 Magnetic Phase Transitions

The effect of pressure on the (isotropic) exchange interaction plays a dominant role in the pressure dependence of the Curie or Néel temperatures of magnetic systems with localized magnetic moments. An increase in J with pressure was derived from measurements of the Kondo effect in "single impurity systems" as rare-earth elements or manganese diluted in noble metals (Schilling 1981). The Kondo temperature T_K in such systems increases under pressure with an almost constant Grüneisen coefficient $\Gamma \sim -10/3$. The values of Γ presented in Table 2 for antiferromagnetic FeO and the ferrimagnetic garnet $Fe_5Gd_3O_{12}$ were derived using Eqn. (6). They are very close to the characteristic values of Γ for the single impurity systems and they confirm the localized character of the magnetic moments in these materials.

The very small pressure-induced changes of T_C presented in Table 2 verify the above mentioned stability of the magnetic state in pure iron, cobalt, and nickel metals in the b.c.c., h.c.p., and f.c.c. crystal structures, respectively. However, a relatively low critical pressure $P_C \sim 10\,GPa$ for the disappearance of magnetism can be derived, Eqn. (4), for the Fe-based alloys with the f.c.c. crystal structure or the iron-based intermetallics with the f.c.c.-like near-neighbor arrangement of atoms. The compressibility values $\kappa_{300\,K}$ in Table 2 correspond to the ferro- or ferrimagnetic compressibility κ_f in materials with $T_C > 300\,K$ and, hence, they comprise the magnetic contributions, κ_m, proportional to the spontaneous magnetostriction ω_S, see Eqn. (5). The enhanced values of κ_f in the iron-based alloy and intermetallics are almost twice those in pure iron and they reflect the pronounced magnetovolume phenomena in these

Table 2
Curie and Néel temperatures T_C and T_N, $\Gamma = \mathrm{d}\ln T_{C,N}/\mathrm{d}\ln V$, compressibility κ, and spontaneous magnetostriction ω_S of selected magnetic materials under high pressure.

Material	$T_{C,N}$ (K)	$\mathrm{d}T_{C,N}/\mathrm{d}p$ (KGPa^{-1})	Γ	κ_{300K} (GPa^{-1})	ω_S
Ni[a]	627	$+3.6$	-1.1	0.54×10^{-2}	-0.03×10^{-2}
Co[a]	1400	0	0	0.52×10^{-2}	—
Fe[a]	1043	-0.3	0.05	0.59×10^{-2}	0.14×10^{-2}
$Fe_{65}Ni_{35}$[b]	505	-43	9	0.94×10^{-2}	2.2×10^{-2}
$Fe_{72}Pt_{28}$[b]	378	-36	9.7	0.98×10^{-2}	1.6×10^{-2}
Y_2Fe_{17}[c]	302	-38	12	1.05×10^{-2}	1.7×10^{-2}
FeO (antiferro)[a]	188	$+6.5$	-5.3	0.65×10^{-2}	-0.36×10^{-2}
$Fe_5Gd_3O_{12}$ (ferri)[a]	564	$+12.8$	-3.4	0.68×10^{-2}	—
Gd[a]	294	-14	1.8	2.61×10^{-2}	—
UGe_2[d]	52	-12.5	20	1.2×10^{-2}	—
UGa_2[d]	120	$+2.3$	-1.6	1.5×10^{-2}	—

[a]Bloch and Pavlovic (1969).   [b]Oomi and Mori (1981).   [c]Mikulina *et al.* (1999).   [d]Franse *et al.* (1985).
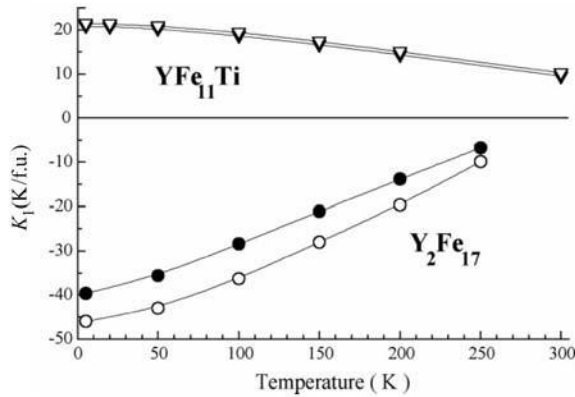
Figure 3
Temperature dependence of anisotropy constant K_1 in $YFe_{11}Ti$ and Y_2Fe_{17} intermetallics at ambient pressure (open symbols) and under high pressure (0.8 GPa) (full symbols).

Figure 4
The dependence of $\mathrm{d}T_C/\mathrm{d}p$ on T_C in the nickel-based alloys, as expressed in Eqn. (9).

materials. The relevant anomalous decrease in T_C under pressure belongs to the Invar characteristics (see *Invar Materials: Phenomena*).

The high negative values of the pressure parameter $\mathrm{d}T_C/\mathrm{d}p$, the spontaneous magnetostriction ω_S, and the compressibility κ_f in the $Fe_{65}Ni_{35}$ and $Fe_{72}Pt_{28}$ alloys and in the Y_2Fe_{17} intermetallics presented in Table 2 are typical for Invar materials.

The model of "strong itinerant ferromagnets" was successfully used to describe the experimental pressure data for nickel and for many crystalline nickel-based alloys with a low content of Cu, Cr, Fe, V, Pd, and Rh, except for the NiMn alloy. The increase of T_C with pressure, i.e., the pressure parameter $\mathrm{d}T_C/\mathrm{d}p$, is proportional to T_C, as seen in Fig. 4. Using Eqn. (9)

the value of $\Gamma \sim -\lambda$ is close to Heine's result $\lambda = 5/3$ (Heine 1967). The same value of Γ was derived also for UGa_2. However, the very pronounced decrease in its magnetic moment under pressure is inconsistent with the discussed model.

3. Concluding Remarks

The development of high-pressure experimental techniques extends the basic thermodynamic framework to the study of pressure-induced phenomena in magnetic systems. New miniature nonmagnetic, nonmetallic pressure cells will allow experiments to be carried out on bulk single crystals under multiextreme conditions—in very high magnetic fields (including pulsed fields up to 100 T), under high

pressure (up to 100 GPa), and at low temperatures (down to mK range).

Studies of pressure-induced phenomena in magnetic systems have become an integral part of research into magnetism. Extraordinary efforts will undoubtedly be made to find a solution to the "traditional" problems and systems: the *f*- and *d*-electron systems, magnetic instabilities in mixed-valence systems (see *Intermediate Valence Systems*), and properties of two-dimensional magnetic structures (see *Bulk Magnetic Materials: Low-dimensional Systems*). There has been an enormous increase in the number of reports on high-pressure research, especially in the relatively new fields of study of the heavy fermions (see *Heavy-fermion Systems*) and non-Fermi liquid systems (see *Non-Fermi Liquid Behavior: Quantum Phase Transitions*).

Bibliography

Bloch D, Pavlovic A S 1969 Magnetically ordered materials at high pressure. In: Bradley R S (ed.) *Advances in High Pressure Research*. Academic Press, London, pp. 41–154

Bridgman P W 1958 *The Physics of High Pressure*. Bell and Sons, London

Buschow K H J 1988 Magnetovolume effects in ternary compounds of novel $RFe_{10}Si$ (R = Nd, Sm, Tb, Ho, Er, Y) intermetallic compounds. *J. Less-Common Metals.* **144**, 65–9

Entel P, Herper H C, Hoffmann E, Nepecks G, Wassermann E F, Acet M, Crisnan V, Akai H 2000 Understanding iron and its alloys from first principles. *Phil. Mag. B* **80**, 141–53

Eremets M I 1996 *High Pressure Experimental Methods*. Oxford University Press, Oxford, UK

Franse J J M, Frings P H, Menovsky A, de Visser A 1985 Magnetism of uranium intermetallics under high pressure. *Physica B* **130**, 180–8

Garfinkel M, Mapother D E 1961 Pressure effect on superconducting lead. *Phys. Rev.* **122**, 459–68

Givord D, Lemaire R 1974 Magnetic transition and anomalous thermal expansion in R_2Fe_{17} compounds. *IEEE Trans. Mag. MAG.* **10**, 109–13

Hayashi K, Mori N 1981 Pressure effect on magnetization of Fe–Ni and Fe–Pt Invar alloys. *Solid State Commun.* **38**, 1057–9

Heine V 1967 s-d Interaction in transition metals. *Phys. Rev.* **153**, 673–82

Kamarad J, Mikulina O, Arnold Z, Garcia-Landa B, Ibarra M R 1999 Magnetization and magnetocrystalline anisotropy of R_2Fe_{17} intermetallics under pressure. *J. Appl. Phys.* **85**, 4874–6

Kanamori J 1963 Electron correlation and ferromagnetism of transition metals. *Progr. Theor. Phys.* **30**, 275–89

Lang N D, Ehrenreich H 1968 Itinerant-electron theory of pressure effect on ferromagnetic transition temperatures: Ni and NiCu alloys. *Phys. Rev.* **168**, 605–22

Mikulina O, Kamarad J, Arnold Z, Garcia-Landa B, Algarabel P A, Ibarra M R 1999 Invar behaviour of Y_2Fe_{17} and $YFe_{11}Ti$ single crystals: magnetic moment of Fe under pressure. *J. Magn. Magn. Mater.* **196–197**, 649–50

Moruzzi V L, Marcus P M 1988 Magnetism in bcc 3d transition metals: onset and approach to the Hund's-rule limit. *Phys. Rev. B* **38**, 1613–20

Oomi G, Mori N 1981 Pressure effect on the spontaneous volume magnetostriction of Fe–Ni and Fe–Pt Invar alloys. *J. Phys. Soc. Jpn.* **50**, 2924–30

Sabiryanov R F, Jaswal S S 1998 Electronic structure and magnetic properties of Y–Fe compounds. *Phys. Rev. B* **57**, 7767–72

Schilling J S 1981 Some recent results in magnetism under high pressure. In: Schilling J S, Shelton R N (eds.) *Physics of Solids under High Pressure*. North-Holland, Amsterdam, pp. 345–56

Sechovsky V, Havela L 1988 Intermetallic compounds of actinides. In: Wohlfarth E P, Buschow K H J (eds.) *Ferromagnetic Materials*. North-Holland, Amsterdam, Vol. 4, pp. 309–491

Sherman W F, Stadtmuller A A 1987 *Experimental Techniques in High Pressure Research*. Wiley, Chichester, UK

Wohlfarth E P 1981 Metallic magnetism under high pressure. In: Schilling J S, Shelton R N (eds.) *Physics of Solids under High Pressure*. North-Holland, Amsterdam, pp. 175–80

Yamamoto K, Endo S, Yamagishi A, Mikami H, Hori H, Date M 1991 A ceramic-type diamond anvil cell for optical measurements at high pressure in pulse magnetic fields. *Rev. Sci. Instrum.* **62**, 2988–90

J. Kamarád
Academy of Sciences of the Czech Republic, Prague Czech Republic

Magnetic Systems: Lattice Geometry-originated Frustration

Frustration of exchange interactions occurs in many magnetic systems owing to various microscopic mechanisms:

(i) Competing long-range exchange interactions (i.e., RKKY interactions) are known to stabilize helicoidal structures in several rare earth compounds.

(ii) Any crystallographic structure containing triangles (f.c.c., triangular lattices, etc.) is frustrated in the presence of nearest-neighbor antiferromagnetic interactions; the two-dimensional kagomé lattice (Fig. 1) and its three-dimensional analogue, the pyrochlore lattice (Fig. 2), are considered as the "most frustrated" structures among existing materials (Liebmann 1986).

(iii) In disordered magnetic systems competition between random ferro- and antiferromagnetic interactions leads to spin-glass (SG) behavior (Mydosh 1993).

Frustration in nondisordered systems has been intensively studied and there are many indications, both theoretical and experimental, that new types of ground states may occur in these systems owing to the large ground-state degeneracy. The main purpose of this article is to give an overview of the different possibilities.
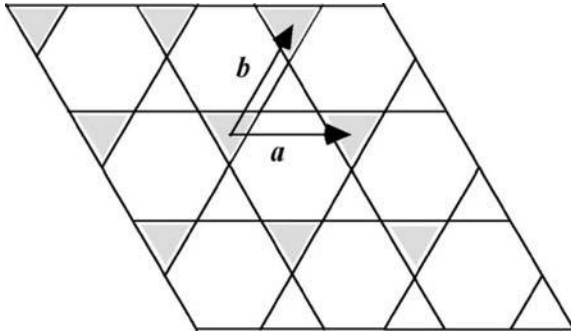
Figure 1
The kagomé lattice: a triangular lattice (generated by the translation vectors *a* and *b*) with a triangular basis (indicated by the shaded triangles).
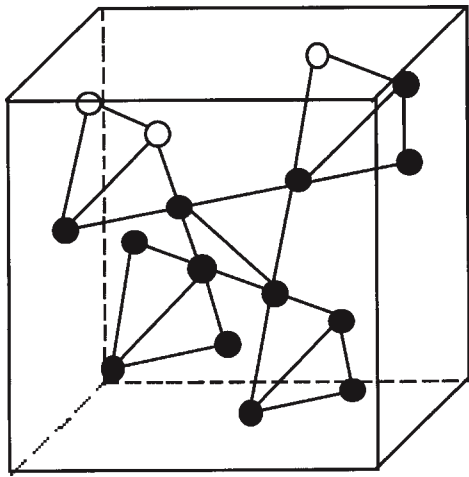
Figure 2
The pyrochlore lattice (f.c.c. lattice with tetrahedral basis).

In addition to the lattice geometry, the range and sign of the interactions and the number of degrees of freedom of local moments are important factors in frustrated systems. These systems are very sensitive to their microscopic characteristics: different behaviors are expected for metallic or insulating systems, as in $3d$ metallic systems where the size of magnetic moments can change, giving rise to an additional degree of freedom; other important parameters are the value of the spin (S) and the strength of magnetic anisotropy. For example, the triangular lattice with classical (equivalent to infinite S) or quantum $S = 1/2$ spins is ordered, but with Ising spins it remains disordered with a finite entropy per site at $T = 0$K.

Frustration can be measured for a given model by several parameters: e.g., when the entropy per site

does not vanish at $T = 0$ K (which contradicts the third law of thermodynamics (Ramirez *et al.* 1999)), its value is a measure of the number of degenerate ground states; another measure is the constraint function, F, defined as the ratio between the ground-state energy, E_g, and the energy of the system if it would be possible to satisfy all pair interactions, E_b, i.e., $F = E_g/E_b$. For a nonfrustrated system, $F = 1$, while in presence of frustration $-1 < F < 1$.

Many frustrated compounds order at low temperature and an empirical measure of frustration can be defined from experiments (Ramirez 1994) as the ratio of the paramagnetic Curie–Weiss temperature, θ_p, which measures the strength of exchange interactions, to the ordering temperature, T_c (which can be any cooperative transition temperature, e.g., Néel or SG transition): $f = |\theta_p|/T_c$. This definition is useful for classifying the frustrated compounds which exhibit any kind of transition; they all correspond to $f > 1$. However, it is not appropriate to a disordered ground state. Values of f larger than 100 are often observed in frustrated compounds. Clearly, a mean field approach cannot be valid for compounds with such large f values.

1. Localized Moments Systems (Gaulin 1994, Harris and Zinkin 1996, Schiffer and Ramirez 1996, Reimers et al. 1991)

1.1 Frustrated Classical Spins Systems

The ground state of localized spin systems is usually well described by minimizing the classical exchange energy. For a Bravais lattice with one magnetic site per unit cell this energy can be written:

$$E = -\sum_{i,j} J(\vec{R}_i - \vec{R}_j)\, \vec{S}_i, \vec{S}_j = -\sum_q J(\vec{q})\, \vec{S}_q \vec{S}_{-q} \quad (1)$$

where $J(\vec{q})$ is the Fourier transform of the exchange interactions $J(\vec{R}_i - \vec{R}_j)$. Thus the ground state is determined by the q value(s) which maximize $J(\vec{q})$. For non-Bravais lattices this procedure can be generalized in the following way. For n magnetic sites per unit cell, the ground state is determined by the largest eigenvalue, $\lambda(\vec{q})$, of a $n \times n$ matrix. However, on the "fully frustrated" pyrochlore (Reimers *et al.* 1991) or kagomé (Harris *et al.* 1992) lattices, the largest eigenvalue, $\lambda(\vec{q})$, is independent of $\vec{q}$ over all the Brillouin zone. In these lattices the magnetic atoms are located on triangles (kagomé) or tetrahedrons (pyrochlore), in such a way that one site is shared by only two elementary clusters (triangles or tetrahedrons). All ground states satisfy the local constraint:

$$\left(\sum_{\text{cluster}} \vec{S}_i\right)^2 = 0 \quad (2)$$

for any elementary cluster. However, this constraint can be satisfied throughout the lattice without inducing any long-range magnetic order. In such a situation, the number of classical ground states increases as the number of sites, N.

It is important to point out that the energy landscape is quite different from that which occurs in an SG state, where the degenerate ground-state configurations are separated by energy barriers. Here, the energy landscape is flat, without any energy barrier between the different states. The thermodynamic properties of such systems are expected to be very different from both conventional ordered magnetic systems (where the ground state is nondegenerate) and SG. The absence of ordering in frustrated lattices is also different from that found in one- and two-dimensional systems, where magnetic correlations develop below the mean field transition temperature but no ordering occurs (or only at $T = 0\,K$) due to entropy effects.

Finally, in some lattices the highest eigenvalue is independent of $\vec{q}$ only along some lines of the Brillouin zone called "degeneration lines." In this case the number of ground states increases only as $N^{1/3}$ and fluctuations beyond mean field solution may induce a phase transition; it has been proposed that such a scenario applies for β-oxygen.

1.2 Possible Ground States in Fully Frustrated Systems

In the mean field approximation, even at $T = 0\,K$, no conventional magnetic long-range order occurs in fully frustrated lattices. Several mechanisms have been proposed which could remove the degeneracy:

• The fluctuations around a particular mean field state contribute to the free energy beyond the mean field approximation. This contribution may change the energy landscape by introducing "valleys." In this case, one ordered state will be selected among all the degenerate states. This phenomenon, called "order by disorder," may occur owing to thermal disorder or to quantum zero point fluctuations or in the presence of a small concentration of impurities.

• Any additional interaction, such as anisotropy, deformations, and dipolar or further-neighbor exchange (Harris *et al.* 1992, Chandra and Coleman 1995), can play an important role in these systems and induce ordering, even if they are much smaller in magnitude than exchange. For quantum spins, more exotic ground states have been proposed, such as dimer, resonant valence bond, nematic, or chiral ordering (Chandra and Coleman 1995). No evidence for such ground states has been found.

Probably, the ground state is a spin-liquid (SL) state, i.e., a singlet state with short-range correlations and a nonzero spin gap. However, the excitation spectrum of these SL states would be different from

nonfrustrated ones (e.g., one-dimensional integer spin chains). In the present case, the singlet–singlet excitations form a continuum starting at zero energy, while in the integer spin chains, the lowest energy excitations have a nonzero gap corresponding to singlet–triplet transitions.

1.3 Examples of Fully Frustrated Compounds

A few kagomé compounds have been studied:

• In $SrCr_{8-x}Ga_{4+x}O_{19}$ (SCGO) (Schiffer and Ramirez 1996), the Cr^{3+} ions ($S = 3/2$) are located both on kagomé planes and on interplane triangular layers. This compound does not order despite its high negative paramagnetic Curie–Weiss temperature, $\theta_p \approx -500\,K$. It exhibits an SG behavior below $T_f = 5\,K$, which could be due to a partial covering of the kagomé planes.

• The chromium and iron jarosites (with $S = 3/2$ and 5/2, respectively) are also two-dimensional kagomé compounds (Wills *et al.* 1998). Both systems order (antiferromagnetic or SG state) at temperatures quite low compared with the Curie–Weiss temperatures, $T_N/\theta_p \approx 0.03$ for chromium and 0.08 for iron jarosites. Moreover, below T_N magnetization is strongly reduced by fluctuations.

• The only example of an integer spin ($S = 1$) kagomé lattice is the organic antiferromagnet m-MPYNN.BF$_4$, which might have an SL ground state (Wada *et al.* 1997).

There are many more compounds exhibiting the three-dimensional pyrochlore structure: the oxides with general formula $A_2B_2O_7$; the spinels AB_2O_4 and $A_2B_2O_4$, where both A and B can be magnetic (rare earth or transition metal) ions; and the fluorides $ABCF_6$. Among these compounds, some exhibit noncollinear magnetic ordering which results from the competition between frustrated interactions and anisotropy. Examples are FeF_3 (Ferey *et al.* 1986), λ-MnO$_2$, $Nd_2Mo_2O_7$, and $Mn_2Sb_2O_7$ (Gaulin 1994), but many of them remain nonmagnetic and have unconventional low-temperature magnetic properties:

• SG-like behavior is observed in many pyrochlores in the absence of any structural disorder (Schiffer and Ramirez 1996).

• Strong, short-range magnetic correlations, as expected in an SL system, are observed in $CsCrNiF_6$ (Harris and Zinkin 1996) and $Li_2Mn_2O_4$.

• A "spin-ice" ground state has been proposed for $Ho_2Ti_2O_7$ and $Dy_2Ti_2O_7$ (Ramirez *et al.* 1999), where the exchange interactions are ferromagnetic but the presence of strong local Ising-like anisotropy leads to a disordered ground state analogous to common water ice.

Finally, the gadolinium gallium garnet $Gd_3Ga_5O_{12}$ (GGG) (Schiffer and Ramirez 1996) belongs to the same class of compounds: the Gd^{3+} ions are located on two interpenetrating corner-sharing triangular

sublattices. It exhibits a complex field-dependent magnetic phase diagram, but there are indications that the zero-field ground state is a SL one (Petrenko *et al.* 1998). Dipolar interactions may also play a role in this compound.

Many of these compounds exhibit an SG-like behavior observed in magnetic response, but specific heat, which probes the low-energy spectrum, is different from normal SG (T^2 behavior instead of T). It is not yet clear whether this behavior is intrinsic to SL states or if it is due to a very small (even undetectable) amount of disorder.

2. Metallic Compounds

2.1 Mixed Magnetic Phases
(Ballou 1998, Yoshimura et al. *1986)*

In itinerant electron antiferromagnets, the amplitude of the magnetic moments can change with respect to external parameters (pressure, temperature, magnetic field, etc.) or to local environment (coordination, interatomic distance, etc.). This additional degree of freedom may lead to nontrivial magnetic phases.

Close to a magnetic–nonmagnetic (M–NM) instability, such amplitude variations occur more easily: frustration can then be lowered or even completely suppressed if some of the magnetic moments vanish. Such mixed phases, where magnetic and nonmagnetic sites coexist, have been observed in several compounds:
- The RMn_2 compounds crystallize in either the C15 cubic (for R = Y, Sm, Gd, Tb, Dy, or Ho) or the C14 hexagonal Laves phase, the first one being similar to the pyrochlore structure (shown in Fig. 2). The manganese magnetic moment depends strongly on the interatomic Mn–Mn distance. This allows stabilization of mixed magnetic phases in $DyMn_2$ (Yoshimura *et al.* 1986), $TbMn_2$ (Ballou *et al.* 1992), and $ThMn_2$, with the concentration of magnetic manganese atoms equal to 1/4 (dysprosium and terbium compounds) and 3/4 (hexagonal thorium compound). The stability of these mixed phases as well as their behavior with temperature or applied fields are well understood in the framework of an itinerant frustrated model close to an M–NM instability (see also *Alloys of 4f (R) and 3d Elements (T): Magnetism*).
- Mixed structures are also observed in a few cerium and uranium compounds. In CeSb (Rossat-Mignod *et al.* 1983) a large number of magnetic phases have been observed and several of them can be described by a stacking of ferromagnetic and nonmagnetic cerium planes. In the triangular UNi_4B (Mentink *et al.* 1994) or kagomé-like CePdAl (Ballou 1998) compounds, the magnetic atoms form chains, one-third of which are nonmagnetic. These compounds are also close to a M–NM instability induced by the Kondo effect. Their observed magnetic

structures can be well explained by a frustrated Kondo lattice model with intersite RKKY exchange interactions of the same order as the Kondo condensation energy T_K.
- A different kind of mixed phase occurs when the instability of the local moments is due to the crystal field scheme in non-Kramers ions. This occurs in $TbRu_2Ge_2$ owing to the small energy difference between the nonmagnetic singlet ground state and the magnetic excited states (Lacroix *et al.* 1998).

All these mixed phases can be modeled within the same pseudo-moment Hamiltonian which includes, in addition to the exchange interaction between the magnetic sites, the energy, Δ, necessary for stabilizing a magnetic moment. In $TbRu_2Ge_2$, Δ is related to crystal field splitting; in the Kondo compounds, $\Delta \approx T_K$, while in the manganese Laves phase, Δ is the stabilization energy of a magnetic moment in an itinerant 3d band. Mixed structures are observed when Δ is of the order of the exchange.

2.2 Itinerant Spin Liquids

In some itinerant systems the absence of magnetic ordering can be attributed to frustration, as in localized frustrated systems, rather than to the instability of band magnetism. This is the case for the cubic Laves phase compound $Y_{0.97}Sc_{0.03}Mn_2$, which remains paramagnetic at low temperature, and shows strong spin fluctuations with short-range magnetic correlations of the order of the interatomic distance. The observed spectrum can be described completely by a localized spin model on a pyrochlore lattice (Canals and Lacroix 1998) indicating that it is the crystal structure that plays the main role in the absence of ordering. Moreover, the signature of a singlet ground state has been observed directly in neutron experiments. The vanishing of the signal in the first Brillouin zone implies that:

$$\chi(\vec{q} = 0) \propto \left(\sum_i \vec{S}_i \right)^2 = 0 \qquad (3)$$

The same behavior occurs in β-manganese, which has a complicated frustrated crystallographic structure formed by corner-sharing triangles and remains paramagnetic at low temperatures (Nakamura *et al.* 1997).

These frustrated metallic systems exhibit large specific heat coefficients, γ ($70\,mJK^{-2}mol^{-1}$ for β-manganese, $180\,mJK^{-2}mol^{-1}$ for $Y_{0.97}Sc_{0.03}Mn_2$), and they are considered as "3d heavy fermions." Much larger values have been measured in the spinel compound LiV_2O_4 where $\gamma = 420\,mJK^{-2}mol^{-1}$ (Kondo *et al.* 1997). However, unlike the usual 4f or 5f heavy fermion systems, the Kondo effect is not observed in these 3d materials. Thus, in the absence of any Kondo effect, such large γ values indicate that the

density of low-energy excitations is large in these itinerant SL states (see *Heavy-fermion Systems*).

3. Summary

Strongly frustrated antiferromagnets may exhibit various unconventional ground states. An SL state can be stabilized in both localized and itinerant systems with frustrated crystallographic structure:

• The understanding of localized SL states has increased considerably, but several aspects need further study, especially the low-temperature dynamics and the difference with conventional SG states. It has been proposed that these systems belong to a new class of "topological spin glasses."

• For metallic SL states, static properties can be described satisfactorily within a localized model, but the dynamics are certainly different ("3*d* heavy fermions"). Also, in various materials close to a magnetic instability, mixed magnetic structures are stabilized.

See also: Bulk Magnetic Materials: Low-dimensional Systems; Electron Systems: Strong Correlations; Magnetic Systems: Disordered; Heavy-fermion Systems; Spin Fluctuations

Bibliography

Ballou R 1998 Geometric frustration in rare earth antiferromagnetic compounds. *J. Alloys Comp* **275–277**, 510–7

Ballou R, Ouladdiaf B, Brown P J, Lacroix C, Nunez-Regueiro M D 1992 Unusual field-induced transition in a frustrated antiferromagnet. *Phys. Rev.* **B 45**, 3158–60

Canals B, Lacroix C 1998 Pyrochlore antiferromagnet: a three-dimensional quantum spin liquid. *Phys. Rev. Lett.* **80**, 2933–6

Chandra P, Coleman P 1995 New outlooks and old dreams in quantum antiferromagnetism. In: *Strongly Interacting Fermions and High T_c Superconductivity, Proc. Les Houches Summer School, session LVI*. North Holland, Amsterdam

Ferey G, de Pape R, Leblanc M, Pannetier J 1986 Ordered magnetic frustration: crystal and magnetic structures of the pyrochlore form of FeF$_3$. *Rev. Chim. Min.* **23**, 474–84

Gaulin B D 1994 Experimental studies of geometrically frustrated magnetic systems. In: Diep H T (ed.) *Magnetic Systems with Competing Interactions*. World Scientific, Singapore, pp. 286–327

Harris A B, Kallin C, Berlinsky A J 1992 Possible Néel orderings in the Kagomé antiferromagnet. *Phys. Rev.* **B 45**, 2899–919

Harris M J, Zinkin M P 1996 Frustration in the pyrochlore antiferromagnets. *Mod. Phys. Lett.* **B 10**, 417–38

Kondo S, Johnston D C, Swenson C A, Borsa F, Mahaja A V, Miller L L, Gu T, Goldman A I, Maple M B, Gajewski D A, Freeman E J, Dilley N R, Dickey R P, Merrin J, Kojima K, Luke G M, Uemura Y J, Chmaissen O, Jorgensen J D 1997 LiV$_2$O$_4$: a heavy fermion transition metal oxide. *Phys. Rev. Lett.* **78**, 3729–32

Lacroix C, Ballou R, Schmitt D 1998 Geometric frustration in rare earth antiferromagnetic compounds. In: Donath M, *et al.* (ed.) *Magnetism and Electronic Correlations in Local Moment Systems: Rare Earth Elements and Compounds*. World Scientific, Singapore, pp. 369–86

Liebmann R 1986 *Statistical mechanics of periodic frustrated Ising systems. Lecture Notes in Physics*, Vol. 251. Springer, Berlin

Mentink S A M, Drost A, Nieuwenhuys G J, Frikkee E, Menovsky A A, Mydosh J A 1994 Magnetic ordering and frustration in hexagonal UNi$_4$B. *Phys. Rev. Lett.* **73**, 1031–4

Mydosh J A 1993 *Spin Glasses: An Experimental Introduction*. Taylor and Francis, London

Nakamura H, Yoshimoto K, Shiga M, Nishi M, Kakurai K 1997 Strong antiferromagnetic spin fluctuations and the quantum spin liquid state in geometrically frustrated β-Mn and the transition to a spin glass state caused by non magnetic impurity. *J. Phys.: Condens. Matter* **9**, 4701–28

Petrenko O A, Ritter C, Yethiraj M, Paul D M 1998 Investigation of the low temperature spin-liquid behavior of the frustrated magnet gadolinium gallium garnet. *Phys. Rev. Lett.* **80**, 4570–3

Ramirez A P 1994 Strongly geometrically frustrated magnets. *Ann. Rev. Mater. Sci.* **24**, 453–80

Ramirez A P, Hayashi A, Cava R J, Siddharthan R, Shastry B S 1999 Zero point entropy in "spin ice." *Nature* **399**, 333–5

Reimers J N, Berlinsky A J, Shi A C 1991 Mean-field approach to magnetic ordering in highly frustrated pyrochlores. *Phys. Rev. B* **43**, 865–78

Rossat-Mignod J, Burlet P, Quezel S, Effantin J M, Delacote D, Bartholin H, Vogt O, Ravot D 1983 Magnetic properties of Ce monopnictides. *J. Magn. Magn. Mater.* **31-34**, 398–404

Schiffer P, Ramirez A P 1996 Recent experimental progress in the study of geometrical magnetic frustration. *Comments Cond. Mat. Phys.* **18**, 21–50

Wada N, Kobayashi T, Yano H, Okuno T, Yamaguchi A, Awaga K 1997 Observation of a spin-gap state in two-dimensional spin-1 Kagomé antiferromagnet m-MPYNN.BF$_4$. *J. Phys. Soc. Jpn.* **66**, 961–4

Wills A S, Harrison A, Mentink S A M, Mason T E, Tun Z 1998 Magnetic correlations in deuterium jarosite, a model S = 5/2 Kagomé antiferromagnet. *Europhys. Lett.* **42**, 325–30

Yoshimura K, Shiga M, Nakamura Y 1986 NMR study of magnetic state of RMn$_2$ intermetallic compounds. *J. Phys. Soc. Jpn.* **55**, 3585–95

C. Lacroix
Laboratoire Louis Néel, CNRS, Grenoble, France

Magnetic Systems: Specific Heat

Historically, specific heat was defined as the heat (δQ) required to rise the temperature (T) of a unit of mass of a substance in a unit of degree, $C_y = \delta Q/\delta T$, where y indicates the control parameters kept constant. This elementary definition worked hand in hand with the development of the thermodynamics because it is directly related to those parameters to be taken into account to describe the state of any physical system, i.e., its energy and temperature.

From the First Law, the heat absorbed by a system is distributed as, $\delta Q = dU + \delta W$, where U is the internal energy and W the work done by the eventual expansion (compression), or by the change in the magnetization (M) under magnetic field (h). If only the thermal component of the system is taken into account (i.e., $dV = 0$), the simple expression $C_v = dU/dT$ is obtained. However, the measurements are normally performed under vacuum (adiabatic) conditions, that implies at constant pressure (C_p). Therefore, $C_p = dH/dT$ is actually measured, where $H = U + pV$ is the enthalpy of the system, which includes the expansion of the system during the heating process. The difference between C_p and C_v is given by $C_p - C_v = TV\alpha^2/\kappa$, where α is the thermal expansion and κ the compressibility (e.g., see Goodstein 1985). Provided that α and κ are nearly temperature independent, this difference becomes negligible at low temperatures. But such is not strictly the case around phase transitions or when T is comparable with the characteristic energy of the system. The same precautions have to be taken with other relations, like the Grüneissen parameter, $\Gamma \sim \kappa\alpha/C_v$, when κ and/or α have significant T dependence and consequently $C_v(T)$ differs from the measured $C_p(T)$.

The Second Law refers to the progressive access to the excited states with the increase of temperature. The measure of that process is evaluated by the entropy, $S(T)$, which is related to δQ through, $dS = \delta Q/T$. Then, specific heat can be expressed as, $C_p = T(dS/dT)_p$, and, therefore, the experimental knowledge of $C_p(T)$ provides a direct measure of the entropy evolution of the system, $S(T) = \int C_p/T \, dT$, i.e., how the system accesses to its thermally excited levels. From this point of view, the specific heat works like a thermal spectrometer, where the excitation is given by δQ and the response by δT. One of the most important aspects of the knowledge of $S(T)$ is that it provides information on the first term of the free energy variation ($dG = -SdT + Vdp - Mdh$). This is the reason why the access to the evolution of $C_p/T(T)$ constitutes one of the basic tools for the characterization of any new system.

1. Contributions to the Specific Heat

Since all allowed states of a system are equally likely, and each component contributes with its own entropy to the total value (i.e., $S(T) = \Sigma_i S_i(T)$), the specific heat provides simultaneous information on the full spectrum of excitations. Then from $C_p/T = dS/dT$ it is possible to compute the contribution of all the components of the system. To extract the information related to each of them requires finding at which range of temperature a specific contribution becomes dominant. According to their respective temperature range of importance, the following typical contributions can be enumerated: (i) nuclear for $T < 0.5\,K$ which are usually recognized by a $C_n \propto T^{-2}$ dependence, (ii)

conduction electrons within the $0.5\,K < T < 4\,K$ range, (iii) when present, heavy fermion (*HF*) quasi-particles dominate the scene up to about $7\,K$, (iv) phonons for about $T > \theta_D/30$, where θ_D is the Debye temperature, (v) magnons, which are related to some magnetic transition and/or anomalies, are dominant up to about $20\,K$, and (vi) Schottky anomalies are well observed when their respective characteristic energies (or associated gaps, Δ) are about $k_B\Delta < 20\,K$. Each of these contributions is related to different statistics, which describe the thermal population of the excited states. For example, Maxwell–Boltzman statistics applies to Schottky-type anomalies (like those originated by nuclear or crystalline electric field (CF) splitting), Fermi–Dirac statistics to the electrons in the band, and Bose–Einstein statistics to phonons, magnons, and other quasi-particles. Since many of these contributions are extensively treated in the literature (e.g., see Gopal 1966) only recent developments related to magnetic properties will be considered in this article.

Conduction electrons can be described as free electrons and their linear contribution to the specific heat, $C_{el} = \gamma T$, is directly proportional to the density of states at the Fermi level, $N(E_f)$ (e.g., see Goodstein 1985). The factor $\gamma \propto N(E_f)$ is the Sommerfeld coefficient, which is constant within the experimental range of temperature. Interaction of band electrons with some quasi-particles (namely phonons, λ_p or magnons, λ_m) dresses the measured γ value, which is then corrected as, $\gamma = \gamma_o (1 + \lambda_p + \lambda_m)$. Experimental values of γ are extracted from a C_p/T versus T^2 representation, as shown in Fig. 1, with γ being the value at $T \to 0$. In pure metals, it ranges between $0.19\,mJ\,mol^{-1}K^{-2}$ and $10\,mJ\,mol^{-1}K^{-2}$ for beryllium and yttrium, respectively (Gopal 1966). These values are strongly enhanced by electron–electron interactions or magnetic correlations, as it occurs in intermediate valent compounds with $10 < \gamma < 80\,mJ\,mol^{-1}K^{-2}$ (e.g., CeIr$_2$, Sereni 1991) or the system showing spin fluctuations with $50 < \gamma < 200\,mJmol^{-1}K^{-2}$ (e.g., UAl$_2$, Stewart 1984). A further increase of this electronic term is observed in heavy fermions, where the γ term becomes up to three orders of magnitude larger than that of a simple metal (e.g., CeCu$_6$, Löhneysen 1995).

Phonon contribution, C_{ph}, is extracted from the slope of a C_p/T versus T^2 representation (see Fig. 1) because $C_p/T = C_{el}/T + C_{ph}/T = \gamma + \beta T^2$, with $\beta = 12\pi^4 k_B N/5\theta_D^3$. This formula is valid up to $T = \theta_D/24$. Some misuse of $\beta \propto N/\theta_D^3$ causes an incorrect evaluation of θ_D as it is strictly valid for pure elements or N atoms of equal mass. This occurs, for example, when it is applied to systems involving components with different masses, where false variation of $\theta_D(T)$ is extracted. A similar situation appears in solids containing a variable number of interstitial atoms without a concomitant change in the measured β. If it were included in N a false variation of $\theta_D(x)$ would be obtained.
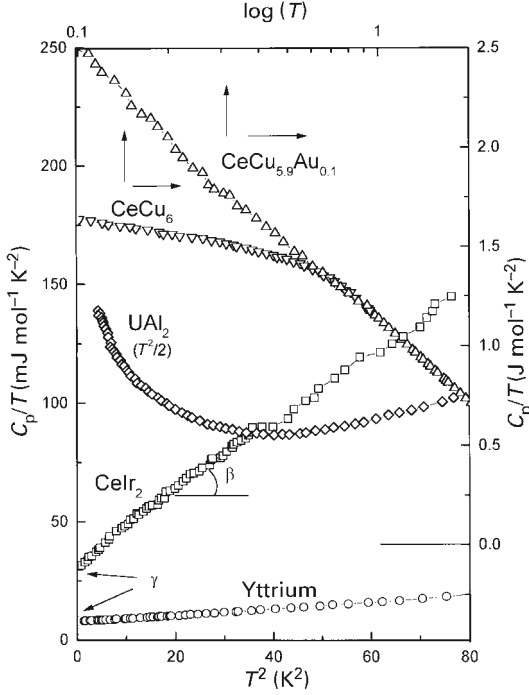
Figure 1
Electronic (γ) and phonon (β) contributions in a $C_p/T = \gamma + \beta T^2$ representation for different systems.

Magnetic contributions, C_m, include a large variety of contributions to $C_p(T)$, which are evaluated as $C_m = C_p - (C_{el} + C_{ph})$. In first glance, contributions related to a magnetically ordered phase and those arising from excitations which do not develop long-range order (LRO) can be distinguished. Others, like nearly or weak magnetic systems, are sometimes difficult to deal with because they appear at the verge of the ordered phase. Section 2 is devoted to magnetic contributions directly related to the ordering transition, followed by one describing the ordered phase itself. Afterwards, other types of magnetic transformations and excitations will be considered.

2. Specific Heat at the Ordered Phase Boundary

As the second derivative of the free energy ($C_p = T\partial^2 G/\partial T^2$), the specific heat defines the order of the phase transition at the critical temperature ($T = T_{ord}$). In the case of a first-order transition the discontinuity in $S(T)$ is reflected in $C_p(T)$ as a divergence at T_{ord}, and the latent heat ($L = T\Delta S$) can be evaluated as, $\int C_p(T)\mathrm{d}T$. Here, L accounts the change of internal energy from one magnetic phase to the other, plus the eventual volume and/or magnetization changes ($L \propto \Delta H$). The Clausius–Clapeyron relationships, $\mathrm{d}T_{ord}/\mathrm{d}p = \Delta V/\Delta S$

and $\mathrm{d}T_{ord}/\mathrm{d}h = \Delta M/\Delta S$ give valuable information about the evolution of the phase transition as a function of the external control parameters.

In solids, most of these transitions are related to a sudden change of volume due to magnetostrictive effects or crystalline symmetry modifications, driven by some strong spin-phonon coupling. Examples of first-order transitions are those observed in dimerized systems, spin-Peirels chains, or quadrupolar splitting. Unfortunately, due to the limited knowledge of the elastic properties of these materials, a detailed description of the process involving a first-order transition can become quite difficult (Stanley 1971). The temperature dependence of $C_p(T)$ close to the transition provides useful information about the microscopic nature of the transition (e.g., dimensionality). The exponent describing the temperature dependence of $C_p(T)$ (with $t = |T - T_{ord}|/T_{ord}$) follows a power law, $t^{-\eta}$, where η is the critical exponent with a value close to zero (e.g., see Stanley 1971).

In a second-order transition a jump in $C_p(T)$, ΔC_p, (like the one shown in Fig. 2) is expected at $T = T_{ord}$ because of the change of the $\mathrm{d}S/\mathrm{d}T$ slope. According to the Ginsburg–Landau (GL) theory, an order parameter (ζ) sets on at $T = T_{ord}$, with infinite initial slope and develops continuously till $T = 0$. Within the scope of the GL theory, the free energy ($G(\Phi)$) shows a minimum of G at $\Phi = \zeta$ and then the variation of $\zeta(T)$ is reflected in $\partial^2 G/\partial T^2$ as a discontinuity or jump in the specific heat. Taking advantage that in ferromagnets ζ corresponds to the spontaneous magnetization $M_s(T)$, a direct observation of that parameter can be done as shown in Fig. 2. Furthermore, as $\Delta U_m \propto M_s^2$ then $C_m(T) \propto \mathrm{d}M_s^2/\mathrm{d}T$ is obtained. In broadened transitions, T_{ord} can be experimentally determined as the temperature where
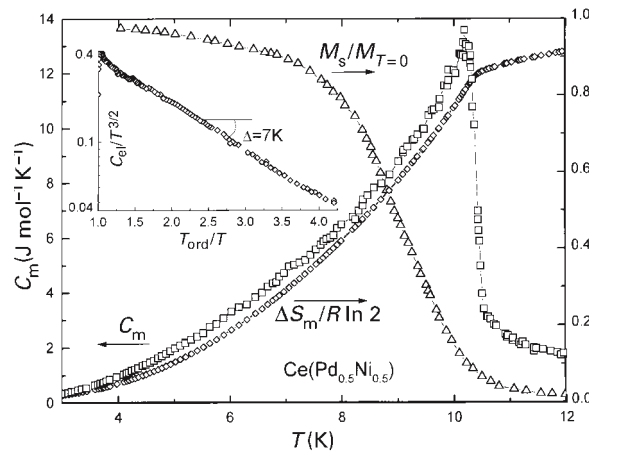
Figure 2
Ferromagnetic example for $\Delta C_m(T_{ord})$ and $C_m(T)$, $\Delta S_m(T)$ and $M_s \propto \zeta(T)$ evolutions. Inset: Arrhenius representation for the magnon gap evaluation.

the maximum slope of the measured $C_m(T \simeq T_{ord})$ anomaly is observed, or more precisely by the entropy compensation criterion around $\Delta C_m(T_{ord})$ (e.g., see Stewart 1984).

Once $\zeta(T)$ develops, any discontinuity implies a jump in $U_m(T)$ and thus the occurrence of a first-order transition. Therefore, in magnetic systems presenting further transformations within their ordered phase, the second-order one is only expected at the paramagnetic phase boundary and first-order ones at lower temperatures, (as observed in $CeRu_2Ge_2$, Wilhelm *et al.* 1999). In some cases first- and second-order transitions occur simultaneously, as in the case of magnetostrictive effects. There, the change of volume (first-order) is triggered by the onset of magnetic order (second-order transition).

2.1 Morphology of the Magnetic Phase Transitions

In a mean field (MF) description of the magnetic transitions the value of $\Delta C_m(T_{ord})$ depends on the momentum J according to, $\Delta C_m(T_{ord}) = 2.5$ $R[(2J+1)^2-1]/[(2J+1)^2+1]$, with a related entropy given by $\Delta S_m = R \ln(2J+1)$. For $J = 1/2$ the respective values are, $\Delta C_m(T_{ord}) = 12.5 \, \text{Jmol}^{-1}\text{K}^{-1}$ and $\Delta S = 5.7 \, \text{Jmol}^{-1}\text{K}^{-1}$, as shown in Fig. 2 for the exemplary compound $Ce(Pd_{0.5}Ni_{0.5})$. Thus, a first-order transition can be recognized when $\Delta C_m(T_{ord})$ clearly exceeds the predicted MF value, as in $CeRu_2Ge_2$ (Wilhelm *et al.* 1999). Concerning the entropy, if it is only due to a discontinuity in $\zeta(T)$, the total entropy will not exceed $\Delta S_m = R \ln(2J+1)$. But, if the first-order transition corresponds to another contribution (e.g., $\Delta V \neq 0$), there is an extra contribution to be taken into account, because $\Delta S_{tot} = \Delta S_m + p\Delta V/T_{ord}$.

2.2 Effects of Magnetic Field, Pressure and Alloying

External magnetic field can be used to distinguish the nature of the magnetic order. In a ferromagnet, the presence of field broadens the transition because of the enhancement of magnetic correlations above T_{ord}. As a consequence $\zeta(T)$ (or $M_s(T)$) does not set on with infinite but with finite slope and from higher temperatures. In an antiferromagnet, the effect of h is quite different because up to a critical field (h_{cr}), where a spin flip is inducted by the applied field, no significant effect should occur and $\Delta C_m(T_{ord})$ is only weakly shifted to lower temperatures. Above h_{cr}, the system will behave like an induced ferromagnet and $C_m(T)$ looks like a Schottky anomaly (see below), which corresponds to a two-level system with the respective parallel and antiparallel spin projection with respect to h. Field effect becomes an important tool in anisotropic systems, because T_{ord} and $\Delta C_m(T_{ord})$ depend on the relative direction between field and magnetic axes.

In view of the mechanical energy involved, the application of external pressure is not expected to produce drastic changes in a magnetic transition by itself, aside from the increase of T_{ord}, due to the reduction of the interatomic distances. However, its effect can be strongly enhanced by other mechanisms such as the hybridization of the local and conduction electron states related to the Kondo effect (e.g., see Sereni 1995). The variation of T_{ord} with pressure is related to $\Delta C_m(T_{ord})$ by the Ehrenfest relation, $dT_{ord}/dp = VT_{ord}\Delta\alpha/\Delta C_m$.

The effect of alloying may produce more important variations in a transition because the chemical potential itself is affected in the substitution process. Local structural pressure and disorder are also typical effects of atomic substitution, with the obvious consequence of the broadening of $\Delta C_m(T_{ord})$. Although pressure and doping are expected to produce similar effects, there are cases showing remarkable differences in $C_m(T)$. Such is the case of the alloyed compound $CeCu_2(Si_{1-x}Ge_x)_2$, where T_{ord} decreases with x, whereas the C_m/T ratio is practically not affected. On the contrary, the application of pressure on the $x = 0.1$ sample does not affect T_{ord}, whereas C_m/T changes significantly (Sparn *et al.* 1998). This different dependence between pressure and doping indicates that the magnetic interaction (i.e., T_{ord}) does not change hand in hand with the amount of condensed degrees of freedom. Knowing $C_m(T,p)$, it is possible to relate this parameter with α through the Maxwell relation, $\partial S/\partial p = -\partial V/\partial T = -\alpha$, as verified in $CeCu_2(Si_{0.9}Ge_{0.1})_2$.

2.3 Low Dimensionality and Anisotropies

It is well known that 1D systems do not develop LRO and their $C_m(T)$ is described as an anomaly. The exact solutions for apparently elementary cases, like those described by Ising (IS) or Heisenberg (HS) models for chains, triangular, or quadratic cases, are not simple and have to be presented as numerical approximations. Nevertheless, the morphology of the phase transition provides some useful information regarding the characteristics of the ordered phase. For example, a 2D-IS lattice is expected to exhibit a logarithmic singularity, $C_m = A \ln t$ on both sides of the transition, with the proportionality factor, A, depending on the type of magnetic lattice (de Jongh and Miedema 1974). The systems approaching the 2D-HS magnetic configuration can be recognized from the evolution of their $\Delta S_m(T)$ because it is predicted that $\Delta S_m(T < T_{ord}) \approx \Delta S_m(T > T_{ord})$. A good complement is to also evaluate $\Delta U_m(T)$ and to compare its distribution above and below T_{ord}. For example, in a 3D-f.c.c. lattice with spins $\frac{1}{2}$, the values are, $(S_\infty - S_{ord})/(R \ln 2) = 0.27$ (HS) or 0.10 (IS) and $(U_\infty - U_{ord})/U_\infty = 0.44$ (HS) or 0.15 (IS), respectively (e.g., see Fisher 1967, Fig. 3).
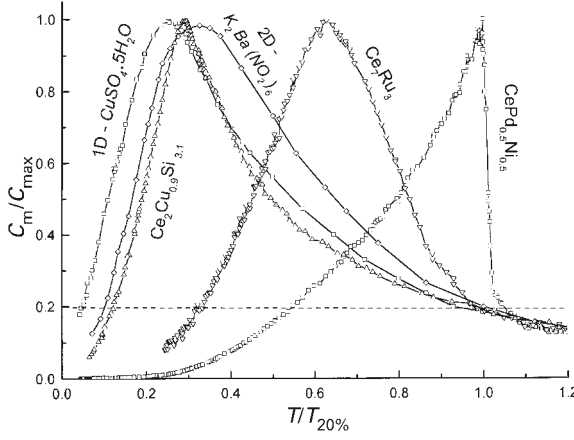
Figure 3
Normalized C_m/C_{max} versus the temperature at which $C_m(T) = 0.2 C_{max}$, $T/T_{20\%}$, to compare the evolution of magnetic correlations in 1D, 2D ($s = 1/2$ Heissenberg) and 3D magnetic systems.

In metallic systems, the anisotropy plays an important role in the magnetic behavior of rare earth compounds because of the CF effect. In these cases the $\Delta S_m(T)$ evolution tends to resemble the one expected for systems with lower symmetry, though the anisotropic $\zeta(T)$ develops in 3D. It is observed for example, that C_m/T versus T is symmetric with respect to the temperature of the maximum of C_m/T. Such a Λ-type transition fulfills the condition for a 2D-HS pattern, $\Delta S_{mag}(T < T_{ord}) \approx \Delta S_{mag}(T > T_{ord})$, despite the 3D behavior which is expected in compounds such as Ce_7Ru_3 or $CeCu_{0.45}Si_{1.55}$ (see Fig. 3). Indeed, for a strict definition of T_{ord}, it must be taken into account that in an antiferromagnet $\Delta U_m(T)$ is proportional to the magnetic correlation strength between spins, $\langle s_i * s_j \rangle^2 \propto \mu_{eff}^2$ (the effective moment). As $\Delta U_m(T) \propto \mu_{eff}^2 \propto \chi(T)T$, the following relation is obtained, $C_m(T) \propto d(\chi T)/dT$ (de Jongh and Miedema 1974). Then, because T_{ord} is defined by the temperature of the maximum variation of $U_m(T)$, it corresponds to the maximum of $C_m(T)$, not to the maximum slope (as in MF transitions).

2.4 Tails ($T > T_{ord}$)

The ideal phase boundary between an LRO phase and the paramagnetic (P) phase is not always well defined in real systems because magnetic fluctuations and/or correlations set on well above T_{ord}. The region where these precursors of the LRO dominate the scenario can be considered as quasi-paramagnetic (QP). From $\chi(T)$, the boundary of such a QP region can be recognized as a deviation from the Curie law, $\chi \propto T^{-1}$. This criterion can be transferred to the specific heat by using the Maxwell relation, $\partial S/\partial h = \partial M/$

Figure 4
Normalized evolution of different systems to their respective paramagnetic states where $C_m T^2 \to B$, after subtracting phonon and excited CF-levels contributions. The Schottky type curve represents the $C_{RF}(T)$ of Ce_2NiGa_7. Inset: comparison of different anomalies around $C_{max}(T_{max})$.

$\partial T \to \gamma/\partial h = \partial^2 M/\partial T^2 = h \partial^2 \chi/\partial T^2$ (Stanley 1971), from which a $C_m \propto T^{-2}$ dependence is deduced for the paramagnetic phase where $\partial M/\partial h = \chi \propto T^{-1}$. Therefore, the $C_m T^2 = B$ condition can be used to define the boundary between P and QP regions. Some selected examples of how the $C_m(T)T^2$ reaches this condition are shown in Fig. 4.

This way of approaching the P-phase can be used to compare the strength of the correlations above T_{ord} in different systems. In Fig. 3, the temperature is normalized to that at which $C_m(T)$ is 1/5 ($= 20\%$) of its maximum value. As shown in Fig. 3, the evolution of quite different magnetic systems at high temperatures nearly coincides in their $C_m \propto T^{-2}$ tendency, though the way they reach their respective C_m^{max} value is very different.

In disordered or frustrated systems or those with low lying spin excitations, LRO may not develop at finite temperature. Nevertheless, the magnetic correlations accounted by the $C_m(T)$ tails can be considered as precursors of a magnetic transition. However, if it orders, the condensed degrees of freedom are taken from the QP state, where magnetic correlations are developing and then $C_m(T > T_{ord})$ can be used as a reference function (C_{RF}). Frequently, these tails are well described by a $C_{RF} \propto -T \ln(T)$ function, which can be independent of doping and pressure (e.g., see Sereni 1998 and references therein).

3. The Magnetically Ordered Phase ($T < T_{ord}$)

The description of the ordered state in a magnetic system is given by the spin wave theory (e.g., see

Akhieza *et al.* 1968). Within this theory there are well defined $C_m(T)$ dependencies, as for example:

(i) ferro- and ferrimagnets with a quadratic ($q = 2$) magnon dispersion-relation, $C_m(T) \propto T^{3/2}$

(ii) antiferromagnets with linear ($q = 1$) magnon dispersion-relation, $C_m(T) \propto T^3$ (note that in these two isotropic cases, the temperature exponent, T^η, is given by $\eta = D/q$, see Gopal 1966)

(iii) under applied or anisotropic molecular fields, an activation energy for the spin waves arises, and then $C_m(T)$ increases exponentially at low temperatures, with an associated gap (Δ_M) in the magnon spectrum. For h applied on the easy axis of anisotropy of a ferromagnet $C_m(T)$ is $\propto T^{1/2} \exp(-\Delta_M/T)$, and for one with easy plane and h perpendicular to it, a $T^{-1/2} \exp(-\Delta_M/T)$ dependence is expected

(iv) In the case of an antiferromagnet, with an easy axis of anisotropy one also gets $C_m(T) \propto T^{-1/2} \exp(-\Delta_M/T)$, whereas for the field perpendicular it is $C_m \propto T^3$

Experimental examples of most of these cases can be found in Sundström (1978) and the inset of Fig. 2.

3.1 Microscopic Character of the Dispersion Relation

The concept of specific heat as a thermal spectrometer is confirmed by its ability to recognize different microscopical dispersion relations (including gaps) in the magnon spectrum. Two illustrative examples are $Ce(Pd_{0.9}Ag_{0.1})$ and $CePd_3Ga_2$. The first shows antiferromagnetic behavior in its $\chi(T)$ macroscopic signal, despite the ferromagnetism of the CePd matrix. Experimentally, $C_m(T) \propto T^{3/2}$ indicates ferromagnetic interactions, in agreement with the positive Curie–Weiss temperature ($\theta_W > 0$). In this case, the disorder introduced by doping makes the reduced ferromagnetic domains to order randomly among them, behaving macroscopically as an antiferromagnet. A mirror-like case is provided by $CePd_3Ga_2$, which orders ferromagnetically at 6 K (Bauer *et al.* 1993) regardless of its Kondo character (Coqblin *et al.* 1996). Nevertheless, $C_m(T) \propto T^3$ is observed for $T < T_{ord}$ indicating the presence of antiferromagnetic interactions, in agreement with the $\theta_W < 0$ value. In this case, frustration effects due to the hexagonal symmetry of the magnetic lattice may explain the difference between the microscopic interaction and the actual type of order. These examples, and those related to the gap detected in the magnon spectrum, confirm the skill of this technique in providing microscopic information within a range of energy of a fraction of degrees (i.e., $\propto 1 \times 10^{-5}$ eV).

4. Transformations and Related Anomalies

Every physical phenomenon has an associated characteristic energy, which leads it to manifest within a certain range of the control parameters. Once that energy scale is identified, a comparative analysis with other effects can be performed. For this purpose, a distinction between phase transition and transformation has to be made. In the first case, the ordering energy ($k_B T_{ord}$) defines a critical value, whereas for the second (e.g., $k_B T_K$ in the Kondo screening or $k_B T_{sg}$ in a spin glass) it only gives a scale of energy where it competes with the thermal-energy $k_B T$. This implies that the condensation of the degrees of freedom occur within an extended range of temperature.

4.1 Kondo Effect

In a diluted magnetic system, where magnetic moments behave as single impurities, there is a spin-spin interaction between the local moment (f) and the conduction electrons (s). This s–f exchange is antiferromagnetic and leads to the formation of a singlet ground state (GS) due to the spin compensation below the Kondo temperature T_K. Such as process is not a phase transition, but a continuous transformation occurring in a logarithmic temperature scale. A consequence of that interaction there is a significant increase of the density of states $N(E_f)$ due to the formation of a virtual-bound state, which is observed in thespecific heat measurements as a strong enhancement of the γ coefficient. The height of this resonant state ($\sim \gamma$) is inversely proportional to its width and, therefore, $\gamma \propto 1/T_K$. The temperature dependence of the Kondo contribution to the specific heat (C_K) is linear at low temperature, has a maximum at $T/T_K = 0.45$ and reaches the T^{-2} dependence at high temperature (e.g., see Bredl 1978). Once the GS is fully formed $\chi(T \rightarrow 0)$ becomes Pauli-like (i.e., $\sim N(E_f)$) and, therefore, $\sim \gamma$. The electronic scattering is also strongly enhanced, producing the characteristic logarithmic increase of the resistivity at low temperature. The problem of the Kondo effect in transport properties is extensively discussed in the chapter *Kondo Systems and Heavy Fermions: Transport Phenomena*.

4.2 Spin Glasses

Magnetic interactions do not develop LRO when randomness distribution inhibits the propagation of the order parameter. In any case, the presence of a mean molecular field at each magnetic moment site is able to freeze a magnetic configuration at a certain temperature, T_{sg}, below which the system behaves in a co-operative manner. This is a simplified picture for a spin glass that becomes more complex when microscopic aspects are considered (e.g., see Mydosh 1993).

Depending on the concentration (x) of the particles carrying the magnetic moment, different regions can be distinguished:

(i) In diluted magnetic systems, the specific heat contribution (C_{sg}) and the characteristic temperature

can be scaled with the impurities concentration, leading to a universal C_{sg}/x vs. T_x dependence. On the $T < T_{sg}$ range, $C_{sg}(T)$ arises linearly with temperature, with a T^2 dependence at $T \to 0$ (i.e., $C_{sg} = aT + bT^2$). For $T \gg T_{sg}$ the expected $C_{sg} \propto T^{-2}$ dependence is verified (Sereni *et al.* 1979 and references therein). Some of these features are illustrated by the $Th_{0.972}Gd_{0.028}$ alloy in the inset of Fig. 4.

(ii) For higher concentrations short-range correlations occur, leading the formation of magnetic clusters. There, the scaling properties are lost and the anomaly can be described by, $C_{cl} = R(\Delta_{cl}/T)^2 e^{\Delta_{cl}/T}/(e^{\Delta_{cl}/T} - 1)^2$, where Δ_{cl} represents the energy gain in the cluster formation, which depends on the magnetic moment, the volume of the cluster, and the energy of anisotropy

(iii) when clusters interact among them a short range order (within the clusters) coexists with the glassy character of the mutual cluster interaction.

4.3 Schottky Anomalies

Another frequent anomaly observed in specific heat measurements is the so-called Schottky anomaly, which is related to the thermal excitations in a level system split by Δ, like in nuclear or electronic GS, where the degeneracy (g_i) is removed by hyperfine (nuclear) or crystalline (electric) fields. Because the thermal population of the levels is governed by Maxwell–Boltzman statistics, the specific heat is described by $C_{Sch} = R(g_i/g_o)(\Delta/T)^2 e^{\Delta/T}/[1 + g_i/g_o e^{\Delta/T}]^2$. For $T \ll \Delta$ one gets $C_{Sch} = R(g_i/g_o)(\Delta/T)^2 e^{\Delta/T}$ and at high temperatures the typical T^{-2} tail appears (Gopal 1966). Because the involved entropy is fixed by the relative degeneracy of the ground and excited levels, $\Delta S = R \ln(g_i/g_o)$, the value of C_{Sch}^{max} and its temperature depend on g_i/g_o and Δ, respectively. In the case where $g_i = g_o$, one can write $C_{Sch}(T) = R(\Delta/2T)^2 \mathrm{sech}(\Delta/2T)^2$. Note that a similar formula was used for $C_{cl}(T)$, where the Bose statistics was applied and thus $C_{cl}(T) = R(\Delta/2T)^2 \mathrm{cosech}(\Delta/2T)^2$.

4.4 Ordering and Anomalies

Magnetic transitions may occur superimposed on these anomalies. In such a case, the fraction of degrees of freedom involved are those not yet condensed into the GS, i.e., $\Delta S(T_{ord})/\Delta S_\infty$. This situation frequently occurs in Kondo systems, where $\Delta C_m(T_{ord})$ is reduced with respect to the expected 1.5R value (e.g., see Bredl *et al.* 1978), when the CF excited levels are still thermally populated or two magnetic configurations compete in the formation of the ordered GS like in $CeNi_xGa_{4-x}$. In the last two cases a $C_{Sch}(T)$-type function plays the role of a reference function, as shown in Fig. 4.

In order to distinguish between a broadened transition and a transformation, some thermodynamic criteria are useful. In a broadened transition, $\Delta S(T)$ should have a change of slope at T_{ord}, reflected in a sudden increase of the negative slope of $\Delta C_m(T)$ by cooling. Alternatively, in a transformation, the $\Delta C_m(T)$ curvature (i.e., $\delta^2 C_m/\delta T^2$) changes monotonously from negative to positive as T decreases.

5. Phases Involving Strongly Correlated Electrons

5.1 The Quasi-paramagnetic Region

In this QP region the magnetic correlations dominate the scenario before the eventual formation of an LRO. When such a situation persists down to very low temperatures, divergencies in $C_m/T(T \to 0)$ are observed because of the enhanced density of low lying spin excitations. Such is the case of Ce-$Cu_{0.9}Au_{0.1}$ shown in Fig. 1 (Löhneysen 1995). A generalized scaling function $C_m/t = -F \log(t) + E$ was proposed for these systems, with $t = T/T_0 (T_0 \propto T_K)$ and $F = 7.2 \, \mathrm{Jmol^{-1}K^2}$ as a universal constant. Besides the logarithmic, algebraic divergencies of the type $C_m/T = \gamma_0 - \gamma_1 T^\eta$ (with $\eta = 1/2$ or 2) were also proposed. Nevertheless, a continuous spectrum of values can be found experimentally in this non-Fermi-liquid (NFL) region (e.g., see Sereni 1998).

Depending on whether the coupling parameter between the local and band electrons spins increases or decreases, the respective low temperature boundary of the QP region is the LRO or the nonmagnetic phase. In the cases where these two phases converge for $T \to 0$, the NFL region becomes narrow and a zero temperature quantum critical point may occur with C_m/T showing some of the predicted T-divergencies (see Löhneysen 1995 and Sparn *et al.* 1998). However, in many cases such a region is quite extended (mostly due to disorder effects) and then a variety of $C_m/T(T \to 0)$ divergencies can be observed (Sereni 1998).

An alternative scenario for incipient magnetic interactions is given by the itinerant magnetism or spin-fluctuations. Due to thermal excitations, spins fluctuate in orientation and amplitude with an associated frequency (ω_{sf}). When $\omega_{sf}^{-1} \propto k_B T_{sf}$ is greater than the thermal energy, the spins look nonmagnetic. On the contrary, at high temperatures thermal fluctuations are more rapid than those of the spins and able to "see" the magnetic component. In this case it is predicted that $C_m/T \propto T^2 \ln(T/T_{sf})$, as shown in Fig. 1 by the exemplary system UAl_2 (Stewart 1984).

5.2 The Nonmagnetic Phase: Heavy Fermions and Intermediate Valent

In a periodic Kondo lattice a narrow electronic band with heavy electrons is responsible for the large γ value. These heavy fermion (HF) quasi-particles present a coherent state identified by a significant

reduction of the electrical resistivity ($\rho = AT^2$) and a strongly enhanced Pauli-like susceptibility (χ). Because in an FL system γ, χ_0 and $A^{1/2}$ are proportional to $N(E_f)$, all these parameters have to be proportional between them. In Fig. 1, the $C_p(T)$ dependence of the HF prototype $CeCu_6$ is shown, with $\gamma = 1.6\,\mathrm{J\,mol^{-1}\,K^{-2}}$. Like for Kondo impurities, $\gamma \propto 1/T_K$ and then its characteristic temperature is deduced to be about 5 K. Indeed, γ depends on temperature like $\gamma(T) = C_K(T)/T$ and, because the Kondo-lattice state is built up from a doublet ground state, the related entropy is also $R \ln 2$.

For large hybridization strength between local and conduction states, both spin and charge components of the wave function are mixed, leading to an intermediate valent (IV) state. In that case, the width of the energy levels becomes comparable to the CF splitting, and then the system gains energy (when $T_K \geqslant \Delta$) by going from a two-fold-degenerated GS (with $J = 1/2$) to the full spin-orbit six-fold-degenerated state (e.g., $J = 5/2$ for Ce). With the consequent increase of the effective level width (T_K) and the reduction of γ (compare $CeCu_6$ with $CeIr_2$ in Fig. 1). In this IV state, the nonmagnetic character comes from the disappearance of the moment due to the 4f-electron delocalization, whereas in the HF state only the spin compensation is involved. Here the FL behavior is fully verified through the Wilson ($\chi_o/\gamma = 0.036\,\mathrm{emu\,K^2\,J^{-1}}$) and Kadowaki–Woods ($A/\gamma^2 = 1 \times 10^{-6}\,\Omega\,\mathrm{cm}\,(\mathrm{J\,K\,mol^{-1}})^{-2}$) ratios, in agreement with the values predicted by the theory (e.g., see Sereni 1991 and references therein). Although the Wilson ratio is claimed to be applicable also for HF systems, the lack of good quantitative determination μ_{eff} of the doublet GS impedes a reliable experimental verification.

The transformation or cross-over from HF to IV states by doping occurs at a cross-over concentration: x_{cr} (Sereni 1995) where most of physical properties (like V, γ, θ_W, ρ, χ) show a change of regime through a change in the concentration dependence. Particulary $\gamma(x)$, shows a maximum at x_{cr}. Although a decrease of $\gamma(x)$ should be expected when going from an HF to an IV regime as T_K increases, the experimental observation indicates that the effective width of the hybridized f level does not evolve monotonously (see Coqblin *et al.* 1996 and references therein). Therefore, the maximum observed in $\gamma(x)$ should be related to the change (increase) of the GS degeneracy from $g_0 = 2$ to 6 (c.f. $J = 5/2$) as mentioned before for cerium ions (Sereni 1995).

6.   Concluding Remarks

This condensed overview on the specific heat of magnetic systems shows some examples of the wide range of information that can be extracted from the experimental study of this thermal parameter. Since it covers macroscopic (thermodynamical) as well as microscopic (e.g., excitation spectrum) properties, it represents one of the basic tools for the characterization of new systems (together with magnetic and transport measurements). Alternatively, since it allows a direct evaluation of the evolution of the entropy with temperature, it gives access to many other thermodynamical parameters through different Maxwell relations. Similar analysis of the specific heat contributions can be applied to other physical phenomena, such as elastic (structural) instabilities, particles diffusion, ferroelectricity, or superconducting properties (see Gopal 1966).

See also: Crystal Field Effects in Intermetallic Compounds: Inelastic Neutron Scattering Results; Electron Systems: Strong Correlations; Heavy-fermion Systems; Intermediate Valence Systems; Magnetic Excitations in Solids; Magnetic Systems: Disordered

Bibliography

Akhieza A I, Bar'yakhtar V G, Peletminskii S V 1968 In: Doniach S (ed.) Thermodynamics of ferromagnets and antiferromagnets. *Spin Waves*. Chap. 6. North Holland, Amsterdam

Bauer E, Hauser R, Gratz E, Schaudy G, Rotter M, Gignoux D, Schmitt 1993 $CePd_2Ga_3$: a new ferromagnetic Kondo lattice. *Z. Phys. B.* **92**, 411–6

Bredl C D, Steglich F, Schotte K D 1978 Specific heat of concentrated Kondo systems. *Z. Phys. B* **29**, 327–40

Coqblin B, Arispe J, Iglesias R J, Lacroix C, Le Hur K 1996 Competition between Kondo and magnetism in heavy fermion compounds. *J. Phys. Soc. Jpn. Suppl. B* **65**, 64–77

de Jongh J L, Miedema A R 1974 Experiments on simple magnetic systems. *Adv. Phys.* **23**, 1–269

Fisher M E 1967 The theory of equilibrium critical phenomena. *Rep. Prog. Phys.* **30**, 698–702

Goodstein D L 1985 *States of Matter*. Dover, New York

Gopal E R 1966 *Specific Heats at Low Temperatures*. Heykood Books, London

Löhneysen H V 1995 Non-fermi-liquid behavior in heavy-fermion systems. *Physica B* **206/207**, 101–7

Mydosh J A 1993 *Spin Glasses: An Experimental Introduction*. Taylor and Francis, London

Sereni J G 1991 Low temperature behavior of cerium compounds. In: Gschneidner K A Jr. Eyring L (eds.) *Handbook on the Physics and Chemistry of Rare Earths*. Elsevier, Amsterdam, Vol. 15 Chap. 98

Sereni J G 1995 Characteristic concentrations in cerium ground state transformations. *Physica B.* **215**, 273–85

Sereni J G 1998 Comparative study of magnetic phase diagrams of Ce compounds. *J. Phys. Soc. Jpn.* **67**, 1767–75

Sereni J G, Huber T E, Luengo C A 1979 Low temperature specific heat of Th–Gd spinglass. *Solid State Commun.* **29**, 671–3

Sparn G, Donnevert L, Hellmann P, Link A, Thomas S, Gegenwart P, Buschinger B, Geibel C, Steglich F 1998 Pressure studies near quantum phase transitions in strongly correlated Ce systems. *Rev. High Pressure Sci. Technol.* **7**, 431–6

Stanley H E 1971 *Introduction to Phase Transition and Chemical Phenomena*. Clarendon, Oxford

Stewart G R 1984 Heavy fermion systems. *Rev. Mod. Phys.* **56**, 755–87

Sundström L J 1978 Low temperature heat capacity of the rare earth. In: Gschneidner K Jr. Eyring L (eds.) *Handbook on the Physics and Chemistry of Rare Earths.* North-Holland, Amsterdam, Vol. 2, Chap. 5

Wilhelm H, Alami-Yadri K, Revaz B, Jaccard D 1999 Detailed investigation of the magnetic diagram of CeRu$_2$Ge$_2$ up to 11 GPa. *Phys. Rev. B* **59**, 3651–60

J. G. Sereni
Centro Atomico Bariloche (CNEA), San Carlos de Bariloche, Argentina

Magnetic Units

The International System of Units, SI (Le Systéme International d'Unités), was adopted by the Conférence Générale des Poids et Mesures in 1960. It is a coherent system founded on seven base units (meter, kilogram, second, ampere, kelvin, mole, and candela) and its use is recommended by the International Union of Pure and Applied Physics (Cohen and Giacomo 1987). Nevertheless, a significant part of the existing literature, particularly concerning magnetism, is still expressed in terms of the electromagnetic (c.g.s.) or the Gaussian systems. Hence, it might be helpful to provide the relationships between the SI and these systems, although it is not intended to advance the use of the latter.

1. Relationship Between SI, c.g.s., and Gaussian Systems

In contrast to the SI system, the c.g.s. system is based on three base units only (centimeter, gram, and second) being appropriate for mechanical problems. The dual nature of the system emerged from the application to electricity and magnetism, where all quantities may be alternatively expressed in either electrostatic units (esu) or electromagnetic units (emu). The electrostatic system defines charge to be a derived quantity based on Coulomb's law for the force between two charges, while the electromagnetic system defines electric current as a derived quantity based on Ampere's law for the force between two electric current elements:

$$\mathbf{F} = k_e \frac{q_1 q_2 \mathbf{r}}{\varepsilon r^3} \quad \mathrm{d}^2\mathbf{F} = k_m \mu \frac{i_1 \mathrm{d}\mathbf{l}_1 \times (i_2 \mathrm{d}\mathbf{l}_2 \times \mathbf{r})}{r^3}$$

In the electrostatic system, $k_e = 1$ is chosen and the permittivity, ε, is defined to be dimensionless and to adopt unity in free space. In the electromagnetic system, $k_m = 1$ is chosen and the permeability, μ, is

defined to be dimensionless and to adopt unity in free space.

One of the main advantages of the SI system is the unification of magnetic quantities with practical electric units of ampere and volt. The unit for current in esu is the statampere (3×10^9 esu s$^{-1} \dot{=} 1$ A) while in emu it is the abampere (1 abampere $\dot{=} 10$ A). For the "mixed" (or "symmetrized") c.g.s. or Gaussian system, all electrical quantities are measured in esu and all magnetic quantities in emu, hence statampere is used here.

The duality is removed in the MKSA or practical system, developed by Maxwell and Giorgi, by introducing the current as an additional base unit without the attempt to express the ampere dimensionally in length, mass, or time. This system is said to be "rationalized," since the prefactors of Coulomb's and Ampere's laws are set equal to $1/4\pi$, while the choice of these prefactors is unity in the c.g.s. and Gaussian systems. This leads to the appearance of factors of 2π and 4π in situations that involve plane geometry and to their absence in situations with spherical or cylindrical symmetry, where these factors might normally be expected in the c.g.s. and Gaussian systems. These systems are therefore called "nonrationalized." Eventually, the SI system was formulated on the basis of the rationalized MKSA system. A comparison of the basic equations (Maxwell's and material equations) of these two systems is given in Table 1, where the quantities in the Gaussian system are indicated with an asterisk and the symbols recommended by IUPAP (Cohen and Giacomo 1987) are used (**E**, electric field; **P**, electric polarization; **H**, magnetic field; **B**, magnetic flux density; **M**, magnetization; χ_m, χ_e, magnetic or electric susceptibility; μ, permeability; ε, permittivity).

As a result of the fourth base unit in the SI and MKSA system, permeability $\mu = \mu_r \mu_0$ and permittivity $\varepsilon = \varepsilon_r \varepsilon_0$ are dimensional physical quantities where ε_0 and μ_0 must fulfill the condition $\varepsilon_0 \mu_0 c^2 = 1$, in order that electrostatics and electromagnetics are coherent. This avoids the asymmetrical introduction of the factor c into the equations for electric and magnetic

Table 1
Maxwell's and material equations.

Gaussian system with three base quantities	SI system with four base quantities
$c\nabla \times \mathbf{E}^* = -\partial\mathbf{B}^*/\partial t$	$\nabla \times \mathbf{E} = -\partial\mathbf{B}/\partial t$
$c\nabla \times \mathbf{H}^* = 4\pi\mathbf{j}^* - \partial\mathbf{D}^*/\partial t$	$\nabla \times \mathbf{H} = \mathbf{j} + \partial\mathbf{D}/\partial t$
$\nabla \cdot \mathbf{D}^* = 4\pi\rho^*$	$\nabla \cdot \mathbf{D} = \rho$
$\nabla \cdot \mathbf{B}^* = 0$	$\nabla \cdot \mathbf{B} = 0$
$\mathbf{D}^* = \varepsilon_r\mathbf{E}^* = \mathbf{E}^* + 4\pi\mathbf{P}^*$	$\mathbf{D} = \varepsilon\mathbf{E} = \varepsilon_0\varepsilon_r\mathbf{E} = \varepsilon_0\mathbf{E} + \mathbf{P}$
$\mathbf{B}^* = \mu_r\mathbf{H}^* = \mathbf{H}^* + 4\pi\mathbf{M}^*$	$\mathbf{B} = \mu\mathbf{H} = \mu_0\mu_r\mathbf{H} = \mu_0(\mathbf{H} + \mathbf{M})$
$\varepsilon_r = 1 + 4\pi\chi_{e}^*$	$\varepsilon_r = 1 + \chi_e$
$\mu_r = 1 + 4\pi\chi_m^*$	$\mu_r = 1 + \chi_m$

quantities. In the SI system the permeability of vacuum is defined to have the value $\mu_0 = 4\pi \times 10^{-7}$ $NA^{-2} = 4\pi \times 10^{-7}$ $Hm^{-1} = 4\pi \times 10^{-7}$ $VsA^{-1}m^{-1}$.

The comparison of the corresponding equations in both systems yield the following relationships: $\sqrt{4\pi/\mu_0} = \mathbf{B}^*/\mathbf{B} = \mathbf{M}/\mathbf{M}^*$; $\sqrt{4\pi\mu_0} = \mathbf{H}^*/\mathbf{H}$; $4\pi = \chi/\chi^*$; $\sqrt{4\pi\varepsilon_0} = \mathbf{E}^*/\mathbf{E} = \rho/\rho^* = \mathbf{j}/\mathbf{j}^* = \mathbf{P}/\mathbf{P}^*$; and $\sqrt{4\pi/\varepsilon_0} = \mathbf{D}^*/\mathbf{D}$, which are useful to convert an *equation* in Gaussian units into the corresponding equation in the SI system and vice versa.

For example, to transform an equation in Gaussian units into SI, replace the quantities with an asterisk by those without an asterisk according to the above relationships (e.g., $\mathbf{B}^* \Rightarrow \mathbf{B}\sqrt{4\pi/\mu_0}$; $w = \frac{1}{2}\mathbf{B} \cdot \mathbf{H}$, $w^* = (1/8\pi)\mathbf{B}^* \cdot \mathbf{H}^*$). Quantities that involve only volume, force, energy, and length transform directly.

2. Definition of the Magnetic Quantities

The magnetic quantities are defined in SI as follows (International Organization for Standardization 1992). The magnetic field strength, $\mathbf{H}$, is a vector quantity, the rotation (curl) of which is equal to the sum of the electric current density and the time derivative of the electric flux density. The magnetic flux density or magnetic induction, $\mathbf{B}$, is a vector quantity such that the force exerted on an element of electric current is equal to the vector product of this element and the magnetic flux density: $\mathbf{F} = I\Delta\mathbf{s} \times \mathbf{B}$. The magnetic moment, $\mathbf{m}$, is a vector quantity, the vector product of which with the magnetic flux density of a homogeneous field is equal to the torque: $\mathbf{m} \times \mathbf{B} = \mathbf{T}$. The International Electrotechnical Commission (IEC) defines also the magnetic dipole moment, $\mathbf{j} = \mu_0\mathbf{m}$. The magnetization as the magnetic moment per unit volume is defined by the relationship $\mathbf{M} = \mathbf{B}/\mu_0 - \mathbf{H}$. The permeability is defined by $\mathbf{B} = \mu\mathbf{H}$ and the relative permeability by $\mu_r = \mu/\mu_0$, where the latter is dimensionless. This is also the case for the magnetic susceptibility defined by $\chi = \mu_r - 1$. The electromagnetic field energy divided by volume is given by $w = \frac{1}{2}\mathbf{E} \cdot \mathbf{D} + \mathbf{B} \cdot \mathbf{H}$.

3. Analogies Between Electric and Magnetic Field Quantities

According to the structure of Maxwell's equations, two types of analogies can be derived for the electric and magnetic field quantities:

(i) The distinction according to the structure of the differential operators (curl and div) leads to the correspondences $\mathbf{E} \leftrightarrow \mathbf{H}$ and $\mathbf{D} \leftrightarrow \mathbf{B}$. This becomes also evident from the integral formulation of Maxwell's relationships, where the electric and magnetic potential differences, $U = \oint \mathbf{E} \cdot d\mathbf{s}$ and $U_m = \oint \mathbf{H} \cdot d\mathbf{s}$, occur as well as the electric flux $\Psi = \oint_{(V)} \mathbf{D} \cdot d\mathbf{A}$ and the magnetic flux $\Phi = \oint_{(V)} \mathbf{B} \cdot d\mathbf{A}$. The electric and magnetic energy densities $w_e = \int \mathbf{E} \cdot d\mathbf{D}$ and $w_m = \int \mathbf{H} \cdot d\mathbf{B}$ also

imply this correspondence. This indicates the primacy of $\mathbf{H}$ based on fictive magnetic surface poles (or "magnetic charges") traditionally used in magnetostatics by analogy with electrostatics. However, this is not a valuable or helpful entry to electromagnetism (see below).

(ii) The distinction by homogeneous and inhomogeneous equations leads to the correspondences $\mathbf{E} \leftrightarrow \mathbf{B}$ and $\mathbf{D} \leftrightarrow \mathbf{H}$, which is also consequent with respect to the influence of matter upon the field quantities: $\nabla \cdot \mathbf{D}$ and $\nabla \times \mathbf{H}$ are determined by the *external* charge and current densities, respectively, and the corresponding equations for $\nabla \cdot \mathbf{E}$ and $\nabla \times \mathbf{B}$ in matter additionally contain polarization charge density $\rho_\mathbf{P} = -\nabla \cdot \mathbf{P}$ and polarization and magnetization current densities $\mathbf{j}_\mathbf{P} = \partial\mathbf{P}/\partial t$ and $\mathbf{j}_\mathbf{M} = \nabla \times \mathbf{M}$, respectively. Thus, the magnetic induction or magnetic flux density, $\mathbf{B}$, is the field in matter.

4. The Primacy of B or H

The codification of the field quantities goes back to Faraday, Maxwell, and their contemporaries. In this tradition the primary magnetic field is $\mathbf{H}$ as the "magnetizing force" now called field strength. The term "magnetic induction" for $\mathbf{B}$ points to the status of a variable quantity that is determined by the sum of $\mathbf{H}$ and $\mathbf{M}$ and corresponds to analogy (i) above. Thus the "coefficient of induced magnetization," χ, is the ratio of $\mathbf{M}$ to $\mathbf{H}$ and the "coefficient of induction," μ, is the ratio of $\mathbf{B}$ to $\mathbf{H}$, named susceptibility and permeability, respectively, by William Thomson (Bennett *et al*. 1976, Goldfarb 1992).

However, as stated in (ii) above the field within magnetized matter is not $\mathbf{H}$ but $\mathbf{B}$, since $\mathbf{B}$ is produced by both the conduction and the Amperian (atomic) currents, while $\mathbf{H}$ has its source in external conduction currents only. Hence, analogy (ii) is more general and those emphasizing the primacy of $\mathbf{B}$ have an excellent viewpoint but are at a historical disadvantage, since the magnetic pole approach has traditionally been used in magnetostatics by analogy with electrostatics.

For the characterization of magnetic materials the traditional approach is usually used because the desired quantity is $\mathbf{M}(\mathbf{H},T)$. The relevant field in a magnetized sample is the *internal field*, $\mathbf{H}$, which occurs in these equations and originates not only from the external field, $\mathbf{H}_{ext}$, but also from the stray- or self-field of the magnetized body. Thus, $\mathbf{H}_{ext}$ has to be corrected by the demagnetizing field $\mathbf{H}_D \equiv -N\mathbf{M}$, where N (or D) is the *demagnetizing factor* and depends on the sample geometry:

$$\mathbf{H} \equiv \mathbf{H}_{int} = \mathbf{H}_{ext} + \mathbf{H}_D = \mathbf{H}_{ext} - N\mathbf{M}$$

Only spheres and ellipsoids have a uniform $\mathbf{M}$ in a uniform $\mathbf{H}_{ext}$ and can therefore be calculated in a closed form while for cylinders and parallelepipeds only approximate N values can be given. The

demagnetizing factors for the three orthogonal axes of any uniformly magnetized body sum up to unity; hence, $N = 1/3$ for a sphere. For a review on demagnetizing factors see, e.g., Chen *et al.* (1991) and Goldfarb (1992).

5. SI System

In the SI system, the relationship between **B**, **H**, and **M** is defined as $\mathbf{B} = \mu_0(\mathbf{H} + \mathbf{M})$ and $\chi = d\mathbf{M}/d\mathbf{H}$. The magnetic polarization $\mathbf{J} = \mu_0\mathbf{M}$ is also a recognized quantity even though it is based on $\mathbf{B} = \mu_0\mathbf{H} + \mathbf{J}$ which is not a defining relationship in SI. The units of **B** and **J** are tesla ($T = Vsm^{-2} = Wbm^{-2}$) and those of **H** and **M** are Am^{-1}; accordingly, χ is dimensionless. **M** and χ are extensive quantities and are based on a unit volume, i.e., the volume magnetization is defined as the magnetic moment (Am^2) per unit volume, which yields Am^{-1}. The volume, however, is usually more difficult to determine with the same precision as the mass and is furthermore temperature dependent. For technical applications, the volume magnetization is the commonly used quantity. In condensed matter physics, however, the temperature dependencies of these quantities are of importance; the mass magnetization (M or σ) and the mass susceptibility (χ_ρ) are preferred although the latter two are not recognized as important SI quantities but are consistent with SI. Their conversion into recognized units requires knowledge of the density as a function of temperature, which is usually not available, in particular for novel materials, at least not with the same precision as the measurement of $M(T)$ or $\chi(T)$. Furthermore, the mass magnetization ($Am^2kg^{-1} = JT^{-1}kg^{-1}$) is preferred to the volume magnetization since atomic quantities such as the magnetic moment per atom, mole, or formula unit (f.u.) can be derived directly. The number, n, of Bohr magnetons per mole (μ_Bmol^{-1}) is simply obtained from the mass magnetization by $Mm_{mol}/N_A\mu_B = Mm_{mol}/5.5849 = n[\mu_Bmol^{-1}]$, where $N_A = 6.0221367 \times 10^{23}\,mol^{-1}$, m_{mol} is the molar mass, and $\mu_B = 9.2740154 \times 10^{-24}\,JT^{-1}$. The same holds also for the effective moment, which is determined from the Curie–Weiss law via $\chi(T)$ measurements.

6. Electromagnetic c.g.s. and Gaussian Systems

In the c.g.s. and Gaussian systems, the defining relationship is $\mathbf{B}^* = \mathbf{H}^* + 4\pi\mathbf{M}^*$. Accordingly, one major property of these systems is that $\mathbf{B}^*$ and $\mathbf{H}^*$ have the same numerical value in empty space, considered as an advantage by some and as a disadvantage by others (e.g., Brown 1984). $\mathbf{B}^*$ is given in gauss (G) and $\mathbf{H}^*$ in oersteds (Oe), which are dimensionally equivalent ($cm^{-1/2}g^{1/2}s^{-1}$). The term $4\pi\mathbf{M}^*$ can be considered as the field in gauss arising from the magnetization of the material, whereas the magnetization, $\mathbf{M}^*$, considered as the magnetic moment per unit volume, differs numerically by the factor of 4π but is dimensionally the same ($emu\,cm^{-3} \doteq ergG^{-1}cm^{-3} = cm^{-1/2}g^{1/2}s^{-1} = G$).

Table 2
Magnetic quantities and conversion from Gaussian to SI units.

Quantity	Symbol	Gaussian system	Conversion factor	SI system
Magnetic flux	Φ	Mx, $G\,cm^2$	10^{-8}	Wb, Vs
Magnetic flux density, magnetic induction	B	G	10^{-4}	T, Wbm^{-2}
Magnetic potential difference, magnetomotoric force	U, F	Gb (gilbert)	$10/4\pi$	A
Magnetic field strength	H	Oe	$1000/4\pi$	Am^{-1}
Volume magnetization	$4\pi M$	G	$1000/4\pi$	Am^{-1}
Volume magnetization	M	$emu\,cm^{-3}$, G	1000	Am^{-1}
Magnetic polarization	J	$emu\,cm^{-3}$, G	$4\pi \times 10^{-4}$	T, Wbm^{-2}
Mass magnetization	M, σ	$emu\,g^{-1}$, $G\,cm^3g^{-1}$	1	Am^2kg^{-1}, $JT^{-1}kg^{-1}$
Magnetic moment	m	emu, $erg\,G^{-1}$	1/1000	Am^2, JT^{-1}
Magnetic dipole moment	j	emu, $erg\,G^{-1}$	$4\pi \times 10^{-10}$	Wbm, Vsm
Volume susceptibility	χ, κ	Dimensionless, $emu\,cm^{-3}$	4π	Dimensionless
Mass susceptibility	χ, κ	$emu\,g^{-1}$, cm^3g^{-1}	$4\pi/1000$	m^3kg^{-1}
Molar susceptibility	χ_{mol}	$emu\,mol^{-1}$, cm^3mol^{-1}	$4\pi \times 10^{-6}$	m^3mol^{-1}
Permeability, $\mu = \mu_0\mu_r$	μ	$\mu^* = \mu_r$	$4\pi \times 10^{-7}$	Hm^{-1}, $VsA^{-1}m^{-1}$
Relative permeability, μ/μ_0	μ_r	Dimensionless	1	Dimensionless
Energy density, energy product	w	$erg\,cm^{-3}$	1/10	Jm^{-3}
Demagnetization factor	N, D	Dimensionless	$1/4\pi$	Dimensionless

Note that emu is not a unit, it is merely an indication that electromagnetic units are in use. This is also evident from the units frequently used for the mass magnetization (emu $g^{-1} \dot{=} erg G^{-1} g^{-1} = G cm^3 g^{-1}$) and the mass susceptibility (emu $g^{-1} = cm^3 g^{-1} =$ emu g^{-1} Oe^{-1}). In terms of base units, the volume susceptibility is dimensionless; however, χ^* is frequently expressed as emu $cm^3 \dot{=} emu\, Oe^{-1} cm^{-3} \dot{=} erg\, Oe^{-1} G^{-1} cm^{-3} = 1$. Accordingly, the notation $4\pi\chi^*$ for the c.g.s. volume susceptibility is numerically equal to the SI volume susceptibility. The permeability is defined in the Gaussian system as the ratio $\mathbf{B}/\mathbf{H}$, hence the Gaussian permeability, μ^*, is identical to the relative permeability in the SI system: $\mu^* = \mu_r = \mu/\mu_0 = 1 + \chi = 1 + 4\pi\chi^*$ (see also the material equations in Table 1).

Table 2 gives numerical factors for the conversion between the two unit systems: multiply the number for the Gaussian quantity by the conversion factor to obtain the number for the SI quantity (e.g., $1\,Mx \times 10^{-8}\,WbMx^{-1} = 10^{-8}\,Wb$). Note that Gaussian and electromagnetic c.g.s. units are the same for magnetic quantities but are different for their electric counterparts.

See also: Perturbed Angular Correlations (PAC)

Bibliography

Bennett L H, Page C H, Schwarzendruber L J 1976 Comments on units in magnetism. In: Becker J J, Lander G H, Rhyne J J (eds.) *AIP Conf. Proc.* American Institute of Physics, New York, Vol. 29, pp. xix–xxi
Brown W F Jr 1984 Tutorial paper on dimensions and units. *IEEE Trans. Magn.* **20**, 112–7
Chen D-X, Brug J A, Goldfarb R B 1991 Demagnetizing factors for cylinders. *IEEE. Trans. Magn.* **27**, 3601–19
Cohen E R, Giacomo P 1987 Symbols, units, nomenclature and fundamental constants in physics. *Physica A* **146**, 1–68
Goldfarb R B 1992 Demagnetizing factors. In: Evetts J (ed.) *Concise Encyclopedia of Magnetic and Superconducting Materials.* Pergamon, Oxford, pp. 103–4
International Organization for Standardization 1992 *Quantities and Units: Part 5. Electricity and Magnetism*, ISO 31-5: 1992(E). ISO, Geneva, Switzerland

G. Hilscher
Institut für Experimentalphysik, TU Wien, Vienna Austria

Magnetic Viscosity

Under the name of magnetic aftereffect (or time-lag in magnetization or magnetic viscosity) everything is included that is connected with the influence of time on magnetization phenomena in ferromagnetic bodies, with the following exceptions (a) the influence of the sample inductance, (b) eddy currents, (c) the irreversible relaxation of chemical or topological microstructure, and (d) relaxation phenomena with characteristic timescales less than 10^{-5} s. Magnetic relaxation phenomena on shorter timescales are dominated by excitation and damping of spin waves, fast motion of domain walls, etc. These phenomena have been extensively investigated by high-frequency resonance experiments (Haas and Callen 1963).

In a typical viscosity experiment the sample has some given magnetic prehistory and the time dependence of magnetization, J, is measured at constant values of temperature, T, and magnetic field, H. In many cases the prehistory begins, as shown in Fig. 1, at some large positive field, H_s, where the sample is in the thermodynamic equilibrium state of magnetic saturation. Then a negative field, H, is applied as fast as possible. The magnetization reacts rapidly (in less than 10^{-5} s) and achieves some value, $J(0)$, on the major demagnetization curve (see Fig. 1(a)). However, now the sample is not in thermal equilibrium and the sudden change of magnetization is followed by a slow relaxation (the aftereffect) on a timescale of seconds, months, or even longer. The first investigation of the magnetic aftereffect was done by J. A. Ewing in the 1880s.

Experimental evidence distinguishes at least four categories of magnetic aftereffects called (a) the reversible aftereffect, (b) the irreversible aftereffect, (c) the anomalous aftereffect, and (d) quantum tunneling of magnetization. Depending on the material investigated and the specific magnetic prehistory of the samples, various types of the time dependence have been observed for the slow relaxation of magnetization. For a large class of experiments a logarithmic time law has been found:

$$J(t) = J(0) + S\ln(1 + t/t_0) \qquad (1)$$

where S is the magnetic viscosity and t_0 is some reference time depending on the sample and on the measuring procedure. The value of t_0 is usually obtained by fitting Eqn. (1) to the experimental data. If t_0 is not appropriately chosen, $J(t)$ will deviate from logarithmic behavior, i.e., in plots such as that of Fig. 1(b), for values of t within an order of magnitude of t_0, the data points will deviate from a straight line. This is not related to the above-mentioned deviations expected for very small values of t ($< 10^{-5}$ s).

Obviously Eqn. (1) is also incorrect for $t \to \infty$. Thus, the magnitude of $J(t)$ cannot exceed the value of the saturation magnetization, J_s, of the material and, for example, at zero field the thermal equilibrium value $J = 0$ has to be achieved for $t \to \infty$. However, the aftereffect is usually small and, in many cases, deviations from Eqn. (1) have not been observed even for times t as long as weeks or months. In the typical example of Fig. 1(b) the relaxation of magnetization over a period of some hours is only a
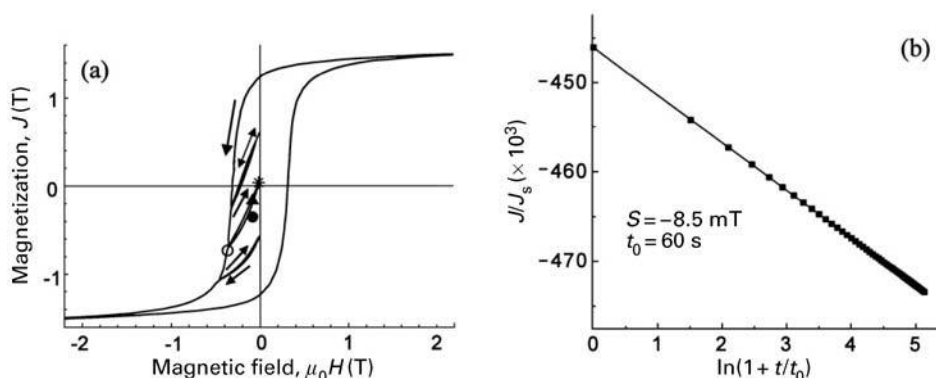
Figure 1
(a) Hysteresis loop of the ferromagnetic material $Nd_4Fe_{77}B_{19}$. The marker ○ is at the coordinate $(H, J(0))$ where the experiment in (b) starts. Also shown are recoil loops beginning at the major demagnetization curve (left-hand branch of the hysteresis loop). The markers ●, ▲, and * characterize the coordinates where the experiments of Figs. 9 and 10 start. (b) Results of a typical viscosity experiment. The parameters S and t_0 are fitted to Eqn. (1); J_s is the magnetization of the previously saturated sample.

few percent. Similar results have been found for all types of ferromagnets ranging from commercial permanent magnets (Givord *et al.* 1987) to the exotic, purely organic soft-magnetic fullerene $TDAE-C_{60}$ (Dunsch *et al.* 1997). Slow relaxation processes similar to the magnetic aftereffect are also known from other fields of physics as the relaxation of remanent magnetization in spin glasses (Huang 1985), the low-frequency dielectric relaxation in ferroelectrics (Jonscher 1983), the elastic aftereffect (found by L. Boltzmann in 1876), or the flux creep in superconductors (Yeshurun *et al.* 1996).

1. Reversible Magnetic Aftereffect

The reversible aftereffect, also called the diffusion or Richter aftereffect, was discovered by G. Richter in 1937 in αFe(C) and interpreted by J. L. Snoek in 1941. This effect is associated with impurity atoms or holes within the ferromagnetic lattice and is observed only in certain substances. In the case of αFe(C) the carbon atoms occupy interstitial sites in the b.c.c. lattice, locally modifying the magnetocrystalline anisotropy in a certain direction (see Fig. 2). When the magnetization is quickly changed owing to a change in the applied magnetic field, the carbon atoms diffuse relatively slowly to a new position. This results in a slow change of the local magnetic anisotropy and, consequently, in a sluggish further change of magnetization. The diffusion aftereffect also occurs if the magnetization is reversibly changed by the magnetic field. If in such a case the field is reversed to its former value, the impurity atoms diffuse back to their former position and the magnetization also relaxes to its former value.
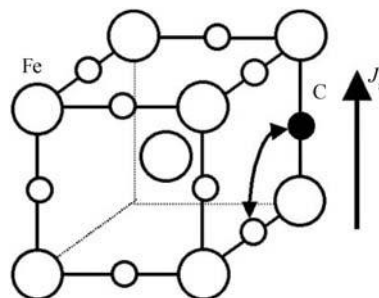
Figure 2
Unit cell of the b.c.c. lattice of αFe(C) with one additional carbon atom (●) which diffuses between interstitial sites (●, ○) thus changing the effective anisotropy experienced by the local magnetization, J_s.

Therefore, this effect is called the reversible aftereffect (Kronmüller 1968). This effect, based on the diffusion of small atoms such as hydrogen, carbon, or nitrogen, has been observed in many crystalline and amorphous alloys as well as intermetallic compounds. An important property of the diffusion aftereffect is that a superposition principle is valid concerning the response of the magnetization, $J(t)$, to previous field jumps, $(\Delta H)_i$, with $i = 1, 2, \ldots$ For viscosity experiments being governed by the reversible aftereffect, a variety of different time dependencies of the relaxing magnetization, $J(t)$, have been reported. This is understandable because, owing to the validity of the superposition principle, the function $J(t)$ can easily be influenced by the magnetic prehistory of the samples.

Depending on the specific selection of the material to be investigated and on the specific magnetic
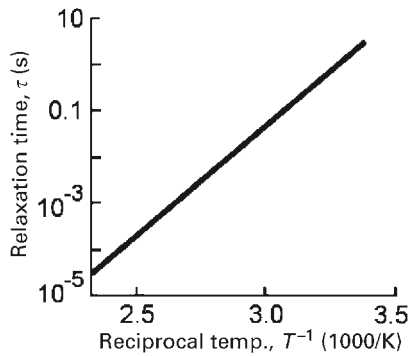
Figure 3
Temperature dependence of the relaxation time τ (according to Eqn. (2)) for an αFe(C) sample (after Chikazumi 1997).

prehistory, a simple exponential time law

$$J(t) = J(0) + J_\tau(1 - e^{-t/\tau}) \qquad (2)$$

with a single relaxation time τ and some constant J_τ, or a sum of such exponential terms or the logarithmic law of Eqn. (1), etc., have been found. As an example, the viscosity experiment on an αFe(C) sample (Chikazumi 1997) can well be described by Eqn. (2), and the temperature dependence of τ is given by

$$\tau = \tau_0 \exp(E/kT) \qquad (3)$$

where k is the Boltzmann constant and τ_0 and E are constants (see Fig. 3). It was shown by H. A. Kramers in 1940 that the Arrhenius formula (Eqn. (3)) results from thermally activated species escaping from a metastable state over an energy barrier E. Obviously the diffusion of carbon in αFe(C) is controlled by such an energy barrier.

2. Irreversible Magnetic Aftereffect

The irreversible aftereffect or fluctuation aftereffect occurs in all ferromagnetic substances and dominates in permanent magnet materials. This effect was discovered by H. Jordan in 1924 who found a field- and a frequency-independent contribution to the losses of a coil with an iron core. The first theoretical analysis of this effect was done by F. Preisach in 1935 who showed that the behavior of the losses is physically equivalent to the logarithmic time law of Eqn. (1) for the magnetization. Preisach also noticed that contrary to the reversible aftereffect, the irreversible aftereffect does not fulfill a superposition principle with respect to a set of succeeding field jumps.

He suggested that the latter effect is based on thermal fluctuations resulting in irreversible changes of magnetization and thus partially destroying the
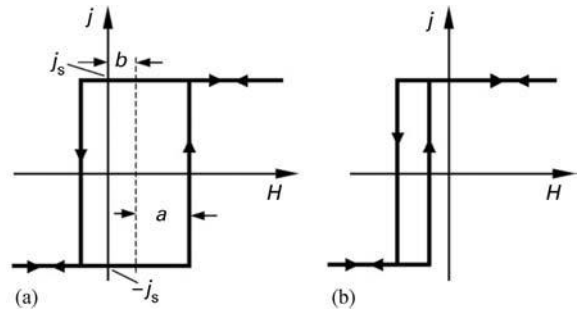
Figure 4
Hysteresis loops of two individual bistable units of a Preisach model with the parameters j_s, a, and b: (a) $b > 0$, $a > b$; (b) $b < 0$, $a < |b|$.

memory of the magnetic prehistory of the sample. Starting with the hypothesis that the irreversible aftereffect and hysteretic magnetization vs. field curves should be based on the same elementary magnetization processes, Preisach introduced a simple model considering ferromagnetic materials as collections of bistable units each of them characterized by its individual rectangular nonsymmetric hysteresis loop (see Fig. 4). If the state of such an individual unit is on its upper branch (j_s) or its lower branch ($-j_s$) and the applied field, H, is near the critical value $b - a$ or $b + a$ (see Fig. 4), respectively, very small changes of H will result in switching of that unit and, consequently, will contribute to an irreversible change of the total magnetization, J, along macroscopic hysteresis curves of the material. In such a critical state of the bistable unit switching will also be caused by small thermal fluctuations, thus contributing to the aftereffect, i.e., to a spontaneous change of J at constant H. There has been a resurgence of interest in Preisach-type models (Bertotti 1998) and they have been widely used to describe hysteresis as well as relaxation phenomena.

The role of thermal fluctuations for the irreversible aftereffect was also emphasized by L. Néel in 1951 who introduced the phenomenological relationship

$$S = \mu_0 \chi_{irr} S_v \qquad (4)$$

where μ is the permeability of vacuum. The irreversible part of the susceptibility, χ_{irr}, has to be determined from the experimental quantities χ (susceptibility) and χ_{rev} (reversible part of the susceptibility) by $\chi_{irr} = \chi - \chi_{rev}$, and the viscosity coefficient, S_v, represents some intrinsic fluctuation field. The typical example of Fig. 5 shows that, as expected, S_v does not vary much on a considered hysteresis curve, contrary to the behavior of χ_{irr} and S. In a theoretical analysis Street *et al.* (1987) found that the quantities in Eqn. (4) depend on the demagnetization factor, D, which characterizes the shape of the sample investigated.
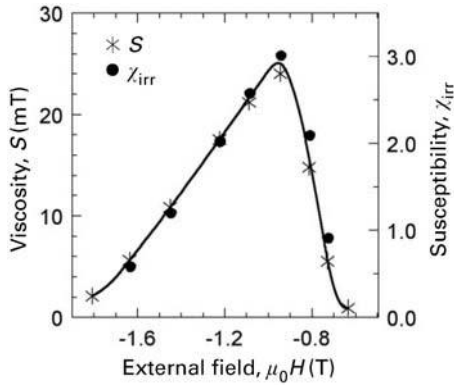
Figure 5
Viscosity, S, and irreversible susceptibility, χ_{irr}, of a sintered NdFeB permanent magnet at 300 K. The measurements are done on the major demagnetization curve (i.e., starting with a high field $\mu_0 H = 5$ T). The maximum of S and χ_{irr} is near the coercive field of the material.

Figure 6
(a) Viscosity coefficient, S_v, (b) susceptibility $\chi = \partial J/\partial H$ and reversible part of the susceptibility, χ_{rev}, vs. polarization, J, for a $Nd_4Fe_{77}B_{19}$ sample (same sample as in Fig. 1), measured on major demagnetization curves for two directions with the demagnetization factors $D = 0.08$ and 0.84. S_v in (a) is calculated according to Eqn. (5) (filled symbols) and Eqn. (4) (open symbols).

Therefore, for $D \neq 0$, Eqn. (4) has to be replaced by

$$S = S_v \frac{\chi_{irr}}{1 - D\chi_{rev}} \tag{5}$$

where now the viscosity coefficient, S_v, is independent of D (in its range $0 \leqslant D \leqslant 1$).

This has been experimentally verified for the "spring-magnet" material $Nd_4Fe_{77}B_{19}$ (Müller *et al.* 1994). As can be seen from Fig. 6 the values of χ_{rev} and χ_{irr} of this material are very sensitive to D, but S_v does not depend much on D if calculated by Eqn. (5). The correlation of the irreversible aftereffect with hysteresis was investigated earlier by J. C. Barbier in 1954 who found a universal relationship between S_v and the coercive field, $_JH_c$, for a large class of materials in which both quantities vary over several orders of magnitude (see Fig. 7). From these observations it can be concluded that the magnetic viscosity, just as the coercivity, depends on details of the chemical and topological microstructure of the material considered and modeling of both quantities will be difficult because these microstructural features have to be taken into account.

One of the few model systems for which the problem of slow magnetic relaxation has been exactly solved is an assembly of uniformly oriented small, spherical, noninteracting ferromagnetic particles of equal size, with uniaxial magnetic anisotropy. The particles are characterized, in the continuum theory called micromagnetism, by their spontaneous magnetization, J_s, anisotropy constant, K, and exchange constant, A. The only microstructural parameter of the model is the particle volume, v (or the corresponding

Figure 7
Barbier plot showing the correlation between the viscosity coefficient, S_v, and the coercive field, $_JH_c$, for a large class of magnetic materials. The straight line corresponds to $S_v \sim {_JH_c^{1.35}}$.

diameter, D). For D less than a critical size

$$D_c = c\mu_0 (AK)^{1/2} J_s^{-2} \tag{6}$$

where c is about 70, the particles are single domain. For example, for $Nd_2Fe_{14}B$ the value of D_c is about 300 nm. Applying Brownian motion theory it has been shown that for sufficiently low temperature, T, and sufficiently large time, t, the relaxation of such a

system is well described by Eqns. (2) and (3) where

$$E = Kv \tag{7}$$

$$\tau_0 = c' \frac{J_s}{K} \frac{\hbar}{\mu_B} \left(\frac{kT}{Kv}\right)^{1/2} \tag{8}$$

where $\hbar$ is Planck's constant, μ_B the Bohr magneton, and c' a number of the order of 1 (Brown 1979, Aharoni 1996). For an $Nd_2Fe_{14}B$ particle of few nanometers in size the room temperature value of τ_0 is about 10^{-11} s. It should be noted that in this approach T enters twice, explicitly in the Arrhenius factor of Eqn. (3) and implicitly via the temperature dependence of the material parameters J_s, K, and A.

For real ferromagnetic materials the exponential decay (Eqn. (2)) of magnetization is usually not observed. An often cited example is shown in Fig. 8, where the time dependence of the magnetization obviously obeys Eqn. (1) and the viscosity, S, strongly decreases with decreasing temperature. It is well known that Eqn. (2) transforms into Eqn. (1) if a relatively broad distribution, $f(E)$, of activation energies has to be taken into account instead of a single value, E (Street and Wooley 1949, Gaunt 1976). An alternative explanation of the origin of logarithmic relaxation observed in many complex systems has been proposed by Chudnovsky and Tejada (1998). They assume that the slow relaxation is governed by some critical state of the system in which the energy barriers in the Arrhenius relationship of Eqn. (3) depend on the relaxing magnetization, J, e.g.,

$$E \sim (J - J_c) \tag{9}$$
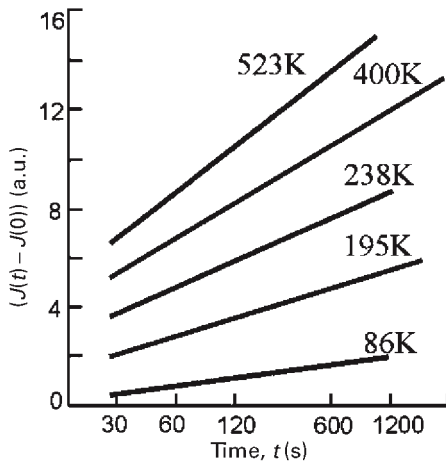
Figure 8
Time dependence of the magnetization of an Alnico permanent magnet measured by Street and Wooley (1949) for various temperatures.

If J exceeds the critical value J_c the fast initial change of $J(t)$ stops and, as time goes on, the magnetization grows logarithmically because the system arrives at greater and greater barriers that are more and more difficult to overcome.

To analyze the magnetic viscosity of arbitrary ferromagnetic materials the concept of an activation volume, v_a, has been introduced by Street and Woolley (1949):

$$v_a J_s S_v = kT \tag{10}$$

According to Eqns. (3) and (7) the energy barrier $E = kT$ being relevant for the activation of a single-domain particle at temperature T can be written as vJ_sK/J_s. A comparison of this expression with Eqn. (10) shows that the anisotropy field, K/J_s, is replaced by Néel's fluctuation field, S_v, from Eqn. (5) and the particle volume, v, by the activation volume, v_a. Theoretical and experimental analysis has revealed that v_a is representative for typical elementary magnetization processes such as nucleation of reverse domains or depinning of domain walls. Its value is typically some hundreds of cubic nanometers and the phenomenological relationship $v_a \sim \delta^3 \sim (A/K)^{3/2}$ has been found, where δ is the domain wall width of the material (Givord *et al.* 1987, Müller *et al.* 1994).

3. Anomalous Aftereffect and Thermal Remagnetization

If a viscosity experiment is dominated by the reversible aftereffect the superposition principle is fulfilled and, consequently, after a sequence of field jumps, $(\Delta H)_i$, with $i = 1, 2, \ldots m$, the rate, $dJ(t)/dt$, may have a sign different from that of the last field jump, $(\Delta H)_m$, or $J(t)$ may even be a nonmonotonic function. The first observation of such a behavior, called the anomalous magnetic aftereffect, was made by A. Mitkevich in 1936 who measured $J(t)$ in $\alpha Fe(C)$ after two field jumps $(\Delta H)_1 < 0$ and $(\Delta H)_2 > 0$ had been applied to the sample.

It had been believed that in viscosity experiments based on the irreversible magnetic aftereffect, the response of magnetization to a sudden change in the applied magnetic field is not very sensitive to the magnetic prehistory of the samples investigated. However, it was shown by Folks *et al.* (1994) by viscosity experiments on recoil curves of a fine-grained, two-phase permanent magnet (similar to the sample of Fig. 1) that some residual information on the magnetic prehistory may be stored even if the superposition principle is not valid. As shown in Fig. 9, the viscosity, S, changes its sign if the starting coordinate of the viscosity experiment is moved along the recoil curve. It should be noted that although the two relaxation curves of Fig. 9 are totally different, the magnetic prehistory of the sample is quite similar for
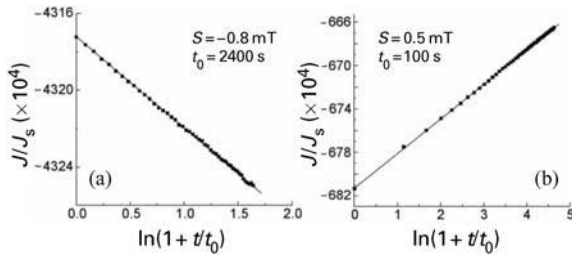
Figure 9
Magnetization, J, vs. time, t, for the sample of Fig. 1 after two field jumps characterized by the markers (a) $\bigcirc$ and $\bullet$ (in Fig. 1) and (b) $\bigcirc$ and $\blacktriangle$ (in Fig. 1) have been applied. The parameters S and t_0 are fitted to Eqn. (1).

Figure 10
Remagnetization phenomena in the sample of Fig. 1 after d.c. field demagnetization characterized by the markers $\bigcirc$ and * (in Fig. 1): (a) spontaneous remagnetization at room temperature (where the sample had been demagnetized); (b) thermal remagnetization.

both cases. The data of both Figs. 9(a) and (b) obey Eqn. (1). However, the magnitude, $|S|$, of the viscosity is considerably smaller compared to the conventional aftereffect experiment of Fig. 1(b). The fit yields very different effective waiting times, t_0, although all the measuring procedures were done on the same timescale. Obviously the large value of t_0 in Fig. 9(a) represents the more complicated magnetic prehistory compared to that corresponding to Fig. 1. If the coordinate on the recoil curve is appropriately chosen the material of Fig. 1 even shows an anomalous magnetic aftereffect, i.e., the magnetization is a nonmonotonic function of time.

The final coordinate * on the recoil curve which starts at the coordinate $\bigcirc$ in Fig. 1(a) represents the d.c.-demagnetized sample. The time dependence of the magnetization of such a sample is shown in Fig. 10(a). As expected from Fig. 9(b) the sample remagnetizes spontaneously, i.e., without an external field. Seemingly the system moves away from the state of thermal equilibrium where the sample magnetization, J, is zero. As shown in Fig. 10(b), a much stronger spontaneous increase of magnetization is observed if the d.c. field-demagnetized sample is heated and subsequently cooled to the starting temperature. This effect is called thermal remagnetization and was discovered by Kavalerova *et al.* (1975) for $SmCo_5$ permanent magnets. In principle, the results of Figs. 9 and 10 are understandable for systems with different relaxation times. If in such a system appropriate initial conditions are realized by an appropriate magnetic history, the magnetization, J, may, in certain periods of time, move away from its equilibrium value and the time dependence, $J(t)$, may be nonmonotonic.

However, as has been pointed out by Preisach and has been proved for small particles (Brown 1979, Aharoni 1996), a remarkable relaxation of J will only be observed if the external field, H, is close to the coercive field of the sample or to some switching field of a subsystem. If, for example, the Preisach units of Fig. 4 are in the state $j = -j_s$, relaxation will only occur if the applied field, H, is close to $(a + b)$, etc.
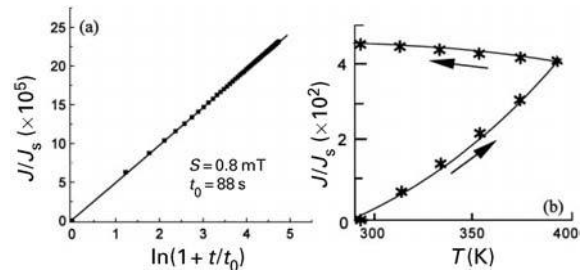
However, it is well known that, for general reasons of symmetry, noninteracting subunits of a system (e.g., particles) have symmetric whysteresis loops. Consequently, in such systems $H > 0$ will always result in $dJ/dt > 0$ and $H < 0$ in $dJ/dt < 0$. Thus the results presented in Figs. 9 and 10 are due to interaction of subunits. The coupling of the subunits can be caused by exchange or by magnetostatic interaction and its effect on slow magnetic relaxation will be particularly pronounced if the Preisach subunits vary much in their "hardness," i.e., in the parameter a in Fig. 4. As a typical example, the so-called spring-magnet material for which the data of Figs. 1, 6, 9, and 10 have been measured consists of a relatively hard and a relatively soft magnetic phase and both phases are assumed to be exchange coupled to each other. (See *Magnets: Remanence-enhanced*)

Hence, if the hard units are predominantly in their upper state $+j_s$, typical soft units will be shifted to the left-hand half of the Preisach plane (see Fig. 4(b)) and even at $H \leqslant 0$ (as in the coordinates $\blacktriangle$ and * in Fig. 1(a)) they may switch from $-j_s$ to $+j_s$ thus contributing to $dJ/dt > 0$ of the sample. The enhancement of this effect by heating (Fig. 10(b)) can be understood by the fact that the anisotropy constant, K (and consequently the parameter a in Fig. 4), decreases more strongly with increasing temperature than the strength of interaction (i.e., parameter b in Fig. 4). Therefore, heating has a similar effect on the subunit in Fig. 4(b) as an increase of the field, H, whereas the relatively hard subunits will not be as much influenced by heating.

The relaxation behavior of a Preisach system (Bertotti 1998) is demonstrated in Fig. 11. The material is described by a probability distribution $p(a, b)$ for the parameters a and b of Fig. 4. In an applied field, H, all Preisach units with $b < H - a$ have the magnetization $+j_s$, those with $b > H + a$ have the magnetization $-j_s$. The state of the remaining units depends on the prehistory of the system. The time dependence of the assembly is determined by the
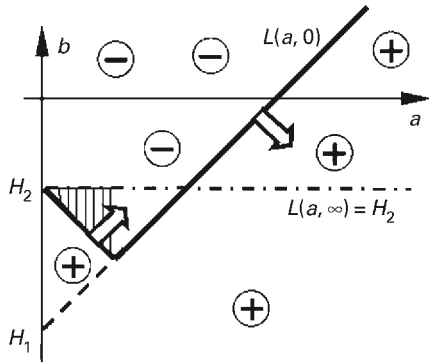
Figure 11
In the Preisach plane (a, b) the state of the collection of units of Fig. 4 is described by the border line $L(a, t)$ separating the units with $+j_s$ (region with + signs) from those with $-j_s$ (regions with – signs). The bold line represents $L(a, t=0)$ immediately after a sequence of field jumps $H = \infty \rightarrow H_1 \rightarrow H_2$ ($H_2 > H_1$, where H_1 corresponds to the marker $\bigcirc$ in Fig. 1). $L(a, \infty)$ is the equilibrium line. $\Rightarrow$ indicates the movement of $L(a, t)$. The units in the hatched region have lower energy barriers than those near the branch of the border line with positive slope.

border line $L(a, t)$, which separates the units with $+j_s$ from those with $-j_s$. This border line and $p(a, b)$ determine the magnetization of the assembly. The border line $L(a, 0)$ for a sequence of field jumps in the applied field from a large positive value of H to H_1 and then to H_2, immediately after the jump to H_2, is shown in Fig. 11 ($H_2 > H_1$, H_1 corresponds to $\bigcirc$ in Fig. 1). The equilibrium state is given by $L(a, \infty) = H_2$ and is reached by a motion of the border line owing to thermally activated reversal processes. The evolution equation for $L(a, t)$ has been derived within generalized thermodynamics, treating the border line as an "internal degree of freedom" and using an Arrhenius-type equation for the magnetization reversal of the single units corresponding to the points (a, b) near the border line. For the sequence of field jumps described above the two branches of the border line $L(a, 0)$ in Fig. 11 result in contributions of different sign to the magnetization change in time. The units with $a < (H_2 - H_1)/2$ (hatched region) have smaller energy barriers than those with $a > (H_2 - H_1)$, and the typical time constants for the units within the hatched region are smaller. Therefore, in the early stages the units in the hatched region will change more rapidly and the magnetization will first move in a positive direction and later it will decrease.

4. Quantum Tunneling of Magnetization

As discussed above, most experimental results on viscosity experiments, e.g., those presented in Figs. 3
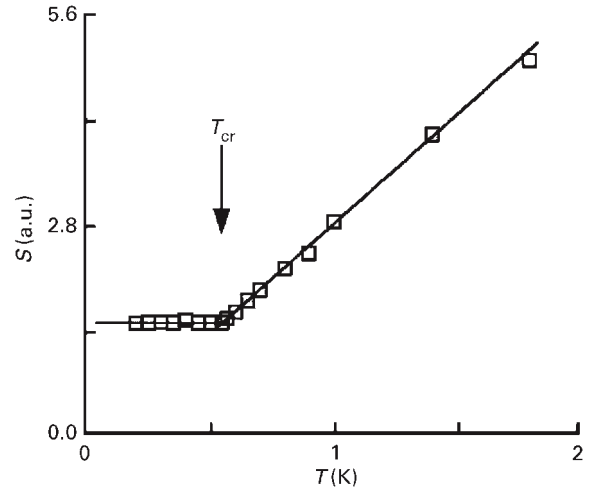
Figure 12
Low-temperature dependence of the magnetic viscosity of a TbFe$_3$ thin film. T_{cr} is the crossover temperature below which quantum tunneling of magnetization is assumed to dominate. The solid lines are guides to the eye (after Chudnovsky and Tejada 1998).

and 8, suggest that the reversible as well as the irreversible magnetic aftereffects are based on thermally activated processes and, consequently, both effects should disappear at very low temperatures. Contrary to this prediction Lambeck (1971) found for various materials that the magnetic viscosity, S, does not go to zero but approaches a finite constant value at low temperatures and it is assumed that the reason for this observation is quantum tunneling through potential barriers, as predicted by H. A. Kramers in 1940 for certain types of metastable states. It has been proved theoretically (Caldeira and Leggett 1981) that for quantum tunneling of macroscopic quantities, such as the magnetization, the tunneling probability may be enhanced by the dissipative coupling of the macroscopic coordinates to the environment. However, it has been shown by Barbara and Gunther (1993) that there are situations (e.g., particular distributions of energy barriers) where a plateau in $S(T)$ can also arise under purely classical thermal activation. In spite of this restriction a finite magnetic viscosity at low temperatures caused by quantum tunneling has been clearly demonstrated for various materials (Chudnovsky and Tejada 1998). For example, the magnetic relaxation in TbFe$_3$ films is found to be perfectly logarithmic and the magnetic viscosity, S, defined by Eqn. (1), indicates a crossover from thermal to temperature-independent relaxation at $T_{cr} = 6$ K (see Fig. 12).

See also: Coercivity Mechanisms; Magnetic Materials: Hard; Magnetic Hysteresis

Bibliography

Aharoni A 1996 *Introduction to the Theory of Ferromagnetism*. Oxford University Press, Oxford

Barbara B, Gunther L 1993 The barrier plot as a tool in magnetic relaxation studies. *J. Magn. Magn. Mater.* **128**, 35–41

Bertotti G 1998 *Hysteresis in Magnetism*. Academic Press, San Diego, CA

Brown W F Jr. 1979 Thermal fluctuations of fine ferromagnetic particles. *IEEE Trans.* **MAG-15**, 1196–208

Caldeira A O, Leggett A J 1981 Influence of dissipation on quantum tunneling in macroscopic systems. *Phys. Rev. Lett.* **46**, 211–4

Chikazumi S 1997 *Physics of Ferromagnetism*. Oxford University Press, Oxford

Chudnovsky E M, Tejada J 1998 *Macroscopic Quantum Tunneling of the Magnetic Moment*. Cambridge University Press, Cambridge

Dunsch L, Eckert D, Fröhner J, Bartl A, Müller K-H 1997 Ferromagnetic hysteresis and aftereffect in polycrystalline TDAE-C_{60}. *J. Appl. Phys.* **81**, 4611–3

Folks L, Feutrill E H, Street R 1994 Observation of magnetic viscosity on recoil curves of exchange spring permanent magnets. In: Manwaring C A F, Jones D G R, Williams A J, Harris I R (eds.) *Proc. 8th Int. Symp. Magnetic Anisotropy and Coercivity in Rare Earth Transition Metal Alloys*. University of Birmingham, Birmingham, UK, pp. 415–21

Gaunt P 1976 Magnetic viscosity in ferromagnets. *Phil. Mag.* **34**, 775–80

Givord D, Lienard A, Tenaud P, Viadieu T 1987 Magnetic viscosity in Nd–Fe–B sintered magnets. *J. Magn. Magn. Mater.* **67**, L281–5

Haas C W, Callen H B 1963 Ferromagnetic relaxation and resonance line widths. In: Rado G T, Suhl H (eds.) *Magnetism*. Academic Press, New York, Vol. I, pp. 449–549

Huang C Y 1985 Some experimental aspects of spin glasses: a review. *J. Magn. Magn. Mater.* **51**, 1–74

Jonscher A K 1983 *Dielectric Relaxation in Solids*. Chelsea Dielectric Press, London

Kavalerova L A, Livschitz B G, Lileev A S, Menushenkov V P 1975 The reversibility of magnetic properties of sintered $SmCo_5$ permanent magnets. *IEEE Trans. Magn.* **MAG-11**, 1673–5

Kronmüller H 1968 *Nachwirkung in Ferromagnetika*. Springer-Verlag, Berlin

Lambeck M 1971 *Barkhauseneffekt und Nachwirkung in Ferromagnetika*. Walter de Gruyter, Berlin

Müller K-H, Eckert D, Handstein A, Wolf M, Wirth S, Martinez L M 1994 Viscosity and magnetization processes in annealed melt-spun $Nd_4Fe_{77}B_{19}$. In: Manwaring C A F, Jones D G R, Williams A J, Harris I R (eds.) *Proc. 8th Int. Symp. Magnetic Anisotropy and Coercivity in Rare Earth Transition Metal Alloys*. University of Birmingham, Birmingham, UK, pp. 179–86

Street R, Day R K, Dunlop J B 1987 Magnetic viscosity in NdFeB and $SmCo_5$ alloys. *J. Magn. Magn. Mater.* **69**, 106–12

Street R, Woolley J C 1949 A study of magnetic viscosity. *Proc. Phys. Soc. A* **62**, 562–72

Yeshurun Y, Malozemoff A P, Shaulov A 1996 Magnetic relaxation in high temperature superconductors. *Rev. Mod. Phys.* **68**, 911–49

K.-H. Müller
IFW Dresden, Germany

Magnetism in Solids: General Introduction

Magnetism represents a class of fascinating physical phenomena that is intimately connected with the behavior of electrons in materials. Nuclear particles with spin also give rise to magnetic phenomena, but these are characterized by a much weaker (nearly 2000 times) magnetic response. This article is mostly devoted to "electronic" magnetism.

Although properties of the lodestone (magnetite) were already known to the Ancient Greeks by 800 BC, magnetism remains even nowadays a field of permanently growing interest. The interest is on the one hand motivated by outstanding magnetic and related electronic properties of novel materials which find frequent use in everyday modern life.

On the other hand, open questions about the electronic structure of materials and its projection in magnetic, magnetoelastic (see *Magnetoelastic Phenomena*), magnetotransport (see *Magnetoresistance: Magnetic and Nonmagnetic Intermetallic*; *Giant Magnetoresistance: Metamagnetic Transitions in Metallic Antiferromagnets*), and magnetocaloric (see *Magnetocaloric Effect: From Theory to Practice*) phenomena represent a serious challenge both to theorists and experimentalists active in research into condensed matter.

For studies of the relationship between magnetism and electronic structure investigation of materials exposed to extreme conditions, such as high magnetic field or high external pressure, is frequently helpful. In the former, the application of a high magnetic fields allows, for example, the determination of the energy of magnetocrystalline anisotropy and exchange interactions between magnetic moments or magnetic-field-induced changes of electronic structure connected, e.g., with itinerant electron metamagnetism (see *Magnetism: High-field* and *Itinerant Electron Systems: Magnetism (Ferromagnetism)*). Application of external pressure, on the other hand, facilitates experiments studying the effects of varying interatomic distances on exchange interactions and other characteristic features of electronic structure (see *Magnetic Systems: External Pressure-induced Phenomena*).

This article is devoted to a brief general introduction to the physics of magnetism in solids. In Sect. 1, basic categories of magnetic behavior of materials are presented phenomenologically. Sections 2 and 3 point to microscopic mechanisms responsible for the bulk magnetic properties. Basic information on magnetic phase transitions and related phenomena is given in Sect. 4, while Sect. 5 focuses on magnetocrystalline anisotropy, its origin, and consequences. Basic models in magnetism are introduced in Sect. 6.

Where desirable, cross-references are given to articles covering particular subjects. For detailed study of various aspects of magnetism in solids several

literature sources are recommended. Besides the extended chapters on magnetism that can be found in widely known text-books on solid-state physics (Kittel 1976, Ashcroft and Mermin 1988), several books concentrating on magnetism are recommended (Chikazumi 1964, Cracknel 1975, Barbara *et al.* 1988, Gilles 1994) including the theory of magnetism (Mattis 1981, Yosida 1996). As a useful reference source the continuously updated series edited by Buschow (e.g., Buschow and Wohlfarth 1993) may be used. In the books listed above information can also be found on further aspects of magnetism in materials.

The most up-to-date information on the research in the field of magnetism can be obtained from numerous journals (e.g., *Journal of Magnetism and Magnetic Materials*, *Physical Review B*, *Europhysics Journal B* (the follower of the *Zeitschrift für Physik B* and *Journal de Physique*), *Journal of Physics: Condensed Matter* and *Journal of Japanese Physical Society*) and at international conferences devoted to physics of magnetism as, e.g., the triennial International Conference of Magnetism (ICM), which was held in 2000 in Recife (Brazil) with proceedings published in the *Journal of Magnetism and Magnetic Materials*; the annual conference of the American Institute of Physics—the Conference on Magnetism and Magnetic Materials (MMM) which has proceedings regularly published in the *Journal of Applied Physics* (the last MMM was held in 2001 in San Antonio). Since different units can still be found in different literature, the reader is referred to *Magnetic Units* for further information.

1. Basic Types of Magnetic Behavior

Initial information on magnetic behavior of a particular material is usually obtained from measurements of the magnetic response of a sample to an applied magnetic field H. The bulk magnetization M is studied by magnetometers that measure the force exerted on a sample in an inhomogeneous external magnetic field or electrical current induced in pick-up coils by moving through a magnetized sample (Cahn and Lifshin 1993, Chikazumi 1964).

The rate of the magnetization change with the magnetic field

$$\vec{M} = \chi \vec{H} \qquad (1)$$

determines the magnetic susceptibility χ. Detailed knowledge of the magnetic field and temperature dependence of magnetization $M(H, T)$ and magnetic susceptibility $\chi(T)$, which are the basic magnetic characteristics of a material, frequently allows the drawing of conclusions about the type of magnetism, especially in simple systems. The basic categories of magnetic behavior of materials are diamagnetism, paramagnetism, ferromagnetism, antiferromagnetism, ferrimagnetism, and metamagnetism.
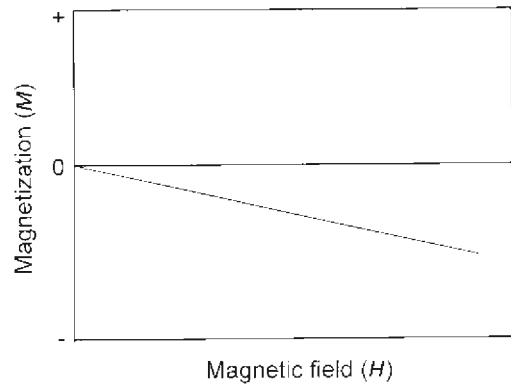
Figure 1
Typical magnetic field dependence of magnetization for a diamagnet (full line).

1.1 Diamagnetism

Regarding the sign of magnetic susceptibility, a negative material response to an external magnetic field ($\chi < 0$) is classified as diamagnetic. If a diamagnet is exposed to an external magnetic field a negative magnetization (see Fig. 1) is induced due to a moving electron charge in a manner described by Lenz's law of electromagnetism. Consequently a negative susceptibility

$$\chi = -\frac{\mu_0 N Z e^2}{6 m_e} \langle r^2 \rangle \qquad (2)$$

is observed, where n is the number of atoms per unit volume, Z is the number of electrons in filled shells per atom, e and m_e are the electronic charge and mass, respectively, $\langle r^2 \rangle$ is the root mean square atomic radius (typically 10^{-21} m), and μ_0 is the permeability of the vacuum.

The susceptibility of a diamagnet is very weak and essentially independent of temperature. Typical examples of diamagnets are copper, silver, gold, bismuth, beryllium, and germanium with values of susceptibility ranging from -5.6×10^{-7} (Ge) to -2.7×10^{-6} (Au). Generally speaking, diamagnetism is present in all substances under applied magnetic field due to inevitable electromagnetic induction in a moving electron charge system. Nevertheless, it can be well detected only in materials containing atoms without permanent magnetic moments. Permanent magnetic moments, which are associated with incomplete *d*- and *f*-electron shells (see Sect. 2 and *Localized 4f and 5f Moments: Magnetism*), yield a much stronger positive susceptibility.

A weak temperature-independent diamagnetic susceptibility (Landau diamagnetism) is produced by conduction electrons in metals (Kittel 1976, Ashcroft and Mermin 1988).

Superconductors exhibit strong diamagnetism with the susceptibility reaching $\chi = -1$ (value for an ideal diamagnet). The diamagnetic susceptibility of a superconductor is strongly temperature-dependent and vanishes at temperatures above the superconducting temperature (Cahn and Lifshin 1993, also see *Electrodynamics of Superconductors: Flux Properties*).

1.2 Paramagnetism

Paramagnets are generally known as materials with atoms (ions) carrying weakly interacting permanent magnetic moments. As a consequence of negligible exchange interactions between moments a true paramagnet shows no sign of magnetic ordering down to the lowest temperatures. In sufficiently low magnetic fields and at not too low temperatures $\mu_B \mu_0 H / k_B T \ll 1$ (k_B is the Boltzmann constant and μ_B is the Bohr magneton). The magnetization of a paramagnet varies linearly with the applied magnetic field yielding a field-independent susceptibility (see Fig. 2).

The magnetic susceptibility of a paramagnet is positive and strongly dependent on temperature. As a rule the susceptibility of a paramagnet follows the Curie law

$$\chi = \frac{C}{T} \qquad (3)$$

where C, the Curie constant, is proportional to the sum of the squares of the effective moments, μ_{eff}, in a unit volume. The effective magnetic moment of an atom characterized by total-angular-momentum quantum number J is:

$$\mu_{eff} = g_J \sqrt{J(J+1)} \mu_B \qquad (4)$$

where g_J is the Landé factor (see *Localized 4f and 5f Moments: Magnetism*). The Curie law implies that the inverse susceptibility of a paramagnet is proportional to temperature as can be seen in Fig. 2.

In higher fields and at lower temperatures the magnetization is no longer a linear function of the magnetic field (and consequently the Curie law is no longer valid) but in many cases can be expressed as:

$$M = M_o B_J(x), \qquad (5)$$

where

$$M_o \approx g_J J \mu_B, \qquad (6)$$

is the maximum attainable magnetization for a material with one type of "magnetic" atoms characterized by J. The function $B_J(x)$ is the Brillouin function of the argument

$$x = \frac{g_J J \mu_0 H \mu_B}{k_B T} \qquad (7)$$

The graphical representation of $B_J(x)$ for several typical values of J is shown in Fig. 3. For further
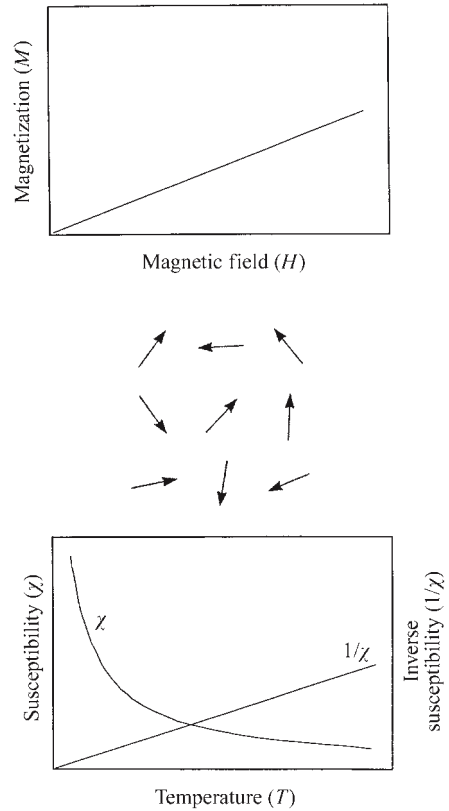
Figure 2
Typical magnetic field dependence of magnetization and temperature dependence of inverse susceptibility for a paramagnet with localized magnetic electrons. The randomly oriented magnetic moments in a paramagnet are illustrated schematically.
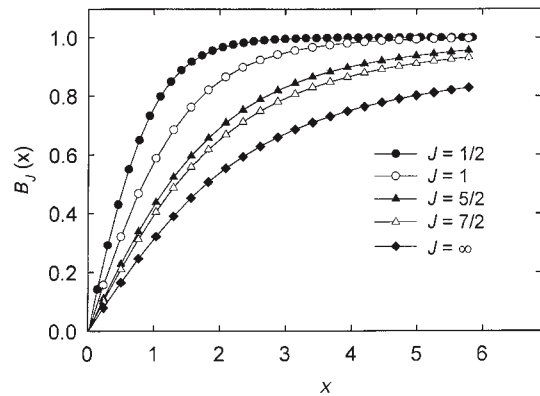
Figure 3
The Brillouin function plotted for several typical values of J.

details see, e.g., Kittel (1976), Ashcroft and Mermin (1988), or Gilles (1994).

In metals the Pauli paramagnetism that is characterized by a nearly temperature-independent susceptibility is also observed. The Pauli susceptibility is proportional to the density of conduction–electron states at the Fermi level E_F. This behavior is a consequence of the magnetic-field-induced splitting of the spin–up and spin–down conduction–electron energy sub-bands (Kittel (1976, Ashcroft and Mermin (1988). The Pauli susceptibility can be strongly enhanced in systems with narrow bands crossed by E_F at a high density of states (see also *Itinerant Electron Systems: Magnetism (Ferromagnetism)* and *Heavy-fermion Systems*).

1.3 Ferromagnetism

In a material with strongly interacting magnetic moments cooperative phenomena can be observed, yielding long-range ordering of magnetic moments (magnetic ordering) at temperatures below a characteristic temperature. The most widely known type of magnetic ordering is ferromagnetism. Ferromagnetic ordering of magnetic moments means that they are aligned parallel to one another (see Fig. 4), which is accomplished by a ferromagnetic exchange interaction (see Sect. 3). The characteristic temperature of a ferromagnet is the Curie temperature (T_C), at which the susceptibility diverges. At temperatures below T_C a spontaneous magnetization (i.e., a finite magnetization existing in zero external magnetic field) emerges. Values of the Curie temperature of some typical ferromagnets are given in Table 1.

At temperatures considerably higher than T_C, the magnetic moments behave as in a paramagnet and the magnetic susceptibility follows the Curie–Weiss law:

$$\chi = \frac{C}{T - \Theta_p} \tag{8}$$
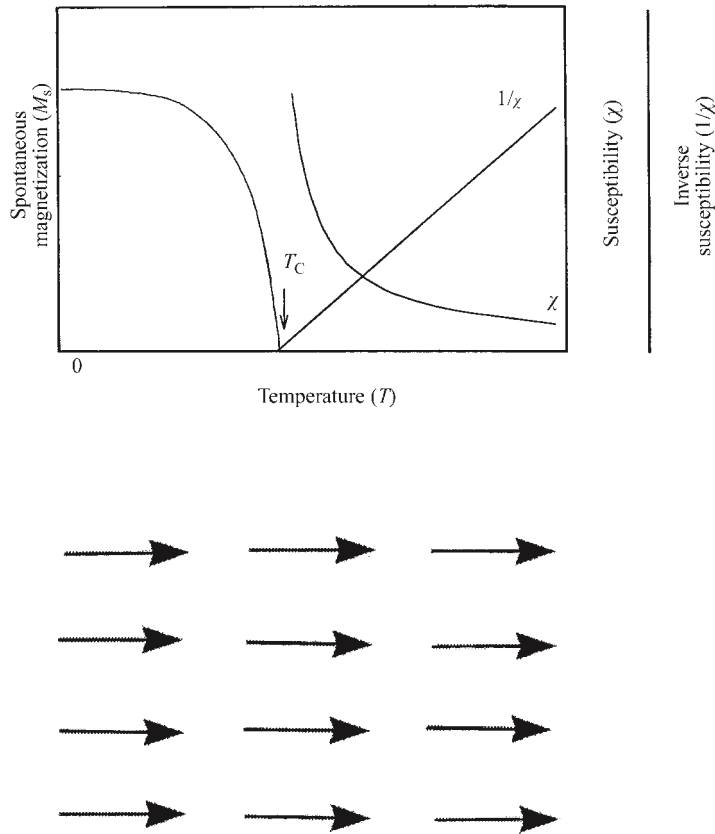
Figure 4
Typical behavior of a ferromagnet: temperature dependence of inverse susceptibility at temperatures above the Curie temperature ($T > T_C$) and spontaneous magnetization at $T < T_C$. The ferromagnetically coupled magnetic moments in a ferromagnet $T < T_C$ are illustrated schematically.

Table 1
Curie temperatures of several typical ferromagnets.

Material	Curie temperature T_C (K)
Iron (Fe)	1043
Cobalt (Co)	1403
Nickel (Ni)	631
Gadolinium (Gd)	293
GdNi$_2$	79
Alnico	1123
SmCo$_5$	993
Nd$_2$Fe$_{14}$B	585

as can be seen in Fig. 4. The parameter Θ_p is called the paramagnetic Curie temperature and in simple ferromagnets $\Theta_p \approx T_C$. Note in relation to the discussion in Sect. 1.2 that in the paramagnetic regime at temperatures close to T_C and in sufficiently high magnetic fields the magnetic field dependence of magnetization becomes strongly nonlinear and the temperature dependence of the susceptibility cannot be described by the Curie–Weiss law.

At temperatures below T_C ferromagnets show several characteristic features. Principally there is the appearance of a spontaneous magnetization (magnetization observed in zero magnetic field) within one domain (see *Magnets, Soft and Hard: Domains*). The spontaneous magnetization increases with decreasing temperature as shown in Fig. 4. A block of a ferromagnet contains, as a rule, a number of domains whose spontaneous magnetizations compensate mutually so that the total bulk magnetization is zero. When a magnetic field is applied, the magnetization increases with increasing field strength and in a sufficiently high field the magnetization saturates at the value of saturated magnetization, M_0, shown schematically in Fig. 5. Ferromagnetic materials exhibit a large variety of magnetization curves which frequently show a hysteresis with respect to the history of application of the magnetic field (see *Magnetic Hysteresis*; *Soft Magnetic Materials: Basics*; *Hard Magnetic Materials, Basic Principles of*). These features of ferromagnets are particularly important in some applications of magnetic materials.

1.4 Antiferromagnetism

In the case of an antiferromagnetic coupling between the neighboring magnetic moments their antiparallel ordering (see Fig. 6) is established at temperatures lower than the Néel temperature T_N. At temperatures higher than T_N, the magnetic moments behave as in a paramagnet and the magnetic susceptibility follows the Curie–Weiss law (Eqn. (5)). However, for ferromagnets $\Theta_p > 0$, and the paramagnetic Curie temperature for simple antiferromagnets is usually negative
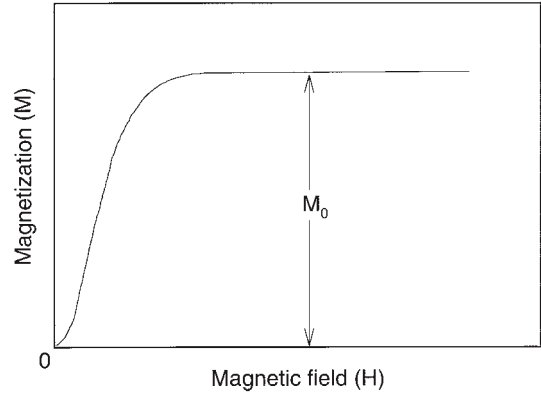
Figure 5
Typical magnetization curve of a ferromagnet (ferrimagnet).
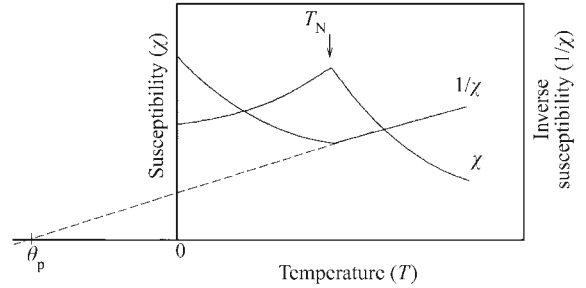
Figure 6
Typical temperature dependence of inverse susceptibility for an antiferromagnet. The antiferromagnetically coupled magnetic moments in an antiferromagnet $T < T_N$ are illustrated schematically.
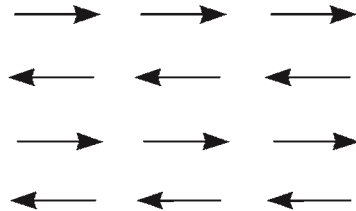
($\Theta_p < 0$). At low temperatures below T_N, the susceptibility decreases (inverse susceptibility increases, as shown in Fig. 6). For simple antiferromagnets the maximum on the $\chi(T)$ curve is located at T_N. In many real systems T_N does not coincide with the susceptibility maximum but with the maximum in $\partial(T\chi)/\partial T$ (Fisher 1962).

In contrast to ferromagnets, antiferromagnets exhibit zero spontaneous magnetization (see also Sect. 3). This is obvious for a simple antiferromagnet in which pairs of magnetic moments coupled in an antiparallel manner mutually compensate. The behavior of a simple antiferromagnet can be understood within the Néel model by considering the antiferromagnet in terms of two interpenetrating ferromagnetic sublattices A and B with an antiparallel coupling of the sublattice magnetizations M_A and M_B ($|M_A| = |M_B|$) (Chikazumi 1964, Barbara *et al.* 1988).

1.5 Ferrimagnetism

Ferrimagnetism is a term that was originally proposed by Néel to describe the magnetic ordering phenomena in ferrites (see *Transition Metal Oxides: Magnetism*), in which Fe ions appear in two different ionic states and hence bear different magnetic moments with mutual antiferromagnetic coupling. The ferrimagnet can be considered in a loose analogy as a two-sublattice antiferromagnet with $|M_A| \neq |M_B|$. In this context ferrimagnets appear sometimes in literature under the name "uncompensated antiferromagnet". As a consequence, a net spontaneous magnetization M_s ($= M_A - M_B$) is observed at temperatures below the ordering temperature T_C. Various types of $M_s(T)$ curves are found for ferrimagnets depending on the temperature variation of sublattice magnetizations. Two types of behavior are shown in Fig. 7.

At temperatures well above T_C, paramagnetic behavior is observed with the magnetic susceptibility following the Curie–Weiss law, usually with a negative value of Θ_p. At a certain temperature interval above T_C, the $1/\chi$ vs. T dependence forms a curve as seen in Fig. 7. This behavior can also be accounted for within the Néel sublattice model.

1.6 Metamagnetism

When a sufficient magnetic field is applied to some materials which exhibit no or a small spontaneous magnetization an abrupt transition to a high magnetization state may be induced (see Fig. 8) (see also Sect. 5.2). The transition is usually called the metamagnetic transition (MT) and the high magnetization state is called metamagnetic because it is a metastable state (it disappears as soon as the magnetic field is removed). There are several rather different mechanisms that cause a MT (see *Magnetic Phase Transitions: Field-induced (Order to Order)*; *Metamagnetism: Itinerant Electrons*; *Magnetism: High-field*). An important parameter of metamagnetism is the critical field H_c at which the MT occurs (H_c is usually associated with the midpoint of the transition). The low field state ($H < H_c$) of a material exhibiting a MT is usually antiferromagnetic, ferrimagnetic, or in some special cases enhanced paramagnetic.
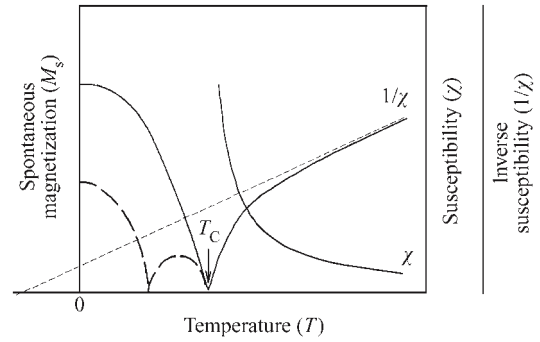
Figure 7
Typical behavior of a ferrimagnet: temperature dependence of inverse susceptibility at temperatures above the Curie temperature ($T > T_C$) and spontaneous magnetization M_s at ($T < T_C$). The antiferromagnetically coupled inequivalent magnetic moments in a ferrimagnet at $T < T_C$ are illustrated schematically. When $M_A \gg M_B$ at all temperatures the $M_s(T)$ resembles a ferromagnet (full line). In some materials a special situation appears due to strongly different temperature dependencies of sublattice magnetization. In particular, if $|M_A| < |M_B|$ for $T_{comp} < T < T_C$, $M_A = -M_B$ and $|M_A| > |M_B|$ for $T < T_{comp}$ (dashed line); at T_{comp}, $M_A = -M_B$, i.e., the sublattice magnetizations compensate and T_{comp} is called the compensation temperature.

1.7 Remarks

Note that diamagnetism of filled electronic shells is an inevitable property of all solids containing atoms (ions) with some filled electronic shells. In metals there is also a weak paramagnetic Pauli susceptibility term (together with the Landau diamagnetic susceptibility) due to conduction electrons that always contributes to magnetic behavior. These weak susceptibility contributions are in materials with permanent magnetic moments usually hidden by the much stronger positive magnetic (paramagnetic, antiferromagnetic, ferrimagnetic, ferromagnetic, etc.) response. Nevertheless, a proper analysis of magnetic data requires that the weak diamagnetic and the Pauli
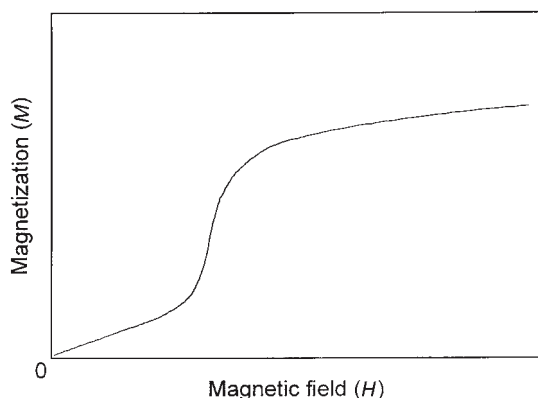
Figure 8
Typical magnetic field dependence of magnetization of a material exhibiting metamagnetism.

paramagnetic terms are also taken into account when not completely negligible.

The bulk magnetization is a sum of individual magnetic moments in the material. Therefore it is obvious that the knowledge of magnetic field and/or temperature dependence of the magnetization (susceptibility) allows only rather limited and frequently ambiguous conclusions to be reached concerning details of the arrangement of magnetic moments, their dynamics, relation to electronic structure, etc. Realistic studies of microscopic aspects of magnetism require the application of methods that use local probes to sense phenomena in the material on the microscopic scale.

Traditionally, the most frequently used microscopic methods in magnetism, especially powerful in studies of magnetic structures and magnetic excitations, are based on various aspects of neutron scattering in materials (Bacon 1975, Squires 1978, Barbara *et al*. 1988) (see *Magnetism: Applications of Synchrotron Radiation*). These experiments are made possible by intensive stationary or pulsed beams of thermal or cold neutrons available at large neutron facilities. Representative examples of reactor based facilities (most of which are open to the external user community) are the Institute-Laue-Langevin (ILL), (http://www.ill.fr), JAERI (http://www.jaeri.go.jp), NIST Research Center (http://rrdjazz.nist.gov/), Oak Ridge, Chalk River Laboratories (http://neutron.nrc.ca/), and Hahn-Meitner-Institut (http://www.hmi.de).

Spallation sources provide high-intensity pulsed neutron beams at various facilities: ISIS (http://www.isis.rl.ac.uk/), LANSCE (http://lansce.lanl.gov), IPNS (http://www.pns.anl.gov/), and SINQ at PSI (http://www1.psi.ch).

Excellent complementary microscopic tools are offered by rapidly developing methods based on x-ray

scattering in magnetic materials (see *Magnetism: Applications of Synchrotron Radiation*). These methods have developed as a result of the high-intensity x-ray beams produced at the most powerful synchrotron facilities, e.g., ESRF (http://www.esrf.fr), NSLS Brookhaven National Laboratory (http://www.nsls.bnl.gov/), and SPRING-8 Himeji.

Fundamental microscopic experiments revealing direct connections between electronic structure and magnetism can be performed using advanced photoemission methods (see *Photoemission: Spin-polarized and Angle-resolved*).

Mössbauer spectroscopy and other methods studying hyperfine interactions, such as NMR, NQR (nuclear quadrupole resonance), and PAC (perturbed angular correlations) (Cahn and Lifshin 1993) (see *Perturbed Angular Correlations (PAC)*), allow the study of magnetic systems probed by a hierarchy of nuclear energy levels which is established partly as a result of hyperfine interactions between the nucleus and the electronic system. Methods exploiting muon spin rotation and relaxation (μSR) offer unique possibilities to observe very small magnetic moments on a level of $10^{-2}\,\mu_B$ as well as various aspects of dynamics of magnetic systems (Schenck and Gygax 1995) (see *Muon Spin Rotation (μSR): Applications in Magnetism*).

The rapid development of theoretical methods and computer codes and the concomitant increase in capacity and speed of modern computers have made realistic *ab initio* calculations of the electronic structure of magnetic materials widely available. Predictions made by such calculations have motivated new experiments focused on particular problems (Brooks and Johanson 1993, Sandratskii 1998) (see *Density Functional Theory: Magnetism*).

2. Magnetic Moments of d and f Transition Elements

An atom (ion) has a net magnetic moment when an inner *d*- or *f*-electron shell is incomplete such that the individual electronic moments within the shell do not cancel completely. In the Periodic Table there are five groups of elements in which this incomplete cancellation occurs: the iron group ($3d$), the palladium group ($4d$), the rare earth (or lanthanide) group ($4f$), the platinum group ($5d$), and the actinide group ($5f$).

Free-atom *d* and *f* electrons possess magnetic moments (Kittel 1976, Ashcroft and Mermin 1988) that are predicted based on the principles of quantum mechanics (see *Transition Metal Oxides: Magnetism* and *Localized 4f and 5f Moments: Magnetism*). When an atom (ion) of a transition element is embedded in a solid, these moments often disappear when the electron orbitals overlap and bond, which leads to delocalization of the *d* or *f* electrons—the electrons become itinerant. Metallic or covalent bonding is
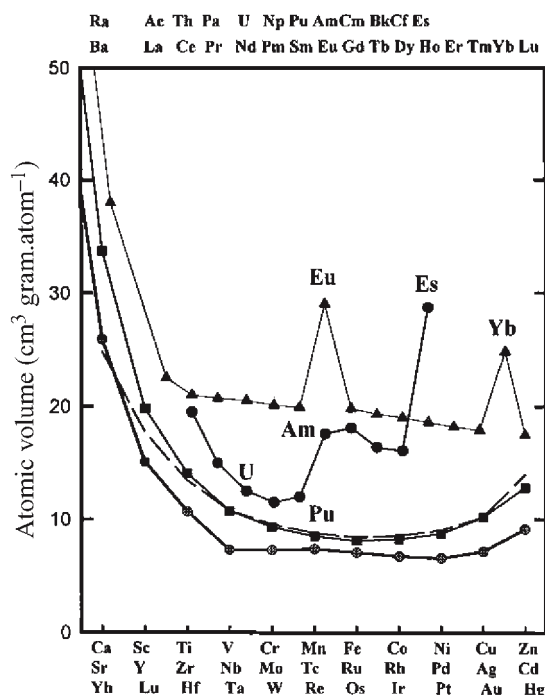
Figure 9
Evolution of atomic volume across 3*d* (hexagons), 4*d* (squares), 5*d* (dashed line), 4*f* (triangles), and 5*f* (circles) transition metal series.

inconsistent with magnetic moments that mostly arise from localized electrons. Onset of this bonding is clearly reflected in a decrease in atomic volume. This effect is well seen in Fig. 9 for transition metals (3*d*, 4*d*, and 5*d*). In the first part of the respective series the bonding states are gradually populated and the ion volume decreases. In the second part the population of antibonding states is associated with a gradual increase in volume. The very weak ion volume variation across the 4*f* series is consistent with localized behavior of 4*f* electrons in most of the lanthanide ions. The actinide series (5*f*) provides an excellent natural example of the crossover between the itinerant character of 5*f* states in elements from thorium to neptunium and localized behavior for these beyond plutonium.

An instructive representation of the evolution of magnetism within the transition-element series between the itinerant and localized character of the *d* and *f* electrons has been presented by Smith and Kmetko (1983) in the "periodic table of transition elements" (see Fig. 10). Note that the sequence of rows in the table is different from the Periodic Table of elements; in particular the series of *f* elements is placed above the transition metal series. The lower left section of the table comprises elements in which the *d* and 5*f* electrons strongly participate in bonding and are itinerant in character. Most of these materials are superconducting. In the top right segment the majority of lanthanides and heavy actinides are located which exhibit localized *f*-electron magnetism.
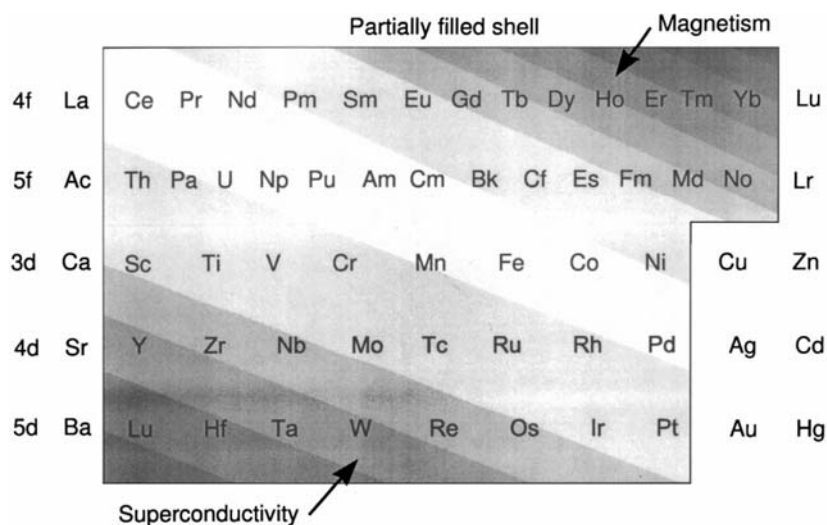
Figure 10
A revisited periodic table of the *f* and *d* transition element series. The periodic table is rearranged with the rare-earth, or lanthanide elements on the top row, the actinides in the second row, and the *d*-electron transition metals below them. Most metals have predictable ground states and become magnetic or superconducting as the temperature is lowered below a characteristic temperature of magnetic ordering or superconducting transition. The low-temperature metallic properties of the elements along the diagonal are difficult to explain because, in the solid-state, their *f* or *d* valence electrons are poised between localization and itinerancy (after Smith and Kmetko 1983).

This together with Fig. 9 suggests that the cross-over to localized behavior can be roughly marked by the diagonal white (and nearly white) region. Crossing this region from left to right can be viewed as a Mott transition from a metallic state to an insulating magnetic state for the relevant *d* and *f* electrons. The cross-over region can be moved to the left or right by embedding ions in appropriate compounds (or by applying external pressure) which yields a reduced or increased overlap of the *d*- or *f*-electron wave-functions. The transition-metal *d* electrons then appear to be localized and bear magnetic moments as a rule in insulators (see *Transition Metal Oxides: Magnetism* and *Pnictides and Chalcogenides: Transition Metal Compounds*). On the other hand, itinerant nonmagnetic 4*f* electrons are found in some specific materials like $CeFe_2$ (Ericksson *et al.* 1988).

The magnetism of localized electron states can be treated theoretically and the observed magnetic moments usually compare well with the calculated values. Nevertheless, the moments of localized electrons in solids may be considerably reduced, due mainly to crystal field interaction, which is particularly effective where there are electrons with larger spatial extensions of wave-functions (see *Localized 4f and 5f Moments: Magnetism*). Also, the itinerant electron states that form energy bands may, under certain conditions, yield magnetic moments and magnetic ordering (see *Itinerant Electron Systems: Magnetism (Ferromagnetism)*, and *Metamagnetism: Itinerant Electrons*).

One of the important control parameters is the relevant bandwidth that plays an important role in determining the type of ground state and the possibility of metamagnetic state of an itinerant electron system. In the cross-over region between localized and itinerant behavior narrow-band materials are located, which are characterized by strongly correlated electrons (see *Electron Systems: Strong Correlations*). The specific electronic properties of strongly correlated electron systems (SCES) in the context of the broad spectrum of metallic systems are schematically summarized in Fig. 11. In the cross-over region a number of exotic phenomena is also frequently observed, for example, the heavy-Fermion behavior (see *Heavy-fermion Systems*) and the intermediate-valence behavior (see *Intermediate Valence Systems*).

The variety of observed magnetic phenomena connected with various stages of "magnetic" electron states between localized and itinerant causes problems in formulating a unified theory of magnetism in materials. Reasonable theoretical approaches are available for the extreme cases: the magnetism of localized electrons (see *Transition Metal Oxides: Magnetism*) and magnetism of itinerant electrons. The intimate relationship between magnetism and electronic structure points to the necessity of applying, in magnetism, methods based on electronic structure theories. The density functional theory (Brooks and Johanson 1993) has been proven to be very successful in providing realistic *ab initio* electronic structure calculations in studies of numerous materials (see *Density Functional Theory: Magnetism*).

3. Ordering of Magnetic Moments

In Sect. 1 ferromagnetism, antiferromagnetism, and ferrimagnetism were introduced phenomenologically. These phenomena are based on long-range ordering of magnetic moments in materials. There are two necessary ingredients of magnetic ordering—magnetic moments and exchange interactions. The latter determine the intersite correlations of magnetic moments.

3.1 Exchange Interactions

The prototype of exchange interaction is the interaction that correlates spins in the hydrogen molecule. (The description can be found in most textbooks on quantum mechanics.) These interactions are electrostatic in origin and lead to a splitting of the energies of the antisymmetric and symmetric orbital states and hence the symmetric ($\uparrow\uparrow$) and antisymmetric ($\uparrow\downarrow$) spin states. This is the case for all exchange interactions.

In Fig. 12 the main types of exchange interactions are reviewed in a schematic illustration. If the magnetic atoms are nearest neighbors in a lattice the direct exchange interaction (nearest-neighbor interaction) can be effective in the case of a sufficient overlap of the relevant *d* or *f* orbitals. The best examples of a direct exchange interaction can be found in the ferromagnetic 3*d* metals Fe, Co, and Ni, which order at high temperatures (see Table 1) but exhibit magnetic moments that are considerably reduced compared with the free-ion values.

In alloys and compounds the magnetic moment-carrying ions are frequently separated by other atoms, allowing various types of weaker indirect exchange interactions to become effective. The weak RKKY interaction between two magnetic atoms in metallic materials is mediated by the conduction electrons polarized when appearing in the vicinity of a magnetic ion (Jensen and Mackintosh 1991) (see *Localized 4f and 5f Moments: Magnetism*). Owing to properties of the conduction electrons the RKKY interaction is long-range and oscillates with respect to the distance from the magnetic ion. As a consequence, the ordered arrangements of magnetic moments (magnetic structures) determined predominantly by the RKKY interaction are complex and have long periodicity in some directions. This type of interaction plays a principal role in the magnetic ordering of highly localized electrons bearing magnetic moments, which are typically found in lanthanides and their compounds. The 4*f* moments in these materials are, as a rule, large and compare well with the free-ion moments but the relevant ordering temperatures are rather low (see $GdNi_2$ in Table 1).
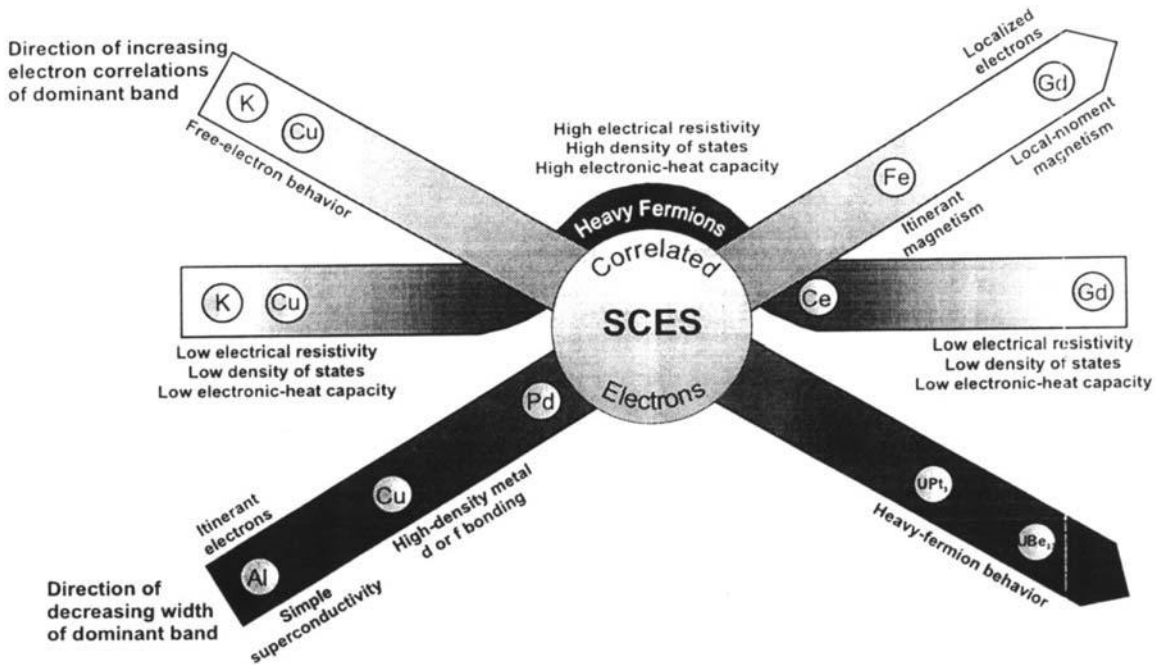
Figure 11

Strongly-correlated electron systems (SCES) at a crossover of electronic properties. The figure summarizes some of the unusual electronic properties of SCES, stemming from the dominant role of their narrow *d*- or *f*-band. Along one diagonal, they stand midway between simple metals, whose conduction electrons are essentially uncorrelated and which exhibit free-electron behavior, and heavy-fermion materials, whose conduction electrons exhibit very strong correlations leading to extremely high effective electron masses. Along the other diagonal, SCES stand at the crossover between materials whose itinerant broad-band electrons form superconducting ground states and magnetic materials, whose fully localized electrons (infinitely narrow band) form local magnetic moments and magnetic ground states. Along the horizontal line, SCES materials are distinguished from the elements on either side by their high resistivity and specific heat, high density of electron states at the Fermi energy, and enhanced electronic mass. Smith and Boring (2000) have presented such a figure originally to point out the electronically unique Pu (plutonium), an actinide metal with strongly correlated 5*f* electrons.

The super-exchange interaction is typical for materials in which the magnetic atoms are surrounded by ligands that do not carry permanent magnetic moments. It has been introduced to describe a situation in magnetic oxides and can be applied to similar ionic materials. A typical example is MnO in which Mn^{2+} ions are separated by an O^{2-} ion. The crystal and magnetic structure of MnO is shown in Fig. 13. The essential ingredient of super-exchange interaction in oxides is that the spin moments of the metal ions on opposite sides of an oxygen ion interact with each other through the *p*-orbit of the oxygen ion (Chikazumi 1964, Barbara *et al*. 1988) (see *Transition Metal Oxides: Magnetism*).

A particular analogy of super-exchange is the indirect exchange in intermetallic materials called "hybridization-mediated exchange interaction" which is frequently reported in actinide intermetallics (Sechovský and Havela 1998). In this case the

interaction between two magnetic ions is mediated by polarization of the valence states of an ion between them (ligand) due to hybridization of relevant magnetic ion and ligand states. Consequently a non-negligible magnetic moment is also observed on the originally nonmagnetic atom (ion).

The idea of a double exchange interaction (Kubo and Ohata 1972) has been introduced to explain ferromagnetism in some perovskite systems containing ions that may possess two different ionic states at crystallographically equivalent sites. The double exchange mechanism became an important issue of the manganese-containing perovskites exhibiting colossal magnetoresistance.

Generally the exchange interaction energy between two ions can be expressed as:

$$H_{ij} = -2J_{ij}\hat{\boldsymbol{S}}_i\hat{\boldsymbol{S}}_j \qquad (9)$$

where J_{ij} is the exchange integral (10^2–10^3 K for direct exchange in 3d metals, 10–10^2 K for indirect exchange and super-exchange), and $\hat{\boldsymbol{S}}_i$, $\hat{\boldsymbol{S}}_j$ are spin operators of the ith and the jth ion. For the whole

system we have the exchange interaction expressed by:

$$H_{ij} = -\sum_{\substack{i,j \\ i \neq j}} J_{ij}\hat{\boldsymbol{S}}_i\hat{\boldsymbol{S}}_j \tag{10}$$

A convenient expression for an exchange interaction is obtained in terms of the molecular field H^{m}. The energy of exchange interactions of an ion with the other ions in a solid can be formally replaced by the energy of the ion's magnetic moment in an external magnetic field, H^{m}, which is called the molecular field (also *mean field*). The molecular field is proportional to the spontaneous magnetization (domain magnetization or sublattice magnetization) such that

$$H^{\mathrm{m}} = \lambda M \tag{11}$$

where the molecular field constant λ is determined by the strength of the exchange interaction.

For example, the molecular field in iron at room temperature is 6.8×10^8 A m^{-1}, which is equivalent to a magnetic induction of 855 T. Introduction of the molecular field allows the theory of magnetization (susceptibility) behavior of ferromagnets, antiferromagnets, and ferrimagnets to be developed easily (Chikazumi 1964, Barbara *et al.* 1988, Gilles 1994) (see *Localized 4f and 5f Moments: Magnetism*). The Curie temperature for a ferromagnet or ferrimagnet, as well as the Néel temperature for an antiferromagnet, is a measure of the sum of the absolute value of molecular-field coefficients (Barbara *et al.* 1988).

Figure 12
Schematic illustration of the main types of exchange interactions (direct, indirect—super-exchange or hybridization-mediated exchange interaction, and RKKY-type indirect exchange interaction mediated by polarized conduction electrons).
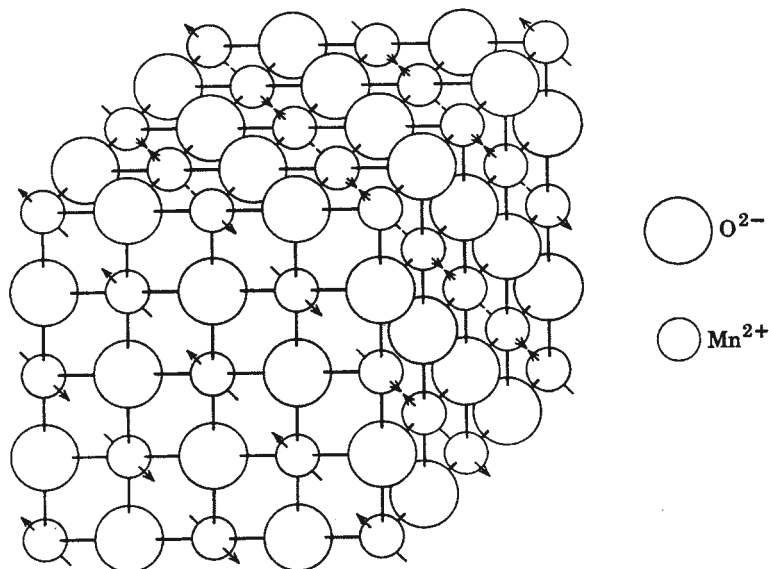
Figure 13
Crystal and magnetic structure of MnO.

3.2 Types of Magnetic Ordering: Magnetic Structures

The character of long-range ordering of magnetic moments is reflected in a magnetic structure that has a certain translational symmetry of equivalent magnetic moments (in analogy to the crystal structure). To determine fully the magnetic structure of a particular material, four basic facts need to be established (Rossat-Mignod 1987):

(i) the ordering temperature below which the magnetic moments develop some type of long-range order (ferromagnetic, or another ordering yielding a spontaneous magnetization, below T_C or antiferromagnetic below T_N);

(ii) the wavevector q that characterizes the modulation of magnetic moments within the structure. If q is equal to the reciprocal lattice vector of the underlying crystal structure, or if it is a simple fraction thereof, the structure is called commensurate. The other magnetic structures are called incommensurate. The incommensurate collinear structure is usually transformed to a commensurate one at low temperatures. Magnetic structures that should be described by more than one q-vector are called "multi-q" structures (Bacon 1975, Barbara *et al.* 1988);

(iii) the orientation of magnetic moments with respect to the crystallographic axis and mutual orientation of neighboring magnetic moments. In this respect a large variety of noncollinear magnetic structures (in which magnetic moments on at least some neighboring magnetic sites are neither parallel nor antiparallel) has been observed besides the collinear structures (in which magnetic moments on neighboring magnetic sites are only either parallel or antiparallel);

(iv) the magnitude of the magnetic moment on each "magnetic" site.

The noncollinear structures usually appear as a result of competition between exchange interactions and the magnetocrystalline anisotropy. Besides extensive experimental investigations of noncollinear magnetic structures using neutron scattering, a theoretical approach using the density functional theory provides realistic results for many systems (Sandratskii 1998).

Long-period magnetic structures appear due to the long-range oscillatory character of exchange interactions, e.g., RKKY-type. The magnetic moments may be rotating, precessing (helical structure), or collinear but modulated with a period given by q. Incommensurate magnetic structures frequently occur due to exchange interactions being strong in only two dimensions while the exchange interaction along the third direction is much weaker. In this case the incommensurate structure emerging below T_N is replaced by a commensurate ordering at lower temperatures.

Effects of RKKY-type interaction are illustrated by the variety of magnetic structures in rare-earth metals (Barbara *et al.* 1988, Jensen and Mackintosh 1991), ranging from ferromagnetism, e.g., the ground state of dysprosium, to various long-period modulated or spiral structures, e.g., erbium (see *Localized 4f and 5f Moments: Magnetism*).

4. Magnetic Phase Transitions

A material that exhibits a long-range magnetic ordering at low temperatures in zero magnetic field is characterized by at least two phases: the high-temperature paramagnetic phase and the magnetically-ordered ground-state phase. In simple systems, the ground-state phase is established immediately below the magnetic-ordering temperature (T_C or T_N). Frequently, the magnetically ordered phase, which appears at temperatures below T_C (or T_N), is different from the ground-state phase. Then one or more magnetic phase transitions are observed at temperatures below T_C (or T_N).

When applying an external magnetic field new magnetic phases can be induced. These phases are usually called metamagnetic and the related magnetic phase transitions with respect to the external magnetic field as the control parameter are called metamagnetic transitions. These transitions are observed in various real antiferromagnets and ferrimagnets (see *Magnetic Phase Transitions: Field-induced (Order to Order)*).

Metamagnetic phase transitions from a paramagnetic state to a magnetically ordered phase can also be found in nearly magnetic itinerant electron systems (Fig. 6) (see *Metamagnetism: Itinerant Electrons*). Further examples can be found in review papers on magnetism in rare-earth intermetallic compounds (Gignoux and Schmitt 1991, 1995) and uranium intermetallics (Sechovský and Havela 1998).

New magnetic phases and magnetic phase transitions may also be induced by applying external pressure (Sechovský and Havela 1998) or by controlled variation of the material composition (see *Magnetic Systems: External Pressure-induced Phenomena*). In the cross-over region between magnetic ordering and the nonmagnetic state rather unusual phenomena are observed at low temperatures (see *Heavy-fermion Systems*).

A phase transition between two magnetic phases can be a first-or second-order type depending on whether it is connected with a discontinuity of the first derivative (e.g., magnetization) or the second derivative (e.g., magnetic susceptibility) of the magnetic part of the free energy, respectively. Magnetic phase transitions in real materials are usually also reflected in transport properties (Sechovský and Havela 1998) (see *Intermetallics: Hall Effect*, *Elemental Rare Earths: Magnetic Structure and Resistance, Correlation of*; *Magnetoresistance: Magnetic and Nonmagnetic Intermetallic*; *Giant Magnetoresistance:*

Metamagnetic Transitions in Metallic Antiferromagnets, and *Rare Earth Intermetallics: Thermopower of Cerium, Samarium, and Europium Compounds*) and in thermodynamic and other material properties (see *Magnetic Systems: Specific Heat*; *Magnetocaloric Effect: From Theory to Practice*; and *Magnetoelastic Phenomena*).

4.1 Magnetic Phase Diagrams

A magnetic phase diagram is a schematic representation of phases adopted by a material over a range of varying parameters. Parameters are usually temperature (T) and external magnetic field (H), external pressure (p), or the concentration of a substituting element (x). These are referred to as H–T, p–T, or x–T magnetic phase diagrams, respectively. Magnetic phase diagrams of simple magnetic systems can contain only two phases: the paramagnetic phase and one magnetically ordered phase. In the case of several competing interactions, especially long-range interactions, the relevant magnetic phase diagram may be rather rich on different phases.

In strongly anisotropic magnetic systems a complete description requires up to three different magnetic phase diagrams, one each for the magnetic fields applied along the three principal crystallographic directions. The compound CeSb (Rossat-Mignod *et al.* 1983, 1990), which crystallizes in one of simplest crystal structure—the cubic NaCl-type, is an excellent example of a very complicated magnetic phase diagram. The enormous number of magnetic
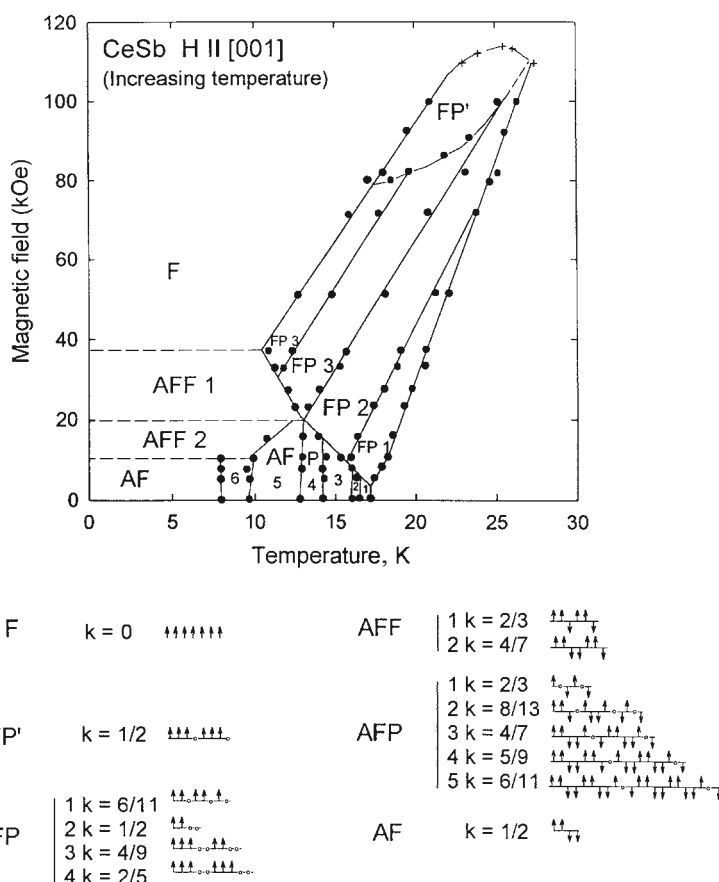
Figure 14
Magnetic phase diagram of CeSb. Orderings in the 15 distinct phases corresponds to commensurate structures which have been classified in three categories: AFF, AFP, and FP phases. The structures are built of ferromagnetic (001) planes of magnetic moments oriented perpendicularly to the planes. The actual structures are realized by complex coupling along the moment direction. Some of the planes sometimes appear frustrated and consequently the moments within them become paramagnetic and the particular plane behaves nonmagnetically (after Rossat-Mignot *et al.* 1983, 1990).

phases characterized by a variety of long-period collinear magnetic structures (see Fig. 14) demonstrates the importance of long-range exchange interactions.

Numerous examples of magnetic phase diagrams of specific materials can be found in other articles (see: *Magnetic Phase Transitions: Field-induced (Order to Order)*, Figs. 1–3, *Metamagnetism: Itinerant Electrons*, Figs. 1 and 6) and in review papers on magnetism in rare-earth intermetallic compounds by Gignoux and Schmitt (1991, 1995) and uranium intermetallics (Sechovský and Havela 1998).

5. *Magnetocrystalline Anisotropy*

Magnetocrystalline anisotropy is manifested by locking magnetic moments in certain crystallographic directions. Anisotropy is one of the most important characteristics of materials considered for permanent magnet applications (see *Magnetic Anisotropy* and *Hard Magnetic Materials, Basic Principles of*). In particular, the anisotropy energy E_A (or the anisotropy field H_A) is one of the key parameters determining the coercive field in ferromagnets. The value of E_A depends on the orientation of magnetization with respect to the crystallographic axes and therefore it can be expressed in terms of directional cosines α_1, α_2, and α_3 of the magnetization vector with respect to the main crystallographic directions [100], [010], and [001], respectively (for a detailed explanation see Chikazumi 1964, Gilles 1994). For cubic crystals such as iron and nickel the magnetocrystalline anisotropy energy is given by:

$$E_A = K_1(\alpha_1^2\alpha_2^2 + \alpha_2^2\alpha_3^2 + \alpha_1^2\alpha_3^2) + K_2\alpha_1^2\alpha_2^2\alpha_3^2 + \dots , \quad (12)$$

where K_i is *the i*th anisotropy constant. For Fe, $K_1 = 4.8 \times 10^4$ Jm^{-3} and $K_2 = \pm 5 \times 10^3$ Jm^{-3}, and for Ni, $K_1 = -4.5 \times 10^3$ Jm^{-3} and $K_2 = 2.34 \times 10^3$ Jm^{-3}; in both cases the values refer to room temperature.

For materials with tetragonal symmetry

$$E_A = K_1\alpha_3^2 + K_2\alpha_3^4 + K_3\alpha_1^4\alpha_2^4. \quad (13)$$

and for hexagonal crystals E_A is usually expressed using the description of magnetization direction by polar angles:

$$E_A = K_{u1}\sin^2\theta + K_{u2}\sin^4\theta + K_{u2}\sin^6\theta$$
$$+ K_3\sin^6\theta\cos6\phi, \quad (14)$$

where θ is the angle with respect to the hexagonal c-axis and ϕ represents the orientation within the basal plane. For cobalt at room temperature $K_{u1} = 4.1 \times 10^5$ Jm^{-3} and $K_{u2} = 1 \times 10^5$ Jm^{-3}.

The easy magnetization direction is associated with the minimum of E_A whereas the maximum of E_A determines the hard magnetization direction. For hexagonal and cubic crystals, the conditions for various types of anisotropy are summarized in Tables 2 and 3.

In localized electron systems the magnetocrystalline anisotropy arises from the single-ion crystal-field interaction between the aspherical *d*- or *f*-charge cloud and the charge distribution surrounding the *d* or *f* ion (crystal field) (see *Crystal Field Effects in Intermetallic Compounds: Inelastic Neutron Scattering Results*). In this context, the magnetocrystalline anisotropy is a consequence of the directional dependence of the energy of a *d*- or *f*-charge cloud in the crystal field. The crystallographic direction associated with the energy minimum determines the easy magnetization direction along which the *d* or *f* magnetic moment preferentially orients with respect to the crystallographic axes. Shape differences of the *d*- or *f*-electron cloud lead to different easy magnetization directions among analogous materials where the *d* or *f* ions experience the same crystal field (Legvold 1980).

The involvement of delocalized 5*f* states in light actinide intermetallics in anisotropic covalent bonding implies an essentially different interaction, the two-ion (5*f*–5*f*) interaction, which plays a major role in the magnetocrystalline anisotropy of actinide materials. An analogous mechanism may account for the magnetocrystalline anisotropy in metallic 3*d* electron magnets (Gignoux and Schmitt 1991). Generally, the existence of an orbital magnetic moment and a strong spin–orbit interaction is a necessary prerequisite for the magnetocrystalline anisotropy mechanisms. In the case of new observations of strong orbital magnetism and consequently very strong magnetocrystalline

Table 3

Summary of magnetocrystalline anisotropy parameters for hexagonal systems.

Easy magnetization direction	[001]	Basal plane
E_A	0	$K_{u1} + K_{u2}$
Conditions for K_{u1}, K_{u2}	$K_{u1} + K_{u2}0$	$K_{u1} + K_{u2} < 0$

Table 2

Summary of magnetocrystalline anisotropy parameters for cubic systems.

Easy magnetization direction	[100]	[010]	[001]
E_A	0	1/4 K$_1$	1/3 K$_1$ + 1/27 K$_1$
Conditions for K_1, K_2	$K_1 > 0$, $K_1 > -1/9K_2$	$0 < K_1 > -4/9K_2$	$0 < K_1 < -1/9K_2$

anisotropy in itinerant electron systems the sophisticated electronic structure calculations (Brooks and Johanson 1993) played a principal role.

6. Basic Models of Magnetism

For the interpretation of magnetic phenomena relevant microscopic models are frequently used. The basic three models are discussed in this section. Equation (9) defines the Heisenberg Hamiltonian of the isotropic exchange interaction between two *S*-state ions (characterized by spin angular momentum *S*) that is the basis of the Heisenberg model. This model is most applicable to materials where the isotropic exchange interaction dominates the crystal-field interaction and there are possible anisotropic exchange interactions.

At the same time, together with the Ising model, it has been one of the standard models for cooperative phenomena and phase transitions. The Ising model is described by the Hamiltonian

$$H_{ij} = -2J_{ij}\hat{\mu}_i\hat{\mu}_j \tag{15}$$

where μ_i is a variable with a value of $+1$ or -1. This Hamiltonian can be regarded as a limiting case of Eqn. (9) in which *S* is assumed to be 1/2 and the exchange coefficient of the transverse component $S_{ix}S_{jx} + S_{iy}S_{jy}$ is negligible. The model is useful for systems where strong uniaxial anisotropy locks the magnetic moments along one crystallographic axis (usually the *z*-axis). On the other hand, the opposite limit of dominating transverse components leads to the XY model expressed by the Hamiltonian

$$H_{ij} = -2J_{ij}(\hat{S}_{ix}\hat{S}_{jx} + \hat{S}_{iy}\hat{S}_{jy}) \tag{16}$$

A possible application of the XY model can be found in materials with strong easy-plane anisotropy.

See also: Alloys of 4*f*(R) and 3*d* (T) Elements: Magnetism; Magnetic Excitations in Solids

Bibliography

Ashcroft N W, Mermin N D 1988 *Solid State Physics*. Saunders College Publishing, New York Chap. 31–3
Bacon G E 1975 *Neutron Diffraction*. Oxford University Press, Oxford
Barbara B, Gignoux D, Vettier C 1988 *Lectures on Modern Magnetism*. Springer, Berlin
Boring A M, Smith J L 2000 Plutonium condensed-matter physics: a survey of theory and experiment. *Los Alamos Sci.* **26**, 42–80
Brooks M S S, Johanson B 1993 Density functional theory of the ground state magnetic properties of rare earths and actinides. In: Buschow K H J (ed.) *Handbook of Magnetic Materials*. North Holland, Amsterdam, pp. 139–230 Vol. 7
Buschow K H J, Wohlfarth E P (eds.) 1993 *Handbook of Magnetic Materials*. Elsevier, Amsterdam
Cahn R W, Lifshin E 1993 *Concise Encyclopedia of Materials Characterization*. Pergamon, Oxford
Chikazumi S 1964 *Physics of Magnetism*. Wiley, New York
Cracknel A P 1975 *Magnetism in Crystalline Solids*. Pergamon Press, Oxford
Eriksson O, Nordstrom L, Brooks M S S, Johansson B 1988 4f-band magnetism in CeFe₂. *Phys. Rev. Lett.* **60**, 2523–6
Fisher M E 1962 Relation between the specific heat and susceptibility of an antiferromagnet. *Phil. Mag.* **7**, 1731
Gignoux D, Schmitt D 1991 Rare earth intermetallics. *J. Magn. Magn. Mater.* **100**, 99–125
Gignoux D, Schmitt D 1995 Metamagnetism and complex magnetic phase diagram of rare earth intermetallics. *J. Alloys Compds.* **225**, 423–31
Gilles J 1994 *Magnetism and Magnetic Materials*. Chapman & Hall, London
Hurd M 1983 Varieties of magnetic order in solids. *Contemp. Phys.* **23**, 469–98
Jensen J, Mackintosh A R 1991 *Rare Earth Magnetism*. Clarendon Press, Oxford
Kittel C 1976 *Introduction to Solid State Physics*. Wiley, New York
Kubo K, Ohata N 1972 A quantum theory of double exchange. *J. Phys. Soc. Jpn.* **33**, 21–32
Legvold S 1980 Rare earth metals and alloys. In: Wohlfarth E P (ed.) *Ferromagnetic Materials*. North Holland, Amsterdam, pp. 184–295
Mattis D C 1981 *The Theory of Magnetism I*. Springer, Berlin
Rossat-Mignod J 1987 Magnetic structures. In: Sköld K, Price D L (eds.) *Methods of Experimental Physics*. Academic Press, New York, Vol. 23, part C, pp. 69
Rossat-Mignod J, Burlet P, Quezel S, Effantin J M, Delaconte D, Bartholin H, Vogt O, Ravot D 1983 Magnetic properties of cerium monopnictides. *J. Magn. Magn. Mater.* **31–4**, 398–404
Rossat-Mignod J, Burlet P, Regnault L P, Vettier C 1990 Neutron scattering and magnetic phase transitions. *J. Magn. Magn. Mater.* **90–1**, 5–16
Sandratskii L M 1998 Noncollinear magnetism in itinerant-electron systems: theory and applications. *Adv. Phys.* **47**, 91–160
Schenck A, Gygax F N 1995 Magnetic materials studied by muon spin rotation spectroscopy. In: Buschow K H J (ed.) *Handbook of Magnetic Materials*. North Holland, Amsterdam, Vol. 9, pp. 57–302
Sechovský V, Havela L 1998 Magnetism of ternary intermetallic compounds of uranium. In: Buschow K H J (ed.) *Handbook of Magnetic Materials*. North Holland, Amsterdam, Vol. 11, pp. 1–289
Smith J L, Bohring A M 2000 Plutonium condensed-matter physics. A survey of theory and experiment. *Los Alamos Sci.* **26**, 90–127
Smith J L, Kmetko E A 1983 Magnetism or bonding: a nearly Periodic Table of transition elements. *J. Less Common Metals* **90**, 83–91
Squires G L 1978 *Introduction to the Theory of Thermal Neutron Scattering*. Cambridge University Press, Cambridge, UK
Yosida K 1996 *Theory of Magnetism*. Springer, Berlin

V. Sechovský
Charles University, Prague, Czech Republic

Magnetism: Applications of Synchrotron Radiation

Magnetism in solids covers a large variety of properties ranging from bulk characteristics of permanent magnets or recording and storage devices to fundamental microscopic phenomena in quantum systems. The measurement of bulk magnetic properties (such as susceptibility, magnetization, and anisotropy) represents the first and necessary step to determine the magnetic state of a material. However, a proper understanding of the magnetic properties requires a knowledge of the electronic ground state. Magnetic moments originate from unpaired electrons; the electron spins interact through various exchange couplings to form ordered spin structures, while the electron orbital moments contribute to the total magnetization via spin–orbit couplings.

Therefore, magnetism depends on electronic properties at the atomic level and/or at the electron band level. The observation of transport properties provides information on the electronic properties. Nevertheless, the understanding of magnetism necessitates the determination of the electronic states that carry the magnetization, and the knowledge of the magnetic order and magnetic interactions at a microscopic level. Local probes (NMR, Mössbauer spectroscopy, μSR) can be exploited to obtain some insight as to the nature of the magnetization. Scattering techniques provide microscopic details about the magnetic sites, the arrangement, and the dynamics of the ordered magnetic moments. (For NMR and Mössbauer spectroscopy see Cahn and Lifshin (1993); for μSR see *Muon Spin Rotation (μSR): Applications in Magnetism*.)

Scattering experiments convey information on spatial Fourier transforms of correlation functions. Diffraction experiments reveal static correlations, including short- and long-range ordered structures, while inelastic scattering experiments are used to observe time-dependent correlations, i.e., fluctuations, normal modes, and collective or localized excitations. The energy range spanned by the excitations is related to the size of the interactions, which are roughly defined by the ordering temperature in the range 1–300 K (0.1–30 meV energy range). However, the energy scales associated with electronic bands are in the electron volt range. An ideally suited scattering probe should cover all these energies. Traditionally neutron scattering is the probe of choice. However, in the past optical effects in the visible range (Faraday and magneto-Kerr effects) have confirmed the existence of interactions between photon polarization and magnetization: the polarization of light is rotated upon transmission through, or reflection from, a magnetized medium.

Similar phenomena (dichroic signals) are observed in soft and hard x-ray absorption experiments, when the photon energy is adjusted near an x-ray absorption edge of a magnetic atom. Reciprocally, x-ray scattering experiments show large resonant enhancements of the scattered intensities yielding count rates in the range 10^4–10^6 photons s^{-1}. These resonant effects in x-ray scattering are superimposed on nonresonant effects, which are much weaker. The developments in the use of x rays rely on tunable photon sources and the scientific interest in the applications of x-ray methods to probe magnetism has increased since the development of modern synchrotron radiation sources.

1. Scattering Probes: Synchrotron X Rays vs. Neutrons

X-ray and neutron scattering techniques are analogous in many ways but their strengths are complementary. Neutrons are considered as the probe of choice for the study of magnetism by means of scattering methods for two reasons (Squires 1978): (a) neutrons possess a spin and the associated neutron magnetic moments couple significantly to the magnetization in materials; and (b) the rather low kinetic energy of neutrons (3–100 meV at reactor sources) allows easy inelastic experiments adapted to magnetic properties. A large fraction of the understanding of microscopic magnetism (magnetic structures, magnetic excitations) comes from neutron scattering results. However, neutron beams have low flux and neutron scattering experiments require large scattering volumes. Furthermore, neutrons as a magnetic probe are sensitive to the total magnetization and do not distinguish readily contributions from different elements, different electronic shells, or spin vs. orbital momentum. Neutrons cannot probe electronic properties.

X rays, when applied to magnetism, suffer from a serious drawback: the nonresonant coupling between the electromagnetic field associated with the photons and the spin and orbital momentum distributions is weak. This interaction was evidenced experimentally in the early 1970s (de Bergevin and Brunel 1972) but was considered as a curiosity until more powerful x-ray sources became available. The reason behind the use of x-ray methods for the study of magnetism arises from the unique properties of x-ray synchrotron radiation: (i) a high brilliance, which gives a large particle flux over an extremely small beam size; (ii) a wide range of photon energy tunability; and (iii) a well-defined polarization state of the emitted radiation. Modern synchrotron sources available worldwide can accommodate different undulators as radiation sources which produce x rays with energy ranging from a few hundred electron volts to 30–40 keV. On the high-energy side, multipole wigglers produce photons up to 300 keV. High brilliances up to 10^{20} photons s^{-1}mm^{-2}mrad^{-2} per 0.1% bandwidth have been reached at the European Synchrotron Radiation Facility (ESRF) in Grenoble, France.

The x-ray polarization is readily tunable, with an almost perfect degree of linear polarization. Special insertion devices are designed to produce elliptically or circularly polarized radiation.

The high photon flux available at synchrotrons compensates for the weakness of the nonresonant magnetic x-ray scattering amplitude, and the easily tuned photon energy has boosted resonant studies. Magnetic resonant x-ray scattering combined with the high brilliance of synchrotron x-ray beams makes it possible to investigate small scattering volumes (microcrystals, thin films, surfaces) or weak magnetic moments (down to $0.01\mu_B$). The resonant process is element selective and electronic shell sensitive, allowing detailed studies of the origin of magnetic moments. The time structure of the synchrotron radiation (x-ray bunches at 357kHz at the ESRF) can be exploited to study the dynamics of magnetic processes in real time down to the nanosecond scale (Bonfim *et al.* 1998).

When used together, x-ray and neutron methods offer a broad range of capabilities and the choice of the technique depends on the details of the problem to be solved. Neutrons are essential in determining magnetic structures (magnetic powder diffraction) and in characterizing magnetic excitations (the observation of magnetic excitations will not be discussed). However, synchrotron x rays provide more information about the electronic character of magnetism (separation of orbital momentum and spin, sensitivity to the electronic shell and to the chemical species). Owing to the properties of synchrotron x-ray beams (brilliance, collimation, time structure), x rays are preferred over neutrons for the investigation of minute samples (surfaces, thin films), time-resolved studies, and high Q-resolution experiments. However, in the case of scattering experiments, the high collimation of synchrotron beams must be matched by the crystalline quality of the materials. As a consequence, only good-quality crystals can be studied; for powder samples, *ab initio* magnetic structure determinations are performed using neutron diffraction.

In the following, the basic character of the interactions of x rays with magnetism is outlined, including a description of the scattering amplitudes (elastic Bragg scattering or diffraction and Compton scattering) and the spin-dependent x-ray absorption methods (magnetic dichroism). Potential applications are indicated and comparison with neutron methods is made when appropriate.

2. Scattering Cross-sections

The x-ray or neutron intensity diffracted by an assembly of atoms is written in terms of an elastic scattering cross-section:

$$\left(\frac{d\sigma}{d\Omega}\right) = \left| \sum_n e^{iQR_n} f_n(k_i, k_f, \hbar\omega) \right|^2 \tag{1}$$

where $\hbar\omega$ is the x-ray energy, k_i and k_f are the incident and scattered wave vectors of the photons, Q is the probe momentum transfer ($Q = k_i - k_f$), and f_n represents the scattering amplitude from the nth atom. Two limiting regimes are distinguished for x rays: the resonant scattering (when the incident photon is close to an absorption edge of a magnetic species in the material) and the nonresonant scattering (when the photon energy is far from any absorption edge). It is convenient to separate the different contributions:

$$f_n(k_i, k_f, \hbar\omega) = f_n^{charge}(Q) + f_n^{nonres}(k_i, k_f)$$
$$+ f_n^{res}(k_i, k_f, \hbar\omega) \tag{2}$$

where f_n^{charge} denotes the familiar Thomson scattering from charge distribution, f_n^{nonres} is the nonresonant magnetic scattering, and all contributions to the resonant scattering are included in f_n^{res}.

The processes discussed here correspond to coherent elastic scattering; there are also inelastic processes, known as Compton scattering, during which photons exchange energy with the scattering system. In such a case, the scattering is incoherent and photons are scattered by individual electrons.

The absorption cross-section, which is measured in spin-dependent absorption experiments, is related to the scattering amplitude in Eqn. (2) through the optical theorem:

$$\sigma_a = 2\lambda \text{Im}[f_n(k_i, k_f, \hbar\omega)] \tag{3}$$

These different cases for x rays are discussed in the following sections. Neutrons are used in the scattering mode only. Furthermore, only the elastic case is considered here.

3. Nonresonant Regime

The nonresonant x-ray regime encompasses coherent Bragg scattering (diffraction) and the Compton inelastic process.

3.1 Nonresonant X-ray Magnetic Bragg Scattering

The nonresonant x-ray magnetic scattering amplitude is written as (Blume and Gibbs 1988):

$$f^{nonres}{}_n(k_i, k_f) = -ir_0 \left(\frac{\hbar\omega}{mc^2}\right)$$
$$\times \left[\frac{1}{2}L_n(Q)A(\varepsilon_i, \varepsilon_f) + S_n(Q)B(\varepsilon_i, \varepsilon_f)\right] \tag{4}$$

where $L_n(Q)$ and $S_n(Q)$ are the Fourier transforms of the orbital momentum and spin magnetization densities (form factors) at the nth site, r_0 is the classical radius of the electron (2.8×10^{-15} m), a standard unit

in atomic scattering processes, and mc^2 is the rest energy of the electron (511 keV). The vector quantities $A(\varepsilon_i, \varepsilon_f)$ and $B(\varepsilon_i, \varepsilon_f)$ depend on the polarization vectors ε_i and ε_f of the incident and scattered wave vectors, respectively; they are not identical and have distinct Q dependencies.

A compact expression has been obtained:

$$f_n^{\text{nonres}}(k_i, k_f) = -ir_0(\bar{\lambda}_e Q)$$

$$\begin{pmatrix} \cos\theta S_2 & -\sin\theta[\cos\theta(S_1 + L_1) \\ & \quad -\sin\theta S_3] \\ \sin\theta[\cos\theta(S_1 + L_1) & \cos\theta[S_2 + 2\sin^2\theta L_2]M \\ \quad +\sin\theta S_3] & \end{pmatrix} \quad (5)$$

where θ is the Bragg angle and $\bar{\lambda}_c$ is the Compton wavelength ($= 3.81 \times 10^{-3}$Å). $L(Q)$ and $S(Q)$ are given by their components ($\alpha = 1,2,3$) in the coordinate system u_1, u_2, u_3, where u_1 is directed along $k_i + k_f$, u_2 is perpendicular to the scattering plane and parallel to $k_i \times k_f$, and u_3 is along Q. The matrix form for $f_n^{nonres}(k_i, k_f)$ is used to describe the polarization dependence. The basis vectors for the polarization ε_i and ε_f correspond to a linear polarization either perpendicular (σ) or parallel (π) to the scattering plane. From Eqn. (5) it can be seen that the contributions from L and S to the total magnetization $M = L + S$ can be obtained separately from magnetic x-ray scattering data. Such a separation is not readily possible in neutron diffraction experiments because neutrons are sensitive to the total moment. It should be noted that $f_n^{nonres}(k_i, k_f)$ is not a spherical tensor formed with $(\varepsilon_i, \varepsilon_f)$ in contrast to the usual Thomson scattering:

$$f_n^{\text{charge}}(Q) = -r_0\rho(Q)\varepsilon_i \cdot \varepsilon_f \quad (6)$$

This difference helps in separating the Thomson charge from purely magnetic x-ray scattering. Comparison of Eqns. (5) and (6) provides a rough estimate for the relative amplitude of magnetic scattering and charge scattering. If all form factors and geometrical factors in $A(\varepsilon_i, \varepsilon_f)$ and $B(\varepsilon_i, \varepsilon_f)$ are set to unity, then:

$$\left|\frac{f_n^{\text{nonres}}}{f_n^{\text{charge}}}\right|^2 \approx (\bar{\lambda}_c \cdot Q)^2 m^2 \left(\frac{N_m}{N}\right)^2 \quad (7)$$

where m is the electron average magnetic moment (expressed in μ_B) and N_m is the number of magnetic electrons compared to the total number of electrons, N, at site n. For conventional diffraction cases, $|Q| = 1$–6 Å^{-1}, $N_m/N = 0.1$, and the ratio of intensities is around 10^{-6}. In practice, this ratio is even smaller because of the geometrical factors in Eqn. (5). This explains why the advent of bright third-generation synchrotron sources has boosted the development

of x-ray techniques by alleviating the consequences of the inherent weakness of nonresonant x-ray magnetic scattering amplitudes.

The neutron counterpart of Eqn. (4) is written as:

$$f_{\text{neutron}}(Q) = f_{\text{nuc}}(Q) + r_0\frac{\gamma}{2}p \cdot (Q \times [Q \times M(Q)]) \quad (8)$$

where p is the neutron beam polarization, γ is the neutron gyromagnetic factor ($= 1.91$), $M(Q)$ is the Fourier transform of the total magnetization, and $f_{\text{nuc}}(Q)$ is the scattering amplitude from the nuclei in the solid. Note that neutrons couple to the Fourier transform $M(Q) = L(Q) + 2S(Q)$ of the total magnetization. The L/S separation can only be achieved by modeling the Q dependence of the two contributions, $L(Q)$ and $S(Q)$.

In the case of ferro- or ferrimagnetic materials, the magnetic Bragg peaks occur at the same positions in reciprocal space as the more intense crystal structure peaks. Interferences between the magnetic scattering amplitude and the scattering amplitude from the crystal structure allow the observation of the magnetic signal. A practical way to extract the magnetic information is to reverse the magnetization direction by applying an alternating magnetic field (reversing the interference term) and to collect the intensity as a function of field orientation; this gives the so-called flipping ratio, R, defined as:

$$R = \frac{I(\uparrow) - I(\downarrow)}{I(\uparrow) + I(\downarrow)}$$

In the x-ray case, because $f_n^{\text{nonres}}(k_i, k_f)$ and $f_n^{charge}(Q)$ are out of phase by $\pi/2$ (Eqns. (4) and (6)), interference only occurs in the case of circular polarization (the ε_i and ε_f vectors are complex) or if the crystal structure factor is imaginary (large absorption and/or noncentrosymmetric structure). In the neutron case, a finite neutron polarization is required to have interference effects. In this case, R is obtained by flipping the polarization of the neutron beam:

$$R = \frac{1 + 2pA(Q) + A(Q)^2}{1 - 2pA(Q) + A(Q)^2}$$

where p is the neutron polarization and

$$A(Q) = \frac{M(Q)}{f_{\text{nuc}}(Q)}$$

Owing to the larger neutron magnetic scattering amplitude, weak magnetic moments $M(Q)$ can be extracted (i.e., field-induced magnetization in paramagnets) provided $f_{\text{nuc}}(Q)$ and p are known accurately. Usually, neutrons can detect magnetic moments down to $0.05\mu_B$. However, x rays have an advantage over neutrons when the sample under investigation is very small, because of the high brilliance of synchrotron sources. Ferromagnetic thin films or multilayers and

interfacial magnetism are routinely studied by means of magnetic x-ray scattering.

In the case of antiferromagnetic systems, the magnetic diffraction peaks occur at positions in reciprocal space that are forbidden for crystal structure reflections, and the limiting factor for detection is the scattered intensity. Figure 1 shows examples of data obtained from third-generation synchrotron sources. Figure 1(a) gives an indication of the scattered intensities available at modern synchrotron sources. Also shown in Fig. 1 are the magnetic form factors $L(Q)$ and $S(Q)$ that have been determined independently by exploiting the polarization dependence of the
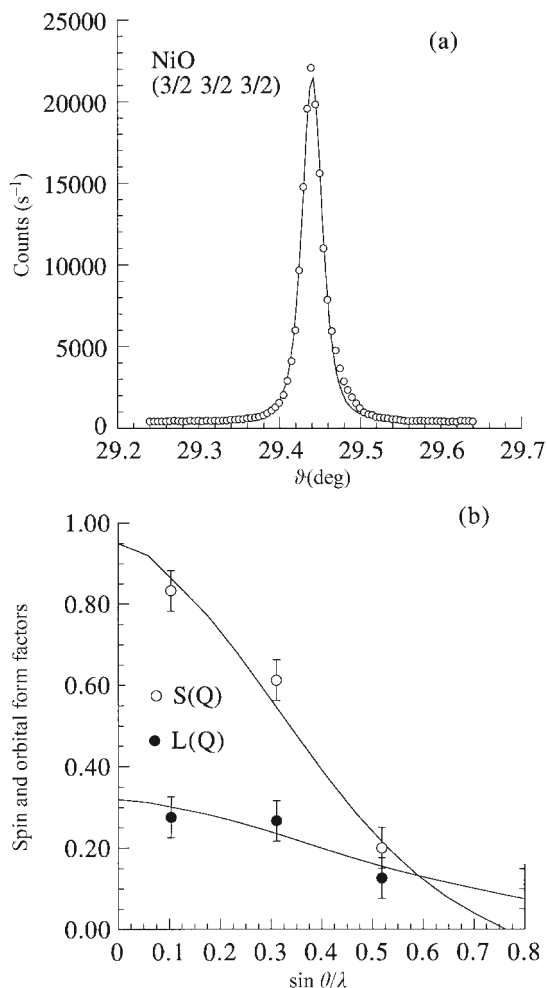
scattering amplitude in Eqn. (5) (Fernandez *et al.* 1998). It is worth noting that at the high-energy limit for Bragg scattering (low Bragg angle θ), the x-ray magnetic scattering is dominated by the spin contribution, whereas the orbital momentum part becomes negligible (Eqn. (5)).

An important aspect of diffraction experiments is the Q-resolution. Owing to the highly collimated beams, synchrotron x-ray experiments allow high Q-resolution conditions which cannot be reached with neutron scattering experiments. This is particularly useful in detecting minute changes in the lattice parameters occurring at magnetic phase transitions due to magnetostriction effects.

3.2 Magnetic Compton Scattering

Inelastic Compton scattering is an incoherent process where the scattering cross-section can be written as (Lovesey and Collins 1996):

$$\frac{d\sigma}{d\Omega d\omega} = N\left(\frac{m}{\hbar k_i}\right)$$
$$\times \left[\left(\frac{d\sigma}{d\Omega}\right)_{charge} J(p_z) + \left(\frac{d\sigma}{d\Omega}\right)_{mag} J_{spin}(p_z)\right] \quad (9a)$$

where $J(p_z)$ is the usual Compton profile (a two-dimensional average perpendicular to the scattering vector of the momentum density). The magnetic Compton profile given by $J_{spin}(p_z) = {}^{1/2}[J_\uparrow(p_z) - J_\downarrow(p_z)]$ is the difference between the profiles of spin-up electrons and spin-down electrons. The differential cross-sections contain geometrical and polarization factors:

$$\left(\frac{d\sigma}{d\Omega}\right)_{Charge} = \frac{1}{2}r^2_0(1 + \cos^2\theta)$$

$$\left(\frac{d\sigma}{d\Omega}\right)_{spin} = -r_0^2 p_c \frac{\hbar\omega}{mc^2}(1 - \cos\theta)(\hat{\mathbf{k}}_i\cos\theta + \hat{\mathbf{k}}_f) \cdot z \quad (9b)$$

where $\mathbf{z}$ is the unit vector parallel the magnetic axis, $\hat{\mathbf{k}}_i$ and $\hat{\mathbf{k}}_f$ are unit vectors along k_i and k_f; and p_c is the degree of circular polarization of the incident x-ray beam. Similarly to the previous discussions on ferromagnets, the magnetic Compton profile is isolated from the total spectrum by reversing either the magnetization direction, $\mathbf{z}$, or the x-ray helicity, p_c. By measuring profiles along several directions, it is possible to reconstruct the three-dimensional spin polarized momentum density and compare it with theoretical electronic band calculations. Only magnetic Compton experiments can supply these experimental confirmations.

Figure 1
Nonresonant magnetic x-ray scattering from NiO. (a) Angular profile of an antiferromagnetic peak. (b) Q-dependence of the spin and orbital moment form factor as extracted from the polarization analysis of experimental data.

4. Resonant Regime

The nonresonant x-ray magnetic scattering amplitude in Eqn. (5) vanishes in the forward direction at $Q = 0$, leading to the absence of magnetic effects in x-ray transmission or x-ray reflection measurements. However, the optical index in the visible region varies with the magnetization direction relative to the light polarization, which is the origin of magneto-optics. In the hard x-ray region, the optical index is very close to unity, and similar effects are not observed. Only near an absorption edge does the x-ray index differ from unity due to the anomalous part of the scattering amplitude, and magnetic effects are detected. The scattering experiments and the absorption methods can be treated in parallel near resonance. Indeed, resonant scattering originates from second-order perturbation processes which can be pictured as the absorption of an incident photon, the creation of a short-lived intermediate state, followed by decay back to the ground state. In the case of elastic scattering, a photon is elastically scattered during the decay. These intermediate states correspond to the promotion of an inner shell electron to a bound or nearly bound level in an outer shell with a high density of states, leaving behind a core hole. The same intermediate levels contribute to the white line in normal x-ray spectroscopy. The outer electronic shells are sensitive to the local symmetry of atomic sites and the scattering amplitude reflects the symmetry of the associated wave functions with respect to the relative orientation of the incident x-ray polarization. When the incident photon energy is tuned to a resonance, the scattering amplitude contains terms which reflect the local symmetry, possibly leading to new Bragg peaks which are forbidden away from resonance (Templeton 1994).

The onset of local magnetic moments is a particular case of symmetry breaking which induces resonant terms in the x-ray scattering amplitude, f_n^{res}, contributing to the total scattering amplitude in Eqn. (2) (Blume 1994). The resonance occurs through electric multipole transitions from a core level into empty electronic shells. The sensitivity to the magnetization arises from the difference in transition probabilities due to the spin polarization of the intermediate states, the spin–orbit couplings, and the exchange interactions. The strength of the resonance is given by the multipole electric transition matrix elements and the spin polarization of the intermediate states. The strongest transition is the electric dipole (E1 with $\Delta l = 1$) contribution; the next strongest is given by the electric quadrupole (E2 with $\Delta l = 2$) contribution, but the relative weakness of the E2 contribution must be balanced with the size of the spin polarization of the associated intermediate states. This is illustrated with the example of 4f and 5f systems. The f electronic states which carry the main magnetic moments are probed directly by E1 transitions at the M_4 and M_5 edges ($3d \rightarrow f$). They are also examined by E2 transitions at the L_2 and L_3 edges ($2p \rightarrow f$); but at the same L_2 and L_3 edges, the d moments, which are polarized by the f electrons, are probed by E1 transitions ($2p \rightarrow d$). This example demonstrates the versatility and the electronic selectivity for the study of the origin of magnetic moments. The resonant process is also chemical selective, because the resonant energy changes with the chemical species and valence state.

The resonant scattering amplitude can be expressed as a series expansion:

$$f_n^{\text{res}}(k_i, k_f, \hbar\omega) = f_{n\text{E1}}^{\text{res}}(k_i, k_f, \hbar\omega)$$
$$+ f_{n\text{E2}}^{\text{res}}(k_i, k_f, \hbar\omega) + \cdots \quad (10a)$$

where $f_{n\text{E}L}^{res}(k_i, k_f, \hbar\omega)$ are contributions from E1 and E2 transitions (Hannon *et al*. 1988).

The E1 contribution to the scattering has the form:

$$f_{n\text{E}1}^{res}(k_i, k_f, \hbar\omega) = F^{(0)} \begin{pmatrix} 1 & 0 \\ 0 & \cos 2\theta \end{pmatrix}$$

$$- iF^{(1)} \begin{pmatrix} 0 & z_1\cos\theta + z_3\sin\theta \\ -z_1\cos\theta + z_3\sin\theta & -z_2\cos\theta \end{pmatrix}$$

$$+ F^{(2)} \begin{pmatrix} z_2^2 & -z_2(z_1\sin\theta - z_3\cos\theta) \\ z_2(z_1\sin\theta + z_3\cos\theta) & \cos^2\theta(z^2_1 tan^2\,\theta + z^2_3) \end{pmatrix}$$
$$(10b)$$

where z_i are components of the moment direction $\mathbf{z}$ in the coordinate system defined above. $F^{(n)}$ are resonant amplitudes which contain a resonant denominator

$$\frac{1}{E_a - E_c + \hbar\omega - i\dfrac{\Gamma}{2}}$$

dipole radial matrix elements $\langle c|r|a \rangle$, and spin polarization of the intermediate states (only in the case of $F^{(1)}$ and $F^{(2)}$) (Hannon *et al*. 1988). E_a, $|a \rangle$ and E_c, $|c \rangle$ are the energies and wave functions of the ground and intermediate states, respectively, and Γ is the inverse lifetime of the intermediate state.

The first term in Eqn. (10b) is independent of $\mathbf{z}$ and does not contribute to the magnetic scattering; it is the usual anomalous x-ray scattering term which contributes to white lines in the fluorescence signal. The second term is linear in $\mathbf{z}$ and contributes to the amplitude of magnetic Bragg peaks. The third term is quadratic in $\mathbf{z}$ and leads to second-order resonant harmonics. More complex terms appear in the E2 contribution, which contains terms up to fourth-order in $\mathbf{z}$ producing third- and fourth-order resonant harmonics.

In order to exploit the resonant enhancement for a given magnetic species, the photon energy is tuned to an absorption edge where the core electron is promoted into the electronic shell that carries the magnetization via the strong E1 transitions. Examples

Table 1
Significant resonances for selected magnetic species.

Magnetic species		Resonance process	Resonant energy	
			Energy (keV)	Wavelength (Å)
3d transition metal	Fe	E1 $p \leftrightarrow d$ L$_2$, L$_3$	0.71	17.5
		E1, E2 $s \leftrightarrow p$, d K	7.1	1.75
5d transition metal	Pt	E1 $p \leftrightarrow d$ L$_2$, L$_3$	11.5–13	1.08–0.95
		E1, E2 $s \leftrightarrow p$, d K	78.4	0.16
4f rare earth	Gd	E1 $d \leftrightarrow f$ M$_4$, M$_5$	1.22–1.19	10.2–10.4
		E1, E2 $p \leftrightarrow d$, f L$_2$, L$_3$	7.9–7.2	1.57–1.72
5f actinide	U	E1 $d \leftrightarrow f$ M$_4$, M$_5$	3.7–3.5	3.35–3.54
		E1, E2 $p \leftrightarrow d$, f L$_2$, L$_3$	20.9–17.2	0.59–0.72

are given in Table 1. Theoretical estimates for the resonant enhancements predict that the resonant scattering amplitude would reach $10r_0$ at the M edges of actinides and even $100r_0$ at the M edges of rare earths, but would be more modest at the L edges of rare earths, around $0.1r_0$. A severe limitation arises from the long wavelengths associated with the strongest resonances. At wavelengths larger than 5Å, diffraction experiments are difficult owing to absorption problems and to the lack of accessible Bragg peaks. In practice, actinide materials are studied at the L$_{2,3}$ and M$_{4,5}$ edges, which allows the study of both the f and d magnetism.

For rare earth materials, resonant scattering experiments are performed at the L$_{2,3}$ edges, where d electrons are probed. In the soft x-ray range the M$_{4,5}$ edges that give access to the f magnetism, allow measurements of magnetic x-ray reflectivity and spin-dependent absorption. The 3d transition metals can be investigated at the L edges, where only reflectivity measurements or studies of artificial multilayers can be performed. The resonant process at the K edge involving p electrons is weak and complex.

Figure 2 shows an example of the resonant enhancement as observed in the antiferromagnetic compound UAs. At the M$_4$ edge of uranium, the resonant enhancement of the x-ray magnetic scattering amplitude has been measured to be $9r_0$ yielding scattered intensities in the 10^6 counts s^{-1} range. Such a large scattering amplitude leads to potential applications, which complement neutron diffraction results, taking advantage of the resonant selectivity and of the large resonant enhancement coupled with the large available x-ray flux. In short, resonant x-ray scattering makes it possible to search for weak signals and to disentangle magnetic properties of different chemical elements or electronic shells. It should be pointed out that the gain in scattered intensity at resonance does not make magnetic powder diffraction experiments readily feasible with x rays, because of absorption and fluorescence effects. Powder neutron diffraction remains the probe of choice for structure determination.
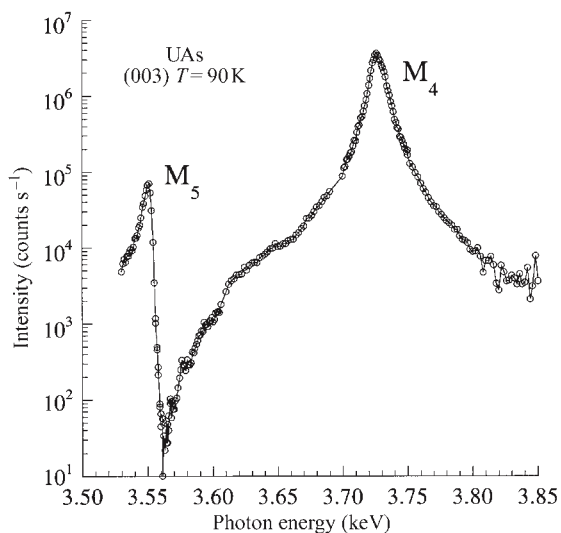
Figure 2
Resonant scattering at the M$_4$ and M$_5$ edges of uranium: resonant enhancement of the antiferromagnetic diffracted intensity in UAs as a function of the incident photon energy. The two resonances are clearly seen. The energy line shape of the intensity corresponds to the sum of two interfering amplitudes with resonant denominators.

Weak scattering signals arise either from small magnetic moments or from small scattering volumes. There exist systems which possess extremely small magnetic moments that neutrons cannot "see" unless a large amount of material is available. Resonant x rays are perfectly suited to studies of such systems with constrained dimensions (microcrystals, surfaces, and interfaces). Magnetic thin films and magnetic surfaces are investigated by using soft x-ray reflectivity (Kao *et al.* 1994, Tonnerre *et al.* 1995) or by scattering methods in the harder x-ray region
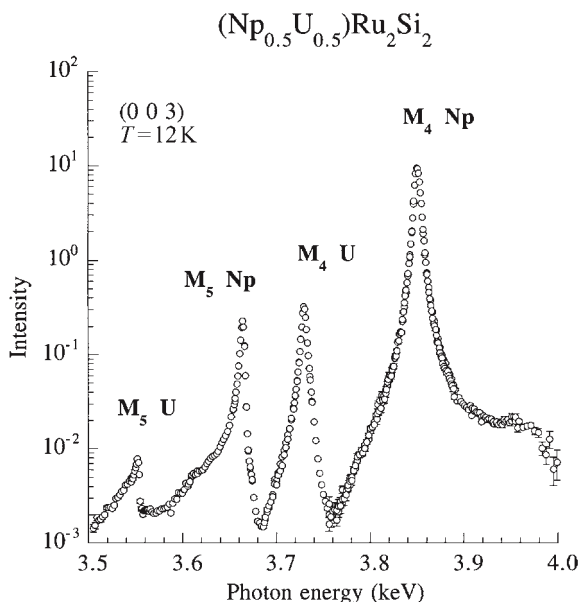
$(Np_{0.5}U_{0.5})Ru_2Si_2$

Figure 3
Demonstration of chemical selectivity. The intensity of the antiferromagnetic intensity from $Np_{0.5}U_{0.5}Ru_2Si_2$ is measured as a function of photon energy around the $M_{4,5}$ edges of uranium and neptunium. At the neptunium M_4 edge the signal arising from the magnetization on the neptunium sites is greater than the uranium contributions by four or five orders of magnitude.

(Watson *et al.* 1996, MacKay *et al.* 1996). The relationship of the magnetic spatial profile and magnetic roughness to the chemical or charge profile can then be determined owing to these enhanced intensities.

The chemical selectivity of resonant x-ray scattering is demonstrated in Fig. 3 which shows the incident photon energy dependence of an antiferromagnetic Bragg peak from a mixed compound, $U_{0.5}Np_{0.5}Ru_2Si_2$, containing two magnetic species, uranium and neptunium. Tuning the photon energy to a given edge (e.g., uranium M_4 edge), turns on the signal from the uranium magnetization, while the neptunium response is extinct (or at least several orders of magnitude weaker). Conversely, data taken at the neptunium M_4 edge probe the behavior of the neptunium moments only. This selectivity of the scattering species constitutes an advantage of x-ray resonant techniques over nonresonant x-ray methods and neutron techniques.

5. Spin Polarized Photon Absorption

The x-ray absorption cross-section is given by the imaginary part of the scattering amplitude at $Q = 0$

and resonant magnetic effects are also seen in absorption measurements. The observed effects are related to the x-ray polarization. The absorption coefficients vary when the easy direction of the magnetization is changed with respect to the incident x-ray polarization or vice versa: this effect is called magnetic linear dichroism. The absorption of circularly polarized x rays depends also on the helicity of the incident photons relative to the direction of the magnetization: this is magnetic circular dichroism (MCD). In all measurements, the magnetic contrast in the absorption process is obtained by changing the relative orientation of the polarization and the magnetization. The observed dichroic signal is taken as the ratio

$$R = \frac{\mu(L) - \mu(R)}{\mu(L) + \mu(R)}$$

where L and R denote the two photon helicities, and μ is the fluorescent signal or the absorption coefficient.

Similarly to the resonant scattering amplitude, the MCD signal is simply proportional to the spin polarized density of states of the intermediate states that are excited during the transition (Schütz *et al.* 1987). However, the orbital moment of the intermediate states is also likely to play a significant role in determining transition probabilities, especially in the cases of localized f-electron states. Indeed, a sum rule for the integral of the dichroic signal (the imaginary part of the magnetic scattering amplitude with $\theta = 0$ in Eqn. (10b) over a given edge has been derived (Thole *et al.* 1992) which allows a determination of the ground state value of the orbital moment in the electronic available states. This sum rule, which is rigorously valid only in the atomic case, has been extended to single electron band models. Furthermore, other sum rules have also been obtained involving expectation values of the spin operators (Carra *et al.* 1993).

Sum rules are derived for the absorption coefficient, related to $f'' = \text{Im}\{f_n(k_f = k_i, \hbar\omega)\}$; equivalent sum rules for the scattering case, where the total scattering amplitude $|f_n|^2$ is measured, would be more difficult to extract. The dichroism methods can bring new information on the ground state electronic properties of magnetic systems. Compared to scattering techniques, absorption methods have two considerable advantages: (a) they can be performed extremely rapidly (only the incident photon energy is varied and nothing else changes); and (b) they do not require single-crystal samples (any type of sample can be studied). However, no information in Q-space is obtained and MCD experiments can only probe magnetized samples, such as ferromagnets and ferrimagnets.

Dichroic effects are studied at low-energy absorption edges (L edges for 3d transition metals and M edges of rare earths) by using fluorescence or electron
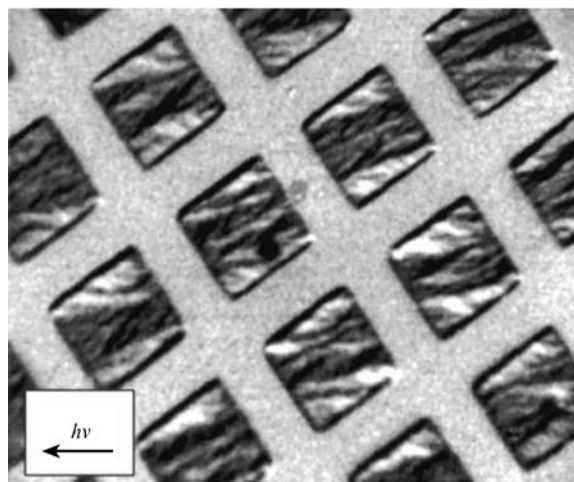
Figure 4
Difference images of magnetic domains in a patterned CoPt multilayer taken at the cobalt L_3 edge. Squares have side length of 20 μm. The arrow indicates the incidence direction of the circularly polarized x rays.

Figure 5
Time response of neodymium magnetization under the application of a pulsed magnetic field of 300 mT.

yield methods. At these energies, experiments are sensitive to the surface state and to the magnetism at surfaces. Local magnetic environments of magnetic species are revealed by magnetic fluorescence spectra. Because of the chemical selectivity, the various components of magnetic alloys and compounds can be studied independently. Even images of ferromagnetic domains have been obtained, leading to technological applications (Schütz *et al*. 1997, Schneider *et al*. 1997). The combined use of MCD methods and x-ray zone played microscopy can provide high-resolution images of ferromagnetic domains with spatial resolution of 50 nm and real time evolution. Figure 4 shows a magnetic domain pattern in a microstructured CoPt multiplayer. The pattern is obtained by subtracting two images recorded at the cobalt L_3 edges with opposite radiation helicity. The resulting contrast arises from the relative orientation of the cobalt magnetization and light incidence. The white (black) areas correspond to regions with magnetization parallel (antiparallel) to the incident light as indicated by the arrow. The magnetization is perpendicular to the incident light in the gray areas.

A very promising application of MCD experiments is the possibility of performing time-resolved studies. The combination of the pulsed time structure of the synchrotron x-ray beam and the fast acquisition rate of MCD allows studies of magnetic dynamics of ferromagnets. The use of energy-dispersive x-ray absorption enables fast dynamics to be studied (down to nanoseconds) over a typical size of 20 μm. An example is given in Fig. 5. The MCD signal has been measured from a complex magnetic system consisting of hard magnetic grains ($Nd_2Fe_{14}B$) embedded in a soft matrix (spring magnet) at the L_2 edge of neodymium. Owing to the selectivity of the MCD method, the neodymium hysteresis cycle can be observed together with the relaxation response of neodymium under the application of a pulse field (Fig. 5). The determination of the relaxation time makes it possible to analyze the different mechanisms driving the coercivity. Other applications include the studies of dynamics of recording or switching devices (Bonfim *et al*. 1998). The uniqueness of the chemical selectivity makes time-resolved MCD an ideal diagnostic probe for the magnetic properties of multicomponent magnetic devices such a spin valves and spring magnets.

6. Future Directions

Synchrotron methods for the study of magnetism have been in use since the early 1980s, and the most remarkable achievements using resonant scattering have been obtained since the early 1990s. New applications have appeared, some of which have arisen owing to the progress in instrumentation and some from a better understanding of the physics. Synchrotron sources and x-ray instruments are likely to improve, yielding new prospects for more applications (studies of microcrystals, coherent effects and magnetic speckles, magnetic inelastic x-ray scattering, time-resolved studies). Theoretical approaches, which have been stimulated by experimental results, will in turn lead to more fundamental applications and studies of the microscopic magnetic properties of solids. Synchrotron x rays will offer new tools for detailed studies of magnetism, which complement neutron scattering techniques.

See also: Magnetic Excitations in Solids; Muon Spin Rotation: Applications in Magnetism; Transparent Rare Earth Compounds: Magnetic Circular Dichroism; Thin Film Magnetism: PEEM Studies

Bibliography

de Bergevin F, Brunel M 1972 Observation of magnetic super-lattice peaks by x-ray diffraction of an antiferromagnetic NiO crystal. *Phys. Lett.* **39A**, 141–2

Blume M 1994 Magnetic effects in anomalous dispersion. In: Materlik G, Sparks C J, Fischer K (eds.) *Resonant Anomalous X-ray Scattering*. Elsevier, Amsterdam

Blume M, Gibbs D 1988 Polarization dependence of magnetic x-ray scattering. *Phys. Rev. B* **37**, 1779–89

Bonfim M, MacKay K, Pizzini S, San Miguel A, Tolentino H, Giles C, Hagelstein M, Baudelet F, Malgrange C, Fontaine A 1998 Nanosecond-resolved XMCD on ID24 at the ESRF to investigate the element-selective dynamics of magnetization switching of Gd–Co amorphous thin film. *J. Synchrotron Rad.* **5**, 750–2

Cahn R W, Lifshin E 1993 *Concise Encyclopedia of Materials Characterization*. Pergamon, Oxford

Carra P, König H, Thole B T, Altarelli M 1993 Magnetic x-ray dichroism: general features of dipolar and quadrupolar spectra. *Physica B* **192**, 182

Fernandez V, Vettier C, de Bergevin F, Giles C, Neubeck W 1998 Observation of orbital momentum in NiO. *Phys. Rev. B* **57**, 7870–6

Hannon J P, Tramell G T, Blume M, Gibbs D 1988 X-ray resonance exchange scattering. *Phys. Rev. Lett.* **61**, 1245–8

Kao C-C, Chen C T, Johnson E D, Hastings J B, Lin H I, Ho G H, Meigs G, Brot J M, Hulbert S L, Idzerda Y U, Vettier C 1994 Dichroic interference effects in circularly polarized soft x-ray resonant magnetic scattering. *Phys. Rev. B* **50**, 9599–602

Lovesey S W, Collins S P 1996 *X-Ray Scattering and Absorption by Magnetic Materials*. Oxford Science, New York

MacKay J F, Terchert C, Savage D E, Lagally M G 1996 Element specific magnetization of buried interfaces by diffuse x-ray resonant magnetic scattering. *Phys. Rev. Lett.* **77**, 3925–8

Schneider C M, Frömter R, Ziethen C, Swiech W, Brookes N B, Schönhense G, Kirschner J 1997 Magnetic domain imaging with a photoemission microscope. *Mater. Res. Soc. Symp. Proc.* **475**, 381–92

Schütz G, Fischer P, Attenkofer K, Ahlers D 1997 New applications of x-ray magnetic circular dichroism. In: Johnson R L, Schmidt-Böcking H, Sonntag B F (eds.) *Proc. X-ray and Inner-Shell Processes*. AIP, Hamburg, Germany, pp. 512–33

Schütz G, Wagner W, Wilhelm W, Kiemle P, Zeller R, Frahm R, Materlik G 1987 Absorption of circularly polarized x rays in iron. *Phys. Rev. Lett.* **58**, 737–40

Squires G L 1978 *Introduction to the Theory of Thermal Neutron Scattering*. Cambridge University Press, Cambridge

Templeton D H 1994 X-ray resonance, then and now. In: Materlik G, Sparks C J, Fischer K (eds.) *Resonant Anomalous X-ray Scattering*. Elsevier, Amsterdam

Thole B T, Carra P, Sette F, van der Laan G 1992 X-ray circular dichroism as a probe of orbital magnetization. *Phys. Rev. Lett.* **68**, 1943–6

Tonnerre J M, Seve L, Raoux D, Rodmacq B, Souille G, Wolfers P 1995 Soft x-ray resonant magnetic scattering from a magnetically coupled Ag/Ni multilayer. *Phys. Rev. Lett.* **75**, 740–3

Watson G M, Gibbs D, Lander G H, Gaulin B D, Berman L E, Matzke H J, Ellis W 1996 X-ray scattering study of the magnetic structure near the (001) surface of UO_2. *Phys. Rev. Lett.* **77**, 751–4

C. Vettier
European Synchrotron Radiation Facility
Grenoble, France

Magnetism: High-field

The effect of an applied magnetic field on matter depends on whether the field is large enough to compete with the magnetic interactions that are present within the material. Only then can a modification of the magnetic state can be induced. The related change in magnetization should be large enough to be observed with sufficient accuracy. High magnetic fields are generated worldwide, in many laboratories and in special user facilities. After a brief review of the techniques that are applied to produce high magnetic fields, this article focuses on a representative selection of the large variety of phenomena that may be observed in the magnetization of magnetic materials when they are exposed to high magnetic fields. Also, the information that can be deduced from the observed high-field behavior will be briefly discussed.

In magnetic materials, the exchange interaction between the magnetic moments generally is the most prominent interaction. Depending on the solid, the exchange interaction may be of different type, and, at temperatures where the thermal energy is lower than the strength of the exchange interaction, will give rise to an ordered structure of the magnetic moments. The strength of the exchange interaction may be expressed in terms of an internal "exchange field" that acts on the magnetic moments and that may be as high as 1000 T. Also, the magnetocrystalline anisotropy in solids may be appreciable and, in specific materials, may be equivalent to a few hundred teslas.

The examples discussed in this article have been taken from the vast body of high-field research that has been carried out on transition metals, rare-earth metals, alloys, and intermetallic compounds. For other specific subjects and other categories of materials in which the response to high magnetic fields may play a significant role, for instance low-dimensional spin systems, critical phenomena, low-dimensional semiconductor structures, heavy-fermion systems, and superconductors, the reader is referred to the articles devoted to these subjects and materials.

1. Production of High Magnetic Fields

Static magnetic fields can be generated by transmitting electrical current through resistive coils that have to be water-cooled in order to remove the dissipated heat or by transmitting current through superconducting coils. In resistive coils, the largest fields made in this way are in the range 30–35 T, whereas in superconducting coils made of conventional superconductors, the maximum field is around 23 T. Larger static magnetic fields (up to 40–45 T) can be generated in hybrid magnets, in which superconducting coils are placed around a water-cooled resistive-coil system, in this way providing a supporting background field of the order of 10 T.

In resistive-coil systems, the value of the highest possible field is mainly determined by the available electrical power and by the limited cooling capacity. In the case of superconducting coils, the main limiting factor is the field at which the coil material looses its superconducting properties and becomes normal. Coils made of high T_c superconductors may lead to significant progress. However, for this to be possible, a number of important technological problems, for instance the production of wire of adequate mechanical strength, have to be solved.

The range of possible fields is appreciably larger if pulsed fields are considered. In pulsed magnets, the coils are energized only for a short time during which the dissipated heat cannot be removed by the cooling water and is mainly absorbed by the coil, which therefore increases in temperature during the pulse. For pulsed fields, the coils are usually energized by capacitor banks or flywheel generators. In practice, two time regimes are distinguished for the duration of the field pulse:

- long pulses with a duration of the order of 10 ms to 1 s that produce fields in the range 60–80 T; and
- short pulses with a duration in the microsecond region that produce fields in the range 100–500 T.

In general, short-pulse experiments are more difficult than long-pulse experiments and, as a consequence, less accurate. Also, in a metallic material, a pulsed magnetic field induces a current that is proportional to the change of the field with time. Therefore, experiments on this important category of solids should be performed in static fields, in fields that are kept constant for a sufficiently long time, or in long-pulse fields that vary only slowly with time. The magnetization measurements presented in this article have been performed in long-pulse fields. Some examples of facilities where long-pulse fields are generated are given in Table 1.

2. 3d Magnetism

In 3d metal-based metallic substances with itinerant electrons, the magnetism arises from electrons that

Table 1
Examples of long-pulse facilities.

Location	Maximum field in length (T in mm)	Pulse length (ms)
KU Leuven	60 in 20; 73 in 10	20; 10
NHMFL Los Alamos	68 in 15; 60 in 32	20; 100
LNCMP Toulouse	61 in 14	200
NRIM Tsukuba	65 in 16	100

occupy allowed states in incompletely filled electron bands that are filled up to the Fermi energy and that can be subdivided into two subbands with opposite spin directions that are equally occupied in the paramagnetic state. In a ferromagnet, and if a magnetic field is applied also in a paramagnetic metal, the two subbands are unequally occupied, thus giving rise to a magnetic moment (see *Itinerant Electron Systems: Magnetism (Ferromagnetism)*). Besides the exchange, the density of electron states at the Fermi level and its energy dependence determine the magnetic response of a metal to an applied magnetic field. In exchange-enhanced (Pauli) paramagnetic substances with a peculiar band structure near the Fermi energy, an applied magnetic field may induce a first-order phase transition from the paramagnetic to the ferromagnetic state. Transitions of this type, from a state with a relatively small magnetic moment to one with a larger moment, are generally denoted as metamagnetic transitions and occur, as discussed below, in many different types of magnetic materials. YCo_2 (Fig. 1) is an example of a nearly ferromagnetic compound that undergoes such a transition at low temperatures at a critical field as high as 69 T, (see *Metamagnetism: Itinerant Electrons*).

3. 4f Magnetism

The rare-earth (R) metals with their partially filled 4f shell and R-based compounds exhibit a large diversity of magnetic structures which result from the competition of the exchange interaction, the crystalline electric field (CEF) interaction, and the quadrupolar interaction, the latter in general being much smaller than the former two (see *Localized 4f and 5f*
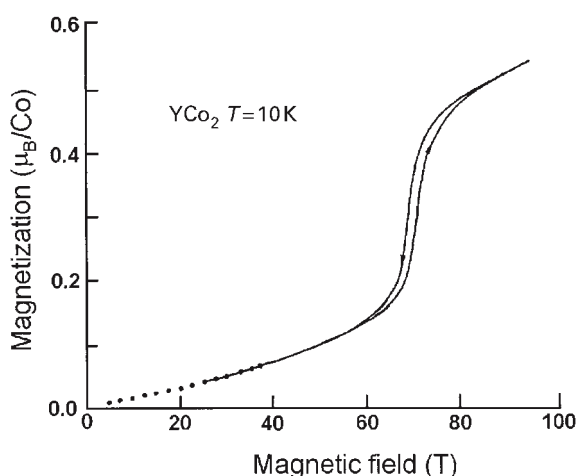
Figure 1
Magnetization of YCo_2 at 10 K (after Duc and Brommer 1999).

Moments: Magnetism). On application of a magnetic field, many R-based compounds exhibit transitions in the magnetization, usually denoted as metamagnetic transitions, examples of which are presented below. For a more detailed survey see Gignoux and Schmitt (1991).

Antiferromagnetic materials with small magnetic anisotropy may, at a certain field value which usually is not very high, exhibit a so-called spin-flop transition in which the collinear antiparallel magnetic moments rotate to a direction perpendicular to the applied field, thereby approximately preserving the collinear structure. This type of metamagnetic transition is often encountered in gadolinium compounds, which generally have small magnetic anisotropy since gadolinium has no orbital moment.

Another type of metamagnetic transition, the spin-flip transition, is found in antiferromagnetic materials with stronger magnetic anisotropy. In this transition, a simple single-step phase transition takes place from the antiferromagnetic state to the forced-ferromagnetic (magnetically saturated) state. A beautiful example is the orthorhombic compound $TbCu_2$ in which the terbium moments form a collinear antiferromagnetic structure with the moments aligned along the a direction. If the field is applied along this direction, a spin-flip occurs in 2 T (Fig. 2). If the field is applied along the b direction, a similar transition is observed at almost 40 T after the antiparallel terbium moments have been rotated from the a to the b direction. In many cases, the magnetization process of antiferromagnetic compounds is more complex and two- (Fig. 3) or multistep metamagnetic processes are involved in reaching the forced-ferromagnetic state.

The occurrence of metamagnetic transitions is not limited to magnetically ordered R-based materials. In Fig. 4, the magnetization of the paramagnetic metal

Figure 3
Magnetization of the hexagonal compound $ErGa_2$ at different temperatures in a magnetic field applied along the c axis (after Gignoux and Schmitt 1991).

Figure 4
Magnetization of praseodymium at 4.2 K in magnetic fields applied along and perpendicular to the c axis (after Gignoux and Schmitt 1991).
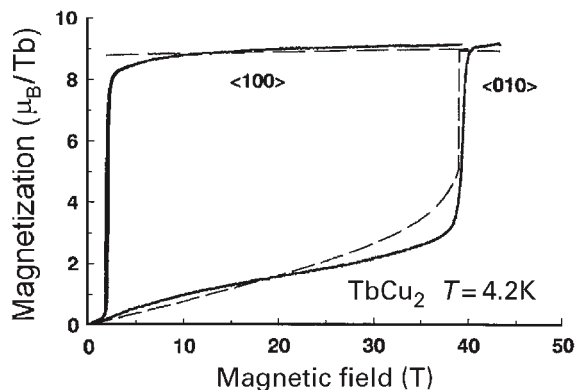
Figure 2
Magnetization of $TbCu_2$ at 4.2 K in magnetic fields applied along the a and b axes (after Andreev *et al.* 1998).

praseodymium is seen to exhibit a metamagnetic transition. This transition can be ascribed to the crossing of two crystal field levels, a singlet which is the ground state in zero field and a magnetic excited

level which has the lowest energy above a certain value of the applied field.

4. 3d–4f Magnetism

Intermetallic compounds of R metals and the late-3d transition (T) metals form a very important class of materials that find numerous applications in e.g., permanent magnets, magnetostrictive devices, magneto-optical recording, etc. In the R–T compounds with T = Fe, Co, the strongest interaction is the 3d–3d interaction which primarily determines the Curie temperature. The 4f–4f interaction is very weak and can be neglected. The 4f–3d interaction, although much weaker than the 3d–3d interaction, is of special importance since by this interaction the strongly anisotropic R sublattice magnetization is coupled to the much less anisotropic T sublattice magnetization. The interaction between 4f and 3d moments is based on an indirect interaction between the 4f and 3d spins, which is antiferromagnetic. This, together with Hund's rules, explains why the magnetic order is ferromagnetic in R–T compounds where R is a lighter element in the series and ferrimagnetic if R is a heavier element (see *Alloys of 4f (R) and 3d (T) Elements: Magnetism*).

The way in which the magnetic moment configuration in R–T compounds is affected by a magnetic field, applied along the principal crystallographic directions of a single crystal, can generally be well described in a molecular-field model with two magnetic sublattices, the R and T sublattices. From such an analysis, quantitative information on the magnetic anisotropy (the crystal field interaction) and on the strength of the 4f–3d interaction can be obtained. Evidently, such information is most readily obtained from magnetization measurements on ferrimagnetic compounds, in which the strict antiparallel configuration of the moments will be affected by a sufficiently high magnetic field.

Single crystals of various classes of R–T compounds with R = Co and Fe have become available, for instance the R_2T_{17} and $R_2T_{14}B$ series, and their magnetization behavior has been investigated systematically in high magnetic fields applied along the main crystallographic directions. The magnetic isotherms at 4.2 K of the ferromagnetic compound $Nd_2Fe_{14}B$ are shown in Fig. 5. In this compound, the magnetic moments on the neodymium and the iron atoms are parallel and the Nd–Fe coupling is sufficiently strong to keep the moments rigidly coupled in the parallel orientation during the magnetization process. Therefore, the magnetic transition observed at about 16 T with the field applied in the [100] direction finds its origin exclusively in the magnetic anisotropy. Transitions like this one can be ascribed to higher-order terms in the anisotropy or, equivalently, to higher-order crystal field coefficients
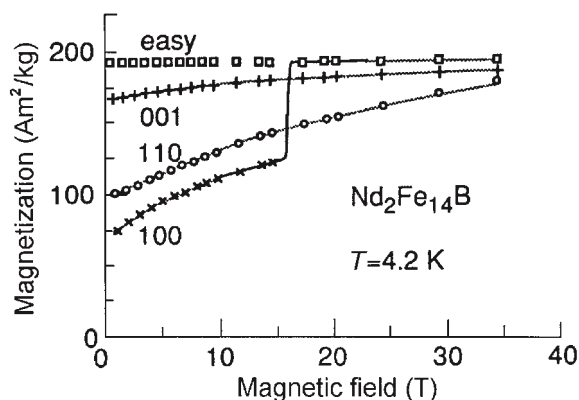
Figure 5
Magnetization of $Nd_2Fe_{14}B$ at 4.2 K in magnetic fields applied along several crystallographic directions (Buschow 1988).
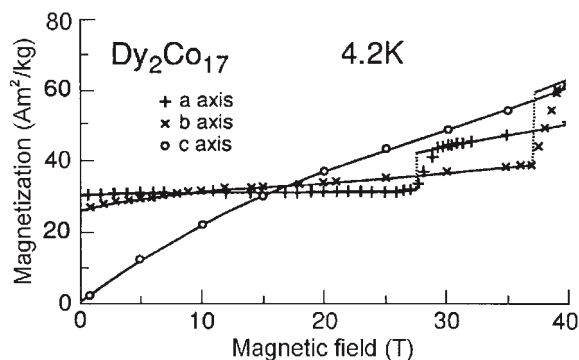
Figure 6
Magnetization of Dy_2Co_{17} at 4.2 K in magnetic fields applied along the three main crystallographic directions (Franse and Radwanski 1993).

and allow for a rather precise determination of these parameters. The transition in $Nd_2Fe_{14}B$ is generally referred to as a first-order magnetization process (FOMP). In $Pr_2Fe_{14}B$, two transitions have been found which are of second-order type (SOMP).

High-field magnetic transitions that are based on the competition between the strength of the applied field and the strength of the 4f–3d exchange interaction have been extensively studied on single crystals of ferrimagnetic R_2Co_{17} and R_2Fe_{17} compounds. As an example, the magnetization of the hexagonal compound Dy_2Co_{17} is shown in Fig. 6, measured with the field along the three principal crystallographic directions. As can be seen, the magnetic anisotropy of Dy_2Co_{17} is of easy-plane type, the dysprosium moments lying along the *a* axis in the basal plane, antiparallel with the cobalt moments, as represented by

751
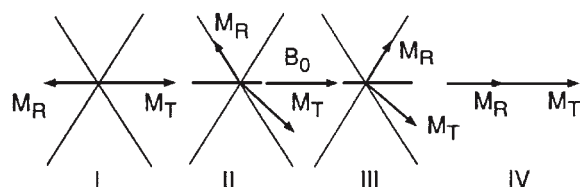
Figure 7
Schematic representation of the various moment configurations in hexagonal ferrimagnetic easy-plane R_2T_{17} compounds.

Figure 8
Magnetization of free powder of $DyCo_{12}B_6$ at 4.2 K (after de Boer 1996).

configuration I in Fig. 7. The resulting magnetization is constant up to about 28 T and equal to the difference of the two sublattice magnetizations. At 28 T the collinear magnetic structure of this ferrimagnet is broken and a transition takes place to a moment configuration (II in Fig. 7) in which the dysprosium moments jump to another easy direction and in which magnetostatic energy is gained at the expense of exchange energy. For the field applied along the *b* axis, this transition takes place at a field strength of about 38 T. The solid lines in Fig. 6 correspond to calculations in terms of a molecular-field model by assuming the existence of two magnetic sublattices, one for the dysprosium and one for the cobalt moments. On the basis of the calculations, for the situation with the field applied along the *a* axis, in total three transitions are expected until the parallel, forced-ferromagnetic arrangement of the two sublattice magnetizations is reached. When the field is applied along the *b* axis, two transitions are expected. Such transitions have been reported for a large number of compounds of several series of R–T compounds, such as the R_2Fe_{17}, R_2Co_{17}, and $R_2Fe_{14}B$ series. Analysis of the magnetization curves has led to knowledge of the crystal field coefficients for these compounds and has provided values for the strength of the 4f–3d interaction (Franse and Radwanski 1993). Also, systematic trends of these parameters have been established.

An experimental method has also been developed to measure directly the strength of the 4f–3d interaction between the R and the T magnetic moments in heavy R–T intermetallic compounds. The method consists of measuring the low-temperature magnetic isotherms in very high magnetic fields of a single crystal or of fine single-crystalline powder particles that can freely rotate in the applied magnetic field. The free-powder magnetization of $DyCo_{12}B_6$ is shown as an example in Fig. 8. In this compound, the breaking of the collinear ferrimagnetic structure starts at about 10 T. The bending of the sublattice moments proceeds smoothly up to about 32 T where the forced ferromagnetic state is reached. The value of the strength of the Dy–Co exchange interaction can be obtained by analyzing the observed magnetization during the bending process in terms of a
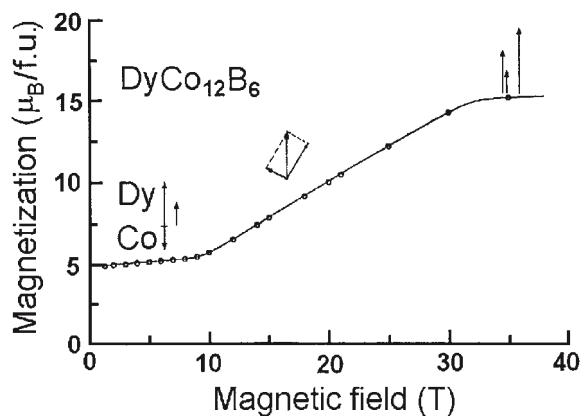
mean-field description. The very simple magnetization process of $DyCo_{12}B_6$ is representative of all R–T intermetallic compounds, in which the magnetic anisotropy of the T sublattice moment is negligible with respect to the R sublattice anisotropy. For these cases, if the crystal can freely rotate in the applied field, the R sublattice moment will remain in its easy direction in the crystal during the entire magnetization process and the magnetization process will be simple.

The magnetization process of $DyCo_{12}B_6$ is very exceptional in the sense that it is completed in experimentally accessible fields. In general, even the value of the field where the bending of the sublattice moments starts is experimentally inaccessible. However, because, as the theoretical description tells, this field is proportional to the difference of the two sublattice moments, the value of this field can be reduced by carrying out suitable chemical substitutions that make the values of the two sublattice moments more similar. This is illustrated in Fig. 9 for Ho_2Fe_{17} in which the iron sublattice moment is larger than the moment of the holmium sublattice and the two sublattice moments can be made more similar by aluminum substitution for iron. In this way the bending process can be brought in an accessible field range, allowing for the determination of the Ho–Fe exchange coupling. Systematic trends of the 4f–3d interaction within and among series of R–T intermetallic compounds could be established on the basis of magnetization measurements on free powders of a large variety of properly substituted R–T systems (Liu *et al.* 1994).

5. 5f Magnetism

Intermetallic compounds that comprise actinides, e.g., uranium, are of special interest since the behavior of
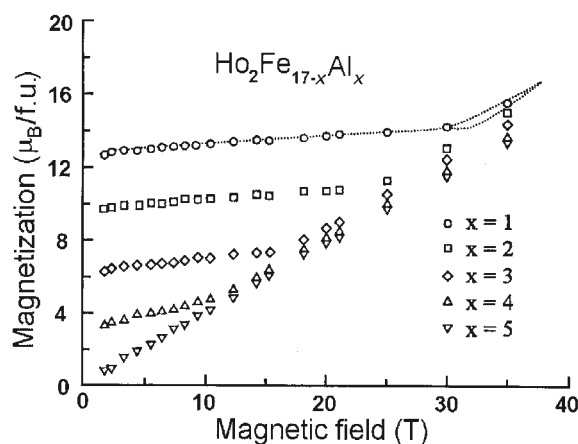
Figure 9
Magnetization of free powder of $Ho_2Fe_{17-x}Al_x$ compounds at 4.2 K (after Zvezdin 1995).
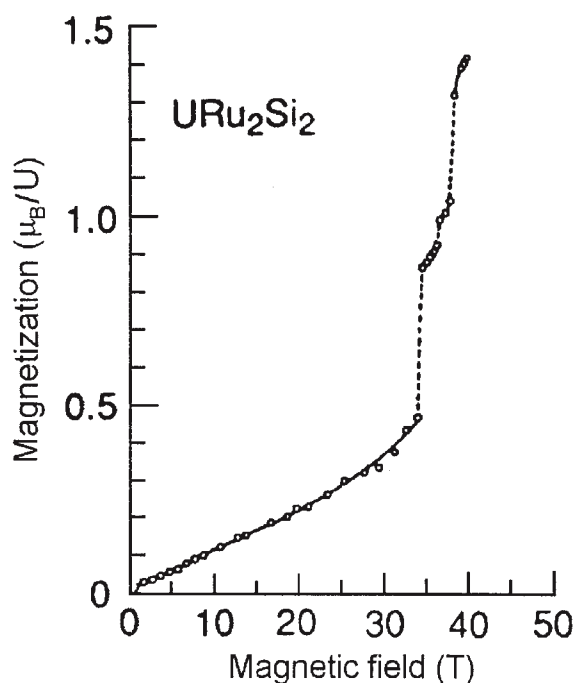
Figure 10
Magnetization of URu_2Si_2 at 4.2 K in magnetic fields applied parallel and perpendicular to the c axis (Sechovsky and Havela 1998).

the 5f electrons is intermediate between itinerant and localized (Sechovsky and Havela 1998). The magnetism of uranium compounds is characterized by complex magnetic structures, unstable magnetic moments, hybridization of the 5f states with d- and p-electron states of the ligand atoms, and extremely large anisotropy that can be associated with this hybridization (see *5f Electron Systems: Magnetic Properties*). The magnetization of the antiferromagnet URu_2Si_2 (Fig. 10) nicely illustrates the very large anisotropy and the richness of field-induced transitions that are encountered in uranium compounds. More examples of the high-field behavior of uranium compounds are given in the review of Sechovsky and Havela (1998).

See also: Magnetism in Solids: General Introduction; Magnetic Measurements: Pulsed Field; Magnetic Phase Transitions: Field-induced (Order to Order)

Bibliography

Andreev A V, Bartashevich M I, Goto T, Divis M, Svoboda P 1998 High-field transition in $TbCu_2$. In: Clark R G (ed.) *Proc. 5th Int. Symp. on Research in High Magnetic Fields*. North-Holland, Amsterdam, pp. 479–82 (*Physica B* **246–247**, 497–82)
Buschow K H J 1988 Permanent magnet materials based on 3d-rich ternary compounds. In: Wohlfarth E P, Buschow K H J (eds.) *Ferromagnetic Materials*. North-Holland, Amsterdam, Vol. 4, pp. 1–129
de Boer F R 1996 The magnetization process in free single-crystalline particles of rare-earth transition-metal compounds. *J. Magn. Magn. Mater.* **159**, 64–70
Duc N H, Brommer P E 1999 Formation of 3d-moments and spin fluctuations in some rare-earth-cobalt compounds. In: Buschow K H J (ed.) *Handbook of Magnetic Materials*. North-Holland, Amsterdam, Vol. 12, pp. 259–394
Franse J J M, Radwanski R J 1993 Magnetic properties of binary rare-earth 3d-transition-metal intermetallic compounds. In: Buschow K H J (ed.) *Handbook of Magnetic Materials*. North-Holland, Amsterdam, Vol. 7, pp. 307–501
Gignoux D, Schmitt D 1991 Rare earth intermetallics. *J. Magn. Magn. Mater.* **100**, 99–125
Gignoux D, Schmitt D 1997 Magnetism of compounds of rare earths with non-magnetic metals. In: Buschow K H J (ed.) *Handbook of Magnetic Materials*. North-Holland, Amsterdam, Vol. 11, pp. 239–413
Liu J P, de Boer F R, de Châtel P F, Coehoorn R, Buschow K H J 1994 On the 4f–3d exchange interaction in intermetallic compounds. *J. Magn. Magn. Mater.* **132**, 159–79
Luong N H, Franse J J M 1993 Magnetic properties of rare earths Cu_2 compounds. In: Buschow K H J (ed.) *Handbook of Magnetic Materials*. North-Holland, Amsterdam, Vol. 8, pp. 415–92
Sechovsky V, Havela L 1998 Magnetism of ternary intermetallic compounds of uranium. In: Buschow K H J (ed.) *Handbook of Magnetic Materials*. North-Holland, Amsterdam, Vol. 11, pp. 1–289
Zvezdin A K 1995 Field induced phase transitions in ferrimagnets. In: Buschow K H J (ed.) *Handbook of Magnetic Materials*. North-Holland, Amsterdam, Vol. 9, pp. 405–543

F. R. de Boer
Universiteit van Amsterdam, Amsterdam
The Netherlands

Magnetization Reversal Dynamics

Many important technological applications involve reversing magnetic moment in a magnetic material within a very short time period. For instance, in computer hard-disk drives, storing a single bit requires reversing the magnetic moments of both the write transducer and the thin film recording medium in a fraction of a nanosecond. Understanding magnetization reversal dynamics is critical in these applications (Bertram and Zhu 1992, Mao 2000, Zhu 2001, Zhu and Zheng 2002).

In general, magnetization reversal in a magnetic material, either of a bulk or thin film, or a particulate form, is always complex. For studying the reversal dynamics, there are many experimental means, including time-resolved Kerr microscopy field *in situ* transmission electron microscopy, field *in situ* scanning electron microscopy with polarization analysis (SEMPA), and field *in situ* magnetic force microscopy (Hubert and Schäfer 2000).

Magnetization reversal dynamics can also be studied via micromagnetic modeling. Combining the gyromagnetic dynamic equation with the classic micromagnetic theory (Strikman and Treves 1963, Brown 1978), the dynamic microscopic magnetization reversal process in a ferromagnetic object can be simulated on a computer or on a cluster of computers (e.g., Zhu 1989). In the modeling, magnetic energy density, E, that includes magnetocrystalline anisotropy energy, magnetostatic energy, ferromagnetic exchange energy, and magnetic potential energy (Zeeman energy), is calculated at each location of the object:

$$E = E_{\text{anisotropy}} + E_{\text{magneto}} + E_{\text{exchange}} + E_{\text{Zeeman}} \quad (1)$$

The effective magnetic field exerted on a local magnetic moment is

$$\mathbf{H} = -\frac{\partial E}{\partial \boldsymbol{M}} = -\left(\frac{\partial E}{\partial \boldsymbol{M}_x} \hat{e}_x + \frac{\partial E}{\partial \boldsymbol{M}_y} \hat{e}_y + \frac{\partial E}{\partial \boldsymbol{M}_z} \hat{e}_z \right) \quad (2)$$

1. Gyromagnetic Equations with Energy Damping

Consider a magnetic moment with magnetization $\boldsymbol{M}$ in a magnetic field $\boldsymbol{H}$. Due to the fact that magnetic moment in a magnetic material arises from electron spin angular momentum and orbital angular momentum, the magnetic moment precesses around the field direction, described by the following torque equation (Landau and Lifshitz 1935):

$$\frac{\mathrm{d}\boldsymbol{M}}{\mathrm{d}t} = -\gamma \boldsymbol{M} \times \boldsymbol{H} \quad (3)$$

where γ is the gyromagnetic constant. In this process, the angle between the magnetic moment and the field

remains unchanged. In other words, the energy of the system is conserved. Any energy dissipation (or often referred to as energy damping) in the system results in a reduction of the angle. To include energy dissipation, one phenomenological form is the Gilbert equation:

$$\frac{\mathrm{d}\boldsymbol{M}}{\mathrm{d}t} = -\gamma \boldsymbol{M} \times \boldsymbol{H} + \frac{\alpha}{M} \boldsymbol{M} \times \frac{\mathrm{d}\boldsymbol{M}}{\mathrm{d}t} \quad (4)$$

where M is the magnitude of the magnetic moment and α is referred to as the damping constant (Gilbert 1955). In this form, the damping motion of the moment direction towards field direction is viscous. The above implicit form of the dynamic equation can be transformed into the following explicit one, known as the Landau–Lifshitz equation (Landau and Lifshitz 1935):

$$\frac{\mathrm{d}\boldsymbol{M}}{\mathrm{d}t} = -\gamma_{\text{L}} \boldsymbol{M} \times \boldsymbol{H} - \frac{\lambda}{M} \boldsymbol{M} \times \boldsymbol{M} \times \boldsymbol{H} \quad (5)$$

with

$$\gamma_{\text{L}} = \frac{\gamma}{1 + \alpha^2} \quad \text{and} \quad \lambda = \frac{\gamma\alpha}{1 + \alpha^2}$$

In both Gilbert and Landau–Lifshitz equations, the magnitude of the magnetic moment is unchanged.

Under the Gilbert equation, if the energy does not depend explicitly on time, the rate of the energy change is given by (Zhu 1989)

$$\frac{\mathrm{d}E}{\mathrm{d}t} = -\mu_0 \frac{\alpha\gamma}{(1 + \alpha^2)M^2} |\boldsymbol{M} \times \boldsymbol{H}|^2 \quad (6)$$

2. Magnetization Reversal of a Uniformly Magnetized Sphere

Consider a uniformly magnetized single-domain magnetic sphere in a magnetic field. At nonzero damping, the magnetic moment of the sphere rotates towards the field direction while precessing around the field direction. The smaller the damping constant α, the greater the number of precession cycles will be before the magnetic moment aligns with the field direction. Figure 1 shows the calculated trajectories according to Eqn. (4) for two different values of the damping constant α. The time duration of the reversal, from near antiparallel direction to the parallel direction, with respect to the field is given by

$$\Delta t = \frac{1 + \alpha^2}{\alpha\gamma(H - H_{\text{s}})} \ln\left(\frac{\tan(\theta_2/2)}{\tan(\theta_1/2)} \right) \quad (7)$$

where θ_2 and θ_1 are the final and initial angles between the magnetic moment and the field whose amplitude is denoted by H, and H_{s} is the switching field threshold (e.g., the anisotropy field). For a given magnetic field whose amplitude is greater than the
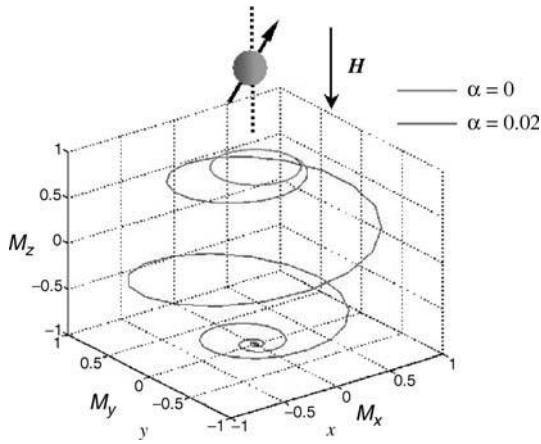
Figure 1
Magnetization trajectory of a uniformly magnetized sphere in a magnetic field. With zero damping, magnetization gyrates around the field direction with a constant moment-to-field angle, and the energy of system is unchanged. With the damping constant nonzero, the magnetization reverses into the field direction while gyrating around the field direction.

switching field threshold, $\alpha = 1$ gives the shortest reversal time (Kikuchi 1956).

3. Magnetization Reversal of a Uniformly Magnetized Thin Film

The dynamic magnetization reversal process in an always uniformly magnetized magnetic thin film is quite different than that in an always uniformly magnetized sphere. For a magnetization reversal with an external magnetic field applied in the film plane, the precession of the magnetic moment around the field direction causes the magnetization to rotate out of plane, generating a demagnetization field normal to the film plane. Subsequently, the magnetization precesses around this demagnetization field, yielding the rotation toward the external field direction within the film plane. Figure 2 shows the trajectories of the magnetization unit vector for the case of $\alpha = 0$ (red curve) and the case of $\alpha = 0.02$ (blue curve). The rotation trajectory of the magnetization vector behaves very much like a pendulum: at zero damping, the magnetization swings like an undamped pendulum. At nonzero damping, the magnetization vector eventually rests along the external field direction.

Note that for a uniformly magnetized thin film, it is the precession of the magnetization that drives the magnetization reversal in the film plane, in contrast to the case of uniformly magnetized sphere. The shortest reversal time for a given external field magnitude
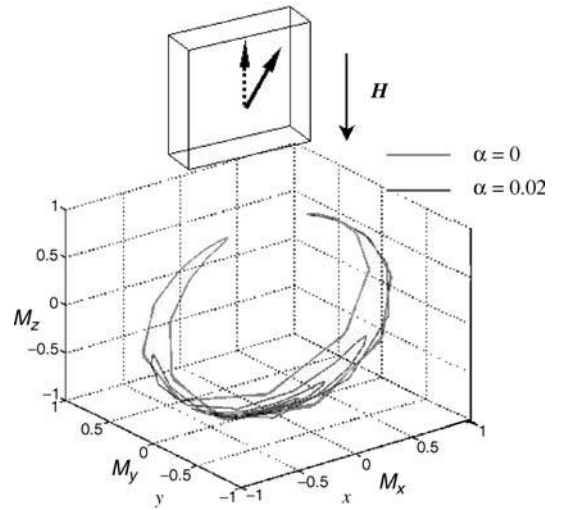
Figure 2
Magnetization reversal of a uniformly magnetized permalloy ($Ni_{81}Fe_{19}$) film for two different values of the damping constant α. The magnetization reversal is really driven by the precession motion of the magnetization.

occurs at a relatively small damping constant depending on the magnitude of the magnetization.

4. Magnetization Reversal of Patterned Magnetic Thin Film Elements

The two magnetization reversal processes described in the previous two sections apply only to objects that have physical dimensions smaller than the exchange length, defined as the square root of the ratio of physical dimension significantly greater than the exchange length:

$$l_{ex} = \sqrt{\frac{A}{M_s^2}} \qquad (8)$$

where A is the exchange stiffness constant and M_s is the saturation magnetization of the material (Brown 1978). For ferromagnetic objects whose physical dimensions are greater than the exchange length, the dynamic magnetization configurations during a magnetization reversal are usually spatially nonuniform. In the case that the ferromagnetic object is a patterned thin film element, the transient reversal process becomes almost independent of the damping constant, except at very final stage of the reversal. Figure 3 shows a dynamic reversal process for a Permalloy thin film elliptical element with a length of $0.6\,\mu m$, a width of $0.3\,\mu m$, and a thickness of $25\,nm$. A damping constant $\alpha = 0$ has been assumed. The
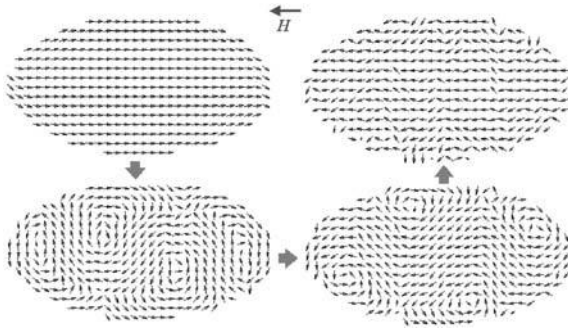
Figure 3
Calculated magnetization reversal process of an elliptical permalloy thin film element. The length of the element is 0.6 μm, width 0.3 μm, and thickness 25 nm. The reversal starts with the formation of four vortices along the edges of the element. The four vortices move across the width of the element, leave magnetization reversed. At the end, spin waves are generated in the reversed element.

Figure 4
The dynamic change of various energy densities during the in-plane magnetization reversal of a patterned nonsingle domain thin film element with zero energy damping ($\alpha = 0$). The reduction of Zeeman energy becomes the ferromagnetic exchange energy and magnetostatic energy stored in the resulted spin waves.

Figure 5
Element-averaged magnetization component along field direction during a magnetization reversal for two energy damping constants $\alpha = 0$ (red) and $\alpha = 0.05$ (blue).

external applied field is assumed to rise exponentially with a rise time $\tau = 0.1$ ns. The reversal starts as four magnetization vortices nucleate along the edges of the element, followed by the motion of the vortices transverse to the field direction, across the film element. As the vortices move out of the opposite edges of the element, the magnetization of the entire element has virtually been reversed, except magnetization still precesses, forming a set of spin waves in the element. Due to the reversal of the magnetization direction, the Zeeman energy has been reduced. Since there is no energy damping during the reversal process, the Zeeman energy has been transformed into the ferromagnetic exchange energy stored in the resulted spin waves. The changes of various energy densities with time during the reversal are plotted in Fig. 4.

The calculation also show that the transient reversal process is virtually unchanged if a small energy damping is introduced during the reversal process and the reversal time becomes essentially independent of the damping constant (Fig. 5). The only difference is that in the case of nonzero energy damping during the reversal process, no spin wave is generated after the completion of the reversal.

For a reversal of a thin film element within the film plane, in the case of zero energy damping, entropy becomes the driving force of the reversal: the generation of the spin wave at the end of the reversal results in an increase of the system's entropy. Note that spin wave is an excellent energy reservoir. Furthermore, a spin wave could directly couple to lattice vibrations, creating an energy-damping path through magnon–phonon interactions.

5. Near-uniform Magnetization Switching

The magnetization reversal process described in the previous section can be characterized as nucleation and motion of magnetization vortices. The formations of the vortices are driven by the relatively high magnetostatic energy since it is significantly reduced in a magnetization vortex due to the magnetization flux closure. When a film becomes sufficiently thin, magnetization vortices longer form and the magnetization reversal becomes near-uniform rotation. Figure 6 shows the magnetization reversal process of a NiFe film element with a size of 0.5 μm × 0.3 μm and a
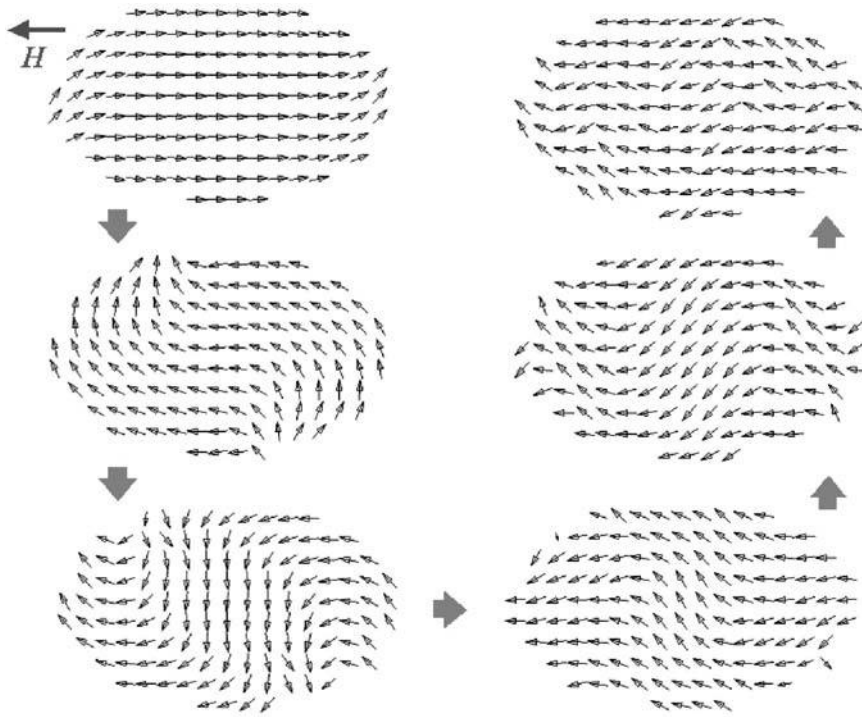
Figure 6
Element-averaged magnetization component along field direction during a magnetization reversal for two energy damping constants $\alpha = 0$ (red) and $\alpha = 0.05$ (blue).
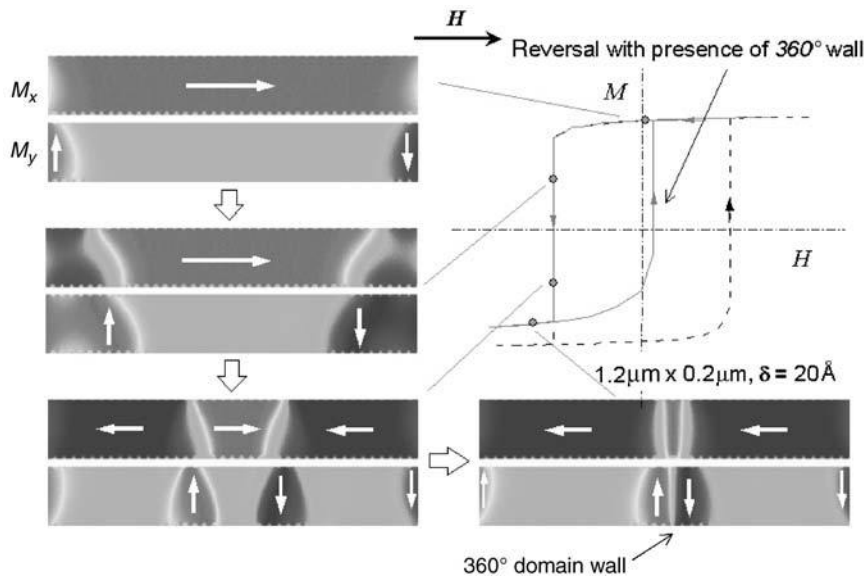
Figure 7
Formation of a 360° domain wall during the reversal of a thin NiFeCo film element that is 1.2 μm × 0.2 μm in size and 2 nm in thickness. The two rows of color pictures at each stage during the reversal represent the longitudinal and the transverse magnetization components, respectively (calculated with $\alpha = 0.02$).

757

thickness only 6 nm. No vortex is present at any stage during the reversal.

6. Effect of the Element Ends

The dynamic magnetization reversal process in a patterned thin film element strongly depends on the element's geometric shape. Reversal of a long rectangular shaped element is particularly interesting. Figure 7 shows a reversal process in a permalloy element with thickness $\delta = 2$ nm. The length and the width of the element are 1.2 μm and 0.2 μm, respectively. The external field is applied along the element length direction. The magnetizations at both ends of the element are oriented parallel to the edges, forming edge domains. The reversal starts from the two ends and expands into the interior of the element via motion of the two domain walls. The magnetization direction within the two domain walls inherits the magnetization directions of the two initial edge domains, which are in the opposite directions in this particular case. As the reversal progresses, the two domain walls move towards each other, forming a 360° domain wall in the middle of the element. The detailed magnetization configuration of the 360° domain wall is shown in Fig. 8. A further significant increase of the field magnitude is needed to move the 360° domain walls out of the side (long) edges. Whereas to reverse the magnetization back with the presence of the 360° domain wall, the critical field magnitude becomes significantly smaller (Fig. 7). The presence of 360° domain wall in the film element is one of the important mechanisms causing nonrepeatable magnetic switching processes.

7. Element of Relatively Large Sizes

Figure 9 shows the calculated magnetization reversal process of a rectangular permalloy thin film element
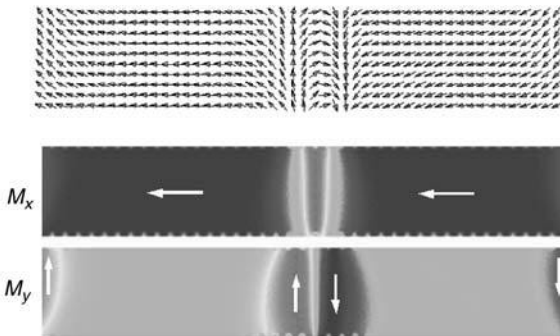
Figure 8
Detailed magnetization configuration of the 360° domain wall of Fig. 7.
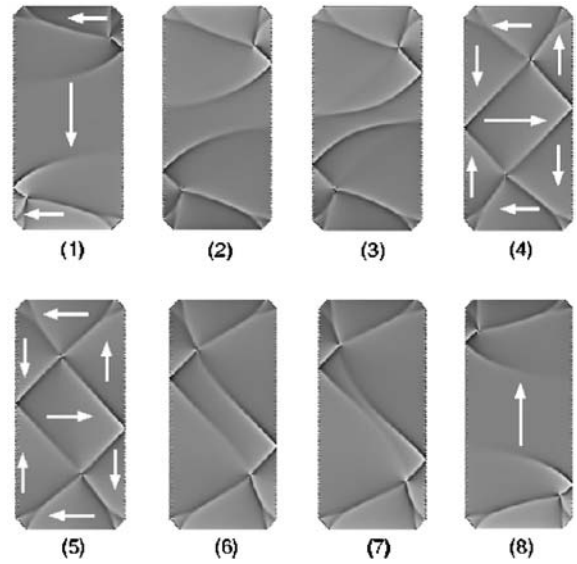
Figure 9
Simulated magnetization reversal process of a permalloy film element of size 10 μm × 5 μm and thickness 30 nm. The gray scale represents the magnetization divergence. An external magnetic field is applied in the element length direction, opposite to the initial magnetization (1) in the center of the element.
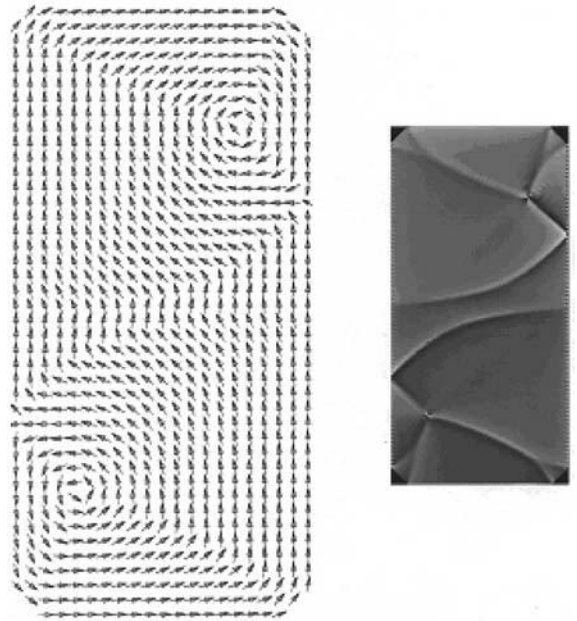
Figure 10
Magnetization vector configuration of a state during the reversal shown in Fig. 9 and its corresponding gray scale representation of the magnetization divergence.
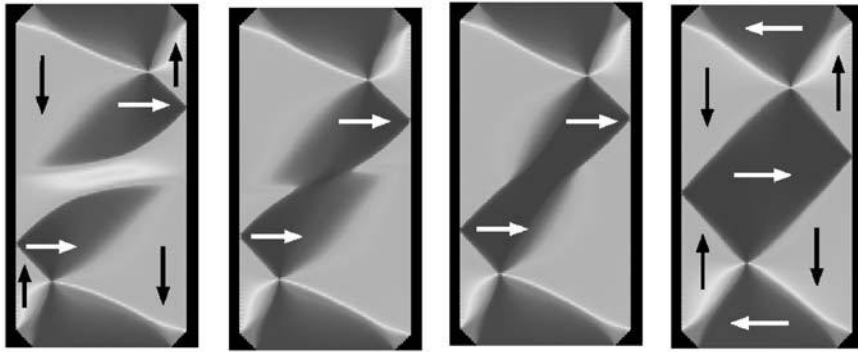
Figure 11
The transient magnetization configurations showing the dynamic formation of the closure domain pattern during the magnetization reversal in Fig. 9. The initial (the extreme left) and the final (the extreme right frame) magnetization states correspond to the states shown in frames (3) and (4) in Fig. 9, respectively. The spectrum of natural light is used to represent the magnetization component in the horizontal direction, with blue indicating the magnetization pointing to right and red to the left.

with size $10\,\mu m \times 5\,\mu m$ and thickness $30\,nm$. The divergence of the magnetization is plotted in gray scale to show the domain walls. Figure 10 shows an example of the exact magnetization pattern corresponding to a wall configuration shown in a gray scale plot. As shown in Fig. 9, from frame (1) to frame (8), the magnetization of the center of the element is completely reversed, from pointing down to pointing up. Prior to the reversal, frame (1) in the figure, there already exist two triangular domains at the top right and bottom left whose magnetizations are already in the reversed (up) direction. As the reversal proceeds, these two reversed domains expand, forcing the formation of the diamond transverse domain in the middle of the element and resulting in the complete flux closure domain configuration shown in frame (4). Continued expansion of the two reverse domains into the entire central area of the element eliminates the transverse diamond domain and the reversal is thus completed.

The formation of the closure domain configuration shown in frame (4) of Fig. 9 is particularly interesting. Figure 11 shows the transient magnetization configurations from the state shown in frame (3) to the state shown in frame (4) of Fig. 9. The connection of the two curved domains forms the central diamond domain in the closure domain configuration.

8. Summary

Magnetization reversal dynamics can be very complicated even in ferromagnetic objects of simple geometric shape. The discovery of the giant magnetoresistance, the advancement of spin-dependent tunneling, and the exploration of spin in semiconductors have sparked recent insurgence on the development of many new types of magnetic devices that utilize magnetic multilayer structures patterned into diminutive dimensions. To facilitate the technological advancements, dynamic micromagnetic modeling will continue to be a powerful tool to obtain critically needed understanding of the magnetization reversal characteristics in these devices and structures.

See also: Longitudinal Media: Fast Switching; Micromagnetics: Basic Principles; Micromagnetics: Finite Element Approach; Magnetic Recording: Patterned Media; Magnetic Recording Media: Particulate Media, Micromagnetic Simulations

Bibliography

Bertram H N, Zhu J -G 1992 Fundamental magnetization processes in thin-film recording media. In: Ehrenreich H, Turnbull D (eds.) *Solid State Physics*. Academic Press, Vol. 46, pp. 271–371

Brown W F Jr 1978 *Micromagnetics*. Krieger, Huntington

Gilbert T L 1955 A lagrangian formulation of the gyromagnetic equation of the magnetization field. *Phys. Rev.* **100**, 1243–53

Hubert A, Schäfer R 2000 *Magnetic Domains*. Springer, pp. 11–104

Kikuchi R 1956 On the minimum of magnetization reversal time. *J. Appl. Phys.* **27**, 1352–7

Landau L, Lifshitz E 1935 On the theory of dispersion of magnetic permeability in ferromagnetic bodies. *Physik. Zeitsch. D. Sowjetunion* **8**, 153–69

Mao C Y 2000 Micromagnetic modeling of thin film write heads for magnetic recording. Ph.D. Dissertation, Carnegie Mellon University, pp. 72–80

Strikman S, Treves D 1963 Micromagnetics. In: Rado G T, Suhl H (eds.) *Magnetism*. Academic Press, Vol. 3, pp. 395–414

Zhu J-G 1989 Interactive phenomena in magnetic thin films. Ph.D. Dissertation, University of California at San Diego, pp. 24–35

Zhu J-G 2001 Micromagnetic modeling of domain structures in magnetic thin films. In: De Graef M, Zhu Y (eds.) *Magnetic Imaging and Its Applications to Materials*. Academic Press, pp. 1–26

Zhu J-G, Zheng Y 2002 The micromagnetics of magnetoresistive random access memory. In: Hillebrands B, Ounadjela K (eds.) *Spin Dynamics in Confined Magnetic Structures I.* Springer, pp. 89–325

J.-G. Zhu

Dept of Electrical & Computer Engineering, Carnegie Mellon University, Pittsburgh, PA 15213-3890, USA

Magnetocaloric Effect: From Theory to Practice

It is known that as an external magnetic field is applied to a magnet under adiabatic conditions (i.e., under the conditions of constant total entropy of the body, $S = $ constant), the initial temperature T of the body may vary due to the magnetocaloric effect (MCE) by the value ΔT. It can result in an increase or in a reduction of the original temperature of a magnetic material. This is a consequence of the variation, under the field, of the internal energy under the influence of an external field of the material possessing a magnetic structure. In 1881 Warburg first discovered MCE as a heat evolution in iron under a magnetic field. In principle, the term MCE should be considered more widely as a description of the processes of entropy variation of the magnetic subsystem.

MCE investigations were shown to yield the kind of information that can hardly be obtained by other techniques. In recent years the interest in investigations of the MCE and the influence of the magnetic field on the entropy has become renewed due to the possibility to obtain information on magnetic phase transitions and the prospects of using some of these materials in magnetic refrigerators (Tishin 1999). The thermodynamic approach is most elaborate for the understanding of the observed phenomena. Also often used are Landau's theory of second-order phase transitions and the mean-field approximation (MFA).

In general, the heat generation and absorption in magnetic materials during adiabatic processes include not only MCE but also elastocaloric effects (ECE). The ECE is a heat emission or absorption at a constant applied magnetic field (in a simple case at zero field) and changing external pressure. If a pressure change takes place under adiabatic conditions then the ECE (like MCE) manifests itself as heating or cooling of a magnet.

1. Elements of Thermodynamic Theory

Considering the total entropy of the system, $S(T, H, p)$, the total differential can be written as:

$$dS = (\partial S/\partial T)_{\mathrm{H,p}}dT + (\partial S/\partial H)_{\mathrm{T,p}}dH + (\partial S/\partial p)_{\mathrm{T,H}}dp \tag{1}$$

where p is the pressure, H is the magnetic field.

For an adiabatic-isobaric process ($dp = 0$) one can obtain from Eqn. (1) with Maxwell's relations the following expression for the temperature change due to the change of the magnetic field (the MCE):

$$dT = -(T/C_{\mathrm{H,p}})(\partial M/\partial T)_{\mathrm{H,p}}dH \tag{2}$$

where $C_{\mathrm{H,p}}$ denotes the specific heat at constant field and pressure (see *Magnetic Systems: Specific Heat*).

The thermodynamic equations obtained above are sufficiently general, since no assumptions as to the structure of the considered system were made. To obtain more concrete results one should know the form of the functions of the free energy of a specific system, which requires some model assumptions. It is known that in ferromagnets normally a second-order phase transition takes place at the Curie point, T_{C}. Belov (1961) adopted the Landau theory of second-order phase transitions to magnetic transitions. According to this theory, the values of the MCE of a ferromagnet which is brought into a magnetic field, H, near the Curie temperature as well as an expression describing the MCE field dependence near the Curie temperature can be calculated.

Above we have considered the MCE in relation to a reversible process of magnetization. Nonreversible magnetothermal effects can arise due to such processes of magnetization as displacement of domain walls and nonreversible rotation of the saturation magnetization, first-order magnetic phase transitions, and Foucalt currents. The nonreversible effects can decrease the sample cooling under adiabatic demagnetization.

The constancy of the total entropy in studies of MCE means (in the case when the total entropy of the magnet can be represented as the sum of three parts: S_{L}, S_{M}, S_{E}—the lattice, magnetic, and electronic entropy, respectively), that as the field is increased from zero up to H it is possible to write:

$$\begin{aligned}
S_{\mathrm{L}}&(T) + S_{\mathrm{M}}(0, T) + S_{\mathrm{E}}(T) \\
&= S_{\mathrm{L}}(T + dT_1) + S_{\mathrm{M}}(H_1, \ T + dT_1) \\
&\quad + S_{\mathrm{E}}(T + dT_1) = \ldots = S_{\mathrm{L}}(T_{i-1} + dT_i) \\
&\quad + S_{\mathrm{M}}(H_i, \ T_{i-1} + dT_i) + S_{\mathrm{E}}(T_{i-1} + dT_i) = \ldots \\
&= S_{\mathrm{L}}(T + \Delta T) + S_{\mathrm{M}}(H, \ T + \Delta T) + S_{\mathrm{E}}(T + \Delta T) \tag{3}
\end{aligned}$$

where dT_i is the infinitesimal gain in the MCE value as the field increases from H_{i-1} up to H_i,
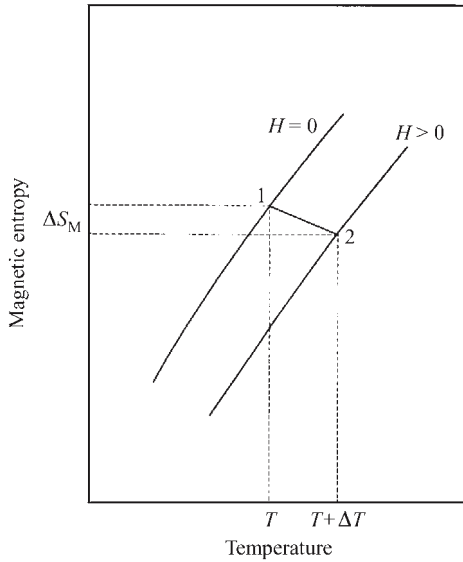
Figure 1
The example of the magnetic entropy curves without magnetic field and at magnetic field $H = $ constant.

$T_i = \mathrm{d}T_i + T_{i-1}$. If the value of $S_E(T)$ has a small change then the Eqn. (3) can be rewritten as:

$$-\Delta S_M(H,\ T) = -(S_M(H,\ T + \Delta T) - S_M(0,\ T))$$
$$= S_L(T + \Delta T) - S_L(T) = \Delta S_L(T) \qquad (4)$$

Thus, as the magnetic entropy is changed by the value $\Delta S_M(H, T)$ (in this case the value of S_M is decreased from point 1 to 2 as shown in Fig. 1) the lattice entropy is decreased by the same amount but with the opposite sign. It should be noted that, as one can see from Eqn. (3), as the field changes, the sum of entropies of the magnetic and lattice subsystems remains constant (at each particular moment of time). At the same time, it seems that the specific part of each contribution to the total entropy of the magnet may vary. In simple one-domain isotropic collinear magnetic structures the field effect is known to result in a stricter alignment of the atomic magnetic moments in the magnetic field direction. Thus, a decrease in magnetic entropy as the field increases (the positive MCE) is usually associated with an increasing order of the magnetic subsystem.

The maximum possible variations in the magnetic entropy for one mole of free ions, as predicted by the theory, is $\Delta S_{max} = -R \ln(2J + 1)$, where R is the universal gas constant and J is the total angular moment. From the classic point of view, the change of S_M is usually related to the rotation of the magnetic moment vectors under influence of the magnetic field (i.e., the S_M decreases with increasing magnetization in classic magnetic materials). In reality, the magnetic

entropy (and consequently the sample temperature) continues to change even in the high field region, just because the probability of atomic magnetic moment deflection from the field direction (due to the thermal fluctuations) remains nonzero even in high magnetic fields.

The magnitude of the isothermal magnetic entropy change, ΔS_M, as well as the total entropy change, ΔS, with the change of magnetic field $\Delta H = H_2 - H_1$ can be calculated from the Maxwell relation on the basis of magnetization data as:

$$\Delta S_M = \int_{H_1}^{H_2} (\partial M(H,T)/\partial T)_H \mathrm{d}H \qquad (5)$$

The magnetic entropy $S_M(H, T)$ can be also calculated as:

$$S_M = \int_0^T (C_M(H,\ T)/T)\mathrm{d}T \qquad (6)$$

where $C_M(H, T)$ is the magnetic heat capacity.

2. Methods of MCE Measurements

At present, there are two main practical methods for the determination of the ΔT value. The first method involves direct measurement of the temperature change $\Delta T(H, T) = T_f - T$ (where T_f is the final temperature) of the sample placed in adiabatic conditions under the influence of an external field. The second way is indirect and based on the calculation of the MCE value on the basis of experimental data on the heat capacity and/or magnetization.

The method of direct measurements of the change in material temperature during the application or removal of a magnetic field by an electromagnet (switch-on technique) has been used for MCE experiments since the 1930s. When the field is produced by an electromagnet the rise time has a maximum value of about a few seconds, while it can be several minutes for a superconducting solenoid. During the field rise a dissipation of heat produced in the sample by the MCE can occur. Estimations show that the field rising time must not be greater than 10 seconds for temperatures above 30 K. This implies that MCE measurements made by a switch-on technique are difficult when using a superconducting solenoid.

Consider as an example the pulsed field setup, as described by Dan'kov *et al.* (1997). The principal scheme of this setup is shown in Fig. 2. Changes of the sample temperature were measured by a copper-constantan thermocouple made of small diameter wires ($\sim 0.05\,\mathrm{mm}$). This provides a small mass of thermocouple (typical weight of the sample is about 1 g) and, consequently, a negligible heat load, which significantly reduces the heat that leaks through the electrical wires. The gadolinium sample, measured by
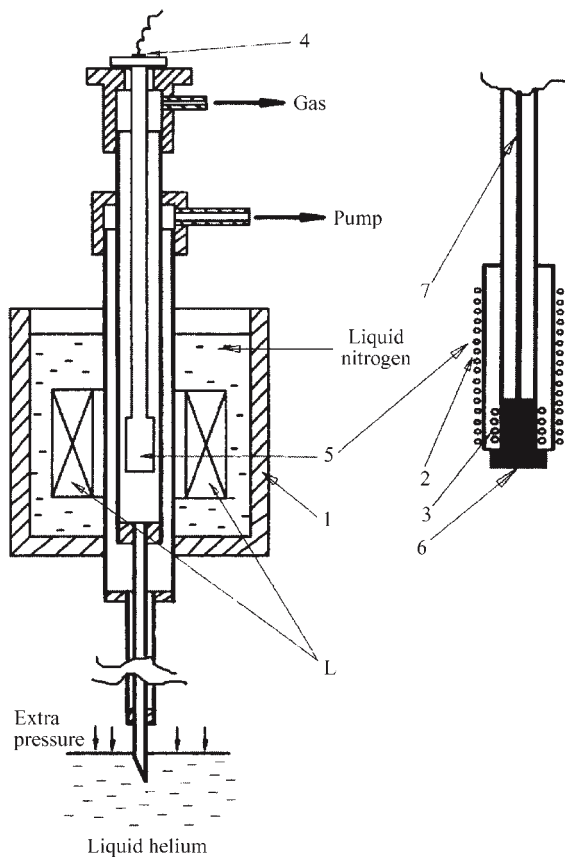
Figure 2
Low temperature part of the experimental pulsed-field setup: (1) liquid nitrogen cryostat, (2) sample heater, (3) field measuring coil, (4) vacuum tight feed through connector, (5) sample holder, (6) sample inside the holder, (7) electrical wiring, and L pulsed solenoid (after Dan'kov *et al.* 1997).

Dan'kov *et al.* (1997) was shaped as a parallelepiped with the dimensions $4 \times 4 \times 10\,\text{mm}$ and cut into two equal parts along the long axes. The thermocouple was placed between the parts in the center of the sample. The magnetic field was created by the solenoid L under the discharge of a battery of capacitors C. This technique made it possible to determine the sample temperature change due to the change of the magnetic field, i.e., the MCE at a given field and temperature.

Experimental data on the magnetic field dependence of the magnetization at constant temperatures allows calculation of the magnetic entropy change by means of Eqn. (5) and the MCE by Eqn. (2).

Another method for the evaluation of ΔS_M is based on the fact that the temperature dependence of the total entropy in the presence of a magnetic field $S(H, T)$ is shifted on the temperature axis relative to the zero-field total entropy $S(0, T)$ to higher temperatures by the value of MCE for a magnetic material under adiabatic conditions. This method is based on the heat capacity measurements and has been proposed by Brown (1976). It allows determination of all parameters required for magnetic refrigeration design.

3. MCE in Different Magnetic Materials

The heavy rare-earth metals (REM) gadolinium to lutetium (except ytterbium) and yttrium have hexagonal close-packed (h.c.p.) crystalline structures. In the magnetically ordered state they display complex magnetic structures (except gadolinium) (see *Alloys of 4f (R) and 3d Elements (T): Magnetism, Localized 4f and 5f Moments: Magnetism*). The MCE and heat capacity of single crystal and polycrystalline samples of heavy REMs have been studied by many authors. The temperature dependence of the MCE of gadolinium obtained by various experimental methods is presented in Fig. 3. A negative MCE is characteristic
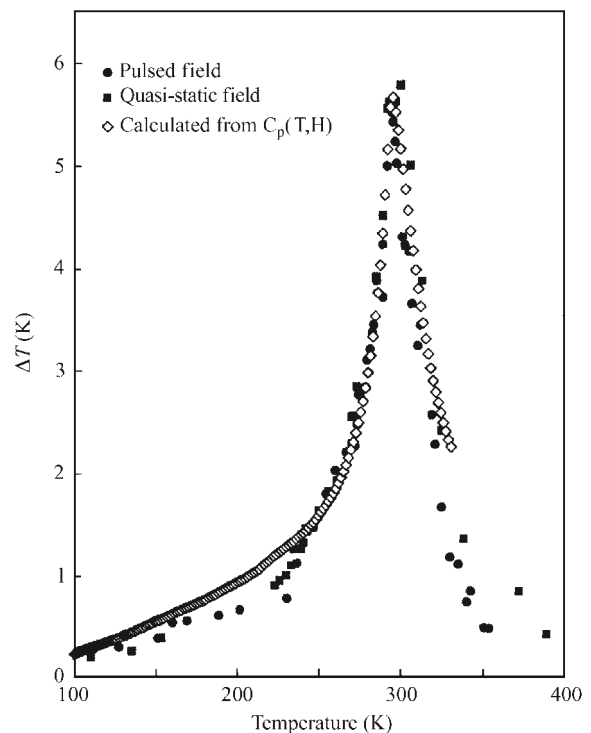
Figure 3
The MCE temperature dependencies of high purity polycrystalline Gd measured directly by quasi-static and pulsed techniques (closed symbols) compared with those determined from the heat capacity (open symbols) for $\Delta H = 20\,\text{kOe}$ (after Dan'kov *et al.* 1997).

of antiferromagnets (e.g., terbium and dysprosium in low magnetic fields), in which the external field reduces the magnetic order rather than enhances it, thus increasing the magnetic entropy.

MCE studies of iron, cobalt, and nickel in fields up to 30 kOe have shown that the magnitude of the MCE near T_C is well described by Eqn. (2). Unlike REMs, in 3d ferromagnets in the same field the maximum of the MCE is fairly sharp. The MCE in iron and cobalt exceeds that of nickel by several fold.

MCE at the first-order transitions (e.g., from ferri- (FI) or ferromagnetism to antiferromagnetism (AFM)) has also been widely studied. Magnetic fields can induce a transition from an AFM structure present below the transition point, to a ferromagnetic one. This is accompanied by sample cooling. In high magnetic field, at the transition from a helicoidal antiferromagnetic state to the ferromagnetic state a positive MCE is observed.

The MCE and magnetic entropy change induced by a magnetic field in thin films prepared on the basis of 3d elements was also measured. MCE is due to the uniform rotation of the spontaneous magnetization. Experimental MCE measurements were made on polycrystalline ferromagnet and single crystalline ferrimagnetic dielectric films.

Investigation of some of oxides showed that the MCE suddenly changes its sign in the low temperature region. An analogous behavior was observed in rare-earth garnets. Such a behavior is related with changes of the ferrimagnetic structure of the rare-earth iron garnets.

The magnetothermal properties of gadolinium gallium garnet (GGG), dysprosium gallium garnet (DGG), and dysprosium aluminum garnet (DAG) were also studied. GGG and DGG have antiferromagnetic ordering below $T_N = 0.8$ K and 0.373 K, respectively. Above T_N they display simple paramagnetic behavior. Rare-earth orthoaluminates (REOA), $RAlO_3$, have an orthorhombically distorted perovskite structure. The magnetic entropy change ΔS_M induced by a field in $GdAlO_3$, $ErAlO_3$, and $DyAlO_3$ was calculated by Kuz'min and Tishin (1991) in the framework of MFA. Kimura $et\ al.$ (1997) determined experimental values of ΔS_M for $RAlO_3$ on the basis of magnetization measurements (see Fig. 4). The experimental results for $DyAlO_3$ and $ErAlO_3$ along the easy axes are in good agreement with the previous calculations. This supports the conclusion that $DyAlO_3$ and $ErAlO_3$ are promising materials for magnetic refrigeration below 20 K as proposed by Kuz'min and Tishin (1991) on the basis of theoretical calculations.

Modern experimental investigations in high magnetic fields of 5 MOe and higher are nowadays nothing extraordinary—the MCE value in such fields can be extremely high. Therefore, the possibility of its influence on the obtained experimental results needs to be accounted for. A computer simulation analysis
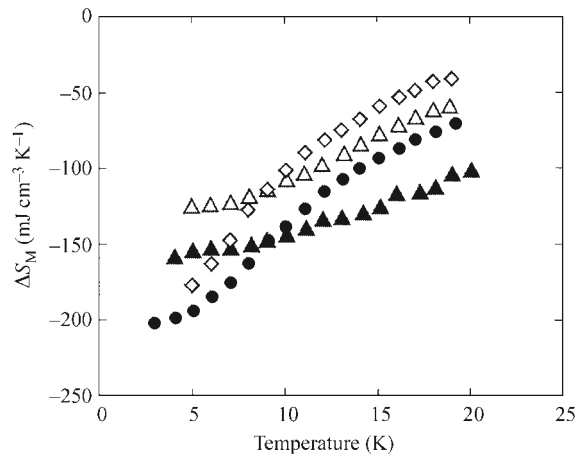
Figure 4
Comparison of ΔS_M temperature dependencies in $DyAlO_3$ (closed triangles) measured along b-axis and in $ErAlO_3$ (closed circles) along c-axis with that in $Gd_3Ga_5O_{12}$ (open diamonds) and $Dy_3Al_5O_{12}$ (open triangles) measured along [111] direction with a magnetic field change of 50 kOe (after Kimura $et\ al.$ 1997).

of the MCE was developed for calculating peak values of the MCE in rare-earth magnets using a mean-field approximation. The study concentrated on the variation of the key thermodynamic parameters such as magnetic field, temperature, and Curie and Debye temperatures of the magnetic materials in a wide range of values. The results of the numerical simulation agree quite well with the experimental data for the heavy lanthanides only for large magnetic fields.

The calculations reveal the fact that if the temperature is high (near 1000 K), saturation of the MCE and magnetic entropy is absent even in the highest magnetic fields (up to 40 MOe), while near the temperature of the phase transition to the paramagnetic state the value of the magnetic entropy saturates in a field of about 10 MOe. The analysis shows that the ΔT_{max} value in the vicinity of the transition point in the series of heavy REMs is directly proportional to the product $g_J J T_{ord}$ and can reach, for example, 254 K in the case of terbium. For more details see Tishin (1999).

4. Magnetic Refrigeration

The MCE is utilized in magnetic refrigeration machines. At the beginning of the century Langevin (1905) demonstrated that changes in the paramagnet magnetization generally resulted in a reversible temperature change. The first experiments to put this idea into practice were carried out in 1933–1934. Investigations in the wide temperature region (from

4.2 K to room temperature and even higher) were started by Brown (1976). Technologically, the current interest in the MCE is connected with the real possibility to employ materials with large MCE values in the phase transition in magnetic refrigerators. The current extensive interest aims to demonstrate that magnetic refrigeration is one of most efficient method of cooling at room temperatures and higher. For instance, the Ames Laboratory (Iowa State University, USA) and the Astronautics Corporation of America have been collaborating and developing an advanced industrial prototype of such a magnetic refrigerator (Zimm *et al.* 1998). In principle, these refrigerators could be used in hydrogen liquefiers, large building air conditioning, vehicle passenger coolers, IR detectors, high-speed computers, and SQUIDs.

At present only REM materials are recognized as appropriate for these purposes. According to Barclay (1994), the REM materials can be used in gas cycle refrigerators as passive regenerators. In magnetic refrigerators they can be applied as working materials (bodies) in externally regenerated or nonregenerative cycles. They can also serve as active magnetic regenerative refrigerators (AMRR).

A regenerator serves to expand a refrigerator temperature span, since the temperature span produced by the adiabatic process itself is insufficient to achieve the desired temperature (especially in the case of magnetic materials). With the help of a regenerator the heat is absorbed from, or returned to, the working material at the various stages of a regenerative thermodynamical cycle.

In the low-temperature region the heat capacity of conventional regenerators in cryogenic refrigerators essentially decreases, since the lattice heat capacity of a solid is proportional to T^3 and the electronic heat capacity in metals is proportional to T. In the refrigerators used for cooling helium gas this leads to a rapid decrease of the refrigerator effectiveness because below about 10 K the volume heat capacity of compressed helium increases. Buschow *et al.* (1975) proposed rare-earth compounds as a possible solution of this problem. The statement was based on the fact that in rare-earth compounds the low magnetic ordering temperatures and the associated heat capacity peaks offer relatively high magnetic contributions to the volume heat capacity. Practical constructions of passive magnetic regenerators using Er_3Ni appeared after investigations of the heat capacity of various R–Ni compounds made by Hashimoto and co-workers (1986). The use of passive magnetic regenerators allowed it to reach 4.2 K and to increase the cooling power.

In magnetic refrigerators a nonregenerative Carnot cycle is used in conjunction with magnetic type regenerative Brayton and Ericsson cycles and with active magnetic regenerator (AMR) cycles (Barclay 1994). A Carnot cycle with a temperature span from T_{cold} to T_{hot} is shown by the rectangle ABCD in the
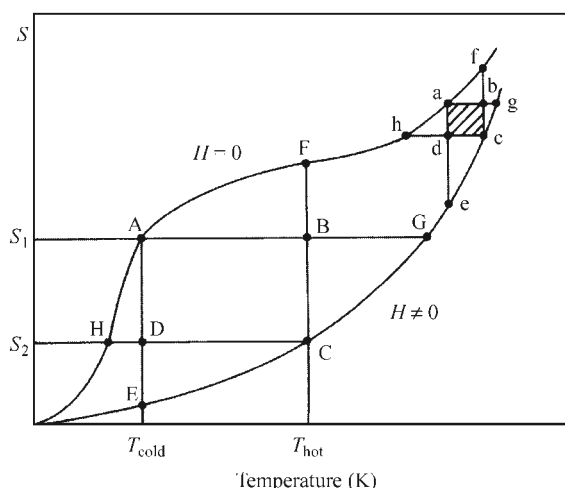
Figure 5
S–T diagram of thermodynamic cycles used for magnetic refrigeration. Two isofield curves are shown: for $H = 0$ and $H > 0$ (after Kuz'min and Tishin 1991).

total entropy—temperature (S–T) diagram in Fig. 5. The heat Q, corresponding to the load during one cycle of refrigeration is equal to $T_{cold}\Delta S_M$. Increasing the temperature span beyond a certain optimal value leads to a significant loss of efficiency as point C in Fig. 5 tends to approach point G and the cycle area becomes narrow. The temperature span of the Carnot cycle for a given T_{cold} and H is limited by the distance AG (i.e., by the MCE at $T = T_{cold}$ and the field change from 0 to H), when Q becomes zero. At temperatures above 20 K the lattice entropy of solids strongly increases, which leads to a decrease of the Carnot cycle area (see rectangle ABCD in Fig. 5). That is why applications of Carnot-type refrigerators are restricted to temperatures region below 20 K.

Magnetic refrigerators operating at higher temperatures have to employ other thermodynamic cycles, including processes at constant magnetic field. Such cycles, as distinct from the Carnot cycle, allow the use of the area between the curves $H = 0$ and $H \neq 0$ in the S–T diagram more fully. The rectangles AFCE and AGCH present the Ericsson and Brayton cycles, respectively. The two cycles differ in the way the field change is accomplished, isothermally in the Ericsson cycle and adiabatically in the Brayton cycle. Realization of isofield processes in both of these cycles requires heat regeneration.

The first room temperature magnetic refrigerator using a regenerative magnetic Ericsson cycle is the device proposed by Brown (1976). The regenerator consists of a vertical column with fluid (0.4 m³, 80% water and 20% alcohol). The magnetic working material immersed in the regenerator consists of 1 mol of

1 mm thick Gd plates, separated by screen wire to allow the regeneration fluid to pass through in the vertical direction. The working material is held stationary in a magnet while the tube containing the fluid oscillates up and down. If initially the regenerator fluid is at room temperature, after about 50 cycles the temperature at the top can reach $+46\,°C$ and the temperature at the bottom can reach $-1\,°C$. The temperature gradient in this device is maintained in the regenerator column.

In the AMR refrigerator the magnetic working material and regenerator are joint in one unit. In this case the temperature gradient exists inside the working material and such a cycle cannot be described by a conventional gas cycle analogue. Consider the AMRR construction proposed by Zimm *et al.* (1998), which is shown in Fig. 6. A magnetic field up to 50 kOe is provided by a helium cooled superconducting solenoid working in the persistent mode. Two beds, each composed of 1.5 kg of gadolinium spheres, are used as the AMR. The spheres have a diameter of 150–300 μm and are made by a plasma-rotating electrode process. The beds are, by turns, moved in and out of the Dewar bore with a magnetic field. Water is used as a heat transfer fluid. The working cycle of the device started with water cooling by blowing it through the demagnetized bed located inside the magnetic area (bottom position in Fig. 6).

Then the water passes through the cold heat exchanger picking up the thermal load from the cooling object. After this the water is blown through the magnetized bed located in the magnetic field area where it absorbs the heat evolved due to the MCE. Next the water passes through the hot heat exchanger, releasing the heat absorbed from the magnetized bed. The cycle is finished by removing the magnetized bed from the magnet and replacing it by the demagnetized one. Such a device, working at 0.17 Hz with a field of 50 kOe in the room temperature range with a temperature span of 5 K, provides a cooling power of 600 W (which is about 100 times better than in previous constructions) with a maximum efficiency of 60 % that of a Carnot process.

The suggestion to use binary and more complicated rare-earth alloys as working bodies for the room temperature region was made by Tishin in 1990. For the application in an ideal Ericsson magnetic regenerator cycle a magnetic working material should have a magnetic entropy change ΔS_M that is constant in the cycle temperature span. The use of terbium–gadolinium and dysprosium–gadolinium alloys as magnetic refrigerators near room temperature is more effective than the use of pure gadolinium.

Hashimoto *et al.* (1986) proposed for a magnetic Ericsson cycle with a temperature span from 10 K to 80 K the use of complex magnetic materials consisting of RAl_2 intermetallic compounds (R = heavy REM). Pecharsky and Gschneidner (1997) proposed the use of the unique behavior of the alloys $Gd_5(Si_xGe_{1-x})_4$ to improve the efficiencies of the magnetic refrigerators.

As mentioned above, refrigerators without regeneration and working with a Carnot cycle can be used below 20 K. Among various oxide compounds $Gd_2Ga_5O_{12}$, $DyAlO_3$, and $ErAlO_3$ are the most suitable working materials for magnetic refrigerators in the temperature range between 2 K and 20 K.

Thus, we have considered the passive and active magnetic refrigerators and materials that can be used for their operation. In conclusion, it is evident that magnetic cooling is a promising technology for the refrigeration industry and may become an important market for the rare-earth industry in the future.

See also: Demagnetization: Nuclear and Adiabatic; Magnetic Refrigeration at Room Temperature

Figure 6
Construction of an AMR refrigerator operating at near room temperature (after Zimm *et al.* 1998).

Bibliography

Barclay J A 1994 Active and passive magnetic regenerator in gas/magnetic refrigerators. *J. Alloys Comp.* **207/208**, 355–61

Belov K P 1961 *Magnetic Transformations*. Consultant Bureau, New York

Brown G V 1976 Magnetic heat pumping near room temperature. *J. Appl. Phys.* **47**, 3673–80

Buschow K H J, Olijhoek J F, Miedema A R 1975 Extremely large heat capacity between 4 and 10 K. *Cryogenics* **15**, 261

Dankov S Y, Tishin A M, Pecharsky V K, Gschneidner K A Jr. 1997 Experimental device for studying the magnetocaloric

effect in pulse magnetic fields. *Rev. Sci. Instrum.* **68**, 2432–7

Hashimoto T 1986 Recent investigations of refrigerant for magnetic refrigerators. *Adv. Cryog. Eng. Mater.* **32**, 261–78

Kimura H, Numazawa T, Sato M, Ikeya T, Fukuda T, Fujioka K 1997 Single crystals of RAlO₃ (R: Dy, Ho and Er) for use in magnetic refrigeration between 4.2 and 20 K. *J. Mater. Sci.* **32**, 5743–7

Kuz'min M D, Tishin A M 1991 Magnetic refrigerants for the 4.2–20 K Region: Garnets or Perovskites? *J. Phys. D* **24**, 2039–44

Langevin M P 1905 Magnetisme et theorie des electrons. *Ann. Chim. Phys.* **5**, 70–113

Pecharsky V K, Gschneidner K A Jr. 1997 Giant magneto-caloric effect in Gd₅(Si₂Ge₂). *Phys. Rev. Lett.* **78**, 4494

Tishin A M 1999 Magnetocaloric effect in the vicinity of phase transitions. In: Buschow K H J (ed.) *Handbook of Magnetic Materials.* North-Holland, Amsterdam, Vol. 12, Chap. 4, pp. 395–524

Warburg E 1881 Magnetische untersuchungen. I. Uber einige wirkungen der coercitivkraft. *Ann. Phys.* **13**, 141–64

Zimm C, Jastrab A, Sternberg A, Pecharsky V, Gschneidner K Jr., Osborn M, Anderson I 1998 Description and performance of a near-room temperature magnetic refrigerator. *Adv. Cryog. Eng.* **43**, 1759

A. M. Tishin
M.V. Lomonosov Moscow State University, Russia

Magnetoelastic Phenomena

Magnetoelasticity is a mutual influence of the magnetic and the elastic properties of materials. It originates from the fact that all main interactions between the atomic magnetic moments in solids depend on the distance between them (e.g., exchange interaction, dipole–dipole interaction, interaction of magnetic moments with crystal electric field). The dimensions, shape, and elastic properties of a sample are influenced by its magnetic state. This is the direct magnetoelastic effect or the magnetostriction (MS). The magnetic properties (magnetization, magnetic ordering temperature, magnetic anisotropy energy) are influenced by the applied and internal mechanical stresses (inverse magnetoelastic effects).

The dependence of a magnetostrictive strain, λ, on the direction of its measurement and the orientation of the magnetization vector (**M**) in a crystal is described by phenomenological formulas specific to a certain crystal symmetry (Clark 1980, Belov *et al.* 1983). For a hexagonal crystal, e.g., cobalt, rare earth (R) metals, and many intermetallic compounds:

$$\lambda = \lambda_1^{\alpha,0}(\beta_x^2 + \beta_y^2) + \lambda_2^{\alpha,0}\beta_z^2 + \lambda_1^{\alpha,2}(\beta_x^2 + \beta_y^2)(\alpha_z^2 - 1/3)$$
$$+ \lambda_2^{\alpha,2}\beta_z^2(\alpha_z^2 - 1/3) + \lambda^{\gamma,2}[0.5(\beta_x^2 - \beta_y^2)(\alpha_x^2 - \alpha_y^2)$$
$$+ 2\alpha_x\beta_x\alpha_y\beta_y] + 2\lambda^{\varepsilon,2}(\alpha_x\beta_x + \alpha_y\beta_y)\alpha_z\beta_z \quad (1)$$

where α_i are the cosines of the magnetization direction, β_i are the cosines of the strain measurement direction, and λ_i are the MS constants. The constants with index α describe the changes in interatomic distances within the basal plane (λ_1^{α}) and along the c-axis (λ_2^{α}) and do not reduce the lattice symmetry. As seen from Eqn. (1), the terms with zero-order constants, $\lambda_i^{\alpha,0}$, do not depend on the magnetization direction and describe the isotropic part of this type of MS, while the terms with second-order constants, $\lambda_i^{\alpha,2}$, correspond to the anisotropic part. A reduction of symmetry is described by the constants with index γ (an orthorhombic distortion in the basal plane) and ε (a deviation from the orthogonality between the basal plane and the c-axis). The MS which reduces the symmetry is essentially anisotropic. The MS modes for hexagonal and cubic crystals are shown in Fig. 1.

For a cubic crystal (e.g., iron and nickel and their alloys, ferrites, RFe₂):

$$\lambda = \lambda^{\alpha,0} + \lambda^{\gamma,2}(\alpha_x^2\beta_x^2 + \alpha_y^2\beta_y^2 + \alpha_z^2\beta_z^2 - 1/3)$$
$$+ 2\lambda^{\varepsilon,2}(\alpha_x\alpha_y\beta_x\beta_y + \alpha_y\alpha_z\beta_y\beta_z + \alpha_x\alpha_z\beta_x\beta_z) \quad (2)$$
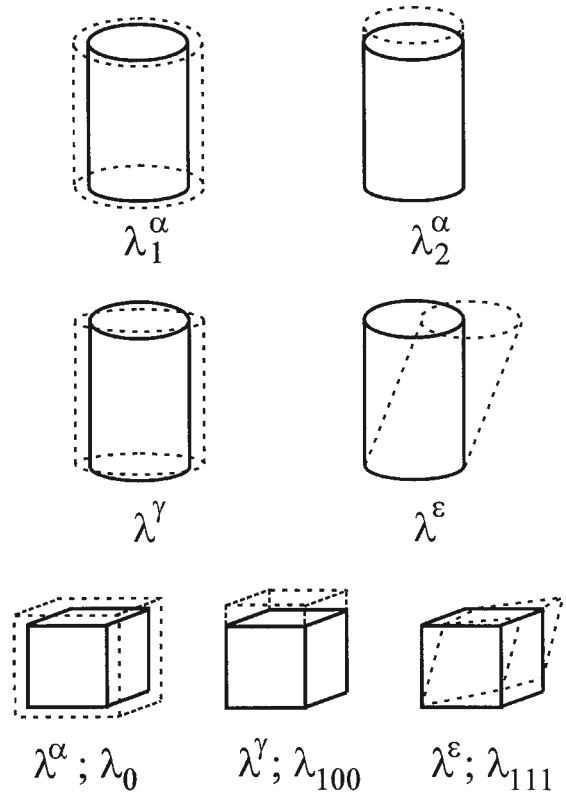
Figure 1
Magnetostriction modes for hexagonal and cubic symmetries.

where $\lambda^{\alpha,0}$ is the isotropic strain which does not depend on the orientation of **M**, $\lambda^{\gamma,2}$ describes the tetragonal distortion, and $\lambda^{\varepsilon,2}$ the rhombohedral distortion of the cubic crystal. Instead of $\lambda^{\alpha,0}$, $\lambda^{\gamma,2}$, and $\lambda^{\varepsilon,2}$, the constants $\lambda_0 = \lambda^{\alpha,0}$, $\lambda_{100} = 2\lambda^{\gamma,2}$, and $\lambda_{111} = 2\lambda^{\varepsilon,2}$ are generally used.

1. Magnetovolume Effects

Figure 2 shows the temperature dependence of lattice parameters of Y_2Fe_{17} (hexagonal crystal structure) and Y_6Fe_{23} (cubic crystal structure) (Givord *et al.* 1971, Andreev 1995 and references therein). The curves in Fig. 2 represent the phonon contribution to the thermal expansion obtained by extrapolation of the paramagnetic behavior into the ferromagnetic range. Below the Curie temperature, T_C, the experimental curves deviate from the extrapolated ones. The differences between the measured and the extrapolated values of the respective lattice parameters
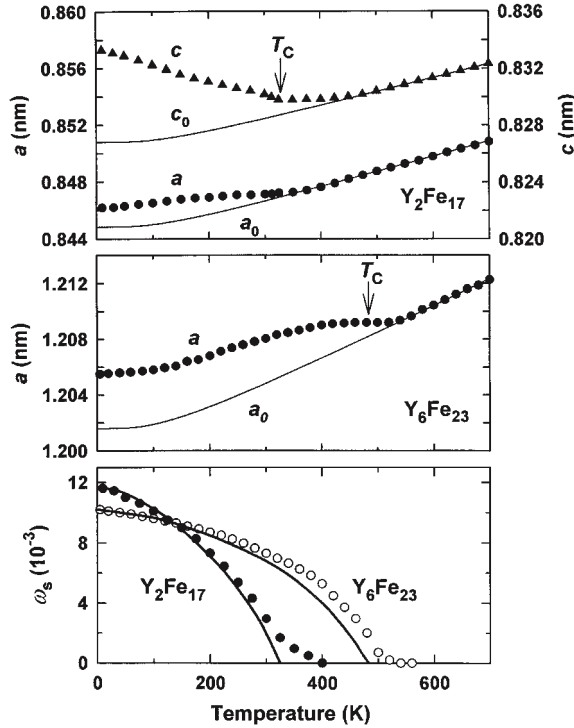
Figure 2
Temperature dependence of lattice parameters a and c of Y_2Fe_{17} and a of Y_6Fe_{23}. The curves are the phonon contribution to the thermal expansion. The arrows indicate the Curie temperature. Bottom: temperature dependence of spontaneous volume magnetostriction ω_s; the lines represent the $\omega_s(T) = \omega_s(0)M_s^2(T)/M_s^2(0)$ dependence.

correspond to the spontaneous linear MS. Both compounds have a negligible anisotropic MS compared to a large isotropic MS. Therefore, the total values of the basal-plane strain, λ_a, and uniaxial strain, λ_c, in Y_2Fe_{17} correspond to the $\lambda_1^{\alpha,0}$ and $\lambda_2^{\alpha,0}$ MS constants, respectively. In cubic Y_6Fe_{23}, the spontaneous MS is described only by $\lambda^{\alpha,0}$. Usually, the spontaneous MS is considered in terms of a volume effect $\omega_s = 2\lambda_1^{\alpha,0} + \lambda_2^{\alpha,0}$ (crystals with a unique axis) and $\omega_s = 3\lambda^{\alpha,0}$ (cubic crystal).

The volume MS has two main origins: the volume dependence of the magnetic moment and the volume dependence of the exchange interactions (du Tremolet de Lacheisserie 1993 and references therein). The first is important in itinerant ferromagnets, where the $3d$ electron states responsible for magnetism generally form an energy band (see *Itinerant Electron Systems: Magnetism (Ferromagnetism)*). The magnetization arises as a result of splitting of sub-bands owing to the exchange interaction (spontaneous effect) or to application of the external magnetic field H (forced, or field-induced effect). The $3d$-band polarization causes an increase in the kinetic energy of electrons. This is compensated by a volume expansion. The increase in kinetic energy is proportional to M^2 to a first approximation. The corresponding volume change can be expressed as:

$$\omega = \Delta V/V = \kappa C M^2 \qquad (3)$$

where κ is the compressibility and C is the magneto-volume coupling constant.

This formula describes the magnetovolume effect in itinerant ferromagnets both in zero field (spontaneous volume MS, ω_s, in this case $M = M_s$, the spontaneous magnetization) and in magnetic field (forced volume MS). In Fig. 2 the temperature dependence of ω_s for Y_2Fe_{17} and Y_6Fe_{23} is compared with M_S^2. A good agreement with Eqn. (3) is seen for a wide temperature range. However, 15–20% of low-temperature ω_s value persists at T_C where M_s becomes zero. Finally, ω_s vanishes at temperatures considerably higher than T_C. Such behavior, typical for compounds with a large magnetovolume effect, is attributed to the existence of a short-range magnetic order in a wide temperature interval above T_C.

The value of ω_s in itinerant ferromagnets is usually positive and sometimes very large. As seen in Fig. 2, it exceeds 1% in Y_2Fe_{17} and Y_6Fe_{23}. Even larger ω_s values, up to 3%, are observed in some $R_2Fe_{14}B$ and $La(Fe,Al)_{13}$ compounds (Andreev 1995 and references therein). The ω_s value can be larger than the phonon contribution below T_C. In such a case the total thermal expansion coefficient becomes very small or even negative (see *Invar Materials: Phenomena*). It is observed in many compounds with low ordering temperatures (<100K) owing to a relatively low phonon contribution. Even a moderate value of ω_s ($\sim 10^{-3}$) is sufficient to exceed the phonon contribution and

produce the Invar-like anomaly in a narrow temperature interval. In some rare cases the Invar effect over a wide temperature interval (including room temperature) can be observed. Besides the above-mentioned iron-rich intermetallics, it occurs also in iron-rich f.c.c. alloys. Other typical examples of systems with large magnetovolume effects are weak itinerant ferromagnets ($ZrZn_2$, $MnSi$) and some antiferromagnetic (AF) alloys and compounds (Cr–Mn, YMn_2) (Nakamura 1983).

The second origin of volume MS, the volume dependence of the exchange interactions, dominates in ferromagnets with a weak volume dependence of the magnetic moment. The isotropic MS constant is then proportional to the magnetic Grüneisen coefficient $\Gamma = (d \ln T_C/d \ln V)$:

$$\lambda^{\alpha,0} \sim \Gamma M^2(H, T) \qquad (4)$$

where M is a volume-independent magnetic moment. The Grüneisen coefficient is usually negative and of the order of unity for most ferromagnets, but sometimes is large and positive for weak itinerant ferromagnets. The absolute value of ω_s in these materials is always much smaller than in Invar alloys. Typical values of ω_s are -1.1×10^{-3} for nickel, -2.7×10^{-3} for iron, and $+2.6 \times 10^{-3}$ for gadolinium (du Tremolet de Lacheisserie 1993).

The forced volume MS (ω_f) has the same physical origins as the spontaneous volume MS. For moderate magnetic fields and temperatures sufficiently lower than T_C, the forced volume MS is associated with the paraprocess and ω_f is a linear function of the applied magnetic field after technical saturation has been achieved. The ω_f values are small for strong ferromagnets at low temperatures ($d\lambda^{\alpha,0}/dH = 4.5 \times 10^{-6} T^{-1}$ for pure iron at 1.5–300 K (du Tremolet de Lacheisserie 1993)) and ω_f usually has a maximum around T_C. Large ω_f values at low temperatures are characteristic of weak itinerant ferromagnets.

A very large ω_f (up to 2%) may be observed at field-induced changes of magnetic structure. This occurs first of all at first-order metamagnetic phase transitions. The field-induced state is ferromagnetic, whereas the initial state can vary. An AF–F transition with large ω_f is observed, for example, in FeRh (Levitin and Ponomarev 1966) and $La(Fe_{0.88}Al_{0.12})_{13}$ (Palstra *et al.* 1985). The transition from a low-moment to a high-moment state is observed in $Sc_{0.25}Ti_{0.75}Fe_2$ (Kido *et al.* 1988), and from the paramagnetic to the F state in the YCo_2- and $LuCo_2$-based alloys (see *Metamagnetism: Itinerant Electrons*). Figure 3 shows the magnetization and MS curves for a polycrystal of $La(Fe_{0.88}Al_{0.12})_{13}$ at 4.2 K. The metamagnetic transition with a wide field hysteresis is accompanied by positive $\omega_f = 1\%$. However, the large ω_f is not a universal feature of a metamagnetic transition. For example, despite the relatively large longitudinal and transverse magnetostrictions
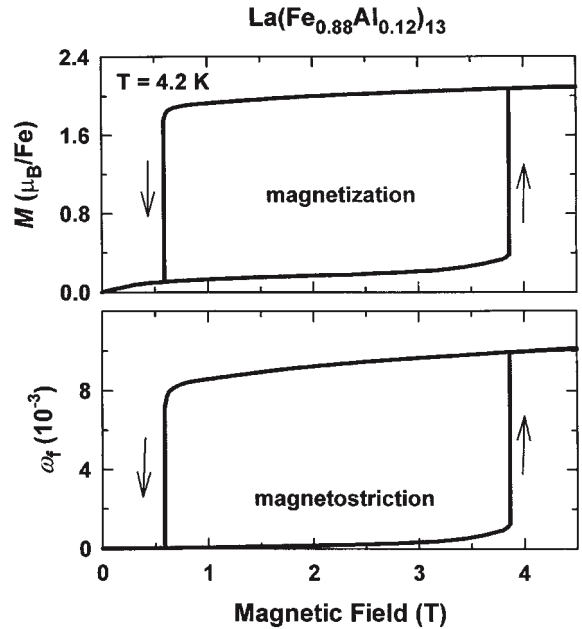
Figure 3
Magnetization and forced volume magnetostriction isotherms for $La(Fe_{0.88}Al_{0.12})_{13}$ at 4.2 K.

accompanying the metamagnetic transition in a single crystal of UNiGa (observed when the magnetic field is applied along the *c*-axis of the hexagonal structure), $\omega_f = 2\lambda_a + \lambda_c$ is negligible due to the mutual cancellation of the linear effects (Andreev *et al.* 1995).

When external pressure is applied to a magnetically ordered material, two magnetoelastic effects occur: changes of the magnitude of magnetic moments and of the energies of moment coupling. For details see *Magnetic Systems: External Pressure-induced Phenomena*.

2. Anisotropic MS

Whereas isotropic (volume) MS depends on the magnitude of magnetic moments and the coupling between them, anisotropic MS describes the changes of dimensions and shape of a sample depending on the orientation of the magnetic moments. Also, the anisotropic MS can be spontaneous or field induced.

The thermal expansion in the magnetically ordered range is affected both by isotropic and by anisotropic MS. The anisotropic MS always causes a reduction of symmetry in the cubic structure. For the hexagonal structure a component of anisotropic MS exists, described by the constants $\lambda_i^{\alpha,2}$ in Eqn. (1), which has no influence on symmetry. Usually, the linear spontaneous strains λ_a and λ_c, which are combinations of $\lambda_i^{\alpha,0}$ and $\lambda_i^{\alpha,2}$, cannot be separated. However, in the
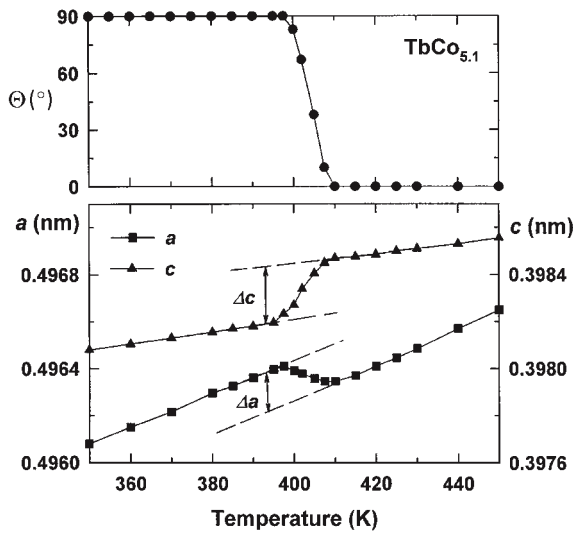
Figure 4
Temperature dependence of the angle Θ between the easy magnetization direction and the c-axis and of the lattice parameters of TbCo$_{5.1}$ in the vicinity of spin reorientation from the basal plane ($\Theta = 90°$) to the uniaxial anisotropy ($\Theta = 0$).

case of a spontaneous spin reorientation each contribution can be clearly distinguished. Figure 4 shows the temperature dependence of lattice parameters of TbCo$_{5.1}$ in the vicinity of the spin reorientation from the basal plane ($\Theta = 90°$) to the c-axis ($\Theta = 0$). The corresponding steps $\Delta a/a$ and $\Delta c/c$ are equal to $\lambda_1^{\alpha,2} \approx -0.3 \times 10^{-3}$ and $\lambda_2^{\alpha,2} \approx 0.6 \times 10^{-3}$, respectively. The volume effect $\Delta\omega_s = 2\lambda_1^{\alpha,2} + \lambda_2^{\alpha,2}$ is thus negligible. For further details see the review of Andreev (1995).

The crystal symmetry is conserved at the magnetic ordering only in the case of uniaxial magnetic anisotropy (the easy magnetization direction is the c-axis in the hexagonal, tetragonal, and rhombohedral structures, or a principal axis in the orthorhombic structure, or the b-axis in the monoclinic structure). Magnetic order with any type of multiaxial anisotropy (in particular, any possible anisotropy in the cubic structure) yields reduced symmetry, which is manifested as a spontaneous distortion. The easy magnetization direction parallel to the $\langle 100 \rangle$ axis in a cubic crystal yields a tetragonal distortion $c/a - 1 = \lambda^{\alpha,2} = 3/2\lambda_{100}$. In the case of the $\langle 111 \rangle$ easy direction, the resulting rhombohedral distortion is characterized by a change of the angle α from $90°$ to a value given by $\cos\alpha = 2\lambda^{\varepsilon,2}/3 = \lambda_{111}$. The orthorhombic distortion in the basal plane of hexagonal crystals as well as the rhombohedral distortion in cubic crystals of the rare earth and actinide compounds can reach values of 10^{-3}–10^{-2} which exceeds by several orders the corresponding values observed in conventional materials based on metals of the iron group.

Note that this so-called "giant MS" is still rather small from a structural viewpoint (e.g., $\lambda_{111} = 10^{-3}$ corresponds to only 3.5 minutes of nonorthogonality between the $\langle 100 \rangle$ axes).

If a magnetic field is applied on a ferromagnet, an anisotropic deformation MS occurs. This effect was discovered by Joule in 1842. Since λ is an even function of H (Eqns. (1) and (2) contain only even degrees of the direction cosines of **M**), $\lambda = 0$ in the case of pure rotation of 180° domains. In a saturated (single-domain) sample, as well as in a uniaxial multidomain sample containing 180° domains only, the Joule MS is caused by a rotation of **M** from the easy direction towards the field direction. The value of λ gradually increases with H and saturates above the anisotropy field H_a.

In materials with multiaxial magnetic anisotropy (e.g., in cubic crystals) the Joule MS is caused first of all by a domain wall displacement leading to redistribution of magnetic phases with noncollinear mutual orientation of **M** and to corresponding reorientation of spontaneous distortions. Since the domain walls are usually moving in relatively low H, the anisotropic MS in samples with multiaxial anisotropy is much more field sensitive and the MS saturates at the field of technical saturation. Such a field dependence is shown in Fig. 5 for annealed pure nickel.
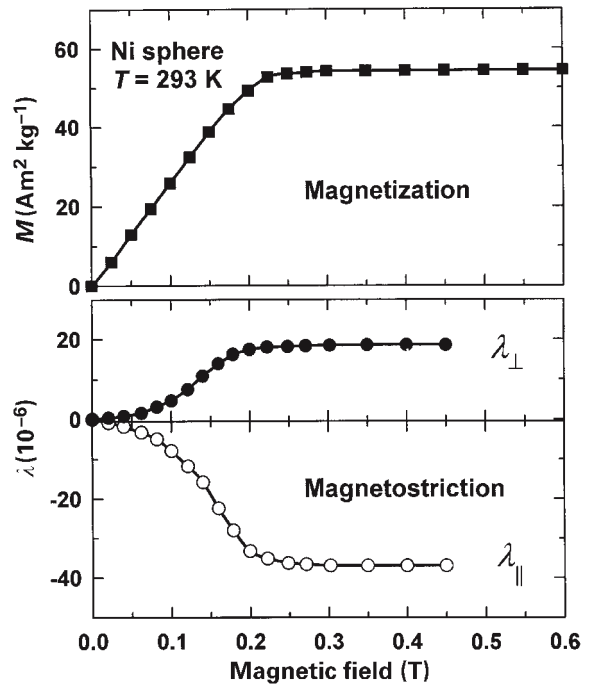
Figure 5
Field dependence of magnetization, M, and longitudinal ($\lambda_\parallel$) and transverse ($\lambda_\perp$) magnetostriction of a nickel polycrystal at room temperature.

When the demagnetized state of a polycrystalline sample before application of the field is isotropic (a random distribution of non-180° magnetic domains over sample volume), the MS measured in the direction parallel to the field, $\lambda_\parallel$, saturates at λ_s which is a characteristic of the material. The corresponding deformation in the perpendicular direction $\lambda_\perp$ saturates at $-\lambda_s/2$ in this case. Generally, the ratio between $\lambda_\parallel$ and $\lambda_\perp$ depends on the magnetic state at zero field because the distribution of the volume over domains is not necessarily random. However, the value $\lambda_s = 2/3(\lambda_\parallel - \lambda_\perp)$ remains independent of the demagnetized state. For a cubic polycrystal (Belov *et al.* 1983):

$$\lambda_s = (2/5)\lambda_{100} + (3/5)\lambda_{111} \qquad (5)$$

Several microscopic mechanisms are responsible for the anisotropic MS (Belov *et al.* 1983). First is the magnetic interaction between a pair of magnetic atoms, which depends on the orientation of the magnetic dipoles relative to the crystallographic axes. The corresponding dipolar MS is essentially anisotropic, but it is usually very small. Second is the MS caused by the variation of the exchange energy with interatomic distances. This mechanism is responsible mainly for the volume MS but can have anisotropic contributions for some substances with low-symmetry lattices. The most prominent mechanism is the interaction between the anisotropic electron shell of an ion and the crystal field (CF). This single-ion MS mechanism is responsible for the so-called giant MS ($\lambda > 10^{-3}$) in many rare earth and actinide compounds.

If the magnetic ion has a nonzero orbital momentum, $\mathbf{M}_L$, the orientation of the total magnetic moment, $\mathbf{M}_J$, by the magnetic field causes the rotation of $\mathbf{M}_L$. The "disturbance" of the crystal field by the rotation of the anisotropic electron shell leads to the anisotropic lattice deformation, i.e., MS. For a simple case of a paramagnet, the relation for the magnetoelastic deformation has been derived:

$$\lambda = AH^2 + CH\tanh(g_j\mu_B H/k_B T) \qquad (6)$$

where A and C are the functions of the direction cosines of the field and the strain. The first term is proportional to Van Vleck susceptibility while the second term reflects the interaction between the magnetic moment and the crystal field. At low H, both terms yield a quadratic dependence of H. The second term saturates at high H.

The single-ion MS caused by the interaction of the 4f shell of R ions with the CF at $T = 0$ can be described by the following (Clark 1980):

$$\lambda(0) = D\alpha J(J - 1/2)\langle r_{4f}^2 \rangle \qquad (7)$$

where D is a coefficient determined by a given crystal lattice, which depends on the CF parameters, the elastic modulus, and the concentration of rare earth ions, α is the Stevens factor that depends on the atomic constants of a 4f ion, $\langle r_{4f}^2 \rangle$ is the average radius squared of the 4f shell, and J is the total angular momentum.

The α factor is determined by the shape of the 4f electron charge cloud. For the 3+ ions of cerium, praseodymium, neodymium, terbium, dysprosium, and holmium $\alpha < 0$ (an oblate 4f cloud), while for samarium, erbium, thulium, and ytterbium $\alpha > 0$ (a prolate 4f cloud) (see *Localized 4f and 5f Moments: Magnetism*). The sign of single-ion MS changes in a series of heavy rare earth ions between holmium and erbium. Similar changes occur in rare earth intermetallic compounds. The MS constants of RFe$_2$ are presented in Table 1 for the ground state (at 4.2K) (adapted from Clark 1980, Belov *et al.* 1983, Andreev 1995). For a particular symmetry, the MS in

Table 1
Magnetostriction constants of RFe$_2$ at 4.2K.[a]

Compound	EMD	μ (μ_B)	λ_{100} ($\times 10^{-3}$)	λ_{111} (exp) ($\times 10^{-3}$)	λ_{111} (calc) ($\times 10^{-3}$)	ω_s ($\times 10^{-3}$)
SmFe$_2$	[110]	3.1	0.03	−4.1	−3.8	
GdFe$_2$	[100]	3.8	0.05[b]	0.05[b]	0	
TbFe$_2$	[111]	5.8		4.5	5.2	
DyFe$_2$	[100]	6.8	−0.07	~3.0[c]	5.0	5.4
HoFe$_2$	[100]	6.9	−0.75	~0.78[c]	1.9	6.3
ErFe$_2$	[111]	6.0		−1.85	−1.85	8.8
TmFe$_2$	[111]	3.7		−3.6	−4.4	
LuFe$_2$	[100]	2.8	−0.09[b]	−0.09[b]	0	4.1
YFe$_2$	[111]	2.8	0.05[b]	0.05[b]	0	2.2
UFe$_2$	[111]	1.2	0.23	3.0	>0	1.6
NpFe$_2$	[111]	2.6		−8.0	<0	

a EMD, easy magnetization direction; μ_m, magnetic moment per formula unit; λ_{100} and λ_{111} (exp), experimentally determined anisotropic magnetostriction constants; λ_{111} (calc), λ_{111} values calculated with Eqn. (7) using the experimental value for ErFe$_2$ to determine D factor; ω_s, spontaneous volume magnetostriction.   b Saturation magnetostriction, λ_s, of polycrystal.   c Values extrapolated to 0K from the high-temperature range (180–300K).

these compounds (except for HoFe$_2$) is determined mainly by λ_{111} ($\lambda_{100} \ll \lambda_{111}$). The λ_{111} values calculated with Eqn. (7) are also given in Table 1. D was determined using the experimental value for ErFe$_2$. The signs of experimental and calculated λ_{111} coincide. The magnitudes also agree satisfactorily. The CF mechanism of giant MS in compounds with nonzero L moment of the R ion is corroborated by the fact that the compounds with nonmagnetic R = Y, Lu, and with gadolinium ($L=0$) exhibit MS of two orders of magnitude less. Giant MS is also observed in UFe$_2$ and NpFe$_2$, the actinide analogues of the RFe$_2$ group (Table 1).

According to the theory of magnetoelastic interaction (Callen and Callen 1963), the field and temperature dependence of the magnetoelastic constant of lth order is determined by the magnetization:

$$\frac{\lambda_l(T,H)}{\lambda_l(0,0)} = \hat{I}_{l+1/2}\{L^{-1}[m(T,H)]\} \qquad (8)$$

where $\hat{I}_{l+1/2}(x) = I_{l+1/2}(x)/I_{1/2}(x)$ is a modified hyperbolic Bessel function and $L^{-1}(m)$ is the inverse Langevin function of the reduced magnetization $m(T, H) = L(x) = \hat{I}_{3/2}(x) = \coth x - 1/x$. Here $x = (\mu_B H_{mol}/k_B T)$ in the molecular field model. In the low-temperature region:

$$\frac{\lambda_l(T,H)}{\lambda_l(0,0)} = m^{l(l+1)/2} \qquad (9)$$

The single-ion model allows one to describe the MS also in the metals of the iron group. The orbital moment of 3d electrons is nearly quenched due to the CF and is usually very small. Nevertheless, the single-ion contribution to the MS exceeds the dipolar contribution in these compounds.

3. Villari Effect

The magnetoelastic effect which is the reverse of the Joule MS, i.e., dependence of the magnetization curve on the mechanical stress was extensively studied by Villari in 1865. The magnetization curves shown in Fig. 6 illustrate the effect of tensile stress in nickel in the longitudinal geometry (magnetization is measured along the tensile stress). At high values of stress, the room-temperature magnetization curves are completely determined by the uniaxial magnetic anisotropy induced by tensile stresses. For an isotropic ferromagnet, the magnetoelastic anisotropy energy can be expressed by (Belov 1987):

$$W_{me} = -\frac{3}{2}\lambda_s \sigma \left(\cos^2\phi - \frac{1}{3} \right) \qquad (10)$$

where σ is a stress, and ϕ represents the angle between **M** and σ. When the stress is positive and the MS is negative (the case of nickel in Fig. 6), W_{me} has
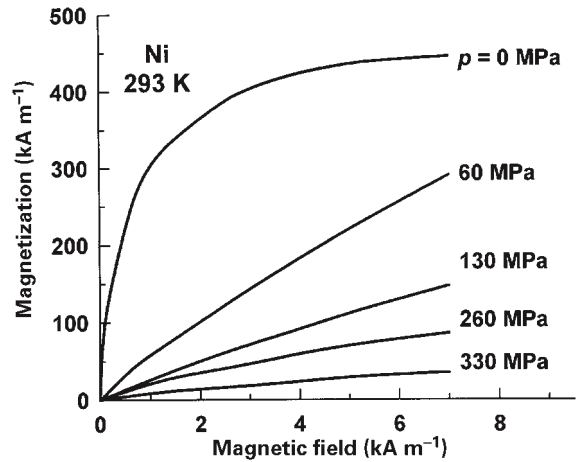
Figure 6
Room-temperature magnetization curves of nickel under varying tensile stresses.

a minimum at $\phi = \pi/2$, i.e., the induced easy magnetization axis lies perpendicular to σ. The direction of σ becomes the hard magnetization axis and therefore the saturation field increases with the stress (Fig. 6). When $\lambda_s \sigma > 0$, the easy magnetization axis is along σ, and the stress makes it easier to reach the saturation of magnetization.

4. Magnetoelastic Contribution to the Magnetic Anisotropy

Even without any external or internal stresses the magnetoelastic coupling modifies the energy of magnetic anisotropy of a crystal. Besides the magnetocrystalline anisotropy, a magnetoelastic anisotropy of the same symmetry appears, which causes additive contributions to the magnetic anisotropy constants. For a cubic crystal, the magnetoelastic contribution to the first anisotropy constant, K_1, can be written as (Belov *et al.* 1983):

$$\Delta K_1 = (9/4)[(c_{11} - c_{12})\lambda_{100}^2 - 2c_{44}\lambda_{111}^2] \qquad (11)$$

where c_{ij} are the elastic constants. The magnetoelastic contribution is responsible for the change of the sign of K_1 in nickel near 480K. In rare earth and actinide compounds the magnetoelastic contribution ΔK_1 is comparable with K_1 and must be taken into account in the description of the magnetization curves and spin-reorientation phase transitions.

5. ΔE Effect

The elastic properties of a ferromagnet may be perturbed by the magnetoelastic coupling. The magnetic

field dependence of the elastic modulus, E (ΔE effect), was discovered by Guillemin in 1846. The ΔE effect is usually described in terms of the ratio $\Delta E/E = (E_0 - E)/E$, where E is the experimentally observed value and E_0 is the value for the case when the elastic stress does not cause magnetization rotation and domain walls movement. In a low-anisotropy material it occurs practically at the field of technical saturation but generally $E \to E_0$ for $H \to \infty$. In ferromagnets, $\Delta E > 0$ and is independent of the sign of λ and σ. A theory of the ΔE effect for isotropic ferromagnets gives the following relations for the limit of very low (LF) and very high (HF) magnetic fields, respectively (du Tremolet de Lacheisserie 1993):

$$\left(\frac{\Delta E}{E}\right)_{LF} = \frac{9\chi_i \lambda_s E_0^2}{5\mu_0 M_s^2}; \quad \left(\frac{\Delta E}{E}\right)_{HF} = \frac{9\lambda_s^2 E_0}{4MH}\sin^2 2\theta \quad (12)$$

where θ is the angle between the internal magnetic field and the axis of measurement of E. A very large ΔE effect may be expected at low H in materials exhibiting a large initial susceptibility, χ_i, and a large λ. Among the giant MS materials, the largest ΔE effects are exhibited by $TbFe_2$ (up to 0.6) and the low-anisotropy alloy $Tb_{0.3}Dy_{0.7}Fe_2$ (up to 1.6). The same value of $\Delta E/E = 1.6$ is observed also in UFe_2. For the high-magnetostrictive Metglass $Fe_{81}B_{13.5}Si_{3.5}C_2$, $\Delta E/E = 15$ (Belov *et al.* 1983 and references therein).

6. Direct and Inverse Wiedemann Effects

When a thin ferromagnetic rod is simultaneously magnetized by a longitudinal field, $H_\parallel$, and by a circular field, $H_\perp$, generated by an electrical current flowing along the sample, the resulting helicoidal magnetic field causes twisting of the rod (the direct Wiedemann effect). For an isotropic wire at a sufficiently low current density, j, and a sufficiently high magnetizing field ($H_\perp \ll H_\parallel$) the twist per unit length, ξ, is given by (du Tremolet de Lacheisserie 1993):

$$\xi = \frac{3\lambda_\perp}{2H_\parallel}j \quad (13)$$

Since, ξ, j, and $H_\parallel$ can be measured with high accuracy, the Wiedemann effect is a valuable method of determination of λ_s in soft ferromagnets.

There are two inverse Wiedemann effects:

(i) The change of the longitudinal magnetization, δM_z, and the appearance of a circular magnetization, M_Φ, in a long ferromagnetic rod magnetized along its length when subjected to a mechanical torque; a voltage appears between the ends of the rod due to a longitudinal electric field associated with the change of the circular magnetization (the Matteuchi effect).

(ii) The change of the circular magnetization, δM_Φ, and the appearance of a longitudinal magnetization, M_z, in a long ferromagnetic rod where an electric current passes when the rod is submitted to a mechanical torque.

7. Linear Magnetostriction. Piezomagnetism

Most ferromagnets and antiferromagnets exhibit a quadratic field dependence of MS in low magnetic fields. However, in low-symmetry materials the thermodynamic potential can contain nonzero terms linearly dependent on the field and on a component of the elastic stress tensor. For 66 magnetic symmetry classes (including 35 of 59 AF classes) a strain varying linearly with applied magnetic field is possible (Birrs 1964). In fact, a linear MS is rarely observed since it is usually masked by much stronger quadratic effects. The odd linear magnetostrain was observed in AF hematite, α-Fe_2O_3, as well as in the orthoferrites $YFeO_3$ and $YCrO_3$ in the region of spin-reorientation transitions (du Tremolet de Lacheisserie 1993 and references therein).

An inverse effect to the linear MS (piezomagnetism) is the appearance of a spontaneous magnetization under external stress. Piezomagnetism is observed in CoF_2, MnF_2, α-Fe_2O_3, and $FeCO_3$ (du Tremolet de Lacheisserie 1993 and references therein).

8. Applications of Magnetoelasticity

Application of isotropic magnetoelastic coupling is limited mainly to the Invar alloys for cases where a low thermal expansion coefficient of the metal is required (e.g., in glass–metal assemblies). Elinvar alloys exhibiting the ΔE effect are employed whenever the elastic properties must be stable over some temperature interval (e.g., a clock spring).

Joule MS is widely used both in static and dynamic devices. The static MS allows the construction of linear actuators offering sufficiently large displacements (20–200µm) and large forces (500–5000 N) at low voltage. Linear actuators are used in micropositioning tools or for damping structures, as well as for components of more complex actuators.

Spring-type magnetostrictive actuators employing the direct Wiedemann effect have been designed for positioning optical units and mechanical parts up to 5Kg: the pieces may be oriented with an accuracy of 10^{-5} degree in a frequency range up to 70Hz.

A magnetic material in an alternating magnetic field undergoes mechanical oscillations due to the MS. A well-known result of such oscillations is the noise of electric power transformers. Therefore, for this and related purposes, the MS should be reduced to as low as possible (zero-MS materials include cobalt-rich amorphous alloys). However, if the MS core has appropriate dimensions, resonance oscillations can appear. Some magnetoelastic materials with sharp resonance (high Q-factor) are used in frequency stabilizers and filters.

Table 2
Saturation magnetostriction, λ_s, magnetomechanical coupling factor, k_{33}, Q-factor, and Curie temperature, T_C, for some magnetostriction materials.

Material	λ_s ($\times 10^6$)	k_{33}	Q-factor	T_C (°C)
Ni	−37	0.25–0.31	700	360
96Ni4Co	−31	0.6		410
87Fe13Al	+ 40	0.32	400	500
49Co49Fe2V	+ 70	0.2–0.4	600	980
$NiFe_2O_4$ + Cu,Co	−26	0.25	2000	590
$Fe_{81}B_{13.5}Si_{3.5}C_2$ Metglas	+ 30	0.97		370
$TbFe_2$	1750	0.35	100	425
$Tb_{0.27}Dy_{0.73}Fe_2$	1000–1500	0.6–0.75	50–200	380

An important area of technical application of magnetostrictive materials is in high-power transducers both for acoustic (loudspeakers, sonars, echo-sounders, defectoscopes, etc.) and for mechanical (welding, sealing, cleaning, cutting, etc.) purposes at typical frequencies below 50 kHz. For these devices the most important property of the material is not the MS, λ, but the magnetostrictivity, $\partial\lambda/\partial H$. A certain amplitude of mechanical oscillation should be reached in as small a magnetic field interval as possible. The relevant parameters are the MS coefficient:

$$h = -\left(\frac{\partial\sigma}{\partial B}\right)_\varepsilon = \frac{E}{\mu}\frac{\partial\lambda}{\partial H} \qquad (14)$$

and the coefficient of sensitivity of a magnetostrictor as an acoustic receiver:

$$d = \left(\frac{\partial B}{\partial\sigma}\right)_H \qquad (15)$$

where H and B are the magnetic field and the magnetic induction, respectively, σ is the mechanical stress, ε is the relative strain, E is the elastic modulus, and μ is the permeability at constant induction (Belov *et al.* 1983).

The transformation of the magnetic energy, U_{magn}, into the elastic energy, U_{elast}, is characterized by the magnetomechanical coupling factor of the sample, $k = \sqrt{(U_{elast}/U_{magn})}$, showing the fraction of U_{magn} which can be converted to U_{elast}. The coupling factor is conventionally obtained by measuring the complex impedance of a coil containing the magnetostrictive material. Generally, it depends on the shape of the sample. In the practically important case when the mechanical motion is parallel to the exciting field, k is specified as k_{33}, a geometry-independent coupling factor characterizing the material (Clark 1980).

In order to select the maximum $\partial\lambda/\partial H$ in the field dependence of λ, a static bias magnetic field is usually applied to the MS core. The elastic energy density can be increased using prestress of a magnetostrictive rod. The best reported magnetostrictive transducers allow one to generate a 3kW acoustic power. For a review

of devices based on materials with giant MS, see Claeyssen *et al.* (1997).

The magnetoelastic characteristics of some materials are presented in Table 2 (adapted from Clark 1980, Tremolet de Lacheisserie 1993, Golyamina 1992). Nickel is a traditional material widely used in magnetomechanical converters. In order to improve the $\partial\lambda/\partial H$ and k_{33} values, alloying components that reduce the magnetocrystalline anisotropy can be added (the alloy 96Ni4Co with compensated anisotropy possesses a k_{33} factor as high as 0.6). Among the magnetostrictive alloys based on iron and cobalt, the best parameters are shown by the alloy 49Co49Fe2V. Owing to its high T_C, the magnetoelastic properties of this alloy are stable over a wide temperature interval. In high-frequency magnetomechanical converters the ferrites are used as core materials owing to their high electrical resistance. The nickel ferrite $NiFe_2O_4$ has relatively high λ_s but k_{33} is small. The k_{33} value and Q-factor increase with the substitution of copper, zinc, and cobalt for nickel. An outstanding value of $k_{33} = 0.97$ has been obtained on the field-annealed Metglas $Fe_{81}B_{13.5}Si_{3.5}C_2$ in a polarizing magnetic field of 50Am^{-1}.

Rare earth intermetallic compounds possess giant MS caused by rare earth ions. The largest room-temperature λ_s is found in $TbFe_2$. However, $\partial\lambda/\partial H$ is low owing to a high magnetocrystalline anisotropy and the λ_s value is achieved only in fields above 2T. The value of $\partial\lambda/\partial H$ can be substantially improved using quasibinary compositions $(Tb_{1-x}Dy_x)Fe_2$ at $x \sim 0.7$ (Terfenol-D) owing to the compensation of the anisotropy constant K_1. This leads to an increase of k_{33} despite a certain decrease of λ_s (Table 2).

See also: Magnetic Systems: External Pressure-induced Phenomena; Invar Materials: Phenomena; Metamagnetism: Itinerant Electrons; Itinerant Electron Systems: Magnetism (Ferromagnetism); Localized 4*f* and 5*f* Moments: Magnetism; Magnetostrictive Materials; Magnetoelasticity in Nanoscale Heterogeneous Materials

Bibliography

Andreev A V 1995 In: Buschow K H J (ed.) *Handbook of Magnetic Materials*. Elsevier, Amsterdam, Vol. 8, pp. 59–187

Andreev A V, Bartashevich M I, Goto T 1995 Magnetostriction of UNiGa at metamagnetic transition. *J. Alloys Compounds* **219**, 267–70

Belov K P 1987 *Magnetostriction Phenomena and Their Technical Applications*. Nauka, Moscow (in Russian)

Belov K P, Kataev G A, Levitin R Z, Nikitin S A, Sokolov V I 1983 Giant magnetostriction. *Sov. Phys. Uspekhi* **26**, 518–42

Birrs R R 1964 In: Wohlfarth E P (ed.) *Selected Topics of Solid State Physics*. North Holland, Amsterdam, Vol. 8

Callen E R, Callen H B 1963 Static magnetoelastic coupling in cubic crystals. *Phys. Rev.* **129**, 578–93

Claeyssen F, Lhermet N, Le Letty R, Bouchillioux P 1997 Actuators, transducers and motors based on giant magnetostrictive materials. *J. Alloys Compounds* **258**, 61–73

Clark A E 1980 In: Wohlfarth E P (ed.) *Ferromagnetic Materials*. Elsevier, Amsterdam, Vol. 1, pp. 531–89

Givord D, Lemaire R, James W J, Moreau J M, Shah J S 1971 Magnetic behavior of rare-earth iron-rich intermetallic compounds. *IEEE Trans. Magn.* **MAG-7**, 657–9

Golyamina I S 1992 In: Prokhorov A M (ed.) *Physical Encyclopedia*. Big Russian Encyclopedia, Moscow, Vol. 3, pp. 8–9 (in Russian)

Kido G, Nakagawa Y, Yamaguchi Y, Nishihara Y 1988 Forced magnetovolume effects in $Sc_{1-x}Ti_xFe_2$ at the ferromagnetic to ferromagnetic transition. *J. Phys.* **49**, C8-251–2

Levitin R Z, Ponomarev B K 1966 Magnetostriction of the metamagnetic FeRh alloy. *Soviet Phys. JETP.* **50**, 1478–83

Nakamura Y 1983 Magnetovolume effects in Laves phase intermetallic compounds. *J. Magn. Magn. Mater.* **31–34**, 829–34

Palstra T T M, Nieuwenhuys G J, Mydosh J A, Buschow K H J 1985 Mictomagnetic, ferromagnetic and antiferromagnetic transitions in $La(Fe_xAl_{1-x})_{13}$ intermetallic compounds. *Phys. Rev. B* **31**, 4622–32

du Tremolet de Lacheisserie E 1993 *Magnetostriction: Theory and Applications of Magnetoelasticity*. CRC Press, Boca Raton, FL

A. V. Andreev
Institute of Physics, Prague, Czech Republic

N. V. Mushnikov
Institute of Metal Physics, Ekaterinburg, Russia

Magnetoelasticity in Nanoscale Heterogeneous Materials

When a material becomes magnetic, the magnetoelastic coupling causes a change in volume, the *volume magnetostriction*, and anisotropic changes in linear dimensions, the *Joule magnetostriction*. The magnetic order, and thus the deformation, can be induced either by a temperature variation (*spontaneous magnetostriction*) or by application of a magnetic field (*forced magnetostriction*). The magnetostriction varies from nearly 1% in rare-earth-based intermetallic compounds to almost zero for iron-based amorphous and nanocrystalline alloys (see *Magnetostrictive Materials*).

The local properties of *nanoscale heterogeneous magnetic systems* do vary in the scale of nanometers, for amorphous materials even on an atomic scale (see *Amorphous and Nanocrystalline Materials*). Heterogeneous materials may exhibit surface (interface) magnetic anisotropy and magnetostriction, negligible in bulk material. For many applications, magnetostrictive thin films are of special interest, because cost-effective mass production is possible. In microelectromechanical systems (MEMSs; see *Micromechanical Systems, Principles of*), thin films exhibiting giant magnetostriction (GMS; see *Thin Films Giant Magnetoresistive*), preferably at low fields, are applied as microactuator elements like cantilevers (see Fig. 1) or membranes, since they combine high-energy output, high-frequency, and remote-control operation. Here, good performers are thin films of rare-earth–transition metal (RT) intermetallic compounds. More recently, attention is also focused on the magnetostrictive properties of perovskite manganites and cobaltates, which are known to exhibit large changes in resistivity upon magnetization (colossal magnetoresistance (CMR); see *Transition Metal Oxides: Magnetism*).

In order to reduce the number of explicit references, for many details we only indicate where references can be found in Duc and Brommer (2002).

1. Magnetoelastic Effects

The free energy of a magnetic substance is the sum of the magnetostatic energy and the "internal" free energy. The magnetostatic energy originates from the
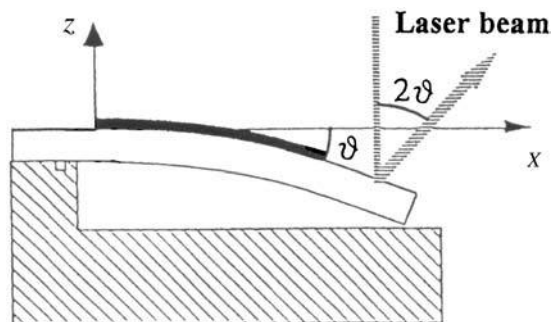
Figure 1
A typical magnetostrictive *cantilever* consists of a thin film deposited on a suitable substrate, which is clamped on the sample holder. The deformation caused by application of a magnetic field can be determined by measuring the deflection of a laser beam.

(long-range) dipolar interactions, giving rise to demagnetizing fields and shape anisotropy. The concurrent deformations depend on the geometry of the sample (hence the name *form effect*), but are small ($\leqslant 10^{-6}$), and often negligible. The "internal" free energy is expanded in the symmetrized strains ε_{xx}, ε_{yy}, ε_{zz}, ε_{xy}, ε_{yz}, ε_{xz}, and the direction cosines of the magnetization α_i ($i = 1, 2, 3$, corresponding to Cartesian coordinates x, y, z, respectively). The free energy is invariant under symmetry transformations, and thus can best be expressed in linear combinations of the strains (e.g., $e = \varepsilon_{xx} + \varepsilon_{yy} + \varepsilon_{zz}$) and polynomials (such as $\alpha_1^2 + \alpha_2^2 + \alpha_3^2 = 1$, $\alpha_1\alpha_2$ or $(\alpha_3^2 - \frac{1}{3})$), which span invariant irreducible subspaces. The strain e mentioned above spans a one-dimensional invariant subspace. For an *n*-dimensional irreducible subspace γ, spanned by strains $\{e_j^\gamma\}$ or polynomials $\{h_j^{\gamma,m}(\boldsymbol{\alpha})\}$ of degree m, with $j = 1, \ldots, n$, a fundamental group-theoretical theorem states that the only (second-order) invariants are $\sum_j (e_j^\gamma)^2$, $\sum_j (h_j^{\gamma,m})^2$, and the bilinear magnetoelastic coupling terms $\sum_j e_j^\gamma h_j^{\gamma,m}(\boldsymbol{\alpha})$. The magnetostrictive strains follow from the minimization of the free energy part $\frac{1}{2}C^\gamma \sum_j (e_j^\gamma)^2 + B^{\gamma,m} \sum_j e_j^\gamma h_j^{\gamma,m}(\boldsymbol{\alpha})$, yielding $e_j^\gamma = -(B^{\gamma,m}/C^\gamma)h_j^{\gamma,m}(\boldsymbol{\alpha})$, governed by the (first-order) "coefficient of magnetostriction" $\lambda^{\gamma,m} = -(B^{\gamma,m}/C^\gamma)$.

As an example, we decompose the free-energy density of an *isotropic* material as $F = F^\alpha + F^\gamma$:

$$F^\alpha = (1/2)C^\alpha e^2/3 + B^{\alpha,0}e/3 \qquad (1a)$$

$$F^\gamma = (1/2)C^\gamma \left[(3/2)\, (\varepsilon_{zz} - e/3)^2 + (1/2)\, (\varepsilon_{xx} - \varepsilon_{yy})^2 \right]$$
$$+ B^{\gamma,2}[(3/2)\, (\varepsilon_{zz} - e/3)\, (\alpha_3^2 - 1/3)$$
$$+ (1/2)\, (\varepsilon_{xx} - \varepsilon_{yy})\, (\alpha_1^2 - \alpha_2^2)] \qquad (1b)$$

Minimizing the free energy results in the *volume magnetostriction* $e = \lambda^{\alpha,0} = -B^{\alpha,0}/C^\alpha$, and the *Joule magnetostriction* components $(\varepsilon_{zz} - e/3) = \lambda^{\gamma,2}(\alpha_3^2 - 1/3)$, and $(\varepsilon_{xx} - \varepsilon_{yy}) = \lambda^{\gamma,2}(\alpha_1^2 - \alpha_2^2)$, with $\lambda^{\gamma,2} = -B^{\gamma,2}/C^\gamma$ (equivalently, for instance, $\varepsilon_{xy} = \lambda^{\gamma,2}\alpha_1\alpha_2$ (cycl.)). Inserting these results in the general expression for the linear expansion, measured in the direction $\boldsymbol{\beta} = (\beta_1, \beta_2, \beta_3)$

$$\Delta\ell/\ell = \varepsilon_{xx}\beta_1^2 + 2\varepsilon_{xy}\beta_1\beta_2 + \text{cycl.} \qquad (2)$$

yields

$$\Delta\ell/\ell = \lambda^{\alpha,0}/3 + \lambda^{\gamma,2}[\{(\alpha_3^2 - 1/3)\, (\beta_3^2 - 1/3) + \text{cycl.}\}$$
$$+ \{2\alpha_1\alpha_2\, \beta_1\beta_2 + \text{cycl.}\}] \qquad (3)$$

From this expression, one defines the "saturated" relative change of length measured along the field direction (common to the magnetization direction) as $\lambda_s = (\Delta\ell/\ell)_\parallel^{\text{sat}} - \lambda^{\alpha,0}/3 = 2\lambda^{\gamma,2}/3$. The relative change in the plane perpendicular to the field would be $-\frac{1}{2}\lambda_s = (\Delta\ell/\ell)_\perp^{\text{sat}} - \lambda^{\alpha,0}/3$. In practice, it is necessary to measure in two perpendicular directions and determine $3\lambda_s/2 = \lambda^{\gamma,2} = [(\Delta\ell/\ell)_\parallel^{\text{sat}} - (\Delta\ell/\ell)_\perp^{\text{sat}}]$.

For uniaxial symmetry, the six strain components are subdivided into two one-dimensional subsets (indicated by the superscript α, and subscripts 1 and 2 for the volume dilatation and the axial deformation, respectively), and two different two-dimensional subsets, indicated by γ for in-plane deformations, and by ε for "skew" deformations. In this case, the magnetostriction can be expressed as

$$\Delta\ell/\ell = \lambda_1^{\alpha,0}/3 + \lambda_2^{\alpha,0}(\beta_3^2 - 1/3)$$
$$+ [\lambda_1^{\alpha,2}/3 + (3/2)\lambda_2^{\alpha,2}(\beta_3^2 - 1/3)](\alpha_3^2 - 1/3)$$
$$+ \lambda^{\gamma,2}[(1/2)\, (\beta_1^2 - \beta_2^2)\, (\alpha_1^2 - \alpha_2^2) + 2\alpha_1\alpha_2\beta_1\beta_2]$$
$$+ 2\lambda^{\varepsilon,2}(\alpha_3\alpha_2\beta_3\beta_2 + \alpha_3\alpha_1\beta_3\beta_1) \qquad (4)$$

Notice here the uniaxial deformation, $\lambda_2^{\alpha,0}$, independent of the direction of the magnetization, and the contribution to the volume magnetostriction, $\lambda_1^{\alpha,2}$, which does depend on the magnetization direction (see fig. 3 in Duc and Brommer 2002, p. 101).

At the surface of an isotropic material the symmetry is reduced from isotropic to uniaxial. The concurrent increase of the necessary number of coefficients (compare Eqns. (4) and (3)) is an example of quite a general rule. This subject is worked out in detail in, for instance, the textbooks written by Du Trémolet de Lacheisserie (1993, 1999).

Most theoretical models for surface anisotropy and magnetostriction are rather phenomenological, based on lower coordination numbers and "missing" pair interactions at the surface. *Ab initio* calculations were reported by Freeman's group (Duc and Brommer 2002, p. 105). Direct experimental evidence of surface magnetoelastic coupling was provided by measuring the strain dependence of the surface magnetization as determined by secondary-electron spin polarization spectroscopy (Duc and Brommer 2002, p. 112).

Since the surface effects contribute "per unit surface area," one defines, for a layer of thickness t, effective parameters such that B^{eff} equals $B^{\text{bulk}} + 2B^{\text{surf}}/t$. Here, the factor 2 is put in, because a layer has two surfaces. In practice, this simple $1/t$ dependence works satisfactorily. For nanocrystallites, both the volume fraction and the "volume-to-surface ratio" of the crystallites (i.e., their radii) must be taken into account.

For higher-order coupling terms, i.e., nonlinear in the strains, analogous symmetry considerations lead to the correct "group-theoretical" invariant magnetoelastic energy contributions. Sander (1999) has shown that for epitaxially grown films, second-order magnetoelastic coupling parameters must be taken into account because of the large "epitaxial" strains due to the mismatch between substrate and film (Duc and Brommer 2002, p. 105)

2. Nanoscale Heterogeneous Structures

2.1 Bulk Material (Ribbons, Thick Films)

Research on bulk giant magnetostrictive materials has been focused on iron-based rare-earth alloys, because they combine a high rare-earth concentration, thus a high magnetostriction, with a high-ordering temperature. The corresponding crystalline RCo_2 compounds are not particularly interesting for applications, because of their lower Curie temperatures: they do exhibit huge magnetostriction, but at low temperatures only.

A high room-temperature magnetostriction was found in Terfenol (polycrystalline $TbFe_2$: Ter for Tb, fe for Fe, nol for Naval Ordnance Laboratory, where it was developed). Terfenol-D (D for Dy: $Tb_xDy_{1-x}Fe_2$, where $x \approx 0.3$) exhibits a reduced magnetic anisotropy, and thus lower (but still rather high) coercivities, together with a large magnetostriction: $\lambda_s \approx 1500 \times 10^{-6}$ ($T_C \approx 650\,K$) (Duc and Brommer 2002, p. 94).

In general, various nanocrystalline structures can be obtained by suitable heat treatments: quenching, (magnetic) annealing. Moreover, the (re)crystallization process can be influenced by additives such as Nb, Mo, Zr, etc. The size of the nanocrystallites determines the surface-to-volume ratio. Combining surface effects and the bulk properties, one can, for instance, achieve low anisotropy (optimal magnetic softness) or minimal magnetostriction (transformers).

2.2 Thin Films

Thin films are often deposited (by sputtering) as an amorphous layer on a substrate. Again, suitable heat treatments can be applied to enhance the properties (e.g., in-plane or perpendicular anisotropy). By controlled recrystallization of Fe-rich amorphous alloys, a material consisting of nanocrystalline grains embedded in an amorphous matrix can be formed (see *Amorphous and Nanocrystalline Materials*). The effective magnetostriction combines the negative contribution of the crystalline phase with the positive contribution of the amorphous phase, whereas in many cases also a surface contribution must be taken into account (see, e.g., the work of Herzer, Szymczak, Ślawska-Waniewska, Żuberek, Gutierez, and others—see Duc and Brommer 2002, p. 168 *ff*).

In amorphous Fe-based thin films, the variation in the Fe–Fe interatomic distance leads to large variations (different signs) of the Fe–Fe exchange interactions, and thus to frustration and freezing of the Fe-moments in different directions: *asperomagnetism* ($M_s > 0$) or *speromagnetism* ($M_s = 0$). Because of the concurrent variation in the local easy axis for the rare-earth moment, in amorphous (Tb,Fe) both the Tb and the Fe subsystem exhibit asperomagnetism (Fig. 2), with reduced subsystem magnetization, and
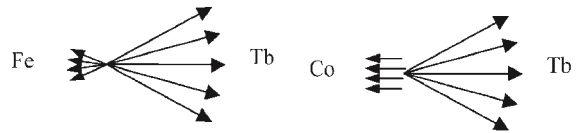
Figure 2
Sperimagnetic structure of amorphous Tb–Fe and Tb–Co.
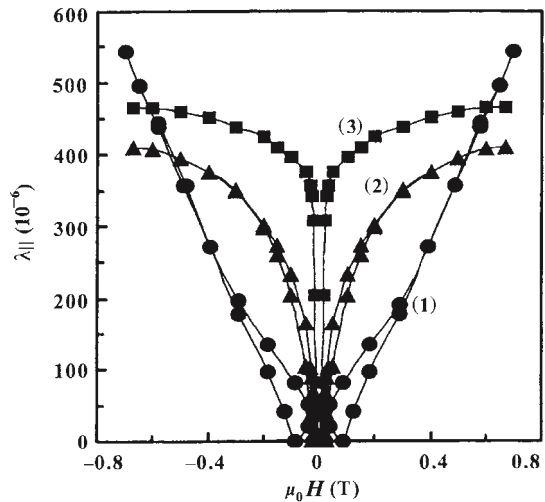
Figure 3
Parallel magnetostrictive hysteresis loops for $Tb(Fe_{0.55}Co_{0.45})_{1.5}$ films: (1) as-deposited film, (2) after annealing at $350\,°C$ and (3) at $450\,°C$ (after Duc *et al.* 2000).

hence magnetostriction. The Curie temperature is lower too. In a-(Tb,Co) only the Tb-subsystem exhibits asperomagnetism (Duc and Brommer 2002, p. 116), whereas the Curie temperature is raised. Because of the important role of the "Laboratoire Louis Néel" in their development, Duc (Duc and Brommer 2002, p. 94) proposed to refer to the a-(Tb,Co) alloys, with composition near $TbCo_2$, as "a-TerCoNéel," by an obvious analogy to TerFeNol, to amorphous Tb-$(Fe,Co)_2$ thin film ($\lambda_s \approx 1020 \times 10^{-6}$) as "a-Terfeconéel," and, adding Dy, to "a-Terfeconéel-D." In Hanoi, amorphous $Tb(Fe_{0.55}Co_{0.45})_{1.5}$, to be named "a-Terfecohan," was developed and found to exhibit already a large magnetostriction ($\lambda_\parallel \approx 340 \times 10^{-6}$) at $\mu_0 H = 20\,mT$ (Fig. 3).

2.3 Sandwich Structures

Sandwich films of the type RT/R′T/RT consist of layers with typical thicknesses of $100\,nm$. Because magnetization or anisotropy differ from one layer to

the next, magnetization reversal occurs at a different field for each layer. An *extended domain wall* (EDW) can be formed at an interface, affecting (reducing) appreciably the magnetostriction because of its relatively large volume. The exchange coupling of the layers can be suppressed by fabricating a thin oxide layer at the interface. The observed jumps in the magnetization curve of a TbCo/NdCo/TbCo sandwich (Givord *et al.*—see Duc and Brommer 2002, p. 165), and the corresponding variations of the observed magnetostriction confirm the process depicted in Fig. 4.

EDW formation has also been observed in TbFe/FeCoBSi multilayers (Quandt and Ludwig—see Duc and Brommer 2002, p. 165) with layer thickness above 20–25 nm (see below).
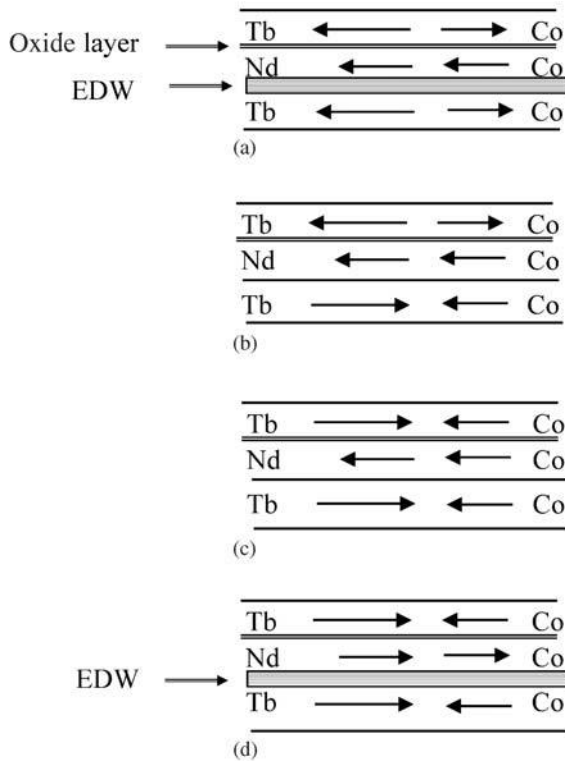
Figure 4
Occurrence of extended domain walls in a TbCo/NdCo/TbCo sandwich film during the magnetization process. A well-defined easy magnetization direction was introduced by annealing in a magnetic field. (a) High negative field: an EDW is formed at the coupling interface to match the antiparallel Co moments; (b) low negative field: the EDW is destroyed when the Co moments are parallel; (c) low positive field: the "uncoupled layer" is switched first; and (d) high positive field: the EDW is necessary again.

2.4 Multilayers

(a) Spacer layers

To reduce coercivity significantly in R–Fe alloys, the crystalline-grain size is desirable to be smaller than the Bloch wall width, i.e., below 5 nm. One can limit the grain growth by depositing, for instance, Nb-layers (0.25 nm) as spacers between 5 nm TbDy-Fe + Zr (Fisher and Winzek—see Duc and Brommer 2002, p. 139). Suitable heat treatment now results in a parallel magnetostriction of 520×10^{-6}, whereas the coercive fields stay distinctively below 100 mT.

Analogous structures may be formed in multilayers when the sharp interfaces are broadened by interdiffusion (Duc and Brommer 2002, p. 151 *ff*).

Notice, that in some cases multilayers (or multi-threaded material) can be produced by repeatedly cold rolling or extrusion (Hai *et al.* 2003).

(b) Magnetostrictive spring magnet type multilayers (MSMMs)

Magnetostrictive, spring magnet type, or rather exchange coupled, multilayers (Fig. 5) combine the large magnetostriction of, for example, a-Tb-(Fe,Co), with the desired soft-magnetic properties and the high magnetization of, for example, (nano)crystalline (Fe,Co). A huge magnetostrictive susceptibility $d\lambda_{\parallel}/dB = 13 \times 10^{-6}\,\text{T}^{-1}$ was reported for {a-Terfecohan/(nano)YFeCo} multilayers (Duc and Brommer 2002, p. 152). The layers must be thin enough (1–20 nm) to prevent EDW formation. Then, the multilayer is one magnetic unit in which the $3d-3d$ exchange interactions ensure parallel coupling of the transition metal moments, antiferromagnetically coupled with the Tb-moments (Duc and Brommer 2002, p. 140 *ff*).

For multilayers, the effective magnetostriction as a function of the thickness t of the magnetic layers has been studied extensively (Duc and Brommer 2002, p. 155 *ff*). As mentioned above, in general the effective
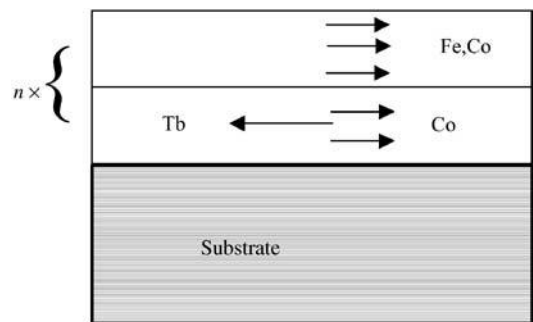
Figure 5
Schematic view of an exchange coupled MSMM (Tb,Co)/(Fe,Co). Layer thickness is 1–20 nm. The repetition number n is of the order of 100.

magnetostriction depends linearly on $1/t$, i.e., $\lambda_{\mathrm{eff}} = \lambda_{\mathrm{bulk}} + 2\lambda_{\mathrm{surf}}/t$.

2.5 Superlattices

Magnetic rare-earth superlattices R/M (M = Y, Lu) are produced by depositing a distinct number of atomic planes per layer. As an example, a $\{\mathrm{Ho}_{31}/\mathrm{Lu}_{19}\}_{50}$ superlattice has 50 layers consisting of 31 Ho and 19 Lu planes (alternatively: $[\mathrm{Ho}_{31}/\mathrm{Lu}_{19}] \times 50$). Remarkable features in these artificial structures are: (i) helical magnetic order (spin density wave) is found to propagate through the (very thin) nonmagnetic layers; (ii) due to epitaxial strains and strains caused by mismatching subsequent layers, the magneto-elastic coupling (B^{γ}) in a superlattice layer may be different from that in the bulk; and (iii) large surface effects are observed (Duc and Brommer 2002, p. 159 *ff*). A magnetic-phase diagram was constructed for $\{\mathrm{Ho}_6\mathrm{Y}_6\}_{100}$ consisting of a ferromagnetic, a fan, and a helical structure. For $\{\mathrm{Ho}_n\mathrm{Lu}_{15}\}_{50}$ superlattices, the relationship $B^{\gamma} = (B^{\gamma}_{\mathrm{vol}} + D\varepsilon)f_1(m) + 2t_{\mathrm{Ho}}^{-1}B^{\gamma}_{\mathrm{surf}}f_2(m)$ appears to describe the observed phenomena satisfactorily as a function of the Ho layer thickness, t_{Ho}, and of the reduced magnetization, m. Here $f_1(m)$ is the general function, derived by Callen and Callen (see Duc and Brommer 2002, p. 161) for a single-ion crystal field contribution, expressing the temperature dependence of the magnetostriction through the temperature dependence of m. $f_2(m)$ is taken to be proportional to m^4 at low temperatures and to m^2 at high temperatures. $B^{\gamma}_{\mathrm{vol}}(= 0.275\,\mathrm{GPa})$ has about the same value as for bulk Ho. $B^{\gamma}_{\mathrm{surf}}/(c/2)\,(= -7.0\,\mathrm{GPa}$, where c is the c-axis parameter of Ho) represents a contribution of opposite sign, large for a thin Ho layer.

2.6 Granular Composites

The recrystallized Fe-rich amorphous alloys, composed of crystalline grains embedded in a residual amorphous matrix, belong to a wide class of heterogeneous structures, ranging from organometallic complexes or metallic clusters deposited on graphite or built-in in polymers on a molecular scale, up to composites consisting of microscale grains embedded either in a metallic binder or in some resin or polymer (see, e.g., Gubin, Kosharov, Herbst, Pinkerton, Duenas, Carman—see Duc and Brommer 2002, p. 168 *ff*). These materials exhibit novel phenomena such as superparamagnetism, giant magnetoresistance, and giant magnetic coercivity (Chien, Hernando, Duc—see Duc and Brommer (2002)). On the one hand, the (nano)crystalline fraction can be manipulated in such a way that zero magnetostriction results (useful for core material), for example, in $\mathrm{Fe}_{90}\mathrm{Hf}_7\mathrm{B}_3$ (Chiriac—see Duc and Brommer (2002)) and $\mathrm{Fe}_{85.5}\mathrm{Zr}_2\mathrm{Nb}_4\mathrm{B}_{8.5}$ ribbons (Makino—see Duc and Brommer (2002)), in as-deposited Fe–Al–O and

$(\mathrm{Co}_{0.94}\mathrm{Fe}_{0.06})$–Al–O films, and, after annealing at $300\,^\circ\mathrm{C}$, also for $(\mathrm{Co}_{0.92}\mathrm{Fe}_{0.08})$–Al–O films (Ohnuma—see Duc and Brommer (2002)). On the other hand, composites containing (microscale) Terfenol-D grains in a nonmetallic binder (epoxy) may optimally have a magnetostrictive response comparable to that of Terfenol-D itself (Duenas and Carman, Armstrong—see Duc and Brommer 2002, p. 173). Such composites are durable and are easily machined into complex shapes.

2.7 Perovskite Manganites and Cobaltates

Huge magnetostriction has been found in perovskite manganites $\mathrm{R}_{1-x}\mathrm{A}_x\mathrm{MnO}_3$ (R: trivalent rare earth; A: divalent cation), cobaltates $\mathrm{R}_{1-x}\mathrm{A}_x\mathrm{CoO}_3$, and some related (doped) layered manganese oxides with formula $(\mathrm{R}_{1-y}\mathrm{A}_y)_{n+1}\mathrm{Mn}_n\mathrm{O}_{3n+1}$ (in particular the highly anisotropic, almost two-dimensional, $n = 2$ members), exhibiting CMR. Thin films of these ceramics can be produced by (pulsed) laser ablation deposition. Consequently, these materials are regarded as possible alternatives for the more conventional RT epitaxially grown thin films. Combination of CMR and magnetostriction may be useful in applications. In general, the phase diagrams are complex, showing different combinations of insulator (or semiconductor)–metal transitions, antiferromagnetic to paramagnetic or ferromagnetic transitions, charge order (influenced by doping), etc. (Duc and Brommer 2002, p. 174 *ff*). These perovskites are included here, because, in some cases, the structure is described as a nanocrystalline heterogeneous composite of ferromagnetic clusters in an antiferromagnetic (semiconducting) matrix (or the other way round).

3. Concluding Remarks

For applications, both zero-magnetostriction (soft-magnetic) materials and materials exhibiting giant magnetostrictive effects (for actuators) are of interest. Reliable magnetostrictive devices (MEMS) have been designed on the basis of Terfenol and Terfenol-D (TbDyFe$_2$). When using amorphous thin films, it is preferable to replace (some) iron by cobalt, because of the asperomagnetic nature of the Fe-subsystem. Magnetoelastic effects in thin films and multilayers are of fundamental interest too, in particular because a better understanding of the magnetoelastic coupling can be obtained by studying surface (interface) effects.

Microactuators and motors have been designed, taking advantage of wireless magnetic excitation, in first instance at room temperature (or higher temperatures). For cryogenic applications, magnetostrictive actuators require low-temperature magnetostrictive materials. In practice, $\mathrm{Tb}_{0.6}\mathrm{Dy}_{0.4}\mathrm{Zn}_1$ (Terzinol) single crystals have been used (Teter—see Duc and Brommer 2002, p. 191), but also perovskites

and rare-earth superlattices must be considered as possible candidates for such applications. Giant magnetostriction has been observed also in high T_C superconductors, e.g., in $Bi_2Sr_2CaCu_2O_8$ single crystals and $YBa_2Cu_3O_7$ ceramics (reviewed by Szymczak 1999).

See also: Magnetic Films: Anisotropy; Magnetic Layers: Anisotropy; Magnetic Microwires: Manufacture, Properties and Applications; Magnetoelastic Phenomena; Magneto-impedance Effects in Metallic Multilayers; Monolayer Films: Magnetism; Multilayers: Interlayer Coupling;

Bibliography

Du Trémolet de Lacheisserie E 1993 *Magnetostriction: Theory and Applications of Magneto-elasticity*. CRC Press, Boca Raton

Du Trémolet de Lacheisserie E 1999 *Magnetism*. Presses Universitaires de Grenoble

Duc N H, Brommer P E 2002 Magnetoelasticity in nanoscale heterogeneous magnetic materials. In: Buschow K H J (ed.) *Handbook of Magnetic Materials*. Elsevier Science, North-Holland, Amsterdam, Vol. 14, p. 89

Duc N H, Danh T M, Thanh H N, Teillet J, Liénard A 2000 Structural, magnetic, Mössbauer and magnetostrictive studies of amorphous $Tb(Fe_{0.55}Co_{0.45})_{1.5}$ films. *J. Phys.: Condens. Matter* **12**, 7957

Hai N H, Dempsey N M, Givord D 2003 Hard magnetic Fe–Pt alloys prepared by cold-deformation. *J. Magn. Magn. Mater.* **262** (3), 353

Sander D 1999 The correlation between mechanical stress and magnetic anisotropy in ultrathin films. *Rep. Progr. Phys.* **62**, 809

Szymczak H 1999 From almost zero magnetostriction to giant magnetostrictive effects: recent results. *J. Magn. Magn. Mater.* **200**, 425

P. E. Brommer and N. H. Duc
University of Amsterdam, Amsterdam
The Netherlands

Magneto-impedance Effects in Metallic Multilayers

Magnetic sensor technology is a strongly growing industry which has been satisfied in some areas by magnetoresistors, giant magnetoresistors (GMRs; see *Giant Magnetoresistance*), fluxgates and other technologies. Giant magneto-impedance (GMI) is a candidate to equal or even overtake some of these emergent sensor systems in terms of performance and lower cost (Mohri *et al.* 1995). The magneto-impedance phenomenon implying a change of the complex resistivity of a ferromagnetic conductor caused by an external magnetic field has been known for more than 50 years. However, a giant change of the impedance of more than 100%, which certain soft magnetic materials exhibit in the presence of a weak external magnetic field (less than 1–10 Oe), has been found quite recently. It was reported (Panina *et al.* 1994) that in CoFeSiB near-zero magnetostrictive amorphous wires and ribbons having a well-defined circumferential (or transverse) anisotropy, the impedance sensitivity to the direct current (d.c.) longitudinal external field is ~ 25–100%/Oe at a frequency of 1–10 MHz. It was also understood that although GMI can be considered as a high-frequency analog to GMR, it has quite a different mechanism. If GMR has a quantum origin, occurring due to a spin-dependent scattering of conductive electrons, GMI is a classical phenomenon that occurs due to a re-distribution of the alternating current (a.c.) density in a magnetic conductor subjected to an external magnetic field. Since then, the research on GMI has expanded rapidly, involving new materials such as magnetic/metallic multilayers, new concepts such as asymmetrical GMI, and excitation at higher frequencies (up to 10 GHz).

Recent progress in GMI technology is related to utilising magnetic/metallic multilayers. Using thin film materials is more preferable in a number of applications, because of compatibility with integrated circuit technology, avoiding soldering problems, and allowing miniaturization. Along with this, the principal advantage of magnetic/metallic multilayers is that the nominal values of the impedance change can be several times larger, reaching 400–600%. It has been reported (Morikawa *et al.* 1997) that in CoSiB/Cu/CoSiB multilayers of 7 μm thick, the impedance change is as large as 340% at a frequency of 10 MHz and a d.c. magnetic field of 9 Oe.

A simple three-layer sandwich film F/M/F consisting of two outer ferromagnetic layers (F) and an inner lead (M), having much higher conductivity ensures large impedance changes under the application of a d.c. magnetic field. As layers F, Co-based amorphous films or NiFe films are typically used since they have a small magnetostriction and good soft magnetic properties. Using noble metals (Cu, Ag, Au) for the inner lead M gives the necessary conductivity ratio (between layers M and F) in the range of 10–50. Since the inner conductivity is much higher, the resistance R of the total structure is determined by that for the layer M and the a.c. current mainly flows along it, whereas the magnetic layers contribute to the inductive part of the impedance. The latter can be considerably larger than R at relatively low frequencies because of a high value of the a.c. permeability which, for certain magnetic configurations, is also sensitive to the d.c. magnetic field.

The problem of calculating the impedance Z in a three-layer film F/M/F can be solved exactly accounting for the skin effect, the a.c. permeability tensor
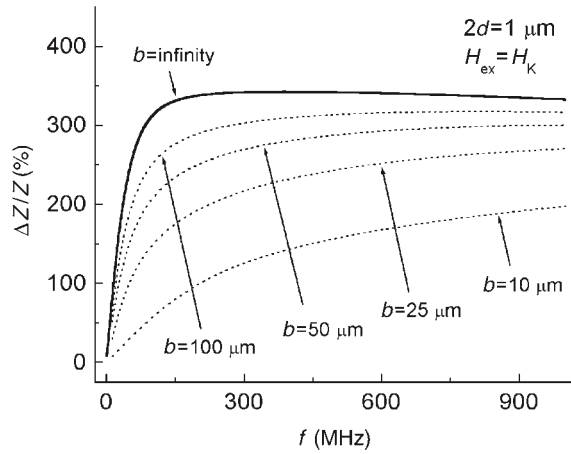
Figure 1
GMI ratio vs. frequency in a sandwich with a transverse anisotropy with the width as a parameter. The total film thickness $2d = 1\,\mu m$.

Figure 2
Real part of the impedance vs. field in NiFe/Au/NiFe films with a transverse anisotropy, $f = 450$–$500\,MHz$.

(Makhnovskiy *et al.* 2000) and the in-plane dimensions (Panina *et al.* 2001). Figure 1 shows the GMI ratio versus frequency for a transverse configuration: the easy axis of the magnetic anisotropy is transverse with respect to the a.c. current, the d.c. magnetic field H_{ex} is applied in parallel with the current. The GMI ratio, defined as a maximal impedance change ratio is expressed as $\Delta Z/Z = |Z(H_K) - Z(0)|/|Z(0)| \cdot 100\%$, where H_K is the anisotropy field. The function $|Z(H_{ex})|$ has a maximum at $H_{ex} \approx H_K$, associated with that for the rotational permeability. Therefore, the GMI ratio introduced gives the maximum impedance change. The magnetic and electric parameters taken for the calculations correspond to amorphous CoFeSiB and Cu sputtered multilayers. For a wide film (film width $b > 100\,\mu m$, thickness $2d = 1\,\mu m$), the GMI is $\sim 300\%$ in a wide frequency range above $50\,MHz$, agreeing well with the experimental data. The GMI ratio is higher for thicker films reaching 600–700% for $2d > 5\,\mu m$ and becomes only $\sim 20\%$ for $2d = 0.1\,\mu m$. With decreasing b below some critical value (depending on the transverse permeability and the thickness of the layers M and F), $\Delta Z/Z$ decreases substantially. This degradation in the GMI behavior is related with the flux leakage across the inner lead (a sort of a.c. demagnetizing). This process is similar to that resulting in a drop in the efficiency of inductive recording heads (Paton 1971).

Figure 2 presents the experimental results for impedance versus field behaviour in a sandwich film with $F = Ni_{80}Fe_{20}$ and $M = Au$. The films are deposited on a glass substrate in the presence of the d.c. transverse field of $\sim 100\,Oe$. After the deposition, the films were annealed to release the stress and finally establish the transverse anisotropy. The field

characteristics have two symmetrical maximums when the external field equals the anisotropy field ($\sim 10\,Oe$). The maximal GMI ratio is in the range of 240% for a frequency of $500\,MHz$. It is smaller than for the case shown in Fig. 1, since the conductivity ratio using NiFe films is also smaller. Yet, the sensitivity is very high ($24\%/Oe$) and using NiFe is practically more preferable.

For application in magnetic sensors, not only high sensitivity but linearity is also important. On the other hand, the characteristics shown in Fig. 2 are not only nonlinear but shaped in a way that the operation near zero field point presents considerable difficulties. A linear response can be obtained using AGMI characteristics. It was proven that in structures with an asymmetric arrangement of the static magnetization (with respect to H_{ex}), the impedance also shows an asymmetric behavior (Panina *et al.* 1999), for example, in multilayers with a cross-anisotropy in the presence of a d.c. bias current I_b (Ueno *et al.* 2000). Here, we present results for NiFe/Au/NiFe multilayers, in which the upper and bottom magnetic films were deposited in cross magnetic fields (by rotating the substrate). Releasing the stress by annealing, a cross-anisotropy film was finally produced. The AGMI characteristics obtained in the presence of the d.c. bias current are given in Fig. 3.

In summary, the GMI effect in multilayers having in principle two soft ferromagnetic films (F) sandwiching a highly conductive lead (M) has significant advantages over that in a single layer. First, the GMI ratio is several times higher ranging within 100–600% for films of 1–$10\,\mu m$ thick. Second, AGMI characteristics needed for linear sensing can be realized using cross-anisotropy films. The application of GMI multilayers in establishing new sensitive and quick response micromagnetic sensors is at an early stage of its development. However, it can be expected that
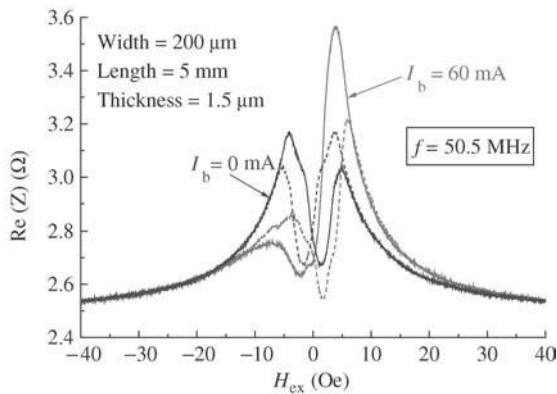
Figure 3
Real part of the impedance in NiFe/Au/NiFe multilayers with cross-anisotropy for a d.c. bias current $I_b = 0$ mA and 60 mA.

significant technical achievements in this field will be made in the foreseeable future.

See also: Amorphous and Nanocrystalline Materials; Magnetic Microwires: Manufacture, Properties and Applications; Magnets Soft; Nanocrystalline Materials: Magnetism

Bibliography

Makhnovskiy D P, Panina L V, Lagar'kov A N, Mohri K 2000 Effect of antisymmetric bias field on magneto-impedance in multilayers with crossed anisotropy. *Sensors and Actuators A* **81**, 106–10

Mohri K, Panina L V, Uchiyama T, Bushida K, Noda M 1995 Sensitive and quick response micro magnetic sensor utilizing magneto-impedance in Co-rich amorphous wires. *IEEE Trans. Magn.* **31**, 1266–75

Morikawa T, Nishibe Y, Yamadera H, Nonomura Y, Takeuchi M, Taga Y 1997 Giant magneto-impedance effects in layered thin films. *IEEE Trans. Magn.* **33**, 4367–72

Panina L V, Mohri K, Bushida K, Noda M 1994 Giant magneto-impedance and magneto-inductive effects in amorphous alloys. *J. Appl. Phys.* **76**, 6198–203

Panina L V, Makhnovskiy D P, Mohri K 1999 Mechanism of asymmetrical magneto-impedance in amorphous wires. *J. Appl. Phys.* **85**, 5444–6

Panina L V, Zarechnuk D, Makhnovskiy D P, Mapps D J 2001 2-D analysis of magneto-impedance in magnetic/metallic multilayers. *J. Appl. Phys.* **89**, 7221–3

Paton A 1971 Analysis of the efficiency of thin-film magnetic recording heads. *J. Appl. Phys.* **42**, 5868–70

Ueno K, Hiramoto H, Mohri K, Uchiyama T, Panina L V 2000 Sensitive asymmetrical MI effect in crossed anisotropy sputtered films. *IEEE Trans. Magn.* **36**, 3448–50

L. V. Panina and D. P. Makhnovskiy
University of Plymouth, UK

Magneto-optic Multilayers

The performance of magneto-optic (MO) media decreases when the wavelength is reduced, and therefore alternatives with high MO output at short wavelengths are needed. Multilayers consisting of very thin cobalt or CoNi and platinum or palladium layers have been developed for this kind of application. A part of a typical multilayer structure is depicted in Fig 1. The circles represent atoms, and the two monolayers of cobalt (4 Å) that are drawn are considered thick layers for application purposes. The stacking in a real multilayer is not perfect, and differs from this schematic representation.

Since the early 1980s elements from large sections of the periodic system have been combined to produce multilayers, which has resulted in a large number of publications. A nonmagnetic interlayer with even better Kerr enhancing properties has been found: platinum. Co/Pt multilayers have a Kerr rotation of up to $0.5°$ at about 300 nm (4.2 eV), are insensitive to corrosion, and owing to the high reflectivity they have a higher figure of merit than the rare-earth (RE) element/transition metal (TM) layers applied in contemporary MO drives. The rewritability is smaller than for RE/TM layers, owing to the higher Curie temperature of Co/Pt multilayers. This Curie temperature is between 300 °C and 400 °C for a good Co/Pt medium. Owing to the high writing temperature that is required, the layers are annealed during each writing process, which can result in a decreasing figure of merit when the material is rewritten many times. Magnetic multilayers have been actively investigated since a perpendicular magnetic anisotropy was found in Co/Pd and Co/Pt multilayers (Carcia *et al*. 1985a). MO applications of Co/Pt and Co/Pd multilayers arose at the end of the 1980s (Zeper *et al*. 1989b, Ochiai *et al*. 1989), with the study of CoNi/Pt multilayers following (Mes *et al*. 1993, Hashimoto *et al*. 1993, Van Drent 1995).
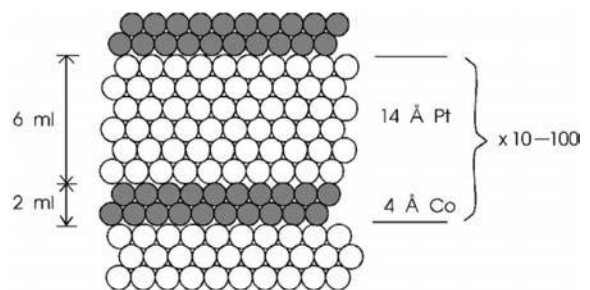
Figure 1
Schematic of part of a multilayer structure. The bilayer consisting of a cobalt and a platinum layer is repeated N times with typically $10 \leqslant N \leqslant 100$.

The Co/Pd, Co/Pt, and CoNi/Pt multilayers discussed in this article meet most of the requirements of the next generation of MO media. MO media use wavelengths from about 820 nm to 680 nm. At shorter wavelengths, the detection of smaller bits is possible as the size of the smallest light spot depends on this wavelength. Reducing the wavelength by a factor of two will increase the density by a factor of 4. Reduction of the wavelength can be achieved with a laser generating blue–green light or by frequency doubling. The Curie temperature is an important system parameter, but the media should also have a large Kerr rotation, perpendicular anisotropy, square hysteresis loop for maximum read signal, and a large coercivity to preserve the written information and allow stable small domains/bits. By tailoring the deposition process, selecting the materials, and designing the layer structure it is possible to make multilayers that feature a high MO output at short wavelengths, good magnetic properties, and a Curie temperature between 250 °C and 300 °C. A comparison between an RE/TM MO recording medium and a Co/Pt one is shown in Fig. 2 by plotting the Kerr rotation. It can be clearly seen that the rotation at smaller wavelengths is much better for the multilayer configuration.

The potential application of Co/Pt and Co/Pd multilayers has motivated numerous studies on their fundamental magnetic, MO, and practical MO recording properties. Co/Pt multilayers are more attractive for MO recording than Co/Pd multilayers because the Kerr effect of the former is larger. The perpendicular magnetic anisotropy (PMA) obtained in magnetic multilayers is mainly attributed to the interface anisotropy. A large Kerr rotation of Co/Pt multilayers at short wavelengths is attributed to polarization of platinum (Weller *et al.* 1993). A large coercivity, H_c (e.g., 3 kOe), with a square hysteresis loop can be obtained in Co/Pt multilayers by many deposition techniques, e.g., using an etched SiN_x underlayer (Suzuki *et al.* 1992). The T_c for Co/Pt multilayers is higher than that of RE/TM media, which leads to a requirement for a higher writing temperature, and results in a smaller number of write/erase cycles before film degradation occurs (Carcia *et al.* 1991a, 1991b). Therefore, it is important to reduce the Curie temperature without significantly reducing the PMA and Kerr rotation. This can be achieved by adding nickel into the cobalt layer to produce a CoNi/Pt multilayer that shows a lower Curie temperature and improved MO recording properties (Mes *et al.* 1993, Hashimoto *et al.* 1993, Hashimoto 1994). Furthermore, a key attribute of MO disks based on RE/TM alloys is their lower optical noise because of their amorphous properties. In contrast, Co/Pt multilayers are crystalline with an average grain size of about 5–10 nm, which causes disk noise as much as 5–7 dB higher than that for RE/TM media (Hashimoto *et al.* 1993). One of the sources of the disk noise is attributed to polarization variations owing to surface roughness and dispersion of the magnetization axis (Hashimoto *et al.* 1993). Therefore, to reduce disk noise, multilayers must be prepared with a smooth surface and small grains having high homogeneity and high degree of the texture along the growth direction.

1. Deposition of Multilayers

Multilayer systems as mentioned above can be prepared by vacuum deposition technologies such as e-beam deposition and sputtering. Because for commercialization a cost-effective manufacturing process is necessary the sputtering process is the most common technology.

Figure 3 shows a schematic of a (magnetron) sputtering system that has been used for the deposition of Co(Ni)/Pt(Pd) multilayers. There are more (at least two) "sputtering guns" mounted in a vacuum chamber. The sputtering guns can be operated using either radio-frequency (RF) or d.c. power. The target material is eroded from the target surface by the incoming positive inert gas ions such as argon, krypton, or xenon (purity 99.999%). Using a different sputter gas has an influence on the structure especially the interface structure of the multilayer. Heavier gas (xenon) reduces the chemical interdiffusion between the magnetic and platinum layer but increases the roughness at the interface compared with using lighter argon gas

Figure 2
Kerr rotation spectra of a 100 nm thick $Co_{22}Pt_{78}$ alloy, a $77 \times (3\,Å\,Co/10\,Å\,Pt)$ multilayer, and a 100 nm thick $Tb_{23.5}(Fe_{90}Co_{10})_{76.5}$ film (Weller *et al.* 1992a).
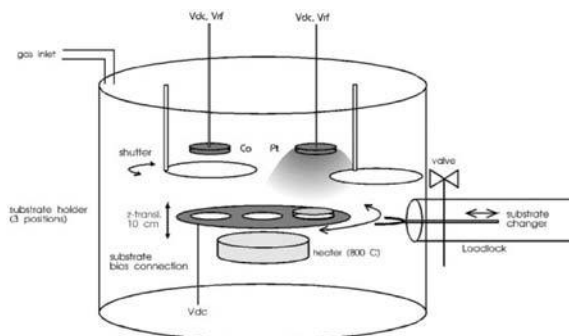
Figure 3
Schematic of the magnetron sputtering system used for the deposition of multilayers.

(Carcia *et al.* 1990, Donnet *et al.* 1996). In this system, RF sputtering leads to slow erosion compared with d.c. sputtering and gives more stable and reproducible results than d.c. sputtering. Therefore, RF sputtering has been used for thin magnetic targets (cobalt or CoNi, 1.5 mm) and d.c. sputtering for thick nonmagnetic targets (platinum and palladium, 3 mm). In most cases, a rather low power of 50 W or 100 W is applied for both RF and d.c. sputtering. For the system in Fig. 3 the frequency of the RF power supply is 13.56 MHz and the reflected power is tuned to be as low as possible (<1 W). The deposition pressure during sputtering varies from system to system. For the system in Fig. 3 most of the samples are deposited at $P_{Ar} = 1.6 \times 10^{-2}$ mbar and 4.0×10^{-2} mbar. During sputtering the substrates can be heated to a few hundred degrees. Also a d.c. bias can be applied to the substrate table to realize a bias sputter deposition that influences the thin-film growth. Moreover the substrate can be sputtered, etched and cleaned before it is deposited. A base pressure of 10^{-9} mbar can be obtained by warming the chamber with the substrate heater. The substrate can be transferred through a load-lock without breaking the vacuum of the process chamber. As a result, the process chamber can be pumped down to a base pressure better than 5×10^{-8} mbar. For sputtering as well as for e-beam evaporation the deposition rates (measured on the substrate) are 1–6 Ås^{-1}. Furthermore, the shutter time, the table rotation, and sputtering pressure are fully controlled by a computer.

2. Thin-film Growth by Sputtering

A transmission electron microscopy (TEM) cross-section of a typical CoNi/Pt multilayer is shown in Fig. 4. This multilayer structure is prepared on a silicon substrate. The first layer is a relatively thick platinum seed layer to obtain a good crystallographic orientation. For this particular purpose the multilayer
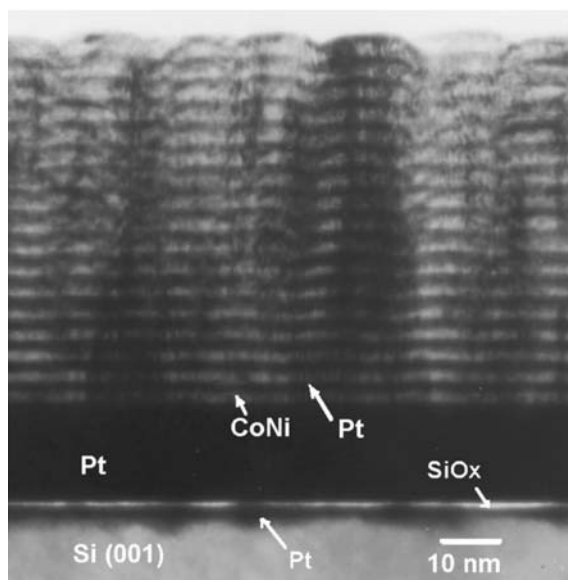
Figure 4
Typical structure of Co(Ni)/Pt multilayers. A cross-sectional TEM image of a $Co_{0.5}Ni_{0.5}$/Pt multilayer with a composition of (Si/24 nm Pt/(3.8 nm CoNi/1.5 nm Pt) × 17).

is made much thicker to demonstrate the growth more clearly. At the bottom, the layers are smooth and flat owing to the smooth and flat surfaces of the substrate and the platinum seed layer. A native SiO_x layer (a bright line) can be seen on the surface of the silicon substrate. The platinum atoms can also be seen in the silicon substrate as indicated in the dark area (platinum silicide formation). Moreover, it clearly shows that the whole stack is composed of individual CoNi (bright) and platinum layers (dark).

In the sputtering process the kinetic energy of the incident atoms plays an important role in the growth of the thin-film microstructure. Consideration of the incident flux energy should include both the sputtered atoms and the gas neutrals reflected from the target. The latter arise from ions, which are accelerated through the plasma sheath and are neutralized on reflection at the target. On their way from the target to the substrate both types of atom are thermalized in the sputtering gas. Their incident energy is therefore considerably lower than their initial kinetic energy. The degree of thermalization is strongly dependent on the deposition pressure, target to substrate distance, target composition, and sputtering gas. Following the calculations of Somekh (1984), the kinetic energy of the incident atoms has been estimated for the case of sputtering of platinum and CoNi. The results are shown in Table 1. Because there is only a small difference in the energies of sputtered platinum with respect to Co/Ni atoms, no discrimination has

Estimated energies of argon neutrals reflected from the targets, $E_{Ar,Pt}$ and $E_{Ar,CoNi}$, and of the sputtered atoms themselves, E_{atoms}, bombarding the substrate as a function of deposition pressure.

p (μbar)	$E_{Ar,Pt}$ (eV)	$E_{Ar,CoNi}$ (eV)	E_{atoms} (eV)
6	90	6	10
12	50	4	6
36	8	0.5	0.1
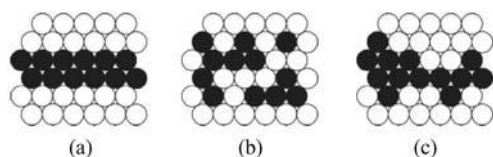
Figure 5
Schematic of three different types of interfaces in multilayers: (a) atomically sharp and smooth; (b) (non-ordered) alloyed; (c) atomically rough.

been made between these two. Clearly, the energetic bombardment of the reflected argon neutrals is dominant when depositing platinum but drastically decreases with increasing argon pressure. The energy of the deposited atoms decreases as well, by as much as two orders of magnitude over this range of argon pressure. Owing to the large variation in the energy of the incident atoms, thin-film growth can be expected to be strongly dependent on the deposition pressure, especially in the case of platinum.

In the case of CoNi/Pt multilayers, Bijker *et al.* (1996) have reported strong effects of the deposition pressure on the microstructure of the multilayers. At high deposition pressure, voids appear in the thin film. The cause of void formation is the high degree of scattering of the sputtered atoms combined with their very low kinetic energy. Obviously, the state of the interfaces in such multilayers will also depend on deposition pressure. Under high-energy bombardment at low argon pressure or at low deposition energies at high argon pressure, alloyed rough interfaces may be expected (see Fig. 5).

The interface conditions between the ferromagnetic layer (Co, CoNi) and nonferromagnetic layer (Pt, Pd) are also strongly dependent on crystallographic structure. In the case of $Co_{50}Ni_{50}$ and platinum they are both f.c.c. metals, but have a lattice mismatch of approximately 10%. Although epitaxial growth cannot be expected, a strong correlation between the textures of the two layers may exist. The interface will then be incoherent and both layers have different and/or inhomogeneous (in-plane) lattice spacing. For Co/Pt

multilayers where f.c.c. to h.c.p. phase transitions may occur in the cobalt layer, several interesting growth features have been revealed by x-ray diffraction (XRD) and high-resolution electron microscopy. Both the interface structure and the crystallographic phase are also highly dependent on the designed layer geometry (i.e., number of bilayers, individual layer thickness, with or without underlayer, etc.). The multilayer structure always exhibits additional superlattice peaks in the diffraction patterns. The periodicity is not related to the crystallographic lattice parameters but to the artificial modulation of the multilayer itself. The structures are always analyzed by both low- and high-angle XRD measurements. The low-angle patterns refer more to the chemical modulation of the multilayers owing to their longer length scale. Carcia (1988) provides information about the interdiffusion of Co/Pd and Co/Pt from low-angle XRD patterns and concludes that Co/Pd sputtered layers do have a sharper chemical interface than Co/Pt layers. The multilayers (Co/Pt, Co/Pd, and CoNi/Pt) grow preferentially with 111 f.c.c. planes normal to the direction of growth. Figure 6 shows a typical high-angle XRD pattern of a $Co_{50}Ni_{50}$/Pt multilayer deposited at an argon pressure of 12 μbar. Two peaks are observed. The largest peak is present between the Pt(111) and $Co_{50}Ni_{50}$(111) lattice positions and indicates a good (111) texture in both the platinum and $Co_{50}Ni_{50}$ layer. Since (111) texture is absent in single $Co_{50}Ni_{50}$ thin films, it may be concluded that the platinum promotes (111) texture in the $Co_{50}Ni_{50}$ layer. The origin of the "multilayer" peak is the artificial layer modulation and its position corresponds to the average lattice spacing in the multilayer.

The dependence of the texture on the deposition conditions can be discussed by analyzing various multilayers by XRD. Figure 7 shows the low-angle
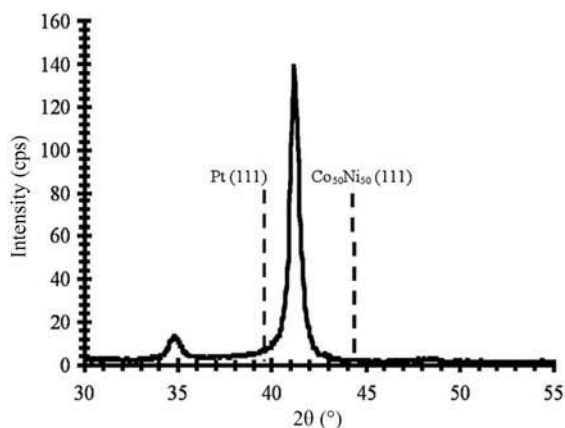
Figure 6
High-angle XRD pattern of a Pt (0.8 nm)/($Co_{50}Ni_{50}$ (0.7 nm)/Pt (0.8 nm)) $\times$ 26 multilayer.
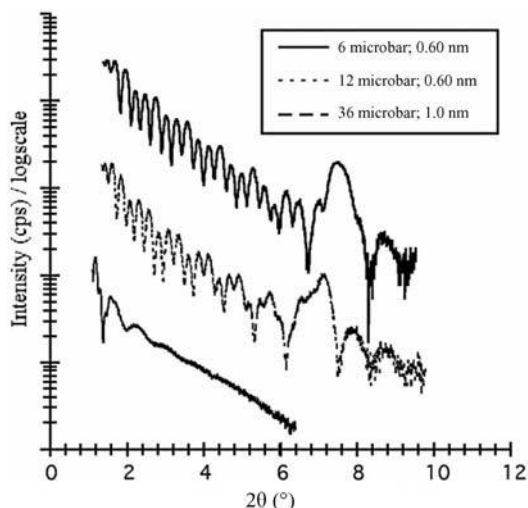
Figure 7
Low-angle XRD patterns of $Co_{50}Ni_{50}/Pt$ multilayers deposited at different pressures (6 μbar, 12 μbar, and 36 μbar and various thickness of CoNi layer as indicated in the legend).

Figure 8
High-angle XRD patterns of $Co_{50}Ni_{50}/Pt$ multilayers with $t_{CoNi} = 6$ Å. The platinum textures (1110) and (200) are indicated around $40°$ and $46°$ (for more details see text).

XRD patterns of three $Co_{50}Ni_{50}/Pt$ multilayers deposited at different argon sputter pressures. For multilayers deposited at 6 μbar and 12 μbar, the first-order Bragg peak owing to the layer modulation is clearly present. The surface roughness obtained from GIXA simulations (the glancing incidence x-ray analysis (GIXA) program is commercial software from Philips Analytical, Almelo, The Netherlands) follows the trend observed for single platinum thin films.

Figure 8 shows high-angle XRD patterns of four different multilayers with a CoNi thickness of 0.6 nm and platinum thickness of 0.7 nm and consisting of 17 multilayers. They are prepared at three different argon pressures of 6 μbar, 12 μbar, and 36 μbar on a 10 nm seed layer. The upper figure is for a sample deposited at 12 μbar, prepared without a seed layer, and consists of nine multilayers.

The diffraction patterns of multilayers deposited on platinum underlayers at 6 μbar and 12 μbar are very similar. The platinum underlayers show good (111) texture and no (200) texture is observed. The multilayers deposited on top of these underlayers also show good (111) texture. The underlayer, multilayer, and satellite peaks have approximately equal intensity. Apparently, microstructural features such as the local variations in thickness (interface roughness) and strain of the individual layers are similar in both conditions. The texture of the platinum underlayer for multilayers deposited at 36 μbar is poor and similar to that of single platinum thin films. The Pt(111) peak of the underlayer is reduced and also the Pt(200) peak is observed. Moreover, the intensity of the multilayer peak is reduced and no satellite peaks are present. This might point to a simple reduction of (111) texture of the multilayers, but also to the presence of larger interface roughness and/or different intralayer strain may contribute to this effect.

The main peak in the diffraction pattern of the multilayer without underlayer is considerably smaller than that of multilayers with underlayer. Probably, the (111) texture is less owing to the bad initial growth as reported for single platinum thin films. This may also explain why the satellite peaks are less sharp. Then, after several bilayers, the interface roughness and interlayer strain seems to be not much different from multilayers deposited with thick underlayers.

3. Magnetic Properties of Multilayers

The most import magnetic properties are magnetization, anisotropy, switching characteristics, coercivity, and the Curie temperature. These are discussed below.

3.1 Magnetization

Certain materials that are not ferromagnetic in their bulk state can become ferromagnetic if placed in close contact with a magnetic "host" material. This happens for platinum and palladium combined with cobalt. Consequently, it has been shown that the magnetization of Co/Pt and Co/Pd multilayers is

enhanced relative to the value of pure cobalt. This is not a new phenomenon because the ferromagnetic polarization of platinum and palladium in diluted alloys with cobalt and iron is well known. It has been reported that e-beam deposited Co (0.3 nm)/Pt (1 nm) layers (Lin *et al.* 1991) have 30% higher magnetization ($1850 \, \text{kAm}^{-1}$) than the pure cobalt value ($1422 \, \text{kAm}^{-1}$). Up to $0.6 \, \mu_B$ induced magnetization to interface palladium is explained in Broeder *et al.* (1987) and $0.9 \, \mu_B$ in Carcia *et al.* (1985a). The induced magnetization depends strongly on how perfect is the interface from a structural as well as from a chemical point of view. The polarization in multilayers seems to be lower than in the alloys, which can be understood by defining the multilayer as a two-dimensional structure. Being magnetic, platinum and palladium also may contribute to the MO activity. The Kerr effects measured at short wavelengths (around 300 nm or 4 eV) for Co/Pt multilayers are much larger than expected, larger even than the Kerr effects measured for a single infinitely thick cobalt layer. The enhancement cannot be attributed to multiple reflections (in the way that dielectric coatings enhance a MO layer (Gamble *et al.* 1985)) because this would result in a noticeable reduction of the reflectivity of the multilayer. Typically the reflectivity is high ($R = 0.4$–0.7 (Zeper 1991)). Another explanation could be that the cobalt layers are so thin that the effect of the reduced number of neighbors becomes apparent. The average magnetic moment per cobalt atom in the bulk is about $1.9 \, \mu_B$, but it might be influenced by the reduced symmetry. Freeman and Wu (1991) calculated enhancements of magnetic moments at the metal surfaces of cobalt, nickel, and iron. The maximum enhancement found for nickel is 23% for a f.c.c. Ni(001) surface, while for cobalt it is 13% for a f.c.c. Co(001) surface. Because very large enhancements are observed (up to a factor of 5 more rotation and ellipticity than is expected from the cobalt alone) the MO activity of platinum should also be considered.

3.2 Magnetic Anisotropy

The origin of perpendicular coercivity is found in the magnetic anisotropy. For the magnetic anisotropy representation a phenomenological formula (Carcia *et al.* 1985a, Draaisma *et al.* 1987) can be written:

$$K_{\text{eff}} = K_v + 2K_s/t_m$$

where K_{eff} is the measured effective anisotropy (including the shape anisotropy, $-\frac{1}{2}\mu_0 M_s^2$), K_v and K_s are the contributions of the volume and interfacial anisotropy of the Néel type, and t_m is the individual layer thickness of the magnetic layers. The result $K_{\text{eff}} > 0$ indicates the easy magnetization axis is perpendicular to the film surface, while $K_{\text{eff}} < 0$ indicates
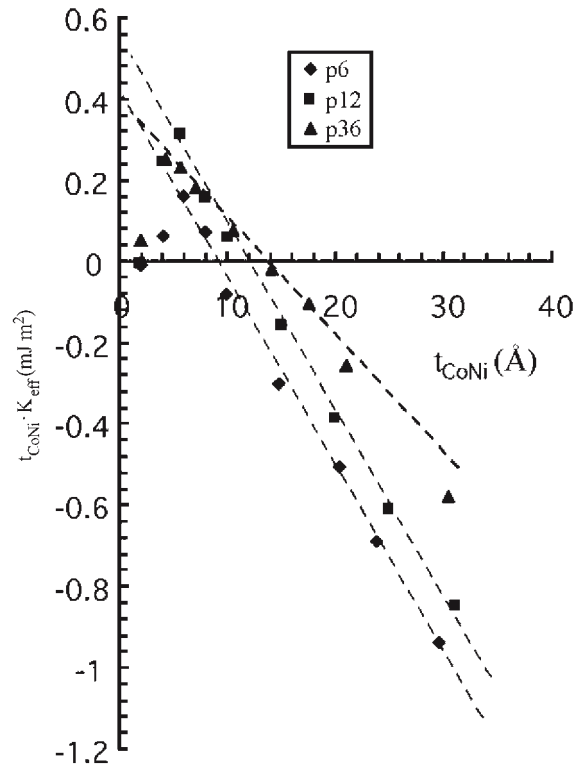
Figure 9
Effective magnetic anisotropy (expressed as) $t_{\text{CoNi}} \times K_{\text{eff}}$ vs. t_{CoNi} for multilayers sputtered with an argon pressure of $6 \, \mu\text{bar}$, $12 \, \mu\text{bar}$, and $36 \, \mu\text{bar}$.

the easy magnetization axis is in the film plane. Figure 9 shows the effective anisotropy of three types of CoNi/Pt multilayers deposited at various argon sputter pressures. They all have a platinum thickness of about 0.7 nm, a platinum seed layer thickness of 10 nm, and consist of 17 bilayers.

Compared to multilayers deposited at intermediate pressure, the interface anisotropy decreases for lower deposition pressures. This may be explained by considering the more energetic bombardment of the multilayer during growth at lower pressure (Carcia *et al.* 1990). This is in agreement with the XRD analysis where no differences between the crystallographic structure of both series is revealed. For multilayers deposited at $36 \, \mu\text{bar}$ the interface anisotropy seems to increase with t_{CoNi}. A likely explanation is the presence of significant interface roughness owing to the low deposition energies of the sputtered atoms (see Table 1). The consequence is that the effective interface area increases with t_{CoNi} and that the measured interface anisotropy should be corrected for this area. Unfortunately, this is not possible. Assuming that for $t_{\text{CoNi}} = 30 \, \text{Å}$ the measured interface

anisotropy is "saturated," it may be concluded that for pressures larger than 12 μbar the true interface anisotropy still increases with pressure. Apparently, this effect dominates the expected reduction of interface anisotropy owing to the presence of (200) grains. Note that the interface roughness is (at least) around the thickness of the platinum layer, i.e., 8 Å. Therefore, the interface anisotropy should also be corrected for the effective platinum coverage, which would give an even larger value. The interface roughness may also explain the apparent decrease of magneto-elastic anisotropy for larger t_{CoNi}. Owing to the large interface roughness and thin platinum layer, the growth of the $Co_{50}Ni_{50}$ layer may be inhomogeneous. Therefore, also strain effects may be inhomogeneous in the $Co_{50}Ni_{50}$ layer. Quantification of these effects is very difficult. The interface structure as a function of deposition pressure has been further characterized (Kirilyuk *et al.* 1998) with magnetization-induced second harmonic generation (MSHG). In general the magnitudes of K_v and K_s depend on the degree of (111) f.c.c. texture of the multilayer. This texture is promoted by using platinum seed layers between the multilayer and the substrate. The explanation of the origin of the perpendicular anisotropy in this type of multilayer is still a matter of debate, although in-depth discussions have been published (Chappert and Bruno 1988, Draaisma *et al.* 1987).

3.3 Coercivity, Nucleation, and Saturation Field

In the case of our multilayers, where the magnetization is reversed by domain wall motion, the origin of coercivity is presumably the imperfection of the layers (Honda *et al.* 1991, Suzuki *et al.* 1992). Magnetically inhomogeneous regions act as pinning centers for the domain walls and thereby hamper their movement through the layer. Suzuki *et al.* (1992) estimated the size of these pinning sites for Co/Pt multilayers with high coercivity and squareness by measurement of H_c, K_u, and M_s as function of temperature (T = 5–400 K). Using the temperature-dependent data in a simple model, Kronmüller *et al.* (1986) found a pinning site diameter of 4 Å for a sample with well-defined [111] orientation and good interfacial sharpness (determined by low- and high-angle XRD) while this diameter increased to 16 Å and 31 Å for less perfect structures. As the magnetic polarization of platinum decays quickly with the distance from the interface, the pinning sites must be located in and nearby the cobalt layers. Therefore, the values of 4 Å and 16 Å are not surprising. The 31 Å diameter pinning site estimate might be due to inhomogeneity in the film plane, in addition to the variation along the film normal (Suzuki *et al.* 1992). When the nucleation field, H_N, is large it can hide both coercivity, H_C, and saturation field, H_S (Zeper *et al.* 1991). On the left-hand side of Fig. 10 the nucleation can be clearly
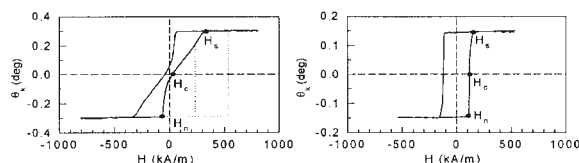
Figure 10
Kerr hysteresis loops of two multilayer samples. Left: sputtered Co/Pt multilayer with clear nucleation field, H_N, coercivity, H_C, and saturation field, H_S. The dotted lines illustrate how H_C and H_S can be hidden when the nucleation field is higher. Right: sputtered $Co_{50}Ni_{50}$/Pt multilayer with unity squareness, where H_C is hidden.

seen as large shoulders occur. At the shoulders the nucleation energy delays the creation of reversed domains. At field H_N a steep transition occurs as here the field is high (low) enough to create the first domains, which immediately stripe out to achieve the energy balance between applied field, part of the layer that is reversed, and the corresponding demagnetizing field. The dotted lines illustrate that first H_C and then H_S will be increased when the nucleation field becomes larger. When the perpendicular anisotropy is high, and the layer is very thin, the hysteresis loop is almost rectangular, as shown on the right-hand side of Fig. 10. Here the coercivity is about the same as the nucleation field. A small tail is found just before H_S and therefore it is assumed that H_S is not "hidden" in this case.

For MO recording, where most of the disk is magnetized in one direction, H_N (not H_C) has to be larger than the writing field. The rectangular ratio $r = H_N/H_C$ should be as close to unity as possible, while H_C should be large. The small pinning sites that are responsible for the coercivity are generated during the sputtering process. Extensive literature about practical rules of thumb to control coercivity is available for Co/Pt multilayers. Initial experiments produced layers with too low a coercivity (300–500 Oe or 25–40 kA m⁻¹), but several ways have been found to enhance coercivity such as by tailoring the argon pressure during deposition, growing the right seed layer, optimizing the multilayer thickness, etc. As mentioned above, the multilayers should have a perpendicular anisotropy, which means an easy axis of magnetization perpendicular to the film surface. The perpendicular anisotropy only occurs if the cobalt or CoNi layers are very thin (Carcia 1988, Carcia *et al.* 1985a, Draaisma *et al.* 1987, Meng 1996, Van Drent 1995).

Figure 11 shows the Kerr rotation hysteresis loops of one series of Co/Pt multilayers with varying cobalt layer thickness, t_{Co}, from 2 Å to 12 Å. The platinum layer thickness and number of bilayers are kept constant, i.e., $t_{Pt} = 7$ Å and $N = 9$. As shown in the loops, the magnetic properties of Co/Pt multilayers are very

787
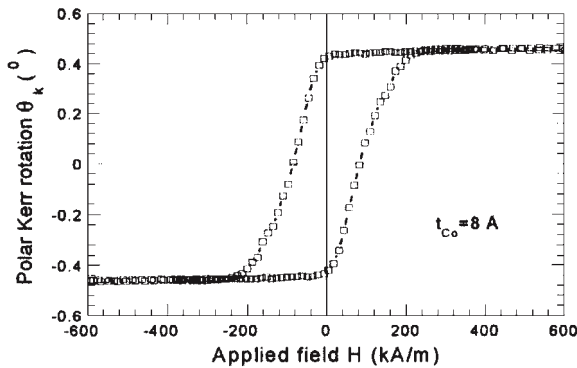
Figure 11
Polar Kerr loops of Co/Pt multilayers with varying cobalt layer thicknesses (series C). The compositions of films are (Si/16 nm Pt/(t_{Co}/7 Å Pt) × 9). The measurements are carried out at room temperature and $\lambda = 300$ nm.

sensitive to t_{Co}, which relies on the sensitivity of the PMA on t_{Co}. For thin cobalt layers the loops are square and the remanent magnetization is equal to the saturation magnetization. The perpendicular coercivity becomes smaller. Similar observations have been made for CoNi/Pt layers (Meng *et al.* 1996c).

(a) Effects of the platinum seed layer on the coercivity

The platinum seed layer contributes to the important effects that increase the perpendicular magnetic anisotropy and the perpendicular coercivity of the multilayers because of the improvement of the f.c.c. $\langle 111 \rangle$ texture (see Fig. 12) (Meng *et al.* 1996b).

Furthermore, a platinum seed layer (thicker than the Kerr information depth) is required for the measurement of the Kerr spectra in order to avoid any influence from the substrates. However, with disks for MO applications, the platinum seed layer must be as thin as possible in order to allow the light to be transmitted through the seed layer without a significant decrease in the light power on the multilayers. Much research has been devoted to the selection of the best seed layer material (Hashimoto and Ochiai 1990), and the seed layer thickness dependence of virtually every multilayer parameter (Zeper 1991). Deposition of the seed layer at elevated temperatures (Shiomi *et al.* 1993b), applying a bias voltage to the substrate table (Honda *et al.* 1991], the influence of soft etch steps on both substrates (Chang and Kryder 1994) and seed layers (Suzuki *et al.* 1992), and the application of transparent ZnO or SiN$_x$ seed layers (Carcia *et al.* 1993, Suzuki *et al.* 1992) have been reported. Transparent seed layers such as ZnO (refractive index $n \sim 2$) enable MO recording from the substrate side, and, when the seed layer thickness is properly chosen, they can act as enhancement layers.
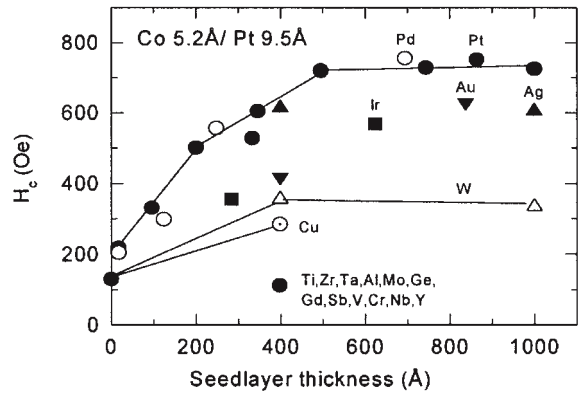
Figure 12
Dependence of coercivity on seed layer material and seed layer thickness (after Hashimoto and Ochiai 1990).
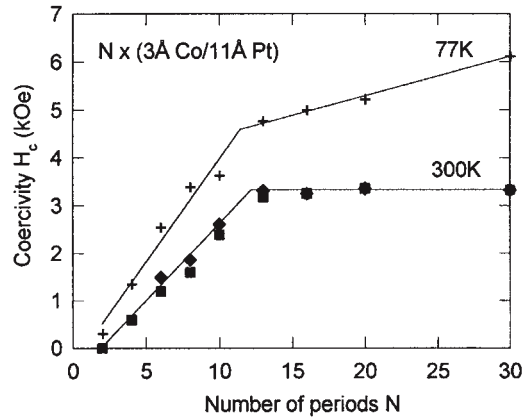
Figure 13
Thickness-dependent coercivity at 77 K and 300 K. Series of sputtered $N \times$ (3 Å Co/11 Å Pt) multilayers as a function of the number of bilayers N (2 [N] 30) measured in the perpendicular direction with polar Kerr and/or AGFM (300 K data) and VSM (77 K data) loops (Weller *et al.* 1992a).

(b) Multilayer thickness and coercivity

When the number of bilayers is increased the coercivity will generally also increase. A good example is given by Weller *et al.* (1992b) where they present the coercivity as a function of the number of bilayers, N (Fig. 13) for $N \times$ (3 Å Co/11 Å Pt) multilayers sputtered with argon at a pressure of 20 μbar on a 80 nm underlayer of SiN$_x$ sputtered at 4 μbar.

Obviously the coercivity increases fast with increasing N when $N < 13$, while it stays constant (300 K) or increases more slowly (77 K) for $N > 13$. An attempt has been made to relate the sharp kink in coercivities around $N = 13$ to the average grain size

(determined from the width of the f.c.c. (111) central Bragg peak in θ–2θ XRD) and to the degree of orientation (measured by the width, $\Delta\theta$, of the rocking curve of the same f.c.c. (111) peak). The average grain size increases smoothly from $D = 7$ nm at $N = 6$ to $D = 15$ nm at $N = 30$ and therefore there is no relationship with the grain size. $\Delta\theta$ does decrease with increasing N, and shows a weak kink between $N = 8$ and $N = 10$. Here too the correlation with H_C is not very convincing. In a study of Zeper *et al.* (1991) the slope of the coercivity vs. N also flattened above $N = 10$, but a sharp kink was not found. Also, Meng (1996) found for CoNi/Pt multilayers an increasing H_C until $N = 16$.

3.4 Curie Temperature

In the thermo-optic writing process a small spot of the medium is heated (by irradiation of laser light) to such a temperature that the coercivity is low enough that the magnetization can be switched by a small magnetic field. In ferromagnetic materials this temperature is close to the Curie temperature (T_c) and therefore T_c is taken as a design parameter, although it might be useful to define a temperature where coercivity becomes zero. A striking example is given by Lin and Do (1990) for a $23 \times (3 \text{ Å Co}/10 \text{ Å Pt})$ multilayer (see Fig. 14), where T_c is about $330\,^\circ$C while the coercivity becomes zero at about $260\,^\circ$C, a difference of $70\,^\circ$C!

Zeper *et al.* (1989a) reported differences of 15–$30\,^\circ$C for Co/Pt multilayers with comparable thickness, while this difference increased to $70\,^\circ$C for a $21 \times (3.6 \text{ Å Co}/16.3 \text{ Å Pt})$ multilayer. Carcia *et al.* (1991b) found a decrease of $30\,^\circ$C for a $(4 \text{ Å Co}/9 \text{ Å Pt})$ multilayer and $50\,^\circ$C for $(4 \text{ Å Co}/19 \text{ Å Pt})$. Apparently this difference increases with increasing interlayer thickness, so it might be attributed to a

decreasing ferromagnetic coupling between the layers. The Curie temperature should preferably be about 450–500 K (180–230 °C). At the lower end it is limited by the environment temperature range to which the medium is subjected and at the upper end by interdiffusion, and thus medium degradation (measured by write–erase cyclability experiments) becomes important. A lower T_c also decreases power requirements for the diode laser in the recorder. Bulk cobalt has a T_c of 1388 K, which is much too high for any type of thermomagnetic recording. The Curie temperatures that are reported for Co/Pt multilayers depend strongly on the layer thickness involved. The dependence on the number of bilayers, N (by coupling through the interlayers), becomes small above $N = 8$, according to a model calculation for Co/Pt multilayers (Bruno 1991). Figure 15 shows various Curie temperatures reported in the literature for Co/Pt multilayers. Here sputtered and evaporated layers with high and low N (where $N > 8$) are all shown on the same graph.

The agreement between the different data sets is generally good and apparently the different preparation methods do not influence T_c strongly. The Curie temperatures reported by Bloemen *et al.* (1991) are extrapolated from temperature-dependent measurements. These extrapolated values are much higher than the values reported by other authors. The reported T_c increases with increasing cobalt thickness. Very thin cobalt layers may not be continuous, thereby lowering M_s and thus T_c. These layers also suffer

Figure 14
Temperature dependence of normalized coercivity and saturated Kerr rotation for a $23 \times (3 \text{ Å Co}/10 \text{ Å Pt})$ multilayer (after Lin and Do 1990).
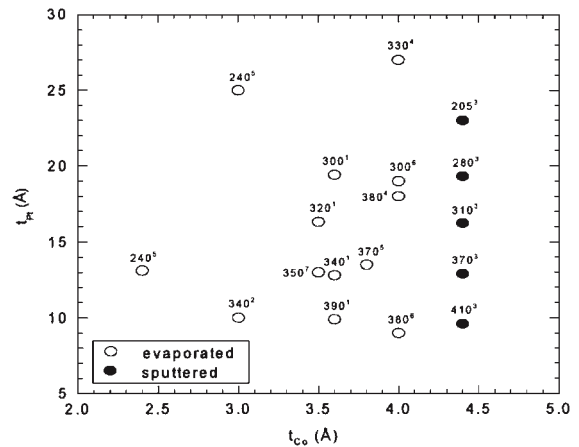
Figure 15
Curie temperatures (°C) reported in the literature for Co/Pt multilayers with varying cobalt and platinum thickness. The small figures above the temperatures denote the following references: 1, Zeper *et al.* (1989b); 2, Lin and Do (1990); 3, Hashimoto (1994); 4, Bloemen *et al.* (1991); 5, van Kesteren and Zeper (1993); 6, Carcia *et al.* 1991a); 7, Mes *et al.* (1993).

from a lower MO output. The increase of Curie temperature with increasing magnetic layer thickness is also in accordance with the random-phase approximation Green function calculations of Bruno (1991) in which he estimates the Curie temperature for ultrathin h.c.p. (0001) cobalt films as a function of the number of atomic planes. T_c of the multilayer decreases with increasing platinum thickness. For a palladium interlayer this effect can be entirely attributed to the strong ferromagnetic coupling through the interlayer, which has a strong exchange-enhanced susceptibility. This coupling is an order of magnitude smaller for platinum interlayers and therefore the strong decrease in Curie temperature with platinum layer thickness cannot be attributed to this coupling (Bruno 1991). Therefore, this platinum thickness dependence might be due to interdiffusion between cobalt and platinum, which are known to form solid solutions. When gold is chosen as the interlayer (gold is insoluble in cobalt, and therefore sharp interfaces are expected) there is almost no dependence of Curie temperature on the gold thickness (Bloemen *et al.* 1991). This result supports the interdiffusion mechanism. Co/Pt layers with good MO properties and good perpendicular anisotropy generally are composed of about 3.5–4.5 Å cobalt and 10–15 Å platinum. The T_c of such a layer is 350–400 °C. The coercivity will vanish at a lower temperature, say 50 °C lower, and therefore the layer has to be heated to 300–350 °C in the writing process. This temperature is higher than desirable. Annealing at 200 °C can lower coercivity (Lin and Do 1990), and therefore the Curie temperature should be lowered by about 100 °C. This could be done by changing the composition of the magnetic layers. This change should not drastically lower the magnetic moment of the magnetic layers because the Kerr rotation scales with the magnetic moment. One way to keep the magnetic moment high is to alloy the cobalt layers with another magnetic element. It has been found that T_c for CoNi/Pt multilayers decreases with decreasing CoNi thickness but increases with decreasing platinum thickness (Meng *et al.* 1996a).

3.5 Thermomagnetic Written Bits

Multilayer disks consisting of Co/Pt have not only been prepared in research laboratories but also commercially (Lin and Do 1990, Sumi *et al.* 1991, Zeper *et al.* 1990, and Hashimoto *et al.* 1990). In MO recording the final bit-size is determined by the properties of the media as well as the writing laser beam. The domain (bit written by laser modulation) becomes smaller as the laser power decreases. This has been measured for Co/Pt multilayer disks (e.g., Greidanus *et al.* 1989) as well as for CoNi/Pt (Meng *et al.* 1996a).

Figure 16 shows an example of written bits in a multilayer with a composition of 1.2 nm platinum
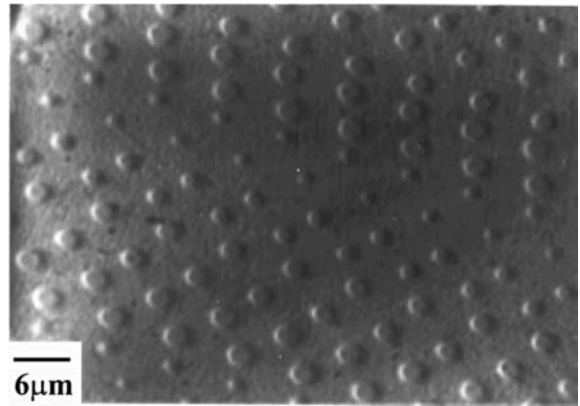
Figure 16
Lorentz microscopy image of written domains in a $Co_{0.5}Ni_{0.5}/Pt$ multilayer with a composition of 12 Å Pt/(5.5 Å CoNi/12 Å Pt) × 20 (sample I) deposited at an argon pressure of 4.0×10^{-2} mbar. The domains shown are written with laser powers of 2.5 mW, 5.0 mW, 7.5 mW, and 10 mW. The writing is performed with a pulse duration of 0.24 µs and a bias field of 50 kAm^{-1}.

seed layer (0.55 nm CoNi/1.2 nm Pt) × 20. The written domains change in size as a function of the laser power. In order to achieve regularly written domains, a large perpendicular coercivity with a square hysteresis loop is required. The optimum thickness in Co(Ni)/Pt multilayers prepared in the author's laboratory has been determined to be about t_{Co} (or $t_{CoNi}) = 5$ Å, $t_{Pt} = 10$ Å, and $N = 10$. An argon sputtering pressure of 1.6×10^{-2} mbar is preferred. The typical magnetic parameters in an optimum CoNi/Pt multilayer are $H_C = 113$ kAm^{-1}, $\Theta_{K,310} = 0.3°$, and $T_c = 255$ °C.

(a) Thermal stability

RE/TM multilayers are sensitive to oxidation while Co/Pd and Co(Ni)/Pt multilayers are very corrosion resistant. It has been shown (Hashimoto and Ochiai 1990, Zeper *et al.* 1991) that a Co/Pt multilayer does not show large changes in H_C and Kerr rotation after being stored for 200 hours at 80 °C and 75% relative humidity. Another important point is the stability of the multilayer structure during thermomagnetic writing. During writing the whole multilayer stack is heated many times locally to much higher temperatures than 80 °C. Various studies (den Broeder *et al.* 1997, Wright *et al.* 1992, Shiomi *et al.* 1993a, Meng 1996) have reported on the structural and chemical changes (diffusion) and changing of the magnetic properties as a function of annealing temperature up to 500 °C. For all multilayers a general result is that below 300 °C only very small changes are observed. Above this temperature depending on the thickness

and preparation technologies changes are reported and at temperature higher than 400 °C a large inter-diffusion takes place and perpendicular anisotropy is very much affected. In the case of CoNi/Pt multilayers two remarkable results have been found during annealing. One is enhancement of coercivity in the annealed multilayers with thinner CoNi layers. Another is enhancement of Kerr rotation in the annealed multilayers having thicker CoNi layers. Based on the reports it is advisable to choose multilayers with switching temperature below 300 °C. In the case of Co/Pt multilayers this means that the cobalt layer must be made thinner, which means that the Kerr rotation becomes smaller. CoNi/Pt multilayers are at least from these viewpoints a better solution.

4. Conclusions

The multilayer structures of Co/Pt are tested and used in very much detail for applications in short-wavelength MO recording. Research on CoNi/Pt multilayers started much later. Based on the published results a remarkable difference between Co/Pt and CoNi/Pt multilayers is the lower Curie temperature in CoNi/Pt. The lower T_c results in lower values for the magnetic properties of CoNi/Pt multilayers but thermomagnetic writing can be more easily performed than in Co/Pt multilayers. The optimal thickness for Co/Pt magnetic layers, regarding magnetic and MO properties, is about 3 Å for cobalt layers, whereas it is 5–6 Å for $Co_{50}Ni_{50}$ layers. In the Co/Pt case, the thinnest platinum layer that still gives a squareness of unity is about 5 Å for 3 Å cobalt layers, and about 7 Å for 5 Å cobalt layers (Hashimoto *et al.* 1990). In the CoNi/Pt case, thinner platinum layers could be applied (down to 2.9 Å platinum for 5 Å $Co_{40}Ni_{60}$ magnetic layers) where the perpendicular anisotropy is still high, the magnetic hysteresis loop has unity squareness and is almost rectangular. The highest Kerr rotation (Θ_K) is found for a 100 Å Pt + 17 × (5 Å $Co_{50}Ni_{50}$/5.9 Å Pt) multilayer sputtered at 40 µbar argon pressure on a Si(111) substrate. The Kerr rotation is 0.48° at 4.6 eV (270 nm), but calculations indicate (Van Drent 1995) that the peak is shifted to higher photon energies because this multilayer is optically thin. According to the calculations, the peak would be 0.46° at 3.8 eV for an optical thick layer (100 instead of 17 repetitions). The calculations also indicate that increasing the seed layer thickness of this sample from 100 Å to 400 Å will shift the peak position back to 4.0 eV, while the Kerr rotation decreases by about 0.01°. The figure of merit (FOM = $R^{1/2}|\Theta_K|$, where R is the reflectivity) is a measure of the MO performance of a given medium. The FOM for CoNi/Pt is calculated for a layer with the highest Kerr rotation.

In Fig. 17 the FOM for the thin CoNi/Pt sample is denoted by open circles. The corresponding reflectivity
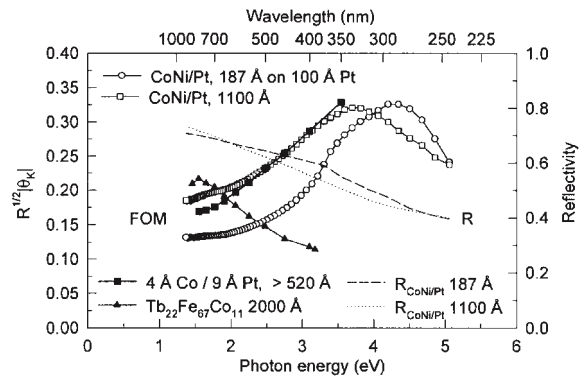
Figure 17
FOM, $R^{1/2}|\Theta_K|$, for several MO layers. Open circles denote the FOM for a 100 Å Pt + 17 × (5 Å $Co_{50}Ni_{50}$/5.9 Å Pt) multilayer on a silicon substrate. The corresponding reflectivity is denoted by the dashed line. Open squares denote the FOM for 100 instead of 17 repetitions. The dotted line denotes the corresponding reflectivity. The FOM for a N × (4 Å Co/9 Å Pt) with $N > 40$ is denoted by filled squares (Zeper 1991). The filled triangles denote the FOM for a conventional MO medium: a 2000 Å $Tb_{22}Fe_{67}Co_{11}$ layer (Hashimoto *et al.* 1990).

is drawn as a dashed line. As this sample is optically thin, comparison to other media is not straightforward. To compare several media, the media should be optically thick, without enhancement layers. Therefore the Kerr rotation, reflectivity, and FOM for a hypothetical 100-bilayer medium based on the thin CoNi/Pt sample are calculated. The MO Voigt constant of the polarized platinum is determined from the measurement data, and a prediction for the Kerr rotation and reflectivity of a 100-bilayer medium is made using this constant. The FOM for the 100-bilayer medium is denoted by open squares, the corresponding reflectivity by the dotted line (Fig. 17). For both $N = 17$ and $N = 100$ the calculated reflectivity is lower by 5–10% than the values measured by Zeper (1991) (not shown in Fig. 17).

These values are compared to the FOM for N × (4 Å Co/9 Å Pt) with $N > 40$ calculated from measured data (Zeper 1991) (filled squares). The FOMs of the Co/Pt and the 100-bilayer CoNi/Pt multilayer overlap in the region 2.4–3.3 eV (375–520 nm). At 3.5 eV the FOM of the Co/Pt multilayer is slightly higher than that for the CoNi/Pt simulation. From these results it is clear that the MO performance of CoNi/Pt multilayers can be made comparable to that of Co/Pt multilayers in the wavelength range of interest. For comparison the FOM of a 2000 Å $Tb_{22}Fe_{67}Co_{11}$ layer (Hashimoto *et al.* 1990) is drawn (filled triangles). The advantage of the multilayers at short wavelengths is evident.

See also: Magnetic Layers: Anisotropy; Magnetic Recording Technologies: Overview; Magneto-optic Recording Materials: Chemical Stability and Life Time; Magneto-optic Recording: Total Film Stack, Layer Configuration; Magneto-optics: Inter- and Intraband Transitions, Microscopic Models of

Bibliography

Bijker M D, Donnet D M, Lodder J C 1996 The effects of sputter pressure on the microstructure of CoNi/Pt multilayers. *J. Magn. Soc. Jpn.* **20** (Suppl. S1), 407–10

Bloemen P J H, de Jonge W J M, den Broeder F J A 1991 The temperature dependence of the magnetization of magnetic multilayers. *J. Magn. Magn. Mater.* **93**, 105

den Broeder F J A, Donkersloot H C, Draaisma H J G, de Jonge W J M 1987 Magnetic properties and structure of Pd/Co and Pd/Fe multilayers. *J. Appl. Phys.* **61**, 4317

den Broeder F J A, Kuiper D, Draaisma H J G 1997 Effects of annealing and ion implantation on the magnetic properties of Pd/Co multilayers containing ultrathin Co. *IEEE Trans. Magn.* **23**, 3696

Bruno P 1991 Theory of the Curie temperature of cobalt-based ferromagnetic ultrathin films and multilayers. *J. Magn. Soc. Jpn.* **15** (Suppl. S1), 15

Carcia P F 1988 Perpendicular magnetic anisotropy in Pd/Co and Pt/Co layered structures. *J. Appl. Phys.* **10**, 55066

Carcia P F, Li Z G, Reilly M, Zeper W B 1993 The magnetic and microstructural properties of Pt/Co multilayers grown on ZnO. *J. Appl. Phys.* **73**, 6424

Carcia P F, Meinhaldt A D, Suna A 1985a Perpendicular anisotropy in Co/Pd thin film layered structures. *Appl. Phys. Lett.* **47**, 178

Carcia P F, Reilly M, Zeper W B, van Kesteren H 1991a *Appl. Phys. Lett.* **58**, 191

Carcia P F, Shah S I, Zeper W P 1990 Effect of energetic bombardment on the magnetic coercivity of sputtered Pt/Co thin film multilayers. *Appl. Phys. Lett.* **56**, 2345

Carcia P F, Suna A, Onn D G, van Antwerp R 1985b Structural, magnetic and electrical properties of thin film Pd/Co layered structures. *Superlattices Microstruct.* **1**, 101

Carcia P F, Zeper W B, van Kesteren H W, Jacobs B A J, Spruit J H M 1991b Materials challenges for metal multilayers as a magneto-optic recording medium. *J. Magn. Soc. Jpn.* **15** (Suppl. S1), 151

Chang C H, Kryder M H 1994 Effect of substrate roughness on microstructure, uniaxial anisotropy and coercivity of Co/Pt multilayer thin films. *J. Appl. Phys.* **75**, 6864

Chappert C, Bruno P 1988 Magnetic anisotropy in metallic ultrathin films and related experiments on Co films. *J. Appl. Phys.* **64**, 5736

Donnet D M, Tsutsumi K, de Haan P, Lodder J C 1996 Effect of sputter gas on the physical and magnetic microstructure of Co/Cu multilayers. *J. Appl. Phys.* **79** (8), 6243–5

Draaisma H J G, de Jonge W J M, den Broeder F J A 1987 Magnetic interface anisotropy in Pd/Co and Pd/Fe multilayers. *J. Magn. Magn. Mater.* **66**, 351

Freeman A J, Wu R 1991 Electronic structure theory of surface, interface and thin-film magnetism. *J. Magn. Magn. Mater.* **100**, 497

Gamble R, Lissberger P H, Parker M R 1985 A simple analysis for the optimization of the normal polar magneto-optical Kerr effect in multilayer coatings containing a magnetic film. *IEEE Trans. Magn.* **5**, 1651–63

Greidanus F J A M, Zeper W B, Jacobs B A J, Spruit J H M, Carcia P F 1989 Magneto-optical recording in Co/Pt multilayers. *Jpn. J. Appl. Phys.* **28** (Suppl. 28–3), 37

Hashimoto S 1994 Adding elements to the Co layer in Co/Pt multilayers. *J. Appl. Phys.* **75**, 438

Hashimoto S, Maesaka A, Fujimoto K, Bessho K 1993 *J. Magn. Magn. Mater.* **121**, 471

Hashimoto S, Ochiai Y 1990 Co/Pt and Co/Pd multilayers as magneto-optical recording materials. *J. Magn. Magn. Mater.* **88**, 211

Hashimoto S, Ochiai Y, Aso K 1990 Ultrathin Co/Pt and Co/Pd multilayered films as magneto-optical recording materials. *J. Appl. Phys.* **67**, 2136

Honda S, Tanimoto H, Ago J, Nawate M, Kusuda T 1991 Origin of coercivity in Co/Pt sputtered multilayers. *J. Appl. Phys.* **70**, 6047

van Kesteren H W, Zeper W B 1993 Controlling the Curie temperature of Co/Pt magneto-optic recording media. *J. Magn. Magn. Mater.* **120**, 271

Kirilyuk A, Rasing Th, Haast M A M, Lodder J C 1998 Probing structure and magnetism of CoNi/Pt interfaces by nonlinear magneto-optics. *Appl. Phys. Lett.* **72**, 2331–3

Kronmüller H, Durst K D, Sagawa M 1986 Analysis of the magnetic hardening mechanism in RE-FeB permanent magnets. *J. Magn. Magn. Mater.* **54/57**, 1055

Lin C J, Do H V 1990 Magneto-optical recording on evaporated Co/Pt multilayer films. *IEEE Trans. Magn.* **26**, 1700

Lin C J, Gorman G L, Lee C H, Farrow R F C, Marinero E E, Do H V, Notarys H, Chien C J 1991 Magnetic structural properties of Co/Pt multilayers. *J. Magn. Magn. Mater.* **93**, 194

Meng Q 1996 Magneto-optical recording media CoNi/Pt and Co/Pt multilayers. Ph.D. thesis, University of Twente

Meng Q, van Drent W P, Lodder J C, Popma Th J A 1996a Curie temperature dependence of magnetic properties of CoNi/Pt multilayer films. *J. Magn. Magn. Mater.* **156**, 296–8

Meng Q, de Haan P, van Drent W P, Lodder J C, Popma Th J A 1996b Effects of Pt seedlayer and Air pressure on magnetic and structural properties of sputtered CoNi/Pt multilayers. *IEEE Trans. Magn.* **32** (5), 4064–6

Meng Q, Lodder J C, Popma Th J A 1996c Magneto-optic Kerr spectroscopy of CoNi/Pt and Co/Pt multilayers. *J. Magn. Soc. Jpn.* **20** (Suppl. S1), 287–90

Mes M, Lodder J C, Takahata T, Moritani I, Imamura N 1993 $Co_xNi_{(1-x)}$/Pt multilayers for magneto-optical recording. *J. Magn. Soc. Jpn.* **17** (Suppl. S1), 44

Ochiai Y, Hashimoto S, Aso K 1989 *IEEE Trans. Magn.* **25**, 3755

Shiomi S, Nakabayashi T, Okada M, Kobayashi T, Masuda M 1993a Magnetic properties and structure of Co/Pt multilayer films evaporated on heated substrates. *Jpn. J. Appl. Phys.* **32**, 791

Shiomi S, Nishimura T, Kobayashi T, Masuda M 1993b Dependence of magnetic properties of Co/Pt multilayers on deposition temperature of Pt buffer layers. *Jpn. J. Appl. Phys.* **32**, L495

Somekh R E 1984 The thermalization of energetic atoms during the sputtering process. *J. Vac. Sci. Technol. B* **2**, 1285–91

Sumi S, Tanase K, Torazawa K, Tsunashima S, Uchiyama S 1991 Multilayer Pt/Co magneto-optic disk. *IEEE Trans. J. Magn. Jap.* **6**, 141

Suzuki T, Notarys H, Dobbertin D C, Lin C J, Weller D, Miller D C, Gorman G 1992 Coercivity mechanism and microstructure of (Co/Pt) multilayers. *IEEE Trans. Magn.* **28**, 2754

Van Drent W 1995 CoNi/Pt multilayers for magneto-optical recording. Ph.D. thesis, University of Twente

Weller D, Brandle H, Gorman G, Lin C J, Notarys H 1992a *Appl. Phys. Lett.* **61**, 2726

Weller D, Farrow R F C, Marks R F, Harp G R, Notarys H, Gorman G 1993 *Mast. Res. Soc. Symp. Proc.* **313**, 791

Weller D, Notarys H, Suzuki T, Gorman G, Logan T, McFadyen I, Chien C J 1992b Thickness dependent coercivity in sputtered Co/Pt multilayers. *IEEE Trans. Magn.* **28**, 2500

Wright C D, Glegg W W, Boudjemultilayerine A, Heyes N A E, Grundy P J, Pollard R J, Greaves S J, Petford-Long A K, Kim Y H, Jakubovics J P 1992 Micro-annealing studies of Pt/Co multilayers for magneto-optic recording applications. *IEEE Trans. Magn.* **28**, 2671

Zeper W B 1991 Magneto-optical recording media based on Co/Pt multilayers. Ph.D thesis, University of Twente

Zeper W B, Greidanus F J A M, Carcia P F 1989a Evaporated Co/Pt layered structures for magneto-optical recording. *IEEE Trans. Magn.* **25**, 3764

Zeper W B, Greidanus F J A M, Carcia P F, Fincher C R 1989b *J. Appl. Phys.* **65**, 4971

Zeper W B, Greidanus F J A M, van Kesteren H W, Jacobs B A J, Spruit J H M, Carcia P F 1990 Co/Pt and Co/Pd multilayers as a new class of Magneto-optical recording materials. *SPIE* **1274**, 282

Zeper W B, van Kesteren H W, Jacobs B A J, Spruit J H M, Carcia P F 1991 Hysteresis, microstructure and magneto-optical recording in Co/Pt and Co/Pd multilayers. *J. Appl. Phys.* **70**, 2264

J. C. Lodder
University of Twente, Enschede, The Netherlands

Magneto-optic Recording Materials: Chemical Stability and Life Time

Thin amorphous rare earth transition metal (RETM) alloys such as (Gd,Tb)–(Fe,Co) and (Gd,Dy)–(Fe,Co) are commonly used as a storage layer in the field of magneto-optical (MO) data storage. These alloys exhibit very good recording properties such as high carrier-to-noise ratio (CNR) and low required write/erase laser powers and fields (Raasch 1993, Raasch *et al.* 1994a, 1994b). Amorphous layers can be prepared by rapid quenching from a liquid phase, evaporation, or sputtering and show a 5–15% lesser density than their crystalline counterparts, depending on composition and preparation conditions (Klahn *et al.* 1990). Amorphous layers have no grain boundaries and composition can be varied continuously. Their advantages compared to polycrystalline materials led to the technical breakthrough of RETM layers in the field of MO data storage. The storage capacity of MO disks has been dramatically increased compared to the first products in 1988. This trend will continue over the next years opening a wide range of applications. The long-term stability is one essential requirement for storage layers.

The stability of RETM films is endangered by crystallization of the amorphous phase, by structural relaxation processes within the amorphous phase, and by selective reactions of the rare earth (RE) atoms, where oxygen is the most critical element. Degradation processes can be monitored by the change of important magnetic properties such as magnetic anisotropy K_u, required magnetic field to reverse the magnetization H_c, Curie temperature T_C, compensation temperature T_{comp}, and saturation magnetization M_s as a function of aging time. The general dependencies of those parameters on composition and preparation conditions are listed in Landolt–Börnstein (Hansen 1988).

1. Crystallization and Structural Relaxation of Thin Amorphous RETM Layers

The amorphous phase is a metastable state, of which the free energy E_{am} is larger than that of the crystalline state E_{cr}. This energy difference is the reason for a phase transition towards the crystalline phase, but a reduction of E_{am} may not result in a better stability. Furthermore, the mobility of atoms, represented by the activation energy dE, dominates the stability of the amorphous phase. For instance, a $Gd_{0.62}Co_{0.38}$ alloy exhibited $dE = 3.3\,\text{eV}$ while $E_{am} - E_{cr} = 0.4\,\text{eV}$ (Buschow 1985). The required energy for atomic rearrangement follows the sequence transition metal (TM) = Fe, Mn, Co, and Ni as well as going from RE = La to RE = Lu. For $RE_{1-x}TM_x$ alloys (RE = Gd, Tb; TM = Fe, Co) with $x = 0.3–0.8$, T_{cr} ranges between 500 K and 900 K with a maximum of $x = 0.35$ ($T_{cr} = 600\,\text{K}$) for Gd–Co alloys (Hansen 1988) and of $x = 0.70$ ($T_{cr} = 900\,\text{K}$) for magnetron-sputtered GdTb–Fe alloys (Klahn *et al.* 1987). The higher T_{cr} of Fe alloys contradicts the former expectations and shows the importance of the preparation process.

It must be taken into consideration that layers sputtered at low argon pressure exhibit an ideal amorphous structure with a small number of crystallization grains and a density close to crystalline layers resulting in a reduced mobility of atoms (Klahn *et al.* 1990). In addition, the heating rate influences T_{cr} which will decrease with decreasing heating rate. The correlation between both parameters is described by Kissinger (1957). A contribution of heating rate implies the possibility of structural changes within the amorphous phase below T_{cr}. These processes are known as structural relaxation processes effecting the near range ordering due to a limited atomic mobility. It is very difficult to comment on the importance of structural relaxation on stability of RETM alloys because this effect has to be separated from oxidation. Nevertheless, Klahn *et al.* (1987) found that structural relaxation mainly affect the coercive energy (required energy to reverse the magnetization), while

other magnetic properties remained nearly constant. This process performs on a logarithmic time scale. The required time to half the coercive energy on an aging temperature of $150\,^\circ\text{C}$ was estimated to be about 17 years though for lower temperatures it would be much longer.

2. Corrosion Kinetics of Thin Amorphous RETM Layers

A large number of elements are able to react with a bare RETM layer. As oxygen is the most critical element, this article will be mainly restricted to oxygen. Klahn *et al.* (1987, 1990) prepared unprotected GdTb–Fe layers of 100 nm thickness on glass substrates by magnetron sputtering and oxidized the samples in a hot dry climate chamber. Oxygen depth profiles were determined after 15 hours by secondary-ion mass spectroscopy (SIMS) as a function of aging temperature. Directly after preparation the layers exhibited a surface oxide layer of about 10 nm thickness consisting of Tb_2O_3 and α-Fe_2O_3. Beneath the surface, a layer was detected with an oxygen saturation level of 25%, enough to oxidize the RE atoms completely and not effecting the TM atoms. The thickness of this partially oxidized layer increases with time and temperature. The remaining layer is magnetically still unaffected. The binding energies for RE–O (Gd–O, $716\,\text{kJmol}^{-1}$; Tb–O, $707\,\text{kJmol}^{-1}$; and Dy–O, $611\,\text{kJmol}^{-1}$) are much larger than for TM–O (Fe–O, $410\,\text{kJmol}^{-1}$ and Co–O, $368\,\text{kJmol}^{-1}$) (Weast 1976). This leads to a strong preference of oxidation of the RE atoms. The energy differences enable a reduction of oxidized TM atoms by RE atoms. Saito *et al.* (1986) established that the oxide of GdTb–Fe consists of RE oxide and b.c.c. Fe clusters.

If the oxygen exposure at higher temperatures continues after complete oxidation of the RE atoms the totally oxidized surface layer will grow into the particular oxidized bulk. The oxidation process can be characterized by an Arrhenian temperature dependency with an activation energy $E_a = 0.3 \pm 0.1\,\text{eV}$, which shows only a weak dependency on composition and preparation (Klahn *et al.* 1990). The oxidation speed decreases considerably with increasing Co content. The most affected quantity is the magnetic anisotropy. Mergel *et al.* (1993) listed data of different additives and its influence on K_u, where a distinction between additives with a metallic bond and those with covalent bonds has to be made. An addition of only 2 at.% oxygen or 4–8 at.% nitrogen will destroy the anisotropy totally. Instead of this, up to 20 at.% of Bi, Pb, Al, Be, or Cr are still acceptable from this point of view (see Sect. 3). Nevertheless, a dilution of the magnetic system will effect T_C, T_{comp}, M_s, and Kerr rotation. The influence of several common additives regarding magnetic and recording properties is discussed elsewhere in more detail (Raasch *et al.* 1995, Raasch 1996).

3. Aging Behavior of Magneto-optical Storage Disks

The weak chemical stability of RETM layers requires additional measures to enhance the environmental stability of the MO layer stack, especially when the MO layers are grown on plastic substrates. Two methods can be applied separately or simultaneously: (i) the use of protective layers, such as SiN or AlN or (ii) doping active elements directly to magnetic layers in order to protect them from further corrosion by passivation of chemical reactions with air or water. If protective layers are grown perfectly, a long-term stability of more than 50 years is obtained. The possibility of local defects within these layers will cause corrosion of the MO layer and can be prevented by using a limited amount of additives though this must be restricted to elements with a metal bond. The magnetism of RETM alloys is caused by the localized $4f$ electrons of the RE and the delocalized $3d$ electrons of TM. Therefore, a differentiation must be made between elements with partly and fully occupied d shells. The addition of metals with partly occupied d shell (Ti, Cr, Nb, Zr, Hf, Ta, and Pt) shows positive effects on the chemical stability. But the large negative effect on the magnetic properties, such as T_C and Kerr rotation, can not be compensated. Elements with fully occupied d shells (Be, Al, and In) show only a minor influence on magnetic properties. In particular, TbFeCo–In layers with In contents of up to 25 at.% exhibit sufficient magnetic properties. Therefore, recording performance simultaneously to a substantial improved environmental stability compared to nondoped RETM layers (Raasch 1996), proven for 150 hours at $85\,^\circ\text{C}$ and 85% relative humidity. The later values represent common accelerated aging test conditions.

See also: Amorphous and Nanocrystalline Materials; Magnetic Films: Anisotropy; Magneto-optical Disks: Thermal Effects; Magneto-optic Recording: Total Film Stack, Layer Configuration

Bibliography

Buschow K H J 1985 Research on amorphous alloys. *Philips Tech. Rev.* **42**, 48–57

Hansen P 1988 Numerical data and functional relationships in science and technology. Crystalline and amorphous films with rare earth and 3d transition elements In: Wijn H P J (ed.) *Landolt–Börnstein*. Springer, Berlin, New Series III 19, pp. 136–287

Kissinger H E 1957 Reaction kinetics in differential thermal analysis. *Anal. Chem.* **29**, 1702–6

Klahn S, Bentin H, Knörr B, Heitmann H, Wilting H 1990 Oxidation kinetics and morphology of dc magnetron sputtered and evaporated amorphous GdTbFe films. *J. Appl. Phys.* **67**, 1442–8

Klahn S, Hartmann M, Witter K, Heitmann H 1987 Structural relaxation and surface induced aging effects of amorphous

GdTbFe films. In: Hernando A, Madurga V, Sanchéz-Trujillo M C, Vazquez M (eds.) *Magnetic Properties of Amorphous Metals*. Elsevier, Amsterdam, pp. 176–8

Mergel D, Heitmann H, Hansen P 1993 Pseudocrystalline model of the magnetic anisotropy in amorphous rare earth transition metal thin films. *Phys. Rev. B* **47**, 882–91

Raasch D 1993 Recording characteristics of Dy–FeCo-based magneto-optical disks in comparison to other MO materials. *IEEE Trans. Magn.* **29**, 34–40

Raasch D 1996 Magnetic and recording properties of amorphous TbFeCo–In thin films. *J. Appl. Phys.* **80**, 2964–7

Raasch D, Bernards J P C, Clausen C, Much G 1995 Magnetic and magneto-optical properties of Tb–FeCo–Cr layers. *J. Magn. Magn. Mater.* **148**, 359–60

Raasch D, Hansen P, Mergel D 1994a Bloch wall energy in (Tb, Nd)–(Fe, Co) thin films. *J. Appl. Phys.* **76**, 8022–4

Raasch D, Reck J, Mathieu C, Hillebrands B 1994b Exchange stiffness constant and wall energy density of amorphous GdTb–FeCo thin films. *J. Appl. Phys.* **76**, 1145–9

Saito N, Togami Y, Morishita T, Sato R 1986 Changes of structure and magnetization of amorphous rare earth transition metal films by annealing. *Jpn. J. Appl. Phys.* **25**, L850–2

Weast R C 1976 *Handbook of Chemistry and Physics*. CRC Press, Cleveland, OH

D. Raasch
Philips Research Laboratories, Aachen, Germany

Magneto-optic Recording: Overwrite and Associated Problems

In the thermomagnetic write process, the magnetic storage layer is locally heated to its Curie temperature (T_C) by a focused laser beam. A magnetic domain is formed during cooling with its magnetization parallel to the direction of the external write field. This process is assisted by the demagnetizing field. Two modes to write information are applied: magnetic field modulation (MFM) and laser intensity modulation (LIM). With MFM, the laser power is kept constant and the magnetic field is switched according to the bit stream. The main issue here is to get sufficiently fast field switching (Lin 1990). With LIM, the laser intensity is modulated under constant external magnetic field. The data rate is higher than with MFM. However, only new domains are written. The old domains have to be erased before, in a separate run, so that there is no direct overwrite.

Two main schemes have been proposed to achieve direct overwrite with laser intensity modulation (LIM–DOW). Both use specifically designed storage media, i.e., a single layer with suitable magnetic properties and exchange-coupled multiple layers (ECMLs), respectively. Circular domains in an exchange-coupled double layer, ECDL, are sketched in Fig. 1.
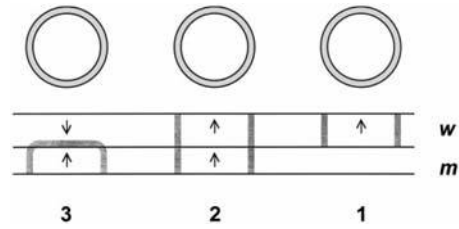
Figure 1
Circular magnetic domains in an exchange-coupled double layer consisting of a write layer *w* and a memory layer *m*. Top view and cross-section. The numbers designate the three steps in DOW.

1. Force Equilibrium at the Domain Wall

The total energy of a cylindrical domain is given by the sum of three energies: wall energy, Zeeman, and demagnetizing energy (Mergel 2000). The radial forces on the domain wall are obtained by differentiating with respect to the radial coordinate r. The pressure on the wall, i.e., the force f_t per unit area of domain wall, is obtained by dividing the radial force by $2\pi r h$, where h is the height of the domain, i.e., in general the thickness of the corresponding layer:

$$f_t = 2\mu_0 M_s[H_a(r) + H_{d1}(r) + (H_{d2}(r))]$$
$$- \left[\frac{\sigma_w}{r} + \frac{\partial \sigma_w}{\partial r} + \left(\frac{\sigma_i}{h}\right)\right] \quad (1)$$

The resulting expressions have the dimension of energy density. The first square brackets enclose the external write field, H_a, and the demagnetizing fields, H_{d1}, due to the domain in one layer, and H_{d2} if there is a second layer. H_{d2} favors parallel orientation of the magnetization in the two layers. The demagnetizing field, H_{d1}, always acts expanding and is given by:

$$H_{d1}(r) = M_s\left(\frac{1}{1 + 3r/2h}\right) \quad (2)$$

Under LIM–DOW conditions, the applied field, H_a, always represents an expanding force. Domain erasure is driven by the contracting wall forces summarized in the second set of square brackets in Eqn. (1). The last term in Eqn. (1), (σ_i/h), arises from an interface wall and has only to be taken into account in exchange-coupled layers.

2. Single-layer DOW

In a single layer, Eqn. (1) applies without the terms $(H_{d2}(r))$ and (σ_i/h). The collapse of domains is achieved by heating to a temperature where the contracting domain wall forces overcome the sum of the

expanding forces, due to the demagnetizing and external write fields, and the coercive field. This is possible if the coercive forces are only moderate, e.g., for GdTb–FeCo, but not for Tb–FeCo, the standard composition. Domain erasure is fostered when the underlayers that are deposited onto the disk before the MO layer are polished because then the wall pinning strength is reduced. Furthermore, the demagnetizing field must be small. The best performance (CNR = 32 dB) in a standard recorder was obtained for 24–25 at.% rare-earth content yielding low magnetization at the erase temperature (Schultz *et al.* 1993).

The principle of single-layer DOW leads to a dilemma. For erasure, on the one hand, the domain walls have to move. During the write process, on the other hand, they must not move because moving domain walls become jagged and increase the write noise (Mergel 2000). This dilemma leads to contradicting requirements for the different steps of recording which could not be solved. For easy and complete domain erasure, materials with low coercive field and low magnetization are needed. Then, however, a write field higher than specified for standard recorders, 200 Oe (16 kAm^{-1}), is needed in order to write domain patterns with a high signal-to-noise ratio. The high field is necessary to assure a force equilibrium with $f_t = 0$ during domain formation in the write process. If $f_t \neq 0$ and the coercive field is low, the domain walls move. However, moving domains become jagged. The write noise increases and the storage density is reduced. Therefore, attempts to achieve a sufficiently high signal-to-noise ratio under realistic recording conditions failed and single-layer DOW has not been implemented on practical disks.

3. DOW in an Exchange-coupled Double Layer

Domains in an exchange-coupled double layer (ECDL) are thermomagnetically created in the three steps illustrated in Fig. 1. An ECDL for direct overwrite consists of a *write layer*, w, into which domains are thermomagnetically written during the write process (step 1) and a *memory layer*, m, into which the domains are copied during cooling below its T_C (step 2). Now common domains extend through both layers. The original domains in the write layer are then erased at room temperature by an initializing field, H_{ini}, of several kOe provided by a permanent magnet (step 3). The reversal of the magnetization of the write layer creates magnetic interface walls.

Domain erasure is supported by the existence of an interface wall. The term (σ_i/h) in Eqn. (1) represents the strongest contracting force due to the small value of h as compared to r. The write temperature is above the T_C of the memory layer, m, such that there is no interface wall during the write process. The contracting forces are much smaller than during erasure such that the dilemma of single-layer overwrite is avoided.
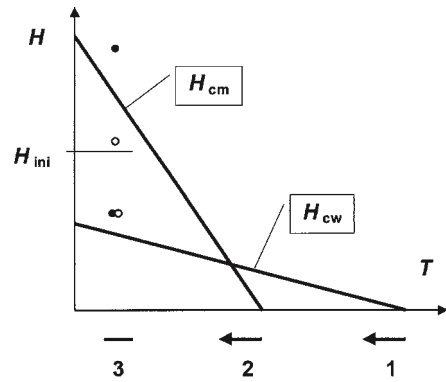
Figure 2
Coercive field of the two layers, write layer, w, and memory layer, m, in an ECDL that allows direct overwrite. The temperature regions of the three steps of DOW are indicated below the T axis. The open circles refer to a P-ECDL and the closed circles refer to an A-ECDL (compare Fig. 4).

Such a write mechanism is possible if there is a cross-over of the $H_c = H_c(T)$ curves of the two layers, as illustrated in Fig. 2 (Saito 2000). At room temperature, the initializing field, H_{ini}, must be between the critical switching fields for the two layers. The creation and annihilation of the interface walls modifies the limits of the write (H_{write}) and initializing (H_{ini}) fields as will be discussed later.

Direct overwrite is achieved by switching the laser power between an erase and a write level. At the erase level, the magnetic layers are heated to a temperature where the coercive energy of the storage layer is reduced below the interface wall energy. The domains are annihilated by outside-in wall motion. At the write level, new domains are written into the write layer.

In order to control the exchange coupling, a thin intermediate layer is interposed between the storage and the write layer. A material with small anisotropy constant, K_u, is chosen such that the wall energy, $\sigma = 4\sqrt{(AK_u)}$, becomes smaller than in the adjacent layers. Then, the interface wall is located the intermediate layer. This allows a wider range of compositions of the other layers. The thickness of the intermediate layer is about 10 nm corresponding to typical wall thicknesses in RE–TM alloys (Mergel 2000).

4. Exchange-coupled Multilayers with a Permanent Magnetic Layer

The external initializing magnet in step 3 can be replaced by an additional permanent magnetic layer, p. The essential parameters of a typical layer stack for such a case are summarized in Table 1 Tsutsumi

Table 1
Composition and properties of a LIM–DOW multilayer.

Layer	Composition	Thickness (nm)	T_C (°C)	H_c (kOe)
m, memory	$Tb_{24}Fe_{70}Co_6$	30	200	12
i, intermediate	$Gd_{32}Fe_{48}Co_{20}$	10		
w, writing	$Dy_{25}Fe_{51}Co_{24}$	30	280	10
s, switching	$Tb_{17}Fe_{79}Co_4$	10	170	2
p, permanent, initializing	$Tb_{24}Fe_{17}Co_{59}$	30	>300	8

Source: Tsutsumi (1993).

Figure 3
Hysteresis loop of an exchange-coupled double layer (b). Single layers (a) layer 1 and (c) layer 2.

(1993). The layer, p, is separated from the write layer, w, by a switching layer, s, that couples w and p when room temperature is approached. The switching layer has a low T_C so that p is decoupled from w during the write process. There are constraints on the thickness of the layers. The total stack should not be thicker than 150 nm to assure sufficient write sensitivity. The thickness of the memory layer should be bigger than 30 nm in order for the MO readout signal not to be affected by the other layers.

5. Reversal Mechanisms in Exchange-coupled Layers

So far, the principal mechanisms of LIM–DOW have been explained. For a discussion of associated problems, the phenomena occurring in exchange-coupled multilayers must be discussed in more detail (Mergel 1993, 2000, Tsunashima 2000, Kobayashi *et al.* 1981).

The reversal mechanisms in ECDLs are complicated. A great variety of hysteresis loops are observed. They are determined by the interface wall energy density, σ_i, the magnetization, M_{sz}, the coercive field, H_{cz}, and the thickness, d_z, of the layers. The different layers are denoted by the index, z. A magnetic reversal takes place when the balance of coercive, Zeeman, and wall energy densities yields a negative value:

$$0 > 2\mu_0 d_z(H_{cz} + v|H_a|)M_{sz} + w\sigma_i, (v, w = \pm 1) \quad (3)$$

$$0 > (H_{cz} + v|H_a|) + wH_{\sigma z} \quad (4)$$

$$H_{\sigma z} = \frac{\sigma_i}{2\mu_0 d_z M_{sz}} \quad (5)$$

with $v = +1$ or -1 when the magnetization is rotated against [ag] or into [in] the external field, respectively, and with $w = +1$ or -1 when an interface wall is created [c] or annihilated [a] by the process, respectively.

The abbreviations in the square brackets [a, c, ag, in] are used to designate magnetic reversal processes. Eqns. (3) and (4) can only be fulfilled when v

or w or both are negative. Three processes are, therefore, allowed and all play a role in LIM–DOW (Mergel 1993)

(i) [c, in, z] Creation of an interface wall by rotation of M_s into the external field.

(ii) [a, in, z] Annihilation of the interface wall with rotation of M_s of layer z into the external field.

(iii) [a, ag, z] Annihilation of the interface wall with rotation of M_s against the external field.

An example of a hysteresis loop of an ECDL is given in Fig. 3(c). The isolated layers are represented by (a) and (b). When the two layers are exchange coupled the following changes may be observed:

(i) Reversal of layer 1 by [a, in, 1] may occur by motion of the interface wall. In such a case, the hysteresis curve becomes sheared.

(ii) The reversal fields are shifted to lower or higher values because domain walls are annihilated or created, respectively.

(iii) Minor loops are not symmetric to zero field but are centered around a value given by

$$H_a = \frac{\sigma_i}{\mu_0 M_{sz} d_z} \quad (6)$$

where M_{sz} and d_z are magnetization and thickness, respectively, of the reversing layer, z. The first two effects have to be taken into account when predicting recording properties of ECDLs from the properties of the isolated layers. The interface wall energy can be determined from Eqn. (6).

In ferrimagnetic RE–TM alloys, the TM moments alone determine the exchange-coupling whereas the magnetization, M_s, that interacts with the external magnetic field, is given by the difference of the TM and RE submagnetizations ($M_{TM} - M_{RE}$). This defines two types of ECDLs (see Fig. 4), A and P. In P-type double layers, M_s is parallel or antiparallel to M_{TM} in both layers. In A-type double layers, M_s is
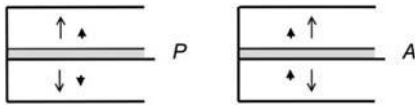
Figure 4
Two types of ECDLs, A and P, based on ferrimagnetic materials. The thin and bold arrows refer to the TM moments and the total magnetization, respectively.

parallel to M_{TM} only in one layer and interface walls exist at infinite external field.

We now apply the reversal systematics to derive the conditions for the LIM–DOW mechanism in ECDLs.

Writing: Avoid [a, ag, w]
Copying: Enable [a, in, m] for P or [a, ag, m] for A, respectively.
Initialization: Enable [c, in, w]: $H_{ini} > H_{cw} + H_{\sigma w}$
Stable domains after initialization:
Avoid [a, in, m], $H_{ini} < H_{cm} - H_{\sigma m}$ for P, inside a circular domain
Avoid [c, in, m], $H_{ini} < H_{cm} + H_{\sigma m}$ for A, outside a circular domain.

The restrictions for the initialization field are indicated in Fig. 2 by circles. The upper limit is higher for A-ECDLs.

6. Media Design

In order to achieve reliable operation, the composition and the thickness of the various layers in a LIM–DOW medium have to be chosen appropriately. In the following, the requirements for the design of a five-layer stack and their implications for the chemical composition of suited RE–TM alloys are schematically summarized. For a typical example see Table 1.

In the memory layer, m, the domains must remain stable under the high initializing field. This implies a high H_c which is achieved by choosing terbium as the dominant rare-earth element. Terbium has a strong spin-orbit coupling that leads to a large anisotropy constant, K_u. H_c increases with K_u with a power between 0.5 and 4. The T_C in the memory layer, m, must be lower than in the write layer, w. Cobalt has a stronger exchange-coupling than iron and leads to a higher T_C in RE–TM alloys. Therefore, w, contains more cobalt than m.

The intermediate layer must have a small wall energy in order for the interface wall to be situated in this layer. This is achieved by a high gadolinium content. Due to lack of spin orbit coupling, gadolinium leads to a low anisotropy constant, K_u, and a low interface wall energy, $\sigma_i = 4\sqrt{(AK_u)}$.

In the write layer, the force on the domain wall must be small during the write process in order to avoid domain wall motion that leads to jagged
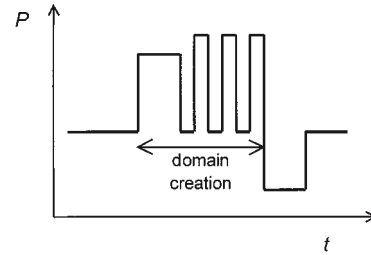
Figure 5
Laser power modulation pattern for DOW on ECMLs in order to avoid thermal interference.

domain boundaries. Dy–FeCo is easily optimized to meet these requirements (Raasch 1993).

The initializing layer must keep a permanent magnetization. A high H_c and a high T_C are needed. They are obtained by high concentrations of terbium and cobalt.

7. Write Pulse Modulation

The temperature profile on the disk is influenced by heat flow from neighboring marks written before or after the considered mark. Therefore, the mark shape depends on the information pattern, and more domain length jitter is generated. This decreases the signal-to-noise ratio and consequently the storage density. The problem could be solved by modifying the modulation scheme of the laser power as shown in Fig. 5 (Saito 2000, Sect. 8.3.5). An assisting power is applied, heating the track to a medium temperature, and shutoff for some time after a domain has been written. This reduces the additionally introduced heat when a domain is written. The write pulse is replaced by a sequence of short pulses such that the write process takes place at a lower temperature.

8. Concluding Remarks

The principle of single-layer DOW leads to contradicting requirements for the different steps of recording. For erasure, on the one hand, the domain walls have to move. During the write process, on the other hand, they should not move because moving domain walls become jagged and increase the write noise. This dilemma could not be solved and the attempts to achieve a sufficiently high signal-to-noise ratio under realistic recording conditions failed.

A typical layer stack for DOW in exchange-coupled layers comprises five layers: a write, a memory, and an initializing layer together with two intermediate layers. The initializing layer has a permanent magnetization. Domain erasure is supported by an interface wall between the write and the memory layer. During the write process, the write layer is magnetically

decoupled from both the initializing and the memory layer and the dilemma of single-layer DOW is avoided.

The relevant magnetic properties like T_C and magnetic wall energy density can be tuned separately for every layer by the composition of the RE–TM alloys. Therefore, overwrite with ECMLs can be implemented in practical disks and yields a good recording performance.

See also: Magneto-optical Disks: Thermal Effects; Magneto-optic Multilayers; Magneto-optic Recording: Total Film Stack, Layer Configuration; Magneto-optical Effects, Enhancement of; Magnetic Recording Technologies: Overview; Super-resolution: Optical and Magnetic Techniques

Bibliography

Gambino R J, Suzuki T (eds.) 2000 *Magneto-optical Recording Materials*. IEEE Press, Piscataway, NJ
Kobayashi T, Tsuji H, Tsunashima S, Uchiyama S 1981 Magnetization process of exchange-coupled ferrimagnetic double-layered films. *Jpn. J. Appl. Phys.* **20**, 2089
Lin C J 1990 Critical assessment of the physics underlying direct overwrite in magneto-optic recording. *J. Appl. Phys.* **67**, 4409–14
Mergel D 1993 Magnetic reversal processes in exchange-coupled double layers. *J. Appl. Phys.* **74**, 4072
Mergel D 2000 Domain dynamics and recording physics. In: Gambino R J, Suzuki T (eds.) *Magneto-optical Recording Materials*. IEEE Press, Piscataway, NJ
Raasch D 1993 Recording characteristics of Dy–FeCo-based magneto-optical disks in comparison to other MO materials. *IEEE Trans. Magn.* **29**, 34
Saito J 2000 Light-intensity modulation direct-overwrite. In: Gambino R J, Suzuki T (eds.) *Magneto-optical Recording Materials*. IEEE Press, Piscataway, NJ, Chap. 8
Schultz M D, Kryder M H, Sekiya M, Chiba K 1993 True direct overwrite in single layer magneto-optical recording. *IEEE Trans. Magn.* **32**, 3772
Tsunashima S 2000 Exchange-coupled films. In: Gambino R J, Suzuki T (eds.) *Magneto-optical Recording Materials*. IEEE press, Piscataway, USA, Chap. 7
Tsutsumi K 1993 Direct overwrite materials for magneto-optical recording. *J. Magn. Magn. Mater.* **120**, 247–53

D. Mergel
Universität Essen, Germany

Magneto-optic Recording: Total Film Stack, Layer Configuration

The currently used rare-earth transition-metal (RE–TM) recording media suffer from two main disadvantages: the RE elements oxidize easily and the polar Kerr effect and consequently the signal strength of the magneto-optic readout decrease significantly at shorter wavelengths. Pt/Co multilayers have advantages relative to RE–TM media in both aspects.

The larger Kerr effect of Pt/Co below a wavelength of 450 nm promises a higher storage density in future recording with blue lasers. However, the recording performance is also determined by several other properties:

- the write sensitivity within the specified ranges of the magnetic field and the laser power
- the magnetic stability of the written domains
- the noise level to get a high signal-to-noise ratio and low error rates
- degradation of the disk after repeated read/write cycles (see *Magneto-optic Recording Materials: Chemical Stability and Life Time*).

In this article, the recording-relevant properties of Pt/Co multilayers are discussed and compared with those of RE–TM media.

1. Magnetic Properties of Pt/Co Multilayers in Comparison with those of RE–TM Films

The saturation magnetization M_s and the coercive field H_c of Pt/Co multilayers are displayed in Fig. 1 as a function of temperature together with M_s of a typical amorphous RE–TM film.

Pt/Co multilayers generally exhibit a higher T_C than amorphous RE–TM films. They need a higher laser power for the thermomagnetic write process and their signal-to-noise ratio of written domains degrades more rapidly with the number of write/erase
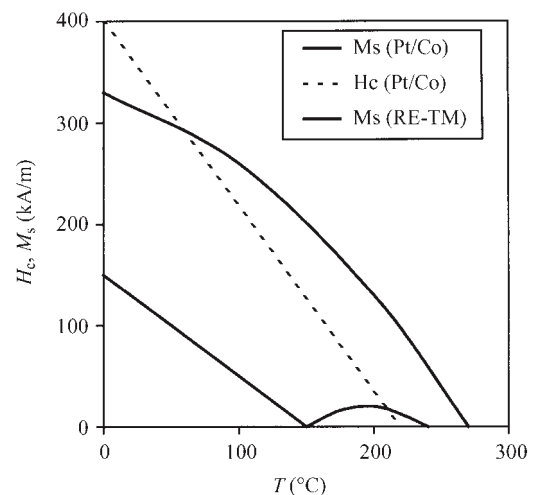
Figure 1
Saturation magnetization M_s and coercive field H_c of a typical (Pt/Co) multilayer as a function of the temperature. For comparison, $M_s(T)$ of a typical RE–TM composition is also shown.

cycles. The Pt layers are typically 0.9 nm thick (five atomic layers). Reducing their thickness lowers T_C, as desired, but also the Kerr angle Θ_K due to less magnetic matter in the total film and thus diminishes the potential advantage of the (Pt/Co) multilayers. Reducing T_C by alloying Ni to Co avoids this problem but still reduces Θ_K at the readout temperature by about 25%.

The M_s of Pt/Co is larger than that of the RE–TM alloys used for MO recording. This leads to stronger demagnetizing effects. The magnetic domains tend to form subdomains and their boundary tends to become curved. Both effects increase the noise of written marks (the write noise). The magnetization of the ferrimagnetic RE–TM alloys is controlled by the choice of the compensation temperature where $M_s = 0$.

The coercive field H_c of Pt/Co multilayers vanishes at about 50 °C below T_C. Wall motion during the first stage of the cooling in the thermomagnetic write process is to be expected. This is a principal disadvantage for recording because wall motion results in jagged domain boundaries and in an increase of the domain length jitter (Mergel 2000, Sect. 6.6).

For MO readout the magnetization must be perpendicular to the substrate. The effective perpendicular anisotropy constant K_{eff} achieves its maximum when the Co layer thickness corresponds to two atomic layers (0.4 nm). In that case all the Co atoms are forming part of Pt/Co interfaces. It was found that a pronounced (111)-f.c.c. texture of the multilayer is needed to get a large K_{eff} but is alone not sufficient. The most decisive feature is the sharpness of the interfaces (Bertero and Sinclair 1994). Any chemical intermixing reduces K_{eff}.

The magnetization M_s, the Kerr angle Θ_K, the Curie temperature T_C, and to a large extent, the anisotropy constant K_{eff} are material properties determined on the subnanometer scale whereas the strength of H_c is strongly determined by the microstructure of the films on the 10 nm scale.

Large values of H_c are obtained for exchange-decoupled grains in combination with a large K_{eff}. The exchange-decoupling can be achieved by a discontinuous microstructure or when the grain boundaries consist of a nonmagnetic phase.

K_{eff} and H_c are sensitive to the details of the deposition process. Evaporated films are characterized by a pronounced (111)-f.c.c. texture with flat interfaces leading to a high K_{eff}. Furthermore, they exhibit a porous columnar structure with physically separated, exchange-decoupled columns or grains so that H_c is large.

The microstructure of Ar-sputtered films is strongly influenced by energetic bombardment by reflected (at Pt) Ar neutrals. This leads to a low H_c due to a dense structure and to a low K_{eff} due to irregular interfaces between Pt and Co (Bertero and Sinclair 1994). Better results are obtained when the films are sputtered with the heavier noble gases Kr or Xe, leading to less severe bombardment, or when they are deposited on well chosen and prepared underlayers.

2. Influence of Underlayers on the Microstructure

A cross-section of a typical MO disk is shown in Fig. 2. There is a capping layer only in some disk designs. Usually a protective layer is deposited on top of the layer stack.

2.1 Pt Underlayers

Pt/Co multilayers exhibit good properties when grown as a (111)-f.c.c. stacking sequence. As the stable phase of Co at room temperature is h.c.p., growth must start with a Pt layer. The thicker this underlayer, the better the (111) texture. However, for substrate-incident readout, the underlayer reduces the signal due to absorption. To give an example, a 5.5 nm thick Pt underlayer diminishes the readout signal (carrier) by 3.5 dB (van Kesteren et al. 1991).

The best magnetic properties of Ar-sputtered (at 1.6 Pa) Pt/Co multilayers were obtained on ultrathin (d_{Pt} about 3 nm), discontinuous Pt underlayers (Carcia et al. 1996). The latter were prepared by d.c. magnetron sputtering followed by ion etching under an rf-bias field. The largest H_c (3.5 kAm^{-1}) and the largest K_{eff} (1.2×10^7 erg cm^{-3}, 1.2 MJ m^{-3}) were obtained for $d_{Pt} = 3.3$ nm before etching. For this thickness the most pronounced superstructure features were observed in x-ray diffractograms. The microstructure of the (Pt/Co) film comprised small (10–20 nm) grains separated by voids and resembled that observed in vapor-deposited films. The etching of the underlayer likely sputtered away some Pt atoms leaving behind highly (111) textured and flat Pt
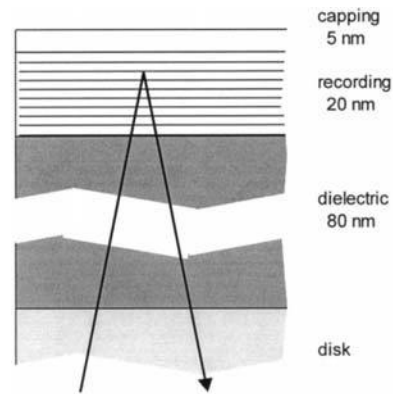
Figure 2
Layer stack comprising a (Pt/Co) recording layer. Not all disk designs comprise a capping layer. There is generally a protection layer on top of the stack.

mesas that served as independent nucleation centers for the multilayers.

For thicker or thinner underlayers the Pt/Co multilayers are structurally less coherent. On thicker underlayers the surface structure becomes continuous. When the underlayers are thinner, the grains are separated but the surface becomes very rough.

2.2 Dielectric Layers

The stack design usually contains a dielectric layer with an index of refraction $n \approx 2$ to get an enhancement of the magneto-optic effects by interference. For RE–TM media only nitrides like Si_3N_4 or AlN can be used due to the tendency of the RE elements to oxidize. For Pt/Co, oxides are also possible and ZnO and In_2O_3 have been attempted. The dielectric underlayers influence the magnetic properties of the Pt/Co multilayers deposited on them. K_{eff} increased to more than 7×10^6 erg cm^{-3} (0.7 MJ m^{-3}) when the underlayer (ZnO and In_2O_3) was sputter-etched at -100 V (Carcia and Suzuki 2000).

ZnO is the most effective in creating a (111)-f.c.c. texture and prevents degradation of the recording properties upon annealing above 300 °C. It has a hexagonal structure and grows preferentially with its c axis (0001) perpendicular to the substrate. The mismatch between the ZnO(0001) and the (Pt/Co)(111) f.c.c. planes is only 1.6% and the multilayers grow epitaxially on ZnO.

The structural and magnetic properties of sputtered (Pt/Co) multilayers depend on the ZnO deposition temperature T_{ZnO} (Carcia *et al.* 1993). K_{eff} was maximum when ZnO was deposited at 150 °C. For $T_{ZnO} \leqslant 200$ °C a continuous microstructure was observed and the magnetic reversal was by wall motion. For $T_{ZnO} = 500$ °C the microstructure is particulate with a better (111)-f.c.c. texture and the magnetization reverses by coherent rotation within the separated grains. However, the perpendicular anisotropy is reduced, correlated with a severe multilayer roughening. This proves that the quality of layering is more important for a large K_{eff} than the texture.

3. Magnetization Reversal

3.1 Magnetic After-effect

In magnetic after-effect experiments, a magnetically saturated specimen is subjected to an inverse magnetic field with a value smaller than H_c and the magnetic relaxation (slow reversal) is observed as a function of the lag time.

For $(Co_{0.6}Ni_{0.4})[0.5 \text{ nm}]Pt[\geqslant 0.6 \text{ nm}]$ multilayers sputtered on a Pt buffer layer, the magnetic after-effect depends on the sputter pressure (Meng *et al.* 1999). Sputtering at low Ar pressure results in dense films. The reversal is dominated by wall motion indicating that the wall propagation field is smaller than the nucleation field. The magnetization pattern is characterized by concatenated small domains. In discontinuous films, grown at high Ar-pressure, a homogeneous nucleation all over the film is observed. Domain wall motion is inhibited and the magnetization reversal occurs by coherent rotation in the isolated grains. The hysteresis curves are sheared, according to the distribution of nucleation energies.

3.2 Mark Structures

The marks in Pt/Co layers can be investigated by scanning magnetic force microscopy (van Kesteren *et al.* 1991). In this technique, a ferromagnetic tip is scanned across the object surface to obtain an image of the magnetization pattern. Pt/Co layers are well suited because they need no protection layer, in contrast to RE–TM layers. This has the advantage that the parameters measured in a recorder, namely the writing conditions and the carrier and noise levels, can be directly related to the magnetic microstructure of the domains on the same disk.

For layers with high magnetization, marks were written even without an applied field, a consequence of the demagnetizing field in the heated area. They contained subdomains because the decrease of the magnetostatic energy is larger than the increase of the total wall energy. Subdomains decrease the readout signal. They furthermore lead to fluctuations in the readout signal and an increase of the write noise. With increasing external field, the subdomains disappear, the carrier increases, and the noise decreases.

For laser intensity modulation, a uniform magnetization of the written marks was only observed for an external write field $H_{ext} > 30$ kA m^{-1} (375 Oe). On these disks, magnetic field modulation always produced irregular domains. This was attributed to the lack of a wall gradient force. The wall gradient force is due to the temperature profile and tends to shift the domain wall into regions of higher temperature, i.e., to the center of the hot spot. This effect balances the expanding demagnetizing force and favors circular domains. For constant laser power, the temperature gradient is much smaller than for modulated laser power.

4. Recording Experiments

In order to estimate the recording performance of a disk, a *carrier* is written. A carrier consists of periodically written marks and produces a signal with 50% duty cycle (up and down signal have the same length). The readout signal is analyzed in a spectrum analyzer. The carrier-to-noise ratio (CNR) is determined as the ratio of the signal and the noise at the write frequency. It depends on the linear velocity of the disk and the residual bandwidth of the spectrum analyzer.
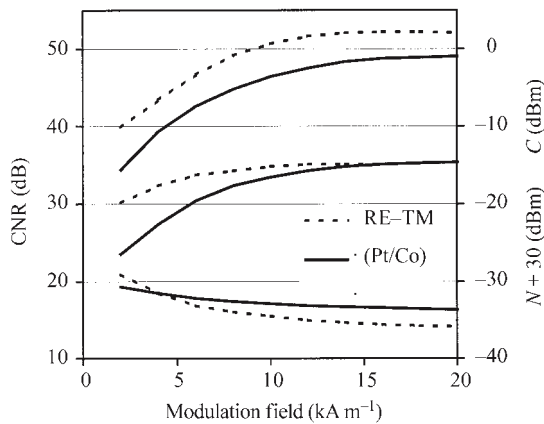
Figure 3
Carrier *C* and noise *N* of a Pt/Co and a GdDyFeCo medium. Laser wavelength 780 nm. Schematically after Teragaki *et al.* (1993).

4.1 Magnetic Field Sensitivity

In Fig. 3, the recording performance of (Pt/Co) and GdDyFeCo media is compared (Teragaki *et al.* 1993). The carrier of Pt/Co saturates at a higher modulation field, 200 Oe (16 kA m^{-1}), instead of 100 Oe (8 kAm^{-1}) for GdDyFeCo. The reason is the higher M_s leading to stronger demagnetizing effects. The higher magnetic field H_{wr} is necessary to obtain complete marks without subdomains although the magnetic reversal starts at a lower field due to a higher Zeeman energy $\mu_0 M_s H_a$.

A high magnetic field sensitivity was obtained in high-M_s films when the formation of subdomains was suppressed by a thin (2–5 nm) RE–TM capping layer, RE-rich and with a high T_C (>280 °C, Ishida *et al.* 1997). This works for $Tb_{14}Fe_{82}Co_4$ ($H_{wr} = 100$ Oe) and for Pt/Co (140 Oe). The CNR obtained with a light wavelength $\lambda = 680$ nm was 2 dB higher for the RE–TM medium. The ferrimagnetic RE–TM-based media have the advantage that the magnetization in the recording relevant temperature region can be optimized towards best recording performance by the choice of the compensation and the Curie temperatures.

4.2 Competition of Carrier-to-noise Ratios

For Pt/Co multilayers, the readout signal at smaller wavelengths is higher than for conventional RE–TM alloys due to a stronger Kerr effect. However, this does not imply automatically a better performance of Pt/Co media and a higher storage density on these media in "blue" recording. The performance of a drive-medium system depends not only on the signal level but also on the various noise levels of the disk and the system noise.
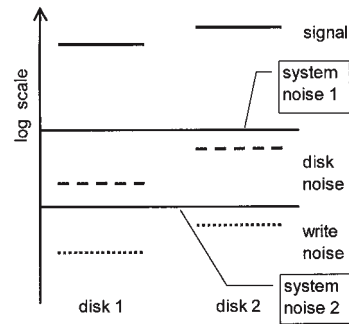
Figure 4
Comparison of signal and noise levels for two competing MO media. Disk 1 has the higher signal level whereas disk 2 has the lower disk noise level. It depends on the level of the system noise which disk exhibits the higher CNR. The CNR is given by the distance between the signal and the highest noise level.

A competition between two disk families, one with a higher signal level, the other with a lower medium noise level is illustrated in Fig. 4. For a large system noise ("1"), disk 2 with the higher signal level yields a relatively better performance, whereas disk 1 with the lower medium noise performs better for a lower system noise ("2"). Therefore, the various noise sources have to be considered in detail when predictions on the recording performance of a medium class are made.

4.3 Noise Sources

The *system noise* is measured on a stationary disk and arises from the light source, the detector, and the electronic circuit. In the first recording experiments with a green laser, the detector noise was initially very strong but its influence on the CNR could be reduced by increasing the laser intensity. Later a specially designed PIN photodetector with a high sensitivity was used (Kaneko *et al.* 1993).

The *disk noise* is the difference between the noise of the rotating and the stationary disk in a magnetically initialized state without magnetic marks. It originates from fluctuations of the polarization due to spatial fluctuations of the magneto-optical properties of the recording layer or due to the roughness of underlayers or the substrate. In Fig. 3, the disk noise is larger for the Pt/Co medium. This is due to additional polarization noise introduced by a nonperfect (111) texture of grain orientations.

The *write noise* is the additional noise measured on a rotating disk with written marks. Both subdomains in the mark and irregularities of the mark edge contribute to the write noise. A higher write noise is expected for Pt/Co media because the domain length jitter is about 40 nm (Teragaki *et al.* 1993) compared

to 15 nm in the best RE–TM media (see Mergel 2000).

The sum of write and disk noise is called *medium noise*. It arises from geometrical irregularities on the disk. As it is readout by the optical system, it is subjected to the optical transfer function. As a consequence, the CNR depends on the mark length that determines the spatial frequency at which the CNR is measured. This effect is important when judging the relative performance of RE–TM and (Pt/Co) media. For marks shorter than 0.5 μm, Pt/Co performs better because the medium noise is suppressed below the system noise by the optical transfer function (Kaneko *et al.* 1993). This corresponds to "system noise 1" in Fig. 4. RE–TM performs better for longer marks due to a lower medium noise, "system noise 2." Therefore, RE–TM media are expected to perform better even for shorter marks when the system noise is reduced (Mergel 2000).

5. Concluding Remarks

Pt/Co media exhibit a high magnetization such that a higher magnetic field is necessary to suppress demagnetizing effects and to obtain saturated marks. The modulation field can be reduced by a thin RE–TM capping layer with high T_C on top of the recording layer. Then, however, the advantage of intrinsic corrosion resistance is lost.

A discontinuous microstructure with exchange-decoupled grains is necessary to obtain a high coercive field H_c. This can be achieved by ion-etched Pt nucleation layers on top of the dielectric layer. Ion-etched dielectric underlayers can promote the spatial coherence and the flatness of the interfaces of Pt/Co multilayers, the key feature to obtain a large perpendicular magnetic anisotropy. ZnO is especially effective because the mismatch of the lattices is only 1.6% and enables heteroepitaxial growth.

The higher signal level of Pt/Co for shorter wavelengths is counteracted by a currently higher medium noise level, both relative to RE–TM. In such a situation, the measured signal-to-noise ratios depend on the details of the recording and readout process. The currently reported domain length jitter is 40 nm as compared to 15 nm for RE–TM resulting in a higher write noise. Therefore, a higher storage density than for RE–TM media cannot be expected in "blue" recording when the system and disk noise are suppressed below the write noise by improved disk manufacturing.

The reason for the large jitter is the temperature dependence of the coercive field, $H_c(T)$. $H_c(T)$ vanishes at 50 °C below the Curie temperature such that the domain walls can easily move in the first stage of the cooling in the thermomagnetic write process and become jagged under nonoptimal recording conditions.

See also: Chemical Stability and Life Time; Magneto-optical Disks: Thermal Effects; Magneto-optical Effects, Enhancement of; Magneto-optic Multilayers; Magneto-optic Recording Materials: Chemical Stability of Life Time; Magneto-optic Recording: Overwrite and Associated Problems; Super-resolution: Optical and Magnetic Techniques

Bibliography

Bertero G A, Sinclair R 1994 Structure–property correlations in Pt/Co multilayers for magneto-optic recording. *J. Magn. Magn. Mater.* **134**, 173–84
Carcia P F, Coulman D, McLean R S, Reilly M 1996 Magnetic and structural properties of nanophase Pt/Co multilayers. *J. Magn. Magn. Mater.* **164**, 411–9
Carcia P F, Li Z G, Reilly M 1993 The magnetic and microstructural properties of Pt/Co multilayers grown on ZnO. *J. Appl. Phys.* **73**, 6424–6
Carcia P F, Suzuki T 2000 New MO recording media based on Pt/Co and Pd/Co multilayers and Pt–Co alloys. In: Gambino R J, Suzuki T (eds.) *Magneto-optical Recording Materials.* IEEE Press, Piscataway, NJ, Chap. 3
Gambino R J, Suzuki T (eds.) 2000 *Magneto-optical Recording Materials.* IEEE Press, Piscataway, NJ
Ishida M, Katsyuama T, Kawase T, Nebashi S, Shimoda T 1997 High magnetic field sensitivity of TbFeCo layer and Pt/Co multilayers with an ultra-thin RE-rich RE–TM layer. *IEEE Trans. Magn.* **33**, 3229–31
Kaneko M, Sabi Y, Ichimura I, Hashimoto S 1993 Magneto-optical recording on Pt/Co and GdFeCo/TbFeCo disks using a green laser. *IEEE Trans. Magn.* **29**, 3766–71
Meng Q, Schuurhuis J R, Ladder J C, Meyer P, Jamet J P, Ferré J 1999 Magnetization reversal processes in CoNi/Pt multilayers. *J. Magn. Soc. Jpn.* **23** (51), 87–90
Mergel D 2000 Domain dynamics and recording physics in magneto-optical recording media. In: Gambino R J, Suzuki T (eds.) *Magneto-optical Recording Materials.* IEEE Press, Piscataway, NJ, Chap. 6
Mergel D, Hansen P, Raasch D 1992 The physical basis of magneto-optical recording. *Proc. SPIE* **1663**, 240–9
Teragaki Y, Kusumoto Y, Sumi S, Torazawa K, Tsunashima S, Uchiyama S 1993 Magnetic field modulation recording on Pt/Co magneto-optical disks. *IEEE Trans. Magn.* **29**, 3796–8
van Kesteren H W, den Boef A J, Zeper W B, Spruit J H M, Jacobs B A J, Carcia P F 1991 Scanning magnetic force microscopy on Co/Pt magneto-optical disks. *J. Appl. Phys.* **70**, 2413–22

D. Mergel
University of Essen, Germany

Magneto-optical Disks: Thermal Effects

In thermomagnetic recording on magneto-optical (MO) data storage media, focused light energy is directed to a moving magnetic film structure to control the local temperature distribution. The magnetic material typically has a strong native anisotropy which

restricts the magnetization alignment perpendicular to the film plane, or nearly so. Owing to the strong temperature dependence of the magnetic properties of the medium, domain reversals that represent a pattern of recorded data can be induced, usually with the aid of an external bias magnetic field. Subsequent to recording, readout of written data is performed by reflecting a focused beam of reduced power from the impressed domain pattern to interrogate the magnetic state of the recorded track by using the MO Kerr effect (see *Faraday and Kerr Rotation: Phenomenological Theory*). The resultant heating of the medium during reading may or may not be instrumental for the proper performance of the readout function, depending on the design of the medium.

1. Regime of Thermal Transport in MO Recording

Much has been published on thermal performance of MO media (McDaniel and Victora 1997, Mansuripur 1995). Normally, the thermal physics involved in treating recording and readout is well within the limits of classical heat conduction in homogeneous media. Therefore, the well-known analysis of classical references (Carslaw and Jaeger 1959) applies, and the complications of microscale heat transport or phase change can be ignored. Even with these simplifications, an MO media designer routinely uses numerical analyses of heat conduction by computer simulation due to the relatively complicated thin film and disk substrate structures involved. Non-numerical thermal analysis methods for moving multilayer thin film stacks, even those on planar substrates, may be too complicated or lack generality for routine engineering design practice (Madison and McDaniel 1989).

Heat conduction in the solid MO film structures obeys the standard diffusion-like differential equation:

$$\nabla^2 T - \frac{1}{\kappa}\frac{\partial T}{\partial t} = \frac{Q(x,y,z,t)}{k}$$
$$= A\exp\{-\beta^2[(x-vt)^2 + y^2]\}$$
$$\times \exp(-\alpha z)\Psi(t) \qquad (1)$$

Here $T(x,y,z,t)$ is the temperature field of interest, $\kappa = k/\rho c$ is the thermal diffusivity, k is the thermal conductivity, ρ is the material mass density, c is the material mass specific heat, v is the moving media velocity, and Q is the thermal power input per volume. In the case of laser beam heating for recording on a typical MO medium thin film structure as shown in Fig. 1, Q should be represented as the Poynting vector energy deposition rate from absorption of the incident electromagnetic beam. The far right side of Eqn. (1) can be used for a simplified case in which a moving beam of Gaussian profile undergoes Beer's law absorption in a single, thick film. α is an absorption coefficient, β is an inverse beam size parameter, and $\Psi(t)$ is an incident beam power-versus-time profile.

Heat diffusion in a thin film structure is frequently described using characteristic lengths and times for the thermal transport described by $L = (\kappa t)^{0.5}$ and $t = L^2/\kappa$. The various film materials in typical MO media structures have very different diffusivities, as indicated in Table 1. Therefore, characteristic lengths and times are most applicable to either single films, or as effective values derived from numeric analyses that weigh together composite results from a realistic, but more complicated structure. Characteristic times in thermal diffusion analysis can also be estimated by relating heat flow to an electrical circuit analogue. If
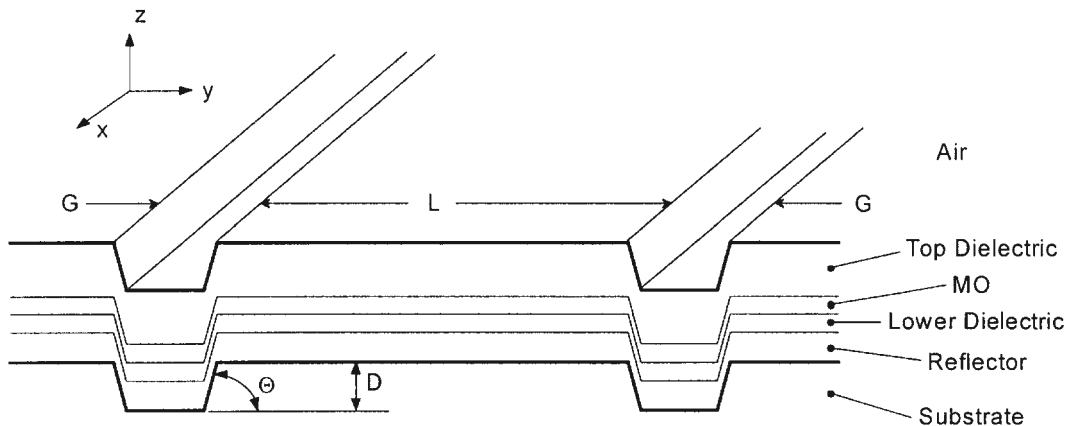
Figure 1
First-surface film stack geometry deposited on a grooved substrate. The geometry of the recording track (land *L*), the inter-track groove *G*, the groove depth *D*, and the groove side wall angle Θ help control heat diffusion.

Table 1
Materials and their properties for a nominal quadrilayer MO structure (see Fig. 1).

Material	Thickness (nm)	n	k_{opt}	k (W m^{-1}K^{-1})	c (J kg^{-1}K^{-1})	ρ (kg m^{-3})	κ (10^{-6} m^{2}s^{-1})
Air	∞	1	0	0.03	1150	1.15	22.7
SiN	85	2.02	0.01	2.0	740	3400	0.79
MO	20	2.4	3.6	7.0	360	7900	2.46
AlX	40	1.8	6.8	25	900	2700	10.3
Polycarbonate	$\sim 10^6$	1.58	0	0.15	300	1200	0.42
glass	$\sim 10^6$	1.5	0	1.0	860	2300	0.51

one relates temperature to voltage, heat flux to current, thermal resistance $R_{th} = L/kA$ (where L and A are effective conductive path length and cross-sectional area, respectively) to electrical resistance, and heat capacity (cm, with m the heat conductor's mass) to electrical capacitance, then the time for the charging of an electrical RC network ($t = RC$) becomes $t = R_{th}cm$. This leads again to the expression $t = L^2/\kappa$.

We note that the thermal constants of the thin films shown in Table 1 may differ considerably from those of the corresponding bulk material, and they may be adjusted considerably by altering the film compositions or deposition processes. One expects higher phonon and electron scattering in thin films due to the effects of layer boundaries and film growth morphology.

In thermomagnetic recording, the thermal energy deposited by an incident light beam should provide locally concentrated heating so that well-controlled magnetic domain reversals are established along a data track. Lateral heat spreading due to media motion (distributed dosing) and thermal diffusion must be limited to enable high resolution writing without excessive cross-write and cross-erase of previously recorded adjacent information. The means available to aid in this purpose are (i) surface topography of the thin films and substrate, (ii) thermal design of the thin film stack, and (iii) the writing strategy employed to apply the radiant energy. In Fig. 1, thermal confinement grooves provide an example of (i), while (ii) is illustrated by the reflector film, which can serve as a heat-sinking layer to minimize lateral heat diffusion. Regarding writing strategy (iii), probably the most important fundamental to remember in the heating of moving thin film structures with focused light beams is the following: *The most efficient heating with the highest resultant thermal gradients is always achieved through the use of short duration, low duty-cycle irradiation pulses* (McDaniel and Victora 1997, McDaniel 1999).

2. Fundamentals of Thermal Design for MO Disk Thin Film Structures

It is evident from Eqn. (1) that the *minimum* lateral extent of a heated region on the MO medium is the width of the incident focused light beam. Disk motion under the beam and lateral thermal diffusion can only enlarge the heated zone. Therefore, to achieve high-resolution, high-performance recording, the MO disk designer must counteract these tendencies with a combination of means as indicated in the previous section. Fortunately, each of the three avenues for control of lateral heat spreading (topography, film design, writing strategy) can be accurately modeled with a numerical computer simulation. The most powerful and flexible of the simulation tools for this purpose provides a solution $T(x,y,z,t)$ in two steps. First, the three-dimensional geometry of the substrate with film coatings (see, for example, Fig. 1) is exposed to a radiant impulse from a prescribed focused beam, and a fully time-developed "thermal impulse solution" is obtained from a finite-element or finite-difference solver operating on Eqn. (1). As long as the thermal problem is defined to be *linear* (material thermal properties independent of temperature; no material phase changes), superposition of the impulse solution in space and time with appropriate weighting according to the input light beam power–time profile will yield the desired final solution $T(x,y,z,t)$, even for a moving beam (McDaniel and Victora 1997, Mansuripur 1995).

Substrate and film topography departing from perfect planarity can increase the impedance to lateral heat flow. This is particularly true if the dominant thermal conduction path(s) is(are) altered or interrupted. For example, in Fig. 1 the side walls of the thermal confinement grooves are likely to have reduced thickness film layers (as measured normal to the local surface) if the incident material species during deposition travel predominantly in the $-z$ direction. Consequently, it is expected that lateral heat conduction can be shaped with features such as those depicted in Fig. 1 (McDaniel 1999), Peng and Mansuripur 2000).

Next, consider the film design issues. The basic physics of thermal transport involves optical absorption of the incident radiation (depending on how film stack reflectance R and absorbance A are split, given the constraint $R + A \approx 1$ in an opaque structure) on a time scale of $< 10^{-12}$ s, followed by diffusion of the

resultant thermal energy by conduction in all directions on time scales ranging from $\sim 10^{-10}$ to 10^{-6} s. Light absorption occurs predominantly in the first film that the incident light encounters that has a large value of k_{opt} (see Table 1). Heat sinking to a reflector layer at the base of the film stack is made increasingly effective by (i) increasing the heat capacity (volume) of the reflector, (ii) increasing the thermal conductivity of the reflector, and (iii) decreasing the thermal resistance between light absorption location and the reflector.

Intuitively, we expect an effective heat sink layer to increase the heat flow in the axial ($-z$) direction away from the light absorption zone, and to diminish the lateral flow. Surrounding the thin, but relatively high thermal conductivity MO layer with insulating dielectric films further suppresses the relative importance of lateral heat flow. Simple analysis of characteristic times for these respective flow directions tells us that the axial channel is at least an order of magnitude faster than the lateral flow channel. This is the primary reason that radiation power input by short-duration, low duty-cycle pulses couples energy efficiently to the fast axial flow channel, and minimizes the (detrimental) effect of the slow lateral flow channel in spreading heat.

3. Issues in Advanced MO Film Designs and Limits of Thermomagnetic Writing

Advanced MO film designs for the attainment of higher performance or areal recording density usually have more complex magnetic film structures than that shown in Fig. 1. In these cases, there typically are two or more magnetic layers with thermally controlled magnetic coupling to each other. Examples of these design structures include light-intensity modulated direct overwrite (LIM-DOW), magnetically induced super-resolution (MSR), and magnetic amplification MO system (MAMMOS). The total thickness of the metallic magnetic layers in these designs (~ 50–100 nm) is much greater than that of the simple, single-layer structure illustrated in Fig. 1 and Table 1. Consequently, the effectiveness of a design strategy utilizing a heat-sinking layer at the base of the film stack is significantly compromised. The incident light is totally absorbed in the thick magnetic layers, and the resultant heat will diffuse laterally with diminished control from the more distant underlying heat sink.

Another inevitable trend for high-performance MO storage media will be the necessity to increase the recording and playback rate. Data throughput rates for rotating memory products are driven higher by increasing the disk rotation rate or increasing the linear bit density along the track, or both. Notice that the former strategy increases the relative linear speed of the write/read beam and the storage medium, while the latter requires improved along-track writing

and reading resolution. The resolution limitations when using an optical stylus whose lateral extent is $W \sim \lambda/NA$ (wavelength/numerical aperture) are well known and obvious. But increasing the linear speed of recording combines with the higher linear bit density to shorten the bit transit time to $\tau \sim L_{bit}/v$. Eventually, τ becomes shorter than the shortest thermal characteristic time of the recording medium, regardless of the aggressiveness of the film thermal design or the writing strategy. At this point, one has lost control of shaping the thermal environment for thermomagnetic writing, and the viability of a recording process based on impressed thermal gradients becomes questionable.

See also: Magneto-optic Recording Materials: Chemical Stability and Life Time; Magneto-optic Recording: Overwrite and Associated Problems; Multilayer Optical Film Modeling; Super-resolution: Optical and Magnetic Techniques

Bibliography

Carslaw H S, Jaeger J C 1959 *Conduction of Heat in Solids.* Oxford University Press, Oxford

Madison M R, McDaniel T W 1989 Temperature distributions produced in an N-layer film structure by static or scanning laser or electron beam with application to MO media. *J. Appl. Phys.* **66**, 5738–48

Mansuripur M 1995 *The Physical Principles of MO Recording.* Cambridge University Press, Cambridge

McDaniel T W 1999 Thermal design of high performance magneto-optical data storage films. Proceedings MORIS '99. *J. Magn. Soc. Jpn.*, **23** Suppl. S1, 251–256

McDaniel T W, Victora R H (eds.) 1997 *Handbook of MO Data Recording.* Noyes, Park Ridge, NJ

Peng C, Mansuripur M 2000 Thermal cross-track cross talk in phase-change optical disk data storage. *J. Appl. Phys.* **88**, 1214–20

T. W. McDaniel
Seagate Research, San Jose, California, USA

Magneto-optical Effects, Enhancement of

The fundamental magneto-optical Kerr and Faraday effects, described phenomenologically in *Faraday and Kerr Rotation: Phenomenological Theory*, are intrinsically very small. However, with modern light sources and signal-processing techniques the various phenomena, discovered originally by Michael Faraday and John Kerr (Faraday 1845, Kerr 1877), can be easily observed. Indeed, with optical modulation techniques, it is possible to detect magneto-optic signals associated with thin layers of magnetic materials that are effectively one atom thick or less. However,

for commercial applications aimed at mass markets, such as magneto-optic memories, the costly use of sophisticated electronic detection techniques and the need to read magnetically stored information very rapidly requires one to optimize the sensitivity with which magneto-optical signals can be detected. The relationship between the size of the magneto-optical effects and the sensitivity with which they can be detected is discussed below. The influence that the various optical and magneto-optical parameters of the material have on the detection process is determined and various techniques are outlined for increasing the size of magneto-optical effects and, in particular, maximizing the sensitivity with which they can be detected. In this article it is not possible to treat all magneto-optic configurations (see *Faraday and Kerr Rotation: Phenomenological Theory*) and we shall concentrate on the polar Kerr effect at normal incidence, since this is most applicable to the developments in magneto-optic data storage systems. However, much of the underlying philosophy of enhancement applies to the alternative situations and, where appropriate, this will be pointed out.

In most instances, whether one is working in reflection (Kerr effect) or transmission (Faraday effect), the magneto-optical signal arises from a magnetization-sensitive polarization change, usually from a linear state to an elliptical state, with the major axis of the polarization ellipse rotated slightly with respect to the incident polarization direction. This of course only applies to the *polar* and *longitudinal* cases and not to the *transverse* case. It is shown in *Faraday and Kerr Rotation: Phenomenological Theory* that the polarization ellipse is the result of the combination of two orthogonal vectors, one optical and the other magneto-optical. These are the Fresnel reflection coefficient, r, and the Kerr coefficient, k, respectively. Under normal circumstances, in thin absorbing films, the condition $|k| \ll |r|$ applies, with the result that a very small, complex magneto-optical rotation, $\hat{\theta}_k$, may be defined as

$$\hat{\theta}_k = \theta_k + \mathrm{i}\varepsilon_k \approx \frac{k}{r} = \left|\frac{k}{r}\right|\cos \Delta_k + \mathrm{i}\left|\frac{k}{r}\right|\sin \Delta_k \qquad (1)$$

where Δ_k is the phase difference between k and r, and θ_k and ε_k are the Kerr rotation and ellipticity, respectively. Intuitively, it seems obvious that the larger this complex rotation the easier it is to detect, and in general this is true. However, as is shown below, one may reduce the reflection coefficient, r, to a value comparable to k with the result that very large rotations could, in principle, be obtained, albeit with very low accompanying reflectivity. It should be made clear, however, that despite the large effective magneto-optical rotations that would result, it is undesirable to have this accompanied by a sample surface that reflects little or no light at all. The role of sample reflectivity, $R(=|r|^2)$, and the associated

magnitude of complex Kerr rotation in determining the sensitivity by which a magneto-optic signal can be detected are clearly of importance, and the way in which each contributes to determining the signal-to-noise ratio in any detection system requires careful attention.

1. Signal-to-noise Ratio

In magneto-optic recording systems, the most common detection method is one that relies on differential detection (Egashira and Yamada 1974) employing two balanced detectors, as shown schematically in Fig. 1. For simplicity the incident radiation is not shown in this diagram. At any given moment the two detectors are, to a very good approximation, balanced in their output by having almost equal light intensities falling on them. The advantage of such a system is that variations in the intensity of the radiation source (often a laser diode) are effectively removed from the differentially amplified output of the two detectors. After traversing the polarizing beam-splitting optics of the system, magneto-optical rotations, induced by magnetization changes in the sample surface, cause small imbalances in the amplified output and this becomes the detected signal. Accompanying this is a series of noise levels whose origins may be fundamental (shot noise), electronic (detector and amplifier noise), or associated with fluctuations of the laser light source. It is the ratio of the signal to the noise level that determines the degree of precision with which the magneto-optical effects can be detected. Atkinson *et al.* (1991) have shown that for such a system the signal-
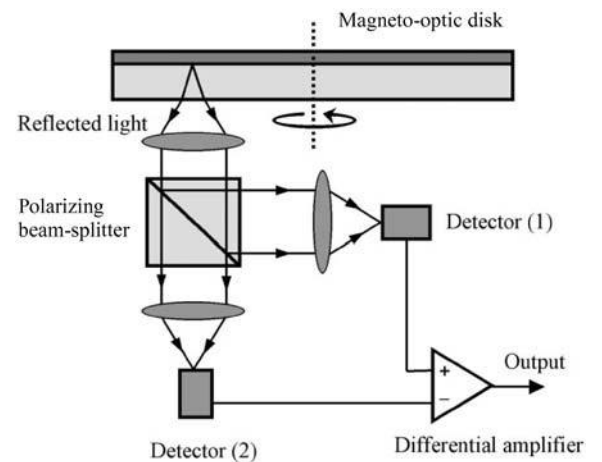
Figure 1
Schematic diagram of a magneto-optic differential readout system.

to-noise power ratio is given by

$$\text{SNR} = \frac{P\psi_k^2 R(1-R)^2 \cos^2 \Delta_k}{\varepsilon + \sigma R + (\lambda+\mu)\psi_k^2 R(1-R)^2 \cos^2 \Delta_k} \quad (2)$$

where

$$|k| = \psi_k(1-R) \quad (3)$$

P is a constant related to the optical read power and quantum efficiency and gain of the detectors, ε is the electronic noise, σ determines the shot-noise level, proportional to disk reflectance, and λ and μ are the laser feedback and medium noise, both of which are assumed to come through the differential detection system in proportion to the Kerr signal.

An important parameter in Eqns. (2) and (3) is ψ_k, known as the potential Kerr coefficient. This parameter, introduced by Gamble *et al.* (1985), may be understood through Eqn. (3) as being the maximum possible amplitude of the Kerr coefficient, produced when the overall system reflectance is reduced to zero. The principles of increasing SNR through magneto-optic enhancement now reduce to three simple requirements. These are to maximize the value of ψ_k for the particular magnetic medium; to ensure zero ellipticity (cos $\Delta_k = \pm 1$); and to do this for a system reflectance that maximizes Eqn. (2) or is compatible with the practical needs of providing sufficient optical feedback for the purposes of tracking. Depending on the levels of the various noise sources, the intensity reflectance can lie between the limits of zero and 33% and is typically 10–20%.

2. Maximizing the Kerr Effect

The most important aspect of magneto-optic enhancement is the maximization of the potential Kerr coefficient and this may be accomplished by the use of a quadrilayer system, as shown in Fig. 2. Enhancement is produced through the use of a high-reflectance mirror placed behind a film of the magnetic medium that is thin enough to allow transmission of the incident radiation. The thickness, d_M, of the magnetic film must therefore be much less than the optical skin depth determined by the absorption coefficient of the material at the design wavelength, λ_0. It is the thickness; the refractive index, n ($= n' + in''$), and magneto-optic parameter, Q ($= Q' + iQ''$), of the magnetic layer; and the reflectance of the mirror that are important in maximizing ψ_k. Indeed its value is unaffected by any optical layers in the system that lie on the side of incidence (e.g., the incident layer).

The mirror itself must satisfy two important requirements: it must have a high-amplitude reflectivity, $|r_m|$, into air; and the phase change, ρ_m, on reflection from the mirror should be controllable.
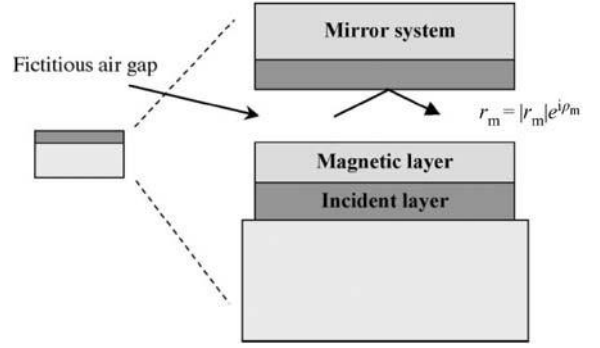
Figure 2
Quadrilayer structure for a magneto-optic disk, showing the reflectivity, r_m, of the mirror system into a fictitious air gap.

This is most easily achieved using an opaque aluminum film separated from the magnetic layer by a low refractive index spacer layer. The spacer layer has little effect on the reflectivity but its thickness, d_s, provides control over ρ_m. It can be shown that the potential Kerr coefficient for such a system is given by (Gamble *et al.* 1985)

$$\psi_k = (1+\Gamma^2)^{1/2} G|Q|/4 \quad (4)$$

where

$$\Gamma = \frac{n''}{n'} \quad (5)$$

and

$$G = G(n', n'', d_M, r_M, \lambda_0) \quad (6)$$

G is a complex gain function derived by Gamble *et al.* (1985). The form of the function can be described graphically by a three-dimensional plot showing how G varies with $|r_m|$ and ρ_m. A typical plot for an absorbing magnetic layer is shown in Fig. 3. It is important to note that this function does not change much with d_M, providing $d_M < $ skin depth, and that many optically absorbing media show similar plots. Even more important to note is that G is a maximum for the largest value of $|r_m|$ but that there is quite a range of values of ρ_m over which G remains relatively high. It is this flexibility in ρ_m that allows us to proceed with simple designs for enhancement.

3. Quadrilayer

At this point there are two ways of proceeding. In the first, called a quadrilayer (Atkinson *et al.* 1991), the thicknesses of the magnetic and spacer layers are adjusted to give a zero reflectance into the medium of the incident layer. This almost always requires a magnetic layer thickness that is less than the skin
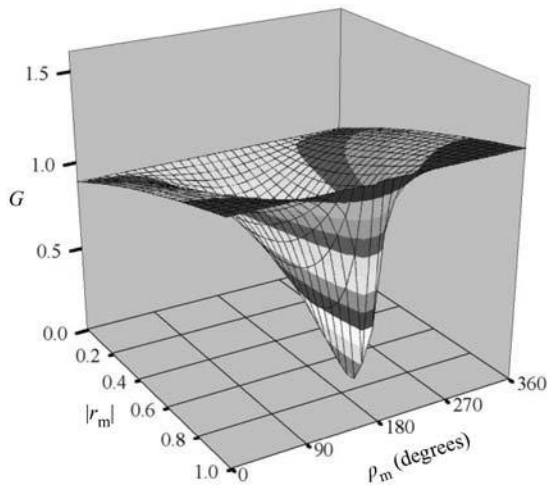
Figure 3
Typical gain function for an absorbing material with $d_M <$ skin depth.

depth and since there is considerable flexibility in the required value of ρ_m, the maximum value of the potential Kerr coefficient is usually achieved quite easily. Having reduced the reflectance from the top of the magnetic layer/mirror system to zero, only the magneto-optical Kerr coefficient, k, remains. The desired finite reflectivity, r, is returned to the system from the single upper surface of the incident layer and is determined by the refractive index of the material of this layer. This combines with the Kerr coefficient to produce a complex Kerr rotation in the usual way. However, the phase, Δ_k, between k and r can be adjusted by varying the thickness of the incident layer and in this way can be set equal to zero or π. This may be done without affecting the value of either k or r.

4. Trilayer

An alternative to the quadrilayer and one that is more practical and adequate for most purposes is the *trilayer* (Atkinson 1993), where the incident layer shown in Fig. 2 is omitted. In this case the overall reflectivity is controlled by the thicknesses of the magnetic and spacer layers. Thus, there are only two variables of the system that can be adjusted to maximize ψ_k, obtain a particular reflectance, and maintain a zero ellipticity. Theoretically it is rarely possible to satisfy all three conditions simultaneously. However, by sacrificing a small percentage in ψ_k and hence maximum Kerr rotation, zero ellipticity can be obtained for a range of reflectances.

The design procedure, based on the use of CoPt, is illustrated graphically in Fig. 4. This shows how the intensity reflectance, R, of the three-layer system
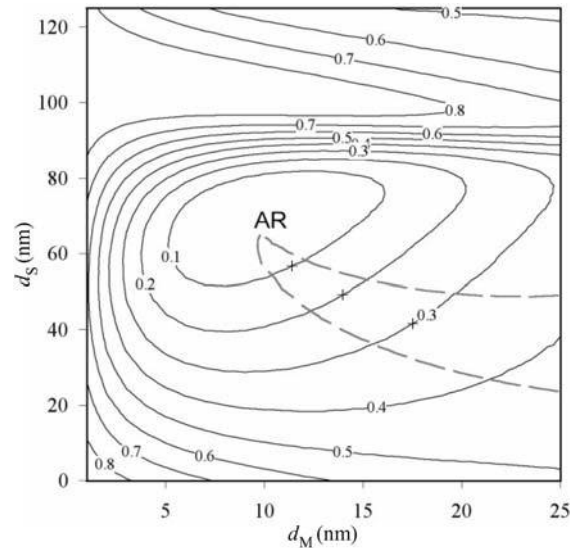
Figure 4
Reflectance (—) and $\cos \Delta_k$ (- - -) contours as a function of the thicknesses of magnetic and spacer layers ($\lambda_0 = 350$ nm).

Table 1
Optical and magneto-optical parameters of materials at $\lambda_0 = 350$ nm.

Material	n'	n''	Q'	Q''
CoPt	1.38	2.84	−0.0138	0.008
SiO$_2$	1.48	0	0	0
Al	0.38	4.23	0	0

varies with the thicknesses d_M and d_s. Also shown in Fig. 4 is a single contour (dashed line) within which $|\cos \Delta_k| > 0.99$. The optical and magneto-optical constants used to generate these contour maps are given in Table 1.

Figure 4 demonstrates how the reflectance of the system can be controlled and that, as required for the quadrilayer design, an antireflection condition can be produced at the point marked AR. It is worth pointing out that the Kerr rotation for such a point would be $\pm 90°$, although the reflectivity of the system would be very low indeed. More important is the area within the dashed contour corresponding to $\cos \Delta_k = -0.99$. Within this region three designs have been marked (+) that would give zero ellipticity for reflectances of 10%, 20%, and 30%.

What is not clear from these figures is the extent to which the designs will achieve optimization of the Kerr rotation through the maximization of the potential Kerr coefficient. In order to check this aspect of the design one must compare the resulting

Trilayer designs corresponding to the three points marked (+) in Fig. 4.

R (%)	d_M (nm)	d_s (nm)	$\lvert k \rvert \times 10^2$	θ_k (°)	$\psi_k/\psi_{k\max}$ (%)
0.1	11.4	56.3	0.9	1.69	96.9
0.2	14.1	48.9	0.8	1.01	97.2
0.3	18.1	42.5	0.7	0.72	96.5

value of ψ_k using Eqns. (4)–(6) and compare this with the absolute maximum possible value, $\psi_{k\max}$. This can be calculated using the same equations combined with the maximum possible value of the G function, $G_{\max}$, which is obtained for a perfect mirror and is given by (Gamble *et al*. 1985)

$$G_{\max} = (1 - \Gamma^{-2})^{1/2} \qquad (7)$$

Because of the insensitivity of the gain function to the mirror reflectance over a range of ρ_m values, it is quite common for the potential Kerr coefficient to be within a few percent of the maximum that would be possible if the design were perfect. This is shown in Table 2 for the three designs marked (+) in Fig. 4 for $R = 0.1$, 0.2, and 0.3.

It may be noted that the extra complexity that would be needed to achieve the perfect enhancement does not usually warrant the additional effort since errors during fabrication of such multilayer systems are likely to lead to imperfections in performance.

5. Enhancement Process

It is useful to obtain a physical understanding of why enhancement of the magneto-optical Kerr effect occurs in the multilayer systems described above. There are two simple reasons for this. First, the overall reflectance is reduced and this clearly leads to an increase in Kerr rotation even if the Kerr coefficient remains unchanged. More importantly, however, for any chosen value of system reflectance, the Kerr coefficient has been increased to the maximum possible value that the intrinsic properties of the magnetic material will allow. This is accomplished through multiple interactions of the radiation with a thin film of the material. This is achieved using a high-reflectance mirror in such a way that all radiation not reflected from the system is absorbed by the magnetic layer. This maximizes the magneto-optic interaction of the incident radiation with the system.

These points are illustrated in Fig. 5, which shows the electric field amplitude and differential absorptance throughout a simple trilayer structure. The design actually corresponds to that indicated in Fig. 4 for $R = 0.1$ at a wavelength of 350 nm. It
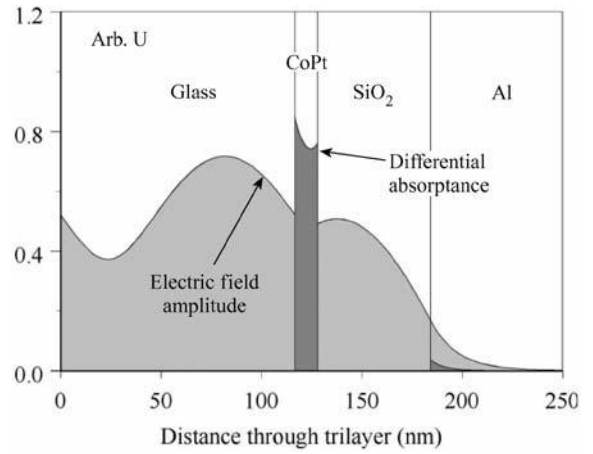
Figure 5
Electric field amplitude and differential absorptance as a function of distance through a trilayer designed for $R = 0.1$.

should be noted that the curve represents the amplitude of the electric wave through the various layers and should not be thought of as a traveling wave. In the incident medium (glass) therefore, we see a standing wave with nonzero nodes resulting from combination of the incident wave and the reflected wave that corresponds to the 10% reflected energy. The fields gradually decrease through the spacer and become very low within the highly reflecting aluminum mirror.

Differential absorptance indicates the variation of optical absorption throughout the system and the total dark area in Fig. 5 corresponds to the total absorption by the trilayer. Most important is the fact that virtually all of the radiation not reflected by the system is absorbed in the magnetic layer. Very little is lost to the mirror, either by absorption or in transmission. It is this fact that results in maximization of the potential Kerr coefficient since all radiation not reflected from the system is available to stimulate the magneto-optical effect.

6. Longitudinal and Transverse Effects

The general principles of enhancement, outlined above for the normal incidence polar Kerr effect, also apply to the longitudinal and transverse effects. In such cases one is working at oblique incidence and account must be taken of the orientation of the polarization state of the incident radiation with respect to the plane of incidence. The longitudinal case has been considered in some detail by Keay and Lissberger (1968). In the transverse case, the effect is usually described in terms of the ratio of the magnetization-sensitive reflectance change, ΔR, to the

usual isotropic intensity reflectance, R, for P-polarized radiation. It is clear that enhancement can be obtained through the control of the reflectivity of the P-polarized state and maximization of the interaction of the radiation with the magnetic layer. The details for these cases will, to some extent, depend on the exact experimental arrangement being used to detect the effects.

7. Summary

An outline has been given of the means by which the normal incidence polar Kerr effect can be enhanced to improve the sensitivity with which it may be detected. The method relies on the use of three- or four-layer systems that control the reflectivity of the coating surface while, at the same time, maximizing the magneto-optical interaction of the radiation with the magnetic medium.

See also: Magneto-optic Recording: Overwrite and Associated Problems; Magneto-optic Recording: Total Film Stack, Layer Configuration; Optical and Magneto-optic Data Storage: Channels and Coding

Bibliography

Atkinson R 1993 Design of magneto-optic phase-optimized trilayer systems for the enhancement of the polar Kerr-effect. *J. Magn. Magn. Mater.* **124**, 178–84

Atkinson R, Salter I W, Xu J 1991 Quadrilayer magneto-optic enhancement with zero Kerr ellipticity. *J. Magn. Magn. Mater.* **102**, 357–64

Egashira K, Yamada T 1974 Kerr-effect enhancement and improvement of readout characteristics in MnBi film memory. *J. Appl. Phys.* **45**, 3643–8

Faraday M 1845 Experimental researches in electricity. *Proc. R. Soc.* **5**, 567–9

Gamble R, Lissberger P H, Parker M R 1985 A simple analysis for the optimization of the normal polar magneto-optical Kerr effect in multilayer coatings containing a magnetic film. *IEEE Trans. Magn.* **21**, 1651–3

Keay D, Lissberger P H 1968 Longitudinal Kerr magneto-optic effect in multilayer structures of dielectric and magnetic films. *Opt. Acta* **15**, 373–88

Kerr J 1877 On rotation of the plane of polarisation by reflection from a magnetic pole. *Philos. Mag.* **3**, 321–43

R. Atkinson
The Queen's University, Belfast, UK

Magneto-optics: Inter- and Intraband Transitions, Microscopic Models of

Magneto-optical methods are widely used to study the magnetic properties of materials. These experiments consider the response of a magnetic medium to
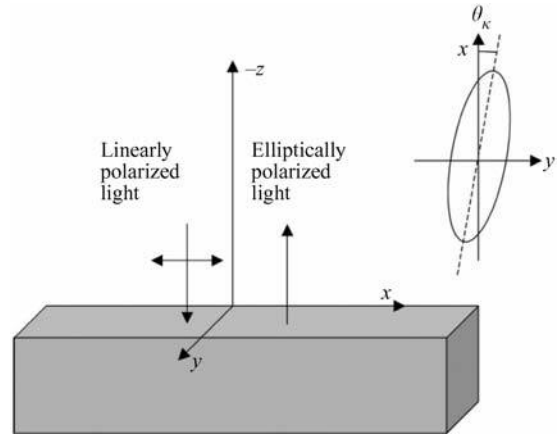
Figure 1
Schematic configuration of polar Kerr effect geometry.

the incident plane polarized light. When linearly polarized light is reflected or refracted it generally becomes elliptically polarized, as shown in Fig. 1. The main axis of the ellipse is rotated through angle θ_k with respect to the polarization direction of the incident light. The magneto-optical Kerr effect (MOKE) considers the reflected light, while the Faraday effect deals with the refracted light. θ_k is called the Kerr/Faraday rotation angle. The other important parameter is the ellipticity (η_k) of the outgoing light.

The discussion below deals primarily with the Kerr effect that can be easily extended to the Faraday effect. To make the analysis of this complex problem somewhat simpler we assume normal incidence of light and assume the z-axis to be normal to the surface of the sample. The light traveling through vacuum or air with refractive index $n = 1$ is reflected from a sample with refractive index n. Let us consider the electric vector of the linearly polarized light.

$$E_{inc} = E_0 \hat{e}_x e^{ikz - i\omega t} \tag{1}$$

where $\hat{e}_x$ is the polarization vector along the x-axis, k is the wave vector, ω is the frequency of the wave, and E_0 is the amplitude. This expression can be rewritten in terms of right and left circularly polarized light as follows:

$$E_{inc} = E_r + E_l \tag{2}$$

where

$$E_{r/l} = E_0(\hat{e}_x \pm i\hat{e}_y)e^{ikz - i\omega t} \tag{3}$$

This wave has equal right and left components.

Using the boundary conditions, the following relation is obtained for the incident, E_{inc}, and the

reflected, E_{refl}, electric vectors:

$$E_{\text{refl}} = \frac{1-n}{1+n} E_{\text{inc}} \qquad (4)$$

Replacing E_{inc} with its right-(n_r) and left-(n_l) circularly polarized components one gets

$$
\begin{aligned}
E_{\text{refl}} &= \frac{1-n_r}{1+n_r} E_{\text{inc,r}} + \frac{1-n_l}{1+n_l} E_{\text{inc,l}} \\
&= \frac{E_0}{2}\left[\frac{1-n_r}{1+n_r}(\hat{e}_x + i\hat{e}_y) + \frac{1-n_l}{1+n_l}(\hat{e}_x - i\hat{e}_y)\right] e^{ikz - i\omega t} \quad (5)
\end{aligned}
$$

which is elliptically polarized light if $n_r \neq n_l$. The Kerr rotation angle and ellipticity are given by

$$
\begin{aligned}
\theta_k &= \frac{\text{Re}(E_{\text{refl}}\hat{e}_y)}{\text{Re}(E_{\text{refl}}\hat{e}_x)} = \text{Im}\frac{n_r - n_l}{1 - n_r n_l}, \\
\eta_k &= \frac{\text{Im}(E_{\text{refl}}\hat{e}_y)}{\text{Re}(E_{\text{refl}}\hat{e}_x)} = \text{Re}\frac{n_r - n_l}{1 - n_r n_l} \qquad (6)
\end{aligned}
$$

The positive sign of the Kerr angle is considered for the rotation from the x-axis to the y-axis. Keep in mind that the direction of propagation for the reflected beam is $-z$.

The corresponding parameters for the Faraday effect are

$$
\begin{aligned}
\theta_F &= \frac{1}{2c}\omega z\,\text{Re}(n_r - n_l), \\
\eta_F &= -\tanh\left(\frac{1}{2c}\omega z\,\text{Im}(n_r - n_l)\right) \qquad (7)
\end{aligned}
$$

where c is the speed of light and z is the distance from the interface. These expressions are valid for $|n_r - n_l| \ll n_r$. We see from these equations that reflected and refracted waves are elliptically polarized due to the difference in the refractive indices of the medium for the left and right polarized light. The index of refraction is related to the dielectric constant ε and conductivity tensor σ as follows:

$$n^2 = \varepsilon = 1 + i\frac{4\pi}{\omega}\sigma \qquad (8)$$

The left-handed ($-$) and the right-handed ($+$) components of the conductivity are given by

$$\sigma^\pm(\omega) = \sigma_{xx}(\omega) \pm i\sigma_{xy}(\omega) \qquad (9)$$

and the conductivity tensor for a medium with three-fold or higher rotational symmetry about the z-axis has the following form:

$$
\sigma = \begin{pmatrix} \sigma_{xx} & \sigma_{xy} & 0 \\ -\sigma_{xy} & \sigma_{xx} & 0 \\ 0 & 0 & \sigma_{xx} \end{pmatrix} \qquad (10)
$$

Combining Eqns. (6), (8)–(10), the Kerr rotation parameters are given by

$$\theta_k = \text{Re}\,\frac{4\pi\sigma_{xy}}{\omega n(1-n^2)}, \quad \eta_k = \text{Im}\,\frac{4\pi\sigma_{xy}}{\omega n(1-n^2)} \quad (11)$$

We see from Eqn. (11) that a system gives rise to the Kerr effect if the off-diagonal component of its conductivity tensor, σ_{xy}, is not zero. Now, the Onsager reciprocal relation $\sigma_{ij}(M) = \sigma_{ji}(-M)$ along with Eqn. (10) gives $\sigma_{xy}(M) = -\sigma_{xy}(-M)$ and $\sigma_{ii}(M) = \sigma_{ii}(-M)$, where M is the magnetization vector along the z-axis. Thus there is no Kerr rotation in a paramagnet or antiferromagnet because $\sigma_{xy}(M) = -\sigma_{xy}(-M)$ leads to an equal and opposite contribution for the identical spin-up and spin-down densities of states. Also, σ_{ii} and σ_{xy} have odd-power and even-power dependence respectively on M. As a result, the rotation parameters are linear functions of M when the higher order terms are neglected. The Kerr rotation for the geometry considered here is known as polar Kerr rotation.

The conductivity tensor is determined by intraband and interband electronic transitions in response to the applied electromagnetic radiation. Thus the computation of the conductivity tensor requires the electronic states of the system. The electronic states are determined by the self-consistent solutions of the one-electron Schrödinger equations

$$(-\Delta + V_{\text{eff}})\psi_{\vec{k}\lambda} = E_{\vec{k}}\psi_{\vec{k}\lambda} \qquad (12)$$

where V_{eff} is the effective potential including spin–orbit interactions, $\vec{k}$ is the wavevector and λ is the band index.

The Drude model is used to calculate the intraband contribution to the diagonal component of the conductivity tensor. The conductivity in this model is given by (Ziman 1972)

$$\sigma^{\text{intra}}(\omega) = \frac{\sigma_0}{1 - i\omega\tau} \qquad (13)$$

where the d.c. conductivity σ_0 is related to the plasma frequency ω_p and the relaxation time τ of the band states by

$$4\pi\sigma_0 = \omega_p^2\tau \qquad (14)$$

The calculated band structure is used to compute ω_p using the following expression (Mazin *et al.* 1989):

$$\omega_p^2 = \frac{4\pi e^2}{\Omega}\sum_{\vec{k}\lambda}|V_{\vec{k}\lambda}|^2\delta(E_{\vec{k}\lambda} - E_F) \qquad (15)$$

where Ω is the volume of the primitive cell of the system and

$$V_{\vec{k}\lambda} = \langle\,\vec{k}\lambda|\nabla|\vec{k}\lambda\,\rangle \qquad (16)$$

is the mean velocity of an electron in state $|k\lambda\rangle$ and E_F is the Fermi energy.

σ_0 and ω_p are used to calculate τ and then $\sigma^{\text{intra}}(\omega)$.

The interband contribution to the conductivity tensor is related to matrix elements of the interaction potential between the electrons and the electromagnetic field given by:

$$H' = \frac{e}{mc} \vec{\pi} \cdot \vec{A} \qquad (17)$$

where A is vector potential and

$$\vec{\pi} = \vec{p} + \frac{\hbar}{4mc^2}\sigma \times \nabla V(r) \qquad (18)$$

with σ as the Pauli spin matrices and $\vec{p}$ as the electron momentum. The second term in $\vec{\pi}$ leads to the spin–flip transitions. It has been found to be negligible compared to the first term and is usually ignored. Treating H' as a perturbation in the random phase approximation, without allowance for the local field effects, the imaginary part of the off-diagonal conductivity tensor is

$$\sigma_{2xy} = \frac{\pi e^2}{4m^2\hbar\omega\Omega} \sum_{\vec{k}\,\lambda\lambda'} \{ |\langle \vec{k}\,\lambda'|\pi^-|\,\vec{k}\,\lambda\rangle|^2$$

$$- |\langle \vec{k}\,\lambda'|\pi^+|\,\vec{k}\,\lambda\rangle|^2 \} \times \delta(\hbar\omega - E_{\lambda\lambda'}) \qquad (19)$$

where π^+ and π^- are electron momentum operators corresponding to right- and left-circularly polarized light and $|\vec{k}\lambda\rangle$ and $|\vec{k}\lambda'\rangle$ are occupied and unoccupied states, respectively (see for example Bennet and Stern 1965, Wang and Callaway 1974). The real part of the diagonal component of the conductivity tensor, σ_{1xx}, is given by a similar expression where π^+ and π^- contributions are added. The Kramers–Kronig dispersion relations are used to find the other parts of these components.

The selection rules for the dipole matrix elements in terms of the orbital quantum numbers (l, m_l) are $\Delta l = \pm 1$ and $\Delta m_l = 1$ for π^+ and $\Delta m_l = -1$ for π^-. In the absence of spin–orbit interactions, π^+ and π^- contributions in Eqn. (19) cancel each other exactly $(\sigma_{xy} = 0)$ due to the degeneracy of the states with magnetic orbital quantum numbers m_l and $-m_l$. As a result there is no Kerr rotation in such a system. Spin–orbit interactions lift the above mentioned degeneracy of the electronic states so that π^+ and π^- contributions no longer cancel each other, giving a finite value for σ_{xy}. Thus a system must have spin moment (asymmetric spin-up and spin-down densities of states) with spin–orbit interactions to produce Kerr rotation.

The off-diagonal components of the conductivity tensor (Eqn. (19)) and hence the Kerr rotation (Eqn. (11)) is determined by the dipole matrix elements between the occupied and unoccupied electronic states

of the same spin separated by the incident photon energy $\hbar\omega$. Since the Kerr parameters are proportional to the off-diagonal component of the conductivity tensor, one can qualitatively try to relate the features in the magneto-optic spectra by assuming the matrix elements in Eqn. (19) to be the same for all transitions. In this case σ_{xy} is proportional to the joint density of states (JDOS) as follows:

$$\sigma_{xy}(\omega) \propto \frac{1}{\omega}\left[\int_{\omega_F-\omega}^{\omega_F} n^\uparrow(\omega')n^\uparrow(\omega+\omega')\mathrm{d}\omega' \right.$$

$$\left. + \int_{\omega_F-\omega}^{\omega_F} n^\downarrow(\omega')n^\downarrow(\omega+\omega')\mathrm{d}\omega' \right] \qquad (20)$$

where $n^{\uparrow,\downarrow}(\omega')$ and $n^{\uparrow,\downarrow}(\omega+\omega')$ are the spin-up($\uparrow$) and spin-down ($\downarrow$) densities of states (DOS) for the occupied and unoccupied states respectively and ω_F refers to the Fermi energy. It must be kept in mind that constant matrix element approximation is inadequate for a quantitative comparison of this rather weak effect.

The magneto-optical materials have been actively studied for several decades in terms of their applications as rewritable data storage devices. The large Kerr rotation allows the increase of signal to noise ratio and as a result the density of recording. Currently, materials with Kerr rotation of about $0.3°$ are used for magneto-optical recording. Research is now concentrated on materials with a Kerr rotation above $0.3°$. Also, the Curie temperature (T_c) should be such that one can easily go above it to write and stay below it to read. Thus, along with the exchange parameters for appropriate T_c, a practical magneto-optical system must have large magnetization and spin–orbit interactions to produce a large enough Kerr rotation. One of the common ways to achieve this combination is by creating a mixture of $3d$ elements with large magnetization and heavy elements with large spin–orbit coupling. The materials currently in use are based on amorphous $(Tb, Gd)_x$ $(Fe, Co)_{1-x}$ ($x = 0.2$–0.3) with Kerr rotation of about 0.2–$0.3°$ around 633 nm wavelength of light (Bloomberg *et al.* 1996).

Finally, as an example of intraband and interband contributions to the Kerr parameters we consider MnBi, an interesting system with one of the largest Kerr rotations known. MnBi has a hexagonal structure with four atoms per unit cell. We have studied the Kerr effect in MnBi using the first-principle relativistic self-consistent band structure calculations. The large magnetization in this system comes from Mn($3.6\,\mu_B$) and Bi is responsible for the appreciable spin–orbit coupling (Sabiryanov and Jaswal 1996).

Figure 2 shows the spin-polarized DOS for MnBi. The major peaks in the DOS are due to the Mn d-states. The interband contribution to the Kerr rotation in MnBi comes primarily from p and d states ($\Delta l = \pm 1$). The Kerr-active region of the
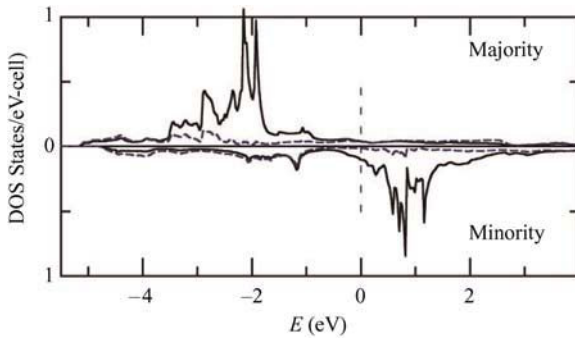
Figure 2
Spin-polarized total and projected DOS of MnBi. The zero on the energy axis corresponds to the Fermi energy.
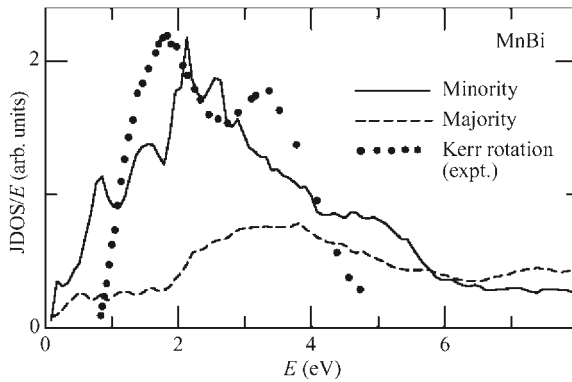
Figure 3
Spin-resolved JDOS of MnBi and the Kerr rotation data from Di *et al.* (1992).

Figure 4
Kerr rotation (θ_k) and ellipticity (η_k) for MnBi. Dots represent the experimental data at 85 K from Di *et al.* (1992). The full line gives the results with interband and intraband contributions while the dashed line corresponds to the interband contribution only.

electromagnetic spectrum for MnBi can be qualitatively seen from the JDOS (Eqn. (20)) for spin-up and spin-down states plotted in Fig. 3. Figure 3 also shows the experimental data for Kerr rotation for MnBi (Di *et al.* 1992). One can see from Fig. 3 that JDOS do a good job of predicting that the Kerr-active region of MnBi is centered around 2–3 eV. The minority spin JDOS has a large peak around 2 eV that arises from a modest peak around 1.4 eV below Fermi energy and a large peak at 0.6 eV above E_F in the DOS of MnBi in Fig. 2. The transitions are between hybrid bands formed by Bi *p*- and Mn *d*-states. The majority-spin JDOS has a small broad peak around 3.3 eV. The transitions from hybrid Bi *p*- and Mn *d*-bands to more dispersed Mn and Bi *sp*-bands are responsible for the smaller second peak in the Kerr rotation angle around 3.3 eV.

For a quantitative comparison, the calculated Kerr rotation and ellipticity are compared with the experimental data in Fig. 4. First, overall there is good

agreement between theory and experiment. The largest Kerr rotation of 2.3° is around 2 eV (630 nm). Figure 4 also shows the calculated Kerr rotation without an intraband contribution. We see that the intraband contribution is appreciable at longer wavelengths but becomes negligible below 600 nm.

In spite of the large Kerr rotation MnBi has not become a data storage device so far. This is because MnBi undergoes structural phase transition from a low-temperature hexagonal ferromagnetic phase to the high-temperature orthorhombic paramagnetic phase near its Curie temperature. This makes it

unsuitable for recording applications. Scientists continue to make efforts to overcome this problem and enable the large Kerr rotation in MnBi to be exploited for data storage applications (Bandaru *et al*. 1998, Sabiryanov and Jaswal 1999).

See also: Density Functional Theory: Magnetism; Magneto-optic Recording: Total Film Stack, Layer Configuration; Magneto-optic Recording: Overwrite and Associated Problems; Magneto-optical Effects, Enhancement of

Bibliography

Bandaru P, Sands T D, Kubota Y, Marinero E E 1998 Decoupling the structural and magnetic phase transitions in magneto-optic MnBi thin films by the partial substitution of Cr for Mn. *Appl. Phys. Lett*. **72**, 2337–9
Bennett H S, Stern E A 1965 Faraday effect in solids. *Phys. Rev*. **137**, 448–61
Bloomberg D S, Naville Connell G A, Mansuripur M 1996 Magnetooptical recording. In: Mee C D, Daniel E D (eds.) *Magnetic Recording Technology*. McGraw-Hill, Boston, Chap. 10, pp. 10.1–10.101
Di G Q, Iwata S, Tsunashima S, Uchiyama S 1992 Magneto-optical Kerr effect of MnBi and MnBiAl films. *J. Magn. Magn. Mater*. **104–7**, 1023–4
Mazin I I, Maksimov Ye G, Rashkeev S N, Uspenskii Yu A 1989 Microscopic calculations of the dielectric response function of metals. In: Golovashkin A I (ed.) *Metal Optics and Superconductivity*. Nova Science, New York, pp. 1–106
Sabiryanov R F, Jaswal S S 1996 Magneto-optical properties of MnBi and MnBiAl. *Phys. Rev. B*. **53**, 313–7
Sabiryanov R F, Jaswal S S 1999 Magneto-optical properties of MnBi doped with Cr. *J. Appl. Phys*. **85**, 5109–11
Wang C S, Callaway J 1974 Band structure of nickel: Spin–orbit coupling, the Fermi surface, and the optical conductivity. *Phys. Rev. B* **9**, 4897–907
Ziman J M 1972 *Principles of the Theory of Solids*. Cambridge University Press, Cambridge, UK

R. F. Sabiryanov and S. S. Jaswal
University of Nebraska, Lincoln, Nebraska, USA

Magnetoresistance in Transition Metal Oxides

If the electrical resistance of a material depends on the strength of the magnetic field which it experiences, then the material is said to show the property of magnetoresistance (MR). This property has many useful applications: it enables magnetic field strength to be deduced from a relatively simple measurement of electrical resistance, and it allows magnetic fields to control the flow of current in a circuit, i.e., a magnetic switch. As recently as 1988, a 50% drop in the resistance of an Fe/Cr multilayer device in a field of 2 T at a temperature of 4.2 K was described as "huge" (Baibich *et al*. 1988). Since that time, considerable progress has been made towards producing a material that shows a larger effect at higher temperatures in weaker fields, with most of the recent research focusing on mixed-metal oxides containing manganese, for example $La_{1-x}Sr_xMnO_3$. The level of success has been such that the word used to describe the magnetoresistance has changed from huge, via giant (GMR), to colossal (CMR), although at the time of writing (2000) the cause of the enhancement is not fully understood. The oxides that have shown the most interesting behavior are described below; a number of more detailed reviews are available (Battle and Rosseinsky 1999, Bishop and Röder 1997, Ramirez 1997, Rao and Cheetham 1997).

1. Perovskites

The seminal paper in the study of MR in mixed-metal oxides was concerned with $Nd_{0.5}Pb_{0.5}MnO_3$ (Kusters *et al*. 1989), a compound that adopts the relatively common, cubic (or pseudo-cubic) perovskite crystal structure. This structure has the general formula ABO_3, with the possibility of substitution on the A site (ideally 12-coordinated by oxide ions) to form $A_{1-x}A'_xBO_3$, or on the B site (6-coordinated) to form $AB_{1-x}B'_xO_3$. Many aspects of the behaviour of A-site substituted $Nd_{0.5}Pb_{0.5}MnO_3$, including the adoption of a perovskite-related structure, have subsequently been shown to be common among MR oxides. The majority of the compounds to be discussed below contain manganese in a mixed valence state, that is, the average oxidation state of the transition-metal cation lies between $+3$ and $+4$, and the average number of electrons in the 3*d* electron shell of each cation is therefore non-integral, lying between 4 and 3 for Mn^{3+} and Mn^{4+} respectively. At temperatures above 200 K, the valence electrons are localized and the electrical conductivity of $Nd_{0.5}Pb_{0.5}MnO_3$ is activated.

However, a transition from an insulating to a metallic state occurs on cooling through 185 K. This is typical of MR oxides, as is the fact that the Curie temperature (T_C), below which the material is ferromagnetic, coincides with the temperature of the metal–insulator (MI) transition. The coexistence of metallic conductivity and ferromagnetism is often accounted for in terms of the double-exchange mechanism (Zener 1951), which argues that the ease of transferring the extra electron associated with a Mn^{3+} cation to a neighboring Mn^{4+} cation, thus establishing a current, is greatest when the outer electrons on the two cations have parallel spins, and that ferromagnetic coupling of the atomic magnetic moments therefore reduces the electrical resistivity. The MR effect is greatest at temperatures slightly above T_C, where the application of a magnetic field

increases the degree of spin alignment in a material which is susceptible to short-range magnetic coupling, thus reducing the spin-scattering of the conduction electrons and effectively moving the MI transition to higher temperatures.

Hence, the resistivity of $Nd_{0.5}Pb_{0.5}MnO_3$ decreases by two orders of magnitude when it is subjected to a field of 11 T at 190 K, with $T_C = 184 \pm 1$ K. This reduction, although large enough to be useful, is occurring at too low a temperature and too high a field to be of practical benefit. In the late 1990s, a great deal of effort was expended in order to shift the region of maximum effect to higher temperatures and to reduce the value of the required field. The perovskites having the general formula $Ln_{1-x}A_xMnO_3$, where Ln is a metal from the lanthanide series and A is an alkaline earth (group II) metal, were studied in great detail. Changes in the value of x produced changes in the mean oxidation state of the manganese cations, and hence changes in the population of the conduction ($3d$) band. They also caused a variation in the mean size of the cations, and hence subtle changes in the details of the crystal structure.

This chemical approach resulted (Urushibara *et al.* 1995) in the observation of 90% MR (defined as $-100[\rho(B)-\rho(0)]/\rho(0)$) at 300 K in $La_{0.875}Sr_{0.175}$ MnO_3, albeit in a field of 15 T. Thus, the temperature problem was solved, but not that of the field strength. It should be noted that the oft-cited chemical similarity of the lanthanide elements cannot be assumed in this research area. The electronic phase diagrams of $Ln_{1-x}A_xMnO_3$ are very sensitive to the particular cations (Ln and A) involved, as well as to their concentration. Although perovskites containing manganese have dominated recent research into MR effects in oxide materials, a number of manganese-free systems have also been studied. One such system (Kobayashi *et al.* 1998) is Sr_2FeMoO_6, a perovskite with an ordered arrangement of two cations over the 6-coordinate sites. This compound is metallic with $T_C \sim 415$ K, and it shows 10% MR in 7 T at 300 K. Note that in analyzing magnetotransport data on these materials there is a need to distinguish between intrinsic MR and spin-dependent intergrain tunnelling effects (Hwang *et al.* 1996), the latter being important in low fields.

2. $n = 2$ Ruddlesden–Popper Phases

The perovskite phases described above are the $n = \infty$ members of the Ruddlesden–Popper family having the general formula $(A, A')_{n+1}(B, B')_nO_{3n+1}$. CMR has also been observed in compounds which correspond to the $n = 2$ member of the series (Fig. 1). In the case of $n = \infty$, a three-dimensional, infinite network of vertex-sharing BO_6 octahedra is present, with the A cations occupying interstices between the octahedra. For $n = 2$, the octahedral network is

(a)

(b)
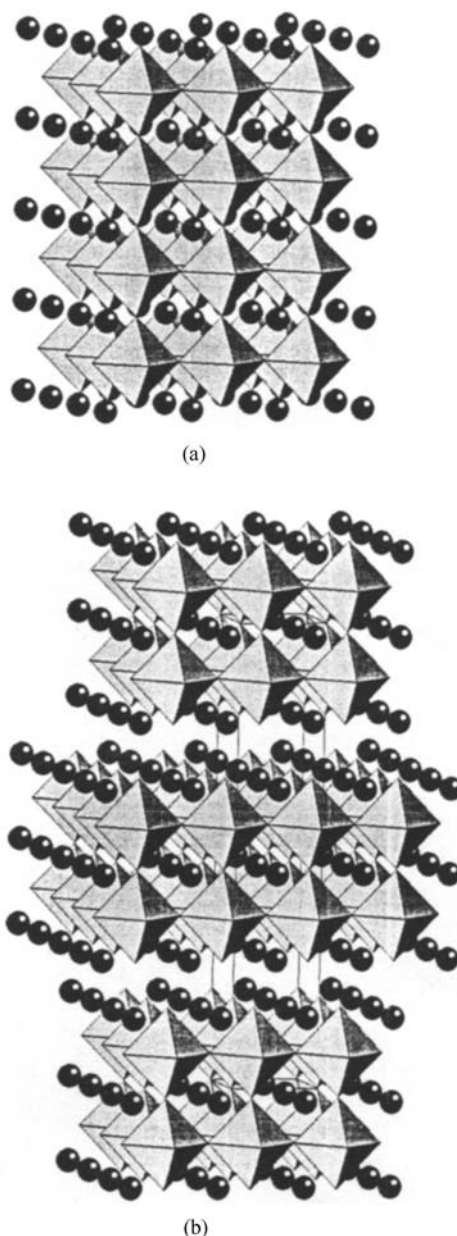
Figure 1
Crystal structures of the Ruddlesden–Popper phases having (a) $n = \infty$ (perovskite) and (b) $n = 2$. MnO_6 octahedra are shown, along with A site cations.

infinite in two dimensions, but it is broken into blocks, each only two (i.e., n) octahedra wide, along the third direction. The two-dimensional nature of this structure introduces anisotropy into the electronic properties of the oxides. $Sr_{1.8}La_{1.2}Mn_2O_7$ was one of the first $n = 2$ compositions to be studied from the

point of view of CMR (Moritomo *et al.* 1996). It was found to show a MI transition coincident with the Curie temperature, $T_C = 126$ K, although the conductivity parallel to the infinite perovskite blocks was two orders of magnitude greater than that in the perpendicular direction.

MR was observed both parallel and perpendicular to the blocks, and the low-field effect was much stronger than had been observed in $n = \infty$ (La, Sr)MnO$_3$; in the two-dimensional material $\rho(0)/\rho(H) = 110\%$ in 0.3 T and $\sim 3000\%$ in 1 T. The chemical sensitivity of these systems is demonstrated by the behavior of Sr$_{1.6}$La$_{1.4}$Mn$_2$O$_7$, which, in contrast to that of Sr$_{1.8}$La$_{1.2}$Mn$_2$O$_7$, is markedly different parallel and perpendicular to the layers (Kimura *et al.* 1996), with the strongest magnetoresistance being in the latter direction. This has lead to comparisons being drawn between the multilayer devices described above and these Ruddlesden–Popper phases, which are now often referred to as "naturally-layered manganites." CMR has been reported in $n = 2$ compositions containing lanthanides other than lanthanum (Battle and Rosseinsky 1999). As in the case of the perovskites, the electronic properties are very sensitive to the atomic number and concentration of the lanthanide; CMR is not observed in compounds containing the smaller lanthanides. It has been shown that the microstructure of these compounds can be very complex (Sloan *et al.* 1998), with intergrowths of $n = \infty$ perovskite breaking up the regular $n = 2$ structure.

3. Other Ruddlesden–Popper Phases

There have been few reports of CMR in $n = 1$ (K$_2$NiF$_4$-like) phases, in which Mn^{3+}/Mn^{4+} charge ordering appears to be common. The most promising system studied to date is perhaps Ca$_{2-x}$Ln$_x$MnO$_4$ ($0 < x < 0.2$, Ln $=$ Pr, Sm, Gd, Ho), with 64% MR being observed in Ca$_{1.92}$Pr$_{0.08}$MnO$_4$ in 7 T at 40 K (Maignan *et al.* 1998). The $n = 3$ phases studied to date have shown lower MR ratios.

4. Pyrochlores

The observation of CMR in the pyrochlore Tl$_2$Mn$_2$O$_7$ (Shimakawa *et al.* 1996) increased the breadth of contemporary magnetotransport research. Tl$_2$Mn$_2$O$_7$ orders ferromagnetically at 142 K, and the MR is largest in this temperature region (86% in 7 T). However, the pyrochlore is metallic both above and below T_C, that is, the onset of ferromagnetic ordering is not accompanied by a MI transition. Furthermore, there is apparently no mixed valency on the manganese sublattice; only Mn^{4+} is present. The CMR observed in this compound is therefore not readily explained by arguments based on double exchange, and it has been shown (Ramirez and Subramanian

1997) that the MR can be increased by doping with scandium to form Tl$_{2-x}$Sc$_x$Mn$_2$O$_7$.

During the last decade of the twentieth century considerable progress was made in improving the magnetotransport properties of mixed-metal oxides. Perovskites that show a practically useful effect at room temperature have been identified; unfortunately the field needed to produce the effect is impractically large. RP phases show an effect at lower fields, but at temperatures too far below ambient to be useful. The remaining challenge is to find new materials that show a colossal effect at high temperatures. These new materials may or may not be perovskite-related, and they may or may not be manganese-based.

See also: Giant Magnetoresistance; Giant Magnetoresistance: Metamagnetic Transitions in Metallic Antiferromagnetics; Magnetoresistance: Anisotropic; Magnetoresistance: Magnetic and Nonmagnet Intermetallics

Bibliography

Baibich M N, Broto J M, Fert A, Dau F N V, Petroff F, Eitenne P, Creuzet G, Friederich A, Chazelas J 1988 Giant magnetoresistance of (001)Fe/(001)Cr magnetic superlattices. *Phys. Rev. Lett.* **61**, 2472–5

Battle P D, Rosseinsky M J 1999 Synthesis, structure, and magnetic properties of $n = 2$ Ruddlesden-Popper manganates. *Curr. Opin. Solid State Mater. Sci.* **4**, 163–70

Bishop A R, Röder H 1997 Theory of colossal magnetoresistance. *Curr. Opin. Solid State Mater. Sci.* **2**, 244–57

Hwang H Y, Cheong S W, Ong N P, Batlogg B 1996 Spin-polarized intergrain tunneling in La$_{2/3}$Sr$_{1/3}$MnO$_3$. *Phys. Rev. Lett.* **77**, 2041–4

Kimura T, Tomioka Y, Kuwahara H, Asamitsu A, Tamura M, Tokura Y 1996 Interplane tunneling magnetoresistance in a layered manganite crystal. *Science* **274**, 1698–701

Kobayashi K L, Kimura T, Sawada H, Terakura K, Tokura Y 1998 Room temperature magnetoresistance in an oxide material with an ordered double perovskite structure. *Nature* **395**, 677–80

Kusters R M, Singleton J, Keen D A, McGreevy R, Hayes W 1989 Magnetoresistance measurements on the magnetic semiconductor Nd$_{0.5}$Pb$_{0.5}$MnO$_3$. *Physica B* **155**, 362–5

Maignan A, Martin C, VanTendeloo G, Hervieu M, Raveau B 1998 Ferromagnetism and magnetoresistance in monolayered manganites Ca$_{2-x}$Ln$_x$MnO$_4$. *J. Mater. Chem.* **8**, 2411–6

Moritomo Y, Asamitsu A, Kuwahara H, Tokura Y 1996 Giant magnetoresistance of manganese oxides with a layered perovskite structure. *Nature* **380**, 141–4

Ramirez A P 1997 Colossal magnetoresistance. *J. Phys.: Condens. Matter* **9**, 8171–99

Ramirez A P, Subramanian M A 1997 Large enhancement of magnetoresistance in Tl$_2$Mn$_2$O$_7$—pyrochlore versus perovskite. *Science* **277**, 546–9

Rao C N R, Cheetham A K 1997 Giant magnetoresistance, charge ordering, and related aspects of manganates and other oxide systems. *Adv. Mater.* **9**, 1009–20

Shimakawa Y, Kubo Y, Manako T 1996 Giant magnetoresistance in Tl$_2$Mn$_2$O$_7$ with the pyrochlore structure. *Nature* **379**, 53–5

Sloan J, Battle P D, Green M A, Rosseinsky M J, Vente J F 1998 A HRTEM study of the Ruddlesden–Popper compositions $Sr_2Ln_2O_7$ (Ln = Y, La, Nd, Eu, Ho). *J. Solid State Chem.* **138**, 135–40

Urushibara A, Moritomo Y, Arima T, Asamitsu A, Kido G, Tokura Y 1995 Insulator–metal transition and giant magnetoresistance in $La_{1-x}Sr_xMnO_3$. *Phys. Rev. B* **51**, 141103–9

Zener C 1951 Interaction between *d*-shells in the transition metals. *Phys. Rev.* **82**, 403–5

P. D. Battle
University of Oxford, UK

Magnetoresistance, Anisotropic

The electrical conductivity of spontaneously magnetized materials depends on the relative orientation of the electrical current and the magnetization. This phenomenon, called anisotropic magnetoresistance (AMR) or spontaneous magnetoresistance anisotropy (SMA), was discovered by Lord Kelvin in the middle of the nineteenth century. However, intensive investigations on AMR started only in the 1950s with the work of Smit (1951) and van Elst (1959). Although technical applications of AMR were suggested in the 1970s, corresponding devices (sensors and read heads for hard disks) (Göpel *et al.* 1989) were not introduced commercially until about 20 years later.

The physical origin of AMR is the reduction of the symmetry of a magnetized material compared to its nonmagnetic state caused by the simultaneous presence of the magnetization and spin–orbit coupling. The first qualitative models to describe AMR were developed by Smit (1951) and Campbell *et al.* (1970) and have been extended subsequently by others. A parameter-free theoretical description of AMR has been published (Banhart and Ebert 1995).

1. Phenomenological Description

For a material that is homogeneously magnetized along the *z*-axis but otherwise isotropic, the conductivity tensor takes the following form (Kleiner 1966, Cracknell 1973):

$$\boldsymbol{\sigma} = \begin{pmatrix} \sigma_\perp & \sigma_H & 0 \\ -\sigma_H & \sigma_\perp & 0 \\ 0 & 0 & \sigma_\parallel \end{pmatrix} \tag{1}$$

with the corresponding resistivity tensor being given by

$$\boldsymbol{\rho} = \begin{pmatrix} \rho_\perp & \rho_H & 0 \\ -\rho_H & \rho_\perp & 0 \\ 0 & 0 & \rho_\parallel \end{pmatrix} \tag{2}$$

The tensor elements $\rho_\perp$ and $\rho_\parallel$ are called transverse and longitudinal electrical resistivity, respectively, with their average

$$\bar{\rho} = \tfrac{2}{3}\rho_\perp + \tfrac{1}{3}\rho_\parallel \tag{3}$$

giving the isotropic resistivity $\bar{\rho}$. Normalizing $\rho_\perp$ and $\rho_\parallel$ using $\bar{\rho}$ leads to the transverse and longitudinal magnetoresistivity, respectively:

$$\left(\frac{\Delta\rho}{\bar{\rho}}\right)_\perp = \frac{\rho_\perp - \bar{\rho}}{\bar{\rho}} \tag{4}$$

$$\left(\frac{\Delta\rho}{\bar{\rho}}\right)_\parallel = \frac{\rho_\parallel - \bar{\rho}}{\bar{\rho}} \tag{5}$$

The difference of these two quantities gives the AMR ratio

$$\frac{\Delta\rho}{\bar{\rho}} = \frac{\rho_\parallel - \rho_\perp}{\bar{\rho}} \tag{6}$$

The off-diagonal element ρ_H of the resistivity tensor is called the Hall resistivity and represents the anomalous or spontaneous Hall effect (Karplus and Luttinger 1954, Smit 1955). The elements of the conductivity tensor $\boldsymbol{\sigma}$ are denoted in an analogous way to those of the resistivity tensor $\boldsymbol{\rho}$ with the following relationships between the various elements:

$$\sigma_\perp = \frac{\rho_\perp}{\rho_\perp^2 + \rho_H^2} \quad \sigma_\parallel = \frac{1}{\rho_\parallel} \quad \sigma_H = \frac{\rho_H}{\rho_\perp^2 + \rho_H^2} \tag{7}$$

$$\rho_\perp = \frac{\sigma_\perp}{\sigma_\perp^2 + \sigma_H^2} \quad \rho_\parallel = \frac{1}{\sigma_\parallel} \quad \rho_H = \frac{\sigma_H}{\sigma_\perp^2 + \sigma_H^2} \tag{8}$$

2. Basic Properties

In principle, the above definitions apply to a single-domain sample. For a multidomain sample one therefore has to apply an external magnetic field to align the magnetization. This may lead, for example, to a variation of $\rho_\perp$ and $\rho_\parallel$ with the field, as shown in Fig. 1 (van Elst 1959). Because the ordinary magnetoresistance is superimposed onto the spontaneous magneto-resistance the proper values $\rho_\perp^0$ and $\rho_\parallel^0$, corresponding to the single-domain state of the sample are obtained by an extrapolation of the high-field data to zero external field.

The simple form given above for the conductivity and resistivity tensors is not restricted to isotropic materials, but applies to any material for which the direction of the magnetization coincides with an at least three-fold rotational symmetry axis (Kleiner 1966, Cracknell 1973). Furthermore, it can be applied without modifications for polycrystalline materials. For less symmetric situations the shape of the tensors in Eqns. (1) and (2) will change. In particular, for single crystals one finds that the AMR varies if the
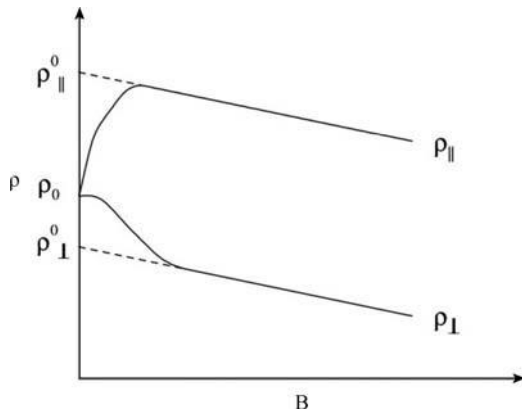
Figure 1
Dependency of the transverse and longitudinal electrical resistivity, $\rho_\perp$ and $\rho_\parallel$, respectively, on an external magnetic field, B.

orientation of the magnetization with respect to the crystal axis is changed (Becker and Döring 1939).

3. Materials and Applications

The AMR effect can be observed in principle in any spontaneously magnetized material. However, most experimental work has been devoted to systems based on the transition metals iron, cobalt, and nickel. In the search for materials with high AMR ratio, diluted and concentrated alloys among these elements, but also with other transition metals (e.g., chromium, vanadium, copper, palladium, and platinum) or non-transition elements (e.g., aluminum, silicon, tin) have been investigated (McGuire and Potter 1975, Dorleijn 1976). Among these systems the highest values for the AMR ratio $\Delta\rho/\bar{\rho}$ have been found for nickel-based alloys.

In particular, a rather simple empirical relationship between the AMR ratio $\Delta\rho/\bar{\rho}$ and the average magnetic moment μ has been found for concentrated binary nickel-based alloys (see Fig. 2 and below). This relationship implies that the AMR ratio can be optimized within certain limits by a suitable choice of the alloy partners and their concentration. An upper limit seems to be given by the data for NiCo alloys and NiFeCo alloys, which show AMR ratios of up to 30% at low temperatures. Unfortunately, the AMR ratio rapidly decreases with increasing temperature. For example, for $Ni_{81}Fe_{19}$ one has $\Delta\rho/\bar{\rho} = 20\%$ at $T = 20\,K$, but only about 3% at $T = 300\,K$.

The AMR effect has also been investigated for a number of amorphous alloy systems, e.g., Fe–Si, Fe–Zr, and Fe–V–B. These amorphous systems are attractive because they can be easily prepared as thin films by various techniques and because their
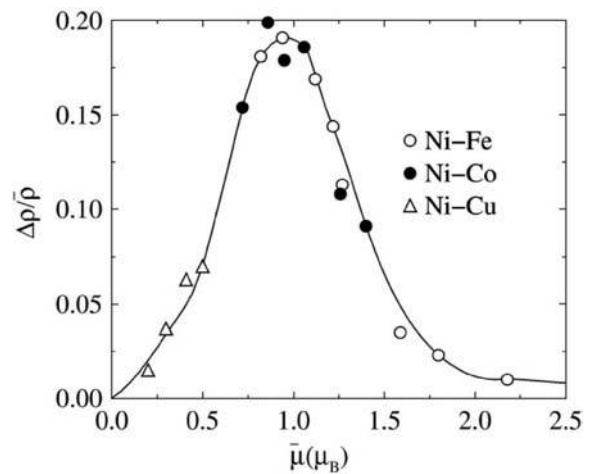
Figure 2
AMR ratio $\Delta\rho/\bar{\rho}$ at 20 K as a function of the average magnetic moment $\bar{\mu}$ for various 3d element alloys (after Wijn 1991).

isotropic resistivity $\bar{\rho}$ is in general almost temperature independent (see *Amorphous Intermetallic Alloys: Resistivity*). Unfortunately, $\bar{\rho}$ is normally quite high (of the order of $100\,\mu\Omega\,cm$) leading to AMR ratios that are usually not much higher than 1%. In contrast to this property of transition metal-based amorphous systems, a very pronounced AMR effect with $\Delta\rho/\bar{\rho}$ up to 26% at low temperature has been found for ferromagnetic amorphous alloys based on uranium and antimony (Freitas and Plaskett 1990). This finding can be ascribed to the strong spin–orbit coupling of uranium (see below).

Although the maximum AMR ratio that can be achieved at room temperature is relatively small, it is nevertheless high enough to be exploited in sensor and storage technology (Göpel *et al.* 1989). Transition metal alloys are very suitable for this purpose, because they can easily be prepared by evaporation or sputtering deposition as thin films. In some cases the resistivity $\bar{\rho}$ of such films can be decreased by up to 30% by tempering. This increases the AMR ratio accordingly leading to a higher output signal for a given input power (Butherus and Nakahara 1985). Further important restrictions for applications are a low magnetostriction and a small coercivity field.

These requirements are extremely well fulfilled by permalloy that is free of magnetostriction at 81 at.% nickel. In addition, it has at this composition a very low coercivity field of about $100\,Am^{-1}$ and a low uniaxial anisotropy energy constant of about $200\,Jm^{-3}$. Although the AMR ratio for the NiFe–alloy system is highest for about 90 at.% nickel and although higher values for $\Delta\rho/\bar{\rho}$ are achieved by other transition metal alloy systems (see above), these suitable properties make $Ni_{81}Fe_{19}$ permalloy the most

commonly used AMR material for applications. According to this situation, industrial research and development aims to optimize the geometry and readout technique of AMR devices instead of searching for more efficient AMR materials (Eijkel and Fluitman 1990).

4. Phenomenological Theories

Transport phenomena in magnetic materials are in general discussed in the framework of two simplifying models (Rossiter 1987). The first is Matthiessen's rule that states that thermal and impurity scattering contribute independently to the electrical resistivity (see *Boltzmann Equation and Scattering Mechanisms*). The two-current model of Mott assumes that the scattering of electrons at impurities in a magnetized sample does not change the electron spin orientation relative to the magnetization, and that the scattering is different for majority and minority spin electrons. This implies that there are two independent currents in a magnetic material with two corresponding subband resistivities, $\rho^{\uparrow}$ and $\rho^{\downarrow}$, that add up to the total resistivity according to

$$\frac{1}{\bar{\rho}} = \frac{1}{\rho^{\downarrow}} + \frac{1}{\rho^{\uparrow}} \tag{9}$$

This approach clearly ignores spin-mixing, e.g., due to finite temperature magnon scattering. This effect is sometimes considered by introducing a parameter $\rho^{\uparrow\downarrow}$ that represents the rate of spin-flip transitions leading to (Fert and Campbell 1968)

$$\bar{\rho} = \frac{\rho^{\downarrow}\rho^{\uparrow} + \rho^{\uparrow\downarrow}(\rho^{\downarrow} + \rho^{\uparrow})}{\rho^{\downarrow} + \rho^{\uparrow} + 4\rho^{\uparrow\downarrow}} \tag{10}$$

The AMR originates from the different scattering rate of electrons that travel parallel or perpendicular to the direction of the magnetization. This is ascribed in general primarily to the spin–orbit coupling. Accordingly, it has been suggested that the AMR ratio can be expressed by (Campbell 1970)

$$\frac{\Delta\rho}{\bar{\rho}} = \gamma(\alpha - 1) \quad \text{with} \quad \alpha = \frac{\rho^{\downarrow}}{\rho^{\uparrow}} \tag{11}$$

where γ, primarily determined by spin–orbit coupling, describes the anisotropy of the spin-resolved resistivities according to

$$\rho_{\parallel}^{\uparrow} = \rho_{\perp}^{\uparrow} + \gamma\rho_{\perp}^{\downarrow}, \quad \rho_{\parallel}^{\downarrow} = \rho_{\perp}^{\downarrow} + \gamma\rho_{\perp}^{\uparrow} \tag{12}$$

In practice one determines the subband resistivities $\rho^{\uparrow(\downarrow)}$ and their ratio α indirectly by measuring deviations from Matthiessen's rule for the temperature dependence of the resistivity or for ternary alloys. The applicability of this model is shown in Fig. 3. Here experimental AMR ratios for various dilute
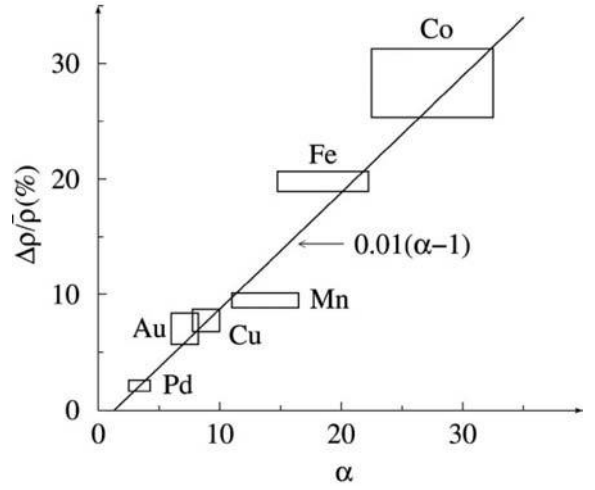
Figure 3
AMR ratio for various dilute nickel alloys NiX, with X = Pd, Au, Cu, Fe, Co (Campbell *et al.* 1970).

nickel alloys are plotted as a function of experimental values for α. Obviously, the data approximately lie on a straight line given by Eqn. (11), if γ is chosen appropriately. However, for alloys for which α is close to unity, pronounced deviations from the behavior shown in Fig. 3 occur. Moreover, first-principles calculations have shown that the measured α is greatly reduced in comparison with values calculated on the basis of the two-current model because spin-mixing mechanisms are always present in real materials. These have been sometimes accounted for by using an extended version of Eqn. (11) (Campbell *et al.* 1970):

$$\frac{\Delta\rho}{\bar{\rho}} = \gamma\frac{(\rho^{\downarrow} - \rho^{\uparrow})\rho^{\downarrow}}{\rho^{\uparrow}\rho^{\downarrow} + \rho^{\uparrow\downarrow}(\rho^{\uparrow} + \rho^{\downarrow})} \tag{13}$$

5. Quantitative Models

The first step towards a quantitative description of AMR was the combination of the model described above with a calculation of the residual electrical resistivity of disordered alloys on the basis of Mott's two-current model (Akai 1977). This questionable approximation could be avoided by the development of a fully relativistic description for the AMR effect (Banhart and Ebert 1995). The starting point of this approach is the formulation of the conductivity tensor as a current–current–correlation function within the Kubo–Greenwood response formalism (Edwards 1958):

$$\sigma_{\mu\mu} = \frac{\hbar}{\pi V_{\text{cryst}}} Tr\langle j_{\mu}\text{Im}G^{+}(E_{\text{F}})j_{\mu}\text{Im}G^{+}(E_{\text{F}})\rangle_{\text{conf}} \tag{14}$$

A similar but somewhat more complex expression can be given for the off-diagonal elements $\sigma_{\mu\nu}$. In Eqn. (14) the underlying electronic structure of the system is described by the retarded electronic Green's function $G^+(E_F)$ for the Fermi energy E_F (Butler 1985). In practice, this is calculated by means of multiple scattering theory.

Model calculations based on Eqn. (14) with the spin–orbit coupling manipulated reveal the role of this relativistic effect for AMR. Its major effect is to mix the minority and majority spin systems. As a consequence the two-current model in its strict sense is obviously not applicable. For the isotropic resistivity $\bar\rho$ it nevertheless gives reasonable results if the spin polarization at the Fermi level is not too high. This applies, for example, for the alloy systems Co_xPd_{1-x} and Co_xPt_{1-x}, while for Fe_xNi_{1-x} inclusion of the spin–orbit coupling increases $\bar\rho$ by up to an order of magnitude compared to a calculation based on the two-current model.

The model calculations also demonstrate that the AMR effect is indeed caused by the spin–orbit coupling with AMR increasing quadratically with its strength. In addition it is found that the spin–orbit coupling causes AMR nearly exclusively via the mixing of the spin systems. This implies in particular that contributions to the AMR due to the spin-diagonal part of the spin–orbit coupling can be neglected.

Use of the formalism described above leads for the conductivity tensor automatically to the structure given by Eqn. (1) that is required from symmetry considerations. As an example of its application, Fig. 4 shows results for the AMR ratio obtained for the alloy system Co_xPd_{1-x} and Co_xPt_{1-x} (without

manipulating the spin–orbit coupling). The satisfying agreement implies that other possible sources of AMR, e.g., magnon scattering processes, can be neglected. Equation (14) has been exploited only to account for the residual resistivity caused by the chemical disorder in alloys. However, it also allows the incorporation of other mechanisms and supplies an appropriate basis to deal with the temperature dependency of AMR.

6. Summary

The AMR effect is a galvanomagnetic effect, which can be observed in any spontaneously magnetized material. Most experimental work that aimed to optimize the AMR ratio of materials applied in sensor and storage technology has been focused on transition metal alloys. For these systems, values for the AMR ratio of up to 30% have been found at low temperatures, with only a few percent remaining at room temperature.

A phenomenological description of the AMR effect is obtained by assuming an anisotropy in the transport properties, represented by a corresponding conductivity tensor. This anisotropy can primarily be ascribed to the presence of the spin–orbit coupling and the magnetic ordering. Starting from this, microscopic descriptions of the AMR effect have been developed. Most of this theoretical work has been based on Mott's two-current model together with the use of some parameters. Modern *ab initio* band structure calculations allow parameter-free calculations of AMR. Corresponding investigations essentially confirm the ideas of the previous more phenomenological work and supply a very detailed understanding for the physical mechanisms giving rise to AMR.

See also: Amorphous Intermetallic Alloys: Resistivity; Giant Magnetoresistance; Giant Magnetoresistance: Metamagnetic Transitions in Metallic Antiferromagnets; Magnetoresistance: Magnetic and Nonmagnetic Intermetallics

Figure 4
AMR ratio $\Delta\rho/\bar\rho$ for the alloy systems Co_xPd_{1-x} and Co_xPt_{1-x} at $T = 0\,K$ calculated by means of Eqn. (14) (filled symbols) and compared to experimental data (Ebert *et al.* 1996).

Bibliography

Akai H 1977 *Physica B* **86–88**, 539–40
Banhart J, Ebert H 1995 *Europhys. Lett.* **32**, 517–22
Becker R, Döring W 1939 *Ferromagnetismus*. Springer-Verlag, Berlin
Butherus A D, Nakahara S 1985 *IEEE Trans. Magn.* **21**, 1301–5
Butler W H 1985 *Phys. Rev. B* **31**, 3260–77
Campbell I A 1970 *Phys. Rev. Lett.* **24**, 269–71
Campbell I A, Fert A, Jaoul O 1970 *Physica C* **3**, S95–101
Cracknell A P 1973 *Phys. Rev. B* **7**, 2145–54
Dorleijn J W F 1976 *Philips Res. Rep.* **31**, 287–410
Ebert H, Banhart J, Vernes A 1996 *Phys. Rev. B* **54**, 8479–86
Edwards S F 1958 *Phil. Mag.* **3**, 1020–31

Eijkel K J M, Fluitman J H J 1990 *IEEE Trans. Magn.* **26**, 311–21

van Elst H C 1959 *Physica* **25**, 708–20

Fert A, Campbell I A 1968 *Phys. Rev. Lett.* **21**, 1190–2

Freitas P P, Plaskett T S 1990 *Phys. Rev. Lett.* **64**, 2184–7

Göpel W, Hesse J, Zemel J N (eds.) 1989 *Magnetic Sensors.* VCH, Weinheim, Germany

Karplus R, Luttinger J M 1954 *Phys. Rev.* **95**, 1154–60

Kleiner W H 1966 *Phys. Rev.* **142**, 318–26

McGuire T R, Potter R I 1975 *IEEE Trans. Magn.* **11**, 1018–38

Rossiter P L 1987 *The Electrical Resistivity of Metals and Alloys.* Cambridge University Press, Cambridge, UK

Smit J 1951 *Physica* **16**, 612–27

Smit J 1955 *Physica* **21**, 877–87

Wijn H P J (ed.) 1991 *Magnetic Properties of Metals d-Elements, Alloys and Compounds.* Springer-Verlag, Berlin

H. Ebert and A. Vernes
Universität München, Munich, Germany

J. Banhart
Fraunhofer-Institut für Angewandte Materialforschung, Bremen, Germany

Magnetoresistance: Magnetic and Nonmagnetic Intermetallics

The theory of the magnetoresistance of metals is concerned with the description of the motion of an electron under the combined influence of externally applied electric and magnetic fields (assuming thermal equilibrium, i.e., $\nabla T = 0$) in the internal periodic potential owing to the ionic lattice. As is discussed in *Boltzmann Equation and Scattering Mechanisms*, an external magnetic field influences the transport phenomena but does not contribute to a current in the same way as an electric field.

The Boltzmann theory will be used for the discussion of the general tendencies of the magnetoresistance.

Ohm's law for the electrical transport in metals in magnetic fields is given by

$$\vec{I} = \overleftrightarrow{\sigma}(T, \vec{B}) \cdot \vec{E} \tag{1}$$

where $\vec{I}$ is the electrical current density, $\vec{E}$ the electric field, and $\overleftrightarrow{\sigma}$ the temperature and magnetic field-dependent conductivity tensor. In the absence of an external magnetic field the conductivity becomes a scalar for a cubic lattice symmetry. If a magnetic field is applied this symmetry is broken, but the Onsager relationships still hold:

$$\sigma_{ij}(\vec{B}) = \sigma_{ji}(-\vec{B}) \tag{2}$$

The conductivity tensor, $\overleftrightarrow{\sigma}(\vec{B})$, for an isotropic (cubic) material with $\vec{B} = (0, 0, B\,\vec{e}_z)$ is given below

from which the corresponding resistivity tensor, $\overleftrightarrow{\rho}(B)$, follows:

$$\overleftrightarrow{\sigma}(B) = \begin{pmatrix} \sigma_{xx}(B) & \sigma_{xy}(B) & 0 \\ -\sigma_{xy}(B) & \sigma_{xx}(B) & 0 \\ 0 & 0 & \sigma_{zz}(B) \end{pmatrix} \rightarrow$$

$$\overleftrightarrow{\rho}(B) = \begin{pmatrix} \rho_{\perp}(B) & \rho_{H}(B) & 0 \\ -\rho_{H}(B) & \rho_{\perp}(B) & 0 \\ 0 & 0 & \rho_{\|}(B) \end{pmatrix} \tag{3}$$

where $\rho_{\perp}$ and $\rho_{\|}$ are the resistivity in a transverse and a longitudinal external magnetic field, respectively, and ρ_H is the Hall resistivity.

The *transverse* and the *longitudinal magnetoresistance* are defined by (respectively):

$$\frac{\Delta\rho_{\perp}}{\rho} = \frac{\rho_{\perp}(T, B) - \rho(T, B = 0)}{\rho(T, B = 0)} \text{ and}$$

$$\frac{\Delta\rho_{\|}}{\rho} = \frac{\rho_{\|}(T, B) - \rho(T, B = 0)}{\rho(T, B = 0)} \tag{4}$$

1. Magnetoresistance in the Scope of the Boltzmann Formalism

In accordance with *Boltzmann Equation and Scattering Mechanisms* we assume that the electrons, moving through the periodic array of the ions in the lattice, can be described by Bloch waves. The semiclassical description of the movement of these packets is given by (see Eqn. (6) of *Boltzmann Equation and Scattering Mechanisms*):

$$\vec{v}_{\gamma} = \frac{1}{\hbar}\vec{\nabla}_k E_{n\sigma}(\vec{k}), \ \frac{\mathrm{d}\vec{k}}{\mathrm{d}t} = +\frac{e}{\hbar}[\vec{E} + (\vec{v}_{\gamma} \times \vec{B})] \tag{5}$$

where $\vec{E}$ and $\vec{B}$ are the electric and the magnetic fields, respectively, and $\vec{v}_{\gamma}$ is the velocity of a conduction electron.

We are looking for a distribution function as a solution of the Boltzmann equation under the simultaneous influence of an electric and a magnetic field. The Boltzmann equation can be written as:

$$\frac{\partial f}{\partial t} + \frac{e}{\hbar}[\vec{E} + (\vec{v}_{\gamma} \times \vec{B})] \cdot \vec{\nabla}_k f + \vec{v}_{\gamma} \cdot \vec{\nabla} f = \left(\frac{\partial f}{\partial t}\right)_{\mathrm{C}} \tag{6}$$

The term on the right-hand side of Eqn. (6) is the collision term, which is given by:

$$\left(\frac{\partial f}{\partial t}\right)_{\mathrm{C}} = \sum_{\gamma}\big\{f(\gamma')[1 - f(\gamma)]P_{\gamma'\rightarrow\gamma} \\ - f(\gamma)[1 - f(\gamma')]P_{\gamma\rightarrow\gamma'}\big\} \tag{7}$$

where $P_{\gamma'\rightarrow\gamma}$ is the quantum mechanical transition rate of an electron per unit time from state γ' to state

γ. Focusing on stationary solutions only and considering small deviations from the equilibrium, a new function, Φ_γ, is then defined through:

$$f = f_0 + f_1 \text{ with } f_1 = -\left(\frac{\partial f_0}{\partial \varepsilon_\gamma}\right)\Phi_\gamma \qquad (8)$$

Equation (6) can be linearized, which then reads (see also Eqn. (36) of *Boltzmann Equation and Scattering Mechanisms*):

$$[C + \Omega]\Phi_\gamma = -e\left(\frac{\partial f_0}{\partial \varepsilon_\gamma}\right)\vec{v}_\gamma \cdot \vec{E} \qquad (9)$$

where C is the *collision operator* and Ω the *magnetic operator*. These operators are defined by (respectively):

$$C\Phi_\gamma = \frac{1}{k_B T}\sum_{\gamma'} W_{\gamma\gamma'}[\Phi_{\gamma'} - \Phi_\gamma] \qquad (10)$$

$$\Omega\Phi_\gamma = -\frac{e}{\hbar}\frac{\partial f_0}{\partial \varepsilon_\gamma}(\vec{v}_\gamma \times \vec{B}) \cdot \vec{\nabla}_k \Phi_\gamma \qquad (11)$$

where

$$W_{\gamma\gamma'} = f_0(\gamma')[1 - f_0(\gamma)]P_{\gamma' \to \gamma} = W_{\gamma'\gamma} \qquad (12)$$

is the symmetric equilibrium transition probability in first order.

1.1 Solution of the Boltzmann Equation

A formal solution for the function Φ_γ of the linearized Boltzmann equation (Eqn. (9)) is given by:

$$\Phi_\gamma = -e[C + \Omega]^{-1}\left(\frac{\partial f_0}{\partial \varepsilon_\gamma}\right)\vec{v}_\gamma \cdot \vec{E} \qquad (13)$$

For the current density it follows that:

$$\vec{I} = e\sum_\gamma \left(\frac{\partial f_0}{\partial \varepsilon_\gamma}\right)\vec{v}_\gamma \Phi_\gamma = -e^2 \sum_\gamma \left(\frac{\partial f_0}{\partial \varepsilon_\gamma}\right)\vec{v}_\gamma[C + \Omega]^{-1}$$
$$\times \left(\frac{\partial f_0}{\partial \varepsilon_\gamma}\right)\vec{v}_\gamma \cdot \vec{E} = \overleftrightarrow{\sigma} \cdot \vec{E} \qquad (14)$$

where e is the charge, $\vec{v}_\gamma$ the drift velocity of the conduction electrons, and $\overleftrightarrow{\sigma}$ is the conductivity tensor.

1.2 Relaxation Time Approximation

In the scope of this concept the collision term is replaced by a function that is proportional to f_1. This function is a measure of the deviation from the thermal equilibrium in the conduction electron distribution weighted by the inverse relaxation time, τ_γ:

$$\left(\frac{\partial f}{\partial t}\right)_C = -\frac{f - f_0}{\tau_\gamma} = -\frac{f_1}{\tau_\gamma} \qquad (15)$$

which is equivalent to setting the collision operator of Eqn. (10) to:

$$C\Phi_\gamma = \left(\frac{\partial f_0}{\partial \varepsilon_\gamma}\right)\frac{1}{\tau_\gamma}\Phi_\gamma \qquad (16)$$

The relaxation time, τ_γ, can be anisotropic in k-space and different for each band.

2. Normal Magnetoresistance

The effect of an external magnetic field on the electrical resistivity can be considered as consisting of two parts. The first originates from the influence of the magnetic field on the conduction electron trajectories. In between collision events the Lorentz force deflects the electrons on their way through the specimen. This mechanism always increases the resistivity with the field. In the following it will be called "normal magnetoresistance." In practice one distinguishes between two limiting cases known as the "low"- and the "high"-field limit. Under usual experimental conditions with polycrystalline sample material one is always in the low-field limit where the conduction electron traverses a path in a plane perpendicular to the B-field and completes only a small arc before being scattered into another state in k-space. In order to provide an example of the influence of a magnetic field on the resistivity, $\rho(T)$ curves of YAl$_2$ at different magnetic fields are shown in Fig. 1. In inset (a) the temperature dependence of the resistivity at low temperatures in different external fields is given. Inset (b) shows the field dependence of the resistivity at different temperatures.
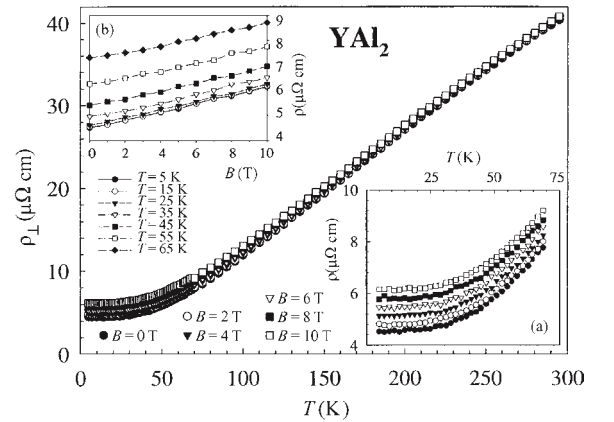
Figure 1
Temperature dependence of the resistivity of YAl$_2$ from 4 K to 300 K in transverse external magnetic fields of various strengths. Inset (a) shows details of the $\rho(B,T)$ curves at low temperatures. Inset (b) shows the field dependence of the resistivity for different temperatures.

2.1 Kohler Rule

Before discussing the temperature variation of the normal magnetoresistance an important and useful rule, the Kohler rule, is discussed. This states that the magnetoresistance can be expressed as

$$\frac{\Delta\rho}{\rho} = \Psi\left(\frac{B}{\rho(B=0,T)}\right) \qquad (17)$$

where Ψ is a general function characteristic of a particular sample material. Rigorously, Eqn. (17) can be justified only if there is a single species of charge carrier (i.e., one conduction band model) and the relaxation time is the same at all points on the Fermi surface. Fortunately the Kohler rule has been found to be a good approximation in many cases where a single scattering mechanism dominates. In the inset of Fig. 2 a so-called Kohler plot of YAl_2 is shown, and it is clear that there are only small deviations from a universal curve at very low temperature ranges. Kohler plots for the two isostructural compounds YAl_2 and YNi_2 have been compared (Gratz *et al.* 1995). In YNi_2 a considerable deviation from the universal curve has been found at lower temperatures for all fields, this being associated with its high residual resistivity. This derives from the impurity scattering, which at low temperature is the dominant relaxation mechanism. However, as the temperature increases the phonon scattering with another relaxation time becomes the dominant scattering mechanism.

The temperature variation of the transverse magnetoresistance ($\Delta\rho_\perp/\rho$) of YAl_2 is shown in Fig. 2. YAl_2 is a representative example of many other nonmagnetic compounds, such as YAg, LuAg, YCu_2, and $LuCu_2$, which show qualitatively a similar
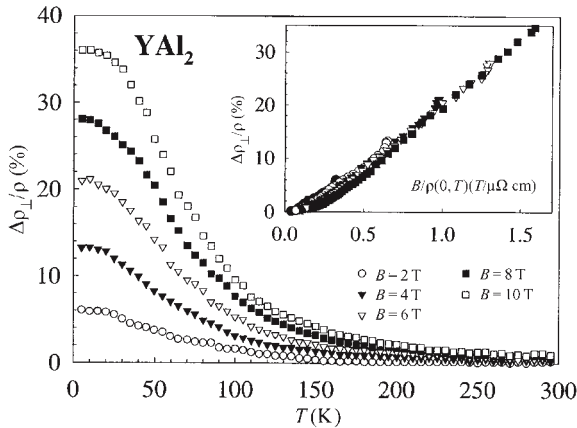
Figure 2
Transverse magnetoresistance of YAl_2 for various field strengths. Inset shows the Kohler plot for YAl_2.

temperature variation of $\Delta\rho_\perp/\rho$ as YAl_2 (Gratz *et al.* 2001). Figure 2 shows that as the temperature increases the influence of the external magnetic field on the resistivity decreases. The increase of $\Delta\rho_\perp/\rho$ with increasing field strength, B, at low temperatures is closely related to the ρ_0 value of the sample, and this may be highlighted with an example. The value of $\Delta\rho_\perp/\rho$ at 4.2 K and 10 T for a YAg sample (cubic CsCl structure, $\rho_0 = 1.8\,\mu\Omega$cm) is 18%. The $\Delta\rho_\perp/\rho$ value for an isostructural sample where 20% of yttrium has been replaced by lutetium ($Y_{0.8}Lu_{0.2}Ag$, i.e., ρ_0 has been increased to $3.6\,\mu\Omega$cm) is only about 6% at 10 T.

2.2 Temperature and Field Dependence of the Normal Magnetoresistance

There have been several successful attempts to calculate the temperature dependence of $\Delta\rho_\perp/\rho$ (e.g., Blatt 1968). In the following a short outline of the model and the underlying assumptions on which such a calculation is based are given (we make use of what is discussed in *Boltzmann Equation and Scattering Mechanisms*).

In accordance with Eqn. (36) of *Boltzmann Equation and Scattering Mechanisms*, we assume an external force, X, in the direction $X \parallel \vec{e}_i$ with $i = x,y,z$:

$$(C+\Omega)\phi_{\gamma i} = Z_{\gamma i} = -\left(\frac{\partial f_0}{\partial\varepsilon_\gamma}\right)v_{\gamma i}X_i \qquad (18)$$

Assuming for the moment that $\Omega = 0$, multiplying from the left by $\phi_{\gamma j}$, and summing over γ we obtain:

$$\sum_\gamma \phi_{\gamma j}C\phi_{\gamma i} = \sum_\gamma Z_{\gamma i}\phi_{\gamma j} = \sum_\gamma \phi_{\gamma i}C\phi_{\gamma j} = \sum_\gamma Z_{\gamma j}\phi_{\gamma i}$$
$$(19)$$

(where the symmetry of the operator C has been used).

The components of the conductivity tensor are given by:

$$\sigma_{ij} = -\frac{e^2}{\mathrm{Vol}X_iX_j}\sum_\gamma(Z_{\gamma i}\phi_{\gamma j} + Z_{\gamma j}\phi_{\gamma i} - \phi_{\gamma i}C\phi_{\gamma j}) \qquad (20)$$

It can be shown that a functional of the form:

$$F_{ij}[\Phi] = -\frac{e^2}{\mathrm{Vol}X_iX_j}\sum_\gamma(Z_{\gamma i}\Phi_{\gamma j} + Z_{\gamma j}\Phi_{\gamma i} - \Phi_{\gamma i}C\Phi_{\gamma j}) \quad (21)$$

takes an extremal value for $\Phi = \phi$ and gives σ_{ij} (see Eqn. (20)). Therefore, one can determine Φ using the variational principle with the functional given by Eqn. (21). Searching for the extremal value of this functional by varying Φ in a subspace one finally obtains an approximation for the conductivity tensor. The application of the variational principle is more

difficult if there exists simultaneously an external magnetic field. However, one can still find a functional which shows an extremal value. In this case one has to make use of the solution of the Boltzmann equation for the two opposite B-field directions B^+ and B^- (see Eqn. (18)):

$$(C + \Omega)\phi_{\gamma i}^+ = -\left(\frac{\partial f_0}{\partial \varepsilon_\gamma}\right) v_{\gamma i} X_i = Z_{\gamma i}$$

$$(C - \Omega)\phi_{\gamma i}^- = -\left(\frac{\partial f_0}{\partial \varepsilon_\gamma}\right) v_{\gamma i} X_i = Z_{\gamma i}$$

The conductivity tensor in the presence of an external magnetic field is similar to that in Eqn. (20) and is given by:

$$\sigma_{ij}(\vec{B}) = -\frac{e^2}{\text{Vol} X_i X_j}$$
$$\times \sum_\gamma [Z_{\gamma i}\phi_{\gamma j}^+ + Z_{\gamma j}\phi_{\gamma i}^- - \phi_{\gamma i}^-(C + \Omega)\phi_{\gamma j}^+] \quad (23)$$

Equation (23) leads to the corresponding functional (see Eqn. (21)):

$$F_{ij}[\Phi_j^+, \Phi_j^-] = -\frac{e^2}{\text{Vol } X_i X_j}$$
$$\times \sum_\gamma [Z_{\gamma i}\Phi_{\gamma j}^+ + Z_{\gamma j}\Phi_{\gamma i}^- - \Phi_{\gamma i}^-(C + \Omega)\Phi_{\gamma j}^+]$$
$$(24)$$

We use for the trial functions the ansatz:

$$\Phi_{\gamma i}^+ = \sum_{m=1}^3 \alpha_{n\sigma}^{im} v_{\gamma m}; \quad \Phi_{\gamma j}^- = \sum_{m=1}^3 \beta_{n\sigma}^{jm} v_{\gamma m} \quad (25)$$

where $v_{\gamma m}$ is a velocity component and the subscripts n and σ are the band index and the spin direction, respectively. A function depending on the parameters α and β follows from the functional. These parameters are determined by:

$$\frac{\partial F_{ij}[\Phi_j^-, \Phi_i^+]}{\partial \alpha_{n\sigma}^{im}} = 0; \quad \frac{\partial F_{ij}[\Phi_j^-, \Phi_i^+]}{\partial \beta_{n\sigma}^{jm}} = 0 \quad (26)$$

Under the assumption of cubic symmetry and two types of charge carriers (two-band model) and a field with an orientation $\vec{B} = {}^0\vec{e}_z B$, one obtains the following for the transverse resistivity:

$$\rho_\perp(B, T) = -\frac{\text{Vol}(X_x)^2}{e^2}$$
$$\times \left\{ \begin{array}{l} \bar{C}_{xx}^{\text{I}} \bar{C}_{xx}^{\text{II}}[(\bar{Z}_{xx}^{\text{I}})^2(\bar{C}_{xx}^{\text{II}}) + (\bar{Z}_{xx}^{\text{II}})^2(\bar{C}_{xx}^{\text{I}})] + \\ [(\bar{Z}_{xx}^{\text{I}})^2(\bar{i}^{\text{II}})^2(\bar{C}_{xx}^{\text{I}}) + (\bar{Z}_{xx}^{\text{II}})^2(\bar{i}^{\text{I}})^2(\bar{C}_{xx}^{\text{II}})]B^2 \end{array} \right\}$$
$$\times \{[(\bar{Z}_{xx}^{\text{I}})^2(\bar{C}_{xx}^{\text{II}}) + (\bar{Z}_{xx}^{\text{II}})^2(\bar{C}_{xx}^{\text{I}})]^2 + [(\bar{Z}_{xx}^{\text{I}})^2 \bar{i}^{\text{II}}$$
$$+ (\bar{Z}_{xx}^{\text{II}})^2 \bar{i}^{\text{I}}]^2 B^2\}^{-1}$$
$$(27)$$

where the superscripts I and II denote the two bands for which the calculation must be performed.

The following abbreviations have been used:

$$\bar{C}_{ij}^{n\sigma} = \text{Vol} \int_{BZ} \frac{\mathrm{d}^3 k}{(2\pi)^3} v_{\gamma i} C v_{\gamma j} \quad (28)$$

$$\bar{Z}_{ij}^{n\sigma} = \text{Vol} \int_{BZ} \frac{\mathrm{d}^3 k}{(2\pi)^3} Z_{\gamma i} v_{\gamma j} \quad (29)$$

$$\bar{i}^{n\sigma} = \bar{i}_{xyxy}^{n\sigma} - \bar{i}_{xxyy}^{n\sigma} \quad (30)$$

$$\bar{i}_{irsj}^{n\sigma} = -\text{Vol}\frac{e}{\hbar c} \int_{BZ} \mathrm{d}^3 k \left(\frac{\partial f_0}{\partial \varepsilon_\gamma}\right) v_{\gamma i} v_{\gamma r} \frac{\partial}{\partial k_s} v_{\gamma j} \quad (31)$$

The resistivity without an external magnetic field ($B = 0$) in a two-band model ($n = \text{I,II}$) is then given by:

$$\rho(B = 0, T) = -\frac{\text{Vol}(X_x)^2}{e^2}$$
$$\times \frac{\bar{C}_{xx}^{\text{I}} \bar{C}_{xx}^{\text{II}}}{[(\bar{Z}_{xx}^{\text{I}})^2(\bar{C}_{xx}^{\text{II}}) + (\bar{Z}_{xx}^{\text{II}})^2(\bar{C}_{xx}^{\text{I}})]} \quad (32)$$

Accordingly, the resistivity for only one conduction band ($n = 1$, $\bar{C}_{xx}^{\text{II}} \to \infty$) is given by:

$$\rho(B = 0, T) = -\frac{\text{Vol}(X_x)^2}{e^2} \frac{\bar{C}_{xx}^{\text{I}}}{(\bar{Z}_{xx}^{\text{I}})^2} =$$
$$-\frac{1}{e^2} \frac{\bar{C}_{xx}}{n\left[\frac{2}{(2\pi)^3} \int \mathrm{d}^3 k \frac{\partial f_0}{\partial \varepsilon_\gamma} v_{\gamma x}^2\right]^2} \quad (33)$$

For the calculation of the transverse magnetoresistance defined by Eqn. (4), we combine Eqns. (27) and (32) and obtain (after extensive calculations, the details of which and a critical discussion of the underlying assumptions are given in Gratz *et al.* (2001)) the following simple relationship:

$$\frac{\Delta \rho_\perp}{\rho} = \frac{B^2}{a[\rho(B = 0, T)]^2 + bB^2} \quad (34)$$

where a and b are field- and temperature-independent parameters, depending on the properties of the two different conduction bands.

2.3 Analysis of Magnetoresistance Data of Nonmagnetic Compounds

From Eqn. (34) it follows that in order to calculate the temperature variation of the transverse classical magnetoresistance one simply needs to know the temperature dependence of the resistivity in zero magnetic field. In order to fit $\Delta \rho_\perp / \rho$ for YAl$_2$ (shown
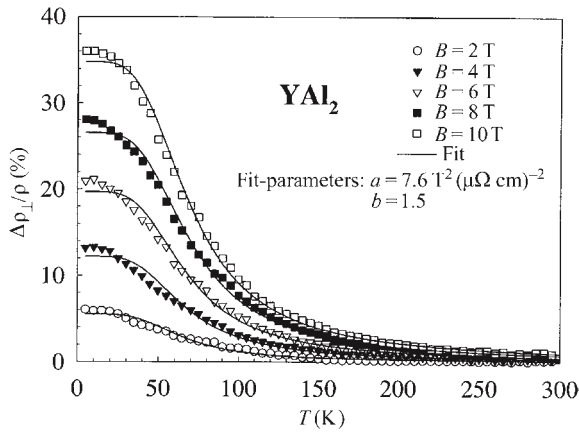
Figure 3
Solid lines are the result of fit procedures of Eqn. (34) (*a* and *b* are the fit parameters in Eqn. (34), see text) to the experimentally determined transverse magnetoresistance data of YAl_2 (symbols).

Figure 4
Anisotropy of the normal magnetoresistance $(\Delta\rho_\perp - \Delta\rho_\parallel)/\rho$. Inset shows the temperature variation of the longitudinal magnetoresistance of YAl_2 for various field strengths.

in Fig. 2) one can use the Bloch–Grüneisen relationship (Eqn. (9) of *Intermetallic Compounds: Electrical Resistivity*):

$$\rho(B=0, T) = \rho_0 + \rho_{ph} = \rho_0 + 4R_\Theta$$
$$\times \left(\frac{T}{\Theta}\right)^5 \int_0^{\Theta/T} \frac{x^5 dx}{(e^x - 1)(1 - e^{-x})} \quad (35)$$

The result of a fit of Eqn. (34) to the experimental data for YAl_2 is given in Fig. 3 by the solid lines. The residual resistivity of the YAl_2 sample is $4.4\,\mu\Omega$cm (see inset (a) of Fig. 1), and the two fit parameters in the Bloch–Grüneisen law are $R_\Theta = 35\,\mu\Omega$cm (this value represents the resistivity at the Debye temperature) and $\Theta = 310$ K (the Debye temperature of YAl_2). The two fit parameters in Eqn. (34) are $a = 7.6\,T^2$ $(\mu\Omega\text{cm})^{-2}$ and $b = 1.5$.

(a) Anisotropy of the normal magnetoresistance
The above calculations concern the transverse magnetoresistance; however, in all of the compounds studied, there is always a smaller but nonvanishing longitudinal magnetoresistance observed. In the inset of Fig. 4 the longitudinal magnetoresistance $(\Delta\rho_\parallel/\rho)$ is shown. The anisotropy of the magnetoresistance, defined as $(\Delta\rho_\perp - \Delta\rho_\parallel)/\rho$, of the YAl_2 sample under consideration is shown in the main part of Fig. 4.

In the case of free electrons occupying a spherical Fermi surface, both the transverse and the longitudinal magnetoresistance vanish identically. For $\Delta\rho_\perp/\rho$ simple arguments can be given, the transverse electric Hall field is just sufficient to compensate for the

deflection produced by the magnetic field. When there are two types of carrier, the resulting Hall field is an average of the two, and therefore cannot exactly compensate for the external magnetic field. For $\Delta\rho_\parallel/\rho$ it can be argued that the electrons travel down the magnetic lines of force, under the influence of the magnetic field, as if the magnetic field does not exist. It is clear from experiments that in order to account for the nonvanishing longitudinal magnetoresistance a more complicated theory must be developed than that provided by Eqn. (27).

3. Magnetoresistance in Ferromagnetic Rare-earth (RE) Compounds

The situation is even more complex in compounds where the RE ions bear magnetic moments, since spin-dependent scattering processes are also involved, below as well as above the magnetic ordering temperature. The resistivity of $GdAl_2$ for various transverse magnetic fields is presented in Fig. 5. The change of the $\rho(T)$ curves with the magnetic field is typical of ferromagnetic compounds. In inset (a) of Fig. 5, the transverse magnetoresistance of $GdAl_2$ in the vicinity of the Curie temperature ($T_C = 168$ K) is shown.

One of the first studies of the magnetic contribution to the resistivity using a mean field theory was made by Kasuya (1968). A comprehensive theoretical treatment of the magnetoresistance in the ferromagnetic and antiferromagnetic state was carried out by Yamada and Takada (1973a, 1973b). In the following we provide a brief calculation of the magnetoresistance in a ferromagnet.
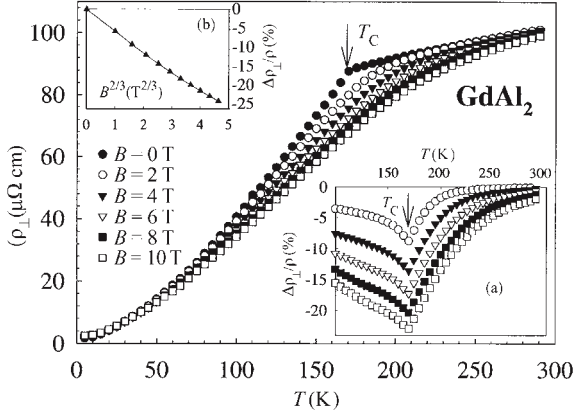
Figure 5
Temperature dependence of the resistivity of GdAl$_2$ from 4 K to 300 K in transverse magnetic fields of various strengths. Inset (a) shows details of the transverse magnetoresistance in the vicinity of the Curie temperature of GdAl$_2$ ($T_C = 168$ K). Inset (b) shows the $B^{2/3}$ dependence of the transverse magnetoresistance of GdAl$_2$ at the Curie temperature.

3.1 Magnetic Scattering in the Molecular Field Approximation

For this calculation we make use of the corresponding equations in *Boltzmann Equation and Scattering Mechanisms*. Combining Eqns. (81a), (84a), and (85a) in a molecular field approximation for a RE element with a total quantum number J, we obtain the following expression for the resistivity owing to spin-dependent scattering:

$$\rho_m(B,T) = C_m \frac{1}{J(J+1)}\left(\langle J_z^2 \rangle - \langle J_z \rangle^2 + \frac{\eta \langle J_z \rangle}{\sinh^2 \eta}\right)$$
(36)

where $\langle \dots \rangle$ denotes the thermodynamical expectation value in the molecular field approximation. Here

$$\langle J_z^2 \rangle = J(J+1) - \langle J_z \rangle \coth \eta$$
(37)

and

$$\langle J_z \rangle = J B_J(2J\eta)$$
(38)

where $B_J(2J\eta)$ is the Brillouin function and η is a function of the reduced temperature, T/T_C, given by:

$$\eta = \frac{T_C}{T}\left[\frac{3}{2J(J+1)}\langle J_z \rangle + \frac{g\mu_B}{2k_B T_C}B\right]$$
(39)

Note that Eqn. (39) differs from Eqn. (83c) of *Boltzmann Equation and Scattering Mechanisms* since an
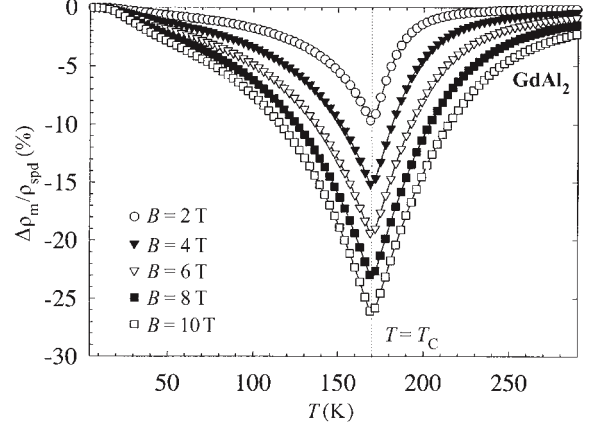
Figure 6
Calculated temperature dependence of the spin-dependent magnetoresistance ($\Delta\rho_m \equiv \rho_m(B,T) - \rho_m(0,T)$) for different field strengths of GdAl$_2$ plotted as $\Delta\rho_m/\rho_{spd}$ vs. T ($\rho(\text{GdAl}_2)_{spd} = 72\,\mu\Omega\text{cm}$, $J = 7/2$).

external magnetic field, B, is now taken into consideration.

The prefactor in Eqn. (36) is given by:

$$C_m = \frac{\pi}{\hbar e^2}\frac{3N|\bar{G}|^2}{\text{Vol}v^2(\varepsilon_F)}(g-1)^2 J(J+1)$$
(40)

In Fig. 7 of *Intermetallic Compounds: Electrical Resistivity* the experimentally determined spin disorder resistivity, ρ_{spd} ($= C_m$, see Eqn. (82a) of *Boltzmann Equation and Scattering Mechanisms*), is shown for some REAl$_2$ and REPt compounds. As can be seen from this figure, ρ_{spd} ($= \rho_m(T > T_C)$) is proportional to the deGennes factor, $(g-1)^2 J(J+1)$, which means that $|\bar{G}|^2$ and $v^2(\varepsilon_F)$ are approximately the same across these series.

By combining Eqns. (36)–(40), $\Delta\rho_m/\rho_{spd}$ can be calculated, which describes the difference in the magnetic (spin-dependent) resistivity with and without an external magnetic field, normalized to ρ_{spd} ($= \rho_m$ ($T \to \infty$)). The formula obtained in this way covers the temperature range below and above T_C and can be calculated for different external magnetic field strengths.

Calculated $\Delta\rho_m/\rho_{spd}$ vs. T curves for GdAl$_2$ ($J = 7/2$, $\rho_{spd} = 72\,\mu\Omega\text{cm}$, $T_C = 168$ K) for various magnetic field strengths are shown in Fig. 6.

The problem with Eqn. (39) is that a value for η is not easily obtained, since η appears also in the argument of the Brillouin function (Eqn. (39) represents an implicit function for η). Furthermore, Eqns. (36) and (37) include η as $\sinh \eta$ and $\coth \eta$, respectively.

For limited temperature regions below and above T_C and at $T = T_C$, simple expressions can be obtained
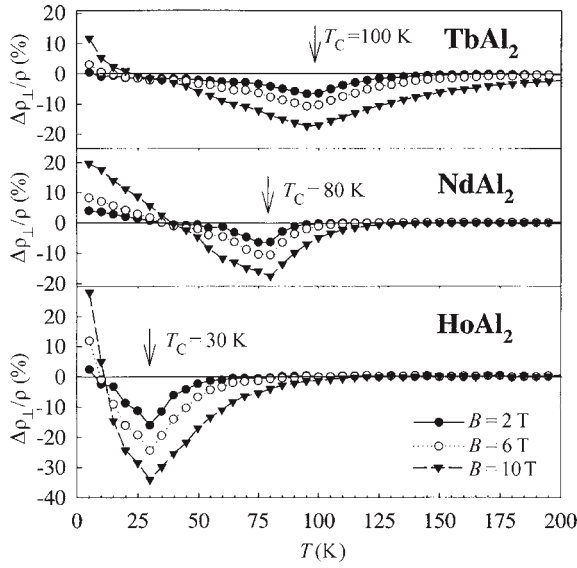
Figure 7
Temperature variation of the transverse magnetoresistance of REAl$_2$ compounds, with decreasing magnetic ordering temperatures and at various field strengths. The positive $\Delta\rho_\perp/\rho$ values towards the low-temperatures region are caused by the normal magnetoresistance, which is superimposed on the negative spin-dependent magnetoresistance.

for $\Delta\rho_m/\rho_{spd}$. There are three basic regions:
(i) Paramagnetic region for $T \gg T_C$:

$$\frac{\Delta\rho_m}{\rho_{spd}} = -C_1 \frac{h^2}{(T/T_C - 1)^2} \qquad (41)$$

where

$$C_1 = \frac{4(J^2 + J + 1)}{9}; \; h = \frac{g\mu_B}{2k_B T_C} B \qquad (42)$$

and under the condition $(T/T_C - 1) \gg h$.
(ii) Magnetically ordered region for $T < T_C$:

$$\frac{\Delta\rho_m}{\rho_{spd}} = -C_1 h \left(\frac{C_2}{1 - T/T_C} \right)^{1/2} \qquad (43)$$

where

$$C_2 = \frac{2(2J^2 + 2J + 1)}{15} \qquad (44)$$

and under the condition $1 \gg [1 - (T/T_C)]^3 \gg h^2$.
(iii) For the increase of the minimum at $T \cong T_C$, with increasing magnetic field:

$$\frac{\Delta\rho_m}{\rho_{spd}} = -C_1 \left(\frac{h}{C_2} \right)^{2/3} \qquad (45)$$

under the condition $[(T/T_C) - 1]^2 \ll h^2$. From Eqn. (45) it follows that $|\Delta\rho_m/\rho_{spd}|$ at T_C increases proportional to $B^{2/3}$.

3.2 Analysis of the Magnetoresistance in Ferromagnetic Compounds

A confirmation of Eqn. (45) is shown in inset (b) of Fig. 5 for GdAl$_2$. It is found that a fit of Eqn. (36) to the experimental data for GdAl$_2$ gives good agreement in the paramagnetic temperature range and in fields up to about 6 T, and below T_C ($= 168$ K) down to roughly 80 K. In order to subtract the normal magnetoresistance from the experimental data, the magnetoresistance of YAl$_2$ (see Fig. 2) is used, which is normalized to the residual resistivity of GdAl$_2$ at the corresponding field strength. (The normalization is necessary, since GdAl$_2$ and YAl$_2$ do not show the same residual resistivity.)

Not such a good agreement is found for other REAl$_2$ compounds, because of the following:
(i) For lower values of T_C in REAl$_2$ compounds, the correction for the normal magnetoresistance becomes more important. In order to demonstrate that the normal magnetoresistance gives rise to positive $\Delta\rho/\rho$ values at low temperatures, data for other magnetic REAl$_2$ compounds (with R = Tb, Nd, or Ho) with decreasing T_C values are presented in Fig. 7.
(ii) Equation (36) is based on the molecular field concept, which is not valid in the spin wave region at low temperatures.
(iii) An influence of the crystal electric field might also play a role in the temperature dependence of $\Delta\rho_m/\rho_{spd}$ and this is not accounted for in Eqn. (36).

A comprehensive discussion of the magnetoresistance in ferromagnetic iron, cobalt, and nickel compounds is given by Campbell and Fert (1982).

(a) Anisotropy of the magnetoresistance in ferromagnetic compounds

In all these compounds the anisotropy curves $((\Delta\rho_\perp - \Delta\rho_\parallel)/\rho$ vs. $T)$ show a sharp change at the onset of the ferromagnetic order. It is interesting to note that $(\Delta\rho_\perp - \Delta\rho_\parallel)/\rho$ for $T < T_C$ is positive for the light REAl$_2$ compounds and mainly negative for the heavy REAl$_2$ compounds (Gratz *et al.* 2001). The problem of the anisotropy of RE impurities in a noble metal matrix has been attributed to hybridization of the valence electron states of the RE impurities with conduction electron states (Lacueva *et al.* 1982).

4. Magnetoresistance in Antiferromagnetic RE Compounds

It is obvious that the situation is more complex in the case of an "antiferromagnetic" spin arrangement, since there are a very large number of possible spin

configurations. The spin arrangements, which in addition depend on the strength (and direction; however, only in a single-crystal sample, see *Elemental Rare Earths: Magnetic Structure and Resistance, Correlation of*) of the applied external field, are most important for the sign and the value of this spin-dependent magnetoresistance. Furthermore, there is an effect associated with the shape of the Fermi surface, which alters in an antiferromagnet, since the spin ordering has a periodicity different from that of the lattice and additional (magnetic) Brillouin zones appear below T_N. This effect is sometimes called the "superzone boundary effect" (Elliott and Wedgwood 1963).

In the paramagnetic state $(T > T_N)$ there is, in principle, no difference to that which occurs in a ferromagnetic material with a negative magnetoresistance at a given temperature above T_N, $\Delta\rho_m / \rho_{spd} \propto - B^2$ (Eqn. (41)).

Yamada and Takada (1973a, 1973b) discussed the field and temperature dependence of $\Delta\rho_m / \rho_{spd}$ for two simple magnetic moment configurations in the antiferromagnetic ordered state. The assumption is made that there are two magnetic sublattices with opposite magnetic moments. These sublattices can have moments aligned either parallel or perpendicular to the external B-field. In the latter case there is no influence of B on $\Delta\rho_m / \rho_{spd}$ if the moments in both sublattices are perpendicular to B (e.g., see the transverse c-axis magnetoresistance in erbium for $T = 60$ K shown in Fig. 5 of *Elemental Rare Earths: Magnetic Structure and Resistance, Correlation of*). In the former case there is an influence on $\Delta\rho_m / \rho_{spd}$, since the external field creates disorder in the sublattice with the opposite oriented spin arrangement (see the transverse a-axis magnetoresistance in erbium for $T = 64$ K in Fig. 4 of *Magnetic Structure and Resistance in Elemental Rare Earths, Correlation of*). Thus, $\Delta\rho_m / \rho_{spd}$ is positive. If the B-field strength (necessary to induce a ferromagnetic spin arrangement) exceeds the critical field, $\Delta\rho_m / \rho_{spd}$ starts to decrease as in a ferromagnet. The corresponding formula derived by Yamada and Takada (1973a) for $T < T_N$ is

$$\frac{\Delta\rho_m}{\rho_{spd}} = \chi_2(T/T_N) \cdot h^2 \qquad (46)$$

where $h = (g\mu_B / 2k_B T_N)B$. The function χ_2 includes an important parameter α ($= V(0)/V(Q)$, where Q is the wave vector of the antiferromagnetic spin arrangement and $V(0)/V(Q)$ describes the relative strength of the nearest-neighbor interaction in the magnetic lattice). The condition for antiferromagnetism is $V(Q) > V(0)$ ($\alpha < 1$) and for ferromagnetism $V(Q) < V(0)$ ($\alpha > 1$). The calculated temperature variation of the function $\chi_2(T/T_N)$ for different α values (according to Eqn. (3.16) in Yamada and Takada (1973a)) is shown in Fig. 8. It can be seen that the discontinuity at T_N increases with increasing α.
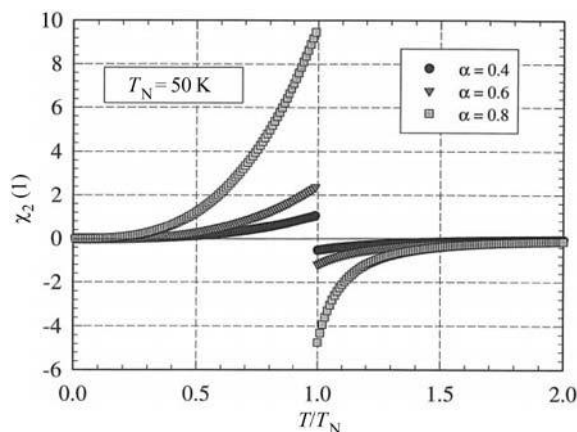
Figure 8
Temperature variation of the function $\chi_2(T/T_N)$ calculated for different α values and for a Neel temperature of 50 K (according to Eqn. (3.16) in Yamada and Takada (1973a)).

4.1 Analysis of the Magnetoresistance in Antiferromagnetic Compounds

In order to give an example of the magnetoresistance of an antiferromagnetic moment configuration, DyAg ($T_N = 56$ K) will be considered. The REAg compounds crystallize in the cubic CsCl-type structure. Neutron diffraction studies show that DyAg has an antiferromagnetic spin arrangement of the $(\pi, \pi, 0)$ type below $T_f = 46.5$ K. At temperatures $T_f < T < T_N$ a sinusoidally modulated spin wave propagation exists along the $\langle 110 \rangle$ direction, polarized in the $\langle 001 \rangle$ direction (Kaneko *et al.* 1987). Figure 9 shows $\Delta\rho_\perp / \rho$ vs. T for DyAg, which is typical of many of these polycrystalline cubic REAg antiferromagnetic compounds. The analysis of these magnetoresistance data, using the above-outlined concept, is shown in the following. For the determination of the function $\chi_2(T/T_N)$ from the $\Delta\rho_\perp / \rho$ data, the magnetoresistance of LuAg is used to correct for the normal magnetoresistance. The function χ_2 thus obtained (using Eqn. (46)) for DyAg is shown in the inset of Fig. 9. Except for the temperature region $T_f < T < T_N$, where there is a sinusoidally modulated spin configuration, the function $\chi_2(T/T_N)$ is basically independent of the magnetic field strength, as it should be. This result exemplifies the correspondence with the calculation shown in Fig. 8 (especially in the paramagnetic range).

For fields smaller than the critical field, in many antiferromagnetic compounds a step-like change of $\Delta\rho / \rho$ at T_N has been observed. The experimental evidence of a discontinuity can serve as a first proof as to whether a noncollinear spin structure appears at the magnetic ordering temperature.
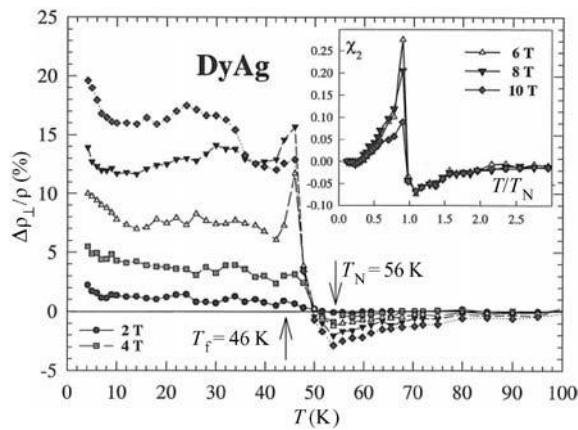
Figure 9

Temperature variation of the transverse magnetoresistance of the cubic antiferromagnetic DyAg compound. $\Delta\rho_\perp/\rho$ vs. T shows the characteristic increase at the onset of the antiferromagnetic ordering. Inset shows the temperature variation of $\chi_2(T/T_N)$ determined from experiment for DyAg. It exemplifies the correspondence with the theoretical χ_2 function shown in Fig. 8. The agreement is less good for the temperature region with the sinusoidally modulated spin configuration ($T_f < T < T_N$).

5. Summary

The influence of an external magnetic field on the resistivity is the subject of this article. The effect of a field on the electrical resistivity can be considered as consisting of two parts. The first originates from the influence of the magnetic field on the conduction electron trajectories owing to the Lorentz force, which deflects the electrons on their way through the specimen. This mechanism always increases the resistivity with increasing field. The other part is owing to the influence of the external magnetic field on the magnetic state and thus on the spin-dependent scattering mechanism. The effect is that in the paramagnetic and the ferromagnetic cases the resistivity decreases with increasing field, whereas in the antiferromagnetic state an increase of the magnetoresistance is in general expected.

Acknowledgments

See also: Amorphous Intermetallic Alloys: Resistivity; Elemental Rare Earths: Magnetic Structure and Resistance, Correlation of; Giant Magnetoresistance; Giant Magnetoresistance: Metamagnetic Transitions in Metallic Antiferromagnetics; Magnetoresistance, Anisotropic; Magnetism in Solids: General Introduction; Localized 4*f* and 5*f* Moments: Magnetism; Alloys of 4*f* (R) and 3*d* (T) Elements: Magnetism; Rare Earth Intermetallics: Thermopower of Cerium, Samarium and Europium Compounds

Bibliography

Blatt F L 1968 *Physics of Electronic Conduction in Solids*. McGraw-Hill, New York
Butcher P N 1973 Basic electron transport theory. In: *Electrons in Crystalline Solids*. IAEA, Vienna, pp. 103–65
Campbell I A, Fert A 1982 Transport properties of ferromagnets. In: Wohlfarth E P (ed.) *Ferromagnetic Materials*. North Holland, Amsterdam, Vol. 3, pp. 747–804
Elliott R J, Wedgwood F A 1963 Theory of the resistivity of the rare earth metals. *Proc. Phys. Soc.* **81**, 846–55
Gratz E, Maikis M, Bauer E, Nowotny H 1995 Magnetoresistance in magnetic and nonmagnetic rare earth compounds. *J. Magn. Magn. Mater.* **140–144**, 111–2
Gratz E, Nowotny H, Hense K, Enser J, Markossian S, Tanaka T 2001 Magnetoresistance in ferro-, antiferro- and nonmagnetic rare earth compounds. To be published
Kaneko T, Yoshida H, Ohashi M, Abe S 1987 Magnetic structure of the intermetallic compound DyAg. *J. Magn. Magn. Mater.* **70**, 277–8
Kasuya T 1968 Effects of s–d interaction on transport phenomena. *Prog. Theor. Phys.* **22**, 227–46
Lacueva G, Levy P M, Fert A 1982 Unified approach to some transport and EPR properties of noble metals with rare-earth impurities. *Phys. Rev. B* **26** (3), 1099–124
Yamada H, Takada S 1973a Magnetoresistance of antiferromagnetic metals due to s–d interaction. *J. Phys. Soc. Jpn.* **34**, 51–7
Yamada H, Takada S 1973b Magnetoresistance due to electron-spin scattering in antiferromagnetic metals at low temperatures. *Prog. Theor. Phys.* **45**, 1401–19

E. Gratz
Technische Universität Wien, Vienna, Austria

Magnetoresistive Heads: Physical Phenomena

Electrical resistivity is a powerful probe of the electronic and physical structure of a material. This sensitivity has resulted in electrical resistance commonly being used to sense indirectly other material properties such as temperature or defect concentration. Electrical resistance can also vary with the magnetic state of the material, magnetoresistance, stimulating the development of magnetoresistive magnetic field sensors that are not compromised by the inherent speed dependence of inductive field sensing. The anisotropic magnetoresistance (AMR) (McGuire and Potter 1975) of bulk ferromagnetic materials has,

until recently, provided the greatest potential for magnetic field sensors.

The development of the technology to create magnetic thin-film structures with layer thicknesses of the order of the electron mean free path led to the discovery of giant magnetoresistance (GMR) (Baibich *et al*. 1988) that promised an increase of one to two orders of magnitude in field sensitivity (see *Giant Magnetoresistance*). GMR sensors are now to be found as the field-sensing element in the read heads of commercial hard disks (Toigo 2000). The origins of GMR lie in the spin-dependent scattering experienced by an electron traveling through the material that results from the spin-polarized electronic band structure of a ferromagnetic material. Both intrinsic and extrinsic factors affect the magnitude and field sensitivity of the GMR.

1. AMR

AMR was first discovered by Lord Kelvin. Due to spin–orbit coupling, the orientation of the electron orbitals in a ferromagnetic material is determined by the direction of the magnetic field (see *Magnetoresistance, Anisotropic*). This results in a greater scattering cross-section for a transport electron when the direction of the current is parallel to the applied field (McGuire and Potter 1975) (see Fig. 1):

$$\rho = \rho_0 + \Delta\rho_{AMR}\cos^2\theta \qquad (1)$$

where θ is the angle between the applied field and the current. This effect is greatest in materials with large spin–orbit coupling such as $Ni_{80}Fe_{20}$ where magnetoresistance values of 4% are possible.

2. Origin of Spin-dependent Transport

The band structure of the free electron like s electrons in ferromagnetic materials is not spin polarized; however, they have the highest mobility and would be expected to be responsible for carrying the majority of the current. However, the 3*d* electrons have the greatest density of states at the Fermi surface and

$$\rho = \rho_0 + \Delta\rho_{AMR}\cos^2\theta \qquad (1)$$
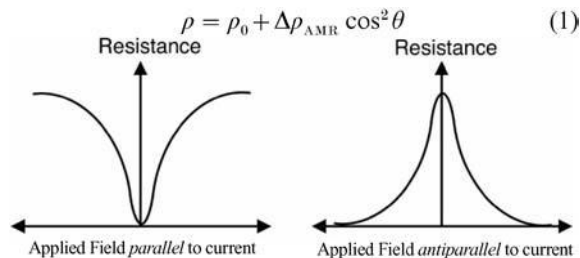
Figure 1
Orientation dependence of AMR.
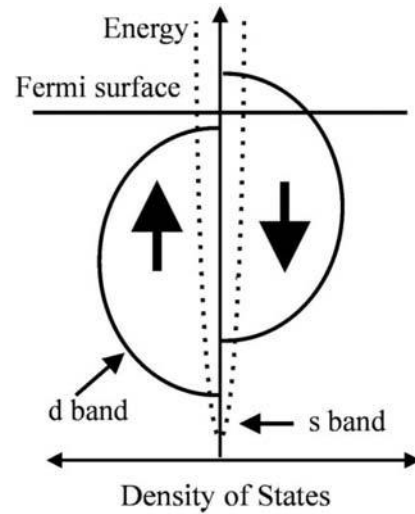
Figure 2
Schematic electronic band structure for a strong ferromagnet, e.g., cobalt.

their band structure is spin split. The probability of electron scattering is proportional to the density of states at the Fermi surface resulting in a probability of s electrons scattering into empty states in the spin split d band and hence spin-dependent scattering. The spin asymmetry parameter is often represented by

$$\alpha = R_\uparrow / R_\downarrow \qquad (2)$$

A schematic diagram of the spin split band structure of a strong ferromagnet such as cobalt and nickel is shown in Fig. 2. In the example shown, the higher density of states at the Fermi level for the spin down band results in a higher probability of scattering for this band and hence a value of α less than unity. Iron is only a weak ferromagnet; however, its band structure is readily modified by distortion of its local electronic environment, for example at a surface or interface. First principles band structure calculations are often necessary to determine the degree of spin-dependent scattering, especially for alloys such as $Ni_{80}Fe_{20}$.

3. GMR

Mott in 1936 determined that the spin quantum number is usually conserved during scattering processes allowing the transport of spin up and spin down electrons to be treated as two parallel spin currents. Taking into account the spin-dependent scattering described in Sect. 2, consider the schematic model shown in Fig. 3.
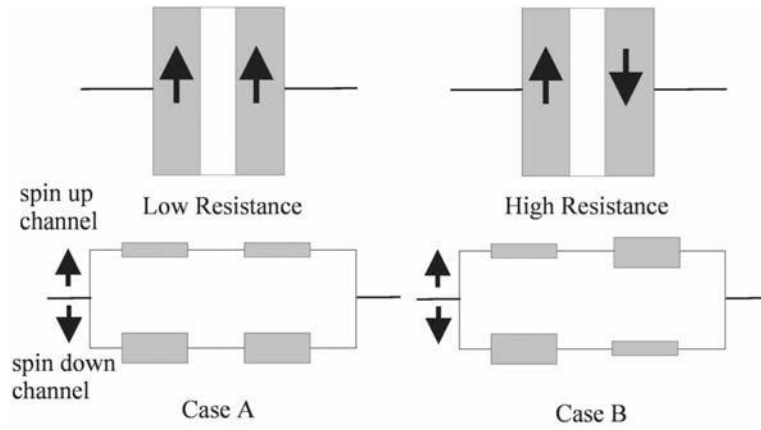
Figure 3
Spin-dependent scattering leading to GMR in a trilayer represented using the resistor model.

The magnetic elements represent regions of saturated magnetization whose relative orientation can be altered as indicated. The resistances of the spin up and spin down channels are modeled as resistors, a larger resistor representing a larger resistance, and are shown acting in parallel in accordance with the Mott two-current model. A current entering the device will contain both spin up and spin down electrons. In case (a) spin up electrons will remain majority electrons throughout their passage and will only be weakly scattered. Spin down electrons, however, will remain minority electrons throughout their passage and will be strongly scattered throughout. The overall resistance in case (a) will therefore be dominated by the low-resistance spin up channel and the current will be spin polarized in the up direction as it emerges.

By contrast, in case (b) where the magnetic regions are misaligned, both the spin up and spin down electrons will spend some time as both majority and minority electrons resulting in a high resistance in both channels. If the device can be switched between these two magnetic states a change in resistance will be observed. The magnetoresistance due to this mechanism can be represented by

$$\frac{R_{\uparrow\downarrow} - R_{\uparrow\uparrow}}{R_{\uparrow\uparrow}} = \frac{(1-\alpha)^2}{4\alpha} \tag{3}$$

where $R_{\uparrow\downarrow}$ ($R_{\uparrow\uparrow}$) is the resistance in the antiparallel (parallel) configuration, and is called GMR. The name refers to the mechanism responsible for the resistance change rather than to the size of the effect itself.

Bulk magnetic material is normally divided up into regions of saturated magnetization called magnetic domains; however, within the domain wall separating domains of different magnetization direction, the local direction of the magnetic moment rotates. As the spin-polarized electrical current travels through the domain wall its spin may be able to rotate about the local direction of magnetization thus quenching any GMR effect (Gregg *et al.* 1996). The thinner the domain wall, the more rapid the rotation of the local moment will be and the lower the probability that the electron spin will be able to precess with the local moment. Therefore, to increase the GMR effect the domain wall should be made as thin as possible. By separating adjacent magnetic domains by a nonmagnetic material the domain wall is effectively removed. This is best achieved in a magnetic multilayer in which the layer thicknesses can be reduced to a few atomic layers.

This was first achieved by Baibich *et al.* (1998) and Binasch *et al.* (1989) in Fe/Cr multilayers; the original data showing GMR for the first time is reproduced in Fig. 4.

Since this initial discovery the subsequent understanding of the underlying mechanisms has enabled GMR of 220% to be achieved at 4.2 K in Fe/Cr multilayers (Schad *et al.* 1994), and at room temperature values of 65% have been realized for Co/Cu multilayers (Parkin *et al.* 1991).

Given that multilayering magnetic and nonmagnetic materials creates a good system for spin-dependent scattering, the choice of materials and the microstructure of the multilayer will determine the maximum value of GMR. However, for effective application as a magnetic field sensor this magnetoresistance must also occur for small changes in applied field. The mechanism by which the multilayer switches between the two magnetic states of parallel and antiparallel alignment of adjacent magnetic layers is therefore crucial in GMR design. Despite their lower magnetoresistance, AMR devices do in fact have quite a good field sensitivity, as a thin film of $Ni_{80}Fe_{20}$, for example, can be switched in fields of only a few tenths of a millitesla.
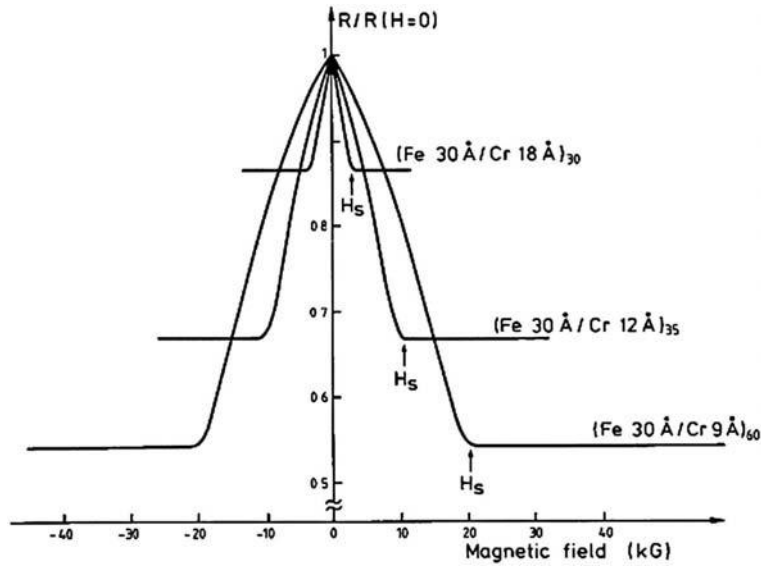
Figure 4
GMR in Fe/Cr multilayers (after Baibich *et al.* 1988).

In the schematic diagram in Fig. 2 the current is shown traveling perpendicular to the layers in the current perpendicular to the plane (CPP) geometry. In this case the resistances of subsequent layers can be added in series and this is the most straightforward type of structure to model theoretically. However, owing to the large cross-sectional area to length aspect ratio, the CPP resistance is extremely small making practical realization more difficult. Superconducting contact pads are often used (Pratt *et al.* 1991) or pillars are formed by etching (Gijs *et al.* 1993) or electrodeposition (Piraux *et al.* 1994) to reduce the cross-section and thereby increase the measurement resistance.

As the electron mean free path in a typical metal multilayer is typically much longer that the thicknesses of the individual layers, it is possible to measure GMR with the current in the plane (CIP) geometry in which the current travels parallel to the layers. In this case the resistances of the layers are added in parallel for each spin current channel. CIP magnetoresistance is practically much easier to measure, as the resistance values are typically a few ohms.

There are now many designs of nanostructures that enable the relative alignment of the magnetic components to be controlled by the application of a magnetic field—some of which are described below. They enable the variation of magnetic field to be controlled according to the following angular-dependent equation:

$$R(\theta) = R(\theta = 0) + \Delta R_{\mathrm{GMR}} \frac{1 - \cos\theta}{2} \qquad (4)$$

where θ is the angle between the magnetization directions of adjacent layers.

3.1 Exchange Coupled Multilayers

GMR was discovered in an Fe/Cr magnetic multilayer whose antiparallel alignment of magnetic layers was the result of interlayer exchange coupling. This coupling is due to spin-dependent reflection coefficients at interfaces setting up a spin density wave in the interlayer. The thickness of the interlayer determines at which point of the spin density wave the next magnetic layer is situated resulting in either antiferromagnetic (antiparallel) alignment or ferromagnetic (parallel alignment) coupling between the magnetic layers (Grünberg *et al.* 1986). This coupling is much stronger than that arising from dipolar interactions. The application of a magnetic field to an antiferromagnetically coupled multilayer will eventually overcome the coupling energy and align the magnetic layers in the direction of the magnetic field.

The relative alignment of the magnetic layers in the multilayer can therefore be altered by the application of a magnetic field resulting in GMR. The disadvantage of an exchange coupled multilayer is that for strong coupling a large field is often required to overcome the exchange coupling resulting in poor field sensitivity of the GMR. In addition, the magnitude and sign of the exchange coupling is very sensitive to interlayer thickness; the coupling typically cycles between ferromagnetic and antiferromagnetic with a period of only 1.1–1.2 nm. This makes

the reproducible manufacture of such systems very demanding and the problem of interdiffusion at the magnetic/nonmagnetic interface very significant (see *Multilayers: Interlayer Coupling*).

3.2 Spin Valves

In a spin valve (Dieny *et al.* 1991a), the exchange coupling between the magnetic layers is suppressed by separating them with a thick nonmagnetic interlayer. One of the magnetic layers is then pinned by, for example, exchange biasing with an antiferromagnet, e.g., FeMn. The other magnetic layer is left free to magnetically switch in a small magnetic field. The most sensitive GMR materials have been made in this way producing values in the region of $18\%\,\text{kAm}^{-1}$ (see *Magnetic Recording Systems: Spin Valves*). Exchange biased multilayers suffer from the relatively low Curie temperature of the antiferromagnet. This limitation has been overcome by replacing the pinning antiferromagnet by an antiferromagnetically coupled multilayer such as Co/Ru (van den Berg *et al.* 1996).

3.3 Heterogeneous Alloys

Layering of the materials is not a requirement for GMR, but the dimensions of the magnetic and nonmagnetic regimes must be on the nanoscale. For example, granular materials will also exhibit GMR (Berkowitz *et al.* 1992, Xiao *et al.* 1992). Such systems are most easily realized using immiscible magnetic and nonmagnetic materials such as CoAg and can readily be prepared by coevaporation, cosputtering, or even mechanical alloying to produce a bulk material with a nanoscale microstructure. The highest resistance is observed when there is the most magnetic disorder at the coercive field. In general, the field sensitivity is not high owing to the relatively high fields often needed to rotate the magnetic moment of small magnetic particles. As the GMR is very sensitive to the moment–moment correlation of neighboring particles, it can be used to probe the magnetic state of the sample (Gregg *et al.* 1996).

3.4 Tunneling Magnetoresistance

If the nonmagnetic layer is replaced by a thin insulator such as Al_2O_3, the quantum mechanical tunneling probability through the insulator will also be spin dependent owing to the number of available states to tunnel into leading to a tunnel magnetoresistance (TMR) (Juliere 1975).

4. Critical Length Scales

The two critical length scales in giant magnetoresistive structures are the electron mean free path and the

spin diffusion length. The spin diffusion length is the length over which the polarization of the electron current is destroyed owing to spin flip scattering. It is related to the momentum mean free path by the following:

$$l_{sd} = \sqrt{v_F \lambda \tau_{\uparrow\downarrow}} \tag{5}$$

where v_F is the Fermi velocity, λ the momentum mean free path, and $\tau_{\uparrow\downarrow}$ the spin flip time.

Typical values for a GMR multilayer are 10 nm for the mean free path and 100–1000 nm for the spin diffusion length in the nonmagnetic material. For a CIP structure, the mean free path is usually the critical parameter as it will control the number of layers an electron will typically encounter in its journey through the multilayer. In a CPP structure, the electron will always sample all the layers in the structure and it is therefore the spin diffusion length that is usually the critical length scale as it determines the degree of polarization of the current as each new interface is reached. In addition, the spin diffusion length in the magnetic layer will affect the degree of polarization of the electron current. Heterogeneous alloys exhibit both CIP and CPP character with the resistances of the magnetic particles adding in both series and parallel. Both length scales are therefore important in these materials.

5. Sources of Electron Scattering

All scattering will reduce the mean free path of the material. All spin-independent scattering, such as scattering in the nonmagnetic layer, will therefore reduce the GMR. This scattering may be the result of the microstructure such as vacancies, defects, interdiffusion, and roughness at the surface or interface or stress and can often be improved by the careful choice of underlayer materials. In a thin film there will also be scattering from the interface with the substrate and the capping layer. Scattering in the ferromagnetic layer or at the interface may be spin dependent and may therefore make a positive contribution to the GMR.

The potential of the scattering process to be spin dependent is interdependent on intrinsic properties such as the band structure, the composition of the multilayer, and its microstructure. Scattering can be spin dependent if there is a matching of the atomic potentials for one spin direction and not in the other; for example, in the Fe/Cr system there is good band matching for the spin down band, but poor matching for the spin up band leading to spin-dependent scattering and GMR. The reverse situation is true for nickel or cobalt at an interface with copper where the spin up band of the ferromagnet is full. Poor structural matching between materials at an interface results in a high dislocation density with high consequent scattering. Note that the highest values

of GMR at room temperature are obtained for the Co/Cu system for which there is good matching of both the electronic and lattice structure.

Additional complications arise for atomic mixing at the interface where the magnetic moment of the alloy thus produced is different to the bulk material, e.g., Ni/Cu (Nicholson *et al.* 1994). This has additional consequences for exchange coupled material where the interdiffusion will also affect the exchange coupling and hence the degree of misalignment of the adjacent magnetic layers. An effective way to benefit from, say, the soft magnetic properties of $Ni_{80}Fe_{20}$, avoid the problems of interdiffusion at the $Ni_{80}Fe_{20}$/Cu interface, and exploit the effective spin-dependent scattering at the well-matched Co/Cu interface is to dust the $Ni_{80}Fe_{20}$/Cu interface with a thin layer of cobalt (Parkin 1993). In general, the band structure at the interface is likely to differ from the bulk making it difficult to predict the performance of a particular interface (Coehoorn 1993, Itoh *et al.* 1993, Nicholson *et al.* 1994).

6. Effect of the Layer Thicknesses

The function of the nonmagnetic layer is to separate the magnetic layers sufficiently to allow independent switching in a spin valve material and in an exchange coupled material to control the interlayer coupling and thereby the degree of magnetic layer misalignment. Increasing the thickness of the nonmagnetic layer beyond what is required to achieve these functions will result in a degradation of the GMR. Typically the nonmagnetic layer has a higher conductivity than the ferromagnet, so in a CIP structure it acts as an effective electrical shunt. Some materials commonly used as nonmagnetic layers such as gold also have a high degree of spin flip scattering resulting from large spin–orbit coupling. This will reduce the spin diffusion length and hence be particularly degrading to the GMR in CPP structures. There is, however, a risk for both CIP and CPP structures in making the nonmagnetic layer too thin owing to the potential for the formation of structural pinholes that will result in direct magnetic coupling between the magnetic layers destroying the magnetic misalignment and with it the GMR (Dieny *et al.* 1991b).

The magnetic layer must be thick enough to effectively spin polarize the current; if it is too thin there will be a high degree of diffuse scattering at the interfaces reducing the mean free path considerably. The GMR will increase with the number of layers until in a CIP structure the mean free path is exceeded; there is therefore also an electrical shunting effect associated with the magnetic layer (Dieny *et al.* 1992).

7. Temperature Dependence

The temperature dependence of the GMR is necessarily connected to the Curie temperature of the magnetic material, and the formation of magnons increases the amount of spin flip scattering as the temperature is increased. The temperature at which the GMR is reduced to zero is lower than the Curie temperature, but related to it. The increased conductivity of the whole magnetic structure at low temperatures results in a reduction of spin-independent scattering, and an increase in the electron mean free path and consequently in an increase in the GMR ratio. For spin valves it is found that the GMR decreases linearly with increased temperature (Dieny *et al.* 1992).

8. Theories of GMR

A model of GMR needs to include spin-dependent scattering probabilities in the bulk, the outer boundaries, and at the interfaces within the structure. As the origin of the spin-dependent scattering derives from the spin splitting of the d band, a truly classical model is incapable of describing the GMR. However, a great deal of physical insight can be gained by incorporating a quantum mechanically derived spin dependence into the scattering parameters of classical theories to form semiclassical models.

The first semiclassical model was that of Camley and Barnas (1989) who used the Boltzmann transport equation. The Fuchs and Sondheimer formulation can be used to take into account the effect of the finite thickness of the thin film. The spin-dependant probability of specular reflection at the outer boundary must be considered and at the interface: transmission, specular reflection, and diffuse scattering must all be taken into account in deriving spin-dependent transmission coefficients. These models lead to the conclusion that in $Ni_{80}Fe_{20}$-based materials spin-dependent scattering within the ferromagnetic layer is dominant, in contrast to cobalt-based multilayers in which the interface is found to dominate. In both cases the detailed microstructure plays a significant role and can be the dominant factor.

Valet and Fert (1993) describe spin-dependent transport using the idea of spin accumulation at the internal interfaces and use a semiclassical formalism of the Boltzmann equation with the addition of spin-dependent electrochemical potentials. These models work well in CPP structures when the spin diffusion lengths in both the ferromagnetic and nonmagnetic layers are much greater than the thicknesses of the individual layers. Pratt *et al.* (1997) have incorporated the spin diffusion length of the ferromagnetic material into a similar model.

Quantum mechanical theories take into account finite size effects on the electronic structure and the transport owing to the presence of a potential barrier, but have been less successful in predicting realistic values of the GMR. Realistic band structures have been successfully incorporated into these models,

most notably by Tsymbal and Pettifor (1996), who considered hybridization of the *sp* and *d* electrons. They considered scattering from spin-independent disorder introduced using the Anderson model, using the Kubo formula. The degree of disorder can be altered as a parameter to obtain typical resistivities for thin-film structures and, for the first time, realistic values obtained for the GMR.

9. Summary and Future Developments

Although the underlying mechanisms of GMR are now understood, accurate predictions are still difficult owing to the significant effect minor changes in electronic band structure and microstructure can have on the spin-dependent scattering. GMR sensors have successfully found a major market for applications most notably as read heads in the data storage industry (Toigo 2000) (see *Magnetic Recording Devices: Inductive Heads, Properties*) and increasingly in a wider range of applications. The latest developments are in magnetic random access memory (MRAM) (Pohm *et al.* 1994) (see *Random Access Memories: Magnetic*) and hybrid spin electronic devices (Gregg *et al.* 1997, Hammar *et al.* 1999) (see *Magnetic Recording Systems: Spin Electronics*). More detailed reviews of GMR can be found in the literature (e.g., Dieny 1994, Gijs and Bauer 1997).

See also: Colossal Magnetoresistance Effects: The Case of Charge-ordered $Pr_{0.5}Ca_{0.5}MnO_3$ Manganite Thin Films; Magnetoresistance in Transition Metal Oxides

Bibliography

Baibich M N, Broto J M, Fert A, Nguyen-Van-Dau F, Petroff F, Etienne P, Creuzet G, Friedrich A, Chazelas J 1988 Giant magnetoresistance of (001)Fe/(001)Cr magnetic superlattices. *Phys. Rev. Lett.* **61**, 2472

Berkowitz A E, Mitchell J R, Carey M J, Young A P, Zhang S, Spada F E, Parker F T, Hutten A, Thomas G 1992 Giant magnetoresistance in heterogeneous Cu–Co alloys. *Phys. Rev. Lett.* **68**, 3745

Binasch G, Grünberg P, Saurenbach F, Zinn W 1989 Enhanced magnetoresistance in layered magnetic structures with antiferromagnetic interlayer exchange. *Phys. Rev. B* **39**, 4828

Camley R E, Barnas J 1989 Theory of giant magnetoresistance effects in magnetic layered structures with antiferromagnetic coupling. *Phys. Rev. Lett.* **63**, 664

Coehoorn R 1993 On the spin dependence of electron scattering at non ideal interfaces. *J. Magn. Magn. Mater.* **121**, 432

Dieny B 1994 Giant magnetoresistance in spin valve multilayers. *J. Magn. Magn. Mater.* **136**, 335

Dieny B, Humbert P, Speriosu V S, Gurney B A 1992 Giant magnetoresistance of magnetically soft sandwiches: dependence on temperature and on layer thickness. *Phys. Rev. B* **45**, 806

Dieny B, Speriosu V S, Gurney B A, Parkin S S P, Wilboit D R, Roche K P, Metin S, Peterson D T, Nadimi S 1991a Spin

valve effect in soft ferromagnetic sandwiches. *J. Magn. Magn. Mater.* **93**, 101–4

Dieny B, Speriosu V S, Parkin S S P, Curney B A, Wilhoit D R, Mauri D 1991b Giant magnetoresistance in soft ferromagnetic multilayers. *Phys. Rev. B* **43**, 1297

Fert A, Valet T, Barnas J 1994 Perpendicular magnetoresistance in magnetic multilayers: theoretical model and discussion. *J. Appl. Phys.* **75**, 6693

Gijs M A M, Bauer G E W 1997 Perpendicular giant magnetoresistance of magnetic multilayers. *Adv. Phys.* **46**, 285

Gijs M A M, Lenezowski S K J, Giesberg J B 1993 Perpendicular giant magnetoresistance of microstructured Fe/Cr magnetic multilayers from 4.2 to 300 K. *Phys. Rev. Lett.* **70**, 3343

Gregg J F, Allen W, Ounadjela K, Viret M, Hehn M, Thompson S M, Coey J M D 1996 Giant magnetoresistance in a single element magnetic thin film. *Phys. Rev. Lett.* **77**, 1580

Gregg J, Allen W, Viart N, Kirschman R, Sirisathitkul C, Schille J, Gester M, Thompson S, Sparks P, Da Costa V, Ounadjela K, Skvarla M 1997 The art of spin electronics. *J. Magn. Magn. Mater.* **175**, 1

Gregg J F, Thompson S M, Dawson S J, Ounadjela K, Staddon R, Hamman J, Fermon C, Saux G, O'Grady K 1994 Effect of magnetic interactions and multiple magnetic phases on the giant magnetoresistance of heterogeneous cobalt-silver thin films. *Phys. Rev. B* **49**, 1064

Grünberg P, Schreiher R, Pang Y, Brodsky M B, Sowers H 1986 Layered magnetic structures: evidence for antiferromagnetic coupling of Fe layers across Cr interlayers. *Phys. Rev. Lett.* **57**, 2442

Hammar P R, Bennet B R, Yang M J, Johnson M 1999 Observation of spin injection at a ferromagnetic–semiconductor interface. *Phys. Rev. Lett.* **83**, 203

Itoh H, Inoue J, Maekawa S 1993 Electronic structure and transport properties in magnetic superlattices. *Phys. Rev. B* **47**, 5809

Juliere M 1975 Tunneling between ferromagnetic films. *Phys. Lett.* **54A**, 225

McGuire T R, Potter R I 1975 Anisotropic magnetoresistance in ferromagnetic 3d alloys. *IEEE Trans. Magn.* **11**, 1018

Nicholson D M C, Butler W H, Zhang X -G, MacLaren J M, Gurney B A, Speriosu V S 1994 Magnetic structure of the spin valve interface. *J. Appl. Phys.* **76**, 6805

Parkin S S P 1993 Origin of enhanced magnetoresistance of magnetic multilayers: spin-dependent scattering from magnetic interface states. *Phys. Rev. Lett.* **71**, 1641

Parkin S S P, Bhadra R, Roche K P 1991 Oscillatory magnetic exchange coupling through thin copper layers. *Phys. Rev. Lett.* **66**, 2152

Piraux L, George J M, Despres J F, Leroy C, Ferain E, Legras R, Ounadjela K, Fert A 1994 Giant magnetoresistance in magnetic multilayered nanowires. *Appl. Phys. Lett.* **65**, 2484

Pohm A V, Beech R S, Bade P A, Chen E Y, Daughton J M 1994 Analysis of 0.1 to 0.3 micron wide, ultra dense giant magnetoresistance memory elements. *IEEE Trans. Magn.* **30**, 4650

Pratt W P, Lee S-F, Slaughter J M, Schroeder P A, Bass J 1991 Perpendicular giant magnetoresistances of Ag/Co multilayers. *Phys. Rev. Lett.* **66**, 3060

Pratt W P Jr, Steenwyk S D, Hsu S Y, Chiang W C, Schaefer A C, Loloee R, Bass J 1997 Perpendicular-current transport in exchange-biased spin-valves. *IEEE Trans. Magn.* **33**, 3505

Schad R, Potter C D, Beliën P, Verbanck G, Moschalkov V V, Bruynseraede Y 1994 Giant magnetoresistance in Fe/Cr superlattices with very thin Fe layers. *Appl. Phys. Lett.* **64**, 3500

Toigo J W 2000 Avoiding a data crunch. *Sci. Am.* **41**, 41

Tsymbal E Y, Pettifor D G 1996 Effects of band structure and spin-independent disorder on conductivity and giant magnetoresistance in Co/Cu and Fe/Cr multilayers. *Phys. Rev. B* **54**, 15314

Valet T, Fert A 1993 Theory of the perpendicular magnetoresistance in magnetic multilayers. *Phys. Rev. B* **48**, 7099

van den Berg H A M, Clemens W, Gieres G, Rupp G, Schelter W, Vieth M 1996 GMR sensor scheme with artificial antiferromagnetic subsystem. *IEEE Trans. Magn.* **32**, 4624

Xiao J Q, Jiang J S, Chien C L 1992 Giant magnetoresistance in non multilayer magnetic systems. *Phys. Rev. Lett.* **68**, 3749

S. M. Thompson
University of York, York, UK

Magnetostrictive Materials

Magnetostriction is the term given to the mechanical deformation induced in a solid substance by the modification of its magnetic state. Inverse magnetostriction refers to the modification of the magnetic state by an applied stress.

These phenomena are significant only in substances which are magnetically ordered or at least close to the onset of a magnetic order, and have practical importance only in those materials which exhibit a spontaneous magnetization, i.e., ferro- or ferrimagnetic materials. Only the latter will be considered in this article.

1. Spontaneous Magnetostriction

Generally speaking, spontaneous magnetostriction is defined as that part of strain which is due to the onset of a magnetic order in a material (du Tremolet de Lacheisserie 1993).

A phenomenological approach consists of treating the onset of spontaneous magnetization as a small perturbation of a hypothetical nonmagnetic state. At a given temperature, the perturbation is entirely defined by the magnetization direction cosines $\alpha_1, \alpha_2, \alpha_3$. The spontaneous magnetostriction tensor $\mathbf{S}$ is then expanded as a function of this perturbation. In a convenient frame (Nye 1957), allowing for time reversal invariance, and using the usual Einstein convention on repeated indices, this gives:

$$S_{ij} = Q_{ijkl}\alpha_k\alpha_l + \text{even higher order terms} (i, j = 1, 2, 3) \tag{1}$$

The tensor $\mathbf{Q}$ and the higher-order tensors are expected to be temperature-dependent. Consideration of the first term only is sufficient to account for the properties of most materials, so that only the form of $\mathbf{Q}$ will be considered in the following. Since $\mathbf{Q}$ is a polar tensor of order 4, it follows the same symmetry rules as the elastic tensors (Nye 1957). Two cases are worth considering: cubic crystals and isotropic materials. In the following, emphasis will be placed on cubic symmetry since it contains the isotropic situation as a special case.

In cubic crystals, the convenient reference frame is obviously the one that coincides with crystallographic axes.

There are only 15 nonzero components of $\mathbf{Q}$ out of which only three are independent, namely

$$Q_{1111} = Q_{2222} = Q_{3333} = Q_{11}$$

$$Q_{1122} = Q_{2211} = Q_{1133} = Q_{3311} = Q_{2233} = Q_{3322} = Q_{12}$$

$$Q_{2323} = Q_{3232} = Q_{1313} = Q_{3131} = Q_{1212} = Q_{2121} = Q_{44} \tag{2}$$

so that the components of spontaneous magnetostriction can now be written as:

$$S_{11} = (Q_{11} - Q_{12})\alpha_1^2 + Q_{12};$$
$$S_{22} = (Q_{11} - Q_{12})\alpha_2^2 + Q_{12};$$
$$S_{33} = (Q_{11} - Q_{12})\alpha_3^2 + Q_{12}$$
$$S_{23} = S_{32} = Q_{44}\alpha_2\alpha_3; \quad S_{13} = S_{31} = Q_{44}\alpha_1\alpha_3;$$
$$S_{12} = S_{21} = Q_{44}\alpha_1\alpha_2 \tag{3}$$

In isotropic material the reference frame can be chosen arbitrarily. The relevant $\mathbf{Q}$ components and the spontaneous magnetostriction are immediately derived from Eqns. (2) and (3), respectively, by expressing the isotropy relation, $Q_{44} = Q_{11} - Q_{12}$.

2. Volume Magnetostriction

The relative volume expansion of a fully saturated sample with respect to the nonmagnetic reference state is $\Delta V/V = S_{11} + S_{22} + S_{33}$, which, from Eqn. (3), turns out to be equal to $Q_{11} + 2Q_{12}$ whatever the orientation $\alpha_1, \alpha_2, \alpha_3$. It can be concluded that in cubic crystals (and therefore in isotropic materials) volume magnetostriction is actually independent of the technical magnetization state and equal to $Q_{11} + 2Q_{12}$.

3. Joule Magnetostriction

Joule magnetostriction is by definition the deformation of a magnetic material which is induced at a fixed temperature by those technical magnetization processes that involve a rotation of the spontaneous magnetization.

It is interesting from an experimental viewpoint to redefine the zero deformation reference state as the isotropic demagnetized state instead of the hypothetical nonmagnetic state. By this, it is meant a multidomain state with an isotropic distribution of

the magnetization orientation and, of course, vanishing average (or technical) magnetization. The strain components as measured with respect to this new reference state (called for convenience spontaneous Joule deformations) are then:

$$S_{11} = (Q_{11} - Q_{12})(\alpha_1^2 - 1/3);$$

$$S_{22} = (Q_{11} - Q_{12})(\alpha_2^2 - l/3);$$

$$S_{33} = (Q_{11} - Q_{12})(\alpha_3^2 - 1/3)$$

$$S_{23} = S_{32} = Q_{44}\alpha_2\alpha_3; \quad S_{13} = S_{31} = Q_{44}\alpha_1\alpha_3;$$

$$S_{12} = S_{21} = Q_{44}\alpha_1\alpha_2 \quad (4)$$

Joule magnetostriction in a cubic crystal may thus be characterized by only two parameters, namely $(Q_{11}-Q_{12})$ and Q_{44}. They can be determined, at least in principle, by measuring the relative elongation $\lambda(\alpha_1,\alpha_2,\alpha_3)$ along various magnetization directions when the sample is brought from the isotropic demagnetized state to the saturated state. Two particular orientations are worth considering, $\langle 100 \rangle$ and $\langle 111 \rangle$: a simple calculation gives

$$\lambda_{100} = 2/3(Q_{11} - Q_{12}); \quad \lambda_{111} = 2/3Q_{44}$$

so that the expression of the spontaneous Joule deformations can be rewritten as:

$$S_1^0 = 3/2\lambda_{100}(\alpha_1^2 - 1/3); \quad S_2^0 = 3/2\lambda_{100}(\alpha_2^2 - 1/3);$$

$$S_3^0 = 3/2\lambda_{100}(\alpha_3^2 - 1/3); \quad S_4^0 = 3\lambda_{111}\alpha_2\alpha_3;$$

$$S_5^0 = 3\lambda_{111}\alpha_1\alpha_3; \quad S_6^0 = 3\lambda_{111}\alpha_1\alpha_3 \quad (5)$$

Here we have used the contracted technical notation for strains (Nye 1957): $S_{11} = S_1$, $S_{22} = S_2$, $S_{33} = S_3$, $S_{23} + S_{32} = S_4$, $S_{13} + S_{31} = S_5$, $S_{12} + S_{21} = S_6$. In practice, due to the difficulty of actual realization of an isotropic demagnetized state, the preferred method of measurement relies on the strain variations caused by controlled modifications of the orientation of fully saturated states (du Tremolet de Lacheisserie 1993).

In isotropic materials, Joule magnetostriction is characterized by only one parameter since $\lambda_{100} = \lambda_{111} = \lambda_s$ where λ_s is called the saturation magnetostriction.

4. Free Energy Density and Other Magnetostrictive Effects

The knowledge of equations of state is essential to most applications of a material. This is related to the knowledge of its free energy density function *F*. The free energy density function of a single domain cubic magnetostrictive crystal at a given temperature can be easily calculated for a given elastic and saturated magnetic state specified by stress components

$T_{11} = T_1$, $T_{22} = T_2$, $T_{33} = T_3$, $T_{23} = T_{32} = T_4$, $T_{13} = T_{31} = T_5$, $T_{12} = T_{21} = T_6$ and magnetization direction cosines α_1, α_2, α_3. Calculation can be made in two different ways. First the crystal is saturated in the specified directions α_1, α_2, α_3 allowing it to deform freely (zero applied stress), so that it takes the spontaneous Joule deformations (Eqn. (5)). Then suitable increasing stresses are applied to the sample in order to bring it reversibly into its specified elastic state while blocking the magnetization. The result is:

$$F = K_0^T(\alpha_1, \alpha_2, \alpha_3) + 1/2s_{11}[T_1^2 + T_2^2 + T_3^2]$$

$$+ s_{12}[T_2T_3 + T_1T_3 + T_1T_2] + 1/2s_{44}$$

$$\times [T_4^2 + T_5^2 + T_6^2] \quad (6)$$

where $K_0^T(\alpha_1, \alpha_2, \alpha_3)$ is the zero stress anisotropy energy of the crystal (defined to within a constant) and the s_{ij} are the elastic compliances at blocked magnetization.

Alternatively, the stress **T** can be applied in the demagnetized state, and then the magnetization is brought to state $\alpha_1,\alpha_2,\alpha_3$ which still produces the spontaneous deformation (Eqn. (5)). Therefore, the total work supplied to the material is:

$$F = 1/2s_{11}[T_1^2 + T_2^2 + T_3^2] + s_{12}[T_2T_3 + T_1T_3 + T_1T_2]$$

$$+ 1/2s_{44}[T_4^2 + T_5^2 + T_6^2] + K_T^T(\alpha_1, \alpha_2, \alpha_3)$$

$$+ 3/2\lambda_{100}[T_1(\alpha_1^2 - 1/3)$$

$$+ T_2(\alpha_2^2 - 1/3) + T_3(\alpha_3^2 - 1/3)]$$

$$+ 3\lambda_{111}[T_4\alpha_2\alpha_3 + T_5\alpha_1\alpha_3 + T_6\alpha_1\alpha_2] \quad (7)$$

A comparison of Eqns. (6) and (7) shows that the anisotropy energy density under stress **T** is given by

$$K_T^T(\alpha_1, \alpha_2, \alpha_3) = \mathbf{K}_0^T(\alpha_1, \alpha_2, \alpha_3) + 3/2\lambda_{100}[T_1(\alpha_1^2 - 1/3)$$

$$+ T_2(\alpha_2^2 - 1/3) + T_3(\alpha_3^2 - 1/3)]$$

$$- 3\lambda_{111}[T_4\alpha_2\alpha_3 + T_5\alpha_1\alpha_3 + T_6\alpha_1\alpha_2] \quad (8)$$

Finally, noticing that $T_i = c_{ij}(S_j - S_j^0)$ where i,j = 1–6, and putting $-3/2 \ (c_{11}-c_{12})\lambda_{100} = B_1$ and $-3c_{44}\lambda_{111} = B_2$, it is easy to obtain from Eqns. (5) and (6):

$$F = K_0^S(\alpha_1, \alpha_2, \alpha_3) + 1/2C_{11}[S_1^2 + S_2^2 + S_3^2]$$

$$+ c_{12}[S_2S_3 + S_1S_3 + S_1S_2]$$

$$+ 1/2c_{44}[S_4^2 + S_5^2 + S_6^2] + B_1[S_1(\alpha_1^2 - 1/3)$$

$$+ S_2(\alpha_2^2 - 1/3)$$

$$+ S_3(\alpha_3^2 - 1/3)] + B_2[S_4\alpha_2\alpha_3 + S_5\alpha_1\alpha_3 + S_6\alpha_1\alpha_2]$$

$$(9)$$

where the c_{ij} are the elastic stiffnesses, and $K_0^S(\alpha_1, \alpha_2, \alpha_3)$ is the anisotropy energy at zero strain which, for

symmetry reasons, has the same form as K_0^T. B_1 and B_2 are called magnetoelastic coupling coefficients.

For an isotropic material, since $\lambda_{100} = \lambda_{111} = \lambda_s$ and $c_{11} - c_{12} = 2c_{44}$, Eqn. (9) reduces to

$$F = K_0^S(\alpha_1, \alpha_2, \alpha_3) + 1/2c_{11}[S_1^2 + S_2^2 + S_3^2]$$
$$+ c_{12}[S_2S_3 + S_1S_3 + S_1S_2] + 1/2c_{44}[S_4^2 + S_5^2 + S_6^2]$$
$$+ B[S_1(\alpha_1^2 - 1/3) + S_2(\alpha_2^2 - 1/3) + S_3(\alpha_3^2 - 1/3)$$
$$+ S_4\alpha_2\alpha_3 + S_5\alpha_1\alpha_3 + S_6\alpha_1\alpha_2] \qquad (10)$$

where $B = -3\lambda_s c_{44}$ is the unique magnetoelastic coupling coefficient.

4.1 Inverse Magnetostrictive Effect

Equation (8) shows that the application of a stress on a magnetostrictive sample induces an additional anisotropy. This is the actual mechanism of the inverse effect since in general this added anisotropy will produce a reorientation of the magnetization.

4.2 ΔE Effect

The effective elastic constants of a magnetostrictive material are generally modified by the application of a static magnetic field (ΔE effect). The reason is that the effective elastic constants are different depending on whether the magnetization is free to rotate (at zero d.c. field) or bound to a given direction (at high d.c. field). Calculation of the ΔE effect is easy only in simple domain configurations. A particularly simple example is that of a single domain cubic crystal bearing an anisotropy of the usual form $K_0^S(\alpha_1, \alpha_2, \alpha_3) = -K_1[\alpha_2^2\alpha_3^2 + \alpha_1^2\alpha_3^2 + \alpha_1^2\alpha_2^2]$ with $K_1 > 0$, magnetized along 100 by a static field H. Starting from Eqn. (9), the differential shear stiffness can be given by

$$\partial T_4/\partial S_4 = \partial T_5/\partial S_5 = c_{44} - B_2^2/(K_1 + 1/2\,\mu_0 M_s H)$$

As expected, it tends to the blocked magnetization value at high field and decreases when the applied field is reduced. A measure of the ΔE effect is the relative variation controlled by the applied field, i.e., $B_2^2/(K_1 c_{44}) = k_{15}$ (Nye 1957). The interest in this parameter and the reason for this notation will be made clear in the next section.

4.3 Nonlinear elasticity

In correlation with the ΔE effect, strong nonlinear elastic effects are also observed in high coupling factor materials. The source of this elastic nonlinearity lies in the nonlinearity of the magnetic response itself. Some calculations can be made for simple single-domain configurations but they will not be developed here.

5. Magnetostriction of Unsaturated States: Piezomagnetic Formulation

Below saturation, the magnetostrictive response of polycrystalline and amorphous materials involves domain processes which can be quite complicated. The usual method, at least for application purposes, is to characterize the material properties only around the relevant bias point as far as possible by phenomenological linear and reversible equations of states.

In general, both a bias field and a bias uniaxial stress are applied to the material along the same direction. The material has then uniaxial symmetry around the bias direction which is taken as axis three of a rectangular frame. In this frame the linearized properties are therefore described by matrix relations that are analogous to those of piezoelectric ceramics (Nye 1957). Taking, for example, differential field **h**, and differential stress **T** as independent variables, the equations of state are written as

$$S = s\mathbf{T} + \mathbf{d} * \mathbf{h}; \quad b = \mathbf{d}\mathbf{T} + g\mathbf{h} \qquad (12)$$

Here, taking advantage of the contracted notation, **T** and the differential strain **S** are six-component vectors whereas **b**, the differential induction, and **h** are three-component vectors. **d** is thus a three line, six columns rectangular matrix. **d*** is actually the transposition of **d**, a consequence of the reversibility assumption.

The form of the piezomagnetic matrix **d** is the same as its piezoelectric analogue, i.e., there are only five nonzero components out of which only three are independent, namely $d_{31} = d_{32}$, $d_{24} = d_{15}$, and d_{33}.

In general in transducer configurations, stress and strain are collinear single-component vectors, as are the field and induction. Vector Eqn. (12) then reduces to a system of two scalar linear equations (no summation on repeated subscripts!):

$$\mathbf{S}_i = \mathbf{s}_{ii}\mathbf{T}_i + \mathbf{d}_{il}\mathbf{h}_l; \quad \mathbf{b}_l = \mathbf{d}_{il}\mathbf{T}_i + \mu_{11}\mathbf{h}_l$$

It is convenient to define a dimensionless coefficient $k_{il} = (d_{il}^2/s_{ii}\,\mu_{11})^{1/2}$ called the magnetomechanical coupling factor. The reason is that its square actually measures the ratio of output to input energy in a static reversible conversion process. By a conversion process, it can define a transformation of magnetic energy into mechanical energy or vice versa. Three useful magnetomechanical coupling factors may be defined in uniaxial magnetostrictors, namely:

$$k_{33} = (d_{33}^2/\mu_{33}s_{33})^{1/2};$$
$$k_{31} = k_{32} = (d_{31}^2/\mu_{33}s_{11})^{1/2}, \quad \text{and}$$
$$k_{15} = k_{24} = (d_{15}^2 s_{44})^{1/2}$$

6. Microscopic Origin of Magnetostriction

Within the model of localized electron ferromagnetism, two microscopic mechanisms are the origin of magnetostriction: exchange interaction between spins, and interaction of a given spin with its local electric field via the spin–orbit coupling. Although it may provide some good clues even in the case of transition metals and alloys, the localized electron model is inadequate for these materials and must be replaced by the band magnetism model. In this model magnetostriction appears as an interaction between the strain and the spin-dependent band structure (du Tremolet de Lacheisserie 1993).

6.1 Spin–Spin Interaction

The dependence of the isotropic Heisenberg exchange on distance between neighboring spins leads to a volume magnetostriction which is generally negative and therefore leads to an enhancement of the lattice thermal expansion. This is the "normal" situation, observed, for example, in pure nickel. The strong positive volume magnetostriction observed in the so-called INVAR alloys is a band magnetism effect and will not be discussed here (see *Invar Materials: Phenomena*).

In addition to the isotropic Heisenberg contribution, the exchange interaction also includes, in general, anisotropic terms of increasing order which depend both on the distance between interacting spins and on the orientation of the bond with respect to spin direction. The orientation dependence is the origin of the magnetic anisotropy energy. Both the distance dependence and the orientation dependence are the origin of Joule magnetostriction.

6.2 Crystal Field Interaction

Ions with a nonspherical electron distribution interact with the nonuniform electric field produced by their neighbors—the so-called crystal field. This interaction can be expanded in terms of orbital multipolar moments and associated field spatial derivatives. For example, the lowest moment is quadrupolar and it is coupled to the first field derivatives (the field gradient tensor). In any case this electrostatic energy depends on the orientation of the electron orbitals with respect to the crystal field and hence the crystal axes (see *Localized 4f and 5f Moments: Magnetism*). In magnetic ions the magnetic moment is either tied to the orbitals or coupled to them by spin–orbit interaction. The final result is that there is a contribution to the free energy of the crystal that depends on the orientation of the spontaneous magnetization with respect to the crystal axes, i.e., an anisotropy energy. The dependence of this anisotropy energy on (anisotropic) strain leads to the Joule magnetostriction. It must be emphasized here that high magnetostriction does not necessarily imply large anisotropy since a function may be zero at a given value of the variable while its derivative is not.

7. Practical Magnetostrictive Materials and their Applications

From a practical point of view it is worth distinguishing four main families of magnetostrictive materials: (i) the so-called INVAR alloys; (ii) the high coupling factor alloys; (iii) the high-saturation magnetostriction alloys; and, finally (iv) the ferrite crystals or ceramics which, in contrast to the previous metallic materials, are almost perfect insulators.

7.1 INVAR Alloys

It was discovered by Guillaume in 1896 that in some alloys of nickel and iron the volume magnetostriction is positive and its temperature dependence just compensates for the normal thermal expansion of the alloy. The result is a metallic alloy bearing a very weak thermal expansion coefficient over a wide temperature range. The applications of these INVAR alloys include very large structures such as methane tankers as well as the most tiny parts of metrology, together with very specific electronic components, such as the masks for high-resolution color TV (du Tremolet de Lacheisserie 1993). A drawback of these materials is that they exhibit a very large forced volume magnetostriction, $\delta V/V \delta H \cong 10^{-10}$ m A^{-1}, preventing their use in a high magnetic field environment.

7.2 High Coupling Factor Alloys

This category includes magnetically soft polycrystalline and amorphous alloys based on iron, nickel, and cobalt. Their saturation magnetostriction is rather low ($\lambda_s < 50 \times 10^{-6}$) and their high coupling factor is rather a consequence of their very low anisotropy.

The most remarkable and useful example of this category of materials is an amorphous alloy known as Metglass 2605 SC with the composition $Fe_{81}B_{13.5}Si_{3.5}C_2$. Due to its fabrication technique (Kavesh 1977), this alloy is available only in the form of a thin ribbon (around 25 μm thick). Table 1 lists some of its relevant characteristics. The last four parameters may be considered as "soft" since they depend strongly on postdeposition treatments which modify all the properties that are related to anisotropy. It is well known that intrinsic anisotropy in amorphous materials is actually a random function of the spatial position with a correlation length typically less than 1 μm. Extrinsic large-scale anisotropy can, however, be induced by appropriate treatments.

Typically, annealing at 642 K for 10 min under a saturating magnetic field parallel to the ribbon plane

Table 1
Some relevant characteristics of Metglass 2605SC.

Young's modulus at blocked magnetization Y_{33}^M (GPa)	200
Curie temperature (K)	643
Spontaneous induction at 300 K (T)	1.61
Saturation magnetostriction at 300 K, 10^{-6}	30
Relative permeability, μ_{33}	20000
Relative permeability μ_{33} under stress bias ($T_{33} = 1$ MPa)	80000
Static magnetostrictivity d_{33} (nm A^{-1})	1000
Magnetomechanical coupling factor k_{33} (under 50 A m^{-1} bias field)	0.97
Young's modulus at free magnetization Y_{33}^H (GPa)	25

induces a uniaxial anisotropy with an easy axis parallel to the applied field. The value of the induced anisotropy field is in the order of 50 A m^{-1}. Such a field-annealed Metglass ribbon has uniaxial symmetry and, as explained in Sect. 5, it may be characterized by differential piezomagnetic parameters around a given bias point. It is usual to take the easy axis as the *z* or "3" axis. Table 1 refers to a field-annealed Metglass alloy in the demagnetized state under zero field and zero stress, unless otherwise specified.

Remarkable points in Table 1 are: (i) an extremely high coupling factor, (ii) a giant ΔE effect (from 25 GPa at zero field up to 200 GPa at high bias field, i.e., at blocked magnetization); and (iii) an extreme sensitivity of permeability to applied stress. However, this is associated with a rather low saturation magnetostriction. All these characteristics make the Metglass alloy a very good candidate for low-power transducer applications (du Tremolet de Lacheisserie 1993, du Tremolet de Lacheisserie *et al.* 1998).

Force transducers make use of the stress dependence of permeability, and more generally of the modification of magnetic response by stress. A significant advantage of these transducers is that since magnetic measurements do not require physical contact with the material, it is quite easy to sense forces acting on moving parts. As an example, consider the noncontact measurements of the torque transmitted by a rotating shaft. A Metglass ribbon is wrapped around the shaft and is submitted to the shearing forces associated with the torque. The ribbon permeability is measured by a fixed coil arrangement placed close to the moving ribbon surface. Permeability must be measured along one of the principal stress directions, in this case at 45° off the shaft axis.

7.3 High-saturation Magnetostriction Alloys

Giant magnetostrictive effects were discovered in 1975 in the intermetallic cubic compound TbFe$_2$,

known as Terfenol (Clark 1980). This alloy exhibits magnetostrictive deformations which are 50 to 100 times larger than the high coupling factor materials. Such a giant magnetostrictive effect can be clearly explained by the localized electron model as a crystal field effect on the rare-earth site. Unfortunately this is obtained at the price of a relatively large anisotropy. Therefore, high driving fields are necessary to generate the magnetostrictive deformation.

The improved alloy Tb$_{0.3}$Dy$_{0.7}$Fe$_2$, known as Terfenol D, still has a very large magnetostriction but a much lower anisotropy. This is because the main contributions to anisotropy, due to terbium and dysprosium, have opposite signs and nearly compensate for each other at this composition, whereas the respective contributions to magnetostriction do not. Table 2 lists some useful room-temperature characteristics of Terfenol and Terfenol D. Even the improved material remains relatively hard and despite the very large saturation magnetostriction, the magnetomechanical coupling factors are definitely lower than those of low-saturation magnetostriction but very soft alloys.

Progress in giant magnetostriction materials has been directed towards the fabrication of highly textured materials and even single crystals (Clark 1986). Potential applications of giant magnetostriction alloys include large displacement transducers and high-power ultrasonic generation. However for static displacement generation, piezoelectric transducers based on PZT ceramics are still the best choice mainly because they do not require a permanent excitation power.

In contrast, Terfenol D is a better candidate than PZT for high-power ultrasonic generation (Claeyssen *et al.* 1988) because it is not brittle and it generates a higher deformation and higher power density. A noticeable disadvantage of these alloys is their metallic electrical conductivity which, due to the so-called skin effect, prevents their use at high frequency.

Giant magnetostriction alloys were also prepared as thin films, with the idea that new specific routes to a vanishing anisotropy could be followed in view of applications to low driving field microactuators (du Tremolet de Lacheisserie *et al.* 1998). Thin films of amorphous Tb$_{1-x}$Dy$_x$(Co$_{0.55}$Fe$_{0.45}$)$_y$ were deposited by Duc *et al.* (1996) using d.c. sputtering. Due to their amorphous structure these films are expected to have a vanishing large-scale magnetic anisotropy together with an isotropic, and still giant, magnetostriction. In practice they always bear some induced anisotropy of various origins. It is preferable in most cases intentionally to induce a homogeneous in-plane uniaxial anisotropy rather than to rely on uncontrolled (and often spatially inhomogeneous) parasitic effects.

This is done both by controlling the sputtering conditions (Quandt *et al.* 1994) and by applying a bias field, either during the deposition itself or during a postdeposition treatment (typically 10 min to 1

Table 2
Main characteristics of Terfenol ($TbFe_2$) and Terfenol D ($Tb_{0.3}Dy_{0.7}Fe_2$). Curie temperature T_c, spontaneous induction $\mu_0 M_s$, saturation magnetostriction λ_s, magnetomechanical coupling factor k_{33}, and static magnetostrictivity d_{33}.

Material	T_c (K)	$\mu_0 M_s$ (T)	$10^6 \lambda_s$	k_{33} max	d_{33} max (nm A^{-1})
$TbFe_2$	698	1.1	1750	0.35	
$Tb_{0.3}Dy_{0.7}Fe_2$	653	1.0	1100	0.6	57

hour at 150–300 °C under a 10000 A m^{-1} field). Films are deposited on substrate plates (silicon or pyrex) of known elastic properties thereby constituting a magnetoelastic bimorph (Klokholm 1976). If the magnetostrictive layer is much thinner than the substrate plate, the magnetostrictive stress at zero deformation, rather than the magnetostrictive deformation at zero stress, can be directly determined (du Tremolet de Lacheisserie and Peuzin 1994). This is done by measuring the curvature and torsion of the magnetoelastic bimorph induced by a known applied field. Magnetostrictive deformation at zero stress can then be calculated by making reasonable estimations of the layer elastic modulus.

For example, in $Tb_{0.32}(Fe_{0.45}Co_{0.55})_{0.68}$, a fairly well-defined easy axis can be induced by an annealing at 250 °C. The elongation, $\lambda(H)$, produced along the in-plane hard direction is then determined as a function of the field H applied along the same direction. Giant magnetostriction is observed with $\lambda(H) = 0.8 \times 10^{-3}$ at $\mu_0 H = 0.3$ T and still $\lambda(H) = 0.3 \times 10^{-3}$ at $\mu_0 H = 0.1$ T. However, these driving fields are still high for microsystem applications. This is due in part to the ferrimagnetic character of these alloys which leads to a rather low spontaneous magnetization ($\mu_0 M_s \cong 0.3$ T) and therefore to a high anisotropy field.

In order to improve further the low field magnetostrictive response, a periodic laminar nanocomposite was fabricated by repeated stacking of a weakly magnetostrictive, but high magnetization, layer of polycrystalline FeCo and a highly magnetostrictive amorphous TbCo layer (Betz 1997). Typical layer thicknesses were about 6 nm and up to hundreds of layers could be stacked by using sequential sputter deposition. As a consequence of the strong exchange coupling between the FeCo and TbCo layers the obtained films behaved as a homogeneous ferromagnetic alloy combining relatively high magnetization and giant magnetostriction. Deformation of up to 0.4×10^{-3} was obtained in a field of only 20 mT. These thin films of giant magnetostriction alloys have given rise to the development of various types of micromechanical devices (du Tremolet de Lacheisserie *et al.* 1998) among which are a micropump (Quandt 1997), a torsional microactuator which is claimed to be free of thermal drift (Betz *et al.* 1996) and a two-dimensional

optical microscanner (Garnier *et al.* 1999). These devices are, however, still at the laboratory level.

7.4 Magnetostrictive Insulators: Ferrites

Two families of magnetoelastic ferrites are worth mentioning from the practical point of view: the spinel ferrites of general formula MFe_2O_4 where M is a metal of the first transition series; and the garnets of general formula $R_3Fe_5O_{12}$ where R is a rare-earth metal or yttrium.

Magnetoelastic spinel ferrites such as $NiFe_2O_4$ and $Ni_{0.98}Co_{0.02}Fe_2O_4$ have a resistivity in excess of $10^4 \Omega.m$, a spontaneous induction of 0.33 T, and a Curie temperature of 863 K. Their spontaneous magnetostriction is comparable with that of high coupling factor materials but since they are somewhat less soft, their magnetomechanical coupling factors are modest (0.2–0.38). These materials face a difficult competition with piezoelectric ceramics.

The garnets, especially $Y_3Fe_5O_{12}$ (YIG), have found many applications in general microwave devices, mostly because they are almost perfect insulators and bear remarkable magnetodynamic properties (von Aulock 1965). Because of their excellent acoustic properties, and despite their rather weak magnetostriction (λ_{100} and λ_{111} are in the order of 10^{-6}), YIG single crystals have been exploited, at least at the laboratory level, in magnetoelastic signal processing devices taking advantage of such effects as magnetic field control of acoustic propagation and coupling between magnetostatic waves and acoustic waves (Auld 1968, 1971).

See also: Magnetoelastic Phenomena; Magnetoelasticity in Nanoscale Heterogenous Materials; Stress Coupled Phenomena: Magnetostriction

Bibliography

Auld B A 1968 *Nonlinear Interaction of Spin Waves and Elastic Waves: Advances in Microwaves*. Academic Press, New York
Auld B A 1971 Magnetostatic and magnetoelastic wave propagation in solids. *Appl. Solid State Sci.* **2**, 1–106
Betz J 1997 Magnetostriction géante de couches minces et microactionneurs magnétostrictifs pour des technologies intégrées. Thesis, University of Grenoble, France

Betz J, Mackay K, Peuzin J, Halstrup B, Lhermet N 1996 Torsion based, drift free magnetostrictive microactuator. In: *Proc. Actuator '96*. Axon Technology Consult GmbH, Bremen, Germany, pp. 283–6

Claeyssen F, Boucher D, Pohlenz C 1988 Application of magnetostrictive rare earth iron alloys to sonar transducers. In: *Proc. Undersea Defence Technology '88*. Microwave Exh. and Pub. Ltd. Ed, London, 711pp

Clark A E 1980 Magnetostrictive rare earth—Fe₂ compounds. In: Wohlfarth E P (ed.) *Ferromagnetic Materials*. North Holland, Amsterdam

Clark A E 1986 Magnetostriction in twinned [112] crystals of $Tb_{0.27}Dy_{0.73}Fe_2$. *IEEE Trans. Magn* **MAG-22**, 973–5

du Tremolet de Lacheisserie E 1993 *Magnetostriction. Theory and Applications of Magnetoelasticity*. CRC Press, Boca Raton, FL

du Tremolet de Lacheisserie E, Mackay K, Betz J, Peuzin J C 1998 From bulk to film magnetostrictive actuators. *J. Alloy. Comp*. 685–91

du Tremolet de Lacheisserie E, Peuzin J C 1994 Magnetostriction and internal stresses in thin films: the cantilever method revisited. *J. Magn. Magn. Mater*. **136**, 189–96

Duc N H, Mackay K, Betz J, Givord D 1996 Giant magnetostriction in amorphous $(Tb_xDy_{1-x})(Fe_{0.45}Co_{0.55})_y$ films. *J. Appl. Phys*. **79**, 973–7

Garnier A, Bourouina T, Fujita H, Hiramoto T, Orsier E, Peuzin J C 1999 Magnetic actuation of bending and torsional vibrations for 2D-optical-scanner application. In: *Proc. 10th Int. Conf. on Solid State Sensors and Actuators*. Sendai, Japan

Kavesh S 1977 In: Leany H S, Gilman J J (eds.) *Metallic glasses*. American Society of Metals, Metals Park, OH

Klokholm E 1976 The measurement of magnetostriction in ferromagnetic thin films. *IEEE Trans. Magn*. **12**, 819–21

Nye J F 1957 *Physical Properties of Crystals*. Clarendon Press, Oxford

Quandt E 1997 Giant magnetostrictive thin film materials and applications. *J. Alloy. Comp*. **258**, 126–32

Quandt E, Gerlach B, Seemann K 1994 Preparation and applications of magnetostrictive thin films. *J. Appl. Phys*. **76**, 7000–2

von Aulock W 1965 *Handbook of Microwave Ferrite Materials*. Academic Press, New York

J. C. Peuzin
Laboratoire Louis Néel, CNRS Grenoble, France

Magnets, Soft and Hard: Magnetic Domains

Below the Curie temperature, the elementary magnetic moments of ferro- and ferrimagnetic materials are spontaneously ordered (see *Magnetism in Solids: General Introduction*). On a mesoscopic scale in the nanometer range, many of these elementary dipoles can be collected in an average value called magnetization, which is represented by a classical vector $\mathbf{M}(\mathbf{r})$ of unit A/m ($\mathbf{r}$ is the position vector). The absolute value of the magnetization vector, given by the saturation magnetization M_s, is a function of temperature alone for all regular magnetic materials, it is constant throughout a (chemically uniform) sample and is largely independent of applied magnetic fields. We can therefore write $\mathbf{M}(\mathbf{r}) = M_s\mathbf{m}(\mathbf{r})$ with $\mathbf{m}^2 = 1$, where $\mathbf{m}(\mathbf{r})$ is the unit vector field of magnetization.

For samples of finite dimensions, this vector field is usually subdivided into magnetic domains, i.e., volumes that are themselves uniformly magnetized to a value equal to M_s along different directions. They are separated by domain walls, in which the magnetization vector continuously rotates on the 10–1000 nm scale to accommodate the change in magnetization orientation between adjacent domains. Domain formation is driven by energy minimization, with the reduction of the stray field energy being responsible for their development above all. The character of a domain pattern depends on the strength and orientation of "easy axes of magnetization" (anisotropy, see also *Magnetic Anisotropy*) relative to the main surfaces of the magnet, but also its shape, dimensions, and physical microstructure are important.

The *magnetic microstructure*, i.e., the arrangement of domains and walls, together with their reaction in external magnetic fields (magnetization processes) determine the macroscopic properties of magnetic materials. Due to the presence of domains, a magnet can accommodate a continuous range of magnetic states that reach from complete demagnetization (if the moments of all domains cancel each other) to saturation in external fields. In *soft magnetic materials*, the magnetic microstructure can easily be modified in small fields either by wall motion or magnetization rotation.

For instance, a high permeability in the core of inductive devices is provided by easily displaceable domain walls leading to a steep magnetization curve, whereas a linear curve for sensor applications requires rotation processes mainly. If major and irreversible rearrangements of domains occur during magnetization, they are responsible for losses and noise in devices, and pinning of domain walls by material imperfections results in hysteresis with coercivity and remanence (see *Magnetic Hysteresis*). Strong pinning or the prevention of domain nucleation causes a high coercivity and leads to *hard magnetic materials* (see *Hard Magnetic Materials, Basic Principles of*).

In Sects. 2 and 3 of this contribution, the basic domain structures in both material classes will be reviewed based on Kerr-microscopical domain studies (see *Kerr Microscopy*), following some introductory remarks on the fundamentals of domains in Sect. 1. Reviews on magnetic materials with emphasis on magnetic microstructure can be found in Cullity (1972), Chikazumi (1997), and O'Handley (2000). A comprehensive review on domains together with an extended bibliography is given in Hubert and Schäfer (1998).

1. Fundamentals of Magnetic Domains

1.1 Energetics of a Ferromagnet

Domain formation is driven by minimization of the total free energy. The relevant magnetic energies are introduced here by showing their effect on the magnetization vector field of (soft) magnetic films (Fig. 1).

(a) Exchange energy

A ferromagnet prefers a parallel alignment of magnetization vectors (Fig. 1(a)). Deviations from this condition invoke an energy penalty, the exchange energy that can be described by a stiffness expression $E_{ex} = A \int (\mathrm{grad}\ \mathbf{m})^2 \mathrm{d}V$ (A is the exchange constant).

(b) Stray field energy

A saturated state as assumed in Fig. 1(a) would cause a magnetic stray field for a finite sample. This can be derived from the material law $\mathbf{B} = \mu_o(\mathbf{H} + \mathbf{M})$ and Maxwell's equation div $\mathbf{B} = 0$ ($\mathbf{B}$ is the magnetic flux density in teslas and $\mathbf{H}$ the magnetic field in amperes per meter), leading to div $\mathbf{H} = -$div $\mathbf{M}$. The sinks and sources of magnetization (div $\mathbf{M}$) may be interpreted as *magnetic charges* (note that magnetic charges never appear isolated but are always balanced by opposite charges, different to electric charges). A field arises from these charges that acts as stray field outside the sample and as demagnetization field in the interior. Volume, interface, and surface charges may be distinguished (Fig. 1(b)), the latter occurring if the magnetization vector is not parallel to a surface or edge. The energy connected to the stray field is $E_{stray} = -0.5\,\mu_o \int \mathbf{H}_{stray} \cdot \mathbf{M} \mathrm{d}V$. It scales with the factor $K_d = M_s^2 \mu_o / 2$ (stray field energy coefficient, units J m^{-3}), which is a measure of the maximum stray field energy density of a material.

If the stray field energy dominates, flux-closed magnetization configurations will develop that tend to avoid stray fields. For the disk in Fig. 1(a), a concentric pattern would be completely charge-free, at the expense of some exchange energy though. Such a continuously flowing, isotropic configuration is in fact observed in anisotropy-free NiFe (Permalloy) disks (Fig. 1(c)).

The existence of "real" domains is, in a conventional picture, connected with the presence of anisotropy, which would favor homogeneously magnetized volumes along "easy directions." However, in thin film elements, domains can also be present in the absence of anisotropy, just induced by the shape as shown in Fig. 1(d) for rectangular and elliptical elements. This follows from the requirement of pole avoidance (Van den Berg 1986): To be completely stray-field-free, the vector field $\mathbf{m}$ must be divergence-free within the element (div $\mathbf{m} = 0$), it must be parallel to the edges and to the film plane, and it must have a constant length ($|\mathbf{m}| = 1$). These
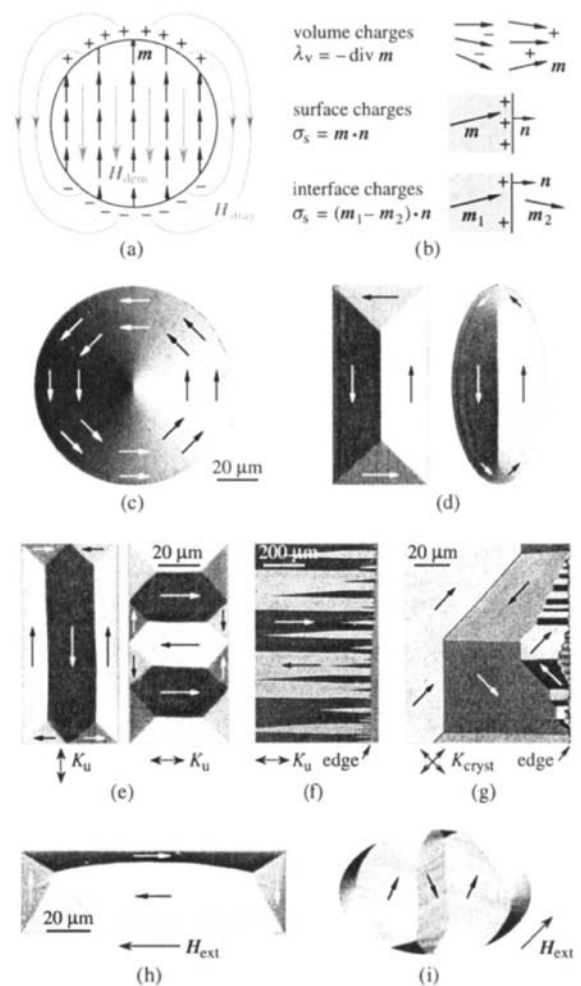
Figure 1

The effect of magnetic energies on domain formation, demonstrated for magnetic films. The magnetic charges (b) of the hypothetical, saturated state in (a) can be avoided by a flux-closed configuration as observed by Kerr microscopy on a Fe$_{81}$Ni$_{19}$ (Permalloy) film disk of 240 nm thickness (c). The shape-induced domains of the anisotropy-free Permalloy elements in (d) are modified by magnetization-induced anisotropies of the order of 100 J/m^3 in (e). The stress-induced anisotropy of the extended amorphous CoFeSiMo-film (f) (thickness 800 nm) is an order of magnitude higher than that of Permalloy, leading to a spike-like closure structure at the film edge. In the (100)-oriented, single-crystalline iron film of 100 nm thickness (g), four domain "phases" are found according to crystal anisotropy. External magnetic fields can cause wall motion and magnetization rotation as shown for 240 nm-thick NiFe elements in (h) and (i), respectively.

requirements can only be met simultaneously if the magnetization stays parallel to the edges on every point along an edge normal, as long as no other edge interferes. Consequently, uniformly magnetized *domain*s result in a certain neighborhood of straight edges. Similar considerations also apply to bulk specimens. However, in most magnetic specimens (especially in bulk magnets) the occurrence of ''regular'' domains and their arrangement is, in fact, strongly connected with the presence of anisotropy.

(c) Anisotropy energy

In most magnetic materials, easy axes do exist that are preferably occupied by the magnetization vector. Deviations cause an anisotropy energy $E_{anis} = K_u \sin^2 \theta$ (for a uniaxial anisotropy, where θ is the angle between easy axis and magnetization, and K_u is the anisotropy constant in J m^{-3}) (see also *Magnetic Anisotropy*).

Anisotropy may have different origins. In the case of Permalloy films, for example, a uniaxial anisotropy may be caused by preferred pair ordering of the atomic nickel and iron components along the local magnetization direction present during film deposition or at annealing (magnetization-induced anisotropy). Well-defined easy axes can be induced by annealing in magnetic fields, leading to oriented basic domains and closure domains at the sample edges to avoid magnetic charges (Fig. 1(e)). The anisotropy energy of the hard-axis closure domains could be reduced by decreasing their volume. This, however, necessarily would decrease the basic domain width at the expense of *domain wall energy*. The wall energy is proportional to $\sqrt{(AK)}$ because in a wall, the magnetization deviates from the anisotropy axes and from parallel arrangement. So the domain structures in the case of Fig. 1(e) are determined by the minimization of anisotropy and wall energy under the constraint of zero stray field energy.

Mechanical stress may induce or modify anisotropies as well, if the magnetostriction constant is different from zero. The stress-induced anisotropy in the amorphous film of Fig. 1(f) is an order of magnitude larger than the magnetization-induced anisotropy of the Permalloy elements in Fig. 1(e). Towards the film edge, the stray field energy is reduced by domain refinement in a spike-like way rather than by closure domains, which would involve considerable anisotropy energy. This mechanism of magnetostatic energy reduction by subdivision of the pole distribution towards an edge or surface is generally found in high-anisotropy, uniaxial materials.

In crystalline materials, the magnetocrystalline anisotropy—the preference of the magnetization vector to align with so-called easy crystal axes—is usually dominating. In the example of Fig. 1(g), two of the $\langle 100 \rangle$ easy axes in a single crystalline iron film are

occupied, leading to a four-phase domain pattern with charge-free $180°$ and $90°$ domain walls.

Another important phenomenon can be seen in Fig. 1(g): the edge of the extended film is misoriented, i.e., it does not contain an easy axis. Here the two requirements of using only easy directions and avoiding stray fields are incompatible. A compromise is found by *domain branching*: towards the film edge, the pattern is refined in several generations of easy-axis-domains, so that the hard-axis closure domains (necessary to completely avoid stray fields) are getting as small as possible. They are restricted to the outermost edge and are not resolved in the image. Far away from the edge, the domains stay wide to save wall energy. The branching process connects the wide and narrow domains in a way that depends on the number of easy directions. In Fig. 1(f), for instance, only two-phase branching is possible due to the uniaxial anisotropy. In the case of a very weak uniaxial anisotropy (Fig. 1(e)), regular closure domains rather than branching may be preferred on misoriented edges. Domain branching also plays a major role in bulk materials if the easy directions are incompatible with the *surface* orientation. For strongly misoriented surfaces, a low energy is achieved by simple domains in the volume and a finely divided surface pattern.

(d) Magnetostrictive energy

A magnetic material with a nonvanishing magnetostriction constant is elongated along the magnetization direction. If the spontaneous deformations of the various parts of a domain pattern do not fit together elastically, a magnetostrictive self-energy arises that can modify the domain arrangement, especially in bulk materials.

(e) Zeeman energy

Applying an external field also adds energy. Domains with magnetization components along the field direction are favored and grow by wall displacement (Fig. 1(h)). In stronger fields, magnetization rotation occurs (Fig. 1(i)).

1.2 Classification of Materials and Domains

The character of a domain pattern is determined by the relative size of anisotropy and stray field energy, defined by the dimensionless material parameter $Q = K/K_d$ (where $K_d = M_s^2 \mu_o / 2$ is the stray field energy coefficient, and K is the effective anisotropy constant). If the stray field energy dominates ($Q \ll 1$), then flux-closed domain patterns develop that avoid stray fields, eventually at the expense of anisotropy energy in closure domains at surfaces if they do not contain an easy axis. A dominating anisotropy energy ($Q \gg 1$) forces the magnetization along easy axes, allowing for magnetic charges.

The ratio Q determines the applicability of a material. A soft magnetic material should have a small value $Q \ll 1$, and strong permanent magnets are often based on materials with $Q \gg 1$. Note, however, that the properties of high and low relative anisotropy are not directly related to magnetic hardness, i.e., to high and low coercivity. Coercivity, as an extrinsic property, depends on additional structural features such as defects, grain boundaries, sample or particle size, and surface irregularities in conjunction with the magnetic microstructure. The intrinsic Q-parameter determines the potential to achieve a desired magnetic hardness (or softness).

1.3 Domain Walls

The characteristic feature of *thin* soft magnetic films (thinner than 30 nm for Permalloy) is the symmetric Néel wall with an in-plane magnetization rotation (Fig. 2(a)). This is a magnetically charged wall, where most of the charges are concentrated in a wall core which scales with the exchange length of the stray-field energy $\sqrt{(A/K_d)}$ ($= 5$ nm for Permalloy). In thick films (thicker than 100 nm for Permalloy), the charged walls are replaced by completely stray-field-free, two-dimensional vortex walls (Fig. 2(b)). The width of the vortex scales with the film thickness.

Above a thickness of the order of $5\sqrt{(A/K)}$ (where K is crystal or an induced anisotropy), a wall structure develops, which is still related to the asymmetric Bloch wall of thick films. Instead of a single vortex in the middle, two vortices are formed in the neighborhood of the surfaces that close most of the magnetic flux arising from the polar magnetization components in the wall interior (Fig. 2(d)). In the volume, this stray-field-free wall assumes a one-dimensional character with a rotation parallel to the wall plane as in a classical Bloch wall (see Fig. 2(c)), and at the surfaces, the magnetization rotates in-plane. Whereas the surface wall width steadily increases with thickness, the interior wall width approaches the classical value of $\pi\sqrt{(A/K)}$. Note that even in low-Q materials the wall width stays finite, because a real soft magnetic material is never completely anisotropy-free, even if it has extremely high permeability. In high-Q materials, the surface vortices are more or less suppressed and the wall approaches the classical Bloch wall structure (c) all through, allowing for magnetic charges at the surfaces.

2. Domains in Soft Magnetic Materials

Soft magnetic materials play a major role as core material in inductive devices. Such devices rely on the high permeability of their cores that reaches values up to one million times the air value. Domain wall displacement is the primary origin of this extraordinary quality of soft magnetic materials. But

(a) Symmetric Néel wall

charge tails   core   charge tails

10 nm Permalloy   20 μm

(b) Asymmetric Bloch wall

(c) Symmetric Bloch wall

domain   wall   domain

(d) Stray-field-free vortex wall

Fe-Si Goss sheet (0.3 mm thick)   FeSiBCuNb nanocrystalline ribbon (25 μm thick)

10 μm
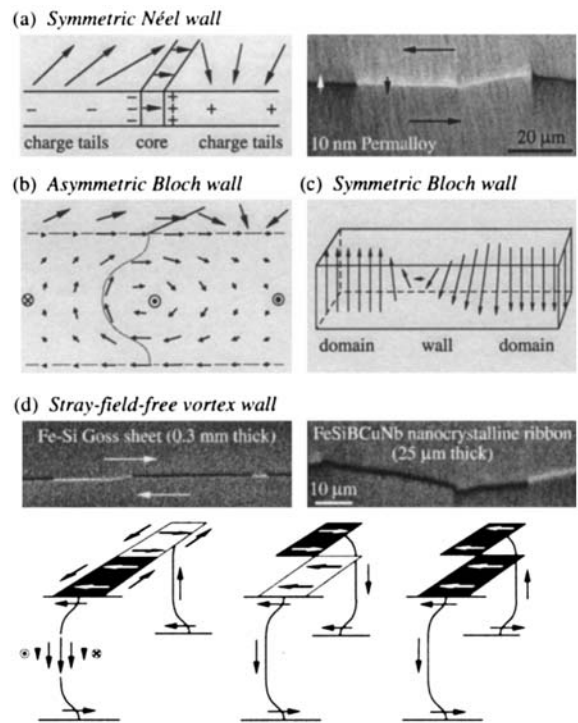
Figure 2
The fundamental types of domain walls in *soft* magnetic materials. In a, b, and d, the surface magnetization and the projection on the cross-section plane is schematically shown together with observations by Kerr microscopy. The black-and-white wall segments are due to different chiralities of the surface magnetization. The magnetic charges of the Néel wall (a) are distributed between a sharply localized core and extremely wide tails, which take over a good part of the rotation. The asymmetric Bloch wall (b) and its derivative for high sample thickness (d) are free of magnetic charges. The slight tilting of some wall segments in (d) is a consequence of the vertical flux, indicating segments of opposite chirality. Those transitions not connected with a kink represent mere "cap switches"—a change in the orientation of the surface vortex without a change in the basic wall chirality. The classical (symmetric) Bloch wall, which is approached in high-Q materials, is sketched in (c) for comparison. Here, the magnetization rotates parallel to the wall plane across the whole sample thickness.

also, magnetization rotation can lead to high permeability if anisotropies are uniform and small. Depending on applications, magnetization processes have to be carefully controlled by selecting proper materials with suitable domain patterns. In high-frequency applications, for instance, wall displacement processes are generally less favorable than rotation

because of the "anomalous" eddy current losses connected with wall motion (see *Magnetic Losses*).

The avoidance of wall motion requires that all 180° walls are oriented perpendicular to the field direction. This can be achieved in ring cores of low-anisotropy materials with a transverse easy axis, showing a linear response with low remanence and coercivity. Irregularities connected with domain wall pinning and domain annihilation or creation processes cause losses in electrical machines and noise in communication and sensor devices. A general rule is: if the character of the magnetic microstructure can be improved in the sense of a more regular domain structure leading to more reversible magnetization processes, a better performance of inductive devices can be achieved.

In this section, the magnetic microstructure of selected soft materials is reviewed. Emphasis will be on equilibrium domains in the field-free state, largely neglecting the rich variety of patterns that occur on application of magnetic fields. The domains in all soft magnetic materials follow the principle of flux closure ($Q \ll 1$), but anisotropy together with the surface orientation has a decisive influence on domain arrangement.

2.1 Grain-oriented Electrical Steel

Grain-oriented transformer material consists of large grains of Fe 3 wt.% Si. They are oriented within a few degrees deviation of the [001] easy direction from the preferred axis of the material. The surfaces of all grains are (110)-related within the same accuracy in misorientation (forming altogether a [001](110) texture, the Goss texture). The sheets are insulated by thin ceramic layers to avoid eddy currents between the sheets and to provide favorable mechanical stress (see also *Steels, Silicon Iron-based: Magnetic Properties*).

The basic domain structure of well-oriented Goss grains consists of wide domains magnetized parallel and antiparallel to the easy [001] direction (grain A in Fig. 3(a)). If the [001] direction is slightly misoriented out of plane (grains B, C), the basic domains are supplemented to reduce the stray field energy: shallow surface domains (lancets) collect the perpendicular flux, which would otherwise emerge from the surface due to the misorientation, and feed it into internal transverse easy-axis domains where it is transported to the other surface of opposite charge polarity or to the neighboring basic domain to be distributed again (Fig. 3(d)). In a variant, the lancets join into combs (grain C) by using a common internal transverse domain that is properly oriented to avoid magnetostrictive energy. Therefore, the combs are aligned along a $\langle 111 \rangle$-axis at the surface.

The magnetization process along the preferred axis occurs by motion of the basic 180° walls. However, during a magnetization cycle, the system of
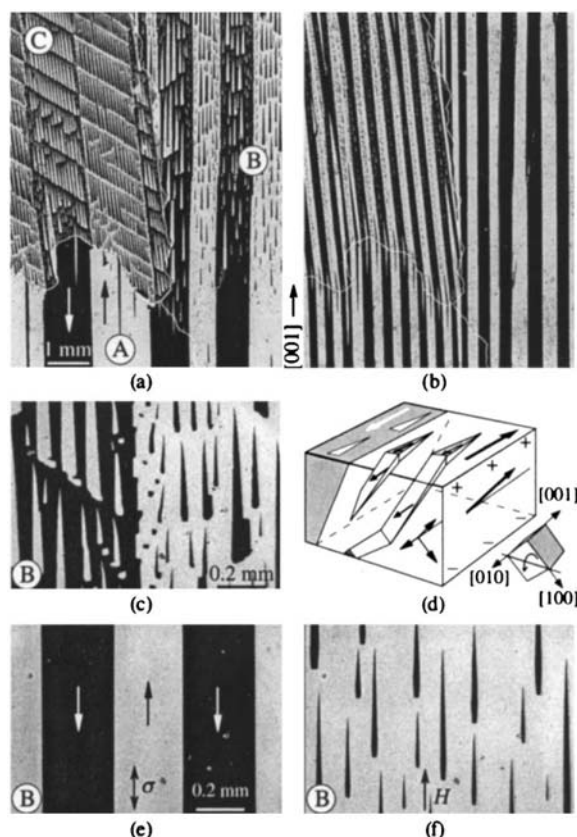
Figure 3
(a) In Goss-textured transformer steel, simple (grain A) or supplemented-bar domains (grains B, C) are observed, depending on the misalignment of the [001] easy axis relative to the surface (that is 0°, 1°, and 2° in grains A, B, C, respectively). Details of grain B are shown at higher magnification in (c) together with a three-dimensional model of a supplementary pattern in (d). A uniaxial tensile stress along the preferred axis (b) largely suppresses the supplementary domains and causes domain refinement in misoriented grains, which also extends to well-oriented grains to maintain flux continuity. The tensile stress of 2 kg mm^{-2} in (b) was applied externally to simulate the stress-effective insulation coating that was removed here to allow for Kerr microscopy. If the basic domains (e) of a stressed grain are wiped out during the magnetization cycle, the supplementary domains return (f). Images (e) and (f) are from the same location, but a field is applied in (f) leading to a relative magnetization of $M/M_s = 0.9$.

supplementary domains is destroyed and rebuilt. The energy bound in the supplementary domains is lost in every cycle, thus forming an important part of hysteresis loss in transformer sheets. Since several nonplanar easy axes are always engaged in

supplementary domain patterns, their generation and annihilation is also connected with magnetostrictive, acoustic noise (note that the magnetostrictive elongation would not change by the motion of a 180° wall).

Two possibilities do exist to avoid the unfavorable supplementary domains. They can be largely suppressed by mechanical tensile stress along the preferred axis (Fig. 3(b)). It magnetostrictively favors the basic domains and wipes out the transversely magnetized domains. The basic domain spacing is then decreased because otherwise the overall stray field energy would rise in the absence of the supplementary domains. The reduced domain width also reduces anomalous eddy current losses, which become important if the basic domain width is larger than the sheet thickness. Fortunately, the planar stress exerted by the stress-effective insulating coating is for the Goss texture equivalent to a uniaxial stress along the preferred axis and will thus suppress supplementary domains. Note, however, that for magnetostatic reasons, the lancet structure reappears when the basic domains are wiped out during the magnetization cycle as is demonstrated in the sequence in Fig. 3(e) and 3(f). This causes extra losses.

It is also possible to avoid supplementary domains completely if a misorientation of better than one degree is achieved. But such a quasi-single-crystalline material would tend to develop very wide basic domains (Fig. 4(a)) with correspondingly large anomalous eddy current losses. The basic domain width can be artificially reduced by scratching or by laser scribing (Fig. 4(b)). The stress introduced locally in this way interrupts the basic domains, acting like an artificial grain boundary (see also *Steels, Silicon Iron-based: Magnetic Properties*).

2.2 Nonoriented Electrical Steel

Figure 5 gives an impression of the huge variety of domains on the surface of nonoriented silicon–iron material commonly used in rotating electrical machines (see also *Steels, Silicon Iron-based: Magnetic Properties*). Domain complexity depends on crystal orientation. Domains in ideal Goss-grains (grain A) or slightly misoriented Goss-grains (grain B) are readily identified by comparison with Fig. 3. In the (100)-oriented grain (C), a simple four-phase surface pattern is found as in the corresponding thin film case (Fig. 1(g)). Note, however, that for a thick sheet also the easy axis perpendicular to the surface will be occupied by internal domains. A slightly misoriented (100) surface (grain D) shows fir-tree domains—a supplementary pattern that distributes the perpendicular flux between neighboring basic domains by shallow surface domains.

With stronger misorientation, the supplementary domain system becomes increasingly complicated

(a) **(b)**

(c)
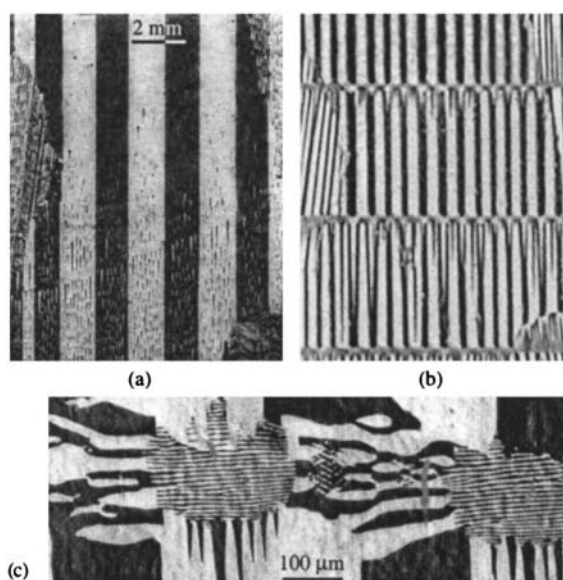
Figure 4
Domain spacing in well-oriented grains (a) can be reduced by laser scribing (b). The stress between the laser spots causes unfavorably oriented domains that interrupt the basic domains (c). Image (b) was obtained by applying a powder emulsion to a laser-treated surface with insulating coating, whereas the Kerr image (a) is from the same location after removing the coating and relieving stress by annealing. Kerr image (c) was obtained before annealing at higher magnification.

(grain E in Fig. 5), and above a critical misorientation, *branched* domain patterns take over (grains F and G in Fig. 5). Branching (see Sect. 1) at the surface of a bulk cubic material occurs in a similar way as shown in Fig. 1(g) for a two-dimensional case, but further possibilities will be added by allowing the third dimension to be used both by the magnetization direction and by the spatial domain structure. The fractal nature of branched patterns with up to four generations of domains is also revealed in the surface pattern of the extremely misoriented grain G (for this (111)-surface the easy axes are aligned at the maximum angle of 54° relative to the surface). Note that in a fine-grained material, not only the orientation of the free surface is important. Even if there might be grains for which this surface is well oriented, there can be inner grain boundaries that are strongly misoriented, consequently dominating the domain pattern in the whole grain.

The bottom images in Fig. 5 give an impression of the complicated domain reorganization processes in misoriented grains when a magnetic field is applied. Only the fact that the branched surface structures are confined to a limited near-surface zone (of about
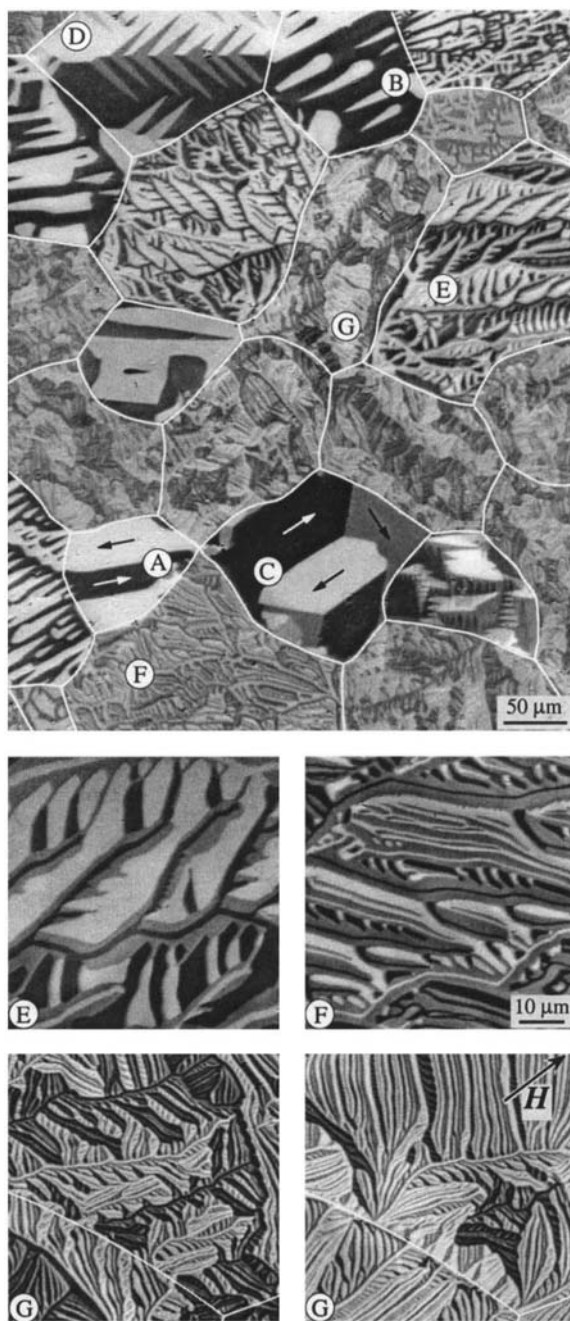
50 μm depth) makes a reasonable permeability in nonoriented material conceivable, which will rely on the underlying (wide) basic domains. The rearrangement of the branched closure pattern causes a kind of friction for the displacement of the basic domain walls and leads to unavoidable hysteresis losses.

2.3 Crystalline High-permeability Materials

Much smaller anisotropies than in silicon–iron material and thus higher permeabilities of more than 100 000 can be reached in NiFe alloys near the 80:20 composition, known as Permalloy or Mumetall. These high-permeability materials are adjusted in composition and heat treatment to reach zeros of first-order anisotropy constant and in the mean magnetostriction constant. Nevertheless, regular domains with clearly delineated domain walls are usually observed within the crystallites of coarse-grained Permalloy (Fig. 6(a)). They scale with the grain size and change from grain to grain, demonstrating the influence of residual crystal anisotropy.
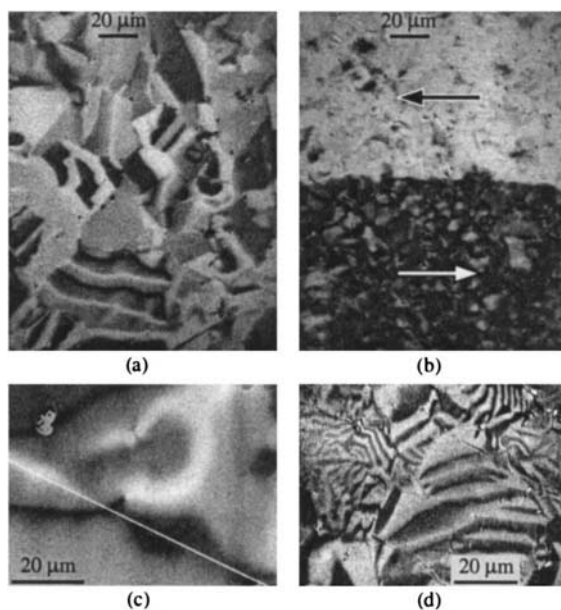
Figure 6
In coarse-grained Permalloy sheets [(a), grain size around 30 μm, thickness 20 μm], regular domains do exist that are correlated over the grain boundaries. Occasionally, domain walls may become dissolved in a continuously rotating magnetization (c), if anisotropy becomes negligibly small. In the fine-grained material [(b), grain size around 13 μm], macroscopic domains extend over many grains and are modulated by the local anisotropies in the grains. A coarse-grained manganese–zinc ferrite is shown in (d).

Figure 5
The domains on the surface of nonoriented electrical steel (thickness 0.5 mm) depend on the orientation of the crystallites. Patterns of selected grains are enlarged below. The images in the bottom row show the same location in a (111)-oriented grain, with a magnetic field applied on the right.

849

Absent are the complex branched surface domains that typically occur in misoriented grains of iron-based material. Only occasionally regular domains may be replaced by a smoothly varying magnetization configuration as actually expected for zero anisotropy (Fig. 6(c)). In fine-grained Permalloy material (Fig. 6(b)), the domain structure resembles that of Permalloy thin films in which the domains extend over the grains (see Fig. 1, and the interpretation in Sect. 2.5). Uniformly magnetized grains are also found in coarse-grained NiFe materials after annealing in magnetic fields. Such regular magnetic microstructures cause reversible magnetization processes and thus low noise in sensor applications.

Similar domains as in coarse-grained Permalloy ribbons are observed in soft magnetic spinel ferrites with a sufficiently large grain size (Fig. 6(d)). Ferrites are prepared by sintering and they are used in high-frequency applications due to their insulating properties (see *Ferrites*). Domain wall processes are important in the whole application range of ferrites up to GHz frequencies.

2.4 Amorphous Ribbons

Amorphous magnetic ribbons are alloys with typically 80% iron, cobalt, or nickel, and 20% "metalloids" like silicon or boron. They are quenched from the melt with a thickness around 20 μm (see *Amorphous and Nanocrystalline Materials*). In application, they compete with high-permeability NiFe alloys. While crystal anisotropy is small in NiFe materials, it cannot exist in metallic glasses by definition. Nevertheless, "regular" domains do exist in such ribbons, again caused by residual anisotropies.

The main source of anisotropy is internal stress, frozen in by the rapid quenching process. The magnetization is coupled to the stress by the magnetostriction constant, so that the domain complexity in as-quenched ribbons depends on magnetostriction as shown in Fig. 7. Two types of domains are typical: wide curved domains that follow a varying in-plane easy axis (caused by dominating tensile stress for positive magnetostriction constant), and narrow fingerprint domains. The fingerprints are closure domains of underlying perpendicular domains, caused by planar compressive stress which induces an easy axis perpendicular to the surface. Internal stress can not only vary laterally, but also in depth. This leads to layered domain structures as demonstrated in Fig. 8. A layered in-plane anisotropy with twisted easy directions is visible in Fig. 7(a).

Even magnetostriction-free metallic glasses show regular (but wide) domains in the as-quenched state (Fig. 7(d)). They are often aligned along the ribbon axis, caused by magnetization-induced anisotropy (see Sect. 1). The easy axis follows the magnetization direction present during quenching, which is frozen in
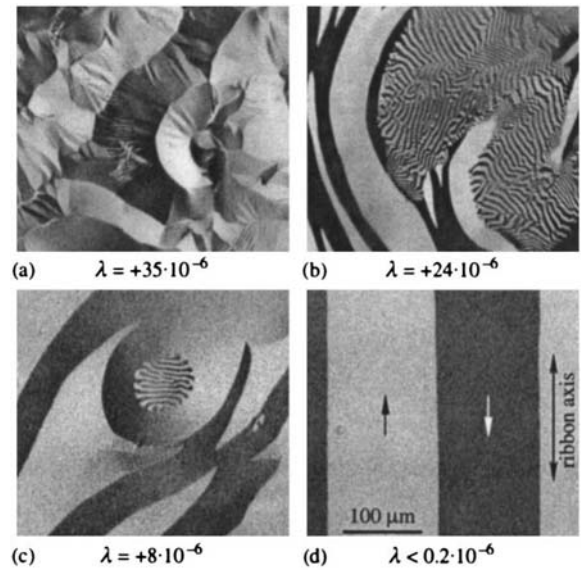
Figure 7
Typical zero-field domain patterns in 20 μm-thick amorphous ribbons of different magnetostriction constant λ.
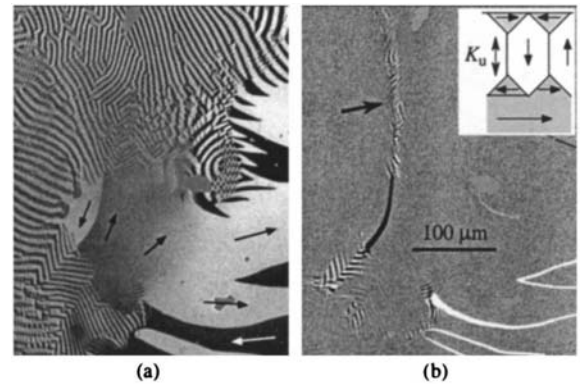
Figure 8
Demagnetized state (a) of a magnetostrictive amorphous ribbon, and the image difference (b) between image (a) and a state where a small magnetic field was applied, showing domain changes. The 180°-wall displacement continues in the area of the fingerprint structure (see arrow in (b)), proving that the fingerprint pattern must be restricted to the surface zone as sketched. Obviously there is a layered stress distribution: compressive stress near the surface and dominating tensile stress underneath.

while cooling through the Curie point and which is along the ribbon axis for magnetostatic reasons. Such induced anisotropies are also present in magnetostrictive materials where it is difficult to separate them

from stress-induced contributions. Residual anisotropies may also be caused by the flow pattern during quenching, by the surface structure of the ribbons (due, for example, to "air bubbles" on the wheel side), and by mechanical creep due to different quenching speed at different ribbon locations.

Controlling anisotropy in metallic glasses is possible. Frozen-in stress can be relaxed by more than 95% by carefully annealing below the crystallization temperature. In addition, annealing can be performed in uniform magnetic fields below the Curie temperature or under external mechanical load. This leads to well-defined anisotropies by the same mechanisms as discussed before. A variety of ordered domain-states is possible in this way (Fig. 9), allowing tailoring of magnetization curves for specific applications. For instance, transverse and perpendicular domains shown in (a) and (e), respectively, are essentially magnetized by rotation in fields along the (vertical) ribbon axis, causing a linear hysteresis curve with only minor domain rearrangement processes. Losses are correspondingly low.

2.5 Nanocrystalline Ribbons

Modern nanocrystalline ribbons with grain sizes in the 10 nm range compete in high-permeability applications with classical Permalloy and amorphous ribbons (see *Amorphous and Nanocrystalline Materials*). The best-known alloy is the FeSiBNbCu system, which consists of nanocrystalline SiFe grains embedded in an amorphous magnetic matrix. Because of the small grain size, the exchange interaction averages over anisotropic properties of the individual grains, so that anisotropy is smoothed out and the material is effectively anisotropy-free (the same mechanism applies to the Permalloy films discussed in Sect. 1 and the fine-grained Permalloy sheets of Sect. 2.3). Together with a very small magnetostriction, excellent soft magnetic properties can be achieved.

Well-defined domains and walls are found in these materials (Fig. 10), which cannot be distinguished at optical resolution from those in metallic glasses. Another class of nanocrystalline materials contains some zirconium and has a higher iron content to obtain a higher saturation magnetization. The patchy modulation of magnetization (Fig. 10(b)) seems to be caused by the effects of the irregular polycrystalline nature of this material. Hard and immobile patch domains are observed when the crystallites are getting too big or if the coupling between the crystal grains is too weak.

3. Domains in Hard Magnetic Materials

The magnetic microstructure of hard magnets is trivial in the permanent magnetic state: the elementary carriers of the magnetic moment, the more-or-less independent grains or particles in these materials,
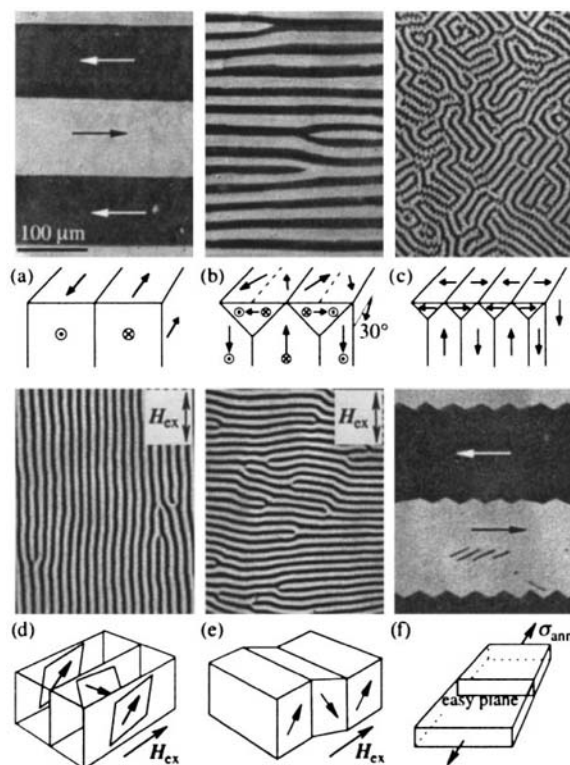
Figure 9
Ordered domain states in metallic glasses after different annealing treatments. The ribbon axis is along the *vertical* direction in all images. Annealing in a field *transverse* to the strip axis results in wide transverse domains (a). A strongly reduced domain width is obtained after annealing in fields perpendicular to the ribbon surface, resulting in an *oblique* (b) or *perpendicular* anisotropy (c) in dependence of the annealing field strength. The orientation of the narrow stripe domains in the case of a perpendicular anisotropy depends on the magnetostriction constant. If the ribbon is demagnetized in an alternating field along its axis, the stripes are oriented parallel to the field axis for a low-magnetostriction material (d) and perpendicular in a high-magnetostriction material (e). This can be explained by the compatibility of magnetostrictive deformations: a positive magnetostriction favors stripe nucleation perpendicular to the field (sketch e) as opposed to parallel stripes (sketch d) in which the deformations are incompatible. The latter is only possible in low-magnetostriction materials and is preferred there because a parallel stripe pattern saves wall energy. The transverse pattern in (f) is obtained by a "creep" annealing treatment under mechanical load. At zero field, the magnetization is forced in the transverse in-plane direction to reduce magnetostatic energy.
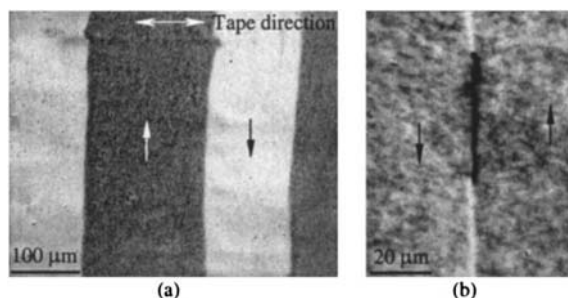
Figure 10
(a) Ordered domain structure on a nanocrystalline FeSiBNbCu-based soft magnetic ring core annealed in a field perpendicular to the tape direction. (b) High-resolution observation on a zirconium-containing nanocrystalline ribbon, showing wall and modulated domain contrast.

keep saturated along a preferred direction in remanence. Domains are not connected to the permanent magnet function and should be completely eliminated to obtain a high coercivity and remanence. They only play a role during switching. Two main classes of permanent magnets must be distinguished: Small-particle magnets and anisotropy-based coarse-grained magnets (see *Hard Magnetic Materials, Basic Principles of*). Most hard magnetic materials rely on a strong uniaxial anisotropy with $Q \gg 1$, as opposed to soft magnetic materials, which typically have a manifold of easy directions.

3.1 Coarse-grained Magnets

In large-grained sintered magnets, two classes can be separated: nucleation- and pinning-type magnets. The difference becomes evident in the initial magnetization curves. Starting from the thermally demagnetized state, every grain in a nucleation-type material contains many domain walls that can be displaced easily (see Fig. 11(a), (b)), leading to a large initial permeability. The permanent magnet properties appear only when the initial domain walls are driven out in a large field (Fig. 11(c)) so that also residual domains, which are a natural consequence of particle shape and localized stray field concentration, are completely annihilated. This requires magnetic fields that may well exceed the saturation field M_s along the preferred axis, in particular for isotropic samples or for misoriented grains in textured material. The magnet can be demagnetized after this step only if new domain walls are nucleated. In contrast, in a pinning-type magnet, the domain walls are effectively pinned by precipitates, leading to a low initial permeability.

Examples of nucleation-type magnets are hexaferrite magnets (see *Alnicos and Hexaferrites*) and
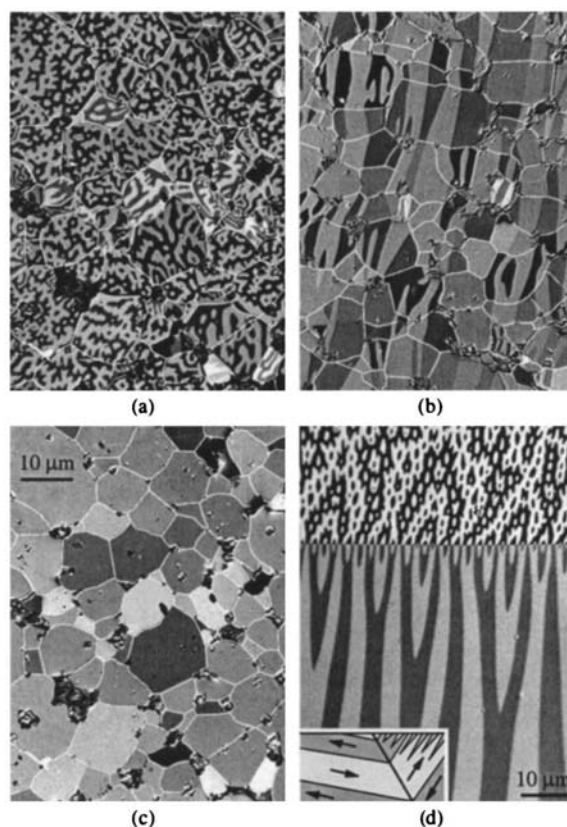
Figure 11
Domains on a sintered NdFeB magnet. (a) The thermally demagnetized state on the basal plane, with the axis of the textured magnet perpendicular to the viewing surface. (b) The same state viewed parallel to the axis reveals the high degree of texture in this material. The grains are magnetostatically coupled as exchange interaction is prevented by a nonmagnetic grain boundary phase. (c) Domain-free, remanent state after applying a saturation pulse [same location as (a)]. The character of the branched domains visible in (a) is displayed in (d) for a large-grained precursor material. The twin grain boundary acts like a mirror for the domains, so that "surface" domains (upper part) and "volume" domains (lower part) show up at the same time (compare Fig. 1(f)).

high-quality rare-earth magnets of the $SmCo_5$ and the $Nd_2Fe_{14}B$ types (see *Magnets: Sintered*). They consist of highly anisotropic grains in a textured, polycrystalline compound, which is prepared in such a way that switching of one grain has little influence on its neighbors. Coercivity is thus primarily given by some mean switching thresholds of the individual grains. Both the initial and the final states of the switching process are essentially saturated in

high-coercivity materials, but the switching process itself traverses a multidomain state (note that the grain size is in the 10 μm range, which is much larger than the single-domain size of about 100 nm).

If the domain walls are narrow due to high crystalline anisotropy, the walls may be effectively pinned by a finely dispersed nonmagnetic phase. The alloy $Sm_2(CoFe)_{17}$ containing copper-rich Co_5Sm precipitates is an example for a high-quality permanent magnet based on this principle. The precipitation phase has a reduced magnetization and exchange constant, so that the domain walls prefer to travel along the platelet-shaped precipitates. The elimination of residual domains plays no role because these domains are pinned (like all others) and the coercivity is determined by the interaction between domain walls and microstructure.

Note that both nucleation and pinning type magnets rely on the high energy and narrow width of their domain walls. A high wall energy makes nucleation of new domains difficult, a narrow wall width favors an effective pinning of walls. The finely divided domains in Fig. 11(a), which are of the two-phase branched type discussed in Sect. 1, can be applied to measure the wall energy. It was shown that the surface domain width of such a pattern stays constant, independent of crystal thickness, whereas the internal domain width increases with thickness. This is determined by an equilibrium between stray field energy and wall energy. From the measurement of the surface domain width, the domain wall energy can conveniently be determined.

3.2 Small-particle and Fine-crystalline Magnets

If a magnetic body becomes very small, it will not contain domain walls and the particle becomes *single-domain*. This occurs when the expense of wall energy becomes greater than the gain of stray field energy. The critical single domain size depends on the Q-parameter and the particle shape. The single domain limit rises with increasing elongation of the particle.

Permanent magnets can also be prepared from such single-domain particles. If the individual particles consist of a low-anisotropy material, they must have an elongated shape to remain single-domain. For such large particles, the danger of thermally activated spontaneous switching (superparamagnetism) is absent. Elongated single-domain particles are therefore thermally stable even if they are completely isolated. Classical examples of this permanent magnet class are the *Alnico* alloys, consisting of fine filaments of a high-saturation FeCo alloy that are embedded into a nonmagnetic NiAl matrix (see *Alnicos and Hexaferrites*).

Modern small-particle magnets are based on high-anisotropy materials that consist of single-domain *grains*. A number of techniques can be used to prepare
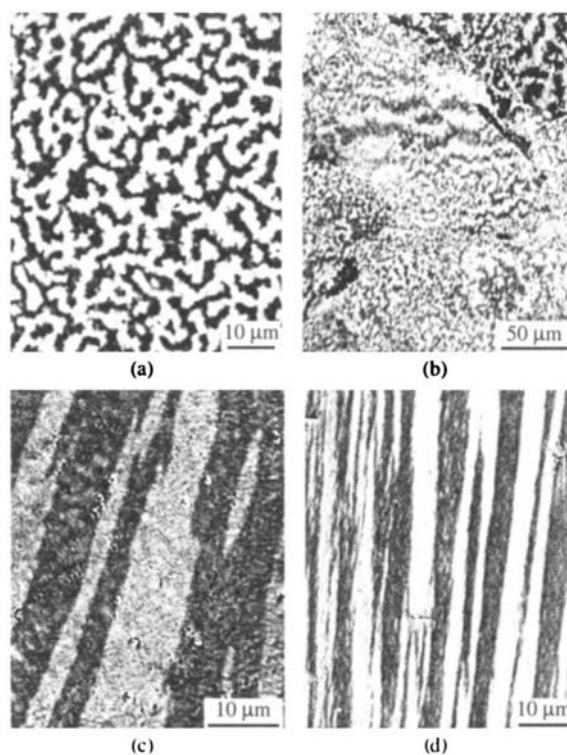
Figure 12
(a) Interaction domains observed on a surface perpendicular to the preferred axis of textured, fine-grained NdFeB material prepared by melt spinning and hot deformation. In the HDDR-processed material (b), the interaction domain width depends on the degree of texture. In (c), the interaction domains are observed parallel to the texture axis in the same material as in (b). (d) Interaction domains on the side face of an oriented Alnico crystal.

fine-crystalline magnets out of precursors such as $Nd_2Fe_{14}B$: rapid quenching and subsequent crystallization, mechanical alloying (see *Magnets: Mechanically Alloyed*), and the HDDR process (see *Magnets: HDDR Processed*). All these methods generate a fine powder with a particle size around 100 μm, which then has to be compacted into solid magnets. Oriented magnets can be produced by "die-upsetting" (see *Textured Magnets: Deformation-induced*). Also by the HDDR process, an anisotropic powder can be produced which can be oriented in a magnetic field.

But even nonoriented fine-crystalline materials remain interesting as a relatively weak exchange interaction between very small grains can lead to an enhanced remanence without a significant loss in coercivity (exchange-enhanced fine-crystalline magnets). The coupling enhances the remanence above the average $M_r = 0.5\,M_s$ of independently oriented

uniaxial grains. A further possibility for achieving high remanence in nonoriented small-grain materials consists of adding a high-saturation soft magnetic phase, which is strongly exchange-coupled to the basic hard magnetic phase if the extension of the soft phase is sufficiently small (see *Magnets: Remanence-enhanced*). The coercivity in these two-phase fine-crystalline magnets is dominated by the hard phase, whereas the high remanence is primarily a consequence of the soft phase.

The magnetization of the grains in fine-grained permanent magnets is strongly correlated. An irregular magnetic microstructure is displayed in the demagnetized state as shown in Fig. 12(a)–(c). The black-and-white contrasts correspond to grain neighborhoods that are magnetized along a certain net magnetization direction. These patterns are predominantly determined by dipolar interactions between the fine grains—an assumption which is justified by the fact that this kind of domains is also observed in small-particle magnets like Alnico (Fig. 12(d)) for which the presence of exchange interaction between the needles can be excluded. To indicate their special nature, they were called "magnetostatic interaction domains." A characteristic feature of interaction domains is their elongated shape extending along the preferred axis of the material as is visible in Fig. 12(c). The "domain boundaries" of the interaction domains can move laterally to some extent by the successive switching of neighboring grains (or particles in case of Alnico), thus providing a certain permeability for the demagnetized state.

3.3 Conclusions

The domain patterns in a variety of soft and hard magnetic (mainly bulk) materials have been reviewed. In both material classes, magnetic domains are formed to reduce the magnetostatic energy of finite samples. The interactions between physical microstructure, easy axes, applied fields, surface orientations, and mechanical stress leads to an enormous variety of domain patterns, only a small fraction of which could be presented by focusing on selected, undisturbed samples.

Although in *soft magnetic materials* the avoidance of magnetic charges is the dominating principle, the domain arrangement is strongly influenced by anisotropy. The orientation of the main surfaces with respect to the easy directions is decisive. If a surface contains easy directions, it is no problem to reconcile pole avoidance with avoiding anisotropy energy by employing the surface-parallel easy directions only. Grain-oriented transformer steel belongs to this class. Here the degrees of freedom for domain formation are strongly reduced and the basic domain patterns are related to those of ideally oriented grains even in the case of small misorientation.

Due to the near-single-crystal nature of this material, its magnetic microstructure is conveniently observable and well understood, so that the losses of transformer steel are steadily reduced by studying and controlling the domain structure. Domain control is also possible in amorphous and nanocrystalline ribbons if the influence of mechanical stress can be avoided. For most other bulk soft magnetic materials—the nonoriented polycrystalline SiFe, NiFe, and ferrite materials—similar possibilities are not available. Observing the complex, often heavily branched domains at the surface of such materials offers only a glimpse at the magnetization processes in the volume.

Domains in hard magnetic materials are only important during switching. In coarse-grained material they are determined by a strong uniaxial anisotropy, and in fine-grained magnets the magnetostatic interaction between small grains results in an inhomogeneous magnetic microstructure called interaction domains.

See also: Coercivity Mechanisms; Ferrite Magnets: Improved Performance; Magnetic Films: Hard

Bibliography

Cullity B D 1972 *Introduction to Magnetic Materials*. Addison-Wesley, Reading, MA

Chikazumi S 1997 *Physics of Ferromagnetism*. Clarendon, Oxford

Hubert A, Schäfer R 1998 *Magnetic Domains. The Analysis of Magnetic Microstructures*. Springer, Berlin

O'Handley R 2000 *Modern Magnetic Materials. Principles and Applications*. Wiley, New York

Van den Berg H 1986 Self-consistent domain theory in soft-ferromagnetic media II. Basic domain structures in thin film objects. *J. Appl. Phys.* **60**, 1104–13

R. Schäfer
Institut für Metallische Werkstoffe, Dresden, Germany

Magnets: Biomedical Applications

This article deals with magnetic substances used inside living beings, particularly humans. The application of magnets in medicine has been known for more than 2500 years. Probably the earliest document dates from about 600 BC and concerns the extraction of an iron arrow tip by means of an extracorporally applied loadstone (Hirschberg 1899). Several publications of pre-Christian centuries described the application of magnetic material as a remedy for a variety of diseases (Häfeli 1998). Nevertheless, it was not before the middle of the twentieth century that the number of different magnetic materials for biomedical applications considerably increased.

1. Natural Magnetic Substances in Humans

The existence of magnetic material, mainly magnetite (Fe_3O_4), in living beings was found for the first time in 1962 (Lowenstam 1962) and later recognized as being responsible for the orientation capabilities of a number of animals. The discovery of small particles consisting of magnetite and maghemite (γ-Fe_2O_3) in human tissue was reported for the first time by Kirschvink *et al.* (1992). There is evidence for some influence of this material with reference to magnetic resonance imaging (MRI), where it may be responsible for contrast alterations. Human tissue is almost completely diamagnetic. There are, however, some paramagnetic substances with high values of susceptibility: hemosiderin and ferritin. These substances are responsible for storage and transport of iron in organisms and can be used for the noninvasive examination of the iron content in the liver (Nielsen *et al.* 1998). Finally, it is worth noting that the magnetic susceptibility of hemoglobin, an important part of red blood cells, changes depending on its oxygenation state. This behavior is used for the so-called blood oxygenation level dependent (BOLD) contrast in functional MRI (Schreiber *et al.* 1998).

2. Bulk Magnets

Important properties of bulk magnets positioned inside a living being concern the force or the torque exerted in magnetic fields on appropriately designed pieces of the material, the magnetic stray field that may be used for monitoring the position of the magnet, and the magnetic losses arising in alternating magnetic fields. All the substances have to be nontoxic. This can be achieved either by the choice of nonpoisonous magnetic materials, as is the case with magnetite, or by covering the magnet with suitable coatings (plastic, gold film, etc.).

2.1 Bulk Magnets for Force or Torque Applications

A magnetic field may be generated by permanent magnets inside the body. Another way is to use fields generated outside the body by coils or permanent magnets. An example of permanent magnets used inside the body is the application in veterinary medicine (Fahlenbrach and Fahlenbrach 1970) where cows are forced to swallow rods of Alnico, a permanent magnetic material, covered with plastic to prevent both the magnet from corrosion and tissues from toxic effects. The magnet remains in one of the stomachs and attracts steel parts often swallowed by the animals together with green fodder or hay. In this way the stomach and intestines are protected against being damaged. The same principle is sometimes also used in human medicine to remove pins, nails, and other steel parts that have been swallowed (Häfeli

1998). Another example concerns the fixation of temporary pacemaker electrodes by hand-held permanent magnets in emergency cases (Paliege *et al.* 1979). Pieces of gold-plated iron wires have been used as tips of flow-in stimulation catheters for this end. Interesting experiments have been performed with certain kinds of catheters that are able to move through blood vessels driven by a combination of a d.c. magnetic field and an a.c. field. These parts consist of a small permanent magnet (barium–ferrite cylinders of a few cubic millimeters) and a flexible plastic tail (Frei *et al.* 1966).

In spite of this fascinating idea these catheters could obviously not be introduced into general medical practice. Guidance of small magnetic probes is being investigated in terms of the so-called magnetic stereotaxis, i.e., the minimally invasive manipulation of a permanent magnet inside the human brain along a path of minimum damage to a position where it can be used to heat a well-defined small region of tissue (e.g., a brain tumor) or to act as a catheter for other purposes. *In vivo* experiments have been successfully performed with animals (Grady *et al.* 1990) and application in humans, e.g., using multiple superconducting coils, looks promising (Meeker *et al.* 1996). Equipment for generating fields outside the body is generally less complicated. However, it was not until the mid-1990s that a piece of permanent magnetic material (Nd–Fe–B disk of 5 mm diameter and 2 mm thickness) was positioned in the stomach and kept there for several hours simply by the force exerted by an external fixed permanent magnet (Gröning *et al.* 1996). The magnetic disk covered by a layer of carnauba wax was part of a tablet designed for osmotically controlled drug release. An interesting application is the magnetic stoma seal for colostomy. It consists of an implanted permanent magnetic ring (Sm–Co covered with titanium) and a suitably formed lid. At first glance this system seems to be very attractive. A critical review of about five years' practice, however, showed a relatively high percentage of incontinence (Schwemmle 1982). Therefore, the conventional technique is still widely used.

2.2 Bulk Magnets for Monitoring

For many years there have been attempts to investigate the motility of the gastrointestinal tract by magnetic monitoring (Forsman 1998) with the aim of avoiding exposure to x rays or other ionizing radiation. However, it was not before 1997 that satisfying results were presented. Weitschies *et al.* (1997) published reliable images of magnetic marker monitoring with a spatial resolution in the millimeter range and a temporal resolution down to 4 ms. The technique uses markers consisting of sucrose pellets coated with a mixture of magnetite and polymethyl methacrylate and enclosed in silicone rubber. After ingestion of

these markers the magnetic stray field outside the body is measured by means of a superconducting quantum interference device (SQUID) and can be used to calculate the actual position of the marker.

However, the technique is a rather expensive one (SQUID array cooled by liquid helium, sophisticated electronics, and a shielded room to reduce background fields by several orders of magnitude). A simpler novel technique is where an extracorporally applied pulsed magnetic field is used to repeatedly align the marker with its magnetic axis. The stray field is measured during the impulse pauses after successively alternating pulses. In this way two essential advantages result: the use of much cheaper conventional field sensors and working without any magnetic shielding, i.e., in a normal environment (Andrä *et al.* 2000). It is worth noting that the same principle can be used to monitor other objects, e.g., the tip of a heart catheter.

2.3 Bulk Magnets for Tissue Heating

One kind of tumor therapy already introduced in clinical practice is the combined treatment by radiation and heat. Here, heating can be realized by eddy currents induced in metallic pieces, so-called thermoseeds, implanted in the tumor region as an array of appropriately positioned needles. Magnetic metals offer the possibility of using magnetic losses with the important advantage of having a mechanism for self-regulation of the maximum temperature by means of the appropriately chosen Curie temperature (Burton *et al.* 1971). In contrast to most other medical applications of magnets, the materials of thermally self-regulating implants are specially designed and consist of nickel alloys with copper, silicon, and palladium, or alloys of Fe–Pt and Pd–Co. A novel principle (Cetas *et al.* 1998) makes use of the field concentration due to the high permeability of a specially composed ferrite material (e.g., containing manganese, zinc, and copper) with a Curie temperature in the range 45–60 °C. The rod-shaped ferrite core is surrounded by a nonmagnetic electrically conductive sheath (e.g., stainless steel), which simultaneously provides biocompatibility.

3. Magnetic Particles

The biomagnetic application of magnetic particles has been known since the late 1950s (Gilchrist *et al.* 1957) but there is now renewed interest. The fields of interest concern contrast media, vascular occlusion, localized heating, targeting of drugs and radiation sources, and cell separation. Most of the modern literature can be found under the keyword "magnetic carriers."

3.1 Magnetic Contrast Agents

An early attempt to use magnetic powders as contrast agents for x-ray investigations was made by Frei *et al.* (1968). Satisfactory visualization was achieved of the gastrointestinal tract by means of commercially available powders (e.g., consisting of magnesium ferrite) even with human volunteers. These investigations were not continued in spite of an advantage over conventional contrast agents, namely the possibility of manipulating the material by external fields during the x-ray investigation. Other studies were concerned with MRI of the abdomen using orally administered superparamagnetic particles consisting of polymer spheres surrounded by iron oxide crystals, each crystal measuring less than 50 nm (Boudghène *et al.* 1993). Dextran-coated superparamagnetic iron oxide particles (presumably magnetite) can be used for cell labeling (Yeh *et al.* 1993), particularly after coupling to special monoclonal antibodies. Other magnetite nanoparticles have already been approved for imaging of liver metastases.

3.2 Vascular Occlusion

Several investigations have been performed with respect to vascular occlusion by means of magnetic particles. One of the first publications deals with the occlusion of intracranial aneurisms (Roth 1969). Iron particles were used and a clinical experiment was performed generating a magnetic thrombus with injected particles exposed to a localized magnetic field of implanted magnets. Vascular occlusion with magnetic particles has also been investigated as a technique for selective infarction of tumors and organs. Mosso and Rand (1973) injected mixtures of carbonyl–iron microspheres with liquid silicone into the renal arteries of dogs. After a certain time, during which the material was held in place by an extracorporally applied magnetic field, vulcanization occurred. Other authors have reported experiments performed without silicone and also found agglomeration by means of the magnetic field.

3.3 Localized Heating

Many attempts have been made to use the heating of magnetic particles in high-frequency magnetic fields for selective treatments of cancer cells within unaffected normal tissue. Gilchrist *et al.* (1957) described this idea and reported on promising experimental results obtained with γ-Fe_2O_3 particles (20–100 nm diameter) administered by injection into different kinds of tissue of dogs from where the particles were carried into the lymph nodes. The hope was to heat the nodes and in this way to destroy lymphatic metastases.

Similarly, the treatment of other tumors seemed to be possible either by direct injection or by transport via blood vessels, particularly the vessels formed by neo-vascularization near growing tumors. A great number of both *in vitro* and *in vivo* experiments has

been carried out since the pioneering work. Magnetic particles of different size (diameters ranging from the so-called multidomain state down to the superparamagnetic region) and different material (magnetite, maghemite, magnetic glass-ceramic, Ba–Co–ferrite, etc.) have been tested. The particles are covered or composed with different organic material or used in the bare state. Reviews of the results (Jordan *et al.* 1993, 1999, Hergt *et al.* 1998, Andrä 1998) show that clinical application cannot yet be applied and several essential problems are still to be solved.

3.4 Magnetic Targeting of Drugs and Radiation Sources

Magnetic drug targeting, i.e., guidance and retention of drug-carrying magnetic particles by means of externally applied magnetic fields, has been investigated since the 1970s. The first clinical experiences with human patients were reported by Kuznetsov *et al.* (1997) who used Fe–C particles combined with anticancer drugs. Lübbe and Bergemann (1997) used magnetic carriers of multidomain particles of Fe_3O_4 coated with starch derivatives and loaded with epirubicin. A concentration of the particles was achieved by means of suitably arranged permanent magnets outside the body of the patient. Magnetic drug targeting may also be used for the localized treatment of thrombosis, as demonstrated by Inada *et al.* (1987) who performed *in vitro* experiments with magnetic enzyme particles consisting of magnetite and polyethylene glucol coupled to urokinase. A further kind of magnetic targeting is the application of particles for the transport of radioisotopes, e.g., ^{90}Y, to the region where the radiation is to be applied. This novel technique was tested in animal experiments by Häfeli *et al.* (1997) who used microspheres (10–30 µm in diameter) consisting of a mixture of polylactic acid and magnetite.

3.5 Magnetic Cell Separation

An already commercially introduced technology is the selective cell separation by means of polymer spheres containing small magnetic particles, so-called magnetic beads. The surface of the beads is coated with different kinds of monoclonal antibodies designed for special selective binding with appropriately prepared biological objects. In this way blood cells, bacteria, or even specific nucleic acid sequences can be isolated and manipulated in special magnetic separation equipment. The magnetic component of the beads in most cases is magnetite. A review of this field can be found in Ugelstad *et al.* (1997).

See also: DNA Microarrays Using Magnetic Labeling and Detection; MRI Contrast Agents; Permanent Magnetic Devices in Otiatria; SQUIDs: Biomedical Applications

Bibliography

Andrä W 1998 Magnetic hyperthermia. In: Andrä W, Nowak H (eds.) *Magnetism in Medicine*. Wiley-VCH, Berlin

Andrä W, Danan H, Kirmße H, Kramer H-H, Saupe P, Schmieg R, Bellemann M 2000 A novel method for real time magnetic marker monitoring in the gastrointestinal tract. *Phys. Med. Biol.* **45**, 3081–93

Boudghène F P, Bach-Gansmo T, Grange J -D, Lame S, Nantois C, Wallays C, Bigot J-M 1993 Contributions of oral magnetic particles in MR imaging of the abdomen with spin-echo and gradient-echo sequences. *JMRI* **3**, 107–12

Burton C, Hill M, Walker E 1971 The RF thermoseed—a thermally self-regulating implant for the production of brain lesions. *IEEE Biomed. Eng.* **BME-18**, 104–9

Cetas T C, Gross E J, Contractor Y 1998 A ferrite core/metallic sheath thermoseed for interstitial thermal therapies. *IEEE Trans. Biomed. Eng.* **45**, 68–77

Fahlenbrach B, Fahlenbrach H 1970 Der Magnetismus in Medizin und Biologie. *Umschau* **14**, 429–33

Forsman M 1998 Magnetism in gastroenterology. In: Andrä W, Nowak H (eds.) *Magnetism in Medicine*. Wiley-VCH, Berlin

Frei E H, Driller J, Neufeld H N, Barr I, Bleiden L, Askenazy H M 1966 The POD and its applications. *Med. Res. Eng.* **5**, 11–8

Frei E H, Gunders E, Pajewsky M, Alkan W J, Eshchar J 1968 Ferrites as contrast material for medical X-ray diagnosis. *J. Appl. Phys.* **39**, 999–1001

Gilchrist R K, Medal R, Shorey W D, Hanselman R C, Parrott J C, Taylor C B 1957 Selective inductive heating of lymph nodes. *Ann. Surgery* **146**, 596–606

Grady M S, Howard III M A, Molloy J A, Ritter R C, Quate E G, Gillies G T 1990 Nonlinear magnetic stereotaxis: three-dimensional, *in vivo* remote magnetic manipulation of a small object in canine brain. *Med. Phys.* **17**, 405–15

Gröning R, Werner M, Berntgen M, Georgaratis M 1996 Per-oral controlled release dosage forms with internal magnets and extracorporal magnetic guidance—investigations into the renal elimination of riboflavin. *Eur. J. Pharm. Biopharm.* **42**, 25–8

Häfeli U 1998 The history of magnetism in medicine. In: Andrä W, Nowak H (eds.) *Magnetism in Medicine*. Wiley-VCH, Berlin

Häfeli U, Pauer G, Macklis R M 1997 Magnetically targeted microspheres for intracavity and intraspinal Y-90 radiotherapy. In: Häfeli U, Schütt W, Teller J, Zborowsky M (eds.) *Scientific and Clinical Applications of Magnetic Carriers*. Plenum, New York

Hergt R, Andrä W, d'Ambly C-G, Hilger I, Kaiser W A, Richter U, Schmidt H-G 1998 Physical limits of hyperthermia using magnetite fine particles. *IEEE Trans. Magn.* **34**, 3745–54

Hirschberg J 1899 Geschichte der Augenheilkunde Engelmann, Leipzig, Vol. 12

Inada Y, Ohwada K, Yoshimoto T, Kojima S, Takahashi K, Kodera Y, Matsushima A, Saito Y 1987 Fibrinolysis by urokinase endowed with magnetic property. *Biochem. Biophys. Res. Commun.* **148**, 392–6

Jordan A, Scholz R, Wust P, Fähling H, Felix R 1999 Magnetic fluid hyperthermia (MHF): cancer treatment with AC magnetic field induced excitation of biocompatible superparamagnetic nanoparticles. *J. Magn. Magn. Mater.* **201**, 413–9

Jordan A, Wust P, Fähling H, John W, Hinz A, Felix R 1993 Inductive heating of ferrimagnetic particles and magnetic fluids: physical evaluation of their potential for hyperthermia. *Int. J. Hyperthermia* **9**, 51–68

Kirschvink J L, Kobayashi-Kirschvink A, Woodford B J 1992 Magnetite biomineralization in the human brain. *Proc. Natl. Acad. Sci. USA* **89**, 7683–7

Kuznetsov A A, Harutyunyan A R, Dobrinsky E K, Filippov V I, Malenkov A G, Vanin A F, Kuznetsov O A 1997 Ferrocarbon particles: preparation and clinical application. In: Häfeli U, Schütt W, Teller J, Zborowsky M (eds.) *Scientific and Clinical Applications of Magnetic Carriers*. Plenum, New York

Lowenstam H A 1962 Magnetite in denticle capping in recent chitons (Polyplacophora). *Geol. Soc. Am. Bull.* **73**, 435–8

Lübbe A S, Bergemann C 1997 Selected preclinical and first clinical experiences with magnetically targeted 4′-epidoxorubicin in patients with advanced solid tumors. In: Häfeli U, Schütt W, Teller J, Zborowsky M (eds.) *Scientific and Clinical Applications of Magnetic Carriers*. Plenum, New York

Meeker D C, Maslen E H, Ritter R C, Creighton F M 1996 Optimal realization of arbitrary forces in a magnetic stereotaxis system. *IEEE Trans. Magn.* **32**, 320–8

Mosso J A, Rand R W 1973 Ferromagnetic silicone vascular occlusion: a technique for selective infarction of tumors and organs. *Ann. Surg.* **178**, 663–8

Nielsen P, Fischer R, Engelhardt R, Dresow B, Gabbe E E 1998 Neue Möglichkeiten in der Diagnose der hereditären Hämochromatose. *Deutsches Ärzteblatt* **95**, B-2262–8

Paliege R, Volkmann H, Andrä W 1979 Magnetische lagefixierung einschwemmbarer Elektrokatheter zur temporären Schrittmachertherapie. *Dt. Gesundh.-Wesen* **50**, 2514–8

Roth D A 1969 Occlusion of intracranial aneurisms by ferromagnetic thrombi. *J. Appl. Phys.* **40**, 1044–5

Schreiber A, Kraemer F M, Janz C, Hennig J 1998 Functional magnetic resonance imaging. In: Andrä W, Nowak H (eds.) *Magnetism in Medicine*. Wiley-VCH, Berlin

Schwemmle K 1982 Colostomie mit Magnetverschluß. *Chirurg* **53**, 547–50

Ugelstad J, Prestvik W, Stenstad P, Kilaas L, Kvalheim G 1997 Selective cell separation with monosized magnetizable polymer beads. In: Andrä W, Nowak H (eds.) *Magnetism in Medicine*. Wiley-VCH, Berlin

Weitschies W, Kötitz R, Cordini D, Trahms L 1997 High-resolution monitoring of the gastro-intestinal transit of a magnetically marked capsule. *J. Pharmaceut. Sci.* **86**, 1218–22

Yeh T-C, Zhang W, Ildstad S T, Ho C 1993 Intracellular labelling of T-cells with superparamagnetic contrast agents. *Magn. Reson. Medicine* **30**, 617–25

W. Andrä and R. Hergt
Institut für Physikalische Hochtechnologie e.V.
Jena, Germany

Magnets: Bonded Permanent Magnets

Bonded magnets are generally prepared by blending coercive powder with a binder followed by compacting or molding the material to the final shape. Because of the presence of the binder the energy product of bonded magnets is always lower than that of their sintered counterparts. However, two great advantages of bonded magnets are their superior mechanical properties and the fact that the magnets can be prepared under net shape conditions. Bonded and sintered magnets of ferrites have been known for many decades. Both types of magnets have very low energy products when compared to sintered rare earth-based magnets. The excellent properties of rare earth-based magnets are, however, accompanied by a high price.

The last decade of the twentieth century saw an increased use of actuators and small electromotors not only of low weight but also of low energy consumption, as in battery-driven motors in particular. There has also been an increased use of electronically controlled, electrically actuated systems in automobiles, especially for critical vehicle control functions. All this and the increased use of electromagnetic devices in the electronic and electric industry has led to an enhanced pressure to find improved or alternative permanent magnet materials lying between the low-cost low-performance ferrite magnets and the high-cost high-performance sintered NdFeB magnets. Bonded NdFeB magnets meet most of the criteria mentioned and their use is growing steadily. For this reason bonded types of rare earth permanent magnets will be discussed below in somewhat more detail.

1. Bonding Technologies

Bonded magnets are generally prepared by blending coercive powder with a binder or by encapsulating coercive powder in a binder, followed by compacting or molding the material to the final shape. The powder of the magnetic materials used in bonded magnets may be ferrites, alnico, samarium cobalt or neodymium–iron–boron. In some cases also hybrid powders are used.

Depending on the binder, the magnets produced may be flexible or rigid. Nitrile rubber or vinyl are commonly used for the former type whereas for the latter type nylon, teflon, polyester, or thermoset epoxies are employed.

There are four main manufacturing routes for bonded magnets: calendering, injection molding, extrusion, and compression bonding.

(i) Calendering involves processing the material between rollers and leads to continuous strips of adjustable thickness and length. This process is schematically shown in Fig. 1. The material used for calendering is usually a mixture of the magnetic powder and a thermoplastic binder. This mixture is processed between rollers forming a continuous strip that may be up to 100 m in length. Magnetic loading can be up to 70% by volume.

(ii) The injection molding process is schematically represented in Fig. 2. This process involves forcing the heated mixture of magnetic powder and thermoplastic binder via tubes into a mold where it is allowed to cool and harden. In this case too, magnetic loading can reach 70%, especially when using powder of spherical shape (Ma *et al.* 2002).
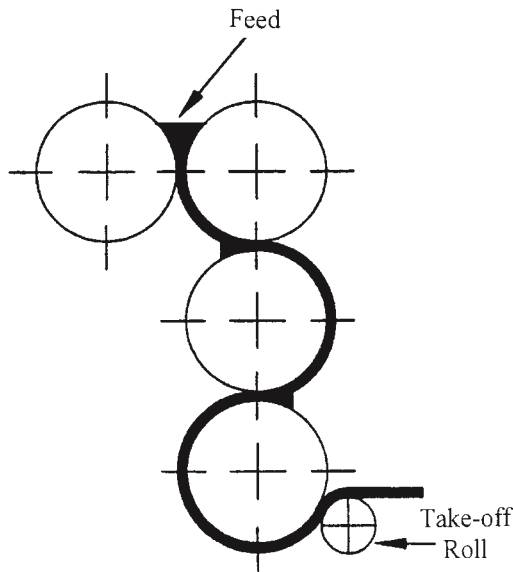
Figure 1
Schematic diagram showing the manufacturing of magnetic strips by calendering (after Ormerod and Constantinides 1997).
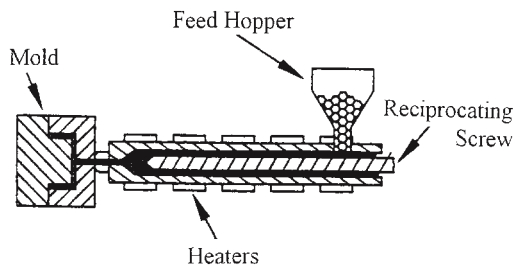
Figure 2
Schematic representation of the injection molding process. This process involves forcing the heated mixture of magnetic powder and thermoplastic binder via tubes into a mold where it is allowed to cool and harden (after Ormerod and Constantinides 1997).

Figure 3
Schematic representation of the extrusion process. The compounded magnetic material is squeezed through an orifice. During the extrusion process the orifice is heated and the profile is controlled as the compounded material cools (after Ormerod and Constantinides 1997).
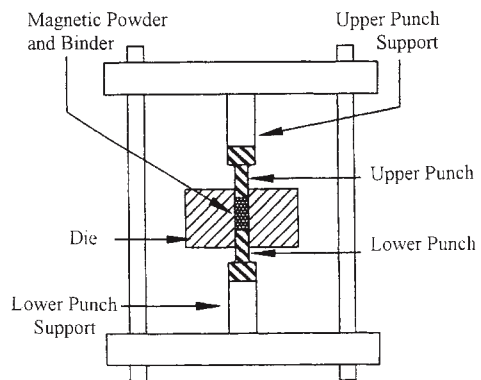
Figure 4
Diagram showing the compression bonding process. The magnetic powder is blended with an epoxy that has been dissolved in an organic solvent. The latter is evaporated during the blending process, leaving the magnetic particles in an epoxy-encapsulated state. The coated powder is flowed into a conventional powder press and compacted into the desired shape. The compacted magnet is finally cured in an oven (after Ormerod and Constantinides 1997).

(iii) Extrusion makes use of an orifice through which the compounded material is squeezed, as illustrated in Fig. 3. During the extrusion process the orifice is heated and the profile is controlled as the compounded material cools. Depending on the binder, the cooled product can be firm, as for flexible end products, or rigid if a nonflexible end product is desired. The loading can reach slightly higher values (up to 75% by volume) than in the two previous cases.

(iv) Compression bonding uses magnetic powder blended with an epoxy that has been liquefied by dissolution in an organic solvent. The latter is evaporated

during the blending process, leaving the magnetic particles in an epoxy-encapsulated state. After drying, the coated powder is flowed into a conventional powder press (Fig. 4) and compacted into the desired shape. Finally, the compacted magnet is cured in an oven at temperatures of around 150–175 °C. This process can reach magnetic loadings up to 80%.

Because of the presence of the binder, the magnetic remanence is always lower than that of the fully dense magnetic material, as obtained, for instance, by sintering. The situation is even less favorable for the energy product, being roughly proportional to the remanence squared. There are, however, obvious advantages. The major advantage is that bonded magnets can be

produced in net shape or near-net shape. Even fairly complicated shapes may be involved, as in injection molding. Another advantage is their superior mechanical properties. Bonded magnets are mainly manufactured from ferrite powder or coercive NdFeB-based powders. Bonded magnets based on NdFeB, owing to their superior intrinsic magnetic properties, offer substantial advantages in terms of size, weight, and performance over bonded ferrite magnets and even over sintered ferrite magnets.

2. The Permanent Magnet Materials

The most common types of magnets used at present are hard ferrite magnets, rare earth-based magnets such as SmCo or NdFeB, and alnico-type magnets. Of these the alnico magnets have only a modest coercivity which leads to nonlinear demagnetization characteristics. For this reason their applicability is very limited compared with the other two types. The hard ferrites have higher coercivities than the alnico magnets and their demagnetizing characteristics are linear. However, the remanence and the concomitant maximum energy product are already low and are further decreased by bonding. Because of their low cost, ferrite magnets are still widely applied, although most of the corresponding magnetic devices are rather bulky and often give far from optimal performance. Ferrite permanent magnets currently dominate automotive and many other applications due to their low cost and proven long-term stability (see *Alnicos and Hexaferrites*).

The rare earth based magnets have high values of coercivity which gives them linear demagnetization characteristics (see *Rare Earth Magnets: Materials*). They have high remanences and typical values of the energy products reached in sintered magnets are 150 kJ m^{-3} for SmCo$_5$, and 300 kJ m^{-3} for Nd$_2$Fe$_{14}$B. The first types of magnets are frequently used in high-temperature applications, which possibility is lost in bonded magnets (see *Magnets: High-temperature*). SmCo$_5$ type magnets are expensive owing to the high price of both samarium and cobalt. The situation is more favorable for NdFeB magnets because neodymium is cheaper than samarium and iron is much cheaper than cobalt, the powder metallurgical processing arts being comparable with those of SmCo$_5$. Hence the performance/price ratio for Nd$_2$Fe$_{14}$B is better than for SmCo$_5$. For this reason the market for sintered Nd$_2$Fe$_{14}$B magnets has flourished and is still growing (see *Magnets: Sintered*).

Although bonded magnets can be manufactured from all of the materials mentioned above, only bonded ferrite magnets and bonded Nd$_2$Fe$_{14}$B magnets have penetrated into the market to an appreciable extent. The ferrites can be easily obtained in powder form (see *Alnicos and Hexaferrites*). A somewhat special processing of the ferrite powders leads to hexagonal platelets that can be easily aligned mechanically during the formation process of flexible bonded magnets. The situation is more difficult in the case of Nd$_2$Fe$_{14}$B, because a simple powder metallurgical route from cast or annealed Nd$_2$Fe$_{14}$B ingots does not generally lead to powders of sufficiently high coercivity for use in bonded magnets. Coercive NdFeB powders can be obtained though by melt spinning. In this technique a fine stream of molten alloy is sprayed onto the outer surface of a rapidly spinning wheel, leading to thin rapidly quenched ribbons or flakes. During the melt spinning the material is protected from oxidation by performing this process in a protective atmosphere or in vacuum. The quenching rate is of the order of 10^5 K s^{-1} and can be varied by changing the rotational speed of the spinning wheel. Different quenching rates lead to different microstructures which in turn determine the magnetic properties of the melt spun material. Optimum melt spinning conditions lead to a nanocrystalline alloy consisting of fine grains (typically 30 nm) of the compound Nd$_2$Fe$_{14}$B, surrounded by a thin layer of a neodymium-rich eutectic phase. In practice, more reliable and reproducible results can be obtained by using a slightly higher quenching rate and subsequently annealing the melt spun material under carefully controlled conditions. The melt spun material is fairly brittle and can be ground to a fine powder suitable for manufacturing bonded magnets. Because the Nd$_2$Fe$_{14}$B grains have a random orientation, these bonded magnets are isotropic. Powder particles of spherical shape flow better in the injection molding process, which allows a higher loading factor. Such powder can be prepared by an inert gas atomization process with typical values for the mean particle diameter of 45 mm. An additional advantage of the atomization process is the high production rate and low processing costs of the powders (Ma *et al.* 2002).

A different route leading to coercive NdFeB powders consists of the so-called HDDR process (see *Magnets: HDDR Processed*). This process involves essentially four steps: **h**ydrogenation of Nd$_2$Fe$_{14}$B at low temperatures, **d**ecomposition of Nd$_2$Fe$_{14}$BH$_x$ into NdH$_{2.7}$ + Fe + Fe$_2$B, **d**esorption of H$_2$ gas from NdH$_{2.7}$, and **r**ecombination of Nd + Fe + Fe$_2$B into Nd$_2$Fe$_{14}$B. This process profits from the fact that the formation of Nd$_2$Fe$_{14}$B grains in the last step is a solid-state reaction and hence proceeds at a rate considerably lower than during solidification from the melt during a normal casting process. The average Nd$_2$Fe$_{14}$B grain size remains in the nanometer range and gives rise to sufficiently large coercivities.

A further advantage is the fact that the HDDR process can successfully be used to obtain anisotropic particles. Takeshita and Nakayama (1992) discovered that additives of zirconium, hafnium, and gallium, in particular, are very effective in producing anisotropic HDDR powder. The amount of additive required is

surprisingly small (for instance, $Nd_{12.5}Fe_{69.9}Co_{11.5}B_6Zr_{0.1}$). Microscopic investigations described by Harris (1992) revealed that large facetted HDDR grains had formed within the original as-cast grain of the alloy. These facetted grains have a common orientation, which is probably the same as that of the original grain. The anisotropic nature of HDDR powders of alloys like $Nd_{12.5}Fe_{75.9}Co_{11.5}B_8Zr_{0.1}$ can thus be visualized by assuming that the HDDR grains have nucleated and grown within an original as-cast grain region from submicron grains, the latter having a common orientation (Harris 1992).

Evidently the effect of the additive is to bring about nucleation centers for nucleation and growth of the HDDR grains, the latter grains having kept the orientation of the original cast grain.

Tomida *et al.* (1996) have used x-ray diffraction to establish a correlation between the anisotropic nature of the ultimate HDDR powder and the amount of $Nd_2Fe_{14}B$ phase remaining unreacted in the hydrogenation process. TEM studies made by Tomida *et al.* on powder hydrogenated under optimum energy product conditions showed that after hydrogenation the powder consists mainly of coarse-grained α-Fe and Fe_2B, with nanocrystalline particles embedded in between. These particles were identified by electron diffraction as NdH_2 particles. However, many of the particles were identified as $Nd_2Fe_{14}B$ particles having a crystallographical orientation almost the same as that of the original cast $Nd_2Fe_{14}B$ grains. Energy-dispersive spectra furthermore showed that these particles are of higher cobalt and gallium concentration than corresponding to the average concentration of the starting alloy. These results have led Tomida *et al.* to propose that this type of nanocrystalline $Nd_2Fe_{14}B$ particles serve as initiation centers in the recombination process and are the origin of the orientational memory effect in HDDR powders.

A different category of materials that appears to be promising is nanocrystalline rare earth-based composite magnets. Under special circumstances, two-phase composite materials can demonstrate a most interesting coercivity behavior. Such a behavior has been described by Kneller and Hawig (1991), who investigated the combined effect of two finely dispersed and mutually exchange-coupled magnetic phases. One of these phases has a large uniaxial anisotropy constant and is able to generate a high coercivity. By contrast, the second phase is magnetically soft. It has a larger magnetic ordering temperature and concomitantly a larger average exchange energy than the hard phase. It is the comparatively high saturation magnetization of the soft phase that, when the latter is exchange coupled to the hard phase, provides a high remanence to the composite magnet. The possibility to prepare magnets showing remanence enhancement has triggered extensive research in this area (see *Magnets: Remanence-enhanced*).

In most of the systems for which remanence enhancement has been reported, the magnetically soft phase is α-Fe or an iron-rich or cobalt-rich alloy. Examples of magnetically hard phases are $Nd_2Fe_{14}B$, $Sm_2Fe_{17}N_3$, Sm_2Co_{17}, and $Nd(Fe,Mo)_{12}N_x$. The microstructures of all these composite magnets have in common that they consist of a very fine distribution of the magnetic particles, falling into the nanometer range. In order to reach this fine distribution various techniques are employed, including melt spinning and mechanical alloying (see *Magnets: Mechanically Alloyed*). This group of materials is referred to as lean rare earth permanent magnets. Their advantages compared with the standard alloys are their excellent corrosion resistance and the fact that they reach saturation in a comparatively low applied field. A disadvantage is their relatively low coercivity. The possibility of using these materials in resin-bonded magnets has been described by Croat (1997).

Another interesting group of materials are interstitially modified R_2Fe_{17} compounds. Although the low Curie temperatures and comparatively low magnetocrystalline anisotropies make the R_2Fe_{17} compounds less attractive for applications as permanent magnet materials, considerable improvements with respect to Curie temperature anisotropy and coercivity have been reached by forming interstitial solid solutions obtained by combining these materials with carbon or nitrogen. The composition of the corresponding ternary nitrides and carbides $R_2Fe_{17}C_x$ and $R_2Fe_{17}N_x$ is generally believed to be restricted to the range $0 \leqslant x \leqslant 3$. More details about the formation ranges and location of the interstitial atoms the lattice are described in the review of Fujii and Sun (1995).

Resin-bonded magnets from nitrogenated Sm_2Fe_{17} powders have been prepared with $BH_{max} = 136 \, kJm^{-3}$, $B_r = 9.0T$, and $\mu_{0B}H_c = 6.5T$. In order to explore the favorably low temperature coefficient of the coercivity in magnet bodies suitable for high-temperature applications Rodewald *et al.* (1993) and Kuhrt *et al.* (1993) have investigated tin- and zinc-bonded magnets. In these cases, however, the obtained remanences were fairly low ($B_r < 0.7$ T).

3. Applications of Bonded Magnets

Bonded ferrite magnets are commercially available in isotropopic and anisotropic grades (see Table 1). The calendered material is commonly called sheet. Sheet magnets are mainly used by screenprinters for advertising specialties, novelties, and picture frames. Sign manufacturers use it for vehicle signs, but there are also medical applications such as needle counters. Extruded profile flexible magnets are called strip. They are used for a variety of gasket applications such as for refrigerator doors, shower doors, and removable storm windows. Other applications are in small

Table 1
Maximum energy products (kJ m^{-3}) of commercially available bonded magnets (from Ormerod and Constantinides 1997).

Magnet powder	Manufacturing route	Magnetic isotropic	Magnetic anisotropic
Ferrite	Calendered	4.0–5.0	11.2–12.8
	Extruded	3.2–4.8	9.6–12.0
	Injection molded	4.0–6.4	12.0–13.6
SmCo	Injection molded		68–76
	Compression		104–136
NdFeB	Calendered	39–41	
	Injection molded	40–42	76–88
	Compression	64–88	112–128

motors and stereo speakers. Injection-molded ferrite magnets are mainly used in automotive applications, office automation, and in small motors. A great advantage of the ferrite magnets is that they are inexpensive and the raw materials are readily available.

Bonded SmCo-type magnets are used in applications where the temperature coefficients of remanence and coercivity have to be low and where a high corrosion resistance is required. Compared to bonded ferrite and NdFeB magnets their market share is low because of the high price of the raw materials.

The majority of bonded NdFeB magnets are used in personal computers but they are also used in a fairly wide range of automotive, consumer, and office products including VCRs, camcorders, and printers, and in smaller appliances such as watches, clocks, timer switches, and cameras. Most of the bonded NdFeB magnets go into various types of electric motors. The most prominent types of electric motors are spindle motors and stepper motors. Stepper motors have fairly small sizes and are characterized by their ability for precise incremental position or speed adjustment with electric pulses from digital controllers. In modern stepper motors, the stators consist of the coils system and the rotors are made of rare earth permanent magnets. The advantage of using rare earth permanent magnets is their high coercivity, which makes it possible to axially magnetize the rotor through the thickness with a large number of poles on the circumference. This allows fairly low step angles. The number of spindle motors produced is lower than the number of stepper motors. Spindle motors are much larger than stepper motors. This is the reason why they still consume a relatively large percentage of bonded NdFeB magnets. The largest application of electric motors is in computer peripherals, where they serve, for instance, as hard disk drive spindle motors, CD-ROM pick-up motors, CD-ROM spindle motors, floppy disk drive spindle motors, and floppy disk head actuators.

For a more detailed discussion of bonded magnet manufacturing, their performance, and their applications the reader is referred to the review articles of Croat (1997), Ormerod and Constantinides (1997), and Ma *et al.* (2002).

See also: Magnetic Materials: Domestic Applications; Textured Magnets: Deformation-induced

Bibliography

Buschow K H J 1997 Magnetism and processing of permanent magnet materials. In: Buschow K H J (ed.) *Magnetic Materials*. Elsevier Science, Amsterdam, Vol. 10. Chap. 4
Croat J J 1997 Current status and future outlook for bonded neodymium permanent magnets. *J. Appl. Phys.* **81**, 4804–9
Fujii H, Sun H 1995 Interstitially modified intermetallics of rare earth and 3d elements. In: Buschow K H J (ed.) *Handbook of Magnetic Materials*. Elsevier Science, Amsterdam, Vol. 9. Chap. 3
Harris I R 1992 The use of hydrogen in the production of Nd-Fe-B-type magnets and in the assessment of Nd-Fe-B-type alloys and permanent magnets—an update. *Proc. 12th Int. Workshop Rare Earth Magnets and their Applications*, Canberra, 1992, pp. 347–71
Kneller E F, Hawig R 1991 The exchange spring magnet: a new material principle for permanent magnets. *IEEE Trans. Magn.* **27**, 3588–600
Kobayashi K, Iriyama T, Imaoka N, Suzuki T, Kato H, Nakagawa Y 1992 Permanent magnet material of Sm$_2$Fe$_{17}$N$_x$ compounds obtained by reaction in NH$_3$-H$_2$ mixture gas atmosphere. *Proc. 12th Int. Workshop Rare Earth Magnets and their Applications, Canberra, 1992*, 32–43
Kuhrt C, Schnitzke K, Schultz L 1993 Development of coercivity in Sm$_2$Fe$_{17}$(N,C)$_x$ magnets by mechanical alloying, solid–gas reaction, and pressure-assisted zinc bonding. *J. Appl. Phys.* **73**, 6026–8
Ma B M, Herchenroeder J W, Smith B, Suda M, Brown D N, Chen Z 2002 Recent developments in bonded NdFeB magnets. *J. Magn. Magn. Mater.* **239**, 418–23
Ormerod J, Constantinides S 1997 Bonded permanent magnets: current status and future opportunities. *J. Appl. Phys.* **81**, 4817–20
Rodewald W, Wal B, Katter M, Veliscescu M, Schrey P 1993 Microstructure and magnetic properties of Zn- or Sn-bonded Sm$_2$Fe$_{17}$N$_x$ magnets. *J. Appl. Phys.* **73**, 5899–901

Takeshita T, Nakayama R 1992 Magnetic properties and microstructures of the Nd-Fe-B magnet powders produced by HDDR process. *Proc. 12th Int. Workshop Rare Earth Magnets and their Applications*, Canberra, 1992, pp. 670–81

Tomida T, Choi P, Maehara Y, Uehara M, Tomizawa H, Hirosawa H 1996 Origin of magnetic anisotropy formation in the HDDR-process of $Nd_2Fe_{14}B$ based alloys. *J. Alloys Compds.* **242**, 129–35

K. H. J. Buschow
University of Amsterdam, Amsterdam
The Netherlands

Magnets: HDDR Processed

The HDDR (hydrogenation–disproportionation–desorption–recombination) process is a method for producing magnetically highly coercive rare-earth (RE) transition-metal (TM) materials by applying a reversible chemical reaction with hydrogen gas (Takeshita and Nakayama 1989, McGuiness *et al.* 1990). In magnets made from rapidly quenched or mechanically alloyed magnets, the high coercivity is achieved by reducing the average grain size of the anisotropic ferromagnetic phase (see *Magnets: Mechanically Alloyed*). The average grain size for the HDDR material is around $0.3\,\mu m$ which is approximately an order of magnitude greater than those of rapidly quenched or mechanically alloyed material. The crucial difference, however, between the HDDR and melt-spun or mechanically alloyed materials is that in the former case it is possible to produce anisotropic powders without applying mechanical deformation.

This article starts with a general description of the HDDR process including the thermodynamic and kinetic aspects. Emphasis will be given in the discussion of possible origins for the anisotropic character of HDDR-treated Nd–Fe–B-based powders, and to technical and economical aspects of preparing magnets from HDDR powders. Finally, an outlook on further prospects of HDDR magnets will be given.

1. General Description of the HDDR Process

Hydrogen is already used very successfully for the hydrogen decrepitation process, which is most effective in terms of producing powders, e.g., for sintered
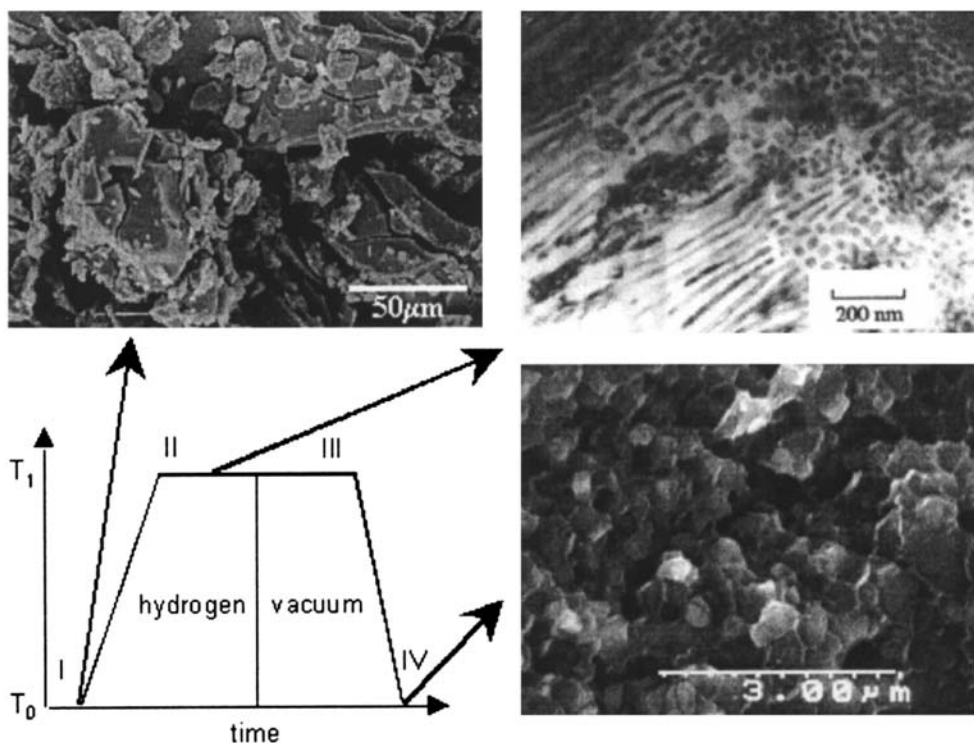
Figure 1
Schematic representation of the HDDR process. Microstructural changes are illustrated by SEM and TEM images of Nd–Fe–B material (I: starting powder after hydrogen decrepitation; II: disproportionated material (TEM); IV: particle fracture surface after HDDR).

magnets (see *Magnets: Sintered*). Another potential application of hydrogen is in the HDDR process. A general schematic representation of this process is given in Fig. 1. In the first step, an AB_n compound (where A is a hydride former, e.g., a RE element) is heated in hydrogen. In many cases, an interstitial hydrogen absorption takes place at lower temperatures, which results in the hydrogen decrepitation of the ingot material and this is predominantly an intergranular fracture process. This decrepitation can be avoided by heating under vacuum and introducing the hydrogen at a temperature where the disproportionation takes place spontaneously. This "solid"-HDDR process is a useful tool for investigations which demand compact samples such as for TEM observations and electric resistivity measurements (Gutfleisch *et al.* 1994). The simplest representation of the exothermic disproportionation reaction is given by:

$$AB_n + (1 \pm \tfrac{1}{2}x)H_2 \rightarrow AH_{2\pm x} + nB + \Delta H \qquad (1)$$
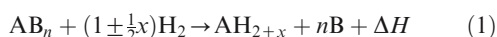
where ΔH is the enthalpy, $+\Delta H$ being an exothermic reaction and $-\Delta H$ an endothermic reaction.

The value of x depends on the precise processing conditions. The second step of the HDDR process is the recombination reaction under vacuum or low hydrogen pressure. The hydrogen is desorbed during stage III and the remaining A-rich regions act as nuclei for the recombination of the original AB_n phase:

$$AH_{2\pm x} + nB \rightarrow AB_n + (1 \pm \tfrac{1}{2}x)H_2 - \Delta H \qquad (2)$$
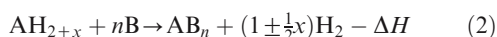
By carefully controlling the process parameters of the recombination reaction, grain sizes of a few hundred nanometers can be obtained. This is of the same order of magnitude as the single domain particle size of magnetically highly anisotropic RE–TM compounds such as $Nd_2Fe_{14}B$ and $SmCo_5$.

2. Thermodynamics and Kinetics

In principle, the HDDR process is applicable to a large number of AB_n-type compounds, e.g., with a RE element as a very strong hydride former A, and a TM and/or another element as nonhydride former B. This is especially true for those compounds with a high RE content and with a relatively low thermodynamic stability.

Figure 2 shows a phase diagram of the hydrogen–AB_n system. It can be seen that, at a sufficient hydrogen pressure $p(H_2)$, the AB_n phase is in a metastable state at room temperature ($T = T_0$). The disproportionated state is the thermodynamically stable state, but the reaction does not take place because of insufficient diffusion of the large A and B atoms. Only when the temperature is raised will the kinetic barrier (dashed line in Fig. 1) be passed and dispro-

Figure 2
Phase diagram of the hydrogen–AB_n system. The disproportionation reaction is given by I→II, the recombination by II→III. No disproportionation will take place for an insufficient hydrogen pressure p_1 (I'→II').
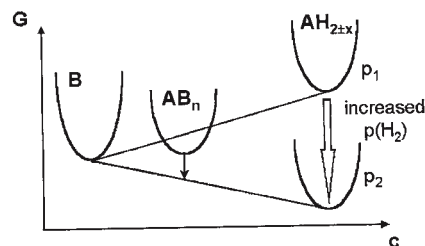
Figure 3
Schematic free enthalpy diagram for the hydrogen–AB_n system at $T = T_1$ according to Fig. 2. A disproportionation of the AB_n compound into $AH_{2\pm x}$ and B is only possible for an increased hydrogen pressure $p_2 > p_1$.

portionation into $AH_{2\pm x}$ and B take place. The kinetic barrier can be lowered by increasing the surface-to-volume ratio of the AB_n material (smaller particles/grains) or by mechanical activation (e.g., reactive milling in hydrogen). A more stable AB_n compound will lead to a narrowed processing window. A higher hydrogen pressure leads to an increased stability of the $AH_{2\pm x}$ hydride and hence the disproportionation of more stable compounds becomes possible (see Fig. 3). The recombination reaction will be initiated by lowering $p(H_2)$ which makes the AB_n phase the preferred thermodynamic choice.

For the RE–TM phases with attractive intrinsic magnetic properties, the phases $Nd_2Fe_{14}B$ and $Sm_2Fe_{17}N_x$ have a relatively low thermal stability and the HDDR process can be applied easily. The

most important example is the HDDR process of $Nd_2Fe_{14}B$:

$$Nd_2Fe_{14}B + (2 \pm x)H_2 \rightarrow 2NdH_{2 \pm x}$$
$$+ 12\alpha\text{-Fe} + Fe_2B + \Delta H \quad (1)'$$

$$2NdH_{2 \pm x} + 12\alpha\text{-Fe} + Fe_2B \rightarrow Nd_2Fe_{14}B$$
$$+ (2 \pm x)H_2 - \Delta H \quad (2)'$$
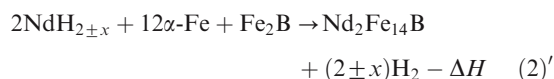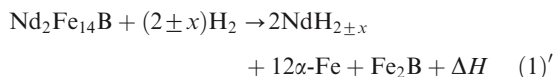
Typical conditions for the disproportionation reaction (Eqn. (1)′) are $T \approx 800\,°C$ and $p \approx 100\,kPa$. The recombination is normally carried out at comparable temperatures under continuous pumping.

The HDDR process is also applicable to the relatively low stability $RE(Fe, X)_{12}$ and $RE_3(Fe, X)_{29}$ materials (e.g., $RE = Nd, Sm; X = Ti, V$). However, in these cases the formation of other phases during recombination is a serious problem. It has been shown that the HDDR process can also be applied to more stable compounds such as $SmCo_5$ and Sm_2Co_{17} when high hydrogen pressure or reactive milling is applied (Kubis *et al.* 1998).

3. Anisotropic Character of HDDR-treated Nd–Fe–B-based Powders

An apparently unique feature of $Nd_2Fe_{14}B$ is the preservation of the anisotropic character of the powder after the HDDR process. A "memory-cell" model suggests nanoscale 2:14:1 phase regions rich in additives such as Co, Ga, or Zr which stabilize the phase. Therefore these regions remain unaffected during the disproportionation reaction and can act as nucleation sites for the recombination reaction. This model is supported by thermodynamic arguments as well as by extensive microstructural investigations. However, there is some evidence that this model is not sufficient: (i) it has, so far, not been possible to maintain the anisotropic character of Sm_2Fe_{17}-type powders after the HDDR process by using additions that stabilize the 2:17 phase in the same manner as the 2:14:1 phase; and (ii) it is possible to obtain anisotropic HDDR powders from ternary Nd–Fe–B materials without the presence of stabilizing additions by applying "solid" disproportionation and recombination in a low hydrogen pressure ("slow" recombination).

As neodymium hydride and α-iron have a cubic crystal structure and do not exhibit preferred crystallographic axes, only the grains of the noncubic iron boride phase remain as possible "memory cells." The absence of the boride phase in the disproportionated state of Sm_2Fe_{17} supports this assumption. A "one-to-one" crystallographic relation between a metastable tetragonal Fe_3B phase and the original 2:14:1 matrix phase has been found in an alloy containing cobalt, gallium, and zirconium (Tomida *et al.*

1999). This Fe_3B phase can also be found in solid-disproportionated ternary Nd–Fe–B materials. The elemental additions appear to stabilize the Fe_3B phase and also to depress excessive grain growth during recombination. Anisotropic powders are harder to obtain from ternary materials probably because the Fe_3B phase is only an intermediate phase in the disproportionation reaction and the subsequent $Fe_3B \rightarrow Fe_2B + Fe$ reaction is not slowed down by the presence of alloying additions. The "slow" recombination at low hydrogen pressures, e.g., $10\,kPa$ at $900\,°C$, enables a better control of grain growth, which is essential for obtaining a high coercivity in ternary Nd–Fe–B materials together with a high degree of texture.

4. Technical and Economical Aspects

The HDDR process is an environmentally friendly and simple method of powder preparation. The combination of hydrogen decrepitation and the HDDR process makes it possible to produce highly coercive Nd–Fe–B-type powders from the ingot starting material in "one run." Additionally, the amount of free α-Fe in cast Nd–Fe–B materials, which has a significant detrimental effect on the magnetic properties, is reduced by the HDDR treatment.

The most sensitive part of the HDDR process is the recombination stage. A scaling up to larger batch sizes leads to the formation of an inhomogeneous microstructure after both processing steps, because of large temperature gradients caused by the strongly exothermic/endothermic character of the disproportionation/recombination reactions. The inhomogeneous microstructure of disproportionated material does not appear to have a great effect on the magnetic properties of isotropic HDDR powders and hence batch sizes of 15 kg are applicable. On the other hand, the batch size for the recombination step has to be limited to about 2 kg in order to avoid large variations in grain size which lead to poor magnetic properties. The application of the slow recombination method could make a significant contribution to solving this technological problem.

The possibility of producing highly coercive powders consisting of nanoscaled grains with a preferred crystallographic orientation is a special feature of the HDDR process that makes it extremely interesting for the cost-effective production of anisotropic hard magnetic powders. However, the degree of texture of HDDR materials is limited as there is always a certain loss of anisotropy after the HDDR treatment of an anisotropic powder. The best properties of HDDR magnets are remanences of about $1.2\,T$ combined with coercivities of $\mu_0 J H_C > 1\,T$, leading to $(BH)_{max}$ values of about $250\,kJm^{-3}$.

There is a large variety of processing routes for isotropic and anisotropic HDDR magnets (for more

details see Gutfleisch and Harris 1998). For example, anisotropic Nd–Fe–B magnets can also be produced by hot pressing and hot deformation of isotropic nanoscaled materials (see *Textured Magnets: Deformation-induced*). It is somewhat harder by this processing route to obtain high coercivities and remanences from HDDR materials compared with the properties obtained from melt-spun and mechanically alloyed materials and this can be attributed to the larger average grain size of the HDDR materials. However, the addition of grain growth inhibiting elements such as zirconium and the integral optimization of HDDR, hot pressing, and deformation still give room for improvements.

5. Future Prospects of the HDDR Process

Applications at moderate temperatures ($\sim 120\,^\circ$C) depend, amongst other things, on low irreversible magnetic losses at these temperatures. There is a question mark over the long-term magnetic stability of HDDR magnets at these temperatures which is much inferior compared with those of melt-spun and sintered magnets. Work is underway to try and improve the performance of the HDDR material.

Of all the known magnetically highly anisotropic RE–TM compounds, only the $RE_2Fe_{14}B$-based materials have been found to exhibit anisotropic features after the HDDR process. Magnets with $RE = Pr$ exhibit promising properties with more relaxed processing conditions compared with those characteristic of $Nd_2Fe_{14}B$. HDDR magnets based on $Pr_2Fe_{14}B$ or $(Nd_{1-x}Pr_x)_2Fe_{14}B$ could be possible alternatives to neodymium-based anisotropic HDDR magnets.

The application of high hydrogen pressures opens the way to preparing a wider range of hard magnets by the HDDR process from highly stable materials such as Sm–Co based compounds. These studies might also help to find new insights into the mechanisms of the HDDR process.

Another way of extending the applications of the HDDR process is the combination with other preparation methods such as ball milling. Reactive milling in hydrogen can lead, after recombination at low temperature, to powders with grain sizes of only a few tens of nanameters. Such materials can exhibit remanence enhancement due to the effect of magnetic exchange coupling (see *Magnets: Mechanically Alloyed* and *Textured Magnets: Deformation-induced*).

See also: Magnetic Materials: Hard; Magnets: Bonded Permanent Magnets

Bibliography

Gutfleisch O, Harris I R 1998 Hydrogen assisted processing of rare earth permanent magnets. In: Schultz L, Müller K H (eds.) *Proc. 15th Int. Workshop on Rare-earth Magnets and their Applications*. Dresden, Germany, pp. 487–506

Gutfleisch O, Martinez N, Verdier M, Harris I R 1994 Phase transformations during the disproportionation stage in the solid HDDR process in a $Nd_{16}Fe_{76}B_8$ alloy. *J. Alloys Compds.* **215**, 227–33

Kubis M, Handstein A, Gutfleisch O, Gebel B, Müller K H, Schultz L 1998 HDDR in Sm–Co—a new method for magnetic hardening of Sm–Co permanent magnets. In: Schultz L, Müller K H (eds.) *Proc. 15th Int. Workshop on Rare-earth Magnets and their Applications*. Dresden, Germany, pp. 527–36

McGuiness P J, Zhang X J, Yin X J, Harris I R 1990 Hydrogenation, disproportionation and desorption (HDD): an effective processing route for Nd–Fe–B-type magnets. *J. Less Common Met.* **162**, 359–65

Takeshita T, Nakayama R 1989 Magnetic properties and microstructure of the NdFeB magnet powder produced by hydrogen treatment. In: Shinjo M (ed.) *Proc. 10th Int. Workshop on Rare-earth Magnets and their Applications*. Kyoto, Japan, pp. 551–7

Tomida T, Sano N, Hanafusa K, Tomizawa H, Hirosawa S 1999 Intermediate hydrogenation phase in the hydrogenation–disproportionation–desorption–recombination process of $Nd_2Fe_{14}B$-based anisotropic powders. *Acta Mater.* **47**, 875–85

I. R. Harris and M. Kubis
University of Birmingham, UK

Magnets: High-temperature

High-temperature permanent magnets with an operating temperature of over $450\,^\circ$C are required for future advanced power systems. Precipitation-hardened 2:17 $Sm(Co_{bal}Fe_wCu_yZr_x)_z$ magnets have large anisotropy fields and a high Curie temperature which make them optimal candidates for such high-temperature applications (Ray 1984). The $Sm(Co_{bal}Fe_wCu_yZr_x)_z$ magnets are characterized by a complex microstructure consisting of a cellular structure superimposed on a lamellar structure, which is formed after a lengthy aging at 800–850 $^\circ$C followed by a slow cooling to 400 $^\circ$C (Hadjipanayis 1996). The cellular/lamellar microstructure is formed during the aging period. Upon slow cooling copper diffusion takes place to the cell boundaries leading to the right microchemistry for optimum domain wall pinning.

The magnets represent a complicated system with four compositional (x, y, w, z) and five heat treating variables. Comprehensive and systematic studies were undertaken on bulk and nanocrystalline rare-earth cobalt-based magnets to understand their behavior and improve their high-temperature performance. These studies led to the development of new high-temperature magnets and to the discovery of some new effects in these magnets (Liu *et al.* 1999,

Tang *et al.* 2000). Also the studies helped to understand further the effects of composition and processing on the magnetic hardening behavior of the magnets, particularly on the coercivity and its temperature dependence. In the following the recent studies on Sm–Co-based high-temperature magnets in both the cast and nanograined powder form are summarized.

1. Bulk Sm(CoFeCuZr)$_z$ Magnets

1.1 Effect of Composition and Processing

In principle, high-temperature magnets must have a high Curie temperature, a high anisotropy field H_A with a small temperature dependence, and high magnetization. In addition the magnets must have the right microstructure for optimum magnetic hardening. Comprehensive studies by Hadjipanayis and co-workers (Liu *et al.* 1999, Tang *et al.* 2000) on the microstructure and the magnetic properties of the precipitation-hardened 2:17 Sm(Co$_{bal}$Fe$_w$Cu$_y$Zr$_x$)$_z$ high-temperature magnets showed that the magnets must not only have a small (70–100 nm) and uniform cellular structure (2:17 cells surrounded by 1:5 cell boundaries) but also the right microchemistry, with a large gradient of copper at the cell boundaries. This is made possible by the presence of a thin lamellar phase (zirconium-rich Z phase), which facilitates the diffusion of copper to the 1:5 cell boundary phase during the slow cooling.

The large difference in copper content across the cell boundaries leads to a steep gradient in domain wall energy, which causes domain wall pinning, and gives rise to high coercivity. The microstructure and microchemistry strongly depend on the composition and processing of the magnets. Lower-ratio z magnets have a smaller cell size (Fig. 1) because of the small percentage of 2:17 phase. A smaller cell size results in a lower coercivity at room temperature with improved temperature dependence (Hadjipanayis 1999). Since copper is concentrated at the 1:5 cell boundaries, an increase in copper content y results in the formation of a greater amount of 1:5 cell boundary phase (and therefore smaller cells) with higher copper content and thus higher room-temperature coercivity. An increase in iron content w results in an increase of the cell size because iron mainly goes into the 2:17 cells.

This leads to higher saturation magnetization magnets, but with a greater temperature dependence of coercivity because of the decrease in both the anisotropy and the Curie temperature of the iron-substituted 2:17 phase (Strnat 1988). The addition of zirconium promotes the formation of the lamellar microstructure, which leads to the optimum uniform microstructure (Tang *et al.* 2000), as explained before. The aging temperature controls the cell size with a higher aging temperature leading to a larger cell
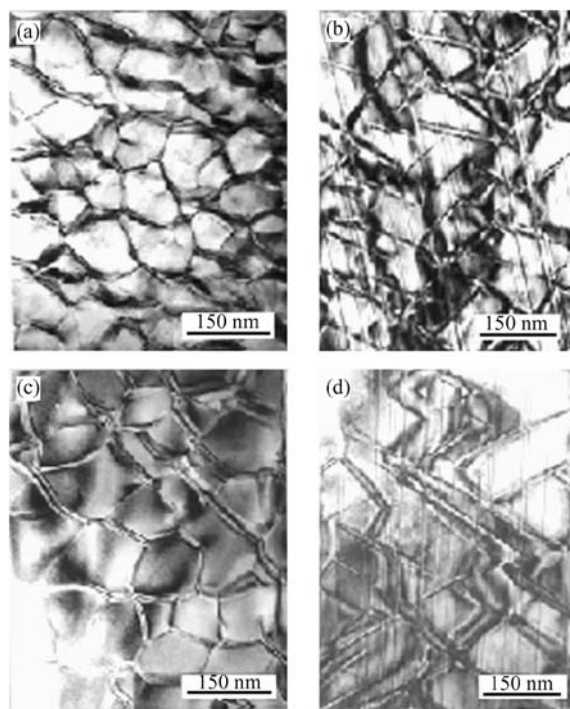
Figure 1
Dependence of cell size on ratio z: (a) and (b) $z = 7.0$; (c) and (d) $z = 8.5$. The left and right figures are microstructures perpendicular and parallel to the c axis of the 2:17 phase, respectively.

size. For a fixed copper content any change in the cell size will alter the copper content in the cell boundaries and therefore drastically affect the coercivity of the magnets and its temperature dependence.

The information derived from the above studies can be used to fine-tune the microstructure and microchemistry of the Sm–Co magnets through adjustments in the composition and processing parameters, and allows the designing of magnets for high-temperature applications.

1.2 New Magnets with a Record High Coercivity of 10 kOe at 500 °C

By changing the ratio z and using an appropriate copper content, new magnets with a coercivity of 10 kOe at 500 °C were developed. Figure 2 shows the temperature dependence of coercivity for the new magnets (A and B) compared with a typical old commercial magnet. For magnet B, with a high ratio z of 8.5 and a copper content of 0.088, the coercivity at room temperature is about 40 kOe. For magnet A, with a low ratio z of 7.0 and a copper content of up to 0.128, a record high coercivity of 10.8 kOe at 500 °C is
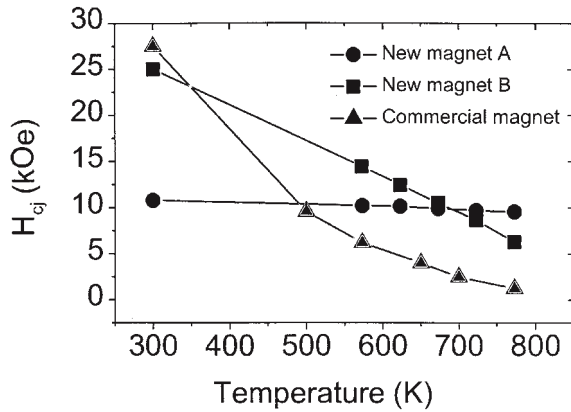
Figure 2
Temperature dependence of coercivity in different magnets.
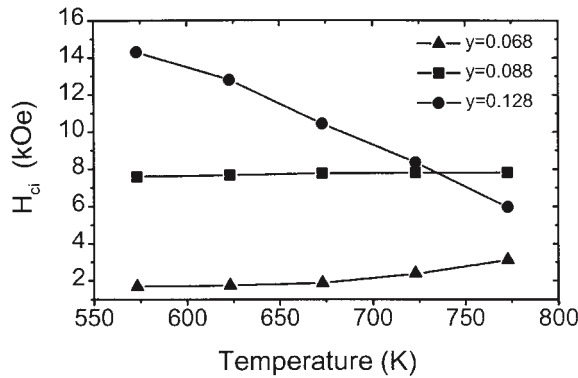
Figure 3
Temperature dependence of coercivity for $Sm(Co_{bal}Fe_{0.1}Cu_yZr_{0.02})_{7.5}$ with different Cu content.

Distance from Center of Cell Boundary (nm)

Figure 4
Nanoprobe analysis of $Sm(Co_{bal}Fe_{0.1}Cu_yZr_{0.02})_{7.5}$ magnets: (a) $y = 0.06$; (b) $y = 0.12$.

obtained. The temperature coefficient of coercivity for magnet A is $-0.03\%\ °C^{-1}$, which is more than eight times smaller than that of magnet B. The new magnets have a better temperature dependence of coercivity than the old commercial magnets. The microstructural data show that the cell size of magnet B is larger than that of magnet A (88 nm vs. 108 nm). These are smaller than the size of commercial magnets which is generally above 120 nm.

1.3 Temperature Dependence of Coercivity Controlled by the Copper Content

The effect of composition on the temperature dependence of coercivity was studied systematically. Figure 3 shows the temperature dependence of coercivity for $Sm(Co_{bal}Fe_{0.1}Cu_yZr_{0.02})_{7.5}$ magnets with

different copper content. The temperature coefficient of coercivity changes from a small positive to a large negative value with increasing copper content from $y = 0.068$ to 0.128. The microstructure of the copper-substituted magnets is similar showing a small decrease in cell size with increasing copper content (from 100 to 80 nm). However, a nanoprobe analysis (Fig. 4) shows that most of the copper goes into the $Sm(Co,Cu)_5$ cell boundary phase. When the copper content in the magnets changes from 0.06 to 0.126, the copper content at the cell boundaries increases from 13.7 to 33.8 at.%.

The difference in the copper content at the cell boundaries leads to a large domain wall energy gradient (associated with the chemical composition gradients) along the cell boundaries and thus to a different intrinsic coercivity, H_c,

$$\mu_o H_c = \mu_o \frac{1}{2J_s} \frac{(\gamma^{1:5} - \gamma^{2:17})}{\delta}$$

where γ is the domain wall energy, J_s the spontaneous magnetization, and δ the 1:5 cell boundary thickness (see *Coercivity Mechanisms*). Moreover, the domain wall energy gradient and effective pinning area in the case of low copper content are much smaller than

in the high-copper-content magnets. Chui (1999) explained the latter behavior in terms of repulsive pinning which leads to the positive temperature coefficient of coercivity. This abnormal temperature dependence of coercivity is of great practical importance, because the temperature coefficient of coercivity can be manipulated by controlling the copper content.

2. Nanograined RE–Co Powders Made by High-energy Mechanical Milling

An alternative way to produce high-performance RE–Co (RE = rare-earth element) high-temperature magnets is to develop a nanoscale microstructure in these magnets. The motivation originates from the well-known size dependence of coercivity which goes through a maximum value at the single-domain size, which is a fraction of a micron for most magnets such as $Nd_2Fe_{14}B$, $Sm_2Fe_{17}(NC)_x$ and Sm_2Co_{17} (Manaf *et al.* 1993, Hadjipanayis 1999). Therefore, high coercivity is expected to develop in magnets with a nanoscale grain size. Furthermore, an enhanced M_r/M_s ratio (>0.5) is also expected in nanoscale isotropic magnets due to the exchange coupling between neighboring nanograins (Fischer and Kronmüller 1999) (see *Magnets: Remanence-enhanced*). The mechanical properties of consolidated nanograin magnets are expected to be greatly improved. In general, the nanostructure can be obtained by using melt-spinning (Coehoorn *et al.* 1989, Manaf *et al.* 1993) and mechanical alloying (Schultz *et al.* 1991, McCormick *et al.* 1998) (see *Magnets: Mechanically Alloyed*).

2.1 Sm–Co-based Nanograined Magnets

Chen *et al.* (2000) carried out systematic studies on the development of nanocrystalline Sm_2Co_{17}-based magnets using mechanical milling. They found that a nanoscale 2:17 phase with an average grain size of about 30 nm is developed within the powders which have an average particle size of about 5 µm. Optimum magnetic properties of $M_s = 110.5$ emu g^{-1}, $M_r = 66.2$ emu g^{-1}, $M_r/M_s = 0.60$, $H_c = 9.6$ kOe, and $(BH)_{max} = 10.8$ MGOe have been obtained in stoichiometric Sm_2Co_{17} powders. The observed magnetic hardening is believed to arise from the high anisotropy of the Sm_2Co_{17} phase and its nanoscale grain size.

A small amount of substitution of zirconium for cobalt significantly increases the coercivity by increasing the anisotropy field of the Sm_2Co_{17} phase. A copper substitution in Zr-containing samples further increases the coercivity by introducing a nanoscale 1:5 phase which forms a uniform mixture with the 2:17 nanograins. This is different from the cellular/lamellar structure observed in bulk magnets with the same composition. The highest coercivity of

20.6 kOe has been obtained in the $Sm_{12}(Co_{0.92}Cu_{0.06}Zr_{0.02})_{88}$ powders. Substituted iron enters the cobalt sublattice sites of the 2:17 structure, leading to an increase of the magnetization but a decrease of the coercivity. An optimum maximum energy product of 14.0 MGOe is obtained in the $Sm_{12}(Co_{0.7}Fe_{0.3})_{88}$ powders.

2.2 PrCo_5 Nanograined Magnets

On the basis of the above results, the studies were extended to the $PrCo_5$ system. $PrCo_5$ is known to have a high magnetization and a strong uniaxial magnetocrystalline anisotropy, and because of this it has attracted much attention as a promising candidate for less-expensive permanent magnets for high-temperature applications since its discovery in the 1960s (Strnat 1967). However, the coercivity developed in $PrCo_5$-based sintered magnets is only 4–7.4 kOe (Velu *et al.* 1989), which is rather low compared with the anisotropy field of 145–170 kOe (Strnat 1988) of the $PrCo_5$ phase. It has been established that magnetically hard nanograined $PrCo_5$-based powders can be successfully synthesized by mechanical milling and subsequent annealing (Chen *et al.* 1999).

As shown in Figs. 5 and 6, a high coercivity of 16.3 kOe along with a high M_r/M_s ratio of 0.66 and medium-strength maximum energy product of 11.6 MGOe has been obtained in stoichiometric $PrCo_5$ powders. A coercivity of 23.7 kOe has been obtained
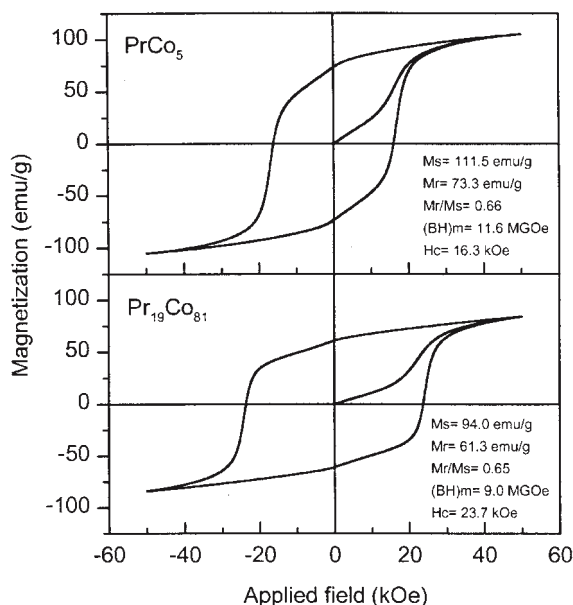
Figure 5
Hysteresis loops of $PrCo_5$ powders.
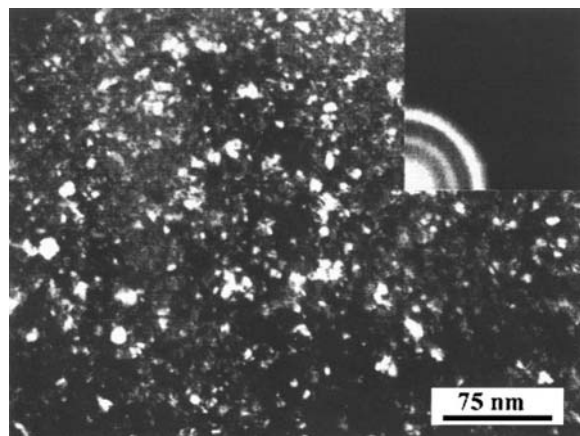
Figure 6
Dark-field TEM image of PrCo$_5$ powders.

in Pr$_{19}$Co$_{81}$ powders, which is the highest coercivity reported for PrCo$_5$-based magnets so far. A uniform PrCo$_5$ microstructure with an average grain size of about 15 nm is developed in the PrCo$_5$-based powders. The nanograined Sm$_2$Co$_{17}$ and PrCo$_5$ powders exhibit an excellent thermal stability. Both have a coercivity of about 5 kOe at 500 °C, which makes these nanostructured magnets promising candidates for high-temperature applications.

3. Conclusions

The microstructure and microchemistry of high-temperature magnets can be finely tuned through adjustments in the composition and processing parameters. For bulk Sm(Co$_{bal}$Fe$_{0.1}$Cu$_y$Zr$_{0.02}$)$_z$ magnets with $z = 7.5$, the temperature coefficient of coercivity changes from a small positive to a large negative value with increasing copper content. Changing the ratio z and using an appropriate copper content lead to a new magnet with a record high coercivity of 10.8 kOe at 500 °C. Its temperature coefficient of coercivity is only –0.03 °C^{-1}, which is much smaller than that of the old commercial magnets. On the other hand, mechanical milling has been found to be an effective technique to produce high-performance nanostructured RE–Co (RE = Sm, Pr) based powders. Magnetic properties of $M_s = 110.5$ emug^{-1}, $M_r = 66.2$ emu g^{-1}, $M_r/M_s = 0.60$, $H_c = 9.6$ kOe, and $(BH)_m = 10.8$ MGOe have been obtained in Sm$_2$Co$_{17}$ powders which have an average grain size of about 30 nm. A high coercivity of 16.3 kOe along with a high M_r/M_s ratio of 0.66 and a medium-high maximum energy product of 11.6 MGOe have been obtained in PrCo$_5$ powders with an average grain size of about 15 nm.

See also: Alnicos and Hexaferrites; Ferrite Magnets: Improved Performance; Magnets: Sintered

Bibliography

Chen Z, Meng-burany X, Hadjipanayis G C 1999 High coercivity in nanostructured PrCo$_5$-based powders produced by mechanical milling and subsequent annealing. *Appl. Phys. Lett.* **75**, 3165–7

Chen Z, Meng-burany X, Hadjipanayis G C 2000 Coercivity in mechanically milled Pr–Co–Zr powders with TbCu$_7$ structure. *J. Appl. Phys.* **87**, 5302–4

Chui S T 1999 Models for the pinning of domain walls in Sm(Co, Fe, Cu, Zr)$_z$ type magnets at finite temperatures. *J. Appl. Phys.* **85**, 4394–6

Coehoorn R, de Mooji D B, de Waard C 1989 Meltspun permanent magnet materials containing Fe$_3$B as the main phase. *J. Magn. Magn. Mater.* **80**, 101–4

Fischer R, Kronmüller H 1999 The role of the exchange interaction in nanocrystalline isotropic Nd$_2$Fe$_{14}$B-magnets. *J. Magn. Magn. Mater.* **191**, 225–33

Hadjipanayis G C 1996 In: Coey J M D (ed.) *Rare-earth Iron Permanent Magnets*. Clarendon, Oxford, UK

Hadjipanayis G C 1999 Nanophase hard magnets. *J. Magn. Magn. Mater.* **200**, 373–91

Liu J F, Zhang Y, Dimitrov D, Hadjipanayis G C 1999 Microstructure and high temperature magnetic properties of Sm(Co, Cu, Fe, Zr)$_z$ ($z = 6.7–9.1$) permanent magnets. *J. Appl. Phys.* **85**, 2800–4

Manaf A, Buckley R A, Davis H A 1993 New nanocrystalline high-remanence Nd–Fe–B alloys by rapid solidification. *J. Magn. Magn. Mater.* **128**, 302–6

McCormick P G, Miao W F, Smith P A I, Ding J, Street R 1998 Mechanically alloyed nanocomposite magnets. *J. Appl. Phys.* **83**, 6256–61

Ray A E 1984 The development of high energy product permanent magnets from 2:17 Re–TM alloys. *IEEE Trans. Magn.* **20**, 1614–8

Schultz L, Schnitzke K, Wecker J, Katter M, Kuhrt C 1991 Permanent magnets by mechanical alloying. *J. Appl. Phys.* **70**, 6339–44

Strnat K J 1967 Legierungen des Kobalt mit seltenen Erdmetallen, eine neue Gruppe aussichtsreicher Dauermagnetwerkstoffe. *Kobalt* **36**, 119–28

Strnat K J 1988 In: Wohlfarth E P, Buschow K H J (eds.) *Ferromagnetic Materials*. North-Holland, Amsterdam Chap. 4

Tang W, Zhang Y, Hadjipanayis G C 2000 Effect of Zr on the microstructure and magnetic properties of Sm(Co$_{bal}$Fe$_{0.1}$Cu$_{0.088}$Zr$_x$)$_{8.5}$. *J. Appl. Phys.* **87**, 399–403

Velu E M T, Obermyer R T, Sankar S G, Wallace W E 1989 PrCo$_5$-based high-energy-density permanent magnets. *J. Less-Common Met.* **148**, 67–71

G. C. Hadjipanayis
University of Delaware, Newark, Delaware, USA

Magnets: Mechanically Alloyed

This contribution presents an overview of the ability of the mechanical alloying process to prepare nanocrystalline rare earth–transition metal (RE-TM) permanent magnet powders.

Reducing the grain size of the hard magnetic phase is an effective way to develop coercivity in RE-TM permanent magnets. Most suitable for the production of fine-grained magnets are nonequilibrium preparation techniques such as rapid quenching (RQ), hydrogenation–disproportionation–desorption– recombination (HDDR) (see *Magnets: HDDR Processed*) or mechanical alloying (MA). The latter method has been established by Schultz *et al.* (1987), where highly coercive NdFeB powders were developed by mechanically alloying the elemental constituents in a planetary ball mill and performing a subsequent heat treatment.

Nowadays, mechanical alloying or mechanical milling (MM, here the initial material is a prealloy) is applied to all technologically interesting hard magnetic systems, of which the iron-based intermetallic phases $Nd_2Fe_{14}B$, $Sm_2Fe_{17}N_x$, and its modified version $Sm_2Fe_{15}Ga_2C_x$ are discussed in this contribution. For an overview of SmCo(Fe) prepared by MA, see Wecker *et al.* (1991) and McCormick *et al.* (1998). Each of the mentioned RE-TM hard magnetic phases has its own advantages and disadvantages concerning the intrinsic properties, the preparation routes or simply the cost of the material (see *Rare Earth Magnets: Materials*). In all cases, mechanical alloying resulting in grain sizes as small as 20 nm leads to an effective magnetic hardening. The nanocrystalline microstructure of mechanically alloyed materials also allows the preparation of exchange-coupled materials, where neighboring grains are magnetically coupled across the grain boundary (Neu *et al.* 1996). This applies to single-phase material as well as to two-phase material, where an additional soft magnetic phase is coupled to the hard phase.

Magnetic materials prepared by MA are isotropic powders. These can be epoxy bonded or cold pressed to give compact magnets, but with a moderate remanence due to the low density and the isotropic easy axis distribution. In some cases, fully dense magnets can be prepared via hot pressing and texture can even be induced by hot deformation (see *Textured Magnets: Deformation-induced*), leading to highly remanent magnets (Schultz *et al.* 1991). The properties, which are very specific for the nanocrystalline microstructure, can also be achieved with rapid quenching. Here, MA is a technologically easy and cost-effective alternative for producing large quantities of powder.

1. The Principle of Mechanical Alloying

For MA, the starting material is sealed under an inert atmosphere in a milling container together with milling balls. The container movement can be a planetary motion, a vibrational motion or a simple rotation in the case of an industrial-sized attritor mill. In the NdFeB system, the intimate mixing and repeated fracturing of the material during milling leads to powder particles with a very fine layered structure of neodymium and iron and small embedded boron particles on a length scale of a few nanometers. A subsequent heat treatment causes a diffusional transformation towards the thermodynamically more stable crystalline intermetallic $Nd_2Fe_{14}B$ phase. The high activation mediated by the milling process (i.e., a large number of dislocations and stress) allows this transformation to take place at temperatures well below the melting temperature and enables the production of nanocrystalline powders.

The actual thermodynamics and kinetics of the process depend on composition, the energy input upon milling, and the choice of the initial material. For higher energy input, the formation of an amorphous phase, coexisting with α-Fe, has been observed upon MA and MM. In all cases, however, the $Nd_2Fe_{14}B$ phase develops only after a heat treatment, so that the optimum choice of annealing temperature T_{ann} and time t_{ann} is of crucial importance. Typically, for low T_{ann} or short t_{ann}, an incomplete phase transformation limits H_c, whereas large grains reduce H_c for too high T_{ann} or too long t_{ann}.

Similar considerations hold for other RE-TM systems. Mechanical alloying of SmFe produces a mixture of nanocrystalline iron and an amorphous phase, which crystallizes into the 2:17-structure upon heating (Schnitzke *et al.* 1990). The same behavior is observed in SmFeGaC (Cao *et al.* 1996), whereas for mechanical milling with higher energy input, full amorphization is observed (Ding *et al.* 1993). In general, the degree of transformation, the occurrence of intermediate phases, and the resulting grain size depend strongly on the annealing treatment.

2. Highly Coercive Powders and Magnets

Besides reducing the grain size, decoupling of the hard magnetic grains is an effective approach to increase H_c. In the $RE_2Fe_{14}B$ system this can be obtained analogous to the case of sintered magnets by choosing a RE content above the stoichiometric value of 11.8 at%, leading to the formation of a RE-rich paramagnetic grain boundary phase. High coercive fields of $\mu_0 H_c = 2.0$ T are reported for a composition close to $Nd_{16}Fe_{76}B_8$ with a remanence $J_r = 0.73$ T (Schultz *et al.* 1991). The reported magnetic data refer to 100% density. The remanence value is slightly below $\frac{1}{2} J_s$ (J_s is the saturation polarization) because of dilution with the additional phase. By substituting dysprosium for neodymium, values of $\mu_0 H_c$ as high as 5.6 T can be obtained (Schultz 1992); the remanence then drops to 0.29 T.
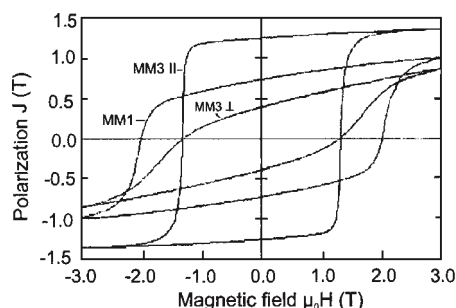
Figure 1
Hysteresis loop of a textured NdFeB magnet (MM3)
prepared via hot pressing and die-upsetting of
mechanically alloyed $Nd_{16}Fe_{76}B_8$-based powder (after
Schultz *et al.* 1991). The magnet is measured parallel and
perpendicular to the press direction. For comparison,
the behavior of the annealed isotropic MA powder is
shown (MM1).

Performing a die-upset experiment with a fully dense,
hot-pressed sample allows the development of texture,
and J_r improves substantially (Fig. 1). With a
$Nd_{16}Fe_{76}B_8$-based composition and additions of cop-
per and gallium, an MA magnet prepared in this way
exhibits $J_r = 1.31$ T, an energy density $(BH)_{max} =
326$ kJm^{-3} and $\mu_0 H_c = 1.2$ T. These values compare
well with those of similar magnets prepared from rap-
idly quenched powders. It is again a property of the
very small grains that allows the effective texturing.

Sm_2Fe_{17} develops uniaxial magnetocrystalline
anisotropy only after modification with interstitial
atoms like carbon or nitrogen, usually introduced by
a solid–gas reaction at temperatures around 500 °C
(Coey and Sun 1990). Schnitzke *et al.* (1990) prepared
$Sm_2Fe_{17}N_x$ powders with $\mu_0 H_c = 2.9$ T by nitriding
nanocrystalline MA Sm_2Fe_{17} powders. The reman-
ence of 0.71 T is in accordance with $J_s = 1.54$ T. Even
higher coercive fields of 4.4 T are reported by Liu
et al. (1994). A systematic study on the different cry-
stallographic modifications of the Sm_2Fe_{17}-nitrides
and their parent alloys is given by Teresiak *et al.*
(1999). The use of the $Sm_2Fe_{17}N_x$-phase is, however,
limited by its low thermal stability. Above 550 °C,
$Sm_2Fe_{17}N_x$ disproportionates into SmN and α-Fe.
Often, small amounts of partly unnitrided soft
Sm_2Fe_{17} or soft α-Fe are present in the material.
For optimization, grain and particle sizes have to be
considered in the kinetics of the solid–gas reaction
(Coey and Smith 1999). The low thermal stability
also prohibits a subsequent hot compaction.

The stability of the carbonized or nitrided Sm_2Fe_{17}
phase can be drastically improved by a substitution
of iron with gallium, silicon or aluminum. Nanocrys-
talline, highly coercive $Sm_2Fe_{17-x}Ga_xC_2$ was pre-
pared by MM with subsequent heat treatment, where
carbon had already been introduced in the prealloy

(Ding *et al.* 1994). The high stability also allows hot
pressing, and fully dense $Sm_2Fe_{15}Ga_2C_2$ magnets
with coercive fields of 1.5 T and remanences of 0.5 T
can be prepared from MA powders (Cao *et al.* 1996).
Texture via die upsetting was not obtained.

3. Exchange-coupled Powders and Magnets

Exchange coupling across the grain boundaries leads
to an enhanced remanence compared to decoupled
single-domain grains due to spin rotation in the grain
boundary region (see *Magnets: Remanence-en-
hanced*). The effect increases with decreasing grain
size. Nanocrystalline single-phase $Nd_2Fe_{14}B$ powders
with exact stoichiometric composition and controlled
grain size were prepared by mechanical milling and
subsequent heat treatment (Neu *et al.* 1999). The
grain-size dependence of the enhancement follows
the prediction of a newly developed micromagnetic
model (Neu *et al.* 1998).

In agreement with the consideration outlined
above, the highest reduced remanence $J_r/J_s = 0.56$ is
found in the $Nd_2Fe_{14}B$ powders with the smallest
average grain size of 33 nm. Smaller grains (21 nm)
were obtained in single-phase $Nd_2(FeCoGaNb)_{14}B$
powders and J_r/J_s was further improved to 0.60.
Suess *et al.* (2000) report even higher reduced re-
manences of 0.68 in mechanically alloyed and hot
pressed $Pr_2Fe_{14}B$ magnets. These experiments show
that exchange coupling, originally discovered in rap-
idly quenched ribbons, is as effective in MA or MM
magnet powders, when a sufficiently small grain size
is achieved.

If a second phase with higher J_s, e.g., iron, is cou-
pled to the hard magnetic phase, the composite ma-
terial shows a collective magnetization behavior, a
further increased remanence, and a decreased but still
considerable coercive field. Both the increase in J_r
and the decrease in H_c scale with the amount of the
soft phase. If, however, owing to large soft grains,
the coupling is insufficient, magnetization reversal is
initiated in the soft grains, coercivity is drastically
reduced, and the demagnetization curve shows a
two-step behavior. Milling of an iron-rich NdFeB
composition and subsequent heat treatment leads to
a $Nd_2Fe_{14}B + \alpha$-Fe composite with sufficiently small
soft grains of about 20–30 nm.

Some additional elements, which dissolve in iron
upon milling but are rejected upon annealing, can
slow down the iron diffusion and therefore further
reduce the iron grain size. Additional elements can
also change the crystallization temperature of the
2:14:1 phase and thereby influence the grain size.
Among the tested elements zirconium, niobium, and
molybdenum are found to improve the coercive field
via a reduced α-Fe grain size (Crespo *et al.* 1997, Cui
et al. 2000). Important to the discussion of grain
sizes and their influence on the magnetic properties is

consideration? of the degree of phase transformation. Especially when the annealing is performed at low temperatures, the advantage of small grain sizes is overcome by a residual amount of amorphous soft phase. There is no lower theoretical limit for grain size of the soft phase to give optimum H_c, but only the experimental difficulty of obtaining both small grains and a complete crystallization.

The substitution of cobalt for iron influences the intrinsic and extrinsic magnetic properties. Milling and annealing leads to the same iron:cobalt ratio in soft and hard phase. Curie temperature and saturation polarization are strongly improved and the remanence is increased. Also J_r/J_s increases, indicating a more effective coupling of the grains, and the coercivity is rather constant. Upon cobalt substitution, a smaller α-(Fe,Co) grain size has been observed (You *et al.* 2000) and owing to the decrease in the magnetocrystalline anisotropy for both phases, an increase in the exchange length l_{ex} is expected. This explains the improved coupling and also the stability of H_c, as the better coupling and the decreased anisotropy level off.

In comparing MA with MM, the second process often leads to better magnetic properties, attributed to a more homogeneous microstructure with a smaller grain size distribution (Miao *et al.* 1996). Consequently, exchange-coupled NdFeB magnet powders prepared by mechanical milling of a master alloy with additional cobalt and grain refining elements show very attractive magnetic properties, with $J_r \approx 1.2$ T, $\mu_0 H_c \approx 0.5$ T and $(BH)_{max} \approx 150$ kJm^{-3} (Fig. 2, Neu 1998). It is also possible to hot-press the as-milled powder and to prepare fully dense magnets with comparable properties (Wecker *et al.* 1995). As a rule

of thumb, in all these materials optimum energy densities are obtained for roughly 20–40 vol.% soft phase, which equals about 7–9 at.% neodymium.

Remanence enhancement in nanocrystalline SmFe-nitrides occurs for a samarium content below 11 at.%. MA of Sm_7Fe_{93} powders, subsequent annealing and nitriding produces a two-phase mixture of $Sm_2Fe_{17}N_x$ and α-Fe with an iron grain size of about 20 nm. The powders show exchange-coupling behavior with a high remanence of $J_r = 1.13$ T and a coercive field of $\mu_0 H_c = 0.39$ T (Ding *et al.* 1993). As H_c depends so critically on the grain size of the soft phase, optimum properties are only achieved in a very small window of the annealing temperature. Successful attempts to refine the α-Fe grain size down to 10–20 nm were reported by O'Donnel and Coey (1997) by adding 2 at.% zirconium or tantalum to a MA Sm_7Fe_{93} powder. The addition of tungsten improves H_c, but without measurable effect on the average grain size (Kaszuwara *et al.* 2000). Here, an increase of the uniaxial anisotropy is assumed, as tungsten is observed to dissolve in the $Sm_2Fe_{17}N_x$ phase. MA two-phase $Sm_2Fe_{14}Ga_3C_2/\alpha$-Fe magnets are discussed in Feutrill *et al.* (1996) with an emphasis on the magnetization behavior of exchange-coupled materials.

4. Conclusions

Mechanical alloying with subsequent heat treatment results in nanocrystalline permanent magnet powders with excellent properties. Hot compaction and hot deformation enables the production of highly anisotropic magnets. The most promising materials for cost effective resin-bonded magnets are isotropic exchange-coupled nanocomposites with high remanences of $J_r \geqslant 1.20$ T and sufficient coercive field $\mu_0 H_c = 0.5$ T, which are based on NdFeCoB or PrFe-CoB. The increase in the Curie temperature due to cobalt allows their use at elevated temperatures. Although diluted, these "lean" hard magnets based on low RE-content can achieve remanences exceeding 0.8 T.

Likewise, the SmFeN/C powders offer Curie temperatures above 450 °C, even without the expensive cobalt. Remanence and energy density, especially in the SmFeMC system, have still to be improved.

Figure 2
Hysteresis loop of exchange-coupled $Nd_8Fe_{78}Co_9Si_1B_4$ magnet powder prepared by mechanical milling of a stoichiometric master alloy blended with iron, cobalt, and silicon powder. Milling and optimum annealing leads to a nanocomposite of 70 vol.% $Nd_2(Fe,Co)_{14}B + 30$ vol.% (α-(Fe, Co)) with grain sizes of about 20 nm (after Neu 1998). $\mu_0 H_c = 0.5$ T, $J_r = 1.19$ T, $(BH)_{max} = 149$ kJm^{-3}.

Bibliography

Cao L, Müller K-H, Handstein A, Grünberger W, Neu V, Schultz L 1996 High-performance $Sm_2Fe_{15}Ga_2C_2$ permanent magnets made by mechanical alloying and hot pressing. *J. Phys. D: Appl. Phys.* **29**, 271–3

Coey J M D, Smith P A I 1999 Magnetic nitrides. *J. Magn. Magn. Mater.* **200**, 405–25

Coey J M D, Sun H 1990 Improved magnetic properties by treatment of iron-based rare earth intermetallic compounds in ammonia. *J. Magn. Magn. Mater.* **87**, L251–4

Crespo P, Neu V, Schultz L 1997 Mechanically alloyed nanocomposite powders of $Nd_2Fe_{14}B/\alpha$-Fe with additional elements. *J. Phys. D: Appl. Phys.* **30**, 2298–303

Cui B Z, Sun X K, Liu W, Zhang Z D, Geng D Y, Zhao X G 2000 Effects of additional elements on the structure and magnetic properties of $Nd_2Fe_{14}B/\alpha$-Fe-type nanocomposite magnets. *J. Phys. D: Appl. Phys.* **33**, 338–44

Ding J, McCormick P G, Street R 1993 Remanence enhancement in mechanically alloyed Sm_7Fe_{93}-nitride. *J. Magn. Magn. Mater.* **124**, 1–4

Ding J, Shen B, McCormick P G, Street R, Wang F 1994 Magnetic hardening of mechanically milled $Sm_2Fe_{14}Ga_3C_2$. *J. Alloys Comp.* **209**, 221–4

Feutrill E H, McCormick P G, Street R 1996 Magnetization behavior in exchange-coupled $Sm_2Fe_{14}Ga_3C_2/\alpha$-Fe. *J. Phys. D: Appl. Phys.* **29**, 2320–6

Kaszuwara W, Leonowicz M, Kozubowski J A 2000 The effect of tungsten addition on the magnetic properties and microstructure of SmFeN-α-Fe nanocomposites. *Mater. Lett.* **42**, 383–6

Liu W, Wang Q, Sun X K, Zhao X, Zhao T, Zhang Z, Chuang Y C 1994 Metastable Sm-Fe-N magnets prepared by mechanical alloying. *J. Magn. Magn. Mater.* **131**, 413–6

McCormick P G, Miao W F, Smith P A I, Ding J, Street R 1998 Mechanically alloyed nanocomposite magnets. *J. Appl. Phys.* **83**, 6256–61

Miao W F, Ding J, McCormick P G, Street R 1996 A comparative study of mechanically alloyed and mechanically milled $Nd_{10}Fe_{84}B_6$. *J. Appl. Phys.* **79**, 2079–83

Neu V 1998 *Exchange-coupled nanocrystalline Nd-Fe-B magnet powders prepared by mechanical alloying*. Dissertation, University of Technology, Dresden

Neu V, Hubert A, Schultz L 1998 Modelling of the enhanced remanence of nanocrystalline, exchange-coupled hard magnetic grains. *J. Magn. Magn. Mater.* **189**, 391–6

Neu V, Klement U, Schäfer R, Eckert J, Schultz L 1996 Remanence enhancement in mechanically alloyed two-phase Nd-Fe-B magnetic material. *Mater. Lett.* **26**, 167–70

Neu V, Schultz L, Bauer H-D 1999 Grain size dependence of remanence enhancement and coercivity in nanocrystalline Nd-Fe-B-powders. *Nanostruct. Mater.* **12**, 769–74

O'Donnel K, Coey J M D 1997 Characterization of hard magnetic two-phase mechanically alloyed $Sm_2Fe_{17}N_3/a$-Fe nanocomposites. *J. Appl. Phys.* **81**, 6310–21

Schnitzke K, Schultz L, Wecker J, Katter M 1990 High coercivity in $Sm_2Fe_{17}N_x$ magnets. *Appl. Phys. Lett.* **57**, 2853–5

Schultz L 1992 Mechanically alloyed permanent magnets. *Mater. Sci. Forum* **88–90**, 687–94

Schultz L, Schnitzke K, Wecker J, Katter M, Kuhrt C 1991 Permanent magnets by mechanical alloying. *J. Appl. Phys.* **70**, 6339–44

Schultz L, Wecker J, Hellstern E 1987 Formation and properties of NdFeB prepared by mechanical alloying and solid-state reaction. *J. Appl. Phys.* **61**, 3583–5

Suess D, Dahlgren M, Schrefl T, Grössinger R, Fidler J 2000 Micromagnetic analysis of remanence and coercivity of nanocrystalline Pr-Fe-B magnets. *J. Appl. Phys.* **87**, 6573–5

Suryanarayana C 2001 Mechanical alloying. *Prog. Mater. Sci.* **46**, 1–184

Teresiak A, Kubis M, Mattern N, Wolf M, Gruner W, Müller K-H 1999 Influence of nitrogenation on structure development and magnetic properties of mechanically alloyed and annealed Sm-Fe powders. *J. Alloys Comp.* **292**, 212–20

Wecker J, Katter M, Schultz L 1991 Mechanically alloyed Sm-Co materials. *J. Appl. Phys.* **69**, 6058–60

Wecker J, Schnitzke K, Cerva H, Grogger W 1995 Nanostructured Nd-Fe-B magnets with enhanced remanence. *Appl. Phys. Lett.* **67**, 563–5

You C, Sun X K, Liu W, Cui B, Zhao X, Zhang Z 2000 Effect of copper and tungsten additions on the structure and magnetic properties of $Nd_2Fe_{14}B/\alpha$-Fe nanocomposite magnets. *J. Phys. D: Appl. Phys.* **33**, 926–31

V. Neu and L. Schultz
Institut für Metallische Werkstoffe, Dresden, Germany

Magnets: Remanence-enhanced

Remanence-enhanced magnets are isotropic hard magnetic materials with remanence exceeding one half of the saturation magnetic polarization expected for a randomly oriented assembly of noninteracting single domain particles of uniaxial magnetic anisotropy. Remanence enhancement is a result of strong ferromagnetic coupling via intergrain exchange interactions among spin magnetic moments belonging to adjacent hard magnetic grains whose sizes are comparable to the ferromagnetic correlation length, or, the "exchange length." Typical exchange lengths in ferromagnets are of the order of a few nanometers. Therefore, remanence-enhanced magnets are normally nanocrystalline.

Typical remanence-enhanced magnets are rapidly solidified $Nd_2Fe_{14}B$-based magnets for which the ratio of remanence to saturation magnetic polarization is about 0.6. Isotropic nanocomposite permanent magnets comprising soft and hard magnetic phases coupled via intergrain exchange interactions are also regarded as remanence-enhanced magnets. In the nanocomposite permanent magnets, the remanence to saturation polarization ratio can be much larger than in the single-phase nanocrystalline magnets because of the small and nonuniaxial magnetocrystalline anisotropy of the soft magnetic phase. Typical examples of this type of magnet include $Fe_3B/Nd_2Fe_{14}B$ and α-Fe/$Nd_2Fe_{14}B$. The demagnetization behavior of both types of remanence-enhanced magnets has been successfully simulated using micromagnetic calculations.

1. Remanence Enhancement in Nearly Single-phase Hard Magnetic Materials

Magnetic hardness of most permanent magnetic materials originates from uniaxial anisotropy, either shape anisotropy or magnetocrystalline anisotropy, of at least one ferromagnetic component phase (see *Magnetic Anisotropy*). The shape anisotropy arises from the direction-dependent magnetostatic energy caused by an elongated shape of a ferromagnetic phase and is of the order of $10^{-1} MJm^{-3}$. On the

other hand, magnetocrystalline anisotropy arises from the electrostatic energy associated with the electron charge distribution of the individual atom which interacts with the electronic charge distribution associated with the crystal. It becomes as large as $22\,MJm^{-3}$. Therefore, most modern permanent magnets are composed of hard magnetic phases such as $MFe_{19}O_{12}$ (M = barium or strontium), $Nd_2Fe_{14}B$, $Sm_2Fe_{17}N_3$, $SmCo_5$, and Sm_2Co_{17} which have a large magnetocrystalline anisotropy.

In the following, an assembly of a large number of single-domain hard magnetic particles of a ferromagnetic material with a uniaxial anisotropy is considered, the easy direction of magnetization being distributed randomly in a three-dimensional space. When a sufficiently large magnetic field is applied in one direction (z-axis), all magnetic moments of all particles will lie on a hemisphere and then the applied field is reduced to zero: the assembly of particles has a remanent magnetization of one half of the total saturation magnetization if there are no interactions among the magnetic moments of the particles (Fig. 1(a)), known as the Stoner-Wohlfarth theorem (Stoner and Wohlfarth 1948). However, if there exist magnetic interactions, either dipolar or exchange interactions, among magnetic moments of the particles, which cause a reduction of the total energy when adjacent particles align their magnetic moment parallel, then the remanent magnetization becomes larger than one half of the total saturation magnetization (Fig. 1(b)). This phenomenon is called remanence enhancement.

Intergranular exchange interactions occurs between atoms belonging to adjacent grains along boundaries. The amount of energy associated with this interaction is proportional to the contact area of these grains. On the other hand, the magnetocrystalline anisotropy energy is proportional to the volume of the grain. These two sources of energy are counteracting with each other. When the local magnetic anisotropy dominates, the effect of exchange coupling can be neglected, and the magnet behaves like a Stoner-Wohlfarth magnet. On the other hand, when exchange coupling is very strong, the local magnetic anisotropy is averaged out and the system behaves like a soft magnetic material. Thus, there exists an intermediate situation in which the system behaves as a remanence-enhanced magnet.

The ratio of these two counteracting energy contributions may be defined as

$$\eta = K_u V / J_e S \qquad (1)$$

where J_e is the effective intergranular exchange constant, $(1/2)S$ the interface surface area per grain, K_u the anisotropy constant, V the volume of a grain, neglecting distributions of values of these quantities. The parameter η is proportional to the grain size. Another parameter which depends on the microstructure of the material is J_e, which depends on the atomic and chemical structure of the grain boundaries.

Figure 2 shows calculated hysteresis loops of model magnets composed of uniform cubic grains characterized by various values of the parameter η. The calculation is based on the hypothesis that the magnetic moment of each cubic cell is represented by a single vector of length $J_s V$, where J_s is the saturation magnetization per unit volume (Fukunaga and Inoue 1992). This figure clearly demonstrates that the remanence ratio increases with increasing exchange interactions (i.e., decreasing η), whereas the coercivity decreases, and that there exists an intermediate strength of exchange coupling with which the magnetic properties in terms of both remanence and coercivity can be optimized. With realistic values of

Figure 1
Schematic illustration of spin direction distribution of (a) a Stoner-Wohlfarth magnet and (b) a remanence-enhanced magnet.
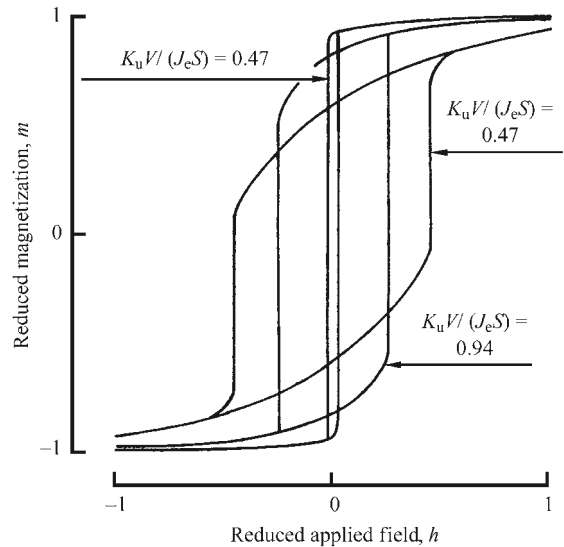
Figure 2
Shapes of full hysteresis loops of single-phase isotropic magnets with different exchange-coupling parameters $\eta = K_u V / J_e S$ (after Fukunaga and Inoue 1992).

K_u and J_e expected for rare earth intermetallic compounds such as $Nd_2Fe_{14}B$, optimum magnetic properties are suggested to be obtained with grain sizes of about 10 nm.

A micromagnetically more accurate description of the mechanism of remanence enhancement needs consideration of directional variation of atomic magnetic moments within a grain. Figure 3 shows the results of two-dimensional finite-element calculations of inhomogeneous regions along grain boundaries of a model system with grain diameters of 10 nm and 20 nm in the remanent state after magnetic
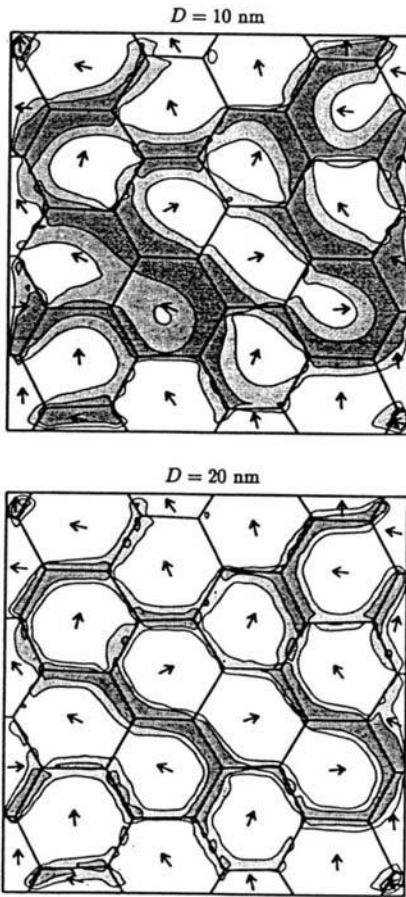
Figure 3
Inhomogeneous regions along grain boundaries in two-dimensional model magnets with different grain sizes using the magnetic parameters of $Nd_2Fe_{14}B$. The arrows indicate the easy direction of magnetization. The shaded areas denote the regions where the magnetic polarization deviates from the local easy direction of magnetization by more than 10 degrees (lighter gray) and 20 degrees (darker gray). Periodic boundary conditions are applied in the calculation (after Schrefl *et al.* 1994).

saturation in one direction (Schrefl *et al.* 1994). The inhomogeneous regions refer to regions in which magnetic moments are largely off from the local easy direction of magnetization. This figure visualizes the effect of grain size on the volume fraction of the inhomogeneous regions in which magnetic moments are inclined towards the common direction of magnetization of the whole magnet.

2. Remanence Enhancement in Nanocomposite Magnets

The class of permanent magnets called nanocomposite permanent magnets or "exchange-spring magnets" (Kneller and Hawig 1991) shows a relatively large remanence of 70–80% of saturation magnetization. These magnets are sometimes considered as remanence-enhanced magnets. One of the reasons that this class of materials maintains such a large fraction of flux density in the remanent state is that they contain a large fraction of nonuniaxial anisotropic phases. The intention to compose a nanocomposite magnet is to increase J_s by combining a hard magnetic phase (phase 1) with other ferromagnetic phases which have a large saturation magnetization (phase 2). Phase 2 does not need to have a large uniaxial anisotropy. Good magnetic properties may be obtained by relying only on strong exchange coupling between the component phases. For instance, b.c.c.-Fe, which is an important component of nanocomposite magnets based on FeNdB or FeSmN systems, has a cubic magnetocrystalline anisotropy.

The remanence ratio of a two-phase isotropic nanocomposite magnet is given by

$$J_r/J_s = [v_1 m_1 J_{s1} + (1 - v_1)m_2 J_{s2}]/J_s \text{with}$$

$$J_s = v_1 J_{s1} + (1 - v_1)J_{s2} \qquad (2)$$

where m_1 and m_2 are the remanence ratios of each component, and J_{s1} and J_{s2} are the saturation magnetizations of phase 1 and phase 2, respectively. For the case in which phase 1 is of uniaxial anisotropy and phase 2 is of planar anisotropy, without any interactions, $m_1 = 0.5$, and $m_2 = 0.79$. For cubic crystals with $\langle 100 \rangle$ easy directions of magnetization (as in b.c.c.-Fe), $m_2 = 0.83$ and for cubic crystals with $\langle 111 \rangle$ easy directions of magnetization (as in f.c.c.-Ni), $m_2 = 0.86$. Therefore, the remanence ratio is always larger than 0.5 for the case of nanocomposite magnets ($v_1 < 1$). A good nanocomposite magnet has a remanence ratio even larger than the value given by Eqn. (2) with the m_1 and m_2 values given above.

3. Processing Methods of Remanence-enhanced Magnets

The nanoscopic structure which is required to realize a measurable remanence enhancement is metastable

in that it contains a high interfacial boundary energy. Commonly used techniques to create such a microstructure utilize the instability of a metastable phase such as an amorphous phase or a mixture of quasi-equilibrium phases. Techniques to create such metastable states include rapid solidification, mechanical alloying (see *Magnets: Mechanically Alloyed*), and vapor deposition (see *Magnetic Films: Hard*). A short heat treatment at sufficiently low temperatures transforms the metastable state into another metastable nanoscopic structure. Another mechanism which may be utilized is the "spinodal decomposition" which is believed to be working in production of the FeAlNiCo type of permanent magnets (see *Alnicos and Hexaferrites*) and in the 2-17 type SmCoFeCuZr-type magnets. However, the main body of existing research has used the rapid solidification technique and, in many cases, a subsequent short annealing at relatively low temperatures in the range between 600 and 700 °C is applied.

In the case of rapid solidification, a continuous strand of a molten alloy is poured onto a circumferential surface of a chilled roll. Pour rate of the molten alloy is regulated by the diameter of an orifice at the bottom of a melt container and by keeping the head pressure of the melt in a certain range. A continuous operation of this process is possible if the melt pour rate can be regulated within the optimum range by supplying melt into the melt container.

The design of the alloy composition involves the addition of small amounts of elements which significantly affect the kinetics of crystallization reactions. Examples are aluminum, silicon, niobium and zirconium in nanocrystalline $Nd_2Fe_{14}B$ (Matsumoto *et al.* 1988) and in $Fe/Nd_2Fe_{14}B$ nanocomposites, and copper in $Fe_3B/Nd_2Fe_{14}B$ nanocomposites (Hirosawa *et al.* 1998). Experiments have indicated that $Nd_2Fe_{14}B$-based nanocrystalline or nanocomposite magnets can be obtained by a single-stage rapid solidification process without further heat treatment (Manaf *et al.* 1991). This process is often called "direct quenching." Another route to produce nearly the same microstructure is to rapidly solidify alloys at a slightly larger cooling rate and apply a subsequent heat treatment. This procedure is often referred as "overquenching and annealing."

The cooling rate during solidification can be controlled by adjusting both the melt pour rate and the substrate (i.e., the chilled roll) speed. The industrially preferred process is the overquenching and annealing route because of a wider processing window in comparison to the direct quenching route. The α-Fe/$SmFe_7N$-type nanocomposites can be produced also by the rapid solidification and annealing route, and a subsequent nitrogenation treatment, which is applied in order to convert the soft magnetic $SmFe_7$ into the hard magnetic $SmFe_7N_x$ phase by a gas-phase interstitial modification of the lattice structure.

The mechanical alloying process is able to produce a metastable mixture of phases and/or elements having a large density of structural defects such as grain boundaries and nonequilibrium vacancies (Schultz *et al.* 1987). On annealing, such a structure of a large internal energy can be transformed into a nanocrystalline or nanocomposite structure. In order to produce a bulk magnet, the resulting mechanically alloyed powder has to be compacted. The metallic materials being processed must be protected in an inert gas atmosphere in order to avoid severe oxidation particularly in the case of rare earth magnets. The mechanical alloying process, therefore, is operated in batch. On a laboratory scale, this process has been successfully used to produce nearly the same material as obtained by the rapid solidification route.

4. Typical Magnetic Properties of Remanence-enhanced Magnets

Some typical examples of remanence-enhanced magnets include $Nd_2Fe_{14}B$, $Fe_3B/Nd_2Fe_{14}B$, α-Fe/$Nd_2Fe_{14}B$, and α-Fe/$SmFe_7N_x$. Single-phase $SmCo_5$- and $Sm_2Fe_{17}N_3$-based materials are usually difficult to process into materials showing a marked remanence enhancement because of the very large uniaxial anisotropy which requires the grain sizes to be very small. Table 1 gives a few examples of remanence-enhanced magnets composed of nearly single phase $Nd_2Fe_{14}B$-type compounds. Typical J_r/J_s values are 0.6. For NdFeB and SmFeN nanocomposites, even higher J_r/J_s values of 0.7 to 0.8 are obtained (Table 2). Figure 4 shows an example of the dependence of

Table 1
Magnetic properties and J_r/J_s ratio of some $Nd_2Fe_{14}B$-based ribbon magnets.

Composition	$(BH)_{max}$ $(kJ\,m^{-3})$	H_{cJ} $(kA\,m^{-1})$	J_r (T)	J_s (T)	J_r/J_s	Reference
$Nd_{13}Fe_{79.3}B_6Si_1Al_{0.7}$	162	891	0.96	N/A	ca. 0.6	Matsumoto *et al.* (1988)
$Nd_{11.8}Fe_{81.0}B_{5.7}Si_{1.7}$	144	874	0.925	1.527	0.606	Clemente *et al.* (1988)
$Nd_{11}Fe_{72}Co_8B_{7.5}V_{1.5}$	153	962	0.926	1.607	0.576	Yamamoto *et al.* (1989)
$Nd_{12}Fe_{82}B_6$	174	1020	1.02	1.58	0.646	Bauer *et al.* (1996)

Table 2
Magnetic properties and J_r/J_s ratio of some nanocomposite magnet ribbons (NdFeB) and powder (SmFeN; a demagnetization correction involved).

Composite phases and their molar fractions	$(BH)_{max}$ (kJ m^{-3})	H_{cJ} (kA m^{-1})	J_r (T)	J_s (T)	J_r/J_s Meas	J_r/J_s Eq. (2)	Reference
$(Fe_3B)_{73}/Fe_{12}/(Nd_2Fe_{14}B)_{15}$	93	240	1.2	1.6	0.75	0.75	Coehoorn *et al.* (1988)
$Fe_{30}/(Nd_2Fe_{14}B)_{70}$	185	416	1.25	1.78	0.70	0.60	Bauer *et al.* (1996)
$Fe_{40}/(Sm_2Fe_{17}N_{2.6})_{60}$	205	310	1.42	1.75	0.81	0.63	Ding *et al.* (1993)
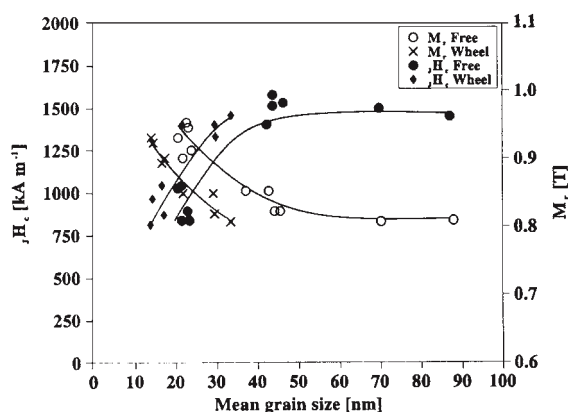
Figure 4
Dependence of remanence and intrinsic coercivity on grain size in $Nd_{13.2}Fe_{79.6}B_6Si_{1.2}$ ribbon magnets (after Manaf *et al.* 1991). ◆ and × represent H_{cJ} and J_r on the wheel side of ribbons and ● and ○ represent H_{cJ} and J_r on the free side of ribbons, respectively.

remanence and intrinsic coercivity on grain size in $Nd_{13.2}Fe_{79.6}B_6Si_{1.2}$ magnets (Manaf *et al.* 1991). A visible remanence enhancement occurs at grain sizes below 40 nm in this example.

Bibliography

Bauer J, Seeger M, Zern A, Kronmueller H 1996 Nanocrystalline FeNdB permanent magnets with enhanced remanence. *J. Appl. Phys.* **80**, 1667–73
Clemente G B, Keem J E, Bradley J P 1988 The microstructural and compositional influence upon HREM behavior in $Nd_2Fe_{14}B$. *J. Appl. Phys.* **64**, 5299–301
Coehoorn R, de Mooij D B, Duchateau J P W B, Buschow K H J 1988 Novel permanent magnetic materials made by rapid quenching. *J. Phys.* **C8**, 669–70
Ding J, McCormick P G, Street R 1993 Remanence enhancement in mechanically alloyed isotropic Sm_7Fe_{93}-nitride. *J. Magn. Magn. Mater.* **124**, 1–4
Fukunaga H, Inoue H 1992 Effect of intergrain exchange interaction on magnetic properties in isotropic NdFeB magnets: Jpn. *J. Appl. Phys.* **31**, 1347–52
Hirosawa S, Kanekiyo H, Uehara M 1998 Magnetic properties of Cr-doped $Fe_3B/Nd_2Fe_{14}B$ nanocomposite hard magnetic materials. *J. Magn. Soc. Jpn.* **22** (Suppl. S1), 325–7
Kneller E F, Hawig R 1991 The exchange-spring magnet: a new material principle for permanent magnets. *IEEE Trans. Magn.* **27**, 3588–600
Manaf A, Buckley R A, Davies H A, Leonowicz M 1991 Enhanced magnetic properties in rapidly solidified NdFeB-based alloys. *J. Magn. Magn. Mater.* **101**, 360–2
Matsumoto F, Sakamoto H, Komiya M, Fujikura M 1988 Effects of silicon and aluminum additions on magnetic properties of rapidly quenched NdFeB permanent magnets. *J. Appl. Phys.* **63**, 3507–9
Schrefl T, Fidler J, Kronmuller H 1994 Remanence and coercivity in isotropic nanocrystalline permanent magnets. *Phys. Rev. B* **49**, 6100–10
Schultz L, Wecker J, Hellstern E 1987 Formation and properties of NdFeB prepared by mechanical alloying and solid state reaction. *J. Appl. Phys.* **53**, 3583–5
Stoner E C, Wohlfarth E P 1948 A mechanism of magnetic hysteresis in heterogeneous alloys. *Philos. Mag. Trans. R. Soc.* **240**, 599–644
Yamamoto H, Nagakura M, Ozawa Y, Katsuno T 1989 Magnetic properties of high-quality melt-spun Nd-Fe-Co-B-V system alloys. In: *Proc. 10th Int. Workshop Rare-Earth Magnets and Their Applications Pt. 1*. The Society of Non-Traditional Technology, Tokyo, pp. 543–50

S. Hirosawa
Sumitomo Special Metals Company, Osaka, Japan

Magnets: Sintered

Sintered magnets are manufactured by powder metallurgy in many shapes and dimensions in large volumes. Besides hard magnetic hexaferrites and Alnico materials (see *Alnicos and Hexaferrites*), mainly rare earth (RE)–transition metal (TM) alloys are applied. By powder metallurgy the magnetocrystalline anisotropy of hard hexaferrites, of samarium (Sm)–cobalt (Co) compounds, $SmCo_5$ as well as modified $Sm_2(Co, Cu, Fe, Zr)_{17}$, and of the neodymium (Nd)–iron (Fe)–boron (B) compound, $Nd_2Fe_{14}B$, can be exploited in order to achieve anisotropic magnets with a high remanent polarization B_R and a strong coercivity H_{cJ} (see *Rare Earth Magnets: Materials*).

The basic principles of the production route, in particular the benefits of the different powder compaction processes and their impact on the

dimensions and magnetic properties are reviewed in this article.

1. Alloying and Powder Processing

Nd–Fe–B or Sm–Co alloys can be prepared from RE metals, mainly neodymium and samarium, transition metals, iron or cobalt, and master-alloys Fe–B, Fe–Nb, or additions, e.g., aluminum, copper, zirconium, etc. Since the RE metals are highly reactive, alloying has to be performed in a vacuum induction furnace. The melting cycle needs careful optimization in order to minimize chemical reactions with the crucible and to prevent oxidation by residual atmospheric gases. The melted alloy is cast into ingots which have a polycrystalline microstructure (see top of Fig. 1).

An alternative alloying route is the calciothermic reduction diffusion (RD) process (Herget 1985). RE oxides, TM powder, and the required additions are mixed with calcium-granulate as a reducing agent. The compacted powders are heated up to 1100 °C in a vacuum, so that the calcium vapor reduces the RE oxide to RE metal. The RE metal diffuses into the TM powder and the RE–TM alloy results, mixed with calcium oxides. After cooling to room temperature the calcium oxides are leached by aqueous solutions. Since the calciothermic RD process uses RE oxides, the materials are more economic, but the final RE–TM alloy-powder contains more impurities than an alloy melted in a vacuum induction furnace.

A recently developed alloying process is *strip casting*. The molten alloy is cast onto a rotating copperroll and is cooled at cooling rates of about $30\,\text{K min}^{-1}$ to approximately 0.3 mm thick flakes (Hirose *et al.* 1998).

The cast ingots, alloy powder particles, or strip cast flakes have a polycrystalline microstructure resulting in a random distribution of the easy-axes of the crystals and hence of the magnetic moments. For achieving a well-defined texture or easy-axis, respectively, powder metallurgy is applied (Fig. 1). The alloys are crushed and milled mechanically or by hydrogen decrepitation to a fine alloy powder (Harris *et al.* 1994). In order to get a perfect alignment in a magnetic field, the powder particles must consist of single crystals. In general alloy powders with a particle size in the range of 3–5 μm meet this condition well. For the production of anisotropic magnets there exists different processing routes that determine the magnetic properties, dimensional tolerances, and processing costs.

2. Compaction Methods

2.1 Cold Isostatically Pressed (CIP) Magnet Blocks

For the production of big blocks the alloy powder is sealed in a rubber mold, aligned in a magnetic field, and pressed isostatically. Since the pressure increases homogeneously from all directions, the alignment of the powder particles is not disturbed significantly during compaction (Fig. 1, left-hand side). The isostatically pressed blocks are sintered to more than 98% of the theoretical density and annealed in order to optimize the magnetic properties.

Hence, isostatically pressed blocks have an excellent texture. The alignment coefficient amounts to about 98% (Rodewald *et al.* 2000). Due to the proper alignment of all magnetic moments, sintered Nd–Fe–B magnets with a remanent polarization of 1.47 T and a coercivity of $9.6\,\text{kA cm}^{-1}$ (12 kOe) can be produced resulting in a maximum energy density of $420\,\text{kJ m}^{-3}$ (53 M GOe). Figure 2 presents the demagnetization curves $J(H)$ and $B(H)$ of such sintered Nd–Fe–B magnets at different temperatures. The temperature coefficients (TC) of the remanent polarization and of the coercivity amount to $-0.11\%\,\text{K}^{-1}$ and $-0.77\%\,\text{K}^{-1}$ in the temperature range of 20–100 °C.

2.2 Axial Field Die-pressed (AP) Net-shape Parts

The manufacturing of parts from isostatically pressed RE magnet blocks needs a lot of machining, which
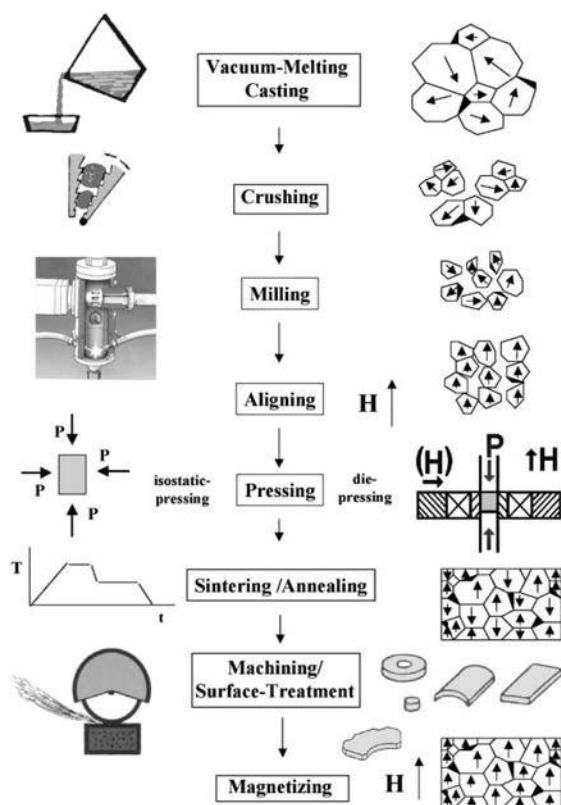
Figure 1
Principles of the different processing routes of sintered RE–TM magnets by powder metallurgy.
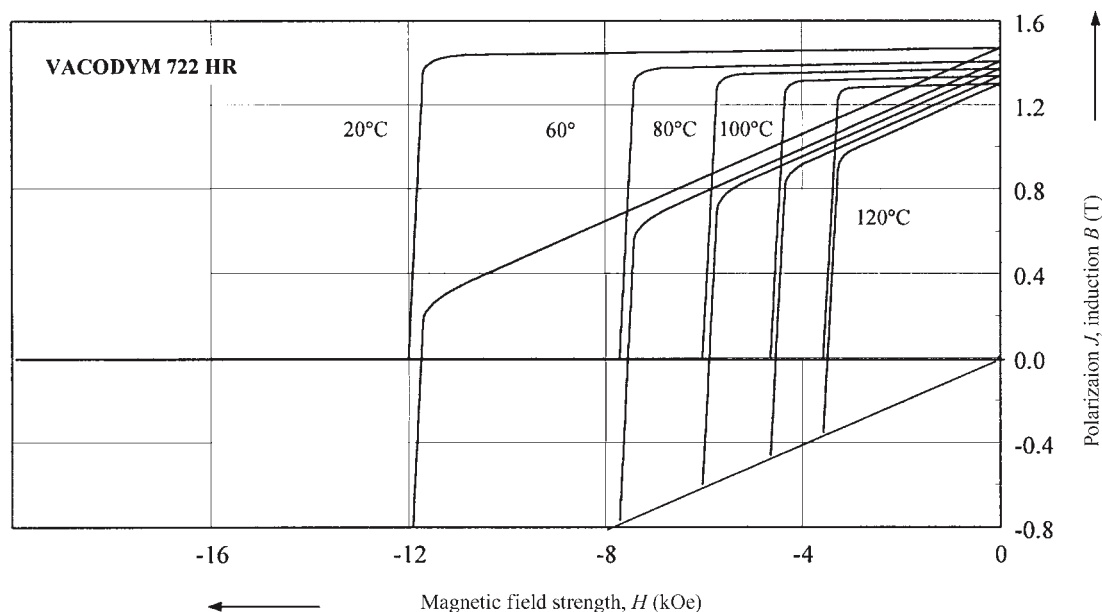
Figure 2
Demagnetization curves $J(H)$ and $B(H)$ at different temperatures of sintered Nd–Fe–B magnets, grade Vacodym 722 HR, with a maximum energy density of $420\,\mathrm{kJ\,m^{-3}}$ ($53\,\mathrm{M\,GOe}$), manufactured by cold isostatic or rubber isostatic pressing, respectively.

increases the processing costs. An alternative route is the production of net-shape parts by die-pressing. The alloy powder is filled into the cavity of a die, aligned by an axial magnetic field and compacted (see Fig. 1, right-hand side). Since the easy-axes of the powder-particles are aligned parallel to the pressing direction, the alignment is disturbed during the compaction. Hence, the remanent polarization of axial field die-pressed magnets is in general about 8% lower in comparison to isostatically pressed magnet blocks.

By axial field die pressing a large variety of dimensions and shapes can be manufactured economically. For instance, net-shape Nd–Fe–B magnets for motor applications achieve a remanent polarization of 1.08 T and a coercivity H_{cJ} (20 °C) of $28.7\,\mathrm{kA\,cm^{-1}}$ (36 kOe) and a maximum energy density of $225\,\mathrm{kJ\,m^{-3}}$ (28 M GOe). At 150 °C, the H_{cJ} of such magnets amount to $12\,\mathrm{kA\,cm^{-1}}$ (15 kOe). The TCs of the remanent polarization and of the coercivity amount to $-0.08\%\,\mathrm{K^{-1}}$ and $-0.51\%\,\mathrm{K^{-1}}$ in the temperature range of 20–100 °C. At room temperature such Nd–Fe–B magnet grades exceed sintered $Sm_2(Co, Cu, Fe, Zr)_{17}$ magnets, but at 200 °C the temperature stability of $Sm_2(Co, Cu, Fe, Zr)_{17}$ magnets is superior.

2.3 Transverse Field Die-pressed (TP) Near Net-shape Parts

Another compaction technology is pressing of parts in a transverse magnetic field (Fig. 1, right-hand side). In this case the alignment of the powder particles is not disturbed so strongly during compaction resulting in a remanent polarization similar to iso-statically pressed magnet blocks. The alignment co-efficients range from 94% to 98% for rectangular blocks and from 93% to 97% for near net-shape parts.

By transverse field die pressing mainly rectangular blocks or near net-shape parts can be manufactured. After sintering, the blocks are cut into thin magnet plates according to customer specifications. However, near net-shape parts will need some contour grinding before cutting. Hence the machining costs increase in comparison to axial field die-pressed magnets.

2.4 Rubber Isostatic Pressing (RIP)

Near net-shape magnet blocks with an excellent texture, i.e., an alignment coefficient similar to that of isostatically pressed blocks, are now manufactured by rubber isostatic pressing (Sagawa *et al.* 2000). The alignment of the precompacted alloy-powder particles in an elastic rubber mold is performed by a set of d.c. and a.c. field pulses with a maximum field strength of $24\,\mathrm{kA\,cm^{-1}}$ (30 kOe) for instance. Afterwards the aligned alloy powder is compacted by axial pressing. But the axial pressing forces are diverted homogeneously by the elastic rubber mold, so that the compaction occurs almost isostatically.
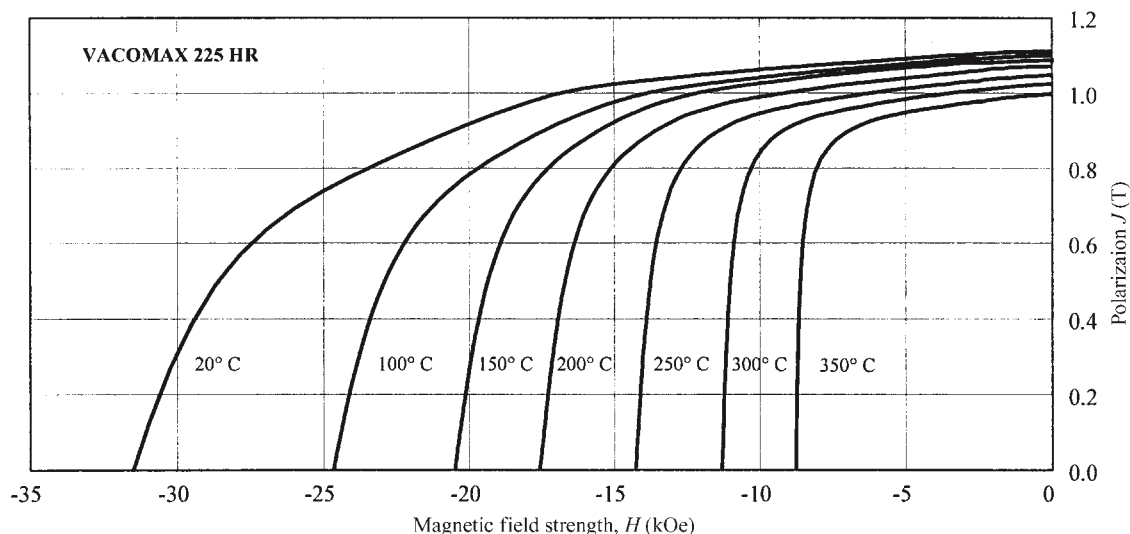
Figure 3
Demagnetization curves $J(H)$ at different temperatures of sintered $Sm_2(Co, Cu, Fe, Zr)_{17}$ magnets, grade Vacomax 225 HR, with a maximum energy density of $225\,kJ\,m^{-3}$ (28 M GOe), manufactured by cold isostatic pressing.

Optimization of the alloy composition, alloy powder milling, aligning and compaction technology, and sintering and annealing treatments now enables the commercial production of near net shape Nd–Fe–B parts with a maximum energy density of $420\,kJ\,m^{-3}$ (53 M GOe). Hence, sintered Nd–Fe–B magnets exploit the magnetic properties of the $Nd_2Fe_{14}B$ compound, $J_s = 1.6$ T, theoretical $(BH)_m = 509\,kJ\,m^{-3}$ (63 M GOe), to more than 80% and have gained a similar maturity as Sm–Co magnets.

3. Samarium–Cobalt Magnets

Although the temperature stability and the corrosion behavior of sintered Nd–Fe–B magnets can be improved by increasing the coercivity and by small additions of aluminum, copper, cobalt, etc., the temperature and corrosion stability of sintered $Sm_2(Co, Cu, Fe, Zr)_{17}$ magnets remains superior at temperatures above 200 °C. The demagnetization curves $J(H)$ at different temperatures of isostatically pressed magnets demonstrate, that at 20 °C the remanent polarization and the coercivity amount to 1.11 T and $25.3\,kA\,cm^{-1}$ (31.6 kOe) resulting in a maximum energy density of $225\,kJ\,m^{-3}$ (28 M GOe, Fig. 3). At 200 °C, $Sm_2(Co, Cu, Fe, Zr)_{17}$ magnets still achieve a coercivity H_{cJ} (200 °C) of $14\,kA\,cm^{-1}$ (17.5 kOe). Maximum continuous operating temperatures up to 350 °C are possible for such magnets. Recently developed $Sm_2(Co, Cu, Fe, Zr)_{17}$ magnets even achieve a straight demagnetization curve $B(H)$ at 550 °C (Walmer *et al.* 2000, see *Magnets: High-temperature*).

4. Concluding Remarks

Powder metallurgy enables the production of sintered net-shape RE–TM magnets for applications in motors, electronic devices, speakers, microphones, a large variety of sensors, bearings, couplings, NMR analysis equipment, MRI tomography, beam guidance devices, magnetic separation, switches, and relays (see *Magnetic Materials: Domestic Applications*).

In order to decrease the processing costs and improve the magnetic performance, the powder processing, aligning and compaction technologies, sintering and annealing treatments, as well as machining and coating processes need continuous optimization. Sintered Nd–Fe–B magnets with a maximum energy density of $420\,kJ\,m^{-3}$ (53 M GOe) have now come into commercial production, while by laboratory facilities a maximum energy density of $444\,kJ\,m^{-3}$ (55 M GOe) has been achieved (Kaneko 2000). In the year 2000, in total about 16000 t of sintered Nd–Fe–B magnets and 1000 t of sintered Sm–Co magnets were produced (Luo 2000).

Besides the production of anisotropic RE–TM magnets by sintering, some alternative processing routes have been developed and evaluated. These include: hot-pressing and hot-deformation of rapidly solidified flakes (Croat *et al.* 1984, Panchanathan 1995), hot-backward extrusion of radially aligned ring-magnets (Yoshikawa *et al.* 1994), hot-rolling (Shimoda *et al.* 1989, Yuri and Ohki 1994, see *Textured Magnets: Deformation-induced*), and vacuum plasma spraying (Overfelt 1986, Rieger *et al.* 2000). But the sintering technologies still meet the technical requirements very efficiently and economically.

Bibliography

Croat J J, Herbst J F, Lee R W, Pinkerton F E 1984 Pr–Fe and Nd–Fe-based materials: a new class of high-performance permanent magnets. *J. Appl. Phys.* **55**, 2078–82

Harris R, McGuiness P, Short C, Book D, Gutfleisch O, Fujita A, Verdier M, Nagel H 1994 The use of hydrogen in the processing and in the characterization of Nd–Fe–B magnets and alloys: an update. *Trans. Mater. Res. Soc. Jpn.* **14B**, 969–74

Herget C 1985 Metallurgical ways to NdFeB alloy—permanent magnets from Co-reduced NdFeB. In: Strnad K J (ed.) *Proc. 8th Int. Workshop on RE Magnets and their Applications.* University of Dayton, OH, pp. 407–22

Hirose Y, Hasegawa H, Sasaki S 1998 Microstructure of strip cast alloys for high performance NdFeB magnets. In: Schultz L, Müller K-H (eds.) *Proc. 15th Int. Workshop on RE Magnets and their Applications.* Dresden, Germany. Werkstoff-Informationsgesellschaft, Frankfurt, Germany, pp. 77–86

Kaneko Y 2000 Rare-earth magnets with high energy products. In: Kaneko H, Homma M, Okada M (eds.) *Proc. 16th Int. Workshop on RE Magnets and their Applications.* Sendai, Japan. Japan Institute of Metals, Sendai, Japan, pp. 83–98

Luo Y 2000 Further development of rare earth magnet industry in China. In: Kaneko H, Homma M, Okada M (eds.) *Proc. 16th Int. Workshop on RE Magnets and their Applications.* Sendai, Japan. Japan Institute of Metals, Sendai, Japan, pp. 31–40

Overfelt R A, Anderson C D, Flanagan W F 1986 Plasma sprayed $Fe_{76}Nd_{16}B_8$ permanent magnets. *Appl. Phys. Lett.* **49**, 1799–801

Panchanathan V 1995 Magnequench magnets status overview. *J. Mater. Eng. Perf.* **4**, 423–9

Rieger G, Wecker J, Rodewald W, Sattler W, Bach F W, Duda T, Unterberg W 2000 Nd–Fe–B permanent magnets (thick films) produced by a vacuum-plasma-spraying process. *J. Appl. Phys.* **87**, 5329–31

Rodewald W, Blank R, Wall B, Reppel G W, Zilg H D 2000 Production of sintered Nd–Fe–B magnets with a maximum energy density of 53 MGOe. In: Kaneko H, Homma M, Okada M (eds.) *Proc. 16th Int. Workshop on RE Magnets and their Applications.* Sendai, Japan. Japan Institute of Metals, Sendai, Japan, pp. 119–26

Sagawa M, Nagata H, Watanabe T, Itani O 2000 Rubber isostatic pressing (RIP) of powders for magnets and other materials. *Mater. Des.* **21**, 243–9

Shimoda T, Akioka K, Kobayashi O, Yamagami T, Ohki T, Miyagawa M 1989 Hot-working behavior of cast Pr–Fe–B magnets. *IEEE Trans. Magn.* **25**, 4099–104

Yoshikawa N, Yamada H, Iwasaki Y, Nagata K, Kasai Y 1994 Magnetic properties and multi-pole magnetizability of a huge radially oriented Nd–Fe–B ring magnet for EV driving motors. In: Manwaring C A, Jones D G E, Williams A J, Harris J R (eds.) *Proc. 13th Int. Workshop on RE Magnets and their Applications.* University of Birmingham, UK, pp. 635–44

Yuri T, Ohki T 1994 Crystal alignment in Pr–Fe–B hot-rolled magnets. In: Manwaring C A, Jones D G E, Williams A J, Harris J R (eds.) *Proc. 13th Int. Workshop on RE Magnets and their Applications.* University of Birmingham, UK, pp. 645–54

Walmer M S, Chen C H, Walmer M H, Liu S, Kuhl E 2000 Magnetic hardening, thermal stability and microstructures for a new class of Sm-TM high temperature magnets. In: Kaneko H, Homma M, Okada M (eds.) *Proc. 16th Int. Workshop on RE Magnets and their Applications.* Sendai, Japan. Japan Institute of Metals, Sendai, Japan, pp. 119–26

W. Rodewald
Vacuumschmelze GmbH, Hanau, Germany

Metal Evaporated Tape

The first generation of commercial Metal-Evaporated (ME) tapes was introduced in 1989 for the Hi-8 video system (Chiba *et al.* 1989, Hokkyo *et al.* 1993) and consisted of an oblique-deposited Co–Ni–O thin film tape. This was followed by the scoopman digital recorder with a stamp-sized cassette (Hinemo and Katahu 1994). In 1993, a new digital video system was proposed (Digital Video Cassette (DVC)) (Yamamitsu *et al.* 1995). This system uses an improved ME tape with a 4 dB higher C/N (Futamoto and Honda 1994). Besides Co–Ni–O-deposited tapes, Co–O films with oblique anisotropy appeared on the market as the tape for DVC (Kawana *et al.* 1995). It is also planned that this type is used for large-capacity data storage tape for computer systems. More than $1\,Gbin^{-2}$ is being developed (Ishida *et al.* 2000) in a helical scanning tape storage system based on Co–O thin film material.

Important in system design is the trade-off between the amount of data reduction, playing time, and cassette size. For both the Hi8 and DVC systems, equivalent metal particle tapes (MP tapes) have been developed which meet these requirements. There is an ongoing competition between MP and ME tapes. In general, ME tape gives a promising signal-to-noise ratio and is a potential candidate for future applications if much smaller tracks will be written (Draaisma *et al.* 1999).

Another advantage of ME tape is that the recording layer thickness can be reduced below 100 nm without changing the magnetic properties too much. Moreover, the properties can be tailored with the deposition parameters of the coating machine. ME tape also has a low noise because of the decreased film thickness (Kagawa *et al.* 1997). The need for extremely small sizes combined with long playing times requires a tape with a very high signal-to-noise ratio and very thin magnetic and total tape thickness. In 1998, a very important paper was published discussing the key issues in the design of magnetic tapes (Richards and Charrock 1998).

Although the paper is not specifically focused on ME tape, most of the issues discussed are directly applicable to it. In the next paragraphs, only the basic
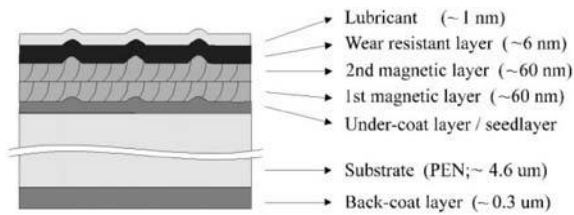
Figure 1
Schematic cross section of an ME tape

Figure 2
Physical principle of the shadowing effect. (a) shows the actual shadowing of the deposited atoms impinging under an angle α with the substrate. In (b) the columnar inclination angle β is shown.

properties of the oblique-deposited magnetic layer, the related microstructure, and the magnetic behavior of ME tape will be discussed. Apart from the development of the magnetic layer, numerous other aspects have also to be considered such as tape mechanics, tape transport, friction and wear, head design, long term stability, etc.

In Fig. 1, a cross-section of an advanced ME tape is shown schematically.

In Fig. 1, two magnetic layers are presented. In recent years ME tape manufacturers have experimented with several magnetic coating layers. One of the reasons is an increased coercivity (by magnetic coupling) of so-called double layers. In Ashton and Thompson (1998), several possibilities are shown which can enhance the magnetic properties. Up to four magnetic sublayers were even reported in Kawana *et al.* (1995).

1. Oblique Evaporation and Columnar Separation

When depositing a thin magnetic layer, by either sputtering or evaporation, a columnar morphology is usually observed (Smith 1995, Abelmann and Lodder 1997). Since these columns are in close contact with each other, a strong exchange coupling between adjacent columns is present resulting in an almost instant switching behavior of the film. This is highly unfavorable for a magnetic recording medium since it prevents writing a stable bit structure with sharp transitions in such a medium, so inducing a columnar separation is necessary to enable the recording of information in a thin magnetic film. One possibility for obtaining this columnar separation is to make use of the so-called shadowing effect as schematically presented in Fig. 2.

From Fig. 2(a) it is observed that due to the height of the initial nuclei, a "shadow" is thrown behind these nuclei and therefore the rest of the vapor flux can not reach the area directly behind them. Since this flux is deposited under an angle with respect to the normal of the substrate, subsequent stages of film growth will result in a tilted columnar morphology, which is schematically shown in Fig. 2(b). Here the columns make an angle β with respect to the normal of the substrate. The relation between both angles is
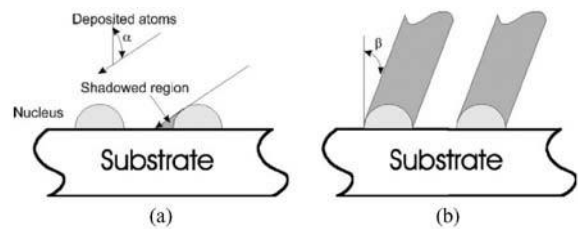
very much determined by the process conditions, i.e., substrate temperature, base pressure, energy of the arriving atoms, etc. (see, e.g., Abelmann and Lodder 1997). In principle, both sputtering (Bijker *et al.* 1997) as well as evaporation can be used in exploiting the effect of shadowing.

In general, atoms tend to migrate across the substrate surface once they have become adatoms. Therefore, the oblique incidence effect might be overcome by the transfer of thermal energy of the substrate to these adatoms, once the substrate temperature becomes high. Hence, low substrate temperatures are beneficial for this type of process. The thin-film morphology of an oblique-deposited magnetic layer with magnetically uncoupled grains can lead to relatively high coercivities. It is known from literature (Feuerstein *et al.* 1985) that the deposited materials iron, cobalt, and nickel show a remarkable increase in coercivity as a function of the angle of incidence (α in Fig. 2). Such an example is shown in Fig. 3. Similar results were reported in Kita *et al.* (1981) for $Co_{62.5}Fe_{37.5}$ and $Co_{30}Ni_{30}$ as well.

The sharp increase in longitudinal coercivity at a high angle of incidence is believed to arise from a strongly reduced exchange coupling between the columns.

2. Manufacturing Process

To produce magnetic tapes, a mass-production equivalent of the mentioned static-angle experiments is schematically shown in Fig. 4.

In this figure, an unwinding and winding reel are shown, which guide the base film over the evaporation source. Therefore, the angle α (from Fig. 2) is changed from 90° to 60° (as indicated in Fig. 4). Thus, instead of making a fixed angle with the atom flux with respect to the substrate, a continuously varying angle of incidence (CVI) is introduced. The use of evaporation has led to the general term metal-evaporated tape or ME tape. The CVI method results in the typical morphology for ME tape, which is shown in Fig. 5.
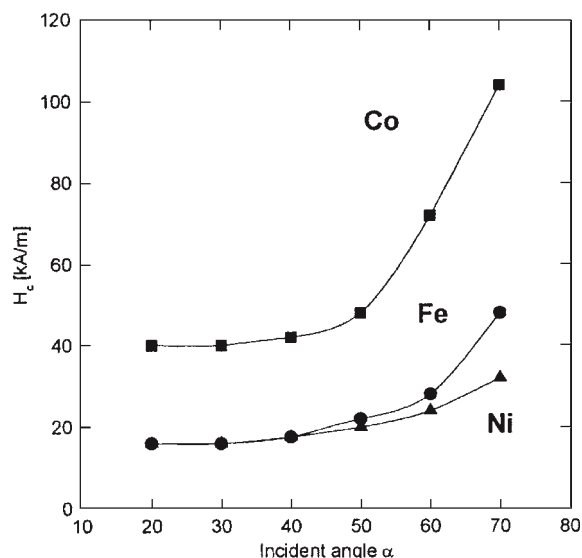
Figure 3
Effect of the angle of incidence of the vapor flux of the three ferromagnetic elements (after Feuerstein *et al.* 1985).
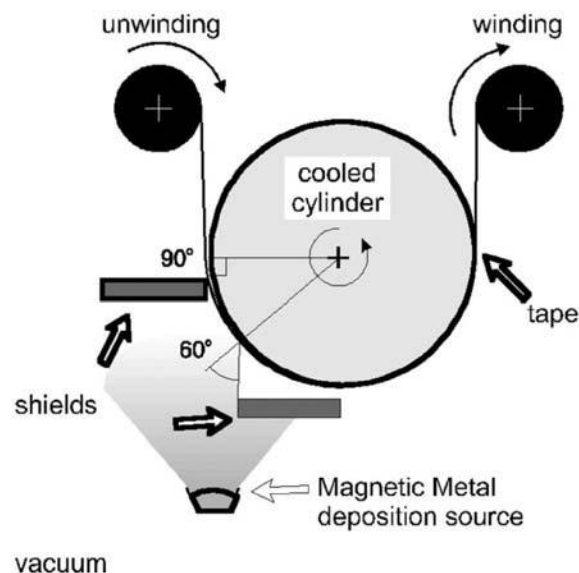
Figure 4
Principle of ME tape mass production.

Comparing the coating thickness and coercivity of ME and metal particle (MP) tapes, it can be concluded that thinner coatings can be achieved with usually better coercivities. Hence, according to the Williams and Compstock (1971) model, smaller
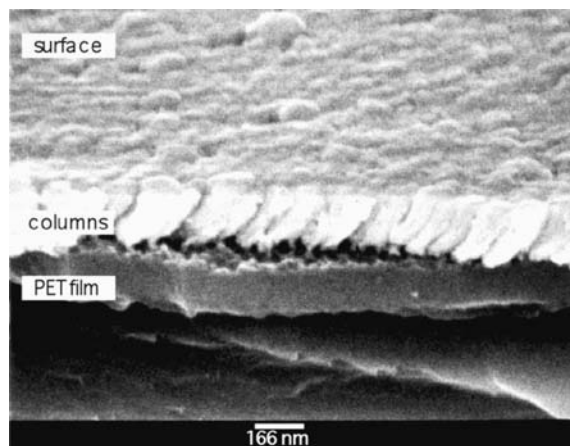
Figure 5
Scanning electron microscope image of an experimental ME tape showing the banana-shaped columnar structure (after Bijker 1998).

values of the transition width (between two written bits) can be achieved. However, recently the particulate coatings have also been improved by developing better particles, which can be better aligned at smaller coating thickness, which have eventually resulted in comparable recording properties (see, e.g., Lalbahadoersing *et al.* 1997, Richter and Veitch 1995). Differences in easy-axis (MP (in-plane) and ME (tilted), and reversal mechanism of MP and ME tape might correspond with a smaller transition length, which results in a better overwrite behavior for ME tape (Lalbahadoersing *et al.* 1997). From the above, the principal process of making ME tapes was made clear.

Many publications can be found about this subject and more detailed information of the subject can be acquired from Luitjens *et al.* (1996), Onodera *et al.* (1996), Kunieda *et al.* (1985), Richter (1993a). Apart from the development of the magnetic thin film or coating, numerous other aspects have also to be considered. These involve issues such as tape mechanics, tape transport, friction and wear, head design, long term stability, etc. When comparing ME tape with the more conventional particulate tape (e.g., Cr_2O_3 and Fe_2O_3), the manufacturing process is the most striking point of difference. As we explained above, ME tape is produced via an evaporation process. In Feuerstein and Mayer (1984), Feuerstein *et al.* (1985), and Wright (1987), several aspects of the vacuum deposition process are shown. In Fig. 6, a cross-section of a typical deposition machine is shown (taken from Feuerstein and Mayer 1984).

In Fig. 6, the base film is unwound from reel (a) via an intermediate coating station (b), towards the oblique deposition zone (c). Here the electron beam (e)
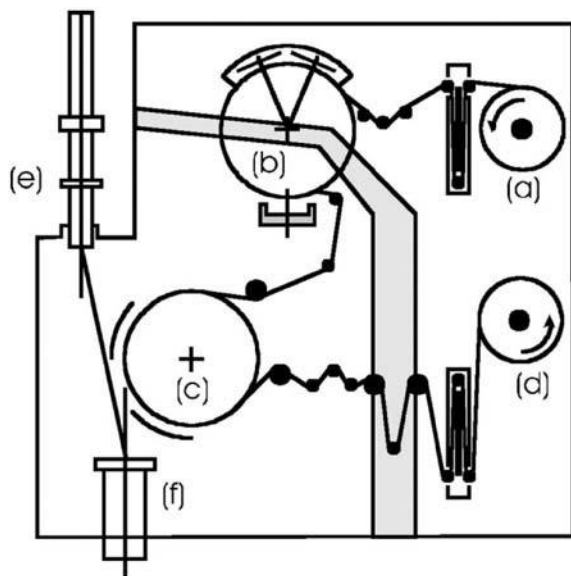
Figure 6
Schematic cross section of a production roll coater. See text for explanation of the items.

evaporates the magnetic material in the crucible (f). Finally, the tape is wound onto a reel (d). Furthermore, a separation between the unwinding zone and the deposition zone is necessary to sustain a reasonable pressure in the deposition zone. The separation is indicated in the figure by the grey area. Some simple calculations can be undertaken to calculate the necessary web speed and the deposition rate. The base material is typically supplied with a width of 1.20 m and a length of 10 km. For these base film lengths, a total coating time of around a few hours is applied. In total, about one hour is needed for pumping, accelerating the web to its full speed, heating up the evaporation source, etc. So, in approximately three hours, the total web length should be coated, which results in a web speed of around $1 \, \text{ms}^{-1}$ or $60 \, \text{m} \, \text{min}^{-1}$. Together with the drum diameter of one meter, and an opening angle of $30°$, the necessary deposition rate can be calculated to be $\sim 0.5 \, \mu\text{m} \, \text{s}^{-1}$. In 1999, Maezawa *et al*. (1999) published data of Co–O tape prepared at deposition rates of $1 \, \mu\text{m/s}$. Such deposition rates require e-beam evaporation sources with astronomically large power consumption.

Usually two e-beam guns are installed in a coater with a web width of 1.20 m (see Leybold 1992). These would be of around 0.5 MW each. The crucible also has a width of around 1.20 m, usually made of a Al_2O_3 ceramic. These large deposition rates require the coating material to be constantly replenished. In the early designs, a rod feed system was designed, but in later designs slugs of coating material were fed via

a vibration system into the melt. This allows the use of a crucible, which can be parked in a separate vacuum chamber during charging of the vacuum machine. This eliminates a complete cooling down of the crucible and saves time. To obtain a homogeneous melt, the e-beams are swept over the melt with a frequency of about 400 Hz. Winding a thin polymer substrate in vacuum conditions is not trivial, let alone in a bi-directional manner. Base films do not necessarily have similar winding characteristics in air compared to vacuum conditions. As modern substrates tend to become thinner and thinner, more sophisticated winding systems are needed. Usually the drum and the winding and unwinding reels are controlled by measuring the torque exerted on the base film. To prevent wrinkling of the base film a slightly V-shaped roll, or capstan, is present in the winding system. Furthermore, when such large rolls of base film are unwound in a vacuum system, they tend to release considerable amounts of water vapor.

3. Microstructure and Magnetic Structure

From Fig. 3 it can be concluded that the necessary high coercivity can only be obtained by oblique deposition if the angle of incidence is very high. Consequently, that is also the area in which the deposition process becomes very inefficient. To overcome this problem depositions are made at smaller angles but with the addition of oxygen during deposition. The result is a very complicated microstructure (see Fig. 7) but with an increase of the coercivity.

The incorporation of the oxygen is hard to understand because companies do have their own specific processes, which are not published. However, in, e.g., Kunieda *et al*. (1985) and Hokkyo *et al*. (1993), the general trends are indicated: an increase in oxygen
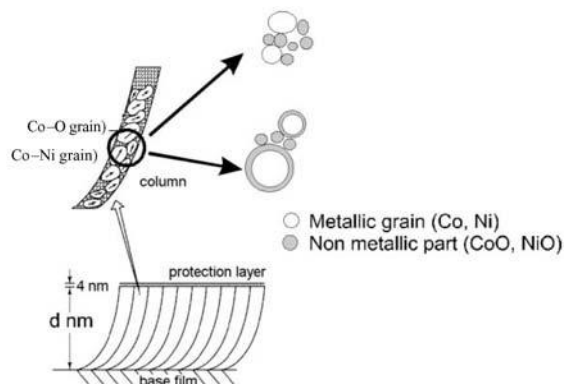
Figure 7
Banana-shaped columnar morphology of ME tape of thickness d. Two possible microstructures are also drawn.

flow, whilst keeping the deposition rate constant, will lead to an increase in longitudinal coercivity (H_c) and a decrease in apparent saturation magnetization (M_s). From Gau *et al.* (1986), a local optimum in H_c as a function of the oxygen flow can be observed. A similar behavior has been observed by Bijker *et al.* (1999).

As can be seen in Fig. 7, apart from an oblique banana-shaped columnar morphology, which is due to the specific deposition geometry, the columns can either exist of ferromagnetic grains in close contact with the nonmetallic grains, or apart from the presence of nonmetallic grains, the ferromagnetic grains have a small oxide skin around them. The oxidation process is most likely diffusion limited (Mujumdar *et al.* 1986), and therefore could explain the correlation between the used deposition rate and the oxygen content in the upper part of the ME tapes which is accompanied by the larger grains sizes in this part of the film as well. This is also reflected by the H_c of the films, which become larger with increasing oxide-shell thickness, thereby reducing the magnetic coupling between the ferromagnetic grains (Bijker 1998). In general, it is not straightforward to relate the microstructure of ME tapes to the switching behavior of the layer. Another distinct property of ME tape is the oblique easy axis of the tape. The easy axis of magnetization is known to exhibit a strong correlation with both the oxygen flow and the deposition geometry. More oxygen leads to increased columnar inclination angles (Nagao *et al.* 1991, Bijker 1998).

The strong relation on the deposition geometry was shown in, e.g., Ogawa *et al.* (1994) and Yano *et al.* (1994). The magnetic anisotropy (see *Magnetic Films: Anisotropy*) is found to be largely due to the shape anisotropy of the columns (see, e.g., Richter and Hibst 1991), although some contribution from the crystal anisotropy may be expected in view of the presence of small h.c.p. cobalt crystallites. The question remains, however, of whether the crystal anisotropy can contribute significantly since all the observed crystals seem to be very small ($\sim 5\,\mathrm{nm}$) and randomly oriented. No clear texture was observed from the microstructural analysis. From the Auger depth-profiling experiments, it becomes clear that an effective magnetization distribution over the film thickness must exist. When the packing density distribution is known as a function of the film thickness, the effective magnetization profile could be calculated. However, judging from the oxygen profile alone, a maximum magnetization is reached in the center section of the tape. A similar conclusion was made in Richter (1993b), although assessed with a combination of recording and VSM measurements. Apart from a distribution of the saturation magnetization, the longitudinal coercivity should also have a distribution over the thickness of the tape, since the columns are better separated in the lower parts of the tape by the geometry of the deposition process. The

aid of oxygen leads to a better lateral decoupling of the columns in the upper parts of the tape.

4. Anisotropy and Recording

The anisotropy is strongly related to the morphology and microstructure of the deposited film. The extreme uniaxial anisotropy associated with the mesoscopic columnar structure in ME tapes gives rise to an oblique recording process which is close to one-dimensional in nature (Nouchi *et al.* 1986).

An oblique easy-axis angle gives rise to asymmetric pulse shapes. Since the columnar structure of ME tape is asymmetrical with respect to the recording head field, it might be expected that the recording behavior is somewhat different in both recording directions. The output spectrum of the Hi8 ME tape is shown in Fig. 8, where indeed a difference in output between the two recording directions is observed.

Similarly, the good and bad recording directions can be understood by considering the projection of the head fields to the oblique medium easy axis in the write process. If writing is assumed to occur at the trailing edge of the head where the field is equal to H_c, in the good direction of head-to-tape motion, the magnitude of the projected total field gradient is larger, leading to sharper transitions (and thus larger output) than the bad direction. The effect of recording in the good and bad direction on the recorded bits can be studied with magnetic force microscopy (MFM) observations.

In Fig. 9, written bits are shown for recording in both directions (see also Luitjens *et al.* 1996, Porthun *et al.* 1998). The same current is used for writing the bits. The distance between transitions (= bit length) is about 0.33 um. The good direction shows sharp bits and track edges (Fig. 9, left). In the less favorable
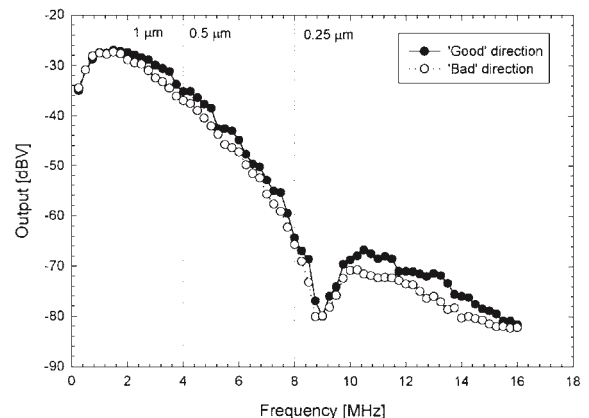
Figure 8
Difference in recording output depending on the recording direction of the Hi8 ME tape.
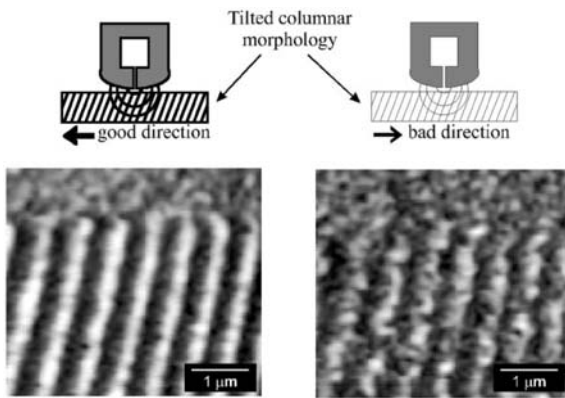
Figure 9
MFM measurements of the recorded magnetization pattern of the Hi8 ME sample in both recording directions. On the left are the bit transitions in the good recording direction; the right hand side shows the transitions in the bad recording direction.

direction, less sharp transitions and interrupted bits are visible (Fig. 9, right). The intrinsic magnetic structures beside the tracks have more or less the same dimensions as the written bits.

The direction, which leads to a higher output, is generally referred to as the good direction. Subsequently the other direction is called the bad direction. The difference is about 4.2 dBV (see Fig. 8). Apart from the effect on output, the read-back pulses are also known to be asymmetric (Krijnen *et al.* 1988).

From Fig. 9 it becomes clear that the transition regions of the bits written in the good direction are far less irregular compared to the image on the right hand side where the bits are written in the bad recording direction. On the right hand side, some sub-domains are visible within the written bit structure and the bits are connected to the outside domain pattern. These irregularities contribute to the lower read-back voltage in the bad recording direction.

Various microscopic models have been developed, e.g., Richter *et al.* (1993). Most macroscopic models of the magnetic reversal process give rise to inverse cosine dependence. Incoherent reversal can be incorporated in a Stoner-Wohlfarth model by appropriate truncation of the switching asteroid (Cramer 1993, Lalbahadoersing 1999). In the limit of very strong interactions, mean-field models are not appropriate. This does not seem to be the case for ME. A key feature which needs to be incorporated, however, are the cooperative interactions (which give rise to very sharp transitions). The results of the different numerical simulations are in good agreement with each other and confirm the earlier-mentioned one-dimensional nature of the recording process in these materials. Both the one-dimensional and the more

sophisticated models indicate that there is little or no improvement in the recorded output signal in ME tape associated with the transition from longitudinal to oblique recording (Stupp *et al.* 1994, Richter *et al.* 1993, Tagawa *et al.* 1991, Cramer 1993).

In Hokkyo *et al.* (1993), a clear relation was demonstrated between the noise level of an ME tape and the oxygen flow. When more oxygen is incorporated into the film, the cobalt grains become smaller and a simultaneous increase of the coercivity suggests a better decoupled structure. Thus, the more oxygen is incorporated, the more cobalt grains per unit of volume exist. From Mallinson (1993, p. 116), the signal-to-noise ratio (SNR) for thin film media is shown to be:

$$\mathrm{SNR} = \tfrac{1}{2} n W \delta \lambda \ (\mathrm{dB}) \qquad (1)$$

with n being the number of particles per unit of volume, W the track width, δ the medium thickness, and λ the recording wavelength. From Eqn. (1) it becomes clear that increasing the number of particles per unit volume will lead to enhanced SNRs. Thus if the art of making fine decoupled cobalt particles is mastered, it will lead to an increase in SNRs.

Some authors have addressed the question of whether there exists exchange coupling over the length of the column, so over the thickness of the tape. Some clue is given by measurements of the activation volume (Richter 1993a, Suzuki and Tajiri 1997). Although care has to be taken with the use of a quantity like the activation volume, it might contribute in the discussion about the role of the exchange coupling. In both articles it was found that switching volumes are generally larger than the crystallites in the columns but smaller than the column size as a whole.

5. Co–Ni(–O) and Co(–O) ME Tape

In the early ME tape, Co–Ni–O is always used as the thin film material. The material is deposited using a continuously varying angle of vapor incidence in an oxygen environment, which leads to the mesoscopic banana-shaped column morphology as shown in Fig. 5. The dependence of the saturation magnetization M_s, coercivity H_c, signal, and noise on the process parameters is discussed in Hokkyo *et al.* (1993). There is a direct relationship between H_c and the O content (due to the increased decoupling of grains) and an inverse relationship between M_s and the O content (due to a reduction in the cobalt content and an increase in the CoO content). To further study the relation between deposition angle, oxygen concentration, magnetic properties, and recording performance, a mini roll coater has been developed (ten Berge *et al.* 1994) and basic experiments have been performed. Auger depth profiling showed that the Co/Ni ratio is constant over the total thickness of the film.

The general picture that emerges from the TEM and XRD analysis is that the ME tapes consist of a banana-shaped columnar structure where small crystallites are the building blocks of the entire column. This has also been established in literature (see, e.g., Hokkyo *et al.* 1993). A schematic representation is given in Fig. 7 as a result of combined TEM and XRD analysis. A similar sketch can be found in Kaneda (1997). In Fig. 10 a TEM cross section is given from a Hi8 Co–Ni(–O) ME tape. From the darkfield observation, the more-or-less homogenous distribution of the small crystals can be observed.

The O concentration is enhanced at the top (30 nm) and the bottom (10 nm). The relation between the deposition rate, the magnetic properties, and structural feature has been studied by ten Berge *et al.* (1994),

Bijker (1998), Bijker *et al.* (1997), and Tohma *et al.* (1997). Between 1993 and 2001, not only Co–Ni–O tapes but also Co–O tapes have been prepared. The so-called advanced ME tape has been produced by oblique deposition of Co–O layers (Futamoto and Honda 1994, Yoshida *et al.* 1994, Sugita *et al.* 1999, Ishida *et al.* 2000). Experimental observations have shown that these films have a microstructure similar to the Co–Ni–O films: an hcp cobalt phase and Co–O crystals of about 5 nm are found. The easy axis of magnetization is about 50 degrees from the tape normal.

These tapes have shown sharp transitions at 100 kfrpi (kilo flux reversal per inch). The high recording densities are a result of the microstructure as well as the higher M_s values (due to the higher cobalt
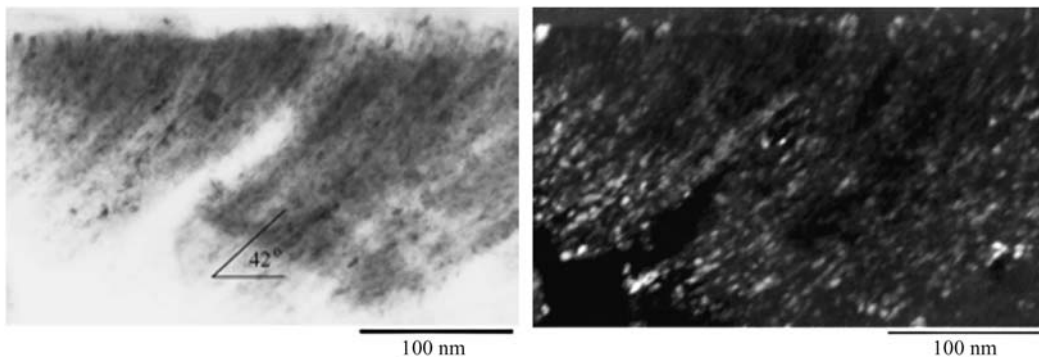
Figure 10
Cross sectional TEM views of a Hi8 ME tape. Both the brightfield (left) and the darkfield (right) are shown. In the brightfield view, the initial columnar inclination angle is also indicated.
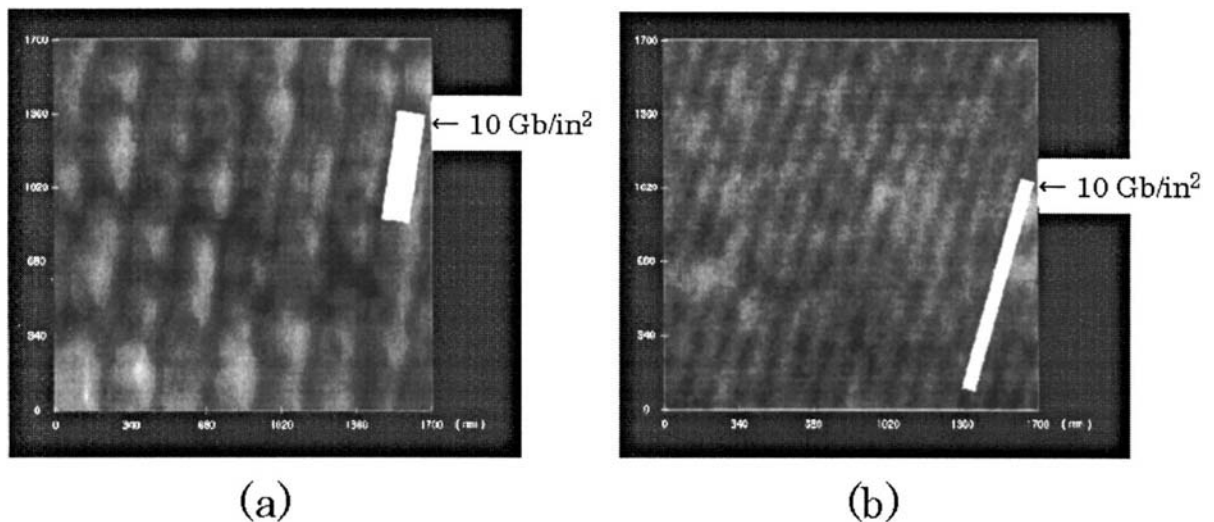
Figure 11
MFM images of the recorded magnetization at 200 kfrpi (a) and 400 kfrpi (b) (after Ishida *et al.* 2000).

content) in these media. In Fig. 11 MFM images are shown (Ishida *et al.* 2000) of the magnetization patterns taken at 200 and 400 kfrpi. The white rectangular regions indicate the bit size corresponding to an areal density of $10\,G\,b\,in^{-2}$. Experimental work has been started (2000) by studying the effect of a CoO underlayer for the Co–O obliquely deposited films. The granular texture of the underlayer promotes separation between the obliquely grown columns and also decreases the size of the columns (Tohma *et al.* 1997).

The difference between Co–Ni–O and Co–O tape is that the latter has higher remanent magnetization and crystalline anisotropy (and thus coercivity). This results in better read/write characteristics and excellent recording performance. This is also due to the very thin DLC protective coatings, which can now be prepared (Yoshida *et al.* 1994, Yoshida *et al.* 1995, Shinohara 1994).

See also: Magnetic Recording: Flexible Media, Tribology; Magnetic Recording: Patterned Media; Magnetic Recording Technologies: Overview; Magnetic Recording: VHS Tapes; Metal Particle versus Metal Evaporated Tape; Micromagnetics: Basic Principles

Bibliography

Abelmann L, Lodder J C 1997 Oblique evaporation and surface diffusion. *Thin Solid Films* **305**, 1–21

Ashton G R, Thompson S J 1998 NML Thin Film Media Final Report, http://www.nta.org/Publications/TechnicalReports/MediaEvaluationAndRD/ThinFilmMediaFinal/

Bijker M D 1998 Oblique sputtered and evaporated magnetic thin films for tape recording. PhD thesis, University of Twente, Enschede, The Netherlands

Bijker M D, Abelmann L, Lodder J C, Popma T J A 1999 The role of oxygen in obliquely deposited tapes. *J. Magn. Magn. Mater*. **193**, 357–61

Bijker M D, Visser E M, Lodder J C, Popma T J A 1997 Oblique sputtered cobalt and Co80Ni20 thin films. *J. Magn. Soc. Jpn*. **21**, 169–72

Chiba K, Sato K, Ebine Y, Sasaki T 1989 Metal-evaporated tape for high band 8 mm video system. *IEEE Trans. Consumer Electron* **35**, 421–8

Cramer H A J 1993 On the hysteresis and the recording process in magnetic media. Ph.D. Thesis, University of Twente, Enschede, The Netherlands

Draaisma E A, Cumpson S R, Jansen T P H G, Hidding P, Luitjens S B 1999 Performance of advanced tapes with DigaMax thin film heads. *J. Magn. Magn. Mater*. **193** (1–3), 384–7

Feuerstein A, Lämmermann H, Mayer M, Ranke H 1985 Videotape manufacture by high-vacuum evaporation aspects of machine technology. *Vacuum* **7**, 277–81

Feuerstein A, Mayer M 1984 High-vacuum evaporation of ferromagnetic materials—a new production technology for magnetic tapes. *IEEE Trans. Magn.* **20** (1), 51–6

Futamoto M, Honda Y 1994 Microstructures and recorded magnetization microstructures of cobalt-based thin film recording media. *J. Magn. Soc. Jpn.* **18** (S1), 485

Gau J S, Spahn R G, Majumdar D 1986 The Role of oxygen in oblique-deposited CoNi thin films. *IEEE Trans. Magn.* **MAG-22** (5), 582–4

Hinemo T, Katahu T 1994 High-density recording magnetic tape recording by nontracking method. *J. Magn. Magn. Mater*. **134**, 255–61

Hokkyo J, Suzuki T, Chiba K, Sato K, Arisaka Y, Sasaki T, Ebine Y 1993 Co-Ni obliquely evaporated tape and its magnetic and recording characteristics. *J. Magn. Magn. Mater*. **120**, 281–5

Ishida T, Tohma K, Yoshida H, Shinohara K 2000 More than 1 Gb/in^2 recording on obliquely oriented thin film tape. *IEEE Trans. Magn.* **36** (1), 183–8

Kagawa K, Okabe A, Yoshida A, Iii T, Sugawara N, Takiguchi M, Okazaki Y, Hayashi K 1997 Recording performance of the combination of magnetoresistive head and thin metal-evaporated tape. *J. Appl. Phys.* **81** (8), 4527–9

Kaneda Y 1997 Tribology of metal-evaporated tape for high-density magnetic recording. *IEEE Trans. Magn.* **33**, 1058–68

Kawana T, Onodera S, Samoto T 1995 Advanced metal-evaporated tape. *IEEE Trans. Magn.* **31** (6), 2865–70

Kita E, Tagawa K, Kamikubota M, Tasaki A 1981 Magnetic recording media prepared by oblique incidence. *IEEE Trans. Magn.* **MAG-17** (6), 3193–5

Krijnen G, Luitjens S B, de Bie R W, Lodder J C 1988 Correlation between anisotropy direction and pulse shape for metal-evaporated tape. *IEEE Trans. Magn.* **24** (2), 1817–9

Kunieda T, Shinohara K, Tomago A 1985 Metal-evaporated video tape. *J. Inst. Electron. Radio Engrs.* **55** (6), 217–22

Lalbahadoersing S 1999 Overwrite and track edges in high-density tape recording: simulation and analysis. PhD Thesis, University of Twente, Enschede, The Netherlands

Lalbahadoersing S, Groenland J P J, Luitjens S, Lodder J C 1997 Comparison of recording properties of ME tape and thin MP tape with respect to overwrite behaviour. *IEEE Trans. Magn.* **35** (5), 3061–3

Leybold Information Brochure 1992 Vacuum web coating, 13-230.02

Luitjens S B, Stupp S E, Lodder J C 1996 Metal-evaporated tape: state of the art and prospects. *J. Magn. Magn. Mater*. **155**, 261–5

Maezawa Y, Yoshida H, Shinohara K 1999 Characteristics of ME tape made at 1 um/s deposition rate. *IEEE Trans. Magn.* **35** (5), 2688–90

Mallinson J C 1993 *The Foundations of Magnetic Recording*. Academic Press, New York

Mujumdar D, Gau J S, Spahn R G 1986 Oxidation behavior of obliquely deposited Co-Ni magnetic thin films. *Thin Solid Films* **145**, 241–7

Nagao M, Yasunaga T, Dohshita H, Kanazawa M, Miura T 1991 Effect of oxygen gas on columnar structures and magnetic properties of Co-O evaporated thin film. *J. Magn. Soc. Jpn*. **15**, (S2), 915–20

Nouchi N, Yoshida H, Shinohara K, Tomago A 1986 Analysis due to vector magnetic field for recording characteristics of ME tape. *IEEE Trans. Magn.* **22** (5), 385

Ogawa Y, Yano A, Kitagaki N, Mizumura T, Okuwaki T, Wakai K 1994 Recording characteristics of obliquely evaporated thin Co-O films. *J. Magnics Soc. Jpn.* **18** (S1), 413–34

Onodera S, Kondo H, Kawana T 1996 Materials for magnetic tape media. *MRS Bull.* **21** (9), 35–41

Porthun S, Abelmann L, Lodder J C 1998 Magnetic force microscopy of thin-film media for high-density magnetic recording. *J. Magn. Magn. Mater*. **182** (1–2), 238–73

Richards D B, Charrock M P 1998 Key issues in the design of magnetic tapes for linear systems of high track density. *IEEE Trans. Magn.* **34** (4), 1878–82

Richter H J 1993a An analysis of magnetization processes in metal-evaporated tape. *IEEE Trans. Magn.* **29** (1), 21–33

Richter H J 1993b Media requirements and recording physics for high-density magnetic recording. *IEEE Trans. Magn.* **29**, 2185

Richter H J, Hibst H 1991 Magnetic characterization of ME tapes: the angular remanence curve. *J. Magn. Magn. Mater.* **95**, 118–22

Richter H J, Veitch R J 1995 Advances in magnetic tapes for high-density information storage. *IEEE Trans. Magn.* **31** (6), 2883–8

Richter H J, Veitch R J, Hibst H, Schildberg H P 1993 Distribution profile of magnetization in ME tape. *IEEE Trans. Magn.* **29** (6), 3754–6

Shinohara 1994 On the durability of carbon-coated ME video tape. *J. Magn. Soc. Jpn.* **18** (S1), 299

Smith D L 1995 *Thin-Film Deposition—Principles and Practice.* McGraw-Hill, New York, Chap. 5

Stupp S E, Cumpson S R, Middleton B K 1994 A quantitative multilayer recording model for media with arbitrary easy-axis orientation. *J. Magn. Soc. Jpn.* **18** (S1), 145

Sugita R, Watahiki T, Muranoi T, Ishida T 1999 Magnetization reversal mechanism of Co-O films with oblique anisotropy. *J. Appl. Phys.* **85** (8), 47144

Suzuki T, Tajiri S 1997 Temperature effect on magnetization stability of thin recording films. *J. Magn. Soc. Jpn.* **21** (S2), 309–12

Tagawa I, Shimizu Y, Nakamura Y 1991 Relationship between H_K distribution of media and high-density recording characteristics. *J. Magn. Soc. Jpn.* **15** (S2), 827

ten Berge P, Abelmann L, Lodder J C, Schrader A, Luitjens S B 1994 Oblique evaporation of $Co_{80}Ni_{20}$ part II: continuously varying angle of vapor incidence. *J. Magn. Soc. Jpn.* **18** (S1), 295–8

Tohma K Siugita R Yoshimoto K Ishida T 1997 Effect of a Co-O underlayer on Co-O films deposited obliquely. IEICE Technical Report MR96-85 (1997–01), pp. 21–8

Williams M Compstock R 1971 An analytical model of the write process in digital magnetic recording, *AIP Conf. Proceedings*, part 1, No. 5, reprinted in R M White, *Introduction to Magnetic Recording*, IEEE Press, New York, 1985, pp. 738–42

Wright M 1987 Recent developments in the production of thin-film magnetic media by electron beam evaporation. *J. Vac. Sci. Technol.* **A5** (1), 57–60

Yamamitsu C, Iketani A, Ohta J, Echina N 1995 An experimental digital VCR for consumer use. *IEEE Trans. Magn.* **31**, 1037

Yano A, Ogawa Y, Kitagaki N 1994 A study on inclination of recorded magnetization in obliquely evaporated Co-O films using the bitter technique. *J. Magn. Soc. Jpn.* **18** (S1), 413–34

Yoshida H, Nishizawa Y, Ouhata H 1995 Reliability of obliquely deposited Co-O thin film with carbon protective layer. *IEEE Trans. Magn.* **31** (6), 2940

Yoshida H, Shinohara K, Odagiri M 1994 Digital recording characteristics of Co-O thin film with protective carbon layer. *J. Magn. Soc. Jpn.* **18** (S1), 439

J. C. Lodder
University of Twente, Enschede, The Netherlands

Metal Hydrides: Electronic Band Structure

Metal–hydrogen systems have been continuously investigated ever since the ability of metallic palladium to absorb large amounts of hydrogen was discovered in 1866. Besides the importance of these systems in fundamental solid-state and materials science, the concern for energy and environmental problems has provided further motivation for studying hydrogen in intermetallic compounds such as $LaNi_5$ since the discovery of the exceptional hydriding properties of this intermetallic by van Vucht *et al.* (1970). Several aspects of the research on metal–hydrogen systems can be found in reviews and books by Mueller *et al.* (1968), Alefeld and Völkl (1978), Buschow *et al.* (1982), Schlapbach (1988, 1992), Fukai (1992), and Wipf (1997).

The insertion of hydrogen in metallic matrices leads to drastic changes in their electronic structure, due in part to structural effects (volume change often accompanied by crystal structure modifications), but mainly due to chemical effects. The presence of hydrogen perturbs the metal–metal bonds and creates new metal–hydrogen interactions, and the additional electrons of the hydrogen atoms modify the electron count and the electronic properties at the Fermi level. For good hydrogen absorbers, the hydrogen per metal atom ratio can vary in a wide range of non-stoichiometry from the solid solution limit to concentrated hydride phases, and the electronic properties at the Fermi level can thus be tuned in a continuous and fascinating way. Electronic band structure studies are useful in understanding, at a microscopic level, the changes in the important physical properties of the matrices on hydrogen uptake such as metal–semiconductor transitions, magnetism, and superconductivity, and thermodynamic properties such as stability, maximum hydrogen absorption capacity, and preferential H site occupancy. A review of the present status, achievements, and limits of the electronic band structure studies of binary transition and rare earth metal hydrides as well as of complex intermetallic hydrides follows, with a particular emphasis on compounds of potential importance for technological applications.

1. Methodologies

The electronic structure problem for a solid involves the study of the light particles, the electrons which, in the Born–Oppenheimer approximation, are assumed to be moving in the electrostatic field of the fixed heavier particles, the nuclei. The energy of the electronic ground state obtained as a function of the fixed nuclei can then be used as a potential energy for the motion of the nuclei.

Since the Schrödinger equation of a system of N interacting particles cannot be solved exactly, it is

usually replaced by an effective Schrödinger equation for one electron moving in the mean field of the other electrons and nuclei. The mean field used for solids is often based on the local density approximation (LDA) of the density functional theory (DFT) developed in the mid-1960s by Hohenberg and Kohn (1964). Besides the electrostatic interactions with the nuclei, this mean field is composed of the Coulomb repulsion due to the electron charge cloud and the exchange and correlation terms; it depends only on the electron density, $\rho(r)$.

In the LDA, the exchange and correlation term is obtained from the many-body theory applied to the electron gas having local density $\rho(r)$. The different *ab initio* techniques used in band structure calculations depend essentially on the approximations used for calculating the effective potential, and on the nature of the basis functions that can be fixed (plane waves, linear combination of atomic orbitals) or energy and potential dependent, as in the augmented plane waves (APW) method. The linear methods such as the linear muffin-tin orbital method (LMTO) and LAPW, use energy-independent basis functions derived from partial waves and combine the advantages of the two methods (see Skriver 1983 and Singh 1994 for reviews); they allow systems of complex structures to be studied using either approximate or full potential treatment. From these studies, total energies, attice parameters, elastic properties, and even fully relaxed structures can, in principle, be obtained. Using the spin-polarization techniques with spin-dependent electron densities, magnetic systems can also be studied.

Improvements beyond the LDA can be included using, for example, the generalized gradient approximation (GGA) and one can correct partly for correlation effects through the so-called GW approximation where G is the exact one-particle Green's function and W the screened Coulomb interaction.

2. Binary Transition Metal Hydrides

In most of the stable metal hydrides, a simple interpretation of the band structure can be obtained in the following way: since the hydrogen potential is more attractive than the metal atom potential, the lowest energy bands result from the hydrogen–metal bonding and H–H antibonding interactions. The number of corresponding bands is usually equal to the number of hydrogen atoms in the unit cell. The extent of the overlap of these states with higher energy metal states depends on a number of factors such as the energy difference between the metal and H orbitals, and the H–H distances; short H–H distances lead to an increase of the overlap due to a destabilization of the H–H antibonding states usually located at the top of the low-energy H-derived bands. The Fermi level position of the hydride depends crucially on the imbalance between the number of hydrogen-induced new states created below the Fermi level of the pure metal and the number of additional electrons per unit cell brought by the hydrogen atoms. This can either lead to a filling of the metal d bands as in the monohydrides, PdH and NiH, or to a depopulation of the pure metal d states in the early transition metal and rare-earth di- and trihydrides.

The electronic structure of rocksalt structure hydrides of transition metals of the end of the series such as palladium and nickel has been investigated since the early 1970s (see Switendick 1978 and Gupta and Schlapbach 1988 for reviews). It has been shown in great detail that the filling of the metal d bands in the stoichiometric hydride, leads to a drastic decrease of the densities of states at the Fermi level and the disappearance of ferromagnetism in nickel and of spin fluctuations of pure palladium. The Fermi surfaces of the monohydrides are topologically similar to those of noble metals; however, the protonic rigid band model is not quantitatively correct. Band structure calculations have been helpful in evaluating the electronic part of the electron–phonon coupling constant λ that controls the superconducting critical temperature T_c in normal superconductors. In PdH ($T_c = 9K$), and its alloys with noble metals, it is the electron–optical phonon coupling that is responsible for the superconducting properties. The role played by the presence of hydrogen s states at the Fermi energy and the low frequencies of the optic modes has been stressed (Jena and Satterthwaite 1983).

Although metal–insulator transitions occurring in bulk yttrium and rare-earth hydrides for hydrogen/metal ratios approaching 3 have been thoroughly investigated (see Vajda 1995 for review), studies of the spectacular optical properties of switchable mirrors based on thin films of YH_x and LaH_x initiated by Huiberts *et al.* (1996) have renewed the interest in the fundamental understanding of the metal–insulator transition as a function of x. The metallic properties of dihydrides of trivalent transition metal are very well accounted for by self-consistent band structure calculations. In the dihydrides, the five valence electrons occupy the two low-energy bands associated with metal–hydrogen and hydrogen–hydrogen bonding and the Fermi level falls at bottom of the metal d bands that accommodate the remaining electron. This feature of the electronic structure of early transition metal hydrides has been often interpreted in terms of a depopulation of the metal d bands in favor of the bonding low energy bands. In fact, in these hydrides the proton is better screened than in PdH or NiH.

In trihydrides of trivalent rare earth, since three M–H and H–H bands are formed below the pure metal d states, a semiconducting or semimetallic behavior is expected for these 6 valence electron systems, depending on the existence of an energy

separation or an overlap of the two manifolds. However, band structure calculations within the LDA (Wang and Chou 1995) lead to a band overlap larger than 1 eV for YH_3 in the hexagonal HoD_3 structure and thus to a metallic state while an optical energy gap of about 2.8 eV is observed in reflection and transmission for YH_3. Although LDA is known to underestimate band gaps in other types of semiconductors or insulators, the discrepancy obtained for YH_3 seems particularly large and led to further interpretations involving broken symmetry structures and many-body effects beyond the LDA. Using parametrized model hamiltonians, Eder *et al.* (1997) showed that strong correlation effects associated with H^- ions can open a substantial gap due to an energy lowering of the H-valence bands; the singlet formed by the two electrons on the H^- ion bears some similarities with the Zhang–Rice singlet coupling two holes in the high-T_c cuprate superconductors. Electromigration experiments of van der Molen *et al.* (2000) tend to be in support of this picture. Ng *et al.* (1999) also found that many-body effects result in a gap due to a narrowing rather than to an energy lowering of the H-derived bands. Other possible mechanisms such as symmetry-breaking distortions due to hydrogen displacements have been considered in particular by Kelly *et al.* (1997) on the basis of minimum energy structures. Although such symmetry breaking can lead to large gaps, these predictions have not been so far confirmed by the neutron diffraction experiments of Udovic *et al.* (1997).

The relevance of the comparison of gaps obtained from band structure calculations that probe only ground state properties and optical gaps that probe symmetry-allowed direct transitions has been questioned by van Gelderen *et al.* (2000). Parameter-free quasiparticle calculations in the GW approximation lead to a gap of 1 eV while inclusion of the electric dipole matrix elements give a larger optical gap of about 3 eV. According to another GW calculation by Miyake *et al.* (2000), the existence of a gap is due to many-body effects, and does not depend on the exact crystal structure; however, the gap is not due to a narrowing of the H-derived bands but rather to an upward shift of the unoccupied yttrium 4*d* states.

Ab initio calculations of the lattice dynamics of YH_3 in the HoD_3 and in symmetry-broken structures by van Gelderen *et al.* (2001), compared with the high-resolution neutron vibrational spectroscopy data of Udovic *et al.* (1997) support the existence of symmetry lowering in YH_3.

Thus, in spite of the most recent developments using state-of-the-art calculations, and experimental data such as neutron scattering and NMR electric field gradient (Zogal *et al.* 2001), the most stable crystal structure and the origin and value of the energy gap of YH_3 are still a matter of debate.

For h.c.p. yttrium, the hydrogen solid solution region has been investigated by Wang and Chou (1994)

by total energy calculations using pseudopotentials (PP) and plane-wave (PW) basis within the LDA. From their total energy calculations, they found that the tetrahedral sites are more stable than the octahedral ones. A study of various pairings of the hydrogen atoms shows, in agreement with experimental data, that the linear ordering of pairs at the tetrahedral sites bridged by a metal atom is favored.

3. Hydrides of Intermetallic Compounds

ZrNi was the first intermetallic compound found to reversibly absorb hydrogen (Libowitz *et al.* 1958), thus opening a new field of investigation. A large amount of experimental research on $LaNi_5$ and related compounds was initiated by the work of van Vucht *et al.* (1970). The development of applications of intermetallics, in particular for energy storage (see Dantzer 1997 for a review), led to the search for new hydrogen-absorbing materials. The hydriding properties of AB-type compounds such as FeTi found by Reilly *et al.* (1974) as well as other intermetallic compounds such as Laves phases AB_2 have been thoroughly investigated. Band structure studies started only in 1982 (see Gupta and Schlapbach 1988 for review of the early work). An increasing number of *ab initio* investigations of these complex structure systems has become available since then. However, theoretical work on the fascinating role of hydrogen on the magnetic properties of intermetallic compounds (see Buschow *et al.* 1982 and Hilscher and Wiesinger 1991 for reviews) remains to be developed.

3.1 Hydrides of AB Compounds

(a) Hydrides of ZrNi and ZrCo

The maximum hydrogen absorption of ZrNi leads to the formation of $ZrNiH_3$ which crystallizes within the CrB-type orthorhombic structure, with a lattice expansion of about 20%. The total density of states (DOS) of the hydride, obtained by LMTO calculations (Gupta 1999) is plotted in Fig. 1. It is characterized as follows. (i) The presence of structure below –4 eV corresponds to metal–hydrogen bonding and H–H interactions. The energy position of this bonding structure agrees with photoemission and x-ray emission data. The contribution of the nickel 3*d* states to the metal–hydrogen bonding is sizeable although it is lower than that of the zirconium 4*d* states. This is due to the larger coordination number of hydrogen with zirconium in the pyramidal Zr_3Ni_2 and the tetrahedral Zr_3Ni sites. (ii) The peak of the DOS centered around –3 eV is mostly due to nickel 3*d* states hybridized with zirconium 4*d*. (iii) The main zirconium 4*d* structure with a weak admixture of nickel 3*d* character is located above the Fermi energy.

The zirconium 4*d* DOS is considerably modified by the presence of hydrogen. The total DOS decreases
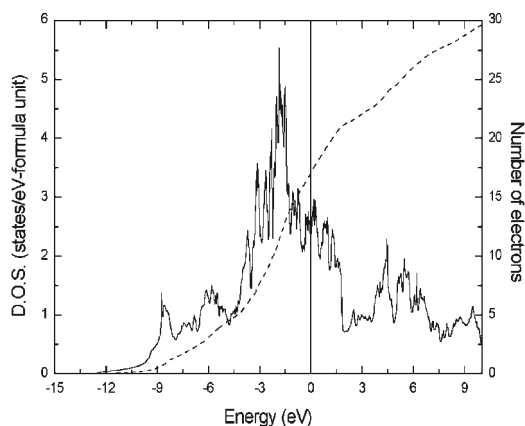
Figure 1
Total density of states of ZrNiH$_3$: solid line, left-hand-side scale; number of electrons, dashed line, right-hand-side scale. The origin of energies is the Fermi energy.

slightly from ZrNi to ZrNiH$_3$; the zirconium d contribution at E_F decreases from 68% in the intermetallic to 62% in its hydride due to the broadening of the zirconium states and a slight lowering of E_F. This feature, which is important for the stability of the hydride, is due to the fact that the Zr–H interaction is strong enough to lower below E_F empty zirconium states of the pure intermetallic compound. In contrast, the Ni–H interaction stabilizes in energy nickel d states already occupied in ZrNi, and thus does not contribute to the lowering of E_F.

A very unusual feature of the ZrNi-H$_2$ system is that the Zr$_4$ (4c) sites that are occupied in triclinic ZrNiH become empty in favor of the pyramidal Zr$_3$Ni$_2$ (4c) and tetrahedral Zr$_3$Ni (8f) sites in ZrNiH$_3$. Total energy calculations were performed for ZrNiH for two possible occupancies of H sites, Zr$_4$ (4c) and Zr$_3$Ni$_2$ (4c). Both sites satisfy the usual geometric criteria of minimum hole size and minimum H–H distances. In agreement with neutron scattering data of Westlake *et al.* (1982), the chemical effect associated with the Zr–H interaction and the Fermi level position result in a greater stability of the Zr$_4$ sites. At higher hydrogen concentration, the repulsive H–H interaction at short distances leads to the site occupancy observed in ZrNiH$_3$.

ZrCo is also a good hydrogen absorber that has been considered since the late 1980s as a possible substitute for uranium for the storage of hydrogen and its radioactive isotope, tritium. ZrCoH$_3$ is isostructural to ZrNiH$_3$. The main differences in the DOS of the two hydrides can be summarized as follows: the cobalt 3d structure is broader and located at higher energy than the nickel 3d peak, leading to a larger overlap with the zirconium 4d states. Since the electron count decreases by one per formula unit

from ZrNiH$_3$ to ZrCoH$_3$, the Fermi level is closer to the cobalt d peak and the total DOS of ZrCoH$_3$ is 30% larger than that of the CsCl structure ZrCo. This indicates a tendency towards magnetic ordering. In ZrCoH$_3$ the metal–hydrogen bonding states are centered around 7 eV below E_F, in agreement with photoemission data reported by Gupta and Schlapbach (1988).

(b)   Hydrides of FeTi and NiTi
FeTi is a Pauli paramagnet of cubic CsCl-type ordered structure. As in isoelectronic and isostructural b.c.c. chromium, the Fermi level falls in the valley of the DOS between occupied d-like bonding states derived primarily from iron and empty d-like antibonding states derived mostly from titanium. In β-FeTiH, hydrogen occupies distorted octahedral Fe$_2$Ti$_4$ sites instead of the more usual tetrahedral sites characteristic of the b.c.c. metals. β-FeTiH has an orthorhombic structure. The analysis of APW band structure calculations shows that the metal–hydrogen bonding states, centered at 9 eV below E_F, are mainly due to the Fe–H interaction that lowers states already filled in the intermetallic. The Ti–H contribution to the bonding is not as large in spite of the greater affinity of hydrogen for titanium; however, this interaction brings new states below E_F. The Fermi level of β-FeTiH is found at higher energy than in FeTi, above the valley of the DOS; the calculated DOS at E_F increases from the intermetallic to its hydride in agreement with the observed increase in the magnetic susceptibility and the electronic specific heat.

The electronic structure of FeTiH$_2$ has been studied ignoring the monoclinic distortion. The low-energy bonding structure grows in width and intensity upon increasing the hydrogen content. The contribution of Ti–H bonding is much larger than in FeTiH since one of the four hydrogen atoms in the unit cell is located closer to two titanium atoms rather than to the iron atoms. The Fermi level of FeTiH$_2$ falls above the valley of the DOS; it is, however, closer to the iron peak than in FeTiH due to the presence of a second H–H derived band at low energies.

Mössbauer isomer shift (IS) experiments reveal a systematic decrease of the s contact electron density at the metal site with hydrogen uptake that cannot be explained by a simple renormalization of the wave-functions due to lattice expansion. Theoretical calculations show that the depletion of the 4s metal states at the iron site is due mostly to the Fe–H bonding contribution.

In the hydride of the shape memory alloy NiTi, the bonding properties are similar to those discussed for FeTi. The hydrogen absorption leads also to an upward shift of the Fermi level and the nesting features of the Fermi surface of NiTi disappear. The premartensitic phase transition of NiTi that arises from the condensation of a soft phonon is believed to be due to

strong electron–phonon coupling of nested electronic states at E_F. No martensitic transformation occurs in the hydride.

3.2 Hydrides of AB_5 (Haucke) Compounds

(a) LaNi$_5$–H$_2$ systems

Several investigations of this system in the solid solution and concentrated hydride phases have been performed since the last review (Gupta and Schlapbach 1988) using the LMTO (Gupta 1998), the tight binding LMTO (Nakamura *et al.* 1998), and plane wave pseudopotential (PW-PP) methods within the GGA (Tatsumi *et al.* 2001).

LaNi$_5$ crystallizes in the hexagonal CaCu$_5$ structure, space group $P6/mmm$, in which the lanthanum atoms occupy the $(1a)$ sites; there are two types of nickel atoms occupying respectively the $(2c)$ sites in the basal lanthanum planes $(z = 0)$, and the $(3g)$ sites in the middle plane $(z = c/2)$. The occupied part of the conduction band is dominated by the nickel $3d$ states with a non-negligible bonding contribution of lanthanum $5d$ states. The main part of the lanthanum $5d$ states is, however, located above the Fermi energy. The $4f$ states are empty; they are very localized at energies 3 eV above E_F. The nickel d bands are not filled and the intermetallic is not a charge transfer compound as shown by core level photoemission spectroscopy, which does not indicate any significant shift in the lanthanum $3d$ and nickel $2p$ core states in LaNi$_5$.

The calculated total DOS is in agreement with XPS data concerning the width of the occupied states and the high emission observed at E_F. The DOS at E_F is high and mostly composed of nickel d states since the lanthanum d contribution is only 4%. This result is in agreement with low-temperature heat capacity measurements which lead to large values of the electronic specific heat coefficient and with magnetic susceptibility data. In spite of the large value of the DOS LaNi$_5$ is found experimentally to be a Pauli paramagnet, although spin polarized band structure calculations (Nakamura *et al.* 1998) lead to a magnetic moment of about 0.6 μ_B per formula unit.

The crystal structure of LaNi$_5$H$_7$ has been repeatedly examined by neutron diffraction (see Percheron-Guégan 1995 for review). Although satisfactory refinements have been obtained in the $P6_3mc$ and the $P31c$ space groups, which differ by the presence of a mirror plane, total energy calculations of Tatsumi *et al.* (2001) favor the $P6_3mc$ structure by 0.34 eV per LaNi$_5$.

The DOS of LaNi$_5$H$_7$ obtained by the LMTO method is shown in Fig. 2. The low-energy structure, extending down to 10 eV below E_F, corresponds to seven bands associated with M–H and H–H interactions. The nickel contribution to the hydrogen bonding is larger than the lanthanum contribution. The
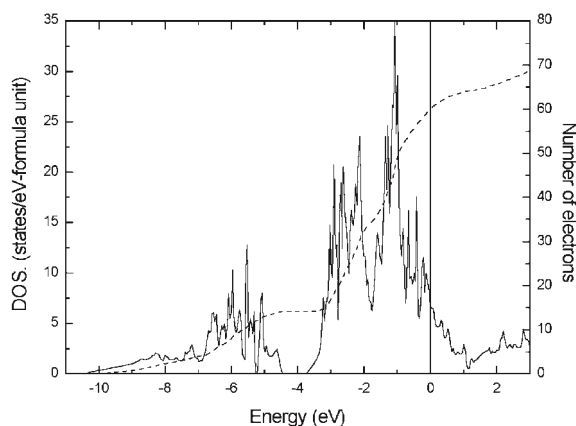
Figure 2
Total density of states of LaNi$_5$H$_7$: solid line, left-handside scale; number of electrons, dashed line, right-handside scale. The origin of energies is the Fermi energy.

nickel d states are not entirely filled in the hydride, and thus the DOS at E_F remains large in the hydride although a decrease is found from its value in the intermetallic in agreement with the trends observed in electronic specific heat and magnetic susceptibility data.

In the solid solution LaNi–H within the $P6/mmm$ space group, five non-equivalent interstices have been proposed as possible H sites. The total energy calculations of Tatsumi *et al.* (2001) for La$_2$Ni$_{10}$H$_1$ using the five possible H site occupancies and including geometry optimization indicate that the $(12n)$ site appears to be the most energetically favorable, in agreement with neutron scattering data.

Experimental values of the heats of formation remain difficult to predict accurately from *ab initio* calculations since they result from the subtraction of very large values of total energies. Nevertheless, using full geometry optimization, Tatsumi *et al.* (2001) obtained a heat of formation of -33 kJ mol^{-1} H$_2$ for the primary solid solution, in rough agreement with experimental data and a heat of formation of -45 kJ mol^{-1} H$_2$ for LaNi$_5$H$_7$, a value that is 30–40% lower than the experimental one.

(b) Effects of substitutions

Substitutions at the lanthanum or nickel sites are used experimentally to modify the thermodynamic properties and play an important role in the selection of the alloys for specific technological applications, since they affect the stability and the maximum hydrogen content (for review see Takeshita *et al.* 1980 and Percheron-Guégan 1995). In order to optimize the choice of intermetallic compound, a better understanding of the role of each alloy constituent on

the electronic properties of the material is crucial. Several semiempirical models (see Griessen and Riesterer 1988 for review) have been proposed for the heat of formation and the heat of solution of metal hydrides and attempts have been made to justify the maximum hydrogen absorption capacity of the matrices. These models show that the energetics of the metal–hydrogen interaction depend both on geometric and electronic factors.

The effect of replacement of nickel by the 3d elements manganese, iron, or cobalt, by an s-p element of the 3d series such as copper, as well as by s-p elements such as aluminum and tin have been investigated by LMTO band structure calculations of ordered systems, thus ignoring the effect of disorder and the possible clustering of substituted elements. Neutron scattering data show that the nickel substitutions considered here occur predominantly at the nickel (3g) sites, in agreement with total energy calculations which indicate that substitutions at the nickel (3g) site are energetically preferred over nickel (2c) by several milliRydberg (mRy). Substitutions of nickel neighbors, M, on the left of the periodic table (M = Mn, Fe, Co) does not just lead to a simple depopulation of the nickel 3d bands. In all the substituted intermetallics a new narrow sub-band, associated with the 3d states of the substituting element M, appears slightly above the nickel d bands. The Fermi level of the substituted intermetallic falls in all cases in the narrow antibonding sub-band of the M element while the main nickel 3d structure is filled. As a consequence, the DOS at the Fermi level increases further from LaNi$_5$ to LaNi$_4$M (M = Mn, Fe, Co) indicating the possibility of magnetic ordering as found in spin-polarized calculations by Yang *et al.* (2000). In contrast, for M = Cu, the copper 3d sub-band is centered below the main nickel d peak in agreement with photoemission data. The substitution of nickel by copper or by an s, p element such as aluminum or tin leads to a decrease of the DOS at E_F associated with the progressive filling of the nickel d bands.

The heats of formation of the substituted alloys LaNi$_4$M (M = Mn, Fe, Co, Cu) have been measured by calorimetric methods. In all cases, the substituted intermetallics are less stable than LaNi$_5$. Band structure calculations indicate that the effect of chemical substitution plays an important role in the observed decreased stability of LaNi$_4$M compared to LaNi$_5$ since the lattice expansion alone accounts for less than 50% of the decohesion of the alloy.

The electronic structures of some hydrides of substituted intermetallic compounds have been studied. In LaNi$_4$CoH$_4$, the Fermi level corresponds to a filling of the main cobalt 3d peak. The maximum hydrogen content appears to be associated with the filling of the cobalt d peak: further shift of the Fermi energy in the lanthanum 4d bands would cost energy since the DOS is not too high.

3.3 Hydrides of AB$_2$ Laves Phases Compounds

Amongst the intermetallic compounds, the Laves phases have been widely investigated in connection with their superconducting and magnetic properties (see Schlapbach 1988 for review), but also as structural materials due to their high melting temperature and high strength, and as hydrogen storage materials. Besides the rich field of potential applications of the Laves phase hydrides, the understanding of the modifications of the electronic and magnetic properties on hydrogen absorption is of fundamental interest. Although electronic structure studies of many cubic (C-15) and hexagonal (C-14 and C-16) intermetallic compounds are available, band structure calculations of the corresponding hydrides remain rather scarce.

(a) Superconducting Laves phases

In the superconducting AB$_2$ Laves phases (A = Zr, Hf, B = V) with superconducting critical temperatures T_c = 8 K for ZrV$_2$ and T_c = 9 K for HfV$_2$, the electron–phonon coupling is expected to be strongly affected by both the lattice expansion and by the change in the nature of the electronic states at E_F on hydrogen absorption.

ZrV$_2$ crystallizes within the C-15 cubic phase above T_m = 100 K; below this temperature it undergoes a rhombohedral distortion (Moncton 1973). The interplay between structural and superconducting transitions also observed in the superconducting A-15 materials was widely discussed in the mid-1970s since they are both indicative of large electron–phonon coupling.

The total density of states of the cubic phase is plotted in Fig. 3. The Fermi energy falls in the transition metal (TM) d bonding bands close to a peak in the DOS. In agreement with previous work by Klein *et al.* (1983), the value of the DOS at E_F is found to be large and dominated by the vanadium 3d contribution, which is about 50% larger than that of the zirconium 4d states. The large value of the DOS at E_F is consistent with the large magnetic susceptibility above T_m, as well as with the value of the electronic specific heat coefficient obtained from low-temperature microcalorimetry. In the rhombohedral phase, due to the symmetry lowering, the Van Hove singularities of the DOS are considerably smoothed. The total DOS at E_F is found to decrease by 35% from its value in the cubic phase, a result consistent with the sharp decrease of the magnetic susceptibility observed at T_m. It is interesting to point out in this connection that two distinct superconducting transitions differing by 1 K have been observed experimentally by Daümer *et al.* (1989) and it has been suggested that the two phases are superconducting, the higher T_c value being attributed to small amounts of untransformed cubic C-15 phase.
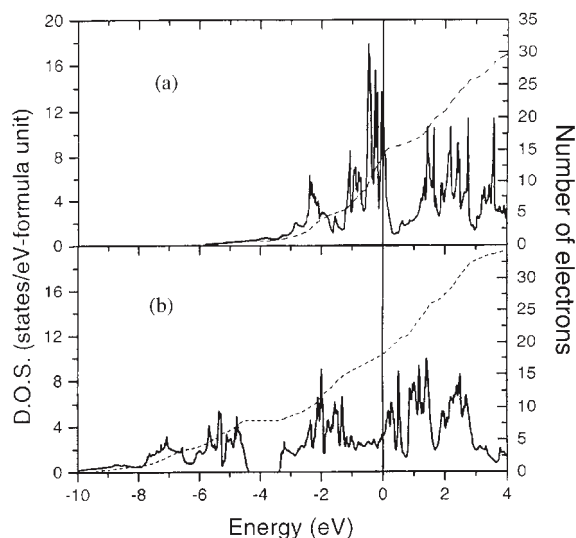
Figure 3
Total density of states: solid line, left-hand-side scale; number of electrons, dashed line, right-hand-side scale. (a) ZrV_2 C-15 cubic phase (b) ZrV_2H_4. The origin of energies is the Fermi energy.

The DOS of ZrV_2H_4 calculated using the structural data of Didisheim *et al.* (1981) in the low-temperature tetragonal phase in which the hydrogen atoms order at one of the Zr_2V_2 sites is plotted in Fig. 3. The metal–hydrogen bonding states form four bands per formula unit, extending from -10.3 eV and -4.4 eV below E_F. The hydrogen interaction with zirconium is slightly larger but of the same order of magnitude than that with the vanadium states. The DOS at E_F is 72% lower than in the pure intermetallic. In the hydride, as in the pure intermetallic, the states at E_F have mostly a vanadium d character. In contrast to the pure intermetallic, the vanadium p contribution at E_F is much smaller since the vanadium p states are rather found to participate in the metal–hydrogen low-energy states.

The band width and structures obtained in the calculated DOS of ZrV_2 and ZrV_2H_4 are in good agreement with UV and x-ray photoemission data of Schlapbach *et al.* (1984) and x-ray emission spectroscopic results.

The results of electronic structure calculations can be used in conjunction with experimental data on the vibrational properties to estimate the electron–phonon coupling constant λ which essentially determines the value of T_c.

Band structure calculations show that the electronic contribution of the electron–acoustic phonon coupling is drastically reduced from the intermetallic to the hydride due to a large decrease of the DOS at E_F and to a reduced value of the vanadium p orbital character of the electronic states. The electronic contribution of the electron–optical phonon is very small because the Fermi level of the hydride falls into the metal d bands unlike in superconducting PdH. For these two reasons, hydrogen absorption leads to the disappearance of the superconducting properties.

(b) Hydrides of magnetic Laves phases

The influence of hydrogen absorption on the magnetic properties of Laves phase AB_2 compounds, where A is a transition or rare earth element and B a magnetic or nonmagnetic transition element, is a very vast and fascinating topic that has been experimentally investigated since the pioneering work of Buschow *et al.* (Buschow and van Diepen 1976, Buschow and Sherwood (1977). Due to the great complexity of the phase diagrams and crystal and magnetic structures observed, *ab initio* investigations of these hydrides remain scarce, particularly for systems involving $4f$ electrons of magnetic rare earths and $3d$ moments on the transition elements, which raise the controversy of the validity of localized versus band models.

The insertion of hydrogen in the matrix is expected to affect the magnetic properties via several factors: magnetism is strongly dependent on interatomic distances that increase by the negative pressure effect associated with hydrogen uptake; in addition, the metal hydrogen bonding and the change in the Fermi level position are expected to strongly modify the magnetic interactions betwen A and B atoms.

We shall discuss here band structure results only on magnetic cubic (C-15) AB_2 compounds (A = Y, B = Mn, Fe) and their hydrides.

YMn_2 is found to be an antiferromagnet: the moments obtained in spin-polarized LMTO calculations, 2.6 μ_B per manganese atom, are in satisfactory agreement with the experimental value of 2.7 μ_B found by (Nakamura *et al.* 1983) and previous LMTO (Pajda *et al.* 1996) and tight-binding Hartree–Fock calculations. The total energy of the antiferromagnetic state is 8 mRy lower than that of the paramagnetic phase and the calculated volume change at the antiferromagnetic–paramagnetic transition agrees with thermal expansion measurements. The hydrogen absorption has been investigated since the work of Buschow *et al.* (Buschow 1976). The band structure of $YMnH_x$ at low ($x = 0.5-1$) (Pajda *et al.* 1996) and high ($x = 4$) hydrogen concentrations has been investigated. Total energies performed for three different hydrogen positions in the low concentration limit favor the tetrahedral A_2B_2 sites, as observed experimentally. The hydrogenated compounds are found to be antiferromagnetic with a small ferrimagnetic component.

At all hydrogen concentrations, the volume expansion leads to an increase of the magnetic moments while the Mn–H bonding interaction tends to decrease the magnetic moment. The change in the magnetic

properties as a function of hydrogen concentration is rather complex (see Goncharenko *et al.* 1997, Latroche *et al.* 2000) and has not yet been fully studied theoretically.

The magnetic properties of YFe_2 obtained from band structure calculations show, in agreement with experimental data of Buschow and van Diepen (1976) and later work, that the intermetallic is ferromagnetic, with a calculated total magnetic moment of 2.86 μ_B compared to the experimental value of 2.9 μ_B. The moment is essentially localized on the iron atoms; however a small ferrimagnetic contribution due to the more delocalized $4d$ orbitals appears on the yttrium sites. Two hydrides YFe_2H_x have been investigated assuming a hydrogen ordering ($x = 3$) by an augmented spherical wave calculation (Paul-Boncour and Percheron-Guégan 1999 and references therein) and by the LMTO method for $x = 4$. For YFe_2H_4 it is found that the 20% lattice expansion leads to an increase of the moment up to 3.93 μ_B while the chemical metal–hydrogen interaction reduces this value as also observed for YFe_2H_3 and YMn_2H_x.

4. Hydrides of Intermetallic Compounds with Transition and Alkali or Alkaline-earth Elements

The search for new storage materials of light weight and good hydrogen absorption capacities, as well as the fundamental interest in hydrides of metals with unusual coordination number or valence, led to the synthesis and characterization of a number of ternary hydrides of general composition $A_xM_yH_z$ where A forms binary insulating hydrides and B forms rather metallic hydrides (see Yvon 1994, Bronger 1995 for reviews).

These hydrides present interesting features from a theoretical point of view due to (i) the possible coexistence of ionic, covalent, and metallic bonding of hydrogen with A and B, (ii) the electrical properties can vary from those of ionic insulators to metallic systems, and (iii) the possibility of finding superconductivity.

4.1 Mg_2NiH_4, Mg_2CoH_5, Mg_2FeH_6 and Related Hydrides

Hydrides of the series A_2MH_6 (A = Mg, Ca, Sr, M = Fe, Ru, Os) crystallize in the cubic K_2PtCl_6 structure while Mg_2CoH_5 and Mg_2NiH_4 are present above 500 K as a high-temperature cubic phase and low-temperature phases of lower symmetry. In the cubic phases the metal lattice is of antifluorite type with large M–M distances. The hydrogen atoms form octahedral cages around the M atom in A_2MH_6 with short M–H distances. The hydrogen positions of the high-temperature phases of Mg_2NiH_4 and Mg_2CoH_5 are believed to result from the thermal average of square planar or tetrahedral configurations around

nickel and square pyramidal arrangement of hydrogen atoms around cobalt. These hydrides correspond to 18 valence electron compounds; the hydrogen content can be increased by a corresponding decrease of the transition metal valence.

The band structures (Gupta and Schlapbach 1988, Orgaz and Gupta 1993, Garcia *et al.* 1999) can be interpreted in terms of coordination chemistry since the M–H cages are weakly coupled. Two types of bonds coexist due to the covalent M–H interactions and the ionic character of the A element. The compounds are found to be insulating. In hydrides with octahedral coordination, A_2MH_6, the gap opens between the three M d-t_{2g} nonbonding and the M d-e_g, hydrogen s antibonding states. In Mg_2NiH_4, with tetrahedral NiH_4 cages, the gap occurs between the five nickel d nonbonding and the Ni–H s antibonding states. In Mg_2CoH_5 with the square pyramidal configuration, the gap appears between the four nonbonding M d and the antibonding $d_{x^2-y^2}$ hydrogen s antibonding states as expected from coordination chemistry. The maximum hydrogen content in these hydrides corresponds to the complete filling of bonding M–H and nonbonding M states, a situation that is known to be energetically favorable. The values of the energy gaps obtained in the LDA calculations are in reasonable agreement with experimental observations although they are expected to be affected by correlation effects in systems with narrow d bands.

4.2 Palladium-based Ternary Hydrides

Since hydrides of palladium and its alloys with filled d bands are superconductors with moderate but sizeable critical temperatures (PdH ($T_c = 9K$), $Pd_{0.55}Cu_{0.45}H_{0.7}$ ($T_c = 16K$)), the synthesis of ternary hydrides of palladium with filled d bands and electronic properties at the Fermi level similar to those of PdH could result in an important electron optical phonon coupling and superconductivty.

Li_2PdH_2 and Na_2PdH_2 have been synthesized by Kadir *et al.* (1991). These hydrides are characterized by a body-centered tetragonal array of linear PdH_2 entities along the c-axis of the tetragonal unit cell, with short Pd–H distances. According to conventional valencies these compounds should be insulating; however, band structure calculations by Gupta (1993) and Switendick (1993) show that these 14 valence electron hydrides are rather semimetallic with a low DOS at E_F associated to a weak overlap between the seven palladium d, hydrogen s derived bands and the eighth band mostly due to lithium or sodium p states.

The crystal structure of K_2PdH_4 is characterized by a b.c.t. array of square planar PdH_4 units with short Pd–H distances; this 16 valence electron hydride is found to be insulating with a gap of 1.8 eV. Its electronic structure can be interpreted in terms of

coordination chemistry of $(PdH_4)^{-4}$ entities, with square planar D_{4h} point group, interacting only weakly, the alkali counterion neutralizing the structure.

Platinum-based compounds such as K_2PtH_4 and Na_2PtH_4 have also been synthesized and characterized. In these hydrides, the PtH_4 units have different orientations than in the palladium-based compounds. These quasimolecular complexes are all found to be insulating (Orgaz and Gupta 2000).

The electronic structure of the palladium-based cubic perovskite structure $APdH_3$ (A = Sr, Eu, Yb) and the complex hydride $PdSr_2LiH_5$ has been investigated in connection with the possible occurrence of superconductivity. In the hydrides $APdH_3$ the electrons of the divalent element are essentially transferred to the Pd–H states, the main part of the d bands of palladium are essentially filled, and the Fermi level falls in the antibonding Pd–H states. These hydrides are metallic with DOSs at E_F as in PdH and noble metals. The crystal structure of the complex $PdSr_2LiH_5$ hydride can be understood from the stacking of cubic perovskite insulating $SrLiH_3$ subunits and defective perovskite $SrPdH_2$. A metallic behavior is found for $PdSr_2LiH_5$. As in $APdH_3$, the essential part of the palladium d states are filled and a non-negligible contribution of the hydrogen s states is found at E_F. A study of the electronic part of the electron–phonon coupling shows that the hydrogen contribution is non-negligible, although it is always smaller than in superconducting PdH. If the optical phonon modes, not yet known, are not too high, hydrides of this family could be potential candidates for superconductivity. Experimentally only $NaPd_3H_2$, which can be viewed as a distorted sodium-substituted palladium hydride, has been found to be superconducting below 2 K, while $CaPd_3H$ is metallic but not superconducting as shown by Rönnebro *et al.* (2000).

5. Perspective

Band structure calculations have greatly improved, at a microscopic level, our understanding of the electronic properties of metal–hydrogen systems. In the near future, further progress needs to be made in the study of compounds of greater structural complexity, in the areas of the thermodynamic and elastic properties, and especially in the rich field of magnetism.

See also: Metal Hydrides: Magnetic Properties

Bibliography

Alefeld G, Völkl J 1978 *Hydrogen in Metals I and II Topics in Applied Physics*, Vols. 28 and 29. Springer, Heidelberg, Germany

Bronger W 1995 Synthesis and structure of new metal hydrides. *J. Alloys Compd.* **229**, 1–9

Buschow K H J 1976 Hydrogen absorption and its effect on the magnetic properties of rare-earth iron intermetallics. *Solid State Commun.* **19**, 421–3

Buschow K H J, Bouten P C, Miedema A R 1982 Hydrides formed from intermetallic compounds of two transition metals. *Rep. Prog. Phys.* **45**, 937–1039

Buschow K H J, Sherwood R C 1977 Magnetic properties and hydrogen absorption in rare-earth intermetallics of the type RMn_2 and R_6Mn_{23}. *J. Appl. Phys.* **48**, 4643–8

Buschow K H J, van Diepen 1976 Effect of hydrogen absorption on the magnetic properties of YFe_2 and $GdFe_2$. *Solid State Commun.* **19**, 79–81

Dantzer P 1997 Metal–hydride technology: a critical review. In: Wipf H (ed.) *Hydrogen in Metals III*. Topics in Applied Physics, Vol. 73. Springer, Berlin, Chap. 7, pp. 279–331

Däumer W, Kahn H R, Köbler U, Lüders C 1989 Temperature-dependent magnetic susceptibility and superconductivity of cubic Laves phase C-15 hydrides. *Phys. Lett. A* **138**, 323–8

Didisheim J J, Yvon K, Fischer P, Tissot 1981 Order-disorder phase transition in $ZrV_2D_{3.6}$. *Solid State Commun.* **38**, 637–41

Eder S J, Pen H F, Sawatzki G A 1997 Kondo-lattice-like effects of hydrogen in transition metals. *Phys. Rev. B* **56**, 10115–20

Fukai Y 1992 *The Metal Hydrogen System, Springer Series in Materials Science*, Vol. 21. Springer, Heidelberg, Germany

Garcia G N, Abriata J P, Sofo J O 1999 Calculation of the electronic and structural properties of cubic Mg_2NiH_4. *Phys. Rev. B* **59**, 11746–54

Goncharenko I N, Mirebeau I, Irodova A V, Suard E 1997 Interplay of magnetic and hydrogen orders in the Laves hydride $YMn_2H_{4.3}$. *Phys. Rev. B* **56**, 2580–4

Griessen R, Riesterer T 1988 Heats of formation models. In: Schlapbach L (ed.) *Hydrogen in Intermetallic Compounds I*, Topics in Applied Physics, Vol. 63. Springer, Heidelberg, Germany, Chap. 6, pp. 221–84

Gupta M 1993 Electronic structure of hydrides containing alkali and alkaline-earth elements. *Z. Phys. Chem.* **181**, 9–18

Gupta M 1998 Effect of substitutions at the nickel site on the electronic structure of $LaNi_5$ and its hydrides. In: Nickel N H, Jackson W B, Bowman R C, Leisure R G (eds.) *MRS Symp. Proc., Symposium: H in Semiconductors and Metals*. Vol. 513. Materials Research Society, Warrendale, PA, pp. 79–84

Gupta M 1999 Electronic structure and stability of hydrides of intermetallic compounds. *J. Alloys Compd.* **293–5**, 190–201

Gupta M, Schlapbach L 1988 Electronic properties. In: Schlapbach L (ed.) *Hydrogen in Intermetallic Compounds I*, Topics in Applied Physics, Vol. 63. Springer, Heidelberg, Germany, Chap. 5, pp. 139–209

Hilscher G, Wiesinger G 1991 Magnetism of hydrides. In: Buschow K H J (ed.) *Magnetic Materials*, Vol. 6. North Holland, Amsterdam

Hohenberg P, Kohn W 1964 Inhomogeneous electron gas. *Phys. Rev.* **136**, B864–71

Huiberts J N, Griessen R, Rector J H, Wijngaarden R J, Dekker J P, de Groot D G, Koeman N J 1996 Yttrium and lanthanum hydride films with switchable optical properties. *Nature (London)* **380**, 231–4

Jena P, Satterthwaite C B 1983 *Electronic Structure and Properties of Hydrogen in Metals, NATO ASI Series*, Vol. 6. Plenum, New York

Kadir K, Kritikos M, Noreus D, Andresen A F 1991 Metallic properties in the series $K_2Pd(II)H_4$, $Na_2Pd(0)H_2$ and $Li_2Pd(0)H_2$ correlated with the stabilization of a formally zero-valent palladium-hydrogen complex. *J. Less-Common Met.* **172–4**, 36–41

Kelly P J, Dekker J P, Stumpf R 1997 Theoretical prediction of the structure of insulating YH$_3$. *Phys. Rev. Lett.* **78**, 1315–8

Klein B M, Pickett W E, Papaconstantopoulos D A 1983 Electronic structure, superconductivity, and magnetism in the C-15 compounds ZrV$_2$, ZrFe$_2$, ZrCo$_2$. *Phys. Rev. B* **27**, 6721–31

Latroche M, Paul-Boncour V, Percheron-Guégan A, Bourée-Vigneron F, André G 2000 Structural and magnetic properties of low D content YMn$_2$ deuteride 2000. *J. Solid State Chem.* **154**, 398–404

Libowitz G G, Hayes H F, Gibb T R P Jr. 1958 The system zirconium–nickel and hydrogen. *J. Phys. Chem.* **62**, 76–9

Miyake T, Aryasetiawan F, Kino H, Terakura K 2000 GW quasiparticle band structure of YH$_3$. *Phys. Rev. B* **61**, 16491–6

Mueller W M, Blackledge J P, Libowitz G G 1968 *Metal Hydrides*. Academic Press, New York

Moncton D E 1973 Lattice transformation in the superconductor ZrV$_2$ by neutron diffraction. *Solid State Commun.* **13**, 1779–82

Nakamura H, Nguyen-Manh D, Pettifor D 1998 Electronic structure and energetics of LaNi$_5$, α-La$_2$Ni$_{10}$H and β-La$_2$Ni$_{10}$H$_{14}$. *J. Alloys Compd.* **281**, 81–91

Nakamura H, Shiga M, Kawano S 1983 Antiferromagnetism of YMn$_2$ intermetallic compound. *Physica B* **120**, 212–5

Ng K K, Zhang F C, Anisimov V I, Rice T M 1999 Theory for metal hydrides with switchable optical properties. *Phys. Rev. B* **59**, 5398–413

Orgaz E, Gupta M 1993 The electronic properties of intermetallic hydrides with the K$_2$PtCl$_6$ structure. *J. Phys.: Condens. Matter* **5**, 6697–718

Orgaz E, Gupta M 2000 Chemical bonding features of the ternary alkali metal platinum and palladium hydrides. *Int. J. Quantum Chem.* **80**, 141–52

Pajda M, Ahuja R, Johansson B, Wills J M, Figiel H, Paja A, Eriksson O 1996 First-principles calculations of the magnetic properties of YMn$_2$ and its hydrides. *J. Phys. Condens. Matter* **8**, 3373–84

Paul-Boncour V, Percheron-Guégan A 1999 The influence of hydrogen on the magnetic properties and electronic structures of intermetallic compounds: YFe$_2$D$_2$ system as an example. *J. Alloys Compd.* **293–5**, 237–42

Percheron-Guégan A 1995 A survey of binary and ternary metal hydride systems. In: Grandjean F, Long G J, Buschow H K J (ed.) *Interstitial Intermetallic Compounds*, NATO ASI Series, Vol. 281. Kluwer, Dordrecht, The Netherlands, Chap. 5, pp. 77–105

Reilly J J, Wiswall R H 1974 Formation and properties of iron titanium hydride. *Inorg. Chem.* **13**, 218

Rönnebro E, Noreus D, Gupta M, Kadir K, Hauback B, Lundqvist P 2000 The crystal structure and electronic structure of CaPd$_3$H. *Mater. Res. Bull.* **35**, 315–23

Schlapbach L 1988 *Hydrogen in Intermetallic Compounds I*, Topics in Applied Physics, Vol. 63. Springer, Heidelberg, Germany

Schlapbach L 1992 *Hydrogen in Intermetallic Compounds II*, Topics in Applied Physics, Vol. 67. Springer, Heidelberg, Germany

Schlapbach L, Osterwalder J, Riesterer T 1984 Recent experimental results on the electronic structure of binary and ternary hydrides. *J. Less-Common Met.* **103**, 295–307

Singh D J 1994 *Plane Waves, Pseudopotentials, and the LAPW Method*. Kluwer, Boston

Skriver H L 1983 *The LMTO Method*, Springer Series in Solid State Sciences, Vol. 417. Springer, Berlin

Switendick A 1978 The change in electronic properties on hydrogen alloying and hydride formation. In: Alefeld G, Völkl J (eds.) *Hydrogen in Metals I*, Topics in Applied Physics, Vol. 28. Springer, Heidelberg, Germany, Chap. 5, pp. 101–29

Switendick A C 1993 The electronic structure of alkali metal-nickel group-hydrogen compounds: Li$_2$PdH$_2$ and K$_2$PdH$_4$. *Z. Phys. Chem.* **181**, 19–25

Takeshita T, Dublon G, McMaster O D, Gschneidner K A 1980 Low temperature heat capacity studies on hydrogen absorbing intermetallic compounds. In: McCarty G J, Rhyne J J, Silver H B (eds.) *Rare Earths in Modern Science and Technology*. Plenum, New York, Vol. 2, p. 563

Tatsumi K, Tanaka I, Inui H, Tanaka K, Yamaguchi M, Adachi H 2001 Atomic structures and energetics of LaNi$_5$-H solid solution and hydrides. *Phys. Rev. B* **64**, 184105

Udovic T J, Rush J J, Huang Q, Rush J J, Anderson I S 1997 Neutron scattering studies of the structure and dynamics of rare-earth hydrides and deuterides. *J. Alloys Compd.* **253–4**, 241–7

Vajda P 1995 Hydrogen in rare-earth metals including RH$_{2+x}$ phases. In: Gschneidner K A (ed.) *Handbook on the Physics and Chemistry of Rare Earths*, Vol. 20. North Holland, Amsterdam, p. 207

Van der Molen S J, Welling M S, Griessen R 2000 Correlated electromigration of H in the switchable mirror YH$_{3-\delta}$. *Phys. Rev. Lett.* **85**, 3882–5

van Gelderen P, Bobbert P A, Kelly P J, Brocks G 2000 Parameter-free quasiparticle calculations for YH$_3$. *Phys. Rev. Lett.* **85**, 2989–92

van Gelderen P, Kelly P J, Brocks G 2001 Phonon spectrum of YH$_3$: evidence for a broken symmetry structure. *Phys. Rev. B* **63**, 100301

Van Vucht J H N, Kuijpers F A, Bruning H C A M 1970 *Philips Res. Rep.* **25**, 133

Wang Yan, Chou M Y 1994 Pseudopotential plane-wave study of α-YH$_x$. *Phys. Rev. B* **49**, 13357–65

Wang Yan, Chou M Y 1995 Structural and electronic properties of hexagonal yttrium trihydride. *Phys. Rev. B* **51**, 7500–7

Westlake D G, Shaked H, Mason P R, McCart B R, Muller M H 1982 Interstitial site occupation in ZrNiH. *J. Less-Common Met.* **88**, 17–23

Wipf H 1997 *Hydrogen in Metals III* Topics in Applied Physics, Vol. 73. Springer, Berlin

Yang J B, Tai C Y, Marasinghe G K, Waddill, Pringle O A, James W J, Kong Y 2000 Structural, electronic, and magnetic properties of LaNi$_{5-x}$T$_x$ (T = Fe, Mn) compounds. *Phys. Rev. B* **63**, 014407

Yvon K 1994 Hydrides: solid state transition metal complexes. In: King R B (ed.) *Encyclopedia of Inorganic Chemistry*. Wiley, New York, pp. 1401–20

Zogal O J, Wolf W, Herzig P, Vuorimäki A H, Ylinen E E, Vajda P 2001 Probing the YD$_3$ structure by ^{2}H NMR electric-field gradients: a comparison with first-principles calculations. *Phys. Rev. B* **64**, 214110

M. Gupta

Université Paris-Sud, Orsay, France

Metal Hydrides: Magnetic Properties

Magnetism in the solid state covers a wide range of phenomena, which are intimately correlated with the localized/delocalized nature of the electrons, the crystal structure, the electronic structure, and the metallurgy

of a given metal or compound. The absorption of hydrogen in a metal or intermetallic compound leads to drastic changes of the electronic structure not only due to volume and structural changes but also due to chemical effects (see *Metal Hydrides: Electronic Band Structure*). In a simplified view the effect of hydrogen absorption upon the magnetic properties in transition metals and their intermetallics is twofold: First, the presence of hydrogen perturbs the metal–metal bonds by creation of metal–hydrogen interactions, and hydrogen contributes two electronic states but only one electron which changes the Fermi level and hence modifies the transition metal moment in the band picture. Second, hydrogen absorption commonly results in a volume expansion (i.e., negative pressure), which influences not only the strength of the magnetic exchange interaction between localized/delocalized electrons but increases also the extent of localization of their associated magnetic moments. In other words, a larger volume implies narrower bands which, on the one hand, gives rise to more localized moments and, on the other hand, may reduce the hybridization of different electronic states present in the host compound. Accordingly, the ground-state properties such as the type of magnetic order (e.g., ferro-, ferri-, antiferromagnetism, etc.), Pauli- or Van Vleck paramagnetism or superconductivity as well as their temperature dependences are significantly changed upon hydrogenation. For experimental and theoretical details, we refer to the comprehensive review articles of Buschow *et al.* (1982), Buschow (1984), Wiesinger and Hilscher (1988, 1991), Vajda (1995), and Pourarian (2002).

For the description of magnetic properties particularly the localized/delocalized nature of the electrons appears to be an important factor. One has to consider two extreme limits.

- The localized limit for which the magnetic moments and their fluctuations are localized in real space (delocalized in reciprocal space). For these systems the Heisenberg model, at least as a prototype, is appropriate where the phenomenological Weiss molecular field is just the exchange interaction which tends to align spins parallel (or antiparallel) when the exchange integral is negative (or positive). Here the carrier of magnetism is a spin and/or an angular momentum yielding localized moments, and the magnetization vanishes at T_C because of disorder between the local moments due to thermal fluctuations. Nevertheless, their absolute value (or amplitude) remains almost independent of temperature. Typical examples are 3*d*-transition metal oxides that are insulators. In these materials, the exchange interaction proceeds via oxygen, which is called superexchange. Another type of compounds with strongly localized moments are rare-earth intermetallics where the localized moment arises from the 4*f*-electrons that are well localized in space and also well screened from the surrounding by 5*s*- and 5*p*-electrons. The magnetic interaction between the 4*f*-moments is mediated by the oscillatory polarized conduction electrons and is called Ruderman–Kittel–Kasuya–Yosida (RKKY) exchange.

- The itinerant limit for which the moments and their fluctuations are delocalized in real space (localized in reciprocal space) with their amplitudes (or magnitude) being strongly temperature dependent. The simplest approach is the Stoner–Wohlfarth itinerant electron model where the magnetic moment is determined by the number of unpaired electrons in the exchange-split spin-up and spin-down bands. With growing temperature the thermal excitations of electron–hole pairs (single-particle excitations) reduce the exchange splitting and thus favor the paramagnetic state at elevated temperature. Consequently, the magnetization disappears if the absolute value of the magnetic moment goes to zero, which happens if the exchange splitting is zero. This model sufficiently describes magnetism in metals at 0 K. Unfortunately, it predicts Curie temperatures (T_C) which are 5–10 times larger than those observed experimentally, because single-particle excitations are not (or only to a reduced extent) responsible for metallic magnetism at elevated temperatures. Accordingly, for quite a long time 3*d*-magnetism has been a controversial topic, where still some problems are not completely settled. The reason for this controversy is the absence of a general agreement upon the microscopic nature of the magnetic excitations at finite temperatures in particular above and below T_C.

To solve these inconsistencies, thermally induced collective excitations of the spin system—as they are well known for localized spins—are included by Moriya to formulate a unified picture of magnetism. A similar and very promising approach by Murata and Doniach was to introduce local and random classical fluctuations of the spin system being excited thermally which are called spin fluctuations. Both models become equivalent at high temperatures and lead to a Curie–Weiss law above T_C and allow the calculation of realistic *ab initio* Curie temperatures (for details see, e.g., Mohn (2003) and references therein).

1. Binary Hydrides of d-metals

Most transition metals form hydrides at sufficiently high pressures of hydrogen. The difficult high-pressure preparation technique and the rather limited hydrogen solubility of *d*-metals constrain the available results, which are reviewed by Antonow (2002). The following binary hydrides were found to exhibit magnetic order: α-MnH$_x$, γ-MnH$_x$ and ε-MnH$_x$ order antiferromagnetically, the latter two with a collinear spin structure ($T_N \gg 300$ K for γ-MnH$_x$ and $T_N \approx 360$ K for ε-MnH$_x$). *Double h.c.p.* ε'-FeH$_x$ ($x \approx 1$) is a ferromagnet with T_C exceeding room temperature, while h.c.p. ε-FeH$_{0.42}$ is

paramagnetic down to 4 K. Hydrides of Co are ferromagnets where, in the ε-hydrides, the moments are aligned along the c-axis and decrease with increasing hydrogen content at a rate of $0.36\mu_B$ per H atom. γ_1-Ni hydride is ferromagnetic and T_C decreases with hydrogen content. The interpretation of the drastic changes of the magnetic properties mainly involves phenomenological and rather qualitative arguments based on the rigid band model. Exceptions are binary and ternary Pd-hydrides where superconductivity is induced by hydrogen absorption (see *Metal Hydrides: Electronic Band Structure*).

2. Binary Hydrides of Rare Earth and Actinides (4f- and 5f-metals)

Contrary to d-metals the rare earths absorb hydrogen readily and form solid solutions and binary hydrides (RH_x) with stoichiometries $x = 2$ and $x = 3$. The generic phase diagram according to Vajda (1995) is displayed in Fig. 1. It consists of three basic parts: (i) the metallic solid solution (α-RH_δ) with H inserted into the tetrahedral interstices of the host metal; (ii) the metallic dihydride β-$RH_{2\delta}$ crystallizing in the f.c.c. fluorite system where two hydrogen atoms occupy the two available tetrahedral sites; (iii) the insulating h.c.p. trihydride γ-$RH_{3-\delta}$ where both tetrahedral sites and one octahedral site are filled up with H. In the case of x approaching 3, metallic
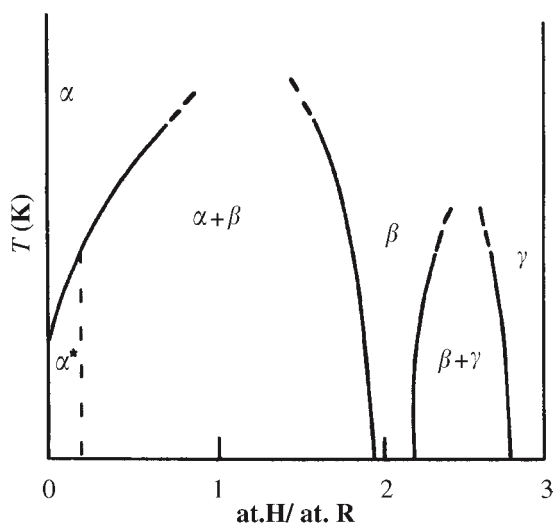
Figure 1
Schematic phase diagram for R–H systems: α, solid solution, α^*, ordered H-sublattice in some R–H solutions; β, dihydride; γ, trihydride (reproduced by permission of Vajda (1995) from *Handbook on the Physics and Chemistry of Rare Earths*, Vol. 20, pp. 207–29; © Elsevier).

conductivity disappears, which has been attributed to the formation of a low-lying s-band with the capacity to hold six valence electrons which has been confirmed to a great extent by band structure calculations. In fact, in this simple view, the number of electrons supplied to the conduction band by one R-atom and three H-atoms is equal at $x = 3$. Since this low-lying bonding band is completely filled up with electrons, in RH_3 conduction electrons are no longer present, prohibiting interactions occurring via the RKKY mechanism. This accounts for the suppression of magnetic interactions to below 3–5 K, where magnetic dipole–dipole interactions become important, which is fairly generally observed, indeed.

Considerable progress has been achieved with respect to the details in off-stoichiometric β- and γ-phases since the discovery of the metal–insulator transitions by Vajda (1995) and the associated optical properties applicable to switchable mirrors (Huiberts *et al.* 1996). The magnetic properties in the rather extended solid solution (α-RH_δ) and dihydride (β-$RH_{2+\delta}$) are significantly affected by ordering interactions between the δ-hydrogens. In the case of magnetic rare earths, this gives rise to various fascinating phenomena caused by the competition between magnetic anisotropy and RKKY interactions on the one hand and the hydrogen sublattice via crystal field interactions on the other. The peculiar quasilinear H–R–H ordering along the c-axis in the α-phase of some h.c.p. rare earth (as well as in Sc and Y) gives rise to the low-temperature ordered α^*–phase which affect the modulated magnetic structures (i.e., sinusoidal or conical) via Fermi surface topology (Vajda 2000). In the β-$RH_{2+\delta}$ phase, the excess δ-hydrogens occupying the octahedral sites in the CaF_2 structure frequently order in a tetragonal hydrogen sublattice corresponding to an $RH_{2.25}$ stoichiometry which modifies the various commensurate and incommensurate magnetic structures, sometimes leading to the appearance of short-range magnetic order or even yielding a breakdown of magnetism.

From the early actinides (Th, Pa, and U), only α- and β-UH_3 order ferromagnetically below ~ 180 K (for a summary, see Wiesinger and Hilscher 1991), while the heavier rare-earth-like actinide hydrides crystallize in the CaF_2 structure. Rather similar behavior is observed for $AH_{2+\delta}$ systems ($A = Np, Pu, Am$) as for the isostructural β-$RH_{2+\delta}$ (Vajda 2000).

3. Hydrides of Intermetallics Containing d-transition Metals and Rare-earth Metals

When a transition metal (TM) is alloyed to a rare earth (R) or a related metal as Y, Sc, and Zr, the R–$3d$ exchange interaction ($3d$–$5d$ overlap) leads to a significant reduction of the TM moment. The strong hydrogen affinity of the R-metals brings about a

decrease of the *3d–5d* overlap in the hydrides. Thus, the absorption of hydrogen frequently cancels this moment depression to a certain degree. This partial restoration of the *3d*-moment is interpreted as a hydrogen-induced screening effect. In R–*3d* intermetallics and their hydrides, where both the R- and the *3d*-elements carry a magnetic moment, we can distinguish between three main types of magnetic interactions which are quite different in nature: (i) between the localized *4f*-moments; (ii) between the more itinerant *3d*-moments; and (iii) between *3d*- and *4f*-moments. Generally, it is observed that these interactions decrease in the following sequence: $3d–3d > 4f–3d > 4f–4f$.

In contrast to binary *4f*-hydrides, for ternary R–*3d* hydrides no similar straightforward arguments can be given about the hydrogen-induced change of the magnetic order. The only statement being generally valid is that upon hydrogen absorption the magnetic order of R–Co and R–Ni compounds is considerably weakened. However, this is only rarely observed in the case of R–Fe compounds. Thus, hydrogen absorption usually weakens the magnetic coupling between *4f*- and the *3d*-moments via the reduction of the *4f–3d* exchange interaction that can lead to substantial changes of the *3d*-transition metal moment in either way. This is explained by a reduced overlap of the *3d*-electron wave functions with the *5d*-like ones due to the narrower bandwidth as a consequence of the hydrogen-induced increase in volume. Furthermore, concentration fluctuations of H-atoms over a few atomic distances may frequently occur leading to a difference in electron concentration between one site and another. This can therefore lead to a varying coupling strength and/or to competing interactions, giving rise to frustration and freezing phenomena at low temperatures. Additionally, a disturbance of the lattice periodicity takes place in the hydrides, reducing the mean free path of the conduction electrons. This leads to a damping of the RKKY conduction electron polarization, which in turn decreases the magnetic coupling strength.

If the magnetic order in R-intermetallics is dominated by *4f*-moments, the concept of an R–H charge transfer by analogy with binary rare-earth hydrides has proved to be a reasonable first approach for explanations of hydrogen-induced changes in magnetism.

In the case where *3d*-magnetism is dominant in the R–*3d* compounds, no general rule can be given. Commonly, hydrogen absorption leads to a loss in *3d*-moment in Ni- and Co-based intermetallics, but to an enhancement of the Fe-moment. For Mn-intermetallics both changes from paramagnetism to ferromagnetism and vice versa are obtained. In Fe-containing intermetallic hydrides the *3d*-states are localized to a greater extent compared to the parent compound. This leads to an enhancement of the molecular field, which, however, is opposed by the influence of the

increased Fe–Fe distance, tending to reduce it. As it is observed experimentally, the former mechanism is apparently the dominating one, yielding an increased or at least an unchanged molecular field constant n_{RFe} upon hydrogenation.

When discussing the hydrogen-induced change of the magnetic properties, one is, among other things, faced with the problem of finding reliable moment data. Frequently, one has to rely on magnetization measurements. The latter may lead to wrong results in those cases, where for experimental reasons (lack of a high field facility), only incomplete saturation has been achieved. Particularly in the case of ternary hydrides, magnetic saturation is difficult to obtain. An alternative way is offered by Mössbauer measurements. However, the problem of correlating the hyperfine field unambiguously with the magnetic moment (particularly in the case of the hydrides) still remains. Only in few cases one can refer to reliable data from neutron diffraction experiments. For a detailed summary of the experimental data in this field, we refer to Yvon and Fischer (1988).

Subsequent to the availability of synchrotron radiation (see *Magnetism: Applications of Synchrotron Radiation*), x-ray absorption (XAS), and x-ray circular magnetic dichroism (XCMD), several studies were devoted to investigations of the electronic states in hydrides. The former simplified approach, where changes of magnetic properties upon hydrogenation were frequently attributed to the influence of hydrogen on the *3d*-sublattice only, has to be modified. On the contrary, an important role is played by the rare earth sublattice through the R(*5d*)–TM(*3d*) hybridization, which is weakened upon hydrogen uptake. XCMD experiments at the $L_{2,3}$ edges of a rare-earth element and K-edge of a *3d*-transition element are particularly suitable to study hydrogen-induced changes of the magnetic properties, since they allow to probe directly the local states of the transition and the rare-earth element. Furthermore, the valence of the latter species can be determined, which in the case of Ce and Yb compounds is of essential importance. x-ray absorption near edge structure (XANES) studies are capable for probing both the electronic unoccupied states and the local structure at a selected site. In particular, L_{III} absorption spectroscopy yields information on inner shell properties, *4f*-occupation numbers, and valence shell properties of rare-earth systems that is related to the magnetic properties of the system. Due to an unstable valence, Ce and Yb compounds are of particular interest in metal hydrogen studies.

4. Hydrides of Mn Compounds

Particularly for Mn-containing ternary hydrides—where mainly RMn$_2$ and R$_6$Mn$_{23}$ have been investigated—no general prediction can be made for the changes in magnetic properties upon hydrogen

uptake. Onset and complete loss of magnetic order after hydrogen absorption are found, as well a substantial reduction of T_C and the magnetization. Moreover, spin glass behavior is frequently obtained for Mn-rich ternary hydrides, which most probably has to be related to the presence of Mn segregations. The reason for these heterogeneous results probably lies in the specific sensitivity of the magnetic properties of Mn compounds upon interatomic distances. Particularly in Mn compounds a critical Mn–Mn distance is of essential importance for the occurrence of magnetic order. In contrast to parent RMn_2 compounds, in the corresponding hydrides the Mn–Mn magnetic interaction dominates and imposes magnetic order in the rare-earth sublattice, with the result that both the R- and Mn-sublattices order at the same temperature. To completely understand the complex process of magnetic ordering present in these compounds, band structure calculations have to be performed and considered.

The Laves-phase compounds RMn_2 have been intensively studied because of their peculiar structural and magnetic properties. Two magnetic sublattices are present: the first one is built up from well-localized $4f$-moments of the rare earth, whereas the second one consists of unstable $3d$ Mn-moments, strongly dependent on the Mn–Mn distance. The topological frustration present in the parent compounds is released when hydrogen is absorbed by forming changes of the local symmetry of the magnetic ions. The hydrogen-induced lattice expansion stabilizes the Mn-moments (Goncharenko *et al.* 1999). Large increases of T_C are observed upon hydrogen uptake. The spin orientation in the hydrides commonly, differs from that observed in the parent compounds and cannot be explained by a unique set of crystal field parameters. This leads to the suggestion that the hydrogen superstructure significantly influences the anisotropy (Cadavez-Peres *et al.* 2001). $CeMn_{1.8}Al_{0.2}$ absorbs more than 4.4 H atoms/f.u., thereby undergoing a volume expansion ($\Delta V/V = 42.5\%$, which is the largest known among metal hydrides). Concomitantly, a metal atom site exchange occurs over a distance of 2.7 Å at room temperature, which is the first of that type observed in Laves phases. The exceptional high mobility of the metal atom substructure is presumably related to the valence transition Ce^{+4} to Ce^{+3}, which is accompanied by a change from Pauli paramagnetism to antiferromagnetic order below 75 K and Curie–Weiss susceptibility above; see Fig. 2 (Filinchuk *et al.* 2003).

5. Hydrides of Fe Compounds

In this case the hydrogen-induced influence on the magnetic properties is less pronounced than in Mn-compounds. Predominantly, the following stoichiometries were studied: R_2Fe_{17}, $RFe_{11}X$, $R_2Fe_{14}B$, R_6Fe_{23},
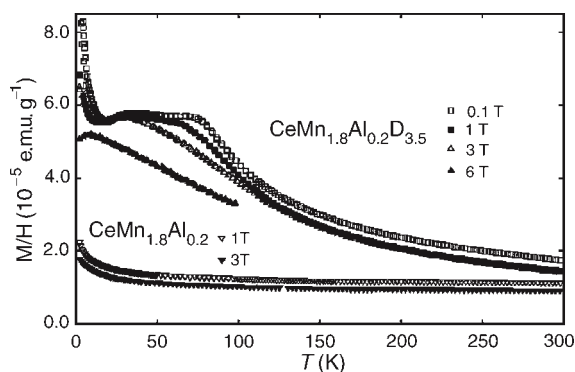
Figure 2
Zero-field cooled susceptibility (M/H) as a function of temperature for $CeMn_{1.8}Al_{0.2}$ and $CeMn_{1.8}Al_{0.2}D_{3.5}$; the antiferromagnetic order of $CeMn_{1.8}Al_{0.2}D_{3.5}$ at about 75 K is shifted to below 10 K at 6 T.

$R_6Fe_{13}X$, RFe_3, RFe_2, and Zr_3Fe. Various neutron diffraction experiments proved that there is an increase of the Fe-sublattice moment after hydrogenation, whereas the rare-earth sublattice moment is generally reduced. The Curie temperature can show changes in either direction; the behavior depends on the amount of Fe in the compound. Compensation points, whenever present in the parent material, are lowered upon the absorption of hydrogen, thus reflecting the reduced rare-earth sublattice contribution to the total magnetic order. In several cases spin reorientations upon hydrogen insertion were found. When the R–Fe exchange is comparable to the local anisotropy energy of the rare earth, the R-moment is strongly coupled to the crystal field axis randomized by the presence of hydrogen. This may lead to a fanning of the R-moments at low temperatures. In that case a hydrogen-induced rise in moment is observed; it only takes place up to a certain hydrogen concentration, beyond which a complete loss of any magnetic order is found, frequently accompanied by complete damage of the lattice periodicity.

A systematic study of almost the whole series $R_2Fe_{17}H_x$ was performed (see, e.g., Grandjean *et al.* 2002). Hydrogen uptake commonly increases the magnetic ordering temperature as well as the saturation magnetization. Spin reorientations present in the parent compound are suppressed by the insertion of hydrogen, an exception being $Pr_2Fe_{17}H_x$. There, hydrogen uptake leads to a slight decrease of the ^{57}Fe hyperfine field. In Ce_2Fe_{17}, on the other hand, the absorption of hydrogen changes the helical magnetic structure into ferromagnetic alignment of the magnetic moments within the basal plane.

While in the context of metal hydrides predominantly polycrystalline materials (mainly powder) are studied, in rare cases (as for RH_x) single crystals of hydrides could be prepared that allow us to study, for

example, the magnetocrystalline anisotropy in $R_2Fe_{17}H_x$ ($x = 0, 3$) crystals (Tereshina *et al.* 2003). In one case (R = Ho) hydrogen induces an FOMP-type transition; for R = Er this transition disappears after the absorption of hydrogen. For R = Tb an easy cone transition is observed upon H-uptake. The experimental results are interpreted on the basis of the orientation of the 4*f*-shell quadrupolar moment with respect to the direction of the electric field gradient due to the charges of the surrounding ions.

Ce exhibits intermediate valence behavior ($v = 3.3$) in $CeFe_{14}BH_x$, $CeFe_{11}H_x$, and $Ce_2Fe_{17}H_x$; this behavior is essentially unaffected by the absorption of hydrogen. This is in contrast to the usual finding that upon hydrogen absorption the significant volume expansion is associated with a change of tetravalent to trivalent Ce. In this case, the increase of the magnetization upon hydriding is not due to a significant Ce 4*f*-contribution via localization of the Ce 4*f*-moment. From XCMD signals a complete 4*f*-delocalized band is obvious, confirming that the itinerant character of the Ce 4*f*-states is also retained in the hydrides. This has to be attributed to the variation of the 3*d*(Fe)–5*d*(Ce) hybridization. It appears that although the hydrogen uptake is due to the H–Ce interatomic chemical attraction, the effect on the physical properties is rather due to a change of the Fe sublattice. The magnetism on the Fe-sites is enhanced upon hydrogen uptake, even if hydrogen is not attracted by Fe-atoms. The large-hydrogen-induced volume increase cannot be attributed to a significant change in the Ce valence; it is mainly due to a relaxation of the stressed Fe–Fe interatomic distances (Isnard *et al.* 1994).

In recent investigations on the high-performance Nd–Fe–B magnets, a group of compounds with the stoichiometry $R_6Fe_{13}X$ was found as an intergranular phase in sintered magnets. Since the Nd–Fe–B magnets are frequently produced via the hydrogen decrepitation (HDDP) process, $R_6Fe_{13}X$ hydrides became a matter of interest. Despite their large Fe-content, the parent compounds exhibit a low net magnetic moment below $1\,\mu_B$/f.u. due to a ferrimagnetic coupling of the moments. Upon hydrogen uptake, these compounds behave as ferromagnetic, exhibiting moments above $25\,\mu_B$/f.u. at room temperature (Leithe-Jasper *et al.* 1996). In the case of X = Sn, it was demonstrated by [119]Sn Mössbauer spectroscopy that a small hyperfine field, being absent in the parent compound, develops at the Mössbauer nuclei upon hydrogenation (Leithe-Jasper *et al.* 1997).

The itinerant metamagnetic transition associated with large magnetocaloric effects in $La(Fe_xSi_{1-x})_{13}$ triggered the investigation of the corresponding hydrides (Fujita *et al.* 2003). Hydrogen absorption increases both T_C and the metamagnetic transition significantly and thus makes $La(Fe_xSi_{1-x})_{13}H_y$ as one of the most promising magnetic refrigerants working in a wide temperature range around room temperature

and in fairly low magnetic fields (see *Magnetic Refrigeration at Room Temperature*).

6. Hydrides of Co Compounds

Compounds with various stoichiometries (R_2Co_{17}, $R_2Co_{14}B$, RCo_5, R_2Co_7, RCo_3, RCo_2) were studied extensively in the past, the results being treated in the reviews cited. In contrast to the corresponding Fe-systems, in all the Co-based systems hydrogen uptake reduces the magnetic order of the Co-sublattice. Values obtained for Curie temperatures and magnetic moments (R as well as Co moments) in the hydride are lower compared to those in their parent counterparts. The hydrides generally show a pronounced resistance against magnetic saturation. With ultra-high fields (up to 110 T) and high-pressure experiments ($P = 12$ kbar), it was possible to estimate the effects of lattice expansion and changes of the electronic structure in $YCo_3H_{1.8}$ and $Y(Co_{0.88}Fe_{0.12})_3H_x$ where itinerant metamagnetic transitions occur from the low-moment to the high-moment state. Upon hydrogen uptake the critical field B_c is substantially reduced (see Fig. 3), whereas upon applying pressure the critical field B_c increases at the rate of $dB/dP = 1.46\,T$ kbar^{-1}. From these data it was concluded that both contributions—the lattice expansion and changes of the electronic structure—are of similar magnitude (Bartashevich 2001), which should be proved by band structure calculations.

Yamamoto *et al.* (2002) reported on an increase of the equilibrium hydrogen pressure as a function of magnetic fields in RCo_5H_x (R = La, Pr, Sm) according to the relation $\ln(P^*/P_0) = 2B\Delta M_S/RT$, where
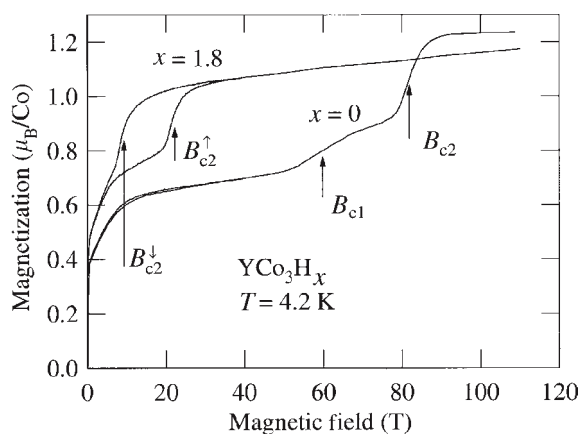
Figure 3
Magnetization as a function of external field for YCo_3 and $YCo_3H_{1.8}$; the arrows indicate the different critical field for the metamagnetic transition (reproduced by permission of Bartashevich *et al.* (2001) from *Physica B* **294–295**, 186–9; © Elsevier).
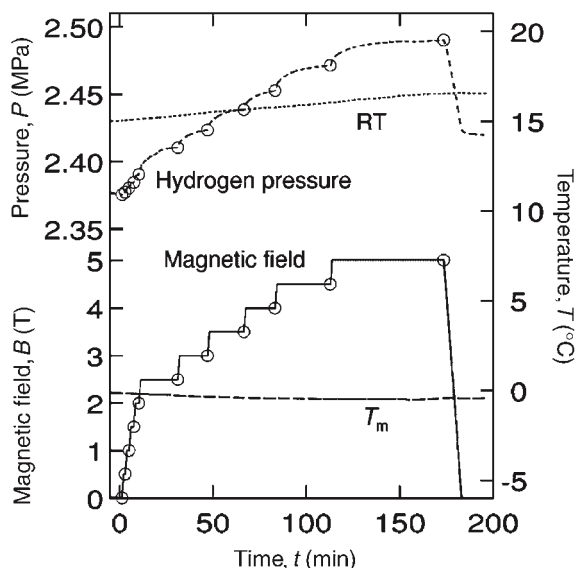
Figure 4
Time variation of magnetic field and hydrogen pressure, sample temperature (dashed line), and room temperature (dotted line) for $PrCo_5H_{4.42}$; the circles indicate the equilibria (reproduced by permission of Yamamoto (2002) from *J. Alloys Compnds.* **330–332**, 56–8; © Elsevier).

P^* and P_0 are the equilibrium hydrogen pressures under a magnetic field B, R is the gas constant is and ΔM_S is the change of the saturation magnetization per desorbed mole of hydrogen. Figure 4 demonstrates the correspondence between the field variation and changes of the hydrogen pressure, the effect of field being largest for the $\beta + \gamma$ region in $PrCo_5H_{4.4}$. In this context, it is worth noting that the magnetic-field-induced change in the heat of reaction was calculated and experimentally proved for some RCo_5H_x systems by the same group (see, e.g., Yamaguchi *et al.* 2002). For a chemical reaction the magnetic field contributes to the chemical potential, yielding magnetothermodynamic effects: as a result, when a magnetic field is applied, the heat of reaction increases in the $\alpha + \beta$ region, whereas it decreases in the $\beta + \gamma$ region for $LaCo_5H_x$.

7. Hydrides of Ni Compounds

In nearly all cases (RNi_5, R_2Ni_7, RNi_3, RNi_2, R_7Ni_3, with R being mainly La and Y) a strong reduction of the magnetic order after hydrogen absorption is obtained, which frequently leads to a complete loss of long-range order. Particularly in these Ni-containing hydrides the precipitation of f.c.c. Ni clusters can be observed. If the parent compound is paramagnetic (as, e.g., $LaNi_5$), the Ni cluster formation is readily

observed in an enhanced susceptibility or even by the onset of magnetic order. The origin of the hydrogen-induced ferromagnetism appears to be the exchange between Ni clusters mediated by the metal–H matrix (Blach and Gray 1997). In the case of Ce-containing intermetallics, the insertion of hydrogen can lead to a change from Kondo- to ferromagnetic behavior as, for example, in $CeNiInH_x$ (Chevalier *et al.* 2002). This is caused by the change of the Ce valence from intermediate in the parent compound to trivalent in the hydride, which is governed by the hydrogen-induced decrease of the hybridization between the Ce $4f$-electrons and the conduction electrons due to the large rise in volume.

See also: Magnetism in Solids: General Introduction; Alloys of $4f$ (R) and $3d$ (T) Elements: Magnetism; Density Functional Theory: Magnetism

Bibliography

Antonov V E 2002 Phase transformations, crystal and magnetic structures of high-pressure hydrides of *d*-metals. *J. Alloys Compnds.* **330–332**, 110–6

Bartashevich M I, Goto T, Yamaguchi M, Yamamoto I 2001 High field and high pressure effect on the field induced metamagnetic transition in $YCo_3H_{1.8}$. *Physica B* **294–295**, 186–9

Blach T P, Gray E, Mac A 1997 Magnetic properties of the $LaNi_5$–H system. *J. Alloys Compnds.* **253–254**, 336–8

Bobet J L, Chevalier B, Weill F, Etourneau J 2002 Magnetic behaviour of the new hydride $CePtAlH_x$. *J. Alloys Compnds.* **330–332**, 373–5

Buschow K H J 1984 Hydrogen absorption in intermetallic compounds. In: Gschneidner Jr. K A, Eyring L (eds.) *Handbook on the Physics and Chemistry of Rare Earths*. North-Holland, Amsterdam

Buschow K H J, Bouten P C P, Miedema A R 1982 Hydrides formed from intermetallic compounds of two transition metals: a special class of ternary alloys. *Rep. Prog. Phys.* **45**, 937–1039

Cadavez-Peres P, Goncharenko I N, Mirebeau I 2001 Competing magnetic anisotropies in mixed rare-earth Laves hydrides. *Phys. Rev. B* **64**, 094419-1–7

Chevalier B, Kahn M L, Bobet J L, Pasturel M, Etourneau J 2002 Occurrence of ferromagnetic transition on hydrogen insertion in the ternary indide $CeNiIn$. *J. Phys.: Condens. Matter* **14**, L365–8

Goncharenko I N, Mirebeau I, Irodova A V, Suard E 1999 Magnetic and hydrogen ordering in the frustrated Laves hydrides $RMn_2H_{4.5}$ (R = Y, Gd, Tb, Dy, Ho): a neutron-diffraction study. *Phys. Rev. B* **59**, 9324–31

Grandjean F, Isnard O, Long G J 2002 Magnetic and Mössbauer spectral evidence for the suppression of the magnetic spin reorientation in Tm_2Fe_{17} by deuterium. *Phys. Rev. B* **65**, 064429-1–10

Filinchuk Y E, Sheptyakov D, Hilscher G, Yvon K 2003 Hydrogen induced valence change and metal atom site exchange at room temperature in the C14 type sub-structure of $CeMn_{1.8}Al_{0.2}H_{4.4}$. *J. Alloys Compnds.* **356–357**, 673–8

Fujita A, Fujieda S, Hasegawa Y, Fukamichi K 2003 Itinerant electron metamagnetic transition and large magnetocaloric effects in $La(Fe_xSi_{1-x})_{13}$ compounds and their hydrides. *Phys. Rev. B* **67**, 104416-1–104416-12

Huiberts J N, Griessen R, Rector H J, Wijngarden R J, Dekker J P, de Groot D G, Koemann N J 1966 Y and La hydride films with switchable optical properties. *Nature (London)* **380**, 231–4

Isnard O, Miraglia S, Fruchart D, Giorgetti C, Pizzini S, Dartyge E, Krill G, Kappler J P 1994 Magnetic study of the $Ce_2Fe_{17}H_x$ compounds: magnetic circular x-ray dichroism, x-ray absorption near-edge structure, magnetization, and diffraction results. *Phys. Rev. B* **49**, 15692–701

Leithe-Jasper A, Skomski R, Qi Q, Coey J M D, Wetzer F, Rogl P 1996 Hydrogen in $RE_6Fe_{13}XH_y$ intermetallic compounds (RE = Pr, Nd; X = Ag, Au, Si, Ge, Sn, Pb). *J. Phys.: Condens. Matter* **8**, 3453–69

Leithe-Jasper A, Rogl P, Wiesinger G, Rainbacher A, Hatzl R, Forsthuber M 1997 A Sn119 Mössbauer study of $RE_6M_{13}Sn$ (RE = La, Pr, Nd; M = Fe, Co). *J. Magn. Magn. Mater*. **170**, 189–200

Mohn P 2003 *Magnetism in the Solid State, Springer Series in Solid State Sciences*. Springer, Berlin, Vol. 134

Pourarian F 2002 Review on the influence of hydrogen on the magnetism of alloys based on rare earth–transition metal systems. *Physica B* **321**, 18–28

Tereshina I S, Nikitin S A, Verbetsky V N, Salamova A A 2003 Magnetocrystalline anisotropy of $R_2Fe_{17}H_x$ (x = 0, 3) single crystals. *J. Alloys Compnds*. **350**, 264–70

Vajda P 1995 Hydrogen in rare earth metals, including RH_{2+x} phases. In: Gschneidner K A Jr., Eyring L (eds.) *Handbook on the Physics and Chemistry of Rare Earths*. North-Holland, Amsterdam, Vol. 20, pp. 207–91

Vajda P 2000 Hydrogen ordering and magnetic phenomena in mostly rare earth based metal hydrogen systems: highlights and open problems. *Physica B* **289–290**, 435–42

Wiesinger G, Hilscher G 1988 Magnetic properties, Mössbauer effect and superconductivity. In: Schlapbach L (ed.) *Topics in Applied Physics (Hydrogen in Intermetallic Compounds I)*. Springer, Berlin, Vol. 63, pp. 285–341

Wiesinger G, Hilscher G 1991 Magnetism of hydrides. In: Buschow K H J (ed.) *Handbook of Magnetic Materials*, North-Holland, Amsterdam, Vol. 6, pp. 511–84

Yamaguchi M, Yamamoto I, Mizusaki S, Ishikawa K 2002 Magnetic field effect on the heat of reaction in metal hydrogen systems. *J. Alloys Compnds*. **330–332**, 48–55

Yamamoto I, Mizusaki S, Ishikawa K, Ishikawa F, Shimazu Y, Yamagushi M 2002 Magnetic field effect on the equilibrium pressure for the $PrCo_5$–H system. *J. Alloys Compnds*. **330–332**, 56–8

Yvon K, Fischer P 1988 Crystal and magnetic structures of ternary metal hydrides: a comprehensive review. In: Schlapbach L (ed.) *Topics in Applied Physics (Hydrogen in Intermetallic Compounds I)*. Springer, Berlin, Vol. 63, pp. 87–138

G. Hilscher and G. Wiesinger
Technische Universität, Wien, Austria

Metal Particle versus Metal Evaporated Tape

Magnetic recording media make up a special class of permanent magnets. Storing information involves switching between different energy states so just as in conventional magnets a high-energy product is desirable. In addition, the need for a high storage density imposes the requirement for media with fine microstructure capable of supporting magnetization patterns on the submicrometer scale. A second, related, special requirement is for an extremely smooth surface finish. This is because spatially varying magnetic fields decay rapidly with distance and therefore the magnetic recording transducer must be kept close to the medium. The design philosophy for finely structured recording media is to take very small magnetic particles having a uniaxial magnetic anisotropy. The particles are too small to support a domain wall (*single-domain particles*) and essentially their rest magnetization can be in only one of two distinct states.

There are two very different commercial approaches to producing media for tape recording. In the first approach, a nonmagnetic base film is coated with an ink containing the magnetic particles and other ingredients. This type of medium is called "*particulate*" and can be found as tape or as floppy disk. The magnetic particles in use are (i) γ-Fe_2O_3, (ii) CrO_2 and cobalt-doped γ-Fe_2O_3, and (iii) metal particle (MP). It is the general consensus that metallic particles are the only particulate media that can sustain very high recording densities.

In the second approach, the recording layer is produced by thin-film deposition techniques, such as evaporation. (Sputtering is not considered a viable alternative because the achievable coating speed is too low.) Metal evaporated (ME) tape is produced by oblique evaporation in an oxygen atmosphere. ME tape is the only thin-film tape commercially available. When ME tape first appeared on the market at the beginning of the 1990s, it greatly outperformed MP tape and appeared to be the only tape medium that could sustain a very high recording density.

1. Recording Potential of ME and MP Tape

Magnetic recording media of either particulate or thin-film type are granular in nature. Fundamentally, the recording potential of a granular medium is related to the number of grains that fit into a bit. Mallinson (1969) pointed out that the maximum signal-to-noise ratio (SNR) is proportional to the particle density in a tape. At read-back, the average magnetization of all magnetic particles in the volume sensed by the read-back head determines the signal, while the deviation from the mean magnetization is noise. Tape media—including ME tape—have a relatively small volumetric packing fraction, typically smaller than 50%. (Even ME tape has a rather low packing fraction (Richter 1993a).) According to Mallinson (1991) the wide-band SNR ratio is given by

$$\text{SNR} \approx \frac{\bar{m}^2 n W \lambda^2}{2\pi(1 - p\bar{m}^2)}, \ \bar{m} = \frac{\bar{M}}{M_r} \tag{1}$$

where λ is the minimum wavelength occurring in the recording system, $\bar{M}$ is the mean magnetization sensed by the head, p is the volumetric packing fraction of the particles in the tape, and n is the number of particles per unit volume. The tape volume sensed by the head is proportional to $W\lambda^2$, which directly appears in Eqn. (1).

Therefore, it is desirable to prepare media with very small particles. Magnetically, extremely small particles—although magnetically ordered—lose their hysteresis, because the energy barriers, ΔE, separating the magnetization states are too small to withstand the thermal energy, $k_B T$ ($k_B = 1.38 \times 10^{-23}\,\mathrm{J\,K^{-1}}$ (Boltzmann's constant) and T is the temperature in kelvin). This leads to a thermally activated process with a relaxation rate, r, given by

$$r = f_0 \exp\left(-\frac{\Delta E}{k_B T}\right) \qquad (2)$$

where f_0 is the "attempt" frequency $\sim 10^{10}\,\mathrm{Hz}$. At zero applied field, the energy barrier, ΔE, is

$$\Delta E = K_1 V \qquad (3)$$

here K_1 is an anisotropy constant and V is the particle volume.

Table 1 gives some material data for ME and MP tape. The main constituent of MP tape particles is iron. The most advanced MP particles are made of an Fe–Co alloy rather than pure iron, because Fe–Co has a somewhat higher saturation magnetization. Moreover, alloying with cobalt improves the corrosion resistance of the metallic particles. MP particles are made needle-like and thus possess shape anisotropy. Since iron and Fe–Co alloys have cubic elementary cells the magnetocrystalline anisotropy can be neglected and is close to zero anyway for the higher cobalt-content Fe–Co alloys. The shape anisotropy fields in Table 1 are calculated assuming elongated ellipsoids of revolution with a ratio of the axes of five. Using the resulting anisotropy constant, $K_1 = \frac{1}{2}(\mu_0 M_s H_A)$, the minimum volume required to

achieve a stable magnetization can be calculated. In the product $\mu_0 M_s H_A$ we see the analogy with the energy product used to characterize permanent magnets. For a lifetime of ~ 10 years, Eqn. (2) yields a required energy barrier of $40\,k_B T$. The magnetic volume given in Table 1 yields an energy barrier of $80\,k_B T$, which provides an adequate margin to tolerate demagnetizing fields and elevated temperatures. Since pure metallic particles are pyrophoric, the particles are surface oxidized. The oxide shell is nonmagnetic and has a thickness of only 3 nm. Therefore, the required (physical) particle volume is significantly larger than the required magnetic volume.

A similar consideration applies to ME tape. Since there is not much information available about the shape of the magnetic subunits, the shape anisotropy contribution has been set to zero. Since ME tape is manufactured in the presence of oxygen, a part of the magnetic layers is oxidized. In contrast to MP tape, the oxidized volume fraction is considerably smaller. The magnetic particle volumes for both types of tape are rather similar, but the physical particle volumes are considerably larger for MP tape. Evidently, the balance between ME and MP tape shifts if the amount of oxygen in either tape can be reduced.

The foregoing analysis is highly simplified and implies that the magnetization reversal process follows the Stoner–Wohlfarth model (Stoner and Wohlfarth 1948). In reality, the magnetization in MP tape switches at lower fields, typically between $150\,\mathrm{kAm^{-1}}$ and $200\,\mathrm{kAm^{-1}}$, which can be because of incoherent switching processes such as curling (Aharoni 1986), or deviations from the ellipsoidal shape (Seberino and Bertram 1999). It has also been reported that the metallic core of MP can consist of several crystallites (Veitch *et al.* 1994), which leads to incoherent magnetization reversal and to a reduced thermal stability. It should also be noted that the coercivity measured in a magnetometer is lower than that at writing. This is an effect of thermally activated magnetization processes and can be derived from Eqn. (2) (Sharrock and McKinney 1981). ME tape does not follow the model of coherent rotation either. Thin films containing

Table 1

Magnetic properties of iron and Fe–Co as used for MP tape, and cobalt and $Co_{0.8}Ni_{0.2}$ as used for ME tape. The shape anisotropy values are calculated assuming an aspect ratio for the particle of five. The magnetic volume represents the minimum volume of the magnetic material to achieve an energy barrier of $80\,k_B T$. For MP tape, a nonmagnetic oxide shell of thickness 3 nm is assumed, for ME tape the volume of the oxide is assumed to be 45% that of the metallic core.

Material	M_s (kA m^{-1})	H_A^{shape} (kAm^{-1})	$H_A^{crystaline}$ (kAm^{-1})	V_{mag} (nm^3)	V_{tot} (nm^3)	l_{tot} (nm)
Fe	1710	712		433	3971	33
Fe$_{0.7}$Co$_{0.3}$	1926	802		341	3552	31
Co$_{80}$Ni$_{0.2}$	1170		584	770	1117	
Co	1436		584	627	910	

cobalt generally contain stacking faults, which reduce the anisotropy and, in particular, the switching field down to values of 100–150 kAm^{-1}. Unlike particulate tape, magnetic exchange interaction between the magnetic subunits cannot be entirely excluded.

Since neither of the two tape materials can be described by the model of coherent rotation, the values for the critical volumes given in Table 1 do not—strictly speaking—apply. Nonetheless, the critical volume for the ME tape "particles" can be expected to be smaller owing to the lesser amount of oxygen built into the tape. This gives ME tape an advantage over MP tape, with an estimated factor of two in critical volume. Applying Eqn. (1), one would therefore expect an advantage of 6 dB in SNR for ME tape over MP tape. The potential gain of ME tape over MP tape is therefore rather moderate (see also Richter and Veitch (1995)).

2. Structure and Manufacture of MP and ME Tapes

2.1 MP Tape

Figure 1 shows a schematic view of the cross-section of standard MP tape. The tape consists of a base film, a back coating, and the magnetic layer. In standard MP tape, the magnetic powder accounts for roughly 40% of the volume of the magnetic layer. In addition to the metal powder, the magnetic layer contains carbon black, abrasive particles of Al_2O_3, dispersants,
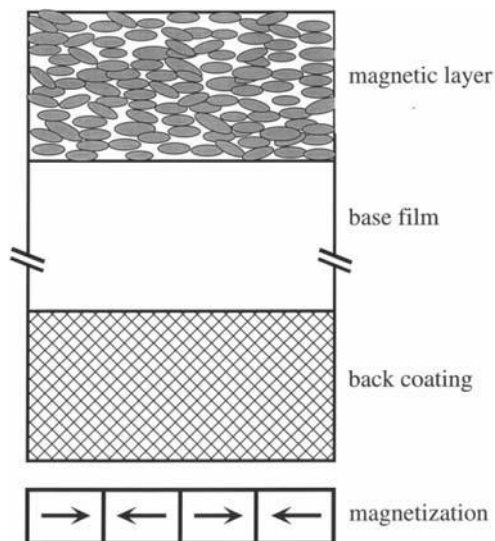
Figure 1
Cross-sectional view of MP tape. The magnetic particles are needle-shaped. The bottom sketch indicates that particulate tapes are magnetized longitudinally.

and lubricants, all held in a plastic binder system. It is essential that the magnetic particles are well dispersed in the coating ink. Very fine MP particles can be better dispersed if a high shear premix or kneading stage is added to the process. Shortly after the coating process, the still wet coating is magnetically oriented. After the alignment, the coating has to dry until the chemical reactions in the binder system are complete. The next step is to "calander" the tape. A calander presses the tape between polished rollers at a high temperature. This treatment results in a compressed magnetic film and, most importantly, in a very smooth surface finish.

2.2 Double-layer Coating of MP Tape

Although double, or even multiple, coating is an old idea, the exciting and reinvigorating developments are more recent. Double-layer MP media have a very thin magnetic layer and a nonmagnetic underlayer that contains very small TiO_2 or $\alpha\text{-}Fe_2O_3$ particles (Inaba *et al.* 1993). The two layers are coated simultaneously. The first commercial product made on this principle was a Hi-8 videotape with considerably improved recording performance. It is not the thinness of the magnetic layer itself—which is about 400 nm for this tape—but the improved surface smoothness that provides the additional output. It has been demonstrated that magnetic layers as thin as 120 nm (Saitoh *et al.* 1995, Richter and Veitch 1995) or even 100 nm (Inaba *et al.* 1998) can be achieved. MP tapes can now virtually match the performance of advanced metal evaporated (AME) tapes of the kind used in the consumer Digital Video system (Inaba *et al.* 1998).

2.3 ME Tape

Figure 2 shows a schematic cross-section of ME tape. The obvious difference between MP and ME tape is the magnetic storage layer. ME tape is manufactured by oblique evaporation of cobalt or $Co_{0.8}Ni_{0.2}$ in an oxygen atmosphere. At the beginning of the evaporation of the layer, the vapor arrives at the substrate at grazing incidence. A film grown at grazing incidence shows uniaxial anisotropy in an oblique direction. These films are porous and it has been found that finished ME tapes can contain as much as 50% voids (Richter 1993a). Roll-coaters operate in a wide range of evaporation angles (continuously varying incidence, CVI (Shinohara *et al.* 1984)), whereby deposition is started at grazing incidence to preserve oblique anisotropy. A CVI process leads to a curved columnar microstructure. The magnetically easy axis is tilted out of the film plane with a tilt angle roughly coinciding with the angle at which the columns start to grow on the base film, typically around 35°. For improvement of particle separation and material yield, the evaporation is performed in the presence

of oxygen. The oxidation of the magnetic material largely removes exchange coupling in ME tape.

Apart from the magnetic layer, there are other differences between ME and MP tape:

(i) For mechanical protection, ME tape typically has a carbon overcoat, which is reactively sputtered. This carbon layer is of the diamond-like carbon (DLC) type and is 5–10 nm thick.

(ii) The lubricant has to be applied as a separate layer on top of the thin-film medium. In MP tape, the pores in the coating serve as reservoirs for the lubricant.

(iii) The surface of the base film, onto which the magnetic layer is deposited in ME tape, carries a thin coating with very small particles. After deposition of the magnetic film, the surface of the magnetic layer then shows "nodules." These nodules are about

10–20 nm high and have a density of 10–50 μm^{-2}. The invention of the nodules has been the technological breakthrough for ME tape. The nodules improve tribology at the expense of an additional spacing loss that sacrifices a small amount of the recording performance.

From a manufacturing point of view, MP tape is very attractive because existing coating technology can be used, whereas ME tape requires a switch to vacuum technology, which is associated with a big investment. Clearly, MP tape is much more economical, and many tape makers have opposed a technology switch to ME tape.

3. Magnetic Properties of MP and ME Tape

Some magnetic parameters of ME and MP tape are summarized in Table 2. Owing to the inclination of the easy axis out of the film plane, the magnetization of the tape is tilted out of the film plane. Initially, little attention was paid to the demagnetization effects present in simple measurements of the magnetic properties. Magnetic properties of regular particulate tapes are measured in the longitudinal direction, which coincides with the alignment direction (i.e., the easy axis of the tape). For ME tape, this standard procedure yields low values for the squareness (ratio of remanent magnetization and saturation magnetization) and large values for the switching field distribution (SFD). The SFD is related to the normalized slope of the hysteresis curve:

$$\text{SFD} = 1 - \frac{H_C dM}{M_r dH}\bigg|_{\text{at } H=H_C}$$

Magnetically, ME tapes did not seem to be very attractive.

If the tape magnetization has a perpendicular component, there is a perpendicular demagnetization field that has to be added *vectorially* to the applied field. The magnetic "particles" in the tape therefore do not "see" the external field alone, rather the vectorial sum of the external field, $\vec{H}_a$, and the film-demagnetizing field, $\vec{H}_d$:

$$\vec{H}_i = \vec{H}_a + \vec{H}_d \tag{4}$$
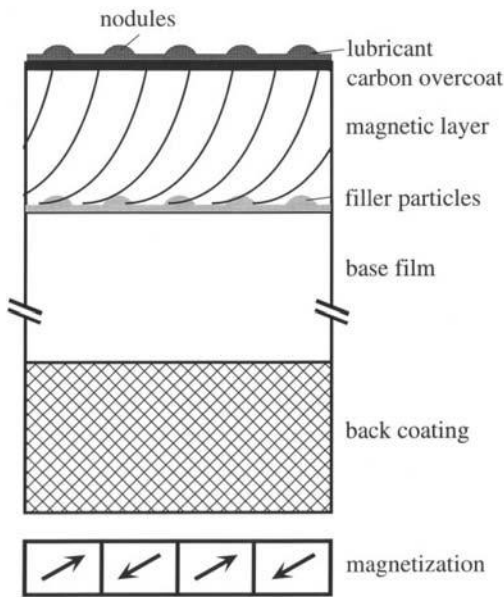
Figure 2
Cross-sectional view of ME tape. The filler particles underneath the magnetic layer give rise to nodules sticking out of the film plane. The easy axis of magnetization is tilted out of the film plane.

Table 2
Magnetic parameters of ME and MP tapes.

Application	Type	M_r (kAm^{-1})	H_c (kAm^{-1})	Coating (μm)	n (1000 μm^{-3})
Hi8 tape	MP	200	120–135	2–3	8
	ME[a]	350	90	0.2	~125
DVC tape	MP	>300	180	0.15	50
	ME[a]	450	135	0.15	~125

a Intrinsic properties.
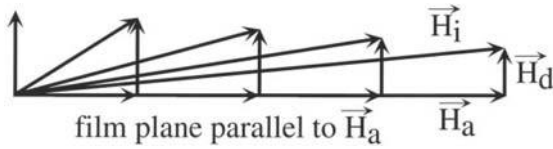
Figure 3
Evolution of internal field during a hysteresis loop measurement of ME tape.

The demagnetizing field is always directed perpendicular to the film plane with $H_d = -M_\perp$, where $M_\perp$ is the perpendicular magnetization of the film. A careful examination shows that during the course of a conventional hysteresis loop measurement in the film plane, the internal field *rotates* when the direction of the external field is held fixed (see Fig. 3). Since a proper hysteresis measurement implies that the applied field direction is not changed, results from a conventional hysteresis loop measurement are highly misleading. Keeping the internal field direction fixed therefore requires that the direction of the external field be continuously adjusted during the measurement. These compensated measurements have been done (Bernards and Cramer 1992, Richter 1993a) and they indicate that the intrinsic properties of ME are excellent: a very square loop with a high squareness and a narrow SFD has been observed.

4. Recording Properties

The ultimate recording potential of ME and MP tape was estimated in Sect. 1. The considerations there imply that the dominant noise source in a recorder is the particle noise of the magnetic medium. In a recorder, however, there are other noise sources present and the absolute output signal of the medium becomes important, especially for inductive readout. This favors high-magnetization media, such as ME and MP tape, and consequently none of the older particulate media are considered for high-density tape recording. The introduction of magnetoresistive (MR) heads, which are more sensitive than inductive heads, de-emphasizes the output requirements.

The most critical parameter in a recording system is the head-to-medium spacing. At read-back, the flux decreases exponentially with distance to the tape surface:

$$\phi \propto \exp(-kz) \Leftrightarrow -55z/\lambda \text{ dB} \tag{5}$$

where z is the distance from the top surface of the medium, $k = 2\pi/\lambda$, and λ is the recorded wavelength of a sinusoidal magnetization.

Equation (5) is called "spacing loss" and is an inevitable consequence of the Laplace equation in two dimensions (Mallinson 1993, Bertram 1994). The derivation assumes that the track width is much larger

than the other dimensions of the recording system, which is the case in all practical recorders. In addition to the reading spacing loss, there is a writing spacing loss. The writing spacing loss is of the order of $45z/\lambda$ dB (Bertram and Niedermeyer 1982), such that the total spacing loss amounts to roughly $100z/\lambda$ dB. In order to reduce head-to-medium spacing, it is therefore required to create a very smooth tape surface. Unfortunately, adhesion occurs between excessively smooth surfaces, so that one has to strike a delicate balance between electrical and mechanical performance.

To achieve a high output, the width of a magnetization transition between regions magnetized in opposite directions needs to be kept as small as possible. To first order, the effect of transition width on the recording output is the same as that of a spacing loss (Bertram 1994). The width of a transition is determined by the following factors:

(i) *Demagnetization*. This occurs at the instant of writing and is proportional to the ratio of remanent magnetization and coercivity of the medium. The first paper to recognize this was that of Williams and Comstock (1971).

(ii) *Particle length ("length loss")*. The transition width cannot be smaller than the length of a particle (Richter and Veitch 1996). Early MP tapes had particle lengths of 150 nm or even longer which affected recording of very short wavelength. Modern MP tapes have particle lengths down to 100 nm and lower such that the length loss effect is small. In addition, smaller particles potentially allow smoother tape surfaces. Shorter lengths will be necessary if the linear recording density is to be increased. Particles of about 60 nm have been made (Hisano and Saito 1998) but they suffer from a poorer SFD.

(iii) *Switching field distribution*. This would determine the transition width if no demagnetization and no limitation by the particle length were present. For ME tape, the SFD can considered to be very small; for MP tape the narrowest values achieved are about 0.2.

(iv) *Coating thickness*. This obviously determines the output of the tape. However, thicker coatings generally produce wider transitions, either caused by greater demagnetization or by geometrical effects (Richter 1997). Examples for some transitions are given in Fig. 4. For many tapes, however, the total thickness of the coating is not at all relevant. The depth of recording is roughly equal to the gap length of the writing head such that the particles at the bottom of a thick magnetic coating remain untouched (partial penetration recording). In addition, spacing loss effects attenuate the contributions from the deeper layers of the tape, especially for short wavelengths. ME tape coatings are 150–200 nm thick, but even those are not fully recorded throughout their depth. It has been shown experimentally and theoretically that thin-film MP tapes do not have a higher

MP tape

medium movement

thin tape

head

ME tape

medium movement

easy axis

head
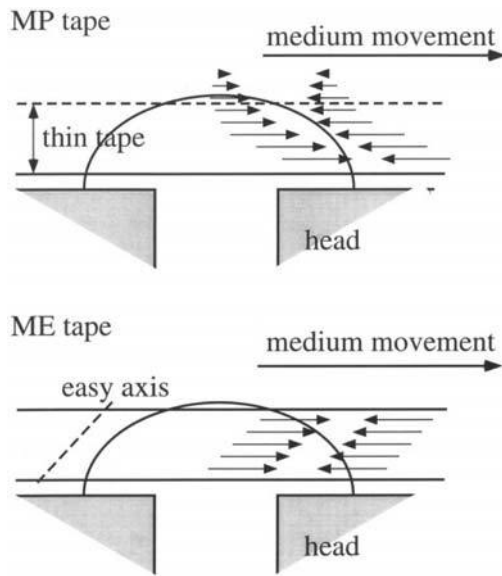
Figure 4
Schematics of recorded transitions for MP and ME tape.
In MP tape, the top layers of the tape are recorded
further downstream, while the opposite is true for ME
tape. The dashed line in the upper figure indicates how
thick is a "thin" MP tape coating.

output at short wavelength than thick tapes (Richter
and Veitch 1995, Richter 1997). On the contrary,
thinner tapes show a lower output for long-wave-
length recording. Thin magnetic coatings are advan-
tageous for overwrite behavior (Richter and Veitch
1995, Veitch *et al*. 1999). For identical coating thick-
ness, ME tape is found to have a much improved
overwrite over MP tape owing to its superior intrinsic
properties and the tilt of the easy axis.

(v) *Direction of the easy axis*. It has been discovered
that ME tape exhibits a recording anisotropy: the
recording output in the two directions differs by
about 6 dB. The high output is observed when the
recording head runs over the medium as shown in
Fig. 4. Modeling results indicate that the optimum tilt
of the easy axis is between $20°$ and $30°$ out of the film
plane and that the output increase over an easy axis
in the tape plane is only moderate (Richter 1993b,
Stupp *et al*. 1994). The oblique recording inherent to
ME tape also reduces nonlinear intersymbol interfer-
ence (Mallinson 1989, Cumpson and Stupp 1997).

5. The Future: ME or MP Tape?

As discussed in Sect. 2, ME tape has a higher re-
cording potential and some other advantages in re-
cording behavior. Apart from the improved
recording performance, ME tape can also be made

thinner. If the base film, for example, has a thickness
of $5 \mu m$, the total thickness of the tape is roughly
$5.2 \mu m$. This has to be contrasted with MP tape,
where the total tape thickness is roughly $6 \mu m$. The
MP tape is thicker because any particulate coating
(double layer, single layer) cannot yet be made thin-
ner than roughly $1 \mu m$, and thus more ME tape than
MP tape can be wound into a given cassette.

However, ME tape can be recorded in only one
direction, which effectively limits its use to helical
scan systems, whereas the major new data storage
systems (Digital Linear Tape and Linear Tape Open)
use serpentine linear recording, reversing direction at
the end of the tape. While ME is simply ruled out for
these systems, it may seem surprising that it has not
been adopted for the latest helical scan data system
DD4. We can conclude that the advantages of ME
tape over MP tape are too small to justify moving to
a new technology. It should not be forgotten that a
technology switch is also associated with risks, and—
although tremendous progress in ME tape has been
made—the tribological properties of particulate tape
still have to be regarded as superior to those of ME
tape. It is therefore likely that MP tape will be the
dominant tape recording medium in the future.

See also: Magnetic Recording: Flexible Media,
Tribology; Magnetic Recording Media: Advanced;
Metal Evaporated Tape; Magnetic Recording Tech-
nologies: Overview

Bibliography

Aharoni A 1986 Perfect and imperfect particles. *IEEE Trans. Magn.* **22**, 478–83
Bernards J P C, Cramer H A J 1991 Vector magnetization of recording media: a new method to compensate for demag-netizing fields. *IEEE Trans. Magn.* **27**, 4873–5
Bertram H N 1994 *Theory of Magnetic Recording*. Cambridge University Press, Cambridge
Bertram H N, Niedermeyer R 1982 The effect of spacing on demagnetization in magnetic recording. *IEEE Trans. Magn.* **18**, 1206–8
Cumpson C R, Stupp S E 1997 Experimental and theoretical studies of nonlinear transition shift in metal evaporated tape. *IEEE Trans. Magn.* **33**, 2968–70
Hisano S, Saito K 1998 Research and development of metal powder for magnetic recording. *J. Magn. Magn. Mater.* **190**, 371–81
Inaba H, Ejiri K, Abe N, Masaki K, Araki H 1993 The ad-vantages of the thin magnetic layer on a metal particulate tape. *IEEE Trans. Magn.* **29**, 3607–12
Inaba H, Ejiri K, Masaki K, Kitahara T 1998 Development of an advanced metal particulate tape. *IEEE Trans. Magn.* **34**, 1666–8
Mallinson J C 1969 Maximum signal-to-noise ratio of a tape recorder. *IEEE Trans. Magn.* **5**, 182–6
Mallinson J C 1989 Proposal concerning high-density digital recording. *IEEE Trans. Magn.* **25**, 3168–9
Mallinson J C 1991 A new theory of recording media noise. *IEEE Trans. Magn.* **27**, 3519–31

Mallinson J C 1993 *The Foundations of Magnetic Recording*, 2nd edn. Academic Press, San Diego, CA

Richter H J 1993a An analysis of magnetization processes in metal evaporated tape. *IEEE Trans. Magn.* **29**, 21–33

Richter H J 1993b An approach to recording on tilted media. *IEEE Trans. Magn.* **29**, 2258–65

Richter H J 1997 A generalized slope model for magnetization transitions. *IEEE Trans. Magn.* **33**, 1073–84

Richter H J, Veitch R J 1995 Advances in magnetic tapes for high density information storage. *IEEE Trans. Magn.* **31**, 2883–8

Richter H J, Veitch R J 1996 A reconsideration of length loss effects. *J. Magn. Magn. Mater*. **155**, 335–7

Saitoh S, Inaba H, Kashiwagi A 1995 Developments and advances in thin layer particulate recording media. *IEEE Trans. Magn.* **31**, 2859–64

Seberino C, Bertram H N 1999 Numerical study of hysteresis and morphology in elongated tape particles. *J. Appl. Phys.* **85**, 5543–5

Sharrock M P, McKinney J T 1981 Kinetic effects in coercivity measurements. *IEEE Trans. Magn.* **17**, 3020–2

Shinohara K, Yoshida H, Odagiri M, Tomago A 1984 Columnar structure and some properties of metal evaporated tape. *IEEE Trans. Magn.* **20**, 824–6

Stoner E C, Wohlfarth E P 1948 A mechanism of magnetic hysteresis in heterogeneous alloys. *Trans. R. Soc.* **A240**, 599–642

Stupp S E, Cumpson S R, Middleton B K 1994 A quantitative multi-layer recording model for media with arbitrary easy axis orientation. *J. Magn. Soc. Jpn.* **18** (Suppl. S1), 145–8

Veitch R J, Ilmer A, Lenz W, Richter V 1999 MP technology for a new generation of magnetic tapes. *J. Magn. Magn. Mater*. **193**, 279–83

Veitch R J, Richter H J, Poganiuch P, Jakusch H, Schwab E 1994 Thermal effects in small metallic particles. *IEEE Trans. Magn.* **30**, 4074–6

Williams M L, Comstock R L 1971 An analytic model of the write process in digital magnetic recording. *AIP Conf. Proc.* **5**, 738–42

H. J. Richter
Seagate Recording Media, Fremont, California, USA

R. J. Veitch
BASF AG, Ludwigshafen, Germany

Metamagnetism: Itinerant Electrons

Itinerant electron metamagnetism (IEM) is a first-order field-induced transition from the paramagnetic state to the ferromagnetic one in itinerant electron systems. This phenomenon is closely related to the instability of ferromagnetism (see *Itinerant Electron Systems: Magnetism (Ferromagnetism)*). Since this phenomenon was predicted to occur by Wohlfarth and Rhodes (1962), many experimental studies using ultrahigh magnetic fields have been done to observe it. Now, many metamagnetic compounds such as pyrites $Co(S_{1-x}Se_x)_2$, Laves phase compounds such as YCo_2, $Y(Co_{1-x}Al_x)_2$, $LuCo_2$, and $Lu(Co_{1-x}Ga_x)_2$ are found. This article first outlines theoretical concepts of IEM and then presents experimental results on the magnetic and electrical properties and magnetovolume effects of these compounds together with alloying and pressure effects on the metamagnetic transition.

1. Theoretical Background

Wohlfarth and Rhodes (1962) first discussed IEM using a Landau-type expression for the free energy of the itinerant electron system based on the Stoner model. They pointed out that IEM is expected to occur in a strongly exchange-enhanced paramagnet with a broad maximum in the temperature dependence of the susceptibility. More detailed conditions for the appearance of IEM at $T = 0$ were given by Shimizu (1982). Later, a theory of IEM at finite temperature, based on the spin fluctuation model, was developed by Moriya (1986) and Yamada (1993).

The magnetic behavior of itinerant electron paramagnets in magnetic fields depends on the shape of the density of states (DOS) near the Fermi level (see *Itinerant Electron Systems: Magnetism (Ferromagnetism)*). The paramagnet does not satisfy the Stoner condition for the appearance of ferromagnetism, $I\rho(\varepsilon_F) > 1$, where I is the exchange energy of electrons and $\rho(\varepsilon_F)$ $(= \rho_\uparrow(\varepsilon_F) + \rho_\downarrow(\varepsilon_F))$ is DOS at the Fermi level ε_F. If $\rho(\varepsilon_F)$ increases with field in a strongly exchange-enhanced paramagnet, however, the Stoner condition will be satisfied in a high magnetic field and a ferromagnetic state will appear. When the function of $\rho(\varepsilon)$ has a positive curvature near ε_F, $\rho(\varepsilon_F)$ increases with field. This is one of the conditions for IEM, as discussed below.

The equation of state for the itinerant electron system at $T = 0$ is written as

$$B = aM + bM^3 + cM^5 \tag{1}$$

where B is the magnetic field, M the magnetic moment, and a the inverse susceptibility χ^{-1} (Shimizu 1982). The coefficients a, b, and c are functions of DOS and its derivatives at ε_F. At a temperature $T > 0$, the coefficients in Eqn. (1) are renormalized by thermal spin fluctuations and the equation is rewritten as

$$B = A(T)M + B(T)M^3 + C(T)M^5 \tag{2}$$

where $A(T)$ is the inverse susceptibility $\chi(T)^{-1}$ (Moriya 1986, Yamada 1993). The coefficients $A(T)$, $B(T)$, and $C(T)$ are functions of a, b, c, and the square of the amplitude of thermally fluctuating moment $\xi(T)^2$. $\xi(T)^2$ is an increasing function of T and proportional to T^2 at low T.

Moriya (1986) determined the magnetic phase diagram for $a > 0$, $b < 0$, and $c > 0$. The negative value of b indicates that the DOS curve has a positive

curvature near the Fermi level. The ground state is paramagnetic for $ac/b^2 > 3/16$. IEM appears under the condition

$$\frac{3}{16} < \frac{ac}{b^2} < \frac{9}{20} \qquad (3)$$

However, IEM does not occur for $ac/b^2 \geqslant 9/20$. For $0 < ac/b^2 < 3/16$, the ground state becomes ferromagnetic even in zero field although the Stoner condition ($a < 0$) is not satisfied. Figure 1 shows the theoretical phase diagram for $a > 0$, $b < 0$, $c > 0$ in the narrow region $0.16 \leqslant ac/b^2 \leqslant 0.21$ near the appearance of ferromagnetism. Since the value of $c\xi(T)^2/|b|$ increases monotonically with increasing T, the ordinate is considered as the T axis. The ferromagnetic transition (FT) occurs on the T_C curve. FT is second order for $0 < ac/b^2 < 5/28$ and first order for $5/28 < ac/b^2 < 3/16$, where the value of T_C abruptly decreases with increasing ac/b^2. The type of FT changes at point T_t on the T_C curve. Note that IEM appears also just above T_C in $5/28 < ac/b^2 < 3/16$. The T_0 line merges into the T_C line at T_t.

The inverse susceptibility is given by the relation (Yamada 1993)

$$\chi^{-1} = a + \frac{5}{3}b\xi(T)^2 + \frac{35}{9}c\xi(T)^4 \qquad (4)$$

Under the condition $ac/b^2 > 5/28$, χ becomes maximum at a temperature $T_{\max}$. Thus, the paramagnetic system with IEM has a broad maximum in $\chi(T)$, which increases in proportion to T^2 at low T. The system with the first-order FT also has a broad maximum in $\chi(T)$ above T_C.

The temperature dependence of the average critical field for IEM is given by

$$B_c(T) = B_c(0) + \frac{1}{16}\sqrt{|b|/3c}\,|b|\,\xi(T)^2 \qquad (5)$$

Therefore, the critical field increases with T as T^2 at low T (Yamada 1993).

2. Observations of Itinerant Electron Metamagnetism

2.1 Laves Phase Compounds MCo_2 (M: Y and Lu)

The Laves phase compounds YCo_2 and $LuCo_2$ are typical $3d$ systems with IEM. $ScCo_2$ is believed to exhibit IEM. These compounds are strongly exchange-enhanced paramagnets. The susceptibility $\chi(T)$ increases with T at low T followed by a maximum at a temperature $T_{\max}$. At high T, $\chi(T)$ obeys the Curie–Weiss law. $\chi(T)$ in the low T region increases in proportion to T^2. The T^2 dependence is caused by the excitation of spin fluctuations and can be explained with Eqn. (4) (Yamada 1993).

Goto *et al.* (1989, 1990) observed IEM in YCo_2 and $LuCo_2$ around 70 T. The magnetization curve of $LuCo_2$ is shown in Fig. 2 (see Fig. 3 for that of YCo_2). In $ScCo_2$, however, IEM does not occur in ultrahigh magnetic fields up to 120 T. The high-field susceptibility of YCo_2 and $LuCo_2$ is very large above

Figure 1
Theoretical phase diagram for $a > 0$, $b < 0$, $c > 0$ in the narrow region $0.16 \leqslant ac/b^2 \leqslant 0.21$ near the appearance of ferromagnetism.
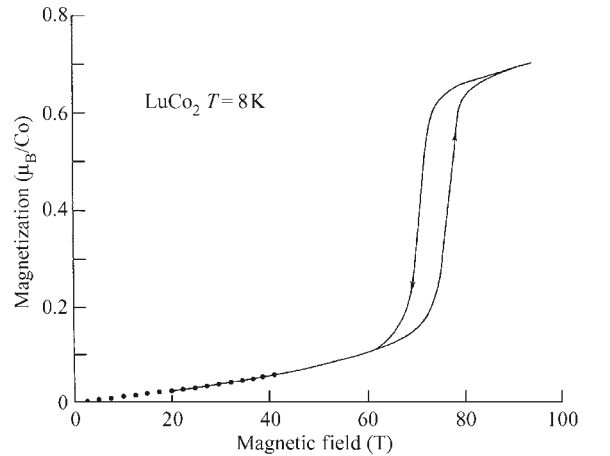
Figure 2
Magnetization curve of $LuCo_2$. The metamagnetic transition can clearly be seen.
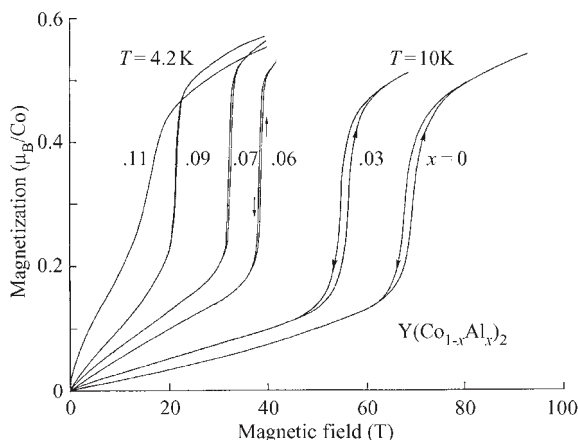
Figure 3
Magnetization curves of paramagnetic $Y(Co_{1-x}Al_x)_2$ with $x \geqslant 0.11$ at low T.

Figure 4
Spontaneous magnetization M_s and the Curie temperature T_C of $Lu(Co_{1-x}Ga_x)_2$.

B_c, which indicates that the magnetization is not completely saturated by the metamagnetic transition (MT). MT is very sharp at low T, but becomes broad with increasing T. The critical temperature for the disappearance of the first-order MT is determined to be $T_0 = 100 \pm 10$ K for YCo_2 (Goto *et al.* 1994).

According to the band model of IEM, the critical field is expected to change sensitively by shifting the position of the Fermi level in the DOS curve. This phenomenon has been examined using samples of $Y(Co_{1-x}M_x)_2$ (M = Fe, Ni, and $Fe_{0.5}Ni_{0.5}$) (Goto *et al.* 1994). Iron substitution shifts the Fermi level to the lower energy side, while nickel substitution shifts it to the higher energy side. With increasing x, B_c decreases in $Y(Co_{1-x}Fe_x)_2$, but increases in $Y(Co_{1-x}Ni_x)_2$. The change of B_c can easily be understood by considering the band structure. Since iron substitution increases the DOS at the Fermi level, the parameter a in Eqn. (1) decreases. This causes the reduction of B_c. However, an increase in B_c is expected by nickel substitution. In the case of doping with equal amount of iron and nickel, no change of B_c is expected. In fact, the observed change of B_c is very small for the doping.

The substitution of aluminum for cobalt in YCo_2 expands the lattice and enhances the susceptibility χ (Yoshimura *et al.* 1985). The position of T_{max} shifts to the low T side and a weak ferromagnetism appears in $Y(Co_{1-x}Al_x)_2$ with $0.12 \leqslant x \leqslant 0.19$. Figure 3 shows the magnetization curves of paramagnetic $Y(Co_{1-x}Al_x)_2$ with $x \geqslant 0.11$ at low T (Goto *et al.* 1994). These compounds exhibit IEM. The average critical field B_c decreases nearly linearly with increasing x and is found to be proportional to T_{max}, $B_c/T_{max} = 0.29$ [T/K] (Goto *et al.* 1994).

The field B_c of $LuCo_2$ also decreases and a ferromagnetic state becomes stable by replacing cobalt with gallium (Murata *et al.* 1993). The critical
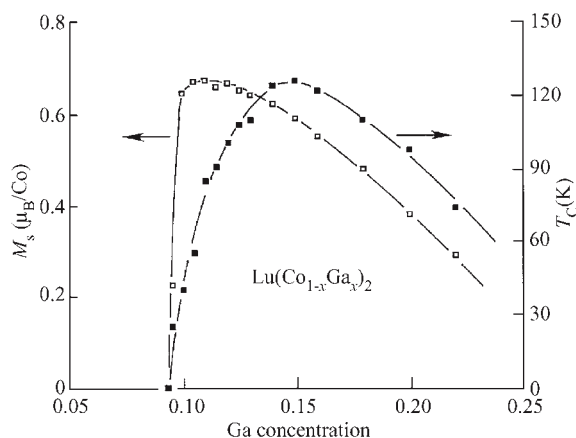
concentration of $Lu(Co_{1-x}Ga_x)_2$ for the onset of ferromagnetism is $x_c \approx 0.095$ (Saito *et al.* 1997). The field-induced moment in the paramagnetic compound is consistent with the spontaneous moment M_s of the ferromagnetic one. Figure 4 shows the value of M_s and T_C as a function of x, which increases abruptly at x_c, where B_c becomes zero (Saito *et al.* 1997). These results imply that the appearance of IEM is related to the instability of ferromagnetism.

When the nonmagnetic M atom in MCo_2 is replaced with magnetic rare earth R, the cobalt moment is induced by the effective field from the R site. The effective field can be evaluated using the relation $B_{eff} = 84(g_J - 1)J$ [T], where g_J is the g-factor of R and J the total angular momentum (Goto *et al.* 1989). The induced cobalt moment is found to increase rapidly at about 70 T, indicating that the effective field produces MT. This value corresponds to the critical field of YCo_2.

2.2 Pyrites $Co(S_{1-x}Se_x)_2$

The CoS_2 compound with the pyrite structure is an itinerant ferromagnet with $T_C \cong 120$ K. The substitution of selenium for sulfur in CoS_2 makes the $3d$ band wider and changes the second-order FT to the first-order one accompanied by a rapid decrease of T_C. The $Co(S_{1-x}Se_x)_2$ compounds with $x \geqslant 0.12$ are paramagnetic and exhibit a broad maximum in $\chi(T)$.

IEM was first observed in paramagnetic $Co(S_{1-x}Se_x)_2$ by Adachi *et al.* (1979). Later, detailed studies were done by Goto *et al.* (1997). Figure 5 shows the magnetization curves of $Co(S_{1-x}Se_x)_2$ for 4.2 K (Goto *et al.* 1997). The average critical field B_c increases linearly with x. The magnetization in the induced ferromagnetic state is consistent with the spontaneous
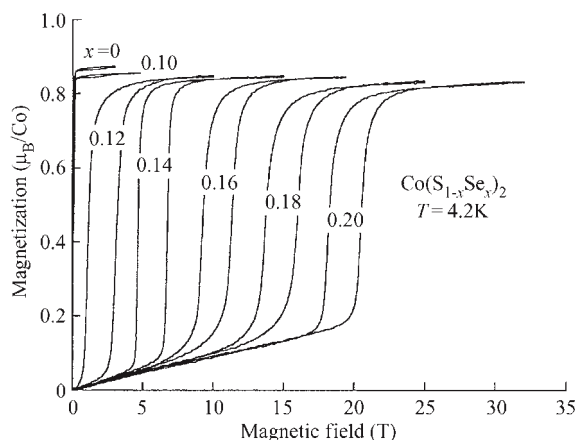
Figure 5
Magnetization curves of $Co(S_{1-x}Se_x)_2$ with $0 \leqslant x \leqslant 0.2$ for 4.2 K.

Figure 7
Magnetization curve of ferromagnetic $Co(S_{0.9}Se_{0.1})_2$ for 4.2 K at various pressures.
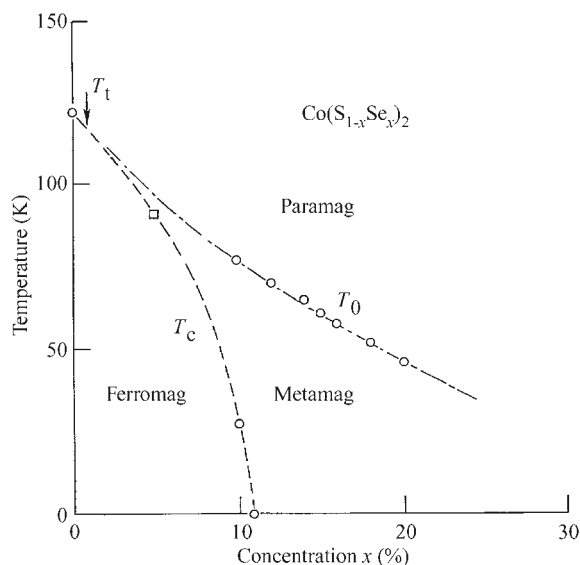
Figure 6
Magnetic phase diagram of $Co(S_{1-x}Se_x)_2$ in the x–T plane.

moment of the ferromagnet. In $Co(S_{0.9}Se_{0.1})_2$ with a first-order FT at 27 K, a metamagnetic transition (MT) is found to appear just above T_C. However, CoS_2 with a second-order FT does not exhibit MT above T_C. The critical field for $0.1 \leqslant x$ shifts in proportion to T^2 as $B_c(x,T) = B_c(x,0) + T^2$ in the low T region $T < 70$ K. The T^2 dependence can be explained by the theory of IEM.

Figure 6 shows the magnetic phase diagram of $Co(S_{1-x}Se_x)_2$ in the x–T plane, where T_0 is the critical
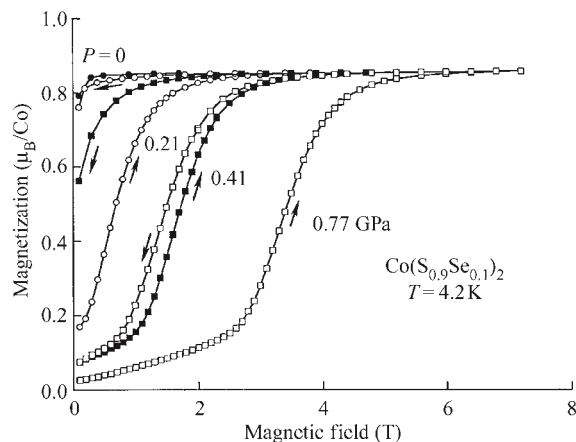
temperature for the disappearance of IEM (Goto *et al.* 1997). The type of FT changes from second-order to first-order at T_t on the T_c curve. The position of T_t can be determined from the critical concentration x_t ($=1\%$) at which $\chi(T_{max})^{-1}$ becomes zero. FT is second-order for $0 \leqslant x < 1\%$, but first-order for $1\% < x < 11\%$. The value of T_C on the first-order phase boundary decreases abruptly with increasing x. MT appears between the T_C and T_0 curves. The experimental phase diagram can be compared with the theoretical one shown in Fig. 1. Since ac/b^2 for $Co(S_{1-x}Se_x)_2$ increases with x, the abscissa of the theoretical phase diagram is considered as the x axis. On the other hand, the ordinate corresponds to the T axis of the phase diagram of $Co(S_{1-x}Se_x)_2$. The theoretical phase diagram reproduces well the experimental one.

3. Pressure Effects

The theoretical phase diagram suggests that the application of high pressure rapidly decreases the value of T_C of the ferromagnet with the first-order transition because ac/b^2 increases with pressure. Figure 7 shows the magnetization curve of ferromagnetic $Co(S_{0.9}Se_{0.1})_2$ for 4.2 K at various pressures (Goto *et al.* 1997). The compound becomes paramagnetic at $P > 0.21$ GPa and exhibits IEM. Similar phenomena were also found in ferromagnetic $Lu(Co_{1-x}Ga_x)_2$ by Goto *et al.* (1994). The critical pressure for the disappearance of ferromagnetism in $Co(S_{0.9}Se_{0.1})_2$ is estimated to be $P_c = 0.25$ GPa from the relation $B_c(P_c) = 0$ at $T = 0$. Since T_C is 27 K at 0 GPa, the pressure effect on T_C is evaluated to be $dT_C/dP = -108$ K/GPa, which is extremely large compared with usual itinerant ferromagnets. The increase of B_c comes mainly from the suppression of the

Stoner enhancement factor. However, the second-order FT is expected to change to the first-order one by the application of pressure. In fact, the FT of CoS_2 changes into the first-order one at 0.4 GPa and MT is found just above T_C for $P > 0.4$ GPa. The application of pressure also affects the susceptibility χ. In $Lu(Co_{0.92}Ga_{0.08})_2$, χ is found to decrease and is accompanied by an increase of T_{max} with increasing P, which is also caused by the suppression of the enhancement factor (Goto *et al.* 1994).

4. Magnetovolume Effects

In the itinerant electron system, the appearance of a magnetic moment M produces a volume magnetostriction $\omega(=\Delta V/V)$, which is related to M, $\omega = nM^2$, where ΔV is the volume change and n is the magnetoelastic coupling constant (see also *Magnetoelastic Phenomena*). Figure 8 shows the magnetostriction curve of $Lu(Co_{0.94}Ga_{0.06})_2$ at 4.2 K in high magnetic fields up to 40 T (Goto and Bartachevich 1998). The volume expands by MT. The estimated value of n is 10.1×10^{-3} $(\mu_B/Co)^2$ in the paramagnetic state and 5.0×10^{-3} $(\mu_B/Co)^2$ in the induced ferromagnetic one. The reduction of n is also found in the $Lu(Co_{1-x}Ga_x)_2$ and $Y(Co_{1-x}Al_x)_2$ systems, originating from the change in the electronic structure of the d electron system caused by MT.

5. Electrical Properties

The spin fluctuation contribution to the electrical resistivity $\rho_{sp}(T)$ has been estimated by subtracting the resistivity of YAl_2 from those of YCo_2, $LuCo_2$, and $ScCo_2$ (Gratz *et al.* 1995). The $\rho_{sp}(T)$ curves increase steeply at low T followed by a maximum. At high T, $\rho_{sp}(T)$ decreases nearly linearly with increasing T. $\rho_{sp}(T)$ in the low T region is proportional to T^2,
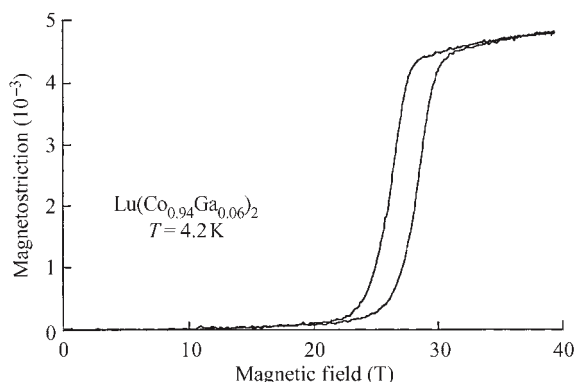
Figure 8
Magnetostriction curve of $Lu(Co_{0.94}Ga_{0.06})_2$ for 4.2 K in high magnetic fields up to 40 T.

$\rho_{sp}(T) = AT^2$. The A/γ ratios (where γ is the coefficient of the electronic specific heat) for these compounds satisfy the Kadowaki–Woods relation, $A/\gamma = 1.0 \times 10^{-5}$ $\mu\Omega$cm $(KmolmJ^{-1})^2$, as well as heavy fermion compounds. This relation can be explained in terms of a spin fluctuation theory (Wada *et al.* 1993). The longitudinal magnetoresistance of $Lu(Co_{0.91}Ga_{0.09})_2$ has been measured at 4.2 K in high magnetic fields (K Murata, unpublished data). Initially the resistance R decreases gradually with increasing field. At MT of 5 T, a large reduction of R by 13% has been observed, which is caused mainly by the suppression of spin fluctuations (see also *Intermetallic Compounds: Electrical Resistivity*).

6. Conclusion

IEM observed in cobalt-based Laves phase compounds and cobalt pyrites originates from a special shape of the DOS curve near the Fermi level, which enhances spin fluctuations at finite temperature. The unusual magnetic properties of these compounds can be explained well with the theory of IEM based on the spin fluctuation model. The metamagnetic transition and the susceptibility are sensitively changed by pressure. Magnetostriction measurements suggest that the electronic structure of the field-induced ferromagnetic state is quite different from that of the paramagnetic state. The electrical resistivity is largely affected by the spin fluctuations.

See also: Itinerant Electron Systems: Magnetism (Ferromagnetism); Spin Fluctuations

Bibliography

Adachi K, Matsui M, Omata Y, Mollymoto H, Motokawa M, Date M 1979 Magnetization of $Co(S_{1-x}Se_x)_2$ under high magnetic field up to 500 kOe. *J. Phys. Soc. Jpn.* **47**, 675–6

Duc N H, Goto T 1999 Itinerant electron metamagnetism of Co sublattice in the lanthanide–cobalt intermetallics. In: Gschneidner Jr. K A, Eyring L (eds.) *Handbook on the Physics and Chemistry of Rare Earths*. Elsevier, Amsterdam, Vol. 26, pp. 177–246

Goto T, Aruga Katori H, Sakakibara T, Mitamura H, Fukamichi K, Murata K 1994 Itinerant electron metamagnetism and related phenomena in Co-based intermetallic compounds (invited). *J. Appl. Phys.* **76**, 6682–7

Goto T, Bartashevich M I 1998 Magnetovolume effects in metamagnetic itinerant-electron systems $Y(Co_{1-x}Al_x)_2$ and $Lu(Co_{1-x}Ga_x)_2$. *J. Phys. Condens. Matter* **10**, 3625–34

Goto T, Fukamichi K, Sakakibara T, Komatsu H 1989 Itinerant electron metamagnetism in YCo_2. *Solid State Commun.* **72**, 945–7

Goto T, Sakakibara T, Murata K, Komatsu H, Fukamichi K 1990 Itinerant electron metamagnetism in YCo_2 and $LuCo_2$. *J. Magn. Magn. Mater.* **90/91**, 700–2

Goto T, Shindo Y, Takahashi H, Ogawa S 1997 Magnetic properties of itinerant metamagnetic system $Co(S_{1-x}Se_x)_2$

under high magnetic fields and high pressure. *Phys. Rev. B* **56**, 14019–28

Gratz E, Resel R, Burkov A T, Bauer E, Markosyan A S, Galatanu A 1995 The transport properties of RCo_2 compounds. *J. Phys. Condens. Matter* **7**, 6687–706

Moriya T 1986 On the possible mechanism for temperature-induced ferromagnetism. *J. Phys. Soc. Jpn.* **55**, 357–66

Murata K, Fukamichi K, Sakakibara T, Goto T, Suzuki K 1993 Itinerant electron metamagnetism and a large decrease in the electronic specific heat coefficient of Laves-phase compounds Lu $(6_{1-x}Ga_x)_2$. *J. Phys. Condens. Matter* **5**, 1525–34

Saito H, Yokoyama T, Fukamichi K 1997 Itinerant-electron metamagnetism and the onset of ferromagnetism in Laves phase $Lu(Co_{1-x}Ga_x)_2$ compounds. *J. Phys. Condens. Matter* **9**, 9333–46

Shimizu M 1982 Itinerant electron metamagnetism. *J. Phys.* **43**, 155–63

Yamada H 1993 Metamagnetic transition and susceptibility maximum in an itinerant-electron system. *Phys. Rev. B* **47**, 11211–9

Yoshimura K, Nakamura Y 1985 New weakly itinerant ferromagnetic system, $Y(Co_{1-x}Al_x)_2$. *Solid State Commun.* **56**, 767–71

Wada H, Shimamura N, Shiga M 1993 Thermal and transport properties of $Hf_{1-x}Ta_xFe_2$. *Phys. Rev. B* 10221–6

Wohlfarth E P, Rhodes P 1962 Collective electron metamagnetism. *Philos. Mag.* **7**, 1817–24

T. Goto
University of Tokyo, Japan

Metrology: Superconducting Cryogenic Current Comparators

The superconducting current comparator (SCC) is a development of the magnetic d.c. comparator (DCC), introduced in 1964 and which operates at room temperature. Initial attempts (Harvey 1972) to develop a superconducting version included enclosing the high μ magnetic core of the DCC in a superconducting shield, but it was soon realized (Sullivan and Dziuba 1974, Grohman *et al.* 1974) that this was unnecessary, the superconducting shield alone was sufficient; in fact the magnetic core could contribute excessive noise to the detector.

The basic operating principle of the SCC relies on the Meissner effect (see *Electrodynamics of Superconductors: Flux Properties*) and can be understood by imagining a very long superconducting tube, open at both ends, and having a thickness greater than the penetration depth of the superconductor. Two separate wires (they need not themselves be superconducting) thread the cylinder. Currents I_1 and I_2 flowing in the wires induce a circulating current $I_s = -(I_1 + I_2)$ in the wall parallel to $I_1 + I_2$ on the inside surface of the cylinder. I_s completes a path round the cylinder creating a magnetic field that is measured with a suitable detector on the outside of the cylinder. If $I_1 = -I_2$ then $I_s = 0$ and, assuming that magnetic field contributions to the detector due to end effects (insufficient length of cylinder) or direct interference from I_1 and I_2 outside the cylinder can be eliminated, the device is a perfect comparator and can be used to compare currents with a sensitivity that depends on the minimum resolution of the detector relative to the magnitude of I_1.

Two versions of the SCC designed to satisfy the criteria outlined above have been described: type I (Sullivan and Dziuba 1974) is the most common so far in the metrology community, and is often described as the "snake swallowing its own tail" comparator; and type II (Grohman *et al.* 1974), a toroidal version of type I, which is more difficult to fabricate but is under development for very high current ($\leqslant 100$ A) and a.c. applications.

1. Type I SCC

The SCC (Fig. 1) comprises a torus (made from Tufnol or machinable glass–ceramic) on which a coil, with as many separate windings as necessary for the intended purpose (e.g., in a typical SCC to be used in an n:1 ($n \leqslant 10$) resistance ratio bridge, there are $n + 2$ windings each having 64 turns), is wound. The windings are NbTi, copper-clad, single-core, insulated superconducting wire with an overall diameter of $\sim 65\,\mu\text{m}$, and impregnated with epoxy glue or
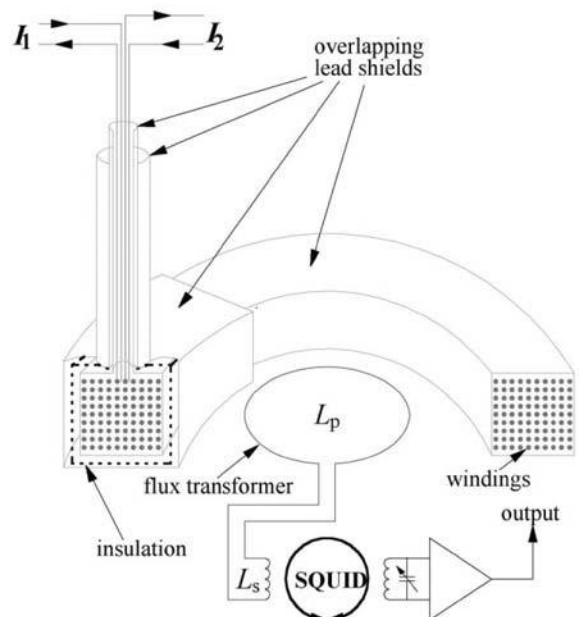
Figure 1
Type I SCC.

otherwise tightly wrapped to prevent movement. The coil is covered with a toroidal superconducting lead shield (0.15 mm thick lead foil carefully soft-soldered to prevent pinholes), with each overlapped turn insulated by thin tape (0.1 mm Kapton). The ends of the windings are brought to the exterior inside 10 cm long, insulated, coaxial lead tubes joined to each turn of the shield. Typically 2.5 overlapped turns are sufficient to meet the requirements set out in the introduction and to obtain the desired accuracy.

The detector coil, with inductance L_p, is wound with superconducting (niobium or NbTi) wire on a Tufnol or machinable glass–ceramic former and inserted coaxially into the middle of the shield. It is connected as a flux transformer to the input coil, inductance L_s, of a d.c. or radio-frequency (RF) superconducting quantum interference device (SQUID). The whole construction, SCC and SQUID, is enclosed in a superconducting shield surrounded by cryoperm, a low-temperature, high μ magnetic shield and lowered into a cryostat containing liquid helium. Optimum flux transfer from the SCC to the SQUID occurs for $L_p \approx L_s$ and a typical sensitivity for a single winding in the SCC is $4.5\,\mu A/\varphi_0$, where φ_0 is the flux quantum. Since an RF SQUID may have a noise sensitivity of $10^{-4}\varphi_0\,\mathrm{Hz}^{-1/2}$, the sensitivity of a 64-turn single winding is approximately $7\,\mathrm{pA\,Hz}^{-1/2}$ and it is relatively easy to detect current inbalances to $\leqslant 1$ part in 10^9.

To check the ratio accuracy of the SCC, equivalent windings are connected in series-opposition and energized with a current large enough to resolve any inbalances. By using a "binary buildup" procedure it is possible to determine the accuracy of any integer ratio. The highest accuracy, reported in 1991 for a 2:1 ratio derived from 10^4 turns per winding, is a few parts in 10^{12}.

2. Type II SCC

In the type I SCC the ratio windings are on the inside of the overlapping superconducting shield and the detector coil sensing flux inbalance on the outside. The topology of the type II SCC is exactly reversed from this, with the detector coil wound toroidally on a former located on the inside of a toroidally shaped superconducting shield with an insulated, overlapped gap region. The ratio windings are also wound toroidally on the outside of the shield and for this reason it is possible for them to carry more current than the type I SCC, without the risk of driving part of the superconducting shield into its normal state. When the detector coil is connected to a SQUID similar to that used for the type I described above, the current sensitivity of a single turn is somewhat less, but since one reason for choosing this design is to compare currents up to 100 A, this is not relevant.

3. SCCs in Resistance Ratio Bridges

The main application of the SCC in metrology is in the measurement of the ratio of two standard resistors R_1 and R_2, which are maintained at precisely controlled temperatures in suitable enclosures. For the most accurate measurements four terminal resistors and an SCC are connected in a bridge arrangement (Delahaye 1978). A fully automated version (Williams and Hartland 1991) is shown in Fig. 2.

Current I_1 from a primary electronic constant current source S_1 flows through resistance R_1 and an in-series primary winding N_1 of a type I SCC. A secondary current $I_2 \approx (N_1/N_2)I_1$, from source S_2, derived from a voltage generated by I_1, is arranged to flow in resistance R_2 and a secondary winding of N_2 turns of the SCC. The two windings of the SCC are connected in opposite senses to produce approximately zero flux, sensed by an RF SQUID closely coupled by a flux transformer to the SCC. Since the relative accuracy of the winding ratio N_1/N_2 is typically smaller than 1 part in 10^{10} any departure in the current ratio I_2/I_1 from that in the winding ratio is corrected by feedback of the SQUID out-of-balance signal to S_2. The ratio R_1/R_2 is determined from the output of the null detector D. This output can also be used to generate a balance current I_b, which flows in
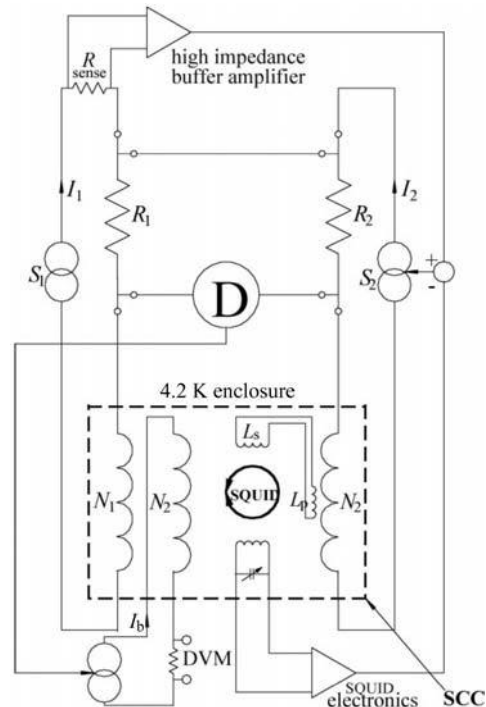
Figure 2
SCC resistance ratio bridge.

an auxiliary winding of N_2 turns of the SCC and brings the detector D to zero balance, so ensuring that the gain stability and linearity of the detector are not significant. Combining the expressions for the detector balance, $R_1I_1 - R_2I_2 = 0$, and for the SCC balance, $(N_1/N_2)I_1 + I_b - I_2 = 0$, one obtains

$$\frac{R_1}{R_2} \cong \frac{N_1}{N_2}\left(1 + \frac{I_b}{I_2}\right)$$

if I_b is small. The current I_b is measured using a resistor and digital voltmeter (DVM), and a large value, accurately known resistor shunting R_2 is used to calibrate I_2. Attention must be paid to the elimination of unwanted leakage currents and that offset currents from the high-impedance buffer amplifier have no significance in the potential circuit.

The operation of the bridge is controlled by a computer, which reverses the direction of I_1 (and I_2) to eliminate the effect of thermal e.m.f.s in the potential circuit, and takes readings of the DVM. For low power dissipation ($\leqslant 1\,\text{mW}$) in R_2, relative random uncertainties (type A) of R_1/R_2 of ~ 1 part in 10^9 can be achieved for measurement times of about 10 minutes.

The SCC bridge is widely used by national laboratories to determine the value of standard resistors in terms of the quantum standard of resistance R_K ($\equiv 25812.807\,\Omega$); to compare quantized Hall resistances fabricated from different materials; and to compare the standard resistors of different national laboratories, with accuracies of a few parts in 10^9. Since 1996 the SCC resistance-ratio bridge has been produced commercially by two companies located in the UK.

See also: Josephson Voltage Standard; SQUIDs: The Instrument

Bibliography

Delahaye F 1978 A double constant current source for a cryogenic current comparator and its applications. *IEEE Trans. Instrum. Meas.* **IM-27**, 426–9

Grohman K, Hahlbolm H D, Lübbig H, Ramin H 1974 Ironless cryogenic current comparator for a.c. and d.c. operations. *IEEE Trans. Instrum. Meas.* **IM-23**, 261–3

Harvey I K 1972 A precise low temperature d.c. ratio transformer. *Rev. Sci. Instrum.* **43**, 1626–9

Sullivan D B, Dziuba R F 1974 Low temperature direct current comparator. *Rev. Sci. Instrum.* **45**, 517–9

Williams J M, Hartland A 1991 An automated cryogenic current comparator resistance ratio bridge. *IEEE Trans. Instrum. Meas.* **IM-40**, 267–70

A. Hartland
National Physical Laboratory, Teddington, UK

Micromagnetics: Basic Principles

A small class of materials exhibit the important property of long range magnetic order. Fundamentally, this arises because of the so-called "exchange energy" which can, under certain circumstances, lead to parallel alignment of neighboring atomic spins. Given the link between the atomic spin and magnetic moment, the spin order gives rise to the observed long range magnetic order. The origin of the long range magnetic order is a fundamental scientific problem which has been studied extensively, both theoretically and experimentally and is now understood in some depth. However, within magnetism there is a major problem when relating fundamental atomic properties to magnetization structures and magnetization reversal mechanisms in bulk materials.

The problem was described vividly by Aharoni (1996) in his discussion of magnetostatic effects. The essential idea is that the material properties are determined by the exchange energy, which in principle is effective on a length scale of subnanometers, and the magnetostatic energy, which has contribution from the boundaries of the material itself and which introduce a different length scale entirely. The challenge of micromagnetics is to develop a formalism in which the macroscopic properties of a material can be simulated including the best approximations to the fundamental atomic behavior of the material.

In brief, the classical approach to micromagnetics replaces the spin by classical vector field which initially allows the determination of magnetostatic fields within the system. In addition to this a different approach to the exchange interaction much be formulated which can replace the quantum mechanical exchange interaction with a formalism appropriate for the limit of continuous material. This, coupled with an energy minimization approach, forms the basis of classical micromagnetics which will be outlined in a later section.

The history of micromagnetics starts with a 1935 paper of Landau and Lifshitz on the structure of a wall between two antiparallel domains, and several papers by Brown around 1940. A detailed treatment of micromagnetism is given by Brown in his 1963 book (Brown 1963).

For many years micromagnetics was limited to the use of standard energy minimization approaches to determine domain structures and classical nucleation theory to determine magnetization reversal mechanisms in systems with ideal geometry. Arguably, the current interest in micromagnetics arises from the availability, from about the mid-1980s onward, of large-scale computing power which enabled the study of more realistic problems which were more amenable to comparison with experimental data.

One important realization during this period was the fact that energy minimization approaches in

principle only determine nucleation fields for the system, and do not predict necessarily correctly the state of the system after magnetization reversal. Consequently, a lot of work has gone into the development of dynamic approaches which use simulations based on the Landau–Lifshitz equation of motion. This is probably the technique in most common use today.

The other area in which considerable development has taken place during the 1990s is that of the calculation of magnetostatic fields, which because of its complexity forms the largest part of most micromagnetic calculations. A number of techniques are available and it is the intention in this review to outline each technique and give consideration to the circumstances under which each one is most applicable.

1. Energy Terms

1.1 Exchange Energy

Exchange energy forms an important part of the covalent bond of many solids and is also responsible for ferromagnetic coupling. The exchange energy is given by

$$E_{exch} = -2J\mathbf{S}_1 \cdot \mathbf{S}_2 \tag{1}$$

where J is referred to as the exchange integral. $\mathbf{S}_1$ and $\mathbf{S}_2$ are the atomic spins. Clearly for ferromagnetic ordering J must be positive. This so-called direct exchange coupling is somewhat idealized and applicable to only a few materials rigorously.

A number of other models exist, including itinerant electron ferromagnetism and indirect exchange interaction or Ruderman–Kittel–Kasuya–Yoshida (RKKY) interaction. Generally speaking, however, Eqn. (1) is the form usually taken for the exchange interaction with the value of J dependent on the detailed atomic properties of the material.

1.2 Anisotropy

The term anisotropy refers to the fact that the properties of a magnetic material are dependent on the directions in which they are measured. Anisotropy makes an important contribution to hysteresis in magnetic materials and is therefore of considerable practical importance. The anisotropy has a number of possible origins.

(a) Crystal or magnetocrystalline anisotropy

This is the only contribution intrinsic to the material. It has its origins at the atomic level. First, in materials with a large anisotropy there is a strong coupling between the spin and orbital angular momenta within an atom. In addition, the atomic orbitals are generally nonspherical.

Because of their shape the orbits prefer to lie in certain crystallographic directions. The spin–orbit

coupling then assures a preferred direction for the magnetization—called the *easy direction*. To rotate the magnetization away from the easy direction costs energy— and *anisotropy energy*. As might be expected the anisotropy energy depends on the lattice structure.

(i) Uniaxial anisotropy occurs in hexagonal crystals such as cobalt.

$$E = KV\sin^2\theta + \text{higher terms} \tag{2}$$

Here θ is the angle between the easy direction and the magnetization, K is the anisotropy constant, and V the volume of the sample. The higher order terms are small and usually neglected. This has one "easy axis" with two energy minima, separated by energy maxima. This energy barrier leads to hysteresis.

(ii) Cubic anisotropy; for example, iron, nickel

$$E/V = K_0 + K_1(\alpha_1^2\alpha_2^2 + \alpha_2^2\alpha_3^2 + \alpha_1^2\alpha_3^2) \tag{3}$$

Here α gives the direction cosine, i.e., the cosine of the angle between the magnetization direction and the crystal axis.

(b) Shape anisotropy

Consider a uniformly magnetized body. By analogy with dielectric materials we can refer to the magnetization (magnetic polarization) creating fictitious "free poles" at the surface.

These lead to a "demagnetizing field" H_d which acts in opposition to $\mathbf{H}$. Figure 1 shows a sample with an anisotropic shape with a magnetic field applied in two perpendicular directions. The energy increases as H_d increases. For an ellipsoid of revolution it can be shown that

$$E = -K_{eff}V\sin^2\theta \tag{4}$$

i.e., the same form as for uniaxial anisotropy. θ is the angle between the long axis of the sample and the magnetization direction. Also,

$$K_{eff} = \tfrac{1}{2}(N_b - N_a)M^2 \tag{5}$$

where $\mathbf{M}$ is the magnetization and N_b and N_a are "demagnetizing factors" in the short axis and long axis directions. N_b and N_a depend on the geometry so that $K_{eff} = 0$ for a sphere and $K_{eff} = M^2/2$ for a needle-like sample.

(c) Stress anisotropy

This arises from the change in atomic structures as a material is deformed. It is related to the phenomenon of "magnetostriction' which is important for sensor applications.

(d) Magnetostatic effects and domain formation

Magnetostatic fields are a natural consequence arising from any magnetization distribution. The
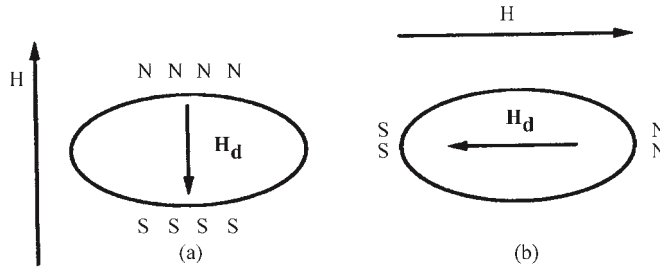
Figure 1
Sample with an anisotropic shape with a magnetic field applied in two perpendicular directions: (a) parallel to the short axis; here the "free poles" are separated by a relatively short distance, leading to a large H_d, (b) parallel to the long axis; poles separated by a smaller distance, which leads to a small value of H_d.

magnetostatic fields are fundamental to the micromagnetic problem and, importantly, introduce another length scale. Magnetostatic effects give rise to magnetization structures on a length scale orders of magnitude greater than atomic spacings. Consequently it is impossible to deal with both magnetostatic and exchange effects rigorously in micromagnetic calculations at least with the current computer facilities. The formulation of the magnetostatic interaction field problem will be given in detail later but for the moment it is simply necessary to introduce the fact that because of magnetostatic fields a magnetized body has a magnetostatic self energy given by

$$E_{mag} = \tfrac{1}{2} N_d M^2 \qquad (6)$$

where N_d is a factor depending on the shape of the sample.

This is, of course, related to the statement (Aharoni 1996) that the energy of a system depends on the boundary of the material. Clearly the energy given by Eqn. (6) can be reduced if the magnetization **M** is reduced. As a result of this the material has a tendency to break into domains in which the magnetization remains at the spontaneous magnetization appropriate for a given material at a given temperature with the domains oriented in such a way as to minimize the overall magnetization and hence the magnetostatic self energy.

However, creating a boundary between two domains also requires energy and the actual domain structure depends on a minimization of the total exchange *and* magnetostatic self-energy. This in a sense was the first application of micromagnetics.

It is interesting to note that as the size of a system reduces the magnetostatic self energy reduces and at some point it becomes energetically unfavorable to form a domain structure since the lowering of the magnetostatic energy is not sufficient to compensate for the energy necessary to create the domain wall. Below this size a sample is referred to as single

domain and here the magnetization processes are dominated by the rotation of the magnetic moment against the anisotropy energy barrier.

2. Foundations of Micromagnetics

It is not possible to neglect any of the three major energy terms, exchange, anisotropy, and magnetostatic. The detailed magnetic behavior of a given material depends on the detailed balance between these energy terms. It is not even possible to add the magnetostatic and anisotropy terms as a perturbation to the exchange energy term and use a quantum mechanical solution of this problem. Currently the only realistic approach is to ignore the atomic nature of matter, to neglect quantum effects, and to use classical physics in a continuum description of a magnetic material.

Essentially, we assume the magnetization to be a continuous vector field **M(r)**, with **r** the position vector. Thus we write

$$\mathbf{M(r)} = M_s \mathbf{m(r)}; \quad \mathbf{m \cdot m} = 1 \qquad (7)$$

where M_s is the saturation magnetization of the material. The basic micromagnetic approach is to formulate the energy in terms of the continuous magnetization vector field and to minimize this energy in order to determine static magnetization structures. Classical nucleation theory can be used to study modes of magnetization reversal and nucleation fields. The energy terms are formulated as follows.

2.1 Anisotropy Energy

This remains a local calculation and is straightforward to carry out using the expressions for either cubic or uniaxial symmetry given earlier.

2.2 Exchange Energy

The exchange energy is essentially short ranged and involves a summation over the nearest neighbors.

Assuming a slowly spatially varying magnetization the exchange energy can be written

$$E_{exch} = JS^2 \sum \phi_{ij}^2 \qquad (8)$$

the summation being carried out over nearest neighbors only. The ϕ_{ij} represents the angle between two neighboring spins i and j. It should be noted that in Eqn. (8) the energy of the state in which all spins are aligned has been subtracted and used as a reference state. This is legitimate as long as it is done consistently. For small angles, $|\phi_{ij}| \approx |\mathbf{m}_i - \mathbf{m}_j|$, a first-order expansion in a Taylor series is

$$|\mathbf{m}_i - \mathbf{m}_j| = |(\mathbf{s}_i \cdot \nabla)\mathbf{m}_j| \qquad (9)$$

where $\mathbf{s}$ is a position vector joining lattice points i and j.

Substituting, Eqn. (9) into Eqn. (10) gives

$$E_{exch} = JS^2 \sum_i \sum_{\mathbf{s}_i} |(\mathbf{s}_i \cdot \nabla)\mathbf{m}_j|^2 \qquad (10)$$

where the second summation is over nearest neighbors. Changing the first summation to an integral over the whole body, the result is that for cubic crystals

$$E_{exch} = \int_V W_e \mathrm{d}V; \quad W_e = A(\nabla \mathbf{M})^2 \qquad (11)$$

where

$$(\nabla \mathbf{M})^2 = (\nabla M_x)^2 + (\nabla M_y)^2 + (\nabla M_z)^2 \qquad (12)$$

The material constant $A = JS^2/a$ for a simple cubic lattice with lattice constant a. This represents a major step in the formulation of micromagnetism: we have related the fundamental atomic properties to the spatial derivatives of the magnetization in the continuum approximation. The atomic properties are included via the exchange integral J which in micromagnetic terms is essentially a phenomenological constant which can be determined from experimental data.

2.3 Magnetostatic Fields

Here we consider only the magnetostatic field arising from the magnetization distribution itself and not any externally applied field which is trivial to add to the overall energy. The magnetostatic or demagnetizing field $\mathbf{H}_d$ is governed by Eqns. (13) and (14)

$$\nabla \times \mathbf{H}_d = 0 \qquad (13)$$

$$\nabla(\mathbf{H}_d + 4\pi\mathbf{M}) = 0 \qquad (14)$$

Eqns. (13) and (14) are written in cgs units, i.e., $\mathbf{B} = \mathbf{H} + 4\pi\mathbf{M}$. Since the curl of $\mathbf{H}_d$ is 0, the demagnetizing field can be derived from a scalar potential,

$$\mathbf{H}_d = -\nabla\phi \qquad (15)$$

Substitution of Eqn. (15) into Eqn. (14) yields

$$\nabla^2\phi = -4\pi\nabla \cdot \mathbf{M} \qquad (16)$$

which because of its analogy with Poisson's equation in electrostatics leads to the definition of a volume magnetic charge density given by

$$\rho = -4\pi\nabla \cdot \mathbf{M} \qquad (17)$$

Thus we can solve for the magnetostatic field by solving for the potential using Eqn. (16) subject to boundary conditions which determine the continuity of the normal component of $\mathbf{B}$ and of the tangential component of $\mathbf{H}_d$.

$$\mathbf{n} \cdot (\mathbf{B}_{ext} - \mathbf{B}_{int}) = 0 \qquad (18)$$

$$\mathbf{n} \times (\mathbf{H}_{d;ext} - \mathbf{H}_{d;int}) = 0 \qquad (19)$$

where $\mathbf{n}$ is a unit vector pointing outward from the surface.

In terms of the scalar potential the equivalent conditions are

$$\phi_{ext} = \phi_{int} \qquad (20)$$

$$\left.\frac{\partial\phi}{\partial n}\right|_{ext} \cdot - \left.\frac{\partial\phi}{\partial n}\right|_{int} = -4\pi\mathbf{M} \cdot \mathbf{n} \qquad (21)$$

Thus again the surface of a bulk magnetized body is determining the overall response of a phenomenon having its origins at the atomic level. Finally we can write expressions for the potential and demagnetizing field as follows:

$$\phi(\mathbf{r}) = -\int_V \frac{\nabla \cdot \mathbf{M}(\mathbf{r}')}{|\mathbf{r} - \mathbf{r}'|}\,\mathrm{d}V' + \int_S \frac{\mathbf{M}(\mathbf{r}') \cdot \mathbf{n}}{|\mathbf{r} - \mathbf{r}'|}\,\mathrm{d}S' \qquad (22)$$

$$\mathbf{H}_d = -\int_V \frac{(\mathbf{r} - \mathbf{r}')\nabla \cdot \mathbf{M}(\mathbf{r}')}{|\mathbf{r} - \mathbf{r}'|^3}\,\mathrm{d}V'$$
$$+ \int_S \frac{(\mathbf{r} - \mathbf{r}')\mathbf{M}(\mathbf{r}') \cdot \mathbf{n}}{|\mathbf{r} - \mathbf{r}'|^3}\,\mathrm{d}S' \qquad (23)$$

The integrals in Eqn. (23) can be interpreted as fields arising from volume and surface change densities $\rho = -4\pi\nabla \cdot \mathbf{M}$ and $\sigma = 4\pi\mathbf{M}(\mathbf{r}) \cdot \mathbf{n}$, respectively.

Although Eqns. (22) and (23) represent elegant closed form solutions for the potential and demagnetizing field, they are not the best form for numerical computation. Essentially, the total energy of the system involves an integral over the volume as follows:

$$E_{mag} = \frac{1}{2}\int_V \mathbf{H}_d \cdot \mathbf{M}\mathrm{d}V \qquad (24)$$

which because of Eqn. (23) involves a six-fold integration. In terms of the numerical problem this involves a scaling with N^2, where N is the number of elements into which the body is discretized. This of course leads to rapid degradation of computational speed with system size and in practice an alternative solution must be found for the calculation of $\mathbf{H}_d$. The techniques involved will be described in detail later.

2.4 Brown's Equations

The final step in the formulation of classical micromagnetics is to minimize the total energy which can be written as follows

$$
\begin{aligned}
E_{tot} \\
= \int_V \left[A(\nabla \mathbf{M})^2 + E_{anis} - M_s \mathbf{m} \cdot \left(\mathbf{H}_a + \frac{\mathbf{H}_d}{2} \right) \right] \mathrm{d}V \quad (25)
\end{aligned}
$$

where $\mathbf{H}_a$ is the externally applied field. Here, E_{anis} is the anisotropy energy density.

The approach uses standard variational principles but the derivation is somewhat protracted. Essentially, setting the first variation of the total energy to zero leads to two equations. The first is a surface equation

$$
2A \left[\mathbf{m} \times \frac{\partial \mathbf{m}}{\partial n} \right] = 0 \Rightarrow \frac{\partial \mathbf{m}}{\partial n} = 0 \quad (26)
$$

since $\mathbf{m} \cdot \partial \mathbf{m} / \partial n = 0$ by virtue of $\mathbf{m} \cdot \mathbf{m} = 1$. The second is a volume equation,

$$
\mathbf{m} \times \left[\frac{2A}{M_s} \nabla^2 \mathbf{m} + \mathbf{H}_d + \mathbf{H}_a + \mathbf{H}_K \right] = 0 \quad (27)
$$

where the anisotropy field $\mathbf{H}_K$ is defined as

$$
\mathbf{H}_K = -\frac{1}{M_s} \frac{\partial E_{anis}}{\partial \mathbf{m}} \quad (28)
$$

Eqn. (27) can be written

$$
\mathbf{m} \times \mathbf{H}_{eff} = 0 \quad (29)
$$

where the effective field $\mathbf{H}_{eff}$ is

$$
\mathbf{H}_{eff} = \frac{2A}{M_s} \nabla^2 \mathbf{m} + \mathbf{H}_d + \mathbf{H}_a + \mathbf{H}_K \quad (30)
$$

Eqn. (27) states that the equilibrium solution is found by making the magnetization lie parallel to the local field. Eqns. (26)–(30) are referred to as Brown's equations and form the basis of the classical micromagnetic approach for the solution of stationary problems.

3. Analytical Solutions

3.1 Stoner–Wohlfarth Theory

Stoner–Wohlfarth (SW) theory is the simplest micromagnetic model since it is assumed that all spins remain collinear thus removing the exchange term. Consider a particle with uniaxial anisotropy and easy axis at some angle ψ to the applied field. The magnetization of the particle has an angle θ to the easy axis and $\theta - \psi$ to the applied field. The magnetic moment of the particle is MV, where V is the particle volume. Assuming that the atomic magnetic moments always remain parallel (coherent rotation) the energy is the sum of the anisotropy and field energies, i.e.,

$$
E = KV\sin^2\theta - MVH\cos(\theta - \psi) \quad (31)
$$

The orientation of the magnetic moment is determined by minimizing the energy E, that is we set $\mathrm{d}E/\mathrm{d}\theta = 0$. This gives

$$
\frac{\mathrm{d}E}{\mathrm{d}\theta} = 2KV\sin\theta\cos\theta + MVH\sin(\theta - \psi) = 0 \quad (32)
$$

In general there are four solutions of Eqn. (32), two minima and two maxima (which separate the minima). We can illustrate the behavior using the special case of $\psi = 0$, that is, the easy axis is aligned with the field, Then Eqn. (32) becomes

$$
2KV\sin\theta\cos\theta + MVH\sin\theta = 0 \quad (33)
$$

Eqn. (33) has a solution at $\sin\theta = 0$, i.e., $\theta = 0$ or π. Further solutions occur at $2KV\cos\theta = -MVH$, so that

$$
\cos\theta = -MH/2K \quad (34)
$$

which are maxima.

These results can be used to illustrate the reversal process in the following way using Fig. 2. A large positive field is first applied to the sample, taking it to point (a) on the hysteresis loop. When the field is reduced to zero the energy maximum stops the system from becoming demagnetized. The magnetization still lies along the easy direction, i.e., in this case parallel to the applied field. This gives a remanent magnetization (point b). In negative fields the magnetization would prefer to reverse, in order to be parallel to the field direction. In order to do this it would have to rotate over the maximum energy, E_{max}. Thus there is an energy barrier to rotation, of value $E_b = E_{max} - E_{min}$. It is straightforward to show that

$$
\begin{aligned}
E_b &= KV \left(1 - \frac{M^2 H^2}{4K^2} \right) - MVH \left(\frac{MH}{2K} \right) - (-MVH) \\
&= KV \left(1 + \frac{M^2 H^2}{4K^2} \right) \quad (35)
\end{aligned}
$$
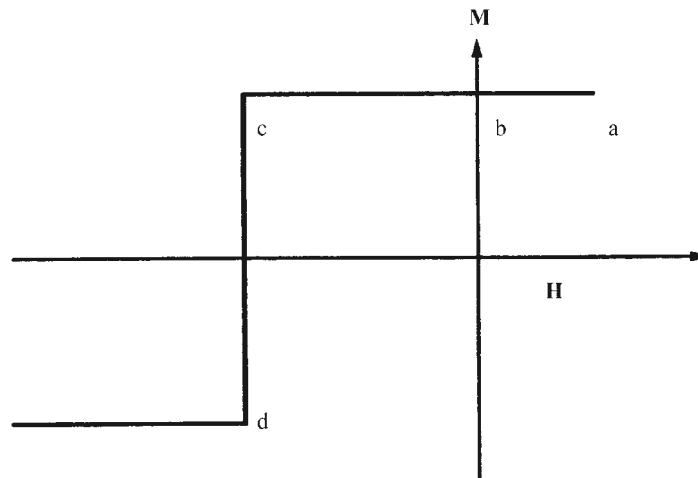
Figure 2
Hysteresis loop for a SW particle with the field applied parallel to the easy axis.

Therefore, the energy barrier becomes zero when $(MH/2K) = 1$, that is, when $H = -2K/M = -H_K$.

At this point, the *coercive force,* the magnetization rotates into the other minimum, i.e., into the field direction (points c to d). Thus H_K is the maximum coercive force for a particle. For a particle oriented at some angle ψ the behavior consists of a mixture of reversible and irreversible rotation.

The coercive force at some angle ψ is less than H_K. For a system of particles with randomly orientated easy axes an average over all orientations gives a hysteresis loop that has a remanence of half the saturation magnetization and a coercivity of $0.479H_K$.

The SW model is still extensively used, especially in materials where the long-range interaction effects are more important than intrinsic grain properties. Generally, agreement with experiment is obtained for a low "effective value" of H_K which takes some account of the nonuniform magnetization processes as is discussed later in relation to thin film simulations.

3.2 The Nucleation Problem

Consider a ferromagnetic body in a magnetic field large enough to cause saturation. The field is slowly reduced to zero and then increased in a negative sense. At some point the original state becomes unstable and the magnetization makes a transition to a new energy minimum. The field at which the state becomes unstable is the "nucleation field." This can be determined analytically for a few simple geometries. In a sense, SW is the simplest nucleation theory. The limitations of nucleation theory can be seen by considering the final state after transition.

In a complex system there may be more than one accessible minimum, rather than the one state of SW theory. Consequently, nucleation theory cannot predict the magnetization curve of anything but the simplest materials and in this sense its predictions are more mathematically than physically interesting. Numerical micromagnetics with its novel techniques for determining the magnetic state at any point of the hysteresis loop is where predictions become accessible to experimental verification.

4. Numerical Micromagnetics

4.1 Calculation of Stationary States: Energy Minimization Versus Dynamic Approach

The first numerical micromagnetic approaches following the resurgence of interest in micromagnetic calculations in the mid-1980s were based essentially on energy minimization. Della Torre (1985, 1986) uses this approach in some calculations on the behavior of elongated particles. The approach works reasonably well but is prone to numerical instabilities.

A more sophisticated minimization technique was developed by Hughes (1983) in studies of longitudinal thin film media consisting of strongly coupled spherical grains (the strong coupling arising from exchange interactions between grains). In these materials strong cooperative reversal is important and a straightforward energy minimization technique was problematical during the magnetization reversal process.

A number of sophisticated energy minimization approaches are possible using standard numerical techniques. For example a number of workers have used conjugate gradient techniques. However, the basic problem arises from the nature of the micromagnetic problem itself. Essentially, it is relatively easy to track

a well-defined energy minimum as it evolves with the magnetic field. This is usually the case, for example, in the decrease from magnetic saturation towards the remanent state where no irreversible behavior occurs. The energy minimum in which the system resides is essentially a local energy minimum on a very complex energy surface. The magnetization reversal process can be seen as the disappearance of the local energy minimum due to the action of a sufficiently large field applied in a sense opposite to the original "positive" saturation direction.

The magnetization reversal process takes place when the minimum in the positive field direction vanishes and the system makes a transition into an energy minimum closer to the negative field direction. If the energy surface has a complex topology it may contain a number of energy minima accessible during the magnetization reversal process. Energy minimization is a very poor technique for predicting the correct minimum.

Magnetization reversal is intrinsically a dynamic phenomenon and in order to predict magnetization states correctly after reversal we should in principle take account of the dynamic behavior of the system as far as is possible. Victora (1987) first used a dynamic approach in studies of longitudinal thin films. The approach is based on the Landau–Lifshitz (L–L) equation of motion of an individual spin, which has the form

$$\frac{\mathrm{d}\mathbf{M}}{\mathrm{d}t} = \gamma_0 \mathbf{M} \times \mathbf{H} - \frac{\alpha \gamma_0}{M_s} \mathbf{M} \times \mathbf{M} \times \mathbf{H} \qquad (36)$$

Here, γ_0 is the gyromagnetic ratio and α is the damping constant. In Eqn. (36) the first term leads to gyromagnetic procession. In the absence of damping this will be eternal and would not lead to the equilibrium state in which the magnetization is parallel to the local field.

The second term represents damping. This ensures that the system eventually reaches the equilibrium position. It should be noted that other forms of the dynamic equation are possible, including the Gilbert form. However, in the limit of small damping, these forms are equivalent although the Gilbert equation is probably more physically correct.

Also, in the limit of large damping, in which case the second term of Eqn. (36) dominates, the Landau–Lifshitz equation is equivalent to a steepest decent energy minimization approach. The L–L equation is the most widely used dynamic approach currently.

Eqn. (36) is easy to solve numerically for a single spin. However, the micromagnetic problem is represented by a set of strongly coupled equations of motions which is a somewhat more difficult numerical problem. The types of system considered can for convenience be considered as of two types.

(i) Weakly coupled systems. Typical examples here might be a set of grains with uniform magnetization coupled by magnetostatic and perhaps weak exchange interactions. For this type of system a simple numerical technique such as the Runge–Kutta approach with adaptive step size will probably suffice.

(ii) Strongly coupled systems. These examples tend to have strong exchange coupling, for example, in the case of studies of nonuniform magnetization processes in a single grain or a set of strongly exchange coupled grains. In terms of the differential equations the system in this case is referred to as "stiff." Although Runge–Kutta will still give a solution, the step size tends to become very small and the computational times involved, increasingly long. It is more usual under these circumstances to use an alternative technique, for example, predictor–corrector algorithms.

The numerical technique essentially entails the determination of the local field $\mathbf{H}$ at each point in the system followed by a determination of the small magnetization changes using Eqn. (36). The whole system is updated simultaneously at each time step after which the local field is recomputed and this procedure is carried out until the system evolves into an equilibrium state. Equilibrium can be determined using a number of criteria:

(i) Magnetization changes at a given step below a certain minimum value, and

(ii) Comparison of the direction of the local magnetization and the local field. Essentially the convergence is determined dependent on the maximum value of $\mathbf{M} \times \mathbf{H}$ for the system.

The technique used depends to some extent on the system studied. In a sense this is the easiest part of numerical micromagnetics. A number of numerical techniques are available for the solution of Eqn. (36) and it is not too difficult to create algorithms based on the dynamic approach which are robust in terms of finding stationary states and also reliable in finding new stationary states after the nucleation of a magnetization reversal event.

Two problems remain however. The first is the determination of the local field $\mathbf{H}$ which is a rather difficult and specific problem on which considerable effort has been expended. However, a further problem is in the microstructure of the material itself and the approximations which need to be made in order to make the problem amenable to a numerical solution whilst retaining some physical realism. The following section considers some aspects of the problem of microstructure in micromagnetics.

4.2 Microstructural Simulations

Numerical micromagnetics involves a discretization of space. The behavior of the spin associated with each small volume element is described by Eqn. (36). Because of the exchange and magnetostatic interactions this leads to a finite set of coupled equations of

motion of the form of Eqn. (36) which have to be solved numerically. The spatial discretization is an important part of the problem.

(a) Particulate systems

Nanostructured particulate systems are essentially of two types. The first is so-called granular magnetic solid, essentially a heterogenous alloy consisting of magnetic particles in a nonmagnetic matrix. This is often produced by sputtering, evaporation, or laser ablation. These systems have a microstructure consisting of relatively randomly distributed grains and can be modeled by placing grains at random into the computational cell. The spatial disorder in this system has been shown (El Hilo *et al.* 1994) to be an important factor in determining the effects of exchange coupling in the materials.

For example, standard micromagnetic calculations with an ordered system lead to an enhancement of the remanent magnetization due to intergranular exchange coupling but also predict a decreased coercive force due to the effects of cooperative magnetization reversal. In a system with a random microstructure, however, the effects of the cooperative reversal are decreased and although the exchange coupling leads to an enhanced remanence the reduction in the scale of the cooperative reversal can also lead to a small enhancement of the coercive force. Consequently, it is important to stress that the microstructure of a material needs to be modeled as realistically as possible.

In the case of particular materials produced by the solidification of a fluid precursor, for example, by the polymerization of a ferrofluid or the production of particulate recording medium from a magnetic dispersion, it is known that magnetostatic interactions are important because they give rise to flux closure and consequent modifications to the microstructure.

Vos *et al.* (1993) have demonstrated the importance of microstructure by comparing the chaining effects which occur in standard particulate media with the behavior of barium ferrite. In the latter case the particles consist of small platelets which tend to form long stacks under the influence of magnetostatic interactions. The calculations of Vos *et al.* indicate very different behavior for the two types of microstructure. However, the actual microstructures used were created using an *ad hoc* procedure.

Chantrell *et al.* (1996) have demonstrated the importance of the correct simulation of microstructure in particulate systems, and have developed a sophisticated molecular dynamic approach Coverdale *et al.* 2001 to the prediction of microstructures.

(b) Granular thin metallic films

Although these are similar to particulate materials in that they consist of well-defined grains, these materials are generally considered as a separate case, essentially because of their different applications and also because they consist, to a first approximation at least, as a single layer of grains.

In these systems, clearly magnetostatic interactions between the metallic grains will be very strong and there is also the possibility of some exchange coupling across grain boundaries. Generally these materials are alloys, for example, of chromium. The intention is that the chromium segregates to grain boundaries giving rise to good magnetic isolation.

The first models of these materials were produced from the mid–1980s onwards and in many ways remain largely unchanged. The models consist of spherical grains which are assumed to rotate coherently and can therefore be treated as a single spin, situated on a regular hexagonal lattice. The reason for this uniformity is that it simplifies the magnetostatic field calculation because fast Fourier transform techniques can be used (as described in the following section).

Many simulations still use this rather idealized model, even though it has been shown that it drastically overestimates the cooperative reversal. Miles and Middleton (1990) were the first to develop a simulation based on an irregular grain structure with a distribution of particle volumes. This and later work (Walmsley *et al.* 1996) demonstrate conclusively that the size of magnetic features in the materials is critically affected by the microstructure and, as one might expect, is significantly smaller in materials with some disorder.

The other problem with the assumed microstructure is the intrinsic assumption of coherent reversal, which means that the intrinsic coercivity (assumed to be due to coherent rotations) is probably overestimated.

The parameters h_{int} and C^* represent the magnetostatic and exchange coupling strengths with respect to the intrinsic coercivity and are empirical parameters which essentially hide the micromagnetic deficiencies of the model. At attempt to produce a realistic microstructure is described by Schrefl and Fidler (1992). The microstructure is produced via a voronoi construction. Essentially this entails, for a two-dimensional system at least, distributing points at random in space and bisecting the line between points to produce grain boundaries. This produces an irregular grain structure and has been used in granular three-dimensional systems (Schrefl and Fidler 1992) and longitudinal thin films (Tako *et al.* 1996).

These models represent the state of the art in terms of microstructural simulations. It is desirable to carry out a discretization of the systems at the subgrain level, since this allows the correct simulation of non-uniform magnetization processes. The uniform mesh is no longer appropriate. Finite element methods are necessary, and are outlined in *Micromagnetics: Finite Element Approach*.

5. *Magnetostatic Field Calculations*

Here we consider relatively common and easily applied approaches. More sophisticated techniques are necessary for calculations using finite elements, and these will be outlined in *Micromagnetics: Finite Element Approach*.

5.1 *Dipole Sum—the Bethe–Peierls–Weiss Approximation*

This is by far the easiest approach to adopt. We start with the interaction field written as

$$\mathbf{H}_i = \sum_{j \neq i} \mathbf{H}_{ij} \tag{37}$$

where

$$\mathbf{H}_{ij} = -\frac{\mathbf{m}_j}{r^3} + \frac{3(\mathbf{m}_j \cdot \mathbf{r})\mathbf{r}}{r^5}$$

is the interaction field at element i due to element j. $\mathbf{m}_i$ and $\mathbf{m}_j$ are the magnetic moments of each element and $\mathbf{r}$ is the spatial separation.

Clearly the determination of fields via Eqn. (37) is an N^2 problem. In order to make the calculation feasible for large systems the usual approximation is to divide the problem into a direct summation over some region V around a given site i and to use a continuum approximation to the field outside this region. For a spherical cut off the result is of the form (in cgs units)

$$\mathbf{H}_i = \sum_{j \in V} \mathbf{H}_{ij} + \frac{4\mathbf{M}}{3} - N_d\mathbf{M} \tag{38}$$

The first term is a direct summation within a region V surrounding i. Outside this region the material is treated as a uniformly magnetized continuous material of magnetization $\mathbf{M}$ (in cgs units). The problem of determining the field at the center of the spherical cut out than reduces to solutions of

$$\mathbf{H}_d = \int_{\partial V} \frac{(\mathbf{r} - \mathbf{r}') \cdot \mathbf{M}(\mathbf{r}')\hat{\mathbf{n}}}{|\mathbf{r} - \mathbf{r}'|^3} \mathrm{d}S \tag{39}$$

over surfaces ∂V representing the inside surface of the cut out region and the outside of the magnetized body. Eqn. (39) follows directly from Eqn. (23) given the assumption of a uniform magnetization, $\nabla \cdot \mathbf{M} = 0$.

The second and third terms in Eqn. (38) are the "Lorentz" and "demagnetizing" fields arising from the internal and external surfaces respectively, with N_d a shape-dependent demagnetizing factor. These factors arise directly from analytical solution of Eqn. (39).

5.2 *Hierarchical Calculation*

The hierarchical approach is a more sophisticated calculation which improves on the Bethe–Peierls–Weiss approximation. Essentially, a dipole sum is

again carried out within a central area around the point at which the field is to be calculated. In the simplest case the remaining material is represented by "cells" of similar size, taken as having a total moment obtained by adding all the moments in the cell. This is then used to calculate the field due to the cell at the central point and a summation of these contributions is taken. This approach was used by Miles and Middleton (1991). It is possible to improve the accuracy by adding higher order (multipole) terms. Such fast multipole methods are often used in electrostatic calculations.

The beauty of the hierarchical calculation is that it can be applied to systems with disordered microstructures which is not easily the case for methods such as the fast Fourier transform, a description of which follows.

5.3 *Fast Fourier Transform Techniques*

This was developed by Mansuripur and Giles (Mansuripur and Giles 1988, Giles *et al.* 1990) specifically for simulation of magneto-optic recording media and has since become widely used. Its advantage is that the use of FFTs give rise to a scaling with $N\ln N$ rather than N^2. The disadvantage is the need for a lattice in order to carry out the discrete Fourier transform. The problem can be formulated in a general way using the following three-dimensional representation formulas:

$$\mathbf{M}(\mathbf{x}) = \sum_{pqr} \mathbf{m}_{pqr} e^{i(\mathbf{k}_{pqr} \cdot \mathbf{x})} \tag{40}$$

$$\phi(\mathbf{x}) = \sum_{pqr} \psi_{pqr} e^{i(\mathbf{k}_{pqr} \cdot \mathbf{x})} \tag{41}$$

Here, $\mathbf{k}_{pqr} = (k_p, k_q, k_r)$ with $k_p = 2\pi p/L_z$, $k_q = 2\pi q/L_y$, $k_r = 2\pi r/L_z$. By substitution into Eqn. (16) and comparing coefficients it is straightforward to show that

$$\phi_{pqr} = -\frac{4\pi i}{|\mathbf{k}_{pqr}|^2} \mathbf{m}_{pqr} \cdot \mathbf{k}_{pqr} \tag{42}$$

Determination of $-\nabla\phi$ then gives the field value.

See also: Coercivity Mechanisms; Magnetic Anisotropy; Magnetic Hysteresis; Micromagnetics: Finite Element Approach

Bibliography

Aharoni A 1996 *Introduction to the Theory of Ferromagnetism.* Clarendon Press, Oxford

Brown W F Jr. 1963 *Micromagnetics*. Interscience, New York

Chantrell R W, Coverdale G N, El-Hilo M, O'Grady K 1996 Modelling of interaction effects in fine particle systems. *J. Magn. Magn. Mater.* **157/158**, 250–5

Coverdale G N, Chantrell K W, Veitch K J 2001 *J. Appl. Phys.* in press

Della Torre E 1985 Fine particle micromagnetics. *IEEE Trans. Magn.* **21**, 1423–5

Della Torre E 1986 Magnetization calculation of fine particles. *IEEE Trans. Magn.* **22**, 484–9

El-Hilo M, O'Grady K, Chantrell K W 1994 The effect of interactions on GMR in granular solids. *J. Appl. Phys.* **76**, 6811–3

Giles K C, Kotiuga P K, Humphrey F B 1990 Three-dimensional micromagnetic simulations on the connection machine. *J. Appl. Phys.* **67**, 5821–3

Hughes G F 1983 Magnetization reversal in cobalt–phosphorous films. *J. Appl. Phys.* **54**, 5306–13

Mansuripur M, Giles K 1988 Demagnetizing field computation for dynamic simulation of the magnetization reversal process. *IEEE Trans. Magn.* **24**, 2326–8

Miles J J, Middleton B K 1990 The role of microstructure in micromagnetic models of longitudinal thin film magnetic media. *IEEE Trans. Magn.* **26**, 2137–9

Miles J J, Middleton B K 1991 A hierarchical model of longitudinal thin film recording media. *J. Magn. Magn. Mater.* **95**, 99–108

Schrefl T, Fidler J 1992 Numerical simulation of magnetization reversal in hard magnetic materials using a finite element method. *J. Magn. Magn. Mater.* **111**, 105–14

Tako K M, Wongsam M, Chantrell K W 1996 Micromagnetics of polycrystalline two-dimensional platelets. *J. Appl. Phys.* **79**, 5767–9

Victora R 1987 Quantitative theory for hysteretic phenomena in CoNi magnetic thin films. *Phys. Rev. Lett.* **58**, 1788

Vos M J, Brott R L, Zhu J G, Carlson L W 1993 Computed hysteresis behaviour and interaction effects in spheroidal particle assemblies. *IEEE Trans. Magn.* **29**, 3652–7

Walmsley N S, Hart A, Parker D A, Chantrell R W, Miles J J 1996 A simulation of the role of physical microstructure on feature sizes in exchange coupled longitudinal thin films. *J. Magn. Magn. Mater.* **155**, 28–30

J. Fidler and T. Schrefl
Vienna University of Technology, Austria

R. W. Chantrell and M. A. Wongsam
University of Durham, UK

Micromagnetics: Finite Element Approach

Since the early 1970s finite element modeling has become increasingly important in such different areas as continuum mechanics, electromagnetic field computation, and computational fluid dynamics. The integration of computer-aided design, finite element processing, and postprocessing methods for visualization of the numerical results makes finite element software a highly flexible tool in industrial research and development. The possibility of solving partial differential equations on irregular-shaped problem domains and of adjusting the spatial resolution using adaptive mesh refinement techniques are among the advantages of the finite element method. The use of the finite element method in micromagnetic simulations allows the realistic physical microstructures to be taken into account, which is a prerequisite for the quantitative prediction of the magnetic properties of thin film recording media or permanent magnets.

Finite element models of the grain structure are obtained from a Voronoi construction and subsequent meshing of the polyhedral regions. Finite element micromagnetic codes have been developed for the calculation of equilibrium states and the simulation of magnetization reversal dynamics. In either case short-range exchange and long-range magnetostatic interactions between the grains considerably influence the magnetic properties. The numerical evaluation of the magnetostatic interaction field makes use of well-established techniques of magnetostatic field calculation based on the finite element or the boundary element method.

Numerical micromagnetics at a subgrain level involves two different length scales which may vary by orders of magnitude. The characteristic magnetic length scale on which the magnetization changes its direction, is given by the exchange length in soft magnetic materials and the domain wall width in hard magnetic materials. For a wide range of magnetic materials, this characteristic length scale is in the order of 5 nm which may be either comparable or significantly smaller than the grain size. Adaptive refinement and coarsening of the finite element mesh enables accurate solutions to be found of the magnetization distribution at a subgrain level.

1. Finite Element Models of Granular Magnets

The simulation of grain growth using a Voronoi construction (Preparata 1985) yields a realistic microstructure for a permanent magnet. Starting from randomly located seed points, the grains are assumed to grow with constant velocity in each direction. Then the grains are given by the Voronoi cells surrounding each point. The Voronoi cell of seed point *i* contains all points in space which are closer to seed point *i* than to any other seed point. In order to avoid strongly irregular-shaped grains, it is possible to divide the model magnet into cubic cells and to choose one seed point within each cell at random. An example is the grain structure of Fig. 1 which is used to simulate the magnetic properties of nanocomposite, permanent magnets.

Different crystallographic orientations and different intrinsic magnetic properties are assigned to each grain. In addition, the grains may be separated by a narrow intergranular phase (Fischer and Kronmüller 1998). Once the polyhedral grain structure is obtained, the grains are further subdivided into finite elements. The magnetization is defined at the nodal points of the finite element mesh. Within each element
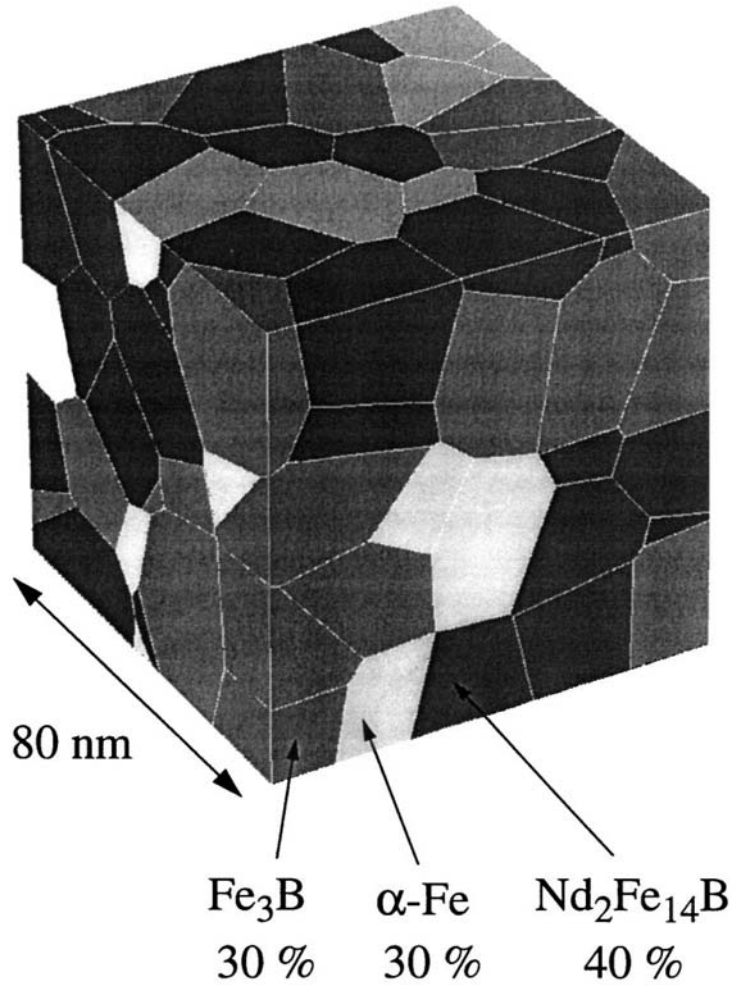
Figure 1
Finite element model of a nanocomposite permanent magnet obtained from a Voronoi construction. The plot gives the grain structure on the surface of a cubic magnet. The different colors refer to magnetically hard ($Nd_2Fe_{14}B$) and (α-Fe, Fe_3B) soft grains.

the magnetization is interpolated by a polynomial function. Thus the magnetization $\mathbf{M(r)}$ may be evaluated everywhere within the model magnet, using the piecewise polynomial interpolation of the magnetization on the finite element mesh. Figure 2(a) illustrates the interpolation of the magnetization using a linear function on a triangular finite element. The magnetization on a point $\mathbf{r}$ within the element

$$\mathbf{M(r)} = (A_1\mathbf{M(r_1)} + A_2\mathbf{M(r_2)} + A_3\mathbf{M(r_3)})/$$

$$(A_1 + A_2 + A_3)$$

$$= (A_1/A)\mathbf{M}_1 + (A_2/A)\mathbf{M}_2 + (A_3/A)\mathbf{M}_3 \quad (1)$$

is the weighted average of the magnetization at the nodal points 1, 2, and 3.
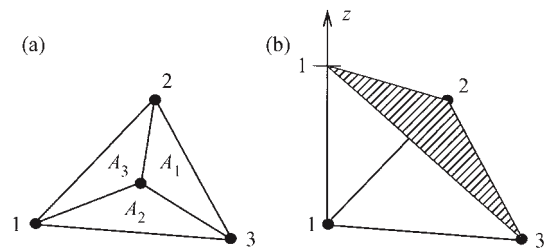
Figure 2
(a) Linear interpolation of the magnetization within a finite element. (b) The hatched area denotes the shape function of node 1, which equals one on node 1 and is zero on all the other nodes of the element.

929

A denotes the total area of the element and A_i are the areas of the subtriangles (see Fig. 2). A similar interpolation scheme applies for tetrahedral elements in three dimensions. The functions $\varphi_i = A_i/A$ are called shape functions. The shape function $\varphi_i(\mathbf{r})$ equals one on the node i and is zero on all the other nodes of the element. The shape function $\varphi_i(\mathbf{r})$ satisfies the conditions

$$\varphi_i(\mathbf{x}_j) = \delta_{ij} \qquad (2)$$

where $\mathbf{r}_j$ denotes the cartesian coordinates of the nodes $j = 1, \ldots, n$. Figure 2(b) depicts the shape function φ_1. The finite element mesh is used to integrate the total magnetic Gibbs free energy over the magnet. The energy integral is then replaced by a sum over cells (triangles, tetrahedrons, hexahedrons, …) and Eqn. (1) is applied to perform the integration of the energy over each cell.

Within the framework of micromagnetism (Brown 1963, Aharoni 1996), the magnitude of **M** is assumed to be a constant over the whole magnet, which depends only on the temperature

$$|\mathbf{M}| = M_s(T) \qquad (3)$$

The linear interpolation, Eqn. (1), does not preserve the magnitude of the magnetization within a finite element. However, the deviation of $|\mathbf{M}|$ from M_s within an element may be used as an error indicator for adaptive refinement schemes. Successive refinement of elements, where $|\mathbf{M}|$ deviates from M_s will lead to a fine mesh in areas with large spatial variation of the magnetization direction. After several refinement steps the constraint, Eqn. (3), will be approximately fulfilled on the entire finite element mesh (see Sect. 5).

2. Total Magnetic Gibbs Free Energy and Effective Field

In numerical micromagnetics generally the following scheme is used in order to calculate a hysteresis loop. At first the model magnet is saturated by applying a high external field. The uniform magnetic state with magnetization pointing parallel to the field direction corresponds to a minimum of the total magnetic Gibbs free energy. The repeated minimization of the energy for decreasing and increasing applied field provides the hysteresis curve. A small change of the external fields alters the energy surface slightly and thus the system is not in equilibrium any more. Unless the change of the external field alters the curvature of the energy surface, the current position of the system will be close to a local minimum of the energy. If the local minimum vanishes as the curvature changes the system has to find its path towards the next local minimum. The Gilbert equation of motion (Gilbert 1955)

$$\frac{\partial \mathbf{M}}{\partial t} = -|\gamma| \mathbf{M} \times \mathbf{H}_{\text{eff}} + \frac{\alpha}{M_s} \mathbf{M} \times \frac{\partial \mathbf{M}}{\partial t} \qquad (4)$$

is believed to describe the physical path the system follows towards equilibrium.

The effective field $\mathbf{H}_{\text{eff}}$ which provides the torque acting on the magnetization is the negative functional derivative of the total magnetic Gibbs free energy, $\mu_0 \mathbf{H}_{\text{eff}} = -\delta E/\delta \mathbf{M}$. The first term on the right hand side of Eqn. (4) describes the gyromagnetic precession, where γ is the gyromagnetic ratio of the free electron spin. The second term describes the dissipation of energy. It causes the magnetization to be become aligned parallel with the effective field as the system proceeds towards equilibrium. α is a dimensional damping parameter. Alternatively, numerical minimization methods may be used to compute the equilibrium states which considerably reduce the computation effort as compared to the numerical integration of the Gilbert equation.

Both static and dynamic micromagnetic finite element calculations start from the discretization of the total magnetic Gibbs free energy

$$E = \int dV \{ e_{\text{ex}}(\mathbf{r}) + e_K(\mathbf{r}) + e_m(\mathbf{r}) + e_z(\mathbf{r}) \} \qquad (5)$$

which is the integral over the sum of the exchange energy density, the magneto-crystalline anisotropy energy density, the magnetostatic energy density, and the Zeeman energy density. When $\mathbf{M}(\mathbf{r})$ is approximated by piecewise polynomial functions on the finite element mesh, the energy functional reduces to an energy function with the nodal values of the magnetization, $\mathbf{M}_i = (M_{x,i}, M_{y,i}, M_{z,i})$, as unknowns. The total energy may be written as

$$E = E(\mathbf{M}(\mathbf{r})) = E(\mathbf{M}_1, \mathbf{M}_2, \ldots, \mathbf{M}_n)$$
$$= E(M_{x,1}, M_{y,1}, M_{z,1}, M_{x,2}, M_{y,2}, M_{z,2}, \ldots,$$
$$M_{x,n}, M_{y,n}, M_{z,n}) \qquad (6)$$

where n is the total number of nodal points. The minimization of Eqn. (6) with respect to the $3n$ variables $M_{x,i}$, $M_{y,i}$, $M_{z,i}$ subject to the constraint $|\mathbf{M}_i| = M_s$ provides an equilibrium distribution of the magnetization.

To satisfy the constraint, Eqn. (3), polar coordinates θ_i, ϕ_i for the magnetization at the node i may be introduced, such that $M_{x,i} = M_s \sin \theta_i, \cos \phi_i$, $M_{y,i} = M_s \sin \theta_i \sin \phi_i$, and $M_{z,i} = M_s \cos \theta_i$. An alternative approach (Koehler 1997) is to normalize the magnetization in the discretized energy function, Eqn. (6), replacing $M_{x,i}$, $M_{y,i}$, $M_{z,i}$ by $M_{x,i}/|\mathbf{M}_i|$, $M_{y,i}/|\mathbf{M}_i|$, $M_{z,i}/|\mathbf{M}_i|$. In both cases, the minimization may be effectively performed using a conjugate gradient method (Gill *et al.* 1993).

Conjugate gradient-based minimization techniques require the gradient of the energy to select the search directions. Using polar coordinates, the gradient of

the energy can be expressed as

$$\frac{\partial E}{\partial \theta_i} = \frac{\partial E}{\partial M_{x,i}} \frac{\partial M_{x,i}}{\partial \theta_i} + \frac{\partial E}{\partial M_{y,i}} \frac{\partial M_{y,i}}{\partial \theta_i} + \frac{\partial E}{\partial M_{z,i}} \frac{\partial M_{z,i}}{\partial \theta_i}$$

$$= - V_i \mu_0 \mathbf{H}_{\text{eff},i} \cdot \frac{\partial \mathbf{M}_i}{\partial \theta_i} \tag{7}$$

$$\frac{\partial E}{\partial \phi_i} = \frac{\partial E}{\partial M_{x,i}} \frac{\partial M_{x,i}}{\partial \phi_i} + \frac{\partial E}{\partial M_{y,i}} \frac{\partial M_{y,i}}{\partial \phi_i} + \frac{\partial E}{\partial M_{z,i}} \frac{\partial M_{z,i}}{\partial \phi_i}$$

$$= - V_i \mu_0 \mathbf{H}_{\text{eff},i} \cdot \frac{\partial \mathbf{M}_i}{\partial \phi_i} \tag{8}$$

In Eqns. (7) and (8) the effective field $\mathbf{H}_{\text{eff}}$ has been introduced. The effective field at the nodal points of the finite element mesh can be calculated within the framework of the box method. The effective field at the nodal point i of the finite element mesh can be approximated by (Gardiner 1985)

$$\mu_0 \mathbf{H}_{\text{eff},i} = - \left(\frac{\delta E}{\delta \mathbf{M}} \right)_i \approx - \frac{1}{V_i} \frac{\partial E}{\partial \mathbf{M}_i} \tag{9}$$

where V_i is the volume of a "box" surrounding the nodal point i. The following conditions hold for the box volumes

$$\sum_i V_i = \int \mathrm{d}V \quad \text{and} \quad V_i \cap V_j = 0 \quad \text{for} \quad i \neq j. \tag{10}$$

3. Magnetostatic Field Calculation

Both static and dynamic micromagnetic calculations are required to evaluate the effective field at the nodal points of the finite element mesh. The effective field is the sum of the exchange field, the anisotropy field, the magnetostatic field, and the external field. The exchange field and the anisotropy field depend only locally on the magnetization or its spatial derivatives and thus may be directly calculated using Eqn. (9). The magnetostatic field depends on the magnetization distribution over the entire magnet. It arises from the nonzero divergence within the grains ("magnetic volume charges") and the intersection of the magnetization with the grain surface ("magnetic surface charges").

Numerical micromagnetics can make use of the well-established methods for the finite element calculation of magnetostatic fields (Silvester and Ferrari 1983). The magnetostatic field either is derived from a magnetic scalar or a magnetic vector potential. The finite element discretization of the corresponding partial differential equation leads to a system of linear equations. Owing to the local character of the equations the corresponding system matrix is symmetric and sparse. State of the art solution techniques for a sparse linear systems consist of a preconditioning step, followed by the iterative solution of the linear system using a conjugate gradient-based method.

For a given finite element mesh the preconditioning of the system matrix has to be done only once, reducing the effort for the subsequent calculations of the magnetostatic field to about $n^{1.3}$, where n is the total number of grid points. Thus the use of the finite element method to treat the auxiliary problem of the magnetostatic field provides an alternative fast solution technique without any restriction on the geometry of the magnetic particles.

3.1 The Magnetostatic Boundary Value Problem

The magnetostatic contribution to the effective field is the negative gradient of the magnetic scalar potential. The magnetic scalar potential satisfies the Poisson equation

$$\nabla^2 U(\mathbf{r}) = \nabla \cdot \mathbf{M}(\mathbf{r}) \tag{11}$$

Outside the magnetic particle $\mathbf{M}$ equals zero and thus Eqn. (11) reduces to the Laplace equation. At the boundary of the magnet Γ the boundary conditions

$$U^{\text{int}} = U^{\text{ext}}, \ (\nabla U^{\text{int}} - \nabla U^{\text{ext}}) \cdot \mathbf{n} = \mathbf{M} \cdot \mathbf{n} \tag{12}$$

hold. Here $\mathbf{n}$ denotes the outward pointing normal unit vector on Γ. The magnetic scalar potential is regular at infinity

$$U \propto 1/\mathbf{r} \quad \text{for} \quad \mathbf{r} \to \infty \tag{13}$$

The Galerkin method is applied to transfer the magnetostatic boundary value problem to a system of linear equations. The partial differential equation, Eqn. (11), is multiplied by test functions φ_i and integrated over the problem domain

$$\int_{\Omega_{\text{int}}} \mathrm{d}V \varphi_i \nabla^2 U(\mathbf{r}) + \int_{\Omega_{\text{ext}}} \mathrm{d}V \varphi_i \nabla^2 U(\mathbf{r})$$

$$= \int_{\Omega_{\text{int}}} \mathrm{d}V \varphi_i \nabla \cdot \mathbf{M}(\mathbf{r}) + \int_{\Omega_{\text{ext}}} \mathrm{d}V \varphi_i \nabla \cdot \mathbf{M}(\mathbf{r}) \tag{14}$$

Here Ω_{int} and Ω_{ext} denote the space within and outside the magnet, respectively. Integration by parts moves the second derivative of the potential and the first derivative of the magnetization vector to the test function

$$\int_{\Gamma} \mathrm{d}S \varphi_i (\nabla U^{\text{int}} - \nabla U^{\text{ext}}) \cdot \mathbf{n} - \int_{\Omega_{\text{int}} \bigcup \Omega_{\text{ext}}} \mathrm{d}V \nabla \varphi_i \nabla U$$

$$= \int_{\Gamma} \mathrm{d}S \varphi_i \mathbf{M} \cdot \mathbf{n} - \int_{\Omega_{\text{int}}} \mathrm{d}V \nabla \varphi_i \cdot \mathbf{M} \tag{15}$$

Substituting the boundary condition, Eqn. (12), into Eqn. (15) the surface integrals cancel.

Within the framework of the Galerkin method, the shape functions φ_i, given by Eqn. (2), are used as test functions. Like the magnetization, the magnetic scalar potential is interpolated by a piecewise polynomial

function over a finite element e

$$U(\mathbf{r}) = \sum_i \varphi_i^e(\mathbf{r}) U_i = \varphi_i^e(\mathbf{r}) U_i \qquad (16)$$

where U_i denote the values of the magnetic scalar potential at the nodes of the element. Then the volume integrals in Eqn. (15) break into sums of integrals over the finite elements

$$\sum_e \int dV \, \nabla \varphi_i \nabla \varphi_j^e U_j = \sum_e \int dV \, \nabla \varphi_i \cdot \varphi_j^e \mathbf{M}_j \qquad (17)$$

The summation over the contributions of the individual finite elements in Eqn. (17) leads the sparse, linear system of equations that gives the potential U_i at the nodes i of the finite element mesh.

3.2 The Open Boundary Problem

In order to impose the regularity condition Eqn. (13), the finite element mesh has to be extended over a large region outside the magnetic particles. As a rule of thumb the distance between the boundary of the external mesh and the particle should be at least five times the extension of the particle (Chen and Conrad 1997). Various other techniques have been proposed to reduce the size of the external mesh or to avoid a discretization of the exterior space. The use of asymptotic boundary conditions (Yang and Fredkin 1998) reduces the size of the external mesh compared to truncation. At the external boundary Robbin conditions are applied, which are derived from a series expansion of the solution of the Laplace equation for U outside the magnet and give the decay rate of the potential at a certain distance from the sample (Khebir *et al.* 1990).

A similar technique that considerably reduces the size of the external mesh is the use of space transformation to evaluate the integral over the exterior space in Eqn. (15). Among the various transformations proposed to treat the open boundary problem, the parallelepipedic shell transformation (Brunotte *et al.* 1992), which maps the external space into shells enclosing the parallelepipedic interior domain, has proved to be most suitable in micromagnetic calculations. The method can be easily incorporated into standard finite element programs transforming the derivatives of the nodal shape functions. This method was applied in static three-dimensional micromagnetic simulations of the magnetic properties of nanocrystalline permanent magnets (Schrefl and Fidler 1998, Fischer and Kronmüller 1998)

An alternative approach for treating the so-called open boundary problem is a hybrid finite element/boundary element method (Fredkin and Koehler 1990, Koehler 1997). The basic concept of this method is to split the magnetic scalar potential into $U = U_1 + U_2$, where the potential U_1 is assumed to solve a closed boundary value problem. Then the equations for U_2 can be derived from Eqns. (11) and (12), which hold for the total potential $U = U_1 + U_2$. The potential U_1 accounts for the divergence of the magnetization and U_2 is required to meet the boundary conditions at the surface of the particle. The latter also carries the magnetostatic interactions between distinct magnetic particles.

The potential U_1 can be computed from the closed boundary value problem

$$\nabla^2 U_1(\mathbf{r}) = \nabla \cdot \mathbf{M}(\mathbf{r}) \quad \text{for} \quad \mathbf{r} \in \Omega_{\text{int}} \qquad (18)$$

$$U_1 = 0 \quad \text{for} \quad \mathbf{r} \in \Omega_{\text{ext}} \qquad (19)$$

$$\nabla U_i \cdot \mathbf{n} = \mathbf{M} \cdot \mathbf{n} \quad \text{for} \quad r \in \Gamma \qquad (20)$$

The potential U_1 is the solution of the Poisson equation within the magnetic particles and equals zero outside the magnets. At the surface of the magnets, natural boundary conditions hold. The potential U_2 satisfies the Laplace equation everywhere

$$\nabla^2 U(\mathbf{r}) = 0 \quad \text{for} \quad \mathbf{r} \in \Omega_{\text{int}} \cup \Omega_{\text{ext}} \qquad (21)$$

and shows a jump at the boundary of the magnetic particles

$$U_2^{\text{int}}(\mathbf{r}) - U_2^{\text{ext}}(\mathbf{r}) = U_1^{\text{int}}(\mathbf{r}), (\nabla U_2^{\text{int}} - \nabla U_2^{\text{ext}}) \cdot \mathbf{n} = 0$$
$$\text{for } \mathbf{r} \in \Gamma \qquad (22)$$

A standard finite element method may be used to solve Eqns. (18)–(22). Eqns. (21) and (22) define a double layer potential which is created by a dipole sheet with magnitude $U_1 \cdot U_2$ can be evaluated using the boundary element method. After discretization, the potential U_2 at the boundary nodes follows from a matrix vector multiplication $U_2 = \mathbf{B} \, U_1$, where $\mathbf{B}$ is a $m \times m$ matrix which relates the m boundary nodes with each other. Once U_2 at the boundary has been calculated, the values of U_2 within in the particles follow from Laplace's equation with Dirichlet boundary conditions, which again can be solved by a standard finite element technique.

The matrix $\mathbf{B}$ depends only on the geometry and the finite element mesh and thus has to be computed only once for a given finite element mesh. Since the hybrid finite element boundary element method does not introduce any approximations, the method is accurate and effective. The use of the boundary element method easily treats the magnetostatic interactions between distinct magnetic particles and requires no mesh outside the magnetic particles. Süß and co-workers (Süß *et al.* 1999) applied the hybrid finite element/boundary element method, in order to simulate the effect of magnetostatic interactions on the reversal dynamics of magnetic nanoelements.

932

3.3 Static Micromagnetics Using a Magnetic Vector Potential

The use of a magnetic scalar potential in micromagnetic calculations, requires the solution of a system of linear equations associated with the magnetostatic boundary value problem, whenever the total magnetic Gibbs free energy or the effective field has to be evaluated. An alternative approach for treating the magnetostatic interactions is the use of a magnetic vector potential. Then micromagnetic problem can be reformulated as an algebraic minimization problem with the nodal values of the magnetization angles θ_i, ϕ_i, and the nodal values of the magnetic vector potential **A** as unknowns. The method applies an alternative function to express the magnetostatic energy.

Brown (1963) proposed an upper bound for the magnetostatic energy

$$\int \mathrm{d}V e_{\mathrm{m}} \leqslant W(\mathbf{A}) = \frac{1}{2\mu_0} \int \mathrm{d}V (\nabla \times \mathbf{A} - \mu_0 \mathbf{M})^2 \quad (23)$$

If minimized with respect to **A**, the functional $W(\mathbf{A})$ reduces to the magnetostatic energy of the magnetization distribution $\mathbf{M}(\mathbf{r})$. Thus it is possible to replace the magnetostatic energy in the total magnetic Gibbs free energy with $W(\mathbf{A})$ and treat **A** as an additional variable. The simultaneous minimization of the energy with respect to **M** and **A** provides the equilibrium configuration of the magnetization (Aharoni 1996). Again spherical coordinates can be introduced to satisfy the constraint (3).

The integral on the right hand side of Eqn. (23) is an integration over the entire space and proper techniques to treat the open boundary problem have to be applied. The first variation of Eqn. (23) gives the unconstrained curl–curl equation for the magnetic vector potential which is the equation commonly solved in magnetostatic field calculations. Thus the use of a magnetic vector potential in numerical micromagnetics treats the magnetostatic field in the very same way as conventional finite element packages for magnetostatic field calculation (Demerdash and Wang 1990).

This method was applied to predict the theoretical limits for the remanence and the coercive field of nanocomposite permanent magnets (Schrefl and Fidler 1998). These magnets consist of a mixture of magnetically hard and soft phases. The complex, multiphase microstructure considerably influences the magnetic properties and thus has to be taken into account in micromagnetic models. Figure 3 gives the numerically calculated demagnetization curves for the $Nd_2Fe_{14}B$ magnet depicted in Fig. 1 as a function of the average grain diameter. Intergrain exchange interactions considerably enhance the remanence compared with the remanence of noninteracting, randomly oriented grains. Figure 4 presents the magnetization distribution in a slice plane for zero applied field and an average grain size of 20 nm.
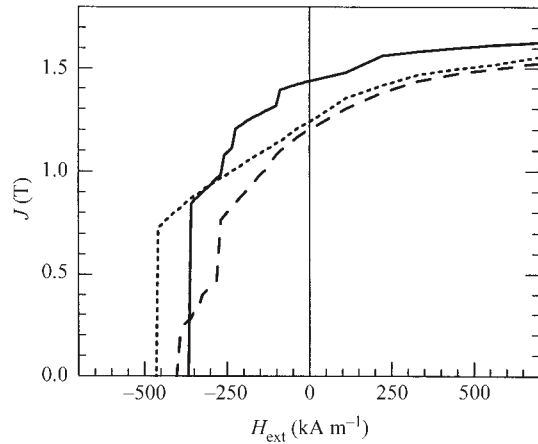
Figure 3
Numerically calculated demagnetization curves as a function of the mean grain size for the nanocomposite magnet of Fig. 1. —, 10 nm; ······, 20 nm; - - - -, 30 nm.

The magnetization remains parallel to the saturation direction within the soft magnetic grains, whereas it rotates towards the direction of the local anisotropy direction within the hard magnetic grains.

4. Dynamic Micromagnetics Using the Finite Element Method

Either a box scheme or the Galerkin method can be applied to discretize the Gilbert equation of motion, Eqn.(4), in space. The Gilbert equation (4) reduces to three ordinary differential equations for each node of the finite element mesh, using the box scheme, Eqn. (9), to approximate the effective field. The resulting system of $3n$ ordinary differential equations describes the motion of the magnetic moments at the nodes of the finite element mesh. The system of ordinary differential equations is commonly solved using a predictor corrector method or a Runge Kutta method for mildly stiff differential equations. Small values of Gilbert damping constant α or complex microstructures will require a time step smaller than 10 fs, if an explicit scheme is used for the time integration. In this highly stiff regime backward difference schemes allow much larger time steps and considerably reduce the required CPU time.

An implicit time integration scheme can be derived, applying the Galerkin method directly to discretize the Gilbert equation (4). A backward difference method (Hindmarsh and Petzold 1995) is used for time integration of the resulting system of ordinary differential equations. Since the stiffness arises mainly from the exchange term, the magnetostatic field can be treated explicitly. During a time interval τ, the Gilbert equation is integrated with a fixed
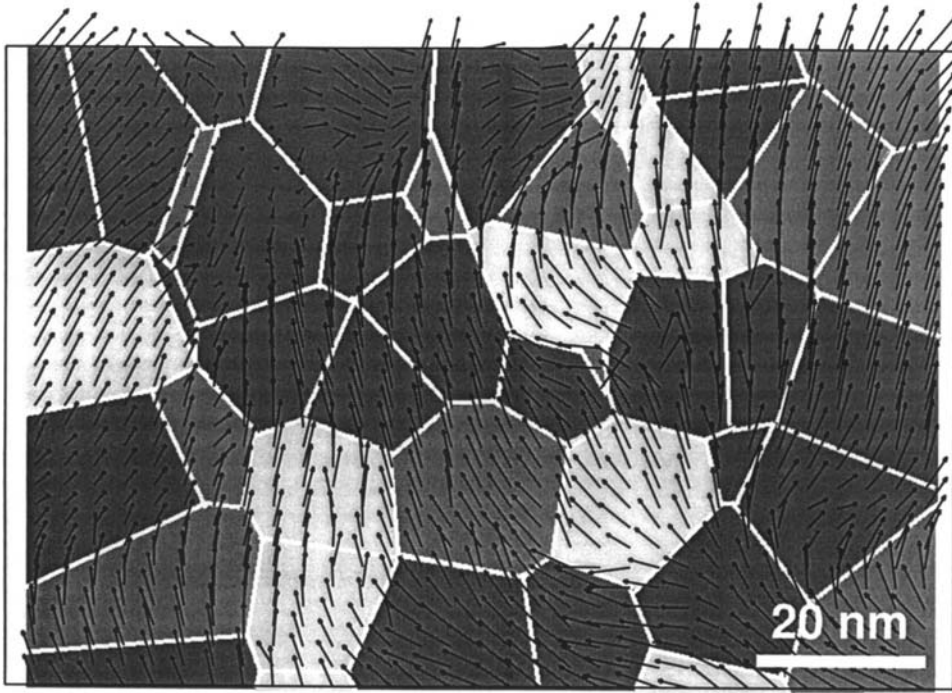
Figure 4
Magnetization distribution within a nanocomposite magnet for zero applied field. The arrows denote the direction of the magnetization in a slice plane parallel to the saturation direction. The mean grain size was 20 nm.

magnetostatic field using a higher order backward difference method. The magnetostatic field is updated after a time τ which is taken to be inversely proportional to the maximum torque $\max_i$, $|\mathbf{M}_i \times \mathbf{H}_{\text{eff},i}|$ over the finite element mesh. The hybrid finite element/ boundary element method is used to calculate the magnetostatic field. Figure 5 presents the flow chart of the semi-implicit time integration scheme. In highly stiff regimes the semi-implicit scheme requires less central processing unit (CPU) time as compared with a Runge–Kutta method, despite the need to solve a system of nonlinear equations at each time step.

A semi-implicit time integration scheme was applied to calculate the magnetization reversal dynamics of patterned Co elements, taking into account the small scale, granular structure of the thin films elements (Schrefl *et al.* 1999). Dynamic micromagnetic calculations using the finite element method and backward difference were originally introduced by Yang (Yang and Fredkin 1996) and applied to the study of magnetization reversal dynamics of interacting ellipsoidal particles (Yang and Fredkin 1998).

5. Adaptive Meshing

The finite element method effectively treats magnetization processes in samples with arbitrary geometries
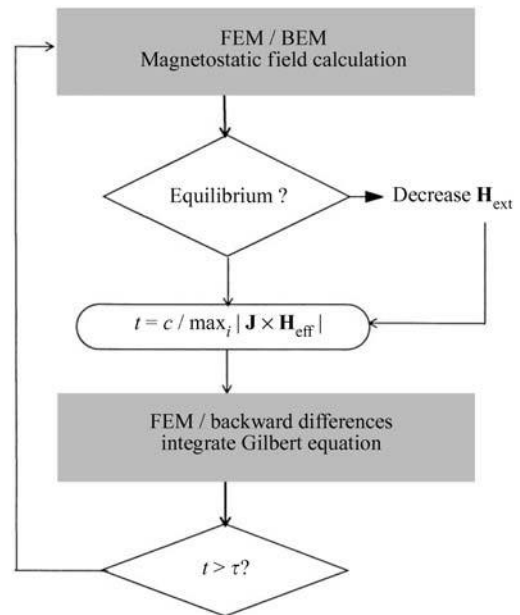
Figure 5
Flow chart of the semi-implicit time integration scheme used to solve the Gilbert equation of motion.

or irregular microstructures. Adaptive refinement schemes allow the magnetization distribution to be solved on a subgrain level, improving the accuracy of the solution while keeping the computational effort to a minimum. Finite element mesh refinement was applied in micromagnetic simulations of longitudinal thin film media (Tako *et al.* 1997), domain structures in soft magnetic thin films (Hertel and Kronmüller 1998), and domain wall motion in permanent magnets (Scholz *et al.* 1999).

6. Refinement Indicators

The discretization of the micromagnetic equations gives rise to two types of discretization error. One is associated with the evaluation of the exchange field, the other arises from the finite element computation of the magnetostatic field. Improvements in the micromagnetic resolution can be made by a uniform increase in the level of discretization. However, this places more computational modes in areas where the magnetization remains uniform. Ideally, it would be most efficient to place new nodes where the error is highest.

The aim of adaptive mesh refinement schemes is to obtain a uniform distribution of the discretization error over the finite element mesh (Penman and Grieve 1987). In order to decide where to refine the mesh, refinement indicators should give a good estimate of the local error. A second criterion for the selection of error estimators for adaptive meshing are the computational costs. Error estimators should be cheap to evaluate and thus error indicators derived from the current finite element solution on an element-by-element basis are preferred. Within the framework of classical micromagnetism the magnitude of the magnetization vector is assumed to be constant.

This condition can only hold at the nodal points of the finite element mesh, using a linear interpolation of the magnetization on a finite element. Bagnérés-Viallix (Bagnérés-Viallix *et al.* 1991) proposed use of the deviations in the length of the magnetization vector from M_s in the center of an element as refinement indicator. The magnetization distribution of a one-dimensional domain wall can be calculated analytically. Thus the true discretization error of the finite element solution can be evaluated. Numerical investigations of one-dimensional mesh refinement showed that the error estimator based on the norm of the magnetization shows the very same functional dependence on the number of finite elements as the true error of the solution.

Refinement indicators that point out the exchange discretization error are usually based on the spatial variation of the magnetization (Hertel and Kronmüller 1998). They identify domain walls, vortices, or magnetic inhomogenities near edges and corners. In

order to consider the discretization error associated with the magnetostatic field calculation, Tako *et al.* (1997) suggested a refinement indicator based on the divergence and curl of both the magnetization and magnetic field. Simulating the magnetization structure of two-dimensional magnetic nanoelements, Ridley *et al.* (1999) showed that this refinement indicator correctly identifies the regions where the true error in the computed magnetic field is high.

6.1 Finite Element Micromagnetics Using Adaptive Mesh Control

In longitudinal thin film media the granular microstructure significantly influences the remanent magnetization distribution. Tako (Tako *et al.* 1997) showed that adaptive refinement clearly improves both the efficiency and accuracy of the computations of magnetization patterns in thin film microstructures obtained form a Voronoi construction. A refinement indicator based on the spatial variation of both magnetization and magnetic field is used to point out elements in which refinement is necessary.

Elements which show a refinement indicator greater than 20% of the maximum value over all elements are subdivided by regular division. The numerical results indicate a significant improvement in the calculated magnetization structure after refinement. The magnetization tends to form vortices which do not fully develop in the coarse grid. With further refinement the structure is allowed a lower energy state to be attained allowing a more complete development of the solenoidal structure. During the refinement process the total energy decreases by about 50% which clearly indicates the success of the refinement indicator.

Hertel and Kronmüller (1998) proposed an r-refinement scheme to resolve vortices in micromagnetic simulations of domain structures in soft magnetic, thin film elements. The discretization error is reduced by moving nodes of the finite element mesh towards regions where higher accuracy is needed. In micromagnetic simulations of domain structures in soft magnetic thin films, this was accomplished by shrinking the elements in regions with strong inhomogeneities. Thus, a high mesh density, which results in a high micromagnetic resolution, was obtained near vortices and domain walls, while keeping the number of elements constant.

In hard magnetic materials the magnetization is uniform within magnetic domains whereas it is highly nonuniform in domain walls, near nucleation sites, vortices, or grain boundaries. A coarse mesh may be sufficient in regions where the magnetization is almost uniform. Local mesh refinement near grain boundaries, domain walls, vortices, and nucleation sites significantly reduces the number of degrees of freedom. As domain walls can move because of external fields,

the discretization has to be adjusted adaptively during the simulation. Scholz *et al.* (1999) presented an algorithm that adapts the finite element mesh to the solution of the Gilbert equation.

Refinement of the tetrahedral mesh at the current wall position and coarsening within the bulk of the domains leads to a high density mesh that moves together with the wall. After each time step, error indicators based on the deviations of $|\mathbf{M}|$ from M_s are calculated for each element. If the maximum error indicator over all elements, η_{max}, exceeds a certain threshold the following refinement scheme is applied: Elements whose error indicators exceeds $0.1\,\eta_{max}$

are marked for refinement, whereas elements with an error indicator lower than $0.01\,\eta_{max}$ are marked for coarsening.

Then, the finite element mesh is refined by subdividing elements, which are marked for refinement. Coarsening is effected by removing finite elements which have been created by an earlier refinement step (Bey 1995). Figure 6 shows the regions of fine mesh at the current wall position during the simulation of domain wall motion in thin $Nd_2Fe_{14}B$ specimens. The wall moves towards the boundary of a misoriented grain, where it remains pinned owing to a reduction in the exchange and anistropy energy stored in the wall.
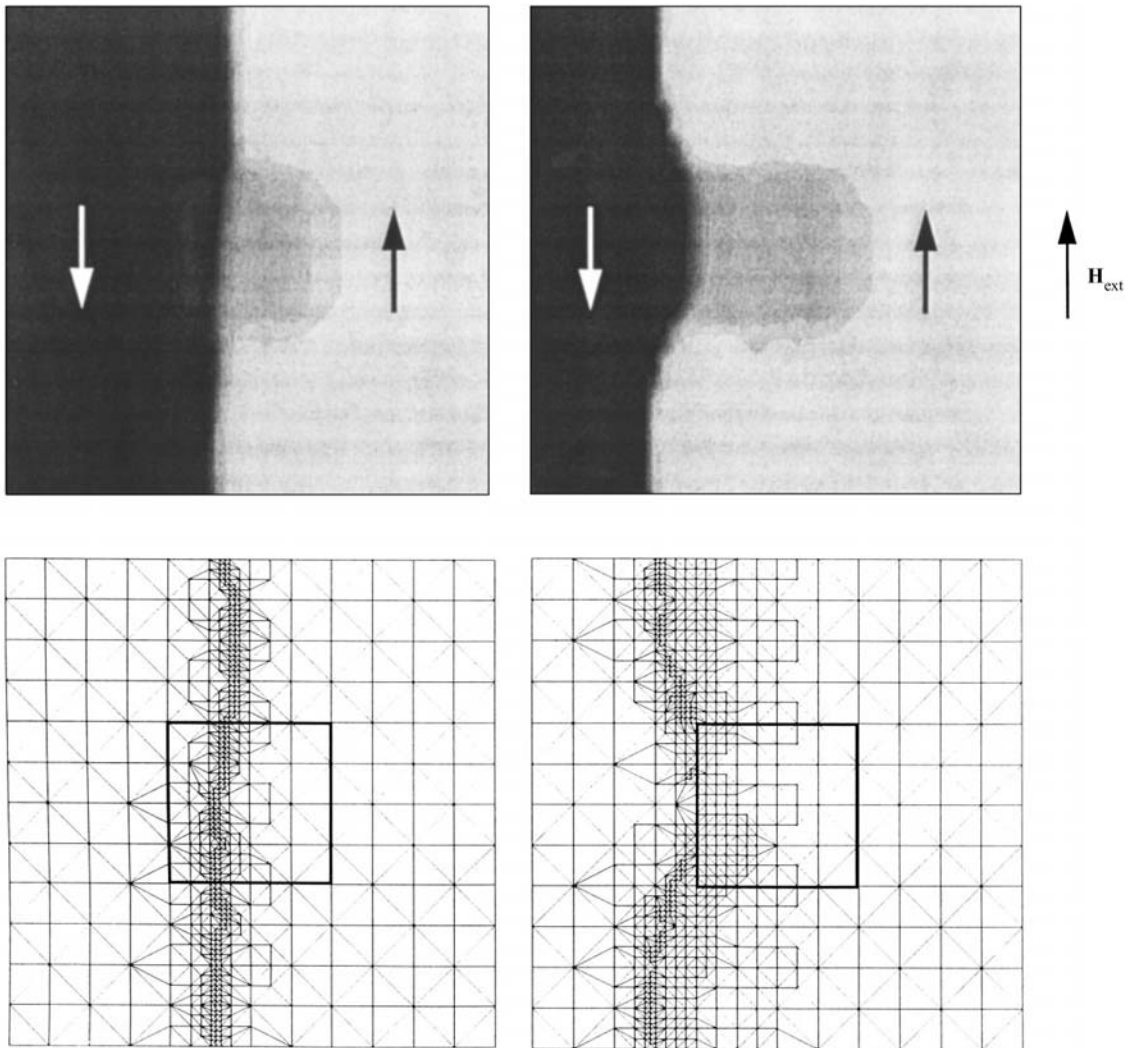
Figure 6
Adaptive mesh refinement: magnetization distribution and corresponding finite element mesh during the simulation of domain wall motion. The wall becomes pinned at the grain boundary of a misoriented grain.

7. Summary

Micromagnetism treats magnetic material as classical continuous media, described by appropriate differential equations governing their static and dynamic behavior. The numerical solution of the governing equations can be effectively performed using finite element and related methods which easily handle complex microstructures. Finite element techniques for an effective solution of the basic static and dynamic equations were compared. These include various methods for treating the so-called open boundary problem in magnetostatic field calculation and discretization schemes that allow sparse matrix methods for the time integration of the equation of motion.

Finite element simulations successfully predict the influence of microstructural features like grain size, particle shape, and edge irregularities on the magnetic properties. Adaptive refinement and coarsening of the mesh controls the discretization error and provides optimal grids for micromagnetic finite element simulation of magnetization processes in longitudinal thin film media, vortex formation in soft magnetic thin films, and of domain wall motion in hard magnetic platelets.

See also: Micromagnetics: Basic Principles

Bibliography

Aharoni A 1996 *Introduction to the Theory of Ferromagnetism*. Clarendon Press, Oxford
Bagnérés-Viallix A, Baras P, Albertini J B 1991 2D and 3D calculations of micromagnetic wall structures using finite elements. *IEEE Trans. Magn.* **27**, 3819–21
Bey J 1995 Tetrahedral grid refinement. *Computing* **55**, 355–78
Brown W F Jr. 1963 *Micromagnetics*. Wiley Interscience, New York
Brunotte X, Meunier G, Imhoff J F 1992 Finite element modeling of unbounded problems using transformations: Rigourous, powerful and easy solutions. *IEEE Trans. Magn.* **28**, 1663–6
Chen Q, Conrad A 1997 A review of finite element open boundary techniques for static and quasi-static electromagnetic field problems. *IEEE Trans. Magn.* **33**, 663–76
Demerdash N A, Wang R 1990 Theoretical and numerical difficulties in 3D vector potential methods in finite element magnetostatic computations. *IEEE Trans. Magn.* **26**, 1656–8
Fischer R, Kronmüller H 1998 Importance of ideal grain boundaries of high remanent composite permanent magnets. *J. Appl. Phys.* **83**, 3271–5
Fredkin D R, Koehler T R 1990 Hybrid method for computing demagnetizing fields. *IEEE Trans. Magn.* **26**, 415–7
Gardiner C W 1985 *Handbook of Stochastic Methods*. Springer, Berlin
Gilbert T L 1955 A Lagrangian formulation of gyromagnetic equation of the magnetization field. *Phys. Rev.* **100**, 1243
Gill P E, Murray W, Wright M H 1993 *Practical Optimization*. Academic Press, London
Hertel R, Kronmüller H 1998 Adaptive finite element mesh refinement techniques in three-dimensional micromagnetic modeling. *IEEE Trans. Magn.* **34**, 3922–30
Hindmarsh A C, Petzold L R 1995 Algorithms and software for ordinary differential equations. Part II: Higher-order methods and software packages. *Comput. Phys.* **9**, 148–55
Khebir A, Kouki A B, Mittra R 1990 Asymptotic boundary for finite element analysis of three-dimensional transmission line discontinuities. *IEEE Trans. Microwave Theory Techniques* **38**, 1427–31
Koehler T R 1997 Hybrid Fem-Bem method for fast micromagnetic calculations. *Physica B* **233**, 302–7
Penman J, Grieve M D 1987 Self adaptive mesh generation technique for the finite element method. *IEEE Proc. A.* **134**, 634–50
Preparata F P 1985 *Computational Geometry*. Springer, New York
Ridley P H W, Roberts G W, Wongsam M A, Chantrell R W 1999 Finite element modelling of nanoelements. *J. Magn. Magn. Mater.* **193**, 423–6
Scholz W, Schrefl T, Fidler J 1999 Mesh refinement in FE-micromagnetics for multidomain $Nd_2Fe_{14}B$ particles. *J. Magn. Magn. Mater.* **196–7**, 933–4
Schrefl T, Fidler J 1998 Modelling of Exchange-spring Permanent Magnets. *J. Magn. Magn. Mater.* **177**, 970–5
Schrefl T, Fidler J, Kirk K J, Chapman J N 1999 Simulation of magnetization reversal in polycrystalline Co elements. *J. Appl. Phys.* **85**, 6169–71
Silvester P P, Ferrari R 1983 *Finite Elements for Electrical Engineers*. Cambridge University Press, Cambridge
Süß D, Schrefl T, Fidler J, Chapman J N 1999 Micromagnetic simulation of the long-range interaction between NiFe nanoelements using BE-method. *J. Magn. Magn. Mater.* **196–7**, 617–9
Tako K M, Schrefl T, Wongsam M A, Chantrell R W 1997 Finite element micromagnetic simulations with adaptive mesh refinement. *J. App. Phys.* **81**, 4082–4
Yang B, Fredkin D R 1996 Dynamical micromagnetics of a ferromagnetic particle – Numerical studies. *J. Appl. Phys.* **79**, 5755–7
Yang B, Fredkin D R 1998 Dynamic micromagnetics by the finite element method. *IEEE Trans. Magn.* **33**, 3842–52

R. W. Chantrell and M. Wongsam
University of Wales, Bangor, UK

J. Fidler and T. Schrefl
Vienna University of Technology, Austria

Monolayer Films: Magnetism

This article is concerned with what changes in magnetic ordering phenomena when the thickness of a single crystal (epitaxial) film is reduced to an atomic scale, i.e., in ultrathin ferromagnetic films (UFF), in epitaxial films consisting of a few atomic layers only. We focus on intrinsic magnetic thin film phenomena, i.e., on those which result from the bare reduction of one of the sample dimensions, and the modified electronic state of surface atoms (surfaces in our sense include interfaces). These intrinsic phenomena are the subject of basic theoretical models. Our approach is

experimental. We report experimental data on intrinsic magnetic properties of model structures, to be discussed in the light of theoretical models. To be concise, we will refer frequently to the more extended review (Gradmann 1993). For further reading see articles in Heinrich and Bland (1994).

Experimental work on UFF crucially depends on the preparation of flat ultrathin epitaxial structures, which is now done preferentially by epitaxial growth in ultra-high vacuum (UHV, pressures of the order 10^{-10} torr. Epitaxial growth is discussed briefly and with emphasis on UFF in Gradmann (1993), in more detail in articles in King and Woodruff (1997). It has been known from diffraction methods for a long time, and visualized in detail by scanning tunneling microscopy (STM), that even the best-grown epitaxial films contain a high level of structural defects. A detailed discussion of the film real structure is beyond the scope of this article (but see articles covering growth phenomena). We choose data from the best available flat epitaxial films. One should have the imperfect structure of even the best epitaxial films in mind.

The intrinsic UFF properties to be discussed in this article are (i) enhanced thermal decrease of magnetic order, as a result of reduced size (size effect, Sect. 1), (ii) changed (ground state) magnetic moments in surfaces (interfaces) (surface effect, Sect. 2) and (iii) outstanding magnetic anisotropies, in particular magnetic surface anisotropies (MSA), and the related, technologically important phenomenon of perpendicular magnetization (Sect. 3). A discussion of the Dead Layers problem will be included in Sects. 1 and 2.

1. Enhanced Thermal Decrease of Magnetic Order (Size Effect)

The basic phenomena of enhanced thermal decrease of magnetic order are shown in Figs. 1 and 2: with decreasing number of atomic layers, D, we observe, as a result of the reduced magnetic coordination, an enhanced thermal decrease of spontaneous magnetization $M_s(T; D)$ (Fig. 1), including a change in shape of the thermal profile, and a monotonic decrease of the Curie temperature $T_c(D)$ (Fig. 2). The full line in Fig. 2 is a power law $(T_c(\infty) - T_c(D)) \propto D^{-\lambda}$ with $\lambda = 1.27$, near the theoretical prediction $\lambda = 1.4$ (Gradmann 1993, p. 52). Qualitatively, the pattern of Figs. 1 and 2 is representative for all UFF systems investigated so far.

A more detailed discussion of thermal decrease of magnetic order is done, as for bulk ferromagnets, separately for the low temperature (spin-wave) regime (roughly $T < T_c/2$) and the critical regime near T_c.

For the spin-wave regime, the main body of available theories was worked out in the 1960s; for a report see Gradmann (1974). In spin-wave theories,
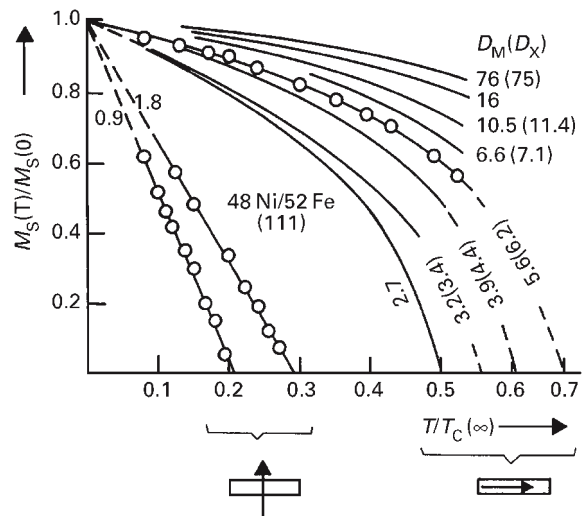
Figure 1
Temperature dependence of magnetization in UFF, of type Cu(111)/48Ni52Fe(111)/Cu(111); number of atomic layers D as parameter (D_M from magnetometry, D_x from x-ray fluorescence). The orientation of magnetization is indicated. Films for $D > 2$ are magnetized in the plane, films for $D < 2$ show perpendicular magnetization (from Gradmann 1974).
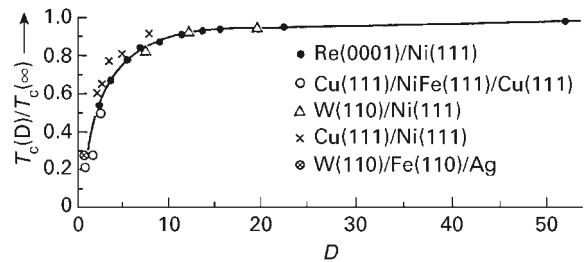
Figure 2
Curie temperatures for densely packed cubic UFF versus the number of atomic layers, D (from Gradmann 1993).

homogeneous ground state magnetization is assumed. The reduced magnetic moment at finite temperatures then is inferred by the finite size (thickness) only. For experimental analysis of this size effect, it is convenient to cast the theoretical results in the form

$$\mu(T; D) \cdot D = \mu_{bulk}(T) \cdot [D - D_{c,size}(T)] \qquad (1)$$

where $\mu(T; D)$ is the magnetic moment per atom in a sample consisting of D atomic layers, and $\mu_{bulk}(T)$ is the bulk moment (Gradmann 1974, Gradmann *et al.*

1997). The size effect is represented by $D_{c,size}(T)$, which turns out to be roughly proportional to T, with a weak (logarithmic) dependence on anisotropies (or external fields) only. Equation (1) can be read in the sense that the size-induced thermal decrease of magnetic moment per area, given by $-\mu_{bulk}(T) \cdot D_{c,size}(T)$, is independent of D. For the limit of a few monolayers thickness, this can be explained from the two-dimensional nature of the spectrum of thermally excitable spin wave states ($k_z \neq 0$ states are frozen). This spectrum is independent of D, and so is the number of excited magnons and therefore the thermal decrease of magnetic moment. The thermal decrease of magnetization therefore scales with $1/D$. For the limit of thick films, the D-independent decrease of magnetic moment per area can be interpreted as resulting from both surfaces, acting independently. In general, Eqn. (1) turns out as a numerical result of spin wave theories; it is confirmed by experiment (Gradmann 1993, Fig. 32).

The enhanced thermal decrease is a result of reduced magnetic coordination in the surface. Accordingly, one expects a local profile, this decrease being strongest in the surface atomic layer. This local structure of thermal decrease can be conveniently discussed in terms of spin wave parameters. For bulk ferromagnets, it is well known that the thermal decrease follows the $T^{3/2}$-law of Bloch, $\mu(T) \propto [1 - \alpha \cdot T^{3/2}]$. Rado noted as early as 1957, in an unpublished conference note, that the spin wave parameter α near the bulk surface should be twofold enhanced in comparison with the bulk, because spin waves show antinodes in the surfaces, and the intensity in the antinode is twice the mean intensity. For bulk surfaces, the Rado enhancement could be confirmed by spin polarized electron scattering. For UFF, conversion electron Mössbauer spectroscopy (CEMS) with monolayer probes of ^{57}Fe showed up as a powerful tool to analyze locally the thermal decrease of magnetic order (Gradmann 1993, pp. 52–60). Surprisingly, the local magnetization in UFF of Fe(110) on W(110) also follows a $T^{3/2}$-law, the only modification being given by a local variation of the spin-wave parameter α. For the monolayer Fe(110), α is 10-fold enhanced. Local profiles of α across UFF have been determined experimentally using CEMS; they show the Rado enhancement near the surface (Gradmann 1993, Figs. 38, 39).

The experimental investigation of the critical temperature regime has been limited so far to the monolayer regime of thickness, in part because for the case of thick films T_c cannot be reached without destroying the film structures, in part because structural inhomogeneities mask the intrinsic critical behavior (finite size tails, caused by islanding of the films see articles on growth phenomena). In the monolayer regime only, basic models of two-dimensional magnetism could be verified for selected epitaxial film systems. In particular, the thermodynamically stable pseudomorphic ML Fe(110) on W(110) has been shown to represent the two-dimensional Ising model with remarkable accuracy. Similarly, the double layer Fe(100) on W(100) represents the two-dimensional xy model. Monolayer magnetism has been reviewed by Elmers (1995), with emphasis on experiments with well-defined ferromagnetic monolayers.

2. Changed Ground State Magnetic Moments in Surfaces (Surface Effect)

The calculation of enhanced (or reduced) magnetic moments in the surfaces of metallic ferromagnets is one of the most interesting applications of first principles band structure theories (Freeman and Wu 1991). The theories apply to the ground state. The calculations usually are performed not for bulk surfaces but for UFF targets. In an analogous way, experimental data for surface magnetic moments are obtained from UFF moments, and their dependence on D, as measured at finite T. An extrapolation to $T = 0$ is required for comparison with theory.

The following scheme has been used for evaluation of UFF moments in terms of surface magnetization (Gradmann 1974, Gradmann *et al.* 1997). We consider magnetic moments per atom, $\mu(T; D) = p(T; D) \cdot \mu_{Bohr}$, expressed by Bohr magneton numbers $p(T; D)$. In extension of Eqn. (1), and changing from moments to magneton numbers, we write

$$p(T; D) \cdot D = p_{bulk}(T) \cdot D + [p_{size}(T) + (p_{surf}^{(1)} + p_{surf}^{(2)})] \tag{2}$$

In using this Ansatz, we assume that the integral excess magnetic surface moments $\mu_{surf}^{(i)} = p_{surf}^{(i)} \cdot \mu_{Bohr}$ can be considered as independent of temperature. In other words, the temperature-dependent size-effected excess magneton numbers $p_{size}(T)$ are superimposed by the temperature-dependent surface-effected ones $p_{surf}^{(i)}$. This approximation seems to be sufficient for the present state of analysis. Some temperature dependence of $p_{surf}^{(i)}$ remains as a correction to be investigated in forthcoming high precision treatments. Equation (2) can be rewritten as

$$p(T; D) \cdot D = p_{bulk}(T)[D - D_c(T)] \tag{3}$$

with

$$D_c(T) = -\frac{[p_{size}(T) + (p_{surf}^{(1)} + p_{surf}^{(2)})]}{p_{bulk}} \tag{4}$$

The experimental analysis consists in plotting the magnetic moment per area, which is proportional to $p(D; T) \cdot D$, versus D. The axial section $D_c(T)$ then is at first glance suggestive of a magnetic dead layer. In this interpretation, it played some historic role in the spectacular work of Liebermann *et al.*

(1970). However, the present analysis shows that this interpretation is misleading and that $D_c(T)$ is nothing but an indication of enhanced decrease of magnetic moments near surfaces, superimposed from surface and size effects. Measured at finite T, an experimental value of $D_c(T)$ is roughly indicative of $T_c(D_c) = T$. In order to obtain absolute values of p_{surf} for some combination of surfaces (interfaces) from magnetometry, one needs to extrapolate to $T = 0$, where p_{size} disappears. This extrapolation is possible because $p_{size}(T)$ is proportional to T (Gradmann 1974, Wagner *et al.* 1997).

An alternative approach to determine p_{surf} is given by evaluation of spin polarized electron diffraction (SPLEED) by dynamical diffraction theories. This difficult approach has been carried out for the two clean surfaces Ni(111) and Fe(110) (Gradmann and Alvarado 1985).

Experimental data for surface excess magneton numbers are shown in Table 1, for selected surfaces. Some theoretical results are included; they show that first principles theories are now able to calculate the surface excess moments correctly. The enhanced surface moment in Fe(110) is explained from band narrowing as a result of reduced number of nearest neighbors. Accordingly, a further reduction of nearest neighbors in steps results in a further increase of magnetic moment by some tenths of a Bohr magneton (Albrecht *et al.* 1992). The coverage by noble metal results in moderate changes of moment below $1\,\mu_B$. Remarkably strong values of p_{surf} are induced by Pd as a substrate or coverage material. Apparently, this results from a magnetic polarization of Pd by the neighboring ferromagnetic film, in tight similarity with the formation of giant moments of polarized Pd around Ni, Fe, and Co impurities in bulk Pd. Interestingly, the polarizability of Pd is enhanced if Pd is not used as a coverage material, but as a substrate which in turn is prepared as an ultrathin epitaxial film on Re(0001) and therefore strained by the Re/PD misfit of 0.3% in the plane (Gradmann 1993, pp. 72–4).

3. Magnetic Anisotropies

For applications, by far the most important properties of UFF are their outstanding magnetic anisotropies. In general, magnetic anisotropies are the magnetic evidence of broken symmetries in the lattice of any magnetic sample. Intrinsic magnetic anisotropies of UFF result from the strong intrinsic anisotropies of their lattice: The anisotropic shape results in the volume type anisotropy of magnetostatic energy, known as magnetic shape anisotropy, which always supports in-plane magnetization. The broken symmetry in both surfaces is the origin of the surface-type magnetic surface anisotropy (MSA) that may support in-plane or perpendicular magnetization. In the latter case, MSA may overcome shape anisotropy, in the very thinnest films, and thus result in perpendicular magnetization (see *Magnetic Films: Anisotropy*).

To be quantitative, we restrict ourselves (i) to the dominating anisotropies that depend on the tilt angle of the magnetization with respect to the surface normal, θ only (out-of-plane anisotropies) and (ii) to the leading term which is proportional to $\cos^2\theta$. For a discussion of in-plane anisotropies and of higher order anisotropies see Fritzsche *et al.* (1994). The temperature dependence of MSA has been discussed by Farle *et al.* (1997).

In the second order out-of-plane approximation, the anisotropic part of the free energy F of an UFF of volume V and area A is given by

$$F = \left[\left(\frac{J_s^2}{2\mu_0} + K_V \right) \cdot V + (K_s^{(1)} + K_s^{(2)}) \cdot A \right] \cos^2\theta \quad (5)$$

The anisotropy constant in brackets is determined for a given film by magnetometric methods (torsion magnetometry, torsion oscillation magnetometry, ferromagnetic resonance, magnetic loop tracing). The volume term is composed of the dipolar shape anisotropy $J_s^2/2\mu_0$ (always positive, easy plane) and an additional crystalline term K_V (of any sign). The

Table 1
Surface excess magneton numbers p_{surf} for selected surfaces (interfaces).

Surface (interface)	p_{surf} experiment; (theory)	Reference
Ni(111)/UHV	$+0.06 \pm 0.12$; (0.11)	Gradmann 1993
Ni(111)/Cu	-0.42 ± 0.04; (-0.42)	Gradmann 1993
Ni(111)/Pd (Pd coverage)	$+0.8 \pm 0.2$	Gradmann 1993
Ni(111)/Pd (Pd substrate, strained)	$+2.0 \pm 0.2$	Gradmann 1993
Fe(110)/UHV	$+0.86 \pm 0.35$; (0.66)	Wagner *et al.* 1997 (Gradmann 1994)
Fe(110)/Pd	$+1.6 \pm 0.4$	Gradmann *et al.* 1997
Fe(100)/Ag	$+0.8 \pm 0.2$	Fullerton *et al.* 1995
Fe(100)/Pd	$+1.7 \pm 0.4$	Fullerton *et al.* 1995

surface term is composed by the surface anisotropy constants $K_s^{(i)}$ of both surfaces ($i = 1; 2$) (we use the notation $\sigma = K_s \cos^2 \theta$ as introduced by Néel (1954) in his pioneering work on MSA; unfortunately, the opposite sign is used in part of the literature after 1980). To separate the volume terms from surface terms, one uses a film series with variable thickness t, all other parameters being fixed (or assumed to be fixed). The separation then is done by plotting F versus t or versus $1/t$. In both cases, a linear plot confirms the Ansatz of Eqn. (5); volume and surface anisotropies can be taken from slopes and axial sections, respectively, in a straightforward manner.

The phenomenological anisotropy constants K_s include all terms that are proportional to the film surface, or scale with $1/t$. The following contributions may be distinguished (Gradmann 1993). (i) Intrinsic MSA results from the bare existence of the surface (interface), by the modified electronic state of surface/interface atoms. It is this contribution that Néel had in mind when proposing the existence of MSA (Néel 1954). Intrinsic MSA is the subject of first principles band structure calculations. Usually, it is the leading MSA contribution. (ii) Dipolar MSA: surface corrections to dipolar energies result both from the atomic structure of an ideal surface and from the roughness of real surfaces. (iii) Crystalline roughness MSA: the electronic state of step and kink atoms is different from surface atoms, resulting in step and kink anisotropies

which roughly are collected in a crystalline roughness contribution. Step anisotropies could be determined for steps on Fe(110) (Gradmann *et al.* 1997). Step anisotropies may enforce or reduce the intrinsic MSA. (iv) Apparent MSA from $1/t$ scaling shape anisotropy: By the size effect discussed in section 1, J_s decreases with decreasing t. It turns out that this results in a contribution to shape anisotropy which scales with $1/t$. (v) Apparent MSA from $1/t$ scaling relaxing strain. For small misfit f, the epitaxial UFF is pseudomorphic with the substrate up to a critical thickness t_c which increases with decreasing f. For $t > t_c$, the misfit is accommodated gradually by misfit dislocations, resulting in a relaxing strain which roughly scales with t_c/t, and in a strain induced anisotropy which scales in the same way. Apparently, this is the most important one of the extrinsic MSA contributions. It disappears in the pseudomorphic range $t > t_c$. Accordingly, intrinsic MSA can be isolated if the analysis is restricted to the pseudomorphic range.

Table 2 shows magnetic surface anisotropy constants K_s for selected interfaces. For comparison with bulk anisotropies, the constants are alternatively given as anisotropy energies per atom, e_s. Shape anisotropies for Ni, Fe, and Co are included in this notation, for comparison. Note that for a couple of interfaces e_s is negative, supporting perpendicular magnetization. Perpendicular magnetization is expected and observed for $e_s^{(1)} + e_s^{(2)} + D \cdot e_s^{\text{shape}} < 0$, if volume type

Table 2

Magnetic surface anisotropy constants, K_s, and surface anisotropy energies per atom, e_s, for selected surfaces (interfaces). Data from sandwich samples on single crystal substrates. Surface energy is defined as $\sigma = K_s \cos^2 \theta$, where θ is the angle between magnetization and surface normal (Néel notation). Data for Ni(111)/Cu, Co(0001)/Cu and Co(0001)/Au from the pseudomorphic range of thickness (intrinsic MSA); this is indicated by bold faces. Shape anisotropies for Ni, Fe, and Co for comparison.

Surface (interface)	K_s (mJ/m^{-2})	e_s (µeV/atom)	Reference
Ni(111)/UHV	+0.33	+109	Gradmann 1993
Ni(111)/Re	+0.29	+95	Gradmann 1993
Ni(111)/Cu	**+0.08**	**+27**	Jungblut *et al.* 1994
Ni, shape		+11.5	
Fe(110)/UHV	−0.97	−390	Gradmann *et al.* 1997
Fe(110)/W	+1.92	+690	Gradmann *et al.* 1997
Fe(110)/Cr	−0.12	−40	Gradmann *et al.* 1997
Fe(110)/Cu	−0.52	−190	Gradmann *et al.* 1997
Fe(110)/Ag	−0.82	−300	Gradmann *et al.* 1997
Fe(110)/Au	−0.72	−260	Gradmann *et al.* 1997
Fe(110)/Au; $T = 10$ K	−0.69	−250	Lugert and Bayreuther 1989
Fe, shape		+140	
Co(0001)/UHV	+0.28	+95	Kohlhepp *et al.* 1995
Co(0001)/Cu	**−0.18**	**−61**	Kohlhepp *et al.* 1993
Co(0001)/Ag	−0.42	−82	Kohlhepp *et al.* 1995
Co(0001)/Au	**−0.37**	**−126**	Kohlhepp *et al.* 1993
Co(0001)/Pd	−0.92	−312	Purcell *et al.* 1992
Co(0001)/Pt	−1.15	−392	McGee *et al.* 1993
Co, shape		+90	

anisotropies can be neglected ($e_s^{(i)}$ and e_s^{shape} are anisotropy energies per atom for interface (i) and for shape anisotropy, respectively). For Co(0001), negative volume type magnetocrystalline and strain anisotropies support perpendicular magnetization. Co(0001) therefore is the most important magnetic part of perpendicularly magnetized multilayers.

Whereas a separation of the different MSA contributions discussed above is not possible in general, the intrinsic MSA is usually considered as leading contribution. For the systems shown in Table 2 in bold faces, the pseudomorphic range has been used. Accordingly, they represent the intrinsic MSA to a good approximation. Higher order terms of MSA (Kohlhepp and Gradmann 1995) are not considered in the data. Because they enter the measurement differently for different methods, the omission of higher order anisotropies creates an uncertainty of the order of 10% in the data. The MSA constants in Table 2 therefore must not be taken as high precision natural constants, but rather as useful parameters to describe a complex variety of anisotropy phenomena in a reasonable model.

4. Conclusions

We have shown for representative examples that magnetic order in ultrathin ferromagnetic films (UFF) deviates from the bulk case by an enhanced thermal decrease of magnetic order, by modified moments in the surfaces and by strong surface-specific anisotropies, which may induce the technologically important phenomenon of perpendicular magnetization. Other interesting aspects of UFF magnetism, like the opportunity to epitaxially prepare magnetic matter in metastable states which do not exist in bulk (fcc Fe, bcc Co, for a review see Prinz (1991)), and to study their magnetic properties, could not be discussed. We focused on metallic ferromagnets on metallic substrates. There is presently strong interest in extending the field to nonmetallic, in particular semiconducting substrates.

New preparation methods like pulsed laser deposition (PLD), in combination with structural testing by scanning tunnel microscopy (STM) open new aspects of the field (Ohresser *et al.* 1999). UFF are important as building blocks for existing and forthcoming magnetic multilayers and nanostructures and the bewildering rich magnetic ordering in them.

See also: Magnetic Layers: Anisotropy; Thin Film Magnetism: Band Calculations; Thin Film Magnetism: PEEM Studies

Bibliography

Albrecht M, Gradmann U, Furubayashi T, Harrison W A 1992 Magnetic moments in rough Fe-surfaces. *Europhys. Lett.* **20**, 65–70

Elmers H J 1995 Ferromagnetic monolayers. *Int. J. Mod. Physics* **9**, 3115–80

Farle M, Platow W, Anisimov A N, Schulz B, Baberschke K 1997 The temperature dependence of magnetic anisotropy in ultra-thin films. *J. Magn. Magn. Mat.* **165**, 74–7

Freeman A J, Wu R 1991 Electronic band structure theory of surface, interface, and thin-film magnetism. *J. Magn. Magn. Mat.* **100**, 497–514

Fritzsche H, Elmers H J, Gradmann U 1994 Magnetic anisotropies of Fe(110) interfaces. *J. Magn. Magn. Mat.* **135**, 343–54

Fullerton E, Stoeffler D, Ounadjela K, Heinrich B, Celinski Z, Bland J A C 1995 Structure and magnetism of epitaxially strained Pd(001) films on Fe(001): experiment and theory. *Phys. Rev. B* **51**, 6364–78

Gradmann U 1974 Ferromagnetism near surfaces and in thin films. *Appl. Phys.* **3**, 161–78

Gradmann U 1993 Magnetism in ultrathin transition metal films. In: Buschow K H J (ed.) *Handbook of Magnetic Materials*. Elsevier Science Publishers, Amsterdam, Vol. 7, pp. 1–96

Gradmann U 1994 Magnetic properties of single crystal surfaces. In: Maddung O, Martienssen W (eds.) Landolt Börnstein New Series, III, **24** (5), 506–19

Gradmann U, Alvarado S F 1985 Elastic spin-polarized low energy electron scattering from magnetic surfaces. In: Feder R (ed.) *Polarized Electrons in Surface Physics*. World Scientific, Singapore, pp. 321–52

Gradmann U, Dürkop T, Elmers H J 1997 Magnetic moments and anisotropies in smooth and rough surfaces and interfaces. *J. Magn. Magn. Mat.* **165**, 56–61

Gradmann U, Müller J 1968 Very thin (2–200 Å) ferromagnetic NiFe films. *J. Appl. Phys.* **39**, 1379–81

Heinrich B, Bland J A C 1994 *Ultrathin Magnetic Structures*. Springer, Berlin

Jungblut R, Johnson M T, de Stegge J, Reinders A, den Broeder F J A 1994 Orientational and structural dependence of magnetic anisotropy of Cu/Ni/Cu sandwiches: Misfit interface anisotropy. *J. Appl. Phys.* **75**, 6424–6

King D A, Woodruff D P (eds.) 1997 *Growth and Properties of Ultrathin Epitaxial Layers*. Elsevier, Amsterdam

Kohlhepp J, Elmers H J, Gradmann U 1993 Magnetic interface anisotropies of Co/Cu(111) and Co/Au(111) interfaces from ultrathin Co-films on Cu(111). *J. Magn. Magn. Mater.* **121**, 487–9

Kohlhepp J, Gradmann U 1995 Magnetic surface anisotropies of Co(0001)-based interfaces from *in situ* magnetometry of Co-films on Pd(111), covered with ultrathin films of Pd and Ag. *J. Magn. Magn. Mat.* **139**, 347–54

Liebermann L, Clinton J, Edwards D M, Mathon J 1970 Dead layers in ferromagnetic transition metals. *Phys. Rev. Lett.* **25**, 232–5

Lugert G, Bayreuther G 1989 evidence for perpendicular magnetic anisotropy in Fe(110) epitaxial films in the monolayer range on gold. *Thin Solid Films.* **175**, 311–6

McGee N W, Johnson M T, de Vries J J, aan de Stegge J 1993 Localized Kerr study of the magnetic properties of an ultrathin epitaxial Co wedge grown on Pt(111). *J. Appl. Phys.* **73**, 3418–25

Néel L 1954 Anisotropie magnétique superficielle et surstructures d'orientation. *J. Physique Rad.* **15**, 225–39

Ohresser P, Shen J, Barthel J, Zheng M, Mohan C V, Klaua M, Kirschner J 1999 Growth, structure and magnetism of fcc Fe ultrathin films on Cu(111) by PLD. *Phys. Rev. B* **59**, 3696–706

Prinz G A 1991 Metastability in epitaxial magnetic metal films. *J. Magn. Magn. Mat.* **100**, 469–80

Purcell S T, Johnson M T, McGee N W E, Zeper W B, Hoving W 1992 Spatially resolved magneto-optical investigation of the perpendicular anisotropy in a wedge-shaped ultrathin epitaxial Co layer on Pd(111). *J. Magn. Magn. Mater.* **113**, 257–63

Wagner K, Weber N, Elmers H J, Gradmann U 1997 Magnetization of free Fe(110) surfaces from thin film magnetometry. *J. Magn. Magn. Mat.* **167**, 21–6

U. Gradmann
MPI Mikrostrukturphysik, Halle, Germany

Mössbauer Spectrometry

Since the discovery of recoil-free γ-ray resonance emission and absorption in solids by R. L. Mössbauer (1958), this phenomenon, termed the Mössbauer effect, has been developed as a useful spectroscopic method to study various solids. Although its principles look somewhat complicated, today's Mössbauer spectroscopy is no longer a strange and difficult method. Usually, as sketched in Fig. 1, γ-rays from a radioactive source placed on a moving stage pass through a foil specimen and an absorption spectrum is recorded. The data are analyzed in terms of the hyperfine interactions between the γ-absorbing nuclei in the specimen and the surrounding electrons and atoms, and give useful information on the phases, the crystalline and bonding states, and the atomic, magnetic, electronic, and defect structures.

Before introducing the principles and techniques of Mössbauer spectroscopy, here is a simple explanation of the Mössbauer effect. As is shown on the left-hand side of Fig. 2, when an excited nuclear state drops to the ground level by emitting a γ-ray, a recoil motion of the nucleus will reduce the γ-ray's energy, E_0, by the amount of the recoil energy, $Mv^2/2$, where M is
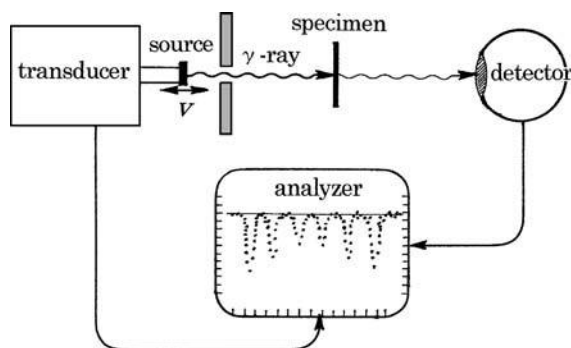
Figure 1
Alignment of apparatus for Mössbauer spectroscopy.
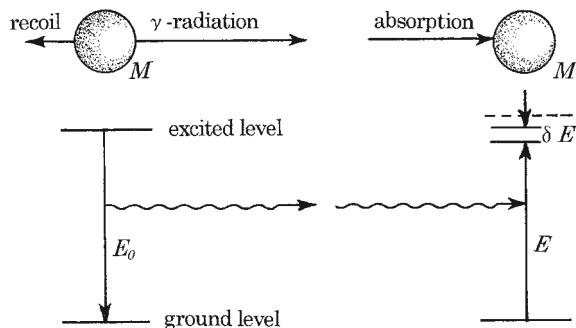
Figure 2
Relation between γ-ray emission and absorption by nuclei and the recoil reaction.

the nuclear mass and v the recoil velocity. The γ-ray emitted in this way would not be absorbed by a nearby nucleus of the same species in the ground level because of the energy deficit. By the laws of momentum and energy conservation are given

$$MV = M(V + v) + \frac{E}{c} \quad \text{and} \tag{1}$$

$$\frac{MV^2}{2} + E_0 = \frac{M(V + v)^2}{2} + E \tag{2}$$

where V is the initial velocity given to the nucleus prior to the emission, E is the energy of the emitted γ-ray which is different from E_0, c is the light velocity, and E/c is the γ-ray's momentum. From the two equations, the decrease of the γ-ray energy is given as

$$\delta E = E_0 - E = \frac{E^2}{2Mc^2} - \frac{EV}{c} \tag{3}$$

The first term on the right-hand side is the recoil energy and the last term is the Doppler effect produced by V. The latter could compensate the former to maintain the γ-ray's energy as E_0, but the necessary Doppler velocity will be of the order of $100\,\mathrm{ms}^{-1}$ in ordinary cases; this is difficult to reproduce and control at the usual laboratory scale. In addition, for absorption, another Doppler effect-aided supplement of energy is needed.

In the actual situation, however, a nucleus in a solid is bound by the surrounding electrons, which are also bound to its neighboring atoms by chemical bonds. This will make the mass, M, in Eqn. (3) extremely large so that the recoil energy will be effectively zero. This is the essential feature of the recoil-free emission and absorption of γ-rays discovered by Mössbauer. More exactly, the problem must be treated by lattice dynamics in quantum theory, taking into account the coupling between the recoil

motion and lattice phonons to find the probability, f, of recoil-free reactions.

1. Principles and Elements of Mössbauer Spectroscopy

The actual situation at nuclear levels is more complicated than the above and the γ-ray absorption will not always take place, even in the recoil-free condition, because the levels' small shifts and splits occur to produce detuning against the γ-ray energy. The modified level structure, called the hyperfine structure, arises from the interactions with environmental electronic configurations. This difficulty in tuning or resonance was solved by Mössbauer himself by changing and controlling the incident γ-ray's energy with a tiny Doppler motion to offset the shifts and splits. As already stated, using the Doppler motion to compensate the recoil energy is unnecessary, but the Doppler velocity used by Mössbauer is an indispensable tool for the spectroscopy.

The necessary relative Doppler motion between the γ-ray source and the specimen is given by a moving stage on a transducer shown in Fig. 1. A velocity of $\pm 10\,\mathrm{mm\,s^{-1}}$ corresponds to about $\pm 10^{-7}$ eV in practical cases which is as small as 10^{-4} times the above mentioned recoil energy but large enough to cover the ordinary range of hyperfine energies. The given Doppler velocity is registered in the abscissa of a display screen in Fig. 1 as the energy scale, and the amount of γ-ray transmission at each velocity is recorded in the ordinate. In the real experimental setup a function generator, a high voltage supply, a multichannel pulse height analyzer, and amplifiers are necessary. Reflection-type spectroscopy is also possible by utilizing conversion electrons or conversion x rays. The data analysis is done by computer.

In addition to the most popular and useful ^{57}Fe isotope with ^{57}Co source (^{57}Co decays by electron capture to an excited level of ^{57}Fe), ^{119}Sn, ^{121}Sb, ^{125}Te, ^{129}I, ^{151}Eu, ^{161}Dy, ^{197}Au, ^{237}Np, and some ten more isotopes are available, using suitable radioisotope sources. In addition, monochromatized synchrotron orbital radiation has become available as a γ-ray source.

In order to analyze the obtained spectra, at least three elements of the hyperfine structure—the isomer shift, the quadrupole splitting, and the nuclear Zeeman splitting—must be considered. A downward arrow at the upper left corner of Fig. 3 indicates the transition from the first excited level to the ground level of ^{57}Fe formed from ^{57}Co, resulting in the emission of a 14.4 keV γ-ray to be absorbed by another stable ^{57}Fe nucleus in the specimen.

However, Coulomb interactions between the nuclear and electron charges always exist, the amounts of which are different between the excited and ground states and between the source and the specimen. The
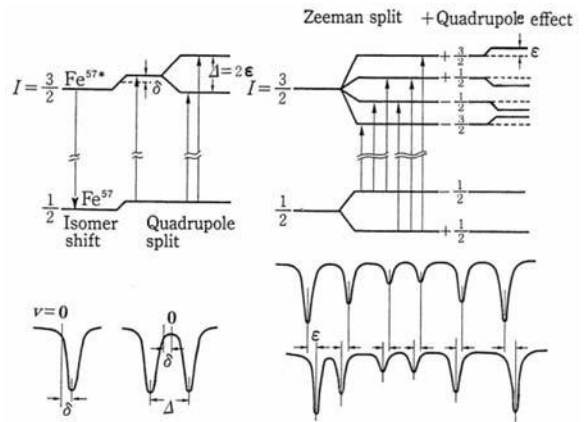
Figure 3
Schematic presentation of hyperfine structures, possible level transitions, Mössbauer parameters, and Mössbauer spectra expected from them.

difference between the emission and absorption energy is the isomer shift, δ, which is given as

$$\delta = \frac{C\Delta R}{R}\left(|\Psi_A(0)|^2 - |\Psi_S(0)|^2\right) \qquad (4)$$

where C is a certain constant, ΔR is the nuclear radius difference between the excited and ground states, and $\Psi_A(0)$ and $\Psi_S(0)$ are the wave functions of s electrons of the absorber (specimen) and the source, respectively. The isomer shift δ can be measured as the deviation of the center of the absorption peak in the Doppler velocity scale, as the lower left schematic shows. It yields information, through the s electron density $|\Psi(0)|^2$, on the phases, atom coordinations, chemical bonds, ionic states, alloying states, etc.

A nucleus with a spin state greater than $\frac{1}{2}$ has an electric quadrupole moment. When such a nucleus is placed in an electric field gradient, the electric quadrupole interaction makes the nuclear level split. In the case of ^{57}Fe, the excited level with the spin $I = \frac{3}{2}$ splits into two and the ground level with $I = \frac{1}{2}$ does not split, as the level schematics in the upper part and the lower middle spectrum in Fig. 3 show. The amount of splitting is given by

$$\Delta = 2\varepsilon = \pm\frac{eQV_{zz}}{2}\left(1 + \frac{\eta^2}{3}\right)^{1/2} \qquad (5)$$

where e is the electron charge, Q the nuclear quadrupole moment, V_{zz} the principal axis component of the field gradient, and η an asymmetry parameter of the field. By measuring the lattice asymmetry and distortion Δ, the effects of coordinating atoms, a charged impurity nearby, clustering of atoms, etc., can be studied.

Another important hyperfine interaction is the nuclear Zeeman effect, by which a nuclear level with a spin I is split into $(2I+1)$ levels when placed in a magnetic field. In the case of ^{57}Fe, the excited level splits into four and the ground level into two. There are six possible transitions between them, giving rise to a six-line spectrum, as the right-hand parts of Fig. 3 show. The peak height ratios are normally 3:2:1:1:2:3. The eigenvalues of the splits are given by

$$E_{\mathrm{m}} = -\frac{\mu H_i m_I}{I} \qquad (6)$$

where μ is the nuclear moment, H_i is the internal magnetic field, and m_I is the magnetic quantum number. Equation (6) shows that H_i is obtained from the total breadth of the sextet spectrum. It is 330 kOe in pure iron at room temperature. As the temperature increases, the total breadth decreases due to the flipping of atom moments, and disappears at the Curie point T_c. When coupled with the quadrupole effect, the sextet becomes asymmetrical as shown by the right-hand lowest spectrum. The Zeeman splitting gives information on various kinds of magnetic states.

The lineshape of each spectral component is of the Lorentzian type, and the linewidth is different for different nuclides. It is influenced by alloying and instrumental errors too. The recoil-free fraction f and, therefore, the peak height decreases with increasing temperature. The temperature dependence of f and δ give us the Debye temperature of the material. When thermally assisted atomic jumps take place, the linewidth exhibits another increase, $\Delta\Gamma$, from which the diffusion constant D can be measured.

The total absorption area, A, is another important parameter directly connected with the amount of the Mössbauer atoms and the recoil free fraction, f. When polarized γ-rays are used to see the magnetic spin orientations in the specimen, one more parameter, θ_{m}, the angle between the beam and the spin orientation, is needed.

2. Typical Examples of Mössbauer Studies in Material Science

Figure 4 shows a simple example of ^{57}Fe Mössbauer spectroscopy to study the tempering process of steel. After being water-quenched from the f.c.c. austenite phase, 1.6 wt.% carbon steel at room temperature shows a spectrum consisting of a large paramagnetic single absorption peak from the retained austenite γ phase ($\delta = -0.01\,\mathrm{mms}^{-1}$) and six line ferromagnetic peaks from the martensite α_{m} phase ($\delta = +0.01\,\mathrm{mms}^{-1}$, $\Delta = 0.01\,\mathrm{mms}^{-1}$, $H_i = 334\,\mathrm{kOe}$). The subpeaks and shoulders as well as line broadening arise from the influence of the interstitial carbon atoms. Tempering for 30 min at 210 °C makes the spectrum sharper, and tempering at 280 °C causes a
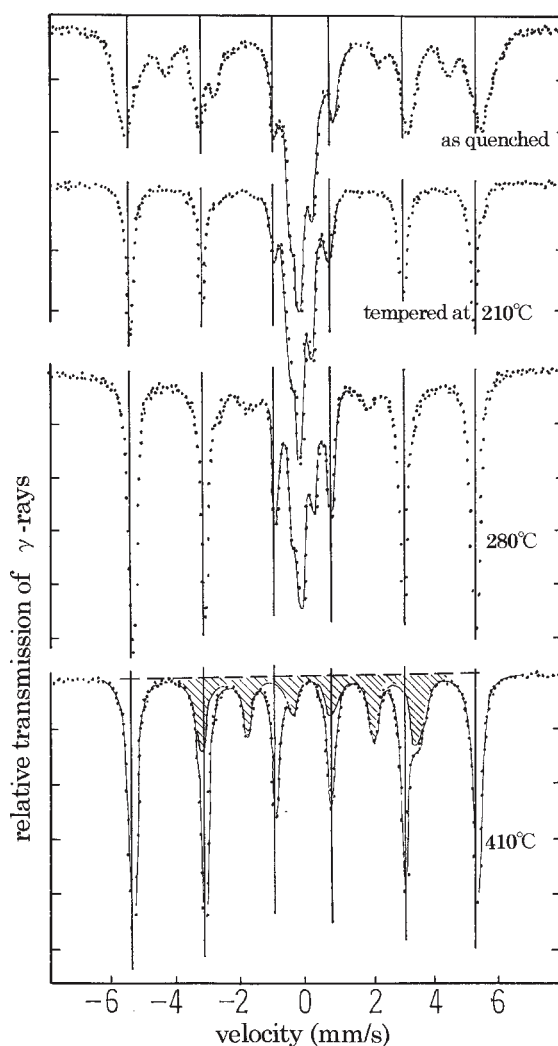
Figure 4

Mössbauer spectra obtained from the water-quenched and tempered plain carbon steel containing 1.6 wt.% carbon.

noticeable decrease of the central peak due to the austenite decomposition. Some new subpeaks emerge too. After 410 °C annealing the spectrum shows no austenite but clear ferromagnetic cementite (θ; Fe_3C) precipitates, corresponding to the separated and shadowed component ($\delta = +0.18\,\mathrm{mms}^{-1}$, $\Delta = 0.01\,\mathrm{mms}^{-1}$, $H_i = 208\,\mathrm{kOe}$) in the figure. In such a way the structure and behavior of materials can be studied.

Another popular material is magnetite, α-Fe_3O_4, which appears not only in materials science but also in earth, biological, and medical sciences. Magnetite has the inverse spinel structure, in which the tetrahedral (A) sites are occupied by Fe^{3+} ions and the octahedral (B) sites by the mixture of Fe^{3+} and Fe^{2+}
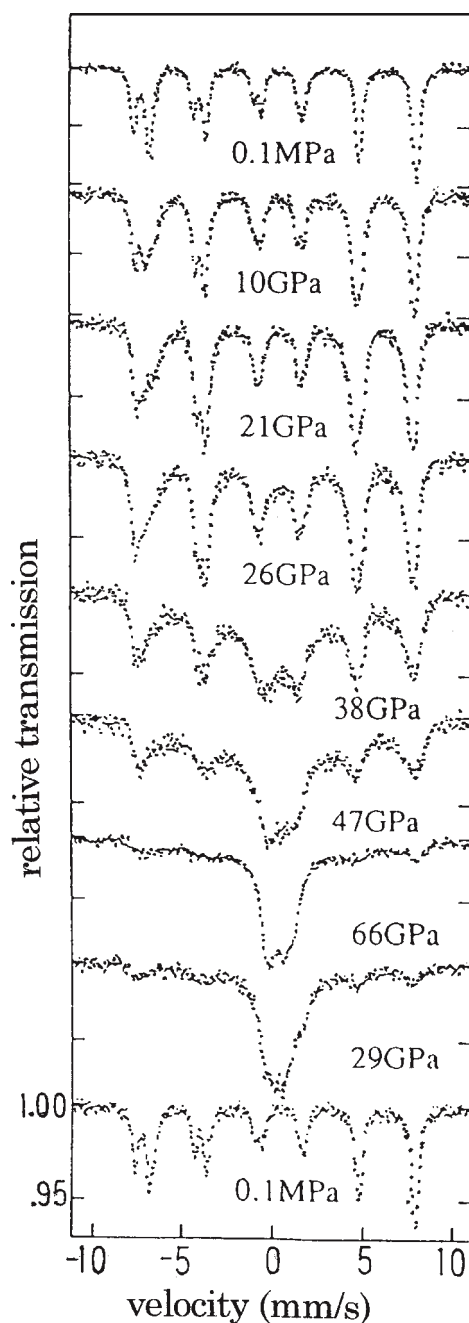
Figure 5
Mössbauer spectra of magnetite (α-Fe_3O_4) under high pressures (after Pasternak *et al.* 1994).

ions, effectively giving the averaged ionic value, $Fe^{2.5+}$.

As an unusual example, a Mössbauer study of magnetite under high pressures, utilizing a special diamond anvil cell, is shown in Fig. 5 (Pasternak *et al.* 1994). Under low pressures, the ^{57}Fe spectrum exhibits a two-component ferromagnetic pattern, corresponding to the two different ionic states, as the uppermost spectrum shows. The outer smaller component arises from Fe^{3+} ($\delta = +0.26\,mms^{-1}$, $\Delta = 0\,mms^{-1}$, $H_i = 490\,kOe$), and the inner larger one from $Fe^{2.5+}$ ($\delta = +0.67\,mms^{-1}$, $\Delta = 0\,mms^{-1}$, $H_i = 455\,kOe$). Under 26 GPa and higher pressures, a paramagnetic new phase with two-site iron appears ($\Delta = 0.3\,mms^{-1}$). An *in situ* dispersion-type x-ray analysis on the same specimen shows a monoclinic two-site structure. By lowering the pressure from 66 GPa, the reverse transition takes place with hysteresis, as the lower part of the figure shows.

Noticeable progress of Mössbauer spectroscopy has been achieved not only in the automation of measurement and analysis but also in methodology (Fujita 1999) including high-pressure and high-temperature measurement up to 1800 K (Fujita and Yoshida 1997), and simultaneous measurement of γ-rays, conversion electrons, and x-rays (Gonser 1998), and use of synchrotron orbital radiation (Gerdau *et al.* 1985). Many applications have been carried out with metals, ceramics, semiconductors, glasses, and other pure and compound materials, with further extension to biology, medicine, archeology, mineralogy, mining, etc.

Bibliography

Fujita F E 1999 Recent developments in Mössbauer spectroscopy. *Contemp. Phys.* **40**, 323–37
Fujita F E, Yoshida Y 1997 Mössbauer spectroscopy of high-temperature materials. *Prog. Mater. Sci.* **42**, 159–75
Gerdau E, Rüffer R, Winkler H, Tolksdorf W, Klages C P, Hannon J P 1985 Nuclear Bragg diffraction of synchrotron radiation in yttrium iron garnet. *Phys. Rev. Lett.* **54**, 835–8
Gonser U 1998 Mössbauer spectroscopy in materials science. In: Fujita F E (ed.) *Physics of New Materials,* 2nd edn. Springer, Heidelberg, Germany, Chap. 9, pp. 269–300
Mössbauer R L 1958 Kernresonanzfluoreszenz von Gamma-strahlung in ^{191}Ir. *Z. Phys.* **151**, 124–43
Pasternak M P, Nasu S, Wada K, Endo S 1994 High-pressure phase of magnetite. *Phys. Rev. B* **50**, 6446–9

F. E. Fujita
Osaka University, Machikane, Toyonaka, Japan

MRI Contrast Agents

Magnetic resonance imaging (MRI) is a powerful clinical modality in diagnostic medicine. The contrast agents are paramagnetic materials, used for improving the efficiency of MRI investigations. The MRI technique is based on the behavior of protons in

the body (mainly water protons) when exposed to magnetic fields (typically 0.5–1.5 T). The magnetic moments of protons align parallel to or antiparallel to the magnetic field direction. Since the number of spins aligned parallel is a little higher than the number aligned antiparallel, a macroscopic magnetization vector (MMV) is formed parallel to the external field (B_0). When a short radiofrequency pulse (B_1) is applied at right angles to B_0, some nuclei enter a higher energy state and the MMV flips into the transverse plane. In a receiver coil situated in the transverse plane, the precessing MMV induces a voltage which produces the MRI signal.

When the radiofrequency pulse is switched off, the excited protons lose energy and the MMV realigns with B_0. This process is called relaxation. The loss of energy may take place via interaction between the protons and the surrounding molecules, characterized by the time constant T_1, the longitudinal relaxation time. The decay of the MMV in the transverse plane occurs through energy exchange between the neighboring protons and because of inhomogeneities in B_0, characterized by the time constant T_2, the transverse relaxation time. The reciprocals of the relaxation times, $1/T_1$ and $1/T_2$, are referred to as the relaxation rates.

The intensity of MRI signals is proportional to the proton density and T_1^{-1} and inversely related to T_2^{-1}. To obtain the MR image, the signals emitted by different volume elements of the body are spatially located in three dimensions with the use of magnetic field gradients. The differences in the signal intensities of the neighboring volume elements in a slice of the body result in the image contrast. The parameters influencing the signal intensity are often different in normal and diseased tissues, which leads to differences in the image contrast.

MRI was introduced as a noninvasive diagnostic tool, but certain clinical problems necessitated the use of exogenous materials, called contrast enhancement agents (CAs), which increase the differences in the signal intensities. The CAs are paramagnetic compounds which produce fluctuating magnetic fields in the proximity of protons in the body, resulting in shorter T_1 and T_2 values (faster relaxation). The CAs known so far can be divided into three groups (see also *Nuclear Magnetic Resonance Spectrometry*).

1. Paramagnetic Metal Complexes

For shortening the relaxation times of protons the most effective metal ions are Gd^{3+}, Fe^{3+}, and Mn^{2+}, each of which has a half-filled electron shell, a large magnetic moment and a relatively long electron spin relaxation time ($\sim 10^{-9}$ s). The aquo-metal ions are toxic; in order to decrease the toxicity, the ions are used in the form of complexes, which are well tolerated. In clinical practice, virtually only complexes
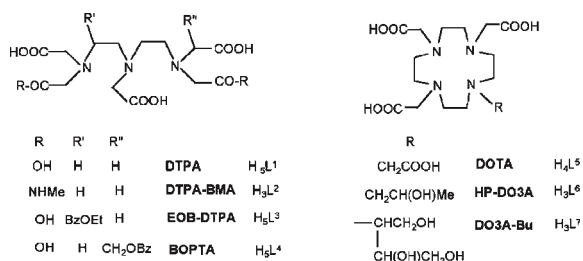
Figure 1
Formulas of ligands used for complexation of Gd^{3+}.

of Gd^{3+} are used (the commercially available Mn^{2+}-dipyridoxyl-diphosphate is of merely marginal importance).

The complexes used as CAs must meet the following requirements: lack of toxicity, high water solubility, low osmolality, high relaxation enhancement effect, high thermodynamic and kinetic stability, quick excretability, and specific *in vivo* distribution. The ligands used for the complexation of Gd^{3+} are the open-chain DTPA, the macrocyclic DOTA, and their derivatives (Fig. 1).

The stability constants of the Gd^{3+} complexes formed with the ligands L^1–L^7 are very high (log $K_{GdL} \approx 22$–26). The only exception is GdL^2 (log $K_{GdL^2} = 16.85$), but L^2 is highly selective for Gd^{3+} as compared with endogenous ions such as Zn^{2+}.

The ligands used are all octadentate in their Gd^{3+} complexes. The ninth coordination site of the Gd^{3+} is occupied by an H_2O molecule. The protons of this molecule rapidly relax in the first coordination sphere and the fast exchange of this H_2O with the bulk water results in the transfer of the paramagnetic effect of Gd^{3+} to the surrounding water protons. To express the relaxation effect of paramagnetic compounds, the term relaxivity is used. The relaxivity ($1/T_{1,2}$, $mM^{-1}s^{-1}$) is the increase in the proton relaxation rate when the concentration of the CA increases by 1mM. It is about 3.5–4.5 $mM^{-1}s^{-1}$ (at 20 MHz) for the clinically used CAs. The relaxivity of Gd^{3+} complexes is comprised of inner sphere relaxation (R_i) and outer sphere relaxation (R_o). R_i is proportional to the number of H_2O molecules in the inner sphere, the magnetic moment of the central ion, and a correlation time, which depends on the tumbling rate of the complex, on the electron spin relaxation time of the Gd^{3+} ion, and on the lifetime of water protons in the inner sphere, while the relaxation decreases in proportion to the sixth power of the Gd^{3+}-proton distance. R_o depends on the diffusion rates of the complex and the water molecules. The contributions of the R_i and R_o to the measured relaxivity are approximately equal.

The Gd^{3+} complexes are prepared by dissolving Gd^{III} oxide, hydroxide, or carbonate together with

the protonated ligands. The negative charges of the complexes formed with L^1, L^3, L^4, and L^5 are neutralized by the protonated *N*-methyl-meglumine cation. The commercial products contain about 5% Ca^{2+} complex, in order to diminish the release of free Gd^{3+} in the body. The CAs are administered to the patients intravenously in 0.5MGdL solution, which can be painful, particularly in the case of the charged complexes, because of the high osmolality. To diminish this problem, nonionic compounds (GdL^2, GdL^6, and GdL^7) have been developed. The Gd^{3+} complexes decrease the T_1 values of protons more significantly than the T_2 values, and they are used in T_1-weighted imaging to increase the signal intensity. The usual dose of GdL complexes is 0.1–0.3 mmolkg^{-1} body weight. The low molecular weight CAs distribute rapidly in the extracellular space of the body. However, due to the fast diffusion of the water molecules through the cell membranes, the CAs shorten the T_1 and T_2 values of protons also in the intracellular space.

The Gd^{3+} complexes formed with the ligands L^1, L^2, L^5, L^6, and L^7 are hydrophilic and are excreted through the kidneys into the urine ($t_{1/2} = 1.6$h). The lipophilic GdL^2 and GdL^3 are excreted partly through the liver and bile and can be used to image the liver. The tolerance to the CAs depends on the selectivity of the ligands for Gd^{3+} over the endogenous ions (Ca^{2+}, Zn^{2+}, Cu^{2+}, etc.), which is expressed as the ratio of the conditional stability constants at physiological pH. A more important factor is the kinetic stability. Both the spontaneous and H^+-assisted dissociation of the complexes GdL and the direct exchange reactions with the endogenous ions and ligands must occur extremely slowly.

The Gd^{3+} complexes formed with the macrocyclic ligands L^5, L^6, and L^7 are extremely inert under physiological conditions. The complexes of DTPA and its derivatives are not so sluggish but, because of the rapid excretion, the amount of the Gd^{3+} released in the body is very low and the CAs are safe.

2. Superparamagnetic Particles

Superparamagnetic materials used as CAs are composed of single-domain crystals (mainly Fe_3O_4) which have much larger susceptibilities than those of paramagnetic compounds. The particles used are coated with a thin dextran or siloxane layer. They primarily shorten the T_2 values by creating large magnetic field inhomogeneities.

The relaxation effect and biodistribution depend greatly on the size of the particles. Particles larger than 50 nm have a short half-life in the blood and are localized mainly in the liver and spleen, from where the exretion is slow ($t_{1/2} \approx 3$–4 days). Ultrasmall superparamagnetic iron oxide particles (USPIO, < 50 nm) reside in the blood pool for a longer time ($t_{1/2} \approx 200$ min) and can be used as intravascular CAs for both T_2- and T_1-weighted images. USPIO agents have a more widespread tissue biodistribution, as they are taken up by the liver, spleen, marrow, and lymph nodes. Thus, the potential use and development of the USPIO agents is of great importance.

3. Stable Free Radicals

Nitroxide free radicals (NFRs) have one unpaired electron, localized in a nitrogen–oxygen bond. The six-membered ring piperidine nitroxides produce larger relaxivities than the five-membered ring pyrrolidine nitroxides. In animal experiments, however, pyrrolidine nitroxides are more resistant to reduction by chemical and enzymatic processes. The relaxation enhancement of the NFRs is much lower than that of paramagnetic complexes. Thus, the clinical use of NFRs seems less probable.

4. Future Developments

The main directions in the research and development of CAs are the increase of relaxivity and the creation of organ-specific materials. The attachment of Gd^{3+} complexes to macromolecules (proteins, dendrimers, etc.) results in higher relaxivities due to the slower rotation of the molecules. Such CAs are transferred more slowly from the intravascular space and can be used in MR angiography. The Gd^{3+} complexes of "porphyrin-like" ligands produce very high relaxivities. Some MRI agents can be used to quantify specific enzymatic activity. The development of CAs for T_2-weighted images opens up new vistas. Potentially, the complexes of Dy^{3+} are the most interesting; these result in large proton chemical shifts and significantly shorten the T_2 values, and they are planned to be used as "susceptibility agents."

Bibliography

Aime S, Botta M, Fasano M, Terreno M 1998 Lanthanide chelates for NMR biomedical applications. *Chem. Soc. Rev.* **27**, 19–29

Lauffer R B 1987 Paramagnetic metal complexes as water proton relaxation agents for NMR imaging: theory and design. *Chem. Rev.* **87**, 901–27

Tweedle M F 1989 Relaxation agents in NMR imaging. In: Bünzli J-C G, Choppin G R (eds.) *Lanthanide Probes in Life Chemical and Earth Sciences*. Elsevier, Amsterdam, pp. 127–79

Westbrook C, Kaut C 1993 *MRI in Practice*. Blackwell Science, Oxford, UK

E. Brücher

Lajos Kossuth University, Debrecen, Hungary

Multilayer Optical Film Modeling

Optical multilayer thin film technologies have many applications ranging from complex high-performance mirrors, filters, and polarizers, to simple single-layer anti-reflection coatings. The design of optical coatings and calculation of their properties is a well-established science and several books (Macleod 1969, Heavens 1991) and substantial articles (Lissberger 1970) have been written on the topic.

More recently, the properties of multilayers have been exploited in the area of information storage with the introduction of CD–RW/DVD (rewritable Compact Disk/Digital Versatile Disk) optical technologies and rewritable magneto-optical systems such as the audio mini-disc. The optimization of these systems requires an understanding of the interaction of light with thin film multilayer media and an appreciation of the factors that determine the ultimate performance of any optical data readout system (see *Magneto-optical Effects, Enhancement of*). For such applications calculation of the optical and magneto-optical properties of the multilayers is crucial. The important properties are the intensity reflectance and transmittance in the optical case, and the Kerr and Faraday effects in the magneto-optical case (see *Faraday and Kerr Rotation: Phenomenological Theory*). To determine these it is necessary first to calculate reflection, transmission, Kerr, and Faraday amplitude coefficients (r, t, k, and f, respectively), which are different for each of the orthogonal p and s component polarization states.

In general, the calculation of optical and magneto-optical properties of a magnetic multilayer stack is complicated, particularly where the magnetization vector may be in an arbitrary direction. However, it is possible to simplify this problem considerably by treating such a system as a linear superposition of three principal magneto-optic configurations. These are the polar, longitudinal, and transverse configurations, which have been defined elsewhere (see *Faraday and Kerr Rotation: Phenomenological Theory*). A further simplification is possible for the polar configuration at normal incidence, which is a case particularly relevant to magneto-optical recording. In this instance, the optical and magneto-optical properties may be readily found using a simple reiterative technique normally applied to optical calculations.

In the space of this short article it is not possible or appropriate to give a detailed derivation of the mathematical formulations necessary for a complete description of all linear, first-order optical and magneto-optical effects. However, it is intended to give sufficient information, together with appropriate references, to enable the reader to understand the basic methods used for thin film and multilayer calculations.

The discussion commences with the simplest case of the reiterative reflectance formula and the normal incidence polar Kerr effect. Following this, a more general analysis is given that leads to a 4×4 characteristic matrix method that, whilst applicable to straightforward optical media, also applies to magnetic media and which is convenient for dealing with many-layered systems.

1. The Permittivity Tensor

The interaction between an electromagnetic wave and magnetic medium depends on the frequency-dependent magnetic and electric response of the material. In general, this response is quantified through material equations expressed in terms of the relative permeability, μ_r, and the relative permittivity, ε_r. At the high frequencies of optical radiation, the magnetic interaction is negligible and μ_r is equal to its free space value of unity. Consequently, the medium response is described entirely by the permittivity. For an optically isotropic system, the relative permittivity is a scalar quantity. For a magnetic material, the unique direction of the magnetization vector imposes an anisotropy on the system and the permittivity becomes a skew-symmetric tensor. In general, if the direction of magnetization is defined by the unit vector, $\hat{\underline{\mathbf{m}}} = m_x \hat{\mathbf{i}} + m_y \hat{\mathbf{j}} + m_z \hat{\mathbf{k}}$, then the first-order permittivity tensor for any direction is

$$[\varepsilon_r] = n^2 \begin{bmatrix} 1 & -im_z Q & im_y Q \\ im_z Q & 1 & -im_x Q \\ -im_y Q & im_x Q & 1 \end{bmatrix} \quad (1)$$

where n is the isotropic complex refractive index and Q is the complex *magneto-optical Voigt parameter*, which is responsible for magneto-optical effects. In most cases $|Q| \sim 1 \times 10^{-3}$, and for this reason higher order terms in Q, that may appear in Eqn. (1) have been omitted.

The effect of the above permittivity tensor is to introduce an optical anisotropy that results in the propagation of particular magneto-optical modes within the medium. In general, these modes are rather complicated to visualize. However, for the special case of a light wave traveling parallel to the magnetization vector there are two simple modes, both circularly polarized but with opposite senses, i.e., one is right handed and the other is left handed. These modes propagate within the medium experiencing refractive indices n_+ and n_-, respectively. The two refractive indices differ from each other by an amount of the order of Q and the medium is said to exhibit *circular birefringence*. Consequently, the circularly polarized modes propagate through the medium at different velocities and are attenuated at different rates. The result is a change in the overall

polarization state of light on transmission or reflection from the medium and this constitutes a magneto-optical effect.

For the present case, where the permittivity tensor is described by Eqn. (1), the magneto-optical behavior is said to be *gyroelectric*. In cases where the magnetic permeability becomes important, circular birefringence may also arise out of a similar anisotropy in the permeability tensor $[\mu_r]$ and there may be a contribution to the magneto-optical behavior which is *gyromagnetic*. For further information on gyromagnetic modeling see Smith (1965) and Hunt (1966).

2. The Reiterative Reflectance Formula

When *s* or *p* polarized light of wavelength λ_0 is incident on the surface of a thin film, it is partly reflected and partly transmitted according to the well-known Fresnel equations. The transmitted light propagates into the film and may be attenuated depending on the imaginary part of the refractive index. If the film is nonabsorbing or sufficiently thin, the light undergoes multiple reflections as it travels back and forth within the film (Fig. 1). Consequently, the calculation of the net amplitude reflectance r_1 and transmittance t_1 involves a multiple beam summation that, for either *s* or *p* states, results in (Heavens 1991, pp. 55–9):

$$r_1 = \frac{r_{01} + r_2 e^{i2\rho_1}}{1 + r_{01} r_2 e^{i2\rho_1}}$$

$$t_1 = \frac{t_{01} t_2 e^{i\rho_1}}{1 + r_{01} r_2 e^{i2\rho_1}} \qquad (2)$$

where $\rho_1 = 2\pi n_1 d_1 / \lambda_0$ is the phase thickness of the film, $r_{01}, r_{12} (= r_2)$ and t_{01}, t_{12} are the amplitude coefficients at the two interfaces. Equations (2a) and (2b) may be applied reiteratively, extending the calculation to the amplitude reflectance and transmittance for multiple layers. In this case the reflectance at the upper boundary of the *l*th layer is:

$$r_l = \frac{r_{l-1,l} + r_{l+1} e^{i2\rho_l}}{1 + r_{l-1,l} r_{l+1} e^{i2\rho_l}} \qquad (3)$$
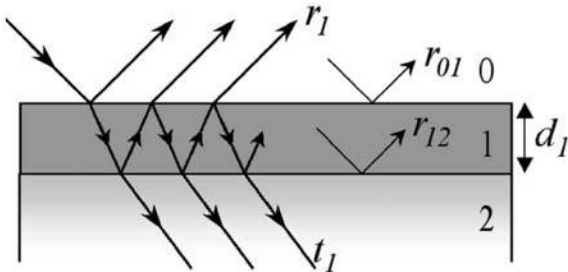
Figure 1
Multiple reflections in a single layer.

with a similar expression for transmittance. The calculation begins at the substrate and is applied repeatedly, layer by layer, toward the incident medium. At each stage in the calculation, r_{l+1} is the system reflectance calculated in the previous step and $r_{l-1,l}$ is the Fresnel amplitude reflectance at a boundary between two semi-infinite media.

The method may be applied to the calculation of the magneto-optical polar Kerr effects at normal incidence. As mentioned in Sect. 1, the light can be expected to propagate as two circularly polarized modes encountering refractive indices n_+ and n_-. The latter are related to the Voigt parameter Q, and the isotropic refractive index n, by $n_\pm = n(1 \pm Q/2)$. Each of these modes gives rise to separate Fresnel reflection coefficients such that:

$$r_{\pm l-1,l} = \frac{n_{l-1} - n_{\pm l}}{n_{l-1} + n_{\pm l}} \qquad (4)$$

It follows that for a stack containing several magnetic layers, the reiterative scheme must be applied twice to determine the two amplitude reflection coefficients $r(n_+)$ and $r(n_-)$. The magneto-optical Kerr effect is then determined from the Kerr amplitude coefficient (see Sect. 3.4), which is related to the differential reflectance, $\delta r = r(n_+) - r(n_-)$, such that:

$$k = i\frac{\delta r}{2} \qquad (5)$$

This approach was applied by Gamble *et al.* (1985) to the optimization of polar Kerr effects in multilayers containing a single magnetic film. It has particular relevance to the design of magneto-optical recording media, which is dealt with in article *Magneto-optical Effects, Enhancement of*.

3. The Characteristic Matrix Method

So far the discussion has been limited to the specific and simple case of light propagating parallel or anti-parallel to the magnetization, as for the polar configuration at normal incidence. In this case, the light propagates as two circularly polarized modes with different velocities and attenuating at different rates according to the refractive indices n_+ and n_-, giving rise to magneto-optical effects. A more general solution to the propagation of radiation in a magnetic medium requires the general mode structure to be determined for magnetization in an arbitrary direction and for any angle of incidence. This is usually done for a single layer in the three principal configurations and then the analysis is extended to multi-layered systems. The analysis is outlined below.

All electromagnetic fields that exist within any medium must satisfy Maxwell's equations and the 3D

wave equation:

$$\nabla(\nabla \cdot \underline{\mathbf{E}}) - \nabla^2 \underline{\mathbf{E}} = -\mu_0 \frac{\partial^2 \underline{\mathbf{D}}}{\partial t^2} \tag{6}$$

where

$$\underline{\mathbf{D}} = \varepsilon_0[\varepsilon_r]\underline{\mathbf{E}} \tag{7}$$

It is assumed that the solutions to the equation are plane waves of angular frequency, ω, described by:

$$\underline{\mathbf{E}} = \underline{\mathbf{E}}_0 \exp i(\underline{\mathbf{p}} \cdot \underline{\mathbf{r}} - \omega t) \tag{8}$$

where $\underline{\mathbf{E}}_0$ is the electric field amplitude, $\underline{\mathbf{p}}$ is the propagation vector, and $\underline{\mathbf{r}}$ is a position vector. For convenience, the Cartesian coordinate system is arranged so that the plane of incidence is always in the x–z plane (Fig. 2). The vectors $\mathbf{r}$ and $\mathbf{p}$ then reduce to:

$$\underline{\mathbf{r}} = x\underline{\mathbf{i}} + z\underline{\mathbf{k}} \tag{9}$$

and

$$\underline{\mathbf{p}} = p_x\underline{\mathbf{i}} + p_z\underline{\mathbf{k}} = \frac{2\pi}{\lambda_0}n(\alpha\underline{\mathbf{i}} + \gamma\underline{\mathbf{k}}) \tag{10}$$

where α and γ are direction cosines ($\alpha^2 + \gamma^2 = 1$) as shown in Fig. 2 and λ_0 is the free space wavelength. Where there is no magneto-optical behavior, p_z has two values, associated with positive and negative going waves with respect to the z-direction of the coordinate system. If magneto-optical activity exists, then for the polar and longitudinal configurations each of these waves propagates as two distinct modes that are convenient to label $p_z^\pm$. For each of these modes there are corresponding refractive indices $n_\pm$ and direction cosines $\gamma_\pm, \alpha_\pm$. In the polar case, for example, these are given by:

$$n_\pm = n(1 \pm \gamma Q/2) \tag{11}$$

$$\gamma_\pm = \gamma(1 \pm \alpha^2 Q/2\gamma)$$
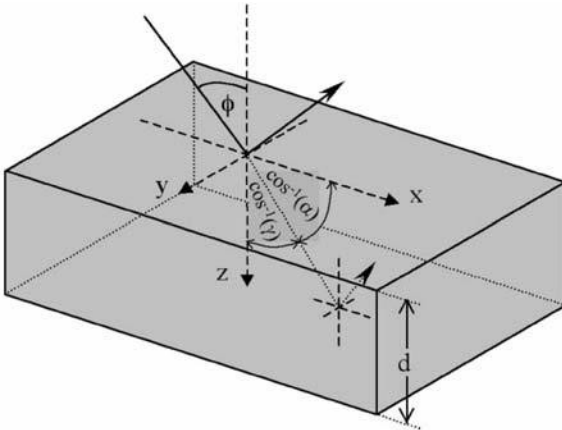
Figure 2
Conventions applied in the characteristic matrix model.

where α, γ, and n are the isotropic values that would apply if the magnetization were reduced to zero. Similar expressions to Eqns. (11a) and (11b) also exist for the longitudinal case.

For the transverse configuration, the magnetization is in the y direction (Fig. 2), perpendicular to the direction in which the light is traveling. The result is that the light propagates as a single mode peculiar to the p polarization state and consequently the magneto-optical effects are different from the other configurations.

The electric and magnetic fields, $\underline{E}$ and $\underline{H}$, corresponding to these modes of propagation in the medium are determined using Eqn. (6) and Maxwell's equations, which are common to all electromagnetic phenomena. Generally, each field has three components corresponding to the three principal directions x, y, and z. A full appreciation of the form of these fields requires knowledge of all three components. However, for the purposes of thin film and multilayer calculations, it is only necessary to determine those components lying in the plane of the film (i.e., the x–y plane). The laws of electromagnetism require these electric and magnetic field components, that are tangential to the layer boundaries, to be continuous across the interfaces. This very important boundary condition means that the tangential field components provide a correlation between electromagnetic fields in adjacent materials and will be discussed further in Sect. 3.3. Again, taking the polar case as an example, the tangential fields are:

$$E_x = Ae^{i\delta_+} + Be^{i\delta_-} + Ce^{-i\delta_+} + De^{-i\delta_-}$$

$$H_y = \frac{i}{Z\gamma}(AV_+e^{i\delta_+} + BV_-e^{i\delta_-} - CV_+e^{-i\delta_+} - DV_-e^{-i\delta_-})$$

$$E_y = \frac{i}{\gamma}(Ae^{i\delta_+} + Be^{i\delta_-} + Ce^{-i\delta_+} + De^{-i\delta_-})$$

$$H_z = -\frac{i}{Z}(AV_+e^{i\delta_+} - BV_-e^{i\delta_-} - CV_+e^{-i\delta_+} + DV_-e^{-i\delta_-})$$

$$\tag{12}$$

where

$$V_\pm = \left(1 \pm \frac{Q}{2\gamma}\right)$$

and

$$\delta_\pm = \frac{2\pi}{\lambda_0} n\gamma V_\pm z$$

and A, B, C, and D are arbitrary constants. The exponents in t and x have been omitted from the above expressions since the conditions must be satisfied for all time and every point on the interface. This leads to the well-known Snell's law and a common term that may be removed from each expression in Eqns. (12a)–(12d). The sign of the exponents of the partial

waves indicate the direction of propagation with the positive and negative signs indicating positive and negative going waves, respectively. The subscript signs correspond to the two magneto-optical modes that, of course, are magnetization dependent.

It is worth pointing out that in the polar case at normal incidence ($\alpha = 0$, $\gamma = 1$, $E_z = 0$) the electric field (E_x, E_y), reduces to two counter-rotating circularly polarized modes ($Ae^{i\delta_+}$, $-iAe^{i\delta_+}$) and ($Be^{i\delta_-}$, $-iBe^{i\delta_-}$). Furthermore, it is clear from Eqn. (11b) that $\gamma_\pm = 1$ and the two corresponding refractive indices are $n_\pm = n (1 \pm Q/2)$. This, of course, is the basis for the differential reflectance approach to the calculation of the polar Kerr effect.

At oblique incidence, for both polar and longitudinal configuration, the modes propagate in two directions $\gamma_\pm$ and are no longer circular but elliptical. In addition, each has field components in the direction of propagation and so can no longer be regarded as transverse electromagnetic (TEM) waves. In the transverse case the mode propagates in a single direction γ and is linearly polarized in the p plane. Again, there are field components both perpendicular and parallel to the direction of propagation in the magnetic medium and the mode of propagation is not a simple TEM mode.

The tangential field components are determined as a function of distance along the z direction, as demonstrated by Eqns. (12a)–(12d) specifically for the polar configuration. Consequently, the equations relate the tangential field components at one boundary of a thin film, placed at $z = 0$ for example, to those at the other boundary at the film thickness $z = d$. It is possible to express this relationship conveniently in matrix form such that:

$$(F_z = 0) = [C](F_z = d) \tag{13}$$

where (F) is a column matrix whose elements are E_x, H_y, E_y, and H_x and $[C]$ is a 4×4 matrix that is characteristic of the film.

Each of the three principal magneto-optical configurations requires a different characteristic matrix. Moreover, each matrix may be decomposed into separate isotropic and anisotropic parts such that:

$$[C]_{P,L,T} = [C]_I + g_{P,L,T}[G]_{P,L,T} \tag{14}$$

where the subscripts refer to the principle configurations. The isotropic matrix $[C]_I$, corresponding to optical behavior of the film, would completely characterize the film if the relative permittivity ε_r was a scalar quantity, i.e., if there was no magneto-optical activity. Hence, it remains the same for all three magneto-optical configurations. The anisotropic matrix accounts for the gyroelectric properties of the medium and leads to calculations of observed magneto-optical effects. To completely characterize the film optically and magneto-optically four

characteristic matrices must be determined in all; an isotropic matrix and three anisotropic matrices corresponding to each of the three magneto-optical configurations. In the proceeding sections the details for each of these matrices will be given.

3.1 The Isotropic Matrix

The isotropic matrix has the form:

$$[C]_I = \begin{bmatrix} C_{11} & C_{12} & 0 & 0 \\ C_{21} & C_{11} & 0 & 0 \\ 0 & 0 & C_{11} & C_{34} \\ 0 & 0 & C_{43} & C_{11} \end{bmatrix} \tag{15}$$

So there are five different elements, which are:

$$
\begin{aligned}
C_{11} &= \cos(\rho) \\
C_{12} &= -iZ\gamma \sin(\rho) \\
C_{21} &= -i \sin(\rho)/Z\gamma \\
C_{34} &= Z \sin(\rho)/\gamma \quad C_{43} = \gamma \sin(\rho)/Z
\end{aligned} \tag{16}
$$

where ρ is the phase thickness:

$$\rho = p_z d \tag{17}$$

and the optical impedance Z, has units of ohms and relates E and H such that $E = ZH$. The optical impedance may be related to the refractive index of the material through

$$Z = Z_0/n \tag{18}$$

where Z_0 is the optical impedance of free space and has the value 376.7 ohms. The direction cosines, α and γ, are related to the angle of incidence, φ, through Snell's law.

An important feature of the isotropic matrix is that it comprises two 2×2 submatrices $[I]_p$ and $[I]_s$ so that:

$$[C]_I = \begin{bmatrix} [I]_p & [0] \\ [0] & [I]_s \end{bmatrix} \tag{19}$$

These are associated specifically with either p polarized light or s polarized light. Consequently the p and s modes do not interact and can be treated separately.

Note that Eqn. (2a) for single layer reflectance may be derived using the isotropic matrix, the summation and matrix methods being completely consistent (Lissberger 1970). This is to be expected as both techniques are based on Maxwell equations and employ the same assumptions and boundary conditions (Heavens 1991, pp. 49–53).

Table 1

The elements of the gyroelectric characteristic matrices where $c = \cos(\rho)$ and $s = \sin(\rho)$. The parameters ρ and Z are given by Eqns. (17) and (18), respectively. The direction cosines γ and α are determined using Snell's law.

	g	G_{11}	G_{13}	G_{14}	G_{23}	G_{24}
Polar	$Q/2$	0	$i\rho s$	$(Z/\gamma)(\rho c - s)$	$-(\rho c + s)/(Z\gamma)$	$-i(\rho s/\gamma^2)$
Longitudinal	$(Q/2)(\gamma/\alpha)$	0	$-(\rho c + s)$	$-i(Z/\gamma)\,\rho s$	$i(\rho s/Z\gamma)$	$(\rho c - s)/\gamma^2$
Transverse	$Q(\gamma/\alpha)$	s	0	0	0	0

3.2 The Gyroelectric Matrices

The characteristic matrices for the polar and longitudinal configurations have the same form:

$$[C]_{P,L} = [C]_I + g_{P,L} \begin{bmatrix} 0 & 0 & G_{13} & G_{14} \\ 0 & 0 & G_{23} & G_{24} \\ G_{24} & G_{14} & 0 & 0 \\ G_{23} & G_{13} & 0 & 0 \end{bmatrix} \quad (20)$$

Thus, there are only four different gyroelectric elements for each of the configurations and these are summarized in Table 1, where the parameters ρ and Z are calculated according to Eqns. (17) and (18).

The magneto-optical behavior for the transverse configuration is different to the other two cases. For a *s* polarized excitation, where the electric field oscillates along the direction of magnetization, there is no gyroelectric effect. Thus the transverse effect is induced by *p* polarized light only. Like the isotropic case, there is no interaction between *p* and *s* modes; so, the gyroelectric effect is a linear *p* polarized effect stimulated by a *p* polarized excitation. It is, therefore, not surprising that the transverse characteristic matrix has a much closer resemblance to the characteristic matrix for isotropic media:

$$[C]_T = [C]_I + g_T \begin{bmatrix} G_{11} & 0 & 0 & 0 \\ 0 & -G_{11} & 0 & 0 \\ 0 & 0 & 0 & 0 \\ 0 & 0 & 0 & 0 \end{bmatrix} \quad (21)$$

The gyroelectric part of the transverse matrix is much simpler than for the longitudinal and polar configurations, there being only two diagonal elements with the same magnitude but opposite sign (Table 1).

3.3 The Characteristic Matrix Method and Multilayers

Up to now the discussion has dealt with the characteristic matrix and how it relates the tangential field components at the two extremities of a film (Eqn. (13)). It is appropriate to remember that the tangential field components only are being considered
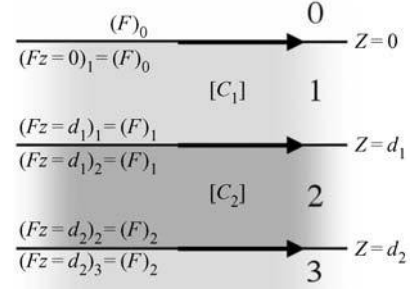
Figure 3
The concept behind the characteristic matrix model.

because at an interface they are continuous. Consequently, it is possible to relate the tangential electric and magnetic fields between adjacent layers and ultimately between the layers in a multilayer.

This may be illustrated by considering Fig. 3, which shows how the boundary conditions effect the field matrix (F). Considering layer one first, at the $z = 0$ boundary between medium zero and layer one, $(F_{z=0}) = (F)_0$. By renaming the field matrix at the second interface $(F)_1$, Eqn. (13) may be rewritten:

$$(F)_0 = [C]_1 (F)_1 \quad (22)$$

The tangential fields in medium zero and layer one have been related using the characteristics matrix for the layer $[C]_1$. Considering layer two, it is clear that a similar analysis may be applied to relate the tangential fields in layers one and two so that $(F)_1 = [C]_2 (F)_2$. This leads to the conclusion that the fields in medium zero and layer two may also be related by multiplying the characteristic matrices of the two layers:

$$(F)_0 = [C]_1 [C]_2 (F)_2 \quad (23)$$

Therein lies the basis for multilayer matrix calculations in that for a stack of L layers deposited on a substrate S in an ambient 0, the tangential fields at

the interfaces with the ambient and substrate are related by multiplying together all the characteristics matrices of the layers comprising the stack:

$$(F)_0 = \prod_{i=1}^{L} [C]_i (F)_S \qquad (24)$$

Note that Eqn. (24) is of the same form as Eqn. (22) and consequently describes the multilayer as a single layer of characteristic matrix $[C]_M = \prod [C]_i$. To the first order, $[C]_M$ has the same form as the characteristic matrix for the single layers comprising the multilayer. For magneto-optic calculations, multiplying together the single layer matrices results in higher order terms in Q appearing in the isotropic part of $[C]_M$ which are usually negligible. However, it is better to remove these terms completely and this may be done using a relatively simple scheme devised by Atkinson and Lissberger (1993).

3.4 The Calculation of Optical and Magneto-optical Effects

It remains to calculate the optical and magneto-optical amplitude coefficients. The amplitude coefficients are related to the s and p polarized electric fields of the incident, reflected, and transmitted light (Fig. 4) such that:

$$r_{p,s} = \frac{E^-_{O\,p,s}}{E^+_{O\,p,s}}$$

$$t_{p,s} = \frac{E^+_{S\,p,s}}{E^+_{O\,p,s}}$$

$$k_{p,s} = \frac{E^-_{O\,p,s}}{E^+_{O\,s,p}}$$

$$f_{p,s} = \frac{E^+_{S\,p,s}}{E^+_{O\,s,p}} \qquad (25)$$

the O and S subscripts indicating the fields in the incident and substrate media, respectively, the $+$ and $-$ superscripts indicating direction of propagation. Consequently, it is necessary to express the tangential fields as p and s electric field components. It should be remembered that the net tangential field is a
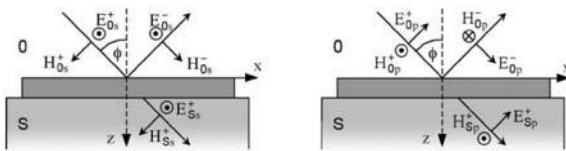
Figure 4
The s and p polarized electric and magnetic field components on reflection and transmission.

summation of the negative and positive going waves at the interface. With reference to Fig. 4, and using $E = ZH$, the boundary field matrix may be expressed in terms of the s and p components of the electric fields:

$$(F) = \begin{pmatrix} E_x \\ H_y \\ E_y \\ H_x \end{pmatrix} = \begin{pmatrix} (E^+_p + E^-_p)\gamma \\ (E^+_p - E^-_p)/Z \\ E^+_s + E^-_s \\ -(E^+_s - E^-_s)\gamma/Z \end{pmatrix} \qquad (26)$$

The characteristic matrix equation, may then be related to the p and s electric field components in the incident medium and the substrate:

$$\begin{pmatrix} (E^+_{Op} + E^-_{Op})\gamma_0 \\ (E^+_{Op} - E^-_{Op})/Z_0 \\ E^+_{Os} + E^-_{Os} \\ -(E^+_{Os} - E^-_{Os})\gamma_0/Z_0 \end{pmatrix} = [C] \begin{pmatrix} E^+_{Sp}\gamma_S \\ E^+_{Sp}/Z_S \\ E^+_{Ss} \\ -E^+_{Ss}\gamma_S/Z_S \end{pmatrix} \qquad (27)$$

The optical and magneto-optical coefficients, as defined by Eqns. (25a)–(25d), are determined by solving the relatively simple set of simultaneous equations represented by Eqn. (27).

The polar and longitudinal effects take the form of a change in the state of polarization known as the complex Kerr rotation in reflection and complex Faraday rotation in transmission. In both cases, the induced magneto-optical components, orthogonal to the incident linear polarization state, result in elliptically polarized light. The complex rotations are related to the amplitude coefficients ratios $k_{p,s}/r_{s,p}$ and $f_{p,s}/t_{s,p}$ as previously mentioned. The transverse effect is an exception in that it is a p polarized effect induced by a p polarized excitation. In this case, the effect is detected as a change in reflectance or transmittance. For details on how to determine the magneto-optical effects from the amplitude coefficients see article *Faraday and Kerr Rotation: Phenomenological Theory*.

4. Concluding Remarks

Accurate modeling of the interaction of light with multilayered recording media is important for the purposes of characterization and performance optimization. The two methods described are well-established and founded on Maxwell's equations and are consistent with each other. Both methods calculate the optical and magneto-optical amplitude coefficients, which are related to observable effects. The material parameters required for the calculations are the thickness, refractive index, and magneto-optical parameter for each layer constituting the multilayer.

The first method is a phenomenological approach where light undergoes a series of multiple reflections

within the media. It provides a relatively uncomplicated way to perform optical calculations but for the magneto-optical case is limited to the polar Kerr effect at normal incidence. The second, a matrix method, is a more general approach and is conveniently used for multilayer systems.

See also: Magneto-optic Effects, Enhancement of; Magneto-optic Multilayers; Magneto-optic Recording: Total Film Stack, Layer Configuration

Bibliography

Atkinson R, Lissberger P H 1993 Correct formulation of first-order magneto-optical effects in multilayer thin films on terms of characteristic matrices and derivation of a related superposition principle. *J. Magn. Magn. Mater.* **118**, 271–7

Gamble R, Lissberger P H, Parker M R 1985 A simple analysis for the optimization of normal Polar magneto-optical Kerr effect in multilayer coatings containing a magnetic film. *IEEE Trans. Magn.* **21**, 1651–3

Heavens O S 1991 *Optical Properties of Thin Solid Films*. Dover Publications Inc, New York

Hunt R P 1966 Magneto-optic scattering from thin solid films. *J. Appl. Phys.* **38**, 1652–71

Lissberger P H 1970 Optical applications of dielectric thin films. *Rep. Prog. Phys.* **33**, 197–268

Macleod H A 1969 *Thin-film Optical Filters*. Hilger, London

Smith D O 1965 Magneto-optical scattering from multilayer magnetic and dielectric films. Part 1. General theory. *Opt. Acta* **12**, 13–45

Zvezdin A K, Kotov V A 1997 *Modern Magneto-optics and Magneto-optical Materials*. IOP Publishing Ltd, Bristol, UK

W. R. Hendren
Queen's University of Belfast, UK

Multilayers: Interlayer Coupling

The exchange coupling of magnetic films across metallic interlayers was first observed in 1986 for dysprosium and gadolinium films separated by yttrium interlayers, and for iron films separated by chromium interlayers (Salamon *et al.* 1986, Majkrzak *et al.* 1986, Grünberg *et al.* 1986. For ferromagnetic films like those of gadolinium and iron, the coupling leads to parallel or antiparallel alignment of the magnetizations on opposite sides of the interlayer, depending on the interlayer thickness D, as seen in Figs. 1(a) and 1(b) respectively. For obvious reasons, the coupling leading to (a) is called "ferromagnetic"(F), and to (b) "antiferromagnetic" (AF). For films with helical magnetic structure like dysprosium, the coupling leads to an angle, ψ, between the magnetic moments on both sides of the yttrium interlayer, which depends on the yttrium thickness, as seen in Fig. 1(c). The actual alignment is also affected by other interactions, like
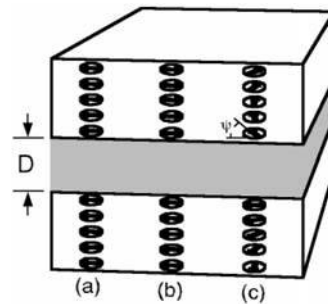
Figure 1
Coupling between magnetic films across metallic interlayer (dark shaded). Encircled arrows indicate moments in monolayer sheets parallel to the interfaces. The arrows indicate ferromagnetic coupling across the interlayer in (a) and antiferromagnetic coupling in (b). The magnetic coupling of films with a helical magnetic structure shown in (c) leads to a phase angle ψ.

anisotropy or an external field, H_{ext}. Large enough fields, H_{ext}, overcome the coupling and align the magnetizations parallel.

In 1990, it was established (Parkin *et al.* 1990) that the oscillation of the magnetic coupling between F and AF alignment, as a function of interlayer thickness, is a general phenomenon of transition metal ferromagnets separated by nonmagnetic interlayers. Previously oscillations had only been seen for gadolinium separated by yttrium. The discovery in 1988 of the giant magnetoresistance (GMR) effect in the Fe/Cr system (see *Giant Magnetoresistance*) led to enhanced interest in the magnetic coupling of transition metal ferromagnets, because of the many applications of GMR.

1. Theoretical Models

Interlayer exchange coupling is believed to be an indirect exchange interaction mediated by the conduction electrons of the spacer layer. It is closely related to the Ruderman–Kittel–Kasuya–Yoshida (RKKY) interaction between localized moments mediated by the conduction electrons of a host metal. The essential ingredients of the RKKY interaction, a localized spin-polarized perturbation and a sharp Fermi surface, lead to the well-known coupling oscillations. Like the exchange coupling in the rare earth metals themselves, the magnetic coupling of gadolinium, dysprosium, holmium, and erbium through yttrium and lutetium spacer layers has been described by the RKKY interaction.

For transition metal ferromagnets separated by paramagnetic interlayers, the description of the coupling needs to be modified. A phenomenological description of the coupling proposed to explain the

experimental observations (Bürgler *et al.* 2001) gives the interlayer coupling energy, E_i, per unit area as:

$$E_i = -J_1\cos(\theta) - J_2\cos^2(\theta) \qquad (1)$$

Here θ is the angle between the magnetizations $\vec{M}_1$ and $\vec{M}_2$ of the films on both sides of the spacer layer. The parameters J_1 and J_2 describe the type and the strength of the coupling. If the term with J_1 dominates, then from the minima of Eqn. (1) the coupling is F (AF) for positive (negative) J_1. If the term with J_2 dominates and is negative, we obtain 90° coupling. The first term of Eqn. (1) is often called the bilinear coupling, and the second the biquadratic coupling.

The microscopic mechanism leading to the bilinear exchange coupling J_1 has essentially the same physical origin as the RKKY interaction. However, one must consider the itinerant nature of electrons in transition metal ferromagnets, which gives rise to the spin-split band structure and spin-dependent reflectivities at the paramagnet/ferromagnet interfaces. The spin-dependent reflectivity is illustrated in Fig. 2(a), where it is assumed that electrons with their spins parallel (antiparallel) to the magnetizations $\vec{M}_1$ and $\vec{M}_2$ are weakly (strongly) reflected at these interfaces.

This spin-dependent reflection at the interfaces gives rise to spin-dependent quantum well states that cause an oscillatory polarization in the interlayer. As a result, there are spin-dependent interference effects like the formation of standing electron waves for certain interlayer thicknesses as indicated in Fig. 2(a). Due to the similarity of the arrangement in Fig. 2(a) with an optical Fabry Perot interferometer, this is sometimes also called the Fabry Perot model of oscillatory coupling. Oscillations in the coupling, observed as the thickness of a magnetic layer or other overlayer is varied, are explained by additional spin-dependent interference effects.
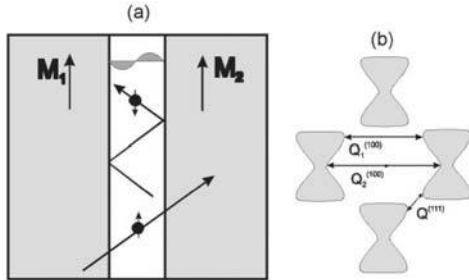
Figure 2
(a) Illustration of spin-dependent reflectivity at the nonmagnetic/magnetic interfaces for the explanation of oscillatory coupling; (b) a cross section of the gold Fermi surface with critical spanning vectors in the [100] and [111] directions.

The predominant contribution to the coupling is from electrons with wave vectors, Q_i, that are critical spanning vectors of the Fermi surface of the interlayer material, i.e., vectors in the direction perpendicular to the interface that connect two sheets of the Fermi surface parallel to each other. For the Fermi surface of gold shown in Fig. 2(b), there are two such vectors in the [100] and one vector in the [111] direction. The periods of the oscillatory coupling are given by $\Lambda = 2\pi/Q_i$ and thus are determined solely by the electronic properties of the interlayer material.

This quantum well model leads to the following dependence of J_1^i of Eqn. (1), connected with the ith Fermi surface spanning vector Q_i, on the interlayer thickness D:

$$J_1^i = J_0^i \sin(Q_i D + \phi_i)/D^2 \qquad (2)$$

The amplitude J_0^i includes Fermi surface geometry factors and interface reflection probabilities. Good parallelism of the parts of the Fermi surface at the endpoints of a critical spanning vector will contribute to large amplitudes of the corresponding oscillatory coupling. This so-called "nesting" effect results in a decrease of the coupling with interlayer thickness as D^{-1} rather than the more typical D^{-2}.

If, due to favorable band matching, electrons with one spin have good transmission at the interfaces, and with the other spin have good reflection, then the result will be large amplitudes in oscillatory coupling strength. This is thought to be the case for the coupling of cobalt across rhodium and ruthenium interlayers (see Table 1). In principle, the quantum well model can be extended to nonmetallic spacers using a complex Fermi surface, but materials difficulties have limited experimental work in this area.

The theoretical description of magnetic coupling assumes perfect interfaces. Experimentally, there is always some disorder at the interfaces. The interaction of Eqn. (2) is defined at each discrete interlayer thickness $D = nd$, where d is the spacing of neighboring atomic layers in the interlayer. The direction of magnetization in a magnetic layer can only change over a finite lateral distance l, comparable to a domain wall width. If there are interlayer thickness fluctuations on a lateral length scale smaller than this magnetic response length l, the observed coupling strength is an average over regions of different thickness:

$$\bar{J}_1(t) = \sum_i \sum_n P(t, n) J_i(n) \qquad (3)$$

where $P(t, n)$ is the fraction of the interlayer area that is n layers thick when the average thickness is t. Short-period oscillations of the coupling are averaged out more readily than long-period oscillations, and therefore are only observed in samples with relatively smooth interfaces. Thickness fluctuations, and also

Table 1
Observed coupling strengths and periods.

Sample	Maximum strength $|J_1 + J_2|$ (mJ m^{-2}) at (thickness (nm))	Periods in ML (nm)
Co/Cu/Co (100)	0.4 (1.2)	2.6 (0.47), 8 (1.45)
Co/Cu/Co (110)	0.7 (0.85)	9.8 (1.25)
Co/Cu/Co (111)	1.1 (0.85)	5.5 (1.15)
Fe/Au/Fe (100)	0.85 (0.82)	2.5 (0.51), 8.6 (1.75)
Fe/Cr/Fe (100)	> 1.5 (1.3)	2.1 (0.3), 12 (1.73)
Fe/Mn/Fe (100)	0.14 (1.32)	2 (0.33)
Co/Ru (0001)	6 (0.6)	5.1 (1.1)
Co/Rh/Co (111)	34 (0.48)	2.7 (0.6)
Co/Os (111-text'd)	0.55 (0.9)	7 (1.5)
Co/Ir (111)	2.05 (0.5)	4.5 (1.0)

interfacial disorder on a finer scale due to alloying, lead to a measured magnetic coupling that is weaker than that expected theoretically.

Although J_2 of the biquadratic coupling term in Eqn. (1) can be of intrinsic origin, most experimental results to date are well explained by a model in which the biquadratic coupling is an extrinsic effect due to the thickness fluctuations of the interlayer. For example, if the bilinear coupling varies spatially due to the thickness fluctuations, the sum of the intralayer coupling energy (exchange stiffness) and interlayer coupling energies is minimized when the magnetizations of the layers fluctuate about their average directions. The energy is lowered the most when the average magnetizations of the two layers are perpendicular. This biquadratic coupling leads to observation of 90° coupling when the average bilinear coupling is small.

The RKKY description of magnetic coupling in rare-earth multilayers and the quantum well model of coupling in transition metal multilayers assume that the electrons in the spacer layers are noninteracting. At the other extreme, the electrons of the interlayer may be strongly interacting, as for example local moments coupled to each other in antiferromagnetic manganese. A phenomenological model for this situation, known as the torsion or proximity model, has been proposed (Slonczewski 1995) that treats the magnetic nature of the spacer layer and predicts slightly different observable behavior.

The appropriate description of the coupling may fall between the assumed noninteracting electrons of the interlayer in the RKKY and the quantum well models and the strongly coupled local moments of the torsion model. A model including an induced spin density wave was proposed to explain experiments on the coupling of dysprosium through yttrium and lutetium. There is also strong evidence from the temperature dependence of the coupling in an iron whisker-based Fe/Cr/Fe trilayer that the chromium electrons are in an interacting, itinerant, spin density wave state (Pierce *et al*. 1999).

2. Experimental Methods and Examples

Polarized neutron diffraction provided the initial evidence for the oscillatory exchange coupling of superlattices of gadolinium layers separated by yttrium interlayers. These measurements were supplemented by magnetization measurements that show the remanent magnetization and the saturation magnetization oscillating as a function of yttrium thickness.

The coupling of rare earths with complex spin structures like dysprosium, holmium, and erbium through interlayers of yttrium and lutetium can be studied with unpolarized neutron diffraction, because there are distinct magnetic scattering peaks deriving from the incommensurate magnetic order. The phase and chirality of the helical spin structure of dysprosium is preserved through yttrium spacer layers over 10 nm thick in superlattices grown along the c-axis direction. The stronger coupling found for c-axis superlattices, compared to a- or b-axis structures, was attributed to the directional properties of the interlayer Fermi surface.

Superlattices, as well as simpler trilayer structures, have been used to investigate the coupling of transition-metal ferromagnets. As an alternative to preparing many superlattices or trilayer samples, each with a specific interlayer thickness, it is possible with a trilayer to grow the spacer layer in the form of a wedge with continuously varying thickness. An example of such a structure is shown in Fig. 3(a).

The periods of the oscillatory interlayer coupling can be determined from the variation of the magnetic domains with changing thickness of the interlayer wedge. The domains can be detected optically with the magneto-optic Kerr effect, or by means of spin-polarized electrons using scanning electron microscopy with polarization analysis (SEMPA).
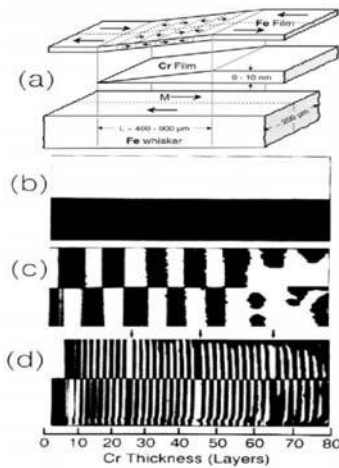
Figure 3
Magnetic domains in Fe/Cr/Fe samples seen by means of SEMPA, which display oscillatory coupling. Sketch of the sample seen in part (a); domains are observed in the bare whisker substrate (b); and in the upper iron film grown at 30 °C (c), and at 350 °C (d) (after Unguris *et al.* 1991).

Figures 3(b)-3(d) displays SEMPA magnetization images in which the black (white) regions correspond to magnetization to the left (right). Note that in part (b), the bare iron whisker displays two domains with a 180° wall in between. Parts (c) and (d) show domains in the upper iron film, separated from the whisker by a chromium spacer grown at an iron whisker substrate temperature of 30 °C and 350 °C, respectively. At 350 °C, the chromium grows in a layer-by-layer mode, forming a very smooth interface, while the lower temperature leads to a rougher chromium growth.

The striking difference in the magnetic domain patterns of parts (c) and (d) of Fig. 3 indicates how thickness fluctuations affect which periods of the magnetic coupling can be observed. For the near ideal growth in (d), both a short- and long-period coupling can be observed, with the short period clearly dominating. In (c), the short-period coupling is averaged out by thickness fluctuations as described by Eqn. (3), and only the long period is observed. The long and short periods were determined to be 12 ML and 2.1 ML respectively. The short-period oscillations derive from a wave vector connecting strongly nested regions of the chromium Fermi surface. The slight difference between this Fermi surface critical spanning wave vector and the lattice wave vector leads to phase slips in the short-period oscillations at the chromium thicknesses indicated by arrows.

For a measurement of coupling strengths, it is necessary to apply a magnetic field. The simplest and

most frequently employed method is a measurement of the remagnetization curve, where the strength of the coupling is determined from the field required to switch from AF to F coupling. A measurement essentially of this type can be made in parallel with a sample structure as in Fig. 3(a) by using magneto-optical microscopy; the coupling strength is determined from the external field required to switch the antiferromagnetically coupled domains, causing them to disappear. Alternatively, one can measure the magnetic coupling by determining the frequency shifts of coupled spin wave modes, which represent the restoring forces caused by the coupling.

Remagnetization curves from trilayers consisting of two 6 nm f.c.c. cobalt films separated by two different thicknesses of copper are displayed in Fig. 4. The coupling is ferromagnetic in Fig. 4(a) and the films always reverse their magnetizations in unison. In Fig. 4(b), the strength of the antiferromagnetic coupling is determined by the field, H_{flip}, where the coupling changes from AF to F. In order to measure the strength of the coupling in ferromagnetically coupled regions by remagnetization curves, it is necessary to resort to a technique known as "spin engineering." To measure the coupling between two ferromagnetic films, F_1 and F_2, across an interlayer I, an additional thick ferromagnetic film, F_0, is added, such that it is strongly antiferromagnetically coupled to F_1 by using a proper interlayer, I_0, as shown in Fig 5. F_1 and F_2 can be held with their magnetizations opposite to the external field, H, until H overcomes the ferromagnetic coupling and reverses the magnetization of F_2,
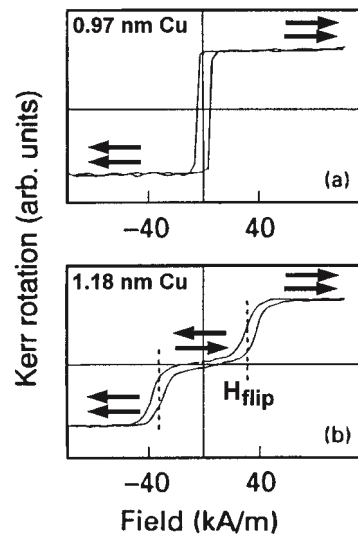
Figure 4
Remagnetization curves of a Co/Cu/Co trilayer structure: (a) with ferromagnetic coupling; (b) with antiferromagnetic coupling.
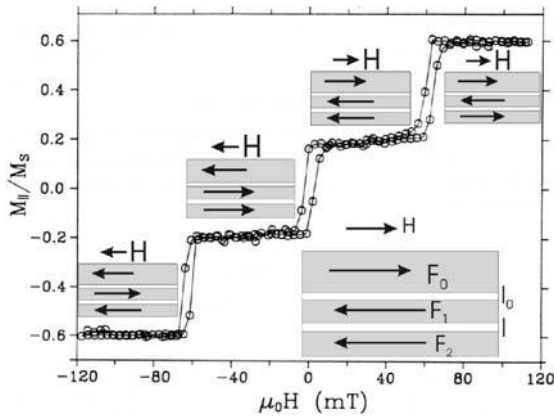
Figure 5
Structure (lower right side) and typical remagnetization curve of a Fe/Au/Fe sample with spin engineering.
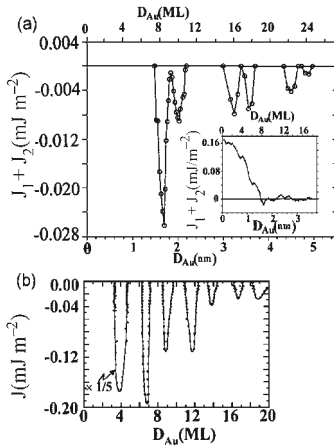
Figure 6
Coupling strength as a function of thickness in Fe/Au(wedge)/Fe on (a) Ag-buffered GaAs substrate; (b) on Fe whisker. The inset in (a) includes ranges where the coupling is ferromagnetic.

thereby determining the ferromagnetic coupling across I.

In Fig. 6(a) we see the result of an evaluation of remagnetization curves for a $Fe/Au_{wedge}/Fe$ structure grown on a silver-buffered GaAs(100) substrate. The spin engineering technique has been used to determine the positive values of the coupling. The coupling is strongly ferromagnetic in Fig. 6(a) for small d_{Au}, probably due to pinholes and magnetic bridges. For increasing d_{Au} ferromagnetic coupling quickly decreases, until there are oscillations around zero. Two periods of oscillation are superimposed with an amplitude that is attenuated as a function of the interlayer thickness.

Measurements of the coupling strength in a $Fe/Au_{wedge}/Fe$ trilayer grown on an iron whisker, by observing the disappearance of antiferromagnetically coupled domains in a Kerr microscope, are shown in Fig. 6(b). Two periods of oscillatory coupling, 2.48 ML and 8.6 ML, were determined from the data. Both the samples used in Figs. 6(a) and 6(b) were grown very carefully; the stronger coupling for the iron whisker sample is indicative of the better growth occurring naturally on that substrate. The data of Fig. 6(b) were further analyzed, taking into account thickness fluctuations to obtain "unaveraged" values to compare with theory; the coupling strength for the short- and long-period oscillations was found to be 60% and 15% of that calculated respectively.

In Table 1 we have compiled some measured values for interlayer coupling strengths and periods. As shown in Fig. 3, the thickness fluctuations can obscure the short period oscillations by averaging but do not change the periods, which are determined by the interlayer Fermi surface. On the other hand, the thickness fluctuations dramatically affect the coupling strength, as seen from Fig. 6, and thus the values listed in Table 1 are representative coupling strengths for specific samples. Table 1 gives the maximum observed coupling strength, $|J_1 + J_2|$, and the spacer layer thickness in ML (in nanometers) at which it was measured. The coupling strength also decreases with increasing temperature.

3. Applications

Applications of interlayer exchange coupling have been suggested. For example, antiferromagnetic coupling can be used in "artificial" antiferromagnets (van den Berg *et al.* 1996), i.e., layered structures of ferromagnetic films, coupled strongly antiferromagnetically, such that the total moment disappears. The advantage of such a structure as compared to a
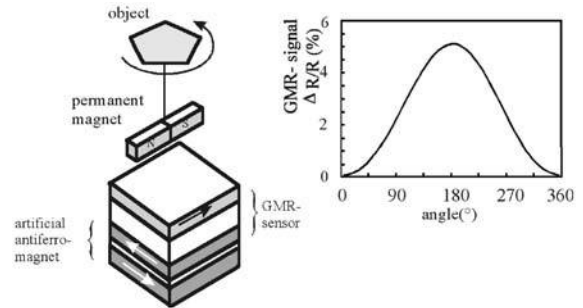
Figure 7
Sensor for the measurement of the rotational angle of an object by means of the GMR effect, which makes use of an artificial antiferromagnet on the basis of antiferromagnetic coupling.

natural antiferromagnet is that in this way it is easier to prepare an uncompensated surface with a net magnetic moment. This is of interest in the context of "exchange anisotropy" used for pinning the magnetization unidirectionally. At the surface of a natural antiferromagnet the moment can be largely compensated, due to surface roughness or other irregularities. Artificial antiferromagnets can replace natural ones, for example, in field sensors, where they are used to shift remagnetization curves using the exchange anisotropy effect. The application is displayed in the case of a rotational GMR type sensor in Fig. 7.

See also: Magneto-optic Multilayers

Bibliography

Bruno P 1995 Theory of interlayer magnetic coupling. *Phys. Rev. B* **52**, 411–39

Bürgler D, Demokritov S, Grünberg P, Johnson M 2001 Interlayer exchange coupling in transition metal systems. In: Buschow K H J (ed.) *Magnetic Materials: Vol. 13*. Elsevier, Amsterdam

Demokritov S O 1998 Biquadratic interlayer coupling in layered magnetic systems. *J. Phys. D: Appl. Phys.* **31**, 925–41

Grünberg P, Schreiber R, Pang Y, Brodsky M B, Sowers H 1986 Layered magnetic structures: evidence for antiferromagnetic coupling of Fe layers across Cr interlayers. *Phys. Rev. Lett.* **57**, 2442–5

Majkrzak C F, Cable J W, Kwo J, Hong M, Mc Whan D B, Yafet Y, Waszczak J V, Vettier C 1986 Observation of a magnetic antiphase domain structure with long-range order in a synthetic Gd-Y superlattice. *Phys. Rev. Lett.* **56**, 2700–3

Majkrzak C F, Kwo J, Hong M, Yafet Y, Doon Gibbs, Chien C L, Bohr J 1991 Magnetic rare earth superlattices. *Adv Phys.* **40**, 99–189

Parkin S S P, More N, Roche K P 1990 Oscillations in exchange coupling and magnetoresistance in metallic superlattice structures: Co/Ru, Co/Cr and Fe/Cr. *Phys. Rev. Lett.* **64**, 2304–7

Pierce D T, Unguris J, Celotta R J, Stiles M D 1999 Effect of roughness, frustration, and antiferromagnetic order on magnetic coupling of Fe/Cr multilayers. *J. Magn. Magn. Mater.* **200**, 290–321

Rhyne J J, Erwin R W, Borchers J, Salamon M B, Du R, Flynn C P 1989 Neutron scattering studies of rare earth magnetic multilayers. *Physica B* **159**, 111–28

Rührig M, Schäfer R, Hubert A, Mosler R, Wolf J A, Demokritov S, Grünberg P 1991 Domain observations in Fe-Cr-Fe layered structures: evidence for a biquadratic coupling effect. *Phys. Stat. Solidi A* **125**, 635–56

Salamon M B, Sinha S, Rhyne J J, Cunningham J E, Erwin R W, Borchers J, Flynn C P 1986 Long range incommensurate magnetic order in a Dy–Y multilayer. *Phys. Rev. Lett.* **56**, 259–62

Slonczewski J C 1995 Overview of interlayer exchange theory. *J. Magn. Magn. Mater.* **150**, 13–24

Stiles M D 1999 Interlayer exchange coupling. *J. Magn. Magn. Mater.* **200**, 322–37

Unguris J, Celotta R J, Pierce D T 1991 Observation of two different oscillation periods in the exchange coupling of Fe/Cr/Fe(100). *Phys. Rev. Lett.* **67**, 140–3

van den Berg H A M, Clemens W, Gieres G, Rupp G, Schelter W, Vieth M 1996 GMR sensor scheme with artificial antiferromagnetic subsystem. *IEEE Trans. Magn.* **32** (5), 4624–6

P. A. Grünberg
Forschungszentrun Jülich, Germany

D. T. Pierce
*National Institute of Standards and Technology
Gaithersburg, Maryland, USA*

Muon Spin Rotation (μSR): Applications in Magnetism

Following the pioneer work by Gurevich *et al.* in 1972, demonstrating the possibility to use polarized positive muons in the field of metal physics, numerous experiments using the *Muon Spin Rotation/ Relaxation* (μSR) technique have been successfully undertaken with special emphasis on the study of magnetic phenomena in matter. Although some experimental and theoretical problems remain to be solved, it is fair to say that the μSR technique became widely recognized as a mature technique able to furnish a complementary point of view when investigating magnetism in matter.

The interest on this novel technique is based on the complementarity between the particular information extracted from the μSR studies and the one obtained from either more classical microscopic techniques (e.g., neutron diffraction, nuclear magnetic resonance (NMR), and Mössbauer spectroscopy) or bulk studies such as specific heat or magnetic susceptibility measurements. The details of the technique itself are extensively discussed in numerous review articles (e.g., Schenck 1985) and correspondingly, several articles provide extensive reviews of the magnetic materials investigated by μSR spectroscopy (e.g., Schenck and Gygax 1995, Dalmas de Réotier and Yaouanc 1997). A concise description of the method can be also found in Cox and Stoneham 1993.

1. The μSR Signal—The Basics

A polarized μ^+ beam is obtained by collecting the muons produced via the two-body decay of positive pions. Due to the zero value of the pion spin, the muon beam is 100% polarized (helicity -1) in the pion frame. After the implantation into the sample, the muons are decelerated within 100 ps and come to rest at an interstitial site without any significant loss of polarization. Subsequently, if the μ^+ are subject to magnetic interactions, their polarization becomes time dependent ($\mathbf{P}_\mu(t)$). Due to the weak decay of the muon (average lifetime $\tau_\mu \sim 2.2\,\mu s$), the time

evolution of $\mathbf{P}_\mu(t)$ can be deduced by measuring the distribution as a function of time of the positron emitted after the muon decay (the positron is emitted preferentially along the direction of the decaying muon spin). In the time differential μSR technique, repeated measurements ($\sim 1 \times 10^7$) are made of the time interval between the μ^+ implantation into the sample and the detection in a particular direction of the emitted positron.

The time histogram of the collected intervals has the form

$$N_{e+}(t) = B + N_0 e^{-\frac{t}{\tau_\mu}}\left[1 + A\frac{P_\mu(t)}{P_\mu(0)}\right] \qquad (1)$$

where the last part of the second term represents the asymmetric positron emission (with typically $A \sim 0.3$). B is a time-independent background, N_0 is a normalization constant, and the exponential accounts for the decay of the μ^+. $P_\mu(t)$ is defined as the projection of $\mathbf{P}_\mu(t)$ along the direction of the initial polarization, i.e., $P_\mu(t) = \mathbf{P}_\mu(t) \cdot \mathbf{P}_\mu(0)/P_\mu(0) = G(t)P_\mu(0)$, where $G(t)$ reflects the normalized μ^+ spin auto-correlation function

$$G(t) = \frac{\langle \mathbf{S}(t) \cdot \mathbf{S}(0) \rangle}{S(0)^2} \qquad (2)$$

which depends on the average value, distribution, and time evolution of the internal fields and, therefore, contains all the physics of the magnetic interactions of the μ^+ inside the sample.

Equation (1) can therefore be written as:

$$N_{e+}(t) = B + N_0 e^{-\frac{t}{\tau_\mu}}[1 + AG(t)] \qquad (3)$$

where $AG(t)$ is often called the μSR signal and the envelop of $G(t)$ is known as the μ^+ depolarization function. In the case of static local magnetic fields ($\mathbf{B}_\mu$) at the μ^+ site, $G(t)$ is given by:

$$G(t) = \int f(\mathbf{B}_\mu)[\cos^2\theta + \sin^2\theta \cos(\gamma_\mu B_\mu t)]d\mathbf{B}_\mu \qquad (4)$$

where $f(\mathbf{B}_\mu)$ is the magnetic field distribution function, θ is the angle between the local field and $\mathbf{P}_\mu(0)$, $B_\mu = |\mathbf{B}_\mu|$ and $\gamma_\mu/(2\pi) = 13.553879$ (± 0.7 ppm) kHzG^{-1} is the gyromagnetic ratio of the muon. Therefore, the careful analysis of the μSR signal will provide information on the local field distribution at the interstitial site where the muon came at rest.

1.1 Transverse-field (TF) Technique—Muon Spin Rotation

For this technique, an external field $\mathbf{H}_{ext}$ is applied perpendicular to the initial muon polarization $\mathbf{P}_\mu(0)$. $\mathbf{P}_\mu(t)$ processes around the total field $\mathbf{B}_\mu$ at the muon site, the value of which can be extracted from the oscillatory component of $G(t)$, recalling that the μ^+ frequency $\nu_\mu = \omega/(2\pi) = \gamma_\mu B_\mu/(2\pi)$. In addition to the determination of the muon Knight shift, this technique allows one to gain more insight on the inhomogeneous field distribution at the muon site caused by static fields and on the presence of $1/T_2$ processes responsible for homogeneous line broadening.

1.2 Zero-field (ZF) and Longitudinal-field (LF) Techniques—Muon Spin Relaxation

With the ZF technique one monitors the time evolution of the muon ensemble under the action of internal magnetic fields. This technique is widely utilized to measure the spontaneous μ^+ Larmor frequencies in magnetically ordered phases, providing information about the values of the static moment and the type of magnetic structures. The observation of spontaneous μ^+ frequencies is, however, limited to systems where the presence of static electronic moments produces well-defined local fields at the μ^+ stopping site. Hence, the μ^+ spin autocorrelation function $G(t)$ depends sensitively on details of the magnetic structure and of course on the μ^+ stopping site.

In a ZF experiment, a depolarization can occur due to the presence either of a static distribution of internal fields arising from static nuclear or electronic dipole fields, or of a time dependence of the internal fields at the muon site. This time dependence may arise from a fluctuation of the magnetic moments or from muon diffusion. In contrast, in a LF configuration (i.e., $\mathbf{H}_{ext} \| \mathbf{P}_\mu(0)$), by choosing $\mathbf{H}_{ext}$ to be stronger than the internal fields, the muon's states "up" and "down" are eigenstates of the Zeeman Hamiltonian and any inhomogeneous (static) distribution of the internal fields will not affect the time evolution of the μ^+ polarization, which will remain constant. This behavior reflects the decoupling of the μ^+ spin from the static internal fields. Hence, to pinpoint the origin of the depolarization, decoupling experiments in a longitudinal fields are routinely performed.

2. Why Muons?

There are several advantages in using the μSR technique to study magnetic systems.

(i) Due to the large muon magnetic moment ($\mu_\mu = 8.89 \mu_N$), the technique is sensitive to extremely small internal fields (down to $\sim 1 \times 10^{-5}$ T) and, therefore, can probe local magnetic fields which can be nuclear or electronic in nature.

(ii) The local probe character of the muon makes μSR very sensitive to spatially inhomogeneous magnetic properties. Hence the occurrence of different phases in the sample will be reflected by different

components in the µSR signal, i.e.,

$$AG(t) = \sum_i A_i G_i(t) \qquad (5)$$

(iii) A careful analysis of the amplitude A_i of these components furnishes a direct measure of the fraction of the sample involved in a particular phase (with the condition $\Sigma_i A_i = A$). Similarly, µSR is a powerful tool when magnetic order is of short range and/or random nature where neutron experiments will fail.

(iv) In addition, the µSR technique can be utilized to check the coexistence of different types of ground states at the microscopic level.

(v) In magnetic phases, the possibility given by µSR to independently extract the value of the ordered static moment and the sample volume involved in the magnetic phase allows one to overcome a shortcoming of other techniques (such as the neutron scattering technique) for which these two parameters are strongly coupled, therefore, hampering their absolute determination.

(vi) Since no applied field is necessary to polarize the spin of the implanted muons, µSR measurements can be made in the absence of a perturbative external field.

(vii) The muon is a spin-$\frac{1}{2}$ particle and consequently is free of quadrupolar interactions. This greatly simplifies the analysis of µSR, with a reduced set of adjustable parameters.

In the following, some exemplary studies illustrating some of the above described advantages of the µSR technique will be briefly discussed.

2.1 Small Values of the Ordered Magnetic Moments

The capability of µSR to detect weak static magnetism has been illustrated by the discovery of magnetic ground states in so-called *heavy-fermion* systems that were long considered examples of Fermi-liquid paramagnets. In these systems, composed by local magnetic moments, the competition between the demagnetizing on-site Kondo interaction and the intersite Ruderman–Kittel–Kasuya–Yosida interaction leads to a richness of different ground states (see also *Heavy-fermion Systems*; *Kondo Systems and Heavy Fermions: Transport Phenomena*). An example is the occurrence of itinerant magnetism of the heavy quasiparticles, which is characterized by extremely small static magnetic moments (of the order of $1 \times 10^{-3} \mu_B$).

Figure 1 exhibits the depolarization rate of µSR spectra obtained in zero-applied field for the heavy-fermion compound $CeRu_2Si_2$ (Amato *et al.* 1994). Below 2 K, the depolarization rate exhibits a significant increase corresponding to an enhancement of the field spread at the μ^+ site of the order of 2×10^{-5} T, which originates from the electronic moments. Considering that the different magnetic structures observed in isostructural compounds with
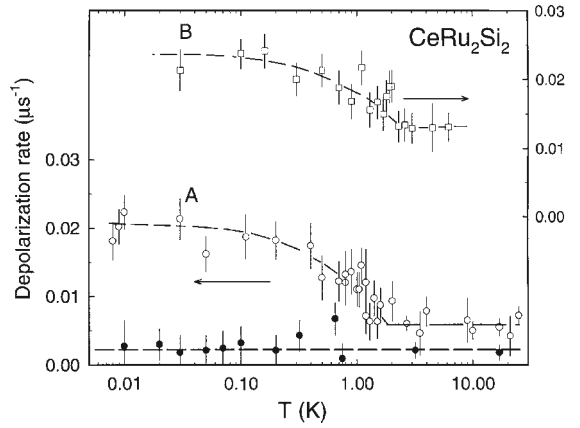
Figure 1
Temperature dependence of the ZF (open symbols) and LF ($B_{ext} = 0.6$ T, closed symbols) depolarization rates in $CeRu_2Si_2$ measured in two monocrystalline samples (A and B). The initial μ^+-polarization was along the tetragonal *c*-axis.

light rare earth metals lead to nonzero net dipole field at the μ^+ site, it was concluded that the field distribution with zero average value detected by µSR in $CeRu_2Si_2$ was due to static Ce moments of the order of $\mu_s \sim 1 \times 10^{-3} \mu_B$/Ce ordering in a complicated (possibly incommensurate) structure.

2.2 Coexisting Phases

In different classes of systems, the question of the coexistence of magnetism and superconductivity has attracted considerable attention. This is, for example, the case for the heavy-fermion compounds where both ground states are found to microscopically coexist for U-based systems and to occur in different domains in Ce-based systems. Such a conclusion was mainly extracted from µSR studies by carefully analyzing the potential presence of different components in the spectra which could reflect the coexistence in a sample of domains with different magnetic properties (muons stopping in different domains will contribute to different components of the signal.)

An interesting example of such studies is provided by the measurements on the heavy-fermion compound $CeCu_2Si_2$ (Feyerherm *et al.* 1997) which, at the opposite of what was concluded from thermodynamic studies only, gave strong evidence *against* a microscopic coexistence of superconductivity and magnetism. The conclusions drawn from the zero-field µSR data are based on the observation of two components in the μ^+ depolarization function (see Fig. 2). One of the components shows a fast relaxation and is associated with magnetic domains developing below ~ 1.3 K. The other exhibits a slow relaxation
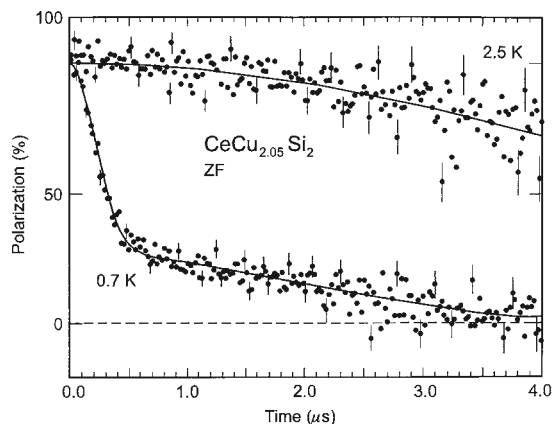
Figure 2
Time evolution of the μ^+ polarization measured in zero-field in a $CeCu_{2.05}Si_2$ sample at low temperature. Note the clear two-component structure of the signal measured below 1 K.

and reflects paramagnetic domains which become superconducting below ~ 0.6 K. Systematic μSR studies have shown that the increase of the magnetic fraction (i.e., the amplitude A_i of the corresponding component of the μSR signal) is strongly sample dependent and that the amount of magnetic phase is closely related to the sample-dependent size of the specific heat jump at the superconducting transition.

2.3 Short-range Magnetism

In the family of the high T_c (and magnetically related) compounds, some significant information was obtained from the μSR technique. In addition to the first indication of magnetic order in several compounds, the μSR technique has played a key role in the elucidation of phase diagrams due to its capability to detect short-range and random magnetism. An example is the studies on $La_2CuO_{4-\delta}$, for which the appearance of magnetism depends on the exact oxygen content (the input of O^{2-} removes electrons and creates holes in the system). Whereas some oxygen deficiency stabilizes the magnetic state, an excess of oxygen suppresses the antiferromagnetic order and eventually leads to superconductivity. Figure 3 shows the spontaneous muon spin precession frequency (ν_μ) observed in zero field for different samples of $La_2CuO_{4-\delta}$ (Uemura *et al.* 1988). Since ν_μ is proportional to the value of the static copper moment (μ_s), the data indicate that μ_s changes only within $\sim 15\%$ for the different samples despite the large difference in the ordering temperatures (from 15 K to 300 K). This is in contrast to results from neutron scattering on three different monocrystalline samples (see Fig. 4) from which a sublattice
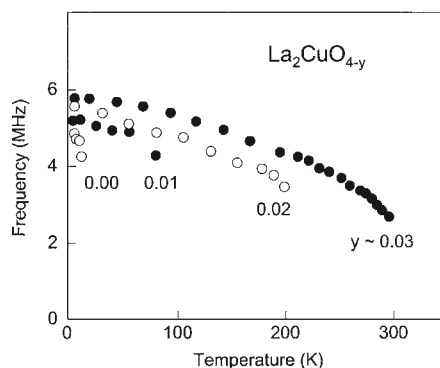
Figure 3
Temperature dependence of the spontaneous muon-spin precession frequency in La_2CuO_{2-y} for various y (from Uemura *et al.* 1988).
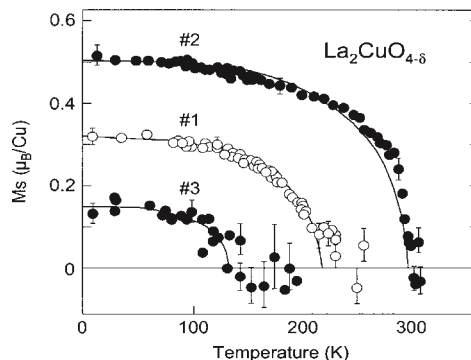
Figure 4
Sublattice magnetization derived from the magnetic Bragg-peak intensity of neutron scattering experiments on $La_2CuO_{2-\delta}$ samples with various δ (see Uemura *et al.* 1988 for details).

magnetization was derived from the intensity of the magnetic Bragg peaks, assuming that the whole volume exhibits long-range magnetism.

The difference between μSR and neutron results can be understood by considering the muon as a point-like probe in *real* space. Therefore, the field at the muon site will be mostly due to its neighboring copper moments, even if the spatial correlation characterizing the magnetic order may be short range. In contrast, the elastic magnetic scattering intensity measured in a neutron scattering experiment will probe the magnetic ordering in *reciprocal* space and will, therefore, only appear when the spatial 3D ordering is long range. It can, therefore, be concluded that the difference between μSR and neutron results is mainly due to a loss of long-range magnetism with increasing oxygen content (i.e., with increasing hole

concentration) introducing frustrations in the magnetic CuO_2 planes. Consequently, the value of the static copper moment extracted from the neutron data for samples with low T_N is systematically underestimated due to the reduced fraction of the specimen exhibiting long-range magnetic order.

3. Intrinsic Difficulties of the Technique

The analysis of the μSR results can be hampered by several potential difficulties.

- To extract quantitative information, the knowledge of the muon stopping site is usually mandatory. To determine it unambiguously, precise Knight-shift measurements are necessary along the principal crystallographic directions. Therefore, and in addition to the intrinsic difficulties of such measurements, the muon site determination requires single crystals, which might be difficult to obtain for given compounds or alloys.

- Another potential problem is the presence of μ^+ diffusion. Fortunately, observations show that diffusion is usually restricted to high temperatures. Since most aspects of magnetic phenomena occur at low temperature, μ^+ diffusion will usually be of limited concern.

- An intrinsic problem of μSR is the addition of an extra positive charge in the lattice. This leads to a modified local charge distribution, due to the screening of the muon's positive charge, and to a slight lattice relaxation, reflected by a small shift in the position of the nearest neighbor ions. This latter effect can be exactly quantified by a careful comparison between the data and simple theoretical calculations.

- Another, more disturbing, effect of the implantation of a positive charge in the lattice is that the modification of the local charge density can possibly affect the crystal electric field (CEF) of the neighboring atoms (see *Localized 4f and 5f Moments: Magnetism*). In systems based on rare-earth or actinides elements (for which the splitting of the ground state due to CEF is rather small) this effect could lead to a slight change of the atomic magnetic susceptibility for the neighboring ions. It has been shown that this effect can be important for singlet ground-state systems where the splitting between the excited states and the singlet ground state is very low (i.e., $< 1\,meV$). It is, therefore, of primary importance to compare systematically, in each particular case, the atomic susceptibility sensed by the interstitial muon to the bulk susceptibility, to detect the potential presence of such muon-induced effects.

4. Future Developments

4.1 Low Energy Muons

Thin films, nanomaterials, and multilayered compounds have emerged as significant elements in science and technology. In response to the need of novel techniques to investigate the magnetic properties of these objects, the development of muon beams with energy in the range of one eV to several keV was needed. In this direction, promising results have been obtained by slowing down energetic muons in appropriate moderators consisting of a thin layer of a van der Waals gas frozen on a substrate (Morenzoni 1997). The availability of epithermal polarized muons, therefore, opens the possibility to extend the μSR technique to the study of thin films and surfaces.

4.2 Muon on Request

Another promising evolution of the technique has been the development of a muon on request setup, combining, for the case of time-differential μSR experiments, the advantages of continuous and pulsed muon beams (Abela *et al.* 1999). Although continuous muon beams possess a good time resolution, limited mainly by the design of the detectors, the presence of random background in the positron histograms limits the useful time interval to about $10\,\mu s$, excluding investigations of slow relaxation processes. On contrast, pulsed muon beams deliver many muons per pulse at low repetition rate ($\ll 1/\tau_\mu$) essentially without background on the histograms. However, the time resolution for such beams is strongly limited by the finite length of the muon pulses.

A method to solve the background problem at continuous beam is to extract *one* muon at a time out of a continuous beam by means of a fast-switching electrostatic deflector, on request from a μSR instrument. Since the positron histograms obtained are essentially background free, this system opens, due to the high time resolution, the unique possibility of studying slow relaxation phenomena in high magnetic fields.

See also: Electron Systems: Strong Correlations; Heavy-fermion Systems; Localized 4f and 5f Moments: Magnetism; Magnetism in Solids: General Introduction

Bibliography

Abela R, Amato A, Baines C, Donath X, Erne R, George D C, Herlach D, Irminer G, Reid I D, Renker D, Solt G, Suhi D, Werner M, Zimmermann U 1999 Muons on request (MORE): combining advantages of continuous and pulsed beam. *Hyperfine Inter.* **121**, 575–8

Amato A, Feyerherm R, Gygax F N, Schenck A, Flouquet J, Lejay P 1994 Ultrasmall-moment static magnetism in $CeRu_2Si_2$. *Phys. Rev. B.* **50**, 619–22

Cox S F J, Stoneham A M 1993 Muon beams used for studying the solid state. In: Cahn R W, Lifshin E (eds.) *Concise Encyclopedia of Material Characterization.* Pergamon, Oxford

Dalmas de Réotier P, Yaouanc A 1997 Muon spin rotation and relaxation in magnetic materials. *J. Phys. Condens. Matter* **9**, 9113–66

Feyerherm R, Amato A, Geibel C, Gygax F N, Hellmann P, Heffner R H, MacLaughlin D E, Müller Reisener R, Nieuwenhuys G J, Schenck A, Steglich F 1997 Competition between magnetism and superconductivity in $CeCu_2Si_2$. *Phys. Rev. B* **56**, 699–710

Gurevich I I, Meleshko E A, Muratova I A, Nikolsky B A, Roganov V S, Selivanov V I, Sokolov B V 1972 Dipole interactions and diffusion of μ^+ meson in copper. *Phys. Lett. A* **40**, 143–4

Morenzoni E 1997 Low energy muons as probes of thin films and surfaces. *Appl. Magn. Res.* **13**, 215–29

Schenck A 1985 *Muon Spin Rotation Spectroscopy*. Hilger, Bristol, UK

Schenck A, Gygax F N 1995 Magnetic materials studied by muon spin spectroscopy. In: Buschow K H J (ed.) *Handbook of Magnetic Materials*. Elsevier, Amsterdam, Vol. 9, pp. 57–302

Uemura Y J, Kossler W J, Kempton J R, Yu X H, Schone H E, Opie D, Stronach C E, Brewer J H, Kiefl R F, Kreitzman S R, Luke G M, Riseman T, Williams D L, Ansaldo E J, Endoh Y, Kudo E, Yamada K, Johnston D C, Alvarez M, Goshorn D P, Hidaka Y, Oda M, Enomoto Y, Suzuki M, Murakami T 1988 Comparison between muon spin rotation and neutron scattering studies on the 3-dimensional magnetic ordering of $La_2CuO_{4-\delta}$. *Physica C* **153–5**, 769–70

A. Amato
Paul Scherrer Institute, Villigen, Switzerland

This page intentionally left blank

N

Nanocrystalline Materials: Magnetism

It is well known that the microstructure, noticeably the grain size, essentially determines the hysteresis loop of a ferromagnetic material. Figure 1 summarizes the typical variation of the coercivity, H_c, over the whole range of structural correlation lengths starting from atomic distances in amorphous alloys over grain sizes, D, in the nanometer region up to macroscopic grain sizes. The permeability shows an analogous behavior being essentially inversely proportional to H_c. The $1/D$-dependence of coercivity for large grain sizes (Pfeifer and Radeloff 1980) reflects the conventional rule that good soft magnetic properties require very large grains ($D > 100 \, \mu m$). Thus, the reduction of particle size to the region of the domain wall width increases H_c towards a maximum controlled by the anisotropies present. Accordingly, fine-particle systems have been mostly discussed as hard magnetic materials (Luborsky 1961). The lowest coercivities, however, are again found for the smallest structural correlation lengths, as in amorphous alloys ("grain size" of the order of atomic distances) and in nanocrystalline alloys for grain sizes $D < 20$nm. The extraordinary D^6-dependence of coercivity at small grain sizes, moreover, demonstrates how close soft and hard magnetic behavior actually can be. Indeed, the soft magnetic behavior on which we will focus in this article is only one manifestation of the novel and extraordinary magnetic properties that can be realized by establishing structural features on the nanometer scale. Thus, nanocrystalline microstructures
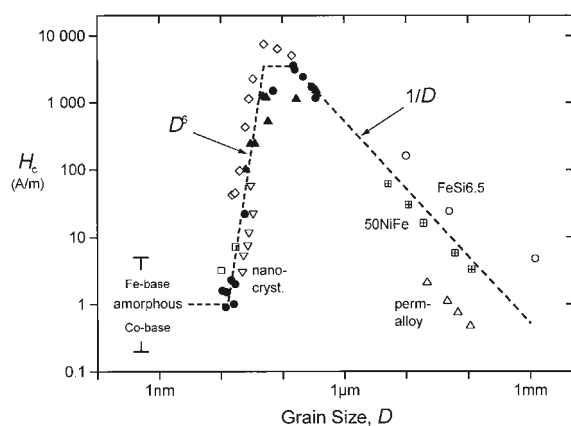
are also of great interest because of their ability to enhance the properties of rare earth hard magnets (Buschow 1997).

The decrease of coercivity shown in Fig. 1 for small grain sizes has to be distinguished from superparamagnetic phenomena, i.e., the well-known decrease of coercivity in small, isolated or weakly coupled particles owing to thermal excitation (Kneller 1969, Luborsky 1961). In the present case we deal with small ferromagnetic crystallites well coupled by exchange interaction which results in low coercivity and, unlike superparamagnetic particles, in a simultaneously high permeability.

The most prominent examples of soft magnetic nanocrystalline materials are devitrified glassy Fe–Cu–Nb–Si–B alloys (Yoshizawa *et al.* 1988); further examples are devitrified Fe–(Cu)–Zr–B alloys (Suzuki *et al.* 1991) or Fe–Hf–C thin films (Hasegawa and Saito 1991). The alloy composition originally proposed and subsequently not much changed is $Fe_{73.5}Cu_1Nb_3Si_{13.5}B_9$ and can be considered as a typical FeSiB metallic glass composition with additions of copper and niobium. The material is produced by rapid solidification of an originally amorphous ribbon, typically $20 \, \mu m$ thick, which is subsequently annealed above its crystallization temperature. The resulting microstructure is characterized by randomly oriented, ultrafine grains of b.c.c. Fe–20at.% Si with typical grain sizes of 10–15nm, hereafter referred to as nanocrystalline. The grains are embedded in a residual amorphous matrix which occupies about 20–30% of the volume and separates the crystallites at a distance of about 1–2 nm. The formation of this particular structure is ascribed to the combined effects of copper and niobium (or other group 4 to 6 elements) and their low solubility in b.c.c. iron. Copper promotes the nucleation of the b.c.c. grains, while niobium hinders their growth and at the same time inhibits the formation of boride compounds. The structure and the associated magnetic properties are astonishingly insensitive to the precise annealing conditions over a wide range of annealing temperatures between about 500 °C and 600 °C. Only annealing at higher temperatures leads first to the precipitation of borides and subsequently to grain coarsening, both of which deteriorate the soft magnetic properties (Herzer 1997).

This article reviews the key mechanisms relevant to the soft magnetic properties in the nanocrystalline region. The materials highlighted will be the Fe–Cu–Nb–Si–B alloys which are widely used. They are of particular interest because of their superior soft magnetic properties compared to those of permalloys and cobalt-based amorphous alloys. The general features, however, also apply to other nanocrystalline magnetic materials.

Figure 1
Coercivity, H_c, vs. grain size, D, for various soft magnetic metallic alloys: Fe–Nb–Si–B (▲), Fe–Cu–Nb–Si–B (●), Fe–Cu–V–Si–B (▽), Fe–Zr–B (□), Fe–Co–Zr (◇), NiFe alloys (⊞, △), and Fe–6.5wt.% Si (○).

1. Magnetocrystalline Anisotropy and Exchange Energy

The major requirement for superior soft magnetic behavior generally is a low or vanishing magnetocrystalline anisotropy. For example, in b.c.c. Fe–20at.% Si, the constituent phase in nanocrystalline $Fe_{73.5}Cu_1Nb_3Si_{13.5}B_9$, the anisotropy constant is $K_1 \approx 8 kJm^{-3}$, i.e., far too large to explain the low coercivity ($H_c < 1 Am^{-1}$) and high permeability ($\mu_i \approx 10^5$) by itself.

The key to understanding is that the effective anisotropy contribution of the small, randomly oriented b.c.c. grains is essentially reduced by exchange interaction. The critical scale where the exchange energy starts to balance the anisotropy energy is given by:

$$L_0 = \sqrt{A/K_1} \qquad (1)$$

where A is the exchange stiffness constant, which is about $L_0 \approx 35nm$ for the material parameters of b.c.c. Fe–20at.% Si. L_0 represents the minimum length scale over which the direction of the magnetic moments can vary appreciably and, for example, determines the order of the domain wall width. Thus, if the grain size, D, is reduced below L_0, the magnetization does not follow the randomly oriented easy axis of the individual grains, but increasingly is forced to align parallel by exchange interaction. As a consequence, the effective anisotropy is an average over several grains and, thus, considerably reduced in magnitude.

1.1 The Random Anisotropy Model

The degree to which the magnetocrystalline anisotropy is finally averaged out has been successfully addressed in terms of the so-called random anisotropy model (Herzer 1990), which was originally developed in order to explain the soft magnetic properties of amorphous ferromagnets by Alben *et al.* (1978). The basic idea starts from an assembly of exchange coupled grains of size D and volume fraction v_{cr}, with magnetocrystalline anisotropies oriented at random and embedded in an ideally soft ferromagnetic matrix. The effective anisotropy constant, $\langle K \rangle$, relevant to the magnetization process results from averaging over the $N = v_{cr}(L_{ex}/D)^3$ grains within the ferromagnetic correlation volume, $V = L_{ex}^3$, determined by the exchange length, L_{ex}, i.e., the scale on which exchange interaction forces the magnetic moments to align parallel. For a finite number, N, of grains within the exchange volume, there will be always some easiest direction determined by statistical fluctuations. Thus, the averaged anisotropy energy density, $\langle K \rangle$, is determined by the mean fluctuation amplitude of the anisotropy energy of the N grains:

$$\langle K \rangle \approx \frac{v_{cr}K_1}{\sqrt{N}} = \sqrt{v_{cr}}K_1(D/L_{ex})^{3/2} \qquad (2)$$

As the local magnetocrystalline anisotropies are averaged out this way, the scale on which exchange interaction dominates expands at the same time. Thus, the exchange length, L_{ex}, has to be renormalized by substituting $\langle K \rangle$ for K_1 in Eqn. (1); i.e., L_{ex} is self-consistently related to the averaged anisotropy by:

$$L_{ex} = \sqrt{A/\langle K \rangle} \qquad (3)$$

The combination of Eqns. (2) and (3) then yields for grain sizes smaller than the exchange length:

$$\langle K \rangle \approx v_{cr}^2 K_1(D/L_0)^6 = v_{cr}^2 D^6 K_1^4 / A^3 \qquad (4)$$

The most significant feature predicted by the random anisotropy model is the strong variation of the effective anisotropy, $\langle K \rangle$, with the sixth power of the grain size. Thus, for $D \approx L_0/3$, i.e., grain sizes of the order of 10–15 nm, the magnetocrystalline anisotropy is reduced by three orders of magnitude towards a few joules per cubic meter, i.e., small enough to enable superior soft magnetic behavior. Correspondingly, the renormalized exchange length, L_{ex}, expands into the micrometer region and, thus, is almost two orders of magnitude larger than the natural exchange length L_0. High-resolution Kerr effect studies of nanocrystalline $Fe_{73.5}Cu_1Nb_3Si_{13.5}B_9$ indeed reveal very wide domain widths of approximately $2 \mu m$ (Schäfer *et al.* 1991).

If there are no other anisotropies, coercivity and initial permeability are closely related to $\langle K \rangle$ by:

$$H_c = p_c\frac{\langle K \rangle}{J_s}; \ \mu_i = p_\mu\frac{J_s^2}{\mu_0\langle K \rangle} \qquad (5)$$

where J_s is the average saturation magnetization of the material, and p_c and p_μ are dimensionless prefactors close to unity. These relations, obvious for coherent magnetization rotation, in the region $D \ll L_{ex}$, also apply for domain wall displacements—actually, on the scale of the 10nm small grains the magnetization vector appears to rotate coherently if a $2 \mu m$ ($\approx L_{ex}$) wide domain wall passes by.

The predictions of the random anisotropy model provide a good guiding principle through the magnetic properties for grain sizes below about $L_0 \approx 40$–50nm. Thus, the D^6-dependence is well reflected in the coercivity (Fig. 1) and the initial permeability (Herzer 1997).

1.2 Remanence Enhancement

The hysteresis loops for $D < L_0$ typically show an enhanced remanence ($J_r/J_s > 0.90$), which is another very characteristic feature for the dominance of exchange interaction in this small grain size region. Actually, this remanence enhancement by exchange interaction is most attractive for novel, isotropic, nanoscale hard magnets (Buschow 1997). Yet at the smallest grain sizes, when the random anisotropy is

sufficiently washed out, more long-range uniaxial anisotropies take over and the remanence ratio decreases again to values around 0.5. Relevant to this are magnetoelastic and field-induced anisotropies, which limit the benefit of further grain size reduction (dashed horizontal line in Fig. 1 for $D < 10$nm). For further details of remanence enhancement in hard magnetic materials see *Magnets: Remanence-enhanced*.

1.3 Grain Coupling

The crucial role of the exchange interaction for the magnetic softening at $D < L_0$ also becomes most evident from the temperature dependence of the magnetic properties, shown in Fig. 2. Thus, when the temperature approaches the Curie temperature, T_c, of the intergranular amorphous phase ($T_c^{am} \sim 200$–$300\,°C$), which is much lower than the T_c of the b.c.c. grains ($T_c \sim 600\,°C$), the exchange coupling between the crystallites is largely reduced. As a consequence, the initial permeability then decreases by almost two orders of magnitude and the coercivity increases correspondingly. Simultaneously the domain structure changes from wide domains to a pattern of small, irregular domains (Schäfer *et al.* 1991).

With increasing measuring temperature the coercivity reaches a maximum and, finally, decreases towards zero. Interestingly, the latter occurs at a temperature ($560\,°C$) below T_c ($607\,°C$) of the b.c.c. grains. This indicates the transition to superparamagnetic behavior, which has been confirmed by a more detailed analysis of Lachowicz and Slawska-Waniewska (1994).

Thus, we find within a single sample a variety of phenomena ranging from soft, to hard, to finally superparamagnetic behavior being controlled by the strength of the interaction between the particles.

2. Magnetostriction

Given a vanishing magnetocrystalline anisotropy, the next important requirement for excellent soft magnetic properties is the absence of magnetostriction in order to minimize magnetoelastic anisotropies. Indeed, it is a feature of nanocrystalline iron-based alloys that the phases formed can lead to low or vanishing saturation magnetostriction, λ_s (Fig. 3). This is responsible for the increase of initial permeability up to one order of magnitude upon formation of the nanocrystalline state.

The behavior of λ_s can be understood from the balance of the magnetostriction among the α-FeSi grains and the residual amorphous matrix:

$$\lambda_s = v_{cr}\lambda_s^{FeSi} + (1 - v_{cr})\lambda_s^{am} \qquad (6)$$

Thus, near-zero magnetostriction in nanocrystalline iron-based alloys requires a large crystalline volume fraction, v_{cr}, with negative magnetostriction in order to compensate for the high positive value of the amorphous iron-based matrix. This is achieved either by a high silicon content in the b.c.c. grains ($\lambda_s^{FeSi} \approx -6 \times 10^{-6}$ for α-Fe$_{80}$Si$_{20}$) as in the Fe–Cu–Nb–Si–B system, or if the grains consist of pure α-iron ($\lambda_s^{FeSi} \approx -4 \times 10^{-6}$) as in Fe–(Cu)–Zr–B.

An important point to stress is that this balance of local magnetostriction constants to zero really results in stress-insensitivity of the magnetic properties as,

Figure 2
Initial permeability, μ_i, and coercivity, H_c, of nanocrystalline Fe$_{73.5}$Cu$_1$Nb$_3$Si$_{13.5}$B$_9$ (annealed 1h at $540\,°C + 4$h at $350\,°C$ in a transverse magnetic field) vs. measuring temperature (measuring frequency $f = 50$Hz). The arrows indicate the Curie temperatures of the residual amorphous matrix ($T_c^{am} = 291\,°C$) and the b.c.c. grains ($T_c^{FeSi} = 607\,°C$).

Fe–Cu$_1$Nb$_3$Si$_x$B$_{2-x}$ with Si+B = ○ 18.5 □ 20.5 ● 22.5 ◇ 23.5 at%
△ Fe–Cu$_1$Si$_x$Nb$_{6.7}$B$_{13}$ ▲ Fe$_{84}$Nb$_7$B$_9$ ▽ Fe–Cu$_{0.1}$Zr$_{6.7}$B$_{2.6}$
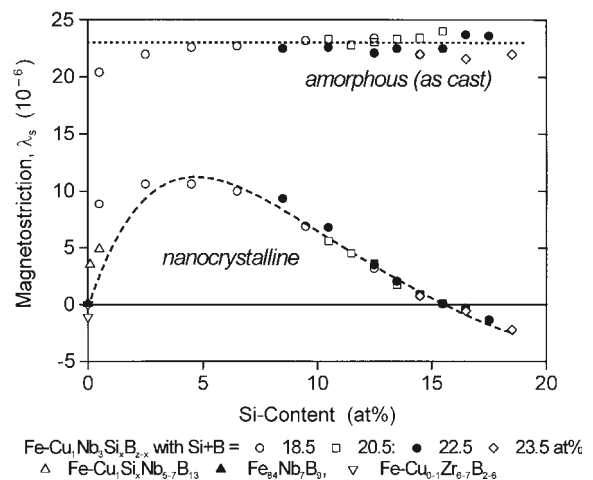
Figure 3
Saturation magnetostriction, λ_s, of Fe–Cu–Nb–Si–B alloys for the amorphous and nanocrystalline state as a function of silicon content.

for example, in Co(Fe)-based amorphous alloys. This is again a consequence of the averaging effect of exchange interaction for structural correlation lengths much smaller than the domain wall width. The situation thus contrasts with that for large-grained crystalline systems, where an average zero saturation magnetostriction does generally not imply stress-insensitivity of the hysteresis loop.

3. Applications

Another requirement for soft magnetic materials is that the shape of the hysteresis loop should be able to be varied according to the demands of various applications. Like in other soft magnetic materials, this can be realized in nanocrystalline alloys by magnetic field annealing, which induces an easy axis parallel to the applied field by atomic pair ordering. The resulting almost perfectly shaped loops indicate that the induced anisotropy clearly dominates over the other anisotropy contributions. Still, the anisotropy constant, K_u, can be tailored small enough in order to achieve the highest permeabilities (Fig. 4).

The anisotropy is primarily induced in the b.c.c. grains and depends upon the crystalline fraction, the silicon content, and the annealing conditions. In particular, the existence of a DO_3 superlattice structure at high silicon contents is the key factor such that K_u is relatively small despite of the high T_c. The kinetics of anisotropy formation is significantly slower than in the amorphous state. As a consequence, the nanocrystalline alloys exhibit an excellent thermal stability of their magnetic properties surpassing by far those of amorphous alloys and even permalloys, which allow elevated application temperatures up to about $150\,^{\circ}$C (see *Amorphous and Nanocrystalline Materials*).

The electrical resistivity of nanocrystalline materials is around $50\,\mu\Omega$cm for Fe–(Cu)–Zr–B alloys, but as high as $115\,\mu\Omega$cm in the case of Fe–Cu–Nb–Si–B alloys owing to the high silicon content in the b.c.c. grains. Combined with the low ribbon thickness inherent to the production process, this yields a favorable frequency dependence of permeability and low losses even at elevated frequencies, as in amorphous cobalt-based alloys.

The relatively inexpensive base composition (iron) and an established production technique coupled with the extraordinary combination of material properties discussed above means these materials can be used for a wide range of applications, such as magnetic cores for ground-fault interrupters, common mode chokes, and high-frequency transformers.

See also: Amorphous and Nanocrystalline Materials; Magnets, Soft and Hard: Magnetic Domains

Bibliography

Alben R, Becker J J, Chi M C 1978 Random anisotropy in amorphous ferromagnets. *J. Appl. Phys.* **49**, 1653–8

Buschow K H 1997 Magnetism and processing of permanent magnet materials. In: Buschow K H (ed.) *Handbook of Magnetic Materials*. Elsevier, Amsterdam, Vol. 10, pp. 463–593

Hasegawa N, Saito M 1991 Structural and soft magnetic properties of carbide-dispersed microcrystalline films with high thermal stability. In: *Proc. Int. Symp. 3d Transition–Semi Metal Thin Films, Magnetism and Processing*. Japan Society for the Promotion of Science, Sendai, Japan, pp. 165–74

Herzer G 1990 Grain size dependence of coercivity and permeability in nanocrystalline ferromagnets. *IEEE Trans. Magn.* **26**, 1397–402

Herzer G 1997 Nanocrystalline soft magnetic alloys. In: Buschow K H (ed.) *Handbook of Magnetic Materials*. Elsevier, Amsterdam, Vol. 10, pp. 415–62

Kneller E 1969 Fine particle theory. In: Berkowitz A E, Kneller E (eds.) *Magnetism and Metallurgy*. Academic Press, New York, pp. 365–471

Lachowicz H K, Slawska-Waniewska A 1994 Coexistence of various magnetic phases in nanocrystalline Fe-based metallic glasses. *J. Magn. Magn. Mat.* **133**, 238–42

Luborsky F E 1961 High coercive materials. *J. Appl. Phys.* **32**, 171S–83S

Pfeifer F, Radeloff C 1980 Soft magnetic Ni–Fe and Co–Fe alloys—some physical and metallurgical aspects. *J. Magn. Magn. Mat.* **19**, 190–207

Schäfer R, Hubert A, Herzer G 1991 Domain observation on nanocrystalline material. *J. Appl. Phys.* **69**, 5325–7

Suzuki K, Makino A, Inoue A, Masumoto T 1991 Soft magnetic properties of nanocrystalline bcc Fe–Zr–B and
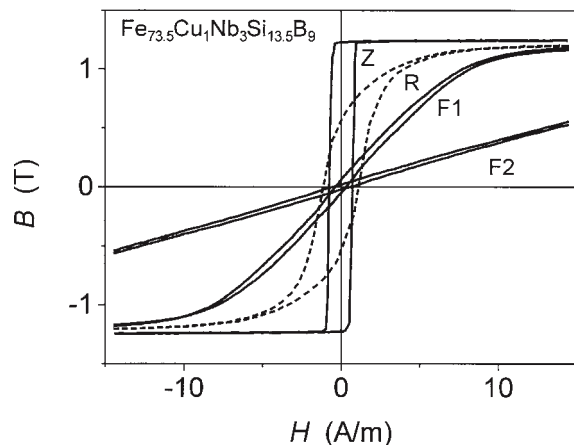
Figure 4
DC hysteresis loops of nanocrystalline Fe$_{73.5}$Cu$_1$Nb$_3$Si$_{13.5}$B$_9$ annealed for 1h at 540 $^{\circ}$C without (R) and with a magnetic field applied parallel (Z) and transverse (F2; $K_u = 20\,\mathrm{Jm^{-3}}$, $\mu = 30 \times 10^3$) to the magnetic path. Sample F1 ($K_u = 6\,\mathrm{Jm^{-3}}$, $\mu = 100 \times 10^3$) was first crystallized at 540 $^{\circ}$C and subsequently transverse field annealed at 350 $^{\circ}$C.

Fe-M–B–Cu (M = transition metal) alloys with high saturation magnetization. *J. Appl. Phys.* **70**, 6232–7

Yoshizawa Y, Oguma S, Yamauchi K 1988 New Fe-based soft magnetic alloys composed of ultrafine grain structure. *J. Appl. Phys.* **64**, 6044–6

G. Herzer
Vacuumschmelze GmbH, Hanau, Germany

Nanosized Particle Systems, Magnetometry on

New techniques for performing and interpreting magnetization measurements can be used on nanosized particle systems. In this article measurements using magnetometers such as a Faraday balance, SQUID, or vibrating sample magnetometer are considered. Their aim is to obtain information about the magnetic properties of the entire sample but also if possible about the system constituents—the particles. This article will focus on two measurement strategies.

First, the magnetization M ($B =$ const., T) is measured vs. temperature T at a constant external magnetic field B. Before the measurement the sample is placed in a (high) magnetic field to "prepare" a well-defined low-temperature magnetic state (LTMS). As an example of LTMS which can be "prepared" in a definite and reproducible way we introduce the new idea of PHFC (positive high-field cooling) which for particles exhibiting magnetic anisoptropy energy opens attractive possibilities for measuring the magnetic moment of the particles and their anisotropy energy. After reaching this LTMS a (weak) magnetic field is applied and the magnetization during the warming up process (field warming = FW) is recorded.

The susceptibility vs. temperature derived from adjacent FW magnetization curves $M(B, T)$ and $M(B + \Delta B, T)$ exhibits a maximum at a temperature determined only by the particles' magnetic moment and the mean field applied, i.e., $B + \Delta B/2$.

The theory of superparamagnetism is applicable after PHFC in the limit of high enough magnetic fields and leads to a simple formula allowing the determination of the magnetic moment of the particles without any calibration of the magnetometer. After the PHFC process the magnetic anisotropy energy influences the starting magnetization for each applied (low) magnetic field differently before the FW measurement.

Second, the magnetization $M(T =$ const., B) is measured vs. field at a constant temperature. Before this, the sample must be completely demagnetized. The initial magnetization curve is measured till reaching saturation. Subsequently, the hysteresis loop is measured. A useful criterion for the particle–particle interaction can easily be obtained relating the initial magnetization with the branches of the hysteresis loop.

1. Nanosized Single-domain Particles

Every modern textbook on magnetism (e.g., Craik 1995) deals with single-domain particles. The maximum size for such single-domain particles is determined by the so-called magnetic exchange length as summarized by Hernando (1999). From data obtained on popular ferromagnets it follows that this typical length scale is of the order of nanometers. Such nanosized particles considered in this article are of great technical importance because of their wide use in magnetic data storage technology.

1.1 Ideal Particle Systems

The properties of ideal particles considered in this article are as follows. All particles are single domain. The magnetization of one particle should (in a first approximation) be temperature independent. This means that the exchange coupling between the atoms inside the particle is very high. The magnetization of a particle will change its direction with respect to the particle body in a homogeneous way (coherent reversal). It will fluctuate like a single magnetic moment with a value of the order of $(10^4–10^5)\mu_B$. The particles do not exhibit any anisotropy energy (no easy axes of magnetization) and there is also no magnetic particle–particle interaction. Additionally it is assumed that the particles are all of the same size, i.e., no size distribution and therefore no distribution of particle magnetic moments. Such particle systems are superparamagnetic. For such particle systems there has for a long time existed a theory for their magnetic properties in thermodynamic equilibrium. Their magnetization will be described by the Langevin function considered later. The calculations presented in this article are performed with such ideal particle properties.

It has been shown that one of the features of real particle systems is that in the limiting case of high enough external magnetic fields this Langevin theory can be used to describe and evaluate their properties from measured magnetization and/or susceptibility curves (Hesse *et al.* 2000).

1.2 Stoner–Wohlfarth Particle Systems

A strong improvement in the physical understanding of the magnetic properties of particle systems can be achieved by introducing ideal particles with anisotropy energy, the Stoner–Wohlfarth model (Stoner and Wohlfarth 1948, Hesse *et al.* 2000).

The system may consist of particles with a homogeneous magnetization and a prolate ellipsoid shape. Without an external magnetic field the magnetization will point into the long direction (polar axis) of an ellipsoid of revolution. Both directions along this polar axis are equivalent. This fact is called uniaxial or bidirectional anisotropy (see *Magnetic Anisotropy*). From the shape of the particle there follows a difference in the magnetic stray dipole field energy when the magnetization is pointing parallel to the polar axis or perpendicular to it (see *Magnetic Layers: Anisotropy*). This anisotropy energy is described by the product KV where the constant K is the anisotropy energy density and V is the volume of the particle (Stoner and Wohlfarth 1948, Craik 1995, Hesse *et al.* 2002).

The angle-dependent part of the energy E concerning the particle's magnetization is given by a competition of the anisotropy energy (see *Magnetic Anisotropy*) and the Zeeman energy with maximum values KV and BM_0V, respectively. With a magnetic moment of the particle equal to $\mu = M_0V$ (M_0 is the saturation value of the magnetization) in the external magnetic field B and a fixed easy direction this energy becomes:

$$E(\alpha, \gamma) = -KV\cos^2(\gamma - \alpha) - M_0VB\cos(\alpha)B_{\text{switch}}$$
$$= \frac{2K}{M_0}; \qquad \gamma = 0 \qquad (1)$$

where α is the angle between the magnetization vector M of the particle and the applied magnetic field B, and γ represents the angle between the easy direction and B (see also Fig. 2, below). If $0 < B < B_{\text{switch}}$ the energy $E(\alpha,\gamma)$ in Eqn. (1) exhibits two minima where the deeper one corresponds to the parallel orientation of the magnetization vector to the external field. If $B > B_{\text{switch}}$ only one minimum exists and in thermal equilibrium all magnetization vectors point in the field direction. This situation will be used in the PHFC process described later.

1.3 Real Particle Systems

When performing magnetization measurements, experimentalists generally have to deal with real particle systems. Even if these particles satisfy the condition of being single domain, many complicating features in comparison to the ideal particles will appear from the following facts. There will be a distribution of particle sizes. As a consequence the system will exhibit a distribution of magnetic moments and a distribution of particle anisotropy energies. In the case of anisotropy there will be a distribution of easy axis orientations. Additionally, particle–particle interactions can be expected. The magnetization of a particle will not change its orientation by a uniform rotation process but will more or less perform a curling process (Aharony 1966).

All these complications will disturb the picture of an ideal superparamagnet. In real particle systems the magnetization of one particle will depend on temperature (internal particle excitations) which must be considered when the temperatures for magnetization measurements approach the Curie temperature of the particle material.

2. Basic Superparamagnetism

The basic theory of (super)paramagnetism deals with the magnetization $M(B, T)$ of a very large number of identical particles (number density per unit volume N) with a magnetic moment μ measured in the direction of an external magnetic field B in the state of thermodynamic equilibrium at a temperature T. For particles with large magnetic moments, the quantization of angular momentum can be neglected and therefore the Langevin function $L(x)$ can be used for describing the system. M_0 is the saturation value of the magnetization for $T \to 0$ or $B \to \infty$ and

$$x = \frac{\mu B}{k_B T} \equiv \frac{T_{\text{B-field}}}{T}$$

All relevant formulas are summarized as follows:

$$M(T, B) = M_0 L(x);$$
$$M_0 = \mu N L(x) = \coth(x) - \frac{1}{x};$$
$$x = \frac{\mu B}{k_B T} \equiv \frac{T_{\text{B-field}}}{T} \qquad (2)$$

In the following examples experiments on real particle systems (described in detail in Hesse *et al.* 2000, 2002) will be presented. The results are compared with calculations based on the Langevin paramagnetism. The parameters assumed for calculations are chosen to be close to the properties of the real particle system. For simplicity the following abbreviations are introduced: in cases where the anisotropy energy KV is in competition with the magnetic energy $\mu B = M_0VB$ we use their temperature equivalents defined as $KV = k_B T_{\text{aniso}}$ and $\mu B = k_B T_{\text{B-field}}$.

3. Susceptibility Versus Temperature

Besides the magnetization, the susceptibility is a very important and informative quantity. If the system in question is in thermodynamic equilibrium at the temperature T in the magnetic field B the susceptibility χ is a measure of the change of magnetization when we increase the magnetic field by an amount ΔB. In the exact mathematical limit ΔB must tend to zero. In laboratory practice a finite small ΔB can be accepted. Then, the susceptibility χ_{lab} is obtained. The dimensionless susceptibility is in the case of the

Langevin function describing the paramagnetism accompanied by a susceptibility function $H(x)$. The theory is summarized in the following equations:

$$\chi(T, B = B_{\text{applied}}) = \mu_0 \lim_{\Delta B \to 0} \left[\frac{M(T, B + \Delta B) - M(B)}{\Delta B} \right]$$

$$\chi(T, B = B_{\text{applied}}) = \mu_0 \left[\frac{\partial M}{\partial B} \right]_{B=B_{\text{applied}}} = \mu_0 \frac{\mu N}{B}$$

$$\begin{aligned} H(x) H(x) &= x \left\{ \left[1 - (\coth x)^2 \right] \right. \\ &\quad \left. + \left(\frac{1}{x} \right)^2 \right\} \chi_{\text{lab}} \left(T, B + \frac{\Delta B}{2} \right) \\ &= \mu_0 \left[\frac{M(T, B + \Delta B) - M(B)}{\Delta B} \right] \\ &\quad \times \chi_{\text{initial}}(T) = \chi(T, B_{\text{applied}} = 0) \\ &= \mu_0 \left[\frac{\Delta M}{\Delta B} \right]_{B=0} \end{aligned} \quad (3)$$

Considering the course of the susceptibility vs. temperature T (at constant magnetic field B) it is obvious that this function exhibits a maximum. This maximum corresponds to a temperature T_{max}. This fact is not well known because for "classic" paramagnets with atomic moments of the order of one Bohr magneton and an external magnetic field of 1 T we expect $T_{\text{max}} = 0.35$ K. Kunkel *et al.* (1988) demonstrated the existence of a maximum in experiments on paramagnets exhibiting magnetic moments of the order of 1 μ_B by performing measurements in high magnetic fields.

The situation changes dramatically if we consider modern nanosized materials with magnetic particles exhibiting moments of the order of $(10^4 - 10^5)\mu_B$. From the properties of the susceptibility function $H(x)$ it follows that

$$1.9 k_B T_{\text{max}} = \mu B \frac{T_{\text{max}}}{[K]} = n \frac{\mu_{\text{Bohr}}}{1.9 k_B} \frac{B}{[T]} = 0.354 n \frac{B}{[T]} \quad (4)$$

where the square brackets [ ] serve to indicate that the units used to measure temperature and field are kelvin and tesla, respectively. The (dimensionless) number of Bohr magnetons is indicated by n. For example, if $n = 10^5$ and $B = 1$ mT we find $T_{\text{max}} = 35.4$ K. Of course, T_{max} is proportional to the magnetic field applied. A useful feature of the formula is that it allows the determination of the particles' magnetic moment from T_{max} without any calibration of the magnetometer.

This simple and valuable law holds for ideal paramagnets, for particles without any anisotropy energy, without interaction, and without any size distribution. Can such a theory be of value for real particle systems, for real experiments? It has been shown (Hesse *et al.* 2000) that in the limit of high applied external magnetic fields the theory of ideal superparamagnets becomes applicable. To achieve this it is necessary to prepare the low-temperature magnetic state (LTMS) of the particle system in a quasiparamagnetic state by the process of positive high-field cooling (PHFC).

4. The Positive High-field Cooling Process and the Quasi-paramagnetic Low-temperature State

As mentioned above, the particles considered must be fixed in space. We cool down the sample to low temperatures in an applied field $B > B_{\text{switch}}$ starting from high temperatures. The result is that all magnetic moments are pointing parallel to the external magnetic field (in the positive direction). For the magnetization measurement we lower the field value to $B_{\text{low}} < B_{\text{switch}}$ and start the FW (field warming) process. As a consequence of the PHFC the projections of all magnetic moments show a component in the (positive) field direction.

This way the blocking behavior is eliminated. Heating up this LTMS persists up to rather high temperatures, which exceed the usual blocking temperature due to the stabilization of the magnetic moment direction by the magnetic field. Such LTMS is named the quasiparamagnetic state.

After the PHFC process performing FW magnetization measurements in different B_{low} magnetic fields the maxima in the susceptibility (Fig. 1) and the particles' anisotropy energy (Fig. 3) become visible. In Fig. 1(a) two calculated magnetization curves $M(B)$ and $M(B + \Delta B)$ vs. temperature are presented. The resulting susceptibility is derived as χ_{lab} from the difference $(M(B + \Delta B) - M(B))$ and clearly shows the expected maximum. In the calculation a magnetic moment of $\mu = 10^4 \mu_B$ was assumed, together with $B = 15$ mT and $B + \Delta B = 18$ mT corresponding to values of $T_{B-\text{field}}$ of 100 K and 120 K, respectively. In Fig. 1(b) results of measurements performed on nickel nanoparticles fixed in an aluminum oxide matrix are presented. The susceptibility was derived from adjacent curves of magnetization. One can clearly observe the maximum of the susceptibility and its shift towards higher temperatures with increasing magnetic field. The details are described by Hesse *et al.* 2000).

5. Magnetization and Anisotropy

Next it will be shown that the PHFC process offers a rather simple way to measure the particles' magnetic anisotropy energy. For simplicity in the first step it is assumed that the sample is textured. This means that all particles are oriented parallel to each other with respect to their easy axis of magnetization. All the easy axes have the same angle with respect to the magnetic field (Fig. 2). The Stoner–Wohlfarth model is chosen
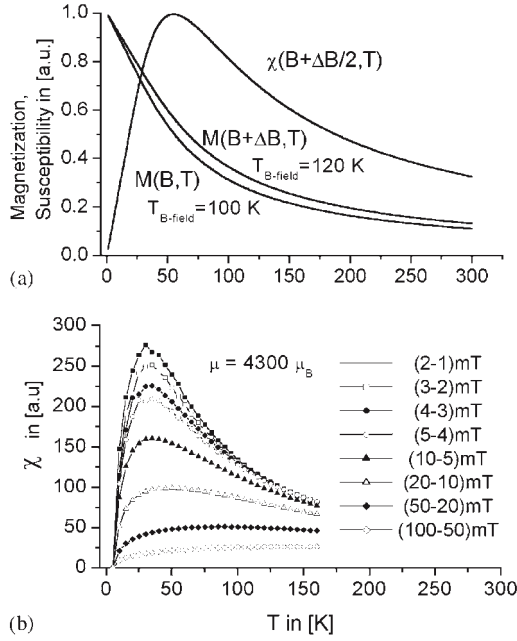
Figure 1
(a) Calculated magnetization $M(B)$ and $M(B + \Delta B)$ vs. temperature and the resulting susceptibility exhibiting a maximum. In the calculation a magnetic moment of $\mu = 10^4 \mu_B$ and $B = 15$ mT, $B + \Delta B = 18$ mT were assumed corresponding to $T_{B-field}$ of 100 K and 120 K, respectively. (b) The susceptibility χ_{Lab} derived from FW magnetization measurements after PHFC (presented in Fig. 3) performed on nickel nanoparticles. The field differences used for χ_{lab} calculations are indicated. The maximum of the susceptibility and its shift with increasing magnetic field towards higher temperatures can be observed. The sample details are described by Hesse *et al.* (2000).

Figure 2
The vector model to explain the influence of the anisotropy after the PHFC process in the quasiparamagnetic state. (a) A Stoner–Wohlfarth particle with its easy direction, the external magnetic field B, and the equilibrium position of the particle's magnetization vector. (b) Here the anisotropy energy is replaced by an anisotropy field. The resulting magnetic field acting in the direction of the particle's magnetization vector can be calculated using Eqns. (5).

for a more detailed description. If the angle between the applied external magnetic field and the easy axis is γ, the projection of the magnetization vector at very low temperature along the applied magnetic field (in the quasiparamagnetic state) becomes $M_0 \cos \alpha$ (see Fig. 2). In order to calculate the temperature dependence of the magnetization observed in the following FW process intuitive formulae (Eqns. (5)) are proposed. Here a function $L^*(x)$ is used:

$$
\begin{aligned}
M(B, T) &= N\mu \cos(\alpha) L^* \left(\frac{\mu B_{res}}{k_B T} \right) B_{res} \\
&= \sqrt{(B + B_{aniso} \cos\gamma)^2 + (B_{aniso} \sin\gamma)^2} \cos\alpha \\
&= \frac{B + B_{aniso} \cos\gamma}{\sqrt{(B + B_{aniso} \cos\gamma)^2 + (B_{aniso} \sin\gamma)^2}} \mu B_{aniso} \\
&= k_B T_{aniso} = KV
\end{aligned}
\tag{5}
$$

The anisotropy influence (after PHFC) is taken into account by an anisotropy field B_{aniso}. The influence of the anisotropy energy is represented by two factors, the anisotropy field B_{aniso} and the angle γ between the applied external magnetic field and the easy axis. The thermal fluctuation of the magnetization vectors will be described by a Langevin-like function $L^*(x)$ labelled with an asterisk. This asterisk means that this function is not identical to $L(x)$ defined in Eqn. (2). It is necessary to take into consideration thermal fluctuations of the magnetization vector within a limited range of angles due to the confinement of the magnetization vector in the potential minimum caused by the anisotropy energy. In addition, "back jumps" of the magnetization vector into the second energy minimum (where the magnetization vector has a negative component with respect to the applied magnetic field) must be considered.

In Fig. 3(a) calculated magnetization curves are presented using $L(x)$ instead of the analytically unknown $L^*(x)$. The experimental results presented

(a)

(b)
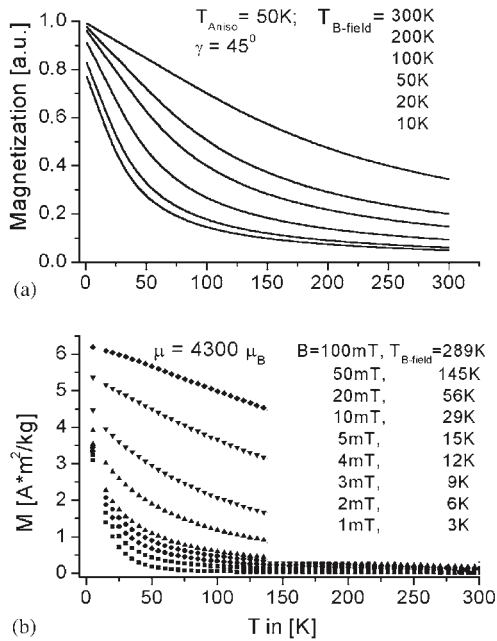
Figure 3
(a) Calculated magnetization M versus temperature for a Stoner–Wohlfarth particle system with easy axes oriented at 45° with respect to the magnetic field applied. The field values and the particle anisotropy are given in equivalent temperatures as defined in the text. (b) The FW magnetization measured after PHFC on nickel nanoparticles in the fields indicated. $T_{B-field}$ also is given calculated for particles with $\mu = 4300\mu_B$. The offsets in the lowest temperature value of the magnetization due to the anisotropy can be observed. The sample details are described by Hesse *et al.* (2000).

in Fig. 3(b) prove the validity of this approach. A Stoner–Wohlfarth particle system with easy axes oriented at 45° with respect to the magnetic field applied was assumed. The field values and the particle anisotropy are given in equivalent temperatures as defined in the text. In the lower part of Fig. 3(b) the magnetization measured on nickel nanoparticles after PHFC in the fields indicated (and their equivalent temperatures) are presented. One can clearly observe offsets in the magnetization values due to the presence of anisotropy. Details are described by Hesse *et al.* 2000).

6. The Hysteresis Loop

Using the property that a Stoner–Wohlfarth particle has no explicit initial magnetization curve, Thamm and Hesse (1996) proposed an alternative method to the well known Henkel plot (Henkel 1964) in order to study the interactions between single–domain

particles. This proposal is justified exactly for particles with uniaxial anisotropy. For such systems it is only necessary to measure first the initial magnetization curve of the completely demagnetized sample and then the hysteresis loop (see *Magnetic Hysteresis*). In an ensemble of a large number of spatially fixed noninteracting particles with uniaxial anisotropy and randomly distributed easy axes, there are always pairs of particles with magnetization vectors in opposite directions. The resulting normalized hysteresis loop of such a pair represents the mean value caused by the summation of the magnetization of each particle. As a consequence an initial curve m_{IC} will appear which is exactly half of the sum of the upper m_{UC} and the lower branch m_{LC}:

$$m_{IC} = \tfrac{1}{2}(m_{LC} + m_{UC})\quad \Delta m = m_{IC} - \tfrac{1}{2}(m_{LC} + m_{UC}) \quad (6)$$

Δm is zero for noninteracting Stoner–Wohlfarth particles.

A finite value of Δm may be caused by interactions between the particles or by the violation of the criteria for Stoner–Wohlfarth particles. An example presenting a measured initial magnetization curve together with the hysteresis loop is given in Fig. 4. The details are

(a)

(b)
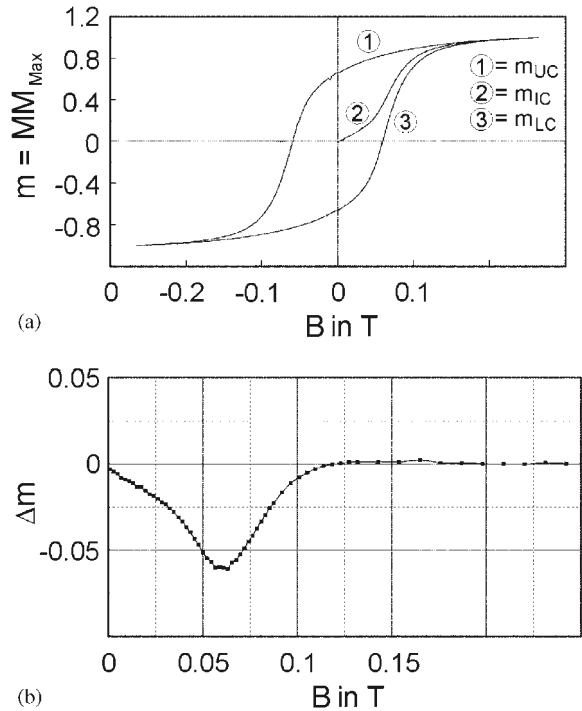
Figure 4
(a) Measured (normalized) initial magnetization curve together with the hysteresis loop. (b) The Thamm–Hesse plot as derived from the measurement in the upper part indicating particle–particle interaction.

described by Thamm and Hesse 1998. There is still no general theoretical justification for Δm in the case of particles with multiaxial anisotropy energy. Nevertheless a nonzero deviation Δm and its dependence on the applied magnetic field $\Delta m(B)$ will bear information about the particle–particle interaction. The dependence of $\Delta m(B)$ can be derived from one measured initial magnetization curve and the hysteresis loop, which is much faster and easier to do than the measurement of the rather popular Henkel plot (Henkel 1964), which hides the field dependence of Δm.

7. Concluding Remarks

Nanosized single-domain magnetic particles open new possibilities in performing and interpreting magnetization measurements. If the particles are fixed in space and exhibit magnetic anisotropy energy it is possible to bring them into a well-defined new low-temperature magnetic state. This can be achieved by the PHFC process. After that the particle's magnetization possesses a component pointing parallel to the applied magnetic field. This LTMS is called quasiparamagnetic. When measuring the magnetization versus temperature in a constant (weak) external magnetic field starting at low temperatures from a quasiparamagnetic state, the susceptibility exhibits a maximum. From the temperature of this maximum a direct determination of the (mean) particle magnetic moment is possible without any calibration. In the magnetization values measured for the LTMS in different (weak) magnetic fields the anisotropy becomes visible and can be determined. This new technique of performing magnetic measurements will enable experimentalists to distinguish between reversible superparamagnetic and irreversible or thermally stable behavior as reported by Chantrell *et al.* (2000).

All measurement procedures and considerations will hold for modern artificially produced arrays of particles or for systems exhibiting self-organized structures as well. Here a large variety of measurement possibilities will appear depending on the direction of the sample with respect to the magnetic field used for the PHFC process.

In the case when the hysteresis loop is measured at constant temperature it is recommended to start the measurement from a completely demagnetized state of the sample. Then the initial magnetization curve must be determined first and subsequently both branches of the hysteresis loop. A simple and useful criterion for the particle–particle interaction can be obtained by plotting the deviation Δm vs. applied magnetic field.

See also: Ferrofluids: Introduction; Magnetic Recording Materials: Tape Particles, Magnetic Properties; Magnetic Recording Technologies: Overview; Nanocrystalline Materials: Magnetism; Thin Films: Domain Formation

Bibliography

Aharony A 1966 Magnetization curling. *Phys. Stat. Solidi* **16**, 3–42

Chantrell R W, Walmsley N, Gore J, Maylin M 2000 Calculation of the susceptibility of interacting superparamagnetic particles. *Phys. Rev. B* **63**, 024410 (1-14)

Craik D 1995 *Magnetism—Principles and Applications*. Wiley, Chichester, UK

Henkel O 1964 Remanenzverhalten und Wechselwirkungen in hartmagnetischen Teilchenkollektiven. *Phys. Stat. Solidi* **7**, 919–29

Hernando A 1999 Magnetic properties and spin disorder in nanocrystalline materials. *J. Phys.: Condens. Matter* **11**, 9455–82

Hesse J, Bremers H, Hupe O, Veith M, Fritscher E W, Valtchev K 2000 Different susceptibilities of nanosized single-domain particles derived from magnetization measurements. *J. Magn. Magn. Mater.* **212**, 153–67

Hesse J, Pütter S, Michele O, Bremers H, Hupe O, Hartung H, Eichler M 2002 Probing magnetism of nanosized single domain particle systems. *Phys. Stat. Solidi (a)* **189**, 481–94

Kunkel H P, Roshko R M, Williams G 1988 Field-dependent susceptibility of a paramagnet. *Phys. Rev. B* **37**, 5880–3

Stoner E C, Wohlfarth E P 1948 A mechanism of magnetic hysteresis in heterogeneous alloys. *Philos. Trans. R. Soc. London* **240A**, 599–642

Thamm S, Hesse J 1996 A simple plot indicating interactions between single-domain particles. *J. Magn. Magn. Mater.* **154**, 254–62

Thamm S, Hesse J 1998 The remanence of a Stoner–Wohlfarth particle ensemble as a function of the demagnetization process. *J. Magn. Magn. Mater.* **184**, 245–55

J. Hesse
Technische Universität Braunschweig, Germany

NDT Techniques: Magnetic

Recent years have seen rapid developments in the use of magnetic measurement techniques for materials evaluation. These range from the use of macroscopic hysteresis measurements through microscopic Barkhausen effect measurements down to nanometer scale magnetic force microscopy. Magnetic methods can be used to address two main classes of problems in materials evaluation: detection of defects, and determination of intrinsic properties. It is now one of the fastest-developing fields in materials evaluation due in part to the development of computer models that have made it possible to interpret the results of magnetic measurements in terms of changes in stress or in the structure of materials.

1. Macroscopic Scale: Magnetic Hysteresis

On the macroscopic scale, all ferromagnetic materials exhibit hysteresis in the variation of flux density B

with magnetic field H (Jiles 1998). The hysteretic properties such as permeability, coercivity, remanence, and hysteresis loss are known to be sensitive to stress, strain, grain size, heat treatment, and the presence of a second phase. In addition, the measurement of hysteresis yields a number of independent parameters, each of which changes to some degree with stress, strain, and microstructure. Since several independent parameters are needed in general to separate effects of stress from microstructure, hysteresis measurements are ideally suited for materials evaluation because the necessary parameters can be obtained from a single measurement.

The effects of elastic stress on hysteresis have been reported by a number of investigators. Stress changes the shape of the hysteresis loop as shown in Fig. 1. However, interpretation of results is difficult without a working model of hysteresis, since none of the direct hysteresis parameters such as coercivity, remanence, initial permeability, or hysteresis loss is uniquely related to a single physical property. It is clear that any model used for interpretation of nondestructive evaluation results such as effects of stress, elastic and plastic strain, creep and fatigue should have as few

parameters as is reasonably possible. The stress or strain dependence of these parameters can then be determined. Some success has been achieved with a magneto-mechanical model based on an effective field due to stress (Sablik *et al.* 1993) and this can be used to predict and interpret the magnetic hysteresis properties under stress.

2. Microscopic Scale: Barkhausen Effect

On the microscopic scale the magnetic Barkhausen effect (MBE) consists of discontinuous changes in flux density, known as Barkhausen jumps, as shown in Fig. 2. These are caused by sudden irreversible motion of magnetic domain walls when they break away from pinning sites as the magnetic field H changes. There are five mechanisms by which MBE is caused: (i) discontinuous, irreversible domain wall motion; (ii) discontinuous rotation within a domain; (iii) appearance and disappearance of Néel peaks; (iv) inversion of magnetization in single-domain particles; (v) displacement of Bloch or Néel lines in two 180° walls with oppositely directed magnetizations.
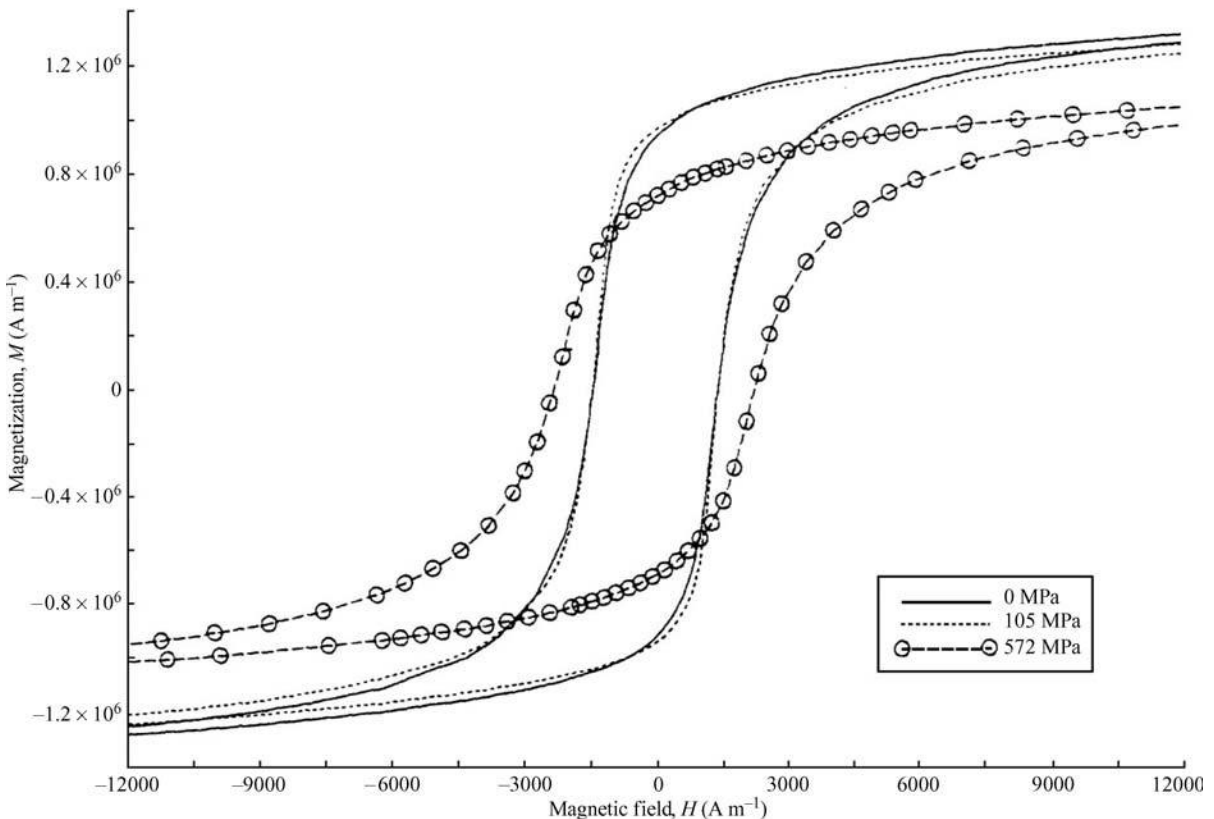
Figure 1
Changes in the hysteresis curve caused by stress (after Makar and Tanner 1998).
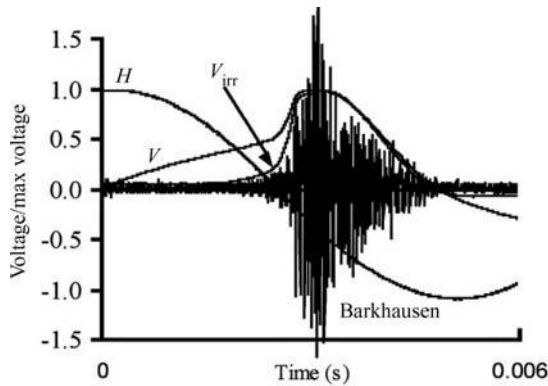
Figure 2
Barkhausen signal shown as voltage against time. The time dependence of magnetic field H, voltage in flux coil V, and envelope of irreversible component of voltage in flux coil V_{irr} are also shown on the same time scale.

The Barkhausen pulse height distribution is dependent on stress and the number density and nature of pinning sites within the material (Mandal *et al.* 1999). The pinning sites are inhomogeneities in the material such as grain boundaries, dislocations, or precipitates of a second phase with different magnetic properties from the matrix material. Most Barkhausen activity occurs close to the coercive field H_c. Double peaks in the count rate can occur and the location and size of the peaks can shift as a result of changes in the defect distribution so that two specimens of the same material with different defect distributions have different Barkhausen spectra.

Barkhausen signals are sensitive to stress as shown in Fig. 3. MBE measurements are used for the nondestructive evaluation of stress. All ferromagnetic NDE methods are sensitive to both mechanical stress and the microstructure of the material and therefore, in order to determine stress, it is necessary to use several independent measurement parameters. It has been found that Barkhausen effect, incremental permeability, X-ray diffraction, and hardness measurements were successful in estimating residual stress. Changes in the density of dislocations affect the MBE signals and MBE can be used to distinguish between microstructures, which cannot be distinguished on the basis of optical microscopy.

The effect of fatigue by cyclic loading on the root mean square value of MBE signals has shown that residual strains in unloaded specimens could be identified, although changes occurring under fatigue cycling were complicated so that the Barkhausen signals could not be simply related to the applied load. However, the median Barkhausen pulse amplitude can be used to assess whether the applied stress amplitude is above or below the fatigue limit.
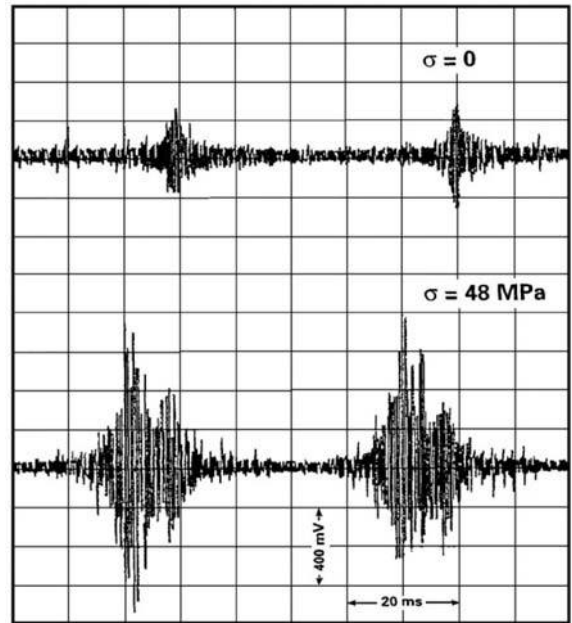
Figure 3
Changes in Barkhausen emissions as a result of applied tensile stress.

3. Nanoscopic Scale: Magnetic Force Microscopy

In order to evaluate the variation of materials properties from one location to the next, magnetic imaging techniques can be used. For example, the variation of magnetic field strength across the surface of a material can be used to produce a two-dimensional image. This could be used to identify unusual regions of a material, which may have defects or be otherwise damaged, or simply to investigate the spatial variation of magnetization.

The magnetic force microscope samples the magnetic field gradients close to the surface of the specimen over a scanning range of typically $10–100\,\mu m$. The method (see *Magnetic Force Microscopy*) is basically a scanning force probe technique detecting magnetic forces between the magnetized tip of the microscope and a test specimen, as shown in Fig. 4. The magnetic force microscope can be used to detect both static and dynamic magnetic fields on the surface of a specimen. In the original device, a spatial resolution of 100 nm was demonstrated. Today, spatial resolutions of 50 nm are routine, and claims of resolutions down to 10 nm are made in some cases (Dahlberg and Proksch 1999). This method is therefore useful for characterizing magnetic materials on length scales from typically 10 nm up to $100\,\mu m$.

The image formed as a result of magnetic force microscopy is obtained by measuring the force or the
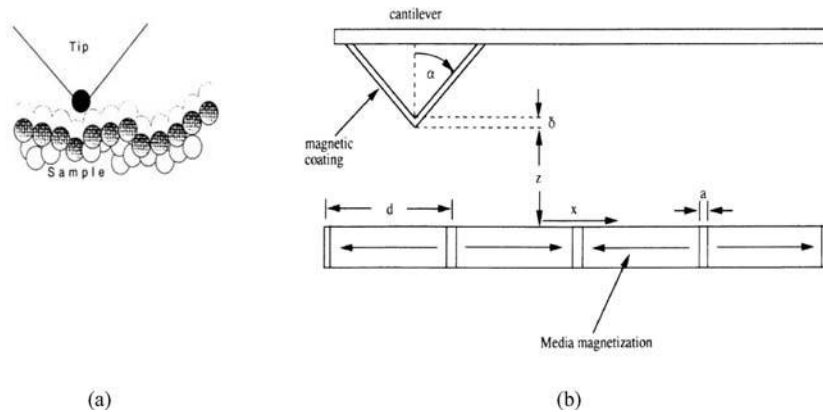
Figure 4
(a) Magnetic probe tip scanning over the surface of a material. (b) Schematic of the cantilever arrangement supporting the probe tip.

force gradient. The images formed can be used to study magnetic structures such as domain walls, closure domains, Bloch lines and, in the case of magnetic recording media, intentionally magnetized regions of a material. It is in the area of magnetic recording media that the magnetic force microscope is finding most applications. The ability to resolve features at length scales down to 50 nm, with little or no surface preparation required, and under ambient atmosphere conditions makes this technique ideal for practical high-resolution magnetic evaluation of material surfaces.

4. Conclusions

The increasing demand for characterization of magnetic materials indicates that there will be a continual growth of interest in the available magnetic evaluation methods in the next few years. A variety of magnetic methods for characterization and evaluation of materials is available. Some techniques are designed to determine intrinsic properties of materials and these include the Barkhausen effect for surface characterization and hysteresis measurements for determination of bulk properties. These methods all offer wide scope for future development because of their sensitivity to material treatment, particularly the presence of different material phases, chemical composition and material deformation in its various forms: elastic and plastic strain, fatigue, dislocation density, and creep stress. Another major group of magnetic techniques has been developed to detect and characterize inhomogeneities, including defects, in materials. These techniques include such methods as magnetic particle inspection, magnetic flux leakage determination, and magnetic force microscopy. Magnetic force microscopy, an ultra high-resolution imaging method, can be used to produce an image of the magnetic field at the surface of a test specimen with resolutions down to 10 nm.

See also: SQUIDs: Nondestructive Testing

Bibliography

Dahlberg E D, Proksch R 1999 Magnetic microscopies: the new additions. *J. Magn. Magn. Mater.* **200**, 720
Jiles D C 1998 *Introduction to Magnetism and Magnetic Materials.* Chapman and Hall, London
Magni A, Beatrice C, Durin G, Bertotti G 1999 Stochastic theory of hysteresis. *Br. J. Appl. Phys.* **86**, 3253
Makar J M, Tanner B K 1998 The effect of stresses approaching and exceeding the yield point on the magnetic properties of high strength pearlitic steels. *NDT&E Int.* **31**, 117
Mandal K, Dufour D, Atherton D L 1999 Use of magnetic Barkhausen effect noise and magnetic flux leakage signals for analysis of defects in pipeline steel. *IEEE Trans. Magn.* **35**, 2007
Sablik M J, Rubin S W, Riley L A, Jiles D C, Kaminski D A, Biner S B 1993 A model for hysteretic magnetic properties under the application of noncoaxial stress and field. *Br. J. Appl. Phys.* **74**, 480

D. C. Jiles
Iowa State University, Ames, Iowa, USA

Non-Fermi Liquid Behavior: Quantum Phase Transitions

The Landau theory of Fermi liquids has been very successful in describing even complex metals such as heavy-fermion systems. However, under certain conditions this model is not capable of explaining the observed thermodynamic and transport properties of metals. Several origins of such non-Fermi liquid behavior are possible, e.g., a magnetic instability leading

to a quantum phase transition, or single-ion effects as the multichannel Kondo effect or a distribution of Kondo temperatures.

1. Classical and Quantum Phase Transitions

Magnetic phase transitions—like many other types of phase transition (PT)—are usually observed by varying the temperature (T) and monitoring changes in thermodynamic quantities like the magnetic susceptibility, the specific heat, or other properties (see *Magnetism in Solids: General Introduction*). Second-order transitions where the first derivatives of the free energy (i.e., the magnetization or entropy) vary continuously are strongly influenced by thermal fluctuations. These fluctuations determine how, at the critical temperature (T_c), the system goes from a disordered state for $T > T_c$, to a magnetically ordered state at $T < T_c$. The fluctuations diverge spatially as T_c is approached, as characterized by the correlation length ($\xi \sim |T - T_c|^{-\nu}$) with a critical exponent (ν), and have a typical lifetime given by $\tau \sim \xi^z$, where z is called the dynamical critical exponent.

Renormalization group theory predicts that the static properties near a PT depend only on a few parameters, namely the spatial dimension of the system (d), the symmetry of the order parameter (OP), and the range of the interaction leading to magnetic order. These parameters determine the universality class of the system. For magnetic systems, the OP is usually the spontaneous magnetization—for antiferromagnets and incommensurate magnets, the staggered magnetization—which is zero above T_c and acquires a finite value below T_c. In many cases, e.g., when the magnetic moments are spatially localized, the symmetry of the OP is described completely by the number (n) of its components, i.e., $n = 1$ (Ising model), $n = 2$ (XY model), or $n = 3$ (Heisenberg model).

While the critical behavior of static properties such as the specific heat or magnetization for these examples is entirely determined by the universality classes, the dynamic behavior within a given class may differ depending on z. Fluctuations can actually suppress a PT altogether; the easier it is to generate fluctuations (i.e., the larger n is), the more PT is suppressed. A PT to long-range order is only possible above a lower critical dimension (d_L) where $d_L = 2$ for $n = 3$, $d_L = 2$ for $n = 2$, and $d_L = 1$ for $n = 1$. (For $n = 2$ and $d = 2$ a special type of PT, the Kosterlitz–Thouless transition, exists.) On the other hand, there is an upper critical dimension (d_U) above which fluctuations in local-moment systems are deemed unimportant because they effectively average out (with $d_U = 4$ for a wide range of models). In general, for $d > d_U$, mean field theory (MFT) is sufficient to describe the PT.

In certain cases, T_c can be driven to zero by some external parameter (δ). The picture of a "classical" phase transition (CPT) has to be modified when T_c

vanishes at a critical value δ_c. At $T = 0$, only quantum fluctuations are possible—for instance at the transition from a paramagnet to an ordered magnet. For such a quantum phase transition (QPT), the relevant length scales and time scales of these fluctuations are coupled via the uncertainty principle, leading to the time entering as additional z dimensions. Formally, the inverse temperature corresponds to an imaginary time, hence the system acquires its full effective dimensionality ($d_{eff} = d + z$) only at $T = 0$ (Sondhi *et al.* 1997). The added time dimensions drive the system towards mean field behavior, where above $d_{eff} = 4$ only Gaussian fluctuations are observed and genuine critical behavior is absent. However, the static properties in all cases of a QPT are influenced by z. This leads to a behavior even at finite T close to δ_c, which is distinctly different from that at a CPT. A particularly interesting QPT is that depicted in Fig. 1 where an itinerant electron system is driven towards (or away from) magnetic order by δ. While far from δ_c, the low-temperature properties of the system can be described in the framework of a Fermi liquid (see *Heavy-Fermion Systems*), unusual "non-Fermi liquid" (NFL) behavior is observed at finite T around δ_c. This QPT has been observed in weakly magnetic transition metal compounds (Sect. 2.2) and in heavy-fermion systems based on rare earths or actinides (Sect. 2.3). On the other hand, NFL behavior in metals does not necessarily arise from proximity to a magnetic instability. Single-ion effects such as the multichannel Kondo effect (Sect. 3.1) or a distribution of Kondo temperatures (Sect. 3.2) may also lead to NFL-like properties.

An example of a QPT in an insulating solid is provided by the dipolar-coupled Ising magnet, e.g., $LiHo_xY_{1-x}F_4$, in a transverse magnetic field (Rosenbaum 1996).
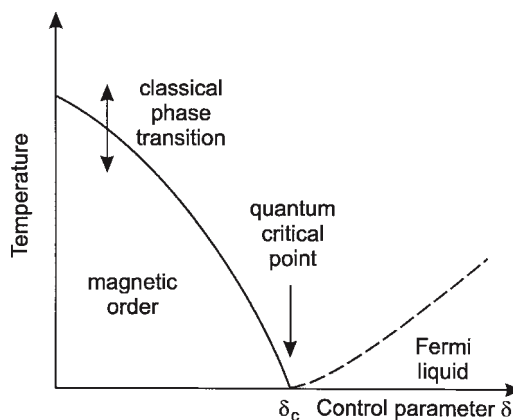
Figure 1
Schematic phase diagram of a metal with an instability towards magnetic order driven by a control parameter (δ) which may be pressure or composition.

2. Quantum Phase Transitions and Non-Fermi Liquid Behavior in Metallic Magnets

2.1 Fermi Liquids

In a metal, the conduction electrons interact with each other due to their Coulomb repulsion. At the same time, there is a strong correlation by virtue of the Pauli priniciple, which states that two electrons (or, more generally, two indistinguishable fermions, i.e., particles with half-integer spin) cannot be in the same quantum state. Much of the complexity of the interacting system may be captured in terms of the physics of a non-interacting electron gas. For $kT \ll E_F$, the specific heat of a non-interacting electron system is given by $C = \gamma_0 T$ with $\gamma_0 = (\pi^2 k^2 / 3) N(E_F)$ where $N(E_F)$ is the density of levels at the Fermi energy E_F and k the Boltzmann constant.

The Pauli spin susceptibility is independent of T, $\chi_0 = \mu_0 \mu_B^2 N(E_F)$ where $\mu_0 = 4\pi \times 10^{-7}$ Vs/Am and μ_B is the Bohr magneton. The contribution to the electrical resistivity due to electron–electron (e–e) scattering is given by $\rho_{e-e} = c \times (kT/E_F)^2$ where c is a microscopic scattering cross section.

Assuming a one-to-one correspondence between the excitations of an interacting electron system (termed "quasiparticles") and of the non-interacting electron gas, Landau postulated that the low-T properties for the interacting system obey the same laws as for the Fermi gas, with a renormalized effective mass m^* (with respect to the free-electron mass m_0) and a few additional parameters taking account of the residual interactions among the quasiparticles. This special case of an interacting electron system that can be obtained from the non-interacting Fermi gas by adiabatically turning on the interaction, is called a (Landau) Fermi liquid. In such a Fermi liquid (FL), the specific heat is given by $C = \gamma T = (m^*/m_0)\gamma_0 T$, the spin susceptibility by $\chi = \chi_0 (m^*/m_0)(1 + F_0^a)$ where F_0^a is an additional Landau parameter, and the resistivity ρ_{e-e} is again $\sim (kT/E_F)^2$ where E_F may be modified due to the interactions.

2.2 Weak Itinerant Magnets

Besides the traditional itinerant magnets like Fe, Co, Ni with rather large Curie temperatures T_c and ordered magnetic moments of the order of $1\mu_B$, there exist a number of intermetallic transition metal compounds and alloys with low T_c and ordered moments of only a small fraction of $1\mu_B$ (see *Itinerant Electron Systems: Magnetism (Ferromagnetism)*). ExaN 1mples of these weak itinerant magnets are MnSi, ZrZn$_2$, and YMn$_2$. In some of these materials, the magnetic order can be suppressed by hydrostatic pressure (p) which serves as a control parameter (cf. Fig. 1). Figure 2 shows, as an example, resistivity data for MnSi, which at ambient pressure is an incommensurate magnet with $T_c = 30$ K. Because of the
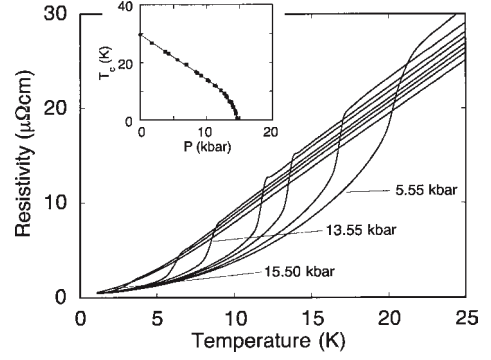
Figure 2
Resistivity $\rho(T)$ of MnSi at various pressures p. Inset shows the magnetic transitions temperature $T_c(p)$ as obtained from the kink in $\rho(T)$ (adapted by permission of American Physical Society from *Phys. Rev. B*, 1997, **55**, 8330–8).

large $2\pi/Q$ ($= 190$ Å), MnSi is often described as an effective ferromagnet (FM).

The onset of magnetic order is seen as a kink in the electrical resistivity $\rho(T)$ (Fig. 2) (Pfleiderer *et al.* 1997). T_c falls monotonically with p and tends to zero at $p_c = 14.6$ kbar, the critical pressure of the magnetic QPT. For $p > p_c$, $\rho(T) = \rho_0 + \beta T^m$ with m between 1.5 and 1.6 is observed over a large T range. This NFL-like behavior ($m < 2$) arises from a long-range interaction between quasiparticles, mediated by overdamped spin fluctuations. Assuming a space- and time-dependent magnetization $\mathbf{m}(\mathbf{r}, t)$, which is treated as a molecular field, the imaginary part of the susceptibility is given by:

$$\chi''(\boldsymbol{q}, \omega) = \omega \chi_{\boldsymbol{q}} \Gamma_{\boldsymbol{q}} / (\omega^2 + \Gamma_{\boldsymbol{q}}^2) \tag{1}$$

where $\Gamma_{\boldsymbol{q}}$ describes the temporal relaxation rate of the Fourier component $\mathbf{m_q}(t)$ of $\mathbf{m}(\mathbf{r}, t)$. For cubic, nearly ferromagnetic materials, $q = |\mathbf{q}|$ and:

$$\Gamma_{\boldsymbol{q}} = \gamma q^n (\chi^{-1} + c q^2) \tag{2}$$

where γ and c are constants, and χ is the T dependent uniform ($q = 0$) susceptibility.

The case $n = 1$ corresponds to damping by quasiparticles in a homogeneous FL. As the QPT is approached, $\chi^{-1} \to 0$ and $\Gamma_{\mathbf{q}} \sim q^3$, i.e., $z = 3$. Assuming that $\hbar \Gamma_q = kT$, the temperature dependence of ρ, varying as T^m, is given by $m = (d+2)/z$. This is in fair agreement with the behavior of MnSi. T_c is predicted by this model to vary as $T_c \sim |p - p_c|^{3/4}$, which is consistent with experimental results not too close to p_c (inset of Fig. 2). The stronger dependence of T_c on $|p - p_c|$ in the vicinity of p_c might signal a first-order transition, in which case the fluctuations are cut off.

In an antiferromagnet (AF), the critical fluctuations are not centered at $\mathbf{q} \approx 0$, but at the AF

Table 1
Predictions of the QGL model for the temperature dependence of the linear specific-heat coefficient C/T and the electrical resistivity ρ at the QPT.

	$d=3$		$d=2$	
	$z=3$ (FM)	$z=2$ (AF)	$z=3$ (FM)	$z=2$ (AF)
C/T	$\sim -\ln(T/T_0)$	$\sim \gamma - \beta\sqrt{T}$	$\sim T^{-1/3}$	$\sim -\ln(T/T_0)$
ρ	$\sim T^{5/3}$	$\sim T^{3/2}$	$\sim T^{4/3}$	$\sim T$

wavevector $\mathbf{Q}$, which is of the order of the dimension of the Brillouin zone. Hence:

$$\Gamma_{\mathbf{Q}+\mathbf{q}} = \gamma_{\mathbf{Q}}(\chi_{\mathbf{Q}}^{-1} + c'q^2) \qquad (3)$$

The exponent n is effectively zero, and hence for $\chi_{\mathbf{Q}}^{-1} \to 0$ at the transition, $\Gamma_{\mathbf{Q}+\mathbf{q}} \sim q^2$ is obtained, i.e., $z=2$ leading to $m = d/z$. For the MFT described here, sometimes termed quantum Ginzburg–Landau (QGL) model, it is required that $d + z > 4$.

The above description of a QPT involving long-range interactions between quasiparticles (Moriya 1985, Lonzarich and Taillefer 1985, Lonzarich 1997) can also be derived in a more sophisticated renormalization-group treatment (Hertz 1976, Millis 1993). The results for the limiting behavior of ρ and C in the QGL model are listed in Table 1.

There is an additional caveat for AF metals at the QPT. The simple expectation $m = 1.5$ ignores the fact that the scattering of quasiparticles by fluctuations occurs only on those parts of the Fermi surface that are connected by $\mathbf{Q}$. However, this scattering may be "short-circuited" by quasiparticles on other parts of the Fermi surface. As was shown by Rosch (1999), an asymptotic FL-like T^2 dependence for $T \to 0$ is only obtained for extremely pure samples without impurity scattering. Impure samples yield $m = 1.5$, while effective exponents $1 \lesssim m \lesssim 2$ can be obtained in a wide T region for samples of moderate and high purity. The different T dependences are due to the existence of two scattering processes with different $\mathbf{q}$ dependences—strongly anisotropic scattering by magnetic fluctuations and isotropic impurity scattering.

2.3 Heavy-fermion Systems

Heavy-fermion systems (HFS), with an (often) regular sub-lattice of $4f$ or $5f$ atoms, notably Ce, Yb, or U, are close to a magnetic instability giving way to long-range magnetic order arising from the interaction between the $4f$ or $5f$ magnetic moments via the conduction electrons (see *Heavy-fermion Systems*). It is instructive to consider the case of an isolated magnetic impurity in a nonmagnetic metallic host where a strong hybridization between conduction electrons and f electrons may lead to a complete screening of

the magnetic moment by the former, resulting in a singlet ground state. This can be described by the Kondo Hamiltonian $H = -J\mathbf{S}\mathbf{s}$ where $\mathbf{S}$ is the impurity spin and $\mathbf{s}$ the conduction-electron spin, with an effective antiferromagnetic exchange interaction (J) (see *Electron Systems: Strong Correlations*).

At sufficiently low T well below the characteristic Kondo temperature T_K, a local FL is formed around the magnetic impurity. In a simplified picture, HFS can be thought of as a lattice-coherent superposition of these local FLs. Hence at low T, most HFS can be described within the framework of FL theory with, however, a very large effective mass m^* derived from the huge linear specific heat coefficient ($\gamma := C/T$) and a correspondingly large Pauli susceptibility (χ), both being only weakly dependent on T. The contribution $\rho_{el-el} \sim (T/T_K)^2$ is observable in HFS because $T_K \sim 10$ K is much smaller than E_F in typical metals.

The competition between on-site Kondo interaction quenching the $4f$ or $5f$ localized magnetic moments and intersite Ruderman–Kittel–Kasuya–Yosida (RKKY) interaction between these moments via the conduction electrons allows for nonmagnetic or magnetically ordered ground states in HFS. This competition is governed by a single parameter, namely the effective exchange constant (J), which enters the characteristic energy scales $kT_K \sim \exp(-1/N(E_F)J)$ and $kT_{RKKY} \sim J^2N(E_F)$ for Kondo and RKKY interactions, respectively. The strength of J is usually tuned by composition or pressure. Because of the exponential dependence of kT_K on J (which depends on the hybridization), volume changes are often the dominant effect in producing the magnetic–nonmagnetic transition. The hybridization can of course be strongly affected when alloying with non-isoelectronic ligands.

A large number of investigations have been carried out on HFS close to the magnetic instability. NFL behavior, i.e., deviations from the FL predictions in the low-T thermodynamic and transport properties has been reported for many systems. The main observations in many cases are a specific heat coefficient (γ) exhibiting a logarithmic T dependence, saturating towards low T in a number of systems, and a T^m dependence of the electrical resistivity (ρ) with $m < 2$. There are relatively few magnetization studies. The most decisive probe for magnetic fluctuations near a QPT, inelastic neutron scattering (INS), has only been employed for a few systems so far.

Since many of the HFS are driven through the QPT by changing the composition (hence introducing disorder), its effect on the critical behavior is an important issue. One has to distinguish between disorder by dilution of the $4f$ or $5f$ site as, e.g., in $Ce_{1-x}La_xRu_2Si_2$, or by altering the ligand configuration as for example in $CeCu_{6-x}Au_x$. In the first case, a "Kondo hole" introduced by dilution might lead to substantial quasiparticle scattering and ultimate loss of coherence. In the second case, the Ce atoms

experience different local environments and this may lead to different local Kondo temperatures. In $CeCu_{6-x}Au_x$, the QPT was tuned both by composition and pressure, with no difference in the functional $C(T)$ and $\rho(T)$ dependencies. Disorder may, however, play an important role in other systems (Sect. 3.2).

Practically, all HFS systems investigated so far are close to an AF instability (as opposed to a FM instability). A number of systems, notably $Ce_{1-x}La_x Ru_2Si_2$, have been compared in detail with the QGL model (Table 1). Long-range AF is introduced into $CeRu_2Si_2$ by moderate La doping. The behavior near the QPT, occurring for $x_c \approx 0.075$, is broadly consistent with expectation, although some differences between INS-derived and specific heat-derived parameters remain (Raymond *et al.* 1997). In $CeCu_{6-x}Au_x$ (the most extensively studied system up to now), the QPT can be tuned by the Au concentration (x), again by virtue of a weakening of J upon expansion of the $CeCu_6$ lattice. At the critical concentration $x_c \approx 0.1$, NFL behavior occurs with $\gamma = a \ln(T_0/T)$ over nearly two decades in T (Fig. 3), and $\rho \approx \rho_0 + AT$ between 0.02 K and 0.5 K.

These T dependences can be understood in terms of the spin-fluctuation model when two-dimensional critical fluctuations coupled to quasiparticles with three-dimensional dynamics are assumed. Indeed,

INS experiments for $x = 0.1$ reveal quasi-one-dimensional features in the dynamical structure factor ($S(\mathbf{q}, E = \text{const.})$) which correspond to quasi-two-dimensional "rods" in real space (Stockert *et al.* 1998). Here the neutron energy transfer was $E = 0.15$ meV. For strictly two-dimensional fluctuations, the system would be at the upper critical dimension since $d_{\text{eff}} = d + z = 4$.

The energy dependence of the critical fluctuations measured at $\mathbf{Q} = (0.8, 0, 0)$ has revealed an anomalous scaling with E and T of the imaginary part of the dynamical susceptibility $\chi''(\mathbf{q}, E, T) = S(\mathbf{q}, E, T) \times (1 - \exp(-E/kT))$ (Schröder *et al.* 1998), i.e., $\chi''(E, T) = T^{-\alpha}g(E/kT)$ with $\alpha = 0.74$ (Fig. 4). The scaling function g is consistent with a simple form of the dynamical susceptibility:

$$\chi(\mathbf{q}, E, T) = c(f(\mathbf{q}) + (-iE + bT)^\alpha)^{-1} \qquad (4)$$

where c and b are constants. The anomalous T dependence of the uniform static magnetic susceptibility has initially been described as $\chi(0, 0, T) = \chi_0(1 - BT^{1/2})$ between 0.08 K and 3 K, but can be modeled up to 7 K by $\chi = c'(\chi_0^{-1} + b''T^\alpha)^{-1}$ with $\alpha = 0.8$ (Schröder *et al.* 1998). The fact that α as obtained from INS for $\mathbf{Q} = (0.8, 0, 0)$ is equal to α ($q = 0, E = 0$) may imply that (i) the non local physics is contained in $f(\mathbf{q})$ which vanishes as $\mathbf{q} \to \mathbf{Q}$ where $\mathbf{Q}$ is a critical vector, i.e., belonging to the quasi-one-dimensional features of $S(\mathbf{q}, E = \text{const})$, and (ii) the anomalous scaling exponent is a local property since it appears to be independent of $\mathbf{q}$. This "local" behavior is, however, different from a simple local Lorentzian fluctuation spectrum that would be described by $\alpha = 1$.

The QPT in $CeCu_{6-x}Au_x$ has not only been tuned by x but also by pressure. Fig. 3 shows that samples with $x > x_c$ can be driven to the QPT, i.e., $T_N = 0$ by appropriate hydrostatic pressure (p). Near the QPT, C

Figure 3
Specific heat C of $CeCu_{6-x}Au_x$ plotted as C/T vs. log T for different hydrostatic pressures p. Note that when $T_N = 0$, i.e., for $x = 0.3$ at 8.2 kbar and for $x = 0.2$ at 4.1 kbar, the C/T curve falls on the same "universal curve" as for $x = 0.1$ where $T_N = 0$ at ambient pressure. Here a pressure of 6.0 kbar leads to Fermi-liquid behavior $C/T \approx$ const. Dashed line indicates C/T for $CeCu_6$. Inset shows the Néel temperature T_N vs. x at $p = 0$ (reproduced by permission of Elsevier Science from *J. Magn. Magn. Mater.*, 1999, **200**, 532–51).

Figure 4
Scaling plot inelastic neutron-scattering data for $CeCu_{5.9}Au_{0.1}$ at $q = (0.8, 0, 0)$ vs. E/k_BT. The inset shows how the quality of the scaling collapse varies with α in Eqn. (5). Solid line in the main part corresponds to a fit with $\alpha = 0.74$ (reproduced by permission of American Physical Society from *Phys. Rev. Lett.*, 1998, **80**, 5623–6).

is identical for all samples. Likewise, the sample with $x = 0.1$ can be driven by p away from the QPT towards FL behavior $C/T \approx$ const. approximately followed by pure CeCu$_6$. The linear $T_N(p)$ and $T_N(x)$ dependencies are in agreement with the scenario of two-dimensional fluctuations. The detailed mechanism of how local moments and long-range fluctuations work together to produce the unique quantum-critical behavior of CeCu$_{6-x}$Au$_x$ has yet to be disentangled.

Tuning of the QPT in the related system Ce-Cu$_{6-x}$Ag$_x$ by a magnetic field has been inferred from C and ρ (Heuser *et al.* 1998) with T dependencies compatible with the QGL scenario with $d = 3$ and $z = 2$ (Table 1), although this scenario does not include a magnetic field.

A number of stoichiometric HFS where the QPT can be tuned by pressure have also been investigated, e.g., CeCu$_2$Si$_2$ with its intriguing—but not yet fully understood—interplay between superconductivity (SC) and magnetism (see *Heavy-fermion Systems*). A particularly interesting case is CePd$_2$Si$_2$ (Fig. 5), which in a small p range where T_N is suppressed to zero, exhibits SC below a large T-range of NFL behavior (Mathur *et al.* 1998). Analogous behavior was found for CeIn$_3$. This is suggestive of spin-fluctuation

mediated SC. Up to now, however, only resistivity measurements have been reported, and the detailed interplay between superconductivity and AF order is not yet known. Even more intriguing is the recent observation of superconductivity in ferromagnetic UGe$_2$ (Saxena *et al.* 2000).

3. Non-Fermi Liquid Behavior due to Single-ion Effects

3.1 Multichannel Kondo Effect

Perfect screening of the magnetic moment via the Kondo effect leads to a local FL around a magnetic impurity in a metal. In general, however, several conduction-electron channels (N) may be present and the Kondo Hamiltonian reads $H = \Sigma_{\alpha=1}^{N} J_\alpha \mathbf{S} \mathbf{s}^\alpha$, where α is the channel index (Schlottmann and Sacramento 1993). For $N < 2S$, the screening is not complete; $N = 2S$ leads to perfect screening for $T \to 0$. In the case of degenerate channels, $J_\alpha = J$ for all α, the impurity spin will be overscreened if $N > 2S$.

For the special case $S = 1/2$ and $N = 2$, NFL behavior is predicted with $C/T \sim \chi \sim -\ln(T/T_K)$ and $\rho \sim 1 - (T/T_K)^{1/2}$ for $T \to 0$. Up to now, the experimental evidence for NFL behavior by overscreening of the magnetic moment of an impurity has been scarce.

In a more general sense, the Kondo effect may also pertain to orbital degrees of freedom of an impurity acting as a pseudospin instead of the spin. This is discussed for the interaction of conduction electrons with tunneling states, first in amorphous metals and later in metallic nanoconstrictions (van Delft *et al.* 1998). In these cases, the two channels are provided by the spectator spin of the conduction electrons. For certain rare-earth and actinide metals, a quadrupolar Kondo effect (QKE) has been considered (Cox and Jarrell 1996), where the pseudospin of the impurity is the quadrupolar moment arising from the aspherical charge distribution of the 4f or 5f electrons.

Again, the two channels are provided by the spin degeneracy of the conduction electrons. Indeed, the NFL anomalies as first reported for U$_{0.2}$Y$_{0.8}$Pd$_3$ (Seaman *et al.* 1991) were suggested to arise from the QKE. Here, NFL anomalies persist to rather dilute U alloys (Maple *et al.* 1995), thus favoring the single-ion QKE model. On the other hand, the NFL behavior might be due to an AF instability (Andraka and Tsvelik 1991), supported by long-range AF order in U$_{0.4}$Y$_{0.6}$Pd$_3$. In addition, a divergence of the quadrupolar susceptibility for $T \to 0$ as predicted for the QKE scenario was not found. Hence the situation for U$_x$Y$_{1-x}$Pd$_3$ is not clear.

The clearest signature of a QKE is found in U$_{1-x}$Th$_x$Be$_{13}$ (Aliev *et al.* 1996). In U$_{1-x}$Th$_x$Pd$_2$Al$_3$, single-ion scaling of NFL properties compatible with the QKE is observed, while U$_{1-x}$Y$_x$Pd$_2$Al$_3$ exhibits

Figure 5
Temperature–pressure phase diagram of a high-purity CePd$_2$Si$_2$ single crystal. Superconductivity appears below T_c in a narrow window where the Néel temperature T_N tends to absolute zero. For clarity, the values of T_c have been scaled by a factor of three, and the origin of the inset has been set at 5 K below absolute zero. The inset shows that the resistivity ρ exhibits a $T^{1.2}$ dependence on temperature over a wide T range (reproduced by permission of Macmillan from *Nature*, 1998, **394**, 39–43).

signatures of a magnetic instability around $x_c = 0.7$ whence the NFL properties in this case might be due to a QPT (Maple *et al.* 1999).

3.2 Distribution of Kondo Temperatures

Features of NFL behavior may arise from a quite different single-ion scenario, i.e., a distribution of Kondo temperatures ($P(T_K)$) in disordered systems. Fluctuations in J or the local $N(E_F)$ near a disorder-induced metal–insulator transition may lead to a wide distribution of $P(T_K)$. Indeed, the specific heat of heavily doped Si:P on the metallic side of the transition shows a contribution $\Delta C \sim T^\alpha$ with $\alpha \approx 0.2$, which is attributed to $P(T_K)$ (Lakner *et al.* 1994). Here the local moments arise from the statistical distribution of P donor atoms in the single crystalline host, with a distribution of hybridization strengths to the conduction electrons and hence of J. In the case of heavy-fermion solid solutions, the statistical distribution of atoms may lead to a distribution of T_K, as first put forward for the case of $UCu_{5-x}Pd_x$ ($x = 1$ and 1.5) on the basis of NMR measurements which directly showed a distribution of Knight shifts, viz., Kondo temperatures (Bernal *et al.* 1996). Even for a rather narrow distribution of J and/or $N(E_F)$, a broad $P(T_K)$ with a finite value for $T_K \to 0$ may occur because of the exponential dependence of T_K on J and $N(E_F)$.

On the other hand, an interesting single-ion NFL scaling was found in the dynamic structure factor $S(q, \omega)$ determined from INS (Aronson *et al.* 1995). This system is also at the verge of a magnetic instability as evident from spin-glass behavior at the lowest temperatures (Vollmer *et al.* 1997). A model combining the proximity to a magnetic instability and disorder, the so-called Griffiths phase model, has been tested for a number of U systems (de Andrade *et al.* 1998).

See also: Magnetic Excitations in Solids

Bibliography

Aliev F G, Vieira S, Villar R, Moshchalkov V V 1996 The quadrupolar Kondo ground state in $U_{1-x}Th_xBe_{13}$. *J. Phys.: Condens. Matter* **8**, 9807–23

Andraka B, Tsvelik A M 1991 Observation of non-Fermi-liquid behavior in $U_{0.2}Y_{0.8}Pd_3$. *Phys. Rev. Lett.* **67**, 2886–9

Aronson M C, Osborn R, Robinson R A, Lynn J W, Chau R, Seaman C L, Maple M B 1995 Non-fermi-liquid scaling of the magnetic response in $UCu_{5-x}Pd_x$ ($x = 1, 1.5$). *Phys. Rev. Lett.* **75**, 725–8

Bernal O O, MacLaughlin D E, Amato A, Feyerherm R, Gygax F N, Schenck A, Heffner R H, Le L P, Nieuwenhuys G J, Andraka B, v. Löhneysen H, Stockert O, Ott H R 1996 Kondo disorder and non-fermi-liquid behavior in $UCu_{5-x}Pd_x$ and $CeCu_{5.9}Au_{0.1}$. *Phys. Rev. B* **54**, 13000–16

Cox D L, Jarrell M 1996 The two-channel Kondo route to non-fermi-liquid metals. *J. Phys.: Condens. Matter.* **8**, 9825–53

de Andrade M C, Chau R, Dickey R P, Dilley N R, Freeman E J, Gajewski D A, Maple M B, Movshovich R, Castro Neto A H, Castilla G, Jones B A 1998 Evidence for a common physical description of non-fermi-liquid behavior in chemically substituted f-electron systems. *Phys. Rev. Lett.* **81**, 5620–3

Hertz J 1976 Quantum critical phenomena. *Phys. Rev. B* **14**, 1165–84

Heuser K, Scheidt E W, Schreiner T, Stewart G R 1998 Inducement of non-Fermi-liquid behavior with a magnetic field. *Phys. Rev. B* **58**, R15959–61

Lakner M, v. Löhneysen H, Langenfeld A, Wölfle P 1994 Localized magnetic moments in Si:P near the metal-insulator transition. *Phys. Rev. B* **50**, 17064–73

Lonzarich G G, Taillefer L 1985 Effect of spin fluctuations on the magnetic equation of state of ferromagnetic or nearly ferromagnetic metals. *J. Phys. C* **18**, 4339–71

Lonzarich G G 1997 The magnetic electron. In: Springford M (ed.) *Electron*. Cambridge University Press, Cambridge, pp. 109–47

Maple M B, de Andrade M C, Herrmann J, Dalichaouch Y, Gajewski D A, Seaman C L, Chau R, Movshovich R, Aronson M C, Osborn R 1995 Non Fermi liquid ground states in strongly correlated f-electron materials. *J. Low Temp. Phys.* **99**, 223–49

Maple M B, Amann A, Dickey R P, Freeman E J, Sirvent C, de Andrade M C, Dilley N R 1999 Non-fermi-liquid regimes in low-temperature phase diagrams of the systems $U_{1-x}M_xPd_2Al_3$ (M = Y, Th). *Physica B* **281–2**, 332–6

Mathur N D, Grosche F M, Julian S R, Walker J R, Freye D M, Haselwimmer R K W, Lonzarich G G 1998 Magnetically mediated superconductivity in heavy-fermion compounds. *Nature* **394**, 39–43

Millis A J 1993 Effect of nonzero temperature on quantum critical points in itinerant fermion systems. *Phys. Rev. B* **48**, 7183–96

Moriya T 1985 *Spin Fluctuations in Itinerant Electron Systems*. Springer, Berlin

Pfleiderer C, McMullan G J, Julian S R, Lonzarich G G 1997 Magnetic quantum phase transition in MnSi under hydrostatic pressure. *Phys. Rev. B* **55**, 8330–8

Raymond S, Regnault L P, Kambe S, Mignot J M, Lejay P, Flouquet J 1997 Magnetic correlations in $Ce_{0.925}La_{0.075}Ru_2Si_2$. *J. Low Temp. Phys.* **109**, 205–24

Rosch A 1999 Interplay of disorder and spin fluctuations in the resistivity near a quantum critical point. *Phys. Rev. Lett.* **82**, 4280–3

Rosenbaum T F 1996 Quantum magnets and glasses. *J. Phys.: Condens. Matter* **8**, 9759–72

Saxena S S, Agarwal P, Ahilan K, Grosche F M, Haselwimmer R K W, Steiner M J, Pugh E, Walker I R, Julian S R, Monthoux P, Lonzarich G G, Huxley A, Sheikin I, Braithwaite D, Flouquet J 2000 Superconductivity on the border of itinerant-electron ferromagnetism in UGe_2. *Nature* **406**, 587–92

Schlottmann P, Sacramento P D 1993 Multichannel Kondo problem and some applications. *Adv. Phys.* **42**, 641–82

Schröder A, Aeppli G, Bucher E, Ramazashvili R, Coleman P 1998 Scaling of magnetic fluctuations near a quantum phase transition. *Phys. Rev. Lett.* **80**, 5623–6

Seaman C L, Maple M B, Lee B W, Ghamaty S, Torikachvili M S, Kang J-S, Liu L Z, Allen J W, Cox D L 1998 Evidence for non-fermi-liquid behavior in the Kondo alloy $Y_{1-x}U_xPd_3$. *Phys. Rev. Lett.* **67**, 2882–5

Sondhi S L, Girvin S M, Carini J P, Shahar D 1997 Continuous quantum phase transitions. *Rev. Mod. Phys.* **69**, 315–33

Stockert O, v. Löhneysen H, Rosch A, Pyka N, Loewenhaupt M 1998 Two-dimensional fluctuations at the quantum-critical point of CeCu$_{6-x}$Au$_x$. *Phys. Rev. Lett.* **80**, 5627–30

v. Löhneysen H 1999 Fermi-liquid instability at magnetic-nonmagnetic phase transitions. *J. Magn. Magn. Mater.* **200**, 532–51

Vollmer R, Mock S, Pietrus T, v. Löhneysen H, Chau R, Maple M B 1997 Specific heat and magnetic susceptibility of UCu$_4$Pd at very low temperatures. *Physica B* **230–2**, 603–5

van Delft J, Ralph D C, Buhrman R A, Upadhyay S K, Louie R N, Ludwig A W W, Ambegaokar V 1998 The two-channel Kondo model. I. Review of experimental evidence for its realization in metal nanoconstrictions. *Ann. Phys. (New York)* **263**, 1–55

H. v. Löhneysen
Universität Karlsruhe, Germany

Nonlinear Magneto-optics

Just as linear magneto-optics describes the interaction of polarized light with magnetic (or magnetized) materials, nonlinear magneto-optics describes their nonlinear optical response. Physically, magneto-optical (MO) effects are related to the breaking of the time-reversal operation (see *Faraday and Kerr Rotation: Phenomenological Theory*). This leads to well-known phenomena such as the Faraday effect and magnetic circular dichroism in transmission and the magneto-optical Kerr effect (MOKE) in reflection. Similarly, nonlinear MO effects are related to a combination of time-reversal symmetry breaking with the breaking of space-inversion symmetry (at least within the electric dipole approximation).

The Faraday and Kerr effects have been known for over a century. However, the field of nonlinear magneto-optics started much more recently with the prediction (Pan *et al.* 1989) of magnetization-induced contributions to the nonlinear optical response of magnetic surfaces and interfaces. This was followed by experimental observation of such effects by Reif *et al.* (1991) for an Fe surface and by Spierings *et al.* (1993) for Au/Co interfaces. (Actually, first predictions of possible nonlinear MO effects were already published as early as 1967 by Lajzerowicz and Vallade (1967) for antiferromagnetic materials and by Akhemiev *et al.* (1985) for magnetic crystals. The "revival" and recent strong development of nonlinear magneto-optics is clearly related to the enormous interest in the study and applications of magnetic multilayers and nanostructures and by the development of solid state mode-locked femto second lasers that are particularly suitable for these kinds of studies (Rasing 1998).

Apart from the nonlinear optical equivalents of the Faraday and Kerr effects, the higher order optical response also leads to new nonlinear MO phenomena that have no equivalence in linear magneto-optics,

e.g., transverse Faraday and Kerr effects that are linear in magnetization (Pavlov *et al.* 1997, Wierenga *et al.* 1995), the breaking of the equivalence between magnetization reversal, the change of light helicity (Kirilyuk *et al.* 2000b), and the sensitivity for antiferromagnetic ordering (Fiebig *et al.* 1995).

1. Theory

An incident electromagnetic wave can induce a polarization in a medium that serves as a source for the transmitted and reflected light. This polarization **P** can be written in the electric dipole approximation as an expansion in powers of the electric field **E**(ω) of the incident wave:

$$P_i = \chi_{ij}^{(1)} E_j(\omega) + \chi_{ijk}^{(2)} E_j(\omega) E_k(\omega) + \cdots \quad (1)$$

The tensor $\chi^{(1)}$ is the linear optical susceptibility, leading to the linear reflection and refraction of light. The second term describes nonlinear optical effects such as *second harmonic generation*. In the presence of a magnetization **M** both $\chi^{(1)}$ and $\chi^{(2)}$ should be further expanded in powers of **M**:

$$\chi^{(1)} = \chi_0^{(1)} + \frac{\delta\chi^{(1)}}{\delta\mathbf{M}}\mathbf{M} + \cdots \quad (2a)$$

$$\chi^{(2)} = \chi_0^{(2)} + \frac{\delta\chi^{(2)}}{\delta\mathbf{M}}\mathbf{M} + \cdots \quad (2b)$$

The first term in both Eqns 2(a) and 2(b) could be thought of as describing purely crystallographic effects while the second one only exists in the presence of magnetization. In principle in both cases the magnetic contribution is described by a higher rank tensor; in practice these magnetic contributions can be written as effective $\chi^{(1)}$ and $\chi^{(2)}$ components, respectively. For example, a nonzero magnetization along the $\hat{z}$-axis of an optically isotropic material yield nonzero components $\chi_{xy}^{(1)} = -\chi_{xy}^{(1)}$ that lead to linear MO effects that are proportional to the ratio $\chi_{xy}^{(1)}/\chi_{zz}^{(1)}$.

The crystallographic nonlinear optical tensor $\chi^{(2)}$ is only nonzero in media without inversion symmetry. Consequently, for isotropic media, $\chi^{(2)}$ only gives a contribution from surfaces and interfaces where the inversion symmetry is broken. The presence of a magnetization does not affect the inversion symmetry (as **M** is an axial vector) but does lower the symmetry of $\chi^{(2)}$ and consequently leads to new nonzero, nonlinear susceptibility components. These elements can be derived in a straightforward way and are summarized in Table 1 for the standard longitudinal, transversal, and polar MO configurations (Rasing 1998).

From Table 1, the effects of magnetization-induced second harmonic generation (MSHG) can directly be understood. For example, in the longitudinal configuration, an *s*-polarized (parallel to y) input

Table 1
The nonzero $\chi^{(2)}$ components for the longitudinal ($\mathbf{M} \| x$), transversal ($\mathbf{M} \| y$), and polar ($\mathbf{M} \| z$) MO configurations (xz is the plane of incidence). For convenience, only the indices are indicated. The odd components are indicated in bold.

	P_{in}	S_{in}	
$\mathbf{M} \| x$	xxz, zxx, zzz	zyy	P_{out}
	yxx, yzz	**yyy**	S_{out}
$\mathbf{M} \| y$	xzx, zxx, zzz, **xxx, xzz, zzx**	zyy, **xyy**	P_{out}
			S_{out}
$\mathbf{M} \| z$	xxz, zxx, zzz	zyy	P_{out}
	yzx		S_{out}

beam will give rise to one even component ($\chi^{(2)}_{zyy}$) and one odd component ($\chi^{(2)}_{zyy}$). The even term will yield a *p*-polarized and the odd term an *s*-polarized field, respectively. Thus, the output polarization can be varied by changing the direction of $\mathbf{M}$, yielding a nonlinear Kerr rotation $\theta_k^{(2)} \sim \arctan(\chi^{(2)}_{yyy}/\chi^{(2)}_{zyy})$ in the same way as in linear magneto-optics, but with values for $\theta_k^{(2)}$ that are three orders of magnitude larger than the linear equivalent (Koopmans *et al.* 1995). Similarly, it follows from Table 1 that in the transverse geometry both *s*- and *p*-polarized input beams will always generate a *p*-polarized output. Consequently, as in linear MOKE, there is no nonlinear Kerr rotation. However, in contrast to the linear case, there is a strong magnetization-induced intensity change, that is *linear* in the magnetization.

Table 1 shows another important difference between the linear and the nonlinear MO effects. Whereas in both cases the MO effects are proportional to a ratio between odd and even tensor components, in the linear case the odd components are small off-diagonal elements. In the nonlinear case the odd components are of a similar type as the even ones (compare the components in Table 1). This fact, which is also supported by calculations of $\chi^{(2)}$ based on spin-dependent band structure (Hübner and Benneman 1989) is responsible for the very strong nonlinear MO effects that have been observed in various experiments and that are typically three orders of magnitude larger than the linear equivalents.

The relation between the nonlinear MO susceptibility and the spin-dependent band structure can be written as:

$$\chi^{(2)}_{ijk}(2\omega)$$
$$\propto \sum_{a,b,c} \frac{\langle a|i|c \rangle \langle c|j|b \rangle \langle b|k|a \rangle}{(2\hbar\omega - E_{ca} + i\hbar\Gamma_{ca})(\hbar\omega - E_{ba} + i\hbar\Gamma_{ba})} \quad (3)$$

Equation (3) shows that spectroscopic MSHG experiments in principle allow the probing of the spin-dependent surface or interface density of electronic

states which is not only of fundamental interest but also highly relevant for the understanding of spin-dependent tunneling processes in magnetic tunnel junctions (de Boer *et al.* 1998).

All the effects so far have been described within the electric dipole approximation only. An extension to include higher order contributions to the nonlinear MO response can be found in Rasing (1998), whereas the application of magnetization-induced sum frequency generation can be found in Kirilyuk *et al.* (2000a).

2. Experimental Considerations

For each polarization combination, the total MSHG response from a magnetic material can be simplified by

$$\mathbf{P}(2\omega, \pm M) = (\chi^{even}_{eff}(\pm\mathbf{M}) \pm \chi^{odd}_{eff}(\pm M))E^2_\omega \quad (4)$$

where χ^{even}_{eff} and χ^{odd}_{eff} are effective tensor components that are even and odd in the magnetization and describe the crystallographic and magnetic contributions to the total response, respectively. As both these contributions are complex quantities, the total (MSHG) signal is thus given by

$$I(2\omega) \sim |\chi^{even}_{eff}|^2 + |\chi^{odd}_{eff}|^2 \pm 2|\chi^{even}_{eff}||\chi^{odd}_{eff}|\cos\Delta\Phi \quad (5)$$

where $\Delta\Phi$ is the phase difference between the two contributions. The importance of the latter is obvious: when $\Delta\Phi = \Pi/2$, the interference term is zero and changing the magnetization direction will have no effect on the total MSHG signal.

Though generally phase information is lost in intensity measurements, fortunately $\Delta\Phi$ can be measured quite easily in nonlinear optics by using interference techniques (Stolle *et al.* 1997). The latter can also be exploited in the case where there is only a purely odd response by adding a nonmagnetic reference signal, as it is the interference between even and odd terms that gives rise to the nonlinear MO effects.

Though MSHG signals give large relative MO effects, being a nonlinear optical technique the absolute intensities are rather small (10–10^4 photons sec^{-1}). However, they are easily detectable with modern photon counting or charge coupled devices (CCD), though care should be taken to filter out the two signal versus the much stronger fundamental signal at ω (see Fig. 1).

Because of the simplicity of the experimental configuration coupled with the large effects, the transverse geometry is often used for experimental studies. One can then define a magnetic contrast or asymmetry as:

$$A = \frac{I(2\omega, +\mathbf{M}) - I(2\omega, -\mathbf{M})}{I(2\omega, +\mathbf{M}) + I(2\omega, -\mathbf{M})} \quad (6a)$$

$$= \frac{2|\chi^{odd}_{eff}|/|\chi^{even}_{eff}|}{1 + |\chi^{odd}_{eff}\chi^{odd}_{eff}|^2} \cos\Delta\Phi \quad (6b)$$
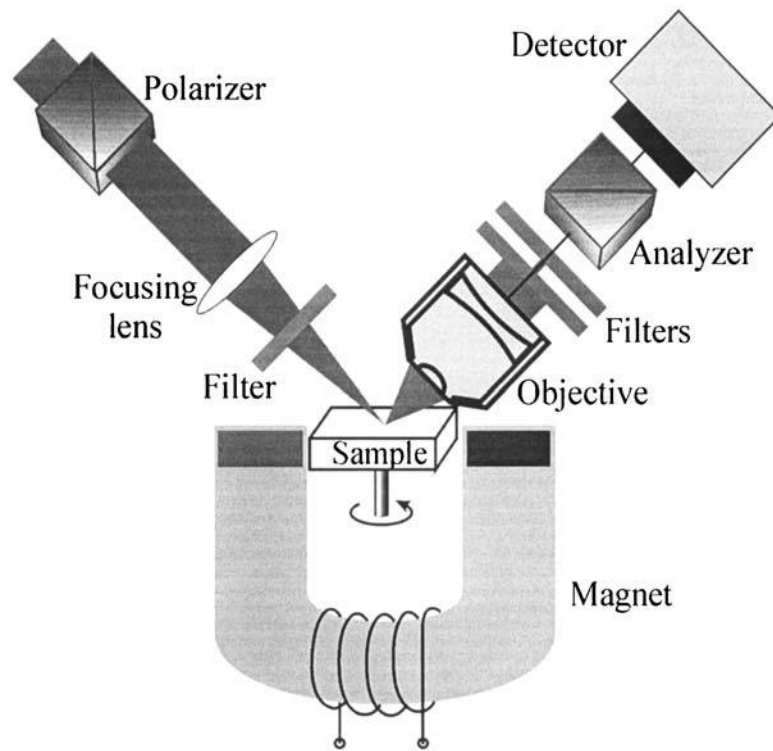
Figure 1
Schematic configuration for nonlinear MO experiments. Photomultipliers or CCD cameras (for domain imaging) can be used as detectors.

Because *A* is normalized with respect to the total SHG intensity, it does not depend on the intensity or shape of the fundamental light pulses, nor on the spectral properties of optical components such as filters in the optical setup. Together with the already mentioned simplicity, this makes *A* a useful parameter for quantitative investigations. One should, however, realize that the appearance of large effects that result from the large magnetic tensor components also means that, in contrast to most linear MO effects, the nonlinear effects are often not simply proportional to the magnetization as directly follows from Eqns (5) and (6). This can for example strongly affect the shape of MSHG loops (see Veenstra 2000).

3. Symmetry Considerations

As a second-order nonlinear optical technique described by a third-rank tensor, MSHG can be exploited to probe other changes in symmetry, e.g., the appearance of steps on vicinal surfaces (Leermakers in press), magnetic moments at step edges (Jin *et al.* 1998), and the changes (phase transitions) in these properties. Because of the use of femtosecond laser sources for these experiments the latter can be performed with unprecedented time resolution. This has already led to exciting results, such as the disappearance of magnetic order within picoseconds, by using strong, but ultrashort, excitation pulses (Hohlfeld *et al.* 1999).

Since the MSHG response originates from the interference of both crystallographic (even) and magnetic (odd) contributions to the nonlinear optical response, a detailed analysis of the symmetry properties of the MSHG signal can provide deeper insight into both the crystallographic and magnetic symmetry of crystalline material. Experimentally this is done by using various polarization combinations (both circular and linear) in combination with azimuthal rotation dependence of the MSHG signal. These effects have been beautifully demonstrated for magnetic garnets (Pavlov *et al.* 1997, Kirilyuk *et al.* 1999) and for hexagonal manganites (Fiebig *et al.* 2000a), where in the last case even very complicated noncollinear spin structures could unambiguously be resolved. In both classes of material, the power of MSHG to probe the local spin structure, i.e., to do domain microscopy has been demonstrated as well (Fiebig *et al.* 2000b, Kirilyuk *et al.* 1997).

4. Concluding Remarks

Nonlinear Magneto-optics, or more specifically, MSHG has yielded an interesting and powerful new technique to investigate the magnetic structure of materials. The higher order optical response gives, in particular, the possibility of probing magnetic ordering in otherwise complicated or inaccessible structures (such as buried magnetic interfaces or antiferromagnetic materials) and has been shown to lead to intrinsically new effects. Therefore, this new area of magneto-optics is not only interesting from a fundamental point of view but it will also be quite important for applications such as the investigations of magnetic nanostructures and the spin dynamics in these systems.

5. Acknowledgments

Bibliography

Akhemiev N N, Borisov S B, Zvezdin A K, Lyubchanskii I L, Melikhov Y V 1985 Nonlinear optical susceptibility of magnetically ordered crystals. *Sov. Phys. Solid State* **27**, 650–2

Boer de P K, Wijs de G A, Groot de R A 1998 Reversed spin polarization at the Co(001)-HfO₂(001) interface. *Phys. Rev. B* **58**, 15422–5

Fiebig M, Fröhlich D, Kohn K, Leute St, Lottermoser Th, Pavlov V V, Pisarev R V 2000a Determination of the magnetic symmetry of hexagonal manganites by second harmonic generation. *Phys. Rev. Lett.* **84**, 5620–3

Fiebig M, Fröhlich D, Lottermoser Th 2000b Spin-angle topography of hexagonal manganites by magnetic second-harmonic generation. *Appl. Phys. Lett.* **77**, 4401–3

Fiebig M, Fröhlich D, Sluyterman v L G, Pisarev R V 1995 Domain topography of antiferromagnetic Cr_2O_3 by second-harmonic generation. *Appl. Phys. Lett.* **66**, 2906–8

Hohlfeld J, Güdde J, Conrad U, Dühr O, Korn G, Matthias E 1999 Ultrafast magnetization dynamics of nickel. *Appl. Physics B* **68**, 505–10

Hübner W, Bennemann K H 1989 Nonlinear magneto-optical Kerr effect on a nickel surface. *Phys. Rev. B* **40**, 5973–9

Jin Q J, Regensburger H, Vollmer R, Kirschner J 1998 Periodic oscillations of the surface magnetization during the growth of Co films on Cu(001). *Phys. Rev. Lett.* **80**, 4056–9

Kirilyuk V, Kirilyuk A, Rasing Th 1997 A combined nonlinear and linear magneto-optical microscopy. *Appl. Phys. Lett.* **70**, 2306–8

Kirilyuk A, Knippels G M H, Meer van der A F G, Renard S, Rasing Th, Heskamp L R, Lodder J C 2000a Observation of strong magnetic effects in visible-infrared sum frequence generation from magnetic structures. *Phys. Rev. B* **62**, R783–6

Kirilyuk A, Pavlov V V, Pisarev R V, Rasing Th 2000b Asymmetry of second harmonic generation in magnetic thin films under circular optical excitation. *Phys. Rev. B* **61**, R3796–9

Kirilyuk A, Pisarev R V, Gridnev V N, Pavlov V V, Rasing Th 1999 Nonlinear optics on magnetic materials. *J. Magn. Soc. Jpn.* **23**, 346–51

Koopmans B, Groot Koerkamp M, Rasing Th, Berg vd H 1995 Observation of large Kerr angles in the nonlinear optical response from magnetic multilayers. *Phys. Rev. Lett.* **74**, 3692–5

Lajzerowicz J, Vallade M 1967 Génération du second harmonique dans les substances magnétiques ordonnées. *C. R. Acad. Sci Paris* **264**, 1819–21

Leermakers R, Keen A M, Nguyen van Daub F, Rasing Th 2001 A magneto-optical study of Co on step bunched vicinal substrates. (In press)

Pan R P, Wei H D, Shen Y R 1989 Optical second-harmonic generation from magnetized surfaces. *Phys. Rev. B* **39**, 1229–34

Pavlov V V, Pisarev R V, Kirilyuk A, Rasing Th 1997 Observation of a transversal nonlinear magneto-optical effect in thin magnetic garnet films. *Phys. Rev. Lett.* **78**, 2004–7

Rasing 1998 Nonlinear Magneto-Optical Studies of Ultrathin Films and Multilayers. In: Benneman K H (ed.) *Optics in Metals.* Oxford University Press, Oxford, pp. 132–218 Chap. 3

Reif J, Zink J C, Schneider C M, Kirschner J 1991 Effects of surface magnetism on optical 2nd harmonic-generation. *Phys. Rev. Lett.* **67**, 2878–81

Spierings G, Koutsos V, Wierenga H A, Prins M W J, Abraham D, Rasing Th 1993 Optical second harmonic generation study of interface magnetism. *Surf. Sci.* **287**, 747–749; *J. Magn. Magn. Mater.* **121**, 109

Stolle R, Veenstra K J, Manders F, Rasing Th, Berg vd H 1997 Breaking of time-reversal symmetry probed by optical second-harmonic generation. *Phys. Rev. B* **55**, R4925–7

Veenstra K J 2000 Phase Sensitive Nonlinear Magneto-Optical Spectroscopy, Ph.D. thesis, University of Nijmegen, The Netherlands

Veenstra K J, Petukhov A V, Jurdik E, Rasing Th 2000 Strong surface state effects in the nonlinear magneto-optical response of Ni(110). *Phys. Rev. Lett.* **84**, 2002–5

Wierenga H A, Jong de W, Prins M W J, Rasing Th, Vollmer R, Kirilyuk A, Schwabe H, Kirschner J 1995 Interface magnetism and possible quantum well oscillations in ultrathin Co/Cu films observed by magnetization induced second harmonic generation. *Phys. Rev. Lett.* **74**, 1462–5

Th. Rasing
University of Nijmegen, Nijmegen
The Netherlands

Nuclear Magnetic Resonance Spectrometry

Nuclear magnetic resonance (NMR) spectroscopy is an analytical technique used extensively in the molecular structure determination of organic, organometallic, biological, and inorganic materials. As the name implies, NMR is concerned with the magnetic properties of atomic nuclei, which give rise to the observed phenomenon. In an NMR experiment, samples are placed in a strong, homogeneous magnetic field and radio-frequency (RF) electromagnetic

energy is applied. Particular nuclei absorb this energy at sharply defined frequencies; this signal is then detected, amplified, and presented as a frequency spectrum. NMR of hydrogen nuclei in bulk materials was first observed in 1946 independently by the research groups of Bloch at Stanford and Purcell at Harvard, for which they received the 1952 Nobel Prize for Physics. It was quickly realized that liquid samples give much narrower peaks with significantly improved resolution of peaks in the spectrum.

The discovery of the *chemical shift*, i.e., the dependence of the resonance frequency of a given nucleus on its specific chemical environment in the molecule, established NMR as a fundamental tool for structure determination. The three most important types of information obtained in a high-resolution NMR spectrum are frequency, area, and multiplicity of the resonance lines. The exact resonance frequency of a nucleus is characteristic of its local electronic environment and is measured against a reference peak in the sample. The area under the resonance line can be integrated to give quantitative information about the relative number of nuclei giving rise to each peak. Peaks may be split into multiple lines owing to scalar (spin–spin) coupling with neighboring nuclei. This interaction occurs through the electrons of the bonding network and is due to the different combinations of spin orientations that neighboring nuclei can adopt. The splitting pattern indicates structural information about the neighboring nuclei.

Advances in instrument hardware since the late 1960s have significantly enhanced the sensitivity and resolution of NMR spectroscopy. As a result, spectra may be obtained of solutions of low concentration, nuclei may be observed that have very low natural abundance, and resolution of structural features is greatly improved. Whereas during the first 20 years after its discovery NMR applications were mostly limited to proton nuclei, modern spectrometers can in principle observe any nucleus, limited only by restrictions of its magnetic properties. Furthermore, developments in software and RF pulse sequence programming have dramatically extended the range and power of NMR experiments. Methods exist to map out fully by NMR the structure of an organic molecule for example. Although methods have also been established to obtain high-resolution NMR spectra of solid materials, the differences in the techniques are sufficient to require that this be a topic for a separate article (see *Solids, Nuclear Magnetic Resonance of*).

1. Principles

Both classical and quantum mechanical descriptions may be used to describe the NMR phenomenon. Since each approach has certain advantages, some features of each will be used in this discussion.

While all atomic nuclei possess charge and mass, some have magnetic moments and angular momentum and therefore behave as spinning bodies. Nuclei with even mass and atomic number have no nuclear spin and therefore do not exhibit the NMR phenomenon. These include the common isotopes ^{12}C, ^{28}Si, and ^{16}O. Of the remaining nuclei, those with odd mass numbers and even nuclear charge numbers have spin quantum numbers, I, which are odd-integral multiples of $\frac{1}{2}$, whereas those with even mass numbers and odd nuclear charge have integral values of I. The nuclear angular momentum is given by $I(h/2\pi)$, where h is Planck's constant. The magnetic moment, μ, is proportional to the angular momentum by a factor γ, called the *magnetogyric ratio*, which is characteristic of a given nucleus:

$$\mu = \gamma h I / 2\pi \tag{1}$$

A set of magnetic quantum numbers given by the series

$$m = I,\ (I-1),\ (I-2),\ \ldots, -I \tag{2}$$

describes the allowed values of the magnetic moment vector. Thus, there are $(2I+1)$ possible spin states for a given nucleus. For the simplest case of those nuclei with $I = \frac{1}{2}$ this corresponds to two spin states. These spin states are degenerate in the absence of a magnetic field, but they correspond to states of different potential energy in the presence of a uniform magnetic field, H_0. For spin-$\frac{1}{2}$ nuclei the two spin states correspond to the magnetic moment aligned either with or against the applied magnetic field ($m = +\frac{1}{2}$ or $m = -\frac{1}{2}$). Inducing and detecting transitions between these two states form the basis of NMR experiments.

The interaction between the applied magnetic field, H_0, and the nuclear magnetic moment, μ, causes precession of the nucleus about the direction of the applied field. The frequency of precession is given by the Larmor equation:

$$v_0 = \gamma / 2\pi H_0 \tag{3}$$

where v_0 is the Larmor frequency of a nucleus and is linearly dependent on the strength of the magnetic field, H_0. If a small magnetic field, H_1, is applied perpendicular to H_0, and made to rotate at a frequency of v_0, energy is absorbed from the H_1 field into the spin system. This is the resonance condition. If H_1 is rotating at any frequency other than v_0, no net absorption of energy occurs. The Larmor frequency is very different for individual nuclei. For example, in a magnetic field of 11.75 T the Larmor frequencies are 500.10 MHz for ^1H, 470.48 MHz for ^{19}F, 125.75 MHz for ^{13}C, 50.67 MHz for ^{15}N, 99.35 MHz for ^{29}Si, and 202.44 MHz for ^{31}P. Although there are a few nuclei whose Larmor frequencies are close enough to overlap frequency ranges, in

general only one nuclear species at a time is observed in a given spectrum.

The separation of the energy levels is small, and at equilibrium there is only a slight excess of nuclei in the lower energy spin state as given by the Boltzmann population distribution. Since NMR experiments are dependent on this small population to produce a signal, NMR is relatively insensitive compared with some other spectroscopic techniques. Once energy transfer occurs into the spin system, the process by which the nuclei re-establish a Boltzmann population distribution is called spin–lattice relaxation. This process is dependent on the presence of fluctuating local magnetic fields. Several common mechanisms of spin–lattice relaxation include interactions with neighboring magnetic nuclei, free rotation of a functional group or molecule, the presence of significant anisotropy in the chemical shift (see Sect. 3), and interactions through scalar coupling (see Sect. 4) with another rapidly relaxing nucleus. Spin–lattice relaxation times, T_1, for most common nuclei are in the range $0 \cdot 1$–$20 \, \text{s}$, but much smaller or greater T_1 values are also possible.

The ease of observing NMR signals for different nuclei is dependent on I, γ, and the natural abundance of the isotope. In general, nuclei with $I = \frac{1}{2}$ produce spectra with the narrowest lines. Nuclei with $I > \frac{1}{2}$ possess electric quadrupole moments which can significantly shorten relaxation times and broaden resonance lines. For this reason these nuclei are generally less suitable for traditional NMR experiments. The magnetogyric ratio is a fundamental constant of the nucleus, which determines the frequency and inherent sensitivity of the nucleus to the NMR experiment. In general, spin-$\frac{1}{2}$ nuclei with a high γ value and reasonable natural abundance are easily observed by NMR spectroscopy. Examples of nuclei with 100% natural abundance which fit this description are ^{1}H, ^{19}F, and ^{31}P.

2. Instrumentation and Experimental Details

Figure 1 shows a block diagram of a typical NMR spectrometer. In most modern NMR spectrometers the magnetic field is generated by a superconducting magnet. The sample is placed into the NMR probe which is located in the center of a homogenous region of the magnet. The spectrometer console provides at least three RF channels which are transmitted into the probe. The *observe channel* supplies the observe RF for the nucleus of interest and receives the signal back from the sample. The decoupler channel is used to irradiate another nucleus in the sample other than the one being observed. The *lock circuit* conducts a separate NMR experiment that continually measures another resonance, typically deuterium (^{2}H), and adjusts for minor drift in the magnetic field. This ensures long-term stability of high-resolution NMR experiments. Modern spectrometers typically employ two computers, one for data acquisition and processing and another for spectrometer control.

Both liquid and solid samples are normally dissolved in a deuterated solvent such as chloroform-d which provides a signal for the lock circuit. The liquid sample is placed in a capped, thin-walled glass tube, which is typically either 5 mm or 10 mm in diameter, although microsample probes are also available.
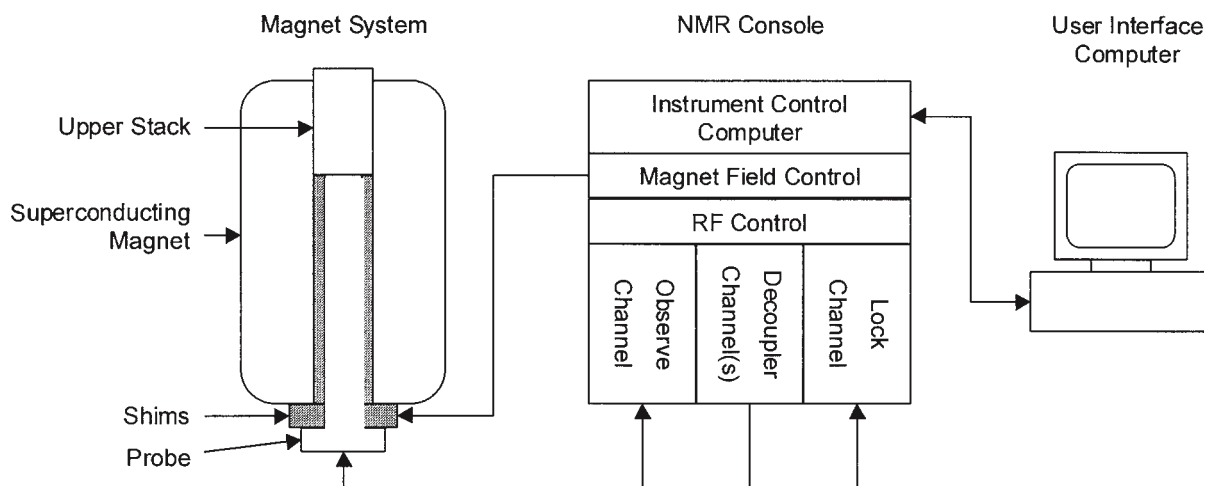
Figure 1

Block diagram of a typical NMR spectrometer. The sample is introduced through the upper stack of the magnet into the probe. The shims are used to optimize the homogeneity of the magnetic field around the sample. Instrument operation is carried out from the NMR console through the user interface computer.

3. Chemical Shifts

As mentioned above, nuclei of a given type do not all exhibit transitions at exactly the same frequency. Each nucleus is surrounded by an electron cloud, and the motion of these electrons creates a secondary magnetic field which tends to oppose the applied magnetic field; chemical shift differences arise because this local electron density varies depending on the electronegativity of the atoms attached to the nucleus and the type of bonding in which it is involved (e.g., single vs. multiple bonds). Thus, the higher the electron density about a nucleus, the greater the secondary magnetic field, or *shielding* effect. The effect of the nearest neighboring atoms or functional groups is usually most important. It is these small differences in resonance frequency among the chemically different nuclei in a sample that help identify the specific structures present.

The peak positions are determined using an internal standard which may be either a peak from another material added to the sample or from the deuterated solvent in the case of ^{13}C or ^{1}H NMR. These positions are reported relative to the position of a reference material. Although NMR data are measured in frequency units, Hz, they are usually reported in the dimensionless units of ppm which is independent of the magnetic field strength. Since the resonance frequencies are directly proportional to magnetic field strength, this is achieved by taking the difference in frequency between the peak and the standard (in Hz), multiplying by 10^6 and dividing by the operating frequency of the spectrometer, v_0. This dimensionless chemical shift is given the symbol δ:

$$\delta = 10^6 (v_{\text{sample}} - n_{\text{ref}})/v_0 \qquad (4)$$

Using these chemical shifts permits comparisons to be made of data acquired on instruments of different magnetic field strength. As an example of a typical spectrum, Fig. 2 shows the ^{1}H NMR spectrum of ethylbenzene. It contains four sets of resonance lines from *low field* to *high field*, or left to right: a singlet, a quartet, and another singlet. The last singlet is due to the protons of tetramethylsilane (TMS), $(CH_3)_4Si$, which is commonly used as the standard for ^{1}H, ^{13}C, and ^{29}Si NMR. By convention, the chemical shift for the standard is set to 0 ppm.

4. Proton NMR

Consider the ^{1}H NMR spectrum shown in Fig. 2. The dominant features of the spectrum are the presence of the singlet at $\delta = 7.2$ ppm (phenyl ring protons), triplet at $\delta = 1.2$ ppm (methyl protons), and quartet at $\delta = 2.6$ ppm (methylene protons). The neighboring group affects more than just the chemical shift of a peak: in the case of the methyl group, for example, the neighboring methylene group not only affects the
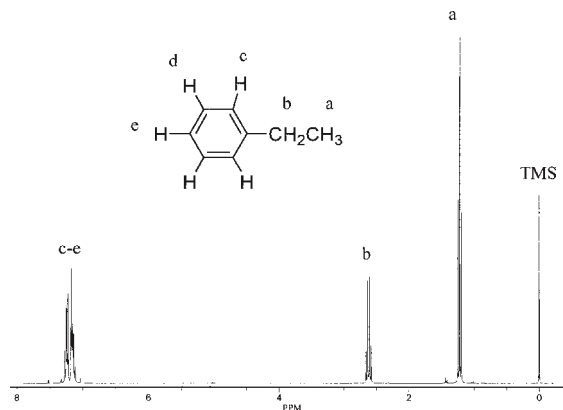
Figure 2
Proton NMR spectrum (300 MHz) of ethylbenzene. Assignments to the protons in the structure are shown. The internal standard is TMS, which is set to a chemical shift of 0 ppm.

position of the resonance line but causes the peak to be split into a triplet as well. The explanation for this phenomenon, called spin–spin splitting, lies in the fact that the neighboring protons may also be in different orientations with respect to the applied magnetic field. Since the proton is a nucleus with $I = \frac{1}{2}$, two possible spin states exist for each proton. Depending on whether the neighboring nuclear spin is aligned with (parallel) or opposed to (antiparallel) the proton at resonance, it will either increase or decrease the net magnetic field experienced by the observed proton. This gives rise to slight differences in energy levels and thus different resonance lines. In the case of the methylene protons of ethylbenzene, three combinations of the orientations ($\uparrow\uparrow$, $\uparrow\downarrow = \downarrow\uparrow$, $\downarrow\downarrow$) of the two spins are possible for the neighboring nuclei producing a 1:2:1 triplet for the methyl protons. Spin–spin splitting is a primary characteristic of ^{1}H NMR. These interactions are said to be electron coupled since they operate through the bonding network; the effect is quite strong over the first few bonds but diminishes greatly thereafter.

The number of lines produced by spin–spin coupling is given by

$$\text{Multiplicity} = 2nI + 1 \qquad (5)$$

where n is the number of protons in the neighboring group and I is the spin quantum number. The separation between the lines of a multiplet is referred to as the coupling constant, J. This value, expressed in frequency units (Hz), reflects the magnitude of the spin–spin interaction and is independent of the applied magnetic field. Characteristic coupling constants are of great value in structure elucidation. Factors that influence the magnitude of the coupling

constant include bond order, electronegativity of the substituents on the coupled nuclei, and bond angles.

To determine if two nuclei are coupled to each other, a double resonance experiment can be performed. In this type of experiment, two RF fields are simultaneously applied to the sample: one is used to observe the spectrum in the normal manner, and the other is a perturbing field applied at the resonance frequency of another nucleus that is suspected to be coupled to the one of interest. If the perturbing (or *decoupling*) field is sufficiently strong the nucleus of interest appears as if it is no longer coupled. In the spectrum of ethylbenzene, for example, if the decoupling field is applied at the resonance frequency of the methylene protons, the methyl proton triplet collapses to a single peak. Similarly, irradiating at the center of the methyl proton resonance causes the methylene proton quartet to collapse to a singlet. The perturbation of coupled spins to determine connectivity in a molecule is a key feature in a number of more advanced NMR techniques.

5. Carbon-13 NMR

The sensitivity of the ^{13}C nucleus is a factor of approximately 6000 lower than that of ^{1}H owing to its smaller magnetogyric ratio and low natural abundance of 1.1%. Although ^{13}C spectra were obtained as early as the 1950s (Lauterbur 1957), significant growth in the application of ^{13}C NMR and other low-sensitivity nuclei did not occur until after the introduction of the pulsed Fourier transform method (Ernst and Anderson 1966).

The resulting dramatic reduction in the amount of time necessary for data acquisition allowed ^{13}C NMR spectroscopy to become a routine tool for probing molecular structure. The rare occurrence of the isotope greatly simplifies ^{13}C NMR spectra by eliminating the spin–spin coupling (^{13}C–^{13}C) that is so dominant in ^{1}H NMR spectra.

Further simplification of ^{13}C spectra is achieved by removing the scalar coupling between ^{13}C and ^{1}H by double-resonance decoupling over the ^{1}H chemical shift range. In the resultant spectrum, each line corresponds to a magnetically unique carbon atom in the sample. The relatively large ^{13}C chemical shift range, which is about 20 times that of ^{1}H, affords excellent resolution of even structurally quite similar atoms. As an example of a typical spectrum, Fig. 3 shows the ^{13}C spectrum of ethylbenzene. Note that all six structurally unique carbon atoms give resonances that are well resolved from each other.

The ability to differentiate structures in ^{13}C NMR is facilitated by the fact that the major factors governing ^{13}C nuclear shieldings are well established. Experimentally, it has been found that substituent effects on ^{13}C chemical shifts are largely additive. Semiempirical methods, therefore, are usually successful in
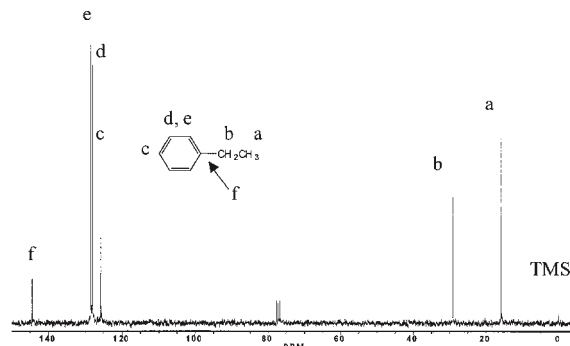
Figure 3
Carbon-13 NMR spectrum of ethylbenzene with assignments of the peaks to the carbons in the structure. Note that each unique carbon atom produces a different peak in the spectrum.

predicting these shifts. The largest variation in ^{13}C chemical shifts occurs with direct substitution by highly electronegative elements such as oxygen and fluorine. The hybridization at carbon also strongly affects the position of the resonance line. Carbon–carbon double bonds (C=C), for example, typically appear in the region 90–160 ppm from TMS, whereas carbon–carbon single bonds (C–C) usually occur in the range 0–90 ppm from TMS.

6. Other Nuclei

Prior to 1970 the bulk of NMR studies concerned the proton. The rest of the interest at that time was divided among the high-sensitivity nuclei ^{19}F, ^{31}P, and ^{11}B. Since then, studies involving virtually all observable NMR nuclei have been carried out. Extensive compilations of chemical shift data can be found for the nuclei mentioned above as well as ^{14}N, ^{15}N, ^{17}O, ^{29}Si, ^{195}Pt, ^{119}Sn, among others.

7. Quantitative NMR

NMR can be readily made quantitative since there are no response factors or matrix effects that need to be considered. In principle this means that the area under each peak in a spectrum is proportional to the number of nuclei of that type that are present in the molecular structure. In practice, however, several factors must be taken into account to obtain quantitative data.

In the data acquisition parameters, a sufficiently wide spectral width needs to be used to ensure a uniform level of RF power has been applied across the range of interest. Two other factors can distort the intensities of the peaks in the spectrum. Perturbations of the populations can occur when nuclei other than protons are observed and proton decoupling is used.

This is called the nuclear Overhauser effect (NOE). The NOE can be eliminated by turning the proton decoupler *off* during the delay between RF pulses (*gated decoupling*) to allow the normal equilibrium populations to be established. The second factor that must be considered is the spin–lattice relaxation time of the nuclei. For quantitative analysis it is necessary to use a sufficient delay between RF pulses to ensure that all nuclei are fully relaxed before the next RF pulse is applied. This may be seconds, or even minutes, and could hinder rapid acquisition of spectra. A small amount of a *paramagnetic relaxation reagent*, such as tris(acetylacetonato) chromium(III), is added to shorten the relaxation times of nuclei other than protons. Relaxation reagents provide an extremely efficient pathway for nuclear spins to return to the ground state through electron–nuclear dipole–dipole relaxation produced by the unpaired electron of the reagent. Thus, for quantitative analysis by NMR of nuclei other than protons, a small amount (50–75 mg) of a relaxation reagent should be added to the solution if possible to reduce T_1, gated decoupling should be used to eliminate any residual NOE, and a sufficiently long relaxation delay must be employed to permit complete relaxation of the nuclei. For protons it is sufficient simply to use a relaxation delay of appropriate length. Frequently the T_1 values of the nuclei of interest are measured and a relaxation delay of five times the largest T_1 is used.

8. Two-dimensional NMR

A major development in NMR was the introduction of the concept of two-dimensional NMR spectroscopy (2D NMR) in the early 1970s (Jeener 1971). In the standard one-dimensional NMR experiment the application of a RF pulse results in the nuclear magnetic moments precessing about the direction of the magnetic field. This response to the RF pulse induces a signal in the receiver coil of the probe which is monitored for a period of time (the *acquisition time*). Thus, the detected NMR signal (or *free-induction decay*, *FID*) is a function of a single time variable. Fourier transformation of this signal produces the normal one-dimensional frequency spectrum.

If the spin system is allowed to evolve under another set of experimental conditions (e.g., the length of time the proton decoupler is on) for a period of time prior to detection of the FID, and if this *evolution period* is varied systematically, the NMR signal is now a function of two time variables. The data are collected as a series of FIDs, each of which has the same acquisition time, t_2, but a different evolution period, t_1. Two Fourier transformations are performed on this data matrix, one on the rows of the matrix (t_1), and the second on the columns of the data (t_2). The result of this process is now a matrix (the two-dimensional spectrum) which is a function of two
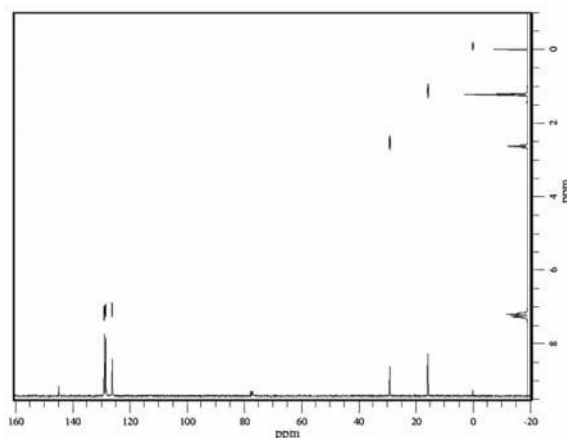
Figure 4
Two-dimensional heteronuclear (^{1}H–^{13}C) chemical shift correlation (HETCOR) plot showing connectivities between carbon nuclei and their directly bonded protons.

frequencies, v_1 and v_2, and for which the intensity of the signal at each pair of frequencies is a third dimension. The specific identity of these frequencies depends on the two-dimensional experiment performed. Some of the applications include *heteronuclear and homonuclear correlation spectroscopies* in which pairs of coupled nuclei are identified through scalar coupling (both short and long range), *J-resolved spectroscopy* in which the coupling patterns and chemical shifts are separated and shown on different axes, and *exchange spectroscopy* in which nuclei involved in chemical exchange can be identified.

An example of a two-dimensional heteronuclear (^{1}H–^{13}C) chemical shift correlation (HETCOR) spectrum of ethylbenzene is shown in Fig. 4. The proton spectrum is shown on the *y*-axis and the carbon spectrum is shown along the *x*-axis. The two-dimensional contour plot shows peaks at the intersections of directly coupled carbon and proton nuclei. Note that the ^{13}C resonance at 145 ppm has no directly bonded proton so there is no peak at that position in the two-dimensional plot.

See also: High-temperature Superconductors, Cuprate: Magnetic Properties by NMR/NQR; Nuclear Resonance Scattering; Solids, Nuclear Magnetic Resonance of

Bibliography

Bax A 1982 *Two-Dimensional Nuclear Magnetic Resonance in Liquids*. Delft University Press, Dordrecht, The Netherlands

Becker E D 1980 *High Resolution NMR, Theory and Chemical Applications*, 2nd edn. Academic Press, New York

Berger S, Braun S, Kalinowski H-O 1997 *NMR Spectroscopy of the Non-Metallic Elements*. Wiley, Chichester, UK

Breitmaier E, Voelter W 1987 *Carbon-13 NMR Spectroscopy, High-Resolution Methods and Applications*, 3rd edn. VCH, New York

Croasmun W R, Carlson R M K (eds.) 1987 *Two-Dimensional NMR Spectroscopy, Applications for Chemists and Biochemists*, Methods in Stereochemical Analysis. VCH, Weinheim, Germany, Vol. 9

Crutchfield M M, Dungan C H, Letcher J H, Mark V, Van Wazer J R 1967 *Topics in Phosphorus Chemistry: Vol. 5. P^{31} Nuclear Magnetic Resonance*. Wiley, New York

Ernst R R, Anderson W A 1966 *Rev. Sci. Instrum.* **37**, 93

Gorenstein D G (ed.) 1984 *Phosphorus-31 NMR, Principles and Applications*. Academic Press, New York

Harris R K 1983 *Nuclear Magnetic Resonance Spectroscopy, A Physicochemical View*. Pitman, Marshfield, MA

Harris R K, Mann B E 1978 *NMR and the Periodic Table*. Academic Press, New York

Jeener J 1971 Ampére International Summer School II, Basko Polje, Yugoslavia

Kalinowski H-O, Berger S, Braun S 1988 *Carbon-13 NMR Spectroscopy*. Wiley, Chichester, UK

Lauterbur P C 1957 *J. Chem. Phys.* **26**, 217

Quin L D, Verkade J G (eds.) 1994 *Phosphorus-31 NMR Spectral Properties in Compound Characterization and Structural Analysis*. VCH, New York

E. A. Williams
*General Electric Company, Niskayuna
New York, USA*

Nuclear Resonance Scattering

Nuclear resonance scattering (NRS) with synchrotron radiation combines the outstanding properties of Mössbauer spectroscopy (see *Mössbauer Spectrometry*) with those of synchrotron radiation. Since its first observation in 1984 (Gerdau *et al.* 1985) a rapid development of the technique and its applications followed which has just been reviewed (Gerdau and de Waard 2000). Thanks to the outstanding properties of third generation synchrotron radiation sources, NRS has nowadays become an established spectroscopy on an atomistic scale which is element and even isotope sensitive and nondestructive. Applications comprise two main fields, "hyperfine spectroscopy" and "structural dynamics." In hyperfine spectroscopy NRS is complementary to other nuclear techniques and yields useful information on atomic, magnetic, and electric properties and structures. Those fields of applications benefit most which exploit the specific properties of synchrotron radiation:

applications to high pressure, to grazing incidence geometry (surfaces and multilayers), to single crystals, and to very small samples. Structural dynamics on a ps to μs timescale as free or jump diffusion as well as rotational motions can directly be measured in the time domain by nuclear quasi-elastic scattering techniques. On the fast timescale the (partial) density of phonon states is directly accessible by nuclear inelastic scattering.

1. Principles of Nuclear Resonance Scattering

Nuclear resonance scattering is a resonant x-ray scattering technique in the time domain. It is based on the Mössbauer effect and the scattering proceeds via the Mössbauer level whereas Mössbauer spectroscopy is an absorption spectroscopy and is normally carried out in the energy domain. Both are, in principle, connected by the Heisenberg uncertainty principle.

In case of Mössbauer spectroscopy (see *Mössbauer Spectrometry*) a radioactive source provides the γ-quanta which are very sharp in energy (neV-μeV) and by varying the energy one measures absorption spectra behind the sample. In nuclear resonance scattering an x-ray pulse from a synchrotron radiation source which is very sharp in time ($\sim 100\,ps$) and very broad in energy (white radiation) excites the nuclear levels in the sample. The successive decay of these levels gives rise to an exponential intensity decay in time. This decay corresponds to the Lorentzian line in Mössbauer absorption spectroscopy.

There are several techniques utilizing nuclear resonance scattering: nuclear forward scattering (NFS), nuclear quasi-elastic scattering (NQES), nuclear Bragg diffraction (NBD), nuclear reflectometry (NR, for the investigation of surfaces and multilayers), nuclear small angle scattering (NSAS, measuring for example, magnetic domain structures), nuclear inelastic scattering (NIS), and synchrotron radiation-based perturbed angular correlation (SRPAC). In the following a short introduction will be given to the main fields: nuclear forward scattering, nuclear quasi-elastic scattering, and nuclear inelastic scattering (see Fig. 1).

1.1 Nuclear Forward Scattering

Nuclear forward scattering (and nuclear reflectometry) has the closest analogy to Mössbauer spectroscopy; in fact, it is its scattering variant. The main domain is the determination of hyperfine parameters such as internal magnetic fields (magnetic hyperfine field), electric field gradients, isomer shifts, and the Lamb-Mössbauer factor (f_{LM}).

The setup for NFS (see Fig. 1) also looks very similar to a standard set-up for Mössbauer spectroscopy (see *Mössbauer Spectrometry*). However, while Mössbauer spectroscopy is an absorption spectroscopy (one γ-quantum is absorbed by one nucleus)
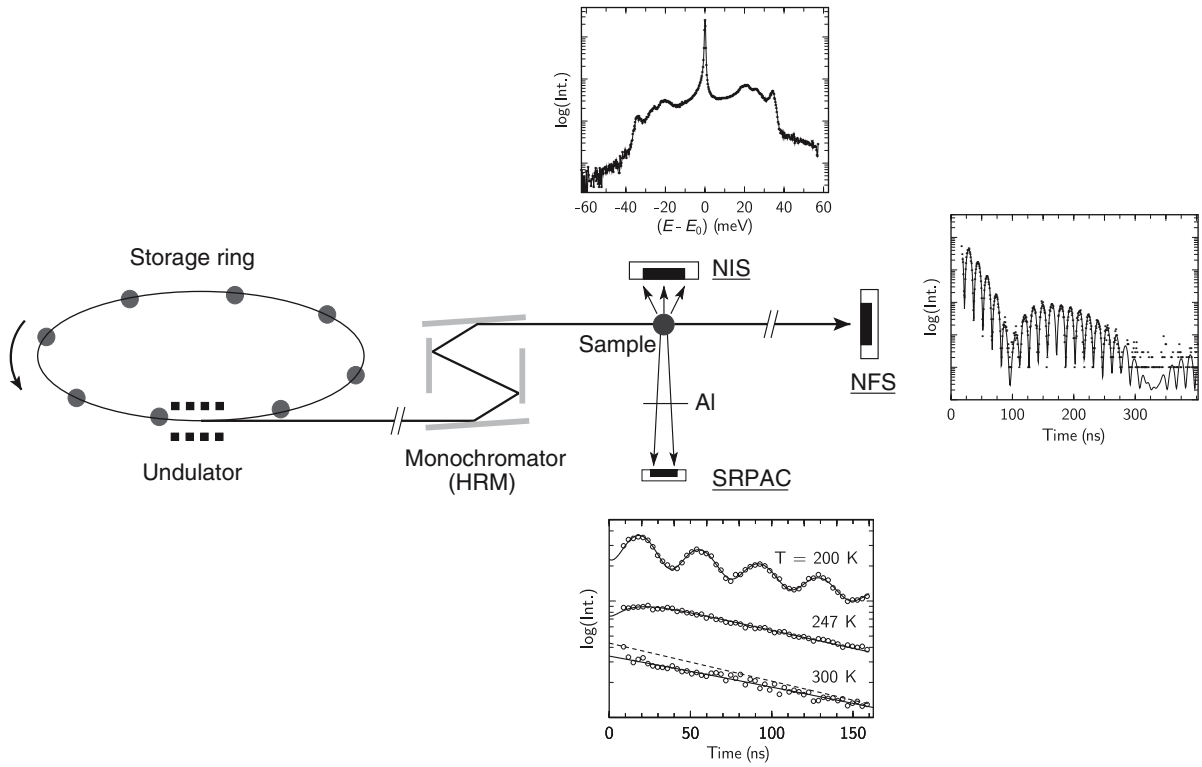
Figure 1
Scheme of the setup for some techniques in NRS: NFS, NIS, and SRPAC. Furthermore, the corresponding time and energy spectra are schematically shown measured by the detectors for NFS, SRPAC, and NIS. The storage ring is operated in "few bunch" mode with e.g. 176 ns spacing between adjacent buckets (red bullets). The undulator produces the well-collimated synchrotron radiation which is monochromized at the nuclear resonances by a high resolution monochromator, HRM (bandwidth $\Delta E \approx$ meV). Finally the radiation impinges the sample. Depending on the scattering process and the scattering geometry different techniques are exploited. Variable sample environments allow for the combination of high/low temperature, high pressure, and external magnetic field.

NFS is a scattering spectroscopy. The "white" synchrotron radiation excites all Mössbauer levels in the sample and creates a "coherent collective nuclear state". In the static case this nuclear state will decay in the forward direction giving rise to an excess of intensity at delayed times (see Fig. 1, NFS). The timescale is determined by the lifetime τ_0 of the involved nuclear level. Multiple scattering may influence the measured time response giving rise to "dynamical beats." Furthermore, in case of split nuclear levels due to hyperfine interaction (electric, magnetic) an additional interference pattern, the so-called "quantum beat" structure is superimposed.

(a) Dynamical beats
For samples with a large effective thickness, $t_{\text{eff}} = n_{\text{MB}} d \sigma_0 f_{\text{LM}}$, with n_{MB} the density of Mössbauer nuclei, d the geometrical thickness, σ_0 the resonant

Mössbauer cross section, and f_{LM} the Lamb–Mössbauer factor, a speed-up effect is observed and dynamical beats (Bessel beats) show up in the time spectra.

In Fig. 2 the situation is shown for Mössbauer and NFS spectra. For a thin sample, $t_{\text{eff}} = 1$, we have a single Lorentzian line in the Mössbauer spectrum which corresponds to an exponential decay in the NFS spectrum (Fig. 2(a),(b), dotted lines). Increasing the effective thickness ($t_{\text{eff}} = 25$) the Mössbauer line becomes much wider and non-Lorentzian (Fig. 2(a), solid line). In the NFS spectrum (Fig. 2(b), solid line) we observe two features: (i) a speed-up, showing up as an increase in intensity at early times (from 10^7 to 10^9 units in the present example) and (ii) a dynamical beat structure is superimposed to the decay. From this beat structure the effective thickness and by this f_{LM} can very precisely be determined.
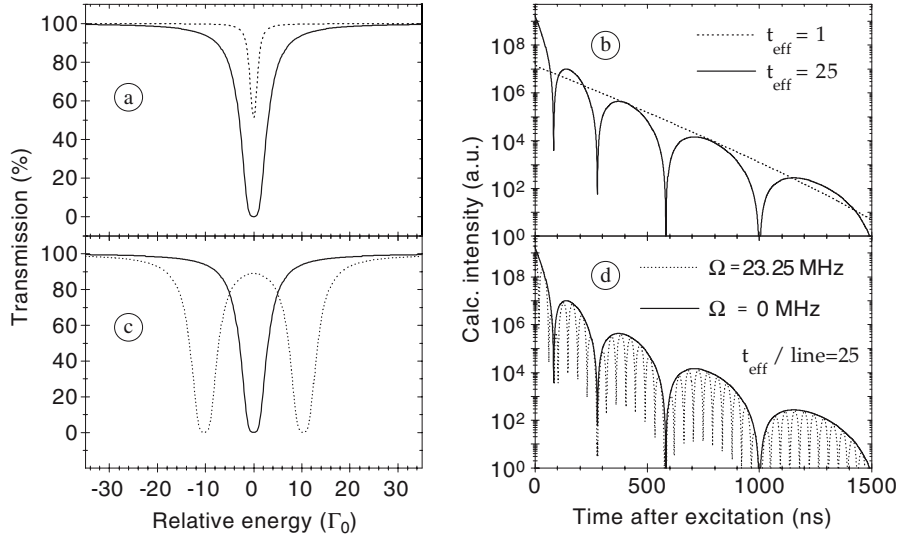
Figure 2
Simulations of corresponding spectra of Mössbauer spectroscopy (left panel, with $\Gamma_0 = \hbar/\tau_0$) and NFS (right panel) for thin ($t_{eff} = 1$) and thick ($t_{eff} = 25$) samples. For the single lines (panel a) the thin sample leads to an exponential decay whereas the spectrum from the thick sample is further modulated by the dynamical beats (panel b). In panel c the energy spectra of a thick sample ($t_{eff} = 25$) with one (solid line) and two (dotted line) transition lines, respectively, are shown. In panel d the corresponding time spectra are shown. The sample with the two lines shows in addition to the dynamical beats the fast, equidistant quantum beat structure with frequency Ω superimposed (from Grünsteudel 1998).

(b) Quantum beats

As is well known (see *Mössbauer Spectrometry*) hyperfine interaction might split the nuclear levels. In Mössbauer spectroscopy several absorption lines reveal this splitting whereas in NRS an interference pattern, the quantum beat structure, shows up.

In case of quadrupolar interaction the excited nuclear state (e.g., in case of ^{57}Fe) splits to the $\pm 3/2$ and $\pm 1/2$ levels. This gives rise to two absorption lines in Mössbauer spectroscopy (see dotted line in Fig. 2(c)). The corresponding spectrum in NFS shows up as an interference pattern of these two transitions with a single frequency Ω of the quantum beats (see dotted line in Fig. 2(d)). Due to the thick sample with an effective thickness $t_{eff} = 25$, the dynamical beat structure strongly modulates the quantum beats as an envelope. It is clearly seen that the quantum beat structure is equidistantly spaced whereas for the dynamical beat structure the distance of the minima increases with time. This can be described in a good approximation by

$$I_{NFS}(t) \propto \frac{t_{eff}}{t/\tau_0} \, \cos^2\left(\frac{\Omega t}{2}\right) e^{-t/\tau_0} \cdot J_1\left(\sqrt{4t_{eff}t/\tau_0}\right)^2 \quad (1)$$

The term $\cos^2(\frac{1}{2}\Omega t)$ describes the quantum beats and the Bessel function J_1 the dynamical beats. For comparison the unsplit case is shown as solid lines in

the same figures. Changing the strength of the hyperfine interaction will result in a different splitting and correspondingly in a different quantum beat frequency Ω.

In the case of magnetic hyperfine interaction, full splitting of the nuclear levels occurs giving rise to six nuclear transitions and correspondingly to six absorption lines in Mössbauer spectroscopy with ^{57}Fe (see *Mössbauer Spectrometry*). In NRS spectroscopy a more detailed interference pattern will result. Contrary to Mössbauer spectroscopy where the γ-rays from the radioactive source are normally unpolarized now the x-rays from the synchrotron radiation source are highly linearly polarized. This feature strongly modifies the time spectra which are displayed in Fig. 3. The important parameters are the orientation of the three vectors with respect to each other, the wave vector $\vec{k}$, the polarization vector $\vec{E}$, and the hyperfine field vector $\vec{H}$.

If all three vectors are perpendicular to each other a simple quantum beat pattern with one single frequency and high contrast results originating from the two $\Delta m = 0$ transitions (Fig. 3a).

A similar spectrum with only one frequency, however, with less contrast appears when $\vec{H} \| \vec{k}$. In this case the two $\Delta m = +1$ and the two $\Delta m = -1$ transitions interfere independently giving rise to left and right hand circular polarization (Fig. 3c).
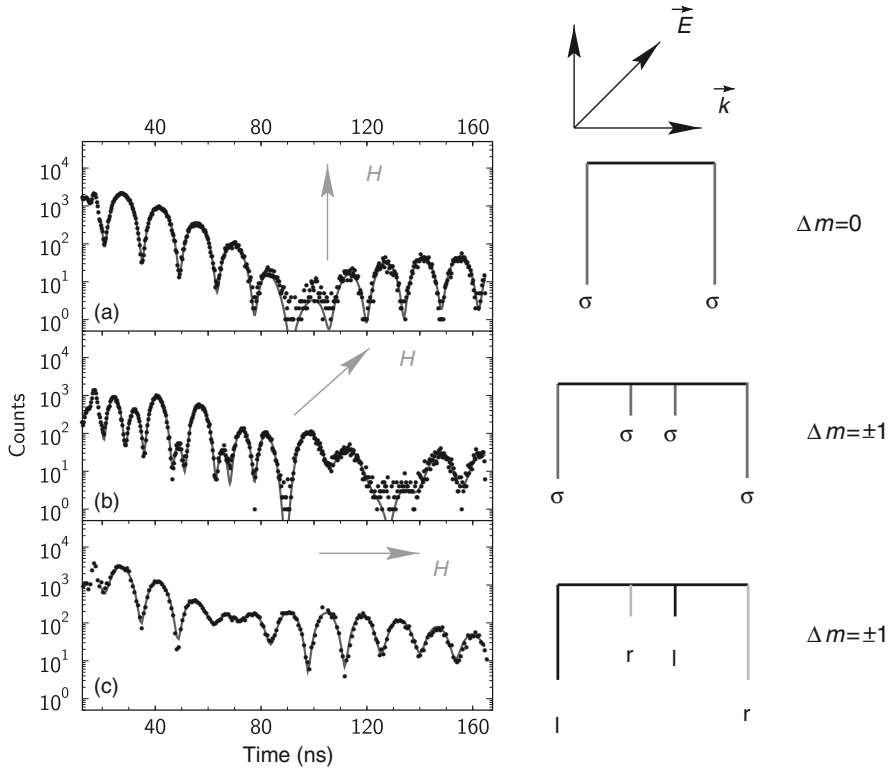
Figure 3
Left panel: Measured time spectra of iron (NFS) in case of magnetic hyperfine interaction for various alignments of the hyperfine field $\vec{H}$ with respect to the wave vector $\vec{k}$ and the polarization $\vec{E}$. Solid lines are fits according to the full theory. Right panel: nuclear transition lines with their polarization state, $\sigma - \sigma$ linearly polarized, l and r left- and right-hand circular polarized, respectively. Δm—change of magnetic quantum number (reproduced with permission from Leupold *et al.* (2003); © Kluwer Academic Publisher).

Finally, for $\vec{H} \| \vec{E}$ all $\Delta m = \pm 1$ transitions interfere giving rise to a more complicated spectrum which is sigma polarized (Fig. 3b). The slow overall modulation is caused by dynamical beats due to the finite effective thickness.

1.2 Nuclear Quasi-elastic Scattering

Nuclear quasi-elastic scattering measures structural dynamics on a ps to μs timescale. The coherent and the incoherent channel can be utilized. In the first case, the coherent channel, the Lamb–Mössbauer factor has to be greater than zero ($f_{LM} > 0$). The setup is the same as in NFS (see Fig. 1). The incoming x-ray pulse creates a coherent collective nuclear state which decays in the static case in forward direction. Dynamics, for example, the jump of a Mössbauer nucleus from one atomic site to another (in space and angle, see Dattagupta (1976) for example), destroys this state. As a consequence no x-ray is scattered in forward direction, i.e., the measured intensity in the

NFS detector is decreased at later times. We will get an "accelerated decay" or a "damping" of the NFS intensity $I_{NFS}(t)$ which might be described in a simplified picture by

$$I(t) \propto I_{NFS}(t) e^{-2\lambda_t t} \, e^{-\lambda_r t} \qquad (2)$$

The first exponential is related to the van Hove self-intermediate function with λ_t being the translational relaxation rate and the second one to the rotational correlation function with λ_r being the rotational relaxation rate. In the second case, the incoherent channel, the scattering is independent of the Lamb-Mössbauer factor, f_{LM}. The setup (see Fig. 1) is similar as in traditional time differential perturbed angular correlation (see *Perturbed Angular Correlations (PAC)*) spectroscopy. Therefore the technique is called synchrotron radiation-based perturbed angular correlation, SRPAC. The incoming x-ray pulse selectively excites a single nucleus which decays in the static case with an angular distribution according to the anisotropy parameter, A_{22}. Dynamics, for

example, rotational motion monitored by the electric hyperfine interaction $\hbar\Omega$, changes this distribution and gives rise to a damping of the intensity signal. The scattering intensity can be written as

$$I = I_0\, e^{-t/\tau_0}\{1 - A_{22}G_{22}(t)\} \tag{3}$$

with A_{22} the anisotropy and angular term and G_{22} the perturbation factor. It reduces in the slow approximation to

$$G_{22}(t) \propto e^{-\lambda_r t}\ \cos^2\left(\frac{\Omega t}{2}\right) \tag{4}$$

and in the fast approximation to

$$G_{22}(t) \propto e^{-(\Omega^2/\lambda_r)t} \tag{5}$$

Combining both techniques the translational and rotational relaxation rates can be separately extracted.

1.3 Nuclear Inelastic Scattering

Nuclear inelastic scattering is a very recent method in order to measure directly the (partial) density of phonon states (Seto *et al.* 1995; Sturhahn *et al.* 1995; Chumakov *et al.* 1995). The principle setup is shown in Fig. 1. The synchrotron radiation is monochromized by a scanning high resolution monochromator (HRM) with (sub-)meV ($1\,\mathrm{meV} = 0.24\,\mathrm{THz}$) energy resolution. At resonance the x-ray pulse creates a coherent collective nuclear state as in NFS which decays either in forward direction or incoherently, due to internal conversion, spin flop etc., in the entire solid angle of 4π. This feature gives a simple and effective method at hand to measure the instrumental function (detector NFS) in parallel with the inelastic spectrum (detector NIS). While scanning the HRM the nuclear resonance can only be excited when at the same time a phonon is excited or annihilated. In NIS this is a purely incoherent process with the consequence of a perfect averaging over the momentum $\vec{q}$. The successive nuclear decay proceeds as a single exponential in the entire solid angle covered by the "4π"-detector (detector NIS). In practice only a solid angle of about π can be achieved.

As an example the energy dependence of nuclear inelastic scattering of synchrotron radiation in a polycrystalline α-iron sample at room temperature is shown as a function of energy of the incident radiation (Fig. 4). The central peak corresponds to elastic scattering. The structure beyond the central peak shows the energy spectrum of inelastic scattering, accompanied either by creation ($E > 0$) or by annihilation ($E < 0$) of phonons. At ambient temperature one may recognize various contributions to the energy spectrum, which correspond to inelastic scattering accompanied by excitation or annihilation of different number of phonons. The normalized probability
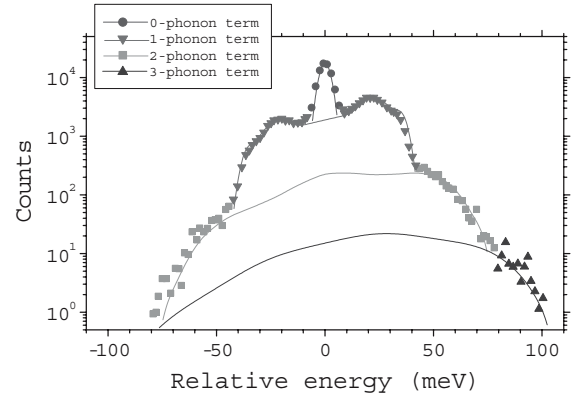
Figure 4
Expansion of the energy spectrum of nuclear inelastic scattering of synchrotron radiation in α-iron in multiphonon terms. The data were taken at room temperature. Different symbols show the regions of the spectra, where the corresponding contributions are dominant. The lines are the calculations according to Eqns. (6)–(8) and convoluted with the instrumental function of the monochromator (reproduced with permission from Chumakov and Sturhahn (1999); © Kluwer Academic Publisher).

of nuclear inelastic scattering $W(E)$ can be decomposed in terms of a multiphonon expansion (Singwi and Sjölander 1960)

$$W(E) = f_{\mathrm{LM}}\left(\delta(E) + \sum_{n=1}^{\infty} S_n(E)\right) \tag{6}$$

The Dirac δ-function $\delta(E)$ describes the elastic part of scattering (zero-phonon term), and the nth term of the series $S_n(E)$ represents the inelastic scattering accompanied by creation (annihilation) of n phonons. The one-phonon term is given by

$$S_1(E) = \frac{E_{\mathrm{R}} \cdot g(|E|)}{E \cdot (1 - e^{-\beta E})} \tag{7}$$

and the subsequent terms under harmonic approximation may be found through the recursive relation:

$$S_n(E) = \frac{1}{n}\int_{-\infty}^{\infty} S_1(E')S_{n-1}(E - E')\,\mathrm{d}E' \tag{8}$$

Here $\beta = (k_{\mathrm{B}}T)^{-1}$ with k_{B} the Boltzmann constant, T the temperature, $E_{\mathrm{R}} = \hbar^2 k^2/2M$ the recoil energy of a free nucleus, k the wave vector of the x-ray quantum, M the mass of the atom. The function $g(E)$ is the normalized density of phonon states

$$g(E) = V_0\frac{1}{(2\pi)^3}\sum_j \int \mathrm{d}\vec{q}\,\delta[E - \hbar\omega_j(\vec{q})] \tag{9}$$

where V_0 is the volume of unit cell, index j numerates the branches of the dispersion relation $\hbar\omega_j(\vec{q})$, $\vec{q}$ is the phonon momentum, and the integral is taken within the first Brillouin zone. The detailed theory of nuclear inelastic scattering has been published by several authors (Singwi and Sjölander 1960; Kohn *et al.* 1998, Sturhahn and Kohn 1999).

From the density of phonon states other (thermo)dynamic quantities can be derived as the vibrational contribution to the internal energy, lattice specific heat at constant volume and pressure, vibrational entropy. From the sum rules (Lipkin 1999) the density of phonon states, f_{LM} and the mean square displacement, the mean kinetic energy, the mean force constant, and the second order Doppler shift can be determined.

In summary, NIS gives direct access to the density of phonon states and various (thermo)dynamic quantities. It is complementary to methods as inelastic neutron, x-ray, and light scattering. In those techniques mainly dispersion relations which are fitted to a model are measured and in a final step the density of phonon states can be derived.

2. Applications

2.1 Applications to High Pressure

High-pressure applications are one of the domains which benefit most from the outstanding properties of synchrotron radiation. The small beam size allows one to work with samples much smaller than 100 μm

in diameter. In that case state-of-the-art diamond anvil cells (DAC) are able to reach pressures far above the 100 GPa regime, those pressures which are common in the center of the Earth. The small divergence of the beam allows sophisticated sample environments, *in situ* pressure calibration and diffraction studies for the determination of the induced volume change with pressure. In the following example iron metal has been investigated by NFS and NIS in order to follow over the pressure-induced phase transition magnetic order (via the hyperfine field) and structural dynamics (via the partial phonon DOS).

(a) Iron metal

Recently, the high-pressure behaviour of iron gained much interest due to unusual superconductivity and due to simulations of the inner core of the Earth and improved technical developments in high-pressure research. It is well known that α-iron undergoes under pressure a magnetic and structural phase transition to the hexagonal closed-packed (h.c.p.) phase of iron (ε-iron) in the pressure range of 10–22 GPa at ambient temperature.

A 2.5 μm thick iron foil enriched to 95% in ^{57}Fe was pressurized in a DAC (Grünsteudel 1997). Figure 5 shows the NFS spectra for various pressures. A small external magnetic field (0.6 T) aligned the internal field perpendicular to the incoming wave vector $\vec{k}$ and the polarization $\vec{E}$ (the case discussed in Fig. 3a). At 3 GPa the spectrum reveals iron in the pure α-phase. The regular quantum beat pattern shows a single frequency from which a hyperfine field
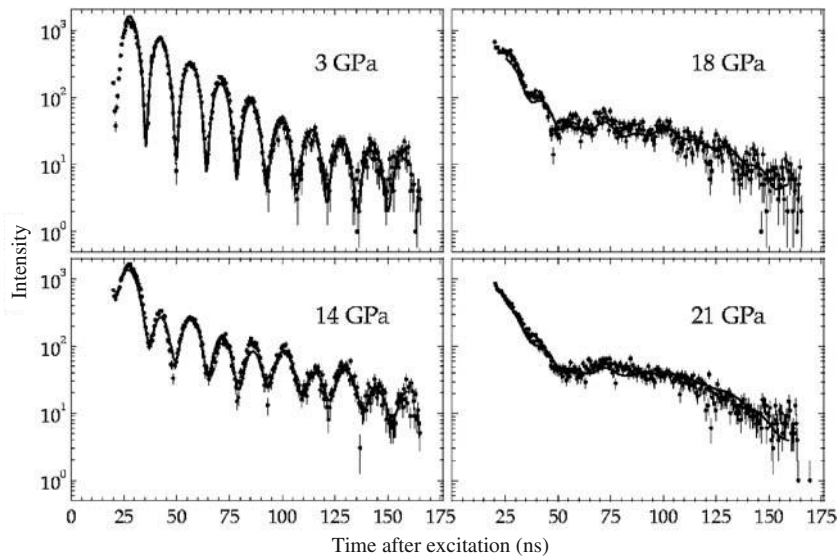
Figure 5
Time spectra of NFS from the pressure induced α→ε transition in Fe at various pressures (from Grünsteudel 1997).

of 32.4 T can be derived. Taking into account the polarizing external field of 0.6 T the internal field becomes 33.0 T (in case of iron the external and internal field align antiparallel). At 14 GPa the influence of the ε-phase is already quite pronounced. With a further increase in pressure the influence of the nonmagnetic ε-phase becomes dominant. At 21 GPa the sample is almost completely in the ε-phase. Now the NFS spectrum is modified only by a single Bessel minimum at 50 ns which originates from the increased effective thickness in comparison to that of the magnetically split one.

With the same sample, NIS spectra have been recorded and the densities of phonon states have been extracted (Lübbers *et al.* 2000b). Examples at ambient pressure and at 42 GPa are displayed in Fig. 6. All spectral features of the density of phonon states of ε-Fe are shifted to higher energies with respect to α-Fe revealing a hardening of the lattice vibrations. Several thermodynamical properties have been derived as f_{LM} and the mean-square displacement, respectively, the mean phonon energy and the corresponding Debye temperature, the lattice contribution to the specific heat c_V, the internal energy, entropy, and the mean force constant. Finally, from the low-energy part of the density of phonon states the average velocity of sound v_{av} (Fig. 6 inset) has been derived according to the relation

$$g(E) = \frac{V}{2\pi^2\hbar^3 v_{av}^3}E^2 \qquad (10)$$
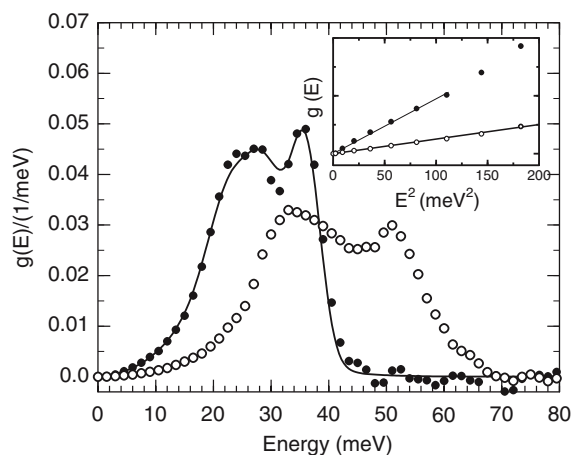
Figure 6
Phonon density of states from the pressure induced $\alpha \to \varepsilon$ transition in Fe at ambient pressure (solid circles) and 42 GPa (open circles). The solid line represents the DOS from neutron scattering. The inset displays the corresponding low energy part for the determination of sound velocities. Here the solid lines represent a linear fit to the data (reprinted with permission from Lübbers *et al.* (2000b); © AAAS).

with V the volume per Fe atom. Extensions to higher pressures have been reported (Mao *et al.* 2001) and investigations undertaken to account for anisotropies (Lübbers *et al.* 2000a). These sound velocity data have been complemented by recent data-from inelastic x-ray scattering and in the very high-pressure regime by those from shock waves and in the low-pressure regime by those from neutron scattering.

2.2 Applications to Nano-structured Material

The understanding of magnetism of self-organized nano-structures and clusters gained much attention because of fundamental aspects of nanoscale magnetic ordering in general and possible applications in high-density magnetic storage and magnetoelectronics.

(a) Iron on W (110)
As an example the perpendicular spin orientation in ultrasmall Fe islands on W (110) will be discussed (Röhlsberger *et al.* 2001). Ultrasmall pseudomorphic Fe islands on an atomically clean W (110) crystal have been prepared by thermal evaporation of Fe enriched to 95% in ^{57}Fe. The coverage of the Fe islands was 0.57 which is slightly below the percolation limit. Their average diameter was determined to be 2.0 nm. A coating of five monolayers of Ag prevents the sample from contamination. Figure 7 left panel displays the time spectra taken in grazing incidence geometry between 300 K and 4.5 K. The right panel of Fig. 7 shows the determined weight of the magnetic component. It increases with decreasing temperature. This can be attributed to superparamagnetic relaxation of the magnetic moments. At high temperatures the magnetization of small particles is subject to fast thermal fluctuations so that the effective magnetic hyperfine field averages to zero. The transition from the fast relaxation regime to the magnetically ordered state occurs at about 50 K. However, it is a very broad transition certainly due to the size distribution of the islands. The modulation in the time spectra is characteristic for a perpendicular magnetization. This result is quite remarkable because Fe films on W (110) are known to be magnetized in-plane for coverages of more than 0.6.

(b) Exchange-coupled thin films
Exchange-coupling between soft- and hard-magnetic phases (see *Multilayers: Interlayer Coupling*) plays an important role in the engineering of novel functional magnetic nanostructures. There exist some micromagnetical models describing this behavior (see *Magnets: Remanence-enhanced*), however, due to methodological difficulties there exist nearly no direct measurements of the actual spin structure. Utilizing the technique of probe layers, i.e., inserting ^{57}Fe in various depths of the thin film (see Fig. 8),
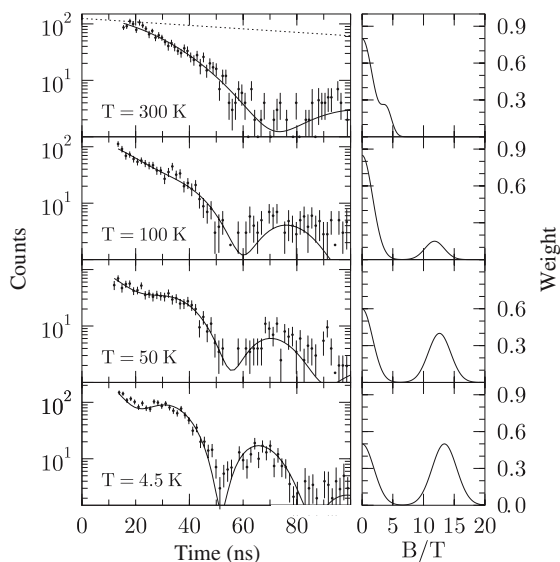
Figure 7
Time spectra of nuclear resonant grazing-incidence reflection from ultrasmall ^{57}Fe islands on W (110). The modulation of the intensity is attributed to a perpendicular magnetization of the Fe islands. The solid lines are the results of simulations. The right panel displays the probability density for the hyperfine field distribution that was obtained from the simulations (reprinted figure with permission from Röhlsberger *et al.* (2001); © by the American Physical Society).
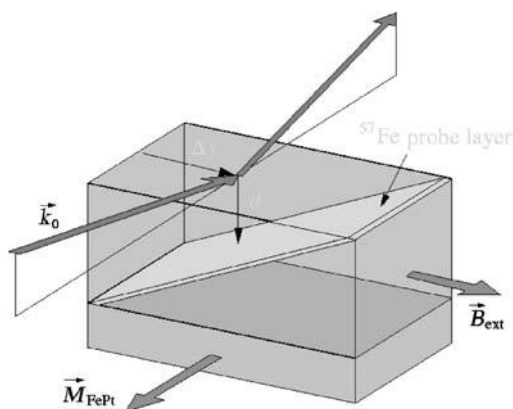
Figure 8
Scattering geometry of the sample (11 nm Fe on FePt). The incoming x-ray beam with wavevector $\vec{k}_0$ impinges the sample at a lateral position Δy probing the spin structure via the wedge-shaped ^{57}Fe probe layer (0.7 nm) at depth d (reprinted figure with permission from Röhlsberger *et al.* (2002); © by the American Physical Society).

NRS directly probes the actual spin structure in various depths by selectively exciting the ^{57}Fe layer at various lateral positions (Röhlsberger *et al.* 2002). The sample investigated here is a bilayer system consisting of 11 nm Fe on 30 nm $Fe_{55}Pt_{45}$ in the hard-magnetic tetragonal $L1_0$ phase. A wedge-shaped 0.7 nm thick ^{57}Fe film with a slope of 0.5 nm/mm has been produced. Different depths d in the sample can thus be probed by adjusting the displacement Δy of the sample transversely to the incident beam. The sample was magnetically saturated in an external field of 2.3 T so that the remanent magnetization $\vec{M}_{FePt}$ of the $Fe_{55}Pt_{45}$ layer was oriented along $\vec{k}_0$, as shown in Fig. 8. Time spectra at 4 K with selected in-plane external fields $\vec{B}_{ext}$ perpendicular to $\vec{k}_0$ were taken at various displacements of Δy. Evaluation of the spectra reveals the depth dependence of the rotation of the magnetization in the Fe film (see Fig. 9).

2.3 Applications to Disordered Systems

NRS techniques are well suited for the investigation of the dynamics of disordered systems over a huge timescale. Whereas NIS covers the fast regime of phonons, NQES techniques complement the investigations to the slow time regime (10^5–10^{10} Hz). The technique of probe molecules allows for the investigation of glasses which do not contain Mössbauer atoms and, furthermore, when carefully chosen, allows for mode selectivity as collective and noncollective modes, respectively. In the following example, the glass forming dibutyl phthalate (DBP), with a glass temperature $T_g = 178$ K, was investigated by NFS (sensitive to translational and rotational dynamics) and SRPAC (sensitive only to rotational dynamics) (Sergueev *et al.* 2003). Ferrocene was used as probe molecules. NFS spectroscopy is applicable as long as the Lamb–Mössbauer factor f_{LM} is greater than zero, which holds in this case up to 210 K. SRPAC, on the other hand, does not depend on f_{LM} and can be applied in the entire temperature regime (see Fig. 10). At the lower temperatures, the SRPAC intensity follows an exponential decay modulated by quantum beats. In the regime of slow relaxation, the beats are damped at a rate proportional to rotational relaxation (see Eqn. (4)). Similar quantum beats modulate the decay of the NFS intensity, where the damping depends on the sum of rotational and translational relaxation (see Eqn. (2)). At higher temperatures, in the regime of fast relaxation, only SRPAC spectra can be measured. From these spectra relaxation rates have been determined. Below 190 K the data sets from both techniques coincide, which means that translational dynamics is absent in the experimental time window. Above 190 K the NFS data begin to deviate from the SRPAC data because translational dynamics is activated. From these results the pure translational relaxation rates have been derived.
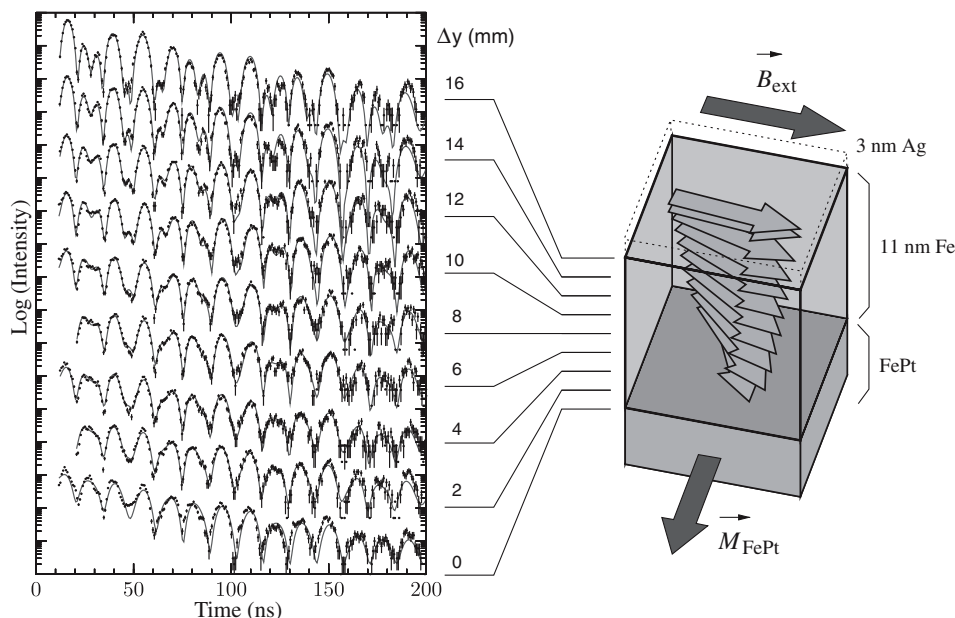
Figure 9
Left panel: Time spectra of nuclear resonant grazing-incidence reflection from the probe layer ($\vec{B}_{ext} = 160$ mT and at 4 K). Right panel: Image of the derived spin structure (blue arrows) of the iron layer (reprinted figure with permission from Röhlsberger *et al.* (2002); © by the American Physical Society).
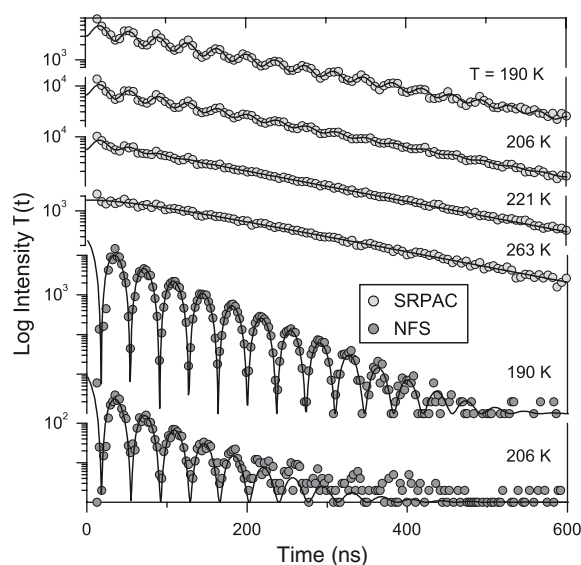
Figure 10
Time spectra of SRPAC and NFS for several temperatures from ferrocene in DBP. The solid lines show the fit according to the full theory (from Sergueev *et al.* 2003).

2.4   Summary

With the advent of powerful synchrotron radiation sources around the world as APS (Argonne, USA), SPring-8 (Harima, Japan), and ESRF (Grenoble, France) nuclear resonance scattering techniques became a rapid growing spectroscopy with unique applications in various fields. The probe molecule/layer technique, the application of sophisticated sample environments, and the possibility of applying various NRS techniques simultaneously makes this spectroscopy a unique tool. The previous typical examples demonstrate the versatility and huge potential of the technique. Even when these examples focused on ^{57}Fe for the sake of simplicity the tunable (in energy) synchrotron radiation allows for a convenient and routine access to various Mössbauer isotopes.

See also: Magnetism: Applications of Synchrotron Radiation; Magnetic Excitations in Solids

Bibliography

Chumakov A I, Rüffer R, Grünsteudel H, Grünsteudel H F, Grübel G, Metge J, Leupold O, Goodwin H 1995 Energy dependence of nuclear recoil measured with incoherent nuclear scattering. *Europhys. Lett.* **30**, 427–30

Chumakov A I, Sturhahn W 1999 Experimental aspects of inelastic nuclear resonance scattering. *Hyperfine Interactions* **123/124**, 781–808

Dattagupta S 1976 Effect of molecular motions in liquids on Mössbauer relaxation spectra. *Phys. Rev. B* **14**, 1329–32

Gerdau E, de Waard H (eds.) 1999/2000 *Nuclear Resonant Scattering of Synchrotron Radiation*. Baltzer Science Publishers

Gerdau E, Rüffer R, Winkler H, Tolkdorf W, Klages C, Hannon J P 1985 Nuclear Bragg diffraction of synchrotron radiation in yttrium iron garnet. *Phys. Rev. Lett.* **54**, 835–8

Grünsteudel H 1998 *Nuclear Resonant Scattering of Synchrotron Radiation on Iron Containing Biomimetic Compounds*. PhD thesis, Medizinische Universiät zu Lübeck, Lübeck

Grünsteudel HF 1997 *Der α-ε-Übergang in Eisen als Beispiel für nukleare Vorwärtsstreuung von Synchrotronstrahlung an Proben unter hohem Druck*. PhD thesis, Universiät Paderborn, Paderborn

Kohn V G, Chumakov A I, Rüffer R 1998 Nuclear resonant inelastic absorption of synchrotron radiation in an anisotropic single crystal. *Phys. Rev. B* **58**, 8437–44

Leupold O, Rupprecht K, Wortmann G 2003 Electronic and magnetic transitions in europium compounds studied by nuclear forward scattering of synchrotron radiation. *Structural Chemistry* **14**, 97–107

Lipkin H J 1999 Mössbauer sum rules for use with synchrotron sources. *Hyperfine Interactions* **123/124**, 349–66

Lübbers R, Giefers H, Rupprecht K, Wortmann G, Chumakov A I 2000a High-pressure phonon spectroscopy of oriented hcp iron. *ESRF Highlights* 2000, 48–9

Lübbers R, Grünsteudel H F, Chumakov A I, Wortmann G 2000b Density of phonon states in iron at high pressure. *Science* **287**, 1250–2

Mao H K, Xu J, Struzhkin V V, Shu J, Hemley R J, Sturhahn W, Hu M Y, Alp E E, Vocadlo L, Alfé D, Price G D, Gillan M J, Schwoerer-Böhning M, Häusermann D, Eng P, Shen G, Giefers H, Lübbers R, Wortmann G 2001 Phonon density of states of iron up to 153 gigapascal. *Science* **292**, 914–6

Röhlsberger R, Bansmann J, Senz V, Jonas K-L, Bettac A, Leupold O, Rüffer R, Burkel E, Meiwes-Broer K-H 2001 Perpendicular spin orientation in ultrasmall Fe islands on W(110). *Phys. Rev. Lett.* **86**, 5597–600

Röhlsberger R, Thomas H, Schlage K, Burkel E, Leupold O, Rüffer R 2002 Imaging the magnetic spin structure of exchange-coupled thin films. *Phys. Rev. Lett.* **89**, 237201

Sergueev I, van Bürck U, Chumakov A I, Asthalter T, Smirnov G V, Franz H, Rüffer R, Petry W 2003 Rotational and translational dynamics studied by nuclear resonant scattering. *ESRF Highlights* 2003, 12–3

Seto M, Yoda Y, Kikuta S, Zhang X, Ando M 1995 Observation of nuclear resonant scattering accompanied by phonon excitation using synchrotron radiation. *Phys. Rev. Lett.* **74**, 3828–31

Singwi K, Sjölander A 1960 Resonance absorption of nuclear gamma rays and the dynamics of atomic motions. *Phys. Rev.* **120**, 1093–102

Sturhahn W, Kohn V G 1999 Theoretical aspects of incoherent nuclear resonant scattering. *Hyperfine Interactions* **123/124**, 367–99

Sturhahn W, Toellner T, Alp E E, Zhang X, Ando M, Yoda Y, Kikuta S, Seto M, Kimball C, Dabrowski B 1995 Phonon density of states measured by inelastic nuclear resonant scattering. *Phys. Rev. Lett.* **74**, 3832–5

R. Rüffer
ESRF, Grenoble, France

O

Optical and Magneto-optic Data Storage: Channels and Coding

The data path of an optical recording system is effectively a communications channel with certain bandwidth and noise characteristics. Data to be recorded must pass through this channel and, on replay, must emerge unaltered. The vehicle to navigate the data through the channel is a recording code (also known as a modulation code or channel code). The recording code converts data to an appropriate format to pass through the channel and be recovered as the original data on replay.

The frequency response of the channel falls off sharply at high frequencies. Therefore, if the signal representing "raw" data contains high-frequency components then these will not be recorded. Because the binary data to be recorded cannot be predicted it is likely that the signal representing the data contains a broad spectrum of frequencies ranging from very low to very high. Consequently, the recording code converts the frequency spectrum of the signal to be recorded to a form that matches the response of the recording channel.

An important function of a recording code is to enable the regeneration of a timebase for effective re-timing of the signal during playback. There will be differences between the speed of the disk during record and playback. It is essential, therefore, to have a timebase signal that is accurately synchronized to the rate at which data are read from the disk. In effect, the recording code combines the data to be recorded with a clock signal on recording. At replay the clock signal is extracted and used to control a phase-locked-loop circuit that provides the timebase.

For a given channel bandwidth the correct choice of code can increase storage density above that of an uncoded system. A common coding technique is "non return to zero immediate" (NRZI): binary one is represented as a signal-level transition and zero as no transition. However, there is a limit to how close transitions can be packed together in an attempt to increase storage density. Too close and their mutual proximity begins to affect the ability of the detection scheme to resolve them. The recording code introduces constraints that define the separation of transitions. Consequently, for a given track length, a greater number of code bits can be stored compared to data bits. Although it takes more code bits to represent a given number of data bits, i.e., the code rate is less than one, the result is a higher data-recording density.

1. Bandwidth

The upper cut-off frequency of an optical-disk channel is a function of the laser wavelength (λ), the track velocity (v) and the numerical aperture (NA) and is given by $2\mathrm{NA}v/\lambda$, (Heemskerk and Immink 1982). Since the laser-spot diameter (D), is equal to $0.5\lambda/\mathrm{NA}$ (Bouwhuis *et al.* 1985) the cut-off frequency becomes v/D. The number of bits that can be stored on a disk depends on the size of the laser-spot and is approximately equal to nA/D^2, where A is the area of the disk and n is the number of bits that can be resolved within the spot. This latter variable can be maximized through proper selection of recording code.

Whilst, in principle, the channel response extends down to d.c. it is prudent to limit its response at the lower frequencies. This minimizes the adverse effect that the low-frequency power components in the replayed signal may have on the laser servo system. Also, to reduce the effect of disk-surface blemishes, which can detrimentally affect the replay signal, it is necessary to employ a high-pass filter in the replay channel that removes the lower frequencies. Other considerations are the use of transformers, which do not pass d.c. levels, in the replay channel.

2. d, k Constraint

One function of the code is to ensure that there are never long periods of time during which there are no transitions or that transitions do not occur too close together. These codes are classed as run-length limited (RLL).

The minimum distance between two transitions is the d constraint, whilst maximum distance is k. The d and k values determine the performance of the code. Ideally d should be low to permit high-density recording but, given a finite laser-spot size, d cannot be so low that it cannot be resolved. Also, intersymbol interference (ISI) and inter-track cross-talk increase with reducing d. The constraint value k cannot be too large since frequent changes in the replayed signal are necessary to synchronize a timebase that re-times the replayed data.

The d,k constraints of a code can be represented by a finite-state transition diagram (FSTD) (Shannon 1948; Franaszek 1970). Figure 1 is an FSTD for a code with constraint 1,3. The dotted paths in the diagram represent no level change in the code; solid lines represent a level change, either zero to one or one to zero. In moving from one state to another it is seen that there must be at least one zero and a maximum of three zeros between two changes.
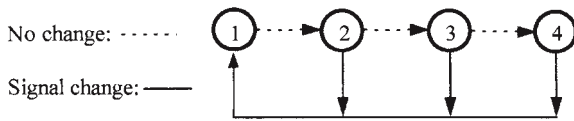
Figure 1
Finite-state transition diagram for 1,3 *d,k* constraint.

Figure 2
Running digital sum (RDS) of coded sequence.

3. Channel Capacity

The maximum rate, *R*, at which information can be transmitted reliably through a channel is limited by the channel capacity *C*. The capacity of a channel perturbed by white noise is given by Shannon (1948):

$$C = W\log(1 + P/N)\text{bits s}^{-1} \tag{1}$$

Where *W* is bandwidth and *P/N* is signal-to-noise ratio. For *R < C*, information may be transmitted at an arbitrarily low error rate. The actual error rate for high *R* is governed by the quality of the channel and the ingenuity of the coding scheme employed.

Shannon also defined capacity for a discrete noiseless channel in units of user bits per channel bit (Shannon 1948):

$$C = \lim_{T \to \infty} \log_2 \frac{N(T)}{T} \tag{2}$$

where *N(T)* is the number of allowed signals of duration *T*. This reduces to $\log_2 \lambda$ where λ is the largest root of the equation $\lambda^{k+1} - \lambda^{k-d} - x + 1 = 0$ and *d* and *k* are the constraint parameters of the code defined above. The equation is derived from a consideration of the finite-state-timing diagram (FSTD) of the code and its associated state transition matrix (Siegel 1985, Immink *et al.* 1998).

In a recording code, *m* data bits are mapped into *n* code bits to give a code with rate *R = m/n*, where $m/n \leqslant 1$. The maximum theoretical code rate is known as the capacity of the code. The efficiency of a code is usually measured in terms of how near to *C* the actual rate is.

4. Code Spectra/Equalization

Data to be recorded will be derived from a number of diverse sources and, as such, cannot be predicted. The various patterns of bits that are likely can be simulated, however, using a pseudorandom binary sequence (PRBS). If the PRBS is long it will contain virtually all the binary combinations that the recording system is likely to encounter. Assuming such a random sequence of data, the frequency spectrum of the ensuing coded sequence is useful in assessing code performance. Since the optical channel response falls off rapidly at high frequency, the high-frequency components of a code's spectrum should be low.
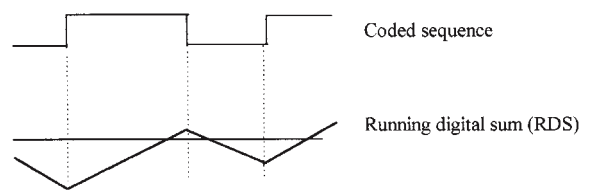
Also, the low-frequency components should have low amplitude with a null at d.c.

Some codes are not absolutely d.c.-free: there may be a slight dc component that will vary with the sequence of the signal being recorded. A measure of the d.c.-content in the coded signal is the running digital sum (RDS). The RDS is the running integral of the coded signal, assuming +1 is integrated when the signal is high and −1 when it is low (Fig. 2). The RDS is effectively the arithmetic sum of the area under the graph of the integral; this should be kept low for efficient operation. The digital sum variation (DSV) represents the limits of the RDS graph. The d.c. content of a code is said to be bounded provided the DSV does not extend to infinity.

A closer match between the response of the channel and the spectrum of the code may be achieved through equalization. Equalization is the process of modifying the channel's frequency response or changing the spectral content of the signal to be recorded to more closely match the response of the channel. Here, the channel is taken to include the write and read electronics. One technique is to include a filter in the channel to shape the spectrum of the code.

5. Examples of Code

In the two-thirds rate code of Horiguchi and Morita (1976) two data bits are represented by three code bits. The *d,k* value is (1,7), which gives a code capacity of 0.679.

The code adopted for the audio compact disk (CD) specification (and for the mini-disk) is known as eight-to-fourteen modulation (EFM) (Heemskerk and Immink 1982). In EFM, eight data bits are coded into 14 code bits. However, in order to control the d.c. content of the code, three merging bits are added after the coding process to produce a coded symbol 17 bits long—hence the true rate is 8/17. Whilst the merging bits minimize the DSV, the *d,k* value of (2,10) is maintained.

An improved version of EFM, EFMPlus (Immink 1995) has been adopted for the digital versatile disk (DVD). This has the same *d,k* value as EFM but the rate is higher at 8/16. Eight data bits are coded into codewords of 16 bits using a look-up table of

codewords. Rather than using merging bits to control d.c. content, substitute codeword sequences are available at the encoder as an alternative to the main table of codewords. During the encoding process, codewords are taken either from the main look-up table or from the substitute table in order to keep the DSV at a minimum. The reduction of one bit in the codeword yields an improvement of 6–7% in information density compared to the EFM code.

6. Signal Detection

The basic method of determining the binary value of the replayed analogue signal is to employ peak detection. With peak detection the replayed signal is compared with a level threshold and a binary value registered accordingly. This is satisfactory for low to medium density systems but if the storage density was to be increased, inter-symbol interference would cause signal distortion in the replayed signal. This distortion would severely impair the detection process. For very high-density systems, therefore, partial response maximum likelihood (PRML) (Siegel 1991) is usually employed. In a PRML scheme the channel response is tightly controlled. This tight control permits the ISI-induced signal distortion to be predicted, thus enabling the corresponding binary values to be determined in line with the replayed signal.

With peak detection a great deal of information is wasted once the decision process is made. A more effective, albeit more complex, method is maximum likelihood detection. The principle behind maximum likelihood detection is that all possible sequences of replayed signal are known to the detector. As each sequence is replayed it is compared to all the known sequences: the one with the best match is the one most likely to be the correct one. A disadvantage is that for a reasonably long replayed sequence the detection process would take too long. Viterbi detection (Viterbi 1967) is a maximum likelihood detection algorithm that reduces detection time by comparing the replayed signal sequence "on-the-fly." Reserved judgements are made on sections of the replayed signal as to the likelihood of it representing a certain bit pattern. The decision to incorporate certain combinations of bits in the detected sequence depends not only on the current signal being decoded but also on previous evaluations: the k constraint of the recording code can be used to force decisions. The result is a detector that gives superior performance compared to peak detection.

7. Comments

The classical work on communications channels by Shannon can be applied to optical recording systems, since the latter is effectively a transmit-now, receive-later communications system. Unlike a communications system, however, the signal power of a recording system cannot be increased indefinitely in order to improve performance.

A binary-data signal comprises two related components: amplitude and time. These must be replicated faithfully on replay to reconstitute the recorded signal: this is a function of the recording code. A further requirement of a code is to increase storage density. However, the dual goals of achieving high density together with reliable timebase regeneration are contradictory. Hence, many codes have been developed in an attempt to resolve these contradictions. The code designer must balance the storage gains to be delivered by a code against the need for reliable operation and cost of implementation.

The signal that is ultimately recorded is derived from the information data, to which has been added data for error correction, timing, synchronization, and sundry other purposes. There is no one "supreme" code with all the best characteristics: many different recording codes are in use, each designed for a specific application. No small consideration is the practical implementation of a code.

The recording codes in general use are single-dimension codes, where a serial sequence of data is coded. In an attempt to resolve the contradictory requirements of a code, two-dimensional codes have been examined (Davey *et al.* 1998). These codes capitalize on the areal format of recorded data. Mutually related information is encoded in two dimensions. This information is recovered at replay to support effective detection. This concept can be extended further to a third dimension. Such codes may be suitable for application to multilayer disks such as the current DVD, which has two layers, and future generations that may possibly have many layers.

See also: Magneto-optic Recording: Overwrite and Associated Problems; Magneto-optic Recording: Total Film Stack, Layer Configuration

Bibliography

Bouwhuis G, *et al.* 1985 *Principles of Optical Disc Systems.* Hilger, Bristol, UK

Davey P J, Donnelly T, Mapps D J 1998 Two-dimensional coding for a multi-track recording system to combat inter-track interference. *IEEE Trans. Magnetics.* **34** (4), 1949–51

Franaszek P A 1970 Sequence state methods of run-length-limited coding. *IBM J. Res. Dev.* **14** (4),

Heemskerk J P J, Immink K A S 1982 Compact disc: system aspects and modulation. *Philips Tech. Rev.* **40** (6), 157–64

Horiguchi T, Morita K 1976 An optimisation of modulation codes in digital recording. *IEEE Trans. Magn.* **12** (6), 740–2

Immink K E S *Coding Techniques for Digital Recorders.* Prentice Hall, Englewood Cliffs, NJ

Immink K A S 1995 EFMPlus: The coding format of the multimedia compact disc. *IEEE Trans. Consumer Electron.* **41** (3), 491–7

Immink K A S, Siegel P H, Wolf J K 1998 Codes for digital recorders. *IEEE Trans. Inf. Theory.* **44** (6), 2260–99

Shannon C E 1948 A mathematical theory of communication. *Bell Syst. Tech. J.* **27** (3), 379–423

Siegel P H 1985 Recording codes for digital magnetic storage. *IEEE Trans. Magn* (5), 1344–9

Siegel P H 1991 Recording codes for PRML. *Digest Magnetic Recording Conf. (MRC 91)*, paper F-2H

Siegel P H, Wolf J K 1991 Modulation coding for information storage. *IEEE Commun. Magn.* (Dec), 1344–9

Viterbi A J 1967 Error bounds for convolutional codes and an asymptotically optimum decoding algorithm. *IEEE Trans. Inf. Th.* **IT-13**, 260–9

Watkinson J 1990 *Coding for Digital Recording*. Focal Press, London

T. Donnelly
University of Plymouth, Plymouth, UK

P

Permanent Magnet Assemblies

Modern permanent magnets are ideally suited to generate magnetic fields of magnitudes comparable to their spontaneous polarization, J_s. These fields can be static or variable, uniform or nonuniform. They are generated by permanent magnet structures that demand no continual expenditure of energy for their operation, and dispense with the elaborate cooling systems required by resistive or superconducting electromagnets. Furthermore, the permanent magnet assemblies are compact and can offer the significant advantage of flux confinement in the region of interest. Permanent magnets are now competitive with electromagnets for generating fields of up to about 2 T. More generally, when a high field with a rapid spatial variation is required, they may offer the only practicable solution.

The polarization, J, of a modern hard magnet (Skomski and Cugat 1999) deviates little from its remanent or saturation value, J_s, far into the second quadrant of the hysteresis loop, before switching at the coercive field, H_c (see *Rare Earth Magnets: Materials*, *Magnets: Sintered*). The plot of the polarization of the magnet as a function of the magnetic field, H, acting on it is almost rectangular in shape, as indicated in Fig. 1. The intrinsic spontaneous polarization of $SrFe_{12}O_{19}$ is 0.47 T, for example, and that
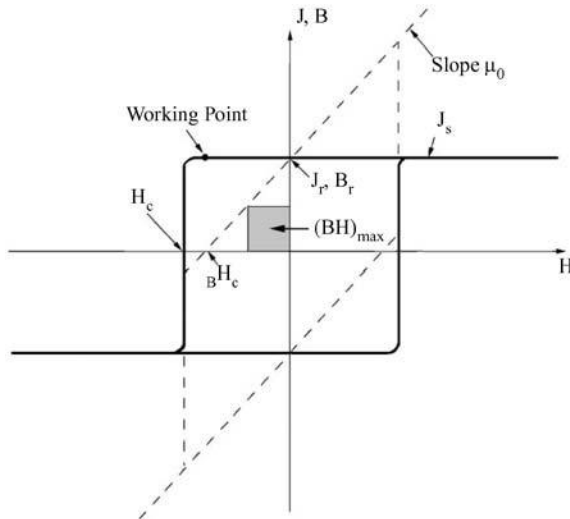
of $Nd_2Fe_{14}B$ is 1.61 T. Values of the remanent polarization of typical sintered magnets are given in Table 1. They are typically 10–20% less than the spontaneous polarization of the pure hard phase due to imperfect crystallite alignment and the presence of secondary phases necessary to develop coercivity. The magnetic flux density, B, is related to the H-field (magnetizing force) and polarization by $B = \mu_0 H + J$ so that in free space, where $J = 0$, the relation between B and H is simply $B = \mu_0 H$.

The purpose of any permanent magnet assembly is to deliver magnetic flux into a region of space adjacent to the magnet known as the *airgap*, creating a magnetic field, $B_g(r)$, in this region. Maximum energy product, $(BH)_{max}$, defined on the B:H loop of Fig. 1, is equivalent to twice the energy stored in the field in the airgap, $(1/2\mu_0) \int B_g^2 d\tau$. The energy product provides a convenient measure of the efficiency of the magnet material for generating airgap fields. In the case of an ideal rectangular hysteresis loop with $\mu_0 H_c > J_r/2$, the maximum possible energy product, $(BH)_{max}$, is $J_r^2/4\mu_0$.

In the structures described below, the airgap is often a cylindrical cavity surrounded by magnets. The fields achieved in the airgap scale with, but are not limited by the polarization of the magnets. Ideally, the field generated is the product of a geometric constant, $K(r)$, for the structure and the remanence of the magnet, J_r.

$$K(r) = B_g(r)/J_r \qquad (1)$$

When $K > 1$, the magnetic structure achieves flux concentration.

Permanent magnet structures are produced by assembling blocks of rare-earth magnets (see *Magnets: Sintered*) or ferrite magnets (see *Alnicos and Hexaferrites*; *Ferrite Magnets: Improved Performance*) in any desired orientation. These magnets with their wide, rectangular hysteresis loops have the property that the field of one magnet does not significantly perturb the magnetization of its neighbors. The magnet blocks behave essentially as if they are rigid and transparent. This follows because the longitudinal susceptibility is zero for a rectangular hysteresis loop; the slope of the $B(H)$ curve is μ_0, as for free space.

The transverse susceptibility, $J_s/\mu_0 H_a$, is only of order 0.1, since the anisotropy field, H_a, is much greater than the magnetization (Table 1). Hence, for example, the directions of magnetization of two blocks of $SmCo_5$ in contact with their easy-axes perpendicular will deviate by less than a degree from the easy-axes. The assumption of rigidity and transparency of the magnetization greatly simplifies the design of magnetic circuits. Errors in the calculated airgap

Figure 1
The $J(H)$ hysteresis loop of an ideal permanent magnet. The corresponding $B(H)$ loop is shown by the dotted line. $(BH)_{max}$ is indicated by the area of the shaded region.

Table 1
Properties of typical oriented sintered ferrite and rare earth magnets.

Compound	T_C (°C)	H_a (MA m^{-1})	J_r (T)	H_c (MA m^{-1})	$(BH)_{max}$ (kJ m^{-3})	T_{max} (°C)
$BaFe_{12}O_{19}$	450	1.1	0.41	0.27	34	300
$SmCo_5$	720	32	0.88	1.70	150	250
Sm_2Co_{17}	827	5.1	1.08	0.80	100	350
$Nd_2Fe_{14}B$	312	6.1	1.28	1.00	300	150
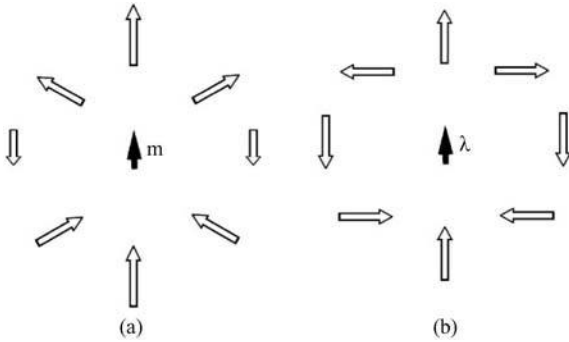
Figure 2
Comparison of the magnetic field pattern produced by (a) a point dipole with moment m and (b) a line dipole with moment λ per unit length.

flux density arising from this approximation are usually no more than a few percent.

Permanent magnet structures have been devised to generate fields that are uniform, nonuniform, or time varying.

1. Uniform Fields

It is not quite obvious that a permanent magnet can be used to generate a uniform field, as the magnetic field produced by a small bar magnet or point dipole of moment, m (A m^2), is nonuniform and anisotropic as shown in Fig. 2(a). This field at a general point $r(r, \theta, \phi)$, relative to the axis of the dipole is given in polar co-ordinates as

$$H_r = 2m\cos\theta/4\pi r^3; H_\theta = m\sin\theta/4\pi r^3; H_\phi = 0 \quad (2)$$

Both the magnitude and direction of H depend on $r(r,\theta,\phi)$. Nonetheless, a uniform field may be achieved over some region of space by assembling segments of magnetic material, each magnetized in a different direction, such that their individual contributions combine to yield a field which is uniform in some confined region.

One approach is to build the structure from long segments whose fields approximate those of line dipoles of length, L, and dipole moment, λ (A m), per unit length. The field due to such a line dipole, in the limit of infinite length, is given by

$$H_r = \lambda\cos\theta/2\pi r^2; \; H_\theta = \lambda\sin\theta/2\pi r^2; \; H_\phi = 0 \quad (3)$$

Thus the magnitude of H, $\sqrt{(H_r^2 + H_\theta^2 + H_\phi^2)}$, at a distance, r, from each segment is actually independent of θ, while its direction everywhere makes an angle, 2θ, with the orientation of the magnet as shown in Fig. 2(b).

By assembling a long, cylindrical magnet with a hollow bore from many individual segments, it is possible to create a field which is uniform within the bore. By choosing the orientation of each segment appropriately, their individual fields will all add at the center of the bore. Such segments can be assembled according to many different prescriptions. Some designs are shown in Fig. 3. The efficiency, ε, of a particular cylindrical magnet structure generating a uniform field in an airgap of cross-section, A_g, is defined as

$$\varepsilon = K^2 A_g / A_m \quad (4)$$

where A_m is the magnet cross-section and K (Eqn. (1)) is now independent of r. A reasonably efficient structure has $\varepsilon \approx 0.1$. The theoretical limit on ε is 0.25 (Jensen and Abele 1996).

In the transverse field design shown in Fig. 3(a), the outer surface is an equipotential with no perpendicular stray field outside the surface and the flux density in the airgap is $0.293B_r$ provided $t/r = \sqrt{2} - 1$. Multiples of this field can be obtained by nesting similar structures, each with the same t/r ratio, one inside the other. These designs find application in nuclear magnetic resonance imaging (MRI). Highly homogeneous fields (better that one part in 1×10^5) are required for NMR applications. The generated fields must be shimmed with small magnets or pieces of soft ferromagnetic material in order to meet this specification. Also popular for NMR applications is the design shown in Fig. 3(b), which consists of two flat cuboid magnets and a soft iron return path (such a return
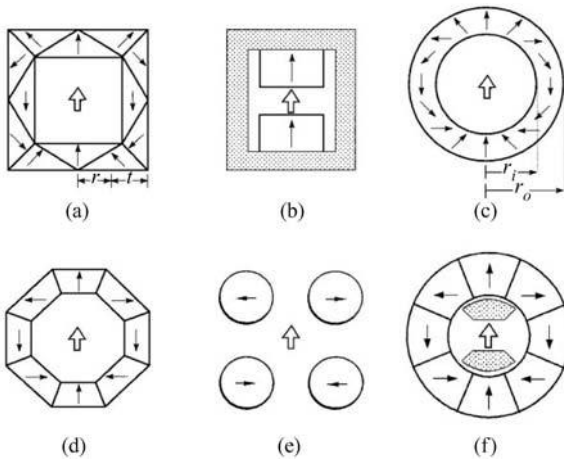
Figure 3
Cross-sections of some permanent magnet structures that generate a uniform magnetic field in the airgap in the direction indicated by the hollow arrow. The magnets are unshaded, with an arrow to show the direction of magnetization. Shaded material is soft iron.

path is often referred to as a *yoke*). Permanent magnet flux sources supply fields of order 0.3 T in whole-body scanners for medical imaging. NMR spectrometers with permanent magnets flux sources are also beginning to be used for quality control in the food, polymer, and construction industries.

Figure 3(c) illustrates another design, known as the *Halbach cylinder* or *dipole ring*, where the direction of magnetization at any point in the cylinder is at 2θ from the vertical axis, and its magnitude remains constant at all points. In the case of a cylinder of infinite length, this configuration yields a uniform magnetic field in the y direction within the cylinder bore. The flux density in the airgap is given by Eqn. (1) with

$$K = \ln (r_o/r_i) \tag{5}$$

where r_i and r_o are the inner and outer radii of the cylinder, respectively. Unlike the structure of Fig. 3(a), the radii, r_i and r_o, can take any values without creating a stray field outside the cylinder.

In practice a continuously varying magnetization pattern is not easily achieved. A more common approach is to approximate the ideal configuration with a finite number, N, of uniformly magnetized segments as illustrated in Fig. 3(d) for $N = 8$. In this case, the field is reduced by a factor, $[\sin(2\pi/N)]/(2\pi/N)$, which is included on the right-hand side of Eqn. (5). However, cylinders with as few as eight segments can still generate 90% of the ideal field.

As a further approximation to the ideal design, the cylinders are never infinitely long; their length, z, is typically comparable to their diameter. The geometrical constant, K, in Eqn. (4) is further reduced by an amount (Zijlstra 1985)

$$\Delta K = (z/2)[1/z_o - 1/z_i] + \ln ((z + z_o)/(z + z_i)) \tag{6}$$

where $z_o = (z^2 + r_o^2)^{1/2}$ and $z_i = (z^2 + r_i^2)^{1/2}$. For example, the flux density at the center of an octagonal cylinder with $r_i = 12$ mm, $r_o = 40$ mm, and length 80 mm made of a grade of Nd–Fe–B having $B_r = 1.20$ T is actually 1.25 T, compared to the value of 1.44 T calculated from Eqns. (1) and (5). Note that the flux in the airgap exceeds the remanence in a circuit which uses no iron, which illustrates the idea of magnetic flux concentration.

These cylindrical structures are useful for producing fields in bores ranging in diameter from a few millimeters to several hundred millimeters. Large structures, like that shown in Fig. 4, are used for industrial-scale materials processing and space-based experiments.

Soft iron can be introduced into a permanent magnet circuit either to provide a return path for the flux (Fig. 3(b)), or to concentrate the flux in the airgap (Fig. 3(f)), thereby creating a larger uniform field in a smaller volume. The field generated by the permanent magnet structure should be sufficient to saturate the soft segments. Pure iron ($J_s = 2.15$ T) or permendur ($J_s = 2.43$ T) may be used. In no case can the additional flux density exceed the polarization of the soft material, and in typical structures it will only be a fraction of this value, depending on the segment shape.

Assemblies composed of pairs of magnetized wedges allow great flexibility in the shape of the cavity while offering efficiencies comparable to those of Halbach cylinders (Jensen and Abele 1999).

A different simplification of the basic structure uses transversely magnetized cylindrical rods, as shown in Fig. 3(e) (Coey and Cugat 1994). This allows both longitudinal and transverse access to the cavity. The geometrical constant at the center for a set of n rods, which are just touching, is

$$K = (n/2)\sin^2(\pi/n) \tag{7}$$

By increasing n, the central region in which the field is uniform is enlarged, but the magnitude of the field itself is reduced.

Uniform fields can also be generated in spherical cavities using the same principles as for cylindrical cavities (Leupold 1996). A uniform field is generated in a spherical cavity when the magnitude of the polarization of a volume element in a hollow spherical magnet structure is kept constant, but its orientation varies as $(2\theta, \phi)$ where (r, θ, ϕ) are its polar
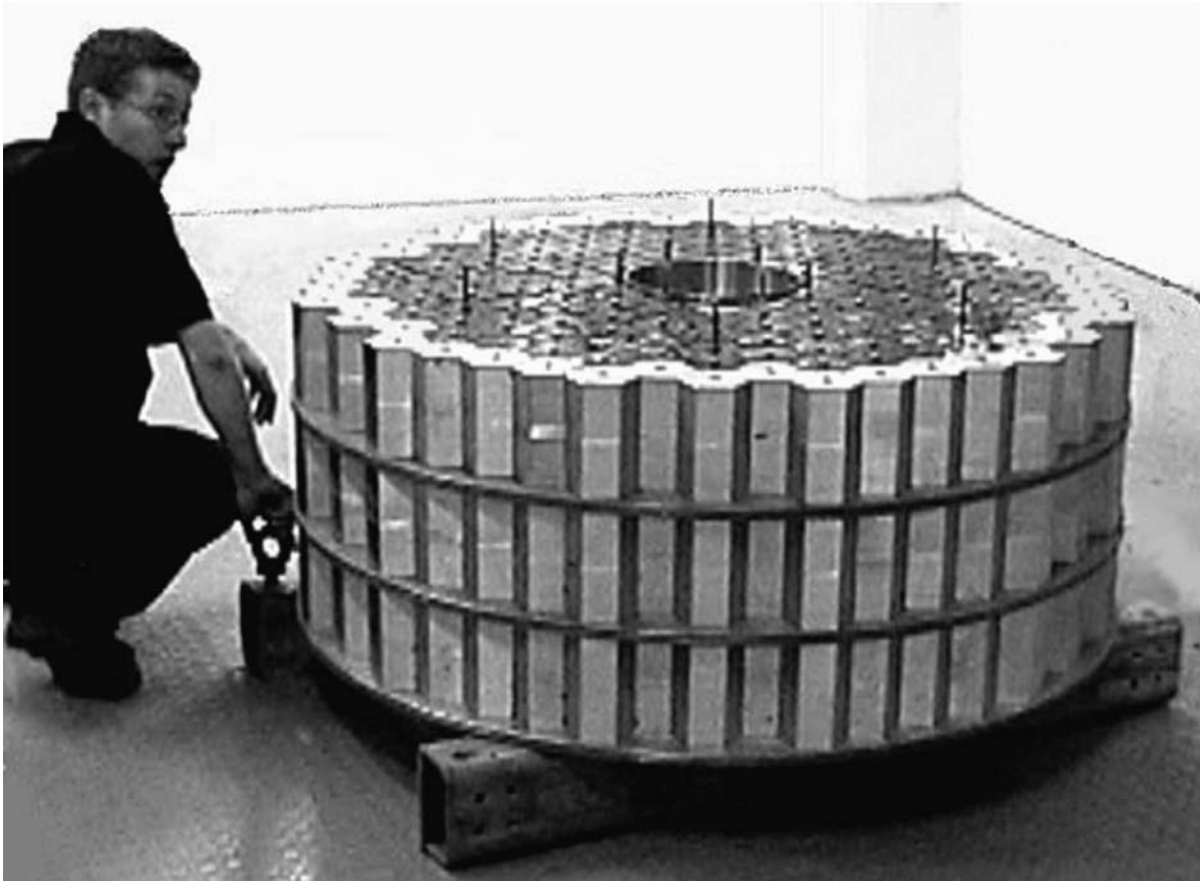
Figure 4
A large permanent magnet structure producing a field of 1 T in a bore of diameter 250 mm (photo by courtesy of Magnetic Solutions Ltd).

coordinates. The resulting geometric constant is

$$K = (4/3)\ln (r_o/r_i) \qquad (8)$$

The field is one-third higher than for a Halbach cylinder of comparable dimensions. Access to the field is by diametral holes bored into the central space, which do not perturb the field significantly provided their radius is less than $r_i/4$. An example is illustrated in Fig. 5.

The upper limit to the fields that can be generated using permanent magnets is about 5 T. This is set in part by the coercivity of the material, as the vertical segments in Fig. 3 are subject to a reverse H-field equal to the field in the bore. But there is also a practical size limitation imposed by the exponential increase in dimension of Eqn. (5). Admitting a material existed with $B_r = 1.5$ T and $\mu_o H_c = 5$ T, the outer diameter required to achieve 5 T in a 25 mm bore

would be 700 mm. Such a structure of 400 mm in height would weigh about 1 t.

2. Nonuniform Fields

The ability of rare-earth permanent magnets to generate complex flux patterns with rapid spatial variation $(\nabla B > 100\,\mathrm{Tm}^{-1})$ is unsurpassed by any electromagnetic device. The solenoid needed to generate a field equivalent to that of a long magnet with $J \sim 1$ T, would require an Amperian surface current of about $800\,\mathrm{kAm}^{-1}$. Whether resistive or superconducting, it would have to be several centimeters in diameter in order to accommodate the requisite ampere-turns. No such limitations exist for permanent magnet dimensions.

The cylindrical configurations of Fig. 3 may be modified to produce a variety of inhomogeneous
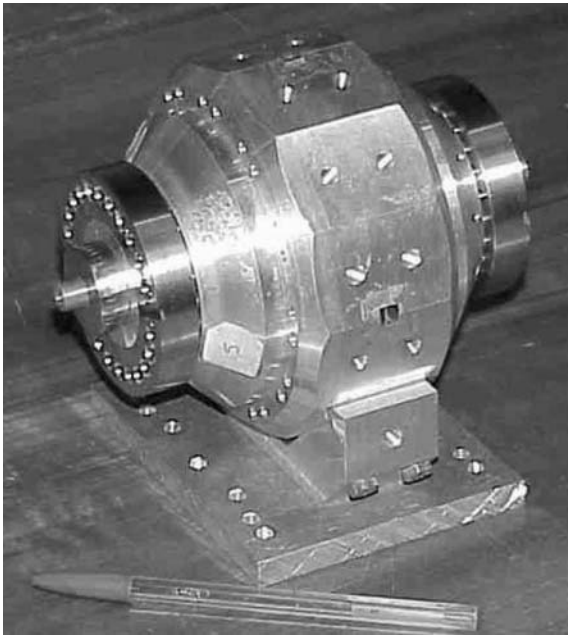
Figure 5
A spherical permanent magnet structure that produces a field of 4.5 T in a spherical cavity of diameter 2 mm (after Cugat and Bloch 1998).
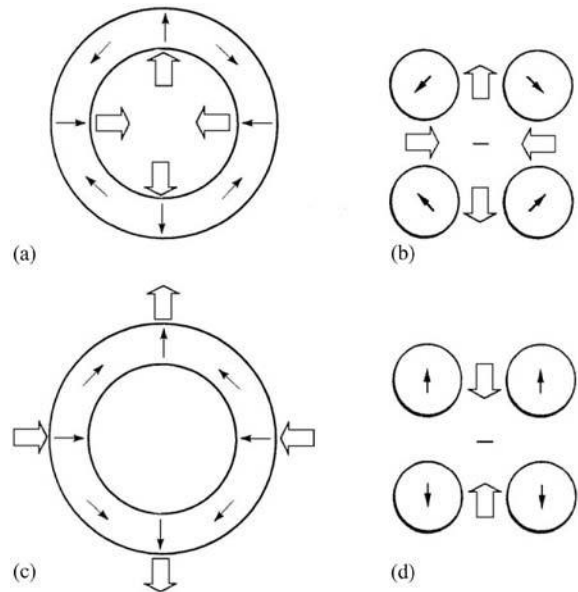
Figure 6
Cross-sections of some permanent magnet structures that generate nonuniform magnetic fields: (a) and (b) a quadrupole field, (c) an external quadrupole field and, (d) a field gradient.

fields. Some examples are shown in Fig. 6. Multipole fields such as quadrupole fields are particularly useful for charged-particle beam control (Halbach 1980). Various multipole fields are generated by having the orientation of the magnets in the ring vary as $(1 + (n/2))\theta$, where $n = 2$ for a dipole field (Fig. 3(c)), $n = 4$ for a quadrupole field (Fig. 6(a)), $n = 6$ for a hexapole field and so on. The field at the center of the quadrupole is zero, but whenever the particle beam deviates it experiences an increasing field which causes its trajectory to curve back to the center. A simplified four-rod structure, which also produces a quadrupole field, is shown in Fig. 6(b).

A different type of permanent magnet structure creates an inhomogeneous magnetic field along the axis of the magnet, which may be the direction of motion of a charged particle beam. Microwave power tubes such as the travelling wave tube are designed to keep the electrons moving in a narrow beam over the length of the tube and focusing them at the end while coupling energy from an external helical coil. Originally this was achieved by applying a uniform axial field from a resistive solenoid, but the design with permanent magnets focusing by a periodic axial field in Fig. 7(a) is just as effective, and represents a great saving in weight and power when $SmCo_5$ magnets are used.

One period of the structure in Fig. 7(a) generates an axial gradient field, also known as a *cusp* field.
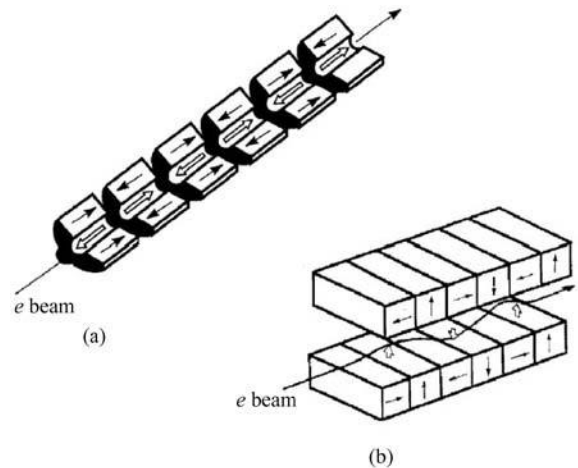
Figure 7
Permanent magnet structures that create spatially varying magnetic fields for particle beam control.
(a) A microwave power tube and (b) a wiggler magnet for synchrotron radiation.

Uses of these fields include the stabilization of molten metal flows.

Insertion devices for generating intense beams of hard radiation (UV and x-ray) from energetic

electron beams in synchrotron sources use a periodic transverse field. These devices are known as *wigglers*, since they cause the electrons to travel in a sinuous path. Similar assemblies are used in free-electron lasers. A design, which includes segments alternately magnetized in parallel and antiparallel directions to concentrate the flux, is shown in Fig. 7(b).

A variant of the normal multipole Halbach configuration is the external Halbach configuration where the orientation varies as $(1-(n/2))\theta$. The multipole field is then produced outside the cylinder. The case of $n=4$ (illustrated in Fig. 6(c)) produces a quadrupole field outside the cylinder and zero field inside. The external Halbach designs are useful for the rotors of permanent magnet electric motors.

Other arrangements of cylindrical magnets (Fig. 6(d)) produce a uniform magnetic field gradient along a particular direction. Field gradients are especially useful for exerting forces on other magnets, or on paramagnetic or diamagnetic material. The force on a magnet of moment, m, is $F=-\nabla(m.B)$ whereas the expression for a nonferromagnetic material is $F=-(1/2\mu_0)\chi V\nabla B^2$, where V is the sample volume and χ is the susceptibility. Field gradients of the order of $100\,\mathrm{Tm}^{-1}$ producing separation forces of the order of $1\times10^8\,\mathrm{Nm}^{-3}$ are used in open gradient magnetic separators to sort ferrous and nonferrous scrap or select minerals from crushed ore on the basis of their magnetic susceptibility.

Some magnetic levitation schemes exploit the nonuniform fields produced by permanent magnets. Diamagnetic material can be levitated against gravity when ∇B^2 is of the order of $100\,\mathrm{T}^2\mathrm{m}^{-1}$, which can be achieved with permanent magnets in volumes of the order of $1\,\mathrm{mm}^3$. A magnet can remain suspended in the vertical field gradient of another magnet provided it lies between two horizontal diamagnetic plates.

Many types of contactless bearings and couplings use permanent magnet structures (Yonnet 1996). The linear bearing illustrated in Fig. 8(a) provides levitation along a track, but lateral constraint of the suspended member is required. It is impracticable to equip a great length of track with permanent magnets. Thus, levitation of vehicles may be provided by repulsion from eddy currents generated in a track of metal plates, or by attraction of the magnets on the vehicle to a suspended iron rail. The simplest rotary bearings are made of two ring-shaped magnets in repulsion. Some configurations (Fig. 8(b)) provide radial restoring force provided the axis is prevented from shifting or twisting. Others support a load in the axial direction (Fig. 8(c)), but must be prevented from moving in the radial direction. Magnetic bearings are simple, cheap, and reliable. They are best suited to high-speed rotary suspensions as in flywheels or turbopumps.

Figure 8(d) shows the design of a simple rotary coupling and Fig. 8(e) is a magnetic gear. These are useful for transmitting motion across the wall of a
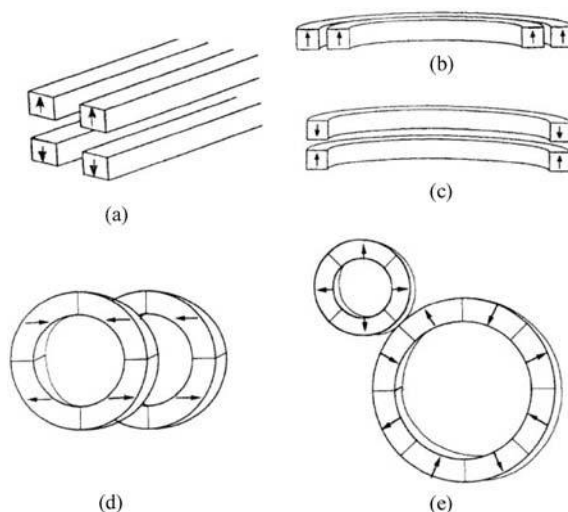
Figure 8
Some magnetic bearings and couplings: (a) is a linear bearing, (b) and (c) are rotary bearings, (d) is a rotating coupling, and (e) is a magnetic gear.
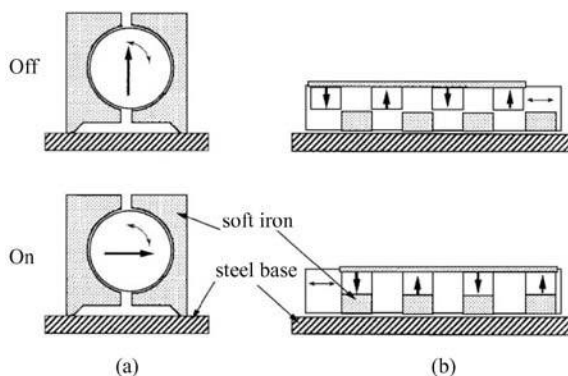
Figure 9
Two designs for switchable magnets.

chamber operating in vacuum or in an aggressive environment. Forces in bearings and couplings depend quadratically on the remanence of the magnets, so it is advantageous to select material with a large polarization and a large coercivity, in case of slippage. Torques of the order of $10\,\mathrm{Nm}$ may be achieved in couplings a few centimeters in dimension.

3. Variable Fields

Fields can be varied by changing the airgap, or by some movement of the magnets in a structure with respect to each other. The working point is displaced

as the magnets move. A simple type of variable flux source is a switchable magnet (Fig. 9). These are often used in holding devices, where a strong force is exerted on a piece of ferrous metal in contact with the magnet. The working point shifts from the open circuit point to the remanence point where $H = 0$ as the circuit is closed. The maximum force that can be exerted at the face of a magnet of area A_m, where the flux density is B_m, is $A_m B_m^2 / 2\mu_0$. Forces of up to $40\,\mathrm{N\,cm^{-2}}$ can be achieved for $B_m = 1\,\mathrm{T}$.

Simple force applications in catches and closures consume large amounts of sintered ferrite. Polymer bonded ferrite magnetized in strips of alternating polarity with a pitch of about 2 mm is widely used for fixing signs and light objects to steel panels.

To create a variable uniform field, two Halbach cylinders of the type shown in Fig. 3(d) each with the same radius ratio can be nested one inside the other, as shown in Fig. 10(a) (Leupold 1996). Then by rotating them through an angle, $\pm\alpha$, about their common axis, a variable field, $2\cos\alpha J_r \ln(r_o/r_i)$, is generated. There would be no torque needed to rotate two ideal Halbach cylinders, but in practice some torque arises from the segmented structure and end effects (Ní Mhíocháin *et al.* 1999).

Another solution is to rotate the rods in the device of Fig. 3(e), as demonstrated in Fig. 10(b) (Cugat *et al.* 1994). By gearing a mangle with an even number of rods so that the alternate rods rotate clockwise and anticlockwise through an angle, α, the field varies as $B_{max}\cos\alpha$. Further simplification is possible with a magnetic mirror, a horizontal sheet of soft iron containing the axis of symmetry that produces an inverted image of the magnets, halving the number of rods required. The torque needed to vary the field in a mangle increases with a decreasing

Figure 10
Structures for producing continuously variable magnetic fields. (a) A nested pair of Halbach cylinders and (b) a rotating mangle.

Figure 11
A 2.0 T permanent magnet flux source based on the structure of Fig. 10(a) (photo by courtesy of Magnetic Solutions Ltd).

number of rods. A movable axial field gradient can be achieved with nonuniformly magnetized rods (Grönefeld 1998).

These permanent magnet variable flux sources are compact and particularly convenient since they can be driven by stepping or servo-motors and they have none of the high power and cooling requirements of a comparable electromagnet. For example, the flux source illustrated in Fig. 11 uses 20 kg of Nd–Fe–B magnets of the design shown in Fig. 10(a) to generate fields up to 2.0 T in a 25 mm bore. Large rotating or alternating fields can be generated by continuously rotating the magnets. Permanent magnet variable flux sources are expected to displace resistive electromagnets to generate fields of up to about 2 T, but they cannot compete with superconducting solenoids in the higher field range.

4. Concluding Remarks

Permanent magnet structures are well suited to generate uniform fields, which are static or variable, as well as multipole field patterns and field gradients with rapid spatial variation. The advantages of permanent magnets are their compactness and energy efficiency—no power supplies or cooling systems are required. Their limitations lie in the maximum fields that they can generate which are determined by the remanence and coercivity of existing permanent magnet materials. Remanences of currently available grades of rare-earth magnets are in the range 0.9–1.4 T. There is little prospect that future materials development will extend the upper limit beyond 2 T.

The field produced by any permanent magnet structure scales with remanence from Eqn. (1). Designs with $K \sim 1$ are compact and efficient, and can achieve flux concentration, but designs with $K > 1.5$ are inefficient in the sense that the ratio of the volume of the magnet to the volume of the cavity increases exponentially with B_g.

The practical limit to the fields that can be generated with permanent magnets is about 5 T. For fields in the range 2 mT to 2 T, a permanent magnet assembly is often the best solution. Fields variable in both magnitude and direction are obtained by somehow rotating the magnets, as in the nested Halbach cylinder systems or in the magnetic mangle. In this field range, permanent magnet flux sources are set to replace the venerable iron-core electromagnet.

As regards spatially varying fields, static field gradients, ∇B, of up to $100 \, \text{T m}^{-1}$ or more can be achieved with permanent magnets in very small volumes. Here there is no electrical solution to rival the Amperian surface currents associated with a magnetization of order $1 \, \text{MA m}^{-1}$.

See also: Magnetic Levitation: Materials and Processes; Magnetic Materials: Domestic Applications;

Permanent Magnets: Sensor Applications; Superconducting Permanent Magnets: Potential Applications

Bibliography

Coey J M D, Cugat O 1994 Construction and evaluation of permanent magnet variable flux sources. In: Manwaring C A F, Jones D G R, Williams A J, Harris I R (eds.) *Proc.13th Int. Workshop on Rare Earth Magnets and their Applications*. Birmingham, UK, pp. 41–54

Cugat O, Bloch F 1998 4-Tesla permanent magnet flux source. In: Schultz L, Müller K-H (eds.) *Proc.15th Int. Workshop on Rare Earth Magnets and their Applications*. MAT-INFO, Dresden, Germany, pp. 853–9

Cugat O, Hansson P, Coey J M D 1994 Permanent magnet variable flux sources. *IEEE Trans. Magn.* **30**, 4602–4

Grönefeld M 1998 New concepts in magnetic couplings derived from Halbach configurations. In: Schultz L, Müller K-H (ed.) *Proc. 15th Int. Workshop on Rare Earth Magnets and their Applications*. MAT-INFO, Dresden, Germany, pp. 807–14

Halbach K 1980 Design of permanent multipole magnets with oriented rare earth cobalt material. *Nucl. Inst. Meth.* **169**, 1–10

Jensen J H, Abele M G 1996 Maximally efficient permanent-magnet structures. *J. Appl. Phys.* **79**, 1157–63

Jensen J H, Abele M G 1999 Closed wedge magnets. *IEEE Trans. Magn.* **35**, 4192–9

Leupold H A 1996 Static applications. In: Coey J M D (ed.) *Rare-earth Iron Permanent Magnets*. Oxford University Press, pp. 381–429

Ní Mhíocháin T R, Weaire D, McMurry S M, Coey J M D 1999 Analysis of torque in nested magnetic cylinders. *J. Appl. Phys.* **86**, 6412–24

Skomski R, Cugat O 1999 *Permanent Magnetism*. IOP Publishing, Bristol, UK

Yonnet J-P 1996 Magnetomechanical devices. In: Coey J M D (ed.) *Rare-earth Iron Permanent Magnets*. Oxford University Press, pp. 430–51

Zijlstra H 1985 Permanent magnet systems for NMR tomography. *Philips J. Res.* **40**, 259–88

J. M. D. Coey and T. R. Ní Mhíocháin
University of Dublin, Ireland

Permanent Magnet Materials: Neutron Experiments

The crystallographic and magnetic properties of materials exhibiting hard magnet characteristics can be simultaneously analyzed by the use of neutron scattering techniques. After an introduction to the different structural, microstructural, and magnetic parameters that are determining factors for optimal intrinsic and extrinsic magnetic properties, the main principles of neutron scattering, both nuclear and magnetic aspects, are discussed in detail in this article. Specific techniques are reviewed, together

with pertinent examples underlining the advantages of neutron scattering.

Modern, powerful hard magnetic materials are of metallic type. They are based on compounds combining the magnetic characteristics of transition metals and rare-earth metals, mainly cobalt or iron combined with samarium, neodymium, or praseodymium. In the crystal structures of these magnetic compounds, the densest sublattice (d elements) provides a high magnetization and supports strong exchange forces, resulting in a high Curie temperature. As important is the less dense rare-earth metal sublattice that couples ferromagnetically with cobalt or iron in the case of the light 4f elements and which provides strongly anisotropic crystal electric field (CEF) parameters, forcing to a marked easy axis behavior of the magnetic structure (see *Localized 4f and 5f Moments: Magnetism* and *Alloys of 4f (R) and 3d (T) Elements: Magnetism*).

In all cases, more than these two elements are needed to stabilize the hard magnetic main phase (e.g., boron in $Nd_2Fe_{14}B$, nitrogen in $Sm_2Fe_{17}N$, etc.) or to stabilize a highly coercive microstructure (e.g., multiphase systems as in the complex $Sm(Co–Fe–Cu–Zr)_{8.5}$ magnets) (see *Rare Earth Magnets: Materials*). Either the atomic long-range ordering that defines the crystal structures or the microcrystalline aspects of the multiphase systems must be measured in combination with the magnetic structure ordering parameters (strength and orientation of the moments, crystal field terms, etc.) and critically analyzed before the highest level of properties can be developed.

Many different techniques are used systematically to obtain the best knowledge of both the intrinsic and the extrinsic properties of the intermetallic or interstitially modified materials showing potentially good magnetic performances. These techniques are chosen specifically, over a wide range of analyses, to characterize bulk magnets (material at gram and centimeter scales), to check the micrometric to submicrometric range of properties (multiphase structures, domain structure), to study the impact of dense arrangements (atoms, coordination) from the nanoscale to the bond scale, or to perform spectroscopic analysis of the orbital (ground) states. Indeed there are many more possible investigation methods, tools, and techniques that can be used to characterize magnetic materials. However, because of wide application ranges, neutron scattering techniques appear to be highly valuable for the systematic characterization of the crystal as well as the magnetic ordering parameters, on the basis of the typical and multipurpose aspects of the interaction of neutrons with atoms and their magnetic moments.

1. Neutron Scattering, Sources, Principles, and Characteristics

Two main types of generators have been developed for the production of intense neutron beams (typically 10^{10}–10^{14} neutrons s^{-1}). The so-called conventional reactor is based on the continuous fission process of ^{235}U nuclei ($\sim 2\,MeV$) with an excess of neutrons of about 1 for 2.5 emitted if a critical mass of fissile core is used. In the pulsed type of source, neutrons are produced from heavy atoms (Pb, ^{238}U, etc.) by strongly accelerated ($\sim 1\,GeV$) pulses of protons (spallation source). For example, very short pulses ($100\,\mu s$) of 20–40 neutrons per proton are radiated periodically ($10\,ms$). In all cases, the neutron energy (velocity) is moderated within appropriate materials. Reactor-type neutron sources are installed worldwide.

The most powerful one is the European HFR-ILL at Grenoble, France. Only a few machines of the pulsed type are operating (in the USA, the UK, Russia, and Japan), with ISIS at Didcot, UK, being the most powerful one. In this article, rather than focusing on the respective merits of each type of neutron generator, the critical differences in the use of neutrons for scattering within materials are discussed. From the Maxwellian shape of the energy spectrum issued from the source, in most cases a monochromatic neutron beam has to be selected by using crystalline monochromators or by creating kinetically controlled pulses by speed selectors (e.g., wheel-choppers). The multifaceted nature of the neutron takes advantage of the physical characteristics as expressed in Table 1.

Owing to these fundamental equivalences, for a neutron beam of wavelength $\lambda = 1.8\,\text{Å}$, i.e., suitable for scattering in crystalline compounds (interatomic distances of 1–2 Å), the neutron speed is $2200\,ms^{-1}$ and the energy is 25 meV, corresponding to an equivalent temperature of 300 K. Hence, these neutrons are called thermal neutrons. At low temperature ($T \sim 20\,K$) a moderator placed close to the reactor core allows for the use of so-called cold neutrons with a longer wavelength of 30–50 Å. A high-temperature ($T > 2000\,K$) target allows for neutrons with a shorter wavelength of less than 0.4 Å.

The first interaction of neutrons with matter (which is not the most interesting one from the point of view of magnetic properties) consists of a nuclear

Table 1

Relationships between the characteristic parameters of free neutrons.

Wave vector: $\mathbf{k}$ (nm^{-1}); wavelength: $\lambda = 2\delta/\mathbf{k}$ (nm, Å); momentum: $\mathbf{p} = \hbar\mathbf{k}$; celerity: $\mathbf{v} = (\hbar/m)\mathbf{k}$ (km s^{-1})

Energy: $E = (\hbar^2/2m)k^2 = mv^2/2 = 5.2267v^2 = (h^2/2m)(1/\lambda^2) = 0.81799/\lambda^2$

$1\,meV = 1.6022 \times 10^{-22}$ J $= 11.6045$ K $= 0.2418 \times 10^{12}$ Hz

Thermal neutron (300 K): celerity $= 2200\,ms^{-1}$; energy $= 25$ meV; wavelength $= 1.8$ Å

resonance and capture phenomenon, represented by an absorption cross-section, σ_a. Except for some isotopes (^{113}Cd, ^{157}Gd, ^{164}Dy, etc.), for most elements the corresponding cross-section remains negligible. It should be noted that the absorption is minimal far from the resonance energy.

The two main scattering processes of thermal neutrons in solid-state materials that exhibit magnetic properties are of the dipolar type.

The first process is nuclear scattering. This results from the interaction of the neutron spin, $n_s = \frac{1}{2}$, with the nuclear spin, I. The corresponding nuclear potential is effective at a distance of the same magnitude as that of the nucleus dimensions. Two intermediate scattering lengths, a_+ and a_-, are associated with the final states $I + \frac{1}{2}$ and $I - \frac{1}{2}$. Together they establish the coherent part of the scattering length $b_c = a_+(I+1)/(2I+1) + a_-(I)/(2I+1)$ and the incoherent part $b_i = (a_+ - a_-)/(2I+1)$. Practically, the coherent scattering process in combination with structured multicentered materials yields discrete intensities depending on the structure factor that is determined by the atomic arrangement. These scattering intensities can interfere constructively, whereas the incoherent scattering, which has isotropically distributed diffuse intensities, cannot interfere. However, considering the dynamic diffusion of a light element (e.g., hydrogen as a proton), incoherent scattering by this particle can be analyzed using a time and position resolving technique.

The second process is magnetic electron scattering. This results from the interaction of the neutron spin with the spin, **s**, and orbital, **l** (if any), vectors attached to the electrons. It can be described in terms of the total atomic spin, S, and orbital, L, components. The diffusion length is $f_M = 2m/\hbar^2(\mathbf{M}_n \wedge \mathbf{e}) \cdot (\mathbf{M}_e \wedge \mathbf{e})$, where **e** is the unit vector and $\mathbf{M}_n$ and $\mathbf{M}_e$ are the magnetic moments of the neutron and the electron, respectively, along the scattering vector (e.g., perpendicular to the diffraction plane). The magnetically scattered amplitude strongly depends on the orientation of the easy magnetic axis in relation to the normal of the diffraction plane (in-plane vs. out-of-plane components of the moments). If the magnetic field is strong enough to align the moments along the scattering vector, the magnetic contribution to diffraction can vanish.

If the neutron beam polarization level is $\boldsymbol{\sigma}_n$ (e.g., as diffracted on a ferromagnetic single-domain single crystal), coherency effects can be observed between both the nuclear and the magnetically scattered waves. This can be expressed by the total cross-section:

$$\sigma_t = b_c^2 + p_M^2 q^2 - 2b_c p_M \mathbf{q} \cdot \boldsymbol{\sigma}_n$$

where p_M is proportional to f_M and **q** is the scattering vector.

There are several important peculiarities to point out. Because of the point-type potential of the

nuclear interaction, the nuclear cross-section of diffusion results in a quasi-constant diffusion (Fermi) length. Since it is a nuclear characteristic (isotope characteristic), very large differences exist between the elemental Fermi lengths, revealing marked contrasts, e.g., for crystal structure determination. Successive d (and f) metals are different from each other and, in the same manner, most of the interstitial light elements are good scatterers. Table 2 compares selected cross-section amplitudes (Sears 1984).

Contrary to the nuclear scattering, the magnetic scattering related to the magnetic electron density, i.e., the magnetic scattering cross-section, decreases with the momentum transfer, Q, well approximated by Gaussian profiles (Brown 1992), which may reveal localized to itinerant aspects of the electron density. For a completely disordered moment distribution (paramagnetic state with no short-range correlations), independent of the initial polarization state of the beam, a diffuse magnetic (incoherent) scattered intensity is found that adds to the nuclear contribution. For a polarized neutron beam, successive measurements of the scattered intensity for two states of polarization (up and down, the scattering vector being horizontal) allow one to determine very accurately the spatial spin density, if the nuclear crystal structure is known. It should be noted that, if the magnetic structure exhibits unpolarized components, a depolarization effect is induced that can be successfully adopted in the polarization analysis technique to detect weak deviations from ferromagnetism.

The scattering processes as described above are of the elastic type (no energy exchange). Since the kinetic energy of thermal neutrons is of the same order of magnitude as that of the excitation processes of matter (phonons, atom diffusion, magnons, crystal field levels, etc.), inelastic scattering experiments can provide valuable information on the correlation energies or the dynamics of atom movements. Inelastic scattering leads to a change (initial to final states) of the neutron energy, where the opposite energy corresponds to the phonon or magnon frequency change $\hbar\omega$. $\mathbf{Q} = \mathbf{k}_f - \mathbf{k}_i = 2\delta\mathbf{R} + \mathbf{q}$ allows one to localize scattered neutrons with a typical intensity given by a double differential (space and energy resolved) scattering cross-section. $\mathbf{Q}$ is the scattering vector, $\mathbf{R}$ a reciprocal lattice vector, $\mathbf{q}$ the wave vector of the excitation, and $\mathbf{k}_i$ and $\mathbf{k}_f$ are the initial and final wave vectors. For such purposes, an analyzer is placed behind the sample to check the spatial and energy dispersion profile.

2. Applications of Neutron Scattering to Hard Magnetic Materials

Except for anomalously absorbing nuclei, the penetration depth of neutrons is particularly large (a few centimeters), several orders of magnitude larger than

Table 2
Absorption and scattering neutron cross-sections of selected elements or isotopes.

Element/isotope	Z (x rays)	PCT (%)	σ_a (barns)	b_c (Fermi)	B (Fermi)
^{1}H	1	99.985	0.33	−3.74	25.21
^{2}H	1	0.015	0.33	6.67	2.04
^{10}B	5	20	3837	−0.1−i(1.06)	−4.7+i(1.23)
^{11}B	5	80	0.005	6.65	−1.31
C	6		0.003	5.65	0.0
N	7		1.90	9.38	0.0
Mn	25		13.3	−3.73	1.79
Fe	26		2.56	9.54	0.0
Co	27		17.18	2.50	−6.2
Ni	28		4.49	10.3	0.0
^{58}Ni	28	68.27	4.6	14.4	0.0
^{80}Ni	28	26.10	2.9	2.8	0.0
Cd	48		2520	5.1−i(0.7)	0.0
Pr	59		11.5	4.45	−0.36
Nd	60		50.5	7.69	0.0
Sm	62		5670	4.2−i(1.58)	0.0
^{149}Sm	62	13.9	40140	24−i(11.2)	28−i(9.84)
Gd	64		48890	9.5−i(13.59)	0.0
^{157}Gd	64	15.7	254000	11−i(70.6)	26−i(54.7)
Tb	65		23.4	7.38	−0.17
Dy	66		940	18.9−i(0.26)	0.0
^{164}Dy	66	28.1	2650	49.4−i(0.74)	0.0
Ho	67		64.7	8.08	−1.7
Th	90		7.37	9.84	0.0

Source: Sears (1984).

for x rays (micrometers). It is worth noting that large samples and thick-walled sample holders and vessels can be used, for example, to investigate fundamental as well as extrinsic magnetic properties, even those sensitive to external pressure, high temperature, corrosion, etc. Examples selected from the literature are discussed below, in order to illustrate the multiple applications of neutron scattering to magnetic materials.

2.1 Crystal Structure Determination

(a) Powder diffraction

Neutron diffraction on powdered samples is a powerful technique that allows in most cases for the determination of the crystal structure of the compound more easily than by using x-ray powder diffractometry, owing to the excellent contrast in the scattering cross-sections, as shown in Table 2. For such purposes, it is recommended to use a high-resolution neutron diffractometer that consists of banks of a large number of individual detectors equipped with selective collimators. The crystal structure of $Nd_2Fe_{14}B$, especially the position of the light boron, was solved for the first time (Herbst *et al.* 1984) using neutron diffraction on a powdered sample. Parallel to

this, the crystal structure was also solved by using x-ray single-crystal four-circle diffractometry (Shoemaker *et al.* 1984, Givord *et al.* 1984). The location of light hydrogen (deuterium) atoms inserted in four types of adjacent tetrahedral sites in $Y_2Fe_{14}BD_{4.8}$ was determined by means of a good-resolution position-sensitive neutron detector (Fruchart *et al.* 1984).

The scheme of the successive filling of the sites, that was found later to depend on the nature of the rare-earth element, was determined using a geometrical model that allowed the prediction of the maximum hydrogen uptake. When the interstitial ternaries $R_2Fe_{17}X_x$ (R = rare earth; X = C, N, H) were found to exhibit potentially high magnetic performances, neutron diffraction on powdered samples was the unique technique to ascertain the position and the stoichiometry (x) of the light element. From volumetric or barymetric gas absorption experiments, it was suggested for a long time that particularly large amounts of X elements (up to nine for hydrogen, up to six for carbon and nitrogen) can be inserted into the 2-17 metal lattice to improve the Curie temperature, the magnetization, and other magnetic properties. From neutron diffraction experiments, it was definitively shown that, at maximum, three carbon or nitrogen and 5 (= 3 + 2) hydrogen atoms per formula unit occupy well-defined 2R–4Fe octahedral sites,

two extra hydrogen atoms occupying smaller 4R–3Fe tetrahedral sites (Isnard *et al.* 1990).

This was confirmed by Koyama and Fujii (2000) for $N_2Fe_{17}N_3$. It is also of interest to analyze the cell parameter expansion, not only on light element insertion but also when other elements are substituted for iron in order to modify the bond lengths. The location of these elements as a function of their concentration provides interesting arguments for a better understanding of the modification of the bulk magnetic characteristics that are volume dependent. This has been systematized for titanium, cobalt, manganese, gallium, silicon, etc., establishing reliable schemes of substitution (Mishra *et al.* 1996).

For some resonantly absorbing elements (dysprosium), either the use of a two-wall cylindrical sample holder at $\lambda = 1-2.5\,\text{Å}$ or the use of very short wavelengths ($\lambda = 0.5\,\text{Å}$) gives the most convenient conditions to record rather good data on powdered samples, e.g., gadolinium or samarium.

(b)   Single-crystal diffractometry

The most precise technique to use for crystal structure determination is four-circle diffractometry. However, this requires rather large single crystals. Spheres of 1.5–2.5 mm in diameter of $R_2Fe_{14}B$ ($R = Y$, Nd, Ho, Er) have been cut by spark erosion from large crystals and systematically studied by neutron diffraction. Precise information about the atomic positions and interatomic distances has been obtained for these dense iron compounds (Wolfers *et al.* 1996). Ancillary equipment can be used to perform experiments under special external conditions, e.g., very low or high temperatures, uniaxial stress, or high pressures.

(c)   Small-angle and diffuse scattering

The small-angle neutron scattering (SANS) technique using long neutron wavelengths (10–20 Å) allows one to investigate intermediate-size domains in the structure, for example, as formed by segregation effects. Only a few examples using SANS have been reported, e.g., the segregation rates of cobalt and copper in $Sm(Co-Cu)_5$ alloys that markedly influence the intrinsic and extrinsic hard magnetic properties of the binaries. In the RFe_5Al_7 series, a clustering tendency of iron is evident from classical powder diffraction experiments by the analysis of diffuse scattering phenomena, since the atomic clustering influences the magnetic correlation scheme (Schäfer *et al.* 1994).

2.2   Magnetic Structure Determination

Neutron powder diffraction is a convenient technique for the measurement of the local magnetic moment characteristics. The higher the counting rate, the better are the refined values. For such a purpose, an instrument typically has a position-sensitive detector (PSD) providing a high counting rate at a sufficiently long wavelength that enables one to record the significant magnetic source signal within the aperture of the detector array. At HFR-ILL, Grenoble, and at LLB, Saclay, there are optimized instruments allowing one to measure diffraction patterns with a high statistic in the time range of minutes up to a few hours. It is recommended to record at least one high-resolution diffraction pattern in a large range of **Q** spacings using a dedicated diffractometer that provides precise crystal structure parameters. Moreover, the excellent counting rate of the banana-type PSD allows one to perform time- and temperature-resolved experiments in order to determine accurately the changes in the magnetic moments, e.g., for $R_2Fe_{14}B$ ($R = Nd$, Ho, Er), as well as for $RFe_{12-x}T_x$ ($R = Dy$) in the range of the Curie temperature or possible spin reorientation temperatures (SRTs).

When single crystals are available, the four-circle technique remains by far the best for detailed crystal and magnetic structure determinations, as demonstrated for the $R_2Fe_{14}B$ series ($R = Y$, Nd, Ho, Er) (Wolfers *et al.* 1996). After appropriate corrections (e.g., absorption or multidomain corrections), precise fittings to the data (several thousand recorded Bragg peaks) lead to detailed pictures of almost ferromagnetic but noncollinear magnetic structures accompanied by the small-atom displacements (and crystal symmetry lowering) related to the important magnetoelastic forces existing in these compounds.

Another method, polarized neutron diffraction (PND), can be used to investigate the magnetic structure of truly ferromagnetic and very large single crystals, e.g., $Y_2Fe_{14}B$ (Givord *et al.* 1985). With this technique, and in the case where the data collection statistics are good enough, a Fourier transformation allows one to plot spin density projections, thus revealing local but weak magnetic polarization effects or temperature-induced changes of density moment setting on cobalt atoms in $ThCo_5$ (Givord *et al.* 1977).

Using thermal neutrons it seemed impossible to analyze the magnetic structures of one of the archetypal magnetic compounds, $SmCo_5$. However, using short wavelengths of 0.4–0.5 Å, in order to reduce the nuclear absorption, precise PND experiments have allowed the calculation of the magnetic form factors of cobalt and samarium, the latter being very different at 4 K and 300 K: the samarium moment is much smaller at room temperature than at low temperature (Givord *et al.* 1979). Further analyses show that the form factors of *L* and *S* type show quite different radial shapes for samarium. Accounting for the opposite orbital and spin contributions in the magnetic moment of samarium yields an anomalous thermal behavior with a crossover temperature estimated as 350 K. Modeling of the appropriate Hamiltonian, considering the large exchange forces and the mixed

CEF multiplets of the samarium ground state, allows one to determine exchange and CEF parameters from a fit to the experimentally obtained form factors. Furthermore, the exchange field and the second-, fourth-, and sixth-order CEF parameters have been calculated, respectively, as $175 \pm 25\,K$, $-200 \pm 50\,K$, $0 \pm 50\,K$, and $50 \pm 50\,K$ (Givord *et al.* 1979), which are in good agreement with values deduced from magnetization experiments and corresponding calculations.

For the parent compound YCo_5, a PND study has permitted the determination of the origin of a very large magnetocrystalline anisotropy, which is not related to the nonmagnetic yttrium but to one of the two cobalt sites (Co_{II}), which exhibits a particularly high orbital contribution and is attributed to its peculiar and asymmetric environment (Schweizer and Tasset 1980).

2.3 Magnetic Excitations

Dynamic excitation spectra have been recorded for different series of intermetallics belonging to the different classes of hard magnetic materials. For the $R_2Fe_{14}B$ series of materials, inelastic neutron scattering (INS) was first performed on powder samples (Loewenhaupt *et al.* 1988). For $R = Y$ and Ce, only phonon scattering is identified. For $R = Nd$, Dy, and Er, resonances of magnetic origin are observed. These are attributed to magnon-like excitations for the latter two compounds, since they markedly increase with temperature (dominant Zeeman field, negligible CEF). For the neodymium compound, two well-defined and equivalent peaks (22 meV and 36 meV) are assigned to the two nonequivalent neodymium sites in terms of CEF effects. From the thermal dependence, it is concluded that the neodymium moment corresponding to the larger CEF signature is poorly affected by the SRT, contrary to the other neodymium site that is sensitive to SRT conditions as sharing the weakest CEF level. This approximate model cannot be considered to agree well with the accurate magnetic structure determination (Wolfers *et al.* 1996) refined from single-crystal data collection.

Subsequent INS experiments on $Nd_2Fe_{14}B$ single crystals (Mayer *et al.* 1992) did not show the existence of lines at 22–36 meV. However, low-energy lines (magnon dispersion) were analyzed on the basis of torque effects acting on the magnetic moments driven by effective exchange and anisotropy fields. The authors proposed a strong influence of long-range interactions in relation to an itinerant character of the iron magnetism.

The R_2Zn_{17} compounds are isotypic with the magnetic R_2Co_{17} compounds. However, owing to the simplest magnetic situation (here only R is magnetic), the CEF excitations were analyzed first (Garcia-Landa 1994). In the low-energy region (<15 meV)

several peaks were confirmed to be of CEF origin; then the noninteracting spins were described using a pure CEF model. For $R = Er$, ($T_{SR} = 1.4\,K$, $T_N = 1.6\,K$) a set of CEF parameters was determined, of which the dominant one is the negative second-order term of less than 2 K, thus agreeing with a magnetically easy plane behavior.

Magnetic excitations have been investigated in detail in some R_2T_{17} compounds (T = transition metal) (Clausen and Lebech 1982). The spin wave dispersion relationships have been interpreted with a linear spin model comprising a Heisenberg exchange term and single-ion CEF anisotropy terms. Experiments performed on Dy_2Co_{17} single crystals using the IN8-ILL spectrometer (Colpa *et al.* 1989) have been analyzed using a complete Hamiltonian with respect to the R–R exchange interaction, which is often considered negligible if compared to the T–T and R–T ones. Since there are some discrepancies between the assignment of a highly dispersive mode that is associated with the Co–Co exchange forces, both the exchange and the CEF characteristic energies have been deduced. For Dy_2Co_{17}, the values are: $J_{TT} \sim 200\,K$, $J_{RT} \sim 25\,K$, $J_{RR} \sim 0.2\,K$, CEF_R parameters ~ 28 to $6\,K$, and T-anisotropy parameter $\sim 6\,K$. They are in good agreement with the high-field magnetization fittings (Givord *et al.* 1977) as compared to those obtained by NPD for $SmCo_5$.

2.4 Atom Dynamics

The quasielastic neutron scattering (QNS) technique based on space and time self-correlation of a single nucleus, which is supposed to move within the compound, is practically restricted to studying either the motion processes of this nucleus (e.g., hydrogen) or the fast rotation of some molecules. This becomes possible owing to a very high incoherent scattering length. For the present purposes, it can be used to analyze the living time of a proton within interstitial sites and the related energy of hopping. A typical application could be the analysis of the diffusion mode of protons, i.e., during either the hydrogen decrepitation or the HDDR (hydrogen decomposition–dehydrogenation–recombination) processes (diffusion, nucleation, wall interface mechanisms, etc.) (see *Magnets: HDDR Processed*). The analysis of the data could be somewhat difficult owing to the rather large unit cell and the multiple and different interstitial sites. However, the questions concerning the diffusion mechanisms have been partly solved, as explained below.

2.5 Phase Transformation Analysis from Resolved Diffraction Experiments

So far only structural and magnetic fundamental trends of the main compounds forming magnet

materials have been considered. However, magnetic properties are much improved by particularly fine-designed microstructures resulting from well-defined thermal or mechanical treatments. *In situ* neutron diffraction experiments performed with PSD instruments with high counting rates have allowed the determination and optimization of chemical and physical treatments leading to the best extrinsic properties. Some typical examples are given below.

Temperature- and time-dependent neutron diffraction experiments confirm the maximum hydrogen uptake in the $Nd_2Fe_{17}H_x$ unit cell, and its distribution onto the two accessible sites (tetrahedral and octahedral types). The preferential chemical attraction favors the larger and space repartited octahedrons (Isnard *et al.* 1990). The cell parameter expansion is determined and the behavior of a critically short Fe–Fe distance is refined. A clear correlation between the hydrogen occupation rates of the sites is established, the corresponding changes of the Fe–Fe distances and the nonlinear increase of the Curie temperature have been attributed to an increase of the exchange parameters.

Similar experiments performed with hydrides (deuterides were chosen to avoid the strong incoherent scattering of hydrogen), as well as with carbides and nitrides, allow the assertion of the existence of an extended solid solution in the 2-17 and 1-12 hydride and carbide phase diagrams and a two-phase behavior in nitrides (Fruchart *et al.* 1994).

Using a dedicated sample holder connected to a hydrogen (deuterium) cylinder and gas pressure sensors, time (kinetics), pressure level (or vacuum), and temperature (slopes and plateaus) dependent neutron diffraction experiments have been performed. For example, they permit the analysis of the structural aspects and the chemical phase transformations when the HDDR route is applied. This process is one of the most powerful ways to form a strongly coercive microstructure in micrometer-sized powders as used for bonded magnet technology (Liesert *et al.* 1997).

Neutron diffraction using PSD techniques is well suited to reproduce the high-temperature thermal and annealing treatments on real magnetic materials. *In situ* experiments permit the correlation of known dilatometric results with phase and structure transformations in bulk materials. Finally, using a high counting rate PSD, such as the D20 diffractometer at ILL, one can extract significant crystal structure and kinetic information in reasonable times even from only a tiny amount of material (a few micrometers thick), e.g., surface corrosion of material at moderate temperature, under specific atmospheres.

2.6 Texture and Microstructure Analysis of Magnets

Cradle circle equipment can be used to analyze the texture parameters (relative grain orientation of the main phase). The orientation of the grains is a critical parameter to form fully anisotropic magnets, thus providing high levels of induction, i.e., large energy products. Texturing of microcrystalline assemblies can be achieved by using different routes depending on the final state (use) of the magnet. The well-known fully dense sintered magnets are treated at a high temperature under high stress (see *Magnets: Sintered*). A preferential orientation of isotropic microcrystalline particles can be achieved by die up-setting and high-temperature fast forging (see *Textured Magnets: Deformation-induced*).

Neutron diffraction texture analysis is a good tool for examining the surfaces as well as the core of large samples (sampling size of a few cubic millimeters) after the material submitted to high stress. Different types of magnetic material can be checked using texture analysis. Using this technique, it has been shown for Nd–Fe–B materials, that fast forging at high temperature is very efficient in order to align most of the microcrystallite axes along the forging direction. These axes are initially in-plane aligned as a result of the book-mold procedure used during cooling the magnet material (Rivoirard *et al.* 2000). Moreover, the effectiveness of the metallurgical procedure is correlated to a ductile-to-brittle phase transformation and to rheological phenomena existing in the range 850–950 °C.

2.7 Laue and Reflectometry Methods

The white-beam technique of the Laue method should be mentioned. Again, owing to the excellent penetration ability of the neutron, the Laue method can be efficiently used to analyze macro- and micro-ordered materials. The first obvious use of a neutron diffraction Laue setup is to control the quality and the orientation of a single crystal within its full volume before other investigations (INS, PND, four-circle, etc.). With one exposure many details of large parts of the reciprocal space can be analyzed and evidence of, for example, twins, defects, dislocations, and strain fields can be obtained. The same method has been used to determine the temperature, magnetic field, and even pressure dependence of magnetic domains up to the limit of resolution of the camera film, i.e., a few micrometers (Tanner *et al.* 1992).

Because new materials are designed for integrated purposes and the needs of densified media for recording (e.g., using hard magnetic compounds), materials science is more and more concerned with nanoscale samples. Neutron reflectometry is a very interesting technique not only for providing information on the quality of thin-layer samples (crystalline and magnetic roughness) but also for analyzing the interface magnetic coupling, the superstructure magnetic ordering reflecting the competition between exchange forces, polarization effects via conduction

electrons, or large magnetocrystalline anisotropy of interfaces. As the scattered signals are of nuclear or magnetic origin, or both, the effectiveness of magnetic reflectometry takes advantage of polarized neutron beams and polarization analysis techniques.

3. Conclusion

Scattering methods using thermal neutrons are particularly well suited to deliver unique information on magnetic materials, and more particularly on those expected to show potential as high-performance magnets. Such magnetic materials are composed of transition and rare-earth metals, but often also contain further elements in rather small amounts. The large dimensional range (from electrons or orbitals to micro- and centimeter scales) can be treated using a very wide range of powerful techniques. This allows not only the characterization of static parameters, but also of dynamics and excitation phenomena, thus effectively providing typical energies. Both aspects are associated with the intrinsic quantities, such as magnetization, exchange forces, and CEF strengths.

Many extrinsic but critical quantities can also be analyzed, especially those being relevant for chemical procedures, processes, microstructure optimization, etc. The multipurpose neutron scattering techniques as such have no equivalent, especially because of their efficiency in depth penetration, contrary to x-ray techniques. Owing to the increasing neutron fluxes and to the correspondingly improved detection techniques, more and more detailed information can be obtained. Hence, either microintegrated materials or microstructured functional materials can be investigated to satisfy the interest in these materials. It can be very fruitful to combine the neutron investigation methods as described here with more conventional, laboratory-scale techniques to support the production of new, hard magnetic materials.

See also: Crystal Field Effects in Intermetallic Compounds: Inelastic Neutron Scattering Results; Magnetic Excitations in Solids

Bibliography

Brown P J 1992 Magnetic form factors. In: Wilson A J C (ed.) *International Tables for Crystallography*. Kluwer, London, pp. 391–9

Clausen K N, Lebech B 1982 *J. Phys. C: Solid State Phys.* **15**, 5095

Colpa J H P, Sinnema S, Frings P H, Franse J J, Radvanski R J 1989 *J. Phys. Cond. Matter* **1**, 2047

Fruchart D, Isnard O, Miraglia S, Pontonnier L, Soubeyroux J L, Fruchart R 1994 R_2Fe_{17} and RM_{12} carbide and carbonitride synthesis from heavy hydrocarbon compounds. *J. Alloys Comp.* **203**, 157–63

Fruchart D, Wolfers P, Vuillet P, Yaouanc A, Fruchart R, L'Héritier P 1984 Structural and magnetic properties of $RE_2Fe_{14}B$ hydrides. In: Mitchell I V (ed.) *Nd–Fe Permanent Magnets: Their Present and Future Applications*. CEC, Brussels, Belgium, pp. 173–8

Garcia-Landa B 1994 *Doctoral thesis*. University of Zaragoza, Spain

Givord D, Laforest J, Lemaire R 1977 Magnetic transition in $ThCo_5$ due to change of Co-moment. *Physica B* **86–88B**, 204–6

Givord D, Laforest J, Schweizer J, Tasset F 1979 *J. Appl. Phys.* **50**, 2008

Givord D, Li H S, Moreau J M 1984 *Solid State Commun.* **50**, 497

Givord D, Li H S, Tasset F 1985 Polarized neutron study of the compounds $Y_2Fe_{14}B$ and $Nd_2Fe_{14}B$. *J. Appl. Phys.* **57**, 4100–2

Herbst J F, Croat J J, Pinkerton F E, Yelon W B 1984 *Phys. Rev. B* **29**, 4176

Isnard O, Miraglia S, Soubeyroux J L, Fruchart D, Stergiou A 1990 Neutron diffraction study of the structural and magnetic properties of the $R_2Fe_{17}H_x(D_x)$ ternary compounds (R = Ce, Nd and Ho). *J. Less-Common Metals.* **162**, 273–84

Koyama K, Fujii H 2000 Nitrogen gas–solid reaction process and basic magnetism of the interstitially modified rare-earth 3d transition-metal nitrides $R_2Fe_{17}N_3$ (R = Y, Ce, Nd, Sm) and $Y_2Co_{17}N_3$. *Phys. Rev. B* **61**, 9475–93

Liesert S, Fruchart D, de Rango P, Soubeyroux J L 1997 The hydrogenation–disproportionation—desorption–recombination process of $Nd_2Fe_{14}B$ studied by in-situ neutron diffraction and thermomagnetic measurements. *J. Alloys Comp.* **253–254**, 140–3

Loewenhaupt M, Prager M, Murani A P, Hoenig H E 1988 Inelastic neutron scattering on $RE_2Fe_{14}B$ (RE = Y, Ce, Nd, Dy and Er). *J. Magn. Magn. Mater.* **76–77**, 408–10

Mayer H M, Steiner M, Stüsser N, Weinfurter W, Dorner B, Lindgård P A, Clausen K N, Hock S, Verhoef R 1992 Inelastic neutron scattering measurements on $Nd_2Fe_{14}B$ and $Y_2Fe_{14}B$ single crystals. *J. Magn. Magn. Mater.* **104–107**, 1295–7

Mishra S R, Long G L, Pringle O A, Middleton D P, Hu Z, Yelon W B, Grandjean F, Buschow K H J 1996 A magnetic neutron diffraction, and Mössbauer spectral study of the $Ce_2Fe_{17−x}Al_x$ solid solutions. *J. Appl. Phys.* **79**, 3145–55

Rivoirard S, Fruchart D, de Rango P, de la Perrier B âthie R, Chateigner D 2000 *Proc. 6th Int. Workshop on Rare-Earth Magnets and their Applications*. Sendaï, Japan

Schäfer W, Kockelmann W, Will G, Fischer P, Gal J 1994 Atomic distribution in $RFe_xAl_{12−x}$ compounds with R = Tb, Dy, Ho, Er, Tm and Fe concentrations $x \lambda 5$ studied by neutron diffraction. *J. Alloys Comp.* **207**, 316–20

Schweizer J, Tasset F 1980 *J. Phys. F: Metal Phys.* **10**, 2799

Sears, V F 1984 AECL report 8490. Atomic Energy of Canada

Shoemaker D P, Shoemaker C B, Fruchart R 1984 The structure of a new magnetic phase related to the sigma phase: iron neodymium boride $Nd_2Fe_{14}B$. *Acta Crystallogr.* **C40**, 1665–8

Tanner B K, Baruchel J, Abell J S 1992 Internal magnetic domain structure changes in thick $TbAl_2$ crystals revealed by polarized neutron topography. *J. Magn. Magn. Mater.* **104**, 317–8

Wolfers P, Obbade S, Fruchart D, Verhoef R 1996 Precise crystal and magnetic structure determinations: I. A neutron diffraction study of $Nd_2Fe_{14}B$ at 20 K. *J. Alloys Comp.* **242**, 74–9

D. Fruchart
Laboratoire de Cristallographie du CNRS, Grenoble France

Permanent Magnetic Devices in Otiatria

Inflammatory diseases of middle ear often result in partial or complete destruction of its sound conducting elements: perforation of tympanic membrane, damage to or destruction of ossicles (hammer, anvil, stirrup) (Fig. 1; Kobrak *et al.* 1963, Wullstein *et al.* 1972, Williams and Rouf 1978, Ferris *et al.* 1998, Kuvnetsov *et al.* 2001). This typically leads to significant deterioration or complete loss of hearing. Prosthesing of such miniature elements in a narrow passage, while preserving the physiological level of signal transduction and protecting the inner ear from overloading, is a challenging task for the surgeon and imposes rigorous requirements on materials for such
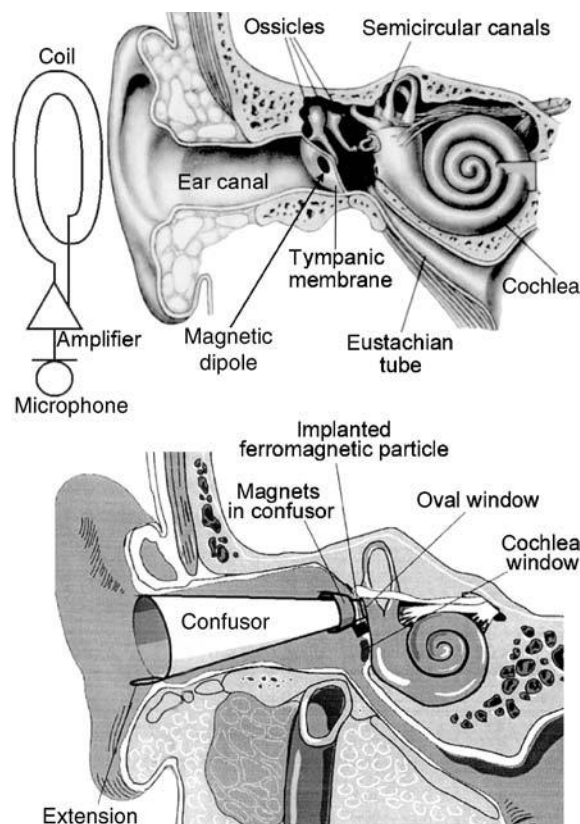
Figure 1
Main elements of a human ear and one of the schemes of hearing rehabilitation using an implanted miniature permanent magnet (top). The magnet is vibrated by an external alternating magnetic field of sound frequency and generates acoustic perceptions for the patient. Application of a removable confusor in patients with total absence of the middle ear sound conducting system (bottom).

prostheses. Application of modern magnetic materials such as $SmCo_5$ and NdFeB (see *Rare Earth Magnets: Materials* and *Magnets: Sintered*) makes it possible to manufacture miniature magnets with high magnetic energy. These magnets can produce mechanical forces, typical for middle ear, even in magnetic systems with open magnetic circuits. A human ear can hear sounds with intensities of up to 120 dB ($L = 20 \log(P/P_0)$), where $P_0 = 2 \times 10^{-5}$ N m^{-2} is the audibility threshold, L is the sound intensity level). So, the maximum sound pressure P on the tympanic membrane can be estimated to be 20 N m^{-2}, and, therefore, maximum forces in the middle ear do not exceed 0.001–0.1 N. Such forces can be achieved by permanent magnets with masses 0.01–10 g, which are close to that of ossicles (several grams). These small magnets can be produced in practically any size and shape, be covered with biologically inert materials and their magnetization can be precisely controlled. Elastic magnets can also be manufactured (see *Magnets: Bonded Permanent Magnets*). Thus, a variety of functional prostheses of middle ear elements based on such miniature magnets can be created.

1. Tympanic Membrane Prosthesing

Tympanic membrane prosthesing in outpatients with dry perforative otitis media can be achieved using two thin sheets of a magnetic elastomer (rare-earth alloy particles, embedded in a biocompatible plastic, e.g., silicone). The prosthesing procedure includes insertion of one compactly rolled sheet of the magnetic elastomer through the tympanic membrane perforation into the inner ear cavity, where it is unfolded using a special tool (S) (Dmitriev and Yunin 1988). A second magnetic sheet is applied from the outer side of the tympanic membrane. The two sheets attract each other, sealing the perforation. This procedure has lead to 15–25 dB improvement in hearing of 27 patients with two-sided dry perforative otitis media and regeneration of tympanic membranes in two patients.

2. Magnetic Prostheses of Ossicles

All known types of the ossicular implants form jointless junctions, which dramatically changes the middle ear acoustic impedance. Permanent magnet-based selforganizing prosthetic devices can preserve the physiological mechanism of sound conduction in the middle ear and simplify surgeons' work. For example, an anvil prosthesis consists of a horseshoe-shaped ferromagnetic element inserted under the stirrup arch and a magnet-containing stem, attached either to the hammer or to the tympanic or artificial membrane (Kuznetsov *et al.* 1983a, 1983b, 2001). The two parts attach to each other by magnetic forces, forming a slip-free magnetic junction between them,

while the anvil-stirrup joint remains physiologically flexible. Nonmagnetic elements of the prostheses are made of rigid and light weight carbon fiber-based materials. Flexibility of the construction prevents overloading of the inner ear. Hearing improvement (20–40 dB of sound conductivity) was observed in 25 of 30 patients with chronic suppurative otitis media, who were implanted with anvil prostheses, and in 24 of 30 patients with stirrup prostheses (up to 35 dB). Prostheses of ossicles with magnetic elements also allow to vibromassage the middle ear system by an external alternating magnetic field, preventing immobilization of the prosthesis due to conjunctive tissue formation.

3. Prosthesing of the Middle Ear Sound Conducting System after a Radical Surgery

In patients with completely destroyed middle ear sound conducting system, but an intact inner ear, hearing rehabilitation requires both adjustment of the prosthesis impedance with the impedance of the inner ear and shielding of the round window. Magnetically soft ferromagnetic particles (steel X13) were implanted under the cicatrical tissue of oval window area in postoperative patients with chronic suppurative otitis media, impermeable auditory tube and total absence of the sound conducting system (Kuznetsov *et al.* 1982, Palchun *et al.* 1982). A removable elastic confusor, containing small permanent magnets, was attached to the cochlea window by magnetic forces (Fig. 1). This confusor focuses sound pressure on the oval window while shielding the round window. Since magnetic forces guide the confusor to the proper position during insertion into the ear canal, this procedure can be done by the patient. Confusor prosthesing provided up to 35 dB decrease in air conduction thresholds in 18 patients, which is approximately two times better, than traditional techniques such as shielding of the round window by oiled cotton tampons or by silicone-based foam "otopen" (Wullstein *et al.* 1972, Williams and Rouf 1978).

4. Excitation of Acoustic Vibrations in the Middle Ear Using Sound Frequency Alternating Magnetic Field Action on a Magnetic Element in the Sound Conducting System

Implantation of miniature permanent magnets into nonmagnetic biological structures of middle ear makes it possible to transform sound frequency alternating magnetic fields into mechanical stimuli, which can be perceived by the patient as acoustic signals (Fig. 1; Kuzhetsov *et al.* 1983a, 1983b, 2001, Dmitriev *et al.* 1986, 1988).

Many coils can generate suitable alternating magnetic fields, but a flat, spiral coil, concealed under

clothes on the patient's shoulder appears to be the most promising. It can generate a sound frequency alternating magnetic field from 10^{-2} Oe to 10 Oe in the ear cavity, providing adequate mechanical stimuli. Due to a relatively large distance from the coil to the ear, the field in the ear cavity is practically uniform: $\nabla B \approx 10^{-6}$ Oe cm^{-1}. The force F acting on the magnetic moment m is proportional to ∇B: $F = (m\nabla)B$, while the torque M acting on the same magnetic moment is proportional to H: $M = m \times H$. Therefore, in such field a magnetic dipole will oscillate mostly tangentially. Elements of the middle ear sound conducting system (ossicles, stirrup base) normally also move predominantly tangentially. Thus, the movements of the magnet can simulate movements of the ossicles in a normal ear and provide acoustic stimuli for the patient.

Depending on the degree of the middle ear deterioration, the location of the magnet varies: it can be either glued to the remaining tympanic membrane, or attached to ossicles (or be a part of an ossicle prosthesis), or implanted into the cicatrical tissue on the oval window surface after a radical operation. The latter was the most common technique and was used in 11 patients. Biocompatible 5–50 mg SmCo$_5$ monocrystals were used. To increase the coercive force and retentivity, the monocrystals were treated by a shock wave before magnetization (Kuznetsov *et al.* 1977). Significant rehabilitation efficiency in patients with hearing thresholds of up to 70 dB was observed after such operations. The patients were monitored for several years and no negative effects of the magnets or magnetic fields on the tissues and the processes in the ear were detected.

Attaching a magnet to the tympanic membrane in patients with an intact middle ear, but a reduced sensitivity of the inner ear, and vibrating it with an external alternating magnetic field can provide additional mechanical stimulation. Extensive experimental studies were done on cadaver material to optimize the magnet size to provide a natural level of sound pressure on the tympanic membrane. Optimal magnet size was found to be 56 mg (Dmitriev and Aknesov 1992). This technique provides a significant improvement of sound perception for all tested magnet locations and solves cosmetic problems of hearing rehabilitation (no wires, earpiece).

5. Magnetically Controlled Implantable Devices for Restoration of Inner Ear Function in Ménière's Disease Patients

Ménière's disease (labyrinth hydrops) is a serious inner ear disease, characterized by an increase of the hydrostatic pressure of intralabyrinth fluids, leading to irreversible destruction of hearing and vestibular functions. This ailment is treated by draining the excess endolymph from the labyrinth to normalize

the pressure using several types of implantable drainage devices, thus eliminating vertigo and preserving the remaining hearing level (Kobrak 1963).

Unfortunately, opening thresholds of these devices cannot be adjusted after implantation and the pressure in the labyrinth cannot be maintained at the level, optimum for the particular patient. Two types of implantable magnetic valves for draining endolymphatic sack were developed and tested (Kuznetsov *et al.* 1985, Yunin *et al.* 1984). Core elements of the valves are rare-earth permanent magnets and magnetic elastomers. Different compositions of magnetic particles (barium hexaferrite and/or rare-earth alloys) imbedded in silicone enable to create elastomers with a wide variety of magnetic properties. Magnetic elastomers were attracted to each other or permanent magnets and closed the endolymph outflow. The devices were grafted into the inner ear of the patients. During an attack, a postoperative patient can open the type I valve and decrease the endolymph pressure by bringing a magnet close to the implanted valve. Once the magnet is removed, the valve closes. Type II valves open automatically when the endolymph pressure exceeds a certain threshold. The valve opening threshold can be adjusted after grafting of the device by changing magnetization of the elastomer using an external impulse magnetization device. Thus, a physician can optimize the endolymph pressure for each particular patient and adjust it to a comfortable level in response to the patient's condition without surgery. Elastomers in the valves can be vibrated by external alternative magnetic field, preventing clogging of the valve due to conjunctive tissue formation and allowing active pumping of endolymph if necessary.

Six patients were implanted with type I valves, and another five received type II valves. The patients were monitored for more than seven years and demonstrated stable improvement in their condition: vertigo attacks were controlled by the valves, hearing levels were maintained. The patients were able to work and live normal lives.

6. Concluding Remarks

A variety of implantable prostheses of middle ear structures based on permanent magnets and using magneto-mechanical forces for their operation were developed for treating middle ear ailments and hearing rehabilitation. Methods of surgical application of the devices were developed and in clinical trials more than 85% of 127 patients with different degrees of middle ear system degradation have shown stable improvement. This promising technology increases reliability of functional results, but needs further development and approval of regulatory authorities (FDA, etc.) for wider clinical trials and use.

Bibliography

Dmitriev N S, Aknesov Yu A 1992 Principle measurement scheme of transductional properties of permanent magnets. *Current Problems of Clinical Otolaryngology*. Irkutsk, Russia, p. 355

Dmitriev N S, Yunin A M 1988 *USSR Patent* 1421332

Dmitriev N S, Yunin A M, Kuznetsov A A 1986 *USSR Patent* 1237170

Ferris P, Prendergast P J, Rice H J, Blayney A W 1998 Finite element modeling of prostheses for ossicular chain reconstruction. *J. Biomech.* **31**, 130

Kobrak H G 1963 *Middle Ear*. Medicina, Moscow

Kuznetsov A A, Nikiforov A K, Adadurov G A, Mishin D D 1977 Magnetic Properties of $SmCo_5$ monocrystals Subjected to Shock waves. *Izvestia Visshih Uchebnyh Zavedenii (Physics)* **5**, 137–9

Kuznetsov A A, Dmitriev N S, Palchun V T, Yunin A M 1982 *USSR Patent* 950374

Kuznetsov A A, Dmitriev N S, Yunin A M 1983a *USSR Patent* 1076114

Kuznetsov A A, Dmitriev N S, Yunin A M, Kazakova Z I 1983b *USSR Patent* 1041110

Kuznetsov A A, Yunin A M, Palchun V T, Dmitriev N S 1985 *USSR Patent* 1159572

Kuznetsov A A, Yunin A M, Dmitriev N S, Palchun V T 2001 Applications of Magnetic devices in otiatria. *JMMM* **225**, 202–8

Palchun V T, Dmitriev N S, Kuznetsov A A, Yunin A M 1982 *USSR Patent* 971287

Williams D F, Rouf R 1978 *Implants in surgery*. Medicina, Moscow

Wullstein H L 1972 *Hearing Improvement Operations*. Medicina, Moscow

Yunin A M, Kuznetsov A A, Palchun V T, Dmitriev N S 1984 *USSR Patent* 1151141

A. A. Kuznetsov, N. S. Dmitriev, M. Yunin, A. Savichev and O. A. Kuznetsov
University of Missouri at Columbia, USA

Permanent Magnets: Corrosion Properties

The rare-earth permanent magnets, particularly Nd–Fe–B magnets, possess outstanding magnetic properties and therefore have grown rapidly in production (see *Rare Earth Magnets: Materials*; *Magnets: Sintered*). However, their poor corrosion resistance (Jacobson and Kim 1987) has limited their applications. This article discusses the corrosion mechanism of Nd–Fe–B magnets and methods to improve their corrosion resistance.

1. Corrosion Mechanism

Permanent magnets based on Nd–Fe–B are very sensitive to various corrosive environments. The great sensitivity to corrosion is caused by the considerable amount of rare-earth element in their composition,

since the electromotive forces of rare-earth elements are much larger than those of iron. Normally, Nd–Fe–B magnets consist of three phases: (i) the main $Nd_2Fe_{14}B$ phase; (ii) a neodymium-rich (usually Nd_4Fe) phase, and (iii) a boron-rich phase. From the electrical point of view, such a contact of three different metallic phases with great differences in electrochemical activity must promote rapid corrosion. Nakamura *et al.* (1989) measured the electrode potentials of the different phases in 1 N HCl solution.

Because the Nd-rich phase has a much lower electrode potential than the $Nd_2Fe_{14}B$ phase, a selective corrosion of the Nd-rich phase occurs by forming a local cell between the $Nd_2Fe_{14}B$ and Nd-rich phases. Therefore, the grain boundary phase corrosion is dominant rather than uniform corrosion for sintered Nd–Fe–B magnets, a fact made evident by microstructural observation. The corrosion rate decreases as the Nd content (or volume fraction of Nd-rich phase) decreases. On the other hand, with the increase of cathodic polarization in strong acid, the hydrogen reduction reaction produces hydrogen atoms at the cathode that can diffuse into the base metal and cause embrittlement, and therefore the rate of Nd–Fe–B magnet dissolution increases (Bala and Szymura 1991). The abnormal dissolution (mechanical degradation) rate increases linearly with the square root of the hydrogen evolution current density.

Since the Nd–Fe–B magnets are generally used in atmospheric environments, various accelerated corrosion environment tests were employed in order to predict the service life of the magnet in ambient environments. The accelerated corrosion environments include: hot–dry air, hot–humidity, high-pressure steam, and salted spray.

The kinetics of oxidation of Nd–Fe–B alloy magnets in air at elevated temperatures (80–200 °C) exhibit an exponential weight gain (Turek *et al.* 1994, LeBreton and Teillet 1990). Quick initial oxidation of the intergranular Nd-rich phases is followed by oxidation of the $Nd_2Fe_{14}B$ phase. The oxidation products are Nd_2O_3, $NdFeO_3$, Fe_3O_4, and an inhomogeneous phase close to α-Fe.

When Nd–Fe–B magnets are exposed to a hot–humid environment (50–90 °C, 50–90% relative humidity) (LeBreton and Teillet 1990), the magnet is disintegrated but the $Nd_2Fe_{14}B$ phase is generally unaffected. The oxidation occurs in the Nd-rich region, producing Nd_2O_3 and $Nd(OH)_3$ as is evidenced by x-ray diffraction. This disintegration increases as temperature and relative humidity increase.

A more accelerated corrosion test is carried out in a high-pressure steam vessel (McGuiness *et al.* 1994, Kim *et al.* 1996). In an autoclave (or PCT) test, grains of the $Nd_2Fe_{14}B$ phase have fallen apart from the magnet. X-ray diffraction patterns on the loose particles exhibit mainly $Nd_2Fe_{14}B$ peaks with small $Nd(OH)_3$ peaks indicating that the oxidation product is $Nd(OH)_3$ and the $Nd_2Fe_{14}B$ remains unspoiled.
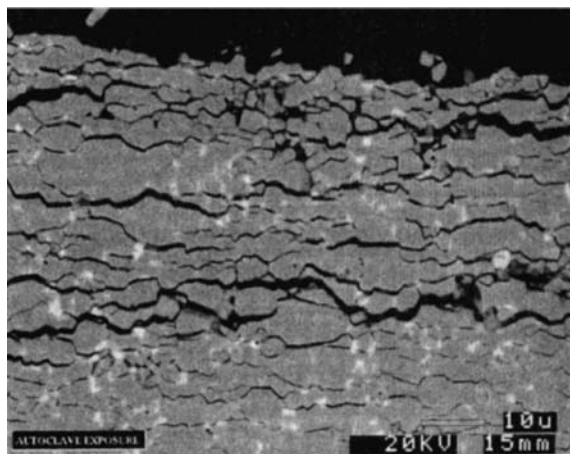
Figure 1
SEM micrograph of a Nd–Fe–B magnet subjected to an autoclave test (Kim *et al.* 1996).

Macroscopic disintegration was observed on both magnetic pole faces of the magnetically aligned and sintered Nd–Fe–B magnet after exposure to an autoclave environment at 115 °C and 2 bar, which is similar to the conditions of hydrogen decrepitation of the magnet. The microstructure underneath the disintegration surface shows plate-like cracking perpendicular to the magnetic orientation as shown in Fig. 1.

The microstructure of hydrogen-decrepitated samples shows similar cracking patterns. There is undoubtedly anisotropic corrosion and hydrogen decrepitation behavior in anisotropic Nd–Fe–B magnets. The similarity between these two corrosion processes infers a common corrosion mechanism. As described before, the hydrogen evolution during cathodic polarization of Nd–Fe–B in strong acid causes mechanical degradation (abnormal dissolution), and thus hydrogen decrepitation is involved and plays an important role in the corrosion mechanism. Hydrogen may be generated in the autoclave test from the decomposition of water vapor:

$$3H_2O + Nd \rightarrow Nd(OH)_3 + 3H$$
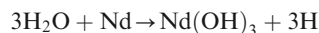
Thus, the corrosion mechanism for Nd–Fe–B magnets in the heat and humidity of the autoclave test starts with a surface reaction of water vapor with the Nd-rich grain boundary phase. The generated hydrogen atoms diffuse along the grain boundaries into the interior of the magnet. Some of the hydrogen reacts with the Nd-rich grain boundary phase, causing volume expansion of this phase ($3H + Nd \rightarrow NdH_3$) and the rest goes into the $Nd_2Fe_{14}B$ matrix ($xH + Nd_2Fe_{14}B \rightarrow Nd_2Fe_{14}BH_x$). The corrosion product of $Nd_2Fe_{14}B$ characterized by x-ray diffraction reveals that a significant expansion of the lattice has taken

place (McGuiness *et al.* 1994). Volume expansion of the Nd-rich phase and lattice expansion of the $Nd_2Fe_{14}B$ phase results in the removal of the $Nd_2Fe_{14}B$ matrix phase grains. The subsurface cracks provide the path for reacting species (water vapor) to the inside of the Nd-rich phase, which accelerates the corrosion reaction. This corrosion reaction increases as the amount of Nd-rich phase in the Nd–Fe–B magnet increases.

2. Improvement of Corrosion Resistance

As discussed in Sect. 1, the large difference in the electrochemical potential between the Nd-rich and $Nd_2Fe_{14}B$ phases promotes a rapid corrosion reaction. The grain boundary also provides the diffusion path of reacting species such as hydrogen atoms. Improvement of corrosion resistance can therefore be achieved by increasing the electrode potential of the Nd-rich phase as close as possible to that of the $Nd_2Fe_{14}B$ phase and by minimizing the Nd-rich region.

Partial substitution of iron by cobalt is reported substantially to improve the corrosion resistance by forming the Nd_3Co phase in the Nd-rich grain boundary, particularly in a hot–humid environment (Tokunara and Hirosawa 1991, Kim and Camp 1996). The electrode potential of Nd_3Co is higher than that of the Nd_4Fe phase and is close to the $Nd_2Fe_{14}B$ phase (Nakamura *et al.* 1989). The corrosion rate of Nd–Dy–Fe–Co–B–Mo sintered magnets, as monitored by weight loss in PCT, is shown in Fig. 2. This corrosion rate decreases as the cobalt content increases to 5 at.% Co.

It is noted that a cobalt addition by itself deteriorates the coercivity although it improves the corrosion resistance and Curie temperature. Therefore, various additional elements combined with cobalt were investigated in order to compensate for the negative effect of reducing coercivity by cobalt. Elements including Al, Ga, Cu, Sn, Cr, Zr, Nb, V, Mo, or W combined with Co are found to increase the coercivity. Because of these additions, the corrosion resistance is further improved. Particularly, a combined addition of cobalt and copper substantially improves both the corrosion resistance and the coercivity without reduction of the energy product (Kim and Camp 1996).

Nickel or Ni and Co additions are also reported to improve significantly the corrosion resistance (Bala *et al.* 1990). The segregation of nickel to the intergranular Nd-rich phase would reduce the electrochemical difference among the phases yielding good corrosion resistance. It is noted, however, that a nickel addition deteriorates coercivity and reduces the Curie temperature. A further small addition of titanium in a Nd–(Fe,Co,Ni)–B alloy enhances the coercivity to a moderate level. Vanadium or molyb-
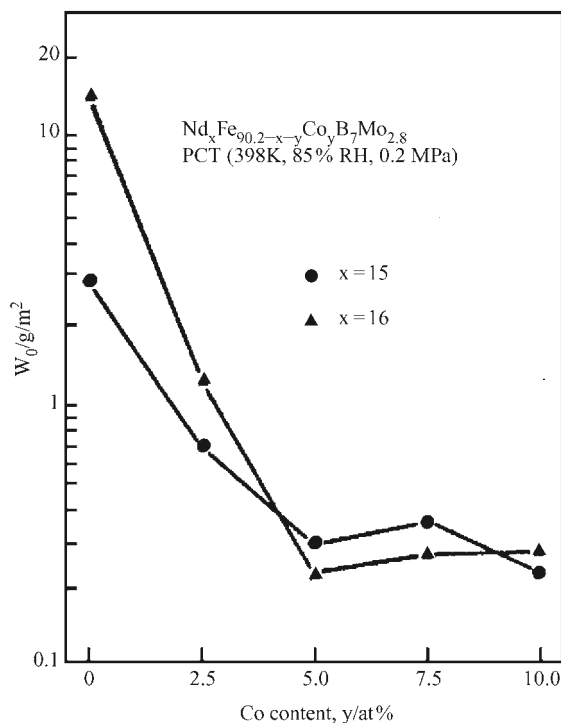
Figure 2
Weight loss per unit area of uncoated magnets in PCT for 130 ks as a function of cobalt content (Tokunara and Hirosawa 1991).

denum additions were also reported to improve coercivity and corrosion resistance by forming intergranular precipitates (Fe–M_{2-}-B_2), but at the expense of the energy product (Hirosawa *et al.* 1990).

A partial replacement of Nd by dysprosium or terbium in Nd–Fe–B magnets also improves the corrosion resistance. The lowering of the total rare-earth amount in Nd–Fe–B magnets increases the volume fraction of the $Nd_2Fe_{14}B$ phase and thus raises the electrode potential, which improves the corrosion resistance (Tokunara and Hirosawa 1991). Chromate etching on the surface of the magnet dissolves the Nd-rich surface phase. This eliminates the reaction site, which also improves the corrosion resistance (Kim 1989).

In addition, increasing density and minimizing porosity also improves the corrosion resistance. The corrosion current reportedly increases as the porosity increases in the magnet. A vacuum impregnation of the surface porosity was reported to improve the corrosion resistance (Stevenson and Stevenson 1988). The microstructure of Nd–Fe–B magnets also affects their corrosion behavior. Nanostructured melt-spun ribbons exhibit a uniform corrosion, while the sintered magnets exhibit a localized corrosion of the

Nd-rich grain boundary phase (Nakamura *et al.* 1989). The latter has a lower electrode potential and thus a poorer corrosion resistance. Hot-worked Nd–Fe–B magnets also exhibit better corrosion resistance than the sintered magnets (Nozieres and Taylor 1990).

A postmachining heat treatment of Nd–Fe–B sintered magnets at 600–1000 °C in a vacuum or in a very low oxygen environment formed a very thin oxidation layer on the surface and thus improved the corrosion resistance in hot–humid environments (Imaizumi *et al.* 1987).

3. Corrosion Protection

The corrosion resistance is further improved by applying corrosion protection layers on the surface of the magnet (Mitchell 1990). Various depositing materials can be put on the magnet surface by using various techniques. Plating can be described as the deposition of a material from a solution. There are two main types of plating: one is electrolytic or electroless plating and the second is electropainting. The most common coating is electrolytic or electroless plating of Ni, Sn, Cu, or combinations of these, because of ease of mass production, economic process, and durability.

However, an adjusted pretreatment to inhibit a reaction of nickel with the magnet is needed because Nd–Fe–B magnets may absorb hydrogen during the plating process causing cracking and, thus, failure of adherence of the layer to the magnet. Nickel plating usually exhibits a good corrosion resistance in hot–humid environments but a poor resistance in salt-spray environments. The cathodically deposited electropaint coating is also very popular because of its ease for mass production. The electropaint coating usually exhibits an excellent corrosion resistance in salt-spray environments and a moderate resistance in hot–humid environments.

Vapor deposition generally refers to the deposition of a material on to a substrate by use of the gaseous phase of the depositing material. There are several forms of vapor deposition as physical, chemical, and spray deposition. Among them the aluminum-ion vapor deposit coating is important for achieving a high corrosion resistance. It provides the highest degree of protection against hot–humid environments and exhibits a moderately good resistance to salt-spray.

See also: Magnets: High-temperature; Magnets: Remanence-enhanced

Bibliography

Bala H, Szymura S 1991 An electrochemical investigation of dissolution of Nd–Fe–B magnets in acid-solution under cathodic polarization. *Corros. Sci.* **32**, 953–63

Bala H, Szymura S, Wyslocki J J 1990 Corrosion characteristics of $Nd_2Fe_{14-x}Ni_xB$ permanent magnets. *IEEE Trans. Magn.* **26**, 2646–8

Hirosawa S, Tomizawa H, Mino S, Hamamura A 1990 High-coercivity Nd–Fe–B-type permanent magnets with less dysprosium. *IEEE Trans. Magn.* **26**, 1960–2

Imaizumi N, Inoue N, Takahashi K 1987 Effects of post-matching heat treatment on the magnetic properties and the corrosion of NdFeB magnets. *IEEE Trans. Magn.* **23**, 3610–2

Jacobson J, Kim A 1987 Oxidation behavior of Nd–Fe–B magnets. *J. Appl. Phys.* **61**, 3763–5

Kim A S 1989 *J. Mater. Eng.* **11**, 95

Kim A S, Camp F E 1996 High performance NdFeB magnets. *J. Appl. Phys.* **79**, 5035–9

Kim A S, Camp F E, Lizzi T 1996 Hydrogen induced corrosion mechanism in NdFeB magnets. *J. Appl. Phys.* **79**, 4840–2

LeBreton J M, Teillet J 1990 Oxidation of (Nd,Dy)FeB permanent magnets investigated by ^{57}Fe Mossbauer spectroscopy. *IEEE Trans. Magn.* **26**, 2652–4

McGuiness P J, Fitzpatrick L, Yartys V A, Harris I R 1994 Anisotropic hydrogen decrepitation and corrosion behavior in NdFeB magnets. *J. Alloy Comp.* **206**, L7–10

Mitchell P 1990 Corrosion protection of NdFeB magnets. *IEEE Trans. Magn.* **26**, 1933–5

Nakamura H, Fukuno A, Yoneyama T 1989 In: *Proc. 10th Int. Workshop on Rare Earth Magnets and their Applications.* Kyoto, Japan, p. 315

Nozieres J P, Taylor D W 1990 Corrosion resistance of hot-worked NdFeB permanent magnets. *J. Less-Com. Metals.* **162**, L1–5

Stevenson M, Stevenson J Jr 1988 *Metal Finishing* **86**, 93

Tokunara K, Hirosawa S 1991 *J. Appl. Phys.* **79**, 5521

Turek K, Liszkowski P, Figiel 1994 The kinetics of oxidation of Nd–Fe–B powders. *IEEE Trans. Magn.* **29**, 2782–4

A. S. Kim
JAHWA Electronics Co., Ltd., Choong-Book Korea

Permanent Magnets: Microstructure

The microstructure of rare earth permanent magnet materials is defined by the type, the structure and the number of phases, by the size, shape and the topological arrangement of the individual phase regions and their interfaces, and by the type, structure and geometry of lattice defects. In the following, several examples of TEM micrographs will show the differences between various types of rare earth magnets (see *Rare Earth Magnets: Materials*). The importance of newly developed permanent magnetic materials in many electro-, magnetomechanical and electronic applications can be attributed to the drastic improvement of microstructure related properties, such as the magnetic energy density product and the coercive field.

The rare earth intermetallic phases with a high uniaxial magnetocrystalline anisotropy (see *Magnetic*

Anisotropy), such as $SmCo_5$, Sm_2Co_{17}, and $Nd_2Fe_{14}B$ are the basis for high-performance rare earth magnets. Samarium–cobalt magnets exhibit the highest coercive fields $_JH_c$ and (Nd,Dy)–(Fe,Co)–B:(Al,Cu, Ga) magnets show the highest value of remanence B_r and energy density product $(BH)_{max}$ obtained so far. Rare earth magnets are divided into the group of the so-called single phase, nucleation-controlled magnets, based on the $SmCo_5$ or $Nd_2Fe_{14}B$ hard magnetic phases, and the group of domain wall pinning controlled, multiphase magnets (see *Coercivity Mechanisms*). Two-phase magnets, which are nowadays also used in high-temperature advanced power applications consist of a continuous $Sm(Co,Cu)_{5-7}$ cellular precipitation structure within a $Sm_2(Co,Fe)_{17}$ matrix phase. Nanocrystalline rare earth magnets exhibit microstructures of single phase, two phase and multiphase character, in which the inhomogeneous magnetization behavior near the intergranular regions can create remanence enhancement (see *Magnets: Remanence-enhanced*).

High-performance rare earth permanent magnets are produced with different composition and by various processing techniques (Strnat 1988, Herbst 1991), which influence the complex, multiphase microstructure of the magnets, such as size and shape of grains, the orientation of the easy axes of the grains and the distribution of phases. The formation and distribution of the phases is determined by the composition of the magnets and the annealing treatment. The grain size of the magnets and the alignment of the grains especially strongly depend on the processing parameters:

- grain sizes in the range between 10 nm and 500 nm are obtained by melt-spinning, mechanical alloying (see *Magnets: Mechanically Alloyed*) and the HDDR (hydrogenation-disproportionation-desorption-recombination) process (see *Magnets: HDDR Processed*),
- sintered (see *Magnets: Sintered*) and hot worked magnets (see *Textured Magnets: Deformation-induced*) exhibit grain sizes above 1 μm.

The hysteresis properties of the magnets are governed by a combination of the intrinsic properties of the material, such as saturation polarization J_s, magnetic exchange and magnetocrystalline anisotropy of various phases, and the influence of the microstructure on the magnetization reversal process (see *Magnetic Hysteresis*). The intergranular structure between the grains plays a significant role in determining the magnetic properties, thus a detailed understanding of the microstructure and of the grain boundaries is necessary. Magnetic domain structures (see *Magnets, Soft and Hard: Domains*), which are a result of the occurrence of magnetic stray fields, are directly influenced by the microstructural features.

The direct observation of microstructure and magnetic domain structure leads to a deeper insight into the origin of the coercivity of rare earth magnets.

Advanced analytical methods, such as high-resolution electron microscopy (see *Magnetic Materials: Transmission Electron Microscopy*), magnetic force microscopy (see *Magnetic Force Microscopy*), position sensitive 3D atom probe, and other techniques have been used to study rare earth magnets. Modeling of magnetic materials is performed at various levels and becomes more important as computer power is improved. Numerical 3D micromagnetic simulations of the magnetization reversal process incorporate realistic microstructures. Advanced analytical investigations and future simulations should be able to predict optimal microstructures and properties for given hard and soft magnetic materials (Fidler and Schrefl 2000).

1. Nucleation-controlled Magnets

The basic microstuctural feature of polycrystalline $SmCo_5$- or $Nd_2Fe_{14}B$-based magnets is the individual hard magnetic grain with its size, shape, and orientation parameters. The ideal microstructure of the so-called single phase magnets consists of aligned single-domain hard magnetic particles. Strictly speaking, these magnets show a complex, multiphase microstructure with various types of intergranular phases according to their phase diagram and phase relations. The amount of each phase and their distribution within polyphase materials are perhaps the most complex of the microstuctural parameters. The occurrence of the multiphase microstructure is one of the reasons why the coercive field of the magnets according to the magnetocrystalline anisotropy field of the hard phase, such as 30700 kAm^{-1} for $SmCo_5$ and 6050 kAm^{-1} for $Nd_2Fe_{14}B$, is never reached in practice.

The microstructure of single phase, anisotropic $SmCo_5$-type magnets consists of grains oriented parallel to the alignment direction. Most of the $SmCo_5$ grain interiors show a low defect density. The grain diameter exceeds the theoretical single domain size and is in the order of 5–10 μm. Besides $SmCo_5$ grains, grains with densely packed, parallel stacking faults perpendicular to the hexagonal c-axis are observed. Such basal stacking faults correspond to a transformation of the $SmCo_5$ crystal structure into the samarium-rich Sm_2Co_7 and Sm_5Co_{19} structure types. Using high-resolution electron microscopy together with x-ray microanalysis, the different polytypes and structural modifications of these samarium-rich phases are characterized. Incoherent precipitates with diameters up to 0.5 μm were identified as Sm_2O_3 or CaO inclusions. The electron micrograph of Fig. 1 shows a defect-free $SmCo_5$ grain separated into magnetic domains in the demagnetized state.

In $SmCo_5$-type sintered magnets, the coercivity is determined by the nucleation field of reversed domains which is lower than the coercivity of a
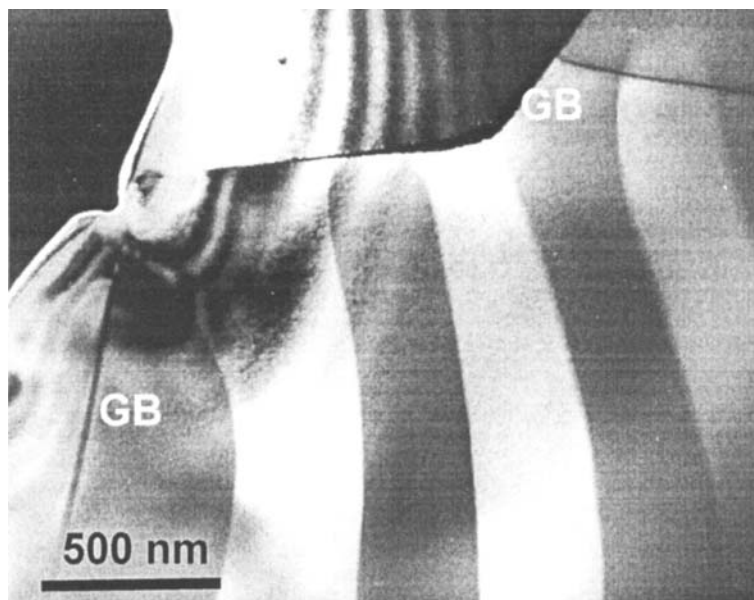
Figure 1
Lorentz electron micrograph showing the magnetic domain configuration in the demagnetized state of a sintered SmCo$_5$ magnet. The coercivity mechanism is controlled by nucleation and expansion of reversed domains.

magnetically saturated particle with a single domain structure and nucleation by the expansion field of the reversed domains. The nucleation of reversed domains takes place in regions with low magnetocrystalline anisotropy. Rare earth-rich precipitates mainly deteriorate the $_JH_c$ of the final magnet. The formation of these phases is due to the addition of a rare earth-rich sintering aid phase before the sintering process. The coercivity can be improved by adding small amounts of transition metal powders or transition metal oxides. TEM studies show that the chemical composition, the size distribution, and the impurity content (oxygen content) of the starting powder material are important factors for the magnetic properties of SmCo$_5$-type sintered magnets. For lower-cost magnets, samarium is partly substituted by a mixture of cerium–mischmetal elements or, for improved magnetic properties, by praseodymium, thus three groups of SmCo$_5$-type sintered magnets are distinguished:
- (CeMM,Sm)Co$_5$ low J_s, low $(BH)_{max}$,
- SmCo$_5$ high $_JH_c$,
- (Pr,Sm)Co$_5$ high $(BH)_{max}$.

Microstructural investigations on sintered magnets of the type (CeMM,Sm)Co$_5$ and (Pr,Sm)Co$_5$ showed similar results as in the case of SmCo$_5$ sintered magnets. The corresponding x-ray spectra of the different phases showed a mixture of rare earth elements due to their ratio of the nominal composition of the magnet.

2. Doped and Substituted Nd$_2$Fe$_{14}$B Magnets

The coercive field of high-performance Nd$_2$Fe$_{14}$B-based magnets is determined by the uniaxial magnetocrystalline anisotropy as well as by the magnetostatic and exchange interactions between neighboring hard magnetic grains. The long-range dipolar interactions between misaligned grains are more pronounced in large-grained magnets, whereas short-range exchange coupling reduces the coercive field in small-grained magnets. Different substituent (S1, S2) and dopant (M1, M2) elements influence the microstructure, coercivity, and corrosion resistance of advanced (Nd,S1)–(Fe,S2)–B:(M1,M2) magnets. The multicomponent composition of the magnets leads to the formation of nonmagnetic and soft magnetic phases.

Generally, two types of substituent elements, which replace the rare earth element or the transition element sites in the hard magnetic phase, and two types of dopant elements were found. Selected substituent elements replace the neodymium atoms (S1 = Dy,Tb) and the iron atoms (S2 = Co,Ni,Cr), respectively, in the hard magnetic phase and considerably change intrinsic properties, such as the spontaneous polarization, the Curie temperature, and the magnetocrystalline anisotropy. The main difference between substituent and dopant elements is the solubility range within the Nd$_2$Fe$_{14}$B phase. Investigations performed on sintered, melt-spun, mechanically alloyed, and hot-worked magnets have shown that two

different types of dopants can be distinguished independently of the processing route. Depending on the type, the dopant elements form additional intergranular rare earth-containing or boride phases (Fidler and Schrefl 1996):

- *Type 1 dopants* (M1 = aluminum, copper, gallium, germanium) form binary or ternary neodymium-containing phases.
- *Type 2 dopants* (M2 = titanium, zirconium; vanadium, molybdenum; niobium, tungsten) form binary or ternary boride phases.

In summary, the following phases were identified by TEM investigations:

- Primary hard magnetic phase: $Nd_2Fe_{14}B$.
- Secondary phases:

neodymium-rich liquid sintering phase, stabilized by some amount of oxygen and iron

$Nd_{1+\varepsilon}Fe_4B_4$

M1-Nd	(CuNd, GaNd$_3$, Ga$_3$Nd$_5$)
M1-Fe-Nd	(M1$_{1+x}$Fe$_{13-x}$Nd$_6$)
M2-B	(TiB$_2$, ZrB$_2$)
M2-Fe-B	(V$_{2-x}$Fe$_{1+x}$B$_2$, Mo$_{2-x}$Fe$_{1+x}$B$_2$, NbFeB, WFeB)
α-Fe	
Oxide-phases	(Nd$_2$O$_3$, …).
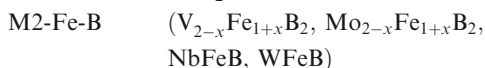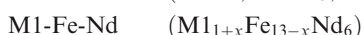
- Additional phases in Dy- and Co-substituted and M1- and M2-doped magnets:
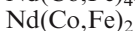
$Nd(Co,Fe)_4B$
$Nd(Co,Fe)_2$
Nd_3Co
dysprosium-containing phases.

Intergranular phases change the coupling behavior between the hard magnetic grains. Nonmagnetic phases eliminate the direct exchange interaction and also reduce the long-range magnetostatic coupling between the hard magnetic grains; both effects lead to an increase of coercivity. The formation of intermetallic, soft magnetic Nd(Fe,S2) phases, such as the Laves type Nd(Fe,S2)$_2$-phase, deteriorate the coercivity of the magnets. If dopant elements M1 or M2 are added to NdFeB, the coercivity is generally increased and the corrosion resistance (see *Permanent Magnets: Corrosion Properties*) is improved. This is the case if the neodymium-rich intergranular phase is replaced by other phases, such as $AlFe_{13}Nd_6$ and Nd_3Co, especially in large-grained sintered magnets. The TEM micrograph of Fig. 2 shows the additional intergranular $Al_1Fe_{13}Nd_6$ and Nd_3Co phases in a Nd(Fe,Co)B:(Al,Mo) magnet. On the other hand, the decrease of the volume fraction of the hard magnetic phase within the magnet decreases the remanence.

The processing route of the magnet strongly influences the grain size and grain size distribution. The coercive field in sintered magnets strongly depends on the sintering parameters, such as temperature and time. Nanocrystalline and submicron magnets are obtained by the melt-spinning route, by mechanical alloying, or by the HDDR process. Hot pressing and die upsetting of NdFeB ribbon materials reveals a densely packed, anisotropic magnetic material. Platelet-shaped grains with diameters less than 1 μm are
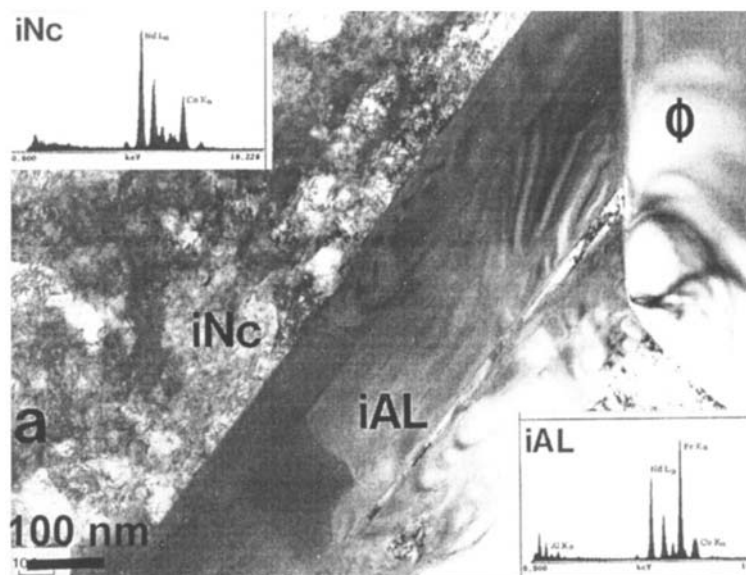
Figure 2
TEM micrograph showing intergranular phases, $Al_1Fe_{13}Nd_6$ (iAL) and Nd_3Co (iNc), besides the $Nd_2(Fe,Co)_{14}B$ (Φ) phase in a Nd-(Fe,Co)-B:(Al,Mo) magnet.

observed by TEM investigations. The degree of orientation of the platelets, which are stacked transverse to the press direction with the easy c-axes perpendicular to the face of each grain, determines the remanence and coercive field of the magnet.

The degree of alignment, size and shape of the grains, and the intergranular regions within the ribbons control the macroscopic magnetic properties. Die-upsetting modifies the spheroidal grains (Mishra 1987) after hot pressing to platelets as shown in the TEM micrographs of Fig. 3(a). Misaligned grains, which are clearly visible, deteriorate the remanence. The c-axis for each grain runs perpendicular to the straight elongated edge. A neodymium-rich phase is found among the platelet-shaped grains as a fine layer between the straight edges or as pockets at the end of the platelets or between the misaligned and aligned grains. On the other hand, the magnets with a lower remanence show a microstructure with more equiaxed grains. In most of the melt-spun magnets, regions with abnormally grown, large grains are found. Some of these grains are fully developed, platelet-shaped grains (see *Textured Magnets: Deformation-induced*).

NdFeB sintered magnets possessing outstanding magnetic properties have succeeded in becoming a major permanent magnet material since their invention in 1983 (see *Magnets: Sintered*). The drastic increase of the energy density product of newly developed $Nd_2Fe_{14}B$-based magnets enabled the invention of many new applications of permanent magnets. Applications of highest energy density magnets ($> 400 \, kJm^{-3}$) are expanding (see *Magnetic Materials: Domestic Applications*; *Permanent Magnets: Sensor Applications*). These magnets are produced by a conventional powder metallurgical process which is essentially based on alloy melting, coarse milling, pulverizing, pressing in a magnetic field, sintering, heat treating and surface coating. The theoretical value of the maximum energy product of $Nd_2Fe_{14}B$-based magnets is calculated to be $512 \, kJm^{-3}$ assuming 100% perfect alignment and 100% volume fraction of the hard phase. In order to densify the magnets up to the theoretical density, it is very important to control the composition of magnets thus generating a sufficient amount of liquid phase at sintering. Several authors (Kaneko 1999), have reportedly obtained NdFeB-based magnets with $400 \, kJm^{-3}$ energy density product by:

- keeping the oxygen content low,
- using the powder mixing technique,
- increasing the magnetizing field and reducing the pressure during compaction,
- using the rubber isostatic pressing (RIP) technique to improve the orientation of the particles in the green compact to obtain sintered magnets with perfect orientation.

In RIP, magnet powder is subjected to such a strong pulsed field just before the compaction that the powder in the rubber mold is thoroughly oriented (Sagawa and Nagata 1993). Then the powder is compacted isostatically, while the orientation is
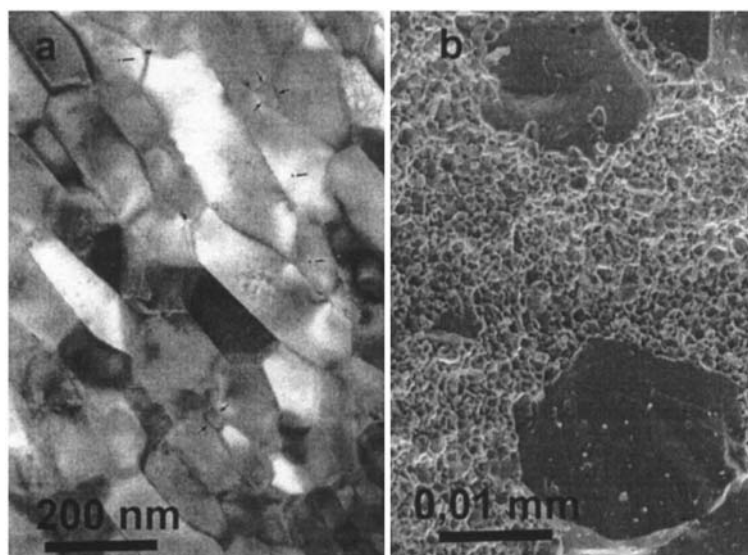
Figure 3
(a) TEM micrograph of a hot-pressed and die-upset $Nd_{14}Fe_{72}Co_7B_6Ga_1$ magnet. (b) SEM micrograph of a fractured surface showing the abnormally grown grains in a sintered $Nd_{13.7}Fe_{bal}B_{5.95}Cu_{0.03}Al_{0.7}$ magnet.

completely kept. The misalignment of the hard magnetic grains with a diameter of 2–5 μm is in the best case of the order of less than 14°. The oxygen content of the magnets has to be reduced from values of 4000–6000 ppm to a value <1000 ppm. A high oxygen content is one limiting factor to decreasing the neodymium content in order to improve the volume fraction of the hard magnetic phase. The squareness of the demagnetization curve and the coercive field drastically decrease as abnormal grain growth (AGG) of the $Nd_2Fe_{14}B$ grains occurs (Rodewald *et al.* 1997). The influence of oxygen on the hard magnetic properties is more complex. The oxygen content strongly affects the AGG, and the magnets with higher oxygen content have the higher critical temperature at which the AGG occurs. The SEM micrograph of Fig. 3(b) shows abnormally grown hard magnetic grains embedded within a matrix of grains with a diameter of 3–5 μm. Even the sintering process influences the degree of misalignment of the grains. Lowest misalignment is obtained by isostatic die pressing (11–14°), followed by transverse field die pressing (18–20°), and axial field die pressing (25–27°).

3. Pinning Controlled Sm(Co,Cu,Fe,Zr)$_{7.5–8}$ Magnets

Copper-containing cobalt-rare earth magnets with a composition of $Sm(Co,Fe,Cu,Zr)_{6–8}$ exhibit domain wall pinning controlled magnetization curves. TEM investigations show a fine cell morphology with about 50 nm × 200 nm in size. The rhombic cells of the type $Sm_2(Co,Fe)_{17}$ are separated by a $Sm(Co, Cu)_{5–7}$-cell boundary phase (Fig. 4(a)). The development of the continuous, cellular precipitation structure is controlled by the growth process and the chemical redistribution process and is determined by the direction of zero deformation strains due to the lattice misfit between the different phases. The cellular precipitation structure is formed during the isothermal aging procedure, whereas the chemical redistribution of the transition metals during the step aging procedure increases the coercivity of the final magnet. Growth of the cell structure occurs primarily during the isothermal aging procedure and involves the diffusion of samarium. In magnets with high coercivities (>1000 kAm^{-1}), thin platelets are found perpendicular to the hexagonal c-axis.

Contrary to high-coercivity magnets which contain large crystallographic twins, a microtwinning within the cell interior phase is observed by high-resolution electron microscopy in low-coercivity magnets (<500 kAm^{-1}) (Fig. 4(b)). The compositional difference between the cell boundary phase and the cell interior phase and therefore the difference in magnetocrystalline anisotropy energy of the two phases determines the coercive field. The platelet phase predominately acts as a diffusion path for the transition metals and leads to a better chemical redistribution after the isothermal aging treatment and, therefore, to a higher coercivity of the magnet. Impurities,
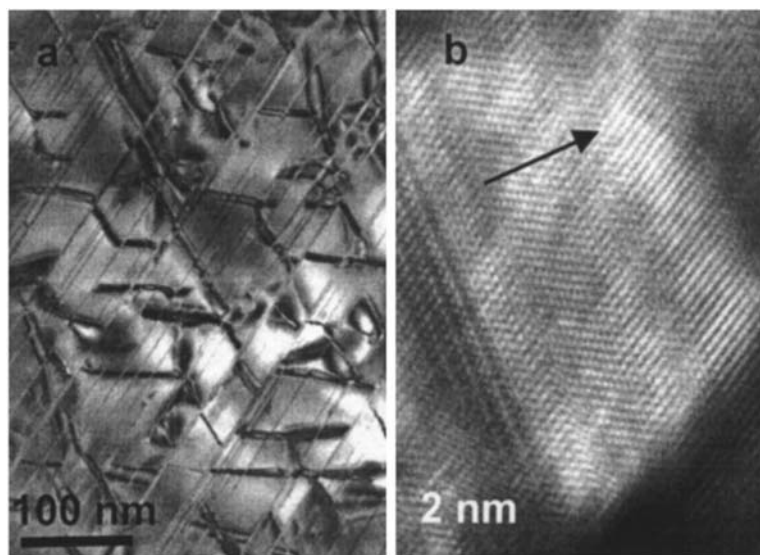
Figure 4
(a) TEM micrograph showing the multiphase cellular microstructure of a precipitation-hardened Sm(Co,Cu,Fe,Zr)$_{7–8}$ magnet. (b) High-resolution image showing microtwinning behavior of the cell matrix phase of a low coercivity magnet.

primarily oxygen or carbon, lead to the formation of macroscopic precipitates of the Sm_2O_3, ZrC, TiC, etc., and therefore impede the formation of the plate-let phase and finally impede the chemical redistribu-tion process.

A new series of magnets with H_c up to 1050 kAm^{-1} at 400 °C has been developed by Chen *et al.* (1998). These magnets have low temperature coefficients of H_c and a straight line *B* vs. *H* (extrinsic) demagnet-ization curve up to 550 °C. High copper-, low iron- and a higher samarium-concentration were found to contribute to high coercivity at high temperatures (see *Magnets: High-temperature*).

4. Nanocrystalline, Composite $Nd_2Fe_{14}B/$ (α-Fe,Fe$_3$B) Magnets

Exchange interactions between neighboring soft and hard grains lead to remanence enhancement of iso-tropically oriented grains in nanocrystalline compos-ite magnets (Kneller and Hawig 1991, Coehoorn *et al.* 1989). Nanocrystalline, single-phase NdFeB magnets with isotropic alignment show an enhance-ment of remanence by more than 40% as compared to the remanence of noninteracting particles, if the grain size is of the order of 10–30 nm (Fig. 5(a)). Numerical micromagnetic calculations have revealed that the interplay of magnetostatic and exchange in-teractions between neighboring grains influence the

coercive field and remanence considerably (Fidler and Schrefl 2000). Soft magnetic grains in two- or multi-phase composite permanent magnets cause a high polarization. Hard magnetic grains induce a large coercivity provided that the particles are small and strongly exchange-coupled. The coercive field shows a maximum at an average grain size of 15–20 nm. Intergrain exchange interactions override the magnetocrystalline anisotropy of the $Nd_2Fe_{14}B$ grains for smaller grains, whereas exchange harden-ing of the soft phases becomes less effective for larger grains.

The magnetization distribution at zero applied field for different grain sizes clearly shows that remanence enhancement increases with decreasing grain size. Owing to the competitive effects of magnetocrystal-line anisotropy and intergrain exchange interactions, the magnetization of the hard magnetic grains sig-nificantly deviates from the local easy axis for a grain size $D \leqslant 20$ nm. As a consequence, coercivity drops, since intergrain exchange interactions help to over-come the energy barrier for magnetization reversal. With increasing grain size the magnetization becomes nonuniform, following either the magnetocrystalline anisotropy direction within the hard magnetic grains or forming a flux closure structure in soft magnetic regions. Neighboring α-Fe and Fe$_3$B grains may form large continuous areas of soft magnetic phase, where magnetostatic effects will determine the preferred di-rection of the magnetization. The large soft magnetic
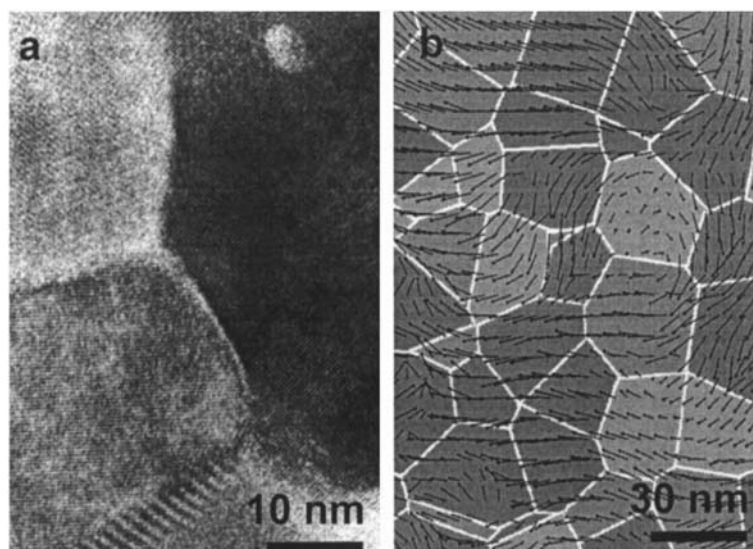
Figure 5
(a) High-resolution electron micrograph of a nanocrystalline, single-phase Nd-Fe-B magnet with isotropic alignment.
(b) Calculated magnetization distribution with a vortex-like structure in a slice plane of a 40 vol.% $Nd_2Fe_{14}B$, 30 vol.% α-Fe, and 30 vol.% Fe$_3$B magnet with a mean grain size of 30 nm for zero applied field. The magnetic polarization remains parallel to the saturation direction within the soft magnetic grains, whereas it rotates towards the direction of the local anisotropy direction within the hard magnetic grains.

regions deteriorate the squareness of the demagnetization curve and cause a decrease of the coercive field for $D > 20$ nm. A vortex-like magnetic state with vanishing net magnetization will form within the soft magnetic phase if the diameter of the soft magnetic region exceeds 80 nm. Figure 5(b) presents the calculated magnetization distribution in a slice plane of a 40 vol.% $Nd_2Fe_{14}B$, 30 vol.% α-Fe, and 30 vol.% Fe_3B magnet with a mean grain size of 30 nm for zero applied field. The magnetic polarization remains parallel to the saturation direction within the soft magnetic grains, whereas it rotates towards the direction of the local anisotropy direction within the hard magnetic grains (see *Magnets: Remanence-enhanced*).

5. Summary

Microstructural parameters, such as grain size, shape of grains, crystal structure, crystal defects, orientation, and composition of various phases are different in $SmCo_5$-, Sm_2Co_{17}-, and $Nd_2Fe_{14}B$-based permanent magnet materials. The complex microstructure considerably influences the magnetic reversal process. Detailed TEM analysis revealed various additional binary and ternary phases in the intergranular region between hard magnetic grains in doped and substituted NdFeB magnets. Intergranular phases change the coupling behavior between the hard magnetic grains. Nonmagnetic phases eliminate the direct exchange interaction and also reduce the long-range magnetostatic coupling between the hard magnetic grains; both effects lead to an increase of the coercive field. The neodymium-rich intergranular phase is necessary for the liquid phase sintering process, but deteriorates the corrosion stability and reduces the remanence.

In order to improve coercivity, remanence, and energy density, it is necessary to increase the volume fraction of the hard magnetic phase by decreasing the amount of oxygen, neodymium and pores, and to improve the degree of alignment of the $Nd_2Fe_{14}B$ grains. Oxygen is partly dissolved in the neodymium-rich intergranular phase. By reducing the amount of oxygen (< 1000 ppm), abnormal grain growth during sintering becomes more severe. The difference in magnetic domain wall energy in precipitation-hardened $Sm(Co,Cu)_5/Sm_2(Co,Fe)_{17}$ multiphase magnets is the main factor determining coercivity. The inhomogeneous magnetization behavior near the intergranular regions of nanocrystalline rare earth magnets, which is directly responsible for remanence and coercivity, is strongly influenced by the microstructural parameters.

Bibliography

Chen C H, Walmer M S, Walmer M H, Liu S 1998 Sm_2(Co,Fe,Cu,Zr)$_{17}$ magnets for use at temperature $> 400\,°C$. *J. Appl. Phys.* **83**, 6706–8

Coehoorn R, Mooij D B, Waard C D E 1989 Melt-spun permanent magnet materials containing Fe_3B as the main phase. *J. Magn. Magn. Mater.* **80**, 101–7

Fidler J, Schrefl T 1996 Overview of NdFeB magnets and coercivity. *J. Appl. Phys.* **79**, 5029–34

Fidler J, Schrefl T 2000 Micromagnetic modeling—the current state of the art. *J. Phys. D: Appl. Phys.* **33**, R135–R156

Herbst J F 1991 $R_2Fe_{14}B$ materials: Intrinsic properties and technological aspects. *Rev. Mod. Phys.* **63**, 819–98

Kaneko Y 2000 Highest performance of NdFeB magnet over 55 MGOe. *IEEE Magn.* **36**, 3275–8

Kneller E F, Hawig R 1991 The exchange-spring magnet: a new material principle for permanent magnets. *IEEE Trans. Magn.* **27**, 3588–600

Mishra R K 1987 Microstructure of hot-pressed and die-upset NdFeB magnets. *J. Appl. Phys.* **62**, 967

Rodewald W, Wall B, Fernengel W 1997 Grain growth kinetics in sintered NdFeB magnets. *IEEE Trans. Magn.* **33**, 3841–3

Sagawa M, Nagata H 1993 Novel processing technology for permanent magnets. *IEEE Trans. Magn.* **29**, 2747–51

Strnat K J 1988 *Rare Earth–Cobalt Permanent Magnets. Ferromagnetic Materials.* Elsevier, Oxford, Vol. 4 pp. 131–209

J. Fidler
Vienna University of Technology, Wien, Austria

Permanent Magnets: Sensor Applications

Sensors for the detection of magnetic fields in combination with a permanent magnet (actuator) are used in a variety of applications to measure the relative position/angle between mechanical parts (Roters 1941, Akoun and Yonnet 1984). Generally speaking these applications are divided into switches (e.g., end control of a linear unit) and analog or incremental continuous measurement. A common example for the latter group is all kinds of speed or position control in electrical machines (Adenot *et al.* 1996).

Magnetic switches as compared to mechanical micro-switches have no moving parts (except reed switches). Therefore, their main advantage is the theoretically infinite lifetime. In the case of continuous positioning or rotation measurement magnetic sensors are in competition with optical methods. While the latter allow a more accurate positioning measurement, the magnetic systems are less sensitive to dust and external influence. The advantages and drawbacks of competing methods have to be evaluated carefully.

This article describes the functionality of sensors, the design methods for the layout and optimization of actuating magnets in sensor applications, typical applications, as well as magnet examples with field specifications.

1. Magnetic Sensors

1.1 Reed Switches

The direct correspondents to mechanical micro-switches are reed switches. In these devices two ferromagnetic contacts are sealed in a glass tube in an inert atmosphere. An external field serves to magnetize the contacts and they are attracted by their induced magnetic poles. Thus the contact will be closed. The external field to close the switch is commonly given in ampere turns defining the number of turns of a long solenoid per mm length multiplied by the required electric current necessary to close the switch. Typical values are 8–80 ampere-turns. The field threshold to open the switch again when the field is reduced is normally about 20–60% below the closing field.

The hysteresis between closing and opening is determined by the magnetic hardness of the contact material and by the geometry of the whole switch. Thus to reduce the switching hysteresis a very low coercive, magnetic material has to be used for the contacts and the switching distance between the two contacts has to be minimized. As an example Table 1 describes the switching behavior of a 15 ampere-turns switch driven by different AlNiCo 35/5 rods.

1.2 Hall Probes

Hall effect sensors are based on a thin film of semiconducting material (typically indium arsenide) in which a voltage perpendicular to an applied current and an applied magnetic field appears (Fig. 1). This voltage is a direct measure of the magnetic field as long as the current is constant. These kinds of sensors with typical dimensions of the sensitive element of $0.6\,\text{mm} \times 0.2\,\text{mm}$ are often combined with an amplifier. A following Schmitt trigger transforms the analogue signal to a digital signal if required. The switching hysteresis is normally smaller than for reed switches. For analogue sensors compensation is necessary for the temperature drift and for nonlinearity effects.

If multipole fields with a small pole pitch are to be detected by Hall probes it is necessary to keep in
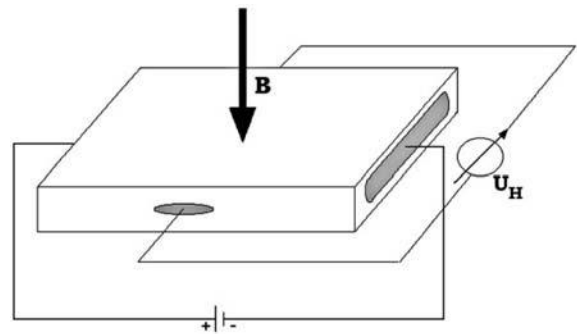
Figure 1
Schematic view of a Hall probe.

Table 1
Switching distance *d* of AlNiCo magnets for 15 ampere-turns reed switch $\varnothing 2.5 \times 18$.

AlNiCo 35/5 (≃ AlNiCo 500) axially magnetized	Contacts long		Contacts short		Contacts bent	
	ON	OFF	ON	OFF	ON	OFF
Dimensions (mm)	(mm)	(mm)	(mm)	(mm)	(mm)	(mm)
$\varnothing 2.5 \times 12.0$	12.0	16.5	11.0	14.5	10.0	12.0
$\varnothing 3.1 \times 15.0$	16.0	21.0	15.5	19.5	15.0	18.5
$\varnothing 4.0 \times 20.0$	25.0	31.5	22.5	28.5	21.5	26.5
$\varnothing 5.0 \times 21.0$	29.5	36.5	26.5	32.5	25.0	31.0
$\varnothing 6.0 \times 25.0$	38.0	48.0	33.5	41.5	31.5	38.0

mind that the magnetic field is averaged over the size of the sensitive area in the element and thus measuring results are dependent on the sensor type. In a chip housing the Hall probe is typically 0.3–0.8 mm behind the surface of the housing.

1.3 XMR Sensors

Magnetoresistance (MR) sensors use the field dependence of the electric resistance in a conducting or a semiconducting probe. While conventional MR effects are rather small in most semiconductors (about 1–3%), there has been a renaissance of these kind of sensors due to extremely large MR effects (XMR sensors), called *anisotropic* MR (AMR) (see *Magnetoresistance, Anisotropic*), *giant* MR (GMR) and, *colossal* MR (CMR) (see *Giant Magnetoresistance*). Even though the traditional MR effect has been used to measure the field strength, MR and XMR sensors are now, and in the near future will be more and more used to measure field angles by evaluating the change of resistivity in two directions. The principle of this method is shown in Fig. 2.

The in-plane magnetic field is measured in two Wheatstone bridges tilted at an angle of 45°. The measured voltages phase 1 and phase 2 correspond to the magnetic field angle φ by phase $1 = k\cos(2\varphi)$ and phase $2 = k\sin(2\varphi)$.

The normal working range of sensors is about 10–100 kAm^{-1}. Smaller fields can lead to deviations from the simple correlation between the field strength and the measured voltage while higher fields can irreversibly destroy some sensors.
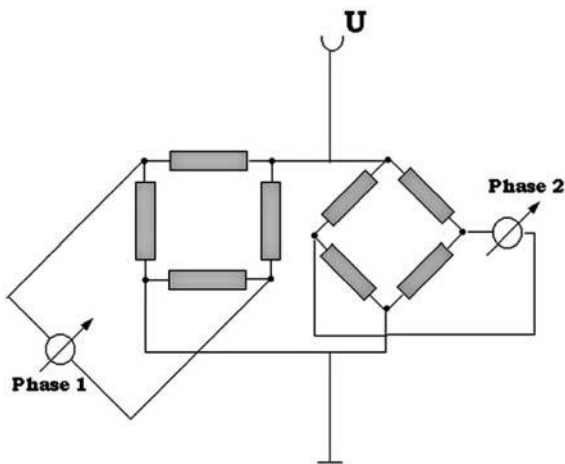
Figure 2
Schematic view of angular measurement with MR sensors.

1.4 Proximity Sensors

These kinds of sensors are used in many kinds of automation. The approach of a ferromagnetic or conducting part to a coil is detected by the changed inductance of the coil. The coil forms a part of an LC circuit of which the frequency is measured with a high accuracy.

1.5 Induction Coils

In dynamical devices rotating with a constant speed the induced voltage in a coil can be evaluated to determine the angular position of a spindle. Typically multipole magnets are fixed to a spindle and the rotation speed can be detected by either the amplitude of the induced a.c. voltage or by counting the periods of this voltage. This method is used for speed control in tool machines and in washing machines.

1.6 Impulse Wire Sensors

In these, also called *Wiegand* sensors, a wire with a single magnetic domain is magnetically reversed and one corresponding large Barkhausen jump is detected by a coil (Rauscher and Radeloff 1991).

1.7 Permanent Magnetic Linear Contactless Displacement

Permanent magnetic linear contactless displacement (PLCD) sensors use the change of induction of a locally saturated soft magnetic core. Even though it was introduced in the 1980s this principle is restricted to a few applications.

2. Field Design for Sensor Applications

Most of the traditional methods (e.g., finite element method, FEM; finite difference method, FDM; and boundary integral method, BIM) to calculate magnetic fields are not appropriate for the design of configurations in sensor applications. On the one hand the open magnetic circuit of a singular permanent magnet does not require complicated numeric calculations for simply shaped magnets like rods or bar magnets. The field of these magnets can be calculated analytically. On the other hand most applications work with multipole magnets for which the calculated field depends greatly on the magnetic model of the magnet. In these cases it is necessary to take into account that a multipole magnetized magnet or, even more complicated, a multipole oriented anisotropic magnet has different magnetic material properties and direction of magnetization in each point within a magnet.

Traditional models in which the magnet is homogeneously magnetized in one direction are no longer

applicable. It is thus necessary to calculate the magnetic properties and the magnetization direction within each element of the permanent magnet from the circumstances during production or magnetization. The melt flow orientation simulation (MFOS) used to calculate the resulting magnetic field, therefore, consists of two analyzing steps. In a first step the magnetic field of the production tools are evaluated using conventional numerical methods. From the resulting field the distribution of magnetic material properties and the state of magnetization can be deduced for each point within the permanent magnet. In a second analysis these values are used to calculate the magnetic field that is produced by the final permanent magnet.

With this method crucial magnetic properties like the steepness of the transition between a north and a south pole or the irregular switching patterns or special magnetic shapes can be designed on the computer

and can be compared to the required values without changing any dimension of the magnet. This method is demonstrated in Fig. 3.

2.1 Axially Magnetized Permanent Magnets for Sensors

For the easy case of simply shaped magnets magnetized in one direction the field of bar-shaped, disc-shaped, or ring-shaped magnets can be calculated analytically by the formulas shown in Fig. 4. All these fields approach the dipole characteristic at larger distances as shown in Fig. 5.

Figure 5
Field profile of the magnets in Fig. 4.

Figure 3
Principle of MFOS. The orienting field (from coil $+I$, $-I$) is calculated and the actual magnetization state in each element of the oriented magnet is simulated to calculate the resulting field.
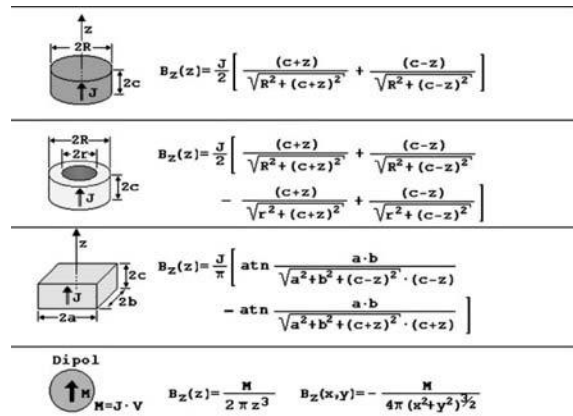
Figure 4
Analytical field of simply shaped permanent magnets.
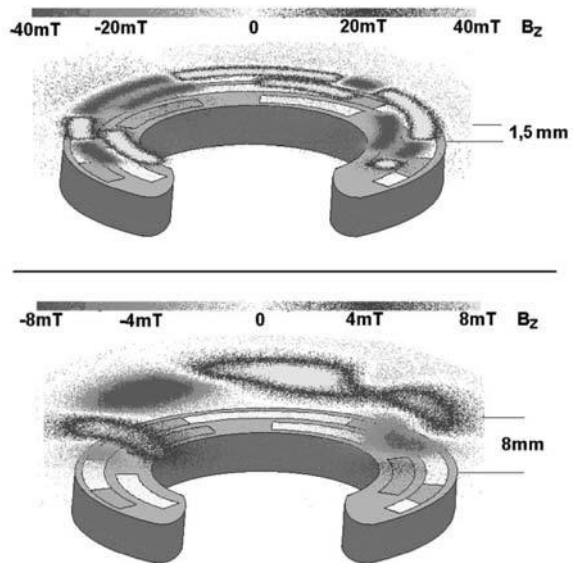
Figure 6
Field 1.5 mm and 4 mm above an irregularly magnetized permanent magnet.

2.2 Multipole Magnets and Irregularly Magnetized Permanent Magnets for Sensors

Traditionally an isotropic permanent magnet material can be magnetized in a multipole pattern. In most cases isotropic ferrite rings are magnetized in an *n* pole pattern on the circumference with a multipole coil supplied with a high current pulse of some microseconds. A large number of these magnets have been substituted by polymer-bonded anisotropic magnets. By injection molding of permanent magnet powder in a polymer matrix it is possible to orientate the powder particles during the injection process and thus to form a magnet with multipole anisotropy. These magnets are often magnetized due to the orientating field during the injection process. However, a final pulsed magnetic field can improve the magnetization by about 5–10%.

As an example Fig. 6 shows a permanent magnet magnetized on two radii in an irregular pattern for switching two sensors. By numerical simulation it is shown that the distance from the magnet to the sensitive Hall element has to be < 1.5 mm. This is not due to the too low field at a distance > 1.5 mm but due to the diffuse reflection of the magnetization pattern at a larger distance.

See also: Permanent Magnet Assemblies

Bibliography

Adenot S, Yonnet J-P, Foggia A 1996 Angular position sensors with permanent magnets. In: *Proc 14th Int. Workshop on Rare Earth Magnets and their Applications*, Sao Paulo. World Scientific, Singapore, pp. 624–31

Akoun G, Yonnet J P 1984 3D analytical calculation of the forces exerted between two cuboidal magnets. *IEEE Trans. Magn.* **20** 1962–4

Grönefeld M 1990 Grundlagen und anwendungen von permanentmagneten, kunststoffgebundene magnete. In: Förster H, Hanitsch R (eds.) *Magnetische Werkstoffe*. Verlag, Cologne, Germany

Rauscher G, Radeloff C 1991 Large Barkhausen jump in composite wires. *IEEE Trans. Magn.* **27**, 5238–40

Roters H C 1941 *Electromagnetic Devices*. Wiley, New York, p. 166

M. Grönefeld
Magnetfabrik Bonn GmbH, Bonn, Germany

Perovskites: Resistivity Behavior

Many compounds with perovskite structure are dielectrics and the temperature dependence of the resistivity $\rho(T)$ is of no interest. However, there is a large class of perovskite compounds in which a

metal–insulator transition (MIT) takes place. Such perovskite compounds have the chemical formula $Ln_{1-x}A_xBO_3$, where Ln is a rare-earth atom and A is a bivalent atom and B may be manganese, nickel, cobalt, titanium, or vanadium. The MIT can occur as a consequence of a change in the concentration of A (especially for manganites $Ln_{1-x}A_xMnO_3$). In addition changes in temperature or an external magnetic field may also induce a metal–insulator transition. In spite of the apparent similarity of the $\rho(T)$ dependencies at the MIT, the underlying physical mechanisms that cause these transitions for different compounds are different. Following Imada *et al.* (1998), we will divide these compounds into three classes which exhibit a MIT controlled by:

(i) double exchange
(ii) bandwidth, and
(iii) band filling.

The crystal structure for all these compounds is a distorted cubic one. However, the distortions can be of various types and, therefore, they have a different effect on the band structure. The usual distortions have orthorhombic Pbnm or rhombohedral $R\bar{3}C$ lattice symmetry for the compounds in question, and the unit cell of the perovskite lattice is shown at Fig. 1.

The substitution of a bivalent element A for Ln in the compounds $LnBO_3$ leads to an increase in current carriers (holes) and this has a direct effect on the resistivity. Similarly, a deficiency (x) of Ln in $Ln_{1-x}BO_3$ affects the resistivity; these compounds being
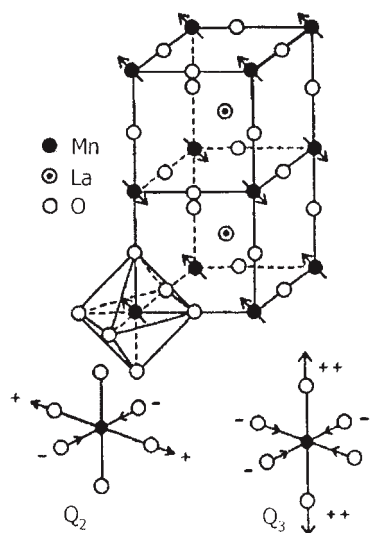
Figure 1
The ideal cubic perovskite structure, showing the AF type A order for $LaMnO_3$. In the actual structure the oxygen octahedron is distorted by a combination of the breathing mode (Q_1), the basal-plane distortion mode (Q_2), and the octahedral stretching mode (Q_3) in addition to a small rotation of the octahedron.
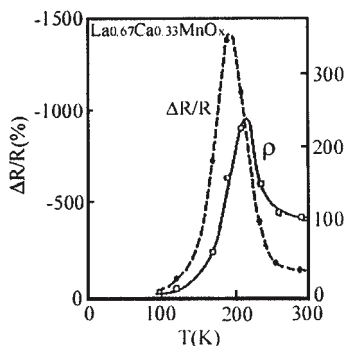
related to ionic conductors and their ionic mobility is
high at high temperatures. These deficiency com-
pounds can exist in a rather broad range of chemical
composition. In both cases a lattice distortion takes
place due to difference in size between Ln and A (or
vacancy) atoms.

The application of a magnetic field can induce a
MIT or shift the temperature at which it occurs; such
changes can cause the resistivity of some manganite
compounds to decrease by several orders of magni-
tude. This effect was discovered in 1993 (von Helmot
et al. 1993, Jin *et al*. 1994) and was named the co-
lossal magnetoresistive effect (CMR). Figure 2 shows
the temperature dependence of the resistivity, $\rho(T)$,
and magnetoresistance $\Delta R/R$ for a thin film sample of
$La_{0.67}Ca_{0.33}MnO_3$. The decrease in the resistance can
be as high as a field of 1000 in a field of 6 T at 200 K.
The physical properties of all compounds with per-
ovskite structure are very sensitive to the method of
preparation and the occurrence of defects.

The interest in these materials arises from the
prospect of their use in various electronic devices
controlled by magnetic field, examples of which are
magnetic field sensors and more specifically spin
transistors. These CMR materials have also been
found to have a large magneto-optical Faraday ef-
fect, and some new effects have been observed for
these materials in experiments with spin polarized
tunneling in superconductors.

1. Double Exchange System

1.1 Doped Rare-earth Manganites

The compounds $Ln_{1-x}A_xMnO_3$ have rather complex
phase diagrams, and consequently different proper-
ties for different compositions. In compounds such as
$La_{1-x}A_xMnO_3$ (A = Ca, Sr, Ba, Pb; $0.2 < x < 0.4$) at
some temperature, T_m, the MIT takes place even
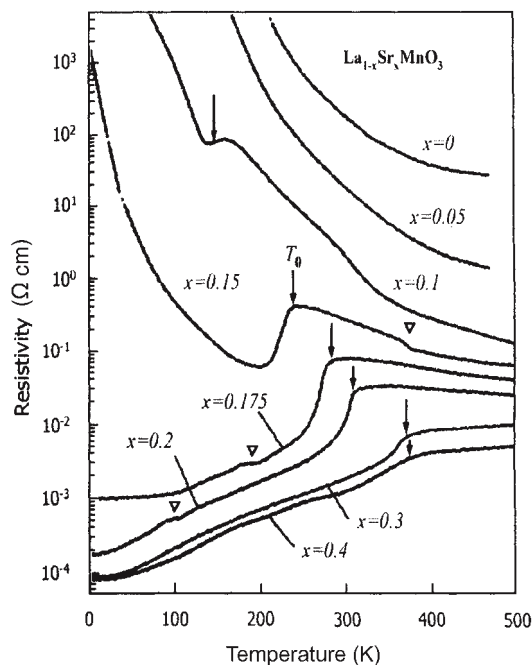
Figure 3
Temperature dependence of resistivity for
$La_{1-x}Sr_xMnO_3$ crystals. Arrows indicate the critical
temperature for the ferromagnetic phase transition.
Anomalies indicated by open triangles are due to the
structural transition (after Urushibara *et al*. 1995).

without an external magnetic field (Fig. 2 and 3). In
other compounds, such as $Pr_{0.7}Ca_{0.3}MnO_3$ the MIT
is induced by a magnetic field (Fig. 4). In this instance
the change of $\rho(T)$ is closely connected with a change
in the magnetic structure.

The maximum in $\rho(T)$ is situated near the Curie
temperature, T_C. In addition, $\rho(T)$ and $\Delta R/R$ are also
sensitive to changes in the lattice parameter. Values
of $\Delta R/R$ for thin films and ceramic polycrystalline
samples are found to be much larger than those ob-
served for the corresponding single crystal samples
with high sample quality. This is especially so in low
magnetic fields. It has been shown that in polycrystals
and thin films, the main contribution to the magne-
toresistance in low magnetic fields derives from the
grain boundaries. A change in magnetic order often
results in a change of crystal structure in a com-
pound. A deformation of the crystal lattice in the
manganites can also be due to the Jahn-Teller (JT)
effect of Mn^{3+}.

Due to the complexity of these compounds there
can be no exhaustive explanation of the CMR effects
in the manganites. These compounds belong to the
class of strongly correlated systems in which electro-
nic, magnetic, and lattice subsystems are intimately
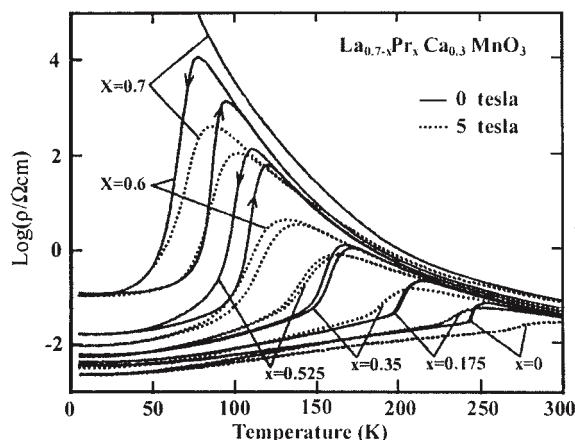
Figure 4
Temperature dependence of resistivity ρ for
$La_{0.7-x}Pr_xCa_{0.3}MnO_3$ compound without and in
magnetic field of 5 T (after Hwang *et al.* 1995).

Figure 5
Diagram of the double exchange model.

linked. The presence of a strong isotopic effect can be taken as evidence for the important role played by the electron–phonon interaction. The main theories adopted to explain the MIT and CMR effects in manganites are based on the concept of double exchange and take account of the Jahn-Teller effect.

1.2 Double Exchange Model

The properties of the doped rare-earth manganites were first discussed by Zener (1951) using a model based on double exchange. A more detailed consideration of the model was made by Anderson and Hasegawa (1955). The double exchange represents a kind of indirect exchange between cations with their charge states differing by one and linked through an anion. In the case of the manganites the manganese ions, Mn^{3+} and Mn^{4+}, interact through an O^{2-} (Fig. 5). The extra electron has an equal probability of being at the first or second Mn site.

That is, the configurations, Mn^{3+}–O^{2-}–Mn^{4+} and Mn^{4+}–O^{2-}–Mn^{3+}, are equivalent and the ground state of the system is degenerate. So between Mn^{3+} and Mn^{4+} ions a resonance bond exists resulting from electron transfer. This in turn leads to an energy lowering that depends on the mutual orientation of the cation spins **S1** and **S2**. As a consequence of this degeneracy the spin of the transferred electron in the lowest energy state must have the same orientation as **S1** and **S2,** and thus this indirect exchange is ferromagnetic. As was shown by Anderson and Hasegawa (1955), the energy gain is $2b \cos(\Theta/2)$, where Θ is the angle between **S1** and **S2** spins (Fig. 5), and b is expressed through the transfer integral from the first to the second manganese ion.

From the discussion above, it follows that if there is a distribution of Mn^{3+} and Mn^{4+} ions within the crystal, there can be electron transfer between these ions and a tendency to orient their spins in a ferromagnetic (FM) manner; there will be a feedback between these processes. The FM ordering of the compound leads to an increase in the conductivity, and the application of an external magnetic field leads to an enhancement of FM ordering resulting in an increase of the conductivity. In the case of $Pr_{0.7}Ca_{0.3}MnO_3$ (Fig. 4), an antiferromagnetic compound, an external magnetic field results in a FM state and produces a metal–insulator transition.

A detailed consideration (Millis *et al.* 1995) of the role of double exchange in the manganites exhibiting CMR has revealed that this model does not adequately explain the behavior of the resistivity. Other models have been proposed that take into account a strong electron–phonon interaction that results in polaron formation. In the report of Millis *et al.* (1995) it was suggested that the cause for such polaron formation is splitting of outer level e_g of Mn^{3+} ion when static or dynamic Jahn-Teller lattice distortion takes place.

1.3 The Jahn-Teller Effect

The Jahn-Teller (JT) effect involves the partial removal of the d-electron degeneracy for atoms in a crystal field, and results in reduction of symmetry of the lattice. Since the ground state of the system has an unstable orbital degeneracy, this degeneracy can be removed by lowering of the self-symmetry when a deformation of the surrounding of the ions occurs, which in turn leads to a reduction in the crystal field energy and removal of the degeneracy.

In the case of the rare-earth manganites with perovskite structure, manganese ions are surrounded by an octahedron consisting of six oxygen ions (Fig. 1). The Mn^{3+} ion with electronic configuration d^4 in a field with octahedral symmetry has a half-filled low-lying threefold level t_{2g} (d^3) and a higher-lying

twofold level e_g containing one electron. Such a configuration is the effect of strong exchange coupling where, according to the Hund's rule, all spins are oriented parallel. As a result of this, there is an effective hole in one of the orbitals of the cation which results in stronger screening from both anions along this orbital axis. Consequently, if the state $d_{x^2-y^2}$ is unfilled, there is an elongation of the octahedron along its axis ($c > a$). If, however, the state d_{z^2} is unfilled there is a distortion in the perpendicular direction (Fig. 1) and in this case $c < a$. These distortions involve the removal of the d-level degeneracy and a reduction in the energy.

If a crystal contains a sufficient number of JT ions, then a co-operative ordering of the distorted polyhedrons may arise such that the crystal symmetry and the energy is lowered. Such crystal distortions can only take place at sufficiently low temperatures. As the temperature increases the crystal undergoes a phase transition at which the lattice symmetry makes increase. For low concentration of JT ions and at elevated temperatures a dynamical JT effect may occur. This consists of an interaction between the local electron configuration distortions and the lattice vibrations (phonons). As a result of this interaction the local distortion can be removed, and the symmetry surrounding the cation becomes cubic when averaged over time. In the doped rare-earth manganites the dynamical JT effect can occur due to the charge transfer between Mn^{3+} and Mn^{4+} ions.

1.4 Bond Directions

The change of conductivity and MIT in the manganites is also connected with orbital overlap. In the interaction between two cations through the anion (C-A-C), there is a weak overlap of cation orbitals, and the anion fulfils a connecting function. This interaction depends on the nature of the interacting atoms, and is displayed in an anisotropy of the $3d$ cation orbitals, the interaction depending on the distance between atoms and on the bond angle of C-A-C. A correlation between the C-A-C bond angle and the nature of the magnetic ordering has been observed, and found to determine the metal–insulator transition. For ferromagnetic compounds the C-A-C angle is approximately $180°$. Doping of a basic compound by atoms with different size results in a change of the C-A-C bond angle. They may have consequences for the MIT.

1.5 The Role of Inhomogeneity

Also, it has also been demonstrated that structural and chemical inhomogeneities play an important role, and this becomes very important when the concentration, x, of a doped element A is small.

It was suggested by Gor'kov (1998) that Coulombic forces result in holes becoming localized near dopants, which makes the formation of conducting clusters along these charged centers a major factor in resistivity behavior of manganites. A charge transfer in the cluster is possible due to the double exchange and the localization is due to the JT effect. This is demonstrated in the data for $La_{1-x}Sr_xMnO_3$ (Fig. 3), where the transition between two kinds of $\rho(T)$ dependence occurs at $x \sim 0.16$. This corresponds to a percolation threshold for a three-dimensional system of random conducting links. Thus the FM phase and metallic-like conductivity arise in percolating clusters which develop when the dopant concentration increases.

1.6 Resistivity Behavior in the Metallic Region

For manganites compounds that undergo the MIT in a particular concentration range, for example for $0.2 < x < 0.4$ in the $La_{1-x}Sr_xMnO_3$ system (Urushibara *et al.* 1995) or for $La_{0.67}(Pb,Ca)_{0.33}MnO_3$ compound (Jaime *et al.* 1998), the resistivity can be described by $\rho(T) = \rho_o + AT^2$ in a fairly wide temperature range (from 10 K to 200 K, Fig. 6). The nature of such resistivity behavior remains unclear, due mainly to the lack of detailed experiments performed on good quality, single crystal samples. Several mechanisms may be held responsible for the T^2-dependence.

Amongst these are electron–electron scattering, electron–magnon scattering, and a peculiar electron–
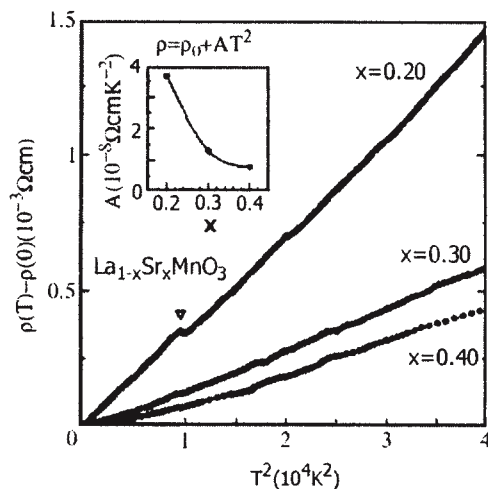
Figure 6
Temperature dependence of resistivity in the low-temperature region ($T < 200$ K) for $La_{1-x}Sr_xCoO_3$ crystals. The T^2 dependence of resistivity was observed. Inset: shows the coefficient A against the nominal hole concentration x. (after Urushibara *et al.* 1995).

phonon interaction due to specific features of the Fermi surface. It has been shown (Jaime *et al.* 1998) that the Kadowaki–Woods relation, $A = C\gamma^2$, where γ is the coefficient of the electronic specific heat and C a universal constant, $C = 10^{-5}\,\mu\Omega\,\mathrm{cm}\,(\mathrm{molKmJ}^{-1})^2$, is not fulfilled in these compounds. This relation provides an anomalously large value that rules out the electron–electron scattering mechanism. In addition the AT^2 value for 200 K is more than ten times greater than the ρ_o value, being as high as $\sim 5\,\mu\Omega\,\mathrm{cm}$ for the best samples. Therefore any reliable method determining the scattering mechanisms remains absent at the present time.

2. Bandwidth-controlled MIT Systems

2.1 $Ln_{1-x}A_xNiO_3$

The compounds, $LnNiO_3$, exist for all lanthanide elements and have pseudocubic perovskite structure, which is rhombohedral $R\bar{3}C$ for $LaNiO_3$ and orthorhombic Pbnm for the other rare earths (Medarde 1997). The temperature dependence of $\rho(T)$ for $LaNiO_3$ may be described as metallic ($\mathrm{d}\rho/\mathrm{d}T > 0$) in the temperature range $T = 0.4$–$300\,\mathrm{K}$ (Gayathri *et al.* 1999), but other compounds experience a MIT at a certain $T_\mathrm{M\text{-}I}$ and $\rho(T)$ exhibits semiconductor behaviour ($\mathrm{d}\rho/\mathrm{d}T < 0$) (Fig. 7). The evolution of $T_\mathrm{M\text{-}I}$ along the compound series can be correlated with the degree of deviation of each compound from the ideal perovskite structure, which increases as lanthanum is replaced by the smaller-size rare earth ions.

The metal–insulator transition occurs close to an antiferromagnetic transition, and the formation of ordered spin structures is attributed to the formation of an orbital superlattice. However, in spite of there

Figure 7
Temperature dependence of electrical resistance for $LaNiO_3$, $PrNiO_3$, $NdNiO_3$, $SmNiO_3$ compounds showing their metal–insulator transitions (after Medarde 1997).

being nominally one electron in the e_g orbital, as in $LaMnO_3$, no evidence for Jahn-Teller distortion has been found. The 3-D magnetic ordering consists of alternating converted bilayers AA(AA)AA(AA) … along the [001] direction, with AA and (AA) representing the magnetic arrangement of nickel moments in adjacent (001) planes. The coexistence of F and AF interactions, which is revealed in the ordered spin structure, suggests the existence of an orbital superlattice such as the regular occupation of either $d_{x^2-y^2}$ or $d_{3z^2-r^2}$ type orbitals.

The relevant parameter controlling the transition at $T_\mathrm{M\text{-}I}$ and the Néel temperature, T_N, as well as the stability of different crystallographic structures found along the compound series is the Ni-O-Ni superexchange bond angle Θ. The insulating state of $LnNiO_3$ should be classified as a charge-transfer insulator, i.e., the MIT takes place due to the opening of a charge-transfer type gap below $T_\mathrm{M\text{-}I}$. The high valency of the Ni^{3+} ions in $LnNiO_3$ makes its charge transfer energy Δ as small as $\sim 1\,\mathrm{eV}$ and stabilizes its low-spin configuration $t_{2g\uparrow}t_{2g\downarrow}e_{g\uparrow}$. In this system the ground state has a strong mixture of d^7, d^8L, and d^9L^2 configurations, resulting in a net d-electron number as large as $n_d = 7.8$. The nickel magnetic moment is found to be $\sim 0.91\,\mu_\mathrm{B}$, close to the ionic value of $1\,\mu_\mathrm{B}$, and this is a result of the charge transfer which occurs from O $2p$ orbitals to $e_{g\uparrow}$ and $e_{g\downarrow}$ orbitals in Ni^{3+}. One electron is involved in the hybridization between the t_{2g} and e_g orbitals on the mean field level, so there is no pair-transfer contribution in the high-spin Ni^{3+} ion because the spin is fully polarized (Imada *et al.* 1998).

For $LaNiO_{3-x}$ compounds the $\rho(T)$ behavior changes with x increasing, and as the number of vacancies increases $\rho(T)$ may be approximated by $\exp(-T_\mathrm{o}/T^{1/4})$. This is in accord with the Mott dependence for disordered systems with random thermally activated hopping, and $\sim \exp(-Q/T)$ for the ordered vacancies state ($x = 0.5$) (Sanchesz *et al.* 1996).

For a small oxygen deficiency, x, the resistivity $\rho(T)$ shows a power-law dependence $\rho(T) = \rho_\mathrm{o} + \alpha T^{1.5} + \beta f(T)$, where $f(T)$ is a function leading to a linear temperature dependence at high temperature ($T > 200\,\mathrm{K}$) and to a T^n-dependence ($n > 2$) at low temperatures. ρ_o is the residual resistivity and α and β are constants (Gayathri *et al.* 1999). The $T^{1.5}$ term implies that the power-law exponent is greater than unity even at the highest temperatures. Such a strong dependence can arise from scattering involving optical phonons in the system. The most metallic sample has a clear positive magnetoresistance (MR) which progressively becomes negative as the oxygen deficiency increases. The positive MR may arise from a band-like contribution, whilst the negative MR, observed for the oxygen-deficient samples, arises from the weak-localization contribution and is not due to any magnetic interactions.
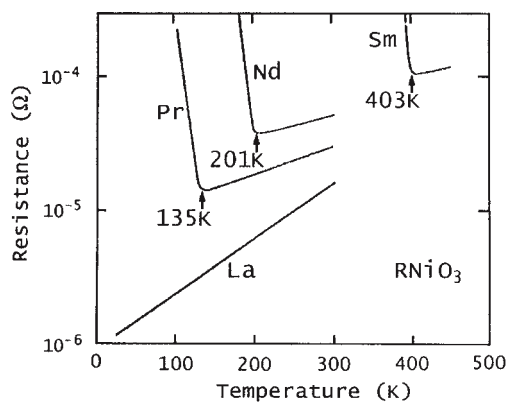
3. Filling-controlled MIT Systems

3.1 $Ln_{1-x}A_xTiO_3$

The compound $LnTiO_3$ is a typical Mott–Hubbard insulator with Ti^{3+} in a d^1 configuration, and the A content, x, represents the nominal "hole" concentration per titanium site or equivalently the $3d$ band filling (n) is given by $n = 1 - x$. The crystalline structure is an orthorhombically distorted perovskite. The Ti-O-Ti bond angle distortion, which affects the transfer energy (t) of the $3d$ electron or the one electron bandwidth (W), depends critically on the ionic radii (Ln, A) or on the tolerance factor. With decreasing size of the Ln ion, $LnTiO_3$ changes from an antiferromagnetic (AFM) insulator ($LaTiO_3$) to a ferromagnetic (FM) insulator ($YTiO_3$). The t_{2g} configuration in the nearly cubic $LaTiO_3$ is in the quadruply degenerate spin-orbit ground state.

This develops into two states with have antiparallel orbital and spin moments (both directed in the [111] direction) and alternating between nearest neighbors, which results in this G-type AFM state. An increase in the distortion induces greater hybridization between neighboring xy, yz, and zx orbitals, leading to an enhancement of the AFM orbital exchange as well as the FM exchange. This enhancement derives from Hund's rule coupling (Imada *et al.* 1998). The magnetic ordering favors the Jahn-Teller distortion, and the t_{2g} level is split into two low-lying levels and one higher level. At each site one of the two lower orbitals is occupied so that the neighboring orbitals are approximately orthogonal to each other with their spins FM aligned.

Filling control in the $3d$ band can be achieved by partially replacing the trivalent ions with divalent calcium or strontium ions. In Fig. 8 the temperature dependencies of the resistivity $\rho(T)$ for $CeTiO_{3+y/2}$ and $Ce_{1-x}A_xTiO_3$ are shown. For $CeTiO_{3+y/2}$, which has a relatively weak electron correlation, only a small amount of hole doping is sufficient to destroy the AFM state and cause the MIT. The compound $Ce_{1-x}Sr_xTiO_3$ ($0.04 < x < 0.4$) is similar to $La_{1-x}Sr_xTiO_3$, and $\rho(T)$ manifests metallic behavior which can be modeled over a wide temperature interval by $\rho(T) = \rho_0 + AT^2$ (ρ_0 is a residual resistivity and A is a constant) (Fig. 9). This T^2 dependence of the resistivity is reminiscent of the dominant electron–electron scattering process, and the Kadowaki–Woods relation $A = C\gamma^2$ is fulfilled for these compounds. It must be noted that the model holds for rather high temperatures (up to 300 K). The coefficient A becomes enhanced as the Mott–Hubbard insulator state is approached from the metallic side.
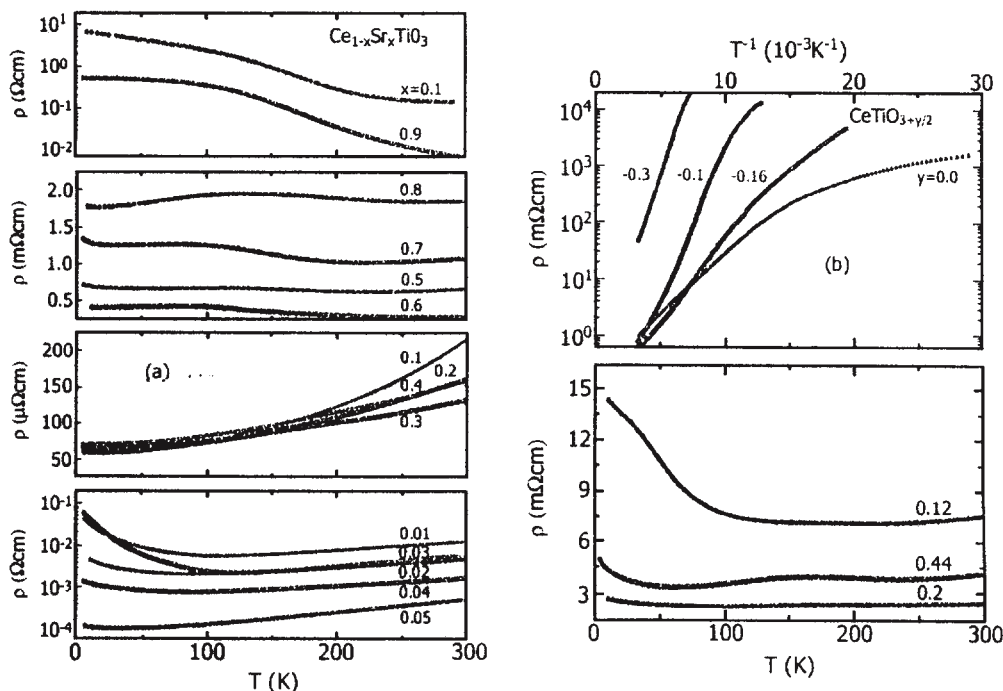
Figure 8
Temperature dependence of electrical resistivity, ρ, of (a) $Ce_{1-x}Sr_xTiO_3$ and (b) $CeTiO_{3+y/2}$ (after Onoda and Yasumoto 1997).
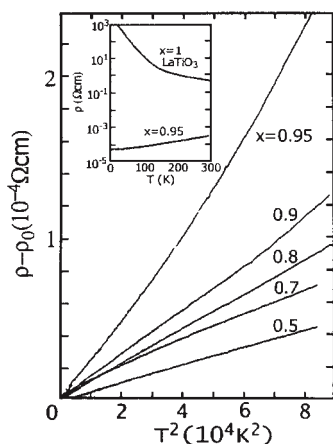
Figure 9
Temperature dependence of resistivity, ρ, in $Sr_{1-x}La_xTiO_3$; ρ, is plotted vs. T^2. The inset shows ρ vs. T plots in the nonmetallic $x=1$ (La_xTiO_3) and metallic $x=0.95$ samples (after Tokura *et al.* 1993).

Figure 10
Temperature dependence of resistivity, ρ in $La_{1-x}Sr_xVO_3$ (after Inaba *et al.* 1995).

3.2 $Ln_{1-x}A_xVO_3$

The parent compound $LnVO_3$ has a tetragonal structure for $Ln=La$, Ce and perovskite structure, with an orthorhombic distortion for the other lanthanides. $LnVO_3$ is a typical Mott–Hubbard insulator and undergoes an AFM transition at temperatures between 120 K and 150 K. The AFM phase is accompanied by a spin canting, giving rise to a weak ferromagnetic component.

With hole doping by partial substitution of divalent ions for rare earth ions, the insulating AFM phase is suppressed. In Fig. 10 one can see that $\rho(T)$ changes from activation type to metallic-like behavior for $x>0.2$. With hole doping, the charge-transfer gap shifts to a lower energy mainly due to the shift in the $2p$ band, and the Mott–Hubbard gap is closed. In the metallic region $\rho(T)$ (Fig. 11) can be well expressed by the relation $\rho(T)=\rho_0+AT^{1.5}$. The $T^{1.5}$ dependence of the resistivity can be interpreted in terms of the strong Curie-like enhancement of the spin susceptibility due to strong antiferromagnetic spin fluctuations (Inaba *et al.* 1995).

3.3 $Ln_{1-x}A_xCoO_3$

The ground state of $LaCoO_3$ is a nonmagnetic insulator and the predominant configuration of the d-electrons is $3d^6$ for Co^{3+} which fully occupy the t_{2g} level resulting from crystal field splitting (10 Dq); this slightly exceeds the Hund's rule coupling energy. With an increase of the temperature the compounds undergo a spin-state transition from a nonmagnetic (t_{2g}^6, $S=0$) to a paramagnetic state ($t_{2g}^5 e_{2g}^1$, $S=1$ or

Figure 11
Temperature dependence of resistivity, ρ, of samples of $La_{1-x}Sr_xVO_3$ near the metal–insulator phase boundary; ρ is plotted vs. $T^{1.5}$. (after Inaba *et al.* 1995).

$t_{2g}^4 e_{2g}^2$, $S=2$). A small amount of hole doping gives rise not only to a decrease in resistivity but also to a large change of magnetic susceptibility (Imada *et al.* 1998). A hole, with O $2p$-state character, causes a
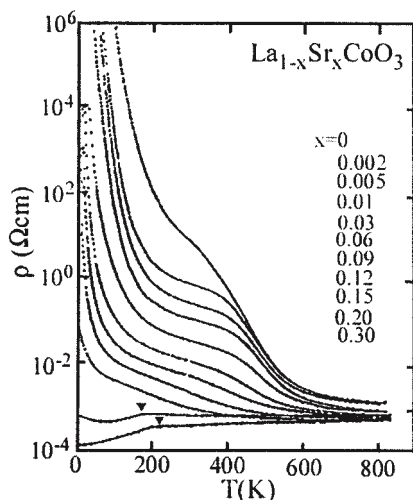
Figure 12
Temperature dependence of resistivity, ρ, in $La_{1-x}Sr_xCoO_3$ with various doping levels. Triangles represent the FM transition temperature (after Imada *et al.* 1998).

local spin-state transition (low spin to intermediate spin) over 10–16 cobalt sites around deriving from strong $2p\sigma-3de_g$ hybridization. Such a large spin polaron is a precursor state for the FM metallic state in $La_{1-x}Sr_xCoO_3$ ($x>0.2$).

The resistivity $\rho(T)$ decreases with increasing x and the behavior of $\rho(T)$ changes abruptly around the composition $x=0.2$ (Fig. 12). The resistivity for $x<0.2$ follows the dependence $\rho(T)=\rho_0\exp[(T_0/T)^n]$, where $n=S$. This is the signature of variable range hopping in the presence of a Coulomb gap within the density of states, and it seems to be a consequence of the cluster nature of the magnetic spins. In compounds with $x>0.2$, the FM as well as the metallic behavior is related to the formation of Co^{4+} ions following from Sr^{2+} substitution. The macroscopic metallic state is formed through percolation. As the temperature is reduced to below approximately 100 K, the spin-state transition will drive most of the Co^{3+} ions into the low-spin state, thus gradually localizing the carriers in the FM clusters (Fig. 13).

Metallic cobaltite compounds show negative magnetoresistance (MR), the highest value of MR is observed close to T_c. The value of the MR is much
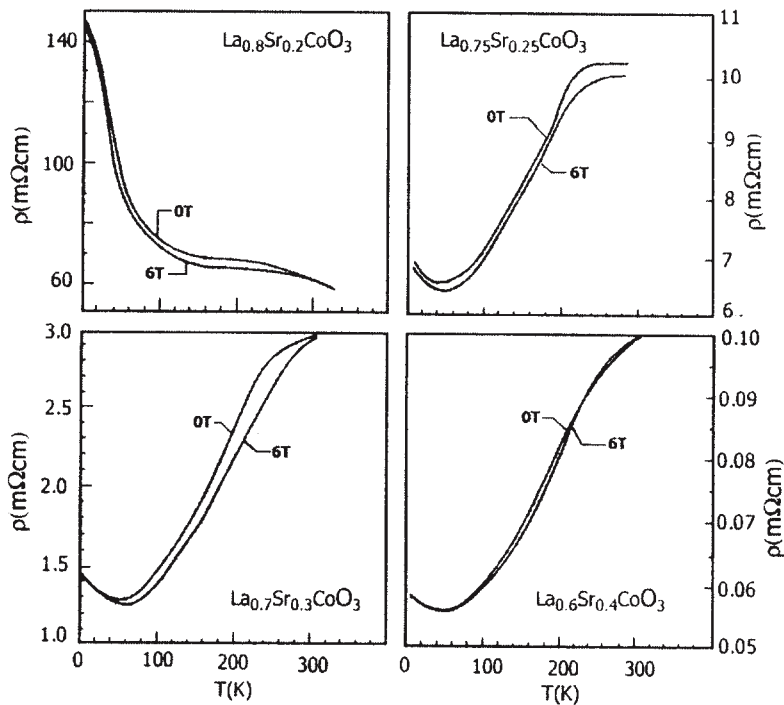
Figure 13
Temperature dependence of resistivity, ρ, in zero field (0 T) and in the field of 6 teslas (6 T) for $La_{1-x}Sr_xCoO_3$ compounds (after Mahendiran and Raychaudhuri 1996).

smaller than that observed for the manganites. The negative MR derives from suppression of spin-disorder scattering due to the application of an external magnetic field. The spin-fluctuation scattering is strongest near T_c and the negative MR also is at a maximum. In conclusion $La_{1-x}Sr_xCoO_3$ is described as a filling-controlled system since the doped holes not only act as metallic carriers but also induce a ferromagnetic moment.

4. Summary

The resistivity behavior of the compounds with perovskite structure show similar features in spite of different mechanisms. The presence of Jahn-Teller ions involves a structural distortion that leads to band splitting. Magnetic interactions also play a very important role, and these compounds are strongly-correlated systems in which electron, lattice, and magnetic degrees of freedom act together to determine their physical properties including resistivity. The peculiarities of the resistivity behavior depend not only on a specific physical mechanism but also on the sample quality. A detailed study of these compounds demands fabrication of samples with perfect structure in order to separate properties intrinsic to the compound from properties associated with the preparation conditions and various defects.

See also: Colossal Magnetoresistance Effects: The case of Charge-ordered $Pr_{0.5}Ca_{0.5}MnO_3$ Manganite Thin Films; Giant Magnetoresistance; Magnetoresistance: Magnetic and Nonmagnetic Intermetallics; Magnetoresistance in Transition Metal Oxides; Transition Metal Oxides: Magnetism

Bibliography

Anderson P W, Hasegawa H 1955 Consideration of double exchange. *Phys. Rev.* **100**, 675–81
Gayathri N, Raychaudhuri A K, Xu X Q, Peng J L, Greene R L 1999 Magnetoresistance of the metallic perovskite oxide $LaNiO_{3-\delta}$. *J. Phys. Condens. Matter* **11**, 2901–7
Gor'kov L P 1998 Lattice and magnetic effects in doped manganites. *Uspehi Fizicheskih Nauk (Russia)* **168**, 665–71
Hwang H Y, Cheong S W, Radaelli P G, Marezio M, Batlogg B 1995 Lattice effects on the magnetoresistance in doped $LaMnO_3$. *Phys. Rev. Lett.* **75**, 914–7
Imada M, Fujimori A, Tokura Y 1998 Metal-insulator transitions. *Rev. Mod. Phys.* **70**, 1039–263
Inaba F, Arima T, Ishikawa T, Katsufuji T, Tokura Y 1995 Change of electronic properties on the doping-induced insulator-metal transition in $La_{1-x}Sr_xVO_3$. *Phys. Rev. B* **52**, R2221–4
Jaime M, Lin M, Salamon N B, Han P D 1998 Low-temperature electrical transport and double exchange in $La_{0.67}(Pb,Ca)_{0.33}MnO_3$. *Phys. Rev. B* **58**, R5801–4
Jin S, Tiefel T H, McCormack M, Fastnacht R A, Ramesh R, Chen L H 1994 Thousand-fold change in resistivity in magnetoresistance La-Ca-Mn-O films. *Science* **264**, 413–5
Mahendiran R, Raychaudhuri A K 1996 Magnetoresistance of the spin-state-transition compound $La_{1-x}Sr_xCoO_3$. *Phys. Rev. B* **54**, 16044–52
Medarde M 1997 Structural, magnetic and electronic properties of $RNiO_3$ perovskites (R = rare earth). *J. Phys. Condens. Matter* **9**, 1679–707
Millis A J, Littlewood P B, Shraiman B I 1995 Double exchange alone does not explain the resistivity of $La_{1-x}Sr_xCoO_3$. *Phys. Rev. Lett.* **74**, 5144–7
Onoda M, Yasumoto M 1997 Electronic states of perovskite-type $Ce_{1-x}Sr_xTiO_3$ and $CeTiO_{3+y/2}$ systems with a metal-insulator transition. *J. Phys. Condens. Matter* **9**, 5623–34
Sanchesz R D, Causa M T, Caneiro A, Butera A, Vallet-Regi M, Sayagues M J, Gonzalez-Calbert J, Garcia-Sanz F, Rivas J 1996 Metal–insulator transition in oxygen-deficient $LaNiO_{3-x}$ perovskites. *Phys. Rev. B* **54**, 16574–8
Tokura Y, Taguchi Y, Okada Y, Arima T, Kumagai T, Iye Y 1993 Filling dependence of electronic properties on the verge of metal—Mott-insulator transitions in of $Sr_{1-x}La_xTiO_3$. *Phys. Rev. Lett.* **70**, 2126–9
Urushibara U, Moritomo U, Arima T, Asamitsu A, Kido G, Tokura Y 1995 Insulator–metal transition and giant magnetoresistance in $La_{1-x}Sr_xCoO_3$. *Phys. Rev. B* **51**, 14103–9
Von Helmot R, Wecker J, Holzapfel B, Schulz L, Samwer K 1993 Giant negative magnetoresistance in perovskitelike $La_{2/3}Ba_{1/3}MnO_x$ ferromagnetic films. *Phys. Rev. Lett.* **71**, 2331–3
Zener C 1951 Interaction between the d-shells in the transition metals. II. Ferromagnetic compounds of manganese with perovskite structure. *Phys. Rev.* **82**, 403–5

Y. M. Mukovskii
*Moscow State Steel and Alloys Institute
Moscow, Russia*

Perturbed Angular Correlations (PAC)

Among the numerous experimental techniques available for studying solids, techniques focused on hyperfine interactions form a subclass that probes a material at the smallest possible length scale. After an outline of the basic principles of hyperfine interactions, the perturbed angular correlation (PAC) method is described and compared with the widely used Mössbauer technique (Cahn and Lifshin 1993). Particular attention is paid to information that can be obtained from PAC experiments. The extended applicability of the method enabled by employing advanced *ab initio* theories is also discussed. Finally, a PAC study of Fe/Cr multilayers is given as an example.

1. Hyperfine Interactions

The simplest nonrelativistic quantum mechanical interpretation of an atom is based on an infinitely massive and point-like nucleus, and ignoring interactions between electrons. This leads to the well-known hydrogen-like electron energy levels, with a

characteristic separation of a few electron volts. Including electron–electron interactions and relativistic effects produce both a shift and degeneracy lifting of these levels on a millielectron volt scale. The resulting energy level scheme is called the fine structure. An even more subtle correction to these levels—the hyperfine structure—stems from the nucleus not being point-like. Deviation from a point can occur both in real space and in spin space.

In the former case, the simplest nontrivial example is a description of the charge density within the nucleus as a deformed sphere (prolate or oblate), which can be characterized by the nuclear quadrupole moment, Q. In spin space, the smallest deviation from a point is described by the nuclear magnetic dipole moment, μ. The interaction of both nuclear moments Q and μ with the surrounding electrons leads to a hyperfine structure in the electron energy levels, on a scale of 10^{-12} eV. As we are dealing here with an interaction, exactly the same hyperfine structure will occur both in the *electronic* and in the *nuclear* energy levels. The PAC technique is based on the hyperfine structure of nuclear energy levels.

The hyperfine interaction operates over a very short range. It is determined by the nuclear wave functions—which are only nonzero inside and close to the nucleus—and the tails of the (valence) electron wave functions that reach the nucleus. As a consequence, bonding effects on the valence electrons caused by the atom being contained in a molecule, liquid, or solid are transferred to the nuclear hyperfine structure. Hence, measurements of a hyperfine structure provide information on the chemical environment of a particular atom. For research in magnetism, the interaction of the nuclear magnetic moment with the magnetic field due to surrounding electron spins is important.

This interaction is mainly given by the Fermi contact term, which describes a nucleus embedded in a homogeneous magnetic medium due to the net s electron spin density, $m(0)$, at the nucleus (in a relativistic approach p electrons can also penetrate the nucleus). The magnetic field generated this way at a nucleus is called the magnetic hyperfine field, B_{hf}, and is given by:

$$B_{hf} = \frac{8\pi}{3}\mu_0\mu_B m(0) \qquad (1)$$

where μ_0 is the permeability of vacuum and μ_B the Bohr magneton. The splitting of nuclear energy levels is related to B_{hf} by:

$$\Delta E_{hf} = \frac{\mu}{I}B_{hf} \qquad (2)$$

where μ is the magnetic dipole moment of the nucleus and I its spin quantum number. Apart from the Fermi contact term, other (and usually smaller) contributions to the hyperfine field originate in orbital and spin motion of electrons.

2. Measuring Hyperfine Interactions by PAC

Several experimental techniques based on different principles are available to measure the magnetic hyperfine interaction. In Mössbauer spectroscopy (MS) recoilless emission and absorption of a Doppler-shifted γ-ray by a radioactive nucleus is exploited. Time differential perturbed angular correlation (TDPAC or PAC) spectroscopy uses the reorientation of an oriented ensemble of nuclei under the influence of a hyperfine field (Schatz and Weidinger 1996, Catchen 1995). It needs a radioactive nucleus with a subsequent emission of two γ-rays in its decay scheme. Nuclei emit γ-rays preferentially along their spin direction. Hence, detecting the first of the two γ-rays by a fixed detector selects an ensemble of nuclei with their spin oriented preferentially along this detector axis.

If a hyperfine field is present, the hyperfine-split nuclear Zeeman levels are repopulated by the hyperfine interaction. This repopulation is equivalent to a reorientation of the nuclear spin, an effect which in a semiclassical picture is called the Larmor precession of the nuclear spin around the direction of the hyperfine field. Hence, the frequency of this rotation can be monitored by detection of the second γ-ray by a second detector, making a fixed angle with the first one. After data reduction, the resulting function, called $R(t)$, is proportional to the time evolution of the emission probability of the second γ-ray in a given direction and clearly shows the spin precession (Fig. 1). The relation between the observed precession frequency, ν, and the hyperfine field is:

$$\nu = \frac{\mu}{hI}B_{hf} \qquad (3)$$

where h is Planck's constant. Information which can be obtained by analyzing $R(t)$ is discussed in Sect. 4.

3. A Comparison Between PAC and MS

Owing to the fast electronics needed to perform a PAC measurement (note that the time scale in Fig. 1 is in the nanosecond range) this method is less used than its "sister" technique MS. Nevertheless, PAC has some advantages over MS. It is insensitive to temperature, in contrast to MS where the recoilless fraction is strongly temperature dependent and prevents the use of MS at too high a temperature. Therefore, PAC is better suited to follow phenomena as a function of temperature. The number of radioactive nuclei which are needed is orders of magnitude lower than for MS. An absolute amount of 10^{11}–10^{12} PAC probes is sufficient. Hence, if the studied nucleus represents an impurity in a material, it has a
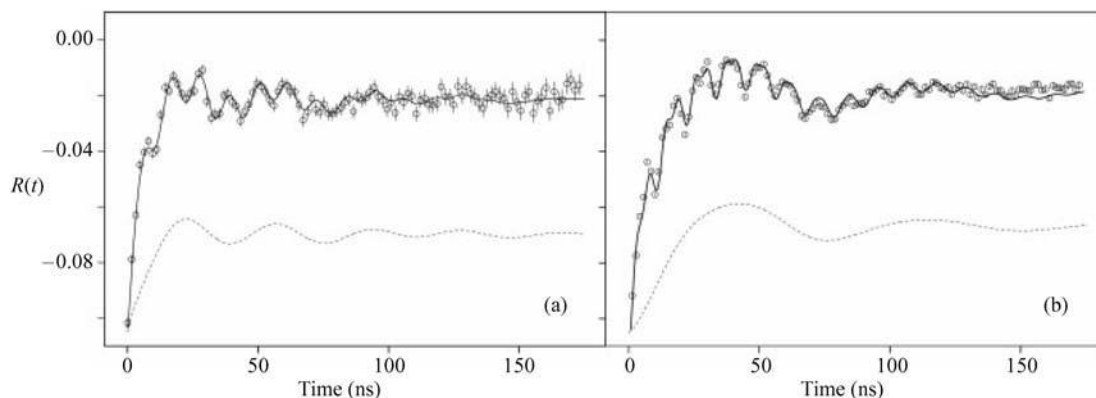
Figure 1
PAC measurements at 289 K for two different orientations (with respect to the detectors) of a Fe/Cr multilayer with an iron thickness of 2 nm and a chromium thickness of 7.5 nm.

negligible effect on the matrix. However, there are some disadvantages.

If interactions become too strong, the oscillations in $R(t)$ become too fast to detect. Therefore, there is an upper limit to the interaction strength detectable by PAC. If the interaction is too weak, a single oscillation takes longer than the time interval where enough data can be gathered. This determines the lower limit of the detectable interaction strengths. In MS only such a lower limit is present. Another advantage of MS is that it can measure the s electron density in the nucleus by the isomer shift, a quantity not probed by PAC. Finally, PAC is suited for some nuclei which are inaccessible by MS and vice versa (the most common PAC nuclei are ^{111}Cd (parent ^{111}In), ^{181}Ta (parent ^{181}Hf), and ^{100}Pd (parent ^{100}Rh)). The above aspects of PAC and MS indicate that the two methods are complementary.

4. Information Obtained in a PAC Experiment

4.1 Site Occupation

The $R(t)$ function is characteristic for a specific environment felt by the probe nucleus. If two or more distinct environments are present, the measured $R(t)$ is a sum of the $R(t)$ functions due to each environment. The distinct sites can, for example, be non-equivalent lattice positions, a substitutional and an interstitial position, or a surface and a bulk position. Unraveling a measured $R(t)$ function into the partial $R(t)$ functions from which it is built, and assigning these to a specific position in the sample makes it possible to track their occupation by probe atoms. This enables, for example, a study of the formation and migration of defect complexes as a function of temperature.

4.2 Magnitude of the Magnetic Hyperfine Field

The frequencies of an $R(t)$ function are proportional to the Larmor precession frequency, and hence to the strength of the magnetic hyperfine field. Quantitative information on the hyperfine field is useful for, e.g., position assignment (see Sect. 4.1). Also, it can help to determine the type of magnetic order, or at least to exclude some possibilities. For example, a probe nucleus symmetrically surrounded by neighbors with antiferromagnetically coupled magnetic moments will probably feel a zero or tiny hyperfine field, whereas this field should be considerably higher if all neighbors have their magnetic moments coupled ferromagnetically. Since the hyperfine field is very sensitive to electronic structure, PAC experiments also provide the possibility of testing *ab initio* electronic theories.

4.3 Orientation of the Magnetic Hyperfine Field

The general formalism of PAC shows that a probe nucleus with nuclear spin $I = 5/2$ (^{111}Cd) at a unique position and feeling a single magnetic hyperfine field generates two frequencies in $R(t)$, i.e., ν and 2ν. Their amplitude in a Fourier analysis of $R(t)$ is related to the absolute direction of the hyperfine field with respect to the detector setup. If the hyperfine field is perpendicular to the detector plane, only 2ν is present. If B_{hf} makes an angle of $30°$ with the detector plane and of $45°$ with the first γ-ray detector, then the ratio $\nu/2\nu$ is 3/1.

4.4 Distributions

The measured $R(t)$ function usually shows an amplitude vanishing for $t > 500$ ns. The reason is that the hyperfine field—and hence the frequencies making up

$R(t)$—is not an infinitely sharply determined quantity. Small intrinsic effects, such as vibrational motion of the probe atom, can cause slight changes in the environments, which will show up as a damping of $R(t)$ described by mainly Lorentzian or Gaussian distributions on the frequencies in its Fourier spectrum. For such intrinsic effects, the damping is generally very weak. If, however, severe perturbations of the environments are present, e.g., lattice defects, vacancies, impurities, $R(t)$ will die out much faster. Determining the amount of distribution can therefore tell how pure the environment of the probe is on the atomic scale. Another use of the distribution is discussed in Sect. 6.

5. Theoretical Understanding of Hyperfine Fields

A very important problem when using any nuclear technique is to relate a measured hyperfine field (which is a very local quantity) to particular chemical and physical properties of the neighborhood of the probe nucleus, and even of the material as a whole. This problem was for long dealt with in a rather crude, phenomenological way. It took until the early 1990s to be solved, when *ab initio* methods with quantitative predicting power were developed. Major work was carried out by Blaha *et al.* (1999) within the framework of density functional theory (DFT, see *Density Functional Theory: Magnetism*). By using the full potential felt by the electrons and solving the resulting Kohn–Sham equation by the linearized augmented plane wave (LAPW) method, the tails of the electron wave functions near the nucleus can be calculated with a sufficient accuracy to obtain the hyperfine field. The method has been implemented in the computer code WIEN, which is a standard tool for calculating hyperfine fields in a variety of materials.

6. Example

To illustrate PAC measurements, thin Fe/Cr multilayers are discussed as a case study (Meersschaut *et al.* 1995).

Bulk b.c.c. chromium is known to have an exotic type of antiferromagnetic order: a spin density wave (SDW). The moments are oriented along the 100 direction and moments at neighboring atoms are antiparallel. But instead of displaying the same magnitude of moment everywhere in the crystal, as is usual in an antiferromagnet, in chromium the moment magnitude is sinusoidally modulated with a period of approximately 20 lattice units. Between 311K and 123K the moments are perpendicular to the propagation direction of the wave (transverse SDW). Below 123K the moments are parallel to the propagation direction (longitudinal SDW).

An interesting question as to the magnetic order and the character of the SDW arises when thin chromium layers are considered with a thickness approaching the period of the SDW. Will the SDW survive or not? If so, will it be transverse or longitudinal? Will the chromium moments keep their original 100 direction? To examine this, ^{111}In nuclei were implanted into a multilayer containing several Fe/Cr bilayers, grown with the 100 direction perpendicular to the layer. The ^{111}In probe atom is known to take substitutional lattice sites in both the chromium and iron layers, where they decay with a lifetime of 2.81 days into the PAC nucleus [111]Cd. The latter nucleus interacts with a hyperfine field generated by the surrounding cadmium electrons, which is directed along the cadmium moment (the moment of the diamagnetic cadmium atom is induced by, and hence is parallel to, the surrounding chromium moments).

The $R(t)$ function of two PAC measurements is shown in Fig. 1. In Fig. 1(a) the multilayer is parallel to the detector plane and in Fig. 1(b) it is perpendicular to it. In both $R(t)$ functions contributions from a slow and a fast frequency are visible. The slow frequency belongs to [111]Cd nuclei in a chromium environment and the fast one to an iron environment. The line through the data points is a best fit, with the chromium contribution to it shown in the lower curves. From the change in frequencies when the multilayer is tilted from Figs. 1(a) to (b), it can be deduced that the hyperfine field on cadmium in chromium—and therefore the chromium magnetization—is oriented perpendicular to the plane of the multilayer, and hence along the 100 direction. Moreover, the $R(t)$ function belonging to chromium positions is not a pure sine wave but a Bessel function. Theory shows that this typical shape appears when the nuclei each experience a different hyperfine field corresponding to an Overhauser distribution in frequency space and a sine wave in real space: solid proof that the SDW is present in this type of Fe/Cr multilayer. Furthermore it has been shown—first by PAC and later by neutron scattering and transport methods—that the SDW is longitudinal and disappears below a critical chromium thickness.

See also: Mössbauer Spectrometry; Nuclear Magnetic Resonance Spectrometry

Bibliography

Blaha P, Schwarz K, Luitz J 1999 *WIEN97, A Full Potential Linearized Augmented Plane Wave Package for Calculating Crystal Properties*. Karlheinz Schwarz, Vienna (updated version of Blaha P, Schwarz K, Sorantin P, Trickey S B *Comp. Phys. Commun.* **59**, 399–415)

Cahn R W, Lifshin E 1993 *Concise Encyclopedia of Materials Characterization*. Pergamon, Oxford, UK

Catchen G L 1995 PAC: renaissance of a nuclear technique. *MRS Bull.* (July), 37–46

Meersschaut J, Dekoster J, Schad R, Beliën P, Rots M 1995 Spin density wave instability for chromium in Fe/Cr(100) multilayers. *Phys. Rev. Lett.* **75**, 1638–41

Schatz G, Weidinger A 1996 *Nuclear Condensed Matter Physics*. Wiley, New York, Chap. 5

S. Cottenier
Katholieke Universiteit Leuven, Belgium

Photoemission: Spin-polarized and Angle-resolved

Magnetism arises from the spins of electrons in partially filled outer shells of atoms in a solid which interact with each other via the exchange interaction. In a paramagnetic material all electronic states are degenerate with respect to spin, and consequently are occupied by two electrons, one with spin up and one with spin down. The exchange interaction lifts this degeneracy, lowering the energies of spin up, and raising those of spin down states. The energy difference between these states is the exchange splitting. Therefore, the spin-polarized electronic (band) structure is the key ingredient for understanding magnetism (see *Density Functional Theory: Magnetism*). Photoemission is commonly used to probe the electronic structure of solids. By also analyzing the spin polarization of the photoelectrons, information on the spin-polarized band structure is obtained. One speaks of electron spin polarization if one can find a direction in space with respect to which the two possible spin states are not equally populated. For ferromagnetically ordered materials, this direction is naturally the magnetization direction. The exchange splitting between majority and minority states of the same symmetry can be measured directly by spin-polarized photoemission.

From temperature-dependent measurements, the change of the band structure on approaching the Curie temperature can be compared with various models of the ferro- to paramagnetic phase transition. The exchange coupling of ultrathin layers adsorbed on ferromagnetic surfaces can be studied. The origin of oscillating interlayer exchange coupling between ferromagnetic layers via a nonferromagnetic interlayer was clarified by spin-resolved photoemission. The degree of spin polarization at the Fermi level is important for devices utilizing spin-dependent transport phenomena. Core-level photoelectron spectra also show spin polarization which can be used as an *element-specific* indicator for magnetic order. While such spectra involving inner shell excitations do not give direct evidence on the spin-polarized electronic structure of the partially filled outer (valence) states, which are the source of magnetism, indirect information is contained in the line shape, the degree of spin polarization, and the presence of satellites. An important aspect of spin-polarized core level spectroscopy is the possibility of characterizing the relative spin orientation of different species in a multicomponent sample because core-level spectra occur with different excitation energies.

Spin-dependent mean free paths and photoelectron diffraction effects may have an influence on the measured spin-resolved photoemission spectra. Apart from a magnetic ground state, spin–orbit interaction gives rise to spin polarization in photoelectron spectra. While for valence states this is, in most cases, a relatively small effect, the large spin orbit interaction encountered for ionized inner shells with nonzero orbital momentum will in general give rise to significant spin polarization, both for magnetic and nonmagnetic systems. By choosing a suitable geometry this effect may be avoided, so that only the exchange-related effect remains. Alternatively, for magnetic systems the combined influence of the exchange and spin orbit interactions leads to magnetic dichroism. The continuous background of secondary electrons also is spin-polarized, and the degree of polarization at low energies can be related to the ground state magnetic moment.

1. Angle-resolved Photoemission

In a photoemission (PE) experiment, UV or soft x-rays are used to excite electrons from a sample. In the excitation process the photon is annihilated, and energy conservation requires that the total energy is unchanged,

$$E_i + h\nu = E_f + E_{kin} \tag{1}$$

where E_i and E_f are the energies of the initial and final state of the sample, E_{kin} is the energy of the photoelectron, and $h\nu$ is energy of the photon (Kevan 1992, Hüfner 1995). The difference between E_i and E_f is conventionally termed binding energy E_B. It is determined from the photon energy chosen for the experiment and the measured kinetic energy of the photoelectron,

$$E_B = h\nu - E_{kin} - \phi_A \tag{2}$$

where ϕ_A is the work function of the sample. The kinetic energies are usually measured by electrostatic analyzers. For solid metallic samples, the most weakly bound electrons are those at the Fermi level. Therefore, the highest kinetic energy photoelectrons are generated by ejecting electrons from states at the Fermi level E_F, and this cut-off is used as reference (zero) for binding energies such that

$$E_B = E_{kin} - E_{kin}(E_F) \tag{3}$$

In addition to energy conservation, momentum also has to be conserved. The relationship between electron energy and momentum, i.e., the band structure, leads to pronounced angular dependencies. In angle-resolved photoemission, the energy distribution of the photoelectrons is measured as a function of emission angle in order to obtain information on the band structure. For making the connection between measured angle-resolved PE spectra and the band structure, the sample has to be a single crystal. Maxima in photoelectron spectra arise whenever the photon energy matches the energy difference between an occupied state and an unoccupied state in the band structure. The components of the photoelectron wave vector parallel ($k_\parallel$) and perpendicular ($k_\perp$) to the surface are

$$k_\parallel[k_\perp] = (2mE_{kin}/h^2)^{1/2} \times \sin\theta[\times\cos\theta]$$

$$= 0.5123 \times (E_{kin}/1\text{eV})^{1/2}\text{Å}^{-1} \times \sin\theta[\times\cos\theta] \quad (4)$$

where m is the electron mass, and θ the emission angle measured to the surface normal. The parallel component is conserved (to within a reciprocal lattice vector) for photoelectrons crossing the surface, so that $k_\parallel$ measured in vacuum is identical to that in the solid.

To interpret the perpendicular photoelectron wave vector component $k_\perp$ measured in vacuum, the relationship between E and k in the solid and the way in which the wave functions in the solid and in vacuum are matched have to be known. Structures in PE spectra are interpreted assuming that the momentum is retained within the excitation ("vertical" or "direct transitions"). With increasing final state energy, the allowed final states become more dense, and the finite angular acceptance of photoelectron spectrometers integrates over an electron momentum range comparable to the Brillouin zone. Spectra taken under such conditions may be interpreted in terms of density of states, which can be obtained from the momentum-resolved band structure by integration in k-space. Angular variations may then still arise from diffraction effects, because the photoelectrons are scattered by the regular array of atoms in the crystal lattice.

2. Electron Spin Analysis

Electron spin polarization P is defined as

$$P = (N_{up} - N_{down})/(N_{up} + N_{down}) \quad (5)$$

where N_{up} and N_{down} are the numbers of electrons with spin parallel and antiparallel to a chosen quantization axis. For magnetic materials the quantization axis is the direction of sample magnetization. To measure photoelectron spin polarization, the energy-analyzed photoelectrons are subjected to a spin-dependent scattering process (Kessler 1985,

Feder 1985). The majority of spin polarimeters derive their spin dependence from spin–orbit interaction. The spin of the free electron may couple to the angular momentum in the scattering process, which gives rise to a spin-dependent contribution to the scattering potential. This spin-dependent contribution is generally small. A sizable magnitude of this effect is usually only found for conditions where the mean scattering cross section is small, so that the spin-dependent part becomes significant. In general a compromise has to be found between the requirements of a large analyzing power and a large mean scattering cross section. For spin–orbit based detectors it is possible in principle to measure both transverse spin components simultaneously.

The optimum scattering energy for so-called Mott detectors is around 100 kV, and this provides scattering asymmetries between 0.2 and 0.3. Mott detectors have been designed and are commercially available with scattering energies of around 30 kV. The lower scattering energy reduces the size, complexity, and cost of such a detector at the expense of lower asymmetries and scattering efficiency. Low energy scattering is employed either in a LEED type arrangement where spin–orbit interaction influences the scattering efficiency for higher-order LEED beams scattered from the surface of a heavy material, or in diffuse scattering off a polycrystalline target composed of a heavy element. Finally, scattering off the surface of a magnetized single crystal of iron has been exploited for spin analysis (Hillebrecht *et al.* 1992). This technique offers a superior performance in comparison to Mott detectors. However, it is much more complicated as it requires careful preparation of the scattering target. Details are summarized in Table 1, and can be drawn from the literature.

3. Technical Aspects

The elastic mean free path for electrons in solids is of the order of 0.5 to 5 nm. Therefore, photoemission is a highly surface-sensitive technique. Clean surfaces are prepared in ultrahigh vacuum, e.g., by sputtering and annealing, cleaving, or deposition. In order to correlate the angular dependencies of photoemission with the band structure, single crystalline samples are required. To exploit fully the potential of the technique, tunable, monochromatic, and polarized light is needed, which is readily available at synchrotron radiation sources. Because of the limited elastic mean free path, photoelectrons undergo numerous inelastic scattering processes, generating secondary electrons with reduced energy. This leads to a continuous background of secondary electrons. For ferromagnetic materials, this background is also spin-polarized (Kisker *et al.* 1982). Photoemission experiments have to be carried out on remanently magnetized samples, and the influence of stray fields on the electron

Table 1

Characteristic parameters of spin polarimeters. If no orientation for the scattering target is given, a polycrystalline one is used. The spin asymmetry is given by the difference of differential scattering cross sections for the two channels corresponding to up and down spin electrons, normalized to the sum. The figure of merit, given by the square of the spin asymmetry times the average scattering cross section, is a measure for the performance of a spin detector; to reach a certain statistical uncertainty, the data acqusition time varies as the reciprocal of the figure of merit. For the LEED polarimeters, the performance depends on the crystalline quality of the surface. For VLEED, the polarization is determined by sequential measurements with reversed target magnetization, which halves the figure of merit (included).

Type of spin polarimeter	Operating energy (eV)	Scattering target	Spin asymmetry	Figure of merit $\times 10^{-4}$
Mott detector	10^5	Au	0.25	1
Medim energy Mott detector	$2–4 \times 10^{-4}$	Au	0.2	0.2
Diffuse scattering	150–300	Au	0.07–0.11	1
LEED	105	W(100)	0.27	1.6
VLEED	12	Fe(100)	0.2–0.4	5–10

trajectories has to be excluded. Ultrathin films grown *in situ* are easy to magnetize within the film plane, and have negligible stray fields.

4. 3d Ferromagnets

Figure 1 shows spin-resolved photoemission spectra for iron, cobalt, and nickel taken in normal emission with 20 eV photons (21.2 eV for cobalt) from single crystal surfaces. With calculated band structures available, the features in the spectra can be attributed to transitions from specific occupied bands, allowing determination of the exchange splitting. In general, a large number of spectra is taken with different photon energies or for different emission geometries. The shifts of the peaks observed in such data sets allow determination of the dispersion of the electronic bands.

The spectrum for iron (Kisker *et al.* 1985) shows a majority peak at 2.6 eV, which is present with small shifts in binding energy (BE) for all photon energies. The minority spectrum shows only a weak structure at the Fermi level, which is attributed to indirect transitions. The dispersion of the bands close to E_F causes a majority spin polarization for photon energies below 33 eV, switching to minority for higher photon energies.

For the spectrum of h.c.p.-cobalt (Getzlaff *et al.* 1996), the minority peak is caused by transitions from bands of Δ_9 and Δ_7 symmetry, which cross the Fermi level and consequently have a high density of states at E_F. The peak in the majority spectrum appears at slightly higher BE. By analyzing the energy and angle dependence of these structures, an exchange splitting of 1.6 eV is found, in agreement with calculations.

The spectrum of Ni(110) shows only a sharp structure at the Fermi level (Ono *et al.* 1998). At different photon energies, features up to about 3 eV BE are

observed. This suggests that the bandwidth is smaller by 30% than the calculated bandwidth. This is ascribed to correlation (self energy) effects, which tend to narrow the bands. The majority and minority peaks have different binding energies. This reflects directly the exchange splitting, 0.12 eV in this case. Furthermore, the exchange splitting varies between 0.1 and 0.4 eV for different points in the Brillouin zone.

For some applications of ultrathin magnetic films, a large spin polarization at the Fermi level is desired. For this purpose, the stabilization of magnetic materials in different phases is of interest as it permits the tailoring of magnetic properties at surfaces or interfaces for specific applications. Electronic structure calculations suggest that f.c.c.-Fe may show widely different magnetic properties for small variations of lattice constant, ranging from nonmagnetic to antiferro- and ferromagnetic states. The ferromagnetic f.c.c. phase is expected to have a higher magnetic moment than the b.c.c. phase, and may possibly be a strong ferromagnet, i.e., show complete (100%) spin polarization at the Fermi level. Figure 2 shows the evolution of the spin-polarized electronic structure of iron with different crystal structures (Kläsges *et al.* 1998); f.c.c.-iron is grown on f.c.c.-cobalt, which can be grown in f.c.c.-structure f.c.c.-Cu(100) up to several hundred monolayers (ML). The initial spectrum shows the spin-resolved spectrum of cobalt in the f.c.c. phase. Close to E_F, one finds a minority polarization, and at higher BEs the spin polarization changes to majority. The spectrum for f.c.c.-Fe (3 monolayer film) shows a majority peak at 2.9 eV and a minority peak at 0.4 eV. This 2.5 eV splitting can be interpreted as an exchange splitting. The increased magnitude of this splitting shows that the magnetic moment is indeed increased compared with the bulk b.c.c. value.

The reduced spin polarization for the 6 ML film shows that the major part of the film is ferromagnetically aligned to the substrate. Nevertheless, the

sp-PES for Fe, Co, Ni
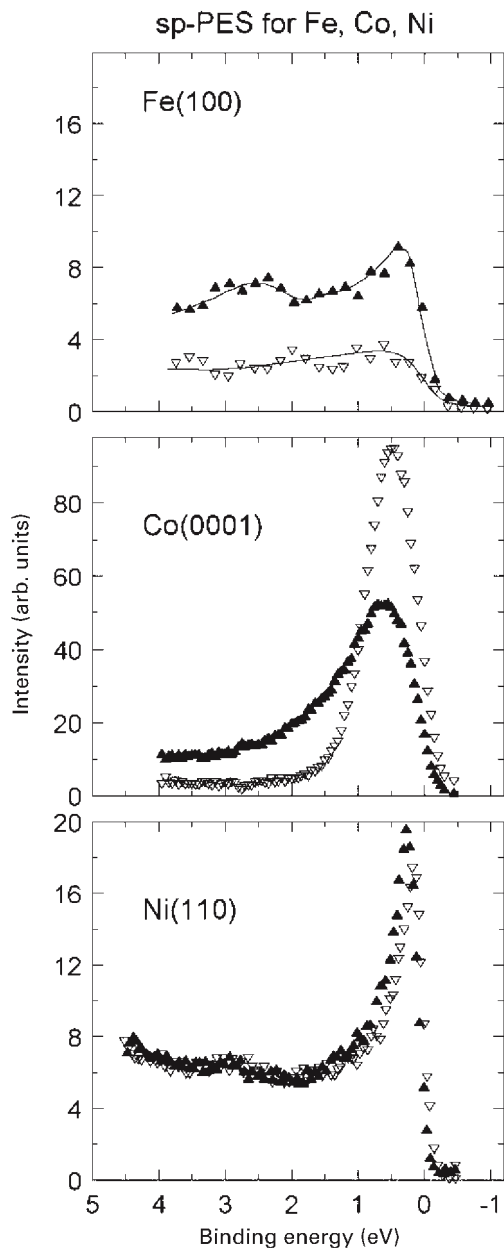
Figure 1
Spin-resolved photoemission spectra for the 3d ferromagnets, taken with 20 eV photons (21.2 eV for cobalt) in normal emission: data for Fe(100) with normal light incidence (from Kisker *et al.* 1985); for Co(0001) light incidence under 30° to surface normal, magnetization in the surface plane (Getzlaff *et al.* 1996); for Ni(110) light incidence 20° to surface normal (Ono *et al.* 1998). For all examples filled triangles pointing up represent majority spin electrons, empty triangles pointing down are for minority spin electrons.
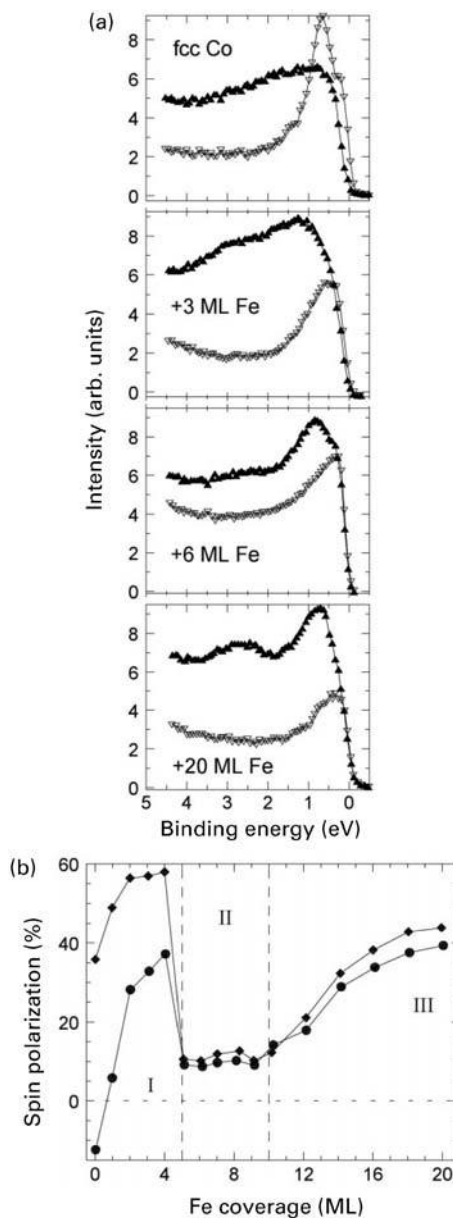
Figure 2
(a) Evolution of spin-resolved photoemission spectra for Fe films grown on f.c.c. Co(100); photon energy 34 eV, normal emission, plane-polarized light under 45° incidence; (b) spin polarization data for Fe films grown on f.c.c.-cobalt, derived from the spectra in Fig. 2(a). The polarization shows three thickness regimes, which are associated with f.c.c.-Fe (area I), a distorted Fe phase with low moment (area II), and finally a transition to b.c.c.-Fe (area III); circles for spin polarization at 0.8 eV binding energy, diamonds for 1.8 eV (from Kläsges *et al.* 1998).

finite spin polarization demonstrates that the surface layer is still ferromagnetically aligned to the cobalt magnetization. A fraction of the surface layer is still in the high moment state, as can be seen from the weak structure between 2 and 3 eV. For coverages above 10 ML, the whole film reverts to the thermodynamically stable b.c.c. structure. The polarization increases, as the whole film orders ferromagnetically; however, the exchange splitting of about 2.2 eV is typical for the b.c.c. moment. Figure 2(b) shows the polarization measured at different points in the spectrum, which tracks very well the magnetic moments derived from other experiments.

5. Ferro- to Paramagnetic Transition

Figure 3 shows the change of the spin-resolved PE spectrum of b.c.c.-Fe with temperature (Kisker *et al.* 1984). The key issue for such studies is to gain an insight into the underlying physics of the transition from the para- to the ferromagnetic state. While the spin-averaged spectra do not change significantly on heating to $0.85\,T_C$, the spin-resolved data show significant changes: the minority peak at 0.4 eV BE loses intensity and becomes broader, and the majority spin peak at 2.6 eV also loses intensity, with nearly unchanged width and BE. The results show that the exchange splitting is of the order of 2 eV, and does not change significantly on approaching the Curie temperature.

Figure 4 shows similar temperature-dependent data for Ni(110) (Hopster *et al.* 1983). The data clearly show a scaling of the exchange splitting proportional to the macroscopic magnetization with increasing temperature, in agreement with the Stoner model. In contrast, these results are inconsistent with a so-called local band model, where the decrease of the magnetization is caused by transverse fluctuations of microscopic regions which still have the full temperature-independent exchange splitting. By choosing different excitation conditions, Fujii *et al.* (1995) probed a different region of the Brillouin zone. The results showed aspects of both types of behavior: an exchange-splitting decreasing with temperature, and a contribution of the local band model with temperature-independent exchange splitting.

Spin- and angle-resolved photoemission of elemental 3d ferromagnets has shown that, depending on the material, different mechanisms are responsible for the ferro- to paramagnetic transition. The small changes of the exchange splitting observed for iron can apparently be understood within a local band model, while the temperature-dependent exchange splitting found for nickel can be explained within the Stoner model (see *Itinerant Electron Systems: Magnetism (Ferromagnetism)*). This does not rule out that in each case the nondominant mechanism is to some extent in operation (Kisker 1984, Fujii *et al.* 1995).
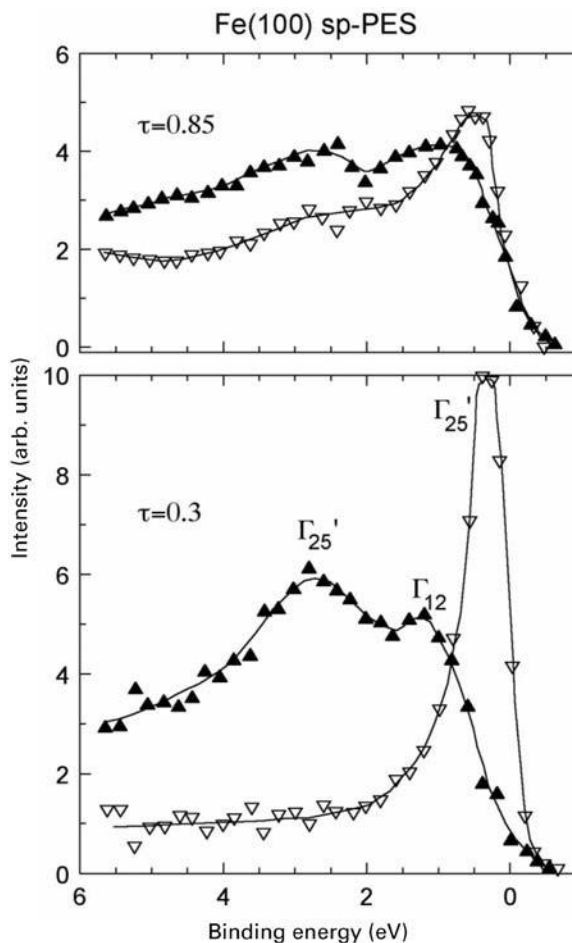
Figure 3
Evolution of the spin-polarized photoemission spectrum of Fe(100) on approaching the Curie temperature $T_C = 1043$ K (Kisker *et al.* 1984). Photon energy 60 eV, normal emission, s-polarized light; lower panel for temperatures $\tau = T/T_C = 0.3$, upper for $\tau = T/T_C = 0.85$; triangles pointing up for majority states.

6. Quantum Well States

The magnetization between two ultrathin films, forming a sandwich with a nonmagnetic layer in-between, may be coupled by exchange interaction via the nonmagnetic interlayer (Grünberg *et al.* 1986). The coupling strength oscillates periodically with interlayer thickness between ferro- and antiferromagnetic coupling, and furthermore decays with interlayer thickness. The most widely used material combinations are Fe–Cr and f.c.c.-Co–Cu (Parkin 1994). The thickness of the interlayer is up to about 20 monolayers. The coupling can be understood in terms of a modified RKKY theory (see *Magnetism in Solids: General*

Ni(100) sp-PES near Tc

Introduction), which was originally proposed to describe the interaction between magnetic impurities in nonmagnetic host materials. In this picture, the oscillation period of the coupling is related to the size and shape of the Fermi surface of the nonmagnetic interlayer. The oscillation period is given by $2\pi/k_N$, where k_N is a Fermi surface nesting vector of the bulk band structure of the interlayer material. The small thickness of the interlayer may lead to quantization of the bulk bands in the direction normal to the film. This affects in particular the sp-like states of copper, which in bulk copper metal are free electron-like. Figure 5 shows spin-resolved photoemission spectra

Figure 4
Evolution of the normal emission spin-polarized photoemission spectrum of Ni(110) on approaching the Curie temperature $T_C = 627$ K; $\tau = T/T_C$; photon energy 16.8 eV, probing the X point (Hopster *et al.* 1983).
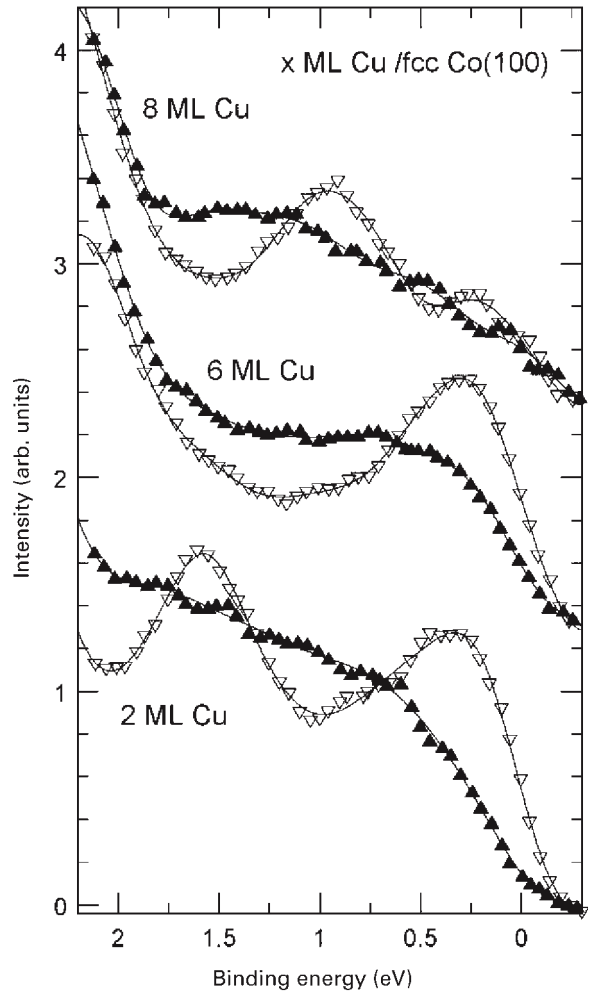
Figure 5
Spin-resolved photoemission from sp-like quantum well states of ultrathin copper grown on f.c.c.-Co(100) (Garrison *et al.* 1993).

for ultrathin copper films on Co(100) (Garrison *et al.* 1993).

The copper d states have binding energies of 2 V or more, so that the region shown is dominated by copper sp-like states (with some residual emission from cobalt d states for the lowest copper coverage). The minority (with respect to cobalt majority) spectra show clearly discrete states that occur with different binding energies for different coverages. In contrast, the majority states do not show discrete states, indicating that the quantum well states are strongly minority-polarized. Depending on the thickness of the copper layer, the quantum well states occur at different energies for certain thicknesses at the Fermi level. The intensity and spin polarization at the Fermi level oscillate with thickness, and this oscillation correlates directly with the oscillation of the interlayer exchange coupling between two f.c.c.-Co films separated by a copper film (Carbone *et al.* 1993). These experiments show that the spin polarization of the quantum well states induced by the confining magnetic interface causes the interlayer exchange coupling.

7. Spin-resolved Photoemission from Core Levels

Inner shells are completely filled, and consequently the total spin and angular momentum is always zero. This means that the integrated spectrum should have no spin polarization. However, ejection of an electron from an inner shell generates a hole which has a spin and, if one is not looking at an s level, an angular momentum. In a magnetic system, the spin of the core hole couples to the spin of valence electrons, and this may lead to different excitation energies depending on the spin of the photoelectron. From studies of the 3d ferromagnets it is known that at the leading edge of a core level spectrum one always finds minority spin polarization. One may state this as a generalized Hund's rule (see *Magnetism in Solids: General Introduction*), because minority spin for the photoelectron means that the spin of the remaining shell from which one electron is removed has majority character, i.e., is parallel to the spin of the majority electrons. Core level spin polarization can be used as an element-specific indicator of magnetic order. For a number of nonferromagnetic elements theoretical calculations predict a ferromagnetic ground state for a monolayer film of this element.

A famous example is antiferromagnetic chromium, which in the bulk has a mean magnetic moment of $0.6\,\mu_B$. For a chromium monolayer on iron an enhanced moment of $3.6\,\mu_B$ was derived, with ferromagnetic order within the chromium layer, coupled antiferromagnetically to the ferromagnetic iron substrate. Figure 6 shows a spin-resolved chromium 3p photoemission spectrum taken for a monolayer (0.15 nm) of chromium on Fe(100) (Hillebrecht *et al.*
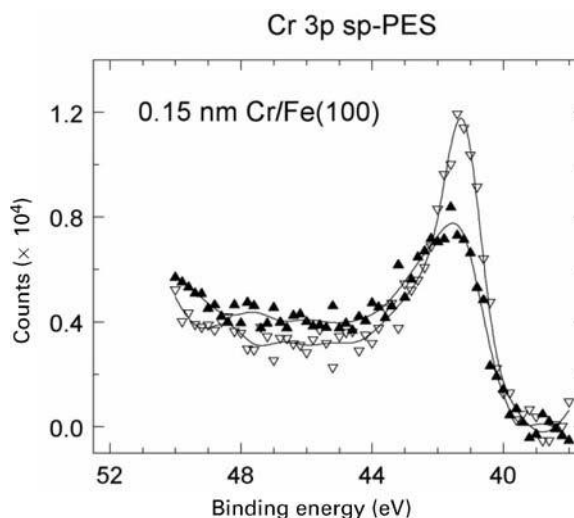
Figure 6
Spin-resolved 3p core level photoemission for 1.5 nm Cr/Fe(100) (from Hillebrecht *et al.* 1992). Photon energy 117 eV, normal incidence and emission. A constant background, matched to the spectrum on the low binding energy side, was substracted from the spectrum.

1992). The spectrum shows a large spin polarization, which is opposite to that of the 3p spectrum of the iron substrate. This demonstrates the antiferromagnetic coupling between the iron surface and the chromium overlayer. The magnitude of the chromium 3p polarization indicates that the chromium moment is smaller than the predicted $3.6\,\mu_B$. This is caused by structural intermixing between chromium and iron atoms occurring during chromium deposition, leading to a higher chromium coordination.

Bibliography

Carbone C, Vescovo E, Rader O, Gudat W, Eberhardt W 1993 Exchange split quantum well states of a noble metal film on a magnetic substrate. *Phys. Rev. Lett.* **71**, 2805–8

Feder R 1985 *Polarized Electrons at Surfaces*. World Scientific, Singapore

Fujii J, Kakizaki A, Shimada K, Ono K, Kinoshita T, Fukutani H 1995 Temperature dependence of the spin- and angle-resolved valence band photoemission spectra of Ni(110). *Solid State Commun.* **94**, 391–5

Garrison K, Chang Y, Johnson P D 1993 Spin polarisation of quantum well states in copper thin films deposited on a Co(001) substrate. *Phys. Rev. Lett.* **71**, 2801–5

Getzlaff M, Bansmann J, Braun J, Schönhense G 1996 Spin resolved photoemission study of Co(0001) films. *J. Magn. Magn. Mater.* **161**, 70–88

Grünberg P, Schreiber R, Pang Y, Brodsky M B, Sowers H 1986 Layered magnetic structures: evidence for antiferromagnetic coupling of Fe layers across Cr interlayers. *Phys. Rev. Lett.* **57**, 2442–5

Hillebrecht F U, Roth C, Jungblut R, Kisker E, Bringer A 1992 Antiferromagnetic coupling of a Cr overlayer to Fe(100). *Europhys. Lett.* **19**, 711–6

Hopster H, Raue R, Güntherodt G, Kisker E, Clauberg R, Campagna M 1983 Temperature dependence of the exchange splitting in Ni studied by spin-polarized photoemission. *Phys. Rev. Lett.* **51**, 829–32

Hüfner S 1995 *Photoelectron Spectroscopy*. Springer, Berlin

Kessler J 1985 *Polarized Electrons*, 2nd edn. Springer, Berlin

Kevan S D 1992 *Angle-resolved Photoemission: Theory and Current Applications*. Elsevier, Amsterdam

Kisker E 1984 Photoemission and finite temperature magnetism of Fe and Ni. *J. Magn. Magn. Mater.* **45**, 23–32

Kisker E, Gudat W, Schröder K 1982 Observation of a high-spin polarization of secondary electrons from single crystal Fe and Co. *Solid State Commun.* **44**, 591–5

Kisker E, Schröder K, Campagna M, Gudat W 1984 Temperature dependence of the exchange splitting of Fe by spin resolved photoemission with synchrotron radiation. *Phys. Rev. Lett.* **52**, 2285–8

Kisker E, Schröder K, Gudat W, Campagna M 1985 Spin polarized angle resolved photoemission study of the electronic structure of Fe(100) as a function of temperature. *Phys. Rev. B* **31**, 329–39

Kläsges R, Schmitz D, Carbone C, Eberhardt W, Kachel T 1998 Surface magnetism and electronic structure of ultrathin fcc Fe films. *Solid State Commun.* **107**, 13–8

Ono K, Kakizaki A, Tanaka K, Shimada K, Saitoh Y, Shendohda T 1998 Electron correlation effects in ferromagnetic Ni observed by spin- and angle-resolved photoemission. *Solid State Commun.* **107**, 153–7

Parkin S S P 1994 Giant magnetoresistance and oscillatory interlayer exchange coupling in polycrystalline transition metal multilayers. In: Heinrich B, Bland J A C (eds.) 1994 *Ultrathin Magnetic Structures*. Springer, Berlin, Vol. 2

F. U. Hillebrecht
Heinrich-Heine-Universität Düsseldorf, Germany

Photomagnetism of Molecular Systems

Photoreactivity is a widespread phenomenon in organic and inorganic chemistry. A compound may change its structural and/or electronic properties under light irradiation. Light-induced charge separation or *cis–trans* isomerization processes under light are well-known examples. A phase transformation may occur, with or without hysteresis. If the light-induced new phase possesses sufficiently long lifetime and differs in optical and/or magnetic properties such that it can be easily detected by optical or magnetic means, the material bears the potential for possible technical applications in switching or display devices.

This article deals with light-induced changes of the magnetic and/or optical properties of transition metal compounds to long lived metastable states. Figure 1 sketches the general situation: A complex compound with ground state spin S and orbital momentum Γ
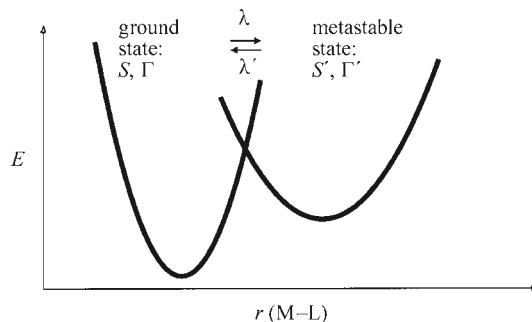
Figure 1
Schematic representation of the potential wells for the ground state with quantum numbers S and Γ and metastable state (S' and Γ') for a transition metal compound. The switching process between these states may be provoked by irradiation with light of wavelength λ, or λ' for the reverse process.

converts under light of wavelength λ, to a more or less metastable state with different spin and orbital momentum S' and Γ'. The metastable state lies higher in energy and usually has weaker metal–ligand (M–L) bonds and accordingly longer bond lengths r(M–L) than the ground state. This is the consequence of an increasing population of antibonding molecular orbitals and simultaneously decreasing population of weakly π-backbonding molecular orbitals. The energy barrier between the potential wells governs the lifetime of the metastable state, which in turn depends on the horizontal and vertical displacements relative to each other. Switching back from the metastable state to the ground state may be possible by using light of different wavelength λ'. The two-potential-well scheme of Fig. 1 refers to transition metal complexes with strong and intermediate field strength ligands. In weak-field complexes the potential with the longer M–L bond length would be the ground state, but light-induced switching is still possible.

There are various classes of transition metal compounds which all show light sensitive electronic structure changes accompanied by drastic changes of their magnetic and/or optical properties. Among the best known and extensively studied systems are those exhibiting:

- metal-centered thermal spin transition, e.g., spin crossover (SC) complexes of iron(II);
- metal-to-ligand charge transfer, e.g., nitroprusside complexes;
- metal-to-metal charge transfer, e.g., Prussian blue analogues;
- ligand isomerization with change of spin state, e.g., stilbenoid complexes;
- valence tautomerism, e.g., catecholate complexes of cobalt(II).

1. LIESST and Related Phenomena

The abbreviation LIESST refers to the phenomenon of light-induced excited spin state trapping, which was discovered in 1984 on $[Fe(ptz)_6](BF_4)_2$ (ptz = 1-propyl-tetrazole), an iron(II) coordination compound known to exhibit thermal spin transition between high-spin (HS, $^5T_2$) and low-spin (LS, $^1A_1$) states (see *Spin Transition Compounds* (Decurtins *et al.* 1984). The material, as a single-crystal, polycrystalline, or embedded in a polymer foil, converts from the LS to the HS state by irradiation with green light into the $^1A_1 \rightarrow {}^1T_{1,2}$ absorption band, followed by two successive intersystem crossing (ISC) processes $^1T_{1,2} \rightarrow {}^3T_{1,2} \rightarrow {}^5T_2$ to populate the HS state $^5T_2$. Radiative decay $^5T_2 \rightarrow {}^1A_1$ is spin and parity forbidden, and due to the considerably larger M–L bond distance in the HS state as compared to the LS state, which builds up an energy barrier between the potential wells of the two states (see Fig. 1), the lifetime of the metastable LIESST state can be very long (e.g., weeks at 20 K in the case of $[Fe(ptz)_6](BF_4)_2$) (Gütlich *et al.* 1994).

Thermal relaxation of the metastable LIESST state does not occur in a classical manner by passing over the barrier, but by nonadiabatic tunneling through the barrier, whereby the observed temperature dependence of the relaxation rate is due to thermal population of the vibronic levels of the $^5T_2$ manifold (Hauser 1995). Optical switching back from the $^5T_2$ LIESST state to the $^1A_1$ ground state is also possible by irradiation with red light for the initial excitation $^5T_2 \rightarrow {}^5E$ followed by two ISC processes $^5E \rightarrow {}^3T_{1,2} \rightarrow {}^1A_1$ (Hauser 1991). It has been found that LIESST and reverse LIESST may be observed with all iron(II) compounds exhibiting thermal SC, a major difference, however, being the lifetime of the light-induced LIESST state at a given temperature, which depends on the ligand field strength, viz., the weaker the ligand field strength, the smaller the difference ΔE^0_{HL} between the lowest vibronic levels of the HS and LS states, the longer the lifetime of the LIESST state. LIESST has also been observed in Langmuir–Blodgett thin films (Letard *et al.* 1999).

More recently, photophysical phenomena in iron(II) SC systems, which are related to LIESST have been observed. If a sample is continuously irradiated with green light while the temperature is raised and then lowered again, a thermal hysteresis may develop; this phenomenon has been termed light-induced thermal hysteresis (Desaix *et al.* 1998). In another case existing thermal hysteresis of an iron(II) SC compound was observed to shift to lower temperatures under continuous irradiation with green light, and to higher temperatures with red light (light-perturbed thermal hysteresis) (Renz *et al.* 2000). Finally there is the SOXIESST (soft x-ray induced excited spin state trapping) which uses a source of soft x rays to initiate the $^1A_1 \rightarrow {}^5T_2$ transition (Collison *et al.* 1997), but the relaxation mechanism should be the same as for LIESST.

2. NIESST Effect

The acronym NIESST stands for nuclear decay-induced excited spin state trapping. This phenomenon is closely related to LIESST, as it makes use of the nuclear decay and its energy release as an intrinsic molecular excitation source, whereas LIESST is the result of irradiation with an external visible light source. Thus the initial step of electronic excitation is different, but the final step of ligand field state relaxations has been found to be the same for both phenomena.

^{57}Fe Mössbauer emission (ME) spectroscopy has been a most elegant tool for the observation of metastable ligand field states at ca. 100 ns after electron capture decay of $^{57}Co(EC)^{57}Fe$ in transition metals compounds (Sano *et al.* 1984). A ^{57}Co labeled compound is used as the Mössbauer source at variable temperatures vs. $K_4[Fe(CN)_6]$ as a single-line absorber. If ^{57}Co is embedded in strong field surroundings, which causes LS behavior in the corresponding iron(II) compound like the *tris*-phen or *tris*-bpy complexes (phen = 1,10-phenanthroline; bpy = 2,2′-bipyridine), one observes the nucleogenic $^{57}Fe^{II}$ ions in LS ($^1A_1$) state at room temperature, which is the ground state in the corresponding synthesized iron(II) compound. Below ca. 200 K, however, one observes typical $^{57}Fe^{II}$-HS resonances in the ME spectra with increasing intensity towards lower temperatures at the expense of the $^{57}Fe^{II}$-LS resonances. In iron(II) SC systems with weaker ligand field strength one observes no more $^{57}Fe^{II}$-LS resonances in the ME spectra, even at very low temperatures where the corresponding synthesized iron(II) complex has already turned to the LS ($^1A_1$) ground state. The trapped HS state of the nucleogenic $^{57}Fe^{II}$ ion was found to have very similar lifetimes as the corresponding LIESST state under comparable conditions (Deisenroth *et al.* 1998). It was, therefore, concluded that NIESST and LIESST are closely related phenomena. Whereas the LIESST effect bears basically the potential for practical applications, NIESST is evidently of more academic interest and has contributed much to a deeper knowledge of mechanistic aspects in hot atom chemistry in the solid state.

3. Stilbenoid Complexes

Another elegant way to change spin states of some transition metal molecular compounds can be achieved using the well-known *cis–trans* photoisomerization of stilbenoid units incorporated as ligand molecules. This effect, called ligand driven light-induced spin change (LD-LISC), was first observed on the iron(II) complex $[Fe(stpy)_4(NCBPh_3)_2]$

(stpy = 4-styrylpyridine) (Boillot *et al.* 1996). This compound undergoes sharp thermal spin transition around ca. 190 K under its *trans* form whereas the *cis* form remains permanently HS. This is the consequence of the different ligand field strength for these two forms due to the different conformations of the coordinated ligand. Irradiation of a thin film of *trans*-[Fe(stpy)$_4$(NCBPh$_3$)$_2$] with UV light around 140 K, that is in the LS area, resulted in a LS→HS conversion which was followed by absorption spectroscopy. This transformation was found to be incomplete, probably due to the rigidity of the matrix at this temperature. Thus light irradiation affords a *cis–trans* isomerization of the ligand with subsequent spin transition at the iron(II) center as a consequence of a change in ligand field strength.

It has recently become possible to observe the LD-LISC effect at room temperature for [Fe(4-methyl-4′-trans-styryl-bpy)$_2$(NCS)$_2$] (Boillot *et al.* 1999) and also for some iron(III) complexes but only in solution. The limiting point of this phenomenon is that it has for now only been observed in thin films or in solution, the reason being the enormous space required for the photoisomerization to proceed. This weak point regarding practical applications could be overcome by implementation of these photosensitive materials in organized media on the mesoscopic scale, such as Langmuir–Blodgett films, which is actually in progress.

4. Nitrosyl Complexes

The discovery of light-induced long lived metastable states ($> 1 \times 10^9$ s) in Na$_2$[Fe(CN)$_5$(NO)].2H$_2$O (Hauser *et al.* 1977) represents an important step in view of possible applications for optical information storage and data recording. Irradiating a single crystal of sodium nitroprusside (SNP) below typically 100 K with green light results in the subsequent population of two metastable states (MS$_1$ and MS$_2$) accompanied by a color change. It was also proved that it is possible to go from MS$_1$ to MS$_2$ with red light and more generally, that all possible photoswitching pathways between the ground state, MS$_1$ and MS$_2$, are accessible using an appropriate wavelength. Upon heating, radiationless relaxation is observed around ca. 200 K (MS$_1$) and 150 K (MS$_2$). The photoswitching mechanism involves a two-step process: a charge transfer transition from the metal *d* orbital to an antibonding π^* NO ligand orbital followed by a relaxation into the metastable potential minima. It may also involve a reorientation of the nitrosyl group atoms upon photoexcitation. This possibility as well as the origin of the longevity of the metastable states is still debated. It should be mentioned that the photo switching of SNP differs from the LIESST phenomenon as the ground state and the metastable states are diamagnetic and as no change of the lattice constants is observed during the photoexcitation.

The existence of photo-induced metastable states is not restricted to SNP. It has also been found for instance for related complexes such as XY[Fe(CN)$_5$(NO)]$_2$.10H$_2$O (X = Rb or Cs), K$_2$[Ru(CN)$_5$(NO)].2H$_2$O and for K$_2$[RuCl$_5$(NO)] (Woike *et al.* 1990); this latter compound points out the crucial role of the nitrosyl group for the photoswitching process.

Thus, SNP and its derivatives represent an appealing class of photochromic compounds, which are suitable for optical memory devices with a very high storage capacity and for holographic information storage (Haussühl *et al.* 1995). It is noteworthy that the effect is not limited to solids but also occurs in glassy matrices. Research efforts are currently underway towards materials with a faster population velocity and high decay temperatures. Chemical modification of the SNP system in a controlled manner might be the appropriate way to reach this exciting goal.

5. Prussian Blue Analogues

The design of molecular magnets with high Curie temperature (T_c) which can be switched by light represents a challenging topic in materials science. Particular attention has been devoted to the Prussian blue family, which can show spontaneous magnetization above room temperature (Ferlay *et al.* 1995). Soon after, the first photo-switchable, cobalt–iron cyanide was reported (Sato *et al.* 1996). K$_{0.2}$Co$_{1.4}$[Fe(CN)$_6$].6.9H$_2$O possesses an f.c.c. structure in which cobalt(II) ions are bridged to iron(III) ions via cyano groups with a few cobalt(III)–iron(II) diamagnetic pairs also being present. Irradiation of a powdered sample with red light at 5 K results in an increase in the magnetization together with a rise of T_c from 16 K to 19 K. This light-induced magnetization remains trapped at 5 K for several days in the dark. Switching back to the ground state was achieved by raising the temperature to 150 K or by irradiation with blue light.

Before the excitation, the cobalt(III) and iron(II) ions are in their diamagnetic LS states ($S = 0$ for both). Excitation with red light induces an electron transfer from the iron to the cobalt leading to cobalt(II) ions in the HS state ($S = 3/2$) and iron(III) ions in the LS state ($S = 1/2$), which couple antiferromagnetically. More interesting is that the reverse electron transfer is accessible with blue light. The local electron transfer switches increases the number of magnetic neighbors and as a result the ordering temperature (Verdaguer 1996). The key role of this phenomenon is not only the presence of Co^{III}–Fe^{II} diamagnetic pairs but also crystal defects which render the network flexible and allow the extension of the light-induced electron transfer.

From an application viewpoint, the slow switching process (a few nanometers), as well as the low

temperature range of the observation of the phenomenon, are the weak points of this system. Anyhow, it represents the first example of fine-tuning of long-range magnetic ordering by light. Photomagnetic studies on related materials using different alkali cations are in progress to further explore this fascinating phenomenon.

6. Concluding Remarks

The photo-control of the magnetic and optical properties remains a challenging topic in material science in view of the possible implementation in optical switching and memory devices. Various examples belonging to this appealing class of materials have been covered in this article. There are no doubts that a sizeable number of new compounds, as well as new photophysical phenomena, may emerge in the near future from this rapidly evolving field. We can, for instance, mention a novel composite material comprising Prussian blue intercalated into photoresponsive vesicles based on azobenzene moieties, whose magnetic properties can be controlled by photoillumination (Einaga *et al.* 1999) or a nitrosyl derivative, *trans*-[Ru(en)$_2$(H$_2$O)(NO)]Cl$_3$ (en = ethylenediamine) which show a remarkably long lived metastable state up to 267 K (Kawano *et al.* 2000).

Bibliography

Boillot M-L, Chantraine S, Zarembowitch J, Lallemand J-Y, Prunet J 1999 First ligand-driven, light-induced spin change at room temperature in a transition-metal molecular compound. *New J. Chem.*, 179–83

Boillot M-L, Roux C, Audiére J-P, Dausse A, Zarembowitch J 1996 Ligand-driven light-induced spin change in transition-metal complexes: selection of an appropriate system and first evidence of the effect, in Fe^{II}(4-styrylpyridine)$_4$(NCBPh$_3$)$_2$. *Inorg. Chem.* **35**, 3975–80

Collison D, Garner C D, McGrath C M, Mosselmans J F, Roper M D, Seddon J M W, Sinn E, Young N A 1997 Soft X-ray induced excited spin state trapping and soft X-ray photochemistry at the iron L-2, L-3 edge in [Fe(phen)$_2$ (NCS)$_2$] and [Fe(phen)$_2$(NCSe)$_2$] (phen = 1,10-phenanthroline). *J. Chem. Soc. Dalton Trans.* 4371–6

Decurtins S, Gütlich P, Köhler C P, Spiering H, Hauser A 1984 Light-induced excited spin state trapping in a transition metal complex. *Chem. Phys. Lett.* **105**, 1–4

Deisenroth S, Spiering H, Nagy D L, Gütlich P 1998 Lamb–Mössbauer factor of electronically excited molecular states measured by time-differential Mössbauer emission spectroscopy. *Hyperfine Interact.* **113**, 351–5

Desaix A, Roubeau O, Jeftic J, Haasnoot J G, Boukheddaden K, Codjovi E, Linares M, Nogues M, Varret F 1998 Light-induced bistability in spin transition solids leading to thermal and optical hysteresis. *Eur. Phys. B* **6**, 183–93

Einaga Y, Sato O, Iyoda T, Fujishima A, Hashimoto K 1999 Photofunctional vesicles containing Prussian blue and azobenzene. *J. Am. Chem. Soc.* **121**, 3745–50

Ferlay S, Mallah T, Ouahes R, Veillet P, Verdaguer M 1995 A room-temperature organometallic magnet based on Prussian blue. *Nature* **378**, 701–3

Gütlich P, Hauser A, Spiering H 1994 Thermal and optical switching of iron(II) complexes. *Angew. Chem. Int. Ed. Engl.* **33**, 2024–54

Hauser A 1995 Intersystem crossing in iron(II) coordination compounds: a model process between classical and quantum mechanical behaviour. *Comments Inorg. Chem.* **17**, 17–40

Hauser U, Oestereich V, Rohrweck H D 1977 On optical dispersion in transparent molecular systems. *Z. Phys. A* **280**, 17–25

Haussühl S, Schetter G, Woike Th 1995 Nitroprussides, a new group of materials for holographic information storage on the basis of metastable electronic states. *Opt. Comm.* **114**, 219–22

Kawano M, Ishikawa A, Morioka Y, Tomizawa H, Miki E -i, Ohashi Y 2000 X-ray diffraction and spectroscopic studies of the light-induced metastable state of a ethylenediamine nitrosyl ruthenium complex. *J. Chem. Soc. Dalton Trans.* 2425–31

Letard J-F, Nguyen O, Soyer H, Mingotaud C, Delhaés P, Kahn O 1999 First evidence of the LIESST effect in a Langmuir–Blodgett film. *Inorg. Chem.* **38**, 3020–1

Renz F, Spiering H, Goodwin H A, Gütlich P 2000 Light perturbed hysteresis in an iron(II) crossover compound observed by the Mössbauer effect. *Hyperfine Interact.* **126**, 155–8

Sano H, Gütlich P 1984 Hot atom chemistry in relation to Mössbauer emission spectroscopy. In: Matsuura T (ed.) *Hot Atom Chemistry*. Kodanski, Tokyo, pp. 265–302

Sato O, Iyoda T, Fujishima A, Hashimoto K 1996 Photoinduced magnetization of a cobalt–iron cyanide. *Science* **272**, 704–5

Verdaguer M 1996 Molecular electronics emerge from molecular magnetism. *Science* **272**, 698–9

Woike Th, Zöllner H, Krasser W 1990 Raman-spectroscopic and differential scanning calorimetric studies of the light induced metastable states in K$_2$[RuCl$_5$NO]. *Solid State Commun.* **73**, 149–52

P. Gütlich and Y. Garcia
Institut für Anorganische Chemie und Analytische Chemie, Johannes-Gutenberg Universität, Mainz Germany

Pnictides and Chalcogenides: Transition Metal Compounds

Research on the magnetic properties of 3d transition metal pnictides and chalcogenides has advanced enormously. Realistic energy band calculations as well as experimental techniques such as photoemission spectroscopy are available and play an important role in clarifying the variety of magnetic and related electronic characteristics. Chalcogens (M) (pnicogens (M′)), elements from the 6a (5a) group of the periodic table, have a valence electron configuration ns^2np^4 (ns^2np^3). The former group includes oxygen, sulfur, selenium, tellurium, and polonium and the latter nitrogen, phosphorus, arsenic, antimony, and bismuth. Chalcogens and pnicogens form many compounds with 3d elements. The total number

of transition metal (T) pnictides $T_nM'_m$ and chalcogenides T_nM_m exceeds 150. This article does not include oxides (see *Transition Metal Oxides: Magnetism*), nitrides, or polonides.

The generally stronger electronegativity of chalcogens compared to pnicogens implies two principal differences between chalcogenides and pnictides. First, in chalcogenides like Fe_7Se_8 and Fe_3Se_4 ordering of vacancies in the crystals often occurs, whereas in pnictides vacancies are generally absent. A second important difference is observed in the magnetic and electronic characteristics. For example, NiS is antiferromagnetic with a nickel magnetic moment of $1.7\mu_B$ and undergoes a nonmetal to metal transition at $T = 263K$, whereas NiAs is a weakly paramagnetic metal. The most interesting chalcogenides and pnictides are of the types TM, TM′, TM_2, and T_2M'. This article briefly reviews the magnetic and electronic properties mainly of the typical compounds mentioned above. Further details can be found in the review by Beckman and Lundgren (1991).

1. Chalcogenides

1.1 Pyrite-type Compounds of TM_2

A pyrite-type structure is adopted by the TM_2 compounds with manganese, iron, cobalt, nickel, and copper. The nearest neighbor sulfur atoms to iron in FeS_2 are shown in Fig. 1. The 3d orbitals in the octahedral crystal field are split into the three $d\varepsilon$ (or t_{2g}) and two $d\gamma$ (or e_g) orbitals. The distorted octahedron
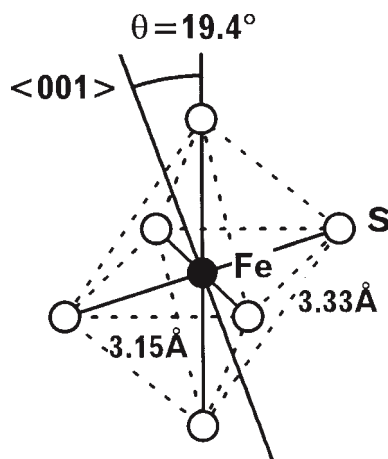
Figure 1
The iron atom in FeS_2 with the cubic pyrite-type crystal structure (space group $Pa3$) is surrounded octahedrally by six nearest neighbor sulfur atoms with the same Fe–S distance of 2.29Å. Two sides of the rectangle are not equal. If the position parameter, u, is just 0.5, the octahedron becomes perfect with $\theta = 0$.

and the influence from more distant neighbors cause further splitting of the $d\varepsilon$ and $d\gamma$ orbitals. The related energy levels are broadened into energy bands owing to the mixing with s and p orbitals of the neighboring atoms. The MnM_2 compounds have lattice parameters several percent larger than the other TM_2 compounds. Owing to strong electron correlation, they do not form energy bands and become antiferromagnetic with a local manganese magnetic moment of $5\mu_B$ in the high-spin state of the $d\varepsilon^3$ and $d\gamma^2$ configuration.

The Néel temperature, T_N, is 48K, 47K, and 87K for MnS_2, $MnSe_2$, and $MnTe_2$, respectively (Ishikawa and Miura 1991). Energy band calculations performed by Bullet (1982) for TS_2 with T = Fe, Co, Ni, Cu, and Zn are successful in explaining the magnetic and electric properties such as Pauli paramagnetic and semiconductive FeS_2 and ferromagnetic and metallic CoS_2, etc. However, the band calculations cannot explain semiconductive NiS_2 (antiferromagnetic with a nickel moment of $1.17\mu_B$). Note that the band description is not relevant for this strongly correlated electron system.

The band calculations predict NiS_2 to be a Mott–Hubbard insulator because of the existence of a half-filled 3d band at the Fermi level. Also, NiS_2 is regarded as an insulator of the charge-transfer type (Fujimori *et al.* 1996, 1997). Since the nickel atom appears in the octahedral surrounding as in Fig. 1, p–d charge transfer is likely to occur. The photoemission spectrum of NiS_2 has been explained by a cluster model with a charge transfer energy of 1.8eV, a d–d electron correlation energy, U, of 3.3eV, and a p–d transfer integral, $pd\sigma$, of −1.5eV.

Both CoS_2 and $CoSe_2$ are metallic. The former is ferromagnetic with $T_C = 125K$ and a cobalt magnetic moment of $0.85\mu_B$, and the latter is apparently a Curie–Weiss-type paramagnet. The solid solutions $Co(S_xSe_{1-x})_2$ in the composition region $0.12 \leqslant x \leqslant 0.4$ show a very interesting metamagnetic transition at $T = 4.2K$ (Adachi *et al.* 1970, 1979). The metamagnetism was successfully explained based on the energy band structure (Takahashi and Tano 1982). The magnetic characteristics of $Co(S_xSe_{1-x})_2$ at finite temperature are typical examples for which the self-consistent renormalization (SCR) theory is applied (Moriya 1979).

1.2 TM Compounds and Related Types

The TM compounds, which crystallize mainly as a hexagonal NiAs-type structure (Fig. 2(a)), often contain vacancies at the T site, and the crystal becomes distorted owing to vacancy ordering. Therefore, the magnetic and electrical properties of TM compounds are generally complex. For example, within the Fe–S system, FeS, $Fe_{1-x}S$ with $x < 0.075$, and Fe_7S_8 compounds have been found. The magnetic and electrical properties of such materials depend on the type of
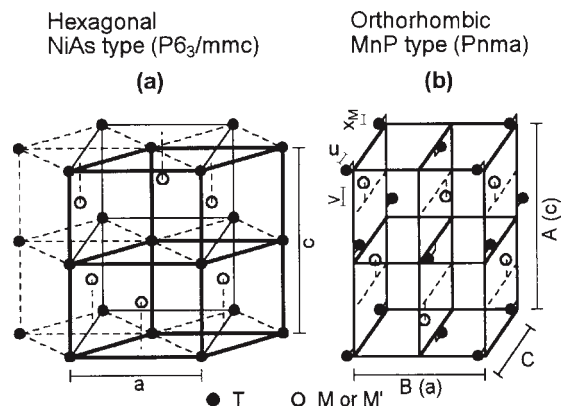
Figure 2
Crystal structures of (a) the hexagonal NiAs-type structure and (b) the orthorhombic MnP-type structure. The MnP- becomes the NiAs-type structure if $C = \sqrt{3}B/2$ and $U = V = X_M = 0$. The parameter δ, which expresses a degree of the distortion from the hexagonal to the orthorhombic structure, is defined as $\delta = (C - \sqrt{3}B)/\sqrt{3}B$. The parameters U, V, and δ are generally less than 0.05, and X_M is negligibly small in general. The lattice parameters A, B, and C in (b) correspond to c, a, and b ($= \sqrt{3}a/2$) in (a), respectively.

vacancy order, which varies with temperature as well as with the composition. Other known compounds with vacancies are Fe_7Se_8, Fe_3Se_4, Cr_7Te_8, Cr_3Te_4, and Cr_2Te_3. Generally, the TM systems with T = V, Cr, and M = S, Se show crystallographic similarities with the Cr–Te system.

The antiferromagnetic compound FeS with $T_N = 598$K undergoes an interesting transition at $T_\alpha = 420$K, which is called the α transition. At T_α the lattice parameters, magnetic susceptibility, and electrical resistivity measured along the c-axis ($\rho_\parallel \cong 0.2\Omega$cm for $T \lesssim T_\alpha$) change very sharply, while the resistivity perpendicular to the c-axis ($\rho_\parallel \cong 10^{-3}\Omega$cm) does not change significantly, and $\rho_\parallel \cong \rho_\perp$ for $T \gtrsim T_\alpha$ (Wijn 1990). The coefficient of the electronic specific heat, γ, has been found to be zero within experimental error (Kobayashi *et al.* 1999), which suggests that FeS is an insulator at low temperatures. T_α of the $Fe_{1-x}S$ compounds is strongly concentration dependent. The mechanism responsible for the α transition is still not clear.

NiS shows an insulator to metal transition at $T_t = 263$K with increasing temperature. The low-temperature phase is antiferromagnetic with a nickel magnetic moment of $1.7\mu_B$ and the high-temperature phase is paramagnetic. The insulator phase is known to be of a charge transfer type and it is considered to be at the metal–insulator boundary. An energy gap of 0.1eV has been obtained for NiS (Fujimori *et al.* 1996). The paramagnetic state of NiS is not

considered to be of a usual Pauli type (Takahashi and Kanamori 1991).

2. Pnictides

All the 3d pnictides are metallic with resistivities of the order of 10^{-3}–$10^{-4}\Omega$cm at 300 K, and their magnetic properties are described by the itinerant electron model. TM′ and T_2M' compounds are reviewed here. The TM′ compounds mainly crystallize either as NiAs-or MnP-type structures (Fig. 2), while the T_2M' compounds crystallize as Cu_2Sb- or Fe_2P-type structures (Fruchart *et al.* 1969). The most interesting are the TM′ compounds. The magnetic moment per transition metal atom is displayed as a function of the lattice parameter for T = Mn and Cr in Fig. 3. Manganese pnictides are generally ferromagnetic, while chromium ones are antiferromagnetic except for Pauli paramagnetic CrP. The B-axis of CrP (the B-axis corresponds to the a-axis of the hexagonal NiAs-type structure; see also Fig. 2 and its caption.) is about 25% smaller than the a-axis of CrSb, while the c-axis (or the A-axis) of the chromium pnictides shown in Fig. 3 remains within about 2% variation. Therefore, μ_{Cr} seems to be a reasonable function of a (or B).

Somewhat analogous features are observed for manganese pnictides (Fig. 3). These findings imply somewhat the existence of a critical separation where the spontaneous atomic magnetic moment changes drastically. The crossover is located around MnAs
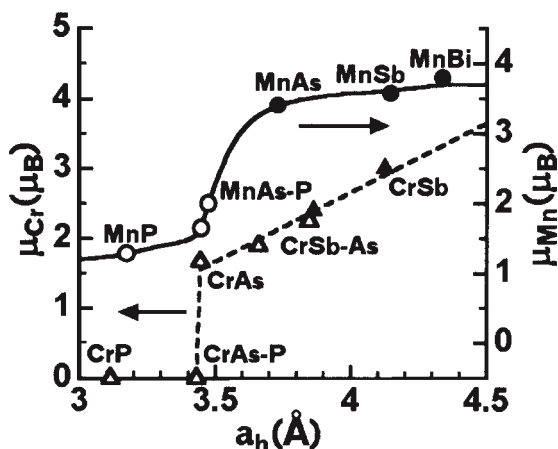
Figure 3
Relationship between the magnetic moment per T atom and the lattice parameter a_h, where a_h means either the a-axis in (a) or the B-axis in (b) of Fig. 2. The filled and the open circles and triangles are the values for the NiAs- and the MnP-type structures, respectively. The data are taken from Wijn (1990) and Kallel *et al.* (1974).
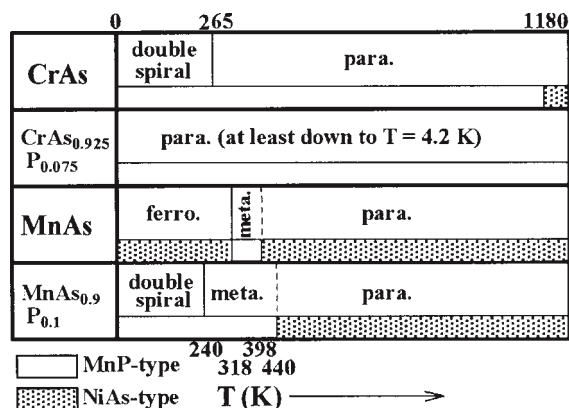
Figure 4
Some examples of the temperature dependences of magnetic and crystallographic properties of the pnictides (Wijn 1990, Selte *et al.* 1975).

Figure 5
Temperature dependences of magnetizations at constant fields for MnAs and $MnAs_{0.9}P_{0.1}$. See also main text.

and CrAs. This conclusion is corroborated by the fact that both MnAs and CrAs undergo a first-order transition at $T = 318$ K and 265 K, respectively, where the magnetic order disappears, accompanied by an abrupt shrinkage of the *a*- or *B*-axis. Besides, the magnetic properties of MnAs and CrAs are also very sensitive to substitutions of other elements. Typical examples are summarized in Fig. 4. A substitution of only 7.5% of phosphorus for arsenic in CrAs yields a collapse of the double spiral magnetic order (Selte *et al.* 1975). The *B*-axis of CrAs extrapolated to $T = 0$ K is about 6.1% (or 0.21Å) larger than that of nonmagnetic $CrAs_{0.9}P_{0.1}$ (Suzuki and Ido 1993).

The substitution of phosphorus for arsenic in MnAs also has a strong effect on magnetic properties. Magnetic properties and the various phase transitions in these materials have been explained in the framework of energy band calculations together with SCR theory (Motizuki and Katoh 1984). A large field effect on the magnetic properties is shown in Fig. 5. At temperatures in the paramagnetic region of 240 K $< T < T_t$, a metamagnetic (field-induced) transition accompanied by a crystallographic transition from the MnP- to the NiAs-type structure is observed. The mechanism responsible for the various phase transitions mentioned above has not been fully clarified.

Mn_2Sb with the tetragonal Cu_2Sb-type structure is ferrimagnetic with $T_C = 550$ K. This compound is interesting because of the strong effect of substitutions of other elements such as chromium for manganese. For example, $Mn_{1.9}Cr_{0.1}Sb$ undergoes a first-order transition from antiferromagnetic to ferrimagnetic order at $T = 300$ K with increasing temperature. The magnetic structures in the Cu_2Sb-type compounds have been explained on the basis of energy band calculations (Shirai and Motizuki 1992).
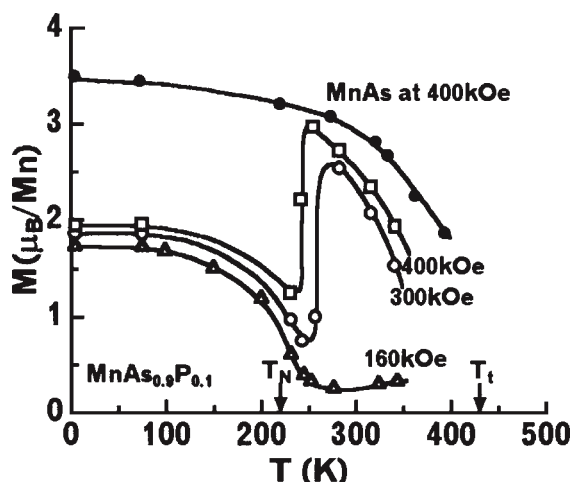
The ground state magnetic and electrical properties of $3d$ metal chalcogenides and pnictides can be explained on the basis of the electronic structures. However, numerous phase transitions induced at finite temperatures by the external field and/or by the temperature change remain unexplained theoretically. Detailed band calculations should be extended to compounds with complex magnetic structures such as CrAs, etc. SCR theory has been exploited to explain the magnetic properties at finite temperatures.

Some magnetic and electrical properties often depend strongly on the crystallographic states, especially for the chalcogenides. In addition to the application of new experimental techniques, preparation of single crystals and polycrystals with well-controlled composition and the related better experimental data may enhance progress in this field. High-pressure studies in the area up to about 10GPa may throw new light on the physics of these materials.

See also: Magnetic Refrigeration at Room Temperature; Magnetism in Solids: General Introduction; Transition Metal Oxides: Magnetism

Bibliography

Adachi K, Matuura M, Ohashi M, Kawai M 1979 Further investigations of magnetic properties of $Co(S_xSe_{1-x})_2$ $(0 \leqslant x \leqslant 1)$. *J. Phys. Soc. Jpn.* **46**, 1474–82

Adachi K, Sato K, Matsui M 1970 New type metamagnetism in $Co(S_xSe_{1-x})_2$: exchange-compensated paramagnetism. *J. Phys. Soc. Jpn.* **29**, 323–32

Beckman O, Lundgren L 1991 Compounds of transition elements with nonmetals. In: Buschow K H J (ed.) *Handbook of*

Magnetic Materials. North-Holland, Amsterdam, Vol. 6, Chap. 3

Bullett D W 1982 Electronic structure of 3d pyrite-and marcasite-type sulphides. *J. Phys.* **C15**, 6163–74

Fruchart R, Roger A, Senateur J P 1969 Crystallographic and magnetic properties of solid solutions of the phosphides. *J. Appl. Phys.* **40**, 1250–7

Fujimori A, Mamiya K, Mizokawa T 1997 Photoemission spectroscopy of correlated transition-metal compounds in the charge transfer regime. *Physica* **B237–238**, 137–41

Fujimori A, Mamiya K, Mizokawa T, Miyadai T, Sekiguchi T, Takahashi H, Mori N 1996 Resonant photoemission study of pyrite-type NiS_2, CoS_2 and FeS_2. *Phys. Rev. B* **54**, 16329–32

Ishikawa Y, Miura N 1991 *Physics and Engineering Application of Magnetism,* Solid State Science 92. Springer, Berlin

Kallel A, Boller H, Bertaut E F 1974 Helimagnetism in MnP-type compounds: MnP, FeP, and $CrAs_{1-x}Sb_x$ mixed crystals. *J. Phys. Chem. Solids* **35**, 1139–52

Katoh K, Motizuki K 1984 Role of spin fluctuation in spontaneous magneto-volume effect of intermetallic compounds MnAs and $MnAs_{1-x}P_x$. *J. Phys. Soc. Jpn.* **53**, 3166–71

Kobayashi H, Nozue T, Matsumura T, Suzuki T, Kamimura T 1999 The low temperature specific heat of FeS and $M_{0.875}X$ (M = Fe, Co; X = S, Se) with a NiAs-like structure. *J. Phys. Condens. Matter* **11**, 8673–9

Moriya T 1979 Recent progress in the theory of spin fluctuations in itinerant electron magnets. *J. Magn. Magn. Mater.* **14**, 1–46

Motizuki K, Katoh K 1984 Spin fluctuation theory of intermetallic compound MnAs. *J. Phys. Soc. Jpn.* **53**, 735–46

Selte K, Hjersing H, Kjekshus A, Andresen A F, Fischer P 1975 Magnetic structures and properties of $CrAs_{1-x}P_x$. *Acta Chem. Scand.* **A29**, 695–8

Shirai M, Motizuki K 1992 In: Kotani A, Suzuki N (eds.) *Recent Advances in Magnetism of Transition Metal Compounds.* World Scientific, Singapore, pp. 67–77

Suzuki T, Ido H 1993 Magnetic–nonmagnetic transition in CrAs and related compounds. *J. Appl. Phys.* **73**, 5686–8

Takahashi M, Kanamori J 1991 Electron correlation in Ni compounds. *J. Phys. Soc. Jpn.* **60**, 3154–61

Takahashi Y, Tano M 1982 The metamagnetism and temperature dependence of the magnetic susceptibility of $Co(S_xSe_{1-x})_2$. *J. Phys. Soc. Jpn.* **51**, 1792–8

Wijn H P J (ed.) 1990 *Landolt-Börnstein New Series*. Springer, Berlin, Group III, Vol. 27a

H. Ido
Tohoku Gakuin University, Tagajo City, Japan

R

Radiation and Particle Detectors

Superconducting radiation and particle detectors measure the energy deposited by photons or particles that interact with the detector. Superconducting detectors measure this energy with orders of magnitude more accuracy than semiconductor detectors. Most superconducting photon and particle detectors operate at temperatures below 1 K. At this low temperature, the energy deposited by the photons and particles of interest is not obscured by the thermal energy of the detector. It is the low temperature of operation that allows superconducting detectors to measure the energy of each incident photon or particle with high precision.

Superconducting radiation and particle detectors are energy dispersive, that is, they provide spectral information by measuring the energy of particles or photons absorbed in the active volume of the detector. Superconducting detectors can often be constructed so that almost every incident particle or photon interacts with the detector. Thus, these detectors can provide a combination of high resolution and high quantum efficiency which is not available in more conventional detectors.

The quest for new detectors with high resolution and high efficiency has been strongly motivated by x-ray astrophysics. However, superconducting detectors are now being developed to study astronomical objects at energies from the infrared to gamma-rays. Superconducting x-ray detectors are also being developed for laboratory plasma experiments and the measurement of nuclear materials. These detectors are being used to improve x-ray fluorescence analysis of many types of materials ranging from integrated circuits to proteins. Superconducting detectors are also used to search for proposed weakly interacting massive particles (WIMPs), which may compose the "dark matter" of the universe. They may also be useful for studying ions and very large molecules.

Various detector designs have been developed which take advantage of the unique thermal and electrical properties of low-temperature superconductors.

1. Microcalorimeters

A microcalorimeter is a small detector used to measure the total energy of incident photons or particles. As illustrated in Fig. 1, the device consists of an absorber, which is heated by individual photons or particles, and a thermal sensor, which measures the resulting change in temperature. The absorber and thermal sensor are in good thermal contact, while the assembly is isolated from the cold bath by a weak thermal link. The temperature rise due to an incident
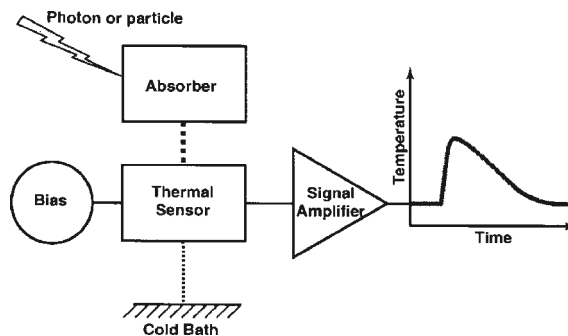
Figure 1
Schematic diagram of a microcalorimeter photon or particle detector.

particle is $\Delta T = E/C$ where E is its energy and C is the heat capacity of the device. A typical microcalorimeter operates at 0.1 K where its heat capacity can be so small that even optical photons will raise the temperature by a significant amount.

In addition to having a low heat capacity absorber, the microcalorimeter must include a sensitive thermal sensor. Thermistors have provided the best results to date. The sensitivity of the thermistor is typically parameterized by α

$$\alpha \equiv \frac{T}{R}\frac{dR}{dT} \tag{1}$$

If a low-noise amplifier is used such that the dominant noise contributions are from the thermal fluctuations in the detector and the Johnson noise in the thermistor, then the limit to the accuracy one can measure the energy is

$$\Delta E_{\mathrm{FWHM}} = \xi 2.35\sqrt{k_B T^2 C} \tag{2}$$

where k_B is the Boltzmann constant and ξ is a prefactor that depends on α and the power dissipated in the detector by the bias circuit.

For semiconducting thermistors, $\alpha \sim -5$ and $\xi \sim 3$. Values of $\xi < 1$, and therefore better energy resolution, can be achieved with a superconducting transition-edge sensor (TES). A TES is a superconducting film operated at the transition between the superconducting and normal state where the change in resistance versus temperature is very steep and $\alpha > 100$ can be obtained. The transition temperature of a TES can be tuned to almost any value with the proper combination of superconducting and normal metals. When the photon or particle deposits energy in the microcalorimeter, the temperature quickly increases, and then returns to the operating temperature. The

time constant for a device operating without bias power is C/G where G is the thermal conductivity of the weak link. When bias power is applied to the thermistor, electrothermal feedback can significantly lengthen or shorten the pulse.

For the TES, a constant voltage bias is usually used. With a constant voltage bias, V, the detector is heated above the base temperature by the bias power $P = V^2/R$. When the detector is heated by a photon or particle, its temperature increases, thereby increasing the resistance, R, of the TES. This increase in R decreases the bias power providing negative electrothermal feedback. This feedback reduces the pulse length. For a TES device with a large α, electrothermal feedback can shorten the pulse time by more than an order of magnitude. In this case, the prefactor in Eqn. (2) is given by $\xi \approx 2.5/\sqrt{\alpha}$, which can be much less than one. A high-bandwidth ($>1\,MHz$) superconducting quantum interference device (SQUID) current amplifier is typically used to operate the low-resistance voltage-biased TES detectors.

While the resolution achieved with microcalorimeters has been remarkable, the results are not generally limited by Eqn. (2). For instance, Eqn. (2) assumes that 100% of the photon or particle energy is converted to heat in the absorber. In real devices, however, some of the particle's energy can either excite long-lived states in the absorber material, or leave the detector before being measured by the thermal sensor. In both cases, the energy resolution is degraded. For optimal results, one must therefore find absorber materials with good photon or particle absorption properties, low specific heat, and good thermalization properties. Insulators and semiconductors can have very low specific heat, but statistical fluctuations in the generation of long-lived electronic states typically degrades the energy resolution to a much worse value than Eqn. (2). Good results, however, have been obtained with high-purity germanium and silicon when all the trapping centers are filled by infrared photon excitation prior to the measurement. Normal metals have excellent thermalization, but they also contain much more specific heat. Semimetals, bismuth in particular, provide an excellent combination of good thermalization with low specific heat. Superconductors cooled far below their transition temperature have low specific heat, and their small energy gap can minimize statistical fluctuations from trapped states. Tin appears to work exceptionally well.

X-ray microcalorimeters are typically $<1\,mm^2$ in area, and several microns thick. When cooled to $T \sim 0.1\,K$, resolutions of about 5 eV full width at half maximum (FWHM) have been obtained at 6 keV, and 2 eV at 1.4 keV. The response time of these devices generally limits their count rate to a few 100 counts per second. These results have been achieved with TES devices and with germanium neutron-transmutation-doped thermistors attached to tin-foil absorbers by epoxy. For comparison, a good energy-dispersive semiconductor detector has a resolution 20 times worse, about 110 eV FWHM at 6 keV. Optical TES devices have also been developed, where $400\,\mu m^2$ pixels operating at $T \sim 80\,mK$ provide single photon counting with a resolving power of about 15, and count rates as high as 3.0×10^4 counts per second. Another thermal sensor under development uses the change in magnetization of a paramagnetic material. A resolution of 13 eV FWHM at 6 keV has been obtained using an erbium-doped gold sensor and a $0.01\,mm^2$ gold absorber.

Larger microcalorimeters are being developed to improve our understanding of the nonbaryonic matter of the universe. When a proposed WIMP particle scatters off a nucleus in a semiconductor crystal, the energy transferred to the detector is divided between electron–hole pairs and thermal energy. By measuring both the electron–hole pairs, and the prompt phonons, dark-matter detectors can differentiate nuclear-recoil events from electron-recoil events which tend to produce more electron–holes for a given energy input. This allows electron-recoil events due to background radiation to be excluded from the measurement, increasing the sensitivity to WIMPs by two orders of magnitude. A similar differentiation has been achieved by comparing the scintillation light and thermal energy collected when photons and particles scatter in calcium tungstate crystals. Despite their modest size ($<1\,kg$), superconducting WIMP detectors have achieved more sensitivity than much more massive detectors operating at higher temperatures where it is not possible to reject background interactions to such a high degree.

2. Superconducting Tunnel Junctions

The superconducting tunnel junction (STJ) detector typically consists of a superconductor-insulator-superconductor (SIS) thin-film structure where the insulator is a very thin ($\sim 2\,nm$) native-oxide layer, usually Al_2O_3. The STJ is cooled below 1/10 of the superconducting transition temperature to condense almost all its electrons into Cooper pairs. An incident photon or particle breaks some of these Cooper pairs and produces electronic excitations called quasiparticles. When the Josephson current is suppressed by a magnetic field and the junction is biased at a nonzero voltage, these excess quasiparticles tunnel through the insulating barrier, producing a current pulse (see *Josephson Junctions: Low-T_c*). The number of quasiparticles produced is $N_{qp} = E/\varepsilon$, where ε is the average energy required to produce a quasiparticle. For most superconductors, $\varepsilon \approx 1.7\Delta$ where Δ is the superconducting energy gap (see *Electrodynamics of Superconductors: Flux Properties*; *Electrodynamics of Superconductors: Weakly Coupled*). Quasiparticle can tunnel back and forth through the barrier of an

STJ detector and this multiple tunneling can increase the measured signal.

If a low-noise amplifier is used such that the total noise in the measurement is dominated by the statistical fluctuations in the generation and tunneling of quasiparticles, then the resolution of the STJ detector would be limited by

$$\Delta E_{\text{FWHM}} = 2.35\sqrt{E\varepsilon(F + F')} \qquad (3)$$

Where F is the so-called Fano factor that parameterizes the statistical fluctuations in the generation of quasiparticles, and F' is a term which describes the noise associated with the variations in how many times each quasiparticle tunnels through the barrier. Monte Carlo simulations find that $F \approx 0.2$ for most superconductors. The total integrated current measured with the device is $Q = nN_{\text{qp}}$ where n is the average number of times a quasiparticle tunnels through the barrier. Typically $n = \Gamma_{\text{tun}}.\tau_{\text{life}}$ where Γ_{tun} is the tunneling rate, and $.\tau_{\text{life}}$ is the quasiparticle lifetime. For a symmetric STJ detector with multiple tunneling, $F' = 1 + 1/n$. Thus the multiple tunneling of quasiparticles can produce a bigger signal, but usually increases the statistical noise.

In general, a high tunnel rate, Γ_{tun}, will produce larger signals and better results. The tunnel rate is inversely proportional to the barrier thickness and the thickness of the superconductor. The barrier can be only so thin before it becomes leaky, allowing resistive current flow and excess noise. A thin superconductor will have a high tunnel rate, but poor x-ray absorption efficiency. It is possible, however, to use two or more superconductors to concentrate the quasiparticles from a larger absorbing layer into a thinner layer next to the tunnel barrier. If the superconducting energy gap of the absorbing layer (typically niobium or tantalum) is larger than the energy gap of the layer next to the tunnel barrier (typically aluminum), then quasiparticles created in the higher-gap material can emit a phonon while in the lower-gap material. As illustrated in Fig. 2, the quasiparticle is then trapped in the lower gap material close to the barrier. Quasiparticle trapping can be used to improve the performance of an STJ x-ray detector.

In general, STJ photon detectors have not achieved the resolution described in Eqn. (3), but the discrepancy is mostly understood. STJ detectors are generally operated with room-temperature current or charge amplifiers. The noise contribution from these amplifiers depends on the resistance of the STJ. This noise contribution is typically measured during intervals when no photons strike the detector. When this quiescent noise estimate is subtracted in quadrature from the measured resolution, the estimated intrinsic resolution can approach the limit in Eqn. (3). Better agreement is obtained with measurements of the electronic noise contribution when a photon
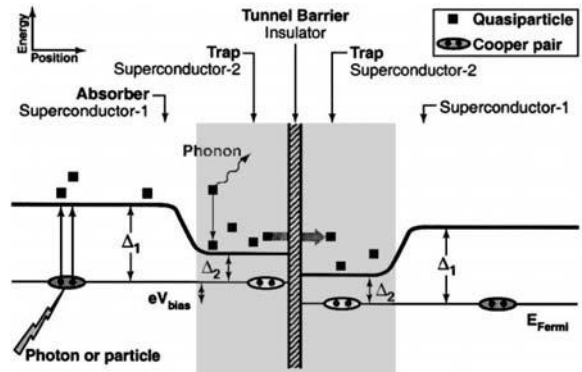
Figure 2
Energy levels in a symmetric superconducting tunnel junction photon or particle detector.

strikes the detector. The quasiparticles created by the photon causes a reduction in the STJ's resistance and an increase in electronic noise. This increase tends to bring the measurements into closer agreement with the limit described in Eqn. (3).

Five-layer STJ detectors of $Nb/Al/Al_2O_3/Al/Nb$ and $Ta/Al/Al_2O_3/Al/Ta$ have successfully been implemented as both x-ray and optical detectors. For x-rays below 1 keV, these detectors have good absorption efficiency and resolution between 2 eV FWHM and 10 eV FWHM, and can operate at temperatures as warm as 0.5 K. At 6 keV, the resolution achieved is about 25 eV FWHM, and the efficiency of these detectors is not as good. A notable exception is a $Al/Al_2O_3/Al$ STJ coupled to a lead film through a thick insulating barrier. In this case, the photon energy is converted to phonons in the lead, which pass through the insulator into the aluminum where the phonons break Cooper pairs. A resolution of 12 eV FWHM at 6vkeV was obtained with this device, and the lead film provides very high absorption efficiency even at 6 keV. Compared to the calorimeters developed so far, the STJ detectors can operate at higher count rates. STJ x-ray detectors have been operated at count rates up to 2.0×10^4 counts per second with little degradation in energy resolution. STJ detectors have also been successfully implemented to measure individual optical photons with a resolving power of about 15.

Quasiparticle trapping is a widely used technique to collect quasiparticles at various locations on a superconducting film or crystal. When a photon or particle interacts with the superconductor, the resulting quasiparticles will diffuse throughout the material, until recombining or becoming trapped. If most of the quasiparticles end up in the trapping centers adjacent to STJs, then both the energy and the position of the absorption event can be determined. Position-sensitive detectors have been successfully fabricated in both one and two-dimensional geometries. An energy

resolution of 13 eV FWHM at 6 keV and a spatial resolution of 0.5 μm in a 20 μm length has been obtained with an epitaxial tantalum strip detector with STJs at each end. The detector response time is limited by the diffusion of quasiparticles in the epitaxial film, and the lifetime of the quasiparticles trapped near the STJs. The count rate capability of these imaging strips is typically less than 1000 counts per second. Similar systems have also been shown to work with optical photons.

3. Hybrid Detectors

Microcalorimeters and STJ detectors have been combined in several interesting ways. One example is the aluminum STJ described above with a lead absorber. In some WIMP detectors, pads of aluminum are deposited on semiconducting crystals. Each aluminum pad is coupled to a TES. When a photon or particle is absorbed in the crystal, nonequilibrium phonons are generated as well as electron–hole pairs. The phonons are absorbed in the aluminum pads where they break Cooper pairs creating excess quasiparticles. These quasiparticles then diffuse in the aluminum and collect in the TES. The quasiparticles heat the TES, creating a current pulse in the amplifier.

Another interesting hybrid detector is the normal metal-insulator-superconductor (NIS) tunnel junction microcalorimeter. In this detector the photon or particle heats the electrons in the normal-metal film. This heating causes more electrons to tunnel through the insulating barrier into the superconductor. This current pulse is measured using a SQUID current amplifier. While the NIS tunnel junction uses tunneling, it is the temperature rise of the electrons in the normal metal that determines its ultimate performance. The resolution is thus limited by the microcalorimeter Eqn. (2) with $\xi \sim 1.3$. The best energy resolution obtained with an NIS tunnel junction microcalorimeter is 22 eV FWHM at 6 keV.

An interesting feature of the NIS tunnel junction is that the tunneling of hot electrons out of the normal metal is a cooling process. If the energy of these electrons can be removed from the system, the temperature of the normal metal can be lowered below the bath temperature. This property has been exploited to build microrefrigerators from NIS tunnel junctions. These microrefrigerators may be useful for cooling detectors or other small low-power devices from 0.3 K to 0.1 K, or from 0.1 K to as low 20 mK.

4. Superconducting Granules

A superheated superconducting granule (SSG) particle detector consists of small type-one superconducting spheres suspended in a dielectric. The spheres are cooled below their transition temperature, and then a magnetic field is applied. The magnetic field is adjusted to a value just below the field required to drive the spheres into their normal state. In this configuration, a small temperature increase within a sphere will cause the sphere to undergo a sudden phase transition to the normal state. When a sphere is in the superconducting state, the magnetic field is screened from its interior by the Meissner effect. During the phase transition to the normal state, the magnetic field penetrates the sphere. This results in a sudden change in magnetic flux, which can be measured by coils surrounding the spheres. Small (30 μm in diameter) spheres of tin or zinc are typically used. At 0.1 K, the heat capacity of these spheres is small enough that only a few electron volts of energy are needed to produce a phase transition.

Unlike microcalorimeters which measure the total energy deposited, SSGs measure only that the energy deposited was above a certain threshold. Some energy information from a constant source can be obtained by scanning the magnetic field. The sensitivity of the SSG particle detector is limited by variations from sphere to sphere in the energy required to produce a phase transition. Various fabrication techniques have been developed which provide a threshold accuracy of about 2%. With this accuracy, it is possible to distinguish between ionizing particles that induce several spheres to undergo phase transitions, and nuclear recoils that excite only one sphere. Detectors with billions of spheres are used for WIMP-search experiments.

See also: SQUIDs: The Instrument; SQUIDs: Amplifiers

Bibliography

Booth N E, Cabrera B, Fiorini E 1996 Low-temperature particle detectors. *Annu. Rev. Nucl. Part. Sci.* **46**, 471–532

de Korte P, Peacock T (eds.) 2000 Proceedings of the 8th International Workshop on Low-temperature Detectors (LTD-8). *Nucl. Instrum. Methods A.* **444**

Frank M, Hiller L J, le Grand J B, Mears C A, Labov S E, Lindeman M A, Netel H, Chow D, Barfknecht A T 1998 Energy resolution and high count rate performance of superconducting tunnel junction x-ray spectrometers. *Rev. Sci. Instrum.* **69**, 25–31

Kraus H 1996 Superconductive bolometers and calorimeters. *Supercond. Sci. Technol.* **9**, 827–42

Moseley S H, Mather J C, McCammon D 1984 Thermal detectors as x-ray spectrometers. *J. Appl. Phys.* **56**, 1257–62

Pretzl K 2000 Cryogenic calorimeters in astro and particle physics. *Nucl. Instrum. Methods A* **454**, 114–27

Wollman D A, Irwin K D, Hilton G C, Dulcie L L, Newbury D E, Martinis J M 1997 High-resolution, energy-dispersive microcalorimeter spectrometer for x-ray microanalysis. *J. Microsc.* **188**, 196–223

S. E. Labov and J. N. Ullom
Lawrence Livermore National Laboratory, Livermore California, USA

Random Access Memories: Magnetic

A variety of magnetic random access memory (MRAM) technologies have been explored over a period of many decades. Their advantages include an unlimited number of read-write cycles, random access to any address, radiation hardness, and nonvolatility (namely, the state of the memory does not require periodic refreshing and is maintained even when power is removed from the memory).

MRAM was originally in use for 30–40 years as magnetic core memory, which was then the only affordable RAM, although very labor-intensive and having a high cost per bit, before the advent of static RAM (SRAM) and dynamic RAM (DRAM) in the form of integrated circuits. It should be noted that while core memory has disappeared from most computers, there are still a number of applications for it in specialized systems, primarily military and space systems. Early interest, centered on magnetic bubble technology, was not successful, and involved an upper layer of permalloy patterned into a T-I bar structure and a lower layer of a garnet material with a single anisotropy direction perpendicular to the surface. Magnetic thin films were considered as an alternative to core memory. Since about the early 1990s, there has been a renewed interest in MRAMs by replacing thin film with anisotropic magnetoresistive (MR) bit structures. However, these nonvolatile memory technologies are of comparatively poor performance and thus limited in their applications. The small number of suppliers would be a concern for systems requiring long-term maintenance or likely upgrade (Jorgensen 1979, Daughton 1992).

The demand for nonvolatile radiation-hard memory has continued with additional pressures for higher density, lower power, higher speeds, and lower cost per bit. The present efforts to develop mainly three different versions of nonvolatile solid-state memories are a response to this. First, an MRAM using the spin-valve (SV) effect has been shown to have a fast switching signal (see *Magnetic Recording Systems: Spin Valves*). Second, an erasable programmable read-only memory (EPROM) employing the Hall effect to detect the fringe field of a ferromagnetic storage element has also been proposed. The third development underway is so-called spin-dependent tunneling (SDT) MRAM. This article reviews progress in MRAMs and outlines the prospects for future developments.

1. MRAM Using the Spin-valve Effect

MRAM using the spin-valve (SV) effect is evolved from that using the MR effect. A spin-valve is composed of two ferromagnetic (FM) layers (such as Permalloy or cobalt) with a spacer layer of a non-magnetic conductor (typically copper). In principle, in the sandwich structures exhibiting the SV effect the resistance is lower when alternate magnetizations are parallel than when they are antiparallel (Daughton and Chen 1993, Matsuyama *et al*. 1997). The access time of the MRAM depends on sense signal, and currently this is limited by the 2% MR thin-film materials used today. The improvement in sensing time with larger signals is roughly equal to the square of improvement in signal. This is because, for a given signal-to-noise ratio (SNR), the sense system bandwidth may be increased by the square of the sense signal improvement. A 10-fold improvement in signal is possible with SV materials, and this would improve read access times of the densest MRAMs to about the same level as DRAMs (Daughton 1992).

Figure 1 is an MRAM architecture using the FM(hard)–conductor–FM(soft) SV sandwich proposed by Wang and coworkers in 1995 (Wang and Nakamura 1995a). This memory requires SV bit lines and word lines. In an SV sandwich there are two kinds of ferromagnetic layers, which possess different coercivities. As shown in Fig. 2, this memory operates on the general principle of storing a binary datum in the magnetically hard layer (cobalt) and sensing its remanent state by switching the magnetically soft layer (NiFe) in such a way that the magnetic state of the hard layer remains unaltered. The parallel and antiparallel states between magnetizations will give a different readout.

Addressing any desired element in a two-dimensional array is a basic requirement for MRAMs. This is realized by means of the "astroid-shaped" switching characteristics of a uniaxial anisotropic ferromagnetic thin film. As depicted in Fig. 3, the switching field in the longitudinal direction is lowered when a transverse field is applied. The word lines and bit lines,
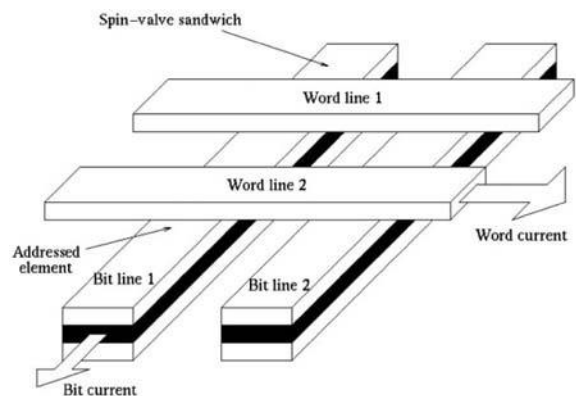
Figure 1
SV-MRAM architecture using SV sandwich. The word lines and SV bit lines, which are orthogonal to each other, are used for selection purposes. The shorting bars between elements to reduce the bit line resistance are not shown in this figure.
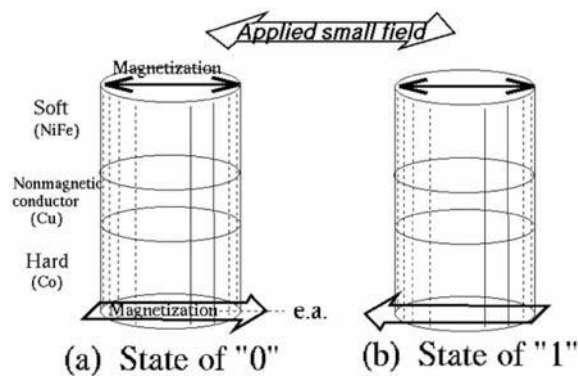
Figure 2
Schematic drawing of SV-MRAM. This memory operates on the general principle of storing binary datum in the magnetically hard layer (e.g., Co) and sensing its remanent state by switching the magnetically soft layer (e.g., NiFe) in such a way that the magnetic state of the hard layer remains unaltered (after Wang and Nakamura 1995a). The parallel and antiparallel states between magnetizations will give a different readout (spin-valve effect).
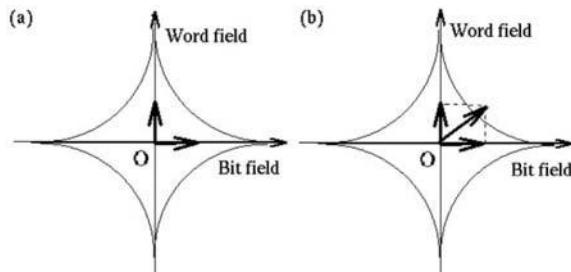
Figure 3
How to address a desired element in a two-dimensional array with the aid of astroid-shaped switching characteristics? (a) Neither the word field (with selected value) nor the bit field (with selected value) by themselves are able to switch the element; (b) both fields act together to produce a combined field vector greater than the switching threshold of the addressed element.

which are orthogonal to each other, are used for selection purpose (see Fig. 1). A word current passes through one of the word lines and a bit current through one of the bit lines. The bit current is assumed to flow mainly along the intermediate layer (e.g., copper) of the SV sandwich owing to its large conductivity. These two currents combine at one and only one intersection point, i.e., the addressed element. As depicted in Fig. 3(a), neither the word field (current) with selected value nor the bit field (current) with selected value is by itself able to switch the
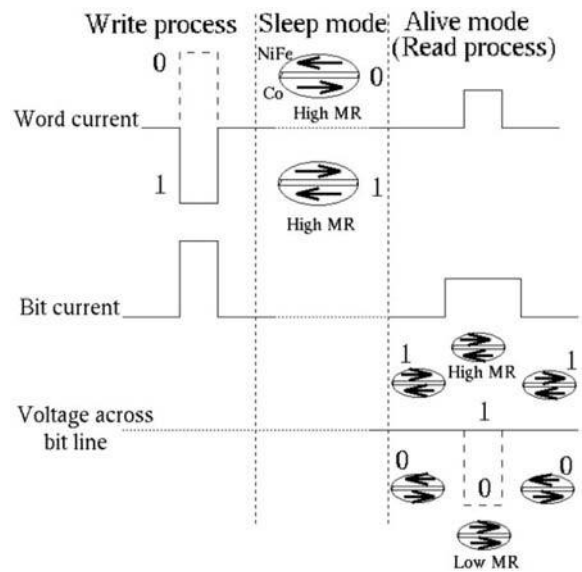
Figure 4
Magnetization configuration of an SV-MRAM element and its expected writing and reading timing diagram. In the absence of external field (sleep mode), the alternate magnetizations are antiparallel due to the inter-layer antiferromagnetic coupling.

element. In Fig. 3(b), if both fields act together, they are able to produce a combined field vector greater than the switching threshold of the addressed element. In such a way, a writing or re-writing operation is realized (Wang and Nakamura 1996a).

Magnetization configuration of an SV-MRAM element and its expected writing and reading timing diagram is shown in Fig. 4. During a write operation, the sign of the word current will define the stored bit value, "0" or "1." In the absence of external field (sleep mode), the alternate magnetizations are anti-parallel, owing to the interlayer antiferromagnetic coupling, giving small self-demagnetizing fields and small external stray fields on nearby memory elements, both of which could help with element stability. During a read operation (alive mode), data readout is performed by monitoring the voltage response of the SV bit line against a positive word current, whose value is not sufficient to switch the hard layer, but switches the soft layer if it opposes the soft layer's magnetization. A different voltage, depending on whether a "0" or "1" is stored, should appear across that SV bit line. In the experimental pulse sequence (Wang and Nakamura 1995a), the sense current applied into the bit line is 5 mA and a sense output voltage of 8 mV appears. The read/write energy is quite low. Furthermore, the test indicates that a stable readout state involving 3×10^8 repeated reversals, by field cycling, of the soft layer's

magnetization is achieved, without gradual decay and eventual erasure of the hard layer's magnetization. Thus this SV-MRAM is confirmed to have a non-destructive readout (NDRO) property.

2. EPROM Using Hall Effect

An erasable programmable read-only memory (EPROM) using the Hall effect to detect the direction of magnetic moment of a ferromagnetic storage element has been proposed by Timoshkov *et al.*, as shown in Fig. 5 (Timoshkov *et al.* 1996). The magnetic film of high coercivity and perpendicular anisotropy is used for data storage, and the Hall element for data reading. The insulating layer between them produces electrical isolation of the functional layers. The data recording process is realized by magnetizing the perpendicular anisotropy layer. The magnetic flux B_Z of this layer penetrates through the Hall element, and the data read process is carried out by the Hall effect in the semiconductor material. The read time for such a memory is limited only by the relaxation time of the Hall effect processes and is equal to 10^{-12}–10^{-13} second. The equation for the Hall voltage U_X is

$$U_X = r_{\rm H}\frac{I_Y B_Z}{ned}f(l/a) \qquad (1)$$

where $r_{\rm H}$ is the Hall factor depending on prevalent scattering mechanism of the carriers, 1.18–1.93; I_Y is the sense current; e is unit electric charge, 1.6×10^{-19} C; n and d are the carrier concentration in the semiconductor (data reading) layer and its width respectively; and $f(l/a)$ is a correction function, which is
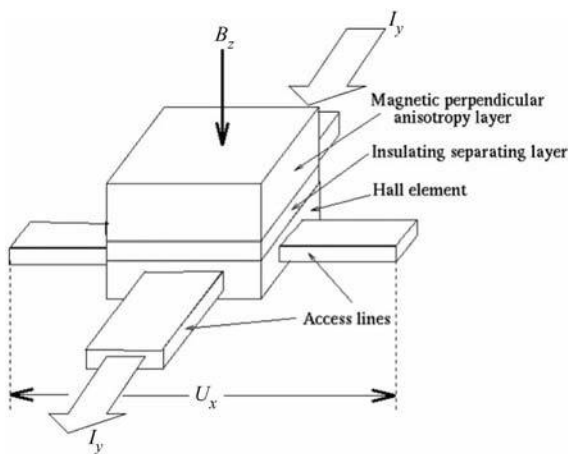
Figure 5
An EPROM using the Hall effect to detect the direction of magnetic moment of a ferromagnetic perpendicular storage element (after Timoshkov *et al.* 1996).

equal to 0.90–0.95 for a reasonable ratio of the length to the width of the data reading layer $l/a = 2-3$.

3. MRAM Using Spin-dependent Tunneling (SDT) Effect

The SDT effect (Julliere 1975, Miyazaki and Tezuka 1995, Moodera *et al.* 1995, Boeck 1998) is a special current-perpendicular-to-plane (CPP) giant magneto-resistance (GMR) effect, based on FM–tunnel–barrier–FM spin-polarized junctions. The tunneling resistance between two ferromagnetic metal layers that are separated by a thin insulator depends on the relative orientation of the magnetization of each layer.

Work by Wang *et al.* on the MRAM using the SDT effect began in 1994 (Wang and Nakamura 1995b, 1996b), and led initially to the successful fabrication of a 2×2 bit SDT-MRAM, based on Co/Al_2O_3/80NiFe tunnel junctions. Figure 6 is its scanning electron microscopy (SEM) picture and schematic. The chiplet has eight contact pads, which provides the required flexibility in connecting the test site to the peripheral select/drive circuitry. The spin-tunneling junction dimensions varied between 2 and 50 μm. All the spin tunneling samples Co(100 nm)/Al_2O_3(3–8 nm)/80NiFe(100 nm) were prepared by radio frequency (rf) sputtering with argon. The intermediate Al_2O_3 was formed by oxidation in the atmosphere. Uniaxial magneto-crystalline anisotropy in ferromagnetic films, important both for memory storage and for the way that a bit is selected, was induced by a magnetic field applied during sputtering. Contact windows were opened in the insulator to allow the orthogonal top leads and bottom leads to access the junctions directly. The top leads are visible as brighter regions in the SEM picture, whereas the bottom leads are darker.

As shown in Fig. 7, the structure of the SDT-MRAM is relatively simple, compared with the semiconductor memories. Having an active memory-cell transistor, flash EEPROMs (electrically erasable programmable ROMs) typify semiconductor memories. The minimum element area of a tunneling cell is 4.84 λ^2, where λ is the resolution limit of the lithography used to fabricate the memory elements. Progress in photolithography technology should enable the reduction of λ beyond the 200 nm limit (Daughton 1992). Compared with the minimum size of a memory-element transistor, over $10\lambda^2$ (also shown in Fig. 7), the SDT-MRAM can potentially be at least twice as dense.

The spin-tunneling junction was designed with a circular shape to benefit the formation of single-domain structure, based on the micromagnetic simulation result (He and Wang 1999), as shown in Fig. 8. For each MRAM element there should exist only two possible states of magnetization, e.g., left and right. Clearly this is the case for an elliptic or circular
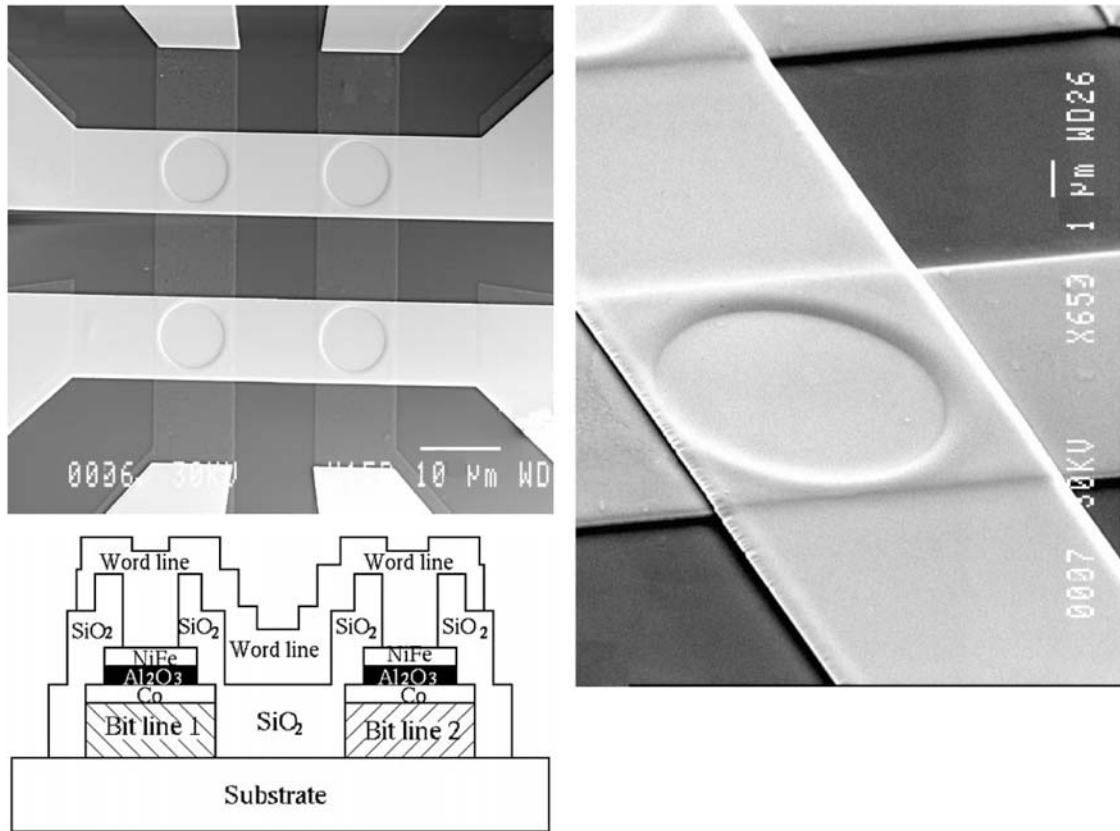
Figure 6
SEM micrographs of a 2×2 bit SDT-MRAM chiplet showing the test site containing 8 contact pads and 4 circular tunnel junctions, each $10\,\mu m$ in diameter, the schematic cross-section (note the CPP structure) and a single-tunnel junction bit. The top leads are visible as bright regions in SEM whereas the orthogonal bottom leads are darker (after Wang and Nakamura 1996b).

island. In detail, for a single domain island one can be sure that the island switches completely in a proper writing process. A multi-domain state found in the square patterned island would lead to a miscellaneous logic in a one bit per island recording system. This is because more than two states are possible and the island might not have switched completely after writing. As a consequence, the magnetization of the island becomes unstable and the result of a next writing process may be unpredictable.

An isolated memory element was tested. Figure 9 illustrates the R(H) response's minor loops operating in the mode in which only the magnetically soft layer is switched by applying a field of $\pm 1.6\,\mathrm{kA\,m^{-1}}$ and the sample is initially saturated by $+3.2\,\mathrm{kA\,m^{-1}}$. Note that the MR hysteresis at zero field represents different magnetization combinations, thereby yielding different resistance values.

The on-chip parallel write/read operations were successfully performed. Writing the information involves a switching of the soft layer's magnetization, ideally without affecting the reference (hard) layer's magnetization. (In a memory device, independent switching of the magnetically soft layer is achieved by making the other layer either magnetically hard or exchange-biased by an antiferromagnetic layer, e.g., MnFe.) Reading the information only requires a measurement of magnetoresistance. An output voltage change of $96\,\mathrm{mV}$, as shown in Fig. 10, between the binary bit states against a sine-wave sense voltage of $160\,\mathrm{mV}$, $1\,\mathrm{MHz}$ has been observed. This is a reproducible readout state.

Ultra-dense magnetic solid-state MRAMs will probably be limited by the minimum signal level. As a comparison, we first deduce the signal level in conventional current-in-plane (CIP)-type MR or SV MRAM. Its signal is given by

$$\mathrm{Signal_{CIP}} = fJ_{\max}\lambda\Delta\rho \qquad (2)$$
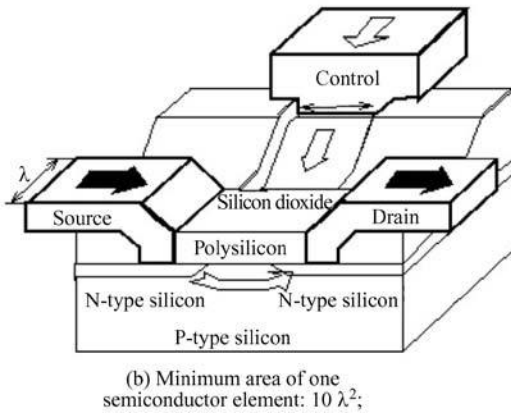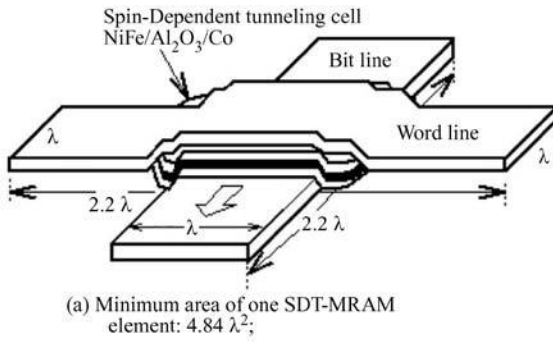
Figure 7
Structure comparison of the SDT-MRAM and the semiconductor memory. In (b) a field effect transistor (FET) comprises a source and a drain contact to send current through a semiconductor channel and a gate control to modulate the carrier density in the channel. Here λ is the resolution limit of the lithography used to fabricate the memory elements.

where f is a factor smaller than one which depends on the mode of storing and sensing information, J_{max} is the maximum current per cross-sectional area allowed by thermal dissipation, and $\Delta\rho$ is the change of resistivity. Thus at the maximum current density, the signal level is proportional to the element size λ. As the storage density increases, the signal level will decrease. In contrast, the signal of SDT-MRAM results in

$$\text{Signal}_{\text{CPP}} = fJ_{max}t\Delta\rho \qquad (3)$$

where t is the total thickness of the spin-tunneling junction. As illustrated in Fig. 11, at a maximum sense current density, the signal level of SDT-MRAM is obviously independent of its cross-sectional area λ^2. This result is so attractive that the density of SDT-MRAM should not be limited by signal degradation. It is suggested that density-independent signal level is
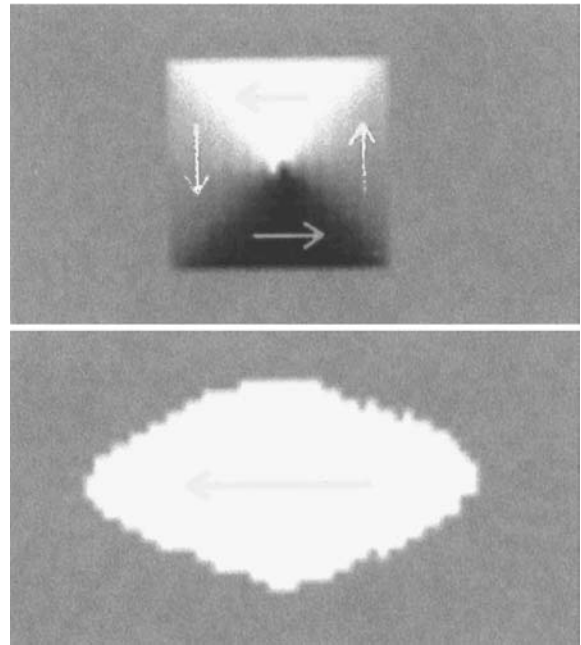
Figure 8
Demagnetized states of patterned islands with different shapes. The brightness stands for the left magnetization direction and the darkness for the right (after He and Wang 1999).

Figure 9
Measured resistance versus applied field R(H) for $Co/Al_2O_3/80NiFe$. The applied field is limited at $\pm 1.6\,\text{kA m}^{-1}$ and the sample is initially saturated by $+3.2\,\text{kA m}^{-1}$. Note that the MR hysteresis at zero field represents different magnetization combinations thereby yielding different magnetoresistances (after Wang and Nakamura 1995b).
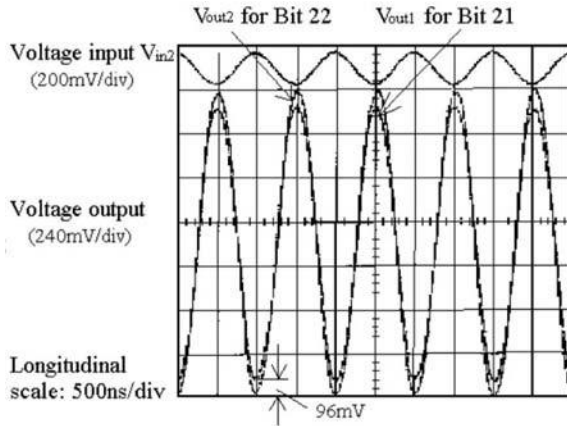
Figure 10
Reproducible read waveform. An output voltage change of 96 mV (after an amplifier) between the binary bit states against a sine-wave voltage excitation (the above) of 160 mV, 1 MHz has been observed. The vertical scale is 1.2 V/div and the horizontal scale is 500 ns/div.

the biggest advantage of CPP-type SDT-MRAM, compared with CIP-type MR or SV MRAM.

It is pointed out that the SDT-MRAM's signal remains constant while the CIP MRAM's signal drops with increasing density. However, the Johnson noise with SDT-MRAM may become a limiting factor in scaling the MRAM element to submicron sizes because this component of noise becomes increasingly important and may even dominate the total noise. What matters for practical application is SNR. Even the larger signals available from SV structures do not make SV-MRAM attractive for mainstream RAM applications. In order to achieve reasonable memory array densities many SV elements (of number n) have to be electrically connected in series, which means that the actual signal available when reading one particular element is MR/n (see Fig. 1 for reference). Thus, a severe practical problem is encountered that ultra-dense CIP SV-MRAM will be limited by low SNR. By contrast, as illustrated in Fig. 6, the high MR signal from the individual junction element can be fully utilized in a cross-point architecture by connecting each element in parallel. In this case, the SNR in an n bit $\times$ n bit SDT-MRAM is independent of n, which is normally a big number. As a result, although SNR in both CIP and CPP MRAMs falls with increasing density, the SNR for the CPP SDT-MRAM remains much larger than for the CIP type MR or SVMRAM.

So far, the experimental results of SDT-MRAM are only for a low-density case in that only 2×2 bit elements are included. For a dense or ultra-dense MRAM, the cross-talk from an addressed element to adjacent elements may cause mis-selection and creep problems (after many such disturbances the magnetic
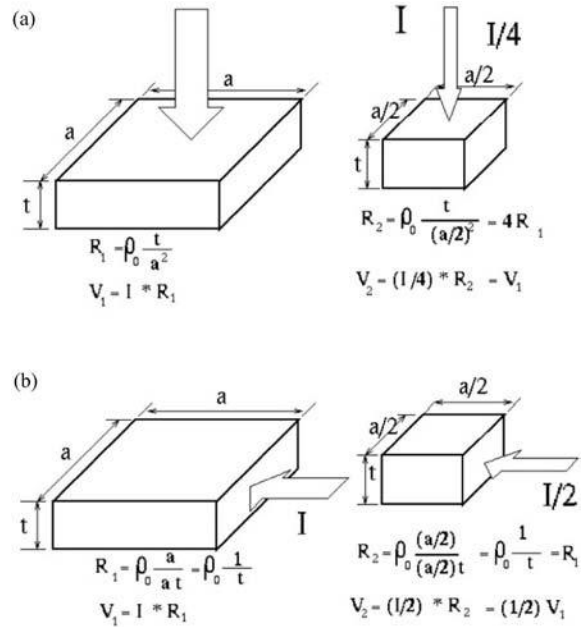
Figure 11
Halving the dimension of an MRAM cell will cause different results on signal amplitude. In the CPP design of (a), signal remains; in the CIP design of (b), signal drops by a factor of 2. Note that both (a) and (b) are at a maximum sense current density.

state of these bits creeps either to some intermediate state or may completely reverse). Note also that the driving field required to switch the layer increases as a result of the decreased length of the element, owing to the demagnetization effect. To address these issues, a finite element method (FEM) was used to study the electromagnetic behavior of SDT-MRAM (Wang *et al*. 1997). Three keepered SDT-MRAM designs have been considered, as shown in Fig. 12. A low-cost conventional keeperless MRAM design (Fig. 12(a)) is taken as our reference. To localize the field, an improved partially keepered MRAM design (Fig. 12(b)) differs from the reference MRAM by the addition of partial keepers, with high permeability, above the bit lines and underneath the word lines. The third design, known as the continuously keepered MRAM design, is shown in Fig. 12(c). In this design, additional continuous keepers with 0.1 μm thickness are formed. It was hypothesized that the drive field would be confined within the nearly closed keeper, effectively enhancing the driving field and reducing interference between adjacent cells. The continuously keepered MRAM design was found to reduce the cross-talk by a factor of five and reduce the driving current by a factor of four, compared with a conventional keeperless design, which will be the most favored approach for achieving 10^9 bits cm^{-2} areal density.
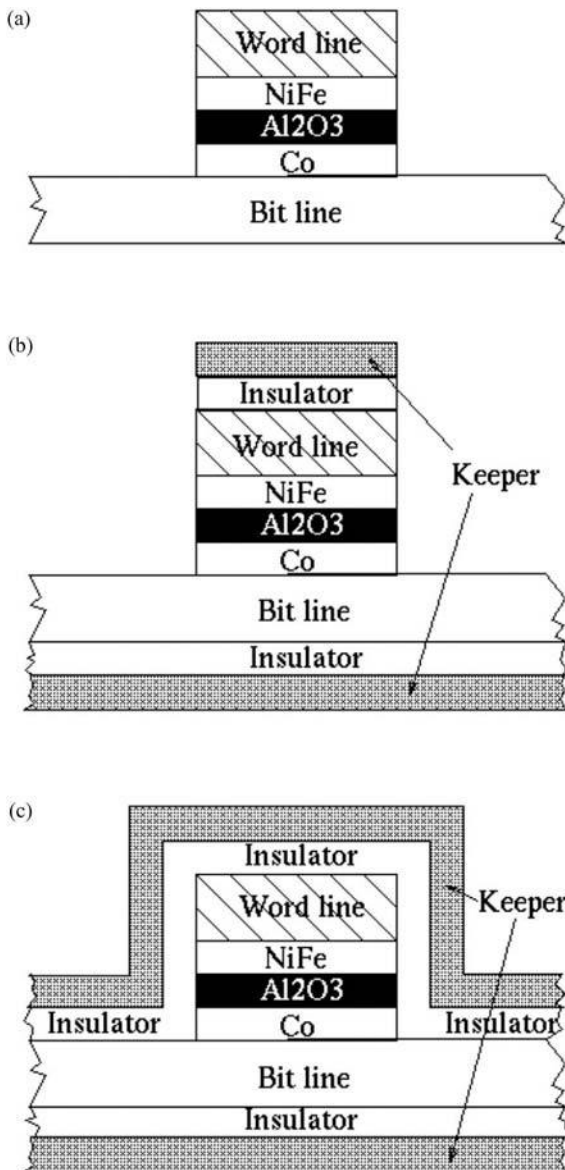
Figure 12
Three keepered SDT-MRAM designs: (a) conventional keeper-less MRAM design; (b) improved partially keepered MRAM design; (c) further improved continuously keepered MRAM design (after Wang *et al*. 1997).

Figure 13
The position of SDT-MRAM in various data storage devices.

4. Conclusions

Read-access time and storage density are the twin keys to computer data storage devices. Although new electronic devices, processor organizations and software systems have contributed to enormous advances in computer technology, they would have been worthless without the faster and denser memories that were developed with them. The SDT-MRAM outlined here, the most promising candidate for magnetic nonvolatile memory, is likely to achieve very high densities. From Fig. 13 it can be seen that SDT-MRAM, which is simply structured, may in some applications potentially exhibit excellent properties superior to semiconductor memories and/or magnetic disks. In particular, the density-independent signal level is the biggest advantage of CPP-type SDT-MRAM, compared with the conventional CIP-type MR or SV MRAM, whose signal level is inversely proportional to the square root of the storage density. Furthermore, it has also been demonstrated that although the Johnson noise makes a large contribution to the total noise, it does not significantly degrade the performance of the device, because the SNR for the SDT-MRAM remains much larger than for the CIP MR or SV MRAM even at high storage density.

Another important parameter for SDT-MRAM is the intrinsic RC time constant of the device. Because of the insulator between electrodes, junctions also act as a parallel plate capacitor. The reason that the RC time constant is important for memory application is because of speed limitations in reading data from a memory element. The RC time constant is independent of the area of the junction and exponentially dependent on the thickness of the barrier and can be reduced until the processing difficulties with thin barriers prevent further reduction in thickness. For modern MRAM applications, the equivalent

resistance for SDT devices must be at the lower end of the resistance range. Parkin *et al*. found that the resistance-area products of magnetic tunnel junctions can be varied from $10^9\,\Omega\mu m^2$ to as low as $60\,\Omega\mu m^2$ by varying the aluminum thickness and properly oxidizing it (Parkin *et al*. 1999). Incomplete oxidation leads to the presence of metallic aluminum in the barrier, which results in a rapid suppression of the tunnel junction magnetoresistance. Based on these facts, the RC time constant for the junctions should be of the order of nanoseconds (Wong *et al*. 1998, Sousa *et al*. 1999). Nevertheless, such a SDT-MRAM has to be read with a silicon sense amplifier. This means a mixed silicon-tunneling structure: the X-Y decoders/sense amplifiers in an array in silicon with "holes" to be filled in by tunneling array. Thus, the speed of the device will probably be limited by silicon technology. (Today, the speed of experimental silicon devices has improved to 1 ns and will be expected to dip below this in future.) There is no significant access-time advantage for the tunneling design as compared to the bipolar devices.

As well as the continuing developments which are always to be expected in semiconductor memory technology, it is also interesting to note other novel technologies, such as the spin-dependent tunneling (SDT) effect. In the immediate future DRAM will continue as the densest semiconductor memory, but MRAM using the SDT effect looks set to take the lead in the medium and longer term and is a very important development for applications where nonvolatility, higher density, radiation hardness and lower power are required. Prototypes are out, technology is maturing, and the advances mentioned in this article would speed up the pace of the application of MRAM, since a microstructured junction might serve as a high-capacity and low-power substitute for conventional semi-conductor memories.

Bibliography

Boeck J D 1998 Switching with hot spins. *Science* **281**, 357–9
Daughton J M 1992 Magnetoresistive memory technology. *Thin Solid Films* 162–216
Daughton J M, Chen Y J 1993 GMR materials for low field applications. *IEEE Trans. Magn*. **29** (6), 2705–10
He L, Wang F Z 1999 Size and shape effects of patterned polycrystalline islands. *Intermag* **HC-09**
Jorgensen F 1979 *The Complete Handbook of Magnetic Recording*. Blue Ridge, Summit, PA
Julliere M 1975 Tunneling between ferromagnetic films. *Phys. Lett. A* **54**, 225–6
Matsuyama K, Asada H, Ikeda K, Taniguchi K 1997 Low current magnetic-RAM memory operation with a high sensitive spin valve material. *IEEE Trans. Magn*. **33** (5), 3283–5
Miyazaki T, Tezuka N 1995 Giant magnetic tunneling effect in a Fe/Al$_2$O$_3$/Fe junction. *J. Magn. Magn. Mater*. **L231–4**, 139
Moodera J S, Kinder L R, Wong T M, Meservey R 1995 Large magnetoresistance at room temperature in ferromagnetic thin film tunnel junctions. *Phys. Rev. Lett*. **74** (16), 3273–6

Parkin S S, Roche K P, Samant M G, Rice P M, Beyers R B, Scheuerlein, O'Sullivan E J, Brown S L, Bucchigano J, Abraham D W, Lu Y, Rooks M, Trouilloud P L, Wanner R A Gallagher W J 1999 Exchange-biased magnetic tunnel junctions and application to nonvolatile magnetic random access memory. *J. Appl. Phys*. **85**(8)
Sousa R C, Freitas P P, Chu V, Conde J 1999 Vertical integration of a spin dependent tunnel junction with an amorphous Si diode for MRAM applications. *Intermag* **HA-03**
Timoshkov Y, Khomenok V Danko V Kurmashev V 1996 The memory element. *Russ. Fed. Pat*. N.2036517
Wang F Z, Mapps D, He L, Clegg W W, Nakamura Y 1997 Feasibility of ultra-dense spin-tunneling random access memory (STram). *IEEE Trans. Magn*. 33 (6), 4498–512
Wang F Z, Nakamura Y 1995a A new type of memory using GMR effect. *IEICE Gen. Conf. Proc. C-502*. Fukuoka, Japan
Wang F Z, Nakamura Y 1995b Perpendicular GMR random access memory using magnetic tunneling effect. *J. Magn. Soc. Jpn*. **19** (S2), 108–11
Wang F Z, Nakamura Y 1996a Design, simulation, and realization of solid state memory element using the weakly coupled GMR effect. *IEEE Trans. Magn*. **32** (2), 520–6
Wang F Z, Nakamura Y 1996b Spin tunneling random access memory (STram). *IEEE Trans. Magn*. **32** (5), 4022–4
Wong P K, Evetts J E, Blamire G 1998 High conductance small area magnetoresistive tunnel junctions. *Appl. Phys. Lett*. **73** (3), 384–6

F. Z. Wang
University of North London, UK

Rare Earth Intermetallics: Thermopower of Cerium, Samarium, and Europium Compounds

The thermoelectric power, *S*, is known as a transport property that is very sensitive to details of the electronic structure at the Fermi energy. Cerium compounds exhibit widely different types of anomalous physical properties owing to the hybridization of cerium 4*f* electrons and conduction electrons. There is already an accumulation of experimental data for *S* for a large number of cerium compounds; however, there has been no review article concerning these data, as far as is known. The aim of this article is to give an overview and discussion of these data for *S* for different types of cerium compounds.

This article is based on previous review papers by Sakurai (1993), and Sakurai *et al*. (1996). Anomalous physical properties of cerium compounds are of interest with respect to highly correlated electron systems (see *Electron Systems: Strong Correlations*). Doniach (1977) considered a competition of two interactions: the Kondo interaction between the cerium 4*f* electrons and the conduction electrons (characteristic temperature T_K) and the RKKY interaction between the 4*f* electrons on different lattice sites via the conduction electrons (characteristic temperature T_N

for an antiferromagnet or T_C for a ferromagnet). The former interaction causes the cerium $4f$ electrons and the conduction electrons to form a hybridized nonmagnetic singlet state for temperatures $T < T_K$, but the cerium $4f$ electrons regain their magnetic moment for $T > T_K$. The latter interaction gives rise to an antiferromagnetic state of the cerium $4f$ electrons for $T < T_N$ (or a ferromagnetic state for $T < T_C$) and to a paramagnetic state with a random orientation of the magnetic moments for T_N (or T_C) $< T$.

These characteristic temperatures T_K and T_N (or T_C) are exemplified in Fig. 1 as functions of the hybridization strength, J, between the cerium $4f$ electrons and the conduction electrons. We can distinguish in Fig. 1 four regions, I–IV, where cerium compounds have distinctly different physical properties. In region I, where $T_K \gg T_N$ (or T_C), cerium compounds are in a fluctuating or intermediate valence state, thus exhibiting no magnetic moment in a wide temperature range $T < T_K$. In region II, with $T_K \approx T_N$ or T_C, the compounds lose the magnetic moment of their localized Ce^{3+} ions owing to the hybridization between the cerium $4f$ electrons and the conduction electrons, and the effective masses of the electrons become very large (heavy fermion) for $T < T_K$. In region III, where T_K is slightly smaller than T_N, cerium compounds order magnetically with reduced ordered moments owing to the Kondo effect. Finally, in region IV, where $T_K \ll T_N$, cerium compounds are in an almost unperturbed antiferromagnetic state with the magnetic moment determined from crystal field effects experienced by the local Ce^{3+} ion.

The $S(T)$ curves for a CeNi single crystal are shown in Fig. 2 as a typical compound of region I together with the nonmagnetic LaNi reference sample
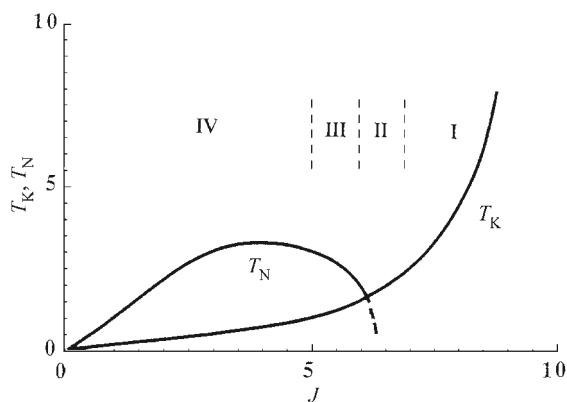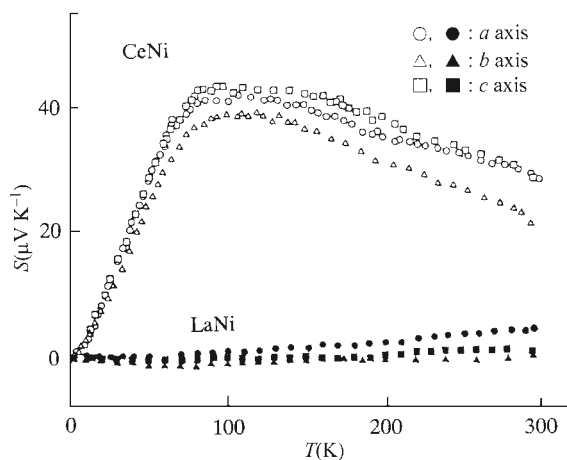
Figure 2
S of an intermediate valence compound CeNi and its nonmagnetic counterpart LaNi (single crystals) along three crystal axes plotted as a function of temperature, T.

(Sakurai *et al.* 1996). The absolute values of S for LaNi along the three principal axes of the orthorhombic crystal are small, and the $S(T)$ curves behave nearly linearly. This behavior can be approximated by the linear relationship $S(T) = aT$, where $a = \text{const.}$ over a wide temperature range. This formula can be derived from the Boltzmann equation for normal metals (see also *Boltzmann Equation and Scattering Mechanisms*, and *Kondo Systems and Heavy Fermions: Transport Phenomena*), with the constant a basically representing conduction electron properties at the Fermi level, described by the density of states (DOS) function (Ziman 1960).

On the contrary, the absolute values of S for CeNi along the three principal axes are much larger than those for LaNi, and the $S(T)$ curves exhibit broad peaks with maximums around 100 K, indicating that a is not a constant but depends on T. An enhancement of the DOS takes place at the Fermi level owing to the formation of nonmagnetic Kondo singlets at low temperatures. Thus, a is much larger for CeNi than for LaNi. With the increase of T, the thermal excitation breaks the Kondo state causing a gradual recovery of the cerium magnetic moments, hence the value of a decreases. A gradual recovery of the Curie–Weiss law is known to take place when T is larger than the temperature of the maximum in S vs. T. In this scenario the Kondo interaction predominates by far over the RKKY interaction, and the effect of the crystalline electric field (CEF) has not been taken into account. Additional examples of these types of materials are $CeSn_3$, $CePd_3$, $CeNiAl_4$, and $CeNi_2Ge_2$ (Sakurai *et al.* 1996).

The $S(T)$ curves of $CeCu_6$ (Onuki and Komatsubara 1987) and CePtIn (Fujii *et al.* 1987) are shown in

Figure 1
Kondo temperature, T_K, and the Neel temperatures, T_N, plotted as a function of the hybridization, J, between cerium $4f$ electron and the conduction electron band (after Doniach 1977).
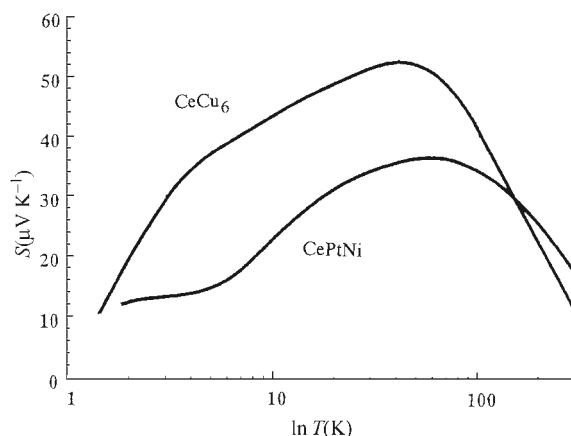
Figure 3
S of two polycrystalline heavy fermion compounds
CeCu$_6$ and CePtNi plotted as a function of $\ln T$.

Fig. 3 as typical compounds of region II. Both compounds exhibit T_K values of only a few kelvin without any magnetic order but they are characterized by a very large enhancement of the electronic specific heat, γ, at low temperatures. The two curves in Fig. 3 resemble each other, showing a large and broad maximum at 50–70 K with shoulders at around 5 K. For temperatures $T > T_K$, the cerium 4f electrons are in a local and dilute ionic state and experience a CEF with the Kondo effect acting as a small perturbation. The RKKY interaction can be neglected. The Seebeck coefficient in this parameter region has been theoretically investigated by Bhattacharjee and Coqblin (1976) and Kashiba *et al.* (1986). According to these calculations a positive peak of the $S(T)$ curve is expected at a temperature around about 1/3 to 1/6 of the overall CEF splitting. The main S peaks of the two compounds in Fig. 3 are ascribed to interplay of the Kondo effect and CEF effect splitting. The main peaks for the two compounds in Fig. 3 are reminiscent of the peak of CeNi in Fig. 2; however, they are of different origins.

The following discussion concerns the initial slope of S vs. T for $T \to 0$. It is well known that $S \to 0$ for $T \to 0$ and the initial slope of $S(T \to 0)$ reflects details of the DOS at $E = E_F$ (Ziman 1960). For CeCu$_6$ and CePtIn a very large value of $10\,\mu\mathrm{VK}^{-2}$ is observed. In comparison, the value for CeNi in Fig. 2 is around $0.5\,\mu\mathrm{V}K^{-2}$ and the value for LaNi, the reference sample for CeNi, is around $0.01\,\mu\mathrm{VK}^{-2}$. Thus, the initial slope of $S(T)$ is apparently closely related to the electronic specific heat, γ.

The initial slope of S is plotted in Fig. 4 as a function of γ for several cerium compounds belonging to regions I and II. They are CeSn$_3$, CeNi, CePd$_3$, CeNiIn, and CeNiAl$_4$ in region I, and CeCu$_6$, Ce$_{0.1}$La$_{0.9}$Cu$_6$, CeInCu$_2$, CePtIn, CeCu$_3$Ga$_2$,

CeCu$_3$A1$_2$, CeCu$_4$Al, and CeCu$_4$Ga in region II (Sakurai 1993).

The estimation of the initial slope of S is noted to depend on the temperature range of measurements especially for the compounds belonging to region II. When the value for CeCu$_6$ in Fig. 3 is estimated from the temperature range above the shoulder around 5 K, the value becomes smaller. $S(T)$ measurements performed for CeCu$_6$ down to 10 mK show another structure below 1 K and the establishment of the relationships $S = aT$ and $\rho = cT^2$ ($c = $ const.) is possible only in a very low temperature range, below 30 mK (Sato *et al.* 1987). The initial slope of S estimated below 30 mK approaches a value of $30\,\mu\mathrm{VK}^{-2}$. Thus, in Fig. 4 the values obtained for cerium compounds belonging to region II for the different temperature ranges are plotted separately (Sakurai 1993).

The proportionality between the initial slope dS/dT for $T \to 0$ and the electronic specific heat coefficient, γ, is confirmed by the experiment, as shown in Fig. 4. In view of the difficulties of obtaining an accurate estimation of the initial slope of S, the scatter of points near the origin of Fig. 4 is not significantly important. The very large initial slope of $S(T)$ for the cerium compounds in region II is a direct consequence of the DOS at the Fermi level for $T < T_K$ originating from the hybridization of the cerium 4f electrons and the conduction electrons mediated by the Kondo interaction.

According to the theory of Kawakami *et al.* (1987) for the Kondo interaction of dilute cerium impurity systems, the initial slope of S and γ exhibit the same enhancement factor at low temperatures. It has been demonstrated that the initial slope of S originates from the asymmetry of the conduction electron state density at the Fermi energy but may also depend on additional interactions of the conduction electron system.

In region III the cerium compounds are so-called Kondo antiferromagnets showing both the Kondo effect and a long-range antiferromagnetic order. Only a few systems are known with a ferromagnetic ground state.

The $S(T)$ curves of CePdSn and CePtSn are given as examples of Kondo antiferromagnets (Sakurai *et al.* 1996). Both compounds show antiferromagnetic order below 7 K, and are characterized by a Kondo resistivity behavior. The $S(T)$ curves of the two compounds shown in Fig. 5 have maximums around 100 K and minimums at around 20 K. The positive peaks are ascribed to the Kondo effect in the presence of the CEF splitting of the ground state multiplet level of the cerium 4f electron, similarly to the positive peaks for CeCu$_6$ and CePtIn.

The narrow minimums at low temperatures are characteristic of cerium compounds in region III. The position of the minimums is typically two or three times larger than the ordering temperature, T_N, and hence can be taken as an experimental
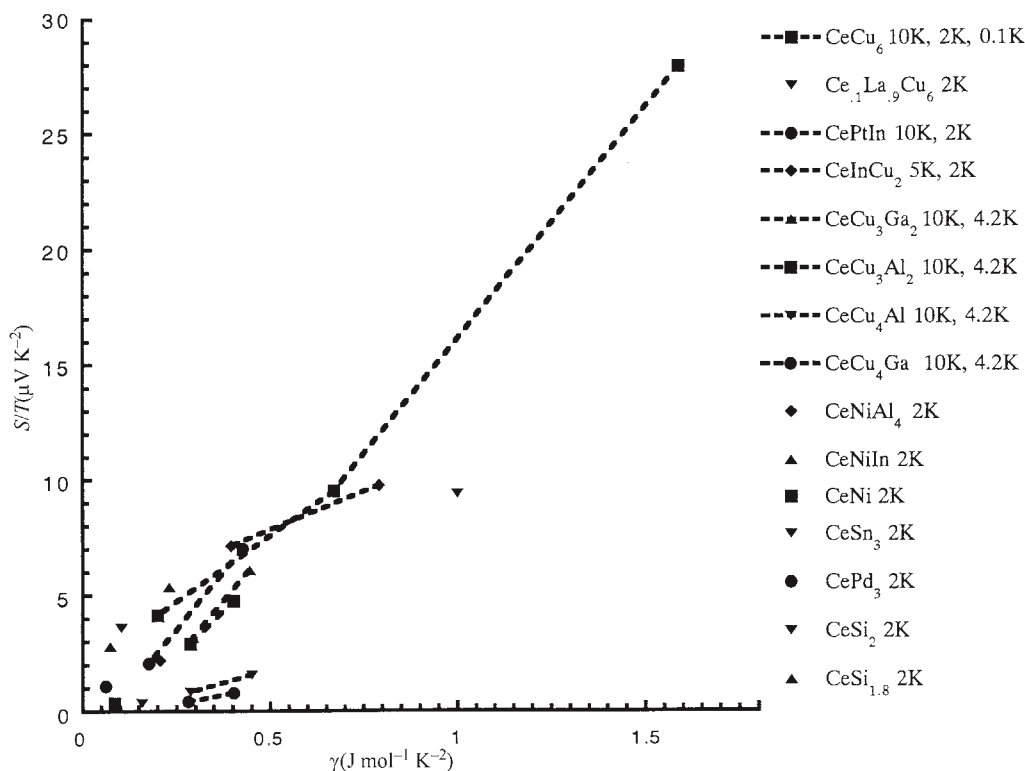
Figure 4
Initial slope of the thermoelectric power S/T at $T = 0$ plotted as a function of the electronic specific heat coefficient, γ, for several heavy fermion and intermediate valence compounds (see text for details).

indication of the onset of short-range antiferromagnetic correlations.

According to Fischer (1989), a resonance term in S appears for cerium compounds having strong magnetic correlations between the cerium moments. This term gives rise to a negative $S(T)$ contribution centered around $T^* = \Gamma/k_B$, where Γ is the half width of the quasi-elastic peak deduced by inelastic neutron scattering, which is a measure of the correlation between the cerium moments. Thus, it is concluded that the resonance term of S proposed by Fischer (1989) gives a theoretical explanation of the minimums in S vs. T, which seems to originate from the onset of short-range antiferromagnetic correlations. S vs. T curves similar to those shown in Fig. 5 have been observed in many Kondo antiferromagnets, e.g., in $CeAl_2$, $CePb_3$, $CeCu_2$, $CePtGa$, $CePtGe$, $CeCu_2Ge_2$, $CePd_2Si_2$, and many others (Sakurai *et al.* 1996).

Various cerium compounds belonging to region II show $S(T)$ behavior typical for systems of region III. Examples are $CeAl_3$ (Jaccard and Flouquet 1987), $CeCu_2Si_2$ (Jaccard *et al.* 1985), and $CeRu_2Si_2$ (Amato *et al.* 1988). These compounds are characterized by a very large enhancement of γ with no long-range

antiferromagnetic order. In spite of the absence of long-range magnetic order in $CeRu_2Si_2$, the existence of short-range magnetic correlation has been verified by neutron scattering experiments (Regnault *et al.* 1988). The minimum in the S vs. T curve for this compound is observed along the *c*-axis but not along the *a*-axis.

The transition of the $S(T)$ behavior from one region to another is sometimes clear and well defined. A striking evolution of $S(T)$ emerges from high-pressure studies of S vs. T. The deep minimum in $S(T)$ for $CeCu_2Si_2$ centered around $20\,K$ at zero pressure vanishes rapidly with pressure and the $S(T)$ curve shows positive values with a steep initial slope at higher pressures (Jaccard *et al.* 1985). The application of pressure (and hence a decrease of the interatomic distance) increases the hybridization between the cerium $4f$ band states and the conduction band states, and thus a change takes place from region III into region II.

Similar changes of the $S(T)$ behavior follow also from chemical pressure, realized by alloying a compound with an isomorphous one having a slightly smaller or larger unit cell volume. The $S(T)$ behavior
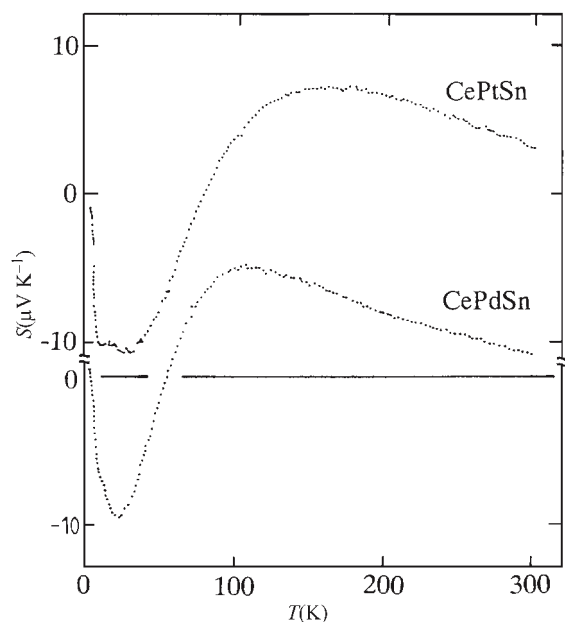
Figure 5
S of two antiferromagnetic Kondo compounds CePdSn and CePtSn plotted as a function of temperature.

Figure 6
S of an antiferromagnetic compound $CePd_2Sn_2$ having no Kondo character and its nonmagnetic counterpart $LaPd_2Sn_2$ plotted as a function of temperature, T.

of $CePb_3$ belonging to region III changes in the pseudobinary system $Ce(Pb_{1-x}Sn_x)_3$ towards region II (Sakurai *et al.* 1996), and with further addition of tin, into region I. A similar change of the S behavior from region III to region II has also been reported for $Ce(Cu_{1-x}Al_x)_5$ and $Ce(Cu_{1-x}Ga_x)_5$ (Bauer 1991). In contrast, a reverse change of the S behavior from region II to region III has been reported for $Ce(Cu_{1-x}Au_x)_6$ (Bauer 1991), owing to the negative chemical pressure produced by the gold substitution.

Typical features of regions II and III frequently coexist. The measurement of $S(T)$ for CePdSn has been carried out down to $0.3\,K$ (Huo *et al.* 1999). According to this experiment, a second positive peak of $S(T)$ at around $1\,K$ is found, in addition to the positive and negative peaks shown in Fig. 4. The appearance of this peak may be associated with a weak enhancement of γ of the compound occurring along with antiferromagnetic order.

Finally, Fig. 6 shows the $S(T)$ curve of $CePd_2Sn_2$ (Sakurai *et al.* 1996) as an example of cerium compounds in region IV. The compound has a T_N value of $0.5\,K$, and no Kondo behavior is observed in its resistivity. The $S(T)$ curve is smooth and corresponds to small absolute value. It resembles that of the nonmagnetic counterpart $LaPd_2Sn_2$. Thus, the cerium $4f$ electrons in the compound are in well-localized states without significant hybridization with the conduction band states. Similar $S(T)$ curves have been reported for $CeMg_3$ (Sakurai *et al.* 1996).

The thermoelectric power, S, is surely a property that reflects very sensitively the various natures of the hybridization between cerium $4f$ electron states and conduction electron states, and it has been demonstrated that each of the four regions of the diagram of Doniach (1977) for the cerium compounds has a very different and characteristic behavior of the $S(T)$ curve. However, as discussed above, the boundaries between different regions are not always strictly defined and may well be changed by applying pressure or by alloying.

Moreover, four temperature parameters, T_K, T_N, T^*, and Γ, have been used to discuss the S behavior, while the parameters of Doniach's diagram are only the first two. Thus, the descriptions given above are for the purpose of a general qualitative overview, and it is known that many exceptional cases exist.

See also: Magnetic Fields: Thermoelectric Power

Bibliography

Amato A, Jaccard D, Sierro J, Lapierre F, Haen P, Lejay P, Flouquet J 1988 Thermopower and magneto-thermopower of $CeRu_2Si_2$ single crystals. *J. Magn. Magn. Mater.* **76/77**, 263–4
Bhattacharjee A K, Coqblin B 1976 Thermoelectric power of compounds with cerium: influence of the crystalline field on the Kondo effect. *Phys. Rev. B* **13**, 3441–51
Bauer E 1991 Anomalous properties of Ce–Cu- and Yb–Cu-based compounds. *Adv. Phys.* **40**, 417–537
Doniach S 1977 The Kondo lattice and weak antiferromagnetism. *Physica B* **91**, 231–4
Fischer K H 1989 Thermoelectric power of heavy-fermion compounds. *Z. Phys. B* **76**, 314–26

Fujii H, Uwatoko Y, Akayama M, Satoh K, Maeno Y, Fujita T, Sakurai J, Kamimura H, Okamoto T 1987 Magnetic and transport properties of new Kondo compounds CeTIn (T, Ni, Pd and Pt). *Jpn. J. Appl. Phys. Suppl.* **26-3**, 549–50

Huo D X, Mori K, Kuwai T, Kondo H, Isikawa Y, Sakurai J 1999 RKKY interaction and Kondo effect in (Ce,La)PdSn. *J. Phys. Soc. Jpn.* **68**, 3377–82

Jaccard D, Flouquet J 1987 Transport properties of heavy fermion systems. *Helv. Phys. Acta* **60**, 108–21

Jaccard D, Mignot J M, Bellarbi B, Benoit A, Braun H F, Sierro J 1985 High pressure transport coefficients of the heavy-fermion superconductor CeCu$_2$Si$_2$. *J. Magn. Magn. Mater.* **47/48**, 23–9

Kashiba S I, Maekawa S, Tachiki M, Takahashi S 1986 Effect of crystal field on Kondo resistivity in Ce compounds. *J. Phys. Soc. Jpn.* **55**, 1341–9

Kawakami N, Usuki T, Okiji A 1987 Thermoelectric power of the Anderson model at low temperature. *J. Phys. Soc. Jpn.* **56**, 1539–45

Onuki Y, Komatsubara T 1987 Heavy fermion state in CeCu$_6$. *J. Magn. Magn. Mater.* **63/64**, 281–8

Regnault L P, Erkelens W A C, Rossat-Mignot J, Lejay P, Flouquet J 1988 Neutron scattering study of the heavy-fermion compound CeRu$_2$Si$_2$. *Phys. Rev. B* **38**, 4481–7

Sakurai J 1993 Several aspects on thermopower of Ce compounds. In: Oomi G, Fujii H, Fujita T (eds.) *Transport and Thermal Properties of f-Electron Systems.* Plenum, New York, pp. 165–73

Sakurai J, Takagi H, Taniguchi S, Kuwai T, Isikawa Y, Tholence J L 1996 Transport properties of CeNi$_2$Sn$_2$ and CePd$_2$Sn$_2$: thermoelectric behaviour of Kondo antiferromagnetic compounds. *J. Phys. Soc. Jpn.* **65** (Suppl. B), 49–56

Sato H, Zhao J, Pratt W P Jr, Onuki Y, Komatsubara T 1987 The transport properties of heavy-fermion compound CeCu$_6$ down to 14 mK. *Phys. Rev. B* **36**, 8841–4

Ziman J M 1960 *Electrons and Phonons.* Oxford University Press, Oxford

J. Sakurai
Toyama University, Japan

Rare Earth Magnets: Materials

Rare-earth permanent magnets (RPMS) are based on intermetallic compounds of rare-earth metals (R) and the transition metals iron or cobalt. The auspicious combination of properties of the rare-earth sublattice and the 3d sublattice lead to the spectacular development in hard magnetic materials: the former providing the high magnetic anisotropy, the latter the high Curie temperature and magnetization. The two most relevant classes of RPMs in application are based on (i) samarium and cobalt which exhibit very high coercivities and low temperature coefficients, and (ii) neodymium, iron, and boron which are un-rivalled in terms of its maximum energy product.

In the present article a brief review will be given of these two compounds, but also of the other recently discovered hard magnetic iron-rich compounds such as ThMn$_{12}$-type compounds and the interstitial solid solutions of nitrogen and carbon in R$_2$Fe$_{17}$-type compounds. The most relevant intrinsic magnetic properties and micromagnetic parameters (for definition see *Hard Magnetic Materials, Basic Principles of*) of these compounds are listed in Table 1. Summaries of novel developments in manufacturing routes, with special emphasis on nanostructured magnets, will be given in the following sections.

The development of NdFeB-type alloys as starting materials for permanent magnets was triggered by both Sumitomo Special Metals (using the powder metallurgical route, Sagawa *et al.* 1984) and General Motors (employing the rapid quenching method, Croat *et al.* 1984). The usefulness of the tetragonal Nd$_2$Fe$_{14}$B-type compounds (see Fig. 1) led to numerous detailed investigations of the Nd–Fe–B system. Three stable ternary phases can be found: Nd$_2$Fe$_{14}$B (Φ), Nd$_{1+\varepsilon}$Fe$_4$B$_4$ (η), and Nd$_5$Fe$_2$B$_6$ (ρ). An instructive presentation of the ternary Nd–Fe–B system with low boron concentrations is given in the liquidus projection shown in Fig. 2, which marks the binary phases, ternary phases, and the important reactions (elucidated in the caption). The Φ phase is located in a region where γ-Fe is the primary solidification product.

The peritectic formation of the Φ phase at 1180 °C will be incomplete in a standard casting process as residues of primary Fe dendrites are left in the Φ grains, the latter in turn being surrounded by neodymium-rich liquid which will solidify at its eutectic temperature of 630 °C. The presence of the iron crystals is detrimental to the magnet's performance. This has important consequences for the manufacturing of this class of magnets. The analogous PrFeB-based compounds are of particular relevance for hot-deformed magnets and low-temperature applications as they show no spin reorientation down to 4.2 K (which occurs at 135 K for Nd$_2$Fe$_{14}$B), but have also been used more recently for melt-spun and HDDR (see *Magnets: HDDR Processed*) materials.

The intrinsic magnetic properties of the related Nd$_2$Fe$_{14}$C are very similar to those of the corresponding borides: the magnetocrystalline anisotropy is slightly higher and the Curie temperature and magnetization slightly lower (see Table 1). The formation of the R$_2$Fe$_{14}$C compound proceeds via a peritectoid reaction from the R$_2$Fe$_{17}$C$_2$ and RFeC phases. This solid-state transformation temperature can be increased very effectively with small boron substitutions for carbon (Eisses *et al.* 1991) and a better control of the microstructure ("ingot magnets") compared to the NdFeB system is possible.

Unlike the Nd$_2$Fe$_{14}$B phase, the hexagonal SmCo$_5$ compound (Strnat *et al.* 1967) with the CaCu$_5$ structure shows a relatively large homogeneity region in the Sm–Co phase diagram (Cataldo *et al.* 1996) as shown in Fig. 3. This region, however, becomes asymmetric when approaching the peritectic melting

Table 1

Structure type, intrinsic magnetic properties (Curie temperature T_C, anisotropy field $H_A = (2K_1 + 4K_2)/\mu_0 M_S$, anisotropy constant K_1, saturation magnetization M_S, upper limit of energy density $(BH)_{max} = \mu_0 M_s^2/4$), domain wall width δ_w, and critical single-domain particle size d_c of important permanent magnet compounds and for comparison α-Fe and $F_{23}B_6$ (note: cubic structure) as well as Fe_3B (in-plane anisotropy).

Compound	Structure type	T_C (K)	$\mu_0 H_A$ (T)	K_1 (MJ m^{-3})	$\mu_0 M_S$ (T)	$\mu_0 M_S^2/4$ (kJ m^{-3})	δ_w (nm)	d_c (μm)
$Nd_2Fe_{14}B$	Tetragonal $Nd_2Fe_{14}B$	585	6.7	5	1.60	516	4.2	0.3
$Pr_2Fe_{14}B$	$Nd_2Fe_{14}B$	565	8.7	5	1.56	484	$\sim$4	$\sim$0.3
$Nd_2Fe_{14}C$	$Nd_2Fe_{14}B$	532	9.5		1.41	396	$\sim$4	$\sim$0.3
$SmCo_5$	Hexagonal $CaCu_5$	993	40	17	1.05	219	3.7	1.7
Sm_2Co_{17}	Rhombohedral 1 Th_2Zn_{17}	1100	6.5	3.3	1.30	336	8.6	0.5
$Sm_2Fe_{17}N_3$	Th_2Zn_{17}	749	21	8.8	1.54	472	3.6	0.4
$Sm_2Fe_{17}C_3$	Th_2Zn_{17}	668	16	7.4	1.45	418		$\sim$0.3
$Sm_3Fe_{26.7}V_{2.3}N_4$	Monoclinic $Nd_3(Fe,V)_{29}$	683	12		1.33	352		$\sim$0.3
$(Sm_{0.75}Zr_{0.25})(Fe_{0.7}Co_{0.3})_{10}N_x$	Hexagonal $TbCu_7$	877	7.7		1.7	575		$\sim$0.3
$NdFe_{10}V_2N_y$	Tetragonal $ThMn_{12}$	743	10		1.11	245		$\sim$0.3
$Sm(Fe_{11}Ti)$	$ThMn_{12}$	584	10.5	4.8	1.14	259	4.0	0.4
α-Fe	b.c.c.	1043		0.046	2.16	928	30	0.007
$Fe_{23}B_6$	Cubic	698		0.01	1.7			
Fe_3B	Tetragonal	786	$\sim$0.4	-0.32	1.62		20	

Nd Fe B

4f **4g** 4e 4c 8j$_1$ 8j$_2$ 16k$_1$ 16k$_2$ 4f
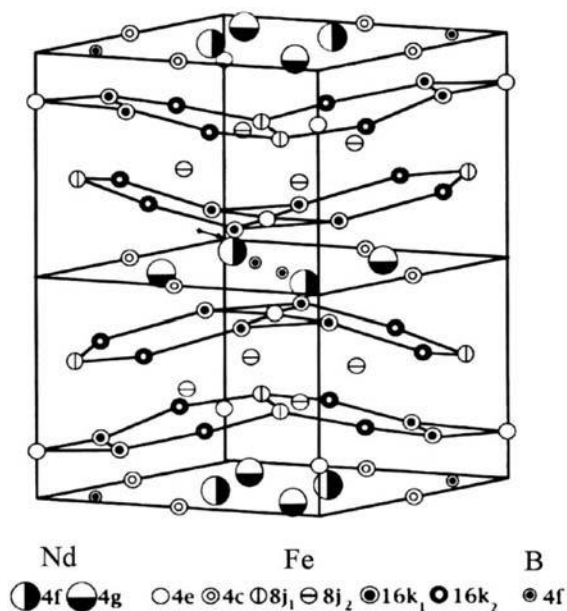
Figure 1
The tetragonal $Nd_2Fe_{14}B$ structure (after Coey 1996).

temperature of 1292 °C. $SmCo_5$ magnets obtained by liquid-phase sintering are characterized by their high Curie temperatures and coercivities.

Commercially produced Sm–Co-type sintered magnets based on the 2:17 phase have usually a composition close to $Sm(Co, Fe, Cu, Zr)_{7.5}$. The most outstanding properties of this class of magnets are their very high Curie temperature and the low temperature coefficients of remanence and coercivity at elevated temperatures (recently up to 500 °C) in addition to their excellent corrosion characteristics. A major drawback is the use of costly Co metal. The homogeneity region of the 2:17 phase narrows with decreasing temperature and a fine cellular network of $SmCo_5$ phase precipitates from a single phase metastable precursor on appropriate low-temperature annealing ($\sim$800 °C). The cell interior with a rhombohedral 2:17 (Th_2Zn_{17}-type) structure shows twin boundaries in the basal plane and a so-called *platelet or z phase* rich in zirconium is also observed parallel to the basal plane.

The rhombohedral structure can be derived from the $SmCo_5$ structure by an ordered substitution of a dumb-bell of cobalt atoms for one-third of the samarium atoms. Unlike the $SmCo_5$ and $Nd_2Fe_{14}B$ magnets, which show a nucleation controlled
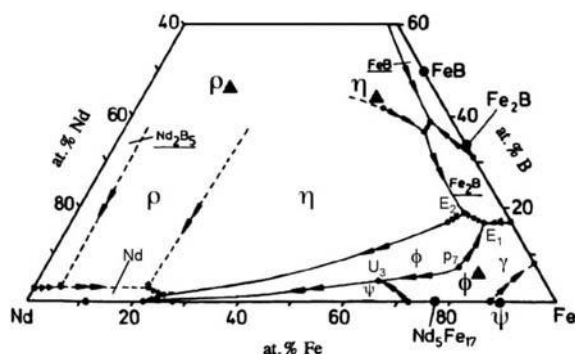
Figure 2
Liquidus projection of the Nd–Fe–B system. Important reactions are p$_7$ (1180 °C: L + γ-Fe $\rightarrow \Phi$), U$_3$ (1130 °C: L + γ-Fe $\rightarrow \Phi$ + ψ(Nd$_2$Fe$_{17}$)), e$_4$ (1115 °C: L $\rightarrow \eta + \Phi$), E$_1$ (1105 °C: L $\rightarrow \Phi$ + + γ-Fe + Fe$_2$B), and E$_2$ (1095 °C: L $\rightarrow \eta + \Phi$ + Fe$_2$B) (after Knoch *et al.* 1994).
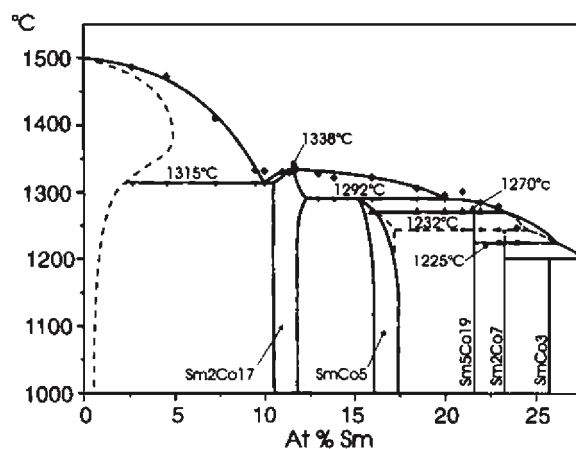
Figure 3
Sm–Co phase diagram (after Cataldo *et al.* 1996).

coercivity mechanism, a pinning controlled mechanism (see *Coercivity Mechanisms*) is dominant for the 2:17-type and the copper and zirconium additions are needed for an effective magnetic precipitation hardening achieved by an elaborated heat treatment. Finally, Fe addition is used in order to increase the remanence. Numerous detailed investigations on, for example, the location of the zirconium atoms in the Th$_2$Zn$_{17}$ structure and the sequence of solid-state transformations on aging have been carried out (see Ray and Liu 1992, Kumar 1988).

Interstitial nitrogen or carbon in rhombohedral R$_2$Fe$_{17}$ (Th$_2$Zn$_{17}$ structure) compounds changes the magnetic properties dramatically because not only the Curie temperature is increased due to the lattice expansion (in the case of nitrogen in Sm$_2$Fe$_{17}$ a 6%

volume expansion and an increase in T_C from 116 °C to 476 °C are observed) but also the crystalline electric field created by the nitrogen or carbon atoms, which occupy the large interstitial 9e sites, changes the magnetocrystalline anisotropy from easy-plane to easy-axis (Coey and Sun 1990). The corresponding R$_2$Fe$_{17}$Z$_x$ (0 $\leqslant x \leqslant$ 3) nitrides and carbides are, in contrast to the binary R$_2$Fe$_{17}$ compounds, promising candidates for permanent magnetic materials. Ternary carbides R$_2$Fe$_{17}$C$_x$ ($x \leqslant$ 1.5) can be prepared by standard casting techniques, higher carbon concentrations can be achieved by either substituting gallium for part of the iron in cast materials or by exposing fine particles of the binary compound to hydrocarbon gases at elevated temperatures (Skomski *et al.* 1995, Fuji and Sun 1995).

Similarly, a simple gas-phase nitrogenation can be carried out at 1 bar nitrogen gas and temperatures of about 400–500 °C. The absorption of nitrogen atoms takes place once the temperature is high enough to overcome the activation energy for the absorption process. This gas–solid reaction consists of adsorption of the gas molecules, their dissociation and subsequent chemisorption of, for example, nitrogen atoms, and long-range diffusion into the metal matrix. A detailed understanding of this irreversible nitrogenation process is necessary in order to optimize the final magnetic properties. It is still a matter of discussion whether in a thermodynamic equilibrium a solid solution or ternary nitrides with fully nitrided and nonnitrided layers are obtained. The relatively slow diffusion of the nitrogen atoms into the matrix makes it necessary to use fine ground particles.

Microcracks and grain boundaries provide fast diffusion paths so that shorter annealing times and lower temperatures can be used. However, the latter remain critical processing parameters as a decomposition in RN and Fe is the preferred reaction from a thermodynamical point of view. Long-range diffusion of metal atoms is required for this reaction and insufficient kinetics make the preparation of ternary nitrides possible despite the metastability of the latter compared to the binary nitride and iron metal. The limited thermal stability of the ternary nitrides restricts the applicability of this class of compounds to metal or polymer bonded magnets. The decomposition temperature can be increased by additions such as silicon or gallium and generally it can be stated that the carbides are superior to the nitrides in terms of their thermal stability. Very small grain sizes are needed for highly coercive powders and the appropriate processing routes have been reviewed by Müller *et al.* (1996).

The tetragonal Fe-rich RFe$_{12-x}$M$_x$ compounds (ThMn$_{12}$ structure) with M = Ti, V, Cr, and Mo, etc., are another family of materials with potential for permanent magnet applications. Their magnetocrystalline anisotropy is once again determined by the superposition of the Fe and R sublattice anisotropies.

The contribution of the Fe sublattice has the same magnitude as in the $Nd_2Fe_{14}B$ compounds and favors the tetragonal c-axis as the magnetically easy direction. But the crystal field-induced R sublattice anisotropy differs in sign and magnitude leaving only samarium as a suitable R element because for the other R elements either the c-axis is not favored or an antiparallel coupling to the Fe sublattice is observed.

$SmFe_{12-x}M_x$, magnetically hardened by melt-spinning or mechanical alloying (see *Magnets: Mechanically Alloyed*) shows high coercivity and Curie temperature but the remanence is somewhat low compared to $Nd_2Fe_{14}B$. Interstitial nitrogen, introduced using analogous procedures as described above, leads to a sign reversal of the R sublattice anisotropy and thus, of the second-order crystal field parameter. The consequence is that now the samarium-based compounds show easy-plane and the neodymium-based compounds easy-axis magnetocrystalline anisotropy. Nitrogen charging is limited to one nitrogen atom per formula unit and good results have been obtained for $Nd_{10}Fe_{75}V_{15}N_x$ (Wang *et al.* 1992). For more details the reader is referred to reviews by Buschow (1991, 1997) and Fuji and Sun (1995).

The monoclinic structure of the $R_3(Fe,M)_{29}$-type compounds can be described as alternating stack of 1:12 and 2:17 units which also present modifications of the $CaCu_5$ structure (e.g., Yang *et al.* 1994). Again, an enhancement of the Curie temperature, saturation magnetization, and a change to easy-axis magnetocrystalline anisotropy is observed upon nitrogenation. In terms of practical use the $Sm_3(Fe,V)_{29}N_4$ material appears to be most promising, having an anisotropy field and Curie temperature higher than $Nd_2Fe_{14}B$ and a slightly lower saturation at room temperature (Hu *et al.* 1996).

Finally, the interesting group of materials with the hexagonal $TbCu_7$-type structure (derived from the Th_2Zn_{17} structure but without long-range ordering) is worth mentioning. These metastable compounds can be prepared by nonequilibrium processing and it has been reported that, for example, zirconium substitution for the rare-earth atom facilitates the formation of this structure and the hard magnetic properties are dramatically improved upon nitrogenation (e.g., $(Sm_{0.75}Zr_{0.25})(Fe_{0.7}Co_{0.3})_{10}N_x$, Sakurada *et al.* 1996).

In the twentieth century, the $(BH)_{max}$ doubled approximately every 12 years (see *Hard Magnetic Materials, Basic Principles of*). Nowadays about 90% of the limit for the energy density $(BH)_{max}$ (based on the $Nd_2Fe_{14}B$ phase) can be achieved in commercially produced sintered Nd–Fe–B grades (see *Magnets: Sintered*). At the end of 2000, however, it appeared that the search for novel hard magnetic compounds, helped by a basic understanding of the crystal field parameters, had somewhat stagnated and no further breakthrough is in sight. On the other hand, only a small number of ternary and quaternary systems has been investigated so far.

See also: Ferrite Magnets: Improved Performance; Magnetic Films: Hard

Bibliography

Buschow K H J 1991 Permanent magnet materials based on tetragonal rare earth compounds of the type $RFe_{12-x}M_x$. *J. Magn. Magn. Mater.* **100**, 79–89

Buschow K H J 1997 *Handbook of Magnetic Materials*. Elsevier, Amsterdam, Vol. 10, Chap. 4

Cataldo L, Lefevre A, Ducret F, Cohen-Adat M Th, Allibert C H, Valignat N 1996 Binary system Sm–Co: revision of the phase diagram in the Co rich field. *J. Alloys Comp.* **241**, 216–23

Coey J M D 1996 *Rare Earth Iron Permanent Magnets*. Clarendon, Oxford, UK

Coey J M D, Sun H 1990 Improved magnetic properties by treatment of iron-based rare earth intermetallic compounds in ammonia. *J. Magn. Magn. Mater.* **87**, L251–4

Croat J J, Herbst J F, Lee R W, Pinkerton F E 1984 Pr–Fe and Nd–Fe-based materials: A new class of high-performance permanent magnets. *J. Appl. Phys.* **55**, 2078–82

Eisses J, de Mooij D B, Buschow K H J, Martinek G 1991 Towards an easy production route for isotropic rare earth based permanent magnets. *J. Less-Common Met.* **171**, 17–25

Fuji H, Sun H 1995 *Handbook of Magnetic Materials*. Elsevier, Amsterdam, Vol. 9, Chap. 3

Hu Z, Yelon W B, Kaogirou O, Psycharis V 1996 Site occupancy and lattice changes on nitrogenation in $Nd_3Fe_{29-x}Ti_xN_y$. *J. Appl. Phys.* **80**, 2955–9

Knoch K G, Reinsch R, Petzow G 1994 The Nd–Fe–B phase diagram and the primary solidification of $Nd_2Fe_{14}B$. In: Harris I R, *et al.* (eds.) *Proc. 13th Int. Workshop on RE Magnets and their Applications*. Birmingham, UK, pp. 503–10

Kumar K 1988 $RETM_5$ and RE_2TM_{17} permanent magnets development. *J. Appl. Phys.* **63**, R13–57

Müller K H, Cao L, Dempsey N M, Wendhausen P A P 1996 Sm_2Fe_{17} interstitial magnets. *J. Appl. Phys.* **79**, 5045–50

Ray A E, Liu S 1992 Recent progress in 2:17 type permanent magnets. In: *Proc. 12th Int. Workshop on RE Magnets and their Applications*. University of Western Australia, Canberra, Australia, pp. 552–73

Sagawa M, Fujimori S, Togawa M, Matsuura Y 1984 New material for permanent magnets on a base of Nd and Fe. *J. Appl. Phys.* **55**, 2083–7

Sakurada S, Tsutai A, Hirai T, Yanagida Y, Sahashi M, Abe S, Kaneko T 1996 Structural and magnetic properties of rapidly quenched (R, Zr)(Fe, Co)$_{10}N_x$ (R = Nd, Sm). *J. Appl. Phys.* **79**, 4611–3

Skomski R, Brennan S, Wirth S 1995 *Interstitial Metallic Alloys*. NATO-ASI Series E, Vol. 281, Chap. 16

Strnat K, Hoffer G, Olson J, Ostertag W, Becker J J 1967 A family of new cobalt-base permanent magnetic materials. *J. Appl. Phys.* **38**, 1001–2

Wang Y Z, Hadjipanayis G C, Kim A, Sellmyer D J, Yelon W B 1992 Structure and magnetic properties of $RFe_{10}V_2N_x$ compounds. *J. Magn. Magn. Mater.* **104–107**, 1132–4

Yang F-M, Nasunjilegal B, Wang J-L, Pan H-Y, Qing W-D, Hu B-P, Wang Y-Z, Liu G-C, Li H-S, Cadogan J M 1994 Magnetic properties of a novel $Sm_3(Fe,Ti)_{29}N_y$ nitride. *J. Appl. Phys.* **76**, 1971–3

O. Gutfleisch
IFW Dresden, Germany

S

Single-molecule Magnets

Molecular objects containing a large, but finite, number of magnetic centers whose magnetization relaxes slowly at low temperature are commonly called single-molecule magnets (SMMs) (Aromi *et al.* 1998). In a sense this is a misnomer, because the term magnet must rigorously apply only to systems in which the spin correlation length diverges, i.e., goes to infinity, and this is clearly not possible in a cluster with a finite size. However, the term is evocative, and it can be used, provided its true meaning is understood.

The first compound to show SMM behavior (Sessoli *et al.* 1993) was $[Mn_{12}O_{12}(CH_3COO)_{16}(H_2O)_4]$. $4H_2O$ (Mn12Ac), which has a ground $S = 10$ state and a large Ising-type anisotropy. The barrier for the reorientation of the magnetization is $\sim 65K$, as shown in Fig. 1. The discrete levels in the potential wells are a clear indication of the quantum nature of the system. Classically the reorientation of the magnetization can occur by overcoming the barrier, and indeed below 15K the relaxation time of the magnetization becomes very long: at 1.5K it is 40 years. Therefore, Mn12Ac behaves like a bulk magnet and shows magnetic hysteresis as shown in Fig. 2. At zero field the magnetization may be either positive or negative, depending on the history of the sample.

Therefore, the SMM is bistable, and in principle it becomes possible to store information in one single molecule. Further, the hysteresis shows quantum effects (Friedman *et al.* 1996, Thomas *et al.* 1996) associated with the small size of the molecule. In fact the magnetization of a quantum object can reorient itself also by tunneling below the barrier. Evidence
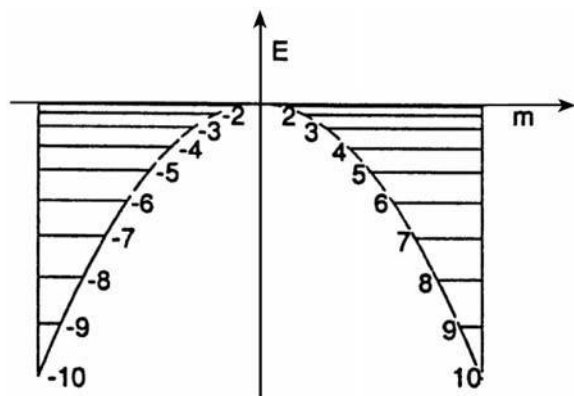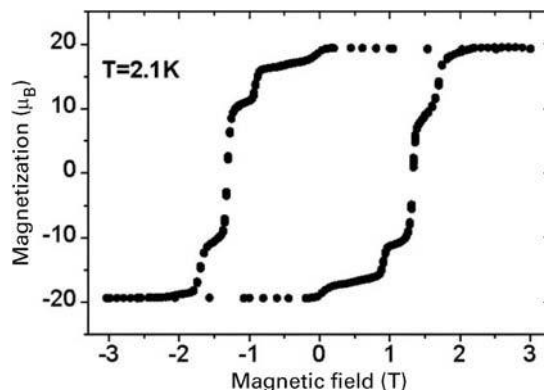
Figure 2
Magnetic hysteresis of a single crystal of Mn12Ac at 2.1K. The magnetic field is parallel to the tetragonal axis of the cluster.

for this behavior is provided by the hysteresis loop of Fig. 2. In fact the flat regions in the hysteresis curve correspond to slow relaxation of the magnetization while the steps correspond to comparatively faster relaxation. The steps occur at $H_i = 0.4$ T, where $i = 0,1,\ldots$. At zero field, pairs of $\pm M$ levels, as depicted in Fig. 1, have the same energy: under these conditions tunneling is possible, and the relaxation time of the magnetization becomes comparatively fast. When a field is applied the levels change their energies and the degeneracy is lost, quenching the tunneling and lengthening the relaxation time. Since some of the levels increase their energies, and others decrease, at some given field pairs of levels will again become degenerate, allowing tunneling and shortening the relaxation time. The fields at which the crossings occur can be calculated once the energies of the levels are known in zero field, and they compare very well with the H_i fields defined above.

The tunneling mechanism described above is a thermally activated one, in the sense that it does not occur within the lowest $M = \pm 10$ levels, but between higher M levels which are thermally populated. In order to observe tunneling a transverse field is needed, which effectively couples the pairs of resonating levels. Mn12Ac has crystal-imposed tetragonal symmetry; therefore only hexadecupolar transverse anisotropy is allowed. Therefore, it is very small and the tunneling process is rather inefficient. In fact at low temperature, where only the lowest $M = \pm 10$ levels are thermally populated, no unambiguous evidence of direct tunneling is found and the relaxation time is very long. Matters have been found to be different in another cluster characterized by an $S = 10$

Figure 1
Energy levels and anisotropy barrier of the ground $S = 10$ state of Mn12Ac. The levels are labeled by the M component of the total spin S ($-M \leqslant S \leqslant M$).

ground state, $[Fe_8(tacn)_6O_2(OH)_{12}]Br_8$ (Fe8). Like Mn12Ac, the cluster also has Ising-type anisotropy, but with a non-negligible transverse quadrupolar anisotropy (Barra *et al.* 1996). The barrier is smaller than in Mn12Ac, $\sim 25K$, and the relaxation times are shorter. Below 300mK the relaxation time of the magnetization becomes independent of temperature showing that the pure tunneling regime is achieved for this system (Sangregorio *et al.* 1997).

The detailed mechanism of tunneling is still a matter of debate, but magnetic nuclei, through the so-called hyperfine interaction, are expected to play an important role. Experiments in which the nonmagnetic nuclei of iron are substituted by the magnetic ^{57}Fe, $I = 1/2$, show that the relaxation rate of the magnetization increases in the quantum regime, confirming that the magnetic nuclei are needed to assist the tunneling. A further confirmation came from a partially deuterated sample in which the relaxation time became longer, in agreement with the lower magnetism of deuterons compared to protons.

The main advantages of SMMs compared with other types of magnetic nanoparticles is that they are absolutely monodisperse, all identical to each other, perfectly known from crystal structure data, and their properties can be fine-tuned through the techniques of molecular chemistry. They have allowed for the first time the observation of quantum phenomena in mesoscopic matter that had been long looked for but had not been unambiguously proved experimentally. Beyond the quantum tunneling effects described above these systems have provided for the first time a confirmation of the Berry phase in magnets (Wernsdorfer and Sessoli 1999). This effect, which is similar to the Aharonov–Bohm effect in conductors, had been suggested to be operative in magnets (Garg 1998) but could not be confirmed until Fe8 became available. Therefore, SMMs can indeed provide a rich new physics, at the border between quantum and classical approaches.

In perspective, SMMs might be considered for applications in memory storage. Further, if the conditions for observing quantum coherence are met, they might be used for hardware for quantum computers. The other developments to be expected are the synthesis of larger clusters, which will be investigated for a large number of different properties, which can make them appealing for biocompatibility (for magnetic resonance imaging contrast agents, for instance, or for magnetic drug delivery).

The conditions for obtaining more efficient SMMs, i.e., systems operating at higher temperatures, are reasonably well understood. It is necessary to have molecules with S values as high as possible in the ground state, with a high Ising-type magnetic anisotropy. In order to reach this goal it would be preferable to assemble individual magnetic centers with a large spin, like iron(III) or manganese(II) ($S = 5/2$), and manganese(III) or iron(II) ($S = 2$). In order to

have high magnetic anisotropy it is useful to start from anisotropic centers. This can be achieved, for instance, by using Jahn–Teller distorted ions like manganese(III). Many attempts are being made to synthesize larger clusters that match these requirements. Some success has been achieved, not only by making obvious chemical variations on the Mn12Ac and Fe8 molecules, but also looking for new systems. This has been achieved using other metal ions, like nickel(II), chromium(III), and vanadium(III). It must be stressed that, although it may be easier to reach high-spin states starting from individual large spins, organic approaches can also be used. Several high-spin molecules have been obtained in this way, though with small anisotropy. However, if efficient strategies are developed for synthesizing large polymers, then the organic approach might turn out to be rewarding.

Bibliography

Aromi G, Aubin S M J, Bolcar M A, Christou G, Eppley H J, Folting K, Hendrickson D N, Huffman J C, Squire R C, Tsai H L 1998 Manganese carboxylate clusters: from structural aesthetics to single-molecule magnets. *Polyhedron* **17**, 3005–20

Barra A L, Debrunner P, Gatteschi D, Schulz Ch E, Sessoli R 1996 Superparamagnetic-like behavior in an octanuclear iron cluster. *Europhys. Lett.* **35**, 133–8

Friedman J R, Sarachik M P, Tejada J, Ziolo R 1996 Macroscopic measurement of resonant magnetization tunneling in high-spin molecules. *Phys. Rev. Lett.* **76**, 3830–3

Garg A 1998 Lattice distortion mediated paramagnetic relaxation in high-spin high-symmetry molecular magnets. *Phys. Rev. Lett.* **81**, 1513–6

Sangregorio C, Ohm T, Paulsen C, Sessoli R, Gatteschi D 1997 Quantum tunneling of the magnetization in an iron cluster nanomagnet. *Phys. Rev. Lett.* **78**, 4645–8

Sessoli R, Gatteschi D, Caneschi A, Novak M A 1993 Magnetic bistability in a metal-ion cluster. *Nature (London)* **365**, 141–3

Thomas L, Lionti F, Ballou R, Gatteschi D, Sessoli R, Barbara B 1996 Macroscopic quantum tunneling of magnetization in a single crystal of nanomagnets. *Nature (London)* **383**, 145–7

Wernsdorfer W, Sessoli R 1999 Quantum phase interference and parity effects in magnetic molecular clusters. *Science* **284**, 133–5

D. Gatteschi
University of Florence, Italy

Solids, Nuclear Magnetic Resonance of

The nuclear magnetic resonance (NMR) phenomenon was discovered in the mid-twentieth century. At about the same time, two different research groups showed that when samples were placed in a strong, homogeneous magnetic (applied) field, the sample could absorb and emit radiofrequency (RF) energy (Purcell *et al.* 1946, Bloch *et al.* 1947). A solid

material (paraffin) was one of the first samples used in the measurement of nuclear magnetic resonance; however, a wide resonance linewidth prevented any detailed interpretation of the spectra. Researchers quickly realized liquid samples provided substantially improved spectral resolution. With liquid samples and improvements in instrumentation that quickly followed, the chemical shift was discovered, along with the discovery of scalar (spin–spin or "through-bond") coupling. Chemical shifts are small perturbations of the exact resonance frequency of a given nucleus caused by differences in the electronic environment of the individual nuclei. Usually very small, chemical shifts are typically measured in parts per million (ppm) relative to the resonance position of some standard. Magnetic nuclei that share common electrons can couple with each other, giving rise to scalar coupling. This spin–spin coupling gives rise to fine structure (splittings) of the resonances of the nuclei involved. Of course, the discovery of these two NMR perturbations provided chemists with a powerful technique for obtaining structural information on liquid samples. In a short time commercial instrumentation was made available to chemists for the study of liquid or solution samples. Many experiments were developed which exploited chemical shifts and scalar coupling to obtain detailed structural information. NMR of solids was left to a relative few NMR research laboratories.

Work in this area was difficult and slow going, owing to enormous sensitivity and resolution problems caused mainly by two factors. First, magnetic nuclei in solid samples interact with each other through their magnetic dipole moments. This dipolar, through-space interaction can be much stronger than the through-bond, scalar interactions. The strength of the dipolar interaction is proportional to

$$\frac{3\cos^2\theta}{r^3} \tag{1}$$

where θ is the angle between a vector connecting the two interacting nuclei and the applied field, and r is their interatomic distance. Thus, the exact resonance position of any nucleus depends on the position of the neighboring magnetic nuclei relative to the applied field direction. The exact magnetic field experienced by any particular nucleus will vary from molecule to molecule in any sample which is less than a perfect single crystal. These dipole–dipole interactions make it impossible to observe abundant spins (like protons) at high resolution in a solid by conventional NMR techniques. Usually, proton linewidths are broadened so all fine structure is hidden. In liquids however, rapid tumbling quickly averages Eqn. (1) over all possible values of θ, effectively zeroing the dipolar effect.

A second possible source of broadening in solids is another orientation effect and is caused by the elec-

tronic environment of nuclei. Electrons near a nucleus shield it from the applied field causing slight perturbations in the resonance positions. This effect gives rise to the chemical shift, the most important perturbation of the magnetic resonance interaction. Electron density, however, may not be homogeneously distributed about a nucleus. In those cases where the electron density is not homogeneous about a nucleus, there will be an orientation dependence of the shielding. This results in another broadening effect in randomly oriented solids called chemical shift anisotropy (CSA). So, in a solid where the molecules are randomly oriented, chemical shifts (both the isotropic and anisotropic parts) and dipolar interactions with other nuclei cause resonance lines to broaden and overlap. (This broadened spectrum is actually made up of many narrower lines at slightly different chemical shifts due to these orientation effects.) For a more formal discussion of these effects see Yannoni (1982). Pines *et al.* (1973) published their discovery that nuclear magnetization could be transferred from an abundant higher spin, I, to a rare lower spin, S, in solid samples through a technique they called cross-polarization (CP).

An initial $90°$ pulse on the abundant spins is followed immediately by a strong RF field parallel (or antiparallel) to the abundant spin magnetization. This parallel RF field prevents the sample abundant spin magnetization from returning to its equilibrium position and this is called a "spin lock." Magnetization then transfers to the rare spins by simultaneously applying a RF field to these rare spins, which meets the Hartmann–Hahn condition (Hartmann and Hahn 1962):

$$H_I\gamma_I = H_S\gamma_S \tag{2}$$

where γ is the magnetogyric ratio and H is the applied field strength of the spins. In the absence of any relaxation, the magnetization of the rare spins is enhanced by a factor of γ_I/γ_S beyond the magnetization expected for a conventional NMR experiment (a simple $90°$ pulse). During this CP contact time, the rare spin magnetization grows at an exponential rate characterized by the time constant T_{IS} (curve (a) of Fig. 1). Relaxation effects will diminish this enhancement factor. As CP progresses, magnetization is exponentially decaying in a time characterized by $T_{1\rho}$ (curve (b) of Fig. 1). As long as $T_{1\rho} > T_{CP}$, the observed enhancement as a function of CP time, t, is just

$$\frac{\exp\left(-\dfrac{t}{T_{1\rho}}\right) - \exp\left(-\dfrac{t}{T_{CP}}\right)}{1 - \dfrac{T_{CP}}{T_{1\rho}}} \tag{3}$$

(curve (c) of Fig. 1).
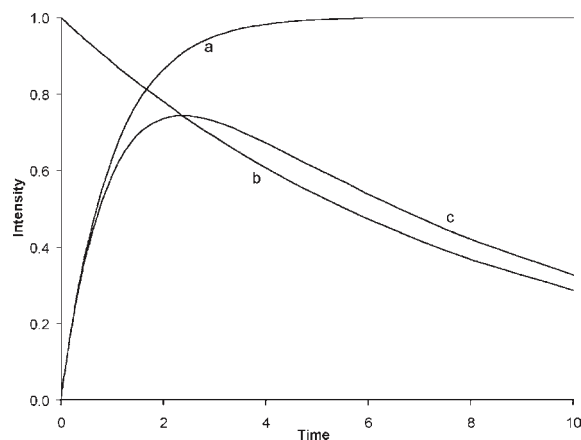
Figure 1
The theoretical CP dynamics are shown. Curve (a) illustrates the expected rare spin magnetization as a function of CP time in the absence of relaxation effects. The single exponential curve is characterized by a time constant, T_{IS}, the CP time. Curve (b) represents spin (either rare or abundant) relaxation. The exponential curve is characterized by a time constant, $T_{1\rho}$, which in this specific example is eight times the CP time constant. Curve (c), which is the expected rare spin magnetization as a function of CP time, is the combination of curves (a) and (b). The time axis is in units of T_{IS} while the enhancement axis is in units of γ_I/γ_S, the theoretical maximum. Notice that for this example, maximum enhancement is achieved at a CP time of about $2.38 \times T_{IS}$ and is about 74% of the theoretical maximum.

As Fig. 2 and Table 1 illustrate, this relaxation effect can have a significant effect on the observed enhancement. It follows from Eqn. (3) that maximum enhancement is at a CP time of

$$\frac{\ln\left(\dfrac{T_{1\rho}}{T_{CP}}\right)}{\dfrac{1}{T_{CP}} - \dfrac{1}{T_{1\rho}}}$$

Besides this potential enhancement in magnetization, and therefore signal strength, CP offers another benefit: the CP process can be repeated after the abundant spin relaxes, irrespective of the state of the rare spin magnetization and/or relaxation rate. Of course, this is because the rare spin magnetization is totally derived from the abundant spins. Pines *et al*. (1973) also showed that a significant improvement in resolution could be achieved by decoupling the abundant spin during the acquisition of the rare spin signal. Schaefer *et al*. (1975) showed that if the CP experiment is performed while the solid sample is spinning
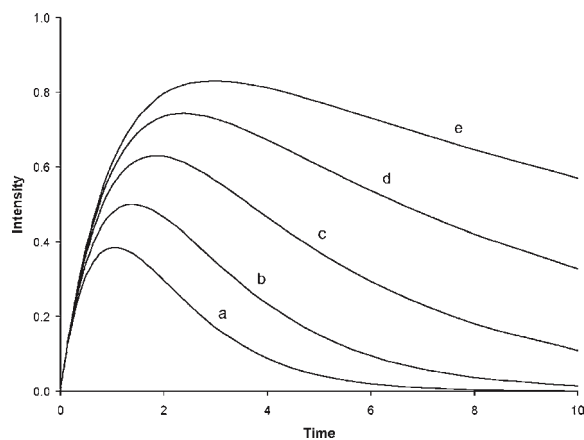
Figure 2
A family of curves showing the CP magnetization as a function of CP time. In each curve T_{IS} is constant and $T_{1\rho}$ is varied. The ratio $T_{1\rho}/T_{IS}$ for each curve is: (a) 1.1, (b) 2.0, (c) 4.0, (d) 8.0, and (e) 16.0. Axis units are as in Fig. 1.

Table 1
The time of occurrence and the value of the maximum enhancement of CP for various values of $T_{1\rho}/T_{IS}$.

$T_{1\rho}/T_{IS}$	t_{max}/T_{IS}	Enhancement[a] (%)
1.1	1.05	38
2.0	1.39	50
4.0	1.85	63
8.0	2.38	74
16.0	2.96	83

a The enhancement is a percentage of the theoretical maximum, γ_I/γ_S.

at a sufficiently high rate (several thousand revolutions per second) at an orientation where Eqn. (1) is zero (magic-angle spinning, MAS), resolution approaching that of liquid samples can be obtained. A sample that is spinning at a rate larger than the CSA causes the CSA of each individual spin to be averaged to the isotropic chemical shift value. If the spinning rate is less than the CSA, spinning sidebands are observed. Figure 3 shows the effect of sample spinning rate on the ^{13}C cross-polarization magic-angle spinning (CPMAS) spectrum of General Electric Lexan (bisphenol A polycarbonate) resin. The top spectrum was obtained at high sample spinning and has minimal spinning sidebands. The bottom spectrum was obtained without sample spinning and shows broad, overlapped resonances. It can be seen from the middle spectrum, obtained at moderate spinning speeds, that the intensities of the spinning sidebands approximately mimic the shape of the nonspinning line shapes.
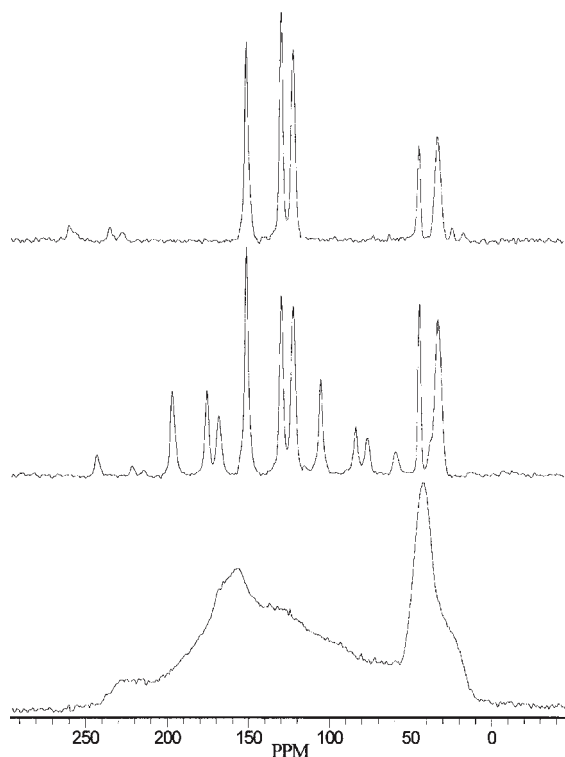
Figure 3
^{13}C CP spectra of a sample of GE Lexan resin are shown spinning at three different rates. All spectra were obtained with a 2.5 ms CP with $\gamma_C H_C = \gamma_H H_H = 55$ kHz. With the sample spinning at 7940 Hz, the top spectrum shows only minor spinning sidebands. For the center spectrum, the sample was spun at 3460 Hz and shows many sidebands. The chemical shift anisotropies of the aromatic resonances at 150–100 ppm are much larger than the aliphatic resonances at 50–20 ppm. The lower spectrum was obtained without spinning, showing overlapping resonances severely broadened by chemical shift anisotropy.

These important discoveries and the work on which they are based provide the foundation for the most popular form of high-resolution solid-state NMR, the CPMAS experiment. Conditions for the high-resolution observation of abundant spins (i.e., protons) were worked out later and combined MAS with multiple pulses during the acquisition of the signal (homonuclear decoupling) and will not be discussed in this article.

1. General Instrumentation

While the requirements for CPMAS NMR are similar to those for liquid NMR, there are several important differences. Superconducting magnets provide stable, high-field, high-homogeneity applied fields for the NMR experiment. In fact, the quality of modern superconducting magnets is such that field/frequency stabilization (NMR lock) is not required. Room temperature access for the CPMAS probe is typically larger than for liquids NMR because of the special geometry and the higher RF power handling requirements, requiring physically larger electronic components. Also, due to the limited resolution of the typical CPMAS spectrum and the bulky and unusual geometry of the probe, room temperature homogeneity shim coils have only a modest impact on spectra quality and have been omitted on some solids-only NMR spectrometers.

RF field strength requirements for CPMAS NMR are typically 1–2 orders of magnitude higher than for liquid NMR resulting in power requirements ranging from almost 100 W to several kilowatts depending on the probe efficiency. The CPMAS probe is the most unique part of a solids NMR spectrometer. Several different designs are commercially available and all share the following features:

• A sample spinning system consisting of a rotor (spinner) made of a high-strength material to hold the sample. Turbine-like impellers are part of the rotor so that it may be spun by pressurized gas flowing over these features.

• A stator (spinner housing) which provides pressurized gas through a bearing surface in which the rotor will spin. The stator is mounted in the probe so that the sample spins at the magic angle (about 54.7°) relative to the applied magnetic field.

• A double-tuned RF coil (usually part of the stator) with suitable tuning circuitry to couple efficiently the high-power transmitters to the coil, resulting in the highest possible RF field strengths.

In addition, the probe may have other features such as spin rate detectors (analog or digital), spin rate controllers, or variable temperature control.

2. Sample Requirements

Spectra of solid samples from a variety of sources can be successfully observed by CPMAS NMR. Obvious choices are crystalline, polycrystalline, and amorphous solids as well as plastics and liquid crystalline materials. Clathrates, inclusion complexes, composites, mixtures, melts, and other compounded materials are also possible. Powdered or granular material is easiest to spin, although anything which fits into the rotor will usually work. Physically large samples need to be reduced in size until particles are smaller than the inner dimensions of the rotor (internal diameters are typically 2–20 mm). Large particles are usually more difficult to spin and sometimes require some signal-free balancing material. With some constraints and care, spectra of highly viscous fluids and gels

(e.g., concentrated biological fluids, solutions and suspensions, and petrophysical fluids) can be run. In cases where spinning might eliminate liquid from the sample, they can be spun in special sealed or lined rotors. Materials that conduct electricity are usually not suitable for MAS. However, in some cases these samples can be spun by diluting the material with an appropriate insulator. In addition, samples which efficiently turn RF energy into heat present special problems. Because of the high RF power levels involved, an extremely low RF duty cycle is used and this usually limits the resolution of the detected signal.

3. Applications

In the simplest CPMAS experiment, chemical shift information of the rare spin nuclei is obtained. Alemany *et al.* (1983a) have shown that for most simple organic compounds, a 2.25 ms CP contact time will result in near-quantitative ^{13}C NMR intensities, making it routine to obtain reliable integration data. Quantitative results are often difficult or impossible to obtain in the case of multiphase compounds. This is especially true for engineered plastics that often are made up of at least two different components that have different physical properties, blended or bonded together to achieve a desirable physical performance.

For example, consider a silicone heat-cured elastomer that is made up of a very-long-chain, low-modulus, lightly cross-linked dimethylsiloxane polymer and a high-modulus fumed silica filler. Chemically, the fumed silica filler is submicrometersized amorphous silicon dioxide particles with the surface of the particles covered with hydroxide groups. The ^{29}Si CPMAS spectrum of a heat-cured elastomer is shown at the top of Fig. 4. The dimethylsiloxane polymer is observed as the sharp resonance at -23.5 ppm. The fumed silica is observed as two broad resonances below -100 ppm. The resonance at -113 ppm is from the amorphous fumed silica and the resonance at -103 ppm is from the surface silicon, directly bonded to the surface hydroxyl groups. Broad peaks at -21.5, -35.8, -57.2, and -66.8 ppm are due to various special methyl siloxanes found on the surface of the fumed silica. The bottom spectrum of Fig. 4 shows what is observed with a simple Bloch-decay experiment, i.e., not using CP. Because the ^{29}Si nuclei relax very slowly, this spectrum was acquired with very long relaxation times between acquisitions. The bottom Bloch-decay experiment more accurately represents the quantitative distribution of silicon in the sample. For this nearly quantitative spectrum, only the dimethylsiloxane polymer and fumed silica peaks are observed. The fumed silica peaks more quantitatively represent the distribution of silicon atoms between
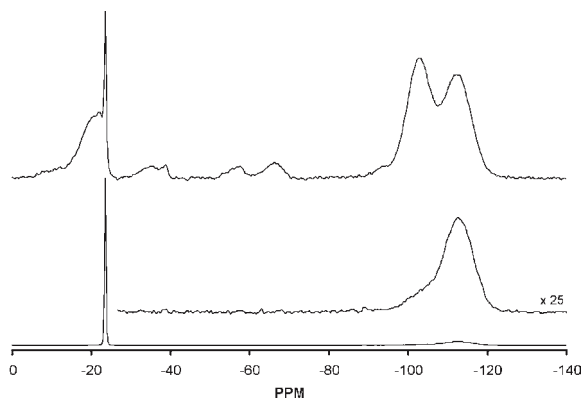
Figure 4
A comparison of ^{29}Si spectra is illustrated with and without CP for a heat-cured elastomer. The top spectrum is the CPMAS spectrum obtained with a 5 ms CP time, acquiring 10^5 scans with a 2 s relaxation time. The bottom spectrum was obtained with a simple ^{29}Si 90° pulse. A 25-fold expansion of the high-field region is shown in the center. As in the CPMAS spectrum, high-powered proton decoupling was applied during the acquisition of the signal and the sample was spun at the magic angle at 7200 Hz. For this Bloch-decay spectrum, 1388 scans were acquired with a 150 s relaxation time. Each spectrum was acquired over several days.

the surface and core of the fumed silica particles, with the surface peak just observable as a shoulder to the dominant core silica resonance. Owing to the limited number of acquisitions for this spectrum, the special surface methyl siloxanes cannot even be observed.

The CP intensity for the silicon in the dimethylsiloxane polymer and the silica particles is not quantitative for different reasons. The polymer undergoes labile motion, interfering with CP from the methyl ^{1}H nuclei to the ^{29}Si nuclei resulting in a very long T_{CP}. Thus, only a very weak signal is observed from the polymer. The silica is immobile owing to the very high molecular weight and the three-dimensional structure of the resin making up the particle and should cross-polarize readily. However, the core silica resonance at -113 ppm cross-polarizes poorly because it does not have any ^{1}H nuclei nearby to provide polarization. It is not possible to obtain a quantitative CPMAS spectrum by lengthening the CP contact time. While a longer CP time would result in a stronger, more quantitative polymer resonance, the relatively short $T_{1\rho}$ of the silica would result in near-zero CP intensity from the silica. These kinds of problems are typically encountered when trying to obtain quantitative CP spectra of multiphase samples. Nonetheless, CPMAS spectra can be quite useful for these kinds of samples. In the case of the heat-cured elastomer illustrated here, the CPMAS

spectrum is very sensitive to the surface of the fumed silica and is a valuable research tool for understanding polymer–filler interactions at or near the filler surface.

While typical CPMAS resolution routinely obtained is still a couple of orders of magnitude poorer than that obtained in liquid NMR, it is usually possible to identify most chemical types of the rare spins. However, it is usually impossible to identify a unique chemical type in the presence of other similar chemical types due to the limited resolution. Successful strategies for the analysis of chemical processes in solids usually involve a comparison of the CPMAS spectra of related materials. For example, researchers have been able to deduce the chemical mechanism of the curing process of urea–formaldehyde (Maciel *et al.* 1983) and phenolic (Bryson *et al.* 1983) resins by comparing ^{13}C CPMAS spectra of resin samples subjected to different curing times. In the case of polymers, crystalline–amorphous morphology may be discernable through an analysis of observed line shapes. A variety of relaxation measurements can be performed in order to obtain information about molecular motion, micro- and macrostructure, and morphology. The abundant spin as well as the rare spin dynamics can be observed through the rare spin magnetization, along with the dynamics of magnetization transfer. Especially sensitive to lower frequency motions, measurement of $T_{1\rho}$ has been useful in the study of macromolecules (Belfiore *et al.* 1983).

Homonuclear decoupling technology has made available special decoupling sequences that selectively disable homonuclear dipole–dipole interactions. Applied to the abundant spins, several new solids techniques were developed. If the abundant spin dipole–dipole interaction is sufficiently weak, application of homonuclear decoupling makes it possible to observe (and use) scalar coupling between the rare and abundant spins. For example, Zilm and Grant (1982) have observed ^{13}C—^{1}H scalar coupling in adamantane and hexamethylbenzene. In another example, Terao *et al.* (1982) have used ^{13}C—^{1}H scalar coupling in camphor to obtain *j*-resolved ^{13}C spectra. While these and other similar results are very interesting, most solid samples do not have the required weak dipole–dipole interaction to allow the scalar coupling to be observed and/or exploited. In another more useful application of homonuclear decoupling, a two-dimensional experiment has been developed in which each rare spin becomes a sensitive probe of its local dipolar environment (Munowitz *et al.* 1981, Schaefer *et al.* 1983). In this experiment, multiple data sets are collected. In each sequential data set an evolving period of homonuclear decoupling is applied to the abundant spins before the detection of the rare spin signal. Projecting the processed data along the evolution axis shows a normal CPMAS spectrum. Slices along the evolution direction show the local dipolar field for each of the resolved nuclei. Because

of Eqn. (1) and because of the rare spin resolution typically achievable, these spectra can be rich in distance and geometry information.

4. Limitations

While CPMAS NMR can approach the resolution of the NMR of liquids, it is typical for a CPMAS spectrum resolution to be limited to several ppm. Amorphous materials and polymers may have a distribution of isotropic chemical shifts for individual carbons due to a variety of carbon environments in the solid matrix. It has been shown that polymers that have undergone severe mechanical stress have broadened CPMAS spectra. VanderHart *et al.* (1981) have published a comprehensive study of resolution limitations of CPMAS NMR. The idea of applying continuous, unmodulated decoupling to the abundant spins during the acquisition of the NMR signal is to remove the dipolar effect of those nuclei, leaving only CSA as a source of broadening. This is difficult to achieve in practice as there is always some nonzero residual dipolar coupling. Bennett *et al.* (1995) described a simple phase modulation of the decoupling RF field that shows significant improvement over unmodulated decoupling.

The CPMAS technique relies upon the premise that equilibrium magnetization of the abundant spins is many times larger than that of the rare spins and those rare spins do not interact with each other. Systems containing rare spins that share a chemical bond present new problems. For example, a sample that contains a high enrichment of ^{13}C will show particularly broad carbon resonances as they interact with one another through their dipolar fields. Another more common situation that can limit resolution is the presence of quadrupolar nuclei. These nuclei orient their quadrupole moments in their molecular environment and can generate a powerful magnetic field along their quadrupole moments. This additional field adds to the applied field and modifies other spin interactions, resulting in line broadening (Naito *et al.* 1981). This effect can be minimized by increasing the applied field strength which decreases the relative contribution of the field generated by the quadrupolar nucleus (Maciel *et al.* 1983). Of course, this solution is not always available if no higher field NMR spectrometer with solid-sample capability is accessible. Even if higher field instruments are available, other complications can arise in very-high-field CPMAS NMR. As the applied field is increased, so does CSA, requiring higher sample spinning rates to obtain pure isotropic resonances and a minimum of spinning sidebands. More sidebands make spectral interpretation more difficult. When spinning rates begin to approach the magnitude of the Hartmann–Hahn RF field, this mechanical motion will begin to interfere with the CP dynamics, resulting in lower CP efficiency, until finally

no signal can be observed (Wind *et al.* 1988). In these cases, obtaining a spectrum with sample spinning sidebands is usually preferred. Alternatively, Dixon (1981) has devised a CPMAS NMR experiment to separate spinning sidebands from isotropic resonances, although this experiment may not always produce the desired results, sometimes distorting intensities due to relaxation effects.

Finally, in some cases, CP spin dynamics may not be suitable for a successful experiment. As shown in Fig. 2, if the $T_{1\rho}/T_{IS}$ ratio is too small, CP may become difficult or impossible to detect (Alemany *et al.* 1983b).

5. Summary

While ^{13}C and ^{29}Si CPMAS NMR was the focus of this discussion, other nuclei can be observed, including ^{15}N, ^{119}Sn, and ^{31}P. It is also possible to generate CP intensity from nuclei other than ^{1}H. For example, ^{13}C—^{19}F CPMAS spectra can be obtained for fluorinated polymers. In a number of respects CPMAS NMR is experimentally more demanding than conventional liquid NMR. However, CPMAS NMR is invaluable in the study of solids, providing both static (structural) and dynamic (motional) information. While there are some samples which cannot be studied by CPMAS NMR, this technique can be applied to a wide variety of materials, regardless of purity, crystallinity, or other physical attributes.

Acknowledgments

See also: High-temperature Superconductors, Cuprate: Magnetic Properties by NMR/NQR; Nuclear Magnetic Resonance Spectrometry; Nuclear Resonance Scattering

Bibliography

Alemany L B, Grant D M, Pugmire R J, Alger T D, Zilm K W 1983a Cross polarization and magic angle sample spinning NMR spectra of model organic compounds: 1. Highly protonated molecules. *J. Am. Chem. Soc.* **105**, 2133–41

Alemany L B, Grant D M, Pugmire R J, Alger T D, Zilm K W 1983b Cross polarization and magic angle sample spinning NMR spectra of model organic compounds: 2. Molecules of low or remote protonation. *J. Am. Chem. Soc.* **105**, 2142–7

Belfiore L A, Henrichs P M, Massa D J, Zumbulyadis N, Rothwell W P, Cooper S L 1983 Molecular dynamics of polycarbonate–diluent systems: applications of high-resolution carbon-13 solid-state NMR. *Macromolecules* **16**, 1744–53

Bennett A E, Reinstra C M, Auger M, Lakshmi K V, Griffin R G 1995 Heteronuclear decoupling in rotating solids. *J. Chem. Phys.* **103**, 6951–8

Bloch F, Hansen W W, Packard M 1947 The nuclear induction experiment. *Phys. Rev.* **70**, 474–85

Bryson R L, Hatfield G R, Early T A, Palmer A R, Maciel G E 1983 ^{13}C NMR studies of solid phenolic resins using cross polarization and magic-angle spinning. *Macromolecules* **16**, 1669–72

Dixon W T 1981 Spinning-side band-free NMR spectra. *J. Magn. Reson.* **44**, 220–3

Hartmann S R, Hahn E L 1962 Nuclear double resonance in the rotating frame. *Phys. Rev.* **128**, 2042–53

Maciel G E, Szeverenyi N M, Early T A, Myers G E 1983 ^{13}C NMR studies of solid urea–formaldehyde resins using cross polarization and magic-angle spinning. *Macromolecules* **16**, 598–604

Munowitz M G, Griffin R G, Bodenhausen G, Huang T H 1981 Two-dimensional rotational spin-echo nuclear magnetic resonance in solids: correlation of chemical shift and dipolar interactions. *J. Am. Chem. Soc.* **103**, 2529–33

Naito A, Ganapathy S, McDowell C A 1981 High resolution solid state ^{13}C NMR spectra of carbons bonded to nitrogen in a sample spinning at the magic angle. *J. Chem. Phys.* **74**, 5393–7

Pines A, Gibby M G, Waugh J S 1973 Proton-enhanced NMR of dilute spins in solids. *J. Chem. Phys.* **59**, 569–90

Purcell E M, Torrey H C, Pound R V 1946 Resonance absorption by nuclear magnetic resonance. *Phys. Rev.* **69**, 37–8

Schaefer J, McKay R A, Stejskal E O 1983 Dipolar rotational spin-echo ^{13}C NMR of polymers. *J. Magnetic Resonance* **52**, 123–9

Schaefer J, Stejskal E O, Buchdahl R 1975 High-resolution carbon-13 nuclear magnetic resonance study of some solid, glassy polymers. *Macromolecules* **8**, 291–6

Terao T, Miura H, Saika A 1982 Simplification and assignment of carbon-13 spectra by using J-resolved NMR spectroscopy in solids. *J. Am. Chem. Soc.* **104**, 5228–9

VanderHart D L, Earl W L, Garroway A N 1981 Resolution in ^{13}C NMR of organic solids using high-power proton decoupling and magic-angle sample spinning. *J. Magn. Reson.* **44**, 361–401

Wind R A, Dec S F, Lock H, Maciel G E 1988 ^{13}C/MAS and high-speed magic-angle spinning. *J. Magn. Reson.* **79**, 136–9

Yannoni C S 1982 High-resolution NMR in solids: the CPMAS experiment. *Acc. Chem. Res.* **15**, 201–8

Zilm K W, Grant D M 1982 High-resolution NMR spectra with J couplings in solids. *J. Magn. Reson.* **48**, 524–6

T. A. Early
General Electric Company, Niskayuna
New York, USA

Spin Fluctuations

1. Introduction

In general, the term spin fluctuations refers to fluctuations of the magnetic (electron spin) moment in magnetic systems, both ordered and paramagnetic ones. In the ground state (zero temperature, zero

applied magnetic field $H = 0$) of a ferromagnetic system of local moments, for instance, all moments are oriented in the same direction. Above a critical temperature, the Curie temperature T_C, the system is paramagnetic. At low temperatures, the excitations from the ground state can well be described as spin waves or magnons, that is, as independent collective excitations obeying Bose–Einstein statistics. With increasing temperature (T), the absolute value of the "long-time averaged" magnetization (M) decreases as $M = M_0 - \alpha T^{3/2}$ (Bloch's $T^{3/2}$ law). The local, momentary magnetization, $M_t(r)$, i.e. the short-time average over a small volume around r, is written as $M_t(r) = M + m_t(r)$, where $m_t(r)$, or simply $m(r)$, represents the random, time-dependent deviation, or fluctuation. The components along the direction of M, chosen as the z direction, $m_z(r)$, are referred to as "longitudinal" fluctuations, the components in the xy-plane, $m_x(r)$, $m_y(r)$, as "transverse" ones. In this temperature range, the transverse fluctuations can be described either as spin fluctuations or equivalently as magnons. The length scale, over which averaging can be performed without blurring out the deviations, is determined by the so-called "correlation length." With increasing temperature, apart from the fact that the spin waves can no longer be considered as independent excitations, the magnitude and the correlation length of the fluctuations increase. In the neighborhood of the transition temperature, the critical fluctuations are dominant, and the correlation length tends to infinity. In this "critical region," "renormalization group" techniques can be applied, leading to the so-called "scaling laws." At still higher temperatures, the correlation length gradually decreases down to an atomic scale. The system then behaves as a collection of independent local atomic moments.

For some specific models (e.g., the Ising model), spin fluctuations can be visualized by computer simulation (see, e.g., http://www.physics.cornell.edu/sss/Ising/Ising.html).

The behavior of spin fluctuations in an itinerant-electron band system is qualitatively the same. In the paramagnetic state, the fluctuations (heavily damped collective excitations) were originally called "paramagnons." A large effect of spin fluctuations is expected for strongly enhanced paramagnets (on the verge of becoming magnetically ordered, see next section). If, moreover, the number of electrons (or holes) in the itinerant band is low, at high temperatures the fluctuations may effectively cause the (local) band to be (momentarily) fully polarized. Then, the system even roughly behaves as a system of local moments. This is illustrated in Fig. 1, showing the resistivity of the strongly enhanced paramagnets Pd, Np, and Pu, as analyzed by Jullien *et al.* (1974). The spin fluctuation contribution is obtained by subtracting the resistivity of a suitable, "normal" metal (Ag in the Pd case, Th for Np and Pu). In local-
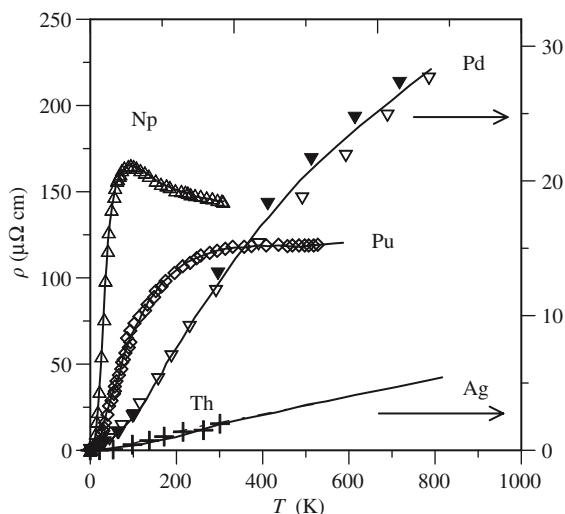
Figure 1
The resistivity of Pd, Np, and Pu as a function of temperature. The solid lines through the data points show the sum of the calculated spin fluctuation contribution and an experimentally determined, suitable "nonmagnetic" background (Ag for Pd and Th for Np and Pu; notice the difference in scales, chosen such that the background contributions coincide). For data and details, see Jullien *et al.* (1974).

moment systems, the "spin disorder scattering" is saturated at high temperatures. Evidently, such saturation may occur in itinerant-electron systems as well. Jullien *et al.* fitted the calculated spin fluctuation contribution by fitting the spectrum of the fluctuations with wave vector q and frequency ω, i.e. of the dynamical susceptibility $\chi(q,\omega)$, applying the "fluctuation – dissipation" theorem.

This theorem is applied in most of the sophisticated spin fluctuation models, indeed. Each mode, (q,ω), behaves as a harmonic oscillator obeying Bose–Einstein statistics. Consequently, one may distinguish zero-point fluctuations (or quantum fluctuations) and thermal fluctuations. The different models are based on different approximations for the quantum fluctuations (as being dependent on the magnetization, for instance), for the change-over from spin wave behavior at low temperatures to fluctuating behavior at higher temperatures, for the necessary cut-off wave vector in the spectrum, for the difference between longitudinal and transverse fluctuations, and so on.

The occurrence of spin fluctuations is by no means restricted to simple ferromagnetic materials. They play an important role in antiferromagnetic and ferrimagnetic materials as well. The interplay of local (rare-earth) moments and an itinerant-electron matrix may enhance the effect of spin fluctuations (see, e.g., Duc and Brommer (1999) for details). In

magnetic perovskites (manganites, cobaltates) magnetic order may compete with charge order, giving rise to a very rich phase diagram. Spin fluctuations can play a decisive role in this competition. In high-T_C superconductors, spin fluctuations are supposed to provide the necessary "glue" for electron pairing, playing the role of the phonons (lattice distortions, electron–phonon coupling) in the more conventional superconductors. In strongly correlated electron systems and Kondo systems, at low temperatures a collective (excited) state may be formed, giving rise to spin fluctuations too. At the so-called spin fluctuation temperature, the collective state is destroyed and the particular fluctuations do not play a role any more.

Nevertheless, here attention will be focused on itinerant-electron systems, mainly because the interest in spin fluctuations started with a long-standing controversy about the relative importance, in these systems, of, on the one hand, collective spin fluctuations and, on the other hand, independent single-particle excitations.

2. Free-energy Considerations

In the Landau theory of second-order phase transitions (see *Phase Transitions, Landau Theory of*), the free energy is expanded as a function of the order parameter, here the magnetic moment M:

$$F_{\text{magn}} = \frac{1}{2} AM^2 + \frac{1}{4} BM^4 + \cdots \frac{1}{6} CM^6 + \cdots \quad (1)$$

In the Stoner–Edwards–Wohlfarth (SEW) model for itinerant electrons (see, e.g., Brommer and Franse 1990, and references therein), one takes $A = A_b - \lambda$, where A_b, like B and C, depends on the band parameters, and where λ represents the exchange energy $-(1/2)\lambda M^2$. The equilibrium condition $\partial F_{\text{magn}}/\partial M = \mu_0 H$ leads to

$$\mu_0 H = AM + BM^3 + CM^5 + \cdots \quad (2a)$$

or, written in the "Arrott–Kouvel" form

$$\mu_0 H/M = A + BM^2 + CM^4 + \cdots \quad (2b)$$

2.1 Arrott Plots

For very weak itinerant ferromagnets (VWIF), the M^4 term is ignored ($B > 0$, for stability). As an example, some M^2 versus $\mu_0 H/M$ plots, so-called Arrott plots, are shown for $Ni_{42.9}Pt_{57.1}$ in Fig. 2. The deviations from the straight lines, at low M^2 and $\mu_0 H/M$ values, are ascribed to concentration variations (see Brommer and Franse 1990). Such straight Arrott plots were often considered as proof for a negligible spin fluctuation contribution.
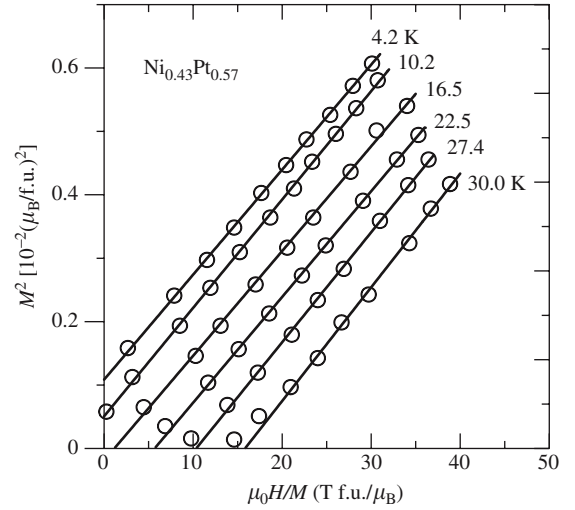
Figure 2
Arrott plots for $Ni_{0.43}Pt_{0.57}$. The straight lines represent the equation of state (Eqn. (2b)) $\mu_0 H/M = A + BM^2$ (for data and details see Brommer and Franse 1990, p. 352).

Spontaneous order ($M \neq 0$ for $H = 0$) occurs when the Landau coefficient A is negative, with $M^2 = -A/B > 0$. When A is positive, the system is paramagnetic, and A is the inverse initial susceptibility. Applying Fermi–Dirac statistics for the independent, single-electron excitations, the temperature dependence of the "Landau co-efficients" A, B, C, and so on, can be determined. In the simplest model (see, e.g., Shimizu 1981 or Brommer and Franse 1990 for a much more elaborate approach), only A_b is taken to be temperature dependent:

$$A_b(T) = A_b(0)(1 + T^2/T_F^2) \quad (3)$$

For a simple itinerant-band structure with Fermi level E_F, T_F is a temperature in the order of the Fermi temperature E_F/k_B.

2.2 Stoner Enhancement

The exchange interaction enhances the paramagnetic susceptibility by the "Stoner enhancement" factor S, defined as

$$S = A_b(0)/A(0) = A_b(0)/[A_b(0) - \lambda] = 1/(1 - \bar{I}) \quad (4)$$

The last equality expresses the enhancement factor conventionally as a function of the Stoner parameter $\bar{I} (= \lambda/A_b(0) = N(E_F)I)$, where $N(E_F)$ is the density of states at the Fermi level of the itinerant band (recall that the Pauli susceptibility $A_b(0)^{-1}$ is proportional to this density of states). I is again a measure for the exchange interaction. Since the unenhanced

inverse (Pauli) susceptibility A_b is positive, the system can only become ferromagnetic for a positive λ of sufficient magnitude. Note that for an itinerant ferromagnet S is negative ($\bar{I} > 1$: the Stoner criterion). Since $A_b(T)$ increases with increasing temperature, the first Landau coefficient in the Stoner model, $A_{St}(T) = [A_b(T) - \lambda] = A_b(0)(1 - \bar{I} + T^2/T_F^2)$ will eventually change sign, and the system becomes paramagnetic (see also Eqn. (7), next section).

2.3 Incorporating Spin Fluctuations

In a simplified version of the Moriya (1985) "self-consistent renormalization" (SCR) treatment of the spin fluctuations, the terms M^{2n}, in Eqn. (1), are replaced by $\langle |M_t(r)|^{2n} \rangle = \langle |M + m(r)|^{2n} \rangle$. Taking the spatial average ($\langle \rangle$) in the homogeneous case, and omitting higher-order terms, one finds for the coefficient of the M^2 term:

$$
\begin{aligned}
A(T) &= A_{St}(T) + B(3m_z^2 + m_x^2 + m_y^2) \\
&= A_{St}(T) + (5/3)B\,m^2(T)
\end{aligned}
\tag{5}
$$

The second equality holds for an isotropic system near T_C, with $m_z^2 = m_x^2 = m_y^2 = m^2(T)/3$.

In the VWIF system under consideration, the spin fluctuation term in Eqn. (5) is positive, and consequently the change of sign will occur at a lower (Curie) temperature. This explanation for the apparent low Curie temperatures of the itinerant-electron systems was a great success of the spin fluctuation theory (see next section).

Band parameters (and thus the Landau co-efficients A_{St}, B,...) can be deduced from band calculations with still increasing accuracy. The necessity to consider also the spin fluctuations is clearly demonstrated by Aguayo *et al.* (2004) in a comparison of the "prototype" itinerant-electron systems Ni_3Al and Ni_3Ga. Since both systems are Ni-based, the exchange parameter λ or I will be about the same for these compounds. The density of states is larger in Ni_3Ga. Hence, one would expect Ni_3Ga to be the more enhanced (or more ferromagnetic) compound (because $\bar{I} = N(E_F)I$ is larger in Eqn. (4)). The opposite is true. Now, according to their calculations the q-dependence of the dynamic susceptibility is weaker in Ni_3Ga. Consequently, there are more spin fluctuations, and the positive contribution to $A(T)$ will be larger (see Eqn. (5)). In fact, Ni_3Ga even remains paramagnetic down to $0\,K$!

2.4 Magnetovolume Effects

Differentiating the magnetic free energy (Eqn. (1)) yields the "magnetic pressure" P_m as

$$
VP_m = \frac{1}{2}A_\omega M^2 + \frac{1}{4}B_\omega M^4 + \cdots
$$

where, $A_\omega = \partial \ln A(V, T)/\partial \ln V$, and analogously. Henceforth, the volume dependence of B (and higher Landau co-efficients) will be ignored. Incorporating the spin fluctuations, one finds the (relative) "magnetic volume" $\omega_m = V_m/V$ as

$$
\omega_m = -\kappa P_m = -\frac{1}{2}(\kappa A_{St,\omega}/V)[M^2 + m^2]
\tag{6}
$$

where, κ is the compressibility. The magnetic volume is proportional to $[M^2 + m^2]$, so there will be a contribution even in the paramagnetic state ($M = 0$).

2.5 Metamagnetic Transitions

In the Laves phase RCo_2 type compounds (R: rare earth, Y), the Co 3d-subsystem is a metamagnetic, itinerant-electron system. For YCo_2, an applied magnetic field exceeding $\sim 70\,T$ induces a jump of the Co moment up to $\sim 0.5\,\mu_B/Co$. Substitution of Al for Co stabilizes this "high-spin" state. $Y(Co_{1-x}Al_x)$ is paramagnetic for $x = 0.075$, but the moment jumps to $\sim 0.6\,\mu_B/Co$ at the metamagnetic transition field of $33\,T$ (see upper panel of Fig. 5). This behavior can be described by the free-energy expression, Eqn. (1), when the Landau coefficient A is positive, whereas B is negative, and C is again positive for stability (see dashed fitting curve in Fig. 5; see also further discussion in Sect. 4).

According to Eqn. (5), in such a system with $B < 0$, the spin fluctuation contribution in $A(T)$ would be negative, so would promote the transition. Stability criteria have been discussed extensively by Yamada *et al.* (2003). The order parameter (M) in Eqn. (1) can be taken to be the amplitude of the relevant antiferromagnetic ordering mode (staggered magnetization). So, the formalism can be applied to antiferromagnetic systems too. For $T > T_N$ ($\approx 100\,K$), YMn_2 is an itinerant-electron paramagnet in which the Mn atoms have no magnetic moment. For $T < T_N$, the Mn subsystem becomes antiferromagnetic, with a large moment ($2.7\,\mu_B/Mn$) and a large volume increase (5%). On the basis of their band structure calculations, and including magnetovolume coupling terms in the free energy expression, Nakada *et al.* (2004) conclude that the Mn subsystem in itself would not order at all: spin fluctuations are necessary to "stabilize" the ordered system (see also Sect. 4).

2.6 Beyond SCR

There have been many attempts to develop the spin fluctuation theory beyond the Moriya SCR level. Noteworthy are the papers by Takahashi and colleagues, e.g., Takahashi (2001), in which the important role of the zero-point or quantum fluctuations is stressed. Kaul and co-workers claim to have found a solution for the transition from the low-temperature spin wave regime to the critical regime around T_C,

and provide and elaborately analyze experiments on mainly Ni_3Al and related compounds (see, e.g., Kaul 1999 and Semwal and Kaul 2002).

3. The Curie Temperature of a Very Weak Itinerant Ferromagnet

According to the Landau theory for second-order phase transitions, the ordering transition occurs when $A(T)$ changes sign (see Eqn. (1), case $B>0$). For an itinerant ferromagnet, $A(T)$ [$= A_{St}(T)$] is given by

$$A_{St}(T) = A_b(0)(1 - \bar{I} + T^2/T_F^2)$$
$$= (A_b(0)/|S|)(-1 + |S|T^2/T_F^2) \qquad (7)$$

$A_{St}(T)$ vanishes at the "Stoner temperature" $T_{St} = T_F/|S|^{1/2}$. When spin fluctuations are taken into account, $A(T)$ is given by Eqn. (5). In the simple treatment here, the temperature dependence of B is neglected. Moreover, in the discussion on the Curie temperature only the behavior of $m^2(T)$ in the neighborhood of T_C is needed. Here, the relation $m^2(T) \sim T^{4/3}$ is generally accepted. Then, with Eqns. (3) and (5), one may write

$$A(T) = A(0) + a_{St}(T/T_0)^2 + a_{sf}(T/T_0)^{4/3} \qquad (8)$$

where T_0 is an arbitrary reference temperature, for ferromagnetic materials often chosen equal to T_C. As an example, Fig. 3 shows an analysis of the temperature dependence of the Landau parameter $A(T)$ for a series of $(Ni,Pd)_3Al$ compounds (data taken from fig. 5 in Brommer and Franse 1990). In fact, in order to obtain a consistent fit for all the curves, a term $\sim T^4$ has been added and the contribution of the spin fluctuation (i.e., the coefficient a_{St} in Eqn. (7)) was assumed to be the same for all compounds. According to this analysis, the contributions of the Stoner T^2 term and the "spin fluctuation" $T^{4/3}$ term are of equal importance. It is easy to imagine that, for this kind of experimental results, reasonable fits could be obtained for a pure Stoner model as well as for a pure Moriya (spin fluctuation) model. Historically, in the debate on the importance of spin fluctuations versus Stoner excitations, it is understandable that the analysis of such measurements never convinced an opponent (for some more details see Brommer and Franse 1990).

Figure 3
Analysis of the first Landau coefficient $A(T)$ for some $(Ni,Pd)Al_3$ compounds. Extending Eqn. (7), the solid lines represent fitting results according to:
$A(T) = A(0) + a_{2St}(T/T_0)^2 + a_{4St}(T/T_0)^4 + a_{sf}(T/T_0)^{4/3}$.
With, arbitrarily, $T_0 = 40\,K$ the fitting results for $Ni_{60}Pd_{15}Al_{25}$ are: $A(0) = 12.25\,TNi/\mu_B$, $a_{2St} = 25.6\,TNi/\mu_B$; $a_{4St} = 0.37\,TNi/\mu_B$, $a_{sf} = 27.36\,TNi/\mu_B$, giving directly the relative importance of these contributions in the total value of $65.6\,TNi/\mu_B$ at $T = T_0 = 40\,K$.

Figure 4
Schematic illustration of the reduction of the Curie temperature: $A(T)/A(0)$ [$= M^2/M_0^2$] is plotted vs. $t = T/T_C$. The solid lines represent $A_{St}(T)/A(0) = 1 - T^2/T_{St}^2$ (Stoner model). The skew dashed line represents the contribution of the spin fluctuations, $(5/3)Bm^2(T)/|A(0)| = (1-p)t^{4/3}$, for $p = 0.5$. Here, p is the relative contribution of the Stoner excitations in $A(T_C)$. $p = 0$: Moriya model (Stoner excitations completely ignored), $p = 0.08$, value quoted for MnSi; $p = 0.5$: possible value for $ZrZn_2$ and Ni_3Al (see Brommer and Franse (1990), table 5).

A striking success of the spin fluctuation approach was the explanation of the reduction of the Curie temperature with respect to the Stoner temperature. This is shown schematically in Fig. 4. With respect to the Stoner temperature, the Curie temperature is reduced by a factor $t_{St} = T_{St}/T_C \ [= 1/\sqrt{p}]$, which is infinite for the pure Moriya model, 12.5 for MnSi ($p = 0.08$) and perhaps about a factor $\sqrt{2}$ for $ZrZn_2$ and Ni_3Al, for which the value $p = 0.5$ is adopted here.
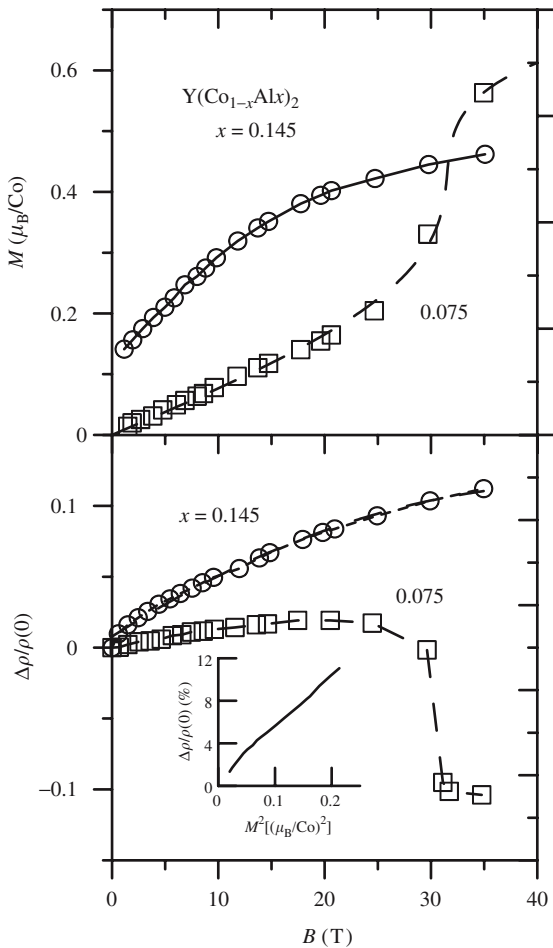
Figure 5
Magnetic moment per Co (upper panel) and the relative magnetoresistivity for the ferromagnetic (stabilized) compound $Y(Co_{0.855}Al_{0.145})_2$ and the metamagnetic compound $Y(Co_{0.925}Al_{0.075})_2$. The dashed line in the upper panel represents the fitting with Eqn. 2(a) for $x = 0.075$, with $A > 0$, $B < 0$, $C > 0$. The other lines are guides to the eye only. The inset in the lower panel shows the proportionality $\Delta\rho/\rho \sim M^2$ for $x = 0.145$, i.e., for the stabilized compound.

4. Volume Effects

4.1 Separation of Volume Effects and Spin Fluctuation Contributions

Many itinerant-electron systems are based on transition metal ions, which are known to exhibit large magnetoelastic effects (see Eqn. (6)). The volume change may influence the properties of the material, for instance, the resistivity. Then, it may be difficult to distinguish the volume effect from the spin fluctuation effect. Figure 5 shows an attempt to separate the effects for two $Y(Co,Al)_2$ compounds. $Y(Co_{1-x}Al_x)$ is ferromagnetic for $x = 0.145$. The magnetic moment increases gradually from $\sim 0.1 \, \mu_B/Co$ up to $\sim 0.5 \, \mu_B/Co$ when the applied field is increased from $0\,T$ to $40\,T$. It exhibits a positive magnetoresistance, proportional to M^2, and thus interpreted as a (or the) volume effect. For the metamagnetic compound ($x = 0.075$), the sharp drop in the magnetoresistance, accompanying the comparable, but now jump-like, increase of the Co moment, is ascribed to the suppression of the spin fluctuations, evidently exceeding the concurrent volume effect.

4.2 Huge Thermal Expansion in YMn_2 and $(Nd,Lu)Mn_2$

Magnetovolume effects are very clear in YMn_2 and related Laves phase compounds (already discussed
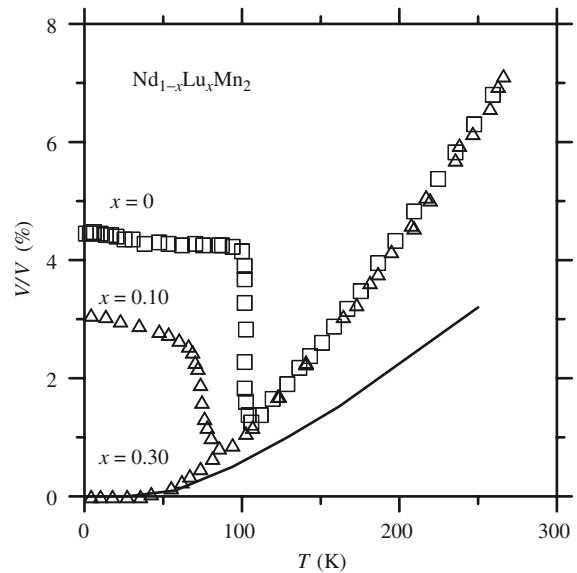
Figure 6
Thermal expansion of some $Nd_{1-x}Lu_xMn_2$ compounds ($x = 0.00$, 0.10, and 0.30). The solid line indicates the background thermal expansion (electronic and lattice contributions). The excess volume is assumed to be due to the magnetic Mn moment. For $T > T_N$, the excess thermal expansion is ascribed to spin fluctuations.

above). The large jump in the Mn moment at T_N leads to a large jump in the volume, and concurrently to a large thermal hysteresis ($\approx 20\,K$), clearly indicating a first-order transition. For $T > T_N$, a large thermal expansivity is found. This is ascribed to spin fluctuations in the (paramagnetic) Mn subsystem. On the basis of a combined analysis of specific-heat data and thermal-expansion for the related alloying system $(Nd,Lu)Mn_2$, Kim-Ngan *et al.* (1994) succeeded to separate the contribution of the spin fluctuations from the lattice contribution and other, electronic, contributions (Fig. 6). The excess volume is assumed to be due to the magnetic Mn moment. When for the antiferromagnetically ordered Mn-system at low temperatures the Mn moment is taken as $2.7\,\mu_B/$Mn, the mean fluctuating Mn moment would be $\sim 2.5\,\mu_B/$Mn at room temperature. So, the fluctuating Mn moments are quite comparable with local atomic moments (of fixed magnitude).

See also: Electron Systems: Strong Correlations; Itinerant Electron Systems: Magnetism (Ferromagnetism); Magnetoelastic Phenomena; Metamagnetism: Itinerant Electrons

Bibliography

Aguayo A, Mazin I I, Singh D J 2004 Why Ni_3Al is an itinerant ferromagnet but Ni_3Ga is not. *Phys. Rev. Lett.* **92**, 147201_1–4
Brommer P E, Franse J J M 1990 Strongly enhanced itinerant intermetallics and alloys. In: Buschow K H J, Wohlfarth E P (eds.) *Ferromagnetic Materials*. Elsevier (North-Holland), Amsterdam, Vol. 5, pp. 323–96
Duc N H, Brommer P E 1999 3D-Moments and spin fluctuations in some rare-earth – cobalt compounds. In: Buschow K H J (ed.) *Handbook of Magnetic Materials*. Elsevier, Amsterdam, vol. 12, pp. 259–394
Jullien R, Béal-Monod M T, Coqblin B 1974 Resistivity of nearly magnetic metals at high temperatures: Application to neptunium and plutonium. *Phys. Rev. B* **9**, 1441–57
Kaul S N 1999 Spin fluctuation theory for weak itinerant-electron ferromagnets: revisited. *J. Phys.: Condens. Matter* **11**, 7597–614
Kim-Ngan N H, Brommer P E, Franse J J M 1994 Spin fluctuations in the $(Nd,Lu)Mn_2$ system. *IEEE Transactions on Magnetics* **30**, 866–8
Moriya T 1985 *Spin Fluctuations in Itinerant Electron Magnetism*. Springer, Berlin
Nakada K, Shimizu H, Yamada H, Harima H 2004 Magnetic properties and Fermi surface of YMn_2. *J. Magn. Magn. Mater.* **262**, 374–81
Semwal A, Kaul S N 2002 Effect of site disorder on the asymptotic critical behaviour of $Ni_{75}Al_{25}$. *J. Phys.: Condens. Matter* **14**, 5829–47
Shimizu M 1981 Itinerant electron magnetism. *Rep. Prog. Phys.* **44**, 329–409
Takahashi Y 2001 Quantum spin fluctuation theory of the magnetic equation of state of weak itinerant-electron ferromagnets. *J. Phys.: Condens. Matter* **13**, 6323–58
Yamada H, Fukamichi K, Goto T 2003 Recent advances of itinerant-electron metamagnetism and related properties of intermetallic compounds. *Physica B* **327**, 148–54

P. E. Brommer
Van der Waals-Zeeman Instituut, Universiteit van Amsterdam, Amsterdam, The Netherlands

Spin Transition Compounds

Octahedral complexes of transition metal ions with configurations d^4–d^7 exist in either the high-spin (HS) or low-spin (LS) state, depending on the nature of the ligand field. In weak fields the ground state is HS, the d electrons being distributed over the t_{2g} and e_g sets, whereas strong fields stabilize the LS state, the t_{2g} set being completely occupied before electrons are added to the e_g set (Fig. 1). For iron(II), for example,
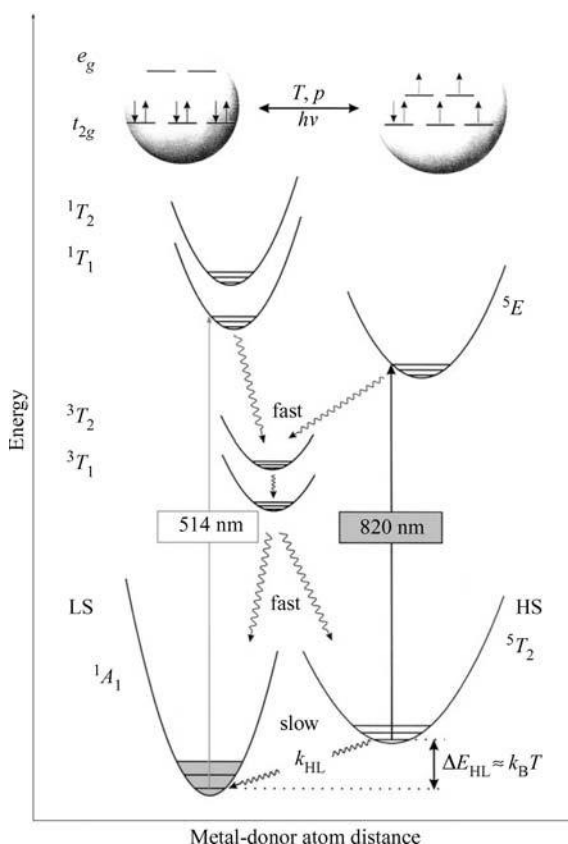
Figure 1
Representation of the interconversion of HS and LS states for iron(II) and the mechanism of the LIESST effect.

the two states are illustrated by $[Fe(H_2O)_6]^{2+}$, configuration $(t_{2g})^4(e_g)^2$, and $[Fe(CN)_6]^{4-}$, configuration $(t_{2g})^6$. For intermediate fields the energy difference between the lowest vibronic levels of the potential wells of the two states may be sufficiently small such that application of some relatively minor external perturbation effects a change in the state. This phenomenon is known as a spin transition (ST) or spin crossover. Materials which display STs are of interest because of their potential in electronic devices for applications such as data storage and displays. The first transitions were observed in the 1930s in iron(III) dithiocarbamates and these were later extensively studied in the 1960s (Martin and White 1968). Although STs have been observed for all the configurations d^4-d^7 for the first transition series, the greatest number has been reported for iron(II) (Gütlich *et al.* 1994).

1. Occurrence and Detection of Spin Transitions

A change in spin state effects fundamental changes in the electronic configuration and thus will affect all those properties of the system which depend on electronic structure. The most important of these are magnetism, color, and structure. In HS Fe^{II}, electrons partly occupy both the antibonding e_g set and the nonbonding or weakly bonding t_{2g} set, whereas in LS Fe^{II} only the t_{2g} set is occupied. This allows closer approach of the donor atoms in the LS state and hence a HS→LS spin transition is accompanied by a significant structural change involving a contraction in the metal–donor atom distances of about 0.2Å or 10%. For solid systems this change in molecular dimensions may bring about fundamental changes in the crystal lattice. For this reason STs in solid systems can follow a number of different paths. These differ principally in the degree of cooperativity associated with the transition. When this is low the transition will be gradual or continuous, but as cooperativity increases the transition becomes more abrupt and may be associated with a phase change and hysteresis. In some instances two-step transitions have been observed, while in others residual fractions of HS or LS species persist at the extremities of the transition.

An ST may be monitored and an ST curve (HS fraction vs. *T*) constructed by a variety of techniques. The curve reflects the nature of the change in population of the HS state with change in temperature. For iron(II), Mössbauer spectroscopy is particularly suitable for characterizing an ST since the spectral parameters associated with the HS and LS states clearly differ and the timescale of the technique generally allows the detection and evaluation of the separate spin states in the course of the transition.

Although the criterion for the occurrence of an ST may appear very restrictive, a large number (>150)

of systems have been characterized. The majority are $Fe^{II}N_6$ systems involving heterocyclic donors. The first synthetic system, $Fe(phen)_2(NCS)_2$ (phen = 1,10-phenanthroline), was identified by König and Madeja (1966). Since then many species of similar composition have been shown to undergo transitions. In addition, derivatives of simple unidentate ligands such as isoxazole and tetrazoles, along with multidentate and polynuclear systems are known. Two strategies are widely effective in fine-tuning the field strength of model ligands so as to bring it into the crossover region:

(i) Incorporation of chemical substituents. If the substituent is adjacent to a donor atom this will destabilize the singlet state by hindering the close approach of the metal atom and is illustrated by $[Fe(mephen)_3]^{2+}$ (mephen = 2-methyl-1,10-phenanthroline) which is HS at room temperature but undergoes a transition to LS at low temperatures, in contrast to the unsubstituted $[Fe(phen)_3]^{2+}$ which is LS. Where the substituent is remote from the donor atom electronic effects may stabilize either state.

(ii) The replacement of six-membered heterocycles by five-membered ones. The principal effect here is to reduce both the σ-donor and π-acceptor character of the system, thus favoring the quintet state, illustrated by the spin crossover behavior of $[Fe(pyim)_3]^{2+}$ (pyim = 2-(pyridin-2-yl)imidazole), in contrast to the completely LS nature of $[Fe(bpy)_3]^{2+}$ (bpy = 2,2′-bipyridine).

2. Solution and Solid-state Behavior

STs are observed for systems in both solution and solid states, though the one system will not necessarily display a transition in both phases. In solution, interactions between the molecules undergoing spin change are virtually negligible and thus the course of the transition can be described by a Boltzmann distribution over all HS vibronic states and the LS state. The driving force for the transition is the considerable entropy gain of ~ 50–$80\,J\,mol^{-1}\,K^{-1}$ for the LS→HS conversion, made up of a magnetic component, $\Delta S_{mag} = R[\ln(2S+1)_{HS} - \ln(2S+1)_{LS}]$, $\sim 13\,J\,mol^{-1}\,K^{-1}$, and a larger vibrational entropy contribution arising from the much higher degeneracies in the HS state. The enthalpy change for the LS→HS conversion is typically 6–$15\,kJ\,mol^{-1}$ and is associated primarily with rearrangement of the coordination sphere (metal–donor atom bond length increase). In the solid state there is electron–phonon coupling between the molecules changing spin state, resulting in cooperative interactions of varying degrees.

One of the most successful models for ST behavior takes as its basis the change in the metal–donor atom distance accompanying a transition (Spiering and Willenbacher 1989). It is proposed that such a

significant change at every "point defect" where an ST occurs sets up pressure (an "image pressure") which is communicated to the surroundings via phonon interactions. In the course of the ST, at many point defects the lattice expands and accelerates the ST in other metal centers. Thus, the nature of the cooperative interactions in a solid is elastic, and the model uses typical quantities from elasticity theory, e.g., bulk modulus and Poisson ratio, to account for the experimental results.

3. Effect of Pressure

The effect of increased pressure is to favor the HS→ LS conversion because of the smaller volume of the LS form. From both solution studies and crystal structure determinations, ΔV has been estimated as typically 50Å^3 per octahedral unit. The study of the effects of high pressure on the course of STs in solid samples has revealed some subtle effects which include displacement of the transition temperature, change in the width of the hysteresis loop, and changes in the residual fractions of HS and LS species at the extremes of the temperature range for the transition (Ksenofontov *et al.* 1999).

4. Effect of Light

It has been observed that an Fe^{II} spin crossover compound in the LS state is converted by light into the metastable HS state with virtually infinite lifetime at sufficiently low temperatures (Decurtins *et al.* 1984). This phenomenon became known as the light-induced excited spin state trapping (LIESST) effect. Later it was found that the reverse process is also possible. The mechanism for these photo-switching processes, a common feature of most Fe^{II} spin crossover systems, is shown in Fig. 1. Green light is used for the spin allowed excitation $^1A_1 \rightarrow {}^1T_1$. A fast relaxation cascading over two successive intersystem crossing steps, $^1T_1 \rightarrow {}^3T_1 \rightarrow {}^5T_2$, populates the metastable $^5T_2$ state. Reverse LIESST is achieved by application of red light whereby the $^5T_2$ state is excited to the ^5E state with two subsequent intersystem crossing processes $^5E \rightarrow {}^3T_1 \rightarrow {}^1A_1$. As demonstrated by Hauser (1991), photo-switching from LS to HS is also possible via $^1A_1 \rightarrow {}^3T_1 \rightarrow {}^5T_2$. LIESST can be induced in spin crossover molecules embedded in polymer films and in KBr pellets, in addition to solid samples. It is worth noting that LIESST has also been observed for the conversion of a HS ground state to a metastable LS state by red light (Poganiuch *et al.* 1990).

The effect of light on spin crossover systems is being pursued vigorously and a number of phenomena have been reported. These include: light-induced thermal hysteresis (LITH), the effect of raising and lowering temperature under constant irradiation (Desaix *et al.* 1998); light-perturbed thermal hysteresis (LPTH), whereby the hysteresis associated with an ST is shifted to either lower or higher temperatures under irradiation of different wavelengths (Renz *et al.* 2000); and ligand-driven light-induced spin crossover (LD-LISC), whereby irradiation effects a *cis–trans* isomerization of the ligand, with subsequent ST at the Fe^{II} center as a consequence of a change in field strength (Boillot *et al.* 1999).

5. Applications

The existence of hysteresis is a prerequisite for bistability, which in turn offers the potential for technical applications of ST systems such as thermal switches and sensors. Furthermore, the drastic color change generally accompanying an ST is promising for applications in displays (Kahn and Launay 1988).

The remarkable changes of ST behavior under applied pressure can be exploited in pressure sensors for applications where remote sensing of pressure could be achieved by a color change in a spin crossover material. The light-induced switching phenomena described above also offer much promise. Data storage using spin crossover materials, although now limited to low-temperature regions, may eventually play a role in holographic devices. Orientational experiments on "transient grids" of a HS/LS lattice have yielded highly promising refractive index results. The switching rates in the subnanosecond region at ambient temperatures may be a promising basis for optical switches. Patents covering these aspects have been registered.

6. Future Developments

Research on ST compounds has grown enormously both from a chemical point of view, allowing the more-or-less controlled synthesis of new materials with special properties, and regarding physical characterization using powerful techniques. Aspects which are the focus of many research groups include:

- synergism (coupling) of magnetic exchange between metal centers and ST at the metal atom; and

- detailed structural characterization of metastable states; important findings on the lattice parameters of a system in a LIESST-generated metastable state have emerged and detailed structural studies will allow greater understanding of light-induced phenomena in general.

See also: Photomagnetism of Molecular Systems

Bibliography

Boillot M-L, Chantraine S, Zarembowitch J, Lallemand J-Y, Prunet J 1999 First ligand-driven, light-induced spin change

at room temperature in a transition-metal molecular compound. *New J. Chem.* 179–83

Decurtins S, Gütlich P, Köhler C P, Spiering H, Hauser A 1984 Light-induced excited spin state trapping in a transition metal complex. *Chem. Phys. Lett.* **105**, 1–4

Desaix A, Robeau O, Jeftic J, Haasnoot J G, Boukheddaden K, Codjovi E, Linares J, Nogues M, Varret F 1998 Light-induced bistability in spin transition solids leading to thermal and optical hysteresis. *Eur. Phys. J.* **B6**, 183–93

Gütlich P, Hauser A, Spiering H 1994 Thermal and optical switching of iron(II) complexes. *Angew. Chem. Int. Ed. Engl.* **33**, 2024–54

Hauser A 1991 Intersystem crossing in Fe(II) coordination compounds. *Coord. Chem. Rev.* **111**, 275–90

Kahn O, Launay J P 1988 Molecular bistabilty: an overview. *Chemtronics* **3**, 140

König E, Madeja K 1966 Unusual magnetic behaviour of some iron(II)–bis(1,10-phenanthroline) complexes. *Chem. Commun.* **61**

Ksenofontov V, Spiering H, Schreiner A, Levchenko G, Goodwin H A, Gütlich P 1999 The influence of hydrostatic pressure on hysteresis phase transition in spin crossover compounds. *J. Phys. Chem. Solids* **60**, 393–9

Martin R L, White A H 1968 The nature of the transition between high-spin and low-spin octahedral complexes of the transition metals. *Trans. Met. Chem.* **4**, 113

Poganiuch P, Decurtins S, Gütlich P 1990 Thermal- and light-induced spin transition in [Fe(mtz)$_6$][BF$_4$]$_2$. First successful formation of a metastable low-spin state by irradiation with light at low temperatures. *J. Am. Chem. Soc.* **112**, 3270–8

Renz F, Spiering H, Goodwin H A, Gütlich P 2000 Light perturbed hysteresis in an iron(II) crossover compound observed by the Mössbauer effect. *Hyperfine Int.* in press

Spiering H, Willenbacher N J 1989 Elastic interaction of high-spin and low-spin complex molecules in spin crossover compounds. *J. Phys.: Condens. Matter* **1**, 10089–105

P. Gütlich
Johannes Gutenberg Universität, Mainz, Germany

H. A. Goodwin
University of New South Wales, Sydney, Australia

Spintronics in Semiconductor Nanostructures

Spintronics is a relatively new field of electronics which has been rapidly developing over the past few years. In order to understand the potential of this new kind of electronics, it is useful to consider the basic properties of the electron. One of these properties is the charge, which has been exploited up to now in conventional semiconductor electronics. The charge of a single electron is constant and local changes of charge can only happen via a current. However, the electron also has a second property, namely the spin. The spin can be seen as an angular momentum which—corresponding to a rotating charge—also induces a magnetic moment. Much in contrast to a macroscopic angular momentum the spin can only have two different (opposite) directions. It is quantized, with the axis of quantization given by an external magnetic field. So, whereas the electron charge has a constant value, the spin of an electron can have two different values called spin-up and spin-down which can be "flipped" from one value to the other. This property allows for the local creation of a spin population without a current (in contrast to a charge) but it also means that a spin population can vanish over time, while a charge population in the absence of a current cannot.

A well-known effect based on spin is ferromagnetism. In normal materials the spin of the electrons is distributed statistically. This means that 50% of the electrons have spin-up and 50% have spin-down. In ferromagnetic materials such as Fe, Co, or Ni, it is energetically favorable for a majority of the electrons to have the same spin direction. In this case the material exhibits a macroscopic magnetic moment and produces an external magnetic field. Until the mid-1980s, access to the magnetic properties was possible only via the magnetic field, using inductive pickup coils like in tape storage or computer disk applications.

In 1987 the situation changed, when a new effect was discovered. Baibich *et al*. (1988), Binasch *et al*. (1989), and Valet and Fert (1993) discovered that metallic multilayers (see *Multilayers: Interlayer Coupling*) composed of magnetic and nonmagnetic metals can exhibit a so-called giant magnetoresistance (see *Giant Magnetoresistance*). When an external magnetic field is applied to the system, the resistance of the layers decreases. It was soon thereafter determined that the effect was based on the spin polarization of the carriers. The spin polarization of the carriers in a material β is a macroscopic quantity giving the average spin population of the electronic system:

$$\beta = \frac{n^{\uparrow} - n^{\downarrow}}{n^{\uparrow} + n^{\downarrow}} \qquad (1)$$

where $n^{\uparrow}$ and $n^{\downarrow}$ are the number of carriers with spin-up and spin-down, respectively. It is clearly visible that for a nonmagnetic material β is 0. In a conventional ferromagnetic material, its value can be up to 40%.

If we assume the same mobility for spin-up and spin-down electrons, without loss of generality, we can assume

$$\beta = \frac{\rho^{\uparrow} - \rho^{\downarrow}}{\rho^{\uparrow} + \rho^{\downarrow}} \qquad (2)$$

where ρ is the local conductivity.

In a homogeneous material this spin polarization can give rise to a spin-polarized current. As long as spin flips are neglected, we can derive two equations

for the spin-up and spin-down current, respectively:

$$\vec{j}^{\uparrow\downarrow} = \vec{E}\rho^{\uparrow\downarrow} \qquad (3)$$

The spin polarization of the currents α is then defined as

$$\alpha = \frac{j^{\uparrow} - j^{\downarrow}}{j^{\uparrow} + j^{\downarrow}} \qquad (4)$$

This corresponds to a picture in which two spin channels exist, which can be seen as fully spin-polarized noninteracting resistors. However, it is clear that the voltage applied to both resistors is always the same, because the interaction of electrons with an electric field is independent from spin, and current contacts are typically not spin selective. A spin-polarized current can thus only be obtained in a material where the carriers are already spin polarized.

The picture changes dramatically, when hybrid structures consisting of both spin-polarized and unpolarized materials are investigated. In this case, the continuity of the respective spin currents has to be maintained, unless a strong spin scattering is present. For a ferromagnet/nonmagnet/ferromagnet (FM/NM/FM) trilayer system this leads to the so-called two-current model, in which two spin channels are present. Each channel consists of three resistors, two for the two ferromagnets and one for the nonmagnetic material (Fig. 1). When the two magnetic layers are magnetized in parallel, the two spin channels have a different total resistance. When the alignment is antiparallel, the resistances of the spin channels are equal. Calculating the total resistance of the system yields different values for parallel and antiparallel alignment. The value for the parallel alignment is always lower than for the antiparallel alignment. This effect is termed giant magnetoresistance (GMR). Besides the appearance of a magnetoresistance, a second effect is also present; in the antiparallel state, the current through both spin channels is equal. However, in the parallel state, the two spin currents are different yielding a spin-polarized current in the nonmagnetic material.

The spin polarization of the current in the parallel state is equal to

$$\alpha = \beta \frac{R_{\text{fm}}}{R_{\text{sc}}} \frac{2}{2(R_{\text{fm}}/R_{\text{sc}}) + (1 - \beta^2)} \qquad (5)$$

and the normalized difference in resistance between the parallel and the antiparallel state is

$$\alpha = \frac{\beta^2}{1 - \beta^2} \frac{R_{\text{fm}}^2}{R_{\text{sc}}^2} \frac{2}{4(R_{\text{fm}}^2/R_{\text{sc}}^2) + 2(R_{\text{fm}}/R_{\text{sc}}) + (1 - \beta^2)} \qquad (6)$$

GMR quickly made its way into applications like hard-disk read heads and field sensors (see *Magnetic Recording Systems: Spin Valves*) and also seemed
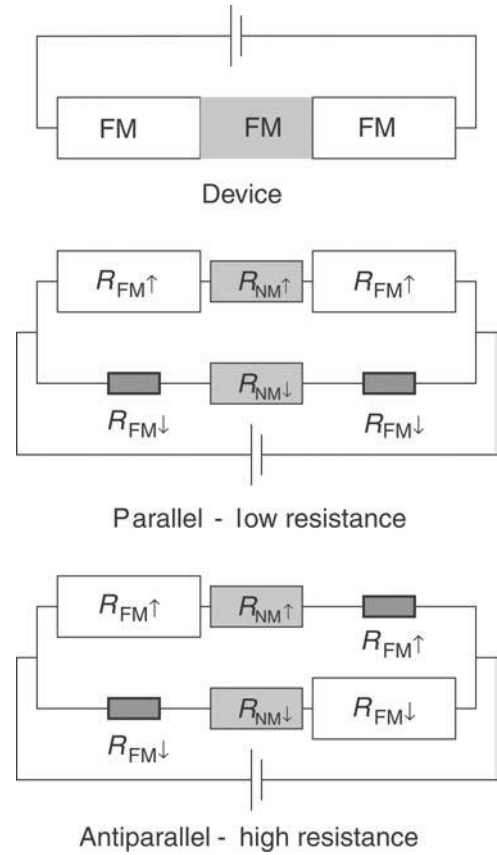
Figure 1
Resistor model (two-current model) for the semiconductor device with two ferromagnetic contacts (up), showing the configuration of the parallel and of the antiparallel magnetization of the contacts. The depicted size of the resistors indicates the higher and lower resistance of spin-up and spin-down channel, respectively. A straightforward calculation shows that the total resistance in the parallel configuration is lower than in the antiparallel case.

desirable for integrating spin-based devices into conventional electronics.

However, in metal-based devices high values for GMR can only be achieved when the thickness of the nonmagnetic material is only a few Å, a fact which limits the device resistance to fractions of an Ω and is incompatible with existing CMOS technology. Furthermore, these small dimensions leave no room for the manipulation of the spin. Indeed in 1990 a new concept for a semiconductor device for spin manipulation was published by Datta and Das in which a spin-polarized current through a semiconductor can be modulated by an electrostatic gate via the spin-orbit coupling. This device has come to be known as

the *Datta-transistor* (Datta and Das 1990). The authors claimed that the spin-polarized current should be obtained by using a GMR-like geometry with ferromagnetic metal contacts on a semiconductor mesa. Furthermore, optical experiments indicated that extremely long spin lifetimes and large spin-flip lengths can be obtained in semiconductors (Kikkawa and Awschalom 1999). Motivated by these results several research groups for more than half a decade tried to achieve the injection of a spin-polarized current (spin injection) into a semiconductor, however, without any results that could not be interpreted as side effects like magnetoresistance or Hall effect (Monzon and Roukes 1999).

The explanation for this failure is simple. If we replace the nonmagnetic metal in the GMR configuration (Fig. 1) by a semiconductor, it seems on first sight that the picture does not change. However, using real numbers for the resistance values shows that in comparison to the resistance of the semiconductor, the resistance of the ferromagnet can be neglected. Even when the spin polarization of the ferromagnet is 80% or 90%, the difference in resistance of both spin channels will be too low to induce any difference in the current of the two spin channels, and any current through the semiconductor remains unpolarized.

In Eqn. (5) this corresponds to $R_{fm} \ll R_{sc}$. This problem was first discussed in Schmidt *et al.* (2000) where the calculation was extended to a local description, in which spin flips in the ferromagnetic material are taken into account. In this case, the outcome is similar, only the resistance R_{fm} is replaced by λ_{fm}/σ_{fm} which is the resistance of a sheet of the ferromagnet with the thickness of the spin-flip length. The spin polarization of the current in the semiconductor is thus proportional to the spin polarization of the ferromagnet β; however, it is reduced by a factor of $(\lambda_{fm}/\sigma_{fm})/(x_0/\sigma_{sc})$ where x_0 and σ_{sc} are the length and conductivity of the semiconductor, respectively.

It seems obvious that one way to circumvent this conductance mismatch is to increase the value of λ_{fm}/σ_{fm}; however, ferromagnetic materials typically have a small spin-flip length and an extremely high resistivity would be needed, which will deteriorate the electrical properties of a device. One way to achieve such a high resistance contact has been discussed by Rashba (2000) and by Fert *et al.* (2001). Less obvious is the use of fully spin-polarized materials (see *Half-metallic Magnetism*) with $\beta = 1$. In this limit we obtain $\alpha = 1$ independent from the resistivity and the spin-flip length in the materials. This is possible because one of the spin channels is now completely blocked due to the absence of carriers.

Approximately at the same time as the conductance mismatch was identified, new experiments based on a different class of magnetic materials were published. When semiconductors are doped with magnetic ions (e.g., Mn or Fe), they can become ferromagnetic or strongly paramagnetic (see *Dilute Magnetic Semiconductors*). ZnMnSe is an example of these so-called dilute magnetic semiconductors (DMSs). Without external magnetic fields, the Mn-spins are not aligned or are antiferromagnetically coupled. However, at low temperatures and in an external magnetic field the material exhibits a giant Zeeman splitting. The *g*-factor can be larger than 100, leading to a splitting of the conduction band of up to 20 meV. At low temperatures, where kT is smaller than the Zeeman splitting, the population of the two spin levels can be expressed by a Boltzmann factor. The upper spin level is thus completely depopulated and the material should act as a perfect spin aligning contact.

The first proof of high-efficiency spin injection using dilute magnetic semiconductors was obtained in 1999 using a light emitting diode (LED) fitted with a DMS contact. When an electron and a hole recombine in GaAs and emit a photon, the polarization of this photon is related to the spins of the hole and the electron via the quantum mechanical selection rules. When unpolarized holes recombine with spin-polarized electrons, there are two possibilities. In case light and heavy holes are degenerate, the circular optical polarization of the emitted photons is

$$P_{\text{circ}}^{\text{opt}} = \frac{\sigma^+ - \sigma^-}{\sigma^+ + \sigma^-} = \frac{(3n^\uparrow + n^\downarrow) - (3n^\downarrow + n^\uparrow)}{(3n^\uparrow + n^\downarrow) + (3n^\downarrow + n^\uparrow)}$$
$$= \frac{1n^\uparrow - n^\downarrow}{2n^\uparrow + n^\downarrow} = \frac{1}{2}\alpha \qquad (7)$$

When the degeneracy is lifted the circular optical polarization is equal to the electron spin polarization. A GaAs LED which is fed with unpolarized holes from the p-side and with spin-polarized electrons from the n-side will thus emit light with a circular polarization which is directly proportional to the electron spin polarization. Such a diode was fabricated (Fig. 2) and characterized at low temperature and in moderate magnetic fields between 0 T and 5 T. The hole confinement in the diode was weak in order to insure degenerate hole states. Figure 3 shows a typical electroluminescence (EL) spectrum of a spin LED. The maximum polarization obtained in the experiment was up to 46% indicating an electron spin polarization of more than 90% (Fiederling *et al.* 1999). A similar experiment was performed using ferromagnetic GaMnAs, however, with a strongly reduced efficiency (Ohno *et al.* 1999).

When DMSs are used as spin aligners however, electrical detection of spin-polarized transport is more difficult than for ferromagnets. The paramagnetic behavior makes it virtually impossible to achieve two small contacts with antiparallel magnetization and thus excludes GMR-like experiments. In addition, the magnitude of magnetoresistance effects due to spin injection is typically proportional to the square of the spin injection efficiency (Eqn. (6)).
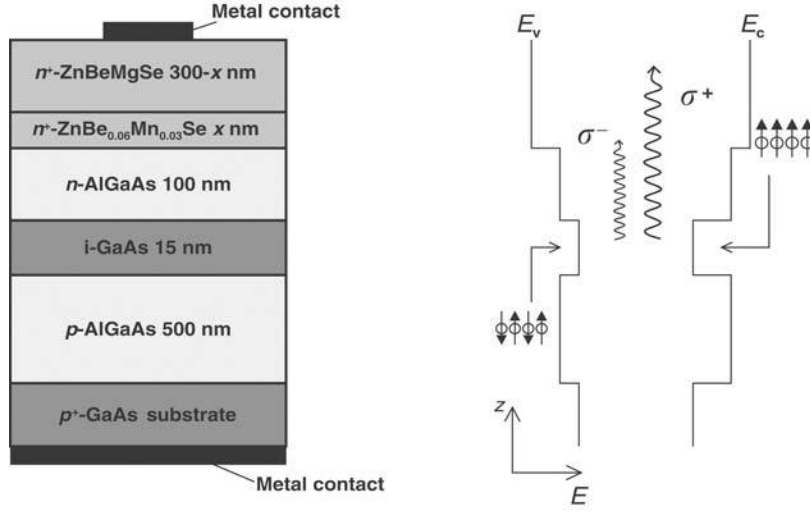
Figure 2
Layer sequence (left) and band structure (right) of the spin aligner LED. The device consists of a GaAs/AlGaAs LED which has a spin aligning *n*-contact. The electrons are aligned in the II–VI-layer and recombine in the GaAs with unpolarized holes coming from the GaAs substrate.
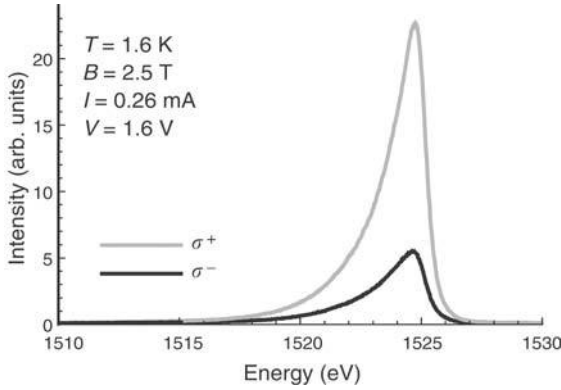
Figure 3
EL spectrum of a typical spin LED. The signal is strongly polarized.

While the latter would not present too big a problem due to the high spin injection efficiency demonstrated in the optical experiment, the realization of GMR could only be achieved using very small contacts with small ferromagnetic bias magnets that are difficult to realize.

However, the splitting of the electrochemical potentials which is always present in spin injection experiments can be used in electrical detection of the spin injection effect. When a nonmagnetic semiconductor is fitted with two dilute magnetic semiconductor contacts and a voltage is applied, a new

magnetoresistance effect can be observed. While the DMS is not magnetized, current through the sample will lead to an identical slope for the electrochemical potentials of spin-up and spin-down electrons in the nonmagnetic semiconductor (NMS) (Fig. 4(a)). As soon as the DMS is magnetized, the electrochemical potentials will split at the interfaces leading to a kind of boundary resistance (Fig. 4(b)).

Much in contrast to giant magnetoresistance, this boundary resistance persists even if the spacing between the contacts is larger than the spin-flip length in the NMS (the effect can also be present in a single contact geometry). This boundary resistance will appear as a magnetoresistance, which can be up to 100% of the resistance of the NMS. The increase of the resistance can be attributed to the nonequilibrium distribution of spin currents in the spin channels of the NMS. At the boundary, one spin channel is suppressed over the range of the spin-flip length, reducing the total conductivity. In the ideal case of full spin polarization and no spin scattering, one spin channel is completely suppressed throughout the NMS leading to a reduction of the conductivity by a factor of 2. For a finite spacing of the contacts, the magnetoresistance can be shown to be

$$\frac{\Delta R}{R_{sc}} = \beta^2 \frac{\lambda_{dms}}{\sigma_{dms}} \frac{\sigma_{sc}}{x_0}$$
$$\times \frac{2}{\frac{\lambda_{dms}}{\sigma_{dms}} \frac{\sigma_{sc}}{\lambda_{sc}}(1 + e^{-x_0/\lambda_{sc}}) + 2\frac{\lambda_{dms}}{\sigma_{dms}} \frac{\sigma_{sc}}{x_0} e^{-x_0/\lambda_{sc}} + 1 - \beta^2}$$

(8)
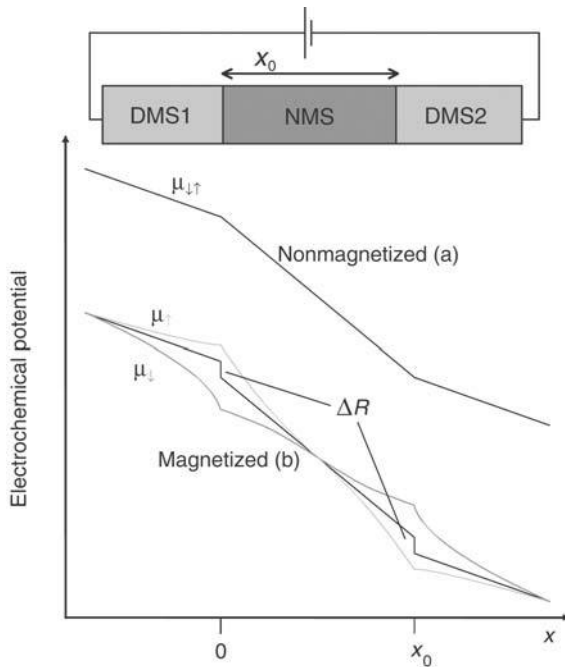
Figure 4
Schematic drawing of the device with two DMS contacts and plot of the electrochemical potentials for the two spin channels. Without applied magnetic field (a) the potentials are identical. As soon as a magnetic field is applied (b) the potentials split at the interfaces.

The effect has been observed experimentally in an all II–VI semiconductor structure where the NMS was ZnBeSe and the DMS was ZnBeMnSe. The observed effect was up to 25% of the total device resistance (Schmidt *et al.* 2001). The deviation from 100% can be explained by the fact that the contact spacing in this experiment was much larger than the expected spin scattering length in ZnBeSe.

Meanwhile, different experiments using optical detection and based on ferromagnetic metal contacts with tunnel barriers have been published (Motsnyi *et al.* 2002, Zhu *et al.* 2001). Although the efficiency obtained is not as high as in the case of DMS contacts, they show that based on a detailed understanding of the phenomena, novel approaches can lead towards room-temperature applications. In addition, over the past years a large research effort has been initiated and is ongoing which is dedicated to highly spin-polarized materials that are ferromagnetic at room temperature. These could replace DMSs and still maintain the same spin injection efficiency that is needed for device applications.

Bibliography

Baibich M N, Broto J M, Fert A 1988 Giant magnetoresistance of (001)Fe/(001)Cr magnetic superlattices. *Phys. Rev. Lett.* **61**, 2472

Binasch G, Grünberg P, Saurenbach F, Zinn W 1989 Enhanced magnetoresistance in layered structures with antiferromagnetic interlayer exchange. *Phys. Rev. B* **39**, 4828

Datta S, Das B 1990 Electronic analog of the electrooptic modulator. *Appl. Phys. Lett.* **56** (7), 665

Fert A, Jaffres H 2001 Conditions for efficient spin injection from a ferromagnetic metal into a semiconductor. *Phys. Rev. B* **64**, 184420

Fiederling R, Keim M, Reuscher G, Ossau W, Schmidt G, Waag A, Molenkamp L W 1999 Injection and detection of a spin-polarized current in a light-emitting diode. *Nature* (London) **402**, 787

Kikkawa J M, Awschalom D D 1999 Lateral drag of spin coherence in gallium arsenide. *Nature* **397**, 139–41

Monzon F G, Roukes M L 1999 Spin injection and the local Hall effect in InAs quantum wells. *JMMM* **198–199**, 632

Motsnyi V F, De Boeck J, Das J, Van Roy W, Borghs G, Goovaerts E, Safarov V I 2002 Electrical spin injection in a ferromagnet/tunnel barrier/semiconductor heterostructure. *Appl. Phys. Lett.* **81** (2), 265

Ohno Y, Young D K, Beschoten B, Matsukura F, Ohno H, Awschalom D D 1999 Electrical spin injection in a ferromagnetic semiconductor heterostructure. *Nature* **402**, 790

Rashba E I 2000 Theory of electrical spin injection: tunnel contacts as a solution of the conductivity mismatch problem. *Phys. Rev. B* **62**, R16267

Schmidt G, Ferrand D, Molenkamp L W, Filip A T, van Wees B J 2000 Fundamental obstacle for electrical spin injection from a ferromagnetic metal into a diffusive semiconductor. *Phys. Rev. B* **62**, R4790

Schmidt G, Richter G, Grabs P, Gould C, Ferrand D, Molenkamp L W 2001 Large magnetoresistance effect due to spin injection into a nonmagnetic semiconductor. *Phys. Rev. Lett.* **87**, 227203

Valet T, Fert A 1993 Theory of the perpendicular magnetoresistance in magnetic multilayers. *Phys. Rev. B* **48** (10), 7099

Zhu H J, Ramsteiner M, Kostial H, Wassermeier M, Schonherr H P, Ploog K H 2001 Room-temperature spin injection from Fe into GaAs. *Phys. Rev. Lett.* **87** (1), 016601

G. Schmidt
Universität Würzburg, Germany

SQUIDs: Amplifiers

Radio-frequency (RF) amplifiers virtually always involve semiconductors as active elements. Noise temperatures of about 2 K can be achieved with these devices at frequencies of several hundred megahertz (Bradley 1999), when the amplifier is cooled to liquid helium temperatures. Cooling the amplifier to still lower temperatures does not reduce the noise temperature further because of intrinsic noise sources in

the transistor. It is also questionable whether a transistor can be cooled to, say, 1 K because of the relatively large power dissipation.

At least at frequencies of several hundred megahertz, better results can be obtained by using a d.c. superconducting quantum interference device (SQUID) as an RF amplifier. For this device, the noise temperature continues to decrease linearly with the bath temperature as it is lowered to about 0.1 K (Wellstood *et al.* 1994). This is because the power dissipation in the SQUID is orders of magnitude lower than for a transistor, and because the only intrinsic noise source at frequencies above a few hertz is Nyquist noise in the shunts of the junctions.

1. Conventional d.c. SQUID Amplifier

The conventional d.c. SQUID amplifier (Hilbert and Clarke 1985) consists of two resistively shunted Josephson junctions (see *Josephson Junctions: Low-T_c*, *Josephson Junctions: High-T_c*) incorporated into a square washer of inductance L over which is deposited a superconducting input coil of n turns with inductance $L_i \approx n^2 L$. The SQUID is current and flux biased so that the flux to voltage transfer function, $V_\Phi = \partial V / \partial \Phi$, is close to a maximum. A signal current I_i in the input coil generates a flux $M_i I_i$ in the SQUID and an output voltage $V_0 \approx M_i I_i V_\Phi$ across it, where M_i is the mutual inductance between the input coil and the SQUID. With sufficiently large M_i and V_Φ, a relatively high gain can be obtained in this configuration. The conventional flux locked loop operation of the SQUID, which is used to linearize its transfer function, cannot be realized for the required high-frequency operation. This means that the amplitude of the input signal is limited to currents that produce flux changes in the SQUID of less than about $\Phi_0/4$. Fortunately, in most high-frequency applications the input signal amplitude is much less than that. If a SQUID with a flux noise of $10^{-6}\Phi_0\text{Hz}^{-1/2}$ is used one can still achieve a dynamic range of nearly 120 dBHz$^{-1/2}$. Larger flux changes, caused, for example, by 50 Hz or 60 Hz fields, can easily be compensated by operating the SQUID in a slow flux locked loop, which maintains the flux bias at odd multiples of $\Phi_0/4$.

Using a SQUID amplifier with an input circuit tuned to 93 MHz, Hilbert and Clarke (1985) achieved a gain of about 18 dB and a noise temperature of about 1.5 K for a bath temperature of 4.2 K. Above 100 MHz, however, parasitic capacitance, C_p, between the input coil of inductance L_i and the SQUID produces self-resonances and severely reduces the gain. The $L_i C_p$ parallel resonance can be moved to higher frequencies by reducing the number of turns, reducing their width, or increasing the thickness of the insulating layer that separates the coil from the SQUID. However, reducing the number of turns may reduce the mutual inductance between the coil and the SQUID to a value that is too small to produce a satisfactory gain. For the same reason the size of the SQUID hole should be made as large as possible (e.g., 200 μm × 200 μm).

Takami *et al.* (1989) have described a SQUID amplifier in which the input circuit is tuned to the desired resonant frequency by adjusting the thickness of the insulating layer between the SQUID and coil, thus varying the parasitic capacitance. To match the high resistance of the parallel $L_i C_p$ circuit to the 50 Ω signal source, the signal is coupled to the coil by a small (3 pF) capacitor. This scheme leads to a relatively high quality factor, Q, of the $L_i C_p$ circuit, a high input current at the resonant frequency, and thus a high gain. Gains have been measured of up to 23 dB at 150 MHz, and a noise temperature of about 0.7 K for a bath temperature of 4.2 K. Unfortunately, the high Q of the resonant circuit decreases the bandwidth to about 1% of the operating frequency, which for many applications is too small. Increasing the bandwidth by decreasing Q decreases the gain. Nevertheless, for narrow-band applications such as NMR, this coupling scheme provides a high gain, low noise amplifier for frequencies of up to a few hundred megahertz.

If operation at higher frequencies is required, the parasitic capacitance either has to be reduced or its influence removed with a resonance technique. Reducing the capacitance can be achieved by placing the input coil inside the SQUID hole. Because of the decreased coupling between coil and SQUID, however, the gain is quite small. Tarasov *et al.* (1995) have made a SQUID amplifier in this way, and reported gains of 8 dB at 700 MHz and a noise temperature of about 1.5 K. In an alternative design, Prokopenko *et al.* (1999) used a SQUID amplifier with a series resonant input circuit to achieve a gain of 10 dB at 3.8 GHz and a noise temperature of 5 K.

2. SQUID Amplifier with Microstrip Input Coupling

An alternative way of achieving high gains and low noise temperatures at high frequencies is to take advantage of the parasitic capacitance, by operating the input coil of a d.c. SQUID as a microstrip resonator. The input signal is no longer coupled to the two ends of the input coil, but rather between one end of the coil and the SQUID loop, which acts as a ground plane for the coil; the other end of the coil is left open. The microstrip resonator is thus formed by the inductance of the input coil and its ground plane and the capacitance between them. In this configuration, the parasitic capacitance no longer prevents currents from flowing through the coil.

For the case in which the impedance, Z_s, of the source coupled to one end of the microstrip is larger than its characteristic impedance, Z_0, and the other

end of the input coil is left open, the fundamental resonance occurs when the length, l, of the microstrip is equal to half the wavelength of the RF signal. In this mode, the microstrip resonator is analogous to a parallel tuned circuit and, neglecting losses in the microstrip and the SQUID, one calculates a quality factor $Q = \pi Z_s/2Z_0$. At the resonant frequency the current fed into the resonator is amplified by Q, producing a magnetic flux that is coupled into the SQUID via a mutual inductance $M_s = \alpha(LL_s)^{1/2}$, where L_s is the microstrip inductance and α the coupling coefficient. One selects the resonant frequency by appropriate choice of the length of the coil. Q, which determines the bandwidth of the amplifier, can be varied by selecting the characteristic impedance of the microstrip; i.e., by choosing an appropriate width of the turns of the coil and thickness and dielectric constant of the insulating layer between the coil and SQUID. One has to keep in mind, however, that reducing Q will increase the bandwidth and lower the gain, since the resonant current amplification is proportional to Q.

Since the conventional washer SQUID is an asymmetric device (the two Josephson junctions are situated close together rather than on opposite sides of the SQUID loop), one can either ground the washer or ground the counter electrode close to the Josephson junctions. Using the washer as ground plane for the input coil suggests one should ground the washer. However, it is also possible to ground the counter electrode and have the washer at output potential. In this case, depending on the sign of V_Φ (which determines the phase shift between input and output of the amplifier), one can obtain either a negative or positive feedback from the output to the input, and using positive feedback, the gain of such amplifiers can be enhanced substantially.

Using this configuration, Mück *et al.* (1998) measured gains of 20 dB up to a frequency of 1.3 GHz. Noise temperatures as low as 100 mK (at 400 MHz) have been measured when the SQUID is cooled to 0.4 K (André *et al.* 1999). This noise temperature is only about a factor of three above the quantum limit. The intrinsic noise temperature of the amplifier is typically 1/4 of the bath temperature, T, and, within measurement errors, scales with T.

The microstrip amplifier can be tuned by means of a varactor diode, which is connected to the open end of the microstrip. Changing the capacitance of the varactor diode by an applied d.c. voltage enables one to reduce the resonant frequency of the amplifier by nearly a factor of two. If gains higher than 20 dB are desired, two amplifiers can be connected in cascade.

3. Conclusion

For applications requiring extremely low noise temperatures at frequencies of several hundred megahertz

and above, an RF amplifier based on a d.c. SQUID is a promising alternative to semiconductor amplifiers. Such applications include intermediate frequency amplifiers for superconductor–insulator–superconductor (SIS) mixers, NMR, or Axion detectors. Gains of more than 20 dB at frequencies exceeding 1 GHz have been obtained with such amplifiers and noise temperatures as low as 100 mK. An exciting possibility is the expectation that the quantum limit could be reached with a d.c. SQUID amplifier cooled to about 100 mK. A challenge for future work is the extension to higher frequencies. It should be possible to operate a SQUID amplifier at frequencies exceeding 10 GHz, probably by modifying the geometry of the SQUID from the square washer format to, perhaps, an in-line configuration. One may hope that the design and testing of such SQUID amplifiers will be undertaken in the not-too-distant future.

See also: SQUIDs: The Instrument

Bibliography

André M -O, Mück M, Clarke J, Gail J, Heiden C 1999 Microstrip d.c. SQUID radio frequency amplifier with tenth-kelvin noise temperature. *Appl. Phys. Lett.* **75**, 698–700

Bradley R F 1999 Cryogenic, low noise, balanced amplifiers for the 300–1200 MHz band using heterostructure field-effect transistors. *Nucl. Phys. B (Proc. Suppl.)* **72**, 137–44

Hilbert C, Clarke J 1985 DC SQUIDs as radio frequency amplifiers. *J. Low Temp. Phys.* **61**, 263–80

Mück M, André M -O, Clarke J, Gail J, Heiden C 1998 Radio frequency amplifier based on a niobium d.c. SQUID with microstrip input coupling. *Appl. Phys. Lett.* **72**, 2885–7

Prokopenko G V, Balashov D M, Shitov S V, Koshelets V P, Mygind J 1999 Two-stage S-band d.c. SQUID amplifier. *IEEE Trans. Appl. Supercond.* **AS-9**, in press

Takami T, Noguchi T, Hamanaka H 1989 A d.c. SQUID r.f. amplifier. *IEEE Trans. Mag* **MAG-25**, 1030–3

Tarasov M A, Prokopenko G V, Koshelets V P, Lapitskaya I L, Filippenko L V 1995 Integrated r.f. amplifier based on d.c. SQUID. *IEEE Trans. Appl. Supercond.* **AS-5**, 3226–9

Wellstood F C, Urbina C, Clarke J 1994 Hot-electron effects in metals. *Phys. Rev. B* **49**, 5942–55

M. Mück
Institut für Angewandte Physik der Justus-Liebig-Universität Giessen, Germany

SQUIDs: Biomedical Applications

A major application of SQUID systems (see *SQUIDs: The Instrument*) is in biomagnetism, a discipline where the faint magnetic fields associated with electrophysiological functions of the heart, brain, nerves, or muscles are detected with the ultrahigh field sensitivity of SQUIDs. Biomedical investigations
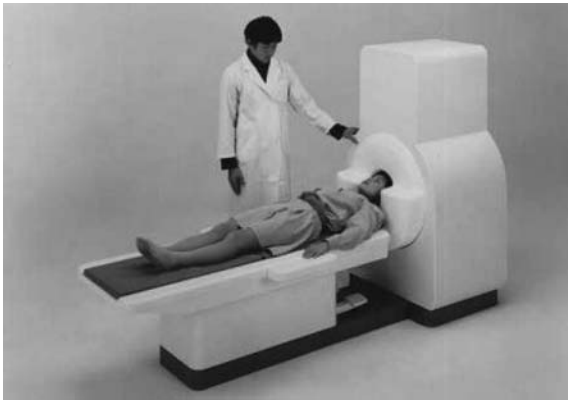
Figure 1
SQUID system for magnetoencephalographic investigations.

with magnetic markers or magnetic nanoparticles have also contributed to biomagnetic research. The magnetic fields under investigation in biomagnetism are very weak. Signal amplitudes that are typically measured are in the range 10^{-9}–10^{-14} T in a frequency range from d.c. to 1 kHz. This requires the sensitivity to magnetic fields that only SQUIDs provide. In addition, very efficient methods for suppressing electric and magnetic interference have to be used.

Modern biomagnetic systems are very complex. With only a few exceptions they are operated in a magnetically shielded room and contain up to 300 low-T_c SQUID sensors maintained at liquid helium temperatures in nonmagnetic fiberglass-reinforced epoxy dewars. Data acquisition, computation, and visualization of results require state-of-the-art information technology. High-T_c SQUIDs and liquid nitrogen cooling are a future prospect and could reduce system complexity and costs.

Figure 1 shows a typical system for magnetoencephalographic investigations. The patient's head is positioned in a helmet-shaped dewar with SQUID sensors fixed inside at the dewar wall in the vicinity of the head.

This article introduces several typical applications. Because of space limitations, only a few instructive examples of biomagnetic applications are covered here to demonstrate the broad spectrum of benefits of biomagnetic SQUID systems. More detailed overviews can be found elsewhere (e.g., Baumgartner *et al.* 1995, Weinstock 1996, Wikswo 1995).

1. Gastroenterology

From the physical and analytical point of view, this application is the simplest to handle. The source to be detected is a small magnetic sample, which may be easily modeled as a magnetic dipole with well-known specifications. Thus, if this magnetized sample is prepared and coated in an appropriate manner such that it can be administered without harm, then its passage through the gastrointestinal tract of a person may be monitored with a SQUID system provided with an algorithm to reconstruct the path of the pellet from field measurement results. Weitschies *et al.* (1997) provide further details of this method.

2. Peripheral Nerves

Another biomagnetic application that relies on a comparatively simple modeling of the source is the investigation of peripheral nerve function. The signal transmission through the nerve fiber may be modeled as an extended current segment, i.e., by a multipole expansion. If the spatiotemporal magnetic field distribution over the nerve is measured with a multichannel SQUID system, then the reconstruction of the current path may be well approximated.

In practice, difficulties result from the poor signal-to-noise ratio commonly accompanying these experiments. Even with the most sensitive SQUID systems available an averaging of up to 10^4 stimuli is necessary to recover the relevant magnetic field signal from the noise. Particularly, the heart signal interferes strongly and has to be eliminated by advanced methods of signal processing. Nevertheless, Mackert *et al.* (1998) have been able to detect the blocking of nerve signal transmission.

3. Magnetoencephalography (MEG)

MEG is the most successful application of biomagnetic systems from the scientific and the commercial point of view. In 1998 more than 50 multichannel SQUID systems were installed and used for MEG investigations worldwide. The latest system generation contains more than 300 SQUID channels.

Most applications concern fundamental physiological and psychological brain research. Clinical applications concern preoperative evaluation and mapping of brain functions and localization of epileptic foci of patients suffering from epilepsy. For an overview on various aspects of MEG see Lounasma *et al.* (1996).

Technologically demanding is the construction of a nonmagnetic helmet-shaped dewar with a close warm/cold distance between the scalp and the pickup coils of the SQUID. Another difficulty is to provide a spatially high density of sensor positions without signal cross-talk between the channels.

While all MEG SQUID systems are made using low-T_c technology, there is hope that high-T_c technology should overcome many of the problems mentioned above. The field sensitivity of high-T_c SQUID systems has already proved sufficient for brain research. Somatosensory-evoked cortical fields have

been detected with a high-T_c SQUID (Drung *et al.* 1996) having a white noise of $< 10\,\mathrm{fTHz}^{-1/2}$.

4. Magnetocardiography (MCG)

Although the maximum amplitude of MCG signals is 1–2 orders of magnitudes higher than typical MEG signals it is necessary to achieve a similarly good signal-to-noise ratio, as the relevant signal components may be of comparably small amplitude. Clinically interesting applications are seen in the field of risk stratification of sudden heart death and myocardial vitality.

One way to derive relevant information from magnetic field maps is to recognize specific patterns or features in the field maps that can be considered as a "fingerprint" or "signature" of certain physiological or pathophysiological functions in which the physician is interested and wants to discriminate. A common approach is then to quantify these signatures by derived characteristic factors. For instance, patients who suffer from coronary artery heart disease, and thus have a high risk of a sudden heart death, show distinctive alterations in magnetic field maps compared to those of normal subjects. The factors mentioned above reflect these alterations and give a valuable indication as to this risk.

5. Source Localization

Many applications demand a "localization" of the physiological or pathophysiological function looked for. Technically, this requires a reconstruction of the current density distribution, the "source," that generated the measured magnetic field pattern. Mathematically, this inverse problem, i.e., the calculation of the source distribution with the help of measured field values, is a so-called ill-posed problem, because principally no unique solution exists. However, with the aid of appropriate models an acceptable approximation of the source may be derived. The most common model is the equivalent current dipole, which is of good value in mapping localized brain functions such as evoked cognitive responses.

A more sophisticated algorithm (Fuchs *et al.* 1995 pp. 320–5) models the current density distribution of the investigated brain or heart function by many small current dipoles distributed over the cortex or the heart ventricle only at such positions that come into question on physiological grounds. In this way, the possible solutions of the inverse problem are effectively constrained. The proper anatomic geometry is derived from magnetic resonance imaging.

6. Towards Unshielded SQUID Systems

In order to suppress noise due to magnetic fields generated, for example, from power line hum, electric street cars, etc., biomagnetic systems are commonly operated in shielded rooms with thick walls consisting of several layers of mu-metal. Such shielded rooms make SQUID systems very expensive and prohibit a wider distribution of biomagnetic methods. Therefore, many approaches have been tried to reduce the need for passive shielding.

One way is to use gradiometer concepts, i.e., instead of measuring with one magnetometer the magnetic flux at one position, one determines the difference of magnetic flux of two adjacent positions (i.e., the approximation of the gradient of the magnetic field). As the source to be investigated is close to the sensors it provides a strong gradient as compared to a distant interfering source and thus the source signals are enhanced with respect to the interference.

Gradiometric configurations may be achieved with appropriately formed pick-up coils: vertical or planar gradiometers. Another way is to use two magnetometers and subtract their signals from each other electronically, thus forming "electronic" gradiometers. Similarly "software" gradiometers may be designed.

A modern solution is to configure the SQUIDs to form a reference system that provides all signal information for a sophisticated algorithm, which then generates the appropriate compensation signals to each of the SQUIDs in the measurement plane of a multichannel system. At sites with only moderate interference, such systems have successfully demonstrated an unshielded performance. However, in urban or clinical environments a passive shield may still be necessary. For a detailed analysis of the topic of interference discrimination see Vrba (1996 pp. 117–78).

With HTS SQUIDs unshielded operation is even more difficult owing to the sensitivity to trapped and moving flux lines in the high-T_c material, particularly if the sensors are cooled and moved in the earth's magnetic field.

See also: SQUIDs: The Instrument; SQUIDs: Nondestructive Testing

Bibliography

Baumgartner C, Deecke L, Stroink G, Williamson S J (eds.) 1995 *Biomagnetism: Fundamental Research and Clinical Applications*. IOS, Amsterdam

Drung D, Ludwig F, Müller W, Steinhoff U, Trahms L, Koch H, Shen Y Q, Jensen M B, Vase P, Holst T, Freltoft T, Curio G 1996 Integrated $YBa_2Cu_3O_{7-x}$ magnetometer for biomagnetic measurements. *Appl. Phys. Lett.* **68**, 1421–3

Fuchs M, Wagner M, Wischmann H -A, Dössel O 1995 Cortical current imaging by morphologically constrained reconstructions. In: Baumgartner C, Deecke L, Stroink G, Williamson S J (eds.) *Biomagnetism: Fundamental Research and Clinical Applications*. IOS, Amsterdam

Lounasma O V, Hämäläinen M, Hari R, Salmelin R 1996 Information processing in the human brain: magnetoencephalographic approach. *Proc. Natl. Acad. Sci. USA* **93**, 8809–15

Mackert B M, Curio G, Burghoff M, Trahms L, Marx P 1998 Magnetoneurographic 3D localisation of conduction blocks in patients with unilateral S1 root compression. *Electroenceph. Clin. Neurophys.* **109**, 315–20

Vrba J 1996 SQUID gradiometers in real environments. In: Weinstock H (ed.) *SQUID Sensors: Fundamentals, Fabrication and Applications,* NATO ASI Series E, Applied Science 329. Kluwer, Amsterdam

Weinstock H (ed.) 1996 *SQUID Sensors: Fundamentals, Fabrication and Applications,* NATO ASI Series E, Applied Science 329. Kluwer, Amsterdam

Weitschies W, Kötitz R, Cordini D, Trahms L 1997 High-resolution monitoring of the gastrointestinal transit of a magnetically marked capsule. *J. Pharmaceut. Sci.* **66**, 1218–22

Wikswo J P 1995 SQUID magnetometers for biomagnetism and nondestructive testing: important questions and initial answers. *IEEE Trans. Appl. Supercond.* **5**, 74–120

H. Koch
*Physikalisch-Technische Bundesanstalt
Berlin, Germany*

SQUIDs: Magnetic Microscopy

Magnetic fields above sample surfaces can be imaged using a superconducting quantum interference device (SQUID) in a scanning SQUID microscope (SSM). Both low critical temperature (low T_c) SQUIDs (which have better sensitivity) and high T_c SQUIDs (which can be operated at higher temperatures) (Koelle *et al.* 1999) have been used as SSM sensors. The best low T_c SQUIDs have a flux noise of $\sim 2 \times 10^{-6} \Phi_0 \mathrm{Hz}^{-1/2}$, where $\Phi_0 = h/2e = 2.07 \times 10^{-15}$ Wb is the superconducting magnetic flux quantum. A SQUID magnetometer with this noise and a $100\,\mu\mathrm{m}^2$ pickup area can detect magnetic fields of $\sim 40\,\mathrm{pTHz}^{-1/2}$, a dipole source of $\sim 2500\,\mu_B \mathrm{Hz}^{-1/2}$, a monopole source (e.g., a superconducting vortex) of $\sim 2.5 \times 10^{-6}\Phi_0 \mathrm{Hz}^{-1/2}$, and a current line source of $\sim 1\,\mathrm{nAHz}^{-1/2}$. Smaller pickup areas are more sensitive for a dipole field source, while larger pickup areas are more sensitive for a current line source. The spatial resolution is about the size of the effective area, if the source–pickup area spacing is smaller than this size.

Many schemes have been used to scan the sample and couple magnetic fields into the SQUID (Kirtley and Wikswo 1999). Either (i) both sample and SQUID are cold (Figs. 1(a)–(c)), or (ii) the SQUID is cold but the sample is at room temperature (Figs. 1(d)–(f)). The second method has the advantage of not requiring sample cooling, with some sacrifice in spatial resolution. In either case, a bare SQUID (Figs. 1(a) and (d)), a SQUID inductively coupled with a superconducting pickup loop (Figs. 1(b) and (e)), or a superconducting pickup
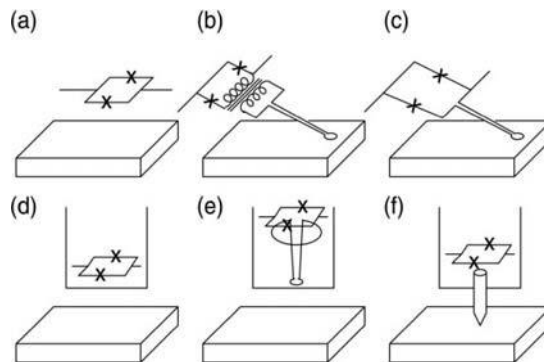
Figure 1
Various strategies for scanning the sample relative to the SQUID.

loop integrated into the SQUID design (Fig. 1(c)) can be used to detect the sample magnetic field. In Fig. 1(f), a ferromagnetic tip is used to couple flux from a room temperature sample to a cooled SQUID.

While early systems connected discrete SQUIDs to hand-wound pickup coils, integrated SQUID sensors are now commonplace. In these devices, commonly Nb–AlO_x–Nb thin-film SQUIDs, the SQUID junctions, shunt resistors, and modulation coil are connected to the pickup coil through a well-shielded, low-inductance lead structure. Pickup loop sizes as small as $4\,\mu\mathrm{m}$ in diameter have been fabricated: modeling indicates that pickup areas as small as $1\,\mu\mathrm{m}^2$ can be effectively attained. SQUIDs using microbridges as the Josephson weak links (micro-SQUIDs) (Wernsdorfer *et al.* 1996) have been fabricated as small as $1\,\mu\mathrm{m}$ in diameter. These micro-SQUIDs have two orders of magnitude higher flux noise than the best tunnel junction SQUIDs, but can be operated in higher ambient magnetic fields. Most SSMs scan the sample relative to the SQUID mechanically. While not as stiff or as fast as piezoelectric scanners, mechanical scanning affords much larger scan areas ($\sim 1\,\mathrm{cm}$ as compared to $\sim 100\,\mu\mathrm{m}$).

SSMs have been used in a number of applications in the fields of biomagnetism, corrosion science, nondestructive evaluation, and superconductivity (Wikswo 1995). Two applications in this last area will be briefly described here.

Exploration of novel superconductors often results in samples with small superconducting concentrations. The SSM is an ideal tool to image samples to determine which parts are superconducting. Figure 2 shows an example (Scott *et al.* 1997). Comparison of optical (Fig. 2(a)) and SSM (Fig. 2(b)) images of a diffusion couple of $Sr_2CuO_3 + 0.05$ $KClO_3$ processed at high temperatures and pressures shows that certain regions (the dark gray areas labeled (e) in Fig. 2(a)) are superconducting. These regions are determined by electron microprobe to be $Sr_3Cu_2O_5Cl$.
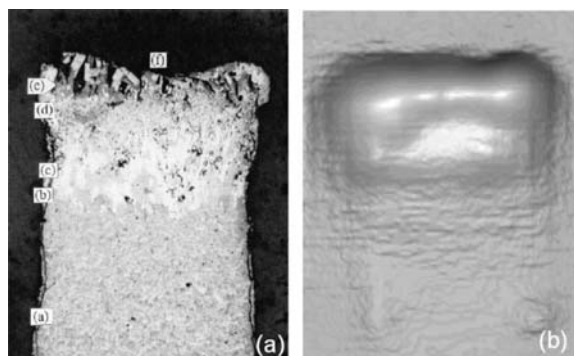
Figure 2
(a) Optical micrograph and (b) SQUID microscope image of a partially superconducting sample. The bright areas in (b) are superconducting (after Scott *et al.* 1997).

Figure 3
SQUID microscope image of thin-film YBCO rings. The presence of a half-flux quantum in the central ring indicates that YBCO has predominantly d-wave pairing symmetry (after Tsuei *et al.* 1994).

The SSM has also played a central role in phase-sensitive tests of the pairing symmetry of the high T_c cuprate superconductors. While conventional superconductors have symmetric or s-wave pairing, there is now good evidence that several optimally doped cuprates have predominantly $d_{x^2-y^2}$ symmetry (see the polar plots in Fig. 3) (Scalapino 1995). With such momentum-dependent sign changes, SQUIDs can be designed with junction supercurrents that destructively interfere at zero applied field, rather than constructively interfering, as for conventional SQUIDs. The first phase-sensitive tests measured the interference patterns of such specially constructed SQUIDs (van Harlingen 1995).

Other phase-sensitive tests have employed the SSM (Tsuei *et al.* 1994, Mathai *et al.* 1995). Figure 3 is a SSM image of four thin-film, 58 μm diameter rings of the high T_c cuprate superconductor YBa$_2$Cu$_3$O$_{7-\delta}$ (YBCO) epitaxially grown on a tricrystal substrate of SrTiO$_3$. The tricrystal geometry produces a high-energy, frustrated state for a d-wave superconductor. This frustrated state is relaxed by spontaneously generating a supercurrent around the ring, which produces a half-integer multiple of the superconducting flux quantum ($(n+1/2)\Phi_0$, where n is an integer) threading the ring. The SQUID image of Fig. 3 is of the sample cooled in zero field. The three outer control rings have no flux trapped in them; the central frustrated ring has $\Phi_0/2$. A number of optimally doped cuprate high T_c superconductors exhibit the half-flux quantum effect in this geometry, and therefore presumably have predominantly d-wave pairing symmetry.

In summary, magnetic microscopy with SQUIDs has the advantage of high sensitivity, but the disadvantages of the requirement of a cooled sensor and relatively modest spatial resolution. Progress is being made in improved instruments with warmed samples, and with higher spatial resolution.
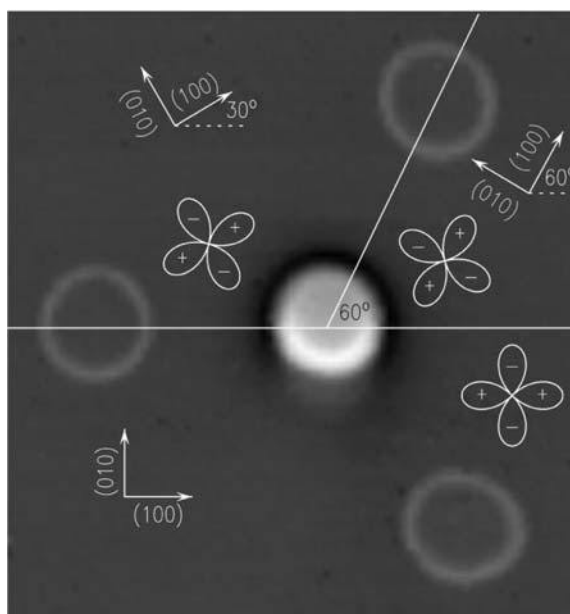
See also: SQUIDs: The Instrument; Magnetic Force Microscopy; Magnetic Materials: Transmission Electron Microscopy; Kerr Microscopy

Bibliography

Kirtley J R, Wikswo J P Jr. 1999 Scanning SQUID microscopy. *Annu. Rev. Mater. Sci.* **29**, 117–48

Koelle D, Kleiner R, Ludwig F, Dantsker E, Clarke J 1999 High transition temperature superconducting quantum interference devices. *Rev. Mod. Phys.* **71**, 631–86

Mathai A, Gim Y, Black R C, Amar A, Wellstood F C 1995 Experimental proof of a time-reversal-invariant order parameter with a π shift in YBa$_2$Cu$_3$O$_{7-\delta}$. *Phys. Rev. Lett.* **74**, 4523–6

Scalapino D J 1995 The case for $d_{x^2-y^2}$ pairing in the cuprate superconductors. *Phys. Rep.* **250**, 329–65

Scott B A, Kirtley J R, Walker D, Chen B H, Wang H 1997 Application of scanning SQUID petrology to high-pressure materials science. *Nature* **389**, 164–7

Tsuei C C, Kirtley J R, Chi C C, Yu-Jahnes L S, Gupta A, Shaw T, Sun J Z, Ketchen M B 1994 Pairing symmetry and flux quantization in a tricrystal superconducting ring of YBa$_2$Cu$_3$O$_{7-\delta}$. *Phys. Rev. Lett.* **73**, 593–6

van Harlingen D J 1995 Phase-sensitive tests of the symmetry of the pairing state in the high-temperature superconductors—evidence for $d_{x^2-y^2}$ symmetry. *Rev. Mod. Phys.* **67**, 515–35

Wernsdorfer W, Doudin B, Mailly C, Hasselbach K, Benoit A, Meier J, Ansermet J-Ph, Barbara B 1996 Nucleation of the

magnetization reversal in individual nanosized nickel wires. *Phys. Rev. Lett.* **77**, 1873–6

Wikswo J P Jr. 1995 SQUID magnetometers for biomagnetism and nondestructive testing: important questions and initial answers. *IEEE Trans. Appl. Supercond.* **5**, 74–121

J. R. Kirtley
IBM Research, Yorktown Heights, New York, USA

SQUIDs: Nondestructive Testing

The need for inspection has been recognized ever since people began to build machines. Nondestructive evaluation (NDE) techniques that can find hidden flaws are ultrasonics, radiography, and electromagnetic techniques (see *Nondestructive Testing and Evaluation: Overview*). Commonly used magnetic field sensors in NDE are induction coils, Hall probes, and magnetoresistors. Induction coils are versatile; however, they have the inherent disadvantage of measuring only the time derivative of the magnetic field. This requires high signal frequencies for good performance. Following the development of SQUID sensors, many research groups have shown the use of SQUIDs (see *SQUIDs: The Instrument*) in conjunction with electromagnetic NDE (e.g., see reviews by Donaldson *et al*. 1996, Jenks *et al*. 1997). The advantages of SQUIDs include high field sensitivity, wide bandwidth, and, possibly most important, very broad dynamic range in conjunction with excellent linearity.

1. Eddy Current Inspection

Eddy current testing by inductive sensors is an important NDE technique, especially for layered structures. The penetration depth of the electromagnetic excitation wave, the so-called skin depth, $\delta_0 = 1/\sqrt{\pi\sigma\mu f}$, restricts the depth at which flaws can be found. For a plane wave excitation with frequency f of a medium with conductivity σ and permeability μ, δ_0 denotes the depth of material where the amplitude is attenuated by $1/e$ and the phase is rotated by π. Thus, the phase lag of the response signal contains information about the flaw depth. In contrast to conventional techniques, SQUID systems offer a high sensitivity at low excitation frequencies, permitting the detection of deeper flaws, and a high linearity, allowing quantitative evaluation of magnetic field maps from the structure investigated. Several research groups have developed LTS as well as HTS SQUID systems for eddy current testing (e.g., Ma and Wikswo 1993, Podney 1995, Tavrin *et al*. 1996, Cochran *et al*. 1995).

Nondestructive testing (NDT) of new and aging aircraft structures is essential for flight safety and for keeping inspection costs low. Eddy current testing is a
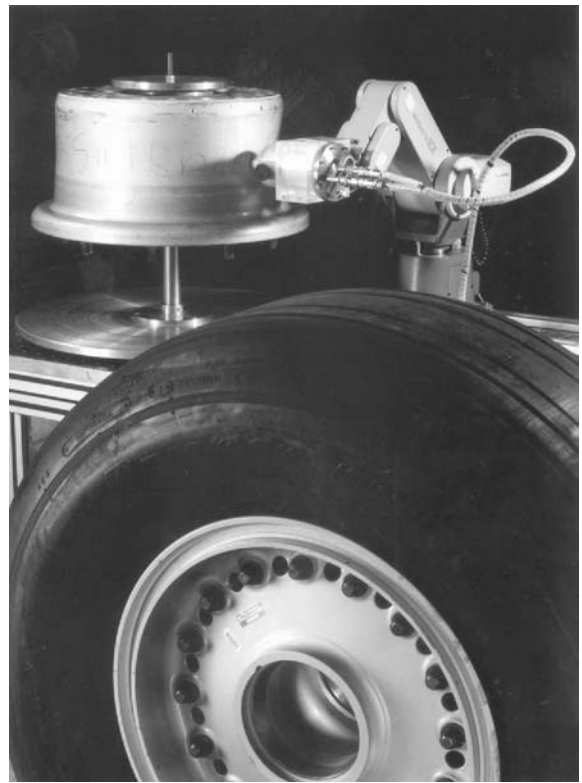
Figure 1
Automated wheel-testing system.

widely used NDT method in aircraft maintenance. The applicability of HTS SQUID magnetometers to aircraft testing has been demonstrated by Kreutzbruck *et al*. (1997). Mobile HTS SQUID planar gradiometers with orientation-independent cooling have been developed for eddy current testing of ''second layer'' cracks and corrosion in aircraft fuselages (Krause *et al*. 1997).

The detection of deep cracks in aircraft wheels is one example of the application of HTS SQUIDs to NDT (Hohmann *et al*. 1999). Figure 1 shows the main parts of a wheel-testing unit. The system consists of a rotating table, a robot, and a sensor head. A planar SQUID gradiometer has been integrated with a commercial Joule–Thomson cryocooler, providing liquid nitrogen-free SQUID cooling. For the generation of eddy currents in the sample, a double-D configuration of induction coils is used. Figure 2 shows the measurement of flaws in an aircraft wheel.

2. Magnetic Flux Leakage

Surface or subsurface flaws in ferromagnetic materials are usually detected by magnetizing the test object
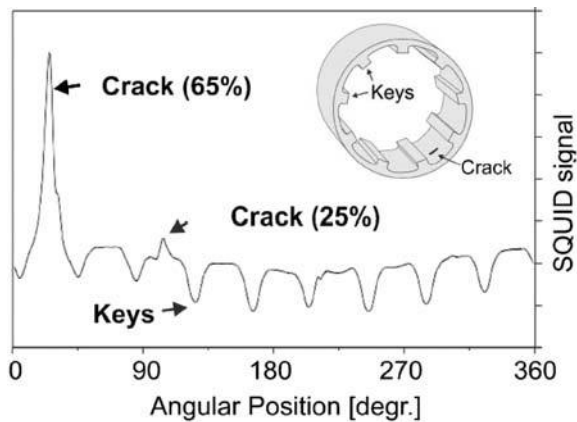
Figure 2
SQUID measurement of an aircraft wheel. Two inner flaws that penetrate the wall thickness by 65% and 25% are detected.

and monitoring the magnetic flux leakage (MFL) above the surface. Open voids lead to a strong enhancement of the outside stray field due to the local absence of a high permeability flux guide. Subsurface voids affect the local permeability (magnetization) of the material and, therefore, also the local stray field. These stray fields are observed either while continuously magnetizing the object or by measuring the remanent magnetization. Local changes in the stray field are mapped by means of scanning the magnetic field sensor over the metal.

The MFL technique has been used for the detection of cracks in steel reinforcement rods (rebars) in concrete structures such as bridges or roofs of buildings (Sawade *et al*. 1997). Owing to hydrogen-induced stress and corrosion, cracks and other damage to prestressed concrete members can occur. The rebars are magnetized longitudinally during a scan with a yoke magnet. In the center of the yoke, the stray field is picked up by HTS SQUIDs, having a greater linearity and dynamic range than conventional Hall

Figure 3
Inspection of a German highway bridge using a SQUID system.

probe magnetometers, also incorporated into the same scanner. With this system, dangerous cracks were detected in a German freeway bridge with running car traffic (see Fig. 3). Subsequent opening of the concrete at the detected location confirmed the findings, and the bridge had to be decommissioned and demolished.

3. Detection of Ferromagnetic Particles

The first certified commercial use of HTS SQUIDs in everyday NDE was the detection of ferrous inclusions in premagnetized aircraft gas turbine disks, fabricated from a special nonmagnetic alloy. The presence of such inclusions may cause cracks in these critical parts, and may eventually lead to engine failure. Tavrin *et al.* (1999) used a second-order unshielded axial gradiometer for determination of the mass, radial position, and depth of small ferromagnetic inclusions in the disk. The disk is slowly rotated on a turntable while the gradiometer is moved radially by a mechanically stable arm. The measurements of remanent magnetization at two different axial distances from the disk surface are used to calculate the magnetic particle depth using the dipolar $1/R^3$ scaling law. The approximate particle mass is then determined from its dipole strength. A particle mass of 1 mg is reliably measurable in the depth range up to 70 mm.

Another approach to the problem of ferromagnetic inclusion detection has been presented by Panaitov *et al.* (1999). A SQUID vector reference is used in a first-order electronic gradiometer to compensate for the disturbances of unshielded environments. Samples with small particles of different sizes and

magnetic moments are placed on a scanning table and moved underneath the gradiometer sensor and the axial component of the d.c. magnetic field is recorded. By fitting the measured field profile to a dipole law, the amplitude of the magnetic moment and the distance from the sensor to the particle is determined. Figure 4 shows an example of the measured particle field profile and the dipole fit to the trace.

4. Outlook

Ideally, the end user would like a tomography-like three-dimensional analysis of the material under test, an image of the sample. This requires the solution of the three-dimensional inverse problem: the determination of the source distribution inside an object by measuring the magnetic fields at a few locations outside (cf. Wikswo 1996). Practical implementation of these imaging techniques is expected to become available in the future.

See also: SQUIDs: Biomedical Applications; SQUIDs: The Instrument

Bibliography

Cochran S, Donaldson G B, Carr C, McKirdy D McA, Walker M E, Klein U, McNab A, Kuznik J 1995 Recent progress in SQUIDs as sensors for electromagnetic NDE. In: Collins R, Dover W D, Bowler J R, Miya K (eds.) *NDT of Materials*. IOS, Amsterdam, pp. 53–64

Donaldson G B, Cochran A, McKirdy D McA 1996 The use of SQUIDs for nondestructive evaluation. In: Weinstock H (ed.) *SQUID Sensors*. Kluwer, Dordrecht, The Netherlands, pp. 599–628

Hohmann R, Maus M, Lomparski D, Grüneklee M, Zhang Y, Krause H J, Bousack H, Braginski A I, Heiden C 1999 Aircraft wheel testing with machine-cooled HTS SQUID gradiometer system. *IEEE Trans. Appl. Supercond.* **9**, 3801–4

Jenks W G, Sadeghi S S H, Wikswo J P 1997 SQUIDs for nondestructive evaluation. *J. Phys. D* **30**, 293–323

Krause H J *et al.* 1997 Mobile HTS SQUID systems for eddy current testing of aircraft. In: Thompson D O, Chimenti D E (eds.) *Rev. Prog. QNDE 16*. Plenum, New York, pp. 1053–60

Kreutzbruck Mv, Tröll J, Mück M, Heiden C 1997 Experiments on eddy current NDE HTS rf SQUIDs. *IEEE Trans. Appl. Supercond.* **7**, 3279–82

Ma Y P, Wikswo J P 1993 Imaging subsurface defects using a SQUID magnetometer. In: Thompson D O, Chimenti D E (eds.) *Rev. Prog. QNDE 12*. Plenum, New York, pp. 1137–43

Panaitov G, Zhang Y, Wang S G, Wolters N, Zhang L H, Otto R, Schubert J, Zander W, Soltner H, Bick M, Krause H J, Bousack H 1999 An HTS SQUID magnetometer using coplanar resonator with vector reference for operators in unshielded environment. In: Obradors X (ed.) *Applied Superconductivity*. Institute of Physics, Bristol, UK, pp. 449–52

Podney W N 1995 Eddy current evaluation of airframes using refrigerated SQUIDs. *IEEE Trans. Appl. Supercond.* **5**, 2490–2

Sawade G, Gampe U, Krause H J 1997 Non-destructive examination using a SQUID magnetometer. In: Forde M T
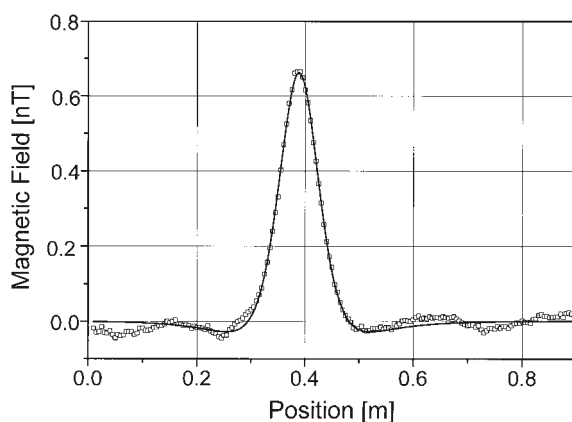
Figure 4
Signal of a small magnetic particle, measured with a SQUID gradiometer (squares). From the dipole fit (line) the moment of particle is found to be 2.6×10^{-6} Am^2, with a minimum distance to the sensor of 87 mm.

(ed.) *Proc. 7th Int. Conf. on Structural Faults and Repair.* Engineering Technical Press, Edinburgh, UK, pp. 401–6

Tavrin Y, Krause H J, Wolf W, Glyantsev V, Schubert J, Zander W, Bousack H 1996 Eddy current technique with high-temperature SQUID for non-destructive evaluation of non-magnetic metallic structures. *Cryogenics* **36**, 83–6

Tavrin Y, Siegel M, Hinken J H 1999 Standard method for detection of magnetic defects in aircraft engine discs using an HTS SQUID gradiometer. *IEEE Trans. Appl. Supercond.* **9**, 3809–12

Wikswo J P 1996 The magnetic inverse problem for NDE. In: Weinstock H (ed.) *SQUID Sensors*. Kluwer, Dordrecht, The Netherlands, pp. 629–95

H. Bousack, R. Hohmann, H.-J. Krause
G. Panaitov and Y. Zhang
Forschungszentrum Jülich, Germany

SQUIDs: The Instrument

The superconducting quantum interference device (SQUID) is exquisitely sensitive to tiny changes in magnetic flux. It can be configured as a very sensitive magnetometer or magnetic field gradiometer, but it can also be used in a wide variety of other applications, for example to measure tiny voltages, to detect very small magnetic moments, and to amplify radio-frequency (RF) signals.

There are two basic types of SQUID. The first, the d.c. SQUID—so called because it operates with a static bias current—consists of two Josephson junctions (see *Josephson Junctions: Low-T_c* and *Josephson Junctions: High-T_c*) connected in parallel on a superconducting loop. When the magnetic flux threading the loop is changed, the maximum supercurrent the device is able to sustain (the "critical current") oscillates with a period of one flux quantum, $\Phi_0 \equiv h/2e \approx 2.07 \times 10^{-15}$ Wb (see *Electrodynamics of Superconductors: Flux Properties*).

The origin of this effect lies in the flux-induced changes in the phases of the superconducting order parameter across the two junctions in a way that is analogous to the two-slit interference experiment in optics: hence the acronym SQUID. This effect was first observed by Jaklevic *et al.* (1964), and practical—if somewhat primitive—devices quickly followed. By measuring the change in voltage across the current-biased SQUID, one can detect changes in magnetic flux corresponding to a minute fraction of a flux quantum.

The second type of device, the RF SQUID, appeared in 1970, and involves a single Josephson junction incorporated into a superconducting loop (Mercereau 1970, Zimmerman *et al.* 1970). The loop is inductively coupled to the inductance of a resonant circuit that is excited at RFs. The RF voltage across the resonant circuit is periodic in the flux threading the loop with a period, Φ_0, enabling one to detect changes in flux in much the same way as with the d.c. SQUID. RF SQUIDs made from machined blocks of niobium became popular in the early 1970s. However, the development of the thin-film d.c. SQUID in 1976 and the subsequent development of techniques to fabricate thin-film niobium SQUIDs on a wafer scale using microfabrication techniques borrowed from the semiconductor industry resulted in the dominance of this kind of device for low-transition-temperature (T_c) superconductors. These devices are mostly used at liquid helium temperatures (4.2 K) or lower.

The advent of high-T_c superconductivity in 1986 led numerous research groups to adopt the SQUID as a vehicle to develop their thin-film and multilayer processing technologies. A wide variety of devices grew from this effort, based on thin films of $YBa_2Cu_3O_{7-x}$ (YBCO), resulting in a viable device technology at liquid nitrogen temperatures (77 K). Although most groups have preferred the d.c. SQUID, its advantage in sensitivity over the RF SQUID is less marked than in the case of low-T_c devices.

This article first outlines the principles of the d.c. SQUID, and then describes practical low-T_c devices and their operation and performance. The principle of the superconducting flux transformer is introduced, and its use in magnetometers and gradiometers is discussed. The fabrication and performance of high-T_c SQUIDs, magnetometers, and gradiometers are described. The principles, fabrication, operation, and performance of high-T_c RF SQUIDs are discussed, and their application as magnetometers and gradiometers is described (Barone 1992, Clarke 1996, Koelle *et al.* 1999).

1. Low-T_c d.c. SQUIDs

Figure 1(a) shows the configuration of the d.c. SQUID. Generally, each of the two Josephson junctions is resistively shunted so that the current–voltage (I–V) characteristic is nonhysteretic, as shown in Fig. 1(b). As one changes the magnetic flux, Φ, threading the loop, the critical current and the I–V
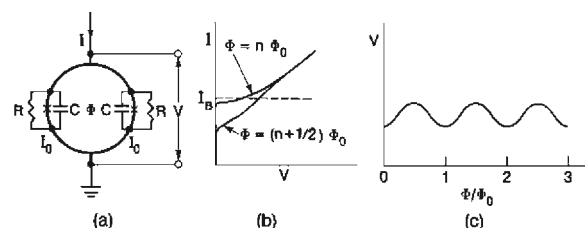
Figure 1
d.c. SQUID: (a) schematic; (b) I–V characteristic; (c) V vs. Φ/Φ_0 at constant bias current I_B.

characteristic oscillate between the two extremes shown with a period, Φ_0. Thus, when the SQUID is biased with a constant current, I_B, the voltage across the SQUID is periodic in Φ, as shown in Fig. 1(c). One operates the SQUID with the bias current adjusted to maximize the amplitude of the voltage oscillations, and the static flux is adjusted to $(n \pm \frac{1}{4})\Phi_0$ (n is an integer) to obtain the maximum transfer function, $V_\Phi \equiv |\partial V/\partial \Phi|_{I_B}$. One measures a flux change $\delta\Phi \ll \Phi_0$ simply by detecting the resulting change in the voltage.

The behavior of the SQUID can be represented by a set of nonlinear equations involving the current and flux biases, the inductance, L, of the SQUID loop, the critical current, I_0, shunt resistance, R, and capacitance, C, of the two Josephson junctions, the phase difference across each junction, the voltage across the SQUID, and the Nyquist noise generated by each shunt resistor (Tesche and Clarke 1977). To avoid hysteresis in the I–V characteristic, the junction parameters must satisfy the constraint $\beta_c = 2\pi I_0 R^2 C / \Phi_0 \lesssim 1$. There have been extensive computer simulations of these equations in order to obtain parameters that optimize the performance of the SQUID.

These simulations reveal that thermal noise causes the performance of the device to deteriorate significantly unless the magnetic energy per flux quantum, $\Phi_0^2/2L$, exceeds about $40k_BT$. At 4.2 K this constraint places an upper limit on L of about 1 nH. The simulations yield values of V_Φ and the power spectral density of the voltage noise, $S_V(f)$. From $S_V(f)$ one can obtain the power spectral density of the flux noise, $S_\Phi(f) \equiv S_V(f)/V_\Phi^2$, and the so-called flux noise energy, $\varepsilon(f) = S_\Phi(f)/2L$. The value of $\varepsilon(f)$ is minimized when $\beta_L \equiv 2LI_0/\Phi_0 \approx 1$. For optimum β_L one finds $V_\Phi \approx R/L$, $S_V(f) \approx 16k_BTR$, and

$$\varepsilon(f) \approx 16k_BT(LC/\beta_c)^{1/2}; \beta_c \lesssim 1 \qquad (1)$$

In addition, there is a current noise in the SQUID loop that often should be taken into account when the SQUID is coupled to an input circuit.

Equation (1) gives a clear prescription for reducing $\varepsilon(f)$: one should reduce T, L, and C. In practice, the design of SQUIDs is a compromise between these requirements and other practical considerations. For example, for photolithographically patterned tunnel junctions, C will be not less than a few tenths of a picofarad, and in order to couple flux efficiently to the SQUID loop, its inductance should be greater than a few tens of picohenries. The majority of d.c. SQUIDs in use involve a niobium square washer as the loop and two resistively shunted Nb–Al$_x$O$_y$–Nb tunnel junctions (Fig. 2). The signal to be measured is coupled in via a niobium spiral coil deposited over the washer, with an intervening insulating layer; this arrangement provides efficient magnetic coupling between the coil and the washer (Ketchen and Jaycox 1982). In typical devices, L is in the range 50–200 pH, I_0 in the range 5–20 μA, and R in the range 3–10 Ω. There are typically $n = 10$–50 turns on the coil. The self-inductance of the coil and its mutual inductance to the loop are approximately n^2L and nL, respectively. These devices are fabricated on silicon substrates using standard photolithographic patterning techniques. The SQUID is often enclosed in a hermetically sealed assembly, and surrounded by a niobium shield to exclude ambient magnetic field fluctuations.

Most SQUIDs are used to measure signals at frequencies up to a few kilohertz, and are invariably operated in a flux-locked loop (Fig. 3). The output current of the amplifier chain is fed into a coil coupled to the SQUID so as to maintain the flux threading it at a constant value. This feedback system produces a linear response to an input magnetic flux,
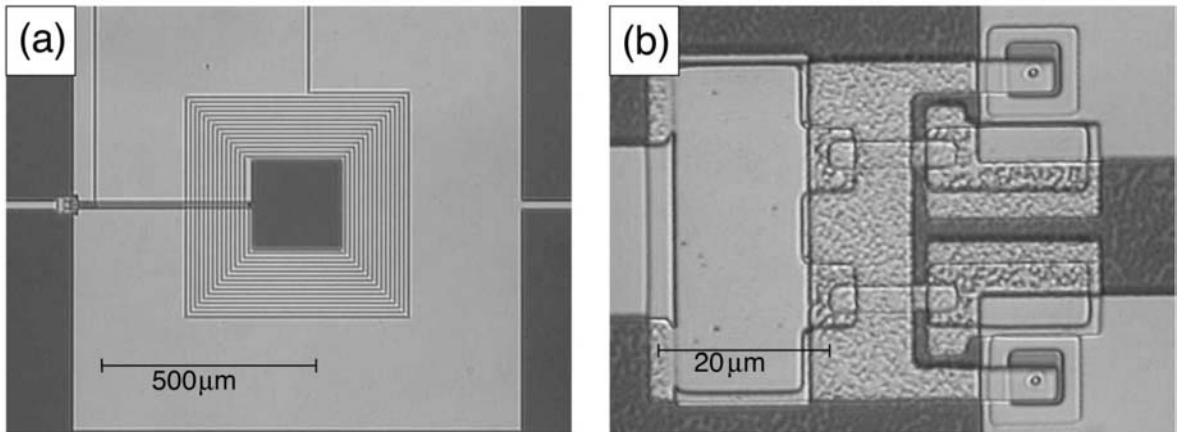
Figure 2
(a) d.c. SQUID with 15-turn input coil. (b) Area to left of SQUID washer showing the two junctions and shunt resistors (courtesy of Xiaofan Meng and Robert McDermott).
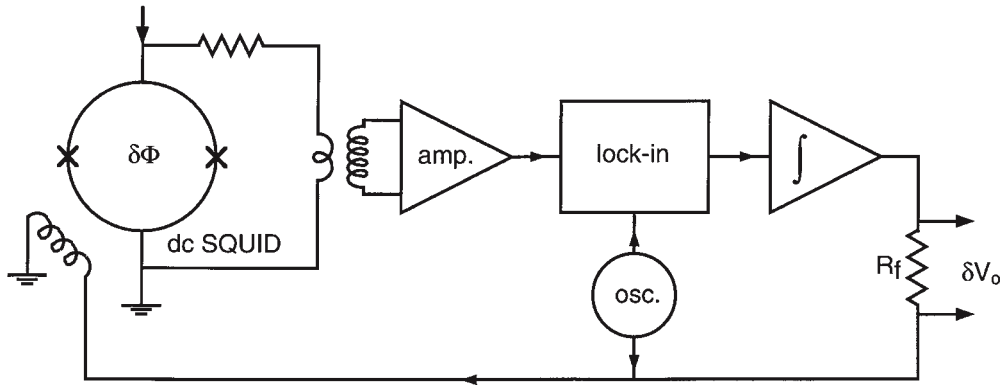
Figure 3
Flux-locked loop for d.c. SQUID.

even though it may correspond to many flux quanta, while enabling one to detect a flux change that is much less than one flux quantum.

There are a number of different detection and feedback systems (Drung 1996). The most widely used scheme, shown in Fig. 3, involves the application of a modulating flux, $\Phi_m \cos 2\pi f_m t$, to the SQUID, where $\Phi_m = \Phi_0/4$ and f_m is typically 100 kHz. The resulting alternating voltage across the SQUID is amplified by a transformer (often cooled) and a chain of amplifiers, and is then lock-in detected at frequency f_m. If the applied flux in the SQUID is $n\Phi_0$, the V–Φ curve is symmetric about this local minimum, the voltage contains components only at $2f_m$, and the output of the lock-in is zero. When the flux is changed to $n\Phi_0 + \delta\Phi$, there will be a component at f_m and an output from the lock-in. After integration, this signal is fed back to the SQUID via a resistor, R_f; the voltage across this resistor is proportional to $\delta\Phi$.

A second popular scheme is "direct readout," in which the SQUID is coupled directly to a low-noise amplifier. The signal from the amplifier is integrated and fed back to a coil coupled to the SQUID as in the flux modulation scheme.

Since the amplifier voltage noise is significantly higher than the intrinsic SQUID noise, the transfer function of the SQUID is enhanced by "additional positive feedback." In this technique, the terminals of the SQUID are connected across a resistor in series with a coil that, in turn, is inductively coupled to the SQUID. When the SQUID is current biased, a change in the voltage across it due to an applied flux generates a current in the shunting network and hence a flux in the SQUID that supports the applied flux. This scheme has the advantage of relatively simple electronics, and can operate at frequencies up to about 10 MHz.

The performance of the d.c. SQUID can be summarized as follows. At 4.2 K the better devices have a flux noise, $S_\Phi^{1/2}(f)$, of 1–2 $\mu\Phi_0$ Hz$^{-1/2}$, corresponding to a noise energy of around $100\hbar$, at frequencies down to roughly 1 Hz; at lower frequencies $S_\Phi^{1/2}(f)$ scales approximately as $1/f^{1/2}$. With properly designed electronics, the measured white noise is largely intrinsic to the SQUID, and its value is in good agreement with computer simulations. Other parameters are determined by the flux-locked loop. For flux-modulated electronics, the bandwidth is typically 0–50 kHz, the dynamic range is 10^7, and the slew rate is up to $10^7\Phi_0$ s^{-1}.

2. Flux Transformer

Although the SQUID is very sensitive to magnetic flux, because of its small area it is not as sensitive to magnetic fields as one would like for many applications. For this reason, to make a sensitive magnetometer the input coil of the SQUID is connected to an external superconducting circuit to form a flux transformer. Figure 4(a) shows the configuration of a magnetometer. The inductance of the large area pickup loop is approximately matched to the inductance of the much smaller input coil of the SQUID. Some flux transformers involve a loop of niobium wire bonded to the input coil of the SQUID; others consist of a thin niobium film coupled to the input coil and fabricated along with the SQUID to make an integrated device. A typical flux transformer enhances the magnetic field sensitivity by 1–2 orders of magnitude, and the best devices achieve a resolution of 1–2 fT Hz$^{-1/2}$ at frequencies above a few hertz.

To detect weak signals in a magnetically noisy environment, most notably in biomagnetic measurements, one generally uses a flux transformer configured as a gradiometer, for example the first-derivative axial gradiometer shown in Fig. 4(b). The gradiometer attenuates magnetic noise from sources at distances much greater than its baseline—the separation
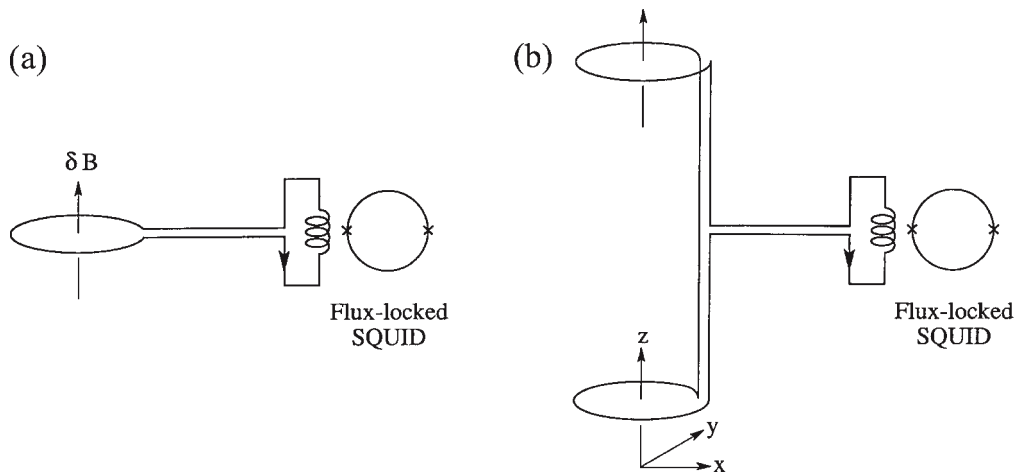
Figure 4
Wire-wound superconducting flux transformers: (a) magnetometer; (b) first-derivative axial gradiometer.

of its pickup loops—while leaving signals at a distance less than its baseline largely unattenuated. Second-derivative axial gradiometers are also used, as are thin-film planar gradiometers measuring off-diagonal gradients.

3. Low-T_c SQUIDs as High-frequency Amplifiers

Low-T_c SQUIDs can be operated at frequencies up to about 100 MHz (see *SQUIDs: Amplifiers*), and have been used as sensitive detectors of NMR and nuclear quadrupole resonance. In this application, the SQUID is operated open loop, with the static flux adjusted to optimize V_Φ. At 100 MHz gains of about 20 dB and noise temperatures of about 1 K have been achieved (Hilbert and Clarke 1985).

A subsequent configuration—the so-called "microstrip SQUID amplifier"—has been realized to amplify signals up to about 1 GHz (Mück *et al.* 1998). In this device the signal is coupled between one end of the spiral input coil and the SQUID washer (Fig. 2), which form a microstrip. When the signal frequency corresponds to the half-wavelength resonance in the microstrip, gains of up to 25 dB have been achieved. Cooled to 20 mK, such amplifiers have noise temperatures close to the quantum limit.

4. High-T_c d.c. SQUIDs

Most high-T_c SQUIDs (Koelle *et al.* 1999) are intended for operation at 77 K. The constraint $\Phi_0^2/2L \gtrsim 40 k_B T$ imposes an upper limit on L of about 50 pH; at this value the constraint $\beta_L \approx 1$ implies $I_0 \approx 20\,\mu A$. All practical high-T_c d.c. SQUIDs are fabricated from thin films of YBCO, deposited by laser ablation, sputtering, or co-evaporation. The major remaining difficulty in the fabrication of these devices is the lack of a reproducible junction technology that produces acceptable parameters at 77 K. The most commonly used junctions involve grain boundaries, formed by the epitaxial growth of the film either on bicrystal substrates or over a step patterned in the substrate, which is usually SrTiO$_3$. The film crossing the grain boundary is patterned to a width of 1–2 μm. Although the results are generally satisfactory, the yield of junctions with acceptable parameters is smaller than is desirable. These junctions do have the virtue of simplicity in that the entire SQUID is patterned in a single layer of YBCO, most usually by ion milling. A dozen or so devices with 500 μm × 500 μm washers can be patterned on a 10 mm × 10 mm substrate.

Compared with their low-T_c counterparts, high-T_c grain boundary junctions produce high levels of $1/f$ noise. Fortunately, this noise can be greatly reduced in the d.c. SQUID by a scheme in which the bias current is reversed, typically at a few kilohertz. The noise of high-T_c SQUIDs varies more widely than that of low-T_c SQUIDs, reflecting the variability in the junction parameters. The best devices achieve a flux noise of about $5\,\mu\Phi_0\,Hz^{-1/2}$ at frequencies down to about 1 Hz, corresponding to a noise energy of $10^{-30}\,J\,Hz^{-1}$, or a little better. For reasons that remain unclear, noise energies are typically an order of magnitude higher than the computed values. Since the flux-locked loop is similar to that used for low-T_c devices, with the addition of bias reversal, comparable values of dynamic range, frequency response, and slew rate are achieved.

The small area of high-T_c SQUIDs mandates the use of a flux transformer for sensitive magnetometers. One approach is to use a configuration much like that of Fig. 2. Although integrated devices of this kind

have been successfully fabricated, the difficulty of obtaining appropriate junction parameters and a fully epitaxial YBCO–SrTiO$_3$–YBCO multilayer on the same substrate has led to low yields. As a result, many groups have resorted to a flip-chip technology in which the SQUID and flux transformer are made on separate chips that are pressed together face-to-face, separated by a thin insulating layer. The best of these magnetometers achieves a white noise below $10\,fT\,Hz^{-1/2}$; however, all these multilayer structures exhibit $1/f$ noise, which increases the noise to, typically, $30\,fT\,Hz^{-1/2}$ at 1 Hz. An alternative approach, illustrated in Fig. 5, is the so-called "directly coupled magnetometer," which has the advantage of being patterned in a single YBCO layer. A current induced in the large area pickup loop by a magnetic field is injected directly into the body of the SQUID. The magnetic field noise of the best devices, about $30\,fT\,Hz^{-1/2}$, remains constant at frequencies down to about 1 Hz.

Various configurations of gradiometers have been fabricated and tested. Given that suitable high-T_c wire is not available, hardware gradiometers are invariably planar structures that measure off-diagonal gradients. The best of these has a baseline of about 50 mm, and attenuates uniform magnetic fields by roughly 10^3. In an alternative approach one subtracts the signals from high-T_c magnetometers electronically to form first or second derivatives.

An important issue with high-T_c devices is their operation in an ambient magnetic field, such as that of the earth. When a high-T_c film is field cooled, flux vortices may enter; thermally induced hopping of these vortices can produce large levels of $1/f$ noise. This problem is largely overcome by ensuring that the film has a narrow linewidth, formed, for example, by patterning it with holes or slots.

5. High-T_c RF SQUIDs

The RF SQUID (Fig. 6(a)) consists of a single Josephson junction integrated into a superconducting loop
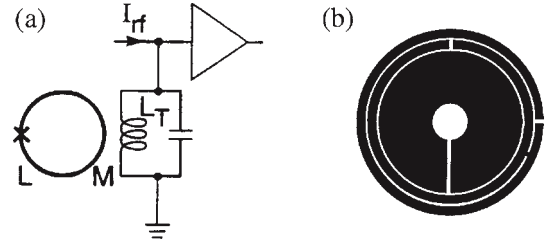
that is inductively coupled to the inductance, L_T, of an *LC* resonant (tank) circuit. The tank circuit is driven by a current at frequency $\omega_{RF}/2\pi$, and the resultant RF voltage is periodic in the flux applied to the SQUID with period Φ_0. The RF can range from 20 MHz up to 10 GHz. The RF amplitude is demodulated, and this signal is amplified, integrated, and fed back to flux lock the SQUID as in Fig. 3.

Operation of the RF SQUID relies on the fact that the applied flux, Φ, which induces a supercurrent around the loop, in general differs from the total flux, Φ_T. There are two distinct modes of operation. For $\beta'_L \equiv 2\pi L I_0/\Phi_0 > 1$, the plot of Φ_T vs. Φ is hysteretic. Energy is dissipated each time an RF cycle traverses a hysteresis loop; the number of these traversals per unit time is periodic in Φ. As a result, the quality factor of the tank circuit and hence the voltage across it at constant RF current are also periodic in Φ. However, for $\beta'_L < 1$ there is no hysteresis and no dissipation. Rather, the SQUID behaves as a parametric inductance, modulating the effective inductance and hence the resonant frequency of the tank circuit as the flux is varied. Consequently, at constant drive frequency the RF voltage is again periodic in Φ.

In the hysteretic regime, for an optimized RF SQUID the noise energy is given by (Chesca 1998)

$$\varepsilon(f) \approx (LI_0^2/2\omega_{RF})(2\pi k_B T/I_0\Phi_0)^{4/3} \qquad (2)$$

Note that ε scales inversely with ω_{RF}, implying that higher frequency operation results in lower noise. In the nonhysteretic regime, ε also scales as $1/\omega_{RF}$ up to the limiting value $\omega_{RF} = R/L$, at which frequency, under optimum conditions (Chesca 1998), one obtains

$$\varepsilon(f) \approx 3k_B T/(\beta'_L)^2(R/L) \qquad (3)$$

Equations (2) and (3) show that $\varepsilon(f)$ increases with T. For low-T_c SQUIDs, however, the noise temperature of the amplifier coupled to the tank circuit is often much higher than the bath temperature so that

the system noise is much greater than the intrinsic noise. This is one reason why the d.c. SQUID is preferred. When the temperature is raised to 77 K the intrinsic noise of the d.c. SQUID increases, while the effective system noise temperature of the RF SQUID changes little. As a result, at 77 K the noise energy of the RF SQUID, operated at gigahertz frequencies, is not very different from that of the d.c. SQUID.

The first generation of RF SQUIDs involved thin-film YBCO washers containing a central hole and a slit connected by one (or often two) grain boundary junctions. The washer was inductively coupled to a tank circuit, excited at frequencies that ranged from 20 MHz to 200 MHz. The magnetic field sensitivity could be enhanced by means of a flux concentrator, made from bulk YBCO, or a single-layer flux transformer. The most sensitive of these devices achieved a magnetic field noise below 30 fT Hz$^{-1/2}$ at frequencies down to about 1 Hz. However, the large size of these magnetometers—up to 50 mm across—limited their applicability. Subsequently, operation at higher frequencies, 1–3 GHz, was achieved by replacing the lumped tank circuit with a microwave resonator. In the design shown in Fig. 6(b) the circular RF SQUID (not shown) is flip-chip coupled to the YBCO resonator, which consists of a flux concentrator surrounded by two coplanar lines (Zhang *et al.* 1998). The relative position of the gaps in these lines and of the connection between them enables one to adjust the resonant frequency. This configuration is straightforward to fabricate, involving the fabrication of a single-layer RF SQUID on one chip and of a single-layer resonator on the other. The best white noise achieved is below 20 fT Hz$^{-1/2}$; however, the level of 1/f noise is high, about 100 fT Hz$^{-1/2}$ at 1 Hz. More sophisticated devices with a multiturn flux transformer integrated with the resonator have also been developed.

A detailed comparison of the measured and predicted noise of the RF SQUID has proved difficult, partly because it is difficult to determine the critical current accurately so that it is not clear whether β'_L is greater or less than unity. It is likely that some devices are operated in a mixed mode in which the flux-dependent RF signal is produced by variations in both dissipation and inductance. RF SQUIDs have been configured as gradiometers using both thin-film structures and electronic subtraction of magnetometers.

6. Final Remarks

The technology of low-T_c d.c. SQUIDs, based on Nb–Al$_x$O$_y$–Nb tunnel junctions, is highly developed, enabling one to fabricate reproducible devices in quantity on 2–4 in (5–10 cm) silicon washers. The sensitivity of these devices as magnetometers, around 1 fT Hz$^{-1/2}$, surpasses the demands of virtually all applications. Thus, there is little research on low-T_c d.c. SQUIDs themselves, at least for low-frequency applications, although there are ongoing efforts to make the associated electronics less expensive, particularly for systems with large numbers of channels. The emphasis is much more on applications, most notably in biomagnetism (Hämäläinen *et al.* 1993, Vrba 1996) (see *SQUIDs: Biomedical Applications*), nondestructive evaluation (Wikswo 1995) (see *SQUIDs: Nondestructive Testing*), NMR (Greenberg 1998) (see *SQUIDs: Amplifiers*), and a vast array of basic science experiments.

In the high-T_c arena, the magnetic field sensitivity achieved for d.c. SQUIDs is not vastly greater than for RF SQUIDs. However, presumably because of the complexity of the microwave system required for the RF SQUID, most groups prefer the d.c. SQUID. In contrast to the low-T_c situation, there is not yet a satisfactory high-T_c junction technology; most devices rely on grain boundary junctions. The white flux noise of d.c. SQUIDs is unlikely to be reduced significantly until better junctions—with a higher I_0R product—are realized. The 1/f noise of single-layer devices is satisfactorily low, but in the case of multilayer structures—which have the lowest white noise—it remains higher than is desirable. It is to be hoped that work to improve the crystalline quality of multilayers and of film edges will reduce the 1/f noise. Further investment is also required to manufacture high-T_c SQUIDs in reasonable quantities, and thus reduce their price. However, despite these remaining problems high-T_c SQUIDs are now exploited in various applications, for example magnetocardiology (see *SQUIDs: Biomedical Applications*), nondestructive evaluation (see *SQUIDs: Nondestructive Testing*), and magnetic microscopy (see *SQUIDs: Magnetic Microscopy*).

Bibliography

Barone A (ed.) 1992 *Principles and Applications of Superconducting Quantum Interference Devices*. World Scientific, Singapore

Chesca B 1998 Theory of RF SQUIDs operating in the presence of large thermal fluctuations. *J. Low Temp. Phys.* **110**, 963–1001

Clarke J 1996 SQUID fundamentals. In: Weinstock H (ed.) *SQUID Sensors: Fundamentals, Fabrication and Applications*. Kluwer, Dordrecht, The Netherlands, Chap. 1, pp. 1–62

Drung D 1996 Advanced SQUID read-out electronics. In: Weinstock H (ed.) *SQUID Sensors: Fundamentals, Fabrication and Applications*. Kluwer, Dordrecht, The Netherlands

Greenberg Ya S 1998 Application of superconducting quantum interference devices to nuclear magnetic resonance. *Rev. Mod. Phys.* **70**, 175–222

Hämäläinen M, Hari R, Ilmoniemi J, Knuutila J, Lounasmaa O V 1993 Magnetoencephalography—theory, instrumentation, and applications to noninvasive studies of the working human brain. *Rev. Mod. Phys.* **65**, 413–97

Hilbert C, Clarke J 1985 DC SQUIDs as radio frequency amplifiers. *J. Low Temp. Phys.* **61**, 263–80

Jaklevic R C, Lambe J, Silver A H, Mercereau J E 1964 Quantum interference effects in Josephson tunneling. *Phys. Rev. Lett.* **12**, 159–60

Ketchen M B, Jaycox J M 1982 Ultra-low noise tunnel junction d.c. SQUID with a tightly coupled planar input coil. *Appl. Phys. Lett.* **40**, 736–8

Koelle D, Kleiner R, Ludwig F, Dantsker E, Clarke J 1999 High-transition-temperature superconducting quantum interference devices. *Rev. Mod. Phys.* **71**, 631–84

Koelle D, Miklich A H, Ludwig F, Dantsker E, Nemeth D T, Clarke J 1993 DC SQUID magnetometers from single layers of $YBa_2Cu_3O_{7-x}$. *Appl. Phys. Lett.* **63**, 2271–3

Mercereau J E 1970 Superconducting magnetometers. *Rev. Phys. Appl.* **5**, 13–20

Mück M, André M-O, Clarke J, Gail J, Heiden C 1998 Radio-frequency amplifier based on a niobium d.c. superconducting quantum interference device with microstrip input coupling. *Appl. Phys. Lett.* **72**, 2885–7

Tesche C D, Clarke J 1977 DC SQUID: noise and optimization. *J. Low Temp. Phys.* **27**, 301–31

Vrba J 1996 SQUID gradiometers in real environments. In: Weinstock H (ed.) *SQUID Sensors: Fundamentals, Fabrication and Applications.* Kluwer, Dordrecht, The Netherlands

Wikswo J P Jr 1995 SQUID magnetometers for biomagnetism and nondestructive testing: important questions and initial answers. *IEEE Trans. Appl. Supercond.* **5**, 74–120

Zhang Y, Yi H R, Schubert J, Zander W, Banzet M, Braginski A I 1998 A design of planar multi-turn flux transformers for radio frequency SQUID magnetometers. *Appl. Phys. Lett.* **72**, 2029–31

Zimmerman J E, Thiene P, Harding J T 1970 Design and operation of stable rf-biased superconducting point-contact quantum devices, and a note on the properties of perfectly clean metal contacts. *J. Appl. Phys.* **41**, 1572–80

J. Clarke

University of California, Berkeley, California, USA

Steels, Silicon Iron-based: Magnetic Properties

Electrical steels are used in the cores of electromagnetic devices such as motors, generators, and transformers because of the ability of ferromagnetic materials to magnify the magnetic effects of current-carrying coils (see *Magnets Soft and Hard: Magnetic Domains*). Of the available ferromagnetic materials, iron and its alloys offer the best cost beneficial performance. The torque of a motor is proportional to B^2, where B is the intensity of magnetization operating between its stationary and moving parts. Because of this square law relationship even small gains in B lead to useful increases in torque and thus output power.

In the case of transformers, the large magnetizations available from iron enable voltage transformations to be carried out by windings of an acceptable size. The voltage appearing at a transformer winding is related to the rate of flux change $d\Phi/dt$ for the core and is normally of sine form so that operation at high peak flux levels is important.

It is clear that for steels to be of the most use for electrical machines a high working induction is desired, as close as practicable to the approximately 2 T at which iron becomes saturated.

At the same time a high permeability (ratio of B to H) or flux magnifying property is desired. The effective permeability of iron reduces as saturation is approached leading to heavier demands on magnetizing current.

Additionally the duties of core steel must be executed without serious wastage of energy within the metal (called power loss or core loss) due to the periodic magnetic reversals involved in use.

The range of electrical steels available has arisen out of the appropriate compromises struck between these factors. Different types of steel suit different applications (see Table 1).

1. Reduction of Power Loss

One of the primary sources of power loss within an electrical steel is eddy current loss (see *Magnetic Losses*). If a solid iron core is placed within a magnetizing coil the iron core itself provides short-circuited current paths in which so-called induced "eddy currents" can flow. These waste energy as heat and also produce magnetic fields which oppose the magnetization (Lenz's law effects) so that penetration of flux to the centre of the core is inhibited. Eddy currents can be radically reduced by splitting up the core into laminae which restricts the flow of eddy currents (Fig. 1). There are limits to the degree of lamination which can be applied set by the cost of rolling steel to reduced thickness and the complexity of handling this material for core building. Inevitably as thinner steel is used the effective space occupancy of the metal reduces since a pile of plates can never have the same mass as solid metal of the same superficial dimensions.

Further the need to insulate laminae from each other by applying coatings reduces the effective space occupancy. Overall the effect is to reduce the apparent saturation induction of the core. Lamination creates much more metal surface, and surfaces produce power loss due to domain wall pinning.

A second means of restraining eddy currents is the use of alloying elements added to iron. Adding some 3% of silicon to iron raises its resistivity fourfold. Many other elements have been tried as resistivity raisers (e.g., aluminum) but silicon has proved to be the most useful. Adding silicon certainly reduces eddy currents (and so power loss) but the resulting alloys are more difficult to roll and harder to punch into laminations. Further, added silicon dilutes the iron

Table 1
Typical electrical steels.

Type of steel	Thickness	Power loss	Conventional density (g cm^{-3})	Relative permeability	Usage
Non-oriented motor grade requiring customer anneal	0.65 mm	7.0 W kg^{-1} $\hat{B}$ 1.5 T, 50 Hz	7.85	3000 at 1.5 T	Small
Non-oriented superior motor grade, requiring customer anneal	0.5 mm	3.8 W kg^{-1} $\hat{B}$ 1.5 T, 50 Hz	7.85	3000 at 1.5 T	Small/medium motors
Non oriented fully annealed	0.5 mm	5.3 W kg^{-1} $\hat{B}$ 1.5 T, 50 Hz	7.75	1620 at 1.5 T	Larger rotating machines small transformers
Non oriented fully annealed	0.35 mm	2.25 W kg^{-1} $\hat{B}$ 1.5 T, 50 Hz	7.60	660 at 1.5 T	Large rotating machines
Grain oriented steel (CGO)	0.27 mm	0.78 W kg^{-1} $\hat{B}$ 1.5 T, 50 Hz	7.65	1.83 T at 800 A m^{-1} Rel μ 1830 at 1.83 T	Transformers
High permeability grain oriented steel	0.27 mm	0.98 W kg^{-1} $\hat{B}$ 1.7 T, 50 Hz	7.65	1.93 T at 800 A m^{-1} Rel μ 1930 at 1.93 T	Transformers
Relay soft iron	1.0 mm	–	7.85	Coercive field strength	56–80 A m^{-1}

Volts $\propto$ cross section,   Resistance $\propto$ Periphery,   Current $\propto \dfrac{\text{Area}}{\text{Periphery}}$,   Power $\propto$ I^{2}R

Whole section: $1 \propto \dfrac{A^2}{4A}$ i.e. $\dfrac{A}{4}$, $R \propto 4A$ so $1^2R \propto \dfrac{A^3}{4}$

One quarter section:
$1 \propto \dfrac{A \times A/4}{5A/2}$ i.e. $\dfrac{A}{10}$, $R \propto (2A + 2A/4)$ i.e. 2.5A, so $1^2R \propto \dfrac{A^3}{40}$

So for four quarters: Power $\propto \dfrac{A^3}{10}$ in total i.e. $2\frac{1}{2}$-times less than for the whole.

Power for 100 sections by a similar route is 50 times less than for full solid.
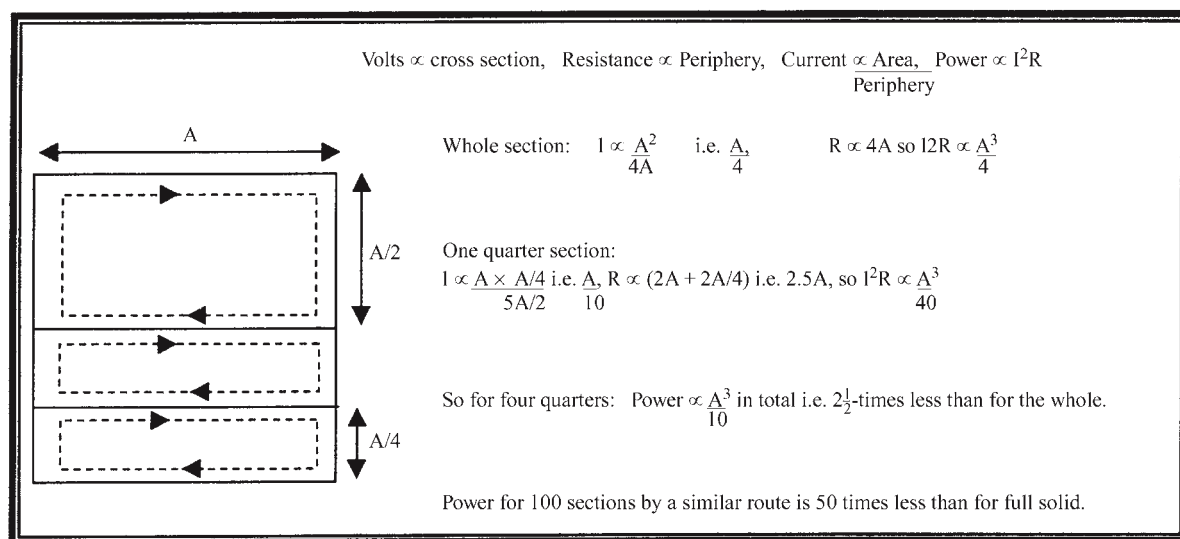
Figure 1
Lamination restrains eddy currents and reduces power wastage—a simplified model.

present and reduces saturation magnetization and high field permeability.

A second major component of power loss is hysteresis loss. If a plot is made of *B* vs. *H* over a cycle of magnetization then the area of the resulting *B–H* loop represents lost energy. The mechanism of this so-called "hysteresis loss" relates to the fact that the magnetization in iron functions via ferromagnetic domain wall motion (see *Magnetic Hysteresis*). Easy domain wall motion is impeded by non-magnetic inclusions in the steel, stressed regions and unfavorable surface states. Clearly it is advantageous for the steel
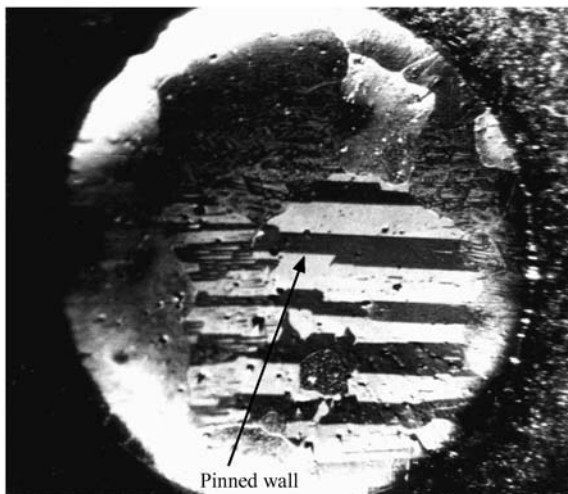
Figure 2
Magneto-optic image of ferromagnetic domains.

to be inclusion-free (high purity) and free from stress. Domain wall pinning occurs at surfaces so that no more surface than is appropriate should be created (i.e., steel not too thin). The bonding of coatings to steel can produce effective roughness at the coating/steel interface which pins domain walls and adds to hysteresis loss. Figure 2 shows the domain structure in an electrical steel in which a domain wall is clearly shown with part of its length pinned.

A further contribution to loss reduction comes from increasing grain size of the steel. With larger grains (crystallites) there is less grain boundary per unit volume. Grain boundaries are prime domain wall pinning sites. Special rolling and heat treatment regimes are used to promote grain growth. Appropriate heat treatments also relieve stress.

Permeability (in certain directions) can be enhanced by growing grains in which the easy direction of magnetization of the iron lattice (Fig. 3) is caused to lie along the direction in which magnetization is desired. This process of "grain orientation" is commonly based on the creation of directionally organized impurity particles, which act to inhibit grain growth in directions other than that desired. To perform this operation, impurities are purposely added to steel at the melting stage (e.g., manganese sulfide, aluminum nitride) so that during subsequent metallurgical operations grains with easy directions of magnetic response in the rolling direction of production are grown preferentially. Figure 4 shows the orientation for the most used Goss grains system.

The statistics of grain growth require that if only certain nuclei are allowed to grow, then from a reduced population the resulting grains will be large. In so-called conventional grain oriented (CGO) steel grains are some 3–4 mm across in metal 0.27 mm
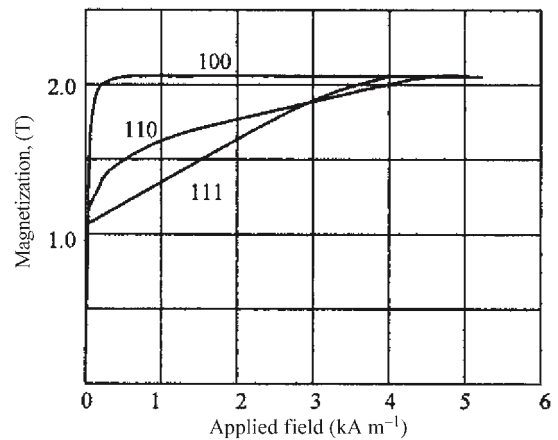
The 100 direction is the easy cube edge direction
The 110 is the hard cube face diagonal direction
The 111 is the hardest cube body body diagonal direction.

Figure 3
Responses to magnetizing fields of different crystal directions.
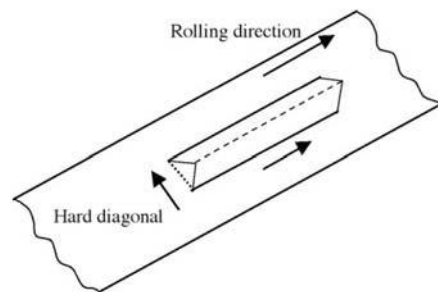
Figure 4
A "Goss-oriented" crystal's relationship to the sheet rolling direction.

thick. The easy direction of magnetization of the grains lies within a spread of a few degrees about the rolling direction.

The desire to get the very highest in-rolling-direction permeability from steel has led to the devising of better and better grain growth inhibitors so that the so-called "improved oriented steel" can have a directionality spread of only 1–2°. This precision has arisen from the requirement that only super-accurately oriented nuclei grow. The growth statistics now lead to grains, which may be 2–3 cm across. This sounds good as orientation is excellent and grain boundaries are few.

However, the magnetic energy considerations within a grain dictate that large grains support wide domain wall spacings. With a wide domain wall spacing walls must move more rapidly to execute the required

1125

flux reversal. A rapidly moving domain wall is a dissipative item due to the micro eddy currents induced by its movement.

This effect can be countered to some degree by creating artificial grain boundaries and reducing the domain wall spacing. Such artificial grain boundaries can be created by lines of mechanical damage or stress, or even gross displacement of metal at the steel surface. Such domain refinement can use laser treatments, spark ablation, ball scribing, etc., to give the desired effect. Figure 5 shows the effect of domain refinement.

The addition of silicon not only restrains eddy currents but improves medium-field permeability and reduces the tendency for losses to rise over time due to the occurrence of fine precipitates within grains.

It is often suggested that eddy current losses increase with the square of frequency of excitation and hysteresis losses linearly. However, complex domain interactions produce losses in excess of this simple model. From the point of view of machine-design engineers, losses are fairly well described by the equation:

$$\text{Loss} = Af + Bf^2 \ (f = \text{frequency}).$$

Here A is a coefficient linked to hysteresis, though not exclusively, and it is increased by the effects of stress and impurities. B is a coefficient influenced by material thickness and resistivity, but also by domain wall spacing.

In general power loss increases with the amplitude of magnetization and the hysteresis component rises with approximately the 1.6 power of $B_{\max}$. This is a useful indicator within the normal range of magnetizations.

2. Steel for Transformers

The production of grain orientation is very valuable for materials destined for use in transformers since unidirectional flux is employed (except at joints and corners). In cores where the percentage of corner region is relatively high conventional grain oriented steel may be preferred as the less exact orientation eases flux rotation at corners. Figure 6 shows cores of differing aspect ratio. Where the long limbs and smaller percentage of corner is used the super-oriented steel can be best exploited. It is usual to employ super-oriented steel at higher working inductions ($B_{\max}$ 1.7 T and above) than is usual for CGO ($B_{\max} \approx 1.5$ T). However, in any system over voltage can more rapidly take steel operating at $B_{\max}$ 1.7 T into technical saturation when severe unwanted magnetizing currents will flow.

3. Steel for Rotating Machines

Grain orientation of the Goss type is unsuitable for the cores of most motors and generators where properties need to be equal at all angles in the plane
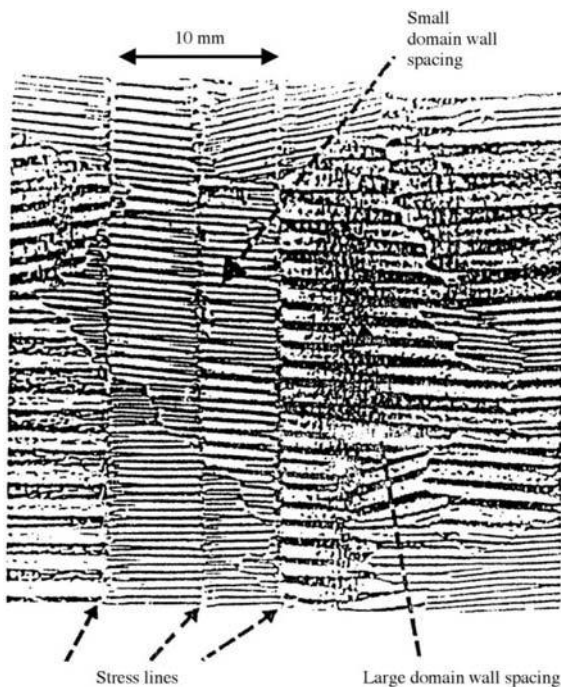
Figure 5
Example of domain refinement.
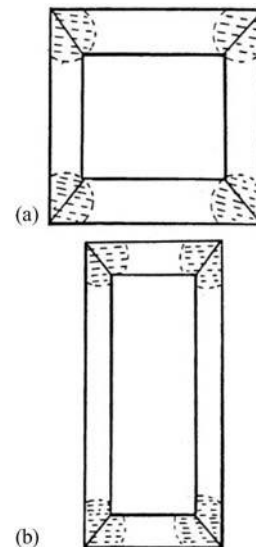
Figure 6
(a) A core with low aspect ratio, (b) a core with high aspect ratio.

of the sheet. Here the benefits of lamination and added silicon still apply and enhanced purity with large grains is desirable. Large grains can be produced by two main methods.

3.1 Long Hot Anneal

Steel strip can be annealed at about 1000 °C in a strand anneal line so that grains may grow to some tens of microns in diameter. Combined with a moderate amount of added silicon, e.g., 1–3%, a good core material is produced which is nearly isotropic. After such an anneal the steel is soft but the added silicon raises hardness to a degree where stamping into motor laminations is fairly convenient.

3.2 Critical Grain Growth

Here strip steel is annealed in a strand anneal line then given a small amount of cold rolling, reducing thickness by about 8%. This is just enough cold work to build in sufficient strain energy to provide "explosive" grain growth when the metal is re-heat treated at about 800 °C. This can usefully be applied after stamping of the steel which was done while still hard from cold rolling. The removal of stamping stress is combined with the beneficial effects of critical grain growth.

3.3 Decarburization

A strand anneal conducted in wet hydrogen, e.g., 800 °C and a dew point of 65 °C enables dissolved carbon to be removed down to some 0.003%. This practice helps reduce hysteresis loss.

Further, end users can make the final post-stamping anneal a decarburizing anneal. In recent years it has become possible to reduce carbon to very low levels at the steel making stage of production so that anneals can be conducted in a neutral gas, e.g., nitrogen. The application of a wet hydrogen anneal when carbon is already low can damage the metal by the production of sub-surface oxidation which harms permeability.

A wide range of highly developed methods exists for the management of lamination annealing for stress removal and decarburization.

4. Coatings

A variety of coatings are used on electrical steels. On grain oriented steel a magnesium oxide coating is applied to the steel before final anneal so that the sulfur which was introduced to control grain growth for orientation can be finally removed. This coating reacts with the silicon in the steel to yield a magnesium silicate glass, which is both insulative and able to apply tension to the steel substrate due to the low thermal expansivity of the glass A supplementary tensile coating may be applied on top of the glass. Tension in the steel refines the ferromagnetic domain structure and reduces power loss. Non-oriented steel may be given a fully organic coating which aids stamping (no further anneal used), or it may require a mixed organic/inorganic coating, part of which survives anneal.

For small machines, e.g., below kilowatt size, interlaminar insulation is not very dependent on applied coatings and provided that stamping burrs do not create unwanted current paths losses do not rise unduly.

A suitable coating can prevent sticking of laminations when these are annealed in stacks. More recently coatings have been developed which are able to survive cold rolling aimed at eventual critical grain growth so that the overall process is simplified.

5. Relay Steels

Electrical steels are normally classified by power loss, and further by permeability. Unalloyed iron intended for use in electromechanical relays is classified by coercive force. (H needed to bring B to zero after full magnetization in ampere-meters). Table 1 shows some typical properties of electrical steels.

6. Conclusions

Silicon–iron alloys represent the most widely used and most cost beneficial core materials for devices used in electric power handling.

See also: Magnetic Steels

Bibliography

Beckley P 1999 Modern steels for transformers and machines. *IEE Eng. Sci. J.* (Aug), 149–59
Beckley P, Thompson J E 1970 Influence of inclusions on domain wall motion and power loss. *Proc. IE* **117** (Nov), 2194–200

P. Beckley
Newport, UK

Stress Coupled Phenomena: Magnetostriction

In terms of a simple atomic description the equilibrium distances between the constituents of solid matter are mainly determined by forces between electric charges and the thermal energy. These distances can

be altered by externally applied mechanical forces resulting in deformations usually described by the tensor of strains ε. In substances exhibiting an ordered structure of atomic magnetic moments the magnetic interaction energy contributes to the total energy and causes additional deformations ε_M. For a ferromagnetic substance with spontaneous magnetization, M_S, these magnetically caused deformations have an isotropic part, resulting in volume changes proportional to M_S^2 (Néel 1937) and an anisotropic part (depending on the direction of M_S). ε_M is connected with the elastic tensor by means of so-called magneto-elastic coupling constants. If M_S is rotated, e.g., by an external magnetic field, the deformations ε_M are changed resulting in macroscopic deformations, Δl, of a sample, often denoted as magnetostriction.

1. Volume Magnetostriction ($\lambda_V = \Delta V / V$)

This type of magnetostriction can be observed in cases where M_S is altered either by strong magnetic fields or near the temperature of a magnetic phase transition, e.g., the Curie temperature for ferromagnets. In most cases λ_V is proportional to the magnetic field strength H. In practicable magnetic fields the slope λ_V/H is small ($\sim 10^{-13}$–10^{-12} $\dot{m}/A^{-1}$). Near the Curie temperature T_C, however, M_S can be considerably enhanced by moderate fields. Recently, values of $\lambda_V/H \approx 10^{-8}$ $\dot{m}/A^{-1}$ were reported for La(Fe$_{0.88}$Si$_{0.12}$)$_{13}$ at $T = 200\,K$ (Fujita and Fukamichi 1999). On the other hand, M_S changes dramatically with temperature near T_C for a constant field and may induce volume changes equal to or larger than the thermal expansion.

2. Joule Magnetostriction $\lambda_J = (\Delta l / l)_{anis}$

The anisotropic part of magnetic deformations was discovered by Joule more than 150 years ago and is therefore often called Joule magnetostriction. In polycrystalline materials with statistically distributed crystalline axes it depends on the angle θ between $\langle M_S \rangle$ and the measuring direction where $\langle M_S \rangle$ is the volume averaged spontaneous magnetization:

$$\lambda_J = (3/2)\lambda_S(\cos^2\theta - \langle\cos^2\theta_0\rangle)$$

Here λ_S denotes the saturation value of λ and $\langle\cos^2\theta_0\rangle$ is the mean value of $\cos^2\theta$ in the initial state. In a single crystal $(\Delta l/l)_{anis}$ additionally depends on the direction of M_S with respect to the crystalline lattice and is, therefore, described by several anisotropy constants λ_n depending on the lattice type as well as on the material. Cubic materials, e.g., iron, nickel, and many alloys, are described by two constants λ_{100} and λ_{111} measured for the cases where the direction of M_S, and that of the measurement, are parallel to the lattice directions [100] and [111], respectively. Therefore,

$$\lambda_J = (3/2)\lambda_{100}[(\alpha_x^2\beta_x^2 + \alpha_y^2\beta_y^2 + \alpha_z^2\beta_z^2) - 1/3]$$
$$+ 3\lambda_{111}(\alpha_x\alpha_y\beta_x\beta_y + \alpha_y\alpha_z\beta_y\beta_z + \alpha_z\alpha_x\beta_z\beta_x)$$

where α_i and β_i are the direction cosines of M_S and the measurement direction with respect to the crystal axes, respectively. Usually λ_n values are of different magnitude and may even have opposite signs. A typical example is iron with $\lambda_{100} = 24 \times 10^{-6}$ and $\lambda_{111} = -22 \times 10^{-6}$. Iron often serves as illustration of the apparently complicated dependence of λ_J as a function of the field strength. The behavior can simply be explained in terms of magnetic domains. According to the magnetocrystalline anisotropy of iron in small fields the magnetization inside each domain is essentially parallel to one of the three $\langle 100 \rangle$ axes and gets closer to the field direction by shifting the walls between differently oriented $\langle 100 \rangle$ domains, this results in a positive $\Delta l/l$. With an increasing field strength, however, M_S is rotated away from the $\langle 100 \rangle$ direction. Then, due to the higher probability to find one of the four $\langle 111 \rangle$ axes near the field direction, the negative contribution of λ_{111} dominates the initial positive change.

3. Theory

3.1 Phenomenological Approaches

The simplest way to describe magnetostrictive effects is through mathematical phenomenology: to calculate the dependence of magnetization M and strain ε on magnetic field H and stress σ one introduces the so called path-dependent differentials (PDD), the integration of which over the material history should recover the correct M and ε behavior. The goal is to construct these PDDs using as few adjustable parameters as possible and yet with enough predictive power to make this approach useful.

By a "physical" macroscopic treatment of magnetostriction the magnetization M is presented as the sum of reversible M_r and irreversible M_{irr} contributions. M_r can then be expressed as a function of the effective field H_{eff}, which, in turn, depends on the magnetization state and elastic stress. The changes of M_{irr} can be due to various dissipative processes, e.g., domain wall motion. The theory in its simplest form (for an isotropic material) results in a system of nonlinear equations that depend on M and magnetostriction $\lambda(M)$ (which is also assumed to exhibit hysteresis). The input parameters of the theory (besides the standard material characteristics) are, e.g., the pinning constant and the initial magnetic susceptibility (Sablik and Jiles 1993).

The "microscopic" approach, which should be able to predict not only the average properties of

magnetostrictive materials but also their microscopic features, is based on the minimization of the magneto-elastic free energy, written as a function of the magnetization $\mathbf{M(r)}$ and deformation $\varepsilon(\mathbf{r})$ of a magnetic body (James and Kinderlehrer 1994). The energy minimization itself can be carried out either analytically (for simplest cases) or numerically. However, numerical methods, which would allow self-consistent computations of magnetization structures and deformation fields in a general three-dimensional case, are not yet available.

3.2 Ab Initio *Calculations*

First principles calculations of magnetostriction constants are now possible for two kinds of magnetic materials:

(i) In transition metals like iron, cobalt, and nickel, where itinerant electrons are responsible for magnetic order, the spin-orbit coupling which leads to the magnetostrictive effects is weak and can be treated using the perturbation theory. Due to the complicated band structure of transition metals, corresponding numerical calculations of the magnetocrystalline anisotropy energy E_{MCA} (its derivative, with respect to the lattice strain ε, provides information about the magnetostriction constant λ) are very tedious. However, due to recent methodological progress, monotonic and numerically stable dependencies of $E_{\mathrm{MCA}}(\varepsilon)$ can be obtained (Wu *et al.* 1998) leading to a reasonable quantitative agreement (within 15–30%) between the experimentally measured λ-values and theoretical results.

(ii) In most rare earth elements magnetic properties are dominated by localized *f*-electrons, and the corresponding spin-orbit coupling is so large that the opposite limit of infinite coupling is a good basis for the calculations. In this limit the charge density of the *f*-shell is assumed to follow the orientation of the atomic magnetic moment in an applied field. Due to the strong anisotropy of this charge density, a large lattice distortion occurs on rotation of these *f*-electron clouds, thus leading to huge magnetostriction. Corresponding *ab initio* calculations (Buck and Fähnle 1998) require the determination of the equilibrium lattice constants of rare earth compounds when the sample magnetic moment is oriented along various crystallographic directions. Magnetostriction λ can then be determined from the relative difference between these constants. Unfortunately, a comparison with experimental data is difficult at present due to their relatively poor quality.

4. Applications

Volume magnetostriction can be used to adjust the thermal expansion coefficient in certain temperature regions, e.g., for invar and covar alloys. The latter is widely used for metal-glass seals and in large cooling cells for liquid hydrogen shipping. Joule magnetostriction was initially used for ultrasound generators and is, at present, applied in many other systems as well. A material composed of two compounds each consisting of a rare earth element and iron is specially designed for the generation of large elongations at room temperature in small magnetic fields. One of them ($TbFe_2$) yields a giant saturation magnetostriction. It needs, however, a high magnetic field strength. The other ($DyFe_2$) is added to $TbFe_2$ in order to make the combination magnetically soft. The optimized substance containing about 70% $DyFe_2$ yields a $\lambda_S \approx 2 \times 10^{-3}$ at room temperature in a moderate magnetic field and is, therefore, an ideal material for actuators and transducers. Recently, a plan was conceived which would achieve a high magnetostriction combined with a high saturation magnetization. This can be realized by using multilayers consisting of thin films of amorphous TbFe and films of Fe–Co alloys (Quandt and Ludwig 1999). These systems are tailored for applications in optical scanners, micro-valves, linear and rotation micro-motors and micro-pumps. It should be pointed out that this class of substances provides a conversion factor from magnetic to mechanical energy of nearly one.

5. New Effects in Thin Films and Multilayers

In ultra thin films and multilayers new effects, due to interfaces and large strains, were found. Interfaces give a remarkable contribution to the magneto-elastic coupling at film thicknesses smaller than several nm resulting, e.g., in nearly magnetostriction free $Co_{50}Fe_{50}$ films at a film thickness of about 1.6 nm. $Co_{50}Fe_{50}$ is an alloy with the high saturation magnetostriction of 80×10^{-6} in the bulk state. In polycrystalline iron films the saturation magnetostriction changes its sign at a film thickness of 5 nm. In systems where, due to epitaxial growth, giant strains in the range of several percent can be obtained, higher order magneto-elastic coupling coefficients are observed (Sander *et al.* 1999). Their magnitude is comparable even with the usually dominating linear ones. Triggered by these new experimental findings both the scientific and the practical importance of magnetostriction effects have recently received considerable attention.

See also: Magneto-elasticity in Nanoscale Heterogenous Materials; Magnetostrictive Materials

Bibliography

Buck S, Fähnle M 1998 *Ab initio* calculation of the giant magnetostriction in Te and Er. *Phys. Rev.* **B57**, R14044–7
Chikazumi S 1997 *Physics of Ferromagnetism.* Clarendon, Oxford

Engdahl G (ed.) 1999 *Handbook of Giant Magnetostrictive Materials: Physics and Device Applications*. Academic Press, London

Fujita A, Fukamichi K 1999 Giant volume magnetostriction due to the itinerant electron metamagnetic transition in La(Fe–Si)$_{13}$ compounds. *IEEE Trans Magn* **MAG-35**, 3796–801

Hubert A, Schäfer R 1998 *Magnetic Domains*. Springer, Berlin

James R D, Kinderlehrer D 1994 Theory of magnetostriction with application to Terfenol-D. *J. Appl. Phys.* **76**, 7012–4

Néel L 1937 Études sur le moment et le champ moléculaire des ferromagnétiques. *Ann. Phys.* **8**, 237–308

Quandt E, Ludwig A 1999 Giant magnetostrictive multilayers. *J. Appl. Phys.* **85**, 6232–7

Sablik M, Jiles D C 1993 Coupled magnetoelastic theory of magnetic and magnetostrictive hysteresis. *IEEE Trans. Magn* **MAG-29**, 2113–23

Sander D, Enders A, Kirschner J 1999 Stress and magnetic properties of surfaces and ultrathin films. *J. Magn. Magn. Mater.* **200**, 439–55

Tremolet de Lacheisserie E du, 1993 *Theory and Applications of Magnetoelasticity*. CRC Press, Boca Raton, FL

Wassermann E F 1990 Invar: moment-volume instabilities in transition metals and alloys. In: Buschow K H J, Wohlfarth E P (eds.) *Ferromagnetic Materials*. North-Holland, Amsterdam, Vol. 5, Chap. 3, pp. 237–322

Wu R Q, Chen L J, Shick A, Freeman A J 1998 First principles determination of magnetocrystalline anisotropy and magnetostriction in bulk and thin film transition metals. *J. Magn. Magn. Mater* **177–81**, 1216–9

W. Andrae and R. Mattheis
IPHT Jena, Germany

D. Berkov
Innovent, Jena, Germany

Superconducting Machines: Energy Distribution Components

Most of the potential applications of superconductivity in power systems benefit from zero resistance and high critical current densities in the superconducting state thus reducing losses and size of components, for example the generator, transformer, cable (see *Superconducting Wires and Cables: Low-field Applications*), SMES (superconducting magnetic energy storage) and motor. But, there is also a potential application which utilizes the transition from the superconducting to the normal-conducting state in order to limit fault currents. The device is usually referred to as a superconducting fault current limiter (SCFCL).

1. Superconducting Transformer

Transformers are major components of power systems. They allow generation, transmission, and distribution of electrical energy at different voltage levels, leading to economical benefits.

Replacing the copper windings in transformers by a superconductor (SC) offers several opportunities. First it offers reduction in losses, owing to the zero resistance of the conductor. Second it offers reduction of size and weight. Because of higher current densities, the mass of conductor needed can be very small. By applying more winding turns/length in the coils, the amount of iron can be reduced as well. Even iron-free transformers might become feasible. Third, large conventional power transformers are oil-cooled. A superconducting transformer would be more environmentally benign.

In a conventional transformer design the SC will be exposed to alternating magnetic fields up to about 0.3 T. In designs with increased winding turns/length (to reduce iron volume) an even higher magnetic field (B) would be reached. The main challenges for the SC material are high j_c losses, low ac losses at high B, and low cost. Since transformers generate losses not only in the conductor but also in the iron core, it is advisable to leave the core of an SC transformer at room temperature, where cooling is cheaper. Such a design however, poses serious requirements on the cryostat, which would need a warm bore and should ideally be made of nonmagnetic and electrically insulating material in order to avoid additional losses.

1.1 Status of Research

Several SC transformers based on LTS have been built in the past, having a rated power of a few 100 kV A. Commercially available LTS (low temperature superconductor) wires meet technical and economical needs (j_c about 50 kA cm^{-2}, a.c. losses $< 10^{-5}$ W A^{-1} m^{-1} at 0.1 T. However, commercialization of LTS transformers has so far been prohibited by the rather high cooling costs, mainly caused by thermal losses through cryostat and current leads.

HTS offers the opportunity to operate SC transformers at 77 K, which could reduce cooling costs to an acceptable level. But, HTS (high temperature superconductor) wires are not nearly as mature as the LTS wires. At present Bi2223 wire is the only HTS available of sufficient length, which could be operated at 77 K. First prototypes based on these materials have been built. A 630 kV A prototype has already been operated for one year under realistic conditions. Even though the technical feasibility has been proven, the present Bi2223 wire will hardly allow a commercial SC transformer to be built.

At present the 77 K field dependence of j_c (j_c(B)), of the wire is too strong and the a.c. losses and wire costs are too high. J_c(B) can be improved by operating the transformer at a lower temperature, which of course increases cooling costs. Bi2223 conductors with reduced a.c. losses are under development. The

maximum acceptable losses are in the order of $10^{-4}\,\mathrm{W\,A^{-1}\,m^{-1}}$ at $0.1\,\mathrm{T}$; present values are about 10 times higher.

YBCO ($YBa_2Cu_3O_{7-x}$) tapes, even though only available at length of few meters, offer better $j_c(B)$ and potentially lower cost. The a.c. losses in magnetic fields parallel to the YBCO tape will be negligible. However, it will be a great challenge to reduce the losses due to perpendicular field components (occurring mainly at the end of the coils) to an acceptable value. Nevertheless, considering the status of early twenty-first century technology, the material seems to have the highest potential for transformer applications.

2. Superconducting Fault Current Limiter

In electric power systems short circuits might be caused by aged or accidentally damaged insulation or by lightning striking an overhead line. The subsequent fault current is only limited by the impedance of the system between location of fault and power sources. All components of the power system have to be designed to withstand the stresses caused by a short circuit. The higher the fault current anticipated, the higher the costs for the equipment.

Many approaches for realising fault current limiters (FCL) have been based on components with strongly nonlinear current–voltage characteristics (e.g., semiconductors, iron-core reactors, and superconductors). Among the nonlinear materials, superconductors stand out because of their unique transition from zero to finite resistance. FCLs which utilize this transition will be referred to as superconducting fault current limiters (SCFCLs). FCLs which are based on other concepts but might still use SC, e.g., in order to realize low-loss coils, will not be discussed here. There are essentially two concepts in SCFCLs, i.e., the "resistive" and the "shielded core" concepts.

2.1 Resistive SCFCL

The most straightforward concept in an SCFCL is the so called "resistive SCFCL" in which the SC is directly connected in series to the line to be protected. For cooling, the SC might be immersed in a coolant (e.g., liquid helium for LTS or liquid nitrogen for HTS), which is chilled by using a refrigerator.

The cross-section of the SC is determined such that, at nominal current, the SC is operated inside the superconducting state, i.e., at zero resistance, so that its interference with the network is negligible. However, the SC only has true zero impedance for direct current (d.c.)-currents. For the more common a.c. applications the finite length of the SC leads to a finite reactance and the alternating magnetic field generated by the current produces a.c. losses. They both depend very strongly on the geometry of the SC, and can be reduced by optimized conductor architecture, e.g., in the coils with windings in opposite directions or meander structures.

In case of a fault, the increase in j will drive the SC out of the superconducting region into a flux–flow regime. The rapidly increasing resistance limits the current to a value below the unlimited prospective fault current. The actual limitation behavior depends very much on the length of the SC and also on the type of SC material. The three main different limitation behaviors can be realized by just varying the length of the same SC material.

First, by using a very long conductor, the electric field $E = $ (line voltage)/(conductor length), to which the SC is exposed during the fault will be very small. Thus, the corresponding current density will exceed the nominal value only by a little. The power density $E.j$ dissipated in the SC will be negligible so that the SC will essentially not warm up (curve 1 in Fig. 1). This "constant temperature" design gives a very good limitation. However, the long length of the conductor will be prohibitively expensive and cause rather high a.c. losses.

The other extreme design would be using a rather short conductor, leading to a relatively large E during the fault. As the fault occurs, the current will increase essentially unlimited by the small resistivity of the flux–flow regime and only limited by the impedance of the power system. However, because of the very high $E.j$ dissipated in the SC, the material will heat up rapidly and, after a few $100\,\mu s$, will become normal conducting and limit the fault current close to or even below the nominal value (curve 3 of Fig. 1). This "fast heating" design needs a rather small amount of SC material. However, the height of the first peak still depends on the unlimited prospective fault current, and instantaneous recovery to normal operation is not possible, since the SC first has to cool down. Furthermore, severe over voltages may arise from the abrupt current reduction, caused by the rapid transition into the normal-conducting state. Last, but not least, the high $E.j$ value during the fault might lead to the SC being damaged.

Using a conductor of intermediate length will lead to an intermediate poor density dissipation in the SC. For the first $10\,\mathrm{ms}$ the maximum of the fault current will be limited to several times (e.g., 5–10) that of the nominal current. The SC will keep warming up and after a few tens of milliseconds will enter the normal conducting region ("slow heating" design, curve 2 in Fig. 1).

2.2 Hot Spots

In the above discussion it is assumed that during the limitation process the voltage drop is uniform over the whole length of the conductor. In reality,
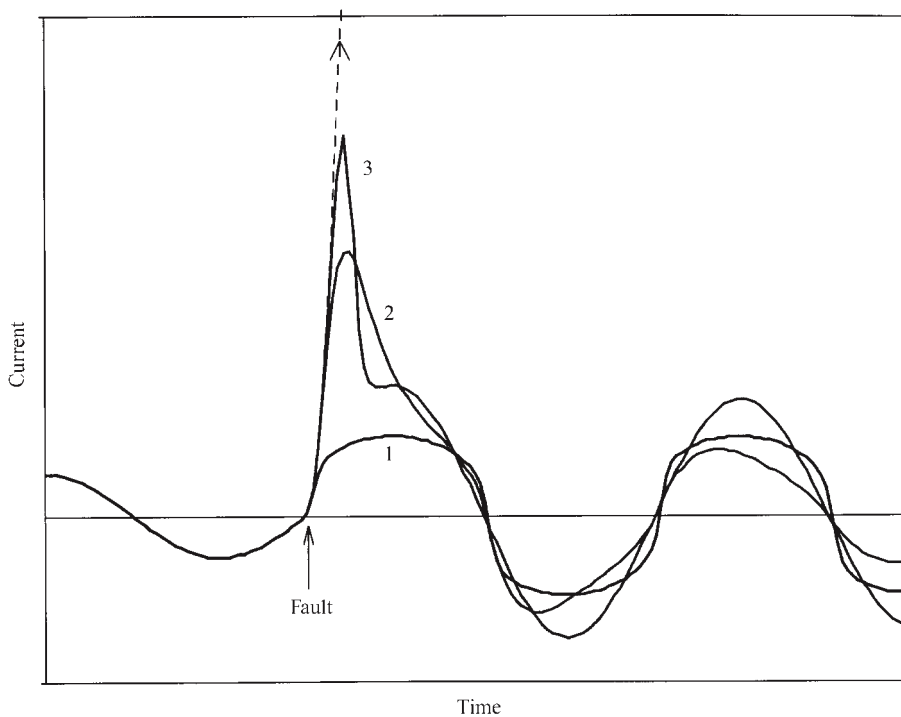
Figure 1
Different designs offer different current limitation behaviors. 1, Constant temperature; 2, slow heating; 3, fast heating.

however, SC tends to develop thermal instabilities called "hot spots," which are due to the strong current and temperature dependence of their resistance. The common measure for reducing the problem is to attach a normal conducting "bypass" or "shunt" in close electrical contact to the SC, which allows the current to bypass the hot spot. Of course, the bypass reduces the total normal resistance of the conductor, which might have to be compensated by increased length. It should be noted that the problem of excessive heating will also limit the maximum possible electric field to which the conductor can be exposed during the fault, i.e., it will also set a lower limit for the length of the SC.

2.3   Shielded Core SCFCL

The second concept in a SCFCL is often referred to as the "shielded core." In this concept the SC is not connected galvanically in the line, but magnetically. The device is essentially a transformer, with its primary normal conducting coil connected in series to the line to be protected, while the secondary side is a superconducting tube (i.e., a one turn coil). In normal operation the iron core sees no magnetic field because it is completely shielded by the SC, thus the name "shielded core." Because of the inductive coupling

between the line and the SC, the device is sometimes also referred to as an "inductive SCFCL." The voltage on the secondary is reduced by the number of the turns of the primary coil, while the current is increased by the same factor. The SC on the secondary has to be designed for these values. Assuming an ideal transformer, the SCFCL will behave exactly like a resistive SCFCL.

In order to achieve a certain limitation behavior, both types of SCFCL need the same amount of a certain SC material. Compared to the resistive SCFCL, the shielded core SCFCL shows the disadvantage of being only applicable for a.c. currents and having a much larger size and weight. On the other hand it needs no current leads, which is especially attractive for high current applications, since the losses of the leads are proportional to their current-carrying capability.

2.4   Status of Research

Several SCFCL prototypes with a rated power of several MVA have been realized based on LTS following the resistive concept. Because of the high j_c and low heat capacity of LTS the "fast heating" design was the "natural" choice. However, like in the

case of the transformer, commercialization has so far been prohibited by the rather high cooling costs.

To date, the largest HTS SCFCL prototype that has been built utilizes Bi-2212 bulk material. ABB has realized a three-phase 1.2 MV A prototype based on tubes of this material. For ceramic HTS, this geometry is usually more easily realized than long length conductors. The device is of the "shielded core" and "slow heating" type, it was successfully operated for one year under realistic conditions in a Swiss hydropower plant.

Because of their high critical current density ($1 \, \mathrm{MA \, cm^{-2}}$) YBCO films are especially suitable for the "fast heating design." Siemens has demonstrated a resistive 300 kV A model based on this material. The films were deposited on planar ceramic substrates, covered with a gold bypass, and patterned into meander.

Bi2223 wires are at present not particularly suitable for SCFCL, because of the low normal resistivity of the Ag-matrix. However, if this resistivity could be increased, the wire would be quite suitable for resistive SCFCL and could even allow for the incorporation of "current limitation" functionality in other devices. Following this approach, a project led by ABB in partnership with American Superconductor and Electricité de France has been launched to develop a current limiting transformer.

See also: Superconducting Machines: Energy Storage

Bibliography

Fevrier A, Tavergnier J P, Laumond Y, Bekhaled M 1988 Preliminary test on a superconducting power transformer. *IEEE Trans. Magn.* **24**, 1477–80
Gromoll B, Ries G, Schmidt W, Kraemer H P, Seebacher B, Utz B, Nies R, Neumueller H W, Balzer E, Fissher S, Heismann B 1999 Resistive fault current limiters with YBCO films–100 kV A functional model. *IEEE Trans. Appl. Supercond.* **9**, 656–9
Hoernfeldt S, Albertsson O, Bonmann D, Koenig F 1993 Power transformer with superconducting windings. *IEEE Trans. Magn.* **29**, 3556–8
Paul W, Chen M 1998 Superconducting control for surge currents. *IEEE Spectrum* **May**, 49–54
Paul W, Lakner M, Rhyner J, Unternährer P, Baumann Th, Chen M, Widenhorn L, Guérig A 1997 Test of 1.2 MV A high-T_c superconducting fault current limiter. *Supercond. Sci. Technol.* **10**, 914–8
Schwenterly S W, McConnel B W, Demko J A, Fadnek A, Hsu J, List F A, Walker M S, Hazelton D W, Murray F S, *et al.* 1999 *IEEE Trans. Appl. Supercond.* **9**, 680–4
Seeber B (ed.) 1998 *Handbook of Applied Superconductivity* IOP Publishing, Vol. 2, pp. 1613–26 and 1691–1702
Verhaege T, Cottevieille C, Estop P, Quemener M, Tavergnier J P, Bekhaled M, Bencharab C, Bonnet P, Laumond Y, Pham V D, Poumarede C, Therond P G 1996 Experiments with a high voltage (40 kV) superconducting fault current limiter. *Cryogenics* **36**, 521–6
Yazawa T, Yoneda E, Nomura S, Tsurunaga K, Urata M, Ohkuma T, Honjo S, Iwata Y, Hara T 1997 Experiments with a 6.6 kV A/1 kA single-phase superconducting fault current limiter. In: Rogalla H, Blank D H A (eds.) *Proceedings of EUCAS 1997, Third European Conference on Applied Superconductivity*. Institute of Physics Conference Series Number 158. Institute of Physics, Bristol, Vol. 2, pp. 1183–6
Zueger H 1998 630 KVA high temperature superconducting transformer. *Cryogenics* **38**, 1169–72

W. Paul
ABB Corporate Research Ltd, Baden-Daettwil Switzerland

Superconducting Machines: Energy Storage

Superconducting magnetic energy storage (SMES) is an emerging technology offering tremendous benefits to the electric power industry. Many years after its conception (Ferrier 1970), SMES is still not widely implemented and its commercial viability is only slowly being established.

1. Principles of Operation

Electric power has always been available on instant demand with a high degree of reliability, flexibility, and control; however, it has never been easy to store in large quantities on a cost-effective and environmentally sound basis.

In SMES, electric energy is stored by circulating a current in a superconducting coil, or inductor. Because no conversion of energy to other forms is involved (e.g., mechanical or chemical), round-trip efficiency can be very high. The energy stored in a d.c. inductor is given by

$$E = \frac{1}{2} L I^2 \qquad (1)$$

where E is the stored energy, L is the inductance of the coil (which depends on coil geometry), and I is the circulated current.

As an energy storage device, SMES is a relatively simple concept. It stores electric energy in the magnetic field generated by d.c. current flowing through a coiled wire. If the coils were wound using a conventional wire such as copper, the magnetic energy would be dissipated as heat owing to the resistance of the wire. However, if the wire is superconducting (no resistance), then energy can be stored in a persistent mode, virtually indefinitely, until required.

The SMES coil, a d.c. device, is usually connected to its load (typically an a.c. device) via an a.c./d.c. converter, or "power conditioning system" (PCS).

The architecture of the PCS varies depending on the application, but in general is based on standard semiconductor power switches in arrangements to maximize reliability, efficiency, and controllability.

The only loss associated with magnetic storage is the power needed to keep the coil cryogenically cooled as required by the superconductor. Additionally, there are minor losses associated with power transfers through the a.c./d.c. converter. Overall efficiency of a SMES system is heavily dependent on size (stored energy) and power rating, as well as on duty cycle, but in general SMES units can be much more efficient than many other systems for energy storage.

2. Applications

In terms of energy storage, SMES competes with other technologies such as batteries, flywheels, and capacitors. The choice of technology is determined by economics (cost) when considering all angles: system performance, capital and operating costs of the unit, reliability and maintainability, environmental and disposal costs, insurance, etc.

SMES is particularly attractive in comparison to other options in cases where a high power/energy ratio is needed (sharp pulses), or when the power pulse repetition rate is high (e.g., tens or even hundreds of pulses per day).

Pulsed power loads such as electromagnetic launch (for military or space applications) could be enabled through the implementation of a SMES system. Buffering pulsating loads in general is a high-payoff application of SMES.

In the electric power sector SMES has two major applications: power quality enhancement, and transmission-related services. Power quality enhancement refers to the ability of SMES systems to sit idle and connected between a load and its utility supply line to ''buffer'' and ''filter'' power quality disturbances such as voltage sags and spikes, harmonic distortions, or frequency problems coming through the utility distribution network. Certain applications needing very sensitive loads (such as is required in semiconductor processing plants) can derive great benefit from access to ''clean'' power and thus pay the premium in price over other storage technologies. At the lower end of stored energy and power (a few megajoules and few megawatts) this is already a commercial application of SMES, with the prospect of capturing a larger market with the development of larger units.

The electric utility industry, being deregulated in most parts of the world, could also be major market for this technology. The applicability of SMES to the utility sector goes well beyond energy storage (daily load leveling). Some of these applications are:

- increased transmission capacity through enhanced line stability;
- spinning reserve;
- leveling of renewable energy sources;
- voltage control;
- frequency control;
- subsynchronous frequency damping;
- wide-area generation control; and
- black start.

Power and energy ratings needed for each of these application vary, from a few hundred megajoules to provide transmission line stabilization, to possibly many gigajoules in the case of spinning reserve for a large network.

In transmission stabilization, a SMES unit is strategically located within a high-voltage network to inject active and/or reactive power on demand to dampen voltage fluctuations that can cause the triggering of protective relays. These fluctuations are usually the result of large generation plants or loads tripping and creating instabilities that cause large-area blackouts. In spinning reserve a SMES unit can act as a infinitely controllable generating unit (with the added benefit of also acting as a ''sink'') to enhance flexibility of dispatch and to provide that extra cushion need to run a transmission network without the need of having ''idling'' plants with the concomitant environmental penalty.

In a fully deregulated utility industry (something not yet achieved) SMES will be an integral part of the network.

3. Technology Development

The status of SMES in terms of its development and application has been reviewed by Hassenzahl (1989) and by Luongo (1996). The early years of SMES development were mostly devoted to system studies and to determining optimum configurations. During the 1980s the technology saw an increase in activity with the implementation of programs that led to actual hardware being produced. During the 1990s there was somewhat of a retrenchment in terms of development, with relatively few full demonstration programs.

In the early 1980s a 30 MJ SMES unit was installed and tested at the Bonneville Power Authority transmission grid in the USA to demonstrate its ability to dampen subsynchronous resonant frequencies (Rogers *et al.* 1983). Also during the 1980s the US Department of Defense funded the design and development of components needed to build a large-scale SMES units that would serve as pulsed power supplies to military systems. These activities yielded a number of advances in terms of innovative designs and the actual fabrication and testing of major SMES components. Among the advances was the development of a very high-current cable-in-conduit conductor, shown in Fig. 1, rated at 200 kA (at 1.8 K and 5 T), and which was actually tested in short
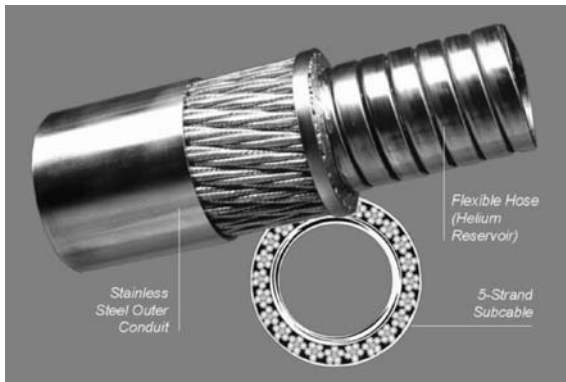
Figure 1
High-current cable-in-conduit conductor.

samples under operating condition to its quench current of 300 kA (Peck *et al*. 1994).

In the 1990s most of the development activity took place in Japan with a focus on transmission stability applications as well as the construction and testing of a large SMES model coil (Hamajima 1999).

Previous experience with SMES notwithstanding, it is safe to say that this technology is still in need of an integrated large-scale demonstration under actual operating conditions (e.g., utility environment) before its widespread acceptance in the market.

4. Outlook

Despite its great promise and many years of development, SMES is far from being the commercial success once envisioned. Even though the technology is making some inroads into the marketplace (at the lower end of storage/power ratings), it is far from mature or being widely accepted. The main stumbling block for wider dissemination of SMES is not technical, but rather economic. The extremely high cost of superconducting devices does not justify the economic benefits that could be accrued in most applications. The advent of high-temperature superconductor (HTS) materials has done little to advance the deployment of SMES. Major reductions in the price of these superconductors would be needed before they can make an impact on the commercial viability of SMES. Operation at higher temperature alone does not justify adoption of HTS materials, as operating costs are typically a small component of lifecycle cost for SMES units of practical size.

Continued advances in SMES technology are nevertheless likely. One-of-a-kind units for specific applications will give SMES opportunities to demonstrate its benefits. Through this evolutionary chain of development SMES will some day take its promised role in the electric power industry.

See also: Superconducting Permanent Magnets: Potential Applications; Superconducting Permanent Magnets: Principles and Results

Bibliography

Ferrier M 1970 Stockage d'energie dans un enroulement supraconducteur. *Low Temperature and Electric Power*. Pergamon, Oxford, UK , pp. 425–32
Hamajima T 1999 Test results of the SMES model coil—pulse performance. *Cryogenics* **39**, 351–7
Hassenzahl W V 1989 Superconducting magnetic energy storage. *IEEE Trans. Magnetics* **25**, 750–8
Luongo C A 1996 Superconducting storage systems: an overview. *IEEE Trans. Magnetics* **32**, 2214–23
Peck S D, Zeigler J, Luongo C A 1994 Tests on a 200 kA cable-in-conduit conductor for SMES. *IEEE Trans. Appl. Supercond.* **4**, 199–204
Rogers J D, *et al*. 1983 30-MJ SMES system for electric utility transmission stabilization. *Proc. IEEE* **71**, 1099–107

C. A. Luongo
*National High Magnetic Field Laboratory
Tallahassee, Florida, USA*

Superconducting Materials, Types of

In 1911 the Dutch physicist Heike Kamerlingh Onnes (Onnes 1911) observed during studies of the electric properties of pure metals at temperatures near absolute zero (0 K or $-273.15\,°C$), that the resistance of a mercury wire dropped precipitously when cooled to below $4.2\,K$ ($-268.95\,°C$). He soon recognized this to be the manifestation of a new state of matter "which on account of its extraordinary electrical properties may be called the superconducting state."

For over 20 years after the discovery of superconductivity, this new state was believed to be just an ideal conductor that loses its resistance below a distinct temperature, the so-called critical temperature, T_c. In the year 1933, Meissner and Ochsenfeld (1933) discovered that magnetic fields are excluded from the inside of a superconductor even on cooling in a constant magnetic field that could not be explained by classical electrodynamics. This effect is known today as the Meissner–Ochsenfeld effect.

Bardeen, Cooper, and Schrieffer published their comprehensive theory of superconductivity in 1957 (Bardeen *et al*. 1957). The salient point of the so-called BCS theory is the attractive electron interaction mediated by phonons. By that virtue, two electrons couple to form so-called Cooper pairs, which act in a fundamentally different way from single electrons. Being quasi-particles with integer spin, Cooper pairs follow the Bose–Einstein statistics

which allows them to condense into a single quantum mechanical state, with all Cooper pairs having the same wave function. Thus, superconductivity is often referred to as a macroscopic quantum phenomenon. The BCS theory was very successful in predicting the critical temperature of a material and provided an explanation for the isotope effect, according to which the critical temperature shifts as a function of the isotopic mass of chemical elements.

With the discovery of materials showing transition temperatures near and above 100 K, it became evident that the BCS theory would not be adequate to describe this new class of superconductors, known as high-temperature superconductors, in contrast to the term "low-temperature superconductor" which comprises all superconductors with critical temperatures below about 30 K. Experiments gave evidence that the charge carriers of superconductivity are Cooper pairs. But, the question about the nature of the force that keeps the Cooper pairs together is still a matter of investigation.

Since the first observation of superconductivity in mercury, thousands of compounds and alloys were investigated with respect to their superconducting properties. In Fig. 1 the fever curve of superconductivity is shown, which is marked by the highest critical temperature known during that time. Since 1993, several new superconductors have been found. None of them, however, have surpassed the world champion $HgBa_2Ca_2Cu_3O_8$ exhibiting a T_c of 138 K at ambient pressure, and 164 K at an isostatic pressure of 23 GPa.

1. Type 1 Superconductors

Type 1 superconductors—also known as the "soft" superconductors—are characterized by a very sharp transition to a superconducting state at T_c, and by "perfect" Meissner–Ochsenfeld effect up to the so-called critical field, B_c. Above B_c, the material becomes normal conducting. Even here, the transition is very sharp (Fig. 2). The value of B_c is temperature dependent and reaches zero at T_c. However, the magnetic field is not repelled at the surface of the superconductor, but penetrates it within a 10^{-8}–10^{-7} m thick surface layer causing screening electric currents in the surface layer. These currents generate a magnetic field which is anti-polarized to the external field. This phenomenon is the reason for the well-known levitation effect of a permanent magnet above a superconductor, or vice versa.

The so-called penetration depth, λ, of the external magnetic field is a material property. It also is temperature dependent and increases asymptotically towards T_c. At the particular field B_c relatively thick normal and superconducting domains running parallel to the field can coexist, known as the intermediate state.

2. Type 2 Superconductors

Type 2 superconductors—also known as the "hard" superconductors—differ from Type 1 in that their transition from a normal to a superconducting state is gradual across a region of "mixed state" behavior.
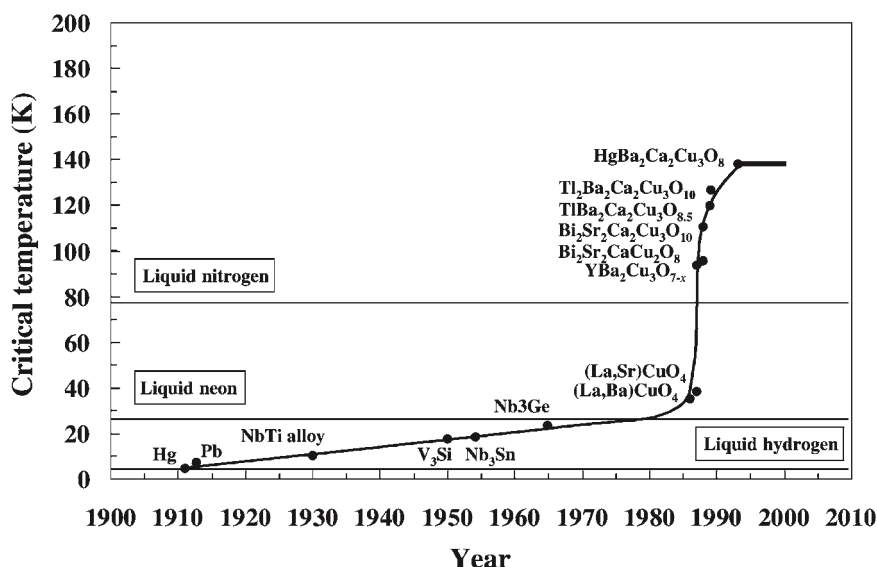
Figure 1
Maximum critical temperature vs. time.
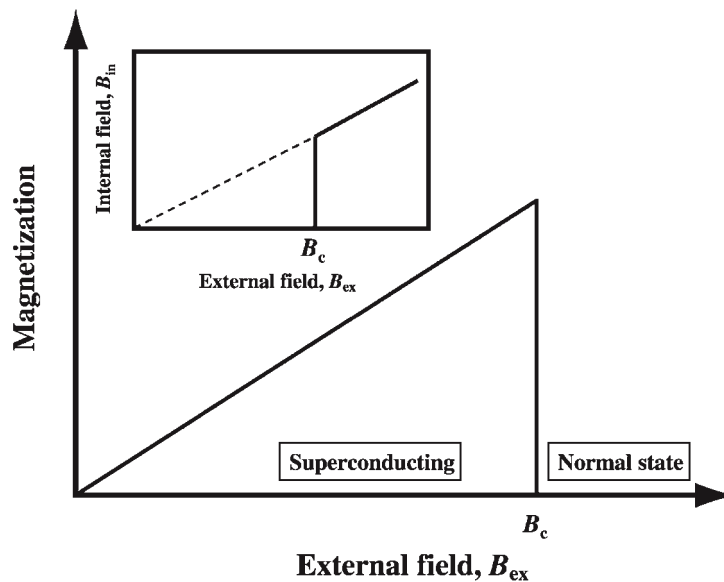
Figure 2
Magnetization of a Type 1 superconductor vs. the external field, B_{ex}. Insert: Magnetic field within a Type 1 superconductor, B_{in}, vs. the external field, B_{ex}.

A Type 2 superconductor exhibits a very different behavior in an external magnetic field compared to the Type 1 superconductors. At low external fields, like the Type 1 superconductor it repels the magnetic field up to the lower critical field, B_{c1}. This region is also called the "Meissner phase." Above B_{c1}, regularly divided quantified flux vortices or flux lines enter the material up to the so-called upper critical field, B_{c2} (Fig. 3). In the region between B_{c1} and B_{c2}, superconducting and nonsuperconducting areas with trapped magnetic flux lines are present (Fig. 4). With increasing magnetic fields, the trapped flux lines move closer together and more trapped flux lines occur, so that the superconducting volume decreases and that of the nonsuperconducting increases (see *Electrodynamics of Superconductors: Flux Properties*). The region is called the "Shubnikov phase" or the mixed state. The values of B_{c1} and B_{c2} are also temperature dependent and decrease with increasing temperature. At T_c both values, B_{c1} and B_{c2}, are zero (Fig. 5).

3. Critical Current Density

Both categories of superconductors, Types 1 and 2, can carry large electric currents up to a certain value which is called the critical current density, J_c ($A\,cm^{-2}$). Above J_c, the superconductor becomes normal conducting. J_c is dependent on both the temperature and the external magnetic field. At T_c or B_c (Type 1) or B_{c2} (Type 2) the value of J_c is zero and the

superconductor becomes normal conducting (Fig. 6). Superconductors show characteristic current vs. voltage behavior. At a current below J_c the voltage is zero. Above J_c, as in a metal, the voltage increases with the current (Fig. 7).

In the mixed state, when an electric current is transported through the superconductor due to the Lorenz force, the trapped flux lines can move through the superconductor causing dissipation of the current and a warming of the superconductor. This phenomenon can result in a rapid transition into the normal conducting state. Therefore, the value of J_c is significantly lower in the Shubnikov phase compared to the Meissner phase. However, the flux lines can be pinned by so-called pinning centers, which are defects with different dimensions within the superconductor. For example, point defects (zero dimension), dislocation lines (one dimension), twin planes (two dimensions), and second phases (three dimensions). The flux lines remain pinned until the Lorenz force surpasses the pinning force of the defect.

4. Superconducting Materials

Except for the elements vanadium, technetium, and niobium, the Type 2 category of superconductors includes compounds and alloys. Niobium ($T_c = 9.2\,K$), especially when alloyed with titanium (Nb0.7Ti0.3: $T_c = 9.8\,K$), exhibits the highest critical temperature of all elements. Although superconductors with higher
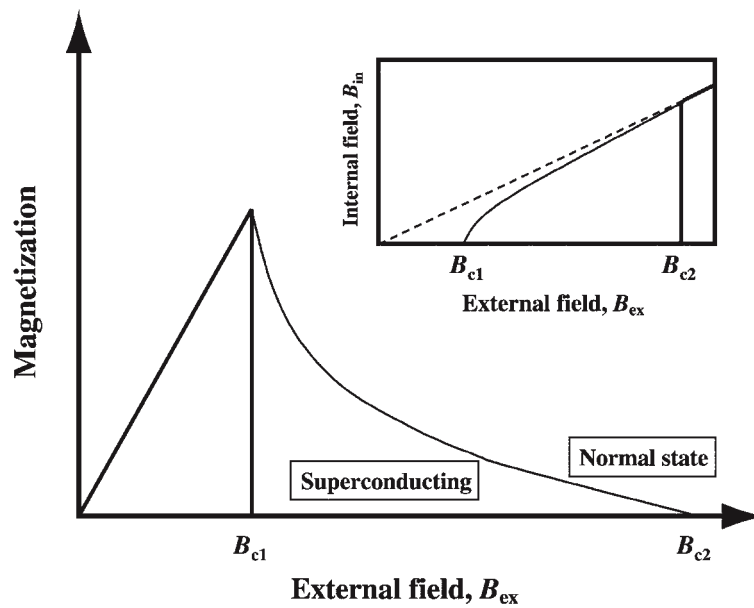
Figure 3
Magnetization of a Type 2 superconductor vs. the external field, B_{ex}. Insert: Magnetic field within a Type 2 superconductor, B_{in}, vs. the external field, B_{ex}.
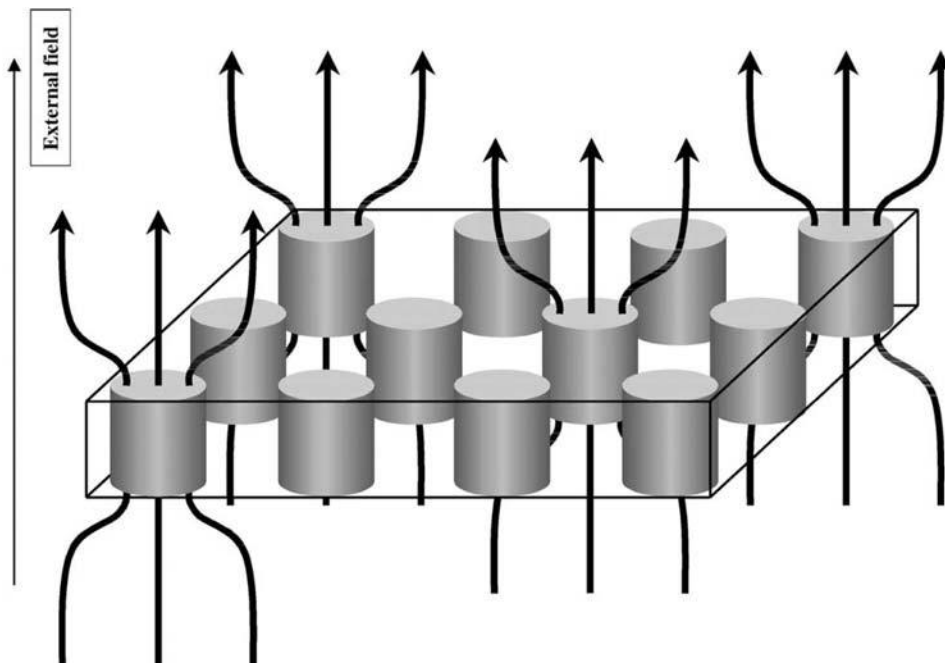
Figure 4
Type 2 superconductor with trapped flux lines vortex.

T_c are available, until now, most commercially available superconducting magnets operating below about 5 T are based on NbTi wires, due to its comparably low price and excellent manufacturing qualities. During the late 1940s and early 1950s, compounds were found with T_c values in the range of 10–20 K. These compounds belong to the β-tungsten structure family, also named A15 phases or A_3B structure. The unit cell of the structure consists of a cube with the B atoms entering each corner of the cube. The A atoms
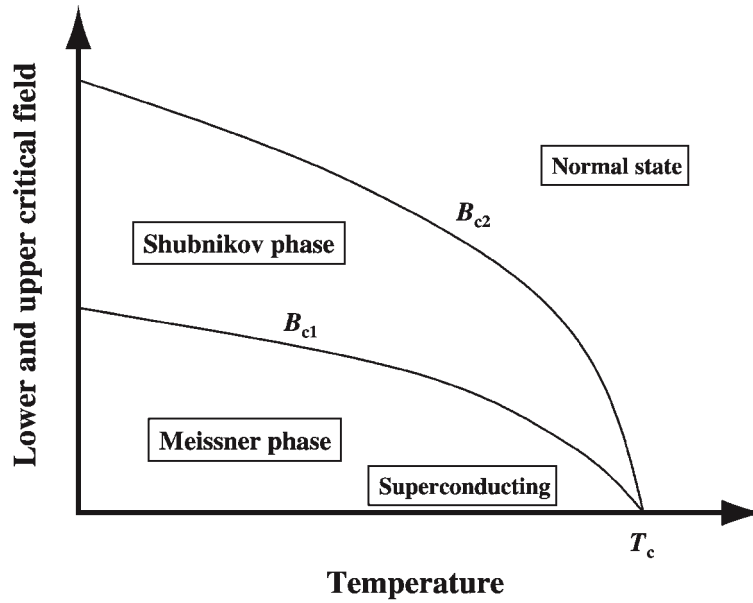
Figure 5
Lower and upper critical field of a Type 2 superconductor vs. the temperature.
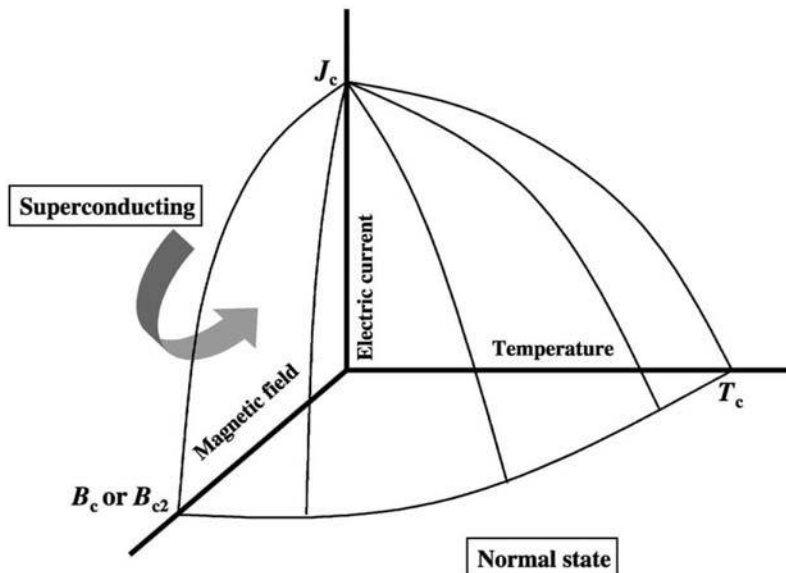
Figure 6
Critical current density, J_c, vs. the temperature and the external magnetic field.

enter the planes of the cube, and so form lines parallel to each crystallographic direction of the crystal (Fig. 8). It is believed that this extraordinary structural feature is mainly responsible for the relatively high T_cs of the compounds. Due to technological considerations with respect to processing and fabrication, only Nb_3Sn ($T_c = 18.1$ K) is used for the manufacturing of wires for high field (>5 T) superconducting magnets.

MgB_2 has been found to be superconducting at a T_c of 39 K and a B_{c2} at about 11 T. This new Type 2 superconductor has a hexagonal structure (AB_2) with $a = 3.086$ Å and $c = 3.524$ Å. Although the compound has quite low T_c and B_{c2} values (about 15 T at 4.2 K and 10 T at 20 K), it is of considerable interest for the processing of wires used for the construction of superconducting magnets operating at 1–2 T and 20 K, due to its comparably low price and excellent workability. In addition, it is hoped that besides MgB_2 other superconducting compounds of this new class of superconductors with T_cs much higher than 39 K will be found.

Superconductivity has been found in different materials (Table 1), which indicates that superconductivity is not only related to one or two structural types, but may occur everywhere.

4.1 High-temperature Superconducting Cuprates

Since the first high temperature superconductor (HTSC) based on copper oxide with the composition $La_{0.85}Ba_{0.115}CuO_3$ was found, a variety of high-temperature superconductors have been synthesized. They
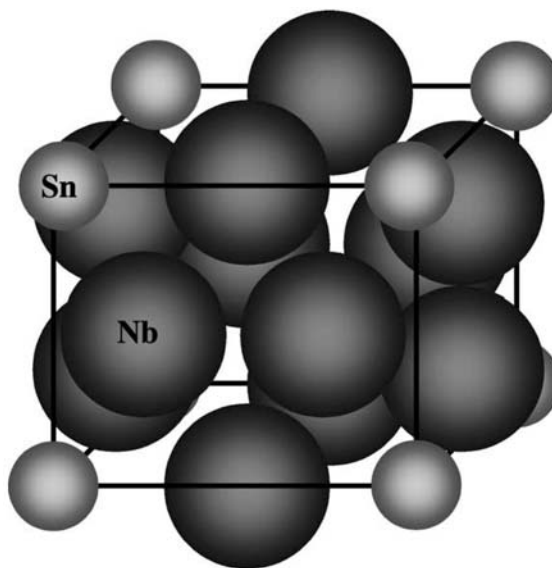
Figure 8
Crystal structure of A15 phases (Nb_3Sn).

all share a single structural feature, namely superconducting two-dimensional sheets of CuO_2 consisting of corner-shared CuO_4 units. The sheets are separated by a nonsuperconducting layer which supplies the sheets with charge carriers. The HTSCs can be divided into three major groups: (i) $REEBa_2Cu_3O_{7-x}$ (123 type);
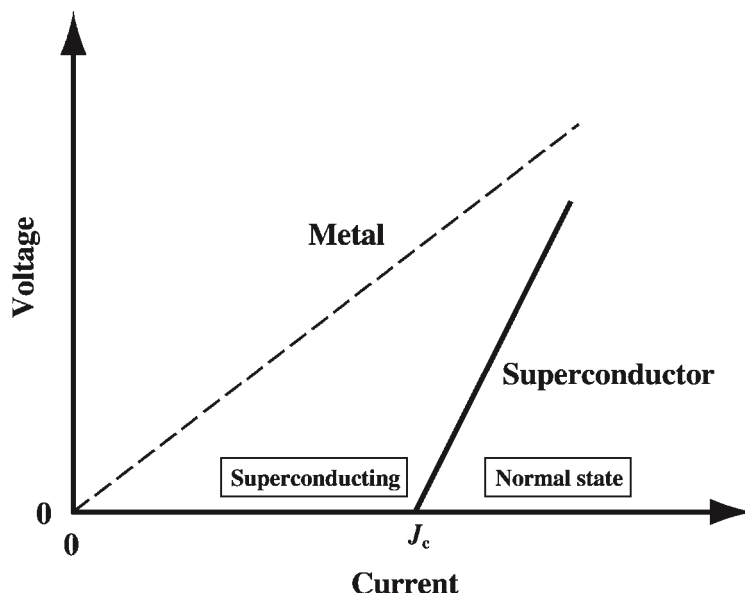
Figure 7
Current–voltage characteristic of a superconductor.

Table 1
Superconducting elements, alloys, and compounds.

Material	Temperature (K)	Material	Temperature (K)
Elements		*A15 phases*	
Carbon (C)	15	Nb_3Ge	23.2
Lead (Pb)	7.2	Nb_3Si	19
Lanthanum (La)	4.9	Nb_3Al	19
Tantalum (Ta)	4.47	Nb_3Sn	18.1
Mercury (Hg)	4.15	V_3Si	17.1
Tin (Sn)	3.72	Ta_3Pb	17
Indium (In)	3.40	V_3Ga	16.8
Thallium (Tl)	1.70	Nb_3Ga	14.5
Rhenium (Re)	1.697	V_3In	13.9
Protactinium (Pa)	1.40		
Thorium (Th)	1.38	*High-temperature superconductors*	
Aluminum (Al)	1.175	$HgBa_2Ca_2Cu_3O_8$	138
Gallium (Ga)	1.10	$HgBa_2CaCu_2O_6$	124
Gadolinium (Gd)	1.083	$HgBa_2CuO_4$	98
Molybdenum (Mo)	0.915	$Tl_2Ba_2Ca_2Cu_3O_{10}$	127
Zinc (Zn)	0.85	$TlBa_2Ca_2Cu_3O_9$	123
Osmium (Os)	0.66	$TlBa_2Ca_3Cu_4O_{11}$	112
Zirconium (Zr)	0.61	$Tl_2Ba_2Ca_3Cu_4O_{12}$	112
Americium (Am)	0.60	$Bi_2Sr_2Ca_2Cu_3O_{10}$	110
Cadmium (Cd)	0.517	$Bi_2Sr_2CaCu_2O_8$	
Ruthenium (Ru)	0.49	$Bi_2Sr_2CuO_6$	20
Titanium (Ti)	0.40	$Ca_{1-x}Sr_xCuO_2$ (at about 5 GPa)	110
Uranium (U)	0.20	$TmBa_2Cu_3O_7$	90
Hafnium (Hf)	0.128	$GdBa_2Cu_3O_7$	94
Iridium (Ir)	0.1125	$YBa_2Cu_3O_7$	93
Lutetium (Lu)	0.100	$Pb_2Sr_2YCu_3O_8$	70
Beryllium (Be)	0.026	$GaSr_2(Y, Ca)Cu_2O_7$	70
Tungsten (W)	0.0154	$La_{1.85}Ba_{.15}CuO_4$	35
Platinum (Pt)	0.0019	$(Nd,Sr,Ce)_2CuO_4$	35
Rhodium (Rh)	0.000325	$Pb_2(Sr,La)_2Cu_2O_6$	32
		$La_{1.85}Sr_{0.15}CuO_4$	38
Metals and alloys			
Nb0.6Ti0.4	9.8	*Various superconductors*	
Nb	9.25	Cs_3C_{60}	40
Tc	7.80	MgB_2	39
V	5.40	$Ba_{0.6}K_{0.4}BiO_3$	30
		YNi_2B_2C	15.5
		$LiTiO_2$	13

(ii) $AB_2Ca_{n-1}Cu_nO_{2n+2.5}$ (1223 type); (iii) $A_2B_2Ca_{n-1}Cu_nO_{2n+4}$ (2223 type) with REE = rare earth elements; A = Bi, Tl, Hg; B = Sr, Ba. The phases have a pronounced layered structure which is visible both microscopically (Fig. 9) and macroscopically (Fig. 10). Due to the significantly different parameters of the a, b, and c axis, the crystallization rate in direction of the a,b plane is about 10^2–10^3 times faster than in c direction.

Compared with low-temperature superconductors of Type 2, the cuprates behave very differently with respect to their superconducting properties vs. the temperature. Their resistivity transition is broader and the breadth increases rapidly with the applied field. This means that there is a region below B_{c2} where the material shows a substantial electrical resistance, although the material is superconducting with respect to quantum mechanical considerations. This region is shown in Fig. 11 between B_{c2} and the irreversibility line, B_{irr}. Below B_{irr} the resistance of the material is zero. The substantial resistance above B_{irr} corresponds to very easy flux flow.

The layered structure also implies a pronounced anisotropy of the properties, causing the so-called
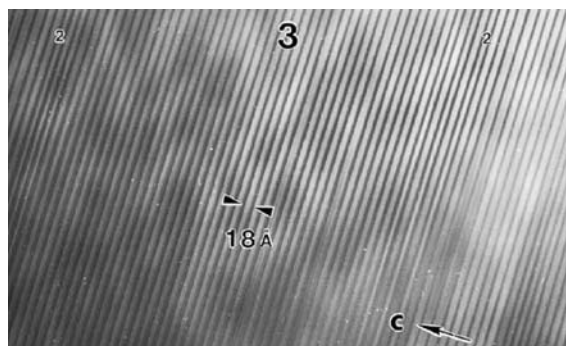
Figure 9
Transmission electron microscopic image of a
$Bi_2Sr_2Ca_2Cu_3O_{10}$ crystal. Dark layers: BiO bilayers,
light gray layers: $Sr_2Ca_2Cu_3O_7$. (3) area with
$Bi_2Sr_2Ca_2Cu_3O_{10}$ structure; (2) Stacking faults with
$Bi_2Sr_2CaCu_2O_8$ structure. (C) crystallographic c axis.
18 Å represent a half unit cell of $Bi_2Sr_2Ca_2Cu_3O_{10}$.

''two-dimensional superconductivity'' parallel to the
a,b plane. For example, the critical current density as
well as the B_{c1} and B_{c2} values of the compounds, are
significantly greater parallel to the a,b plane than
parallel to the c axis (Fig. 12). In addition, due to the
almost complete decoupling of the CuO_2 sheets by
the nonsuperconducting (Bi, Tl, Hg)O sheets, the
HTSCs behave very differently within an applied
magnetic field. At temperatures below about 30 K

flux lines are formed above B_{c1} like in the Type 2 low-
temperature superconductors. Above that tempera-
ture, the flux lines disappear and separated, almost
two-dimensional, flux disks, the so-called pancake
vortices, are formed within the CuO_2 sheets (Fig. 13).
The coupling between the pancakes is very weak, es-
pecially at high temperatures, for example 77 K (boil-
ing point of liquid nitrogen), so that the pancakes are
moving independently from the neighboring pancake
of the next CuO_2 sheet when a Lorenz force is ap-
plied. Pinning of these pancakes is almost impossible
and therefore, the J_c decreases significantly in an ap-
plied magnetic field (Fig. 14).

4.2 The Compound $YBa_2Cu_3O_{7-x}$

One of the main important high temperature super-
conducting cuprates is the compound $YBa_2Cu_3O_{7-x}$,
better known as the ''123 phase'' ($T_c = 93$ K). The
123 phase is characterized by a Cu–O sublattice con-
sisting of the CuO_2 sheets parallel to the crystallo-
graphic a–b plane, and Cu–O chains parallel to the
crystallographic a axis (Fig. 15). The yttrium atom
enters the center of the unit cell, and separates the
Cu–O sheets. At temperatures of above 700 °C the
compound is tetragonal with a = 3.857 Å and
c = 11.839 Å. Below that temperature, the phase be-
comes orthorhombic with a = 3.885 Å, b = 3.818 Å,
and c = 11.680 Å due to the introduction of excess
oxygen into the Cu–O chains.
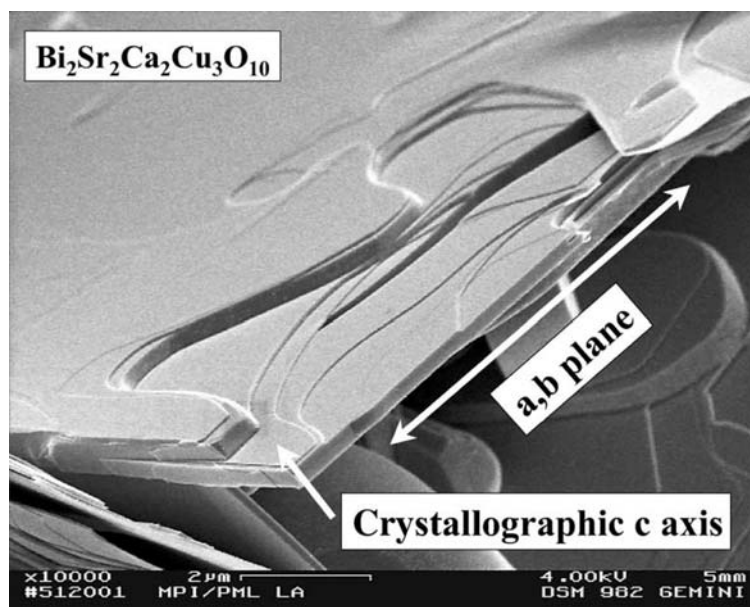
Figure 10
Scanning electron microscopic image of a $Bi_2Sr_2Ca_2Cu_3O_{10}$ crystal showing the extreme anisotropy in grain
dimension.
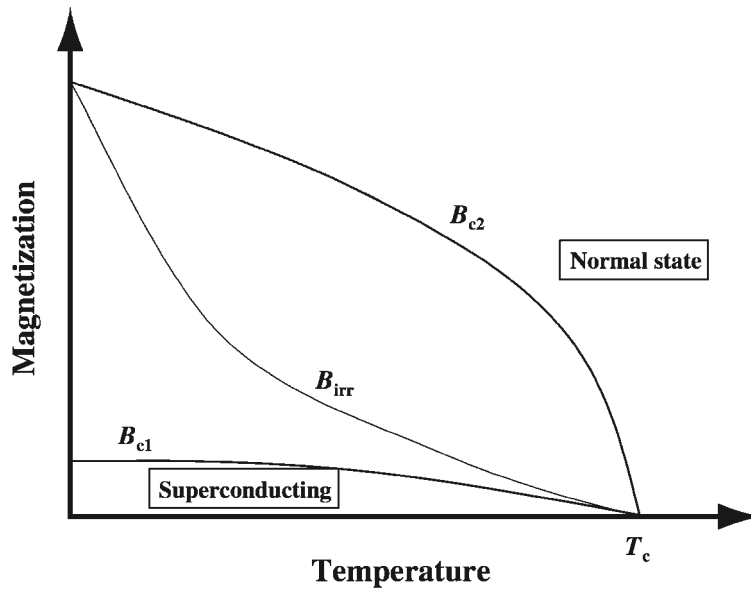
Figure 11
B_{c111}, B_{c2}, and B_{irr} vs. the temperature.
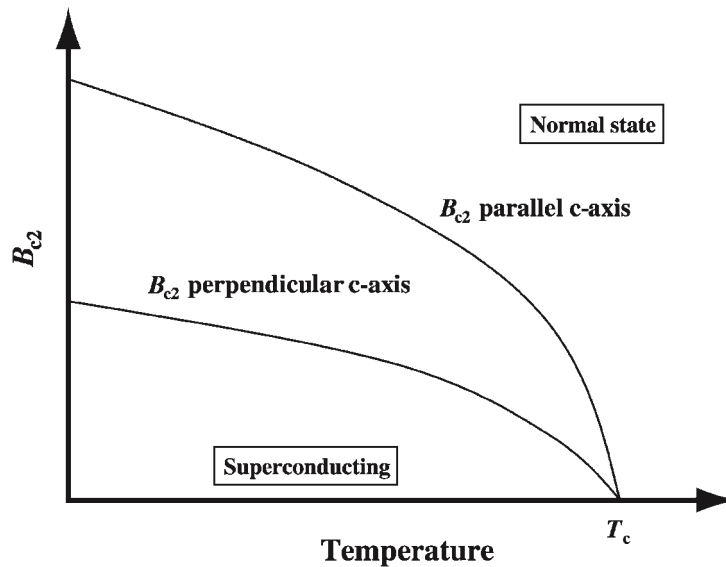
Figure 12
Schematic drawing of the upper critical field vs. temperature parallel and perpendicular to the crystallographic c axis showing the pronounced anisotropy of the superconducting properties of the HTSCs.

The phase transformation is combined with a formation of elastic twins parallel to the crystallographic [110] plane. This phenomenon makes it easy to distinguish between the tetragonal and orthorhombic 123 phase using a microscope and polarized light (Fig. 16). Tetragonal $YBa_2Cu_3O_6$ is nonsuperconducting. With increasing oxygen content the compound becomes superconducting at about $YBa_2Cu_3O_{6.3}$. Maximum T_c is reached at $YBa_2Cu_3O_{6.93}$. A further increase of the oxygen content decreases T_c.
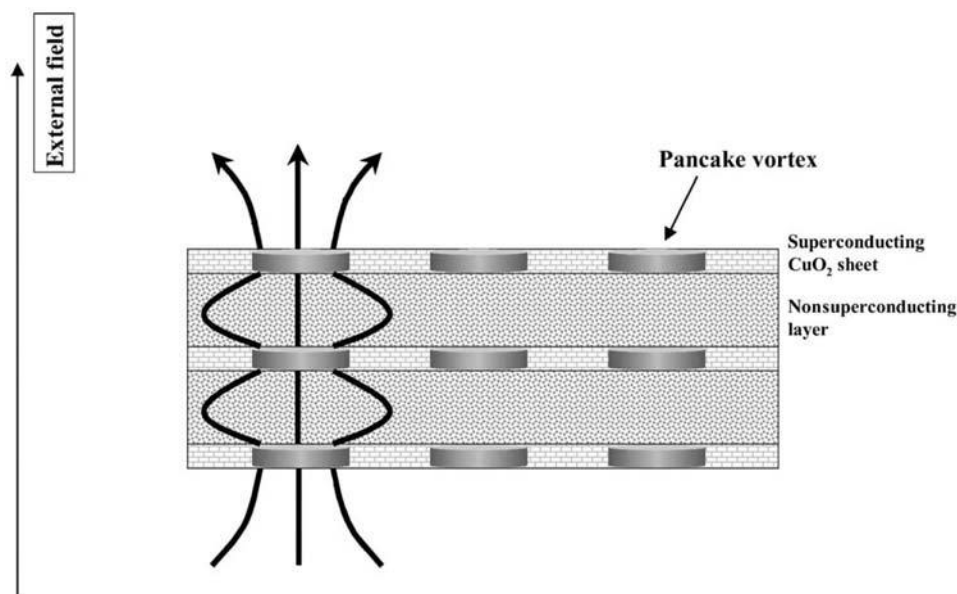
Figure 13
Pancake vortex in a HTSC parallel to the CuO_2 sheets.
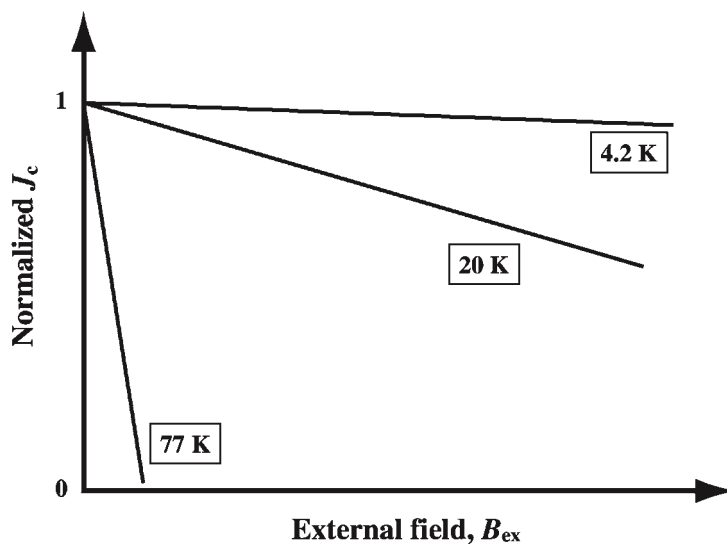
Figure 14
Schematic drawing of the influence of the external field, B_{ex}, on the J_c value of HTSCs at different temperatures.

4.3 The 1223 and 2223 Type Compounds

The compounds have layered structures parallel to the crystallographic a,b plane, consisting of (Bi,Tl, Hg)O-layers which alternate with perovskite-like $B_2Ca_{n-1}Cu_nO_{1+2n}$ units as illustrated in Fig. 17. The $Sr_2Ca_{n-1}Cu_nO_{1+2n}$ units contain the CuO_2 sheets which are oriented parallel to the a,b plane. The $n = 2$ phase (1212 or 2212 phase) is characterized by two CuO_2 sheets and the $n = 3$ phase (1223 and 2223 phase) by three CuO_2 sheets, respectively. Thus, the general structure of all members of the series consist of CuO_2 sheets, that are separated by calcium (for $n > 1$) and covered in the c direction by (Ba,Sr)O
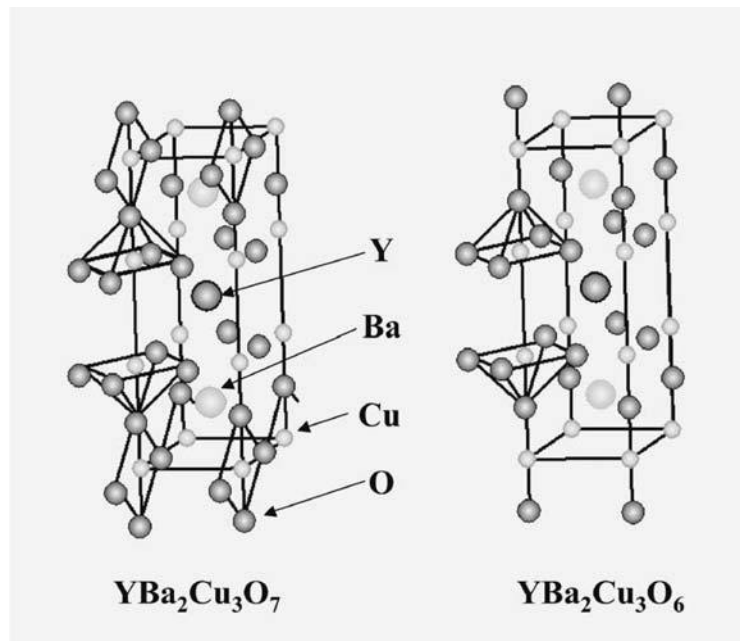
Figure 15
Crystal structure of tetragonal, nonsuperconducting $YBa_2Cu_3O_6$, and orthorhombic, superconducting $YBa_2Cu_3O_7$.
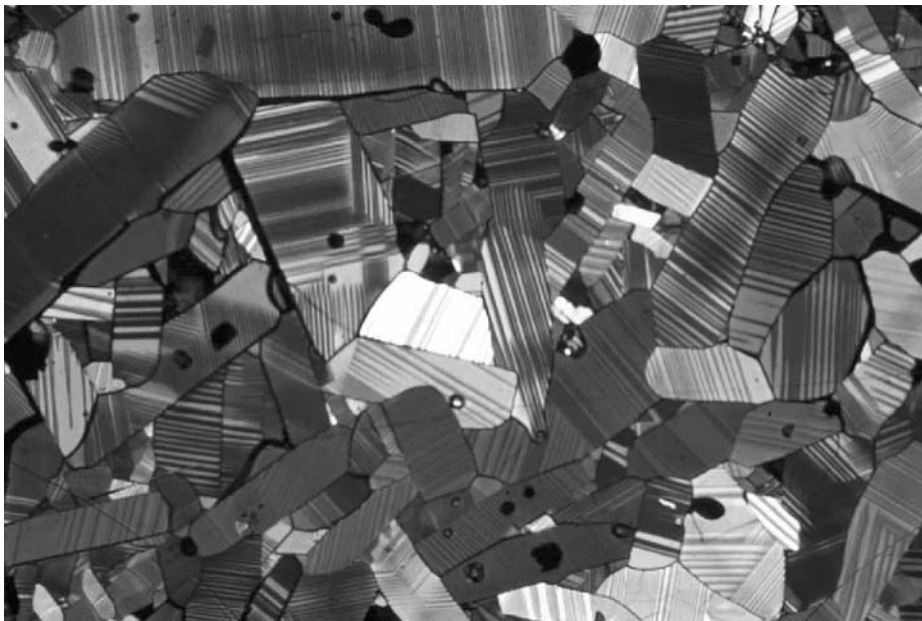
Figure 16
Micrograph of a 123 ceramic using an optical microscope and polarized light showing the [110] twin boundaries in 123 grains.
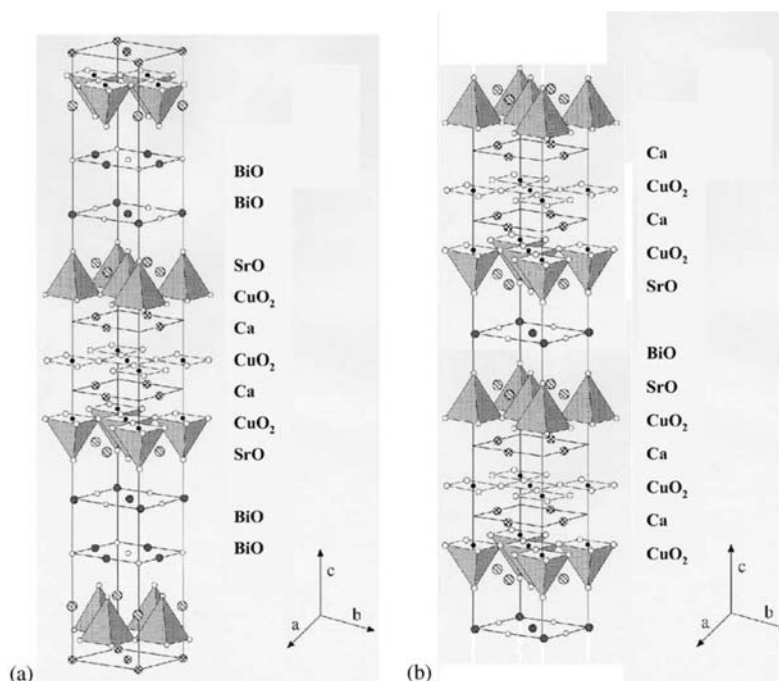
Figure 17
(a) Crystal structure of the $A_2B_2Ca_2Cu_3O_{10}$ type HTSC with A = Bi, Tl, Hg, and B = Sr, Ba. (b) Crystal structure of the $AB_2Ca_2Cu_3O_{10}$ type HTSC with A = Tl, Hg, and B = Sr, Ba.

sheets. These perovskite-like units alternate in c direction with the (Bi, Tl, Hg)O-layers.

The T_cs of the compounds are dependent on the oxygen content and, like the 123 phase, they exhibit a maximum T_c at a certain oxygen content. However, none of them become nonsuperconducting at low oxygen contents, and the dependence of T_c is very different from compound to compound.

See also: Electrodynamics of Superconductors: Weakly Coupled; Superconducting Thin Films: Materials, Preparation, and Properties; Superconducting Thin Films: Multilayers; Superconducting Permanent Magnets: Principles and Results

Bibliography

Bardeen J, Cooper N L, Schrieffer J R 1957 Theory of superconductivity. *Phys. Rev.* **108**, 1175–204
Cava R J 2001 Oxide superconductors. *J. Am. Ceram. Soc.* **83**, 5–28
Flükiger R 1991 A15 compound superconductors. In: *Advances in Materials Science and Engineering*. Pergamon, Oxford
Ginsberg D M (ed.) 1989 *Physical Properties of High Temperature Superconductors*. World Scientific, Singapore
Lynn J W (ed.) 1990 *High Temperature Superconductivity*. Springer, New York
Matthias B T, Geballe T H, Compton V B 1965 Superconductivity. *Rev. Mod. Phys.* **35**, 1–23
Meissner W, Ochsenfeld R 1933 *Naturwissenschaften.* **21**, 787
Onnes H K 1911 *Comm. Phys. Lab. Univ. Leiden, Suppl.* No. 34
Park C, Snyder R L 1995 Structures of high-temperature cuprate superconductors. *J. Am. Ceram. Soc.* **78**, 3171–94
Tinkham M 1975 *Introduction to Superconductivity*. McGraw-Hill, New York (extended edn. 1995)

P. Majewski
Max-Planck-Institut für Metallforschung
Stuttgart, Germany

Superconducting Materials: BCS and Phenomenological Theories

At very low temperatures many metals and alloys undergo a second-order phase transition to a superconducting state in which there is no resistance to flow of electricity. Superconductors exhibit other remarkable phenomena such as exclusion of magnetic flux from the interior (the Meissner effect) and flux quantization. Phenomenological theories were developed to describe semiquantitatively different aspects of superconductivity, including the Gorter–Casimir

two-fluid model for thermal properties and the London theory for electromagnetic properties. In spite of many attempts, it was nearly 50 years from the discovery of superconductivity in 1911 before a microscopic theory based on pairing of electrons was derived from quantum mechanics. The theory has been able to account quantitatively for most properties of superconductors as well as to predict new unexpected phenomena. Transition temperatures can be derived essentially from first principles for the simpler metals, but the theory has been less successful in predicting new compounds with high transition temperatures.

1. Outline of Phenomenological Theories

Superconductivity was discovered by Kamerlingh Onnes, only three years after he had liquefied helium. He found that the resistance of a rod of frozen mercury drops suddenly to zero when cooled to near the boiling point of helium (4.2 K). It was soon found that superconductivity is a common phenomena, exhibited by many metals, alloys, and intermetallic compounds when cooled below a critical temperature T_c. To show that the resistance really vanishes, Onnes showed that a persistent current flows indefinitely in a ring or solenoid with no voltage applied. In steady state, the electric field in a superconductor vanishes ($E = 0$).

It was not until 1933 that Meissner discovered a property that is even more basic; a superconductor excludes a magnetic field ($B = 0$). If a sphere or other simply connected body is placed in a magnetic field and cooled below T_c, the flux in the interior is expelled. If the field were applied when the sphere is in the superconducting state, currents would be set up near the surface to keep the flux inside from changing. They would flow indefinitely, so that B would remain zero in the interior. What Meissner showed is that the state with the flux excluded is the unique thermodynamically stable state of a superconductor. Thus the currents flowing near the surface that counteract the external field are stable, not metastable.

Early attempts to account for the vanishing resistance were aimed at trying to understand why the electrons making up the supercurrent flow are not scattered as they are in the normal state. After the discovery of the Meissner effect, the focus shifted to the nature of the phase transition in the electronic structure that could lead to such remarkable properties.

Superconductivity can be understood only in terms of quantum theory; superconductors are quantum systems on a macroscopic scale. The current flowing around a superconducting ring is quantized such that the total magnetic flux threading the ring is an integral multiple of a flux unit, $\Phi_0 = h/2e = 2.07 \times 10^{-15}$ Wb.

There is a critical magnetic field as well as a critical temperature. Because flux is excluded from the interior, there is an increase in magnetic energy of $\frac{1}{2}\mu_0 H^2$ per unit volume, where H is the applied field. When this magnetic energy more than makes up for the free energy differences $G_s(0)$–G_n between superconducting and normal phases in the absence of a field, the system reverts to normal. Thus the critical magnetic field H_c is given by

$$\tfrac{1}{2}\mu_0 H_c^2 = G_n - G_s(0) \tag{1}$$

The free energy difference and critical fields decrease with increasing temperature and vanish at the critical temperature T_c. There is an approximate law of corresponding states:

$$H_c = H_0(1 - (T/T_c)^2) \tag{2}$$

where H_0 is the critical field at $T = 0$ K. Equation (1) gives a relation between $H_c(T)$ and the thermodynamic quantities, such as heat capacity, that can be derived from the free energy. Experiments in the early 1930s by Keesom and co-workers at Leiden verified these relations experimentally.

In 1934, Gorter and Casimir showed that Eqn. (2) and other properties could be accounted for by a phenomenological two-fluid model in which there is an electron charge density $\rho_s(\rho_s = n_s e)$ associated with the superfluid condensate and a density ρ_n associated with electrons excited out of the condensate and subject to the usual scattering processes, with the total density $\rho = \rho_s + \rho_n$. The total current is then $J = \rho_s v_s + \rho_n v_n$, where v_s and v_n are the velocities of the two components. In the absence of an electric field, $v_n = 0$ and $J_s = \rho_s v_s$. There is no entropy associated with ρ_s, so a supercurrent carries no entropy.

A little later, in 1935, F. London and H. London proposed their famous phenomenological equations to describe the electrodynamics of superconductors. To account for infinite conductivity and the Meissner effect, they added to Maxwell's equations an equation relating the current to magnetic field:

$$J_s(r) = -A(r)/\Lambda \tag{3}$$

where $\Lambda = m/n_s e^2 \mu_0$ and A is the vector potential expressed in a gauge such that $\nabla.A = 0$. The time derivative gives the usual equation for acceleration of the electron in an electric field in the absence of dissipation. Equation (3) leads in addition to the Meissner effect.

F. London suggested that superconductivity is a quantum phenomenon associated with the rigidity of the wave function describing the response of the system to changes of the momentum p of electrons in a magnetic field. The current is given by a sum over all electrons of $e\langle p - eA \rangle/m$ averaged over the wave function of the superconducting condensate.

Equation (3) follows if $\langle \boldsymbol{p} \rangle = 0$ even in the presence of a magnetic field (described in the London gauge). In a normal metal $\langle \boldsymbol{p} \rangle$ changes in such a way that $\langle \boldsymbol{p} - eA \rangle$ is very small, giving just the small Landau diamagnetism. Particularly in his book, published in 1950, London emphasized that the rigidity of the wave functions in a magnetic field could arise from a long-range order in the momentum distribution of the electrons.

According to the London theory, the shielding currents near the surface of a superconductor in a magnetic field flow in a layer of average thickness determined by a penetration depth $\lambda = \lambda_L = \Lambda^{1/2}$, determined by n_s, the density of superconducting electrons. In the late 1940s, Pippard, working at Cambridge, found that the penetration depth increases markedly with added impurities. Impurities decrease the scattering mean free path of electrons in the normal state but have little effect on their density. For this and other reasons, he proposed a nonlocal form of the London relation in Eqn. (3) in which $J_s(r)$ is given by an integral of $A(r)$ over a region surrounding the point r of size determined by a coherence distance ξ. If l is the electron mean free path,

$$\xi^{-1} = \xi_0^{-1} + l^{-1} \qquad (4)$$

where ξ_0 is the coherence distance in the pure metal, typically of order 10^{-7} m.

About the same time (1950), Ginzburg and Landau proposed a different sort of modification of the London equations. They were interested in trying to understand the energy of the boundary between superconducting and normal domains in the intermediate state. The intermediate state consists of a series of normal and superconducting domains in the form of slabs parallel to the applied field. The field $\boldsymbol{B}$ is equal to the critical field in the normal domains and vanishes in the interior of the superconducting domains. The change from $n_s = 0$ in the normal domains to the equilibrium value in the superconducting domains occurs gradually across the boundary over a distance determined by the two lengths in the problem, ξ and λ.

Thus they needed to have a theory that describes changes of $n_s(r)$ in space. Further, in accord with Landau's theory of second-order phase transitions, they described the ordered low-temperature phase by an order parameter that vanishes as $T \to T_c$. Ginzburg and Landau showed remarkable insight in proposing on phenomenological grounds that the order parameter be a complex function $\Psi(r) = |\Psi(r)| \exp[i\varphi(r)]$ with amplitude and phase. The order parameter describes both the density n_s and the velocity v_s of superconducting condensate:

$$\left. \begin{array}{l} n_s^* = |\Psi(r)|^2 \\ m^* v_s = \hbar \nabla \varphi(r) - e^* A(r) \end{array} \right\} \qquad (5)$$

Because of pairing, it is now known that $m^* = 2\,m$, $e^* = 2e$ and $n_s^* = n_s/2$.

Since $\Psi(r)$ must be single valued, the line integral of $\nabla \varphi$ around a closed loop must be a multiple of 2π. If the loop is in the interior of a superconductor where $v_s = 0$ (such as around the interior of a torus containing a persistent current), the enclosed flux $\Phi = \oint A.dl = (h/e^*) \oint \nabla \varphi dl$ must be a multiple of a flux unit $\Phi_0 = h/e^*$.

By expanding the free energy in powers of $\Psi(r)$, they derived a nonlinear Schrödinger-like equation to determine $\Psi(r)$. This equation was coupled with Maxwell's equations to determine $\Psi(r)$ and thus the supercurrent flow subject to appropriate boundary conditions. The expansion is presumed to be valid just below T_c where $\Psi(r)$ is small. They used the equations to determine the boundary energy as well as other properties of superconductors.

To have a Meissner effect, the boundary energy must be larger than a critical value. Otherwise the superconductor could break up into a structure with very thin normal regions that would allow the flux to penetrate a distance λ on either side. The decrease in magnetic energy from the flux penetration would more than compensate for the higher free energy of the normal regions. Ginzburg and Landau found that the criterion could be described by a parameter $\kappa = \lambda/\xi$. If $\kappa < 1/\sqrt{2}$, the superconductor is stable against normal domain formation for all fields less than H_c and there is a perfect Meissner effect. If $\kappa > 1/\sqrt{2}$, the flux begins to penetrate when the field is greater than a lower critical field $H_{c1} < H_c$, but the metal remains superconducting up to a higher critical field, $H_{c2} > H_c$. Since magnetic flux can penetrate for $H_{c1} < H < H_{c2}$, the increase in magnetic energy is less than that for a complete Meissner effect, so that the transition to the normal state does not occur until the higher critical field is reached. The upper critical field H_{c2} may be as large as 20 T or greater for some intermetallic compounds. High-field superconducting magnet wire is made with such materials.

Superconductors with $\kappa < 1/\sqrt{2}$ that exhibit a perfect Meissner effect are called type I, those with $\kappa > 1/\sqrt{2}$ are called type II. Type-II superconductors were first investigated by Shubnikov at Kharkov in the Soviet Union in 1937 and 1938. His work stopped when he fell victim to a purge.

It was first thought that flux penetrates type-II superconductors through thin layers of normal domains as it does in the intermediate state. Then Abrikosov derived another solution, published in 1957, of the Ginzburg–Landau equations that he interpreted as a periodic array of quantized vortex lines. The order parameter $\Psi(r)$ goes to zero on the axis of the lines. Supercurrent circulating around the axis gives rise to one unit of flux Φ_0. With this theory, Abrikosov was able to account in a quantitative way for the magnetization curves observed by Shubnikov.

In addition to the Ginzburg–Landau theory, the year 1950 was notable for the experimental discovery that T_c depends on isotopic mass (indicating that the motion of the ions in the metal must be involved) and H. Fröhlich's independent suggestion that interactions between electrons and lattice vibrations (or their quanta, phonons) are responsible for superconductivity. Results of the experiments could be accounted for if T_c varies inversely with the square root of the isotopic mass.

Onnes just missed discovering the isotope effect 30 years earlier. He attempted to detect a difference in critical temperature between ordinary lead and lead that came from radioactive decay of uranium. However, his measurements were not sufficiently precise to find the small difference in T_c arising from the slight difference in mass of the lead nuclei from the two sources.

Attempts by Fröhlich and by Bardeen in 1950 to explain superconductivity in terms of changes in the energy of individual electrons from interaction with the phonons failed. Pines and Bardeen showed that the electron–phonon interaction leads to an effective attractive interaction for electrons which have energies within a phonon energy of the Fermi energy E_F. It was thought that it would be necessary to take this attractive interaction into account in a successful theory.

2. Pairing Theory of Superconductivity

In 1957, Bardeen, Cooper and Schrieffer gave a theory of superconductivity based on pairing of electrons in the superconducting ground state. Pairing occurs in such a way as to take advantage of the attractive phonon-induced interaction between electrons. An energy gap for quasiparticle excitations appears at the Fermi surface, in confirmation of experiments in the early 1950s of heat capacity and of thermal conductivity. The theory, known as the BCS theory from the initials of the authors, has been successful in accounting in quantitative detail for a wide variety of properties of superconductors, including the isotope effect, the Meissner effect, persistent currents, a second-order phase transition, an expression for the supercurrent in the form suggested by Pippard, penetration depths and their temperature dependence, and other electromagnetic and thermal properties.

Normal metals are well described by a Fermi sea of electrons and quasiparticle excitations of electrons from the sea. Each quasiparticle state is defined by a wave vector $\boldsymbol{k}$ and spin σ. At $T = 0\,\mathrm{K}$, all states with energies less than the Fermi energy E_F are occupied; those above are unoccupied. Low-lying excited configurations can be described by the wave vectors of the occupied states above E_F and unoccupied states or holes below E_F. If the energy ξ_k is measured from the Fermi energy, the total excitation energy is given by

$$W_{\mathrm{exc}} = \sum_{\substack{\mathrm{occ} \\ k > k_F}} \xi_k + \sum_{\substack{\mathrm{occ} \\ k < k_F}} |\xi_k| \qquad (6)$$

Self-energies from effects of coulomb and phonon interactions are included in the quasiparticle energies ξ_k.

According to BCS, the ground-state wave function of the superconducting condensate is a linear combination of a selected set of wave functions Ψ_i of low-lying excited configurations of the normal metal:

$$\Psi_s = \sum a_i \Psi_i \qquad (7)$$

The configurations Ψ_i which enter the sum are restricted to those in which the normal quasiparticle states are occupied in pairs of opposite spin and momentum $(\boldsymbol{k}\uparrow, -\boldsymbol{k}\downarrow)$, such that if in a given configuration one of the two states is occupied, the other is also. An interaction between electrons gives matrix elements between two configurations in which a pair $\boldsymbol{k} \equiv (\boldsymbol{k}\uparrow, -\boldsymbol{k}\downarrow)$ is occupied and the pair $\boldsymbol{k}'$ unoccupied in one configuration and $\boldsymbol{k}'$ occupied and $\boldsymbol{k}$ unoccupied in the other. With paired configurations, the phases of the wave functions can be chosen so that all matrix elements between such configurations are negative for an attractive interaction V. If the coefficients a_i have the same sign or phase, the matrix elements V_{ij} add coherently to give a negative contribution to the energy:

$$\int \Psi_s^* V \Psi_s d\tau = \sum a_i^* a_j V_{ij} \qquad (8)$$

The wave function in Eqn. (7) was written by BCS in terms of creation operators, $c_{k\sigma}^*$ for putting a particle in the state $\boldsymbol{k}$, σ:

$$\Psi_s = \prod_k (u_k + v_k c_{k\uparrow}^* c_{-k\downarrow}^*) \Psi_0 = \sum_N a_N \psi_N \qquad (9)$$

Here v_k^2 is the probability that the pair $(\boldsymbol{k}\uparrow, -\boldsymbol{k}\downarrow)$ is occupied and $u_k^2 = 1 - v_k^2$ is the probability that it is unoccupied. The wave function is not an eigenstate of the number of pairs N, but the coefficients u_k and v_k can be chosen so that the distribution is sharply peaked about the number in the normal ground state below E_F.

For a simple model in which it is assumed that $V_{ij} = -V$ for $|\xi_k| < \hbar\omega_{\mathrm{ph}}$ and zero otherwise, where $\hbar\omega_{\mathrm{ph}}$ is an average phonon energy, the following results are obtained by a variational method:

$$u_k^2 = 1 - v_k^2 = \frac{1}{2}\left(1 + \frac{\xi_k}{E_k}\right) \qquad (10a)$$

$$E_k = (\xi_k^2 + \Delta^2)^{1/2} \quad \text{for} \quad |\xi_k| < \hbar\omega_{\mathrm{ph}} \qquad (10b)$$

$$\Delta = 2\hbar\omega_{\mathrm{ph}} \exp[-1/N(0)V] \qquad (10c)$$

$$G_s - G_N = -\tfrac{1}{2}N(0)\Delta^2 \qquad (10d)$$

where $N(0)$ is the normal state density of states at the Fermi level.

A superconductor has a set of quasiparticle excitations in one-to-one correspondence with those of the normal metal. The energy of such an excitation is E_k, corresponding to that of a particle above the Fermi sea or a hole below. Since excitations are formed in pairs from the ground state, the minimum energy required for creating a pair of excitations at the Fermi surface is the energy gap 2Δ.

The probability that a state k is occupied at finite temperatures is given by the Fermi function

$$f_k = \frac{1}{1 + \exp(\beta E_k)} \qquad (11)$$

where $\beta^{-1} = k_B T$. The gap parameter Δ decreases with increasing temperature and goes to zero at the critical temperature T_c. The value of $\Delta(T)$ can be found from the equation

$$1 = N(0)V \int_0^{\hbar\omega_{ph}} \frac{(1 - 2f_k)d\xi_k}{E_k} \qquad (12)$$

This equation is commonly referred to as the BCS gap equation. Near T_c, $\Delta(T)/\Delta(0) \simeq 1.74[1 - (T/T_c)^2]^{1/2}$. The gap goes to zero as $T \to T_c$ and there are no solutions for $T > T_c$. The value of T_c is given by

$$k_B T_c = 1.13\hbar\omega_{ph} \exp[-1/N(0)V] \qquad (13)$$

The energy gap at $T = 0$ is proportional to T_c:

$$E_g = 2\Delta(0) = 3.52 k_B T_c \qquad (14)$$

In this weak coupling approximation there is only one parameter, $\Delta(0)$ or $k_B T_c$, rather than two, $\hbar\omega_{ph}$ and $N(0)V$. Weak coupling means that $k_B T_c$ is very small compared with the phonon energies so that the phonon spectrum is not important. In this limit there is a law of corresponding states since everything scales with T_c. Strong coupling and effects of coulomb interactions will be discussed later.

With a ground state and set of quasiparticle excitations it is possible to calculate transition probabilities and various response functions without much more difficulty than for normal metals. The main complications arise from coherence factors that are a result of the pairing. In normal metals scattering from $k\sigma$ to $k'\sigma'$ is independent in first approximation from all other scattering. In a superconductor it is possible to go from $k\uparrow$ to $k'\uparrow$ either directly or by scattering from $-k'\downarrow$ to $-k\uparrow$ and these two contributions must be added coherently. Depending on the nature of the scattering, they add constructively or destructively.

The coherence factors can be calculated most easily by a reformulation of the BCS theory given independently by Valatin and by Bogoliubov. They define quasiparticle operators for a superconductor as linear combinations of creation and destruction operators for normal quasiparticles:

$$\gamma_{k\uparrow}^* = u_k c_{k\uparrow}^* - v_k c_{-k\downarrow} \qquad (15a)$$

$$\gamma_{-k\downarrow}^* = u_k c_{-k\downarrow}^* + v_k c_{k\uparrow} \qquad (15b)$$

These operators do not conserve particle number and are designed to operate on wave functions of the type of Eqn. (9) that are not eigenstates of the number of pairs N. The ground state Ψ_s is the vacuum state for quasiparticle excitations:

$$\gamma_{k\uparrow}\Psi_s = \gamma_{-k\downarrow}\Psi_s = 0 \qquad (16)$$

When there is current flow, the paired states $(k_1\uparrow, k_2\downarrow)$ all have precisely the same momentum $p_s = \hbar(k_1 + k_2)$ so that any pair can be scattered into another pair. There is thus a long-range order of the momentum distribution as envisaged by London. Individual electrons can be scattered, but such scattering does not change the common momentum of the paired states.

As in the Ginzburg–Landau theory, the canonical momentum p_s can be expressed as the gradient of a phase φ (see *Josephson Effects in Weak Links*). There is an arbitrary phase factor in the ground-state wave function since v_k can be replaced by $v_k \exp(i\varphi)$ without changing the energy. The degenerate wave function is an eigenstate of phase

$$\Psi_s(\varphi) = \prod_k (u_k + v_k \exp(i\varphi) c_{k\uparrow}^* c_{-k\downarrow}^*)\Psi_0$$

$$= \sum_N a_N \exp(iN\varphi)\Psi_N \qquad (17)$$

The phase and the number of pairs N are conjugate variables, with $N_{op} = -i\partial/\partial\varphi$. If the number of pairs is fixed, the phase is undetermined. The phase corresponds to that of the Ginzburg–Landau theory, with $p_s = \hbar\nabla\varphi$ the momentum of a pair.

It was trying to understand whether phase differences between two superconductors connected by a weak link could be observed that led Josephson to predict that a supercurrent should flow through a tunnel junction separating two superconductors differing in phase. The importance of phase as a variable describing the superconducting state had been stressed by Anderson. The Josephson effect was first observed by Anderson and Rowell. It has led to many practical applications.

3. Gor'kov–Eliashberg Formulation

Not long after the first publications of the BCS theory, Gor'kov used the method of thermal Green's functions to treat problems in which there is a space variation of the order parameter $\Delta(r)$ as well as

problems in which there is strong coupling so that it is necessary to include the energy dependence of Δ. One of his first applications was to show that the theory reduces to the Ginzburg–Landau theory near T_c, with $\Delta(r)$ playing the role of the order parameter $\Psi(r)$. An important difference is that the charge of a pair, $2e$, replaces the electronic charge e.

Eliashberg used the Gor'kov formulation to derive a gap equation sufficiently general to include strong coupling. The electron–phonon interaction enters the integral equation in the form $\alpha^2(\omega)F(\omega)$, where $F(\omega)d\omega$ gives the number of phonons with energies in the interval $\hbar d\omega$ and $\alpha(\omega)$ is the electron–phonon coupling constant averaged over all directions in space. There are two coupled integral equations for $\Delta(\omega)$ and for the mass renormalization factor $Z_s(\omega)$ from the electron–phonon interaction, both of which are in general complex.

For weak coupling, Z_s is the same as Z_n and is the factor by which the density of states in energy is enhanced by the electron–phonon interaction. Expressed in terms of an interaction parameter λ, $Z_s = Z_n = 1 + \lambda$ where

$$\lambda = 2 \int_0^\infty \alpha^2(\omega)F(\omega)d\omega/\omega \qquad (18)$$

The parameter λ corresponds to $N(0)V_{ph}$ of the BCS theory, with the phonon energy $\hbar\omega_{ph}$, defined by

$$\hbar\omega_{ph} = 2 \int_0^\infty \alpha^2(\omega)F(\omega)d\omega/\lambda \qquad (19)$$

The repulsive Coulomb interaction between electrons can be included by renormalizing the screened interaction V_c to the same energy range as the phonons. The interaction constant $\mu = N(0)\langle V_c \rangle$ for scattering between states extending over an energy of the order of E_F from the Fermi surface is replaced by a renormalized constant

$$\mu^* = \mu/[1 + \mu \ln(E_F/\hbar\omega_{ph})] \qquad (20)$$

for scattering within an energy $\hbar\omega_{ph}$ of E_F. Virtual scattering to states outside of this range is included in the renormalized interaction. The expression for T_c for weak coupling is then

$$k_B T_c = 1.13\hbar\omega_{ph} \exp[-1/(\lambda - \mu^*)] \qquad (21)$$

Normally, μ^* varies only slowly with electron density and is typically in the range 0.10–0.15. It may, however, change the exponent α in the isotope effect $T_c \sim M^{-\alpha}$ from the value $\frac{1}{2}$ because μ^* can vary with isotopic mass through its dependence on $\hbar\omega_{ph}$.

McMillan used the Eliashberg equations to calculate T_c for a series of transition metals and found that the results could be fitted approximately by the semiempirical expression

$$k_B T_c = \left(\frac{\Theta_D}{1.45}\right)\exp\left[-\frac{1.04(1 + \lambda)}{[\lambda - \mu^*(1 + 0.62\lambda)]}\right] \qquad (22)$$

where Θ_D is the Debye temperature. Values of λ range from about 0.25 for metals with low T_c to above 1.25 for strongly coupled superconductors with high T_c.

Metals and compounds with high T_c are those with a reasonably large λ and high phonon energies as defined by Eqn. (19). It is difficult to find materials that satisfy both criteria because a large λ is usually associated with a soft lattice and consequently low phonon frequencies. Examples of soft metals are mercury ($T_c \simeq 4.2\,\text{K}$) and lead ($T_c \simeq 7.2\,\text{K}$). A high density of states $N(0)$ such as is found with transition metals is helpful, but within a range of alloys it is often found that λ increases inversely with the density of states. The matrix elements of the electron–phonon coupling go in the opposite direction and more than compensate for the decrease in $N(0)$. Materials with high T_c have been discovered by empirical methods rather than by suggestions from theory.

The Gor'kov–Eliashberg theory has been used to calculate T_c essentially from first principles for simple metals and alloys such as aluminum (weak coupling), tin (moderate coupling) and lead (strong coupling). The phonon spectra are derived from neutron scattering data and a pseudopotential method is used to calculate $\alpha^2(\omega)$. The good agreement with experimental values leaves little doubt about the basic validity of the theory.

Of even greater interest is the application of equations to derive $\alpha^2(\omega)F(\omega)$ empirically from the current–voltage characteristics of a tunnel junction between a normal metal (N) and the superconductor (S) separated by a thin insulating layer. At low temperatures $(dI/dV)_{NS}$ is portional to the density of states in the superconductor. The ratio to the conductance measured when both sides are normal is for a voltage V corresponding to $eV = E = \hbar\omega$

$$\left(\frac{dI}{dV}\right)_{NS} \bigg/ \left(\frac{dI}{dV}\right)_{NN} = \frac{N_S(E)}{N(0)} = \frac{E}{(E^2 - \Delta^2)^{1/2}} \qquad (23)$$

where $N(0)$ is the uniform density of states in the normal metal and the expression on the right is for weak coupling. The current vanishes when $E < \Delta$.

For strong coupling, when $\Delta(E)$ is complex, Schrieffer and co-workers showed that

$$\frac{N_S(E)}{N(0)} = \text{Re}\left\{\frac{E}{[E^2 - \Delta(E)^2]^{1/2}}\right\} \qquad (24)$$

If the conductance is measured over a broad energy range, Kramers–Krönig relations can be used to determine both the real and imaginary parts of $\Delta(E)$ and thus the complete Green's functions required to

calculate equilibrium and transport properties. This procedure has given excellent agreement between theory and experiment, even when there is strong coupling.

McMillan devised a computer program to determine $\alpha^2(\omega)F(\omega)$ directly from tunnelling data with use of the Eliashberg integral equations. This method has been used for a large number of superconducting elements and compounds to obtain detailed information about $\alpha^2(\omega)F(\omega)$ and its variation with energy. It is necessary to estimate μ^* from the electron density; the only other variable in the equations is then $\alpha^2(\omega)F(\omega)$. Generally, the peaks of $\alpha^2(\omega)F(\omega)$ coincide with the peaks of the phonon density of states $F(\omega)$ measured by neutron scattering.

4. Basic Features and Extensions of the Pairing Theory

At low temperatures, the normal state is described as a weakly interacting gas of quasiparticles and phonons. The quasiparticles correspond to electrons above or holes below the Fermi surface.

The fully renormalized quasiparticles are in one-to-one correspondence with those of a gas of non-interacting particles. Because of interactions, the quasiparticle excitations are not exact eigenstates of the normal metal but have a finite lifetime. According to the Landau Fermi liquid theory, the lifetime varies at low temperature as ω^{-2}, where ω is the quasiparticle energy relative to that of the Fermi surface. Thus the approximation treating the quasiparticles as independent becomes better and better as the temperature is decreased.

The wave functions of the superconducting state are described by linear combinations of low-lying normal-state configurations. If the energies of the normal-state configurations are derived empirically, the free energy difference between normal and superconducting states may be derived with far greater precision than would be possible by a first-principles calculation of either phase by itself.

What is needed is the matrix element for scattering of a pair of quasiparticles in state $(\mathbf{k}_1, \mathbf{k}_2)$ to $(\mathbf{k}'_1, \mathbf{k}'_2)$ with conservation of wave vector:

$$\mathbf{k}_1 + \mathbf{k}_2 \rightarrow \mathbf{k}'_1 + \mathbf{k}'_2 \tag{25}$$

When the interaction is mediated by the electron–phonon interaction it may be regarded as occurring in two steps:

$$\mathbf{k}_1 \rightarrow \mathbf{k}'_1 + \mathbf{q}_{\mathrm{ph}} \tag{26a}$$

$$\mathbf{k}_2 + \mathbf{q}_{\mathrm{ph}} \rightarrow \mathbf{k}'_2 \tag{26b}$$

where $\mathbf{q}_{\mathrm{ph}}$ is the wave vector of the phonon. An alternative process is the same as in Eqn. (26) with $\mathbf{k}_1$ and $\mathbf{k}_2$ interchanged. Energy is conserved only in the

final step. The superconducting phase is formed from a subset of low-lying normal configurations between which the matrix elements are predominantly negative, corresponding to an attractive interaction.

The quasiparticles in the subset are associated in pairs each of which has exactly the same momentum as every other pair. When there is no current flow the paired states have opposite spin and momentum.

One of the earliest extensions of the original BCS theory, by Mattis and Bardeen, was to include effects of a scattering mean free path l. In this case, the momentum $\mathbf{k}$ is not a good quantum number to describe the quasiparticles. A quasiparticle state $\psi \uparrow$ is paired with the time-reversed state $\psi^* \downarrow$. The main effect is to replace the inverse of the Pippard distance, ξ_0^{-1}, with $\xi^{-1} + l^{-1}$, as in Eqn. (4).

Not long after the microscopic theory was published suggestions were made to get an attractive interaction between quasiparticles other than that mediated by phonons. These are not necessarily alternatives to the phonon mechanism but may supplement it so as to enhance the transition temperature. Although none has been firmly established, it is likely that something besides phonons is required to account for the high transition temperature of compounds with copper oxide layers, first discovered by Bednorz and Müller.

Other low-lying excitations that have been suggested are, like phonons, defined by a wave vector. They include excitons (creation of electron–hole pairs), acoustic plasmons (in a ground state with equal numbers of conduction electrons and holes in overlapping bands) and spin and charge-density wave excitations (where there is nesting of opposite faces of the Fermi surface).

Little and, independently, Ginzburg suggested an exciton mechanism in which there is physical separation of the excited electron–hole pair and the carriers that give the current flow. Little suggested conduction in linear chains surrounded by polarizable side chains. Ginzburg suggested layer structures with conductive layers alternating with polarizable layers in which the electron–hole excitations take place.

Both may have found realizations in two classes of compounds with abnormally high superconducting transition temperatures, although it is still far from certain that it is the exciton mechanism that is responsible. Ginzburg's suggested geometry is similar to that of the high-T_c copper oxide layer structures. Little's is similar to that of organic linear-chain compounds that have been found by Williams and co-workers to have transition temperatures as high as 13 K. However it has been found that in both systems the normal metal is not described by a simple Fermi liquid. More radical departures from the usual BCS theory than getting enhanced attractive interactions may be required. In both systems, experiments indicate that in the normal state the reciprocal of the quasiparticle lifetime varies as ω rather than as ω^2.

The energy gap in planar directions in the high-T_c oxides is about $8k_BT_c$, much larger than the BCS value of $3.52\,k_BT_c$ for weak coupling. Some extensions and changes of the BCS theory are required to account for the high-T_c oxides and organic linear-chain superconductors. It is uncertain whether or not these changes are minor or require a major restructuring of the theory.

5. Applications to Other Areas of Physics

The concepts and mathematical methods of the theory of superconductivity have been applied successfully to the superfluid phase of liquid helium of isotopic mass three, to the structure of nuclei, to pulsars and neutron stars and to the elementary particles of high-energy physics. Liquid ^{3}He, like electrons in metals, obeys Fermi–Dirac statistics. The liquid undergoes a pairing transition to a superfluid phase below 3 mK. The pairing is of parallel spins in a triplet state ($S=1$) rather than the singlet spin pairing ($S=0$) that occurs with electrons in superconducting metals. Extensions of superconductivity theory have been applied with great success to account for the pairing energy of neutrons and protons in nuclei. The pairing energy gap decreases with increasing atomic number. The biggest superfluid objects in the universe are pulsars and neutron stars in which there is evidence that both neutrons and protons undergo pairing transitions.

To define the state of a superconductor it is necessary to specify the superfluid velocity v_s in addition to the other macroscopic variables, such as temperature and pressure. This is associated with what is called broken-gauge symmetry. Analogous concepts are now being used widely to better understand the structure of the particles (elementary excitations) of high-energy physics.

See also: Amorphous Superconductors; Coherence Length, Proximity Effect and Fluctuations; Electrodynamics of Superconductors: Flux Properties; Electrodynamics of Superconductors: Weakly Coupled; Superconducting Thin Films: Materials, Preparation and Properties; Superconducting Thin Films: Multilayers

Bibliography

Bardeen J 1973 Electron–phonon interactions and superconductivity. In: Haken H, Wagner M (eds.) 1973 *Cooperative Phenomena*. Springer, Berlin
Bardeen J, Schrieffer J R 1961 Recent developments in superconductivity. In: Gorter C J (ed.) 1961 *Progress in Low Temperature Physics*, Vol. 3. North-Holland Amsterdam
Chilton F (ed.) 1971 *Superconductivity: Proc. Int. Conf. Science of Superconductivity*. North-Holland, Amsterdam
de Gennes P G 1966 *Superconductivity in Metals and Alloys*. Benjamin, New York
London F 1950 *Superfluids*, Vol. 1. Wiley, London
Parks R D (ed.) 1969 *Superconductivity*, Vols. 1, 2. Dekker, New York
Rickayzen G 1965 *Theory of Superconductivity*. Wiley, London
Shoenberg D 1952 *Superconductivity*. Cambridge University Press, Cambridge
Schrieffer J R 1964 *Theory of Superconductivity*. Benjamin, New York
Tinkham M 1975 *Introduction to Superconductivity*. McGraw-Hill, New York

J. Bardeen
University of Illinois, Urbana, Illinois, USA

Superconducting Materials: Irradiation Effects

Irradiating superconducting materials changes their physical properties, such as critical temperature, T_c, critical current, J_c, and critical magnetic field, H_c (Brown 1981). Therefore, irradiation effects on superconducting materials are important to the technological applications and basic understanding of superconductivity. These effects depend on the material and the nature of the radiation itself. The radiation source can be x- or γ-rays, electrons, fast or thermal neutrons, or light or heavy ions. The irradiation effects depend on the type of radiation source, radiation energy, flux density, and accumulated dosage. From a technological point of view, fast neutrons and γ-rays are the principal radiation sources. Both γ-rays and neutrons interact with materials through electrically charged particles—electrons, light or heavy recoil ions, or charged reaction products in transmutations. Ion irradiation can be well controlled for energy, dose, damage type and density, irradiation temperature, and damage orientation, etc., to provide an understanding of the physical processes occurring in a material. Therefore, the emphasis of this article is placed on irradiation effects caused by ions.

1. Energy Loss and Defect Formation

Energy loss is the most important factor in ion–solid interactions, because it is a measure of the capacity of a particle to deposit energy within a material. Energy loss is a material property, which is a function of the mass, atomic number, and energy of the particle. Figure 1 shows the energy dependence of electronic and nuclear energy loss of various ions in a typical high-temperature superconductor (HTS), namely $YBa_2Cu_3O_7$. Ions of hydrogen, helium, bromine, tin, and gold are used for illustration.

Energy loss–energy dependence
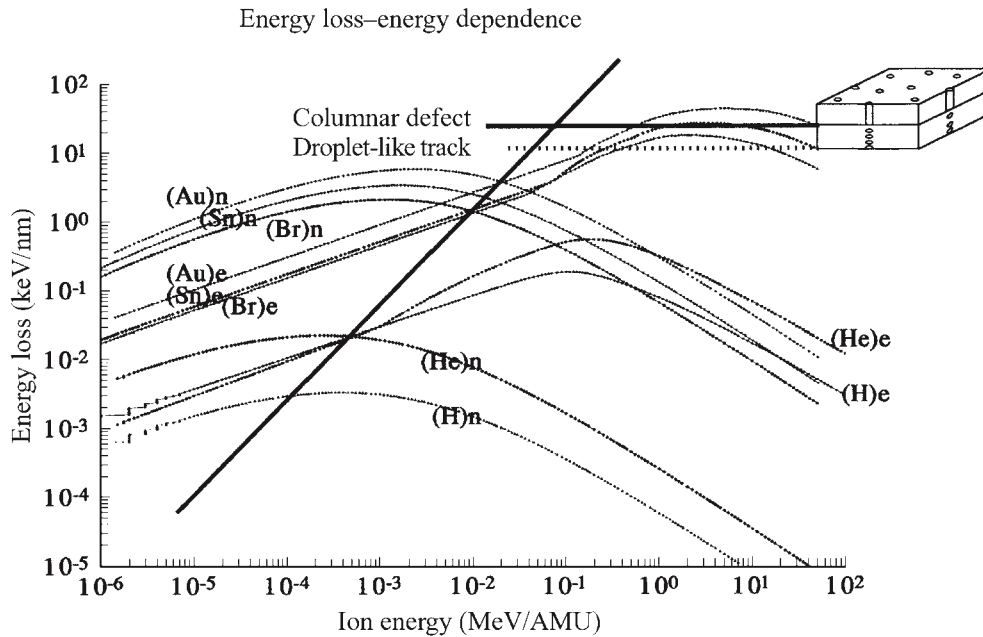
Figure 1
Defect formation in different energy loss regions and its dependence on incident particle energy. See text for details.

Energy loss is expressed in units of $keV\,nm^{-1}$ and the ion energy is normalized by the mass number of the projectile. Subscripts "n" and "e" label the nuclear and electronic energy loss, respectively, for a given ion in the HTS. Figure 1 has three straight lines that mark the approximate boundary of different regions of significance. The upper left area of the inclined line is a region where nuclear energy loss is greater than electronic energy loss. In this region, the energy of the projectile is transferred to the material via collisions that displace the target atoms, creating point defects. When the energy of the recoiled atoms is high enough, these recoiled atoms will subsequently strike others, creating a collision cascade.

At higher ion energy (across the inclined straight line in Fig. 1), the energy loss is dominated by the ionization and excitation of the electrons of the target material with consequential diluted defect formation, which has very little effect on the properties of superconductors. However, for heavy ions of GeV energies, when the electronic energy loss is close to the maximum, the highly striped multicharged heavy ions can interact with and set in motion a large number of target electrons. This dense ionization in a small area will leave a high density of atomic disorders owing to a thermal spike (Szenes 1996). At electronic energy losses higher than $11\,keV\,nm^{-1}$ in YBCO (marked as a horizontal dotted straight line in Fig. 1), local defects with high densities of atom disorders may form droplet-like and discontinuous columnar defects

along the fast ion track. Above a critical electronic energy loss between $28\,keV\,nm^{-1}$ and $35\,keV\,nm^{-1}$ (marked as a horizontal straight line in Fig. 1), entirely continuous amorphous tracks with diameters of a few nanometers are produced along the ion path (Wheeler *et al.* 1993). Different effects on superconductivity will result from these defects. Before we correlate the defect structure with the superconductor properties, we need to understand the magnetic properties of type II superconductors.

2. Defects and Pinning Centers in Type II Superconductors

HTSs and all the technologically relevant conventional superconductors are type II superconductors. In these materials, the magnetic field penetrates in the form of an array of flux lines called superconducting vortices (Blatter *et al.* 1994). These vortices are string-like objects consisting of a central core (whose radius is approximately the coherence length, ξ), where the order parameter, $\psi(r)$, is depressed, surrounded by supercurrents extending over a larger distance. In a defect-free superconductor, the ground state of the vortex array is a triangular Abrikosov lattice. As electric currents exert force on the vortices, any transport current density, J, results in a dissipative vortex motion (i.e., finite resistance) and the most relevant property for application is lost.

Crystallographic defects may locally depress $\psi(r)$. If a core sits on one of these defects, the energy of the vortex decreases. This position-dependent energy distorts the lattice and produces vortex pinning, i.e., flux line motion is prevented until J surpasses J_c.

Controlling the structure of defects in the material is thus the key for the optimization of vortex pinning. The relationship between the elementary pinning force, f_p, of one defect and J_c is rather complex, but several basic rules exist (Ullmaier 1975). First, the best pinners are those defects that are just large enough to accommodate a vortex core, of transverse size $\sim \xi$. Second, to increase the total pinning force the density of defects should be large. Finally, defects elongated along the H direction (columnar defects) are particularly appropriate, as they are able to confine large portions of a core.

3. Irradiation Effects in Superconductors

The methods of optimizing pinning in conventional superconductors have improved (Brown 1981). The inclusion of nonsuperconducting particles (as in Nb–Ti wires) or the introduction of dislocations by metallurgical techniques are well-known procedures. Amorphous superconductors are less sensitive to radiation damage, owing to the absence of pre-irradiation crystalline order. Irradiation of clean materials with very low initial J_c has been used as a tool to investigate vortex pinning in samples with a well-characterized structure of defects.

The very small ξ of HTSs (~ 1–2 nm) suggests that irradiation may be a very appropriate tool for pinning enhancement. The small ξ and the lack of ductility prevent the use of many metallurgical techniques to create defects. The controlled generation of defects by irradiation is a powerful tool in exploring the novel properties of the vortex matter.

Irradiation of HTSs with light particles, which produce a random distribution of localized defects (Civale 1993), reduces T_c and increases the normal state resistivity. The initial $dT_c/d\Phi$ for different ions and energies is proportional to the nuclear energy loss rate, confirming that damage is only due to atomic collisions. For higher Φ the defective regions start to merge, and T_c decreases faster.

Vortex pinning effects of irradiation in HTSs are best explored in high-quality single crystals, where weak links are absent and J_c before irradiation is low. The introduction of random defects in HTS crystals enhances J_c, and cascade defects generated by fast neutrons are very effective. In YBCO, for instance, J_c may increase by an order of magnitude (up to $\sim 10^7$ A cm^{-2}) at 5 K and H of a few tesla, and by two orders of magnitude (up to $\sim 10^5$ A cm^{-2}) at 77 K and low H. Protons of 2–3 MeV produce similar results. J_c increases with Φ at low doses, reaches a broad maximum, and eventually drops abruptly at

the Φ range where T_c also starts to collapse. As expected, optimum J_c occurs when the distance between defects is a few times the value of ξ. The damage produced by electrons in the 1–3 MeV energy range, which consists mostly of point defects (Frenkel pairs), also produces a small, but still considerable increase in J_c in YBCO and Bi-2212.

Aligned columnar defects (CD) produced by heavy-ion irradiation are the strongest pinning centers in HTSs, because of simple geometrical reasons (Civale 1993). First, they can confine the whole length of the core, gaining a large pinning energy without the energy cost of an elastic distortion. Second, their diameter (5–10 nm) is appropriate to exert a very large pinning force (Wheeler *et al.* 1993). The advantage with respect to random defects is dramatic at high T and H. For instance, for YBCO at 77 K and 5 T, $J_c > 10^5$ A cm^{-2} can be obtained. The density of CD can be expressed in terms of the equivalent *matching field*, the field at which the CD and vortex densities are the same.

CD generate uniaxial pinning, i.e., the J_c increase is anisotropic, being largest when H is parallel to the tracks. Uniaxial pinning gives rise to the lock-in effect (Blatter *et al.* 1994): in the solid phase, H can be tilted away from the direction of the tracks by a finite angle and the vortices will still remain trapped in the CD. Irradiation of Bi-2212 and Bi-2223 with ~ 1 GeV protons has been used to produce fission of the bismuth nuclei (Civale 1993). The damage created by the fission fragments consists of amorphous tracks similar to the aligned CD, but randomly oriented. These isotropic distributions of CD also produce large increases in J_c, with the technological advantage that the penetration range of the protons is large (~ 50 cm), in contrast to the few micrometers of heavy ions. Similar fission damage has been introduced in uranium-doped YBCO by irradiation with thermal neutrons.

See also: High-temperature Superconductors: Thin Film and Multilayers; Superconducting Materials: Types of; Superconducting Permanent Magnets: Principles and Results

Bibliography

Blatter G, Feigel'man M V, Geshkenbein V B, Larkin A I, Vinokur V M 1994 Vortices in high temperature superconductors. *Rev. Mod. Phys.* **66**, 1125–388

Brown B S 1981 Radiation effects in superconducting fusion-magnet materials. *J. Nucl. Mater.* **97**, 1–14

Civale L 1993 In: Jin S (ed.) *Processing and Properties of High T_c Superconductors*. World Scientific, Singapore, pp. 299–369

Szenes G 1996 Formation of columnar defects in high-T_c superconductors by swift heavy ions. *Phys. Rev. B* **54**, 12458–63

Ullmaier H 1975 *Irreversible Properties of Type II Superconductors*. Springer, Berlin

Wheeler R, Kirk M A, Marwick A D, Civale L, Holtzberg F H 1993 Columnar defects in YBCO induced by irradiation with high energy heavy ions. *Appl. Phys. Lett.* **63**, 1573–5

W. K. Chu and J. Liu
University of Houston, Houston, Texas, USA

L. Civale
*Comisión Nacional de Energía Atómica, Bariloche
Argentina*

Superconducting Microwave Applications: Filters

1. Fundamentals of Microwave Absorption of High-temperature Superconductors

The microwave response of a superconductor can be understood by two physical phenomena. First, by the Meissner effect (see any textbook on superconductivity, e.g. Waldram 1996), which causes any magnetic field applied to the surface of a superconductor to decrease exponentially inside the superconductor on the length scale of the London penetration depth λ_L, which is about 160 nm for the most relevant high-temperature superconductor (HTS) compound $YBa_2Cu_3O_7$ (called "YBCO") at $T \to 0$. The London penetration depth increases with temperature according to $[\lambda_L(0)/\lambda_L(T)]^{-2} \approx 1 - (T/T_c)^2$ (T_c = transition temperature, with $T_c = 92$ K for YBCO). As T approaches T_c, $\lambda_L(T)$ converges to the normal metal skin depth. Below about $0.8T_c$, $\lambda_L(T)$ is nearly frequency independent up to several hundred gigahertz.

The second fact is that at finite temperatures below T_c, Cooper pairs (corresponding to "ballistic" charge carriers without dissipation) and quasi-particles (corresponding to normal conducting charge carriers obeying Ohm's law with a temperature dependent conductivity $\sigma_1(T)$) coexist (see, e.g., Klein 1997). According to this simple physical picture, the electrodynamic response of a superconductor can be described by a complex valued conductivity:

$$\sigma = \sigma_1(T) - i\sigma_2(T) = \sigma_1(T) - \frac{i}{\omega\mu_0\lambda_L^2(T)} \quad (1)$$

The imaginary part of the conductivity corresponds to the inductive response of the Cooper pairs. The explicit relationship between σ_2 and λ_L follows from the London equations. It should be emphasized that the rigorous treatment of the electrodynamic response of a superconductor requires a quantum mechanical treatment based on BCS theory including some peculiarities of high-temperature superconducting oxides (Klein 1997, Hein 1999). In the context of this article, only a basic understanding of the microwave response

being necessary for the understanding of superconducting filters can be provided. At microwave frequencies $\sigma_1 \ll \sigma_2$ holds true resulting in a simple expression for the surface resistance and reactance of a superconductor (by a Taylor expansion of Eqn. (1)):

$$R_s = \frac{1}{2}\,\omega^2\mu_0^2\sigma_1(T)\lambda_L^3(T); \quad X_s(T) = \omega\mu_0\lambda_L(T) \quad (2)$$

In contrast to normal metals, the surface resistance exhibits a quadratic frequency dependence. The absolute values for thin films of YBCO at a temperature of 77 K are shown in Fig. 1. According to this data, there is a clear advantage by orders of magnitude for using HTS for the whole range of microwave communications bands. Above 77 K, R_s increases strongly towards the critical temperature due to the strong increase of the London penetration depth. Below 77 K, R_s decreases gradually towards zero temperature by less than one order of magnitude.

The surface resistance data discussed so far correspond to the linear regime corresponding to low levels of microwave magnetic fields. For higher field levels corresponding to higher values of the stored field energy, nonlinearities occur resulting either in an increase of R_s and/or intermodulation distortion (Hein 1999). This is of particular importance, because—as a result of magnetic field displacement—planar conductors possess a strongly peaked edge current
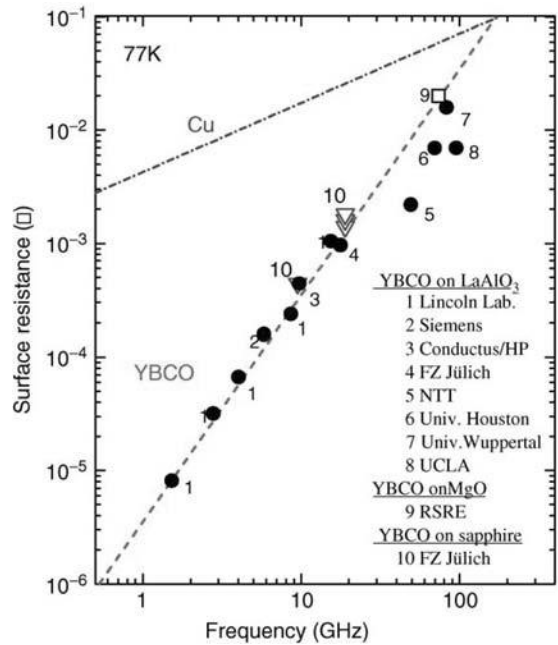
Figure 1
Measured surface resistance of epitaxially grown YBCO films grown at different laboratories at $T = 77$ K in comparison to that of copper.

density (enhanced by about one order of magnitude). This effect can only be avoided by employing "edge current free" modes in circular disk or ring resonators. Typically, intermodulation distortion as well as a field dependent surface resistance occurs at field levels, which depend strongly on the film quality. As an example, misoriented grains in the strongly anisotropic materials and grain boundaries give rise to strong nonlinearities.

The nonlinear effects in HTS films are strongly temperature dependent, in particular close to T_c (Klein 1997, Hein 1999). Therefore, operation temperatures of 50–65 K are more favourable than 77 K. As discussed in Sect. 5, temperatures in this range can be attained by low-power closed-cycle cryocoolers.

2. Technology of High-temperature Superconducting Thin Film Devices

In most cases, HTS planar microwave devices rely on epitaxially grown films of YBCO grown by vacuum deposition techniques. Nonvacuum techniques like spraying or sol–gel (Alford *et al.* 1997) represent very challenging developments with the focus on low-cost production. However, the properties of such films are still behind that of epitaxial film. However, for some applications like coating of large area microwave cavities for base-station filters, HTS thick films are in use (Remilliard *et al.* 2001). For a review about the growth of YBCO films see Wördenweber (1999).

Apart from YBCO, thin films with reasonable microwave properties have been prepared from the thallium-based compounds $Tl_2Ba_2CaCu_2O_8$ ($T_c \approx$ 105 K) and $Tl_2Ba_2Ca_2Cu_3O_{10}$ ($T_c \approx 115$ K) (Klein 1997, Wördenweber 1999). For the thallium-based and the more recently discovered mercury-based compounds with T_c values up to 140 K, epitaxial growth is very difficult because of the volatility of thallium and mercury, respectively.

HTS films with reasonable and qualified microwave properties can be grown on wafers up to a diameter greater than 4 in; the most common sizes are 2 in and 3 in for microwave applications (Wördenweber 1999). A very important step was the preparation of double-sided coatings, which have turned out to be essential for planar microwave devices, where the ground plane needs to be superconducting in order to achieve high quality factors.

Substrates for planar HTS microwave devices need to fulfil the criteria for expitaxial growth plus moderated values of the dielectric constant ($\varepsilon_r \leqslant 25$) and a low level of dielectric losses (tan $\delta \leqslant 10^{-5}$). The most commonly used substrate materials are lanthanum aluminate ($LaAlO_3$, $\varepsilon_r \approx 23$), magnesium oxide (MgO, $\varepsilon_r \approx 10$) and sapphire (Al_2O_3, $\varepsilon_r \approx 10$) (see Krupka *et al.* 1994, Zuccaro *et al.* 1997).

The fabrication of a planar microwave device is based on a patterning process. As a first step, masks are prepared according to the layout of the structure. A conventional photolithographic procedure based on a photoresist layer followed by chemical or ion beam etching is applied for patterning of the HTS wafers. In order to provide electrical contacts to microstrip connectors and to the housing, the HTS films are often covered with an *in situ* gold layer prior to patterning. The feature sizes are typically not smaller than 10 μm, but due to RF current crowding at the edges, the performance of planar microwave devices becomes quite sensitive to the quality of the patterning process. After process optimization no significant degradation of the microwave properties remains.

3. Planar HTS Resonators

Typically, the building blocks of HTS filters are planar HTS resonators. In general, a microwave resonator is characterized by its resonant frequency f_0, its unloaded quality factor Q_0 of the selected resonant mode(s), and its spectrum of spurious modes.

The unloaded quality factor of a resonator is determined by the stored energy W and the dissipated power P_{diss}

$$Q_0 = \frac{2\pi f_0 W}{P_{diss}} \tag{3}$$

P_{diss} contains loss contribution from the circuit layer and the unpatterned ground plane, dielectric losses from the substrate materials in use, and radiation losses (or metal losses from the housing). The dielectric losses are characterized by the loss tangent tan δ of the substrate material. Neglecting radiation losses, the unloaded quality factor is given by

$$\frac{1}{Q_0} = \kappa \tan \delta + \frac{R_s}{G}; \quad \kappa = \frac{\varepsilon_r \int_S \boldsymbol{E}^2 \mathrm{d}V}{\int_{V-S} \boldsymbol{E}^2 \mathrm{d}V + \varepsilon_r \int_S \boldsymbol{E}^2 \mathrm{d}V};$$
$$G = \frac{\omega \mu_0 \int_V \boldsymbol{H}^2 \mathrm{d}V}{\int_C \boldsymbol{H}^2 \mathrm{d}A} \tag{4}$$

with κ representing the filling factor indicating the normalized fraction of electric field energy stored in the dielectric substrate (S). Typically, κ values are slightly smaller than 1. The quantity G is a geometric factor (in Ω) representing the surface integral of the squared RF magnetic field over the conducting parts (C). In case of planar resonators G is roughly proportional to the substrate thickness. For conventional metals, the dielectric losses are small in comparison to metal losses. For HTS resonators, substrate losses can play a significant role. The integrals in Eqn. (4) with subscript "V" are volume integrals over the entire volume of the resonator, i.e., substrate plus housing.

Figure 2 shows typical examples of HTS planar resonators which have been used as building blocks of multipole filter structures. Planar HTS resonators
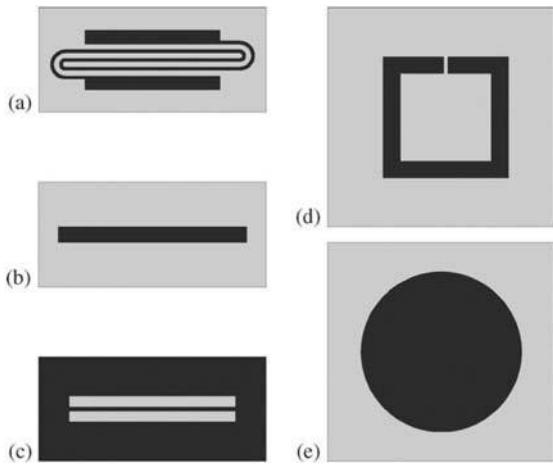
Figure 2
Typical planar resonators being used as building blocks for planar HTS filters: quasi-lumped element (a), (design by Superconductor Technologies Inc.), microstrip (b), coplanar waveguide (c), folded microstrip with integrated capacitors (d), and two-dimensional disk resonator (e). Omitting the capacitive gap in the folded microstrip design (d) leads to a ring resonator (if circular shaped), which also represents a quite commonly used microstrip resonator design.

are either formed by segments of quasi-TEM (transverse electromagnetic) transmission lines defining the resonances to be at frequencies where the length L equals a multiple of half a guided wavelength (b,c) or lumped element resonators each composed of a discrete inductor L and capacitor C (see (a) and (Hieng *et al.* 2001)) with its resonance at a frequency $f = 1/[2\pi(LC)^{1/2}]$. In many cases hybrids of lumped elements and microstrip lines are used, e.g., folded microstrip lines disrupted by a capacitive gap (d) (Hong *et al.* 1999). In order to obtain a high value of Q for microstrip and lumped element structures, the ground plane needs to be formed by a HTS film, e.g., in general double-sided films are required in order to achieve ultimate performance. As an alternative, coplanar resonators have been used (c) with some compromise on Q in comparison to microstrip lines of the same size but with the advantage of single sided coating. However, until now no high performance multipole filters based on coplanar resonators have been built. For the highest Q and ultimate power handling capability circular two-dimensional disk resonators excited in the TM_{010}-mode have been used (e), also requiring double sided coating (Kolesov *et al.* 1997).

The structures shown in Fig. 2 are generally not restricted to superconductors, but only here the achievable quality factors are comparable or higher than the ones of bulky cavities or dielectric resonators

at room temperature. Therefore, there is strong potential in high-temperature superconductor technology for the miniaturization of high-performance microwave devices and circuits.

4. Planar Multipole Filter Topologies

The class of microwave filters which can mostly benefit from HTS technology is characterized by some common structural features ("topologies").

Filters of this class are passive and reciprocal two-ports, where the incident power is transmitted within certain frequency intervals (passbands) and reflected within the stopbands. Rejection in the stopbands is achieved by reflection. Unavoidable dissipation causes a degradation of the filter performance. For a given amount of dissipation, the degree of degradation depends on the filter parameters. In turn, this determines whether an HTS realization is beneficial or not.

In the most common filter topology all resonators are identical, possessing the same resonant frequency f_0 in the uncoupled state. A structure where input and output ports are coupled via one resonator only, represent a one-pole filter with a Lorentzian shaped transmission characteristic. If losses can be neglected, the frequency bandwidth (frequency interval where the transmission factor is higher than a prescribed value) of a one-pole filter is controlled by the strength of the coupling between resonator and ports. In order to achieve a frequency response closer to the rectangular frequency response of an ideal filter, a multiple-resonant (multipole) filter structure needs to be employed. In the most common filter topology, multiple-resonant structures are realized by a set of identical resonators of unperturbed resonant frequency f_0, which are mutually coupled. Mutual coupling of N resonators results in a splitting into N (in general) different frequencies. In the case that each resonator supports two orthogonal resonant modes (dual-mode resonator), N represents the number of operational modes.

Each coupling path (direct connection between resonator i and j) is characterized by its coupling coefficient k_{ij}, which is related to the frequency splitting of f_0 into f_e and f_o for the even and odd mode, respectively, by $k_{ij} = (f_e - f_o)/f_0$. In the special case of pure adjacent resonator coupling ($k_{i,j} = 0$ for $i \neq j \pm 1$), a single chain between input and output port is formed. This allows one to approximate a rectangular bandpass response with transition width δf decreasing with increasing order N (see Fig. 3). Different approximations for the insertion loss response are possible. The most popular is the Chebyshev response with equal-ripple response of the (reflective) passband insertion loss (Matthaei *et al.* 1980). The required order (number of resonators or operational modes) increases with increasing ratio between the passband width Δf and the transition
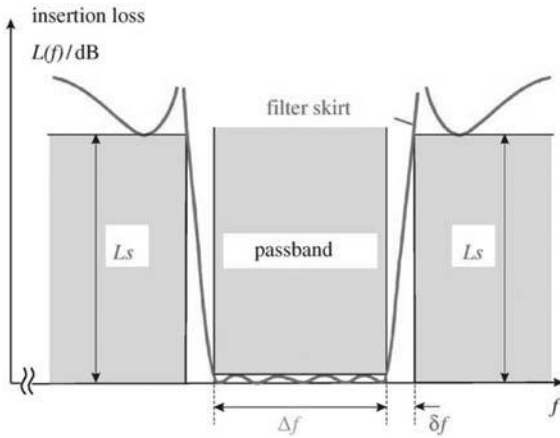
Figure 3
Typical frequency response of a passband filter with 2
transmission zeros in the stopbands
(Δf = passband width, δf = transition width).

width δf. For a given order N the transition width δf
can be further reduced by introducing transmission
zeros in the stopband close to the band-edge. These
transmission zeros cannot be realized if the coupling
topology is restricted to adjacent resonator coupling.
Additional coupling between non-adjacent resona-
tors ("crosscouplings") with appropriate coupling
sign and strength is required. Filters with cross-cou-
plings are characterized by the ratio between the
number of transmission zeros at finite frequencies
and the filter order and referred to as quasi-elliptic or
elliptic filters (Fig. 4) (Klauda *et al.* 2000).

In analogy to spectral-analysis where frequency res-
olution increases with integration time, the skirt steep-
ness (in dB MHz^{-1}) of a filter determines the minimum
time duration in which the signal has to be stored in
the filter structure. This time duration τ can be de-
scribed by means of the frequency-dependent group
delay which is the frequency derivative of the trans-
mission phase and corresponds to the delay of a nar-
rowband (bandwidth approaching zero) pulse passing
through the filter. The group delay time τ allows for a
simple relationship between the field energy W stored
in the resonators to the incident power P_{inc}.

$$W = \tau P_{inc} \qquad (5)$$

Up to now, degradations of the filter response caused
by losses were ignored. The in-band insertion loss L_{diss}

$$\frac{L_{diss}}{dB} = 10 \log\left(\frac{P_{in}}{P_{out}}\right) = 10 \log\left(1 + \frac{\omega\tau}{Q}\right) \qquad (6)$$

is increased due to the finite unloaded quality factor Q
by an amount which is proportional to the group de-
lay. The insertion loss is associated with an unwanted
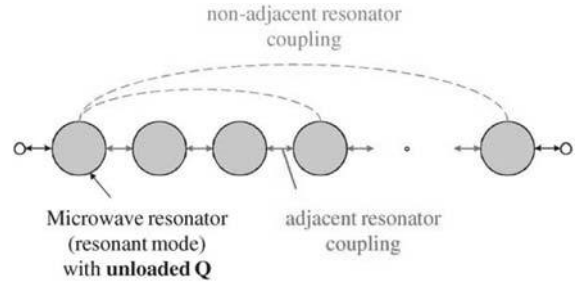
Figure 4
Filter topology with resonators, adjacent resonator
coupling, and non-adjacent resonator coupling (cross-
coupling).

power reduction of in-band signals as well as with an
unwanted amplitude distortion caused by the frequen-
cy dependence of τ. The latter effect leads to a round-
ing of the insertion loss response at frequencies close to
the band edge where the group delay has a maximum.

Therefore, the achievable skirt steepness for a
bandpass filter depends on the unloaded quality fac-
tor and on the filter topology (Klauda *et al.* 2000):

$$S < 4 \times 10^{-3}\frac{Q_0\xi}{f} \qquad (7)$$

The dimensionless quantity ξ has a value of 0.33 for
Chebyshev and 1 for elliptic filters (the values for
quasi-elliptic filters are in between) (where S is meas-
ured in dB MHz^{-1} and f in GHz).

5. Planar High-temperature Superconducting Filters and Subsystems

5.1 Filters

Since the late 1990s, tremendous progress has been
achieved in the development of HTS planar filters
and their integration in subsystems, mostly for base
stations in mobile communication (Willemsen 2001).
For HTS planar filters the resonator types shown in
Fig. 2 and others have been used. The main emphasis
was to develop filters for base stations with steep
skirts coming as close as possible to the Q-require-
ments discussed in the previous section. In most cas-
es, these are (quasi) elliptic filters with 8–17 poles or
Chebyshev filters with up to 30 poles.

Figure 5 shows an example of an eight-pole quasi-
elliptic filter based on folded microstrip resonators
similar to "c" in Fig. 2. In this case of monomode
resonators, coupling coefficients of different signs
were achieved by changing between electric and mag-
netic field coupling of the resonators. For a 17-pole
elliptic filter at 1.8 GHz with 5% relative bandwidth
(resonator $Q_0 = 50.000$ at 65 K) a steepness of skirts
of 85 dB MHz^{-1} was demonstrated (Fig. 6). Such a
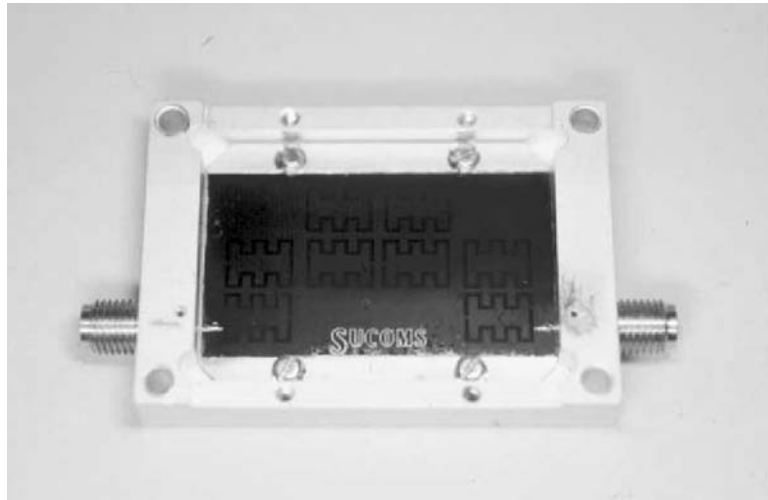
Figure 5
Example of an HTS-planar filter with 8 poles and quasi-elliptic characteristic (from Hong *et al*. 1999).
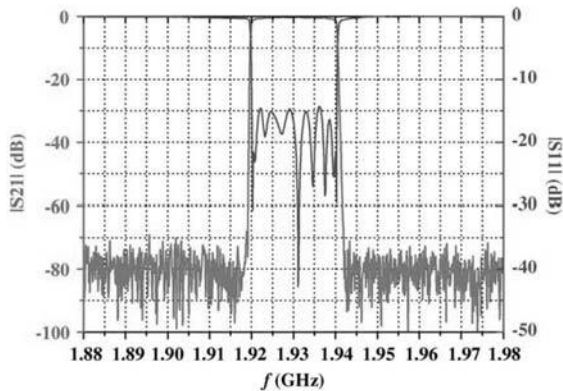
Figure 6
Measured characteristic of a HTS planar 17-pole elliptic filter (from Kolesov *et al*. 2000).

high performance cannot be achieved with any other filter technology.

In addition, high quality filters based on microstrip resonators have been developed for C-band satellite transponders. Figure 7 shows a three channel IMUX test module developed at Bosch SatCom GmbH in Germany. This test module, which is considered to be part of a space experiment, consists of three HTS quasi-elliptic eight-pole channel filters, cryogenic circulators, a cryogenic preamplifier, and a wide band HTS input filter (Klauda *et al*. 2000).

Due to the nonlinear surface resistance of HTS films (see Sect. 1) power handling of HTS filters is limited. In general, one can claim that planar HTS filters with edge-parallel currents in their resonators can handle power levels in the mW range without
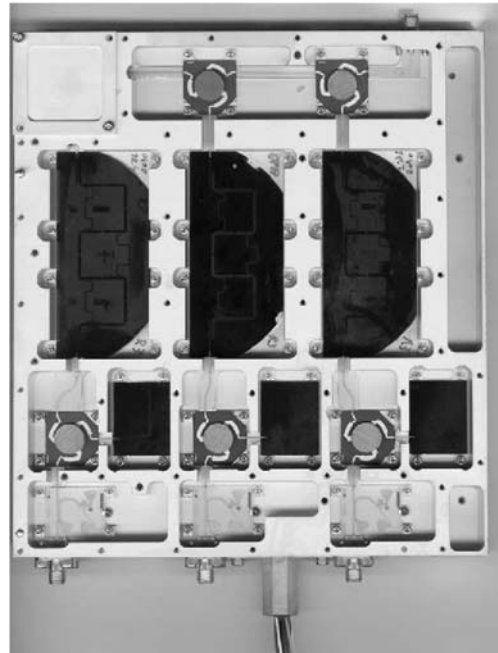
Figure 7
Photograph of a three-channel IMUX module based on HTS planar filters as part of a cryogenic C-band satellite transponder. The HTS filters are indicated as large black squares (from Klauda *et al*. 2000).

significant intermodulation distortions. Applications to transmit circuits with typical power levels of several 10 W can only be handled by employing the edge-current free disk resonator.

5.2 Subsystems

The most important "enabling technology" for applications of HTS in telecommunications is cryotechnology. Cooling by liquid nitrogen is unacceptable, because the amount of maintenance for each base station should be as small as possible. The situation for satellite communications is even more severe, because the lifetime of a geostationary satellite is at least 10 yr.

The most convenient way of cooling is to use Stirling-type closed-cycle refrigerators consisting of a small stainless steel compressor with helium gas pressure of a few bar and a cold finger with a displacer inside, both connected by a thin stainless steel tube. Typically, a compressor with an a.c. 50 Hz power consumption of 100–200 W with the size of one or two beer cans provides a cooling power of 3–10 W at 77 K, which is the typical amount of cooling power needed for a HTS subsystem, consisting of about three filters and one cryogenic LNA (low-noise amplifier). For the sake of filter performance the base station subsystems are operating between 60 K and 70 K, and the satellite systems at 77 K because cooler efficiency is a crucial parameter with respect to system mass reduction (Klauda *et al.* 2000, Willemsen 2001).

Figure 8 shows a commercial system for potential use in wireless base stations (Kolesov *et al.* 2000). The filters are assembled inside a Dewar vacuum (left side), the metal cylinder in the right part of the assembly is the compressor of the Stirling-type refrigerator.

In 2002, companies are focussing on improving the coolers with respect to lifetime (currently about 3–5 yr for continuous operation) and cost reduction.

Figure 8
Commercial HTS subsystem for potential use in base stations. The filters and the LNA are inside a Dewar vacuum (left side), the metal cylinder in the right part of the assembly is the compressor of the Stirling-type refrigerator (from Kolesov *et al.* 2000).

6. Tuneable and Switchable Filters

Tuneable and switchable filters are supposed to have a strong potential for future receiver front-ends. First, for military communications systems, most flexible interference suppression is an important issue. Second, for future mobile communication systems beyond the currently installed third-generation systems, most flexible allocation of bandwidth may require high-performance reconfigurable filters (see also Sect. 7).

In general, the figure-of-merit (FOM) of a tuneable resonator is given by

$$\text{FOM} = \frac{\Delta f}{f} \, Q \qquad (8)$$

with $\Delta f/f$ being the relative frequency tuning range and Q the unloaded quality factor of the resonator.

The most commonly investigated techniques which can be used for HTS tuneable devices are based on ferroelectrics and ferrites. For the future also micromechanical switches (MEMS) are considered to be relevant for planar HTS circuits (see, e.g., Rebeiz *et al.* 2001).

6.1 Ferroelectric Varactors

These are very attractive for the integration with passive HTS microwave circuits because of the agile dielectric materials which can be grown as epitaxial heterostructures with YBCO. The current efforts are concentrated on thin films of $SrTiO_3$ ($SrTiO_3$ does not exhibit a ferroelectric phase transition but the temperature dependence of the permittivity exhibits a Curie–Weiss law similar to ferroelectric above its Curie temperature). Thin films exhibit lower ε_r values in comparison to the bulk single crystals, but a stronger tuneability above about 60 K. Similarly, the dielectric losses at microwave frequencies are in the range of 10^{-2} (see, e.g., Petrov *et al.* 1998) in comparison to several 10^{-4} for bulk single crystals (Vendik *et al.* 1998).

The FOMs achieved at microwave frequencies for single varactors or tuneable resonators are in the range of about 100. Figure 9(a) shows an example of a planar HTS resonator incorporating a ferroelectric varactor based on a YBCO/$SrTiO_3$ multilayer structure. With such resonators a tuneability by about 10% was achieved (Marcilhac *et al.* 2001, B Marcilhac, private communication). Such resonators can be used to construct multipole bandpass filters (Fig. 9(b)).

6.2 Ferrites

These represent a very common way of frequency tuning utilizing the magnetic field and magnetization dependence of a permeability tensor. In general, the microwave properties of a ferrite biased by a d.c. magnetic field H_0 in *z*-direction are defined by the
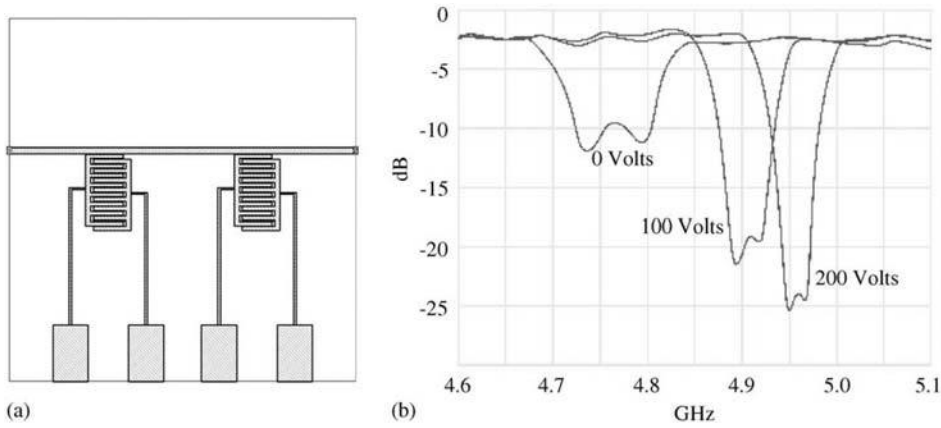
Figure 9
Tuneable lumped element 2-pole bandpass filter based on a $SrTiO_3$ loaded interdigited capacitor (a) and experimental result for measured filter response (b) (from Marcilhac *et al*. 2001).

permeability tensor which is in the lossless case (see, e.g., Pozar 1998)

$$[\mu] = \begin{bmatrix} \mu & i\kappa & 0 \\ -i\kappa & \mu & 0 \\ 0 & 0 & \mu_0 \end{bmatrix}$$

with $\mu = \mu_0 \left(1 + \dfrac{\omega_0\omega_m}{\omega_0^2 - \omega_m^2}\right)$ and $\kappa = \mu_0 \dfrac{\omega\omega_m}{\omega_0^2 - \omega_m^2}$ (9)

The angular frequencies $\omega_0 = \mu_0\gamma H_0$ and $\omega_s = \mu_0\gamma M_s$ are proportional to the external magnetic field H_0 and the saturation magnetization M_s with $\gamma = 1.759 \times 10^{11}$ C kg^{-1} being the gyromagnetic ratio. This proportionality corresponds to a ratio of 2.8 MHz G^{-1} between the value of frequency $f = \omega/2\pi$ and magnetic field.

Large tuning ranges can be achieved by exploiting the ferrimagnetic resonance ($\omega = \omega_0$) in a YIG sphere. However, the losses are quite high and therefore combinations with HTS are not worth considering. In addition, high magnetic fields applied during operation may result in a significant degradation of the surface resistance of the employed HTS film. One attractive possibility is to use latching devices, where the magnetization of the ferrite can be switched between the remanent magnetization values $-M_r$ and $+M_r$ (usually slightly lower than M_s) employing short current pulses applied through a coil. This principle has been employed successfully for the realization of planar HTS phase shifters (Oates *et al*. 1997). Tuneable resonators and simple Chebyshev filters with a small number of poles have been demonstrated, the FOM values are about several hundred.

However, there are several drawbacks associated with ferrimagnetic tuning:
(i) The growth of HTS on ceramic YIG or other ferrites is difficult because no epitaxial growth can be achieved; epitaxial growth of single crystal YIG substrates has been achieved, but the substrates are very expensive and only available in small dimensions. Therefore, the working solutions rely on flip-chip assemblies.
(ii) The particular form of the μ-tensor sets strong limits on possible tuning and phase shifting topologies.
(iii) Experimentally, the losses below about 5 GHz increase dramatically due to ferrimagnetic resonance losses of partially magnetized segments of the ferrite material in use (M_s of YIG corresponds to 4.9 GHz). As an alternative to YIG, Ga- or Al-doped YIG with lower values of M_s have been used (Yeo and Lancaster 2001). One of the challenges is the development and optimization of ferrites with tailored properties at cryogenic temperatures.

7. Impact of High-temperature Superconducting Subsystems for Future Microwave Systems

The superior performance of HTS filters, namely high selectivity combined with a very low passband insertion loss can be used to enhance the performance of receiver front ends with respect to both interference resistivity as well as a reduced receiver noise figure.

Receiver front-ends are analogue subsystems, placed in between the antenna ports and the analogue-to-digital converters (ADCs). Their function comprises pre-amplification, down-conversion and some filter functions. It is important to distinguish between the different filter functions. Channel (carrier) selection and/or separation in principle can be performed by analogue filters in the microwave or the intermediate frequency (IF) section, or by software-controlled digital filters in the digital part. In 2002, analogue channel selection in the IF represents the best choice. Future receivers are expected to utilize

more and more digital channel selection ("software defined radio"). Transparent transponders with signal processing exclusively in the microwave regime represent an exception from this trend. In contrast to channel selection, other filter functions need to be performed in the microwave regime. These functions are the suppression of image reception in superheterodyne receivers and the rejection of strong out-of-band interferers. The second function stems from the necessity to prevent strong interfering signals from entering the LNAs and mixers, where they would cause saturation, desensitisation, and intermodulation effects due to the nonlinear response of these active devices.

Cryogenic units for base-transceiver stations (BTS) of wireless communication networks became commercially available in the late 1990s. These units comprise HTS bandpass filters followed by cryogenic LNAs, both integrated in an enclosed vacuum which incorporates the cryocooler. In order to meet the different requirements associated with frequency allocation in a first-generation analogue and second- and third-generation digital systems, these systems are available for different center frequencies and bandwidths, as well as with multiple passbands and with narrowband stopbands embedded in wider passbands. The number of filter-LNA chains in one cryogenic unit equals the number of antenna ports (sector antennas and diversity antennas) implemented in a one BTS.

For the evaluation of system benefits offered by cryogenic front-ends, the issue of a significantly improved interference suppression due to steeper filter skirts and the issue of an improved sensitivity due to the reduced receiver noise figure should be clearly distinguished. The first feature becomes significant in the case of wireless systems which have to operate in areas with strongly interfering systems with unwanted signals at frequencies closely spaced to the edge frequencies of the desired signal. Here, the improved selectivity is transformed into a lower intermodulation noise level and hence into improving the quality of service.

Alternatively, this advantage can be transformed into reduced guard-band widths and hence in an enhanced spectral efficiency and capacity.

In case of spread-spectrum systems, like the third-generation W-CDMA standard, HTS stopband filters with extremely narrow bandwidths can be used to reject narrowband interferers falling into the wideband operational frequency band.

The reduced receiver noise figure of cryogenic filter-LNA configurations originates from three different effects, namely the reduced noise temperature of the cooled LNA, the reduced thermal noise of the filter due to the lower physical temperature, and the reduced contribution of the amplifier noise due to the decreased passband insertion loss of the filter. Reduced receiver noise becomes important in noise-limited

situations (e.g., rural areas), where it transforms into a lower number of required BTSs or an improved coverage for a fixed number of BTSs. Typically, the noise figure of a BTS with the cryogenic front end at the ground (noise figure degeneration due to lossy cable between antenna and front-end) resembles the noise figure of a conventional, but mast-mounted front-end.

See also: High-temperature Superconductors: Thin Films and Multilayers; Superconducting Radiation Sensors

Bibliography

Alford N Mc N, Penn S J, Button T W 1997 High-temperature superconducting thick films. *Supercond. Sci. Technol.* **10**, 169–85

Hein M 1999 High-temperature superconductor thin films at microwave frequencies. In: *Tracts in Modern Physics*. Springer, New York, Vol. 155

Hieng T S, Huang F, Lancaster M J 2001 Highly miniature HTS microwave filters. *IEEE Trans. Appl. Supercond.* **11**, 349–52

Hong J-S, Lancaster M J, Greed R B, Voyce D, Jedamzik D, Holland J A, Chaloupka H J, Mage J -C 1999 Thin film HTS passive microwave components for advanced communications systems. *IEEE Trans. Appl. Supercond.* **9**, 3839–96

Klauda M, Kaesser T, Mayer B, Neumann Ch, Schnell F, Aminov B, Baumfalk A, Chaloupka H, Kolesov S, Piel H, Klein N, Schornstein S, Bareiss M 2000 Superconductors and cryogenics for future communication systems. *IEEE Trans. Micro. Theory Tech.* **48**, 1227–39

Klein N 1997 Electrodynamic properties of oxide superconductors. Juelich report, July 3773, Post-doctoral thesis, Juelich Research Centre, Germany

Kolesov S, Aminov B, Kaiser T, Kreiskott S, Piel H, Pupeter N, Wagner R, Wehler D, Medelius H, Draganic Z, Chaloupka H 2000 Cryogenic BTS receiver front end demonstrator *Proc. 30th European Microwave Conf.*, Vol. 3, pp. 230–2

Kolesov S, Chaloupka H, Baumfalk A, Kaiser T 1997 Planar HTS structures for high-power applications in communication systems. *J. Supercond.* **10**, 179–87

Krupka J, Geyer R G, Kuhn M, Hinken J H 1994 Dielectric properties of single crystals of Al_2O_3, $LaAlO_3$, $NdGaO_3$, $SrTiO_3$, and MgO at cryogenic temperatures. *IEEE Trans. Micro. Theory Tech.* **42**, 1886–90

Marcilhac B, Crete D G, Lemaitre Y, Mansart D, Mage J C, Bouzehoua C, Jacquet E, Woodall P, Countur J P 2001 Frequency agile microwave devices based on Y-Ba-Cu-O/Sr-Ti-O/La-Al-O structures. *IEEE Trans. Appl. Supercond.* **11**, 438–41

Matthaei G, Young L, Jones E M T 1980 *Microwave Filters, Impedance-matching Networks and Coupling Structures*. Artech House, Dedham

Oates D E, Dionne G F, Temme D H, Weiss J A 1997 Superconductor ferrite phase shifters and circulators. *IEEE Trans. Appl. Supercond.* **7**, 2347–50

Petrov P K, Carlsson E F, Larsson P, Friesel M, Ivanov Z G 1998 Improved $SrTiO_3$ multilayers for microwave application: growth and properties. *J. Appl. Phys.* **84**, 3134–40

Pozar D M 1998 *Microwave Engineering*. John Wiley, New York

Rebeiz G M, Muldavin J B 2001 RF MEMS switches and switch circuits. *IEEE Microwave Magazine* 59–71 and http://www.eecs.umich.edu/rebeiz/Current_Research.html

Remilliard S K, Abdelmonem A, Radzikowski P O, Lazzaro N D, Applegate D S 2001 Field deployable microwave filters made from superconductive thick films. *J. Supercond.* **14**, 47–56

Vendik O G, Ter-Martirosyan L T, Zubko S P 1998 Microwave losses in incipient ferroelectrics as functions of the temperature and the biasing field. *J. Appl. Phys.* **84**, 993–8

Waldram J R 1996 *Superconductivity of Metals and Cuprates.* Institute of Physics, Bristol

Willemsen B A 2001 HTS filter subsystems for wireless telecommunications. *IEEE Trans. Appl. Supercond.* **11**, 60–7

Wördenweber R 1999 Growth of high-Tc thin films. *Supercond. Sci. Technol.* **12**, R86–R102

Yeo K S K, Lancaster M J 2001 High-temperature superconducting ferrite phase shifter latching structures. *IEEE Trans. Appl. Supercond.* **11**, 430–3

Zuccaro C, Winter M, Klein N, Urban K 1997 Microwave absorption in single crystals of lanthanum aluminate. *J. Appl. Phys.* **82**, 5695–704

N. Klein
Jülich Research Center, Germany

H. Chaloupka
University of Wuppertal, Germany

Superconducting Permanent Magnets: Potential Applications

When high-temperature superconductivity (HTS) was discovered, it became possible to construct electrical machines without high cryotechnic expenditure which was necessary with classical superconductors. Bulk superconductors (see *Superconducting Permanent Magnets: Principles and Results*) could be used for different types of electrical motors, e.g., hysteresis motors, reluctance motors, and trapped field motors (Kovalev *et al.* 2000, Oswald *et al.* 1998, Barnes *et al.* 2000).

While the hysteresis motor is an asynchronous motor type, the others are synchronous motors. For those drives the rotors move synchronously with the rotating field. The superconductors arranged in the rotors of synchronous motors are exposed to a d.c. field, if only the fundamental wave is considered. However, the rotating field has no pure sine-wave form, it contains higher harmonics, causing hysteresis losses and perhaps also eddy current losses in the penetration depth of the magnetic field.

With reluctance motors, the solid superconductor is used as a diamagnet which has to exclude the quadrature axis field, if possible, totally. In case of the trapped field motor, the solid superconductor works as a permanent magnet; here the strength of the trapped field is decisive and important for the power density of the motor. These principal considerations are not only true for rotating, but also for linear, drives where there is a linear moving field instead of a rotating field.

1. Theoretical Considerations

The intrinsic moment M_i of a rotating field machine is normally dominated by the air gap field B and the ampere turns per meter A_s in the stator. Additionally, the phase angle ε between the phasor of the main field and the ampere turns per length plays an important role:

$$M_i = CBA \cos \varepsilon \qquad (1)$$

Here, C is a machine constant including the motor geometry and the winding parameters. The phasor of the main field consists of the vector addition of the rotor field B_r and the stator field B_s. For rotors with permanent magnets B_r is essentially larger than B_s and $\varepsilon < 20°$. Consequently:

$$M_i \sim CB_r A_s \qquad (2)$$

Therefore, high values for B_r result in the case of equivalent motor dimensions in relatively high torques. The advantage of trapped field motors must depend on improved values of the rotor field according to Eqn. (2).

2. Comparison with Conventional Motors

The possible advantages of superconductive permanent magnets being used in electrical machines become obvious in a comparison with conventional motors. Here, especially the comparison with permanent magnet motors with rare-earth elements has to be discussed. Permanent magnets of the composition Nd–Fe–B have remanence field strengths of approximately 1.2–1.5 T, coercive field strengths of 800–$900 \, \text{kAm}^{-1}$, and maximum energy densities of $400 \, \text{kWsm}^{-3}$. In the air gap of such permanent magnet motors, we obtain mean operating field strengths of 0.7–0.8 T. The strength of the air gap field determines according to Eqn. (2) the power density of a motor.

Permanent magnet motors have also a high power factor compared with other motor types, e.g., asynchronous motors, and principally no losses in the field-generating part. Both advantages allow a small motor size and an appropriately high dynamic of the motors. Superconductive permanent magnet motors certainly become interesting when their power density is significantly higher than that of normal permanent magnet motors. If it is possible to trap very high fields in the superconductors, motors could be designed

without magnetic yoke in the stator and, therefore, avoid hysteresis and eddy current losses in the iron. Consequently the size and the weight of the motor could be reduced significantly.

If superconductive permanent magnets are used, the field geometry which results from the local current density in the form of a Bean cone (see *Superconducting Permanent Magnets: Principles and Results*) differs from the rectangular field shape of conventional permanent magnets. Comparing these different motor types, this difference must be taken into account and yields a possible disadvantage of superconductive permanent magnets.

3. Further Developments

The present developments on bulk superconductors concentrate on the improvement of the current densities at possibly high operating temperatures, and on the manufacturing of large single domain structures. Large geometries are absolutely necessary for the construction of medium- and large-size motors. Superconductive connections across grain boundaries can perhaps become useful with a view to larger structures.

The current density in the superconductor and its geometry determine the achievable magnetic induction. The current density can be increased in bulk superconductors by decreasing the operating temperature. But, consequently the effort for the cooling system will increase significantly. Trapped field motors need a magnetizing facility that has to be integrated in the motor. Superconductive permanent magnets must be recharged in the superconductive state, i.e., at a low temperature after every period of heating up. This certainly creates a technical problem that requires an appropriate effort.

4. Possible Fields of Application

4.1 Motors

Electrical machines with superconductive permanent magnets are certainly of advantage if they offer a higher power density and simultaneously a high degree of efficiency in comparison with conventional solutions. Here all those applications are of special interest where the volume of the motor and its weight play a decisive role, e.g., in case of high-accelerated vehicles or in airplanes and rockets. Apart from that, fields of application exist where the cryotechnique is already available, e.g., in case of liquid gas pumps. The power density is also important with linear motors as servo drives, because the rotor mass directly influences the power need of these drives. This is particularly true for positioning drives, the moving cycle of which is essentially composed of only quick positive and negative accelerations.

At the present level of technique, the necessary cryotechnique is certainly still a serious obstacle for many possible applications. In future, however, the advantages of superconductive drives will lead step-by-step to industrial applications.

4.2 Magnetic Bearings, Fly Wheels, and Maglevs

The combination of HTS and permanent magnets, e.g., rare-earth magnets, can be used in magnet bearings, fly wheels, and magnetically levitated transport systems (Maglevs, Proceedings of ASC 1998, Proceedings of EUCAS 1999). The forces achieved depend on the superconducting currents and the field of the permanent magnet as discussed before. The higher the current density in the superconductor the higher are the levitating forces for fly wheels and for Maglev, and the restoring force in the case of bearings. For ideal conditions, i.e., an infinite current density in the superconductor, the area of which is large compared to the area of the permanent magnet, the force density is given by

$$f_x = \frac{B_s^2}{2\mu_0} \tag{3}$$

where B_s is the field produced by the permanent magnet on the surface of the superconductor.

In the case of $B_s = 0.5\,\text{T}$ the force density is about $10\,\text{Ncm}^{-2}$.

Superconductive magnetic bearings are advantageous for very high rotating speeds, as they are nearly absolutely friction-free. However, the stiffness of such bearings, measured as force per deflection, must still be distinctly improved before their application in electric drives.

As Eqn. (3) shows, much higher force densities can be achieved using superconducting permanent magnets with trapped fields significantly higher than 1 T.

See also: Magnetic Levitation: Materials and Processes; Magnetic Levitation: Superconducting Bearings; Superconducting Machines: Energy Storage

Bibliography

Barnes G J, McCulloch M D, Dew-Hughes D 2000 Computer modelling of electric motors containing bulk type II superconducting materials in the rotor. In: Obradors X, Sandiumenge F, Fontcuberta J (eds.) *Applied Superconductivity 1999*. Institute of Physics Conference Series. IOP Publishing, Bristol, UK, pp. 1075–8

Kovalev L K, Ilushin K V, Penkin V T, Koneev S M A, Poltavets V N, Larionoff A E, Modestov K A, Larionoff S A, Gawalek W, Habisreuther T, Oswald B, Best K J, Strasser T 2000 Hysteresis and reluctance electric machines with bulk HTS elements. Recent results and future developments. In: Obradors X, Sandiumenge F, Fontcuberta J (eds.) *Applied*

Superconductivity 1999. Institute of Physics Conference Series. IOP Publishing, Bristol, UK, pp. 1037–42

Oswald B, Krone M, Söll M, Strasser T, Oswald J, Best K J, Gawalek W, Kovalev L 1998 Superconducting reluctance motors with YBCO bulk material. *IEEE Trans. Appl. Supercond.* **9**, 1201–4

Proceedings of ASC, Palm Springs 1998 *IEEE Trans. Applied Superconductivity*, Vol. 9

Proceedings of EUCAS 1999 In: Obradors X, Sandiumenge F, Fontcuberta J (eds.) *Applied Superconductivity 1999*. Institute of Physics Conference Series. IOP Publishing, Bristol, UK,

B. Oswald
Oswald Elektromotorenbau GmbH
Miltenberg, Germany

Superconducting Permanent Magnets: Principles and Results

Bulk type II superconductors are able to trap magnetic fields and to act as permanent magnets. The trapped fields are generated by superconducting persistent currents circulating macroscopically within the superconductor. The main feature of the resulting field distribution is a maximum trapped field B_o in the center of the superconducting domain. High trapped fields B_o in bulk superconductors require a high critical current density of the supercurrents and large superconducting domains. Several melt-processing techniques were developed in the last years of the twentieth century to produce superconducting permanent magnets from bulk high temperature superconductors (HTS) as $YBa_2Cu_3O_{7-x}$ (YBCO), $SmBa_2Cu_3O_{7-x}$ (Sm-123), and $GdBa_2Cu_3O_{7-x}$ (Gd-123).

Trapped fields B_o up to 2.1 T can be obtained at the temperature of liquid nitrogen on the surface of HTS disks several centimeters in diameter. Higher trapped fields were observed at lower temperatures due to the increasing critical current density. However, the trapped field is limited by the mechanical properties of the material, because Lorentz forces cause considerable tensile stresses during the magnetization procedure and can cause cracking of the material. To avoid cracking, HTS disks can be reinforced by steel tubes which produce a compressive stress on the superconductor after cooling from 300 K to the measuring temperature. Mechanical properties are also improved by the addition of silver. Very high trapped fields beyond 10 T have been achieved in this way in bulk YBCO material at temperatures between about 20 and 40 K.

The influence of flux creep on the properties of superconducting permanent magnets will be discussed. Furthermore, levitation forces between superconductors and permanent magnets will be considered.

1. Type II Superconductors and Trapped Fields

1.1 Field Profile

The magnetization vs. field dependence of a type II superconductor is shown in Fig. 1. In the Meissner state ($B_a < B_{c1}$ with B_{c1} as the lower critical field), a superconducting surface current screens off the external magnetic field B_a so that the magnetic induction B in the bulk superconductor vanishes. In the mixed state between B_{c1} and the upper critical field B_{c2}, magnetic flux penetrates the superconductor in the form of flux lines, each containing one quantum of magnetic flux $\phi_o = 2.1 \times 10^{-15}\,\mathrm{T\,m^2}$. A flux line is composed of a normal conducting core of radius ξ (coherence length) and a surrounding circulating supercurrent region where the magnetic field and the supercurrents fall off within a distance λ (London penetration depth). In the absence of defects, the flux lines form a triangular lattice. As the external field B_a increases towards B_{c2}, the size of the superconducting region between the cores of the flux lines shrinks to zero, and the sample shows a continuous transition to the normal state. The $M(B_a)$ dependence of a defect-free type II superconductor is reversible and after switching off the external field no magnetic flux is trapped within the superconductor.

The $M(B_a)$ dependence becomes highly irreversible if the superconductor contains defects like dislocations, precipitates, etc., which interact with the flux lines. The interaction force between the defects in the material and the flux line lattice, the volume pinning force F_p, balances the driving force $F_L = j_c \times B = 1/\mu_o(\mathrm{rot}\,B \times B)$ acting on the flux lines due to the density gradient of flux lines. According to the concept of the critical state (Bean 1962), the gradient of the magnetic field has its maximum value $1/\mu_o\,\mathrm{d}B/\mathrm{d}r = j_c$ within regions of the superconductor penetrated by the field, or $\mathrm{d}B/\mathrm{d}r = 0$ for those regions that never felt the magnetic field.

The resulting field distribution for increasing external field is shown in the lower inset of Fig. 1. Neglecting the field dependence of the critical current density, the field within the superconductor decreases linearly with increasing distance from the sample edge. As the external field is reduced, the gradient of the local field near to the sample edge changes its sign, but has the same absolute value as before. The resulting field profile for decreasing external field is shown in the upper inset of Fig. 1. The magnetization becomes positive because a field is trapped in the superconductor by the pinning effect.

The field profile after switching off the external field is shown in Fig. 2. The trapped field decreases linearly from its maximum value B_o at the center of the sample to zero at the edge of the sample. The gradient of this field profile is determined by the pinning force of the defects acting on the flux lines. Therefore, the maximum trapped field B_o of a superconducting permanent
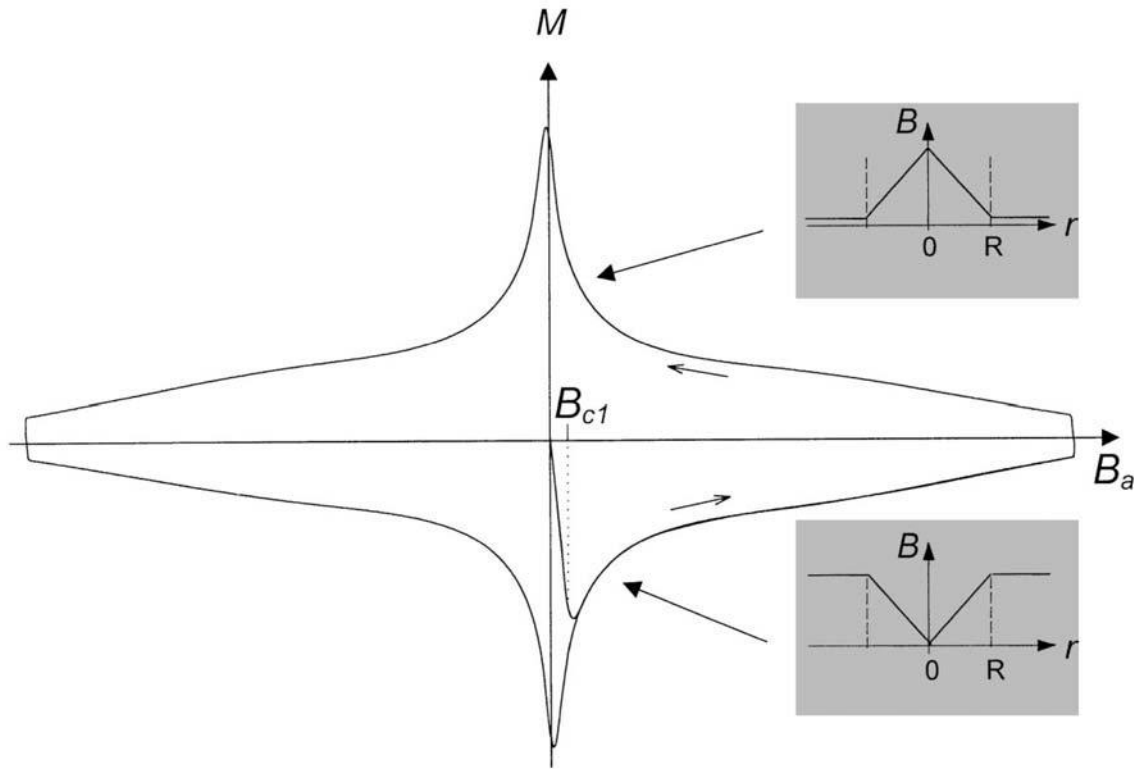
Figure 1
Magnetization vs. applied magnetic field of a type II superconductor. In the two insets the typical field distribution within the superconductor (radius R) is shown for increasing (lower inset) and decreasing (upper inset) magnetic field assuming a field-independent critical current density.

magnet depends on the critical current density j_c of the supercurrents and the radius R of the current loops. For a cylindrical sample of infinite length, B_o is given by

$$B_o/\mu_o = j_c R \tag{1}$$

Using $j_c = 10^4 \, \text{A cm}^{-2}$ and $R = 1 \, \text{cm}$, Eqn. (1) gives a maximum trapped field $B_o = 12.6 \, \text{T}$ within the superconductor or in the gap between two long superconducting samples. The trapped field on the surface of a long superconducting sample is half as large as this value, hence $B_o = 6.3 \, \text{T}$. It should be noted that the results obtained from Eqn. (1) overestimate the trapped field, because a field-independent critical current density is assumed, whereas in real superconductors, the critical current density decreases with increasing magnetic field. Nevertheless, this approximation gives an idea about the relation between the critical current density and the trapped field in superconducting permanent magnets.

The field profile of a YBCO disk (Fig. 3) is shown in Fig. 4. The curved shape of the distribution of the

trapped field in bulk YBCO superconductors can be calculated taking into account the field dependence of the critical current density of the supercurrents as was demonstrated by Klupsch *et al.* (1997).

1.2 Trapped Fields in Low- and High-temperature Superconductors

Trapped fields in low-temperature superconductors have been investigated at the temperature of liquid helium. In a niobium hollow cylinder, magnetic fields up to $0.26 \, \text{T}$ have been trapped (Garwin *et al.* 1973). Higher magnetic fields up to $2.2 \, \text{T}$ were permanently trapped at $4.2 \, \text{K}$ in a hollow cylinder consisting of copper-clad Nb_3Sn ribbons (Rabinowitz *et al.* 1977). However, the trapped field in bulk superconductors at low temperatures was found to be strongly limited by thermomagnetic instabilities resulting in flux jumps. An initial thermal disturbance in the critical state caused, for example, by the motion of magnetic flux during increasing external field, reduces the critical current. The released magnetic energy changes unstably into thermal energy as the external field
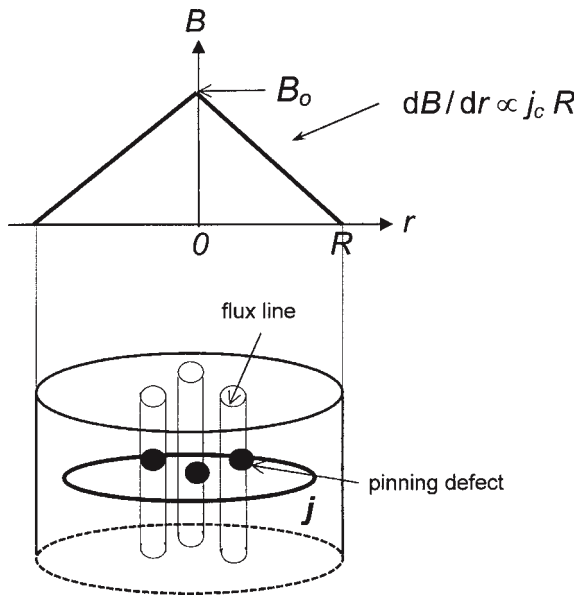
Figure 2
Field profile of a type II superconductor for a constant critical current density after switching of the external magnetic field and schematic view showing the circulating supercurrent (current density j) and pinned flux lines within the superconductor.

Figure 3
Melt-textured YBCO disk with a Sm-123 seed crystal in the centre of the disk.

exceeds a certain value B_j which depends on the specific heat of the superconductor. The low specific heat of superconductors at helium temperatures reduces their instability field B_j to very low values, limiting the trappable field in the bulk superconductor.

Figure 4
Typical field profile of a YBCO disk measured at 77 K (after Fuchs *et al.* 2000).

The discovery of high-temperature superconductors (HTS) stimulated new activities in the field of superconducting permanent magnets in bulk material. Because of the large specific heat of HTS at liquid nitrogen temperature, the instability field B_j becomes much larger than at 4.2 K. A second advantage of HTS is that the use of liquid nitrogen instead of helium as coolant of the superconductor makes the handling of superconducting permanent magnets much easier. However, HTS have several peculiarities that make the preparation of bulk material with high critical current densities rather difficult. The primary problems with these materials are their extremely small coherence length, their large anisotropy, and their brittleness.

A key parameter for the performance of superconductors for applications is the coherence length which determines the size of the normally conducting core of the flux lines. In order to control the motion of flux lines one needs a microstructure with defects as small as the coherence length. The extremely small coherence length of HTS, which for YBCO is only 1.8 nm, is the reason that defects as grain boundaries—which are very beneficial in low temperature superconductors because they act as pinning defects—serve now as weak links and limit the critical current, especially in the presence of an external magnetic field.

The crystal structure of HTS is highly anisotropic, which has implications for both the physical and mechanical properties. The electrical conductivity is highly anisotropic with much higher conductivity

within the CuO_2 planes than perpendicular to the planes. Therefore, supercurrents can flow only within the CuO_2 planes, i.e., the trapped field generated by these supercurrents is directed along the c-axis.

The brittleness of HTS is mainly caused by the anisotropy of the mechanical properties. For YBCO in particular, the anisotropic expansion coefficient results in large stresses causing microcracking because, by cooling from the crystal formation temperature to the superconducting transition temperature, the lattice contracts far more along the a, b planes than perpendicular to the planes. Microcracking is a central issue to be solved for any application of YBCO and especially for superconducting permanent magnets in which large Lorentz forces arise by the interaction between magnetic fields and supercurrents.

2. Trapped Fields in Bulk HTS at $T = 77\,K$

YBCO has a superconducting transition temperature T_c of about 91 K. The critical current density of bulk, polycrystalline YBCO material with randomly oriented grains is strongly limited by its pronounced weak link behavior. Only very small currents are able to flow across the grain boundaries, especially if a magnetic field is applied. Weak links can be avoided by growing large grains using melt-processing techniques. Several techniques have been found to be suitable for the growth of large single-domain YBCO material without high-angle grain boundaries (Murakami 1993, McGuinn 1995, Krabbes et al. 1997).

In most cases, seed crystals (Sm-123 or MgO) are used in order to orientate the c-axis of the YBCO sample perpendicular to the plane surface of the sample. Large superconducting domains with a c-axis texture can be produced in this way. A single-domain YBCO sample 35 mm in diameter with a Sm-123 crystal on top of the sample is shown in Fig. 3. In the present state of the art, the upper limit of bulk, single-domain YBCO samples is about 10 cm in diameter.

The simplest way to control the grain structure is to investigate the distribution of the trapped field at 77 K. By applying a magnetic field in the c-direction, flux lines penetrate the material and supercurrents are induced in the a, b plane of the YBCO sample which is cooled by liquid nitrogen. After switching off the applied field, the distribution of the trapped field in the superconductor is scanned by means of a Hall sensor with a small active area. An example for the field profile obtained for a single-domain YBCO sample is shown in Fig. 4.

It was mentioned above that the main problem in obtaining high critical current densities in YBCO is to create a defined microstructure with defects as small as the coherence length. But also the identification of the relevant defects in bulk YBCO which are responsible for pinning is difficult. Usually, different kinds of pinning defects of different size as normal conducting Y_2BaCuO_5 (Y-211) precipitates, arrays of stacking faults, dislocations and twin boundaries are present in the material.

The role of the different defects for the pinning effect in melt-textured YBCO material has been investigated very extensively and several review articles of the subject are available (Murakami 1992, McGuinn 1995). The Y-211 precipitates which can be observed by light microscopy have rather large extensions between about 0.5 and 20 μm compared with the diameter $2\xi = 3.6$ nm of flux lines in YBCO at 77 K. However, pinning at the interface between the superconducting matrix and the large Y-123 precipitates due to the abrupt change of the order parameter over a short distance can explain many j_c results found for melt-textured YBCO, as was pointed out by Murakami (1992).

Flux pinning can be improved by radiation-induced columnar defects using heavy ions of high energy. However, these defects are limited to a relatively thin layer of a few tens of microns near to the surface of the sample. In order to introduce strong pinning defects into bulk superconductors, [235]U-doped YBCO material was irradiated with thermal neutrons (Weinstein et al. 1994). Columnar defects were produced by fission in the bulk material and these defects were almost of optimum size with a diameter of about 5 nm. High critical current densities up to $8.5 \times 10^4\,A\,cm^{-2}$ and trapped fields up to 2.1 T were obtained on the surface of a single YBCO sample 20 mm in diameter at 77 K (Weinstein et al. 1996). For comparison, the best trapped field results at 77 K for nonirradiated bulk YBCO are in the range slightly above 1 T (Walter et al. 2000, Krabbes et al. 2000). Very promising results have recently been reported for bulk Nd-123 and Sm-123 material. Trapped fields up to 2.1 T (Ikuta et al. 1999) were achieved at 77 K for Sm-123 disks.

3. Relaxation Effects in Bulk YBCO

As was mentioned in Sect. 1.1, a large gradient of the field profile in superconductors requires pinned flux lines. However, pinned flux lines can also be thermally activated at a finite temperature and hop from one pinning defect to the other driven by the Lorentz force. Thermally activated flux motion or flux creep tends to reduce the field gradient and, therefore, the maximum trapped field B_o in the superconductor.

Flux creep effects are small at low temperatures and for high pinning energies. For HTS, flux creep becomes extremely large at 77 K, since kT is about 20 times larger than at 4.2 K. Therefore, in HTS the flux lattice is much more mobile than in low-temperature superconductors and there are large portions of the H–T plane where extremely large flux creep effects are observed.

For 77 K, typical relaxation rates of $d(B/B_o)/d(\ln t/t_o) \approx -0.05$ were reported for melt-textured

YBCO (Weinstein *et al.* 1996), i.e., the trapped field B_o reduces by about 5% per time decade. Hence, flux creep seems to be a serious problem for superconducting permanent magnets. However, successful reduction of the relaxation rate was achieved by cooling the YBCO sample by several degrees during or after activation. Investigating a YBCO mini-magnet with $B_o = 4.3$ T at 65 K, the creep rate was found to lower by factors of 6, 197, or $\geqslant 1000$ by decreasing the temperature for $\Delta T = 2$ K, 4 K, and 6 K, respectively, after activation (Weinstein *et al.* 1996).

4. Limiting Factors for Superconducting Permanent Magnets in Different Temperature Ranges

The simplest way to enhance trapped fields in YBCO is to work at temperatures below 77 K using the higher critical current density and pinning force at lower temperatures. As the trapped field increases, the mechanical properties of the material also become important, because large forces act on the superconductor during the magnetizing procedure. Since the flux lines are pinned on defects within the superconductor, a force is transferred to the crystal lattice where the pinning defects are embedded. As a result of these body forces, the material undergoes macroscopic mechanical deformations during the magnetizing procedure. Magnetoelastic effects in HTS have been reviewed by Johansen (2000).

A trapped field in the superconductor is connected to a tensile stress, which causes cracking of the disk if the tensile strength of the material is reached. The different limitations of the trapped field of a melt-textured YBCO sample are illustrated in Fig. 5. In the
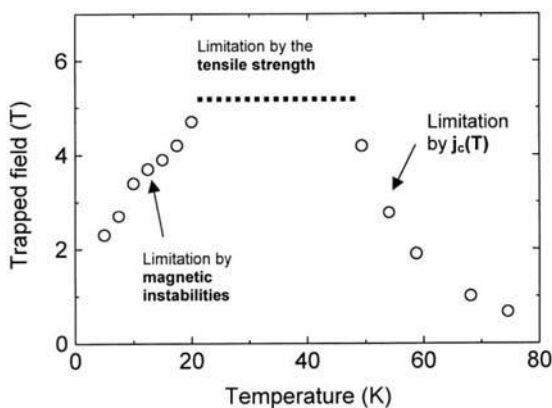
Figure 5
Schematic representation of the temperature dependence of the maximum trapped field B_o of a YBCO disk showing the limitations of B_o in different temperature ranges.

temperature range between about 50 K and T_c, the trapped field is determined by the pinning properties of the material and the size of the superconducting domains. At temperatures around and below about 50 K, the trapped field is limited by the mechanical properties of the superconductor. Thermomagnetic instabilities become predominant at temperatures below 20 K. In this region the trapped field is strongly reduced by flux jumps (Wenger 2000).

The limitations of the trapped field in the ranges of high and low temperatures have been discussed in the previous chapters. In the following, the limitation of the trapped field by mechanical properties and several possibilities to overcome this problem will be considered in more detail.

5. Very High Trapped Fields in Bulk YBCO Below 77 K

The temperature dependence of the maximum trapped field is usually measured in superconducting magnets. For magnetizing the bulk YBCO sample, a magnetic field is applied at a temperature above T_c and the sample is cooled to the measuring temperature. Then, the magnetic field is reduced to zero and B_o is recorded by means of a Hall probe. However, at high trapped fields, large magnetic tensile stresses act on the superconductor during this procedure resulting in cracking of the material which is indicated by a sudden decrease of the signal of the Hall probe during the magnetizing procedure. A visual inspection of damaged samples shows in some cases one crack on the surface of the sample, but sometimes no crack is visible.

The crack within the superconductor can be easily detected by a field profile measurement at 77 K (Fuchs *et al.* 1997). A typical example is shown in Fig. 6. The crack divides the disk into two superconducting domains. Currents can flow only within the superconducting domains, but not across the boundary between the two domains.

The distribution of the tensile stress within a bulk superconductor during the activation process was calculated by Ren *et al.* (1995) for long cylindrical samples. Later, this model was extended to arbitrary lengths of cylindrical samples (Johansen 1999). According to these models, the maximum tensile stress σ_m occurs at the center of the sample and increases with the square of the trapped field B_o.

The tensile strength σ_{max} of a damaged sample can be estimated from the applied magnetic field at which cracking was observed using the theoretical $\sigma_m(B_a)$ dependence predicted by the stress model. A typical value for the tensile strength of melt-textured YBCO is $\sigma_{max} \sim 40$ MPa (Ren *et al.* 1995), which is more than one order of magnitude lower than the tensile strength of metallic low-temperature superconductors originating from small cracks in melt-textured
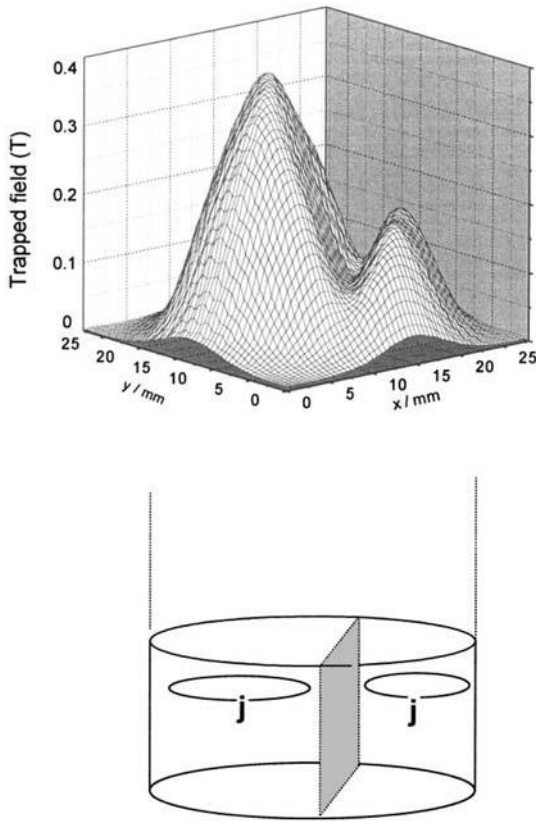
Figure 6
Typical field profile of a damaged YBCO disk after
cracking (top panel) and schematic view of the
corresponding two superconducting domains and the
circulating supercurrents (bottom panel).

YBCO, limiting the tensile strength of the material.
The cracks start to propagate when the external stress
reaches the fracture toughness K_c of the material. The
tensile strength depends in this case on K_c and the
initial size a of the largest crack according to the re-
lation (Paker 1981)

$$K_c \sim \sigma_{max}(\pi a)^{0.5} \qquad (2)$$

Typical values of the fracture toughness of melt-
textured YBCO are in the range of $K_c \sim$
(1–2) $MPa\,m^{1/2}$ (Schätzle *et al.* 1999). The fracture
toughness was found to increase by the incorporation
of ductile particles impeding the propagation of the
cracks. In YBCO containing ductile silver precipi-
tates, an enhancement up to $K_c \sim 2.4\,MPa\,m^{1/2}$ was
reported compared with $K_c \sim 1.9\,MPa\,m^{1/2}$ in samples
without silver inclusions (Schätzle *et al.* 1999). It
was also reported that YBCO samples can be rein-
forced against the tensile stress by placing them into
steel tubes. Steel has a larger coefficient of thermal
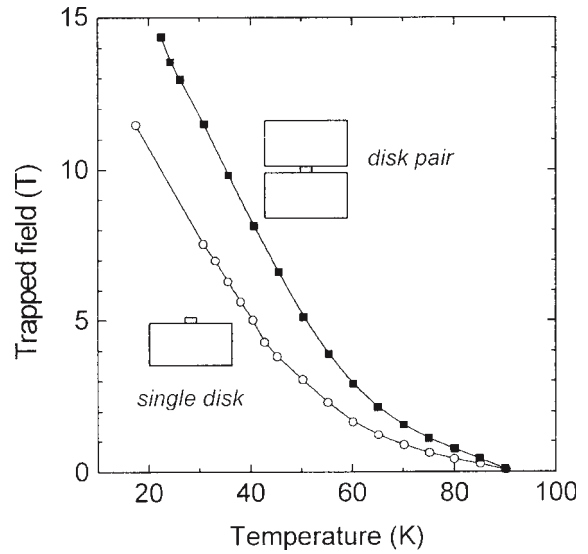
Figure 7
Temperature dependence of the maximum trapped field
B_o for YBCO disks containing 10 wt.% Ag: $\bigcirc$, single
YBCO disk, $\blacksquare$, YBCO disk-pair. In both cases a
bandage made of a steel tube filled with epoxy was used
(after Fuchs *et al.* 2000).

expansion than YBCO in the a, b plane resulting in a
compressive stress after cooling the sample from
300 K to the measuring temperature $\leqslant 77$ K. Using a
steel tube, the trapped field of YBCO disks with silver
inclusions could be enhanced to values of $B_o = 11.4$ T
(at 17 K) and of $B_o = 14.3$ T (at 22 K) on the surface
of a single YBCO sample, and in the gap between two
YBCO samples, respectively (Fig. 7) (Fuchs *et al.*
2000). In both cases, the YBCO disks had a diameter
of 25 mm.

For comparison, trapped fields up to 10.1 T at 42 K
have been reported by Weinstein *et al.* (1996) for a
YBCO mini-magnet without silver additions and
without mechanical reinforcement. This mini-magnet
consisted of stacked irradiated YBCO tiles.

6. Levitation Forces

One of the most fascinating features associated with
HTS is the stable levitation of a permanent magnet
over a bulk HTS. This levitation is completely pas-
sive, because the magnetic flux surrounding the per-
manent magnet is pinned by defects within the
superconductor. On the other hand, stable levitation
is not possible for two permanent magnets and,
therefore, conventional magnetic bearings require
an active feedback control in order to stabilize the
levitation. Passive superconducting bearings consist-
ing of a superconductor and a permanent magnet are
one of the most promising applications of bulk
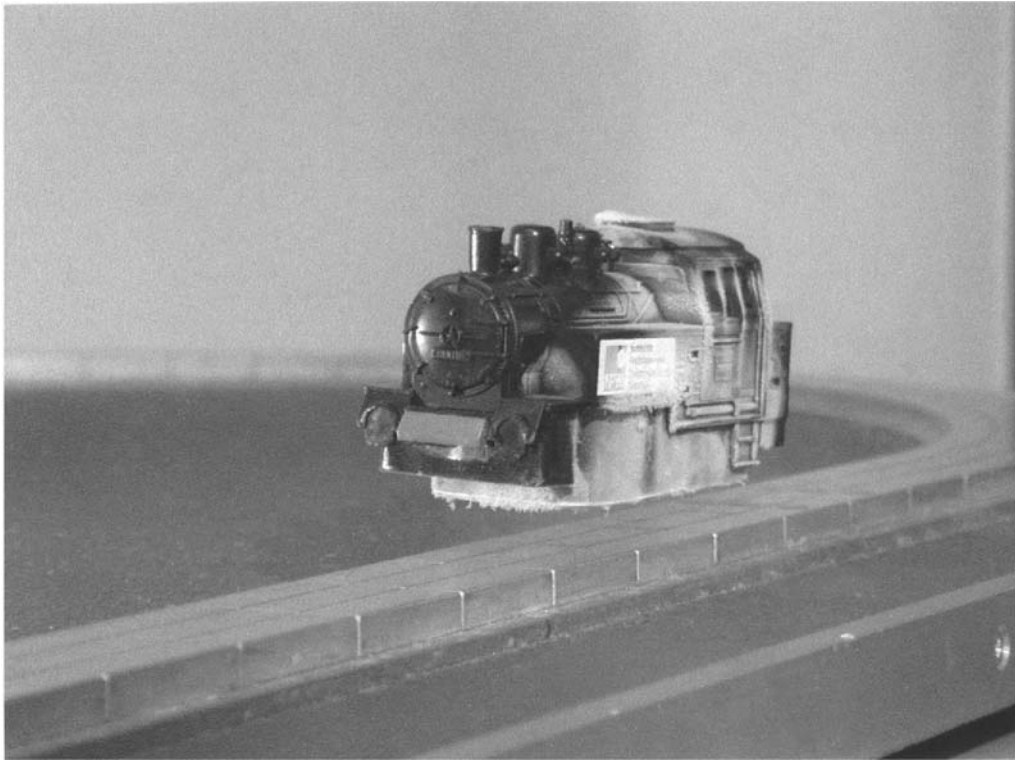
Figure 8
Model railway with steam locomotive equipped with two superconducting permanent magnets and cooled with liquid nitrogen as demonstration of stable levitation.

YBCO. They can be used in flywheels for energy storage, in motors for liquid gas pumps and for transportation systems (see *Superconducting Permanent Magnets: Potential Applications*). The possibility of linear transportation is nicely demonstrated by a model railway, where an old-fashioned steam locomotive equipped with superconducting permanent magnets and cooled with liquid nitrogen runs contactless and frictionless on a magnetic track (Fig. 8).

The levitation force between a permanent magnet and a superconductor cooled in the field of the magnet and containing a trapped magnetic flux can be written as

$$F \propto j_c R \mathrm{d}B/\mathrm{d}x \qquad (3)$$

where R is the size of the current loops in the superconductor and $\mathrm{d}B/\mathrm{d}x$ is the field gradient produced by the permanent magnet within the superconductor.

As the superconductor approaches the permanent magnet after zero field cooling, the repulsive levitation force increases and reaches a maximum value for a small distance. Typical values of the maximum levitation force F between a samarium–cobalt permanent magnet (diameter 25 mm) and YBCO disks are between 50 and 90 N (Gruss *et al.* 1999) at 77 K. The corresponding levitation pressure F/A (A = area of the permanent magnet) varies between 10 and 18 N cm^{-2}.

The levitation pressure of this type of superconducting magnetic bearings is mainly limited by the surface field of the available permanent magnets, which is lower than the maximum trapped field of YBCO at 77 K. Therefore, the bulk YBCO can not be magnetized up to the maximum value of the trapped field, especially in the temperature range below 77 K, where the trapped field of the superconductor becomes yet higher.

The upper limit of the levitation force achievable for a given permanent magnet would be obtained for an ideal superconductor of infinite size and infinitely large critical current density perfectly shielding the magnetic field of the permanent magnet. The resulting levitation force corresponds to the force between two permanent magnets and is given by (Teshima *et al.* 1996)

$$F_{\max} = AB_s^2/2\mu_o \qquad (4)$$

where B_s is the surface field of the permanent magnet. For a permanent magnet with $B_s = 0.4$ T, the

maximum achievable levitation pressure is $F_{max}/A = B_s^2/2\mu_O = 25\,\mathrm{N\,cm^{-2}}$. The experimental values for YBCO samples mentioned above achieve 50–72% of this upper limit. Much larger levitation pressures up to $5000\,\mathrm{N\,cm^{-2}}$ are expected if a superconducting permanent magnet with a trapped field as high as 11 T were to be used instead of a conventional permanent magnet.

The most important problem which has to be solved in order to realize YBCO magnets for superconducting permanent magnets or for other applications at temperatures lower than 77 K is to magnetize the superconductor. Pulsed magnetic fields can be used for magnetizing YBCO disks, however, large viscous forces act on the penetrating magnetic flux, especially in the case of short rise times ($\sim 1\,\mathrm{ms}$) of the pulsed field. Therefore, (i) higher pulsed fields are needed in order to trap the same magnetic field in the superconductor as by applying a static field and (ii) heat generation due to the rapid motion of magnetic flux strongly reduces the trapped field achievable at temperatures lower than 77 K (Yanagi *et al.* 1998). At 77 K, promising results were achieved by using pulsed fields with a relatively long rise time of 16 ms (Gruss *et al.* 1999).

7. Conclusions

These new superconducting permanent magnets form a new class of ultrahigh performance permanent magnets. The trapped flux density can be higher by an order of magnitude compared to the remanence of the best ferromagnetic permanent magnets (see *Rare Earth Magnets: Materials*). Since stored magnetic energies and forces scale quadratically with the trapped flux density, these new "cold magnets" offer magnetic energies and forces two orders of magnitude higher than conventional magnets, reaching completely new fields of applications accessible for permanent magnets. Two examples are the rotational frictionless support, i.e., superconducting magnetic bearings, and frictionless linear transportation. The latter should allow transportation of extremely heavy goods which can not easily be moved by wheeled systems, like concrete ports or moving bridges. Additionally, contactless transportation, which does not create any wear debris, can be advantageously used in clean rooms in the microelectronics industry (for further reading, see *Superconducting Permanent Magnets: Potential Applications*).

See also: Superconducting Machines: Energy Storage; Magnetic Levitation: Superconducting Bearings

Bibliography

Bean C P 1962 Magnetization of hard superconductors. *Phys. Rev. Lett.* **8**, 250

Fuchs G, Krabbes G, Schätzle P, Gruss S, Stoye P, Staiger T, Müller K-H, Fink J, Schultz L 1997 High trapped fields in bulk $YBa_2Cu_3O_{7-\delta}$ samples at temperatures around 50 K. *Appl. Phys. Lett.* **70**, 117–9

Fuchs G, Schätzle P, Krabbes G, Gruss S, Verges P, Müller K-H, Fink J, Schultz L 2000 Trapped magnetic field larger than 14 Tesla in bulk $YBa_2Cu_3O_{7-x}$. *Appl. Phys. Lett.* **76**, 2107–9

Garwin E L, Rabinowitz M, Frankel D J 1973 Permanent multipole magnetic fields stored in superconductors. *Appl. Phys. Lett.* **22**, 599–600

Gruss S, Fuchs G, Krabbes G, Schätzle P, Fink J, Müller K-H, Schultz L 1999 High trapped fields in melt-textured $YBa_2Cu_3O_{7-\delta}$. *IEEE Trans. Appl. Supercond.* **9**, 2070–3

Ikuta H, Mase A, Mizutani U, Yanagi Y, Yoshikawa M, Itoh Y, Oka T 1999 Very high trapped field in melt-processed SmBaCuO. *IEEE Trans. Appl. Supercond.* **9**, 2219–22

Johansen T H 1999 Flux-pinning-induced stress and strain in superconductors: Case of a long circular cylinder. *Phys. Rev. B* **60**, 1–14

Johansen T H 2000 Flux-pinning-induced stress and magnetostriction in bulk superconductors. *Supercond. Sci. Technol.* **13**, R121–37

Klupsch T, Strasser T, Habisreuther T, Gawalek W, Gruss S, May H, Palka R, Mora Serrano F J 1997 Field mapping characterization for axially magnetized superconducting cylinders in the remanent critical state: theory and experiment. *J. Appl. Phys.* **82**, 3035–41

Krabbes G, Schätzle P, Bieger W, Fuchs G, Wiesner U, Stöver G 1997 Thermodynamically controlled melt processing to improve bulk materials. *IEEE Trans. Appl. Supercond.* **7**, 1735–8

Krabbes G, Fuchs G, Schätzle P, Gruss S, Park J W, Hardinghaus F, Stöver G, Hayn R, Drechsler S-L, Fahr T 2000 Zinc doping of $YBa_2Cu_3O_7$ in melt-textured materials: peak effect and high trapped fields. *Physica C* **330**, 181–90

McGuinn P 1995 Bulk processing and charactrization of $YBa_2Cu_3O_{6+x}$. In: Donglu S (ed.) *High Temperature Superconducting Materials Science and Engineering*. Elsevier, Amsterdam, pp. 345–82, Chap. 8

Murakami M 1992 Melt processing. In: Murakami M (ed.) *Melt Processed High-Temperature Superconductors*. World Scientific, Singapore, pp. 21–44, Chap. 3

Murakami M 1993 Melt processing, flux pinning and levitation. In: Jin S (ed.) *Processing and Properties of High T_c Superconductors*. World Scientific, Singapore, Vol. 1, pp. 215–68, Chap. 6

Paker A P 1981 *The Mechanics of Fracture and Fatigue, An Introduction*. E & F N Spon, London

Rabinowitz M, Arrowsmith H W, Dahlgren S D 1977 Dependence of maximum trappable field on superconducting Nb_3Sn cylinder wall thickness. *Appl. Phys. Lett.* **30**, 607–9

Ren Y R, Weinstein R, Liu J, Sawh R P, Foster C 1995 Damage caused by magnetic pressure at high trapped field in quasi-permanent magnets composed of melt-textured YBaCuO superconductors. *Physica C* **251**, 15

Schätzle P, Krabbes G, Gruss S, Fuchs G 1999 YBCO/Ag bulk material by melt crystallization for cryomagnetic applications. *IEEE Trans. Appl. Supercond.* **9**, 2022–5

Teshima H, Morita M, Hashimoto M 1996 Comparison of the levitation forces of melt-processed YBaCuO superconductors for different magnets. *Physica C* **269**, 15–21

Walter H, Delemare M P, Bringmann B, Leenders A, Freyhardt H C 2000 Melt-textured YBaCuO with high trapped fields up to 1.3 T at 77 K. *J. Mater. Res.* **15**, 1231–4

Weinstein R, Liu J, Ren Y, Sawh R, Parks D, Foster C, Obot V 1996 Very high trapped fields: cracking, creep, and pinning

centers. In: Batlogg B, Chu C W, Chu W K, Gubser D U, Müller K A (eds.) *Proc. 10th Anniversary HTS Workshop on Physics, Materials and Applications.* World Scientific, Singapore, pp. 625–8

Weinstein R, Ren Y, Liu J, Chen I G, Sawh R, Parks D, Foster C, Obot V 1994 Progress in J_c, pinning and grain size for trapped field magnets. In: Fujita T, Shiohara Y (eds.) *Advances in Superconductivity IV.* Springer, Tokyo, pp. 855

Wenger C. 2000 Untersuchung der thermodynamischen Stabilität des schmelztexturierten $YBa_2Cu_3O_{7-x}$—Materials (Investigation of the thermodynamic stability of melt-textured $YBa_2Cu_3O_{7-x}$ material), Ph.D. thesis. Technical University Dresden, Germany

Yanagi Y, Itoh Y, Yoshikawa M, Oka T, Terasaki A, Ikuta H, Mizutani U 1998 Pulsed-field magnetization of YBaCuO superconducting bulk magnet cooled by refrigerator. In: Osamura K, Hirabayashi I (eds.) *Advances in Superconductivity X.* Springer, Tokyo, pp. 941–4

G. Fuchs and L. Schultz
Institut für Metallische Werkstoffe, Dresden, Germany

Superconducting Radiation Sensor Applications: Detectors and Mixers

Superconducting detectors and mixers belong to the wide class of small-scale applications of superconductivity. They are used in measurements of weak radiating electromagnetic fields and nuclear radiation. Superconductivity offers various basic principles for effective radiation detection. Several devices have been developed, exploiting the different features of the condensed matter in the superconducting state:

(i) heating by the absorption of radiation, which is sensitively detected by a superconducting device;

(ii) creation of nonthermal excitations by the absorption of radiation and their collection by a superconducting device;

(iii) capability of active superconducting devices of processing high-frequency electromagnetic waves.

The most relevant types of superconducting sensors for radiation detection are microcalorimeters, superconducting tunnel junction detectors, and mixers. Superconducting detectors are developed for visible, ultraviolet, and x-ray single-photon detection. They can also be applied in detecting large-mass molecules or nuclear radiation, like electrons, α-particles, and neutrons. Mixers are typically used in measurements of electromagnetic radiation in the infrared and millimeter wavelength regions.

The major motivation for using superconducting sensors is their superior sensitivity. The detection of very small energy deposition (high sensitivity) with high energy resolution (i.e., the capability of distinguishing slightly different energies) is achieved by operating the sensors at low temperatures, where lattice vibrations (phonons) and excitation energy are more than one hundred times smaller.

The need for detectors with advanced performance is a continuous request from frontier experiments in elementary particle physics and astronomy. The progress in the development of both sensors and complementary technologies (cryogenics, in particular) opens the possibility of using these sensors in a novel generation of spectrometers for microanalysis of materials in civil applications (laboratory and industrial measurements).

1. Superconducting Microcalorimeters

Microcalorimeters have been developed for x-ray astronomy to detect single-photon events from faint sources in the energy range 0.1–10 keV (1 eV = 1.602×10^{-19} J). A microcalorimeter consists of an absorber in thermal contact with a thermometer (see Fig. 1). The energy (E) of the incident radiation, typically one photon, is converted to heat in the absorber, leading to a temperature rise $\Delta T = E/C$, where C is the total heat capacity of the absorber and the thermometer. The temperature rise is read by the thermometer and indicates the radiation energy. Any microcalorimeter must have a low heat capacity mass to absorb incident radiation, a weak link to a low-temperature heat sink which provides the thermal isolation needed for a temperature rise to occur, and a thermometer with a high sensitivity to measure change in temperature. In a microcalorimeter, one exploits the fact that the heat capacity of superconductors or pure dielectric crystals becomes small at low temperatures (50–100 mK). Thus, the temperature rise can be measured by resistive thermometers (thermistors), for which a change in the electrical resistance accompanies a change in temperature. Thermistors are characterized by their sensitivity, $\alpha = \mathrm{d}(\log R)/\mathrm{d}(\log T)$, where R is the electrical resistance and T is the temperature. In an ideal thermistor-based calorimeter, the energy resolution, ΔE, scales as $T(C/|\alpha|)^{1/2}$ so that low operating temperatures and heat capacities contribute to achieve good energy resolution.

Two types of thermistors are used in microcalorimeters: doped semiconductor thermistors and transition edge sensors (TES). Microcalorimeters of neutron transmutation doped (NTD) germanium thermistors paired with superconducting tin absorbers have provided an energy resolution of $\Delta E = 5.2$ eV at $E = 5.9$ keV (Alessandrello *et al.* 1999). TES are thin superconducting films deposited on the absorber. The temperature rise is measured by the TES which works in the region of its normal-to-superconductor phase transition (see *Superconducting Materials, Types of*), where the temperature dependence of the resistance is steep. TES are made from superconductors (aluminum, titanium, tungsten, or proximity bilayers, like Al/Ag, Ir/Au, Mo/Au), with transition temperatures in the range 50–100 mK (see Fig. 2).
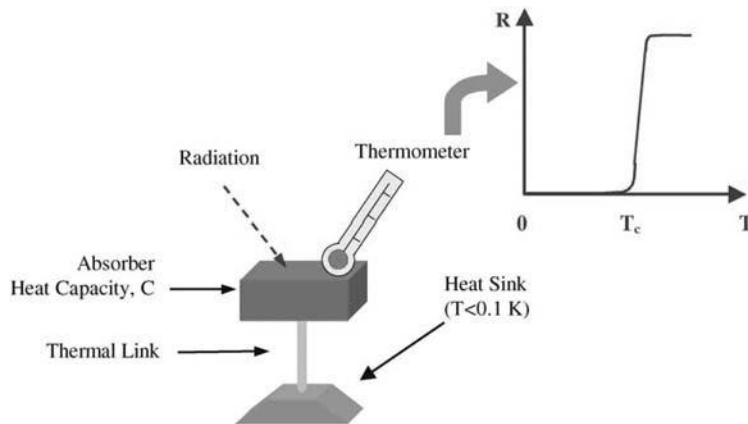
Figure 1
Sketch of a microcalorimeter with the resistance vs. temperature curve of a TES thermometer.
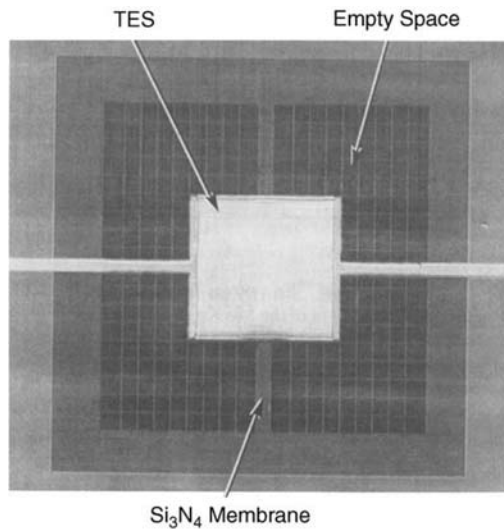
Figure 2
A Mo–Cu TES microcalorimeter on a Si_3N_4 membrane patterned as a "fly-swatter." The TES has dimensions $400 \times 400\,\mu m$. The large bars are $50\,\mu m$ wide, and the small bars are $5\,\mu m$ wide on $50\,\mu m$ centers. The device was fabricated at NIST, Boulder, CO, USA (from Irwin *et al.* 2000, reprinted with permission from Elsevier Science Ltd.).

Because the transition from the normal to the superconducting state occurs over a very narrow temperature range, a TES is a much more sensitive thermometer than a semiconductor thermistor. The advantage of TES-based devices is that a large volume of normal metals, off-limits to semiconductor-based microcalorimeters, can be used. The rapid and efficient thermalization of metal absorbers allows better energy resolution and faster detector response.

TES microcalorimeters achieved energy resolution $\Delta E < 4.7\,eV$ at $E = 6\,keV$ and $\Delta E = 2.38\,eV$ at $E = 1.5\,keV$, with count rates in excess of 500 counts per second.

2. Superconducting Tunnel Junction Detectors

A superconducting tunnel junction (STJ) consists of two superconducting thin films ($\sim 200\,nm$ in thickness) separated by a very thin insulating barrier ($\sim 1\,nm$ in thickness) (see the sketch in Fig. 3). Typically used superconductors are niobium, tantalum, or aluminum. Normal electrons (so-called quasiparticles) can flow across the barrier via quantum tunneling processes. In STJ detectors, one exploits the fact that the energy gap of a superconductor is of the order of millielectronvolts, so that millions of electrons can be created after a complex energy cascade following the absorption of a single x-ray photon. The amount of created charge is proportional to the energy of the absorbed radiation. The absorber of an STJ detector can be either one of the two junction electrodes or a separate superconductor which injects the STJ with the excitations in the form of electrons or high-energy phonons.

The nonequilibrium electronic charges produced by the radiation diffuse and flow across the tunneling barrier of the STJ, where they are measured as an extra tunneling current. The tunneling barrier is made transparent to improve tunneling so that STJs are physically the same as the more widely known Josephson tunnel junctions (see *Josephson Junctions: High-T$_c$*; *Josephson Junctions: Low-T$_c$*), but the Josephson supercurrent is suppressed by applying a weak magnetic field. STJs are biased in the subgap region of the current–voltage characteristics and are operated at very low temperature ($T \sim T_c/10$) in order to reduce the thermal population of electrons and the recombination
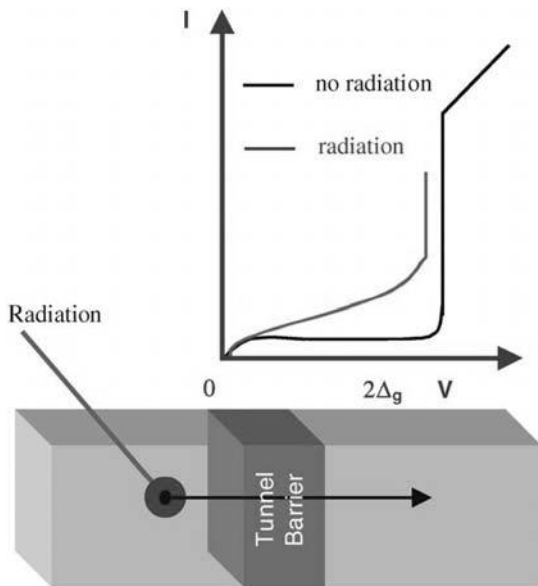
Figure 3
Sketch of a STJ with the corresponding current–voltage (*I–V*) curves with and without radiation. The red curve shows the increased tunneling current with respect to the dark condition (black curve).

of the extra electrons. Compared with semiconductor detectors, the very high number of charges generated gives rise to improved energy resolution and detection threshold. Intrinsic energy resolution of few electronvolts at 6 keV is possible and 12 eV has been measured in Al-STJ (Angeloher *et al.* 2001).

STJs are nonthermal, single-particle detectors. In nonthermal detectors, the nonequilibrium distribution of excitations is detected before it relaxes. This feature makes STJs particularly suitable in high-count-rate applications (5000 counts per second can be achieved). Similarly to TES, STJ detectors were developed to answer the demanding request of x-ray astronomy for high-energy resolution detectors. However, they are also capable of detecting single photons with lower energy, like ultraviolet and visible photons. At these short wavelengths, thousands of electrons are still created in a superconductor, sufficient to generate an appreciable pulse signal. Imaging can be obtained by arrays of STJ pixels (see Fig. 4).

3. Superconducting Mixers for Infrared Detection

Infrared and millimeter wave radiation detectors are realized by several superconducting devices, like STJs (in this context often called superconductor insulator superconductor (SIS) junctions), Josephson junctions, or hot electron bolometers. Applications in radioastronomy, in passive molecular spectroscopy
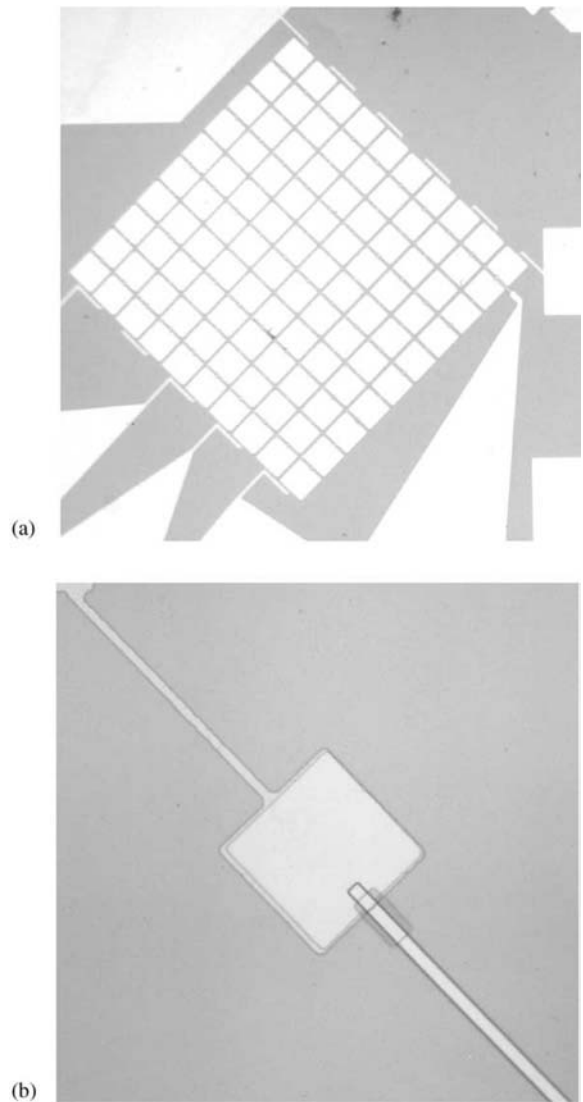
Figure 4
(a) A 10×10 array of STJs. Each STJ has dimensions $100 \times 100 \, \mu m$. (b) A single STJ detector on a silicon substrate patterned as an "island." The STJ has dimensions $50 \times 50 \, \mu m$, and the narrow wirings are $3 \, \mu m$ wide. (The devices were fabricated at CNR-Istituto di Cibernetica, Pozzuoli, Naples, Italy.)

for environmental monitoring and air quality control, have been developed. Infrared and millimeter wavelengths correspond to energy values too low ($\sim meV$) for single photon detection and to frequencies too high ($\sim 0.1 \, GHz$–$10 \, THz$) where amplification and processing of electronic signals are difficult. In this case a useful concept is the mixing to down-convert high-frequency (HF) signals. In heterodyne mixers

the HF signal, which has to be detected, is mixed with a laboratory local oscillator (LO), at a slightly different frequency, to give a low difference frequency signal (IF) that can be amplified and studied by conventional devices. In the output signal the information about the frequency and the phase of the incoming signal is preserved. The spectral resolution is limited only by the line width of the LO. The conversion efficiency (ratio between the power of incoming signal to the power at IF signal) and the noise temperature (equivalent noise level added by the mixer during the conversion process) characterize the performance of the mixer. Superconducting mixers have one common advantage over conventional (Schottky) mixers, namely extremely low LO power requirements (of the order of nanowatts).

SIS mixers are the technology of choice in the range 40–800 GHz. These receivers are now in daily use in several millimeter-wavelength telescopes in observatories. SIS mixers are based on the photon-assisted tunneling process and exploit the strong nonlinearity of the SIS current–voltage characteristics. SIS mixers exhibit the best performance (conversion efficiency close to unity and noise temperature close to the quantum limit, $T_n = 50 - 170$ K). However, their operation is limited to the frequency range below the gap frequency of superconductor. This is about 700 GHz for niobium and slightly above 1 THz for NbN.

Josephson effect mixers, with photon-assisted tunneling of Cooper pairs of electrons as the underlying operational mechanism, show moderate performance ($T_n = 1200 - 2000$ K), but they can be fabricated using the high transition temperature superconductors (HTS). HTS allow the use of liquid nitrogen ($T = 77$ K) as coolant or cryogen-free cryocoolers, so that they are specifically indicated for space applications.

Hot-electron bolometers (HEBs) can also be operated as mixers in heterodyne receivers. Intrinsically, frequency-independent performance and no gap limitation predestinates these type of mixers for operation at very high frequencies, around and well above 1 THz. Two concepts of HEB mixer materials are exploited: phonon-cooled bolometers (relying typically on NbN, $T_n = 400 - 2000$ K) and diffusion-cooled HEB (fabricated mostly of Nb, $T_n = 650$ K).

4. Conclusions

Superconducting sensors are undergoing continuous evolution. The above overviewed sensors are not exhaustive of devices under development. The reader is referred to the literature for a complete review of the subject (Booth *et al.* 1996, De Korte and Peacock 2000)

An interesting perspective for applications is represented by spectrometry for high-sensitivity microanalysis. This is due to the fact that both superconducting microcalorimeters and STJ detectors have surpassed the ultimate energy resolution of semiconductor detectors ($\Delta E = 120$ eV at $E = 6$ keV), which are typically used in x-ray fluorescence energy-dispersive spectrometers (EDS). The improved energy resolution of superconducting sensors combined with their fast count rate makes possible the realization of spectrometers having the energy resolution of Bragg crystals used in wavelength-dispersive spectrometers as well as the fast operation mode and the simplicity of use of EDS-like instruments (Wollman *et al.* 1997). Furthermore, the detection principle of TES and STJ detectors is heat transfer rather than ionization. This opens the possibility of an efficient detection of very slow massive ions like macromolecules (biopolymers, proteins, DNA fragments) and neutral particles (neutrons). The sensitivity allows high throughput, even in the presence of dilute samples with traces of significant elements. To exploit this property, time-of-flight mass spectrometers equipped with superconducting detectors have been proposed (Hilton *et al.* 1998).

See also: Radiation and Particle Detectors; SQUIDs: The Instrument; Superconducting Thin Films: Materials, Preparation, and Properties; Superconducting Thin Films: Multilayers

Bibliography

Alessandrello A, Beeman J W, Broffiero C, Cremonesi O, Fiorini E, Giuliani A, Haller E E, Monfardini A, Nucciotti A, Pavan M, Pessina G, Previstali E, Canotti L 1999 High energy resolution bolometer for nuclear physics and x-ray spectroscopy. *Phys. Rev. Lett.* **82**, 513–6

Angeloher G, Hettl P, Huber M, Jochum J, Feilitzch F v, Mossbauer R L 2001 Energy resolution of 12 eV at 5.9 keV from AI-superconducting tunnel junction detectors. *J. Appl. Phys.* **89**, 1425–9

Booth N E, Cabrera B, Fiorini E 1996 Low temperature particle detectors. *Annu. Rev. Nucl. Part. Sci.* **46**, 471–532

De Korte P, Peacock T (eds.) 2000 *Proc. 8th Int. Workshop on Low Temperature Detectors. Nucl. Instr. Methods A* **444**

Hilton G C, Martinis J M, Wollman D A, Irwin K D, Dulcie L L, Gerber D, Gillevet P M, Twerenbold D 1998 Impact energy measurement in time-of-flight mass spectrometry with cryogenic microcalorimeters. *Nature.* **391**, 672–5

Irwin K D, Hilton G C, Martinis J M, Deiker S, Bergren N, Nam S W, Rudman D A, Wollman D A 2000 *Proc. 8th Int. Workshop on Low Temperature Detectors. Nucl. Instr. Methods A* **444**, 184–7

Qing Hu, Richards P L 1990 Quasiparticle mixers and detectors. In: Ruggiero S T, Rudman D A (eds.) *Superconducting Devices.* Academic Press, London, Chap. 5, pp. 169–96

Wollman D A, Irwin K D, Hilton G C, Dulcie L L, Newbury D E, Martinis J M 1997 High-resolution, energy-dispersive microcalorimeter spectrometer for x-ray microanalysis. *J. Microscopy* **188**, 196–222

R. Cristiano
CNR-Institute of Cybernetics, Naples, Italy

Superconducting Thin Films: Materials, Preparation, and Properties

The crystal structures of high T_c superconductors are described in this article together with the deposition methods used to produce high-quality films of these materials. This article complements *High-temperature Superconductors: Thin Films and Multilayers*. It is impossible to include all of the important work contributed by the large number of groups active in this rapidly progressing field. Additional information can be found in reviews of high T_c materials and depo-

sition methods (Humphreys *et al*. 1990, Eckstein and Bozovic 1995, Schlom and Harris 1995, Matijasevic and Bozovic 1996, Fisk and Sarrao 1997, Wördenweber 1999).

1. Materials

1.1 Crystal Structures and Types of Building Layers

All high T_c superconductors have perovskite-related structures. The crystal structure of perovskite ($CaTiO_3$) and some of the better-known high T_c superconductors are shown in Fig. 1. All high T_c
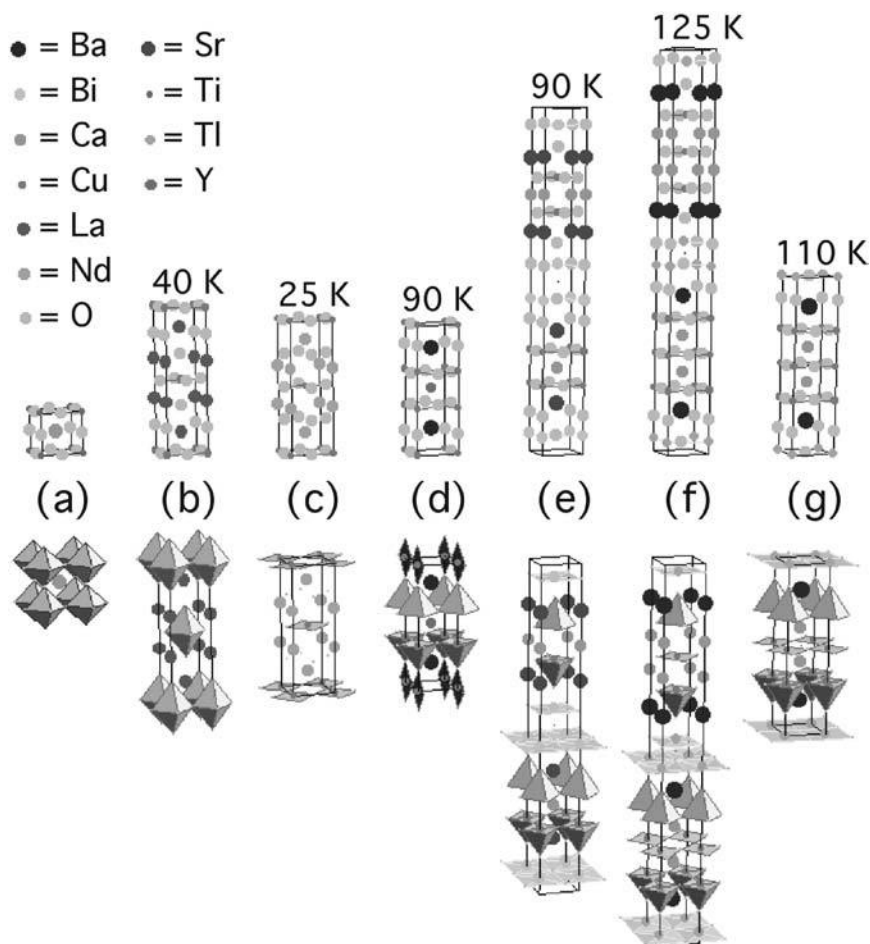
Figure 1
Crystal structure of (a) perovskite ($CaTiO_3$) and some of the better known high T_c superconductors: (b) $(La,Sr)_2CuO_4$, (c) $(Nd,Ce)_2CuO_4$, (d) $YBa_2Cu_3O_{7-\delta}$, (e) $Bi_2Sr_2CaCu_2O_8$, (f) $Tl_2Ba_2Ca_2Cu_3O_{10}$, and (g) $TlBa_2Ca_2Cu_3O_9$. Two equivalent representations of these crystal structures are shown: the atomic positions (above) and the copper coordination polyhedrons (below). The oxygen atoms occupy the vertices of the copper coordination polyhedrons. The tetragonal subcells of the $(La,Sr)_2CuO_4$ and $Bi_2Sr_2CaCu_2O_{8+\delta}$ structures are shown for clarity and to illustrate the similarities between these perovskite-related phases. The approximate superconducting transition temperatures are also shown.

structures can be assembled from a relatively small number of more fundamental layer types (Tokura and Arima 1990), referred to as building layers (Schlom and Harris 1995). A common feature of the crystal structures of all known copper-containing high T_c superconductors is the presence of CuO_2 layers. The CuO_2 layers are separated from one another along the c-axis of the crystal structure by various intervening layers, the known types of which are shown in Fig. 2. By stacking the building layers shown in Fig. 2 on top of one another along the c-axis direction, all known copper-containing high T_c structures can be assembled.

There is only one other known oxide superconductor with a relatively high T_c that does not contain CuO_2 layers, $(Ba,K)BiO_3$, which has a T_c of about 30 K (Cava *et al*. 1988). Like the structurally related solid solution $Ba(Pb,Bi)O_3$ with T_c of approximately 13 K (Sleight *et al*. 1975), $(Ba,K)BiO_3$ has a simple cubic perovskite structure, shown in Fig. 1, with bismuth occupying the octahedrally coordinated titanium position and barium and potassium occupying the larger calcium site. From a building layer standpoint, $(Ba,K)BiO_3$ consists of alternating BiO_2 and $(Ba,K)O$ building layers.

Although high T_c phases are commonly referred to by formulas implying that they are stoichiometric, e.g., $Bi_2Sr_2CaCu_2O_8$, this is an oversimplification. In reality, significant cation mixing, anion vacancies, or cation vacancies often occur within the building layers, with several percent mixing quite common in some layers, although not within the CuO_2 layers. For example, site-sensitive structural refinement of a single crystal of the high T_c superconductor Bi_2Sr_2-$CaCu_2O_8$ has determined that its overall composition
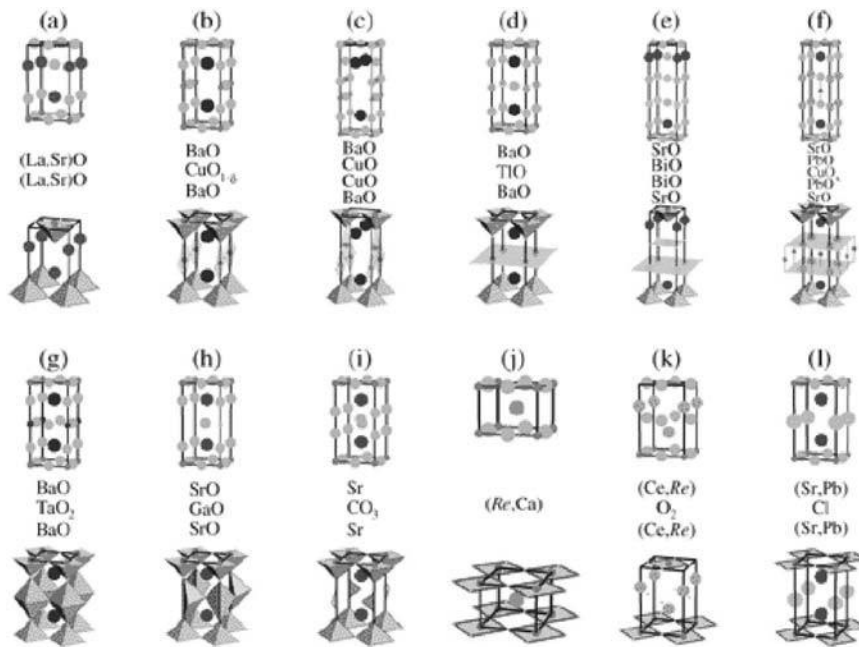
Figure 2
Building layers of all known layered CuO_2 structures: (a) [(La,Sr)O–(La,Sr)O] or [(Sr,Ca)(Br,Cl)–(Sr,Ca)(Br,Cl)]*, (b) [BaO–CuO$_{1-\delta}$–BaO], (c) [BaO–CuO–CuO–BaO], (d) [BaO–TlO–BaO] or [BaO–HgO$_x$–BaO] or [SrO–(Bi,Cu)O$_x$–SrO] or [SrO–(Bi,Cd)O–SrO] or [SrO–(Pb,Sr)O–SrO] or [SrO–(Pb,Cu)O$_x$–SrO] or [SrO–(Pb,Cd)O–SrO] or [SrO–(Ce,Cu)O$_x$–SrO]* or [SrO–(Ce,Cd)O–SrO], (e) [BaO–TlO–TlO–BaO] or [BaO–HgO$_x$–HgO$_x$–BaO] or [SrO–BiO–BiO–SrO] or [(Ba,Sr)O–(Pb,Cu)O$_x$–(Pb,Cu)O$_x$–(Ba,Sr)O], (f) [SrO–PbO–CuO$_x$–PbO–SrO], (g) [LaO–SnO$_2$–LaO]* or [BaO–TaO$_2$–BaO]* or [SrO–TaO$_2$–SrO] or [SrO–NbO$_2$–SrO], (h) [SrO–GaO–SrO] or [SrO-CoO–SrO]* or [SrO–AlO–SrO]*, (i) [Sr–CO$_3$–Sr] or [(*Re*,Ba)–BO$_3$–(*Re*,Ba)] where *Re* is a rare earth ion, (j) [(*Re*,Ca)], (k) [(Ce,*Re*)–O$_2$–(Ce,*Re*)], and (l) [(Sr,Pb)–Cl–(Sr,Pb)]*. The tetragonal subcell of each building layer is outlined. CuO_2 layers are shown above and below each building layer to illustrate their attachment positions. Partial substitution for the constituents of these basic building layers is frequently possible and may be used for doping purposes (e.g., Bi ↔ Pb, Tl ↔ Pb, Sr ↔ Ba, Sr ↔ La, Sr ↔ Ca, Ca ↔ Re). Most of these building layers are constituents of the copper-containing high T_c superconductors discovered to date. Those intervening layers known to occur between CuO_2 layers, but so far not constituents of superconducting structures, are marked with an asterisk (reproduced by permission of Noyes Publications from ''Molecular Beam Epitaxy: Applications to Key Materials,'' 1995, pp. 505–622).

is $Bi_{2.15}Sr_{1.92}Ca_{0.75}Cu_2O_{8.1}$ with the "calcium site" occupied by 75% calcium, 19% strontium, and 6% bismuth (Petricek *et al.* 1990, Coppens *et al.* 1991). Other sites in the crystal structure also show cation mixing, although to a lesser extent.

Nonstoichiometry is an important aspect of high T_c superconductors. For some phases, the adjustable nonstoichiometry (solid solution) within a particular building layer is explicitly stated, e.g., $(La,Sr)_2CuO_4$, $(Nd,Ce)_2CuO_4$, $YBa_2Cu_3O_{7-\delta}$, and $(Ba,K)BiO_3$. As described below, nonstoichiometry in the building layers provides charge carriers via chemical doping. Pure $Bi_2Sr_2CaCu_2O_8$ would not be superconducting, since the average oxidation state of copper would be exactly $+2$ and there would be no charge carriers, whereas $Bi_{2.15}Sr_{1.92}Ca_{0.75}Cu_2O_{8.1}$ is superconducting and the average oxidation state of copper is $+2.21$.

1.2 Chemical Doping

In addition to structural control, realizing the optimal carrier concentration in the CuO_2 layers is a crucial part of the synthesis of high T_c materials. The building layers surrounding the CuO_2 layers serve as "charge reservoirs" to dope the CuO_2 layers by chemical means (Cava 1990). Doping the CuO_2 layers with holes or electrons is a necessary, although not sufficient, condition for achieving superconductivity in these materials. A convenient method for charge counting to assess chemical doping is through the use of the concept of oxidation states. Note that the oxidation state of an ion is not the same as the true charge on the ion. For simplicity, the oxidation state of an oxygen ion (O) is defined to be –2; hence, in order to quantify the doping of the CuO_2 layers, it is sufficient to know the oxidation state of copper. The average oxidation state of copper is determined from the phase composition, the standard oxidation states of the remaining ions (e.g., Sr^{2+}, La^{3+}, etc.), and the condition of charge neutrality. For example, in $La_{2-x}Sr_xCuO_4$ the average oxidation state of copper is $(2+x)$, and in $Nd_{2-x}Ce_xCuO_4$ (where Ce^{4+} is present) it is $(2-x)$.

In the parent compounds, La_2CuO_4 and Nd_2CuO_4, where no chemical doping is present ($x=0$), the oxidation state of copper is $+2$ and the compounds are not superconducting. As x increases and the parent compounds are doped, charge carriers (holes) enter the CuO_2 layers and the average oxidation state of copper deviates from $+2$. Some high T_c compounds contain elements that may assume a variety of oxidation states (e.g., bismuth, lead, thallium, or mercury); these must be known in order to determine the oxidation state of copper in the CuO_2 layers. The same is true for compounds with nonequivalent copper sites, e.g., those that contain $CuO_{1-\delta}$ "chains" (see Fig. 2(b)).

The oxidation state of copper is greater than 2 for *p*-type superconductors and less than 2 for *n*-type superconductors. The amount of charge transferred from the surrounding (charge reservoir) building layers to the CuO_2 layers is given by the deviation of the oxidation state of copper from $+2$. One can also talk of the deviation of the oxidation state of each CuO_2 unit from -2: $[CuO_2]^{-2+\delta}$, where δ is positive for hole-doped (*p*-type) and negative for electron-doped (*n*-type) superconductors. (While the two jargons are mathematically equivalent, the latter may be closer to the physical reality: in high T_c cuprates, the holes in CuO_2 layers reside in states of predominantly O $2p$ character, with relatively small admixture of Cu $3d$ (Nücker *et al.* 1988).) Studies of the maximization of T_c with doping (Tokura *et al.* 1988, Torrance *et al.* 1988, Tokura *et al.* 1989, Shafer and Penney 1990, Rao 1991) have revealed that a maximum T_c for each structure occurs at about $|\delta| \approx 0.2$, as shown in Fig. 3 for several *p*-type superconductors.

1.3 Minimum Oxygen Partial Pressure for $YBa_2Cu_3O_{7-\delta}$ Stability

While some high T_c superconductors are thermodynamically stable at high temperatures and may be quenched to avoid decomposition, others (e.g., $YBa_2Cu_3O_7$) are not stable at any temperature or pressure (Sleight 1991). Their synthesis is commonly achieved by first forming a thermodynamically stable parent structure (e.g., $YBa_2Cu_3O_6$) and subsequently
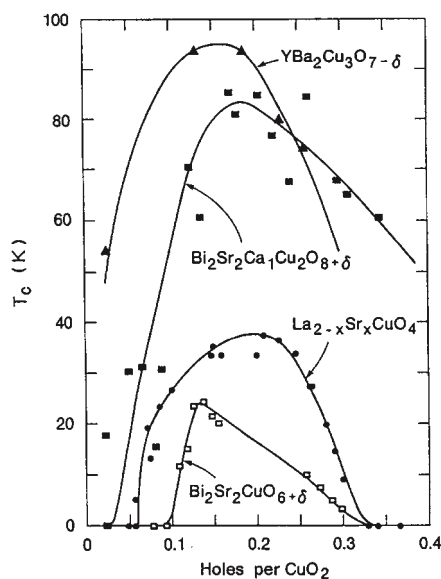
Figure 3
T_c as a function of hole concentration, n_h, per CuO_2 unit for various high T_c superconductors as determined by chemical titration (reproduced by permission of World Scientific from *Mod. Phys. Lett. B* 1992, **6**, 555–71).

altering its composition after the sample has been cooled to a temperature where the parent structure is kinetically prevented from decomposing (e.g., by venting the deposition chamber with oxygen as the film cools from its growth temperature).

It is for this reason that the growth of $YBa_2Cu_3O_{7-\delta}$ films with $\delta \approx 0$ involves a minimum of two steps: (i) formation of the $YBa_2Cu_3O_6$ parent structure and (ii) oxidation of this parent structure to $YBa_2Cu_3O_7$. For $YBa_2Cu_3O_{7-\delta}$, temperatures in the vicinity of 700 °C and 400 °C are used for these two steps, respectively. The latter temperature is low enough to kinetically prevent the decomposition of

$YBa_2Cu_3O_{7-\delta}$, but high enough that the kinetics of oxygen uptake are rapid (Shi and Capone 1988).

The minimum P_{O_2} at which a desired high T_c structure (or its parent structure) is thermodynamically stable is a major constraint in thin-film synthesis by vacuum deposition methods. The lines d_1, m_1, and d_2 shown in Fig. 4 bound the region in which the oxygen-deficient parent structure of $YBa_2Cu_3O_{7-\delta}$ is stable as a function of substrate temperature and oxygen pressure. The lines were established for bulk $YBa_2Cu_3O_{7-\delta}$ (Lindemer *et al.* 1991); however, the region in which $YBa_2Cu_3O_{7-\delta}$ films may be deposited is the same for deposition techniques that use molecular oxygen
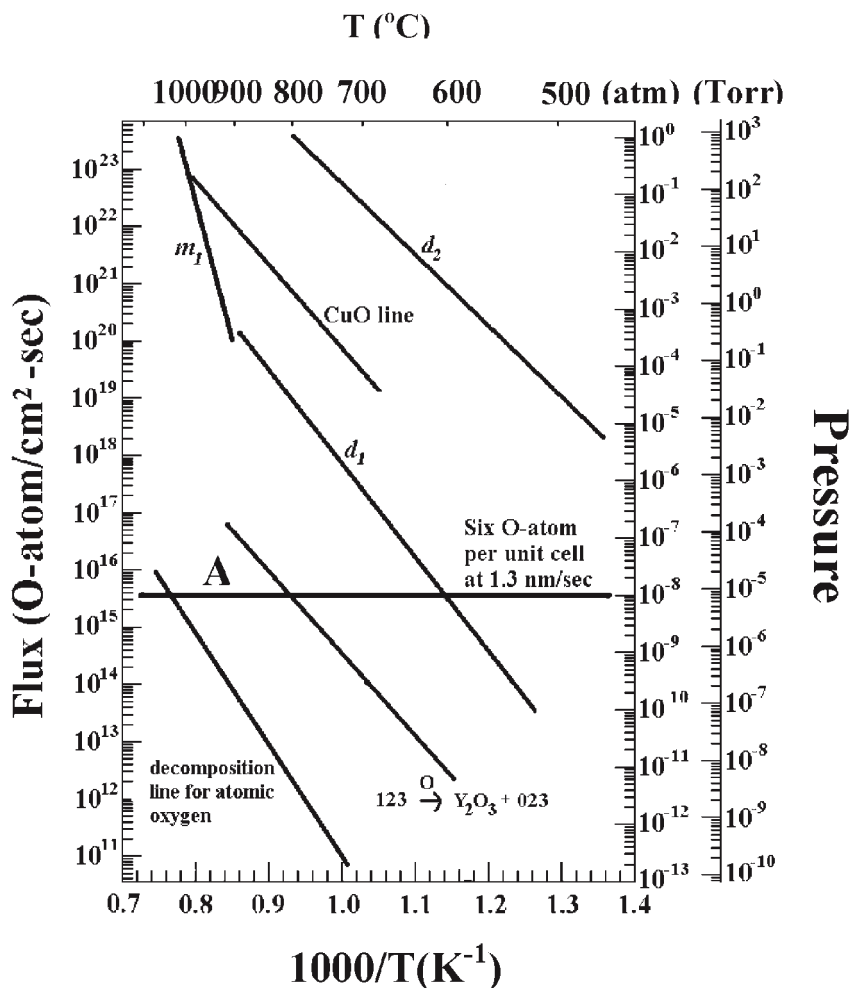
Figure 4
Temperature and oxidant pressure dependence of the region in which $YBa_2Cu_3O_{7-\delta}$ is stable. In molecular oxygen, $YBa_2Cu_3O_{7-\delta}$ is stable in the region bounded by d_1, m_1, and d_2. In atomic oxygen, it is stable in the region between the lowest two lines. The horizontal line A shows where the incident oxidant flux is just six oxygen atoms per unit cell for a $YBa_2Cu_3O_{7-\delta}$ growth rate of 1.3 nms^{-1} (reproduced by permission of Elsevier Science from *J. Cryst. Growth* 2001, **225**, 183–9).

(Hammond and Bormann 1989). This constraint is particularly restrictive in the case of molecular beam epitaxy (MBE) growth, where one must keep the background gas pressure low in order to maintain the long mean free path necessary for MBE. This has necessitated the use of activated oxygen species such as ozone, atomic oxygen, and NO_2 (Nonaka *et al.* 1995, Schlom and Harris 1995).

The approximate lines that bound the region of $YBa_2Cu_3O_{7-\delta}$ stability when grown using atomic oxygen are also shown in Fig. 4. In addition to providing a growth environment that lies within the region in which $YBa_2Cu_3O_{7-\delta}$ is stable, it is also necessary for the oxidant flux to be sufficient to supply the six oxygen atoms per unit cell needed to form $YBa_2Cu_3O_{7-\delta}$. This minimum flux depends on the film growth rate and is shown by line A in Fig. 4 for a $YBa_2Cu_3O_{7-\delta}$ growth rate of $1.3\,nms^{-1}$.

2. Deposition Methods

In what follows, the key techniques for deposition of thin films of high T_c superconductors are described. Note that the quoted deposition conditions are specific for these materials. The key limiting factor here is the necessity to fully oxidize copper, which requires film growth either under a relatively high partial pressure of oxygen, or using more reactive oxidants. This requirement has prompted attempts at deposition under unusual thermodynamic conditions, as well as the development of a range of new hardware tools. The latter include special heaters that are oxidation resistant, mechanisms for shuttling the film during deposition back and forth between neighboring low-pressure (deposition) and high-pressure (oxidation) zones, ozone distillation systems and oxygen plasma sources for delivery of activated oxygen to high-vacuum chambers, differentially pumped analytical tools, etc.

2.1 Sputtering

For the thin-film deposition of high T_c superconductors by sputtering, one makes use of discharge in a gas, typically argon, plus oxygen to oxidize the film. The gas pressure is most frequently kept in the range 50–700 mtorr. The plasma is generated by an electric field, either d.c. or a.c. The ions from the plasma hit the surface of a target and eject from it mainly neutral atoms. These are collected onto a substrate, which is usually heated to promote crystallization. The composition of the film is largely determined by the stoichiometry of the target, which can involve a single element or a mixture of elements.

Soon after the discovery of high T_c superconductors, sputtering from a single compound target was applied with success to grow high T_c superconductor thin films, and this remains one of the simplest and most popular methods to grow such films. Good-quality films of $La_{1.85}Sr_{0.15}CuO_4$, $YBa_2Cu_3O_{7-\delta}$ (both *c*- and *a*-axis oriented), $Bi_2Sr_2CaCu_2O_8$, etc., have been deposited in this way (Suzuki and Murakami 1987, Xi *et al.* 1989, Eom *et al.* 1989, Wagner *et al.* 1993). A common problem is resputtering of the film by negatively charged oxygen ions and the resulting degradation of the film, but this can be overcome by using higher gas pressure (Poppe *et al.* 1988) or off-axis sputtering (Eom *et al.* 1990) as shown in Fig. 5.

More advanced sputtering systems contain several targets. The substrate is moved from target to target to make multilayers. Using multi-element targets and switching from one to another, superlattices have been made of $(YBa_2Cu_3O_{7-\delta})_n(PrBa_2Cu_3O_{7-\delta})_m$ (Triscone *et al.* 1990, Jakob *et al.* 1994) and $(Bi_2Sr_2CaCu_2O_8)_n(Bi_2Sr_2CuO_6)_m$ (Li *et al.* 1994) with remarkable crystalline coherence.

2.2 Pulsed Laser Deposition

In pulsed laser deposition (PLD), a short-wavelength laser—most frequently a KrF excimer laser ($\lambda = 248\,nm$)—is focused onto a target to ablate material. Some of this ablated material reaches and deposits on the substrate (Dijkkamp *et al.* 1987). Like sputtering, PLD is generally done under a substantial pressure, typically 100–300 mtorr, during deposition. Unlike sputtering, argon is not necessary for the process so pure oxygen is usually used. Apart from the stoichiometry of the target, the composition of the resulting film may depend on the target-to-substrate distance, the pressure, the laser fluence (energy per illuminated area on the target per pulse), etc. Nevertheless, PLD is also a very simple technique that generally produces good results fast; in particular, it is well suited to switching from one material to another. A frequent problem is the occurrence of micrometer-sized particulates ("boulders") that are observed in the films. Various solutions to this problem have been proposed, such as using off-axis PLD.

More advanced PLD systems have also been built, and many of these include multiple, interchangeable targets. Efforts have been made to extend PLD to large-area substrates, by rotation and translations of both the target and substrate. Finally, by using ozone or NO_2, either of which is much more reactive than O_2, PLD has been performed under high-vacuum conditions (Tabata *et al.* 1989, Koinuma and Yoshimoto 1994). Here, the key advantage is that one can use *in situ* analytical tools such as reflection high-energy electron diffraction (RHEED) to monitor the crystallinity and morphology of the surface of the growing film. This has been accomplished more simply at the pressures conventionally used for PLD by differential pumping of the RHEED electron gun (see Fig. 6) (Rijnders *et al.* 1997). The growth of individual

(a) 90° Off-Axis
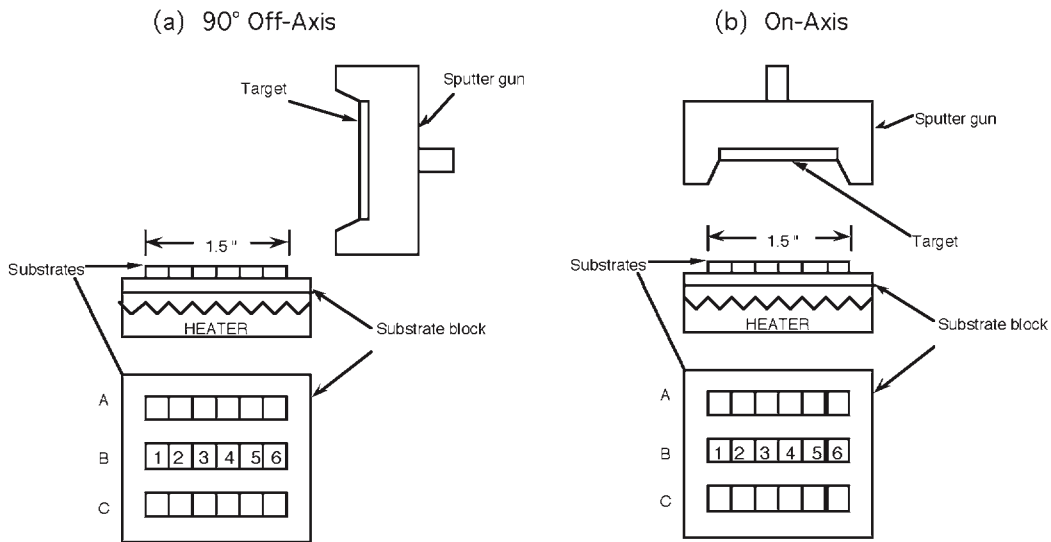
(b) On-Axis

Figure 5
Schematics of (a) 90° off-axis and (b) on-axis sputtering from a single target, onto an array of substrates, to study the compositional spread (reproduced by permission of Elsevier Science from *Physica C*, 1990, **171**, 354–82).
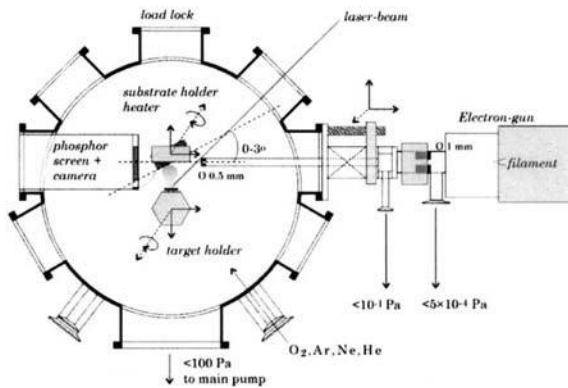
Figure 6
Schematic of a PLD system, equipped with an *in situ* RHEED probe (reproduced by permission of the American Institute of Physics from *Appl. Phys. Lett.* 1997, **70**, 1888–90).

Figure 7
Schematic of a reactive thermal evaporation system, with a high oxygen pressure pocket (reproduced by permission of SPIE from "Oxide Superconductor Physics and Nano-engineering II," 1996, pp. 154–9).

monolayers and the engineering of new structures at the atomic-layer level have been achieved using PLD in this way.

2.3 Reactive Evaporation

The simplest variant of reactive evaporation is the use of resistively heated metallic "boats" as thermal sources of metal atoms. The evaporation rates are controlled by tuning the current, and monitored by quartz crystal microbalances (QCMs). One effective implementation of this technique, shown in Fig. 7, uses a black-body-type rotating disk heater, which has an "oxidation pocket" with a very narrow opening (Kinder *et al.* 1996). This allows for a relatively high pressure inside the oxidation pocket ($\sim 10^{-2}$ torr), and a low pressure in the rest of the chamber ($\sim 10^{-4}$ torr), which extends the lifetime and stability of the thermal evaporation sources. This is the preferred technique for the deposition of uniform $YBa_2Cu_3O_{7-\delta}$ films over large-area wafers (up to 9 in (23 cm) in diameter). The method also has a comparatively high throughput and is cost effective.

2.4 Molecular Beam Epitaxy

The coherence length in high T_c superconductors is very short, a couple of nanometers at most. To fabricate good active devices such as Josephson junctions, one thus needs a capability to deposit ultrathin layers, with perfect interfaces. This becomes even more critical when one is concerned with large-scale integration where the devices have to get denser and smaller, while the uniformity demands increase.

One of the most successful techniques that enables one to control the film deposition at an atomic-layer level, for high T_c superconductors as well as for other complex oxides, is reactive MBE (Eckstein and Bozovic 1995, Schlom and Harris 1995). It is similar to reactive evaporation, except that (i) the pressure during deposition must be low enough such that the mean free path of the depositing species (atoms or molecules) is longer than the source-to-substrate distance and (ii) the chamber walls must be cold enough such that the metal atoms or molecules that collide with them are not re-emitted. Under such conditions (typically 10^{-5} torr or less), the supply of the desired species, in whatever overlapping or nonoverlapping order desired, can be precisely controlled.

The molecular beams are chopped by mechanical shutters, and the timing is computer controlled. Radiatively heated effusion cells are typically used to provide molecular beams of the elemental constituents of the materials to be grown (see Fig. 8). For atomic-layer engineering, it is not enough to monitor relative ratios; one needs an absolute measurement of the atomic fluxes. For this purpose, spectroscopic techniques such as measurements of absorption or emission of visible or UV characteristic radiation from the atomic beams have been used with success, usually in addition to the more conventional QCMs.

Using MBE, a variety of high T_c superconductor heterostructures have been fabricated, including tri-layer Josephson junctions (known also as planar or sandwich junctions). The superconductive electrodes are made of $Bi_2Sr_2CaCu_2O_8$, $YBa_2Cu_3O_{7-\delta}$ (both c- and a-axis oriented), or $La_{1.85}Sr_{0.15}CuO_4$. For the barrier layers, various materials have been used including titanates and manganites, with the layer thickness down to one unit cell. High T_c superconductor layers of one unit cell thickness have also been fabricated with T_c equal to bulk samples, as well as various superlattices, and even some novel, artificial high T_c superconducting compounds (Bozovic *et al.* 1994, Schlom and Harris 1995).

2.5 Other Techniques

Some of the high T_c superconductors with the highest T_c contain highly volatile (and toxic) elements, such as mercury or thallium. The techniques described above
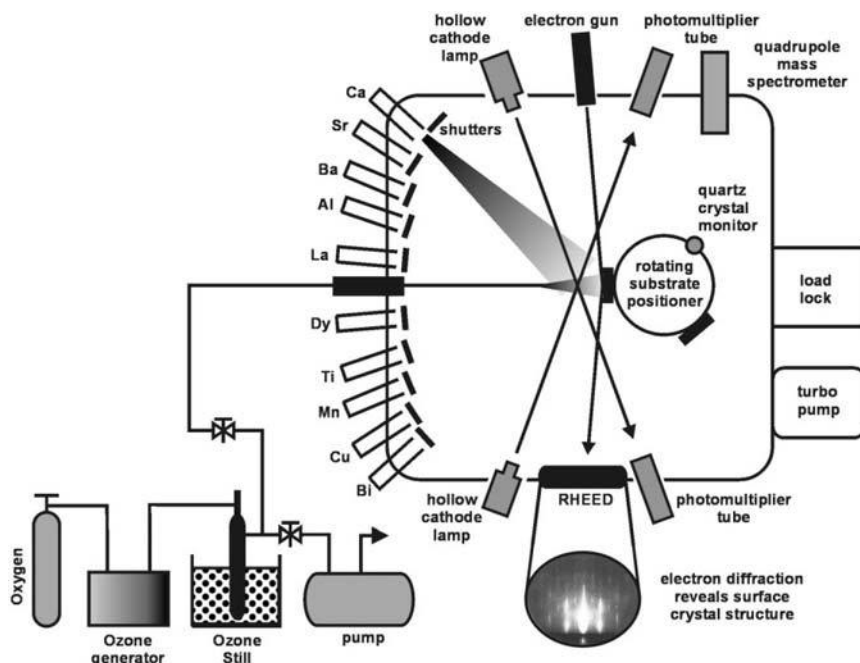
Figure 8
Schematic of an MBE system for atomic-layer synthesis of oxide superconductors (reproduced by permission of Annual Reviews Inc. from *Annu. Rev. Mater. Sci.*, 1995, **25**, 679–709).

are not well suited for handling such elements. For this reason, special approaches have been adopted: either a two-step process, where the precursor film is deposited first, and then postannealed (*ex situ*) under a high vapor pressure of thallium or mercury, or a single-step (*in situ*) process where sputtering of the precursor and high-rate thermal evaporation of thallium are applied simultaneously (Tsuei *et al.* 1994, Myers *et al.* 1994).

Several techniques have allowed films with excellent in-plane texture to be realized on polycrystalline substrates of practical importance. One method makes use of ion beam-assisted deposition (IBAD) to create an in-plane oriented buffer layer of yttria-stabilized cubic zirconia (Iijima *et al.* 1992) or MgO (Wang *et al.* 1997) on the underlying substrate. Films of high T_c superconductors are then epitaxially grown on top of this buffer layer. Another method, which has achieved comparable in-plane texture to IBAD, uses rolling and annealing to achieve texturing in metal strips, e.g., nickel, that are then used as substrates for film deposition (Goyal *et al.* 1996, Norton *et al.* 1996). The freedom from single-crystal substrates that these techniques bring offers flexibility for the integration of high T_c superconductor films with other materials and forms the basis of a growing coated-conductor technology (see *Superconducting Wires and Cables: Low-field Applications*).

Other techniques, such as metal-organic chemical vapor deposition (MOCVD), etc., have also been applied with success to grow high T_c superconductor thin films, but they are less widespread.

3. Summary and Outlook

As discussed in this article, films and multilayers containing a great number of high T_c compounds are now grown routinely and have exceptional properties (see *High-temperature Superconductors: Thin Films and Multilayers*)—quite an accomplishment, given that high T_c superconductivity was discovered only in 1986. Multilayers have progressed from combining known materials to literally engineering new materials at the atomic-layer level.

The progress achieved and the knowledge acquired will be applied in the future to the growth of films and heterostructures of other oxide or nitride compounds, into which high T_c superconducting films will be embedded. As in semiconductors, through doping and material selection, the functionality of individual layers can be tailored in heterostructures. It is expected that the challenges and the potential benefits of such heterostructures will stimulate further improvements in the control of film growth.

Acknowledgments

Bibliography

Bozovic I, Eckstein J N, Virshup G F, Chaiken A, Wall M, Howell R, Fluss M 1994 Atomic-layer engineering of cuprate superconductors. *J. Supercond.* **7**, 187–95

Cava R J 1990 Structural chemistry and the local charge picture of copper oxide superconductors. *Science* **247**, 656–62

Cava R J, Batlogg B, Krajewski J J, Farrow R, Rupp L W Jr., White A E, Short K, Peck W F, Kometani T 1988 Superconductivity near 30 K without copper: the $Ba_{0.6}K_{0.4}BiO_3$ perovskite. *Nature* **332**, 814–6

Coppens P, Lee P, Gao Y, Sheu H -S 1991 Application of the selective atom diffraction method to the cation distribution in high T_c bismuth cuprates. *J. Phys. Chem. Solids* **52**, 1267–72

Dijkkamp D, Venkatesan T, Wu X D, Shaheen S A, Jisrawi N, Min-Lee Y H, McLean W L, Croft M 1987 Preparation of Y–Ba–Cu oxide superconductor thin films using pulsed laser evaporation from high T_c bulk material. *Appl. Phys. Lett.* **51**, 619–21

Eckstein J, Bozovic I 1995 High-temperature superconducting multilayers and heterostructures grown by atomic layer-by-layer molecular beam epitaxy. *Annu. Rev. Mater. Sci.* **25**, 679–709

Eom C B, Sun J Z, Lairson B M, Streiffer S K, Marshall A F, Yamamoto K, Anlage S M, Bravman J C, Geballe T H, Laderman S S, Taber R 1990 Synthesis and properties of $YBa_2Cu_3O_7$ thin films grown in situ by 90° off-axis single magnetron sputtering. *Physica C* **171**, 354–82

Eom C B, Sun J Z, Yamamoto K, Marshall A F, Luther K E, Geballe T H, Laderman S S 1989 In situ grown $YBa_2Cu_3O_{7-\delta}$ thin films from single-target magnetron sputtering. *Appl. Phys. Lett.* **55**, 595–7

Fisk Z, Sarrao J L 1997 The new generation high-temperature superconductors. *Annu. Rev. Mater. Sci.* **27**, 35–67

Goyal A, Norton D P, Budai J D, Paranthaman M, Specht E D, Kroeger D M, Christen D K, He Q, Saffian B, List F A, Lee D F, Martin P M, Klabunde C E, Hartfield E, Sikka V K 1996 High critical current density superconducting tapes by epitaxial deposition of $YBa_2Cu_3O_x$ thick films on biaxially textured metals. *Appl. Phys. Lett.* **69**, 1795–7

Hammond R H, Bormann R 1989 Correlation between the in situ growth conditions of YBCO thin films and the thermodynamic stability criteria. *Physica C* **162–164**, 703–4

Humphreys R G, Satchell J S, Chew N G, Edwards J A, Goodyear S W, Blenkinsop S E, Dosser O D, Cullis A G

1990 Physical vapour deposition techniques for the growth of $YBa_2Cu_3O_{7-\delta}$ thin films. *Supercond. Sci. Technol.* **3**, 38–52

Iijima Y, Tanabe N, Kohno O, Ikeno Y 1992 In-plane aligned $YBa_2Cu_3O_{7-x}$ thin films deposited on polycrystalline metallic substrates. *Appl. Phys. Lett.* **60**, 769–71

Jakob G, Hahn T, Kluge T, Wagner P, Adrian H 1994 Characterization of $YBa_2Cu_3O_7/PrBa_2Cu_3O_7$ Superlattices. *J. Supercond.* **7**, 197–200

Jo W, Peng L S-J, Wang W, Ohnishi T, Marshall A F, Hammond R H, Beasley M R, Peterson E J 2001 Thermodynamic stability and kinetics of Y–Ba–Cu–O film growth at high rates in atomic and molecular oxygen. *J. Cryst. Growth* **225**, 183–9

Kinder H, Berberich P, Prusseit W, Semerad R, Utz B 1996 Very large area $YBa_2Cu_3O_7$ film deposition. In: Bozovic I, Pavuna D (eds.) *Oxide Superconductor Physics and Nano-Engineering II*, SPIE Proc. 2697. SPIE, Belingham, pp. 154–9

Koinuma H, Yoshimoto M 1994 Controlled formation of oxide materials by laser molecular beam epitaxy. *Appl. Surf. Sci.* **75**, 308–19

Li Z, Rifi H, Vaures A, Megtert S, Raffy H 1994 Synthesis of $Bi_2Sr_2CaCu_2O_8/Bi_2Sr_2CuO_6$ superlattices with a T_c enhancement effect. *Phys. Rev. Lett.* **72**, 4033–6

Lindemer T B, Washburn F A, MacDougall C S, Feenstra R, Cavin O B 1991 Decomposition of $YBa_2Cu_3O_{7-\delta}$ and $YBa_2Cu_4O_8$ for $p_{O2} \leqslant 0.1$ MPa. *Physica C* **178**, 93–104

Mannhart J 1992 Changes in the superconducting properties of high-T_c cuprates produced by applied electric fields. *Mod. Phys. Lett. B* **6**, 555–71

Matijasevic V, Bozovic I 1996 Thin film processes for high-temperature superconductors. *Current Opinion Solid State Mater. Sci.* **1**, 47–53

Myers K E, Face D W, Kountz D J, Nestlerode J P 1994 Superconducting and epitaxial $(Tl,Pb)Sr_2Ca_{1-x}$ $Y_xCu_2O_7$ thin films by in situ deposition. *Appl. Phys. Lett.* **65**, 490–2

Nonaka H, Ichimura S, Shimizu T, Arai K 1995 Development of oxidation sources in preparation of high-T_c oxide superconductor thin films using the molecular beam epitaxy method. *Crit. Rev. Solid State Mater. Sci.* **20**, 285–338

Norton D P, Goyal A, Budai J D, Christen D K, Kroeger D M, Specht E D, He Q, Saffian B, Paranthaman M, Klabunde C E, Lee D F, Sales B C, List F A 1996 Epitaxial $YBa_2Cu_3O_7$ on biaxially textured nickel (001): an approach to superconducting tapes with high critical current density. *Science* **274**, 755–7

Nücker N, Fink J, Fuggle J C, Durham P J, Temmerman W M 1988 Evidence for holes on oxygen sites in the high-T_c superconductors $La_{2-x}Sr_xCuO_4$ and $YBa_2Cu_3O_{7-y}$. *Phys. Rev. B* **37**, 5158–63

Petricek V, Gao Y, Lee P, Coppens P 1990 X-ray analysis of the incommensurate modulation in the 2:2:1:2 Bi–Sr–Ca–Cu–O superconductor including the oxygen atoms. *Phys. Rev. B* **42**, 387–92

Poppe U, Schubert J, Arons R R, Evers W, Freiburg C H, Reichert W, Schmidt K, Sybertz W, Urban K 1988 Direct production of crystalline superconducting thin films of $YBa_2Cu_3O_7$ by high-pressure oxygen sputtering. *Solid State Commun.* **66**, 661–5

Rao C N R 1991 The Blackett memorial lecture, 1991: chemical insights into high-temperature superconductors. *Phil. Trans. R. Soc. London, Ser. A* **336**, 595–624

Rijnders G J H M, Koster G J, Blank D H A, Rogalla H 1997 In situ monitoring during pulsed laser deposition of complex oxides using reflection high energy electron diffraction under high oxygen pressure. *Appl. Phys. Lett.* **70**, 1888–90

Schlom D G, Harris J S Jr 1995 MBE growth of high T_c superconductors. In: Farrow R F C (ed.) *Molecular Beam Epitaxy: Applications to Key Materials*. Noyes, Park Ridge, NJ, pp. 505–622

Shafer M W, Penney T 1990 Hole, T_c relationships in superconducting oxides. *Eur. J. Solid State Inorg. Chem.* **27**, 191–220

Shi D, Capone D W II 1988 60–90 K superconducting phase transition in $YBa_2Cu_3O_{7-\delta}$. *Appl. Phys. Lett.* **53**, 159–61

Sleight A W 1991 Synthesis of oxide superconductors. *Physics Today* **44** (6), 24–30

Sleight A W, Gillson J L, Bierstedt P E 1975 High-temperature superconductivity in the $BaPb_{1-x}BixO_3$ system. *Solid State Commun.* **17**, 27–8

Suzuki M, Murakami T 1987 Hall effect in superconducting $(La_{1-x}Sr_x)_2CuO_4$ single crystal thin films. *Jpn. J. Appl. Phys., Part 2.* **26**, L524–5

Tabata H, Kawai T, Kanai M, Murata O, Kawai S 1989 Tailored thin films of superconducting Bi–Sr–Ca–Cu–O oxide prepared by excimer laser ablation technique. *Jpn. J. Appl. Phys., Part 2.* **28**, L823–6

Tokura Y, Arima T 1990 New classification method for layered copper oxide compounds and its application to design of new high T_c superconductors. *Jpn. J. Appl. Phys., Part 1.* **29**, 2388–402

Tokura Y, Takagi H, Uchida S 1989 A superconducting copper oxide compound with electrons as the charge carriers. *Nature* **337**, 345–7

Tokura Y, Torrance J B, Huang T C, Nazzal A I 1988 Broader perspective on the high-temperature superconducting $YBa_2Cu_3O_y$ system: the real role of the oxygen content. *Phys. Rev. B* **38**, 7156–9

Torrance J B, Tokura Y, Nazzal A I, Bezinge A, Huang T C, Parkin S S P 1988 Anomalous disappearance of high-T_c superconductivity at high hole concentration in metallic $La_{2-x}Sr_xCuO_4$. *Phys. Rev. Lett.* **61**, 1127–30

Triscone J-M, Fischer Ø, Brunner O, Antognazza L, Kent A D, Karkut M G 1990 $YBa_2Cu_3O_7/PrBa_2Cu_3O_7$ superlattices: properties of ultrathin superconducting layers separated by insulating layers. *Phys. Rev. Lett.* **64**, 804–7

Tsuei C C, Gupta A, Trafas G, Mitzi D 1994 Superconducting mercury-based cuprate films with a zero-resistance transition temperature of 124 kelvin. *Science* **263**, 1259–61

Wagner P, Hilmer F, Frey U, Adrian H, Steinborn T, Ranno L, Elschner A, Heyvaert I, Bruynseraede Y 1993 Preparation and structural characterization of thin epitaxial $Bi_2Sr_2CaCu_2O_{8+\delta}$ films with T_c in the 90 K range. *Physica C* **215**, 123–31

Wang C P, Do K B, Beasley M R, Geballe T H, Hammond R H 1997 Deposition of in-plane textured MgO on amorphous Si_3N_4 substrates by ion beam-assisted deposition and comparisons with ion beam-assisted deposited yttria-stabilized zirconia. *Appl. Phys. Lett.* **71**, 2955–7

Wördenweber R 1999 Growth of high-T_c thin films. *Supercond. Sci. Technol.* **12**, R86–102

Xi X X, Linker G, Meyer O, Nold E, Obst B, Ratzel F, Smithey R, Strehlau B, Weschenfelder F, Geerk J 1989 Superconducting and structural properties of YBaCuO thin films deposited by inverted cylindrical magnetron sputtering. *Z. Phys. B* **74**, 13–9

I. Bozovic
OXXEL GmbH, Bremen, Germany

D. G. Schlom
*Penn State University, University Park
Pennsylvania, USA*

Superconducting Thin Films: Multilayers

Over the years superconducting multilayer technology has been developed either for scientific curiosity or for technological applications. One of the simplest multilayer structures is the superlattice where superconducting layers and nonsuperconducting layers alternate either in a periodic order or in a nonperiodic special order. The nonsuperconducting layers are usually normal materials that can allow some coupling between the superconducting layers. Without any further processing, these superlattices have been used for investigation of their superconducting properties. The main scientific interest has been the interaction between the superconducting layers as a function of their coupling strength. Most studies were on artificially made two-dimensional superconducting structures before the discovery of high-temperature superconductivity (HTS) in 1987.

Some of the investigations of the superlattices have led to important technological discoveries, one of which being Nb/Al:Al$_2$O$_3$/Nb tunnel junctions. While the tunneling phenomena were being studied in Nb/Al superlattices, the idea of using the proximity effect between niobium and aluminum was considered and the excellent barrier properties of Al$_2$O$_3$ were discovered. This tunnel junction technology has been very important in low T_c superconducting (LTS) electronics since the early 1980s.

While most low T_c superconductors are based on conventional metals, the discovery of HTS has brought on a completely new class of materials, namely the metal oxides in complex perovskite structures. These new oxide materials require new deposition and processing techniques.

This article describes the deposition and processing technology of superconducting multilayers and their applications for the case of high T_c superconducting materials. The LTS case will be briefly mentioned for comparison.

1. Deposition Technology

1.1 LTS Multilayers

When lead was used before niobium was introduced to LTS technology, the preferred thin-film deposition technique was evaporation, because the soft lead was almost impossible to sputter. However, when the more refractory niobium material is used, sputtering techniques are possible, although the evaporation technique continues to be used, especially for careful epitaxial growth of niobium thin films. The sputtering technique for niobium is found to be very reliable once ultrahigh vacuum and stress-free deposition conditions are obtained.

The majority of niobium growth is for polycrystalline thin films and the adjacent nonsuperconducting layers are also polycrystalline. For many technological applications SiO$_2$ is used as the insulating layer between the niobium wiring layers, and chemical vapor deposition techniques are often used to take advantage of the developments made in the semiconductor industry. LTS technology based on metals is very similar to that of metallization in the semiconductor industry.

The sputtering, evaporation, and chemical vapor deposition techniques mentioned above are standard methods used throughout the electronics industry (see *High-temperature Superconductors: Thin Films and Multilayers*).

1.2 High T_c Superconducting Multilayers

High T_c superconductors, discovered in 1987, turned out to be very complex metal oxides that had to be grown in high-oxygen environments (greater than 1 mtorr) and at high temperatures (greater than 700 °C). Laser ablation, or pulsed laser deposition (PLD), is a newer technique that has gained much popularity because it is ideally suited for deposition at a high oxygen pressure. The relative ease of this technique in depositing multicomponent oxides makes it especially effective for exploring new materials for HTS electronics, such as epitaxial dielectrics or barrier layers. A short-wavelength (170–260 nm) excimer laser is focused onto a rotating target of the material to be deposited. At the energy of the laser beam (0.1–2 J per pulse) the matter emitted from the target forms a plume that carries it to the substrate at supersonic velocities. In general, a higher gas pressure is required during laser ablation owing to the very high energy of the vaporized material from the surface of the target. The laser plume glows brightly from the target and deposition is usually done near the end of the plume, about 5 cm away. As in the case of sputtering, the various species scatter differently and therefore the "sweet spot" of the deposition process is relatively small, usually 1–2 cm, depending on the geometry. The deposition rate per laser pulse ranges from a fraction of an angstrom to a few angstroms. The technique is fairly reproducible and has been used extensively for research and development purposes. Although other techniques are potentially more manufacture-friendly, laser ablation is very actively used for prototyping multilayer devices made up of several complex materials, such as superconductors, dielectrics, ferroelectric oxides, magnetic oxides, and other conducting oxides.

A particular problem associated with PLD is the deposition of micrometer-sized droplets, so-called "boulders," on the grown film. These particles originate at the target and are emitted from the action of the laser pulse. A variety of procedures have been used to reduce this problem so that the boulder density can be very low in the best films. Such procedures

include target preparation, such as frequent polishing, defocusing the laser spot, mechanically chopping the plume, or spatially filtering the beam. The quality of multilayers made by PLD depends on being able to reduce these boulder problems.

Although PLD can produce relatively high deposition rates (up to tens of nanometers per second), the area on which one deposits is relatively small. A straightforward way to increase the deposition area is to scan wafers over the plume either by moving the substrate vertically and horizontally or by rotating the substrate. Another scheme uses a rotating cylindrical target with a linear laser profile to obtain larger deposition areas.

Another major difficulty of these techniques is the uniform heating of large wafers. Most of the heating methods for small-area laser ablation mount a substrate on a heated metal surface with silver paste, which is difficult to extend to larger sizes. In order to overcome this difficulty of heating a large wafer, an off-axis laser ablation technique has been developed. A large wafer (2–3 in (5–8 cm)) can be mounted parallel to the direction of the plume inside a relatively simple black-body-like heater. The deposition takes place when the atoms collide with the background pressure and are scattered to the surface of the wafer. By rotating the wafer and selecting an appropriate pressure for the geometry, a fairly uniform deposition can be achieved over 2 in (5 cm) wafers. This technique allows for simultaneous deposition on both surfaces of the wafer, which is an important benefit for microwave applications requiring a ground plane. A drawback of this technique is its low deposition rate because of the off-axis geometry. Typical conditions for 2 in (5 cm) wafer deposition results in a deposition rate lower by about a factor of 10 than that for on-axis deposition. However, the added advantage of off-axis laser ablation is the reduction of the boulder density, especially important for multilayer work.

By using a laser fluence just enough to evaporate a few atomic layers of the target in a low-oxygen environment (less than 10^{-4} torr) and at the same time by using a sequence of metal or metal oxide targets, one can obtain a process similar to molecular beam epitaxy (MBE) by evaporation, here called laser-MBE. Some *in situ* diagnostic tools can then be used to characterize the growth of the materials. This technique has mainly been used to grow artificially layered superconducting materials, such as the infinite-layered superconductor.

2. Processing Technology

2.1 LTS Multilayers

LTS multilayer technology has made significant progress since the 1980s, mainly in Japan, based on niobium thin films primarily for SQUID and high-speed digital circuit applications. The main challenge has been to define the junction structure, the Nb/Al:Al$_2$O$_3$/Nb trilayer, without degrading the uniformity of its properties. A new process of defining the junction area by anodization rather than etching has been invented and is a very reliable process for minimizing the damage along the edges of the trilayer structure.

A reactive ion etching process of niobium uses a fluorine-based gas such as CF_4. By using dielectrics such as SiO_2, multilayer structures including a ground plane, a trilayer structure, and wiring layers have been fabricated.

2.2 High T_c Superconducting Multilayers

Unlike polycrystalline niobium, HTS multilayer structures need to be epitaxial mainly because of a large anisotropy and the weak grain boundaries of HTS materials. Epitaxial growth requires a high-temperature deposition of each material and this complicates the heating methods. No large-area (>1 in (2.5 cm)) HTS multilayer process is available, although fairly complicated structures including a ground plane and edge junctions have been successfully fabricated (see *High-temperature Superconductors: Thin Films and Multilayers*; *Films and Multilayers: Conventional Superconducting*).

Of several HTS materials, YBa$_2$Cu$_3$O$_{7-x}$ (YBCO) is the most frequently used material for multilayer work. This is because the anisotropy of YBCO is the smallest of all HTS materials and YBCO is least susceptible to the damage caused by etching. It is inevitable that a patterned multilayer structure will require a current path perpendicular to the substrate. A weak current-handling capability in this direction, namely a large anisotropy, will cause a problem in such a multilayer structure. In order to minimize the sudden current flow in the perpendicular direction, edges have to be patterned in such a way that the edge angle is very small ($<20°$), although this will make the edge area wider.

Unfortunately, no good reactive etching method for these complex metal oxides has been found, and a dry ion beam milling (usually by an argon ion beam) technique has been the primary method for etching. Several wet etching methods have been found but they have not been very popular because of severe undercut below the photoresist during the etching process. During dry ion beam etching, the YBCO material is cooled by a thermal contact with a water-cooled plate in order not to lose oxygen when heated in vacuum. A line width as small as 1 µm has been found to carry high critical current density by this method.

YBCO is a semistable material at room temperature, and when it is bombarded with high-energy particles, such as argon ions, it starts to lose oxygen and then the materials becomes amorphous. This has

been observed during transmission electron microscope sample preparation. However, the lost oxygen can be restored by annealing the material in an oxygen ambient at about 400–500 °C where the oxygen intake is maximum. One can also restore the ion beam-damaged crystallinity by annealing the material around 800 °C in the appropriate oxygen environment (usually around 100 mtorr). Especially for multilayer work in which one relies on the epitaxial growth of the subsequent layer on top of the edges, the restoration of the crystalline quality after etching is a very crucial step.

YBCO loses oxygen when heated but regains it during cooling in an oxygen environment at 400–500 °C. This means that if one grows a second epitaxial layer, through which the oxygen diffusion is very slow at 400–500 °C, on top of the first YBCO layer, the resulting structure will have an oxygen-deficient YBCO layer. This is because the oxygen cannot diffuse through the dielectric layer to get to the bottom YBCO layer. This problem gets worse as one develops a more perfect dielectric layer because defects such as grain boundaries or oxygen vacancies in the dielectric layer are often the channels for oxygen diffusion.

The most frequently used dielectric layers are $SrTiO_3$, $LaAlO_3$, Sr_2AlTaO_6, or Sr_2AlNbO_6. These all have a perovskite structure, similar to YBCO, allowing epitaxial growth adjacent to YBCO. Of these dielectric materials, $SrTiO_3$ is the easiest to deposit and the first that was developed. However, the high dielectric loss of $SrTiO_3$ does not allow its use for high-speed circuits. Other similar dielectric materials with low dielectric loss, such as $LaAlO_3$, Sr_2AlTaO_6, and Sr_2AlNbO_6, were later developed. However, all these dielectric materials have low oxygen diffusion rate problems especially when a better material with fewer defects is grown.

Materials that have exactly the same structure as YBCO but are not superconducting have been used in multilayer structures. These include $PrBa_2Cu_3O_{7-x}$ and doped YBCO. They have the advantage of having an identically layered structure, which allows for perfectly matched growth from the edges. In addition, they have an almost identical oxygen diffusion rate, resulting in a fully oxygenated YBCO layer underneath. However, their insulating properties are far from ideal, making them impossible for use as dielectric layers. For this reason, these materials have been used mainly for barriers for Josephson junctions (see *Josephson Junctions: High-T_c*).

Because of its anisotropy, a Josephson junction process for YBCO has been developed in an edge junction geometry. The process requires forming a low-angle slope for the first YBCO layer and then depositing the barrier layer and the second YBCO layer on top of it. As mentioned above, restoration of the crystallinity after etching is critical in allowing for

good epitaxial growth of the subsequent barrier and YBCO layers. A technique to modify the edge and convert the interface region into an insulating phase by annealing them in a different environment has been developed.

It remains to be seen how much further HTS multilayer technology will be developed. The answer to this may lie in the prospects for its application in the future.

3. Applications

3.1 LTS Multilayers

LTS multilayer technology has been used for developing SQUID sensors. Multilayer flux transformers or gradiometers coupled with trilayer tunnel junctions have been successfully developed and are used in practical SQUID instruments. In the case of high-speed electronic circuits, both the voltage state logic and the single-flux quantum logic require multilayer technology and niobium mutilayer technology is being used to demonstrate many high-speed circuits (see *SQUIDs: The Instrument*).

3.2 High T_c Superconducting Multilayers

Unfortunately, the use of HTS technology for SQUID applications is by its single-layer process. Multilayered flux transformers for SQUID applications have been demonstrated, but the extra low-frequency noise does not improve its performance over that of single-layered flux transformers.

For microwave applications, double layers of HTS materials on both sides of a wafer are used. One of these layers is the ground plane in a microstrip geometry. It is very likely that many microwave applications of this multilayer technology will be developed with the proliferation of wireless communication. It remains to be seen how this will affect HTS multilayer technology.

A few very simple multilayer HTS digital circuits of the single-flux quantum logic kind have been demonstrated in spite of the many problems described above (see *Superconductors: Rapid Single Flux Quantum (RSFQ) Logic*).

See also: Superconducting Microwave Applications: Filters; Superconducting Thin Films: Materials, Preparation and Properties

Bibliography

Shinjo T, Takada T (eds.) 1987 *Metallic Superlattices: Artificially Structured Materials*. Elsevier, Amsterdam

K. Char
Seoul National University, South Korea

Superconducting Wires and Cables: High-field Applications

The performance of superconducting wires is fundamentally limited by the magnetic flux density or field, the current density, and the operating temperature, while the magnet applications are limited by current, voltage, and stored energy. Thus the term "high-field applications" is really a generalization for high-performance applications, involving all of these conductor and magnet constraints. As a rule, high field is easiest to obtain in small bores and at low temperatures. This article reviews progress in strands and cables that improves the performance capabilities of large-scale superconducting applications.

All high-current and many high-field superconducting applications use conductors that are made up of cables with multiple strands. A large variety of cable topologies have been used, but two are the most common. High-energy physics multipole (dipole, quadrupole, etc.) magnets generally use Rutherford cables, a high aspect ratio topology with two layers, and a highly regular cabling and crossover pattern. Large energy storage, fusion research, and detector magnets more frequently use cable-in-conduit conductors (CICC), round cables that are built up from smaller round subcables, then compacted into a square or low aspect ratio conduit. The two cable types are illustrated in Fig. 1.

Rutherford cables are favored for multipole magnets, because they can achieve tighter bends with lower conductor strain, while multipole magnets are characterized by modest bore sizes and high length-to-minimum-bend-radius ratios. Cable-in-conduit conductors are favored for the larger bore fusion,

(a) Rutherford Cable

(b) Kapton/Glass Cable Insulation

(c) Multistage Cable
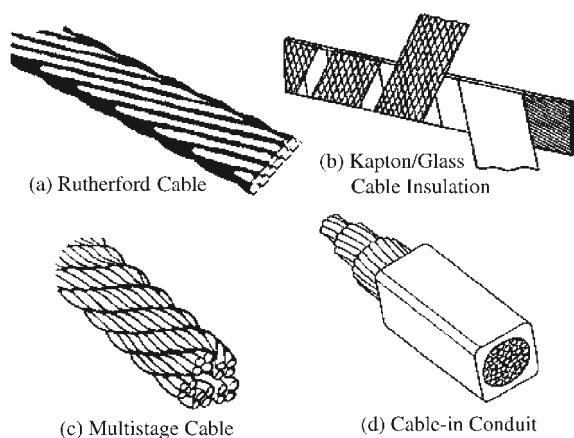
(d) Cable-in Conduit

Figure 1
Cable types: (a) simple Rutherford cable, (b) Rutherford cable with kapton/glass insulating wrap, (c) multistage circular cable, (d) cable-in-conduit.

detector, and superconducting magnetic energy storage (SMES) magnets, because of their ability to be built up to nearly unlimited current-carrying capabilities, making them most appropriate for very large, high-energy applications. CICC conductors have been built and tested up to 200 kA for large SMES applications (Peck and Michels 1991) and large magnets have been tested to 80 kA (ITER 2001).

1. Strand

Commercial and scientific applications of superconducting cables are dominated by niobium titanium (NbTi). NbTi, the first practical superconducting material for large-scale applications, is strong, ductile, and relatively inexpensive. The production of NbTi strand is approximately 200 t per year. The largest commercial application is medical magnetic resonance imaging (MRI) magnets, while scientific applications are currently dominated by production of the Large Hadron Collider at CERN (Perin 1991). NbTi magnets have been built with peak flux densities ranging from under 1 T to peaks of 8–9 T at 4.2 K (the boiling temperature of liquid helium) and 9–11 T at 1.8 K (Perin 1991) (near the lambda point of superfluid helium). NbTi is a mature technology, which has slowly been improving, so that it is now possible to purchase large quantities with critical current densities of 3000 A mm^{-2} at 5 T and 4.2 K.

All other magnet applications use Nb$_3$Sn with an annual production of approximately 2.5 tonnes per year. Nb$_3$Sn is used in nuclear magnetic resonance and open MRI magnets. Scientific applications include next-generation magnets for high-energy physics and fusion, including 20 t of Nb$_3$Sn in the KSTAR tokamak being built in South Korea (Lee *et al.* 1999) and an equivalent amount for the recently tested ITER CS Model Coil in Japan (Martovetsky *et al.* 2001). Nb$_3$Sn cables have been used in large pulsed cables up to 13 T (Tsuji *et al.* 2001), dipole magnets up to 14.7 T (Gourlay *et al.* 2001), small solenoids up to 17 T (Takeo *et al.* 1987), and inserts up to 21 T. Nb$_3$Sn has superior critical temperature and field, but it is an order of magnitude more expensive than NbTi, requires a long heat treatment at 600–700 °C to become superconducting, and is brittle, requiring great care in handling during fabrication and cooldown to the cryogenic operating temperature.

However, the conductor development program for a high-field Very Large Hadron Collider (VLHC) has achieved spectacular progress in critical current density, which has risen over just a few years from 700 A mm^{-2} to 2900 A mm^{-2} at 4.2 K and 12 T. Significant progress in the programme's goal of reducing the cost of Nb$_3$Sn in large quantities from \$1000 to \$200 kg^{-1} would make several new high-field applications possible.

New materials have been proposed, but have not yet had practical impact on high-field magnet

applications. The two most widely studied high-temperature superconductor materials, BSSCO-2223 (bismuth strontium calcium copper oxide) and YBCO (yttrium barium copper oxide), are not available as strands. Artificial pinning center strands have been proposed as an alternative to NbTi, because of superior properties at low field and projected low manufacturing costs (Rudziak *et al.* 1995). Nb_3Al, which has been proposed as an alternative to Nb_3Sn, has similar critical properties, but much lower strain sensitivities.

A recently tested Nb_3Al cable has shown performance at 13 T and 46 kA that equals that of previous generation Nb_3Sn and with less degradation over time (Takeuchi 2001). BSSCO-2212 strands have been proposed as high-temperature superconductors, paradoxically because of their superior performance at low temperature and high field. Cables using BSSCO-2212 have achieved 10 kA. None of these alternative strands have demonstrated the existence of more than niche markets and, despite impressive progress, they remain single vendor prototypes. A new strand material that may have a better opportunity to "break out" into commercialization is the recently discovered medium-temperature MgB_2, which benefits from being potentially inexpensive to manufacture, lightweight, and ductile, although its critical temperature is lower than BSSCO or YBCO, while its critical field is lower than Nb_3Sn.

State-of-the-art performance of the different strands is listed in Table 1.

2. Rutherford Cable

The Rutherford cable is a two-layer cable of round or square strands, whose high aspect ratio allows winding around the relatively tight radii of constricted end turns in magnets with long straight sections. The simplest form of the Rutherford cable is a two-layer cable with uniform superconducting strand placement and uniform crossover of strands. Several variations of these two forms have been built into a number of historic high-field magnets. Some of these historic cables are illustrated in Fig. 2. Rutherford

(a) LCTIGC/GE (Cable w/Copper core)
(b) LDX F-Coil (Cable-in-Copper C-channel)
(c) LCT Hitachi (Cable-in-Copper U_channel)
(d) LCT Euralom (Cable-in-coduit w/Steelcore)
(e) LHD TF (Cable wA1 stabilizer in copper housing)
(f) T-15 (Cable w/core, housing and external channels)
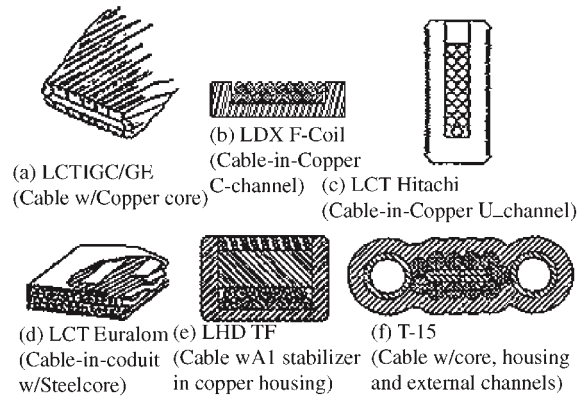
Figure 2
Historic Rutherford cable design options, drawn to scale: (a) large coil task, IGC/General Electric, cable with a copper core; (b) levitated dipole experiment floating coil, cable in a copper C-channel; (c) large coil task, Hitachi, cable in a copper U-channel; (d) large coil task, EURATOM/Vacuumschmelze, cable-in-conduit with an insulated steel core; (e) large helical device, cable with an aluminum stabilizer in a copper housing; (f) T-15 tokamak, cable with core in a housing and external cooling channels.

cables can be compacted for higher strength and packing factor, and "keystoned" so that a winding can fit without gaps on a circumference. As shown in Fig. 2, they can be reinforced by a central core—either steel to add strength and reduce losses, or copper to improve stability and quench protection (Beard *et al.* 1988).

Figure 2 also shows how a Rutherford cable can be inserted horizontally or vertically into a copper channel, improving strength, stability, and protection (Beard *et al.* 1988, Schultz *et al.* 1999). It also shows cables that functionally resemble a CICC, by being inserted into a sealed can with forced-flow helium circulating directly through the conductor or through side-channels (Beard *et al.* 1988, Chernoplekov and Monoszon 1982). The two-layer configuration can

Table 1
State-of-the-art strands.

Parameter	Units	Value	Name/reference
J_{cnonCu} (4.2 K, 5 T, NbTi)	A mm^{-2}	3800	SSC, OST 14 μm, Furukawa 2.5 μm
J_{cnonCu} (4.2 K, 12 T, Nb_3Sn)	A mm^{-2}	2900	Scanlan
J_{cnonCu} (4.2 K, 20 T, Nb_3Al)	A mm^{-2}	650	Sumption, DOE HEP (Sumption *et al.* 2002)
J_{cnonAg} (4.2 K, 0 T, BSSCO-2212)	A mm^{-2}	2000	Showa, manufacturer's literature
Nstrands/cable (CICC)		1440	ITER Russian PF insert coil (ITER 2000)
Nstrands/cable (Rutherford)		47	LBNL D20
		60	LBNL/Fermilab 2002 (not used in magnet)

also benefit from the ability to achieve a highly regular cabling pattern and near-uniform contact resistances, permitting analysis of cable supercurrents. Cables with as many as 47 strands have been used in high-energy physics dipole magnets (McInturff *et al.* 1997).

Since Rutherford cables are typically used in quasi-steady-state applications, they are usually designed for low contact resistance between strands. The specification for the Large Hadron Collider (Perin 1991) is $10\,\mu\Omega$ per contact. Such a low contact resistance tends to be dominated by the oxide layer on the strand surface. In Tevatron (Cooper and Fisk 1983) and HERA (Meinke 1991), the strands are covered by a thin layer of SnAg (5%) to reduce surface resistance. For applications requiring a significant ramp rate, such as injector magnets, a compromise has to be made between good current transfer for stability and good resistance for low losses. This can usually be accomplished by a thin steel core in the center of the cable, allowing strand–strand current transfer, while eliminating large circulating currents.

3. CICC

Although it has many variants, the cable-in-conduit conductor (CICC) concept has changed little since its invention in the 1960s. Strands are cabled into successive stages, called subcables, in which typically 3–6 subcables are bundled into the next larger cable stage. Cables with as many as 1440 strands have been built up in this manner (ITER 2001). The cable is then jacketed, i.e., inserted into a helium-tight conduit that provides support against winding and Lorentz loads, as well as being a pressure vessel for helium coolant. The most common CICC is a simple circular cable, inserted into a conduit that is squared off with Turks-head rollers, then welded together, either with a continuous seam weld or by orbital welding of discrete sections of pipe. The aspect ratio can be higher than one, when this improves the overall winding packing factor.

A circular conduit has the dual advantage of being indifferent to angular position due to any twist during winding or transitions and it also has the lowest stress multiplier for holding internal helium pressure. However, it is incapable of sustaining much compression from radial loads in the winding pack, and has a low packing factor, so that it must be placed in a scalloped structural plate. The cable may have a central coolant hole (Tsuji *et al.* 2001), or it can be placed in a thin inner conduit, leaving four unobstructed cusps in the corners (Steeves *et al.* 1989), so that the hydraulic path will have a larger hydraulic diameter and less friction, allowing the removal of higher heat loads. This philosophy can be extended to where the central hole is much larger than the cable space for very long channels or when needed to allow conduction cooling by superfluid helium (Peck and
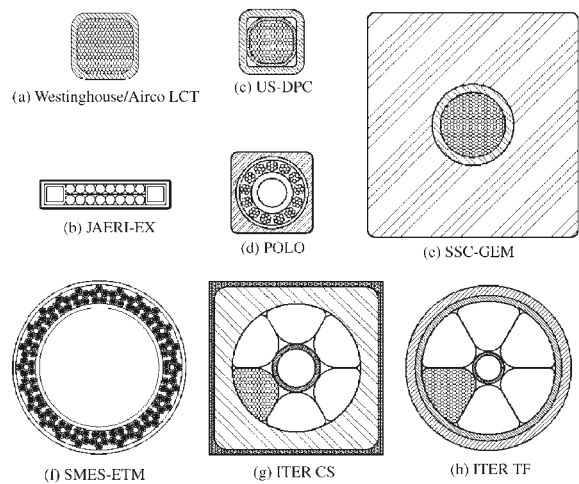
Figure 3

Historic cable-in-conduit design options, drawn to scale: (a) large coil task, Westinghouse/AIRCO, Nb_3Sn; (b) dual purpose coil, Japan Atomic Energy Research Institute, cable-in-conduit with through cable and external cooling channels; (c) US dual purpose coil, central CICC in thick walled conduit and corner channels; (d) POLO, insulated subcable, dual channel CICC; (e) SSC GEM detector, cable in thin steel tube in thick aluminum conduit; (f) superconducting magnetic energy storage-engineering test magnet, large central channel; (g) International Thermonuclear Experimental Reactor (ITER) central solenoid, thick conduit, central cooling channel; (h) ITER toroidal field magnets, thin conduit in plate, central cooling channel.

Michels 1991). Historic examples of these design options are illustrated in Fig. 3.

CICC has several structural, electrical, and conductor cooling advantages. The conduit can be a high-strength superalloy and the winding pack can be completely potted, giving both mechanical rigidity and high electrical integrity. The cable is in direct contact with helium coolant with a high wetted perimeter and can utilize the much higher enthalpy of the helium to give it an energy margin against disturbances that is orders of magnitude higher than a dry magnet. The disadvantages of CICC are the additional cost of the conduit, closure welds, and cable insertion, local stress concentrations in the conduit walls, the need for a forced-flow refrigerator, and the need for electrical isolation from the helium headers. Because of the nearly unlimited ability to build up the cable to high currents and the demonstration of electrical isolation to 25 kV, CICC is favored in large-bore, high-energy storage magnets.

Progress in conduit design and manufacture has included (i) the development of reliable closure welds, (ii) conduit materials and welds with high strength

and toughness, even after being subjected to long superconductor heat treatments, and (iii) conduit materials with a good thermal contraction match to the superconductor. Reliable seam welds were demonstrated in thick JBK-75 (Beard *et al.* 1988) and Incoloy (Steeves *et al.* 1989) conduits in the 1980s. The International Thermonuclear Experimental Reactor (ITER), which would have required hundreds of kilometers of high current cable, developed orbital welding techniques with two advantages. The total length of welds in the system was greatly reduced and the welds were fully inspectable, before the insertion of cable.

ITER has also demonstrated excellent performance in high-current cables using Incoloy 908 and titanium alloy (Martovetsky *et al.* 2001). Incoloy 908 has the dual advantages of a good thermal contraction match with Nb_3Sn and higher strength and toughness than stainless steel conduits, after a long heat treatment. Titanium puts the lowest strain in the superconductor of any practical material. Both Incoloy 908 and titanium alloy require tight control of the atmosphere during heat treatment to avoid severe embrittlement during heat treatment. Less-expensive 304 and 316LN stainless steels have been used with NbTi and a low-carbon 316 has been developed to survive the Nb_3Sn heat treatment (Miller *et al.* 1994).

4. State-of-the-art Magnets and Future Progress

Several metrics are available for measuring state-of-the-art performance from magnets using strands and cables. These include magnets of solenoidal, toroidal, and multipole topologies, achieving the highest field, the highest current density for the current and voltage, the highest superconducting pinning force (current density-field product), and the highest average stress (e.g., the current density-field-radius product in a solenoid). International experts were surveyed for this article, and the highest historic values of these metrics that were identified are listed in Table 2.

Further improvements in high-field superconducting strands and cables will probably be driven by steady increases in the critical current density, temperature, and field of the strands. It should also be possible to significantly lower the manufacturing costs of all of the advanced strand materials, when they are produced in commercial quantities. The same potential for reducing costs with quantity exists for the advanced conduit materials desired for CICCs with heat-treated strands. The copper needed for the protection of CICC magnets should be reduced by the development of internal heaters and sensors with high signal/noise ratios. Advances in the understanding and performance of cables are expected if fully

Table 2
State-of-the-art performance: cable and magnet.

Parameter	Units	Value	Name/reference
B_{max} (solenoid)	T	23.4	NRIM NMR (Kiyoshi *et al.* 2000)
B_{max} (cryocooled solenoid)	T	15.0	INRC, Tohoko U. (Watanabe and Motokawa 2000)
B_{max} (NbTi dipole)	T	10.15	SSC/LBNL D-19
B_{max} (NbTi solenoid)	T	10.1	MIT Hybrid III (Iwasa *et al.* 1993)
B_{max} (NbTi/CICC, 1.8 K)	T	11.1	Euratom LCT (Darweschsad *et al.* 1999)
B_{max} (Nb_3Sn/CICC, 1.8 K)	T	14.1	NHMFL 45 T Outsert (Miller *et al.* 1994)
B_{max} (pulsed coil, > 1 T s^{-1})	T	13	ITER CS model coil
B_{max} (pulsed coil, > 5 T s^{-1})	T	6.7	DPC-EX (Ando *et al.* 1994)
B_{max} (dipole)	T	14.7	LBNL RD-3 (Gourlay *et al.* 2001)
B_{max} (quadrupole)	T	9.63	LHC KEK low-beta quad
B_{grad} (quadrupole)	T m^{-1}	260	LHC MQY Oxford/Cern IR (Strait 2001)
W_m/M_{cold}	kJ kg^{-1}	11.8	CMS solenoid detector (Herve 2000)
I_{cond} (CICC)	kA	200	SMES/ETM (Walker *et al.* 1990)
I_{cond} (dipole)	kA	19.8	U. Twente 11 T (den Ouden *et al.* 1997)
V_{term}	kV	23	POLO (Darweschad *et al.* 1997)
J_{wp} (dipole/quadrupole)	A mm^{-2}	560	LLNL APC HCX prototype (Martovetsky *et al.* 2002)
J_{wp} (solenoid)	A mm^{-2}	415	9.5 T Cryocool outsert (Shen *et al.* 2001)
J_{nonCu} (dipole/quadrupole)	A mm^{-2}	2349	LHC low I insertion quad (Lucas *et al.* 2000)
J_{Cu} (solenoid)	A mm^{-2}	1343	9.5 T Cryocool outsert
J_{Cu} (solenoid/CICC)	A mm^{-2}	550	US-DPC (Painter *et al.* 1992)
J_{Cu} (dipole/quadrupole))	A mm^{-2}	1550	LLNL APC HCX prototype
J_{wp} (dipole)	A mm^{-2}	1627	LBNL D20, outer
$J_{wp}B_{max}R_1$ (solenoid)	MPa	220	NHMFL 45 T outsert (Miller *et al.* 1994)
$J_{wp}B_{max}R_{av}$ (solenoid)	MPa	335	NHMFL 45 T outsert
$R_{bore}^2 B_o^2$ (quadrupole)	m^2 T^2	0.73	TJNAF Hall C Q2

predictive codes become available for calculating supercurrent evolution in each individual strand of a cable, providing reliable predictions of cable losses and individual strand recovery performance.

See also: Superconducting Materials, Types of; Superconducting Wires and Cables: Low-field Applications; Superconducting Wires and Cables: Materials and Processing; Superconducting Permanent Magnets: Potential Applications

Bibliography

Ando T, Nakajima H, Sasaki T-Y, Hiyama T, Takahashi Y, Nishi M, Yoshida K, Okuno K, Kato T, Sugimoto M, Isono T, Kawano K, Koizumi N, Hamada K, Oshikiri M, Sasaki T, Wadayma Y, Miyake A, Iwamoto S, Takahashi T, Ebisu H, Hosono T, Yamamoto K, Yasukawa Y, Tsukamoto H, Hanawa H, Seki S, Wakabayashi H, Tsuji H, Takayasu M, Turck B, Wuchuner F 1994 The second test results on the Nb_3Sn demo poloidal coil (DPC-EX). *Adv. Cryogenic Eng.* **39**, 335–41

Beard D S, Klose W, Shimamoto S, Vecsey G, Haubenreich P N, Komarek P, Shimamoto S, Dresner L, Fietz W A, Kato T, Lubell M S, Lue J W, Luton J N, Maurer W, Okuno K, Schwenterly S W, Takahashi Y, Ulbricht A R, Zichy J A 1988 The IEA Large Coil Task: development of superconducting toroidal field magnets for fusion power. *Fusion Eng. Des.* **7**, 1–229 (special issue)

Chernoplekov N A, Monoszon N A 1982 T-15 facility and tests. *IEEE Trans. Magn.* **23**, 826–30

Cooper W E, Fisk H E 1983 Fermilab Tevatron quadrupoles''. *IEEE Trans. Magn.* **19**, 1372–5

Darweschsad M, Fink S, Friesinger G, Gruenhagen A, Heller R, Hofmann A, Herz W, Komarek P, Maurer W, Noether G, Rietzschel K, Schleinkofer G, Suesser M, Ulbricht A, Wuechner F, Zahn G 1999 Test of the EURATOM LCT coil (NbTi conductor) with forced flow He II. *Fusion Eng. Des.* **45**, 361–75

Darweschsad M, Friesinger G, Heller R, Irmisch M, Kathol H, Komarek P, Maurer W, Nöther G, Schleinkofer G, Schmidt C, Sihler Ch, Süßer M, Ulbricht A, Wüchner F 1997 Development and test of the poloidal field prototype coil POLO at Forschungszentrum Karlsruhe. *Fusion Eng. Des.* **36**, 227–50

Gourlay S A, Benjegerdes B, Bish P, Byfford D, Caspi S, Chow K, Dietderich D, Gupta R, Hafalia R, Hannaford R, Harnden W, Higley H, Jackson A, Lietzke A, Liggins N, McInturff A, Millos G, O'Neill J, Palmerston E, Sabbi G, Scanlan R, Swanson J 2001 Fabrication and test of Nb_3Sn racetrack coils at high field. *IEEE Trans. Appl. Supercond.* **11** (1), 2164–7

Herve A 2000 The CMS detector magnet. *IEEE Trans. Appl. Supercond.* **10** (1), 389–94

ITER Design Group 2000 *Technical Basis for the ITER FEAT Outline Design*. ITER EDA Documentation Series No. 19. IAEA, Vienna

ITER TFMC Operation and Testing Group 2001 First results of test of the ITER toroidal field model coil in the TOSKA facility of Forschungszentrum Karlsruhe. (in press)

Iwasa Y, Leupold M J, Weggel R J, Williams J E C, Itoh S 1993 Hybrid III: the system, test results, the next step. *IEEE Trans. Appl. Supercond.* **3** (1), 58–65

Kiyoshi T, Kosuge M, Yuyama M, Nagai H, Wada H, Kitaguchi H, Okada M, Tanaka K, Wakuda T, Ohata K, Sato J 2000 Generation of 23.4 T using two Bi-2212 insert coils. *IEEE Trans. Appl. Supercond.* **10** (1), 472–7

Lee G S, Kim J, Hwang S M, Chang C S, Chang H Y, Cho M H 1999 The design of the KSTAR tokamak. *Fusion Eng. Des.* **46**, 405–24

Lucas J, Kirby G A, Ostojic R, Rodrigeuz-Mateos F, Krischel D, Schillo M 2000 Design and construction of a 1 m model of the Low Current Superconducting Quadrupole for the LHC insertions. *IEEE Trans. Appl. Supercond.* **10** (1), 150–3

Martovetsky N, Manahan R, Lietzke A 2002 Development of superconducting focusing quadrupole for heavy ion driver. *Magnet Technology Conf. MT-17*, Geneva, Sept 24–28, 2001

Martovetsky N, Michael P, Minervini J, Radovinsky A, Takayasu M, Thome R, Ando T, Isono T, Kato T, Nakajima H, Nishijima G, Nunoya Y, Sugimoto M, Takahashi Y, Tsuji H, Bessette D, Okuno K, Ricci M 2001 ITER CS model coil and CS insert test results. *IEEE Trans. Appl. Supercond.* **11** (1), 2030–3

McInturff A D, Benjegerdes R, Bish P, Caspi S, Chow K, Dell'Orco D, Dietderich D, Hannaford R, Harnden W, Higley H, Lietzke A, Morrison L, Morrison M, Scanlan R, Smithwick J, Taylor C, van Oort J 1997 Test results for a high field (13 T) Nb_3Sn dipole. *Proc. Particle Accelerator Conference*, Vancouver, Canada, May 12–16, 1997, pp. 3212–14

Meinke R 1991 Superconducting magnet system for HERA. *IEEE Trans. Magn.* **27**, 1728–31

Miller J R, Bird M D, Bole S, Bonito-Oliva A, Eyssa Y, Kenney W J, Painter T A, Schneider-Muntau H-J, Summers L T, Van Sciver S W, Welton S, Wood R J, Williams J E C, Bobrov E, Iwasa Y, Leupold M, Stejskal V, Weggel R 1994 An overview of the 45-T hybrid magnet system for the new national high magnetic field laboratory. *IEEE Trans. Magn.* **30** (4), 1563–70

den Ouden A, Wessel S, Krooshoop E, ten Kate H 1997 Application of Nb_3Sn superconductors in high-field accelerator magnets. *IEEE Trans. Appl. Supercond.* (June), 733–8

Painter T A, et al. 1992 Test data from the US Demonstration Poloidal Coil Experiment. *MIT Plasma Fusion Center Report*, PFC/RR-91-1, pp. 1–281

Peck S D, Michels P H 1991 Test results from the 200 kA SMES/ETM conductor. *IEEE Trans. Magn.* **27** (2), 1724–7

Perin R 1991 The superconducting magnet system for the LHC. *IEEE Trans. Magn.* **27**, 1735–40

Rudziak M K, Seuntjens J M, Renaud C V, Wong T, Wong J 1995 Development of APC Nb-Ti composite conductors at Supercon, Inc. *IEEE Trans. Appl. Supercond.* **5** (2), 404–7

Schultz J H, Kesner J, Minervini J V, Radovinsky A, Pourrahimi S, Smith B, Thomas P, Wang P W, Zhukovsky A, Myatt R O, Kochan S, Mauel M 1999 The levitated dipole experiment (LDX) magnet system. *IEEE Trans. Appl. Supercond.* **9** (2), 378–81

Shen W, Coffey M, McGhee W 2001 Development of 9.5 T NbTi cryogen-free magnet''. *IEEE Trans. Appl. Supercond.* **11** (1), 2619–22

Steeves M M, Hoenig M O, Takayasu M, Randall R N, Tracey J E, Hale J R, Morra M M, Hwang I, Marti P 1989 Progress in the manufacture of the US-DPC test coil. *IEEE Trans. Magn.* **25** (2), 2089–92

Strait J 2001 Very high gradient quadrupoles. *Proc. 2001 Particle Accelerator Conf.*, Chicago, IL, pp. 176–80

Sumption M D, Buta F, Collings E W, Tomsic M, Austen A, Gregory E, Parrell J, Hong S, Zhang Y, Scanlan R M 2002 Nb_3Al strand processing transport properties and cabling. *Proc. Applied Superconductivity Conf.*, Houston, TX, Aug 2002, to be published

Takeo M, Funaki K, Sato S, Yamafuji K, Iwakuma M, Hiramatsu M, Matsumoto K, Hamada M 1987 A 17 tesla superconducting magnet with multifilamentary superconductors. *IEEE Trans. Magn.* **23** (2), 565–8

Takeuchi T 2001 Nb₃Al conductors. *Magnet Technology Conf. MT-17*, Geneva, Sept 24–28, 2001

Tsuji H, Okuno K, Thome R, Salpietro E, Egorov S, Martovetsky N, Ricci M, Zanino R, Zahn G, Martinez A, Vecsey G, Arai K, Ishigooka T, Kato T, Ando T, Takahashi Y, Nakajima H, Hiyama T, Sugimoto M, Hosogane N, Matsukawa M, Miura Y, Terakado T, Okano J, Shimada K, Yamashita M, Isono T, Koizumi N, Kawano K, Oshikiri M, Nunoya Y, Matsui K, Tsuchiya Y, Nishijima G, Kubo H, Shimba T, Hara E, Imahashi K, Uno Y, Ohuchi T, Ohtsu K, Okayama J, Kawasaki T, Kawabe M, Seki S, Takano K, Takaya Y, Tajiri F, Tsutsumi F, Nakamura T, Hanawa H, Wakabayashi H, Shimizu T, Kuramochi K, Omine T, Tamiya T, Harada J, Nishii K, Huguet M, Mitchell N, Bessette D, Minervini J, Vieira R, Michael P, Takayasu M, Bevilacqua G, Maix R, Manahan R, Jayakumar R, Savoldi L, Herz W, Ninomiya A 2000 Progress of the ITER Central Solenoid Model Coil Program. *IAEA-CN-77, 18th IAEA Energy Conf.*, Sorrento, Italy, 4-10, IAEA 2001, pp. 354–61

Walker D L, *et al.* 1990 Design of a 200 kA conductor for superconducting magnetic energy storage (SMES). *Adv. Cryogenic Eng.* **35**, 573–9

Watanabe K, Motokawa M 2000 Cryogen-free high field superconducting magnets. *IEEE Trans. Appl. Supercond.* **10** (1), 489–94

J. H. Schultz
Massachusetts Institute of Technology, Cambridge MA, USA

Superconducting Wires and Cables: Low-field Applications

The discovery in 1986 of high-temperature superconductors (HTSs) with the prospect for operation at liquid nitrogen temperature (77 K) or above provided new impetus for superconducting electric power applications. HTS materials also exhibit higher heat capacity than low-temperature superconductor (LTS) materials that markedly improves their electrical stability, i.e., "normalization" of the superconducting state, during thermal transients. The higher transition temperatures also ease the refrigeration requirements and facilitate cryogenic operation (Blaugher 1996).

1. Cables

Type II superconductors available in the shape of wires and tapes appear as almost "natural" candidates for such electrotechnical applications as power transmission cables. Traditionally, network engineers have relied on increasing voltage to transmit a larger amount of power. Superconducting cables have the capability of carrying much higher currents, so providing the opportunity for reducing the number of circuits, or using lower voltage rating.

In the 1980s a significant research effort, including design studies and experimental activity, was devoted to the assessment of power cables based on low T_c, liquid-helium-cooled materials. Such research led to the conclusion that, although technically attractive, such cables were not economically viable, unless for very high transmitted power, above 2–5 GVA. The main cause for this was identified as the projected cost of refrigeration, which resulted from the high cost and low efficiency of liquid helium, combined with the intrinsically unfavorable geometry (very high surface to volume ratio) of cables. Since 1986 the availability of the new class of high T_c superconducting materials, potentially suitable for (far more effective) cooling with liquid nitrogen, has therefore given a renewed impetus to the development of superconducting power cables.

A range of applications is envisaged. A few instances worth mentioning are the upgrading of existing underground circuits, the matching of the power rating of an overhead line for sections to be relocated underground, and the elimination of intermediate voltage transformations in urban distribution networks.

The expected benefits include, for example, increased transmission efficiency (energy saving, improved stability of high-power circuits), drastic reduction of electromagnetic pollution, an effective solution to the expanded energy demand in congested metropolitan areas, etc.

Development activities are underway in several countries, and include both feasibility studies and experimental work with prototype fabrication and testing. In a number of such experiments, prototype terminations and joints are also being developed. The lengths of such prototypes range from a few meters to more than a hundred meters (Norman *et al.* 1999, Kelley *et al.* 1999).

The first experimental installations of a three-phase superconducting connection in a "real" environment are being realized in the USA. Actually, one link made with cold dielectric (CD) cables (see below) fabricated by SouthWire has already been installed at an industrial plant, and another link, made by Pirelli based on a warm dielectric (WD) design (see below), was planned to be installed in a part of a utility (Detroit Edison) network by the end of 2001.

As type II superconductors show true zero resistance only under d.c. conditions, d.c. cables would appear as the "natural" way of best exploiting HTS materials, by achieving a virtually zero dissipation in the conductor, in addition to negligible dielectric losses. In fact, most power lines transmit a.c. power, and so a.c. designs are also typically assumed for superconducting cables. These are in turn generally classified, according to two main choices that can be made regarding electrical insulation, into "warm" or "cold" dielectric types.
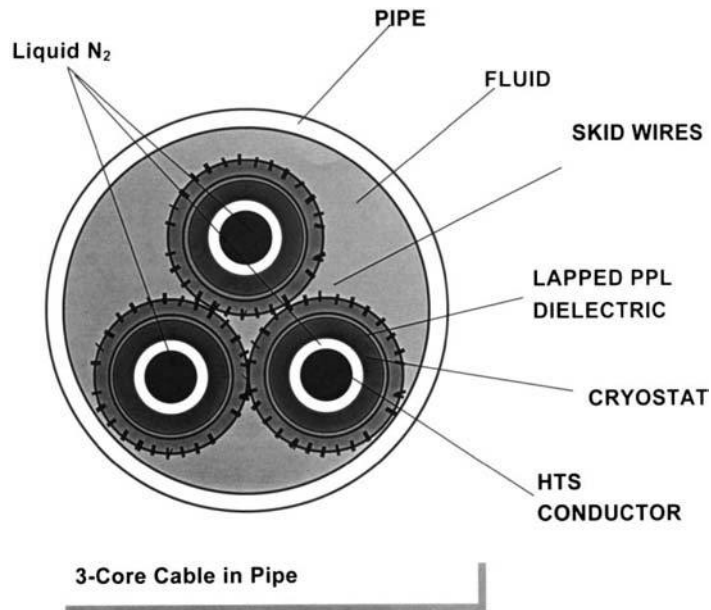
Figure 1
Example of a three-phase WD cable in a pipe.

In the WD cable design (Fig. 1), the HTS, made up of one or more layers of current-carrying HTS tapes, is enclosed in a cryogenic environment (the so-called "cryostat"), which in turn is covered by conventional dielectric materials.

This design has several advantages, such as:

• it has similar performance and requires similar installation procedures as a conventional cable.

• it can carry, at the same level of losses, more than twice the power of a conventional cable.

• it uses already developed dielectric materials.

• it needs accessories, both termination and joint, that can be derived in a relatively easy way from conventional ones.

• it requires fewer HTS tapes than the CD coaxial design.

In the CD design, two coaxial HTS conductors, separated by a dielectric at liquid nitrogen temperature, are enclosed in the cryostat (Fig. 2).

This approach, which is characterized by the presence of a superconducting "sheath" that acts as a return path for the current and cancels out the external magnetic field, represents the best technical solution for very high-power transmission. It allows one to:

• transmit a large amount of power with reduced losses in "compact" cable systems, eliminating a.c. losses due to external magnetic field of the other phases; and

• eliminate eddy current losses in metallic components, allowing installation close to other cables in service.
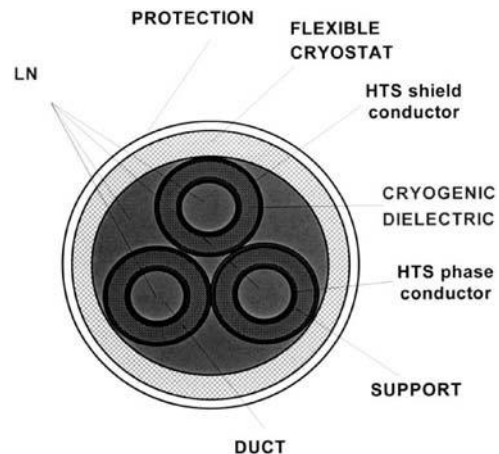
Figure 2
Example of a three-phase CD cable in a pipe.

However, it requires about twice the amount of superconducting material compared to the WD design, and requires a suitable cryogenic insulation in addition to the development of specific accessories.

Generally, the design of the conductor of a superconducting cable includes a multilayer stranded

structure around a suitable former of adequate internal dimension.

Optimization of the conductor involves several parameters such as the tape laying angle, the laying tension, the use of binding and/or insulating materials between superconducting layers, the number of tapes and layers, and the former material and dimensions to comply with both electrical and mechanical constraints during fabrication, handling, and service.

Cable manufacturing requires that the superconducting materials are available in the shape of long, flexible wires. Most of the cable prototypes fabricated have been made with BSCCO 2223 tapes typically a few millimeters wide, with a thickness of a few tenths of a millimeter.

For the optimization of the overall electrical and mechanical performance, superconducting tapes are made with a "multifilamentary" structure, with the number of filaments typically ranging from a few tens to over a hundred.

It is worth remarking that the long length required for a wire to be used in cable technology also imposes obvious constraints in terms of performance uniformity. This in turn requires a very good control of the processing parameters (mechanical, "chemical," and thermal) throughout the whole wire fabrication process.

The development of flexible tapes with biaxially textured YBCO, being pursued in the USA, Europe, and Japan with promising results, has not yet reached a stage as to allow the manufacturing of long prototypes. The possibility of replacing BSCCO sintered tapes with YBCO thick films deposited on a flexible substrate is, however, considered extremely interesting for cable applications. In fact, provided that the performances already demonstrated on shorter lengths can be maintained to a significant extent over kilometer-long tapes, the use of YBCO is expected to provide an important improvement in terms of cost-effectiveness, and will therefore possibly give further impetus to the development of superconducting cables.

2. Fault Current Limiter

A fault current limiter (FCL) is, in principle, a device that is capable of protecting a power grid from very high surge currents that can arise when a fault (short circuit) occurs anywhere in the grid. As such fault currents are expected to increase with increasing grid interconnection, which is presently a worldwide trend, the need for an effective protection will become more necessary. The problem has been solved partially with the use of nonsuperconducting devices as circuit breakers, fuses, high-impedance transformers, etc, which in general have some drawbacks such as increased operating losses or at least nonideal efficiency. In fact, there is no direct "equivalent" for a superconducting FCL among conventional, nonsuperconducting power components.

A superconducting device can take advantage of the unique property of superconducting materials to undergo a rapid transition to normal state upon a quench, and therefore can in principle offer ideal performance in terms of fast response, fast recovery, and zero impedance throughout normal operation.

As it did for cables, and substantially for the same reasons (insufficient cost-efficiency with low T_c materials), the discovery of HTSs has given new impetus to research activities on FCL development in Europe, the USA, Israel, and Japan. Such activities include design studies as well as demonstrations of small- to full-scale prototypes (Leung 1997).

Various design approaches are considered, namely:

- "Resistive," i.e., the superconducting device is connected directly in series with the power line. The sudden increase of current due to a fault would induce the superconductor-to-normal transition of the material, hence increasing the impedance of the line.
- "Inductive," or "screened core," when the superconductor is *magnetically* (and not galvanically) connected to the line. Such a device is substantially based on a transformer, which has a superconducting shielding tube as the secondary. Under fault conditions the HTS becomes unable to screen the magnetic field generated by the primary coil and the flux penetrates into the iron core thus increasing suddenly the impedance of the device. Different from the resistive type, the HTS component will experience higher current but at lower voltage and does not need current contacts.
- "Hybrid," which is also based on a transformer configuration that includes a resistive superconducting element combined with resistive or inductive shunts.

The different designs are typically based on different superconducting materials. Being studied for FCL applications are BSCCO 2212, BSCCO 2223, and YBCO, in various shapes, namely wires, bulk, and films.

Long tapes with good uniformity are available in the case of a composite tape with BSCCO 2223, which would therefore be a candidate for resistive FCLs. Unfortunately, the composite includes a high-conductivity matrix, which poses severe limits on the efficiency of a type of device based on such tapes. Tapes made with YBCO films deposited on a high-resistivity metallic substrate are available only in short lengths, but, assuming that kilometer-long tapes can be produced, they could represent a good candidate for that purpose. An alternative approach has already been demonstrated with prototypes of resistive FCLs made with YBCO thick films deposited on nonmetallic substrates in a suitable pattern.

YBCO films have also been used as the resistive element in a prototype of a hybrid (with inductive shunt) type of FCL. BSCCO 2212 is more suitable for the manufacture of large pieces, and has been used in prototypes of inductive FCLs in the shape of bulk cylinders.

In general, key material features of superconducting elements for both resistive- and hybrid-type FCLs are essentially their critical current density and normal state resistivity, which determine the required length of the element and the amount of power that will be generated during quench transition, and the sharpness of the superconducting-to-normal transition, which determines the time response of the device.

Other extremely important requirements concern the stability of the superconducting element against the creation of "hot spots" and subsequent thermal instability. From this viewpoint, thin films on non-metallic substrates imply a different design approach compared to tapes with a metallic matrix or substrate.

As a general consideration, however, it must be noted that there will never be a universal superconducting FCL, since depending on its location inside the network the requirements in terms of recovery, limitation current, and protection coordination are very different. The requirements for the material are also very different. There will therefore probably be opportunities for different materials to be implemented in different types of FCLs in the future.

See also: Superconducting Wires and Cables: High-field Applications; Superconducting Wires and Cables: Materials and Processing

Bibliography

Blaugher R D 1996 Superconducting electric power applications. *Adv. Cryogenic Eng.* **42**, 883–98
Kelley N, Cinquemani P, Belcher P, Wen Y, Nassi M, Corsaro P, Ladié P, Norman S R, Rahman M M 1999 Applications of HTS cables to power transmission: state of the art and opportunities. In: *Proc. IEEE Transmission and Distribution Conf.* IEEEE, Piscataway, NJ, Vol. 1, pp. 13–19
Leung E 1997 Surge protection for power grids. *IEEE Spectrum* July, 26–30
Norman S R, Ladié P, Nassi M, Schroth R 1999 Latest development of high temperature superconducting cable systems. In: *Proc. Jicable '99*. Jicable, Versailles, France, paper A3.5, pp. 97–102

L. Gherardi
Pirelli Cavi e Sistemi Spa, Milan, Italy

Superconducting Wires and Cables: Materials and Processing

1. Introduction

The phenomenon of superconductivity was first observed in 1912 in the laboratory of Heike Kamerlingh Onnes, at the University of Leiden (Holland). At low temperatures certain materials ($\sim$ 800 superconducting

compounds have been recently tabulated by Poole and Farach 2000) suddenly lose their resistance to the flow of electricity. The phenomenon remained a laboratory curiosity until 1954 when G. B. Yntema at the University of Illinois made the first successful superconducting magnet. At that point, magnet performance fell well below that predicted by the properties of the superconductor. The slow progress can be partially attributed to (i) the difficulty in obtaining the extremely low temperatures required and (ii) the lack of understanding of how to create electrically and thermally stable wires from superconductors. The primary limitation, however, was that the superconducting phenomenon was not only limited to low temperatures but also to a restricted range of electrical current density and magnetic field and that the range of these properties was particularly limited in early superconductors. The maximum values of temperature, electrical current, and magnetic field are interdependent and, when plotted in three axes, form a "critical surface" (Fig. 1). Those early superconductors, such as Pb, In, and Hg are classified as type I superconductors. These are superconductors in which magnetic flux is excluded from their bulk and the critical current density is limited to a surface layer of approximately one-tenth of a micrometer. The maximum fields in which these superconductors can operate are usually less that 0.1 T (similar to the flux density between the poles of a horseshoe permanent magnet). These limitations make type-I superconductors impractical for wire and cable applications. All "technical superconductors," i.e., superconductors that can be readily fabricated into wires and cables for high-current applications, are type-II superconductors. In type-II superconductors, magnetic flux penetrates the bulk of the superconductor to form individual flux
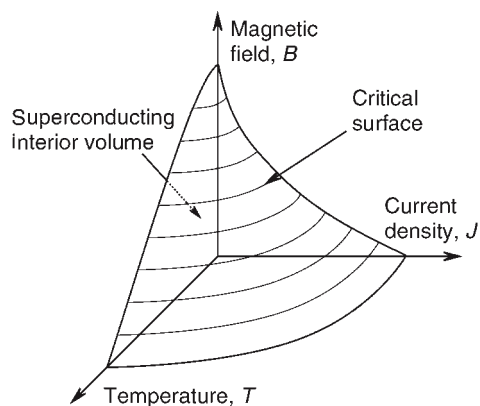
Figure 1
Schematic illustration of the critical surface for a type-II superconductor. The applied field (B), the temperature (T), and the current density (J) must be maintained below the critical surface in order to retain superconductivity.

quanta (see *Electrodynamics of Superconductors: Flux Properties*). In the most widely used technical superconductors, Nb–Ti and Nb$_3$Sn, the upper critical fields are 13 T and 27 T, respectively, and current densities $>10^9$ A m^{-2} can be carried (compared to $\sim 10^7$ A m^{-2} for domestic Cu wire). In Fig. 2, the critical current densities at 4.2 K are compared for strands or tapes that are fabricated in lengths of more than 100 m. The temperature range is still limited (the critical temperatures for Nb–Ti and Nb$_3$Sn are 10 K and 18 K, respectively), but for many applications the cost of insulation and refrigeration is more than offset by the reduced energy costs resulting from nonresistive current flow. Because the amount of energy lost in current flow through a superconducting magnet is extremely low, it can be operated without a power supply once the magnet has been charged. This mode of operation, termed "persistent" is very desirable for MRI and NMR applications because the current flow (and consequently the field) is very stable. Liquid He is now readily available and provides cooling to 4.2 K at atmospheric pressure and as low as 1.8 K at reduced pressure. Recent advances in insulation and refrigeration technology have also made the application of superconductors more widespread. The discovery of

high-temperature superconductivity (HTS) superconductors (ceramic superconductors with critical temperatures above the boiling point of liquid nitrogen (77 K) in 1986 (see *High-temperature Superconductors: Thin Films and Multilayers*)) dramatically increased interest in the application of superconductivity. The discovery of superconductivity at 39 K in MgB$_2$ in 2001 further extended the temperature range for intermetallic superconductors.

Superconductors must be formed into composite wires in order for them to be used in high-current applications and these wires may also be cabled. The wide variety of mechanical properties of superconductors: the range from strong ductile alloys like Nb–Ti to brittle ceramics such as HTS superconductors means that the wire processing routes vary greatly. Of the HTS superconductors only one, Bi-2212, is manufactured in round-wire form and HTS superconductors are more commonly manufactured as multifilamentary tapes. The brittle superconductors cannot undergo wire drawing and are consequently mechanically processed in the form of ductile precursors or fine powders that are reacted to form the final superconductor. For Nb–Ti, the alloy can be cold-worked to a remarkable extent but heat treatments are also applied during processing in order to introduce a second phase into the microstructure that will ultimately pin the fluxoids in the final wire. Because of these variations, the types of processing will be introduced separately and by superconducting material. There are, however, key components that are common to all superconducting strands.

2. General Strand Requirements

2.1 Matrix and Filaments

Superconducting wires are almost always of a multifilamentary design in which individual continuous filaments (<30 μm in diameter) are embedded in a high-conductivity matrix. When conditions in a localized region of a superconductor exceed the critical surface conditions, that area will start to conduct resistively and produce local heating. The resulting heat and current transfer will start a cascade effect and result in a rapid transition of the whole superconductor to the normal state. The ability to transfer heat and current away from localized regions by sub-dividing the filaments into a high-conductivity matrix was a key step towards producing practical superconductors. The primary components of cryogenic stabilization were not formulated until the mid-1960s (Stekley and Zar 1965). The most desirable matrices are Cu or Al, but Ag is required for the processing of HTS superconductors where oxygen diffusion through the matrix is required during heat treatment. External stabilizer is often added after heat treatment; this is particularly the case for Al, which has thermal and density advantages over Cu, but is difficult to
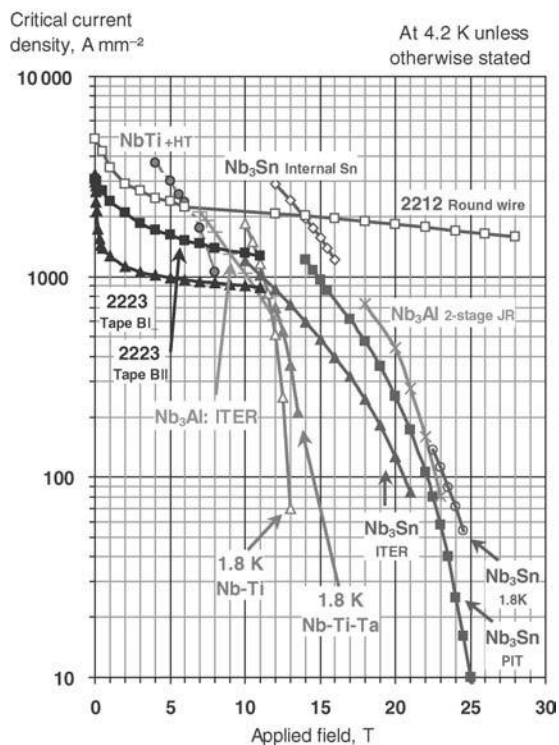
Figure 2
Comparison of critical current densities (at 4.2 K unless otherwise stated) available in strands and tapes of more than 100 m.

fabricate as the matrix of a composite wire. In addition to stability requirements, fine filaments also serve the purpose of limiting hysteretic loss, not only for a.c. applications but also for d.c. applications. The filament diameter requirements for a.c. applications are quite severe with desired filament diameters of less than 1 μm. For a.c. applications, a Cu–Ni matrix is often used to reduce proximity coupling of the filaments.

2.2 Filament Uniformity

As the critical current per unit cross-sectional area is limited by the material properties, the amount of current that can be carried by an individual filament is reduced if the filament is locally necked to a smaller diameter. Current may be locally transferred to adjacent filaments, but there is a broadening of the critical current transition and a reduction in time that the strand may be operated in the persistent mode (crucial for MRI application). With final filament diameters of less than 20 μm often required, this imposes a very high level of quality control on the processing of the strands. The degree of filament uniformity is reflected in the sharpness of the superconducting transition with increasing current. In the early stages of the resistive transition; the curve of voltage, V, against current, I, can be described by the power law:

$$V \propto I^n \qquad (1)$$

The value of n (the transition index) decreases with field; the more uniform the filament cross-sectional areas, the more linear the decrease in n-value and the higher the initial low field value (Warnes and Larbalestier 1986). An electric field, E, is generated along the superconductor carrying a current density, J, that is related to the critical current density of the superconductor J_c at field E_c by the transition index, n:

$$E = E_c(J/J_c)^n \qquad (2)$$

For composites based on Nb–Ti strands, the value of n (5 T) can be 50–100, in Nb_3Sn for NMR application the values are in the range of 40–80. The high n-values in Nb–Ti strands correspond to variations in filament cross-sectional area of less than 2% (coefficient of variation) (Lee and Larbalestier 1993). In HTS superconductors the range of available n-values is presently only 10–20 and persistent mode operation is not feasible under these conditions.

2.3 Critical Current Density and Flux Pinning

Pure annealed superconductors do not carry very much current because once current passes through the superconductor, a Lorentz force is induced on the flux lines. When they move, the flux line lattice (FLL) dissipates energy and the superconductor eventually

goes "normal" (see *Electrodynamics of Superconductors: Flux Properties*; *Superconducting Materials: Irradiation Effects*). The flux lines, however, can be held in place by defects in the superconductor, a process termed "flux pinning." In A15 based superconductors (such as Nb_3Sn), increasing the grain boundary density has been shown to increase critical current density (Scanlan *et al.* 1975, Ochiai *et al.* 1986). In Nb–Ti a linear increase in critical current density is observed with vol.% of α-Ti precipitate (Lee *et al.* 1990). Consequently, the introduction of pinning defects and the refinement of grain size are key elements to the success of technical superconductors.

2.4 Twisting

Twisting of the strand about its drawing axis is typically required to reduce flux-jump instability caused by varying external fields, and to reduce eddy-current losses. The twisting is ideally applied just before a multifilamentary strand has reached final size, so that the twist can be locked into place by a further die-pass. The higher the expected rate of change of field, the tighter the required twist pitch. For the relatively steady-state dipole magnets for the Superconducting Supercollider, ~80 rotations along the drawing axis per meter were required, for a.c. application with a similarly sized strand the number of twists per meter might be 300. Typically, twist pitches cannot be higher than 8 times the wire diameter, and normally a twist pitch of 10–20 times the diameter is used.

2.5 Final Shaping and Cladding

The final cross-section of the strand can be controlled by die shape and size or by using independently adjusted rollers operating along the strand surface. In this way, square or rectangular cross-section filaments can be produced. Alternatively, the strand can by inserted into a channel in a larger form, most commonly a rectangular aluminum external stabilizer.

2.6 Cabling

Individual strands can be cabled or braided together to form a conductor with a higher current carrying capacity. The most common design for Nb–Ti magnets is the Rutherford cable, which consists of a fully transposed, flat cable. Using this approach, high-aspect-ratio cables can be produced with as many as 46 strands (Scanlan *et al.* 1997). Strands may also be drawn into a larger conduit or combined with external stabilizers. A cross-section of a cable-in-conduit-conductor (CICC) is shown in Fig 3. As in the single strand-in-channel aluminum process, multiple strands have been applied to surface channels in circular cross-section aluminum rods.
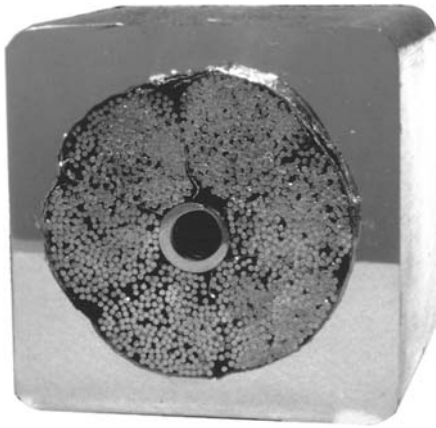
Figure 3
CICC: this 51 mm diameter Incoloy® jacketed cable contains 6 sub-cables; each containing 180 Nb₃Sn based superconducting strands.

2.7 Length-dependent Parameters

Both commercial Nb–Ti and Nb₃Sn strands are made in lengths of over a kilometer and variations can occur over the length of the strand, due to differences in mechanical properties of the components and bonding of the monofilaments that occurred during mechanical reduction. In Nb–Ti variations in critical current, I_c, along the length of strands can be directly correlated with variations in Cu/Nb–Ti ratio along the length as shown by Kanithi *et al.* (1990). In their study of strands developed for the Superconducting Supercollider project, they showed that the variation in I_c (due to variations in the intrinsic superconducting properties, the strand diameter and Cu/Nb–Ti ratio as well as measurement error) was more than twice the variation seen in J_c (due to just the intrinsic superconducting properties and measurement error). As HTS-based strands are still in their production infancy, a different phenomenon is observed: as production length is increased, the overall I_c declines because it is very difficult to maintain the ideal conditions (grain alignment, heat treatment temperature, low porosity) necessary for good HTS strand over long lengths.

3. Superconducting Strand and Cable Manufacture by Material

3.1 Nb–Ti

(a) Alloy composition
Nb–Ti has become the dominant commercial superconductor, because it can be economically manufactured in a strong and ductile form with both high current density and high resistive transition index.

The starting point for fabrication of Nb–Ti strand is an alloy of between 46.5 wt.% Ti and 50 wt.% Ti. Decreasing Ti over this range increases both the critical temperature, T_c, and the upper critical field, H_{c2} (which at 4.2 K has a maximum value of 11.5 T at 44 wt.% Ti). The increase in T_c and H_{c2}, however, is offset by a decrease in the amount of Ti available for precipitation of the α-Ti phase desired for flux pinning and high critical density. The composition of the Nb–Ti also affects the precipitate morphology: if the α-Ti is formed at grain boundary intersections, it tends to be uniform in size and distribution and does not significantly affect strand ductility. Higher Ti compositions, however, also produce fine distributions of Widmanstätten-type precipitation in the grain interiors resulting in both a nonuniform microstructure and a significant hardening of the Nb–Ti. As all these factors are sensitive to composition, it is very important to start with a homogeneous alloy. With final filament diameters well below 0.05 mm, the alloy must also be free of unmelted Nb or nonductile inclusions that may result in filament and ultimately strand breakage. Although the large difference in the melting points of Ti and Nb makes this a difficult alloy to manufacture, homogeneity levels in commercial Nb–47 wt.% Ti alloys are now typically much better than ±1.5 wt.% Ti. Impurity content has been traditionally kept low and consistent, but recent work has shown that increasing the allowable content of iron can considerably refine the precipitate size without adversely affecting the precipitate volume (Smathers *et al.* 1996).

(b) Extrusion and billet assembly
The (as-cast) Nb–Ti ingot is (hot forged) to the required diameter and then annealed in the single phase β region (~2 h at 870 °C). For fine filament Cu matrix composites, the Nb–Ti ingot is then sealed inside a high-purity Cu extrusion can, that subsequently (warm-extruded) forms a (well-bonded) monofilament. Monofilament production billets ready for extrusion are shown in Fig. 4. Billet assembly is performed in a clean environment, in order to avoid introducing particles that would not co-deform to the sub-0.05 mm filament size. Where high critical current densities and fine filaments are desired, an Nb diffusion barrier is wrapped around the Nb–Ti rods in order to inhibit the formation of brittle Cu–Ti intermetallics during heat treatment (Wilson 1972). The monofilament is then reduced in diameter by wire drawing, typically finishing with a hexagonal die to produce filaments that can be efficiently (restacked). The thickness of Cu around the Nb–Ti at this stage is important because it determines the spacing between Nb–Ti filaments when Cu/Nb–Ti monofilaments are stacked together. For optimum mechanical stability in Nb–Ti/Cu multifilamentary composites, a filament spacing to filament diameter (s/d) ratio of 0.15–0.20 is

Figure 4
Monofilament Cu-clad Nb–Ti extrusion billets being inspected after welding (image courtesy of Hem Kanithi, Outokumpu Advanced Superconductors Inc.).

ideal (Gregory *et al.* 1987). Usually, additional stabilizer is required and that may be added by increasing the wall thickness of the extrusion can or adding a central core of stabilizer. For d.c. magnet application, it has been established by Ghosh *et al.* (1987) that a minimum Cu thickness of 0.4–0.5 μm is required to reduce the magnetization associated with proximity filament coupling. For s/d ratios of 0.15–0.20, the minimum Cu thickness requirement limits the minimum filament diameter to ~ 3 μm when using a pure Cu matrix. If smaller filaments are required, Ni or Mn can be added to the Cu between the filaments (Hlasnik *et al.* 1985, Cave *et al.* 1989, Kreilick *et al.* 1988).

The monofilament is then restacked inside another Cu extrusion can to form the final multifilamentary composite. The size of this extrusion can be up to 330 mm in diameter with a weight of 400 kg. As many as 4000 filaments may be assembled in one extrusion. Alternatively, large numbers of fine filaments can be produced by restacking a previously extruded multifilamentary billet. Using this approach, strands with up to 40 000 filaments have been manufactured. Where a small number of large filaments are desired (typically for low-field MRI application), Nb–Ti rods can be directly inserted into gun-drilled holes in a solid high-purity Cu extrusion billet. Warm extrusion helps bond the composite, as much of the subsequent processing involves cold work by wire drawing, and the resulting strain introduces into the Nb–Ti an essential element in developing the high critical current microstructure.

(c)   Precipitation heat treatment
Such a treatment is applied after sufficient cold work has been carried out following the multifilamentary

extrusion. If too little cold work is applied before heat treatment, Widmanstätten-type precipitation will occur, causing increased hardness (reducing drawability) and producing a non-optimum precipitate size and distribution. Lee *et al.* (1989) found that the amount of (prestrain) required increases linearly with wt.% Ti. Consequently, a higher prestrain is required to suppress Widmanstätten-type precipitation in a chemically inhomogeneous alloy than would be required in a homogeneous alloy. For Nb–47 wt.% Ti, the required prestrain is ~ 5 but this rises steeply to 9 for a 55 wt.% Ti alloy. Heat treatments are typically at 375–420 °C, ranging from 20 h to 80 h in duration. Multiple heat treatment and drawing cycles are required to produce high critical current densities (Cheng-ren *et al.* 1983). Whereas an initial heat treatment will only yield ~ 10 vol.% precipitate, by applying additional cold work strain, the effect of the slow diffusion rate at these temperatures is again overcome and more precipitate is produced. Second and third heat treatments typically yield 15 vol.% and 20 vol.% of α-Ti precipitate, respectively. The strain between heat treatments is 0.8–1.5 and at least three heat treatments are usually applied. A linear relationship between the optimized critical current density and the volume of precipitate Nb–47 wt.% Ti alloys has been established by Lee *et al.* (1990) 20% volume of α-Ti precipitate is sufficient to produce a critical current density of > 3000 A mm^{-2} at 5 T, 4.2 K. Increasing Ti content increases the precipitation rate and amount, but higher pre-strains are required if good ductility and long piece length is to be maintained. Alternatively, the pinning sites can be introduced mechanically by hand-assembling the desired microstructure at a large size, in the same way as the multifilamentary billets are assembled, and then reducing the dimension to match the fluxoid spacing by multiple restacking and drawing cycles. This approach is called APC for artificial pinning center. With APC strand, no additional heat treatment is necessary and a greater flexibility is possible in the microstructural components. Despite superior low field (< 5 T) performance, the APC approach has not reached commercialization because of the costs associated with the multiple restacking approach.

(d)   Final wire drawing
After final heat treatment the α-Ti precipitates are roughly equiaxed in transverse cross-section, 100–200 nm in diameter with an extension along the wire axis giving an aspect ratio of 5–20. The extensive final wire drawing (an engineering true strain of 5), however, produces a plain strain condition in the b.c.c. β-Nb–Ti, which is supported by (inter-curling) of the Nb–Ti grains. This results in distortion of the α-Ti precipitates into densely folded sheets during final wire drawing (Fig. 5(a)). The folding process rapidly decreases the precipitate thickness and spacing with a
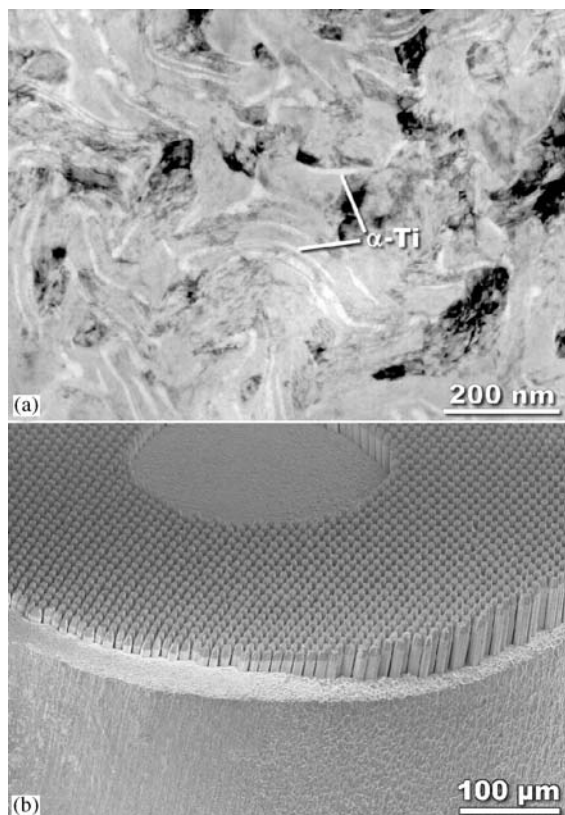
Figure 5
(a) Transmission electron microscope image of high
critical current density Nb–Ti microstructure with
folded sheets of α-Ti precipitate. (b) Etched cross-section
of Nb–Ti-based superconducting strand fabricated by
IGC-AS (now Outokumpu Advanced Superconductors)
for the Interaction Region Quadrapole Magnets of the
Large Hadron Collider at CERN.

dependence of $d^{1.6}$ (where d is the strand diameter)
and increases the precipitate length per area with a
dependence of $d^{-1.6}$, as measured by Meingast *et al.*
(1989). The critical current density increases as the
microstructure is refined until it reaches a peak, after
which there is a steady decline. The peak in critical
current density for a monofilament or a multifil-
amentary strand with uniform filaments occurs at a
final strain of ~ 5. If the filaments are nonuniform in
cross-section (sausaged), the peak occurs earlier and
at a lower critical current density. A strand that has a
premature (and lowered) peak in critical current den-
sity during final drawing is described as "extrinsically
limited" because it has not attained the intrinsic crit-
ical current density of the microstructure. The most
common source of extrinsic limitation is sausaging of
the filaments, due to intermetallic formation or lack

of bonding between the components of the compos-
ite. A high-performance strand (Fig. 5(b)) has saus-
aging reduced to a very low level—a coefficient of
variation for the filament cross-section of $\sim 2\%$.
With tight quality control, uniform properties and
piece lengths exceeding 10 km should be expected.

3.2 Nb_3Sn

Nb_3Sn is the second most widely used superconduc-
tor and has a higher upper critical temperature
(18.2 K) than Nb–Ti. It is one of several A15 struc-
ture compounds that are superconducting. Other A15
superconductors of interest include Nb_3Al (T_c of
19.1 K) and Nb_3Ge (T_c of 23.2). Nb_3Al has been
manufactured in long lengths and has a better strain
tolerance than Nb_3Sn and better performance at a
very high field (>22 T) making it important to high-
field NMR inserts. Nb_3Al is much more complex and
expensive to fabricate than Nb_3Sn because of the
mechanical differences between Nb and Al and be-
cause the optimum Nb_3Al composition for a A15
structure, can only be formed by high temperature
processing ($>1000\,^\circ$C). Nb_3Sn, on the other hand, is
widely manufactured and has shown sufficient strain
tolerance in practice to be used successfully in very
large solenoids such as the ITER CS model coil which
stored 640 MJ of energy (Kato *et al.* 2001) and high-
field (>21 T) inserts for NMR application (Kiyoshi
et al. 2001). Because A15 materials are brittle, all
production routes use ductile precursors that are heat
treated to form the A15 at final size by solid-state
diffusion. At an early stage it was found that the
presence of Cu greatly aids the formation of Nb_3Sn at
temperatures below 800 °C. It has also been found
that adding Ti (0.7–1 wt.%) or Ta (7.5 wt.%) im-
proves the critical current density at high fields
(>12 T).

The three basic production routes currently used
by commercial Nb_3Sn vendors—the bronze process,
the internal Sn, and the powder-in-tube (PIT) fabri-
cation techniques—are illustrated in Fig. 6. The in-
ternal Sn process may use a jelly roll of Cu and Nb
sheets, as illustrated in Fig. 6, or may use Nb (or Nb
alloy) rods in a Cu matrix as shown in Fig. 7.

(a) Bronze process
For MRI application the most common route is the
"bronze process" in which Nb alloy rods are first clad
in high-purity ductile Cu–Sn bronze and then assem-
bled inside another Cu–Sn tube in a way similar to
the production of Nb–Ti filaments in Cu for Nb–Ti
strand. As with Nb–Ti alloy, multiple restacks can be
used to increase the filament number. Under heat
treatment (typically 650–725 °C) the Sn from the
bronze reacts with the Nb to form the superconduct-
ing A15 compound. As the Cu–Sn alloy does not act
as a stabilizer, additional high-purity Cu must be

Bronze process

Modified jelly roll

Powder-in-tube
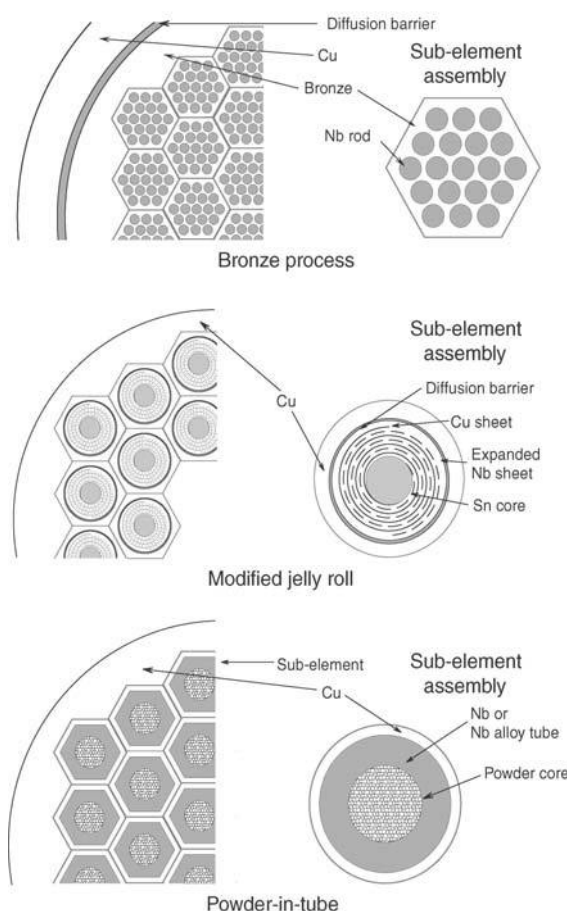
Figure 6
Schematic illustration comparing the bronze process, modified jelly roll (internal Sn), and PIT fabrication techniques for Nb_3Sn-based superconducting strand.

Figure 7
Transverse cross-section of a rod-process internal Sn Nb_3Sn strand prior to diffusion heat treatment. This strand was designed for high critical current density by IGC-AS (now Outokumpu Advanced Superconductors).

added outside, and/or inside the bronze–Nb filament composite, with a Ta and/or Nb diffusion barrier to eliminate Sn contamination of the stabilizer. An example of a bronze–process strand is shown in Fig. 8. Vanadium has also been used as a barrier but results in a reduced critical current density. This process can yield a strand with a very high uniformity in filament size and distribution, which makes it an ideal product for high-field NMR and other applications where a minimum of hysteresis loss is desired. The bronze, however, quickly work hardens during wire drawing and must be annealed frequently in order to maintain strand ductility, this extra processing step significantly increasing the cost of the strand. The Sn content in the composite is also limited by the amount of Sn (< 15 wt.% Sn) that can be added to bronze while maintaining ductility. The impact of insufficient Sn is most noticeable on critical current density. Recent developments in the bronze process have centered on the use of specially processed high Sn bronzes (up to 16 wt.% Sn) that have good ductility and high homogeneity (Sakamoto *et al.* 2000) (Fig. 9).

(b) Internal Sn process
Higher Sn content and higher critical current density can be achieved by keeping the Sn separate from the Cu during strand fabrication. This is the basis for the internal Sn process which places an Sn core inside an Nb–filament/Cu matrix. The Sn core can be alloyed as a carrier for the Nb_3Sn allowing-element or to improve the mechanical properties of the soft Sn. Strands produced by this process have achieved the highest critical current densities for Nb_3Sn (in excess of 2400 A mm^{-2} in the non-stabilizer package). The high critical current densities are achieved, in part, by reducing the amount of Cu in the Cu/filament/Sn package and the resulting reduction in filament coupling results in an undesirable increase in filament coupling. There are two distinct sub-categories of internal Sn process strand based on the form of the Nb filaments. In the "rod-in-tube" (RIT) process internal Sn–Nb filaments are assembled by inserting rods of Nb into pre-drilled holes in a Cu billet. The second internal Sn method is termed modified jelly-roll (MJR) and used an expanded metal sheet of Nb co-wrapped with a Cu sheet to create the individual Nb
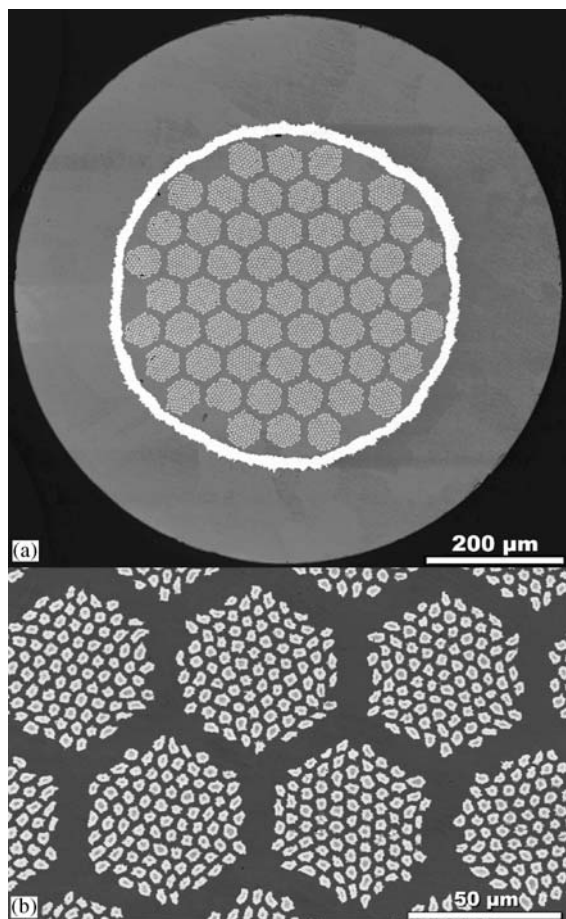
Figure 8
Bronze process Nb₃Sn strand fabricated by
Vacuumschmelze for ITER shown in (a) full cross-
section and (b) in filament detail. The filaments have a
central unreacted core of Nb.

filaments in a Cu matrix. Both of these techniques
achieve very high current densities, but limitations to
the sizes of the billets (because of the restricted depth
of the gun-drilled holes for rod-process and size lim-
itations to deforming the MJR stacks) means that
billet sizes are typically only 20 kg and processing
costs are subsequently much higher than for Sn. As in
the bronze process, the individual Cu–Nb–Sn sub-
elements are clad in a diffusion barrier (Ta or Nb or
TaNb alloy) to prevent poisioning of the Cu stabilizer
by Sn diffusion. Sn diffuses rapidly through Cu at the
temperatures used for the A15 forming heat treat-
ment (up to 700 °C) and barrier integrity is conse-
quently of great concern. The heat treatment of the
strands to form the A15 phase is preceded by multiple
lower-temperature steps designed to combine the Sn
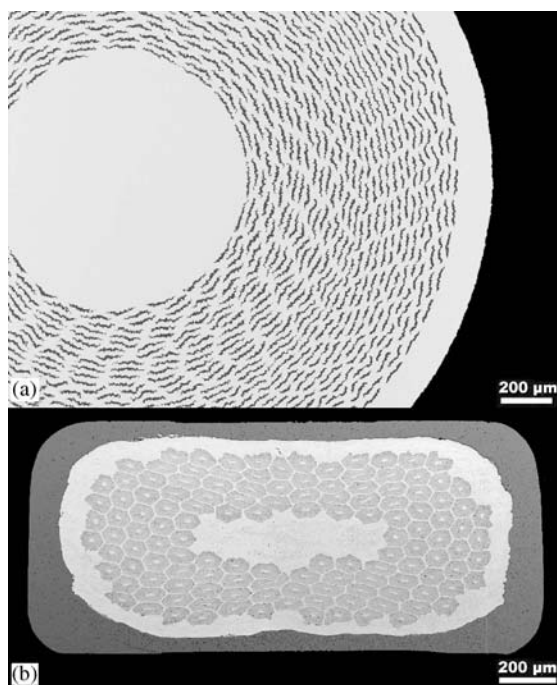
Figure 9
(a) Precursor jelly-roll of Al and Nb fabricated by
Oxford Advanced Superconductors. (b)
Multifilamentary Nb₃Al tape fabricated by the National
Institute for Materials Science in Japan from a rapidly
heated and cooled composite of jelly-roll precursors
(fabricated by Hitachi Wire and Cable).

with the Cu without Sn melting. Both the RIT and
MJR technique can also be used to fabricate precur-
sor strand for Nb₃Al production.

(c) PIT process
Nb₃Sn may also be formed from higher Sn content
Nb–Sn phases (Nb₆Sn₅ and NbSn₂) by inserting the
intermetallics in powder form into tubes of Nb and
reacting at 650–700 °C. The presence of Cu is also
required to allow the formation of the A15 phases in
the 650–700 °C temperature range in which fine grain
size is maintained (Lefranc and Muller 1976). Ele-
mental Sn is also added to improve the Sn-to-Nb ra-
tio. No low-temperature heat treatment is required
for these strands and the A15 formation heat treat-
ment takes a relatively short time, 50–75 h (180–
270 ks). This process uses the best combination of
high critical current densities (> 2200 A mm⁻² at 12 T
and 4.2 K in the nonstabilizer volume) and low effec-
tive filament diameter (as low as 30 μm in high critical
current density strand). The process is used to man-
ufacture small quantities for demanding applications

1205

(Lindenhovius *et al.* 2000) and has not received the cost benefits of commercial scale-up. The PIT technique can also be used for MgB_2, Bi-2223, and YBCO, but porosity is an issue for these conductors when fabricated by this technique.

3.3 Nb_3Al

Nb_3Al has not achieved commercial strand status, but it can be described as a technical superconductor as it has been fabricated into high performance and uniform kilometer lengths that have in turn been fabricated into full-scale devices. At magnetic fields above 20 T, critical current densities can be obtained that are comparable to the best Nb_3Sn strands and useful critical current densities (>100 A mm^{-2} nonstabilizer) can be achieved above 24 T. Perhaps the most important feature of Nb_3Al is the high strain tolerance of the Nb_3Al strands compared to Nb_3Sn. One ton (total length of 210 km) of mass-produced "jelly-roll" process strand (Yamada *et al.* 1994) was manufactured for the 13 T–46 kA Nb_3Al insert for the ITER Central Solenoid model coil. The jelly-roll of Nb and Al is created by co-winding sheets of Nb and Al together on an oxygen-free pure copper core. This will eventually become an individual filament in the final multifilamentary strand. The assembled jelly-roll and core are inserted into an oxygen-free pure copper tube to create an extrusion billet. After hydrostatic extrusion, the billet is drawn down to a small enough size that it can be restacked to create a multifilamentary billet. The billet is hydrostatically extruded and drawn for a second time, to the desired strand diameter size. The extrusion and restack process reduces the thickness of the Nb–Al layers in the filaments to less than 1 μm. The production yield rate for the ITER insert strand was 70% for strands longer than 1.5 km. The final strand is heat treated (800 °C for 10 h is typical) to produce Nb_3Al. The critical current densities obtained by this technique are ~ 600 A mm^{-2} at 12 T and 4.2 K (Hosono *et al.* 2002).

The highest critical fields and critical temperatures for Nb_3Al are based around high-temperature heat treatments and rapid cooling. In the rapid-heating, quenching, and transformation (RHQT) (Iijima *et al.* 1997) process Nb/Al composites (MJR or RIT) are resistance heated to 1900–2000 °C and then rapidly quenched into a molten Ga bath at 40–50 °C producing a metastable b.c.c. supersaturated solid solution, $Nb(Al)_{ss}$, inside an Nb matrix. The heating time is ~ 0.1 s. The $Nb(Al)_{ss}$ has excellent ductility and the strand can consequently be mechanically clad or cabled with Cu at this stage and the stabilized strand may also be wound into device form. The $Nb(Al)_{ss}$ is then transformed to Nb_3Al at 800 °C. Both the critical temperature, T_c, of ~ 17.8 K and the critical magnetic field, B_{c2}, of ~ 26 T are 0.7 K and 4 T lower for RHQT composites than the highest values obtained by laser

or electron beam irradiation processed Nb_3Al (Takeuchi *et al.* 2000) and this difference has been attributed (Kikuchi *et al.* 2001a) to stacking faults formed in the A15 phase. Two successful modifications to the basic RHQT technique specifically address the stacking fault issue. In the double rapidly heating/quenching technique (DRHQ), the standard RHQT process is followed, but instead of a conventional low temperature (<1000 °C) transformation heat treatment, a second RHQ process produces the A15 phase and this is followed by a long-range ordering heat treatment at 800 °C for ~ 12 h (Kikuchi *et al.* 2001b). The T_c for these stacking fault free strands has been measured at 18.4 K, which suggests very good stoichiometry. Furthermore, a critical current density of 135 A mm^{-2} was obtained at 25 T (Kikuchi *et al.* 2002). A disadvantage of this technique is that the brittle A15 phase is formed during high-temperature processing. Alternatively, the transformation-heat-based up-quenching technique (TRUQ), follows the initial RHQ of the RHQT process with a short heating step to 1000 °C. At this temperature, the heat released by local transformation from the $Nb(Al)_{ss}$ to the A15 phase produces a rapid local heating and propagation of the reaction along the length of the strand. As the self-heating is localized to the A15 volume, the heat is quickly dissipated after reaction across the Nb and stabilizer volumes, so that external Cu stabilizer applied after the initial RHQ process is not melted (Takeuchi *et al.* 2000).

3.4 HTS Superconductors

HTS superconductors have demanded great interest because of their ability to superconduct with relatively inexpensive liquid nitrogen cooling and their impressive high-field performance. HTS wires and tapes have not achieved the same commercial impact as LTS strands, however, because of the relative difficulty of producing long, low-cost lengths of conductor. The primary sources of this difficulty are the anisotropy in their superconducting behavior and the barrier to current flow presented by high-angle grain boundaries in these materials. Consequently, the strands must be fabricated with a remarkable degree of grain alignment. Further complicating the process is a high sensitivity to heat treatment temperature (<1 °C control must be exerted across the entire strand length for Bi-2212) and a need for oxygen diffusion into the HTS composite during fabrication. This second requirement effectively means that silver must be used as the superconducting strand stabilizer. Of the HTS superconductors, only Bi-2212 can be readily made into round-wire form strand. All the other HTS superconductors require a tape format. $(Bi,Pb)_2Sr_2Ca_2Cu_3O_x$ based conductors have been shown to be capable of application to superconducting power cables, magnetic energy-storage devices,

transformers, fault current limiters and motors, but widespread application will require significant cost reduction in processing. YBCO-based superconductors have the highest recorded critical current densities, but at present there is no viable wire production technique available for YBCO and critical current densities fall rapidly with superconductor thickness above 0.5 μm and with length beyond 1 μm.

(a) Bi-2223

$(Bi,Pb)_2Sr_2Ca_2Cu_3O_x$ ("Bi-2223") is most readily fabricated using PIT techniques very similar to those used for Nb_3Sn, with Ag replacing the Cu tubes used for Nb_3Sn. In addition to standard wire drawing techniques, groove rolling is also incorporated to bring powder-filled monofilaments to restack size. Hot extrusion can then be used to bond the multifilamentary composite while increasing the powder density and reducing the billet diameter. Extrusion is followed by further drawing and groove rolling, and finally rolling into tape. As a conventionally mechanically processed material, this is readily scalable to large production quantities. The key issue is to increase the connectivity between the grains of the conductor. The prospect of two- to fivefold improvements in the performance of the present process, coupled to cost reductions triggered by significant scale-up and alternative routes such as overpressure processing (Rikel *et al.* 2001) or melt processing (Flükiger *et al.* 2001) could accelerate the early penetration of superconducting technology into the utility network.

Demonstration HTS transmission cable projects have utilized Bi-2223 strand including test installations at Detroit Edison and Southwire in the USA. For the Detroit–Edison project, a conductor was fabricated by American Superconductor that used four layers of Ag-sheathed Bi-2223 tapes (29 km in total), each tape having an average critical current of ~ 118 A d.c. at 77 K. The tapes utilized oxide-dispersion-strengthened silver matrices as well as stainless steel reinforcement added to both sides of the HTS tape (Masur *et al.* 2001). For the Southwire project, 30 m cables were produced from PIT Bi-2223 tapes manufactured by IGC. The measured critical current for the cables was 2980 A at 77 K (Sinha *et al.* 2001).

(b) MgB₂

Since its discovery in early 2001, MgB_2 has generated much interest as it has the highest T_c (39 K) of any intermetallic superconductor and has the lowest cost components. Like Bi-2223, MgB_2 wires or tapes can use essentially the same technology as that used for Nb_3Sn PIT composites. PIT offers a scaleable technology for future production of kilometer-length MgB_2 and has already been exploited for strand fabrication (Jin *et al.* 2001, Grasso *et al.* 2001). The perpendicular irreversibility field is less than that for Nb_3Sn, the most widely used intermetallic superconductor, and this may restrict MgB_2 to applications of lower field.

4. Summary

Nb–Ti and Nb_3Sn superconductors are well established as commercial superconductors with stable markets for NMR and MRI devices as well as high magnetic field testing equipment. Future markets in fusion reactors, accelerator magnets, and energy storage drive further developments. The strain tolerance of Nb_3Al should maintain interest in this material for high-field applications where conductor cost is not an issue. The ability to use liquid nitrogen as a coolant for HTS conductors, such as Bi-2223, is important for applications such as power transmission lines that are not well suited for low temperature refrigeration. Further performance improvement and cost reduction will be required before HTS strands are economically viable. MgB_2 offers the potential of a low-cost superconductor for the future that, while not being able to use liquid nitrogen cooling, is still able to benefit from reduced refrigeration costs due to its high T_c.

See also: Superconducting Wires and Cables: Low-field Applications; Superconducting Wires and Cables: High-field Applications; Superconducting Materials: Irradiation Effects

Bibliography

Cave J R, Fevrier A, Verhaege T, Lacaze A, Laumond Y 1989 Reduction of AC loss in ultra-fine multifilamentary NbTi wires. *IEEE Trans. Magn.* **25**, 1945–8

Cheng-ren Li, Xiao-zu Wu, Nong Zhou 1983 NbTi superconducting composite with high critical current density. *IEEE Trans. Magn.* **19**, 284–7

Flükiger R, Giannini E, Lomello-Tafin M, Dhallé M, Walker E 2001 Phase formation in Bi,Pb(2223) tapes. *IEEE Trans. Appl. Superconduct.* **11**, 3393–8

Ghosh A K, Sampson W B, Gregory E, Kreilick T S 1987 Anomalous low field magnetization in fine filament NbTi conductors. *IEEE Trans. Magn.* **23**, 1724–7

Grasso G, Malagoli A, Ferdeghini C, Roncallo S, Braccini V, Siri A S, Cimberle M R 2001 Large transport critical currents in unsintered MgB_2 superconducting tapes. *Appl. Phys. Lett.* **79**, 230–2

Gregory E, Kreilick T S, Wong J, Ghosh A K, Sampson W B 1987 Importance of spacing in the development of high current densities in multifilamentary superconductors. *Cryogenics* **27**, 178–82

Hlasnik I, Takacs S, Burjak V P, Majoros M, Krajcik J, Krempasty L, Polak M, Jergei M, Korneeva T A, Mironova O N, Ivan I 1985 Properties of superconducting NbTi superfine filament composites with diameter $0.1 \leqslant$ μm. *Cryogenics* **25**, 558–64

Hosono F, Iwaki G, Kikuchi K, Ishida S, Ando T, Kizu K, Miura Y, Sakasai A 2002 Production of a 11 km long jelly roll processed Nb_3Al strand with high copper ratio of 4 for fusion magnets. *IEEE Trans. Appl. Superconduct.* **12**, 1037–40

Iijima Y, Kosuge Y M, Takeuchi T, Inoue K 1997 Nb$_3$Al multi-filamentary wires continuously fabricated by rapid-quenching. *Adv. Cryogenic Eng.* **42**, 1447–54

Jin S, Mavoori H, Bower C, van Dover R B 2001 High critical current in iron-clad superconducting MgB$_2$ wires. *Nature* **411**, 563–5

Kanithi H, Erdmann M, Valaris P, Krahula F, Lusk R, Gregory E, Zeitlin B 1990 A status report on the development of inner and outer conductors for the SSC dipole and quadrupole magnets. In: McAshan M (ed.) *Supercollider 2*. Plenum, New York, pp. 601–9

Kato T, *et al.* 2001 First test results for the ITER central solenoid model coil. *Fusion Eng. Design* **56–57**, 59–70

Kikuchi A, Iijima Y, Inoue K 2001a Microstructures of rapidly-heated/quenched and transformed Nb$_3$Al multifilamentary superconducting wires. *IEEE Trans. Appl. Superconduct.* **11**, 3615–8

Kikuchi A, Iijima Y, Inoue K 2001b Nb$_3$Al conductor fabricated by DRHQ (double rapidly-heating/quenching) process. *IEEE Trans. Superconduct.* **11**, 3968–71

Kikuchi A, Iijima Y, Inoue K, Kosuge M 2002 New Nb$_3$Al conductor made by DRHQ process. *Adv. Cryogenic Eng.* **48**, 1025–33

Kiyoshi T, Sato A, Takeuchi T, Itoh K, Matsumoto S, Ozaki O, Wada H, Yoshikawa M, Kamikado T, Ito S, Miki T, Hase T, Hamada M, Hayashi S, Kawate Y, Hirose R 2001 Development and operation of superconducting NMR magnet beyond 900 MHz. *IEEE Trans. Appl. Superconduct.* **11**, 2347–50

Kreilick T S, Gregory E, Scanlan R M, Ghosh A K, Sampson W B, Collings E W 1988 Reduction of coupling in fine filamentary Cu/NbTi composites by the addition of manganese to the matrix. *Adv. Cryogenic Eng.* **34**, 895–900

Lee P J, Larbalestier D C 1993 An examination of the properties of SSC Phase II R and D strands. *IEEE Trans. Appl. Superconduct.* **3**, 833–41

Lee P J, McKinnell J C, Larbalestier D C 1989 Progress in the understanding and manipulation in high J_c Nb–Ti alloy composites. In: Murakami Y (ed.) *Proc. New Developments in Applied Superconductivity*. World Scientific Press, pp. 357–62

Lee P J, McKinnell J C, Larbalestier D C 1990 Restricted novel heat treatments for obtaining high J_c in Nb–46.5 wt.%Ti. *Adv. Cryogenic Eng. (Mater.)* **36**, 287–94

Lefranc G, Muller A 1976 Effect of copper additions to superconducting niobium–tin sinter material. *J. Less Common Metals* **45**, 339–42

Lindenhovius J L H, Hornsveld E M, den-Ouden A, Wessel W A J, ten-Kate H H J 2000 Powder-in-tube (PIT) Nb$_3$Sn conductors for high-field magnets. *IEEE Trans. Appl. Superconduct.* **10**, 975–8

Masur L, Parker D, Tanner M, Podtburg E, Buczek D, Scudiere J, Caracino P, Spreafico S, Corsaro P, Nassi M 2001 Long length manufacturing of high performance BSCCO–2223 tape for the Detroit Edison Power Cable Project. *IEEE Trans. Appl. Superconduct.* **11**, 3256–60

Meingast C, Lee P J, Larbalestier D C 1989 Quantitative description of a high J_c Nb–Ti superconductor during its final optimization strain: I. Microstructure, T_c, H_{c2} and resistivity. *J. Appl. Phys.* **66**, 5962–70

Ochiai S, Uehara T, Osamura K 1986 Tensile strength and flux pinning force of superconducting Nb$_3$Sn compounds as a function of grain size. *J. Mat. Sci.* **21**, 1020–6

Patnaik S, Cooley L D, Gurevich A, Polyanskii A A, Jiang J, Cai X Y, Squitieri A A, Naus M T, Lee M K, Choi J H, Belenky L, Bu S D, Letteri J, Song X, Schlom D G, Babcock S E, Eom C B, Hellstrom E E, Larbalestier D C 2001 Electronic anisotropy, magnetic field-temperature phase diagram and their dependence on resistivity in *c*-axis oriented MgB$_2$ thin films. *Supercond. Sci. Technol.* **14**, 315–9

Poole C P, Farach H A 2000 Tabulations and correlations of transition temperatures of classical superconductors. *J. Superconduct.* **13**, 47–60

Rikel M O, Williams R K, Cai X Y, Polyanskii A A, Jiang J, Wesolowski D, Hellstrom E E, Larbalestier D C, DeMoranville K, Riley G N, Jr., 2001 Overpressure processing Bi2223/Ag tapes. *IEEE Trans. Appl. Superconduct.* **11**, 3026–9

Sakamoto H, Higuchi M, Endoh S, Kimura A, Wada K, Meguro S, Ikeda M 2000 Very high critical current density of bronze-processed (Nb,Ti)$_3$Sn superconducting wire. *IEEE Trans. Appl. Superconduct.* **10**, 971–4

Scanlan R M, Fietz W A, Koch E F 1975 Flux pinning centres in superconducting Nb$_3$Sn. *J. Appl. Phys.* **46**, 2244–9

Scanlan R, McInturff A D, Taylor C E, Caspi S, Dell'Orco D, Higley H, Gourlay S, Bossert R, Brandt J, Zlobin A V 1997 Design and fabrication of a high aspect ratio cable for a high gradient quadrupole magnet. *IEEE Trans. Appl. Superconduct.* **7**, 936–8

Sinha U K, Lindsay D T, Hughey R L, Jr., Stovall J P, Gouge M J, Lue J W, Haldar P, Selvamanickam V, Vo N 2001 Development and test of world's first industrial high temperature superconducting (HTS) power cable. *Power Eng. Soc. Winter Meeting, IEEE* **2**, 442–7

Smathers D B, Leonard D A, Kanithi H C, Hong S, Warnes W H, Lee P J 1996 Improved niobium 47 wt.% titanium composition by iron addition. *Mater. Trans.* (Japanese Institute of Metals) **37**, 519–26

Stekly Z J J, Zar J L 1965 Stable superconducting coils. *IEEE Trans. Nucl. Sci.* **12**, 367–72

Takeuchi T, Banno N, Fukuzaki T, Wada H 2000 Large improvement in high-field critical current densities of Nb$_3$Al conductors by the transformation-heat-based up-quenching method. *Supercond. Sci. Technol.* **13**, L11–4

Warnes W H, Larbalestier D C 1986 Critical current distributions in superconducting composites. *Cryogenics* **26**, 643–53

Wilson M N 1972 Filamentary composite superconductors for pulsed magnets. *Proc. 1972 Appl. Superconduct. Conference,* IEEE, pp. 385–8

Yamada Y, Ayai N, Takahishi K, Sata K, Sugimoto M, Ando T, Takahashi Y, Nishi M 1994 Development of Nb$_3$Al/Cu Multifilamentary Superconductors. *Adv. Cryogen. Eng.* **40**, 907–14

P. J. Lee
The University of Wisconsin, Madison, WI, USA

Superconductors: Borocarbides

Superconductivity in quaternary rare-earth transition-metal borocarbides (*RT*BC) has been found in 1994 (Nagarajan *et al.* 1994, Cava *et al.* 1994). With the invention of these materials the new LuNi$_2$B$_2$C-type structure (see Fig. 1), space group I4/*mmm*, has been discovered which can be considered as the well-known ThCr$_2$Si$_2$ type interstitially modified by carbon. The RT_2B$_2$C compounds are the $n = 1$ (so-called
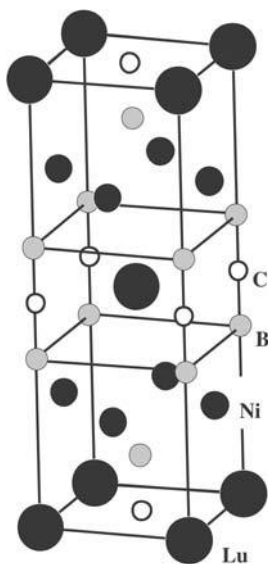
Figure 1
LuNi$_2$B$_2$C-type crystal structure.

Table 1
Compounds with the LuNi$_2$B$_2$C-type structure.

CeCo$_2$B$_2$C	HoCo$_2$B$_2$C	NdRh$_2$B$_2$C	ThRh$_2$B$_2$C
CeNi$_2$B$_2$C	**HoNi$_2$B$_2$C**	PrNi$_2$B$_2$C	**TmNi$_2$B$_2$C**
CePt$_2$B$_2$C	HoRh$_2$B$_2$C	**PrPt$_2$B$_2$C**	UNi$_2$B$_2$C
CeRh$_2$B$_2$C	LaIr$_2$B$_2$C	PrRh$_2$B$_2$C	URh$_2$B$_2$C
DyNi$_2$B$_2$C	LaNi$_2$B$_2$C	**ScNi$_2$B$_2$C**	YCo$_2$B$_2$C
DyPt$_2$B$_2$C	**LaPd$_2$B$_2$C**	SmNi$_2$B$_2$C	**YNi$_2$B$_2$C**
DyRh$_2$B$_2$C	**LaPt$_2$B$_2$C**	SmRh$_2$B$_2$C	**YPd$_2$B$_2$C**
ErNi$_2$B$_2$C	LaRh$_2$B$_2$C	TbNi$_2$B$_2$C	**YPt$_2$B$_2$C**
ErRh$_2$B$_2$C	LuCo$_2$B$_2$C	TbRh$_2$B$_2$C	**YRu$_2$B$_2$C**
GdCo$_2$B$_2$C	**LuNi$_2$B$_2$C**	**ThNi$_2$B$_2$C**	YbNi$_2$B$_2$C
GdNi$_2$B$_2$C	NdNi$_2$B$_2$C	**ThPd$_2$B$_2$C**	
GdRh$_2$B$_2$C	NdPt$_2$B$_2$C	**ThPt$_2$B$_2$C**	

Superconductors are printed in bold face.

single layer) variants of $(RC)_nT_2B_2$ structures where nRC layers alternate with single T_2B$_2$ layers. Details on the properties of these and related compounds can be found in the review articles listed in the Bibliography. Table 1 summarizes the known superconducting and non-superconducting RTBC compounds of LuNi$_2$B$_2$C-type structure where R stands for 4f- and 5f-elements as well as for Sc, Y, and La. Among them YPd$_2$B$_2$C has the highest superconducting transition temperature $T_c \approx 23$ K. However, no single-phase samples could be prepared of this particular compound so far. The growth of very high quality single crystals of various RTBC almost immediately after their discovery has had a profound impact on the quality of the work performed.

For certain combinations of elements R and T, superconductivity and antiferromagnetic order have been found to coexist. The magnetic moments in these materials are localized at the R-sites whereas the Ni d-electrons are nearly nonpolarized. A striking feature distinguishing the superconducting RTBC from other superconductors known until 1994 is that the magnetic ordering temperature T_N is comparable with T_c (see Fig. 2), i.e., the magnetic energy is comparable with the superconducting condensation energy. Therefore, the investigation of these compounds is expected to result in new insights into the interplay of superconductivity and magnetism. The high values of T_N demand that in RTBC, different from the situation in high-T_c cuprates and the classical magnetic superconductors, exchange coupling between the rare-earth magnetic moments is the dominant magnetic interaction rather than magnetostatic interaction. Obviously the exchange is mediated by conduction electrons. Consequently, also the interaction between the magnetic moments and the conduction electrons must be relatively strong. Figure 2 shows a linear scaling of T_N and, roughly approximated, also of T_c with the de Gennes factor DG $= (g-1)^2 J(J+1)$ of the R^{3+} Hunds' rule ground state where g is the Landé factor and J the total angular momentum. Such so-called de Gennes scaling, at the same time for T_N and T_c, is due to the fact that both effects, antiferromagnetism and the suppression of
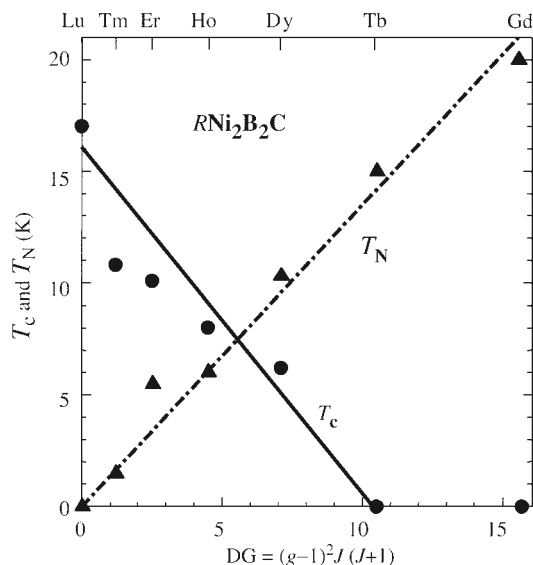
Figure 2
Critical temperatures for superconductivity, T_c, and for antiferromagnetic ordering, T_N, of RNi$_2$B$_2$C
compounds with $R =$ Lu, Tm, Er, Ho, Dy, Tb, and Gd. DG, g, and J are explained in the text. The straight lines represent rough linear approximations.

superconductivity, are governed by the exchange interaction of the conduction electrons with the *R* 4*f*-electrons. According to Fig. 2 YbNi$_2$B$_2$C should be a superconductor becoming antiferromagnetically ordered at sufficiently low temperatures. In this compound, however, hybridization of 4*f*-electrons with the conduction electrons connected with correlation effects results in heavy fermion behavior and suppression of superconductivity.

The *RT*BC superconductors have been classified as phonon-mediated type II superconductors (see *Superconducting Materials, Types of*) in the clean limit (i.e., the mean free path of the unpaired electrons is large compared to the coherence length of the Cooper pairs). They are *s*-wave superconductors with a strongly anisotropic energy gap. Their superconducting and magnetic properties can only be understood by taking into account details of the electronic structure and of the electron–phonon interaction. Thus, the positive curvature of the upper critical field H_{c2} as a function of temperature *T* of LuNi$_2$B$_2$C (see Fig. 3) is due to a strong dispersion of the Fermi velocity and can be well described in a two-band model. The critical temperature T_c is governed by nested regions of the Fermi surface. In the case of antiferromagnetically ordered *RT*BC, these nesting features induce peculiarities in the magnetic long-range order which is also strongly influenced by crystalline electric fields (CEFs). The interplay of itinerant-electron-mediated exchange and CEF results in a large variety of types of antiferromagnetic structures with temperature-dependent spin reorientation transitions as well as (field-dependent) metamagnetic transitions.

Figure 4
Temperature dependence of the upper critical field H_{c2} for TmNi$_2$B$_2$C and ErNi$_2$B$_2$C single crystals. Circles: $H\|a$; triangles: $H\|c$ (after Canfield and Bud'ko 2001).

As expected these clean-limit superconductors show an anisotropy of $H_{c2}(T)$ due to the anisotropy of the Fermi surface. In *RT*BC superconductors with magnetic *R*-elements antiferromagnetic order causes further contributions to the anisotropy of $H_{c2}(T)$ as can be seen in Fig. 4. ErNi$_2$B$_2$C and TmNi$_2$B$_2$C even show a different sign in the anisotropy of their H_{c2}, which obviously is connected with the different directions of the *R* magnetic moments in these two compounds.

In most known type II superconductors the flux line lattice does not depend on the symmetry of the crystal lattice and is hexagonal as described by the standard London or Ginzburg–Landau model. In *RT*BC superconductors, however, hexagonal-to-square vortex–lattice transitions have been observed, depending on strength and direction of the applied magnetic field as well as on temperature.

See also: Electrodynamics of Superconductors: Flux Properties; Films and Multilayers: Conventional Superconducting; High-temperature Superconductors: Thin Films and Multilayers; High-temperature Superconductors: Transport Phenomena; High-T_c Superconductors: Electronic Structure; Superconducting Materials, Types of

Figure 3
$H_{c2}(T)$ of an LuNi$_2$B$_2$C single crystal measured parallel to the tetragonal *c*-axis ($\bigcirc$). The solid curve was calculated using a two-band model. Dashed line: isotropic single-band model (Shulga *et al*. 1998).

Bibliography

Canfield P C, Bud'ko S L 2001 Effects of local moment magnetism on the superconducting properties of RNi$_2$B$_2$C compounds. In: Müller K-H, Narozhnyi V N (eds.) *Rare Earth Transition Metal Borocarbides (Nitrides): Superconducting, Magnetic and Normal State Properties*. Kluwer Academic, Dordrecht, pp. 33–44

Cava R J, Takagi H, Batlogg B, Zandbergen H W, Krajewski J J, Peck W F, Jr., van Dover R B, Felder R J, Siegrist T, Mizuhashi K, Lee J O, Eisaki H, Carter S A, Uchida S 1994 Superconductivity at 23 K in yttrium palladium boride carbide. *Nature* **367**, 146–8

Hilscher G, Michor H 1999 Superconductivity and magnetism in quaternary borocarbides and boronitrides. In: Narlikar A V (ed.) *Studies on High Temperature Superconductors*. Nova Science, New York, Vol. 28, pp. 241–86

Lynn J W, Skanthakumar S, Huang Q, Sinha S K, Hossain Z, Gupta L C, Nagarajan R, Godart C 1997 Magnetic order and crystal structure in the superconducting $R\text{Ni}_2\text{B}_2\text{C}$ materials. *Phys. Rev. B* **55**, 6584–98

Müller K -H, Fuchs G, Drechsler S-L, Narozhnyi V N 2002 Magnetic and superconducting properties of rare earth borocarbides of the type $R\text{Ni}_2\text{B}_2\text{C}$. In: Buschow K H J (ed.) *Handbook of Magnetic Materials*. Elsevier, Amsterdam, Vol. 14, pp. 199–305

Nagarajan R, Mazumdar Ch, Hossain Z, Dhar S K, Gopalakrishnan K V, Gupta L C, Godart C, Padalia B D, Vijayaraghavan R 1994 Bulk superconductivity at an elevated temperature ($T_c \approx 12$ K) in a nickel containing alloy system Y–Ni–B–C. *Phys. Rev. Lett.* **72**, 274–7

Shulga S V, Drechsler S -L, Fuchs G, Müller K-H, Winzer K, Heinecke M, Krug K 1998 Upper critical field peculiarities of superconducting $Y\text{Ni}_2\text{B}_2\text{C}$ and $Lu\text{Ni}_2\text{B}_2\text{C}$. *Phys. Rev. Lett.* **80**, 1730–3

K.-H. Müller and V. N. Narozhnyi
IFW, Dresden, Germany

Superconductors: Rapid Single Flux Quantum (RSFQ) Logic

RSFQ superconductor digital devices were first suggested in 1985 and developed experimentally mostly in the 1990s; for detailed reviews see Likharev and Semenov (1991) and Bunyk *et al*. (2003). In comparison with the previous generation of superconductor logic, RSFQ logic offers a considerably higher speed (up to 800 GHz for simple niobium-based digital circuits) and much lower power dissipation (of the order of 10^{-18} J bit^{-1} at liquid helium temperatures) at comparable parameter margins (of the order of $\pm 30\%$). Because of these advantages, RSFQ logic is a focus of research and development work, despite the fact that its successful implementation requires higher circuit design standards.

1. Physical Basis

RSFQ circuit operation is based on the natural property of superconductors to quantize magnetic flux $\Phi = \int B_n dA$ through any closed superconducting loop in multiples of the flux quantum Φ_0:

$$\Phi = n\Phi_0, \ \Phi_0 \equiv h/2e \approx 2 \times 10^{-15} \text{ Wb},$$
$$n = 0, \ \pm 1, \ \pm 2, \ \dots \quad (1)$$

Evidently, digital bits can be coded by certain values of the integer n; e.g., the flux states with $n = 0$ and $n = 1$ may be used to present binary zero and unity, respectively. If the superconducting loop is made of a bulk superconductor, switching between the different flux states would require the suppression and restoration of superconductivity in at least some cross-section of the loop; the latter process would take too much time (~ 100 ps for the most popular superconducting material, niobium). However, if the loop is interrupted with one or more Josephson junctions (see *Josephson Junctions: Low-T_c*, *Josephson Junctions: High-T_c*), switching may be performed much faster (in a fraction of a picosecond for niobium).

Figure 1(a) shows the simplest single flux quantum (SFQ) circuit with just one Josephson junction. Stationary states of this system can be analyzed by combining the equation for Josephson supercurrent, $I = I_C \sin\varphi$, where φ is the Josephson phase drop across the junction, with the usual equation for the total magnetic flux through the loop, $\Phi = \Phi_{ex} - LI$, where L is the loop inductance, and Φ_{ex} is the external magnetic flux. (In electronic circuits it is frequently convenient to create this flux by passing an external current through a part of the loop: $\Phi_{ex} = MI_{ex}$, where M is the inductance of this common part.) Taking into account the fundamental relationship $\varphi = 2\pi\Phi/\Phi_0$, these equations may be readily solved together to give the stationary relationship between Φ and Φ_{ex}. This relationship shows that if the LI_C product is
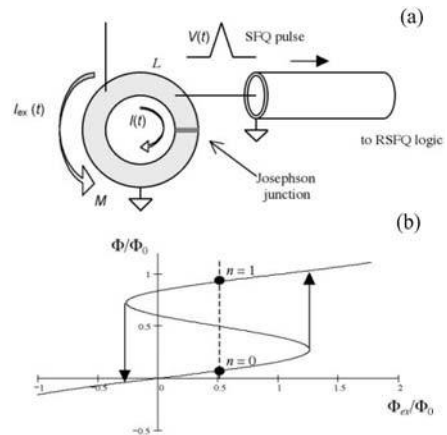
Figure 1
(a) Simplest SFQ circuit ("RF SQUID" or "DC/SFQ converter") serving as an SFQ pulse generator. (b) Total magnetic flux Φ in the circuit as a function of applied flux Φ_{ex} for a value of $LI_C = \Phi_0$, typical for RSFQ circuits. Arrows indicate flux-state switching at critical values of the external field. The middle branch (with negative slope) corresponds to unstable states. Filled points show two stable states at the equilibrating value $\Phi_{ex} = \Phi_0/2$.

large enough ($> \Phi_0/2\pi$), the Josephson phase difference φ (and hence the total magnetic flux Φ and persistent current I) may have several stable stationary states for the same external field Φ_{ex}, with the difference close to Φ_0 (see Fig. 1(b)). By fixing a d.c. flux bias at $\Phi_0/2$, one can work with just two states ($n = 0$ and $n = 1$) with equal energy and stability.

Switching between the states may be achieved by changing Φ_{ex} beyond a critical value at which one of the stationary states disappears (see arrows in Fig. 1(b)). In order to avoid irreproducible multiflux switching events, the Josephson junction has to be overdamped (i.e., the McCumber–Stewart parameter β_C to be less than 1), for example by using external shunting by normal thin film. In practice, β_C is made close to 1; in this case the switching time is minimal and is close to 3 units of

$$\tau_C = \Phi_0/2\pi I_C R_N \qquad (2)$$

where I_C is the junction critical current and R_N the normal resistance. For typical Josephson junctions the switching duration is a few picoseconds. According to Faraday's law $V = d\Phi/dt$, during the switching, a short voltage pulse with the quantized area

$$\int V(t)dt = \Delta\Phi \approx \Phi_0 \approx 2\ mV \times ps \qquad (3)$$

is formed across the junction (Fig. 1(a)). In RSFQ circuits these "SFQ pulses," with amplitudes of the order of 1 mV, are passed to other devices causing their switching.

Figure 2 shows the basic RSFQ circuit, the set–reset ("RS" or "D") flip-flop. Its quantizing loop with inductance $L \approx \Phi_0/I_C$ includes two (rather than one) Josephson junctions, but its characteristics are nevertheless almost identical to those shown in Fig. 1. The supply current (DC IN) is close to, but smaller than,

the total critical current $2I_C$ of Josephson junctions 1 and 2, so that it creates Josephson phase drops $\varphi_{1,2} < \pi/2$ across these junctions. Owing to its asymmetric injection, the same d.c. current also creates a magnetic bias Φ_{ex} close to $\Phi_0/2$ in the loop. Because of this bias, the loop has two equilibrated flux states: $n = 0$ (with the additional persistent current $I_p \approx \Phi_0/2I_C$ circulating counterclockwise) and $n = 1$ (I_p of the same magnitude, but circulating clockwise).

Let the device be initially in state $n = 0$, so that the d.c. supply current I_{dc} and the persistent current add in junction 1, and bias it subcritically ($\varphi_1 \sim \pi/3$). When an SFQ pulse SET IN arrives from the left input terminal, it pushes the applied flux beyond the critical value (cf. Fig. 1(b)). As a result, the phase φ_1 leaps by $\sim 2\pi$, and the flux changes by $\sim \Phi_0$, i.e., the system switches from its flux state 0 to state 1 (with persistent current clockwise). Similarly, an SFQ pulse arriving from the right input (RESET IN) provides the reset of the device (i.e., switching from 1 to 0). Simultaneously the latter process develops an output pulse SFQ OUT, because the Josephson phase across junction 2 leaps by 2π. This pulse may now go to other RSFQ devices.

Other logic gates ("elementary cells") of the RSFQ family also have one or several coupled quantizing loops, each interrupted with 2–4 Josephson junctions. A detailed description of the available cells is available on the Internet (Bunyk *et al.* 1999). The following important features are common for all cells:

• the flux state is stored in the cell until it is reset by another pulse; hence each elementary cell can be considered as a combination of a logic gate and a latch in one device ("clocked gate");

• the reset pulse not only triggers the output pulse, but also restores the device to its initial state, so that the shortest distance between the set and reset pulses may be just slightly longer than the width of the pulse—just a few picoseconds for niobium-based devices; and

• the d.c. bias current provides the necessary energy amplification of the SFQ pulses, thus compensating for the inevitable energy loss in the passive transmission lines and shunting conductances of the Josephson junctions.

When ultrafast processing of digital information in an RSFQ circuit is completed, the results may be transferred to the usual (voltage-level) form using a "SFQ/DC converter" circuit which uses a d.c. SQUID (see SQUIDS: The Instrument) to sense the flux state of the output RSFQ cell—in practice, galvanically coupled versions of such an SFQ/DC converter are used. The resulting d.c. voltage signal, with a swing of several hundred microvolts, can be amplified by a latching superconductor circuit to a few millivolts, extracted from the cryo-region using a copper cable, and amplified to the standard semiconductor transistor level of a few volts by inexpensive room-temperature semiconductor amplifiers.

Figure 2
Simplest RSFQ logic cell, RS flip flop (crosses denote Josephson junctions). Its basic mode of operation is described in the text. Additional junctions $1'$ and $2'$ are necessary to avoid possible detrimental back action of the device on the input circuits. For example, if the pulse SET IN arrives when the flip-flop is in state 1 and junction 1 carries low current (d.c. supply current and persistent current subtract in the left branch of the loop), then junction $1'$ performs the 2π leap of the Josephson phase, and the pulse is not reflected back to the source.

Input interfaces for RSFQ circuits are even simpler, because the energy of RSFQ signals is much less than that of standard room-temperature electronics signals. For example, even the single-junction circuit shown in Fig. 1(a) may serve as the input stage ("DC/SFQ converter"), although its parameter margins may be improved by using two additional Josephson junctions.

2. Status

After a slow start in Russia, in the early 1990s intensive RSFQ technology development was begun at several US universities and corporate research and development groups, using both low-temperature superconducting (LTS) and high-temperature superconducting (HTS) materials. A few years later, several European groups started work on RSFQ circuits, mostly using HTS materials. In the late 1990s several Japanese groups started a five-year program focused on LTS RSFQ technology.

This progress has allowed the implementation of several relatively complex LTS RSFQ circuits with 1000–2000 Josephson junctions each, mostly using the 3.5 μm niobium trilayer fabrication technology of HYPRES Inc. (e.g., see Fig. 3). The maximum clock speed for this technology ranges from 20 GHz for VLSI circuits to 70 GHz for simple digital devices. The speed is inversely proportional to the linear junction size, so that for deep-submicrometer niobium trilayer technology the corresponding clock frequencies may reach approximately 150 GHz and

800 GHz, respectively (for details see Likharev 1999, Bunyk *et al.* 2003). Figure 4 shows an example of such an ultrafast device, a digital frequency divider (T flip-flop) tested to operate up to 770 GHz (Chen *et al.* 1999).

During the 1990s several simple HTS RSFQ circuits (with up to 30 Josephson junctions) designed for demonstration purposes were implemented and tested at temperatures from 4.2 K to 77 K (e.g., see Fig. 5). Unfortunately, both experiments (Ruck *et al.* 1999) and calculations (Likharev 1999, Bunyk *et al.* 2003) indicate that thermal fluctuations impose an upper bound for VLSI RSFQ circuits using HTS materials (copper oxides) at about 10 K if a low bit error rate ($<10^{-10}$) is a requirement. The potential advantage of HTS Josephson junctions is that they may have a higher $I_C R_N$ product and hence provide a higher operation speed than LTS junctions (see Eqn. (2)). However, the HTS thin-film junction fabrication methods developed so far do not deliver on this promise. Moreover, these methods still do not provide sufficiently low critical current spreads. As a result, by the end of the 1990s the development of HTS RSFQ technology was not continued by most research groups.
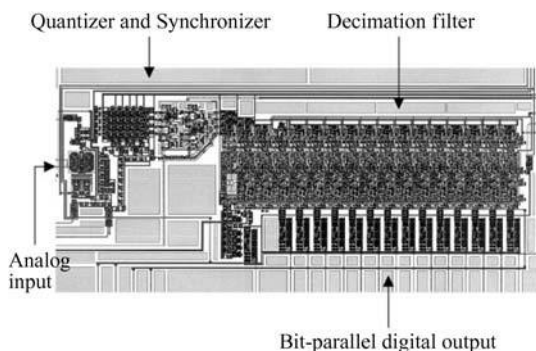
Figure 3
RSFQ analog-to-digital converter designed and tested by a HYPRES/SUNY collaboration (Rylov *et al.* 1998). The circuit has close to 3000 Josephson junctions, the total power consumption being below 1 mW, with an active area of 7 mm × 2 mm. By 2001 the spur-free dynamic range of the device had been improved to reach 12:3 effective bits for a 175 Mbps effective sampling rate, better than for any reported semiconductor transistor ADC.
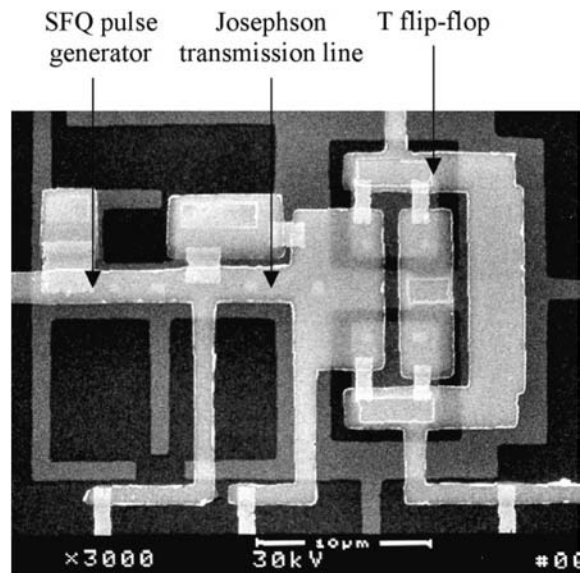
Figure 4
Scanning electron microscope image of an RSFQ test circuit including a digital frequency divider (DFD) with 0.5 μm, externally shunted niobium trilayer junctions. This device could operate up to 750 GHz, while 770 GHz has been reached using its version with 0.3 μm self-shunted junctions (after Chen *et al.* 1999). The power dissipated by the divider is just 1.5 μW, some 5×10^4 times lower than for the fastest reported semiconductor DFD operating below 70 GHz.
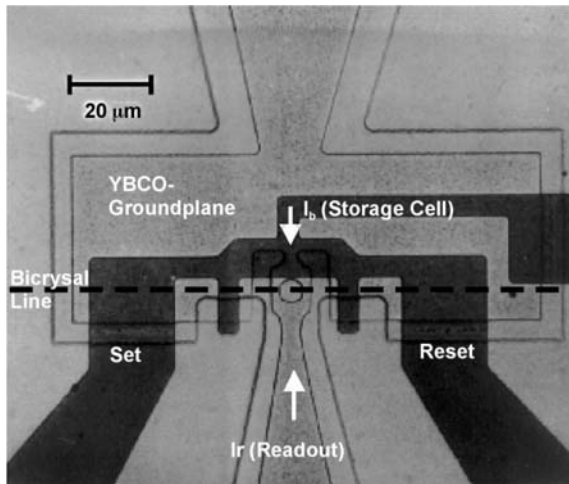
Figure 5
Scanning electron microscope image of a simple 14-junction HTS RSFQ circuit (two DC/SFQ converters, two Josephson transmission lines, an RS flip-flop, and an SFQ/DC converter) fabricated using two YBCO layers, which could operate up to 77 K (after Ruck *et al.* 1999).

3. Application Prospects

RSFQ circuits using submicrometer junctions are some 100 times faster than similar modern CMOS circuits. Even more importantly, RSFQ devices dissipate much less power energy per bit (about 10^5 times less without taking into account refrigeration, and 30–300 times less including the refrigeration needs). One more important advantage of LTS RSFQ circuits is that their fabrication technology is much simpler that that of CMOS or digital circuits based on other modern materials (SiGe, GaAs, InP, etc.).

However, the necessity of deep refrigeration of RSFQ circuits limits their possible applications to a few narrow, though important, niches of the digital electronics market. These applications (Tables 1 and 2) can be divided into two major categories:
- circuits that may be competitive at the existing (or slightly upgraded) level of LTS fabrication technology; and
- applications that would require the transfer to submicrometer, VLSI technology.

Despite the relative simplicity of LTS fabrication, the cost of a pilot line for RSFQ VLSI circuits has been crudely estimated at $\times$ 30 million. Towards the end of 1999 the most important prospective driver of RSFQ technology was the so-called Hybrid Technologies Multi-Threaded (HTMT) computing project started in the USA (Fig. 6). In this project, an RSFQ subsystem will be responsible for all "number-crunching," as

Table 1
Possible applications of LTS RSFQ logic devices: 3.5 μm technology with $< 10^3$ junctions per chip.

Circuit	Expected performance examples
A/D converters	14 bits at 60 MHz; noise: 3 db
Digital SQUIDs	Noise: 1 f THz$^{-1/2}$ at 10^{10} Φ_0 s^{-1}
D/A converters	10 bits at 18 GHz, 100 mV
D.c. and a.c. calibrators	10 V at 30 MHz, 10 ppb
Digital signal correlators	1 bit at 1 024 channels, 16 Gbps; 8 bits at 8 channels, 128 Gbps

Table 2
Possible applications of LTS RSFQ logic devices: 0.4 μm technology with $\sim 10^6$ junctions per chip.

System	Expected performance examples
Communication digital switching cores	100 Gbps at 128 channels; 1 chip, 0.1 W at 4 K
Digital signal processors	100 gigaflops; 1 chip, 0.1 W at 4 K
High-end workstations and servers	1 teraflops; 4 processors, 0.5 W at 4 K
Petaflops-scale computing systems	1 petaflops; 4000 processors, 250 W at 4 K

well as for interprocessor communication networks (Dorojevets *et al.* 1999).

4. Material Issues

For the reasons outlined in *Sect. 2*, only LTS-based RSFQ circuits are being seriously developed. The leading role here belongs to the niobium trilayer technology that was developed during the 1980s (e.g., Hasuo *et al.* 1988). In this technology, the tunnel barrier of a Josephson junction is formed by thermal oxidation of a thin (< 10 nm) aluminum layer deposited on the base niobium film. After a few minutes of oxidation in dry oxygen at a pressure of a few millitorr (Miller *et al.* 1993), a niobium counter electrode film is deposited without vacuum breaking, thus preventing any contact between aluminum and water vapor. The junctions fabricated using this technique may exhibit very high reproducibility (random spreads of the order of 1%) even for subnanometer
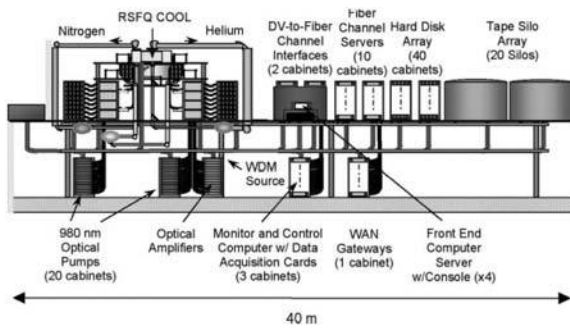
Figure 6
Preliminary design of the HTMT petaflops-scale computer room. Note that despite the RSFQ "COOL" subsystem being responsible for all the "number crunching," it occupies $< 1 \, m^3$, just a tiny fraction of the whole machine size. This compactness is possible owing to the extremely low power dissipation of RSFQ circuits, and is very important for providing very low (20 ns) interprocessor communication latency (courtesy of J. Morookian and L. Bergman, Jet Propulsion Laboratory).

aluminum oxide barriers providing very high critical current density j_c (well beyond $1 \, kAcm^{-2}$).

The important issues in the development of this technology include its extension to higher j_c (up to $100 \, kAcm^{-2}$), which is necessary for self-shunted operation of Josephson junctions with maximum speed, while retaining the low critical current spreads. A related issue is the chemical–mechanical polishing of the junction counter electrode, necessary for submicrometer junction definition, without disturbing the ultrathin aluminum oxide layer. Despite considerable progress in these directions (Miller *et al.* 1993, Chen *et al.* 1999, Patel and Lukens 1999), high j_c RSFQ circuits of sufficiently high integration scale have yet to be developed.

For some (especially space-platform) applications the increase of operation temperature to $\sim 10 \, K$ is important, because of higher refrigeration efficiency. Niobium nitride-based Josephson junctions with MgO tunnel barriers capable of operating at such temperatures have been demonstrated (e.g., Kerber *et al.* 1997, and references therein), but their fabrication technology has to be further advanced to enable VLSI circuit integration.

See also: Josephson Junctions: High-T_c; Superconducting Materials: Types of; Superconducting Thin Films: Materials, Preparation and Properties

Bibliography

Bunyk P, Likharev K, Litskevitch P, Rylyakov A, Zinoviev D 1999 RSFQ cell library; available at: gamayun.physics.sunysb.edu/RSFQ/Lib/

Bunyk P, Leung M, Spargo J, Dorojevets M 2003 Flux-1 RSFQ Microprocessor: Physical design and test results. *IEEE Trans. Appl. Supercond.* **13**, 433–6

Chen W, Rylyakov A, Patel V, Lukens J, Likharev K 1999 Rapid single flux quantum T-flip flop operating up to 770 GHz. *IEEE Trans. Appl. Supercond.* **9**, 3212–5

Dorojevets M, Bunyk P, Zinoviev D, Likharev K 1999 COOL-0: design for RSFQ subsystem for petaflops computing. *IEEE Trans. Appl. Supercond.* **9**, 3606–14

Hasuo S, Imamura T, Fujimaki N 1988 Recent advances in Josephson junction devices. *Fujitsu Techn. J.* **24**, 284–92

Kerber G, Abelson L, Elmadjian R, Hanaya, Ladizinsky E 1997 An improved NbN integrated circuit process featuring thick NbN ground plane and lower parasitic circuit inductances. *IEEE Trans. Appl. Supercond.* **7**, 2638–43

Likharev K 1999 Superconductor devices for ultrafast computing. In: Weinstock H (ed.) *Applications of Superconductors.* Kluwer, Dordrecht, The Netherlands, pp. 247–93

Likharev K, Semenov V 1991 RSFQ logic/memory family: a new Josephson junction technology for sub-terahertz-clock-frequency digital systems. *IEEE Trans. Appl. Supercond.* **1**, 3–26

Miller R, Mallison W, Kleinsasser A, Delin K, Macedo E 1993 Niobium trilayer Josephson tunnel junctions with ultra-high critical current densities. *Appl. Phys. Lett.* **63**, 1423–5

Patel V, Lukens J 1999 Self-shunted Nb/AlO$_x$/Nb Josephson junctions. *IEEE Trans. Appl. Supercond.* **9**, 3247–50

Ruck B, Chong Y, Dittman R, Engenhart A, Oelze B, Sodtke E, Siegel M 1999 Measurement of the error rate of single flux quantum circuits with high-temperature superconductors. *IEEE Trans. Appl. Supercond.* **9**, 3850–3

Rylov S, Brock D, Gaidarenko D, Kirichenko A, Vogt J, Semenov V 1998 High resolution ADC using phase modulation–demodulation architecture. *IEEE Trans. Appl. Supercond.* **9**, 3016–9

K. K. Libharev
State University of New York, Stony Brook
New York, USA

Super-resolution: Optical and Magnetic Techniques

In optical recording, an optical head focuses the beam from a semiconductor laser to produce a probe spot on the recording medium. The focused spot has a Gaussian intensity profile and a width determined ultimately by the laws of diffraction. When limited only by diffraction, the diameter of the spot is directly proportional to the wavelength of the laser radiation, and inversely proportional to the numerical aperture (NA) of the objective lens. If the width of the spot (d) is taken as the distance between the half power points, then in the diffraction limit $d \cong 0.56\lambda/NA$. In magneto-optics, as with most optical recording technologies, it is, however, possible to write "marks" much smaller than the total width of the diffraction-limited spot

(see *Magneto-optical Effects, Enhancement of*). As shown in Fig. 1, this may be achieved by exploiting the thermal nature of the write mechanism used by all current recording systems, and involves making the correct choice of the critical write temperature in conjunction with optimization of the thermal response or write sensitivity of the medium.

The resolution on readout, however, remains constrained by the total width of the beam, so that the density at which information can be stored is determined by the rate at which the depth of modulation (signal) falls as recorded marks are packed closer. When the minimum separation between recorded marks is reduced to half the diameter of the focused spot, the signal falls to zero. Therefore it is the readout process that limits the density at which information can be stored. At least three separate technologies are under active development with a view to overcoming this limitation, and they all rely heavily on the material and material processing for their successful operation.

The optical recording industry foresees (News Letter no. 4 OITDA 1998) the need for a technology in which the areal densities approach 1 Tbyte in^{-2} by 2010. Since the launch of optical storage products, an intensive global research effort has driven down the wavelength of semiconductor laser diodes from around 800 nm to the 400 nm devices announced (Nichia Corporation Japan 1999) early in 1999. However, these developments alone only improve the resolution by a factor of four. Moreover, they have impacted primarily on the CD-ROM or other read-only formats, since the shorter wavelength

(≈ 650 nm) laser devices installed have been slow to realize the power required for high-speed writing.

The other parameter governing the resolution of an optical head is its numerical aperture. Unfortunately, the improvements of a similar order that might be achieved by increasing the numerical aperture become increasingly difficult to implement as the NA approaches its limiting value (1 in. air), while constrained to conventional optics by other system requirements. The NA of current systems remains limited to a value of around 0.55–0.65. It is clear that to realize the density figures quoted above will involve development of techniques that can bypass the diffraction limit. The optical and magnetic super-resolution techniques discussed here offer that very possibility, but implemented by very different means.

The simplest way of achieving optical resolution beyond the diffraction limit is to operate in what is known as the near-field regime, placing an aperture defining the required resolution between the laser source and the sample. Providing the aperture-to-sample separation is maintained at only a small fraction of the laser wavelength, then the resolution is determined by the diameter of the aperture and not by diffraction. Perhaps the best early demonstration of this technique is the work of Betzig *et al.* (1987) using metallized optical fibers tapered to an aperture of only 40 nm using access technology borrowed from scanning probe microscopy. Such techniques are of course very inefficient in their utilization of optical energy, and although more recent demonstrations (Hosaka *et al.* 1996) have achieved readout data rates of 10 MHz for phase-change recording using this principle, because of the current speed of their access they will not be considered further.

1. Magnetic Super-resolution

"Magnetically induced super-resolution" (MSR) as originally conceived is the term applied to various techniques developed to overcome the diffraction limit by creating, in the surface of the moving medium, an "effective dynamic aperture" much smaller than the width of the readout beam. This technique, first proposed by Sony (Ohta *et al.* 1991), is realized in a similar fashion to the direct overwrite (DOW) by light intensity modulation (LIM) technology conceived earlier by Nikon (Saito *et al.* 1987). The deposition process is controlled to produce a medium having a complex multilayer structure of magnetic films that are coupled to each other magnetostatically or, more commonly, through the exchange interaction. At the same time, the unique compositional dependence of the properties of various amorphous rare-earth–transition metal (RE-TM) alloys such as TbFeCo, GdFe, GdFeCo, etc., is exploited to control their Curie temperature, coercivity, and switching field (see *Magneto-optic Recording Materials: Chemical Stability and Life*

Figure 1
Writing below the diffraction limit.

Time). The composition of each of the different coupled layers that comprise the medium is varied, so that its magnetic and thermomagnetic behavior is precisely tailored to a specific task within the MSR readout process. Activation of these different characteristics is achieved by using a somewhat higher laser power than employed for conventional readout, in conjunction with an applied magnetic readout field.

To appreciate the working principle of MSR systems, consider a basic three-layer medium such as shown in Fig. 2 consisting of a conventional storage layer, an intermediate or transfer layer, and a readout layer. Domains representing the stored data pattern are written conventionally into the storage layer, which has a high Curie temperature and a very large coercivity. An identical pattern becomes imprinted on to the readout layer by exchange coupling through the intermediate or transfer layer. The readout layer also has a high Curie temperature, but its coercivity is small, less than that of the applied readout field (H_r). It is also made thick enough so that the readout beam only interrogates this layer—no energy is allowed to reflect back from the storage layer to the detection system. As the beam tracks across recorded data, it produces in the medium a temperature profile that has the basic Gaussian profile of a laser beam, distorted in the direction of the medium's motion (Fig. 3). The Curie temperature of the intermediate layer is less than the temperature reached by the medium in the hottest part of the beam profile. In this region the data pattern in the readout layer is thus temporarily decoupled from the storage layer, and aligns instead with the readout field H_r.
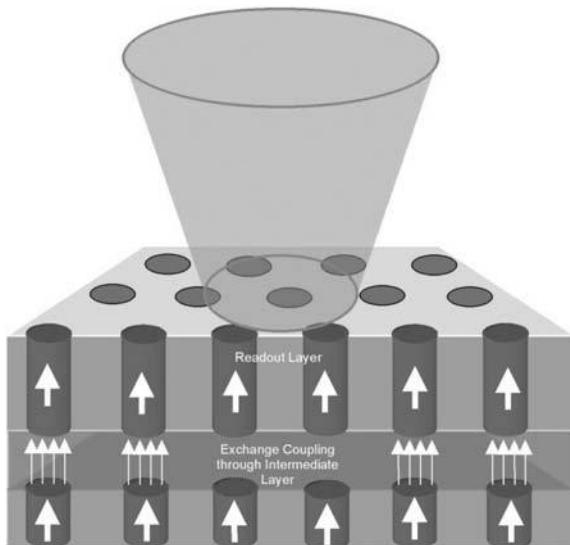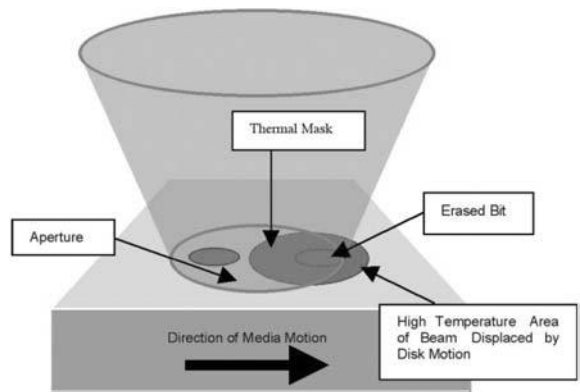
Figure 3
Reduced aperture and thermal mask in front aperture detection (FAD).

The data pattern under this part of the beam is effectively erased, creating a region that behaves as an active optical mask inserted into the beam in the plane of the surface. Magneto-optic information is therefore read out only with that portion of the focused laser spot that is reflected from the cooler part of the irradiated surface. This is crescent-shaped, as can be seen in Fig. 3. It is the width of the crescent, typically only one-third the width of the focused spot, along the track that now determines the resolution. After the beam has passed a given portion of data, the medium cools and the erased pattern is re-established as the coupling between the surface readout layer and the lower undisturbed storage layer is restored. Throughout this process, the integrity of the data in the storage layer is ensured by the high Curie temperature and coercivity of this layer. In a similar fashion, the high Curie temperature of the readout layer maintains the signal quality of the data being read out in the cooler aperture in the medium. Although Figs. 2 and 3 show the operation of the system with pulse position recording, it is also compatible with pulse length recording and magnetic field modulation, when the written domains themselves become crescent-shaped.

The basic system described above is characterized by the high-temperature mask trailing the detection aperture, and is therefore known as front aperture detection (FAD). Since it was first conceived it has been extensively developed and refined. For example, it is immediately obvious that if the relative positions of the mask and aperture could be reversed, then not only would the improved resolution be retained, but the mask would now cover adjacent tracks, precluding crosstalk and permitting higher track densities and/or land-and-groove recording. This is achieved in rear aperture detection (RAD), though usually at the expense of introducing an additional initializing field. In its most sophisticated embodiment, RAD can be

Figure 2
Trilayer exchange-couple MSR medium.

implemented as a double-mask system that further reduces the aperture and improves the resolution.

Finally, there is center aperture detection (CAD), in which the temperature dependence of the anisotropy of certain of the RE-TM alloys is exploited. The composition of the readout layer is made such that the magnetization lies in plane at ambient temperature, but rotates out of plane at much higher temperatures. A polar Kerr readout signal is therefore only detected from the very center of the temperature profile formed by the beam in the medium. The cooler areas are effectively masked since, as the magnetization still lies in plane, they display no polar rotation. A major benefit of this system is that it requires no additional fields applied during readout.

For a more extensive description of MSR technology, the reader is directed to the review by Kaneko and Nakaoki (1996). Recent achievements of the double-mask or CAD-MSR technology include the 2 Gbyte capacity, 90 mm disk reported by Fujitsu (Shono 1999) and the 9 Gbyte, 120 mm disk reported by Sharp (Murakami *et al.* 1996). Despite these successes, a major drawback of the MSR principle is that the signal level decreases with reducing aperture size, since an ever-reducing portion of the focused spot is actually used to detect the tiny domains. By 1996, it had become apparent that a more sophisticated system would be required to read out domains below about 0.2 μm in diameter.

2. Magnetically Amplifying Magneto-optic System

The magnetic amplifying magneto-optic system (MA-MMOS) was proposed by researchers at Hitachi and Sanyo (Awano *et al.* 1996) to address the problems of reducing signal level in MSR systems. Again this is a multilayer system, with the functions of storage and readout separated into mutually coupled layers whose properties are tailored to their specific task through the correct combination of rare-earth and transition metal elements. In MAMMOS media, the coupling between layers is almost exclusively magnetostatic and the working principle is relatively straightforward.

The stable diameter (d_o) of a cylindrical reverse domain written into a perpendicular recording medium is determined by the balance of forces acting on it. Energy stored in the domain walls acts to collapse the domain, but is opposed by the resistance to wall motion provided by the coercivity. In the case of domains so small that MAMMOS is required for readout, the ratio of the thickness of the medium to the stable domain diameter in general becomes such that it is also necessary to take account of the contribution of the magnetostatic energy to the stability of the system. The demagnetizing field associated with a reversed domain acts with the coercive field to oppose the collapsing field and stabilize the bit at a smaller

diameter. Previous studies (Callan and Josephs 1977, Honda *et al.* 1981) have treated these two opposing forces by combining them into an effective field (H_{eff}), with stable domains being obtained when this effective field is less than the coercive field ($H_{eff} < H_c$). In these circumstances, application of an alternating external applied field (H_{appl}) synchronized with the system data clock, and aligned to alternately either assist or cancel the coercive field, will expand or collapse any domain.

Data domains written in the storage layer with diameters as little as one-tenth of the full width of the readout beam are resolved on readout by first copying each in turn to the readout layer. There they are then temporarily expanded, so that each one fills or overfills the beam to produce signal levels approaching 100% saturation. The readout sequence may be understood by reference to Fig. 4. In Fig. 4(a), the instantaneous applied field is in a direction and of a magnitude such that it opposes coupling between the storage layer and the readout layer, so that there are no data domains in the readout layer. As H_{appl} passes through zero, as shown in Fig. 4(b), coupling is established and a domain is copied to the readout layer. H_{appl} now increases to a maximum in the direction that assists the coercive field and opposes the collapsing field. The copied domain is therefore caused to expand to a size that is readily detectable (Fig. 4(c)). During the opposite half of the applied field cycle, H_{appl} again passes through zero when the domain is shrunk to its original size, before finally being fully collapsed and expelled from the readout layer as the cycle completes (Fig. 4).

Recent demonstrations of the potential of MA-MMOS technology have included a carrier-to-noise ratio (CNR) of more than 50 db from 0.2 μm domains (Takagi *et al.* 1999), the observation of a MAMMOS signal from 0.04 μm domains (Takagi *et al.* 1999), and the combining of light intensity modulation direct overwrite with MAMMOS readout (Tokunaga *et al.* 1999).
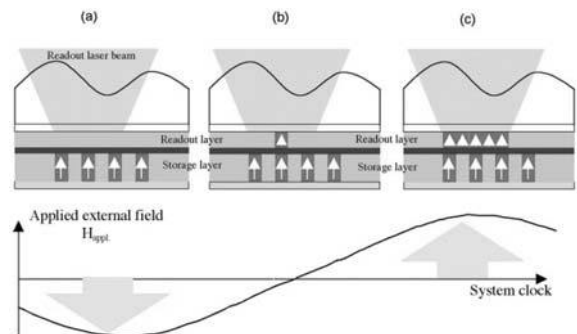
Figure 4
Basic MAMMOS mechanism using a.c. applied field synchronized to system clock.

3. *Optical Super-resolution*

Optical super-resolution refers to a suite of techniques that seek to increase the resolving power of an optical head by circumventing the limiting value of 1 for the NA in air of conventional objective lenses. The principle employed is analogous to the use of oil immersion objectives in microscopy. A solid immersion lens (SIL) with a high refractive index in the form of a hemisphere or truncated super-sphere in used in conjunction with a conventional objective having NA of around 0.5. Figure 5 shows the simple case in which a conventional low NA objective is used to focus the beam at the center of the flat face of a SIL having hemispherical form. In this arrangement all rays enter the SIL along its radii and are undeviated or diffracted. Thus, although the angle subtended by the cone of incident rays is unchanged, the NA ($= n \times \sin \theta$) of the composite system is increased by a factor n, since final incidence to focus is now through a medium having a refractive index greater than air. The focused spot size is consequently reduced by a factor n, where n is typically in the range 1.9–2.3. Adoption of the super-sphere offers yet further potential improvement.

It is well known (Nussbaum and Phillips 1976) that a beam directed through a sphere of radius r is focused to a point free of both spherical aberration and coma at a distance r/n below the center of the sphere. If the material below the point of focus is removed, as shown in Fig. 6, we have a situation similar to the

Figure 6
Supersphere SIL.

simple hemisphere. However, the peripheral rays defining the NA that were originally converging at ϕ_1 now converge at a larger angle ϕ_2, given by $n \times \sin^{-1} \phi_1$, to a new focus at the center of the plane of truncation. The effective NA is in this case therefore increased by a factor of n^2, since the beam is again also incident through a media of refractive index n. Used in conjunction with blue lasers, this technology offers the potential to resolve domains as small as 100 nm. It is not, however, without its problems. Total internal reflection means that only a small part of the cone of radiation forming the focused spot can exit into air for coupling into the disk media. In order that adequate field propagates in the air gap between the lens and media, it is necessary to rely heavily on the evanescent wave whose intensity drops rapidly away from the lens surface. Implementation of the full potential of this technique therefore requires operating in the near-field regime, with the air gap ideally much less than the wavelength of the radiation.

Outside the near-field limit, i.e., at lens-to-media separations of around two to three wavelengths, the technology does make attainment of NA equal to 1

Figure 5
Hemispherical solid immersion lens (SIL).

a practical possibility, however. Of course, head gaps of these dimensions make it necessary to abandon some of the major advantages of optical disk technology. The large separations between head and media, and between the point of focus on actual recording media and the disk surface adjacent to the environment, can no longer be supported. The SIL must be flown like the head in a conventional magnetic hard drive, but considerably closer to the recording surface. In these circumstances, integration of the write coil on the same slider carrying the SIL is a natural step. Optical access to the actual recording medium can no longer be protected through the substrate and front-surface media a thin dielectric overcoat must be used. Fortunately, the refractive indices of the common protective overcoats such as silicon nitride match reasonably well to those of SILs. In general, it is also necessary, because of the extreme intensity in the very small spot, to desensitize the medium. A fuller treatment of near-field optics is given elsewhere in this encyclopedia.

See also: Magneto-optical Effects: Enhancement of; Magneto-optic Recording: Overwrite and Associated Problems; Magneto-optic Recording: Total Film Stack, Layer Configuration; Optical and Magneto-optic Data Storage: Channels and Coding

Bibliography

Awano H, Ohnuki S, Shirai H, Ohta N, Yamaguchi A, Sumi S, Torazawa K 1996 *Appl. Phys. Lett.* **69** (27), 4257–9
Betzig E, Isaacson M, Lewis A 1987 *Appl. Phys. Lett.* **51**, 2088
Callan H, Josephs R M 1971 *J. Appl. Phys.* **42**, 1977
Honda S, Ueda K, Kusuda T 1981 *J. Appl. Phys.* **52**, 2295
Hosaka S, Shintani T, Kikukawa A, Imura R 1996 *J. Magn. Soc. Jpn.* **20** (S1), 79–82
Kaneko M, Nakaoki A 1996 *J. Magn. Soc. Jpn.* **20** (S1), 7–12
Murakami Y, Maeda S, Takhashi A, Tanaka Y, Watanabe T 1996 *J. Magn. Soc. Jpn.* **23** (S1), 181–4
News Letter no. 4 (Jan 1998) www.oitda.or.jp/Optoelectronic Industry and Technology Development Association (OITDA), Japan
Nichia Corporation, Japan, Blue Laser model NLHV500A October 1999
Nussbaum A, Phillips R A 1976 *Contemporary Optics for Scientists and Engineers*. Prentice-Hall, Englewood Cliffs, NJ, pp. 88–90
Ohta M, Fukumoto A, Aratani K, Kaneko M, Watanabe K 1991 *J. Magn. Soc. Jpn.* **15** (S1), 319–22
Saito J, Sato M, Matsumoto H, Akasaka H 1987 *Jpn. J. Appl. Phys.* **26** (suppl. 4), 155
Shono K 1999 *J. Magn. Soc. Jpn.* **23** (S1), 177–80
Takagi N, Mitani K, Awano H, Shimazaki K, Ohta N 1999 *J. Magn. Soc. Jpn.* **23** (S1), 161–4
Tokunaga T, Fujii Y, Yamada K 1999 *J. Magn. Soc. Jpn.* **23** (S1), 169–72

D. M. Newman
Centre for Data Storage Materials
Coventry University, UK

T

Textured Magnets: Deformation-induced

There are two different processes for producing anisotropic rare earth–transition metal–boron (RE–TM–B) magnets with high energy density. One is the conventional technique of powder metallurgy (see *Magnets: Sintered*). The crystal alignment is achieved by applying an external magnetic field during the cold-pressing stage. The alternative processing route is hot deformation of cast alloys or of fine-grained powder, the latter consolidated previously by hot pressing. The hot working process produces grain alignment along the c-axis perpendicular to the plastic flow direction. The key for understanding the formability of the inherently brittle alloys is the presence of the RE-rich grain boundary phase, which is liquid at the deformation temperature ($>700\,^{\circ}$C). It is conceivable that the liquid grain boundary phase can annihilate microcracks created during the deformation. However, a liquid cannot resist high tensile stresses. Therefore, the deformation must be performed under compressive stress.

1. Deformation of Cast Alloys

Permanent magnet production by hot deformation of cast alloys promises to be a potentially simpler and more economical option in comparison with the sintering route because of the troublesome handling of magnetic powder that is extremely sensitive to oxygen contamination.

The simplest deformation method is upsetting of cylindrical specimens between two punches. Extensive hot-pressing experiments performed by Shimoda *et al.* (1989) revealed that Pr–Fe–B alloys with the composition $Pr_{17}Fe_{79}B_4$ are particularly suitable for hot deformation. Hot pressing at $1000\,^{\circ}$C with strain rates of 10^{-4}–$10^{-3}\,s^{-1}$ introduces a preferred magnetization direction parallel to the press direction. Additionally, the magnetic alignment is closely related to the structure of the cast ingots and the direction of principal stress. The appropriate structure is a columnar structure in which the c-axis of the hard magnetic $Pr_2Fe_{14}B$ phase (2:14:1 or Φ phase) is in the plane perpendicular to the crystal growth direction. Therefore, the principal stress during deformation should also be perpendicular to the growth direction. Inserting the cylindrical specimens into an iron ring prevents cracking up to strain rates of $10^{-1}\,s^{-1}$ as well as squeezing out the liquid intergranular phase. Additionally, increasing the strain rate results in a grain refinement and with a consequent enhancement of the coercivity.

Studies concerning additive elements show that copper addition is effective in increasing coercivity and in improving the magnetic alignment. Microstructural studies reveal that copper (i) refines the as-cast grain size and (ii) reduces the melting point of the praseodymium-rich phase. Copper probably leads to a better wetting behavior and separation of the hard magnetic grains. In the studies of Shimoda *et al.* (1989) the magnetic properties of hot-pressed and annealed $Pr_{17}Fe_{76.5}B_5Cu_{1.5}$ magnets were as follows: remanence, $B_r = 1.25$ T; intrinsic coercivity, $_iH_c = 796$ kA m^{-1}; and maximum energy product, $(BH)_{max} = 288$ kJ m^{-3}.

Hot rolling of RE–TM–B alloys has been studied by Ohki *et al.* (1989). The essential feature of the hot rolling is a high strain rate (1–10 s^{-1}), which makes this process very suitable for mass production. The optimum rolling temperature is about $950\,^{\circ}$C. Regarding the optimum structure, it is found that the primary crystallization of iron is necessary for the formation of fine-grained Φ crystallites during the following peritectic reaction. Optimum magnetic properties demand a postdeformation heat treatment that is beneficial to both the coercivity and the remanence. Regarding Pr–Fe–B alloys, the following maximum values have been achieved: $(BH)_{max} = 340$ kJ m^{-3} and $_iH_c = 1194$ kA m^{-1}. Concerning neodymium-based alloys, the maximum published values are: $(BH)_{max} = 269$ kJm^{-3} and $_iH_c = 525$ kA m^{-1}. Hot rolling of ingots is also used for the preparation of anisotropic powder suited for bonded magnets (Hinz *et al.* 1994).

Extrusion of RE–TM–B alloys results in magnets with radial c-axis orientation. Nozieres *et al.* (1988) carried out extrusion experiments with large ingots, cast in an iron sheath. Energy products in the range 120–160 kJ m^{-3} have been obtained.

Regarding the mechanism of deformation and texturing, the microstructural feature of the hot deformation of cast alloys is the marked grain refinement. It is assumed that the crystal alignment is related to rotation of the grain debris in the liquid intergranular phase. The start of the alignment is supported by the plate-like shape anisotropy with its c-axis perpendicular to the larger and flat surface of the dendritic grains (Yuri and Ohki 1994). During the deformation process the cracking occurs preferentially along the c-plane of the main phase, resulting in an enhancement of the plate-like shape anisotropy and the rotation of the grains. In a later stage the rotation of the grains is accompanied by an irregular cracking at the surface of the grains. This generates significant amounts of small and unaligned grain debris. Postdeformation heat treatment results in grain growth with dissolution of the small and unaligned grains and in blunting of the sharp edges of the large grains.

2. Deformation of Powder Precursors

The possibility of an alignment of compacted melt-spun RE–TM–B powder precursors by hot

deformation was discovered by Lee *et al.* (1985). In the first step a fully dense isotropic precursor must be produced by hot pressing. The high densification is possible because the RE-rich grain boundary phase is liquid in the applied temperature range from 700 °C to 750 °C. In the second step the deformation of the precursor takes place at temperatures between 750 °C and 800 °C. In the case of the die-upset method, this step can be accomplished by transferring the sample to an oversized die cavity (Fig. 1). The deformation leads to an anisotropic magnet with the alignment parallel to the pressing direction.

Optimizing the composition in the Nd–Fe–B ternary system involves a compromise between maximizing the volume fraction of the $Nd_2Fe_{14}B$ phase and providing excess neodymium for the grain boundary phase. According to Nozawa *et al.* (1988) the optimum composition of die-upset magnets is in the range $Nd_{13.5-14}Fe_{80.5-80}B_6$. Because the coercivity is reduced after hot deformation of ternary alloys, the effect of additional elements has been investigated. A 0.5 at.% gallium addition proves to be favorable leading to a coercivity enhancement of up to $1600 \, kA \, m^{-1}$ and also a relatively small reduction in remanence (Nozawa *et al.* 1988). The partial substitution of cobalt for iron leads to an enhancement of the Curie temperature of the magnetic main phase and, therefore, to better thermomagnetic stability of the magnets. According to Yoshida *et al.* (1991) the addition of cerium or silicon has a positive effect on the workability.

For melt spinning, a high quench rate should prevent the formation of coarse grains on the wheel-free surface of the ribbons. Surface velocities of $30-34 \, m \, s^{-1}$ lead to an optimum alignment after upsetting (Fuerst and Brewer 1993). Concerning the deformation conditions, increasing the die-upset level results in an enhancement of the alignment up to a height reduction of about 75%. The optimum deformation temperature is in the range 750–800 °C and the optimum strain rate is $10^{-2}-10^{-1} \, s^{-1}$. Die-upset magnets are commercially available. The energy product of the different grades ranges from about $255 \, kJ \, m^{-3}$ to $340 \, kJ \, m^{-3}$ and the intrinsic coercivity ranges from $955 \, kA \, m^{-1}$ to $1670 \, kA \, m^{-1}$ (Panchanathan 1995). The published maximum energy product is about $400 \, kJ \, m^{-3}$. Saito *et al.* (1998) investigated the magnetic properties of amorphous powder consolidated by shock compression. Die-upset magnets with the composition $Nd_{13.5}(Fe_{0.975}Co_{0.025})_{80}Ga_{0.5}B_6$ show a maximum energy product of $433 \, kJ \, m^{-3}$ and an intrinsic coercivity of $995 \, kA \, m^{-1}$ offer optimal deformation.

Mechanically alloyed powder (see *Magnets: Mechanically Alloyed*) and HDDR powder (see *Magnets: HDDR Processed*) compacts can also be used as precursors for the successful production of die-upset magnets (e.g., Schultz *et al.* 1991). A comparison of deformation and magnetic properties has been given by Kirchner *et al.* (1998) (Fig. 2).

The hot deformation of fine-grained powder precursors is also suited to produce radially oriented ring magnets by backward extrusion (Croat 1989). Magnets with different dimensions and energy products of more than $280 \, kJ \, m^{-3}$ are commercially available. The process seems to be especially attractive because the magnetic properties of rings surpass those of ring
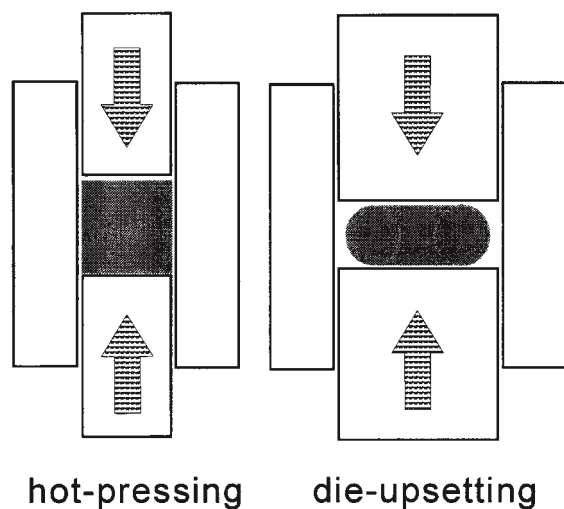
Figure 1
Schematic representation of the preparation of RE–TM–B magnets from fine-grained powder by hot pressing (isotropic magnet) and subsequent hot die-upsetting (anisotropic magnet).
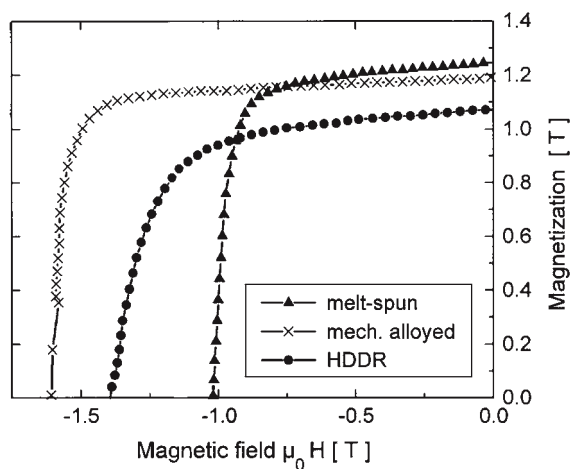
Figure 2
Demagnetization curves measured along the texture axis of die-upset Nd–Fe–B magnets produced from melt-spun (▲), mechanically alloyed (×), and HDDR powders (●) (after Kirchner *et al.* 1998).

magnets made from sintered material, especially at small dimensions. Backward extruded ring magnets do not quite reach the maximum properties of die-upset magnets. The reason is the inherent inhomogeneity of the deformation process, which results in inhomogeneous properties in the cross-section of the rings (Grünberger *et al.* 1996).

 Contrary to cast ingots, microstructural investigations in fine-grained alloys show the formation of flat platelet-shaped grains which are larger than those of the starting material (e.g., Lee *et al.* 1985). Therefore, it is consequent to discuss diffusion-supported mechanisms for deformation and texturing. It is believed that deformation and alignment are produced by a combination of grain boundary sliding and anisotropic grain growth caused by the inherent anisotropy of the crystal growth of the tetragonal Φ phase or by the anisotropy of the elastic properties. Lewis *et al.* (1997) published a survey of the existing literature in this field. Grünberger (1998) investigated the applicability of the model of solution precipitation creep. This is based on the transport of matter in the liquid intergranular phase caused by the local dependence of the solution equilibrium between solid and liquid on the local stress state. Because the local stress state depends on the elastic properties, the anisotropy of the latter can contribute to the development of texture. The kinetic analysis of the strain rate stress relationships of die-upset experiments indicates an interface-controlled process.

See also: Magnetic Materials: Hard; Magnets: Bonded Permanent Magnets; Magnets: Remanence-enhanced; Magnets: Sintered

Bibliography

Croat J J 1989 Current status of rapidly solidified Nd–Fe–B permanent magnets. *IEEE Trans. Magn.* **25**, 3550–4
Fuerst C D, Brewer E G 1993 High-remanence rapidly solidified Nd–Fe–B: die-upset magnets. *J. Appl. Phys.* **73**, 5751–6
Grünberger W 1998 The solution-precipitation creep—a model for deformation and texturing mechanisms of nanocrystalline NdFeB alloys. In: *Proc. 15th Int. Workshop on Rare-Earth Magnets and Their Applications*. Dresden, Germany, pp. 333–48
Grünberger W, Hinz D, Schläfer D, Schultz L 1996 Microstructure, texture, and magnetic properties of backward extruded NdFeB ring magnets. *J. Magn. Magn. Mater.* **157/158**, 41–2
Hinz D, Handstein A, Harris I R 1994 Microstructure and magnetic properties of anisotropic NdFeB powders from hot rolled ingots by HD process. *IEEE Trans. Magn.* **30**, 601–3
Kirchner A, Grünberger W, Gutfleisch O, Neu V, Müller K-H, Schultz L 1998 A comparison of the magnetic properties and deformation behaviour of Nd–Fe–B magnets made from melt-spun, mechanically alloyed and HDDR powders. *J. Phys. D: Appl. Phys.* **31**, 1660–6
Lee R W, Brewer E G, Schaffel N A 1985 Processing of neodymium–iron–boron melt-spun ribbons to fully dense magnets. *IEEE Trans. Magn.* **21**, 1958–63
Lewis L H, Thurston T R, Panchanathan V, Wildgruber U, Welch D O 1997 Spatial texture distribution in thermomechanically deformed 2-14-1-based magnets. *J. Appl. Phys.* **82**, 3430–41
Nozawa Y, Iwasaki K, Tanigawa S, Tokunaga M, Harada H 1988 Nd–Fe–B die-upset and anisotropic bonded magnets. *J. Appl. Phys.* **64**, 5285–9
Nozieres J P, Perrier de la Bathie R, Gavinet J 1988 A novel process for rare earth–iron–boron permanent magnets preparation. *J. Physique* **49** (C8), 667–8
Ohki T, Yuri T, Miyagawa M, Takahashi Y, Yoshida C, Kambe S, Higashi M, Itayama K 1989 A new method of producing Pr–Fe–B base hard magnetic materials. In: *Proc. 10th Int. Workshop on Rare-Earth Magnets and Their Applications*. pp. 399–408 Kyoto, Japan
Panchanathan V 1995 Magnequench magnets status overview. *J. Mater. Eng. Perform.* **4**, 423–9
Saito T, Fujita, M, Kuji T, Fukuoka K, Syono Y 1998 The development of high performance Nd–Fe–Co–Ga–B die upset magnets. *J. Appl. Phys.* **83**, 6390–2
Schultz L, Schnitzke K, Wecker J, Katter M, Kuhrt C 1991 Permanent magnets by mechanical alloying. *J. Appl. Phys.* **70**, 6339–44
Shimoda T, Akioka K, Kobayashi O, Yamagami T, Ohki T, Miyagawa M, Yuri T 1989 Hot-working behavior of cast Pr–Fe–B magnets. *IEEE Trans. Magn.* **25**, 4099–104
Yoshida Y, Kasai Y, Watanabe T, Shibata S, Panchanathan V, Croat J J 1991 Hot workability of melt-spun Nd–Fe–B magnets. *J. Appl. Phys.* **69**, 5841–3
Yuri T, Ohki T 1994 In: *Crystal alignment in Pr–Fe–B hot-rolled magnet. Proc. 14th Int. Workshop on Rare-Earth Magnets and Their Applications*, pp. 645–54 Birmingham, UK

W. Grünberger
*Institut für Festkörper- und Werkstofforschung
Dresden, Germany*

Thin Film Magnetism: Band Calculations

The understanding and design of complex magnetic nanostructures is one of the current frontiers in magnetism. Research in this field is stimulated by its interesting fundamental physics as well as applications today and in the future in the field of data storage and magnetoelectronics. New experimental techniques, like molecular beam epitaxy and spin-polarized electron spectroscopy techniques, for growth and characterization of the nanostructures go hand-in-hand with powerful theoretical methods and provide a great deal of insight into these phenomena. Ab initio calculations based on density functional theory play a crucial role for the microscopic understanding of fundamental magnetic properties, such as magnetization and magnetic order.

1. Spin-density Functional Theory

Ab initio calculation means that the system under consideration is described without any free parameter.

The problem that needs to be solved is the many-body problem of a system formed by interacting electrons and nuclei. With the Born–Oppenheimer approximation (Born and Oppenheimer 1927) the problem can be reduced to a system of N interacting electrons moving in the electrostatic potential V_{ext} caused by the nuclei

$$H = \sum_{i=1}^{N} \left(-\frac{\hbar^2}{2m} \right) \frac{\partial^2}{\partial \mathbf{r}_i^2} + \sum_{i=1}^{N} V_{ext}(\mathbf{r}_i) + \frac{1}{2} \sum_{i \neq j}^{N} \frac{\varepsilon^2}{|\mathbf{r}_i - \mathbf{r}_j|} \quad (1)$$

where $\varepsilon^2 = e^2/4\pi\varepsilon_o$. ε_o is the dielectric constant. $\mathbf{r}_i$ is the position of electron i while all other constants have their traditional meaning. Depending on the boundary conditions used for the external potential, systems with arbitrary dimensions like atoms or clusters, wires, slabs, or bulk materials can be described (Fig. 1) Atoms and clusters are considered to be quasi one-dimensional and are finite in all spatial directions. Wires are confined in two directions and are translational invariant in the third, slabs are finite in one direction and periodically repeated in the other two directions, and bulk systems are translational invariant in all spatial directions.

Density functional theory (Hohenberg and Kohn 1964, Kohn and Sham 1965, Sham and Kohn 1966) constitutes the main underlying basis for the solution of this problem. In the generalization of density functional theory to magnetic systems (Rajagopal 1980, Hedin and Lundqvist 1971, Barth and Hedin 1972, Moruzzi *et al.* 1978, Gunnarsson and Lundqvist 1976, Gunnarsson *et al.* 1972), the so-called spin density functional theory, one distinguishes between two types of electrons, namely the majority electrons ($\sigma = +$) and the minority electrons ($\sigma = -$) whose spin is in and opposite to the direction of magnetization, respectively. In addition to the Coulomb potential of the nuclei the electrons experience an extra contribution $\pm \mu_B H$ due to an external field H. the spin degeneracy is lifted. As a consequence the majority electrons are more attracted than the minority electrons. Contributions from orbital momenta and from spin–orbit coupling are neglected, giving an adequate approximation for itinerant magnetism.

The two types of particles are represented by spin-dependent densities $n^+(\mathbf{r})$ and $n^-(\mathbf{r})$, leading accordingly to the following functional for the ground state energy

$$E[n^+, n^-] = T[n] + \int d^3 r V_{ext}(\mathbf{r}) n(\mathbf{r}) + U[n] + E_{xc}[n^+, n^-] \quad (2)$$

where $T[n]$ is the functional of the kinetic energy for a set of N noninteracting electrons of density $n(\mathbf{r})$. $U[n]$ is the classical Hartree energy

$$U[n] = \frac{1}{2} \int d^3 r n(\mathbf{r}) \int d^3 r' n(\mathbf{r}') \frac{\varepsilon^2}{|\mathbf{r} - \mathbf{r}'|} \quad (3)$$

and $E_{xc}[n^+, n^-]$ the exchange-correlation energy which includes all many-body interactions, exchange and correlation, in an effective way. The total density is given by

$$n(\mathbf{r}) = n^+(\mathbf{r}) + n^-(\mathbf{r}) \quad (4)$$

and the magnetization density is given by

$$m(\mathbf{r}) = n^+(\mathbf{r}) - n^-(\mathbf{r}) \quad (5)$$

Clearly, the ground state energy is a functional of both spin-dependent densities, $E[n^+, n^-]$. Using spin-dependent densities in terms of single-particle wave functions $\varphi_k^\sigma(\mathbf{r})$

$$n^\sigma(\mathbf{r}) = \sum_k |\varphi_k^\sigma(\mathbf{r})|^2 \quad (6)$$

the variation of the ground state energy yields the spin-dependent Kohn–Sham equations

$$\left[-\frac{\hbar^2}{2m} \frac{\partial^2}{\partial \mathbf{r}^2} + V^\sigma(\mathbf{r}) \right] \varphi_k^\sigma(\mathbf{r}) = E_k^\sigma \varphi_k^\sigma(\mathbf{r}) \quad (7)$$

and, by analogy with the spin-independent case an effective though spin-dependent potential follows as

$$V^\sigma = V_{ext}(\mathbf{r}) + \int d^3 r' n(\mathbf{r}') \frac{\varepsilon^2}{|\mathbf{r} - \mathbf{r}'|} + V_{xc}^\sigma(\mathbf{r}) \quad (8)$$

with

$$V_{xc}^\sigma = \frac{\delta E_{xc}}{\delta n \pm (\mathbf{r})}$$

Under the local spin density approximation (LSDA), the exchange-correlation energy (Barth and Hedin 1972, Moruzzi *et al.* 1978) is written as Eqn. (9)

$$E_{xc}[n^+, n^-] \approx \int d^3 r (n^+(\mathbf{r}) + n^-(\mathbf{r})) \times \varepsilon_{xc}^{hom}(n^+(\mathbf{r}), n^-(\mathbf{r})) \quad (9)$$

and

$$V_{xc}^\sigma \approx \left[\frac{\partial}{\partial n \pm}(n^+ + n^-) \, \varepsilon_{xc}^{hom}(n^+, n^-) \right]_{n^\sigma = n^\sigma(\mathbf{r})} \quad (10)$$

Figure 1
Dimension of the systems under consideration. Zero-dimensional clusters, one-dimensional wires, two-dimensional slabs, and three-dimensional bulk systems.

Different approximations of the local density and the local spin density functional (Hedin and Lundqvist 1971, Barth and Hedin 1972, Moruzzi *et al.* 1978, Vosko *et al.* 1980) have been used. They lead to variations within the error of the local density or spin density approximation itself.

2. Stoner Model of Ferromagnetism

The one-particle nature of the Kohn–Sham equation (Eqn.(7)) allows a Stoner-like model to be derived for ferromagnetism (Vosko and Perdew 1975, Gunnarsson 1976, Janak 1977, Stoner 1938, Blügel 1995). Starting from the assumption that the magnetization density $m(\mathbf{r})$ is a small parameter compared to the density $n(\mathbf{r})$, the exchange and correlation potential V_{xc} can be expanded in powers of $m(\mathbf{r})$. The linear approximation yields

$$V_{xc}^{\pm} = V_{xc}^0 \mp m(\mathbf{r})\tilde{V}(n(\mathbf{r})), \quad \tilde{V} > 0 \qquad (11)$$

where V_{xc}^{σ} is the exchange-correlation potential for the nonmagnetic case. As a consequence, the majority of electrons experience a more attractive potential as minority electrons. In the Stoner model this potential shift is expressed in terms of a constant

$$V_{xc}^{\pm} = V_{xc}^0 \mp \tfrac{1}{2}IM, \quad M = \int_{V_{atom}} \mathrm{d}\mathbf{r}\, m(\mathbf{r}) \qquad (12)$$

with the local atomic moment M and the Stoner parameter I. In the case of ferromagnetism M is the same for all atoms. As a consequence of the constant potential shift in Eqn. (12), the single particle wave functions $\varphi_k^{\sigma}(\mathbf{r})$ (Eqn. (7)) do not change with respect to the nonmagnetic wavefunctions, while the eigenvalues E_k are shifted rigidly downwards or upwards

$$\varphi_k^{\pm}(\mathbf{r}) = \varphi_k^0(\mathbf{r}) \quad \text{and} \quad E_k^{\pm} = E_k \mp \tfrac{1}{2}IM \qquad (13)$$

This is the so-called spin–split bandstructure (Fig. 2). The symmetric energy shift is transferred to the spin-dependent density of states

$$n^{\sigma}(E) = n(E \pm \tfrac{1}{2}IM) \qquad (14)$$

with respect to the density of states of the nonmagnetic system $n(E)$ (Fig. 2). Integration over all occupied states up to the Fermi energy E_F gives the number of electrons

$$N = \int^{E_F} \mathrm{d}E(n^0(E + \tfrac{1}{2}IM) + n^0(E - \tfrac{1}{2}IM) \qquad (15)$$

and the moment per atom

$$M = \int^{E_F} \mathrm{d}E(n^0(E + \tfrac{1}{2}IM) - n^0(E - \tfrac{1}{2}IM)) \qquad (16)$$

Since the density of the nonmagnetic system n^0 and the number of electrons N are known, the Fermi energy E_F and the moment M can be obtained from the self-consistent solution of Eqns. (15) and (16). As a sufficient condition for a ferromagnetic solution the Stoner criterion

$$In^0(E_F) > 1 \qquad (17)$$

can be derived. Large Stoner parameters or exchange integrals I and large density of states at the Fermi energy $n^0(E_F)$ favor ferromagnetism. The corresponding parameters deduced from a nonspin-polarized calculation are shown in Table 1 (Gunnarsson 1976, Janak 1977). Obviously, the Stoner criterion is only fulfilled for Fe, Co, and Ni, precisely those metals that show ferromagnetism. Fig. 3 shows the densities of states for Fe, Co, and Ni computed by means of a spin-density functional calculation. The results show the dominating contribution of the 3d electrons. The density of states is exchange split and otherwise very complicated. The spin-up and spin-down densities of states remain, however, very similar which confirms the validity of a Stoner model.

The corresponding spin moments in comparison to experimental results for spin moments and total moments are given in Table 2. The exchange integral I is an interatomic property that depends on the type of
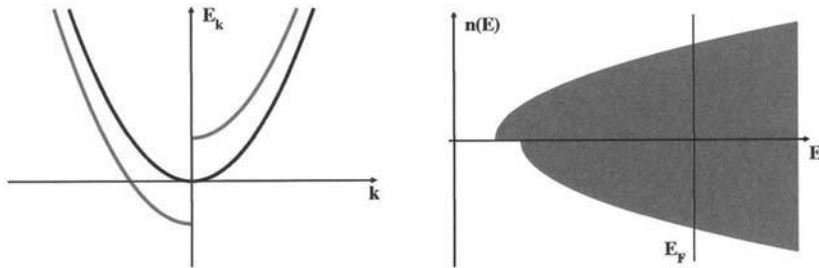
Figure 2
Spin–split band structure and density of states for free electrons; majority and minority bands are shifted downwards and upwards, respectively.

Table 1
Density of states $n(E_F)$ (in eV^{-1}) at the Fermi energy calculated for nonmagnetic systems, Stoner parameter I (in eV), and $In(E_F)$ (Gunnarsson 1976, Janak 1977).

Metal	Na	Al	Cr	Mn	Fe	Co	Ni	Cu	Pd	Pt
$n(E_F)$	0.23	0.21	0.35	0.77	1.54	1.72	2.02	0.14	1.14	0.79
I	1.82	1.22	0.76	0.82	0.93	0.99	1.01	0.73	0.68	0.63
$In(E_F)$	0.41	0.25	0.27	0.63	1.43	1.70	2.04	0.11	0.78	0.50
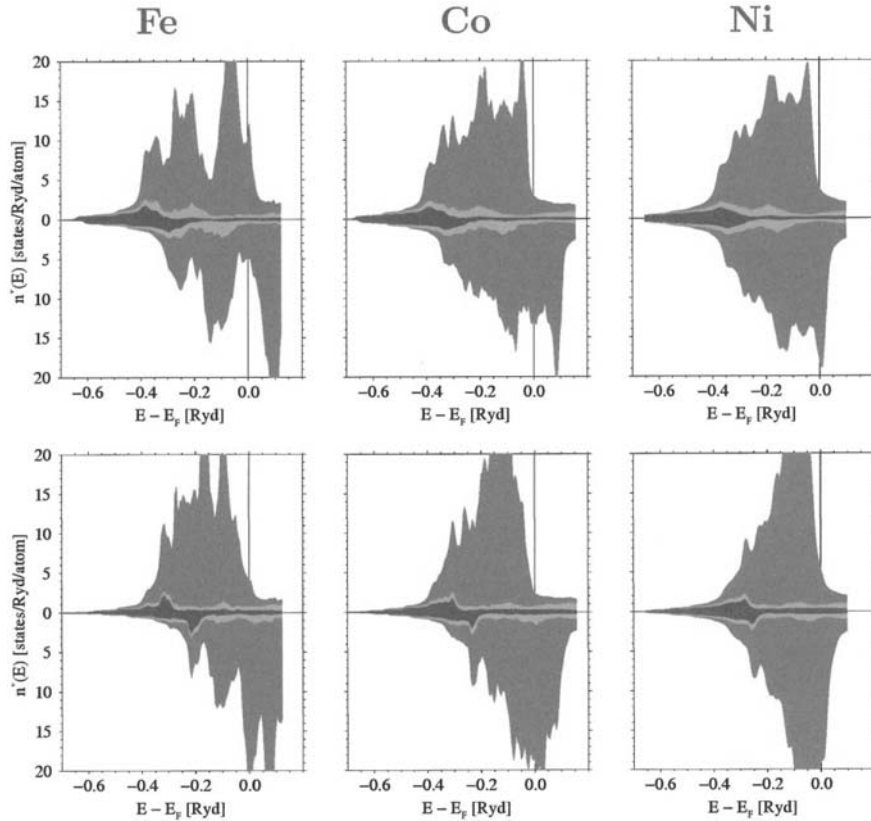
Figure 3
Spin–polarized density of states of Fe, Co, and Ni in a bulk phase (upper panel) and for the corresponding atom in a (100) surface (lower panel). The shades denote the contribution of s (darkest), p (lightest), and d electrons (medium shade).

Table 2
Magnetic moments (μ_B atom) for Fe, Co, and Ni calculated in the LSDA approximation (Moruzzi *et al.* 1978) in comparison to experimental values for the spin moment and the total moment.

Metal	M_{LSDA}	M_{spin}	M
Fe	2.15	2.12	2.22
Co	1.56	1.57	1.71
Ni	0.59	0.55	0.61

atom but is independent on structure and environment. According to Gunnarsson (1976) and Janak (1977) the exchange integrals of the transition metals have the following trend

$$I_{3d} > I_{4d} > I_{5d} \tag{18}$$

The density of states at the Fermi level is reciprocal with the bandwidth

$$n(E_F) \sim W \tag{19}$$
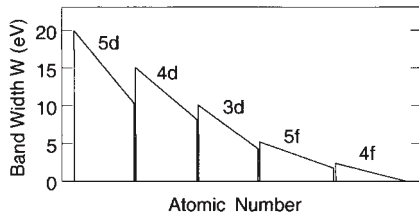
Figure 4
Trend in the bandwidth of the transition metal, lanthanides and actinides as a function of the atomic number.

The stronger the electrons are localized, the smaller the bandwidth, the larger is the density of states. The bandwidth is zero in the atomic limit. The Stoner criterion is always fulfilled. The magnetic moment is determined by Hunds rule. If we restrict our further considerations to the tightly bound d electrons of transition metals, the bandwidth can be expressed by means of a tight-binding model

$$W_{\mathrm{d}} = 2\sqrt{N_{nn}}h_{\mathrm{d}}(R_{nn}) \qquad (20)$$

According to this approximation the bandwidth depends on the overlap integral or hopping matrix element h_{d} of the d electrons and the number of nearest neighbor atoms or coordination number N_{nn}. The overlap integral h_{d} is element specific, is determined by the overlap of the d wavefunctinos, and, of course, is reciprocal with the nearest neighbor distance R_{nn}. The trend in the transition metals follows the relation

$$h_{3\mathrm{d}} < h_{4\mathrm{d}} < h_{5\mathrm{d}} \;\Rightarrow\; W_{3\mathrm{d}} < W_{4\mathrm{d}} < W_{5\mathrm{d}}$$
$$\Rightarrow\; n_{3\mathrm{d}} > n_{4\mathrm{d}} > n_{5\mathrm{d}} \qquad (21)$$

In Fig. 4 the general trend of the bandwidths of transition metals, lanthanides, and actinides is shown (Blügel 1995).

3. Magnetism in Reduced Dimensions

Understanding magnetism in low-dimensional systems looks rather straightforward. The simplest low-dimensional system is the isolated atom, for which it is known that nearly all transition metal atoms have magnetic moments. The magnetism is well described by Hund's rules. On the other hand, it is known that among the transition metals only five remain mag-

netic in their bulk crystalline phase: Co and Ni are ferromagnetic, Cr is antiferromagnetic, and Mn and Fe are ferromagnetic or antiferromagnetic depending on their crystal structure. Low-dimensional transition metals, that is interfaces, surfaces, ultrathin films, and monolayers, should behave between these two extremes. As a consequence an enormous number of ab initio calculations have been performed in this field in the 1990s (Blügel 1995, Weinert and Blügel 1993, Asada *et al.* 1999).

Following the considerations above a reduction of the coordination number N_{nn} would cause band narrowing and would enhance the tendency towards magnetism due to the Stoner criterion.

The reduction of the coordination number, however, can be achieved by a reduction in the dimension of the system under consideration. An fcc crystal has a coordination number of $N_{\mathrm{fcc}} = 12$, an atom of the (100) surface of the same crystal is surrounded by eight atoms $N_{(100)} = 8$, and the monolayer atoms have only four nearest neighbors, $N_{\mathrm{ML}} = 4$. Keeping the nearest neighbor distance and the overlap integrals fixed, the density of states and the bandwidths would obey the following relation

$$n_{\mathrm{fcc}} : n_{(100)} : n_{\mathrm{ML}} = \frac{1}{W_{\mathrm{fcc}}} : \frac{1}{W_{(100)}} : \frac{1}{W_{\mathrm{ML}}}$$
$$= 1 : 1.22 : 1.73 \qquad (22)$$

The reduction in the coordination number is hence the origin of the enhancement of magnetism at interfaces, surfaces, and for monolayers or ultrathin films. As a consequence these systems offer the opportunity to find totally new magnetic materials.

For the ab initio description of surfaces and ultrathin magnetic films, different geometries are used. In a superlattice the metallic films are separated by vacuum layers but otherwise are periodically repeated in all spatial directions. Surface geometry consists of semi-infinite metal and vacuum parts whereas slab geometry is a freestanding metal film embedded in vacuum layers (Fig. 5).

Figure 3 shows the local densities of states for Fe, Co, and Ni (100) surfaces computed by means of a spin-density functional calculation. The comparison of bulk (upper panel) and surface (lower panel) density of states illustrates the effect of band narrowing clearly. Enhancement of the magnetic moments at the surface in comparison to the bulk material is given in Table 3.

Figure 5
Superlattice, semi-infinite surface system, and slab.

Table 3
Magnetic moments (μ_B atom) for Fe, Co, and Ni calculated in LSDA approximation (Blügel 1995) for (100) and (110) surfaces in comparison to bulk moments (Moruzzi *et al.* 1978).

Metal	M_{LSDA}	$M_{(100)}$	$M_{(110)}$
Fe	2.15	2.88	2.43
Co	1.56	1.85	—
Ni	0.59	0.68	0.74

The magnetic moment of the Ni (110) surface is higher than for the (100) surface. The results for Fe are opposite. This behavior is related to the surface orientation, which determines the coordination number and the next nearest neighbor distance between the surface atoms. The largest magnetic moment will be obtained for the most open surface. Ni is an fcc system: the low-index surface (110) is the most open, (100) is intermediate, and (111) is the closed packed surface. The trend for bcc systems is opposite. Fe is a bcc system.

It is implied in the discussion so far that the co-ordination number is the crucial feature in interface magnetism but this is not the whole truth. The following features have to be taken into account to achieve a quantitative description. First of all, the point symmetry of a surface is lower in comparison to the bulk system. Symmetry reduction causes level splitting, changes the shape of the density of states, and is unfavourable for magnetism. Second, the relaxation of the charge density at the surface changes hybridization at the surface and causes a redistribution of spectral density. As a consequence, a relative shift of the sp band against the d band and/or a change of spectral weight is obtained (see Fig. 3). The number of d states is changed. As a result magnetism can be enhanced or reduced (see Ni). The neglect of these interplaying effects have caused confusion in the past in the field of surface and interface magnetism. But they are readily included in self-consistent electronic structure calculations.

4. Ground State Magnetic Order

Based on the calculation of the total energy (Eqn. (10)), ab initio electronic structure calculations provide a perfect tool for investigating the magnetic order. Comparison of the total energy for different magnetic configurations ΔE allows a systematic search of the magnetic order in the ground state.

As an example, the magnetic order of 3d transition metal monolayers on top of a Cu substrate was investigated (Blügel 1995). The total energy of a ferromagnetic configuration E^F is compared to the total energy of an antiferromagnetic configuration E^{AF} (Fig. 6). The energy differences

$$\Delta E = E^{AF} - E^F \qquad (23)$$

are shown in Fig. 7. Fe, Co, and Ni layers prefer ferromagnetic, whereas V, Cr, and Mn prefer an antiferromagnetic order.

This is an arbitrary example chosen to demonstrate the method. Similar calculations can be applied to various other problems concerning the magnetic configuration, for example surface steps and edges or
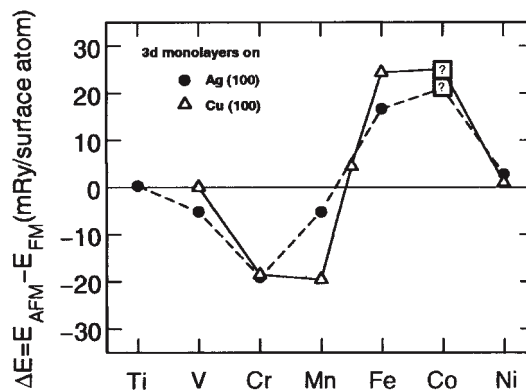
Figure 7
Total energy difference per atom for a ferromagnetic and antiferromagnetic phase for 3d monolayers on a △, Cu (100) and ●, Ag (100) substrate.

Figure 6
Schematic representation of ferromagnetic and c (2 × 2) antiferromagnetic order of a monolayer film grown as an overlayer on a fcc (001) substrate.

surface alloys (Freyss *et al.* 1996) also including non-collinear magnetic order (Sandratskii 1998)

The capability of this method was nicely confirmed by experimental observation of the local magnetic order in surface alloys by means of spin-polarized scanning tunneling spectroscopy (Heinze *et al.* 2000).

See also: Monolayer Films: Magnetism; Density Functional Theory: Magnetism; Itinerant Electron Systems: Magnetism (Ferromagnetism); Multilayers: Interlayer Coupling

Bibliography

Asada T, Bihlmayer G, Handschuh S, Heinze S, Kurz Ph, Blügel S 1999 *J. Phys.: Condens. Matter*. **11**, 9347
Barth U V, Hedin L 1972 *J. Phys. C* **5**, 1629
Blügel S 1995 *Habilitation*. RWTA, Aachen
Born M, Oppenheimer J R 1927 *Ann. Phys.* **84**, 457
Freyss M, Stoeffler D, Dreyssé 1996 *Phys. Rev. B* **54**, 12677
Gunnarsson O 1976 *J. Phys. F: Met. Phys.* **6**, 587
Gunnarsson O, Lundqvist B I 1976 *Phys. Rev. B* **13**, 4274
Gunnarsson O, Lundqvist B I, Lundqvist S 1972 *Solid State Commun.* **11**, 149
Hedin L, Lundqvist B 1971 *J. Phys. C* **4**, 2064
Heinze S, Bode M, Kubetzka A, Pietzsch O, Nie X, Bluegel S, Wiesendanger R 2000 *Science* **288**, 1805
Hohenberg P, Kohn W 1964 *Phys. Rev.* **136**, 864
Janak J F 1977 *Phys. Rev. B* **16**, 255
Kohn W, Sham L J 1965 *Phys. Rev.* **140**, 1133
Moruzzi V R, Janak J F, Williams A R 1978 *Calculated Electronic Properties of Metals*. Pergamon Press, New York
Rajagopal A K 1980 *Adv. Chem. Phys.* **41**, 59
Sandratskii L M 1998 *Adv. Phys.* **47**, 91
Sham L J, Kohn W 1966 *Phys. Rev.* **145**, 561
Stoner E C 1938 *Proc. R. Soc. London* **165**, 372
Vosko S H, Perdew J P 1975 *Can. J. Phys.* **53**, 1385
Vosko S H, Wilk L, Nussair N 1980 *Can. J. Phys.* **58**, 1200
Weinert M, Blügel S 1993 In: Bennet L H, Watson R E (eds.) *Magnetic Multilayers*. World Scientific, Singapore

I. Mertig
Technische Universität Dresden, Germany

Thin Film Magnetism: PEEM Studies

A Photoemission Electron Microscope (PEEM) images photo and/or secondary electrons, which are generated at the surface of a solid sample by the absorption of x-ray or ultraviolet (UV) radiation. Depending on the wavelength of the radiation different contrast mechanisms are present, providing information on the elemental and chemical composition, and the electronic and magnetic properties of the material. Magnetic domain imaging is a major application of the PEEM technique, exploiting strong x-ray magnetic dichroism effects, e.g., at the L edges of the magnetic 3*d* transition metals (e.g., Cr, Mn, Fe, Co, Ni). For a comparison with other domain imaging techniques see *Kerr Microscopy*, *Magnetic Materials: Transmission Electron Microscopy*, *Magnetic Force Microscopy*, and references therein.

The PEEM technique stands out against other magnetic imaging techniques through its surface sensitivity and element specificity, making PEEM an ideal tool for the investigation of ultra-thin magnetic films, multi-layers, and alloys. In contrast to other high resolution, magnetic imaging techniques, PEEM is also sensitive to antiferromagnetic order. The spatial resolution of PEEM for magnetic domain imaging is typically about 50–100 nm, which positions PEEM between Transmission Electron Microscopy and optical techniques, such as Kerr Microscopy.

1. Photoemission Electron Microscopy

PEEM was first used in the 1930s and has since then matured into an established surface science technique (Stöhr *et al.* 1993, Tonner *et al.* 1995, Stöhr *et al.* 1998, Anders *et al.* 1999). PEEM is closely related to the Low Energy Electron Microscope (LEEM) and the Spin-polarized Low-energy Electron Microscope (SPLEEM), which were pioneered by Bauer (1994) and Duden and Bauer (1998). All three techniques utilize low-energy electrons to form an image representing physical properties of the sample surface. LEEM and SPLEEM image diffracted low-energy electrons and thereby provide information on the local crystallographic (LEEM) and magnetic (SPLEEM) structure of the surface of a crystalline sample. PEEM, in contrast, images electrons generated by photoionization and therefore is not limited to the study of crystalline samples (see also *Photoemission: Spin-polarized and Angle-resolved*). As light sources, UV gas discharge lamps, UV lasers, and synchrotron radiation sources have been used. Synchrotron radiation offers the important advantage of tunability of the wavelength of the illumination, thereby allowing a selection between various mechanisms of contrast. X-ray PEEM thus combines aspects of spectroscopic and microscopic methods and is called a spectromicroscopy technique.

A typical PEEM setup using synchrotron radiation from a bending magnet is shown in Fig. 1 (Anders *et al.* 1999, Scholl *et al.* 2002). X rays pass through a moveable aperture, which selects the polarization of the radiation. A spherical grating monochromator and an exit slit monochromatize and focus the beam onto the sample. A schematic kinetic energy spectrum of the emitted electrons after x-ray absorption is shown in Fig. 2(a). Photoemission lines appear at high kinetic energy, followed by a broad tail of secondary electrons which peak at low energies close to the work function cut-off. PEEM microscopes usually accept the total electron yield without prior
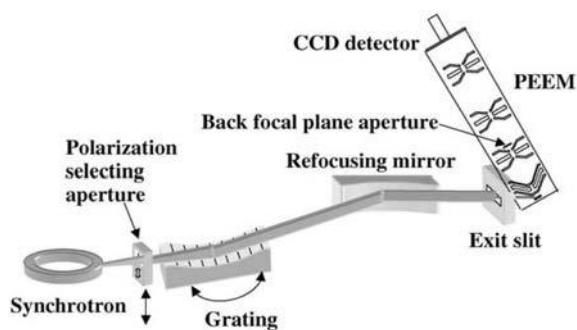
Figure 1
PEEM-2 Photoemission Electron Microscope and x-ray beamline at the Advanced Light Source, USA. X rays are monochromatized by a spherical grating and focused into a $30 \times 30 \ \mu m^2$ spot on the sample. The electron microscope column produces a magnified image of the local x-ray absorption on a phosphor, which is imaged by a slow-scan CCD camera.
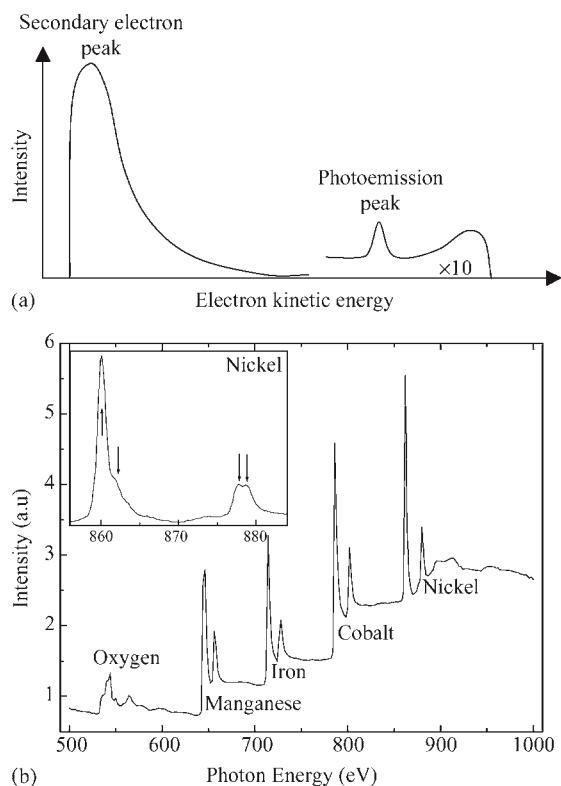
Figure 2
(a) Energy spectrum of emitted electrons after the absorption of x-rays. (b) X-ray absorption spectrum measured in total electron yield of a Co/FeMn/NiO sample. The absorption fine structure at the Ni L_2 peak (inset) results from the presence of nickel oxide.

energy discrimination. The sampling depth of PEEM correlates with the mean free path of low energy electrons in the studied material and lies typically between 2 nm and 5 nm for metals.

The emitted electrons are accelerated in the strong electric field between the sample and the first microscope lens ($\sim 10^4 \ V \ mm^{-1}$), and are then imaged with magnification by electron optics, consisting of typically 2–4 electrostatic or magnetic lenses. A back focal plane aperture limits the angular spread of the transmitted electrons and also acts as a simple energy filter, reducing the chromatic and spherical aberrations of the microscope. Projector lenses magnify and focus the image onto the electron detector, typically an electron sensitive phosphor and/or a channelplate detector, producing a visible image. Deflector and stigmator elements in the microscope steer the electron beam and correct for eventual mechanical misalignments. Using synchrotron radiation microscopes, has achieved a spatial resolution close to 20 nm (Anders *et al.* 1999).

2. Contrast Mechanisms

Contrast in PEEM results from local variations in the light absorption, the work function, and the topography of the sample. Topographic structures such as edges, bulges, and holes locally distort the electric field close to the sample and modulate the image intensity. Work function contrast arises from inhomogeneities in the surface composition and thereby the work function. This contrast mechanism is particularly strong using UV radiation close to the work function cut-off.

Chemical, magnetic, and elemental contrast arises from Near Edge X-ray Absorption Fine Structure (NEXAFS), which is discussed in more detail in *Surface Chemistry: Electron Yield Spectroscopy* (Ormerod 2001). As an example, an x-ray absorption spectrum of a Co/FeMn/NiO multi-layer is shown in Fig. 2(b). Different elements in a material can be identified by their characteristic core hole binding energies and absorption edges. The fine structure close to the absorption edge—the inset shows the Ni $L_{2,3}$ edge—can be further analyzed, providing information about the chemical and magnetic state of the material. For example, the multiplet structure at the L edges, marked by arrows in Fig. 2(b), is characteristic for nickel oxide (Regan *et al.* 2001).

PEEM microscopes are typically used in three modes of operation: (i) full-field imaging, (ii) local spectroscopy, and (iii) spectromicroscopy. In the full-field imaging mode images are acquired at fixed photon energy. In the local spectroscopy mode local x-ray absorption spectra are acquired in predefined regions by scanning the photon energy and using the spatial resolution provided by the PEEM electron optics. In the spectromicroscopy mode, stacks of

PEEM images are acquired as a function of photon energy, generating a three-dimensional dataset with two lateral and one energy dimension.

3. X-ray Magnetic Linear and Circular Dichroism

X-ray Magnetic Circular Dichroism (XMCD) and X-ray Magnetic Linear Dichroism (XMLD) are established spectroscopic x-ray techniques, which are widely used for the investigation of ferromagnetic and antiferromagnetic surfaces and thin films (Thole *et al.* 1985, Schütz *et al.* 1987, Alders *et al.* 1998, see also *Magnetism: Applications of Synchrotron Radiation*). Both methods probe the modification of the electronic structure of a material in the presence of magnetic order, resulting in an intensity variation of the near edge x-ray absorption fine structure. X-ray magnetic dichroism has been extensively used at $2p$ to $3d$ transitions ($L_{2,3}$ edge) in $3d$ transition metals, exploiting the strong spin–orbit interaction of $2p$ core levels and the strong exchange splitting of $3d$ valence levels (Schütz *et al.* 1987). More recently XMLD has been applied in studies of collinear antiferromagnets (e.g., Alders *et al.* 1998). In order to illustrate the appearance of both dichroism effects, x-ray absorption spectra are shown in Fig. 3, measured in single microscopic magnetic domains on a $Co/LaFeO_3$ bilayer.

The sample was grown by molecular beam epitaxy (MBE) on a $SrTiO_3(001)$ substrate (Scholl *et al.* 2000). The relative in-plane orientation of the photon polarization and the sample magnetization are shown on the right. The size of the XMCD effect in ferromagnetic Co, which appears as a variation of the L_3 and L_2 resonance intensities, depending on the relative orientation of the sample magnetization $\mathbf{M}$ and the circular x-ray polarization direction $\mathbf{P}$, is a measure for the element specific, atomic, spin, and orbital moment and the angle enclosed by the magnetization and the polarization vector: $\Delta I \sim |\mathbf{M}| \cos \angle (\mathbf{M}, \mathbf{P})$ (Fig. 3(a)). Alternatively, XMLD is particularly useful for the investigation of collinear antiferromagnetism because it probes an anisotropic electronic structure. Ideal antiferromagnets do not show XMCD because they are magnetically compensated. The absorption spectrum of the antiferromagnetically ordered Fe atoms in $LaFeO_3$ shows a change in the relative intensity of the L_3 and L_2 multiplet peaks due to XMLD, depending on the relative orientation of the $LaFeO_3$ magnetic axis and the linear x-ray polarization (Fig. 3(b)). The size of the effect is again a measure for the element specific, atomic, magnetic moment $\mathbf{M}$, and the angle enclosed by the spin axis $\mathbf{A}$ and the linear polarization vector $\mathbf{E}$: $\Delta I \sim |\mathbf{M}^2| [1 - 2\cos^2 \angle (\mathbf{A}, \mathbf{E})]$.

XMCD was first applied to ferromagnetic domain imaging in a pioneering work in 1993 (Stöhr *et al.* 1993). More recently, microscopic antiferromagnetic
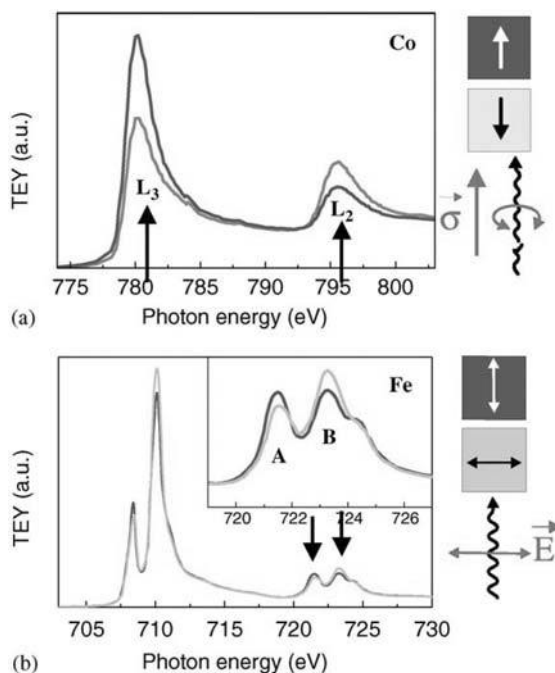
Figure 3
(a) X-ray Magnetic Circular Dichroism (XMCD) and (b) Linear Dichroism (XMLD) spectra of 1.2 nm Co/40 nm $LaFeO_3/SrTiO_3(001)$. The $LaFeO_3$ spectrum was acquired at the Fe edge. The spectra show opposite dichroism effects (a) at the L_3 and L_2 resonance in the ferromagnet Co (XMCD) and (b) at the L_2 multiplet peaks A and B in the antiferromagnet $LaFeO_3$ (XMLD).

domains have been imaged for the first time using XMLD (Scholl *et al.* 2000, Nolting *et al.* 2000). For the study of ferromagnetic domains in transition metal ferromagnets, e.g., Co, images are acquired with the photon energy tuned to the peak of the L_3 and L_2 resonances. The ratio image acquired with circular polarization is the XMCD image (Fig. 4(a)). Alternatively, images acquired with opposite polarization can be divided. Dividing PEEM images acquired with linear polarization at the magnetically sensitive peaks A and B at the L_2 edge of the antiferromagnet $LaFeO_3$ generates the XMLD image, representing the antiferromagnetic domain structure of a material (Fig. 4(b)).

Different colors in the XMCD and XMLD image correspond to different directions of the magnetic moment. In Co (top) we distinguish three classes of domains, which have magnetizations pointing up (shown here as the darkest shade), down (lightest shade), and left or right (medium shade, not distinguished in this measurement geometry). The XMLD image of $LaFeO_3$ shows two classes of domains with the in-plane projection of the atomic magnetic
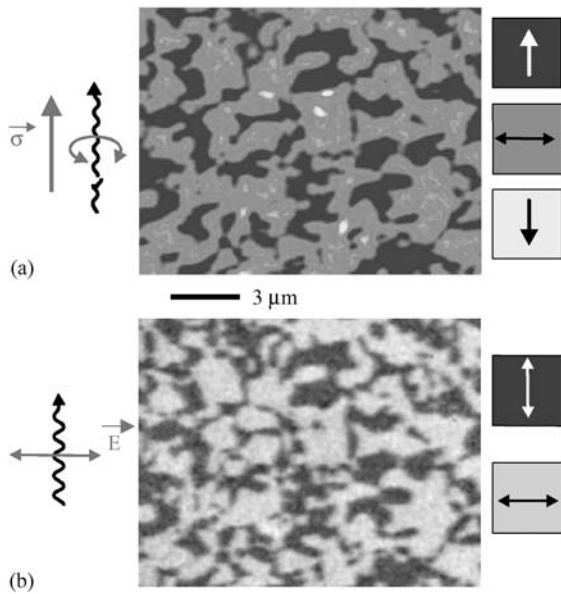
Figure 4
X-ray magnetic dichroism images of (a) the ferromagnetic domain structure in Co and (b) the antiferromagnetic domain structure in $LaFeO_3$ in a $Co/LaFeO_3/SrTiO_3(001)$ multilayer sample. Different shades refer to different domain orientations as indicated in the boxes. The images demonstrate a parallel orientation of the in-plane component of the Fe and Co moment due to interfacial exchange coupling.

moments pointing up down (darker shade) and left-right (lighter shade). Note that the shown images were acquired at identical sample positions, making use of the element specificity of x-ray PEEM. The correspondence between the two domain structures indicates a uniaxial interface exchange coupling of sufficient strength, aligning the magnetization in the ferromagnet with the in-plane component of the magnetic axis in the antiferromagnet.

4. Imaging of Local Exchange Bias

One important application of domain imaging using the PEEM technique is the study of exchange biased thin film systems. Exchange bias at a ferromagnet/antiferromagnet interface leads to a unidirectional anisotropy of the ferromagnetic layer, pinning its magnetization into a preferred direction (Meiklejohn and Bean 1956); see also *Magnetic Films: Anisotropy*. This pinning is employed in magneto-electronic devices for stabilization of the magnetization in a magnetic reference layer. The major application of this effect is in magnetic hard disk heads containing a read element based on the giant magnetoresistance

phenomenon (see *Giant Magnetoresistance* and *Magnetic Recording Technologies: Overview*). The unique combination of elemental specificity, surface sensitivity, and ferro- and antiferromagnetic contrast of PEEM allows studying the magnetic structure directly at the interface between two coupled layers, providing crucial insight into the microscopic coupling mechanism (Ohldag *et al.* 2001). The unidirectional pinning of the magnetization in a ferromagnet in contact with an antiferromagnet can be made visible by PEEM as shown in Fig. 5.

XMCD images of a ferromagnetic Co layer on La-FeO_3 were acquired in remanence as function of the applied magnetic field. Figure 5 shows a subset of a field series, containing about 30 images. The strong uniaxial interface coupling to the AFM prevents a permanent rotation of the horizontally oriented magnetic domains (gray), which have a magnetization oriented perpendicular to the field direction. Vertically
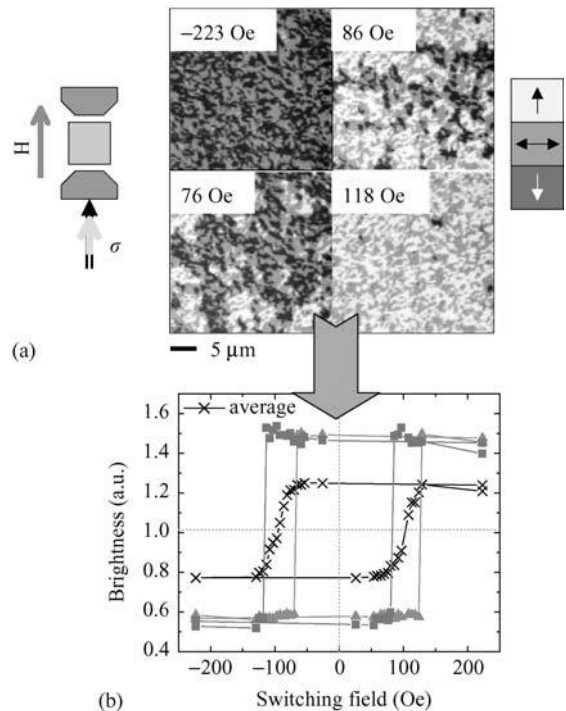
Figure 5
(a) Magnetization reversal of Co layer pinned by $LaFeO_3$ underlayer. The images were acquired in remanence after applying magnetic field pulses of increasing strength. The correspondence of magnetization direction to domain brightness is illustrated on the right. (b) Local hysteresis loops were calculated in single domains, showing exchange bias of opposite sign (triangles/squares). The average loop (crosses) was acquired by averaging the XMCD intensity over the whole PEEM field of view.

oriented domains, which have an easy axis along the magnetic field, switch from black to white at about 100 Oe, indicating the reversal of the magnetization parallel to the applied field. Remanent hysteresis loops of two individual domains are shown at the bottom of Fig. 5. The two representative loops show a relative shift of the plus/minus and minus/plus switching fields of about 50 Oe. This corresponds to a positive (negative) exchange bias field in the triangles (squares) domain of $+25$ (-25) Oe. Averaging over a large number of domains yields the average loop (black).

5. Conclusion

In comparison to other domain imaging techniques x-ray PEEM stands out by its ability to separately study the chemical, electronic, and magnetic properties of different materials in a layered or alloyed material. The moderate surface sensitivity of the technique permits the investigation of ultrathin multilayers but at the same time PEEM is sufficiently sensitive to detect sub-monolayer amounts of magnetic moments. The spatial resolution of PEEM can be further improved by aberration correction. Implementation of correction techniques promises an improvement of the spatial resolution close to the physical limit of 1–2 nm. Another future application of PEEM is the investigation of dynamical magnetic processes, such as spin precession and magnetization reversal, utilizing the pulsed structure of synchrotron sources.

Bibliography

Alders D, Tjeng L H, Voogt F C, Hibma T, Sawatzky G A, Chen C T, Vogel J, Sacchi M, Iacobucci S 1998 Temperature and thickness dependence of magnetic moments in NiO epitaxial films. *Phys. Rev. B* **57**, 11623–31

Anders S, Padmore H A, Duarte R M, Renner T, Stammler Th, Scholl A, Scheinfein M R, Stöhr J, Séve L, Sinkovic B 1999 Photoemission electron microscope for the study of magnetic materials. *Rev. Sci. Instrum.* **70**, 3973–81

Bauer E 1994 Low-energy electron microscopy. *Rep. Prog. Phys.* **57**, 895–938

Duden T, Bauer E 1998 Spin-polarized low-energy electron microscopy. *Sur. Rev. Lett.* **5**, 1213–9

Meiklejohn W H, Bean C P 1956 New magnetic anisotropy. *Phys. Rev.* **102**, 1413–4

Nolting F, Scholl A, Stöhr J, Seo J W, Fompeyrine J, Siegwart H, Locquet J-P, Anders S, Lüning J, Fullerton E E, Toney M F, Scheinfein M R, Padmore H A 2000 Direct observation of the alignment of ferromagnetic spins by antiferromagnetic spins. *Nature* **405**, 767–9

Ohldag H, Regan T J, Stöhr J, Scholl A, Nolting F, Lüning J, Stamm C, Anders S, White R L 2001 Spectroscopic identification and direct imaging of interfacial magnetic spins. *Phys. Rev. Lett.* **87**, 247201/1–4

Ormerod R M 2001 Surface Chemistry: Electron Yield Spectroscopy. In Buschow K H J, Cahn R W, Flemings M C, Ilschner B, Kramer E J, Mahajan S (eds.) Encyclopedia of Materials: Science and Technology, Elsevier, Oxford, Vol. 9, pp. 9006–8

Regan T J, Ohldag H, Stamm C, Nolting F, Lüning J, Stöhr J, White R L 2001 Chemical effects at metal/oxide interfaces studied by x-ray-absorption spectroscopy. *Phys. Rev. B* **64**, 214422/1–11

Scholl A, Ohldag H, Nolting F, Stöhr J, Padmore H A 2002 X-ray photoemission electron microscopy, a tool for the investigation of complex magnetic structures. *Rev. Sci. Instrum.* **73**, 1362–8

Scholl A, Stöhr J, Lüning J, Seo J W, Fompeyrine J, Siegwart H, Locquet J-P, Nolting F, Anders S, Fullerton E E, Scheinfein M R, Padmore H A 2000 Observation of antiferromagnetic domains in epitaxial thin films. *Science* **287**, 1014–6

Schütz G, Wagner W, Wilhelm W, Kienle P, Zeller R, Frahm R, Materlik G 1987 Absorption of circularly polarized x rays in iron. *Phys. Rev. Lett.* **58**, 737–40

Stöhr J, Padmore H A, Anders S, Stammler T, Scheinfein M R 1998 Principles of x-ray magnetic dichroism spectromicroscopy. *Surf. Rev. Lett.* **5**, 1297–308

Stöhr J, Wu Y, Hermsmeier B D, Samant M G, Harp G R, Koranda S, Dunham D, Tonner B P 1993 Element specific magnetic microscopy with circularly polarized x rays. *Science* **259**, 658–61

Thole B T, Laan G, van der Sawatzky G A 1985 Strong magnetic dichroism predicted in the $M_{4,5}$ x-ray absorption spectra of magnetic rare-earth materials. *Phys. Rev. Lett.* **55**, 2086–8

Tonner B P, Dunham D, Droubay T, Kikuma J, Denlinger J, Rotenberg E, Warwick A 1995 The development of electron spectromicroscopy. *J. Electron Spectrosc. Rel. Phenom.* **75**, 309–32

A. Scholl
Lawrence Berkeley National Laboratory, Berkeley California, USA

Thin Films, Multilayers and Devices, Superconducting

Thin films are an essential part of all electronic technologies. This is particularly true for superconducting instrumentation, sensors and electronics, in which the active devices themselves are made from deposited films, often a sequence of films made as a multilayer structure. This is in contrast to some semiconductor technologies, in which devices are often created by doping of bulk single crystals, say silicon or GaAs, and are then linked together with interconnects and to passive components (capacitors, resistors) that are made from deposited films. In the most highly developed superconducting technology, namely Josephson junction circuits operating at 4.2 K, the entire circuit of junctions, resistors, capacitors, insulators and interconnects is made from films that are deposited at room temperature (a significant difference from semiconductor processing, which is carried out at high temperatures). Thus, the control of thin-film processes

is especially critical to the success of superconducting electronics technologies. The important film synthesis methods, the properties of superconducting films and the devices made from them are the subjects of this article, which therefore forms a link between articles that are concerned predominantly with different materials or physical phenomena and articles that deal with low-current applications.

The very significant differences between low-temperature superconducting (LTS) materials and high-temperature superconducting (HTS) materials have already resulted in some divergence in the approaches being used to make, understand and use LTS and HTS films. In each section of this article LTS films will be described first, then the differences in the HTS cases will be identified. It is important to note that LTS film studies and technology date from the late 1950s and are, hence, well established, whereas HTS films are very recent and the field is subject to rapid change.

1. Thin Films

1.1 Thin-film Synthesis

The various deposition methods that are available to make thin films of all kinds can be readily used for superconductors. These methods are thermal and electron-beam evaporation and sputtering. Many elemental superconductors that have been used for both science and applications studies (e.g., lead, tin, indium, aluminum, zinc) can be made as films by the simplest methods, which is thermal evaporation in a moderate vacuum (10^{-4} Pa or 10^{-6} torr) onto a substrate at room temperature. The nature of the substrate is not critical, glass is quite adequate. Alloys of these elements can be made by evaporation from two sources or sometimes (e.g., PbBi) from a single source.

Films of greater technological interest (e.g., niobium, tantalum and their alloys with other transition metals) are not easy to evaporate thermally, but electron-beam evaporation and sputtering are straightforward for such materials. Magnetron sputtering sources have become the method of choice for the niobium films used in Josephson circuits. Alloys can be made from a sputtering target of the appropriate composition. The superconducting properties of transition metals are more sensitive to impurities, such as oxygen, than the s–p metals and a better vacuum system must be used, say $\leqslant 10^{-6}$ Pa (10^{-8} torr). The transition metals make excellent getters, so placing a liquid-nitrogen-cooled surface near the substrate very effectively lowers the system pressure. The substrate temperature can be 300 K for niobium film deposition, but the resistance ratio of clean films made at this temperature will be limited by the grain size. Higher substrate temperatures are needed for some transition metals (e.g., tantalum) and to increase the

grain size of niobium. In particular, high-quality epitaxial films with long electronic mean free paths, such as those used in SIS particle detectors, and epitaxial superlattices with mean free paths extending over many layers (see later) are grown at temperatures as high as 800 °C.

To form films of compounds based on niobium which have higher critical temperatures, such as NbN, NbCN and the family of A15 compounds Nb_3Sn, Nb_3Ge, Nbj_3Al (see *Superconducting Materials; Types of*) somewhat more complicated methods are used. The nitrides and carbonitrides, which are important materials for Josephson circuits operating at 8–10 K, are made by sputtering niobium targets in argon plus nitrogen or nitrogen plus methane onto substrates at 100–1000 °C (Braginski and Talvacchio 1990). The A15 compounds have generally been made by coevaporation from electron-beam sources, say niobium and tin, but cosputtering from multiple targets or sputtering from a single mixed target can also be used. The geometry of the evaporation sources (see Fig. 1) creates a spread of compositions across an array of substrates (Hammond 1975). This allows measurements to explore the effects of stoichiometry on the physical properties of the films. To form the crystalline structure of the compound, a heated substrate has to be used. Typical optimum temperatures are 880 °C for Nb_3Sn, 900 °C for Nb_3Ge. These high deposition temperatures have limited the interest in A15 compounds for electronics applications, although values over 700 °C are now accepted as necessary for HTS films.
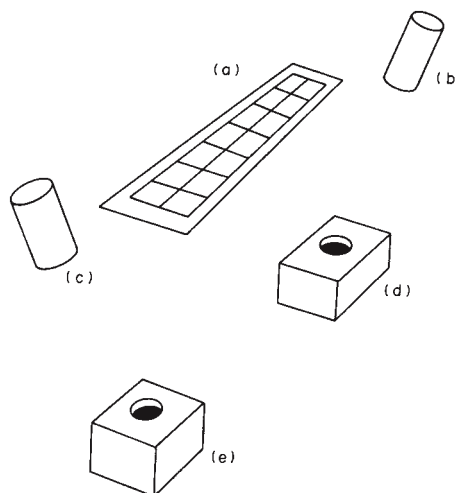
Figure 1
Arrangement of sources and substrates to achieve a spread of compositions: (a) array of substrates heated to 800 °C; (b) niobium deposition-rate monitor; (c) tin deposition-rate monitor; (d) niobium electron-beam source; and (e) tin electron-beam source.

To prepare films of the HTS materials, many of the techniques described in this section are being used (see *High-temperature Superconductors: Thin Films and Multilayers*). The presence of three elements plus oxygen in the HTS materials leads to increased complexity of the deposition systems, particularly those for cosputtering, sequential sputtering (a fraction of a monolayer of each material is deposited sequentially and repeated many times), coevaporation (MBE) and sequential evaporation. Two comparatively simple methods have quickly become popular and reproducibly yield very-high-quality films. These are off-axis sputtering (Eom *et al.* 1989) and laser ablation (Inam *et al.* 1988). As in the case of A15 compounds, HTS films are deposited at high temperatures (600–750 °C) with the best films being made at $\geqslant 700$ °C. Unlike the transition metals, HTS films are deposited in high oxygen pressures (sometimes 250 Pa) and, hence, the base pressure of the vacuum system is less relevant. One film process that is widespread for semiconductors, chemical vapor deposition (Li *et al.* 1991), is being tried for HTSs with some success. It has the potential to be a commercial process for films of large area. At present typical film substrate sizes are 4 in or 5 in diameter wafers for niobium circuits, with plans in one laboratory to move to 8 in and 2 in diameter for HTS devices.

A very significant difference between LTS and HTS films is in the choice of substrates. Epitaxy between the substrate and film is essential for HTS materials, hence, a very much more limited choice of substrates is available. Because of the high deposition temperatures, substrates for both HTS and A15 films must not react chemically with the film at temperatures up to around 800 °C. For most LTS films this is not a consideration, but for those applications requiring epitaxial films with long electronic mean free paths, the substrate again must be chosen to have a good lattice match and to be nonreactive.

1.2 Film characterization

Given the possibility that impurities introduced into films during deposition will change their properties from those exhibited by bulk samples of the same material, characterization is an important part of thin-film research. Important measurements include: the resistivity of the film at 300 K, which will be increased by impurities and disorder; the resistivity ratio between 300 K and (say) 10 K, which is strongly reduced by impurities and electron scattering from the film surfaces; the transition temperature T_c, which is generally decreased by impurities but can sometimes be increased by disorder; the critical current density J_c, which can be most easily measured by making a constriction in the film; the stoichiometry, which can be determined by Rutherford backscattering, inductively coupled plasma spectroscopy or en-

ergy/wavelength dispersive x-ray analysis; and the crystalline perfection, which is studied by x-ray scattering or channelling techniques.

Of these characterization techniques, one of the simplest and most informative is the measurement of resistivity and resistivity ratio (ρ_{300K}/ρ_{10K}). For example, $\rho_{300K} \simeq 15 \,\mu\Omega$ cm for niobium implies an electronic mean free path of 3 nm. As phonon scattering is reduced with decreasing temperature, scattering from grain boundaries and lattice defects (or the film surface) becomes dominant, for films deposited in a poor vacuum system scattering by included impurities becomes important. Thus, a resistivity ratio of 7 implies a mean free path at 10 K of 21 nm, whereas 50 implies 150 nm. The ratios of 7 and 50 are typical of niobium films made on room-temperature and heated substrates. If the film thicknesses are larger than the mean free path, the resistivity ratio is an immediate indicator of film quality. In some epitaxial niobium films, resistivity ratios as large as 300–400 in 2 μm thick films have been reported. For many materials (e.g., silver, niobium, molybdenum, tin, gallium) precision deposition techniques enable films to be deposited with mean free paths that are so long at low temperatures that the resistance ratio is generally limited by surface scattering, unless the films become very thick.

These measurements are commonly used for both LTS and HTS superconducting films. In the HTS case, an important additional parameter of interest is the surface impedance R_s at frequencies in the range from 1 GHz to 100 GHz. The importance of microwave applications of HTS films has created the need to measure R_s from 4.2 K to at least 77 K (see *Superconducting Microwave Applications: Filters*). As R_s for good HTS films is at least an order of magnitude below that of copper, a copper cavity cannot be used for the measurements at 77 K. A niobium cavity can be used at 4.2 K. No standard measurement method exists, but a technique which determines the Q of a resonator made of two HTS films facing each other is becoming popular (Taber 1990).

1.3 Physical Properties of Films

Many of the properties of superconducting films are discussed in other articles, in that they are identical to those of the bulk material. However, thin films are often used in preference to single crystals or polycrystalline samples, for three reasons. First, they allow certain experiments to be carried out more easily. Examples are high-frequency properties, where a film can be prepared with a smooth clean surface more easily than the bulk; nonequilibrium properties, where the sample volume can be made small; Josephson effects in weak links (see *Electrodynamics of Superconductors: Weakly Coupled*), which are most easily defined in films; tunnelling spectroscopy for

which tunnel junctions are prepared by oxidizing clean film surfaces; and proximity effect studies, in that films can easily be made with thickness comparable to a coherence length (at least in LTS materials).

The second reason for using films for scientific studies is that they can be made to exhibit properties that are different from those of the same bulk material. These differences can arise because of dimensional effects, as films can be grown very thin in the dimension normal to the substrate and can be patterned to be small in the plane. When the thickness of the film is less than the coherence length, it becomes two dimensional, in that its properties cannot vary in the direction normal to its surfaces. These dimensional (including dimensional crossover effects) effects will be discussed in Sect. 2.

Another difference between film and bulk materials can be created because the structure and electronic properties of the film are changed by the deposition process. This is generally a result of crystalline disorder (see *Superconducting Materials: Irradiation Effects*). If the film is deposited on a substrate that is too cold to allow ordering to occur, a very-small-grained or even amorphous film can result (see *Amorphous Superconductors*). An early example was the nonsuperconducting semimetal bismuth, which became superconducting up to 6 K when deposited on a substrate held at 4.2 K. The T_c of gallium is similarly raised from 1.1 K to 8.5 K by such "quench condensation." Such films were the first amorphous metals (Brandt and Ginzburg 1960, Buckel Gey 1963). Aluminum films can have a T_c up to 6 K compared to the bulk 1.2 K, the T_c depending largely on the conditions of deposition and the strain induced by the substrate. Such changes in T_c are due to modification of both the phonon spectrum and the density of electronic states of the material. In crystalline transition metals, with their well known dependence of T_c on electron-to-atom ratio (see *Superconducting Materials: Types of*), a remarkably different dependence is observed when films are deposited at low temperatures to make them amorphous. Such quench-condensed films have high resistivities and small resistance ratios (close to 1).

A third reason for using films is for superconducting applications in devices and electronics, as described later in this article and in other more specific contributions on particular application areas.

The same reasons for interest in the physical properties of LTS films apply to HTS materials. However, the radically different properties of the HTS oxides do create some different results. For example, the oxides have anisotropic and very short coherence lengths. Most HTS films are grown with the c-axis normal to the substrate, with the copper oxide sheets in the plane of the substrate. The c-axis coherence length is only a few tenths of nanometers. Thus, the surfaces of HTS films, unlike their LTS counterparts,

are most unlikely to have properties representative of the bulk material (even those properties along the c axis). This is because any change in stoichiometry, for example loss of oxygen, or disorder, including that due to surface reconstruction of the lattice, can affect a surface layer whose thickness is comparable to, or greater than, a coherence length. Thus, any experiments that are surface sensitive, such as tunnelling, proximity effects and photoemission studies, are unlikely to measure bulk properties of HTS materials in measurents on c-axis films. Recently, films with other orientations have been deposited (see *High-temperature Superconductors: Thin Films and Multilayers*); measurements on these films are likely to reveal more of the bulk properties of HTS materials. In LTS materials the coherence length is generally much longer than the thickness of any surface layer, although niobium and A15 films can exhibit problems of surface degradation unless care is taken.

Effects of dimensionality are also different in HTS materials, in that even in the bulk they are strongly anisotropic and can be considered pseudo two dimensional. It is also not possible to produce films thinner than the coherence length along the c axis. The coherence length is only 4 nm in the a–b plane of YBCO, so even a-axis films are difficult to make thin compared to this length. The effect on physical properties of making the films thin is most easily studied in superlattices (see Sect. 2) but remarkably thin HTS films have been made that remain superconducting to quite high temperatures.

The properties of both films and bulk HTS materials can differ significantly from optimum values, particularly due to loss of oxygen, to crystalline disorder and to doping effects. The trend of these effects is to decrease T_c and increase resistivity until the material becomes insulating at low temperatures (Greene and Bagley 1990).

There is one parameter that is very different in films compared to bulk single crystals, especially in the case of YBCO. This is the value of critical current J_c. All good HTS films with T_c close to 90 K, independent of their method of preparation, have J_c values at all temperatures $< T_c$ much higher than those for single crystals. It appears that a pinning center is rather readily produced in thin films that is difficult to reproduce in crystals and that this defect is common to all "high quality" YBCO films to date.

2. Superlattices

As an object of scientific study, multilayers or superlattices are an interesting class of "engineered" materials in the fields of semiconductors, magnetism (see *Thin Film Magnetism: PEEM Studies*), optics, x-ray optics and superconductivity (Shinjo and Takeda 1987). They are made by sequentially depositing two or more materials many times (e.g., ABABAB...).

The individual film thicknesses of A and B approach one atomic layer in some cases. This repetition of the film sequence distinguishes them from the multilayer device structures to be discussed later.

In semiconductors the long electron wavelength (~ 10 nm) implies that the bulk electronic band structure can be radically changed in the direction normal to the layers of a superlattice, once the individual layers have thickness comparable to this wavelength. This regime is relatively straightforward to reach with current growth capabilities such as MBE. Thus, semiconductor superlattices have become a field of intense activity, for both their research interest and device potential. In metals, the short electron wavelength (a few tenths of nanometers) implies that such band structure changes cannot be observed. When metals become superconducting, however, the electron wavelength is replaced by the coherence length as the important length parameter. In LTS materials, it is easy to make superlattices with layer thickness much less than coherence lengths (typically tens of nanometers). Hence, there is scientific interest in superconducting superlattices, in which the components A and B can be superconductor (A) with another superconductor, metal, semiconductor or insulator (B).

It is important to note that in HTS superlattices, at least those with c axis normal to the substrate, it is again not possible to make the layer thickness thinner than the coherence length, which is only a few tenths of nanometers. If the HTS materials were strictly two dimensional, layering them into a superlattice should have no effect on T_c unless structural effects occurred (see later).

Unlike semiconductor superlattices, at present there are no important devices made from superconducting superlattices (in contrast to multilayer device structures), although the Nb/Al–Al oxide–Nb trilayer process that is now the metallization of choice for Josephson circuits was a direct result of studies of tunnelling in niobium–aluminum superlattices (Geerk *et al.* 1982).

2.1 Superlattice Synthesis

The vacuum equipment that is commercially available makes it relatively easy to prepare superconducting superlattices. A substrate is exposed to alternating sources of materials, for example by moving shutters in front of electron-beam sources, or by rotating or oscillating the substrate in front of two sputtering sources. Magnetron sputtering sources are particularly suitable because of the stability of their deposition rate. It is often important to heat the substrate, as the resulting films (e.g., niobium, tantalum) will then have larger grain size, longer electron mean free path and longer coherence lengths. Superlattices of HTS materials have been made by the same methods. Obviously a heated substrate ($\sim 700\,^\circ$C) is always

necessary. In addition, laser deposition lends itself ideally to the synthesis of HTS superlattices. Two targets are moved alternately into the focus of the laser beam and the layer thickness is controlled by the number of laser shots allowed to impinge on each target (Lowndes *et al.* 1990).

2.2 Superlattice Characterization

As a superlattice has an additional periodicity of the structure in the growth direction, which is superimposed on the crystal lattice spacing, an important measurement is the standard θ–2θ x-ray scan. An example is shown in Fig. 2, where the subsidiary maxima are due to x-ray reflections from the superlattice (Somekh *et al.* 1989). The position of these maxima can be used to determine the superlattice wavelength (the sum of the A and B layer thicknesses) and their intensities are related to the interfacial roughness between layers.

Another important measurement is simply the net resistivity of the superlattice (in the case of two metals). If the electron mean free path is long, that is, the electrons move freely through the interfaces between A and B, then the resistivity will have a value between the values of A and B in their bulk form. However, if the electrons are scattered at the interfaces, or if the films themselves become structurally disordered due to the layering process or to strain, then the resistivity will be higher than the values of A or B. Even in superlattices of superconductors with other materials (insulators, semiconductors), or in HTS superlattices, the resistivity and resistance ratio are very important parameters to measure.

Transmission electron microscopy can yield elegant pictures of superlattices and can be used to give the orientation of the individual layers or grains
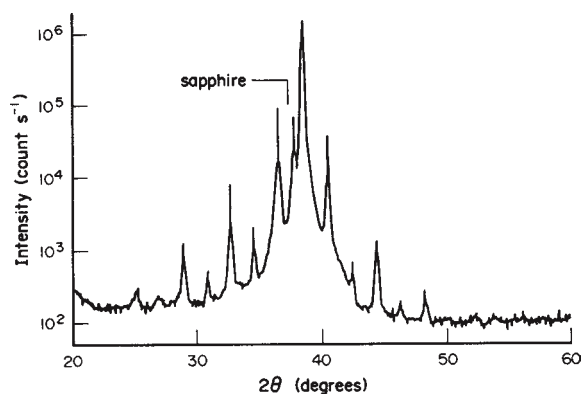
Figure 2
CuK alpha x-ray trace of niobium–tantalum epitaxial multilayer (4.9 nm wavelength) grown on A-plane sapphire to give (110) niobium–tantalum epitaxy; from the superlattice intensities the interface roughness can be estimated at 0.22 nm (after Somekh *et al.* 1989).

within the layers. In the HTS materials, the layered nature of the oxide structure gives even more striking results. One example shows that within the one layer there is a very abrupt change from YBCO to PrBCO, presumably the result of ledge growth of the layers of unit cell dimensions, that is, the layer was growing as one unit cell of YBCO say when the source was changed to PrBCO, which continued the growth to complete the layer. This ledge growth is also clearly evident in scanning tunnelling microscope profiles of the surface of YBCO films (not superlattices), in which the layers of one unit cell in height are shown around screw growth dislocations.

2.3 Physical Properties of Superlattices

The superconducting property of LTS superlattices that has received by far the greatest attention is the upper critical field H_{c2}, measured with the field applied parallel to the layers. This is because the dimensionality of the superconducting state is readily determined from the form of the dependence of H_{c2} on temperature T.

As an example, consider the specific case of a superlattice of niobium–germanium (germanium films are insulators at low temperatures) (Ruggiero *et al.* 1982). If the niobium layers are thick ($t \gg \xi$), then the superlattice behaves like bulk niobium, that is, it is three dimensional. If the niobium layers are thin ($t \ll \xi$), and the germanium is thick, then the niobium layers are isolated from each other and are two dimensional. However, if the niobium layers are again, thin, and the germanium layers are thin enough to allow appreciable coupling by tunnelling between the niobium layers, then bulk three-dimensional behavior is again recovered, as the superlattice appears again as uniform material over the length scale of ξ. Interesting crossover effects have been observed as a function of temperature, in that the coherence length is much longer near T_c than it is at lower temperatures. Hence, it is possible to find two regimes, one at higher temperatures where $\xi > t$ and three-dimensional behavior is observed and another at low temperatures with $\xi < t$ that exhibits two-dimensional behavior. As these two regimes have different temperature dependences of H_{c2}, namely $H_{c2} \simeq T_c - T$ for three dimensions and $H_{c2} \simeq (T_c - T)^{1/2}$ for two dimensions, the crossover between them is observed in the plot of H_{c2} vs T (see Fig. 3). These regimes can be thought of as the situations where the cores of the flux vortices either extend across multiple layers as Abrikosov vortices (three dimensional) or sit between the niobium layers in the germanium layers as Josephson vortices (two dimensional).

A second type of superlattice utilizes superconducting and normal metals (e.g., SNSNSN...). The coupling between the S layers is by the proximity effect induced in the N layer. A widely studied example is niobium–copper superlattices, in which one unusual
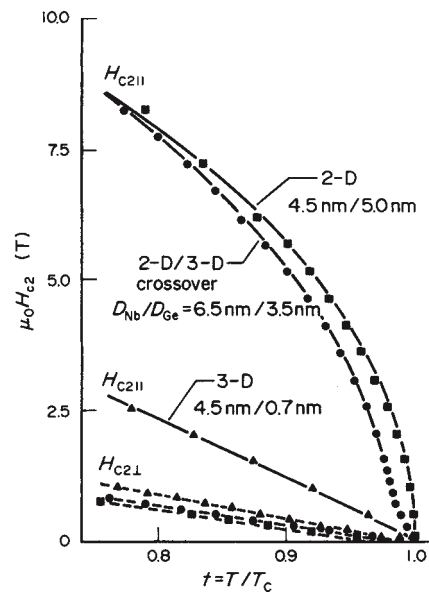
Figure 3
Upper critical fields near T_c for Nb–Ge multilayers. Systematically varying the germanium thickness between the two-dimensional niobium layers effects a progression from anisotropic three-dimensional behavior [$H_{c2\parallel}(T) \sim (T_c - T)$] to "crossover" behavior and finally to decoupled two-dimensional behavior [$H_{c2\parallel}(T) \sim (T_c - T)^{1/2}$] (after Ruggiero *et al.* 1980).

effect occurs for small periods ($\lesssim 2$ nm). Both the niobium and copper layers appear to become disordered, with a strong increase in resistivity, a decrease in resistance ratio and decrease in the T_c of the niobium. Dimensional crossover effects can also be observed in SN superlattices as the N layer becomes longer than its effective coherence length, which in copper in niobium–copper superlattices was demonstrated to be about 20 nm (Banerjee *et al.* 1983).

More recently, a further novel transition was predicted (Takahashi and Tachiki 1986) and observed (Karkut *et al.* 1988) in superlattices of two superconductors with very similar T_c but with very different mean free paths, for example, niobium and a niobium–titanium alloy. In this case two crossover transitions were observed. Near T_c the vortices are located in the niobium–titanium but are large enough to extend across the niobium (three dimensional, $H_c \simeq (T_c - T)$). At a lower temperature ξ_{Nb} becomes less that t_{Nb} and the vortices relocate into the niobium layers and are confined within them (two dimensional, $H_{c2} \simeq (T_c - T^{1/2})$) (see Fig. 4). At even lower temperatures, ξ_{NbTi} becomes $< t_{NbTi}$ and the vortices become two dimensional within the niobium–titanium layers, which have a very high H_{c2}.

Work on HTS superlattices is naturally at an earlier stage, although the layered nature of the oxide

Figure 5
Critical temperature of $(YBCO)_M/(PrBCO)_N$ superconducting multilayers ($m = 1$ to 8 unit cells thick) vs the separating PrBCO layer thickness: Δ, eight-cell YBCO; $\square$, four-cell YBCO; $\blacktriangle$, three-cell YBCO; $\blacksquare$, two-cell YBCO; $\bullet$, single-cell YBCO (after Lowndes *et al.* 1990).

Figure 4
(a) Theoretical temperature dependence of the parallel critical fields for a multilayer SS'SS'SS'… . The dashed and dash-dotted curves indicate the upper critical fields when the superconducting order parameter nucleates in the S and S' layers respectively. The observable $H_{c2\parallel}$ is the higher one of the two critical fields at each temperature. The point (T^{*}, H^{*}) is a multicritical crossover point, d is the layer thickness and D is the diffusivity (after Takahashi and Tachiki 1986). (b) Resistive measurements of $H_{c2\parallel}$ vs $t(= T/T_c)$ for Nb/NbTi superlattices with layers of equal thickness showing behavior at t^{*} for samples with different wavelength Λ (after Karkut *et al.* 1988).

materials has allowed superlattices of very impressive perfection to be grown. Perhaps the most interesting question to be answered to date is the value of T_c as the individual HTS layers are made thinner and as

the coupling across an intermediate layer is made weaker. The intermediate layer is, for example, PrBCO which is a lattice-matched oxide that is a Mott insulator that exhibits high electrical resistivity at low temperatures. The results of Fig. 5 show that even layers of YBCO that are one unit cell thick have a T_c of 20 K when widely separated (Lowndes *et al.* 1990). The T_c increases as the coupling increases, reaching 56 K when the PrBCO is one unit cell thick.

It is evident that HTS materials with a pronounced perovskite layer structure behave in many respects as intrinsic atomic-scale multilayers, the alternating layers being the copper oxide planes (S) and the redox spacer layers (N or I) (see *Superconducting Materials: Types of*). In the more complex HTS materials the doping levels on the two types of layer may be varied independently, their character changing from …SNSNSN… to …SISISIS… depending on the preparation conditions. The interpretation and modelling of HTS materials as intrinsic multilayer structures is currently an active area of considerable importance both for their basic physical properties and for their behavior in magnetic fields.

3. Superconducting Device Structures

Superconducting devices are rather simple structures compared to those that are commonplace in semiconductor technology. This perhaps reflects the orders

of magnitude difference in commitments of time, personnel and funds to the two fields since the mid-1940s, which are themselves measures of the relative commercial importance of the two fields to date. Some superconducting devices can be made in a single film of material, the most common uses two films and the most complex requires only three. Despite this, they perform logic functions faster than the most advanced semiconductor devices and at a level of power dissipation which is orders of magnitude smaller (see *Thin Films, Multilayers and Devices, Superconducting*). Whether they will ever become more complex, or indeed need to do so, is an open question.

3.1 Tunnel Junctions and Weak Link Structures

Superconductors are affected strongly by magnetic fields and only weakly by electric fields. This magnetic field sensitivity is the basis for many electronic devices. In a superconducting film, or film adjacent to a superconductor, a local region is produced where the superconducting state can be controlled by external magnetic fields. The cryotron (Buck 1956), which was the earliest superconducting electron device, used this principle. This device, which was invented in 1954 and therefore predates the Josephson effect, used two films (see Fig. 6) separated by an insulator. A current through the control film created a magnetic field which switched the second film from its superconducting to its normal state. Recovery from the normal state was not fast (by modern standards). With the discovery of the Josephson

effect (see Josephson 1962) a much faster device became possible. The Josephson junction (see Fig. 7) consists of two superconducting films separated by a thin insulator (< 1.5 nm thick). This insulator allows the tunnelling of pairs of electrons (the Josephson current) and single electrons (the quasiparticle current). These result in the tunnelling currents shown in Fig. 8 as a function of the voltage across the insulator. For an ideal junction there would be a discontinuous jump at $2\Delta/e$ and an exponentially small subgap tunnelling current proportional to $\exp(-\Delta/k_{\rm B}T)$ (Van Duzer and Turner 1981). In real systems there is a smearing due to lifetime effects and non-uniformity in the films. In addition there is invariably a subgap leakage current. The sources of subgap leakage vary from device to device and depend very
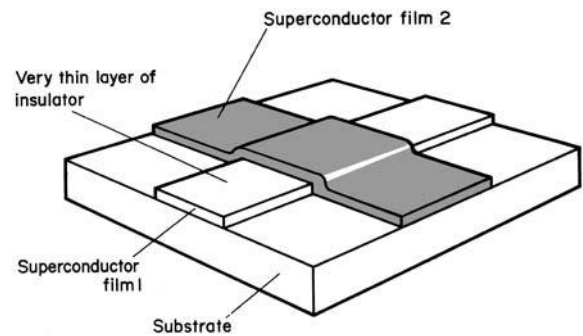
Figure 7
Josephson junction (SIS tunnel junction).
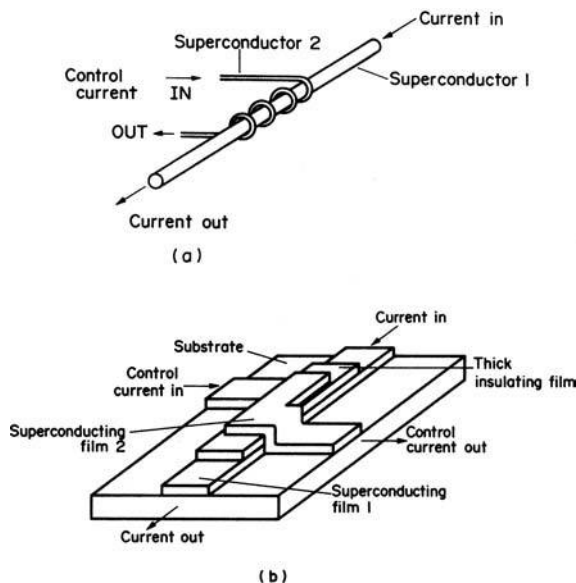
Figure 6
Cryotron types: (a) wire-wound type, (b) thin-film type.
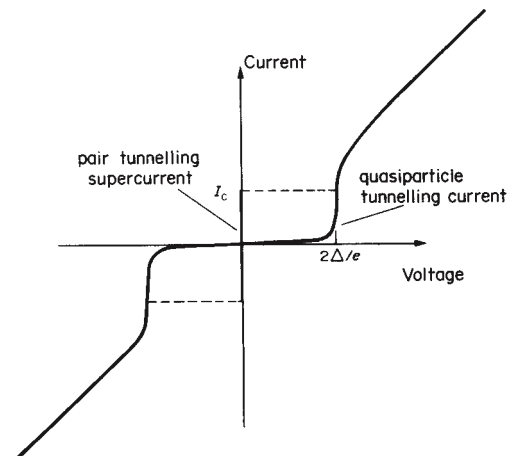
Figure 8
I–V characteristic of Josephson junction for the case where the two superconducting films have the same energy-gap parameter Δ, the characteristic shows some subgap leakage current.

much on the fabrication of the device. Leakage can for instance arise from electron states within the tunnel barrier, or pinholes in the barrier itself. At low temperatures for very-high-quality low-leakage barriers, small subgap currents due to two-particle or many-particle tunnelling can be observed (Kirk *et al.* 1991). If a small magnetic field is applied to the junction parallel to the films, the Josephson current is reduced to zero when one quantum of magnetic flux is in the area given by the width of the junction multiplied by the sum of the London penetration depths of the two films (Rowell 1963). In practical devices, this is about 0.1–1 mT. It is important to realize that, in contrast to the cryotron, it is only the Josephson current that is switched off by the magnetic field. The two films comprising the junction remain entirely superconducting at these low magnetic fields. In addition to control by magnetic field, the junction can also be switched by increasing the current until the maximum Josephson current is exceeded.

The Josephson tunnel junction has become the device of choice for LTS electronic, instrument and sensor applications (Ruggiero and Rudman 1990). It is fast and consumes little power. Its modern form, made from Nb/Al–Al oxide–Nb, is described in detail in *SQUIDs; Biomedical Applications; SQUIDs: The Instrument; Josephson Voltage Standard; Josephson: Junctions: Low-T_c*

Soon after the theoretical discovery and experimental verification of the Josephson tunnel junction, it was realized that Josephson effects could be observed in many even simpler structures, which are now collectively known as weak links (Anderson and Dayem 1964). No tunnelling occurs in any of these structures, they rely instead on creating a region of weak coupling between two superconductors by various means other than an oxide layer. Some examples are shown in Fig. 9. The simplest is a contact between a pointed wire of one superconductor and a second bulk superconductor ("point contact"). The thin-film

version is a small constriction defined in a film (a "weak link", "bridge" or "microbridge"). A "variable thickness bridge" has the constriction both thinner and narrower than the surroundings (banks). The coupling region can also be made from a normal metal, which is made weakly superconducting by the proximity effect (SNS junction).

In all these Josephson weak link devices, the length of the coupling region must be comparable to the superconducting coherence length in that region. In LTS materials and normal metals, standard film growth and lithographic techniques can produce features of the sizes required (generally $\lesssim 1\,\mu m$). In HTS materials, this is obviously not possible.

Unlike the semiconducting transistor, superconducting devices do not have gain. At a fixed current level, they simply switch between the zero voltage and finite voltage states with application of magnetic field. A few three-terminal devices have been investigated that are more transistorlike in design, but not yet in operation (Kleinsasser and Gallagher 1990). One example is the superconducting FET (see Fig. 10), in which two closely spaced superconducting contacts induce a weak coupling region on the surface of a semiconductor by the proximity effect. This superconducting channel is then switched on and off by application of an electric field from the gate. To date, large gate voltages are required to achieve switching and the devices are not practical.

As of mid-1991, the device scene in HTS materials is one of great activity and some uncertainty. All the devices made in LTS materials are being investigated, with varied levels of success. It is clear that the short coherence lengths of the HTS materials creates a real challenge in device design and processing. It does seem likely that junctions of the weak link type will emerge as more important than tunnel junctions, at least in those HTS materials with $T_c > 77\,K$. The reasons for this will be given later.

One HTS device has been created which has no LTS counterpart. A control line modulates the flux density in a weakened region of a second film (channel). It can be called a flux-flow cryotron (Martens *et al.* 1991) in that the channel is switched from zero resistance into its flux flow state, rather than into its normal state. Its value in interface circuits has already
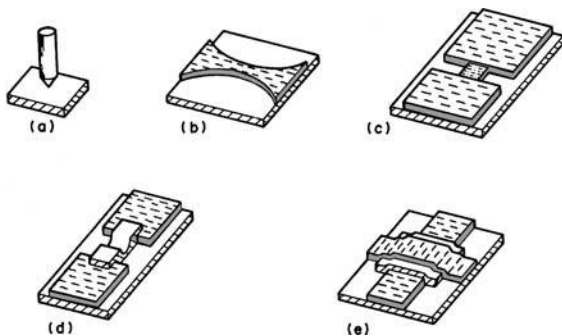
Figure 9
Josephson weak link structures: (a) point contact, (b) constriction, (c) variable thickness bridge, (d) SNS planar and (e) SNS sandwich.
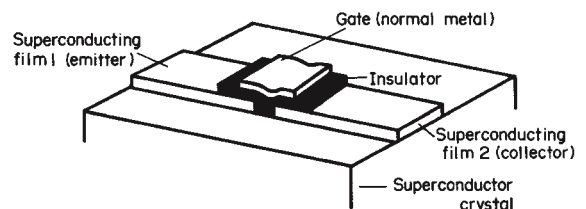
Figure 10
Superconducting three-terminal device (FET type).

been demonstrated, in that its output voltage is quite large (tens to hundreds of millivolts).

3.2 Device Processing: LTSs

The LTS weak link devices are relatively easy to make with current lithographic techniques. Optical, electron-beam and ion-beam patterning have all been used to create the weak regions of dimensions 1 μm or less in a variety of materials. The details will not be discussed here.

Tunnel junctions exhibiting quasiparticle tunnelling were first made in the late 1950s by the very simple process of evaporating a strip of aluminum film using a shadow mask, exposing it to the air for a short time (~ 1 min), then evaporating a crossing strip of lead to produce an Al–Al oxide–Pb tunnel junction (Giaever 1960). The brief exposure to air grows the required thickness of aluminum oxide (~ 1.5 nm) which completely covers the aluminum film even over relatively large areas of a few square millimeters. It is important that there are no defects or "pinholes" in the oxide, otherwise a metallic short circuit occurs. This basic oxidation process has been used for the vast majority of tunnel junctions made on many different materials, and is used in the current commercial process.

Other materials that have been used to make oxide tunnel junctions include lead, tin, niobium, tantalum and the alloys and A15 compounds of niobium. In some cases the oxidation is not so easy as it is for aluminum and heating in oxygen is required. Because of its relatively high T_c (7.2 K), lead and its alloys received many years of study as the metallizations for Josephson circuits. The problems that were encountered illustrate the difference between the research mode of making a few successful junctions for scientific study, and a manufacturing mode of reproducibly making circuits that require many thousands of junctions. The variation of critical current density across these junctions must be small and they must survive both shelf storage and many thermal shocks as they are cycled from 300 K to 4.2 K and back to 300 K. Because of the failure of lead, no satisfactory metallization for Josephson circuits existed for 20 years (1963–1983). Niobium was an obvious choice ($T_c = 9.2$ K), but oxidation of niobium itself produces a mixture of oxides with insulating, semiconducting and even metallic properties. There is probably also degradation of the niobium film surface. This problem was finally solved by immediately depositing a thin layer (< 10 nm) of aluminum on top of the niobium film in the same vacuum system, then oxidizing the aluminum to form an aluminum oxide, rather than niobium oxide, tunnel barrier (Geerk et al. 1982).

Such "artificial" barriers have been used for a number of other materials that do not readily oxidize themselves. The best known example is MgO, which
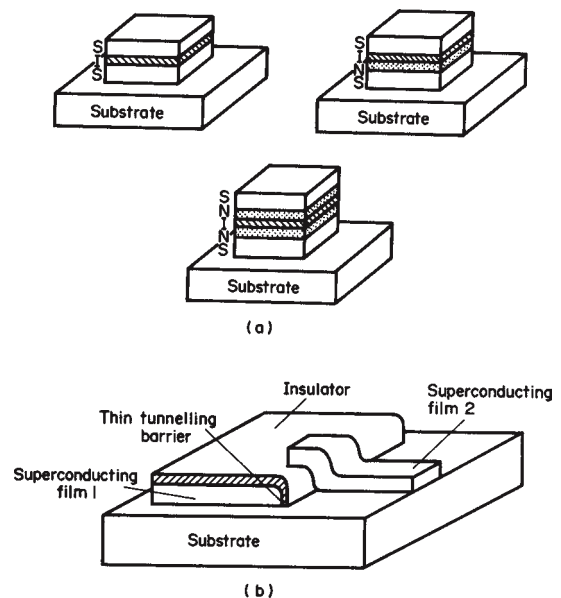
Figure 11
(a) Three types of multilayer sandwich structure Josephson junction, SIS, SNIS and SNINS; (b) edge-type Josephson junction.

is deposited as a thin layer on top of NbN to form NbN–MgO–NbN tunnel junctions (Shoji et al. 1985). The different types of "sandwich" tunnel junctions are shown in Fig. 11.

The sizes of sandwich junctions can be as small as $1 \mu m \times 1 \mu m$ using standard optical lithography and submicrometer sizes using deep-UV sources. Another way to make very small junctions is to oxidize the edge of a film that has been cut by ion milling. Such an "edge junction" is shown in Fig. 11. The small capacitance of such structures makes them suitable for high-frequency SIS detectors used in radio astronomy studies.

3.3 Device Processing: HTSs

The new oxide materials with $T_c > 77$ K are demanding the invention of a new device technology. They readily form tunnel junctions with counterelectrodes of low-T_c materials (Geerk et al. 1988), either because their surfaces lose oxygen and become insulating, or because the counterelectrode itself (e.g., lead) removes the oxygen to form the insulator. However, such junctions have no technological value. Obviously there is no Josephson current until the temperature is below T_c of the counter electrode and, at least to date (1991), none of them exhibits the I–V characteristic of Fig. 8 with well-defined Josephson current and energy gap. This comment applies to all the
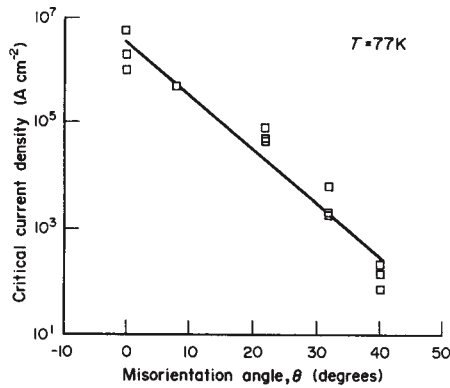
Figure 12
Variation of critical current density with misorientation angle for grain boundaries in YBCO films on yttria-stabilized zirconia (YSZ) substrates.
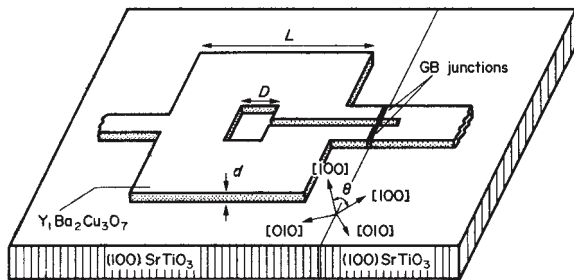
Figure 13
Bicrystal SQUID structure with grain boundary junctions.
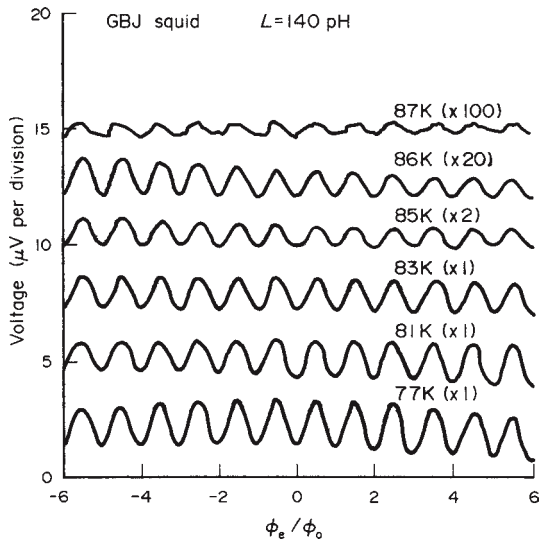
Figure 14
Field modulation of bicrystal SQUID illustrated in Fig. 13 for temperatures between 77 K and 87 K.
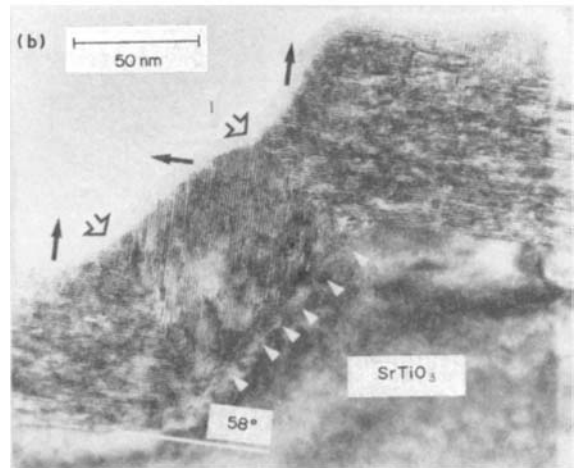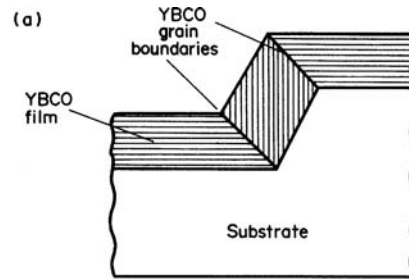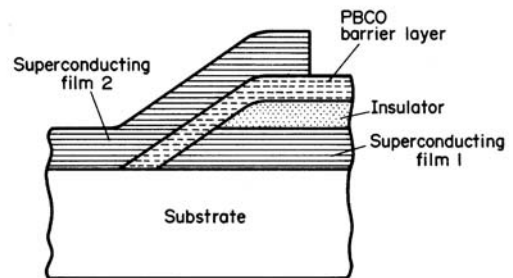
Figure 15
(a) Schematic of steep step junction with two grain boundaries, (b) electron micrograph of 58° step junction in a YBCO film on SrTiO$_3$ (after Jia *et al.* 1991) and (c) schematic of a shallow step junction with a normal PrBCO layer.

anisotropic oxides. Whether it is an intrinsic property remains to be seen.

The isotropic oxides (e.g., BaPbBi oxide, BaKBi oxide) are strikingly different. A "classical" *I–V* characteristic of the type shown in Fig. 8 has been observed by simply touching a BKBO single crystal to a BKBO film and work is underway to produce similar results in a thin-film sandwich structure. At

present, the maximum T_c in an isotropic oxide superconductor is about 30 K. However, this would allow a Josephson technology similar to that developed for niobium to be used at 12–15 K, well within the range of closed cycle refrigerators of reasonable cost. Thus, these isotropic oxides might become important metallizations for electronics applications.

In the absence of any useful tunnel junctions in HTS materials, the weak link devices are of more importance than they were in the LTS field (although it is true that most of the SQUID-based LTS magnetometers that have been sold have in fact used such weak links rather than tunnel junctions). A great variety of device structures are being investigated at present (mid-1991). Many of them make SQUIDs operating at 77 K. Whether any of them will become the basis of a genuine circuit technology remains to be seen. They include SNS devices where the N layer

can be silver (or silver–gold alloy). In one geometry the silver covers a break in the HTS film induced by a step in the substrate. Other N layers are semiconducting and "metallic" oxides, in various geometries (Simon 1991). The possible presence of a proximity effect in such oxides is an interesting issue.

To define a weak link constriction, or region of reduced J_c and T_c, of a size comparable to the very short coherence lengths, is difficult in HTS materials. However, electron-beam writing and focused ion-beam milling have been used with some success, and the use of patterning by a scanning tunnelling microscope has been proposed. In one structure nature itself seems to provide a structure of the correct dimensions, namely a boundary between two grains in the film. The cleanest examples of such devices are grain boundary junctions grown on substrates that were cut and deliberately misaligned in the plane by
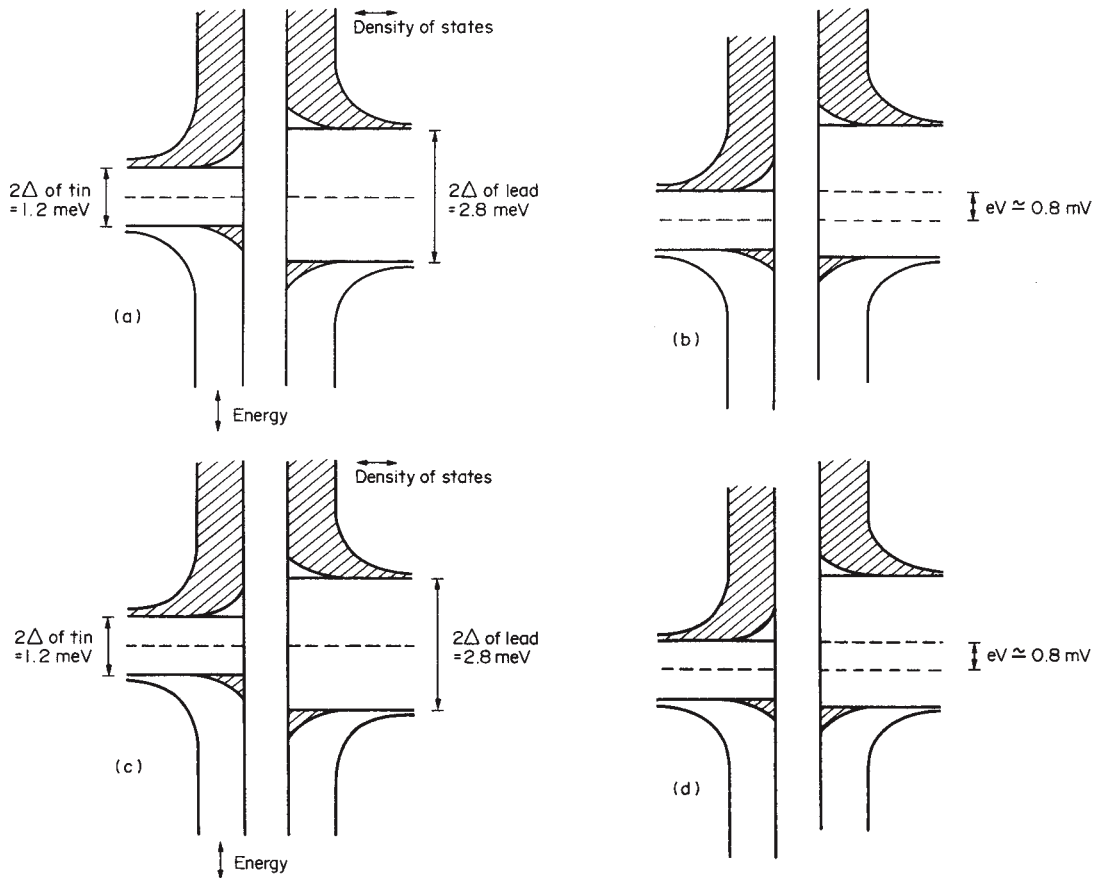
Figure 16

The density of filled and empty quasiparticle states for lead and tin superconducting layers on each side of a tunnel barrier. An applied voltage V leads to a relative displacement of the density of state diagrams, the voltage corresponding to the gap 2Δ is $2\Delta/e$: (a) zero applied voltage; (b) $eV = \Delta_{Pb} - \Delta_{Sn} \simeq 0.8$ mV; (c) $\Delta_{Pb} - \Delta_{Sn} < eV < \Delta_{Pb} + \Delta_{Sn}$, $eV \simeq 1.4$ mV; and (d) $eV = \Delta_{Pb} + \Delta_{Sn} \simeq 2.0$ mV.
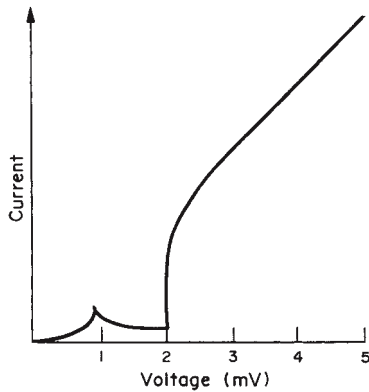
Figure 17
The current–voltage characteristic for the tunnelling of quasiparticles in an Sn–I–Pb junction.

various tilt angles (Gross *et al.* 1990a). The film, growing epitaxially, replicates the orientation of the substrate. On yttria-stabilized zirconia substrates, the critical current drops exponentially with angle, by four orders of magnitude as the angle is increased from 0 to 40° (see Fig. 12) (Ivanov *et al.* 1991). SQUIDs of YBCO showing modulation with magnetic field up to 87 K have been produced with such grain boundary junctions (Gross *et al.* 1990b). (See Fig. 13, which shows the structure, Fig. 14 demonstrating the modulation and also the article *Josephson Junctions: High-T_c*.)

A step geometry has also been used to form weak link HTS junctions (see Fig. 15). If the angle of the step is steep ($\theta > 45°$) single or multiple grain boundaries form at the discontinuity in the substrate surface (Fig. 15a,b). For shallow junctions ($\theta < 35°$) the epitaxy is preserved at the step and an SNS junction can be formed by depositing a heteroepitaxial layer of normal PrBCO (Fig. 15c) (Gao *et al.* 1991). In this junction films are grown with the *c* axis normal to the substrate so that the tunnelling current is in the *ab* plane, the direction with longest coherence length.

An alternative process called biepitaxy creates a grain boundary in the film by control of the in-plane epitaxy using seed and buffer layers (Char *et al.* 1991a), rather than by changing the substrate orientation. This process could allow complex circuits of grain boundary junctions to be demonstrated, as the junction can be located at any point on a single-crystal substrate. The first integrated SQUID magnetometer fabricated on one chip used such biepitaxial grain boundary junctions (Char *et al.* 1991b).

3.4 Properties of Devices

The ideal BCS current–voltage characteristic of LTS tunnel junctions can be readily understood by the use of semiconductorlike diagrams in which the filled and
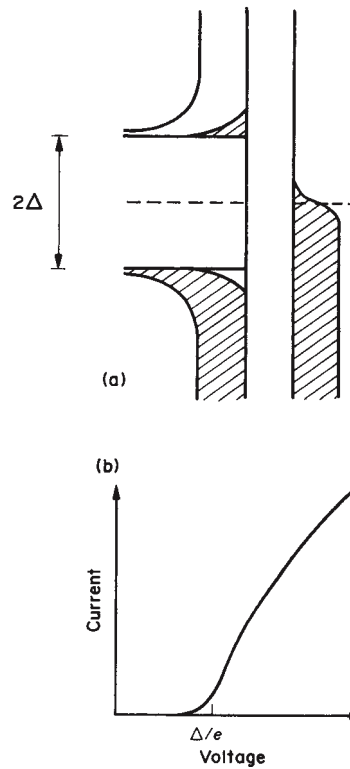
Figure 18
SIN tunnel junction: (a) density of filled and empty states at zero applied voltage, and (b) current–voltage characteristic at finite temperature.

empty quasiparticle states are shown at an energy 2Δ apart and have $(E^2 - \Delta^2)^{1/2}$ energy dependencies of the density of states (see Fig. 16). The superconducting pairs are shown at the Fermi level, the midpoint of the gap. The effect of an applied voltage *V* is simply to slide the Fermi levels and thus the whole gap structures relative to each other by a distance *eV*. The effect of temperature is included by a thermal distribution over only the quasiparticle states.

The most interesting case is that of two superconductors with different energy gaps, say tin and lead to be specific. The T_c values are 3.7 K and 7.2 K, and the energy-gap parameters $\Delta = 0.6$ meV and 1.4 meV, respectively or $2\Delta = 1.2$ meV and 2.8 meV. The density of states diagrams are then as shown in Fig. 16a at zero voltage and a temperature significantly below the T_c of tin. As the voltage is increased, a maximum in current occurs at $eV = \Delta_{Pb} - \Delta_{Sn}$ (Fig. 16b), but the current then decreases for larger voltages. This is because the current is the integral over the filled and empty states that are aligned with each other, which is smaller in Fig. 16c than in Fig. 16b. A sudden increase in current occurs for $eV = \Delta_{Pb} + \Delta_{Sn}$ in Fig. 16d. In theory, this should be a discontinuous
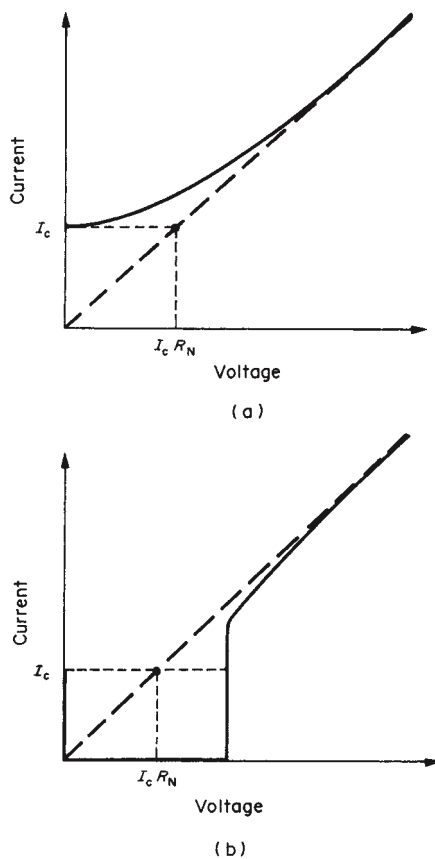
Figure 19
(a) The current–voltage characteristic for a weak link with a resistively shunted junction RSJ type transition, the $I_C R_N$ product for the weak link is indicated; and (b) $I_C R_N$ product for Josephson tunnel junction.

jump in current at any temperature, but in practice it has a slight width due to lifetime effects and nonuniformities in the films.

At high voltages, the current–voltage characteristic approaches that of the normal state. The quasiparticle branch of the characteristic is shown in Fig. 17; the complete characteristic, including the Josephson current of pairs flowing at $V = 0$ exhibits the main features of Fig. 8. Another interesting case is the S–I–N junction, where N is a normal metal, for which the density of states diagram and I–V characteristic are shown in Fig. 18. The reader should be able to recreate the I–V characteristics by following the process of sliding the density of states as described.

In weak link devices, as there is no tunnelling, there is no signature of the energy gap in the I–V characteristic. In many such devices, the I–V characteristic resembles that for a tunnel junction with a low-resistance shunt across it, the resistively and capacitatively shunted junction (RCSJ) (see

Electrodynamics of Superconductors: Weakly Coupled). The I–V characteristic then appears as in Fig. 19.

An important "figure of merit" for both LTS and HTS devices of both tunnelling and weak link types is the $I_C R_N$ product, which is the voltage defined in Fig. 19. It is related to the signal voltage that is available in a SQUID or circuit. Obviously it should be large (millivolts). It can be $\leqslant 3\,\text{mV}$ in niobium tunnel junctions, but in many HTS devices, especially the SNS type, it is very small (e.g., tens of microvolts). This makes such structures less interesting for practical applications.

A second figure of merit, used for tunnel junctions, is a measure of the subgap leakage current that flows for voltages less than the energy gap compared with the current that would flow at the same voltage in the normal state. This can be expressed as the ratio R_S/R_N calculated at some defined voltage (e.g., $2\,\text{mV}$ for niobium devices), or as a voltage V_m defined as R_S times the critical current I_c. In an ideal junction, this current is only due to quasiparticles that are thermally excited above the gap. Hence, at temperatures small compared with T_c, it should be very small. For example, for Pb–I–Pb junctions at 1 K values for R_S/R_N of 10^5 have been observed. For Nb–I–Nb at 4.2 K most of the subgap current is thermally excited and the ratio is about 20–25. Values lower than this indicate a poor quality junction with some non-tunnelling leakage paths for the excess current. The most obvious possibility is a small pinhole in the tunnel barrier.

4. Concluding Remarks

The discovery of the HTS oxides raises interesting questions of how LTS and HTS junction technologies will be used, assuming that the latter can be developed. There are strong signs that this will happen. In some areas of application, it seems likely that HTS and LTS technologies will compete with each other, as they do with silicon and GaAs in some cases.

In one example, the most sensitive SQUIDs for measuring magnetic signals from the brain might well remain at 4.2 K, whereas for other measurements, where portability of the equipment is needed (e.g., nondestructive evaluation of pipes) 77 K operation will be favored.

The majority of the digital circuits that have been built with niobium tunnel junctions employ "voltage state logic," in which the two states of the junction are at zero voltage and about 2.9 mV. Power dissipation is the product of the current and this voltage for the time that the junction remains switched. If HTS junctions of the same type could be made, the advantages of the low power dissipation of superconducting technology would be partly lost. The voltage (gap) would be ten times larger, and the current also ten times larger (to scale with the operating temperature); hence, the power would be 100 times larger.

However, there is a class of superconducting circuits, known as QFP (quantum flux parametron) or SFQ (single flux quantum) circuits, that avoid this problem and, hence, regain the advantage of the very low power dissipation of Josephson technology, even at temperatures up to 77 K. The basic circuit element is the SQUID and power is dissipated only when a quantum of flux (which is the bit of information in QFP) moves in or out of the SQUID loop. The momentary voltage pulse is the bit of information in SFQ circuits. Such circuits do not need Josephson junctions of the type shown in Fig. 8; in fact they can use weak link devices. Thus, they appear to be the most likely candidates for initial demonstrations of HTS high-speed electronics.

Another divergence between LTS and HTS that is already becoming apparent is the extensive use of fully epitaxial multilayer devices in HTS. In this materials aspect, HTS begins to resemble III–V semiconductor technology much more than it does conventional superconductor (niobium) technology. As an example, an integrated HTS SQUID magnetometer has been fabricated which utilized 15 epitaxial oxide layers of superconductors and insulators, plus a final silver contact layer (see Char *et al.* 1991a). Indeed, the field of superconducting thin films, multilayers and devices is changing and progressing rapidly.

See also: Films and Multilayers: Conventional Superconducting; Metrology: Superconducting Cryogenic Current Comparators; Superconducting Machines: Energy Distribution Components; Superconduction Radiation Sensors; Superconducting Thin Films: Materials, Preparation and Properties; Superconducting Wires and Cables: Materials and Processing

Bibliography

Anderson P W, Dayem A H 1964 *Phys. Rev. Lett.* **13**, 195

Banerjee I, Yang Q S, Falco C M, Schuller I K 1983 Anisotropic critical fields in superconducting superlattices. *Phys. Rev. B* **28**, 5037–40

Braginski A I, Talvacchio J 1990. In: Ruggiero S T, Rudman D A (eds.) 1990 *Superconducting Devices*. Academic Press, San Diego, CA, Chap. 8, p. 273

Brandt N B, Ginzburg N I 1960 *Zh. Eksp. Teor. Fiz.* **39**, 1554

Buck D A 1956 *Proc. IRE* **44**, 482

Buckel W, Gey W 1963 *Z. Phys.* **176**, 336

Char K, Colclough M S, Garrison S M, Newman N, Zaharchuk G 1991a Biepitaxial grain-boundary junctions in YBa$_2$Cu$_3$O$_7$. *Appl. Phys. Lett.* **59**, 733–5

Char K, Colclough M S, Lee L P, Zaharchuk G 1991b Extension of the biepitaxial Josephson junction process to various substrates. *Appl. Phys. Lett.* **59**, 2177–9

Eom C B, Sun J Z, Yamamoto K, Marshall A F, Luther K E, Geballe T H, Cadermann S S 1989 *In situ* grown YBa$_2$Cu$_3$O$_{7-\delta}$ thin films from single-target magnetron sputtering. *Appl. Phys. Lett.* **55** (6), 595–7

Gao J, Aarnink W A M, Gerritsma G J, Veldhuis D, Rogalla H 1991 Preparation and properties of all high T_c SNS-type edge dc SQUIDS. *IEEE Trans. Magn.* **27**, 3062–5

Geerk J, Gurvitch M, McWhan D B, Rowell J M 1982 *Physica* **109**, 1775

Geerk J, Xi X X, Linker G 1988 Electron tunnelling into thin films of Y$_1$Ba$_2$Cu$_3$O$_7$. *Z. Phys. B* **73**, 329–36

Giaever I 1960 *Phys. Rev. Lett.* **5**, 147

Greene L H, Bagley B G 1990 In: Ginsberg D M (ed.) 1990 *Physical Properties of High Temperature Superconductors II*. World Scientific, Singapore, p. 509

Gross R, Chaudhari P, Dimos D, Gupta A, Koren G 1990a Thermally activated phase slippage in higher T_c grain boundary Josephson junctions. *Phys. Rev. Lett.* **64**, 228–31

Gross R, Chaudhari P, Kawasaki M, Ketchen M B, Gupta A 1990 Low noise YBa$_2$Cu$_3$O$_{7-\delta}$ grain boundary junction dc SQUIDS. *Appl. Phys. Lett.* **57**, 727–9

Hammond R H 1975 *IEEE Trans. Magn.* **11**, 201

Inam A, Hegde M S, Wu X D, Venkatesan T, England P, Miceli P F, Chase E W, Chang C C, Tarascon J M, Wachtman J B 1988 As-deposited High-T_c and J_c superconducting thin films made at low temperatures. *Appl. Phys. Lett.* **53**, 908–9

Ivanov Z G, Nilsson P A, Winkler D, Brorsson G, Claeson T 1991 *Proc. SQUID 1991* (in press)

Jia C L, Kabius B, Urban K, Herrman K, Cui G J, Schubert J, Zander W, Braginski A I, Heiden C 1991 Microstructure of epitaxial YBa$_2$Cu$_3$O$_7$ films on step edge SrTiO$_3$ substrates. *Physica C* **175**, 545–54

Josephson B D 1962 *Phys. Lett.* **1**, 251

Karkut M G, Matijaservic V, Antognazza L, Triscone J-M, Missert N, Beasley M R, Fischer Ø 1988 Anomalous upper critical fields of superconducting multilayers—verification of the Takahashi–Tachiki effect. *Phys. Rev. Lett.* **60**, 1751–4

Kirk E C G, Blamire M G, Somekh R E, Evetts J E, Van Vechten D, Lovellette M N 1991 Ultra-high quality Nb/ AlO$_x$/Nb tunnel junctions with epitaxial base layers. *IEEE Trans. Magn.* **27**, 3137–40

Kleinsasser A W, Gallagher W J 1990 In: Ruggiero S T, Rudman D A (eds.) 1990 *Superconducting Devices*. Academic Press, San Diego, CA, Chap. 9, p. 325

Li Y Q, Zhao J, Chern C S, Huang W, Kulesha G A, Lu P, Gallois B, Norris P, Kear B, Cosandey F 1991 High critical current densities in YBa$_2$Cu$_3$O$_{7-x}$ thin films formed by metallorganic chemical vapor deposition at 730 °C. *Appl. Phys. Lett.* **58**, 648–50

Lowndes D H, Norton D P, Budai J D 1990 Superconductivity in nonsymmetric epitaxial YBa$_2$Cu$_3$O$_{7-x}$/PrBa$_3$Cu$_3$O$_{7-x}$ superlattices—the superconducting behavior of Cu–O bilayers. *Phys. Rev. Lett.* **65**, 1160–3

Martens J S, Ginley D S, Beyer J B, Nordman J E, Hohenwarter G K G 1991 A Josephson junction to FET high-speed line driver made of TlCaBaCuO. *IEEE Trans. Magn.* **27**, 3284–8

Rowell J M 1963 *Phys. Rev. Lett.* **11**, 200

Ruggiero S T, Barbee T W, Beasley M R 1980 *Phys. Rev. Lett.* **45**, 1299

Ruggiero S T, Barbee T W, Beasley M R 1982 *Phys. Rev. B* **26**, 4894

Ruggiero S T, Rudman D A (eds.) 1990 *Superconducting Devices*. Academic Press, San Diego, CA

Shinjo T, Takeda T 1987 *Metallic Superlattices*. Elsevier, Amsterdam

Shoji A, Aoyagi M, Kosaka S, Shinokik F, Hayakawa H 1985 Niobium nitride Josephson tunnel junctions with magnesium oxide barriers. *Appl. Phys. Lett.* **46**, 1098–100

Simon R 1991 High-T_c thin films and electronic devices. *Phys. Today* **44** (6), 64–70

Somekh R E, Shih W C, Dyrbye K, Huang K H, Baxter C S 1989 *The Sputter Deposition of Metal Multilayers*, X-Ray Instrumentation, SPIE Vol. 1140. Society of Photo-Optical Instrumentation Engineers, Bellingham, WA, pp. 453–63

Taber R C 1990 A parallel plate resonator technique for microwave loss measurements on superconductors. *Rev. Sci. Instrum.* **61**, 2200–6

Takahashi S, Tachiki M 1986 Theory of the upper critical field of superconducting superlattices. *Phys. Rev. B* **33**, 4620–31

Van Duzer T, Turner C W 1981 *Principles of Superconductive Devices and Circuits*. Elsevier, Amsterdam

J. M. Rowell

Conductus Inc., Sunnyvale, California, USA

Thin Films: Domain Formation

Soft magnetic films and nanostructures are of interest for applications as sensors and storage material. Most desirable are single-domain structures that switch their magnetization at a certain field by fast coherent rotation. These ideal films, so far, have not been produced; the films tend to break up into domains along the magnetization loop. The formation of domains in soft magnetic films and nanostructures has to be understood for the discussion of the magnetic properties of the films and nanostructures and how to select them for applications.

A desirable ideal state of the magnetization in thin ferromagnetic films is the single-domain state in which at remanence the magnetization is directed along an easy axis. Application of an external field should cause coherent rotation of the magnetization towards the applied field. Magnetization reversal is expected by spontaneous switching at a critical field. Nature does not follow these idealized assumptions.

For discussing the static equilibrium state of the magnetization in a real sample one has to consider the integral minimum of all magnetic energies: the Zeeman energy $\varepsilon_H = -\vec{H}\vec{M}$ of the sample in an applied field; the crystalline anisotropy energy ε_K; the uniaxial anisotropy energy ε_{K_u}; the magnetostrictive anisotropy energy ε_σ; the exchange anisotropy ε_{ex}; the external demagnetizing self-energy $\varepsilon_{dext} = -(1/2)\vec{H}_{dext}\vec{M}$, where $\vec{H}_{dext}$ is the demagnetizing field from magnetic poles at the film boundaries; the intrinsic demagnetizing self-energy $\varepsilon_{dint} = -(1/2)\vec{H}_{dint}\vec{M}$, where $\vec{H}_{dint}$ is the demagnetizing field resulting from intrinsic magnetization divergencies; the surface anisotropy σ_s; and the wall energy σ_w (Kittel 1949, Craik and Tebble 1965).

All of these energy densities have to be integrated over the volume of the film. Their minimum gives the

stable state of magnetization distribution in the film. This problem is treated in the field of micromagnetism.

Experimental observation of domains gives a first indication of how to approximate this difficult problem, which is then reduced to the domain theory, in which the domains are separated by walls and homogeneous magnetization is assumed within domains (Kittel 1949).

The methods of domain observation have increased in sensitivity and resolution over the years. They include the Bitter pattern, magneto-optical Faraday and Kerr rotation, Lorentz microscopy, spin polarized photoemission of electrons, and x-ray dichroism (Hubert and Schäfer 1998). These methods will not be discussed in this article.

Why is the single-domain state of a film not a state of lowest energy? Why does the film break up into domains?

(i) The film size is finite. Magnetic poles at the boundaries cannot be avoided in the single-domain state, leading to strong magnetic self-energy. The total magnetic energy is decreased when this self-energy is decreased by domain formation. The additional increase in energy owing to domain wall energy is smaller than the decrease of the self-energy.

(ii) Nonideal films, for instance polycrystalline films, show fluctuation of the direction of the local magnetization around the mean direction, the so-called magnetization ripple (Hoffmann 1968). In some cases this ripple is responsible for nucleation of domains. The ripple prevents a coherent switching of single domains.

Domain formation in thin films is many and varied. It can be explained in the best way by discussing soft magnetic thin films with uniaxial magnetic anisotropy, which are applied as magnetic sensors. The uniaxial anisotropy results from film deposition in the presence of a magnetic field parallel to the film plane or from field annealing below the Curie temperature of the deposited film. In both cases the direction of the applied field introduces an easy axis of the magnetization parallel to the applied field. Permalloy ($Ni_{91}Fe_{19}$) is the typical material used for soft magnetic uniaxial films.

1. The Single-domain Theory of Stoner and Wohlfarth

The magnetization reversal of ideal uniaxial films is theoretically described by the Stoner–Wohlfarth single-domain theory (Stoner and Wohlfarth 1948, Cohen 1969, Prutton 1964), in which an ideal uniaxial film with homogeneous in-plane magnetization is assumed.

The in-plane magnetization loops with applied field in the easy or hard direction are calculated from the minimum of the Zeeman energy, $-\vec{M}\vec{H}$, and the
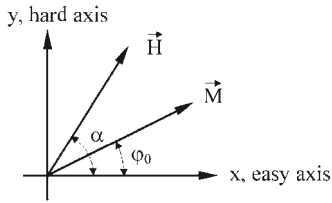
Figure 1
System of coordinates and angles.
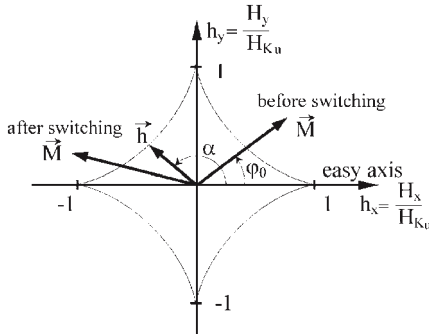
Figure 2
Stoner–Wohlfarth astroid.

Figure 3
Magnetization loops of uniaxial films: (a) easy axis;
(b) hard axis.

uniaxial anisotropy energy, $K_u \sin^2 \varphi_0$ (Fig. 1), leading to

$$\frac{\partial \varepsilon}{\partial \varphi_0} = \frac{\partial}{\partial \varphi_0}[-HM \cos(\alpha - \varphi_0) + K_u \sin^2 \varphi_0]$$
$$= -HM \sin(\alpha - \varphi_0) + 2K_u \sin\varphi_0 \cos \varphi_0 = 0 \quad (1)$$

for the equilibrium state.

Introducing the anisotropy field $H_{K_u} = 2K_u/M$, which is characteristic for uniaxial films, the equilibrium state is given by

$$h \sin(\alpha - \varphi_0) + \cos \varphi_0 \sin \varphi_0 = 0 \quad (2)$$

The field $h = H/H_{K_u} = HM/2K_u$ is the applied field in units of H_{K_u}, which will be used in the following discussions.

The effective field, $h(\alpha)$, in units of H_{K_u}, is given by

$$\frac{1}{2K_u}\frac{\partial^2 \varepsilon}{\partial \varphi_0^2} = h(\alpha) = h \cos(\alpha - \varphi_0) + \cos 2\varphi_0 \quad (3)$$

which determines the stability of the magnetization. Stable states require $h(\alpha) > 0$; instability, i.e. switching, occurs for $h(\alpha) = 0$ (Hoffmann 1966, 1968).

The equation

$$h(\alpha) = h \cos(\alpha - \varphi_0) + \cos 2\varphi_0 = 0 \quad (3a)$$

describes the well-known Stoner–Wohlfarth astroid (Fig. 2) (Stoner and Wohlfarth 1948, Cohen 1969, Prutton 1964).

On applying a field $\vec{H}$ at an angle α to the easy axis, for which the magnetization at $H = 0$ was originally saturated, the magnetization is coherently rotated by an angle φ_0 from the easy axis. As soon as the applied field $\vec{H}$ crosses the astroid, the magnetization switches spontaneously by coherent rotation into a new stable state (Fig. 2).

In the special case of applying the field along the easy axis, the magnetization remains stable in the original state, until at $H = -H_{K_u}$ it switches spontaneously to the antiparallel direction by coherent rotation (Fig. 3(a)). These two stable states, switched at H_{K_u}, make uniaxial films desirable for magnetic storage. Unfortunately, in reality, coherent switching along the easy axis is not observed. Instead, the magnetization of the films breaks up into domains, and magnetization reversal is completed by domain wall motion with coercive force $|H_c| < |H_{K_u}|$ (see Figs. 10(a) and (b)).

In the special case of applying the field along the hard axis, the magnetization rotates continuously from the easy axis against the direction of the applied field, until at $H = H_{K_u}$ the magnetization is saturated in this direction. The expected magnetization loop is given in Fig. 3(b). In this way the uniaxial film is used as a field sensor (see also *Coercivity Mechanisms*).

2. Magnetization Ripple

In discussing magnetization reversal in real polycrystalline films or in single-crystalline films, including defects, one has to include inhomogeneous local anisotropies, such as crystalline anisotropy and magnetostriction of the crystallites. These local anisotropies lead to deviations, φ, of the local direction of the magnetization from the mean direction φ_0. The magnetization is no longer homogeneous over the entire film. The fluctuations are coupled in elliptical areas over many crystallites. The major axis of the coupling ellipse is always directed perpendicular to the mean magnetization and is determined by dipolar coupling. The minor axis, parallel to the mean magnetization, is determined by the exchange length.

The fluctuation φ can be seen in images obtained by Lorentz microscopy (Fig. 4). This "magnetization ripple" (Hoffmann 1966, 1968, Cohen 1969) dominates
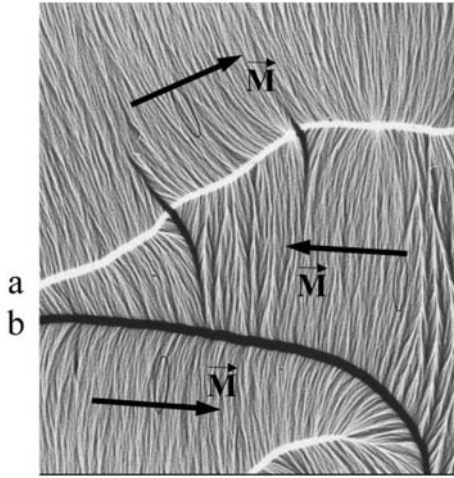
Figure 4
Lorentz image with magnetization ripple, Bloch wall, and cross-tie wall (courtesy of J. Zweck).

the magnetization reversal in fields along the hard axis and is responsible for the formation of domains. The model of homogeneous magnetization of ideal single-domain films is no longer applicable. The fluctuations, φ, of the magnetization cause magnetic divergencies, leading to intrinsic demagnetizing fields. Furthermore, exchange energy has to be taken into account. Assuming a two-dimensional thin film with infinite diameter, the total energy density depends on the site $\vec{r}$:

$$\varepsilon(\vec{r}) = \varepsilon_H + \varepsilon_{K_u} + \varepsilon_d(\vec{r}) + \varepsilon_{ex}(\vec{r}) + \varepsilon_{loc}(\vec{r}) \qquad (4)$$

and is now the sum of the Zeeman energy ε_H, the uniaxial anisotropy energy ε_{K_u}, the intrinsic demagnetizing energy $\varepsilon_d(\vec{r})$, the exchange energy $\varepsilon_{ex}(\vec{r})$, and the local energy $\varepsilon_{loc}(\vec{r})$.

Instead of Eqns. (1) and (2), the following variational problems have to be solved. For the equilibrium state:

$$\delta \iiint \varepsilon(\vec{r'})\mathrm{d}V' = 0 \qquad (5)$$

and for the effective field:

$$h_{eff}(\vec{r}) = \frac{1}{2K_u}\delta^2 \iiint \varepsilon(\vec{r'})\mathrm{d}V' \qquad (6)$$

Solving Eqn. (5) first gives the mean direction φ_0 of the magnetization, which is the same as in the single-domain theory.

Furthermore, solution of Eqn. (5) leads to a quantitative description of the ripple angle, φ, and the ripple wavelength, λ. The r.m.s. value $\sqrt{\overline{\varphi^2}}$ depends on the local anisotropies and the applied field; λ depends on the exchange constant and the applied field. On

decreasing the applied field H from saturation towards the Stoner–Wohlfarth astroid, both the ripple angle, φ, and the ripple wavelength, λ, increase (Fig. 5).

Solution of Eqn. (6) leads to a quantitative description of the intrinsic demagnetizing field caused by the ripple (Hoffmann 1966). The effective intrinsic demagnetizing field is aligned parallel or antiparallel to the mean magnetization (Fig. 6). This oscillation causes local instabilities as soon as $h_{eff}(\vec{r}) = 0$, leading to ripple blocking. This is most important for domain formation owing to the existence of the ripple. Blocking means that the mean direction of the magnetization no longer follows the Stoner–Wohlfarth single-domain behavior. The film splits into domains and hysteresis is observed.

The blocking curve is now the critical curve (Fig. 7) for magnetization reversal in thin films. On increasing the reversed applied field, the field vector can never approach the Stoner–Wohlfarth astroid (curve a) before crossing the blocking curve (curve b). This is a fundamental statement of ripple theory. The magnetization of a real film with uniaxial anisotropy can never be switched by coherent rotation. The magnetization breaks up into domains. Magnetization reversal is completed by domain wall motion. This theoretical prediction has been confirmed by many experiments. The Stoner–Wohlfarth model can be applied only to the region outside the blocking curve.
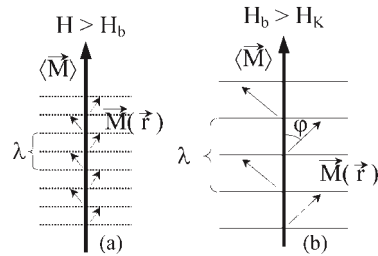
Figure 5
Magnetization ripple: (a) free ripple state; (b) ripple at blocking field H_b.
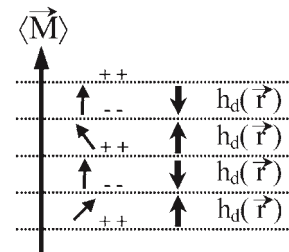
Figure 6
Intrinsic demagnetizing field of the ripple.
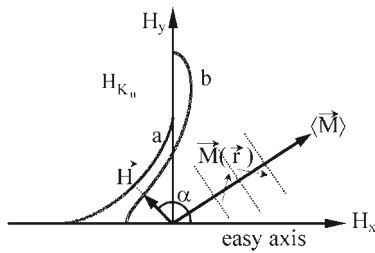
Figure 7
Critical curves for magnetization reversal: (a) Stoner–
Wohlfarth astroid; (b) blocking curve.
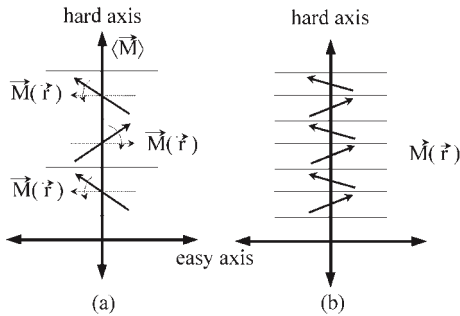
Figure 8
Magnetization ripple during reversal along the hard
axis. Ripple at the blocking field. Film with (a) low local
anisotropies and (b) large local anisotropies.

3. Magnetization Reversal in Fields Along the Hard Axis

Magnetization reversal along the hard or easy axis is
of special interest. In the case of high-quality films
(low local anisotropies), the magnetization loop in
the hard axis direction may appear as in Fig. 3(b) as a
straight line. In this case the intrinsic demagnetizing
field is small. The ripple wavelength at blocking,
which determines the domain width, is large. Each
domain then behaves like a Stoner–Wohlfarth single
domain. Reversal occurs by clockwise and counter-
clockwise rotation of the magnetization within each
domain (Fig. 8(a)). The remanence is zero.

In the case of larger local anisotropies the intrinsic
demagnetizing field is stronger. The ripple wave-
length at blocking is smaller (Fig. 8(b)). Magnetiza-
tion reversal within the domains is affected by the
demagnetizing field. Hysteresis is observed. The re-
manence is larger than zero.

4. Magnetization Reversal in Fields Along the Easy Axis

During magnetization reversal along the easy axis
some more effects have to be discussed. Owing to the
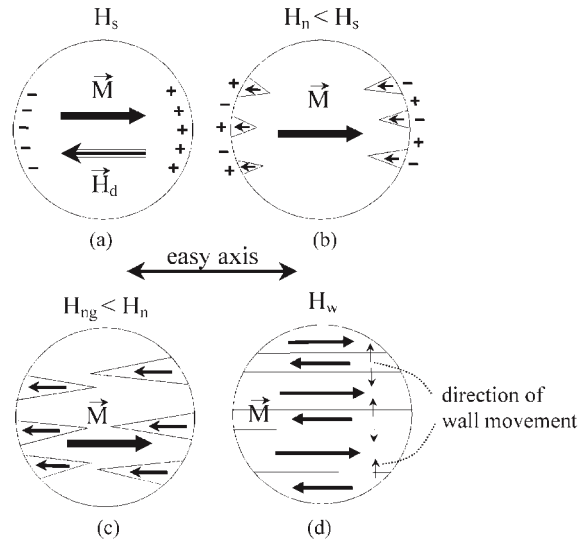
Figure 9
Stages of magnetization reversal along the easy axis: (a)
saturation in applied field H_s; (b) nucleation of reversed
domain at decreasing applied field; (c) growth of the
nuclei; (d) formation of walls and wall movement.

finite size of the films, at saturation magnetic poles at
the edge of the film create an external demagnetizing
field H_d (Fig. 9(a)), which need not be discussed dur-
ing hard axis reversal.

The demagnetizing field is antiparallel to the mag-
netization. It is strongest at the film edge. Decreasing
the applied field below the saturation field leads to
nucleation of reversed domains at the nucleation field
H_n (Fig. 9(b)). This reduces the total demagnetizing
field and consequently the demagnetizing self-energy.

On decreasing the applied field further, the re-
versed nuclei grow (at H_{ng}) (Fig. 9(c)) and finally
form domains (Fig. 9(d)). The magnetization reversal
is finalized by domain wall movement that starts at
H_w. The reversal always starts with nucleation at H_n.
The shape of the magnetization loop depends on the
strengths of H_n, H_{ng}, and H_w. The ripple is present in
all cases but the mentioned fields dominate the do-
main formation and the magnetization reversal, since
these fields are effective before ripple blocking occurs.

Two characteristic types of magnetization loops
are observed, depending on the geometry and quality
of the film:

(i) $H_n > H_{ng} > H_w > H_c$, which leads to a magnet-
ization loop in the easy axis direction as shown in
Fig. 10(a); and

(ii) $H_n <$ all other fields, which leads to a magnet-
ization loop as shown in Fig. 10(b); in this case the
applied field H has to be reversed from the saturation
direction to nucleate the reversed domains, which
immediately grow to larger domains and saturate the
magnetization by domain wall movement.
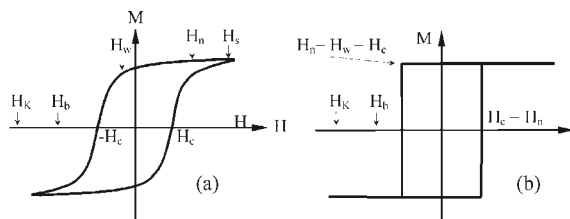
Figure 10
Magnetization loops dominated (a) by the field necessary for wall movement and (b) by the nucleation field.
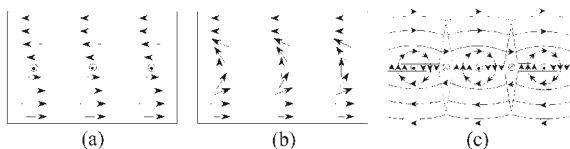
Figure 11
Domain walls in thin films: (a) Bloch wall; (b) Néel wall; (c) cross-tie wall.

The magnetization loop of Fig. 10(b) is similar to that along the easy axis of the Stoner–Wohlfarth single-domain theory (Fig. 2(a)) where magnetization reversal is given by coherent switching. In real films coherent switching at H_{K_u} can never occur, as explained by the blocking curve (Fig. 7). Domains are formed and magnetization reversal occurs by domain wall movement. This is very clearly seen, since $|H_c| < |H_{K_u}|$ in all cases. The magnetization reversal in isotropic films with zero uniaxial anisotropy is the same as described above for the easy axis reversal.

In general, the single-domain theory is valid only outside the blocking curve (Fig. 7). The films can be used as sensors without hysteresis, as long as the magnetic field vector does not cross the blocking curve. Coherent switching is impossible.

5. Domain Walls

Three types of walls are observed in thin films, depending on the film thickness (Kittel 1949, Hubert and Schäfer 1998, Middelhoek 1961). Examples are given below for permalloy films.

(i) Bloch wall, film thickness $d > 50$ nm (Fig. 11(a)). Inside of the walls the magnetic moments rotate around the normal of the walls, avoiding magnetic divergences and stray fields parallel to the film plane. Stray fields perpendicular to the film plane result from magnetic poles at the film surface.

(ii) Néel wall, film thickness $d < 25$ nm (Fig. 11(b)). For thinner films the magnetic self-energy of poles at
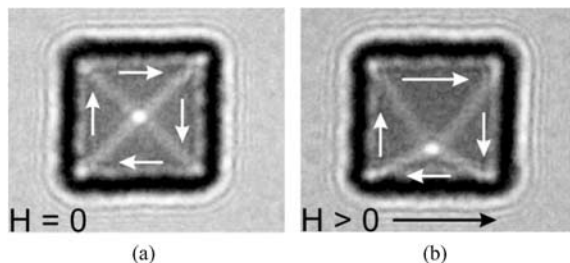
Figure 12
Landau–Lifshitz configuration of domains of a squared nanostructure, observed by Lorentz microscopy: (a) remanence; (b) in an applied field (courtesy of M. Schneider).

the film surface is too strong. Within the wall the magnetic moments rotate in the film plane, avoiding the magnetic poles at the surfaces. Instead, the wall creates magnetic divergencies, which increase the wall energy.

(iii) Cross-tie wall, film thickness ~ 25–50 nm (Fig. 11(c)). This type of wall is a transition between the Néel and Bloch walls.

6. Magnetization Reversal in Nanostructures

Domain formation in nanostructures is governed by the external demagnetizing field from the film edge. In the remanent state domains are formed to avoid the demagnetizing field.

6.1 Rectangular Nanostructures

Rectangular nanostructures show in the remanent state the ideal Landau–Lifshitz domain configuration that is shown in the Lorentz image of Fig. 12(a). Applying a magnetic field causes an increase of the domain with magnetization parallel to the field and a decrease of the domain with antiparallel magnetization. The vortex in the center of the film is shifted perpendicular to the applied field (Fig. 12(b)).

6.2 Circular Nanostructures

To avoid the demagnetizing field from the edges of the circular nanostructures in the remanent state the magnetization forms a circular flux closure with a vortex in the center of the nanostructure. Figures 13(a) and (b) show the Lorentz image of rotation of the magnetization. Increasing an applied field shifts the vortex perpendicular to the applied field with respect to the film edge (Fig. 13(c)). At the saturation field H_s the vortex collapses. This saturation field is larger than the demagnetizing field H_d at saturation. Decreasing the applied field to zero again leads to circular flux
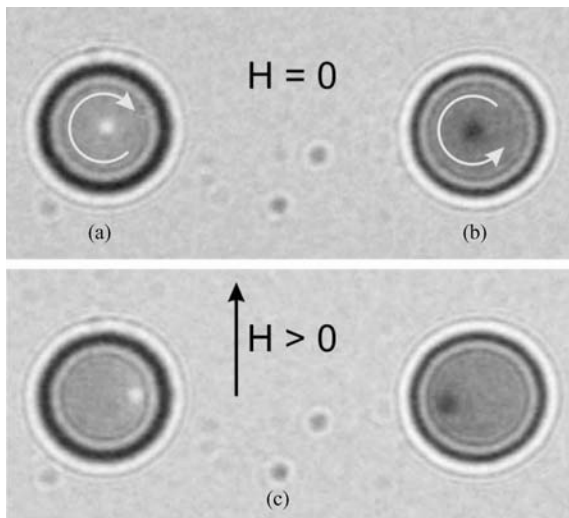
Figure 13
Circular nanostructures (height 15 nm, diameter 600 nm) observed by Lorentz microscopy. The bright and dark spots are vortices. (a) Counterclockwise flux closure at remanence, vortex in the center of the circle. (b) Clockwise flux closure at remanence. (c) Applied field $\vec{H}$: shift of the vortices perpendicular to $\vec{H}$ towards the edge of the nanostructure (courtesy of M. Schneider).
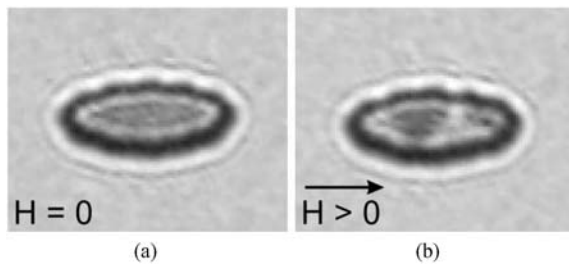
Figure 14
Lorentz microscopy image of elliptical nanostructures: (a) at remanence after saturation along the major axis; (b) in applied reverse field (courtesy of M. Schneider).

closure with a vortex in the center of the structure (see Figs. 13(a) and (b)).

6.3 Elliptical Nanostructures

The shape anisotropy of elliptical nanostructures leads to an easy axis along the major axis. After saturation along the easy axis the structure remains in a single-domain state at zero field (Fig. 14(a)). On applying a reverse field the magnetization breaks up into domains (Fig. 14(b)). Saturation in the reverse field occurs by domain wall motion. These structures are of interest for magnetic storage. For this purpose

the formation of domains during magnetization reversal has to be avoided. Much work is in progress to overcome this reversal problem.

7. Conclusion

The interest in ferromagnetic films is rapidly growing because of their application as field sensors in various modes, as magnetic storage material for floppy disks, as nanostructures in MRAMs, and as giant magnetic resistance elements in many applications. In cases of single-domain behavior stability at remanence and after switching the magnetization from one stable state to another is desired. Difficulties arise because of domain formation in the films and nanostructures. This article shows that in any nonideal soft magnetic film domain formation is unavoidable. Future investigations will try to overcome this problem instead of neglecting it.

See also: Longitudinal Media: Fast Switching; Magnets, Soft and Hard: Domains; Magnetic Films: Anisotropy; Magnetic Layers: Anisotropy; Monolayer Films: Magnetism

Bibliography

Cohen M S 1969 In: Chopra K L (ed.) *Thin Film Phenomena*. McGraw-Hill, New York, 608 ff
Craik D J, Tebble R S 1965 *Ferromagnetism and Ferromagnetic Domains*. North-Holland, Amsterdam
Hoffmann H 1966 Stray fields in thin magnetic films. *IEEE Trans. Magn.* **MAG 2**, 566–70
Hoffmann H 1968 Theory of magnetization ripple. *IEEE Trans. Magn.* **MAG 4**, 32–8
Hubert A, Schäfer R 1998 *Magnetic Domains*. Springer, Berlin, p. 11 ff
Kittel C 1949 Physical theory of ferromagnetic domains. *Rev. Mod. Phys.* **21**, 541–83
Middelhoek S 1961 Ferromagnetic domains in thin Ni–Fe films. Ph.D. thesis, University of Amsterdam
Prutton M 1964 *Thin Ferromagnetic Films*. Butterworth, Washington, DC
Stoner E C, Wohlfarth E P 1948 A mechanism of magnetic hysteresis in heterogeneous alloys. *Phil. Trans. R. Soc.* **A250**, 599–642

H. Hoffmann
Universität Regensburg, Germany

Thin Films: Giant Magnetostrictive

Interest in giant magnetostrictive materials in thin film form has grown rapidly over the past few years, owing to their potential as actuators for powerful transducer systems in microsystems, e.g., laser scanners,

micropumps, and ultrasonic motors (Quandt 2000). The development of the corresponding room temperature giant magnetostrictive thin film materials is based on rare earth–transition metal alloys. In general, the rare earth iron-based alloys offer the best chance of developing giant magnetostriction at room temperature or above, since the highly aspherical 4*f* orbitals of the rare earths remain in an oriented state, owing to the strong coupling between the rare earth and the iron moments, resulting in this large room-temperature magnetostriction.

An important task in developing giant magnetostrictive materials has been optimization of magnetostriction to magnetic anisotropy ratio, in order to attain large strains at moderate magnetic fields. In bulk materials it was achieved by using cubic compounds—the rare earth–Fe$_2$ Laves phases—in which the second order anisotropy constant vanishes, also by Tb–Dy alloying in order to compensate the fourth order anisotropy constant (Clark 1980). In the case of thin films, amorphous $(Tb,Dy)_x(Fe,Co)_{1-x}$ films (Duc *et al*. 1996) or especially novel TbFe/FeCo multilayers (Quandt and Ludwig 1999) represent the most promising approaches to combine soft magnetic and giant magnetostrictive properties.

Special attention has to be paid to the sign of the magnetostriction. While terbium-based materials exhibit positive magnetostriction, which means that this material expands in the direction of the external field, samarium-based materials behave in the opposite way, thus allowing an easy design of magnetostrictive bimorphs, which enables the realization of stress- or temperature-compensated bending actuators while further enhancing the overall effect.

The fabrication of giant magnetostrictive thin films was originally realized only by PVD techniques, the most prominently used being magnetron sputtering (Quandt 2000) with either mosaic-type or composite targets as well as multitarget arrangements. Other PVD techniques include electron beam evaporation, laser ablation and ion beam sputtering. The amorphous films are generally deposited onto unheated or cooled substrates, while for crystalline films heated substrates for a single-step process are used as an alternative to a post-deposition crystallization treatment.

For applications, the orientation of the magnetic easy axis and of the domains in the demagnetized state is of special importance, because maximum magnetostriction is only obtained by 90° rotations of the magnetic domains while 180° rotations do not result in any magnetostrictive strain. Considering that magnetostrictive thin film actuators are in general driven by a single magnetic field, the direction of which is fixed in relation to the actuator and in-plane in order to avoid large demagnetization losses, the optimized demagnetized state should consist of domains with an in-plane easy axis being oriented perpendicular to the driving field direction. This initial state can be obtained by a post-deposition annealing

process under an in-plane magnetic field which is oriented under 90° towards the driving field direction (Ludwig and Quandt 2000).

Another possibility to influence the direction of the magnetic easy axis of a magnetostrictive film is directly related to the film's stress. Considering the minimum of the magnetoelastic energy for an isotropic ferromagnet

$$E_{me} = -\tfrac{3}{2}\sigma\lambda_s\cos^2\alpha$$

the orientation of the magnetic easy axis (α: angle between the directions of the magnetization and of the application of the stress) depends on the sign of the film stress σ for a material with a given saturation magnetostriction λ_s. This equation implies an in-plane magnetic easy axis for a positive product $\sigma\lambda_s$, while a negative product results in a perpendicular anisotropy. Therefore, in the case of positive magnetostrictive-like terbium-based or FeCo films, tensile stress is required for in-plane anisotropy, whereas negative magnetostrictive samarium-based films should be deposited with compressive stress to result in the same anisotropy. As the sign and the magnitude of the film's stress can be controlled by the fabrication conditions, the thermal expansion coefficient of the substrate, or by stress annealing, an in-plane magnetic easy axis can be adjusted, in general, for all thin film materials.

The in-plane magnetoelastic coupling coefficient b or the magnetostriction λ can be measured by the common cantilevered substrate technique using the formula of du Trémolet de Lachesserie and Peuzin, resulting in:

$$b = \frac{\alpha}{L}\frac{h_s^2}{h_f}\frac{E_s}{6(1+v_s)}; \ \lambda = \frac{-b(1+v_f)}{E_f}$$

where α is the deflection angle of the cantilever as a function of applied field, L is the free length of the cantilever, E_s and v_s are the Young's modulus and Poisson's ratio for the substrate, and h_s, h_f are the thicknesses of the substrate and film, respectively.

In the following sections, amorphous, nanocrystalline and multilayered state-of-the-art giant magnetostrictive materials in thin film form with positive and negative magnetostriction and applications of these materials are discussed.

1. Amorphous Films

Use of amorphous materials is an important approach to lowering macroscopic anisotropy. In amorphous magnetic rare earth–iron alloys, the contribution of the rare earth–iron interaction results in the formation of a sperimagnetic structure with an ordering temperature above room temperature. In the case of positive magnetostrictive materials, TbFe thin films have been fabricated in a wide composition

range. It was found that increasing the rare earth content compared to the Laves phase composition results in the highest low-field magnetostriction in amorphous thin film materials. Assuming the same local environment in the amorphous compared to the crystalline state, a further approach to reduce the remaining anisotropy should be achievable by Tb/Dy substitution, which was investigated for a wide composition range for rare earth–iron or rare earth–cobalt thin film materials. This approach leads to a further reduction in the magnetic saturation field, but the lower Curie temperature due to the dysprosium alloying leads to a significant reduction in the saturation magnetostriction resulting in no or only a very small gain in low-field magnetostrictive strain of these ternary films.

Since the Curie temperature of amorphous TbFe is still quite low and is thus detrimental to giant magnetostriction to be obtained at higher temperatures, another interesting approach is related to the amorphous TbCo or TbFeCo alloys. Although the crystalline Laves phase $TbCo_2$ orders below 300 K, the ordering temperatures in amorphous TbCo alloys are raised up to 600 K depending on the composition, owing to a strongly ferromagnetically coupled cobalt sublattice with a sperimagnetic structure. In particular, amorphous films of the system Tb–Dy–Fe–Co exhibit very high room temperature magnetostrictions, exceeding 1000×10^{-6}. Comparison with other amorphous terbium-based thin film materials is shown in Fig. 1.

While $SmFe_2$ bulk materials are normally not considered as actuator materials, owing to the tensile stress required in these materials in order to achieve a suitable alignment of the magnetic domains, this situation is different in thin film bending transducers, which can easier be stressed with different signs. Therefore, amorphous Sm–Fe and Sm–Fe–B thin
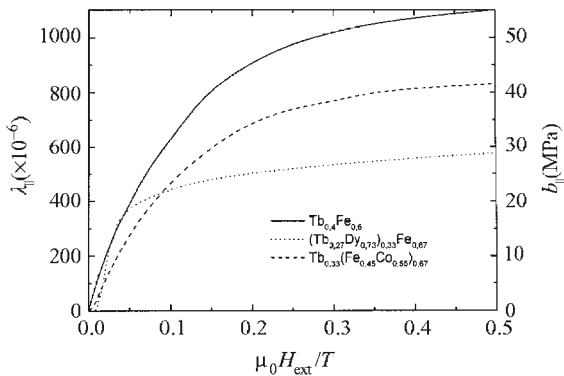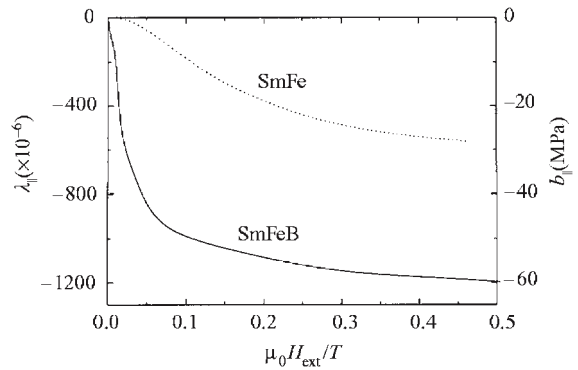
Figure 2
In-plane magnetostriction and magnetoelastic coupling coefficient of amorphous $Sm_{0.4}Fe_{0.6}$ and $Sm_{0.368}Fe_{0.626}B_{0.006}$ films.

films have been investigated over a wide compositional range, showing interesting giant magnetostriction at low external fields, especially in the case of Sm–Fe–B with a boron content of approximately 0.8 at.% (Lim *et al.* 1998), which is shown in Fig. 2 in comparison to an amorphous SmFe thin film.

2. Nanocrystalline Materials

The major drawback of all amorphous materials are their low Curie temperatures, leading to a limited temperature range of use and to large temperature coefficients of the magnetostriction at room temperature. Since the Laves phase $TbFe_2$ orders at 711 K (Clark 1980), crystallized films of the composition $(Tb_{0.3}Dy_{0.7})Fe_2$ have been investigated in some detail. In general, it has been found that crystallization is accompanied by a coercivity of at least 70 mT, thus requiring large magnetic driving fields. A possibility to overcome these limitations is related to the control of the grain size of the magnetic thin film material, as the random anisotropy model predicts a decrease of the coercivity with the grain size provided that the grain size is smaller than the ferromagnetic exchange length (Winzek *et al.* 1999).

Therefore, giant magnetostrictive materials with nanocrystalline grain structure should allow the combination of high Curie temperatures with soft magnetic properties. In particular, three approaches to realize a nanocrystalline grain structure have been reported: control of the crystallization temperature, addition of additives to enhance grain nucleation, and the use of multilayer structures to limit the grain growth in normal direction. The most promising result has been obtained for TbDyFe/Nb multilayers having a Curie temperature of 560 K and a saturation magnetostriction of 550×10^{-6}. Their hysteresis is significantly reduced compared to crystalline single

Figure 1
In-plane magnetostriction and magnetoelastic coupling coefficient of amorphous $Tb_{0.4}Fe_{0.6}$, $(Tb_{0.27}Dy_{0.73})_{0.33}Fe_{0.67}$, and $Tb_{0.33}(Fe_{0.45}Co_{0.55})_{0.67}$ films.
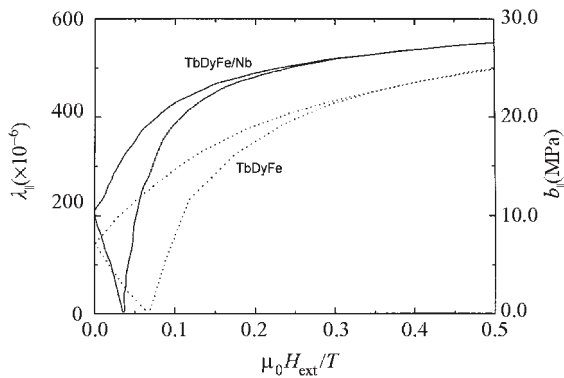
Figure 3
In-plane magnetostriction and magnetoelastic coupling coefficient of nanocrystalline $(Tb_{0.27}Dy_{0.73})_{0.33}Fe_{0.67}$ films and $(Tb_{0.27}Dy_{0.73})_{0.33}Fe_{0.67}/Nb$ multilayers.

Figure 4
Low-field magnetostriction and magnetoelastic coupling coefficient of $Tb_{0.4}Fe_{0.6}/Fe_{0.5}Co_{0.5}$ multilayers in comparison to $Tb_{0.4}Fe_{0.6}$ amorphous single layers.

layer materials (Fig. 3), but still reaches 35 mT under optimized preparation conditions.

3. Multilayers

Since the magnetic saturation field is proportional to the ratio of the anisotropy and the saturation magnetization, an alternative approach is based on an increase of the saturation magnetization of these materials. The amorphous rare earth transition metal materials used up to now have rather low magnetizations, owing to their ferrimagnetic nature. For the compositions of interest the rare earth moments dominate and thus any decrease of their content will further reduce the magnetization, while an increase results in a lowering of the Curie temperature and consequently a lowering of the room temperature magnetization. However, using multilayers it is possible to engineer new composite materials with properties which overcome these limitations (Quandt and Ludwig 1999).

To create such a composite, two materials have to be combined: one material is the giant magnetostrictive amorphous TbFe alloy, while the other is magnetically soft and has a very high magnetization and, preferably, a considerable magnetostriction itself (e.g., FeCo). Fabricating these layers with thicknesses smaller than the ferromagnetic exchange length and the domain wall width, domain wall formation at the interfaces is prevented and the magnetic properties of such an exchange-coupled multilayer system are determined by the average of those of each individual layer. Although it was found that the layers couple anti-parallelly, an enhancement of the overall magnetization is achievable for certain thickness ratios. Together with the reduction in anisotropy this increase in magnetization results in a significant reduction in the magnetic saturation field. Figure 4
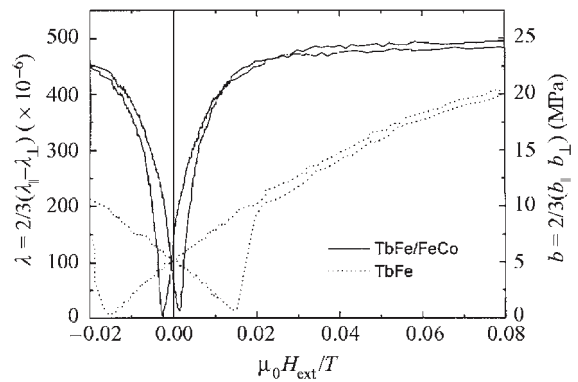
compares the low field magnetoelastic coupling coefficient of an optimized TbFe/FeCo multilayer with a state-of-the-art amorphous TbFe single layer film.

Furthermore, these types of multilayers show two effects which are of interest for the realization of smart actuators: both a significant change of the Young's modulus and of the electrical resistivity with the magnetic field. The Young's moduli of the multilayers exhibit a distinct increase with the applied magnetic field, of approximately 20% in the case of an annealed TbFe/FeCo multilayer, while this effect is smaller and requires higher magnetic fields in the case of the corresponding amorphous TbFe single-layer materials. The magnetoresistive effect is approximately 0.2% being developed in the same field range as the films' magnetostriction.

4. Applications

Giant magnetostrictive materials in thin film form have predominantly been used as various micro-actuators for applications in microsystem technology (Ludwig and Quandt 2000). Their working principle is based on a bending transducer which consists of a film/substrate compound with the substrate being, in general, non-magnetostrictive. Different geometries and boundary conditions are common, the most important being cantilevers, membranes and plates. Upon magnetization the magnetostriction in the film causes the film/substrate compound to bend, similar to the bending of a bimetallic transducer. Commonly, the most important feature of these micro-actuators is their remote-controlled operation. In the following, some examples of these magnetostrictive thin film transducers are explained in more detail.

In the case of cantilevers different applications have been realized, normally by using silicon micro-machining for the fabrication of the cantilevers. The large

bending or deflection of these cantilevers was applied for fluid jet deflectors controlling up to $500\,\mathrm{mls}^{-1}$, for magnetic field measurements by detecting the deflection of the cantilever optically, as well as for optical two-dimensional micro-mirrors which employ bending and torsional vibrations driven by two differently oriented magnetic fields. Furthermore, special attention was paid to the development of thermal drift-free actuators either realized by a special design of the micromachined substrate or by combining positive and negative magnetostrictive materials in a bimorph structure.

Magnetostrictive membranes have been used for fluidic micro-components such as micro-valves or micro-pumps, whereas the deflection of the membrane is used either to close or to open the valve outlet or to induce a pressure rise in the pumping chamber. Free plates with magnetostrictive coatings have been employed for the realization of travelling machines or for ultrasonic motors. Both linear and rotating standing wave motors were realized with micro-machined silicon or titanium substrates using a propulsion mechanism of vibrating teeth on a friction layer. The ultrasonic motors were operated by a.c. magnetic fields in combination with a magnetic bias field.

As a completely different application, giant magnetostrictive thin films can be used in scanning probe microscopy for magnetic field imaging. This technique has been demonstrated in the case of the magnetic field distribution of a hard-disk read–write head by coating this device and measuring the magnetic field induced change in the thickness of the coating due to the magnetostriction.

These different applications demonstrate the potential that giant magnetostrictive thin film materials have for the realization of micro-actuators and micro–sensors. It is expected that further application areas can be addressed by using the novel giant magnetostrictive multilayers, owing to their higher magnetostrictive susceptibility, their higher Curie temperature and their additional features, e.g., their change of resistivity and Young's modulus in a magnetic field.

See also: Magnetoelastic Phenomena; Magnetostrictive Materials; Magnetoelasticity in Nanoscale Heterogeneous Materials

Bibliography

Clark A E 1980 Magnetostrictive rare earth–Fe$_2$ compounds. In: Wohlfarth E P (ed.) *Ferromagnetic Materials*. Elsevier, Amsterdam, Vol. 1, pp. 531–86

Duc N H, Mackay K, Betz J, Givord D 1996 Giant magnetostriction in amorphous $(Tb_{1-x}Dy_x)(Fe_{0.45}Co_{0.55})_y$ films. *J. Appl. Phys.* **79**, 973–6

Lim S H, Choi Y S, Han S H, Kim H J, Shima T, Fujimori H 1998 Magnetostriction of Sm-Fe and Sm-Fe-B thin films fabricated by RF magnetron sputtering. *J. Magn. Magn. Mater.* **189**, 1–8

Ludwig A, Quandt E 2000 Giant magnetostrictive thin films for applications in microelectromechanical systems. *J. Appl. Phys.* **87**, 4691–5

Quandt E 2000 Giant magnetostrictive thin film technologies. In: Engdahl G (ed.) *Handbook of Giant Magnetostrictive Materials*. Academic Press, San Diego, pp. 323–43

Quandt E, Ludwig A 1999 Giant magnetostrictive multilayers. *J. Appl. Phys.* **85**, 6232–7

Winzek B, Hirscher M, Kronmüller H 1999 Crystallization of sputter-deposited giant-magnetostrictive TbDyFeM (M = Mo, Zr) films and multilayers. *J. Alloys Comp.* **283**, 78

E. Quandt
Stiftung Caesar, Bonn, Germany

Transition Metal Oxides: Magnetism

For practical applications the most important magnetic transition metal oxides are ferrites. In addition, manganites with perovskite structure and chromium dioxide are also important. Oxides in which magnetism is connected with the presence of *f* electrons are discussed elsewhere (see *Localized 4f and 5f Moments: Magnetism*).

A convenient feature of ferrites is that their magnetic properties can be well controlled. This is connected with the fact that the magnetic part of the free energy has a good approximation in a single ion character, i.e., it is a sum of the contributions of individual ions present in the system. As a rule there are several crystallographic sublattices occupied by cations with a large number of possible combinations of cation types and concentrations. By choosing the proper combination the desired properties may be then achieved.

There are numerous reviews of magnetism and the properties of transition metal oxides. A good review with an accent on applications was written by McCurrie (1994). Ferrites with the spinel structure were considered by Krupička and Novák (1982) and Brabers (1995), while those with the garnet and magnetoplumbite structure were discussed by Winkler (1981) and Kojima (1982), respectively. Recent experimental results for the mixed valence manganites were reviewed by Ramirez (1997).

1. Basic Interactions of Localized Electrons

In most of the magnetic oxides the 3*d* electrons of the iron group transition metal ions may be treated as localized. The exceptions are usually connected with the mixed valence, i.e., with the presence of two different valence states of the same atom on crystallographically equivalent sites. Even in these cases, however, the localized picture provides a convenient starting point. The interactions important for the

magnetism of systems with localized 3*d* electrons are discussed below.

1.1 Intra-atomic Coulomb Interaction

This interaction makes the occupation of an orbital state by two electrons with opposite spins energetically unfavorable. A consequence is the First Hund's rule according to which the ground state of a free ion corresponds to the maximal total spin S. Between terms having the same S, the term with the maximum total angular momentum L is energetically most stable (Second Hund's rule). The energy intervals between terms characterized by their L and S values are of the order of electron volts. In particular the ground state of the Fe^{3+} ion is ^6S ($S = 5/2$, $L = 0$) and the first excited term ^4G ($S = 3/2$; $L = 4$) is at $\sim 4\,eV$.

1.2 Crystal and Ligand Field

In crystals the electrons of a magnetic ion are subjected to the electrostatic crystal field and due to the covalency the 2*s* and 2*p* electrons of oxygen ligands are transferred to the empty states of the magnetic ion. Both these effects lead to the splitting of the energy levels of the ion. The corresponding interaction has a single electron character and it is described by an effective Hamiltonian:

$$\hat{H}_{CF} = \sum_{k=0}^{2l} \sum_{q=-k}^{k} B_{k,q} \hat{t}_{k,q} \tag{1}$$

where $B_{k,q}$ is the crystal field coefficient and $\hat{t}_{k,q}$ is the one electron irreducible tensor operator, which can be expressed in terms of the electron orbital momentum operator $\vec{l}$. The Hamiltonian $\hat{H}_{CF}$ reflects the local symmetry of the ion site. For the *d* electrons ($l = 2$), in the important case of the octahedral symmetry, Eqn. (1) reduces to:

$$\hat{H}_{CF} = \frac{B_4}{60}[35\hat{l}_z^4 - 30l(l+1)\hat{l}_z^2 + 25\hat{l}_z^2$$
$$- 6l(l+1) + 3l^2(l+1)^2 + \tfrac{5}{2}(\hat{l}_+^4 + \hat{l}_-^4)] \tag{2}$$

which splits a quintuplet of *d*-orbital states into a lower lying triplet, denoted as t_{2g}, and doublet e_g. The splitting between the doublet and the triplet is of the order of electronvolts and $\hat{H}_{CF}$ is thus comparable to the intra-atomic Coulomb interaction. In the tetrahedral symmetry the quintuplet is again split into a doublet e and a triplet t_2, with the doublet having a lower energy. If the local symmetry is lower than cubic, more terms are present in $\hat{H}_{CF}$ causing additional splitting of the orbital states.

1.3 Spin-orbit Coupling

The spin-orbit coupling is an intra-atomic relativistic interaction, which couples the electron spin with its orbital momentum. It may be approximated by:

$$\hat{H}_{ls} = \zeta(\vec{l} \; \vec{s}) \tag{3}$$

For the iron group ions the spin-orbit coupling parameter ζ is of the order of 1×10^{-2}–$1 \times 10^{-1}\,eV$ and $\hat{H}_{ls}$ is thus smaller compared to the intra-atomic Coulomb and crystal field interactions.

1.4 Vibronic Interaction, Jahn–Teller Effect

The vibronic (electron–lattice) interaction is especially important for ions, which have the orbitally degenerate ground state in the given crystal environment. As shown by Jahn and Teller a coupling term, linear in displacement of ions ("force"), then appears in the Hamiltonian. In the static treatment, which neglects the kinetic energy of ions, the local symmetry is then lowered by a spontaneous distortion of the environment (static Jahn–Teller effect). The static treatment is appropriate for systems with a large concentration of Jahn–Teller ions, where the co-operative interaction leads to lowering of the crystal symmetry. If a Jahn–Teller ion is isolated in an otherwise ideal lattice, the symmetry of its environment remains unchanged. However, in wave functions the electron and lattice coordinates become inexorably mixed, leading to a significant modification of the behavior observed, e.g., the spin-orbit coupling is quenched (dynamic Jahn–Teller effect).

Examples of ions exhibiting strong Jahn–Teller effects are Mn^{3+}, Cr^{2+}, and Cu^{2+} ions in the octahedral co-ordination and the tetrahedral Fe^{2+} ion.

1.5 Exchange Interaction

The dominant mechanisms of the exchange interaction in magnetic oxides are connected with the transfer of electrons between the magnetic ions via the intervening oxygen ligands. Such "supertransfer" depends on the mutual orientation of the spins and on the occupations of the electron orbitals. Owing to the Pauli principle, the transfer can occur in the case of half-filled orbitals only for antiparallel spins, hence the antiparallel spin orientation is favored. This is the strongest exchange mechanism in ferrites leading to ferrimagnetism or antiferromagnetism. If one of the orbitals in question is empty, transfer of electrons with both spin orientations is allowed, but, because of the intra-atomic exchange interaction (First Hund's rule), the parallel orientation is preferred. This mechanism thus leads to ferromagnetic ordering. A particular case of the latter interaction occurs when the two orbital states have the same energy, as in the manganite perovskites with mixed Mn^{3+}–Mn^{4+} valence. The Mn^{3+}–Mn^{4+} pair may be treated as Mn^{4+}–$Mn^{4+} + e^-$ with the Mn^{4+} centers being equivalent. The tendency to ferromagnetism is then

strong, and the interaction is in this case called the double exchange (e.g., Kubo and Ohata 1972).

The exchange interactions listed above are isotropic and the corresponding effective Hamiltonian has the Heisenberg form:

$$\hat{H}_{ex} = -\sum_i \sum_{j \neq i} J_{ij} \vec{S}_i \vec{S}_j \qquad (4)$$

For the double exchange this form is only a rough approximation, because the biquadratic and higher-order terms are important too. The exchange integral J_{ij} is a sensitive function of the angle between the M_i-oxygen and the M_j-oxygen bonds in the M_i-oxygen-M_j triad and it also depends on the orbital states in question. In particular, if either the M_i or the M_j cation has an orbitally degenerate state, J_{ij} must be treated as an operator in the orbital space.

In combination with the spin-orbit and crystal-field terms the exchange interaction (Eqn. (4)) yields anisotropic terms in the effective Hamiltonian, which may be expressed in the pseudodipolar or/and Dzyaloshinski–Moriya form:

$$\hat{H}_{psdip} = \vec{S}_i \bar{T} \vec{S}_j; \quad \hat{H}_{DM} = D[\vec{S}_i, \vec{S}_j] \qquad (5)$$

where $\bar{T}$ is a traceless tensor (e.g., Kanamori 1963).

2. Crystal and Magnetic Structure

A convenient representation of the crystal structures of the magnetic oxides is provided by the interconnected polyhedra as showed in Figs. 1(a)–(d). The centers of the polyhedrons (tetrahedrons, octahedrons, dodecahedrons, or bipyramids) are occupied by the cations, while the oxygen ligands are situated in their corners.

2.1 Spinels

Spinel ferrites MFe_2O_4 have a cubic crystal symmetry with eight formula units in the unit cell. There are two cation sublattices—tetrahedral (A) and octahedral (B). In spinel ferrites with a normal structure (e.g., $Zn^{2+}[Fe_2^{3+}]O_4)M^{2+}$ ions occupy the A sublattice, while the B sublattice is filled by the Fe^{3+} ions. In the inverse spinel ferrites the M^{2+} ions are in the B sublattice (M = Ni, Co, or Fe). For M = Mn, Mg, or Cu the M ions are in both the A and B sublattice and their distribution may be influenced by the thermal treatment. The Fe^{3+} ions may be substituted by other trivalent magnetic (Mn^{3+}, or Cr^{3+}) or nonmagnetic (Ga^{3+}, or Al^{3+}) ions. Other possibilities are represented by the Li-ferrite, $Fe^{3+}[Li_{0.5}^{1+}Fe_{1.5}^{3+}]O_4$, and maghemite, γ-Fe_2O_3-$Fe^{3+}[\square_{1/3}Fe_{5/3}^{3+}]O_4$ (where $\square$ represents the cation vacancy).

The dominating magnetic coupling in the spinel ferrites is the antiferromagnetic A–B superexchange interaction, leading to ferrimagnetic ordering. The magnetic structure of nickel ferrite is thus:

↓ ↓ ↓ ↓ ↓ ↓ ↓ ↓

8 Fe^{3+} ($5\mu_B$) on A sites

↑ ↑ ↑ ↑ ↑ ↑ ↑ ↑ ↟ ↟ ↟ ↟ ↟ ↟ ↟ ↟

8 Fe^{3+} ($5\mu_B$) and 8 Ni^{2+} ($2\mu_B$) on B sites
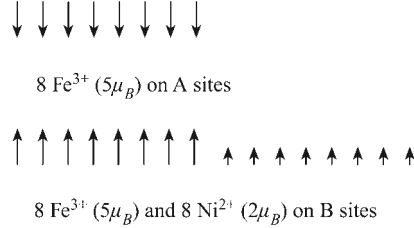
2.2 Garnets

The ferrites with the garnet structure $R_3Fe_5O_{12}$ (R may be, for example, yttrium, trivalent rare-earth ion, or bismuth) are cubic compounds with eight formula units in the unit cell. The Fe^{3+} ions occupy 16 tetrahedral (d) sites and 24 octahedral (a) sites. The R^{3+} ions fill 24 dodecahedral (c) sites. The ion distribution is thus $\{R_3^{3+}\}[Fe_2^{3+}](Fe_3^{3+})O_{12}^{2-}$. Iron can be *fully* substituted by some other trivalent cations (e.g., Al^{3+}, or Ga^{3+}), or *partly* by tetravalent (Si^{4+}, or Ge^{4+}) or bivalent (Co^{2+}, or Mg^{2+}) ions. If the substitute is not trivalent, the charge neutrality is maintained by the change of the iron valence. The bivalent cations (e.g., Ca^{2+}, Sr^{2+}, or Mn^{2+}) may also enter the c sublattice.

The dominating magnetic coupling in the garnet ferrites is the antiferromagnetic a–d superexchange interaction, leading to a ferrimagnetic ordering of Fe(a) and Fe(d) spins. The spin of the rare-earth ions on the c sublattice is antiparallel to the Fe(d) spin. The magnetic structure of $Gd_3Fe_5O_{12}$ is:

↓ ↓   ↓ ↓ ↓

2 Fe^{3+} ($5\mu_B$) on a sites; 3 Gd^{3+} ($7\mu_B$) on c sites

↑ ↑ ↑

3 Fe^{3+} ($5\mu_B$) on d sites
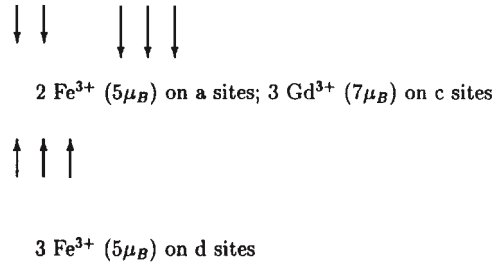
Gd^{3+} is an *S*-state ion with zero-orbital momentum in the ground state. The exchange interactions in $Gd_3Fe_5O_{12}$ are thus isotropic and the magnetic structure is collinear. In other rare-earth iron garnets the magnetic moments of individual R^{3+} ions are not parallel to the magnetization forming so called umbrella structure.

2.3 Hexagonal Ferrites

The most important hexagonal ferrites $M_2Fe_{12}O_{19}$ (M = Ba, Sr, or Pb) have the magnetoplumbite structure. The unit cell contains two formula units, and
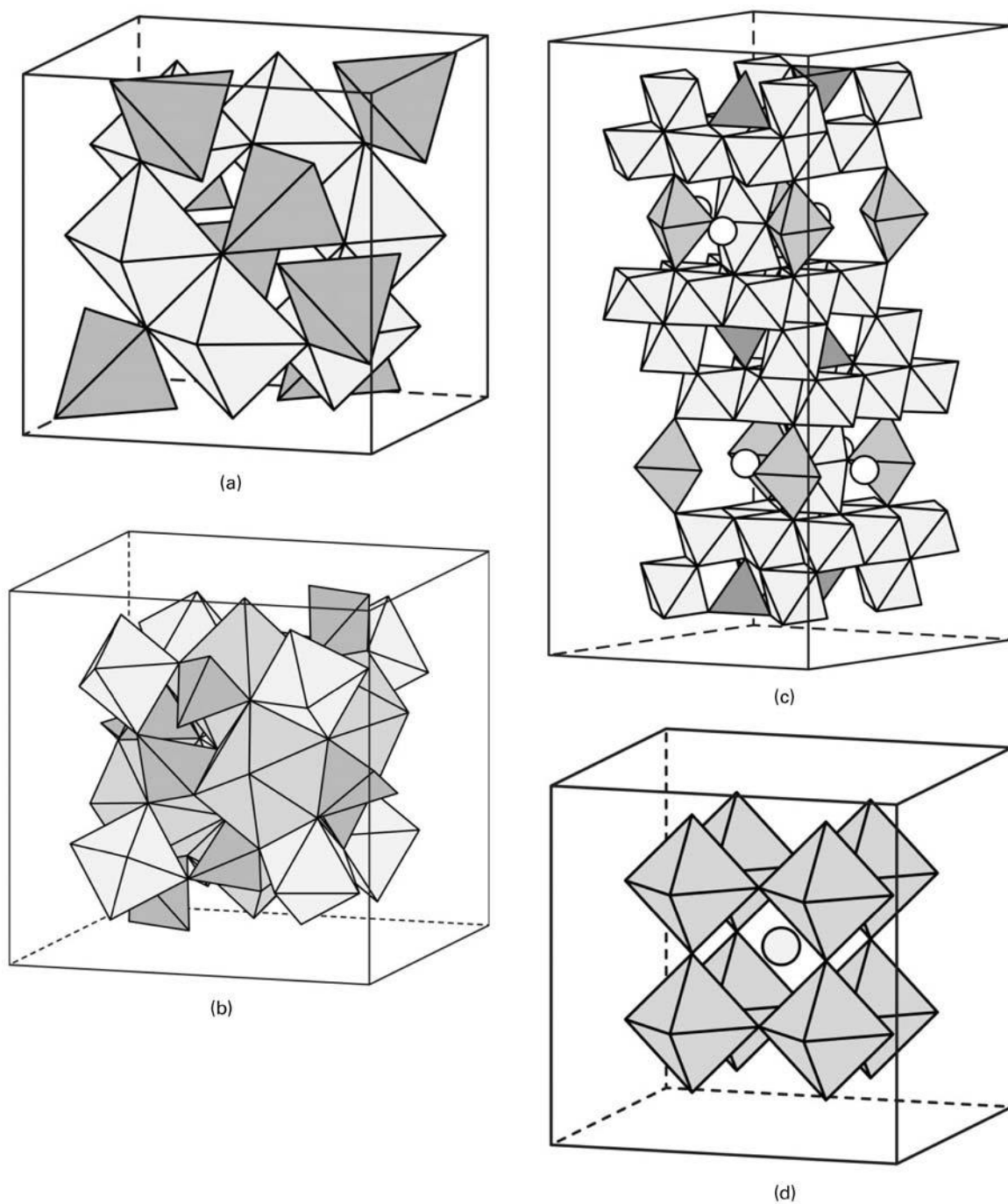
Figure 1
The arrangement of the polyhedrons surrounding the 3d metal ions in the (a) spinel, (b) garnet, (c) M-hexaferrite, and (d) perovskite crystal structures. For garnet the dodecahedrons of the R ions are also shown. For M-hexaferrite and perovskite structures the cation sites, which are not occupied by the 3d metal ions, are represented by circles.

Table 1
Fe sublattices in $MFe_{12}O_{19}$. Two alternative notations for sublattices used in the literature are given.

Sublattice	Fe1 2a	Fe2 4e (2b)	Fe3 4f1	Fe4 4f2	Fe5 12k
Coordination	Octahedral	Bipyramidal	Tetrahedral	Octahedral	Octahedral
Spin	Up	Up	Down	Down	Up

can be divided into four blocks designated as **SRS*R***. The **S** block has the spinel structure, while symmetry of **R** is rhombohedral. Asterisk means a rotation of the block by π around the hexagonal axis. There are five sublattices occupied by Fe^{3+} ions. The superexchange interactions, all of an antiferromagnetic character (Novák *et al.* 1989), lead to a collinear ferrimagnetic ordering of spins (Table 1). Substitution of various cations in all the Fe sublattices as well as in the M sublattice can be made. Technological applications of these materials are described in *Alnicos and Hexaferrites*.

Hexagonal ferrites with a more complicated structure contain a hexagonal block **T**, in addition to blocks **R** and **S**. Examples are W, Y and Z hexaferrites with the chemical compositions $BaM_2Fe_{16}O_{27}$, $Ba_2M_2Fe_{12}O_{22}$, and $Ba_3M_2Fe_{24}O_{41}$, respectively.

2.4 Perovskites

The most important transition metal perovskites are orthoferrites $RFeO_3$ (where R is yttrium or a rare-earth ion) and mixed valence manganites $R_{1-x}M_xMnO_3$ (where M is a bivalent or monovalent cation such as Ca^{2+}, Sr^{2+}, Ba^{2+}, Pb^{2+}, Na^+, and K^+). All these compounds have a distorted perovskite structure. The Fe^{3+}, Mn^{3+}, and Mn^{4+} ions are octahedrally coordinated while the R and M ions have 12 oxygen ligands. The orthoferrites are basically antiferromagnetic, but there is a weak ferromagnetism due to a canting (about $0.5°$) of the antiferromagnetically oriented Fe^{3+} spins.

In manganites containing bivalent M ions the ion distribution is $(R_{1-x}^{3+}M_x^{2+})(Mn_{1-x}^{3+}Mn_x^{4+})O_3^{2-}$. If x is smaller than ≈ 0.1 an antiferrodistortive ordering of the local Jahn–Teller deformations associated with the Mn^{3+} ions exists. The systems are nonmetallic and antiferromagnetic. For higher M concentrations the double-exchange interaction prevails over the superexchange, the systems are then metallic-like and ferromagnetic. The Curie temperature depends on the difference of R^{3+} and M^{2+} ionic radii and it reaches $\sim 370\,K$ in the (LaSr) system. A rich phase diagram exists for $x \approx 0.5$. Depending on the R^{3+} and M^{2+} cations the system may exhibit a Mn^{3+}–Mn^{4+} charge ordering and it is then nonmetallic and antiferromagnetically ordered. In other cases ferromagnetic ordering and the metallic-like conductivity is observed.

2.5 Chromium Dioxide

CrO_2 has a rutile structure with two formula units per unit cell. It is an unusual transition metal oxide as it is ferromagnetic, rather than ferrimagnetic. The tetravalent state of chromium is expected with the electron configuration $[Ar]3d^2$. The magnetic moment per unit cell is then $4\,\mu_B$ (assuming that the orbital angular momentum is quenched by the crystal field) in reasonable agreement with the experimental data.

3. Important Properties

3.1 Temperature Dependence of Magnetization

In the molecular field approach the temperature dependence of the sublattice magnetizations of a ferrimagnetic system is calculated from the coupled system of equations:

$$\vec{B}_\alpha = \sum_\beta \lambda_{\alpha\beta}\vec{M}_\beta; \quad M_\alpha(T) = M_\alpha(0)\boldsymbol{B}_{S_\alpha}(x_\alpha);$$

$$x_\alpha = (g_\alpha\mu_B S_\alpha/kT)B_\alpha \tag{6}$$

where $\vec{M}_\alpha$ is the magnetization of the sublattice α, $\lambda_{\alpha\beta}$ are the molecular field coefficients, connected with the exchange integrals J_{ij} (see Eqn. (4)) by:

$$\lambda_{\alpha\beta} = \frac{2z_{ij}J_{ij}}{n_j g_i g_j \mu_B^2} \tag{7}$$

the site $i(j)$ belongs to the sublattice $\alpha(\beta)$, z_{ij} is the number of neighbors, n_j is the number of j-type sites for whatever is the quantity of material to which the magnetization is related. g_i, $g_j \approx 2$ are the respective g-factors. $\boldsymbol{B}_S$ is the Brillouin function. For a ferrimagnetic system with two magnetic sublattices, three possible types of the $M(T)$ dependence are obtained (Fig. 2).

In systems where the double exchange dominates, the molecular field approach leads to a different set of equations (see Kubo and Ohata 1972). The $M(T)$ dependence is more convex, compared to a system described by the Heisenberg–Hamiltonian.

3.2 Magnetocrystalline Anisotropy

The main mechanism which gives rise to the magnetocrystalline anisotropy originates from the interplay
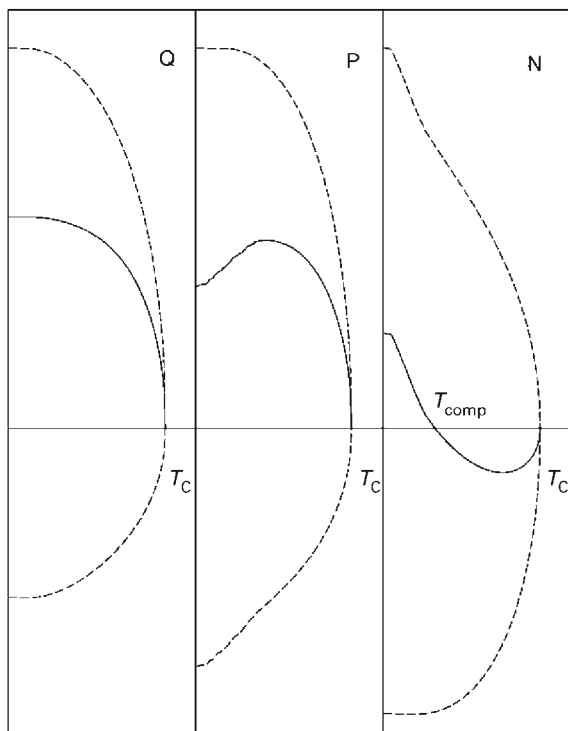
Figure 2
Three types of temperature dependence of the magnetization in a two-sublattice ferrimagnet. Dashed curves correspond to the magnetizations of the sublattices. Full curve is the total magnetization. T_{comp} denotes the compensation temperature.

of the crystal field, spin-orbit, and exchange interactions. The anisotropic part of the free energy then has a single ion character, i.e., it may be expressed as the sum of the contributions of individual magnetic ions, present in the system, the same holds also for the anisotropy constants. A large contribution give ions the orbital moment of which is not quenched by the crystal field. Examples are the Co^{2+} and Fe^{2+} ions in the octahedral co-ordination and all trivalent lanthanide ions, with the exception of La^{3+}, Gd^{3+}, and Lu^{3+}.

The temperature dependence of the single ion contribution k to the anisotropy constant follows the $l(l+1)/2$ law:

$$\frac{k(T)}{k(0)} = \left[\frac{m(T)}{m(0)}\right]^{l(l+1)/2} \qquad (8)$$

where $m(T)$ is the magnetic moment of the ion at temperature T, $l = 2$ and 4 for the first anisotropy constant in the axial and cubic symmetry, respectively.

In systems with symmetry lower than cubic the dipolar and anisotropic exchange interactions may also contribute to the magnetocrystalline anisotropy. In many ferrites with nominally cubic symmetry an axial magnetocrystalline anisotropy may be induced by annealing the system in a magnetic field.

3.3 Electrical Conductivity and Magnetoresistance

In many transition metal oxides the same cation may exist in several different valence states. Such a 'mixed valence' situation is connected with the presence of oxygen or cation vacancies and/or caused by cation substitution. An example is the $Y_3Fe_5O_{12}$ garnet (YIG), in which all cations are trivalent, providing the system is ideally stoichiometric. Substitution of Si^{4+} for Fe^{3+} in the tetrahedral sublattice then induces the change of valency of the octahedral Fe ion $Fe^{3+} \rightarrow Fe^{2+}$.

The charge carriers are in most cases described as polarons (electrons or electron holes plus the lattice distortion) moving by hopping or in a band. The electrical conductivity may be of n-type (e.g., YIG:Si) or p-type (e.g., YIG:Ca) and it can be very low in nearly stoichiometric compounds (10^{-11} c in YIG at 300 K, see Winkler 1981). A special case is represented by magnetite $(Fe^{3+})[Fe^{3+} Fe^{2+}]O_3$ with the equal number of ferrous and ferric cations in the octahedral sublattice. The d.c. conductivity of Fe_3O_4 is larger than $10^2 \Omega^{-1}cm^{-1}$ at 300 K.

The importance of the ferromagnetic, metallic-like mixed valence manganites (see Sect.2.4) is increasing. Above T_C the conductivity in these compounds has a hopping character, while below T_C it is metallic-like. At temperatures close to T_C an external magnetic field markedly influences the spin configuration and has a large effect on the electrical conductivity, leading to "colossal" magnetoresistance.

3.4 Optical and Magneto-optical Properties

At long wavelengths $\lambda > 1.5\,\mu m$ the optical absorption in ferrites is mainly caused by the lattice vibrations. Between ~ 1.5–$5.0\,\mu m$ the so-called infrared window exists, in which the absorption coefficient α can be very low ($\alpha < 0.03\,cm^{-1}$ for the yttrium iron garnet). At shorter wavelengths the absorption increases due to the electronic transitions between the states of the transition metal ions as well as the charge transfer transitions involving the oxygen ligands. If the rare earth ions are present, characteristic absorption bands appear in the far infrared region. The absorption is also very sensitive to the presence of the charge carriers (Fe^{2+} or Fe^{4+} ions).

The rotation of the plane of linearly polarized light (Faraday effect) was most thoroughly studied in garnet ferrites (see Winkler 1981). The specific Faraday rotation θ_F lies in the range from 1×10^2–$1 \times 10^5\,°cm^{-1}$ and it depends on the wavelength of the light beam, temperature, composition of the

garnet, external magnetic field, etc. θ_F is strongly enhanced by the presence of the Bi^{3+} ion in the dodecahedral sublattice.

See also: Growth and Magnetic Properties of YIG Films; Perovskites: Resistivity Behavior

Bibliography

Brabers V A M 1995 Progress in spinel ferrite research. In: Buschow K H J (ed.) *Handbook of Magnetic Materials*. Elsevier, Amsterdam, Vol. 8, pp. 189–234

Kanamori J 1963 Anisotropy and magnetorestriction of ferromagnetic and antiferromagnetic materials. In: Rado G T, Suhl S (eds.) *Magnetism*. Academic Press, New York, Vol. 1, pp. 127–203

Kojima H 1982 Fundamental properties of hexagonal ferrites with magnetoplumbite structure. In: Wohlfarth E P (ed.) *Ferromagnetic Materials*. North-Holland, Amsterdam, Vol. 3, pp. 305–92

Krupička S, Novák P 1982 Oxide spinels. In: Wohlfarth E P (ed.) *Ferromagnetic Materials*. North-Holland, Amsterdam, Vol. 3, pp. 189–304

Kubo K, Ohata N 1972 A quantum theory of double exchange I. *J. Phys. Soc. Jap*. **33**, 21–32

McCurrie R A 1994 *Ferromagnetic Materials Structure and Properties*. Academic Press, London

Novák P, Idland K, Zalesskij A V, Krivenko V G, Kunevitch A V 1989 Magnons and sublattice magnetizations in hexagonal Ba ferrite. *J. Phys. Condens. Matter* **1**, 8171–9

Ramirez A P 1997 Colossal Magnetoresistance. *J. Phys. Condens. Matter* **9**, 8171–99

Winkler G 1981 Magnetic garnets. *Vieweg Tracts in Pure and Applied Physics*, Vol. 5. Vieweg & Sohn, Braunschweig, Germany, Vol. 5

P. Novák
Institute of Physics ASCR, Prague, Czech Republic

Transparent Rare Earth Compounds: Magnetic Circular Dichroism

Magnetic circular dichroism (MCD) is the difference in molar absorptivities for left and right circularly polarized light, $\Delta\varepsilon = (\varepsilon_{LCP} - \varepsilon_{RCP})$, and is measured as a function of frequency (or wavenumber) on samples placed in a longitudinal magnetic field. In this chapter, MCD spectroscopy of transparent rare-earth compounds in the solid and liquid state is described, with special emphasis on the MCD spectra of trivalent europium ions. The majority of the MCD studies on trivalent rare-earth ions have been devoted to the Eu^{3+} ion. The trivalent Eu^{3+} ion ($4f^6$ electronic configuration) has the advantage of a nondegenerate ground state ($^7F_0$) and the presence of excited states with a small total angular momentum J (e.g. $^5D_1$ and $^5D_2$). This makes the MCD spectrum of Eu^{3+}

relatively easy to interpret, in comparison with the MCD spectra of the other trivalent rare-earth ions. The Eu^{3+} MCD spectrum is dominated by signals which have the shape of the first derivative of a Gauss-curve. These signals are the so-called *A*-terms. An *A*-term can have a positive or negative sign. A positive *A*-term has its positive lob at the high wavenumber side of the spectrum.

In this case, the absorption of left circularly polarized light takes place at a higher energy (or wavenumber) than the absorption of right circularly polarized light. For a negative *A*-term, the reverse is true. As will be discussed further, the sign of the *A*-terms in the MCD spectrum depends on the symmetry of the first coordination sphere around the Eu^{3+} ion. The information obtained by MCD is similar to what can be extracted from a classical Zeeman spectroscopy experiment, where the splitting and mixing of energy levels in a magnetic field are studied. However, MCD can also be measured in the case of broad absorption bands. Typical MCD applications are the assignment of electronic transitions, measurement of the Zeeman splitting, investigation of magnetic and symmetry properties of electronic states, polarization studies and testing the reliability of crystal-field wave functions and intensity parameters. An MCD spectrum has a higher information content than the corresponding absorption spectrum, since in addition to the intensity, the MCD signal is characterized by a sign (positive or negative). MCD is an excellent method for detecting the presence of overlapping transitions in the absorption spectrum. The method is very sensitive to changes in the electronic structure, and therefore to changes in the physical structure.

1. Measurement of MCD Spectra

The measurement of MCD spectra is rather similar to the measurement of absorption spectra. The primary differences are that the radiation incident on the sample must be circularly polarized and that the sample is placed in a longitudinal magnetic field (magnetic field lines parallel to the light beam). Most magnetic circular dichroism spectrometers are circular dichroism spectrometers extended with a magnet, although some instruments are especially designed for MCD measurements. A permanent magnet, electromagnet or superconducting magnet can be used. The permanent magnet has the disadvantage that the magnetic field is rather weak and that the magnetic field cannot be switched off for CD measurements. An electromagnet is often the best choice, because it can produce a moderate magnetic field (ca. 1 T), it can be switched off and it is simple in use. A superconducting magnet can provide a strong magnetic field (typically 5–7 T), but cooling with liquid helium is necessary. The light beam from the light source is first linearly polarized and then circularly polarized

by a Pockels cell or photoelastic modulator. Typically, MCD instruments have a single-beam setup.

There are some constraints on the samples which can be used in MCD measurements. The circular polarization of the incident light beam may only be altered by sample absorption, resulting in elliptically polarized light. This means that MCD can only be recorded for optical isotropic samples or in an isotropic direction for anisotropic samples. Solutions will give no problems. Cubic crystals and especially glasses have to be checked for the absence of internal stress. Uniaxial crystals can be measured along the unique optic axis. In this case, adequate orientation of the sample is crucial. In principle, MCD spectra of biaxial crystals cannot be measured. Finally, it is difficult to record the MCD spectrum of powdered samples, because of the effects of light scattering.

MCD data are obtained with an MCD spectrometer in terms of *ellipticities* θ (in millidegrees). The relation between θ and $\Delta\varepsilon$ is given by the expression:

$$\theta = \frac{33000\Delta\varepsilon}{lC} \tag{1}$$

where l is the optical path length (in cm) and C is the concentration (in molL^{-1}).

2. Basis MCD Theory

An elaborate discussion of the theory of MCD can be found in the work of Stephens (1970, 1974, 1976) and of Piepho and Schatz (1983). MCD spectra find their origin in the magnetically induced optical activity, due to the Zeeman effect. The Zeeman effect predicts that all the energy level degeneracy is lifted in the presence of a magnetic field. In the case of a rare-earth ion coordinated by ligands according to a defined geometry, the energy levels in question are the levels obtained after introduction of the crystal-field perturbation on the free-ion levels. The Hamiltonian of such a system can be written as:

$$H = H_0 + H'_{\text{ER}} + H'_{\text{SOC}} + H'_{\text{CF}} + H'_{\text{Zeeman}} \tag{2}$$

where H_0 is the Hamiltonian in the central-field approximation, H'_{ER} is the electron repulsion Hamiltonian (the prime indicates that the Hamiltonian describes a perturbation), H'_{SOC} is the spin-orbit coupling Hamiltonian, H'_{CF} is the crystal-field Hamiltonian and H'_{Zeeman} is the Zeeman Hamiltonian. The wavefunctions are those which diagonalize the total Hamiltonian (including the Zeeman effect). In an MCD measurement, the magnetic field is applied parallel to the propagation direction of the light. The propagation direction is called z; therefore the magnetic field component to be considered is $\mathbf{H}_z$. In a crystal with the principal site symmetry axis parallel to z, the Zeeman levels are described and labeled with respect to this z-axis.

According to a notation used by Judd (1962), the Zeeman levels of the ground state can be written as:

$$\langle A_\alpha | = \sum_M \langle 4f^N \psi JM | a_M \tag{3}$$

where A is a crystal field level with Zeeman component α, a_M are coefficients, $4f^N$ indicates the $4f^N$ configuration with N electrons in the valence shell, ψ is an additional quantum number, J is the total angular momentum, and M is the z-component of J. For the excited state, an analogous expression can be written:

$$|A'_{\alpha'}\rangle = \sum_{M'} a'_{M'} |4f^N \psi'J' M'\rangle \tag{4}$$

For the discussion of the MCD signals it is sufficient to consider only the M quantum numbers:

$$\langle A_\alpha | = \sum_M \langle M | a_M \tag{5}$$

$$|A'_{a'}\rangle = \sum_{M'} a'_{M'} |M'\rangle \tag{6}$$

If the rare-earth ions are in an uniaxial single crystal with the main symmetry axis parallel to the propagation direction of the light, light absorption only takes place in the xy plane. For an electric dipole transition, the operators are:

absorption of RCP :

$$m_{+1} = \frac{-1}{\sqrt{2}}(m_x + im_y) = -|e|D^{(1)}_{+1} \tag{7}$$

absorption of LCP :

$$m_{-1} = \frac{1}{\sqrt{2}}(m_x - im_y) = -|e|D^{(1)}_{-1} \tag{8}$$

where m_x, m_y are the electric dipole operators for light polarized according to the x or y directions, and $|e|$ is the absolute charge of the electron. $D^{(1)}_\rho$ is a tensor of rank 1, with polarization numbers $\rho = +1$ for RCP and $\rho = -1$ for LCP. In the case of a magnetic dipole transition, the operators are:

absorption of RCP :

$$\mu_{+1} = \frac{-1}{\sqrt{2}}(\mu_x + i\mu_y) = \frac{-|e|}{2mc}(L + 2S)^{(1)}_{+1} \tag{9}$$

absorption of LCP :

$$\mu_{-1} = \frac{1}{\sqrt{2}}(\mu_x - i\mu_y) = \frac{-|e|}{2mc}(L + 2S)^{(1)}_{-1} \tag{10}$$

where m is the electron mass, c is the speed of light, L is the orbital angular momentum and S is the spin angular momentum. Since the Zeeman components are characterized by the quantum numbers M, one can understand that circularly polarized light induces transitions between Zeeman levels. Depending on the quantum number M of the ground state $\langle A_\alpha |$ and

the quantum number M' of the excited state $|A'_{\alpha'}\rangle$, either left circularly polarized light (LCP, $\rho = -1$) or right circularly polarized light (RCP, $\rho = +1$) can be absorbed preferentially. The conditions for absorption in terms of M, M' and ρ can be formulated by *selection rules*.

The relative order of the splitting of a J-level by a magnetic field in its M components is defined by the Landé-factor g:

$$g = 1 + \frac{J(J+1) - L(L+1) + S(S+1)}{2J(J+1)} \quad (11)$$

If g is positive, the *sign of the A-term* of Eu^{3+} is determined by the *sign of the M' quantum number* used to label the Zeeman level to which *left circularly polarized light* is absorbed. If g is negative, the absorption of right circularly polarized light has to be evaluated. For the observable $^{2S+1}L_J$ levels of Eu^{3+}, g is always positive.

3. MCD Selection Rules

3.1 Electric Dipole Transitions

Although no electric dipole transitions can occur for Eu^{3+}, it is instructive to start with this case. The classical example to illustrate the MCD signal of an electric dipole transition is the $^1P \leftarrow ^1S$ transition. In a magnetic field, the ^1P state splits into three components: $^1P_{+1}$ ($|M'\rangle = |+1\rangle$), $^1P_0$ ($|M'\rangle = |0\rangle$) and $^1P_{-1}$ ($|M'\rangle = |-1\rangle$). The selection rule, which can be obtained by evaluating 3j symbols in the transition moment integral, is:

$$\Delta M = M' - M = -\rho \quad (12)$$

When the ground state is characterized by $\langle M| = \langle 0|$, as in the case of $^1S_0$, the selection rule is reduced to:

$$\Delta M = M' = -\rho \quad (13)$$

In other terms, left circularly polarized light ($\rho = -1$) is absorbed to the upper Zeeman component characterized by $|M'\rangle = |+1\rangle$ (g is positive). For the same reason, right circularly polarized light is absorbed to the lower Zeeman component $|M'\rangle = |-1\rangle$. The corresponding MCD signal will be a positive A-term.

3.2 Magnetic Dipole Transitions

The same considerations as for an electric dipole transition, lead to the selection rule for a magnetic dipole transition:

$$\Delta M = M' - M = -\rho \quad (14)$$

which can be rewritten in the case that the ground state is characterized by $\langle M| = \langle 0|$, to:

$$\Delta M = M' = -\rho \quad (15)$$
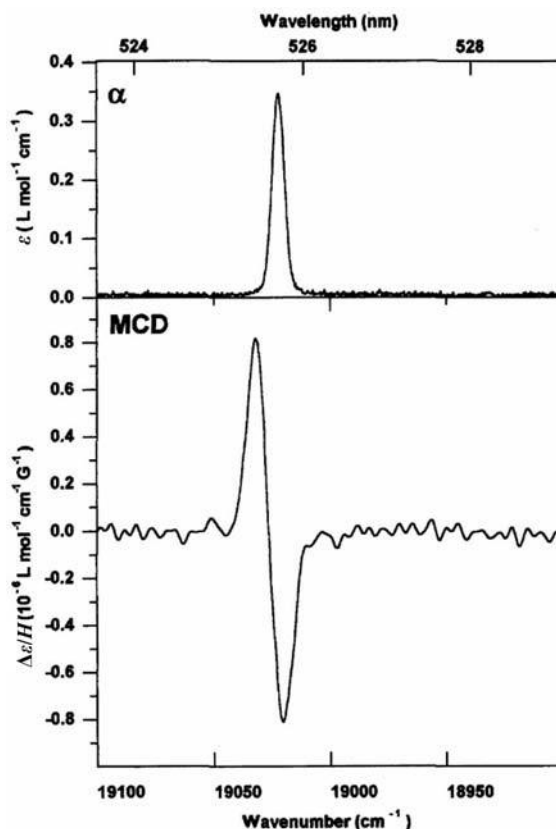
Figure 1
MCD and axial absorption spectra of the $^5D_1 \leftarrow ^7F_0$ magnetic dipole transition of $LiYF_4{:}Eu^{3+}$ at ambient temperature. The A-term has a positive sign.

The MCD selection rules for electric dipole and magnetic dipole transitions are thus the same. A positive A-term is observed if the Zeeman component $|+1\rangle$ is at a higher energy than the $|-1\rangle$ component. An example is the magnetic dipole transition $^5D_1 \leftarrow ^7F_0$ in the MCD spectrum of Eu^{3+} (at ca. $19000\,cm^{-1}$), which always shows a positive A-term. It has been suggested to use this transition as a sign reference transition, in order to see if the magnetic field lines are parallel or antiparallel to the magnetic field lines (Görller-Walrand 1985). The MCD and axial absorption spectrum of the $^5D_1 \leftarrow ^7F_0$ transition in $LiYF_4{:}Eu^{3+}$ is shown in Fig. 1.

3.3 Induced Electric Dipole Transitions

According to the Judd–Ofelt theory (Judd 1962, Ofelt 1962), the occurrence of intraconfigurational f–f transitions is explained by nonsymmetric interactions which mix states of opposite parity into the $4f^N$

configuration. A simple mechanism is the coupling of states of opposite parity by the effect of the odd terms in the crystal-Hamiltonian H_{CF}:

$$H_{CF}^{odd} = -|e|V^{odd} = \sum_{k,q} B_q^k D_q^{(k)} \qquad (16)$$

where B_q^k is a crystal-field parameter and $D_q^{(k)}$ is a tensor of rank k (k is odd) (Görller-Walrand and Binnemans 1996). The important point is that, depending on the values of k and q which are determined by the first coordination sphere around the lanthanide ion, mixing occurs between states of opposite parity and the Zeeman components, which are characterized by linear combinations of $\langle M|$ functions in the ground state and by linear combinations of $|M'\rangle$ functions in the excited state. The selection rule for an induced electric dipole transition is

$$\Delta M = M' - M = -(\rho + q) \qquad (17)$$

In the case where the ground state is characterized by $\langle M| = \langle 0|$, as for the $^7F_0$ ground state of Eu^{3+}, the selection rule is simplified to:

$$\Delta M = M' = -(\rho + q) \qquad (18)$$

The sign of the A-term is identical to the sign of the M' value that satisfied the selection rule for $\rho = -1$. Whereas the sign of the A-term of an electric dipole transition or a magnetic dipole transition is only dependent on the free-ion properties, the sign of the A-term of an induced electric dipole transition depends on the site symmetry of the lanthanide ion (Görller-Walrand and Fluyt-Adriaens 1985; Görller-Walrand *et al.* 1985). The selection rules are valid for the intermediate coupling scheme (J is a good quantum number), but relaxation of the selection rules can occur when J-mixing is strong.

4. Use of MCD for Site Symmetry Determination

The sign of the MCD-signal of the induced electric dipole transition $^5D_2 \leftarrow {}^7F_0$ (at ca. 21500 cm^{-1}) can be used to probe the site symmetry of the Eu^{3+} ion and the type of the idealized coordination polyhedron. A positive A-term is found for the Eu^{3+} ion in a C_{4v} symmetry ($q=0$), whereas a negative A-term is expected for D_{2d} ($q=\pm 2$) and D_{3h} symmetry ($q=\pm 3$). It is not possible to discriminate between D_{2d} and D_{3h} symmetry on the basis of the sign of the $^5D_2 \leftarrow {}^7F_0$ transition alone, but in the case of D_{3h} symmetry, the MCD signal of the $^5D_2 \leftarrow {}^7F_0$ transition is twice as intense as the intensity of the MCD signal of the $^5D_1 \leftarrow {}^7F_0$ transition, whereas in the case of D_{2d} symmetry the two MCD signals have an equal intensity. Ideally, C_{4v} is the symmetry of a monocapped square antiprism (coordination number, CN = 9) or of a distorted square antiprism (CN = 8). D_{3h} is the symmetry of a tricapped trigonal prism (CN = 9) and D_{2d} is the symmetry of a

dodecahedron (CN = 8). These coordination polyhedra are the most often observed coordination polyhedra of lanthanide complexes.

5. Check of the Reliability of Intensity Parameters

The spectral intensities of magnetic dipole transitions can be calculated exactly, provided that a good set of wavefunctions is available. The spectral intensities of induced electric dipole transitions in the absorption spectrum for lanthanide ions in single crystals are commonly parametrized in terms of $B_{\lambda kq}$ or A_{tp}^{λ} intensity parameters (Görller-Walrand and Binnemans 1998). Since these parameters are related to the experimental dipole strength by nonlinear equations, solution of the problem is not straightforward. The sign of the parameters is indeterminate: a change of all the signs of the parameters will result in exactly the same calculated dipole strength. The extracted parameter set depends largely on the chosen starting values. Different parameter sets may give the same figure of merit for the calculated dipole strengths. It is very difficult to select the most adequate set of intensity parameters. Simulation of the MCD spectrum can help. Calculation of the MCD signals does not require more parameters than the crystal field and intensity parameters extracted from the absorption spectrum. If these parameters are adequate, they should allow a good simulation of the MCD spectrum. In the past, the MCD spectrum was often described by the Faraday parameters or MCD parameters A_1, B_0 and C_0 (Stephens 1970). In the Stephens-formalism several approximations are made, and these are not always valid for lanthanide systems, especially not for single crystals. An assumption is, for instance, that the Zeeman splitting is small compared to the crystal field splitting within a multiplet. This is not true for small crystal field splittings and a strong magnetic field. The Zeeman effect cannot be considered as a small perturbation compared to the crystal field effect.

Not only do the free ion and the crystal field Hamiltonian have to be included in the total Hamiltonian, but also the Zeeman Hamiltonian (as described in Sect. 2). After diagonalization, the Zeeman levels are directly found, instead of the crystal field levels. The MCD of a transition is calculated as the difference in intensity between the absorption of left circularly polarized to the Zeeman levels of a $^{2S+1}L_J$ term and the absorption of right circularly polarized light (Fluyt *et al.* 1996). The MCD of a transition has to be reported as an intensity difference. A positive sign indicates that left circularly polarized light is absorbed more effectively than right circularly polarized light. A negative sign indicates the opposite. In the case of overlapping bands, the band width of the curves used for the simulation will affect the overall appearance of the MCD signal to a

large extent. For single crystals, a Lorentzian shape function often gives the best results for the graphical simulation.

MCD can sometimes be used to detect transitions that are not resolved in the absorption spectrum. A condition is that the MCD signals of transitions to the closely spaced crystal field levels, which give rise to overlapping absorption bands, have an opposite sign. However, if the MCD signals of the transitions to the nearly degenerate crystal field levels have the same sign, the MCD spectrum is not advantageous.

6. MCD of Bioinorganic Compounds and Macrocyclic Complexes

Because lanthanide ions can subsitute for Ca^{2+} in different proteins, it was suggested that MCD spectroscopy of lanthanide-substituted proteins could be used to probe the Ca^{2+} active sites of these proteins. The fact that Ca^{2+} active sites were being probed by luminescence spectroscopy after Eu^{3+} or Tb^{3+} substitution, and the sensitivity of the MCD spectrum towards small changes in the environment of the coordinated lanthanide ions, suggested that MCD could be a good technique to study the metal-ion site structure. In the past, several MCD studies were devoted to lanthanide ions (mainly Nd^{3+}) bound to proteins, but these studies were qualitative in nature, pointing to the differences of the MCD spectra of lanthanide ions in aqueous solution and of protein–lanthanide complexes. The use of MCD spectroscopy of lanthanide ions in bioinorganic chemistry has been reviewed (Dooley and Dawson 1984), but there has been little activity in this research field.

Bibliography

Dooley D M, Dawson J H 1984 Bioinorganic applications of magnetic circular dichroism spectroscopy: copper, rare-earth ions, cobalt and non-heme iron systems. *Coord. Chem. Rev.* **60**, 1–66

Fluyt L, Couwenberg I, Lambaerts H, Binnemans K, Görller-Walrand C, Reid M F 1996 Magnetic circular dichroism of $Na_3Nd(ODA)_3 \cdot 2NaClO_4 \cdot 6H_2O$. *J. Chem. Phys.* **105**, 6117–27

Görller-Walrand C 1985 Eu^{3+} as an MCD probe? *Chem. Phys. Lett.* **115**, 333–4

Görller-Walrand C, Behets M, Porcher P, Laursen I 1985 Selection rules in rare earth MCD spectra. An experimental confirmation. *J. Chem. Phys.* **83**, 4329–37

Görller-Walrand C, Binnemans K 1996 Rationalization of Crystal Field Parametrization. In: Gschneidner K A Jr, Eyring L. *Handbook on the Physics and Chemistry of Rare Earths*. North Holland, Amsterdam, Vol. 23, Chap. 155, pp. 121–283

Görller-Walrand C, Binnemans K 1998 Spectral intensities of *f–f* transitions. In: Gschneidner K A Jr, Eyring L. *Handbook on the Physics and Chemistry of Rare Earths*. North-Holland, Amsterdam, Vol. 25, Chap. 167, pp. 101–264

Görller-Walrand C, Fluyt-Adriaens L 1985 Selection rules for rare-earth magnetic circular dichroism spectra. *J. Less-Common Met.* **112**, 175–91

Judd B R 1962 Optical absorption intensities of rare-earth ions. *Phys. Rev.* **127**, 750–61

Ofelt G S 1962 Intensities of crystal spectra of rare-earth ions. *J. Chem. Phys.* **37**, 511–20

Piepho S B, Schatz P N 1983 *Group Theory in Spectroscopy. With Applications to Magnetic Circular Dichroism*. Wiley, New York

Stephens P J 1970 Theory of magnetic circular dichroism. *J. Chem. Phys.* **52**, 3489–516

Stephens P J 1974 Magnetic circular dichroism. *Annu. Rev. Phys. Chem.* **25**, 201–32

Stephens P J 1976 Magnetic circular dichroism. *Adv. Chem. Phys.* **25**, 197–264

C. Görller-Walrand and K. Binnemans
K.U. Leuven, Heverlee, Belgium

This page intentionally left blank

LIST OF CONTRIBUTORS

Contributors are listed in alphabetical order together with their addresses. Titles of articles that they have authored follow in alphabetical order. Where articles are coauthored, this has been indicated by an asterisk preceding the title.

Amato, A.
Paul Scherrer Institute, Villigen, Switzerland
Muon Spin Rotation (µSR): Applications in Magnetism

Andrä, W.
Institut für Physikalische Hochtechnologie e.V. Jena Germany
*Magnets: Biomedical Applications
*Stress Coupled Phenomena: Magnetostriction

Andreev, A. V.
Institute of Physics, Prague, Czech Republic
*Magnetoelastic Phenomena

Atkinson, R.
The Queen's University, Belfast, UK
Faraday and Kerr Rotation: Phenomenological Theory
Magneto-optical Effects, Enhancement of

Aziz, M. M.
University of Manchester, Manchester, UK
*Magnetic Recording: Rigid Media, Recording Properties

Bain, J. A.
Carnegie Mellon University, Pittsburgh Pennsylvania, USA
Magnetic Recording Devices: Inductive Heads, Properties

Banhart, J.
Fraunhofer-Institut für Angewandte Materialforschung, Bremen, Germany
*Magnetoresistance, Anisotropic

Bardeen, J.
University of Illinois, Urbana, Illinois, USA
Superconducting Materials: BCS and Phenomenological Theories

Barthélémy, A.
UMR CNRS-Thomson CSF and Université Paris Sud, Orsay, France
*Giant Magnetoresistance

Battle, P. D.
University of Oxford, UK
Magnetoresistance in Transition Metal Oxides

Bauer, E.
Institut für Experimentalphysik, Wien, Austria
Intermediate Valence Systems
Kondo Systems and Heavy Fermions: Transport Phenomena

Beckley, P.
Newport, UK
Steels, Silicon Iron-based: Magnetic Properties

Berkov, D.
Innovent, Jena, Germany
*Stress Coupled Phenomena: Magnetostriction

Bertotti, G.
Istituto Elettrotecnico Nazionale Galileo Ferraris Turin, Italy
Magnetic Losses

Bhushan, B.
Ohio State University, Columbus, Ohio, USA
Magnetic Recording Devices: Head/Medium Interface

Binnemans, K.
K.U. Leuven, Heverlee, Belgium
*Transparent Rare Earth Compounds: Magnetic Circular Dichroism

Bissell, P. R.
University of Central Lancashire, Preston, UK
Magnetic Recording: VHS Tapes
Magnetic Recording Materials: Tape Particles, Magnetic Properties

Bousack, H.
Forschungszentrum Jülich, Germany
*SQUIDs: Nondestructive Testing

Bozovic, I.
OXXEL GmbH, Bremen, Germany
*Superconducting Thin Films: Materials, Preparation, and Properties

Brinkmann, D.
University of Zurich, Switzerland
High-temperature Superconductors, Cuprate: Magnetic Properties by NMR/NQR

Brommer, P. E.
University of Amsterdam, Amsterdam
The Netherlands
*Magnetoelasticity in Nanoscale Heterogeneous
   Materials*

Brommer, P. E.
Van der Waals-Zeeman Instituut, Universiteit van
Amsterdam, Amsterdam, The Netherlands
Spin Fluctuations

Brooks, M. S. S.
European Commission Joint Research Centre
Karlsruhe, Germany
Density Functional Theory: Magnetism

Brücher, E.
Lajos Kossuth University, Debrecen, Hungary
MRI Contrast Agents

Brück, E.
University of Amsterdam, Amsterdam
The Netherlands
Magnetic Refrigeration at Room Temperature

Burkov, A. T.
Russian Academy of Sciences, St Petersburg, Russia
Magnetic Fields: Thermoelectric Power

Buschow, K. H. J.
University of Amsterdam, Amsterdam
The Netherlands
Alnicos and Hexaferrites
Magnetic Materials: Hard
Magnets: Bonded Permanent Magnets

Campbell, I.
Université Paris Sud, Orsay, France
Magnetic Systems: Disordered

Cascales, C.
Instituto de Ciencia de Materiales de Madrid
Spain
*Crystal Field and Magnetic Properties, Relationship
   between*

Chaloupka, H.
University of Wuppertal, Germany
Superconducting Microwave Applications: Filters

Chantrell, R. W.
University of Durham, UK
Micromagnetics: Basic Principles

Chantrell, R. W.
University of Wales, Bangor, UK
Micromagnetics: Finite Element Approach

Chapman, J. N.
University of Glasgow, UK
*Magnetic Materials: Transmission Electron
   Microscopy*

Char, K.
Seoul National University, South Korea
Superconducting Thin Films: Multilayers

Charles, S. W.
University of Wales, Bangor, UK
Ferrofluids: Preparation and Physical Properties

Chu, W. K.
University of Houston, Houston, Texas, USA
*Superconducting Materials: Irradiation
   Effects*

Civale, L.
Comisión Nacional de Energía Atómica, Bariloche
Argentina
Superconducting Materials: Irradiation Effects

Clarke, J.
University of California, Berkeley, California, USA
SQUIDs: The Instrument

Coey, J. M. D.
University of Dublin, Ireland
Permanent Magnet Assemblies

Collocott, S. J.
CSIRO Telecommunications and Industrial Physics
Lindfield, Australia
Magnetic Materials: Domestic Applications

Coqblin, B.
Université Paris-Sud, Orsay, France
Electron Systems: Strong Correlations

Cottenier, S.
Katholieke Universiteit Leuven, Belgium
Perturbed Angular Correlations (PAC)

Coverdale, G. N.
University of Durham, County Durham, UK
*Magnetic Recording: Particulate Media, Micromagnetic
   Simulations*

Crespo, P.
Instituto de Magnetismo Aplicado, Universidad
Complutense de Madrid-RENFE, Spain
Magnetic Hysteresis

Cristiano, R.
CNR-Institute of Cybernetics, Naples, Italy
*Superconducting Radiation Sensor Applications:
   Detectors and Mixers*

Cugat, O.
Laboratoire d'Electrotechnique de Grenoble UMR
5529 INPG/UJF – CNRS ENSIEG – BP 46 F-38402
Saint-Martin-d'Heres Cedex, France
Magnetic Micro-actuators (MAGMAS)

Cywinski, R.
University of Leeds, Leeds, UK
Amorphous Intermetallic Alloys: Resistivity

de Boer, F. R.
Universiteit van Amsterdam, Amsterdam
The Netherlands
Magnetism: High-field

de Groot, R. A.
University of Nijmegen, The Netherlands
Half-metallic Magnetism

Delamare, J.
Laboratoire d'Electrotechnique de Grenoble UMR
5529 INPG/UJF – CNRS ENSIEG – BP 46 F-38402
Saint-Martin-d'Heres Cedex, France
*Magnetic Micro-actuators (MAGMAS)

Deutscher, G.
Tel Aviv University, Tel Aviv, Israel
Coherence Length, Proximity Effect and Fluctuations

Dietl, T.
Institute of Physics, Warsaw, Poland
Dilute Magnetic Semiconductors

Diviš, M.
Charles University, Czech Republic
Localized 4f and 5f Moments: Magnetism

Dmitriev, N. S.
University of Missouri at Columbia, USA
*Permanent Magnetic Devices in Otiatria

Donnelly, T.
University of Plymouth, Plymouth, UK
*Optical and Magneto-optic Data Storage: Channels
and Coding*

Doyle, W. D.
The University of Alabama, Alabama, USA
Magnetic Recording Devices: Future Technologies

Duc, N. H.
University of Amsterdam, Amsterdam
The Netherlands
**Magnetoelasticity in Nanoscale Heterogeneous
Materials*

Early, T. A.
General Electric Company, Niskayuna
New York, USA
Solids, Nuclear Magnetic Resonance of

Ebert, H.
Universität München, Munich, Germany
*Magnetoresistance, Anisotropic

Ellerby, M.
University College, London, UK
*Elemental Rare Earths: Magnetic Structure and
Resistance, Correlation of*

Eschrig, H.
Institute of Solid State and Materials Research
Dresden, Germany
High-T_c Superconductors: Electronic Structure

Fähler, S.
IFW Dresden, Germany
*Magnetic Films: Hard

Fert, A.
UMR CNRS-Thomson CSF and Université Paris
Sud, Orsay, France
*Giant Magnetoresistance

Fidler, J.
Vienna University of Technology, Austria
*Micromagnetics: Basic Principles
*Micromagnetics: Finite Element Approach
Permanent Magnets: Microstructure

Fiorani, D.
Institute of Materials Chemistry, C.N.R.
Rome, Italy
*Ferrofluids: Magnetic Properties

Fruchart, D.
Laboratoire de Cristallographie du CNRS, Grenoble
France
*Permanent Magnet Materials: Neutron
Experiments*

Fuchs, G.
Institut für Metallische Werkstoffe, Dresden
Germany
Magnetic Levitation: Superconducting Bearings
**Superconducting Permanent Magnets: Principles and
Results*

Fujii, T.
Murata Manufacturing Company Ltd., Shiga
Japan
*Growth and Magnetic Properties of YIG Films

Fujita, F. E.
Osaka University, Machikane, Toyonaka, Japan
Mössbauer Spectrometry

Fukushima, H.
Honda-cho, Chiba, Japan
**Longitudinal and Perpendicular Recording: Thermal
Stability*

Garcia, Y.
Institut für Anorganische Chemie und Analytische
Chemie, Johannes-Gutenberg Universität, Mainz
Germany
*Photomagnetism of Molecular Systems

Gatteschi, D.
University of Florence, Italy
Single-molecule Magnets

Geyer, R. G.
National Institute of Standards and Technology
Boulder, Colorado, USA
Ferrite Ceramics at Microwave Frequencies

Gherardi, L.
Pirelli Cavi e Sistemi Spa, Milan, Italy
Superconducting Wires and Cables: Low-field
Applications

González, A.
Instituto de Magnetismo Aplicado, Universidad
Complutense de Madrid-RENFE, Spain
*Magnetic Hysteresis

Goodwin, H. A.
University of New South Wales, Sydney
Australia
Spin Transition Compounds

Görller-Walrand, C.
K.U. Leuven, Heverlee, Belgium
Transparent Rare Earth Compounds: Magnetic
Circular Dichroism

Goto, T.
University of Tokyo, Japan
Metamagnetism: Itinerant Electrons

Gradmann, U.
MPI Mikrostrukturphysik, Halle, Germany
Monolayer Films: Magnetism

Gratz, E.
Technische Universität Wien, Vienna, Austria
Boltzmann Equation and Scattering
Mechanisms
Intermetallic Compounds: Electrical Resistivity
Magnetoresistance: Magnetic and Nonmagnetic
Intermetallics

Gregg, J.
University of Oxford, Oxford, UK
Magnetic Recording Systems: Spin Electronics

Griscom, D. L.
Naval Research Laboratory, Washington, DC
USA
Amorphous Materials: Electron Spin Resonance

Grönefeld, M.
Magnetfabrik Bonn GmbH, Bonn, Germany
Permanent Magnets: Sensor Applications

Grössinger, R.
Technische Universität Wien, Vienna, Austria
Magnetic Measurements: Pulsed Field
Magnetic Measurements: Quasistatic and ac

Grünberg, P. A.
Forschungszentrun Jülich, Germany
Multilayers: Interlayer Coupling

Grünberger, W.
Institut für Festkörper- und Werkstofforschung
Dresden, Germany
Textured Magnets: Deformation-induced

Grundy, P. J.
University of Salford, Manchester, UK
Magnetic Layers: Anisotropy
Magnetic Recording: Rigid Media, Preparation

Gupta, M.
Université Paris-Sud, Orsay, France
Metal Hydrides: Electronic Band Structure

Gutfleisch, O.
IFW, Dresden, Germany
Hard Magnetic Materials, Basic Principles of
Rare Earth Magnets: Materials

Gütlich, P.
Institut für Anorganische Chemie und Analytische
Chemie, Johannes-Gutenberg Universität, Mainz
Germany
Photomagnetism of Molecular Systems
Spin Transition Compounds

Hadjipanayis, G. C.
University of Delaware, Newark, Delaware, USA
Magnets: High-temperature

Harris, I. R.
University of Birmingham, UK
Magnets: HDDR Processed

Hartland, A.
National Physical Laboratory, Teddington, UK
Metrology: Superconducting Cryogenic Current
Comparators

Havela, L.
Charles University, Prague, Czech Republic
5f Electron Systems: Magnetic Properties

Hayashi, N.
University of Electrocommunications, Tokyo, Japan
Longitudinal and Perpendicular Recording: Thermal
Stability

Hellman, F.
University of California, San Diego, California USA
Magnetic Films: Anisotropy

Hendren, W. R.
Queen's University of Belfast, UK
Multilayer Optical Film Modeling

Hergt, R.
Institut für Physikalische Hochtechnologie e.V. Jena
Germany
Magnets: Biomedical Applications

Hernando, A.
Instituto de Magnetismo Aplicado, Universidad
Complutense de Madrid-RENFE, Spain
Magnetic Hysteresis
Magnetic Microwires: Manufacture, Properties, and
Applications

Herzer, G.
Vacuumschmelze GmbH, Hanau, Germany
Amorphous and Nanocrystalline Materials
Nanocrystalline Materials: Magnetism

Hesse, J.
Technische Universität Braunschweig, Germany
Nanosized Particle Systems, Magnetometry on

Hillebrecht, F. U.
Heinrich-Heine-Universität Düsseldorf
Germany
Photoemission: Spin-polarized and Angle-resolved

Hilscher, G.
Institut für Experimentalphysik, TU Wien, Vienna
Austria
Magnetic Units

Hilscher, G.
Technische Universität, Wien, Austria
Metal Hydrides: Magnetic Properties

Hirosawa, S.
Sumitomo Special Metals Company, Osaka
Japan
Magnets: Remanence-enhanced

Hobby, P.
Philmore Group Limited, Monmouthshire
UK
Magnetic Recording Media: Advanced

Hoffmann, H.
Universität Regensburg, Germany
Thin Films: Domain Formation

Hohmann, R.
Forschungszentrum Jülich, Germany
SQUIDs: Nondestructive Testing

Huebener, R. P.
University of Tübingen, Germany
High-temperature Superconductors: Transport
Phenomena

Ido, H.
Tohoku Gakuin University, Tagajo City, Japan
Pnictides and Chalcogenides: Transition Metal
Compounds

Indeck, R. S.
Washington University, St. Louis, Missouri, USA
Magnetic Recording Measurements

Jaswal, S. S.
University of Nebraska, Lincoln, Nebraska, USA
Magneto-optics: Inter- and Intraband Transitions,
Microscopic Models of

Jiles, D. C.
Iowa State University, Ames, Iowa, USA
NDT Techniques: Magnetic

Kamarád, J.
Academy of Sciences of the Czech Republic, Prague
Czech Republic
Magnetic Systems: External Pressure-induced
Phenomena

Kamiyama, S.
Akita Prefectural University Honjo, Japan
Ferrohydrodynamics

Kanert, O.
Universität Dortmund, Germany
Amorphous Materials: Nuclear Spin Relaxation

Kes, P. H.
Leiden University, The Netherlands
Electrodynamics of Superconductors: Flux Properties

Kilcoyne, S. H.
University of Leeds, Leeds, UK
Amorphous Intermetallic Alloys: Resistivity

Kim, A. S.
JAHWA Electronics Co., Ltd., Choong-Book, Korea
Permanent Magnets: Corrosion Properties

Kirchmayr, H.
Vienna University of Technology, Austria
Magnetic Anisotropy

Kirtley, J. R.
IBM Research, Yorktown Heights, New York
USA
SQUIDs: Magnetic Microscopy

Klein, N.
Jülich Research Center, Germany
Superconducting Microwave Applications: Filters

Koch, H.
Physikalisch-Technische Bundesanstalt, Berlin
Germany
SQUIDs: Biomedical Applications

Kools, F.
Carbone Lorraine-Ferrites, Evreux, France
Ferrite Magnets: Improved Performance

Krause, H.-J.
Forschungszentrum Jülich, Germany
SQUIDs: Nondestructive Testing

Kronmüller, H.
Max-Planck-Institut für Metallforschung, Stuttgart
Germany
Coercivity Mechanisms

Kubis, M.
University of Birmingham, UK
Magnets: HDDR Processed

Kupriyanov, M.
Moscow State University, Russia
Electrodynamics of Superconductors: Weakly Coupled

Kuznetsov, A. A.
University of Missouri at Columbia, USA
*Permanent Magnetic Devices in Otiatria

Kuznetsov, O. A.
University of Missouri at Columbia, USA
*Permanent Magnetic Devices in Otiatria

Labov, S. E.
Lawrence Livermore National Laboratory
Livermore California, USA
*Radiation and Particle Detectors

Lacroix, C.
Laboratoire Louis Néel, CNRS, Grenoble, France
*Magnetic Systems: Lattice Geometry-originated
    Frustration*

Lane, A. M.
University of Alabama, Tuscaloosa, Alabama
USA
*Magnetic Recording Media: Particulate
    Dispersions

Lee, P. J.
The University of Wisconsin, Madison, WI, USA
*Superconducting Wires and Cables: Materials and
    Processing*

Li, Y.
Read-Rite Corporation, Fremont, California, USA
*Magnetic Recording Technologies: Overview

Libharev, K. K.
State University of New York, Stony Brook
New York, USA
*Superconductors: Rapid Single Flux Quantum
    (RSFQ) Logic*

Lindroos, V. K.
Helsinki University of Technology, Laboratory of
Physical Metallurgy and Materials Science, P.O. Box
6200 (Vuorimiehentie 2A), FIN-02015 HUT Espoo
Finland
*Giant Magnetostrictive Materials

Liu, J.
University of Houston, Houston, Texas, USA
*Superconducting Materials: Irradiation Effects

Lodder, J. C.
University of Twente, Enschede, The Netherlands
Magneto-optic Multilayers
Metal Evaporated Tape

Loewenhaupt, M.
IAPD, Dresden, Germany
Magnetic Excitations in Solids

Löhneysen, H. v.
Universität Karlsruhe, Germany
*Non-Fermi Liquid Behavior: Quantum Phase
    Transitions*

Luongo, C. A.
National High Magnetic Field Laboratory
Tallahassee, Florida, USA
Superconducting Machines: Energy Storage

Majewski, P.
Max-Planck-Institut für Metallforschung, Stuttgart
Germany
Superconducting Materials, Types of

Makhnovskiy, D. P.
University of Plymouth, UK
*Magneto-impedance Effects in Metallic
    Multilayers

Mannhart, J.
Universität Augsburg, Germany
*High-temperature Superconductors: Thin Films and
    Multilayers

Marín, P.
Instituto de Magnetismo Aplicado, Universidad
Complutense de Madrid-RENFE, Spain
*Magnetic Hysteresis
*Magnetic Microwires: Manufacture, Properties, and
    Applications

Markosyan, A. S.
Czech Academy of Sciences, Prague, Czech Republic
and Moscow State University, Russia
Alloys of 4f (R) and 3d (T) Elements: Magnetism

Matijasevic, V.
Oxxel GmbH, Germany
*Films and Multilayers: Conventional
    Superconducting*

Mattheis, R.
IPHT Jena, Germany
*Stress Coupled Phenomena: Magnetostriction

McDaniel, T. W.
Seagate Research, San Jose, California, USA
Magneto-optical Disks: Thermal Effects

McHenry, M. E.
Carnegie Mellon University, Pittsburgh
Pennsylvania, USA
Magnetic Steels

Menon, A. K.
Read-Rite Corporation, Fremont, California
USA
*Magnetic Recording Technologies: Overview

Mergel, D.
University of Essen, Germany
*Magneto-optic Recording: Overwrite and Associated
    Problems*
*Magneto-optic Recording: Total Film Stack, Layer
    Configuration*

Mertig, I.
Technische Universität Dresden, Germany
Thin Film Magnetism: Band Calculations

Middleton, B. K.
University of Manchester, Manchester, UK
*Magnetic Recording: Rigid Media, Recording
*   Properties*

Miltat, J.
Université Paris-Sud, Orsay, France
*Magnetic Force Microscopy

Mohn, P.
Technische Universität Wien, Austria
Itinerant Electron Systems: Magnetism
*   (Ferromagnetism)*

Morel, A.
St Pierre d'Allevard, France
*Ferrite Magnets: Improved Performance

Moze, O.
Modena University, Italy
Crystal Field Effects in Intermetallic Compounds:
*   Inelastic Neutron Scattering Results*

Mück, M.
Institut für Angewandte Physik der Justus-Liebig-
Universität, Giessen, Germany
SQUIDs: Amplifiers

Mukovskii, Y. M.
Moscow State Steel and Alloys Institute
Moscow, Russia
Perovskites: Resistivity Behavior

Müller, K.-H.
IFW Dresden, Germany
Magnetic Viscosity
*Superconductors: Borocarbides

Muller, M. W.
Washington University, St. Louis, Missouri
USA
*Magnetic Recording Measurements

Mushnikov, N. V.
Institute of Metal Physics, Ekaterinburg, Russia
*Magnetoelastic Phenomena

Nagao, M.
Tokyo Institute of Technology, Yokohama, Japan
*Magnetic Properties of Dislocations

Nakatani, Y.
University of Electrocommunications
Tokyo, Japan
*Longitudinal and Perpendicular Recording: Thermal
*   Stability*

Narozhnyi, V. N.
IFW, Dresden, Germany
*Superconductors: Borocarbides

Nekvasil, V.
Institute of Physics, ASCR, Prague
Czech Republic
Localized 4f and 5f Moments: Magnetism

Neu, V.
Institut für Metallische Werkstoffe
Dresden, Germany
*Magnets: Mechanically Alloyed

Newman, D. M.
Centre for Data Storage Materials Coventry
University, UK
Super-resolution: Optical and Magnetic
*   Techniques*

Nguyen Van Dau, F.
UMR CNRS-Thomson CSF, Orsay, France
*Giant Magnetoresistance

Niemeyer, J.
Physikalisch-Technische Bundesanstalt
Braunschweig, Germany
Josephson Voltage Standard

Nikles, D. E.
University of Alabama, Tuscaloosa, Alabama
USA
*Magnetic Recording Media: Particulate Dispersions

Ní Mhíocháin, T. R.
University of Dublin, Ireland
*Permanent Magnet Assemblies

Novák, P.
Institute of Physics ASCR, Prague
Czech Republic
Transition Metal Oxides: Magnetism

Nowotny, H.
Vienna University of Technology, Austria
*Boltzmann Equation and Scattering
*   Mechanisms*

Obradors, X.
Institut de Ciéncia de Materials de Barcelona
Spain
*Magnetic Levitation: Materials and Processes

Odenbach, S.
Universität Bremen, Germany
Ferrofluids: Neutron Scattering Studies

Ohta, M.
Niigata University, Niigata City, Japan
ESR Dosimetry: Use of Rare Earth Ions

Ōnuki, Y.
Osaka University, Japan
*Intermetallics: Hall Effect
Magnetic Systems: De Haas–van Alphen Studies of
*   Fermi Surface*

Oswald, B.
Oswald Elektromotorenbau GmbH, Miltenberg
Germany
*Superconducting Permanent Magnets: Potential
    Applications*

Panaitov, G.
Forschungszentrum Jülich, Germany
*SQUIDs: Nondestructive Testing

Panina, L. V.
University of Plymouth, UK
**Magneto-impedance Effects in Metallic
    Multilayers*

Paul, W.
ABB Corporate Research Ltd, Baden-Daettwil
Switzerland
*Superconducting Machines: Energy Distribution
    Components*

Petford-Long, A. K.
University of Oxford, Oxford, UK
Magnetic Recording Systems: Spin Valves

Peuzin, J. C.
Laboratoire Louis Néel, CNRS Grenoble, France
Magnetostrictive Materials

Pierce, D. T.
National Institute of Standards and Technology
Gaithersburg, Maryland, USA
*Multilayers: Interlayer Coupling

Popova, M. N.
Russian Academy of Sciences, Moscow, Russia
*High-resolution Fourier Transform Spectroscopy:
    Application to Magnetic Insulators*

Porcher, P.
Laboratoire de Chimie Appliquée de l'Etat Solide
Paris, France
*Electronic Configurations of 3d, 4f, and 5f Elements:
    Properties and Simulation*

Prellier, W.
Laboratoire CRISMAT CNRS UMR 6508 6
Boulevard du Marechal Juin F-14050 Caen Cedex
France
*Colossal Magnetoresistance Effects: The Case of
    Charge-ordered $Pr_{0.5}Ca_{0.5}MnO_3$ Manganite Thin
    Films*

Puig, T.
Institut de Ciéncia de Materials de Barcelona
Spain
*Magnetic Levitation: Materials and Processes

Quandt, E.
Center of Advanced European Studies and Research
Bonn, Germany
Actuator Materials for Small-scale Devices

Quandt, E.
Stiftung Caesar, Bonn, Germany
Thin Films: Giant Magnetostrictive

Raasch, D.
Philips Research Laboratories, Aachen, Germany
*Magneto-optic Recording Materials: Chemical
    Stability and Life Time*

Raj, K.
Ferrofluidics Corporation, Nashua, New Hampshire
USA
Ferrofluids: Applications

Rasing, Th.
University of Nijmegen, Nijmegen, The Netherlands
Nonlinear Magneto-optics

Regnault, L. P.
CEA, Grenoble, France
Bulk Magnetic Materials: Low-dimensional Systems

Reyne, G.
Laboratoire d'Electrotechnique INPG BP 46 F-38402
Saint Martin d'Heres Grenoble Cedex France
*Magnetic Micro-actuators (MAGMAS)

Richter, H. J.
Seagate Recording Media, Fremont, California, USA
Longitudinal Media: Fast Switching
*Metal Particle versus Metal Evaporated Tape

Richter, M.
Institut für Festkörper- und Werkstofforschung
Dresden, Germany
*Density Functional Theory: Magnetism

Rodewald, W.
Vacuumschmelze GmbH, Hanau, Germany
Magnets: Sintered

Rogalla, H.
University of Twente, Enschede, The Netherlands
Josephson Junctions: High-T_c

Rosensweig, R. E.
Fondation de l'Ecole Normale Supérieure
Paris, France
Ferrofluids: Introduction

Ross, C. A.
Massachusetts Institute of Technology, Cambridge
Massachusetts, USA
Magnetic Recording: Patterned Media

Rosseinsky, M. J.
University of Liverpool, UK
Fulleride Superconductors

Rottmayer, R. E.
Seagate Research, Pittsburgh, Pennsylvania, USA
*Magnetic Recording Heads: Historical Perspective
    and Background*

Rowell, J. M.
Conductus Inc., Sunnyvale, California, USA
Thin Films, Multilayers and Devices, Superconducting

Rüffer, R.
ESRF, Grenoble, France
Nuclear Resonance Scattering

Sabiryanov, R. F.
University of Nebraska, Lincoln, Nebraska, USA
*Magneto-optics: Inter- and Intraband Transitions, Microscopic Models of

Sáez-Puche, R.
Universidad Complutense de Madrid, Spain
Crystal Field and Magnetic Properties, Relationship between

Sakabe, Y.
Murata Manufacturing Company Ltd., Shiga Japan
*Growth and Magnetic Properties of YIG Films

Sakurai, J.
Toyama University, Japan
Rare Earth Intermetallics: Thermopower of Cerium, Samarium, and Europium Compounds

Sandratskii, L. M.
Institut für Festkörperphysik, Technische Universität Darmstadt, Germany
*Density Functional Theory: Magnetism

Sato, A.
Tokyo Institute of Technology, Yokohama, Japan
*Magnetic Properties of Dislocations

Sato, H.
Tokyo Metropolitan University, Japan
Giant Magnetoresistance: Metamagnetic Transitions in Metallic Antiferromagnets
*Intermetallics: Hall Effect

Sato, R.
Technische Universität Wien, Vienna, Austria
*Magnetic Measurements: Quasistatic and ac

Savichev, A.
University of Missouri at Columbia, USA
*Permanent Magnetic Devices in Otiatria

Schäfer, R.
Institut für Metallische Werkstoffe, Dresden, Germany
Kerr Microscopy
Magnets, Soft and Hard: Magnetic Domains

Schlom, D. G.
Penn State University, University Park Pennsylvania, USA
*High-temperature Superconductors: Thin Films and Multilayers
*Superconducting Thin Films: Materials, Preparation, and Properties

Schlom, D. G.
Universität Augsburg, Germany
*High-temperature Superconductors: Thin Films and Multilayers

Schmidt, G.
Universität Würzburg, Germany
Spintronics in Semiconductor Nanostructures

Scholl, A.
Lawrence Berkeley National Laboratory, Berkeley California, USA
Thin Film Magnetism: PEEM Studies

Schrefl, T.
Vienna University of Technology Austria
*Micromagnetics: Basic Principles
*Micromagnetics: Finite Element Approach

Schultz, J. H.
Massachusetts Institute of Technology, Cambridge MA, USA
Superconducting Wires and Cables: High-field Applications

Schultz, L.
Institut für Metallische Werkstoffe, Dresden Germany
*Magnetic Films: Hard
*Magnets: Mechanically Alloyed
*Superconducting Permanent Magnets: Principles and Results

Sebek, J.
Institute of Physics ASCR, Prague Czech Republic
Demagnetization: Nuclear and Adiabatic

Sechovský, V.
Charles University, Prague, Czech Republic
Magnetism in Solids: General Introduction

Sereni, J. G.
Centro Atomico Bariloche (CNEA), San Carlos de Bariloche, Argentina
Magnetic Systems: Specific Heat

Shoji, A.
Electrotechnical Laboratory, Tsukuba Japan
Josephson Junctions: Low-T_c

Söderberg, O.
Helsinki University of Technology, Laboratory of Physical Metallurgy and Materials Science, P.O. Box 6200 (Vuorimiehentie 2A), FIN-02015 HUT Espoo Finland
*Giant Magnetostrictive Materials

Sozinov, A.
Helsinki University of Technology, Laboratory of Physical Metallurgy and Materials Science, P.O. Box 6200 (Vuorimiehentie 2A), FIN-02015 HUT Espoo Finland
*Giant Magnetostrictive Materials

Spiess, H. W.
Max-Planck-Institut für Polymerforschung Mainz, Germany
Amorphous Materials: Nuclear Magnetic Resonance, New Techniques

Spratt, G.
Hewlett Packard, Boise, USA
*Magnetic Recording Media: Advanced

Steglich, F.
Max-Planck-Institut für Chemische Physik fester Stoffe, Dresden, Germany
*Heavy-fermion Systems

Sullivan, J. L.
Aston University, Birmingham, UK
Magnetic Recording: Flexible Media, Tribology

Süllow, S.
Technische Universität Braunschweig Germany
*Heavy-fermion Systems

Talke, F. E.
University of California, San Diego, La Jolla California, USA
Magnetic Recording: Rigid Media, Tribology

Tamanaha, Cy. R.
Geo-Centers, Washington, DC, USA
DNA Microarrays using Magnetic Labeling and Detection

Terrones, H.
Instituto Potosino de investigación Científica y Technológica, San Luis Potosí, Mexico
*Fullerene Formation

Terrones, M.
University of Sussex, Brighton, UK
*Fullerene Formation

Thiaville, A.
Université Paris-Sud, Orsay, France
*Magnetic Force Microscopy

Thompson, S. M.
University of York, York, UK
Magnetoresistive Heads: Physical Phenomena

Tishin, A. M.
M.V. Lomonosov Moscow State University Russia
Magnetocaloric Effect: From Theory to Practice

Tronc, E.
C.N.R.S., Université Pierre et Marie Curie, Paris France
*Ferrofluids: Magnetic Properties

Tsuei, C. C.
IBM, Yorktown Heights, New York, USA
Amorphous Superconductors

Uesaka, Y.
Nihon University, Fukushima, Japan
*Longitudinal and Perpendicular Recording: Thermal Stability

Ullom, J. N.
Lawrence Livermore National Laboratory Livermore California, USA
*Radiation and Particle Detectors

van der Zaag, P. J.
Philips Research Laboratories, Eindhoven The Netherlands
Ferrites

Veitch, R. J.
BASF AG, Ludwigshafen, Germany
*Metal Particle versus Metal Evaporated Tape

Vernes, A.
Universität München, Munich, Germany
*Magnetoresistance, Anisotropic

Vettier, C.
European Synchrotron Radiation Facility Grenoble, France
Magnetism: Applications of Synchrotron Radiation

Wang, F. Z.
University of North London, UK
Random Access Memories: Magnetic

Wassermann, E. F.
Gerhard-Mercator-Universität, Duisburg Germany
Invar Materials: Phenomena

Whitman, Lloyd J.
Naval Research Laboratory, Washington, DC USA
DNA Microarrays using Magnetic Labeling and Detection

Wiesinger, G.
Technische Universität, Wien, Austria
*Metal Hydrides: Magnetic Properties

Williams, E. A.
General Electric Company, Niskayuna New York, USA
Nuclear Magnetic Resonance Spectrometry

Wongsam, M.
University of Wales, Bangor, UK
*Micromagnetics: Finite Element Approach

Wongsam, M. A.
University of Durham, UK
*Micromagnetics: Basic Principles

Yagasaki, K.
University of the Ryukyus, Okinawa, Japan
*Magnetic Fields: Thermoelectric Power

Yunin, M.
University of Missouri at Columbia, USA
*Permanent Magnetic Devices in Otiatria

Zhang, Y.
Forschungszentrum Jülich, Germany
*SQUIDs: Nondestructive Testing

Zhu, J.-G.
Dept of Electrical & Computer Engineering,
Carnegie Mellon University, Pittsburgh,
PA 15213-3890, USA
Magnetization Reversal Dynamics

Zvezdin, A. K.
Russian Academy of Sciences, Moscow, Russia
*Magnetic Phase Transitions: Field-induced
  (Order to Order)*

This page intentionally left blank

SUBJECT INDEX

The Subject Index has been compiled to assist the reader in locating all references to a particular topic in the Encyclopedia. Index entries are filed in letter-by-letter sequence, and arranged in set-out style with up to three levels of heading. Major coverage of a subject is indicated by ***bold italic*** page numbers. Page numbers followed by *T* (or *F*) refer to Tables (or Figures). *See* references point the user to preferred terms; *see also* references indicate terms of related interest. Every effort has been made to make the index as comprehensive as possible and to standardize the terms used.

This page intentionally left blank